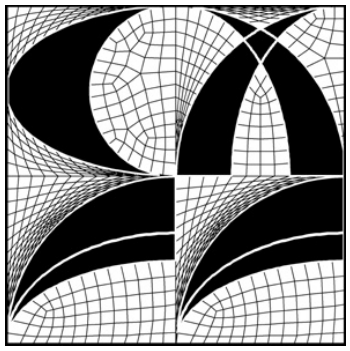

Conference on
Modelling Fluid Flow
CMFF'12
September 4-7, 2012

The 15th Event of international Conference Series
on Fluid Flow Technologies Held in Budapest

CONFERENCE PROCEEDINGS

CD-ROM

Edited by
J. Vad

Department of Fluid Mechanics
Budapest University of Technology and Economics

2012

Proceedings of the Conference on Modelling Fluid Flow
Budapest University of Technology and Economics, Hungary 2012

Edited by J. Vad

CD-ROM ISBN 978-963-08-4588-5

Published by the Department of Fluid Mechanics
Budapest University of Technology and Economics
H–1111 Budapest, Bertalan L. u. 4–6., Hungary
Tel: +36 1 463 40 72
Fax: +36 1 463 34 64
e-mail: vad@ara.bme.hu
www.ara.bme.hu

Local Organising Committee

Chairman:	Dr. J. Vad, Budapest (H)
Secretary:	Ms. A. Rákai, Budapest (H)
Members:	Dr. Gy. Paál, Budapest (H)
	Prof. Sz. Szabó, Miskolc (H)
	Prof. T. Lajos, Budapest (H)

Organising Institution

Department of Fluid Mechanics, Budapest University of Technology and Economics

Co-operating Organisations

Department of Hydrodynamic Systems, Budapest University of Technology and Economics
Department of Fluid and Heat Engineering, University of Miskolc
Scientific Society of Mechanical Engineers (Flow Technology Section)
Committee of Fluid Mechanics and Thermodynamics of the Hungarian Academy of Sciences
The Japan Society of Mechanical Engineers
Visualization Society of Japan

Editor

Associate Prof. János Vad, PhD.
Department of Fluid Mechanics, Budapest University of Technology and Economics

Conference Organisation

International Scientific and Programme Committee (ISPC)

Chairman:	Prof. D. Thevenin, Magdeburg (D)
Honorary Chairman:	Univ. Prof. Dr.-Ing. habil. R. Schilling, Munich (D)
Review Chairman:	Prof. L. Baranyi, Miskolc (H)
Members:	

Prof. R. S. Abhari, Zürich (CH)
Prof. B. J. Boersma, Delft (NL)
Prof. A. R. J. Borges, Lisbon (P)
Dr. B. P. M. van Esch, Eindhoven (NL)
Dr. Á. Fáy, Miskolc (H)
Prof. L. Fuchs, Lund (S)
Dr. T. Gausz, Budapest (H)
Prof. B. J. Geurts, Twente (NL)
Prof. V. Goriatchev, Tver (RUS)
Prof. R. Grundmann, Dresden (D)
Prof. G. Halász, Budapest (H)
Prof. H. Jaberg, Graz (A)
Dr. L. Kalmár, Miskolc (H)
Prof. G. Kosyna, Braunschweig (D)
Prof. K. Kozel, Prague (CZ)
Dr. G. Kristóf, Budapest (H)
Prof. H. Kuhlmann, Vienna (A)
Dr. L. Kullmann, Budapest (H)
Prof. J. Kumicak, Kosice (SK)
Prof. I. R. Lewis, Newcastle-upon-Tyne (UK)
Prof. M. Leschziner, London (UK)
Prof. N. C. Markatos, Athens (GR)
Prof. M. Nedeljkovic, Belgrade (SRB)
Prof. H. Nørstrud, Trondheim (N)
Prof. A. Okajima, Kanazawa (J)
Prof. F. Rispoli, Rome (I)
Prof. R. Rohatynski, Zielona Góra (PL)
Prof. W. Schneider, Vienna (A)
Dr. E. Shapiro, Cranfield (UK)
Prof. M. Shirakashi, Nagaoka (J)
Prof. S. J. Song, Seoul (KR)
Prof. R. Susan-Resiga, Timisoara (RO)
Prof. T. Takahashi, Nagaoka (J)
Dr. T. Verstraete, Sint-Genesius-Rode (B)
Prof. T. Weidinger, Budapest (H)

Table of Contents
Volume I.

Invited Lectures

Workshop
Optimization of wind turbines

Workshop
Boundary layer problems, similarity solutions

Atmospheric flows

Biomedical flows

Diffusers. Nozzles. Jets

External fluid dynamics

Internal flows

Liquid applications, water pollution and treatment

Multiple phases and components

Reactive flows

Turbomachinery

Vibration, acoustics

Wall-bounded flows

Modelling related to wind engineering, aerodynamics, and meteorology

---

Addenda
Invited Lectures

Authors' Index

Preface

The present conference is the 15^{th} event in a successful series of conferences establishing and maintaining relationships among experts all over the world working in research and development related to fluid machinery for five decades.

Since 2003 the scope of the events has been extended. According to their new name: CMFF (Conference on Modelling Fluid Flow), they respond to challenges in the rapidly developing fields of fluid mechanics. The conferences are unique events designed to provoke and establish interactive symbiosis and efficient synergy of numerical flow simulation and physical modelling of flow processes using advanced measurement methods. It aims at defining the state of the art in CFD and advanced measuring techniques, inspiring both research and practical applications by promoting interaction between scientists and practitioners working in the computational and experimental fluid dynamics field.

The organiser for this conference is the Department of Fluid Mechanics at the Budapest University of Technology and Economics, supported by the Department of Hydrodynamic Systems at the same University, and by the Department of Fluid and Heat Engineering at the University of Miskolc. Cooperating organisations are: Flow Technology Section of the Scientific Society of Mechanical Engineers in Hungary, Committee of Fluid Mechanics and Thermodynamics of the Hungarian Academy of Sciences, the Japan Society of Mechanical Engineers, and the Visualisation Society of Japan.

Authors from more than 30 countries submitted about 160 papers. After careful reviewing, 123 session papers have been published in the printed Proceedings, containing 2 invited lectures and 6 workshop papers as well. The organisation of review of the session papers has been supported by the members of the International Scientific and Programme Committee, with involvement of invited experts, thus guaranteeing the high level of publications in the Proceedings.

A considerable portion of the publications reports the concerted application of CFD and modern experimental techniques. It is our pleasure that despite the extension of conference profile, the traditional topic appears again as a focal point: a large portion of the sessions deal with fluid machinery. Simultaneously, recently emerging technologies such as Large Eddy Simulation and Computational Aero-Acoustics show increasing significance in the technical programme of the Conference.

The editor thanks the authors for their valuable contribution.

Budapest, on 4 September 2012

Dr. János Vad

Invited Lectures

Conference on Modelling Fluid Flow (CMFF'12)
The 15th International Conference on Fluid Flow Technologies
Budapest, Hungary, September 4-7, 2012

THE ROLE OF LES IN UNSTEADY GROUND VEHICLE AERODYNAMICS

Siniša Krajnović

Vehicle Aerodynamics Laboratory, Department of Applied Mechanics, Chalmers University of Technology, Gothenburg, Sweden, www.tfd.chalmers.se/~sinisa, E-mail: sinisa@chalmers.se

ABSTRACT

The paper discusses how LES can be used to increase our knowledge of vehicle aerodynamics flows and improve the aerodynamic performance of vehicles. Applications of gusty flows and flow control are used to demonstrate the LES applications in vehicle aerodynamics. The LES simulations of gusty flows gives insight into the underlying flow mechanisms for hysteresis, phase shift and overshoot of aerodynamic forces and moments observed between the quasi-steady and dynamic tests. The LES of flow control applications show that LES can be used to explore the flow control processes of trailing vortices produced with vortex generators, moving surface boundary-layer control and a small cylinder used as a local disturbance of the shear layer behind a bluff body.

Keywords: crosswind stability, flow control, LES, vehicle aerodynamics

INTRODUCTION

Prediction of flows around ground vehicles such as cars, trucks, buses or trains, is mainly done today using RANS methods, where the prediction is strongly dependent on the capability of the turbulence model used. Unfortunately, despite the many years of development in turbulence modeling and the success of RANS in predictions of a large number of flows, there is currently no turbulence model that can deal with regions of separation flow around vehicles, such as wake, wheelhouse cavity, underbody etc. These flows are simply too complicated for turbulence modeling. They contain a wide spectrum of turbulent scales and a variation of flow features, which makes it difficult (if not impossible) to design a turbulence model that can produce accurate prediction. The technique of large eddy simulation (LES) has been used since the 1990s for various bluff body flows, and the first LES of vehicle-like bluff body flow was presented by Krajnović and Davidson [1, 2] in 2001. The body used in [1, 2] was an extremely simplified geometry of a bus and the Reynolds number was 10^5 based on the vehicle height and the inlet velocity. Although the geometry was so simple, the results of the simulation showed the potential of LES for understanding the flow physics in external vehicle aerodynamics. However, that simulation showed several challenges in performing LES of ground vehicle flows. Simulating a few seconds of flow with LES is computer intensive because both the spatial and temporal resolution must be sufficient for an accurate prediction. The vast amount of the results from an LES leads to another challenge in postprocessing and analysis of the results. Finally, the computational effort required to predict a flow around real ground vehicles at operational Reynolds numbers is huge, mainly due to the requirement of resolving near-wall coherent structures, and simulations of this kind will not be possible for at least a decade. Nevertheless, the LES offers us an opportunity to study the flows around (at least simplified) ground vehicles and moderate Reynolds numbers with a kind of magnifying glass that can help us to develop new knowledge about these flows.

The author has used LES for over a decade for numerical experiments in flows around simplified ground vehicles. LES was used for predictions of flows around simplified cars [3, 4, 5], buses [2] and trains [6, 7, 8, 9, 10]. Detailed flows around a wheel in a wheelhouse [11], around a simplified A-pillar of a vehicle and vehicles influenced by wind gusts [12] have been studied. The present paper will present several recent applications of LES in vehicle aerodynamics ranging from prediction of wake flows and crosswind stability to flow control applications. A review of LES work in external vehicle aerodynamics between 2000 and 2009 is presented in [13].

1. CROSSWIND STABILITY

Understanding the effects of unsteady winds of flows around vehicles is very important because of the safety risks that they pose. The unsteady character of the flow (often with a moving vehicle and a sudden change of wind) makes the prediction

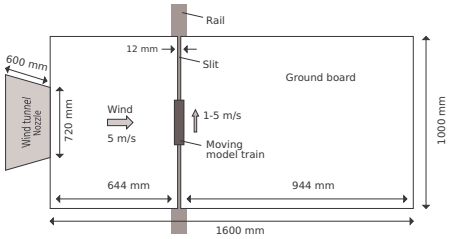

Figure 1. Schematic view from above of the experimental set-up

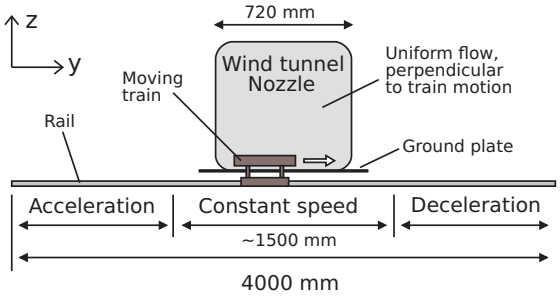

Figure 2. Illustration of the crosswind scenario.

impossible with RANS methods. Furthermore, the practical limitations of experimental facilities restrict the experimental investigations. LES seams to be a good numerical tool for exploring these flows at moderate Reynolds numbers, and recent studies are presented in the text below. One key question related to the validity of the standard experimental studies with crosswind flows was explored in the work presented here. The experiments are normally performed with a stationary model in the wind tunnel while the crosswind flow is applied. The model can either be placed at one position or its position can be varied in several experiments (so called quasi-steady experiments). The question is whether the results of such experiments using static models are relevant to a dynamic change of the crosswind flows around real vehicles. The following text will illustrate the usage of LES to answer the question of the validity of the stationary experiments.

1.1. COMPARISON OF FLOWS WITH STEADY AND UNSTEADY WINDS

The aim of this study was to explore the differences between the results obtained in the dynamic and the stationary tests with crosswind flows. For that purpose, the flow from the experimental study by Suzuki et al. [14] with a moving model through a wind generated by a wind tunnel nozzle was studied. Although the geometry was simple (see Figs. 1-3) and the Reynolds number low (Re = 22615 based on the model height and the inlet velocity), the existence of the experimental data enabled the validation of the LES results before they were used to explain the differences in the flows. The simplified train geometry used in the present work is a cuboid mounted on two support cylinders, as shown in Fig. 3. The model was mounted on two supporting cylinders that are pulled by a mechanical mechanism along a slit shown in Fig. 1. The constant speed of the model is obtained only during approximately twice the width of the wind tunnel nozzle (see Fig. 2). Before the region of constant speed, the model is accelerated and the test region is followed by deceleration (Fig. 2). The positions of the pressure holes at which the experimental data were collected are shown in Fig. 3.

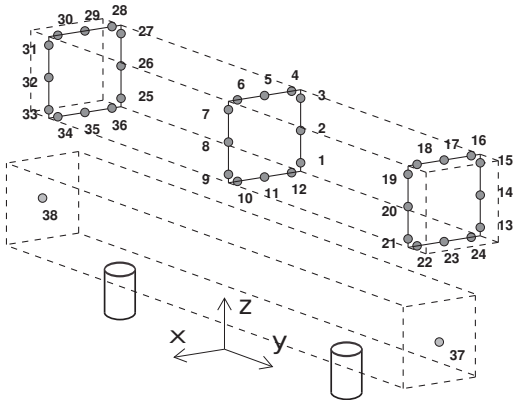

Figure 3. The geometry of the body with the points on the train body where the pressure is measured during the experiment.

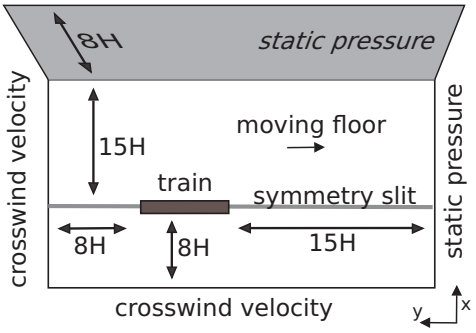

Figure 4. Computational domain with dimensions and boundary conditions.

1.1.1. Numerical simulations and boundary conditions

The train velocity of 5 m/s was studied; this simulation is referred to as an LES of the dynamic case. Another LES simulation was made of the case with steady boundary conditions and the crosswind at a yaw angle of 45^o and an amplitude of 7.07 m/s, corresponding to the maximum amplitude of the crosswind that the train experiences in the dynamic case. The set-up studied in this simulation corresponds to a train that is influenced by a constant crosswind of 5 m/s while traveling at speed of 5 m/s. The moving ground is applied in the simulation, resulting in a relative velocity between the train and the ground. This is thus not the same as a simulation of the flow around a train that is stationary and influenced by a crosswind (as is often the case in wind tunnel experiments).

In the experimental study by Suzuki et al. [14], a model train at a scale of 1/60th was moved along a 4-m linear guide rail placed in front of a wind tunnel nozzle. The train in the present numerical work is stationary, and the influence of the wind gust in the LES of the dynamic case is simulated by changing boundary conditions. The dynamic case simulation is first run with only one inlet and a constant velocity profile at the inlet of -5 m/s. When the flow has developed, the wind profile condition is applied on one lateral wall and the inlet of the domain. This is done by changing the slip lateral boundary condition and the inlet constant streamwise velocity to the wind profile boundary conditions (described below). The resulting wind gust boundary condition is a function in space that changes in time.

The wind gust profile has a maximum velocity equal to the velocity of the steady crosswind, and it moves along the domain with a speed of 5 m/s. Thus, with the length of the train model of 0.3284 m and the width of the wind gust profile equal to the width of the wind tunnel nozzle of 0.72 m, the duration of the wind gust is around 0.21 s.

The velocity profile moves with a negative velocity (i.e. -5 m/s in the y-direction.) The y component of velocity $V = -5$ m/s is therefore prescribed on the left and lower inlets in Fig. 4. The no-slip boundary condition with a velocity of -5 m/s in the y-direction is applied. As seen in Fig. 1, there is a slit in the ground board in the experimental set-up. This slit is slightly wider than the support cylinders in Fig. 3 that connect the train model to the carriage that brings the train forward. The presence of the slit in the numerical simulation was modeled using a symmetry boundary condition in the isolated region of the slit. The outlet and the upper (in Fig. 4) lateral walls have a static pressure boundary condition. The roof of the domain has a symmetry boundary condition. Velocity data for the wind tunnel profile are available at the position of the train from the experiment when the train was not present in the tunnel. The average turbulent intensity

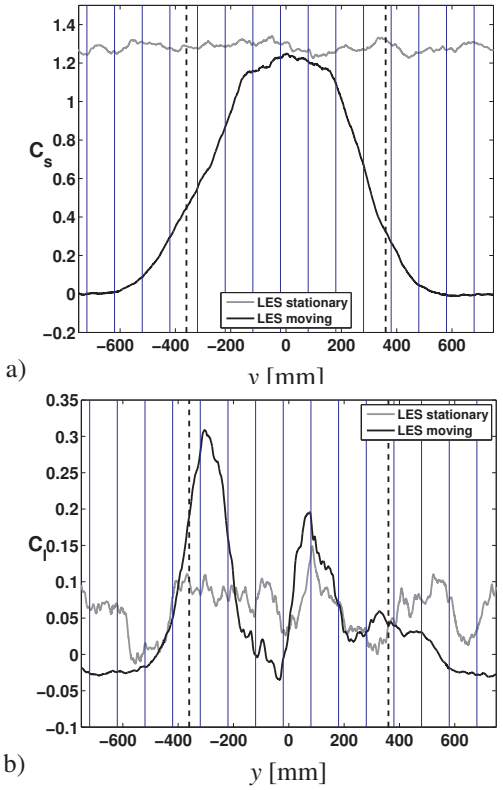

Figure 5. a) Side force coefficient C_s, during passage of the wind tunnel nozzle; b) Lift force coefficient C_l, during passage of the wind tunnel nozzle. The extension of the wind tunnel nozzle is indicated by dashed lines

at the inlet of the wind tunnel used in the experiments was low (less than 1%). A velocity profile from the experiment, constant in time, was thus used as the inlet boundary condition in the present LES.

The boundary conditions in the LES of the stationary case are identical to those in the dynamic case except at the inlet and the lower lateral wall (in Fig. 4), where a constant velocity of 7.07 m/s was applied at a yaw angle of 45^o.

1.1.2. Forces and moments

The aerodynamic moments are computed with respect to the coordinate system with the origin set at the ground plane in the middle between the supporting cylinders (Fig. 3). The yawing moment, (C_{YM}), the rolling moment, (C_{RM}), and the pitching moment, (C_{PM}), are defined as moments around the z-, y- and x-axes, respectively. The aerodynamic forces are normalized with the dynamic pressure and the cross section area of the train in the y-direction. Furthermore, the distance between the supporting cylinders was used for normalization of the aerodynamic moments.

The coefficients of the aerodynamic forces and moments are shown in Figs. 5-7. Starting with the side force coefficient, it can be observed that the transient force coefficient is lower than the value

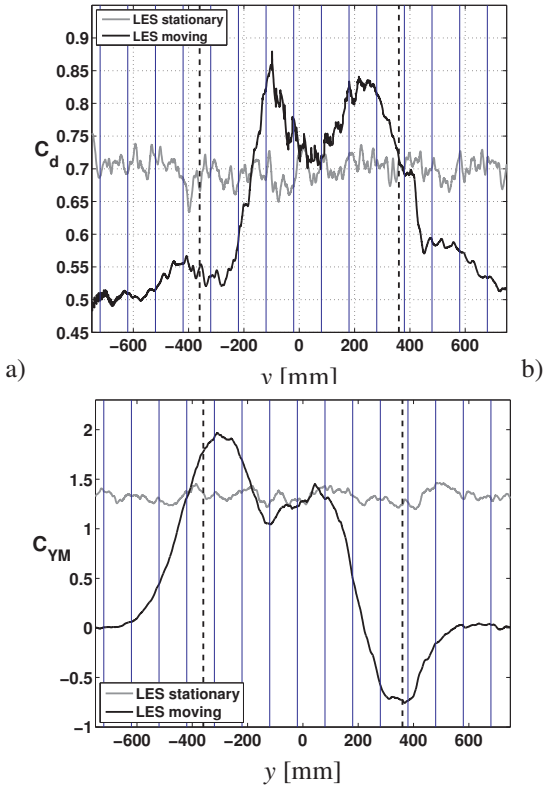

Figure 6. a) Drag force coefficient C_d, during passage of the wind tunnel nozzle; b) Yawing moment coefficient C_{YM}, during passage of the wind tunnel nozzle. The extension of the wind tunnel nozzle is indicated by dashed lines

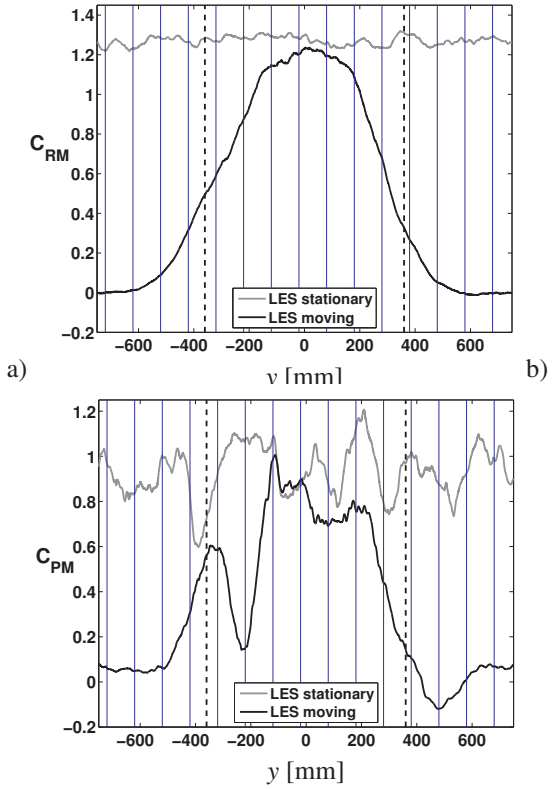

Figure 7. a) Rolling moment coefficient C_{RM}, during passage of the wind tunnel nozzle; b) Pitching moment coefficient C_{PM}, during passage of the wind tunnel nozzle. The extension of the wind tunnel nozzle is indicated by dashed lines

from the steady case. A similar observation was made by Passmore et al. [15], although their experiment simulated different transient changes of the wind profile (they used an oscillating aerofoil gust generator to simulate the transient aerodynamic effect). The transient lift force coefficient exceeds the static value by as much as 200% (Fig. 5b). The overshoot in the transient yawing moment coefficient by as much as 30% as compared to the static value is shown in Fig. 6b. A similar value was found in [15]. Note also that the two peaks in the transient lift force and yawing moment occur at approximately the same y positions. The drag force coefficient of the transient case (Fig. 6a) exceeds that of the static case by approximately 20%, but the peaks come later as compared to those for the lift force and yawing moment. On the other hand, the transient rolling and pitching moments are lower than the corresponding static values (Fig. 7). Results of the LES presented show clear differences in the resulting maximum of the aerodynamic forces and moments between the dynamic and steady cases. The differences in the predictions are particularly important for the yawing moment because that coefficient has a large impact on the crosswind stability and thereby on the safety of vehicles. The results of the present investigations show an overshoot in the dynamic case of approximately 30% compared to the steady case, indicating the importance of simulating correct flow conditions.

1.2. Hysteresis and phase shift between the quasi-steady and dynamic tests

Tests using dynamic flow conditions have shown different forces and moment from those found in steady flow conditions; hysteresis effects and a phase shift in force and moment signals were also observed. The differences in flows between steady and transient flow conditions are expected to be a result of a lag in the response of the flow to continuous changes in the position of the vehicle when truly transient flow conditions are applied.

The example described in the following section demonstrates the usage of LES for exploration of the flow physics of an experiment in which the vehicle is exposed to steady wind during continuous changes in the yaw angle.

1.2.1. Description of the set-up

The flow around the body studied in the experiment by Chometon et al. [16] is studied here. Krajnović et al. [17] made LES of the flow around the body at quasi-steady conditions (yaw angles of 10^o, 20^o and 30^o). The results presented in [17] showed that LES is better suited than RANS or DES for the flow around the body studied here.

The model is shown in Fig. 8. It has a length of L = 675 mm and a width of W = 240 mm. The maximum height is H = 192 mm.

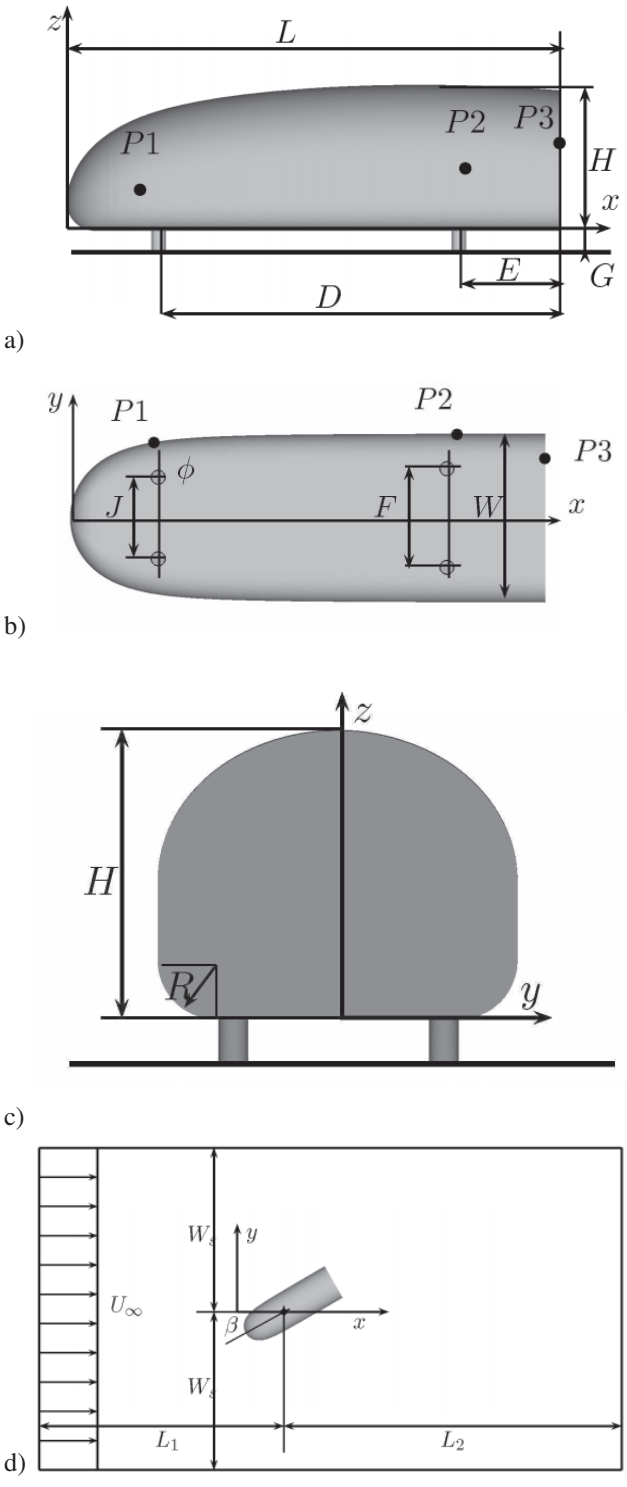

Figure 8. a-c) Geometry of the body. d) Sketch of the models' set-up in the computational domain.

Krajnović et al. [12] made a LES simulation of the flow around this model when it was exposed to periodic oscillations around its vertical axis. The Reynolds number based on the incoming velocity and the car length in [12] was $Re = 9 \times 10^5$. This is the same Reynolds number as in the experimental study by Chometon et al. [16]. The model in the experimental study was placed on a turntable that allowed the model to oscillate with an amplitude of 10^o around the vertical axis. The yaw angle of the model was continuously varied between -10^o and 10^o, both in experiments [16] and in the present LES. The frequency of the oscillation was 2 Hz corresponding to a Strouhal number of $St = fL/U_\infty = 0.068$ in the present LES. U_∞ is the inlet velocity.

Figure 9 shows a comparison between the present LES and experimental data [18] of the wall pressure at positions of pressure taps P1 and P2 (see Fig. 8). The LES results are shown for each oscillating sweep (thin gray curves) and as ensemble averaged (averaged over three oscillating sweeps) curves (thick black curves).

The first observation in Fig. 9 is that both the experimental data and the LES results oscillate during the sweep of the model. The agreement of the LES results with the experimental data is good for pressure taps P1 and P2.

Figure 10 shows the data from LES using the dynamic flow conditions and the quasi-steady experimental data for the drag and the side force coefficients. Here, the LES data are presented for three sweeps between the $\beta = 10^o$ and $\beta = -10^o$ and back together with their ensemble-averaged curves. The figure shows that the LES (using dynamic flow conditions) data and the quasi-steady experimental data are different and that the dynamic data primarly exhibit higher values, especially for small yaw angles. The second observation from Figs. 9 and 10 is that the evolutions of the wall pressure coefficient and the aerodynamic forces both show the existence of the hysteresis phenomenon.

All signals of the pressure and the forces show hysteresis effects in their behavior in the two parts of the sweep between the extreme yaw angles $\beta = 10^o$ and $\beta = -10^o$. This behavior results in different values of the surface pressure and the aerodynamic forces for the same yaw angle position but for different halves of the rotation sweep. These differences were found to be largest for small yaw angles. Furthermore, the pressure and the force signals show the existence of hysteresis, where the influence of the body oscillations on the surrounding flow and the resulting aerodynamic forces is experienced with a certain delay in time.

This results in a phase shift of the curves in Fig. 10a. Note that the phase shift is present in both halves of the sweep. A phase shift of this kind causes differences in data between the two halves of the rotation sweep and between the quasi-steady and

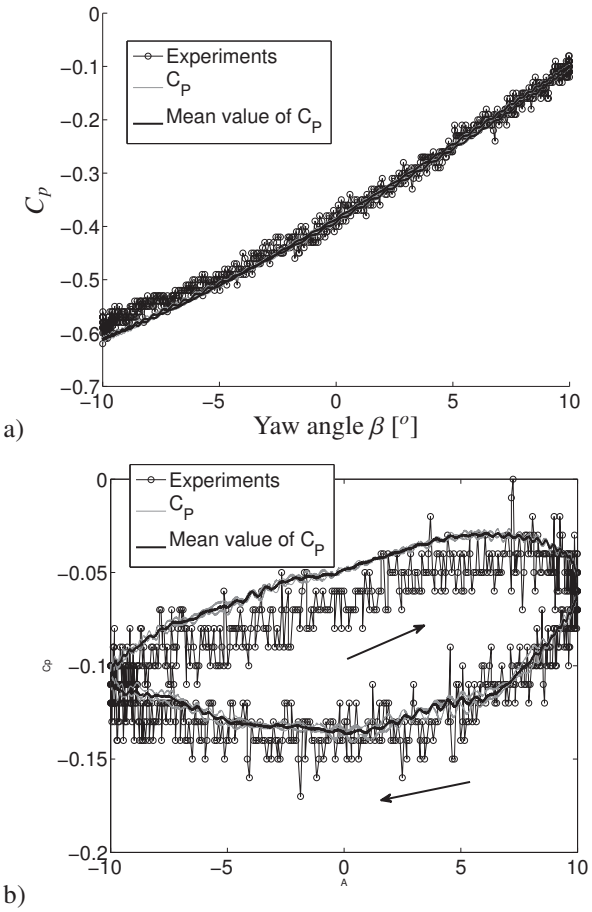

Figure 9. Comparison between the present LES and experimental data of the C_p values at points a P1 and b) P2.

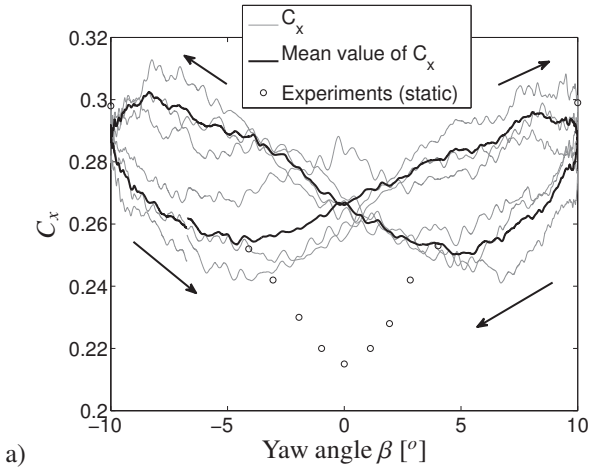

a)

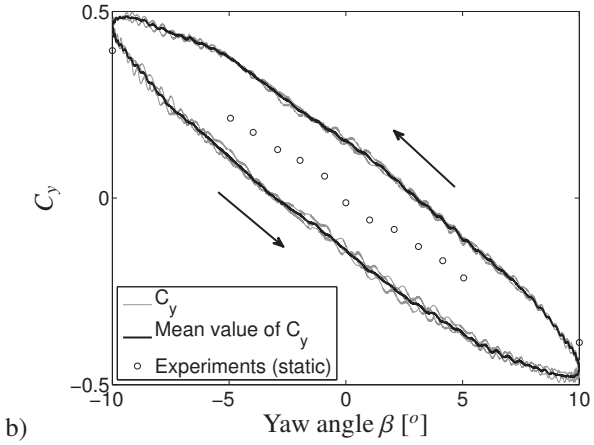

b)

Figure 10. Comparison of the a) drag coefficient C_x and b) side force coefficient C_y.

a)

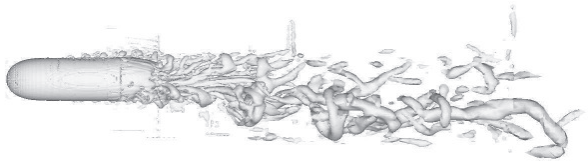

b)

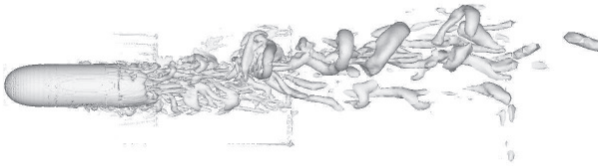

c)

Figure 11. Iso-surface of the second invariant of the velocity gradient tensor $Q = 2 \times 10^4$ for position $\beta = 0^o$. LES of a) quasi-steady flow; b) dynamic flow for increasing β; c) dynamic flow for decreasing β.

dynamic data. The hysteresis effect can be explained by the evolution of the flow during the sweep. As the body experiences a solid body rotation, the surrounding flow tries to follow up. The delay in the reaction of the flow to the body rotation is caused by the nature of the surrounding fluid, however, and is due to the inertia effects of the flow when the sign of the rotation is changed.

Figure 11 shows comparisons of the flow structures from the present LES using quasi-static and dynamic (oscillating body) flow conditions for the yaw angle of $\beta = 0^o$. Owing to a lack of space, only one angle is chosen. Differences in flows between the quasi-static and dynamic flow conditions were found at all yaw angle positions, however. Figure 11 shows that, at a yaw angle of 0^o, the hairpin vortices on the lee side of the body are

thinner in the quasi-static case than in the oscillating case.

This difference affects the surface pressure on the body and thereby the aerodynamic forces and moments. The wake behind the base of the body is also influenced by the oscillations of the model. As seen in Fig. 11b and c, there is a curvature in the shape of the wake viewed from above when the model is oscillating. This is explained by a time lag in the response of the wake to the body oscillation. While the wake develops around the symmetry plane of the body in the LES using quasi-static flow conditions, the dynamic flow conditions result in a shift of the flow structures on the side of the symmetry plane of the domain in which the body is rotating.

2. FLOW CONTROL

Modulation of the flow surrounding vehicles by different means of flow control has received great attention in recent years. Particularly interesting is flow control of the flow behind trailers of trucks, where practical constraints prevent aerodynamic shaping of the geometry. There are also other regions of flow where flow control can show great potential. If we consider only trucks, there is room for improvement in several regions, such as in front of the truck, in the gap between the truck and a trailer or between two trailers, the wake behind a truck etc. The flow of passenger cars can also be influenced using different means of flow control, and here we shall consider one passive strategy using cylindrical vortex generators on the rear end of the vehicle [19] and another using a cylindrical body to influence the shear layer behind a bluff body [20].

Krajnović et al. [21] used blowing or suction to influence the A-pillar trailing vortices. The LES presented in [21] showed that it is a suitable tool for predicting the flow control process of the vortex breakdown of the trailing vortex formed around the A-pillar.

LES of the active flow control of the wake flow behind a D-shaped body relevant for a truck were presented by Krajnović and Fernandes [22]. Another recently presented control strategy by Han and Krajnovic [23] used the momentum injection through Moving Surface Boundary-layer Control (MSBC) to influence the flow around a cube. The following section will present some results of that study.

2.1. LES of the MSBC

The idea behind the MSBC technique is to decrease the relative motion between the surface and the free stream to delay the growth of the boundary layer and thereby prevent or delay flow separation of boundary layers. Alternatively, injection of the momentum into the existing boundary layer can be done as a part of MSBC. Han and Krajnovic [23] used LES to study the flow around a cube at two

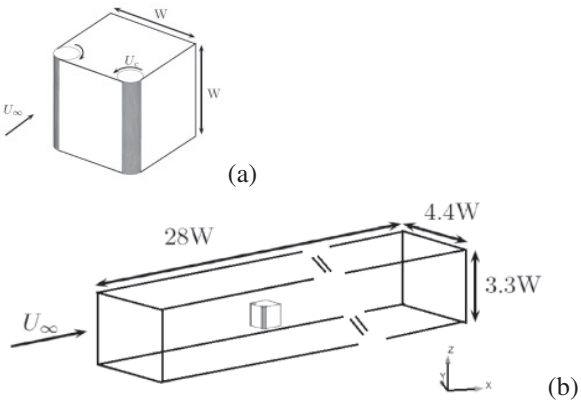

Figure 12. The geometry of the cube (a), the computational domain (b).

yaw angles of the flow, 0^o and 30^o. The cube was equipped with two rotating cylinders (Fig. 12), and the idea was to use rotation of the cylinders to reduce the relative velocity between the surface and the flow.

The geometry of the cube and its placement inside the computational domain is shown in Fig. 12. The length of the side of the cube is $W = 203mm$, and the rotating cylinders at two adjacent vertical surfaces have a diameter of $D_r = 50.8mm$. The wind tunnel has a span of $4.4W$ and a height of $3.3W$. The cube is placed in the middle of the span at a height of $1.0W$ from the floor. The center of the cube is located $8W$ from the inlet and $20W$ from the outlet. The inlet velocity, U_0, is $5m/s$, resulting in $Re = 6.7 \times 10^4$ based on the height of the cube, W. No-slip boundary conditions are imposed on the surfaces of the cube except on the control device (the shaded surfaces in Figure 12(a)), where a tangential velocity of $U_c = 2U_0$ is applied to simulate the rotating cylinders with the direction of rotation indicated by the arrows in Figure 12(a). The LES showed that the drag coefficient was reduced for both yaw angles when the MSBC was applied. The rotating cylinders were efficient in removing the separation of boundary layers on the lateral sides of the cube, as seen in Fig. 13 in the case of 0^o yaw angle. This resulted in a change of the surface pressure and shear forces and drag reduction of some 6.2%. The more separated flow at a 30^o yaw experienced a more dramatic change of the flow (see Fig. 14) when the flow controlled was applied. The resulting drag was reduced by 45.3%. Unfortunately, such a drastic change in flow topology led to an increase in the yaw moment of approximately 44.7%, which is disadvantageous for lateral stability. This first LES of MSBC illustrates the potential of the technique and motivates further studies of flows with a combination of several bluff bodies in tandem representing wagons of the train or a tractor and trailer.

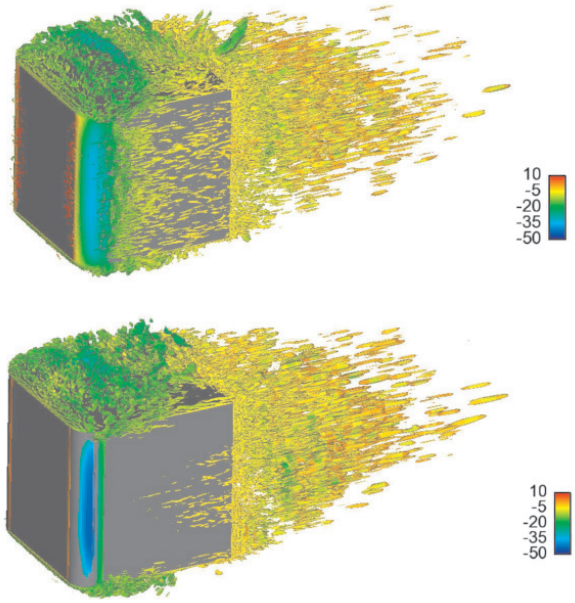

Figure 13. Iso-surface of the second invariant of the velocity gradient ($Q = 1.0\times10^5$) in the case of a 0° yaw angle: non-rotating case (left) and rotating case (right), colored by the pressure.

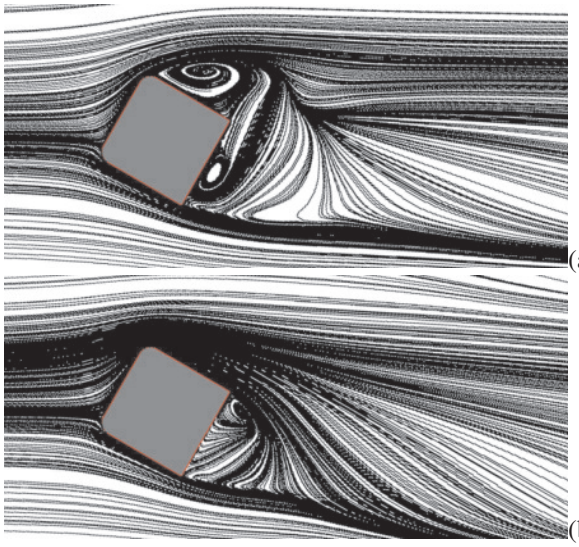

Figure 14. Time-averaged streamlines for the non-rotating case (a) and the rotating case (b) in the case of a 30° yaw angle. Top view in the middle plane of the cube

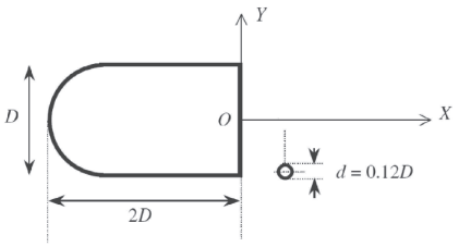

Figure 15. Arrangement of the main bluff body and the control cylinder in one xOy plane

2.2. LES of the passive flow control around a D-shaped body

LES with the Coherent Structure Model was used in [20] to study a passive flow control around a two-dimensional D-shaped bluff body at a Reynolds number of 13 000 based on the incoming velocity and the height of the body. A small circular control cylinder located in the near-wake region behind the bluff body is employed as a local disturbance of the shear layer and the wake. The main bluff body is a symmetric cylinder with a leading face profiled as a semi-circle followed by a flat trailing plane (see Figure 15). The height of the main body is $D = 25mm$ and the length is $L = 50mm$. The small control cylinder has a circular cross-section with a diameter of $d = 3mm$, and its center is located at the position of $(0.4D, -0.46D)$ in the xOy plane. The free-stream velocity is $U_0 = 8m/s$ at the inlet, resulting in a Reynolds number of 13 000 based on the height of the main body, $D = 25mm$. The computational domain has a height of $16D$, which is consistent with the experiment [24]. The main body is placed at the middle of the total height. A span of $4D$ is used in the numerical simulations.

Figure 16 shows the comparison of an iso-surface of the second invariant of the velocity gradient Q between the natural and the controlled flows. The natural flow in Fig. 16a shows strong von Karman vortex shedding. The small control cylinder is immersed in the shear layer behind the body. As it disturbs the shear layers development, it influences development of the wake. The resulting vortex shedding in the controlled flow is damped in Fig. 16b, and the wake is elongated. The result of this elongated wake is an increase in the surface pressure on the base of the body and a reduction of drag by some 27.6% compared with the controlled flow.

2.3. Prediction of flow control with vortex generators

One way to influence the boundary layer separation is to produce streamwise vortices by vortex generators, for example. The function of these longitudinal vortices is to sweep the high-energy air from the inviscid portion of the flow field or higher portion of the boundary layer to the inner parts of the

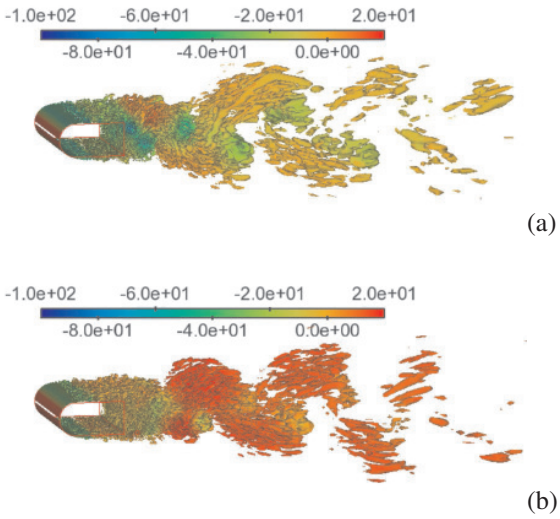

Figure 16. Iso-surface of the second invariant of the velocity gradient ($Q = 1.0 \times 10^5$): natural case (left) and controlled case (right), colored by pressure.

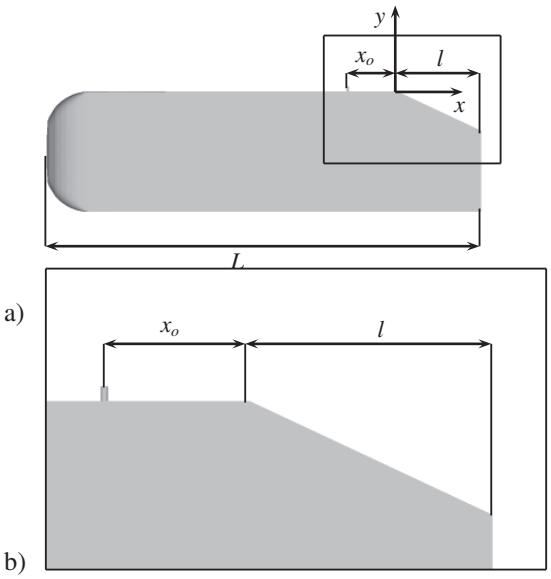

Figure 17. a) Shape of the Ahmed body b) Zoom of the rear of the geometry.

boundary layer. The separation is delayed as energy is added from the high-energy air to the retarded air inside the boundary layer, leading to an increased base pressure and lower drag of the vehicle.

The passive flow control case studied in [19] is that of the generic car model called the Ahmed body that was previously studied in both experimental (e.g. Ahmed [25], Lienhart et al. [26]) and numerical work (Krajnović and Davidson [3, 4, 5, 27]). The angle of the rear slanted surface was 25^o, and the free-stream velocity was 20 m/s, resulting in a Reynolds number based on the model length, L, of $Re_L = 1.35 \times 10^6$. The geometry of the model is presented in Figs. 17 and 18. In a previous experimental study, Pujals et al. [28] used cylindrical roughness elements, presented in Fig. 19, to force the large-scale streaks. They studied several configurations of the cylinders, changing the height of the cylinders, k, their diameter, d, the spanwise spacing, λ_z, and the distance from the roughness to the rear slanted surface of the body, x_o. The experimental study of Pujals et al. [28] showed that the configuration of the roughness with 16 cylinders and $\lambda_z = 24$mm, $d = 6$mm, $k = 12$mm and $x_o = 120$mm resulted in a maximum reduction of drag of approximately 10% . That configuration of the cylindrical roughness was chosen in the present study.

The drag reduction as a result of the passive flow control applied on the Ahmed body is quantified in the present work by ΔC_d, defined as $\Delta C_d = 2\frac{C_d C_d^o}{C_d + C_d^o}$, where C_d^o and C_d are the time-averaged drag coefficients of the natural and controlled flows, respectively. The same quantity was computed in the experimental work of Pujals et al. [28].

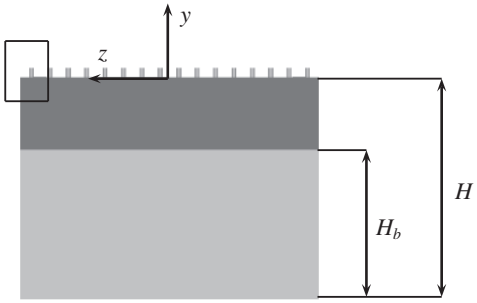

Figure 18. Ahmed body seen from behind.

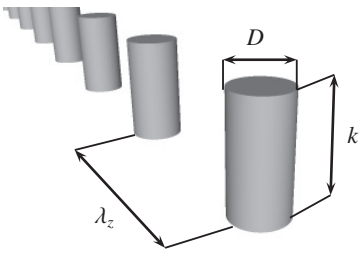

Figure 19. The relevant parameters of the cylindrical roughness elements.

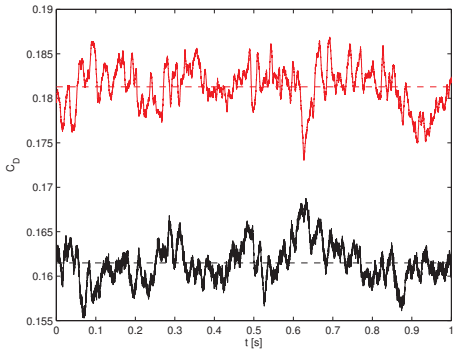

Figure 20. Comparison of the drag coefficient between the natural (red curve) and actuated flows (black curve)

The time histories of the drag coefficients for the LES predictions are given in Fig. 20. We find that $\Delta C_d^{LES} = 11.7\%$. The value obtained in the experiments of Pujals et al. [28] was around $\Delta C_d^{EXP} = 10\%$, which is close to the present LES prediction. Figure 21 shows a comparison of the LES predictions of the flow around the rear end of the Ahmed body between the natural and the controlled flows. A similar as in the previous prediction at different Reynolds number, the present LES produced a reattachment of the flow on the rear slanted surface in the natural flow (Fig. 21a). Figure 21b shows that the separation bubble on the slanted surface becomes thinner in the LES prediction of the actuated flow. As a result of that, the angle of the flow falling down above the slanted surface in the near wake is changed and the near wake is elongated. This is the same phenomenon as is observed in the experimental investigation of Pujals et al. [28]. The actuated flow shown in Fig. 21b produces a much thinner separation bubble on the slanted surface, and the near-wake separation bubble is elongated. This is the desired consequence of the flow control strategy applied here, as an elongated near-wake separation bubble results in higher surface pressure on the vertical base of the Ahmed body.

3. CONCLUSIONS

Large eddy simulation is a technique that has great potential as a tool for obtaining fundamental knowledge about vehicle flows. It is not a technique for predicting aerodynamic forces and moment for vehicles at operational Reynolds numbers. Although attempts have been made by some engineers to run LES codes at Reynolds numbers of real vehicles, the resulting calculations cannot be regarded in the name of LES. The failure of such calculations to resolve not only important near-wall coherent structures but, probably much more, important turbulent motion will lead to false flow predictions.

An appropriate usage of LES requires resolution of the near-wall streaks that are important for a

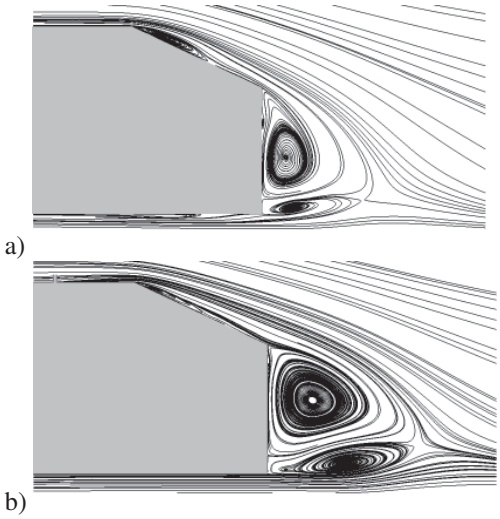

Figure 21. Streamlines projected onto the symmetry plane from the LES; a) natural flow and b) controlled flow

maintenance of turbulence, and their resolution requirements mean a necessarily substantial reduction of Reynolds number of the flow compared to that around real vehicles. However, if the Reynolds number used in the LES is chosen with caution it is possible to make an extrapolation of the results of the simulation. A good example of this kind of approach is [3, 4], where the sharp edge separations made possible a reduction of the Reynolds number by a factor of four. The choice of appropriate Reynolds number is by no means an easy task and requires validations with experimental data at different Reynolds number regimes. This paper presents a choice of the LES application in vehicle aerodynamics by the author, including gusty flows and flow control. Gusty flows are natural candidates for LES because of the absence of other CFD techniques that can do the job and because of difficulties associated with moving models and gusty flows in experimental tests. Flow control is a perfect example where understanding of the flow and of the flow-control mechanisms is a must for the flow control strategy to be efficient. The examples in this paper were of the open-loop flow control type but, in the real world, the flow control must be able to adjust to the flow conditions, which change as a result of so many things, from atmospheric conditions, changes in driving conditions (speed, acceleration) to interactions with other vehicles and objects (such as overtaking).This means that the control loop must be closed and include information about the flow evolution. Making this kind of a closed-loop control strategy operational will require the development of simpler models than evaluations of Navier-Stokes equations. However, the LES has a natural place in the process of the development of such simpler models.

Beside the two examples of LES usage described

above, there are other good candidates for LES applications in vehicle aerodynamics. Understanding the platooning effects when vehicles travel in convoys is one. There is great interest in mastering the technique of platooning as a way to make transports more energy efficient and environmentally friendly. The knowledge required to produce autonomic systems that can safely run convoys of vehicles requires a deep understanding of complicated flow processes with multiple vehicles moving in flows that interact with flows around other vehicles.

ACKNOWLEDGEMENTS

The work presented here was funded by Trafikverket and the Chalmers Sustainable Transport Initiative. The authors are grateful to AVL List GmbH for providing the licenses for the AVL FIRE solver for the project. Computation time at SNIC (the Swedish National Infrastructure for Computing) at the Center for Scientific Computing at Chalmers (C3SE) is gratefully acknowledged.

References

[1] Krajnović, S. and Davidson, L. 2001 "Large eddy simulation of the flow around a ground vehicle body". *SAE 2001 World Congress*, SAE Paper 2001-01-0702, Detroit, Michigan, USA.

[2] Krajnović, S. and Davidson, L. 2003 "Numerical Study of the Flow Around the Bus-Shaped Body". *ASME: Journal of Fluids Engineering*, Vol. 125, pp. 500–509.

[3] Krajnović, S. and Davidson, L. 2005 "Flow around a simplified car, Part 1: Large eddy simulation". *ASME: Journal of Fluids Engineering*, Vol. 127, pp. 907–918.

[4] Krajnović, S. and Davidson, L. 2005 "Flow around a simplified car, Part 2: Understanding the Flow". *ASME: Journal of Fluids Engineering*, Vol. 127, pp. 919–928.

[5] Krajnović, S. and Davidson, L. 2005 "Influence of Floor Motions in Wind Tunnels on the Aerodynamics of Road Vehicles,". *Journal of Wind Engineering and Industrial Aerodynamics*, Vol. 93,9, pp. 677–696.

[6] Hemida, H. and Krajnović, S. 2008 "LES study of the influence of train nose shape on the flow structures under cross-wind conditions". *ASME: Journal of Fluids Engineering*, Vol. 130, p. .

[7] Hemida, H. and Krajnović, S. 2009 "Exploring Flow Structures Around a Simplified ICE2 Train Subjected to a 30 Degree Side Wind Using Large-Eddy Simulation". *Journal of Engineering Applications of Computational Fluid Mechanics*, Vol. 3(1), pp. 28–41.

[8] Diedrichs, B., Berg, M., Stichel, S., and Krajnović, S. 2007 "Vehicle dynamics of a high-speed passenger car due to aerodynamics inside tunnels". *I MECH E Part F Journal of Rail and Rapid Transit*, Vol. 221, pp. 527–545.

[9] Diedrichs, B., Krajnović, S., and Berg, M. 2008 "On tail vibrations of very high-speed trains cruising inside tunnels". *Engineering Applications of Computational Fluid Mechanics*, Vol. 2(1), pp. pp. 51–75.

[10] Osth, J. and Krajnović, S. 2012 "Large Eddy Simulation of the Flow around one Single-Stacked Container Freight Wagon". Pombo, J. (ed.), *Proceedings of the First International Conference on Railway Technology: Research, Development and Maintenance,Paper 16,doi:10.4203/ccp.98.162*, Civil-Comp Press, Stirlingshire, UK,.

[11] Krajnović, S., Sarmast, S., and Basara, B. 2011 "Numerical Investigation of the Flow Around a Simplified Wheel in a Wheelhouse". *ASME: Journal of Fluids Engineering*, Vol. 133, p. 111001.

[12] Krajnović, S., Bengtsson, A., and Basara, B. 2011 "Large Eddy Simulation Investigation of the Hysteresis Effects in the Flow Around an Oscillating Ground Vehicle". *ASME: Journal of Fluids Engineering*, Vol. 133, p. 121103.

[13] Krajnović, S. 2009 "LES of Flows Around Ground Vehicles and Other Bluff Bodies". *Philosophical Transactions of The Royal Society A*, Vol. 367 (1899), pp. 2917–2930.

[14] Suzuki, M., Nakade, K., and Suzuki, M. 2009 "A wind tunnel test for railway vehicle under cross wind using a moving model rig". *The 18th Transportation and Logistics Conference, pp.231–232*.

[15] M., P., S., R., and A., I. 2001 "An experimental study of unsteady vehicle aerodynamics". *IMechE*, Vol. 215,D, pp. 779–788.

[16] Chometon, F., Strzelecki, A., Ferrand, V., Dechipre, H., Dufour, P., Gohlke, M., and Herbert, V. 2005 "Experimental study of unsteady wakes behind an oscillating car model.". *SAE Technical Paper No. 2005-01-0604*, p. .

[17] Krajnović, S. and Sarmast, S. 2010 "Numerical investigation of the influence of side winds on a simplified car at various yaw angles". *3rd Joint US-European Fluids Engineering Summer Meeting, Symposium on Issues and Perspectives in Ground Vehicle Flows*, FEDSM-ICNMM2010-30766, August 1-5, Montreal, Canada.

[18] Guilmineau, E. and Chometon, F. 2008 "Numerical and Experimental Analysis of Unsteady Separated Flow behind an Oscillating Car Model". *SAE paper 2008-01-0738*, p. .

[19] Krajnović, S. and Han, X. 2012 "LES and PANS of passive and active control of flows around generic vehicle bodies". *Seventh International Conference on Computational Fluid Dynamics (ICCFD7)*, Big Island, Hawaii.

[20] Han, X. and Krajnović, S. 2012 "Numerical investigation of passive flow control around a D-shaped bluff body". *Turbulence, Heat and Mass Transfer 7*, Begell House, Inc.

[21] Krajnović, S., Osth, J., and Basara, B. 2011 "LES study of breakdown control of A-pillar vortex". *International Journal of Flow Control*, Vol. 2, No. 4, pp. 237–257.

[22] Krajnović, S. and Fernandes, J. 2011 "Numerical Simulation of the Flow Around a Simplified Vehicle Model with Active Flow Control". *Int. J. Heat and Fluid Flow*, Vol. 32 (1), pp. 192–200.

[23] Han, X. and Krajnović, S. 2012 "Large eddy simulation of flow control around a cube subjected to momentum injection". *Turbulence, Heat and Mass Transfer 7*, Begell House, Inc.

[24] Parezanovic, V. and Cadot., O. 2012 "Experimental sensitivity analysis of the global properties of a two-dimensional turbulent wake". *Journal of Fluid Mechanics*, Vol. doi:10.1017/jfm.2011.495.

[25] Ahmed, S. R., Ramm, G., and Faltin, G. 1984 "Some Salient Features of the Time Averaged Ground Vehicle Wake", SAE Paper 840300.

[26] Lienhart, H. and Becker, S. 2003 "Flow and Turbulent Structure in the Wake of a Simplified Car Model", SAE Paper 2003-01-0656.

[27] Krajnović, S. and Basara, B. 2010 "LES of the Flow around Ahmed Body with Active Flow Control". Deville, D., Le, T.-H., and Sagaut, P. (eds.), *Turbulence and Interactions, Notes on Numerical Fluid Mechanics*, vol. 110, pp. 247–254, Springer-Verlag Berlin Heidelberg.

[28] Pujals, G., Depardon, S., and Cossu, C. 2010 "Drag reduction of a 3D bluff body using coherent streamwise streaks". *Experiments in Fluids*, Vol. 49, pp. 1085–1094.

Conference on Modelling Fluid Flow (CMFF'12)
The 15th International Conference on Fluid Flow Technologies
Budapest, Hungary, September 4-7, 2012

PROFESSOR N.YE. JOUKOWSKI, HIS LIFE, WORK AND DEVELOPMENT OF HIS IDEAS IN TSAGI

Victor V. VYSHINSKY[1]

[1] Corresponding Author. Department of Aeromechanics and Flight Engineering, Moscow Institute of Physics and Technology (State University). Gagarin St. 16, Joukowski (Zhukovsky), Moscow Region, Russia, 140181. Tel.: +7 495 5568421, Fax: +7 495 5568417, E-mail: vyshinsky@falt.ru

ABSTRACT

The article gives a brief biography of Prof. N.Ye. Joukowski, in particular, describes his years of study and the first years of his work, acquaintance with European scientists. The brief information on the scientific heritage of the scientist, his wide range of interests in matters of theory and practice is given. The articles on the theory of aviation are separately considered.

The most significant results of the scientist's research are given: the famous lift theorem, Chaplygin-Joukowski postulate (Kutta-Joukowski condition), the aerodynamic Joukowski airfoils.

N.Ye. Joukowski created the first in Russia wind tunnels. On the basis of this experimental equipment the scientific school was formed. Aerodynamic laboratories at Moscow University and at Imperial Moscow Technical School were created. Under the leadership of Joukowski and with the help of the funds of D.P. Ryabushinsky the first aerodynamic institute in Europe was founded. The apotheosis of this activity was the creation of the Central Aerohydrodynamic Institute (TsAGI).

The results of the development of Joukowski's ideas in TsAGI are given.

Keywords: Aerodynamics, Chaplygin-Joukowski postulate, Joukowski's airfoils, lift force.

1. INTRODUCTION

N.Ye. Joukowski managed, inherently, to lay the foundation of modern aerodynamics of airfoils and wings. During the period of 1902-1909, independently of W.M. Kutta (1867-1944) and F.W. Lanchester (1868-1946), he developed the mathematical basis of the theory of the lift force in two-dimensional case. The results presented in his papers (1904-1912) were included in all monographs on aero and fluid mechanics.

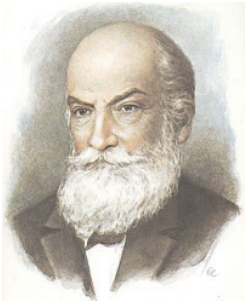

N.Ye. Joukowski

2. A BRIEF BIOGRAPHICAL SKETCH

Nikolai Joukowski was born on the 5th of January in 1847 in the village of Orekhovo Pokrovsky uyezd, (now the Vladimir region). His father, Yegor Ivanovich Joukowski, was descended from the small gentry. He was an educated railway engineer (in 1832 he graduated from the best in those years higher technical military school – St. Petersburg Institute of Railways Corps).

Yegor Ivanovich and Anna Nikolaevna Joukowski

Nikolai Yegorovich Joukowski spent his childhood in the village, where he came back many times throughout his life.

2.1. Years of study and the first years of work

After finishing Fourth Moscow Classical Gymnasium (1858-1864) with honors (magna cum laude) Joukowski entered Moscow State University. In 1868 he graduated from the Department of Physics and Mathematics, majoring in Applied Mathematics.

Since 1870 he taught physics at Second Moscow Girls' Gymnasium, since 1872 – mathematics at Imperial Moscow Technical School (IMTS), which he linked his life to forever. In 1874 N.Ye. Joukowski was appointed associate professor at the Department of Analytical Mechanics in IMTS. In 1878, the department of theoretical mechanics was established, which he headed until his death.

In 1876, Nikolay Yegorovich Joukowski published his first work – a master's thesis, "Kinematics of fluid body" (VIII volume of the collection of Mathematics), which he brilliantly defended on the 13th of October in Moscow University. His opponents were Professors V.Ya. Tsinger and F.A. Sludsky. Relying on the analytic and geometric method, he made things clear in a very difficult question on the motion of fluid particle.

Fourth Moscow Classical Gymnasium (years of study 1858-64)

Moscow State University (years of study 1864-68, professor's work 1885-1921)

2.2. Acquaintance with European scientists

A business trip to the polytechnic schools of Germany and France in 1877 had a great influence on the further evolution of Joukowski in the sphere of science, development of scientific views, assessment of various fields in the areas of mathematics and mechanics.

At that time the French school of mathematics and mechanics was in the prime of its glory. Suffice it to list the mathematicians and the mechanicians, members of the Paris Academy of Sciences: Michel Chasles, Charles Hermite, Joseph Liouville, Joseph Serret, Pierre Ossian Bonnet, Victor Alexandre Puiseux, Jean Claude Bouquet, Adhemar Jean Claude Barre de Saint-Venant, Henry Ame Resal, Urbain Jean Joseph Le Verrier [1].

In 1895 in Germany Joukowski watched the flights of gliders of German engineer and aviator Otto Lilienthal (1848-1896) and then talked to him about the ways of aeronautics development. Touched by the attention of professor Joukowski, Lilienthal presented him with his glider.

Lilienthal's glider

This glider was later used by the members of the aeronautic circle in IMTS, then it became an exhibit in the museum of N.Ye. Joukowski. Carrying out his experiments with gliders N.Ye. Joukowski developed his special technique to manufacture them, mainly, from silk and rush.

The first published work was followed by the next ones, always original and profound in its content.

Lilienthal's glider in the Joukowski museum (picture of the author, 2012)

2.3. The scientist's range of interests

The scientific heritage of Joukowski is 194 works. Including 18 works on hydrodynamics, 4 – on the hydrodynamic lubrication theory, 22 – on aerodynamics, 22 – on hydraulics, 21 – on aeronautics, 40 – on theoretical mechanics, 23 – on practical mechanics, 5 – on the theory of strength of materials, etc. [1]. Some of them are represented in Figure 1. The subject of his work was theoretical, analytical and applied mechanics. He studied:

theory of

- electrical engineering;
- gyroscopes, instrument engineering;
- planetary orbits determination…

theory and practice of

- the movement of solids and liquids;
- hydraulic engineering, e.g. theoretical and practical issues of water supply, paper "On the hydraulic shock in water pipes", 1899 (Fig. 1a), translated into European languages, N.Ye. Joukowski stated a complete theory that took into account the compressibility of water, the material of pipes, and which revealed the pressure waves arisen in pipes: these studies enabled to determine the location of the accident without leaving the water-pump station;
- artillery;
- shipbuilding…

practice

- movement of groundwater, water filtration in the dams;
- engineering industry;
- snowdrifts on the railways...

His works, which served as a basis for further development of aviation, are most emphasized.

In 1882 for the study "On the strength of movement" a doctorate in applied mathematics was conferred on him. Opponents were Professors F.A. Sludsky, V.Ya. Tsinger, A.U. Davidov. Since 1885 Joukowski taught theoretical mechanics at Moscow University, since 1888 he was a professor of Applied Mathematics Department.

While teaching Joukowski conducted scientific research. As the main theme he chose the motion of bodies in a fluid or gas, which eventually made him the founder of theoretical and experimental aeromechanics. He conducted experiments without assistance, constructed wings for the tests. He had to test first wings, tying them to himself and then picking up speed on a bike.

In 1885, Joukowski did research "On the motion of a rigid body with cavities filled with homogeneous dropping liquid." The developed method also allowed conducting calculations for the bodies which cavities are not completely filled with fluid. For this work Moscow University awarded to Joukowski Professor Brashmon Prize.

In 1890, the scientist began to develop the theory of determining the lift force of a wing or a propeller ("Toward the Theory of Flying"). In October 1891, at the meeting of the Moscow Mathematical Society he made a report "On birds' soaring" (Fig. 1a) published in 1892. In the work he researched birds soaring to climb and for the first time he calculated the possible flight paths, including the famous "loop," which was first carried out in 1913 by pilot P.N. Nesterov. In this work the first flight paths of birds and airplanes are given, derived on the basis of mathematical calculations.

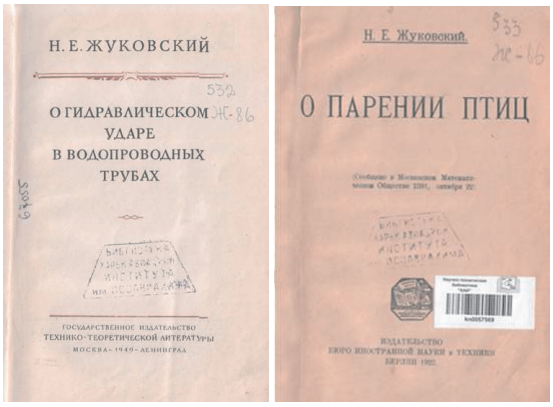

Figure 1a. "On the hydraulic shock in water pipes", "On birds' soaring"

In 1894, Joukowski was elected a corresponding member of the St. Petersburg Academy of Sciences, in 1900 he was nominated as a candidate for full membership in the Academy, but he withdrew his candidacy, not wanting to give up teaching at Moscow University and IMTS, because the election would have meant moving to St. Petersburg.

2.4. Papers on the theory of aviation

Relying on the experimental data of Lilienthal, Joukowski in his paper "On the most advantageous slope angle of airplanes" (1897) showed how, based on polar of airplane, to choose the optimum angle of attack in economical mode of horizontal flight of an airplane.

The works that followed [2, 3]:

"On the winged propellers" – 1898.

"On Aeronautics" – 1898.

"On the net load raised by helicopter" – 1904 (one of the fundamental for the calculation of rotary-wing aircraft).

"On the fall in the air of light, elongated bodies, rotating around its longitudinal axis" – 1906 (relying on the experiments, the scientist suggested the idea about the vortical nature of the lift force of an airplane wing [4]).

"On the bound vortices" – 1906 (N.Ye. Joukowski discovered the origin of the lift force of the airfoil and gave an exact formula for calculating it – the famous Joukowski theorem, which determines the proportionality between the

lift force acting on a body in plane-parallel flow of ideal incompressible fluid and the velocity circulation around it [5]).

"The theory of a propeller screw with large number of blades" – 1907.

"On the contours of lifting surfaces of airplanes" – 1910 [6] (Fig. 1c).

"Theoretical foundations of aeronautics" – 1910-1912 (Fig. 1b).

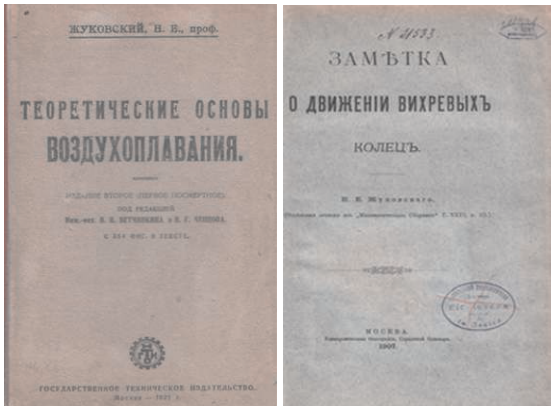

Figure 1b. "Theoretical foundations of aeronautics", "About vortex rings motion"

Figure 1c. "On the contours of lifting surfaces of Antoinette type", "The vortex theory of screw propeller"

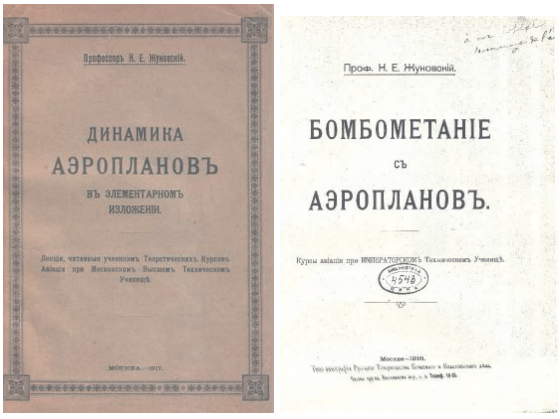

Figure 1d. "The dynamics of airplanes", "Bombing from airplanes"

"Geometrische Untersuchungen über die Kutta'sche Strömung" (Dutch) "Geometric study of the Kutta's flow" – 1911-1912.

In papers of 1910-1911 period together with S.A. Chaplygin, N.Ye. Joukowski solved the problem of determining the value of velocity circulation for the aerofoil with a sharp trailing edge, which formed the basis of theoretical aerodynamics. Mathematical apparatus was developed for solving the problems of the flow past an airplane wing, the theory of the wing of infinite span was proposed.

"The vortex theory of screw propeller" – 1912-1915 (Fig. 1c).

"The dynamics of airplanes" – 1913-1917 (Fig. 1d).

"Bombing from airplanes" – 1916 (he was the first in Russia to research aerial bombs, Fig. 1d).

"Aerodynamic calculation of airplanes" – 1917.

2.5. Last years of his life

In 1912 at the age of 95 his mother, Anna Nikolaevna, died. Over 65 years Nikolay Joukowski was under her constant care and tutelage. He had two children: daughter, Elena (1894-1920) was married to B.N. Yuriev, a disciple of N.Ye. Joukowski. His son Sergei (1900-1924) was a student of Air Force Academy. His children's mother, N.S. Sergeeva (1870-1904), was not married to N.Ye. Joukowski.

Nadejda Sergeevna Sergeeva

N.Ye. Joukowski with daughter Elena, son Sergei

Severe emotional experience caused by the death of his daughter undermined his health completely. He died (because of stroke) in a health center in Usovo on March 17, 1921 at the age of 74.

There are no direct descendants of N. Ye. Joukowski.

2. THE MOST SIGNIFICANT RESULTS

2.1. Lift theorem

"The pressure force of the flow, oncoming at the speed $\underline{V_\infty}$ and flowing around the contour with a circulation Γ, is expressed as follows:

$$\underline{Y} = -i\rho\Gamma\underline{V_\infty}\ell \qquad (1)$$

The direction of this force is determined if one rotates the vector $\underline{V_\infty}$ at a right angle in the direction opposite to the velocity circulation" (Figure 2) [6, 7]. Here ℓ is a wing span.

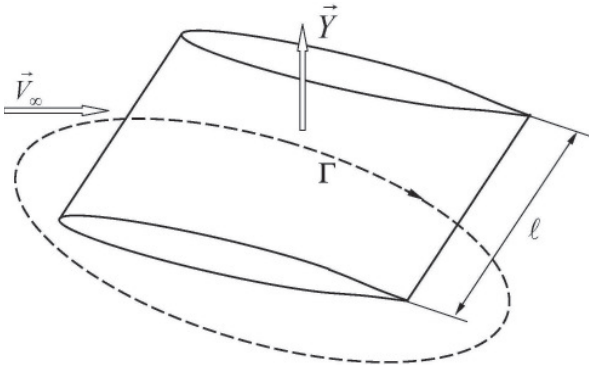

Figure 2. Theorem on the lift force

This formula was derived independently by W.M. Kutta in 1902.

2.2. Chaplygin-Joukowski postulate

The second important result, Chaplygin-Joukowski condition, which in the foreign literature known as Kutta-Joukowski condition. The solution of the problem of plane-parallel incompressible ideal fluid flow around a body is not unique (Neumann boundary-value problem for the Laplace equation) and can be obtained at an arbitrary value of the velocity circulation.

In 1909 S.A. Chaplygin formulated the following postulate: among an infinite number of theoretically possible smooth flows around an airfoil with the corner point on the trailing edge it is the flow with a finite velocity at this point that actually occurs.

In terms of an ideal fluid this statement is taken for granted. It is applicable for airfoils with the cuspidal point on the trailing edge of the contour. In case of a corner point on the trailing edge the latter is a point of the flow stagnation, that is, the velocities calculated from both sides are set to zero. Further studies explained the origin of this postulate by the influence of viscous forces. The large pressure gradients at a sharp trailing edge, arising with the value of the circulation that does not conform to Chaplygin-Joukowski postulate, lead to the flow separation and vorticity shedding into a flow behind the airfoil. Vorticity affects the airfoil flow in such a way that it shifts the trailing point of the flow to a sharp trailing edge (Figure 3). This process ends when the trailing point of the flow coincides with the trailing edge, i.e. Chaplygin-Joukowski postulate is fulfilled. Application of this hypothesis makes the determination of the lift force purely a mathematical problem.

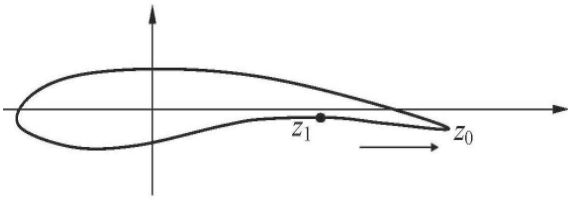

Figure 3. Chaplygin-Joukowski postulate

Despite the fact that this postulate was formulated by S.A. Chaplygin, it also fairly has the name of N.Ye. Joukowski, who used it earlier when considering specific hydrodynamic problems. In particular, in the paper "On the bound vortices" [5], this postulate was used to obtain a unique solution of the problem of detached flow of a plate placed across the flow in the simulation of separation by two point vortices.

2.3. Joukowski's airfoils

The third important contribution to theoretical aerodynamics made by N.Ye. Joukowski was the introduction of a special function of a complex variable, which bears his name, and the research of the problem of flow for the airfoils of special shape with the help of this function (Joukowski airfoils). Joukowski was the first who got an analytic solution to the problem of flow around series of airfoils of finite thickness with a sharp trailing edge. He also obtained an expression for the lift force of such airfoils [6, 7, 8].

In accordance with the method of conformal maps, if analytic function $w = f(z)$ of complex variable $z = x + iy$ with the normalization conditions $f(\infty) = \infty$, $f'(\infty) = 1$ is known, realizing a conformal mapping of the area outside contour C in plane Z to the area outside the circle of radius a in the plane W, the solution to the problem of flow past the contour C by potential flow of an ideal incompressible fluid with the velocity $\underline{V_\infty}$ is written in the analytical form:

$$\Phi(z) = \overline{\underline{V_\infty}} f(z) + \frac{V_\infty a^2}{f(z)} + \frac{\Gamma}{2\pi i} \mathrm{Ln}\, f(z), \qquad (2)$$

where $\Phi(z) = \varphi(z) + i\psi(z)$ – a complex flow potential, Γ – velocity circulation determined from Chaplygin-Joukowski postulate, a horizontal bar denotes complex conjugate value, $\underline{V} = \overline{\Phi'(z)}$.

Finding the mapping function $f(z)$ for an arbitrary contour is a complex task and is usually sought in the form of a segment of the Laurent series. However, if one sets oneself some specific form of the function $f(z)$, corresponding to the contours of interest, the calculation of the flow past such contours can be easily implemented using the formula (2). N.Ye. Joukowski considered a complex function:

$$z = \frac{1}{2}\left(w + \frac{a^2}{w}\right), \qquad (3)$$

which can also be written as

$$\frac{z-a}{z+a} = \left(\frac{w-a}{w+a}\right)^2 \qquad (3.1)$$

or

$$w = f(z) = z + \sqrt{z^2 - a^2}\ . \qquad (3.2)$$

Joukowski function is considered in all the monographs on the theory of analytical functions and conformal maps. It transforms circles in the plane of the variable W into different contours in plane Z, subject to the location of the circle in plane W. In particular, a circle of radius a centered at the origin of the coordinates in plane W is transformed into a flat plate of the length $2a$ along the real axis in plane Z. A circle of radius $\rho_0 > a$ with the center at the origin of the coordinates in plane W is transformed into an ellipse in plane Z with focuses at points $z = \pm a$ and with eccentricity which depends on the value of ρ_0. The circle in plane W with its center on the imaginary axis passing through the points $w = \pm a$, corresponds to the arc of the circle in plane Z (see Figure 4). Here

$$\alpha = 2\mathrm{arctg}\frac{h}{a}$$

is the angle between the tangent to the arc ACB in the point $z = a$ and x-axes,

$$\beta = \pi/2 - \alpha/2\ .$$

The calculation of the flow past such flat bodies with the help of Joukowski function presents no difficulty.

Very important in terms of aerodynamic applications is that Joukowski scrutinized other contours, which were the result of a circle transformation by means of Joukowski function. Thus, if the center of the circle in plane W is shifted relative to the origin of coordinates and the circle passes through the point $w = a$ and the point $w = -a$ is located inside it, then in plane Z this circle, in general, conforms to asymmetric contour with a sharp trailing edge and similar to an airfoil of an airplane. This contour is called Joukowski airfoil. In particular case when the center of the circle in plane W is on the real axis, in plane Z a symmetric relative to the real axis contour comes out which is called Joukowski rudder.

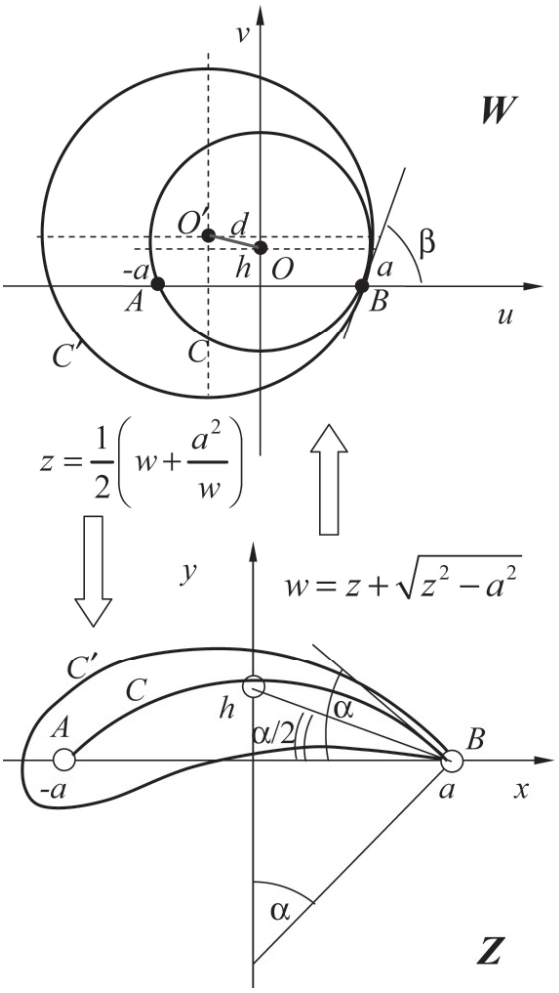

Figure 4. Joukowski transformation

Thus, N.Ye. Joukowski was the first who obtained an analytical solution to the problem of the flow past a family of airfoils of finite thickness with a sharp trailing edge. It was he, who derived a formula for the lift force Y, acting on such profiles Eqs. (1, 4):

$$\Gamma = -2\pi V_\infty \left(\sqrt{a^2 + h^2} + d\right)\sin(\vartheta + \alpha/2), \qquad (4)$$

$$|\underline{Y}| = 2\pi\rho V_\infty^2 \left(\sqrt{a^2 + h^2} + d\right)\left|\sin(\vartheta + \alpha/2)\right|,$$

where ρ – fluid density, V_∞ – upstream velocity, ϑ – angle of attack.

3. EXPERIMENTAL RESEARCH

In 1891 at Moscow State University Joukowski built a wind tunnel with a diameter of the test section of 2 feet. The method for determining the lift force of an airfoil without using the aerodynamic balance was developed, the so-called method "floor-ceiling", whereby the measurement of velocities on the upper and lower walls of a wind tunnel and calculation of velocity circulation allows to determine the lift force using the theorem of Joukowski.

In 1902 Joukowski managed to build a small wind tunnel at Moscow University with a square cross-section of 0.75 × 0.75 m, 7 m long and with a flow velocity of 1.5 to 20 m/sec. With assistants he created the instruments and methods of measuring the pressure distribution along the contour of an aerodynamic body.

In this wind tunnel numerous tests were conducted. The most important ones were researches of windage center, dependence drag of the ball on the speed, air friction drag on solid walls.

4. FOUNDATION OF THE SCHOOL

N.Ye. Joukowski founded his own school, the best representative of which was Sergei Alekseevich Chaplygin, who brilliantly continued the work of Joukowski in the future.

Since 1889 at Moscow University under the direction of Joukowski different researches on aeronautics and aviation were conducted, the models of aircrafts were studied and tested. He attracted young people, worked together with students, acted as an organizer of public initiatives in the sphere of aviation and aeronautics.

In 1904 with the help of the funds of D.P. Ryabushinsky in the estate of the Ryabushinskys, Kuchino, near Moscow, under the leadership of Joukowski the first aerodynamic institute in Europe was founded, where a group of his disciples were engaged in the research of the basis of future aircraft construction. Wind tunnel in the institute in Kuchino is represented in Figure 5.

Thinking of creating a base for experiments, in 1909 N.Ye. Joukowski built a new wind tunnel with the internal diameter of 1.6 m and the length of 10 m in Moscow University (Figure 6). For several decades, all studies on aerodynamics were carried out in that tunnel.

In 1909 N.Ye. Joukowski organized an aeronautic circle under IMTS, which many eminent Russian scientists in the sphere of theoretical and practical aviation and aeronautics sprang from. In 1910 he managed to organize an aerodynamic laboratory under IMTS (Figure 7).

In 1911, by the 40th anniversary of teaching IMTS confirmed Joukowski's appointment as a mechanical engineer and presented him with a golden engineering sign. Joukowski was very happy to wear this adornment – quite unusual for the professors of theoretical mechanics at that time. It must be said that at that time the notions "scientist", "engineer," "teacher" were very different and that is often incomprehensible to a modern engineering-technical worker.

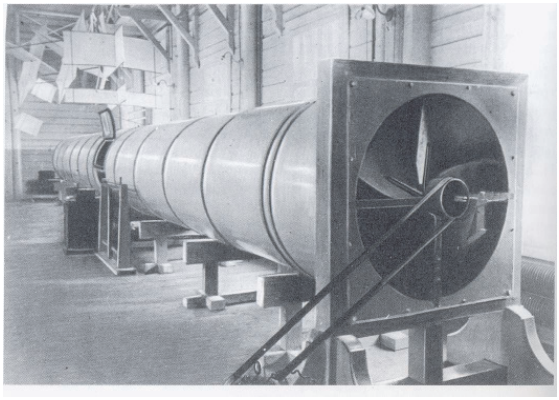

Figure 5. Wind tunnel in the institute in Kuchino (length 14.5 m, diameter 1.2 m, V = 6 m/s)

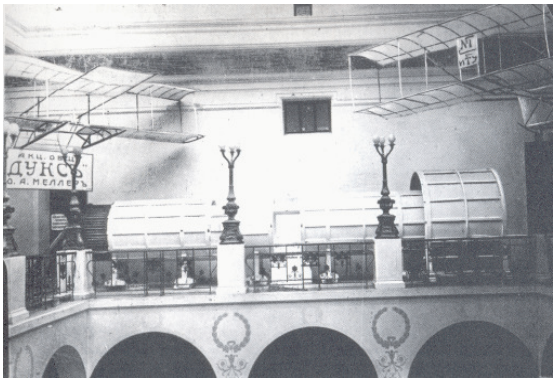

Figure 6. Wind tunnel of Moscow University

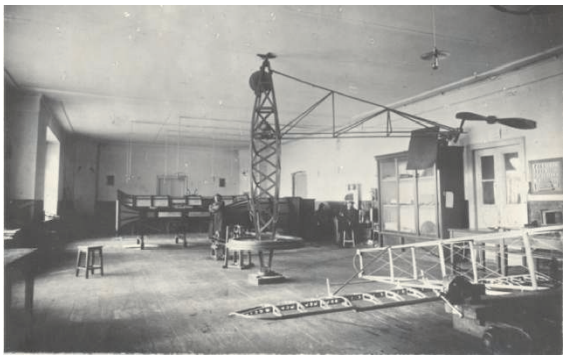

Figure 7. Aerodynamic laboratory at IMTS

N.Ye. Joukowski did not confine himself to studying the problems and training engineers. He became one of the first teachers to the pilots of incipient aviation. Since 1913 he taught at "short

theoretical courses of aviation" created at IMTS for pilot-officers, since the beginning of the 1st World War – he taught at the courses for volunteer pilots.

5. FOUNDATION OF TSAGI

In 1916 the scientist organized at IMTS Aviation design-testing bureau, where the foundation of aerodynamics and calculation of aircraft strength were developed. A.N. Tupolev was at the head of Aerodynamic calculation department. If the flight dynamics answers the questions how to pilot a plane correctly, what forces act on it during the flight, what rules must be observed when performing aerobatics, then the aerodynamic calculation is to answer the question what flight data one or another airplane will recieve subject to the selected wing airfoil, engine power, fuselage shape, tail units, struts, stays, etc. It was these calculations that the most engineers building the aircraft needed. What will the speed, the rate of climb, altitude, landing speed for a certain aircraft be – these are the most burning questions for each aircraft designer.

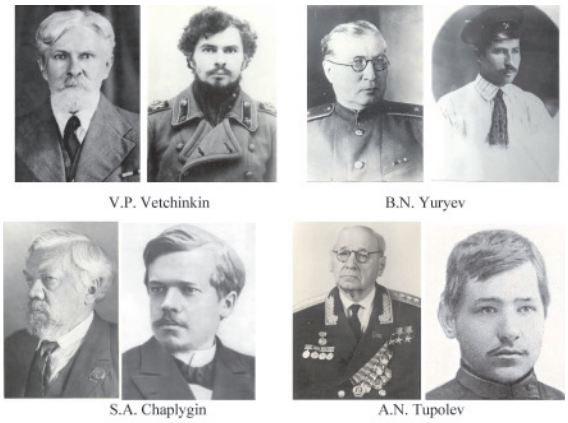

Zhukovsky's disciples – organizers and first directors of subdivisions of TsAGI

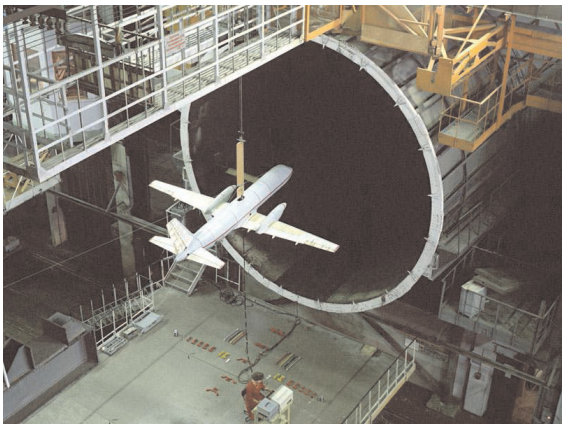

Figure 8. Experiments in T–104 subsonic wind tunnel of TsAGI (*V* = 10–120 m/s)

In 1918, bringing together around himself the leading figures in the sphere of aircrafts, N.Ye. Joukowski proposed to set up a powerful aerodynamic state institute. On the 15th of December, 1918 the history of the Central Aerohydrodynamic Institute (TsAGI), which deserved international fame and was named after N.Ye. Joukowski after his death, began. Figures 8-10 illustrate some test facilities of TsAGI.

N.Ye. Joukowski was also the founder of the oldest higher education institution of aviation of the country, Air Force Engineering Academy named after N.Ye. Joukowski. Since September 1920 he was its Rector.

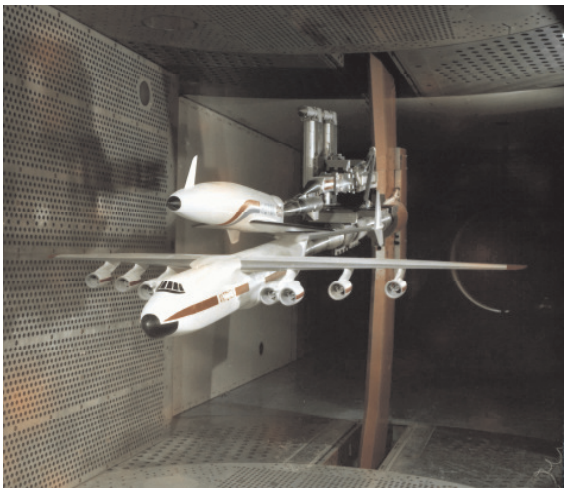

Figure 9. Experiments in T-128 transonic wind tunnel of TsAGI (M = 0.15–1.7, test section 2.75×2.75 m)

Figure 10. Tests of full-size structures in static test room of TsAGI

6. DEVELOPMENT OF THE IDEAS OF PROF. N.YE. JOUKOWSKI IN TSAGI

6.1. Generalizations of Joukowski theorem

1. The Joukowski theorem for adiabatic flows of compressible gas is true if the values for density

and velocity are understood as the proper values in the undisturbed flow. Brief description of this generalization is presented in the paper of F.I. Frankl and M.V. Keldysh [9].

2. The Joukowski theorem is also true for the case of the flow around flat airfoil cascades, if V is the arithmetical mean of velocity vectors far in front of and behind the cascade. These results were received in the work of L.I. Sedov [10].

S.A. Chaplygin, head of the scientific seminar, and the participants – followers of Joukowski's ideas (the author of this paper used the lectures of professor N.V. Zvolinsky)

3. The Joukowski theorem is proved and widely used "in the small" when considering the flow round a thin lifting surface. Proof of this theorem and its wide application in the theory of the wing may be found in the monograph of S.M. Belotserkovsky [11].

4. The Joukowski theorem is also true for the elements of a thin surface, performing spatial unsteady motion, if the lift force is understood as a load on this element, and the velocity – as the relative velocity at the given instant of time at the selected point of the lifting surface. Main results and applications are presented in monograph [12].

By creating the lift force theory N.Ye. Joukowski laid the foundation of modern theoretical and applied aerodynamics. Development of his ideas is the basis for solving many specific aerohydrodynamic problems of great practical importance. These ideas gave rise to a strong trend in the development of the theory of singular and hypersingular integrals [13]. Well known method of the discrete vortices (MDV) utilizes this theory as the theoretical basis.

Thanks to the scientific studies of N.Ye. Joukowski and his disciples the lift force theory has become a cornerstone of modern aerohydromechanics. Everlasting practical value of the obtained exact solutions to the problem of the flow round an airfoil section is that they are suitable for testing the generated approximate numerical methods.

6.2. Application of the Chaplygin-Joukowski postulate in computational methods

The Chaplygin-Joukowski postulate is an essential element in the formulation of the boundary value problem of flow past a body and in one form or another is present in almost all analytical and numerical methods for solving flow problems. In numerical methods, this postulate can assume many mathematically equivalent forms, for example:

– in solving flow problems by the method of hydrodynamic singularities or boundary element (the method of discrete vortices, panel methods) placed the condition of bringing of the vortices strength at the trailing edge to zero or the continuity of the double layer (layer of hydrodynamic dipoles) is set;

– the condition of given direction of the flow shedding in the trailing edge is stipulated, for example, along the bisector of the angle between the tangents to the airfoil's contour at the trailing edge;

– the condition that the pressure equality on the upper and lower surfaces of an airfoil or wing in tending to the trailing edge is stipulated.

When solving the problems of viscous flow past bodies by the approaches based on the model of viscous-innviscous interaction, it appears that in formulating the boundary value problem for the external innviscous flow and making the boundary conditions at a sharp trailing edge there should be non-zero differential pressure.

Despite the differences in the wording of the conditions at a sharp trailing edge, they are called the Chaplygin-Joukowski conditions and reflect the fact that some additional condition is needed, which determines the value of circulation, for a unique solution to the problem of flow past flat bodies.

6.3. Application of the Joukowski transformation in theoretical aerodynamics

The Joukowski transformation and the Joukowski airfoil have been widely used in theoretical aerodynamics. The solution obtained by N.Ye. Joukowski is used to verify the accuracy of methods of computing the flow about arbitrary airfoils.

Another application of the Joukowski transformation is due to the fact that some computing methods converge poorly in a close location of vortex layers in the area of a thin trailing edge of an airfoil. Preliminary application of the Joukowski transformation allow to distinguish singularity explicitly, to eliminate this defect and create a method that provides rapid convergence of the iterative solution process.

A similar transformation is used when applying the method of conformal maps to calculate an airfoil of arbitrary shape. In this case the flow area in plane Z around an arbitrary contour is transformed into an area outside some contour in plane W by the Joukowski transformation. If a streamlined airfoil is the Joukowski airfoil, in plane W it corresponds to a circle. In general, a contour is obtained which is close to a circle. The mapping of this contour close to a circle on a circle in the complex plane Ω is sought in the form of a segment of the series. Currently efficient numerical method for expanding functions into Fourier series is developed and the summation of these series (fast Fourier transformation), which allows to determine the unknown coefficients of the series. The application of the Joukowski transformation at the first stage provides a fast convergence of the series and allows us to do with a relatively small number of terms of the series.

The Joukowski transformation (3) gives airfoils with a cuspidal point in the trailing edge. The generalization of the Joukowski transformation is the transformation of the form:

$$\left(\frac{z-a}{z+a}\right)=\left(\frac{w-a}{w+a}\right)^{2-\frac{\tau}{\pi}}, \qquad (5)$$

which gives the airfoils with the angle τ between the tangents to the upper and lower surfaces of the airfoil at the trailing edge. These profiles are called the generalized Joukowski airfoils or the Karman-Trefftz airfoils [14]. If $\tau = 0$, the transformation (5) turns into the Joukowski transformation (3.1). This transformation is used instead of (3.1) in the method of calculating the flow about an arbitrary airfoil by the method of conformal maps.

The Joukowski transformation and the generalized Joukowski transformation together with the method of conformal maps have been used in the calculation of the flow past airfoils and wings by a compressible gas. In this case, the equations of gas flow are non-linear (Euler equation or full equation for the velocity potential). Finite-difference numerical methods of solving these equations require the generation of computational grid in the nodes or cells of which the unknown values of gas-dynamic quantities are defined. If we make a conformal map of airfoils or stream-oriented cross sections of a wing of finite span to the circle, then the grid formed by the lines r = const, θ = const in a polar coordinate system (r, θ) corresponds to a curvilinear mesh in the initial area of the flow.

The advantage of such a mesh is its orthogonality, which simplifies writing equations in a curvilinear coordinate system and improves the accuracy of calculations. In addition, the solution to the problem of the incompressible fluid flow around a given contour, which is obtained as a byproduct of this approach, can be used as a good initial approximation for the iterative procedure of solving the problem of the compressible gas flow. Such an approach to solving problems of calculating the compressible gas flow is used in a number of studies (e.g. [15-16]).

6.4. Effect of heat exchange on lifting properties of a wing of finite aspect ratio at subsonic speed

In the paper [17], the momentum conservation law for a continuous medium is used to study the aerodynamic forces acting on a wing of finite span at subsonic speeds under the heat exchange with the medium. An analytical expression for the principal vector of aerodynamic forces in view of heat transfer, allowing, in particular, to investigate the effect of heat exchange on the lifting properties of the wing is obtained. The computation studies of aerodynamic characteristics of a wing of finite span in the framework of a boundary-value problem for the Reynolds-averaged Navier-Stokes equations, fully confirmed the results of analytical studies on the effect of heat exchange on the lift force [18].

Increase of the lift force at a fixed angle of attack can be obtained by cooling the upper surface of an aerodynamic body. Decrease of the lift force can be obtained by heating the upper surface (or supplying heat from the side of the upper surface).

6.5. Joukowski method of approximate solutions to technical problems

In his practice N.Ye. Joukowski was guided by the principle: "the art of mechanics is to produce integrable equations". Approximation is not in mathematics, but in the "mechanical" setting of difficult technical problems and thus in obtaining simple solutions. This principle was developed by his disciples, this approach is still kept and is being

used in TsAGI, which allows solving complex problems on the basis of relatively weak computing machinery and measuring equipment.

7. CONCLUSION

Classical mechanics is generally accepted to repose on the works of Isaac Newton, Johann Kepler, ... theoretical fluid dynamics – on the works of Academicians of St. Petersburg Academy Daniel Bernoulli (period of living in Russia 1725-1733) and Leonhard Euler (periods of living in Russia 1727-1741, 1766-1783). List of the scientists, of course, one can continue, but "the main terms of expansion" in this appreciation are unquestionable.

As well, a relatively young science – computational fluid dynamics reposes on the works of N.Ye. Joukowski and W.M. Kutta.

ACKNOWLEDGEMENTS

The author is particularly grateful to professor S.V. Lyapunov (TsAGI named after professor N.Ye. Joukowski) and professor V.T. Kalugin (Moscow State Technical University named after N.Er. Baumann, former IMTU), who assisted in the writing of this article.

REFERENCES

[1] Ed. Byushgens, G.S., 2007, *Joukowski, N.Ye.*, Moscow: Federal State Unitary Enterprise Central Aerohydrodynamics Institute after prof. N.Ye. Joukowski (in Russian).

[2] Joukowski, N.Ye., 1937, "The screws. Windmills. A wind tunnel", *The Complete Works*, Vol. 5, Ed. V.P. Vetchinkin, Moscow, Leningrad: Chief. ed. of aviation lit. (in Russian).

[3] Joukowski, N.Ye., 1937, "Vortices. The theory of the wing. Aviation", *The Complete Works*, Vol. 6, Ed. A.P. Kotelnikov, Moscow, Leningrad: Chief. ed. of aviation lit. (in Russian).

[4] Joukowski, N.Ye., 1949, "On the fall in the air light, oblong bodies, rotating about their longitudinal axis", *Collected Works*, Vol.4, Gostekhizdat (in Russian).

[5] Joukowski, N.Ye., 1949, "On the bound vortices", *Collected Works*, Vol. 4, Gostekhizdat (in Russian).

[6] Joukowski, N.Ye., 1949, "On the contours of supporting surfaces of airplanes", *Collected Works*, Vol. 4, Gostekhizdat (in Russian).

[7] Joukowski, N.Ye., 1910, "Über die Konturen der Tragflächen der Drachenflieger", *Z.F.M.,* b. 1, s. 281.

[8] Joukowski, N.Ye., 1949, "Determination of the pressure of plane-parallel flow of fluid on the contour, which in the limit transforms into a straight-line segment", *Collected Works*, Vol. 4, Gostekhizdat (in Russian).

[9] Frankl, F.I., and Keldysh, M.V., 1934, "Neumann exterior problem for nonlinear elliptic equations with the application to the wing theory in a compressible gas", Proc. *USSR Academy of Sciences, math. ser*., No. 4 (in Russian).

[10] Sedov, L.I., 1939, *The theory of plane motions of an ideal fluid*, Publ. Oborongiz (in Russian).

[11] Belotserkovsky, S.M., 1965, *A thin lifting surface in a subsonic gas flow,* Moscow, "Nauka" (in Russian).

[12] Belotserkovsky, S.M., Skripach, B.K., and Tabachnikov, V.G., 1971, *Wing in an unsteady gas flow,* Moscow, "Nauka" (in Russian).

[13] Belotserkovsky, S.M., 1985, *Numerical methods in singular integral equations and their applications in aerodynamics, the theory of elasticity, electrodynamics,* Moscow: "Nauka" (in Russian).

[14] Von Karman, T., and Trefftz, E., 1918, "Potentialströmung um gegebene Tragflächenguerschuitte", *Z.Flugtechn. Motorluftsch*., 9, pp. 111-116.

[15] Ives, D.C., 1982, *Conformal grid generation. Numerical grid generation*, ed. by J.F. Tompson, North-Holland, Amsterdam.

[16] Lyapunov, S.V., 1991, "A short-time method for solving the Euler equations in the problem of transonic flow around an airfoil", *Math. modeling*, No. 4 (in Russian).

[17] Petrov, A.S., 2009, "Lift force and induced drag of a finite span wing in the flow of a viscid compressible gas at subsonic speed", "*Uchyonye Zapiski TsAGI*", Vol. XL, No. 5, pp. 16-28 (in Russian).

[18] Petrov, A.S. Vyshinsky, V.V., and Vu Thanh Trung, 2011, "Aerodynamic characteristics of wing airfoil with taking into account heat exchange with the flow of the viscous compressible gas at subsonic speeds", Proc. *XV International Symposium "Methods of discrete singularities in the problems of mathematical physics"*. Kharkov-Kherson, pp. 115-118 (in Russian).

Workshop
Optimization of wind turbines

Conference on Modelling Fluid Flow (CMFF'12)
The 15th International Conference on Fluid Flow Technologies
Budapest, Hungary, September 4-7, 2012

CFD AND BEM OPTIMIZATION OF HORIZONTAL AXIS WIND TURBINES IN A MULTIFIDELITY PERSPECTIVE

Fabio De Bellis[1], Luciano A. Catalano[2]

[1] Corresponding Author. Department of Mechanics, Mathematics and Management, Polytechnic University of Bari. Via G. Re David 200, 70125 Bari Italy. E-mail: debellis@imedado.poliba.it
[2] Department of Mechanics, Mathematics and Management, Polytechnic University of Bari. E-mail: catalano@poliba.it

ABSTRACT

The optimization of wind turbines is currently not as common as gas turbines or compressors optimization. In the present paper, the design of a stall regulated horizontal axis wind turbine has been performed employing two different simulation techniques in an optimization framework: Computational Fluid Dynamics (CFD) and Blade Element Momentum (BEM). Starting from the previous works available in the literature, the advantages and disadvantages of both techniques have been analyzed considering the development of the Pareto front and the optimization results. Different objectives and the capability of analyzing different blade shapes have also been considered.

The similarity between CFD and BEM results for conventional blades suggest to employ a combination of the two simulation techniques in a multifidelity approach in the future optimizations.

Keywords: optimization, CFD, BEM, horizontal axis wind turbines.

NOMENCLATURE

a	[-]	axial induction facor
a'	[-]	tangential induction facor
B	[-]	number of blades
c_i	[m]	chord of the i-th section
C_d	[-]	drag coefficient
C_l	[-]	lift coefficient
C_N	[-]	normal force coefficient
C_T	[-]	tangential force coefficient
F	[-]	tip loss factor
F_T	[N]	tangential force
M	[Nm]	torque
r	[m]	radial coordinate
R	[m]	blade span
V_0	[m/s]	free stream velocity

Greek

Φ	[°]	local angle of attack
ρ	[kg/m^3]	air density
σ	[-]	solidity
ω	[rad]	rotational speed

1. INTRODUCTION

The need for wind turbines optimization is well justified both from the academic and the industry point of view. Starting from the latter, the exponential growth of this sector in the last years and in the future fully justifies (and often explicitly requests) improved, innovative, optimized wind turbines. Interestingly, such demand is not limited to the large commercial applications, but also applies to the small turbines producing few kilowatts. From the scientific standpoint, it should be initially highlighted that there are few works available in the literature dealing with this topic; such consideration is particularly significant considering the great number of optimization works published in other research fields, for example gas turbines or compressor stages [1-4]. Many publications on wind turbine optimization focused their attention on the optimization of the installation site matching or on the control systems [5, 6], but there are very few works available in the literature about the optimization of the turbine design by itself [7-10]. Additionally, such latter papers employed Blade Element Momentum (BEM) method to evaluate the performance of the turbine, mainly due to its low computational cost. However,

it should be recalled that BEM is a simplified simulation method, since it is based on the 'no radial dependency' hypothesis [11]: each radial section in the spanwise direction is treated independently from the others in a bi-dimensional way, thus neglecting the existence of radial flows. Although some empirical corrections were introduced in order to take into account the rotational and radial effects (Prandtl and Glauert corrections), the 3D performance of a given blade is basically obtained simply adding the force and moment components of each section calculated as standing alone.

Strictly speaking, the only fully 3D, turbulent, rotational and viscous simulation technique available is Computational Fluid Dynamics (CFD), but at the price of a computational cost some orders of magnitude greater than BEM. Nevertheless, given the continuous improvements of CFD and the even more increasing growth of computational resources available, CFD optimizations of wind turbines are nowadays certainly likely to be studied in depth.

In a past work, the authors developed and validated a CFD procedure able to efficiently cope with the conflicting requirements of simulation accuracy and computational cost [12]. With such tool, the authors demonstrated the feasibility of 3D CFD optimization applied to the design of conventional and non-conventional blade of horizontal axis wind turbines [13, 14].

In the present paper, the results obtained with the abovementioned CFD optimizations have been compared with those achieved employing BEM instead. The purpose of the study is to highlight the differences of the two simulation techniques, but also the mutual advantages when applied to HAWT optimization.

The next section describes the methodologies adopted both for the simulations (CFD and BEM) and the optimization, whilst the most relevant results are presented before the conclusions.

2. METHODOLOGY

This section provides the most significant details about the methodology employed during both the simulation and the optimization process. Coherently with the scope of the paper, the simulation description is differentiated between CFD and BEM methodology in two separate subsections, whereas the employed optimization strategies are presented in a third subsection.

2.1 3D CFD simulation

In a CFD algorithm Navier-Stokes equations are solved locally on each grid cell composing the domain; however, numerical approximations can be significant and computational resources are a serious issue. It was demonstrated in the past that CFD can be successfully employed to assess the aerodynamics of wind turbines [15-20]. Unfortunately, the complexity of the flow field, which is unsteady, rotational, full three dimensional and with high Reynolds numbers, requires severe resources to be simulated with acceptable accuracy by CFD. As a consequence, CFD optimization of wind turbines had not been considered affordable up to now, and no works are available in the literature on this topic. Considering that a "classic" optimization can require tens or even hundreds of evaluations (depending on the numbers of objectives), if a wind turbine CFD optimization has to be performed there are two possibilities: the availability of a huge amount of computational resources (including time) or the development of a CFD simulation technique at the same time affordable and reliable. The latter option was investigated by the authors in a past work [12], where the feasibility of such approach was demonstrated. In that paper the whole CFD process was analyzed and, starting from mesh generation, some simplifications were introduced, such as fully unstructured mesh topology, reduced grid size, incompressible flow assumption, use of wall functions, commercial available CFD package employment. The chosen final settings were the result of a trade-off between numerical accuracy and resources utilized: in this way, the aerodynamic performance of a wind turbine blade was assessed with significantly less computational power. Besides the introduced simplifications, numerical predictions of shaft torque, forces and flow distribution showed a confident agreement with the NREL Phase VI experimental data set [21].

2.2 BEM simulation

A complete description of the classical BEM theory and its theoretical explanations can be found in the [11], but the main features of the theory and implemented in the in-house developed Matlab code are described as follows. As already mentioned, in a BEM code the power (or torque) produced by the rotor is obtained adding the contribution of each radial section:

$$dM = rBF_T dr \tag{1}$$

where the tangential force F_T can be written as a function of the free stream velocity V_0 and the tangential coefficient C_T:

$$dM = \frac{1}{2}\rho B \frac{V_0(1-a)\omega r(1+a')}{\sin\Phi\cos\Phi} c C_T r dr \tag{2}$$

whilst a and a' are axial and tangential induction factor, respectively:

$$a = \frac{1}{\frac{4(\sin\Phi)^2}{\sigma C_N}+1} \tag{3}$$

$$a' = \frac{1}{\frac{4 \sin \Phi \cos \Phi}{\sigma C_T} - 1} \quad (4)$$

Given that B is the number of blades, r the radius of the rotor, ρ the air density and Φ the angle of attack of the relative velocity with the profile section under analysis, the normal and tangential force coefficient are obtained as functions of lift and drag coefficients:

$$C_N = C_l \cos \Phi + C_d \sin \Phi \quad (5)$$

$$C_T = C_l \sin \Phi - C_d \cos \Phi \quad (6)$$

where C_l and C_d have to be known a priori from wind tunnel data or from some other source (which is another relevant drawback of the BEM method).
Finally, the solidity σ can be calculated for each radial section with the following equation:

$$\sigma(r) = \frac{c(r)B}{2\pi r} \quad (7)$$

In order to consider the non-infinite number of blades in the rotot, Prandtl introduced a factor F (tip loss factor) in the fractions at the a and a' equations denominator [22]:

$$F = \frac{2}{\pi} \cos^{-1}(e^{-f}) \quad (8)$$

where f is in turn:

$$f = \frac{B}{2} \frac{R-r}{r \sin \Phi} \quad (9)$$

The effect of the turbulent wake has been considered in the Matlab code through the Buhl version [23] of the Glauert correction [24], in which the axial induction factor is further modified as:

$$a = \frac{18F - 20 - 3\sqrt{C_T(50-36F)+12F(3F-4)}}{36F-50} \quad (10)$$

where F is the Prandtl tip factor.
Finally, post-stall coefficients and 3D rotation correction have been calculated with Viterna [25] equations and the rotation correction proposed by Snel et al. [26], respectively.
Such BEM code has been validated against both the experimental data from NREL and another BEM code, developed by TU Berlin [27], namely the QBLADE software (lift and drag data of the S809 taken from [21]). Figure 1 clearly confirms that the agreement achievable with the developed BEM code is as accurate as the one obtained with the QBLADE software and close to the experimental values. In particular, a very accurate prediction of the shaft torque of the blade has been obtained for low wind velocities, characterized by a non-stalled (attached) flow regime around the blade (up to 10 m/s). When stall occurs there are some discrepancies in the torque curve between the BEM results and the experiments, particularly in the early stall region (between 10 and 15 m/s). However, since the non-perfect agreement is completely coherent with the QBLADE code taken as reference, it can be deduced that the disagreement is probably due to the BEM simulation technique itself, considering that stall is three dimensional process and BEM is based on a 'no radial dependency' assumption.

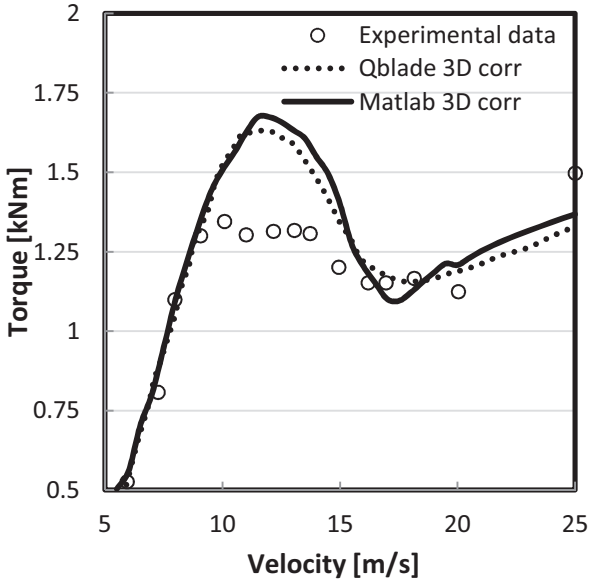

Figure 1. BEM code validation against experiments and QBLADE.

2.3 Optimization

The aim of this paper is to compare CFD and BEM optimization of horizontal axis wind turbine (HAWT) to design HAWT blades subject to some given working conditions and to some constraints.

In order to have a benchmark, it has been chosen to design "a priori" a stalled regulated HAWT with a nominal diameter of 10 m and with the same aerodynamic profile of the NREL Phase VI turbine, i.e. the S809. This has been done for several reasons:

- since the Phase VI turbine has been already studied, both quantitative and qualitative data are available and can be used to draw proficient conclusions;
- by using the same aerodynamic profile, any possible amelioration must be due to the improved design rather than to a better aerodynamic performance of the profile itself;
- to use the same aerodynamic profile reduces the number of parameters, and the optimization is simpler and faster.

Only twist and chord distributions have been varied in the optimization process, being then considered

as the design varibles with a third and first order polynomial, respectively.

Nevertheless, it should be recalled that the aim of the paper is not the optimization of the NREL turbine, but to obtain "from scratch" new design configurations optimized for some given conditions. Such a tool could then be employed at a preliminary design stage to obtain more detailed information about the fluid dynamics features of the turbine blade. In this sense, the comparison with the Phase VI turbine is a "blind comparison" useful to highlight differences and similarities and understand the reasons beneath them "a posteriori". In addition, the exposed method can be applied identically to any size and type of HAWT, since it is in no way limited to the studied example.

The key component in the optimization process is represented by the optimization algorithm itself. Each objective is reinforced by means of a constraint of positivity to enhance optimization convergence, that is, the torque in each wind condition must not be negative (otherwise the blade is not a turbine but an aerodynamic brake). Furthermore, it is convenient to point out that to optimize the shaft torque completely means to optimize the shaft power produced by the wind turbine, since the rotational velocity is constant (stall regulated wind turbine).

In addition to aerodynamic torque maximization, also structural stress minimization is considered in the present work. The so called root bending moment is a common way to consider the most significant structural stresses acting on a wind turbine blade both, both in the textbooks (see [11] and [28]) and in past optimization works based on BEM models. Root bending moment (also referred to as flapwise bending moment) is the moment which tend to deflect the blade out of the rotor plane in the downwind direction (see Figure 2). This quantity is responsible for many other structural assessments, such as blade deflection, fatigue (through vibrations), pylon and gearbox dimensioning. The root bending moment is more significant than the resultant force vector acting in the axial direction, since takes in to account also the redial point of application of each force contribute. As a consequence, the pressure force applied on the tip section of the blade gives a stronger contribute to the resultant bending moment rather if the same force is applied near the root.

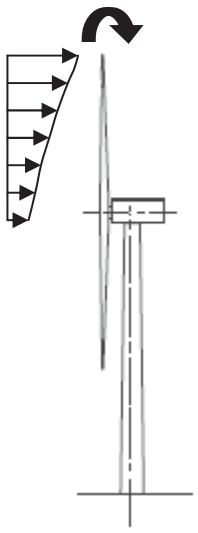

Figure 2. Root bending moment definition.

The tool employed to manage the overall optimization process is the software modeFrontier® by ESTECO, which allows to use several optimization algorithms. The simulations are performed either by Fluent (CFD) or the Matlab code (BEM) and the results extracted and analyzed by the optimizer (proper algorithms have been chosen for each optimization).

The ARMOGA algorithm was originally developed by Sasaki and Obayashi [29]. With respect to traditional genetic algorithms employing selection, crossover and mutation operators to reproduce the natural evolution of species, ARMOGA also uses range adaptation to adjust the search region according to the statistics of the former data stored in an archive. Range adaption then helps reducing the number of time consuming evaluations, particularly in aerodynamic optimizations, where ARMOGA can improve multiple conflicting objectives with a low number of high cost computations. The ARMOGA algorithm has been employed in the initial design optimization of a conventional blade (without structural objectives), whilst the other two application cases have been performed with the NSGA-II algorithm.

The Non-dominated Sorting Genetic Algorithm II (NSGA-II) is an evolutionary algorithm originally developed by professor K. Deb et al. [30] at Kanpur Genetic Algorithms Laboratory (KanGAL). It is an algorithm designed for fast and efficient solutions search, and can use both continuous and discrete variables. Compared with ARMOGA, it performed better since gave faster and more robust results.

3. RESULTS

The most significant results regarding BEM and CFD optimization are shown in this section, dividing the two topic in two sub-sections as done before.

3.1 CFD optimization

In the present optimization, the design of the wind turbine has been performed with the aim of maximizing the aerodynamic shaft torque at two wind velocities at the same time: 7 m/s and 20 m/s. The two wind velocities are representative of attached and stalled flow conditions, again in the perspective of assessing the capability of a CFD optimization in the two cases.
Schematically, there are two objectives:

- Obj1 - maximize low speed torque (max M_7)
- Obj2 - maximize high speed torque (max M_{20})

and two constraints:

- Constr1: $M_7 > 0$ ("turbine" constraint)
- Constr2: $M_{20} > 0$ ("turbine" constraint)

In a multi objective (M.O.) constrained optimization, the selection of the optimum is usually made between the individuals lying on the Pareto Front, that is the set on non-dominated solutions. In Figure 3, the two-dimensional objective space of the proposed M.O. optimization is represented: the individuals generated by the ARMOGA algorithm are spread over the whole plot, but the two red dashed lines define the feasible region in the right-up sector where both constraints are satisfied (a SOBOL Design of Experiments with 10 individuals has been used as initial population).

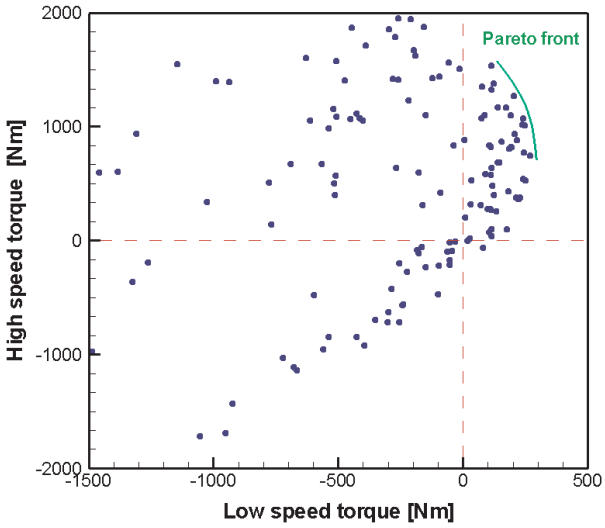

Figure 3. CFD optimization objectives space.

The Pareto Front is shown and joins together the feasible designs able to maximize one objective for a given value of the other objective. Once the Pareto Front has been individuated, the selection of the optimum individual is completely up to the importance given to one objective in relation to the other. In the present study, the best design has been chosen in order to maximize the low speed torque first, and so the optimum is the individual with the highest torque at the lowest wind velocity. This decision can be justified considering that the wind turbine is supposed to spend a larger part of its operational time working at this wind speed condition: consequently, it is more convenient to improve this condition first (it can be also noticed from the plot that the other designs with bigger high speed torque are characterized also by an unacceptable shaft torque at low wind velocity).

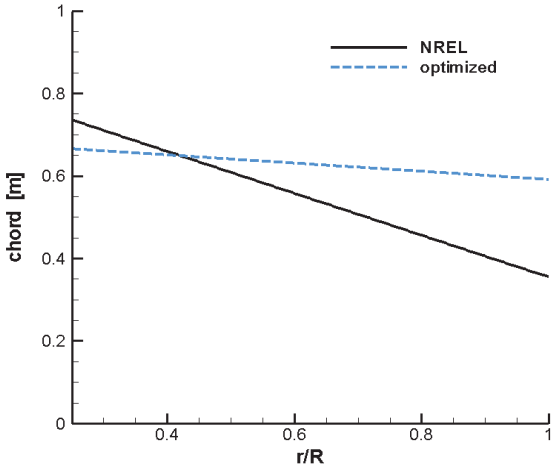

Figure 4. Chord distribution comparison (CFD).

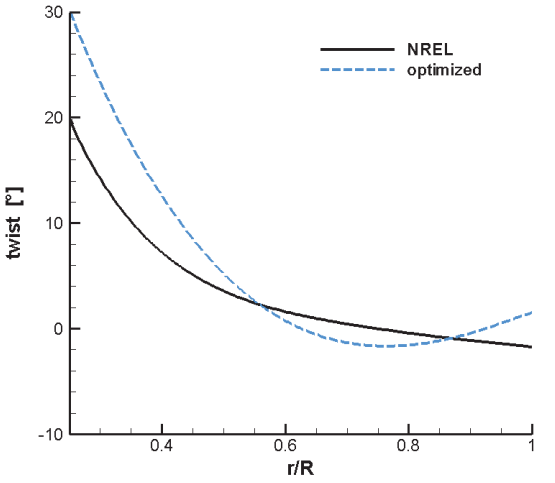

Figure 5. Twist distribution comparison (CFD).

The selected optimum has been compared with the NREL benchmark, again by means of chord, twist (Figure 4) and pressure distributions (Figure 5). The M.O. optimum shows an interesting chord distribution: it is nearly constant (a little bit decreasing actually), and then lower than NREL blade at the root but greater than the benchmark elsewhere.

Twist values of the optimized blade differ from the benchmark especially at the blade root and tip, where the angles are larger. In the mid-span region however, the optimized blade shows smaller angles of attack when compared with the NREL blade. Nevertheless, the increased chord together with changed angles of attack lead to marked torque increase: above 35% in the high speed condition and 7% in the low speed condition on the benchmark. As expected, stalled conditions are more likely to be optimized than attached flow conditions, because CFD becomes more valuable in the former case. Indeed, the optimized design takes advantage of a reduced flow separation when compared with the NREL turbine, thus increasing its performance. This effect can be addressed to the increased angle of attack in that section, as shown in Fig. 5.

It is also interesting to stress that those improvements in blade design have been obtained without even changing the blade profile: future works will concentrate on this issue, and further ameliorations are expected.

The drawbacks of the CFD optimization rely on the CFD simulation: a single design needs 6 hours to be simulated (only for 2 wind velocities), so that the overall optimization took a couple of weeks. Moreover, the Pareto front, although clearly defined, is not fully developed and many designs have been generated (and simulated) in the non-feasible zones.

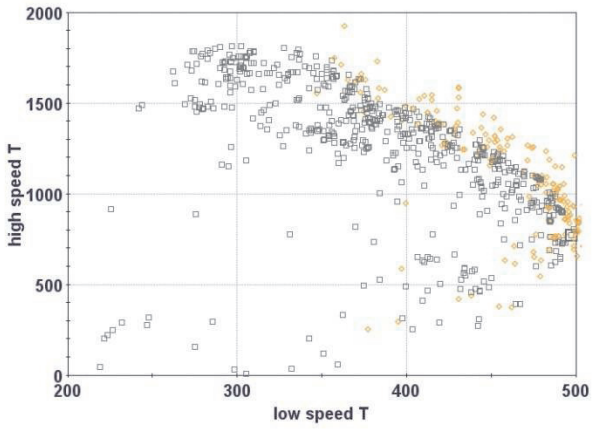

Figure 6. BEM optimization objectives space.

3.2 BEM optimization

The first consideration about BEM optimization is that a single BEM simulation can take no more than few seconds to perform the entire power curve. Keeping this in mind, several different optimization strategies have been explored, with particular attention to the variation of objectives and constraints. Initially, the same optimization criterion employed with the CFD has been replicated using the BEM simulation instead. Therefore, the optimization has the same two objectives of the previous optimization but one additional constraint. This third constraint has been introduced in order to consider also the structural loads usually involved in the design of HAWT. Specifically, a constraint on the maximum accepted root bending moment acting on the blade has been added.
The additional constraint can be then expressed as:

- Constr3: $\text{flap}_{TOT} < 3500$ Nm ("integrity" constraint)

where:

$$\text{flap}_{TOT} = \frac{2 \cdot \text{flap}_7 + \text{flap}_{20}}{3}$$

The weighted average has been introduced because the typical flap bending moment at low speed condition is about a half of the moment at high speed condition, but the blades usually work for a much longer period at low speed condition rather than at high speed, due to the nature of the wind. In order to balance the two contributes then, a weight "2" has been attributed to the flapwise moment at the low speed condition. In this optimization, the NSGA-II algorithm has been employed with a initial population of 15 individuals randomly generated. The results of such optimization are shown in Figure 6, which reports a wider Pareto front than in the CFD case (diamonds are unfeasible designs, circles feasible ones). The very short time needed to simulate each design individual allowed to get a larger number of generations of the genetic algorithm and so more points lying on the Pareto front; as done in the CFD optimization, the feasible individual with the higher low speed torque has been selected.

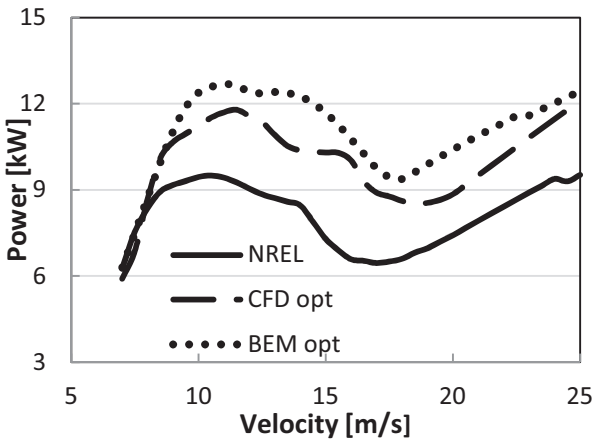

Figure 7. Power curve comparison.

The two optimums generated by the CFD optimization and the BEM optimization are compared in Figure 7 in terms of their power curve and related also to the NREL Phase VI performance

(all power curves obtained with the BEM simulation of the different blades). Two aspects are particularly significant: 1) both the optimized designs are capable of producing more power than the benchmark, about 30% more starting from 10 m/s, and 2) the two power curves show similar trends, altough the BEM optimum is characterized by a higher power curve everywhere. The latter aspect is particularly interesting, since suggests that similar results can be obtained when optimizing with the same objects, indipendently from the simulation techniques.

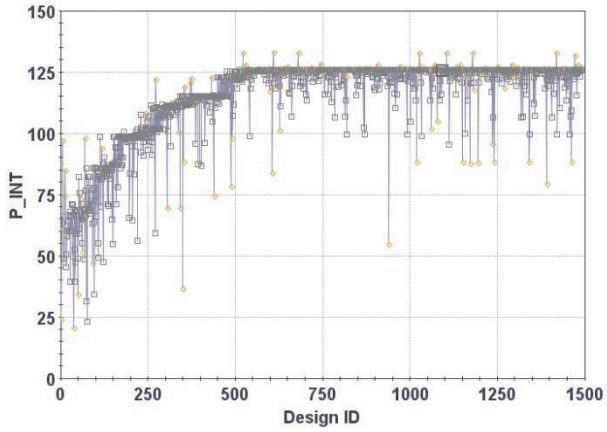

Figure 8. Power integral history chart.

The BEM simulation promptness allowed also to optimize the entire power curve and not only the blade performance at few wind velocities. In fact, in the CFD optimization, only two wind speed have been considered as design condition, but this was done to reduce the computational time, given that each velocity correspond to a different CFD run. With a BEM tool, all wind velocities can be analyzed; however, in a optimization it is mandatory to reduce the number of objectives as much as possible. Thus, it is not likely to have as many objectives as the velocities considered. In order to cluster the results, the numeric integral of the power curve has been employed and defined as the only objective of the optimization, whereas the "integrity" constraint of the previous optimization has been applied. The NSGA-II optimization algorithm has been employed again, with the same DOE and population of the previous BEM optimization. The results of such optimization are reported in Figure 8 in terms of a history chart of the generated designs. As shown in the chart, about 500 designs (30+ generations) were needed to reach the stable plateau, with a linear increase before that. The feasible design with the highest value of the power curve integral has been selected (ID 1091), and its geometry compared with the optimum obtained in the previous BEM optimization. Figure 9 and 10 show the twist and chord distributions of the optimized blades also in relation to the NREL benchmark. The similarities of the two new designs rely on the increased values of chord and twist angle (except at the tip) when compared to the benchmark blade; however, the blade designed by the latter optimization (power curve integral as objective) exasperates in some way the trends already found with the first BEM optimization, reaching a hyperbolic-like trend both for chord and twist.

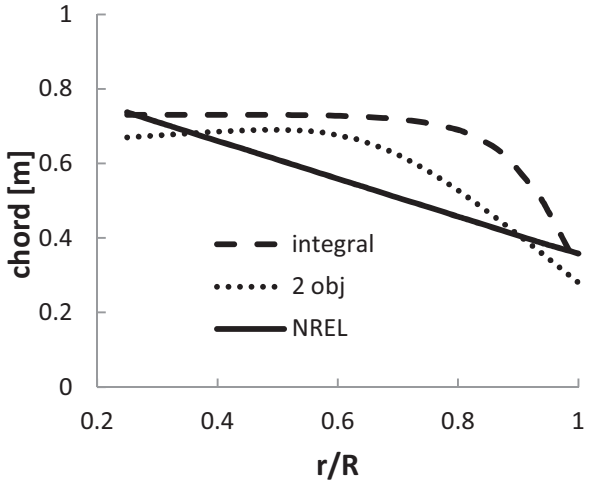

Figure 9. Chord distribution comparison (BEM)

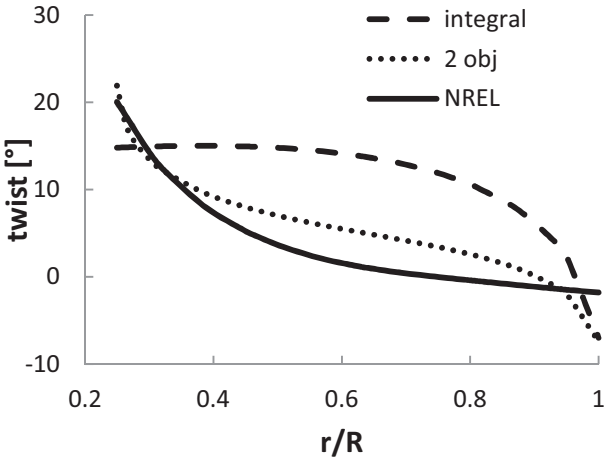

Figure 10. Twist distribution comparison (BEM)

BEM optimization is regarded as a powerful and "cheap" option in the HAWT optimization; nevertheless, it is affected by two main deficiencies: it is not capable of simulating high 3D geometries (i.e.: winglets at the tip and non conventional blades, see Figure 11) and the performance data of the aerodynamic profiles have to be always known in order to run a BEM simluation (which can not always be true, especially for innovative profiles).

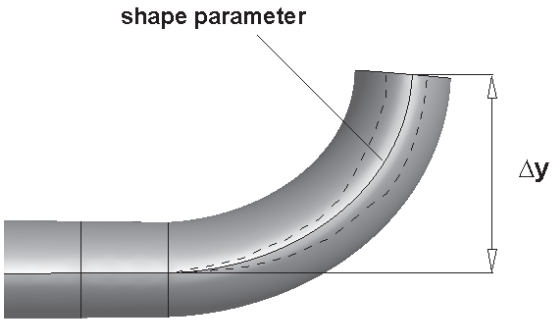

Figure 11. Example of non conventional blade with high 3D geometry (winglet).

4. CONCLUSIONS

In the present paper, both CFD and BEM optimization of HAWT have been considered. Both of them show advantages and disadvantages: potentially, the CFD is more comprehensive and detailed in all configurations, particularly 3D flows and stalled conditions; however, it is also much more time consuming and computational expensive. At the opposite, BEM optimization is extremely fast, being able to simulate a complete power curve in few seconds, but is based on the 'no radial assumption' which limits its application to conventional blades with reduced three dimensional phenomena. Additionally, the lift and drag polar should be known in advance, and this is also a limitation when innovative profiles have to be employed.

For conventional blades, it was found that similar results can be achieved with both CFD and BEM optimization when defining the same objectives: this suggest in the future to take advantage of both techniques combining them in a multifidelity optimization. In fact, the overall optimization could be divided in two steps: an initial phase carried out by the BEM code in which few candidate designs are selected; and a second phase where CFD is employed to accurately choose the best geometry configuration.

ACKNOWLEDGEMENTS

The authors would like to acknowledge the undergraduate student I. Anzivino for its aid in the BEM simulation development.

REFERENCES

[1] Giannakoglou, K.C. (1999), "Designing turbomachinery blades using evolutionary methods", in Proceedings of ASME Turbo Expo 1999, Indianapolis, USA, June 1999, ASME Paper 99-GT-181.

[2] Verstraete, T., Alsahili, Z., and Van den Braembussche, R. A. (2010), "Multi-disciplinary Optimization of a Radial Compressor for Micro Gas Turbine Applications", ASME Journal of Turbomachinery, 132, 3, July 2010.

[3] Verstraete, T., Garreau, M., Alsahili, Z., and Van den Braembussche, R. A. (2007), ""Multi-disciplinary Optimization of a Radial Turbine for Micro Gas Turbine Applications", in Proceedings of the 7th European Conference on Turbomachinery, pp. 667-676, Athens, Greece, 2007.

[4] Milli, A., Shaphar, S. (2008), "Full-Parametric Design system to improve the stage efficiency of a High-Fidelity HP Turbine configuration", in Proceedings of ASME Turbo Expo 2008, Berlin Germany, 2008, GT2008-51348.

[5] Albadi, M.H., El-Saadany, E.F. (2010), "Optimum turbine-site matching", Energy, 35, pp. 3593-3602.

[6] Kongnam, C., Nuchprayoon, S.(2010), "A particle swarm optimization for wind energy control problem", Renewable Energy, 35, pp. 2431-2438.

[7] Fuglsang, P., Madsen, H.A. (1999), "Optimization method for wind turbine rotors", Journal of Wind Engineering and Industrial Aerodynamics, 80, pp. 191-206.

[8] Lanzafame, R., Messina, M. (2007), "Fluid dynamics wind turbine design: Critical analysis, optimization and application of BEM theory", Renewable Energy, 32, pp. 2291–2305.

[9] Hao Xuan, Zhang Weimin, Liu Xiao and Liu Jieping (2008), "Aerodynamic and Aeroacoustic Optimization of Wind Turbine Blade by a Genetic Algorithm", in Proceedings of 46th AIAA Aerospace Sciences Meeting and Exhibit, January 2008, Reno, Nevada, AIAA 2008-1331.

[10] Wang Xudong, Wen Zhong Shen, Wei Jun Zhu and Sørensen, J.K., Chen Jin (2009), "Shape Optimization of Wind Turbine Blades", Wind Energy, 12, pp. 781–803.

[11] Hansen, M.O.L. (2008), "Aerodynamics of Wind Turbines", Earthscan publications, London, UK.

[12] De Bellis, F.; Catalano, L. A., Dadone, A. (2010), "Fast CFD simulation of horizontal axis wind turbine", in Proceedings of ASME Turbo Expo 2010, June 2010, Glasgow, UK, GT2010-22724.

[13] De Bellis F., Catalano L. A. (2011), "Single and Multi Objective CFD Optimization of Horizontal Axis Wind Turbine", GT2011-45607, Proceedings of ASME Turbo Expo 2011: Power for Land, Sea and Air, GT2011, Vancouver, Canada.

[14]De Bellis F., Catalano L. A. (2011), "Multi-disciplinary CFD optimization of conventional and non-conventional HAWT blades", Eurogen 2011, 14-16 September, Capua, Italy.

[15]Hansen, M.O.L., Sørensen, J.N., Voutsinas, S., Sørensen, N., Madsen, H.Aa. (2006), "State of the art in wind turbine aerodynamics and aeroelasticity". Progress in Aerospace Sciences, 42, pp. 285–330.

[16]Sørensen, N.N., Michelsen, J.A., Schreck, S. (2002), "Navier-Stokes predictions of the NREL phase VI rotor in the NASA Ames 80-by-120 wind tunnel", in Proceedings of ASME 2002 Wind Energy Symposium (WIND2002) January 2002 , Reno, Nevada.

[17]Duque, E.P.N., Burklund, M.D., Johnson, W. (2003), "Navier-Stokes and comprehensive analysis performance predictions of the NREL phase VI experiment", Journal of Solar Engineering, 125, pp. 457–467.

[18]Potsdam, M. A., Mavriplis, D. J. (2009), "Unstructured Mesh CFD Aerodynamic Analysis of the NREL Phase VI Rotor", in Proceedings of 47th AIAA Aerospace Sciences Meeting and Exhibit Proceedings, January 2009, Orlando, Florida, AIAA 2009-1221.

[19]Gomez-Iradi, S., Steijl, R., Barakos, G. N. (2009), "Development and Validation of a CFD Technique for the Aerodynamic Analysis of HAWT", Journal of Solar Engineering, 131, 3, August 2009.

[20]Stone, C., Lynch, C. E., Smith, M. J., 2010. "Hybrid RANS/LES Simulations of a Horizontal Axis Wind Turbine". In 48th AIAA Aerospace Sciences Meeting Including the New Horizons Forum and Aerospace Exposition Proceedings, Orlando, Florida, AIAA 2010-459.

[21]Simms, D., Schreck, S., Hand, M., Fingersh, L.J. (2001), "NREL unsteady aerodynamics experiment in the NASA Ames wind tunnel: a comparison of predictions to measurements", NREL/TP-500-29494.

[22]Shen W.Z., Mikkelsen R., Sørensen J.N., Bak C. (2005), "Tip loss corrections for wind turbine computations", Wind Energ. 2005; 8:457–475.

[23]Buhl M.L. (2004), "A New Empirical Relationship Between Thrust Coefficient and Induction Tactor for the Turbulent Windmill State", NREL/TP-500-36834, Golden CO, September 2004.

[24]Glauert H. (1926), "The Analysis of Experimentals Results in the Windmill Brake and Vortex Ring States of an Airscrew" in Volume 1026 of Reports and memoranda, Great Britain Aeronautical Research Committee, H.M. Stationery Office, 1926.

[25]Viterna L.A.-Janetzke D.C. (1982), "Theoretical and Experimental Power from Large Horizontal-Axis Wind Turbines", NASA TM-82944, September 1982.

[26]Snel H.-Houwink R.-Bosschers J. (1994), "Sectional prediction of lift coefficient on rotating wind turbine blades in stall", ECN-C—93-052, Petten, December 1994.

[27]Pechlivanoglou G., Marten D., Nayeri C.N., Paschereit C.O. (2010), "Integration of a WT Blade Design Tool in XFOIL/XFLR5", DEWEK 2010, 17-18 November, Bremen, Germany.

[28]Burton, T., Sharpe, D., Jenkins, N., Bossanyi, E (2001), "Wind Energy Handbook", John Wiley & Sons Ltd..

[29]Sasaki, D., Obayashi, S. (2005), "Efficient Search for Trade-Offs by Adaptive Range Multi-Objective Genetic Algorithms," Journal of Aerospace Computing, Information, and Communication, 2, pp. 44-64.

[30]Deb, K. and Agrawal, R. B. (1995), "Simulated binary crossover for continuous search space", Complex Systems, 9, 115.

Conference on Modelling Fluid Flow (CMFF'12)
The 15th International Conference on Fluid Flow Technologies
Budapest, Hungary, September 4-7, 2012

ROBUST ANALYZING TOOLS FOR WIND TURBINE BLADES COUPLED WITH MULTIOBJECTIVE OPTIMIZATION

D.Perfiliev[1*], J.Hämäläinen[2], J.Backman[1]

[1]Corresponding Author. Laboratory of Fluid Dynamics, Lappeenranta University of Technology, Skinnarilankatu 34, P.O.Box 20, FI-53851 Lappeenranta, Finland. Tel.: + 358 46 572 4533, E-mail: Daniil.Perfiliev@lut.fi, Jari.Backman@lut.fi
[2]Centre of Computational Engineering and Integrated Design (CEID), Lappeenranta University of Technology. E-mail: Jari.Hämäläinen@lut.fi
*Corresponding Author

ABSTRACT

This paper presents recently developed tools for analyzing different wind blade properties brought by its geometric shape and corresponding geographical site characteristics. A set of blade shapes with a certain deviation from the initial geometry was investigated. The results showed that the original geometry can be improved due to individual site wind characteristics and concluded for better aerodynamic efficiency and lower economic expenses.

Keywords: wind turbine blade, BEM corrected, analysis tools, multiobjective optimization, Matlab

NOMENCLATURE

COE	[r.u./MWh]	cost of energy
C_{rotor}	[r.u.]	relative blade cost
AEP	[MWh]	annual energy production
b	[-]	relative fixed cost of the blade
w_{rotor}	[-]	weight parameter
S	[m^2]	blade element surface area
δ	[m]	unidirectional layup thickness
c	[m]	average blade element chord
ρ	[kg/m^3]	air density
R	[m]	rotor radius
η	[-]	electrical efficiency
C_p	[-]	aerodynamic efficiency
T	[h]	annual turbine work hours
H	[m]	tower height
k	[-]	shape factor
A	[m/s]	scale factor
L	[m]	static blade-tower clearance
t_{ply}	[mm]	the unit ply thickness
E	[Pa]	Young's modulus
σ_{ut}	[Pa]	allowable tensile strength
σ_{uc}	[Pa]	allowable compressive strength

Subscripts and Superscripts

BEM	Blade Element Momentum
i	considered blade shape on i-th iteration
or	original blade
$r.u.$	relative units

1. INTRODUCTION

Due to rapid growth of wind industry in recent decades there is a strong need for automation of project development. Therefore scientific and industrial community is working together for development of fast and robust tools for wind turbine design. As wind blades constitute a relatively big share of the total turbine price, even a slight improvement of their technical and economic output can significantly benefit the industry.

A lot of scientific work is related to the optimization of wind blade inner and outer geometry. However it focuses on either improvement of technical efficiency (annual energy production) or points for minimal cost of energy and multiobjective criterions are not widely implemented.

With growing computer capacity the use of complex Computational Fluid Dynamics (CFD) tools for simulation and design of the wind turbine is becoming beneficial. However, engineering approaches for fast and robust analysis of turbine properties are still prevailing in industrial community and continue to improve. For instance, recently updated Blade Element Momentum theory (BEM) provides more accurate and close to practice calculation of aerodynamic efficiency.

To use universal and flexible computational environment all procedures and analysis are done with help of Matlab coding.

2. GENERAL PROCEEDURE OF BLADE SHAPE ANALYSIS

The general procedure includes investigation of the given initial blade shape properties, and then switches to investigation of different combinations

of the blade shape geometrical characteristic, namely the chord distribution, that a on certain range is deviated from the initial one. The theory behind each analysis tool (aerodynamics, economy and mechanics) is coded as separate Matlab file functions and bounded by main file. Iterations that perform investigations of different blade shapes are also conducted within its code, as well as it contains information about initial blade geometry. The rest of needed information, the profile lift and drag properties, is given through a respective structural files.

The structure of all involved Matlab files is presented in Figure 1.

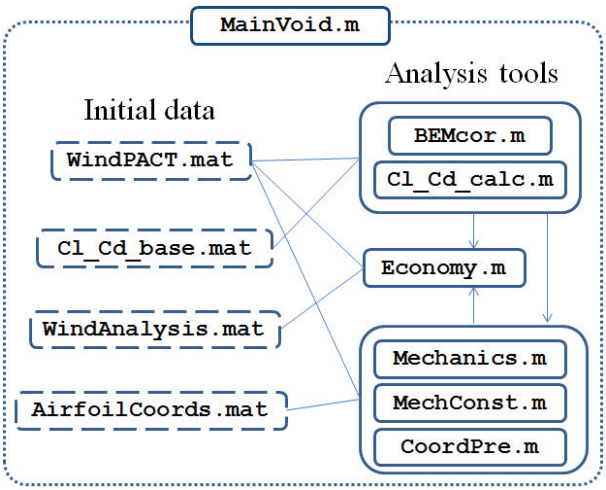

Figure 1. General structure of m-files

2.1. Aerodynamics

Based on the considered blade geometry the aerodynamic blocks calculate total aerodynamic efficiency, induced flap and edgewise torques and forces. The analysis is done for design conditions of the wind speed 7m/s, the tip speed ratio of 6.9 and the pitch of 2 degrees. The values are achieved on the experiment basis with intent to reach maximum aerodynamic efficiency. The same analysis is done for extreme wind conditions, as results of force and torque distributions along the blade span are used later on for mechanical procedures. The extreme wind speed is found based on IEC Standard [1] which states that the 50-year extreme wind speed is five times greater than the yearly averaged one.

The theory behind aerodynamic procedure is Blade Element Momentum Method (BEM) [2, 3]. However it is revised based on the recent research works by RISØ specialists [4] that corrected the classical BEM for two terms: pressure variation from wake rotation and decreased inflow at tip region due to wake expansion.

An advanced technique is applied for the storage of the lift and drag coefficient curves of different airfoil cross sections [5].

2.2. Mechanics

The blade geometry and force distribution for design and extreme wind conditions received from the aerodynamic procedure are used as input for mechanical investigation. The structural layup at the typical blade cross-section is presented in Figure 2.

The main purpose of the mechanical procedure is to find a proper unidirectional layup thickness. The rest of the layups are assumed either fixed or its distribution is described with a trend equation received on the known information about the blade of close size. Information is based on [6]. The procedure is aimed to be improved and will include a proper structural layering for the core and double-bias thicknesses as well.

The unidirectional layup thickness is found to satisfy three limiting conditions: the ultimate strength criterion, the buckling criterion, finally the tip deflection should not be more than two third of static blade-tower clearance, L=3.3m for considered turbine [7, 8]. The equations for criterions are given and explained in [6]. Structural properties like axial stiffness and offsets of the elastic-axis are calculated based on the blade geometry and it is described in [9].

Finally all the layups thicknesses are chosen so that they are an integer multiply of the unit ply thickness of the constituent material. The structural properties of materials are presented in Table 1.

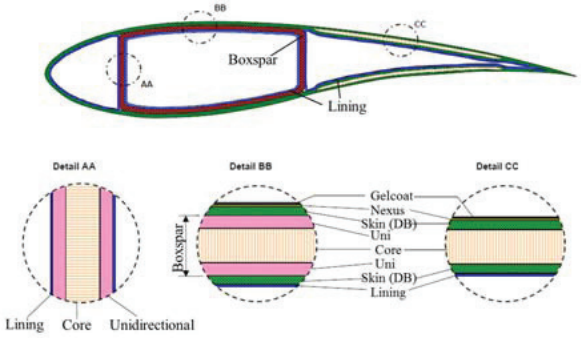

Figure 2. Structural layup of blade cross-section (based on [6])

Table 1. Blade material structural properties

Material	t_{ply} (mm)	E (Pa)	σ_{ut} (Pa)	σ_{uc} (Pa)
Gelcoat	0,381	--	--	--
Nexus	0,51	--	--	--
Double-bias	0,53	1,03E+10	1,51E+8	-1,74E+8
Lining	0,53	1,03E+10	1,51E+8	-1,74E+8
Unidirectional	0,53	3,70E+10	9,86E+8	-7,46E+8
Core	3,125	1,00E+07	--	--

2.3. Economics

The economy analysis is particularly needed to have a basis for the comparison of different blade geometries performance. The approach is based on calculation of the cost of energy function, *COE*:

$$COE = \frac{C_{rotor}}{AEP} \quad (1)$$

where C_{rotor} is the relative cost of production, transportation and erection of the wind turbine rotor; *AEP* is the annual energy production. The respective equations for C_{rotor} in Eq.(2) and *AEP* in Eq.(4).

$$C_{rotor} = b + (1-b)w_{rotor} \quad (2)$$

where b=0.1 is accounted for fixed parts of transportation and manufacturing costs [10]; w_{rotor} is the weight parameter that gives basis for the comparison of the original and considered blade geometries. The weight parameter is calculated as:

$$w_{rotor} = \sum_{i=1}^{n} \frac{S_i \delta_i c_i}{S_{or} \delta_{or} c_{or,i}} \quad (3)$$

where S – blade element surface area; δ – unidirectional layup thickness; c – average chord of blade element.

The annual energy production is calculated with a classical method:

$$AEP = \sum_{i=1}^{n} \frac{\rho V_i^3}{2} \pi R^2 C_p \eta \cdot f_i(V_i) \cdot T \quad (4)$$

where T=8700h; R=35m – rotor radius; C_p – aerodynamic efficiency; η=0.9 – electrical efficiency; ρ=1.229kg/m^3 – air density; $f(V)$ – Weibull wind speed distribution function. In addition the cut-in and cut-out speeds are equal to 3m/s and 25m/s respectively. The rated power equals to 1.5MW as this is the turbine power that is investigated in the study, see later. The turbine is variable speed and has pitch mechanism.

For more information about economic calculations the reader is referred to [11].

3. INVESTIGATION OF BLADE SHAPE SET

A set of blade shapes were investigated to find ways to improve the original blade geometry for operation in the certain wind conditions. The initial blade geometry is based on WindPACT 1.5MW wind turbine. The chord, twist and cross-sectional airfoils of its working, monotonic part are presented in Table 2.

The chord distribution clearly has linear dependence along the span. It was decided to consider a set of linear chord distributions with ±15% of the initial chord of the first cross section. To have clear resultant picture, the adjustment step for iterations is chosen to be 1.5% of the initial chord of first cross section. To clarify see Figure 3.

The chosen location of an island near Vaasa city in Finland has the following wind characteristics of the Weibull distribution: shape factor, k=2.15; scale factor, A=8.11m/s. This information is based on annual data from Finnish wind atlas [12] and adjusted for turbine tower height H=84m [8].

At first the analysis is done for the original blade. Then it is switched for the set of blade shapes on the basis of the different chord distributions that are considered one by one. In that way the connection of efficiency with price is formed.

Table 2. WindPACT 1.5MW blade geometry properties

R, m	Chord, m	Twist, deg	Airfoil
7,88	2,72	79,50	S818
9,63	2,64	80,86	S818
11,38	2,52	82,38	S818
13,13	2,39	83,90	S818
14,88	2,27	85,42	S818
16,63	2,14	86,60	S825
18,38	2,02	87,39	S825
20,13	1,90	87,86	S825
21,88	1,77	88,34	S825
23,63	1,65	88,81	S825
25,38	1,53	89,21	S825
27,13	1,41	89,49	S825
28,88	1,30	89,60	S825
30,63	1,18	89,71	S826
32,38	1,07	89,83	S826
34,13	0,96	89,94	S826

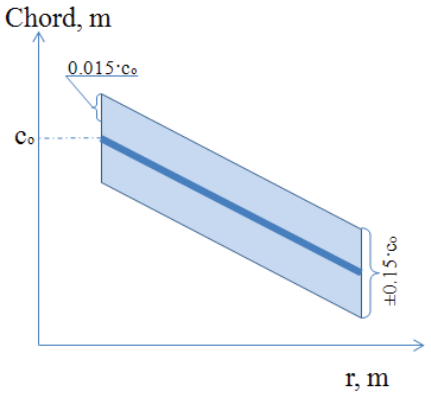

Figure 3. Set of considered chord distributions.

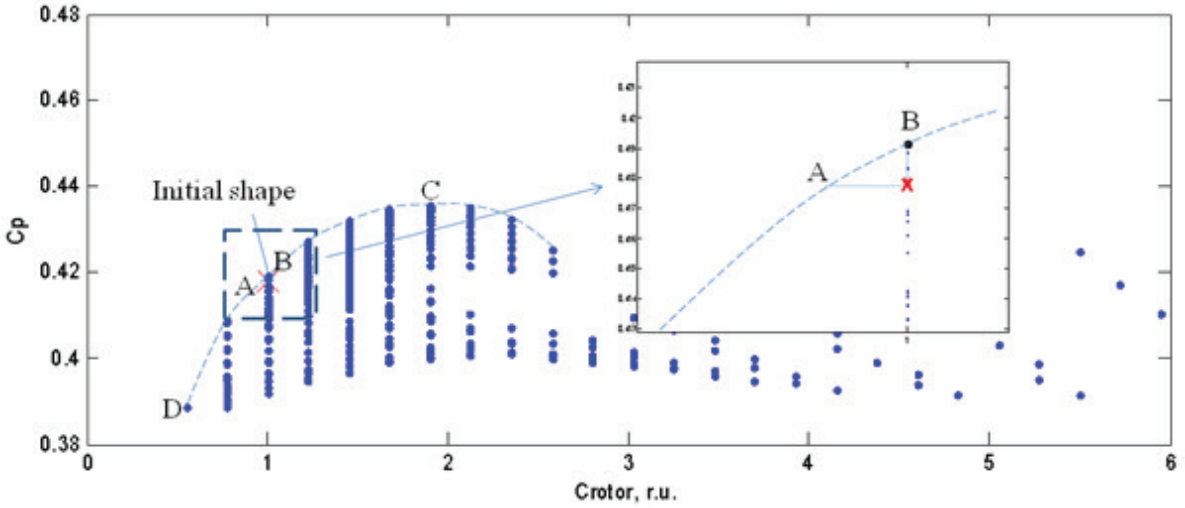

Figure 4. Dependence of aerodynamic efficiency on the relative rotor cost

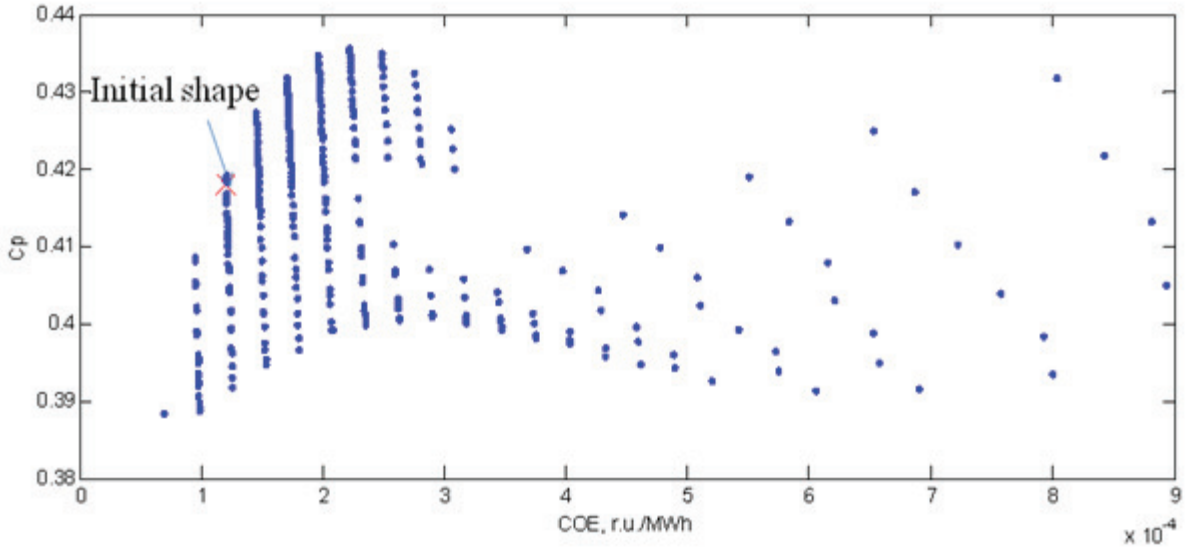

Figure 5. Dependence of aerodynamic efficiency on the cost of energy

3.1. Results and discussions

Figures 4 and 5 show the result of investigation of blade shapes set for the fixed pitch of 2 degrees.

From the figures above it is seen that the initial blade performance can be improved by at least two variants. Variant A gives the same aerodynamic efficiency with less expense. Variant B provides better efficiency at the same level of expense. Two other interesting cases are variants C and D with the highest achievable aerodynamic efficiency and the lowest expenses respectively. The chord distributions for the mentioned cases, as well as the original one are presented in Figure 6.

In practice a designer might look for a compromise variant on the DABC curve somewhere between points B and C.

The received figures show that the analysis tools give illogical results for rotors with very big difference from the original blade shape (on the right side of the plots, not shown here). Experiments showed errors when the chord deviation was set to more than 15%. Investigations for pitch angle less than 1.5 degrees also gave illogical values for aerodynamic efficiency (it went above the Betz limit). These findings are not explained here and require more research in the near future, e.g. comparisons with CFD analysis.

4. SUMMARY

This paper is devoted to the wind turbine blade analysis tools that are used for the geometry shape optimization. Recently developed corrections to the method for calculation of aerodynamic efficiency are implemented. Advanced approaches for airfoil data storage, mechanical calculations and economic analysis are presented. The proposed methodology was used for investigation of set of blade chord distributions presenting various geometry shapes.

Results showed variants for possible improvements of aerodynamic efficiency and cost expenses. The final decision, however, has to be made by designer. Investigation raised questions about unstable results that have to be answered in the future. The next step of research is for inclusion variation of twist distribution and cross-sectional profiles.

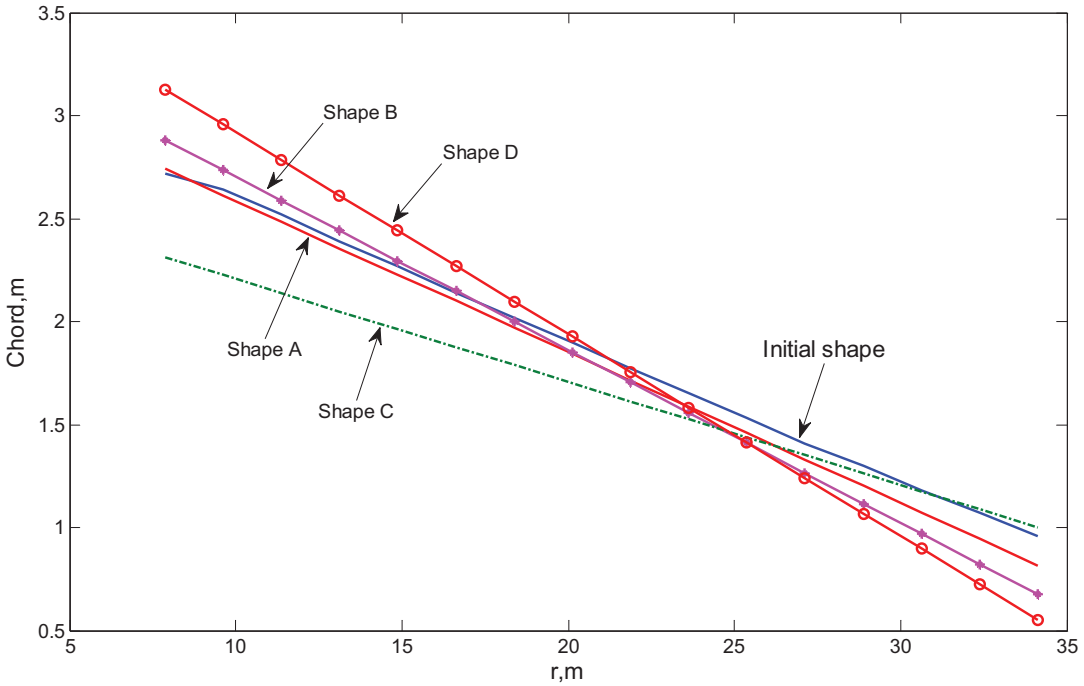

Figure 6. Chord distribution along the span for different variants of the blade shape

ACKNOWLEDGEMENTS

This research work has been carried out in the RENEWTECH project funded by European Regional Development Fund (ERDF).

REFERENCES

[1] IEC 61400-12-1 1st ed., 2005, "Wind turbines – Part 12-1: Power Performance Measurements of Electricity Producing Wind Turbines", *International Electrotechnical Committee*.

[2] Ingram G., 2011, "Wind turbine blade analysis using the Blade Element Momentum Method", http://www.dur.ac.uk/g.l.ingram/download/wind_turbine_design.pdf

[3] Moriarty P.J., Hansen A.C., 2005, "AeroDyn Theory Manual", *Technical report*.

[4] Madsen H.A., Bak C., Døssing M., Mikkelsen R., Øye S., 2010, "Validation and modification of the Blade Element Momentum theory based on comparisons with actuator disc simulations", *Wind Energy*, Vol. 13, pp. 373-389.

[5] Merz K.O., 2011, "Conceptual design of a stall-regulated rotor for a deepwater offshore wind turbine", Doctoral Thesis, Norwegian University of Science and Technology (NTNU), pp.31-35.

[6] Bir G., Migliore P., 2004, "Preliminary structural design of composite blades for two- and three-bladed rotors", *Technical report*.

[7] Tong W., 2010, "Wind power generation and wind turbine design", WIT Press, p. 210.

[8] Malcolm D.J., Hansen A.C., 2002, "WindPACT turbine rotor design study", *Subcontractor report*.

[9] Hansel M.O.L., 2009, "Aerodynamics of wind turbines", *2nd edition*, pp. 107-116.

[10] Wang X., Shen W.Z., Zhu W.J., Sørensen J. N., Chen J., 2009, "Shape optimization of wind turbine blades", Wind Energy, Vol. 12, No. 8, pp. 781-803.

[11]Perfiliev D., 2010, "Optimization of wind blade design including its energetic characteristics", Master Thesis, Lappeenranta University of Technology, pp. 35-41.

[12]Finnish wind atlas, http://www.tuuliatlas.fi/

Conference on Modelling Fluid Flow (CMFF'12)
The 15th International Conference on Fluid Flow Technologies
Budapest, Hungary, September 4-7, 2012

Active stall control solutions for power regulation and load alleviation of large wind turbines

George PECHLIVANOGLOU[1], Christian Navid NAYERI[2], Christian Oliver PASCHEREIT[3]

[1] SMART BLADE GmbH, Zuppinger Staße 14, D- 88213, Ravensburg, Germany. Email: g.pechli@smart-blade.com
[2] Hermann Föttinger Institute, Technical University of Berlin, Müller Breslau Straße 8, D-10623, Berlin, Germany. E-mail: christian.nayeri@tu-berlin.de
[3] Corresponding Author. Hermann Föttinger Institute, Chair of Fluid Dynamics. Technical University of Berlin, Müller Breslau Straße 8, D-10623, Berlin, Germany.Tel.: +49 (0)30 314 23359, Fax: +49 (0)30 314 21101 E-Mail: oliver.paschereit@tu-berlin.de

ABSTRACT

Large wind turbine blades suffer from the effects of high fluctuating aerodynamic loads, which lead to extreme load and power peaks. The existing blade pitch systems are required to operate reliably for several million cycles through the lifetime of the turbine. At the same time they are expected to be fast enough to adapt the blade positions to the current wind regimes. The pitch rates, however, are also limited by the structural integrity and torsional stiffness of the blades thus creating a very complex system control problem. The current paper proposes the use of active stall control elements on the blades for load alleviation and partial power regulation. Vertical and inclined spoilers as well as inflatable stall ribs are parametrically investigated in the wind tunnel and tested on virtual blade simulations. The results of the investigations show that it would be feasible to use such elements as high precision load and power control solutions while maintaining the pitch system for the more drastic power regulation operations.

wind turbine, flow control, stall control, spoilers, stall ribs

NOMENCLATURE

AoA	$[deg]$	angle of attack
BEM	$[-]$	Blade Element Momentum theory
Cl	$[-]$	lift coefficient
Cd	$[-]$	drag coefficient
Cl/Cd	$[-]$	glide ratio
Cp	$[-]$	power coefficient
λ	$[-]$	tip speed ratio
$r.p.m$	$[-]$	rotations per minute

1. INTRODUCTION

The current development of wind energy has led to the production of very large wind turbines equipped with rotorblades of up to 75m in length and a generating capacity of up to 7.5MW. These structures have to operate in highly turbulent atmospheric conditions and have to withstand all the adverse weather phenomena under continuous operation with minimal maintenance for 20 years. The combination of the aforementioned extreme technical requirements together with the extreme cost pressure create a very complex technical problem, which leads to significant technological breakthroughs. Wind turbine blade technology has until now mostly focused on the structures and the improvements in the field of materials, quality control and structural design. The limits however of both the materials and the manufacturing techniques have lead to a development plateau where significant effort and cost is necessary in order to achieve further improvements.

The field of wind turbine engineering which has been generally underdeveloped is that of the advanced aerodynamics and the outer blade surface design. It is obvious that aerodynamics play a major role on the performance of wind turbines. Nevertheless, due to several limitations such as the theoretical and simulation complexity, as well as the poor understanding of complex flow phenomena this field did not develop as much as it was anticipated. Currently efforts are made in order to introduce modifications to the aerodynamic rotorblade designs. A number of researchers around the world concentrate their research efforts on the development of the new generations of rotorblades equipped with advanced aerodynamic solutions. These will allow the passive and active manipulation of the flow in order to achieve higher performance, load reduction and longer service life for the blades. The aim of the current paper is to propose a new

approach for the blade design which will incorporate distributed active stall control elements able to offer load alleviation as well as partial power regulation. Some of these solutions are adapted derivations from the aerospace industry (i.e. spoilers) while others are relatively novel solutions (i.e. stall ribs). The general performance summary of these active stall control solutions was first presented by the authors in 2011[1]. However this paper presents a more detailed analysis which also includes results from wind turbine performance simulations.

2. SPOILERS

2.1. Inclined Spoilers

The use of inclined spoilers as lateral control devices for aircrafts is well established since the beginning of motorized flight. Extensive research has been performed in this field, mostly from aircraft manufacturers and NACA[2]. Many of the existing research results reveal that the performance of the spoilers varies significantly between real life conditions and wind tunnel tests[3]. This is mostly due to the complex aerodynamic phenomena produced by the spoilers.

Spoiler performance varies largely depending on Reynolds number, spoiler design and spoiler deflection angle[3, 4]. Generally small spoiler deflections lead to stable flows with low aeroelastic responses, but also lower lift and drag control. Large spoiler deflections are very effective, but introduce large flow disturbances leading to large instabilities, reversed flows behind the spoiler as well as separation bubbles at the spoiler hinge line [3, 4].

The introduction of spoilers on wind turbine blades is a known technical proposal from the beginning of modern wind turbine development[5, 6, 7]. In contrary to the proposals of the past, modern proposals[8, 9, 10] in the field mostly focus on refined spoiler designs intended to reduce the aerodynamic lift of the blades and thus regulate the wind turbine power while significantly reducing the structural loads.

The actuation of inclined spoilers is a relatively straight-forward process with acceptable technical risk. The actuation can be accomplished with various technical principles utilizing mechanical, electromechanical, pneumatic or hydraulic actuators. The implementation of hydraulic or pneumatic actuators could eliminate possible problems with lightning strikes and is thus preferred by the authors.

The main consideration regarding the operation of wind turbine blades equipped with spoilers is the related uncertainty on their aeroelastic response. NREL[1] researchers performed extensive tests in the past with pultruded rotorblades equipped with spoiler configurations [11] and identified their feasibility despite the fact that further research is necessary in order to successfully implement this solution.

[1]National Renewable Energy Laboratory

2.2. Vertical Spoilers

Some of the early spoiler designs, such as the one proposed in 1935 by J.G. Lee[12] comprised sliding vertical spoilers or rotatably emerging and hinged spoilers [13]. These were named vertical spoilers (Schemp Hirth Spoilers) or dive brakes when used on aircraft structures. Often they comprise vertically deployable or rotating structures[14] (Fig. 1).

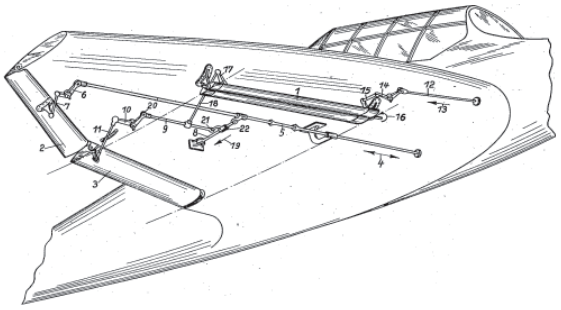

Figure 1. Vertical spoiler (dive brake) configuration proposed by H. Wagner in 1939[14]

Vertical spoilers are used extensively in gliders design as “air brakes” (Fig. 2). The spoilers are then emerging from the wing structure via a simple hinge mechanism[15].

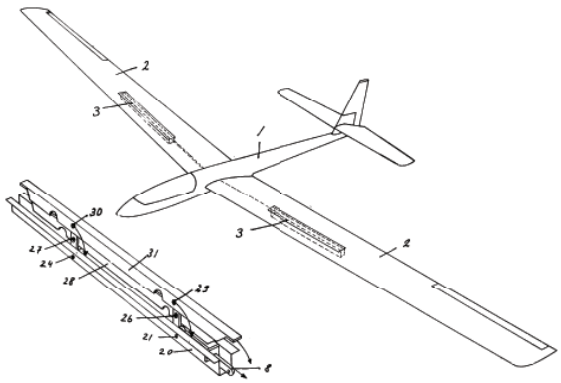

Figure 2. Vertical spoiler configuration implemented on sailplane wing [16]

One of the first extensive investigations of these devices was performed by Jacobs in 1934 and was published in the form of NACA Report 446[17] and NACA Report 449[18] and showed that vertical spoilers of small height (in the range of 10mm) provided significant lift control especially when located near the leading edge on the suction side.

Spoiler shape variations, investigated by NACA[19] show that the flat type vertical spoiler without gap between spoiler and airfoil is the most effective spoiler shape in terms of lift control. However wind tunnel tests performed by the authors show that flat shaped vertical spoilers can lead to aerodynamic flutter and strong noise emissions when

their size exceeds certain limits. Vertical spoilers have in the past been used as emergency brakes on wind turbine blades[7]. However the intention of the authors is to investigate the use of vertical spoilers of the smallest possible size in dynamic mode as aeroelastic load alleviating elements rather as emergency stop devices.

2.3. Stall Ribs

The US Patent documents of Hunter in 1943[20] and Campbell in 1944[21] present an implementation of the flexible stall rib concept on aircrafts. In 1961 Barber[22] proposed an inflatable spoiler at the suction side of an aircraft wing surface which was intended as a stall control solution (Fig. 3).

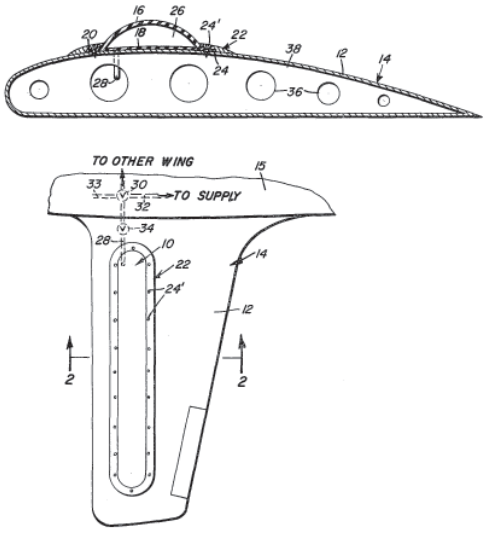

Figure 3. Elastic Stall Rib located at the suction side of an aircraft wing, operating as lateral control element [22]

The proposal for a stall rib system for wind turbine blades was initiated by Holzem in 1990[23]. There the stall rib was an emergency stall device working against over-speed. One of the main benefits of the inflatable stall rib is the simplicity of the actuation mechanism and its control strategy potential. The system can be divided into multiple independent stall rib units in order to increase the actuation precision, the effectiveness and the redundancy of the overall system.

The integration of small stall rib units on wind turbine blade structures is considered a relatively simple procedure with small changes in the blade production process. However due to the aerodynamic sensitivity of the leading edge region the stall ribs have to be smoothly integrated thus achieving a surface without flow disturbances. Due to the sensitivity of the rubber membranes to UV radiation, nature's elements, temperature fluctuations, the modular stall ribs have to be designed in such a way

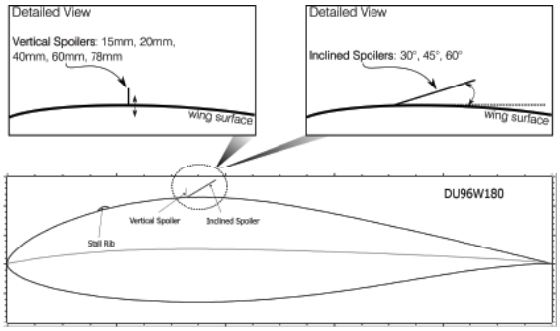

Figure 4. Plot of the DU96W180 airfoil used during the current research project

that they can be easily and replaced without high *O&M* costs.

3. EXPERIMENTAL SETUP

The wind tunnel facility of the HFI, TU Berlin was used for all the experimental investigations. It is a closed loop wind tunnel, powered by a 500 kW speed regulated DC motor. Its test section with a length of 10m and a cross-sectional area of $2 \times 1.4\,\mathrm{m}^2$ has a contraction ratio of 6.25 : 1 and a turbulence level of the free stream below 0.5%. The investigated airfoil was a DU96W180[24] with a chord length of 600 mm. It was connected to an external 6-component balance, de-coupled from the test section, between splitter walls. The splitter walls were installed to eliminate the influence of wind tunnel boundary layer effects with the wing extending over the entire span (a=1.554m) between the walls. The gaps (≈ 0.5 mm) at the sides of the test wing were sealed with thin adhesive tape to reduce the pressure losses at the edges of the airfoil, while maintaining the de-coupling of the balance and the wind tunnel. The Reynolds number based on the chord length was $Re \approx 1.3 \cdot 10^6$ for all the measured configurations.

The stall ribs, vertical and inclined spoilers were tested on the same test wing and were mounted on special mounted positions that allowed for quick configuration variation. The general position of these elements is shown in Fig. 4. Each on of these elements however was also tested in a parametric fashion in order to identify the operational trends and to define a design optimum.

4. EXPERIMENTAL RESULTS

The investigation of the **vertical spoilers** revealed that even a small spoiler height is able to dramatically reduce the performance of the airfoil configuration. As it is shown in Fig. 5 the general effect of the vertical spoiler is not highly affected by the size (height) of the spoiler. The lift variation has a weak correlation with the height of the element. The overall efficiency (glide ratio) remains very close to zero, even for the configurations with very low spoiler height.

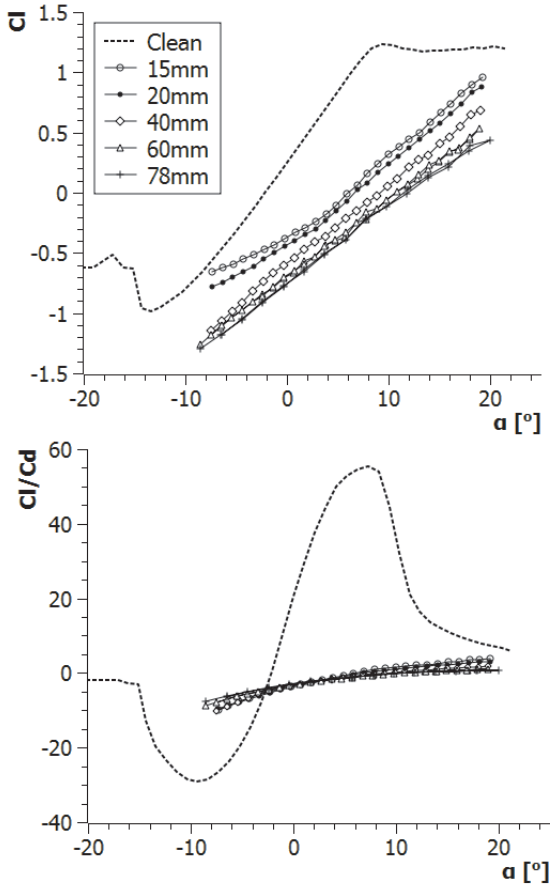

Figure 5. Various configurations of vertical spoilers tested in the wind tunnel

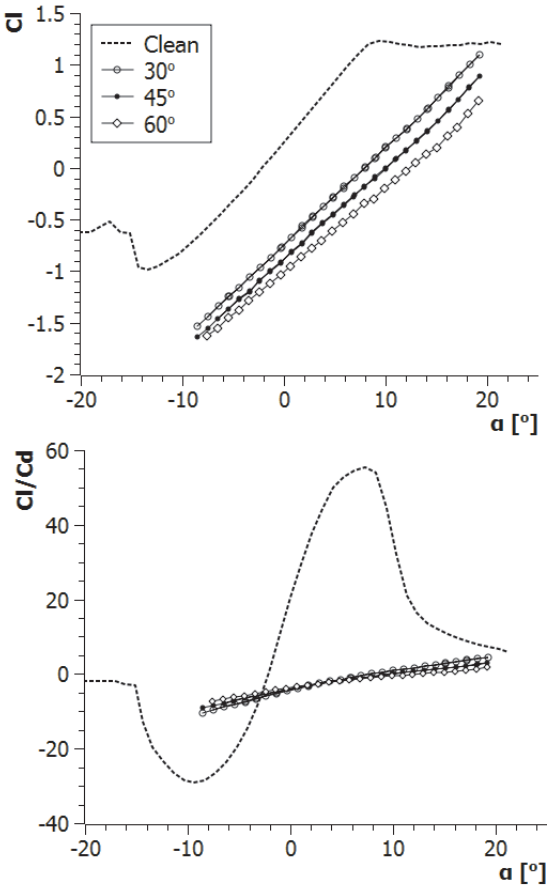

Figure 6. Various configurations of inclined spoilers tested in the wind tunnel

The same trend was observed for the **inclined spoiler** configurations. The impact on the airfoil lift increased with the increase of the inclination, however the efficiency of the airfoil remained extremely low in all configurations (Fig. 6). This is an indication that the lift control in conjunction with the significant drag increase are able to dramatically influence the performance of a wind turbine blade. A comparison of some of the most promising configurations (15mm and 40mm vertical spoiler as well as 30^o inclined spoiler) showed that all the aforementioned setups performed very well as power reduction devices (Fig. 7). At the same time the highest control authority within a wide range of AoA variations was achieved by the 40mm vertical spoiler.

The **stall ribs** that were tested during the investigations included several shapes ranging from the typical dome-shape to a wedge stall rib shape (Fig. 8). This was done in order to identify the effects of shape on the performance of the solutions. Furthermore various positions were tested in order to identify an optimal position for this configuration. It is worth mentioning that the performance of the stall ribs when inactive is another important operational parameter that needs to be taken into consideration. Often the position of such elements is not dictated by

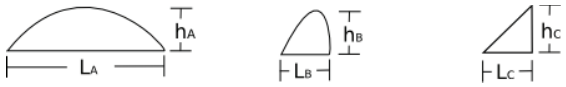

Figure 8. Various configurations of stall ribs

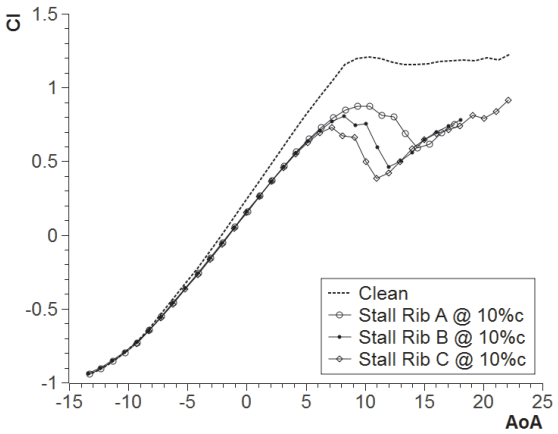

Figure 9. Various configurations of stall ribs measured in the wind tunnel

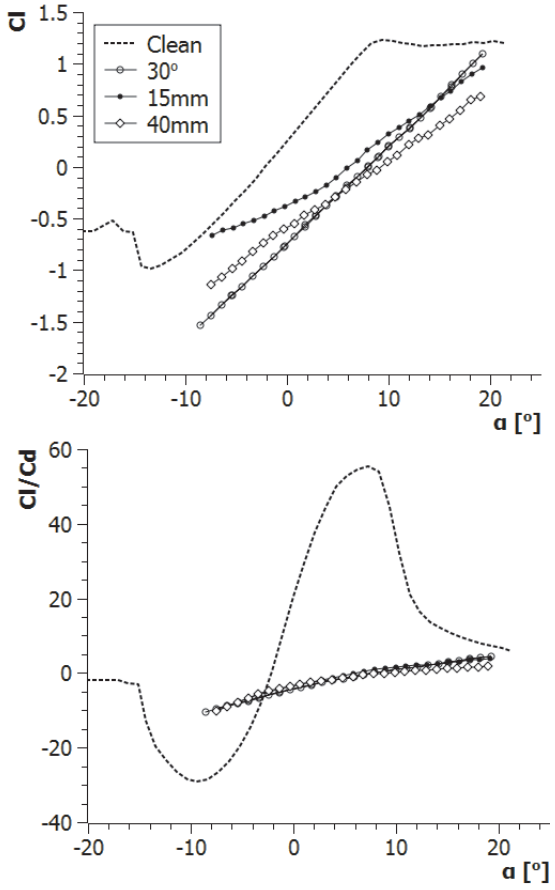

Figure 7. Configurations of inclined and vertical spoilers compared

their optimal operation point during deployment but by their lowest interference position during normal wind turbine operation.

The investigation of various stall rib shapes revealed similar behavior with small variations at the stall point and maximum Cl value (Fig. 9). The investigation of various positions reveals a strong correlation between the stall rib positions and its control authority. It is generally observed that forward placements of the stall ribs lead to relatively limited control authority. Similarly the placement of stall ribs at the 50%c of the blade or further downstream leads to significant control authority reduction. The optimal chordwise position for stall ribs especially for this configuration is identified at aprox. 20%c (Fig. 10). The installation of double upstream and downstream stall ribs offers slightly better performance, which however cannot necessarily justify the additional implementation and manufacturing costs.

In terms of the efficiency of the configuration, the observations of the authors show that a forward placement of the stall rib is more beneficial than a downwind placement (Fig. 11). It is interesting to note that the 20%c placement of the stall ribs creates a very large efficiency peak at negative AoA ranges which might significantly reduce the control authority of the solution. The position which offers the best compromise in this case and for this configuration seems to be aprox. at 10%c – 15%c.

5. BEM SIMULATIONS

The polars measured in the wind tunnel were integrated in a virtual blade design in order to investigate the effect of the active elements on the

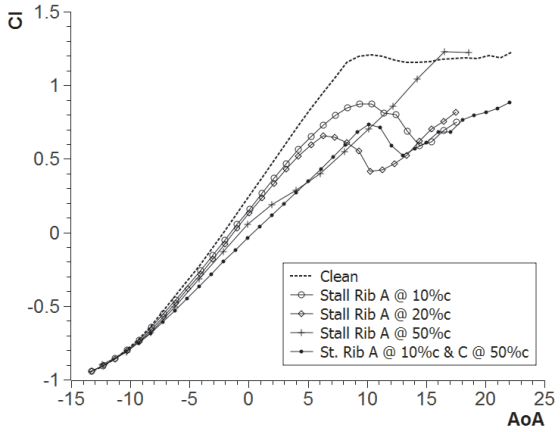

Figure 10. Various positions of stall ribs (Type-A) measured in the wind tunnel

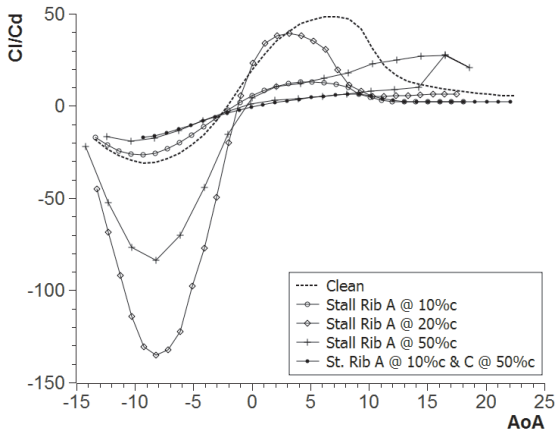

Figure 11. Glide ratio of various positions of stall ribs (Type-A) measured in the wind tunnel

performance of a wind turbine. This blade has a span of 70m and was designed for a 6MW wind turbine. It comprises typical wind turbine airfoils from the DU family[24], developed by TU Delft. The inner 50% of the blade span uses circular sections and DU sections with $35\%, 30\%, 25\%$ and 21% thickness. These sections are not equipped with any passive or active flow control device and remain unchanged throughout the computations. The blade structural twist is kept at an optimal 30^o in order to avoid simulation errors due to post-stall performance at the blade root. The outer 50% of the blade span is equipped with the DU96W180 section. For this section the measured wind tunnel polars with and without stall control elements are used. All the polars were imported in the simulation software QBlade [25] and were extrapolated to 360^o degrees AoA. The non dimensional rotor performance was simulated by means of a steady state BEM computation including tip and root loss corrections. The comparissons presened reffer to the baseline rotor and an alternative rotor with activated stall ribs in order to identify the difference in Cp between the two rotors (Fig. 12).

The simulations revealed that the deployment of stall ribs is able to reduce the rotor efficiency from values above 50% to as low as 15% for the optimal design point (design λ: 9). Similarly the power curve of a virtual wind turbine is also highly affected by the deployment of stall ribs. Figure 13 shows the baseline power curve of a 6MW variable-speed pitch regulated wind turbine compared with the case where the stall ribs are activated. It is apparent that the stall ribs achieve a very high power control authority. At the nominal wind speed of $10m/s$ the activation of the stall ribs is able to reduce the power to less than $\frac{1}{6}$ of the nominally achievable power. For higher wind speeds and for the region where the generator speed variability is exhausted the stall ribs still manage to significantly reduce the generated power. At the high wind region wind turbines usually operate at constant r.p.m. The local AoA therefore increases with the wind speed increase, thus the stall ribs become less effective. Nevertheless it is observed that the stall ribs overall are able to effectively control the power of the turbine for the entire operational spectrum.

The effect of stall ribs on the turbine loads is also significant (Fig. 14). The typical root bending moment peak at the nominal wind speed, observed at the baseline case, is effectively halved with the activation of stall ribs. The axial thrust behavior follows similar pattern with that of the bending moment (thrust curve not shown here). The relative increase of loads (i.e. bending moment) for wind speeds higher than the nominal is simply caused because of the absence of pitch activation during the stall rib simulation. A combination of stall ribs and blade pitch control would of course lead to an even more dramatic load reduction after the nominal wind speed.

The performance of the other active stall control

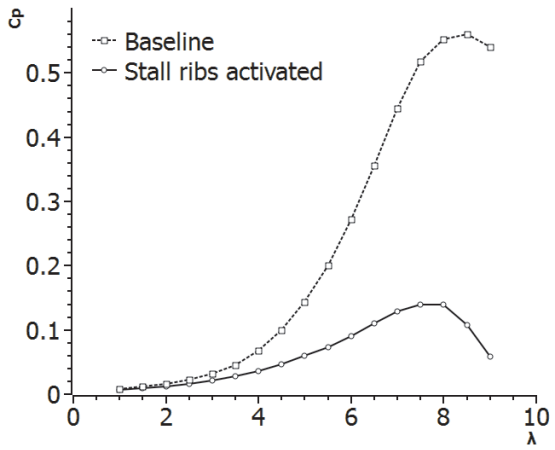

Figure 12. Rotor Cp over λ for the generic 70m blade with and without stall ribs

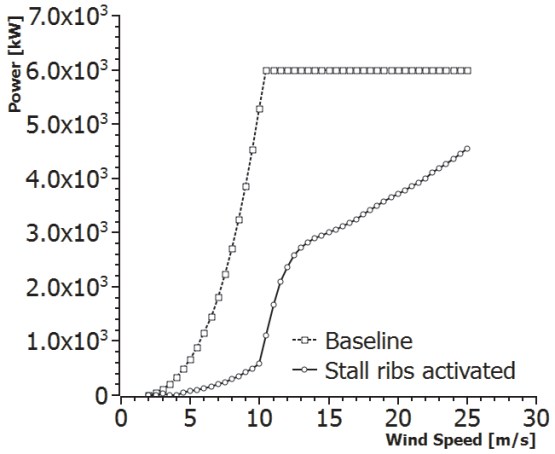

Figure 13. Power curve comparison for a 6MW wind turbine with and without deployed stall ribs

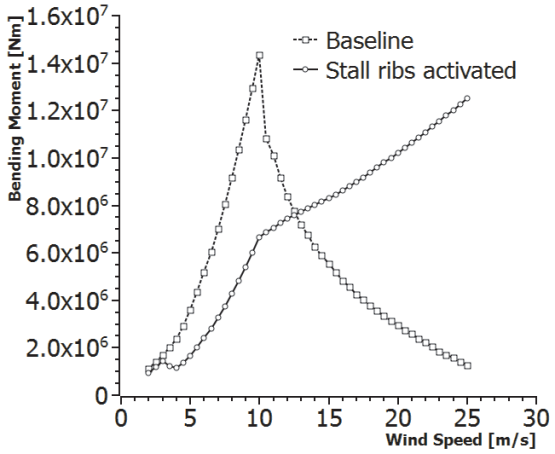

Figure 14. Power curve comparison for a 6MW wind turbine with and without deployed stall ribs

elements such as the vertical and inclined spoilers follows the same trends with the stall ribs and therefore are not presented here for space economy.

6. SUMMARY

The experimental investigations described in this paper are aimed at the characterization of a series of aerodynamic active stall control solutions on dedicated wind turbine airfoils. The goal is to develop active stall control elements as means for load alleviation and partial power regulation for very large wind turbine rotorblades. The aerodynamic performance in combination to the mechanical complexity and ease of integration is taken into account in the element selection process. Parametric wind tunnel investigations were performed in order to identify the optimal configuration and the optimal design parameters of each solution.

The wind tunnel experiments reveal that in order to achieve a significant drop in the airfoil efficiency and regulate the power and the loads, it is sufficient to deploy small-sized spoilers. The use of typical rigid vertical or inclined spoilers is feasible and in this case the required spoiler size or spoiler deflection can be kept to a minimum. Furthermore, non-standard spoiler solutions such as the flexible stall rib concept are proposed. These offer significant advantages over conventional spoilers mostly in the field of system integration and system maintenance complexity. Wind turbine rotorblades are flexible and highly elastic structures susceptible to frequent lightning strikes. It is therefore desired to avoid if possible all electro-mechanical actuators and cabling inside blade structures in order to avoid high maintenance costs and lightning damages. It is therefore possible that pneumatically actuated stall ribs can offer a feasible and attractive load and power control solution.

The performance of stall ribs and other active stall control solutions for load alleviation and partial power regulation systems was demonstrated by means of BEM simulations based on a generic 70m blade design for a 6MW turbine. The implementation of such elements in a multitude of individual spoiler or stall rib units would allow the precise control of flow separation on the blade. Through such a system it would be possible to unload parts of the blade in a very short time in order to avoid the load and power peaks of atmospheric gusts and rapid wind speed variations. At the same time it would be possible to perform the frequent power fine-tuning operations through the stall rib or spoiler units thus utilizing the blade pitch system only for large angle variations at a low pitch rate. This control strategy would be beneficial for both the blade structure as well as for the blade pitch mechanism.

The increased noise emissions due to flow separation which would be caused by such stall control systems would definitely be an issue on

land-based turbines, but this would probably not be the case on offshore wind turbine installations.

ACKNOWLEDGEMENTS

The authors would like to acknowledge the valuable support of Smart Blade GmbH for the completion of this project.

References

[1] Pechlivanoglou, G., Nayeri, C., and Paschereit, C. 2010 "Performance optimization of wind turbine rotors with active flow control". *Proceedings of ASME IGTI Turbo Expo 2011 ASME/IGTI June 6 - 10, 2011, Vancouver, Canada*, ASME.

[2] Fischel, J. and Ivey, M. 1948 *Collection of test data for lateral control with full span flaps*. NACA.

[3] Seetharam, H., Kuhn, W., M.D. Mack, and Bright, J. 1979 "Aerodynamics of spoiler control devices", Vol. AIAA Aircraft Systems and Technology Meeting.

[4] Ostowari, C., W.H. Wentz, and Seetharam, H. 1981 "Effects of design variables on spoiler control effectiveness hinge moments and wake turbulence", Vol. AIAA 19th Aerospace Sciences Meeting.

[5] Chevreau, R. 1952 "Wind motor". *Pat. No. US 2622686*.

[6] Lawson-Tancred, H. 1985 "Wind turbine blades". *Pat. No. US 4692095*.

[7] Hau, E. 2006 *Wind Turbines: Fundamentals, Technologies, Applications, Economics (2nd Edition)*. Springer.

[8] Gollnick, B. 2007 *Untersuchung der Möglichkeiten des Einsatzes von Strömungselementen fur Windenergieanlagen*.

[9] Ramsay, R. R., Janiszewska, J. M., and Gregorek, G. M. 1997 "Wind tunnel testing of an S809 spoiler flap model (for wind turbines)". *AIAA Meeting papers*, Vol. , p. 11.

[10] Stiesdal, H. Pat. No. US 2003/0091436 A1 "Method for regulating a windmill and an apparatus for the use of said method".

[11] Olsen, T., Quandt, G., M.C. Cheney, and Arcidiacono, P. 1999 "Analysis and Tests of Pultruded Blades for Wind Turbine Rotors", Vol. NREL Subcontractor Report.

[12] Lee, J. 1935 "Control device for airplanes". *Pat. No. US 2164531*.

[13] Wagner, H. Pat. No. DE 727732 "An Tragflügeln angeordnete Abreissleisten".

[14] Wagner, H. Pat. No. US 2218128 "Aircraft having its wings provided with disturbing bodies".

[15] Neuhierl, H. Pat. No. DE 7738361 "Stoer oder Bremsklappe fuer Modellflugzeuge".

[16] Thomas, F. and Milgram, J. 1999 *Fundamentals of Sailplane Design*. College Park Press.

[17] Jacobs, N. 1934 "Airfoil section characteristics as affected by protuberances". *NACA*, Vol. Report no. 446.

[18] Jacobs, N. 1934 "Airfoil section characteristics as affected by protuberances of short span". *NACA*, Vol. Report no. 449.

[19] Wenzinger, C. J. 1941 *Tests of round and flat spoilers on a tapered wing in the NACA 19foot pressure wind tunnel*. NACA.

[20] Hunter, W. 1943 "Aerodynamic Brake". *Pat. No. US 2428936*.

[21] Campbell, R. 1944 "Aerodynamic Brake". *Pat. No. US 2400388*.

[22] Barber, E. 1961 "Aircraft wing construction". *Pat. No. US 3136501*.

[23] Holzem, A. 1990 "Wind turbine wing with a pneumatically actuated spoiler". *Pat. No. US 5106265*.

[24] Timmer, W. and van Rooij, R. 2003 "Summary of the delft university wind turbine dedicated airfoils". *AIAA 41st Aerospace Sciences Meeting and Exhibit*, Vol. , p. 11.

[25] Pechlivanoglou, G., Marten, D., Nayeri, C., and Paschereit, C. 2010 "Integration of a wind turbine blade design tool in XFOIL/XFLR5". *Proceedings of DEWEK 2011*, DEWI.

Conference on Modelling Fluid Flow (CMFF'12)
The 15th International Conference on Fluid Flow Technologies
Budapest, Hungary, September 4-7, 2012

NUMERICAL INVESTIGATION OF VERTICAL AXIS WIND TURBINES

Seyed Alireza Ahmadi[1] Gunther Brenner, [2]

[1]Corresponding Author. Institute of Applied Mechanics, Clausthal University, D-38678 Clausthal-Zellerfeld, Adolph-Roemer-Strasse 2A: +49 5323 72 3166, Fax: +49 5323 72 2203, E-mail: saah@tu-clausthal.de
[2]Institute of Applied Mechanics, Clausthal University, D-38678 Clausthal-Zellerfeld, Adolph-Roemer-Strasse 2A: E-mail: gbr@tu-clausthal.de

ABSTRACT

The goal of the present paper is the assessment of tools for aerodynamic design and optimization of vertical axis wind turbines (VAWTs). For optimization and design purposes, fast and computationally inexpensive methods are required. These may be based on integral momentum balances and the actuator disc theory and are known,e.g., as "single stream tube model" or "multiple stream tube model". However, these models suffer from inaccuracies and are not reliable at certain operation conditions since dynamic effects in the flow past the oscillating profile are not or not appropriately considered. Modern CFD methods (Computational Fluid Dynamics) are able to account for these effects more precisely and on a more rigorous level but at significantly larger computational costs. The intention of the present paper is to shed some more light on the dynamics of the flow past a VAWT and how these effects may be incorporated into such parameter models.

CFD, vertical axis wind turbines, model reduction

Nomenclature

A	$[m^2]$	turbine frontal area
C_l	$[-]$	lift coefficient
C_d	$[-]$	drag coefficient
C_p	$[-]$	power coefficient
c	$[m]$	chord length
H	$[m]$	wing span
k^*	$[-]$	non-dimensional oscillation frequency
L	$[m]$	length of computational domain
n	$[-]$	number of wings
N	$[N]$	normal force
q	$[Pa]$	dynamic pressure
T	$[N]$	tangential force
t	$[s]$	time
R	$[m]$	turbine radius
Re	$[-]$	Reynolds number
u	$[m/s]$	velocity
α	$[-]$	angle of attack
β	$[-]$	flow retardation factor
λ	$[-]$	tip speed ratio
ϕ	$[-]$	angle of rotor position
σ	$[-]$	solidity
ω	$[1/s]$	angular velocity

Subscripts and Superscripts

l, t	lift, drag
n, t	normal, tangential
x, y, z	Cartesian coordinates
∞	free stream
$stall$	stall

1 Introduction

Since the Darrieus wind turbine was introduced in 1931 [4], modern VAWTs experienced a changeful development. Between 1975 and 1990, they received a lot of attention and research was focused on large scale VAWTs. In recent years an increasing demand in decentralized power plants is observed renewing the interest in VAWTs. Compared to Horizontal-Axis Wind Turbine (HAWT), the VAWT presents several advantages such as its insensitivity to yaw and wind direction and its increased power output in skewed flow. The VAWT is inherently omnidirectional, and hence obviates the need to provide a yawing mechanism. Due to its simpler configuration, the production costs and service efforts are potentially lower than for HAWT. These observations also have driven the promotion of small scale VAWT. In some sense, the price paid for structural simplicity is aerodynamic complexity: VAWT aerodynamics is inherently unsteady. Dynamic effects are due to the periodically changing apparent flow conditions at the airfoils in Darrieus motion. Both, angle of attack and velocity magnitude undergo significant changes, in particular at low tip speed ratios. This results in periodically changing aerodynamic loads and the continuous reproduction of trailing vortices. This dynamic stall effect may act positively on the power generation [9] but may cause problems such as aeroelastic vibrations or noise due to the interactions between vortices and the blade. Quantifying these effects in the design of VAWTs or optimizing the

design by exploiting the dynamic stall systematically is yet an unsolved issue.

Recent developments in computational methods and computer resources have greatly increased the capabilities of prediction tools which are suitable for the prediction of flows in such rotating machinery. The numerical assessment of the three-dimensional and transient, turbulent flow based on the Reynolds-averaged Navier-Stokes equations (RANS) is in principle possible but requires significant computational effort. Therefore, the design and optimization should be based on simpler parameter models such as the single streamtube model (SSTM) or its variants, double multiple streamtube (DMST) or multiple streamtube model (MSTM) [11]. However, full Navier-Stokes simulations may be used in order to improve the understanding of the flow past a VAWT. Here, in particular the dynamic stall and the mutual interaction of the wings passing the windward and leeward side of the rotor is of interest.

In the present paper, the aerodynamics of a Darrieus type windturbine is analyzed numerically using CFD (Computational Fluid Dynamics) in order to shed some light on power characteristic and dynamic loads. This analysis is intended to bring the discussion concerning the pros and cons of the VAWT onto a more objective level. Besides that, the VAWT may be regarded as a challenging test case in modeling instationary aerodynamics as a base for optimization.

The present paper is organized as follows. In the next section, a brief overview regarding the relevant flow phenomena and the state of the art regarding modeling the flow past a VAWT are presented. Subsequently, the computational methods used in the present study are outlined. Transient, two dimensional results for the flow past a Darrieus rotor are presented in section 5. The results are analyzed in detail and suggestions are made for the improvement of parameter models such as the DMST model. Finally, comparisons with full three-dimensional simulations are presented.

2 Aerodynamic Analysis

Because of the cycloidal motion of the blade of a VAWT, it experiences a continuously oscillating angle of attack (pitching motion) as well as changing magnitude of the apparent flow velocity. The configuration shown in Fig. 1, illustrates these variations. The geometric or local angle of attack is defined as the angle between the profile chord and the local flow direction u_{rel}

$$\alpha = arctan\left(\frac{sin\varphi}{\lambda + cos\varphi}\right). \qquad (1)$$

Here, $\lambda = \omega R/u_\infty$ is the tip speed ratio, u_∞ is the freestream velocity and φ is the azimuth angle. The relative flow velocity u_{rel} depends on the azimuth angle and is calculated as

$$\frac{u_{rel}}{u_\infty} = \sqrt{(\lambda + cos\varphi)^2 + sin^2\varphi}. \qquad (2)$$

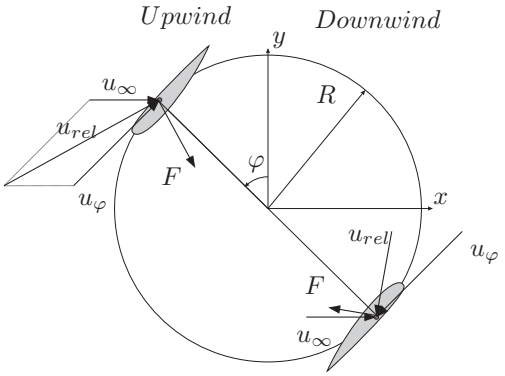

Figure 1: Components of the velocities and forces.

The variation of the flow direction and velocity magnitude causes varying forces on the airfoil and consequently fluctuating circulation in the flow behind the airfoil. During the upstroke motion of the airfoil (increasing angle of attack), the flow past the airfoil attaches to it beyond the steady separation point. Subsequently, a vortex develops at the leading edge and moves along the upper surface of the profile with approximately 22 percent of the ambient velocity [11]. During that passage, this vortex reduces the pressure along the low-pressure surface and increases lift, drag and the pitching loads far in excess of the static counterpart. The vortex finally lifts of the airfoil and a counter-rotating vortex originates from the trailing edge as the airfoil reaches again a neutral position. The vortices shed from the airfoil and are transported with the flow. Depending on the value of the tip-speed ratio, they may interact with the generating airfoil as this airfoil passes through the leeward side of the rotor. The details of the vortex shedding are determined by the airfoil shape, Reynolds number, angle of attack and the oscillation frequency. The oscillation frequency is usually nondimensionalized in terms of freestream velocity and the chord length c, i.e., $k^* = \omega c/2u_\infty$.
A first approach for modeling the aerodynamics of a Darrieus type turbine was presented in [13] based on the streamtube theory. In [10, 12] several improvements leading to the multiple streamtube (MSTM) and DMST have been proposed. The DMST model relies basically on a momentum balance between the aerodynamic forces acting on a profile and the convective transport of momentum in a control volume around the airfoil. Indeed, the mentioned models may be assumed as an adaptation of Betz theory to the particularities of Darrieus motion. The forces on the airfoil may be obtained from aerodynamical databases, which are available for a vast number of profiles. However, these data are usually obtained for constant flow conditions or quasi-static change of angle of attack. It is well known that the dynamic effects are due to the fast varying angle of attack and may change the airfoil characteristics significantly. The stall at high angle of attack is delayed which can lead to higher lift forces than expected for static conditions. In [7] the

particle image velocimetry (PIV) is used to identify the vortex shedding near the airfoil in a stationary and rotating frame of reference. In [5, 6, 8], PIV measurements are used to provide data for validation of CFD results, to determine the loads on blade and to assess the vortex shedding depending on the wing tip geometry.

An important parameter influencing the power characteristic of the turbine is the solidity, defined as the ratio of the chord length of all wings over the radius of the rotor, i.e., $\sigma = n \cdot c/R$. Higher solidity usually shifts the maximum value for power coefficient to smaller tip speed ratios and results in lower efficiency. At low tip speed ratios, a blade does not interact with the air flow passing through the volume swept out by the proceeding blades significantly. But at high tip speed ratios, the rotor blades strongly interact with the wakes, which are generated by the upstream wings [3]. A further important parameter is the angle of incidence of the profile with respect to the circumference. The choice of the profile (maximum camber, distance of maximum camber, maximum thickness etc.) is of importance since it directly enters into the force balance. In that context, it is often claimed that non-symmetric airfoils may cause self-start of the rotor.

3 Single Stream Tube Model (SSTM)

Templin [13] was one of the first researchers who developed a parameter model for VAWTs. This model is based on the actuator disk theory applicable for propellers. In this model, the flow through the turbine is assumed to have a constant velocity. The blades of the turbine is subdivided to small elements in order to apply the momentum theory to each of them. The infinitesimal forces on the blade elements in the normal and circumferential directions and their relevant coefficients are defined as follows

$$\begin{aligned} C_n &= C_l cos\alpha + C_d sin\alpha\,, \\ C_t &= C_l sin\alpha - C_d cos\alpha\,, \\ dN &= C_n qcdz\,, \\ dT &= C_t qcdz\,. \end{aligned} \tag{3}$$

The aerodynamic coefficients can be extracted from experimental databases. In the present work, data for an NACA 4418 profile have been used [1]. The force experienced by one element in the direction of the air flow is then calculated as

$$dF = qc(C_n sin\varphi - C_t cos\varphi)\cdot \tag{4}$$

The total force on a turbine with n blades each of them with chord c in a complete rotation $(0 < \varphi < 2\pi)$ and a blade length z $(-H < z < H)$ is obtained as

$$F = \frac{n \cdot c}{2\pi} \int_{z=-H}^{H} \int_{\varphi=0}^{2\pi} q(C_n sin\varphi - C_t cos\varphi) d\varphi\, dz\cdot \tag{5}$$

It should be noted that usually the static lift and drag coefficients are used to calculate this force and therefore do not reflect dynamic effects. However, to determine trends, such as the influence of the shape of the profile and the solidity of the turbine on the power curve, these models represent valuable results.

4 Computational Model

In the present study, the general purpose CFD code ANSYS CFX is used to compute the flow-field around the rotor. This code is based on the approximate solution of the transient, incompressible and Reynolds averaged Navier-Stokes (RANS) equations. The SST $k-\omega$ model is used to model turbulence in combination with scalable wall functions. CFX employs the finite volume discretization and an implicit solution of the resulting algebraic equations. The time integration is of second order accuracy. The computational domain used in the present investigation is illustrated in Fig. 2. It consists of a stationary outer region sufficiently large to provide suitable boundary conditions far away from the rotor, i.e., $L \approx 10R$. The rotor itself is embedded in an inner rotating domain. Between these domains a general grid interface (GGI) is defined to interpolate the flow-field quantities. Although the interface is designed in such a way that conservation is satisfied, numerical errors are introduced due to interpolation procedures. In order to avoid interference between disturbances which are created by this interface and the flow-field near the blades, a reasonable large distance between the rotor and the interface is considered. Each of the blades is embedded in a C-type grid with circular outer shape. This allows to define a constant pitch angle for the wing, while maintaining a high quality grid near the wing surface. The flow parameters are completely summarized in nondimensional form as the Reynolds number based on the chord length and the freestream velocity ($Re = 400.000$) as well as the ratio chord length over turbine radius ($c/r = 0.2$). The wing is a NACA 4418 profile with zero angle of incidence. At the inlet a constant free stream velocity of $10m/s$ is

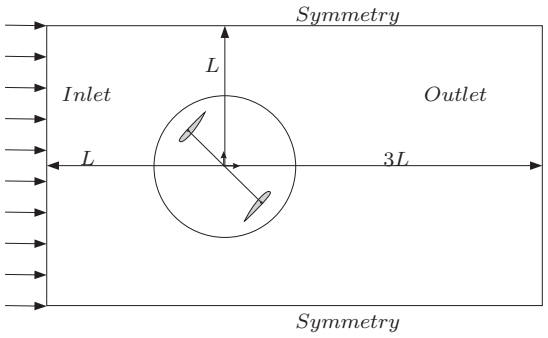

Figure 2: Sketch of the computational domain and boundary conditions.

prescribed. The boundary conditions are shown in Fig. 2. The dimension of the domain as well as the number of elements is checked systematically to demonstrate grid-convergence. The Y^+ criterion is also checked for the final computational grid. Its value is close to unity,

which ensures the appropriateness of the grid quality and size near the blades. The final grid near the turbine and a closeup of the blades are shown in Fig. 3.

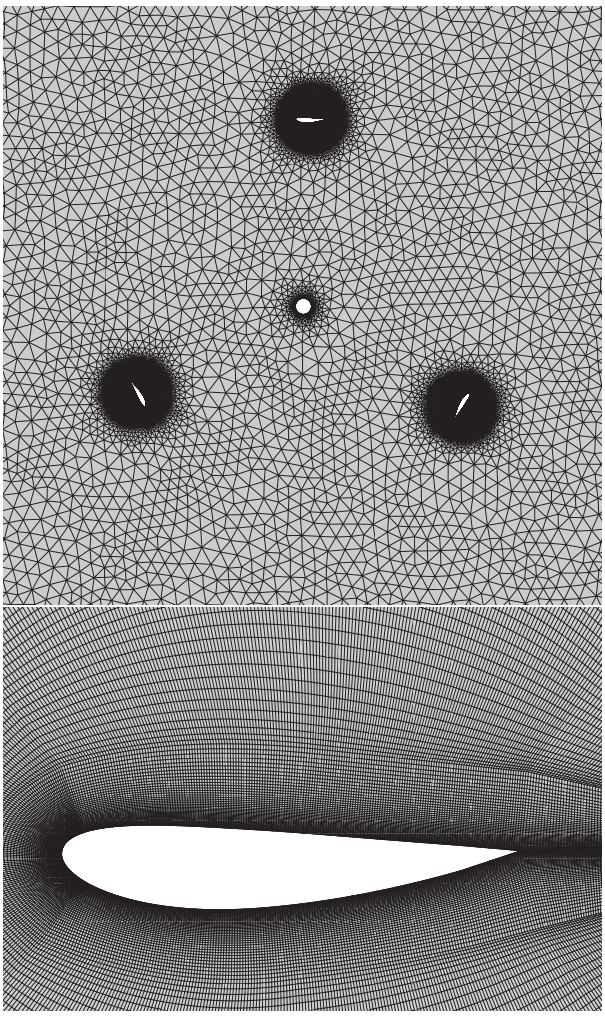

Figure 3: Close-up views of the computational grid around a three blade Darrieus rotor.

5 Results

In the following, results are presented for a typical configuration of a Darrieus rotor. The effect of solidity in the range $\sigma = 0.48$ and $\sigma = 0.72$ on the performance is determined by varying the number of the wings while keeping the chord to radius ratio c/R constant. The variation of the power coefficient versus the tip speed ratio is presented in Fig. 4. As can be seen, increasing the solidity shifts the operating point, i.e., point of the maximum power, to lower values of the tip speed ratio. The efficiency of the turbine predicted is, in very good agreement between the SSTM and the CFD model for low tip speed ratios up to the operating point. For higher values of λ, increasing differences are observed.

It may be suspected, that these differences are due to dynamic effects in the flow which increase as the rotational speed of the rotor increases. In the following, some light will be shed on the phenomena which may cause these deviations. As denoted in [11],

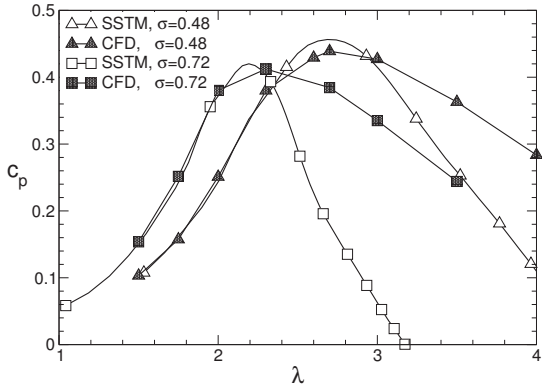

Figure 4: Variation of power coefficient versus tip speed ratio for different solidities.

the aerodynamic performance of a VAWT is affected by various transient effects in the fluid flow and hence strongly depends on the tip speed ratio. At lower values of λ, dynamic stall effects are expected due to the delay of separation when dynamically varying the angle of attack of the profile. At higher tip speed ratios, the mutual interactions between the flow around the wings dominate, i.e., the wake of a leading wing disturbs the flow arriving at the following wing.

The effect of dynamic stall may be quantified by two parameters [2]. On the one hand, the amplitude of the dynamic variation of the angle of attack of the wing should exceed the static stall angle (α_{stall}). The nominal variation of the angle of attack depends on the tip speed ratio according to

$$\alpha_{max} = tan^{-1} \frac{1}{\sqrt{\lambda^2 - 1}}. \tag{6}$$

In Fig. 5 the ratio $\alpha_{max}/\alpha_{stall}$ is plotted versus the tip speed ratio. Here, a static stall angle of 22° for a NACA 4418 profile is considered. Thus, for the present configuration, dynamic stall effects are relevant only for tip speed ratios smaller than about four. The second

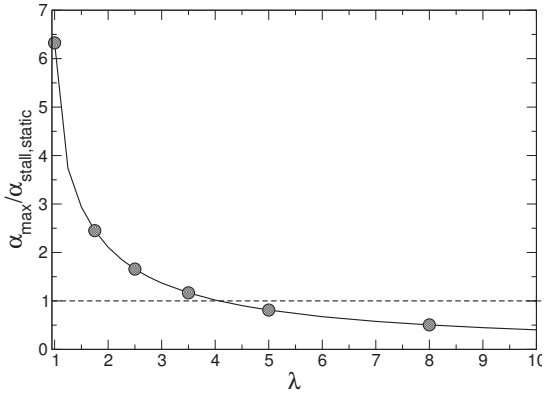

Figure 5: Variation of $\alpha_{max}/\alpha_{stall}$ versus tip speed ratio.

constraint is related to the frequency of variation of

angle of attack. A reduced frequency may be defined as the time scale of the flow passing the profile with chord length c related to the time scale of changing the angle of attack, i.e.,

$$F^* = \frac{\frac{c}{R\omega}}{\frac{2\alpha_{max}}{\dot{\alpha}_{max}}} = \frac{c}{R}\frac{1}{\lambda - 1}\frac{1}{2\alpha_{max}} \,. \qquad (7)$$

According to [2], for reduced frequencies above about 0.2, dynamic stall effects are expected. The evolution of the reduced frequency versus the tip speed ratio is plotted in Fig. 6 for various ratios of c/R. It may be concluded, that the present configuration with $c/R = 0.24$ is quite insensitive with respect to dynamic stall. This explains the quite good agreement of the results of the CFD simulation and the SSTM model at small λs.

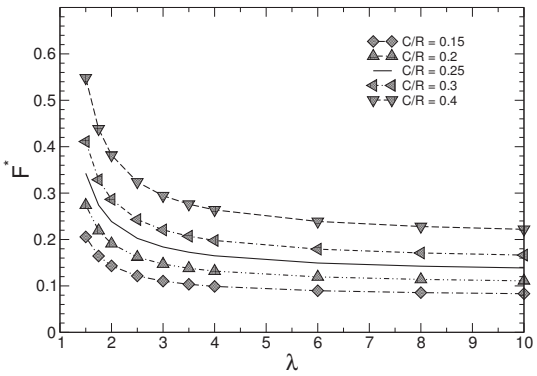

Figure 6: Variation of F^* versus λ.

However, dynamic stall plays only a minor role for higher tip speed ratios and therefore cannot be made responsible for the large deviation of SSTM and CFD predictions in this regime.

Thus, in the following, the mutual interaction between the profiles of the rotor is investigated and quantified. From momentum theory it is well known, that the aerodynamic force exerted on a profile corresponds to a change of momentum and therefore reduces the velocity downstream of the profile. This reduction can be quantified based on the results of the CFD computations by averaging the velocity in the midplane of the rotor during one revolution as follows:

$$u_{ave} = \frac{1}{T}\int_0^T \frac{1}{2R}\int_{-R}^{R} u(x=0,y,t)\, dydt \,. \qquad (8)$$

The ratio of u_{ave} and the freestream velocity is known as the reduction factor β. In the following, the reduction factor obtained from the CFD simulation is compared and discussed with the results from momentum theory, which is part of the solution of the SSTM model. In Fig. 7 show that by increasing tip speed ratio, the reduction factor steadily decreases. From Betz theory it is expected, that the maximum power is obtained for a reduction factor of $\beta = 2/3$. For the present configurations, this corresponds to $\lambda \approx 2$ for the high solidity case, and to $\lambda \approx 2.7$ for the low solidity case, as can be seen from Fig. 7. This is in quite good agreement with the power coefficient presented in Fig. 4. For larger values of λ, there is an increasing discrepancy between the results obtained using CFD and the SSTM model in that the SSTM predicts a much larger decrease of velocity. However, according to the actuator disc theory, there is a minimum value of reduction factor of $\beta = 0.5$. For large values of λ, this limit is asymptotically reached in the CFD simulation. The SSTM model over predicts the flow retardation and consequently predicts too low power coefficients. Thus, it is concluded, that in order to improve the accuracy of momentum models like SSTM, a better representation of the mutual interaction of the wings in wind- and leeward position is required.

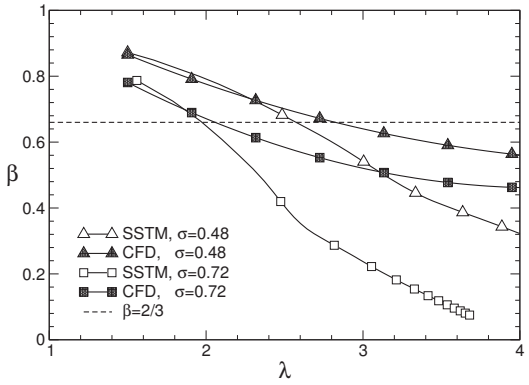

Figure 7: Reduction factor β versus tip speed ratio λ for two solidities.

6 Conclusion and Summary

In the present paper, time-dependant and two dimensional computations of the flow past a vertical H-rotor are presented. Computational fluid dynamics is used to provide detailed data for the verification of simpler parameter models, such as the SSTM model. The latter may be used as a base for further optimization of these turbines. Large discrepancies have been observed between predictions based on the more reliable CFD simulations and the simple parameter model. Although the global power characteristic as well as the maximum power are predicted in quite good agreement, a significant under prediction of the power characteristic by the SSTM model is observed for high values of tip speed ratio. Based on an analysis of the characteristic times and amplitudes of the wing in Darrieus motion, it can be concluded that the delay of the flow separation (dynamic stall) is apparently not responsible for this discrepancy. Instead, it was shown that this is due to the over prediction of the flow retardation in the SSTM model, which is basically an actuator disc model with minor adaptation to the kinematics of the H-rotor. This will be subject to further investigations.

References

[1] Ira H. Abbott and Albert E. von Doenhoff. *"Theory of wing sections"*. Dower Publishing, 1959.

[2] E. Amet, T. Maitre, C. Pellone, and J.-L. Achard. "2D Numerical Simulations of Blade-vortex Interaction in a Darrieus Turbine." *Fluids Engineering*, 131:523–573, 2009.

[3] C. A. Consul, R. H. J. Willden, E. Ferrer, and M. D. McCulloch. "Influence of solidity on the performance of a cross-flow turbine." Uppsala, Sweden, 2009. European Wave and Tidal Energy Conference.

[4] Georges Jean-Marie Darrieus. "Turbine having its rotating shaft transverse to the flow of the current." US patent No. 1.835.018.

[5] Carlos Simão Ferreira, Gerard van Bussel, Fulvio Scarano, and Gijs van Kuik. "PIV visualization of Dynamic stall VAWT and Blade Load Determination". In *Proceedings of the 46th AIAA Aerospace sciences meeting and exhibit, Reno, USA*, pages 1–13, 2008.

[6] Carlos Simão Ferreira, Gerard van Bussel, and Gijs van Kuik. "2D CFD simulation of dynamic stall on a vertical axis wind turbine: verification and validation with PIV measurements". In *Proceedings of the 45th Aerospace sciences meeting and exhibit (AIAA) in Reno*, pages 1–11, 2007.

[7] Nobuyuki Fujisawa and Satoshi Shibuya. "Observations of dynamic stall on Darrieus wind turbine blades". *Journal of Wind Engineering and Industrial Aerodynamics*, 89(2):201–214, 2001.

[8] Claudia Hofemann, Carlos Simão Ferreira, Kristian Dixon, Gerard van Bussel, Gijs van Kuik, and Fulvio Scarano. "3D Stereo PIV Study of the Tip Vortex Evolution on a VAWT". In *Proceedings of the European Wind Energy conference & Exhibition (EWEC) in Brusssels*, pages 1–8, 2008.

[9] R. B. Noll and N. D. Ham. "Effects of dynamic stall on SWECS". *ASME J. Sol. Energy Eingineering*, 104:96–101, 1982.

[10] Ion Paraschivoiu. "Double-Multiple Streamtube Model for Darrieus Wind Turbines". In *Proc. NASA Wind Turbine Dynamics Workshop. Cleveland*, pages 19–24, 1981.

[11] Ion Paraschivoiu. *"Wind Turbine Design with Emphasis on Darrieus Concept"*. Polytechnic International Press, Montreal, Kanada, 2002.

[12] James H. Strickland. "The Darrieus Turbine: A Performance Prediction Model Using Multiple Streamtubes". Sandia Report SAND75-0431, Sandia National Laboratories, 1975.

[13] R. J. Templin. "Aerodynamic performance theory for the NRC vertical axis wind turbine". Technical report, National Research Council Laboratory Technical Report LTR-LA-160, 1974.

Conference on Modelling Fluid Flow (CMFF'12)
The 15th International Conference on Fluid Flow Technologies
Budapest, Hungary, September 4-7, 2012

Optimal Design of a Savonius Turbine

Mohamed H. Mohamed,[1] Gábor Janiga, [2] Dominique Thévenin [3]

[1] Department of Mechanical Power, Faculty of Engineering, Helwan University, P.O. 11718, Cairo, Egypt, E-mail: moh75202@yahoo.de
[2] Corresponding Author. Lab. of Fluid Dynamics and Technical Flows, Univ. of Magdeburg "Otto von Guericke", Germany, E-mail: janiga@ovgu.de
[3] Lab. of Fluid Dynamics and Technical Flows, Univ. of Magdeburg "Otto von Guericke", Germany. E-mail: thevenin@ovgu.de

ABSTRACT

Wind energy and efficiency are two key terms in finding a solution to the world's increasing energy problems and the possible dangers of the climate warming. Available technical designs are not always suitable for low wind-speeds, urban surroundings and high installation densities. Systems derived from the Savonius turbine may be possible converters for such conditions, if they deliver a sufficient efficiency. The present study aims at investigating and improving the output power and the efficiency of the standard Savonius turbine. For this purpose, a modified design is considered, involving simultaneously new blade shapes, an obstacle plate shielding the returning blade and a flow deflector. After checking the impact of design modification, the optimum angle and position of these guiding plates and modified blade shape leading to the highest performance of the Savonius turbine are computed by optimization. This optimization is carried out by coupling an in-house optimization library (OPAL) with an industrial Computational Fluid Dynamics (CFD) code (here ANSYS-Fluent). The optimization process maximizes the output power coefficient and relies on Evolutionary Algorithms. A considerable improvement of the modified Savonius turbine performance (typically 58% relative increase of the power coefficient) has been finally obtained in this manner.

Keywords: Evolutionary Algorithms, Optimization, Savonius turbine, Turbomachines, Wind energy

1. INTRODUCTION

Global energy consumption in the last half century has increased very rapidly and is expected to continue to grow over the next 50 years. However, significant changes are now expected. The past increase rate was stimulated by relatively cheap fossil fuels supporting industrialization in North America, Europe, and Japan. While energy consumption in these countries continues to increase, additional factors are making the picture more complex. It is unclear yet how the required electricity production will be covered.

Many developed and developing countries have realized the importance of wind as an important resource for power generation. Necessary measures are being taken up across the globe to tap this energy for an effective utilization. From an emerging energy source twenty years ago, wind energy has evolved into a mature and booming global business. Associated costs have fallen dramatically over the last 15 years, moving closer to those of conventional energy sources. However, even if the associated technology has been greatly improved during the last decade, the available technical design is not yet adequate to develop reliable wind energy converters for low wind-speeds, reduced inter-turbine spacings and urban environment. Vertical-axis turbines like the Savonius turbine may be suitable converters for such conditions.

S. J. Savonius initially developed the vertical-axis Savonius rotor in the late 1920s. The concept of the conventional rotor is based on cutting a cylinder into two halves along the central plane and then moving the two half cylinders sideways along the cutting plane, so that the cross-section resembles the letter S (Fig. 1). The Savonius rotor, which is a slow-running vertical axis wind machine, has a rather poor efficiency: $C_p = 0.2$ [1] at best. Nevertheless, it can present some advantages for specific applications, in particular due to its simplicity, resulting robustness and low costs. If a sufficient efficiency could be obtained, the Savonius rotor would become a very interesting complementary source of electricity from wind energy.

2. MEASURING PERFORMANCE

Using the notations of Fig. 1, the velocity coefficient (or speed ratio) is first defined as:

$$\lambda = \frac{\omega R}{U} \tag{1}$$

Considering a Savonius rotor of height H, a wind of incoming velocity U, the mechanical power P and the mechanical torque T on the axis of a Savonius turbine, it is possible to write

$$C_p = \frac{P}{\rho R H U^3} \tag{2}$$

and

$$C_m = \frac{T}{\rho R^2 H U^2} \tag{3}$$

where C_p and C_m are respectively the output power coefficient and the torque coefficient of the turbine. In the following sections, the optimization process will consider the output power coefficient C_p as target function for a conventional Savonius set-up (Fig. 1). This conventional configuration of the rotor has been extensively studied in the past. The corresponding values of C_p and C_m have been determined numerically and sometimes experimentally as a function of the speed ratio λ. This has been used to validate extensively our numerical procedure by comparison with published, reference data, as documented in [2, 3].

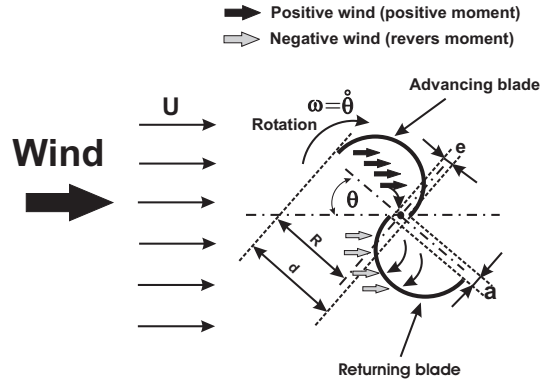

Figure 1. Schematic description and main parameters characterizing a Savonius rotor

3. Work objectives

Many authors have tried to solve the major issues associated to standard Savonius turbines: poor efficiency and self-starting characteristics (see e.g., [4, 5, 6]). Several ideas have been introduced for this purpose. It has been for instance suggested to place a guiding box around the rotor [7]. As an alternative, twisted blades have been proposed and indeed improve the performance of the Savonius turbine [8, 9]. Multi-stage Savonius turbines have been investigated experimentally and theoretically [10, 11] and show again some progress compared to the standard configuration. The installation of an obstacle shielding the returning blade leads also to an increase in turbine performance and to a better self-starting capability [2]. Using simultaneously a second plate as a flow deflector leads to a further increase of the power output for the classical Savonius turbine [3]. Some of the most important results concerning such possible improvements have been summarized in recent publications [2, 12].

Since one of the major advantages of the Savonius turbine is its simplicity and corresponding compactness, robustness and low cost, a modification introducing a high complexity should probably not be retained. Considering the results of all previous studies, some simple guiding or deflecting plate(s) would lead to the best efficiency improvement at the lowest possible cost and complexity. As a possible complement, the shape of these plates and of the turbine blade itself could be modified. Following this line of thought, the present work builds on top of our previous investigations [2, 3, 12], in order to improve the performance of the standard Savonius rotor and generate new designs. In the present study we will thus investigate:

- First, the effect of two guiding plates (obstacle and deflector) for the standard Savonius geometry (Fig. 2a). In this case the internal distances (a and e) will be fixed at standard values, $a/d = 0.0$ and $e/d = 0.027$.
- In a second step we will study simultaneously the effect of guiding plates (obstacle and deflector), blade shape (Fig. 2b) and internal distances between the blades a and e (Fig. 2c).

The guiding plates consist of 1) a deflector plate, employed to obtain the best possible flow conditions for the advancing blade, while 2) the obstacle plate shields partly the returning blade (Fig. 2a). The deflector plate should increase the positive moment, while the obstacle plate will reduce the reverse moment, and as a consequence the total moment of the turbine (moment difference between the advancing and the returning blade) will be increased. Beside this effect of guiding plates, the shape of the rotor as well as the internal distance will be optimized in the second step thanks to a suitable mathematical procedure.

4. Optimization

Optimization of mechanical components is an important aspect underlying many engineering processes; a well-designed system will lead to money saving during the production phase and better machine performance. On the other hand, optimization first makes the engineering step more complex. A truly optimized design mostly requires an increased use of high-performance computing.

Optimization methods attempt to determine the n design variables X_i ($i = 1 \ldots n$) that

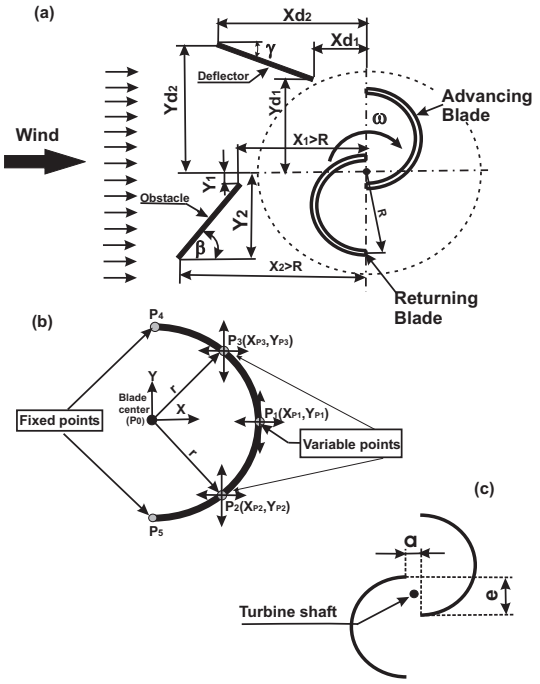

Figure 2. Schematic description of the geometry and free optimization parameters

maximize a user-defined objective function, denoted $OF(V(X_i); X_i)$, where $V(X_i)$ is the solution of the flow equations obtained by Computational Fluid Dynamics (CFD) [13]. In the present paper, the free design variables considered for the optimization will first describe the deflector and obstacle position for classical Savonius turbine. For this purpose, eight parameters are considered ($X_1, Y_1, X_2, Y_2, X_{d1}, Y_{d1}, X_{d2}$ and Y_{d2}), which together are sufficient to obtain clearly the position, length and angles of these guiding plates (see Fig. 2a). In the second step, using an even more aggressive optimization process, we will optimize sixteen parameters simultaneously; eight parameters for guiding plates (same as above), six parameters for describing the blade shape ($X_{p1}, Y_{p1}, X_{p2}, Y_{p2}, X_{p3}$ and Y_{p3}) and two parameters for internal spaces of the turbine, a and e (check all parameters in Fig. 2). The objective function considers only one output of the simulation that should be maximized as far as possible: the output power coefficient C_p. The central goal when designing an improved Savonius turbine is to achieve high efficiency and high power output. Furthermore, it must be kept in mind that turbomachines often operate outside the nominal (or design) conditions. Therefore, after optimizing the configuration for the maximum output power coefficient, known to occur for a speed ratio $\lambda = 0.7$, the full range of useful speed ratios will be considered.

4.1. CFD-based Optimization

An appropriate optimization algorithm must be chosen. A considerable experience is available in our group concerning mathematical optimization relying on CFD evaluations [13]. We therefore employ our own optimization library, OPAL (OPtimization ALgorithms), containing many different optimization techniques. OPAL has already been coupled in the past with different CFD solvers (in-house codes, ANSYS-Fluent, ANSYS-CFX, OpenFOAM) and has been employed successfully to improve a variety of applications, for example heat exchangers [14], burners [15] or turbomachines [3, 12]. Using Evolutionary Algorithms (EA), a very robust procedure can be obtained and local extremal values do not falsify the results. Therefore, the present study relies again on EA. The employed parameters of the algorithm are: a population size in the first generation of 20, a number of generations of 20 for the first case (eight free parameters) and 30 generations for the second case (sixteen free parameters), a survival probability of 50%, average probability 33.3% a crossover probability of 16.7% and a mutation probability of 100% with decreasing mutation amplitude. All further details can be found in [2], where the same procedure has been applied for a simpler configuration.

A fully automatic optimization takes place, using OPAL (decision-maker for the configurations to investigate), the commercial tool Gambit for geometry and grid generation (including quality check) and the industrial CFD code ANSYS-Fluent to compute the flow field around the Savonius turbine. As a result of the CFD computation the output power coefficient is determined, and is stored in a result file. The procedure is automated using journal scripts (Gambit, Fluent) and a master program written in C, calling all codes in the right sequence Fig. 3. By checking the values stored in the result file, OPAL is able to decide how to modify the input parameters, before starting a new iteration. The fully coupled optimization procedure is a complex task, which has been described in detail in previous publications. We thus refer the interested reader to [13] for a complete description of the procedure.

5. NUMERICAL FLOW SIMULATIONS

The optimization procedure can only deliver the right solution, if all evaluations relying on Computational Fluid Dynamics indeed lead to an accurate flow description. From the literature it is known that an accurate CFD simulation of the flow around a Savonius turbine is a challenging task, mainly due to its highly time dependent nature and to the fact that flow separation plays an important role for the efficiency of the system. It is therefore necessary to check the full numerical procedure with great care. Afterwards, the resulting methodology must be validated.

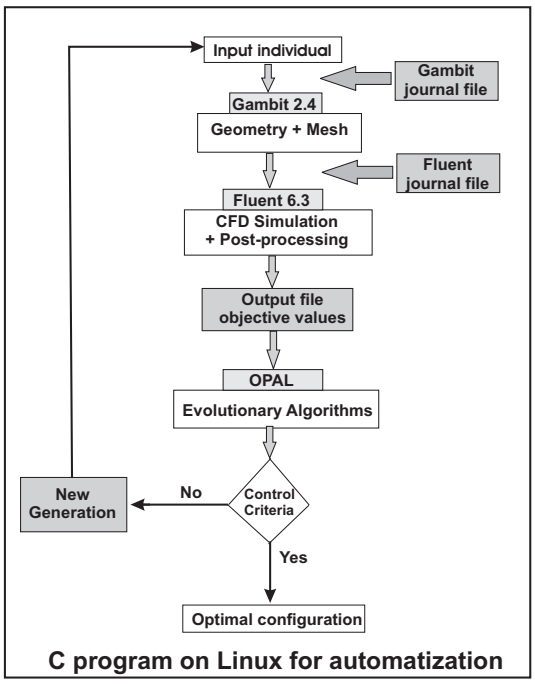

Figure 3. Flow chart for CFD-based optimization using the in-house optimizer OPAL

All flow simulations (denoted also CFD for Computational Fluid Dynamics) presented in this work rely on the industrial software ANSYS-Fluent. The unsteady Reynolds-Averaged Navier-Stokes equations are solved using the SIMPLE (Semi-Implicit Method for Pressure-linked Equations) algorithm for pressure-velocity coupling. The flow variables and all turbulent quantities are discretized in a Finite-Volume formulation using a second-order upwind scheme.

The unsteady flow is solved by using the Sliding Mesh Model (SMM). Three complete revolutions are always computed, using a constant time-step; the first one is used to initiate the correct flow solution, while the flow properties (in particular the power coefficient C_p and the torque coefficient C_m) are obtained by averaging the results during the last two revolutions. It has been checked that the results do not change noticeably by iterating further in time, so that this present combination (one revolution for initializing the flow, plus two revolutions to compute the target function) has been kept throughout (all the details of this selection have been explained in [16, 17]). On a standard PC, one evaluation (i.e., three revolutions for one specific configuration) takes about 270 minutes of computing time.

6. RESULTS AND DISCUSSIONS

Again, CFD-based optimization can only deliver meaningful results, when the CFD evaluations of the different configurations are of sufficient accuracy. Therefore, we first discuss the quality of the CFD model.

6.1. CFD Validation

6.1.1. Grid-independence study

A grid-independence study has been first carried out for one typical geometrical configuration. Several different two-dimensional, unstructured grids of increasing density and quality, composed of $5,000$ up to $120,000$ cells, have been tested for the standard Savonius turbine with specified guiding plates. All grids employing more than $80,000$ cells lead to a relative variation of the output quantity below 1.3% [3]. Since the cost of a CFD evaluation obviously increases rapidly with the number of grid cells, the intermediate grid range between $85,000$ and $95,000$ cells has been retained for all further results shown in the present paper.

6.1.2. Turbulence model selection

In a second step the full numerical procedure and in particular the employed turbulence model have been validated by comparison with published experimental results for a classical Savonius turbine [7]. The influence of the turbulence model is shown in Fig. 4. These results demonstrate the excellent agreement obtained between CFD and experiments for the target function, C_p, when using the realizable $k-\varepsilon$ turbulence model, which is usually recommended for rotating bodies. For the present configuration, two-dimensional simulations are sufficient (no geometry change in the third direction when excluding boundary effects). The employed computational procedure thus appears suitable to predict the performance of the turbine in the investigated range of operation and is now kept for all further simulations.

6.2. Optimization Results

After having checked the accuracy of an individual evaluation relying on CFD, it is now possible to start the optimization procedure. The mathematical optimization procedure described previously (Evolutionary Algorithms relying on automated evaluations through CFD) can now be employed to find the optimal design while taking into account the guiding plates. This is done first for a constant speed ratio $\lambda = 0.7$, considering a fixed incident wind velocity $U = 10$ m/s. This value of λ is retained since it is known from the literature that it corresponds to the zone of peak power coefficient of the conventional Savonius turbine. As explained previously, eight degrees of freedom are first considered simultaneously for the optimization (Fig. 2a). In the second step, and in addition to the eight free parameters of the guiding plates, the blade shape is described by five points; two fixed points (P_4 and P_5) and three movable points (P_1, P_2, P_3). Each point has two coordinates (X_{Pi}, Y_{Pi}) this means we have another six free parameters (X_{P1}, Y_{P1}, X_{P2}, Y_{P2}, X_{P3} and Y_{P3}) (Fig. 2b). Knowing all 5 points, the full blade profile is reconstructed using standard splines (Nonuniform rational B-splines,

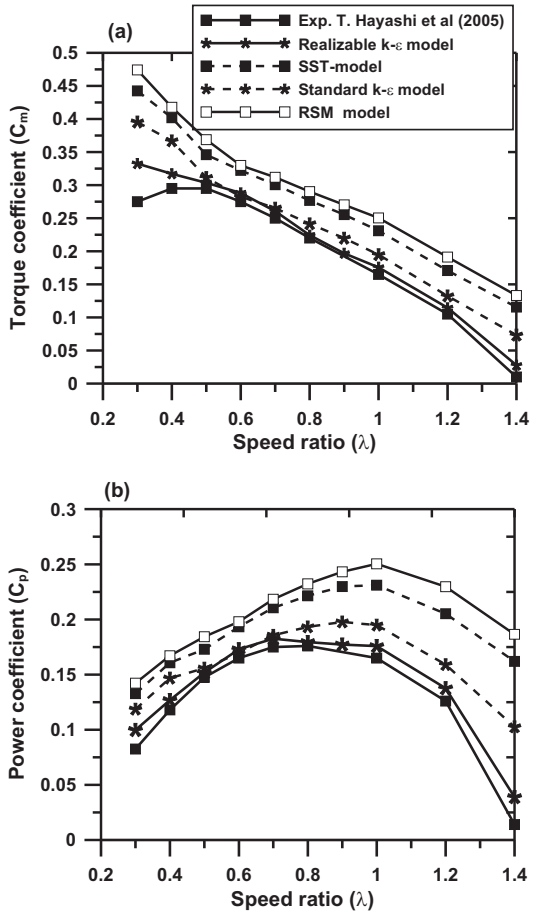

Figure 4. Validation of computational model: a) torque coefficient, b) power coefficient, both compared to published experimental results for a conventional Savonius turbine [7]

NURBS). The order of a NURBS curve defines the number of nearby control points that influence any given point on the curve. The curve is represented mathematically by a polynomial of degree one less than the order of the curve; this means that the spline order is 5 in our case and the degree of the polynomial is 4. Another two free space parameters that describe the internal spaces of the turbine are incorporated in the second step as well (Fig. 2c), leading to sixteen free parameters.

The parameter spaces considered in the optimization are documented in Table 1. These domains are selected to prevent any domain overlap along the X or Y-directions and to keep realistic blade shapes. During the calculations, a circular turbine shaft is included with a fixed radius R_{sh} computed in a standard manner from $R_{sh}/d = 0.029$.

The results presented in Fig. 5a indicate that the considered objective is indeed considerably influenced by the eight first free parameters and thus by the positions, angles and lengths of the guiding plates. As a whole, 210 different geometrical settings have been evaluated by CFD, during 40 days of total computing time on a standard PC. However, the results of Fig. 5b indicate as expected an even larger impact when considerind sixteen free parameters. There, 310 different geometrical settings have been investigated by CFD, requesting two months of total computing time on a standard PC. Note that the user-waiting time could be considerably reduced by carrying out the requested CFD in parallel on a PC cluster [13]. Such a parallel procedure, already implemented in OPAL, has not been used in the present case but could reduce the needed time by orders of magnitude, as demonstrated in other studies.

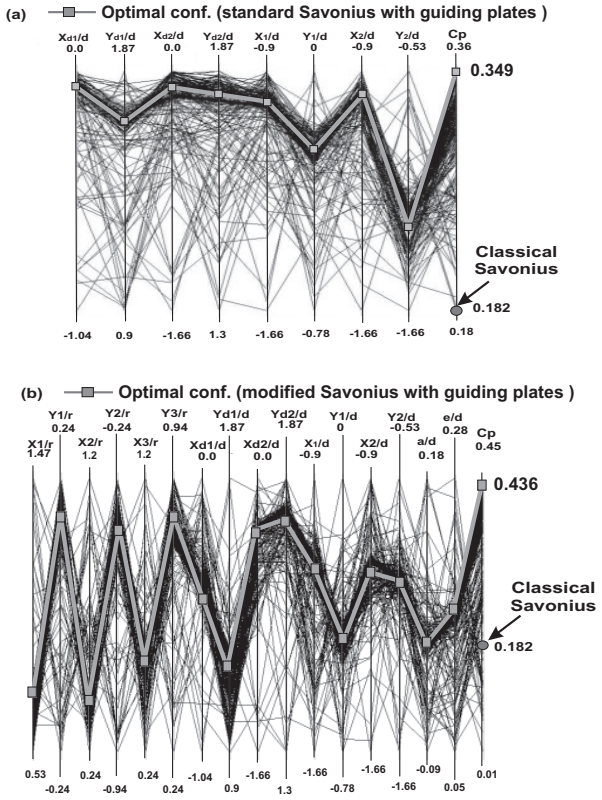

Figure 5. Input parameters of the optimization and power coefficient represented using parallel coordinates. The parameters of the optimal designs are connected with a thick gray line. The power coefficient of the conventional turbine is shown with a gray circle; a) eight free parameters b) sixteen free parameters

The optimal configuration (highest point in the right column in Fig. 5a and Fig. 5b, all corresponding parameters being connected by a thick gray line) can now readily be identified for $\lambda = 0.7$. The optimum parameters are listed in Table 2. In Table 3 the resulting angles and lengths of the guiding plates are summarized.

At $\lambda = 0.7$ the optimal points found by the optimization procedure correspond to an absolute increase of the power coefficient by 0.167 (resp. 0.254) for the first step (resp. second step)

Table 1. Acceptable range for the input parameters (parameter spaces)

	8 free parameters		16 free parameters	
Parameter	Minimum	Maximum	Minimum	Maximum
Blade shape				
X_{P1}/r	–	–	0.53	1.47
Y_{P1}/r	–	–	−0.24	0.24
X_{P2}/r	–	–	0.24	1.2
Y_{P2}/r	–	–	−0.94	−0.24
X_{P3}/r	–	–	0.24	1.2
Y_{P3}/r	–	–	0.24	0.94
Guiding plates				
X_{d1}/d	−1.04	0	−1.04	0
Y_{d1}/d	0.9	1.87	0.9	1.87
X_{d2}/d	−1.66	0	−1.66	0
Y_{d2}/d	1.3	1.87	1.3	1.87
X_1/d	−1.66	−0.9	−1.66	−0.9
Y_1/d	−0.78	0	−0.78	0
X_2/d	−1.66	−0.9	−1.66	−0.9
Y_2/d	−1.66	−0.53	−1.66	−0.53
Internal spaces				
a/d	–	–	−0.09	0.18
e/d	–	–	0.05	0.28

Table 2. Optimum parameter values

Parameter	**8 parameters**	**16 parameters**
Blade shape		
X_{P1}/r	–	0.54822
Y_{P1}/r	–	0.19762
X_{P2}/r	–	0.34849
Y_{P2}/r	–	−0.37885
X_{P3}/r	–	0.54593
Y_{P3}/r	–	0.770346
Guiding plates		
X_{d1}/d	-0.066981	−0.41882
Y_{d1}/d	1.509671	1.24505
X_{d2}/d	-0.17377	−0.3433
Y_{d2}/d	2.28434	2.29074
X_1/d	-1.134209	−1.2828
Y_1/d	-0.286166	−0.4037
X_2/d	-1.0892	−1.27654
Y_2/d	-1.37918	−1.16339
Internal spaces		
a/d	–	−0.00635
e/d	–	0.18286

of the optimization procedure, as shown in Fig. 5. This means a relative increase of the performance (measured by the power output coefficient) by 47.8% for the conventional Savonius rotor with guiding plates and by 58.3% for the modified design.

Note that this new shape of blades (Fig. 6b) is only optimum in combination with the employed guiding plates. Indeed, the modified shape exploits best the flow redirection induced by the two plates. As a consequence, the reverse moment is reduced

Table 3. Optimum angles and lengths for the guiding plates

	8 free parameters		**16 free parameters**	
	Obstacle	**Deflector**	**Obstacle**	**Deflector**
$\beta_{opt.}$	92.35°	-	90.41°	-
$\gamma_{opt.}$	-	82.15°	-	94.13°
$\frac{Lo}{d}$	1.094	-	0.7597	-
$\frac{Ld}{d}$	-	0.782	-	1.048

by the shielding obstacle and the flow has been redirected by the deflector to the advancing blade; simultaneously, the modified shape leads to an increase of the positive moment of the advancing blade.

6.3. Off-design performance

It is now important to check how this gain would change as a function of λ, since such a turbine must be able to work also for off-design conditions. Therefore, the performance of the optimal configurations has been finally computed for the full range of useful λ-values, as shown in Fig. 7. This figure demonstrates that the improvement of both torque coefficient and power output coefficient is observed throughout for all values of λ, compared to the conventional Savonius turbine. The absolute gain for C_p and C_m is even higher for lower λ-values. The relative performance increase compared to the classical Savonius configuration is always higher than 35% in the effective operating range.

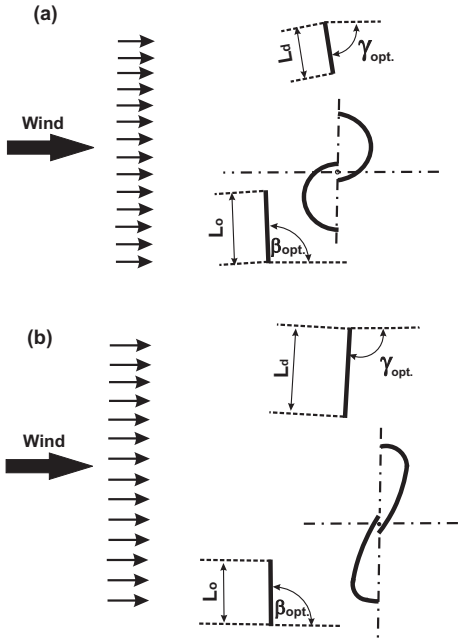

Figure 6. Optimum configurations; a) classical Savonius with guiding plates, b) modified Savonius with guiding plates

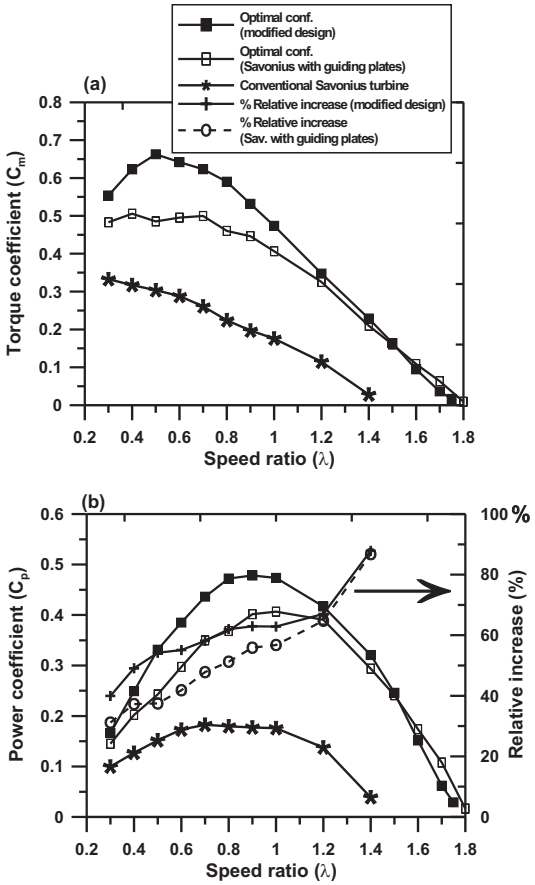

Figure 7. Performance of the optimized configurations (black and empty squares) compared to the conventional Savonius turbine without guiding plates (black star): a: torque coefficient; b: power coefficient. The corresponding relative increase compared to the standard configuration is shown with black plus for the modified design and empty circle for Savonius with guiding plates

7. CONCLUSIONS

This work investigates the optimal aerodynamic performance of modified Savonius turbines using numerical simulations. The standard Savonius turbine is a promising concept for small-scale wind-energy systems, but suffers from a poor efficiency. Therefore, the major objective of the present study was to develop an improved design, leading to higher values of the power coefficient and thus a higher efficiency.

For this purpose, guiding plates have been first introduced to redirect the flow to the advancing blade of a conventional Savonius (semi-cylindrical shape). In a second step, guiding plates, the blade shape (skeleton line) and turbine internal spaces have been optimized simultaneously to get the optimal design derived from a Savonius turbine.

The unsteady solution for the turbulent flow is obtained by accurate CFD simulations. A validation against published experimental measurements has demonstrated that the employed numerical procedure relying on the realizable $k - \varepsilon$ turbulence model can be employed for a quantitative analysis of the performance, provided a sufficiently fine grid is used.

The two cases have been optimized in a fully automatic manner, in order to obtain the best possible performance, as measured by the power coefficient C_p. The optimization relies on Evolutionary Algorithms, while all geometrical configurations are evaluated by CFD. This optimization procedure is able to identify considerably better configurations than the conventional Savonius turbine, leading in particular at $\lambda = 0.7$ to a relative increase of the power output coefficient by 47.8% and 58.3% for Savonius and modified Savonius with guiding plates, respectively. A performance gain of at least 35% is found for the full operating range ($0.3 \leq \lambda \leq 1.4$). This positive effect is also observed for the torque coefficient. The absolute performance of the modified design is higher than the conventional Savonius turbine with guiding plates until $\lambda \simeq 1.2$. Afterwards, the performance becomes approximately similar. As a whole, these optimal configurations appear to be very promising for wind energy generation, in particular in urban areas or developing countries.

References

[1] Menet, J., 2004, "A double-step Savonius rotor for local production of electricity: A design study", *J. Renewable Energy*, Vol. 29, pp. 1843-1862.

[2] Mohamed, M.H., Janiga G., Pap E. and Thévenin, D., 2010, "Optimization of Savonius turbines using an obstacle shielding the returning blade", *J. Renewable Energy*, Vol. 35, pp. 2618-2626.

[3] Mohamed, M.H., Janiga, G., Pap, E. and Thévenin, D., 2009, "Optimal performance of a Savonius turbine using frontal guiding plates", *In Proc. 14th Int. Conference on Modelling Fluid Flow (CMFF'09)*, Budapest, Hungary, pp. 871-879.

[4] Gupta, R., Biswas, A. and Sharma, K.K., 2008, "Comparative study of a three-bucket Savonius rotor with a combined three-bucket Savonius-three-bladed Darrieus rotor", *J. Renewable Energy*, Vol. 33, pp. 1974-1981.

[5] Altan, B.D. and Atýlgan, M., 2008, "An experimental and numerical study on the improvement of the performance of Savonius wind rotor", *Energy Convers. Manage.*, Vol. 49, pp. 3425-3432.

[6] Afungchui, D., Kamoun, B., Helali, A., Djemaa, A., 2010, "The unsteady pressure field and the aerodynamic performances of a Savonius rotor based on the discrete vortex method", *J. Renewable Energy*, Vol. 35, pp. 307-313.

[7] Irabu, K. and Roy, J.N., 2007, "Characteristics of wind power on Savonius rotor using a guide-box tunnel", *Exper. Thermal Fluid Sci.*, Vol. 32, pp. 580-586.

[8] Kamoji, M.A., Kedare, S.B. and Prabhu, S.V., 2009, "Performance tests on helical Savonius rotors", *J. Renewable Energy*, Vol. 34, pp. 521-529.

[9] Saha, U.K. and Rajkumar, M.J., 2006, "On the performance analysis of Savonius rotor with twisted blades", *J. Renewable Energy*, Vol. 31, pp. 1776-1788.

[10] Saha, U.K., Thotla, S. and Maity, D., 2008, "Optimum design configuration of Savonius rotor through wind tunnel experiments", *J. Wind Engineer. Indust. Aerodyn.*, Vol. 96, pp. 1359-1375.

[11] Hayashi, T., Li, Y. and Hara, Y., 2005, "Wind tunnel tests on a different phase three-stage Savonius rotor", *JSME Int. J. Series B: Fluids Thermal Engineer.*, Vol. 48, pp. 9-16.

[12] Mohamed M.H., Janiga G., Pap E. and Thévenin D. "Optimal blade shape of a modified Savonius turbine using an obstacle shielding the returning blade", *Energy Convers. Manage.*, 2011, Vol. 52, 236-242.

[13] Thévenin, D. and Janiga, G., 2008, *Optimization and Computational Fluid Dynamics*, Springer-Verlag, Berlin, Heidelberg.

[14] Hilbert, R., Janiga, G., Baron, R. and Thévenin, D., 2006, "Multiobjective shape optimization of a heat exchanger using parallel genetic algorithms", *Int. J. Heat Mass Transf.*, Vol. 49, pp. 2567-2577.

[15] Janiga, G. and Thévenin, D., 2007, "Reducing the CO emissions in a laminar burner using different numerical optimization methods", *J. Power Energy*, Vol. 221, pp. 647-655.

[16] Mohamed, M.H. and Thévenin,D., 2008, "Performance optimization of a Savonius Turbine Considering Different Shapes for Frontal Guiding Plates", *Tenth International Congress of Fluid Dynamics ASME-ICFDP9, (ICFD10-EG-3026)*, Ain Soukhna, Red Sea, Egypt.

[17] Mohamed, M.H., Janiga, G., Pap, E. and Thévenin, D., 2010, "Optimal Performance of a Modified Three-Blade Savonius Turbine Using Frontal Guiding Plates", *In ASME Turbo Expo Conference*, (GT2010-22538), Scotland, UK.

Workshop
Boundary layer problems, similarity solutions

Conference on Modelling Fluid Flow (CMFF'12)
The 15th International Conference on Fluid Flow Technologies
Budapest, Hungary, September 4-7, 2012

THERMAL BOUNDARY LAYER MODEL OF A NON-NEWTONIAN FLUID OVER MOVING SURFACE WITH A CONVECTIVE SURFACE BOUNDARY CONDITION

Gabriella BOGNÁR[1]

[1] Corresponding Author. Department of Analysis, University of Miskolc, H-3515 Miskolc-Egyetemváros, Hungary. Tel.: +36 46 565111, E-mail: matvbg@uni-miskolc.hu

ABSTRACT

In this paper the classical problem of the steady laminar boundary layer over a moving flat plate in a uniform stream of fluid with convective surface boundary condition is investigated. Both Newtonian and power-law type non-Newtonian fluids are considered. Our aim is to investigate the case when similarity solutions to the hydrodynamic and thermal boundary layers exist. The effect of the parameters on the numerical solutions to the velocity and temperature profiles is examined.

Keywords: boundary layer, convective surface boundary condition, moving surface, non-Newtonian fluid

NOMENCLATURE

$\bar{a}$	convective parameter
f	dimensionless stream function
h_f	heat transfer coefficient
k	thermal conductivity
K	consistency index
n	power-law index
Pr	Prandtl number
Re	local Reynolds number
T	fluid temperature
T_f	hot fluid temperature
T_w	plate temperature
T_∞	ambient temperature
u, v	velocity components along the x and y directions, respectively
U_∞	free stream velocity
x, y	Cartesian coordinates along the plate and normal to it, respectively

Greek symbols

α_t	thermal diffusivity
η	similarity variable
Θ	dimensionless temperature
ρ	fluid density
τ_{xy}	shear stress
ω	positive constant
ψ	stream function

1. INTRODUCTION

The convection flow over a moving plate in a moving fluid has many practical engineering applications such as the cooling of polymer films or sheets and metallic plates on conveyers. Klemp and Acrivos [19] demonstrated a method for integrating the boundary layer equations through a region of reverse flow and applied it to the problem of uniform flow past a parallel flat plate of finite length whose surface has a constant velocity directed opposite to that of the main stream. Similar problems were then considered by Abdelhafez [2], Hussaini, Lakin and Nachman [16], Riley and Weidman [22], Chappidi and Gunnerson [11], Afzal, Badaruddin and Elgarvi [3], Lin and Huang [21], Weidman et al. [24] and Ishak, Nazar, Arifin and Pop [17] among others. The above-mentioned papers confined the problems to Newtonian fluids. Many practical situations demand for fluids that are non-Newtonian in nature such as molten plastics, polymeric liquids, food stuffs and slurries.

Our goal is to investigate the similarity solutions for the steady laminar boundary layer flow of a Newtonian or non-Newtonian fluid over a permeable flat plate in a uniform free stream when the bottom surface of the plate is heated by convection from a hot fluid. We study the boundary layer flow over a moving plate in Ostwald-de-Waele type of non-Newtonian fluids. We show that similarity solutions to the hydrodynamic and

thermal boundary layers are possible if the convective heat transfer associated with the hot fluid on the lower surface of the plate is proportional to a power function of *x*, where *x* is the distance from the leading edge of the solid surface. The equations of momentum and energy are transformed into a system of ordinary differential equations. Numerical solutions are provided and the effects of the parameters are examined on the flow and thermal fields.

2. NEWTONIAN FLUID FLOWS

First we consider a steady, two-dimensional laminar flow of a viscous fluid over a flat plate in a stream of fluid at temperature T_∞ moving over the top surface of the plate with a uniform velocity U_∞. The plate is moving with constant velocity U_w in the same or opposite direction to the free stream. The *x*-axis extends parallel to the surface, while the *y*-axis extends upwards, normal to the surface.

2.1. The Basic Equations

The governing equations are [xx]

$$\frac{\partial u}{\partial x}+\frac{\partial v}{\partial y}=0, \tag{1}$$

$$u\frac{\partial u}{\partial x}+v\frac{\partial u}{\partial y}=\frac{1}{\rho}\frac{\partial \tau_{xy}}{\partial y}, \tag{2}$$

$$u\frac{\partial T}{\partial x}+v\frac{\partial T}{\partial y}=\frac{\partial}{\partial y}\left(\alpha_t\frac{\partial T}{\partial y}\right), \tag{3}$$

where u, v are the velocity components along x and y coordinates, respectively, T is the temperature of the fluid in the boundary layer. Furthermore, for Newtonian fluids the relation between the shear stress and the shear rate is formulated by $\tau_{xy}=\mu\frac{\partial u}{\partial y}$. It is assumed that the bottom surface of the plate is heated by convection from a hot fluid of uniform temperature T_f which provides a heat transfer coefficient h_f. The boundary conditions for the flow field are

i. on the plate surface (no slip and impermeable surface):

$$u(x,0)=-U_w, \tag{4}$$

$$v(x,0)=0, \tag{5}$$

$$-k\frac{\partial T}{\partial y}=h_f(T_f-T_w) \quad \text{at } y=0 \tag{6}$$

where h_f is the heat transfer coefficient, and k denotes the thermal conductivity;

ii. matching with the free stream as $y\to\infty$:

$$u(x,\infty)=U_\infty, \tag{7}$$

$$T(x,\infty)=T_\infty. \tag{8}$$

If T_w denotes the uniform temperature over the top surface of the plate we have the relations: $T_f>T_w>T_\infty$.

The continuity equation (1) is satisfied by introducing a stream function such that

$$u=\frac{\partial \psi}{\partial y} \quad \text{, and} \quad v=-\frac{\partial \psi}{\partial x}.$$

The momentum and energy equations can be transformed into a system of ordinary differential equations by the following transformation

$$\eta=\gamma^{-\frac{1}{2}}(U_\infty)^{\frac{1}{2}}yx^{-\frac{1}{2}},$$

$$\psi(x,y)=\gamma^{\frac{1}{2}}(U_\infty)^{\frac{1}{2}}x^{\frac{1}{2}}f(\eta),$$

$$\Theta(\eta)=\frac{T-T_\infty}{T_f-T_\infty},$$

where $\gamma=\mu/\rho$, η is the similarity variable, $f(\eta)$ is the dimensionless stream function, $\Theta(\eta)$ is the dimensionless temperature. The transformed system of ordinary differential equations is the following:

$$f'''+\frac{1}{2}ff''=0, \tag{9}$$

$$\Theta''(\eta)+\frac{Pr}{2}f(\eta)\Theta'(\eta)=0, \tag{10}$$

where $Pr=\frac{\gamma}{\alpha_t}$ is the Prandtl number. The boundary conditions (4), (5) and (7) are transformed to the following forms:

$$\begin{aligned} &f'(0)=-\lambda,\\ &f(0)=0,\\ &f'(\infty)=\lim_{\eta\to\infty}f'(\eta)=1, \end{aligned} \tag{11}$$

where the prime denotes the differentiation with respect to the similarity variable η, and the velocity ratio parameter is $\lambda = U_w / U_\infty$. Equation (5) is called the Blasius equation. It should be noted that for $\lambda > 0$, the fluid and the plate move in the opposite directions, while they move in the same directions if $\lambda < 0$. The boundary conditions for the thermal field can be formulated as

$$\Theta'(0) = -\bar{a}(1 - \Theta(0)),$$
$$\Theta(\infty) = \lim_{\eta \to \infty} \Theta(\eta) = 0 \qquad (12)$$

under the assumption that the heat transfer coefficient $h_f = cx^{-1/2}$ and $\bar{a} = \frac{c}{k}\left(\frac{\gamma}{U_\infty}\right)^{\frac{1}{2}}$. We note that for Newtonian fluids it was shown in [5, 6, 18] that similarity solutions exist if h_f is proportional to $x^{-1/2}$.

The dimensionless velocity components can be written in the form

$$u(x, y) = U_\infty f'(\eta),$$
$$v(x, y) = \frac{U_\infty}{2} Re_x^{-\frac{1}{2}} (\eta f'(\eta) - f(\eta))$$

and $\eta = Re_x^{\frac{1}{2}} \frac{y}{x}$, where $Re_x = \frac{U_\infty x \rho}{\mu}$ denotes the local Reynolds number.

For $\lambda = 0$ the boundary value problem (9), (11) is the well known Blasius problem. Although this is almost a century old, it is still a topic of active current research (see [1, 4, 10, 12-15, 20, 23]).

The second boundary value problem (10), (12) is to be solved for Θ for different values of parameters Pr and $\bar{a}$.

2.2. Numerical Reslts

We obtained the numerical results using the symbolic algebra software Maple 12. The boundary value problem has been solved by the Runge-Kutta-Felhberg fourth-fifth method for certain values of parameters Pr and $\bar{a}$. Fig. 1 and Fig. 2-3 exhibit the Maple generated numerical solution for the velocity profile and temperature profiles, respectively.

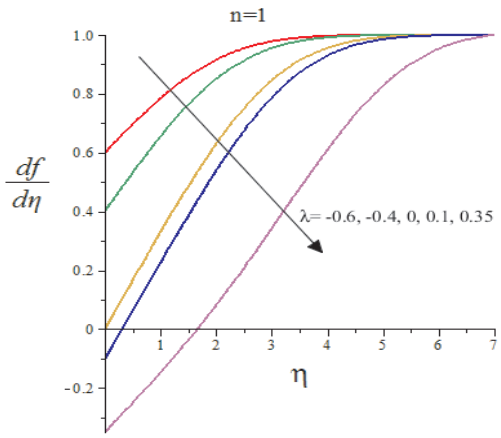

Figure 1. Similarity velocity profiles $f'(\eta)$ $(u(x, y) = U_\infty f'(\eta))$

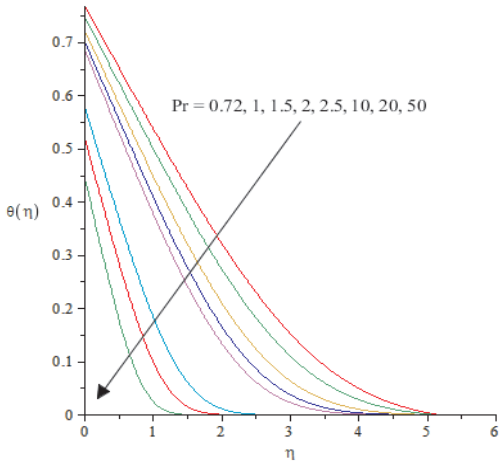

Figure 2. Similarity velocity profiles $\Theta(\eta)$ **for** $\bar{a} = 1$

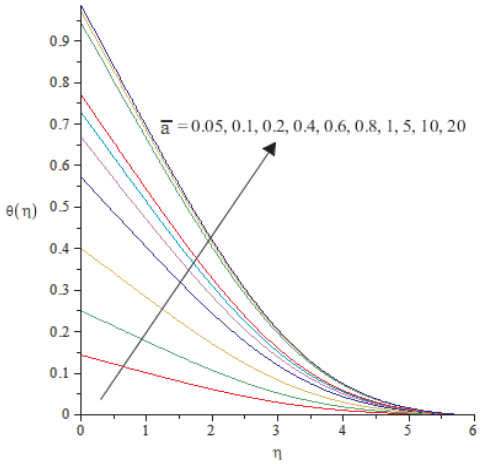

Figure 3. Similarity velocity profiles $\Theta(\eta)$ **for** Pr=0.72

3. NON- NEWTONIAN FLUID FLOWS

In this section, it is assumed that the flow behaviour of a non-Newtonian fluid is described by the Ostwald-de Waele power law model, where the shear stress is related to the strain rate $\frac{\partial u}{\partial y}$ by the expression

$$\tau_{xy} = K\left|\frac{\partial u}{\partial y}\right|^{n-1}\frac{\partial u}{\partial y},$$

where K is the consistency index for non-Newtonian viscosity. Here, n is called power-law index, that is $n<1$ for pseudoplastic, $n=1$ for Newtonian, and $n>1$ for dilatant fluids.

3.1. The Basic Equations

We consider the steady laminar incompressible convection boundary layer flows over a horizontal flat plate moving with uniform velocity U_∞. The governing equations of motion and the energy equations describing the flow can be written by (1)-(3). In equation (3) the thermal diffusivity α_t can be defined as $\alpha_t = \omega\left|\frac{\partial u}{\partial y}\right|^{n-1}$ for $u\neq 0$ (ω positive constant) and $\alpha_t = 0$ for $u=0$ (see [25]). Here the similarity variable η, the dimensionless stream function $f(\eta)$ and the dimensionless temperature $\Theta(\eta)$ are introduced by

$$\eta = \gamma^{-\frac{1}{n+1}}(U_\infty)^{\frac{2-n}{n+1}}\, y\, x^{-\frac{1}{n+1}},$$

$$\gamma = \frac{K}{\rho},$$

$$\psi(x,y) = \gamma^{\frac{1}{n+1}}(U_\infty)^{\frac{2n-1}{n+1}}\, x^{\frac{1}{n+1}} f(\eta),$$

$$\Theta(\eta) = \frac{T-T_\infty}{T_f - T_\infty}.$$

Now, the dimensionless velocity components can be written in the form

$$u(x,y) = U_\infty f'(\eta),$$

$$v(x,y) = \frac{U_\infty}{n+1}Re_x^{-\frac{1}{n+1}}(\eta f'(\eta) - f(\eta)).$$

and $\eta = Re_x^{\frac{1}{n+1}}\frac{y}{x}$, where the local Reynolds number $Re_x = \frac{U_\infty^{2-n}x^n}{\gamma}$.

Similarly, for the dimensionless stream function and the dimensionless temperature the equations (1)-(3) reduce to

$$\left(|f''|^{n-1}f''\right)' + \frac{1}{n+1}f\,f'' = 0 \qquad (13)$$

$$\left(|f''(\eta)|^{n-1}\Theta'(\eta)\right)' + \frac{Pr}{n+1}f(\eta)\Theta'(\eta) = 0 \qquad (14)$$

with boundary conditions (11) and (12) under the assumption that the heat transfer coefficient is $h_f = cx^{-1/(n+1)}$ and $\bar{a} = \frac{c}{k}\left(\frac{\gamma}{U_\infty^{2-n}}\right)^{\frac{1}{n+1}}$.

Equation (13) is called the generalized Blasius equation [7, 9].

3.2. Numerical Results

The solution to (13), (11) for different values of λ are shown in Fig. 4. Fig. 5 exhibits the velocity profiles when the plate moves in the opposite direction as the direction of the fluid flow. The effect of power exponent n for $f'(\eta)$ is demonstrated in Fig. 6.

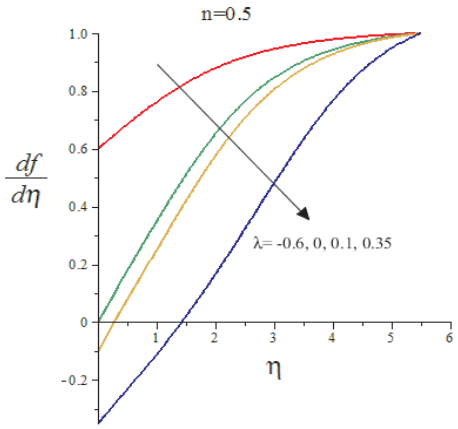

Figure 4. Similarity velocity profiles $f'(\eta)$ ($u(x,y) = U_\infty f'(\eta)$) for *n=0.5*

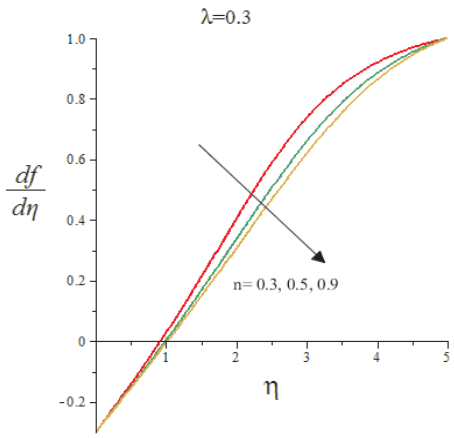

Figure 5. Similarity velocity profiles $f'(\eta)$ for $\lambda = 0.3$

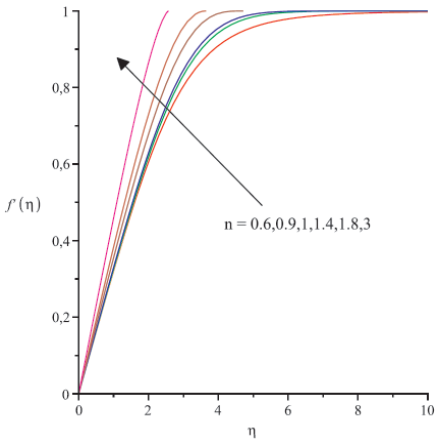

Figure 6. Similarity velocity profiles $f'(\eta)$ for different values of n

The solution for $f(\eta)$, which can be obtained numerically, represents then the solution for the problem of uniform flow past a semi-infinite flat plate with a negative surface velocity relative to the free stream. It is found that $f'(\eta)$ increases monotonically from $-\lambda$ to unity with increasig η. The profiles for $f''(\eta)$, being proportional to the shear stress have a more unusual shape, as shown in Fig. 7-8.

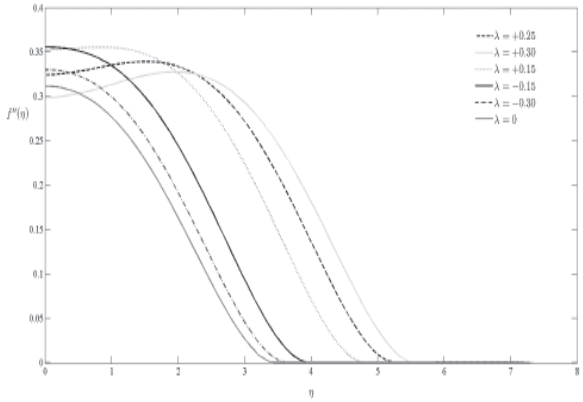

Figure 7. Shear stress profiles for various λ when $n = 1.5$

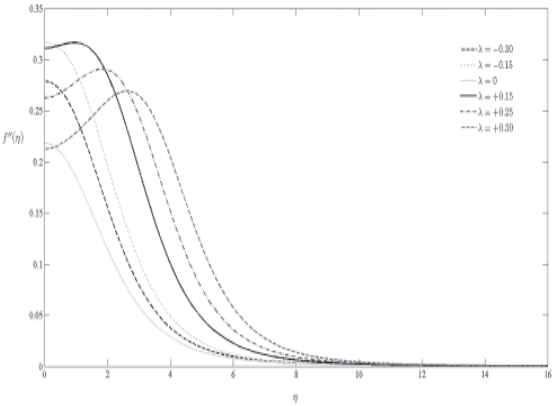

Figure 8. Shear stress profiles for various λ when $n = 0.5$

For non-Newtonian fluids the numerical calculations also show that there is a critical value λ_c for any fixed n such that solution exists only if $\lambda \le \lambda_c$ [8]. The variations of $f''(0)$ and λ_c with λ for different values of n are given in [5]. The determination of $f''(0)$ is important since it has a physical meaning: *drag force* or force due to *skin friction*. It is a fluid dynamic resistive force which is a consequence of the fluid and the pressure distribution on the surface of the object. The *skin friction parameter* $f''(0)$ originates from the non-dimensional *drag coefficient*

$$C_D = (n+1)^{\frac{1}{n+1}} Re^{\frac{-n}{n+1}} [f''(0)]^n .$$

The influences of λ and n on the skin friction parameter are represented in Fig.9. If $\lambda > 0$, Hussaini and Lakin [16] proved that there is a critical value λ_c such that solution exists only if $\lambda \le \lambda_c$. Dual solutions exist for $0 < \lambda < \lambda_c$. The effect of parameter n is presented on the velocity profiles in Fig. 10.

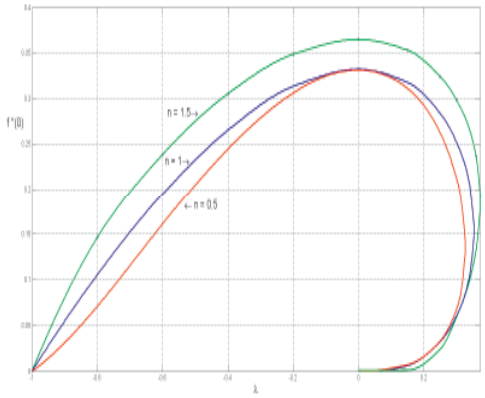

Figure 9. The variation of $f''(0)$ with λ for different values of *n*

Next we examine the effects of the parameters Pr and $\bar{a}$ for $\Theta(\eta)$ in Fig. 11-14.

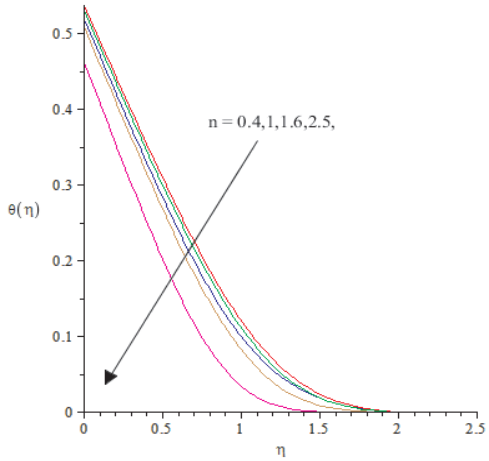

Figure 10. Similarity velocity profiles $\Theta(\eta)$ for Pr=10, $\bar{a} = 0.3$

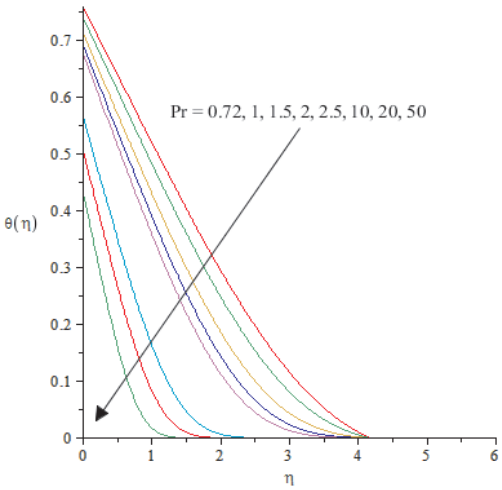

Figure 11. Similarity velocity profiles $\Theta(\eta)$ for $n = 1.2$, $\bar{a} = 1$

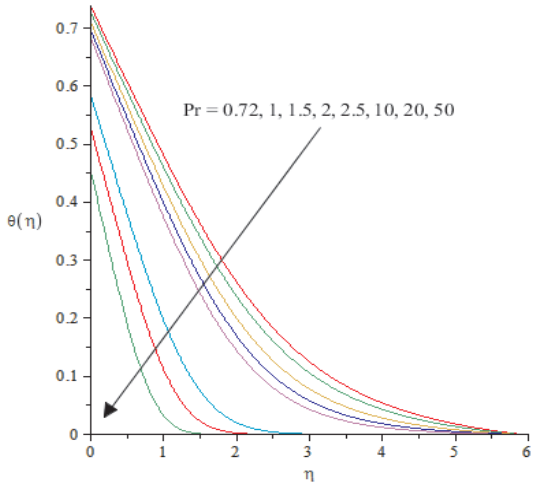

Figure 12. Similarity velocity profiles $\Theta(\eta)$ for $n = 0.4$, $\bar{a} = 1$

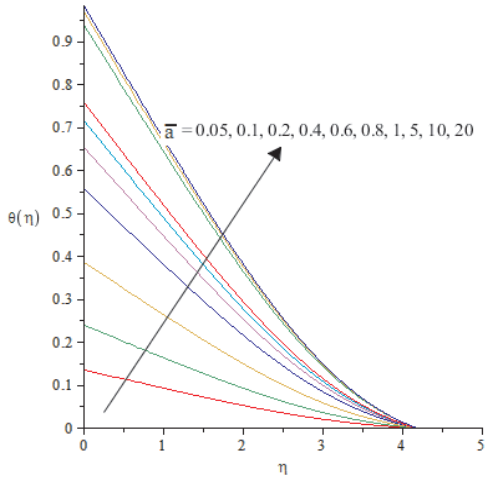

Figure 13. Similarity velocity profiles $\Theta(\eta)$ for $n = 1.2$, Pr=0.72

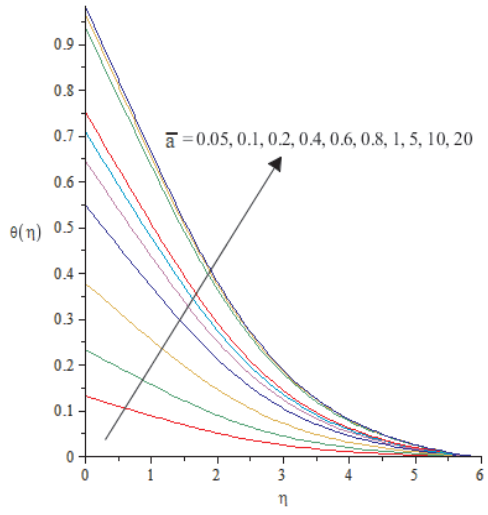

Figure 14. Similarity velocity profiles $\Theta(\eta)$ for $n = 0.5$, Pr=0.72

5. CONCLUSIONS

The numerical solutions exhibit that the velocity gradient is increasing when n is increasing and the plate surface temperature decreases as either Pr or n increases and also when $\overline{a}$ decreases. The temperature gradient at the surface increases as Pr increases, which implies an increase in the heat transfer rate at the surface. We observe that the thermal boundary layer thickness decreases with increasing Prandtl number or increasing power index n, moreover the hydrodynamic boundary layer thickness decreases as n increases. There is no effect of $\overline{a}$ on the thermal boundary layer thickness.

ACKNOWLEDGEMENTS

The described work was carried out as part of the TÁMOP-4.2.2/B-10/1-2010-0008 project in the framework of the New Hungarian Development Plan. The realization of this project is supported by the European Union, co-financed by the European Social Fund.

REFERENCES

[1] Abbasbandy, S., 2007, "A numerical solution of Blasius equation by Adomian's decomposition method and comparison with homotopy perturbation method" *Chaos Solitons Fractals,* Vol. 31, pp. 257–260.

[2] Abdelhafez, T.A., 1985, "Skin friction and heat transfer on a continuous flat surface moving in a parallel free stream" *Int. J. Heat Mass Transfer* 28, pp. 1234-1237.

[3] Afzal,N., Badaruddin, A., Elgarvi A.A., 1993, "Momentum and heat transport on a continuous flat surface moving in a parallel stream", *Int. J. Heat Mass Transfer*, Vol. 36, pp. 3399-3403.

[4] Ahmad, F., 2007, "Degeneracy in the Blasius problem" *Electron J. Differ. Equations*, Vol. 92, pp. 1–8.

[5] Aziz A., 2009, "A similarity solution for laminar thermal boundary layer over a flat plate with a convective surface boundary condition" *Comm. Nonlinear Sci. Numer. Simulat.* Vol. 14, pp. 1064-1068.

[6] Bataller R.C., 2008, "Radiation effects for the Blasius and Sakiadis flows with a convective surface boundary condition" *Appl. Math. Comput.* Vol. 206, pp. 832–840.

[7] Bognár, G., 2009, "Similarity solution of a boundary layer flow for non-Newtonian fluids" *Int. J. Nonlin. Scie. Numer. Simulation*, Vol. 10, pp. 1555-1566.

[8] Bognár, G., 2011, "On similarity solutions to boundary layer problems with upstream moving wall in non-Newtonian power-law fluids" *IMA J. Applied Mathematics,* 2011, pp. 1–17 doi:10.1093/imamat/hxr033

[9] Bognár, G., 2011, "Analytic Solutions to a Boundary Layer Problem for Non-Newtonian Fluid Flow Driven by Power Law Velocity Profile" *WSEAS Transactions on Fluid Mechanics*, Vol. 6, pp. 22-31.

[10] Boyd, J.P., 2008, "The Blasius function: Computations before computers, the value of tricks, undergraduate projects, and open research problems" *SIAM Review,* Vol. 50, pp. 791-804.

[11] Chappidi, P.R., Gunnerson F.S., 1989, "Analysis of heat and momentum transport along a moving surface" Int. *J. Heat Mass Transfer* Vol. 32, pp. 1383-1386.

[12] Cortell, R., 2005, "Numerical solution of the classical Blasius flat-plate problem" *Appl Math Comput* Vol. 170, pp. 706–10.

[13] Fang, T., Guo, F., Lee, C.F., 2006, "A note on the extended Blasius problem" *Appl Math Lett.* Vol. 19, pp. 613–617.

[14] He, J. H., 1999, "Approximate analytical solution of Blasius' equation" *Commun. Nonlinear Sci. Numer. Simulation,* Vol. 4, pp. 75–78.

[15] He, J. H., 2003, "A simple perturbation approach to Blasius equation" *Appl. Math. Comput.,* Vol. 140, pp. 217–222.

[16] Hussaini, M.Y., Lakin, W.D., Nachman, A., 1987, "On similarity solutions of a boundary layer problem with an upstream moving wall" *SIAM J. Appl. Math.* Vol. 47, pp. 699-709.

[17] Ishak, A., Nazar, R., Pop, I., 2007, "Boundary layer flow over a continuously moving thin needle in a parallel free stream" *Chin. Phys. Lett.* Vol..24, pp. 2895-2897.

[18] Ishak A., 2010, "Similarity solution for flow and heat transfer over a permeable surface with convective boundary condition" *Appl. Math. Comput.* Vol. 217, pp. 837-842.

[19] Klemp, J.B., Acrivos, A., 1972, "A method for integrating the boundary-layer equations through a region of reverse flow" *J. Fluid Mech.* Vol. 53, pp. 177-191.

[20] Liao, S.-J., 1999, "An explicit, totally analytic, solution for Blasius viscous flow problems" *Int. J. Non-Lin. Mech.* Vol. 34, pp. 758–778.

[21] Lin, H.S., Huang, S.F., 1994, "Flow and heat transfer of plane surfaces moving in parallel

and reversely to the free stream" *Int. J. Heat Mass Transfer* Vol. 37, pp. 333-336.

[22] Riley, N., Weidman, P.D., 1989, "Multiple solutions of the Falkner-Skan equation for flow past a stretching boundary" *SIAM J. Appl. Math*. Vol. 49, pp. 1350-1358.

[23] Wang, L., 2004, "A new algorithm for solving classical Blasius equation" *Appl Math Comput*. Vol. 157, pp. 1–9.

[24] Weidman, P.D., Kubitschek, D.G., Davis, A.M.J., 2006, "The effect of transpiration on selfsimilar boundary layer flow over moving surfaces" *Int. J. Eng. Sci*. Vol. 44, pp. 730-737.

[25]Zheng L., Zhang X., He J., 2004, "Suitable heat transfer model for self-similar laminar boundary layer in power law fluids" *J. Thermal Science* Vol. 13, pp. 150-154.

Atmospheric flows

Conference on Modelling Fluid Flow (CMFF'12)
The 15th International Conference on Fluid Flow Technologies
Budapest, Hungary, September 4-7, 2012

VALIDATION OF RANS FLOW MODELS WITH FLOW DATA OF AN IDEALISED CENTRAL-EUROPEAN CITY CENTRE, MICHEL-STADT

Anikó RÁKAI[1], Jörg FRANKE[2]

[1] Corresponding Author. Department of Fluid Mechanics, Budapest University of Technology and Economics. Bertalan Lajos u. 4 - 6, H-1111 Budapest, Hungary. Tel.: +36 1 463 2464, Fax: +36 1 463 3464, E-mail: rakai@ara.bme.hu
[2] Institut für Fluid- und Thermodynamik, Universität Siegen, Siegen, Germany. E-mail: joerg.franke@uni-siegen.de

ABSTRACT

Simulation of flow and dispersion in the urban environment with the help of Computational Fluid Dynamics (CFD) is getting more and more popular, thanks to the increase in computer power and, increasingly, the availability of powerful open source software. With CFD, the Reynolds Averaged Navier Stokes (RANS) approach is one of the possibilities to gain results around the buildings at the most interesting location for the urban population.

These RANS models still need to be validated against measured data to increase the acceptance of them. This is equally important for open source software, where mainly the users have to perform and publish validations, and for commercial software, where the code developers should push validation. In this paper validation of the open source code OpenFOAM 1.7.1 against wind tunnel data of the CEDVAL-LES database will be presented. This public database contains flow and dispersion data of an idealised Central-European city centre, called Michel-Stadt. Only results of the flow simulations will be summarized in this work.

The simulations were carried out with the standard and realizable $k-\epsilon$ turbulence model, using different mesh densities and types. The results are compared to the ones obtained with the commercial software Ansys Fluent 13 and the wind tunnel data of two mean velocity components and three Reynolds stress tensor components. For the mean velocities also validation metrics are presented.

Keywords : RANS, urban flow, validation

NOMENCLATURE

Subscripts and Superscripts

H	$[m]$	building height
U	$[m/s]$	streamwise velocity component
UV	$[m^2/s^2]$	Reynolds shear stress component
V	$[m/s]$	lateral velocity component
z	$[m]$	vertical coordinate
z_0	$[m]$	aerodynamic roughness

mean	time average
ref	reference quantity
RMS	root mean square

1. INTRODUCTION

Quality assurance of Computational Wind Engineering can be obtained by proper verification and validation of the codes used. OpenFOAM 1.7.1 has already been validated against the VDI guideline [1] and the Mock Urban Setting Test (MUST) case [2]. In the framework COST 732 [3] several Computational Fluid Dynamics (CFD) codes were tested against the MUST case and a real city, Oklahoma's wind tunnel measurement data, but not OpenFOAM. The two test cases proved to be either too simple or too complex, so a new test case in between was investigated in the Environmental Wind Tunnel Laboratory of the University of Hamburg [4], which is used here for further validation of OpenFOAM 1.7.1.

2. VALIDATION EXPERIMENT Michel-Stadt

The used dataset is part of CEDVAL-LES, a collection of data for validation of Large Eddy Simulation (LES) models (http://www.mi.uni-hamburg.de/Data-Sets.6339.0.html). Several datasets are available with flow and dispersion measurements. Here the Michel-Stadt case will be used and only the flow results will be discussed. The geometry is an idealized Central-European city centre placed in the Atmospheric Boundary Layer (ABL) modelled by roughness elements. Two component velocity data time series (streamwise and lateral components, no vertical component results are available) were collected with Laser Doppler Velocimetry (LDV) in

40 vertical profiles, 2 horizontal planes and 3 street canyon planes (see Figure 1). For the approach flow 3 component measurements were carried out.

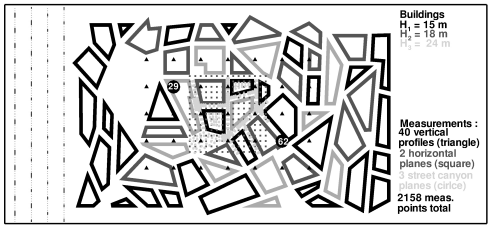

Figure 1. Computational domain with roughness elements, buildings and measurement positions.

3. COMPUTATIONAL SETUP

The computational domain was defined to correspond with the COST 732 Best Practice Guideline [1] (Fig. 1), which resulted in a $1575 \cdot 900 \cdot 168m$ domain, with a distance of the buildings of $11H_3$ from the inflow, $9.4H_3$ from the outflow and at least $6H_3$ from the top boundaries, where $H_3 = 24m$ is the highest buildings' height. The computations were done in full scale, while the experiment was done at a scale of 1:225.

As can also be seen in Fig. 1, four lines of the wind tunnel's roughness elements were included in the mesh as the first buildings are in the wake of them. The height of the roughness elements is 9 and 18 m in full scale, so they are relatively high compared to the buildings and the corresponding aerodynamic roughness height $z_0 = 1.53m$ is unattainable with reasonable meshes as the approach flow resolution would have to be too coarse compared to the resolution of the area of interest. Placing the rougness elements right before the geometry of interest ensures during the measurement that there is no secondary boundary layer development between the roughness elements and the buildings, but it makes it difficult to model the roughness implicitly as a rough wall function. However the effect of inflow roughness also modelled implicitly with z_0 was tested in [5] and no significant effect was shown in the results which suggests that the inner flow structures are much more influenced by the buildings themselves.

Unstructured Delaunay tetrahedral grids were generated in Ansys Icem CFD, with three different resolutions, fine, medium and coarse. To investigate the influence of the mesh type, a polyhedral mesh was generated from each tetrahedral mesh with Ansys Fluent 13. The number of cells of each of the six meshes can be seen in Table 1.

As inflow boundary condition, a power law profile (exponent 0.27, with a reference velocity $U_{ref} = 6.11m/s$ defined at $z_{ref} = 100m$) fitted to the measured velocity values was given. The turbulent kinetic energy and its dissipation profiles were

Table 1. Number of cells of the six meshes (and their abbreviations).

$\cdot 10^6$ cells	coarse	medium	fine
polyhedral	1.73 (P3)	3.21 (P2)	6.17 (P1)
tetrahedral	6.65 (T3)	13.17 (T2)	26.79 (T1)

calculated from the measured approach flow values by their definition and equilibrium assumption. At the top of the domain the measurement values corresponding to that height were fixed. The lateral boundaries were treated as smooth solid walls, as the domain's extension is the same as the wind tunnel width. The floor, roughness elements and buildings were also defined as smooth walls. Standard wall functions were used. As the roughness elements are included in the domain there is no need to use rough wall functions for the approach flow and also the problem of maintaining a horizontally homogenous ABL (Atmospheric Boundary Layer) profile, which is reported [6] to be problematic for this kind of modelling, is avoided.

The Reynolds Averaged Navier Stokes Equations were solved with standard and realizable k-ϵ turbulence model and the SIMPLE method was used for pressure-velocity coupling. Convective terms were first discretised with first order upwind schemes to help convergence, then the momentum divergence terms were changed to the cell limited linear upwind scheme [7]. With second order discretization for all variables in some cases convergence problems arised. When the residuals became unstable, the equations were substantially underrelaxed, which was already necessary for the first order solutions on the polyhedral meshes. The tetra meshes were more robust, in their case the default underrelaxation factors (0.7 for all quantities, except 0.3 for pressure) were sufficient.

In case of the computations with second order terms for all variables the normalized residuals were in some cases low but not stable. In these cases the solver was bounding the values, of k and ϵ to physical positive but very small values as they were becoming negative. This is assumed to cause the oscillation in the normalized residuals. But the maximum and average values of k and ϵ were checked to be stable through several iterations, so these simulations were also evaluated.

The results of the computations were compared to Ansys Fluent calculations where a similar approach was followed, using the second order upwind method [8] for pressure and momentum and the first order upwind method for the turbulence quantities in the final simulations. Contrary to OpenFOAM, the Fluent simulations with polyhedral grids were more stable than the ones with tetrahedral grids. The results compared are the ones with second order discretization for flow variables and first order

for turbulence quantities. More details on the Fluent computations can be found in [9] and [5].

4. RESULTS AND DISCUSSION

The simulation data are obtained at the measurement locations using linear interpolation between cell centre values. The results are presented graphically for two selected vertical profiles (Fig. 1). Profile 29 is in the courtyard of a building block while 62 is on the roof of a building. In addition, hit rates [10] are calculated as validation metric for the streamwise (U_{mean}) and lateral (V_{mean}) mean velocity components. The corresponding Reynolds stress components (U_{RMS}, V_{RMS}, UV) are compared to measurements by scatter plots as information about the experimental confidence intervals is missing for them. The Reynolds stress components of the numerical simulations were obtained from the Boussinesq hypothesis.

Hit rates are used for the quantitative comparison between the simulations and experiments. The hit rate is defined as the ratio of hits to the total number of measurement locations (see Eqn 1) [10]. Here 25% is the allowed relative difference and 0.033 for U_{mean}/U_{ref} and 0.0576 for V_{mean}/U_{ref} are the allowed absolute differences, W [11].

$$q = \frac{1}{N}\sum_{i=1}^{N}\delta_i \tag{1}$$

$$\delta_i = \begin{cases} 1 & \text{for} \quad \left|\frac{P_i - O_i}{O_i}\right| \leq 0.25 \ \text{ or } \ |P_i - O_i| \leq W \\ 0 & \text{for} \quad \text{else} \end{cases} \tag{2}$$

4.1. Comparison of the two solvers

The results of OpenFOAM 1.7 were compared to Ansys Fluent computations as it is a highly validated software for atmospheric flow modelling. As mentioned in section 3 the results of second order discretization only for the mean velocity components were used for comparison, as the main difference in the behaviour of the two solvers could be observed in the convergence. The obtained profiles and hit rates are very similar in case of the same mesh and computational setup. Differences can be due to the different numerical schemes used and the implementation of the turbulence model. Details on the comparison are presented in [9], here only the hit rates are shown in Table 2, which reveals the good agreement between the results.

4.2. Grid independency

The grid independence studies are also presented for the computations with second order discretization for the mean velocity components and first order discretization for the turbulent quantities.

The profiles for the mean velocities show a very good agreement with the measured values in most cases as can be seen for a typical courtyard profile in Figure 2, where the inlet reference velocity and height given in section 3 are used for non-dimensionalisation.

Table 2. Hit rates for OpenFOAM / Fluent

U_{mean}/U_{ref}	coarse	medium	fine
polyhedral	0.66/ 0.64	0.68/ 0.68	0.69/ 0.69
tetrahedral	0.72/ 0.69	0.76/ 0.75	0.76/ 0.75
V_{mean}/U_{ref}	coarse	medium	fine
polyhedral	0.78/ 0.78	0.79/ 0.78	0.78/ 0.78
tetrahedral	0.82/ 0.80	0.82/ 0.82	0.83/ 0.82

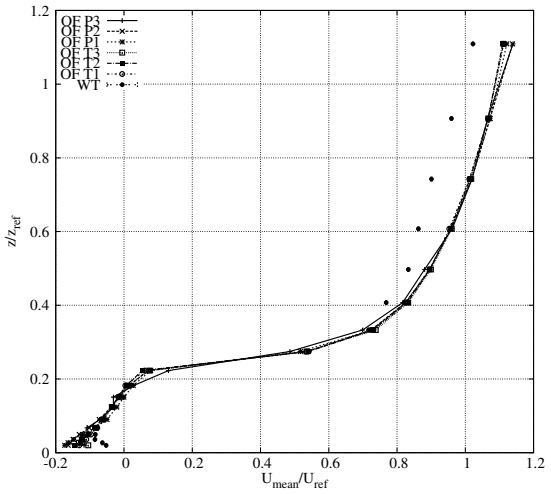

Figure 2. Grid dependence of streamwise velocity at location 29

For the streamwise velocity component there is a clear over-prediction at higher elevation (Fig. 2), due to the speed-up caused by blockage effects, which is even more emphasised in case of the rooftop profile (62, Figure 8). It was investigated with Fluent in a domain with height $11H_3$ by Franke [5], showing that high velocities are reduced but still higher than the experimental ones.

From the hit rate results in Table 2 it can be seen that the simulations are not fully grid independent. The tetrahedral meshes have higher hit rates which is a consequence of the better resolution. Between the medium and fine meshes the change in hit rate is however only very small. The presented values are acceptable according to the VDI guideline [10], which has 0.66 as lower limit for successful validation. These results are similar to the ones obtained by Efthimiou et al. [11] with the commercial code StarCD and in-house code ADREA.

The turbulent quantities show no significant dependency on mesh resolution but the values are highly underpredicted. Further details can be found

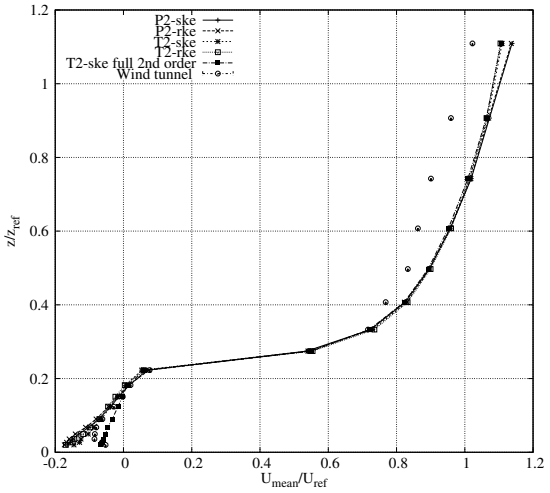

Figure 3. Turbulence model dependence of streamwise velocity at location 29

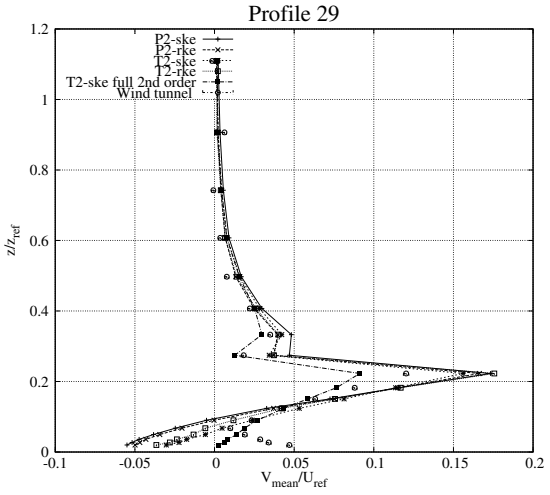

Figure 4. Turbulence model dependence of lateral velocity at location 29

in [9].

4.3. Turbulence model

As the standard $k-\epsilon$ model has realizability problems, for example it can result in non-physical negative normal Reynolds stress components, the realizable $k-\epsilon$ model was also investigated (NB: In the compared measurement positions all normal components were positive also for the standard model.). However, all the results obtained with the realizable model are worse as can be observed, both graphically in all of the profiles and in the computed hit rates (Table 3). A similar experience was reported by Izarra [12] and a contradictory by [2], both for the MUST case. Therefore the applicability of this model or other realizability constraints for the turbulence modelling need further investigation.

In the figures for RMS components (Figures 5, 6, 10 and 11) it can be observed that the profiles for the polyhedral mesh with different turbulence models are very close to each other, while in case of the tetrahedral mesh the turbulence model change causes more different results. The standard profiles are clearly closer to the measurements.

The profiles for the Reynolds stress components suggest that the mesh type and thus the resolution and the discretization scheme (as will be discussed in Section 4.4) has greater effect on the results than the turbulence model in the current implementation.

Table 3. Hit rates for standard/realizable $k-\epsilon$ model

U_{mean}/U_{ref}	coarse	medium	fine
polyhedral	0.66/0.62	0.68/0.64	0.69/0.64
tetrahedral	0.72/0.70	0.76/0.70	0.76/0.72
V_{mean}/U_{ref}	coarse	medium	fine
polyhedral	0.78/ 0.77	0.79/ 0.77	0.78/ 0.76
tetrahedral	0.82/ 0.79	0.82/ 0.79	0.83/ 0.79

From the hit rates in Table 3 it can be assumed that the realizable $k-\epsilon$ model is less sensitive to the mesh resolution as it has more similar, though worse results for all the meshes.

4.4. Discretization schemes

To obtain convergence with second order schemes is not sraightforward for such a complicated geometry and unstructured meshes, as shown in section 3, but as it is assumed to be converged the results of the medium tetrahedral mesh are compared. They are notably better for the fully second order solution which can be seen also in case of the graphical comparison of the profiles of the non-dimensional RMS velocity components, seen in Figure 5, 6, 10 and 11. This is what is expected from the theory of the discretization, but the convergence problems need further investigation in such complicated geometries. Usually a solution is declared converged if the normalized residuals for the variables fall below a certain level ($10e-6$) and level out, i.e. they are flat. In this case for the fully second order simulations these criteria were not met all the time, but the results still seem to be good. The definition of the normalized residual itself differs in solvers, so it is not possible to expect a certain value.

The change in the results from 1st to 2nd order discretization in the turbulence quantities can be observed already in the mean flow variables. The most important change is that the negative V_{mean} values are not present (Figure 4). This is also discussed in Section 4.5.

In Figures 13, 14 and 15 scatter plots of the Reynolds stress components can be seen. These plots are showing the simulation results against the

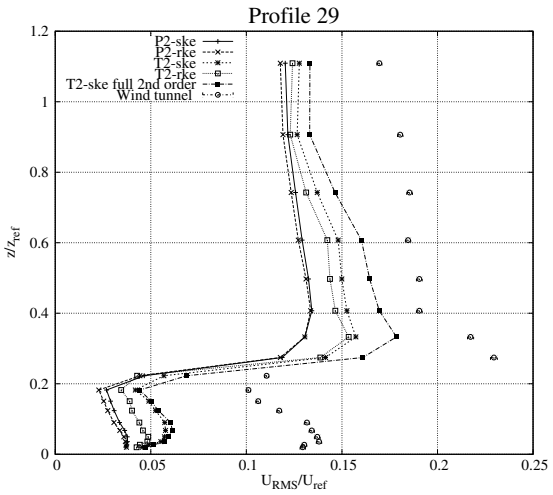

Figure 5. Turbulence model dependence of streamwise velocity fluctuation at location 29

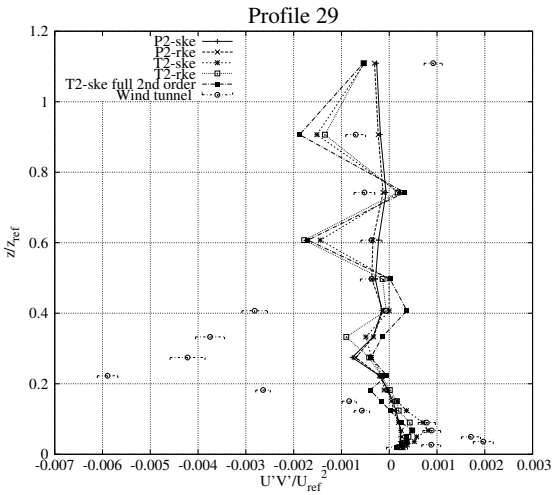

Figure 7. Turbulence model dependence of turbulent shear stress at location 29

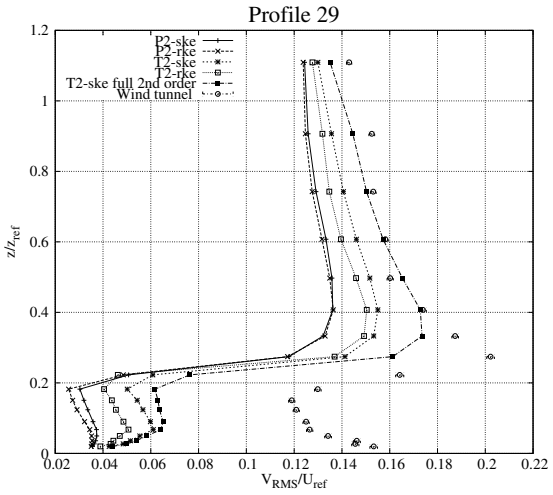

Figure 6. Turbulence model dependence of lateral velocity fluctuation at location 29

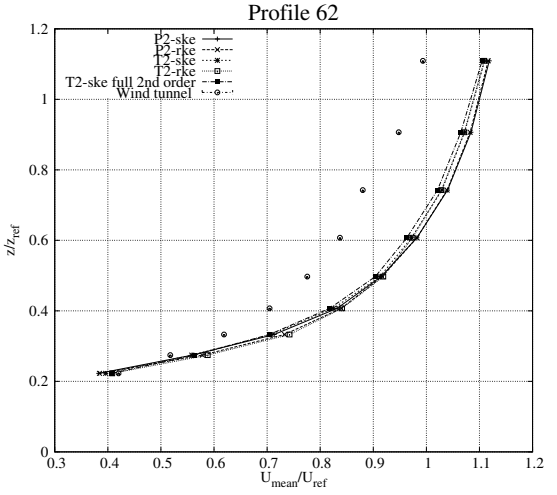

Figure 8. Turbulence model dependence of streamwise velocity at location 62

measurements results. Also the 45 degree line is present in the plots. Points falling on this show perfect match. Lines for a factor of 2 and 0.5 correspondance are also shown which enable to see which values fall between this factor.

Also from the scatter plot of the results, a significant improvement can be observed (Figure 13) for the RMS prediction due to the reduced numerical diffusion, but the underprediction of the values is not solved. The predicted lateral RMS components in Figure 14 look even better, with a considerable amount of points close to the 45 degree line.

It is difficult to draw conclusions about the discretization scheme effects on the Reynolds shear stress components in Figure 15, as the values are very small, an order of magnitude smaller than the normal stresses (RMS values) and show no straightforward trends.

4.5. Comparison of polyhedral and tetrahedral mesh performance

As the computational cost related to CFD applications is also essential, it is also evaluated for the different grid types. The normalized cell numbers, memory consumption and CPU time can be seen in Table 4. They are obtained by dividing the corresponding values by the value of the coarsest polyhedral mesh. This way the increase in mesh number, memory usage and needed CPU time can be easily investigated.

The computations for which these values are presented were carried out on the same cluster architecture with parallel computation on 4 CPUs. The finest mesh was too big to be run on the

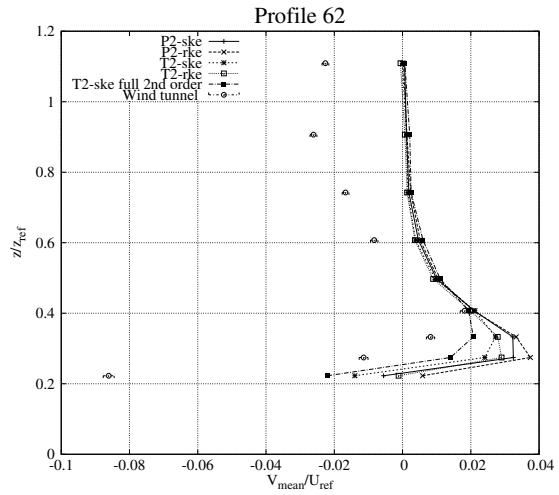

Figure 9. Turbulence model dependence of lateral velocity at location 62

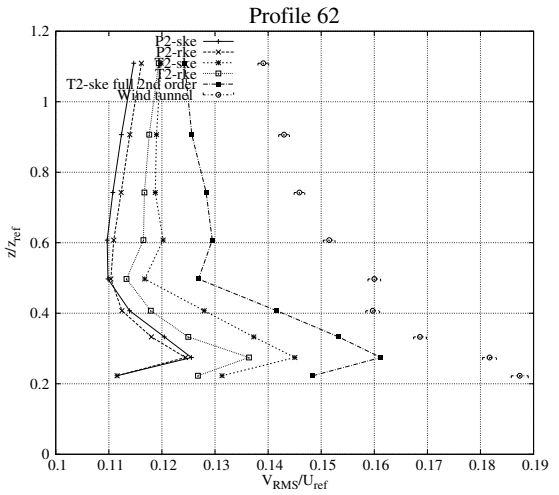

Figure 11. Turbulence model dependence of lateral velocity fluctuation at location 62

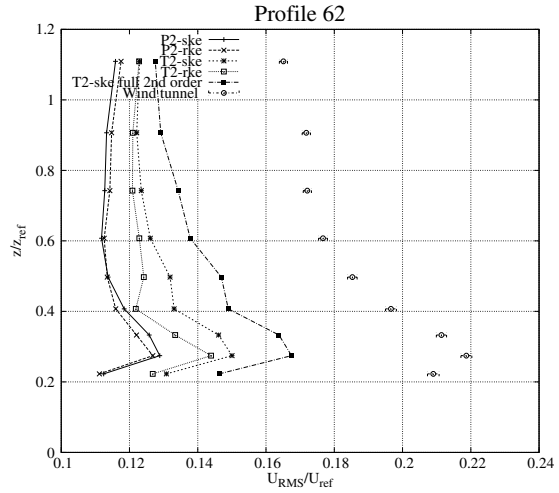

Figure 10. Turbulence model dependence of streamwise velocity fluctuation at location 62

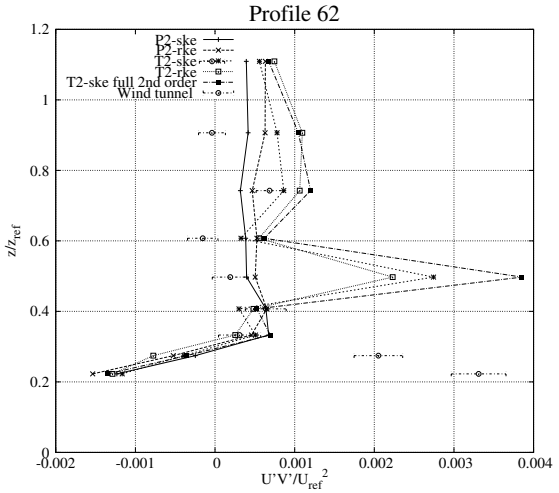

Figure 12. Turbulence model dependence of turbulent shear stress at location 62

same architecture so the corresponding values are not shown. The CPU times are obtained from 500 iterations which is assumed to be enough to compare the pure computational time after startup. The time needed for convergence is not discussed here in detail, but it is also an important factor in evaluating the polyhedral meshes. The simulations on the polyhedral meshes generally converged faster for the first order calculations, but for the second order calculations further investigation is needed.

It can be seen in Table 4 that the polyhedral meshes reduce the cell numbers by about a factor of 4 compared to their ”parent” tetrahedral meshes, and the computational time is reduced by a factor of 5 or more. On the other hand the memory need is only smaller by a factor of 1.5 or less due to the flux calculations on the polyhedral faces, which add up to a higher number. The fine polyhedral and coarse tetrahedral meshes have comparable cell numbers and computational time, but the polyhedral mesh needs more memory. Looking at the results obtained with these two meshes for the hit rates in Table 3, it can be seen that they are similar, with slightly higher values for the tetrahedral mesh. The choice between the two mesh types can be thus decided by a trade-off between computational costs and accuracy. The polyhedral mesh has the potential to decrease the time needed, but with higher memory consumption.

Comparing the mean velocity profiles of the polyhedral and tetrahedral meshes, differences occur close to the ground for the lateral velocity profile. The tetrahedral mesh results are slightly closer to the measurements but still qualitatively wrong with negative velocity components for Profile 29 (Figure

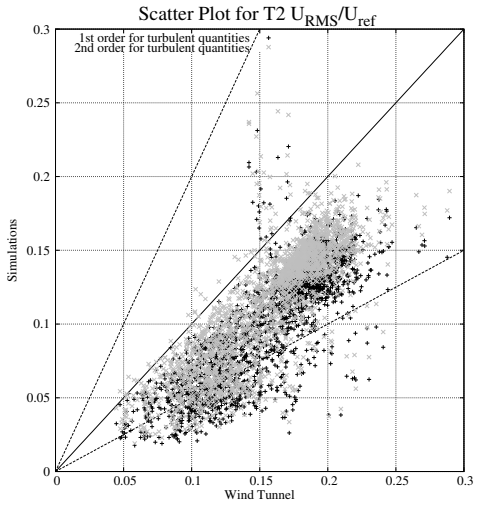

Figure 13. Scatter plot for streamwise RMS values for the T2 mesh with results for discretization scheme change from 1st order to 2nd in turbulent quantities

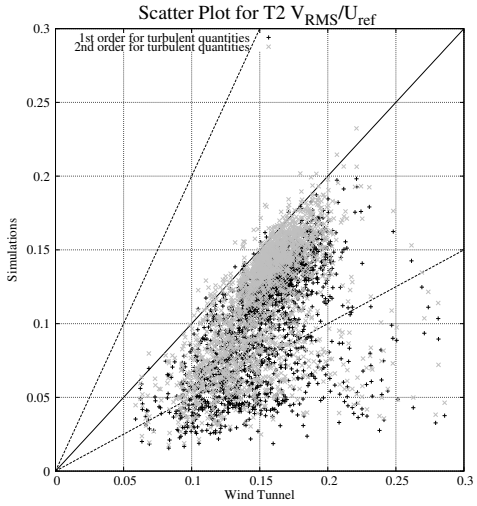

Figure 14. Scatter plot for lateral RMS values for the T2 mesh with results for discretization scheme change from 1st order to 2nd in turbulent quantities

4). This behaviour is changed by the full second order discretization as mentioned in Section 4.4.

In the profile comparison of the turbulent shear stresses in Figure 7 and 12, an unexpected instability appears for the tetrahedral meshes which is more emphasised in the full second order simulation. This needs further investigation, with the convergence issues mentioned already.

5. CONCLUSION

The open source CFD code OpenFOAM 1.7.1 was evaluated with the results of an idealized European city centre geometry, Michel-Stadt. The

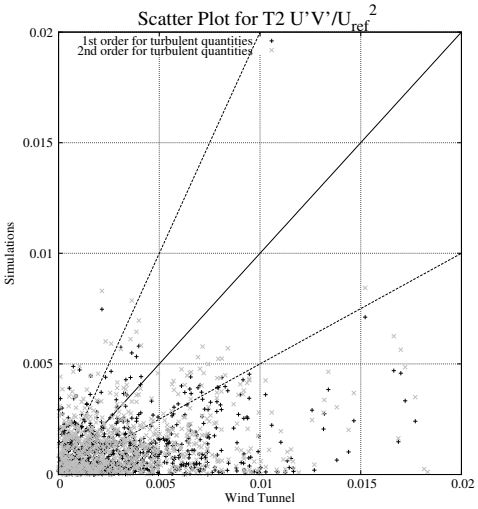

Figure 15. Scatter plot for the turbulent shear stress values for the T2 mesh with results for discretization scheme change from 1st order to 2nd in turbulent quantities

Table 4. Normalized cell number, memory consumption and computational time of the different meshes (the coarsest mesh used for normalization)

	coarse	medium	fine
P cell	1	1.86	3.57
P memory	1	1.62	3.11
P CPU time	1	2.24	5.05
T cell	3.91	7.61	15.49
T memory	1.64	2.76	
T CPU time	5.05	13.00	

results show that generally this solver can be used for urban flow modelling. This was shown by comparing the results to the well validated Ansys Fluent 13 computations and obtaining good agreement.

Two turbulence models were compared, which showed that the standard $k-\epsilon$ model has better results for this case and setup than the realizable $k-\epsilon$ model.

Discretization schemes were also evaluated and the cell limited linear upwind scheme for all variables showed the best agreement with the experimantal results. The convergence criteria for such complicated geometries needs further evaluation.

Tetrahedral and polyhedral meshes were also compared. It was shown that polyhedral meshes can equally be used with an optimal trade-off between computational time, memory consuption and the needed accuracy. This has to be decided for the application in question and should be further investigated.

ACKNOWLEDGEMENTS

The work relates to the scientific programme of the project "Development of quality-oriented and harmonized R+D+I strategy and the functional model at BME". The New Hungary Development Plan (Project ID: TÁMOP-4.2.1/B-09/1/KMR-2010-0002) supports this project.

References

[1] Franke, J., Hellsten, A., Schlunzen, K. H., and Carissimo, B. 2011 "2011 The COST 732 Best Practice Guideline for CFD simulation of flows in the urban environment: a summary". *International Journal of Environment and Pollution*, Vol. 44, No. 1–4, pp. 419–427.

[2] Rákai, A. and Kristóf, G. 2010 "CFD Simulation of Flow over a Mock Urban Setting Using OpenFOAM". *Gépészet 2010: Proceedings of the Seventh Conference on Mechanical Engineering. Budapest, Hungary*.

[3] Schatzmann, M., Olesen, H., and Franke, J. 2010 , "COST 732 model evaluation case studies: Approaches and results.".

[4] Fischer, R., Bastigkeit, I., Leitl, B., and Schatzmann, M. 2010 "Generation of spatio-temporally high resolved datasets for the validation of LES-models simulating flow and dispersion phenomena within the lower atmospheric boundary layer". *Proceedings of The Fifth International Symposium on Computational Wind Engineering (CWE2010), Chapel Hill, North Carolina, USA*.

[5] Franke, J., Laaser, A., Bieker, B., and Kempfer, T. 2012 "Sensitivity analysis of RANS simulations for flow and dispersion in the generic European city centre Michel-stadt". *Proc. 15th International Conference on Fluid Flow Technologies (CMFF'12), Budapest, Hungary*.

[6] Blocken, B., Stathopoulos, T., and Carmeliet, J. 2007 "CFD simulation of the atmospheric boundary layer: wall function problems". *Atmospheric Environment*, Vol. 41, pp. 238–252.

[7] OpenCFD, L. 2010 *OpenFOAM 1.7.1 user manual*.

[8] Ansys 2009 *Ansys Fluent 12.0 Theory Guide*. Ansys Inc.

[9] Rakai, A. and Franke, J. 2012 "Validation of two RANS solvers with flow data of the flat roof Michel-Stadt case". *Proc. 8th International Conference on Air Quality Science and Application, Athens, Greece*.

[10] VDI 2005 , "Environmental Meteorology Prognostic microscale wind field models Evaluation for flow around buildings and obstacles, VDI guideline 3783, Part 9".

[11] Efthimiou, G. C., Hertwig, D., Fischer, R., Harms, F., Bastigkeit, I., Koutsourakis, N., Theodoridis, A., Bartzis, J. G., and Leitl, B. 2011 "Wind flow validation for individual exposure studies". *Proceedings of the 13th International Conference on Wind Engineering (ICWE13), Amsterdam, The Netherlands*.

[12] Izarra, R. 2009 "Second Moment Modelling for the Numerical Simulation of Passive Scalar Dispersion of Air Pollutants in Urban Environments". Ph.D. thesis,

Conference on Modelling Fluid Flow (CMFF'12)
The 15th International Conference on Fluid Flow Technologies
Budapest, Hungary, September 4-7, 2012

SENSITIVITY ANALYSIS OF RANS SIMULATIONS FOR FLOW AND DISPERSION IN THE GENERIC EUROPEAN CITY CENTRE MICHEL-STADT

Jörg FRANKE[1], Alexander LAASER [2], Bastian BIEKER [3], Tobias KEMPFER [4]

[1] Corresponding Author. Institut für Fluid- und Thermodynamik, Universität Siegen. Paul-Bonatz-Str. 9-11, D-56076 Siegen, Germany. Tel.: +49 271 740 4683, Fax: +49 271 740 2666, E-mail: joerg.franke@uni-siegen.de
[2] Institut für Fluid- und Thermodynamik, Universität Siegen. E-mail: alexanderla@gmx.de
[3] Institut für Fluid- und Thermodynamik, Universität Siegen. E-mail: bastian.bieker@student.uni-siegen.de
[4] Institut für Fluid- und Thermodynamik, Universität Siegen. E-mail: tobias.kempfer@student.uni-siegen.de

ABSTRACT

In this work sensitivity results for the flow and dispersion RANS CFD simulations in the generic city model *Michel-Stadt* are presented. Flow results are compared with wind tunnel measurements graphically and with the validation metric hit rate. Concentration results are only compared with other simulation results as experimental data are not yet available. It is found that the flow can be very well predicted with hit rates for mean velocity components above 0.70, using fine hexa- and tetrahedral grids. Polyhedral grids yield lower hit rates. While mesh type and resolution have a large influence on the results, approach flow roughness modelling, wall function selection and Reynolds number do not. Larger changes are observed when changing from the standard to the realizable $k-\varepsilon$ turbulence model, with better results for the standard model. Similar results are obtained for the concentration distribution, where source flow rate, turbulence model and wall function model have only a small influence.

CFD, RANS, urban flow and dispersion, validation

NOMENCLATURE

C	$[-]$	mean concentration
C^*	$[-]$	scaled mean concentration
H	$[m]$	building height
Re	$[-]$	Reynolds number
U	$[m/s]$	streamwise velocity component
V	$[m/s]$	lateral velocity component
$\dot{V}$	$[m^3/s]$	flow rate
k	$[m^2/s^2]$	turbulent kinetic energy
q	$[-]$	hit rate
u'	$[m/s]$	streamwise velocity fluctuation
v'	$[m/s]$	lateral velocity fluctuation
z_0	$[m]$	roughness height
α	$[-]$	power law exponent
ε	$[m/s^3]$	turbulent dissipation rate

Subscripts and Superscripts

a, r	absolute, relative
max, min	maximum, minimum
ref	reference
var	variance
u, v	streamwise, lateral velocity
$\langle\rangle$	temporal mean

1. INTRODUCTION

For the assessment of the predictive capabilities of computational models for flow and dispersion in urban areas, experimental validation data sets of high quality are necessary [1, 2]. For statistically steady RANS models, wind tunnel data are of the largest value, due to their good repeatability and representativeness in space and time, with accordingly small uncertainties. This makes validation more stringent, if numerical model results have to be close to the intervals defining the experimentally determined reality. Due to the normally well characterised approach flow conditions in wind tunnels, also the uncertainties in the numerical simulation results are smaller, as the input uncertainties decrease [3].

Simple building models and realistic city models have been experimentally investigated with numerical model validation in mind. To close the gap between these different complexities, a validation data set of intermediate geometrical complexity was recently generated in the boundary layer wind tunnel of the Meteorological Institute at the University of Hamburg [4]. While this data set is intended for the validation of unsteady Large Eddy Simulations(LES), the also available time averaged measurements are used in the present work for Reynolds Averaged Navier Stokes (RANS) model validation, using the commercial Computational Fluid Dynamics (CFD) code ANSYS FLUENT 13.

It is becoming generally accepted that validation

requires not only the availability of uncertainties in the experimental results, but also an estimate of the uncertainty in numerical simulation results [3]. Sources of these uncertainties are mathematical modelling (e.g. turbulence model), numerical solution (discretisation error, incomplete iterative solution, precision), as well as uncertainties in geometry and the boundary conditions. Methods for the estimation of the different errors and their conversion into uncertainties have been proposed, e.g. [5, 6], and shall also be tested for the present urban fluid mechanics problem in the future. Up to now only a sensitivity analysis with regards to mathematical modelling, boundary conditions, geometry and numerical solution has been performed. The results of this analysis are presented in the following, using graphical comparison with available experimental data and validation metrics.

2. EXPERIMENTAL DATA

Michel-Stadt is a generic European city centre that was studied by Bastigkeit [4] in the boundary layer wind tunnel of the Meteorological Institute at the University of Hamburg. The 1:225 scale model consists of 60 building rings with flat roof in the current investigation, which are irregularly placed as shown in Figure 1. Three different building heights are used, 15, 18 and 24 *m*. These values refer to full scale, which will be used throughout this section. The building width is 15 *m* and two street widths of 18 and 24 *m* are used. The streets, small squares and the one large open space represent 10% of the urban area.

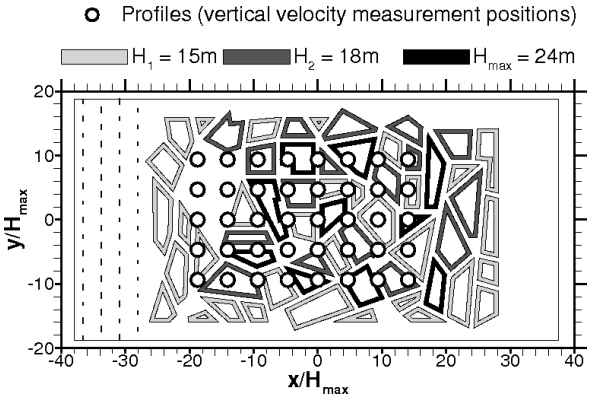

Figure 1: Plan of *Michel-Stadt* with four rows of roughness elements and vertical velocity measurement positions

The city model is approached by a fully developed atmospheric boundary layer flow with large roughness height z_0 = 1.53 *m*. To obtain the large z_0, roughness elements used in the wind tunnel's flow development section have heights of 9 and 18 *m*. They are staggered as shown in Fig. 1, with this arrangement repeating until the vortex generators at the beginning of the flow development section.

The three velocity components of the approach flow were measured with a 2D Laser Doppler Anemometer (LDA). The vertical profile of the mean velocity in flow direction is best approximated by a power law with exponent $\alpha = 0.27$, consistent with the roughness height. The turbulence intensities are also representative of the large roughness. Homogeneity of the flow in the lateral direction has been shown.

In the urban area only the two vertical velocity components were measured with 2D LDA. The 2158 measurement positions are grouped in 40 vertical profiles and five horizontal planes at 2, 9, 18, 27 and 30 *m*. The vertical measurement positions are shown in Fig. 1, the horizontal in Figure 2. At each position the time averaged velocity components U and V, their variances U_{var} and V_{var}, as well as the correlation $\langle u'v' \rangle$ are publicly available in the CEDVAL-LES database [7]. Note that in the database also time series are available, as it is dedicated to validation of time dependent simulations like LES.

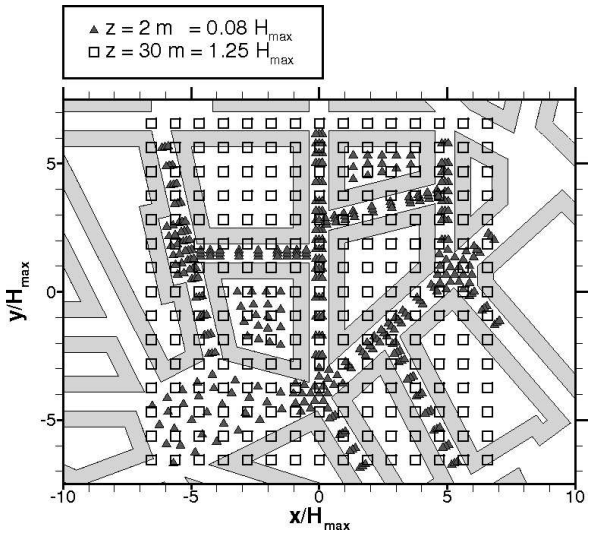

Figure 2: Horizontal velocity measurement positions in street canyons and above buildings

In addition to the velocities, concentrations of continuously released Ethane were measured in the urban area with a fast Flame Ionisation Detector (FID). The background concentration was measured with a standard FID. Like the velocity measurement positions, the concentration measurement positions are grouped in eight vertical profiles and two horizontal planes at 2 and 30 *m*. These positions are shown in Figure 3 together with the location of the continuous release on the roof of a 15 *m* high building. In total there are 188 concentration measurement positions.

Measured concentration time series as well as time averaged concentrations are not yet publicly available in the abovementioned database, but will be in the near future.

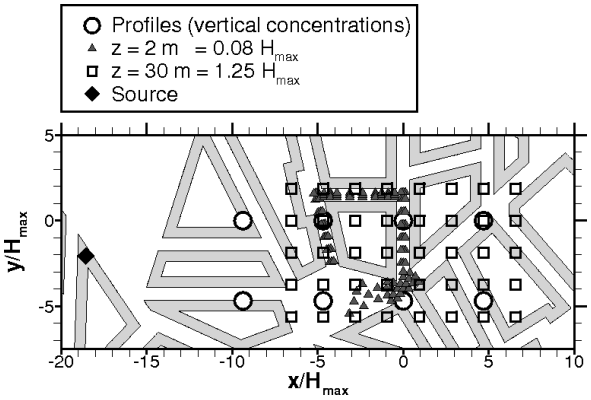

Figure 3: Source position with vertical and horizontal concentration measurement positions

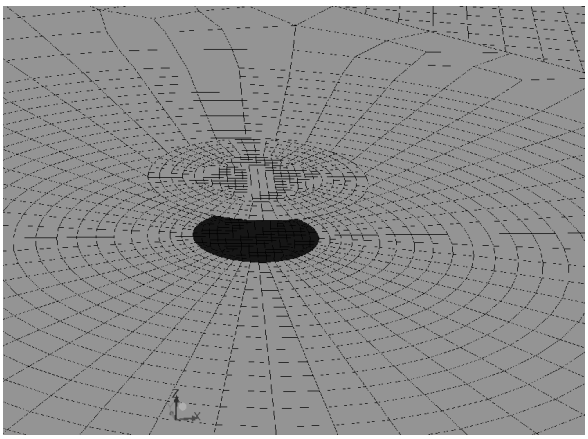

Figure 4: Source geometry in the computational model for hexahedral grid

3. COMPUTATIONAL PARAMETERS

All simulations were performed with ANSYS FLUENT 13. The statistically steady RANS equations with constant fluid properties were solved for the flow field and the concentration distribution calculated with the Reynolds averaged transport equation of a passive scalar.

3.1. Computational domains

From Fig. 1 the horizontal extent of the employed computational domain is visible. The lateral extent is the same as the width of the wind tunnel test section. The flow enters the domain $11H_{max}$ in front of the first buildings. Four rows of roughness elements are explicitly modelled as zero thickness solid walls, except for one case, where they are implicitly modelled by a roughness height z_0.

The outflow plane is located $9H_{max}$ behind the last buildings and the height of the domain used for most simulations is $7H_{max}$. For one simulation the height is extended to $11H_{max}$.

Simulations were run in full and model scale to investigate the Reynolds number influence. Defining the Reynolds number with some reference height z_{ref}, $Re = \rho U_{ref} z_{ref}/\mu$, and assuming identical fluid properties, as well as mean reference velocity U_{ref} at z_{ref} in full and model scale, the full scale Re is 225 times the model Re, i.e. two orders of magnitude higher.

Dispersion calculations were done in model scale only. The source geometry is approximated as circular inlet area with 7 *mm* diameter, also taking a circular plate with 12 *mm* diameter at a vertical distance of 5 *mm* into account, see Figure 4. This vertical momentum reducing plate is again modelled as zero thickness wall.

3.2. Grids

A total of seven unstructured grids, differing in resolution and cell type, were generated in the computational domains. One fine unstructured hexahedral grid was made with ANSYS ICEMCFD 13 by first discretising the entire horizontal bottom plane with unstructured quadrilaterals. This 2D grid layer was then extruded vertically, leading to a fully hexahedral grid. Part of its surface mesh is shown in Fig. 4, and the total number of cells is given in Table 1.

Also with ANSYS ICEMCFD 13 three Delaunay tetrahedral grids were generated. Starting with the fine grid, the medium grid was generated by multiplying the prescribed reference lengths with a factor of 1.5. In the same way the coarse grid was generated from the fine, using a factor of 2.25. By this method the cell numbers are always roughly doubled, when going from the coarse to the medium and then fine grid, cf. Table 1.

Finally, each tetrahedral grid was converted to a polyhedral grid with ANSYS FLUENT 13, leading to a substantial reduction in number of cells by roughly a factor of four, see Table 1. The polyhedral grids therefore require less memory and computing time, compared to the tetrahedral grids.

Table 1: Number of cells in millions

Cell type	coarse (3)	medium (2)	fine (1)
Hexahedra	–	–	22.9
Tetrahedra	6.65	13.2	26.8
Polyhedra	1.73	3.21	6.17

The grids are in the following referred to by the first letter of the cell type and the number of the resolution, e.g. P3 for the coarse polyhedral grid.

3.3. Turbulence models and wall functions

The Reynolds stresses are approximated with the linear Boussinesq hypothesis and closure is achieved with the standard $k-\varepsilon$ (SKE) and realizable $k-\varepsilon$

(RKE) model, as implemented in ANSYS FLUENT 13 [8]. With the SKE model standard wall functions (SWF) and enhanced wall functions (EWF) are used, while for the RKE model simulations were only run with standard wall functions.

For the turbulent scalar flux in the transport equation for the passive scalar, the gradient diffusion model is used with constant turbulent Schmidt number of 0.7.

3.4. Boundary conditions

The inflow boundary conditions were taken from measurements of the approach flow. For the mean velocity in flow direction a power law profile with exponent $\alpha = 0.27$ and reference velocity $U_{ref} = 6.11$ *m/s* at $z_{ref} = 100$ *m* was used, while the measured values for k were directly prescribed, see Figure 5. ε was calculated from these two profiles, assuming equality of production and disspation.

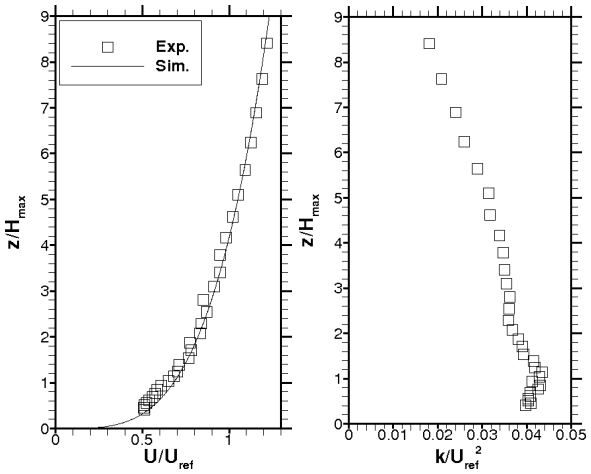

Figure 5: Approach flow profiles of mean velocity component in flow direction (left) and turbulent kinetic energy (right)

At the outflow a constant pressure was prescribed. Lateral boundaries, corresponding to the lateral wind tunnel walls, were treated as smooth walls or as symmetry. At the top boundary either fixed values from the inflow pofiles were used, or symmetry. With explicitly modelled roughness elements the entire bottom boundary of the computational domain and the roughness elements were treated as smooth walls. When the roughness elements were not explicitly modelled in one model scale simulation, the experimentally determined roughness height $z_0 = 6.8 \cdot 10^{-3}$ *m* (model scale) was used on the part of the bottom floor, covered by the roughness elements, cf. Fig. 1. This roughness was converted into a sandgrain roughness [8]. The resulting sandgrain roughness is however larger than the minimum distance of the cell centres from the bottom wall, leading to differing effective roughnesses for the different grids, all smaller than the prescribed roughness.

Building walls were normally treated as smooth. One simulation was performed with rough building walls, using $z_0 = 3.3 \cdot 10^{-5}$ *m*, which is the maximum, usable with the grids.

As concentration boundary conditions a zero gradient was prescribed everywhere, except at the inflow plane, where $C = 0$ was used. At the circular source inlet two flow rates were investigated, $\dot{V}_{min} = 2.64 \cdot 10^{-5} m^3/s$ corresponding to the experimental minimum and $\dot{V}_{max} = 4.31 \cdot 10^{-5} m^3/s$ as the experimental maximum.

3.5. Numerical approximations

All simulations were run with the single precision solver of ANSYS FLUENT 13, using the SIMPLE scheme for pressure velocity coupling. For the flow simulations one to two thousand iterations were initially done with the first order upwind scheme for all convective terms. After switching the approximation to the second order upwind scheme for pressure and momentum, two thousand further iterations were sufficient to reach a converged flow field, which did no longer change with iterations. Convergence with also the convective term of the k and ε equation being approximated with the second order upwind scheme could only be achieved on the fine hexahadral grid.

The dispersion simulations were run after the flow simulations with fixed pressure, velocity, k and ε distributions. After 150 iterations with the first order upwind scheme for the convective term in the scalar transport equation, another 150 were done with the second order upwind scheme, followed by again 150 iterations with the third order MUSCL scheme [8].

Gradients in the cell centres were approximated by two methods. Due to severe convergence problems in the flow simulations with the least square method, especially on the tetrahedral grids, the Green-Gauss node based approximation [8] was chosen for the tetra- and hexahedral grids. For the three polyhedral grids the Green-Gauss cell based approximation [8] had to be employed, as the node based version is not yet available.

The converged results of the flow and concentration fields were tri-linearily interpolated to all measurement positions described in the previous section.

4. RESULTS

The influence of the different parameters on the simulation results is mainly investigated by graphical comparison with experimental data. For the mean velocity components the validation metric hit rate is used in addition. Numerical concentration results are only compared with each other, as experimental data are not yet published.

4.1. Validation metric hit rate

The hit rate q is a global validation metric, used to measure the difference between numerical simulation

results and experimental data. The hit rate is also used for flow fields in the evaluation protocol of COST Action 732 [9, 10]. It is defined as the fraction of hits at all measurement positions N,

$$q = \frac{1}{N} \sum_{n=1}^{N} i_n \quad . \tag{1}$$

A hit, i.e. $i_n = 1$, is obtained at one measurement position n, if either the magnitude of the relative or absolute difference between non-dimensional simulation result, S_n, and non-dimensional experimental result, E_n, is smaller than a prescibed value.

$$i_n = \begin{cases} 1 \text{ if } \frac{|S_n - E_n|}{|E_n|} \leq \Delta_r \text{ or } |S_n - E_n| \leq \Delta_a \\ 0 \text{ else} \end{cases} \tag{2}$$

The allowed relative difference, Δ_r, is usually 0.25 [10]. For the allowed absolute difference, Δ_a, the experimental uncertainty should be used. In the present work uncertainties of 0.033 for U/U_{ref} and 0.0576 for V/U_{ref} are used, following [11]. As no uncertainties are reported for the measured Reynolds stresses, they are not compared by means of the hit rate.

4.2. Flow field

The full scale simulation results with the polyhedral and tetrahedral grids were already presented by [12], in comparison to the results obtained with the open source code OpenFOAM on the same grids. The presented hit rates for the mean velocity components on the tetrahedral grids are reprinted in Table 2, where corresponding results for the full scale simulation with the hexahedral grid are added, as well as results for the tetrahedral grids used in model scale. All simulations use explicit roughness elements, SKE, SWF, smooth lateral walls, fixed values at top, and neglect the concentration source.

Table 2: Hit rates for Reynolds number dependence, full scale / model scale

q_u	coarse	medium	fine
hexahedral	– / –	– / –	0.79 / –
tetrahedral	0.69 / 0.67	0.75 / 0.73	0.75 / 0.73
polyhedral	0.64 / 0.63	0.68 / 0.67	0.69 / 0.68
q_v	coarse	medium	fine
hexahedral	– / –	– / –	0.87 / –
tetrahedral	0.80 / 0.79	0.82 / 0.81	0.82 / 0.81
polyhedral	0.78 / 0.78	0.78 / 0.78	0.78 / 0.77

The results in model scale with the smaller Reynolds number are consistently worse than the results in full scale with the higher Reynolds number, visible from the slightly smaller hit rates. The increase in hit rate with grid refinement is however still valid. The highest hit rates are obtained on the highest quality, hexahedral grid. On this grid model scale simulations were only run with active source. The corresponding hit rates for maximum source flow rate are $q_u = 0.77$ and $q_v = 0.84$, also smaller than the full scale values.

In [12] it was observed that the mean streamwise velocity at the vertical profiles, see Fig. 1, was over-predicted in all simulations. Therefore simulations have been run in a domain that has been extended from $7H_{max}$ to $11H_{max}$, based on the medium tetrahedral grid T2. In addition the lateral and top boundary conditions were varied in the lower domain. From Figure 6 it follows, that the extended domain height (F-E) does reduce the streamwise velocity above the buildings, while leaving the lateral velocity and the variances nearly unaffected. The hit rates are $q_u = 0.73$ and $q_v = 0.82$, cf. Table 2 for corresponding values of the lower full scale domain. Using in the lower domain symmetry at the top (SW), or at the top and the lateral boundaries (SS), does not have a visible influence. The same is true for model (M) and full (F) scale sensitivity, as already shown with the hit rates in Table 2.

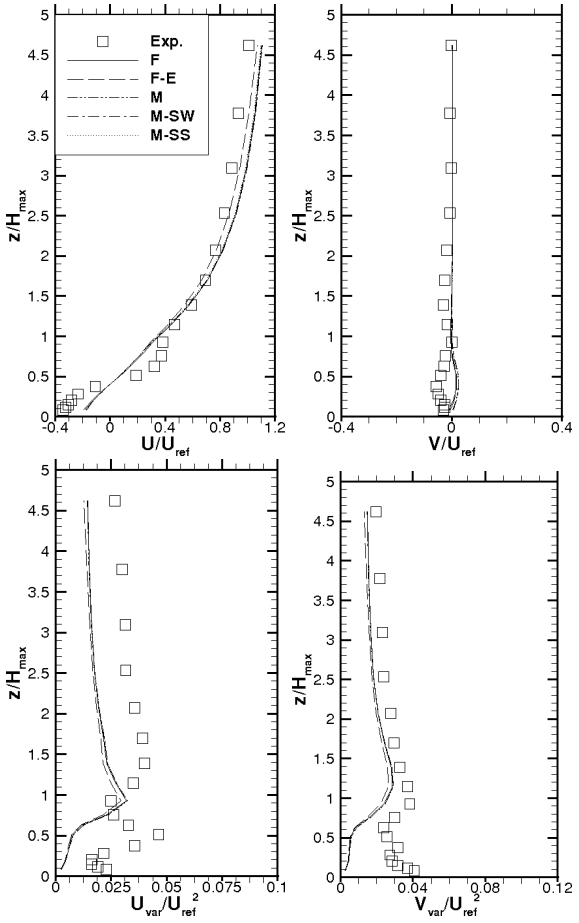

Figure 6: Domain height, top and lateral boundary condition sensitivity at central vertical profile, $(x/H_{max}, y/H_{max}) = (0, 0)$

The influence of the approach flow modelling is shown in Figure 7 with results for the fine tetrahedral grid, T1, again at the central measurement profile. Visually only minor differences can be noted, which is also the case at profiles closer to the roughness elements, which are not shown here. The flow above and in between the buildings is therefore determined by the buildings themselves. For the case with explicit roughness modelling the hit rates are $q_u = 0.73$ and $q_v = 0.81$, which are equal to the ones for the implicit modelling case with z_0. Note that the high hit rates of V/U_{ref} are due to the large absolute allowed difference, shown as error bars in Fig. 7, in relation to the typically small velocity component magnitudes.

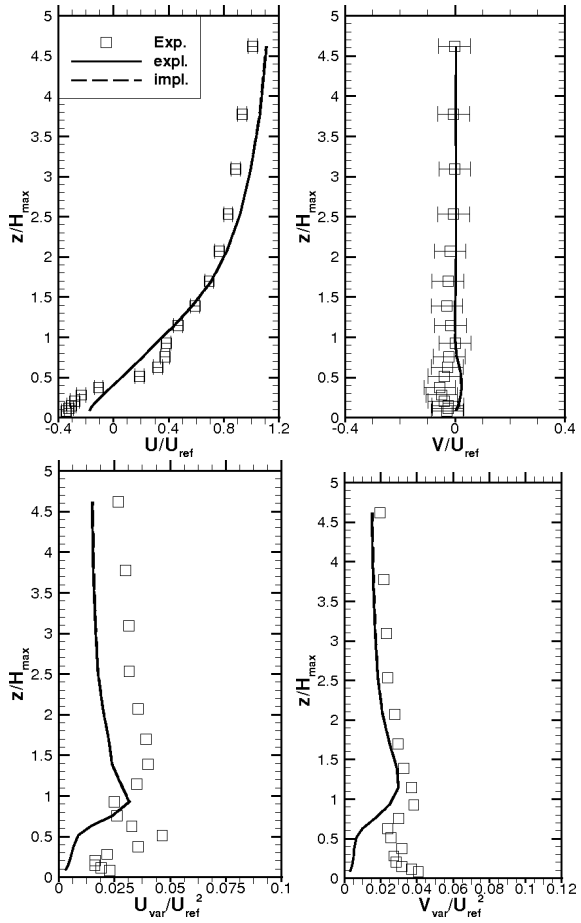

Figure 7: Sensitivity to roughness element modelling at central vertical profile, $(x/H_{max}, y/H_{max}) = (0, 0)$

Investigations of the sensitvity to wall functions were conducted in model scale, as the largest part of the walls without the lateral ones has dimensionless wall distances smaller than 12, e.g. 58%, 41% and 27% for T1, T2 and T3, respectively, rendering the standard wall functions questionable for k and ε modelling. The comparison of the results from standard wall functions with the ones of enhanced wall functions showed no differences in the hit rates and the visual comparison at measurement positions.

The change of turbulence model from SKE to RKE showed worse agreement of RKE results with the experimental data. On the hexahedral grid in model scale the hit rates were reduced from $q_u = 0.77$ and $q_v = 0.84$ with SKE to $q_u = 0.67$ and $q_v = 0.78$ with RKE. These findings are similar to the ones of [13], who used the RKE model with OpenFOAM for Michel-Stadt full scale simulations.

Finally, model scale results with the hexahedral grid are used to visualise the agreement between the measured and predicted flow field in the street canyons. In Figure 8 the experimental and numerically simulated velocity vectors are displayed at the three measurement heights, cf. Figure 2. The drastic change in the flow features is very well reproduced by the simulation, while at some positions with relatively small velocity magnitude significant differences are visible.

4.3. Concentration field

Concentration computations were only done in model scale. As at present no experimental results are available, the computational results are only compared with each other in the form of scatter plots. To that end the computed mean concentrations C are scaled as

$$C^* = \frac{C U_{ref} H_{max}^2}{\dot{V}}, \tag{3}$$

with either the maximum or minimum source flow rate.

The influence of the mesh type and resolution is shown in Figure 9. Compared are tetra- and polyhedral grids when using the maximum source flow rate. It can be seen that changing from fine to medium (T1-T2) and from fine to coarse (T1-T3) has only a small influence on the concentrations with the tetrahedral grid. When changing from the fine tetrahedral to the fine polyhedral grid (T1-P1), the changes are larger, exceeding often 25 %, with the polyhedral grid generally predicting higher concentrations. Larger influences of the resolution are obvious for the polyhedral grid. Changing from fine to medium (P1-P2), the changes in the concentrations are roughly within 25 %, while when going from fine to coarse (P1-P3), sometimes more than 50 % smaller concentrations are predicted on the coarse grid.

The influence of the source flow rate and the numerical approximation of the convective term in the scalar transport equation are shown in Figure 10 for the fine tetrahedral grid. The source flow rate has no visual influence, as well as the change from 2nd order upwind to 3rd order MUSCL. With the first order upwind scheme roughly 25 % lower concentrations are predicted, most likely due to the enhanced numerical diffusion.

Finally, the influence of the hexahedral grid is shown in comparison to the tetra- and polyhedral grid. These results are displayed in Figure 11 together with results of the influence of the turbulence model and the wall functions. The differences in concentrations are much higher when using the fine hexahedral grid

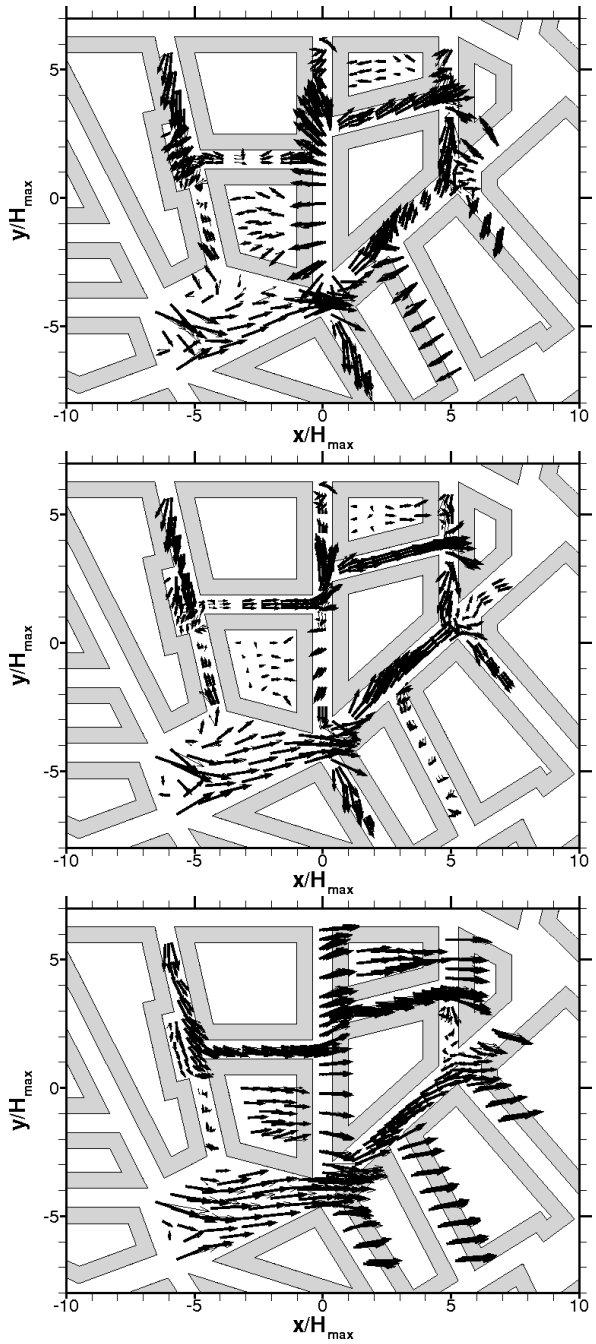

Figure 8: Mean flow field within street canyons at $z/H_{max} = 0.08, 0.38, 0.75$, from top to bottom, corresponding to $z = 2, 9, 18$ *m* in full scale. Fat gray arrows are measured data, thin black arrows simulation results

instead of the fine tetrahedral (H1-T1) or the fine polyhedral (H1-P1), as they are observed in Fig. 9 for the change from tetrahedra to polyhedra (T1-P1).

5. SUMMARY

The sensitivity of the computations of the flow field and concentration distribution in the generic Europaen city centre *Michel-Stadt* to several physical and numerical parameters have been analysed in this

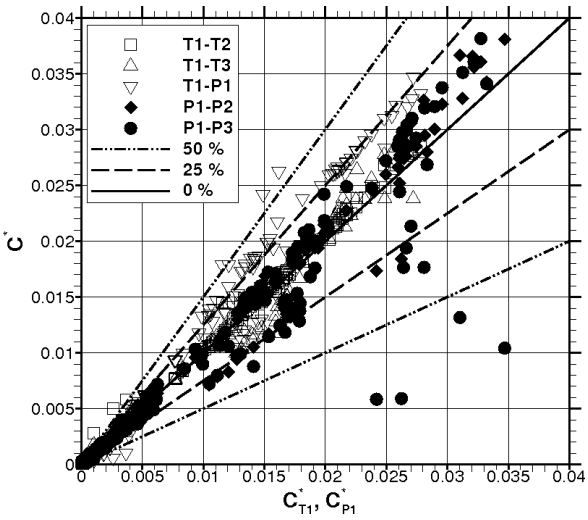

Figure 9: Influence of grid resolution for tetra- and polyhedral grids

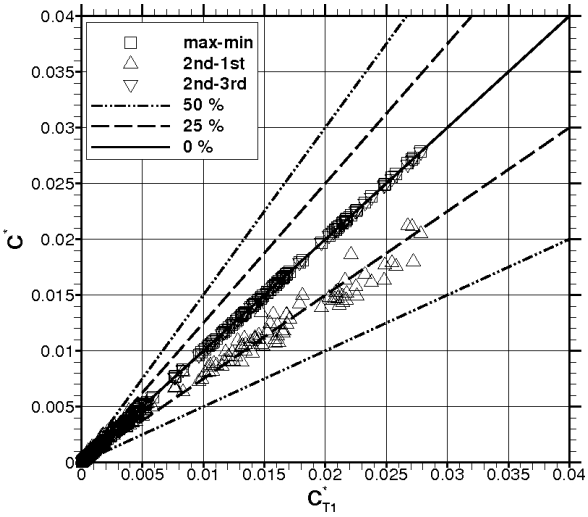

Figure 10: Sensitivity to source flow rate and numerical approximation on fine tetrahedral grid

work. Available measurements were used for assessing the influence of the parameter variations.

For the flow field the main findings are that the results are not very sensitive to changes in the Reynolds number and to changes in wall modelling. Despite the relatively small dimensionless wall distances, resulting differences from standard and enhanced wall modelling are negligible. Most astonishingly, the same is true when comparing results at the measurement positions, obtained on one hand with an approach flow over the explicitly modelled roughness elements, and on the other hand with implicit roughness element modelling by an aerodynamic roughness height, which is smaller than the experimentally observed one, due to the small grid size. The flow over and in between the buildings is therefore predominantly determined by the buildings themselves. The largest influence is due to the grid

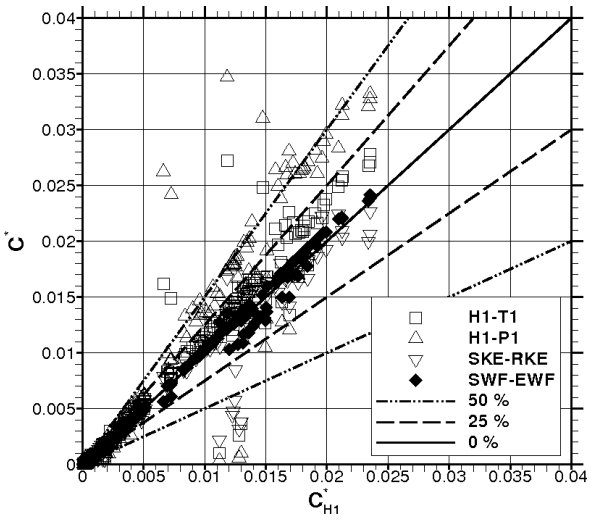

Figure 11: Sensitivity to grid type, as well as turbulence model and wall function on the hexahedral grid

resolution and the turbulence model, with the standard $k-\varepsilon$ model yielding better results than the realizable $k-\varepsilon$ model. With the former hit rates well above 0.70 are obtained for this complex urban geometry.

For the concentrations the abovementioned differences in the flow fields have the largest influence. The variation of the source flow rate by approximately a factor of two does not affect the normalised concentrations at the measurement positions, which are all further away from the source position. The use of the 1st order upwind method in the employed passive scaler transport equation increases the numerical diffusion, leading to lower concentrations at the measurement positions.

When measurements for the mean concentrations are available, a quantitative comparison is possible. This will be based on graphical comparison of the results at measurement positions and on metrics. In addition to the hit rate the usual metrics for dispersion will be used, which are for example the fractional bias, geometric variance or factor of two. The quality of the predictions will be assessed by also testing the recently proposed acceptance criteria for urban dispersion model evaluation by Hanna and Chang [14].

References

[1] Fernando, H., Zajic, D., Di Sabatino, S., Dimitrova, R., Hedquist, B., and Dallman, A. (2011) Flow, turbulence, and pollutant dispersion in urban atmospheres. *Phys. Fluids*, **22**, 051301–1–20.

[2] Schatzmann, M. and Leitl, B. (2011) Issues with validation of urban flow and dispersion CFD models. *J. Wind Eng. Ind. Aerodyn.*, **99**, 169–186.

[3] Roy, J. and Oberkampf, W. (2010) A complete framework for verification, validation, and uncertainty quantification in scientific computing. Tech. rep., AIAA 2010-124.

[4] Bastigkeit, I. (2011) *Erzeugung von Validierungsdaten für wirbelauflösende mikroskalige Strömungs- und Ausbreitungsmodelle*. Ph.D. thesis, Universität Hamburg, Department Geowissenschaften.

[5] Walters, R. and Huyse, L. (2002) Uncertainty analysis for fluid mechanics with applications. Tech. rep., NASA/CR-2002-211449, ICASE Report No. 2002-1.

[6] Congedo, P., Duprat, C., Balarac, G., and Corre, C. (2011) Effects of inlet uncertainties on prediction of turbulent flows using RANS and LES simulations. Tech. rep., AIAA 2011-3869.

[7] Fischer, R., Bastigkeit, I., Leitl, B., and Schatzmann, M. (2010) Generation of spatio-temporally high resolved datasets for the validation of LES-models simulating flow and dispersion phenomena within the lower atmospheric boundary layer. *Proc. 5th International Symposium on Computational Wind Engineering (CWE2010), Chapel Hill, North Carolina, USA*.

[8] Ansys (2009) *Ansys Fluent 12.0 Theory Guide*. Ansys Inc.

[9] Britter, R. and Schatzmann, M. (2007) *Background and justification document to support the model evaluation and protocol document*. COST Office.

[10] Schatzmann, M., Olesen, H., and Franke, J. (2010) *COST 732 Model Evaluation Case Studies: Approach and Results*. COST Office.

[11] Efthimiou, G., Hertwig, D., Fischer, R., Harms, F., Bastigkeit, I., Koutsourakis, N., Theodoridis, A., Bartzis, J., and Leitl, B. (2011) Wind flow validation for individual exposure studies. *Proc. 13th International Conference on Wind Engineering (ICWE13), Amsterdam, The Netherlands*.

[12] Rakai, A. and Franke, J. (2012) Validation of two RANS solvers with flow data of the flat roof Michelstadt case. *Proc. 8th International Conference on Air Quality Science and Application, Athens, Greece*.

[13] Rakai, A. and Franke, J. (2012) Validation of RANS flow models with flow data of an idealised central-European city centre, Michel-Stadt. *Proc. 15th International Conference on Fluid Flow Technologies (CMFF'12), Budapest, Hungary*.

[14] Hanna, S. and Chang, J. (2012) Acceptance criteria for urban dispersion model evaluation. *Meteorol Atmos Phys*, **116**, 133–146.

Conference on Modelling Fluid Flow (CMFF'12)
The 15th International Conference on Fluid Flow Technologies
Budapest, Hungary, September 4-7, 2012

LES Analysis of the Flow Around a Staggered Array of Buildings

Charikleia PAPACHRISTOU,[1] Evgeniy SHAPIRO, [2] Dimitris DRIKAKIS [2]

[1] Lanner Group Limited, Forward House, 17 High Street, Henley-in-Arden, Warwickshire, B95 5AA, UK. E-mail: HPapachristou@lanner.com
[2] Corresponding Author. Ricardo Software, Ricardo UK Limited, ShorehambySea, West Sussex, BN43 5FG, UK. E-mail: evgeniy.shapiro@ricardo.com
[3] Department of Fluid Mechanics and Computational Science, School of Engineering, Cranfield University, Cranfield, UK. E-mail: d.drikakis@cranfield.ac.uk

ABSTRACT

The paper presents a detailed investigation of the flow around a staggered array of buildings using Implicit Large Eddy Simulation. The effect of numerical discretisation on the obtained flow field are highlighted through a comparative evaluation of 2nd and 5th order spatial reconstruction methods. The results are validated against available experimental and DNS data demonstrating favourable performance of the ILES technique. The time-averaged flow field recovered from ILES simulations is then used in order to determine the parameters of the equivalent Atmospheric Boundary Layer (ABL) profile including the zero-plane displacement and roughness height. The results demonstrate that the equivalent ABL parameters are virtually independent of the spatial averaging approach with a negligible variation observed between a 25 stations averaged profile and a 4 stations averaged profile.

Keywords: ABL, ILES, High-order schemes

NOMENCLATURE

d	$[m]$	zero plane displacement
e	$[J/m^3]$	total energy
$\mathbf{E}, \mathbf{F}, \mathbf{G}$	$[-]$	inviscid flux vectors
h	$[m]$	roughness element height
k	$[-]$	von Karman constant
$\mathbf{L}, \mathbf{M}, \mathbf{N}$	$[-]$	viscous flux vectors
p	$[Pa]$	pressure
q	$[W/m^2]$	heat flux
ρ	$[kg/m^3]$	density
τ	$[Pa]$	viscous stress tensor
u, v, w	$[m/s]$	Cartesian velocity components
u_*	$[m/s]$	friction velocity
U_r	$[m/s]$	free stream velocity
z_0	$[m]$	surface roughness

1. INTRODUCTION

Atmospheric Boundary Layer (hereafter ABL) is the lowest part of the atmosphere in which two regions can be identified depending on whether the surface friction effects are negligible or not; the outer and the inner region respectively. In the inner region, air circulates closer to the Earth's surface giving rise to frictional forces which consequently lead to generation of turbulence. Since ABL is characterized as a three dimensional and turbulent layer where significant exchanges of momentum, heat and mass take place between the atmosphere and Earth's surface, the presence of any vegetation or mankind activities such as building structures could only result into an increase in its already complex flow structure. Parameters such as the wind's speed and direction, the local topology and the building characteristics could result into dirrefent scales of turbulence affecting in various extent pedestrian comfort and safety. Thus, proper understanding of the flow mechanisms in urban areas is vital so that its features are accurately predicted when computational methods are used. Computational (e.g. [1, 2, 3]) and experimental (e.g. [4]) representation of ABL in urban areas frequently relies on introduction of artificial roughness, for example through a periodic staggered array of wall mounted obstacles. The two most pertinent questions arising in the CFD modelling of this representation of ABL are these of the accuracy of the simulation and the reduction of extensive CFD data to the engineering approximations, such as the average ABL velocity profile. These issues are the focus of this paper.

Where the accuracy of a CFD simulation is concerned, one of the main sources of uncertainty is associated with the turbulence modelling. Reynolds Averaged Navier Stokes (RANS) turbulence models are arguably, the most widely

used class of turbulence models in building aerodynamics. Despite its popularity though, RANS was demonstrated to be inadequate in predicting complex flow fields either around a single or multiple building models in moderate and high Reynolds numbers [5, 3, 6, 7]. On the other side of the scale, a more accurate prediction of these flows can be obtained with Direct Numerical Simulation (DNS) (e.g. [8]). However, DNS becomes prohibitively expensive for high Reynolds number flows due to the resolution requirements. Over the past two decades, Large Eddy Simulation (LES) has been increasingly adopted as a method of choice for ABL model flows (e.g. [1, 2, 9]). Nonetheless, drawbacks still exist associated with the approach's potential in the field of wall bounded flows. With the scales becoming smaller and smaller in the near wall region, two options are available: either to modify the SGS model or to use wall models. Both options could increase the complexity of the SGS model rapidly and become unaffordable in high Reynolds numbers [10]. Boris et al. [11] introduced the idea of using implicit (ILES) instead of explicit SGS models relying on the dissipation of the numerical scheme to represent correct energy transfer between the scales of the flow. A particular class of ILES methods relying on high-resolution numerical schemes (e.g. [10]) has proven to be quite successful in the modelling of wall-bounded turbulent flows across a wide range of applications (e.g. [12]). Since the implicit SGS model relies on the dissipative properties of the numerical scheme, the comparative analysis of the performance numerical schemes presented in this paper allows to shed light on the turbulent modelling capability of ILES. The second part of the paper addresses the second issue - the reconstruction of the averaged wind velocity profile from the results of the CFD simulation, through the comparative analysis of different averaging and curve fitting approaches.

2. NUMERICAL FRAMEWORK

The flows under investigation are low speed. However, particularly in the context of ILES, it is convenient to utilise a full compressible solver to take full advantage of the shock-capturing schemes developed for compressible flow and tested extensively in ILES context (e.g. [12]). The flow is governed by the system of conservation laws in the differential conservative form given by:

$$\frac{\partial \mathbf{U}}{\partial t} + \frac{\partial \mathbf{E}}{\partial x} + \frac{\partial \mathbf{F}}{\partial y} + \frac{\partial \mathbf{G}}{\partial z} = \frac{\partial \mathbf{L}}{\partial x} + \frac{\partial \mathbf{M}}{\partial y} + \frac{\partial \mathbf{N}}{\partial z}\ , \quad (1)$$

where the vectors of the unknown conservative variables, viscous and inviscid fluxes as follows:

$$\mathbf{U} = \begin{pmatrix} \rho \\ \rho u \\ \rho v \\ \rho w \\ e \end{pmatrix},\ \mathbf{E} = \begin{pmatrix} \rho u \\ \rho u^2 + p \\ \rho v u \\ \rho w u \\ (e+p)u \end{pmatrix},$$

$$\mathbf{F} = \begin{pmatrix} \rho v \\ \rho u v \\ \rho v^2 + p \\ \rho w v \\ (e+p)v \end{pmatrix},\ \mathbf{G} = \begin{pmatrix} \rho w \\ \rho u w \\ \rho v w \\ \rho w^2 + p \\ (e+p)w \end{pmatrix},$$

$$\mathbf{L} = \begin{pmatrix} 0 \\ \tau_{xx} \\ \tau_{xy} \\ \tau_{xz} \\ u\tau_{xx} + v\tau_{xy} + w\tau_{xz} - q_x \end{pmatrix},$$

$$\mathbf{M} = \begin{pmatrix} 0 \\ \tau_{yx} \\ \tau_{yy} \\ \tau_{yz} \\ u\tau_{yx} + v\tau_{yy} + w\tau_{yz} - q_y \end{pmatrix},$$

$$\mathbf{N} = \begin{pmatrix} 0 \\ \tau_{zx} \\ \tau_{zy} \\ \tau_{zz} \\ u\tau_{zx} + v\tau_{zy} + w\tau_{zz} - q_z \end{pmatrix}. \quad (2)$$

The system is closed by the Newtonian stress tensor expression with the viscosity given by Sutherland's law, the Fourier's law expression for the heat flux and ideal gas thermal and caloric equations of state. The block structured CNS3D solver is used to solve the above system in curvilinear coordinates corresponding to the local transformation from (x, y, z) to (i, j, k) space (e.g. [13]). The viscous fluxes **L**, **M** and **N**, are discretised using the second order central difference scheme in (i, j, k) space. The inviscid fluxes are computed using HLLC Riemann solver [14] with the reconstructed left and right states given by either of:

- *Monotonic Upwind Scheme for Scalar Conservation Laws* (MUSCL) scheme [15, 16] with the 2nd order limiter by van Albada (hereafter 2ndVA, [17]) or 5th order limiter by Kim and Kim (hereafter 5thM) [18, 19]
- *Weighted Essentially Non-Oscillatory* (WENO) scheme by Liu et al. in 5th order of accuracy (hereafter 5thWN [20])

The time integration approach used the explicit 3rd order *Total Variation Diminishing* (TVD) Runge-Kutta scheme (e.g. [13]).

The reader is referred to [21] for the complete system of equatons and a detailed description of numerical schemes.

3. PROBLEM FORMULATION

The benchmark case adopted in this paper follows the experimental study by Cheng and

Castro [4] (case C20S in the reference paper), who investigated near-wall flow over a staggered array of wall-mounted obstacles as a representative benchmark for urban ABL. This problem was investigated computationally by a number of authors (e.g. [9],[8]), notably - a DNS study was performed by Coceal et al. [8] providing an excellent opportunity to evaluate performance of ILES. In order to enable the comparison with the DNS study, a periodic section of the roughness domain is used containing four repeating units arranged in a regular staggered manner. Each of those units consists of a one cube (building) a 25% covering area. The size of the domain is L_x x L_y x L_z = 4h x 4h x 4h , where $h = 0.02m$ is the building height (Figure 1).

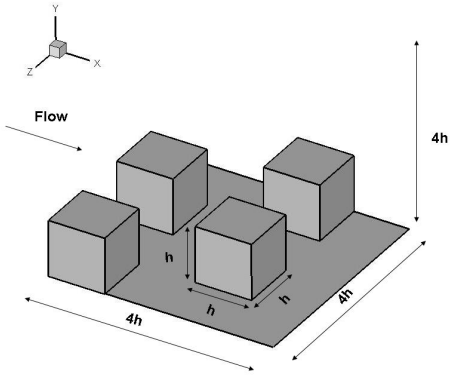

Figure 1. Computational domain

The case is simulated at a Reynolds number Re = 5000 based on the free stream velocity U_r and bulding height h corresponding to the experimental conditions. The Mach number was set equal to 0.2 to speed up the computations for the explicit scheme and the viscosity was adapted to match the Reynolds number of the experiment. The top boundary (along the y- direction) was set to symmetry. The non slip condition was chosen for the lower boundary of the domain and the faces of the buildings. Fully periodic boundary conditions were imposed along the streamwise (x) and spanwise (z) direction to simulate an infinite array of obstacles. Due to the periodic boundary conditions, a constant forcing pressure gradient of $-1.59Pam^{-1}$ is used. The solution was initially run until the stabilisation of the average velocity at several marker points in the domain. The averaged quantities were then assembled over the period of approximately 1400 CPU hours.

The computational mesh was created in the commercial software GridgenV15 using a structured multiblock configuration. The results presented in this paper were obtained using a clustered computational mesh of 16x16x16 nodes per unit cube. The mesh was selected based on the grid sensitivity study (see [21]), as providing an optimal cost/quality ratio. Note that DNS results of [8] were obtained on a mesh of 64x64x64 nodes per unit cube.

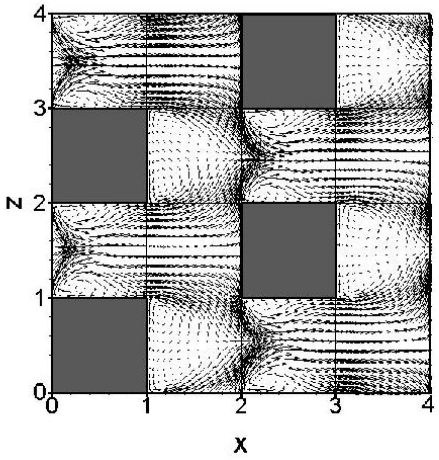

Figure 2. Velocity vectors at xz plane (y=0.5)

4. COMPARISON OF SCHEMES

The structure of the flow field is illustrated by vectors of time-averaged velocity at constant xz-plane. Indicative results obtained using the 5th order MUSCL scheme are shown in Figure (2). The flow enters the computational domain along the streamwise direction and gets redirected by the presence of the buildings. Due to flow separation at the upstream face of the building, a complex vortical structure is formulated around the sides and wake. The flow is redirected along the left and right walls and wraps around each building until it starts weakening further downstream. Finally, the presence of two vortices in very close proximity to the leeward face of the building indicates the existence of legs of the arc-type vortex. Based on the above observations, it can be stated that the flow characteristics resemble those seen in the fundamental case of flow around an isolated obstacle (e.g. [22]. Vortices are also observed near the end of the computational domain; an indication of the near wall region ahead due to the periodic boundary conditions.

The distributions of streamwise velocity u results were compared against Laser Doppler Anemometry experimental data (LDA) [4] and DNS data [8] at four representative locations; over the roof $P0$, $(x, z) = (0.5h, 2.5h)$, at the wake $P1$, $(x, z) = (1.5h, 3.5h)$, in front of the cube $P2$, $(x, z) = (1.5h, 1.5h)$ and in the cavity between the cubes $P3$, $(x, z) = (0.5h, 3.5h)$. Location $P0$ corresponds to the rapid acceleration of flow over the building without recirculation. Wall-normal rake at location $P1$ traverses the recirculation bubble immediately behind the building. Location $P2$ corresponds to the flow being pushed upward by the recirculation bubble in front of the building, Finally at $P3$ - the

flow is slowed down between the two recirculation bubbles between the buildings.

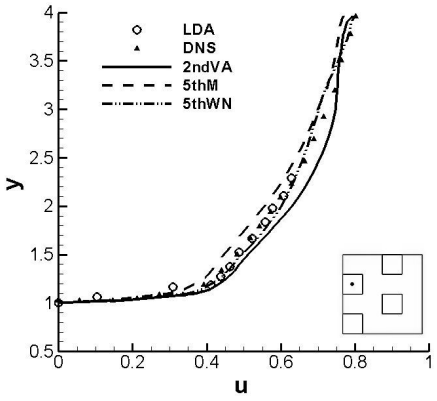

Figure 3. P0: Time averaged velocity profile over the roof of the cube

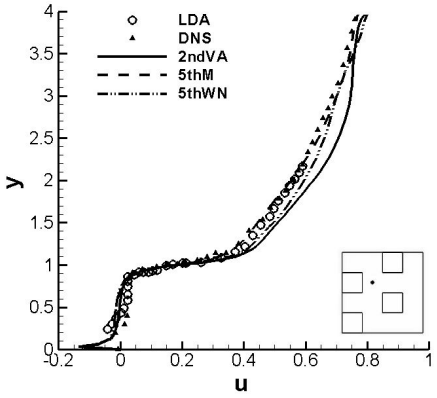

Figure 4. P1: Time averaged velocity profile at the wake of a cube

The comparisons between LDA and computational data are presented in Figures 3- 6. Overall, all simulations are in good agreement with the experimental data. However, based on the velocity comparisons, 5thM scheme provide arguably a better overall fit with 2ndVA scheme predicting a fuller ABL profile in the inertial layer (Figures 3 and 4) and 5thWN scheme - underpredicting the acceleration of flow between the buildings (Figures 5 and 6) by comparison with the experimental data. The recovery to freestream conditions is similar between the schemes. It is also notable that there is virtually no difference between the results in the stagnation region behing the cube (Figure 4.

DNS data of Coceal et al. [8] allows evaluation of ILES performance towards freestream where there is no experimental data available. Figures 3 and 6

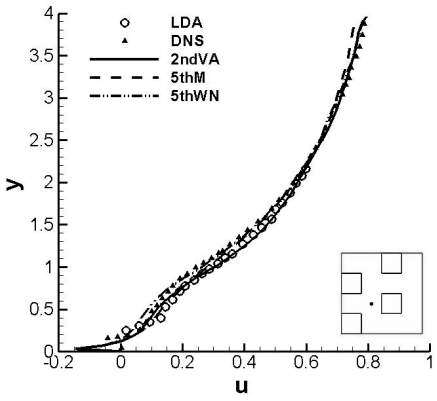

Figure 5. P2: Time averaged velocity profile in front of a cube

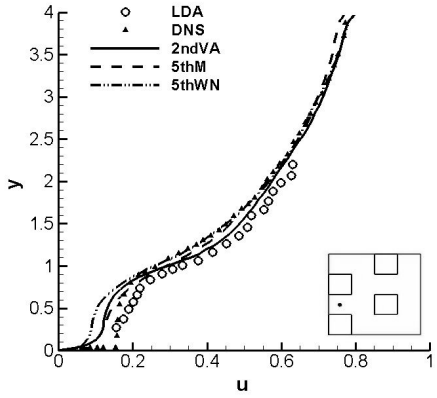

Figure 6. P3: Time averaged velocity profile in the cavity between the cubes

also show comparison with DNS data at points P0 and P3 where there difference between ILES results obtained with different schemes is more pronounced. The results indicate that the fuller ABL profile predicted by 2ndVA scheme is incorrect and the best agreement is with 5thWN at P0 and P3 and 5thM at P1 with both 5th order schemes recovering correct freestream values. At P2 both 5th order schemes are in agreement with DNS data.

Finally, comparisons in terms of Reynolds stresses are given in Figures 7 and 8. Specifically, Figure 7 shows comparisons of Reynolds stresses at P1. The peaks of the stresses in the shear layer are captured with reasonable accuracy by all schemes. Better comparisons are seen as the order of the scheme increases. In Figure 8, the stresses are underpredicted above the height of the cube.

Overall, results obtained with ILES are in a good agreement with DNS and experimental data. The ability of ILES to yield results of accuracy similar to that of DNS is very encouraging. Furthermore the ILES results were obtained on a grid 64 times coarser

than that employed in DNS simulations. The above highlights the appropriateness of applying ILES for this type of flows.

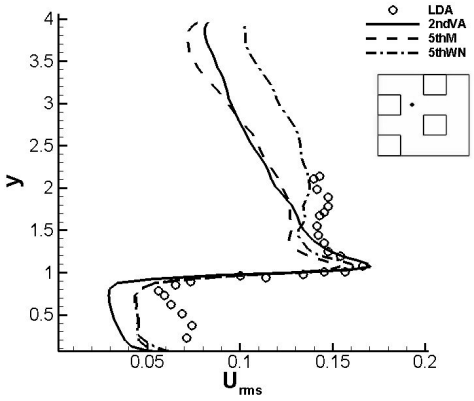

Figure 7. P0: Time averaged velocity profile over the roof of the cube

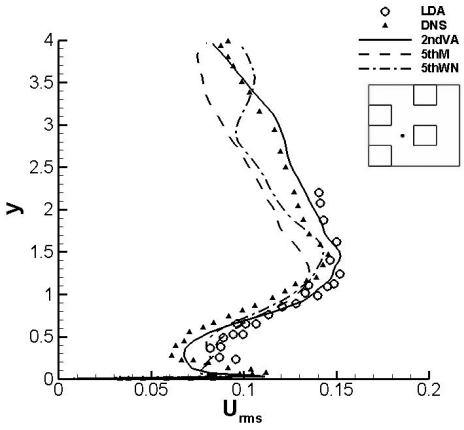

Figure 8. P1: Time averaged velocity profile at the wake of a cube

5. RECONSTRUCTION OF THE LOGARITHMIC ABL PROFILE

Under neutral conditions, the spatially-averaged vertical wind variation within the inertial sublayer can be described by the logarithmic law given given by:

$$u = \frac{u_*}{k} ln\left(\frac{z-d}{z_0}\right) . \quad (3)$$

where d is the zero-plane displacement, z_0 is the roughness length, u_* is the friction velocity and k is the von Karman constant (0.4 in the present study). The parameters included in Eq. 3, have to be recovered from the averaged experimental or computational data. In the reference experimental study [4], Cheng and Castro initially used 25 measurement locations over one geometrically repeating unit as indicated in Figure 9. However, based on the comparisons of velocities and Reynolds stresses resulting from spatial averaging over at 25 line array and 4-line array (highlighted by squares in Figure 9), the authors have decided to use 4-point spatial averaging as the difference was apparenly small. One should note however, that the curve fitting to logarithmic ABL profile is very sensitive to the averaged distribution and visible lack of difference in the average profile does not guarantee negligible difference in the recovered coefficients of the logarithmic profile. Therefore we will include the comparison of the 4-line and 25-line averaged results.

According to Eq. (3), the friction velocity u_* is used as the slope fit in the logarithmic law profile. When the viscous contribution is assumed negligible, u_* can be calculated from the pressure distribution on the front and back faces on the cubes (denoted as $u_*(p)$). In most cases however, a direct measurement of the drag force is not possible and $u_*(\tau)$ is deduced from turbulence shear stress measurements with the best fit provided by taking into account both inertial and roughness sublayers [4]. The zero-plane displacement d and roughness length z_0 are then determined by fitting the logarithmic law using various u_*. A summary of the surface characteristics of the staggered cubical array extracted from the four locations only, is shown in Table 1 as presented in the work of Cheng et al. [4]. The difference in the results highlights the uncertainty of the procedure of determination of the parameters of ABL from experimental measurements. We will use $u_*(\tau)$ fitting for comparison purposes though as the shear stress approach is more common. Note that the actual point where the velocity of the fitted logarithmic ABL is equal to zero for the shear stress fit is located at $z = 0.01751m$ ($z = 0.8755h$).

Table 1. LDA surface characteristics [4].

	$u_*(p)$	$u_*(\tau)$
u_*/U_r	0.0724	0.0635
$d(mm)$	14.5	16.7
$z_0(mm)$	1.33	0.81

As part of the numerical scheme dependency investigation, mean velocity profiles have been obtained with all schemes (either in their original form or modified) at specific locations consistent with the methodology presented in [4]. Typically, in experimental measurements, u_* in Eq. 3 is obtained from the shear stress profile in the inertial sublayer, whereas roughness parameters, independent of the wind speed, are obtained from the curve fitting of the Eq. 3. One of the main differences between the CFD results and experimental results obtained for this flow at the same nominal Reynolds number is the

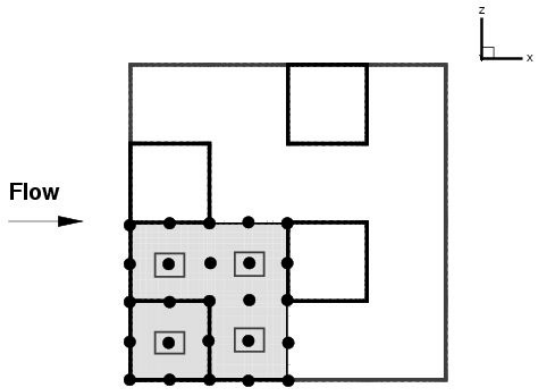

Figure 9. Locations of spatial averaging

value of the friction velocity characterising the wall shear stress. In order to evaluate this difference, the following methodology was adopted in this paper. The roughness parameter z_0 depends only on the roughness geometry (e.g. [23]), therefore it was fixed at the experimental value of $0.81mm$ as the computational array is identical to the one used in the experiment. The velocity profiles were then spatially averaged and fitted into the logarithmic Eq. 3 using linear regression analysis along with the least square fitting to obtain the friction velocity u_* and zero plane displacement d.

The results obtained with different numerical schemes are presented in Table 2. The sensitivity of the results to the averaging approach increases with the decrease of the order of accuracy. The ILES surface parameters exhibit a good agreement with the experimental parameters. Comparing 4-line averaged data between the experiment and computation, best agreement for the friction velocity is given by 5thM scheme (10.4%) and the smallest error in the zero-plane displacement - by 2ndVA scheme (3.1%). Furthermore the difference between the spatial averaging approaches is negligible, which is in line with the experimental findings. All numerical velocity profiles are providing an excellent fit to the logarithmic profile with the R2 goodness of the fit exceeding 0.98 for all cases. Note that all three schemes overpredict the friction velocity.

6. SUMMARY

Implicit Large Eddy Simulation using high-resolution methods was applied to flows around a staggered array of four cubical elements representing buildings. Real urban environment involving separation and reattachment areas due to wind's interaction with buildings or other roughness elements, provides an excellent test case for assessing the accuracy of ILES in predicting such highly complex flows. The investigation

Table 2. ILES surface parameters using the 2-parameter fit

Scheme	2ndVA	5thM	5thWN
25 lines fit			
u_*/U_r	0.0719	0.0701	0.0719
$d(mm)$	17.5	18.3	18.2
R^2	0.99	0.99	0.99
4 lines fit			
u_*/U_r	0.0715	0.0702	0.0718
$d(mm)$	17.2	18.1	18.0
R^2	0.99	0.98	0.99

was performed in stages focusing on the effect of numerical parameters on the solution.

The first stage involved the validation of ILES results against available LDA data in terms of mean velocity profiled at four distinct locations. Comparisons were made also between ILES and DNS data. From the results obtained, it is clear that despite the reduced grid resolution, ILES maintained a reasonable agreement with the LDA and DNS data.

The second stage considered the fitting of the spatially averaged mean velocity data (above the cube) to the logarithmic wind profile. Fitted friction velocity and zero plane displacement were found to be in a good agreement with the experimental data, with the 5th order MUSCL scheme yielding best prediction of the friction velocity. All schemes lead to an excellent fit to the logarithmic velocity profile in the inertial sublayer.

With the accuracy of ILES simulations demonstrated through the direct comparison against DNS and experiment, further analysis of this flow can focus on issues of numerical accuracy and methods of extraction of ABL parameters from the computational data.

References

[1] Kanda, M., Moriwaki, R., and Kasamatsu, F. 2004 "Large-eddy simulation of turbulent organized structures within and above explicitly resolved cube arrays". *Boundary Layer Meteorology*, Vol. 112, pp. 343–368.

[2] Stoesser, T., Mathey, F., Frohlich, J., and Wolfgang, R. 2003 "LES of flow over multiple cubes". *ERCOFTAC Bulletin*.

[3] Tutar, M. and Oguz, G. 2004 "Computational modelling of wind flow around a group of buildings". *International Journal of Computational Fluid Dynamics*, Vol. 18, pp. 651–670.

[4] Cheng, H. and Castro, I. 2002 "Near wall flow over urban-like roughness". *Boundary-Layer Meteorology*, Vol. 104, pp. 229–259.

[5] Ehrhard, J. and Moussiopoulos, N. 2000 “On a new nonlinear turbulence model for simulating flows aroud building-shaped structures”. *Journal of Wind Engineering and Industrial Aerodynamics*, Vol. 88, pp. 91–99.

[6] Murakami, S. 1993 “Comparison of various turbulence models applied to a bluff body”. *Journal of Wind Engineering and Industrial Aerodynamics*, Vol. 46/47, pp. 21–36.

[7] Murakami, S. 1997 “Current status and future trends in computational wind engineering”. *Journal of Wind Engineering and Industrial Aerodynamics*, Vol. 67/68, pp. 3–34.

[8] Coceal, O., Thomas, T., Castro, I., and Belcher, S. 2006 “Mean flow and turbulent statistics over groups of urban-like cubical obstacles.”. *Boundary Layer Meteorology*, Vol. 121, pp. 491–519.

[9] Xie, Z. and Castro, I. 2006 “LES and RANS for turbulent flow over arrays of wall-mounted obstacles”. *Flow Turbulence Combust*, Vol. 76, pp. 291–312.

[10] Grinstein, F., Margolin, L., and Rider, W. 2006 *Implicit Large Eddy Simulation*. Cambridge University Press.

[11] Boris, J. P., Grinstein, F. F., Oran, E. S., and Kolbe, R. L. 1992 “New insights into large eddy simulation”. *Fluid Dynamics Research*, Vol. 10, pp. 199–228.

[12] Drikakis, D., Hahn, M., Mosedale, A., and Thornber, B. 2009 “Large-eddy simulation using hgh-resolution and high-order methods”. *Phylosophical Transaction of the Royal Society*, Vol. 367, pp. 2985–2997.

[13] Drikakis, D. and Rider, W. J. 2004 *High-Resolution Methods for Incompressible and Low-Speed Flows*. Springer.

[14] Toro, E., Spruce, M., and Speares, W. 1992 “Restoration of the contact surface in the HLL Riemann solver”. Tech. Rep. Technical Report COA–9204., College of Aeronautics. Cranfield Institute of Technology. UK.

[15] Kolgan, V. 1972 “Application of the minimum-derivative principle in the construction of finite-difference schemes for numerical analysis of discontinuous solutions in gas dynamics.”. *Transactions of the Central Aerohydrodynamics Institute*, Vol. 3(6), pp. 68–77.

[16] van Leer, B. 1974 “Towards the ultimate conservative difference scheme. Part II: Monotonicity and conservation combined in a second order scheme”. *Journal of Computational Physics*, Vol. 14, pp. 361–370.

[17] van Albada, B. R. W. W. J., G. D.; van Leer 1982 “A comparative study of computational methods in cosmic gas dynamics”. *Astronomy and Astrophysics*, Vol. 108(1), pp. 76–84.

[18] Kim, K. H. and Kim, C. 2005 “Accurate, efficient and monotonic numerical methods for multi-dimensional compressible flows. Part I: Spatial discretization”. *Journal of Computational Physics*, Vol. 208, pp. 527–569.

[19] Kim, K. H. and Kim, C. 2005 “Accurate, efficient and monotonic numerical methods for multi-dimensional compressible flows. Part II: Multi-dimensional limiting process”. *Journal of Computational Physics*, Vol. 208, pp. 570–615.

[20] Liu, X.-D., Osher, S., and Chan, T. 1994 “Weighted Essentially Non-oscillatory Schemes”. *Journal of Computational Phyics*, Vol. 115, pp. 200–212.

[21] Papachristou, C. 2010 “Implicit Large Eddy Simulation of Environmental Urban Flows”. Ph.D. thesis,

[22] Martinuzzi, R. and Tropea, C. 1993 “The flow around surface mounted prismatic obstacles placed in a fully developed channel flow”. *ASME Journal of Fluids Engineering*, Vol. 115, pp. 85–92.

[23] Raupach, M., Antonia, R., and Rajagopalan, S. 1991 “Rough-wall turbulent boundary layers”. *Appl. Mech. Rev*, Vol. 44, pp. 1–25.

Conference on Modelling Fluid Flow (CMFF'12)
The 15th International Conference on Fluid Flow Technologies
Budapest, Hungary, September 4-7, 2012

SPECTRALLY-CONSISTENT REGULARIZATION MODELLING OF WIND FARM BOUNDARY LAYERS

F. Xavier TRIAS[1], David FOLCH[2], Andrey GOROBETS[3,4], Assensi OLIVA[5]

[1]Heat and Mass Transfer Technological Center, Technical University of Catalonia, C/Colom 11 08222 Terrassa, Spain.
Tel.: +34 93 739 81 92, Fax: +34 93 739 89 20, Email: xavi@cttc.upc.edu
[2]Heat and Mass Transfer Technological Center, Technical University of Catalonia, E-mail: davidf@cttc.upc.edu
[3]Heat and Mass Transfer Technological Center, Technical University of Catalonia, E-mail: andrey@cttc.upc.edu
[4]Keldysh Institute of Applied Mathematics, Russian Academy of Sciences, Moscow, Russia.
[5]Heat and Mass Transfer Technological Center, Technical University of Catalonia, E-mail: oliva@cttc.upc.edu

ABSTRACT

The incompressible Navier-Stokes equations constitute an excellent mathematical modelization of turbulence. Unfortunately, attempts at performing direct simulations are limited to relatively low-Reynolds numbers because of the almost numberless small scales produced by the non-linear convective term. Alternatively, a dynamically less complex formulation is proposed here. Namely, regularizations of the Navier-Stokes equations that preserve the symmetry and conservation properties exactly. To do so, both convective and diffusive term are altered in the same vein. In this way, the convective production of small scales is effectively restrained whereas the modified diffusive term introduces a hyperviscosity effect and consequently enhances the destruction of small scales. In practise, the only additional ingredient is a self-adjoint linear filter whose local filter length is determined from the requirement that vortex-stretching must stop at the smallest grid scale. In the present work, the performance of the above-mentioned recent improvements is assessed through application to homogeneous isotropic turbulence, a turbulent channel flow and a turbulent boundary layer. As a final application, regularization modelling will be applied for large-scale numerical simulation of the atmospheric boundary layer through wind farms.

Keywords: Energy conserving, Hyperviscosity, Regularization modelling, Turbulence, Wind power

NOMENCLATURE

$\mathcal{C}(\underline{u},\underline{v})$	convective operator, $(\underline{u}\cdot\nabla)\underline{v}$
$\mathcal{D}\underline{u}$	diffusive operator, $\nu\Delta\underline{u}$
$H_4(\widehat{g}_k)$	overall damping effect introduced in the k-th Fourier-mode
Q	second invariant of S, $-1/2tr(S^2)$
R	third invariant of S, $-1/3tr(S^3)$
Re	Reynolds number
S	strain tensor, $1/2(\nabla\underline{u}+\nabla\underline{u}^T)$
$f_4^\gamma(\widehat{g}_k)$	damping effect introduced by the $\mathcal{C}_4^\gamma$ regularization in the k-th Fourier-mode
$\widehat{g}_k$	k-th Fourier-mode of the convolution kernel of the filter
h	local grid size
$h_4^\gamma(\widehat{g}_k)$	hyper-viscosity effect introduced in the k-th Fourier-mode
k	k-th Fourier-mode
k_c	smallest grid scale
p	pressure
$\underline{u}$	velocity field
α	$\epsilon/\sqrt{24}$
γ , $\tilde{\gamma}$	parameter in $\mathcal{C}_4^\gamma$ model, $\tilde{\gamma}=1/2(1+\gamma)$
ϵ	filter length
ε	dissipation rate of kinetic energy
λ_i	eigenvalues of S, $\lambda_1\leq\lambda_2\leq\lambda_3$
λ_Δ	largest non-zero eigenvalue of the Laplacian operator
ν	kinematic viscosity
$\underline{\omega}$	vorticity, $\nabla\times\underline{u}$

Subscripts and Superscripts

$\overline{(\cdot)}$, $(\cdot)'$	symmetric linear filter and its residual
$\widehat{(\cdot)}$	Fourier transform
$(\cdot)^*$	conjugate transpose

1. INTRODUCTION

The incompressible Navier-Stokes (NS) equations form an excellent mathematical model for turbulent flows. In primitive variables they read

$$\partial_t\underline{u}+\mathcal{C}(\underline{u},\underline{u})=\mathcal{D}\underline{u}-\nabla p\;;\qquad \nabla\cdot\underline{u}=0, \qquad (1)$$

where $\underline{u}$ denotes the velocity field, p represents the pressure, the non-linear convective term is defined by $\mathcal{C}(\underline{u},\underline{v})=(\underline{u}\cdot\nabla)\,\underline{v}$, and the diffusive term reads $\mathcal{D}\underline{u}=\nu\Delta\underline{u}$, where ν is the kinematic viscosity. Preserving the symmetries of the continuous differential operators

when discretizing them has been shown to be a very suitable approach for direct numerical simulation (DNS) (see [1, 2, 3], for instance). Doing so, certain fundamental properties such as the inviscid invariants - kinetic energy, enstrophy (in 2D) and helicity (in 3D) - are exactly preserved in a discrete sense. However, direct simulations at high Reynolds numbers (Re) are not feasible because the convective term produces far too many relevant scales of motion. In the quest for a dynamically less complex formulation we consider regularizations [4, 5, 6] of non-linearity that preserve the symmetry and conservation properties exactly [7]. In this way, the convective production of small scales is effectively restrained in an unconditionally stable manner. In our previous works, we restrict ourselves to the $\mathcal{C}_4$ approximation: the convective term in the NS equations (1) is then replaced by the following $\mathcal{O}(\epsilon^4)$-accurate smooth approximation $\mathcal{C}_4(\underline{u},\underline{v})$ given by

$$\mathcal{C}_4(\underline{u},\underline{v}) = \mathcal{C}(\overline{\underline{u}},\overline{\underline{v}}) + \overline{\mathcal{C}(\overline{\underline{u}},\underline{v}')} + \overline{\mathcal{C}(\underline{u}',\overline{\underline{v}})}, \quad (2)$$

where the prime indicates the residual of the filter, *e.g.* $\underline{u}' = \underline{u} - \overline{\underline{u}}$, which can be explicitly evaluated, and $\overline{(\cdot)}$ represents a symmetric linear filter with filter length ϵ. Therefore, the governing equations result to

$$\partial_t \underline{u}_\epsilon + \mathcal{C}_4(\underline{u}_\epsilon,\underline{u}_\epsilon) = \mathcal{D}\underline{u}_\epsilon - \nabla p_\epsilon; \qquad \nabla\cdot\underline{u}_\epsilon = 0, \quad (3)$$

where the variable names are changed from $\underline{u}$ and p to $\underline{u}_\epsilon$ and p_ϵ, respectively, to stress that the solution of (3) differs from that of (1). Note that the $\mathcal{C}_4$ approximation is also a skew-symmetric operator like the original convective operator. Hence, the same inviscid invariants than the original NS equations are preserved for the new set of partial differential equations (3). The numerical algorithm used to solve the governing equations preserves the symmetries and conservation properties too. In practise, the only additional ingredient is a self-adjoint linear filter [8] whose local filter length is determined from the requirement that vortex-stretching must stop at the smallest grid scale [9]. Altogether, the method constitutes a parameter-free turbulence model that has already been successfully tested for a variety of natural and forced convection configurations (see [7, 9], for instance). However, two main drawbacks have been observed: (i) due to the energy conservation, the model solution tends to display an additional hump in the tail of the spectrum and (ii) for very coarse meshes the damping factor can eventually take very small values. These two issues are addressed in the following section.

2. RESTORING THE GALILEAN INVARIANCE: HYPERVISCOSITY EFFECT

The $\mathcal{C}_4$ regularization preserves all the invariant transformations of the original NS equations, except the Galilean transformation. This is a usual feature for most of the regularizations of the non-linear term [10]. This can always be recover by means of a proper modification of the time-derivative term. With this idea in mind, and following the same principles than in [7], new regularizations have been recently proposed in [11]. Actually, they can be viewed as a generalisation of the regularization methods proposed in [7] where Galilean invariance is partially recovered by means of a modification of the diffusive term. Shortly, by imposing all the symmetries and conservation properties of the original convective operator, $\mathcal{C}(\underline{u},\underline{u})$, and cancelling the second-order terms leads to the following one-parameter fourth-order regularization

$$\mathcal{C}_4^\gamma(\underline{u},\underline{v}) = \frac{1}{2}((\mathcal{C}_4+\mathcal{C}_6)+\gamma(\mathcal{C}_4-\mathcal{C}_6))(\underline{u},\underline{v}). \quad (4)$$

Notice that for $\gamma = 1$ and $\gamma = -1$, $\mathcal{C}_4^\gamma$ becomes respectively the $\mathcal{C}_4$ and $\mathcal{C}_6$ approximations proposed in [7],

$$\mathcal{C}_4(\underline{u},\underline{v}) = \mathcal{C}(\overline{\underline{u}},\overline{\underline{v}}) + \overline{\mathcal{C}(\overline{\underline{u}},\underline{v}')} + \overline{\mathcal{C}(\underline{u}',\overline{\underline{v}})},$$
$$\mathcal{C}_6(\underline{u},\underline{v}) = \mathcal{C}(\overline{\underline{u}},\overline{\underline{v}}) + \mathcal{C}(\overline{\underline{u}},\underline{v}') + \mathcal{C}(\underline{u}',\overline{\underline{v}}) + \overline{\mathcal{C}(\underline{u}',\underline{v}')}.$$

Then, to restore the Galilean invariance we need to replace the time-derivative, $\partial_t\underline{u}_\epsilon$, by the following fourth-order approximation:

$$(\partial_t)_4^\gamma \underline{u}_\epsilon = \partial_t(\underline{u}_\epsilon - 1/2(1+\gamma)\underline{u}_\epsilon'') = \mathcal{G}_4^\gamma(\partial_t\underline{u}_\epsilon), \quad (5)$$

where $\mathcal{G}_4^\gamma(\phi) = \phi - 1/2(1+\gamma)\phi''$. In this case, the new set of PDEs reads

$$(\partial_t)_4^\gamma \underline{u}_\epsilon + \mathcal{C}_4^\gamma(\underline{u}_\epsilon,\underline{u}_\epsilon) = \mathcal{D}\underline{u}_\epsilon - \nabla p_\epsilon. \quad (6)$$

Therefore, Galilean invariance might be restored by simply setting $\gamma = -1$. However, this approach suffers from several practical drawbacks [11]. Another possibility relies on modifying appropriately other terms, *i.e.* viscous dissipation. The energy equation for (6) becomes

$$\frac{d}{dt}(|\underline{u}_\epsilon|^2 - 1/2(1+\gamma)|\underline{u}_\epsilon'|^2) = (\underline{u}_\epsilon, \mathcal{D}\underline{u}_\epsilon) < 0, \quad (7)$$

provided that the filter is self-adjoint, $|\underline{u}|^2 = (\underline{u},\underline{u})$, and the innerproduct of functions is defined in the usual way: $(a,b) = \int_\Omega a\cdot b d\Omega$. Therefore, the modification of time-derivative term (5) constitutes a dissipation model. Recalling that $(\mathcal{G}_4^\gamma)^{-1}(\phi) \approx 2\phi - \mathcal{G}_4^\gamma(\phi) + \mathcal{O}(\epsilon^6)$, we can obtain an energetically almost equivalent set of equations by modifying the viscous diffusive term

$$\partial_t\underline{u}_\epsilon + \mathcal{C}_4^\gamma(\underline{u}_\epsilon,\underline{u}_\epsilon) = \mathcal{D}_4^\gamma\underline{u}_\epsilon - \nabla p_\epsilon, \quad (8)$$

where the linear operator $\mathcal{D}_4^\gamma\underline{u}$ is given by

$$\mathcal{D}_4^\gamma \underline{u} = \mathcal{D}\underline{u} + 1/2(1+\gamma)(\mathcal{D}\underline{u}')'. \quad (9)$$

In this way, we are reinforcing the dissipation by means of a hyperviscosity term. As expected, this basically acts at the tail of the energy spectrum and therefore helps to mitigate the two above-mentioned drawbacks of the original $\mathcal{C}_4$ regularization. Then, to apply the method two parameters still need to be determined; namely, the local filter length, ϵ, and the constant γ. These two issues are addressed in the forthcoming sections 3 and 4, respectively.

3. RESTRAINING THE PRODUCTION OF SMALL SCALES OF MOTION

3.1. Interscale interactions

To study the interscale interactions in more detail, we continue in the spectral space. The spectral representation of the convective term in the NS equations is given by

$$\mathcal{C}(\underline{u},\underline{u})_k = i\Pi(k) \sum_{p+q=k} \hat{u}_p q \hat{u}_q, \quad (10)$$

where $\Pi(k) = I - kk^T/|k|^2$ denotes the projector onto divergence-free velocity fields in the spectral space. Taking the Fourier transform of (8), we obtain the evolution of each Fourier-mode $\hat{u}_k(t)$ of $u_\epsilon(t)$ for the $\{\mathcal{CD}\}_4$ approximation[1]

$$\left(\frac{d}{dt} + h_4^\gamma(\widehat{g}_k)\nu|k|^2\right)\hat{u}_k + i\Pi(k) \sum_{p+q=k} f_4^\gamma\left(\widehat{g}_k, \widehat{g}_p, \widehat{g}_q\right) \hat{u}_p q \hat{v}_q = F_k, \quad (11)$$

where $\widehat{g}_k$ denotes the k-th Fourier-mode of the kernel of the convolution filter, *i.e.*, $\overline{\hat{u}}_k = \widehat{g}_k \hat{u}_k$. The mode $\hat{u}_k$ interacts only with those modes whose wavevectors p and q form a triangle with the vector k. Thus, compared with (10), every triad interaction is multiplied by

$$f_4^\gamma(\widehat{g}_k, \widehat{g}_p, \widehat{g}_q) = (\tilde{\gamma} f_4 + (1-\tilde{\gamma}) f_6)(\widehat{g}_k, \widehat{g}_p, \widehat{g}_q) \quad (12)$$

where $\tilde{\gamma} = 1/2(1+\gamma)$ and f_4 and f_6 are given by

$$f_4(\widehat{g}_k, \widehat{g}_p, \widehat{g}_q) = \widehat{g}_k(\widehat{g}_p + \widehat{g}_q) + \widehat{g}_p\widehat{g}_q - 2\widehat{g}_k\widehat{g}_p\widehat{g}_q \quad (13)$$

$$f_6(\widehat{g}_k, \widehat{g}_p, \widehat{g}_q) = 1 - (1-\widehat{g}_k)(1-\widehat{g}_p)(1-\widehat{g}_q), \quad (14)$$

where $0 < f_n \leq 1$ $(n = 4, 6)$. On the other hand, the k-th Fourier mode of the diffusive term is multiplied by

$$h_4^\gamma(\widehat{g}_k) = 1 + \tilde{\gamma}(1-\widehat{g}_k)^2 \quad (15)$$

where $h_4 \geq 1$. Moreover, since for a generic symmetric convolution filter (see [12], for instance), $\widehat{g}_k = 1 - \alpha^2|k|^2 + \mathcal{O}(\alpha^4)$ with $\alpha^2 = \epsilon^2/24$, the functions f_4^γ and h_4^γ can be approximated by $f_4^\gamma \approx 1 - 1/2(1+\gamma)\alpha^4(|k|^2|p|^2 + |k|^2|q|^2 + |p|^2|q|^2)$ and $h_4 \approx 1 + 1/2(1+\gamma)\alpha^4|k|^4$, respectively. Therefore, the interactions between large scales of motion ($\epsilon|k| < 1$) approximate the NS dynamics up to $\mathcal{O}(\epsilon^4)$. Hence, the triadic interactions between large scales are only slightly altered. All interactions involving longer wavevectors (smaller scales of motion) are reduced. The amount by which the interactions between the wavevector-triple (k, p, q) are lessened depends on the length of the legs of the triangle $k = p + q$. For example, all triadic interactions for which at least two legs are (much) longer than $1/\epsilon$ are (strongly) attenuated; whereas, interactions for which at least two legs are (much) shorter than $1/\epsilon$ are reduced to a small degree only.

[1] Hereafter, for simplicity, the subindex ϵ is dropped.

3.2. Stopping the vortex-stretching mechanism

Taking the curl of Eq.(8) leads to

$$\partial_t \underline{\omega} + \mathcal{C}_4^\gamma(\underline{u},\underline{\omega}) = \mathcal{C}_4^\gamma(\underline{\omega},\underline{u}) + \mathcal{D}_4^\gamma \underline{\omega}. \quad (16)$$

This equation resembles the vorticity equation that results from the NS equations: the only difference is that $\mathcal{C}$ and $\mathcal{D}$ are replaced by their regularizations $\mathcal{C}_4^\gamma$ and $\mathcal{D}_4^\gamma$, respectively. If it happens that the vortex stretching term $\mathcal{C}_4^\gamma(\underline{\omega},\underline{u})$ in Eq.(16) is so strong that the dissipative term $\mathcal{D}_4^\gamma\underline{\omega}$ cannot prevent the intensification of vorticity, smaller vortical structures are produced. Left-multiplying the vorticity transport Eq.(16) by $\underline{\omega}$, we can obtain the evolution of $|\underline{\omega}|^2$. In this way, the vortex-stretching and dissipation term contributions to $\partial_t|\underline{\omega}|^2$ result

$$\underline{\omega}\cdot\mathcal{C}_4^\gamma(\underline{\omega},\underline{u}) \quad \text{and} \quad \underline{\omega}\cdot\mathcal{D}_4^\gamma\underline{\omega}, \quad (17)$$

respectively. In order to prevent local intensification of vorticity, dissipation must dominate the vortex-stretching term contribution at the smallest grid scale, $k_c = \pi/h$. In spectral space, this requirement leads to the following inequality

$$\frac{\hat{\omega}_{k_c}\cdot\mathcal{C}_4^\gamma(\underline{\omega},\underline{u})^*_{k_c} + \mathcal{C}_4^\gamma(\underline{\omega},\underline{u})_{k_c}\cdot\hat{\omega}^*_{k_c}}{2\hat{\omega}_{k_c}\cdot\hat{\omega}^*_{k_c}} \leq h_4^\gamma\left(\hat{g}_k\right)\nu k_c^2, \quad (18)$$

where the vortex-stretching term, $\mathcal{C}_4^\gamma(\underline{\omega},\underline{u})_{k_c}$, is given by

$$\mathcal{C}_4^\gamma(\underline{\omega},\underline{u})_{k_c} = \sum_{p+q=k_c} f_4^\gamma\left(\widehat{g}_{k_c}, \widehat{g}_p, \widehat{g}_q\right)\hat{\omega}_p i q \hat{u}_q. \quad (19)$$

Note that $f_4^\gamma\left(\widehat{g}_{k_c}, \widehat{g}_p, \widehat{g}_q\right)$ depends on the filter length ϵ and, in general, on the wavevectors p and $q = k_c - p$. This makes very difficult to control the damping effect because f_4^γ cannot be taken out of the summation in (19). To avoid this, filters should be constructed from the requirement that the damping effect of all the triadic interactions at the smallest scale must be virtually independent of the interacting pairs, *i.e.*

$$f_4^\gamma(\widehat{g}_{k_c}, \widehat{g}_p, \widehat{g}_q) \approx f_4^\gamma(\widehat{g}_{k_c}). \quad (20)$$

This is a crucial property to control the subtle balance between convection and diffusion in order to stop the vortex-stretching mechanism. This point was addressed in detail by [8]. Then, the overall damping effect at the smallest grid scale, $H_4(\widehat{g}_{k_c}) = f_4^\gamma(\widehat{g}_{k_c})/h_4^\gamma(\widehat{g}_{k_c})$, follows straightforwardly

$$H_4(\widehat{g}_{k_c}) = \frac{2\nu k_c^2 \hat{\omega}_{k_c} \cdot \hat{\omega}^*_{k_c}}{\hat{\omega}_{k_c} \cdot \mathcal{C}(\omega, u)^*_{k_c} + \mathcal{C}(\omega, u)_{k_c} \cdot \hat{\omega}^*_{k_c}}, \quad (21)$$

with the condition that $0 < H_4(\widehat{g}_{k_c}) \leq 1$.

3.3. *From spectral to physical space*

In the previous subsection we applied our analysis on a spectral space. However, the method needs to be applied on a physical domain in $\mathbb{R}^3$. To that end, here we propose to express the overall damping effect, $H_4(\widehat{g}_{k_c})$, as a function of the invariants of the strain tensor, $S(\underline{u}) = 1/2(\nabla \underline{u} + \nabla \underline{u}^T)$. Recalling that the velocity field, u, is solenoidal ($\nabla \cdot \underline{u} = 0$); $tr(S) = 0$ and the characteristic equation of S reads

$$\lambda^3 + Q\lambda + R = 0, \quad (22)$$

where $R = -1/3tr(S^3) = -det(S) = -\lambda_1\lambda_2\lambda_3$ and $Q = -1/2tr(S^2) = -1/2(\lambda_1^2 + \lambda_2^2 + \lambda_3^2)$ are the invariants of S, respectively. We order the eigenvalues of S by $\lambda_1 \leq \lambda_2 \leq \lambda_3$. Let us now consider an arbitrary part of the flow domain Ω with periodic boundary conditions. The innerproduct is defined in the usual way: $(a, b) = \int_\Omega a \cdot b d\Omega$. Then, taking the L^2 innerproduct of (1) with $-\Delta\underline{u}$ leads to the enstrophy equation

$$\frac{1}{2}\frac{d}{dt}|\underline{\omega}|^2 = (\underline{\omega}, \mathcal{C}(\underline{\omega}, \underline{u})) - \nu\left(\nabla\underline{\omega}, \nabla\underline{\omega}\right), \quad (23)$$

where $|\underline{\omega}|^2 = (\underline{\omega}, \underline{\omega})$ and the convective term contribution $(\mathcal{C}(\underline{u}, \underline{\omega}), \underline{\omega}) = 0$ vanishes because of the skew-symmetry of the convective operator. Using the results obtained by [13] and following the same arguments than in [14], it can be shown that the vortex-stretching term can be expressed in terms of the invariant R of $S(u)$

$$(\underline{\omega}, \mathcal{C}(\underline{\omega}, u)) = -\frac{4}{3}\int_\Omega tr(S^3) d\Omega = 4\int_\Omega R d\Omega, \quad (24)$$

and the $L^2(\Omega)$-norm of $\underline{\omega}$ in terms of the invariant Q

$$|\underline{\omega}|^2 = -4\int_\Omega Q d\Omega. \quad (25)$$

Then, the diffusive term can be bounded by

$$(\nabla\underline{\omega}, \nabla\underline{\omega}) = -\left(\underline{\omega}, \Delta\underline{\omega}\right) \leq -\lambda_\Delta\left(\underline{\omega}, \underline{\omega}\right), \quad (26)$$

where $\lambda_\Delta < 0$ is the largest (smallest in absolute value) non-zero eigenvalue of the Laplacian operator Δ on Ω. If we now consider that the domain Ω is a periodic box of volume h, then $\lambda_\Delta = -(\pi/h)^2$. In a numerical simulation h would be related with the local grid size. Then, to prevent a local intensification of vorticity, *i.e.* $|\underline{\omega}|_t \leq 0$, the following inequality must be hold

$$H_4(\widehat{g}_{k_c})\frac{(\underline{\omega}, S\underline{\omega})}{(\underline{\omega}, \underline{\omega})} \leq -\nu\lambda_\Delta, \quad (27)$$

where, in this case, $k_c = \pi/h$. This inequality is the analog to Eq.(21) in physical space. Rayleigh's principle states that

$$\max_{\underline{\omega}\neq 0}\frac{(\underline{\omega}, S\underline{\omega})}{(\underline{\omega}, \underline{\omega})} = \lambda_3, \quad (28)$$

and therefore gives a lower bound for the damping function, $H_4(\widehat{g}_{k_c}) \leq \nu(-\lambda_\Delta/\lambda_3)$. This was the approach consider in our previous work [9]. However, the maximum value is attained only if $\underline{\omega}$ is aligned with the eigenvector corresponding to λ_3, and therefore the convective terms tends to be over-damped. This becomes especially relevant near the walls. In order to overcome this drawback here we propose to rewrite the inequality (27) in terms of the invariants Q and R. From Eqs. (24)-(27) we deduce

$$H_4(\widehat{g}_{k_c}) \leq \nu\lambda_\Delta\frac{Q}{R^+}, \quad (29)$$

where $R^+ = \max\{R, 0\}$ and the overall damping factor $0 < H_4 \leq 1$. Thus, a proper definition of the overall damping factor at the smallest grid scale is given by

$$H_4(\widehat{g}_{k_c}) = \min\left\{\nu\lambda_\Delta\frac{Q}{R^+}, 1\right\}. \quad (30)$$

Notice that the invariant Q is always negative whereas R can be either positive or negative. In terms of the Reynolds number, the quotient of R and Q scales like $R/Q \propto (Re^{3/2})/Re = Re^{1/2}$. Then, recalling that $\lambda_\Delta \propto h^{-2}$, it yields to $H_4(\widehat{g}_{k_c}) \propto h^{-2}Re^{-1}Q/R \propto h^{-2}Re^{-3/2}$. Therefore, we obtain $H_4(\widehat{g}_{k_c}) \to 1$ if $h \propto Re^{-3/4}$. This shows that the model switches off when h approaches to the smallest scale in a turbulent flow. Another interesting feature of the model is that it automatically switches off ($R \to 0$) for laminar flows (no vortex-stretching) and 2D flows ($\lambda_2 = 0 \to R = 0$). The near-wall behaviour of the invariants is given by $R \propto y^3$ and $Q \propto y^0$, respectively, where y is the distance to the wall. Consequently, it results into a model that switches off in the wall.

For convenience, let us now define the ratio between λ_2 and λ_3, $\eta = \lambda_2/\lambda_3$. Note that $\lambda_1 \leq 0$ and $\lambda_3 \geq 0$, whereas the middle eigenvalue, λ_2, can be both positive or negative. Actually, the sign of the invariant $R = -\lambda_1\lambda_2\lambda_3$, λ_2 and η are the same. Then,

recalling that the strain tensor is traceless ($tr(S) = 0$), *i.e.* $\lambda_1 + \lambda_2 + \lambda_3 = 0$, the first eigenvalue can also be written in terms of λ_3 and η: $\lambda_1 = -(1+\eta)\lambda_3$. Then, the ratio Q/R results into $(-Q/R)^{-1} = \lambda_{QR} = (1+\eta)\eta/(\eta^2+\eta+1)\lambda_3$. Here, λ_{QR} can be viewed as the rate of amplification of vorticity at the smallest grid scale. Then, assuming that $|\eta| \ll 1$, $\lambda_{QR} \approx \eta\lambda_3 = \lambda_2$ and therefore it is consistent with the preferential vorticity alignment with the intermediate eigenvector (see the work by [15] and references therein).

4. ON THE DETERMINATION OF γ

A criterion to determine the local filter length, ϵ, has been presented in the previous section. Then, the only parameter that still needs to be determined in Eq.(9) is the constant γ. As stated before, by simply setting $\gamma = -1$, the $\mathcal{C}_4^\gamma$ becomes the sixth-order accurate $\mathcal{C}_6$ regularization and the Galilean invariance is restored without introducing any additional modification in the dissipation term. However, the $\mathcal{C}_6$ approximation itself suffers from a fundamental drawback. Namely, the overall method relies on the fact that Eq.(20) is approximately satisfied and therefore, the damping factor $\mathcal{C}_4^\gamma$ can be taken out of the summation in (19). This is not the case of f_6: notice that since $\widehat{g}_0 = 1$, $f_6(\widehat{g}_{k_c}, \widehat{g}_{k_c}, \widehat{g}_0) = 1$ irrespectively of the value of $\widehat{g}_{k_c}$.

At this point, the 'optimal' value of γ could be determined by means of a trial-and-error numerical procedure. Alternatively, the constant γ can be obtained by assuming that the smallest grid scale $k_c = \pi/h$ lies within the inertial range for a classical Kolmogorov energy spectrum $E(k) = C_K\varepsilon^{2/3}k^{-5/3}$. In such a case, and recalling that $\widehat{g}_k = 1 - \alpha^2|k|^2 + \mathcal{O}(\alpha^4)$, the total dissipation for $k_T \leq k \leq k_c$ can be approximated by the contribution of the following two terms

$$\mathcal{D}_\nu \equiv \nu \int_{k_T}^{k_c} k^2 E(k) dk, \tag{31}$$

$$\mathcal{D}_\nu^{''} \equiv \nu \int_{k_T}^{k_c} k^4\alpha^4 E(k) dk, \tag{32}$$

where $\mathcal{D}_\nu$ is the physical viscous dissipation and $\mathcal{D}_\nu^{''}$ is the additional dissipation introduced by the hyperviscosity term, $(\mathcal{D}u')'$. Hence, integration for a Kolmogorov energy spectrum, the total dissipation within the range $k_T \leq k \leq k_c$ is given by

$$\mathcal{D}_\nu + \tilde{\gamma}\mathcal{D}_\nu^{''} = \frac{3\nu}{16} C_K\varepsilon^{2/3} \left\{ \left(4 + \tilde{\gamma}\alpha^4 k_c^4\right) k_c^{4/3} - \left(4 + \tilde{\gamma}\alpha^4 k_T^4\right) k_T^{4/3} \right\}, \tag{33}$$

where $\tilde{\gamma} = 1/2(1+\gamma)$ has been introduced here for the sake of simplicity. At the tail of the spectrum the following

$$\tilde{H}_4 \approx \frac{\mathcal{D}_\nu + \tilde{\gamma}\mathcal{D}_\nu^{''}}{\varepsilon}, \tag{34}$$

represents the ratio between the total dissipation and the energy transferred from scales larger than k_T to the tail of the spectrum. Let us assume that $\tilde{H}_4 = \mathcal{O}(H_4(\widehat{g}_{k_c}))$ where the overall damping at the smallest grid scale, $H_4(\widehat{g}_{k_c})$, is given by Eq.(30). However, at this point it is more suitable to express it in terms of the invariant Q. To do so, we simply notice that the three roots of the characteristic cubic equation (22) can be computed analytically:

$$\lambda_i = -|S|\sqrt{\frac{1}{3}}\cos\left(\frac{\theta}{3} - \frac{2\pi(i-1)}{3}\right) \qquad i = 1, 2, 3, \tag{35}$$

where $|S| = \sqrt{-4Q}$ and the angle θ is given by

$$\theta = \arccos\left(\frac{1}{2}R \Big/ \sqrt{\left(-\frac{1}{3}Q\right)^3}\right). \tag{36}$$

Since S is symmetric, the eigenvalues must be real-valued, $\lambda_i \in \mathbb{R}$, and, therefore, the invariants Q and R must satisfy

$$27R^2 + 4Q^3 \leq 0 \tag{37}$$

Hence, $\theta \in [0, \pi]$ and the ratio $R^+/-Q$ can be bounded in terms of the invariant Q

$$0 \leq \left(\frac{R^+}{-Q}\right) \leq \sqrt{\frac{4}{27}}\sqrt{-Q}, \tag{38}$$

then, plugging this into Eq.(30) leads to

$$1 \geq H_4(\widehat{g}_\pi) \geq -\sqrt{\frac{27}{4}}\frac{\lambda_\Delta\nu}{\sqrt{-Q}}. \tag{39}$$

On the other hand, for a classical Kolmogorov energy spectrum, the ensemble averaged invariant Q is approximately given by

$$< Q >= -\frac{1}{4}\int_0^{k_c} k^2 E(k) dk \approx -\frac{3}{16} C_K\varepsilon^{2/3}k_c^{4/3}. \tag{40}$$

Finally, combining Eqs.(39) and (40), the energy balance given by Eq.(34) results

$$\frac{-12\lambda_\Delta\nu\varepsilon}{\sqrt{C_K\varepsilon^{2/3}k_c^{4/3}}} \lesssim \mathcal{D}_\nu + \tilde{\gamma}\mathcal{D}_\nu^{''}. \tag{41}$$

Then, plugging Eq.(33) and rearranging terms leads to

$$1 \lesssim \frac{-C_K^{3/2}k_c^2}{32\lambda_\Delta} \left\{ \left(4 + \tilde{\gamma}\alpha^4 k_c^4\right) - \left(4 + \tilde{\gamma}\alpha^4 k_T^4\right) \left(\frac{k_T}{k_c}\right)^{4/3} \right\} k_c^2. \tag{42}$$

Recalling that $\lambda_\Delta = -(\pi/h)^2$, $k_c = \pi/h$ and $\alpha \approx k_c^{-1}$, the previous expression simplifies

$$1 \lesssim \frac{C_K^{3/2}}{32}\left\{(4+\tilde{\gamma}) - \left(4+\tilde{\gamma}\left(\frac{k_T}{k_c}\right)^4\right)\left(\frac{k_T}{k_c}\right)^{4/3}\right\}. \tag{43}$$

Since $k_c > k_T$, we can consider than $4 \gg \tilde{\gamma}(k_T/k_c)^4$, we get a proper bound for $\tilde{\gamma}$,

$$\begin{aligned}\tilde{\gamma} &\gtrsim 4\left\{8C_K^{-3/2} - \left(1-\left(\frac{k_T}{k_c}\right)^{4/3}\right)\right\} \\ &\approx 4\left(8C_K^{-3/2}-1\right).\end{aligned} \tag{44}$$

Hence, for a Kolmogorov constant of $C_K \approx 1.58$ [16] it leads to a lower limit of $\tilde{\gamma} \approx 12.1$ ($\gamma \approx 23.2$). At this point, numerical experiments are needed to confirm this estimation; also to provide more accurate values. To do so, simulation of isotropic turbulence at $Re_\lambda \approx 72$ has been chosen as a first test-case. The code is pseudo-spectral and uses the $3/2$ dealiasing rule. Filters proposed in [8] are applied in spectral space. The total amount of energy in the first two modes is kept constant following the approach proposed in [17]. Figure 1 displays the results for a box size of 16^3 for different values of $\tilde{\gamma}$ from 0 up to 30. As expected, the original hump displayed for $\tilde{\gamma} = 0$ attenuates for increasing values of $\tilde{\gamma}$. Moreover, the lower bound for $\tilde{\gamma}$ given by Eq.(44) is in a fairly good agreement with these numerical tests. Even more important, for $\tilde{\gamma}$ bigger than a certain value, the results are virtually independent on the value of $\tilde{\gamma}$.

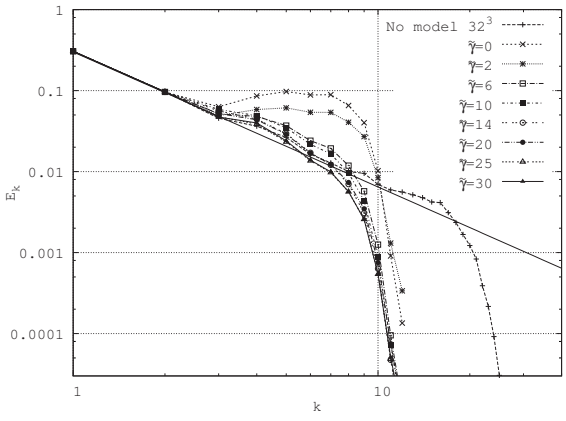

Figure 1. Energy spectra at $Re_\lambda \approx 72$ for different values of $\tilde{\gamma}$ from 0 up to 30.

Figure 2 displays the results obtained for a box size of 64^3 and $Re_\lambda \approx 202$. In this case, the energy-containing and dissipative scales are clearly separated by an inertial range. Again, the hump at the tail of the spectrum attenuates for increasing values of $\tilde{\gamma}$. More importantly, the inertial range is well predicted only for those cases with $\tilde{\gamma} \gtrsim 14$, in relatively good agreement with the lower bound given by Eq.(44). These are still preliminary results and more simulations are needed to confirm these conclusions.

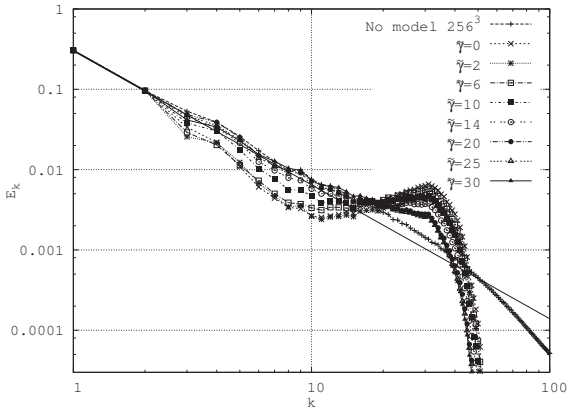

Figure 2. Energy spectra at $Re_\lambda \approx 202$ for different values of $\tilde{\gamma}$ from 0 up to 30.

5. TOWARDS THE SIMULATION OF WIND FARM BOUNDARY LAYERS

The final goal of this work is to perform numerical simulation of atmospheric boundary layer through wind farms. This challenging application can only be achieved by combining the most advanced numerical techniques with reliable turbulence models. Regarding the former, regularization of the Navier-Stokes equations have already been successfully tested for several configurations (see [7, 9], for instance). Furthermore, it is expected that the proposed modifications will result into relevant improvements. With regard to the numerical techniques, the above-described pseudo-spectral algorithm is the most appropriate choice for this type of configurations. Preliminary results for a three-dimensional homogeneous isotropic turbulence have been presented in the previous section. The next test-case is a turbulent channel flow at $Re_\tau = 180$. First results are displayed in Figure 3 together with the classical results obtained by J.Kim *et al.* [18]. This configuration was successfully tested for a $\mathcal{C}_4$ regularization in [7]. Those results also showed an additional hump at the tail of the spectrum. It is expected that the additional hyperviscosity term will improve the results. This will be presented and discussed during the conference.

6. CONCLUDING REMARKS AND FUTURE RESEARCH

Since DNS simulations are not feasible for real-world applications the $\{\mathcal{CD}\}_4^\gamma$-regularization of the NS equations has been proposed as a simulation shortcut: the convective and diffusive operators in the NS equations (1) are replaced by the $\mathcal{O}(\epsilon^4)$-accurate smooth approximation given by Eq.(4) and Eq.(9), respectively. The symmetries and conservation properties of the original convective term are exactly

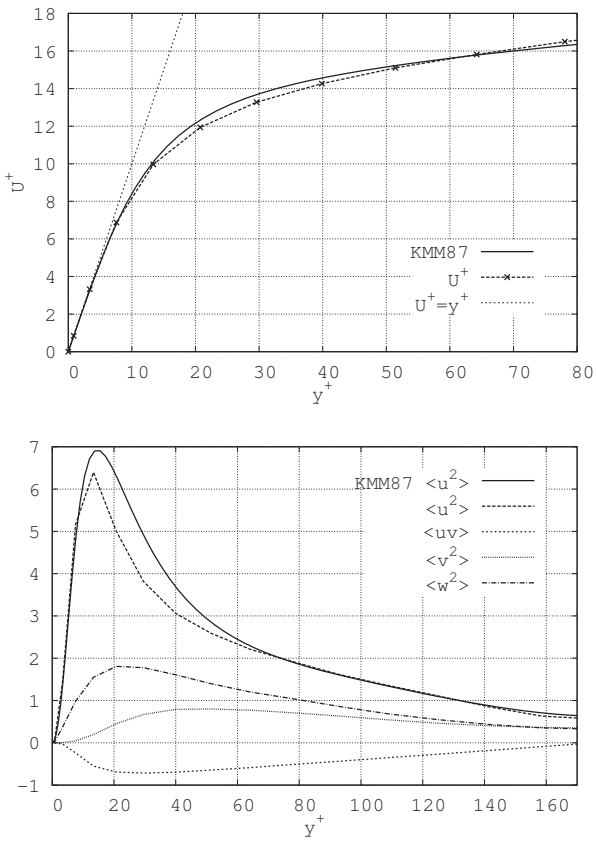

Figure 3. Results for a turbulent channel flow at $Re_\tau = 180$ and grid size $32 \times 32 \times 32$. Top: mean streamwise velocity profile. Bottom: some turbulent statistics. Reference data corresponds with the results published in [18].

preserved. Doing so, the production of smaller and smaller scales of motion is restrained in an unconditionally stable manner. In this way, the new set of equations is dynamically less complex than the original NS equations, and therefore more amenable to be numerically solved. The only additional ingredient is a self-adjoint linear filter whose local filter length is determined from the requirement that vortex-stretching must be stopped at the scale set by the grid. This can be easily satisfied in spectral space via Eq.(21) provided that discrete filter satisfies Eq.(20), *i.e.* the triadic interactions at the smallest scale are virtually independent of the interacting pairs. This was addressed in detail by [8]. However, in physical space it becomes more cumbersome. To circumvent this, here a criterion based on the two invariants, R and Q, of the local strain tensor is used. Doing so, the expected behaviour of a turbulence model is achieved: it switches off (*i.e.* $H_4 = 1$) for laminar flows (no vortex-stretching), 2D flows ($R = 0$) and near the walls.

In the present paper, the parameter γ of Eq.(8) is approximately bounded by assuming a Kolmorogov energy spectrum. This has been addressed in Section 4 where the following bound has been determined:

$$\tilde{\gamma} \gtrsim 4\left(8C_K^{-3/2} - 1\right), \tag{45}$$

where $\tilde{\gamma} = 1/2(1+\gamma)$ and C_K is the Kolmogorov constant. Preliminary simulations for homogeneous isotropic turbulence seems to confirm the adequacy of the bound given by Eq.(45). In this way, the proposed method constitutes a parameter-free turbulence model suitable for complex geometries and flows. Apart from homogeneous isotropic turbulence numerical results evaluating the performance of the $\{\mathcal{CD}\}_4^\gamma$ method for wall-bounded configurations will be presented during the conference. Namely, a turbulent channel flow and a turbulent boundary layer. As a final application, regularization modelling will be applied for large-scale numerical simulation of the atmospheric boundary layer through wind farms. The analysis of these $\{\mathcal{CD}\}_4^\gamma$ regularization models is also part of our future research plans.

ACKNOWLEDGEMENTS

This work has been financially supported by the *Ministerio de Ciencia e Innovación*, Spain (ENE2010-17801) and a Juan de la Cierva postdoctoral contract (JCI-2009-04910) by the *Ministerio de Ciencia e Innovación*. Calculations have been performed on the IBM MareNostrum supercomputer at the Barcelona Supercomputing Center. The authors thankfully acknowledge these institutions.

References

[1] Morinishi, Y., Lund, T., Vasilyev, O., and Moin, P. 1998 "Fully Conservative Higher Order Finite Difference Schemes for Incompressible Flow". *Journal of Computational Physics*, Vol. 143, pp. 90–124.

[2] Vasilyev, O. V. 2000 "High Order Finite Difference Schemes on Non-uniform Meshes with Good Conservation Properties". *Journal of Computational Physics*, Vol. 157, pp. 746–761.

[3] Verstappen, R. W. C. P. and Veldman, A. E. P. 2003 "Symmetry-Preserving Discretization of Turbulent Flow". *Journal of Computational Physics*, Vol. 187, pp. 343–368.

[4] Guermond, J. L., Oden, J. T., and Prudhomme, S. 2004 "Mathematical perspectives on large eddy simulation models for turbulent flows". *Journal of Mathematical Fluid Mechanics*, Vol. 6, pp. 194–248.

[5] Geurts, B. J. and Holm, D. D. 2003 "Regularization modeling for large-eddy simulation". *Physics of Fluids*, Vol. 15, pp. L13–L16.

[6] Guermond, J. L. and Prudhomme, S. 2005 "On the contruction of suitable solutions to the

Navier-Stokes equations and questions regarding the definition of large-eddy simulations". *Physica D*, Vol. 207, pp. 64–78.

[7] Verstappen, R. 2008 "On restraining the production of small scales of motion in a turbulent channel flow". *Computers & Fluids*, Vol. 37, pp. 887–897.

[8] Trias, F. X. and Verstappen, R. W. C. P. 2011 "On the construction of discrete filters for symmetry-preserving regularization models". *Computers & Fluids*, Vol. 40, pp. 139–148.

[9] Trias, F. X., Verstappen, R. W. C. P., Gorobets, A., Soria, M., and Oliva, A. 2010 "Parameter-free symmetry-preserving regularization modeling of a turbulent differentially heated cavity". *Computers & Fluids*, Vol. 39, pp. 1815–1831.

[10] Guermond, J. L., Oden, J. T., and Prudhomme, S. 2003 "An interpretation of the Navier-Stokes-alpha model as a frame-indifferent Leray regularization". *Physica D*, Vol. 177, pp. 23–30.

[11] Trias, F. X., Gorobets, A., Verstappen, R. W. C. P., and Oliva, A. 2011 "Symmetry-preserving regularization of wall-bounded turbulent flows". *13^{th} European Turbulence Conference*, Warsaw, Poland, September, p. .

[12] Carati, D., Winckelmans, G. S., and Jeanmart, H. 1999 "Exact expansions for filtered-scales modelling with a wide class of LES filters". *Direct and Large-Eddy Simulation III*, pp. 213–224, Kluwer.

[13] Chae, D. 2005 "On the spectral dynamics of the deformation tensor and a new a priori estimates for the 3D Euler equations". *Communications in Mathematical Physics*, Vol. 263, pp. 789–801.

[14] Verstappen, R. 2011 "When does eddy viscosity damp subfilter scales sufficiently?". *Journal of Scientific Computing*, Vol. 49, No. 1, pp. 94–110.

[15] Galanti, B., Gibbon, J., and Heritage, M. 1997 "Vorticity alignment results for the three-dimensional Euler and Navier-Stokes equations". *Nonlinearity*, Vol. 10, No. 6, pp. 1675–1694.

[16] Donzis, D. A. and Sreenivasan, K. R. 2010 "The bottleneck effect and the Kolmogorov constant in isotropic turbulence". *Journal of Fluid Mechanics*, Vol. 657, pp. 171–188.

[17] Chen, S., Doolen, G. D., Kraichnan, R. H., and She, Z. 1993 "On statistical correlations between velociy increments and locally averaged dissipation in homogeneous turbulence". *Physics of Fluids A*, Vol. 5, p. 458.

[18] Kim, J., Moin, P., and Moser, R. 1987 "Turbulence statistics in fully developed channel flow at low Reynolds number". *Journal of Fluid Mechanics*, Vol. 177, pp. 133–166.

Conference on Modelling Fluid Flow (CMFF'12)
The 15th International Conference on Fluid Flow Technologies
Budapest, Hungary, September 4-7, 2012

WIND TUNNEL MEASUREMENT ON THE FLOW AND DISPERSION FOR A TURBULENT BOUNDARY LAYER FLOW OVER TWO CONSECUTIVE TRAPEZOIDAL SHAPE OF TERRAINS

Bao-Shi Shiau[1,2], Cheng-Wen Huang[2]

[1] Corresponding Author. Institute of Physics, Academia Sinica, Taipei, Taiwan. Tel.: +886 2 27896749, Fax: +886 2 27889829, E-mail: bsshiau@gate.sinica.edu.tw
[2] Department of Harbor and River Engineering, National Taiwan Ocean University, Keelung, Taiwan. E-mail: b0085@mail.ntou.edu.tw

ABSTRACT

Experimental study on the flow and dispersion characteristics for a turbulent boundary layer flow over two consecutive trapezoidal shape terrains were carried out in the Environmental Wind Tunnel. A thick turbulent boundary layer was generated as the approaching flow. Two consecutive trapezoidal terrain models with upwind and downwind slope angle of 27° and 45° were placed four times of terrain height behind the point source. The source height is the same as the terrain model height. Methane was used as tracer gas and it was mixed with the standard gas. The sampled gas in airbag was analyzed with FID (Flame Ionization Detector) to measure methane concentration. The measurement results show that the wind flow speed-up factor increases around the top surface of trapezoidal shape terrain when the upwind slope angle of trapezoidal shape terrain increases from 27° to 45°. The averaged height of the concentration plume is found to decrease along the upwind slope of trapezoidal shape terrain for slope angles of 27° and 45°. The vertical dispersion parameters of plume along the downstream distance of source increase when the slope angle of terrains changes from 45° to 27°.

Keywords: dispersion, plume, trapezoidal shape of terrain, turbulent boundary layer flow

NOMENCLATURE

a	[-]	power exponent
c	[-]	coefficient
C	[$\mu g/s$]	concentration
Fr	[-]	densimetric Froude number
H	[m]	stack height
K	[-]	dimensionless concentration
K_L	[-]	flow speed-up factor
n	[$1/s$]	frequency
Q	[g/s]	discharge rate
Re	[-]	Reynolds number
U_H	[m/s]	mean velocity at height H
U_{ref}	[m/s]	free stream velocity
z	[m]	height
z_c	[m]	plume averaged height
Z_{ref}	[m]	boundary layer thickness
σ_z	[m]	vertical dispersion parameter

1. INTRODUCTION

The pollution plume dispersion through obstacles is often encountered in the industrial complex, urban or rural region. The variation of topography of the complex terrain plays an important role for simulation of pollutants dispersion problems in environmental wind engineering since the topography change apparently affected the flow structure (MacDonald et al. [1], Crooks et al. [2], Liu et al. [3], Cao and Tamura [4]). Shiau & Hsu [5] and Shiau & Hsieh [6] had studied the flow structure of turbulent boundary layer flow over trapezoid shape of topography. Davison et al. [7] had made field investigation on plume dispersion through large group of obstacles. Hanna et al. [8] made comparison of model simulations with observations of mean flow and turbulence within simple obstacle arrays.

Two consecutives trapezoidal shape of terrains were often existed as the typical case of complex terrain. Experimental study on the dispersion characteristics for wind flow over two consecutives trapezoidal shape terrain can provide data for the validations of numerical simulation on environmental wind engineering problems. In the present study, we conducted wind tunnel experiments to measure on the flow and dispersion characteristics for a turbulent boundary layer flow over two consecutives trapezoidal shape terrains with different slope angles. Effects of the slope angle of the trapezoidal shape terrain on the wind

flow and the plume characteristics, such as plume averaged heigh, dispersion parameters of concentration distributions were investigated.

2. EXPERIMENTAL SET UP AND WORK

The experiments were carried out in the National Taiwan Ocean University's Environmental Wind Tunnel. The wind tunnel test section has a dimension of 2 m wide,1.4 m high, and 12.5 m long. The tunnel is an open suction type and it contracts to the test section with an area ratio of 4:1. The turbulence intensity of empty tunnel in test section is less than 0.5 % at the mean velocity of 5 m/s.

An X-type hot-wire incorporating with the TSI IFA-300 constant temperature anemometer was employed to measure the turbulent flow signals. Output of the analog signals for turbulent flow was digitized at a rate of 4 K Hz each channel through the 12 bit Analog-to–Digital converter. Since none of the analog signals containing significant energy or noise above 1 K Hz, with the Nyquist criteria, a digitizing rate of 2 K Hz was sufficient. The low pass frequency for the analog signals is set as 1 K Hz in all runs of the experiments

Four spires of 140 cm height were equally spaced and properly arranged at the entrance of test section to generate a thick turbulent boundary layer which was used as the approaching flow.

The consecutive trapezoidal shape of two-dimensional terrain model with slope angle of $\theta=27^o$, 45^o are constructed. Figure 1 shows the schematic diagram of the terrain model for slop angle of 27^o and measurement coordination. The origin of the coordination is at which the source located. The source height h=5cm is the same as the terrain height H=5 cm. Four spires of 100 cm height and roughness elements (2 cm x 2 cm x 2cm) are properly arranged on the entrance of test section.

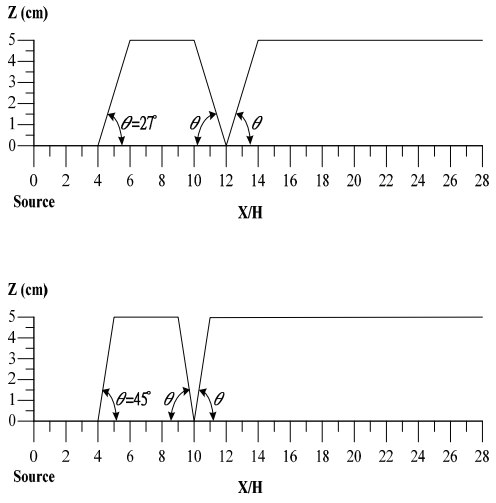

Figure1. Two consecutive trapezoidal shape of slope angle $\theta=27^o$ and $\theta=45^o$ terrain models and the coordinate system

Four spires were placed at the entrance of the wind tunnel test section, and roughness elements succeeded to be arranged of 9 m in length. The fully developed thick turbulent boundary layer was generated as the approaching flow which had the free stream velocity of 4.56 m/s, and boundary layer thickness of about 1 m. The Reynolds number based on the free stream velocity and boundary layer thickness of approaching flow was about $Re=2.93*10^5$.

Methane was used as tracer gas and it mixed with the standard gas. The mixed gas emitted from the stacks as the sources in the experiments. Tracer gas was applied to use as the concentration indicator. The tracer gas was a methane and air mixture with which the volume ratio was 1:9. So tracer gas was slightly lighter than the ambient environment of air. The discharging condition designated by the densimetric Froude number, Fr, and it is defined as:

$$Fr = \frac{U_s}{\sqrt{gD_s[(\rho_s - \rho_a)/\rho_s]}} \quad (1)$$

where U_s is the discharged velocity of tracer gas; g is the gravity; D_s is the inner diameter of stack; ρ_s is the density of tracer gas; ρ_a is the density of ambient air. The discharging condition for tracer gas emitted from the stack in all runs of the present experiment was Fr=100; where U_s=4.44 m/s, $\rho_s - \rho_a$ = 0.055 kg/m^3, D_s =0.0042 m, ρ_s =1.15 kg/m^3, and g=9.81 m/s^2.

The designed rake of sampling tubes was employed to take tracer gas samples. The rake was composed of many tubes. The cam system was applied to accomplish the work of pumping tracer gas. The system was conducted to suck simultaneously the tracer gas through many tubes which one end mounted on the rake, and the the other end were connected to each of the corresponding airbags. Each airbag with of three liters in volume. The sucking procedure lasted for three minutes in each run. The collected tracer gas in each airbag was analyzed using the equipment of FID (Flame Ionization Detector). The methane contained in the sampled tracer gas of each airbag was quickly burned and detected by the FID, and the concentration of the sample was yielded. Figure 2 shows the schematic diagram of the experimental arrangement.

3. RESULTS

3.1. Turbulent boundary layer flow as the approaching flow

Four spires of 100 cm height arranged across the entrance of test section and with roughness

elements (2 cm x 2 cm x 2cm) deployed succeeding in the test section floor for 9 meters long behind the spires. Such arrangements ensure to generate a thick turbulent boundary layer flow. Figure 3 shows the mean velocity profiles of approaching flow. The turbulent boundary layer thickness is of about $Z_{ref} \cong 100$ cm, and the free stream velocity is of $U_{ref} = 4.56$ m/s. The turbulent boundary layer flow mean velocity profile is expressed in power law form as follows:

$$\frac{U}{U_{ref}} = (\frac{Z}{Z_{ref}})^{a} \qquad (2)$$

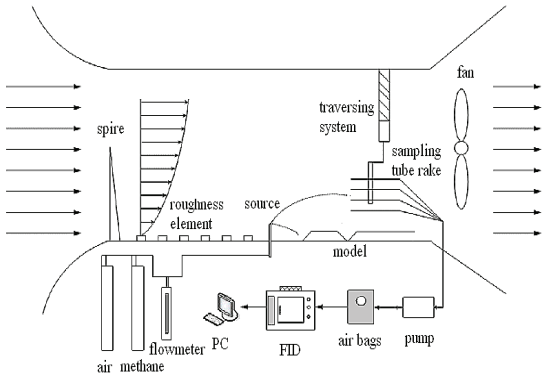

Figure2. Schematic diagram of experimental arrangement

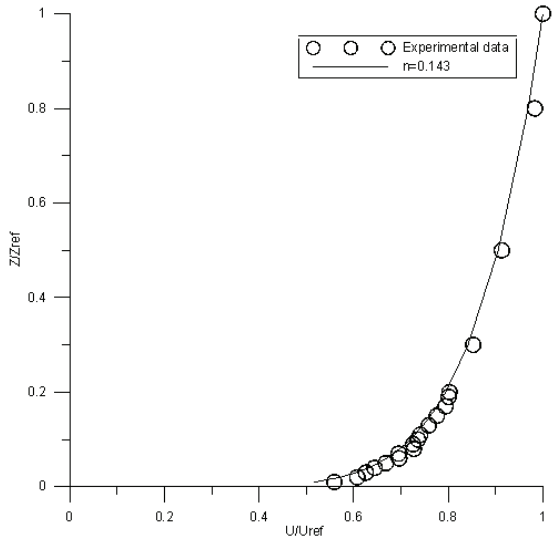

Figure 3. Mean velocity profile of approaching flow

In the present study, the power law with an exponent a=0.143, was simulated as the approaching flow which passed over the two consecutive trapezoidal shapes of terrain model. This value lies in the range of 0.143 to 0.167 as proposed by Counihan [9] for the rural terrain type of neural atmospheric turbulent boundary layer flow.

The longitudinal turbulence intensity profile of approaching flow is shown as Figure 4. The longitudinal turbulence intensity I(u) is defined as the ratio of root mean square of flow velocity fluctuation and the local mean flow speed. The turbulence intensity close to the ground is approximately 15%. Counihan [9] had found that the longitudinal turbulence intensity near the wall in the rural areas fell in the range of 10% to 20 %.

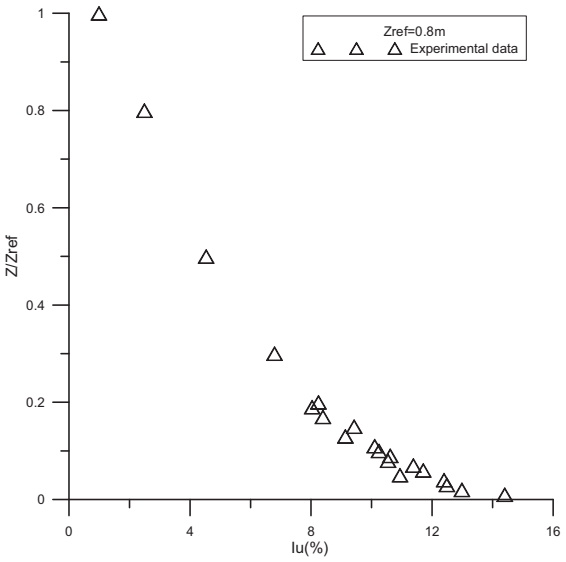

Figure 4. Longitudinal turbulence intensity profile of approaching flow

To ensure the turbulence structure of the simulated approaching flow, the turbulent flow power spectrum is analyzed to show the turbulence power density distribution. The turbulent velocity power spectrum of approaching flow measured at the height Z=0.08m (Z/Z_{ref}=0.08) is shown in Figure 5. Maeda and Makino [10] rewrote the Von-Karman type power spectrum equation (see as follows), and such Von-Karman type power spectrum equation is also plotted and shown in the Figure 5 for comparison.

$$S_u(n) = \frac{2\overline{u'^2}L_x^{\,u}}{U[1+(\frac{2cnL_x^{\,u}}{U})^2]^{\frac{5}{6}}} \qquad (3)$$

In the figure 5, the spectrum density, $S_u(n)$ and frequency, n are normalized, and they are denoted by $US_u(n)/\overline{u'^2}L_x^{\,u}$ and $nL_x^{\,u}/U$, respectively. Here $\overline{u'^2}$ denotes the mean square of longitudinal velocity fluctuation; c is the coefficient of 4.2065; $L_x^{\,u}$ is the integral length scale of longitudinal velocity in x direction (i.e. streamwise direction); U

is the longitudinal mean velocity at the height of *Z*. The integral length scale is obtained by multiplying the integral time scale, T_E with the longitudinal mean velocity, *U*. It is found that present result closes to the Von Karman equation, and the inertia-subrange of turbulence spectrum of approaching flow is with a slope of -5/3 which is in good agreement with the Kolmogorov spectrum law.

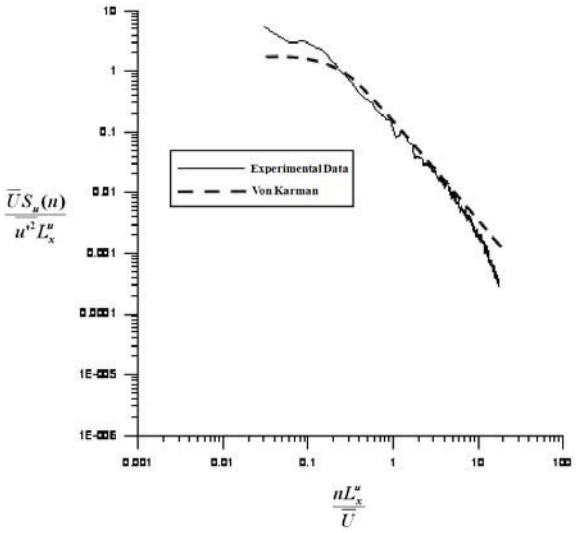

Figure 5. Turbulent flow power spectrum of approaching flow at height z=0.08 m (Z/Z_{ref}=0.08)

3.2. Flow over two consecutives trapezoidal shape of terrains

As the turbulent boundary layer type of approaching flow passed over the two consecutives trapezoidal shape of terrains, the flow was forced to accelerate along the slope surface of embankment. When the accelerated flow comes near the top surface of the terrain, the accelerated flow may reach a stage of the maximum increase of the velocity for the height close to the ground region of the top surface. Then, the flow decelerated and gradually recovered to the original mean velocity profile of the approaching flow along the downwind distance of top surface of the terrain. The acceleration of flow speed is called speed-up.

To investigate the characteristics of flow speed-up phenomenon along the downstream, locations of terrain for different terrain slope angles, we adopted a flow speed-up factor, K_L which is defined as:

$$K_L=[U(z)-U_s(z)]/U_s(z) \quad (4)$$

where *U(z)*: mean velocity at height *z* above the terrain top surface, $U_s(z)$: mean velocity at the same height *z* above the ground level upstream of the terrain.

Figure 6(a) and Figure 6(b) show the flow speed-up factor profiles at different downstream stations of source for two consecutive trapezoidal shape terrains with slope angles of θ=27° and θ=45°. Results reveal that K_L at the height closer to the ground of top surface of first trapezoidal shape of terrain at location X/H=6 for θ=27°, and X/H=5 for θ=45° become significantly larger than the other locations of the first and second terrains. Baker [11] measured the wind over the railway embankments with slope angle θ=27°, he also obtained similar result of the variation for wind flow speed-up parameter.

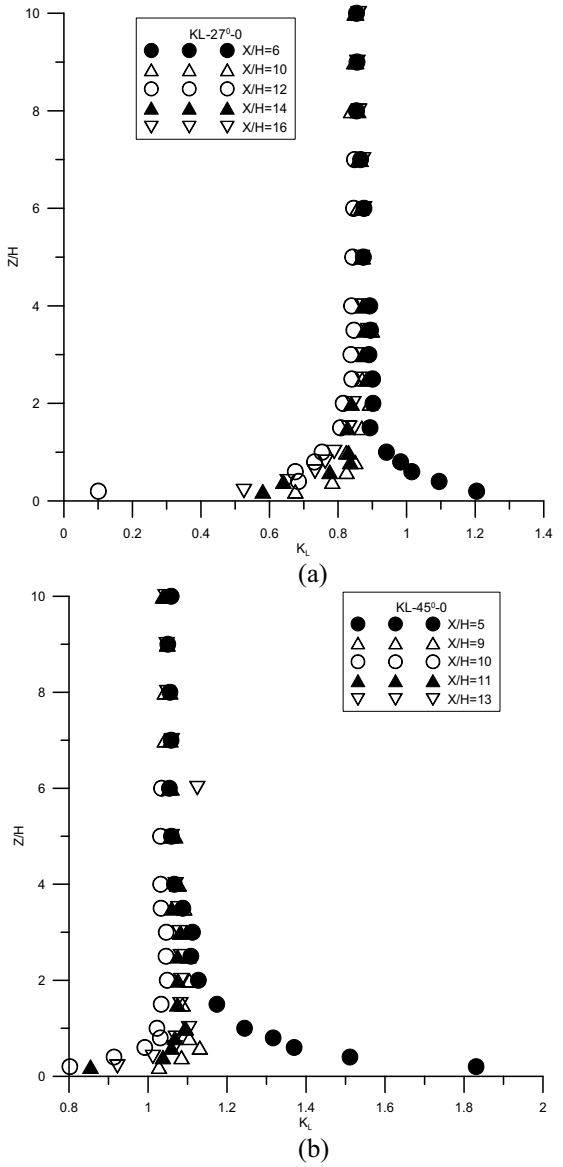

Figure 6. Flow speed-up factor profiles at different downstream stations of source for slope angles of two consecutive trapezoidal shape of terrains; (a) slope angle θ=27°, (b) slope angle θ=45°

Figure 7 showed the comparison of flow speed-up factor K_L profiles along the downstream distance of source for different terrain slope angles. When

approaching flow began to flow along upwind slope of the first trapezoidal shape of terrain, the flow was disturbed due to the change of topography. At the tip of upwind slope of the first terrain (X/H=6 for θ=27°, and X/H=5 for θ=45°), results revealed that the flow speed-up factor increased as increasing the slope angle of first terrain from 27° to 45°. And at the tip of downwind slope of the first terrain (X/H=10 for θ=27°, and X/H=9 for θ=45°), the flow speed-up factor still increased when the slope angle of first terrain changed from 27° to 45°. But the value of flow speed-up factor decreased as flow passed from the tip of upwind slope to the tip of downwind slope of the first trapezoidal shape of terrain. At the toe of the downwind slope of the first terrain or the toe of the upwind slope of the second terrain (X/H=12 for θ=27°, and X/H=10 for θ=45°), the flow speed-up factor decreased as comparing with that of at the tip of upwind slope of the first terrain. At far downstream distance of the source (X/H=14, X/H=16 for θ=27°; and X/H=11, X/H=13 for θ=45°), the flow gradually recovered to the original mean velocity profile of the approaching flow. So the flow speed-up factor profiles close together for different downstream distances.

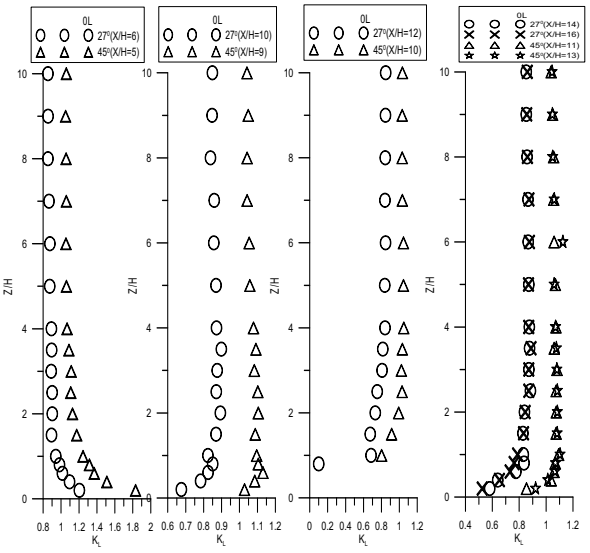

Figure 7. Comparison of K_L profiles at different downstream distance of source for terrains with different slope angles

3.3. Concentration distribution around two consecutive trapezoidal shape terrains

For convenience on the analysis of concentration distribution characteristics, dimensionless concentration parameter, K was used. The concentration, C (μg/s) was scaled with the stack height H=5 cm, emission discharge rate Q=0.070725 g/s, and cross wind speed U_H=3.04 m/s. This yielded dimensionless concentration parameter, $K=CH^2U_H/Q$.

Dimensionless concentration contours in X-Z plane along the downstream of source for two consecutive terrains with slope angles, 27°, and 45° were shown in Fig. 8, and Fig. 9, respectively. Both of the figures show the tracer concentration disperses along the downstream distance of the source. It was found that tracer concentration accumulation occurred at the region of upwind slope of the first trapezoidal shape of terrain and around the region between two terrains for both cases of slope angles, 27°, and 45°.

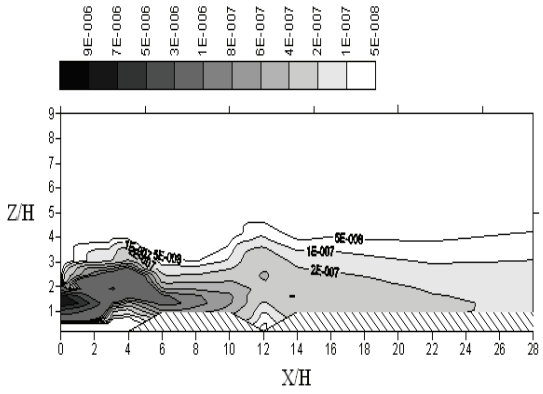

Figure 8. Vertical concentration contours around two consecutive trapezoidal shape terrains for slope angle of 27°

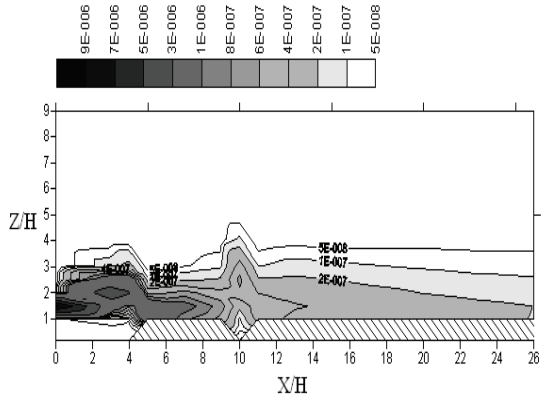

Figure 9. Vertical concentration contours around two consecutive trapezoidal shape terrains for slope angle of 45°

Figure 10 shows the horizontal concentration profiles at different downstream stations of source for two consecutive trapezoidal shape terrains with upwind slope angle of 27°. And Figure 11 shows the horizontal concentration profiles at different downstream stations of source for two consecutive trapezoidal shape terrains with upwind slope angle

of 45°. The solid lines representing theoretical Gaussian distribution of concentration are also shown in Fig.10 and Fig.11 for comparisons.

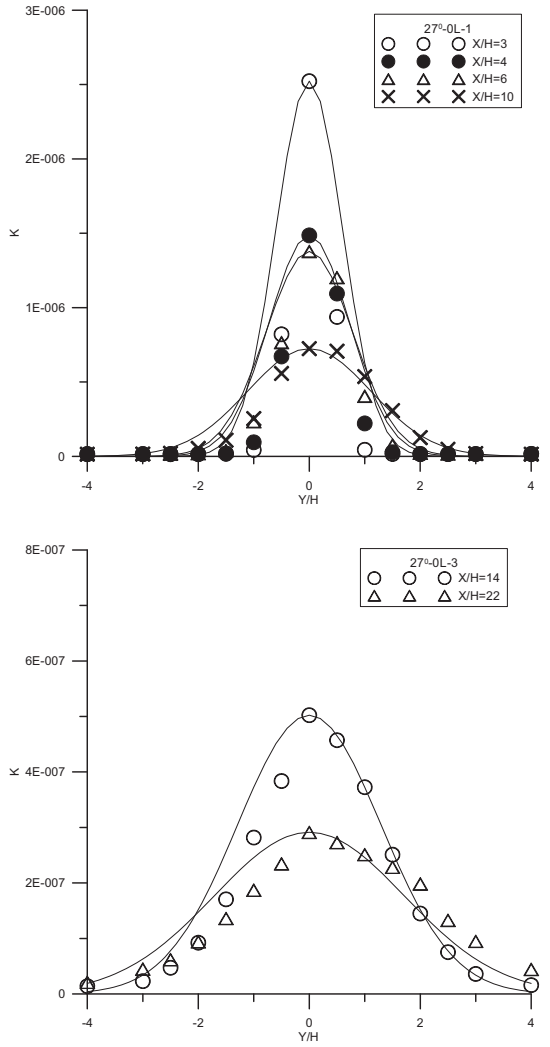

Figure 10. Horizontal concentration profiles along downstream stations of source for two consecutive trapezoidal shape terrains with slope angle of 27°

3.4. Dispersion characteristics

The plume dispersion parameters σ_z designate as the standard deviation of the concentration distributions in vertical direction. The parameter represented the extents of spread for tracer plume in vertical direction. Using the concentration distribution, the dispersion parameter σ_z can be computed as follows:

$$\sigma_z = [(\int_0^\infty z^2 C dz / \int_0^\infty C dz) - z_c^2]^{\frac{1}{2}} \quad (5)$$

where C is the measured tracer concentration; z is the vertical ordinates of Cartesian coordinates. z_c is the locations of centroid for vertical concentration distributions,. z_c also represented as the plume average height. z_c are calculated by

$$z_c = (\int_0^\infty C z dz)/(\int_0^\infty C dz) \quad (6)$$

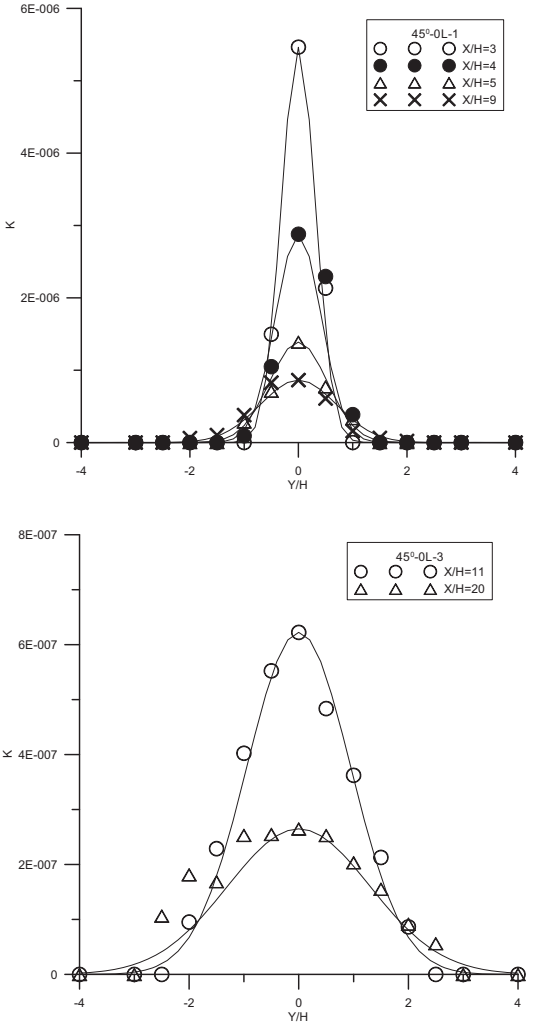

Figure 11. Horizontal concentration profiles along downstream stations of source for two consecutive trapezoidal shape terrains with slope angle of 45°

The plume averaged height variations along with the downstream distance of source for escarpment of different upwind slopes were shown in Figure 12. For both of the slope angles of 27^o and 45^o of terrains, the plume averaged heights increased along the downstream of source (0<X/H<4), but they decreased in the region of upwind slope of the first trapezoidal shape of terrain. At the location where two terrains interacting (X/H=12 for θ=27°, and X/H=10 for θ=45°), the

plume averaged heights reached maximum for both of two cases of slope angles of 27° and 45° of terrains.

Figure 13 shows the vertical dispersion parameters as functions of the downstream distance for two consecutive trapezoidal shape terrains with slop angles 27° and 45°. Results indicate that the vertical dispersion parameters of plume increased along with the downstream distance of source. And the vertical dispersion parameters of plume along with the downstream distance of source are in general slightly larger as the slope angle of terrains decreased from 45° to 27°.

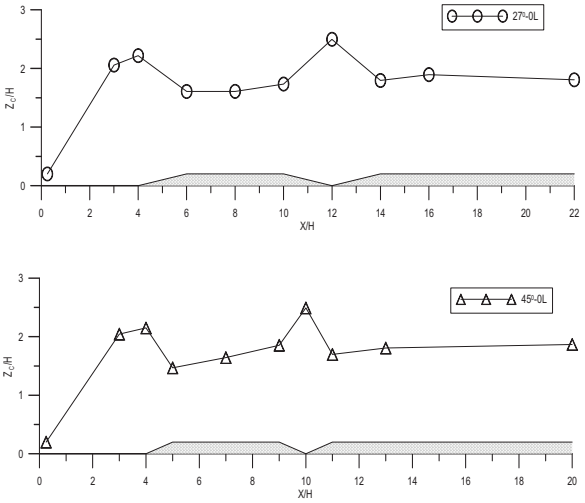

Figure 12. Plume averaged height along the downstream stations of source for two consecutive trapezoidal shape terrains with upwind slope angles of 27° and 45°

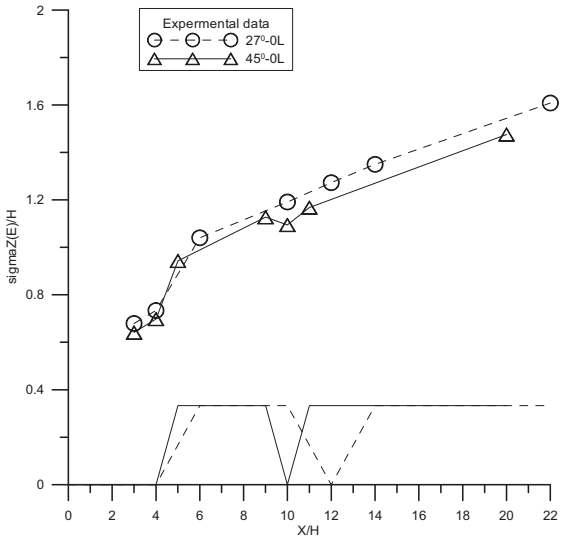

Figure 13. Vertical dispersion parameter as the function of downstream distance of source for two consecutive trapezoidal shape terrains with upwind slope angles of 27° and 45°

4. CONCLUSIONS

Experimental study on the flow and dispersion characteristics for a turbulent boundary layer flow over two consecutive trapezoidal shape terrains were carried out in the environmental wind tunnel. Two consecutive trapezoidal terrain models with upwind and downwind slope angle of 27° and 45° were placed four times of terrain height behind the point source. The source height is the same as the terrain model height. Flow and tracer concentrations were measured and analyzed. Based on the results, conclusions are in summary as:

(1) The wind flow speed-up factor increases around the top surface of trapezoidal shape terrain when the slope angle of trapezoidal shape terrain increases from 27° to 45°.

(2) The averaged height of the concentration plume is found to decrease along the upwind slope of trapezoidal shape terrain for slope angles of 27° and 45°.

(3) The vertical dispersion parameters of plume along with the downstream distance of source increase when the slope angle of terrains changes from 45° to 27°.

ACKNOWLEDGEMENTS

This work has been supported by the Taiwan National Science Council under grant NSC 99-2221-E-019-050.

REFERENCES

[1] MacDonald, R. W., Griffiths, R. F., and Hall, D. J., 1998, "A Comparison of Results from Scaled Field and Wind Tunnel Modelling of Dispersion in Arrays of Obstacles", *Atmos. Environ.*, Vol. 32, No.22, pp.3845-3862.

[2] Crooks, G., and Ramsay, S., 1993. "A Wind Tunnel Study of Mean and Fluctuating Concentrations in a Plume Dispersion over a Two-dimensional Hill", *Boundary Layer Meteoro.*, Vol.66, pp.155-172.

[3] Liu, H., Zhang, B., Sang, J., and Cheng, A. Y.S., 2001. "A Laboratory Simulation of Plume Dispersion in Stratified Atmospheres over Complex Terrain", *J. Wind Engn. and Ind. Aerodyn.*, Vol.89, pp.1-15.

[4] Cao, S. and Tamura, T., 2007, "Effects of Roughness Blocks on Atmospheric Boundary Layer Flow over a Two-dimensional Low Hill with/without Sudden Roughness Change", *J. Wind Engn. and Ind. Aerodyn.*, Vol.95, pp.679-695.

[5] Shiau, B.S., and Hsu, S.C., 2003, "Measurement of the Reynolds Stress Structure and Turbulence Characteristics of the Wind Above a Two-Dimensional Trapezoidal Shape

of Hill," *J. Wind Engn. and Ind. Aerodyn.*, Vol.91, Issue 10, pp.1237-1251.

[6] Shiau, B.S., and Hsieh, C.T., 2002, "Wind Flow Characteristics and Reynolds Stress Structure Around the Two-dimensional Embankment of Trapezoidal Shape with Different Slope Gradient,", *J. Wind Engn. and Ind. Aerodyn.,* Vol.90, Issue 12-15, pp.1645-1656.

[7] Davidson, M.J., Mylne, K.R., Jones, C.D., Philips, J.C., Perkins, R.J., Fung, J.C.H., and Hunt, J.C.R., 1995. "Plume Dispersion through Large Group of Obstacles – a Field Investigation", *Atmos. Environ*., Vol. 29, No.22, pp.3245-3256.

[8] Hanna, S.R., Tehranian, S., Carissimo, B., Macdonald, R.W., and Lohner R., 2002. "Comparison of Model Simulations with Observations of Mean Flow and Turbulence within Simple Obstacle Arrays", *Atmos. Environ*., Vol. 36, pp.5067-5079.

[9] Counihan, J., 1975, "Adiabatic Atmospheric Boundary Layer: A Review and Analysis of Data from the Period 1880-1972", *Atmos. Environ.*, Vol. 9, pp.871-905.

[10] Maeda, J. and Makino, M., 1988, "Power Spectra of Longitudinal and Lateral Wind Speed Near the Ground in Strong Winds", *J. Wind Engn. and Ind. Aerodyn.*, Vol.28, pp.31-40.

[11] Baker, C.J., 1985, "The Determination of Topographical Exposure Factors for Railway Embankments", *J. Wind Engn. and Ind. Aerodyn.*, Vol.21, pp. 89-99.

Biomedical flows

Conference on Modelling Fluid Flow (CMFF'12)
The 15th International Conference on Fluid Flow Technologies
Budapest, Hungary, September 4-7, 2012

NUMERICAL SIMULATION OF THE NANO PARTICLE DEPOSITION USING A THREE-DIMENSIONAL MODEL OF LUNG AIRWAYS

A. F. Tena[1], P. Casan[1], J. Fernandez[2], A. Marcos[2], and R Barrio[3]

[1] Instituto Nacional de Silicosis. C/ Dr Bellmunt. 33006 Oviedo. E-mail: anafertena@gmail.com, pcasan@ins.es
[2] Universidad de Extremadura. Avda de Elvas, 06006 Badajoz, Spain. E-mail: ffrancos@unex.es, acmarcos@unex.es
[3] Universidad de Oviedo. Campus de Viesques 33203 Gijón, Spain. E-mail: barrioraul@uniovi.es

ABSTRACT

One of the main health problems to the urban population is the exposure to air pollution. Suspended particles (made up of soot, smoke, dust and liquid droplets) can cause a wide range of respiratory diseases such as asthma and chronic obstructive pulmonary disease, as well as worsening heart diseases and other conditions. Knowing the particle deposition in realistic models of the human respiratory system is fundamental to prevent these diseases, and this is the objective of this work.

A 3D numerical model of the bronchial tree has been developed, from the trachea to the seventh level bronchioles. The geometry follows the model developed by Weibel and Kitaoka. It has been discretized with a mesh of about one million cells. The Navier-Stokes equations have been solved with a commercial CFD finite volume code.

Keywords: CFD, Lung, Particles.

NOMENCLATURE

CFD	[-]	Computational Fluid Dynamics
COPD	[-]	Chronic Obstructive Pulmonary Disease
DF	[-]	Deposition fraction
DPM	[-]	Discrete Phase Model
SIMPLE	[-]	Semi-Implicit Method for Pressure-Linked Equations
UDF	[-]	User Defined Function
d	[m]	Branch diameter
d_a	[m]	Aerodynamic diameter
d_p	[m]	Particle diameter
n	[-]	Order of the branch
Q	[ℓ/min]	*F*low rate
$\vec{u}$	[m/s]	Velocity vector
$(\nabla \times \vec{u}) \cdot \vec{u}$	[m/s^2]	Helicity
$y+$	[-]	Wall Yplus ($\rho y u_t \ / \ \mu$)
β	[º]	angle

1. INTRODUCTION

In the rush hour in the city, cars, with diesel engines, start up, move for a few meters, slow down and then start again, releasing particles into the atmosphere. Depending on their size, particles can be classified into:

- Particles of aerodynamic diameter between 15 and 100 μm: Particles over 15 μm are deposited by their weight and are rarely inhaled.
- Particles of aerodynamic diameter between 5 and 10 μm: The human nose and trachea filter particles from 10 to 15 μm, preventing its entrance into the lungs.
- Particles of aerodynamic diameter between 2.5 and 5 μm: The cilia of the respiratory epithelium of the trachea expel the captured particles of 3-5 μm through the nasopharynx.
- Particles of aerodynamic diameter less than 2.5 μm. These finer particles are the most important from the standpoint of health.

Aerodynamic diameter is the diameter of a sphere of density 1,000 kg/m^3 that has the same gravitational settling velocity as the particle in question.

$$d_a = d_p \left(\frac{\rho_p}{1{,}000} \right)^{\frac{1}{2}} \tag{1}$$

The effect of particles on health is directly dependent on its size, since the human body is designed to remove larger particles and prevent them from accumulating in the lungs, which are the filters that prevent the passage of particles to the blood stream.

The upper airways consist of the nose, inner nasal cavity, paranasal sinuses, pharynx and larynx. For this work we will focus on the anatomy of the lower airways, which begin at the trachea. The

trachea is divided into two main bronchus. Then each bronchi continue to divide in a dichotomous way, reaching a minimum of 23 generations. Generations 1, 2 and 3 are called bronchi. Generations 4 to 16 are the bronchioles. The latter is called the terminal bronchiole and it is the smallest portion of the airways devoid of alveoli.

The basic objective of the experimental and numerical studies of flow in the lungs is to deepen in the knowledge of the gas exchange (O_2 and CO_2) and in the particle deposition, and optimize the application of pharmaceutical aerosols for the treatment of lung diseases. The deposition of aerosols in the lungs is a non-stationary phenomenon due to the complexity of the lungs' geometry, the existence of interactions between air, water and solids, the cells' mechanics and heat transfer. This means that the velocity, density, pressure or temperature can change over time. Not all phenomena occurring in the lungs' airways can be simulated. Experimental and numerical simplifications are needed, such as considering the airflow as isothermal, rigid ducts (which would be the bronchi), and a spherical shape of the particles.

The earlier studies of particle deposition were based on one-dimensional models based on empirical formulas. One of the pioneering researchers in this field was Martonen [1-2], who proposed in 1982 a system of equations to determine the particle deposition. For its formulation took into account a number of assumptions such as the behaviour of particles in the lung (that are deposited by impaction, sedimentation and diffusion) and the velocity of air in the lungs in function of tidal volume and respiratory rate. In the larger particles the impaction behaviour predominates, while in the smaller ones diffusion is the main behaviour. The intermediate particles tend to deposit by sedimentation because of the effect of gravity.

For over a decade, several studies about the airflow behaviour were performed, starting in the mouth and ending in the alveolar region [3-6]. These studies have mainly focused on isolated sections of the lung, such as the trachea and the first generations of alveolar ducts or sacs.

Current studies are based predominantly in Computational Fluid Dynamics (CFD). Increased computer power has allowed the development of this technique, in which the Navier-Stokes equations are solved in the domain under study. Walters [7] uses a model with a finite number of flow paths, each of which is fully resolved, to provide a detailed description of the entire complex small-scale flowfield. This model was tested for three inspiratory flowrates and compared in terms of pressure drop, flow distribution characteristics, and flow structure with the fully resolved geometry. Robinson [8, 9] focuses her work in studying the three main modes of particle deposition (impact, sedimentation and diffusion) using simplified ducts. The techniques of imaging (e.g., SPECT) can detect with a high degree of resolution the deposition patterns of particles, but not clearly the airway composition. Martonen [10] shows a protocol to aid in the interpretation of these images, where the interior of lung was partitioned into a series of nested shells, each one containing its part of the airways, helping the interpretation of scintigraphy images. To our knowledge, the use of CFD in Spain has been only developed in the Universidad Autónoma de Madrid [11] and in the Universidad de Valladolid [12], although both cases were limited to the upper airways.

This work is part of a broader one, which tries to model the airflow in the lung with all their characteristics: unsteady flow, inhalation and exhalation of particles, common diseases (asthma, bronchitis, etc.). A first step was [13] the construction and simulation of a particular 7-level model, using a single way to study the unsteady flow that occurs during the execution of a spirometry test. The main innovation was the unsteady boundary conditions applied in conjunction with an adaptive time step. Such conditions required the use of two UDF. The fluid dynamic phenomenon of different obstructive diseases, and how it is perceived in the tests, was characterized varying the geometry and the unsteady boundary conditions.

A second step of the investigation is the main objective of this work, to study the lung deposition of inhaled particles through a numerical model. To achieve the overall objective we have established the following specific objectives:

- Preparation of a geometrical model of human airway.
- Preparation of numerical model to determine the airflow through the airway.
- Determining the transport and deposition of particles under different conditions of speed and particle sizes.

2. METHODOLOGY

A 3D numerical model of the bronchial tree has been developed, from the trachea to the seventh level bronchioles with the commercial code Ansys Gambit© [14]. The geometry follows the models developed by Weibel [15] and Kitoaka et al [16].

This model begins at the trachea, which has a length of 12 *cm* and a diameter of around 1.8 *cm*. The right main bronchus is shorter and wider. It leaves the trachea with an angle of 25 to 30 degrees, with a diameter of approximately 1.5 *cm* and a length of 2 *cm*. The left main bronchus leaves the trachea with an angle of approximately 45 degrees. It is substantially longer than the right main bronchus, with an average length of 5 *cm* and a diameter of 1.2 *cm*. Levels 2 and 3 are made with Kitoaka recommendations [16] and the rest following Weibel [15]. The bifurcation angle β was set to 35º

according to the guidelines given in [15]. The dimensions of the built model can be seen in table 1.

Table 1. Model dimensions

Gen n	Branches number	Diam (m)	Lengh (m)	Area (m^2)
0	1	0.01800	0.12000	2.54E-08
1	2	0.01221	0.04782	1.17E-08
2	4	0.00828	0.01906	5.39E-09
3	8	0.00562	0.00760	2.56E-09
4	16	0.00445	0.01267	1.56E-09
5	32	0.00351	0.01069	9.69E-10
6	64	0.00281	0.00901	6.19E-10
7	128	0.00227	0.00761	4.05E-10

The geometry of the bifurcations in the bronchioles at all the generations is created by a similar procedure. The diameter d and the length ℓ, deduced from the relations proposed by Weibel and Kitaoka, are:

$$\begin{cases} d = 0.018\exp(-0.388\,n) & \text{if } n \le 3 \\ d = 0.013\exp\left[-(0.2929 - 0.00624\,n)\,n\right] & \text{if } n > 3 \end{cases} \quad (2)$$

$$\begin{cases} l = 0.12\exp(-0.92\,n) & \text{if } n \le 3 \\ l = 0.025\exp(-0.17\,n) & \text{if } n > 3 \end{cases} \quad (3)$$

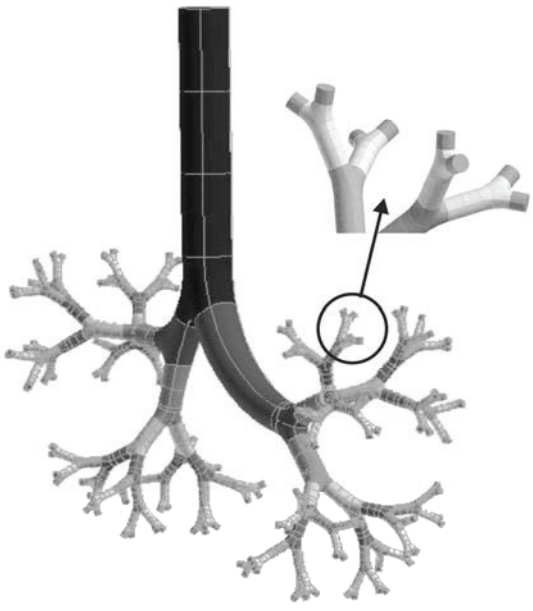

Figure 1. Numerical model geometry from the trachea to the 7th order bronchioles

Figure 1 shows a global image of the model. The complete morphology of the lung can be generated from this model by imposing symmetry at each of the branches. The entire lung is presented in Figure 2 for showing purposes only; of course, the numerical simulation of this complete morphology would be simply unavoidable.

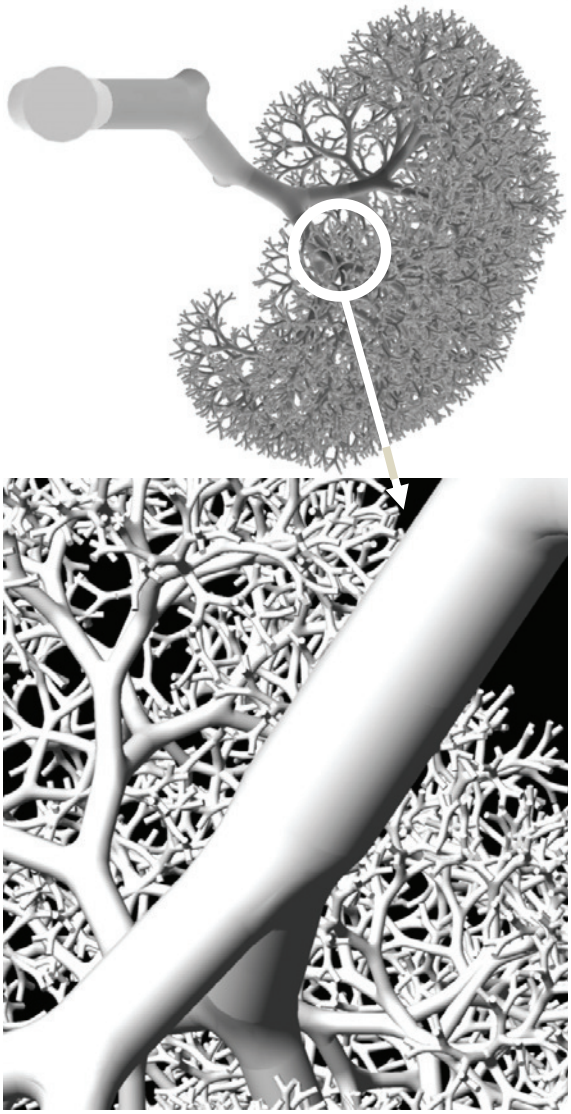

Figure 2. Complete morphology of the lung

Figure 3 shows a detail of the unstructured mesh generated. The model of the lung was meshed with tetrahedral cells due to their better adaptation to complex geometries. The size of the tetrahedrons diminishes while descending from the high-order to the low-order generations. A boundary layer mesh was built before meshing the volumes in order to obtain a better description of the boundary layer in the numerical calculations. The size of the tetrahedrons was consistent with the size of the boundary layer cells. The volume of the cells ranges between $2.96\text{x}10^{-12}$ and $2.01\text{x}10^{-10}$. The maximum equiangle skew was restricted to 0.6 for 97.60% of the cells in the mesh.

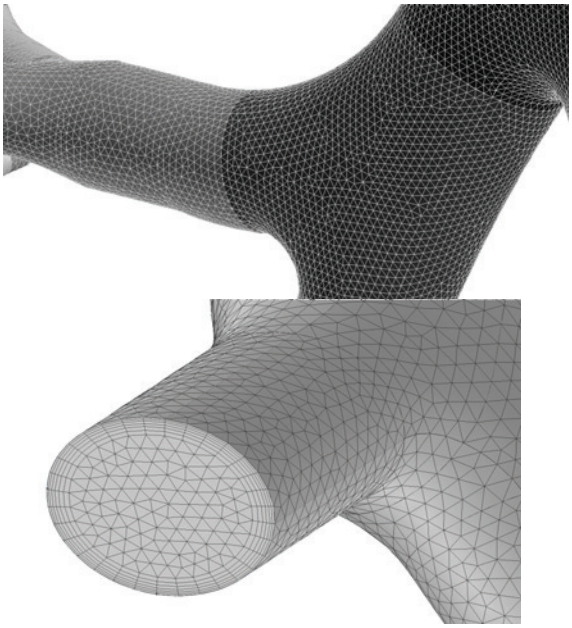

Figure 3. Detail of the mesh

The total number of cells used to begin the simulations was about 10^6, though other meshes of different size ($2x10^6$ and $4x10^6$) were generated in order to investigate the dependence of the numerical predictions. As can be seen in Figure 4, the variation observed in the outlet static pressure rate when considering different mesh sizes is not very significant. For the mesh size used for the calculations (about 1,000,000 cells) this variation is lower than 1.77%, and with 2,000,000 cells is lower than 1.04% compared with the model of 4,000,000 cells.

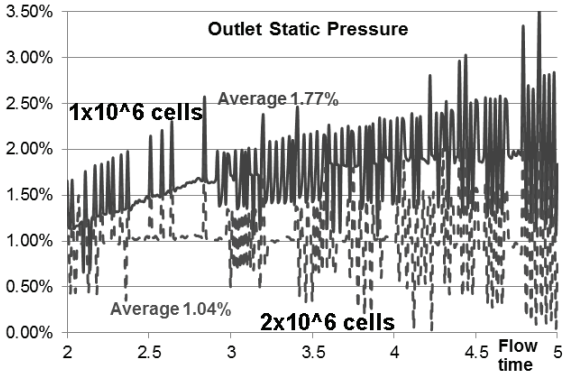

Figure 4. Results of the independence tests

The numerical simulations were performed with the code Ansys Fluent© [17]. This code was used to solve the full steady 3D Reynolds-averaged Navier-Stokes equations by the finite volume method. The fluid used in the calculations was air. The velocities will vary between 0.4 and 8 *m/s*, so the Reynolds number is between $4.93x10^2$ and $9.83x10^3$. The flow was considered as incompressible and turbulent. To effectively address both laminar and turbulent flow conditions, the model used for turbulent closure was the SST k-omega together with the transitional flows option to enable a low-Reynolds-number correction to the turbulent viscosity. This model provides a good approximation to transitional flows because the value of ω does not reach the zero value as the laminar flow limit is approached. Furthermore, the turbulence is simulated all the way to the viscous sublayer, avoiding the use of standard wall functions, which are inaccurate for transitional flows. The pressure-velocity coupling was established by means of the SIMPLE algorithm. Second-order upwind discretizations were used for the convection terms and central difference discretizations were established for the diffusion terms. The $y+$ values were maintained to be on the order of approximately 2 or less at all wall boundaries.

This model has already been tested in the first step of this broad work [13].

The particle trajectory equation can either be solved with the momentum and energy equation for the continuum flow (coupled) or after the momentum and energy equations have converged (uncoupled). The coupled option allows particles to interact with the flow fluid and affect the flow solution. In this case, the uncoupled option was chosen. The inlet boundary condition was mass flow rate, and the outlet boundary condition was pressure outlets. Each of the 128 terminal airway branches were held constant at atmospheric pressure, instead of constant outflow, since the flow rate in the branches is allowed to vary. Convergence was accepted with a criteria of 0.00001 residuals for continuity and each velocity component in the momentum equation. Convergence required about 1,600 iterations and approximately 10 min CPU time.

Once the static simulation has finished, the Discrete Phase Model (DPM) is switched on to predict the trajectory of discrete phase particles. To study particle deposition, the Lagrangian approach was used; particle trajectories were calculated within the steady flow fields of interest as a post processing step. Forces on the particles of interest include drag, pressure gradient, gravity, lift, and Brownian motion. To model the effects of turbulent fluctuations on particle motion, a random walk method has been employed. The tracking parameters used were 50,000 for the "maximum number steps" and 5 for the "step length factor".

Particles are introduced by means of an injection type called surface, specifying particle properties and velocity. The particles must be introduced from a surface close to the entrance (0.1 *mm*) and not near the walls (0.5 *mm*) to avoid the immediate deposition. Robinson [18] founded that 50,000 particles are necessary to minimize random variation in the deposition efficiency predictions due to the randomness of the particle position profile. Figure 5 shows the spatial distribution of particles

employed at the inlet in DPM. Only 188 of the 50,058 particles are shown.

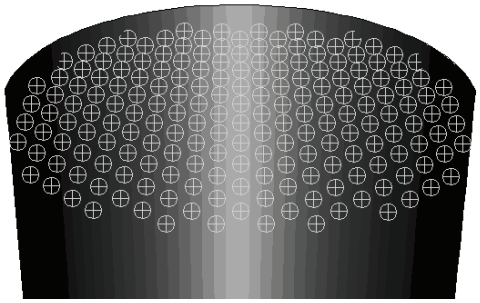

Figure 5. Particles distribution at the inlet.

Deposition is determined by summing up the "trapped" fate particles, which occurs when their centre of mass touches the wall. Fluent also reports the number of incomplete, aborted, or unable to be tracked particles. These numbers can be minimized by adjusting various input parameters.

3. RESULTS

The flow rates tested were 8, 31, 95 and 122 *ℓ/min*, which are equivalent to different respiratory rhythms. The seeding conditions of the particles were:

- Inert material density: 1,000 kg/m^3.
- Particle size: 5 *nm*, 10 *nm*, 50 *nm*, 0.1 μm, 0.2 μm, 0.5 μm, 1 μm, 2 μm, 5 μm, 10 μm and 20 μm.
- Velocity: the same that air.
- Density 0.5%.
- Number of injected particles: 50,058.

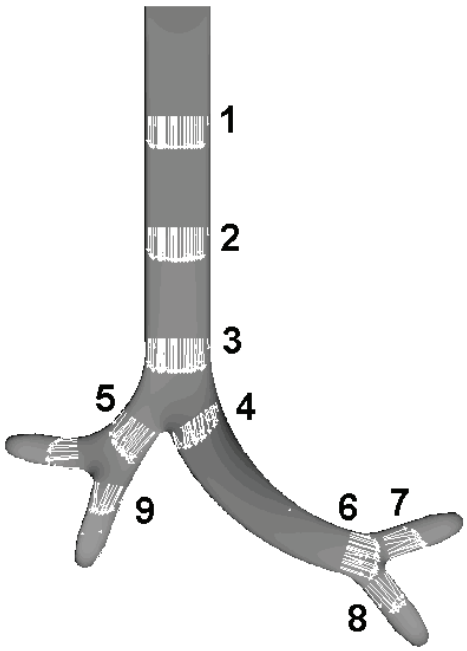

Figure 6. Velocity vectors and contours (range 0-6.5 *m/s*) in the first 3 levels, flowrate 31 *ℓ/min*

Figure 6 shows the velocity contours in the first 3 levels as well as the velocity profiles at several positions.

In figure 7, the helicity inside the lung at various positions is mapped. Helicity is defined by the dot product of the vorticity and the velocity vectors, that is $(\nabla \times \vec{u}) \cdot \vec{u}$. It provides information about the vorticity aligned with the fluid stream. It has been plotted here looking for the secondary flows. The surfaces are tangential planes and two counter-rotating vortices are captured. It can be observed that the vortex centres are kept more or less at the same distance from the lung centre. Only small differences are found at both sides of the centre plane (middle surface in the axis direction).

Because the input boundary condition, the fluid begins to have vorticity at the end of the trachea, which favours the deposition of particles carried by the air.

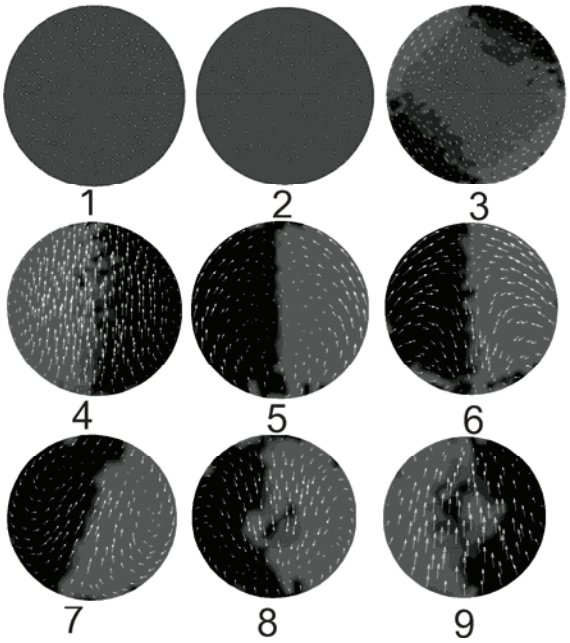

Figure 7. Helicity at various sections (figure 6) in m/s^2, flow rate 31 *ℓ/min*.

The regional deposition of particles can be quantified in terms of the deposition fraction (DF), defined as the mass ratio of deposited particles in a specific region to the particles entering the lung. Here (figure 8) is the ratio of the particles trapped in the first seven levels and entering the lung. These results agree with Dolovich [18], shown in figure 6, except in the range of particles between 0.1 and 2 *microns*, where numerical values are greater than those obtained experimentally. This difference may be due mainly to lung numerical model used, but can also be influenced by the parameters used.

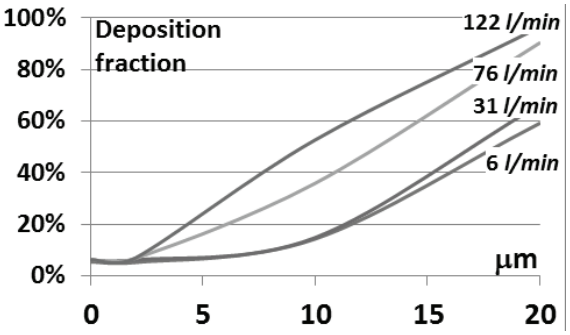

Figure 8. Relationship between particle size and lung deposition. Numerical results.

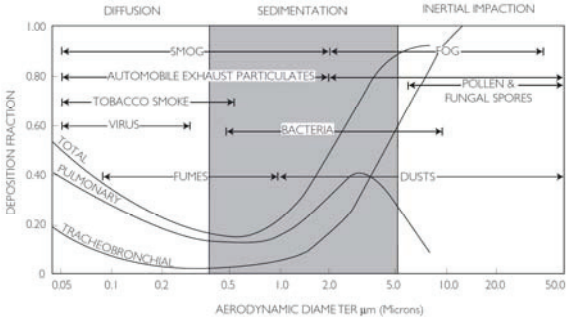

Figure 8. Relationship between particle size and lung deposition. Experimental results (Dolovich et al.).

Figures 9 to 14 show the concentration of the particles (kg/m^2) settled on the duct walls for a flow rate of 31 *ℓ/min* and for all size of particles. Black colour with white border means "high concentration" of settled particles on the wall, and gray colour means absence of settled particles. It can be observed that the number of escaped particles decreases when the particle size increases. This is due to the gravitational force, which also increases, forcing the particles to settle on the walls. In these figures it also can be observed that the black areas reach more distant regions as the particles are smaller.

4. CONCLUSIONS

The distribution of particles in the lung airways depends of its size. Small particles are distributed more uniformly than bigger particles, which follow the mean flow. The main objective of this work, to study the particle transport in the lung from the trachea to level 7 has been achieved. The next step is a combination of this work with the previous one. We will try to determine the particle deposition from the mouth to the level 17 during a respiratory cycle, using a mixture of particles of different sizes. Due to the high number of branches (131,072), it is necessary to work with a single pathway, so the boundary conditions applied in the truncated branches will be very important.

ACKNOWLEDGEMENTS

The authors gratefully acknowledge the financial support provided by Junta de Extremadura and FEDER under project GR10047 and also by Ministerio de Ciencia e Innovación under project DPI 2010-21103-C04-04.

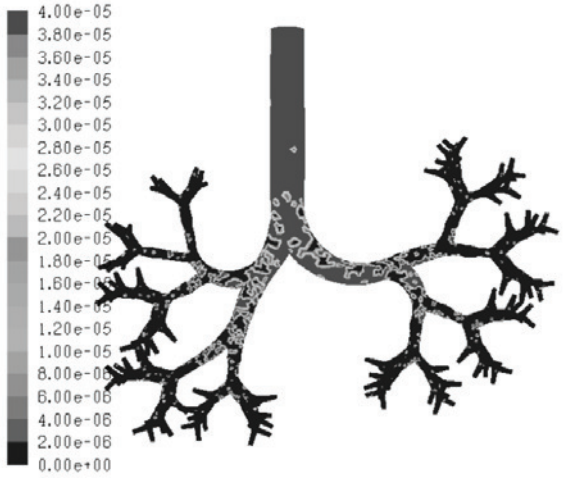

Fig. 9: Flowrate 31 *ℓ/min*, size 1 *pm*

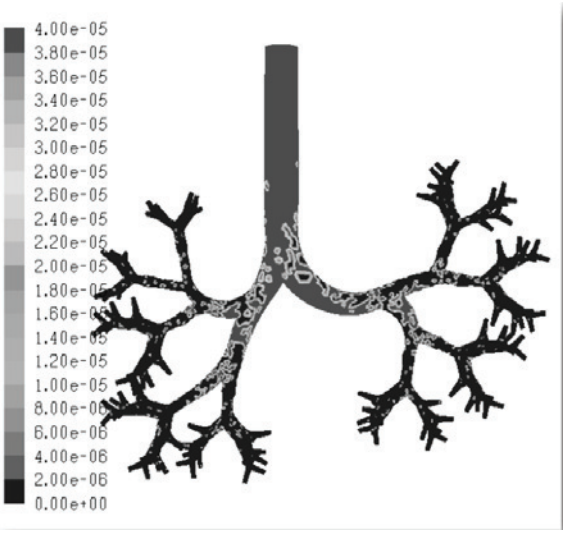

Fig. 10 Flowrate 31 *ℓ/min*, size 1 *nm*

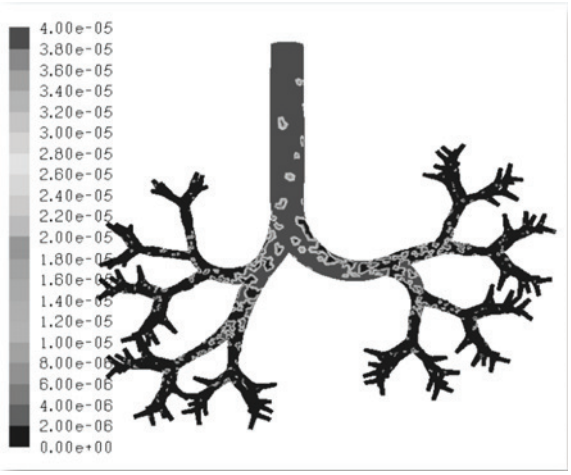

Fig. 11: Flowrate 31 *ℓ/min*, size 1 *μm*

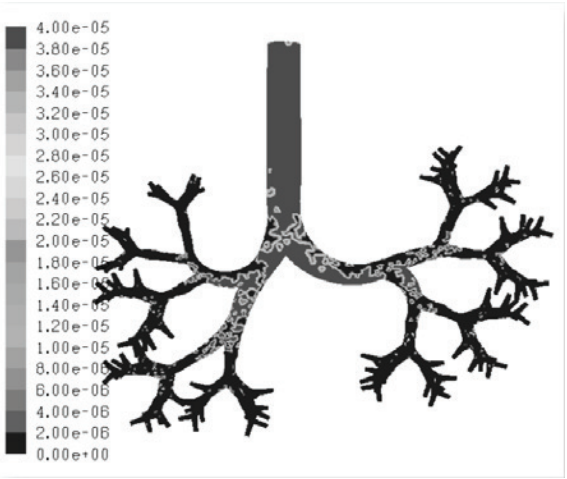

Fig. 12: Flowrate 31 *ℓ/min*, size 5 *μm*

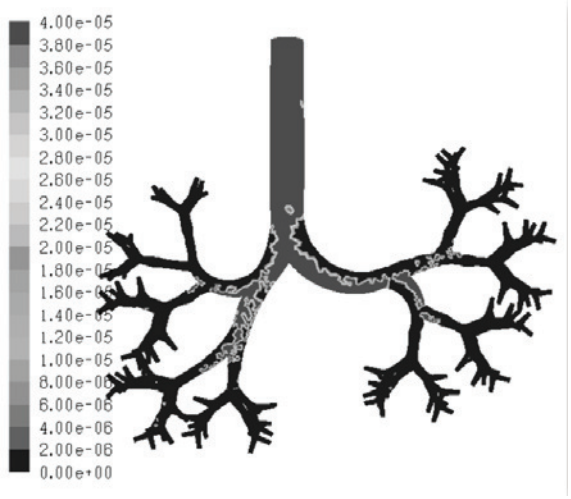

Fig. 13: Flowrate 31 *ℓ/min*, size 10 *μm*

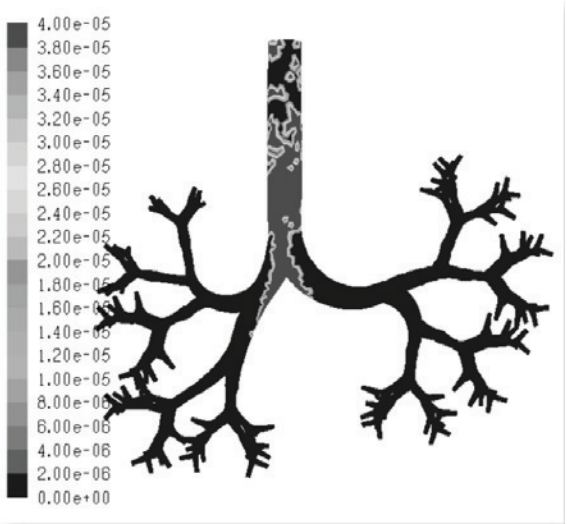

Fig. 14: Flowrate 31 *ℓ/min*, size 50 *μm*

REFERENCES

[1] Martonen TB. Analytical model of hygroscopic particle behavior in human airways. *Bull Math Biol. 1982; 44:425–442*.

[2] Martonen TB, Katz I. Inter-related effects of morphology and ventilation on drug deposition patterns. *STP Pharm Sci. 1994; 4:11–18*.

[3] Adler K, Brucker C. Dynamic flow in a realistic model of the upper human lung airways. *Exp. Fluids. 2007; 43:411–23*.

[4] Ball CG, Uddin M, Pollard A. High resolution turbulence modelling of airflow in an idealised human extrathoracic airway. *Comput. Fluids. 2008; 37:943–64.*

[5] Gemci T, Ponyavin V, Chen Y, Chen H, Collins R. Computational model of airflow in upper 17 generations of human respiratory tract. *J. Biomech. 2008; 41:2047–54*.

[6] Zhang Z, Kleinstreuer C, Kim CS. Airflow and nanoparticle deposition in a 16-generation tracheobronchial airway model. *Ann. Biomed. Eng. 2008; 36:2095–110.*

[7] D. Keith Walters and William H. Luke, A Method for Three-Dimensional Navier-Stokes Simulations of Large-Scale Regions of the Human Lung Airway. *J. Fluids Eng. 132, 051101, 2010*, *vol. 132, 051101-1-8.*

[8] Robinson, RJ., Snyder, P., Oldham MJ. Comparison of Particle Tracking Algorithms in Commercial CFD Packages: Sedimentation and Diffusion. *Inhalation Toxicology, 19:517–531, 2007.*

[9] Robinson, RJ., Snyder, P., Oldham MJ. Comparison of Analytical and Numerical Particle Deposition Using Commercial CFD Packages: Impaction and Sedimentation. *Inhalation Toxicology, 20:485 - 497, 2008.*

[10] Martonen T. B, Schroeter, J.D., Fleming J.S. 3D In Silico Modeling of the Human Respiratory System for Inhaled Drug Delivery and Imaging Analysis. *Journal of Pharmaceutical Sciences, Vol. 96, 603–617, 2007*.

[11] Castro Ruiz Pilar. *Análisis computarizado del flujo aéreo en cavidad nasal. Tesis Doctoral*. Universidad Autónoma de Madrid. 2003.

[12] Quispe Apaclla César, 2010. *Estudio del flujo de aire a través de las fosas nasales en la inspiración y espiración, considerando el intercambio de calor existente. Tesis Doctoral*. Universidad de Valladolid.

[13] Tena, Ana T, Casan, P, Marcos, A, Barrio, R, Blanco, E, 2011. Analysis of the fluid dynamic characteristics of the obstructive pulmonary diseases using a three-dimensional cfd model of the upper conductive zone of the lung airways. *Proceedings of the ECCOMAS. Conference on Simulation and Modeling of Biological Flows, VUB, Brussels, Belgium.*

[14] *Gambit version 2.4.6* (2006). ©ANSYS Inc.

[15] Weibel, E.R., *Morphometry of the human lung*, Springer-Verlag (1963).

[16] Kitaoka H, Takaki R, Suki B. A three-dimensional model of the human tree. *J. Applied Physiology. 1999; 87: 2207-2217*.

[17] *Fluent version 6.3.26* (2006). ©ANSYS Inc.

[18] Robinson, R. J., Oldham, M. J., Clinkenbeard, R. E., and Rai, P. 2006. Experimental and numerical analysis of a 7 generation human replica tracheobronchial model. Ann. Biomed. Eng. 34(3):373–383

[19] Dolovich MB, Newhouse MT. Aerosols. *Generation, methods of administration, and therapeutic applications in asthma. In Allergy. Principles and practice*, 4th edn, eds Middleton E Jr, Reed CE, Ellis EF, Adkinson NF Jr, Yunginger JW, Busse WW. St Louis: Mosby Year Book, Inc., 1993; 712–739.

Conference on Modelling Fluid Flow (CMFF'12)
The 15th International Conference on Fluid Flow Technologies
Budapest, Hungary, September 4-7, 2012

NUMERICAL ANALYSIS FOR THE EFFECT OF DIALYSIS DOSE ON THE NON-NEWTONIAN BLOOD FLOW CHARACTERISTICS IN THE ARTERIOVENOUS GRAFT

Soyoon KIM[1], Hyangkyoung KIM[2], Hong Sun RYOU[3]

[1] School of Mechanical Engineering, Chung-Ang University. E-mail: cutesoykim@gmail.com
[2] School of Medicine, Chung-Ang University. E-mail: hkkim@cau.ac.kr
[3] Corresponding Author. School of Mechanical Engineering, Chung-Ang University. 221 Heuksuk-Dong, Dongjak-Gu, Seoul, Korea. Tel.: +82 2 813 3669, Fax: +82 2 813 3669, E-mail: cfdmec@cau.ac.kr

ABSTRACT

For patients with renal failure, the renal replacement therapies such as haemodialysis, and kidney transplantation are needed. Haemodialysis is widely used to remove the waste products. It is important for efficient haemodialysis to improve a patency rate of the vascular access. Since the complications are related to the flow pattern, haemodynamics in the access is needed to be considered for high patency rate. During the haemodialysis, the blood flow from an artificial kidney affects the flow characteristic in the vascular access. Therefore, methods of haemodialysis have to be set up, but there is no standard clearly.

In this study, the numerical analysis is performed for an effect of the dialysis dose on the flow in the graft. The blood is assumed to be a non-Newtonian fluid using Carreau model. When the dialysis dose is over 40% of the arterial flow rate, both low AWSS and high OSI are appeared at the graft of vein side. This can cause the graft failure such as stenosis. Thus, we suggest that the dose of dialysis under 40% for the arterial flow is appropriate for effective haemodialysis and analyse the effect of non-Newtonian characteristics on the blood flow in the graft.

Keywords: Arteriovenous graft, CFD, Dialysis dose, Haemodialysis, Non-Newtonian fluid, Vascular access

NOMENCLATURE

T	$[s]$	Period
n	[-]	Power law index
p	$[Pa]$	Pressure
t	$[s]$	Time
$\underline{v}$	$[m/s]$	Velocity vector
γ	$[1/s]$	Shear rate
η	$[Pa\ s]$	Apparent viscosity
η_∞	$[Pa\ s]$	Infinite shear viscosity
η_0	$[Pa\ s]$	Zero-shear viscosity
λ	[-]	Time constant
ρ	$[kg/m^3]$	Density
$\underline{\tau}$	$[Pa]$	Shear stress tensor

Subscripts and Superscripts

w	At the wall

1. INTRODUCTION

Chronic kidney disease (CKD) is a loss in renal function over a period of months or years. It often exists together with other conditions such as cardiovascular disease and diabetes. CKD is classified into 5 stages which are defined by level of renal function which is measured by glomerular filtration rate (GFR). Stage 5 CKD can be described as renal failure, also called end stage renal disease (ESRD). In this case, renal replacement therapy such as dialysis treatment or kidney transplantation is required to maintain life [1].

Haemodialysis is one of the dialysis treatments. It is a method for removing waste products such as creatinine and urea. Stable blood flow and accessibility to the vessel are necessary for haemodialysis. To achieve these conditions, a vascular access is constructed. Minimization of complications such as stenosis or thrombosis is required for high patency rate of the vascular access [2]. The arteriovenous fistula (AVF) which means the vascular access is classified into autogenous AVF and prosthetic graft AVF according to vessel attribute. The autogenous AVF is the method that artery and vein are connected directly. It has higher patency rates and lower rates of infection than prosthetic graft AVF. But the autogenous fistula requires at least 6 weeks for maturation before it can be used while the prosthetic graft AVF does not need. If it is difficult to place the autogenous AVF, a prosthetic graft AVF should be considered [3-5].

The prosthetic graft AVF is usually made from polytetrafluorethylene (PTFE). It has advantages that the catheter insertion part is wide and reconstruction is easy. However, there can be complications such as infection, stenosis and thrombosis. Most of all, venous neointimal hyperplasia (VNH) is a major cause of PTFE graft failure and VNH is caused by a stenosis. Graft thrombosis is the cause of 80 % of all vascular access dysfunction. There is a stenosis in over 90 % of thrombosis grafts either at the venous anastomosis or the proximal vein [6-8]. Understanding the mechanism of graft thrombosis can lead to prevent the complications. Early thrombosis is due to technical error like kinking or twisting of the vessel or graft at placement, or an inadequate inflow or outflow of the vascular access [9]. Roy-Chaudhury et al. [7] suggested that macrophages, specific cytokines and angiogenesis within the neointima and adventitia are likely to contribute to the pathogenesis of VNH in graft. Tricht et al. [10] had numerical study on haemodynamic characteristics for the pressure drop according to graft form; furthermore, experiment was conducted for haemodynamic phenomena according to amount and injection flow rate during haemodialysis [11]. Accordingly, causes of thrombosis and stenosis can be explained as three types, that is to say function of endothelial cells, technical problem of constructing AVF, and blood flow characteristics in the AVF.

Also, there are many researches for improving the patency. Niemann et al. [12] studied the characteristics of blood flow about the AVF form which can make the complications minimize. Lei et al. [13] suggested the surgery method for graft model, which can reduce flow interference and verified graft form that could be important factor for irregular flow. Krueger et al. [14] concluded that the patch form could improve the pressure and velocity distributions of blood flow comparing to conventional form, and demonstrated that occurrence of intimal hyperplasia and stenosis could be decreased. Dixon et al. [15] analysed use of aspirin at baseline associated with primary unassisted graft patency. To predict the complications, Tricht et al. [16] experimented the graft for finding the prediction index of stenosis. Also, Kim et al. [17] performed the numerical simulation for the effect of dialysis dose on the blood flow characteristics with Newtonian fluid.

Until now, most of researches are focused on the flow through the anastomosis site. However, the blood flow from the catheter is as much important as the blood flow in the anastomosis. An insertion of catheter or the catheter flow would make the unstable flow, such as turbulent flow, and this can initiate thrombosis or intimal hyperplasia (IH) development [9]. In spite of the effect of catheter blood flow on the haemodynamics in the graft, there is little data for flow in the AVF during dialysis. Thus, the aim of present study is to analyse the flow characteristics of the prosthetic graft AVF considering non-Newtonian characteristics of the blood and to provide the guidelines for optical dialysis dose using the numerical approach.

2. NUMERICAL DETAILS

2.1. Modelling

Generally, the prosthetic graft AVF is the vascular access which connects the artery and vein. Figure 1 shows a schematic geometry of idealized blood vessel after the construction of the access. Diameters of artery, vein and graft are 4.25 *mm*, 6.3 *mm*, 6 *mm* respectively. Length of the artery and the vein before anastomosis is 100 *mm*, which is longer than that of the experimental research [11] in order to obtain numerically stable results.

The computational grid is consisted of the tetrahedral mesh and prism layer and built by ANSYS Meshing Platform (AMP) v13.0. The total number of grid cells is about 180,000 through a grid independence test. The difference of time-averaged wall shear stress (AWSS) at outer line of the graft according to the number of grid cells is within 1.5 %. To calculate the wall shear strress, the size of grid near the wall is 0.1 *mm*.

2.2. Governing Equations

The governing equations for numerical simulation include the continuity equation and the momentum conservation equation as shown as:

$$\frac{\partial \rho}{\partial t} + \nabla \cdot (\rho \vec{v}) = 0 \tag{1}$$

$$\frac{\partial}{\partial t}(\rho \vec{v}) + \nabla \cdot (\rho \vec{v}\vec{v}) = -\nabla p + \nabla \cdot \bar{\bar{\tau}} \tag{2}$$

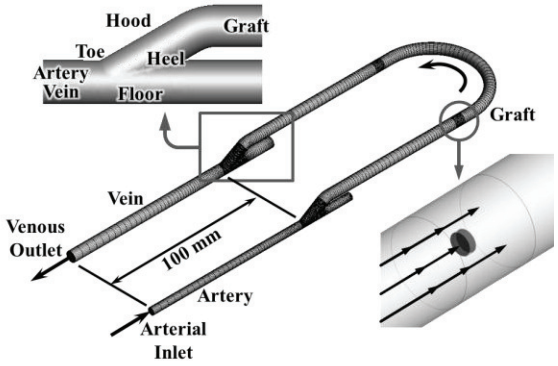

Figure 1. Schematics of the idealized blood vessel after the construction of the access

The vector of fluid velocity is $\vec{v}$ and $\tilde{\tilde{\tau}}$ is the shear stress tensor.

To consider the rheological characteristics of the blood, the constitutive equations for non-Newtonian fluid are required. The second invariant of shear stress tensor is:

$$\tilde{\tilde{\tau}} = \eta\dot{\gamma} \tag{3}$$

We use the Carreau model [18] which is generally known that it is suitable for the blood. Apparent viscosity of the blood using the Carreau model is expressed as:

$$\eta = \eta_{\infty} + (\eta_0 - \eta_{\infty})[1 + (\lambda\dot{\gamma})^2]^{(n-1)/2} \tag{4}$$

In the equation (4), η_0 is the zero-shear viscosity (0.056 *Pa s*), η_{∞} is the infinite shear viscosity (0.00345 *Pa s*), λ is the time constant (0.313 *s*), and n is the power law index (0.356) [18].

Since the maximum Reynolds number is about 1930 using the infinite shear viscosity, it is assumed that the blood flow is laminar, incompressible, and unsteady flow. Density of the working fluid is assumed as 1090 kg/m^3.

2.3. Boundary Conditions

For the blood pulsation, the inlet boundary condition is a time-dependent velocity waveform which is reconstructed with the fast Fourier transform (FFT) of a velocity waveform obtained from in vitro measurements [10] as shown in Figure 2. Mean velocity of the velocity profile is about 1.299 *m/s*. There are 6 cases according to the dialysis dose of 0, 200, 300, 400, 500, 750 *ml/min*. Boundary conditions of catheters are constant velocity considering each dialysis dose. The pressure-outlet boundary condition which means constant pressure of atmospheric pressure is used for the venous outlet.

2.4. Computational Details

The computational fluid dynamics (CFD) simulations for haemodynamics are performed with the commercial CFD software, FLUENT v13.0. For unsteady simulations, the PISO algorithm is used and each time step is 0.002 *s*. To meet the numerical stability, the number of time steps is set to 630, in other words, it is 2 cardiac cycles. Solution time for each case is about 6 hours on a 4-node, parallel, and 3.40GHz Intel i7 system.

2.5. Validation

To validate the results of numerical simulation, pressure distribution in graft is compare with that of experiment [11]. Figure 3 shows that pressure drop

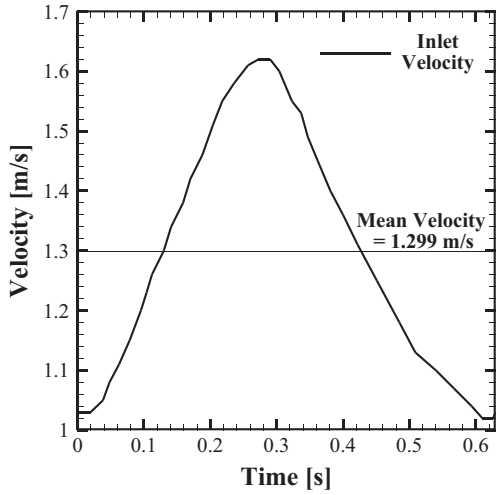

Figure 2. Inlet velocity profile [10]

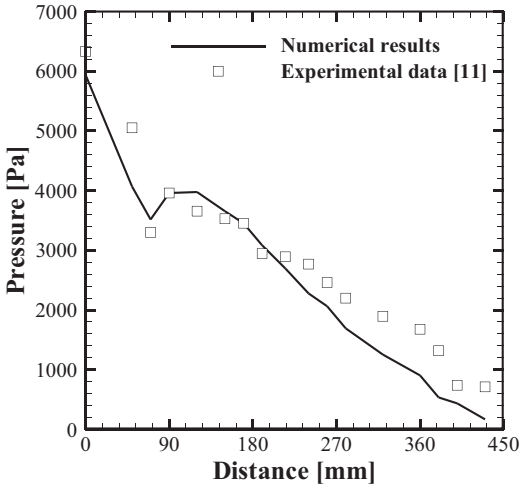

Figure 3. Comparison of mean pressure distribution with experimental data [11] according to the distance from the arterial inlet

in the graft is about 5.83 *kPa*, which has an error of 2.5 %. Locally, there is pressure distribution with the maximum error of 9 %. On the whole, it is confirmed that the distribution of the pressure in graft is similar with the experimental data [11].

3. RESULTS AND DISCUSSIONS

3.1. Pressure

Figure 4 is a distribution of mean pressure according to the distance from the arterial inlet. The cross-sectional average pressure at the arterial inlet without dialysis is 3096.44 *Pa* which is higher than the average pressure with dialysis. As the dialysis dose increases, the pressure drop also decreases linearly. This means that the heart would be under less strain during the dialysis. At anastomosis sites of the artery and the vein, the mean pressure varies locally due to a difference in flow velocity

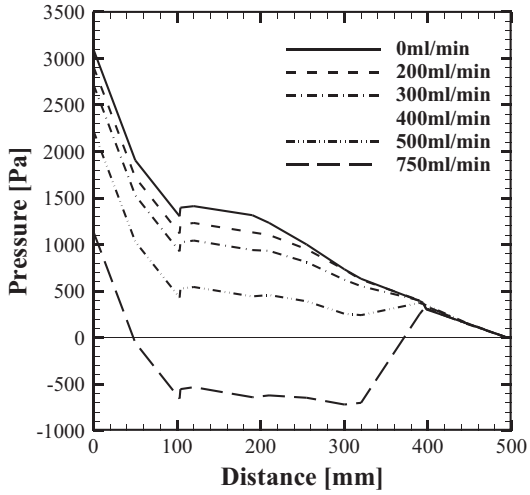

Figure 4. Mean pressure distribution according to the distance from the arterial inlet

according to a change of the cross-sectional area.

When the dialysis dose is over 50 % of the mean blood flow rate (1000 *ml/min*), a negative pressure appears because of an excessive suction of a catheter at the side of the artery (Arterial catheter). The same blood flow rate is provided from the catheter at the side of the vein (Venous catheter) and the pressure becomes higher after venous catheter.

3.2. Time-averaged Wall Shear Stress

Wall shear stress (WSS) is mainly applied to the inner layer of the arterial wall and the vascular Endothelium [19] because the endothelial cells are in direct contact with the blood flow. For the straight blood vessel, WSS is maintained about 1.5 *Pa* because of the autoregulation by the endothelial cells. Continuous exposure of WSS between 35 *Pa* and 40 *Pa* can cause physical damage of endothelial cells [20]. On the other hand, lower WSS, about 10 *Pa* to 30 *Pa*, can increase the permeability of the endothelial cells, damage erythrocytes and cause enhanced adhesiveness or aggregation of the platelet [21, 22]. When WSS is below 1 *Pa*, intimal hyperplasia or atherosclerosis can occur[23, 24]. Therefore, it is necessary for predicting the disease of blood vessel to realize locations of high or low WSS.

As mentioned earilier, the blood flow is the pulsatile flows according to the cardiac impulse. This will indicate that the shear stress on intima, namely endothelial cells, also varies for time. In this study, time-averaged wall shear stress (AWSS) for 1 cardiac cycle is used for analysis and AWSS is defined as:

$$\mathrm{AWSS} = \frac{1}{T}\int_0^T |\vec{\tau}_{\mathrm{w}}|\, dt \qquad (5)$$

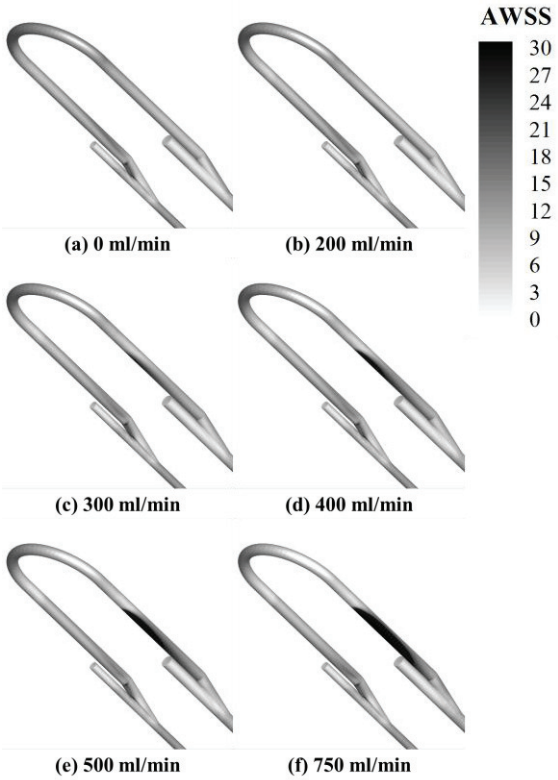

Figure 5. High AWSS distribution

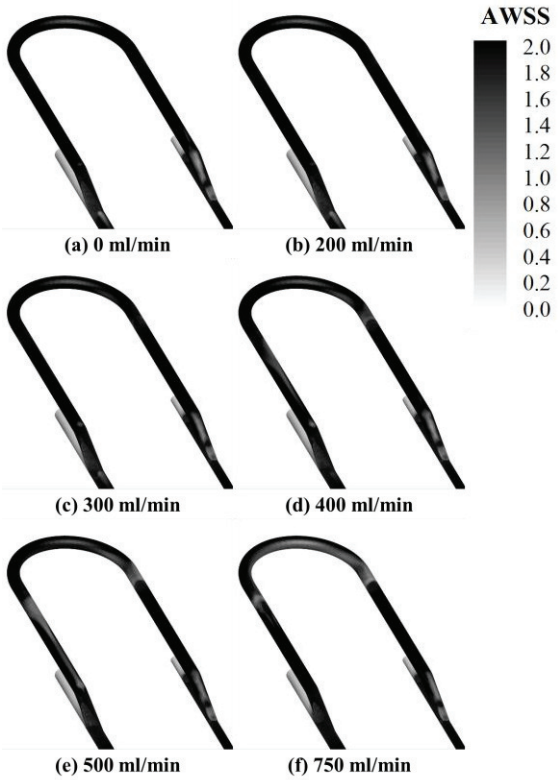

Figure 6. Low AWSS distribution

Figure 5 and 6 represent distributions of AWSS. From Fig. 5, we can indicate the location of higher AWSS. At the heel of the arterial anastomosis

which is an apical region of the bifurcation, there is maximum AWSS because the velocity profile is dramatically skewed toward the apex. Also, higher AWSS appears at a bottom face of the venous graft when the dialysis dose is over 300 *ml/min*. As the dialysis dose increases, the blood flow from the catheter affects the size of high AWSS zone.

Low AWSS below 1 *Pa* appears at the hood of arterial graft because of the circulation flow. When the dialysis dose is 0~200 *ml/min*, a region of low AWSS does not appear except for the arterial hood. Over 300 *ml/min*, AWSS is lower than 1 *Pa* after the suction due to the decrease of the flow rate. As the dialysis dose becomes larger, the larger area of low AWSS appears at the inner part of curved graft enlarges because the main stream of blood flow concentrates on outer side of the graft by the centrifugal force. From these reasons, the velocity profile at the cross-section in the venous graft indicates that the velocity of blood flow increases at the outer side of graft. Since the flow jet from the catheter leans to the bottom side of the graft, the flow with low velocity occurs at the top side of the venous graft. In case of excessive dialysis dose (750 *ml/min*), there is little velocity variation near the top side wall of the venous graft to maintain the flow rate.

3.3. Oscillatory Shear Index and Relative Residence Time

Oscillatory shear index (OSI) is an index which stands for an amount of the shear stress acting on the luminal surface because of the cross flow or reverse flow velocity components during pulsatile flow. From a fluctuation of wall shear stress (WSS), high OSI is associated with a dysfunction of endothelial cells of the blood vessel [25-27]. OSI is defines as:

$$\mathrm{OSI} = \frac{1}{2}\left(1 - \frac{\left|\int_0^T \vec{\tau}_w \, dt\right|}{\int_0^T |\vec{\tau}_w| \, dt}\right) \tag{6}$$

Relative residence time (RRT) as well as OSI is emerging as appropriate tools for atherosclerosis localization[28]. It indicates the residence time that the blood cells such as erythrocytes, leukocytes, and platelets spend at endothelium. RRT is calculated as [29]:

$$\mathrm{RRT} \sim [(1 - 2.0 \times \mathrm{OSI}) \times \mathrm{AWSS}]^{-1} \tag{7}$$

Figure 7 represents distributions of OSI in the graft. High OSI appears locally at the hood of arterial graft because of the circulation flow. Distributions of OSI do not greatly change with dialysis dose below 200 *ml/min*. When the dialysis dose is over 300 *ml/min*, high OSI occurs at the

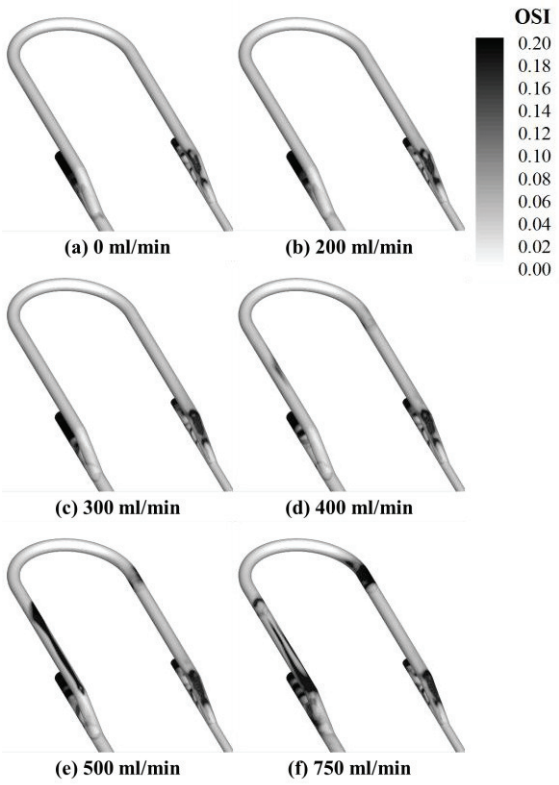

Figure 7. OSI distributions

catheter of the arterial side due to decrease of flow velocity in graft after suction. At the straight part of venous graft, a velocity gradient near the top side of the wall is not large with the dialysis dose below 300 *ml/min*, but high OSI over 0.2 occurs when the dialysis dose is over 400 *ml/min*. In addition, velocity gradient near the wall is not large in case of dialysis dose with 750 *ml/min* because of excessively large flow rate from the catheter. Then a region of high OSI has different pattern at the straight part of the venous graft. It can be concluded that a possibilities of thrombus and stenosis can change with the dialysis dose

RRT distributions are shown in Figure 8. High RRT region is at the straight part of vein side, the curved part after the suction and the arterial anastomosis site. These locations are with low AWSS or high OSI. Therefore, most locations which have possibility of complication can be detected from the RRT distribution more sensitively.

4. CONCLUSION

In this study, an effect of the dialysis dose on the blood flow in the arteriovenous graft is analysed. Therefore, the following conclusions can be drawn.

When the dialysis dose is over 50 % of flow rate in arterial inlet, negative pressure is generated. And the region of low AWSS and high OSI shows up locally after the suction at the arterial graft when the dialysis dose is over 30 % of flow rate. Also, the region of low AWSS appears at the straight part of

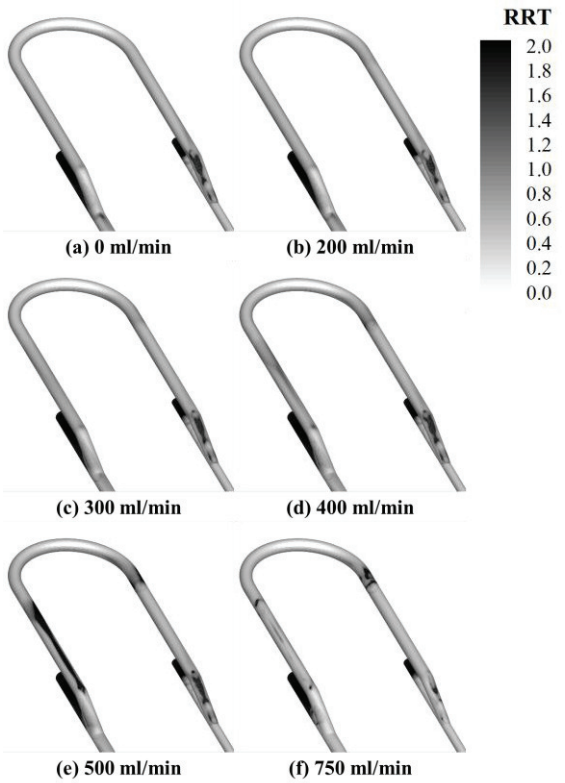

Figure 8. RRT distributions

graft of vein side when the dialysis dose is over 40 % of blood flow rate. In case of excessive dialysis dose (75 % of flow rate), low AWSS occurs at inner side of curve part and this is caused by the reduction of flow rate. Most of locations with low AWSS and high OSI can be detected from the RRT distribution. From these results, it can be predicted that the dialysis dose over 40 % of flow rate is needed to be avoided for higher patency rate.

ACKNOWLEDGEMENTS

This research was supported by Basic Science Research Program through the National Research Foundation of Korea(NRF) funded by the Ministry of Education, Science and Technology(2012-0001465).

REFERENCES

[1] National Collaborating Centre for Chronic Conditions, 2008, *Chronic kidney disease: national clinical guideline for early identification and management in adults in primary and secondary care*, London: Royal College of Physicians.

[2] Wood, J.D., Turenne, M.N., Strawderman, R.L., Young, E.W., Hirth, R.A., Port, F.K., and Held, P.J., 1997, "Vascular access survival among incident hemodialysis patients in the United States", *Am J Kidney Dis*, Vol. 30, pp. 50-57.

[3] Vascular Access 2006 Work Group, 2006, "Clinical practice guidelines for vascular access", *Am J Kidney Dis*, Vol. 48, pp. S248-S273.

[4] Tordoir, J., Canaud, B., Haage, P., Konner, K., Basci, A., Fouque, D., Kooman, J., Martin-Malo, A., Pedrini, L., Pizzarelli, F., Tattersall, J., Vennegoor, M., Wanner, C., Piet M. ter Wee, and Vanholder, R., 2007, "EBPG on vascular access", *Nephrol Dial Transplant*, Vol. 22, pp. ii88-ii117.

[5] Stehman-Breen, C.O., Sherrard, D.J., Gillen, D., and Caps, M., 2000, "Determinants of type and timing of initial permanent hemodialysis vascular access", *Kidney Int*, Vol. 57, pp. 639-645.

[6] Sunil, U., Thanh, N.H., Brott, B.C., Ito, Y., Cheng, C.H., Shih, A.M., Allon, M., and Andreas, S.A., 2005, "Turbulent flow evaluation of the venous needle during hemodialysis", *J Biomech Eng*, Vol. 127, No. 7, pp. 1141-1146.

[7] Roy-Chaudhury, P., Kelly, B.S., Miller, M.A., Reaves, A., Armstrong, J., Nanayakkara, N., and Heffelfinger, S.C., 2001, "Venous neointimal hyperplasia in polytetra fluoroethylene dialysis grafts", *Kidney Int*, Vol. 59, pp.2325-2334.

[8] Beathard, G.A., 1994, "The treatment of vascular access graft dysfunction: a nephrologist's view and experience", *Adv Ren Replace Ther*, Vol. 1, No. 2, pp. 131-147.

[9] Tricht, I.V., Wachter, D.D., Tordoir, J., and Verdonck, P., 2005, "Hemodynamics and complications encountered with arteriovenous fistulas and grafts as vascular access for hemodialysis: A review", *Ann Biomed Eng*, Vol. 33, No. 9, pp. 1142-1157.

[10]Tricht, I.V., Wachter, D.D., Tordoir, J., and Verdonck, P., 2006, "Comparison of the hemodynamics in 6mm and 4-7mm hemodialysis grafts by means of CFD", *J Biomech*, Vol. 39, No. 2, pp. 226-236.

[11]Tricht, I.V., Wachter, D.D., Tordoir, J., Vanhercke, D., and Verdonck, P., 2005, "Experimental analysis of the hemodynamics in punctured vascular access grafts", *ASAIO J*, Vol. 51, pp. 352-359.

[12]Niemann, A.K., Kock, S.A., Nygaard, J.V., Frund, E.T., Petersen, S.E., and Hasenkam, J.M., 2007, "Assessment of hemodynamic conditions in a-v fistulas using CFD", *Excerpt from the Proceedings of the COMSOL Users Conference 2007*.

[13]Lei, M., Archie, J.P., and Kleinstreuer, C., 1997, "Computational design of a bypass graft that minimizes wall shear stress gradients in the region of the distal anastomosis", *J Vasc Surg*, Vol. 25, No. 4, pp. 637-646.

[14]Krueger, U., Zanow, J., and Scholz, H., 2002, "Computational fluid dynamics and vascular access", *Artif Organs*, Vol. 26, No. 7, pp. 571-575.

[15]Dixon, B.S., Beck, G.J., Dember, L.M., Vazquez, M.A., Greenberg, A., Delmez, J.A., Allon, M., Himmelfarb, J., Hu, B., Greene, T., Radeva, M.K., Davidson, I.J., Ikizler, T.A., Braden, G.L., Lawson, J.H., Cotton, J.R.Jr., Kusek, J.W., and Feldman, H.I., 2011, "Use of aspirin associates with longer primary patency of hemodialysis garfts", *J Am Soc Nephrol*, Vol. 22, No. 4, pp. 773-781.

[16]Tricht, I.V., Wachter, D.D., Vanhercke, D., Tordoir, J., and Verdonck, P., 2004, "Assessment of stenosis in vascular access grafts", *Artif Organs*, Vol. 28, No. 7, pp. 617-622.

[17]Kim, J.Y., Ro, K.C. and Ryou, H.S., 2011, "Numerical study on blood flow characteristics in a arteriovenous graft wigth delivered dose during hemodialysis", *Journal of Computational Fluids Engineering*, Vol. 16, No. 4, pp. 84-91.

[18]Cho, Y.I., and Kensey, K.R., 1991, "Effects of the non-Newtonian viscosity of blood on flows in a diseased arterial vessel. Part 1: Steady flows", *Biorheology*, Vol. 28, No. 3-4, pp. 241-262

[19]Papaioannou, T.G., and Stepanadis, C., 2005, "Vascular wall shear stress: Basic principles and methods", *Hellenic J Cardiol*, Vol. 46, pp. 9-15.

[20]Fry, D.L., 1968, "Acute vascular endothelial changes associated with increased blood velocity gradients", *Circ Res*, Vol. 22, No. 2, pp. 165-197.

[21]Fung, Y.C., 1981, *Biomechanics: Mechanical properties of living tissues*, Springer.

[22]Malek, A.M., Alper, S.L., and Izumo, S., 1999, "Hemodynamic shear stress and its role in atherosclerosis", *J Am Med Assoc*, Vol. 282, No. 21, pp. 2035-2042.

[23]Sallam, T.A., Lumsden, A.B., Suggs, W.V., and Ku, D.N., 1996, "Low shear stress promotes intimal hyperplasia thickening", *J Vasc Invest*, Vol. 2, pp. 12-22.

[24]Canneyt, K.V., Pourchez, T., Eloot, S., Guillame, C., Bonnet, A., Segers, P., and Verdonck, P., 2010, "Hemodynamic impact of anastomosis size and angle in side-to-end arteriovenous fistulae; a computer analysis", *J Vasc Acess*, Vol. 11, No. 1, pp. 52-58.

[25]Glor, F.P., Long, Q., Hughes, A.D., Augst, A.D., Ariff, B., Thom, S.A., Verdonck, P.R., and Xu, X.Y., 2003, "Reproducibility study of magnaetic resonance image-based computational fluid dynamics prediction of carotid bifurcation flow", *Ann Biomed Eng*, Vol. 31, No. 2, pp. 142-151.

[26]He, X., and Ku, D.N., 1996, "Pulsatile flow in the human left coronary artery bifurcation: Average conditions", *J Biomech Eng*, Vol. 119, No. 1, pp. 74-82.

[27]Ku, D.N., Giddens, D.P., Zarins, C.K., Glagov, S., 1985, "Pulsatile flow and atherosclerosis in the human carotid bifurcation. Positive correlation between plaque location and low oscillating shear stress", *Arterioscler Thromb Vasc Biol*, Vol. 5, No. 3, pp. 293-302.

[28]Soulis, J.V., Lampri, O.P., Fytanidis, D.K., and Giannoglou, G.D., 2011, "Relative residence time and oscillatory shear index of non-Newtonian flow models in aorta", *2011 10th International Workshop on Biomedical Engineering*, pp. 1-7.

[29]Himburg, H.A., Grzybowski, D.M., Hazel, A.L., LaMack, J.A., Li, X., and Friedman, M.H., 2004, "Spatial comparison between wall shear stress measures and porcine arterial endothelial permeability", *Am J Physiol Heart Circ Physiol*, Vol. 286, pp. 1916-1922.

Conference on Modelling Fluid Flow (CMFF'12)
The 15th International Conference on Fluid Flow Technologies
Budapest, Hungary, September 4-7, 2012

DETAILED COMPARISON OF NUMERICAL FLOW PREDICTIONS IN CEREBRAL ANEURYSMS USING DIFFERENT CFD SOFTWARE

Philipp BERG[1], Gábor JANIGA[1], Dominique THÉVENIN[1]

[1] Department of Fluid Dynamics and Technical Flows, University of Magdeburg. Universitaetsplatz 2, D-39106 Magdeburg, Germany. Tel.: +49 391 67 181 95, Fax: +49 391 67 128 40, E-mail: berg@ovgu.de

ABSTRACT

Within the last decades, Computational Fluid Dynamics (CFD) simulations became increasingly important to investigate flow phenomena that are difficult to analyze experimentally. In the field of medical engineering, for instance concerning blood flows in cerebral aneurysms, computer-based approaches could open up new opportunities to support medical practitioners before high-risk interventions.
The present work compares commercial and open-source CFD software packages in order to determine their reliability for predicting medical blood flows. The haemodynamic simulations were carried out on unstructured as well as block-structured grids of a patient-specific geometry. Blood is treated as an incompressible, isothermal and Newtonian fluid. To provide a realistic inflow condition a time- and space-dependent Womersley velocity profile is implemented.
Several comparisons found that if the geometric complexity allows block-structured mesh generation, hexahedral grids should be preferred in order to predict the blood flow. Steady and unsteady simulations resulted in almost equal parameters for velocity and wall shear stresses at peak pressure. Nevertheless, unsteady flow patterns that may cause remodelling processes of the arterial walls, can only be analysed with unsteady assumptions. Finally, it can be stated that OpenFOAM® is a comparable CFD tool regarding haemodynamic simulations in cerebral aneurysms.

Keywords: cerebral aneurysm, CFD, Fluent, haemodynamics, OpenFOAM

NOMENCLATURE

A	$[m^2]$	surface area
C	$[-]$	Fourier coefficient
f	$[1/s]$	frequency
ICI	$[-]$	inflow concentration index
N	$[-]$	number of elements
P	$[-]$	number of processors
Q	$[m^3/s]$	flow rate
R	$[m]$	mean vessel radius
r	$[m]$	radial coordinate
T	$[s]$	period of the cardiac cycle
TOT	$[s]$	turnover time
t	$[s]$	time
$\underline{U}$	$[m/s]$	absolute velocity vector
w	$[m/s]$	axial velocity component
α	$[-]$	Womersley number
η	$[Pa \cdot s]$	dynamic viscosity
κ	$[-]$	rate of change
ν	$[m^2/s]$	kinematic viscosity
ρ	$[kg/m^3]$	density
Φ	$[-]$	variable
τ	$[Pa]$	wall shear stress
ω	$[1/s]$	angular frequency

Subscripts and Superscripts

A	aneurysm
in	flow direction into the aneurysm
inlet	inflow of the flow domain
k	count index of the Fourier series
max	maximum value
mean	mean value
n	count index of the rate of change
o	ostium

1. INTRODUCTION

In order to investigate highly complex problems Computational Fluid dynamics (CFD) evolved to a sophisticated method to approach the behaviour of flow phenomena and their effects on key parameters. Within the last decades, several advantages were found in contrast to experimental procedures. For instance, numerical methods may be able to consider scales, which cannot be captured experimentally so far. In many cases, high performance computing hardware is less expensive than complex measuring equipment. Additionally, a better reproducibility can be achieved due to a lower systematic error and to a lower influence

of varying process conditions.
These advantages are useful in the field of medical engineering, for instance concerning blood flow in cerebral aneurysms. These are abnormal focal dilatations of weakened arterial walls resulting from a process of remodelling and growing [1]. Without treating or with a wrong treatment an enhanced risk of rupture exists, with rupture leading to heavy disabilities or even a sudden death [2]. Therefore, specific research regarding haemodynamics in cerebral aneurysms is essential. Qualitative observations as well as time-dependent measurements of the velocity components are possible by means of 7-Tesla-Magnetic Resonance Tomography (MRT) [3]. However, investigating the pressure distribution along certain vessel regions or the change of wall shear stresses within a cardiac cycle can only be achieved numerically.
Recent works show that computational techniques are promising in simulating the blood flow in the cerebral aneurysm itself and also the influence on the haemodynamics after treatments like *Coiling* or *Stenting* [4, 5]. Validation of the numerical results by means of digital subtraction angiography (DSA) has been carried out successfully as well [6].
Although those computer-based approaches could open up new opportunities to support medical practitioners before high-risk interventions, even published results should always be questioned critically. Sforza et al. [7] investigated the haemodynamics in intracranial aneurysms in order to identify flow patterns influencing aneurysm progression. After their computations and in vivo observations they found that numerical models tend to be oversimplified and do not reproduce accurately the complex flow structure.
In order to obtain predictions within hours, most numerical simulations rely on numerous assumptions and model reductions, depending on the desired accuracy. Therefore, individual conditions as well as all complex biological regulation mechanisms controlling the human vascular system cannot be considered in standard algorithms at the state of the art. Due to this circumstance, the acceptance of CFD in medicine is still limited in practice, leading to controverse discussions, e.g., regarding the pressure prediction in cerebral aneurysms after treatment with flow diverting devices [8]. Also the wide range of modelled and measured boundary conditions compared in [9] shows reliable computational predictions remain highly challenging.
However, various software packages or in-house algorithms are used and the number of computations considering medical flows increased rapidly over the past years. Those tools are either commercial or contributed through an open-source license. In order to determine their reliability for predicting medical blood flows one of the leading products of each category is chosen and compared afterwards. The commercial CFD solver ANSYS Fluent® as well as the open-source code OpenFOAM®are used to investigate the haemodynamics in a patient-specific cerebral aneurysm. The computations are based on a reconstructed aneurysm geometry measured by means of Magnetic Resonance Imaging (MRI). Both packages use a finite volume method whereby steady as well as unsteady simulations have been carried out to analyse the influence of spatial discretisation. Furthermore, important parameters like accuracy, computational costs, parallel efficiency, problem-specific model extension and user-friendly interfaces are assessed. Finally, conclusions are drawn to highlight strengths and weaknesses of the individual software packages and more generally concerning CFD for haemodynamics.

2. MATERIALS AND METHODS

The following sections demonstrate how the present CFD simulations were set up based on raw patient-specific imaging data. Spatial and temporal discretisation methods as well as post-processing are described in detail.

2.1. Vascular Model

In order to perform the desired blood flow simulations it is necessary to generate a suitable geometry model. Several techniques exist to obtain three-dimensional data of cerebral arteries by means of imaging systems. For instance CTA (Computed Tomography Angiography) scans as well as MRI scans use contrast agents to visualise the blood and therefore the boundaries of the surrounding vessel walls.
The present geometry was obtained by using a DSA, commonly utilized during an operation. The resulting projection consists of two-dimensional data in the first place but a 3D reconstruction is possible when connecting multiple datasets achieved by rotating the C-arm around the patient. At present, such a 3D Rotational Angiography (3DRA) provides the highest local resolution and can be seen as the gold standard in terms of imaging methods. The segmentation of the aneurysm geometry was performed using a seeded region-growth algorithm. Optical artefacts occurring during the imaging process have been eliminated as well. To achieve a high surface quality the segmentation results were transformed into discrete meshes and smoothed afterwards [10].
The resulting cerebral aneurysm was located on the middle cerebral artery (MCA) connected to the circle of Willis, which supplies blood to the brain and ensures an unhindered blood flow into the important parts. Figure (1) presents the shape of the investigated geometry from different points of view. The inflow region is positioned at the bottom and two outlets can be detected on the top.

To identify the influence of the mesh density on several parameters, five unstructured grids were generated with a number of elements ranging from circa 230.000 to 12.5 millions. For the

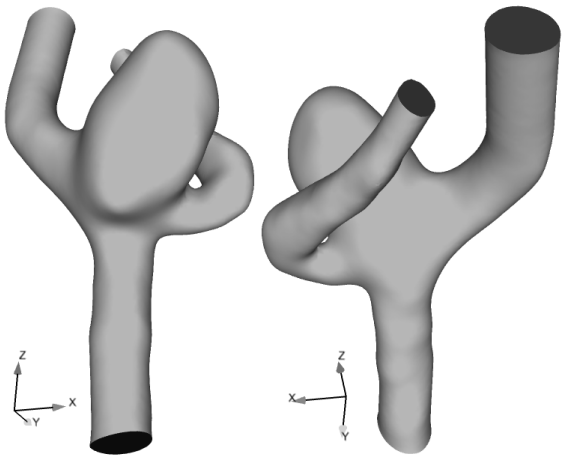

Figure 1: Patient-specific geometry of the investigated cerebral aneurysm

spatial discretisation the commercial meshing software ANSYS ICEM-CFD ® 13.0 (Ansys Inc., Canonsburg, PA, USA) was used. A Delaunay method created the tetrahedral elements with a maximum size ranging from 0.2 to 0.05 mm. Due to the element flexibility even complicated geometries like patient-specific aneurysms are able to be meshed within a short time. In areas of strong changes in geometric direction, especially in the region between the aneurysm sack and the vessel branches local refinements of the meshes were carried out. Therefore, flow patterns are better resolved in these zones. Additionally, three boundary layers of prismatic elements were inserted to ensure a finer resolution close to the vessel wall. Their initial height ranges from 40 to 15 μm and a growth ratio of 1.3 was defined. Corresponding to the previously described meshes presented in Table (1) another five unstructured meshes were generated without boundary layers. Therefore, the necessity of such layers in blood flow simulations can be investigated.

Table 1: Number of elements corresponding to the unstructured meshes without and with prismatic layers at the walls

Mesh number	Number of elem. (without prisms)	Number of elem. (with prisms)
1	228.317	256.723
2	516.230	551.612
3	1.678.508	1.667.308
4	3.142.530	3.016.046
5	12.468.478	12.274.395

To compare results obtained on structured and unstructured grids, another (block-structured) grid was generated consisting of 1.7 million hexahedral elements. The cell growth ratio from the walls to the inner volume was chosen similar to the unstructured one. Figure (2) shows an unstructured mesh with boundary layers (top) and the structured grid (bottom), respectively.

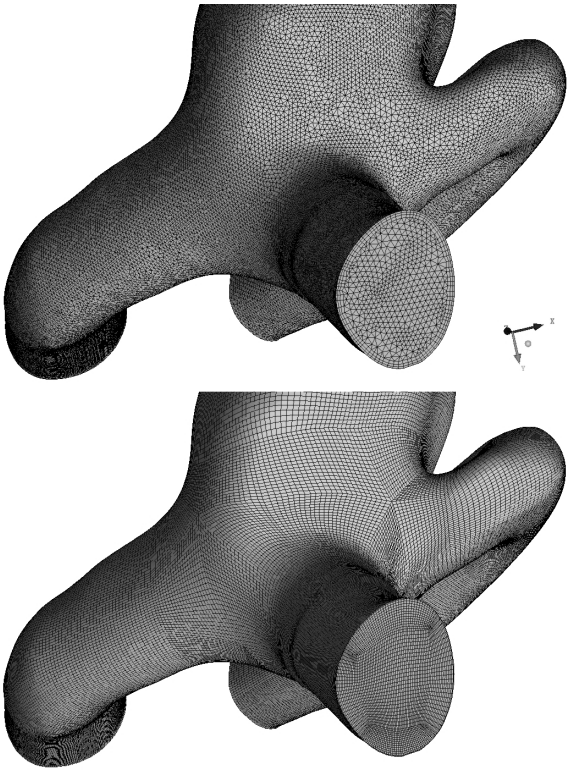

Figure 2: Presentation of unstructured mesh # 3 with boundary layers (top) and the structured mesh (bottom)

2.2. Haemodynamic simulation

Based on the generated meshes steady as well as unsteady haemodynamic simulations were carried out. In all cases blood is treated as an isothermal, incompressible ($\rho = 1055\ \frac{kg}{m^3}$) and Newtonian fluid with a constant dynamic viscosity $\eta = 4.265 \cdot 10^{-3}\ Pa \cdot s$ [11]. Indeed, blood as a suspension of plasma and cellular components shows non-Newtonian behaviour especially at low shear stresses. Previous computations have shown that considering the viscosity dependency with the commonly used *Carreau-Yasuda*-model does not lead to any noticeable differences in the velocity profiles due to the large arterial diameters [12].
Fully developed Womersley velocity profiles are implemented as inflow boundary conditions [13]. In contrast to common parabolic velocity profiles this time- and location-dependent solution considers the pulsatile character of the blood flow. Hence, this analytical approach shows a good agreement with measurements. As given in Eq. (1) the axial velocity component $w(r,t)$ is composed of a steady and an oscillatory part [14] and affected by the mean vessel

radius R, the Bessel functions J_0 and J_1 of the first kind (of order 0 and 1), and the Womersley number α. This dimensionless number characterises the ratio of unsteady acceleration forces to frictional forces (see Eq. (2)) with the angular frequency $\omega = 2\pi f$ and the kinematic viscosity $\nu = \eta/\rho$. With respect to the present study a Womersley number $\alpha = 3.13$ was calculated.

$$w(r,t) = \frac{2C_0}{\pi R^2}\left[1-\left(\frac{r}{R}\right)^2\right] + \sum_{k=1}^{N}\left\{\frac{C_k}{\pi R^2}\left[\frac{1-\frac{J_0\left(\alpha_k \frac{r}{R} i^{3/2}\right)}{J_0\left(\alpha_k i^{3/2}\right)}}{1-\frac{2J_1\left(\alpha_k i^{3/2}\right)}{\alpha_k i^{3/2} J_0\left(\alpha_k i^{3/2}\right)}}\right]\right\} e^{ik\omega t} \quad (1)$$

$$\alpha_k = R\sqrt{\frac{k\cdot\omega}{\nu}} \quad (2)$$

The corresponding synthetically generated flow rate for one cardiac cycle is described by a set of complex Fourier coefficients C_k and presented in Figure (3). The arterial walls are assumed to be rigid and a no-slip boundary condition is defined forcing the velocity component to be zero [15]. Due to a lack of knowledge regarding the pressure variation in the different vessel branches a traction-free condition is imposed at the outlets of the domain.

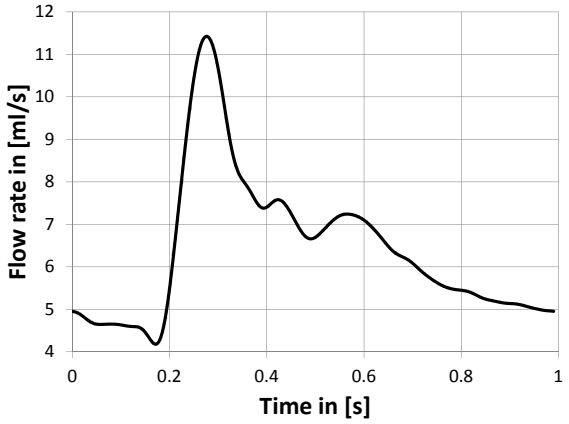

Figure 3: Flow rate for one cardiac cycle (T=0.99 s) corresponding to the inflow boundary condition of unsteady simulations

The governing Navier-Stokes equations were solved using the commercial software package ANSYS Fluent®13.0 and the open-source code SGI OpenFOAM® 2.0.1 (SGI Inc., Fremont, CA, USA), respectively. Both are based on a finite volume method approximating the integral form of these governing equations. For the steady cases a semi-implicit coupling algorithm (SIMPLE) was used to iteratively calculate the pressure and velocity fields. Convergence was obtained when the scaled residuals of pressure and momentum decreased below a value of 10^{-5}. The time-dependent simulations were carried out with a pressure-implicit algorithm (PISO) executing 2 steps of pressure correction within each loop. A constant time step size was chosen as 10^{-3} s according to the stability condition (Courant number ≤ 1), which was estimated in advance. Within each time step scaled residuals of 10^{-4} were demanded. Only the second cardiac cycle was analysed, discarding the first cycle [16].
Due to the high number of element the computational domain has been decomposed in advance in order to simulate in parallel. The Scotch-method was used as a decomposition algorithm leading to domains with equivalent element numbers [17]. All simulations were carried out on the in-house cluster Kármán consisting of 544 computing cores (AMD Quad Core 2.1 GHz) and an InfiniBand network.

2.3. Analysis

The effect of mesh type and resolution on several variables was first investigated. Therefore, in Eq. (3) a rate of change κ was defined describing how a certain averaged parameter Φ changes depending on the number of elements N. A multiplication with 10^8 adjusts κ to a manageable order of magnitude.

$$\kappa_n = \left|\frac{\Phi_{n+1}-\Phi_n}{N_{n+1}-N_n}\right| \cdot 10^8 \quad n = 1\ldots 4 \quad (3)$$

In the scope of this study, the maximum velocity U_{max}, its temporal mean value U_{mean} as well as the mean wall shear stress τ_{mean} were analysed. Additionally, in Eqs. (4) to (5) different criteria commonly used in haemodynamic post-processing were implemented based on the calculated velocity fields. The turnover time (TOT), which is defined by the ratio of the aneurysm volume V_A to the flow rate entering the aneurysm Q_{in} describes how long the blood resides within the sack [12]. Q_{in} is computed using the entering velocity times the inflow area A_{in}, which is part of the total ostium area A_o (area between the aneurysm and the corresponding vessel). The entering blood can be expressed as well by the inflow concentration index (ICI) [18]. Compared to TOT, ICI involves also the flow rate at the inlet of the cerebral artery Q_{inlet}.

$$TOT = \frac{V_A}{Q_{in}} \quad (4)$$

$$ICI = \frac{Q_{in}/Q_{inlet}}{A_{in}/A_o} \quad (5)$$

Post-processing was accomplished with EnSight® 9.2 (CEI Inc., Apex, NC, USA) and

Kitware ParaView® 3.10.1 (Kitware, Inc., Clifton Park, NY, USA).

3. RESULTS

After carrying out the previously described simulations and analyses it is now possible to compare 1) the meshing strategy, 2) the choice of the solver and 3) the importance of temporal variations. Figures (4) to (5) present an exemplary velocity field as well as the corresponding streamlines for a steady case.

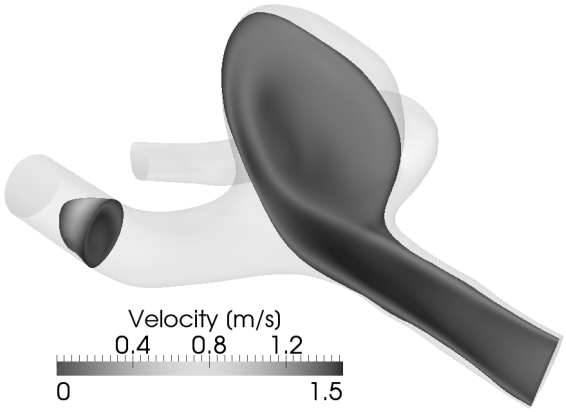

Figure 4: Exemplary velocity distribution within the flow domain based on a block structured mesh

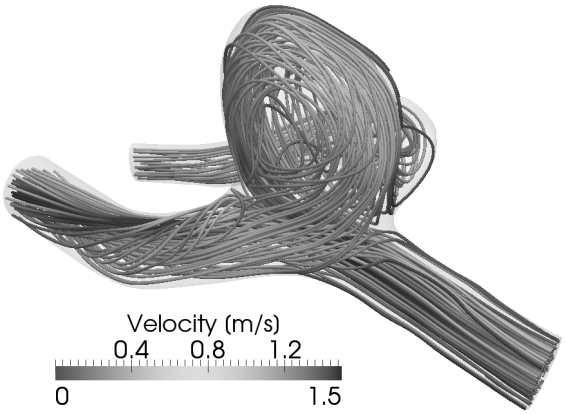

Figure 5: Streamlines corresponding to the velocity field of a block structured simulation

These figures reveal that the flow enters the aneurysm at its bottom and remains close to the aneurysmal wall until it exits sideways back to the arterial branches. Afterwards, approximately 77 % of the mass flow rate remain within the frontal vessel and 23 % leave through the smaller one, respectively. Due to the geometric situation a helical flow pattern develops in the branches resulting in non-parabolic velocity profiles.

3.1. Unstructured vs. Structured

To quantitatively compare the different meshing technologies two variables were derived from steady Fluent® simulations. The spatially averaged velocities U_{mean} as well as the mean wall shear stress τ_{mean} of the unstructured meshes are presented in Table (2) and (3) with their rates of change κ.
With increasing number of elements κ decreases in all cases and indicates only minor variations between the last two considered mesh densities. Comparing unstructured based simulations with and without layers directly, negligible differences appear between U_{mean} (0.17 % - 0.81 %). In contrast, higher deviations occur with respect to τ_{mean} ranging from 11 % to 19.7 %. Considering the resulting values of the block-structured simulation an average velocity of $0.704\ \frac{m}{s}$ and a mean wall shear stress of $29.68\ Pa$ was found which is in good agreement with the results achieved by unstructured meshes with prisms. This shows that the use of boundary layers is highly recommended when analyses regarding the vessel walls are of interest.

Table 2: Rate of change for the unstructured meshes without layers

Nr.	U_{mean} in $[\frac{m}{s}]$	κ in $[\frac{m}{s}]$	τ_{mean} in $[Pa]$	κ in $[Pa]$
1	0.6598	5.4483	35.5745	164.943
2	0.6702	0.9926	35.0995	58.6467
3	0.6814	0.3063	34.4356	28.0244
4	0.6859	0.0572	34.0169	9.11
5	0.6913	-	33.1672	-

Table 3: Rate of change for the unstructured meshes with layers

Nr.	U_{mean} in $[\frac{m}{s}]$	κ in $[\frac{m}{s}]$	τ_{mean} in $[Pa]$	κ in $[Pa]$
1	0.6639	3.9859	28.5623	81.5409
2	0.6756	0.6206	28.8028	32.5714
3	0.6825	0.4131	29.1662	3.8082
4	0.6881	0.0613	29.2176	3.2668
5	0.6939	-	29.52	-

The analyses of additional parameters e.g. regarding pressure distribution or regions of elevated wall shear stresses showed the same tendencies. Hence, it can be concluded for unstructured meshes that the largest changes occur at element numbers smaller than approximately 3 millions. The differences between 3 and 12 million cells are relatively small and the values are closest to those of the block structured mesh. This finding supports the assumption that an increased effort during mesh generation

allows to achieve more accurate results within shorter computational times.

3.2. Fluent vs. OpenFOAM

After identifying the impact of spatial discretisation on several parameters, a comparison of two CFD packages followed. At first the mean velocity of steady computations was investigated and a good agreement between both solvers can be observed. The deviation ranges from 0.12 % at the coarsest mesh density to 0.34 % for mesh # 5. However, the introduced variables TOT and ICI reveal larger differences. The predicted turnover times deviate between 1.4 and 5.8 %. Approximately equal variations occur for the inflow concentration indices ICI (1.3 - 7.1 %).
In addition to the flow variables, the required simulation time using different numbers of processors was assessed. In all cases, Fluent® was faster in reaching the demanded residuals of 10^{-5}. Due to license restrictions with Fluent® only up to 8 cores were considered. While there is no problem for parallelisation with OpenFOAM®, the usage of more processing units leads to a higher communication among the slaves, rapidly decreasing efficiency. In this context, it is always important to analyse the speed-up factor and the parallel efficiency, respectively. Figure (6) shows the corresponding results.

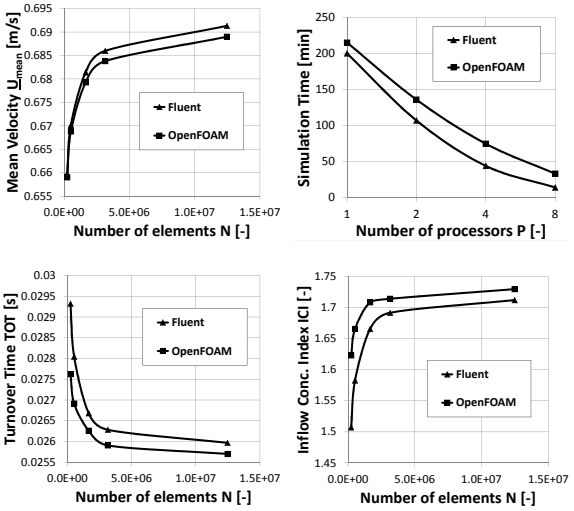

Figure 6: Comparison between ANSYS Fluent® and OpenFOAM®: Mean velocity (top left), simulation time as function of the number of processors for case # 2 (top right), turnover time (bottom left), inflow concentration index (bottom right)

Overall, OpenFOAM® as a freely available open-source software package constitutes a valuable and cost-efficient alternative to Fluent® in order to predict haemodynamics in cerebral aneurysms.

3.3. Steady vs. Unsteady

The mean velocity of the time-depended simulation was temporally averaged over one cardiac cycle and compared to U_{mean} of the steady solution. Only minor differences ($\leq$ 5 %) were noticeable. The same tendencies appear regarding the maximum velocity and the wall shear stresses presented in Figure (7). Elevated regions are predicted in both cases at the transition of vessel and aneurysm and in areas of strong changes in geometric direction. The largest visible differences between both cases occur on the walls of the branches.

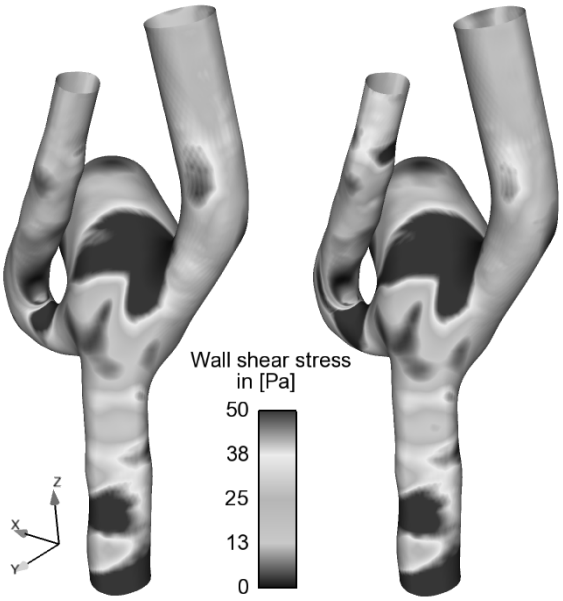

Figure 7: Steady wall shear stress (left) compared to the temporal average of the unsteady simulation (right)

Hence, time-consuming unsteady simulations might be be replaced by steady assumptions when only average information is of interest. However, in order to analyse time-dependent flow patterns, which may be responsible for vessel wall remodelling, unsteady simulations obviously need to be performed. One such example would be the existence of an oscillating flow near the aneurysm dome.

4. CONCLUSION

Firstly, the comparison between unstructured and block structured meshing methodologies shows that significant differences occur depending on the mesh resolution. Although mesh generation of unstructured grids is clearly less time-consuming, a higher resolution is necessary to achieve comparable accuracy. This leads to larger simulation times due to the high number of elements and to a slower convergence by contrast with structured meshes. Hence, higher computational costs will result. If possible, the generation of hexahedral grids is recommended. If

vessel parameters like the wall shear stress or its gradients are needed and a block-structured meshing is too complex, prism layers are essential at the boundaries.
Secondly, it was found that the results achieved by the open-source CFD software OpenFOAM® were in a good agreement with that of Fluent ®, which was only minimally higher in all cases. Although simulation times of OpenFOAM® were slightly higher in order to achieve a converged state, parallelisation is possible with OpenFOAM® without any license restriction. This could be an important factor for an application in clinical workflows where reliable results are often required rapidly before decision-making. In terms of user-friendliness and getting familiar with the necessary steps to set up haemodynamic simulations Fluent® is far more intuitive in particular due to its graphical user interface (GUI). After a reference case has been set up, both software packages are able to derive simulations very quickly and without GUI for instance using a journal file.
The analysis of averaged parameters like the mean velocity or wall shear stresses revealed no major differences between steady and unsteady simulations. Hence, steady simulations may be used to estimate such quantities. In order to investigate fluctuating flow patterns, which may influence the wall properties, time-dependent computations are obviously required.
Overall it can be stated that OpenFOAM® is a competitive CFD tool regarding haemodynamic simulations in cerebral aneurysms. Furthermore, it is worth putting additional effort in the generation of block-structured meshes to achieve afterwards more accurate and stable steady and unsteady simulations. Further investigations aim onto the experimental validation of numerical results. Here, four-dimensional (time dependent velocity vectors) measurements using a 7-Tesla-MRT or Particle Tracking Velocimetry techniques are suitable [19].

ACKNOWLEDGEMENTS

The authors like to express their gratitude to Dr. Oliver Beuing for providing the patient-specific MRT data of the cerebral aneurysm. Special thank also goes to Dipl.-Ing. Mathias Neugebauer who supported the investigations by reconstructing the patient data in order to generate a geometric model.

References

[1] Lasheras, J. (2007) The biomechanics of arterial aneurysms. *Annual Review of Fluid Mechanics*, **39**, 293–319.

[2] Payner, T., Melamed, I., Ansari, S., Leipzig, T., Scott, J., DeNardo, A., Horner, T., Redelman, K., and Cohen-Gadol, A. (2011) Trends over time in the management of 2253 patients with cerebral aneurysms: A single practice experience. *Surgical Neurology International*, **2**, 110–115.

[3] Gasteiger, R., Janiga, G., Stucht, D., Hennemuth, A., Friman, O., Speck, O., Markl, M., and Preim, B. (2011) *Bildverarbeitung für die Medizin 2011*, chap. Vergleich zwischen 7 Tesla 4D PC-MRI-Flussmessung und CFD-Simulation, pp. 304–308. Springer, Berlin Heidelberg New York.

[4] Mitsos, A., Kakalis, N., Ventikos, Y., and Byrne, J. (2008) Haemodynamic simulation of aneurysm coiling in an anatomically accurate computational fluid dynamics model: technical note. *Neuroradiology*, **50**, 341–347.

[5] Ugron, Á., Szikora, I., and Paál, G. (2012) Computer simulation of intracranial aneurysm treatment using densely woven stents. *Proc. 5th European Conference of the International Federation for Medical and Biological Engineering*, pp. 442–445.

[6] Ho, H., Wu, J., and Hunter, P. (2011) *Computational Biomechanics for Medicine*, chap. Blood Flow Simulation in a Giant Intracranial Aneurysm and Its Validation by Digital Subtraction Angiography, pp. 15–26. Springer, Berlin Heidelberg New York.

[7] Sforza, D., Putman, C., and Cebral, J. (2009) Hemodynamics of cerebral aneurysms. *Annual Review of Fluid Mechanics*, **41**, 91–107.

[8] Cebral, J., Mut, F., Raschi, M., Scrivano, E., Ceratto, R., Lylyk, P., and Putman, C. (2011) Aneurysm rupture following treatment with flow-diverting stents: Computational hemodynamics analysis of treatment. *American Journal of Neuroradiology*, **32**, 27–33.

[9] Marzo, A., et al. (2011) Computational hemodynamics in cerebral aneurysms: The effects of modeled versus measured boundary conditions. *Annals of Biomedical Engineering*, **39**, 884–896.

[10] Neugebauer, M., Janiga, G., Beuing, O., Skalej, M., and Preim, B. (2010) Computer-aided modelling of blood flow for the treatment of cerebral aneurysms. *International Journal of Biomedical Engineering and Technology*, **55**, 37–41.

[11] Thews, G., Schmidt, R., and Lang, F. (2000) *Physiologie des Menschen*. Springer, Berlin Heidelberg New York.

[12] Berg, P., Janiga, G., and Thévenin, D. (2011) Investigation of the unsteady blood flow in cerebral aneurysms with stent using the open-source software openfoam. *Proc. Open Source CFD International Conference*.

[13] Womersley, J. (1955) Method for the calculation of velocity, rate of flow and viscous drag in

arteries when the pressure gradient is known. *American Journal of Physiology*, **127**, 553–563.

[14] Nichols, W. and O'Rourke, M. (2005) *McDonald's Blood Flow In Arteries*. Hodder Arnold.

[15] Anor, T., Grinberg, L., Baek, H., Madsen, J., Jayaraman, M., and Karniadakis, G. (2010) Modeling of blood flow in arterial trees. *Systems Biology and Medicine*, **2**, 612–623.

[16] Castro, M., Putman, C., and Cebral, J. (2008) *Computational Hemodynamics of Cerebral Aneurysms - Assessing the Risk of Rupture from Hemodynamic Patterns*. VDM Verlag Dr. Mller, Saarbrcken.

[17] Pellegrini, F. and Roman, J. (1996) Scotch: A software package for static mapping by dual recursive bipartitioning of process and architecture graphs. *Proc. HPCN'96, Brussels, Belgium*.

[18] Cebral, J., Mut, F., Weir, J., and Putman, C. (2011) Quantitative characterization of the hemodynamic environment in ruptured and unruptured brain aneurysms. *American Journal of Neuroradiology*, **32**, 145–151.

[19] Bendicks, C., Tarlet, D., Roloff, C., Bordás, R., Wunderlich, B., Michaelis, B., and Thévenin, D. (2011) Improved 3-d particle tracking velocimetry with colored particles. *Journal of Signal and Information Processing*, **2**, 59–71.

Conference on Modelling Fluid Flow (CMFF'12)
The 15th International Conference on Fluid Flow Technologies
Budapest, Hungary, September 4-7, 2012

INVESTIGATION OF THE VELOCITY FIELD IN A FULL-SCALE ARTIFICIAL MEDICAL MODEL

Zsolt MÁTRAI[3], Christoph ROLOFF[1], Róbert BORDÁS[2], Norbert SZASZÁK[3], Szabó SZILÁRD[3], Dominique THÉVENIN[2]

[1] Corresponding Author. Institute of Fluid Dynamics and Thermodynamics, Otto-von-Guericke-University Magdeburg. Universitaetsplatz 2, 39112 Magdeburg, Germany. Tel.: +49 391 6712336, Fax: +49 391 6712840, E-mail: christoph.roloff@ovgu.de
[2] Institute of Fluid Dynamics and Thermodynamics, Otto-von-Guericke-University Magdeburg, Germany
[3] Department of Fluid and Heat Engineering, University of Miskolc, Hungary

ABSTRACT

The aim of this contribution was to experimentally characterize the flow in the aneurysm of a full-scale medical phantom model for validation of companion numerical simulations. Due to its practical importance, a non-intrusive treatment of brain aneurysm attracts growing interest. To develop suitable treatment options, a better knowledge of the blood flow pattern in the complex geometry of aneurysms and cerebral vasculature is very important.

To get information on the flow around the aneurysm, Laser Doppler Velocimetry (LDV) measurements had already been carried out by our group in a similar model at several cross-sections, considering a pulsating flow. As a complement, the present experimental series were carried out using large-field imaging measurement techniques.

First, 2D-Particle Tracking Velocimetry (PTV) images were recorded and our in-house PTV-algorithm was optimized for the measurement configuration. The flow was seeded by fluorescent tracers and the excitation wave length was filtered out to avoid undesirable Mie scattering. In order to validate the PTV algorithm, the recorded images were also evaluated using a conventional cross-correlation method, like in Particle Image Velocimetry (PIV). Due to the different nature of the two evaluation methods, an interpolation of the Lagrangian (PTV) data into an Eulerian coordinate system (PIV) was required, in order to make a proper comparison between the two evaluation algorithms. The experimental setup, methods, results and conclusions are presented in this work.

Keywords: Cerebral aneurysm, PTV, PIV, blood flow, phantom model

NOMENCLATURE

B	[-]	normalisation constant
C	[-]	contrast threshold
I	[-]	pixel intensity
K	[-]	convolution kernel
K_0	[-]	normalisation constant
n	[-]	refractive index
w	[-]	filter size factor
μ	[$mPa{\cdot}s$]	dynamic viscosity
ρ	[kg/m^3]	density

Subscripts and Superscripts

i,j	pixel coordinates
max	maximum

Abbreviations

CFD	Computational Fluid Dynamics
CT	Computed Tomography
IA	Interrogation area
LDV	Laser Doppler Velocimetry
MMA	Minimum acceleration
MRI	Magnetic Resonance Imaging
PIV	Particle Image Velocimetry
PTV	Particle Tracking Velocimetry
ROI	region of interest
SHA	subarachnoid haemorrhage

1. INTRODUCTION

Abnormal bulges appearing on blood arteries supplying the brain are called cerebral aneurysms. They can be found statistically in two to five percent of the population [1]. Though only about 0.1% of these blood-filled balloons rupture annually, the consequences for the patients are severe. A ruptured cerebral aneurysm causes in 80% to 90% of all cases a subarachnoid haemorrhage (SHA) with a mortality rate of about 60% [2]. Current medical treatment approaches of such saccular aneurysms before rupture are still connected with a high risk for the patient. The

mortality rate 30 days after treatment is almost 18% [3]. Consequently, the decision whether the risk of rupture and its aftermath justify the risky treatment is left to the medical expert. Three main treatments exist to prevent an aneurysm from rupture: 1) surgical clipping of the neck of the aneurysm sac, the most classical but traumatic method, 2) endovascular positioning of filaments (coils) inside the sac to promote thrombosis or 3) stenting of the parent artery to control the blood flow in a favourable manner.

To support the medical decision process, the numerical characterization of flow conditions and altered hemodynamics in stented blood vessels was investigated in joint projects involving in particular the Institute of Neuro-Radiology and the Dpt. of Fluid Dynamics at the University of Magdeburg "Otto von Guericke". The aneurysms are first detected by means of modern visualization techniques like Computed Tomography (CT) and Magnetic Resonance Imaging (MRT) and are later converted into geometry data useable for Computational Fluid Dynamics (CFD). The numerical calculations then deliver patient-specific information to the medical expert.

Accurate CFD calculations require an appropriate knowledge of boundary conditions. Therefore, velocity measurements under unsteady flow conditions have been first carried out in phantom models by means of Laser Doppler Velocimetry. However, such measurements only delivered limited information and with low signal to noise ratio.

The present paper deals with investigations of the flow field conditions using high speed imaging methods, Particle Image Velocimetry (PIV) and Particle Tracking Velocimetry (PTV). Both methods are based on detection of light emitted by sufficiently small tracer particles seeded to the flow. While PIV then calculates the velocities by a displacement correlation between two successive flow images, PTV considers a sequence of several frames and individual particles are tracked both in time and space. The resulting pathlines (trajectories) of PTV provide a Lagrangian description of the flow field.

In the following, we will describe the experimental setup used to perform high speed imaging measurements in an aneurysm phantom model. The basics of the applied image processing methods and the tracking algorithm are introduced. Moreover, flow field results are presented for both the 2D-PTV in the aneurysm sack and the inlet vessel, the latter being used to provide inlet boundary conditions for companion CFD computations. The Lagrangian pathlines are compared to Eulerian PIV velocity vectors by a suitable interpolation. Finally, a conclusion and an outlook for further improvements are given.

2. EXPERIMENTAL SETUP

In the following, the experimental setup of the high speed imaging in the aneurysm phantom model is introduced

2.1. Full-scale phantom model

The first step of the medical procedure is to detect the aneurysm in the brain of the patient. Magnetic Resonance Imaging (MRI) can be used for this purpose. In case of detection, the patient-specific three-dimensional geometry of the local cerebral vasculature is reconstructed from the MRI data and converted into a computational model. On the one hand, this model is a basis for meshing purposes and individual flow investigations using CFD to support medical experts. Additionally, this computational model can be used to create a realistic phantom model by rapid prototyping for experimental investigations.

This experimental model has been built at Fraunhofer IFF (Magdeburg), which is specialized in manufacturing engineering. The construction involves a complex sintering process of the metallic positive model of the blood vessels, the casting of the silicon material around it and finally the melting and discharge of the metal composition to have free blood vessels for the artificial blood.

The dimensions of the phantom model (Figure 1) are roughly 130 *mm* x 110 *mm* x 40 *mm*, while the maximum length inside the aneurysm sac is smaller than 20 *mm*. The sac placed as close as possible to the outside wall of the silicone model in order to minimize light absorption between flow tracers and camera.

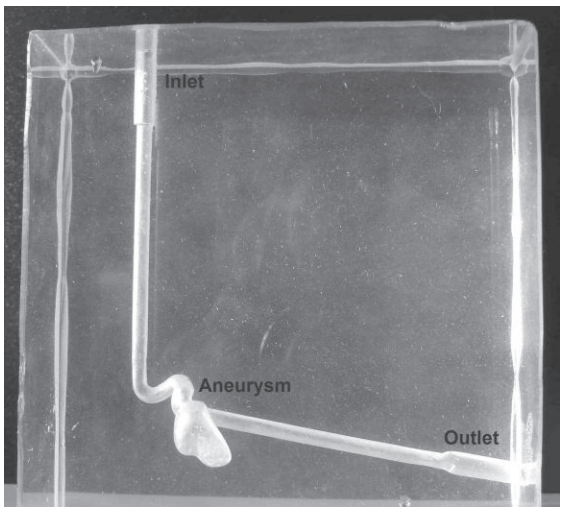

Figure 1. Photograph of the phantom model

The blood-mimicking fluid must fulfil two conditions simultaneously. On the one hand, the viscosity and density of this fluid should be similar to real blood. On the other hand, the refraction indices of the phantom model and of the artificial

blood should match as exactly as possible in order to avoid optical distortions at interfaces from model to fluid.

Finally, a mixture composed of 46.140 *wt%* distilled water, 47.566 *wt%* of glycerine, 6.292 *wt%* of salt and 0.002 *wt%* of xanthan gum particles delivers an excellent artificial blood featuring a viscosity of $\mu = 4.47$ *mPa·s*, a density of $\rho = 1050$ *kg/m³* and an excellent refraction index match with the silicon material of the phantom ($n = 1.41$). Moreover the xanthan gum adds shear-thinning behaviour to the fluid, mimicking real blood even better.

2.2. Optical measurement arrangement

The measurement setup is show in Figure 2. The fluid circuit consisted of the aneurysm phantom model with inlet and outlet through which the artificial blood was pumped. A LabView script controlled the peristaltic tube pump, which performed a pressure slope deduced from standard conditions for human blood cycles at rest (54 *beats/min* with a maximum pressure of 130 *mmHg;* the pressure curve is presented later in Figure 5). The overall pressure range was adjusted by an air chamber (windkessel) placed between pump and phantom model inlet and a pressure indicator recorded the transient pressure data.

The artificial blood was seeded with fluorescent tracer particles for the PTV measurements. They featured a diameter of 10.46 ± 0.18 *µm*, a density of 1,510 *kg/m³* (Melamine Resin) and were labelled with Rhodamine 610 (Rhodamine B) with a maximum emission at 584 *nm*. Fluorescent particles have been chosen to eliminate all reflections that would reduce the signal to noise ratio. The artificial blood including fluorescent particles was stored in a 2 *l* tank and stirred continuously to ensure homogeneous tracer distribution.

Illumination, i.e. excitation of the tracer particles was provided by a continuous Ar-Ion laser (Spectra Physics 2020) with an output power of 3 *W* at a wavelength range from 457.9 to 514.5 *nm*. The beam was formed to a light sheet of approximately 1 *mm* thickness centred in the middle vertical plane of the aneurysm/inlet vessel, which was acceptable for 2D measurements.

In order to carry out PTV with sufficient spatial and temporal resolution, a high speed CMOS camera (LaVision HighSpeedStar 6) was used. With this camera it is possible to record images with 1024 x 1024 *px²* at a frame rate of 5400 *Hz* and 12 *bit* dynamic range. The objective lens was a 60 *mm* Micro-Nikkor with an f-stop of 5.4 to allow a sufficient depth of field over the laser sheet thickness. A high pass filter (cut off 575 *nm*) was used to block unwanted laser reflections. Although the filter cut off and the laser wavelengths were not optimized for the Rhodamine 610 characteristics, the particles emitted sufficient light for our high speed measurements.

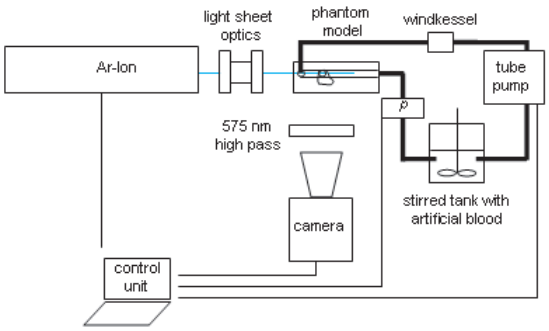

Figure 2. Sketch of the measurement setup

3. PTV

Particle image segmentation and tracking of particles are the main challenges in PTV. A global methodology can hardly be found for each individual application. Therefore, various concepts can be found in literature. In the following, we will give an introduction concerning the procedures applied by our group (realized by MatLab scripts), involving image processing techniques, particle segmentation and 2D-Tracking.

3.1. Particle segmentation

The first step of image processing involves the creation of a suitable mask to define the region of interest (ROI) in the camera images and to exclude any ghost particle detections outside the fluid zone.

Several possible ways for masking can be imagined, e.g. manual spline-drawing of boundaries, appropriate thresholding of an optically non-filtered image or computational long exposure of the ROI. We decided to use the third alternative because it can be transformed to a fully automated routine with only a single individual parameter. Therefore, each pixel of all images of a high speed sequence (typically 5000 images) is checked for its maximum intensity. This pixel value is stored in the masking image and thresholded appropriately. To receive a closed form for the mask and suppress outside noise the binary image is treated with morphological operations: it is eroded and dilated several times and can now be used as ROI-mask. An example masking process is shown in Figure 3.
The second processing step consists of background image subtraction. The background image is processed in a similar manner to masking, but instead of maximum intensity of each pixel it searches for the minimum intensity during one sequence. Consequently, this methodology subtracts the lowest noise level from each pixel and the resulting image is then used for particle image segmentation.

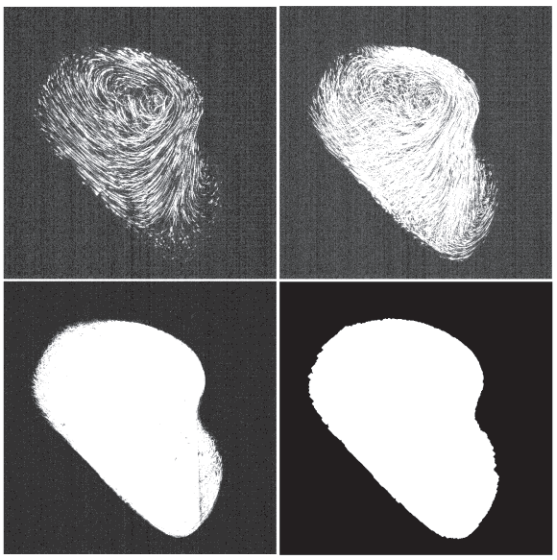

Figure 3. Masking process from upper left to lower right: computational long exposure after 50, after 250, after 5000 images, the final mask

The image segmentation is a composition of two approaches. In order to suppress noise and with regard to the ideal Gaussian character of the particle image we first compute the convolution of the image with a kernel [4]:

$$K(i,j) = \frac{1}{K_0}\left[\frac{1}{B}\exp\left(-\frac{i^2+j^2}{4}\right) - \frac{1}{(2w+1)^2}\right] \quad (1)$$

where the normalization constants are

$$K_0 = \frac{1}{B}\left[\sum_{i=-w}^{w}\exp\left(-\frac{i^2}{2}\right)\right]^2 - \frac{B}{(2w+1)^2} \quad (2)$$

and

$$B = \left[\sum_{i=-w}^{w}\exp\left(-\frac{i^2}{4}\right)\right]^2. \quad (3)$$

The integer value w should be bigger than the particle image radius in pixels and we found $w = 3$ to be appropriate.

The particle segmentation is carried out afterwards via a dynamic threshold segmentation algorithm according to [5]. The algorithm scans the image for local maxima whose intensity is higher than a basic threshold. If a local maximum is found, it is labelled as a part of a particle. From there, a region-growing process starts, which allocates all neighbouring pixels fulfilling two conditions: its intensity $I_{i,j}$ has to be lower than the border pixel lying in direction to the local maximum pixel and its intensity has to be higher than a contrast threshold C:

$$I_{i,j} / I_{\max} > C \quad (4)$$

This algorithm is in principle able to detect and separate overlapping particles and particles of relatively low brightness.

Once all pixels belonging to a particle are found, the particle's position is estimated by computing the centre of mass of the pixel intensity distribution.

3.2. Tracking algorithm

The tracking scheme applied is basically a slightly modified three-frame approach, where the estimation of particle positions is founded on the assumption of minimum acceleration (MMA) between particle positions of three consecutive frames [6,7]. That means that from the two very last positions of an existing trajectory, a velocity is calculated. It is assumed that for the next step this velocity will not change too much, which delivers an estimated position for the future timestep. A radius around this estimate is defined in which we look for particle candidates. The candidate with the lowest distance from the estimate will be considered as new part of the trajectory. In conflict situations of this assignment process, we stop each involved trajectory, as it turned out to be the best alternative [8].

If a particle cannot be assigned to previous trajectories, we start a new one. The next estimate in this case is calculated by the mean displacement of neighbouring existing trajectories (defined by a neighbour radius).

For the very first two frames, where we naturally have no trajectory history yet, we start our estimation with a PIV correlation delivering displacement vectors for interrogation areas (IA) of the flow zone. Particles are assigned to their IA and their individual estimated position in the next frame is computed. The final assignment then uses the Hungarian algorithm, where the total costs are minimized (a cost is defined as the distance from a candidate to the estimate).

The tracking scheme proved very reliable especially as the frame rate of image recording in the aneurysm with 2000 *Hz* is fast enough, so that the displacement of particle between consecutive images is small. However, as it is only applied in 2D, we very often suffer from particle drop out, i.e. that particles leave the laser sheet temporarily or completely. This limits the length of the resulting trajectories but does not perturb the assignment process by itself.

4. RESULTS

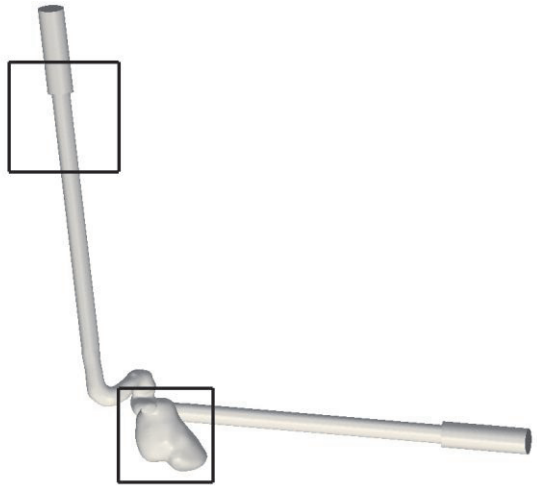

Figure 4. Reconstructed model geometry with marked ROIs for inlet and aneurysm recordings.

In this section 2D-PTV results are presented inside the aneurysm itself and in the inlet tube (see ROIs in Figure 4), which is of special interest, as we are able in this manner to derive velocity profiles as inlet boundary conditions for CFD computations (Figure 5). Velocity vectors are also compared from PTV trajectories to PIV correlation techniques by an Lagrange-Euler transformation using a standard MatLab function.

Figure 5 shows the cross-section averaged velocity at the inlet as a function of time. It can be observed that the determined velocities are in the expected correlation with the measured pressure values.

Three time stamps are selected (around 200, 600 and 1,000 *ms*), where the values are presented in what follows.

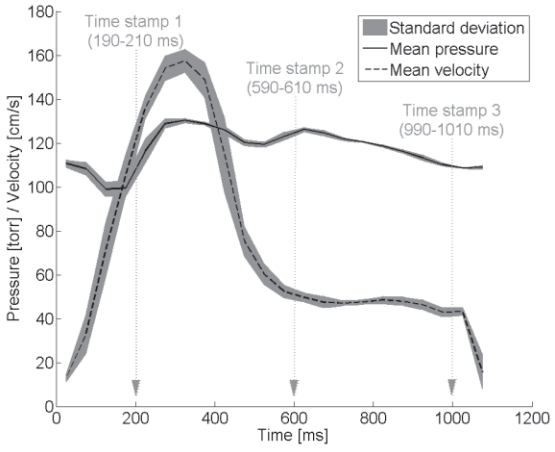

Figure 5. Measured pressure and cross-section mean velocity at the inlet as a function of time during one pulsation (period).

4.1. Aneurysm

The image recording inside the aneurysm was carried out at a frame rate of 2000 *Hz* with an exposure of 1/3000 *s*. These values turned out to be sufficient to get small particle displacements and almost no exposure streaks from motion blurring of the particles. A recording comprises 5000 images, i.e. a total recording time of 2.5 *s*. Consequently, more than two pressure cycles can be observed.

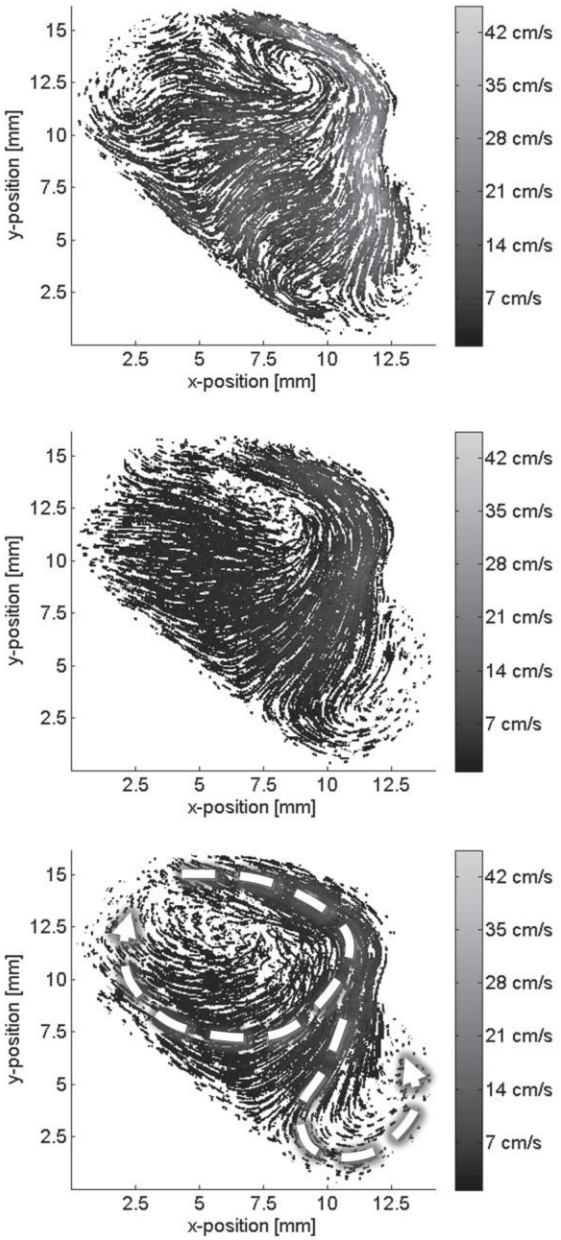

Figure 6. Trajectories in the aneurysm sack. Top: at 190-210 ms, Middle: at 590-610 ms, Bottom: at 990-1010 ms

In each image around 1100 particles can be detected. The tracking scheme computes around 292,000 trajectories with a length distribution according to Table 1. 71.8% of all trajectories

consist of more than two positions, which confirms the reliability of the tracking approach. As mentioned before, one has to consider the two-dimensional character of the measurement, i.e. particle pathlines crossing the laser sheet will only be captured temporarily, leading to short trajectories. 6.1%, i.e. 18,043 trajectories are longer than 50 positions. They are as expected mostly found in low-speed regions of the aneurysm.

Table 1. Trajectory lengths in the aneurysm

2	3	3-10	11-50	>50
28.2%	14.4%	29.5%	21.8%	6.1%

Trajectories of the flow in the aneurysm for three times of the pressure cycle are shown in Figure 6. For convenience, twenty frames before and after the mentioned timestep have been included into consideration and arrows or other markers indicating the trajectory direction have been left out.

As can be observed, there is a fast inflow into the aneurysm around 190-210 *ms* (top). Maximum velocities reach up to 40 *cm/s*. When the pressure cycle shows a declining slope, we observe a reduction of flow speed inside the aneurysm. Lowest velocities can be found around 1050 *ms*, where the pressure also reaches a minimum. Generally, two vortices can be observed: a big, clockwise rotating vortex in the upper part, where the blood enters and leaves the aneurysm, and a smaller, counter-clockwise rotating one in the lower right corner of the sack, where velocities are much lower (sketched in bottom part of Fig. 6).

As a comparison, the Eulerian velocity data, evaluated by direct cross-correlation (DCC) from the PTV recordings is presented in Figure 7 for the previously selected time stamps.

The previously mentioned Lagrange-Euler transformation was applied on the Lagrangian PTV data and the velocities were estimated using a standard Matlab function "TriScatteredInterp" with a linear interpolation method, since higher order interpolation schemes do not necessarily perform better than that of lower order [9]. PTV data were finally interpolated on the same grid, used by PIV evaluations.

To check, how PTV performs, each successively recorded image pair was evaluated by direct cross-correlation (DCC) of an open-source PIV software (PIVlab, version 1.3 by W. Thielicke and E. J. Stamhuis).

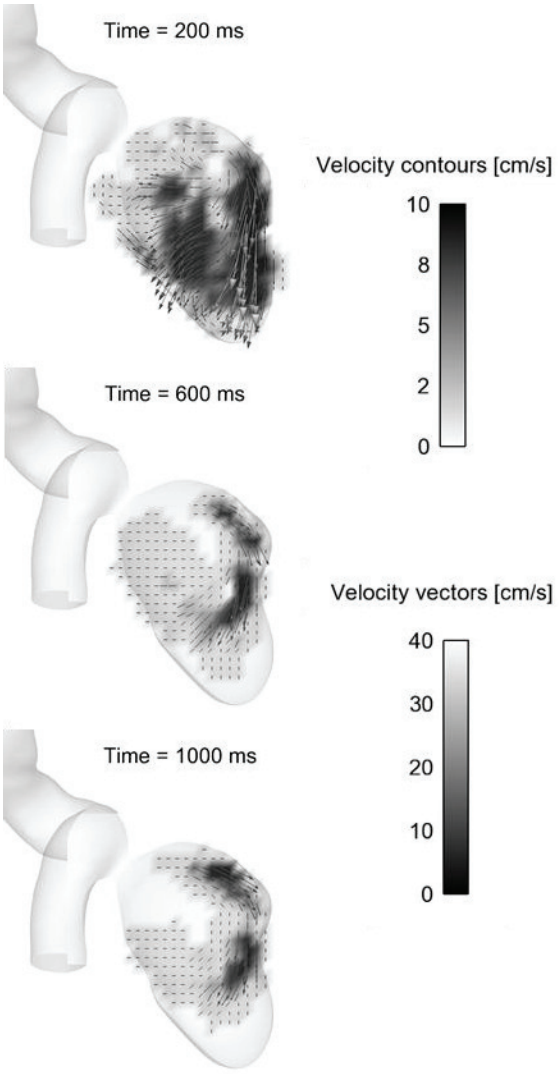

Figure 7. Velocity vectors in the aneurysm for the selected time stamps, derived by DCC from PTV recordings.

The resulting vector field was then compared to that of the interpolated one, derived from the PTV data. The comparison for the time stamp 200 *ms* is presented in Figure 8, where the background (grayscale color-bar) presents the relative deviation of the vectors derived by the two methods. An examination of these deviations showed that discrepancies above 10% are primarily caused by missing PIV vectors, probably due to an insufficient particle seeding density, hindering an effective PIV evaluation. This effect could be suppressed by a 2x2 median filter applied to the vector field derived by DCC.

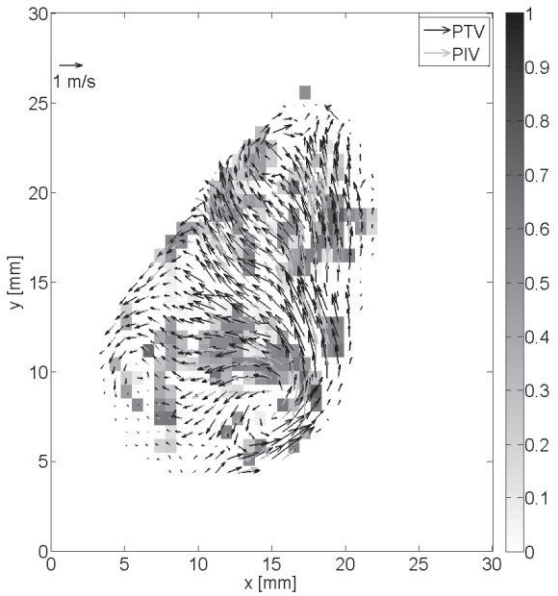

Figure 8. Comparison of velocity vectors derived by interpolation from Lagrangian data and by DCC. The relative difference for the local velocity magnitude is shown with the color-bar.

4.2. Inlet

Because of much higher velocities in the inlet pipe, it was necessary to increase the frame rate up to 4500 *Hz* and to decrease the exposure time down to 40 μs in order to avoid streak lines which may have caused problems for the image processing and particle position estimation. A recording comprises 5400 images. Hence, a complete pressure cycle can be captured (Figure 5).

Table 2. Trajectory lengths in the inlet vessel

2	3	3-10	11-50	>50
32.3%	14.8%	26.5%	21.1%	5.3%

Since we used the same magnification as in the aneurysm, the ROI in each image was much smaller, because of the thin diameter of the inlet vessel. Hence, only 250 particles could be typically found in each image. Two major differences in the flow pattern affect the tracking and have to be considered: on the one hand, the velocities are much higher than in the aneurysm. Even with the doubled frame rate, the tracking becomes more difficult, as the particle displacement increases, while inter-particle distances remain similar. On the other hand, the one-directional and one-dimensional character of the flow facilitates the tracking process considerably. Both effects seem to neutralise each other so that the quantitative distribution of trajectory lengths is comparable to that within the aneurysm. A typical recording comprises about 90,000 trajectories from which more than 67% are longer than two timesteps. 5.3% of all trajectories are longer than 50 timesteps, but can only be found close to the vessel walls, where velocities are slow enough to hinder particles from dropping out of the observation zone of the camera.

The inlet data were also transformed to an Eulerian coordinate system, where cross-section averaged velocity information is presented in Figure 9, as a function of time. At the already selected time stamps 200, 600 and 1,000 *ms*, the Re number was calculated: 1220, 470 and 420, respectively, confirming that the flow is laminar inside the model. The corresponding velocity profiles are presented in Figure 9, together with a steady laminar profile for comparisons. The measured profiles are broader, revealing the shear-thinning property of the artificial blood as well as considerable unsteady effects.

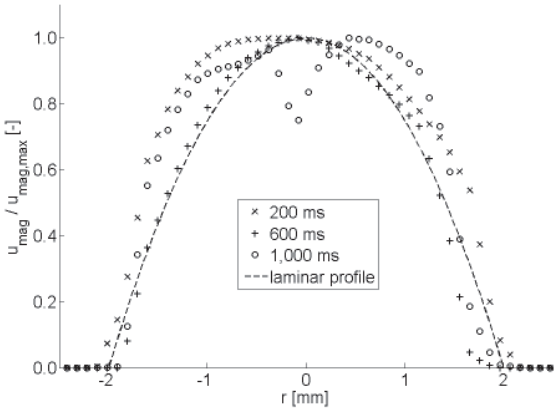

Figure 9. Dimensionless inlet profiles at different time stamps (marked in Figure 5) compared to a steady laminar profile.

5. SUMMARY

This work presents results of 2D-PTV measurements in an artificial full-scale cerebral aneurysm model. PTV measurements were successful and should be soon extended to 3D. The primary aim of the experiments was to deliver inlet boundary conditions and of course validation data for CFD. Since input and output of the numerical simulations occur in an Eulerian frame while PTV experiments supply measurement data in a Lagrangian one, conversion of the data were necessary. PTV results are presented in both points of view and PTV measurements can also be used in this way for a DCC evaluation of the recorded images. Quantitatively, both the results are very similar (relative deviation well below 10%). For a qualitative analysis of flow features, PTV appears much more appropriate, due to the additional information supplied by particle trajectories.

Further work should deal with 3D-particle tracking in such phantom models, using three colour cameras and tracer particles with different wavelength emissions, facilitating correspondence for the same particles on different camera views and time instances.

ACKNOWLEDGEMENTS

This work was carried out as part of the TÁMOP-4.2.1.B-10/2/KONV-2010-0001 project in the framework of the New Hungarian Development Plan. The realisation of this project is supported by the European Union, co-financed by the European Social Fund.

REFERENCES

[1] Kaminogo, M., Yonekura, M. and Shibata, S., 2003, "Incidence and Outcome of Multiple Intracranial Aneurysms in a Defined Population", *Stroke*, Vol. 34(1), pp. 16–21.

[2] Yu, S.C.M., and Zhao, J.B., 1999, "A steady flow analysis on the stented and non-stented sidewall aneurysm models", *Medical Engineering & Physics*, Vol. 21(3), pp. 133–141.

[3] Sadasivan, C., Lieber, B.B., Gounis, M.J., Lopes, D.K., and Hopkins, L.N., 2002, "Angiographic Quantification of Contrast Medium Washout from Cerebral Aneurysms after Stent Placement", *American Journal of Neuroradiology*, Vol. 23(7), pp. 1214–1221.

[4] Crocker, J.C., 1996, "Methods of Digital Video Microscopy for Colloidal Studies", *Journal of Colloid and Interface Science*, Vol. 179, pp. 298-310.

[5] Mikheev, A.V., 2008, "Enhanced particle-tracking velocimetry (EPTV) with a combined two-component pair-matching algorithm", *Measurement Science and Technology*, Vol. 19(8), pp. 085401.

[6] Malik, N.A., 1993, "Particle tracking velocimetry in three-dimensional flows. Part II, Particle tracking", *Experiments in Fluids*, Vol. 15(4/5), p. 279.

[7] Dracos, T.A., 1996, "Three-dimensional velocity and vorticity measuring and image analysis techniques", *Lecture notes from the short course held in Zürich*, ERCOFTAC series, Vol. 4., Kluwer, Dordrecht.

[8] Ouellette, N.T., 2006, "A quantitative study of three-dimensional Lagrangian particle tracking algorithms", *Experiments in Fluids*, Vol. 40(2), pp. 301-313.

[9] Stüer, H., and Blaser, S., 2000, "Interpolation of scattered 3D PTV data to a regular grid", *Flow Turbulence and Combustion*, Vol 64(3), pp. 215-232.

Conference on Modelling Fluid Flow (CMFF'12)
The 15th International Conference on Fluid Flow Technologies
Budapest, Hungary, September 4-7, 2012

A NEW OVERSET GRID ALGORITHM APPLIED TO THE SIMULATION OF FLOWS INVOLVING COMPLEX GEOMETRIES

Tim Craft, Hector Iacovides, Alex Skillen[2]

[1] Computational Fluid Dynamics Group, Modelling and Simulation Centre, School of MACE, The University of Manchester, UK.
[2] Corresponding Author. Email: alex.skillen@manchester.ac.uk

Abstract

The generation of structured grids around complex geometries is generally a difficult task. This task is typically a major bottleneck in the overall solution procedure; however, the overset grid method can be used to relieve much of this burden. An overset grid consists of a set of simple component grids, which can overlap arbitrarily (provided there is sufficient overlap to interpolate from). The union of all simple grids should then delineate the global domain. This allows complex domains to meshed using a series of simple meshes.

A new overset hole cutting algorithm is developed in order to automatically combine the series of simple meshes into an overset domain. It has been shown that for a variety of test cases, continuous and accurate solutions are obtained from one grid to another, which are comparable to experimental data.

Chimera, Complex geometries, Hole cutting, Overset grids, Turbulent flow.

1. Introduction

The majority of flows that are of engineering interest involve complex geometrical domains. Examples of such complex domains range from the flow over an entire aircraft, to internal biomedical flows such as the flow induced by a beating heart. When simulating such problems within a CFD framework, it is first necessary to generate a suitable grid over which the discretised governing equations can be solved. However, the generation of grids around complex geometries poses many challenges. To overcome these challenges, the overset grid method can be used.

In the overset grid method, it is noted that it is not a necessary condition to have grid-block interfaces aligned with one another (in contrast to a block-structured grid arrangement). By relaxing this constraint, the overset meshing technique has the potential to be far simpler at the pre-processing stage than an equivalent block-structured formulation. The method also offers several advantages over unstructured grids. For example, for an unstructured grid cell connectivity information needs to be computed and stored. Expensive gradient reconstruction procedures are also generally required. There are also issues in implementing higher order convection schemes. The hexahedral cell shapes employed in a structured grid are also particularly well suited for efficiently resolving near wall regions. This is particularly important for flows involving turbulence or heat transfer where a fine spatial discritisation is generally required.

The overset method's solution procedure commences by solving the governing equations over one mesh with boundary conditions at internal boundaries obtained by interpolation from a suitable donor mesh. This is then repeated in an iterative manner on all other meshes until convergence is achieved. The main features of an overset CFD code that are unique to the overset formulation are: the interpolation algorithm; and an algorithm that constructs the overall overset grid from the set of component grids. The former algorithm interpolates information from a donor grid, providing boundary condition data at internal boundaries for the grid that is being solved on. The latter algorithm tags each cell on a component grid with an integer code that dictates what type of node is being dealt with. Cells can be standard cells, interpolation cells, or unused cells.

One of the main challenges facing the overset method is the issue of conservation at grid interfaces. Berger [1] presents a conservative interpolation scheme valid for two-dimensional cases where sub-grids are aligned with one another in a very limited number of specific ways. Chesshire and Henshaw [2] extended on the work of Berger by generalising the conservative interpolation method for arbitrarily arranged two-dimensional sub-grids. However, the extension to 3D has not been carried

out and is likely to be prohibitively complex for the general case. Tang et al. [3] propose a semi-conservative approach, in which a discrete approximation to the conservation of mass across overset sub-grids is satisfied. The method is referred to as mass-flux based interpolation (MFBI). Tang et. al. [3], Ge and Sotiropoulos [4], and Kangle and Gang [5] all demonstrate the superiority of MFBI over standard linear interpolation.

In the present study, a new overset algorithm is developed and validated. A new hole cutting algorithm is presented which automatically takes a set of user generated sub-grids and tags all cells appropriately. The hole cutting algorithm is shown to be quick and robust.

2. The overset algorithm

2.1. Inter-grid interpolation

The MFBI algorithm [3] has been used in all simulations presented in this work. This is used in favor of a simple linear interpolation since this authors' investigations [6] have shown that, while non-conservative linear interpolation may generally be satisfactory at grid independence, the MFBI semi-conservative interpolation procedure tends to yield improved convergence rates and lower residual error.

2.2. Hole cutting

The objective of the hole-cutting algorithm is to provide an overset grid from a set of structured sub-grids. This is achieved by tagging each cell on each sub-grid as a standard cell, an interpolation cell, or an unused cell. Standard cells are those on which the discritised governing equations can be solved on using a computational stencil comprising of other standard cells, or interpolation cells only. Interpolation cells are cells in which the values of the primitive variables are obtained through interpolation, and are required in order to provide a complete computational stencil to other standard cells. Unused cells are cells that take no part in the computation at the current time-step.

In general, some cells may lie outside of the computational domain, in which case they must be 'cut', (i.e. tagged as unused). In order to remove cells that lie outside of the computational domain, the first step is to identify any cells that intersect boundaries. The intersection of walls shall be considered here, but the method is equally applicable to other edges of the computational domain, such as inlets, outlets, etc.

A 'wall face' is defined as the quadrilateral face of a cell that has the wall boundary condition applied to it (by the user). To test for intersection of this wall face with any given hexahedral cell, the wall face can be split into two triangles. Similarly, each face of the test cell can be split into two triangles. The intersection test is then decomposed into up to twenty-four triangle-triangle intersection tests. Rapid triangle-triangle intersection testing algorithms can be employed for this purpose, such as those developed for the field of computer games graphics. If an intersection is detected, then the test cell must lie partly outside of the computational domain, and hence should be tagged as an unused cell. Figure 1 illustrates overset grids that may be used for the study of flow around a circular cylinder after applying this step.

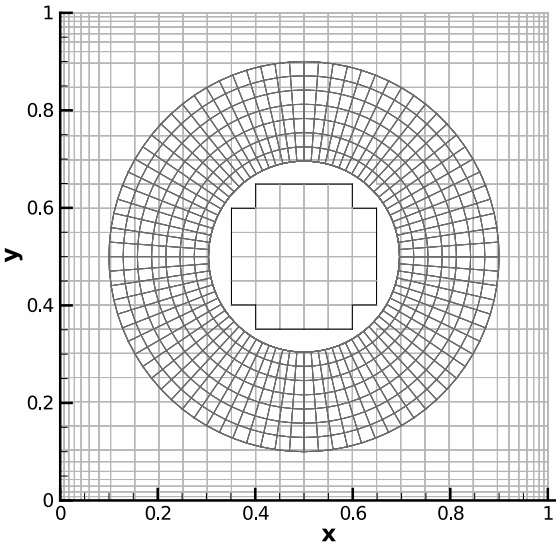

Figure 1. Demonstration grids for flow around a circular cylinder after removing cells that intersect walls.

Once all cells that intersect the edge of the computational domain have been removed, what remains is to remove the cells that lie *fully* outside of the computational domain. This can be achieved by noting that any cells that are adjacent to an unused cell cannot be standard cells (since their computational stencils would be incomplete). They must therefore be either interpolation cells or unused cells. For each cell that is adjacent to an unused cell, identification of a suitable donor grid is attempted (this is achieved by attempting to find interpolation coefficients in the range $[0, 1)$). Where no suitable donor grid can be identified, the cell in question must lie outside the computational domain, and is therefore tagged as unused. Alternatively, if a suitable donor-grid can be identified, the cell is preliminarily tagged as an interpolation cell. By repeating this process until no further changes are made by repeating further, all cells that lie outside of the computational domain will have been tagged as unused, and a valid overset grid will have been attained. Figure 2 shows the outcome of this step.

We now wish to minimise the overlap between grids in order to reduce duplicate computational effort. It has also been shown that minimising the overlap is desirable for solution continuity and convergence rate [6]. To this end, we devise a scoring system for overlapping cells, which will be used to

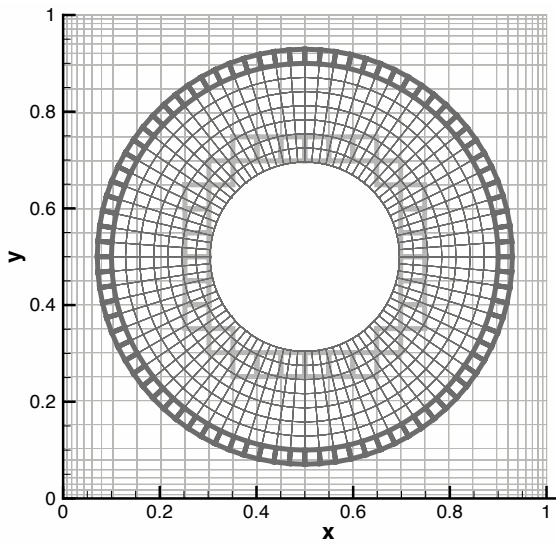

Figure 2. Demonstration grids after removing cells outside of domain. Heavy lines indicate interpolation cells.

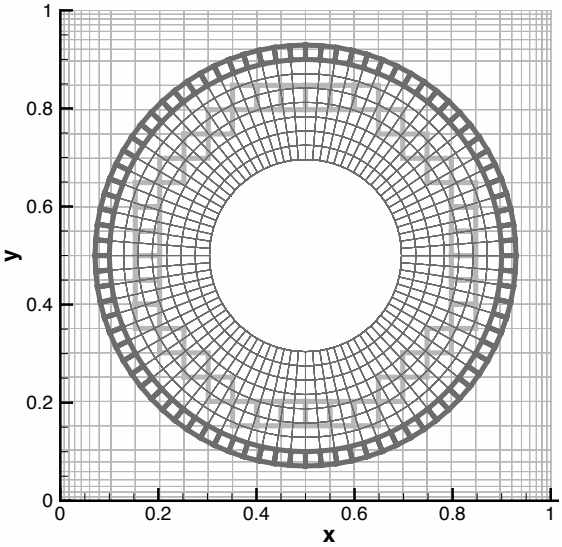

Figure 3. Final demonstration grids for the flow around a circular cylinder. Heavy lines indicate interpolation cells.

determine which of the overlapping cells to remove. Scores are calculated based on a user defined criteria (for example, by preserving cells with the lowest volume).

Consider overlapping sub-grids Ω_A and Ω_B. Initially, we wish to remove the cells on Ω_A that (a) fully overlap Ω_B, (b) score lower than the mean score of the overlapping cells on Ω_B, and (c) do not form part of an interpolation stencil for any of the interpolation cells on any other sub-grid. Any cells on Ω_A that match all three of these criteria may be tagged as unused. Note that the cell's tags on Ω_B are not altered at this stage. The algorithm is as follows:

- Firstly, all the cells on Ω_A that comprise part of the interpolation stencil of interpolation cells on other sub-grids are flagged. Such cells cannot be removed, as to do so would cause an invalid interpolation stencil (one that comprises unused donor cells).

- All cells that are *adjacent to* those previously flagged are also flagged. These adjacent cells also cannot be removed since if they were, the previously flagged cell would necessarily be converted to an interpolation cell in order to provide a complete computational stencil to surrounding standard cells on Ω_A. However, the interpolation from other interpolation cells may be circular, and hence is not permitted.

- For each cell on Ω_A that has not been flagged in the previous steps, the validity of removing the cell is assessed. If the cell were to be removed, any surrounding standard cells would need to be converted to interpolation cells to maintain complete computational stencils. The viability of this conversion is assessed by attempting to find a suitable donor grid for all cells subject to conversion. Where no donor grid can be identified for any one of the candidate conversions, the original cell in question cannot be removed. Where donor stencils can be identified in all cases, the original cell in question may be removed, (but is not removed yet).

- If the cell identified in the previous step may be removed, the cell(s) on the underlying grid that overlap the present cell are identified (this step is done approximately for computational efficiency by simply assessing if any underlying cell's bounding box intersects the bounding box of the present cell). The cell is removed only if its score is greater than the average of that of the cells it overlaps.

The steps above are repeated for each sub-grid in turn. The resulting overset grids for the circular cylinder case are shown in Figure 3. This algorithm is robust, as will be demonstrated by the variety of test cases considered in the next section.

It can be noticed from the preceding description that finding interpolation stencils is an oft required process in this hole cutting algorithm. As a first step, one should check that the bounding box of a candidate interpolation stencil engulfs the interpolation point; if it does not, the candidate interpolation stencil cannot be the correct one. A related process is to test if two bounding boxes intersect one another (this test is performed in order to determine which cell(s) a given cell overlaps). Both the point-in-box and box-box-intersection tests can be performed very rapidly by storing the geometric data in an alternating digital tree data structure, as described by Bonet et al. [7] (note

that the latter algorithm is simply a generalisation of the former since a point can be treated as a box with zero volume). By employing such a structure, search times can generally be reduced from $O(n^2)$ to $O(n \log n)$ time, where n is the number of cells.

We note that the hole cutting algorithm described here involves geometric tests that are independent of one another. For this reason, it is expected that the algorithm would be particularly well suited to solution on GPUs. This extension however is left as future work.

2.3. Grid zipping

For internal flows, a bulk correction is generally required in order to ensure that the mass flux entering the domain via the inlet is exactly balanced by that leaving via the outlet(s). In an overset grid formulation, there is no guarantee that the surface to be integrated over will be made up of just one grid. In general, there may be several such grids overlapping one another arbitrarily. Cells in the overlap region would require a weighting to prevent their contribution being counted twice. However, the calculation of a suitable weighting factor is non-trivial in the general case for cells that *partly* overlap other grids. This would require complex (and costly) geometrical analysis to determine the proportion of the cell that is overlapping.

A simpler method is to remove any overlapping cells from one of the grids completely, and to fill the 'gap' with triangular cells, generating a hybrid surface grid. The underlying primitive variables are then interpolated onto the triangular cells, and the resulting (non-overlapping) surface is integrated over for the purposes of applying a bulk correction. The 'zipper grid' method [8] has been employed here for generating the surface grids over inlets and outlets for the internal flow cases considered.

3. Test Cases

3.1. Flow over a multi element airfoil

Here, the turbulent flow over a two element airfoil is considered. Multi element airfoil configurations pose many challenges in mesh generation. A multi-block structured mesh is generally very challenging to generate. This is particularly true for configurations involving both slats and flaps, or flaps which comprise of more than one component. The benefits of the overset method in this situation are clear. Simple body fitted grids around each airfoil component are independently generated and overlaid onto a 'background grid'. The problem is reduced to one of generating C-shape grids around each component, while the background grid can be Cartesian.

3.1.1. Geometry and computational mesh

Figure 4 shows the geometry of the computational domain. This is the same geometry as that considered experimentally by Adair and Horne [9]. Tunnel walls have been included in the simulations owing to the large model dimensions relative to those of the tunnel, thereby leading to the possibility of significant tunnel wall blocking effects.

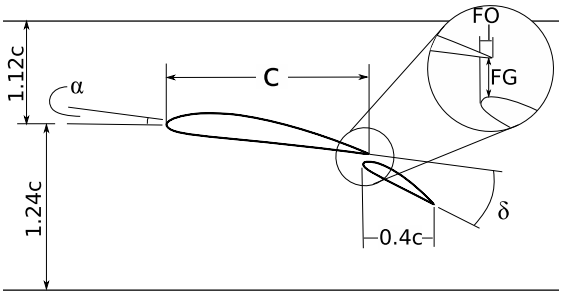

Figure 4. Geometry of two-element airfoil.

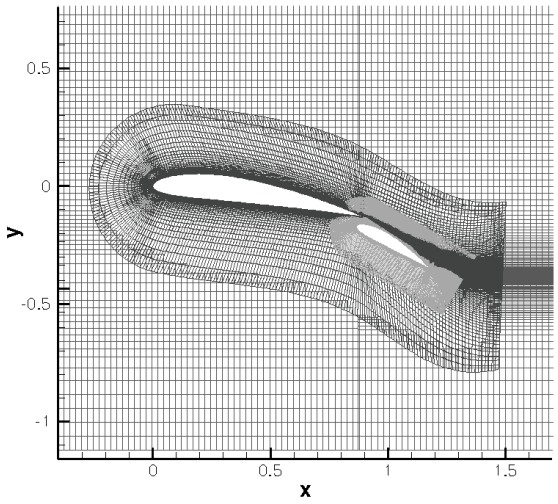

Figure 5. Meshes used for the study of the flow over a two element airfoil.

The two-element airfoil configuration comprises a NACA 4412 main airfoil with a NACA 4415 flap. The flap has a chord length of $0.4c$ (where c is the main airfoil chord length). The location of the flap relative to the main airfoil is specified in terms of the flap gap (FG), the flap overlap (FO), and flap deflection (δ_f) (See Figure 4). The values of FG, FO and δ_f used in the present study are $0.035c$, $0.028c$ and 21.8° respectively. The angle of attack of the main airfoil, α, is set to 8.2°.

A grid comprising around 70,000 cells has been employed. Grid sensitivity tests have been carried out with $120,000$ cells, with no appreciable difference in the solution. Figure 5 shows the grids used. It can be seen from the figure that the hole cutting algorithm has preserved cells with the finest resolution. A total of 4 subgrids have been employed (one for each airfoil component, and two background meshes in order to provide a refinement in the wake). Each subgrid is substantially easier to generate than the 7 blocks used in [10] for the same geometry.

3.1.2. Turbulence modelling

The effects of turbulent momentum transfer are approximated via the use of the low Reynolds number Launder Sharma $k-\epsilon$ model.

3.1.3. Boundary conditions

At the inlet, a uniform velocity has been specified with a magnitude that is consistent with the Reynolds number of 1.8×10^6, based on the main airfoil chord length. Turbulence intensity levels at the inlet have been provided in [9] and are used to approximate the inlet turbulent kinetic energy. The value of ϵ at the inlet was set via a parametric study to ensure good agreement with experimental data at the closest upstream measurement point to the inlet.

At the outlet, the pressure has been set to zero, while a zero gradient conditions have been employed for the turbulence variables and velocity components (with an overall bulk correction applied to the normal component).

The no-slip condition has been used for all walls comprising the airfoil surfaces, while a slip boundary condition has been employed for the tunnel walls (this is equivalent to a symmetry condition and is achieved by enforcing a zero gradient condition for all variables, before setting the wall-normal velocity component to zero). A slip boundary condition is used on the tunnel walls since this provides a reasonable approximation of the blocking effect of the tunnel walls (albeit without the slight additional blocking due to the presence of the thin tunnel wall boundary layers), without requiring one to fully resolve the near wall region. A fully resolved no-slip condition at the tunnel wall would require significantly more computational cells, especially given the low Reynolds number turbulence model variant employed.

3.1.4. Results

An overview of the solution is reported via the use of flow streamlines in Figure 6. It can be seen from the figure that the streamlines are continuous across subgrids.

Figure 7 shows the pressure coefficient on the surface of the airfoil and flap. Comparisons are made with the available experimental data. Here is can be seen that a very good agreement is obtained between the two sets of results. This suggests that the correct lift and moment coefficients have also been captured by the computation. The predicted lift coefficient is equal to 3.28 for the present configuration, while a moment coefficient of $c_m = -0.94$ has been obtained (based on the torque about the quarter chord point). This compares favorably with experimental values of 3.19 and -0.99 for the lift and moment coefficients respectively [9], which were obtained via integration of the measured surface pressure distribution.

The detail of the flow downstream of the main airfoil's trailing edge is assessed by means of three profiles, for which there are also experimental data

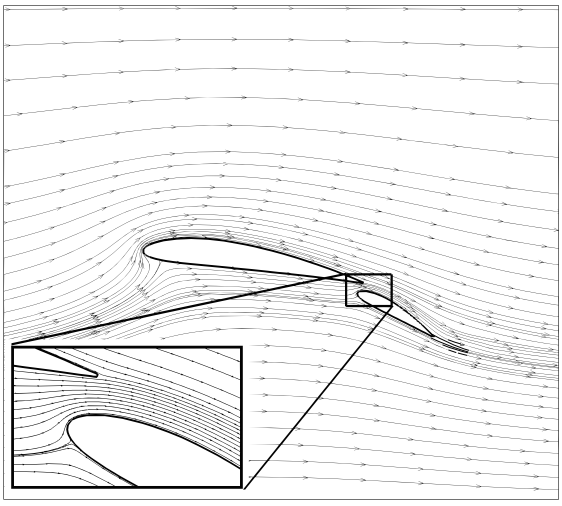

Figure 6. Flow streamlines. Insert shows detail in region of gap.

[9]. Table 1 details the specific location and orientation of each profile.

Figure 8 shows profiles of the streamwise mean velocity component at each of the stations considered. It can be seen that the overall shape of the computed profiles is reasonably close to that of the experimental data for all cases. Note that there is a difference between computed and measured boundary layer thickness, which is likely to be due to the simplicity of the turbulence model employed. Iaccarino and Durbin [10] also reported similar discrepancies for the same geometry when using block-structured grids, despite their use of a more sophisticated turbulence model.

Table 1. Location and orientation of profiles.

Profile	x/c	β (angle from vertical)
1	1.031	14
2	1.308	44
3	1.322	0

3.2. Flow through the human carotid bifurcation

In human anatomy, there are two common carotid arteries; one on the left of the neck, and the other mirroring on the right. It is these two arteries that provide blood to the head. Within the upper neck, the common carotid artery divides into the internal and external carotid arteries, and it is this division that is described as the carotid bifurcation.

The overset grid method is a particularly useful tool for meshing pipe domains. For example, an O-shaped grid can be used to depict the outer portion of the pipe, while the core can be meshed via the use of a separate grid of Cartesian section. This therefore avoids the issues of a grid singularity at the centre of the pipe that would be encountered

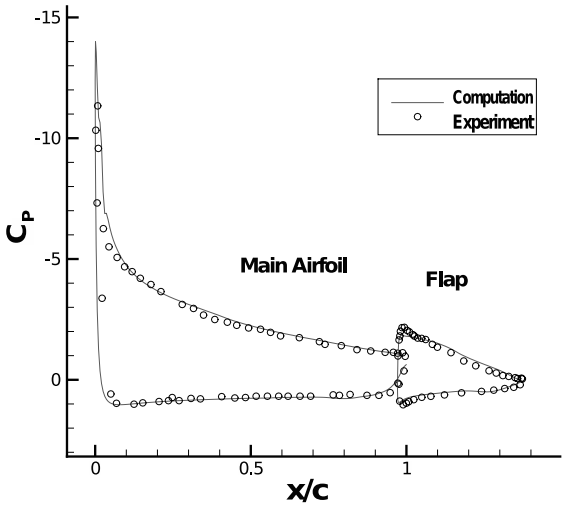

Figure 7. Pressure distribution over main airfoil and flap.

via the use of a single O-shaped block. Complex domain decomposition issues that are encountered when generating a block structured grid are also avoided.

For branching pipe geometries, a block structured grid would be particularly difficult to generate, while the overset method can handle such domains with ease. For this reason, the vast majority of previous studies of the carotid bifurcation (and other similar branching pipe geometries) have tended to use costly unstructured meshes. By using a structured overset grid, highly efficient solution algorithms such as tri-diagonal matrix solvers can be employed. Cell connectivity information also is not required.

3.2.1. Geometry and mesh

The geometry considered here is as close as is possible to that considered experimentally by Bharadvaj *et. al.*, [11] (note there is some ambiguity in the precise geometry in [11], so an exact replica could bot be attained).

A total of five overset sub-grids have been used in the present study to delineate the overall computational domain. The common carotid artery and the internal carotid are both depicted via the use of the same two grids, with the grids bending at the bifurcation in order to cover the internal carotid portion of the domain. An O-grid covers the outer section of the artery, while a separate square-section grid covers the core of the artery. The external carotid artery uses a further two grids, again covering the interior and exterior of the artery via the use of a separate O-grid and square-section grid. A final fifth overset sub-grid has been used at the junction between the external and common carotid arteries in order to transfer information between the two. A total of around 350, 000 active cells have been used to cover the domain (i.e. not including those that are cut

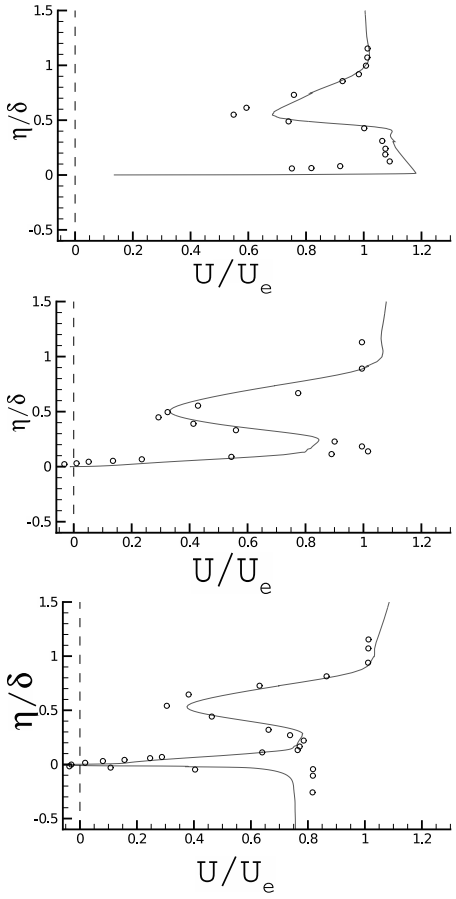

Figure 8. Profiles of the streamwise velocity. Locations stated in Table 1. Profile 1 (top) to Profile 3 (bottom).

by the hole cutting algorithm). This resolution has been arrived at via a detailed grid sensitivity study, details of which are available in [6].

3.2.2. Boundary conditions

The flow Reynolds number is set to either 400 or 800 (based on inlet diameter and bulk inlet velocity) depending on the experimental conditions. No turbulence modelling is necessary in either case. A parabolic inlet profile has been prescribed in order to remain consistent with the fully developed laminar inlet condition of the experiments [12].

At the outlet, a bulk correction algorithm has been applied over zipped surface grids (Section 2.3). The flow division ratio is specified as 70:30 through the internal and external carotid arteries respectively.

All walls have the no-slip condition applied.

3.2.3. Results

An overview of the axial velocity at several profiles through the symmetry plane is reported in Figure 10. Experimental comparison is also provided in the Figure. It can be seen that there is generally a good qualitative agreement between the two sets of results. The figure demonstrates many of the main

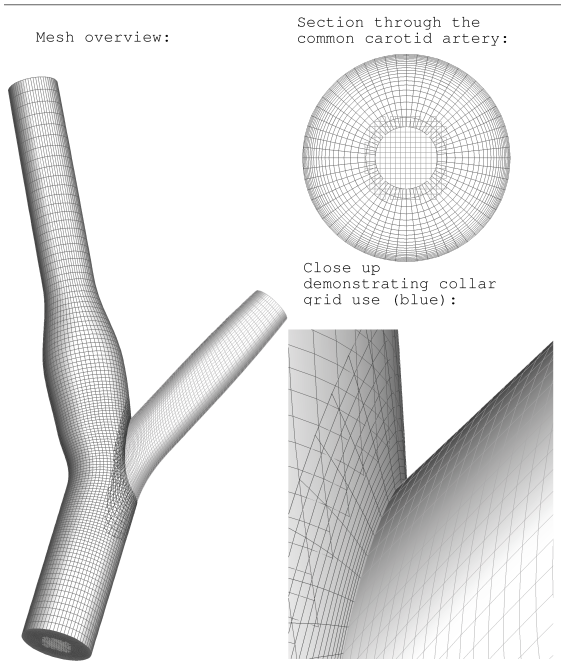

Figure 9. Grids used for carotid bifurcation case.

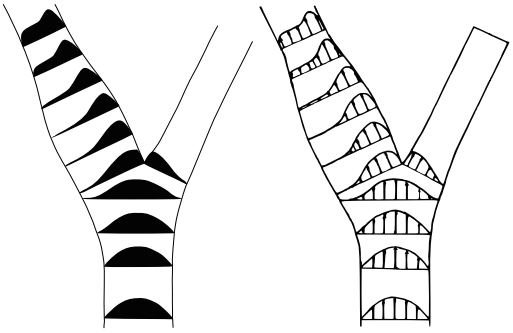

Figure 10. Velocity vectors in the symmetry plane. Computed results (left) are compared with experimental data [12] (right). Re=400.

flow features. Separation in the internal artery's sinus is suggested via the essentially zero velocity gradient near to the common-internal wall.

Figures 11 and 12 provide comparisons of the axial and tangential velocity respectively, at three sections through the internal carotid artery (at the entrance of the sinus, at maximum sinus diameter, and at the conclusion of the sinus). From the latter figure, a strong secondary flow is apparent. This secondary flow results from the axial curvature of the arterial wall. As the fluid follows the curvature of the artery, a pressure gradient acting towards the inner side of the bend is established in order to balance the centrifugal force. The fluid located at the core of the pipe resists bending to the same extent as the fluid that is located closer to the pipe wall due to the high axial-momentum (and inertia) of the former. Conversely, the low axial-momentum fluid located near the top side of the pipe, caused

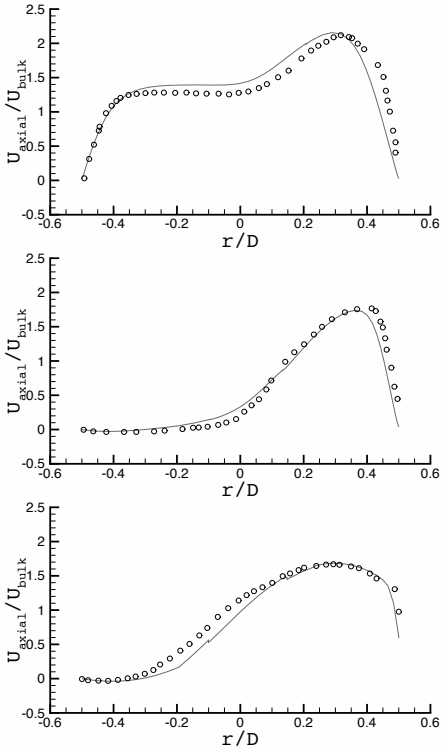

Figure 11. Axial velocity. Entrance to sinus (bottom). Maximum sinus diameter (middle). Conclusion of sinus (top). Re=400. ○, Experiments [12]. ——, Present study.

by the viscous interaction imposed by the no slip condition, is influenced by the pressure gradient to a greater extent than the core fluid, and therefore turns with a smaller radius of curvature. A secondary flow following the circumference of the pipe results, flowing from the outer side to the inner side of the bend. A resultant flow is also established acting against the pressure gradient and along the symmetry plane in order to balance this circumferential flow. The transport of momentum by the secondary flow acts to skew the axial velocity towards the outer side of the bend, as is evident from Figure 11.

Both Figures 11 and 12 shown a good agreement with the experimental data and display continuous solutions across grid interfaces. Any small discrepancies between the solution and the experimental data is likely to be due to geometric ambiguity. The shape of the recirculation region is particularly sensitive to the precise curvature of the artery wall, and hence a small difference in the geometry can have a fairly large affect on the flow.

4. Conclusions

In this paper, details of a new overset algorithm are presented. The algorithm is validated by considering the flow over a two-element airfoil and through a human carotid bifurcation; both very challenging geometries. It is noted that the generation of structured grids around such

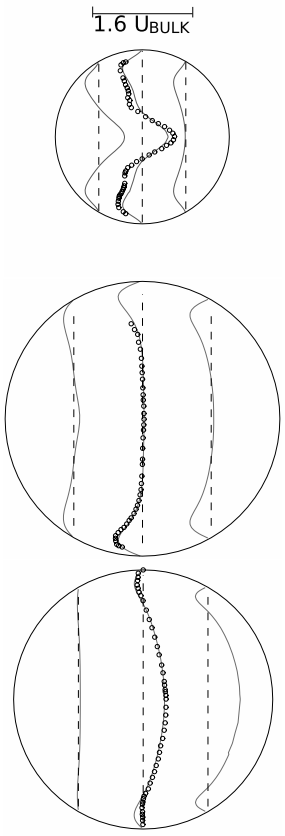

Figure 12. Tangential velocity profiles. Entrance to sinus (bottom). Maximum sinus diameter (middle). Conclusion of sinus (top). Re=800. ∘, Experiments [12]. ——, Present study.

geometries is impractical. This complexity is further compounded if the geometry is further complicated (e.g. by including additional elements or branches for the airfoil or artery respectively). The overset grid method can handle such cases with ease.

The method also provides several advantages over unstructured grids. Namely, the flow solver is typically much more efficient for a structured grid since highly efficient tri-diagonal matrix solvers can be employed in order to solve the linear system. Grid connectivity information is not required for a structured grid since cell connectivity is readily available (this is not true for an unstructured grid). This reduces both memory and CPU overhead. Finally, hexahedral cells that are used in a structured grid formulation are particularly well suited to efficiently resolving a near wall boundary layer; very high aspect ratio calls can be employed in a stable manner since the cells are aligned with the flow direction. The same is not necessarily true for unstructured cells.

For the two test cases considered here, it has been shown that there is a good agreement between computed and measured results. It is also apparent that solution continuity across internal overset interfaces is achieved.

References

[1] M.J. Berger. On conservation at grid interfaces. *SIAM J. Numer. Anal*, 24(5):967–984, 1987.

[2] G. Chesshire and WD Henshaw. A Scheme for Conservative Interpolation on Overlapping Grids. *SIAM Journal on Scientific Computing*, 15:819, 1994.

[3] H.S. Tang, S. Casey Jones, and F. Sotiropoulos. An overset-grid method for 3D unsteady incompressible flows. *J. of Computat. Phys.*, 191(2):567–600, 2003.

[4] L. Ge, S. Lee, F. Sotiropoulos, and T. Sturm. 3D unsteady RANS modeling of complex hydraulic engineering flows. I: Numerical model. *Journal of Hydraulic Engineering*, 131:800, 2005.

[5] S. Kangle, X. Gang. Assessment of an Interface Conservative Algorithm MFBI in a Chimera Grid Flow Solver for Multi-Element Airfoils. In *Proceedings of the World Congress on Engineering*, volume 2. Citeseer, 2009.

[6] A. Skillen. *The overset grid method, applied to the solution of the incompressible Navier-Stokes equations in two and three spatial dimensions.* PhD thesis, The University of Manchester, 2011.

[7] J. Bonet and J. Peraire. An alternating digital tree (ADT) algorithm for 3D geometric searching and intersection problems. *International Journal for Numerical Methods in Engineering*, 31(1):1–17, 1991.

[8] W.M. Chan and P.G. Buning. Zipper grids for force and moment computation on overset grids. *AIAA Journal*, 1995.

[9] D. Adair and WC Horne. Turbulent separated flow over and downstream of a two-element airfoil. *Experiments in Fluids*, 7(8):531–541, 1989.

[10] G. Iaccarino and PA Durbin. Application of the k-ϵ-v2 model to multi-component airfoils. In *Center for Turbulence Research, Proceedings of the Summer Program*, page 23, 1996.

[11] BK Bharadvaj, RF Mabon, and DP Giddens. Steady flow in a model of the human carotid bifurcation. Part I–flow visualization. *Journal of Biomechanics*, 15(5):349–362, 1982.

[12] BK Bharadvaj, RF Mabon, and DP Giddens. Steady flow in a model of the human carotid bifurcation. Part II–Laser-Doppler anemometer measurements. *Journal of Biomechanics*, 15(5):363–365, 1982.

Diffusers. Nozzles. Jets

Conference on Modelling Fluid Flow (CMFF'12)
The 15th International Conference on Fluid Flow Technologies
Budapest, Hungary, September 4-7, 2012

NUMERICAL INVESTIGATION OF THE STEADY SEPARATION INDUCING MECHANISMS IN A PASSAGE DIFFUSER WITH APPLICATION OF TWO-EQUATION TURBULENCE MODELS

Benjamin WILKOSZ[1], Philipp SCHWARZ[2], Nan CHEN[3], Peter JESCHKE[4]
Caitlin SMYTHE[5]

[1] Corresponding Author. Institute of Jet Propulsion and Turbomachinery, RWTH Aachen University. D-52062 Aachen, Germany. Tel.: +49 (0)241 8095 591, Fax: +49 (0)241 8092 229, E-mail: wilkosz@ist.rwth-aachen.de
[2] Institute of Jet Propulsion and Turbomachinery, RWTH Aachen University. E-mail: schwarz@ist.rwth-aachen.de
[3] Institute of Jet Propulsion and Turbomachinery, RWTH Aachen University. E-mail: nan.chen@rwth-aachen.de
[4] Professor. Institute of Jet Propulsion and Turbomachinery, RWTH Aachen University. E-mail: jeschke@ist.rwth-aachen.de
[5] GE Aviation, Lynn, Massachusetts, 01910, United States of America. E-mail: caitlin.smythe@ge.com

ABSTRACT

Subject of the presented paper is the investigation of steady separation inducing mechanisms in a passage diffuser. This diffuser is used in a centrifugal compressor for small aero engines. Furthermore, the impact of two-equation turbulence models on the passage diffuser's separation prediction is analyzed. Steady stage simulations are conducted from which the major separation-inducing flow mechanisms at the channel inlet are identified. Secondly, stand-alone diffuser simulations with simplified inlet conditions, isolating the individual mechanisms, are conducted with four widely used turbulence models ($k-\epsilon$, $k-\omega$, BSL and SST). The coupling between the separation behaviour, the involved mechanisms and the turbulence models can be established. It is found that the counter-rotating vortices, produced by the leading edges of the diffuser, are the dominating mechanism and mainly responsible for the pressure-side (PS) separation. The results of this paper mediate the flow physics of this type of passage diffuser system and thus are essential for diffuser (re)design as well as appropriately choosing two-equation turbulence models.

Keywords: centrifugal compressor, flow separation, passage diffuser, steady CFD, turbulence model

1. NOMENCLATURE

Latin Symbols

A	$[m^2]$	area
C_p	$[-]$	static pressure recovery
$\dot{m}$	$[kg/s]$	mass flow rate
p	$[Pa]$	pressure
R	$[m]$	radius of the Rankine vortex (V_{max})
r	$[m]$	radius from vortex core
S	$[s^{-1}]$	shear strain rate
V	$[m/s]$	absolute velocity
Y	$[m]$	blade-to-blade coordinate
$y+$	$[m]$	dimensionless wall distance

Greek Symbols

δ	$[m,-]$	boundary layer thickness, Kronecker delta
Γ	$[m^2s^{-1}]$	circulation
κ	$[m^2s^{-2}]$	turbulence kinetic energy
μ	$[kgs^{-1}m^{-1}]$	dynamic viscosity
ρ	$[kgm^{-3}]$	density
τ	$[Nm^{-2}]$	stress term
ω	$[s^{-1}]$	turbulence frequency
ξ	[-]	dimensionless diffuser length

Subscripts and Superscripts

i,j,k	tensor components
max	maximum
norm	normalized
red	reduced
ref	reference
sec	secondary
t	total or turbulent
θ	tangential component

Abbreviations

CFD	computational fluid dynamics
PIV	particle image velocimetry
PS,SS	pressure- or suction-side
RANS	Reynolds-Averaged Navier Stokes
SR	separation ratio

2. INTRODUCTION

Compared to an axial compressor, the centrifugal compressor has a higher total pressure ratio and power density. Due to the larger frontal area and aerodynamic advantages over very small axial compressors these types of compressors often find application at last compressor stages in small aero engines. Within a cooperative research project between the Institute for Jet Propulsion and Turbomachinery (IST) at the RWTH Aachen University and GE Aviation a centrifugal compressor stage (Figure 1) is investigated experimentally and numerically. The stage includes an impeller, a GE-patented passage type diffuser [1] and a deswirler. The impeller has a main and a splitter blade. The passage diffuser contains 30 discrete passage drillings. The deswirler includes a bend and a single row of 90 prismatic blades.

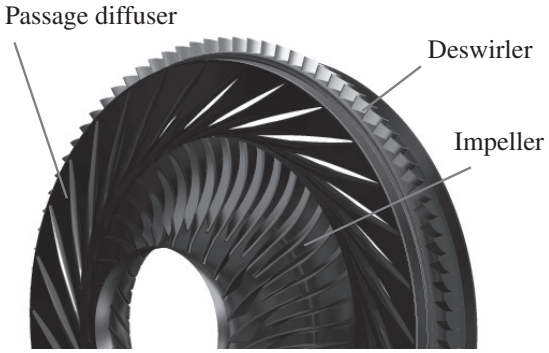

Figure 1: Frontal view of the centrifugal compressor

The aerodynamics of the passage diffuser is the focus of this work. A distinct feature of this diffuser is its inlet region illustrated in Figure 2. It has a vaneless region, a semi-vaneless space and a following passage. Due to the intersection of two neighboring passages elliptical leading edges are formed in the pseudo-vaneless space. These elliptical leading edges or "ridges" work as vortex generators and induce a pair of counter-rotating vortices passing into the throat [2]. These vortices were recorded to reduce the throat blockage and thereby improve the diffusion within the passage [3]. Furthermore, it is shown for the investigated diffusion system that this mechanism plays a major role in the separation behaviour downstream of the throat. The potential of counter-rotating vortices to control flow separation is demonstrated by numerous studies. These vortex generators, either used in a diffuser [4], over a flat-plate [5], or on the suction side of an aircraft wing [6], have been experimentally and numerically proved to be capable of transporting energy-rich fluid from the outer flow into the low-momentum boundary region and thereby providing an impinging impulse to suppress the growth of boundary layer and the associated separation.

Computational Fluid Dynamics (CFD) analyses of highly loaded diffusion systems play a key role in the development of future centrifugal compressors. Due to time-efficiency, steady-state CFD using 3D-RANS techniques is attractive for diffuser design. The correct prediction of the diffuser exit flow is essential for the development of aerodynamically coupled components. Nevertheless, this flow type is still a challenge for modern 3D-RANS simulation methods. In particular the investigated diffusion flow is characterized by a high adverse pressure gradient as a result of the high throat Mach number ($Ma = 0.6$) and a progressive area ratio. Previous experimental investigations showed a PS flow separation over the whole operation range [2], yet steady simulations have generated varying results for the investigated diffuser ([7, 8, 9]). Grates [8] concluded from his numerical investigation, that unsteady effects may be responsible for the found PS separation, but he mentioned that shortcomings of the used mixing plane approach and the coupled incident flow have to be questioned critically. Unsteady PIV investigations [10] as well as internal unsteady CFD investigations [11, 8] showed moderate to small unsteady effects within the channel downstream of the diffusers throat. The presented investigation targets to identify the steady mechanisms responsible for the flow separation and to find out the coupling between the turbulence modeling and these mechanisms.

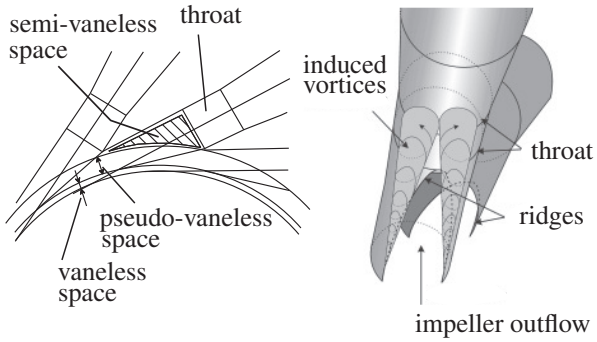

Figure 2: Passage diffuser inlet region

3. METHODS

3.1. Numerical Domain and Grid

The numerical investigation is conducted using the flow solver ANSYS CFX (version 12.1). ANSYS CFX offers the possibility to define complex inlet boundaries as well as a large variety of two-equation turbulence models. Structured meshes created with ANSYS ICEM and TurboGrid are applied.

The stage simulation, shown in Figure 3, contains three domains. It uses a rotor-stator mixing-plane interface to couple the rotating impeller domain and the stationary diffuser domain. At the diffuser inlet, two blocks are incorporated at the front- and backwall to extract the bleed air as described in [9]. The complete stage contains approximately 5.4×10^6 finite elements. The stand-alone diffuser domain, also shown in Figure 3, contains the diffuser domain downstream of the diffusers throat. The throat plane provides a simple

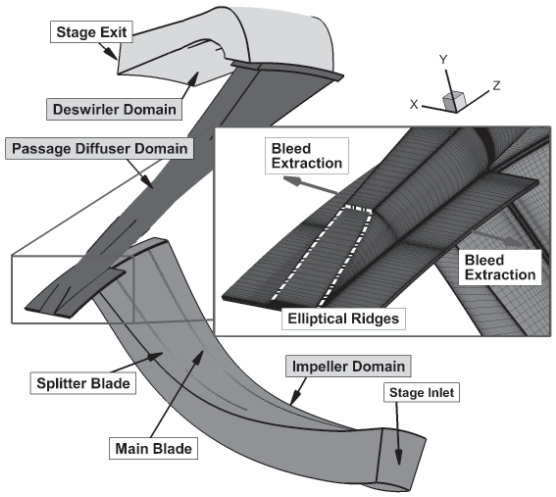

(a) Stage model

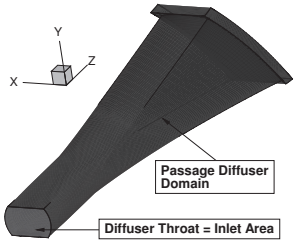

(b) Stand-alone diffuser model

Figure 3: Computational mesh models with detailed views at diffuser inlet regions

inlet plane, on which the single flow mechanisms can be set as boundary conditions. The mesh is refined to obtain y^+ values less than 1.5 to ensure the sufficient resolution of the boundary layer.

3.2. Boundary Conditions

The stage simulation and the stand-alone diffuser simulation are conducted at an operation point slightly towards choke from the stage aerodynamic design point. This operation point is chosen due to the pronounced differences between the simulations with different turbulence models. For the stage simulation the experimentally measured radial total pressure, total temperature and velocity angle profiles are used as inlet conditions. In addition, mass flow rates are set at the stage outlet and bleed extractions. For the stand-alone diffuser simulation, the inlet conditions at the throat are set as an absolute velocity field plus an averaged static pressure and temperature. As outlet condition a static pressure is set. For the extreme cases with the largest boundary layers or vortex strength, these boundary conditions result in an absolute mass flow shift $< 3\%$ and a maximum shift in reduced mass flow $< 1.5\%$. From experimental studies it can be shown that these shifts are within the diffuser operation range as used in the centrifugal stage. Therefor it is considered to be in an acceptable and not responsible for a shift in separation behavior. Figure 4 shows

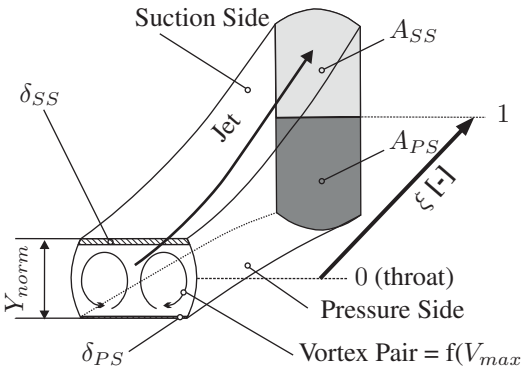

Figure 4: Schematical drawing of the applied inlet conditions and the dimensionless diffuser length ξ

schematically the applied boundary conditions at the throat section for the diffuser stand-alone simulation. To enable the analysis with changing magnitudes of the investigated flow mechanisms (see Section RESULTS) the following inlet conditions are parameterized:

- SS boundary layer modeled as a linear distribution. A boundary layer thickness ($\delta_{SS} = 0.99V_{core}$) is used to set the magnitude of the distortion.
- PS boundary layer modeled as a linear distribution. A boundary layer thickness δ_{PS} is used to set the magnitude of the distortion.
- Counter-rotating vortices modeled as a pair of symmetric Rankine-vortices. To simplify the analysis, the vortices have the same strength. Additionally, the location and the core radius of the vortices are fixed.

The Rankine vortices applied contain a forced vortex component in the central core region ($r \leq R$) and a free vortex component surrounded ($r > R$), which is comparable to the vortices generated by the ridges of the passage diffuser. The equations describing the two counter-rotating Rankine vortices with symmetrical conditions caused by the presence of a pressure-side and suction-side wall are adopted from Pozrikidis [12]. The maximum tangential velocity of the Rankine vortex $V_{\theta,max} = \Gamma/(2\pi R)$ represents the vortex strength and is varied within the investigation.

3.3. Turbulence Models

Four types of widely used two-equation turbulence models ($k-\epsilon$, $k-\omega$, BSL and SST) [13, 14] are applied throughout this work. To close the Reynolds-Averaged-Navier-Stokes equations, the two-equation turbulence models use the Boussinesq approximation to express the Reynolds stress tensor by the gradients of the mean velocity field:

$$\tau_{ij} = \mu_t(S_{ij} - \frac{2}{3}\frac{\partial U_k}{\partial x_k}\delta_{ij}) - \frac{2}{3}\rho k\delta_{ij} \qquad (1)$$

where S_{ij} is the mean strain rate tensor $S_{ij} = \frac{\partial U_i}{\partial x_j} + \frac{\partial U_j}{\partial x_i}$, and k is the turbulent kinetic energy. Yet the problem remains in the prediction of the turbulence eddy viscosity μ_t, which depends on the specific definition of each turbulence model. The $k-\epsilon$ model predicts the eddy viscosity μ_t by connecting the turbulence kinetic energy k with the rate of dissipation ϵ. The $k-\omega$ model introduces a new term, the turbulence frequency ω, to replace the ϵ. Menter [14] proposed two new turbulence models, the BSL model and SST model by combing $k-\epsilon$ and $k-\omega$ together. The two models adopt the formation of $k-\omega$ in the near-wall region and blend into $k-\epsilon$ in the outer boundary layer as well as free shear layer by using a blending function. Menter further pointed out that one important difference between the eddy-viscosity turbulence model and the Reynolds-stress model is that the latter includes the effect of the transport of the principal turbulent shear stress. This deficiency shared by almost all eddy-viscosity turbulence models would result in an over-prediction of eddy viscosity in the boundary layer regions with adverse pressure gradient. Therefore Menter introduced a modification in the definition of eddy viscosity, which results in the new shear-stress transport (SST) turbulence model:

$$\mu_t = \frac{\rho a_1 k}{\max(a_1\omega, SF_2)} \tag{2}$$

where $S = \sqrt{2S_{ij}S_{ij}}$ is the magnitude of strain rate. F_2 is a blending function and is introduced to account for the principal turbulent shear stress. It increases to one at the outer region of the boundary layer and decreases to zero in the free-stream and near wall flow. This modifications reduces μ_t when the ratio of production to dissipation is significantly larger than one, as in case of a boundary layer with adverse pressure gradient and sensitize the boundary layer.

4. RESULTS

4.1. Stage Simulation

Figure 5 shows the normalized reduced 2D-velocity distribution V_{red}/V_{ref} in the midspan-plane of the passage diffuser. The upper figure shows the result from time-averaged PIV measurements taken by Zachau [15]. The lower two figures show the result from the steady stage simulation for the $k-\omega$ and for the SST model. The PIV-measurements show two windows to get optical access to the flow. The first window is positioned between $0.1 < \xi < 0.3$ whereas the second window is positioned between $0.4 < \xi < 1.0$ (Figure 4). The experiment shows a SS orientated area with high momentum fluid ① and a large separation at the pressure side ② . The steady simulation with the $k-\omega$ model agrees with the experimental data, while the flow field with the SST model shows a different separation behaviour. Its high momentum flow is located near the pressure side, rather than near the suction side ③ . A transfer of the high-momentum fluid towards the PS and an early PS weakening ④ can be seen, similar to the $k-\omega$ simulation. However, an abrupt separation at the SS ⑤ dominates the diffusion, resulting in a jet flow near the PS ⑥ .

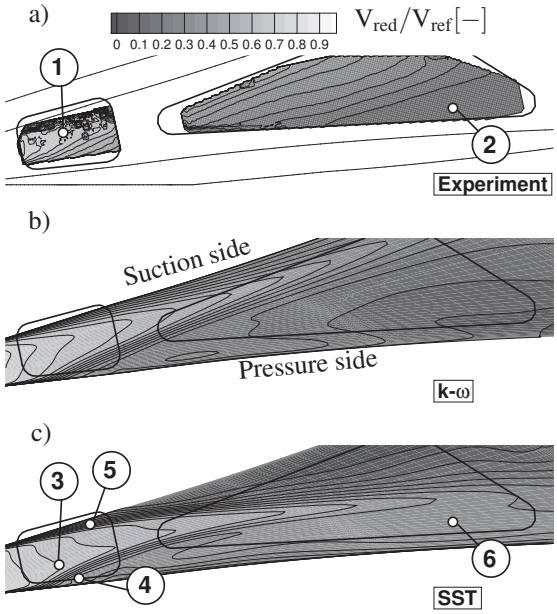

Figure 5: The streamwise velocity contour $V_{red}/V_{ref}[-]$ in the midspan plane of the passage diffuser, a) Experiment; b) $k-\omega$; c) SST

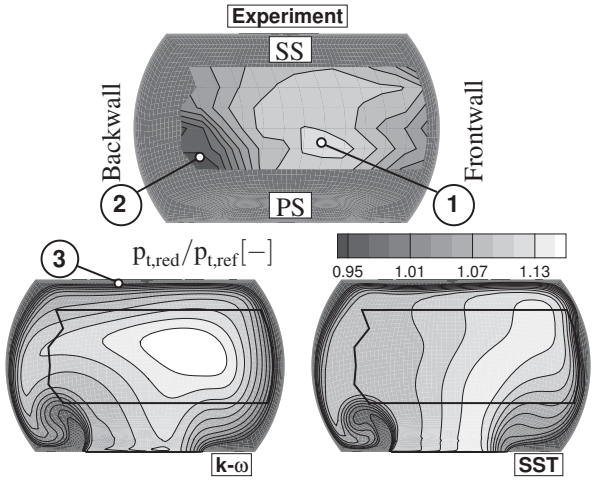

Figure 6: Reduced and normalized total pressure distribution at the diffusers throat

The origin of the secondary flow is found upstream in the diffuser throat. Figure 6 shows the reduced normalized total pressure distributions from CFD together with the related experimental measurements. The total pressure is measured using a pitot probe shortly upstream of the throat at $\xi = -0.057$ due to practical limitations. The total pressure level within

the core region is 5% higher in the CFD simulation. The experiment shows an island type pattern of high momentum fluid slightly orientated towards the front wall in the center region of the passage ① . In the PS back wall corner an area of low momentum fluid can be seen ② , resulting from one of the vortices created by the back wall ridge of the diffuser [9]. From the CFD simulation a thick boundary layer at the SS can be seen ③ . At the PS the boundary layer starts to develop. The $k-\omega$ model captures the structure of the flow field correctly, whereas the SST model shows a weaker pronounced island structure and a less sharply contoured vortex at the back wall.

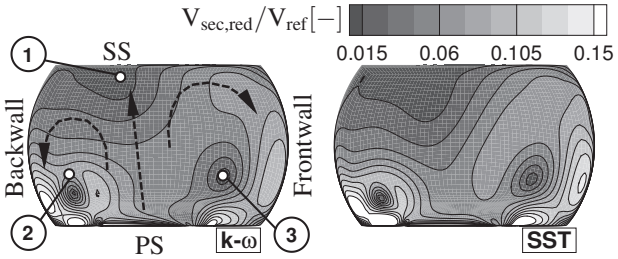

Figure 7: Secondary flow within the diffuser throat

Figure 7 shows the reduced normalized secondary velocity V_{sec} for both turbulence models in the throat. V_{sec} is calculated from the flow vectors projected on the throat surface. For the normalization the core velocity from the primary flow is used. The magnitude of the secondary velocity is about one order less than the core velocity, indicating that it has a significant influence on the flow development downstream. From the V_{sec}-field, a pair of two counter-rotating vortices can be identified. Between the vortices there is a stagnation point ① in V_{sec}. This region is stabilized by the impinging flow towards the SS. At the PS a similar stagnation point develops downstream. However this stagnation point is of destabilizing nature due to the extraction of fluid from the wall and the convection of low-momentum fluid over the front- and back wall toward this region. The character of these vortices reflects the characteristic of the impeller exducer flow. A smaller vortex close to the back wall is evoked by the thin boundary layer from the impeller hub unfurling over the back wall ridge ② . A larger vortex close to the front wall is generated by the thick boundary layer coming from the impeller shroud unfurling over the front wall ridge ③ . The $k-\omega$ and the SST model show a similar build-up for the secondary flow distribution within the throat. From the above results, three steady flow mechanisms influencing the separation behaviour in addition to the conservation of tangential momentum [16] have been identified:

1. SS boundary layer. This boundary layer is relative thick (magnitude: $0.1\ Y_{norm}$) due to the long running length over the suction side before it reaches the throat section. This mechanism stimulates a SS separation (Figure 4: Jet close to pressure side).

2. PS layer. This boundary layer is thin (Magnitude: $0.02\ Y_{norm}$) due to the short running length. Secondly, caused by a negative flow incidence the fluid is accelerated over the front end of the pressure side. The fluid acceleration results in a stable and thin boundary layer. This mechanism stimulates a PS separation (Figure 4: Jet close to suction side).

3. Two counter rotating vortices, evoked by the diffuser's ridges in combination with the curling of the tip-clearance and hub boundary layer. This mechanism is proved to stimulate a PS separation based on the evaluation later by the diffuser simulation (Figure 4: Jet close to suction side).

4.2. Stand-alone Diffuser Simulation

Stand-alone diffuser simulations with either a SS boundary layer, PS boundary layer or counter-rotating vortices are performed to validate the above found mechanisms concerning their impact on the separation. In order to investigate the hierarchy of the mechanisms simulations with combined flow mechanisms are conducted. The starting point is the uniform inlet condition to verify the dominance of the conservation of tangential momentum for all turbulence models. Under these conditions, the fluid in the passage diffuser tends to travel along a logarithmic spiral towards the PS wall, and thus is more prone to evoke a SS separation. For the numerical investigation the thickness of the boundary layer (δ_{PS} or δ_{SS}) is varying from 0 to $0.005\ Y_{norm}$. These values are smaller than the boundary layers from in the stage simulation, however impose a significant impact on the diffuser flow's separation behaviour due to the large momentum thickness and lower wall velocity gradient. For the counter-rotating vortices, the vortex strength V_{core}/V_{ref} is varying from 0 to 0.1. This range covers the maximum V_{sec} found within the stage simulation. As the combined flow mechanisms, the SS and PS boundary layer thicknesses are set as $0.005\ Y_{norm}$ and $0.001\ Y_{norm}$, respectively, so that the ratio of the two magnitudes is comparable to the stage simulation. In addition, the vortex strength V_{core} is increased from 0.075 to 0.15. Since the equivalence of rotational momentum between the real and the simplified vortices is difficult to obtain, a range is used to show the qualitative influence. The separation ratio SR is introduced by the authors to quantify the type and magnitude of separation. The SR, calculated by Eq. 3, reflects the distribution of effective mass flow rate between the PS and SS area of the diffuser channel's outlet and accounts for recirculation. Figure 4 shows schematically a flow field with $SR < 1$, indicating a PS separation.

$$SR = \frac{V_{\text{PS}}}{V_{\text{SS}}} \quad V_{PS/SS} = \frac{\int |\dot{m}| V_\xi \mathrm{d}A_{PS/SS}}{\int |\dot{m}| \mathrm{d}A_{PS/SS}} \quad (3)$$

Figure 8 shows the SR for the diffuser simulation with the PS disturbances (a), counter rotating vortices (b) and the combined conditions (c). Note that without disturbance all the simulations show a $SR > 1$ ① indicating the conservation of tangential momentum is dominant for all cases. With increasing δ_{SS} the SR increases continuously and is not examined here in detail. Both the PS-distortion and the counter-rotating vortices counteract the conservation of tangential momentum. Generally, with increasing PS-distortion and vortex strength (Figure 8(a) - (b)) these mechanisms gradually become dominant and the SR decreases below unity. The SST model reacts more sensitively than the other turbulence models to the changes in inlet conditions. It can be seen that for the SST model with counter-rotating vortices, the SR firstly increases rather than decreases as the other turbulence models do ② . This indicates that the small vortices rather increase the disturbance of the already highly loaded SS boundary layer, possibly caused by the impinging between the vortices and the SS boundary layer. The PS boundary layer is stabilized by the conservation of tangential momentum and is not significantly influenced by the vortices. Only with very high vortex strength the separation switches to the PS. The combined inlet conditions (Figure 8(c)) gives a good indication of the difference in hierarchy of the investigated mechanisms and explains for the behavior earlier seen in Figure 5. Although the boundary layer thickness at the SS is the multiple of the thickness at the PS and together with the conservation of momentum evokes a SS separation, the counter-rotating vortices gradually dominates the separation behaviour ③ . For the SST model, the distortion of the highly loaded SS is more dominant at lower levels of counter-rotating vortices. High levels of vortex strength are necessary to eventually cause a change in the flow separation ④ . The above results show that the correct separation prediction is determined by the balance between the found mechanisms. The dominant factor, the counter-rotating vortices, is the reason for the pressure-side separation found in experimental studies, shown in Figure 5.

As mentioned in the introduction, the correct performance prediction depends on the separation behavior. To illustrate the effect on the performance Figure 9 shows the normalized pressure recovery $C_{p,norm}$ for the channel, calculated as:

$$C_{\text{p,norm}} = \frac{1}{C_{\text{p,ref}}} \frac{p_{\text{s},\xi=1} - p_{\text{s},\xi=0}}{p_{\text{t},\xi=0} - p_{\text{s},\xi=0}} \quad (4)$$

p_t is the mass flow averaged total pressure and p_s is the area averages static pressure. Form Figure 9 it can be concluded, that the pressure recovery varies up to 15% depending on the turbulence model and side as well as degree of the separation. Generally, it can be seen that C_p reaches a maximum close before the SR approaches unity ① . Although the induced boundary layer generates additional losses, the reduction of the SS separation for small values of $\delta_{\text{PS}}/Y_{\text{norm}}$ improves the diffusion and redirection of the flow within the channel ② . Once the separation switches to the PS the pressure recovery decreases rapidly. The counter-rotating vortices lead to higher values of pressure recovery than the PS distortion with equivalent SR. This demonstrates the positive effect of mixing on the diffusion of the flow.

5. ANALYSIS

From the above results it becomes clear, that the identified mechanisms determine the side and magnitude of the separation. However, with the same magnitude of boundary layer distortion and vortex strength, the balance between the mechanisms is different for the SST turbulence model. These differences are very pronounced for the following cases, shown in Figure 8:

- Case I: the pressure-side boundary layer disturbance with $\delta_{PS} = 0.002 Y_{norm}$.
- Case II: the counter-rotating vortices with $\text{V}_{\text{core}}/\text{V}_{\text{ref}} = 0.05[-]$
- Case III: the combined mechanisms with $\text{V}_{\text{core}}/\text{V}_{\text{ref}} = 0.123[-]$

The associated flow field of case III is exemplary shown in Figure 10.

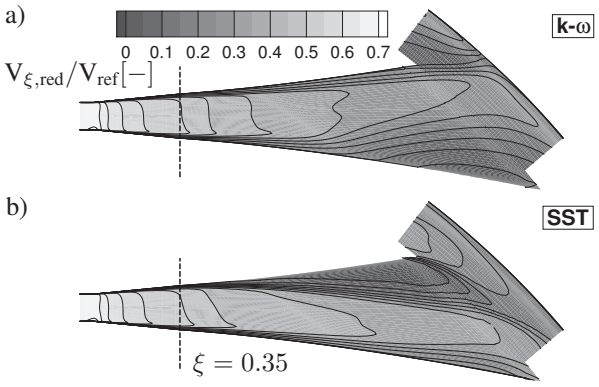

Figure 10: Normalized 2D-velocity in the midspan plane: Case III. a) $k-\omega$**; b) SST**

From the pressure build-up along the diffuser passage, $\xi = 0.4$ can be considered as the location where the discrepancies between the turbulence models become apparent. Upstream of this location, at ξ =0.35, attention is paid to the details of the boundary layer. The turbulence eddy viscosity μ_t plays an important role, because the major difference

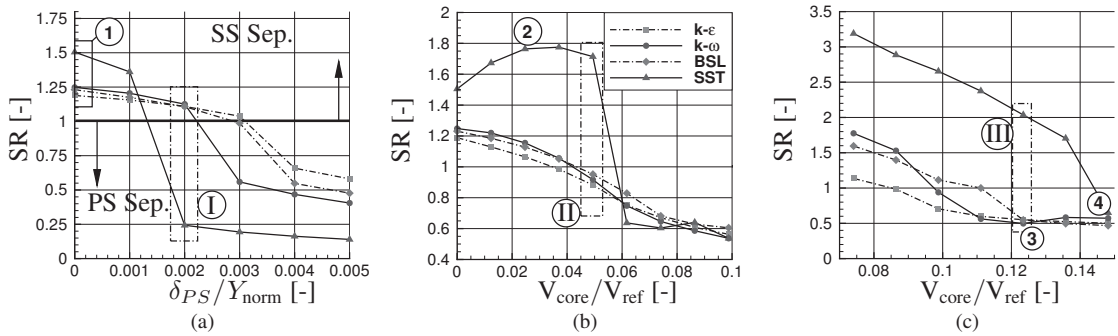

Figure 8: SR **for the diffuser simulation. a) PS boundary layer; b) vortices; c) combined mechanisms.**

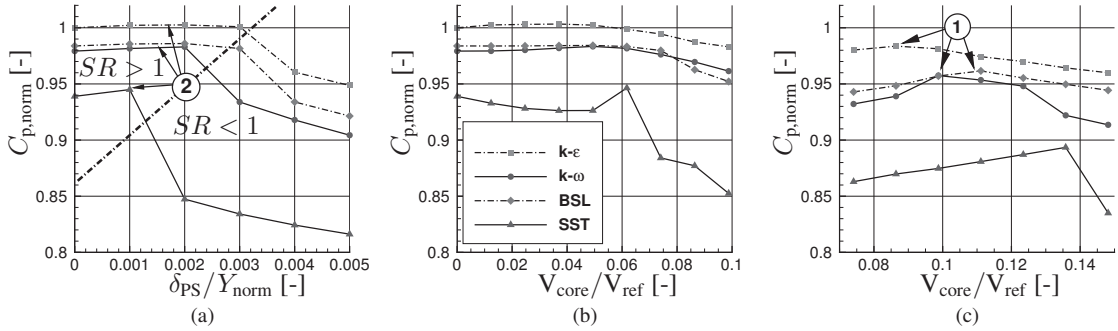

Figure 9: $C_{\mathbf{p,norm}}$ **for the diffuser simulation, a) PS boundary layer; b) vortices; c) combined mechanisms.**

between SST and other used turbulence models is the modification of eddy viscosity realized by a limiter function, as explained in the introduction. To illustrate the effect of the limiter and link the impact with the separation behaviour the relative turbulence eddy viscosity variance $\Delta\mu_t$ is introduced. μ_t is the turbulence eddy viscosity calculated by the turbulence model, and μ_t^* is derived from the original unchanged eddy viscosity definition.

$$\Delta\mu_t = \frac{\mu_t - \mu_t^*}{\mu_t^*} \qquad \mu_t^* = \rho\frac{k}{\omega} \tag{5}$$

Figure 11 shows the relative turbulence eddy viscosity variance $\Delta\mu_t$, the streamwise pressure gradients $\partial p/\partial z$ (normalized), and the boundary layer velocity profiles (normalized) from the PS to the SS in the centerline of the section $\xi = 0.35$ for the flow cases I, II and III (Figure 8). To the right a simplified sketch to illustrate the separation behavior can be seen.

for Case I the influence of the PS boundary layer on $\Delta\mu_t$ can be seen in Figure 11 - ①. Without PS distortion the highly loaded SS shows a stronger decrease in $\Delta\mu_t$. The decrease of the effective viscosity thickens the boundary layer at the PS for the SST model ②, making the boundary layer favourable for separation. Consequently, a stronger adverse pressure gradient is observed at the PS boundary ③, which overrules the mechanism of conservation of tangential momentum and causes a SS separation for the SST model. For the other turbulence models a slightly higher pressure rise at the PS can be seen ④, similar to the SST Model. Nevertheless, the mechanism of conservation of tangential momentum is dominant and evokes a SS separation.

Case II shows the opposite separation behaviour from Case I. A strong decrease of eddy viscosity can be seen at the SS ⑤. This leads to a small increase in boundary layer growth for the SST model ⑦. When comparing the pressure gradients the differences between the different turbulence models become more clearly. Whereas the SST simulation shows the highest pressure gradient towards the SS, the other turbulence models show the highest pressure gradient at the PS ⑥. For the SST simulation the highly loaded SS shows a higher distortion evoked by the interference with the vortices.

Case III looks similar to case II. However the large distortion at the channel's SS causes a strong weakening effect for this boundary layer. The thick SS boundary layer combined with a high pressure gradient at the SS evokes a SS separation for the SST simulation, whereas the other turbulence models show a maximum pressure gradient near the PS of the channel. As in Case II the vortex mechanism dominates the separation behaviour for the $k-\omega$, the $k-\epsilon$ and the BSL model. Again, the SST model is dominated by the weakening of the highly loaded SS boundary layer, rather than the vortex mechanism.

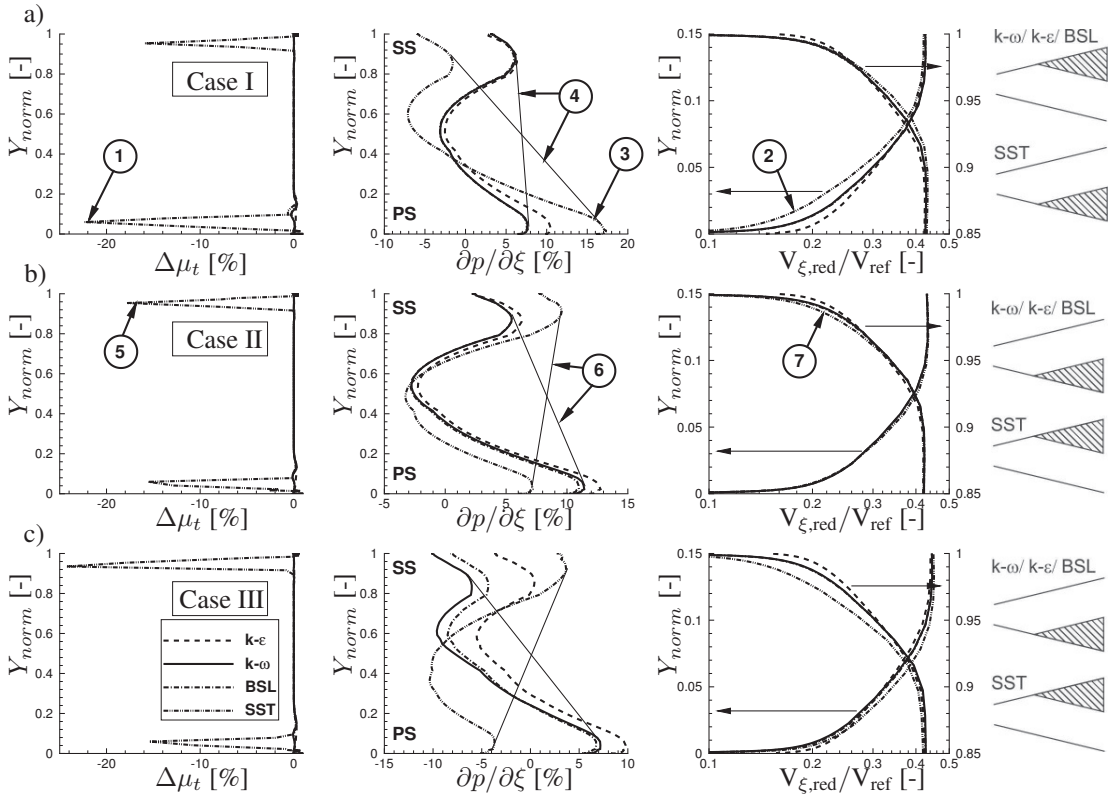

Figure 11: Blade to Blade profiles in the section $\xi = 0.35$, a) PS boundary layer with $\delta_{p.s} = 0.002Y_{\mathbf{norm}}$; b) counter-rotating vortices with $\mathbf{V_{core}/V_{ref}} = 0.05[-]$; c) combined flow mechanisms with $\mathbf{V_{core}/V_{ref}} = 0.123[-]$

6. CONCLUSION

Subject of this paper is the separation behaviour of a highly loaded passage diffuser used in a centrifugal compressor for aero engines. The correct prediction with steady CFD methods has a significant impact on the performance prediction as well as correct redesign procedure for aerodynamically coupled components. However, state of the art 3D-RANS methods with 2-equation turbulence closure models reach their limitations when predicting a flow field with high adverse pressure gradients and separation. Four separation-inducing mechanisms for the investigated diffuser system are identified based on a full steady stage simulation:

1. Conservation of the tangential momentum: This weak mechanism evokes a SS separation.

2. The SS distortion caused by the boundary layer: This mechanism is strong due to the long running length of this boundary layer up to the throat and evokes a SS separation.

3. The PS distortion caused by the boundary layer: This mechanism evokes a PS separation. Although the mechanism is strong, it plays a subordinate role in the investigated case since the running length of the SS boundary layer is short.

4. The counter-rotating vortices transporting the high-momentum core flow toward the SS: This mechanism is determining for the investigated diffuser flow and evokes a PS separation.

Stand-alone diffuser simulations are used to isolate and investigate the single mechanisms. From this the following conclusion can be drawn: *The balance between the mechanisms determines the side and amount of separation for the investigated passage diffuser. Since the SS boundary layer and the counter rotating vortices are dominant for the investigated flow field, the dominance of the counter rotating vortices gives the experimentally confirmed PS separation.* The correct balance between these mechanisms is evident for the $k-\omega$, the $k-\epsilon$ and the BSL models. The mechanisms are differently balanced for the SST model, in which case an over-sensitivity caused by the introduced shear stress term in combination with the presence of an extreme adverse pressure gradient is identified as the root cause for the dominance of the SS boundary layer distortion.

ACKNOWLEDGEMENTS

General Electric Aviation (GEA) funds the Centrifugal Compressor Technology Project at the Institute of Jet Propulsion and Turbomachinery. This is gratefully acknowledged. Further the GEA Compressor and Fan Aero group extensively supports this research. Special thanks go to Zaher Moussa.

References

[1] A.C. Bryans. Diffuser for a centrifugal compressor. *US Patent Number 4,576,550*, page 8, 1986.

[2] U. Zachau, C. Buescher, R. Niehuis, H. Hoenen, D.C. Wisler, and Z. M. Moussa. Experimental investigation of a centrifugal compressor stage with focus on the flow in the pipe diffuser supported by particle image velocimetry (piv) measurements. *GT2008-51538*, 2008.

[3] Ian Bennett. *The Design and Analysis of Pipe Diffusers for Centrifugal Compressors*. PhD thesis, Cranfield Universaty, 1997.

[4] O. Toernblom and A. Johansson. A reynolds stress closure description of separation control with vortex generators in a plane asymmetric diffuser. PHYSICS OF FLUIDS, Mar. 2007.

[5] E. Canepa, D. Lengani, S. Satta, E. Spano, M. Ubaldi, and P. Zunino. Boundary layer separation control on a flat plate with adverse pressure gradients using vortex generators. ASME, May 2006.

[6] G. V. Selby, J. C. Lin, and F. G. Howard. Control of low-speed turbulent separated flow using jet vortex generators. Springer, 1992.

[7] C.V. Wallis, Z.M. Moussa, and B.N. Srivastava. A stage calculation in a centrifugal compressor. In *ICAS2002 CONGRESS*, 2002.

[8] D. R. Grates. *Numerische Simulation der instationaeren Stroemung in einem Radialverdichter mit Pipe-Diffusor*. PhD thesis, RWTH Aachen, 2009.

[9] R. Kunte, P. Schwarz, B. Wilkosz, P. Jeschke, and C. Smythe. Experimental and numerical investigation of tip clearance and bleed effects in a centrifugal compressor stage with pipe diffuser. ASME, Jun. 2011.

[10] R. Kunte. *Experimentelle und numerische Untersuchung eines Radialverdichters mit Pipe Diffusor und Umlenkbeschaufelung f?r eine Triebwerksanwendung*. PhD thesis, RWTH Aachen Institut fuer Strahlantriebe und Turboarbeitsmaschinen, 2011.

[11] E. Findeisen. Numerische pumpgrenzuntersuchung eines radialverdichters mittels stationaerer und instationaerer 3d-rans-simulation. Master's thesis, IST, Fakultaet fuer Maschinenwesen Rheinisch-Westfaelische Technische Hochschule Aachen, Sep. 2011.

[12] C. Pozrikidis. *Fluid Dynamics Theory, Computation and Numerical Simulation*. 2001.

[13] David C. Wilcox. *Turbulence Modeling for CFD*. DCW Industries Inc.; La Canada, California, Nov 1994.

[14] F. R. Menter. Two-equation eddy-viscosity turbulence models for engineering applications. *AIAA Journal*, 32(8):1598–1605, 1994.

[15] U. Zachau. *Experimental Investigation on the Diffuser Flow of a Centrifugal Compressor Stage with Pipe Diffuser*. PhD thesis, RWTH Aachen, 2007.

[16] Bruno Eckert and Erwin Schnell. *Axial- und Radialkompressoren. Anwendung, Theorie, Berechnung*. Springer, Berlin [u.a.], 1961.

Conference on Modelling Fluid Flow (CMFF'12)
The 15th International Conference on Fluid Flow Technologies
Budapest, Hungary, September 4-7, 2012

NUMERICAL ANALYSIS OF HIGH-SPEED LIQUID LITHIUM FREE-SURFACE FLOW

Sergej Gordeev[1], Volker Heinzel[2], Robert Stieglitz[3]

[1] Corresponding Author. Institute for Neutron Physics and Reactor Technology, Karlsruhe Institute for Technology, Hermann v. Helmholtz Platz 1, D76344 Eggenstein, Germany, Phone: +49 721 608 2 3464, Fax: +49 721 608 2 4837, E-mail: sergej.gordeev@kit.edu
[2]Institute for Neutron Physics and Reactor Technology, Karlsruhe Institute for Technology, Germany, volker.heinzel@kit.edu
[3]Institute for Neutron Physics and Reactor Technology, Karlsruhe Institute for Technology, Germany, robert.stieglitz@kit.edu

ABSTRACT

The liquid lithium film thickness facing the Deuterium beam of the International Fusion Material Irradiation Facility (IFMIF) determines the neutron flux to be generated. Hence, apart from its thickness also its spatio-temporal behaviour plays a decisive role in the performance of the target. One aspect contributing to the free surface shape is the evolution of the viscous wall boundary layer at the concave shaped back-wall, which is analysed in this context by means of a CFD LES analysis. In order to validate the model experiments conducted at the Osaka University have been compared with respect to mean and turbulent flow quantities in a broad spectrum of mean flow velocities. Thereby a good qualitative and quantitative agreement has been attained identifying different flow regimes and, moreover, allowing for a more refined, realistic IFMIF target prediction performance.

Keywords: CFD, free surface, LES, liquid metal flow, turbulence.

1. INTRODUCTION

The International Fusion Materials Irradiation Facility (IFMIF) [1] is an accelerator based deuteron-lithium (D - Li) neutron source to simulate the neutron irradiation field in a fusion reactor. The target facing two 5 *MW* rectangular shaped deuteron beams is formed by a high-speed liquid lithium (Li) free-surface film bounded by a concave shaped back-wall. Aside from the neutron production the liquid lithium has the function to remove the deposited beam energy and to cool the back wall structure. Therefore, the Lithium is accelerated in a two step nozzle by a factor 10. Downstream the nozzle exit it flows in a tailrace along the concave target back wall before entering a collector. At the free liquid target surface the pressure is at vacuum similar to that of the beam guide tube. An optimal neutron production requires a target design consisting of nozzle and back-wall that shows a constant film thickness over a large operational range at a simultaneously low fluctuation level of the surface shape caused by the turbulent lithium flow.

1.1. Mechanisms of instabilities on the free surface liquid flow downstream the nozzle exit

Two mechanisms can potentially affect the free surface shape downstream the nozzle exit:

- a boundary layer relaxation at the nozzle exit associated with the evolution of vortex structures close to the free surface;
- an interaction of turbulent vortices generated in the channel core flow with the free surface.

Various visual observations of free surface flows both in water and lithium [2, 3, 4] exhibit a similar and typical behavior. At low nozzle exit velocities with a low turbulence, which is caused by a boundary layer acceleration within the nozzle, a smooth free surface shape is observed. At large mean nozzle exit velocities three different surface shape regimes can be identified in downstream direction. In the immediate vicinity of the nozzle exit the liquid surface remains still smooth. Further downstream surface waves form. Their crests are perpendicular to the mean flow velocity and the crests are arranged almost parallel to each other. The formation of the waves originate from a reorganization of the bulk flow caused by the boundary layer relaxation at the nozzle exit. The amplitude of the wave height continuously growns downstream in a distinct domain, depending on the mean flow velocity. Further downstream this structured wave pattern deteriorates due to dissipative effects caused by viscosity and surface tension As a consequence an irregular shaped wave pattern is observed. If the turbulence intensity of the

bulk flow is moderate, the wave amplitudes are damped downstream by surface tension and gravitation. For increasing velocities both domains the smooth one and the one with a regular formed wave pattern regions shrink and then disappear. Additionally an increasing turbulence intensity causes a rising production of large scale vortex structures in the bulk flow. These in turn interact with the free surface and lead there to a significant deformation. As result, the observable free surface is composed of large cell-like irregular structures super-imposed by small scale patterns.

The onset of the surface waves caused by boundary layer relaxation and by interaction of the bulk turbulence with the free surface can by estimated by means of analytical methods [4, 5, 6]. Although the analytical estimations allow for a qualitative and quantitative description of the free surface behavior, they are not capable to account for all physical phenomena affecting its shape and stability. Here, only CFD measures can provide an insight by a quantification of the different interacting and competing phenomena. Since turbulence models based on Reynolds averaged closure approach can not depict any coherent structures, only large eddy simulations (LES) seem to be a suitable tool to investigate coherent turbulence structures close to the free surface at engineering relevant Reynolds numbers.

This paper focuses on two aspects. At first a validation of the LES technique is conducted by a comparison of simulation results with experimental data. Secondly we analyzing the influence of the initial flow conditions in the bounded nozzle flow on the free surface shape evolution and its stability as a function of the mean jet flow velocity.

1.2. Test section

For the validation experiments in a horizontal lithium free surface flow conducted at the Osaka University [2] are taken, which set-up is depicted in Figure 1. It consists of a two-stage contraction nozzle (70x10 mm^2) and an open horizontal duct. Two view ports located at x=15 *mm* and 175 *mm* downstream the nozzle exit allow an optical access. The free surface shape is either observed by a high speed video camera and height and shape of the surface waves parameters are recorded pointwise using an electro-contact probe. The experiments are conducted for mean nozzle exit velocities up to 15 *m/s* in an argon atmosphere of 0.15 *MPa*. To investigate the impact of the turbulence intensity four different jet mean velocities are analysed, U_0=4, 9, 13 und 15 *m/s*. The dimensionless parameters set relevant for the problem considered are the Reynolds number $Re=U_0 d/\nu$, the Weber number $We=U_0^2 d\ \rho/\sigma$ and Froude number $Fr=U_0/(gd)^{1/2}$ (See tab.1). Here, d is the jet thickness; ρ, σ, and g are the fluid density, surface tension and gravity constant.

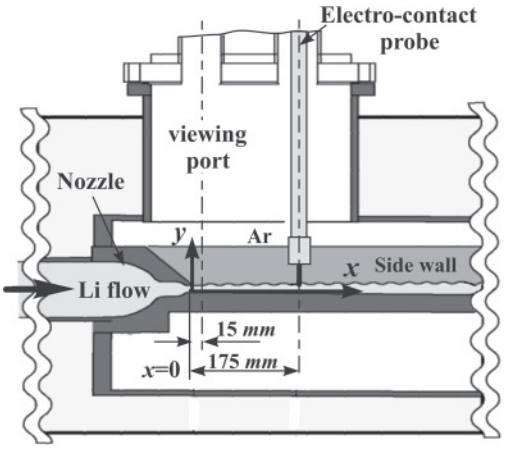

Figure 1. Test section of the lithium loop facility at Osaka University [2]

The analysis of the turbulent boundary layer at the nozzle exit for similar flow conditions has been performed by Itoh et al. [2] based on water experiments with the same nozzle geometry. For U_0=4 *m/s* the acceleration of in the nozzle causes a re-transition from a turbulent into a laminar boundary layer (re-laminarization), while at larger U_0 the laminarization of the boundary layer is still incomplete. In case of U_0=15 *m/s* the turbulent conditions are fully recovered in the short parallel section (5 *mm*) near the nozzle exit.

Table 1. Test conditions

U_0 (*m/s*)	Re	We	Fr
4	0.44 x 10^5	362	9.47
9	1.00 x 10^5	1830	21.3
13	1.44 x 10^5	3820	30.8
15	1.67 x 10^5	5090	35.5

1.3. Numerical method and computational domain

The LES simulations performed use a wall-adapting local eddy-viscosity (WALE) model [7] offered by the CFD code Star-CCM+ [8], which profits from the absence of wall functions or global damping procedures. The model produces an efficient and fast scheme by its algebraic character and offers the capability to predict laminar to turbulent transitions. A Volume of Fluid method (VOF) [9] is used for computing the argon-lithium two-phase flow. To maintain at a sharp liquid gas interface representation of the VOF transport equation solution a High-Resolution Interface Capturing (HRIC) scheme [10] is employed.

The computational domain used is illustrated in Figure 2; it is split into two parts, a wall bounded nozzle flow and the free surface flow domain. Due to computational reasons the free surface flow channel downstream the nozzle exit is limited to

180 *mm*. By employing periodic boundary conditions the spanwise generated grid can be confined to 10 mm in width. The wall bounded nozzle flow is simulated separately using a V2F turbulence model. The results of this simulation in terms of velocity and turbulence distribution at the end of the first contraction part of the nozzle has been used as inlet conditions of the model presented here. Additionally, a synthetic-eddy method to represent the time dependent turbulent inflow boundary conditions is applied. The time step corresponds to a Courant number Co < 0.5 and in all cases approx. $5 \cdot 10^4$ time steps are computed to attain a reasonable statistics. The simulation assumes a constant liquid Lithium temperature of 250 *°C* and an argon atmosphere of 0.15 *MPa*. The thermo-physical data have been taken from [11].

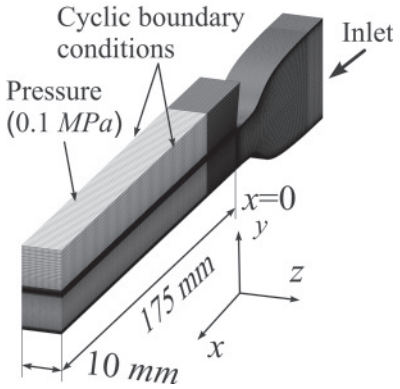

Figure 2. Computational domain used (Grid 3)

1.4. Grid sensitivity study

The mesh used is structured and non-uniform. Three grid topologies, a coarse mesh (grid1), a medium mesh (grid2) and a fine mesh (grid3) are adopted in study the grid sensitivity. The computational mesh of grid1 consists of $3.6 \cdot 10^5$ cells with a cell size close to the free surface is 0.5 *mm* x 0.02 *mm* x 0.4 *mm* in streamwise (x), wall-normal (y) and spanwise (z) direction. Grid2 consists of $2.4 \cdot 10^6$ cells and is generated by a refinement of the channel area of grid1 in all three directions. Finally, in grid3 the cell size in x- and z-direction is further refined so that the cell dimensions correspond to 0.125 *mm* x 0.01 *mm* x 0.1 *mm*. The cells are clustered near the wall, so that the first cell layer is located within the viscous sublayer. For all grid topologies the larger scales ($L=k^{3/2}/\varepsilon$), Taylor length scales ($\lambda=(10\nu k/\varepsilon)^{1/2}$) and Kolmogorov ($\eta=(\nu^3/\varepsilon)^{1/4}$) scales are computed using the V2F model. Here k is the turbulent kinetic energy, ε the dissipation rate of the turbulent kinetic energy and ν the kinematic viscosity.

Figure 3 shows the computed wall-normal distribution of the length scales in the cross section near the nozzle exit for U_0=15 *m/s* and compares it with the grid filter ($\Delta=V^{1/3}$), in which V denotes the cell volume. The data for grid1 are between the larger and Taylor length scales, but closer to the Taylor scale except for the immediate near wall region. Therefore, grid1 seems to be reasonable to simulate the free surface flow as long as wall near effects can be neglected.

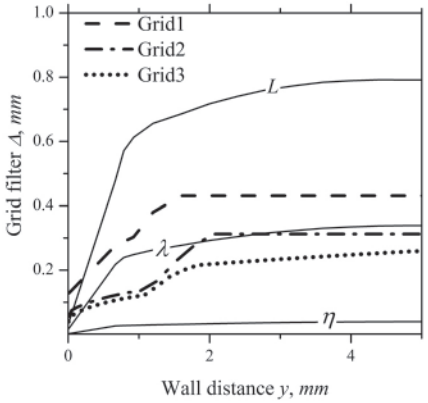

Figure 3. Calculated wall-normal distribution (y) of the length scales in a cross section near the nozzle exit (x=5 *mm*) for U_0=15 *m/s* and compared with the grid filter ($\Delta=V^{1/3}$)

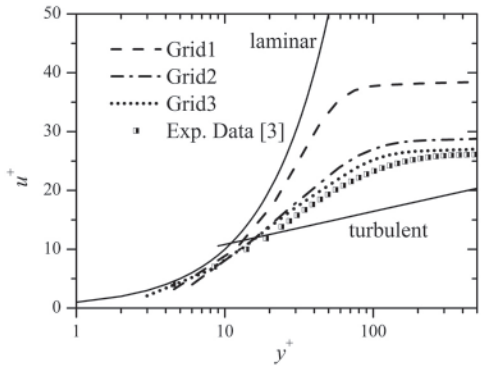

Figure 4. Dimensionless mean velocity near the nozzle exit $u^+(=U/u_\tau)$ as a function of $y^+(=yu_\tau/\nu)$ for U_0=15 *m/s*

In order to study the influence of the grid resolution on the boundary layer behavior the dimensionless mean velocity near the nozzle exit $u^+(=U/u_\tau)$ is calculated as a function of the wall normal dimensionless distance $y^+(=yu_\tau/\nu)$. Here, the friction velocity is defined by $u_\tau=(\tau_w/\rho)^{0.5}$, in which τ_w is the wall shear stress. For U_0=15 *m/s* measured velocity profiles of water experiments [3] are compared with simulation data, which seems to be tolerable since the kinematic viscosity ν of Lithium at 250 *°C* is similar to that of water. Figure 4 shows u^+ as a function of y^+ for all grids. The experimental data exhibit a transitional character of the boundary layer caused by a boundary layer laminarization, which can be well identified by the deviation of the data from the turbulent logarithmic wall law. Figure 4 also illustrates that grid1 is not capable to depict

the transitional character and only fully laminar boundary layer profile are computed. The velocity profiles predicted by grid2 and grid3 reasonably coincide with the experimental data. Thus, for $U_0 \leq 9$ *m/s* reasonable simulations can be conducted using grid2, while larger values of U_0 demand a resolution of grid3.

1.5. Results

The simulation is parallelized using domain decomposition and MPI. The maximal computing time on 8 processors (12 *GB* RAM, 3.2 *GHz* Intel-Core) in case U_0=15 *m/s* for a physical time of 0.15 *s* (ten flow-through times) is approximately 2400 *h* using a time step size of 10^{-6} *s*.

1.5.1. Free surface flow near the nozzle exit

Figure 5 compares visually observed and numerically simulated free surface shapes for different mean nozzle exit velocities in the domain $0<x<120$ *mm* and $0<z<10$ *mm*, where z=0 is the symmetry line in z-direction. Here, regarding the LES the fluid/gas interface is assumed to occur at VOF=0.5. Similar like the experiment the simulation exhibits for U_0=4 *m/s* a smooth free surface shape. For $U_0 \geq 9$ *m/s* a quasi-regular wave pattern is observed both in experiment and simulation. In both the crest lines appearing in the immediate vicinity of the nozzle exist are oriented perpendicular to the mean flow velocity. The structure of the intermittently generated two-dimensional waves is affected by small Λ-shaped waves propagated pointwise along the nozzle edge in streamwise direction. This effect is more pronounced in the experiment, which could be caused by a nozzle edge roughness, which increases the instability close to the nozzle outlet and which is not taken into account in the simulations. Further downstream the nozzle exit not only the the crest height increases but also its structure deteriorates. The surface exhibits an irregular shape. For U_0=15 *m/s* the LES also shows a regular wave pattern of almost parallel aligned crests and valleys near the nozzle exit which can be hardly visually observed in the experiments. This may be also be devoted the surface roughness of the nozzle edge, but also the insufficient resolution of the picture does not allow an exact detection of small scaled structured wave patterns.

Figure 6 shows a comparison of measured [12] and computed wave length near the nozzle exit for mean jet velocities from 5 to 8 *m/s*. The wave lengths detected in the experiment vary between 1.5 and 1 *mm*, and decrease with increasing velocity. Additional experimental data are available from lithium flow measurements conducted by Hassberger [4]. Here, a good agreement between measurements and predictions are obtained.

Figure 7 shows non-dimensional wave number of the experimental results as a function of Weber number based on momentum thickness of boundary layer at the nozzle exit. The non-dimensional wavenumber is defined by $\alpha\delta_2 = 2\pi\delta_2/\lambda$, in which α, δ_2 and λ denote the dimensional wavenumber, the

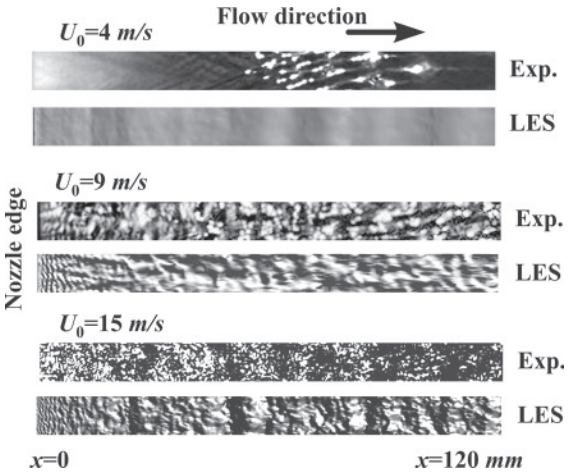

Figure 5. Visualization of Lithium free-surface shape by HSV camera compared to computed instantaneous free surface contour (VOF =0.5)

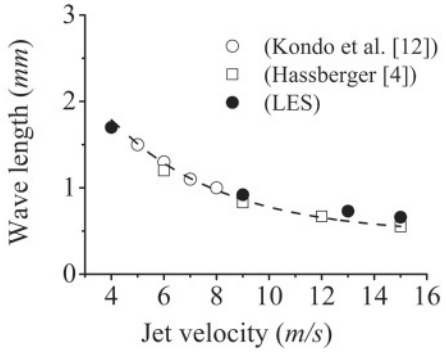

Figure 6. Comparison of the calculated wave length in the outlet area with measurements [4, 10] for jet velocities from 4 to 15 *m/s*

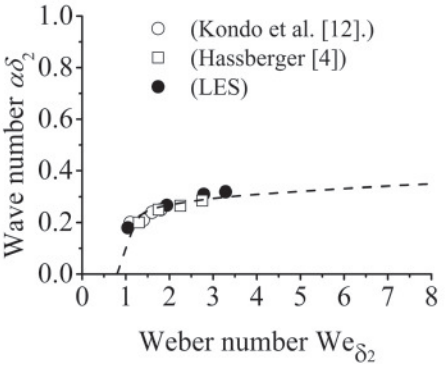

Figure 7. Comparison of measured [4, 10] and simulated dim.-less wave number as a function of $We_{\delta 2}$. Dashed line prediction by linear stability theory

momentum thickness at the nozzle exit and the measured wavelength. The dashed line shows the most unstable wave number predicted by a linear stability theory of the shear layer employing the momentum thickness as a characteristic length scale. Also here the simulations exhibits a good agreement with the measurements both in the absolute value and with respect to a slight increase with $We_{\delta 2}$.

In order to provide a deeper insight of the mechanism for the generation of structured and unstructured surface patterns close to the free surface the Figure 8 visualizes the vortex structures in that domain for two velocities; U_0=4 *m/s* (Fig. 8a) and U_0=15 *m/s* (Fig. 8b). For the visualization of the vortex structure shape the method based on the second invariant of the velocity-gradient tensor Q is used, which is proposed in [13]. This method is capable of extracting low pressure swirl flow associated with a vortex motion. For an incompressible liquid this detection criterion can be written as:

$$Q = \frac{1}{2}\left(|\Omega|^2 - |S|^2\right) > 0 \qquad (1)$$

where S and Ω are the symmetric and anti-symmetric parts of the velocity gradient tensor. A coherent vortex is defined as a region where Q>0.

In both cases two types of vortical structures evolve as Fig. 8 depicts. The first are streamwise aligned Goertler vortices developing on the concave shaped nozzle walls and persisting downstream far beyond the nozzle exit. The second type of emerging surface structures are wavelike spanwise oriented roll cells, which are generated by the relaxation of the velocity profile at the nozzle exit. They travel with the mean flow velocity and remain very close to the free surface.

For U_0=4 *m/s* the boundary layer in the nozzle flow laminarizes due to an acceleration of the mean flow. Therefore, the turbulence intensity of the roll cells is not large enough to affect by its momentum the shape of free surface. Or in other words, the persisting fluctuation intensity of the roll cells can be suppressed by the surface tension. Both vortex structures, that of the roll cells and the Goertler vortices disappear downstream and as a result the free surface shape remains flat. For U_0=15 *m/s* the boundary layer is also influenced by the acceleration and the turbulent vortex structures in the wall bounded flow are suppressed near the concave nozzle wall. However, the generated turbulence intensity near the nozzle edge is considerably larger. It causes an intense generation of vortex structures, which are now capable to impact the free surface stability and alter the surface shape. The axis of the roll cells is nearly perpendicular to the main flow direction and the cells appear in regularly staggered downstream arrangement. The perpendicular arrangement of roll cells and Goertler vortices yields an increased shear within the liquid. This in turn enhances the viscous dissipation and leads to an accelerated deterioration surface wave pattern.

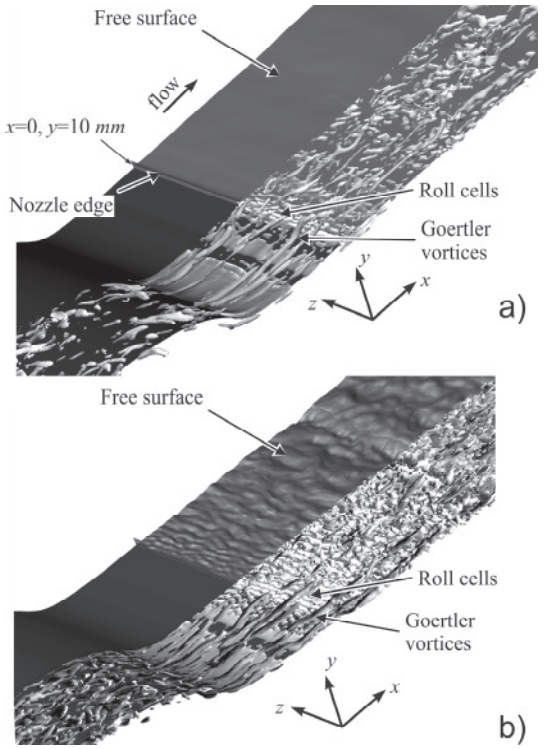

Figure 8. Vortex structures close to free surface downstream the nozzle exit for U_0=4 *m/s* (a), and U_0=15 *m/s* (b). Vortex shape identified based on invariant of the velocity-gradient tensor Q

1.5.2. Free surface flow downstream the nozzle exit (*x*=175 *mm*)

For U_0=4 *m/s* the free surface remains nearly smooth in experiment and simulation. With increasing flow velocity the development of three-dimensional irregular surface structures is detected. Similar like the experimental observations, the simulations show that the formation of large scale cell-like pattern on the free surface (white and black areas in Fig. 5) further downstream is more pronounced for high velocity values. Likely this indicates an interaction between surface and turbulent structures.

Fig. 9 shows the frequency distribution of waves at x=175 *mm* for three mean velocities U_0=9, 13 and 15 *m/s*. In experiments (bar plot) the wave height corresponding to the peak frequency increases from 0.2 *mm* for U_0=9 *m/s* to 0.77 *mm* for U_0=15 *m/s*. The simulations predict a maximum value of the frequency in a small wave range with heights between 0.1 and 0.2 *mm* (dots). For 15 *m/s* (Fig.9c), two peaks of the wave frequencies can be detected. Only the second peak in the large wave region corresponds to the measurements.

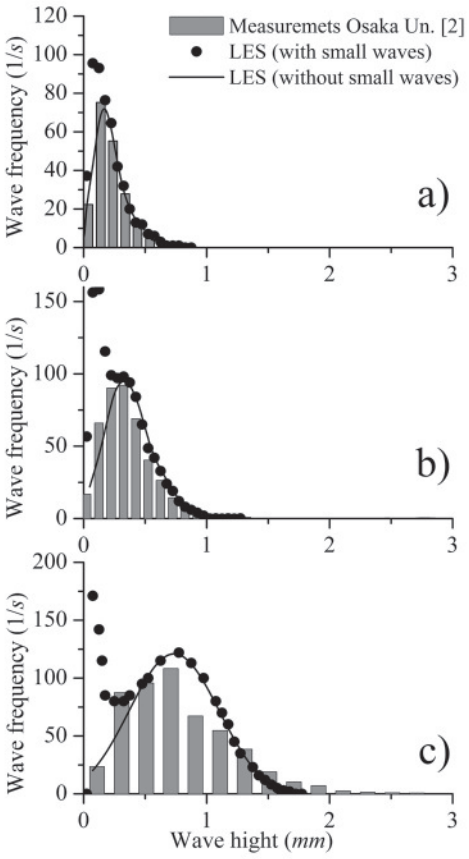

Figure 9. Comparison of measured and computed frequency of surface waves at x=175 *mm* for U_0=9 *m/s* (a), 13 *m/s* (b), 15 *m/s* (c)

In experiments (bar plot) the wave height corresponding to the peak frequency increases from 0.2 *mm* for U_0=9 *m/s* to 0.77 *mm* for U_0=15 *m/s*. The simulations predict a maximum value of the frequency in a small wave range with heights between 0.1 and 0.2 *mm* (dots). For 15 *m/s* (Fig. 9c), two peaks of the wave frequencies can be detected. Only the second peak in the large wave region corresponds to the measurements.The explanation for these deviations can be attributed to the limited accuracy of the measurement technique. The electro-contact probe detects a contact between the liquid lithium and the needle tip inserted into the Lithium in the test section with an increment of 0.1 *mm*. Addtionally, the wetting of the probe needle by the lithium complicates further the exact detection of the interface, which prevents a precise acquisition of small waves on the free surface. Hence, the contribution of small waves is not provided in the statistics of the measurement data. Excluding small waves from the calculation statistics reveals a good agreement with experimental data (solid lines) and supports this argumentation.

The graphs 10 present the non-dimensional mean velocity u^+ and the turbulent intensity distribution of the normalized streamwise velocity u'/U_0 near the wall at x=150 *mm*. For 4 *m/s* $\leq U_0 \leq$ 15 *m/s* the boundary layer exhibits the typical characteristics of a developed turbulent flow. All cases are characterized by high turbulence intensities of about 15% in the near wall domain and all velocity profiles agree with the universal logarithmic profile of turbulent boundary layers. In spite of developed turbulent flow conditions, the free surface behavior downstream the nozzle exit is different depending on the turbulence level in the open channel.

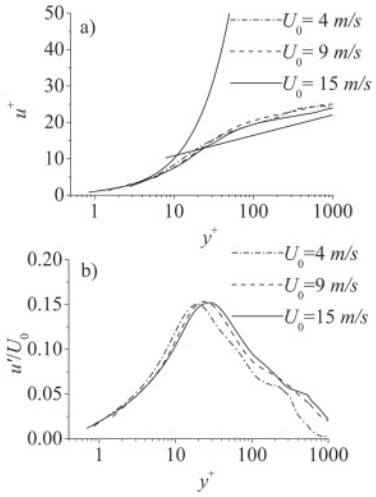

Figure 10. Calculated profiles of the dim.-less mean velocity u^+ (a) and the turb. intensity of the velocity u'/U_0 (b) near the wall at x=150 *mm* as a function of y^+

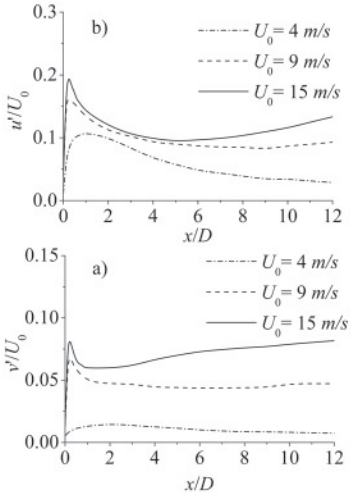

Figure 11. Computed turbulent intensity of the velocity u' (a) and v' (b) for U_0=4, 9 and 15 *m/s*

Figure 11 shows computed streamwise evolution of the turbulence intensity of the velocity components u' and v' for U_0=4, 9 and 15 *m/s*. For U_0=4 and 9 *m/s* the turbulent intensities of both

components exhibits near the nozzle exit first an increase cuased by the boundary layer relaxation. Downstream the turbulent intensity declines. While for 4 *m/s* this decrease of both components is continued far downstream, for 9 *m/s* it remains nearly constant at large *x*/*D*. In case of U_0=15 *m/s*, however, the turbulence intensity reaches a local minimum and then increases monotonically again.

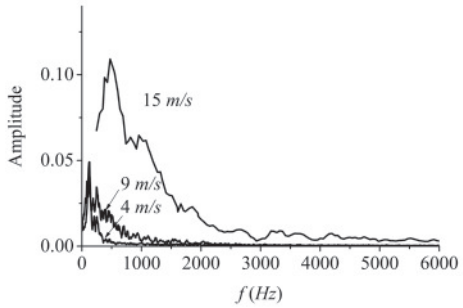

Figure 12. Power spectral density of the flow depth at *x*=175 *mm* for U_0=4, 9 and 15 *m/s*

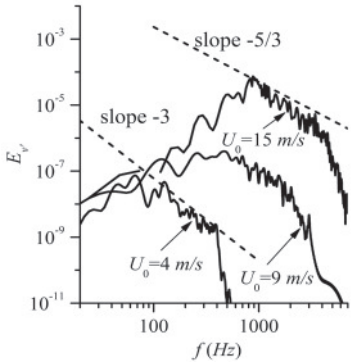

Figure 13. The energy spectra of the free surface velocity in wall normal direction at *x*=175 *mm* for U_0 =4, 9 and 15 *m/s*

The calculations show that a rise in the turbulence level alters both the frequency and amplitude characteristics of the free surface structures. The power spectral density distributions (PSD) of the flow depth at *x*=175 *mm* is shown in Figure 12. A peak region corresponds to the frequency of large scale cell-like patterns on the free surface. In case of U_0=15 *m/s*, the average amplitude of the surface fluctuations grows significantly and the contribution of higher frequencies becomes more pronounced compared to smaller mean flow velocities. The energy spectra of the free surface velocity in wall normal direction at *x*=175 *mm* are shown in Figure 13, where only the frequency range corresponding to the large scale fluctuations of the free surface are plotted.The magnitude of the energy spectra for U_0=15 *m/s* is by factors of $10^{2.5}$ and $10^{3.5}$ higher than for U_0=9 *m/s* and 4 *m/s* respectively. In the range between 9 *m/s* ≤ U_0≤15 *m/s*, the energy spectra follow with respect to the frequency a slope of -5/3, which is associated with isotropic turbulence. For U_0=4 *m/s* the power law shifts to a slope of -3, which is attributed to a more anisotropic turbulence character near the free surface. A cutout of the simulated channel with a spanwise size of 2 *mm* and a streamwise length of 40 *mm* (Fig. 14) illustrates the interaction of the large scale turbulent structures with free surface. The vortical structures are identified by iso-surfaces of *Q*=50000, and the free surface is given by VOF=0.5. For U_0=4 *m/s* (Fig. 14a) the large scale turbulent structures are produced in the boundary layer and transported downstream. These structures are either attached to the wall or separate from the boundary layer and finally dissipate into the bulk flow. Due to the small thickness of the boundary layer they are not able to reach the free surface and hence do not impact its shape. The vortex structures produced by the flow separation at the nozzle exit remain near the freee surface and are transported there downstream. These structures flatten and disintegrate due to viscosity, surface tension and gravitation.

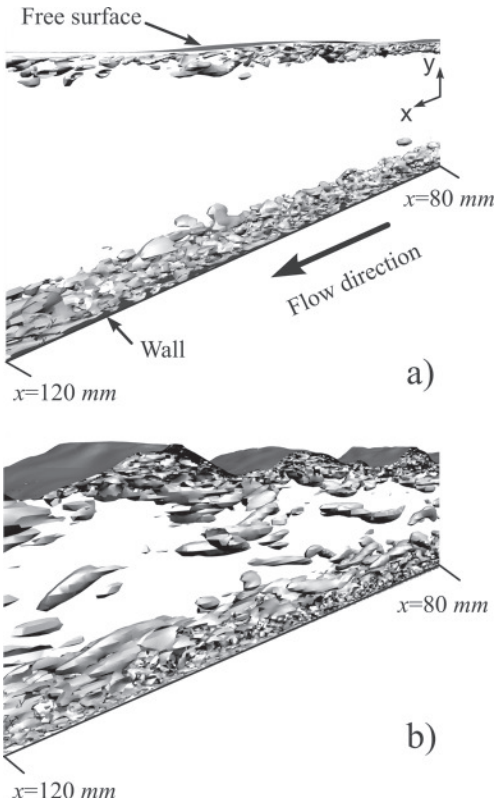

Figure 14. Vortex structures downstream the nozzle exit for U_0=4 *m/s* (a) and U_0=15 *m/s* (b). The vortical structures identified by *Q*=50000, and the free surface by VOF=0.5

For U_0=15 *m/s* (Fig. 14b) an interaction of the large scale vortical structures emerging from the boundary layer with the free surface is apparent.

The vortical structures generated in the turbulent nozzle flow do not completely disappear by the laminarization and are transported downstream. Additionally, the vortex structures are produced in the boundary layer and transferred to the bulk flow. Some of these vortical structures now reach the free surface causing a strong interaction expressed by the generation of large waves. The high turbulence level prevents a dissipation of the relatively small vortex structures produced by the separation from the nozzle. The interaction of these vortices structures with the free surface is mainly responsible for the generation of small ripples and patches.

5. SUMMARY

The aim of this study is numerical investigation of the influence of the initial flow conditions in a convergent nozzle on the free surface stability of a high speed lithium jet and the validation of CFD technique.

Regarding the validation procedure a horizontal lithium free surface flow experiment is chosen, for which different mean velocities from 4 *m/s* $\leq U_0 \leq$ 15 *m/s* are analyzed. A reasonable agreement between numerical data and experimental observation has been attained. The comparison of the wave frequency distribution at x=175 *mm* shows discrepancies between experiment and calculations for small waves, which can be explained by an insufficient accuracy of the measurement technique.

The detailed analysis of the simulation data demonstrates the impact of the boundary layer conditions at the nozzle exit on the free surface shape evolution downstream. It shows that the boundary layer relaxation at the outlet is associated with the appearance of spanwise oriented and streamwise parallel arranged vortices near the free surface, which are responsible for generation of a regular surface wave pattern. The structure of the intermittently generated waves is affected by small Λ-shaped waves propagated pointwise along the nozzle edge in streamwise direction. This wave type is caused by streamwise aligned Goertler vortices, which are developed on the concave nozzle wall and persist downstream from the nozzle exit. For U_0=4 *m/s* the boundary layer within the nozzle flow is relaminarized and the intensity of roll cells generated by the boundary layer relaxation is insufficient to alter the free surface shape. For higher U_0 regular surface waves can be observed in the vicinity of the nozzle exit. With increasing distances from the nozzle exit their wave amplitude at first grows and further downstream dissipation yields to a breakdown of this regular into three-dimensional irregular structures.

At x=175 *mm* for U_0=4 *m/s* the free surface remains nearly smooth. Because of the low turbulence level the vortical structures generated in the boundary layer do not reach the free surface. The vortex structures close to the free surface flatten and dissipate by several mechanisms. For increasing velocities the streamwise extension of the regular wave pattern monotonically shrinks and also the amplitude of the 3D structures height decreases. At high velocities the turbulence generation downstream the nozzle exit results in a strong interaction of coherent turbulent structures with the free surface expressed by the formation of the large scale cell-like patterns on the free surface.

REFERENCES

[1] IFMIF International Team, 2004, "IFMIF Comprehensive Design Report", an Activity of the International Energy Agency Implementing Agreement for a Program of Research and Development on Fusion Materials.

[2] Suzuki, S. et al., 2011, "Overview: Free Surface Measurement with Renewed Nozzle of Osaka Li Loop", *Fus Eng Des*, Vol. 86, pp. 2577-2580.

[3] Itoh, K., Yoshiyuki, T., Nakamura, H., Kukita, Y., 1999, "Initial Free Surface Instabilities on a High-Speed Water Jet Simulating a Liquid-Metal Target", *Fusion Technology*, Vol. 36, pp.69-84.

[4] Hagsberger, J.A., 1983, "Stability of the FMIT High Speed, Free Surface Liquid Jet Flowing Along a Curved Back Wall", Proc. *10th Symposium on Fusion Engineering*, Vol. 2, pp. 1849-1853.

[5] Brennen, C., 1970 "Cavity Surface Wave Patterns and General Appearance", *J Fluid Mech*, Vol. 44, pp. 33-49.

[6] Brocchini, M. and Peregrine, D.H., 2001, "The Dynamics of Strong Turbulence at Free Surfaces. Part 1", *J Fluid Mech*, Vol. 449, 225–254.

[7] Nicoud, F. and Ducros, F., 1999, "Subgrid-Scale Stress Modelling Based on the Square of the Velocity Gradient Tensor", *Flow Turb Combust*, Vol. 62 (3), pp. 183–200.

[8] STAR-CCM+ Version 4.02.011, 2008, *User Guide*, CD adapco Inc., New York.

[9] Brackbill, J. U., Kothe, D. B. and Zemach, C.; 1992, "A Continuum Method for Modelling Surface Tension", *J Comput Phys*, Vol. 100, pp. 335-354

[10] Hirt, C. and Nichols, B., 1981, "Volume of Fluid Method for the Dynamics of Free Boundaries", *J Comp Physics*, Vol. 39, pp. 201-225

[11] Addison, C.C., 1984; *Chemistry of the liquid alkali metals*; Whiley&Sons Inc., ISBN0471905089

[12] Kondo, H. et al., 2005, " Surface Wave on High Speed Liquid Lithium Flow for IFMIF", *Fus Eng Des*, Vol. 75–79, pp. 865–869

[13] Hunt, J.C.R., Wray, C.A.A. and Moin, P., 1988, "Eddies, Streams, and Convergence Zones in Turbulent Flows". *In its Studying Turbulence Using Numerical Simulation Databases*, *2. Proceedings of the 1988 Summer Program*, pp. 193-208, N89-24538 18-34.

Conference on Modelling Fluid Flow (CMFF'12)
The 15th International Conference on Fluid Flow Technologies
Budapest, Hungary, September 4-7, 2012

ON THE EFFECT OF COMBINED STREAMWISE/SPANWISE OSCILLATIONS ON IMPINGING JET HEAT TRANSFER

J. VALLET[1], H. HAJI MOHAMED ALI[2], E. SHAPIRO[3]

[1] Rio Tinto Alcan, Grenoble, France. E-mail: Julien.Vallet@riotinto.com
[2] School of Engineering, Cranfield University, Cranfield, United Kingdom. E-mail: h.hajimohamedali@cranfield.ac.uk
[3] Corresponding Author. Ricardo Software, Ricardo UK Limited, Shoreham–by–Sea, West Sussex, BN43 5FG, UK. E-mail: evgeniy.shapiro@ricardo.com

ABSTRACT

The paper presents a numerical investigation of the effect of combined streamwise and spanwise oscillations on the heat transfer induced by impinging circular jet cooling method. The analysis is carried out using unsteady RANS modelling with the commercial software Fluent 12.1.4 for a nozzle to plate ratio H/D=2.5 and a Reynolds number of 38 000 based on jet diameter, corresponding to experimental validation case of Hoffman et al. (Numerical Heat Transfer, Part B: Fundamentals, 51(6) 2007). Following a comparative study of the accuracy of turbulence models employed, grid dependency and validation study, the effect of the frequency, amplitude and phase shift of spanwise and streamwise excitation is evaluated. The results demonstrate that a substantial improvement of up to 3 times can be obtained in the integral time-averaged Nusselt number in the core region of the of the jet. Furthermore there is an indication of the existence of an optimal point with respect to the amplitude, relative frequency and phase shift of spanwise oscillations.

Keywords: heat transfer, oscillating impinging jets.

1. INTRODUCTION

Jet impingement is used as a heat transfer enhancement mechanism in applications ranging from turbomachinery [1] and electronic components [2] to food processing [3]. The ubiquitous applications of impinging jets can be attributed to the efficiency and flexibility of this heat enhancement method [4].

Heat transfer using steady state impinging jets has been studied extensively by a number of researchers. An excellent review of the available experimental and numerical literature can be found in [5, 6].

A particularly promising modification of this classic mechanism is relying on unsteady modulation of the jet velocity with the aim of increasing peak and integral heat transfer. A number of authors have considered the effects of the signal shape and frequency as well as the Reynolds number and nozzle-to-plate distance (e.g. [7-13]). These studies have indicated that the spanwise forcing can lead to either a small increase (e.g. [14]), substantial increase (e.g. [15-17]) or a decrease (e.g. [11, 12, 18, 19]) of heat transfer, depending on the flow and geometrical parameters. The overall effect of the spanwise forcing on heat transfer depends on the interaction of the forced jet flow with the ambient entrained fluid and the degree of mixing resulting from this interaction prior to the jet reaching the plate.

On the other hand, spanwise or transverse oscillations in impinging jets have received comparatively little attention. A notable exception of this was the study by Camci and Herr [20], who examined the effect of self-oscillating impinging jets and demonstrated a maximal improvement of up to 70%. Furthermore, to the authors' knowledge, a combined effect of streamwise and spanwise oscillations has not been so far considered in a framework of a systematic study. In the following sections, a detailed investigation is presented into the effect of combined streamwise and spanwise modulation, demonstrating the potential for an improvement of the integral heat transfer in the jet core.

2. METHODOLOGY

The geometry was based on the work by Hofmann et al [9, 10] who have studied impinging jet heat transfer experimentally [9] and numerically

[10] in the steady state and unsteady configurations. The unsteady configuration was considered in [10] with the streamwise forcing applied through boundary conditions. The nozzle diameter was set to 25 mm to correspond to the experimental conditions. The experimental study employed two configurations with a high nozzle-to-plate distance of H/D = 10.0 and low nozzle-to-plate distance of H/D = 2.5 respectively and two Reynolds numbers of 124,000 and 34,000 based on the nozzle diameter. In the present paper, the low nozzle-to-plate case is considered at nominal Reynolds number of 34,000. The selection of the experimental case was initially motivated by the presence of the secondary separation in the unforced flow which makes the computational modelling challenging, while the relatively low Reynolds number reduces the grid requirements [10]. A schematic of the computational domain is shown in Fig. 1.

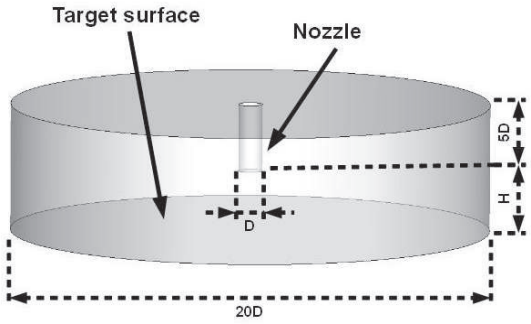

Figure 1. Geometry of the model

For the simulation, it is assumed that the fluid is incompressible with constant density, specific heat and thermal conductivity of the air jet. The viscous heat dissipation is neglected and constant temperature boundary condition is applied to the heated plate.

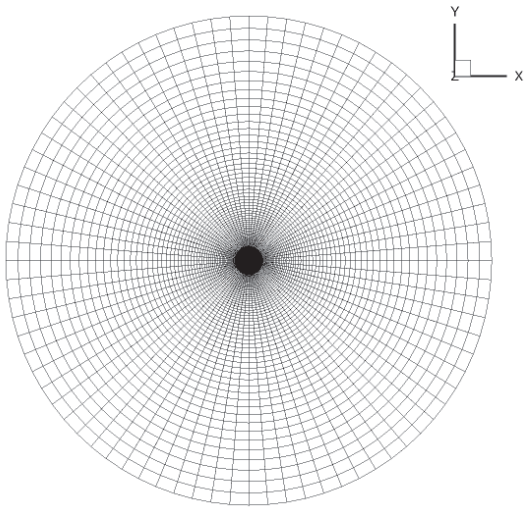

Figure 2. Top view of grid

A block-structured mesh was constructed with clustering employed towards the jet core and the heated plate. A top view of the mesh on the heated plate is presented in Fig. 2. The mesh was wall resolved, employing estimated wall distance of y+=1 based on the flat plate correlation. Grid convergence study was performed for the mesh geometry at three different grid levels of 0.3, 0.64 and 1.4 million cells. The solution exhibited only limited grid dependency on the medium grid, hence the medium grid was selected for the core study. See [21] for more detail.

The velocity inlet boundary condition is set at the outlet of the nozzle using the UDF function in the solver. For the steady case, the parabolic function defined in Eq. 1 was used for simplicity with the maximum inlet velocity, U_o, of 21.35 m.s^{-1}. Parabolic profile was used as a first approximation instead of the plug turbulent flow profile for simplicity. It is also anticipated that the results obtained with the parabolic profile should enhance the sensitivity of peak heat transfer to the velocity modulation as the maximum velocity of the profile is greater than that of the plug profile at the same flow rate. Note that in the experiment the nozzle outlet velocity was closer to a plug flow. For the unsteady case, the velocity inlet is defined for the streamwise and spanwise oscillations according to Eqs. 2 and 3.

$$U_{Z-inlet}(r) = U_o - \frac{U_o r^2}{R^2} \quad (1)$$

Where U_o is the maximum velocity, R is the radius of the inlet pipe and r the radius of the pipe.

$$U_{Z-inlet}(r) = \left[U_o - \frac{U_o r^2}{R^2}\right] [1 + A_{stream} sin(2\pi f_{stream} t)] \quad (2)$$

$$U_{x-inlet} = U_o A_{span} sin(2\pi f_{span} t + \varphi) \quad (3)$$

Where $A_{stream/span}$ is the amplitude of the corresponding oscillations amplitude, f is the oscillation frequency and φ is the phase shift. The turbulent intensity at the inlet is 1% with the lengthscale based on the hydraulic diameter.

The k-epsilon standard turbulence model was used with the Enhanced Wall Treatment., based on validation studies of Vallet [21] and Ul Haq [22].

The flow field was solved using the SIMPLE pressure-correction algorithm with the second order upwind discretisation used for all governing equations and the standard interpolation scheme used for pressure field with the relaxation factors shown in Table 2. The discretisation of gradients is the least squares cell based. Iterations during individual time steps converged to 10^{-3} for all equations except for the energy equation which

converged to 10^{-5}. Implicit 1st order time stepping was used for the time marching of the solution with 20 time steps per period of oscillations, following [23]. The resulting time step was 6.25×10^{-4}s for cases where the frequency of the imposed oscillations was equal to 80Hz, 1.25×10^{-3}s for cases involving 40Hz oscillations.

3. TEST CASES

The test cases for the study are summarised in Table 1. The streamwise oscillations are kept with the same amplitude and frequency of 30% and 40 Hz. The spanwise oscillations are then varied in terms of frequency, amplitude and phase shift. Case 7 corresponds to the reference point without spanwise oscillations.

Table 1: Summary of test cases

	Spanwise		
	Amplitude	Frequency	Phaseshift
Case 1	4.7%	10 Hz	0
Case 2	4.7%	40 Hz	0
Case 3	4.7%	80 Hz	0
Case 4	4.7%	40 Hz	π/4
Case 5	4.7%	40 Hz	π/2
Case 6	30%	40 Hz	0
Case 7	Reference, no spanwise oscillations.		

The amplitude represents the percentage of the U_o as Eq. 1-3.

4. RESULTS

Flow Field

The flow field results of the simulation are shown in this section. Fig. 3 shows the velocity contours, in m/s, of the impinging jet oscillating at 40 Hz streamwise and 40 Hz spanwise at different points of the cycle as well as the contours of the surface heat flux at the plate in W/m^2.

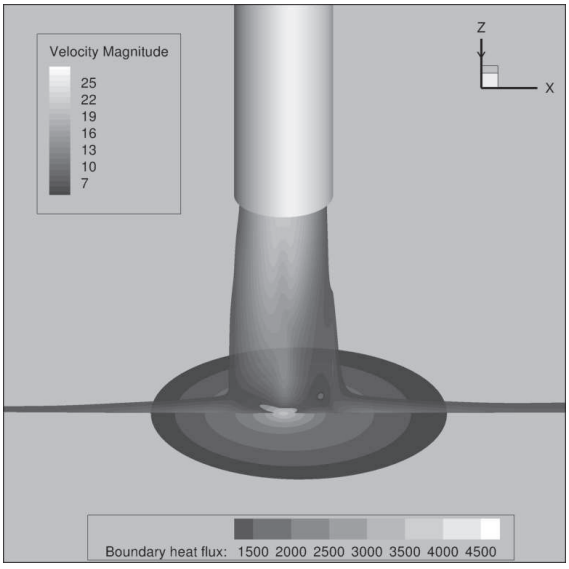

(a) Angle = 0 degrees

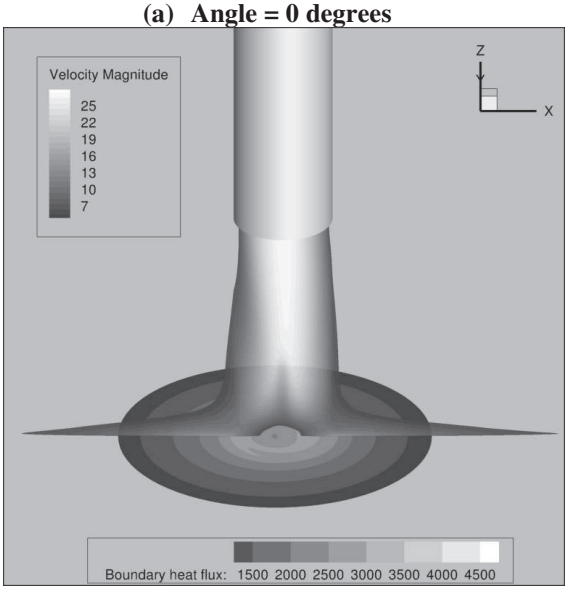

(b) Angle =90 degrees

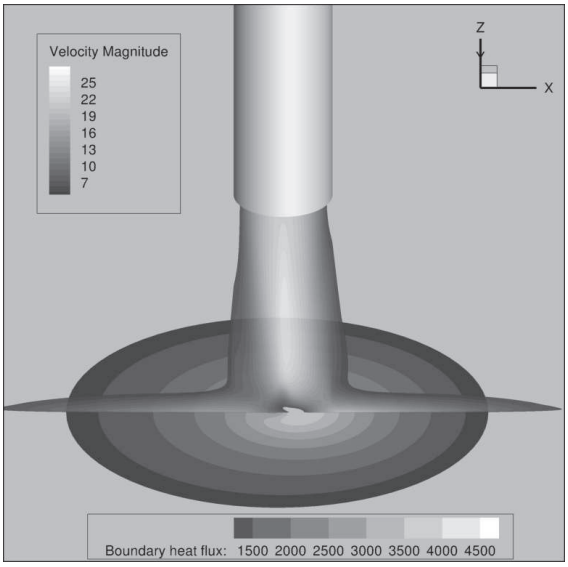

(c) Angle = 180 degrees

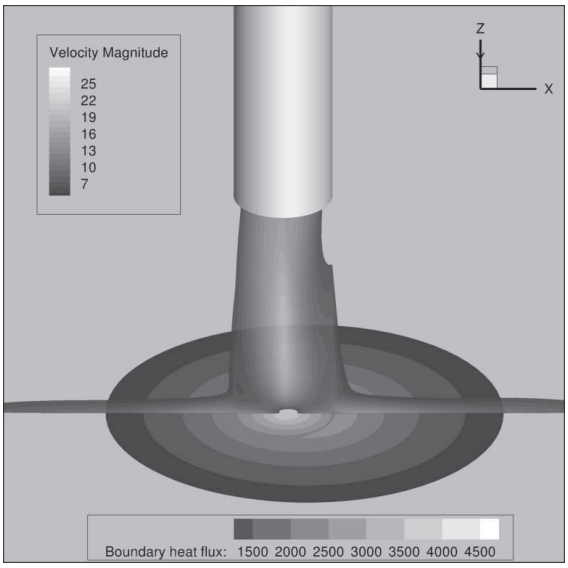

(d) Angle =270 degrees

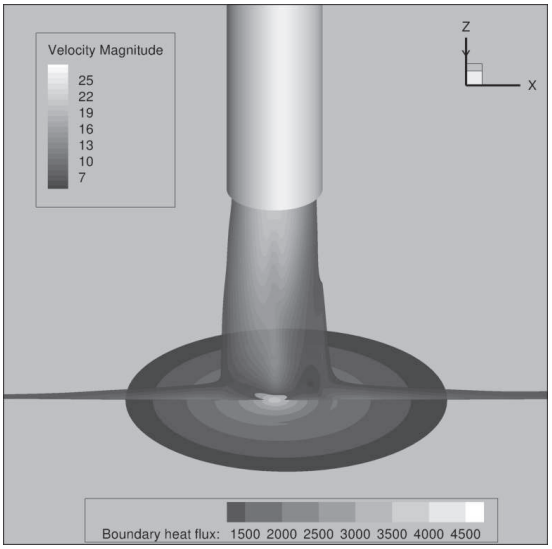

(e) Angle = 360 degrees

Figure 3. Velocity/heat flux contours of impinging jet for 40 Hz streamwise / 40 Hz spanwise oscillations

The jet reaches the maximum streamwise velocity at 90 degrees combined with the maximum positive spanwise deflection. The minimum velocity combined with maximum negative spanwise deflection is reached at 270 degrees.

There is a delay between the fluctuations at the inlet and heat transfer response at the plate due to the time it takes the fluid element to reach the plate. The jet hits the stagnation point at the plate at the bottom and then disperses outwards. The maximum coverage for the heat transfer at the surface occurs at 180 and 270 degrees as indicated by the surface heat flux contours at the plate

At angles 0, 180 and 360 degrees, the nozzle is at the original position and the heat transfer peak returns to the centre of the plate (minus the delay of the jet propagation). The presence of the spanwise modulation affects the position of the heat transfer peak, which sweeps a larger area by comparison with the case where only streamwise oscillations are present. Due to this behaviour, the effectiveness of the heat transfer at the core increases as described in the following section.

Heat Transfer Properties

The effect of the spanwise frequency on the time-averaged Nusselt number in the range of $0 < r/D < 1$ is illustrated in Fig. 4 below. It can be seen that there is an increase in the Nusselt number as the spanwise oscillation were increased from 10 Hz to 40 Hz and a significant drop from 40 Hz to 80 Hz.

This increase shown in Fig. 4 can be further illustrated by the area average time-averaged Nusselt number in the jet core, between 0 and 1 of r/D, summarised in Table 2. Maximum increase in the Spanwise excitation at 40 Hz shows an increase by approximately 9.27% from the results of the jet with no spanwise oscillation.

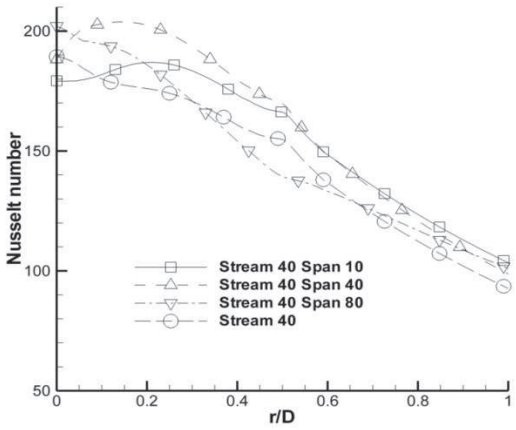

Figure 4. Time-averaged Nusselt number comparison of different spanwise frequencies.

Table 2:Area average of Nu for r/D < 1 at different frequencies.

	Area average Nu	% Diff against Case 7
Case 1	139.19	8.75%
Case 2	139.86	9.27%
Case 3	129.50	1.18%
Case 7	127.99	-

Based on the flow field description and the distribution of the time-averaged Nusselt number, it is possible to identify two conflicting mechanisms in the fluid flow. The forced precession of the jet core is improving heat transfer in the core area by re-distributing the cold air on the heated plate. At the same time, the increase in the motion of the jet through spanwise oscillations enhances the mixing with the ambient air and decreases the momentum of the jet before it reaches the plate more efficiently. This effect decreases the heat transfer in the core of the jet with the increase of the spanwise frequency. It should be noted that with the same bulk average inlet velocity, the increase of heat transfer in the core of the jet is necessarily accompanied by the decrease of the local Nusselt number further away from the core. This highlights the potential of the arrays of jets to further increase of heat transfer through combined spanwise and streamwise oscillations.

The effect of phase shift is shown in Fig. 5. There is a slight variation of the Nusselt number when the phase shift is $\pi/4$ and a decrease when the phase shift is $\pi/2$. This is further quantified in Table 3 where increase of the area average Nusselt number is observed for phase shift $\pi/4$ and a decrease for phase shift $\pi/2$. The latter can be expected as in this case we have the maximum spanwise forcing corresponding to the minimum streamwise velocity deviation, which is not efficient. The mechanism underlying the increase of the area average Nusselt for phase shift of $\pi/4$ is unclear at the moment and requires further

investigation. However, the distribution of the change of the area average Nusselt number with the phase shift points to the existence of the optimal non-zero phase shift for this configuration.

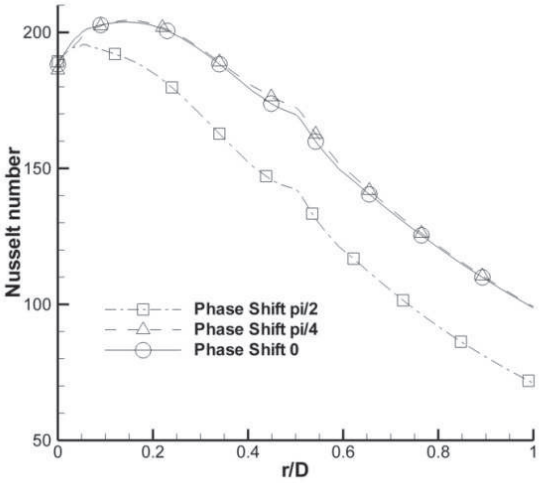

Figure 5. Time-Averaged Nusselt number comparison of different phase shift.

Table 3:Area average of Nu for r/D < 1 at different phase shift.

	Area average Nu	% Diff against Case 2
Case 4	140.94	0.78%
Case 5	112.58	-19.5%
Case 2	139.86	-

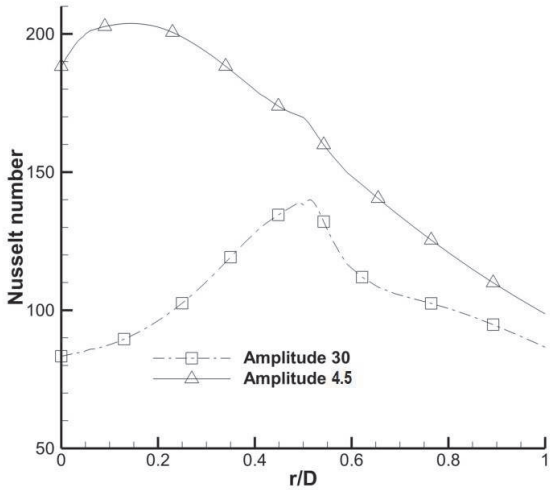

Figure 6. Time-Averaged Nusselt number comparison of different amplitude.

The effects of the change of the amplitude of spanwise oscillations are illustrated in Fig. 6. The time-averaged Nusselt number shows a significant decrease when the amplitude of the spanwise oscillations is increased from 4.7% to 30%. The area average Nusselt for this case decreases by 24% by comparison with the low amplitude forcing. This observation is consistent with the hypothesis about the balance between the mixing of the jet with the ambient surrounding air and corresponding loss of momentum on the one side and the increased area of the interaction between the jet core and the heated plate due to the forcing. The increase in amplitude does not affect significantly the spread of the jet core, whereas it does contribute to the increased mixing before the jet reaches the plate resulting in the overall decrease of the heat transfer.

5. CONCLUSION

A substantial increase of the integral heat transfer has been demonstrated through the combination of the streamwise and spanwise oscillations. For all investigated spanwise frequencies, pulsation increases the heat transfer rates in the stagnation region but decreases the local Nusslet number in the wall jet region. The introduction of the spanwise oscillations tends to increase the heat transfer rates by comparison with streamwise oscillations alone. The apparent explanation is the increased area swept by the jet core as it moves under the spanwise forcing.

The phase shift between the spanwise and streamwise pulsation does not have a substantial positive effect on the heat transfer rates, however a moderate improvement can be achieved. Increase of the oscillation amplitude on the other hand tends to decrease the Nusselt number profile especially in the stagnation region.

The observations made in cause of the simulations support the hypothesis of the competing effect of the momentum diffusion, facilitated by forcing, which has a negative effect on the average heat transfer and the motion of the jet core under forcing, which causes the increase of the average heat transfer. The behaviour of the area average Nusselt number in the points taken in the parametric space of the problem for this study indicates the presence of an optimum point maximising the area average Nusselt number. Further studies of this phenomenon are currently underway at Cranfield University and the possibility of application of formal optimisation methods, required to identify the optimal point and investigate its sensitivity to flow parameters, is being explored.

REFERENCES

[1] Logan, E., and Prasad, R.R., 2005, “Handbook of Turbomachinery”, Marcel Dekker Inc., New York.

[2] Pavlova, A., Amitay, 2006,“Micro-Electronic Cooling Using Synthetic Jet Impingement”, *Journal of Heat Transfer,* vol. 128, no. 9 , pp. 897-907.

[3] Ollson, E. E.M., Tragardh C., 2007, “CFD Modeling Of Jet Impingement During Heating And Cooling Of Foods”, *Computational Fluid*

Dynamics in Food Processing Edited by Da-Wen Sun, CRC Press, Pages 487–500.

[4] Zuckerman, N., Lior, N., 2006, "Jet Impingement Heat Transfer: Physics, Correlations, and Numerical Modeling", *Advances in Heat Transfer*, vol. 39, pp. 565.

[5] Zuckerman, N., Lior, N., 2005 "Impingement Heat Transfer: Correlations and Numerical Modeling", *Journal of Heat Transfer*, vol. 127, no. 5, pp. 544-552.

[6] Jambunathan K., Lai E., Moss M.A., Button B.L., 1992, "A Review Of Heat Transfer Data For A Single Circular Jet Impingement", *Int. Journal Heat Fluid Flow,* vol. 13, pp. 106–115.

[7] Middelberg, G. and Herwig, H., 2009, "Convective Heat Transfer Under Unsteady Impinging Jets: The Effect Of The Shape Of The Unsteadiness", *Heat and Mass Transfer*, Waerme-und Stoffuebertragung, vol. 45, no. 12, pp. 1519-1532.

[8] Ball, H. D. and Nevins, R. G., 1963, "Effects Of Varying The Jet Velocity, Jet Frequency, Wave Form, Impingement Angle, Nozzle-To-Plate Distance And Test Plate Temperature On The Film Coefficient Of Heat Transfer From A Flat Plate To A Pulsating Impinging Jet", *International Heat Transfer Conference*, Coulder, Colo , Aug. 28 - Sept. 1, 1961 and London, England, Jan. 8-12, 1962./ *International Developments in Heat Transfer*, proceedings of the 1961-1962 *Heat Transfer Conference. New York, ASME*, 1963, p. 510-516. 15 refs. Army-supported research; United States.

[9] Hofmann, H. M., Kind, M. and Martin, H., 2007, "Measurements On Steady State Heat Transfer And Flow Structure And New Correlations For Heat And Mass Transfer In Submerged Impinging Jets", *International Journal of Heat and Mass Transfer*, vol. 50, no. 19-20, pp. 3957-3965.

[10] Hofmann, H. M., Kaiser, R., Kind, M. and Martin, H., 2007, "Calculations of Steady and Pulsating Impinging Jets - An Assessment of 13 Widely used Turbulence Models", *International Journal of Heat and Mass Transfer*, vol. 51, no. 6, pp. 565-583.

[11] Hofmann, H. M., Movileanu, D. L., Kind, M. and Martin, H., 2007, "Influence Of A Pulsation On Heat Transfer And Flow Structure In Submerged Impinging Jets", *International Journal of Heat and Mass Transfer*, vol. 50, no. 17-18, pp. 3638-3648.

[12] Mladin, E. C. and Zumbrunnen, D. A., 1995, "Dependence Of Heat Transfer To A Pulsating Stagnation Flow On Pulse Characteristics", vol. 9, no. 1, pp. 181-192.

[13] Poh H.J, Kumar, K. and Mujumdar A.S., 2005, "Heat Transfer From A Pulsed Laminar Impinging Jet", *International Communications in Heat and Mass Transfer*, vol. 32, no. 10, pp. 1317-1324.

[14] Haneda, Y., Tsuchiya, Y., Nakabe, K. and Suzuki, K., 1998, "Enhancement Of Impinging Jet Heat Transfer By Making Use Of Mechano-Fluid Interactive Flow Oscillation", *International Journal of Heat and Fluid Flow*, Vol. 19, no. 2, pp. 115-124.

[15] Mladin, E. C. and Zumbrunnen, D. A., 1997, "Local Convective Heat Transfer To Submerged Pulsating Jets", *International Journal of Heat and Mass Transfer*, vol. 40, no. 14, pp. 3305-3321.

[16] Sailor, D. J., Rohli, D. J. and Fu, Q., 1999, "Effect Of Variable Duty Cycle Flow Pulsations On Heat Transfer Enhancement For An Impinging Air Jet", *International Journal of Heat and Fluid Flow*, vol. 20, no. 6, pp. 574-580.

[17] Zumbrunnen, D.A. and Aziz, M., 1993, "Convective Heat Transfer Enhancement Due To Intermittency In An Impinging Jet", *ASME: Journal of Heat Transfer*, vol. 115, no. 1, pp. 91-98.

[18] Azevedo, L. F. A., Webb, B. W. and Queiroz, M., 1994, "Pulsed Air Jet Impingement Heat Transfer", *Experimental Thermal and Fluid Science*, vol. 8, no. 3, pp. 206-213.

[19] Sheriff, H. S. and Zumbrunnen, D. A., 1994, "Effect Of Flow Pulsations On The Cooling Effectiveness Of An Impinging Jet", *ASME: Journal of Heat Transfer*, vol. 116, no. 4, pp. 886-895.

[20] Camci, Herr, 2002, "Forced Convection Heat Transfer Enhancement using a Self-Oscillating Impinging Planar Jet", *Journal of Heat Transfer*, vol. 124, no. 4, pp. 770-782.

[21] Vallet, J., 2010, "CFD Analysis of Heat Transfer in Oscillating Impinging Jet with Spanwise and Streamwise Oscillations", *MSc thesis*, School of Engineering, Cranfield University, Cranfield.

[22] Ul Haq, A., 2009, "CFD Analysis of Heat Transfer Enhancement in Oscillating Impinging Jet", *MSc thesis*, School of Engineering, Cranfield University, Cranfield.

[23] Behera, R. C., Dutta, P. and Srinivasan, K., 2007, "Numerical Study of Interrupted Impinging Jets for Cooling of Electronics", *Components and Packaging Technologies*, *IEEE*, vol. 30, no. 2, pp. 275-284.

Conference on Modelling Fluid Flow (CMFF'12)
The 15th International Conference on Fluid Flow Technologies
Budapest, Hungary, September 4-7, 2012

OPTIMIZATION OF THE THERMAL AND FLUID DYNAMIC BEHAVIOUR OF AIR CURTAINS. ANALYSIS OF THE PLENUM BY MEANS OF LES

Giraldez H.,[2] Perez Segarra C. D., [1] Rodriguez I., [2] Oliva A. [2]

[1] Corresponding author. Centre Tecnològic de Transferència de Calor (CTTC), Universitat Politècnica de Catalunya (UPC), ETSEIAT, Colom 11, 08222, Terrassa, Barcelona, Spain. Fax: +34 93 739 89 20, e-mail: cttc@cttc.upc.edu
[2] Centre Tecnològic de Transferència de Calor (CTTC), Universitat Politècnica de Catalunya (UPC),

ABSTRACT

The improvement procedure of an air curtain unit (ACU) is described in the present study. The procedure is based on Large Eddy Simulations (LES) and Hot Wire Anemometry (HWA) measurements. Initially, the flow provided by the air curtain is evaluated experimentally according to the AMCA standard [1] and employing HWA technology. The initial measurements indicate an undesired behavior of the device: the velocity at the discharge exhibits a non homogeneous distribution. According to the literature, the efficiency of air curtains is closely related to its capacity to provide an homogeneous jet with high enough velocity and with low turbulence levels [2].

On this study, the criteria for optimization applied to the plenum chamber consist in finding out what design increases both the homogeneity and the mean velocity values produced at the discharge. An air curtain producing a jet with these features will minimize the air interchange between outdoor and indoor spaces.

Alternative plenums are evaluated by means of fully 3D LES. Previous works indicate that a fully three-dimensional treatment is required in the simulations of ACUs [3], due to its no-bidimensional behaviour. The results of the simulations indicate that a more smooth plenum is required to avoid recirculations. The prototype of the designs with the best behavior, according to the simulations, are constructed and its flow are characterized with HWA measurements. The measurements show consistent results with LES. It is concluded that the proposed plenum geometry improves the initial design both in homogeneity and in mean velocity values at the discharge. The downstream jet evolution is characterised with semianalytical and experimental approaches. The code TermoFluids[4] has been used for the simulations of the plenum.

Keywords: air curtain unit, CFD , Hot Wire Anemometry, LES, plenum optimization, WALE

NOMENCLATURE

ν_e	$[m^2/s]$	kinematic eddy viscosity
p	$[m^2/s^2]$	pseudopressure
S	$[m/s]$	rate of stress tensor
Δ	$[m]$	length scale of the filter
u	$[m/s]$	velocity vector
$\overline{\phi}$	-	volume average (ϕ=u,p,...)
C_s,C_w	-	turbulence constants
St	-	Strouhal Number
D	m	Inner curve diameter
f	s^{-1}	Frequency of vortex shedding
g_{ij}	s^{-1}	velocity gradient tensor ij component
δ_{ij}	-	Kronecker symbol
&	s^{-2}	traceless symmetric part of square of g

Subscripts and Superscripts

t	temporal
x, y, z	transversal, spanwise and axial (jet axis) coordinates
-	spatial mean
T	transposed

1. INTRODUCTION

An air curtain unit (ACU) is a device which acts as an ambient separator producing a plane air jet. The entrainment is produced by the difference of temperature and pressure between indoor and outdoor spaces and the presence of wind. In order to minimize the entrainment of external air to the protected indoor space, the jet should have a velocity high enough to counteract these effects. It also must be as homogeneous as possible. The homogeneity of the flow at the discharge affects directly the downstream evolution of the jet. A low level of turbulence is also a desired characteristic in the jet [6].

The part of the ACU that gives the jet its desired characteristics is the plenum. The plenum is an inner chamber which is situated between the fans and the nozzle discharge (see Figure 1).

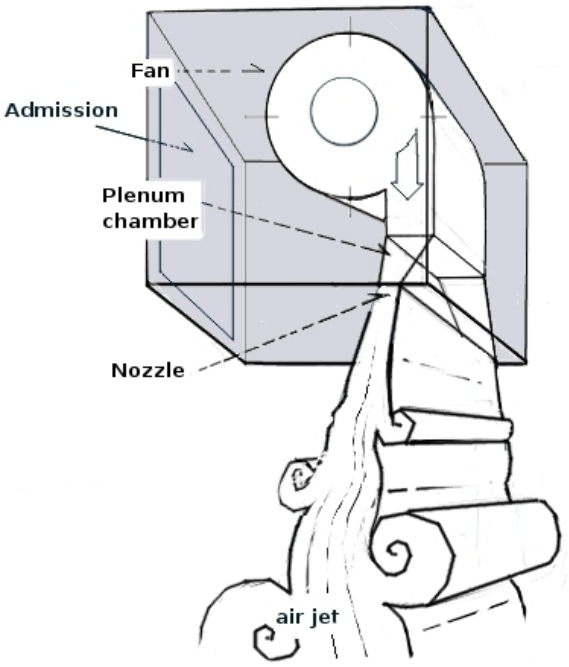

Figure 1. Scheme of the basic parts of an air curtain.

The ACU studied in this paper is characterised according to the AMCA standard [1]. A lack of homogeneity at the discharge is observed in the measurements .

The cause of this behaviour is determined by means of LES, showing that the main cause of inhomogeneity is the fast expansion after the fans outlet. This expansion produces ring vortices, which spreads and affects the discharge and hence the overall efficiency of the device. To solve this problem an alternative plenum design will be evaluated by means of LES.

The best designs according to the simulations are constructed (here refered as m1 and m2 prototypes) and its flow is measured with HWA, so the difference in the flow produced by the plenum modifications can be checked. The HWA measurements show consistent results with the numerical simulations, so the plenum that produces a high homogeneous discharge has also higher downstream velocity values.

The comparation of the energy spectras possibly highlight the effect of the mesh, showing that some peaks at the energy spectra may be produced numerically.

In the economical sense, it is worth notice that the more sofisticated is the plenum design, the more expensive can be its production. This is the main cause that the proposed designs must be quantitative evaluated, in order to ensure that the improvements in efficiency imply higher savings than its associated manufacturing costs.

The numerical techniques employed has been a tool to predict the behaviour of the device and the overall methodology has probed itself as an acceptable procedure to improve ACU designs.

2. METHODOLOGY

The actions carried out consist in:

- Measuring the flow produced by the air curtain with HWA. Identification of possible flow deficiencies.
- Searching the possible causes of the non optimal behaviour with LES. Application to the plenum.
- Proposing alternative plenum designs in order to overcome the persisting deficiencies.
- Prediction of the behaviour of alternative designs with LES.
- Construction and experimental evaluation of the produced air flow with HWA of the bests designs according to the numerical simulations.
- Checking the design by means of comparison with the initial behaviour.

The measurements are carried out according to the AMCA standard requirements.The HWA probes are calibrated at the same laboratory, ensuring the accuracy of the measurements.

The simulations are performed with a high performance parallel code developed by Termofluids S.L.[4], capable of calculations with unstructured three-dimensional meshes, in unsteady conditions and with different LES models (e.g. the Wale model [2]). In the LES models, the larger scales of the turbulence are solved, while the smaller ones are filtered and modelled by means of a turbulent viscosity, which adds the additional transport of momentum contained in the small vortices.

3. EXPERIMENTAL SETUP

An experimental setup to evaluate the flow produced by the ACU is constructed (see Figure 2). The dimensions of the channel are 5 x 1.1 x 1 , with a step of 1 metre between longitudinal measurements, 0.01 metres between transversal measurements. The main parts of the experimental setup are the channel itself, the probe positioning cartesian robot and the HWA system. Obviously, the ACU is fixed at the beginning of the channel.

The experimental setup allows the characterization of the flow in the range between the discharge (z=0m) and the end of the channel itself (z=4m), without external perturbations by the action of the baffles situated at each side of the ACU.

Figure 2. The experimental setup where the HWA measurements are carried out.

The cartesian robot allows a positioning with resolution of 10^{-6}m. The measurements are taken in every transversal section programming the cartesian robot to cover all the required domain in a time interval equal to the adquisition time. The relative movement of the robot do not affect the measurement of the velocity because the probe only captures the components of the velocity which acts in the plane normal to its wire (see Figure 2). The measurements are carried out with unidimensional probes at a sample rate of 1000 Hz, during an adquisition time of 128 s in each test line. The test lines have a length of 1.0 m, covering all the spanwise direction of the ACU discharge and with a separation of 0.01 m between each test line. The separation between measurement planes is 1 m, being the first plane at a distance equal to the nozzle width.

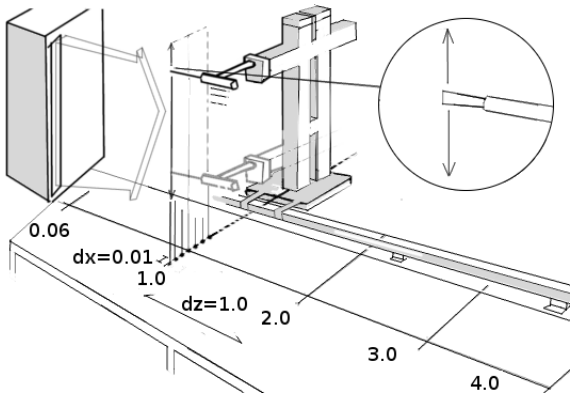

Figure 3. Velocity measurement procedure scheme.

Moreover, adjoint to the probe there is also a termocouple, which allows to correct the discrepances produced by the possible deviations between the ambient temperature in the moment of calibration of the probe and the ambient temperature in the moment of data adquisition.

4. MATHEMATICAL FORMULATION

4.1. Large Eddy Simulation

The spatially filtered equation of momentum used in LES[7] can be written as follows:

$$\partial_t \overline{u} + (\overline{u} \cdot \nabla)\,\overline{u} + \nabla \overline{p} - 2\nu \nabla \cdot S\,(\overline{u}) = \nabla \cdot \left(\overline{u\overline{u}^T} - \overline{uu^T} \right) \tag{1}$$

Modelling the right-hand side in terms of $\overline{u}$ yields a simplified representation of the large eddies.

$$\nabla \cdot \left(\overline{u\overline{u}^T} - \overline{uu^T} \right) = 2\nabla \cdot (\nu_e S\,(\overline{u})) \tag{2}$$

The classical Smagorinsky model [8] is given by

$$\nu_e = c_s^2 \Delta^2 \left| S\,(u) \right| \tag{3}$$

The Smagorinsky model suffers from several shortcomings, one of them is that it predicts a nonvanishing eddy viscosity in regions where the flow is laminar and at no-slip walls.

In order to overcome these defficiencies, in this study the Wall Adapting Local Eddy viscosity (WALE) model [9] will be employed. According to this model the expression for the eddy viscosity is given by

$$\nu_e = (C_w \Delta)^2 \frac{\left(\&_{ij}^d \&_{ij}^d \right)^{3/2}}{\left(\overline{S}_{ij} \overline{S}_{ij} \right)^{5/2} + \left(\&_{ij}^d \&_{ij}^d \right)^{5/4}} \tag{4}$$

where $\&$ is the traceless symmetric part of the square of the velocity gradient tensor:

$$\&_{ij}^d = \frac{1}{2} \left(\overline{g}_{ij}^2 + \overline{g}_{ji}^2 \right) - \frac{1}{3} \delta_{ij} \overline{g}_{kk}^2 \tag{5}$$

$$\overline{g}_{ik}^2 = \overline{g}_{ik} \overline{g}_{kj} \tag{6}$$

and δ_{ij} is the Kronecker delta operator.

It is probed that the WALE model is a better approximation than the classical Smagorinsky model, avoiding the undesired behaviour explained above. A detailed description of the high performance parallel program Termofluids can be found in the bibliography indicated below [4].

5. RESULTS

5.1. Description of the prototypes

In the present study there are three geometries involved: the current plenum geometry and the two modified prototypes, here refered as m1 and m2 designs. It is worth noting that the plenum is the inner chamber which conditiones the air flow, and it is located between the fan and the discharge.

The modified plenum design m1 introduces only an inner curve, in order to isolate and evaluate its

effect (see Fig.4). Additionally, the modified design m2 introduces lateral diffusors and a more thin nozzle discharge (see Fig.7).

The results obtained in every step of the optimization procedure are summarised below.

5.2. HWA measurements of the initial flow field

The measurements allow to determine the mean velocity and the homogeneity of the flow along the air curtain discharge, being those the mean parameters demanded by the AMCA standard [1].

The velocity measurements of the initial design can be seen in table 1. As a consequence of the lack of homogeneity at the discharge, the jet spreads transversally faster, and the decrease of the core velocity is also larger. This characteristic produces a jet too much weak and, hence, a low sealing efficiency. In order to find out the reasons of this undesired behaviour, LES of different plenum designs are evaluated. The analysis of the results of the simulations are following described.

Distance[m]	0.06	1.0	2.0	3.0	4.0
Avg. core vel	12.03	6.55	4.65	3.50	2.47
Uniformity	75%	80%	84%	84%	78%

Table 1. Mean core velocities in function of the distance from the air curtain discharge. Initial design.

5.3. Numerical simulation of the modified plenum geometry m1

A new plenum design is proposed and the simulation of its produced flow is carried out. The meshes employed in the present study are unstructured and each one has roughly 1,8 M control volumes. Once the system has acquired an statistical steady state, the results captured are averaged from that moment and during an interval of time long enough to ensure that the temporal autocorrelation of the signal goes to zero. The inlet boundary condition is emulated situating a previous channel long enough to develope a turbulent profile with a mass flow equal to the provided by the actual fans. The characteristic Reynolds of the simulations is 20.000, defined with the characteristic length of the fan's discharge, its mean velocity and the physical properties of air at ambient temperature (20°C).

It can be seen the presence of strong inhomogeneity of the mean velocity values at the discharge section of the flow. It is produced by a fast expansion after the fans. This recirculation spread down and modifies the whole flow's structure, having a destructive effect in a supposedly ideal bidimensional airjet. To make the jet behaviour more bidimensional further modifications of the plenum are required.

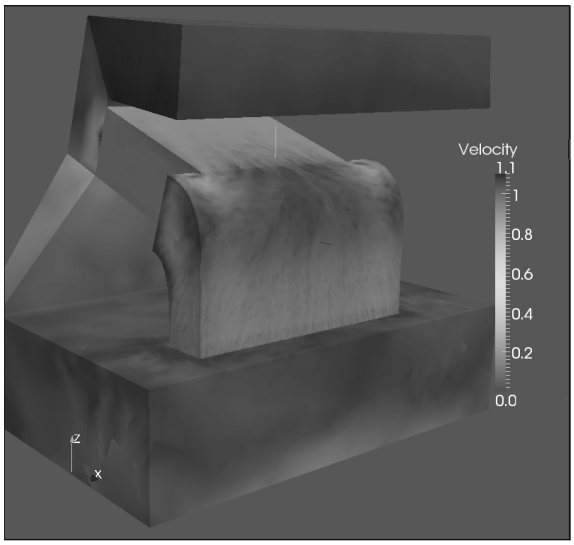

Figure 4. Instantaneous velocity distribution with the modified plenum design m1.

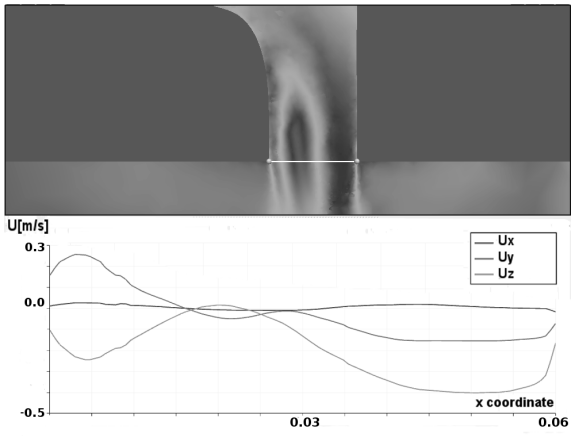

Figure 5. Mean velocity components profile in x middle section of the discharge (see white line on the upper figure) with the modified plenum design m1.

5.4. Numerical simulation of the modified plenum geometry m2

A new design is modelled and the flow produced is predicted by means of LES. The modified plenum m2 includes a smoothing lateral diffusors, that avoid fast changes of section in the path from the fans to the ACU discharge. In the Figures 7 and 8 it can be seen that the initial lack of homogeneity is diminished with this design.

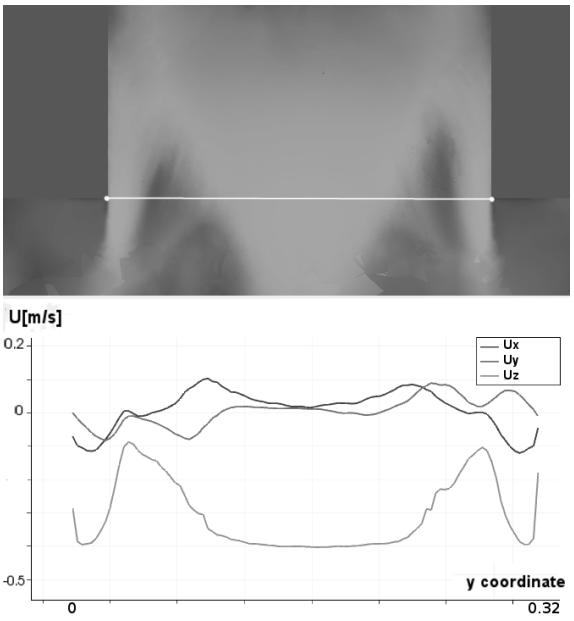

Figure 6. Mean velocity components profile in y middle section of the discharge (see white line on the upper figure) with the modified plenum design m1.

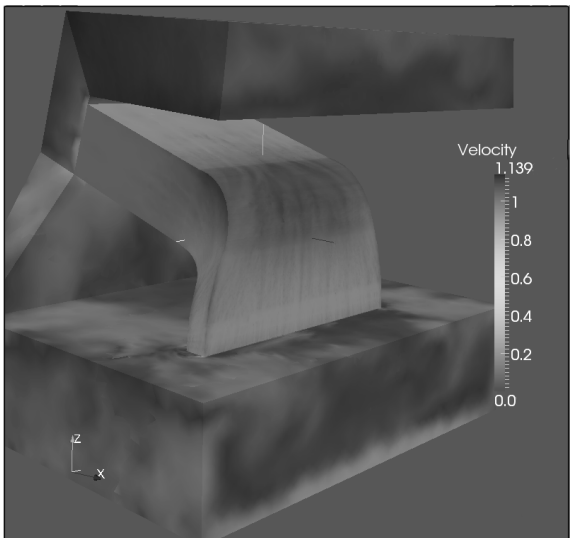

Figure 7. Instantaneous velocity distribution with the modified plenum design m2.

5.5. HWA measurements of the proposed geometries

A prototype of the proposed designs is constructed and evaluated by means of HWA. The results for the model m1 without lateral diffusors are summarized in table 2. The results for the model m2 with lateral diffusors are summarized in table 3.

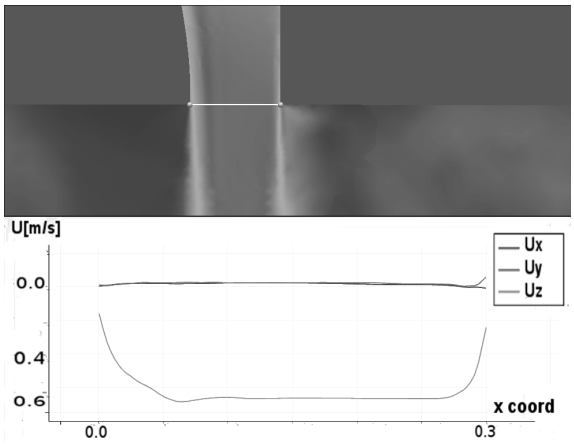

Figure 8. Mean velocity components profile in x middle section of the discharge (see white line on the upper figure) with the modified plenum design m2.

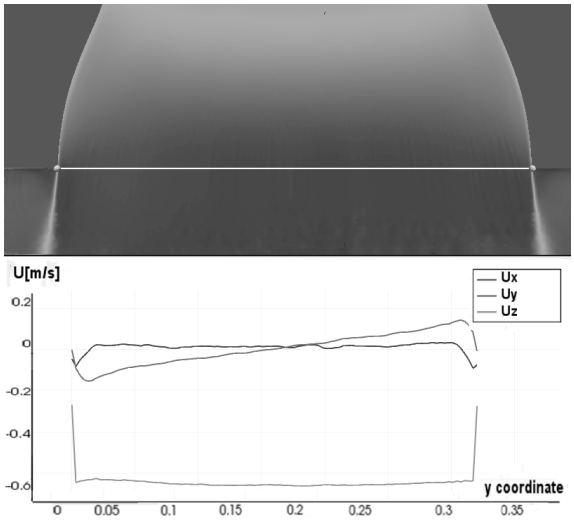

Figure 9. Mean velocity components profile in y middle section of the discharge (see white line on the upper figure) with the modified plenum design m2.

It can be seen in the comparative of table 4 that the new design has a better behavior than the initial design. The modified plenum m1 does not improve much more the results, but after lateral diffusors and a thin nozzle are introduced (modified plenum m2) the results are satisfactory even at the most demanding distance (4 metres from the discharge).

5.6. Experimental and numerical energy spectras

The energy spectra at some locations at the discharge have been studied in order to evaluate the possible coherent strutures of the flow with the proposed design. The energy spectra at the central point of the discharge is presented (see location as white point on Fig. 11). The study is carried out employing the technique of the Lomb periodogram,

Distance[m]	0.06	1.0	2.0	3.0	4.0
Avg. core vel	15.99	6.78	5.09	3.29	3.07
Uniformity	73%	79%	85%	84%	81%

Table 2. Mean core velocities in function of the distance from the air curtain discharge. Prototype without lateral diffusors.

Distance[m]	0.06	1.0	2.0	3.0	4.0
Avg. core vel	17.65	8.85	7.02	5.63	4.4
Uniformity	83%	83%	85%	85%	86%

Table 3. Mean core velocities in function of the distance from the air curtain discharge. Prototype with lateral diffusors and thin nozzle.

Prototype	Initial	m1	m2
Avg. core vel at 4 m	2.47	3.07	4.4
Improvement	-	24%	80%

Table 4. Comparative of the results obtained by the initial geometry and the proposed prototypes.

which generates the energy spectra from an uneven temporal signal [10]. The evaluation of the proposed design m2 indicates a possible vortex shedding in two different frequencies (see Fig. 10). A plausible explanation for this phenomena is that the vortex shedding of low frequency is produced by the lateral ring vortices and the vortex shedding of high frequency is produced by the inner curve (see Fig.12). The observation of the streamlines indicates a similar behavior. In order to check the frequency associated with the vortex shedding produced by the inner curve:

$$St = fD/v \tag{7}$$

So, as the other parameters are known, the frequency associated is

$$f = St * v/D = 0.2 * 20.0/0.3 = 53s^{-1} \tag{8}$$

The spectra obtained experimentally at the same location show a different energy distribution, not appearing the observed peaks. The difference between spectras possibly indicate that the peaks (see Fig. 10 and 11) are numerically induced. Another possibility is that discrepancies are generated by the boundary conditions. The numerical simulations can only partially emulate the real boundary conditions.

The observation of the spectra obtained numerically (see Fig.10) indicates a possible backward cascade of energy from high frequencies. It can also be observed that the -5/3 slope is not an acceptable approximation in the studied region of the spectra. This indicates that the flow exhibits a non isotropic turbulence, possibly due to the proximity of solid walls.

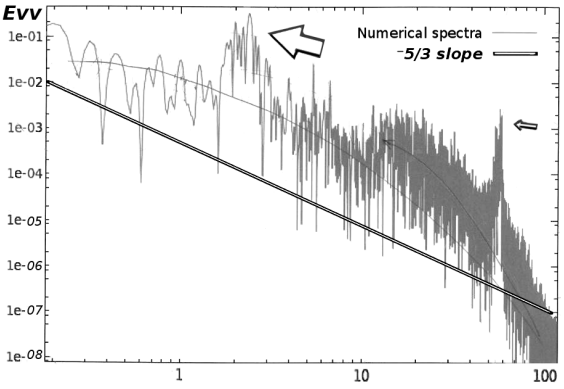

Figure 10. Energy spectra numerically obtained at middle point of the discharge with the modified plenum design m1.

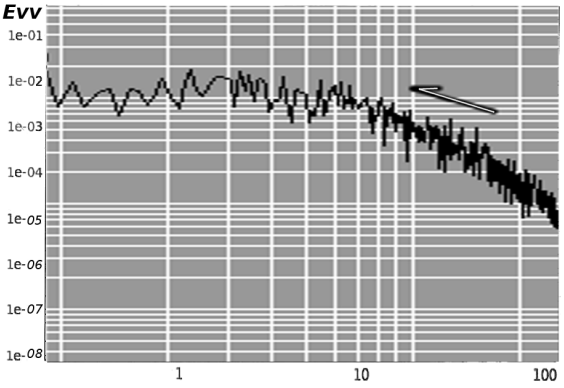

Figure 11. Energy spectra experimentally obtained at middle point of the discharge with the modified plenum design m1.

6. CONCLUSIONS

The airflow ejected by an air curtain has been characterized according to the AMCA standard requirements [1]. The measurements of the flow produced by the initial design has been observed as a non homogeneous, with very low velocity values in some regions. It have been detected by means of LES the main reasons of the problem. Alternative geometries have been numerically characterized and the best candidate according to the predictions has been constructed. The prototype has been checked experimental and numerically, showing concordance between the simulations and the measurements. The prototype of the proposed geometry improves the homogeneity and the mean velocity values in the discharge.

It is worth noting the optimization procedure described here is iterative. It includes experimental measurements, numerical simulations and the production of new prototypes, being the manufacturer an active agent in every cicle.

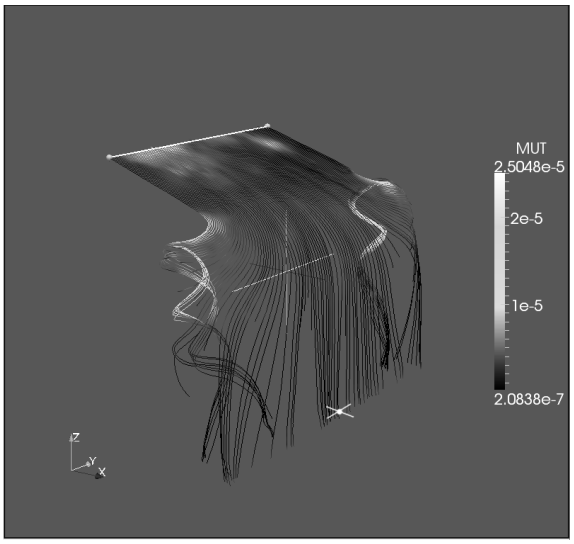

Figure 12. Streamlines obtained with the modified design m1.

The different plenum geometry modifications (both the inner curve and lateral difusors as well) have been checked. After the present study, the air curtain presents a configuration with two major modifications introduced so far: outer and inner curves, and next prototypes may include the lateral diffusors proposed.

LES has been employed in the optimization procedure of the air curtain plenum.

ACKNOWLEDGEMENTS

This work has been financially supported by the Ministerio de Educacion y Ciencia, Spain (Project: 'Development of high performance parallel codes for the optimal design of thermal equipments', reference ENE2010-17801) together with the companies Termofluids and Airtecnics.

References

[1] Air Movement and Control Association International. *"ANSI/AMCA Standard 220-05. Laboratory Methods of Testing Air Curtain Units for Aerodynamic Performance Rating."*, 2005.

[2] K. Sirén. "Technical Dimensioning of a Vertically Upwards Blowing Air Curtain. Part I" *Energy and Buildings*, 35:681–695, 2003.

[3] J. E. Jaramillo, C. D. Pérez-Segarra, A. Oliva, and C. Oliet. "Analysis of the Dynamic Behaviour of Refrigerated Space Using Air Curtains" *Numerical Heat Transfer, Part A*, 55(6):553–573, 2009.

[4] O. Lehmkuhl, C. D. Perez-Segarra, R. Borrell, M. Soria, and A. Oliva. "TERMOFLUIDS: A new Parallel unstructured CFD code for the simulation of turbulent industrial problems on low cost PC Cluster" In *Proceedings of the Parallel CFD 2007 Conference*, pages 1–8, 2007.

[5] J. E. Jaramillo. *"Suitability of Different RANS Models in the Description of Turbulent Forced Convection Flows. Application to Air Curtains"* PhD thesis, Universitat Politècnica de Catalunya, 2008.

[6] A. M. Foster, M. J. Swain, R. Barrett, P. D'Agaro, and S. J. James. "Effectiveness and optimum jet velocity for a plane jet air curtain used to restrict cold room infiltration" *International Journal of Refrigeration*, 29(5):692–699, 2006.

[7] P. Sagaut. *"Large Eddy Simulation for Incompressible Flows"*. Springer-Verlag, 2001.

[8] J. Smagorinsky. "General circulation experiments with the primitive equations, part. I: the basic experiment" *Monthly Weather Rev.*, 91:99–164, 1963.

[9] F. Nicoud and F. Ducros. "Subgrid-scale stress modeling based on the square of the velocity gradient tensor" *Flow, Turbulence and Combustion*, 62:183–200, 1999.

[10] William H. Press, Saul A. Teukolsky, William T. Vetterling, Brian P. Flannery *Numerical Recipes: the art of scientific computing*,689:692, 2007.

Conference on Modelling Fluid Flow (CMFF'12)
The 15th International Conference on Fluid Flow Technologies
Budapest, Hungary, September 4-7, 2012

2D AXISYMMETRIC NUMERICAL SIMULATION AND COMPARISON WITH EXPERIMENTAL DATA OF SWIRLING FLOW IN A CONICAL DIFFUSER WITH FLOW-FEEDBACK CONTROL TECHNIQUE

Constantin TĂNASĂ[1], Alin BOSIOC[2], Romeo SUSAN-RESIGA[3], Sebastian MUNTEAN[4]

[1] Corresponding Author. Department of Hydraulic Machinery, "Politehnica" University of Timisoara. Bv. Mihai Viteazu, No.1, Tel.: +40 256403692, E-mail: costel@mh.mec.upt.ro
[2] Romanian Academy – Timisoara Branch, E-mail: alin@mh.mec.upt.ro
[3] Department of Hydraulic Machinery, "Politehnica" University of Timisoara, E-mail: resiga@mh.mec.upt.ro
[4] Romanian Academy – Timisoara Branch, E-mail: seby@mh.mec.upt.ro

ABSTRACT

In our previous work is introducing the axial water jet injection at the end of the runner crown to mitigate the vortex rope. Around 10% of the main discharge is necessary to mitigate the vortex rope (associated to 70% partial discharge for a real turbine). The axial water jet is supplied with water from upstream. It is not acceptable to bypass the runner with such a large fraction of the turbine discharge because of volumetric losses which appears into the system. By examining the flow on the discharge cone, when the turbine operates at part load, is observed that is an excess of static and total pressure on the cone wall. This conclusion led us to introduce the new flow-feedback control technique (FFCT). This technique does not require any additional energy supply and the turbine efficiency is not affected. The FFCT was implemented on test rig from "Politehnica" University of Timisoara. This paper presents results of a 2D axisymmetric numerical simulation of swirling flow which are compared against experimental ones in two cases: with and without FFCT (numerical velocity profiles and pressure recovery coefficient are compared against the experimentally measured values). The results prove stagnant region mitigation when employing the FFCT.

Keywords: axisymmetric, conical diffuser, flow-feedback, swirling flow.

NOMENCLATURE

D_{throat}	$[m]$	reference diameter from the throat of the convergent - divergent test section
N	[-]	the number of samples
Q	$[m^3/s]$	main discharge
c_p	[-]	pressure recovery coefficient
p	$[kPa]$	static pressure
v	$[m/s]$	velocity

Subscripts and Superscripts

RMS	Random Mean Square
i	index of each samples
s	the number of acquired samples for each set
throat	throat of the test section
–	temporal mean

1. INTRODUCTION

The variable demand of the energy market forces that hydraulic turbine to work at different regimes, which includes the regimes far from the best efficiency point. In particular, for fixed-pitch blades runners (i.e. Francis turbine), the efficiency of the turbine rapidly deteriorates at off-design operating points. Moreover, in the discharge cone downstream the runner a precessing helical vortex (called vortex rope) is developed, with associated severe pressure fluctuations. The vortex rope produces large vibrations in the hydraulic system, breakdowns of the runner blades or leads to power swing phenomenon. Rotation flow phenomenon came to be investigated experimentally in the last decades by many research teams, but CFD technique, came to be applied with conclusive results only in the last two decades. A first numerical analysis of unsteady swirling flow in draft tube cone was made by Ruprecht et al. [1]. The numerical results are compared and validated with the experimental ones. An important step in understanding the phenomenon of partial discharges flow in draft tube cone was performed within the

project FLINDT. Experimental investigations were performed by Ciocan et al. [2]. Pressure pulsations were analyzed on the cone wall, velocity profiles out of the runner and on the cone with LDV and PIV. These data were used to better understand the formation of vortex rope in the draft tube. Also experimental results were compared with those of numerical simulation. Thus the results for numerical simulation of vortex rope precession motion showed that three-dimensional turbulent flow model reproduce quantitatively correct physical phenomenon.

In order to eliminate or to mitigate the instabilities from the draft tube cone different techniques have been implemented in hydraulic turbines. Given by the energy injected in the draft tube cone these methods can be divided into active, passive or semi passive control. If an external energy source is used to mitigate or eliminate the vortex rope, the control is called active. Examples of active control include cone air admission, aeration by the wicket gates trailing edge [3], [4], or tangential water jets [5]. The control involving no additional energy to destroy the vortex rope is called passive. Passive control methods include fins mounted on the cone [6] extending cones mounted on the runner's crown [7] or using J-Grooves [8]. These methods lead to some improvements in reducing the pressure pulsations for a narrow regime but they are not effective or even increase the unwanted effects. Resiga et al. [9] have proposed a novel and robust method to mitigate the vortex rope: a water jet is injected in the crown of the runner, along the discharge cone axis. This technique was investigated on a test rig developed at the "Politehnica" University of Timisoara.

Muntean et al. [10] have performed a 3D numerical analysis of the swirling flow into the test section geometry. The vortex rope computed using numerical simulation has a similar configuration with that observed on experimental test rig. A comparison between experimental results and 2D axisymmetric numerical simulation was performed by Susan-Resiga et al. [11]. This work proved that a 2D axisymmetric simulation is able to capture very well the measured velocity profiles at different levels on the con. Also, it was demonstrated that a 2D axisymmetric simulation is able to capture the formation and development of swirling flow phenomena at levels similar to a 3D numerical simulation. The only observation is that for a 2D axisymmetric simulation the pressure pulsations cannot be investigated, consequently the maximum amplitude peaks cannot be identified. Therefore a 2D axisymmetric numerical simulation can offer as soon as accurate information about the flow in the diffuser cone with or without vortex rope at different flow regimes or applying the new control method. In the case of swirl generator from UPT laboratory, which were made previous experimental measurements, numerical simulation has been investigated by several research groups. Their purpose was to validate the numerical model with experimental results. Petit et al. [12] use OpenFoam code to validate the measured velocity profiles. Entire swirling flow generator along with convergent-divergent test section was investigated three-dimensional. A numerical calculation, which involved comparing and validating the results of the Fluent code was analysis of Ojima et al. [13]. The conclusion of these investigations was that different numerical codes were able to capture the numerical results of the experimental data very well. The drawback of this study is that the time of three-dimensional calculation is large, so it is difficult to calculate a number of operating regimes in a short time. Bosioc in his PhD. thesis [14] has presented the design, implementing and experimental measurements of the axially jet control method. The flow control technique used by Bosioc, requires 10% or more from the main discharge to supply the jet. The water which supplies the jet is taken from upstream with an auxiliary energy source (pump).

The results presented by Bosioc et al. in [14], show that the pressure fluctuations associated to the vortex rope, have a sudden drop when the jet is supply with approximately 11-12% from de main discharge. Obviously it is not acceptable to by-pass the runner with such a large fraction of turbine discharge, because of volumetric losses which appear into the system, and that leads to a decrease of the turbine efficiency.

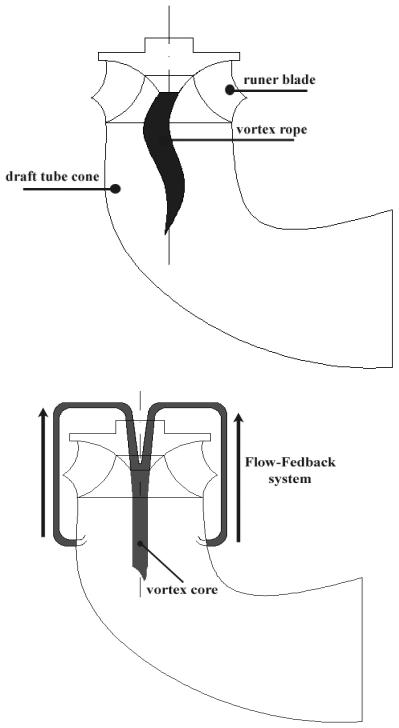

Figure 1. Schematic representation of the vortex rope (up) and water jet injection using FFCT (down), in the conical diffuser

By examining the flow on the discharge cone, when the turbine operates at part load, Resiga et al. [15] have observed an excess of static and total pressure near to the cone wall. This conclusion led him to introduce a new Flow-Feedback Control Technique – FFCT (a passive control method), by taking a fraction of the flow from the cone wall, which is redirected to upstream, for eliminating the vortex rope, by injecting it through the runner crown. This technique does not require any additional energy in order to supply the axial jet. Consequently, the overall turbine efficiency is not decreased (Fig. 1).

The second section of the paper presents the experimental test rig used to generate the swirling flow in a conical diffuser similar with the draft tube cone of a Francis turbine and the FFCT description. The third and the fourth sections present the experimental and numerical investigations of velocity profiles and pressure recovery coefficient. Section five present the results and validation between numerical and experimental data. Section six summarizes the conclusions.

2. TEST RIG

The test rig has some main parts like: swirl generator, test section for measuring pressure filed, another one for measuring velocity profiles with Laser Doppler Velocimetry (LDV), and the twin spiral case with double exit (Fig. 2 - up).

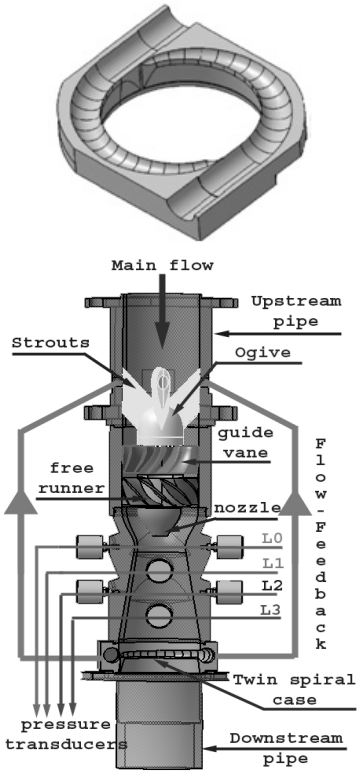

Figure 2. Twin spiral case (up), and cross-section of the assembled test section with flow feedback system (down)

The swirl generator presented by Resiga et al. in [15], has an upstream ogive with four leaned struts, followed by a set of guide vanes and a free runner, and ending with a nozzle (Fig. 2 - down). The ogive supports the entire assembly of the swirl generator and allows the injection of water through the leaned struts.

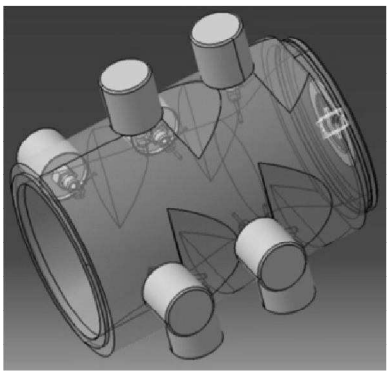

Figure 3. The test section with 8 transducers for pressure field measurements

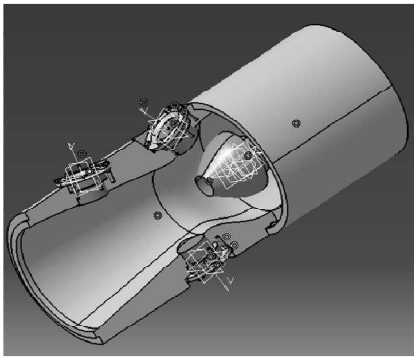

Figure 4. The test section with three optical windows for measuring the velocity profiles with LDV

Two test sections with the same geometry was manufactured, Bosioc et al. [14], in order to measure the velocity and pressure fields, respectively. On the first test section 8 pressure transducers are installed two by two at four levels (L0…L3), Fig. 3. On the second one, three optical windows was installed in order to measure the velocity profiles with Laser Doppler Velocimetry – LDV, Fig. 4. The first window is located in the convergent part of the test section. The second window is displaced on the divergent part near to the throat while the third one near to the exit, respectively. The flow-feedback technique was implemented on the test rig from "Politehnica" University of Timisoara, Tanasa et al. [16]. The main part of the flow-feedback system is a twin spiral case installed downstream to the discharge cone. The spiral case collects the water from the cone outlet and supplies the axial jet through the pipe system (Fig. 2).

3. EXPERIMENTAL INVESTIGATIONS

Two kinds of measurements were performed on the test section: the velocity profiles measurements with LDV (Fig. 5) and pressure measurements in order to assess the pressure recovery coefficient.

The LDV measurements were performed on the test section with the three optical windows, and the pressure was measured on the test section with the 8 pressure transducers, both of them presented in section 2. The experimental data were measured with Dantec Dynamics 2D LDV system with two components (meridional and circumferential velocity). The main characteristics of the optical system are: focal length of the probe 159.6 mm, beam diameter 2.2 mm and the beam spacing 39.2 mm. Two pairs of beams with wavelength of 488 nm and 514.5 nm are generated, and the probe includes a photo multiplier with incorporated amplified. A 3D traversing system is installed for probe positioning within 0.01 mm accuracy on each axis. Measurements were performed with a step of 1 mm, and 15000 samples or 20 seconds acquisition time, which was set before.

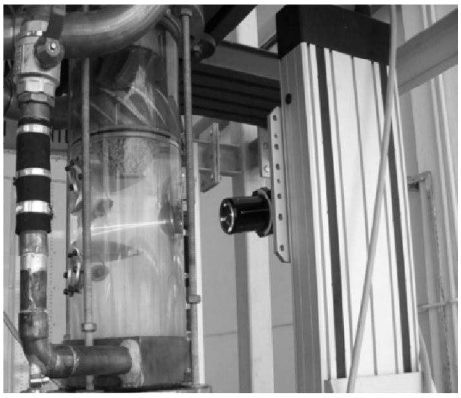

Figure 5. LDV system during the velocity profiles measurements

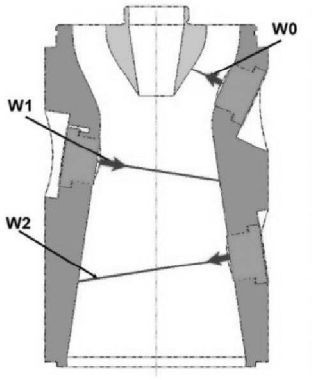

Figure 6. Test section with the three optical windows and the corresponding survey axis for measuring the velocity profiles

In order to reflect the light which is produced by the laser, in the test rig were introduced silver particles with 10 μm mean diameter. Figure 6 present the test section with the optical windows and the location of associate survey axis for the three windows.

The time averaged velocity was calculated with equation:

$$\bar{v} = \sum_{i=0}^{N-1} \frac{1}{N} \cdot v_i \tag{1}$$

where N is number of samples, and v_i the velocity for each sample. The analysed data are presented in dimensionless form, using the following reference values: the minimum diameter of the test section D_{throat} = 0.1 m and the mean velocity at the throat is the discharge velocity corresponding to the discharge Q:

$$v_{throat} = \frac{Q}{\pi \cdot \frac{D_{throat}^2}{4}} \tag{2}$$

where Q is the main flow discharge, and D_{throat} is the throat diameter of the test section.

The plotted velocity profiles for meridian and circumferential velocity have points obtained from experimental investigation with and without FFCT, at overall discharge values Q = 0.03 m^3/sec and Q = 0.025 m^3/sec in dimensionless values and the variation of Random Mean Square Velocity (v_{RMS}) for each point also in dimensionless values. The variation of RMS was calculated with formula:

$$v_{RMS} = \sqrt{\sum_{i=0}^{N-1} \frac{1}{N} \cdot \left(v_i - \bar{v}\right)^2} \tag{3}$$

In order to obtain reliable pressure data we measure 100 sets at discharge value of 0.03 m^3/sec. Each set is acquired using a Lab View program, and corresponds to an acquisition time of 32 seconds at a sampling rate of 256 samples/sec, resulting in 8192 samples of unsteady pressure.

The capacitive pressure transducers have an accuracy of 0.13% within a range of ±1 bar relative pressure. For the investigations reported in this paper we are interested in the time-averaged pressure values, in order to assess the wall pressure recovery for the conical diffuser without and with FFCT. The dimensionless wall pressure recovery coefficient, c_p, is defined as:

$$c_p = \frac{\bar{p} - \bar{p}_{throat}}{\left(\rho \cdot v_{throat}^2\right) / 2} \tag{4}$$

where is the time averaged value of the wall pressure, with the corresponding value at the throat p_{throat}, and v_{throat} defined in Eq. (2). All graphs of

pressure recovery coefficient contain the variation of the RMS which was calculated with formula:

$$p_{RMS} = \sqrt{\sum_{i=1}^{N_s} \frac{1}{N_s} \left(p_i - \bar{p}\right)^2} \qquad (5)$$

where *Ns* is number of acquired samples for each set, in our case *Ns* = 8192 samples, p_i is the measured pressure for each sample. Of course, p_{RMS} is also made dimensionless with respect the kinetic term $\left(\rho \cdot v_{throat}^2\right)/2$.

4. NUMERICAL INVESTIGATIONS

The above experimental investigations offer only a limited amount of data. As a result, in order to understand the complex physics of the decelerated swirling flow we perform numerical simulations as well. As mentioned before, in the present paper we focus on the time-averaged flow field. Therefore, a simplified flow model corresponding to the axisymmetric turbulent swirling flow downstream the free runner of the swirl generator is considered. The 2D axisymmetric domains for numerical simulation are presented in Figure 7 (without FFCT – upper half-plane and with FFCT – lower half-plane). The annular inlet section is considered just downstream the runner blades. Then we have a convergent section up to the hydraulic passage throat, and a conical diffuser ending with a discharge cylindrical pipe. In the numerical domain we have the survey axis where meridian and circumferential velocity profiles are validated against LDV measured ones. First, the swirl generator was analyzed numerically, using a three-dimensional turbulent flow computation. Separate sub domains were considered for the ogive with struts, non-rotating blades, and the free runner [17]. The mixing interface technique was employed to transfer the outlet velocity and turbulence quantities profiles from one sub-domain to the next one in the flow direction.

For numerical simulation both the 3D domain for the swirl generator and 2D domain for the test section is use an unsteady k-ε turbulence model. From the 3D domain of the free runner we impose the velocity profiles in the axisimmetric 2D domain. Since the flow in the conical diffuser is three-dimensional and unsteady due to the development of the precessing vortex rope, one may question the relevance of an axisymmetric flow simulation. This issue was examined by Resiga et al. [11], and we concluded that the axisymmetric flow model accurately describe the circumferentially averaged three-dimensional flow field. For the 2D simulation the governing equations for axisymmetric swirling flows and incompressible fluids were obtained by writing both the continuity and the momentum equations in cylindrical coordinates (z, r, θ).

The continuity equation:

$$\frac{\partial v_z}{\partial z} + \frac{\partial v_r}{\partial r} + \frac{v_r}{r} = 0 \qquad (6)$$

The axial momentum equation:

$$\frac{\partial v_z}{\partial t} + v_z \frac{\partial v_z}{\partial z} + v_r \frac{\partial v_z}{\partial r} = -\frac{1}{\rho}\frac{\partial p}{\partial z} \qquad (7)$$

The radial momentum equation:

$$\frac{\partial v_r}{\partial t} + v_z \frac{\partial v_r}{\partial z} + v_r \frac{\partial v_r}{\partial r} - \frac{v_\theta^2}{r} = -\frac{1}{\rho}\frac{\partial p}{\partial r} \qquad (8)$$

The circumferential momentum equation:

$$\frac{\partial v_\theta}{\partial t} + v_z \frac{\partial v_\theta}{\partial z} + v_r \frac{\partial v_\theta}{\partial r} + \frac{v_r v_\theta}{r} = 0 \qquad (9)$$

At the outlet of the computational domain a radial equilibrium condition is used which involves the radial pressure gradient with the circumferential velocity:

$$\frac{\partial p}{\partial r} = \frac{\rho v_\theta^2}{r} \qquad (10)$$

The effective dynamic viscosity is calculated as the sum at the so called turbulent viscosity μ_T and the molecular viscosity μ. The axisymetric swirling flow model which is implemented in the FLUENT 6.3 code is used with the turbulence model which was described above.

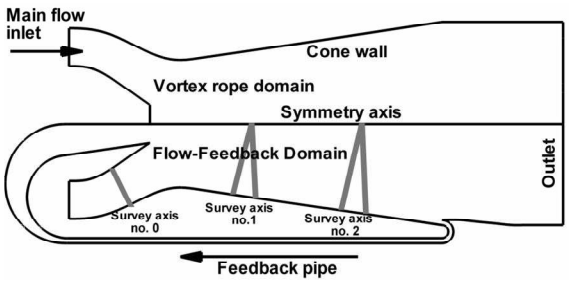

Figure 7. 2D computational domain in a meridian half-plane without FFCT (upper) and with FFCT (lower)

5. RESULTS

Once the numerical solution for the axisymmetric turbulent swirling flow is obtained, we first check the accuracy of the inlet velocity profiles. In doing so, we compare the computed meridian and circumferential velocity profiles with the LDV measurements on the survey axis located in the three windows of the test section. The results of the velocity profiles and pressure recovery coefficient are presented in the dimensionless form

with respect the throat diameter (for the axis) and velocity from the throat test section (see eq. 2 and eq. 4). Figure 8 presents the velocity profiles for window 2, where a very good agreement between computations and measurements it is observed, thus validating the overall accuracy of the 3D flow computation in the bladed region of the swirl generator. The RMS for W0 is 20% for each measured point.

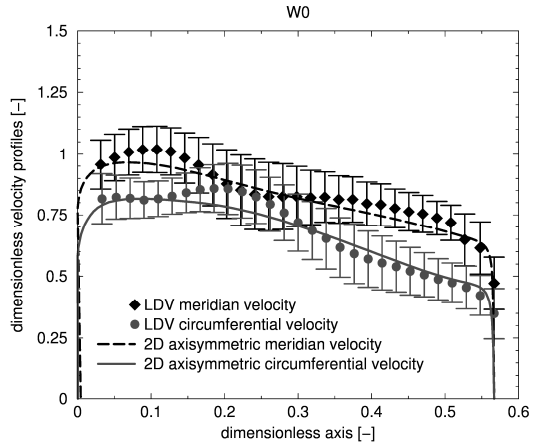

Figure 8. Comparison of velocity profiles between experimental investigation and numerical simulation in the convergent part of the test section (window W0)

For window W1 and window W2 in the case without FFCT the velocity profiles are presented in Figure 9. It can be observed for both windows that it exist a quasi-stagnant region associated to the vortex rope (in the middle part of the survey axis the meridian profile is near to zero value). Nishi et al. [18] shows that the vortex rope evolves from the instability of a vortex sheet which rolls-up as a helical vortex (spiral vortex core) around a central stalled region. This central region is highly oscillating due to the helical vortex precession, but on average it has a vanishing velocity. For both windows W1 and W2, from comparison of meridian and circumferential velocity profiles is observed in the case of numerical analysis, the stagnant region is larger than the experimental one. It seems that the axisymmetric model cannot catch very well the 3D effects of vortex rope from reality. Anyway the profiles from numerical analysis are in the variation of v_{RMS}, for each point. From both circumferential velocity profiles is observed that flow is like a solid body rotation.

In the case with FFCT the velocity profiles are presented in Figure 10. For window W1 is observed that meridian velocity profile has an excess flow up to a double value, as a fact the stagnant region associated to vortex rope is removed. Circumferential velocity profile is placed in the middle part of the axis around zero, meaning that in that area instead of tangential component of the velocity the place is taken by the axial velocity component. Anyway it can be observed that the numerical and experimental results are in a very good agreement. For window W2 it can be observed that the jet generated by the FFCT is not enough to mitigate de vortex rope. To mitigate (and for this window too), the vortex rope, it is more necessary 2% to the jet from nominal flow [11]. Anyway is observed from the meridian velocity profile that the stagnant region is much smaller than in the case of W1, and numerical and experimental velocity profile are in a good agreement.

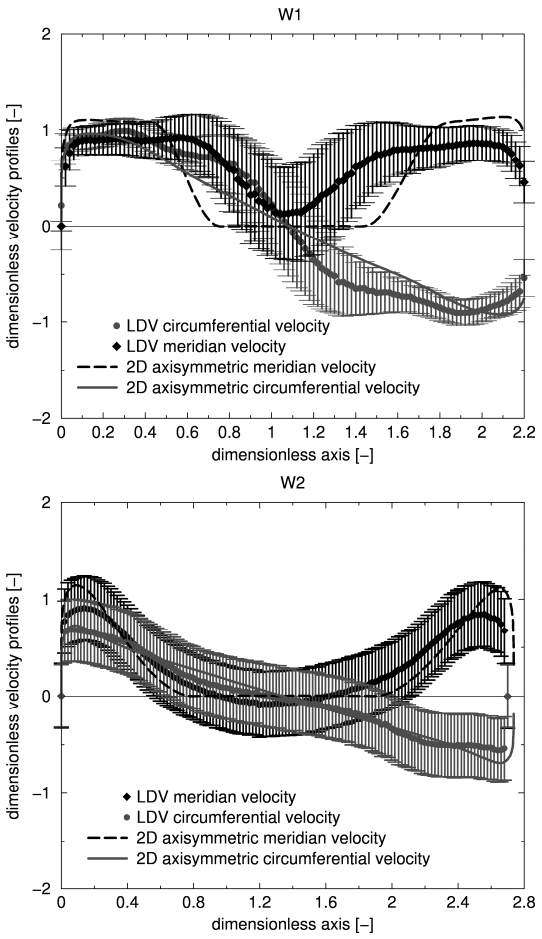

Figure 9. Comparison of velocity profiles for window W1 – up, and window W2 – down, for the case without FFCT

The error band for W0 for each measuring point is 25%, for W1 in the case without FFCT (Fig. 9 - up), is between 25% at the wall of the test section and 50% in the middle part, were the stagnant region is well developed. For W2 in the case without FFCT (Fig. 9 – down), the error band is 50%. In the case with FFCT the error band for W1 is between 5% at the wall and 2% in the middle of the test section. For W2 in the case with FFCT the error band is between 25% at the wall and 30% in the middle. It can be observed, since with employing the FFCT the errors are diminishes.

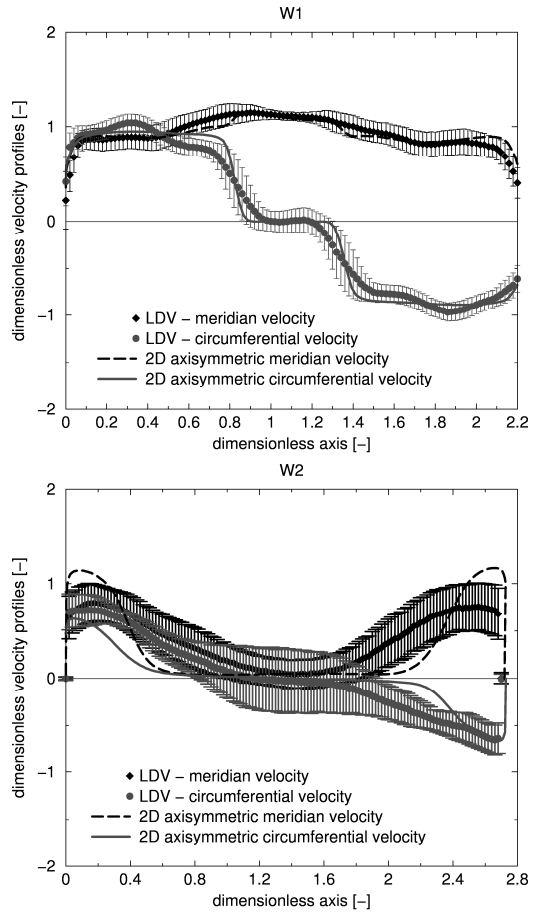

Figure 10. Comparison of velocity profiles for window W1 (up), and window W2 (down), for the case with FFCT

Once the velocity profiles are validated, we focus on the wall pressure recovery coefficient for both flow regimes: without and with FFCT. Figure 11 shows the wall pressure coefficient computed from the axisymmetric turbulent swirling flow simulation and the measured values at the positions indicated in Section 2 – Fig. 2. We see that the wall pressure recovery reaches a value of approximately 0.55 when the decelerated swirling flow has a precessing vortex rope. Once again, in this paper we examine only the time averaged flow field, in order to assess the influence of our flow control approach on the overall diffuser efficiency. The computational results in Fig. 11 (up) agree well, with the measured pressure recovery coefficient, with an overestimation of the experimental value obtained in the middle part of the conical diffuser, at 100 mm distance from the throat. It can be seen that the axial model cannot capture exactly the 3D effects of the vortex rope from reality. We explain this difference by the large amplitude of the pressure fluctuations in this region due to the precessing vortex rope. From the case with FFCT (Fig. 11 – down), it can be observed that wall pressure recovery coefficient increases up to approximately 0.8, this is 45% larger than the previous value of 0.55 without FFCT. Both plots in Fig. 11 include the 2% error band of the main value for each measuring point, calculated with eq. 5. This is an important improvement in the diffuser performance, which for real turbines will lead to a corresponding increase of the overall performance. The numerical results agree well with the measured values of the wall pressure recovery coefficient.

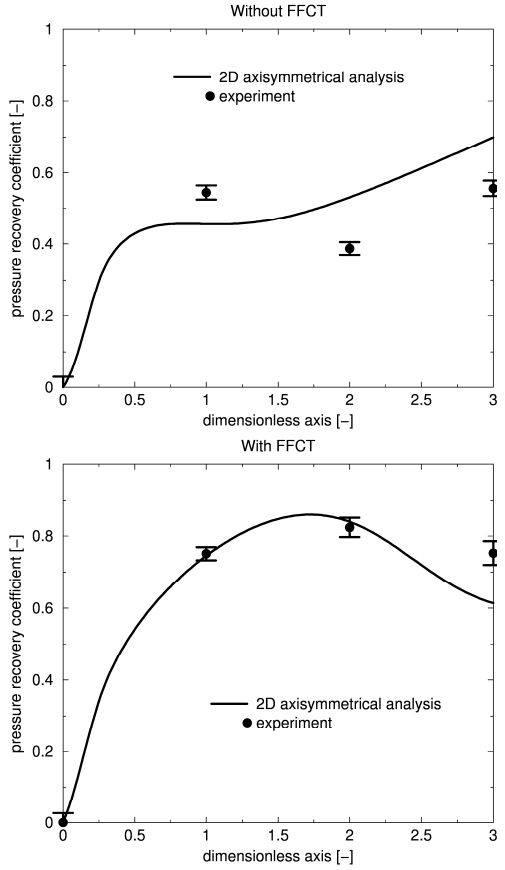

Figure 11. Wall pressure recovery coefficient without FFCT (up) and with FFCT (down)

6. CONCLUSIONS

In this paper the decelerated swirling flow in conical diffuser, with a configuration that mimics the flow in the discharge cone of hydraulic turbines operated at partial discharge is investigated. In particular, it is examine a novel flow control technique (Flow-Feedback), which uses a fraction of the discharge near the cone wall in order to mitigate the vortex rope, and to improve the pressure recovery while reducing the hydraulic losses. The wall pressure recovery measurements on the conical diffuser show that the FFCT leads to a 45% improvement in the first part of the test section. This is extremely useful for hydraulic turbines when operated far from the best efficiency point, leading to a significant overall increase in the performance. In order to elucidate the correlation

between the jet injection with FFCT along the axis and the increase in pressure recovery it is performed numerical simulations of the decelerated turbulent swirling flow using an axisymmetric flow model. The velocity profiles from numerical simulation are validated with very good accuracy against Laser Doppler Velocimetry measurements of the meridian and circumferential velocity profiles on the test section. Also pressure recovery from experiment it is in a good agreement with the numerical one. As it's expected, for the case without FFCT it seems that the axisymmetric model cannot capture with enough accuracy the 3D effects of vortex rope, but an axisymmetric flow from experiment can be validated very well with the numerical one.

ACKNOWLEDGEMENTS

"This work was supported by the CNCSIS PCE 799/2008 project and partially by a grant of the Romanian National Authority for Scientific Research, CNCS – UEFISCDI, project number PN-II-RU-PD-2011-3-0165."

REFERENCES

[1] Ruprecht, A., Helmrich, T., Aschenbrenner, T. and Scherer, T., 2001, „Simulation of pressure surge in a hydro power plant caused by an elbow draft tube", *10th International Meeting of the Workgroup on the Behaviour of Hydraulic Machinery under Steady Oscilatory Conditions*. Trondheim, Norway.

[2] Ciocan, G.D., Iliescu, M., Vu, T.C., Nennemann, B. and Avellan, F., 2007, „Experimental study and numerical simulation of the FLINDT draft tube rotating vortex", *JFE,* 129, pp.146-158.

[3] Thike, R.H., 1981, „Practical solutions for draft tube insatbility", *Water Power and Dam Construction*, 33(2), pp.31-37.

[4] Pappilon, B., Sabourin, M., Couston, M., and Deschenes, C., 2002, "Methods for air admission in hydro turbines", *Proceedings of the 21st IAHR Symposium on Hydraulic Machinery and Systems*, Lausanne, Switzerland, pp. 1-6.

[5] Kjeldsen, M., Olsen, K., Nielsen, T., and Dahlhaug, O., 2006, "Water injection for the mitigation of draft tube pressure pulsations", *IAHR International Meeting of W.G. on Cavitation and Dynamic Problems in Hydraulic Machinery and Systems*, Barcelona, Spain.

[6] Nishi, M., Wang, X. M., Yoshida, K., Takahashi, T., and Tsukamoto, T., 1996, "An Experimental Study on Fins, Their Role in Control of the Draft Tube Surging", *Hydraulic Machinery and Cavitation, in Cabrera, E., et al., eds., Kluwer Academic Publishers*, Dordrecht, The Netherlands, pp. 905-914.

[7] Vevke, T., 2004, "An Experimental Investigation of Draft Tube Flow," *PhD thesis*, Norwegian University of Science and Technology, Trondheim, Norway.

[8] Kurokawa, J., Kajigaya, A., Matusi, J., and Imamura, H., 2000, "Suppression of Swirl in a Conical Diffuser by Use of J-Groove," *Proceedings of the 20th IAHR Symposium on Hydraulic Machinery and Systems*, Charlotte, North Carolina, Paper DY-01.

[9] Susan-Resiga R., Vu T.C., Muntean S., Ciocan G.D., Nennemann B., 2006, „Jet control of the draft tube vortex rope in Francis turbines at partial discharge" Proc. of the *23rd IAHR Symposium on Hydraulic Machinery and Systems*, Yokohama, Japan.

[10] Muntean, S., Nilsson, H. and Susan-Resiga, R., 2009, „3D numerical analysis of the unsteady turbulent swirling flow in a conical diffuser using Fluent and OpenFoam", *In*: *Proceedings of the 3rd IAHR International Meeting of the Workgroup on Cavitation and Dynamic Problems in Hydraulic Machinery and Systems*. Brno, Czech Republic, pp.155-165.

[11] Susan-Resiga, R., Muntean, S., Tanasa, C. and Bosioc, A., 2009, „Three-dimensional versus two-dimensional axisymmetric analysis for decelerated swirling flows", *In*: *The 14th International Conference on Fluid Flow Technologies*. Budapest, Hungary.

[12] Petit, O., Bosioc, A., Nilsson, H., Muntean, S., Susan-Resiga, R., 2011, „Unsteady simulations of the flow in a swirl generator using OpenFoam", *IJFMS*, 4(1).

[13] Ojima, A. and Kamemoto, K., 2010, „Vortex method simulation of 3D and unsteady vortices in a swirling flow apparatus experimented in "Politehnica" University of Timisoara", *In*: *25th IAHR Symposium on Hydraulic Machinery and Systems, Online at: IOP Conf. Series: Earth and Environmental Science*. Timisoara, Romania.

[14] Bosioc, A., 2011, „Controlul curgerii cu rotatie in conul tubului de aspiratie al turbinelo hidraulice", *PhD. Thesis*, Timisoara, Romania.

[15] Susan -Resiga, R., and Muntean S., 2008, "Decelerated Swirling Flow Control in the Discharge Cone of Francis Turbine", *4th International Symposium on Fluid Machinery and Fluid Engineering*, Beijing, China.

[16] Tanasa, C., Bosioc, A., Susan-Resiga, R., and Muntean, S., 2011, "Flow-Feedback for Pressure Fluctuation Mitigation and Pressure Recovery Improvement in a conical diffuser with swirl", *IJFMS*, 4(1), pp. 47-56.

[17] Bosioc, A., Tanasa, C., Muntean, S. and Susan-Resiga, R., 2009, „2D LDV measurements and comparison with axisymmetric flow analysis of swirling flow in a simplified draft tube", *In*: *3rd International Meeting of the Workgroup on Cavitation and Dynamic Problems in Hydraulic Machinery and Systems*. Brno, Czech Republic, pp.551-561.

[18] Nishi, M., Shigenori, M., Takashi, K. and Yosutashi, S., 1982, „Flow regimes in a elbow draft tube", *In*: *IAHR Symposium, Operating Problems of Pump Station and Power Plants*.

External fluid dynamics

Conference on Modelling Fluid Flow (CMFF'12)
The 15th International Conference on Fluid Flow Technologies
Budapest, Hungary, September 4-7, 2012

EXPERIMENTAL DETERMINATION AND DATA PROCESSING OF TRAJECTORIES, DEFORMATION AND BREAKUP OF WATER DROPLETS IMPINGING ON AIRFOILS

Suthyvann SOR[1], Adelaida GARCÍA-MAGARIÑO[2], Jesús MOROTE[3]

[1] Aerodynamics Testing Engineer, Aerodynamics Branch, INTA (National Institute of Aerospace Technology), Carretera de Ajalvir km 4, 28850 Torrejón de Ardoz, Madrid, Spain. Tel.:+34915201641, Fax: +345202033. E-mail: sors@inta.es.
[2] Aerodynamics Testing Engineer, Aerodynamics Branch, INTA (National Institute of Aerospace Technology), Carretera de Ajalvir km 4, 28850 Torrejón de Ardoz, Madrid, Spain. Tel.:+34915201202, Fax: +345202033. E-mail: adelaida.garciamagarino@insa.es.
[3] Research Engineer, Aerodynamics Branch, INTA (National Institute of Aerospace Technology), Carretera de Ajalvir km 4, 28850 Torrejón de Ardoz, Madrid, Spain. Tel.:+34915201807, Fax: +345202033. E-mail: morotej@inta.es.

ABSTRACT

This work presents the methodology and specific software developed for the processing of high speed imaging taken at the rotating rig cell of INTA in cooperation with NASA, to observe the interaction between water droplets and airfoils. The water droplets, with diameters between 250 μm and 1000 μm, impinge on airfoils moving at velocities up to 90 m/s. The image acquisition rate is up to 75000 f.p.s, requiring automatic processing to handle the resulting large amount of frames. The specific Matlab application developed to perform this task can process 250 frames in 20 seconds to obtain positions, areas and equivalent maximum and minimum droplet diameters. An additional 30 seconds post processing period follows to obtain the water droplet velocity and acceleration. The experimentally determined flow field around the airfoil is used to obtain the Bond, Weber and Reynolds numbers as well as the drag coefficient along the path of a given droplet.

Keywords: Droplet Breakup, Droplets, Image Processing, Tracking, Trajectories.

NOMENCLATURE

Bo	[-]	Bond number
C_d	[-]	drag coefficient
D	[m]	droplet diameter
D_{max}	[pix]	droplet maximum diameter
D_{min}	[pix]	droplet minimum diameter
FR	[fr/s]	frame acquisition rate
Mg	[pix/m]	camera magnification
Oxy	[mm]	Cartesian coordinate system. Origin at the initial position of the droplet tracking. x parallel to the stagnation line, positive towards the model motion. and y perpendicular to the x axis vertical
Re	[-]	Reynolds number
U_m	[m/s]	model velocity in earth axes
U_{rd}	[m/s]	slip velocity
We	[-]	Weber number
X_{di}	[m]	droplet position in model axes
d	[mm]	droplet-leading edge distance
f_{di}	[-]	droplet frame number
f_m	[-]	model frame number
t	[s]	time
x_m	[m]	model position in frame axes
x_{di}	[m]	droplet position in frame axes
ρ_a	[kg/m^3]	air density
ρ_w	[kg/m^3]	water density
σ_w	[N/m]	water surface tension

1. INTRODUCTION

Aircraft manufacturers have reported in-flight observation of droplet breakup near the wing surfaces of large transport aircraft. The observation is relevant for in-flight icing phenomena. The breakup of large droplets before impinging on the lifting surfaces gives rise to a set of smaller droplets that in part may surpass the airfoil so affecting the expected ice accretion process. If droplet breakup is a factor in the ice accretion process, current ice accretion codes will need to be modified to account for the breakup phenomena [1-6].

In 2007 the National Aeronautics and Space Administration (NASA) and the Instituto Nacional de Técnica Aeroespacial (INTA) in Madrid, Spain, in a joined cooperative effort, undertook an experimental research program to obtain droplet breakup data on the vicinity of airfoils. A droplet breakup rotating rig [7] was designed and built at the INTA facilities near Madrid. Experiments were

conducted, in collaboration with NASA, in the fall of 2008 [1] and summer of 2011 [8]. The experimental setup and high speed image acquisition system is briefly described in section 2.

The large amount of data obtained from the experimental campaigns recommended the development of a specific Matlab application called SITEA for processing purposes. The application is capable to track individual droplets giving the trajectory, and the maximum, minimum and equivalent droplet diameters. In addition SITEA calculates velocities, accelerations and the non dimensional Reynolds, Bond, and Weber numbers together with the drag coefficient along the stagnation line.

A methodology to classify all the tests data obtained during the campaign was adopted to determine the input to the application. A defined storage format is necessary to perform a later study.

2. EXPERIMENTAL SETUP

The aim of the experiment is the recording of the evolution of droplets impinging on an airfoil. For this purpose, the rotating rig facility of INTA is used [7]. The rig, carrying a fixed airfoil, rotates at controlled velocities giving rise to airfoil impinging velocities up to 90 m/s. The water droplets fall from a monodisperse tap impinging on the airfoil. Images of the droplet evolution just before impact are taken by a high speed camera (75000 f.p.s) using shadowgraph photography technique [9]. A synchronizer system guarantees that images are taken just before the impact.

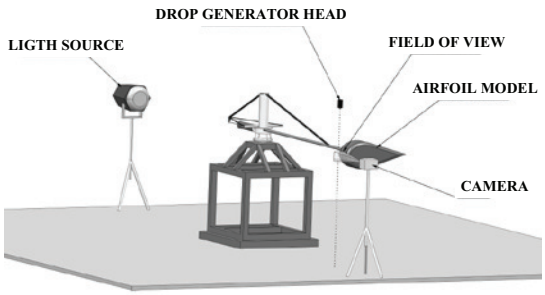

Figure 1. Experimental setup.

Figure 2. Panoramic photo of the experiment in the rotating rig installation.

3. EXPERIMENTAL OBSERVATION

As the airfoil model approaches, the droplets along the stagnation line, initially spherical, become spheroids flattened in the front side and bulging at the rear [10]. Two diameters are characteristic in the images, the maximum and the minimum diameters, corresponding to directions perpendicular and parallel to the stagnation line. On the collision path the minimum diameter decreases while the maximum diameter increases. Breakup occurs when the minimum diameter starts to increase (criteria of minimum diameter). At this moment a growing concavity appears in the rear side, giving the droplet a hat appearance. The brim of the hat blows up turning into a parachute-like shape. This is the type of breakup observed during the present tests [8], however there are additional droplet breakup processes such as bag breakup, vibrational breakup…[11-14].

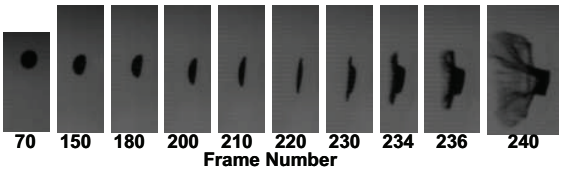

Figure 3. Example of the deformation and breakup of a droplet.

4. PRE-PROCESSING

The large amount of information obtained during the test campaigns and the initial format of the recorded files requires data pre-processing.

Pre-processing consists of the conversion from the video format to a format compatible with Matlab, PNG in this case, and the generation of an Excel file that identifies and contains all the information related to each clip of images to be analyzed by the application. The relevant information for each clip is:

1) Test configuration: model used, model velocity and expected droplet diameter.
2) Frame identification: initial and final frame of the droplet tracking. The final frame corresponds to the moment just before droplet breakup or impingement on the model.
3) Identifying the frame in which model appears.
4) Location and generic name of the files.
5) Number of droplets to analyze in each clip.
6) Acquisition configuration, including acquisition rate and magnification of the camera.

5. PROCESSING. MATLAB APLICATION

SITEA is an application developed in a Matlab environment, designed for quick and efficient determination and processing of trajectories, deformations and breakup of droplets impinging on airfoils. The video processing consists of the

analysis of each clip. The first frame of the clip is processed as follows:

1.-Selection of the droplet to be tracked. Among all the droplets included in the first frame, one is selected to be tracked by marking on the frame a region of interest that includes only that droplet.

2.-Droplet detention. Images are converted to a binary image by a threshold selection, by using the Matlab sentences "graythresh" and "im2bw". "Graythresh" computes a global threshold using Otsu's Method [15] that converts an intensity image to a binary image with "im2bw". Otsu's method chooses the threshold to minimize the intraclass variance of the thresholded black and white pixels. This command works satisfactorily when the background of the image is homogeneous enough. Otherwise it is necessary to homogenize the background first. When the region of interest is relatively small, the background is usually sufficiently homogeneous.

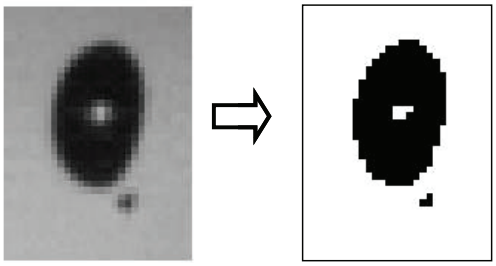

Figure 4. Region of interest converted to binary image.

Attention must be paid to the contrast of the image in order to obtain the correct droplet shape in the binary image. Figure 5 shows an example, of two images of the same glass sphere taken at two illumination and consequently two contrast levels, yielding different binary images.

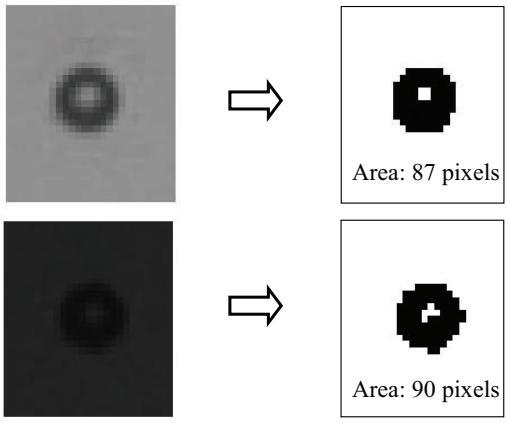

Figure 5. Shadow images of a glass sphere with different illumination. Influence of the image contrast on the binary image conversion.

3.-The binary image is filtered to discard glints and dust images. The filtering process is performed in three steps:

a) Image conversion to negative.

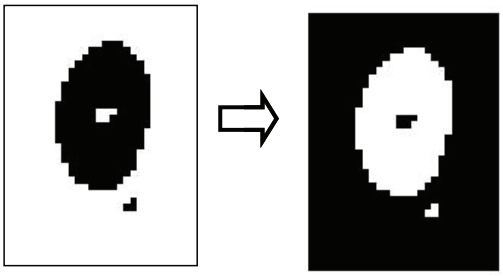

Figure 6. Binary image converted to negative.

b) Dust cleaning. Using the command "bwareaopen" it is possible to eliminate white objects or dots owning areas smaller than a given number of pixels. In the cases studied, all the dust objects were correctly eliminated when the selected number of pixels was a 10% of the expected droplet area.

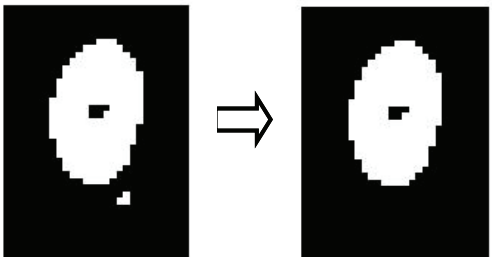

Figure 7. Cleaning dust

c) Glint elimination. White holes in the centre of the droplet due to light glints are removed using the command "imfill".

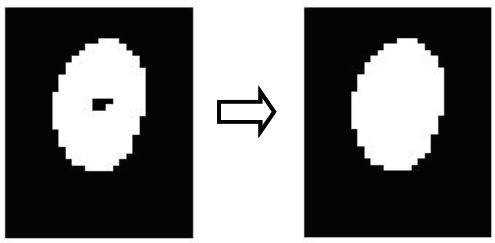

Figure 8. Glints elimination.

4.-·Acquisition of the droplet parameters. The command "regionprops" is used to find the centroid position in the region of interest and the principal properties of the water drop, namely, droplet area, equivalent diameter, and minimum and maximum diameter. The droplet centroid coordinates, initially calculated in the local axes associated to the region of interest, are converted to frame axes. All

calculated data are given in pixels and need to be converted to the international system of units using the camera magnification feature.

The equivalent diameter obtained by the command "regionprops", is the diameter of the circle of the same area as measured in pixels. Since droplets are slightly deformed in the initial tracking image, this equivalent diameter is not the real droplet diameter. The real diameter is calculated on the assumption that droplets become an axisymmetric spheroid during the deformation [10], using the maximum and minimum diameter.

$$D = \sqrt[3]{D_{\max}{}^2 D_{\min}} \tag{1}$$

In the Fig. 9, the evolution of the maximum and minimum diameters, equivalent diameter calculated from the area, and that from Eq. (1) are shown. Note that the droplet diameter calculated from Eq. (1) remains constant during the deformation until breakup onset (criteria of minimum diameter), while the equivalent diameter does not.

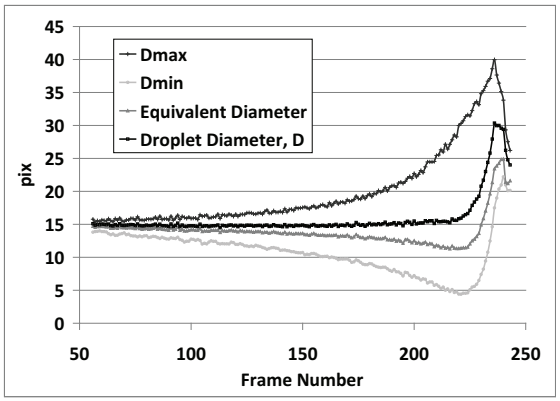

Figure 9. Example of droplets diameters evolution.

For the next frames, the region of interest is an area of the same size as the former but now centred at the position of the droplet in the previous frame. In a similar way each frame is analysed: conversion to binary image, conversion to negative, dust cleaning, glint elimination, acquisition of the droplet parameters and transformation of coordinates from local axes to frame axes.

Following the analysis of all frames, a change of the reference system is made from frame reference to model reference. The velocity of the model and the rate of frame acquisition are constant, so the droplet position in the model reference system is defined by Eq. (2), where f_m is the number of the frame where the leading edge position is measured, f_{di} is the number of the frame where the droplet position is measured, U_m is the model velocity, FR is the rate of frame adquisition, x_{mf} is the leading edge position in f_m , x_{di} is the droplet position in f_{di} , and Mg is the camera magnification.

$$X_{di} = \frac{(f_m - f_{di})}{FR} U_m + \frac{(x_{mf} - x_{di})}{Mg} \tag{2}$$

Droplet evolution is additionally characterised by the acceleration along the trajectory and the non-dimensional parameters: Reynolds, Weber, and Bond Numbers and the Drag Coefficient, appearing all defined in Eqs. (3)-(6). U_{rd} is the slip velocity, D is the droplet diameter, ρ_a is the air density, ρ_w is the droplet density, and σ_w is the water surface tension for the droplet [1].

$$\mathrm{Re} = \frac{\rho_a U_{rd} D}{\mu_a} \tag{3}$$

$$We = \frac{\rho_a U_{rd}{}^2 D}{\sigma_w} \tag{4}$$

$$Bo = \frac{\rho_w D^2}{\sigma_w}\left(\frac{dU_{rd}}{dt}\right) \tag{5}$$

$$C_d = \frac{4}{3}\frac{\rho_w}{\rho_a}\frac{D}{U_{rd}{}^2}\frac{dU_{rd}}{dt} \tag{6}$$

The slip velocity can be calculated from droplet and air velocities. The flow field in front of the model is measured in advance with PIV technique [16]. Droplet velocity and acceleration are calculated from a fit curve of droplet positions.

SITEA additionally gives the droplet breakup starting point. This point is defined in section 3 for the type of breakup observed during the tests (criteria of minimum diameter), and it is obtained by minimizing the fitted function of the droplet minimum diameter evolution. From the beginning of the breakup process, the droplet is no longer compact since a concavity has appeared, and the mass centre and the centroid of the droplet image does not concur.

6. DATA STORAGE

The correct storage of a large amount of data is of vital importance for a later post-processing of results. Two options were considered to save the data: an excel file or a Matlab variable structure. The excel file has the advantage of simplicity of use and access whereas Matlab permits greater capacity for post-processing tasks. The post-processing requirements of this application make the Matlab structure the selected option. However both of them were used leading to a redundancy useful for checking purposes.

7. VALIDATION

In order to validate SITEA, several cases were selected. The evolution of the droplets was tracked

by SITEA and by Spotlight program. Spotlight program is a program developed by NASA addressed to other applications that also tracks the position of droplets. Using Spotlight and calculating manually the rest of parameters, excellent agreement between the two applications was obtained. The development of SITEA embodies additional features to the single droplet trajectory calculation given by Spotlight.

8. COMPUTATIONAL TIME

Running SITEA in a basic computer (Pentium IV, 2800Mhz; 2Gb RAM), the application can process 250 frames in 20 seconds to obtain positions, areas and equivalent maximum and minimum droplet diameters, followed by an additional 30 seconds post processing period to obtain the water droplet velocity and acceleration. The computational time is about a 10% of the pre-processing time. Nevertheless, the total analysis time has been reduced in a 90% compared to the other analysis method.

9. EXAMPLE OF APPLICATION

This section presents an example of application of the method. Once the input panel is filled in with the data of the selected case, the application starts asking for a region of interest. The tracking is shown on the screen for checking purposes.

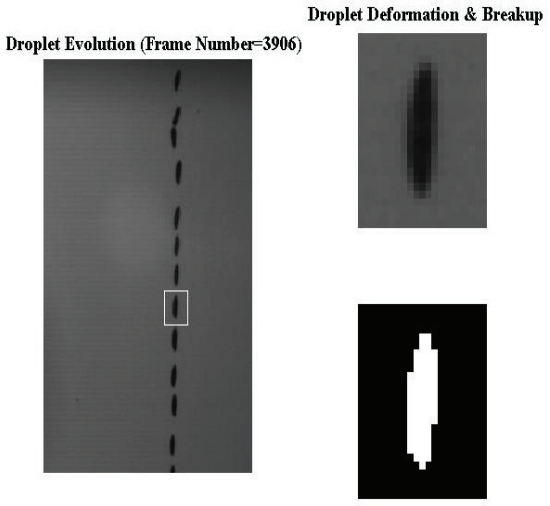

Figure 10. Window showing the tracking evolution of the droplet. On the left each frame with the region of interest marked is shown. On the right the region of interest before and after the image processing.

Once the tracking has finished, an estimate of the horizontal position evolution is shown in a plot. The origin for the Cartesian coordinate is the initial position of droplet tracking and the x axis direction is toward the model motion.

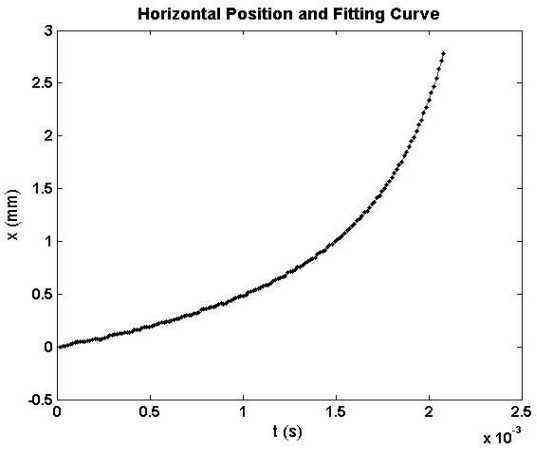

Figure 11. Window showing tracking evolution and fitting curve of the water droplet.

The criterion used for the experimental determination of breakup consists of the finding of the minimum value of the curve of minimum diameter. Accordingly, the minimum diameter is approximated by a curve that allows the determination of the minimum. The evolution of the minimum diameter together with the approximation curve is shown in a new plot for checking purposes.

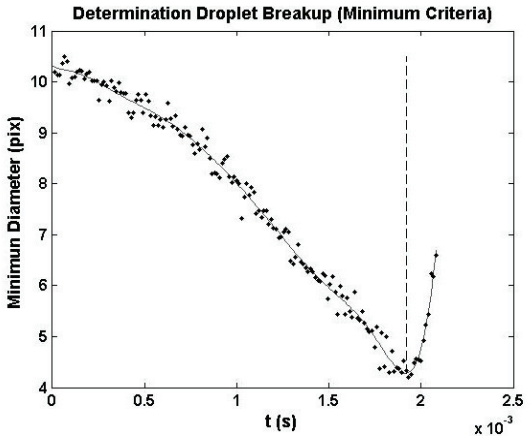

Figure 12. Window showing tracking evolution of the droplet minimum diameter and fitted curve.

The evolution of the droplet trajectory and different shaped parameters are finally displayed for each drop in a single figure.

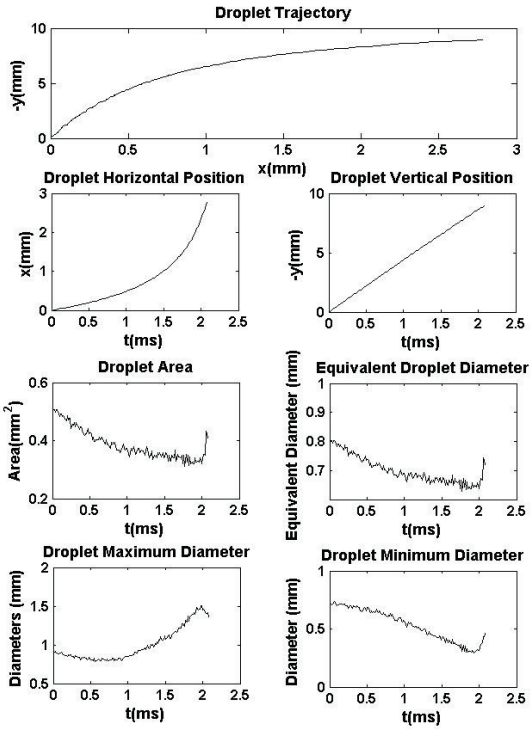

Figure 13. Window showing the summary of the droplet evolution.

Once the evolution of the tracking has been examined in the summary figure, the data are saved including all the dimensionless parameters that are shown in a separate figure.

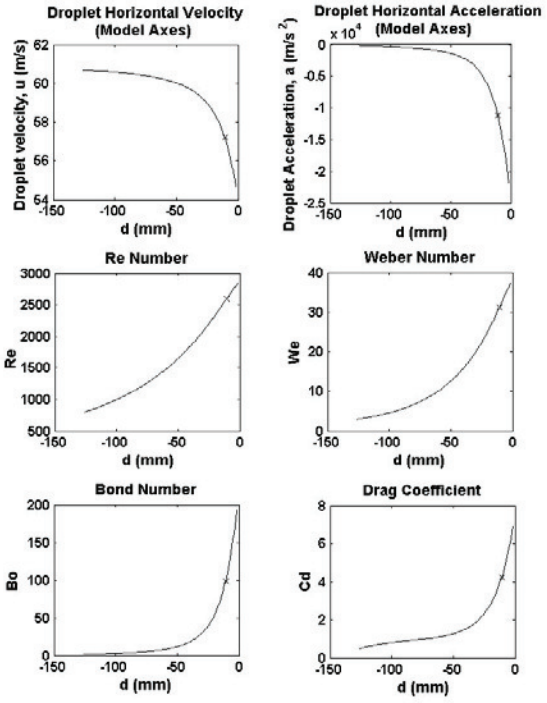

Figure 14. Window showing a summary of all the calculated data. d is the leading edge distance to the droplet.

10. CONCLUSIONS

This paper presents the tracking and analysis system SITEA for which the principal advantage is the required computational time, considerably lower compared to the previous method of analysis.

Another gain of the new application is the threshold selection. In Spotlight the threshold is chosen by the user at the initial step of the analysis and is kept constant along the tracking process. In SITEA, the threshold is calculated by Otsu's Method for the specific region of interest on each frame. This feature implies that the threshold changes along the path of the droplet, representing an advantage in cases where the image's background is not homogenous and the contrast of the image varies. Additionally, the threshold automatic selection by Otsu's method precludes unsatisfactory use of the application by inexperienced operators.

Up to now, more than 3600 droplets have been analysed using SITEA, appearing as a suitable application for processing data in terms of computational cost and efficiency.

Additional levels of automation would result in substantial savings of the time expended in pre-processing tasks. An automatic initial detention and numeration of each droplet could lead to a noticeable reduction of pre-processing data. In this manner leading edge emergence could be detected automatically together with new droplet entrances and departures.

The use of SITEA and future updates allows the cost-efficient fulfilment of a large amount of tests. The experimental results will enable the performance of correlations between different dimensionless parameters and will give a valuable insight to the trajectories, deformations and breakup mechanisms of droplets impinging on airfoils. The experimental information so obtained will improve the prediction capabilities of current ice accretion codes.

ACKNOWLEDGEMENTS

The authors would like to thank Ph.D. Mario Vargas from NASA for his generous support and outstanding help at validating SITEA by making comparisons to Spotlight results. Thanks also to Mrs. Urdiales for her patient work to validate SITEA by running numerous cases.

REFERENCES

[1] Vargas, M., and Feo, A., 2010, "Experimental Observations on the Deformation and Breakup of Water Droplet near the Leading Edge of an Airfoil".*AIAA Atmospheric and Space Environments Conference.* Toronto, Canada. AIAA-2010-7670.

[2] Tan, S.C., 2005, "Effects of Large Droplet Dynamics on Airfoil Impingement

Characteristics", *AIAA Aerospace Sciences Meeting and Exhibit*, Reno, Nevada, AIAA-2005-74.

[3] Luxford, G., Hammond, W., and Ivey, P., 2004, "Role of Droplet Distortion and Breakup in Large Droplet Aircraft Icing", *AIAA Aerospace Sciences Meeting and Exhibit*, Reno, Nevada, AIAA-2004-411

[4] Hasman, R.J., 1984, "The Effect of the Atmospheric Droplet Size Distribution on Aircraft Ice Accretion", *AIAA Aerospace Sciences Meeting*, Reno, Nevada, AIAA-84-0108

[5] Chang, H-P., and Kimble, K.R., 1983 "Influence of Multidroplet Size Distribution on Icing Collection Efficiency", *AIAA Aerospace Sciences Meeting*, Reno, Nevada, AIAA-83-0110

[6] Luxford, G., Hammond, W., and Ivey, P., 2005, "Modelling, Imaging and Measurement of Distortion, Drag and Breakup of Aircraft-Icing Droplets", *AIAA Aerospace Sciences Meeting and Exhibit*, Reno, Nevada, AIAA 2005-71

[7] Feo, A. Vargas, M., and Sor, S., 2011, "Rotating Rig Development for Droplet Deformation/Breakup and Impact Induced by Aerodynamic Surfaces". *SAE International* 2011-38-0087.

[8] Vargas, M., Sor, S., and García-Magariño, A., 2012 "Mechanism of Water Droplet Breakup Near the Leading Edge of an Airfoil", To be published in *AIAA Atmospheric and Space Enviroments Conference*, New Orleans, Lousiana (to be published).

[9] Frohn, A. and Roth, N, 2000, *Dynamics of Droplets*, Springer

[10] Sor, S., and García-Magariño, A. 2012 "Diameter and Axisymmetry Measurements of a Water Droplet Impinging on an Airfoil", *Technical Report* AE-TNO-4420-065-INTA-12

[11] Wierzba, A., 1990, "Deformation and Breakup of Liquid Droplets in a Gas Stream at Nearly Critical Weber Numbers", *Experiments in Fluids* Vol 9, pp 59-64

[12] Dai, Z. and Faeth, G.M. 1999, "Temporal properties of multimode secondary Droplet Breakup", *AIAA Aerospace Sciences Meeting and Exhibit,* Reno, Nevada, AIAA, 99-0333

[13] Tan, S.C., Papadakis, M., Miller, D., Bencic, T., Tate, P., and Laun, M.C., 2007 "Experimental Study of Large Droplet Splashing and Breakup", *AIAA Aerospace Science Meeting and Exhibit*, AIAA 2007-904

[14] Tan, S.C., Papadakis, M.,and Sampath, M.K., 2005, "Computational Study of Large Droplet Breakup in the Vicinity of an Airfoil", *Technical Report,* DOT/FAA/AR-05/42

[15] Otsu, N., 1979, "A threshold Selection Method from Gray-Level Histograms", *IEEE Transactions on systems, man, and cybernetics*, Vol 9, Nr. 1, pp 62-69.

[16] Sor, S., and García-Magariño, A., 2011, "PIV Measurements on Airfoil Model in Rotating Arm", *Technical Report* AE-TNO-4420-091-INTA-11.

Conference on Modelling Fluid Flow (CMFF'12)
The 15th International Conference on Fluid Flow Technologies
Budapest, Hungary, September 4-7, 2012

NUMERICAL SIMULATION OF LOW-SPEED STALL AND ANALYSIS OF TURBULENT WAKE SPECTRA

Philipp Peter GANSEL[1], Sebastian ILLI [2], Thorsten LUTZ [3], Ewald KRÄMER [4]

[1] Corresponding Author. Institute of Aerodynamics and Gas Dynamics, University of Stuttgart. Pfaffenwaldring 21, 70569 Stuttgart, Germany. Tel.: +49 711 685 63416, Fax: +49 711 685 63438, E-mail: gansel@iag.uni-stuttgart.de
[2] E-mail: illi@iag.uni-stuttgart.de
[3] Head of branch "Aircraft aerodynamics". E-mail: lutz@iag.uni-stuttgart.de
[4] Head of Institute. E-mail: kraemer@iag.uni-stuttgart.de

ABSTRACT

At the Institute of Aerodynamics and Gas Dynamics (IAG) numerical studies on the low-speed stall of aircraft wings, the development of the wake and its interaction with the empennage are performed. In the present paper unsteady Reynolds-averaged Navier-Stokes (URANS) calculations as well as highly resolved Delayed Detached-Eddy Simulations (DDES) of the turbulent wake downstream of a boundary layer separation on an airfoil section are described. For these simulations a NACA 0012 airfoil test case with a free stream Mach number of 0.3 and a Reynolds number of 6 million at a high angle of attack was chosen. URANS calculations on different grids and with different turbulence models show that a fine structured discretisation of the wake region facilitates the transport of turbulent viscosity with low dissipation. The DDES approach allows propagation of resolved turbulent structures far downstream of the flow separation. The spectral analysis shows a good agreement of measured and simulated pressure fluctuations in the junction of energy-containing range and inertial sub-range of the spectrum. Furthermore semi-empirical turbulence spectrum models were used to obtain spectral turbulence information from URANS solutions. The resulting turbulent velocity fluctuation spectra are compared to the resolved velocity fluctuations of the DDES.

Keywords: CFD, DDES, stall, spectra, wake

NOMENCLATURE

E_{11}	$[m^3/s^2]$	one-dimensional longitudinal turbulent kinetic energy spectrum
$F+$	$[-]$	reduced frequency
L_{11}	$[m]$	longitudinal integral length scale
Ma	$[-]$	Mach number
R_{11}	$[m^2/s^2]$	spatial velocity autocorrelation
Re	$[-]$	chord Reynolds number
U_∞	$[m/s]$	free stream velocity
c	$[m]$	airfoil chord length
c_l	$[-]$	lift coefficient
c_p	$[-]$	static pressure coefficient
k	$[m^2/s^2]$	specific turbulent kinetic energy
r	$[m]$	distance
t	$[s]$	time
u	$[m/s]$	velocity in x-direction
x, y, z	$[m]$	space coordinates
y_1^+	[-]	dimensionless wall coordinate
α	$[^\circ]$	angle of attack
Δ	$[m]$	maximal cell edge length in the structured wake mesh
ε	$[m^2/s^3]$	dissipation rate of k
κ_1	$[1/m]$	longitudinal wave number
κ_e	$[1/m]$	wave number of the most energy containing eddies
ω	$[1/s]$	turbulent dissipation frequency

Subscripts and Superscripts

$\bar{}$	temporal mean
$'$	fluctuation

1. INTRODUCTION

At the boarders of the flight envelope flow effects occur which still are not completely understood and far from being reproduced correctly by today's numerical methods in industry relevant flow cases. At low Mach numbers and sufficiently high angles of attack large boundary layer separations on the wing cause a rapid lift drop and form a highly unsteady turbulent wake. This phenomenon called low-speed stall is the subject of the presented studies, with a focus on the spectral information in the wake downstream of the separation. The fluctuations can affect the inflow conditions and the flow state of the safety critical horizontal tail plane (htp) [1] or even excite its structural modes.

However, only few published studies concerning transport aircraft configurations deal with turbulent fluctuations in the wake. Whitney et al. [2] developed

an URANS based model to predict htp yaw and roll moment fluctuations measured near low-speed stall. In the German HINVA research project in-flight stall tests with the DLR ATRA aircraft are planned to collect amongst others unsteady pressure signatures on wing and htp as a validation basis for unsteady CFD methods [3]. A couple of investigations of turbulent wake fluctuations have been published in the context of active flow control devices. Seifert and Pack [4] evaluated the spectral content of the turbulent wake of a stalling airfoil with and without periodic blowing near the leading edge by means of unsteady pressure transducers. Wokoeck et al. [5] used PIV measurements of a stalling tail plane airfoil to validate RANS results with different transition prediction methods. Lopez Mejia et al. [6] explored time-averaged and instantaneous vorticity fields around an airfoil with tangentially aligned synthetic jet actuators using an incompressible DDES code (EDDES) and PIV measurements. Since hybrid RANS-LES methods as DES were developed to model massive separation, at first applications concentrated on flows around blunt bodies or airfoils in deep stall [7–9]. Beyond that, Onera performed zonal and delayed DES on three-element airfoils [10–12] and on a civil aircraft type configuration [13]. Nagy et al. [14] conducted zonal RANS-LES and LDA measurements of a fan airfoil with intent to calculate the flow generated noise. In their numerical studies Durrani and Qin [15] compared Reynolds stresses in the boundary layer and the near wake region of an airfoil from DDES, DES, URANS and experiments. Probst and Radespiel [16] applied different DES approaches and showed deficiencies in the prediction of mild trailing edge separation. Stall of a NACA 0012 airfoil was investigated by Lehmkuhl et al. [17] by comparing Direct Numerical Simulation and Large Eddy Simulation (LES) results.

In the presented research three different ways to assess the spectrum of turbulent motions in separated airfoil flow are tested and compared: unsteady RANS calculations with evaluation of the resolved large scale fluctuations of the flow variables, DDES with fine resolution of turbulent fluctuations down to the dissipation range and a tubulence spectrum model based on URANS turbulence model entities.

2. FUNDAMENTALS

2.1. Turbulent Spectrum Model

Proccesses in turbulent flows at high Reynolds numbers can be described by the concept of the energy cascade [18]. It states that turbulence consists of eddies of different sizes. Energy is entered into turbulence at large scales driven by the boundary conditions given as the adjacent flow field, then transferred to successively smaller eddies and finally dissipated to heat at the smallest scale, called the Kolmogorov scale. The so called Kolmogorov hypotheses state that at high Re i) small scale turbulence is locally isotropic, ii) the statistics of turbulent motions are of universal form and uniquely determined by turbulent dissipation rate ε and viscosity and iii) in a certain range of scale the statistics of turbulent motions are independent of viscosity as well and thus solely defined by ε. Accordingly the turbulent spectrum can be devided into the energy-containing range, where big eddies are formed and depend on the flow conditions, the inertial subrange, where energy is passed on to smaller scales by inviscid processes and the dissipation range where viscous effects dominate. The universal functional form of the turbulent spetrum allows to construct models independent of the particular class of flow. Von Kármán developed a turbulent energy spectrum model, wherefrom Lysack and Brungart [19] derived the one-dimensional longitudinal spectrum

$$E_{11}(\kappa_1) = \frac{8.73}{55}\frac{k}{\kappa_\mathrm{e}}\left[1+\left(\frac{\kappa_1}{\kappa_\mathrm{e}}\right)^2\right]^{5/6} \tag{1}$$

with the most energy containing eddies' wave number

$$\kappa_\mathrm{e} = 1.9\frac{\varepsilon}{k^{3/2}} \tag{2}$$

and the turbulent kinetic energy k. When derived from a time and space dependent data sample, $E_{11}(\kappa_1)$ equals twice the Fourier transform of the velocity fluctuation two-point auto-correlation

$$R_{11}(r,t) = \overline{u'(x+r,t)\cdot u'(x,t)} \quad . \tag{3}$$

2.2. Numerical Methods

The calculation of the fluid flow describing incompressible Navier-Stokes equations for industry relevant cases with complex geometries and high Reynolds numbers today is still not affordable, since the number of grid points required for sufficient resolution and the CPU-time needed for computation are proportional to $Re^{9/4}$ and Re^3 respectively [20]. One approach is to decompose the flow variables in the Navier-Stokes equations into a temporal mean value and a time-dependent fluctuation. This leads to the RANS equations which are solved for the mean values. The remaining fluctuation-dependent terms (called Reynolds stresses) are modelled. To determinate the Reynolds stresses eddy viscosity turbulence models are widely used. For the URANS simulations conducted in the presented studies mainly the Menter SST two-equation turbulence [21] model was used. It provides transport equations for k and either its dissipation rate ε (in the free flow) or the dissipation frequency $\omega = \varepsilon/k$ (in near wall flow).

If turbulent fluctuations shall be resolved in the simulations RANS methods are not applicable by definition. DES became popular for flows with large scale boundary layer separation in the recent years.

It combines the advantage of LES to resolve the big turbulent structures with relatively small grid sizes. The outer part of the separated flow is calculated with LES, where the total grid points scale with $Re^{0.4}$ [20]. In the boundary layer, where LES would require much more cells, RANS equations are applied. In contrast to RANS, in LES the Navier-Stokes equations are not averaged in time but spatially filtered, where the filter width is proportional to the biggest cell extension. In the equations terms depending on the residual fluctuations filtered out remain according to the Reynolds stresses in RANS and are named residual or subgrid scale (SGS) stresses. Again they can be modelled using eddy viscosity models, of which the Smagorinsky model is used in the present study.

Spalart et al. [22] presented an implementation of DDES where the SA turbulence model is used in the RANS domain and the SGS model is formulated in such a way that the transport equation can be transfered into the SA model equation by replacing the local grid size by the distance to the nearest wall. A flow dependent blending function controls the application of the different approaches. Nevertheless the adequate selection of the required spatial grid resolution is crucial for correct operation of the hybrid scheme.

3. CONDUCTED SIMULATIONS

3.1. Test Case Description

As a test case wind tunnel tests were chosen from literature with available unsteady measurements in the wake [4]. The analysed NACA 0012 airfoil section with a chord length c of $0.165m$ was tested in a transonic cryogenic wind tunnel under free stream conditions of $Ma = 0.3$ and $Re = 6 \cdot 10^6$. The data chosen for the presented simulations were recorded at an angle of attack of $\alpha = 16°$, where a big turbulent separation area occurs on the airfoil.

Due to the high memory consumption of full flow field solutions, the spectral analysis, which all time steps are required for, was conducted only in three defined points listed in Table 1. Position A is very close to the trailing edge and position B lies approximately in the middle of the wake at a downstream position. In the experiments unsteady pressure transducers were placed in the wake at position C. The origin of the used coordinate system is placed at the airfoil leading edge, the x-axis points towards the trailing edge, the y-axis in span wise direction and the z-axis upwards.

Table 1. Analysed measurement positions

Position	A	B	C
x/c	1.2121	3.3750	3.3750
z/c	0.12121	0.60606	1.2198

3.2. Numerical Setup

The presented simulations have been performed using the unstructured finite volume code TAU (version 2011.1.0) from DLR (German Aerospace Center) [23]. It can handle the mixed-type element hybrid meshes created with the meshing software Gridgen V15.17.

For the URANS calculations the computational domain is a two-dimensional (2d) hybrid mesh with a C-type boundary layer mesh, a big structured wake area and an unstructured farfield region. The boundary layer grids of the three resolution levels fine, medium and coarse have 60 cells in wall normal direction with a first cell size of $y_1^+ \leq 1$ independently of the grid resolution. The wake mesh is directly attached to the boundary layer mesh with a smooth transition of cell size. Table 2 shows cell sizes in the homogeneously structured wake region, overall and surface point counts for the different grid resolutions. To save computational costs, the wake mesh is restricted to the part of the flow field, where the measurement positions are defined and the turbulent wake is assumed to pass through (Figure 1). The farfield boundary distance from the airfoil geometry is $100c$.

Table 2. Point counts and wake region cell size Δ of the used RANS and DES meshes

	RANS			DES
	fine	medium	coarse	
points	219000	94000	47000	$17.8 \cdot 10^6$
surf. pts.	445	243	139	445×81
Δ	0.5% c	1.0% c	2.0% c	0.5% c

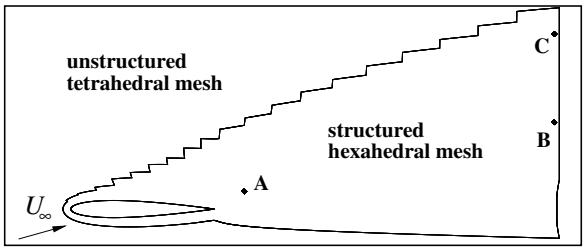

Figure 1. Computational domain with the analysed measurement positions A, B and C

In the URANS simulations the second order Jameson central discretisation scheme was used with matrix dissipation for stabilisation. The dual time stepping method was applied with a physical time step size of $25\mu s$ which is approximately 1/100 times the convective time scale c/U_∞. Amongst others the one equation turbulence model from Spalart and Allmaras [24] in its original formulation (SAO), the shear stress transport model (SST) from Menter [21] and the Reynolds stress model (RSM) implemented in TAU [23] were used as turbulence models. For DDES calculations the structured parts of the fine 2d URANS mesh were extruded span wise by $40\%c$ with the same cell size Δ in y-direction yielding three-dimensional (3d) isotropic structured cells in the wake region. The farfield mesh is filled up with tetrahedra. On the span wise boundary planes periodic conditions were

applied to simulate an infinite wing without any tip or wind tunnel side wall effects. The distance between the periodic planes was chosen as big as possible under consideration of limited computational costs to minimise the error introduced through the forced span wise periodicity of the flow. The numerical schemes were the same as applied to URANS. During one time step of $2.5\mu s$ the flow passes the shortest cells in the wake which, in combination with the isotropically structured mesh, ensures a low dissipation in the propagation of the turbulent wake structures.

4. RESULTS

4.1. URANS Simulations

The analysis of the 2d URANS simulations concentrates on the SST turbulence model because it is used for the semi-empirical turbulent fluctuation spectrum model later. The results with the other eddy-viscosity turbulence models are comparable. In the simulations the boundary layer flow separates from the suction side of the airfoil, as expected from the compared experimental data. The unsteady flow is exactly periodic with a very long main cycle of about 11.5 convective time scales (see Figure 2). Over a big part of this period the separated flow reattaches to the upper surface of the airfoil and forms a separation bubble (see Figure 3 a)). Gradually the separation point is moving upstream and the vortex inside the bubble is getting stronger. This becomes significant in the rising lift coefficient during this phase. There is virtually no large-scale turbulent movement in the wake.

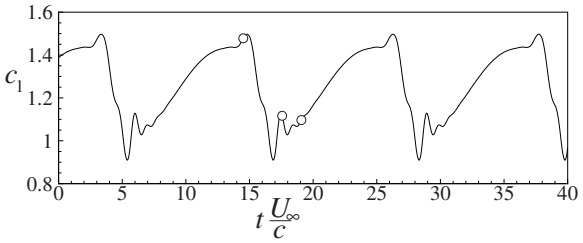

Figure 2. c_l time series of a NACA 0012 airfoil at 16° angle of attack (URANS SST)

At one moment a counter rotating vortex develops behind the separation bubble and a shedding process begins which means a drastic decrease of lift (see Fig. 2). The streamlines in Fig. 3 b) show the flow state shortly after this event. Finally several alternately rotating vortices are shed from the airfoil, the flow reattaches in the upstream part due to the reduced circulation and the remaining small separation bubble starts again to grow and increase the lift (see Fig. 3 c)).

The time-averaged pressure distribution on the airfoil simulated with the three different turbulence models is compared to experimental data in Figure 4. The numerical results lie very close to each other. However, the measurements of Seifert and Pack [4] are qualitatively different. In contrast to the simulations

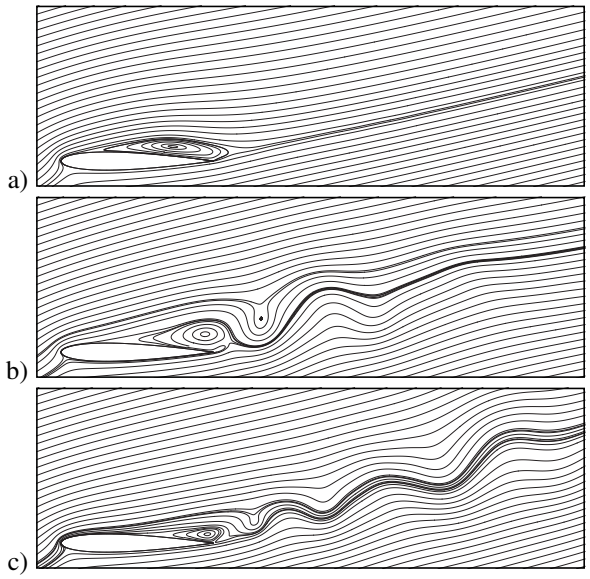

Figure 3. Instantaneous streamlines at a) $t\frac{U_\infty}{c}$ = 14.5, b) 17.5 and c) 19 as highlighted with ∘ in Fig. 2

the airfoil flow is separated over the whole chord length which is expressed in the lower pressure in the rear part of the airfoil. The drop of circulation causes a decrease of the leading edge suction peak and overall lift level. Yet there are older wind tunnel tests conducted by Ladson et al. [25] in the same facility that fit the simulations very good. This leads to the assumption that the test case is exactly at the boarder between those two flow patterns and little disturbances can determine it. Since it is known that eddy-viscosity turbulence models tend to predict boundary layer separation too late in the sense of higher incidence, some calculations at increased α were accomplished. The surface pressure distribution at $\alpha = 18.5°$ was found to be in very good agreement with the experiment of Seifert and Pack (see Fig. 4).

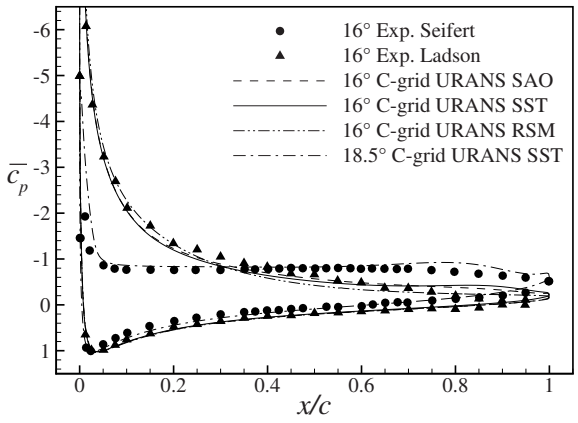

Figure 4. Fine grid URANS mean pressure distributions compared to experimental data

In the comparison of the pressure distribution simulated on the different grids (Figure 5) it can be

seen that with increasing spatial resolution the pressure on the suction side in front of about 25%c is increasing a bit, but decreasing behind that point. On the pressure side there are no noticeable differences.

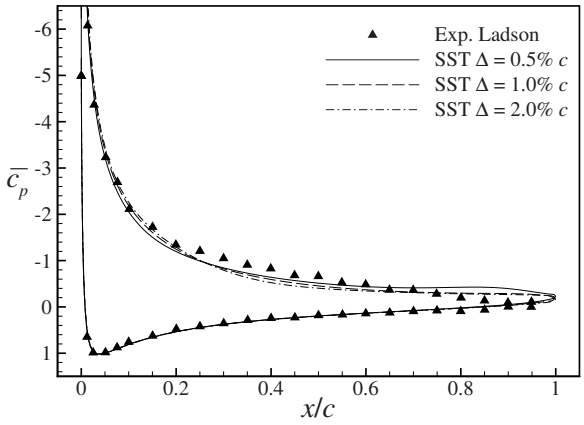

Figure 5. URANS mean c_p with diff. resolutions

The resolved pressure fluctuation spectra at position C in the simulation on the fine and medium grids are dominated by the main flow oscillation seen above in the lift characteristics and its higher harmonics (see Figure 6). The bad results on the coarse mesh can be explained with high numerical dissipation of the fluctuations in the insufficiently resolved wake mesh, since the pressure distributions on the airfoil surface are almost equal for all URANS grids. The medium grid simulation seems to match the experimental data in its peaks, but in terms of grid convergence the peaks of the fine mesh simulations overestimate the amplitudes. Compared to the URANS calculations the experiment shows a smoother spectrum without harmonic peaks. This fact suggests a more continuous vortex shedding progress in the experiment than the URANS simulations show.

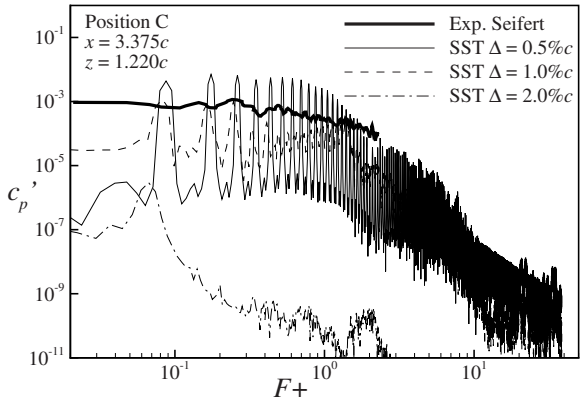

Figure 6. Pressure fluctuations resolved by URANS on fine, medium and coarse meshes

4.2. DDES Calculations

The DDES calculation produces a physically more reasonable flow pattern with continuously shed vortices of different scales. The 3d vortices can be visualised using the λ_2 criterion as illustrated in Figure 7. It is evident that the fine turbulent structures dissipate as soon as they leave the structured wake mesh and enter the coarser areas of the tetrahedra.

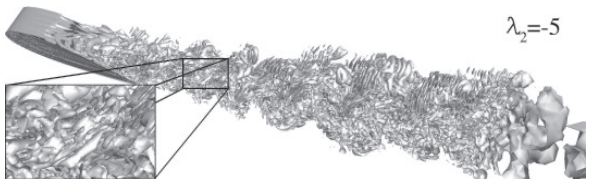

Figure 7. λ_2 iso-surface of turbulenct wake (DDES)

The time-averaged c_p distribution from the DDES shows an earlier and more clearly visible separation point (see Figure 8) than the URANS. It is remarkable that even the RANS simulation with the SAO turbulence model produces a different pressure distribution than DDES, where in the boundary layer enclosing RANS area the same turbulence model is used. This shows the feedback of the separated flow on the boundary layer state.

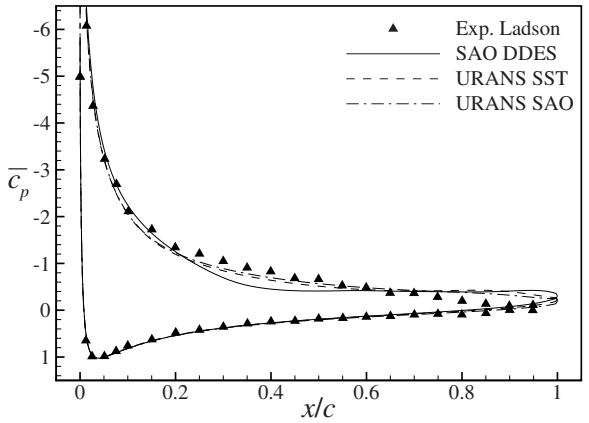

Figure 8. DDES span wise averaged mean c_p compared to URANS and experiment

To give a better insight in the differences of URANS and DDES simulated flow, the instantaneous vorticity in a x-z plane is plotted in Figure 9 (for the URANS plot the same time step was chosen as shown in Fig. 3 c)). While the URANS results show few big discrete vortices the DDES generates structures of different sizes. Furthermore small vortex cores of high vorticity are preserved longer.

The pressure fluctuation spectrum derived from DDES time series at position C is in good agreement with the measurement data (see Figure 10). The spectrum has no outstanding peaks like the URANS spectrum in Fig. 6 which confirms the assumption about the character of the DDES calculated flow. The spectra derived at positions A and B are plotted additionally in Fig. 10. The spectrum at position A shows the highest amplitudes due to its proximity to the airfoil trailing edge where the shedding turbulent

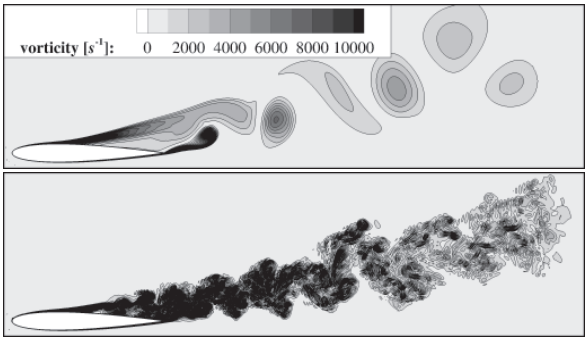

Figure 9. Vorticity in x-z plane from URANS SST (upper picture) and DDES (lower picture)

vortices are formed driven by the boundary conditions. In position B the fluctuation level is already about one order of magnitude smaller because of the decaying processes in the energy cascade and the spreading of the wake while propagated downstream. In point C the amplitudes are even smaller, although in this position the flow has passed roughly the same distance from the airfoil as in point B. However, point C lies close to the boarder of the wake to the outer free stream region where the turbulence intensity is significant lower.

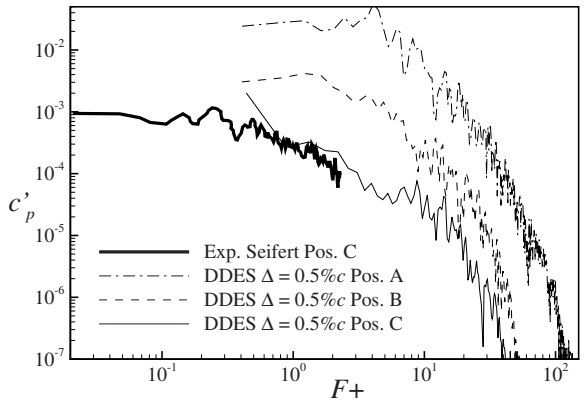

Figure 10. Pressure fluctuations resolved by DDES in wake positions A, B and C

It should be noted in this place that the simulated physical time covered by the DDES calculation is much shorter than in the URANS cases. A total of 6000 physical time steps with 200 inner iterations each were computed within the DDES on 500 computing cores in parallel mode. The last 2000 time steps were considered for spectral analysis after the time averaged flow quantities have reached convergence. Due to the big grid, the small time step size and limited computational resources the spectrum is limited to relatively high frequencies, since the lowest representable frequency is reciprocally proportional to the total time length of the evaluated signal.

One possibility to overcome this problem without adding computational time is to perform the DDES on a coarser mesh with less points and thus bigger time steps. Like shown for URANS (compare fine and medium mesh results in Fig. 6) the same characteristics are expected as with the fine DDES mesh. According studies also discussing different DES formulations are to be published by Illi et al. [26].

Another approach to gain information about the turbulent spectrum is to perform the relatively cheap URANS and model a turbulence spectrum from the turbulent quantities calculated by the turbulence model. This is done for the presented test case in the following section.

4.3. Modelled Fluctuation Spectra

For an applicability assessment of the velocity spectrum model presented by Lysack and Brungart [19] for separated wake flow first the turbulent kinetic energy k and its dissipation range ε were extracted from URANS solutions. For comparison $k = 0.5 \cdot (\overline{u'^2} + \overline{v'^2} + \overline{w'^2})$ also has been calculated from the DDES results and listed in Table 3. Here the amount of turbulence modelled by the SGS model is neglected.

Table 3. Time-averaged turbulent kinetic energy k from URANS SST and DDES

k $[m^2/s^2]$	pos. A	pos. B	pos. C
DDES	678.28	43.670	0.041669
URANS fine	264.90	49.921	6.3069
URANS medium	301.34	44.718	0.33582
URANS coarse	398.00	46.848	0.00047421

The values show that close to the trailing edge (position A) the URANS simulations give a much lower turbulence level than the DDES. Additionally k is increasing with decreasing spatial resolution. At position B in the middle of the wake downstream of the airfoil k is very comparable for all presented simulations. At the boarder of the turbulent wake in point C k is very low and the relative differences between the methods and grid resolutions are in the range of several orders of magnitude.

Utilising Taylor's hypothesis of frozen turbulence the time dependent velocity data logged at A, B and C during the DDES calculation can be transferred into a space domain [18]. The one-dimensional longitudinal velocity spectra $E_{11}(\kappa_1)$ from DDES are derived by duplicating and Fourier transforming R_{11} (Eq. (3)). For URANS $E_{11}(\kappa_1)$ is calculated via Eq. (1).

In Figure 11 $E_{11}(\kappa_1)$ at the different evaluation positions is plotted. As seen from the turbulent kinetic energy in Table 3 the modelled spectra in point A underpredict the DDES calculated amplitudes. At position B in the middle of the wake it is the other way around. In both cases the URANS modelled spectra are almost the same for all grid resolutions. Also the wave number range of the transition region between large scale range and inertial subrange which corresponds to κ_e is in good agreement to the DDES spectra.

In position C the large differences of k in the URANS simulations give a very dissimilar description

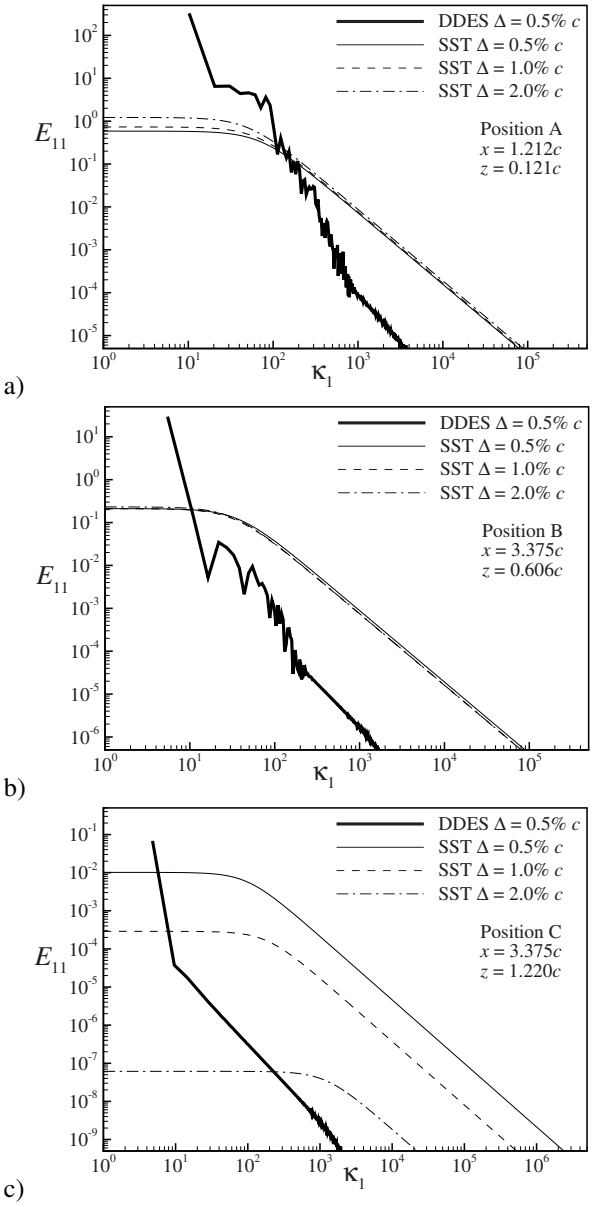

Figure 11. $E_{11}(\kappa_1)$ **from DDES and turbulent fluctuation spectrum model at positions A, B and C**

of the flow and cannot be used for detailed analysis. Also the very low velocity fluctuations in the DDES are not useful for spectral evaluation. Nevertheless the pressure fluctuation spectrum from DDES matches the experimental measurement as shown in the previous section. This fact leads to the assumption that even if the turbulent wake passes by a certain point in such a way that the turbulent vortices are not recognisable in the local velocity, still you can find a significant footprint of the turbulent structures in the pressure.

5. CONCLUSIONS

The presented studies revealed the ability of URANS and DDES calculations to propagate turbulent vortical structures on structured meshes in the wake of the flow past an airfoil in low-speed stall. The dissipation of coherent turbulent structures strongly depends on the local grid cell size in the wake region.

While URANS simulates big discrete periodically shed vortices, DDES shows a continuously forming of turbulent 3d structures of different scales in the wake. Hence evaluated pressure spectra from URANS simulations base on the fundamental frequency of the periodic vortex shedding pattern and its harmonics, whereas DDES calculations give a smooth spectrum which fits the experimental measurements better.

The turbulent spectrum model based on URANS turbulence model entities is able to give a rough estimate of the velocity fluctuation spectrum, at least the wave number of the most energy containing eddies.

Furthermore it could be observed that on the boarder of the wake virtually no meaningful velocity spectrum could be derived from the DDES results, while the measurable pressure fluctuations fit the experimental data. This can be of relevance when simulating the wake of an aircraft with boundary layer separation occurring at the inner wing sections. Even when the wake of the separation passes underneath the htp it can have an effect on the surface pressure distribution and cause unsteady fluctuations in the integral forces.

ACKNOWLEDGEMENTS

The presented studies are part of the HINVA and the ComFliTe project funded by the “German Federal Ministry of Economics and Technology”. Computational resources were kindly provided by the “Leibniz Supercomputing Center” Munich during the DEISA 2 call and the “High Performance Computing Center Stuttgart” within the bwGRiD project [27].

REFERENCES

[1] Havas, J., and Jenaro Rabadan, G., 2009, “Prediction of Horizontal Tail Plane Buffeting Loads”, *Technical Report* IFASD-2009-128.

[2] Whitney, M. J., Seitz, T. J., and Blades, E. L., 2009, “Low-Speed-Stall Tail Buffet Loads Estimation Using Unsteady CFD”, *Technical Report* IFASD-2009-127.

[3] Rudnik, R., Reckzeh, D., and Quest, J., 2012, “HINVA - High lift INflight VAlidation - Project Overview and Status”, Proc. *50th AIAA Aerospace Sciences Meeting including the New Horizons Forum and Aerospace Exposition*, Nashville, TN, AIAA-2012-0106.

[4] Seifert, A., and Pack, L. G., 1999, “Oscillatory Excitation of Unsteady Compressible Flows over Airfoils at Flight Reynolds Numbers”, *Technical Report* AIAA-99-0925.

[5] Wokoeck, R., Grote, A., Krimmelbein, N., Ortmanns, J., Radespiel, R., and Krumbein, A., 2006, “RANS Simulation and Experiments on the Stall Behaviour of a Tailplane Airfoil”, in *New Results in Numerical and Experimental Fluid*

Mechanics V (Rath, H.-J., Holze, C., Heinemann, H.-J., Henke, R., and Hönlinger, H., Eds.), *Notes Num Fluid Mech and Multidisciplinary Design*, Vol. 92, pp. 208–216.

[6] Lopez Mejia, O. D., Moser, R. D., Brzozowski, D. P., and Glezer, A., 2011, "Effects of Trailing-Edge Synthetic Jet Actuation on an Airfoil", *AIAA J*, Vol. 49(8), pp. 1763–1777.

[7] Weinman, K., 2006, "NACA0012 beyond Stall", in *FLOMANIA – A European Initiative on Flow Physics Modelling* (Haase, W., Aupoix, B., Burge, U., and Schwammborn, D., Eds.), pp. 233–246.

[8] Garbaruk, A., Shur, M., Strelets, M., and Travin, A., 2009, "NACA0021 at 60 Incidence", in *DESider – A European Effort on Hybrid RANS-LES Modelling* (Haase, W., Braza, M., and Revell, A., Eds.), pp. 127–139.

[9] Illi, S., Lutz, T., and Krämer, E., 2010, "Simulation of Pressure and Shock Induced Separation using DES Implementations in the DLR-TAU Code", Proc. *Second Symposium "Simulation of Wing and Nacelle Stall"*, Braunschweig, Germany, pp. 127–139.

[10] Deck, S., 2005, "Zonal Detached Eddy Simulation of the Flow around a High-Lift Configuration", *AIAA J*, Vol. 43(11), pp. 2372–2384.

[11] Deck, S., 2009, "Three-Element Airfoil", in *DESider - A European Effort on Hybrid RANS-LES Modelling* (Haase, W., Braza, M., and Revell, A., Eds.), pp. 156–163.

[12] Deck, S., 2011, "Recent Improvements in the Zonal Detached Eddy Simulation (ZDES) Formulation", *Theor Comp Fluid Dyn*, pp. 1–28.

[13] Brunet, V., and Deck, S., 2008, "Zonal-Detached Eddy Simulation of Transonic Buffet on a Civil Aircraft Type Configuration", in *Advances in Hybrid RANS-LES Modelling* (Peng, S.-H., and Haase, W., Eds.), *Notes Num Fluid Mech and Multidisciplinary Design*, Vol. 97, pp. 182–191.

[14] Nagy, L., Lohász, M. M., Régert, T., and Vad, J., 2008, "Hybrid/Zonal RANS/LES Computation of an Airfoil", Proc. *6th International Conference on Mechanical Engineering (Gépészet 2008)*, Budapest, Hungary.

[15] Durrani, N., and Qin, N., 2011, "Behavior of Detached-Eddy Simulations for Mild Airfoil Trailing-Edge Separation", *J Aircraft*, Vol. 48(1), pp. 193–202.

[16] Probst, A., and Radespiel, R., 2010, "A Comparison of Detached-Eddy Simulation and Reynolds-Stress Modelling Applied to the Flow over a Backward-Facing Step and an Airfoil at Stall", Proc. *48th AIAA Aerospace Sciences Meeting including the New Horizons Forum and Aerospace Exposition*, Orlando, FL, AIAA-2010-920.

[17] Lehmkuhl, O., Baez, A., Rodríguez, I., and Pérez-Segarra, C. D., 2011, "Direct Numerical Simulation and Large-Eddy Simulations of the Turbulent Flow around a NACA0012 Airfoil", Proc. *7th International Conference on Comp. Heat and Mass Transfer*, Istanbul, Turkey.

[18] Pope, S. B., 2011, *Turbulent Flows*, Cambridge University Press.

[19] Lysack, P. D., and Brungart, T. A., 2003, "Velocity Spectrum Model for Turbulence Ingestion Noise from Computational-Fluid-Dynamics Calculations", *AIAA J*, Vol. 41(9), pp. 1827–1829.

[20] Blazek, J., 2005, *Computational Fluid Dynamics: Principles and Applications*, Elsevier, 2nd edn.

[21] Menter, F. R., 1994, "Two-Equation Eddy-Viscosity Turbulence Models for Engineering Applications", *AIAA J*, Vol. 32(8), pp. 1598–1605.

[22] Spalart, P. R., Deck, S., Shur, M. L., Squires, K. D., Strelets, M. K., and Travin, A., 2006, "A New Version of Detached-Eddy Simulation, Resistant to Ambiguous Grid Densities", *Theor Comp Fluid Dyn*, Vol. 20(3), pp. 181–195.

[23] German Aerospace Center (DLR), 2011, *TAU-Code User Guide, Release 2011.1.0*.

[24] Spalart, P. R., and Allmaras, S. R., 1992, "A One-Equation Turbulence Model for Aerodynamic Flows", *Technical Report* AIAA-92-0439.

[25] Ladson, C. L., Hill, A. S., and Johnson, W. G., Jr., 1987, "Pressure Distributions from High Reynolds Number Transonic Tests of an NACA 0012 Airfoil in the Langley 0.3-Meter Transonic Cryogenic Tunnel", *Technical Report* NASA-100526.

[26] Illi, S., Gansel, P. P., Lutz, T., and Krämer, E., 2012, "Hybrid RANS-LES Wake Studies of an Airfoil in Stall", *submitted to CEAS Aeronaut J*.

[27] *http://www.bw-grid.de*, member of the German D-Grid initiative, funded by the "Federal Ministry for Education and Research" and the "Ministry for Science, Research and Arts Baden-Württemberg".

Conference on Modelling Fluid Flow (CMFF'12)
The 15th International Conference on Fluid Flow Technologies
Budapest, Hungary, September 4-7, 2012

Turbulence Models in Numerical Simulations of Unsteady Flows

Petr FURMÁNEK,[1] Karel KOZEL[2]

[1] Corresponding Author. Department of Aerodynamics, Aeronautical Research and Test Estabilishment, V mezihoří 2a, Prague, 180 00, Tel.: +420 266 310 121, E-mail: petr.furmanek@fs.cvut.cz
[3] Department of Technical Mathematic, Faculty of Mechanical Engineering, Czech Technical University in Prague. E-mail: Karel.Kozel@fs.cvut.cz

ABSTRACT

The aim of this article is to compare and evaluate usability of the main state-of-the-art turbulence models in numerical simulations of a simple type of unsteady flow. The researched case is turbulent transonic flow over an oscillating NACA 0012 profile, which in its nature resembles a lot of effects with significant influence to the flow field (e.g. flutter). Mathematical model is described by the system of Reynolds-Averaged Navier–Stokes equation, which is solved using the finite volume method. The authors use two different schemes - an in-house developed solver (cell-centred Modified Causon's scheme, which is based on the MacCormack scheme in TVD form) and solver EDGE by the Swedish defence research agency FOI (cell-vertex, uses various types of the Runge–Kutta method combined with the Jameson's artificial dissipation, multi-grid and implicit residual smoothing). The investigated turbulence models are: the one-equation Spalart-Allmaras model, the two-equation Kok's TNT $k-\omega$ model and the EARSM model. The authors come to surprising conclusion that none of the chosen models can be used as a reliable numerical simulation of such a simple case of turbulent flow (at least without any modifications) and propose some possible solutions to this problem.

Keywords: EARSM model, FVM, Kok's TNT model, Spalart–Allmaras model, TVD, unsteady flow.

NOMENCLATURE

M	$[-]$	Mach number
Re	$[-]$	Reynolds number
U	$[m \cdot s^{-1}]$	absolute velocity vector
c_l	$[-]$	lift coefficient
c_m	$[-]$	moment coefficient
c_p	$[-]$	pressure coefficient
f	$[Hz]$	frequency
k	$[m^2 \cdot s^{-2}]$	turbulent kinetic energy
$\tilde{k}$	$[Hz]$	reduced frequency
p	$[Pa]$	pressure
x_{ref}	$[m]$	reference point
α	$[deg]$	pitching angle
Γ	$[-]$	profile defining curve
ρ	$[kg \cdot m^{-3}]$	density
ω	$[s^{-1}]$	specific dissipation rate
$\tilde{\omega}$	$[rad \cdot s^{-1}]$	angular velocity

Subscripts and Superscripts

∞ free-stream values.

1. INTRODUCTION

The unsteady effects play a very important role in external aerodynamics flows. Sometimes even with fatal consequences (e.g. flutter). It is therefore necessary to have reliable simulation tool for such cases. There are many numerical methods (i.e. combinations of numerical schemes, turbulence models and various acceleration techniques) able to model very well the steady turbulence problems. Considering the finite volume method (FVM), the majority of the state-of-the-art numerical schemes for turbulent simulations are based on the system of the Reynolds–Averaged Navier–Stokes equations. This system is however derived with the use of time-averaging, which neglects certain type of unsteadiness. The question remains, how do these methods cope with unsteady flows. The authors chose a simple experimental test case of unsteady transonic flow over the oscillating NACA 0012 profile (which is however similar to the effects appearing in real flows), in order to compare some

of the most commonly used turbulence models in combination with typical FVM schemes.

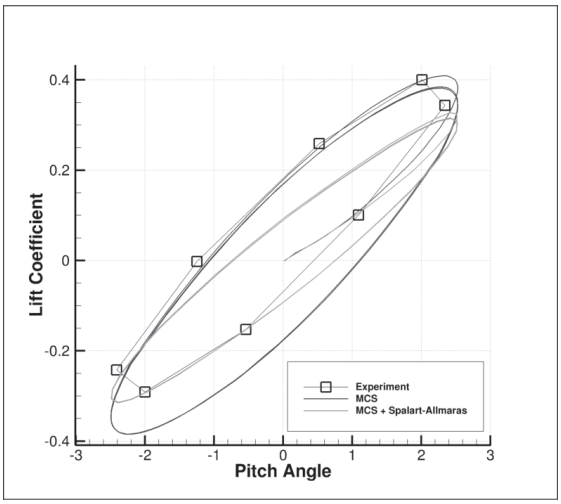

Figure 1. c_l **coefficient, numerical (line) and experimental (discrete line with squares) results. MCS, Spalart-Allmaras.**

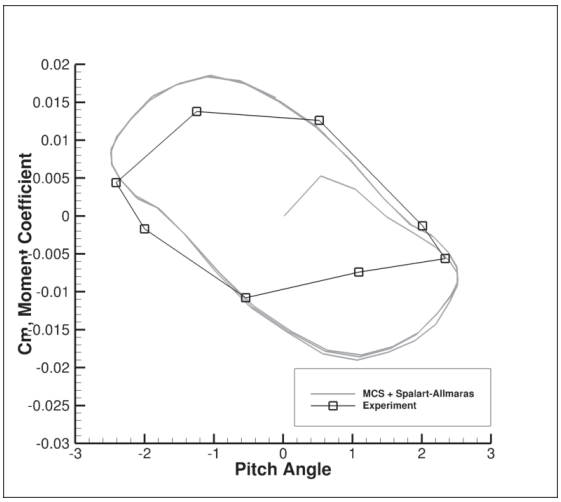

Figure 2. c_m **coefficient, numerical (line) and experimental (discrete line with squares) results. MCS, Spalart-Allmaras.**

2. MODELLED TYPE OF FLOW

The experimental data used in this work are taken from the AGARD report No. 702 [1], particularly from test case denoted as CT5. The profile NACA 0012 oscillates with given frequency $f = 62.5\ Hz$ around the reference point $x_{ref} = [0.25, 0.00]$, which is placed in one quarter of the profile chord (measured from the leading edge). The actual angle of attack is given by the following prescription for pitching angle

$$\alpha(t) = 0.016^\circ + 2.51^\circ sin(\tilde{\omega}t), \tag{1}$$

where angular velocity

$$\tilde{\omega} = \frac{2\tilde{k}U_\infty}{c}, \tag{2}$$

with U_∞ being the free stream velocity, c the chord length and the reduced frequency $\tilde{k} = 0.0814$. The inlet Mach and Reynolds numbers are considered $M_\infty = 0.755, Re = 5.5 \times 10^6$.

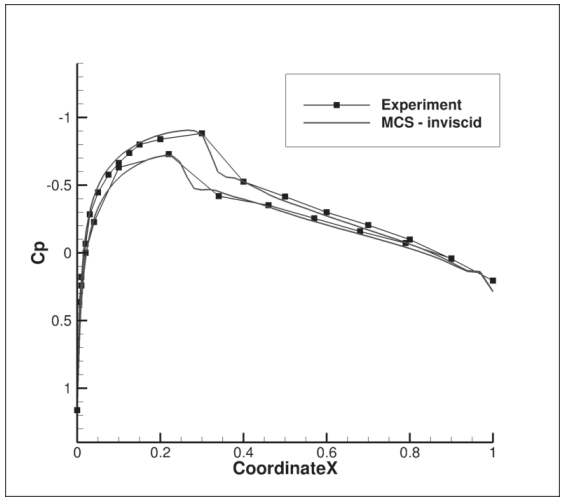

Figure 3. c_p **coefficient during the** 5^{th} **period of oscillatory motion,** $\alpha = 1.09°$**, experimental (line with dots) and numerical (line) results. MCS, inviscid flow.**

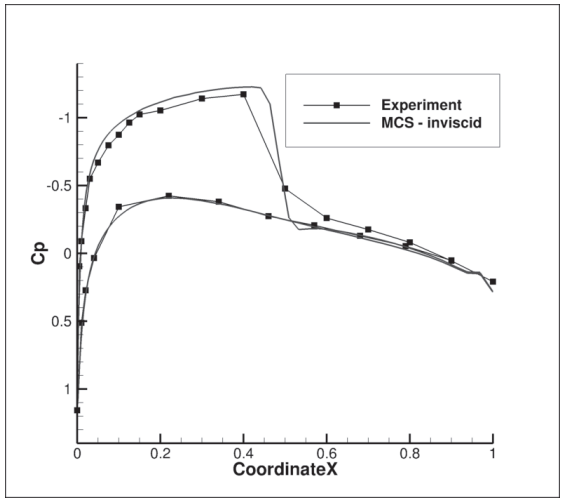

Figure 4. c_p **coefficient during the** 5^{th} **period of oscillatory motion,** $\alpha = 2.34°$**, experimental (line with dots) and numerical (line) results. MCS, inviscid flow.**

3. NUMERICAL METHODS

Most of the numerical results shown in this work were obtained by turbulent simulations. Some older inviscid results already published in [2] are also compared with new numerical data for better

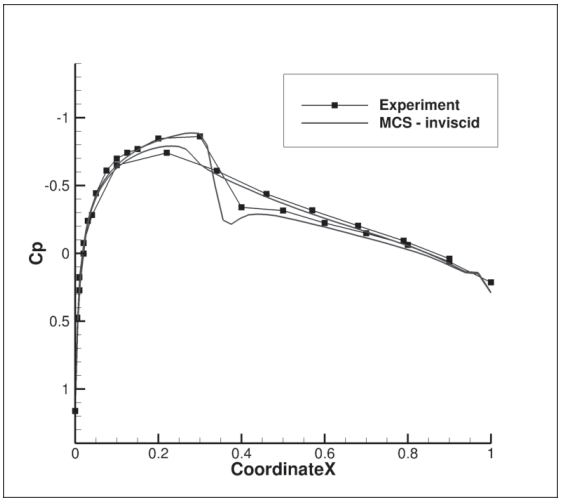

Figure 5. c_p **coefficient during the** 5^{th} **period of oscillatory motion,** $\alpha = -1.25°$**, experimental (line with dots) and numerical (line) results. MCS, inviscid flow.**

understanding to the effects of various turbulence models. Hence two systems of governing equations were used - the RANS for turbulent computations and the system of the Euler equations for the inviscid computations. These systems were solved using two different FVM schemes (an in-house developed code and the solver Edge by the Swedish defence agency FOI). These methods were chosen as representatives of the typical FVM schemes used in nowadays CFD codes. A more detailed description follows.

3.1. Numerical Schemes

The Modified Causon's scheme (MCS): the MCS scheme [3] is derived from the cell-centred TVD form of the classical explicit MacCormack scheme, which is able to deliver very good results. The MCS is not TVD, but in comparison with the full-TVD version it saves approximately 30% of computational memory and power while maintaining almost the same level of accuracy. In order to simulate the turbulence effects, the one-equation Spalart–Allmaras model was employed [4]. The scheme was used in an explicit form and was parallellized with the use of the OpenMP library.

Edge: the Edge flow solver is based on a cell-vertex finite volume scheme. For steady flows, the equations are integrated towards steady state with an explicit multi-stage Runge-Kutta scheme [5]. In order to accelerate convergence, residual smoothing and a multi-grid technique can be employed. Low Mach-number preconditioning is also available. Time-accurate computations are implemented using dual time-stepping: implicit time marching with explicit sub-iterations. Edge is parallellized with the use of the MPI library. For the simulation of turbulence effects were chosen the same models as in the previous case (i.e. the Spalart–Allmaras and the Kok's TNT) and also the Wallin–Johansson EARSM model [6] (based on transport equations of the Hellsten $k - \omega$ model.)

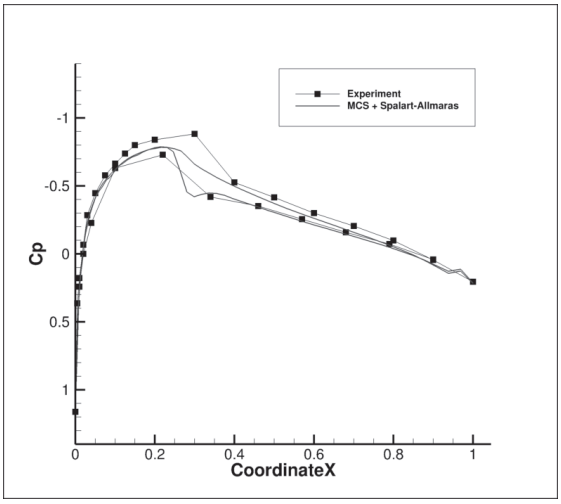

Figure 6. c_p **coefficient during the** 5^{th} **period of oscillatory motion,** $\alpha = 1.09°$**, turbulent flow, experimental (line with dots) and numerical (line) results. MCS, Spalart–Allmaras.**

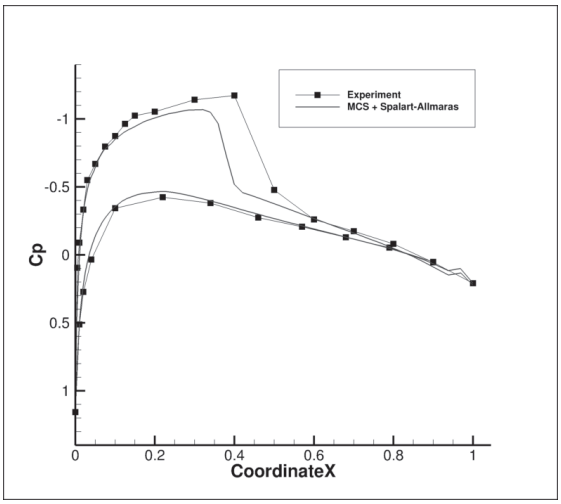

Figure 7. c_p **coefficient during the** 5^{th} **period of oscillatory motion,** $\alpha = 2.34°$**, turbulent flow, experimental (line with dots) and numerical (line) results. MCS, Spalart–Allmaras.**

3.2. Turbulence Models

All the used turbulence models are based on the Boussinesq eddy viscosity hypothesis, which is analogy to the Newtons friction law. As its consequence the additional turbulent stresses in the RANS system are evaluated by augmenting the molecular viscosity with an eddy viscosity. The following models were chosen because they represent widely used industrial standard. Moreover,

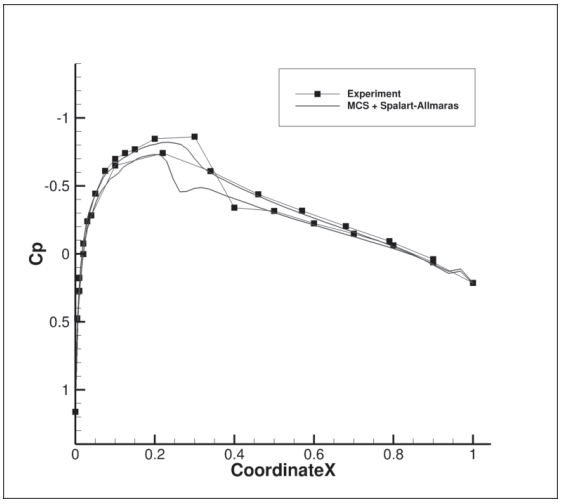

Figure 8. c_p **coefficient during the** 5^{th} **period of oscillatory motion,** $\alpha = -1.25°$**, turbulent flow, experimental (line with dots) and numerical (line) results. MCS, Spalart–Allmaras.**

they have performed well in a number of steady state simulations. The concern of the authors was their performance in combination with the mentioned numerical schemes.

Spalart-Allmaras model: in this model the eddy viscosity is obtained as a solution of one transport equation for viscosity-like variable $\tilde{\nu}$. It was developed for 2D attached wall-bounded flows with only a mild separation. This model is commonly used for aerodynamical turbulence simulation and is calibrated to suit this purpose. For details see [4].

Kok's TNT $k-\omega$ **model:** Kok's TNT model [7] is modification of the standard $k-\omega$ model by Wilcox [8]. It removes dependence of the specific dissipation rate on free-stream values by adding a cross-diffusion term and uses re-calibrated model constants.

EARSM model: Explicit Algebraic Reynolds Stress model was derived as a simplified solution of the turbulence model with transport equations for Reynolds stresses [6]. The main difference from the above-mentioned models based on the Boussinesq hypothesis is non-linear constitutive relation between the tensor of Reynolds stresses and the rate-of-strain tensor. There are more variants of the EARSM model implemented in Edge. The authors used the one based on the transport equations of the Hellsten $k-\omega$ model.

The unsteady motion was implemented using the Arbitrary Lagrangian–Eulerian (ALE) method [9] satisfying the geometric conservation law. Unfortunately, it was not possible to use the same computational meshes for both schemes, because each of the solvers demands different input data format. Each of the meshes however employs layer of the prismatic cells in the closest proximity of the solid wall satisfying the value of $y+ = 1$.

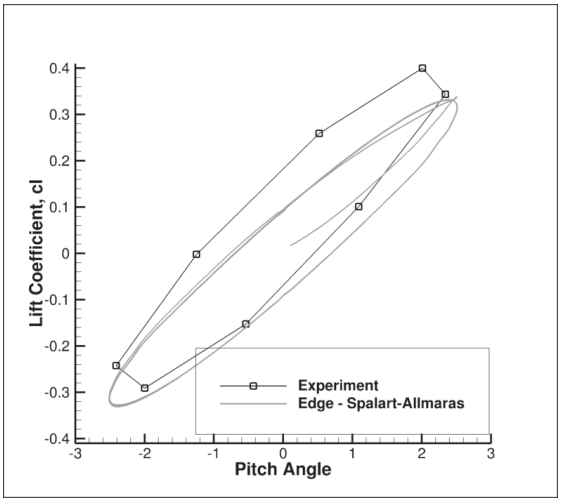

Figure 9. c_l **coefficient, numerical (line) and experimental (line with squares) results. Edge, Spalart-Allmaras.**

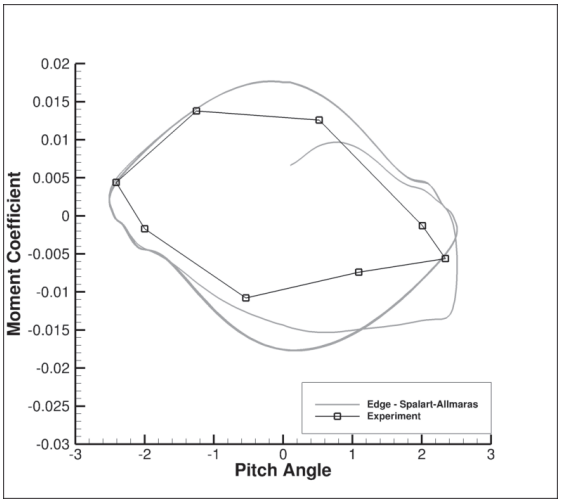

Figure 10. c_m **coefficient, numerical (line) and experimental (line with squares) results. Edge, Spalart-Allmaras.**

4. NUMERICAL RESULTS

Numerical results are shown on behaviour of the lift, pitching moment and pressure coefficients

$$c_l = \frac{\oint_\Gamma p\,dx}{\frac{1}{2}\rho_\infty u_\infty^2}, c_m = \frac{\oint_\Gamma [x - x_{ref}]p\,dx}{\frac{1}{2}\rho_\infty u_\infty^2}, c_p = \frac{p - p_\infty}{\frac{1}{2}\rho_\infty u_\infty^2}$$

where Γ is the curve defining the profile, ρ is density U is total velocity and p is pressure.

All As can be seen in Figures 1 and 3 to 5 the inviscid model corresponds very well to the

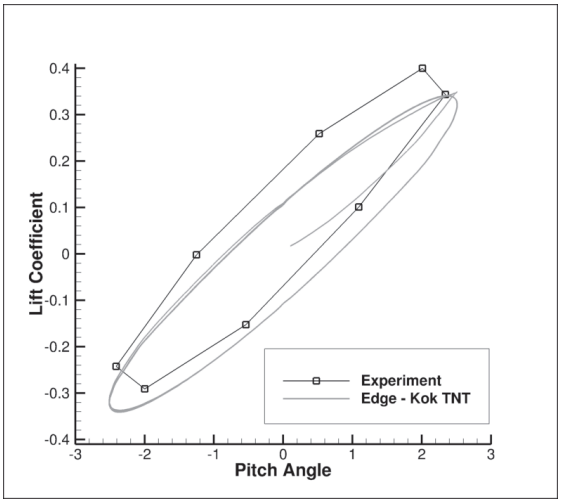

Figure 11. c_l **coefficient, numerical (line) and experimental (line with squares) results. Edge, Kok's TNT.**

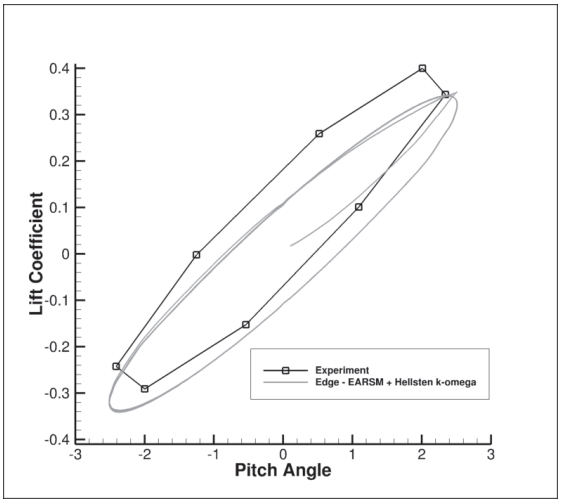

Figure 13. c_l **coefficient, numerical (line) and experimental (line with squares) results. Edge, EARSM.**

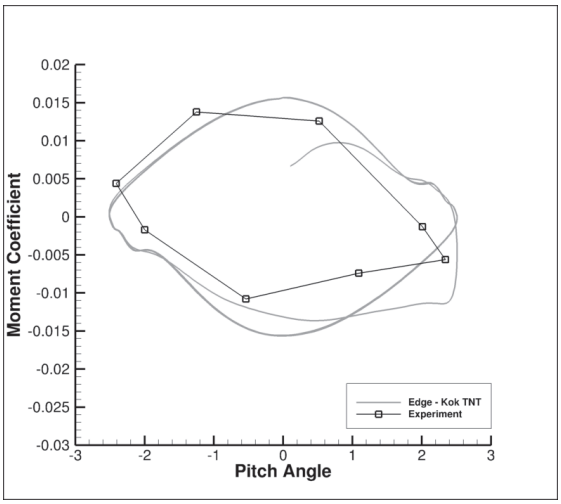

Figure 12. c_m **coefficient, numerical (line) and experimental (line with squares) results. Edge, Kok's TNT.**

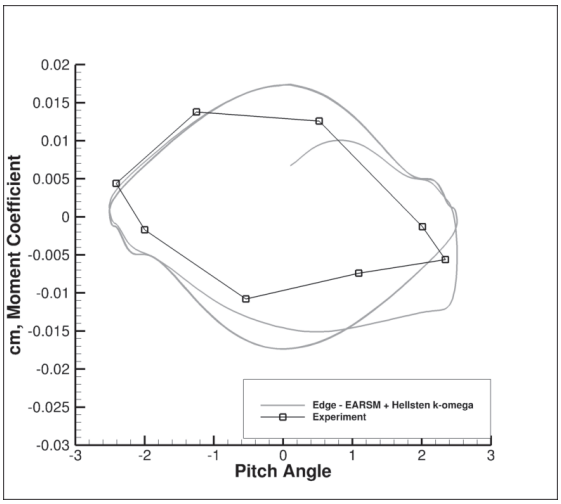

Figure 14. c_m **coefficients, numerical (line) and experimental (line with squares) results. Edge, EARSM.**

experimental simulation. Some slight differences can be observed in the behaviour of the lift coefficient (Figure 1). However, as discussed in [2], in this particular case the experimental data could be put into question as they should be symmetric with the centre of symmetry in point [0,0]. The numerical results fulfil such condition, the experimental do not. The correspondence in the behaviour of the pressure coefficient (Figs. 3 to 5) is very good even for relatively large values of the pitching angle (Figure 4). The situation changes completely if the turbulence modelling is turned on (Figures 6 to 8). Then the results begin to differ very significantly regardless on the combination of numerical method and turbulence model.

The solver Edge delivers a slightly better but still unusable results. The ellipsis of the c_l coefficient has a different slope than the experimental one (Figures 9 to 14), the behaviour of the moment coefficient is also very dissimilar and as in the previous cases, there are great differences between values of the experimental and numerical data in the c_p coefficient behaviour (Figures 15 to 23).

5. CONCLUSION

Considering the shown numerical results it is clear that the chosen type of unsteady flow cannot be simulated using the standard numerical simulation tools, which at the same time can be very precise for steady flow simulation. There are more possible reasons for such a behaviour and so far, the precise one is not known. Nevertheless, based on the tests done by the authors, the influence of the computational grid can be ruled off as the results

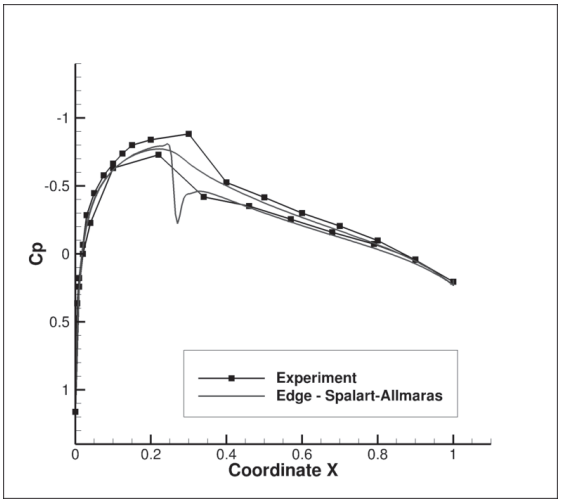

Figure 15. c_p **coefficient during the** 5^{th} **period of oscillatory motion,** $\alpha = 1.09°$**, turbulent flow, experimental (line with dots) and numerical (line) results. Edge, Spalart–Allmaras.**

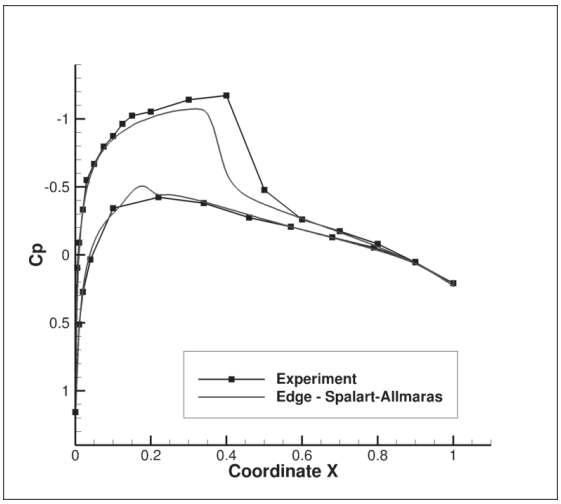

Figure 16. c_p **coefficient during the** 5^{th} **period of oscillatory motion,** $\alpha = 2.34°$**, turbulent flow, experimental (line with dots) and numerical (line) results. Edge, Spalart–Allmaras.**

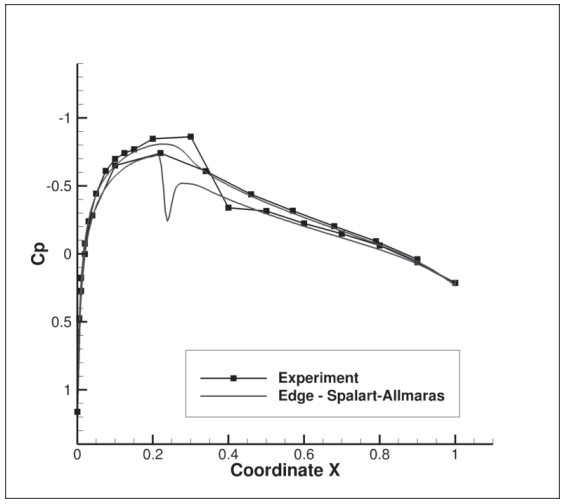

Figure 17. c_p **coefficient during the** 5^{th} **period of oscillatory motion,** $\alpha = -1.25°$**, turbulent flow, experimental (line with dots) and numerical (line) results. Edge, Spalart–Allmaras.**

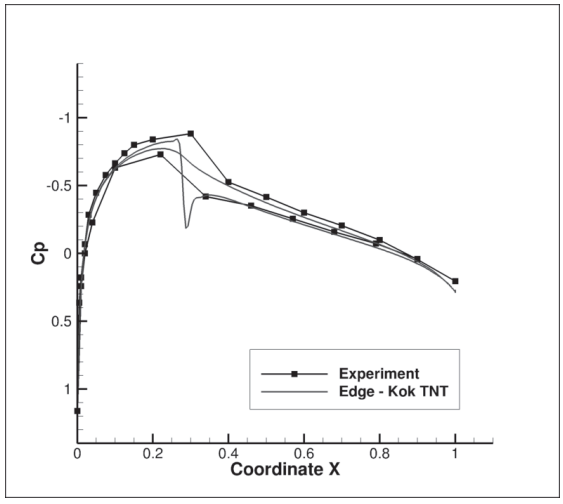

Figure 18. c_p **coefficient during the** 5^{th} **period of oscillatory motion,** $\alpha = 1.09°$**, turbulent flow, experimental (line with dots) and numerical (line) results. Edge, Kok's TNT.**

are bad both on structured and unstructured grids (with very fine resolution in the proximity of the solid wall). The same can be said about the influence of the time-step size, which in the case of the explicit scheme (MCS) was of magnitude 10^{-6} and in the case of the Edge of magnitude 10^{-3}.

The dual-time stepping allows to set smaller (and also larger) values of time-step but no qualitative changes of the results were observed. It is therefore necessary to further investigate the interactions between various types of numerical schemes, turbulence models and unsteady motion modelling techniques (e.g. ALE method). Another effect that deserves a closer investigation is the interaction between unsteady shockwave and turbulent boundary layer. Latest findings indicate necessity of adding time-dependent terms in the transport equations of turbulence models.

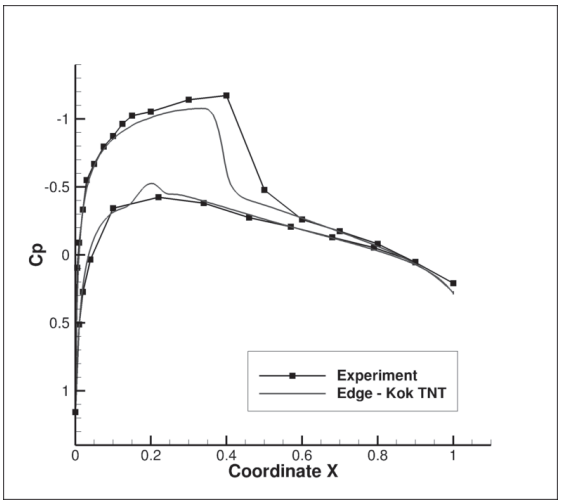

Figure 19. c_p **coefficient during the** 5^{th} **period of oscillatory motion,** $\alpha = 2.34°$**, turbulent flow, experimental (line with dots) and numerical (line) results. Edge, Kok's TNT.**

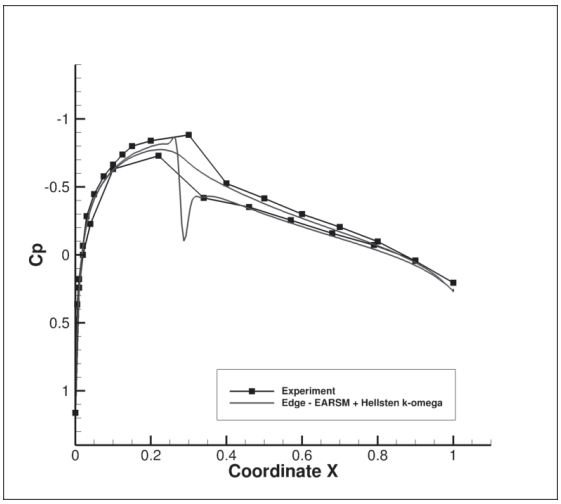

Figure 21. c_p **coefficient during the** 5^{th} **period of oscillatory motion,** $\alpha = 1.09°$**, turbulent flow, experimental (line with dots) and numerical (line) results. Edge, EARSM.**

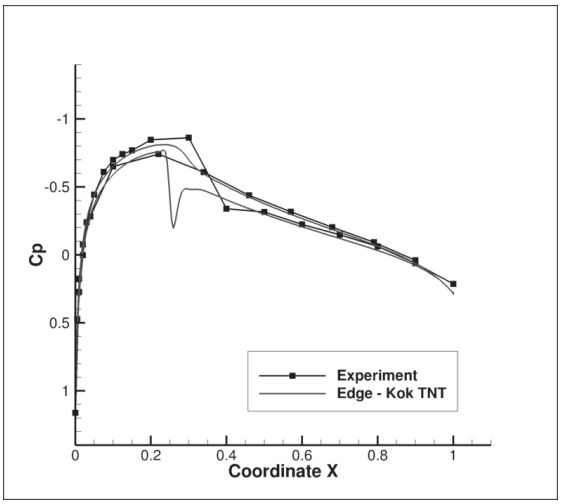

Figure 20. c_p **coefficient during the** 5^{th} **period of oscillatory motion,** $\alpha = -1.25°$**, turbulent flow, experimental (line with dots) and numerical (line) results. Edge, Kok's TNT.**

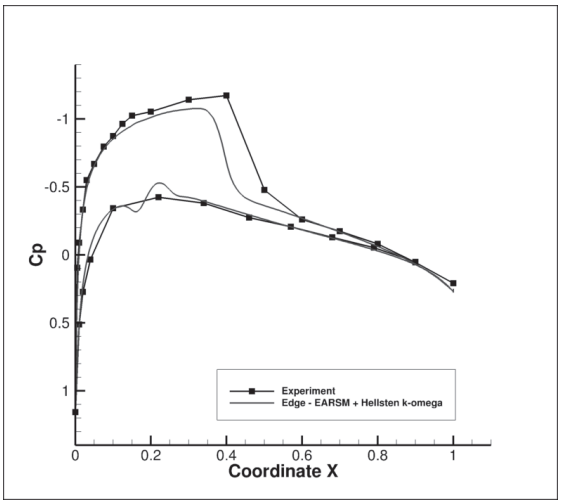

Figure 22. c_p **coefficient during the** 5^{th} **period of oscillatory motion,** $\alpha = 2.34°$**, turbulent flow, experimental (line with dots) and numerical (line) results. Edge, EARSM.**

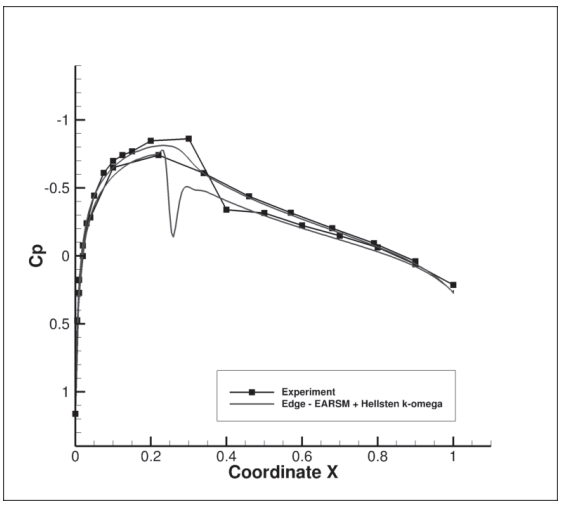

Figure 23. c_p **coefficient during the** 5^{th} **period of oscillatory motion,** $\alpha = -1.25°$**, turbulent flow, experimental (line with dots) and numerical (line) results. Edge, EARSM.**

ACKNOWLEDGEMENTS

This work was partly supported by the grant GACR P101/11/0207, P101/10/1329 and GA201/08/0012.

References

[1] AGARD R-702. 1982, , Compendium of Unsteady Aerodynamic Measurements, Tech. rep.

[2] Furmánek, P., Fürst, J., Kozel, K. 2009 "High Order Finite Volume Schemes for Numerical Solution of Unsteady Flows". *Numerical Mathematics and Advanced Applications 2009*, Springer Verlag Berlin- Heidelberg, ISBN 978-3-642-11794-7, pp. 333-340.

[3] Furmánek, P., Fürst, J., Kozel, K. 2009 "High Order Finite Volume Schemes for Numerical Solution of 2D and 3D Transonic Flows ", *Kybernetika*, Volume 45, No. 4, 567-579.

[4] Eca, L., Hoekstra, M., Hay, A., and Pelletier, D. 2007 "A Manufactured Solution for a Two-Dimensional Steady Wall-Bounded Incompressible Turbulent Flow ", *International Journal of Computational Fluid Dynamics*, Vol. 21, Nos. 3-4, pp. 175-188, 2007.

[5] Jameson A. 1995 "Analysis and Design of Numerical Schemes for Gas Dynamics 1, Artificial Diffusion, Upwind Biasing, Limiters and Their Effect on Accuracy and Multigrid Convergence". RIACS Technical Report 94.15, *International Journal of Computational Fluid Dynamics.* Vol. 4, pp. 171-218.

[6] Franke, M., Wallin, S., Thiele, F. 2005 "Assessment of explicit algebraic Reynolds-stress turbulence models in aerodynamics computations ", *Aerospace Science and Technology*, No. 9.

[7] Kok, J. C. 2000 "Resolving the Dependence on Freestream Values for $k - \omega$ Turbulence Model ", *AIAA Journal*, Vol. 38, No. 7.

[8] Wilcox, D. C. 2008 "Formulation of the $k - \omega$ Turbulence Model Revisited ", *AIAA Journal*, Vol. 46, No. 11.

[9] Donea, J. 1982 "An arbitrary Lagrangian-Eulerian finite element method for transient fluid- structur interactions", *Computational Methods in Apllied Mechanical Engineering*, 33:689-723.

Conference on Modelling Fluid Flow (CMFF'12)
The 15th International Conference on Fluid Flow Technologies
Budapest, Hungary, September 4-7, 2012

AERODYNAMIC ANALYSIS OF AN ISOLATED WHEEL WAKE

Emma CRONER,[1] Guillaume MOTHAY, [2] Christophe SICOT, [3] Hervé BÉZARD [4]

[1] MICHELIN, Centre de technologie Ladoux, Clermont-Ferrand Cedex, 63040, France. Tel.: +33 5 62 25 28 28, Fax: +33 5 62 25 25 83, E-mail: Emma.Croner@onera.fr
[2] Institut Pprime, UPR CNRS 3346, ENSMA, Université de Poitiers. E-mail: guillaume.mothay@etu.ensma.fr
[3] Institut Pprime, UPR CNRS 3346, ENSMA, Université de Poitiers. E-mail: christophe.sicot@lea.ensma.fr
[4] ONERA – The French Aerospace Lab, F-31055, Toulouse, France. E-mail: Herve.Bezard@onera.fr

ABSTRACT

The flow around road vehicles wheels exhibits complex unsteady 3D phenomena, including massive boundary layer separations, recirculation areas and 3D vortical structures. Although the mechanisms generating the wake main vortices have been identified, their exact topology is still indeterminate and a description of their unsteady evolution has not yet been proposed.

The intent of the present paper is to characterize the structure and unsteady motion of an isolated wheel wake. For this purpose, wind tunnel investigations have been carried out with a smooth rotating wheel in contact with a moving belt and compared to URANS simulations based on the geometry used for experiments.

CFD calculations appeared to have successfully predicted the main features of the flow. Particle Image Velocimetry and hot-wire anemometry measurements coupled with numerical simulation results allowed to confirm the origin and the nature of the main vortical structures in the near-wake and to investigate their unsteady behaviour. Results show good agreement with previous knowledge and provide new insight in the unsteady features of the wake.

Keywords: aerodynamics, CFD, hot-wire, PIV, URANS, wheel

NOMENCLATURE

C	$[-]$	force coefficient
D	$[m]$	wheel diameter
f	$[Hz]$	frequency
L	$[m]$	wheel width
V	$[m/s]$	mean velocity vector norm

Subscripts and Superscripts

i	at the inlet of the test section
L, D, S	lift, drag, side force
P	in-plane
x, y, z	axial, transversal, vertical

1 INTRODUCTION

Car wheels are responsible for 20% to 40% of modern vehicles total drag. In addition to the own drag of these bluff bodies, this high contribution is also due to the strong interactions of their wake with the vehicle underbody through pressure modifications. Hence, as body shape optimization reaches its limits, wheels aerodynamics is becoming a major concern in order to reduce fuel consumption and the wake dynamics understanding is therefore essential.

Fackrell & Harvey [8] carried out the first experimental work about an isolated wheel in realistic conditions, namely a rotating wheel in contact with a moving floor. Pressure distribution measured on the wheel surface highlighted two main specificities of the flow. First, upstream of the contact area, the rotating wheel and the moving ground behave like a viscous pump and cause pressure coefficients to rise above 1. A lateral jet stream, referred as *jetting*, is produced to each side of the wheel generating two near-ground vortices. A negative pressure peak downstream of the contact area was predicted but not observed. The second phenomenon, confirmed by smoke visualizations, is the boundary layer separation occuring further upstream on the top of a rotating wheel compared to a stationary one because of the fluid entrainment by the wall. Added to the jetting-vortices effects, this causes the wake of the rotating wheel to be taller and narrower than the one of the stationary wheel.

This pressure distribution analysis was completed by Mears *et al.* [12] who reproduces Fackrell's measurements with modern devices confirming previous observations and revealing the already suggested negative pressure peak.

Most of the following studies emphasized the importance of reproducing realistic rolling conditions to analyse vehicles aerodynamics. Cogotti [5] and Mercker & Berneburg [13] outlined the importance of the wheel and ground motions to ensure a correct wake development and consequently properly estimate the aerodynamic coefficients. The contact between the moving surfaces is indeed the only way to generate the flow features mentioned above. These considerations on isolated wheels were extended to full vehicle configurations by experiments, summarized by Elofsson and Bannister [6]. All authors highlighted the major effect of moving ground and rotating wheels on the vehicle total lift and drag coefficients. In addition, Mlinaric and Sebben [14] emphasized the importance of the contact patch dimensions, especially the transversal one.

In a more general point of view, the main objectives of the authors were to quantify the impact of different elements on the vehicle global aerodynamic performances in order to affirm the necessity or not to take them into account during measurements or numerical simulations. Hence, wheel characteristics such as grooves or deformation were find to deeply affect the car aerodynamics through underbody and base pressure modifications [15]. All experimental works, conducted since the 70', as well as the numerical ones, during the last decade, agreed on the wheels major impact on car aerodynamics and consequently outlined the importance of understanding the flow developing around them.

From consideration of previous works and vortex theory, Mercker & Berneburg [13] suggested a schematic of near-wake vortical structures including the two jetting-vortices, two vortices behind the upper wheel boundary separation – specific to lift bodies – and two weak central vortices created at the rims centers. More recently, Saddington *et al.* [17] revisited this model in the light of Laser Doppler Anemometry (LDV) measurements : the central vortices have not been observed and are supposed to be quickly swept up into the lower and upper ones ; moreover the upper vortices appeared to be weaker and to merge with the jetting-vortices within one diameter downstream of the wheel axis.

The use of Computational Fluid Dynamics (CFD) added a new insight in the understanding of car wheels aerodynamics. The first simulations with isolated wheels [1, 18] tended essentially to demonstrate the CFD ability to predict specific flow features through pressure coefficients comparisons. Besides parametric studies, the following works provided detailed visualizations of the flow around isolated wheels and wheels inserted in wheelhouses. Concerning the rotating wheel, McManus & Zhang [11] proposed a schematic picture of the mean flow structures including an arch-shaped vortex just downstream the top of the wheel instead of two contra-rotative vortices. In contrary, Wäschle *et al.* [19] described the flow topology with a ring vortex on the top and a wake-horseshoe vortex downstream the contact area. He considers that this structure dominates the wake : the massive vortices in the wake lower part come from the merge of the weak jetting-vortices with the powerful wake-horseshoe vortex.

Although the main flow features have already been studied both experimentally and numerically, authors do not yet agree on the exact flow topology surrounding a rotating wheel. Moreover, few numerical studies were conducted with unsteady calculations and, to the author's knowledge, none of them tried to characterize the unsteady behaviour of the wake. Only Basara [1] suggested the presence of a vortex shedding phenomenon and some authors [7, 16] evaluated the drag evolution of a wheel in a wheelhouse. This paper intents to complete actual knowledge by analyzing the wake structures topology and unsteadiness in order to better understand the main vortex dynamics and their impact on aerodynamic forces.

2 EXPERIMENTAL SETTINGS

The wind tunnel test campaign took place in the Aero Concept Engineering (ACE) facility in Magny-Cours, France. Particle Image Velocimetry (PIV) and hot-wire anemometry measurements were used to obtained mean and instantaneous information on velocity field in the wake of an isolated wheel rotating in contact with the ground (see Figure 1).

The ACE wind tunnel featured a 2.35m-wide and 2m-high test section. Hence it was possible to test a full scale wheel assembly which was composed of a strut and a wheel. The strut can be divided into two parts, one mast and one arm, which were linked together by a pivot joint. Both parts got streamlined cross-sections to be as less intrusive as possible. The wheel was carefully aligned with the oncoming flow and only a 0°yaw angle is studied here. The smooth shaped Michelin tire used for this experiment complied with the 205/55/R16 norm thus corresponding to a width of L=0.205m and an external diameter D=0.631m. Both sides of the rim were covered with smooth black carbon plates.

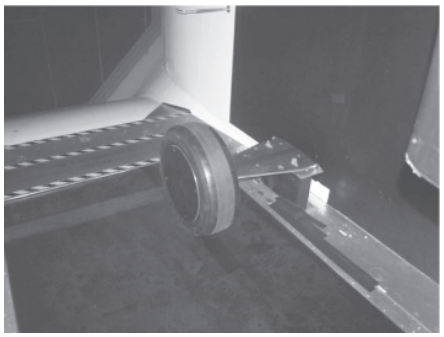

Figure 1: Experimental assembly

In order to fit with real road conditions, the vein was equipped with a moving belt to provide both ground simulation and rotation. A low load level was required so as not to damage the belt but a minimal load was also needed to ensure full contact across the tire tread. Two adjusting screws enabled to set the position of the arm to find the configuration that provided the best compromise between load level and quality of the contact patch. The belt velocity was synchronized with the air free-stream, and the tests were run at the selected value of 22 m/s, corresponding to a Reynolds number based on the wheel diameter of 9.1×10^5. A suction system was placed ahead of the belt in order to remove the boundary layer developed on the lower wall of the convergent.

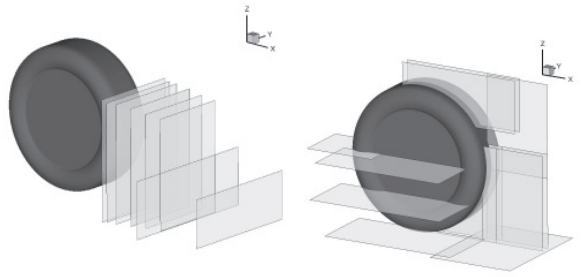

(a) (b)

Figure 2: PIV planes : constant X (a), constant Y and constant Z (b)

A 2D-2C PIV system is used to record the flow velocity field information. Illumination is provided by a double pulsed Nd:YAG laser emitting two pulses of 120 mJ each (laser sheet thickness $\approx$1 mm). An oil generator provides seeding with a mean particle diameter of about 1 μm. Two LaVision CCD cameras with both a 1376$\times$1040 pixel square resolution were used. The pre-processing corresponds to the subtraction of the background image using the minimum value within the set of images. Velocity vectors fields are computed with LaVision 7.2 software. A multipass algorithm with a final interrogation window size of 16$\times$16 pixels and 50% overlapping is applied. For each position in Figure 2, 2000 images pairs were acquired at a frequency of 4 Hz. Consequently, estimated statistical absolute errors for mean and root-mean-square (RMS) values are, respectively [2],$\Delta U \approx 0.004 u_{RMS}$ and $\Delta u_{RMS} \approx 0.03 u_{RMS}$ with a 95% confidence level.

Further investigations were performed in the wake of the rotating wheel using a one-dimensional hot-wire anemometer. The sampling frequency was set at 5 kHz with duration of two minutes for each measurement. The time series data is split into segments of 8092 points with a 50% overlap and a Hamming window is used to compute the modified periodogram of each segment. The purpose of this study was to probe locations that featured vortical structures according to previous PIV measurements. In the plane located at D behind the wheel center, velocities were recorded at different heights above the ground in the median plane and behind the jetting-vortice on the strut-free side.

3 NUMERICAL MODELLING

CFD simulations of the experimental configuration were performed in order to provide a direct comparison between experimental and numerical results. The origin of the cartesian coordinate system is placed at the center of the wheel. The X axis is parallel to the moving floor and oriented downstream, the wheel rotates around the Y axis and the Z axis is vertical. The test section of the wind tunnel is reproduced with the exact moving belt and wheel positions ; only its length has been increased at each extremity to minimize the influence of the boundary conditions. The suction system is replaced by an upstream prolongation of the moving belt in order to suppress the boundary layer.

Calculations are based on an accurate representation of the smooth rotating wheel used for experiments and a simplified version of the strut without links between the mast and the arm. The low load level of the wheel minimizes the tire deformation. Hence, the tire geometry can be approximately obtained by revolution of one profile taking the centrifugal force into account. The ground contact is produced by cutting the wheel at an appropriate ground level providing correct dimensions of the contact patch.

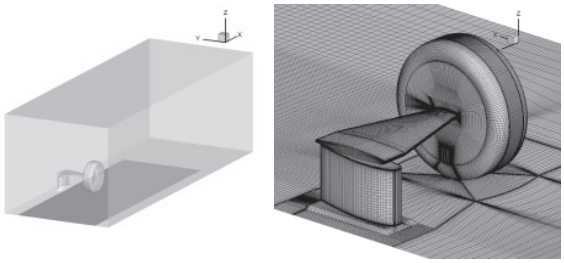

(a) (b)

Figure 3: Computational domain (a) and wheel meshing (b)

Inflow conditions are defined to match experimental ones with a uniform velocity profile at V_i = 22 m/s which gives a Mach number of 0.064 and a Reynolds number based on the wheel diameter of 9.1×10^5. The flow can be considered as fully turbulent. A relative turbulence intensity 0.1% and a viscosity ratio of 10 are defined to calculate turbulence variables at the inlet. At the outlet, constant static pressure is prescribed. A slip boundary condition is specified on the wind tunnel walls to avoid resolving boundary layers along them. The floor, the moving belt, the wheel and the strut surfaces are considered as adiabatic walls with no-slip condition. The moving belt and the wheel velocities are adjusted to match the inflow velocity V_i, with an adequate angular velocity of 69.7 rad/s on the wheel.

The block-structured computational mesh (see Figure 3 (b)) was created with ICEM CFD software. It consists of 9×10^6 hexaedral cells distributed on 4 non-matching subdomains : the main domain around the wheel and 3 smaller ones fitting the support. The minimal cell size at walls enables a correct resolution of the boundary layers according to wall unit values ($y+ \leq 1$).

The ONERA code *elsA* [4] has been used to solve URANS equations by finite volume discretization method. It is to note that RANS solutions cannot converged with fine grids because of the intrinsic unsteadiness of the flow. The ONERA k-kL two-equation turbulence model [3] was chosen for turbulence closure. The spatial discretization uses a second-order accurate upwind scheme and the global time-step used for the explicit time resolution is 10^{-5}s, ensuring a Courant-Friedrichs-Lewy number $CFL \leq 1$ everywhere. Finally, the Weiss-Smith low-Mach preconditioning [20] is applied.

4 RESULTS

4.1 Pressure distribution

An instantaneous pressure coefficient distribution along the wheel center-line in Figure 4 shows that the characteristic features are reproduced. The positive and negative pressure peaks C_{Pmin}= -13.5 and C_{Pmax}= 15.6 around the contact position (θ=90°) characterize the viscous pumping. The upstream boundary layer separation is detected by the local minimum at 278°. As in many other numerical studies [1, 11, 18], the separation is predicted a bit downstream compared to experience (∼290°). The 100°-270°section has already been proved to be strongly unsteady [8], explaining the important discrepancies in this area. For $\theta \leq 90°$, the pressure differences outline higher velocities caused by the lower aspect ratio of the present geometry.

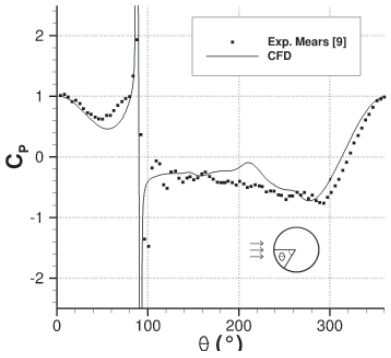

Figure 4: C_P distribution along the wheel center-line

4.2 Analysis of the flow topology

Numerical results are time-averaged over 2×10^5 time-steps and compared to PIV results. The boundary layer separation can be visualized in Figure 5 with a recirculation bubble predicted further downstream by CFD compared to PIV. The position of the separation and the recirculation bubble shape are quasi-steady for each case. Streamlines plotting in the median plane highlights the *downwash* phenomenon : the flow coming from above the wheel is driven downwards by the vortices rotation.

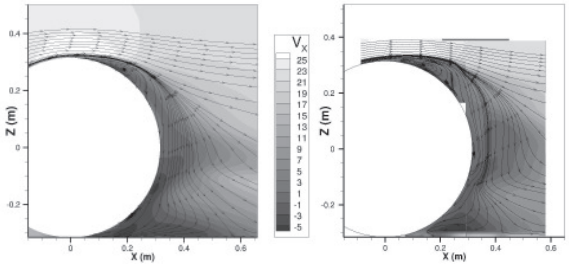

(a) CFD (b) PIV

Figure 5: Streamlines and V_x contours in the plane Y=0

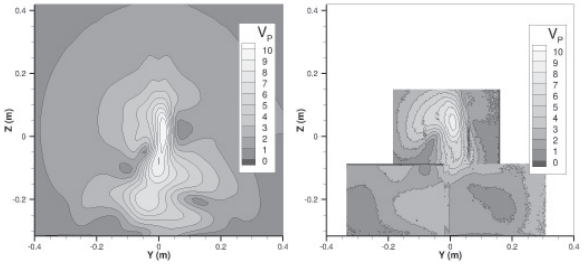

(a) CFD (b) PIV

Figure 6: V_P contours in the plane X=D

The wake dimensions can be observed for different X thanks to in-plane velocity (V_P) contours in Figure 6. This can be completed by the Γ_2 criterion [9] and Q criterion [10] which detect coherent vortical structures for experimental and numerical results respectively. The Q criterion is calculated from all velocity components by $Q = \frac{1}{2}(\|\Omega\|^2 - \|S\|^2)$, where Ω is the vorticity tensor and S the strain-rate tensor. The Γ_2 criterion is based on the flow topology in a 2D area and is therefore suitable for analyzing two-components PIV measurements. The local flow is considered as dominated by the rotation when $Q >> 0$ and $|\Gamma_2| > 2/\pi$. An iso-contour of Q criterion is compared to the Γ_2 criterion contours extracted from PIV in Figure 7. These results, added to the 3D iso-surface of Q criterion in Figure 8, exhibit massive coherent structures and enables the visualization of the wake development.

In the near-wake, namely $X \leq D$, both PIV and CFD results show the presence of secondary vortical structures (**5** and **6** in Figure 7) between the two other pairs : the upper vortices **1** and **2** caused by the boundary layer separation and the near-ground vortices **3** and **4** linked to the jetting. The secondary

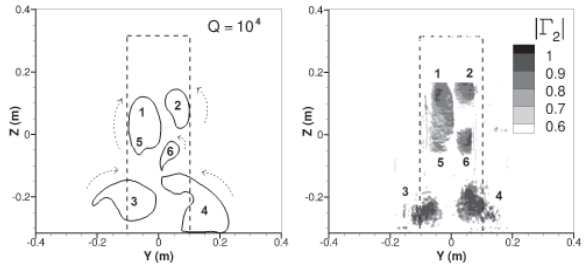

Figure 7: Numerical iso-contour Q=10^4 compared to experimental Γ_2 contours in the plane X=$0.66D$

vortices **5** and **6**, originating from the wheel base, merge either with one upper vortice or with a lower one, resulting in vortex size differences at X=D. The weak vortices suggested to be created on the wheel sides centers are not observed. In addition, as observed by Wäschle *et al.* [19], the two lower vortices does not originate directly from the jetting vortices but are actually connected in a massive wake-horseshoe vortex like the one isolated in Figure 9.

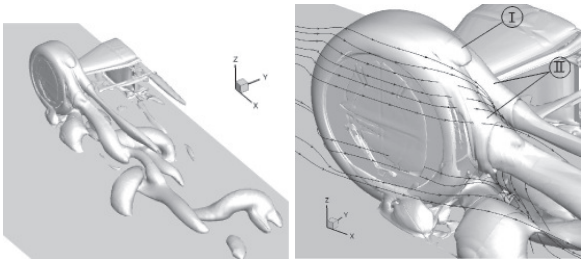

Figure 8: Iso-surface $Q = 1000$ and streamlines

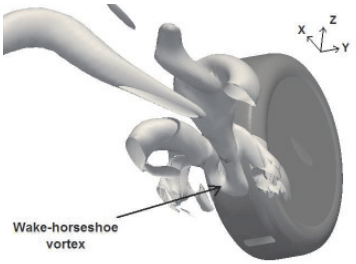

Figure 9: Bottom view of some lower-wake vortical structures ($Q = 10000$)

4.3 Analysis of the flow unsteadiness

4.3.1 Vortical structures

The temporal analysis of an iso-Q criterion surface over one period of 0.08 seconds is plotted Figure 10, where capital letters indicate the dominant structure between the left and right sides. It reveals how the wake 3D vortical structures are created and how the above-mentioned wake-horseshoe vortex is closely related to the jetting phenomenon.

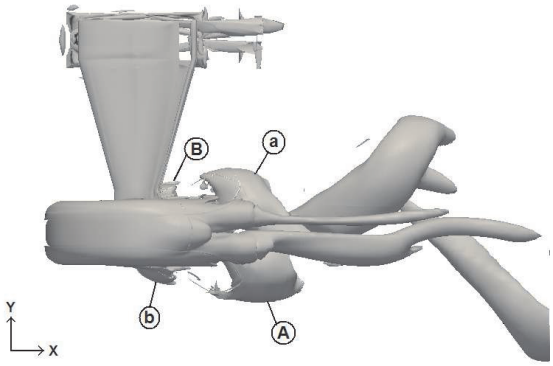

(a) 0 s – C_S max.

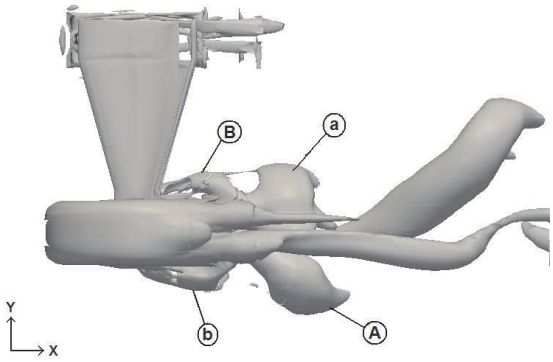

(b) 0.02 s

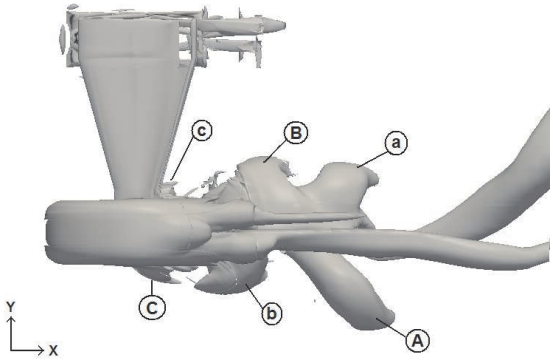

(c) 0.04 s – C_S min.

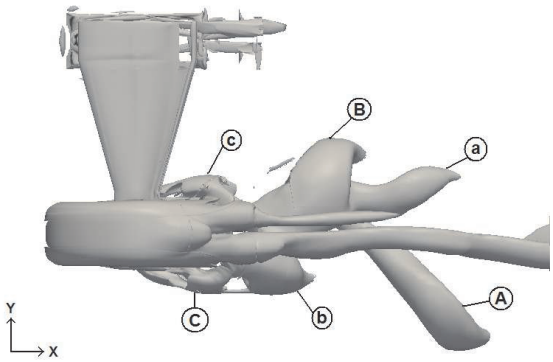

(d) 0.06 s

Figure 10: Top views of iso-surface $Q = 5000$ at 4 instants of the 0.08 second-long period

At t=0 s, the structures **A** and **a** are linked in a wake-horseshoe vortex, attached to the wheel base-surface, while the jetting phenomenon produces **B** and **b**. At the following instant, **B** and **b** start interacting with the highly unsteady wheel base area. When these structures are shed in the wake, at t=0.4 s, they are linked in a new wake-horseshoe vortex and the predominance of **B** is emphasized. In the meantime, **C** and **c** are produced by the jetting. As a result, the massive 3D structures in the wake are created by the interaction between the quasi-symmetric structures originating from the jetting and the unsteady wheel base flow. This issue is discussed in section 5.

4.3.2 Velocity spectra

The flow unsteadiness is now studied at different positions in the wake through velocities evolutions given by numerical calculations and hot-wire anemometry. Velocity spectra are obtained by discrete Fast Fourier Transformations (FFT). Some results are presented in Figures 11 and 12 through Power Spectral Density (PSD) plotting. For each component and each position in the wake, the main frequencies detected by hot-wire anemometry can be divided in two parts : 11.1 Hz and its harmonics on one hand, 14.8 Hz and its harmonics on the other hand. It has been found that the first frequency matches the wheel rotation frequency while the wake dynamics are characterized by 14.8 Hz and its first harmonic, as explained in the section 5. The use of URANS method provides numerical spectra with strong peaks corresponding to the wake main motions. The main frequencies are 12.5 Hz and its harmonics which can be compared to 14.8 Hz. As a result, the temporal characteristics of the numerical wake show good agreement with experiment considering the use of URANS simulations.

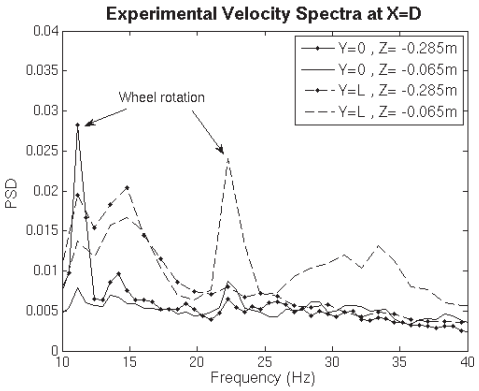

Figure 11: Velocity spectra in the plane X=D for experimental results

The main frequency is now referred as f_1 and its harmonic f_2. In both hot-wire and CFD results, f_1 is predominant in velocity variations for all probes positions in the wake. Time variations are particularly

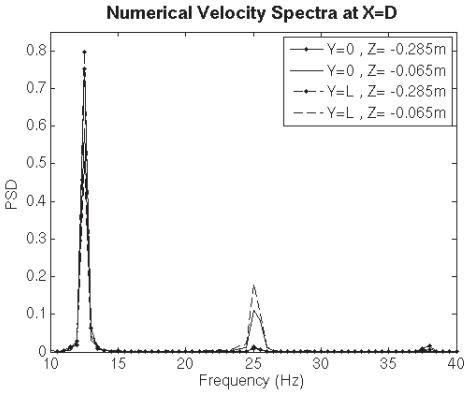

Figure 12: Velocity spectra in the plane X=D for numerical results

significant behind the jetting-vortices near the ground with large V_x and V_y variations. In the median plane, V_y variations remain high while V_x variations decrease. For numerical simulations, additional probes were placed just behind the jetting birth and behind the upper separation in the median plane. The upper separation stability is confirmed, with velocity variations not above 1%, and the area just behind the contact zone is found to be dominated by f_2.

4.3.3 Aerodynamic coefficients

CFD simulations give access to aerodynamic coefficients time evolutions presented in Figure 13, where C_D, C_L and C_S refer respectively to drag, lift and side force coefficients. Spectral analysis of these results reveals the same characteristic frequencies f_1 and f_2 as previously.

The side force coefficient exhibits the largest variations with a dominant frequency equal to f_1=12.5 Hz. This force is most of time negative because of the set-up asymmetry, which also induces a global deviation of the wake in the direction of $Y \geq 0$. Considering this orientation, the wheel behaves just like a asymmetric wing profile producing a negative mean side force. Similarly to the signal in the jetting area, drag and lift coefficients exhibit slightly higher spectral density for f_2=25 Hz.

Moreover, the viscous components of each force was found to be quasi-steady ; consequently, their variations are solely due to pressure modifications.

	C_D	C_L	C_S
Mean value	0.444	0.164	-0.0331
Variations	$\pm$0.0125	$\pm$0.0145	$\pm$0.0775

Table 1: Aerodynamic coefficients

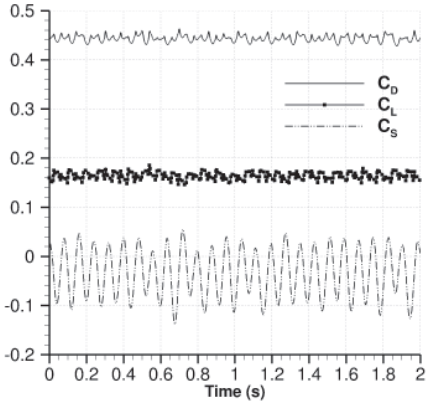

Figure 13: Temporal evolution of aerodynamic coefficients during 2 secondes (2×10^5 time-steps)

5 DISCUSSION

Contours plotting shows good agreement between numerical and PIV results. Despite some area with higher velocities, the structures developed in the wake are well reproduced. CFD results also reproduce the characteristic flow features mentioned in the literature such as the jetting phenomenon. Spectral analysis coupled to the above-mentioned results about the flow topology enables hence to validate the numerical model before carrying out a detailed analysis of the wake dynamics.

The ring vortex suggested by Wäschle *et al.* [19] on the upper-part of the wheel has not been observed. The results show an arch-shaped vortex (**I** in Fig. 8) just downstream the top of the wheel, matching the recirculation bubble in Fig. 5, associated to the highly correlated contra-rotative vortex pair (**II** in Fig. 8). These steady structures are produced by the upper wheel boundary layer separation and the wheel rotation. The vortex pair becomes unsteady only after the downwash when it interacts with the lower part of the wheel wake.

URANS calculation reveals complex structures for the wake lower part. The jetting phenomenon appears to be coupled with the unsteady behaviour of the depression area downstream of the contact between the wheel and the moving belt. On both sides of the contact zone, the jetting vortices are quasi-symmetric and structures are simultaneously shed at f_2 frequency. When they interact with the flow behind the wheel, the jetting vortices lose their symmetry because of the base flow lateral motion, one structure becoming predominant.

For the configuration under consideration, the asymmetry is increased by the one of the global flow caused by the set up. A horseshoe vortex is then created from the interaction of the two structures with the wheel rotation in the base recirculation area. The structures observed in the wake are those shed from this massive horseshoe vortex. For each vortex pair, the weaker side is dissipated far more quickly as seen in Figure 10 (d) with the pairs **A**-**a** and **B**-**b**. The main frequency in the wake is consequently reduced to f_1.

Hence the wake does not exhibit a classical vortex shedding phenomenon similar to those producing the von Kármán vortex street. The structures originating from upstream the contact area are affected by the downstream area and become asymmetric.

The use of CFD enables to get further in the flow understanding by analyzing the effects of vortex dynamics on the aerodynamic coefficients evolutions. The three coefficients time-evolutions are controlled by the wake lower part. The drag and lift coefficients are equally affected by f_1 and f_2 frequencies while the side force coefficient evolution exhibits only one characteristic frequency f_1.

C_D and C_L evolutions appears to be strongly correlated – maximal drag matching minimal lift – and controlled by the vortex pairs shedding frequency f_2. This behaviour is closely related to the nearwake lower part where a pressure decrease induces lower lift and higher drag. Hence, it has been found that maximal drag matches the moment when the jetting vortices interact with the wake-horseshoe vortice and make it become larger (see Figure 10 b and d). This phenomenon can be compared to the observations of Krajnović [16] in the case of a wheel included in a wheelhouse : Large Eddy Simulations (LES) results indicated that an increase in density of flow structures in the wheel wake is visible when the drag is maximal. In contrary, C_S is affected by pressure distributions on the wheel sides and therefore highly depends on the predominance of one jetting vortical structure. The link between the wake and the side force can be illustrated in Figure 10 where (a) occurs for the maximal value of C_S and (c) for the minimal one. The authors suggest that the predominance of one of the two structures is less significant in the case of an isolated wheel without strut. The drag and lift evolutions are therefore essentially controlled by f_2 frequency giving numerical Strouhal numbers of St_W=0.233, based on the wheel width, and St_D=0.717, based on the wheel diameter.

To the authors knowledge, there are few evaluations of Strouhal number in the literature and only for wheels in wheelhouses. URANS results of Damiani *et al.* [7] give St_W=0.22 and Krajnović *et al.* [16] find a dominant peak at St_D=1.39 for the case of a wide wheelhouse. However these studies were carried out at a subcritical Reynolds number ($< 10^6$ [5]) and it is difficult to compare isolated wheel results with those of vehicles. In addition, the characteristic length is not clearly defined. The diameter is adapted to the case of infinite cylinder but in the case of wheels the wake is necessarily affected by the wheel width. Hence, the authors suggest that the characteristic length of a wheel (low aspect ratio cylinder) may be a combination of diameter and width.

CONCLUSION

Wind tunnel testing and numerical modelling were carried out to characterize the wake of an isolated wheel. The CFD model has been able to reproduce both the flow topology and its unsteady behaviour with correct characteristic frequencies. As a result, the vortex dynamics analysis and the identification of their effect on the aerodynamic coefficients add new insight into the unsteady evolution of the wake and the flow surrounding the wheel.

ACKNOWLEDGEMENTS

The authors wish to thank B. Gardarin, the project manager at Michelin ; J. Borée and L.-E. Brizzi of Institut Pprime for having conducted the wind tunnel experiments ; P. Braud of Institut Pprime for his technical assistance throughout the test campaign ; and the Aero Concept Engineering society. The research was supported by Michelin.

References

[1] B. Basara, D. Beader, and V. Przulj. Numerical simulation of the air flow around a rotating wheel. In *3rd MIRA International Vehicle Aerodynamics Conference*, Rugby, UK, October 2000.

[2] L.H. Benedict and R.D. Gould. Towards better uncertainty estimates for turbulence statistics. *Experiments in Fluid*, 22(2):129–136, 1996.

[3] H. Bézard and T. Daris. Calibrating the length-scale equation with an explicit algebraic Reynolds stress model. In *ERCOFTAC International Symposium on Engineering Turbulence Modelling and Experiments - ETMM6*, Sardinia, Italy, May 23-25 2005.

[4] L. Cambier and J.-P. Veuillot. Status of the elsa CFD software for flow simulation and multidisciplinary applications. In *46th AIAA Aerospace Sciences Meeting and Exhibit*, January 7-10.

[5] A. Cogotti. Aerodynamics characteristics of car wheels. *Int. J. of Vehicle Design*, pages 173–196, 1983. Special Publication SP3.

[6] P. Elofsson and M. Bannister. Drag reduction mechanisms due to moving ground and wheel rotation in passenger cars. *SAE Paper*, 2002-01-0531, 2002.

[7] Damiani F., Iaccarino G., Kalitzin G., and Khalighi B. Unsteady flow simulation of wheel-wheelhouse configurations. In *34th AIAA Fluid Dynamics Conference and Exhibit*, Portland, USA, 2004.

[8] J.E. Fackrell and J.K. Harvey. The aerodynamics of an isolated wheel. In *Proceedings of the 2nd AIAA Symposium on the aerodynamics of Sport and Competition Automobiles*, volume 16, pages 119–125, 1974.

[9] L. Graftieaux, M. Michard, and N. Grosjean. Combining PIV, POD and vortex identification algorithms for the study of unsteady turbulent swirling flows. *Measurement Science and Technology*, (12):1422–1429, 2011.

[10] J.C.R. Hunt, A.A. Wray, and P. Moin. Eddies, stream, and convergence zones in turbulent flows. Technical report, Center for Turbulence Research, 1988.

[11] J. McManus and X. Zhang. A computational study of the flow around an isolated wheel in contact with the ground. *Journal of Fluids Engineering*, 128(3):520–530, 2006.

[12] A.P. Mears, R.G. Dominy, and D. B. Sims-Williams. The airflow about an exposed racing wheel. *SAE Paper*, 2002-01-3290, 2002.

[13] E. Mercker and H. Berneburg. On the simulation of road driving of a passenger car in a wind tunnel using a moving belt and rotating wheels. In *3rd International Conference Innovation and Reliability*, Florence, Italy, April 1992.

[14] P. Mlinaric and S. Sebben. Investigation of the influence of tyre deflection and tyre contact patch on cfd predictions of aerodynamic forces on a passenger car. In *7th MIRA International Vehicle Conference*, PN 116-022, 2008.

[15] F. Modlinger, R. Demuth, and N. Adams. Investigations on the realistic modelling of the flow around wheels and wheel arches by CFD. *JSAE Paper*, 20075195, 2007.

[16] Krajnović S., Sarmast S., and Basara B. Numerical investigation of the flow around a simplified wheel in a wheelhouse. *Journal of Fluids Engineering*, 133(111001).

[17] A.J. Saddington, R.D. Knowles, and K. Knowles. Laser Doppler Anemometry measurements in the near-wake of an isolated Formula One wheel. *Experiments in Fluid*, 42(5):671–681, 2007.

[18] A.F. Skea, P.B. Bullen, and J. Qiao. CFD simulations and experimental measurements of the flow over a rotating wheel in a wheel arch. *SAE Paper*, 2000-01-0487, 2000.

[19] A. Wäschle. The influence of rotating wheels on vehicle aerodynamics - Numerical and experimental investigations. *SAE Paper*, 2007-01-0107, 2007.

[20] J.M. Weiss and W.A. Smith. Preconditioning applied to variable and constant density flows. *American Institute of Aeronautics and Astronautics Journal*, 33(11):2050–2057, 1995.

Conference on Modelling Fluid Flow (CMFF'12)
The 15th International Conference on Fluid Flow Technologies
Budapest, Hungary, September 4-7, 2012

Simulations of Flow Around a Simplified Train Model with a Drag Reducding Device using Partially Averaged Navier-Stokes

Jan ÖSTH[1], Siniša KRAJNOVIĆ[2]

[1] Corresponding Author. Division of Fluid Dynamics. Department of Applied Mechanics, Chalmers University of Technology. Hörsalsvägen 7A, SE-412 96 Göteborg, Sweden. Tel.: +46 31 772 13 90, Fax: +46 31 18 09 76, E-mail: ojan@chalmers.se
[2] Division of Fluid Dynamics. Department of Applied Mechanics, Chalmers University of Technology. www.tfd.chalmers.se/~sinisa, E-mail: sinisa@chalmers.se

ABSTRACT

Partially Averaged Navier Stokes is used to simulate the flow around a simple train model. The train model has previously been studied in wind tunnel experiments [1] and has a length to height/width ratio of 7:1. The Reynolds number based on the height of the train model is $0.37 \cdot 10^6$. For this Reynolds number, the flow separates from the curved leading edges on the front then attaches again on the roof and sides forming a boundary layer there before separating in the wake. The first case is of the natural flow around the train model where direct comparison to experimental data of drag coefficient and pressure coefficient are made. In the second case an open cavity is placed on the base of the train model with the aim of reducing the overall drag on the model. The results show that the drag for model with the cavity is reduced by some 10% compared to the drag of the natural case. The agreement to experimental data for the natural case is not perfect but the general features in the flow field are simulated correctly.

Train aerodynamics, PANS, Drag reduction, CFD

NOMENCLATURE

C_D	$[-]$	Drag force coefficient
C_p	$[-]$	Pressure coefficient
F_x	$[N]$	Force in stream wise direction
F_y	$[N]$	Force in span wise direction
f_k	$[-]$	Ratio of unresolved kinetic energy to resolved
f_ϵ	$[-]$	Ratio of unresolved dissipation to resolved
k_u	$[m^2/s^2]$	Unresolved kinetic energy
p_F	$[Pa]$	Filtered pressure
u_i	$[m/s]$	Filtered velocities
ζ_u	$[-]$	Velocity scale ratio
ϵ_u	$[m^2/s^3]$	Unresolved dissipation
ρ	$[kg/m^3]$	Density
ν	$[kg/sm]$	Molecular viscocity
ν_u	$[kg/sm]$	Viscosity of the unresolved scales

HST	High Speed Train
RT	Regional Train
PANS	Partially Averaged Navier-Stokes

1. INTRODUCTION

Aerodynamic issues concerning railway systems are numerous. Aerodynamic noise generated by the train has a negative influence on the environment around the railway system and on the passengers inside the train. Pressure variations in tunnels increase the drag of the train significantly in comparison to open air and can cause considerable ear discomfort for passengers in the train and riding discomfort due to large dynamic oscillation of the train. Pressure waves radiate to the environment from the tunnel exit. The increased driving resistance inside tunnels increase the mechanical stress on the train. The slip stream (a very strong shear layer) formed around the moving train can cause serious accidents to persons or material located on platforms when trains pass by. Cross-winds can cause very serious accidents such as derailment [2]. The aerodynamic drag induced on the train affects the economics of the railway system considerably and limits the maximum speed. High speed trains (HST) are in general shaped in a very good way in regard to minimizing the aerodynamic drag. However, still it is responsible for the consumption of some 40-50% of the total energy put into the railway system during traction [3] for a typical HST. For regional type (RT) of trains, the aerodynamic drag contributes less to the total energy consumption due to the typical lower operational speeds. In general regional trains have a worse shape from an aerodynamic drag minimizing point of view compared to high speed trains. The

contribution to the total aerodynamic drag on a train comes from different areas of the train: skin friction drag along the train body, pantographs and other protruding objects, inter-carriage gaps, brakes, boogies and the pressure difference between the head and the tail of the train, the last one being dominating for RT trains [3].

One way to increase the base pressure and thereby reduce the aerodynamic drag on trains having a square back such as the Bombardier Contessa/X31 train used in southern Sweden could be to place plates forming a cavity on the aft of the train. Such devices has proven to be able to reduce the drag on simplified ground vehicle models in wind tunnel experiments and numerical simulations [4, 5] as well as on real tractor-trailers during over-the-road tests [6, 7].

The work reported in the present paper aims at reducing the drag on a simplified train model by attaching an aft cavity on the base of the train. The investigation method used in the present work is unsteady numerical simulations using the recently proposed hybrid turbulence modeling method Partially Averaged Navier Stokes (PANS). The train model has previously been investigated in wind tunnel experiments by Sakuma & Ido [1]. Two cases are simulated: the natural case and the cavity case. For the natural case, direct comparison with experimental data is possible. For the aft cavity case however, no direct experimental data are available. The outline of the paper is as follows: in Section 2 the train model for the two cases and the reference experiments are described. In Section 3 the PANS equations are presented. In Section 4 the numerical details of the simulations are described. Then follows the results from the simulations in Section 5.1 and in the last Section the results are discussed and the paper is concluded.

2. THE TRAIN MODEL AND REFERENCE EXPERIMENT

The train model used in the numerical investigation in the present paper is taken from the wind tunnel experiments reported in [1] where the large-scale wind tunnel [8] at Railway Technical Research Institute (RTRI) was used . The train model, presented in Fig. 1, is a prismatic bluff body with the height H and width $W = H = 0.56\,m$. The length of the bluff body is $7H$ which thus makes it resemble some RT trains better than other bluff bodies with smaller length-to-height ratio reported in the literature (e.g. [9]). The aim of the extensive experimental study reported in [1] was to investigate how the separation from the leading front edges of the bluff body was affected by different roundings of the front edges for a Reynolds number of $1.9 \cdot 10^6$ and $0.37 \cdot 10^6$ based on the width of the train. The former Reynolds number corresponds roughly to one third of that of a real regional train travelling at 120 km/h.

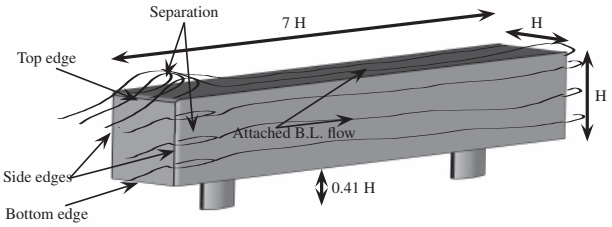

Figure 1. Schematic drawing of the train model and the flow around it at the low Reynoldsnumber $Re_H = 0.37 \cdot 10^6$.

One of the configurations from [1] is choosen for the simulations presented in the present paper. In the choosen configuration the leading top and side edges on the front are rounded using an elliptic profile (see Fig 2). The major axis in the ellipse has length $0.07H$ and the minor axis has length $0.04H$. The bottom edge is not rounded at all and is thus sharp. The model was placed on two egg-shaped supports in the wind tunnel and the model is lifted 0.41 H above the ground. The top and side edges on the rear end of the bluff body are rounded with a circular radius of 0.107H while the bottom edge here is sharp.

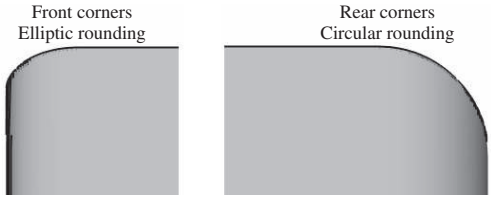

Figure 2. The front and rear corners of the train model, respectively.

For the choosen configuration from [1] which make up the natural case in the present study and $Re_H = 0.37 \cdot 10^6$ the flow separates from the leading edges on the front of the bluff body (see Fig. 1). After a distance of approximately $\approx H$, the flow re-attaches on the top and the sides of the body and an attached boundary layer develops along the body before the flow separates in the wake once again. There are thus three major very difficult flow situations to simulate in this case. If not the separation on the front leading edges are simulated correctly, the boundary layer will not be simulated correctly and that will make it impossible to simulate the separation in the wake in a correct manner. The reported drag coefficient of the bluff body at $Re_H = 0.39 \cdot 10^6$ in the experimental study is $C_D^{low} = 0.86$ and for $Re_H = 1.9 \cdot 10^6$ it is $C_D^{high} = 0.41$ [1]. This significantly smaller drag coefficient for the high Reynolds number is because the flow in that case does not separate from the

leading front edges and thus stays attached all the way to the rear of the bluff body.

2.1. Cavity case: attached open cavity on the base of the train model

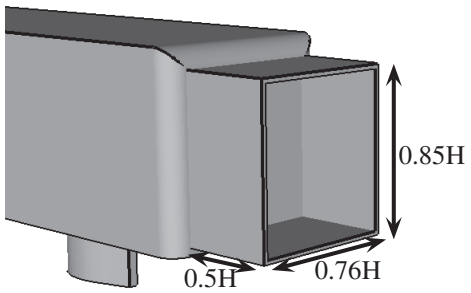

Figure 3. The flaps attached on the base of the train model.

The cavity placed on the aft on the train model is depicted in Fig. 3. The length of the cavity is 0.5 H which corresponds to the length that was found to be optimal in the previously mentioned studies [6, 7] where a cavity was attached on the base of a real tractor-trailer. The inset of the cavity from the bottom edge is 0.06 H corresponding to the optimum value from the studies. The inset from the side and top edges are choosen such that the plates are placed on the end of the curvature on the edges.

3. PANS GOVERNING EQUATIONS

Two crucial parameters in PANS are $f_k = k_u/k$ and $f_\epsilon = \epsilon_u/\epsilon$. The former is the ratio of unresolved kinetic energy to the resolved kinetic energy. The latter is the ratio of unresolved dissipation to the total dissipation in the flow. For the formal derivation and motivation of the PANS method the reader is referred to [10]. Herein, the equations are simply stated. The governing flow equations are the incompressible, partially filtered Navier-Stokes Equations (NSE):

$$\frac{\partial u_i}{\partial x_i} = 0 \tag{1}$$

$$\frac{\partial u_i}{\partial t} + u_j\frac{\partial u_i}{\partial x_j} = -\frac{1}{\rho}\frac{\partial p_F}{\partial x_i} + \frac{\partial}{\partial x_j}(\nu\frac{\partial u_i}{\partial x_j} - \tau(u_i, u_j)) \tag{2}$$

In Eqs. (1) and (2) $u_i = \langle v_i\rangle$ are the partially filtered velocities. v_i are the unfiltered velocities containing all spatial and temporal scales in the flow and $\langle\cdot\rangle$ denotes filtering by an arbitrary filter (in time and space) fulfilling the requirements for averaging invariance [11]. $p_F = \langle p\rangle$ is the partially filtered pressure. $\tau(v_i, v_j) = \langle v_i v_j\rangle - \langle v_i\rangle\langle v_j\rangle$ is the sub-filter scale (SFS) stress which is modelled by the turbulent-viscosity (Boussinesq) assumption:

$$\tau(v_i, v_j) - \frac{2}{3}k_u\delta_{ij} = -2\nu_u S_{ij} \tag{3}$$

In Eq. (3) $k_u = \frac{1}{2}\tau(v_i, v_i)$ is the kinetic energy of the unresolved motion (sub-filter scales) in the flow. $S_{ij} = \frac{1}{2}(\partial u_i/\partial x_j + \partial u_j/\partial x_i)$ is the rate-of-strain tensor of the resolved motion (the partially filtered velocities). ν_u is the eddy viscosity of the unresolved motion. The simulations in this work employs the PANS $k-\epsilon-\zeta-f$ model [12] which previously has been used to simulate the complex unsteady flow around a rudimentary landing gear and for active flow control [13, 14]. ν_u is thus modelled as:

$$\nu_u = C_\mu\zeta_u\frac{k_u^2}{\epsilon_u} \tag{4}$$

Here, $\zeta_u = \overline{v_u^2}/k_u$ is the velocity scale ratio of the unresolved velocity scales $\overline{v_u^2}$ and k_u. $\overline{v_u^2}$ refers to the normal fluctuating component of the velocity field to any no-slip boundary, see Ref. [15] for further details and argumentation for the concept of introducing the normal velocity scale. ϵ_u is the dissipation of the unresolved scales. The four model equations for the quantities in Eq. (4) are:

$$\frac{\partial k_u}{\partial t} + u_j\frac{\partial k_u}{\partial x_j} = (P_u - \epsilon_u) + \frac{\partial}{\partial x_j}[(\nu + \frac{\nu_u}{\sigma_{ku}})\frac{\partial k_u}{\partial x_j}] \tag{5}$$

In Eq. (5) $P_u = -\tau(v_i, v_j)\frac{\partial u_i}{\partial x_j}$ is the production of unresolved kinetic energy which is closed by the relation in Eq. 3.

$$\frac{\partial \epsilon_u}{\partial t} + u_j\frac{\partial \epsilon_u}{\partial x_j} = C_{\epsilon 1}P_u\frac{\epsilon_u}{k_u} - C^*_{\epsilon 2}\frac{\epsilon_u^2}{k_u} + \frac{\partial}{\partial x_j}(\frac{\nu_u}{\sigma_{\epsilon_u}}\frac{\partial \epsilon_u}{\partial x_j}) \tag{6}$$

$$C^*_{\epsilon 2} = C_{\epsilon 1} + \frac{f_k}{f_\epsilon}(C_{\epsilon 2} - C_{\epsilon 1}) \tag{7}$$

$$\sigma_{ku,\epsilon u} = \sigma_{k,\epsilon}\frac{f_k^2}{f_\epsilon} \tag{8}$$

$$C_{\epsilon 1} = 1.4(1 + 0.045/\sqrt{\zeta_u}) \tag{9}$$

$$\frac{\partial \zeta_u}{\partial t} + u_j\frac{\partial \zeta_u}{\partial x_j} = f_u - \frac{\zeta_u}{k_u}P_u + \frac{\zeta_u}{k_u}\epsilon_u(1 - f_k) + \frac{\partial}{\partial x_j}(\frac{\nu_u}{\sigma_{\zeta u}}\frac{\partial \zeta_u}{\partial x_j}) \tag{10}$$

$$L_u^2\nabla^2 f_u - f_u = \frac{1}{T_u}(c_1 + c_2\frac{P_u}{\epsilon_u})(\zeta_u - \frac{2}{3}) \tag{11}$$

The integral length and times scales of the unresolved scales L_u and T_u in Eq. 11 are computed using the unresolved kinetic energy. The parameter f_k is choosen as:

$$f_k(\mathbf{x}) = \frac{1}{\sqrt{C_\mu}}(\frac{\Delta}{\Lambda})^{2/3} \tag{12}$$

Where Δ is the geometric-average grid cell dimension, thus $\Delta = (\Delta x\cdot\Delta y\cdot\Delta z)^{1/3}$ and Λ is the Taylor scale of turbulence. The Taylor scale of turbulence Λ is computed using the resolved and unresolved kinetic energy and dissipation, $\Lambda = (k_u +$

$k_{res})^{1.5}/\epsilon$. f_k is computed in every cell at the end of each timestep. The computed values are then used as fixed values during the next timestep. The values of the constants in the model equations are:

$$C_\mu = 0.22;\ C_{\epsilon 2} = 1.9 \quad (13)$$

$$c_1 = 0.4;\ c_2 = 0.65;\ \sigma_k = 1; \quad (14)$$

$$\sigma_\epsilon = 1.3;\ \sigma_{\zeta_u} = 1.2 \quad (15)$$

4. Numerical set-up

4.1. Numerical method

Equations (1), (2), (5), (6), (10) and (11) are discretized using a commercial finite volume solver, AVL Fire v2010.1 ([16]). The discretization is done using a collocated grid arrangement. The convective fluxes in the momentum equations are approximated by a bounded upwind scheme of second order accurancy. The convective fluxes in the model equations are approximated by an unbounded upwind scheme of second order accurancy. The time marching procedure is done using the implicit second-order accurate three-time level scheme. The pressure is determined by the SIMPLE algorithm ([17]).

4.2. Computational grid

One computational grid is used for each of the cases (natural and cavity). The grids contain only hexa-hedral elements and are constructed with the hexa-blocking method in the grid-generator software Ansys ICEM CFD. The grid for the natural case contains 12 million cells and for the controlled case the grid contrains 14.5 million cells. The grids for the two cases are identical except the necessary difference at the base of the train model where the cavity is attached in the cavity case. The computational grid on the front of the train model is shown in Fig. 4. The size of the wall-adjacent cells in the normal direction from the wall on the train model in the grids is $\Delta n_1 = 0.000045$ H.

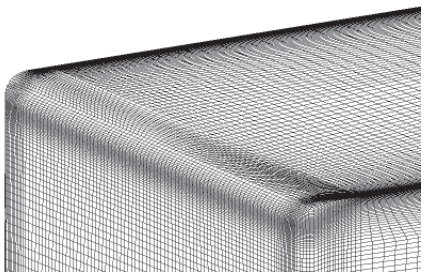

Figure 4. The grid on the front of the train model.

4.3. Computational domain and boundary conditions

The computational domain is presented in Fig. 5. Figure 5a shows the computational domain from the side. The total length of the domain is $35H$. The distances of $8H$ from the inlet to the bluff body and $20H$ after the bluff body are the same lengths as have been used in a number of similar type of unsteady numerical investigations in vehicle aerodynamics [18, 19, 20, 21]. On the inlet, a uniform velocity of $U_\infty = 10\,m/s$ in the x-direction is set. The values of k_u and ϵ_u on the inlet is set such that the ratio of the viscosity of the unresolved scales to the kinematic molecular viscosity is $\nu_u/\nu = 0.3$. On the ground plane the no-slip condition is used together with the velocity component in the x-direction equal to U_∞. This is done in order to precent developement of the boundary layer on the ground plane since in the reference experiments ([1]), the boundary layer was removed by using suction in front of the train.

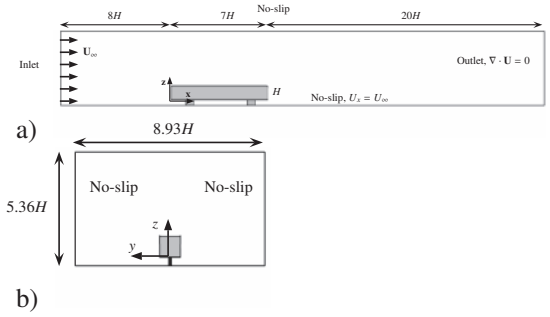

Figure 5. The wind tunnel used in the present numerical investigation. a) side view, b) front view.

The homogeneous Neumann boundary condition is applied on the outlet. On the lateral side and roof the no-slip condition is used. A front view of the computational domain is shown in the bottom figure in Fig. 5. The dimensions of the cross-section corresponds to that of the wind tunnel used in the reference experiments. The blocking ratio is approximately 2%.

4.4. Numerical accurancy: spatial and temporal resolution

The obtained spatial resolution in the simulation is presented in Table (1).

Table 1. Obtained spatial resolution in the simulations. Part I refers to the first 1/3 part of the train, Part II to the middle part of the train and Part III to the last part of the train, respectively.

		$n^+ = nu^*/\nu$	$s^+ = \Delta su^*/\nu$	$x^+ = \Delta xu^*/\nu$
Part I	Mean	0.15	-	-
	Maximum	0.7	100	120
Part II	Mean	0.22	-	-
	Maximum	0.55	140	180
Part III	Mean	0.46	-	-
	Maximum	0.65	300	370

The time step in the simulation was choosen to 0.00015 s in physical time and in convective time units $\Delta t^* = \Delta t U_\infty / L = 0.00038$, where L is the length of the train model. This time step kept the CFL number below unity in all of the cells in the mesh except in a small volume on the curved surface on the front part of the train model where the maximum CFL number reached 2. The simulations were first run for 20 000 time steps in order to let the flow initialize. This corresponds to a fluid particle travelling through the wind tunnel 1.5 times (8 convective time units). After the initial simulation time, the time averaging of the flow properties was started. The averaging in both simulations was done during 50 000 time steps corresponding to 20 convective time units $t^* = t U_\infty / L$.

5. RESULTS

In this section some results from the simulations are presented.

5.1. *Pressure coefficient - comparison with experimental data for natural case*

The pressure coefficient defined as: $C_p = (p_F - p_\infty)/0.5\rho U_\infty$ is presented along a line for the natural case in Fig. 6. The pressure in the simulation follows that in the experiments. However, in the region of separated flow on the roof the negative pressure seems to be underestimate in the simulation compared to in the experiments.

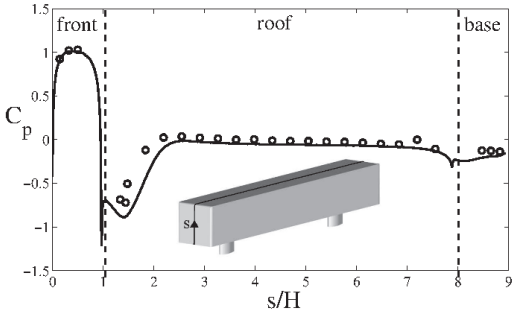

Figure 6. Pressure coefficient along a line s starting at origo along the mid plane of the train model for the natural case.

5.2. *Global quantities*

The time-averaged drag forces from the simulations are presented in Table (2). For the natural case, the drag coefficient is underestimated compared to the experiments by some 10%. The drag coefficient for the cavity case is reduced by some 10% compared to the natural case simulation. The friction part of the drag force was found to be 4% in both cases. The drag coefficient is defined as follows:

$$F_x = \frac{1}{2} C_D \rho U_\infty^2 A_x \tag{16}$$

where ρ is the density of air at 20° and $A_x = \mathrm{H}^2$.

Table 2. Time-averaged aerodynamic forces on the train model. See text for the definition of the drag coefficient.

Aerodynamic coefficients	C_D
Experiment	0.86
Natural	0.78
Controlled	0.70

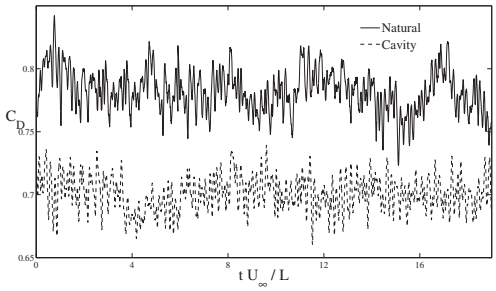

Figure 7. Time-signals of the drag forces for the natural and controlled case.

Time-signals of the drag forces are presented in Fig. 7. The size of the fluctuations in the signal is in the same order for the two cases. The root-mean square value of the drag signal for the natural case is 0.017 and for the cavity case 0.014.

5.3. *Streamlines of the time-averaged flow*

Stream lines of the time-averaged velocity field are presented in Figs. 8 and 9. Figure 8 shows streamlines around the first half of the train model for the two cases. The separation from the leading edges is denoted V_F in the figure. In Fig. 9 the streamlines around the second half of the model are shown. The vortex in the wake is denoted V_W. For the natural case V_W extends a distance H in the streamwise direction from the base, while for the cavity case the length of V_W is 1.5 H.

Streamlines from a top view are shown in a plane cutting the train model at $z = 0.5H$ are shown in Figs. 10 and 11.

In the cavity, an assymmetry is seen in the time-averaged flow field (see Fig. 11 b). This indicates that the flow field has not been averaged for a sufficiently long time to average the low frequency motion of the fluid inside the cavity.

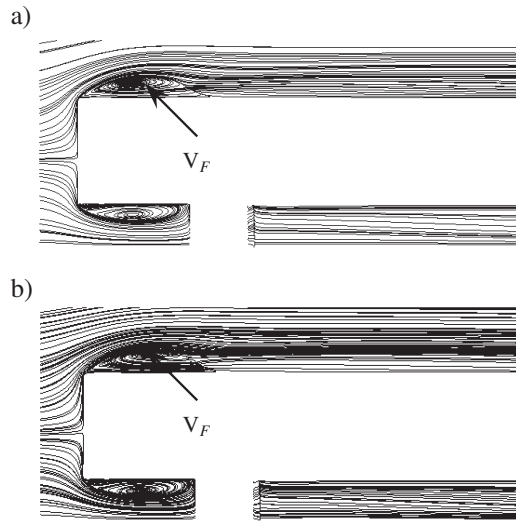

Figure 8. Streamlines of the time-averaged velocity field around the first half of the train model. a) natural case. b) cavity case. Flow is from left to right.

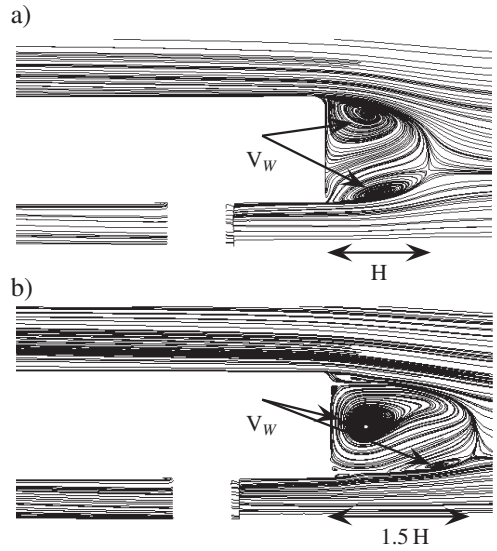

Figure 9. Streamlines of the time-averaged velocity field around the second half of the train model. a) natural case. b) cavity case.

5.4. Pressure coefficient in the wake

The pressure coefficient is shown for the two cases in a cut in the wake behind the train model in Fig. 12. For the natural flow, the value of the pressure coefficient behind the train reaches down to −0.34. For the cavity case on the other hand, the pressure is more evenly distributed in the cavity and the value inside the cavity of the pressure coefficient is −0.08. Around the edges on the outside of the cavity the pressure coefficient is lower.

In Fig. 13 the pressure coefficient on the base face of the train model is shown for the two cases. For the natural case, the pressure is lower on the upper part of the face. For the cavity case the pressure is more evenly spread out inside the cavity. The pressure is increased on the latter case compared to the natural case in correspondence to the decreased value of the drag coefficient for the cavity case.

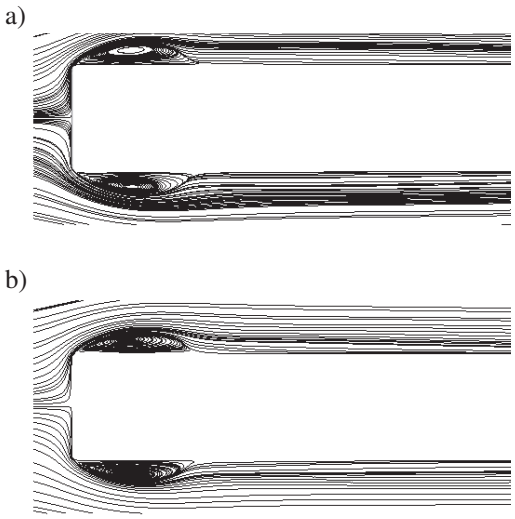

Figure 10. Streamlines of the time-averaged velocity field around the first half of the train model. a) natural case. b) cavity case.

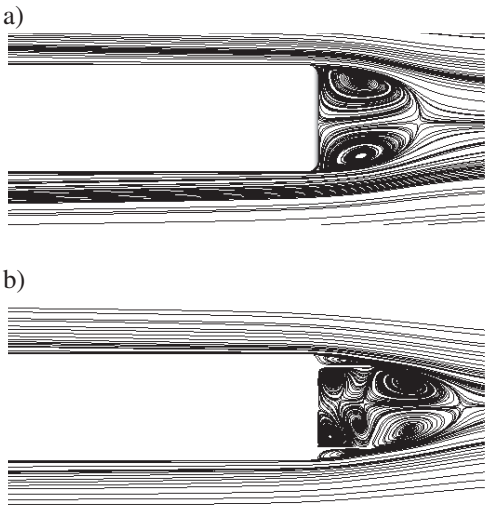

Figure 11. Streamlines of the time-averaged velocity field around the second half of the train model. a) natural case. b) cavity case. View is from above.

6. SUMMARY

In this work two simulations of the flow around a train model have been reported. The flow around the train model has previously been investigated by experiments in wind tunnel. The simulation method employed was the Partially Averaged Navier-Stokes method which is a hybrid method for turbulence modelling. The train model is a prismatic bluff body with rounded edges on the front as well as on the aft. The Reynolds number in the investigation

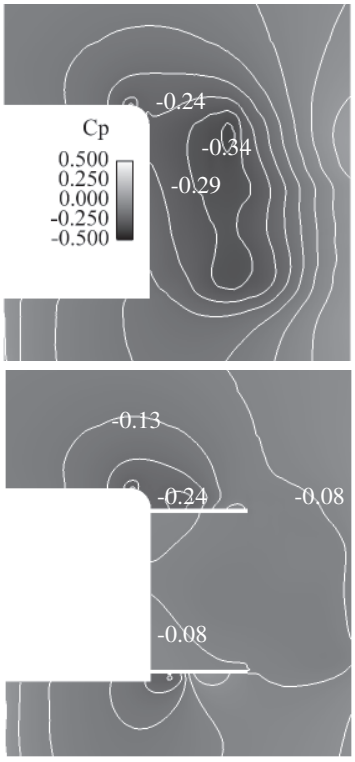

Figure 12. Pressure coefficient in the wake. a) natural case. b) cavity case. Side view.

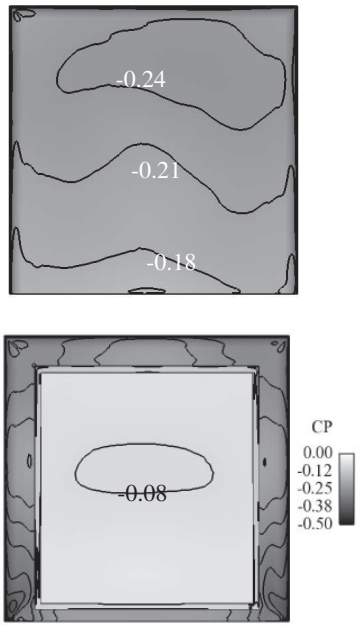

Figure 13. Pressure coefficient on the base of the train model. a) natural case. b) cavity case.

based on the height of the model was $Re_H = 0.37 \cdot 10^6$. In the experiments, for this Reynolds number, the flow separates from the curved leading edges. This separation of the flow was predicted in the simulations as well. Comparison to experimental data for the pressure coefficient along a line in the symmetry plane of the model showed that the general trend was correct in the simulation. However, in the separated region on the roof of the train model the negative pressure was underpredicted in the simulation compared to that in the experiments. This underprediction of the negative pressure in the separated region on the roof might be one reason to why the drag coefficient was predicted to 0.78 in the simulation compared to 0.86 in the experiments. This is because the separation starts already on the front edges and thus negative pressure on the curved edges contributes to a decrease in the over all drag coefficient of the train model. Adding four plates forming an open cavity on the aft on the train model proved to decrease the drag by some 10%. The primary mechanism by which the drag is decreased is that the plates effectively prevents the shear layers separating from the edges on the base of the train model from interacting to each other. This extends the size of the wake formed behind the train model and thereby the pressure inside the wake is increased and the decrease in the drag follows. It was found in the simulation that for the natural flow the wake extends approximately the distance of H behind the train model and with the attached cavity on the aft the wake extends 1.5 H. For higher Reynolds numbers, the reported experimental value of the drag coefficient is lower ($\approx$ 0.4). This is because the flow does not separate from the leading edges in that case. This means that for higher Reynolds number, the placement of a cavity on the aft would lead to a higher relative decrease of the drag coefficient. This is in agreement with the results reported in i.e. [5] where a decreased drag coefficient of 23% was reported by placing a cavity on a ground vehicle bluff body without flow separation on the front of the vehicle model. The PANS $k - \epsilon - \zeta - f$ method has prevously been employed successfully to simulate the challenging unsteady flow around a landing gear [13]. The flow stayed attached on the front of the landing gear at the Reynolds number in that study. The present work shows that PANS is able to simulate the flow for a bluff body with separation from a curved surface at the front.

Acknowledgements

We are grateful to Dr. Yutaka Sakuma at RTRI for providing us with experimental data and geometrical details of the train model. This project is supported financially by Trafikverket (Swedish Transport Administration). Software licenses were provided by AVL List GMBH. Computations were performed at SNIC (Swedish National Infrastructure for Computing) at the Center for Scientific Computing at Chalmers (C3SE), Center for High Performance Computing at KTH (PDC) and National Supercomputer Center (NSC) at LiU.

References

[1] Sakuma, Y. and Ido, A. 2009 “Wind Tunnel Experiments on Reducing Separated Flow Region Around Front Ends of Vehicles on Meter-Gauge Railway Lines”. *Quarterly Report of RTRI*, Vol. 50, No. 1, pp. 20–25.

[2] Raghunathan, R. S., Kim, H.-D., and Setoguchi, T. 2002 “Aerodynamics of high-speed railway train”. *Progress in Aerospace Sciences*, Vol. 38, pp. 469–514.

[3] Orellano, A. and Sperling, S. 2009 “Aerodynamic Improvements and Associated Energy Demand Reduction of Trains”. *The Aerodynamics of Heavy Vehicles II: Trucks, Buses, and Trains*, vol. 41, pp. 219–231, Springer Berlin / Heidelberg.

[4] Khalighi, B., Zhang, S., Koromilas, C., Balkanyi, S. R., Bernal, L. P., Laccarino, G., and Moin, P. 2001 “Experimental and computational study of unsteady flow behind a Bluff Body with a drag reduction device”, SAE Paper 2001-01-1042.

[5] Verzicco, R., Fatica, M., Laccarino, G., and Moin, P. 2002 “Large Eddy Simulation of a road vehicle with drag-reduction devices”. *AIAA Journal*, Vol. 40, pp. 2447–2455.

[6] Coon, J. D. and Visser, K. 2004 “Drag Reduction of a Tractor-Trailer Using Planar Boat Tail Plates”. *The Aerodynamics of Heavy Vehicles: Trucks, Buses, and Trains*, vol. 1, Springer Berlin / Heidelberg.

[7] Grover, K. and Visser, K. D. 2001 “Over-the-road tests of sealed aft cavities on tractor trailers”, SAE Paper 2006-01-3529.

[8] Maeda, T. and Kondo, Y. 2001 “RTRI’s Large-scale Low-noise Wind Tunnel and Wind Tunnel Tests”. *Quarterly Report of RTRI*, Vol. 42, No. 2, pp. 65–70.

[9] Cooper, K. R. 1985 “The effect of Front-Edge Rounding and Rear Edge Shaping on the Aerodynamic Drag of Bluff Vehicles in Ground Proximity”, SAE Paper No. 850288.

[10] Girimaji, S. S. 2006 “Partially-Averaged Navier-Stokes Model for Turbulence: A Reynolds-Averaged Navier-Stokes to Direct Numerical Simulation Bridging Method”. *Journal of Applied Mechanics*, Vol. 73, pp. 413–421.

[11] Germano, M. 1992 “Turbulence: the filtering approach”. *Journal of Fluid Mechanics*, Vol. 238, pp. 325–336.

[12] Basara, B., Krajnović, S., S., G. S., and Pavlovic, Z. 2011 “Partially Averaged Navier-Stokes Method for Turbulence Simulations: Near-Wall Eddy Viscosity Transport Model Implementation”. *AIAA Journal*, Vol. in press, p. DOI: 10.2514/1.J050967.

[13] Krajnović, S., Lárusson, R., Helgason, E., and Basara, B. 2011 “PANS of Rudimentary Landing Gear”. *AIAA Paper AIAA-2011-3109. Nr. 153761*.

[14] Han, X., Krajnovic, S., and Basara, B. 2011 “Study of active flow control for a simplified vehicle model using PANS turbulence model”. *4th Symposium on Hybrid RANS-LES Methods*, September 28-30, Beijing China.

[15] Durbin, P. A. 1991 “Near-Wall Turbulence Closure Modeling Without Damping Functions”. *Theoretical and Computational Fluid Dynamics*, Vol. 3, pp. 1–13.

[16] AVL 2010 . CFD Solver. AVL Fire Manual, v2010.1, edition 11/2010.

[17] Patankar, S. and Spalding, D. 1972 “A calculation procedure for heat, mass and momentum transfer in three-dimensional parabolic flows”. *Int. J. Heat Mass Transfer*, Vol. 15, pp. 1787–1806.

[18] Krajnović, S. 2009 “LES of Flows Around Ground Vehicles and Other Bluff Bodies”. *Philosophical Transactions of the Royal Society A*, Vol. 367, No. 1899, pp. 2917–2930.

[19] Krajnović, S., Östh, J., and Basara, B. 2010 “LES Study of breakdown control of A-pillar vortex”. *Int. J. Flow control*, Vol. 2, No. 4, pp. 237–257.

[20] Krajnović, S., Östh, J., and Basara, B. 9-12 September, 2009 “LES of active flow control around an Ahmed body with Active Flow Control”. *Conference on Modelling Fluid Flow (CMFF’09), The 14th International Conference on Fluid Flow Technologies*, Budapest, Hungary.

[21] Östh, J. and Krajnović, S. 2012 “The flow around a simplified tractor-trailer model studied by Large Eddy Simulation”. *Journal of Wind Engineering and Industrial Aerodynamics*, Vol. 102, pp. 36–47.

Conference on Modelling Fluid Flow (CMFF'12)
The 15th International Conference on Fluid Flow Technologies
Budapest, Hungary, September 4-7, 2012

PIV measurement of the flow past a Generic Car body with wheels at LES applicable Reynolds number

Andras GULYAS[1], Agnes BODOR [2], Tamas REGERT [3], Imre M. JANOSI [4]

[1] Corresponding Author. Department of Fluid Mechanics, Budapest University of Technology and Economics. 1111. Budapest, Bertalan L. u. 4-6. Tel.: +36 1 463 4072, Fax: +36 1 463 3464 E-mail: gulyas@ara.bme.hu
[2] Department of Fluid Mechanics, Budapest University of Technology and Economics. E-mail: agibodor@gmail.com
[3] Ex-member of Department of Fluid Mechanics, Present address: 72 Chaussee de Waterloo, 1640 Rhode-St-Genese, regert@vki.ac.be
[4] von Karman Laboratory of Environmental Flow, Department of Physics of Complex Systems, Eotvos Lorand University. E-mail: janosi@lecso.elte.hu

ABSTRACT

Experiments by using 2D-2C Particle Image Velocimetry (PIV) were carried out and reported concerning the flow field past a generic car body (modified Ahmed body) which is equipped with wheels and wheel-arches. The Reynolds number was chosen to not exceed $2 \cdot 10^5$ based on the height of the Ahmed body which makes it possible to investigate the same configuration by means of Large Eddy Simulation (LES). The wheels were rotating but the ground was stationary. The wheel-ground contact was realized by means of small rectangular openings below the wheels in the ground plane in which the wheels were immersed. The transition contour of the immersed wheels and the ground, as well as the rectangular openings below the wheels were properly sealed to prevent parasite flow and to provide well defined boundary conditions for an upcoming LES investigation. The flow field was investigated in several planes with normal vectors pointing towards the directions normal to the free stream. Mean characteristics of the flow are provided and discussed.

Keywords: Ahmed body, PIV, wheel, vehicle aerodynamics

NOMENCLATURE

d	$[m]$	Diameter of the wheel
D	$[m]$	Diameter of the wheel arch
H	$[m]$	Height of the Ahmed body
X	$[m]$	Lateral coordinate, parallel to ground plane
Y	$[m]$	Streamwise cooridnate
$vmag$	$[m/s]$	Magnitude of velocity
2D-2C		2-dimensional and 2 velocity component PIV system
CFD		Computational Fluid Dynamics
LES		Large Eddy Simulation
RANS		Reynolds-Averaged Navier-Stokes equations based turbulence modelling
PIV		Particle Image Velocimetry

1. INTRODUCTION

The aerodynamic effects of the rotating wheels on road vehicles is a topic of high importance in vehicle aerodynamics. Wheels on vehicles have high impact on both lift and drag coefficients. According to several studies (see e.g. [1, 2, 3]) the presence of wheels and wheel-arches on an aerodynamically optimized passenger car body increases drag and lift by an amount of 30% and 40%, respectively. Due to their functionality, wheels cannot have an aerodynamically favorable shape.

During the last couple of decades, several publications discussed the characteristics of the flow field past isolated wheels [4, 5, 6], wheels in wheel-arches [3, 7, 8, 9] and full cars [1, 2] both on experimental way as well as by Computational Fluid Dynamics (CFD). In case of wheels rotating in wheel-arches the investigated geometry was either complicated [9], not completely representing the case of a conventional car [3, 8] or its details were not open for public access [2, 8].

The intention of the present research is to provide reference data for a car model that has known, simple geometry and is equipped with four wheels rotating in their wheel-arches. The choice of the authors of this paper was made on the well known Ahmed body due to its well documented, simple geometry. The modified Ahmed body was already investigated by means of Reynolds-Averaged Navier-Stokes (RANS) modeling [10]. The differences of the flow field characteristics between the Ahmed body and the modified Ahmed body, based on RANS modelling,

were discussed in [10] the RANS modelling characteristics of such flows were investigated in detail in [11]. To further improve the reliability of the computational results, the need for experimental results arose for the purpose of validation.

It is well known in the research community of bluff bodies (e.g. [12, 13, 14, 15, 16]) that, in spite of its excellent performance in determining the forces acting on bodies, RANS modeling fails when the structure of the flow field is to be analyzed [12, 13, 16]. The only reliable and affordable approach to obtain information concerning the structure of the flow field is Large Eddy Simulation [12, 13]. However, LES requires more and more computational efforts with increasing Reynolds number due to the wide range of appearing vortical structures to be resolved. For this reason the experiments were designed for a maximum Reynolds number of $2 \cdot 10^5$ based on the height of the Ahmed body. Although this Reynolds number is not representative for full scale vehicles, it can serve as a validation case for LES computations.

In the scope of experimental investigations up to now, the applied measurement techniques were force and surface pressure distribution measurements [3, 7, 8, 9] and Laser Doppler Velocimetry (LDV) [2]. PIV experiments were already carried out and published for the case of isolated rotating wheel in [6]. To the authors knowledge, PIV experiments regarding to the flow past a vehicle with wheels and wheel-arches has not been published for research purposes. The Ahmed body with wheels provides a configuration that is open for the public in all its details. The present experiments represent the first step for the determination of the flow field past a realistic, non-confidential road-vehicle configuration. The experimental results help in understanding the main flow features past the wheels and the interaction of the flow past the vehicle and the wheels, on one hand. On the other hand the present experiments targets to provide a database for the validation of numerical simulation results that would lead to an even deeper understanding of the flow features and the mechanisms that lead to such a high increase in both lift and drag due to the presence of wheels. Although the present paper shows only a small fraction of the experimental results, the experiment campaign is in progress to provide a full map of the flow field. Here the authors concentrate mostly on the description of the experiments.

The structure of this paper is the following: in the second section the geometry of the generic car body with wheels is shown in detail. The wind tunnel model and its accuracy is also discussed along with the configuration of the measurement test section. The third section discusses the PIV system setup and the measurement locations illustrating the location of the laser and camera devices. In the fourth section the uncertainty of the results are discussed. The fifth section discusses the measurement locations and configurations and finally the sixth section shows the mean flow field based on the velocity vector fields.

2. THE WIND TUNNEL MODEL

2.1. The generic car body with wheels

The Ahmed-body equipped with wheels was first published by [10], but for the sake of clarity, its structure and dimensions are provided here. As a reference, the Ahmed body with the slant angle of 25 was chosen. The wheels were designed to maintain the same underbody gap as for the original Ahmed body. The geometry of the wheel arches was a half cylinder with a small flat extension downwards. Its diameter and depth was tuned to mimic the size usually found on road vehicles. The geometry of the vehicle and the sizes are shown in Fig. 1 according to the original setup used by [17] and [18]. The sizes of the Ahmed-body are expressed in terms of its height, H and the wheel diameter d ($H = 215mm$ and $d = 108mm$ for the present case). The geometrical axles of the cylinders modelling the wheelhouses of the vehicle were placed in the same location as that of the wheels. The outer vertical surfaces of the wheels were aligned with the side plane of the vehicle model. The wheel axles are cylinders.

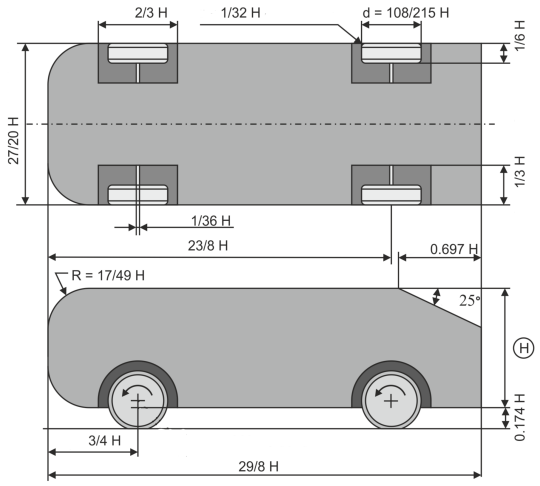

Figure 1. Geometry of the modified generic car body with wheels and wheel arches.

The wind tunnel model can be seen in Fig. 2. Its interior structure can be seen in Fig.2. The vehicle body was built up onto a frame constructed by using commercially available aluminum profiled rods that are fixed to each other by balts. The two sidewalls of the vehicle are made of 11mm thick poly-ethylene sheets. The top face, the slanted surface, the base and the underbody of the vehicle were made of aluminum sheets of 2mm thickness and balted to the 11mm thick faces of the sidewalls. The rounded front face was made of fiber-glass composite material and it is a single piece structure. The model was designed to hang from a strut, thus providing the possibility for rotating wheels with stationary

ground. This configuration is not relevant in practice, but well suitable for validation of computational fluid dynamics [19]. The connector disk can also be well visible in Fig.2. The wheel pairs (front wheel pair and rear wheel pair) were connected to an axle. Each axle was equipped by two deep-groove roller bearings. The casings of the bearings were fixed to the main aluminum frame of the model. Inside the vehicle model, a single-phase AC electric motor was placed and drove the two axles simultaneously by means of belt drive. This solution ensured that both the wheel pairs rotated at the same r.p.m.. The rotation speed was measured by an optical counter device that was also fixed inside the model and watched a marker on the front axle. The signal of the optical counter was transformed into r.p.m. by a digital counter. The single phase engine was regulated by a toroid transformer. To prevent the propagation of any vibration originating at the engine due to any imperfecties of the engine and the connecting elements, the engine mounting points were isolated by rubber sheets. The axle of the engine was connected to the axles of the wheels by means of ribbed belts that also helped the damping of any spurious vibration and ensured the drive of wheels without any slip w.r.t. the engine r.p.m. During the tests, no detectable vibration occurred during the rotation of wheels. The wheels were made of poly-ethylene blocks and were also equilibrated to avoid their vibration on the axles. During the tests there was no detectable vibration observed. Cables of the engine and the r.p.m. measuring device were guided out from the model inside the strut system, thus they were hidden from the flow. The wheel axles crossed the vertical surface of the wheel-arch through a sealed bore that had a physical contact with the axle. This structure prevented any flow leakage between the interior and exterior of the model. The engine was sufficiently powerful to keep the required r.p.m. also in case of having sealing parts that touched the rotating elements. After mounting the top, slanted face, base, underbody and front face elements to the main side walls of the model, model clay was used to fill all eventual gaps. The geometry parameters were fine-tuned when the model was assembled. After filling the micro-gaps and the heads of balts, some layers of two-component filler material was sprayed onto the surface. After a second fine-tuning of the sizes of the model, the surface was polished and painted mat black to accommodate for PIV measurements.

The rotation of the wheels were solved by having no contact with the ground. However, due to the problems in CFD when meshing the wheel-ground contact, it has been chosen to realize a similar structure for the wind tunnel model too. Four rectangular openings slightly larger than the ground contact patch of the wheel when immersed $3mm$ ($0.027d$ where d is the wheel diameter) were formed in the ground plane. Each window was filled by a piece of textile with $5mm$ long impermeably dense

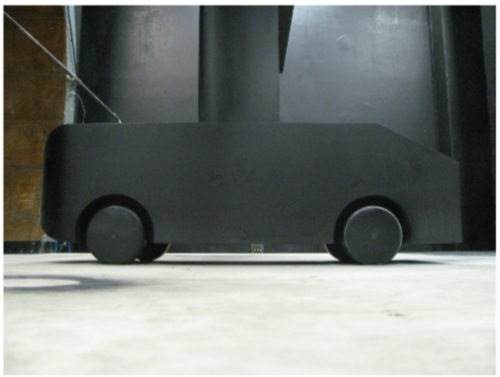

(a)

(b)

Figure 2. Top: Wind tunnel model of the generic car body with wheels. Bottom: Interior structure of the generic car body with wheels (top surface removed).

fur. The fur has filled all the depth of the window up to the plane of the ground. For final tailoring and to ensure the integrity of the ground plane surface, thin tape was used to cover the windows on the top. The tapes were tailored to fit the "simulated" ground-contact contour of the wheels and there was a physical contact between the rotating wheel and the tape contours. This way any possibility for leakage was closed out. The tapes were approximately $0.1mm$ thick and were sticked onto the ground plane. The authors expected negligible effect of this small roughness on the already turbulent boundary layer along the flat ground plane.

2.2. Test section configuration

The overall configuration of the test section can be seen in Fig.3. The nozzle outlet diameter of the Gottingen type wind tunnel is $2.6m$ (for further details of this wind tunnel, see [20]) and the blockage of the vehicle model including the struts and the ground plane construction was computed to be 2.5%. The vehicle model is hanging on a strut system. There is a horizontal strut spanning over the test

section with both of its ends being outside the jet of the wind tunnel. Outside the jet of the test section the horizontal strut is fixed to two vertical steel bars of square cross section. The fixing parts permit the fine adjustments of the "riding height" of the model, which provides a method for immersing the wheels precisely by $3mm$ into the windows in the ground plane. The horizontal strut is a steel bar of square cross section which is covered by a NACA 0015 airfoil envelope with a chord length of $300mm$. In the mid-span of the horizontal strut, a circular cross section steel bar is mounted vertically that holds the vehicle model itself. The vertical strut is also covered by a NACA 0015 airfoil with a chord length of $170mm$. The airfoils were made of glass-fiber composite material and their geometrical accuracy is $0.1mm$. The junction between the two airfoils is the simple perpendicular transition contour between them without any roundings, any additional treatment to make it easy to model by CAD and to mesh for CFD. On the other end of the vertical strut, the airfoil ends simply in the plane of the vehicle's top surface. Here also sharp corners are created to avoid any roundings for providing precise boundary conditions for CFD. It can be also observed that there is a gap between the connector disk and the top face of the vehicle model. It was designed for force measurements but for now, it was filled by model clay for the PIV measurements.

The ground plane was a raw wooden sheet without any polishing treatment on its surface to ensure the development of a turbulent boundary layer with early transition. The ground plane was shifted downwards in flow-normal direction with respect to the center of the wind tunnel outlet nozzle, the leading edge of the ground plane had to be inclined downwards to ensure attached flow. The leading edge has been made of aluminum sheets that were bent by a radius of $3mm$. A section of them can be seen in Fig.4. At the inclination region there is a jump in the curvature that promotes transition but does not lead to detectable separation bubble. Due to this special geometry of the leading edge, the authors decided to carry out measure the inlet velocity profiles in detail at multiple spanwise locations (not reported here).

3. PIV MEASUREMENT SYSTEM

Measurements have been carried out by a non-time-resolved 2D-2C PIV system. The system was distributed by ILA GmbH and consisted of a Solo Nd-Yag laser from New Wave Technology that produces laser pulses with an energy of $15mJ$ and $3-5ns$ duration with a repeatability frequency of $15Hz$ for each cavity. For recording the images, a Pixelfly double shot CCD camera was used. The synchronization was solved by the compact system provided by ILA GmbH. The laser was equipped with a cylindrical lens unit providing a laser sheet. The minimum separation time used during the experiments was $200\mu s$ that was accommodated for the low Reynolds number flow. This time

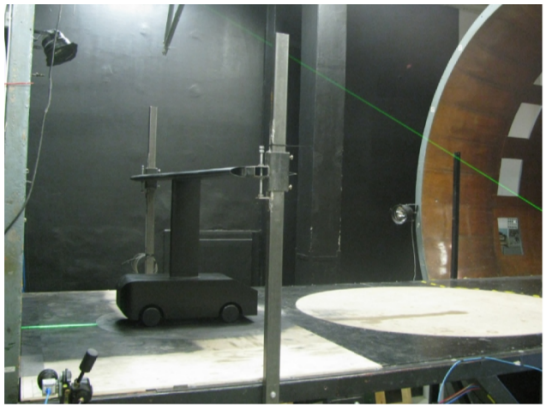

Figure 3. Wind tunnel test section configuration for the PIV experiments.

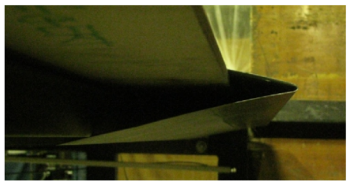

Figure 4. The profile of the leading edge of the ground plane. Flow from right to left.

separation produces approximately a maximum particle displacement of $10pixels$ (approximately $1mm$ for the current magnification) at the high velocity regions for a domain of physical sizes $130mm$x$100mm$. To capture the images, a Nikon $50mm$ objective was used on the camera.

The seeding was provided by using olive oil droplets generated by a commercially available device: TSI 9307-6 six-jet oil droplet generator, that produces droplets with diameters of approximately $1\mu m$. The seeding was injected downstream of the test section into the collector funnel of the wind tunnel. It has passed over the recirculation pipe, through the fan and all turbulence decreasing screens before entering the test section from the inlet nozzle. Thanks to the recirculation of the air in the Gottingen type wind tunnel, sufficient amount of seeding droplets persisted in the wind tunnel for the duration of data acquisition for a given laser sheet position. To characterize the flow field past the generic car body, several laser sheet positions were used and 300 image-pairs were collected for each sheet position. The laser head was mounted onto a 3D electronic traversing system that provided an accuracy of $0.1mm$ regarding the position of the laser sheet. The traversing system and the laser were outside the jet of the wind tunnel.

To provide the required field of view by using the $50mm$ Nikon objective, the camera had to be placed into the flow field in the vicinity of the horizontal part of the strut holding the vehicle model. As the Reynolds number was very low and forces were thus rather weak, the flow did not exert sensible effects on

the camera itself, however, it lead to a risk for the modification of the flow field in the vicinity of the vehicle. The effect of the vicinity of the camera was investigated by observing the flow in the vertical laser sheets with and without the presence of the camera in the flow. The camera was modeled by a wooden block of similar geometry, mounted on the camera holding strut. The results showed that there was no sensible effect of the presence of the camera on the flow field past the vehicle.

To provide laser sheets parallel to the side of the vehicle model, the laser had to be installed inside the wind tunnel jet, downstream the Ahmed body. As the distance of the laser device was 3.2 vehicle lengths from the base of the vehicle, the authors expected backward effect of the device. To investigate the amount of this effect, a sensitivity study has been carried out by varying the distance of the laser from the vehicle and recording image pairs at several locations in the wake of the vehicle. Based on the measurement results, there was no sensible effect of the presence of the laser head on the flow field characteristics.

The axis of the camera lense was mostly perpendicular to the laser sheet, but to ensure the planar measurements, the mapping utility of the VidPIV software (ILA) was applied to de-warp the images to get rid of perspective effects. The authors have chosen to apply the software WiDIM (Window Deformation Iterative Multigrid) [21] to determine the velocity vector fields with the kind permission of the von Karman Institute for Fluid Dynamics, Rhode-Saint-Genese, Belgium, which was found to perform more satisfactory than VidPIV for the present case. The image pairs were processed by an initial window size of 64x64 pixels and two interrogation window refinements and 75% overlapping was imposed to obtain one vector by 4 pixels (for PIV terminology, see e.g. [21]).

4. Uncertainty analysis

The uncertainty analysis covers the discussion of errors originating from the vehicle model, the wind tunnel, the PIV measurement configuration and the determination of displacement field.

4.1. Vehicle model and wind tunnel

The vehicle model consists of several separate parts bolted together by using immersed-head balts. To achieve the most precise sizes, the interior main frame was tailored carefully. The aluminum sheets had an error less than $0.1mm$ regarding their thickness distribution. The poly-ethylene side walls were less accurate thus adjustments at the interior side of them were realized to maintain constant width of the vehicle along its length. The bolts were tightened to a limit where the aluminum sheets were not yet deformed at all. After the extensive surface treatment and finishing, the inaccuracy in size remained below $0.5mm$ in general. It means that for the vehicle sizes the error of the geometry is 0.2% of the vehicle height H, while for the wheels the same error results in 0.46% of the wheel diameter d. The airfoil contours on the struts had an error of $0.1mm$ which means an error of 0.06% of the smaller ($170mm$) chord length for the vertical strut and 0.03% for the bigger ($300mm$) chord length on the horizontal strut. Measurements were carried out for $5m/s$ free-stream velocity that corresponds to a Reynolds number of $7.17 \cdot 10^4$. With the present diameter of the wheel the rotation frequency was set to $15Hz$ (the exact value is $14.74Hz$). The smallest digit on the rotation frequency indicator was $1Hz$, thus the error of the rotation speed of the wheels was maximum 6.7% of the target value. The wind tunnel is driven by a DC electric motor and regularized by sliding resistances. Throughout the measurements, the r.p.m. of the wind tunnel fan was set to produce the same total pressure upstream the convergent channel of the nozzle. The pressure was measured with an accuracy of $1Pa$, that leads to a maximum of 3% error in the measurement of the free stream velocity ($5m/s$).

4.2. PIV processing

The uncertainty of the PIV measurements origins from the quality of the images, the accuracy of the software to determine the displacement field and the properties of the statistical analysis carried out on the results.

The laser sheet was adjusted by turning the cylindrical lens head mounted onto the laser device. The horizontal reference plane was the ground itself. A sheet of paper with a calibration pattern of minimum feature size of $1mm$ was used. Two other alignment references were: the imaginary line connecting the centers of the front and the rear wheel on one side; the top surface of the vehicle. The laser sheet thickness was approximately $1mm$ and the length of the reflection stripe that was used for monitoring horizontality was $200mm$ taking into account an error of the adjusting as $1mm$ at both ends of the laser sheet, the maximum alignment uncertainty is estimated to be $0.57\,^\circ$. The horizontality in the spanwise direction was set on a similar way, but with a calibration plate slightly inclined about the normal direction of the ground plane. In this direction the length of the reflection stripe was $300mm$, yielding a maximum error of $0.38\,^\circ$ for the alignment.

The next source of error is the misalignment between the camera CCD plane and the laser sheet. This error was automatically compensated by the VidPIV software of ILA by using its built-in mapping utility. The mapping is based on marking the four corners of a rectangle on a calibration image and providing the true size of each side. Images are then warped into the plane of the CCD of the camera based on the four corners and the corresponding true sizes.

The magnification of the camera provided particle image sizes of minimum 3 pixels, permitting a good basis for Gaussian fitting for sub-pixel

precision and to avoid peak-locking.

For all the laser sheet positions, the quality of image pairs ensured that the signal to noise ratio was higher than the limit of 2.3 for 91% of the velocity field for each time instant of the top view configuration. The side view configuration suffers from worse signal to noise ratio due to the perturbing effect of the background even after background subtraction.

The accuracy of the magnitude of the displacement vectors determined by using WiDIM [21] has been reported to be $0.1 pixel$. On the physical scale, on average, $1mm = 10 pixel$ was determined, yielding a displacement error of $0.01mm$. The accuracy of the separation time has been found to be approximately $1\mu s$. By using these two errors, the absolute error of the velocity for the case of $10 pixels$ displacement of the particle images is estimated to be $0.06 m/s$ based on the quadratic propagation of errors.

Mainly due to the strong temporal limitations for the research facilities, 300 image pairs were recorded for each laser sheet positions. Being the time realizations uncorrelated with each other and assuming Gaussian distribution of the velocities around the mean value, a simple statistical method was applicable for the estimation of the error of the mean and RMS velocities. The maximum error in the mean quantities is 5% of the freestream velocity (where the maximum error was found at the location where the RMS of velocity reached 20% of the freestream velocity). The maximum error of the RMS quantities is estimated to be 8%.

5. MEASUREMENT LOCATIONS AND CONDITIONS

Measurements were carried out in several laser sheet positions in the vicinity of the front wheel, the rear wheel, the wake, the slanted surface and upstream the body. These locations are indicated in Fig.5. On the side-view images the full wheel and wheelhouse was recorded on an image plane. The reference plane was the side of the vehicle. The first plane is 2.5mm (0.01168H), the second plane was 2.5mm from the first plane. All the other planes were displaced with respect to each other by $5mm$ ($0.0234H$). In total, 14 planes were recorded from side-view.

The results reported here are recorded from top-view of the vehicle. The uppermost plane was located half way between the lower and the upper surface of the vehicle. The planes were then shifted downwards by $10mm$ ($0.0467H$). In total, 14 planes were recorded this way. Here the wheels were recorded from two sections: upstream half and downstream half.

The inlet velocity field has been recorded in three planes: one plane was coincident with the symmetry plane of the vehicle body and it covers the region from the leading edge until the front face of the body. Two planes were recorded between the middle plane of the vehicle and the left edge of the ground plane. The first plane was $0.814H$, the second plane $3.837H$ from the middle plane of the vehicle.

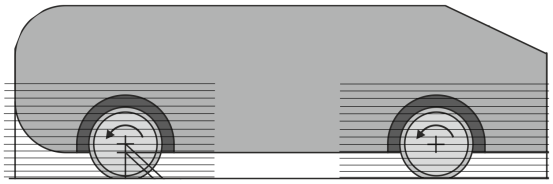

Figure 5. Schematic representation of a part of the slice locations where PIV measurements were taken.

Due to limitations in the extension of this paper, only a fraction of the measured slices are available and discussed, however, the measurement data is available for the public by referring to this paper, via communication to the corresponding author.

The freestream velocity is set to $5m/s$ for all measurements. The results that are reported here correspond to rotating wheels.

6. RESULTS

The mean velocity fields are shown for the region of the front wheel in 6 planes oriented with a vertical normal vector perpendicular to the ground plane and to the direction of the freestream. The represented planes have been chosen as follows: the reference plane is at the height of the center of the wheel. The positions of the planes are at the following distance from the center of the wheel: $-0.185d$, $0.0d$, $0.185d$, $0.37d$, $0.556d$, $0.648d$. It can be seen that the latter two planes are above the wheel but still in the region of the wheel arch opening (the top of the wheel arch opening is situated at $0.664D$ above the center of the wheel). According to preliminary observations the flow that is entering from the underbody of the vehicle is then exiting above the wheel from the wheel arch.

The contours of velocity magnitude and the streamlines of the flow field can be seen in Fig.6 and Fig.7. The flow arrives at a velocity of $5m/s$ to the vehicle and accelerates up to a maximum of $6.7m/s$ along the sides. It can be observed that next to the wheel arch the flow is deflected sideways away from the side of the vehicle. The most amount of deflection is found at the lower part of the wheel (bottom image of Fig.7). The flow in the vicinity of the lower part of the wheel is strongly influenced by the well known vortex pair generated by the so called "jetting" phenomenon at the contact region between the wheel and the ground which is the dominating phenomenon of the flow field when wheels are rotating. Streamlines that are pointing with a large angle with respect to the main flow direction indicate the presence of this strong vortex. Beside and above the center of the wheel the streamlines are more aligned with the free stream direction. This fact indicates that

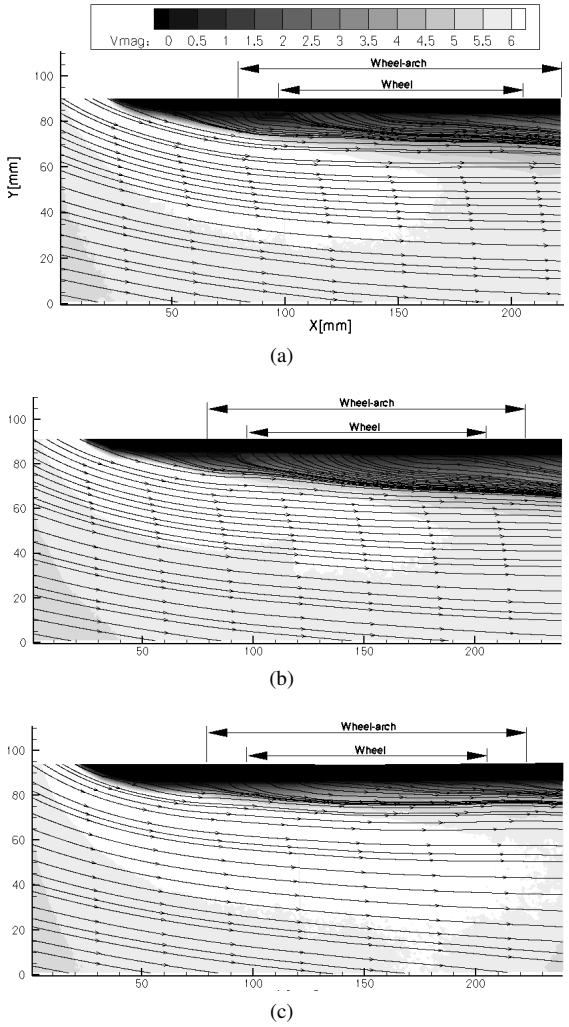

Figure 6. Streamlines with the contours of velocity magnitude $[m/s]$ for horizontal planes beside the front wheel region. From top to bottom the planes are $0.648d$, $0.556d$, $0.37d$ measured from the center of the wheel. Flow from left to right. Contour code and indication of axes on the top image.

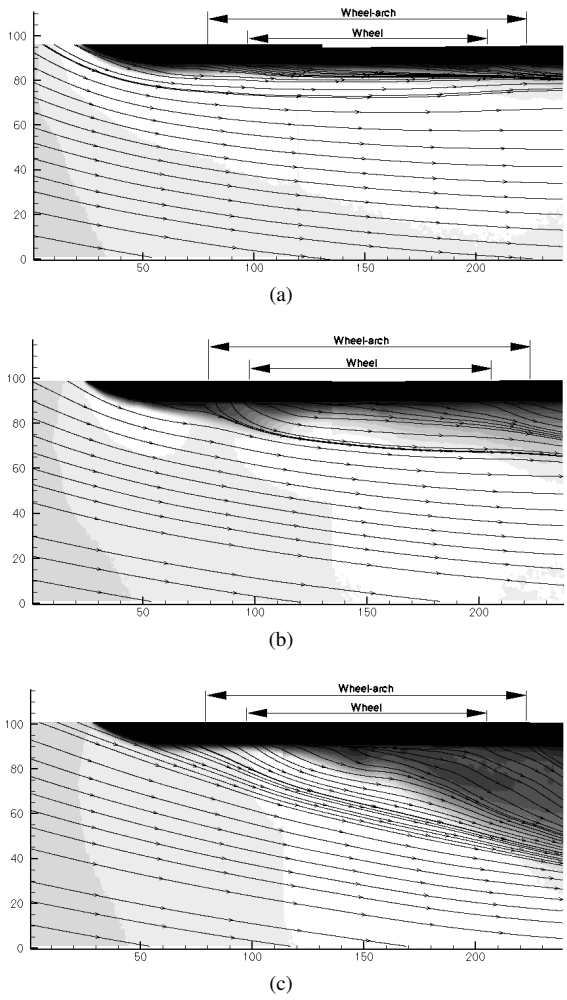

Figure 7. Caption same as Fig.6, except that the planes are $0.185d$, $0.0d$, $-0.185d$ measured from the center of the wheel. Flow from left to right.

the longitudinal vortex that was generated by the "Jetting" phenomenon is weakened already at the height of the center of the wheel. Above the center of the wheel, at $0.185d$ and $0.37d$ it can be seen that the streamlines are turning towards the side of the vehicle in the vicinity of the wheel. This reversion in the direction of streamlines indicates that the top of the longitudinal vortex is reached. Another larger deflection can be observed above the wheel ($0.556d$ and $0.648d$) because the flow is exiting in this region. The flow in general is in a good agreement with the observations of previous works [10, 7, 2].

7. CONCLUSIONS

In the present paper the measurement setup and some representative results of the PIV investigation of an Ahmed body equipped with wheels and wheel arches is presented. The tests were carried out with rotating wheels and stationary ground. The contact between the ground plane and the wheels was modeled by immersing the wheels into the ground plane by $3mm$ and sealing the remaining gaps. The freestream velocity was set to $5m/s$ to stay below a Reynolds number of $7.17 \cdot 10^4$ based on the height of the Ahmed body (measured from the bottom of the Ahmed body). In this paper only the top view of the flow field is presented for the front wheel. Similar measurements were taken for the rear wheel, but these are not presented due to the limited extension of the paper.

ACKNOWLEDGEMENTS

The authors whish to express their thanks to the Theodore von Karman Wind Tunnel Laboratory of the Department of Fluid Mechanics of Budapest University of Technology and Economics for the possibility to carry out these experiments. Special

thanks to Professor Sinisa Krajnovic from the Chalmers University in Geotheborg, Sweden, for the discussion concerning the boundary conditions of the experiments. Special thanks to Tivadar Szavai and Istvan Jezso for the realization of the wind tunnel model. Special thanks to the von Karman Laboratory of Environmental Flow, Department of Physics of Complex Systems, Eotvos Lorand University for the possibility of using their PIV system for the present measurements. Special thanks for the Department of Atomic Physics for lending some necessary optical parts. This work has been supported by the Hungarian National Fund for Science and Research under contract No. OTKA PD 76217 and the New Hungary Development Plan (Project ID: TAMOP 4.2.1/B-09/1/KMR-2010-0002).

References

[1] Eloffson, P. and Bannister, M. 2002 "Drag reduction mechanisms due to moving ground and wheel rotation in passenger cars". *Society for Automotive Engineers*, pp. 185–198, 2002-01-0531.

[2] Waschle, A. 2007 "The Influence of Rotating Wheels on Vehicle Aerodynamics - Numerical and Experimental Investigations". *Society for Automotive Engineers*, pp. 1–14, 2007-01-0107.

[3] Skea, A., Bullen, P., and Qiao, J. 2004 "CFD simulations and experimental measurements of the flow over a rotating wheel in a wheel arch". *Society for Automotive Engineers*, pp. 115–123, 2000-01-0487.

[4] Fackrell, J. E. and Harvey, J. K. 1973 "The flow field and pressure distribution of an isolated road wheel". *Advances in Road Vehicle Aerodynamics*, pp. 155–164.

[5] Mears, A., Dominy, R., and Sims-Williams, D. 2002 "The air flow about an exposed racing wheel". *Society for Automotive Engineers*, pp. 37–43, 2002-01-3290.

[6] Brizzi, L., Noel, A., and Herbert, V. 2004 "Phase average velocity field in the vicinity of an isolated wheel model". Foundation, T. C. G. (ed.), *12th International Symposium on Applications of Laser Techniques to Fluid Mechanics*, paper 29/3.

[7] Fabijanic, J. 1996 "An experimental investigation on wheel-well flows". *Society for Automotive Engineers*, pp. 161–172, 960901.

[8] Axon, L., Garry, K., and Howell, J. 1999 "The Influence of Ground Condition on the Flow Around a Wheel Located Within a Wheelhouse Cavity". *Society for Automotive Engineers*, pp. 149–158, 1999-01-0806.

[9] Cogotti, A. 1983 "Aerodynamic characteristics of car wheel. Impact of Aerodynamics on Vehicle Design". *International Journal of Vehicle Design*, Vol. SP3, pp. 173–196.

[10] Regert, T., Lajos, T., and Schwarczkopf, A. 2007 "The effect of wheels on the characteristics of an Ahmed-body". *Proceedings of the European Automotive CFD Conference*, Frankfurt, July, pp. 57–67.

[11] Regert, T. and Lajos, T. August 2007 "Description of flow field in the wheelhouses of cars". *International Journal of Heat and Fluid Flow*, Vol. 28, No. 4, pp. 616–629.

[12] Krajnovic, S. and Davidson, L. 2005 "Flow around a simplified car, Part 1: Large Eddy Simulation". *Journal of Fluids Engineering*, Vol. 127, pp. 907–918.

[13] Krajnovic, S. and Davidson, L. 2005 "Flow around a simplified car, Part 2: Understanding the flow". *Journal of Fluids Engineering*, Vol. 127, pp. 919–928.

[14] Schmidt, S. and Thiele, F. 2002 "Comparison of numerical methods applied to the flow over wall-mounted cubes". *International Journal of Heat and Fluid Flow*, Vol. 23, pp. 330–339.

[15] Rodi, W. 1997 "Comparison of LES and RANS calculations of the flow around bluff bodies". *Journal of Wind Engineering and Industrial Aerodynamics*, Vol. 69-71, pp. 55–75.

[16] Craft, T. J., Gant, S. E., Iacovides, H., Launder, B. E., and Robinson, C. M. E. 2002 "Computational Methodts Applied to the Study of Flow Around a Simplified Ahmed Car Body (Case 9.4)". *10th ERCOFTAC/IAHR Workshop on Refined Turbulence Modelling*.

[17] Ahmed, S., Ramm, G., and Faltin, G. 1984 "Some salient features of the time-averaged ground vehicle wake". *Society for Automotive Engineers*, pp. 1–31, 840300.

[18] Lienhart, H. and Becker, S. 2003 "Flow and turbulent structure in the wake of a simplified car model". *Society for Automotive Engineers*, pp. 1–8, 2003-01-0656.

[19] at Chalmers University Geotheborg Sweden, S. K. P. "Personal communication".

[20] BME "Theodore von Karman Wind Tunnel Laboratory at Dept. of Fluid Mechanics, Budapest University of Technology and Economics", http://www.karman-wtl.com.

[21] Scarano, F. and Riethmuller, M. 2000 "Advances in iterative multigrid PIV image processing". *Experiments in Fluids*, Vol. 29, pp. 51–60.

Conference on Modelling Fluid Flow (CMFF'12)
The 15th International Conference on Fluid Flow Technologies
Budapest, Hungary, September 4-7, 2012

THE UNSYMMETRIC FLOW AROUND THE AHMED BODY

Walter Meile[1], Thomas Wanker[2], Günter Brenn[3]

[1] Corresponding Author. Institute of Fluid Mechanics and Heat Transfer, Graz University of Technology. Inffeldgasse 25/F, A-8010 Graz, Austria. Tel.: +43 316 873 7343, Fax: +43 316 873 7356, E-mail: meile@fluidmech.tu-graz.ac.at
[2] Institute of Fluid Mechanics and Heat Transfer, Graz University of Technology. E-mail: wanker@bios-bioenergy.at
[3] Institute of Fluid Mechanics and Heat Transfer, Graz University of Technology. E-mail: brenn@fluidmech.tu-graz.ac.at

ABSTRACT

The Ahmed body has become a standard body of reference for aerodynamic flows around passenger vehicles. The literature shows a variety of data and simulations of the flow, in particular for symmetric conditions.

The present paper reports about results from an extensive experimental study of the flow around the Ahmed body for various yawing angles. The Ahmed body was equipped with rear geometries at two different slant angles. The experiments were carried out in the 2*m* model wind tunnel of the institute at Reynolds numbers between $0.69 \cdot 10^6$ and $2.76 \cdot 10^6$. Further to force measurements, the flow was visualized and measured by means of PIV.

The experiments revealed an instability of the flow at a yawing angle around 12°, which leads to temporal fluctuations of forces and moments. The flow turns out to be bi-stable. The temporal characteristics of the change between the two states of flow reveal no periodicity, but rather chaotic behaviour. By simultaneous measurements of forces/moments and flow field the physical reasons for the fluctuating forces were identified.

The paper presents all details of the experiments and the results, which allow the dynamic behaviour of the Ahmed body under asymmetric flow conditions to be explained.

Keywords: Ahmed body, bistable state, measurement of forces and moments, PIV, vehicle aerodynamics

NOMENCLATURE

A	[m^2]	area
F	[N]	force
H	[m]	height
M	[Nm]	moment
R	[m]	radius
Re	[-]	Reynolds number
U_∞	[m/s]	free stream velocity
W	[m]	width
c	[-]	force/moment coefficient
l	[m]	length
p	[Pa]	pressure
u ,v, w	[m/s]	velocity components
x, y, z	[m]	coordinates (wake measurements)
x', y', z'	[m]	coordinates (force measurements)
β	[°]	yawing angle
φ	[°]	slant angle
fso		full scale output

Subscripts and Superscripts

f, r	front, rear axle
s	slant
L, D, S	lift, drag, side force
P, R, Y	pitching, rolling, yawing
Ref	reference
Max	maximum

1. INTRODUCTION

The Ahmed body is a bluff model body of simple shape with basic aerodynamic properties of a vehicle, which has been used for many reference investigations. Experiments with this model body may, e.g., represent the influence of a varying slant angle at the back on the flow structure and on the resulting aerodynamic force components.

The first systematic measurements on the influence of the slant angle in the range between 0° and 40° at a flow velocity of 60 *m/s* ($Re = 4.29 \cdot 10^6$) were carried out using the so-called Morel body [1]. Ahmed et al. [2] carried out measurements with the same boundary conditions, but using a slightly modified body, the Ahmed body. Despite some differences, comparable values of the total aerodynamic drag were obtained for the two bodies. The motivation of both series of investigations was the observation of Janssen and Hucho [3] that the drag strongly varies with the inclination of the slant, reaches a maximum near a critical slant angle of 30°, and drops significantly beyond this angle.

During the past decades the Ahmed body was subject of many experimental investigations where

the aims differed in detail. However, in most cases the focus was on symmetrical flow while the influence of side wind was considered only rarely.

Baxendale et al. [4] measured drag and lift forces of 8 slant configurations under symmetrical conditions in a wind tunnel with a moving belt. Due to the altered experimental conditions the determined force coefficients differ from Ahmed's results, but in principle a similar variation of drag with the slant angle was observed.

Later, surface pressures and drag/lift forces were measured at full scale Reynolds numbers by Bayraktar et al. [5]. Their model was 4.7 times larger than the original Ahmed body, and the investigations included three different slant angles below the critical value, as well as yawing angles up to ±15°. The drag coefficient at the lowest Reynolds number $Re = 4.29 \cdot 10^6$ is in full agreement with Ahmed's results. Due to the larger relative ground clearance the measured lift data are not realistic with respect to the original configuration.

Further measurements on pressure distribution, flow velocity, and turbulence properties of the Ahmed body in symmetric flow were carried out by Lienhart et al. [6]. The air velocity in those experiments was 40 *m/s*. The database (ERCOFTAC) derived from these measurements serves yet for many quantitative comparisons.

Conan et al. [7] performed force measurements in two test-sections and investigated the wake flow with the critical slant angle with the aid of PIV. Drag measurements yielded the usual behaviour with varying slant angle and the change of state at the critical angle (30°) in principle, i.e. states of "low drag" and "high drag". In general the drag was moderately overestimated, except with the 25° slant where the value was 20% larger than Ahmed's data. This is all the more surprising since the Reynolds number was smaller than in the original experiments. However, the flow velocity in the PIV investigations was only 13 *m/s* and, therefore, the change of state could not be reproduced and the drag remained throughout in the "low drag" configuration.

The aim of the present study is to investigate experimentally the aerodynamic behaviour of the Ahmed body under varying geometrical conditions, i.e. with sub- and supercritical slant angles. The acquired experimental data are compared with results of the aforementioned investigations. Emphasis is placed on the behaviour under non-symmetric flow, i.e. with non-zero yawing angle. A complete representation can be found in [8].

2. THE AHMED BODY

The geometrical shape of the Ahmed body investigated is depicted in Figure 1. Despite the considerable deviation of the body geometry from usual vehicles it represents the basic aerodynamic properties of a vehicle, especially in the rear part.

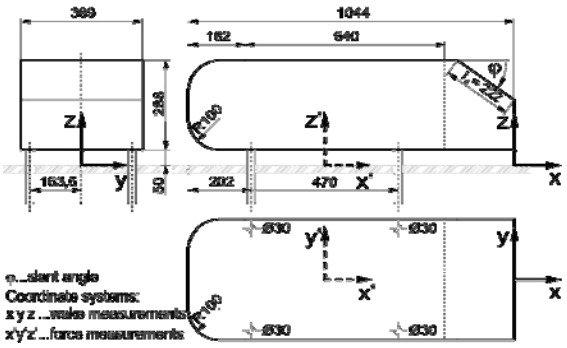

Figure 1. Geometry of the Ahmed body, coordinate systems

According to the results reported in [2], the influence of the front part on the aerodynamic drag is very low, and the influence of the frictional drag does not depend on changes of the slant angle at the back. However, the slant angle has a strong influence on the aerodynamic drag and lift at the back. In symmetrical flow, both the drag and lift coefficients change abruptly at the angle φ =30°. Therefore, this angle is called the critical slant angle.

With increasing slant angle up to φ =30°, an inward rotating pair of vortices with increasing strength is generated near the edges, as observed at fastback vehicles. Therefore, the Ahmed body with a slant angle of 25° belongs to the fastback vehicles, which exhibit very strong inward rotating longitudinal vortices at the C-pillars. These vortices extend far into the wake and generate a field of downwind in the enclosed region. As a consequence, at a slant angle of 25°, the flow is deflected far downward from the roof. The line of flow separation at the sloping back is shifted to the lower part, so that a short and almost closed wake is generated. With increasing distance from the body, the C-pillar vortices approach the ground and move outward. At a slant angle of 30°, i.e., directly before transition to the full squareback flow, this pair of vortices is developed most strongly, and the flow separates at the lower edge of the slant. This produces strong underpressures at that position, so that the aerodynamic drag reaches its maximum in this state ("high drag" configuration). Once the slant angle of 30° is exceeded, the vortex pair bursts, and the flow with a nearly two-dimensional wake ("low drag" configuration) is established [2].

3. EXPERIMENTAL SETUP AND PROCEDURE

3.1 Wind tunnel and techniques

The present investigations were performed in the 2 *m* low-speed aerodynamic wind tunnel of the Institute of Fluid Mechanics and Heat Transfer at Graz University of Technology. This wind tunnel is of the Göttingen type with a ¾-open test section and

closed return. A detailed description is given in [9]. The nozzle outlet cross-section is 2 *m* × 1.46 *m* (*W* x *H*), the maximum wind speed is $v_{Max} \approx 41{,}5$ *m/s*, the non-uniformity of the flow velocity in the usable part of the cross-section is ≤ 0.5 % of the mean value, the longitudinal level of turbulence along the jet axis is ≈ 0.13 %. The static pressure is constant throughout the test section from about 0.8 *m* downstream from the nozzle exit. A sketch of the wind tunnel is depicted in Figure 2.

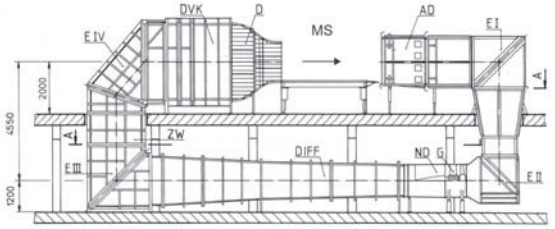

Figure 2. The 2*m* wind tunnel at the ISW

The aerodynamic forces on the body are measured with a six-component platform balance. All load cells are of type Z6-H3 of HBM (200 kg) with an accuracy of 0.05% fso and are operated via an HBM MGCPlus signal conditioner system controlled by the HBM software package CATMAN 5.0. This conditioner system is capable of resolving forces down to ±0.02N. The balance was calibrated following classical procedures during previous investigations on the aerodynamics of ski jumping (e.g. [10]). Due to the calibration, maximum deviations in drag, lift, and moment of ≤ 0.5% of the measured value were achieved.

The wake measurements were performed with PIV. For this purpose a pulsed double cavity Nd:Yag laser system of type *Gemini PIV* from *New Wave Research* was applied. The wavelength is 532 *nm*, the pulse duration 5 *ns*, and the released energy is 200 *mJ* per pulse. The images were recorded with two identical cameras of type High Sense MkII (*Dantec Dynamics*) with 60 *mm* fixed-focus *Nikon* lenses. The CCD-chips have 1344×1024 active pixels at 12 bit depth. The seeding was generated with a smoke generator Fog-smoker 2F using Slow Fog Universal fluid (*Ehle*). The seeding was released in the settling chamber of the wind tunnel from a T-type pipe arrangement.

3.2 The model

The presently used Ahmed body was built from wooden materials in the original dimensions shown in Fig. 1. The rear part was interchangeable, so as to realise the two slant angles to be investigated with the same front part of the body. The model was connected to the balance below the test section floor by cylindrical aluminium stilts, which were fixed by screws on a special mounting support, so that the model could be turned with the balance platform.

3.3 Measurement Program

Steady mean values of forces and moments on the Ahmed body were measured at the 2 slant angles $\varphi = 25°, 35°$, yawing angles in the range $-25° \le \beta \le 25°$ in 2.5° steps, the velocities 10, 20, 30, 40 *m/s* (corresponding to Reynolds numbers $0.69 \cdot 10^6 \le Re \le 2.76 \cdot 10^6$). Furthermore, yawing angles $\beta = \pm 11°, \pm 12°, \pm 13°, \pm 14°$ were investigated with $\varphi = 35°$. In order to achieve steady mean values, three measurements were taken over an integration time of 15 *s* each and were subsequently averaged.

Long-term measurements of forces and moments over a period of 600 *s* with an averaging time of one second were performed at the slant angle $\varphi = 35°$, yawing angles $\beta = \pm 11°, \pm 12°, \pm 13°, \pm 14°$, and with velocities of 30 and 40 *m/s*.

Velocity measurements in the wake were performed at both slant angles, yawing angles $\beta = +5°, 0°, -5°, -10°, -12.5°$, and -15° at a velocity of 30 *m/s*.

3.3.1 Force measurements, data evaluation

The tare loads of the stilts were determined in separate measurement series and subtracted from the full loads. The cross sectional area of the model perpendicular to the longitudinal axis of the test section is small and, therefore, the blockage ratio of the test section at $\beta = 0°$ is 3.8%. But even at yawing angles $\neq 0°$ the blockage is acceptable for achieving meaningful results.

The signals from the six load cells of the balance allow for the derivation of 3 forces and 3 moments with respect to a reference coordinate system. The coordinate system is chosen in accordance with the usual convention. The origin is located on the test section floor, in the centre between the stilts, and the vertical axis is aligned with the axis of the balance. All loads are measured in a wind-fixed system, while, in cases of $\beta \neq 0°$, the forces and moments in a model-fixed system are derived computationally (see Figure 3).

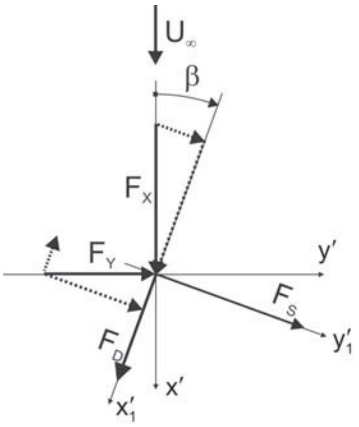

Figure 3. Forces in wind-fixed and model-fixed coordinate systems (exemplarily), definition of β

The following loads are determined: drag (D), lift (L), and side (S) forces, as well as pitching (P), yawing (Y), and rolling (R) moments. From the results, the corresponding coefficients are calculated as follows:

$$c_{D,L,S} = \frac{F_{D,L,S}}{(\rho/2)U_\infty^2 A_{Ref}} \quad (1)$$

$$c_{M(P,Y,R)} = \frac{M_{P,Y,R}}{(\rho/2)U_\infty^2 A_{Ref} l_{Ref}} \quad (2)$$

The reference velocity is the free stream velocity U_∞ in the wind tunnel test section and ρ denotes the density. As usual in aerodynamics, the reference area A_{Ref} was chosen as the cross-sectional area of the model perpendicular to its longitudinal axis. In automotive industry and testing, the track width has been established as the reference length $l_{Ref,1}$ for the rolling moment coefficient, while the wheelbase usually serves as the reference length $l_{Ref,2}$ for the two other moment coefficients. In the present case of the Ahmed body, the reference data are $A_{Ref} = 0.112\ m^2$, $l_{Ref,1} = 0.327\ m$, and $l_{Ref,2} = 0.47\ m$. The Reynolds number is formed with the model length (Fig. 1) as reference.

The lift forces on the front and rear axles ($F_{L,f}$, $F_{L,r}$) are easily determined from the overall lift force F_L and the pitching moment M_P by a balance of forces and moments around the model's side force axis. The corresponding coefficients are derived analogously with the same reference quantities.

3.3.2 Wake measurements

The flow field in the wake of the Ahmed body was investigated in order to associate the aerodynamic loads with the flow behaviour at varying yawing angles and to explain the phenomena observed during the force measurements.

The free stream velocity in the test section was chosen with 30 *m/s*. This value was set for two reasons: (1) PIV measurements are very time consuming and, therefore, a lower velocity reduces the tunnel load significantly and (2) force measurements exhibited that the principal flow behaviour was quite similar at the two higher velocities.

Both cameras were mounted upright one above the other with an overlap of about 12 *mm* in the image plane. This resulted in an image section of 161×412 *mm*, the height being enough to cover the interesting region. This setup was traversed four times in mean flow direction by one image width, resulting in 644 *mm* length of the covered region. In the cross-stream direction, 10 to 12 planes with distances $\Delta y = 40$ *mm* were adjusted as depicted in Figure 4. The reference coordinate system (*x, y, z*) is specified in Fig. 1.

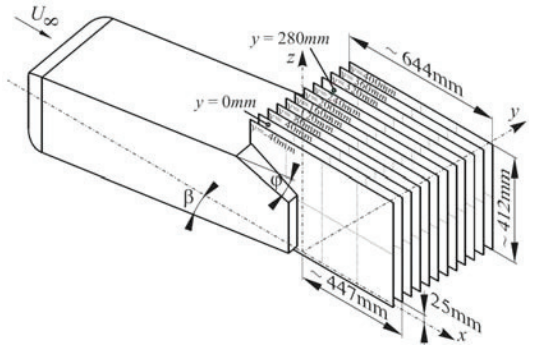

Figure 4. Overview of measurement planes

With this setup two images could be recorded simultaneously. After traversing the system 4 times in the *x*-direction 8 single images had to be composed to yield the final image of the measurement planes. The recording frequency was 5 *Hz*, the recording time was set to 20 *s*, resulting in 100 double frames to be evaluated for the mean velocity distribution.

The program package *Dynamic Studio* 2.10.86 served for data acquisition, while the evaluation was done with the newer version 3.14.35 (both from *Dantec Dynamics*). The evaluation procedure is not described for brevity but it should be mentioned that filtering routines for smoothing the results were avoided. The further data processing was completed using *MATLAB*.

4. RESULTS

In this section the experimental results from the present wind tunnel measurements are compared with corresponding data from the literature. Subsequently, a detailed description of the behaviour of the body under the influence of non-symmetric flow conditions is presented.

4.1 Forces and moments

The dependence of forces on the Reynolds number was investigated for $\varphi = 25°$ in symmetrical flow. Figure 5 depicts $c_D(Re)$.

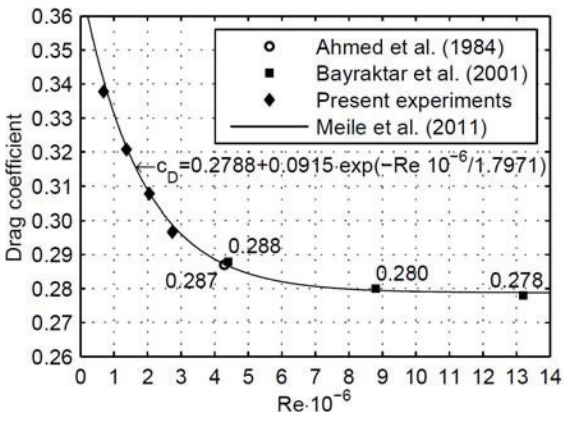

Figure 5. c_D versus Re ($\varphi = 25°$, $\beta = 0°$)

Throughout the investigated regime ($0.69 \cdot 10^6 \leq Re \leq 2.76 \cdot 10^6$) the drag coefficient varies by about 12%. At larger Reynolds numbers, as typical for passenger cars, the variation is much weaker. The data in [5] (max. variation 3.5 %) show the major part of the decrease up to $Re \approx 9 \cdot 10^6$, and a much less pronounced variation with Re above this threshold. The curve fit through the present data (derived in [11]) includes the values reported in [2] and [5] and so extends over one order of magnitude in the Reynolds number. This indicates that the present measurements reproduce the earlier reference data very accurately.

The results under yawing conditions are presented only for the highest velocity (U_∞ = 40 *m/s*), and only positive yawing angles are depicted. The force coefficients for φ = 25° are given in Figure 6, and Figure 7 shows the corresponding results for φ = 35°.

With φ = 25° the drag remains practically constant up to β = 15°, which is in accordance with findings in [5] for much larger Reynolds numbers. In this configuration the lift is positive throughout the whole regime. In symmetrical flow, lift is generated only in the rear part, while the front axle lift is nearly zero. With increasing β, lift is also generated in the front part, which may be ascribed to flow separation in this region. As to be expected, the side force grows continuously with increasing β. The gradient is smaller up to 7.5°, but more pronounced for larger β due to the separation in the front part.

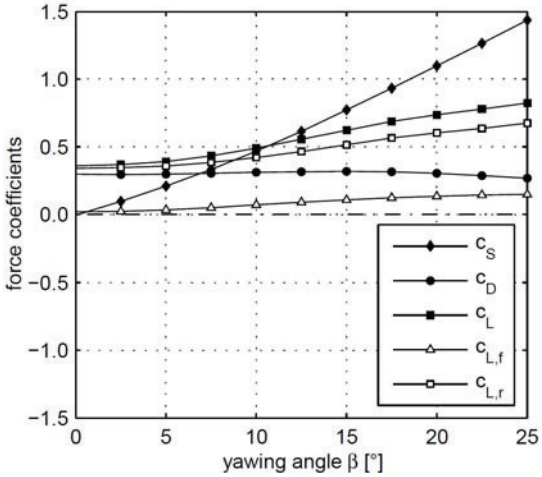

Figure 6. Force coefficients versus yawing angle, φ = 25°, $Re = 2.76 \cdot 10^6$

In contrast to the aforementioned behaviour, the measurements with φ = 35° exhibit a discontinuous slope with a significant change of the forces in the regime 10° ≤ β ≤ 15°. In symmetrical flow, the drag is smaller than with the subcritical slant angle (this is well known), but much larger at yawing angles > 15°. The overall lift is positive throughout the whole regime of β, but notably smaller than with φ = 25°, and practically zero in symmetrical flow. The front axle lift shows only minor variations throughout the whole regime, but the rear axle lift is negative for β < 10°, reaches zero at β = 10°, and exhibits a jump to large positive values in the regime 10° ≤ β ≤ 15°. The overall lift is therefore dominated by the changes near the rear axle. The side force increases again nearly linearly with increasing β, but the significant change of the flow pattern is also resembled by a kink in the slope of the side force.

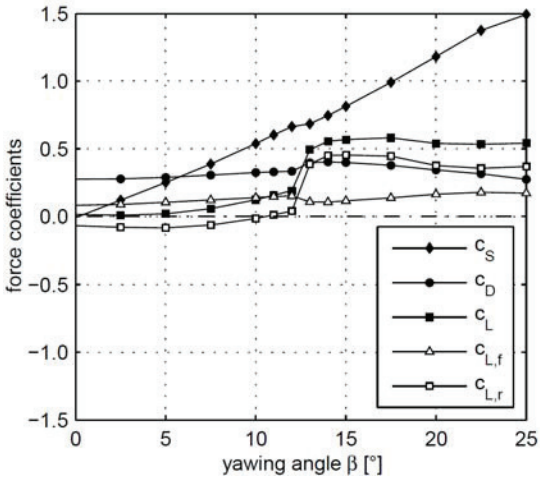

Figure 7. Force coefficients versus yawing angle, φ = 35°, $Re = 2.76 \cdot 10^6$

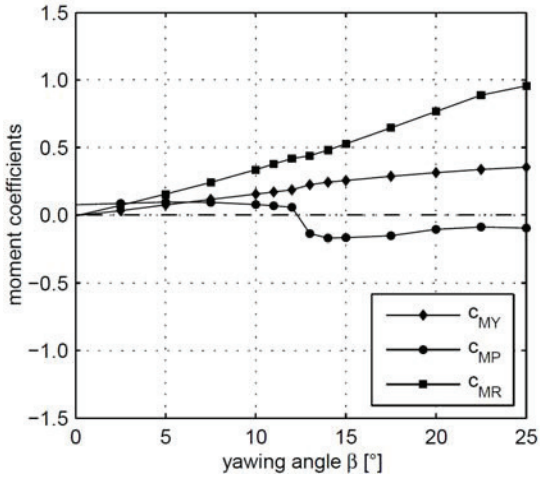

Figure 8. Moment coefficients versus yawing angle, φ = 35°, $Re = 2.76 \cdot 10^6$

The dependence of the moments on the yawing angle is clearly determined by the relation between the forces. With the subcritical slant angle, the rolling and yawing moments are positive at positive yawing angles and vice versa, and increase with β. The pitching moment is always negative (towards the front) due to the distribution of lift among the axles (see Fig. 6). With the supercritical slant angle,

the evolutions of the rolling and yawing moments are similar, but the pitching moment behaves completely different. For $\beta < 11°$ this moment is positive. However, the significant change of the rear axle lift causes the pitching moment to change its sign, as shown in Figure 8.

The observed variations of forces and pitching moment may exert a significant influence on the driving dynamics of the vehicle.

The absolute values of force and moment coefficients at the two lower velocities are not identical, but the principal development is quite similar. At the lowest velocity (10 *m/s*), a different behaviour was detected and, therefore, a Reynolds number influence is evident.

Due to the observed discontinuous variations of the temporal mean values of forces and moments with the supercritical slant it could be concluded that the flow pattern changes significantly in the regime $10° \leq \beta \leq 15°$. Long term measurements should provide a better view on the temporal behaviour of these changes by means of 1 *s* mean values. It was found that, in the negative regime, $\beta \approx -12°$ represents the border case between the two flow patterns, while the changes appear at $\beta \approx +13°$ in the positive regime. Figure 9 depicts data recorded at 40 *m/s*, and only the negative regime of β is described. The scaling of the axes is chosen identical, which allows the magnitude of changes of individual components to be directly compared.

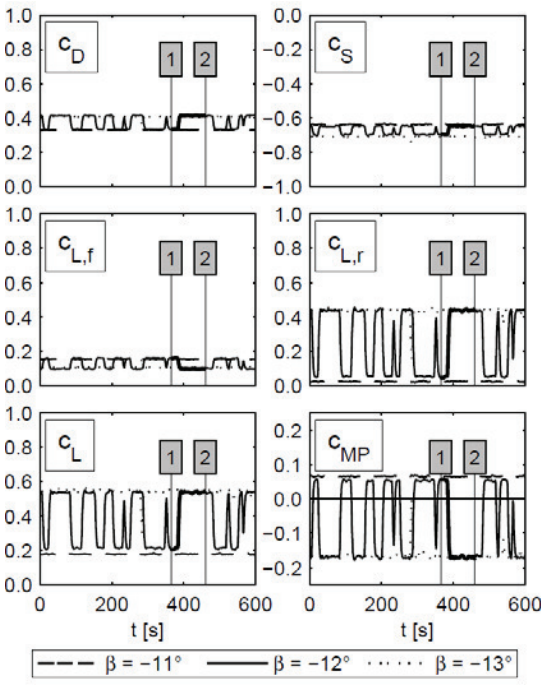

Figure 9. Temporal sequence of force and moment coefficients, $\varphi = 35°$, $Re = 2.76 \cdot 10^6$

Two different states marked with "1" and "2" can be recognized from the diagrams. Both states may remain for several minutes, but may as well disappear after a few seconds. The change appears completely arbitrary, and no distinct frequency can be detected. This leads to the conclusion that there exists a bi-stable state as a limiting case between two flow patterns.

Regarding state "1", drag and lift exhibit a comparably low level. The rear axle lift is practically zero and, therefore, smaller than the front axle lift, which causes a positive pitching moment. This clearly corresponds to observations at lower values of the yawing angle represented by -11° in the diagrams. The side force and the related moments (yawing, rolling) have reached a certain level. If the flow pattern changes into state "2" the overall lift grows to a large value. This is caused by the processes at the rear part, since the rear axle lift increases from nearly zero to a large positive level. Simultaneously, the front axle lift is reduced to a smaller extent and, therefore, the pitching moment exhibits a distinct jump to a negative value.

The variation of drag is smaller, but always in phase with the change of lift. The increase of drag and rear axle lift indicate lower pressure at the slant and base of the model. This, in turn, forces the conclusion that a new inward rotating vortex (C-pillar vortex) is generated at the windward edge of the slant, as known from the subcritical slant. The pressure reduction may be ascribed to the altered flow field caused by this one-sided vortex. From this asymmetric flow field it has been assumed initially that also the (negative) rolling moment should increase. However, the rolling moment decreases a bit, and this can be explained by the complex interaction between the lift and side forces. The absolute value of the side force is much larger than the lift at the actual yawing angle, but is reduced during the change of state. This is due to the reduction of the windage because of the shorter wake, which, in turn, is a result from the vortex formation as known from the subcritical slant.

4.2 Wake measurements

First the wake structure in symmetrical flow was determined for validating the measurements. With $\varphi = 25°$, the flow is attached at the slant and separates at the upper edge of the base. Therefore, the wake is relatively short (~ 200 *mm*). The C-pillar vortices are clearly detectable in the *x,z*-planes at different locations *y* (see Fig. 4) near the side border of the model. In the inner planes ($y \leq$ 120 *mm*) the flow is directed downwards, while upward flow is visible in outer planes ($y \geq 160$ *mm*). The diameter of these vortices grows in the *x*-direction, and the vortices migrate into the wake.

With $\varphi = 35°$, the wake structure is nearly two-dimensional, since no C-pillar vortices occur. The flow separates already at the upper edge of the slant and, therefore, a relatively long wake (~ 350 *mm*) is formed.

For both slant configurations, two counter-rotating vortices with axes perpendicular to the mean flow direction occur. Their size is much smaller with φ = 25°, while the upper vortex extends over the slant and a wide portion of the wake in the case with φ = 35°.

For a quantitative validation, the deduced velocity profiles in several planes were compared with available LDA data of Lienhart et al. [6]. In general, the agreement is excellent for both slant configurations. Minor deviations were found only near solid walls which, however, may be ascribed to reflections during the PIV-measurements.

Under yawing conditions with φ = 25°, the flow pattern for small yawing angles is similar as in symmetrical flow. However, the C-pillar vortex at the windward side is more intense than at the opposite side. At larger yawing angles, the flow pattern is in general similar. Figure 10 depicts the behaviour exemplarily for φ = -12.5°, which can be directly compared to Figs. 11 and 12.

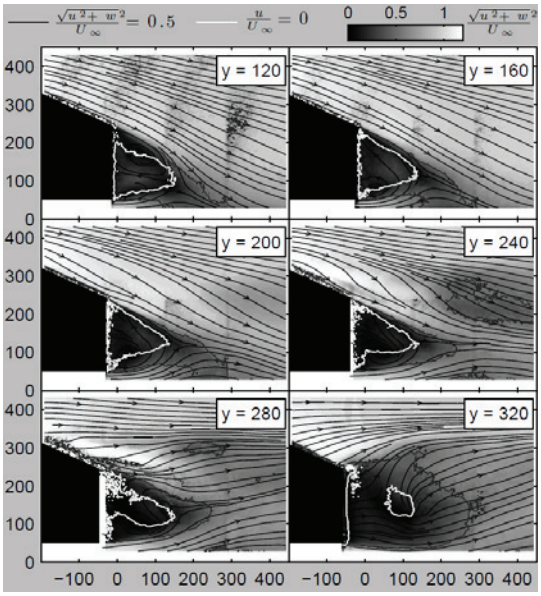

Figure 10. Velocity field and streamlines, β = -12.5°, φ = 25°, *Re* = 2.07·10^6

It is interesting to note that the longitudinal vortex at the windward side is much larger than observed for smaller yawing angles. It is remarkable that the diameter of this vortex is relatively large already in regions above the slant and can, therefore, be identified also in inner planes. This indicates that this vortex must be initiated further upstream in the prismatic middle part of the Ahmed body. Indeed, the formation of longitudinal vortices at the upper long edges of prismatic bodies under yawing conditions is known from other situations like flat-roofed buildings, containers, tanks, etc. At the windward side of the Ahmed body, this vortex rotates in the same direction as the C-pillar vortex, and it can be assumed that it merges with the C-pillar vortex. At the lee-side, both vortices rotate in opposite directions and, hence, the C-pillar vortex is reduced or even vanishes at larger yawing angles. Nevertheless, in all cases the flow remains attached over the slant, and a short wake is formed.

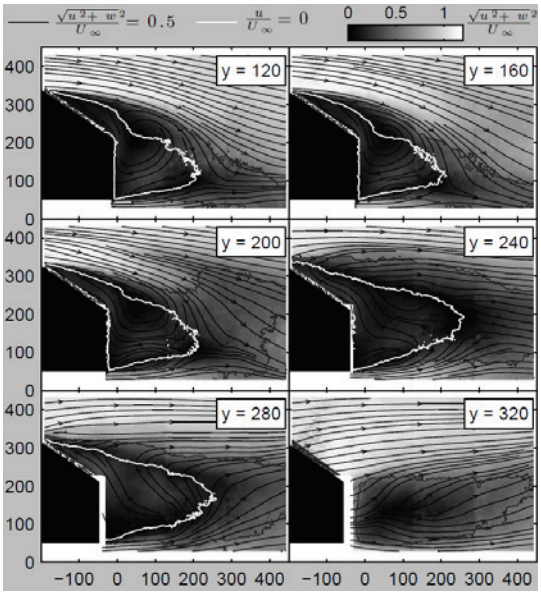

Figure 11. Velocity field and streamlines, β = -12.5°, φ = 35°, *Re* = 2.07·10^6, state "1"

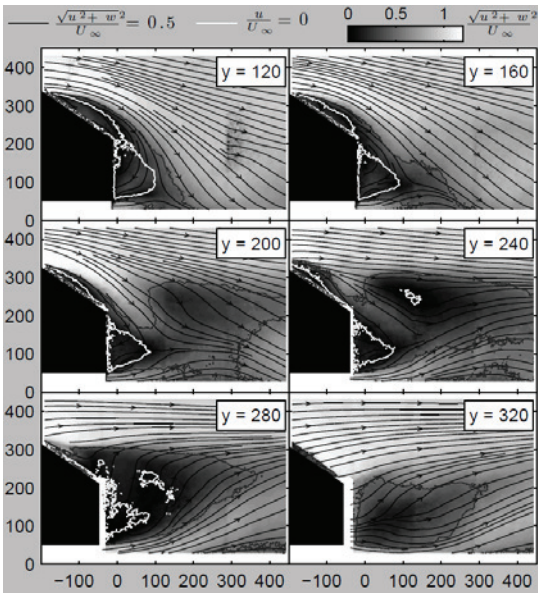

Figure 12. Velocity field and streamlines, β = -12.5°, φ = 35°, *Re* = 2.07·10^6, state "2"

With φ = 35° and at moderate yawing conditions (small β), the flow separates at the upper edge of the slant, and the wake is large. A salient observation is a somehow dented region of the wake in the rear portion of the measurement region. Otherwise, the flow resembles the classical

squareback pattern with a large annular vortex enclosed.

Based on the force measurements it was concluded that the formation of a C-pillar vortex at the windward side causes a change of the flow pattern from squareback to hatchback and, therefore the change of forces. But a change of the wake is already evident at β = -10° by longitudinal vortices emerging from the upper edges of the prismatic part, as mentioned above. Although the flow separates from the upper slant edge, a downwash towards the slant can be recognized since the wake is shorter and appears dented.

The bistable state at the yawing angle $\beta \approx$ -12.5° is of particular interest. In order to clearly distinguish the two states, two separate series of measurements were recorded, while observing the balance readings. Figure 11 corresponds to state"1", and Figure 12 to state "2", as introduced in the previous section. In both Figures the wake is indicated by the line $|v|/U_\infty = 0.5$. The recirculation zone is indicated by the white line $u/U_\infty = 0$.

The flow picture related to state "1" is largely identical with the observations for the smaller $\beta \approx$ -10°. The vortex emerging from the windward roof edge is located above the wake and visible in the planes y = 160 *mm* and y = 200 *mm*. The sense of rotation is clear from the flow direction – downward in the inner region ($y \leq$ 160 *mm*) and upward in the outermost region. The wake region is comparably long.

In state "2", the wake is significantly shorter, and the length is comparable to the wake with the subcritical slant. The flow separates at the upper edge of the slant, but is reattached at least partly to the slanted surface, thereby forming a separation bubble. In this state, the windward roof edge vortex is combined with the C-pillar vortex, which can be recognized in the planes y = 280 *mm* and y = 320 *mm*.

The completely different flow pattern for identical configurations under identical boundary conditions clearly proves that two different flow states exist.

5. SUMMARY

The present experiments provide insight into the aerodynamics of the Ahmed body under yawing conditions. The development of forces and moments with the yawing angle is consistent. With the supercritical slant angle, a bistable state was identified, where significant changes of the flow pattern occur in a narrow regime of yawing angles. This was explained by wake measurements with PIV.

ACKNOWLEDGEMENTS

The authors gratefully acknowledge support from the Fachhochschulstudiengänge Burgenland GmbH, Austria, who provided the complete PIV-System for the present work.

REFERENCES

[1] Morel, T., 1978, „The effect of base slant on the flow pattern and drag of three-dimensional bodies with blunt ends", In: Sovran, G., Morel, T., Mason. W.T. (Eds.) *Aerodynamic drag mechanisms of bluff bodies and road vehicles.* Plenum Press, New York, pp.191-226.

[2] Ahmed, S.R., Ramm, G., and Faltin, G., 1984, „Some salient features of the time-averaged ground vehicle wake", *SAE paper 840300*.

[3] Janssen, L.J., and Hucho, W.H., 1974 „Aerodynamische Formoptimierung der Typen VW-Golf und VW-Scirocco", *Kolloquium über Industrie-Aerodynamik*, Aachen, Part 3, pp. 46-69.

[4] Baxendale, A.J, Graysmith, J.L, Howell, J., and Haynes, T., 1994, „Comparisons between CFD and experimental results for the Ahmed reference model", *RAeS Conference on Vehicle Aerodynamics*, Loughborough, UK, 30.1-30.11.

[5] Bayraktar, I., Landman, D., and Baysal, O., 2001, „Experimental and computational investigation of Ahmed body for ground vehicle aerodynamics", *SAE paper 2001-01-2742*.

[6] Lienhart, H., Stoots, C., and Becker, S., 2000, „Flow and turbulence structures in the wake of a simplified car model (Ahmed model)", *DGLR Fach Symp. der AG STAB*, Universität Stuttgart, November 15–17.

[7] Conan, B., Anthoine, J., and Planquart, P., 2011, „Experimental aerodynamic study of a car-type bluff body", *Exp Fluids* 50, pp. 1273-1284.

[8] Wanker, T., 2011, „Der Ahmed-Körper unter Schräganströmung". *Diploma Thesis, Institute of Fluid Mechanics and Heat Transfer, Graz University of Technology*.

[9] Gretler, W., and Meile, W., 1993, „Der 2m-Windkanal am Institut für Strömungslehre und Gasdynamik der Technischen Universität Graz". *ÖIAZ* 138/3, pp. 90-96.

[10] Reisenberger, E., Meile, W., Brenn, G., and Müller, W., 2004, „Aerodynamic behaviour of prismatic bodies with sharp and rounded edge", *Exp Fluids* 37, pp. 547-558.

[11] Meile, W., Brenn, G., Reppenhagen, A., Lechner, B., and Fuchs, A., 2011, „Experiments and numerical simulations on the aerodynamics of the Ahmed body", *CFD Letters* 3(1), pp. 32-39.

Conference on Modelling Fluid Flow (CMFF'12)
The 15th International Conference on Fluid Flow Technologies
Budapest, Hungary, September 4-7, 2012

FLOW AND TURBULENT STRUCTURES AROUND SIMPLIFIED CAR MODELS

David ALJURE,[1] Ivette RODRIGUEZ, [2] Oriol LEHMKHUL, [2 , 3] Ricard BORRELL, [3] Assensi OLIVA [3]

[1] Corresponding Author. Centre Tecnològic de Transferència de Calor (CTTC) , Universitat Politècnica de Catalunya (UPC). ETSEIAT, Colom 11, 08222, Terrassa, Barcelona, Spain. E-mail: davidal@cttc.upc.edu
[2] Centre Tecnològic de Transferència de Calor (CTTC) , Universitat Politècnica de Catalunya (UPC). ETSEIAT, Colom 11, 08222, Terrassa, Barcelona, Spain. Fax: +34 93 739 89 20. E-mail: cttc@cttc.upc.edu
[3] Termo Fluids, S.L. Av. Jaquard, 97 1-E, 08222 Terrassa (Barcelona), Spain. E-mail: termofluids@termofluids.com

ABSTRACT

External car aerodynamic study has great importance in overall car efficiency and ride stability, making it a key element in successful automotive design. Flow over car geometries fully show three dimensional, unsteady turbulent characteristics. Additionally, vortex shedding, flow reattachment and recirculation bubbles can be found around the buff body. These phenomena greatly influence the key factors in aerodynamic study, the lift and drag coefficients, vital for ride stability and energy efficiency, respectively. The purpose of the present study is to assess and compare the different large scale turbulent flow structures present in car aerodynamics using two basic car geometries.

Flow around two model car geometries is resolved, the Ahmed and the Asmo car. These generic buff bodies reproduce the basic fluid dynamics features of real cars using simplified geometries. Firstly, the flow over both geometries is studied and compared against experimental results to validate the code, afterwards, various LES models are used to study the flow in detail and compare the structures found in both geometries.

Keywords: Automotive aerodynamics, CFD, CLES, Turbulence models.

NOMENCLATURE

c_D	$[-]$	Total drag coefficient
c_L	$[-]$	Total lift coefficient
C	$[-]$	Convective operator matrix
D	$[-]$	Diffusive operator matrix
G	$[-]$	Gradient operator matrix
M	$[-]$	Divergence operator matrix
cP	$[-]$	Adimentional pressure $\frac{P}{\rho U2}$
Q	$[1/s]$	Second invariant of ∇U
u	$[m/s]$	Velocity vector
$urms$	$[m/s]$	Root mean square stream-wise velocity

1. INTRODUCTION

Computational fluid dynamics (CFD) have evolved greatly in the past two decades becoming a vital tool in industrial research, development and investigation. Due to the nature of fluid flows, most practical applications deal with turbulent motion; the modelling of this phenomenon is of vital importance within the CFD industry, where vast resources are invested into researching it. Within the different possible applications of the CFD technology come aerodynamics and automotive design. The automotive industry makes great advances every year; engine performance has increased greatly in the past decade, along with weight reduction and safety measures. External aerodynamics in automotive developments bear increased importance as such advances are made. Aerodynamic resistance increased its relative importance by 124% when an audi r8 automobile was such advances [1]. Additionally, as weight reduction becomes more popular, aerodynamics become more important to ensure vehicle drive stability.

The bodies to be studied using Challenging Large Eddy Simulations (CLES) in the present paper are the widely studied (Lehmkuhl [2], Krajnović [3][4], Minguez [5]) Ahmed car model (with a 25 angle of the rear slanted surface) and the Asmo car model ([6],[7]). The Ahmed body car is a semi-rectangular vehicle with a rounded front and a slanted back. The simplified topology of this model allows easy modelling, meshing and comparisons between experimental and numerical results. The second model, the Asmo car is a model created by Daimler-Benz in the 90's to investigate low drag bodies in automotive aerodynamics.

2. NUMERICAL METHOD

2.1. Domain and Boundary Conditions

The geometries to be studied are the Ahmed car [8] and the Asmo car [7]. The computational domain is a $9.1944 \times 1.87 \times 1.4$m rectangular channel with the front of the car located 2.1014 m downwind from

the inlet boundary. The outlet boundary is at a distance of 6.048 m for the Ahmed car and of 6.282 m for the Asmo car, measured from the rear of the body. To simulate the same case as Lienhart [8] a $\frac{3}{4}$ open wind tunnel was simulated using the following boundary conditions:

- Inlet: The inlet condition is a uniform flow such as the reference Reynold using the model height is $Re = 7.68 \times 10^5$.
- Outlet: A convective outlet boundary condition was used.
- Floor: A no-slip - 0 velocity condition was used for the floor.
- Top, front and back: To complete a open wind tunnel these three boundaries where modelled using a symmetry condition.

2.2. Governing Equations and Discretization

The incompressible-isotherm Navier-Stokes equations are solved:

$$\rho \frac{\partial u}{\partial t} + C(u)u + Du + Gp = 0 \quad (1)$$

$$Mu = 0 \quad (2)$$

where u is the three-dimensional velocity vector field and p is the pressure scalar field. The matrices C, D, G and M are the convective, diffusive, gradient and divergence operators respectively. It is important to note the non-linear relation in the convective term of the equation $C(u)u$. The velocity-pressure coupling is solved by means of a fractional-step algorithm; the temporal discretization for the convective, difusive and derivative parts of equation (1) was made using a second order self-adaptative scheme [9]; whereas a back-ward euler scheme was used for the pressure gradient. The spatial discretization was made on a collocated mesh by means of a conservative scheme similar to that presented by Felten [10] where skew-symmetry is ensured for the convective operator as well as a positive-definite symmetry diffusive operator.

Turbulence modelling is carried out by using different eddie-viscocity models; the wall-adapting local-eddy viscocity (WALE) [11], a WALE model with a variational multiscale approach (VMS) [12], the singular values subgrid model (SIGMA) [13], and the q-r model that uses invariants q and r of the filtered strain tensor to model eddy viscocity (QR) [14].

The simulations have been performed using the TermoFluids high performance parallel code [15] on a hybrid tetra-prism unstructured mesh generated using the Ansys IcemCFD software and ran in the JFF computing cluster in the UPC. METIS software was used for domain partitioning.

3. RESULTS

3.1. Mesh Study

3.1.1. Ahmed Car

First, to validate the code, results of the Ahmed car simulations using the VMS turbulence model were compared to the experimental results obtained by Lienhart [8].

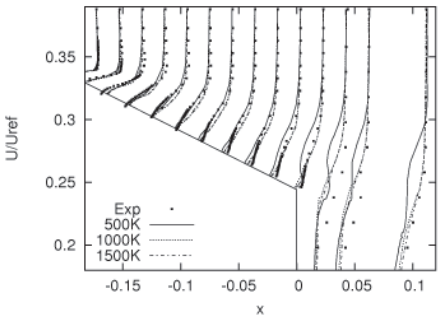

Figure 1: Average stream-wise velocity profiles over the slant wall in the mid plane.

As we can see in figure 1, the obtained results are in good agreement with the experimental results; a mesh of approximately 1×10^6 control volumes shows good results.

3.1.2. Asmo Car

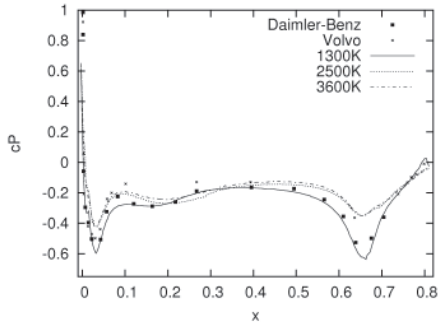

Figure 2: Average pressure coefficient in the underbody

Figure 2 shows the mesh independence of the simulations performed on the Asmo car, it can be seen that a 2.5×10^6 mesh shows good results in agreement with the experiments performed by Volvo [6].

3.2. LES Analysis

Four different LES models were used to analyse the flow over the simplified cars, the QR, WALE, SIGMA and VMS models.

3.2.1. Ahmed Car

The first geometry studied, the Ahmed car, allowed the comparison of the results with the experimental data obtained by Lienhart [8]. Stream-wise velocity

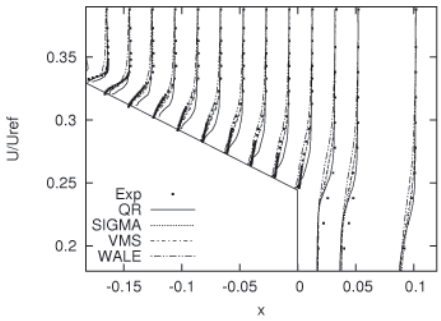

Figure 3: Average stream-wise velocity profiles over the slant wall in the mid plane.

profiles shown in figure 3 evidence that the VMS model and SIGMA model results are closer to the experimental data than the other two models. Moreover, it can be seen that the WALE, SIGMA and VMS models yield good results in the boundary layer of the slant wall, where the QR model fails to predict the flow behaviour correctly. The results in the near wake are a little different, having the QR show the best results.

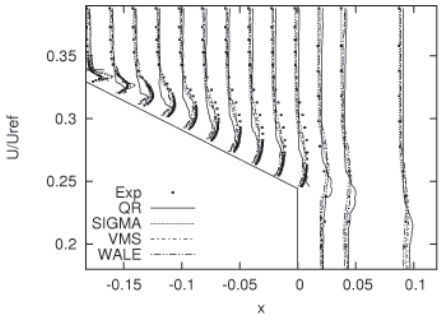

Figure 4: Average stream-wise RMS-velocity profiles over the slant wall in the mid plane.

Figure 4 shows the stream-wise root mean square velicity profile $urms$ along the slant back of the Ahmed model. In this case, the WALE model yielded the best results of all four models. Again the less accurate data is the one resulting from the QR model.

3.2.2. Asmo Car

The same 4 models where used to solve the flow over the Asmo car. As figure 5 shows, the results obtained by the WALE and SIGMA models show the highes error whereas the QR and VMS models results are the better, however fail to fully predict the pressure spikes in the front and back.

3.3. Flow Structures

3.3.1. Lifted streamwise vortices:

According to Townsend's attached eddy hypothesis [16], the average large eddy motion consists of pairs of inviscid parallel roller vortices.

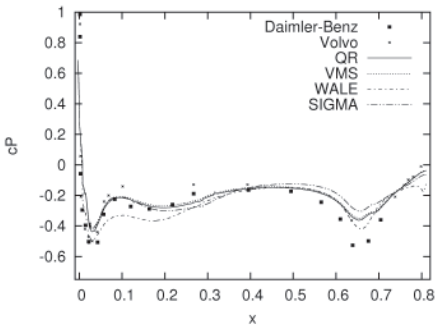

Figure 5: Average pressure coefficient in the underbody

These eddies extract energy from the mean flow through the vortex stretching mechanism. However, when the flow is bounded by a wall, the eddies are restricted and form double-cone eddies. These two structures are ideal, however they bear great resemblance to the structures observed in the wake of the Ahmed car flow. Several authors have discused the different methods to identify vortical structures within the flow [16],among those is the second invariant of the velocity gradient tensor Q:

$$Q = \frac{1}{2}(||W^2|| - ||S^2||) \tag{3}$$

$$W = \frac{1}{2}(\nabla u - (\nabla u)^T \tag{4}$$

$$S = \frac{1}{2}(\nabla u + (\nabla u)^T \tag{5}$$

Figure 6a and 6b show, by means of the second

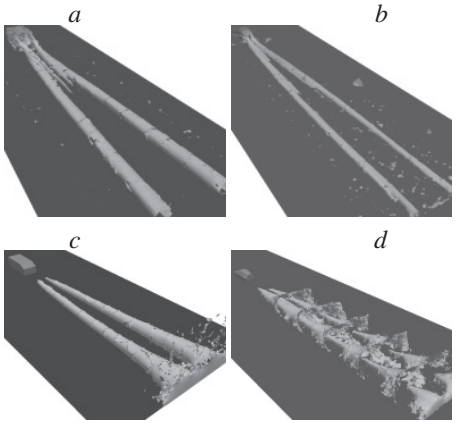

Figure 6: Streamwise vortices (a) Ahmed car Q=0.1 (b) Asmo car Q=0.1 (c) Ahmed car P=0 (d) Asmo car P=(-0.01,0.01)

invariant Q, two longitudinal vortices generating in the back of the cars. The presence of this vortices can also be verified by means of a local presure minimum, shown in figure 6c and 6d. This turbulent structure is found both on the Ahmed and the Asmo geometry, however, when comparing the vortices in both geometries the magnitude and strength of these

structures in the Asmo car is lower, they don't display a strong a profile as the ones present in the Ahmed car. This fact is specially evident in in figures 6c and 6d, where, compared to the pressure isosurface of the Ahmed car, the vortex structure in the Asmo car is not unified, making this eddy much weaker in comparison to the one displayed by the Ahmed body flow. It can also be seen in figure 6 that the lower part of the vortices are bounded by the floor of the channel, thus, restricting the overall size of the eddy. Figure 7 shows the mean streamlines where the main

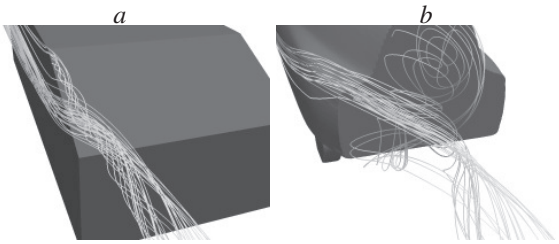

Figure 7: Mean streamlines in the back of the car models

longitudinal vortices are generated. It is important to note that the geometry in both cases is very different, the slant back in the Ahmed body and the curved profile in the Asmo car, however, the vortex generation mechanism seems to be the same. In both cases there is a high speed stream moving along the side wall of the car, a slow speed stream in the back of the car and the main flow travelling along the top of the body. In the Ahmed body the slow speed stream consists of fluid recirculating along the slant wall, whereas in the Asmo car the slow speed stream consist in the main recirculation bubble in the back of the car. The vortex is then generated by the interaccion between these three streams, as the high speed stream passes the end of the side wall it flows towards the mid plane (pushed by the low pressure zone found in the back), crashing into the slow speed stream reducing its speed before colliding against the main flow present close to the midplane (where the pressure has a higher value). This second collision changes the mixed stream direction giving it a twirling motion, and thus, creating the longitudinal vortex[1].

3.3.2. Recirculation Bubble

Figures 8 and 9 show the recirculation bubbles present behind the bodies. The recirculation adimentional length for the Ahmed body is around 0.69H (0.65H in [3]) whereas for the Asmo body is around 0.48H using the body's height as the reference length. Besides from the size, the recirculation bubbles in both bodies differ in shape; in the Ahmed body it is composed of two straight spanwise vortices generated by the flow coming down the slant back and the flow coming from the underbody. In the Asmo body the

[1]The results in this section where obtained using a different mesh containing more control volumes in the wake area

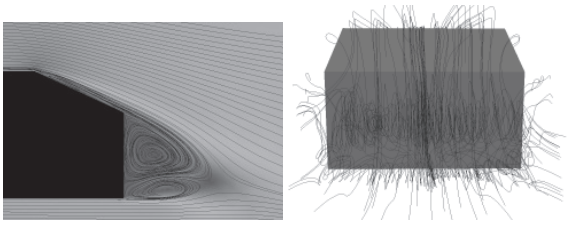

Figure 8: Recirculation bubble behind the Ahmed Body.

vortex takes the shape of a horseshoe thoroidal vortex bounded by the flow coming from the sides and the top of the body. The flow from the underbody, after passing through the diffuser, reduces its speed thus reducing its influence in the recirculation bubble.

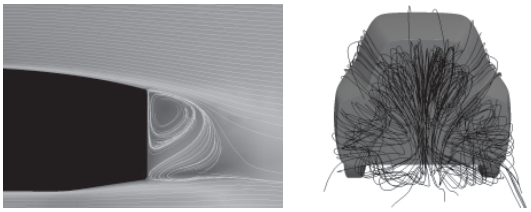

Figure 9: Recirculation bubble behind the Asmo Body.

3.3.3. Pressure Field and Pressure Gradients

Flow detachment is generally identified by a low pressure zone. The places where fluid separation occurs are accompanied by steep pressure gradients that generate vortices and eddies, which in turn augment drag on the aerodynamical body. Other factors afecting the aerodynamic drag, and which are partially responsable for the pressure drag a body experiences, are the high pressure bubbles in the front of the geometry and low pressure bubbles in the back. Figures 10 and 11 show the adimensional pressure cP contours for the two bodies; this figure shows that the pressure gradients present in the Ahmed body are much greater than those present in the Asmo body. Additionally, it can be seen that the Ahmed body has several zones of detachment. Furthermore, the pressure difference around the Ahmed car is greater than that present in the Asmo car.

The mild pressure gradients present in the Asmo body allow the flow to remain attached for most of the car's length, thus producing a smaller wake as seen before. The steeper pressure gradients present in the Ahmed body are strong enough to produce separated flows increasing the size and pressure losses in the wake, thus, increasing the pressure drag.

Figure 12 shows the high pressure and low pressure bubbles around the bodies. The low profile nose of the Asmo car allows the formation of a smoother flow pattern thus diminishing the stagnation in the flow and reducing the size of the high pressure bubble;

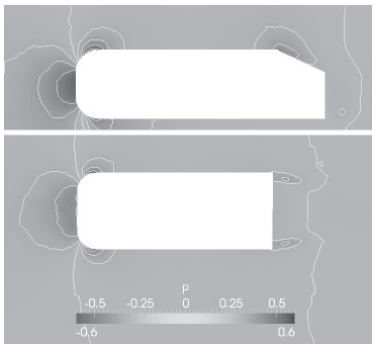

Figure 10: Mean pressure contours in the Ahmed body.

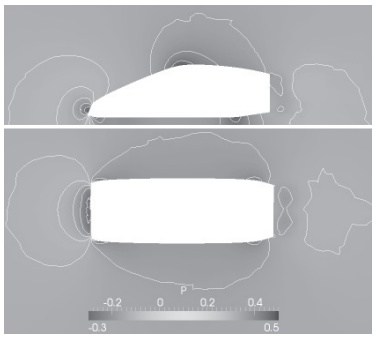

Figure 11: Mean pressure contours in the Asmo Body.

whereas in the Ahmed car the wider nose puts up a bigger resistance to the flow increasing the size of the high pressure bubble. It is also important to notice that at the slant back the edges are in a low pressure zone with high flow separation. This accounts for the formation of the big lifted longitudinal vortices shown before. There is also a mid-body low pressure zone present in both geometries, in the Ahmed car it is found near the front of the car, immediately after the nose, whereas this zone is spread wider in the Asmo geometry, accounting for the smoother pressure gradients present in this geometry.

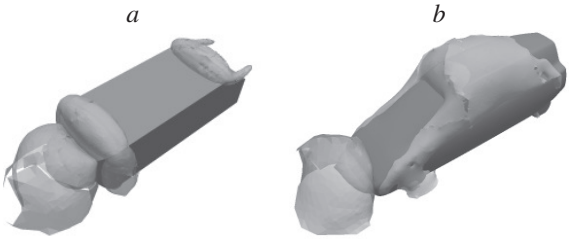

Figure 12: Mean pressure surfaces around the Ahmed and Asmo bodies.

The effects of pressure gradients can be classified in two mayor groups, positive and negative relative to the direction of the flow. These zones can readily be seen on figure 10 and 11.

Figure 13 show the Q isosurfaces in the front of

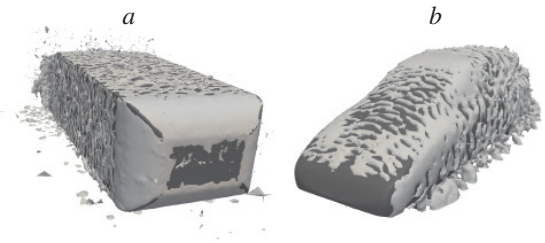

Figure 13: $Q = 20$ instantaneous isosurfaces in the front of the Bodies.

the model cars. The first structure in the front of the Ahmed car is smooth and resembles a laminarized flow. This part of the geometry has a negative pressure gradient (pressure decreases in the direction of the flow); this gradient "pushes" the fluid back, increasing the velocity gradient near the wall, thus, increasing the local wall shear stress. The flow structure in front of the Asmo car is different. After passing the stagnation point (zone with no structure visible), the mild negative pressure gradient along the nose of the car permits the flow to be more stable than that found in the Ahmed car.

As the fluid moves back, it reaches the local pressure minimum and, thus, a zone of positive pressure gradient. Figure 13a shows this point as the transition of the smooth coherent structure to the unstable flow along the top of the car. This zone is characterized by a separation zone and a lower wall shear; figure 13a shows this zone as a collection of small vortical structures away from the wall. Several authors, such as Minguez [5] and Krajnović [3] state there is a recirculation zone here; eventhough the meshes used in the present study are not fine enough for a complete resolution of the flow in this area, evidence (pressure field and coherent structures) suggests the presence of recirculation zone in this place. Further back, the pressure gradient becomes small and the coherent structures in the Ahmed car exhibit the turbulent behaviour to be expected from the streak inestability cycle.

The flow over the Asmo car show very little instabilities, however, evidence of the behaviour explained earlier can be found. As the fluid travels throught the top of the nose it reaches a local pressure minimum. As the fluid closes on this point the pressure gradient becomes larger and a smooth structure, such as the one mentioned earlier, forms. Upon reaching the low pressure point the structure breaks down due to the negative pressure gradient. Furthermore, the vortical structures in the bottom of the car, shown by figure 13b, are vortices shedding around the tyres.

Studying closely figure 13a a small structure, generating in the lower corner of the car, can be seen. As was exposed by Krajnović [4], this vortical structure is generated by the interaction of the boundary layers of the floor and the underbody of the Ahmed car. The presence of the wheels in the Asmo car prevent this

structure from forming.

The flow structures in the back of the car are also very different. The slant back is a geometry feature unique to the Ahmed car and it displays very turbulent flow. Figure 14a shows the Q isosurfaces in this region, it shows small vortical structures forming on the the surface, right at the edge where the slanted surface starts as well as several big vortical structures. The big vortical structures present are the vortices that form the recirculation bubble, the big lifted streamwise vortices (shown earlier) and large horseshoe like vortices shedding from the slant wall.

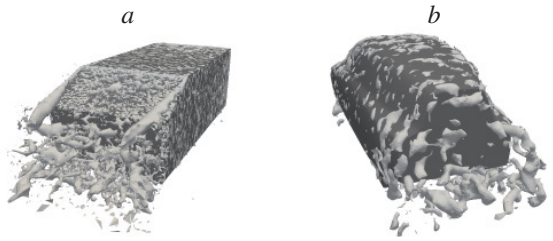

Figure 14: $Q = 200$ instantaneous isosurfaces in the slant back of the (a) Ahmed body (b) Asmo Body

These small vortical structures are the result of the change in surface direction and the subsequent negative pressure gradient this change generates. As was explained earlier, this pressure gradient creates flow instabilities. The combination of the flow instabilities and the geometry present add up to vortex shedding in this section.

The turbulent structures present in the back of the Asmo car are different in shape and size as those seen in the Ahmed car. Figure 14b shows less vortical structures being generated in the back of the car, the vortex shedding phenomenon can be witnessed readily in this geometry; large structures detach from the bottom of the car, as well as small vortices detaching from the wheels, the diffuser and the trailing edge of the car. As it is to expect in flow over buff bodies, both geometries show vortex shedding, however, in the Ahmed car, specially in the slant back, this phenomenon is very strong.

3.4. Drag & Lift Coefficients

As stated earlier, two of the most important aerodynamic parameters are the lift and drag forces. The drag coefficient quantifies the advancing resistance posed by the air (surrounding fluid) onto the vehicle; whereas the lift coefficient cuantifies the force exerted onto the vehicle in the direccion perpendicular to the flow. Reducing the drag coefficient of a vehicle will reduce its overall fuel consumption, reducing the lift coefficient will improve ride stability and cornering performance.

3.4.1. Ahmed Car

Table 1 shows the drag coefficients obtained for the different LES models. The SIGMA model performs well in predicting the drag, specially the pressure, whereas the WALE shows the worst results; furthermore, the VMS and the QR model perform very similarly. All four models perform, when resolving the viscous drag, in a similar fashion. As can be seen in table 2, the Ahmed geometry has a high lift coefficient, it is of the same magnitude as the drag coefficient.

Table 1: Ahmed car drag coefficients

Model	Pressure	Skin friction	Total
VMS	0.302	0.008	0.310
QR	0.301	0.008	0.309
WALE	0.310	0.011	0.321
SIGMA	0.281	0.010	0.292
Exp[17]	–	–	0.298

Table 2: Ahmed car lift coefficients

Model	Pressure	Skin friction ($\times 10^5$)	Total
VMS	0.313	3.8	0.313
QR	0.328	25.6	0.328
WALE	0.256	6.9	0.256
SIGMA	0.313	6.8	0.313

3.4.2. Asmo Car

Table 3: Asmo car drag coefficients

Model	Pressure	Skin friction	Total
VMS	0.154	0.0027	0.157
QR	0.154	0.0027	0.156
WALE	0.168	0.0036	0.171
SIGMA	0.161	0.033	0.164
Exp. Volvo [6]	–	–	0.158

Tables 3 and 4 show the force coefficients on the Asmo geometry. As it can be easily seen, the drag coefficient of the Ahmed car is nearly double the drag coefficient of the Asmo car. The drag coefficient calculated with the VMS and QR models are quite close to the experimental values reported by Volvo. The WALE and SIGMA models slightly overpredict the drag. The QR and VMS models yield very similar lift coefficients, whereas the WALE and the SIGMA report quite different results. Comparing tables 2 and 4 it can be seen that the lift coefficient for the Asmo car is one order of magnitude smaller than the lift coefficient found for the Ahmed car.

4. CONCLUTIONS

CLES simulations where carried out in two different geometries, the Asmo car an the Ahmed car; using 4 different turbulence models, the QR, the VMS, the SIGMA and the WALE (to the authors knowledge,

Table 4: Asmo car lift coefficients

Model	Pressure	Skin friction ($\times 10^5$)	Total
VMS	0.0279	31.7	0.0282
QR	0.0283	31.7	0.0286
WALE	0.0143	22.4	0.0.0145
SIGMA	0.0728	34.3	0.0.0731

this is the first time the SIGMA and VMS models are used in resolving flow around simplified car models). When comparing the results obtained in the Ahmed geometry with the experimental results it can be seen that the agreement in the slanted back is accepable, however, due to the mesh sizes used in the present simulations the results aren't in good agreement with the experimental results in the near wake as other authors with finer meshes have achieved. The results in the underbody of the Asmo car are also in good agreement with experimental results , however, the pressure distribution in the front part has some error.

The coherent structures in the flow around the Asmo car are much weaker and exhibit less turbulent behaviour than those found around the Ahmed car. The biggest structures in the flow, the lifted streamwise longitudinal vortices in the wake, are present in both geometries using the same generation mechanism, however, the geometry features of the Ahmed body allow for the formation of a much stronger vortex.

The recirculation bubble present in both geometries differ both in shape and size; the one present in the Asmo car is smaller, shows a horseshoe shape and is formed by flow coming from the top and the sides of the car; the bubble found in the Ahmed car is formed by two spanwise vortices and is created by the flow coming from the top and the bottom of the geometry. The differences in this structure allow for different magnitudes in the pressure fields, being the pressure behind the Ahmed car lower than that found in the Asmo car.

Another difference in pressure, this time in the nose of the car, is also found, the low profile nose of the Asmo car results in less stagnation and lower pressures in the front. The Asmo car also exibits lower pressure gradients around the entire body, this produces a more laminarized flow around the entire geometry, less vortical structures dettaching and less vortex shedding in its back.

All the differences in the flow features explained in the previous paragraphs account for the results shown in tables 1, 2, 3 and 4; the drag coefficient for the Ahmed car is greater than that calculated around the Asmo car. Additionally, the Ahmed car shows a large positive lift coefficient, opposed to the smaller value found for the Asmo car.

Furthermore, the VSM model was the slowest model of the four tested, restricting the timestep by predicting a higher turbulent viscocity, whereas the QR model was the fastest, permiting a higher timestep due to lower turbulent viscocity. The SIGMA and VSM models performed very similarly and better than the WALE and QR models in the Ahmed car, where the geometry changes and corners heavily influence the flow. VMS and QR models performed well in the Asmo car; however the SIGMA and WALE models didn't, they show problems when dealing with flows heavily influenced by the boundary layer.

ACKNOWLEDGEMENTS

This work has been financially supported by the Ministerio de Educación y Ciencia, Spain (Project: Development of high performance parallel codes for the optimal design of thermal equipments, reference ENE2010-17801) and Termo Fluids S.L.

APPENDIX A: Fine Meshes

All the previous data, with exception to those that show the big lifted streamwise vortices, where done with coarse meshes. The results are satisfactory, however it is important to contrast the results found with finer meshes to ensure their validity. A 6M control volume mesh was used for the Ahmed car and a 4.5M control volume mesh was used for the Asmo car, both using the VMS model.

The turbulent structures around the Ahmed car are quite more complex than those found in the Asmo car. Figure 15 shows the mean Q isosurfaces present around the front of the cars. The structures found in the figure 15a, when compared to 13a are much more complex. The finer mesh allows the resolution of smaller scales thus showing much more structures, however, the structures found in the coarser mesh are consistent with the structures in this section. Figure 13b show the structures present in the Asmo car; also consistent with those found in the finer mesh shown in figure 15b.

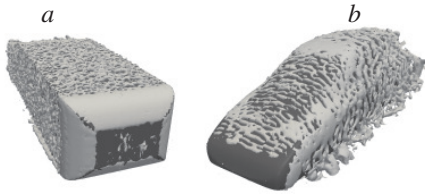

Figure 15: $Q = 20$ **instantaneous isosurfaces in the front of the bodies.**

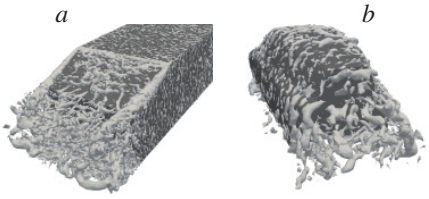

Figure 16: (a) $Q = 200$ **instantaneous isosurfaces in the back of the bodies**

Figures 16 show the structures found in the back of the geometries. Once again, when comparing to figure 14 the main difference is the smaller scales shown in the results from this section; however, the large scale structures found are found in both coarse and fine meshes. It is important to note that vortex shedding is largely influenced by both large and small length scales. As can be seen when comparing figures 16b and 14b, there is a vortex structure shedding from the bottom of the car, the coarse mesh represents it as a single large structure, when in reality it is a collection of different sized structures.

Table 5: Lift and drag coefficients

Geometry	c_D(exp)	c_L
Ahmed Car	$0.2925(0.298)$	0.2950
Asmo Car	$0.1576(0.158)$	0.01646

Finally, the lift and drag coefficients for the fine meshes are shown in table 5. When compared to the results shown in tables 1, 2, 3 and 4 the parameters don't vary much. The force coefficients calculated with the coarser meshes are close to the results obtained in this appendix. When comparing to the experimental results for the Ahmed car [17] and by Volvo [6] for the Asmo car we see that the results obtained for both cars are lower, 1.85% and 0.25% for the Ahmed and Asmo car respectively.

References

[1] Islam, M., 2009, *"Application of OpenFOAM Technology for Vehicle Aerodynamics Development"* OpenFoam Proceedings.

[2] Lehmkuhl, O., Borrell, R., Perez-Segarra, C.D., Oliva, A., and Verstappen, R., 2010, *"LES and Regularization Modeling of the Turbulent Flow Over an Ahmed Car."* ERCOFTAC Workshop.

[3] Krajnović, S., and Davidson, L.,2005, *"Flow Around a Simplified Car: Part1: Large Eddy Simulation"* ASME: Journal of Fluids Engineering, 127, pgs 907-918.

[4] Krajnović S., and Davidson, L., 2005, *"Flow Around a Simplified Car: Part2: Understanding the Flow"* ASME: Journal of Fluids Engineering, 127, pgs 919-928.

[5] Minguez, M., Pasquetti, R., and Serre, E., 2008, *"High Order Large Eddy simulation of flow over the "Ahmed body" car model."* Physics of Fluids 20.

[6] Perzon, S., and Davidson, L., 2000, *"On Transient Modeling of the Flow Around Vehicles Using the Reynolds Equation"* ACFD 2000 Beijing, China, pp 720-727.

[7] Nakashima, T., Tsubokura, M., Nouzawa, T., Nakamura, T., Zhang, H., and Oshima, N., 2008, *"Large-Eddy Simulation of Unsteady Vehicle Aerodynamics and Flow Structures"* BBAA VI International Colloquium on: Bluff Bodies Aerodynamics & Applications Milano, Italy.

[8] Lienhart, H., Stoots, C., and Becker, S., 2000, *"Flow and Turbulence Structures in the Wake of a Simplified Car Model (Ahmed Model)"* DGLR Fach. Symp. der AG STAB, Stuttgart University.

[9] Trias, F., and Lehmkuhl, O., 2011, *"A self-adaptive strategy for the time integration of navier-stokes equations"* Numerical heat transfer, Part B, fundamentals, 60 - 2, pgs. 116-134.

[10] Felten, F.N., and Lund,T. S., 2006, *"Kinetic Energy Conservation Issues Associated with the Collocated Mesh Scheme for Incompressible Flow"*. Journal of Computational Physics, vol. 215, pgs 465-484.

[11] Nicoud, F., and Ducros, F., 1999, *"Subgrid-Scale Stress Modelling Based on the Square of the Velocity Gradient Tensor"*. Flow, Turbulence and Combustion, vol. 62, pgs 183-200.

[12] Lehmkuhl, O., Baez, A., Rodriguez, I., and Perez-Segarra, C.D., 2011, *"Direct Numerical Simulation and Large-Eddy Simulations of the Turbulent Flow Around a NACA-0012 Airfoil"* 7th International Conference on Computational Heat and Mass Transfer.

[13] Nicoud, F., Baya, H., Cabrit, O., Bose, S., and Lee, J., 2011, *"Using Singular Values to Build a Subgrid-Scale Model for Large Eddy Simulations"* Physics of fluids, 23.

[14] Verstappen, R., 2009, *"When does eddy viscosity damp subfilter scales sufficiently?"* Quality and Reliability of Large Eddy Simulations II.

[15] Lehmkuhl, O., Perez-Segarra, C.D., Borrell, R., Soria, M., and Oliva, A., 2007, *"TERMOFLUIDS: A new Parallel unstructured CFD code for the simulation of turbulent industrial problems on low cost PC Cluster"* Proceedings of the Parallel CFD 2007 Conference". Ismail H. Tuncer, p. 1-8.

[16] de Villiers, E., 2006, *"The Potential of Large Eddy Simulation for the Modeling of Wall Bounded Flows"* Department of Mechanical Engineering Imperial College of Science, Technology and Medicine.

[17] Kapadia, S., Roy, S., Vallero, M., Wurtzler, K., and Forsythe, J., 2003, *"Detached-Eddy Simulation Over a Reference Ahmed Car Model"* 41st Aerospace Sciences Meeting and Exhibit.

Conference on Modelling Fluid Flow (CMFF'12)
The 15th International Conference on Fluid Flow Technologies
Budapest, Hungary, September 4-7, 2012

AERODYNAMIC FLOW CHARACTERISTICS AROUND SQUARE CYLINDER WITH GROOVES

(EFFECT OF WIDTH OF GROOVES AND INTERVAL OF GROOVES)

Tomoaki AOYAMA[1], Hiroo OKANAGA[2], Katsumi AOKI[3]

[1] Department of Mechanical Engineering, Tokai University, 4-1-1 Kitakaname, Hiratsuka-shi, Kanagawa, 259-1292 Japan. Tel.: +81-463-58-1211, Fax: +81-463-50-2479, E-mail:1bmkm004@mail.tokai-u.jp
[2] Department of Mechanical Engineering, Tokai University, 4-1-1 Kitakaname, Hiratsuka-shi, Kanagawa, 259-1292 Japan. Tel.: +81-463-58-1211, Fax: +81-463-50-2479, E-mail: okanaga@tokai-u.jp
[3] Department of Mechanical Engineering, Tokai University, 4-1-1 Kitakaname, Hiratsuka-shi, Kanagawa, 259-1292 Japan. Tel.: +81-463-58-1211, Fax: +81-463-50-2479, E-mail: katumi@keyaki.cc.u-tokai.ac.jp

ABSTRACT

The drag and lift of bluff bodies depend on the separation phenomenon from the leading edge. Recently, many studies have discussed the characteristics of flow characteristic around a square cylinder, especially on the shape modification and drag coefficient. We researched square cylinders with grooves on the surface. However, there have been few studies on the effect of groove's interval and width on the characteristics of flow around a square cylinder and its overall effect remains unknown. Therefore in this paper, we investigate the aerodynamic flow characteristics around square cylinder with grooves of various widths and interval. We carried out wind tunnel tests to measure the drag on a square-section cylinder with grooves. We also carried out flow visualization by the Spark tracing method, and PIV analysis by using a circulating water tunnel. As a result, we determined the effect of groove interval and width on characteristics under many conditions. We found that the drag coefficient of a square cylinder with grooves at wide intervals is less than of a square cylinder with narrow interval grooves. Moreover, the interval and width of grooves on the square cylinder also affect the wake area and drag coefficient.

Keywords: Square cylinder with grooves, Drag coefficient, Flow visualization, Spark tracing method, PIV analysis

1. INTRODUCTION

Recently, it is required that high-rise buildings shall not suffer damage due to wind loading. The drag and lift of bluff bodies, such as high-rise buildings, depend on the separation phenomenon from the leading edge. There are lots of researches that discuss about the flow characteristics around the square cylinder [1]-[5].

The aerodynamic forces were changed by the shape of bluff bodies. It is well known that drag forces on square cylinders are reduced by the effects of various shapes of square cylinder. For examples, Naudascher carried out experimental analysis on controlling the flow separation of different corners shapes of square cylinder [6]. In Japan, Mizota and Okajima summarized the relationship between the aspect ratio of the rectangular cylinder and drag coefficient. As a result, the maximum drag coefficient C_D is 3.0 when aspect ratio is at 0.62 [7]. TAMURA and MIYAGI focused on the drag reduction effect of the corner shape. They made the corners of the square cylinder chamfered, and rounded. It is clarified that drag coefficient changed by corner shape [8]. From the experiment results, whereas the drag coefficient C_D of square cylinder is 2.0. The drag coefficient C_D of corner cutting square cylinder is reduced to 1.4 and the drag coefficient C_D of square cylinder with round shape is reduced to 1.3. Additionally, KURATA and YAMATO focused on the drag reduction effect of the corner shape, too. They made the corners of the square cylinder cut-off and the value of C_D also becomes lower than 1.2 in some situation [9]. Furthermore, KOIDE observed the effect of grooves, such as the balcony to the surface of buildings. From the experiment results, the drag coefficient of square cylinder with grooves is smaller than square cylinder without grooves [10], [11]. Moreover, the drag coefficient of square cylinder with grooves can be decreased by changing

the width, depth and interval of the grooves [12]. However, there are only few experiment results about the effect of groove's interval and width on the flow characteristics around the square cylinder and its overall effect remains unknown. Therefore in this paper, we investigate the aerodynamic flow characteristics around square cylinder with various kinds of width and interval of grooves with the measurements of the drag coefficient, particle image velocimetry and flow visualization by Spark tracing method.

2. INSTRUMENTAL APPARATUS

2.1 Drag Measurement

The experimental apparatus shown in Fig 1 with a test section of 400 *mm* × 400 *mm* was used for aerodynamic measurements and flow visualization around the square cylinder. The flow velocity was 30 *m/s* (Re =8.0 × 104). The turbulence intensity in this velocity range of this wind tunnel is 0.3 *%*. The model was placed vertically between two fixed ends - plates to minimize blockage effects. The end - plates were at a distance of 0.5 *mm* ~ 1 *mm* from the test model. The model was attached to a multi component load cell. It contained elements for measuring drag, lift and the yawing moment.

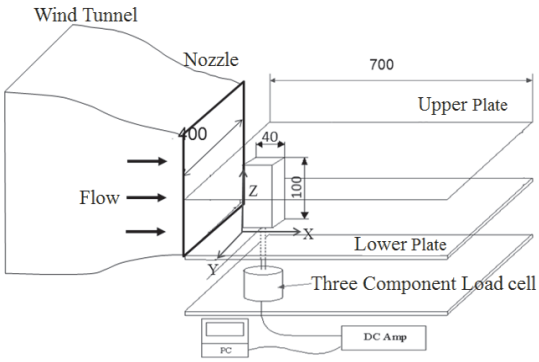

Figure 1. Outlines of experimental apparatus

2.2 Flow Visualization by Spark-tracing Method

Figure 2 shows the experimental apparatus used for the spark tracing method. The pulse generator can generate pulse waves of high voltage electricity. The electricity is stored in a pulse drive unit and then passed through a pulse transformer and a fixed electrode. The electrode material is tungsten, and the diameter of the electrode is 0.3 *mm*. High-voltage/high- frequency pulse generator is employed as the power source adjusted to 250 *kV*, the pulse interval to 150 *μs* and the number of the pulse to 150. The first electric spark from the pulse wave arcs to another electrode over the shortest distance, producing ionized air after the first electric spark. This ionized air moves together with the uniform flow. The second electric spark from the pulse wave passes through this ionized air because the electric resistance of the ionized air is low, and the second electric spark again produces ionized air. The ionized air from the second electric spark moves together with the uniform flow, and the third electric spark moves again through the ionized air from the second electric spark. The flow pattern around the test model can be visualized by repeating this process.

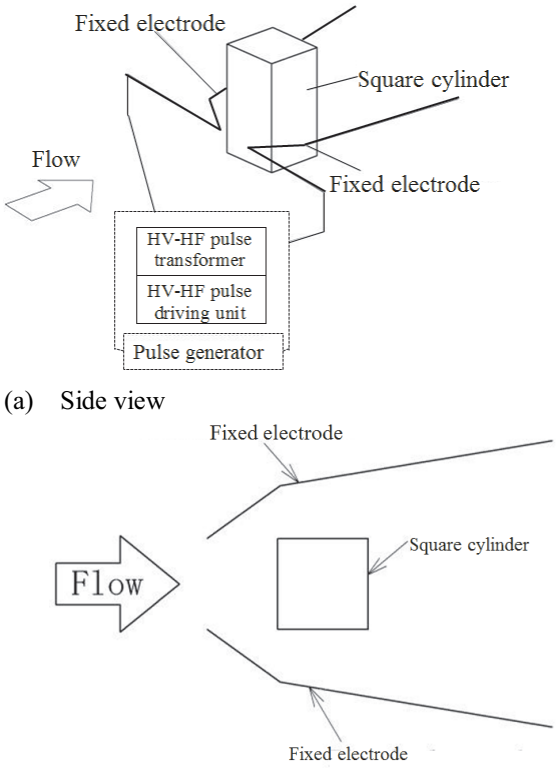

Figure 2. Apparatus for visualization by spark-tracing method

2.3 Flow visualization water tunnels

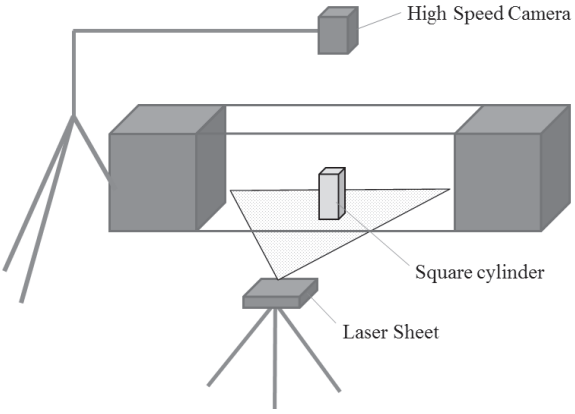

Figure 3. Apparatus for Flow visualization water tunnels

Figure 3 shows the schematic view of the visualization experiment using a laser light sheet and a high speed camera (HAS-500 KATOKOKEN CO, LTD). The tracer particles called Orgasol (average diameter=50 μm) is inserted into the circulating water tunnel in order to observe the flow characteristic around the cylinder. Software of PIV analysis DIPP－FLOW (KATOKOKEN CO, LTD). All experiments were carried out according to the conditions as follows; shuttle speed 1/500 *Sec* and Re=5200. All image of the experiment are analysed by using PIV analysis. In addition, In flow visualization by suspension method, aluminum powder(average diameter=100 μm), Xenon slit-light and a camera with shutter speed of 0.5 is used.

2.4 Model Configurations

The test models which served as the basic structure for the drag measures shown in Fig 4 consisted of ABS synthetic resin of 40 *mm* width *(d)* and 100 *mm* height *(h)*. 7 types of grooved cylinder with the different size of the interval ratio of the grooves *(w/d)* and width ratio *(s/d)* had been used in the experiment. A0 is the frontal projected area square cylinder without grooves, A is the frontal projected area of square cylinder with grooves. The specifications of test models are shown in Table (1). In addition, depth ratio of all square cylinders *(b/d)* is 0.05.

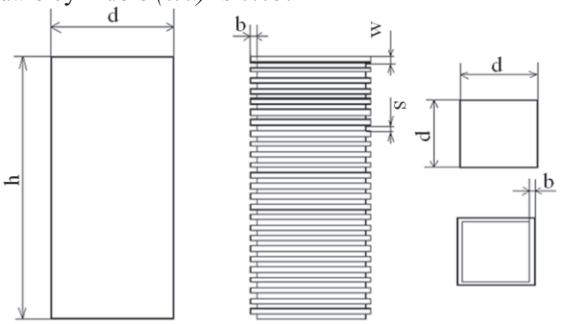

Figure 4. Test model

Table 1. Specification of test models

Type	Grooves		A/A_0
	w/d	*s/d*	
S0	0	0	1.00
S22	0.05	0.05	0.95
S23	0.05	0.075	0.94
S24	0.05	0.10	0.936
S32	0.075	0.05	0.96
S42	0.10	0.05	0.968
S52	0.125	0.05	0.972
S62	0.15	0.05	0.976

3. EXPERIMENTAL RESULTS

3.1 Drag Coefficient

The drag coefficient is expressed as follows:

$$C_D = \frac{2D}{\rho A U^2} \quad (1)$$

Where D is the drag which are calculated from fluid-dynamic forces from the multi component load cell, ρ is the density of air, A is the frontal projected area and U is the uniform velocity.

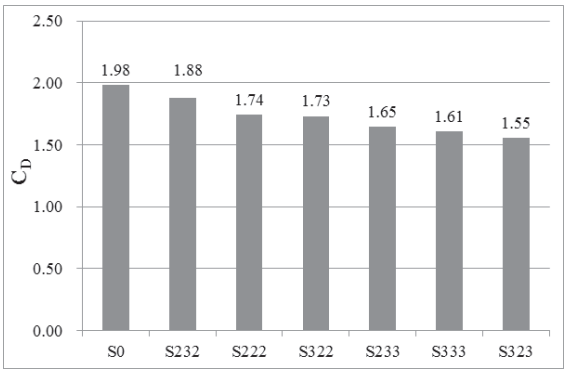

Figure 5. Drag coefficient of Square Cylinders

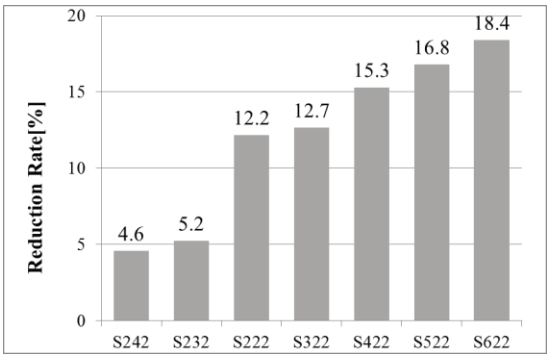

Figure 6. Reduction rate of C_D

Figure 5 shows the drag coefficient of square cylinders and square cylinder with grooves. Fig 6 shows reduction rate of drag coefficient based on the square cylinder coefficient result. From Fig. 5, By applying the groove, the drag coefficient has decreased. In Fig 6, a maximum of 18.4 % of drag coefficient is reduced by grooved cylinder (S62) with compared to square cylinder. In the case of increasing the groove's interval, the drag coefficient is reduced on following order S22, S32, S42, S52, and S62 .However the result of increasing the groove width (S22, S23, S24) shows that the drag reduction rate are increased.

3.2. Flow Visualization of Spark-tracing Method

Figure 7 shows the visualization results obtained by using the spark-tracing method. The visualization result shows the flow pattern around the test models and the wake flow. However, from

the images it is difficult to differentiate the flow characteristic for each one of the cylinder because flow is unsteady. Therefore, M is defined as the distance between the spark and the side of cylinder as shown in Fig 8. Figure 9 shows the relationship between the separation width M taken from the 20 visualization images and the drag coefficient. From the result, the separation width has become smaller in order of S0＞S24＞S23＞S22＞S32＞S42＞S52＞S62 as show in Fig 9. As the drag coefficient reduces, the separation width become closer.

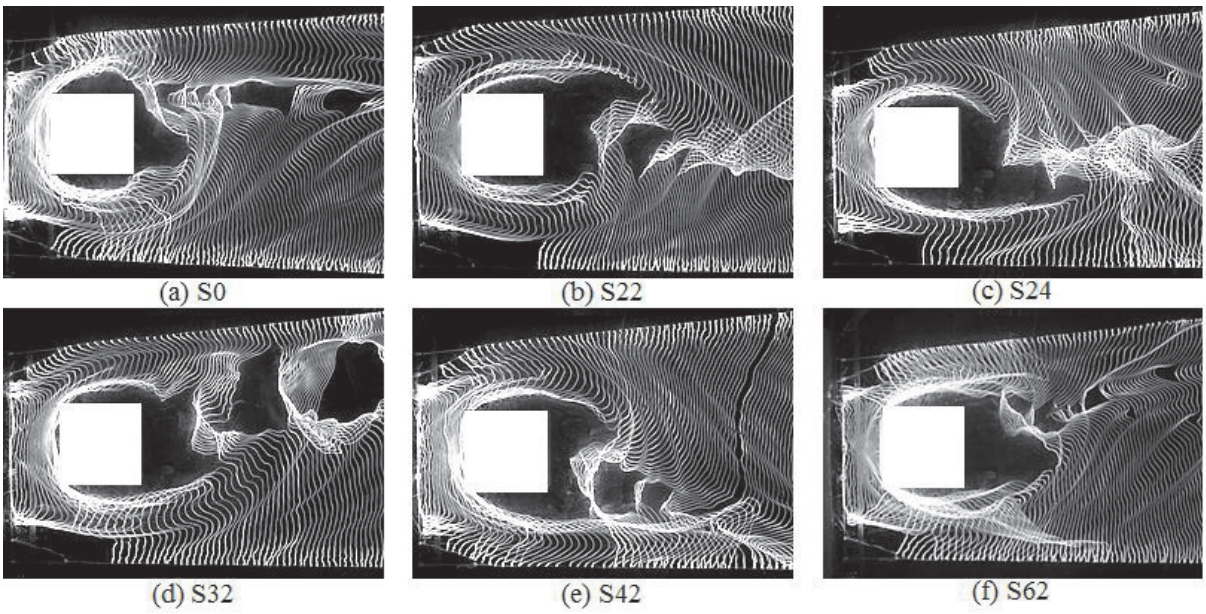

Figure 7. Visualization results around the test models by spark-tracing method

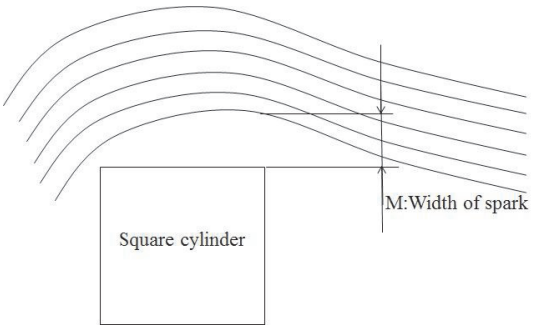

Figure 8. View of spark width from the top of cylinder

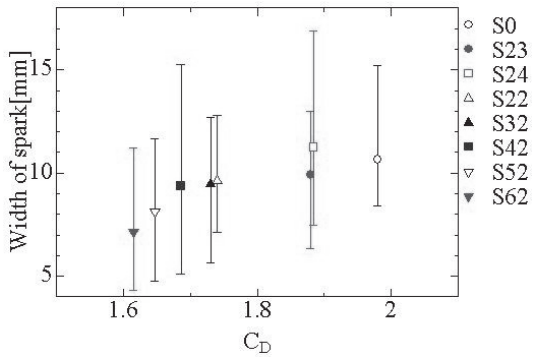

Figure 9. Relationship between C_D and width of spark

3.3. Flow visualization water tunnels

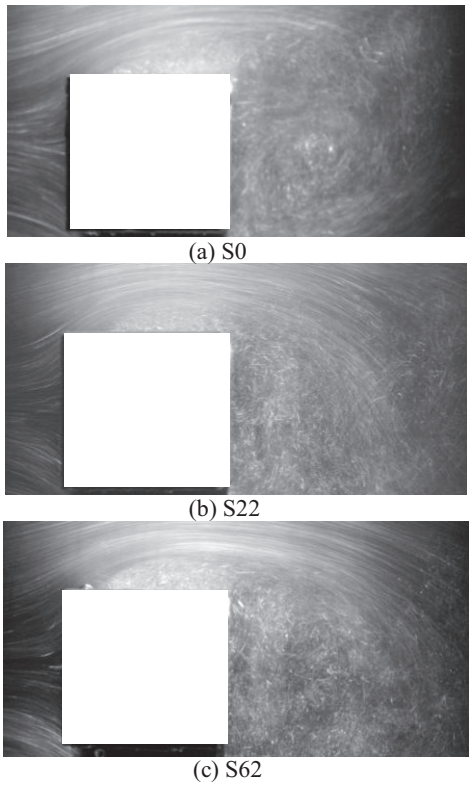

Figure 10. Visualization results around the test models by Aluminium Suspension method

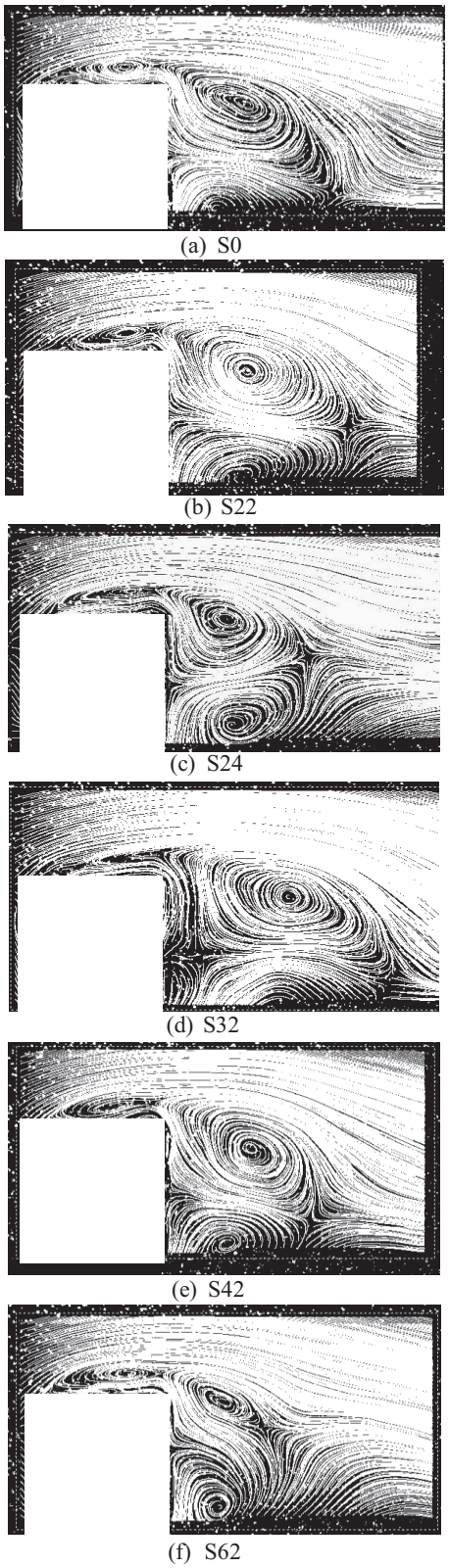

(a) S0

(b) S22

(c) S24

(d) S32

(e) S42

(f) S62

Figure 11. Experimental results from PIV analysis

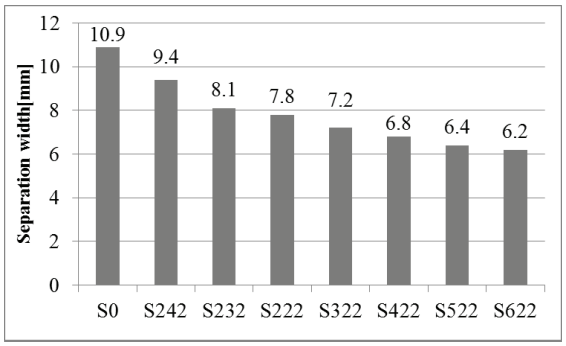

Figure 12. the separation width by PIV analysis

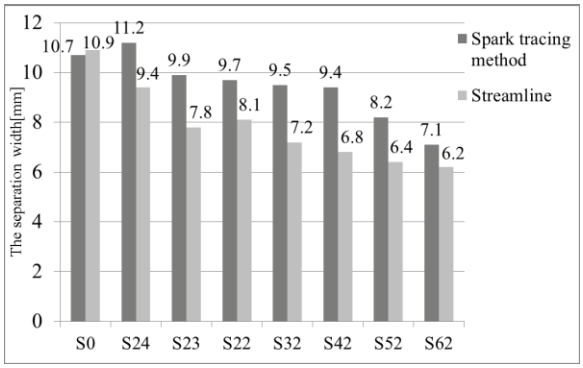

Figure 13. Comparison by the separation width

Figure 10 and Fig. 11 shows the results from the flow visualization by using circulating water tunnels. Fig.10 shows the result of visualization using suspension method and Fig.11 shows the result of streamline using PIV analysis. From the result, the flow separated area between Fig.10 and Fig.11 is similar to each other. Therefore we consider that PIV analysis results possess high reliability. These figures are shown streamlines calculated from the average velocity measured using PIV analysis. From Fig 12, the separation width has become smaller in order of S0＞S24＞23 ＞S22＞S32＞S42＞S52＞S62. In addition, from these figure is observed the existence of the vortex in the separation width area. Based on the comparison between S0 and S62 image, the drag coefficient for the cylinder becomes lower. As the results, separation width area become smaller as the drag coefficient reduces. Figure 13 shows the comparison with the separation width using PIV analysis and using the spark-tracing method. From the result, the separation width shows similar tendency by PIV analysis and visualization results by spark-tracing method.

4. CONCLUSION

In the present study, we investigate the effect of groove's interval and width on the flow characteristics around the square cylinder by measuring the drag coefficient, flow visualization by water tunnel, and spark tracing method. From the experiments result, the flow characteristics of cylinder were concluded as following;

I. In the measurement of aerodynamic forces, the drag coefficients of the all square cylinder with grooves reduce in comparison with the square cylinder without grooves.
II. As the grooves interval of square cylinder become more widely, the drag coefficient decrease. The reduction rate is 18.4 *%* at the maximum when *w/d* is 0.15.
III. As the groove width become more widely, the drag increase.
IV. From the flow visualization by spark-tracing method, the separation width becomes smaller, as the drag coefficient is smaller. The separation width of S62 is smallest, and has a smaller 3.6 *mm* than separation width of S0.
V. From the result of the PIV analysis, as the drag coefficient for the cylinder becomes lower, the produced vortex is smaller. As the conclusion, separation width area become smaller as the drag coefficient reduces.

In conclusion, without changing the square cylinder cross-section shape, the drag coefficient can be reduced by changing the surface structure of the square cylinder. We think that our study can be applied not only to the structure of building but also in industrial -uses such as drag reduction in bluff body.

5. REFERENCES

[1] N.K. Delany, N.E Sorensen, Low-speed drag of cylinders of various shapes, NACA Report 3038, 1953.

[2] B. J. Vickery, Fluctuating lift and drag on a long cylinder of square cross-section in a smooth and in a turbulent stream, J. Fluid Mech., Vol. 25, pp. 481-494, 1966

[3] A. Laneville, I.S. Gartshore and G.V. Parkinson, An explanation of some effects of turbulence on bluff bodies, Proceedings of the Fourth International Conference on Wind Effects on Buildings and Structures, pp333-341, 1975

[4] B. E. Lee, The effect of turbulence on the surface pressure field of a square prism, Journal of Fluid Mechanics, vol. 69, pp263-282, 1975

[5] Kenny C. S. Kwok and Peter A. Bailey, Aerodynamic Devices for Tall Buildings and Structures, Journal of Engineering Mechanics, No.113-3, pp 349-365, 1987.

[6] E. Naudascher, J.R. Weske and B. Fey, Exploratory study on damping of galloping vibrations, Journal of Wind Engineering and Industrial Aerodynamics Vol. 8, Issues 1–2, pp211–222, 1981.

[7] T MIZOTA, A OKAJIMA, Experimental studies of time mean flows around rectangular prismas, Journal of JSCE, No.312, pp 39-47, 1981

[8] T TAMURA and T MIYAGI, The effects of cornier shape on aerodynamic characteristics of a type of square cylinder, J.Struct. Constr. Eng., AIJ, No.514, pp 51-58, 1998 (in Japanese).

[9] M KURATA, H YAMATO, Z YASUTOMI and T KIDA, Effect of Cutout at edges to Drag Reduction of Square Prism with Angle of Attack, Proceedings of JSME, B, No.68-668, pp 1087-1094, 2002 (in Japanese).

[10] M KOIDE, H OKANAGA and K AOKI, Effect of Grooves on the Aerodynamics around Corner cut Square Cylinder, Proceeding of The School of Engineering of Tokai University, Vol.46, No.2, pp.79-84, 2006 (in Japanese).

[11] T IKEDA and H OKANAGA, The Flow Characteristics of Three-Dimensional Flow Around Square Cylinders With Grooves, Proceeding of The School of Engineering of Tokai University, vol.51, No2, pp.121-126, 2011 (in Japanese).

[12] T AOYAMA, H OKANAGA, Flow Visualization around Square Cylinders with Grooves: Effects of Groove Depth, Width and Interval, Vol.51, No.2, pp.127-130, 2011 (in Japanese)

Conference on Modelling Fluid Flow (CMFF'12)
The 15th International Conference on Fluid Flow Technologies
Budapest, Hungary, September 4-7, 2012

HEAT AND ENERGY TRANSFER FROM A CYLINDER PLACED IN AN OSCILLATORY LOW-REYNOLDS NUMBER FLOW

Betti BOLLÓ[1], László BARANYI[2]

[1] Department of Fluid and Heat Engineering, University of Miskolc, Miskolc, Hungary, H-3515 Tel.: +36 46 565-154, Fax: +36 46 565-471, e-mail: aramzb@uni-miskolc.hu
[2] Department of Fluid and Heat Engineering, University of Miskolc, Miskolc, Hungary, e-mail: arambl@uni-miskolc.hu

ABSTRACT

Heat transfer characteristics of a circular cylinder exposed to an oscillating flow are investigated numerically using the commercial software package Ansys Fluent based on the finite volume method (FVM). For in-line oscillation the influence of oscillation amplitude and temperature are analyzed at Reynolds number 120 and for frequency ratio 0.8 in the lock-in domain. For transverse motion the influence of temperature on force coefficients and heat transfer is investigated for Re=100, 120, 140, 160 and 180 and at four oscillation amplitude values at frequency ratio 0.8. Force coefficients, mechanical energy transfer and heat transfer are investigated for these cases.

Keywords: heat transfer, heated cylinder, in-line oscillation, low Reynolds number, Nusselt number, transverse oscillation

NOMENCLATURE

a_0	[-]	cylinder acceleration, nondimensionalised by $\widetilde{U}_m{}^2/d$
A	[-]	amplitude of oscillation, nondimensionalised by d
C_D	[-]	drag coefficient
C_L	[-]	lift coefficient
d	[m]	cylinder diameter
E	[-]	mechanical energy transfer
f	[-]	oscillation frequency, nondimensionalised by $\widetilde{U}_m/d$
f_v	[1/s]	vortex shedding frequency
g	[m/s^2]	acceleration due to gravity
h	[$W/(m^2K)$]	local convective heat transfer coefficient
$\underline{i}$, $\underline{j}$	[-]	unit vectors in x and y directions
k	[$W/(mK)$]	thermal conductivity of the fluid
Nu	[-]	Nusselt number, $Nu=h\,d/k$
P	[-]	a period of a vortex shedding, $1/f$
$\dot{q}$	[W/m^2]	heat flux
r	[-]	radius, nondimensionalised by d
Ri	[-]	Richardson number, $Ri = g\,\beta\,d\left(\widetilde{T}_w-\widetilde{T}_\infty\right)/\widetilde{U}_m^2$
Re	[-]	Reynolds number, $Re=\widetilde{U}_m\,d/\upsilon$
St	[-]	nondimensional vortex shedding frequency, $St=f_v\,d/\widetilde{U}_m$
t	[-]	time, nondimensionalised by $d/\widetilde{U}_m$
$\widetilde{T}$	[K]	absolute temperature
T	[-]	nondimensional temperature, $\left(\widetilde{T}-\widetilde{T}_\infty\right)/\left(\widetilde{T}_w-\widetilde{T}_\infty\right)$
T^*	[-]	temperature ratio, T_w / T_∞
$\widetilde{U}_m$	[m/s]	time-mean free stream velocity
$\underline{v}$	[-]	free stream velocity vector, nondimensionalised by $\widetilde{U}_m$
β	[$1/K$]	thermal expansion coefficient
υ	[m^2/s]	kinematic viscosity

Subscripts and Superscripts

eff	effective
f	film
fb	fixed body
m	time-mean for free stream velocity
rms	root-mean-square value
x, *y*	components in x and y directions
w	wall
0	for cylinder motion
∞	far from the cylinder

1. INTRODUCTION

Flow around cylinders, always a topic of interest, becomes more complicated when oscillation is present, and when heating effects are involved. Such situations occur, for instance, with tube bundles of heat exchangers or hot wire anemometers.

Oscillation commonly occurs in elastically supported structures in wind or under water,

especially oscillation transverse to the main stream. The flow past a circular cylinder oscillating transversely has been studied extensively, even at low Reynolds numbers. Williamson and Roshko [1] experimentally investigated the wake patterns behind an oscillating cylinder at low Reynolds numbers. Lu and Dalton [2] numerically simulated the flow over an oscillating cylinder at *Re*=185 to reproduce the experimental results of Gu et al. [3].

In-line oscillation has been studied experimentally and numerically. Low Reynolds number studies include [4], investigating a broad frequency ratio range numerically at *Re*=200, finding vortex switches. A low-Reynolds number numerical study identified vortex switches for in-line oscillation against oscillation amplitude Baranyi [5] and against frequency ratio ranging from 0.76 to 0.94 [6]. At some critical parameter values, flow pattern switched into a mirror image. An experimental study using in-line oscillatory low Reynolds flow reports on particle image velocimetry measurements obtained in the forced wake of a circular cylinder in a free stream flow with periodic velocity oscillations superimposed upon it [7]. This case is kinematically equivalent to that of a cylinder forced to oscillate in-line with a steady uniform flow.

Another numerical study for in-line cylinder motion at *Re*=200 and frequency ratio 1 is Mureithi et al. [8]. A low order discrete model was developed based on symmetry-equivariance theory. The resulting simple model was found to capture the observed wake dynamics, predicting the sequence of bifurcations found in numerical computations.

For flows over a heated cylinder the fluid properties vary with temperature. This has a significant effect on flow characteristics, especially for the in-line and transverse cylinder motion. Karanth et al. [9] numerically investigated the effects of in-line and of transverse oscillation of the cylinder for *Re*=200 and concluded that the heat transfer rate from the oscillating cylinder increased with increasing of velocity amplitude for both motions. Cheng et al. [10] adopted the same numerical method to study the effect of transverse oscillation on flow patterns and on heat transfer from a cylinder. Their results indicated that the heat transfer increased remarkably as the flow approached the lock-in regime.

The main purpose of the present study is to investigate the effect of cylinder temperature and oscillation amplitude on the heat transfer and mechanical energy transfer *E* between the fluid and the cylinder at the frequency ratio of 0.8 in the lock-in domain. To the best knowledge of the authors the mechanical energy transfer has been investigated for unheated cylinders only [11]. In this study the mechanical energy transfer is also investigated for a heated cylinder for in-line and transverse motions.

For in-line flow oscillation the influence of oscillation amplitude on heat transfer is analysed for a single Reynolds number. Karanth et al. [9] also investigated heat transfer (Nusselt number), but at only the three oscillation amplitude values of 0, 0.25 and 0.5 for in-line motion, while we investigated over 80 oscillation amplitude values at two temperature ratios. For transverse oscillation the force coefficients, *E* and Nusselt number *Nu* versus Reynolds number are investigated at four oscillation amplitudes and five *Re* values.

2. NUMERICAL METHOD

The main set of simulations was carried out using Ansys Fluent commercial software based on the finite volume method (FVM). The two-dimensional (2D), unsteady, laminar, segregated solver is used to solve the incompressible oscillatory flow for the collocated grid arrangement. The second order upwind scheme was used to discretise the convective terms in the momentum equations. The semi-implicit method for the pressure linked equations (SIMPLE) scheme is applied for solving the pressure-velocity coupling.

The physical domain is illustrated in Figure 1. The inner circle represents the cylinder surface with diameter d, the outer circle the far field with diameter d_∞. The origin of the Cartesian coordinates x, y is located in the centre of the cylinder and the positive x-axis is directed downstream. The accuracy of the computed results depends on the computational mesh, the time step, the size and shape of the computational domain. For uniform flow past an unheated stationary circular cylinder the effect of domain size, mesh, and time step was investigated to determine a combination at which the solution is roughly parameter independent [12]. In [13] computational results are compared with those of several studies, finding very good agreement.

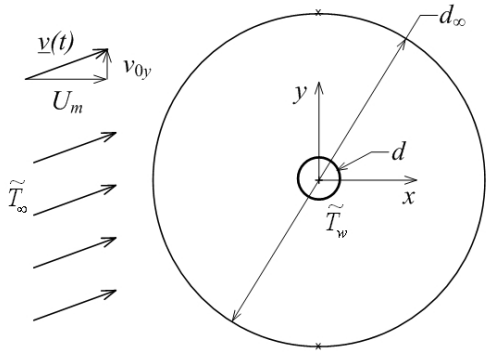

Figure 1. Computational domain

In this study the computational domain is characterised by d_∞/d=180 with mesh points of 361x298 (peripheral x radial), respectively. In the physical domain logarithmically spaced radial cells

are used, providing a fine grid scale near the cylinder wall and a coarse grid in the far field. A dimensionless time step of Δt=0.001 is used.

Flow past a cylinder oscillating in-line with a uniform free stream is modelled by a stationary cylinder combined with an unsteady free stream obtained by the superposition of a uniform flow and an oscillatory flow in in-line direction:

$$\underline{v}(t) = U_m \underline{i} - u_{0x} \underline{i} = U_m \underline{i} + 2\pi f A_x \sin(2\pi f t)\underline{i}. \quad (1)$$

To model the transverse motion, the time-dependent free stream velocity vector can be written as

$$\underline{v}(t) = U_m \underline{i} + v_{0y} \underline{j} = U_m \underline{i} - 2\pi f A_y \cos(2\pi f t)\underline{j}. \quad (2)$$

In Eqs. (1) and (2) everything is nondimensional; t and f are the time and oscillation frequency, U_m is unity, u_{0x} and v_{0y} are the time dependent fluctuating velocities in in-line and transverse directions, respectively. A_x and A_y are the oscillation amplitudes for in-line and transverse motion, and $\underline{i}$, $\underline{j}$ are the unit vectors in x,y directions, respectively. In Fig. 1 velocity vectors are shown for the transverse oscillatory flow.

The nondimensional frequency of oscillation f was set at 0.8 St_0, where St_0 is the nondimensional vortex shedding frequency, or Strouhal number, for a stationary cylinder at that Reynolds number. This frequency ratio value ensures that lock-in condition (vortex shedding frequency equal to that of the cylinder oscillation f) is reached at moderate amplitude values. In this study only locked-in cases were considered. Only one frequency ratio is investigated, due to the computational time needed.

The fluid is air, assumed to be incompressible. Both the absolute ambient temperature $\widetilde{T}_\infty$ and cylinder wall absolute temperature $\widetilde{T}_w$ are assumed to be constant. The temperature ratio T*, which can also be interpreted as a nondimensional wall temperature, is defined as

$$T^* = \widetilde{T}_w / \widetilde{T}_\infty . \quad (3)$$

Four temperature ratios of 0.9, 1.0, 1.1 and 1.5 are investigated. For flows over a heated cylinder the fluid properties such as viscosity, density and thermal conductivity vary with temperature. The dependence of the viscosity on temperature is given by Sutherland's formula [14] and further fluid properties are obtained from [15]. Since the maximal Richardson number Ri was 0.35 for the investigated cases, free convection was neglected, as is standard for Ri < 0.5 [16].

For the unheated cases (T*=1.0) the FVM results are compared with the data of the second author, who used his 2D in-house code based on the finite difference method (FDM). For FDM a non-inertial system fixed to the cylinder is used to compute the 2D low-Reynolds number unsteady flow around a circular cylinder placed in a uniform stream and forced to oscillate in in-line or transverse directions. The governing equations are the nondimensional Navier-Stokes equations for incompressible constant-property Newtonian fluid, the equation of continuity and the Poisson equation for pressure. On the cylinder surface, no-slip boundary condition is used for the velocity and a Neumann type boundary condition is used for the pressure. Potential flow is assumed in the far field. The code is thoroughly tested against experimental and computational results in Baranyi [17].

The FDM code is for a mechanically-oscillated cylinder placed in a uniform stream, while the present FVM simulation is for oscillatory flow around a stationary cylinder. When viewed from a system fixed to the cylinder, these two cases are kinematically identical and can thus be compared.

The shape of the computational domain for the FDM simulation is the same as for the FVM, but the domain size is different: for FDM the domain for in-line motion is d_∞/d=360, while for transverse motion it is d_∞/d=160.

Flow and heat transfer features are of interest in this study. Time-mean (TM) and root-mean-square (rms) values of lift C_L, drag C_D coefficients were evaluated and plotted against the oscillation amplitude or Reynolds number. The lift and drag coefficients shown in this study do not contain inertial forces originating from the system fixed to the accelerating cylinder. Coefficients without inertial forces are often termed 'fixed body' coefficients [2]. The relationship between the two sets of coefficients can be written as

$$C_L = C_{Lfb} + \frac{\pi}{2} a_{0y}, \; C_D = C_{Dfb} + \frac{\pi}{2} a_{0x}, \quad (4)$$

where subscript fb refers to the fixed body (understood in an inertial system fixed to the stationary cylinder) Baranyi [18]. Here a_{0x} and a_{0y} are the dimensionless x and y components of cylinder acceleration. Since these accelerations are periodic their time-mean values vanish, resulting in identical TM values for the two setups. Equation (4) shows that for in-line motion the two lift coefficients are identical, and the drag coefficients are different from each other. For transverse cylinder motion it is exactly the other way round.

The mechanical energy transfer between the fluid and the cylinder for transverse motions was defined in [11] and was extended for two-degree-of-freedom cylinder motion by [17]. The total energy transfer E can be divided into two parts,

$$E = E_1 + E_2 , \quad (5)$$

where E_1 and E_2 are the energy transfer coefficients originating from transverse and in-line motion;

$$E_1 = \int_0^P C_L(t)\,\dot{y}_0(t)\,dt,\; E_2 = \int_0^P C_D(t)\,\dot{x}_0(t)\,dt, \qquad (6)$$

where P is the motion period and x_0 and y_0 are the dimensionless cylinder displacement in x and y directions, respectively, and the over dot means differentiation by time. As can be seen in Eq. (6), for in-line cylinder motion E_1 is zero, so E=E_2; for transverse motion E_2 is zero, so E=E_1.

The heat transfer between the cylinder and the surrounding fluid is determined using the dimensionless, or local Nusselt number, obtained from (see e.g., [19])

$$Nu = \frac{h\,d}{k} = -\left(\frac{\partial T}{\partial r}\right)_{wall}, \qquad (7)$$

where k is the thermal conductivity of the fluid, r is the dimensionless radius. Here T is the dimensionless temperature defined by $\left(\widetilde{T}-\widetilde{T}_\infty\right)/\left(\widetilde{T}_w-\widetilde{T}_\infty\right)$, where $\widetilde{T}$ is the temperature of the fluid in an arbitrary point measured in K, and h is the local convective heat transfer coefficient

$$h = \frac{\dot{q}}{\widetilde{T}_w-\widetilde{T}_\infty}, \qquad (8)$$

where $\dot{q}$ is the heat flux from the cylinder wall to the fluid.

In the present work fluid properties are not constant for heated cylinders so the thermal conductivity of the fluid k also depends on the temperature, which influences the Nusselt number value. The physical properties of the working fluids are evaluated at the free stream temperature $\widetilde{T}_\infty$ or the film temperature $\widetilde{T}_f$, which can be defined as the arithmetic mean of the cylinder wall temperature and the free-stream temperature [20]. Some studies have indicated that the vortex shedding in an air flow can be reduced or even completely suppressed by increasing the cylinder temperature [21, 22]. The temperature variation leads to changes in the kinematic viscosity of fluid, so the local Reynolds number varies in the near field of the heated cylinder. This phenomenon leads to the development of the effective temperature concept, which models the varying kinematic viscosity in the non-isothermal wake behind a heated circular cylinder by defining an effective temperature

$$\widetilde{T}_{eff} = \widetilde{T}_\infty + c\left(\widetilde{T}_w-\widetilde{T}_\infty\right), \qquad (9)$$

where c is a constant. This concept was first introduced by Lecordier et al. [21] and later refined by Wang and Travnicek [16], who successfully correlated their experimental data for Nusselt number and suggested c=0.36. In the present work we use the Nusselt number Nu_{eff}=$Nu(\widetilde{T}_{eff})$ based on the effective temperature $\widetilde{T}_{eff}$, where c = 0.36.

3. RESULTS

In the present study, computations were carried out for in-line and transverse oscillatory flows at a frequency ratio of f/St_0=0.8 in the lock-in domain. This frequency ratio value ensures that lock-in condition is reached at moderate amplitude values. This keeps amplitudes well within the range of reliability of the computational procedure. In addition, it appears that in practice the frequency ratio of oscillating bodies is in the vicinity of unity [11, 23]. For both motions the rms and TM of force coefficients, Nusselt number and the mechanical energy transfer between the fluid and the cylinder are analysed.

3.1 In-line Oscillation

For in-line motion the computations are performed at Re=120 and at two temperature ratios of T*=1.0 and 1.5 with amplitude of oscillation as the independent variable.

Figure 2 shows the time-mean (TM) of lift (and the identical fixed body lift) against the oscillation amplitude for two temperature ratios. For the unheated case (T*=1.0) the results obtained by FVM and FDM are in good agreement. The solution jumps between two states, as was found earlier by [5]. The state curves compare well for the two methods but the location and number of jumps are different. This is not surprising, since the system boundary separating the basins of the two attractors of this nonlinear system can be very complex, and a tiny change in the parameters can trigger a switch to the other attractor of the system [17]. As can also be seen in the figure, the two state curves are mirror images of each other, as was found earlier in [5]. State curves for the heated (T*=1.5) and unheated (T*=1.0) cases are nearly identical. It can also be seen that for increasing temperature ratio the lower boundary of the locked-in domain shifts towards smaller amplitude values. The lock-in domain begins at A_y=0.35 for the unheated case and at A_y=0.305 for T*=1.5.

The rms of drag coefficient is shown in Figure 3 for T*=1.0 and 1.5 at Re=120. The two methods compare well. It can be seen that the rms values increase with both amplitude and temperature ratio.

The mechanical energy transfer E between the fluid and the body was also investigated for in-line flow oscillation. Figure 4 shows E=E_2 against oscillation amplitude A_x at Re=120 for T*=1.0 and 1.5. The values of E were found to be negative in the entire lock-in domain investigated. This means that the fluid acts against the cylinder motion, with a dampening effect. The absolute value of E

increases with amplitude but decreases with temperature ratio. The agreement between FDM and FVM results is very good.

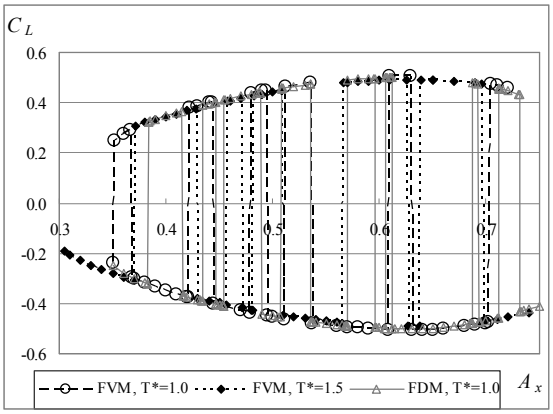

Figure 2. Time-mean of lift versus in-line oscillation amplitude for two temperature ratios

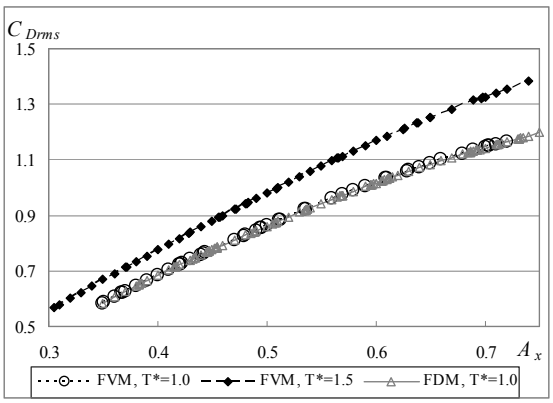

Figure 3. The rms of lift versus in-line oscillation amplitude

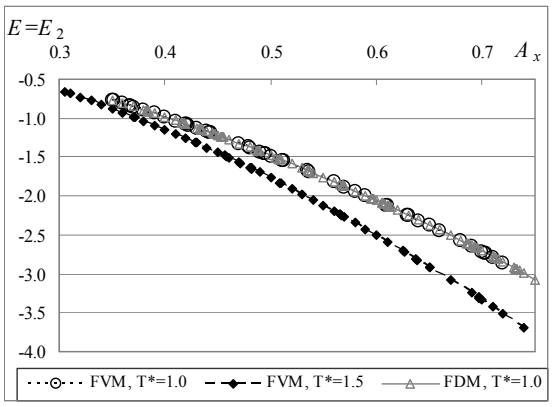

Figure 4. Mechanical energy transfer versus in-line oscillation amplitude

The heat transfer between the cylinder and the surrounding fluid is calculated using the effective Nusselt number Nu_{eff} based on the effective temperature (see Eq. (9)). In a previous study [24] the uniform flow past a heated stationary cylinder (A_x=A_y=0) was investigated and Nu_{eff} agreed well with the experimental data of [16, 22] for different Reynolds numbers.

Figure 5 shows Nu_{eff} versus oscillation amplitude at T*=1.0 and 1.5 for in-line oscillation. It was earlier found that for a heated stationary cylinder Nu_{eff} increases with Re and decreases with T* [24]; here, for in-line motion, a similar tendency was found at given amplitude values for Nu_{eff}. As can be seen in Fig. 5, Nu_{eff} first increases with increasing oscillation amplitude, reaches a maximum value at around A_x=0.55, and then decreases slightly, indicating that higher amplitude values may suppress the temperature effects. This seemingly contradicts the claim of Karanth et al. that Nu_{eff} increases with increasing velocity amplitude [9]. However, in their study of the flow past and heat transfer from a cylinder oscillated in in-line direction at Re=200 they investigated only the three oscillation amplitude values of A_x=0, 0.25 and 0.5, which fall into the rising range.

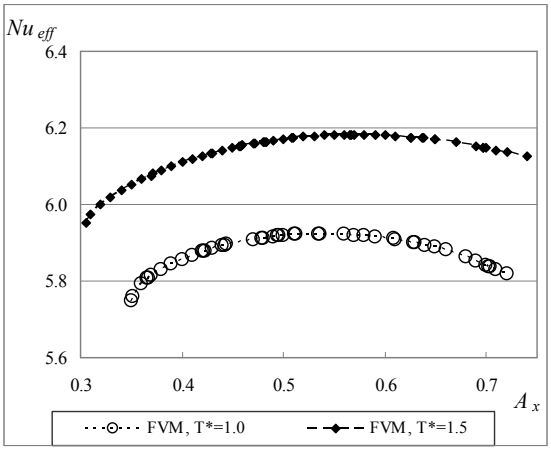

Figure 5. Nu_{eff} versus in-line oscillation amplitude at T*=1.0 and 1.5

3.2 Transverse Oscillation

Here we compare results for an unheated (T*=1.0) cylinder, a cooled cylinder (T*=0.9), and a heated cylinder (T*=1.1 and 1.5). The Reynolds numbers of Re=100, 120, 140, 160 and 180 are investigated at four oscillation amplitude values.

3.2.1. Unheated case

Results at T*=1.0 are given in Figure 6 for the TM of drag obtained by FVM and FDM, while the rms of fixed body lift coefficient is shown in Figure 7. No jumps were found in any curves, similarly to earlier results for a stationary unheated cylinder [5].

The TM of drag (Fig. 6) decreases with increasing Re, but for a given Re, C_D increases with increasing oscillation amplitude. The rms of lift (Fig. 7) increases with increasing oscillation amplitude for a given Re and it increases as well

with increasing *Re* for a given amplitude. The two CFD methods yield practically the same results.

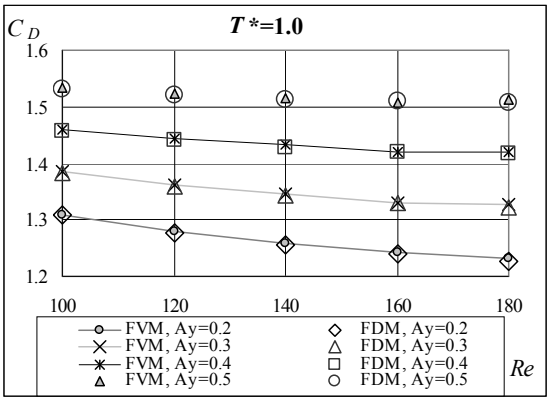

Figure 6. Time-mean of drag versus *Re* at four transverse oscillation amplitudes, *T=1.0**

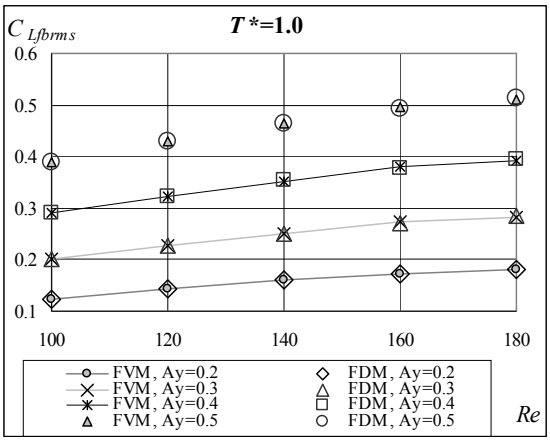

Figure 7. C_{Lfbrms} versus *Re* at four transverse oscillation amplitudes, *T=1.0**

Figure 8 shows the mechanical energy transfer (E=E_1) versus *Re* at different amplitudes for both methods. When the oscillation amplitude is held constant, the value of E increases with *Re*. The two methods yield good agreement.

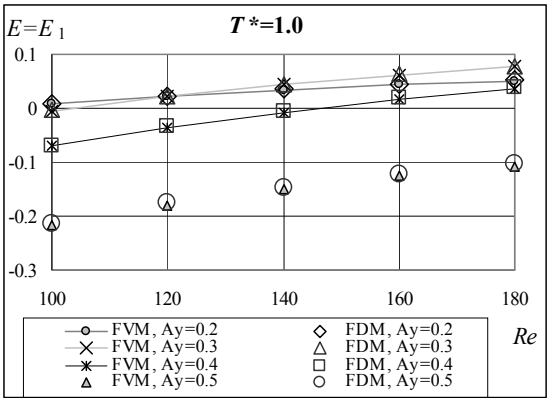

Figure 8. Mechanical energy transfer versus *Re* at four transverse oscillation amplitudes, *T=1.0**

We can see that the E for A_y=0.5 is always negative in the lock-in domain, for A_y=0.2 E is always positive, and the other two curves change from negative to positive E with increasing *Re*. Positive E values mean that energy is added to the cylinder from the fluid, and so flow-induced vibration is liable to occur in the free vibration case. Negative E values, on the other hand, tend to dampen vibration [17].

3.2.2. Heated or cooled cylinder

Although four oscillation amplitudes were investigated, here we present results for only one value, A_y=0.2. Similar trends to the results shown here were found for the other A_y values.

Figure 9 shows the TM of drag against Reynolds number for different temperature ratios. As can be seen in the figure, the drag increases with increasing temperature ratio and decreases with increasing *Re*, similarly to the uniform flow around a stationary heated cylinder [24].

The rms of the fixed body lift coefficient C_{Lfbrms} is shown in Figure 10. Rms increases fairly steadily with increasing *Re.* At a given Reynolds number, C_{Lfbrms} decreases with increasing temperature ratio.

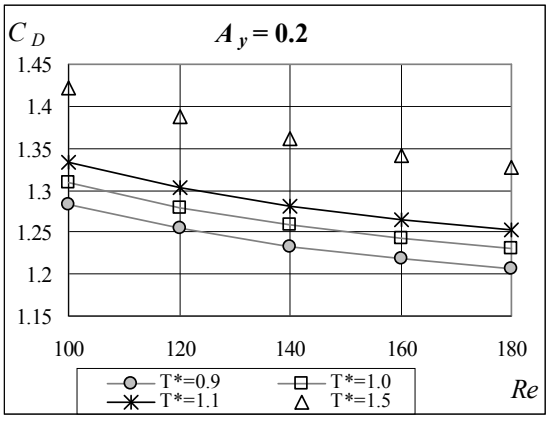

Figure 9. Time-mean of drag versus *Re* at four temperature ratios, A_y=0.2

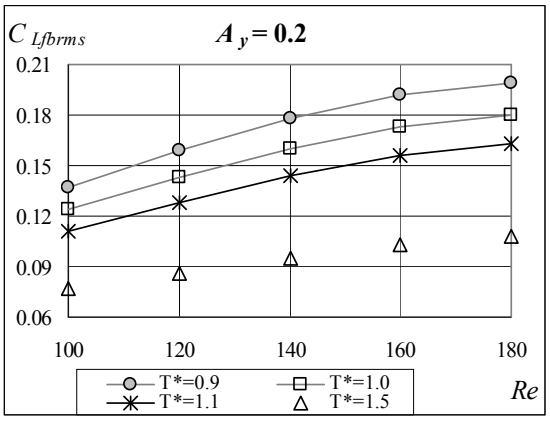

Figure 10. The rms of lift versus *Re* at four temperature ratios, A_y=0.2

Figure 11 shows the mechanical energy transfer (E=E_1) versus Re at different temperature ratios T* for A_y=0.2. It can be seen in the figure that E decreases with increasing T* for a given Re, and is primarily positive in the lock-in domain.

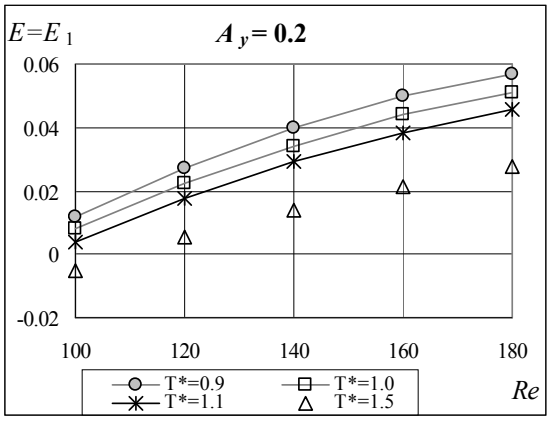

Figure 11. Mechanical energy transfer versus Re at four temperature ratios, A_y=0.2

For transverse motion the heat transfer is also investigated. Figure 12 shows the effective Nusselt number versus Reynolds number for different amplitudes for T*=1.0. Although it was found for in-line motion that the curve of Nu_{eff} is not linear (see Fig. 5), for transverse motion Nu_{eff} increases linearly with oscillation amplitude, similarly to the results of [9]. When the oscillation amplitude is held constant, the value of Nu_{eff} increases linearly with Re. As Re is increased, the distance between the Nu_{eff} curves belonging to different oscillation amplitudes increases slightly.

The effect of temperature ratio on the effective Nusselt number is shown for different amplitude values and different Reynolds numbers in Figure 13. When the oscillation amplitude is held constant Nu_{eff} values increase linearly with Reynolds number. Increasing the temperature lowers Nu_{eff}.

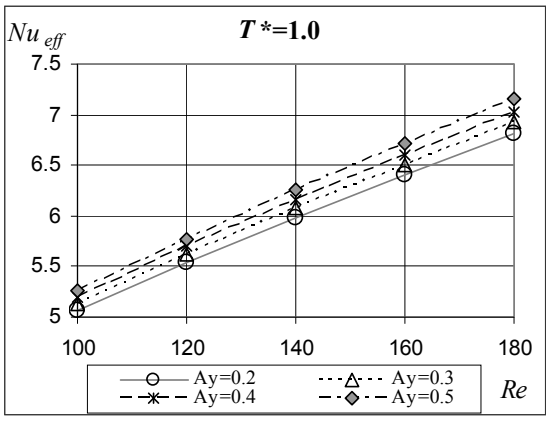

Figure 12. Nu_{eff} versus Re at four transverse oscillation amplitudes, T*=1.0

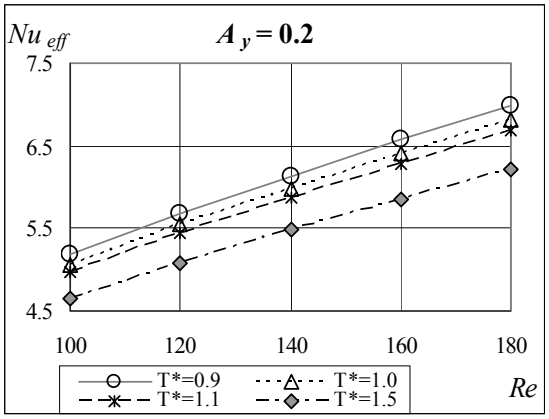

Figure 13. Nu_{eff} versus Re at different T*, A_y=0.2

4. SUMMARY

The present work numerically investigated the effect of temperature ratio (wall temperature over ambient temperature), amplitude of oscillation, and Reynolds number on heat transfer, mechanical energy transfer and force coefficients from a heated circular cylinder placed in oscillating flow in in-line or in transverse direction. For the unheated case the computational results obtained by the finite volume method (Ansys Fluent) are compared with those of a finite difference method, finding good agreement.

For in-line oscillation practically the same state curves are found for unheated and heated cases, but curves of larger temperature ratio shift the lock-in domain to smaller amplitude values.

For a given amplitude value the effective Nusselt number Nu_{eff} decreases with increasing temperature ratio for in-line and transverse oscillation, while with increasing oscillation amplitude for in-line motion Nu_{eff} first increases, reaches a maximum value and then decreases slightly, indicating that higher amplitude values may suppress the temperature effects. For transverse oscillation Nu_{eff} increases linearly with amplitude and with Reynolds number.

The mechanical energy transfer E for in-line motion results is always negative (flow acts against cylinder motion), while for transverse motion both positive (enhancing cylinder motion) and negative values occur. With increasing temperature the value of E decreases for in-line oscillation. For transverse motion the energy transfer increases with Reynolds number for a given amplitude.

A possible further step in the research is the further investigation of the combined effect of oscillation amplitude and surface temperature for a heated cylinder oscillating in-line.

ACKNOWLEDGEMENTS

This study has been supported by the Hungarian National Fund for Science and Research under Project No. OTKA K 76085. The work was carried out as part of the TÁMOP-4.2.1.B-

10/2/KONV-2010-0001 project in the framework of the New Hungarian Development Plan. The realization of this project is supported by the European Union, co-financed by the European Social Fund.

REFERENCES

[1] Williamson, C.H.K., and Roshko, A., 1988, "Vortex formation in the wake of an oscillating cylinder", *Journal of Fluids and Structures*, Vol. 2, pp. 355-381.

[2] Lu, X.Y., and Dalton, C., 1996, "Calculation of the timing of vortex formation from an oscillating cylinder", *Journal of Fluids and Structures*, Vol**.** 10, pp. 527-541.

[3] Gu, W., Chyu, C., and Rockwell, D., 1994, "Timing of vortex formation from an oscillating cylinder", *Physics of Fluids*, Vol. 6, pp. 3677-3682.

[4] Al-Mdallal, Q.M., Lawrence, K.P., and Kocabiyik, S., 2007, "Forced streamwise oscillations of a circular cylinder: Locked-on modes and resulting fluid forces", *Journal of Fluids and Structures,* Vol. 23, pp. 681-701.

[5] Baranyi, L., 2009, "Sudden and gradual alteration of amplitude during the computation for flow around a cylinder oscillating in transverse or in-line direction", *ASME 2009 Pressure Vessels and Piping Conference*, *Symposium on Flow-Induced Vibration*. Prague, Paper No. PVP2009-77463.

[6] Baranyi, L., 2008, "Effect of frequency ratio on the force coefficients of a cylinder oscillated in a uniform stream", Proc. *7th JSME-KSME Thermal and Fluids Engineering Conference*, Sapporo, Japan, Paper No. L132.

[7] Konstantinidis, E., Balabani, S., and Yianneskis, M., 2005, "The timing of vortex shedding in a cylinder wake imposed by periodic inflow perturbations", *Journal of Fluid Mechanics*, Vol. 543, pp. 45-55.

[8] Mureithi, N.W., Huynh, K., and Pham, A., 2009, "Low order model dynamics of the forced cylinder wake", *ASME 2009 Pressure Vessels and Piping Conference*, *Symposium on Flow-Induced Vibration*. Prague, Paper No. PVP2009-78093

[9] Karanth, D., Rankin, G.W., and Sridhar, K., 1994, "A finite difference calculation of forced convective heat transfer from an oscillating cylinder", *International Journal of Heat and Mass Transfer*, Vol. 37, pp. 1619-1630.

[10] Cheng, W.H., Hong, J.L., and Aung, W., 1997, "Numerical prediction of lock-on effect on convective heat transfer from a transversely oscillating circular cylinder", *International Journal of Heat and Mass Transfer*, Vol. 40, pp.1825-1834.

[11] Blackburn, H.M., and Henderson, R.D., 1999, "A study of two-dimensional flow past an oscillating cylinder", *Journal of Fluid Mechanics*, Vol. 385, pp. 255-286.

[12] Bolló, B., 2010, "Grid independence study for flow around a stationary circular cylinder", Proc. *microCAD 2010, International Computer Science Conference*, Miskolc, Hungary, Section F, pp. 1-6.

[13] Bolló, B., and Baranyi, L., 2010, "Computation of low-Reynolds number flow around a stationary circular cylinder", Proc. *7th International Conference on Mechanical Engineering*, Budapest, pp. 891-896.

[14] White, F.M., 1999, *Fluid Mechanics*. 4th ed., McGraw-Hill.

[15] *VDI-Wärmeatlas*, 2002, 9th ed., Springer Verlag.

[16] Wang, A.B., and Trávníček, Z., 2001, "On the linear heat transfer correlation of a heated circular cylinder in laminar crossflow using a new representative temperature concept", *International Journal of Heat and Mass Transfer*, Vol. 44, pp. 4635-4647.

[17] Baranyi, L., 2008, "Numerical simulation of flow around an orbiting cylinder at different ellipticity values", *Journal of Fluids and Structures*, Vol. 24, pp. 883-906.

[18] Baranyi, L., 2005, "Lift and drag evaluation in translating and rotating non-inertial systems", *Journal of Fluids and Structures*, Vol. 20, pp. 25-34.

[19] Baranyi, L., 2003, "Computation of unsteady momentum and heat transfer from a fixed circular cylinder in laminar flow", *Journal of Computational and Applied Mechanics*, Vol. 4, pp. 13-25.

[20] Özisik, M.N., 1985. *Heat Transfer.* McGraw-Hill.

[21] Lecordier, J.C, Hamma, L., and Paranthoën, P., 1991, "The control of vortex shedding behind heated circular cylinder at low Reynolds numbers", *Experiments in Fluids*, Vol. 10, pp. 224-229.

[22] Wang, A.B., Trávníček, Z., and Chia, K.C., 2000, "On the relationship of effective Reynolds number and Strouhal number for the laminar vortex shedding of a heated circular cylinder", *Physics of Fluids*, Vol. 12, pp. 1401-1410.

[23] Kaiktsis, L., Triantafyllou, G.S., and Özbas, M., 2007, "Excitation, inertia, and drag forces on a cylinder vibrating transversely to a steady flow", *Journal of Fluids and Structures*, Vol. 23, pp. 1-21.

[24] Bolló, B., 2010, "Low Reynolds number flow around and heat transfer from a heated circular cylinder", *International Review of Applied Sciences and Engineering*, Vol. 1, pp. 15-20.

Conference on Modelling Fluid Flow (CMFF'12)
The 15th International Conference on Fluid Flow Technologies
Budapest, Hungary, September 4-7, 2012

NUMERICAL INVESTIGATION OF MECHANICAL ENERGY TRANSFER BETWEEN THE FLUID AND A CYLINDER OSCILLATING TRANSVERSE TO THE MAIN STREAM

László BARANYI[1], László DARÓCZY[2]

[1] Corresponding Author. Department of Fluid and Heat Engineering, University of Miskolc, Miskolc-Egyetemváros, H-3515, Hungary
Tel.: +36 46 565 154, Fax: +36 46 565 471, E-mail: arambl@uni-miskolc.hu
[2] University of Miskolc. E-mail: daroczylaszlo@gmail.com

ABSTRACT

This paper deals with the two-dimensional numerical simulation of low-Reynolds number flow past a circular cylinder forced to oscillate transverse to the main stream. The study concentrates on the investigation of mechanical energy transfer E between the fluid and a transversely oscillating cylinder. When E is negative the fluid works to dampen the cylinder oscillation. When E is positive, work is done on the cylinder and this can be a source of vortex-induced vibration (VIV) for free vibration cases. The object of this paper is to identify subdomains in the parameter domain of Reynolds number, oscillation amplitude and frequency ratio (Re, A_y, f/St_0) where the mechanical energy transfer is positive.

Computations are carried out using in-house code based on the finite difference method. Since carrying out the computation even for one point of the three-dimensional domain of (Re, A_y, f) is computationally expensive, the analysed space is limited to Re = 100-180, A_y = 0.1-1.0 and f = (0.6-1.2) St_0, where St_0 is the dimensionless vortex shedding frequency from a stationary cylinder at the same Reynolds number.

Keywords: CFD, circular cylinder, lift, lock-in, low-Reynolds number flow, mechanical energy transfer

NOMENCLATURE

A	[-]	oscillation amplitude, non-dimensionalised by d
C_D	[-]	drag coefficient, $2D/(\rho U^2 d)$
C_L	[-]	lift coefficient, $2L/(\rho U^2 d)$
C_p	[-]	static pressure coefficient
D	[-,N/m]	dilation or divergence, drag force per unit length
E	[-]	mechanical energy transfer
L	[N/m]	lift force per unit length
Re	[-]	Reynolds number, Ud/ν
St	[-]	Strouhal number, $f_v d/U$
T	[-]	cycle period, non-dimensionalised by d/U
U	[m/s]	free stream velocity
a_{0x}, a_{0y}	[-]	cylinder acceleration in x and y directions, non-dimensionalised by U^2/d
d	[m]	cylinder diameter, length scale
f_v	[s^{-1}]	vortex shedding frequency
FR	[-]	frequency ratio, f/St_0
p	[-]	pressure, non-dimensionalised by ρU^2
t	[-]	time, non-dimensionalised by d/U
u,v	[-]	velocities in x, y directions, non-dimensionalised by U
x,y	[-]	Cartesian co-ordinates, non-dimensionalised by d
Δt	[-]	time step, non-dimensionalised by by d/U
ρ	[kg/m^3]	fluid density
ω	[-]	vorticity, $\omega=\partial v/\partial x-\partial u/\partial y$, non-dimensionalised by U/d

Subscripts and Superscripts

D	drag
fb	fixed body
L	lift
pb	base pressure
rms	root-mean-square value
v	vortex
x, y	components in x and y directions
0	for stationary cylinder

1. INTRODUCTION

Flow past oscillating cylinders has been studied widely because of its practical implications. Structures subjected to wind or underwater flows can oscillate, which can have unwanted consequences. Vibration of stacks, silos or tube bundles of heat exchangers are some examples of

fluid-structure interaction. If a cylinder is in forced motion, then the vortex shedding and the interaction between the fluid and the cylinder is affected by factors such as cylinder forcing frequency and the amplitude and direction of oscillation, in addition to the Reynolds number (*Re*) of the flow. Transverse oscillation is most often studied due to its relevance to real life.

When vortices are shed from a bluff body, the induced periodic lift force may lead to large amplitude oscillations, especially when the damping is small and the vortex shedding frequency is near to the natural frequency of the body. As mentioned in [1], since many phenomena in flow-induced vibrations are only weakly dependent on *Re*, they can be fairly accurately simulated even at relatively low Reynolds numbers, such as those in this study.

There are a huge number of papers available for flow past a circular cylinder oscillating transverse to the free stream. In their very famous paper based on a low-Reynolds number experimental investigation of flow past a cylinder in forced motion, Williamson and Roshko [2] determined a map of vortex shedding modes. Blackburn and Henderson for *Re*=500 [3] and for *Re*=200 [4] and Lu and Dalton [5] for *Re*=185 found some vortex switches in transverse oscillation for frequency ratios over 1. Low-Reynolds number numerical studies, based on finite difference method, found no vortex switches for transverse oscillation either against oscillation amplitude [6] or against frequency ratio below subharmonic forcing [7]. The same computational procedure was applied and its results were compared with those of a finite volume based commercial software package for cylinder oscillation in [8], investigating the effect of oscillation amplitude on the force coefficients and on energy transfer. Neither method found vortex switches. For transverse oscillation, both positive and negative values of mechanical energy transfer were obtained. Very good agreement was found between the results of the two methods.

The aim of this study is a systematic investigation in a relatively wide parameter domain of the effect of three important parameters on the force coefficients and on the mechanical energy transfer between the cylinder and the fluid for low Reynolds numbers. These three parameters are the Reynolds number *Re*, oscillation amplitude A_y, and frequency ratio f/St_0. To the best knowledge of the authors such a systematic investigation in the phase space of (*Re*, A_y, f/St_0) is not available in the literature.

2. COMPUTATIONS

Computations were carried out using an in-house code based on the finite difference method.

2.1. Computational method

A non-inertial system fixed to the cylinder is used to compute 2D low-Reynolds number unsteady flow around a circular cylinder placed in a uniform stream and forced to oscillate transversely to the uniform free stream flow. The governing equations are the Navier-Stokes equations for incompressible constant-property Newtonian fluid written in the non-inertial system fixed to the accelerating cylinder, the equation of continuity and a Poisson equation for pressure. All quantities in these equations are non-dimensional. The physical domain consists of two concentric circles with dimensionless radii of R_1 and R_2, where R_1 represents the cylinder surface and R_2 the far field.

No-slip boundary condition is used for the velocity; a Neumann-type boundary condition is applied for pressure on the cylinder surface and potential flow is assumed in the far field. Boundary-fitted co-ordinates are used to accurately impose the boundary conditions. The physical domain is mapped into a rectangular shape computational domain (Fig. 1). With this the mesh of logarithmically spaced elements on the physical plane are transformed to an equidistant mesh on the computational plane. The transformed governing equations with boundary conditions are solved by a finite difference method [9]. Space derivatives are approximated by fourth-order central difference except for the convective terms for which a third-order modified upwind scheme is used. The Poisson equation for pressure is solved by the successive over-relaxation (SOR) method. The equation of motion is integrated explicitly and the continuity equation was satisfied at every time step. For further details see [9].

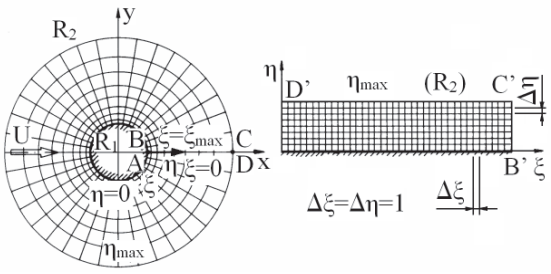

Figure 1. Physical and computational domains

The 2D code developed by the first author has been tested extensively against experimental and computational results (see [9] for details) for both stationary and oscillating cylinders.

The non-dimensional displacement of the centre of the transversely oscillated cylinder is described by

$$y_0(t) = -A_y \sin(2\pi f_y t), \qquad (1)$$

where t is the dimensionless time, A_y and $f_y = f$ are the dimensionless transverse amplitude and frequency of cylinder oscillation, respectively. In this study only locked-in cases are considered, when the frequency of vortex shedding synchronizes with that of the cylinder oscillation.

2.2. Computational setup

In this study we investigated the behaviour of flow past a circular cylinder placed in a uniform stream with its axis perpendicular to the velocity of the main flow. The cylinder is oscillated mechanically transverse to the uniform free stream. Here we concentrate on domains where lock-in occurs and where the mechanical energy transfer is positive. We also investigate the force coefficients within a wide parameter domain (or phase space) of (Re, A_y, f/St_0). Here St_0 is the dimensionless vortex shedding frequency or Strouhal number for a stationary cylinder at that Re. Force coefficients investigated under lock-in conditions are the time mean (TM) and root-mean-square values (rms) of lift (C_L), of drag (C_D), and of base pressure (C_{pb}).

Throughout this paper the lift and drag coefficients used do not contain the inertial forces originated from the non-inertial system fixed to the accelerating cylinder. Coefficients obtained by removing the inertial forces are often termed 'fixed body' coefficients [5]. The relationship between the two sets of coefficients can be written as [10]

$$C_L = C_{Lfb} + \frac{\pi}{2} a_{0y},\ C_D = C_{Dfb} + \frac{\pi}{2} a_{0x}, \qquad (2)$$

where subscript 'fb' refers to the fixed body (understood in an inertial system fixed to the stationary cylinder). In Eq. (2) a_{0x} and a_{0y} denote the acceleration of the cylinder in x and y directions, respectively. Since the inertial terms are T-periodic functions, their time-mean values vanish, resulting in identical TM values for lift and drag in the inertial and non-inertial systems. Naturally the rms value of C_L will be different in the two systems, while C_{Drms} remains the same, as $a_{0x}=0$ for transverse cylinder oscillation (see Eq. (2)).

2.3. Phase space (Re, A_y, FR) and simulation settings

A large number of computations were carried out in order to obtain an appropriate resolution of the three-dimensional phase space (Re, A_y, f/St_0). Computations were carried out for all possible combinations of Re=100, 120, 140, 160 and 180; A_y=0.1, 0.2, 0.3, 0.4, 0.5, 0.6, 0.7, 0.8, 0.9, 1.0; and frequency ratio f/St_0=0.6, 0.7, 0.8, 0.9, 1.0, 1.1, 1.2. The frequency ratio f/St_0 will be denoted by FR for the sake of simplicity. The St_0 values from [11] are St_0= 0.1644, 0.1735, 0.1806, 0.1864, 0.1913 for Re=100, 120, 140, 160, 180, respectively. Besides these points, computations were also carried out for a further 36 points in order to improve the precision of the analysed three dimensional surfaces, making a total of 386 computational points.

All other settings were the same for the simulations. A mesh of 361x292 (peripheral x radial) was used with the ratio of radii of R_2/R_1=160 and the dimensionless time step Δt=0.0005 was used to make the first order temporal discretization scheme accurate. Comparisons with second-order Runge-Kutta discretization results showed that at this small time step the results agree well with each other [12]. Simulations were run for the non-dimensional time of t=600-1000.

Results from the in-house Fortran code were post-processed. The computed results were the mechanical energy transfer E, the time-mean of C_L, C_D, $-C_{pb}$ and the root-mean-square of $C_{L,fb}$, $C_{D,fb}$ only for cases where periodic solution were achieved, i.e. for the lock-in region. Values were collected in an Excel file, automatically exported to an in-house database handler program, and selected cases were exported to a spreadsheet for post-processing with Matlab, where the original set of cases was interpolated to a much finer mesh using the command GRIDDATAN and the command ISOSURFACE was used to visualize surfaces at constant values of the analyzed coefficients [13].

3. RESULTS

Computational results are presented with a focus on mechanical energy transfer between the fluid and the cylinder within the locked-in domain in the investigated phase space.

3.1. Lock-in domain

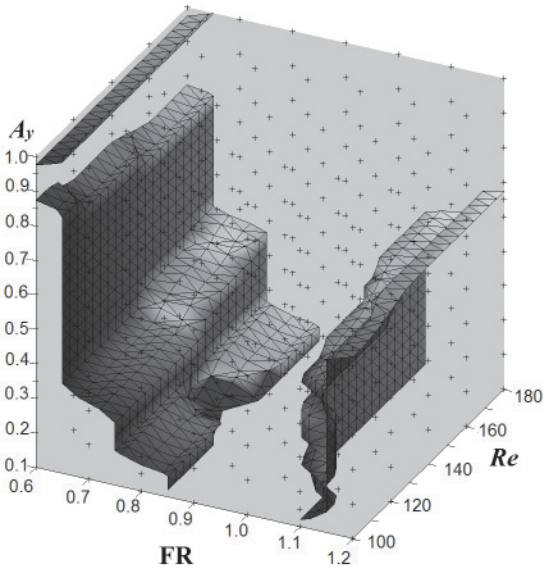

Figure 2. Lock-in region

Out of the 386 analyzed cases lock-in occurred in 252 cases. The lock-in domain displayed in three-dimensional (3D) form in Fig. 2 was plotted only approximately, with the isosurface being drawn for the value of 0.5 (where 1 represented cases in the lock-in region, and 0 otherwise). Naturally, due to computing limitations, the interpolated surfaces are not precise representations of the lock-in–not lock-in boundary, but still these rough boundaries are basically sufficient for our needs. The refinement of these boundaries could be a further step in our research. A more careful determination of the lock-in boundaries for a transversely oscillating cylinder at *Re*=180 is found e.g., in [14].

3.2. Mechanical energy transfer

The mechanical energy transfer E between fluid and a transversely oscillated cylinder is determined when the fluid is already periodic. E was defined in [3] as

$$E = \int_0^T C_{\mathrm{L}}(t)\, v_{0\mathrm{y}}(t)\, \mathrm{d}\, t, \qquad (3)$$

where v_{0y} is the cylinder velocity, t and T are the dimensionless time and time period, respectively. E is positive when work is done on the cylinder and negative when work is done on the fluid by the cylinder.

Figure 3 shows the mechanical energy transfer E against frequency ratio FR for different amplitude values A_y within the lock-in domain at *Re*=180. As can be seen in the figure, E is negative for the largest part of the phase space. For large amplitude values E is negative and its absolute value increases with FR. Small positive values can be seen only for FR between 0.8 and 1.0 and amplitudes below 0.6. Curves for smaller *Re* numbers are similar.

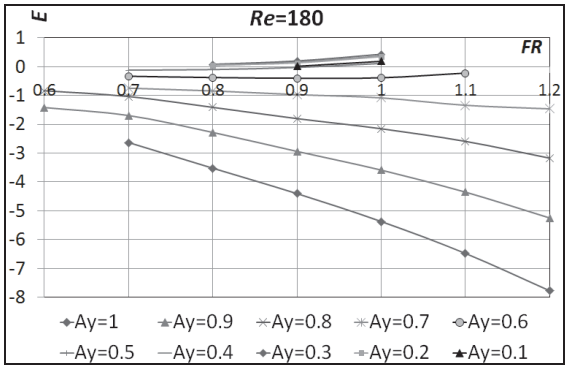

Figure 3. Mechanical energy transfer; *Re*=180

Figure 4 shows part of the same diagram for positive E values. E increases with increasing FR and rather surprisingly the effect of oscillation amplitude reveals no clear tendency: the lowest and second lowest amplitudes belong to 0.5 and 0.1, respectively. Figures 5 and 6 show the corresponding curves for *Re*=140 and 100, respectively. A careful look at the three figures reveals that the tendencies are basically the same; this was true for all Reynolds numbers investigated.

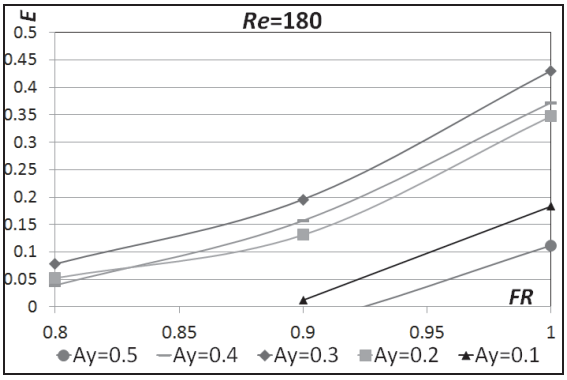

Figure 4. Positive mechanical energy transfer; *Re*=180

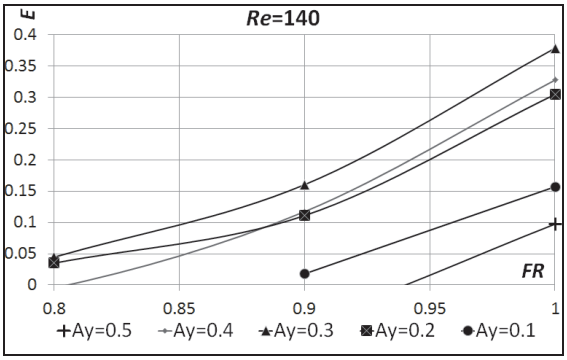

Figure 5. Positive mechanical energy transfer; *Re*=140

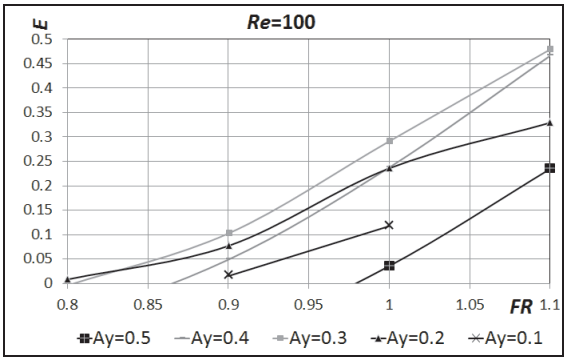

Figure 6. Positive mechanical energy transfer; *Re*=100

Figure 7 shows E against oscillation amplitude A_y for different frequency ratios FR within the lock-in domain at *Re*=100. As can be seen, E is negative again for the largest part of the phase space. For large amplitude values E is negative and its absolute value increases with FR. Small positive values can be seen only for amplitudes below 0.6. Curves for larger *Re* numbers are similar. Interestingly, there is

a special point in the figure which practically all curves go through (A_y≈0.65 and E≈ -0.6).

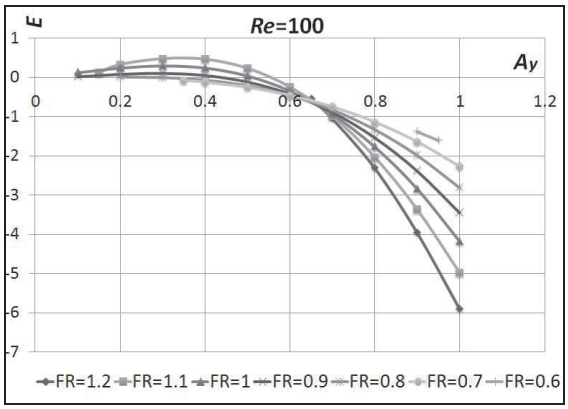

Figure 7. Mechanical energy transfer; *Re*=100

Figure 8 shows the part of Fig. 7 where E values are positive. It can be seen that E has a maximum for each curve at around A_y =0.3 and that E increases with increasing FR (as can also be seen in Figs. 4-6). The largest computed E value in the investigated domain can be seen in Fig. 8; its value is 0.4794 and belongs to Re=100, FR=1.1 and A_y=0.3. The same point can also be seen in Fig. 5. Figures 9 and 10 show the corresponding curves for Re=140 and 180, respectively. It can be seen that Figs. 8-10 are very similar to each other, and that the Reynolds number effect is not strong at all, supporting the findings in [1]. Curves belonging to the same frequency ratio shift to somewhat higher E values for larger Re values, forming a clear trend, unlike that seen for A_y in Figs. 4-6. Figures belonging to all Re values investigated are similar to each other.

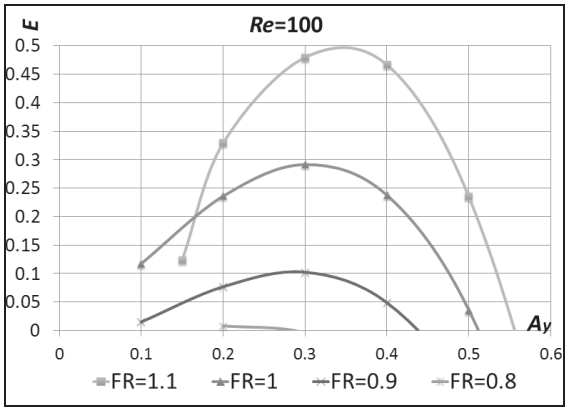

Figure 8. Positive mechanical energy transfer; *Re*=100

The clear tendency can be deducted from the figures that larger amplitudes usually result in larger energy transfer from the cylinder to the fluid. However, at lower amplitudes this behaviour becomes less obvious, and a domain of positive energy transfer can be identified.

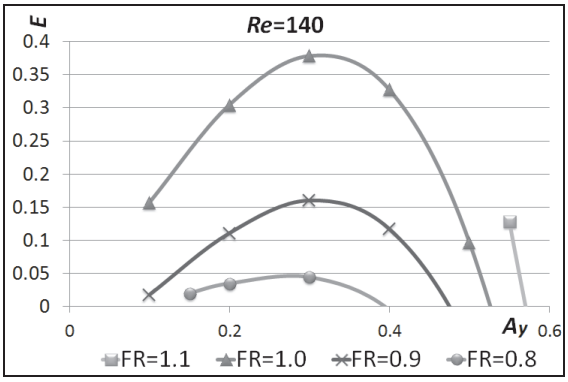

Figure 9. Positive mechanical energy transfer; *Re*=140

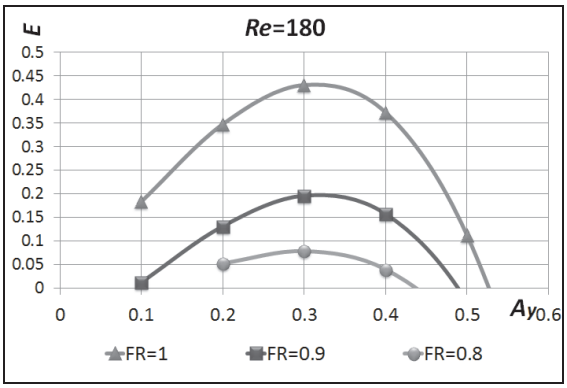

Figure 10. Positive mechanical energy transfer; *Re*=180

The mechanical energy transfer results introduced in Figs. 3-10 are also represented by isosurfaces in the 3D phase space shown in Fig. 11. Isosurfaces of E = -7, -4, -1.2, -0.5, 0, 0.1, 0.25 and 0.4 are shown in the figure, as well as the border of the lock-in region. Figure 12 shows the same E isosurfaces from a different view.

Interestingly, the region of phase space where the mechanical energy transfer is positive and relatively large is close to the upper border of the lock-in region. This behaviour may contribute to vortex-induced vibrations.

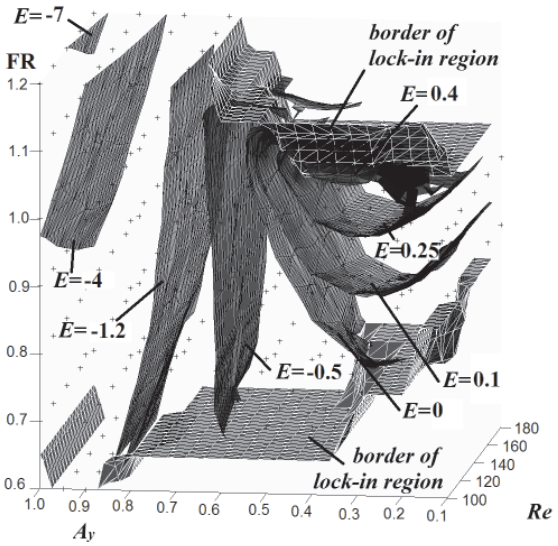

Figure 11. Isosurfaces of mechanical energy transfer

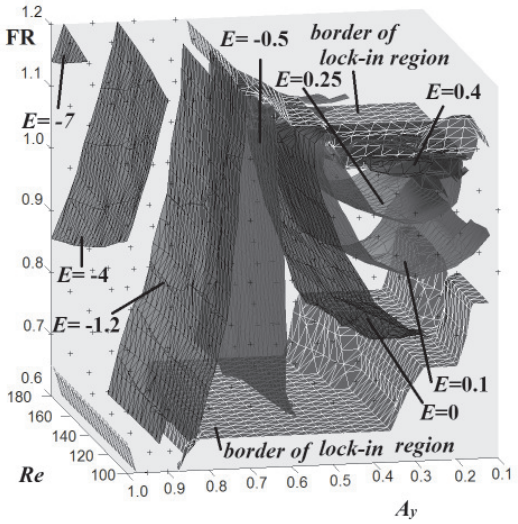

Figure 12. Isosurfaces of mechanical energy transfer

3.3. Time-mean of drag coefficient

The TM of drag in the lock-in domain increases quite regularly when plotted against oscillation amplitude, as can be seen in the example for an intermediate *Re* value of 140, shown in Fig. 13. The curves belonging to different frequency ratios show increasing drag with increasing *FR*. Figure 14 displays the TM of drag against the frequency ratio for different oscillation amplitude values. With the exception of the curve for A_y=0.8 at higher *FR* values, once again the drag tends to increase with increasing A_y and *FR*. The effect of Reynolds number is rather weak, as can be seen in the isosurfaces of drag shown in Fig. 15.

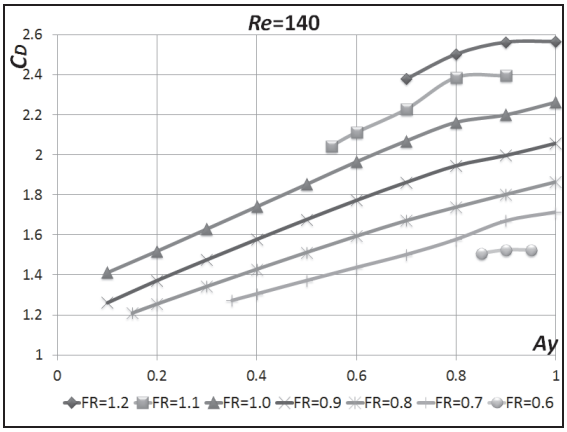

Figure 13. Drag coefficient against oscillation amplitude, *Re*=140

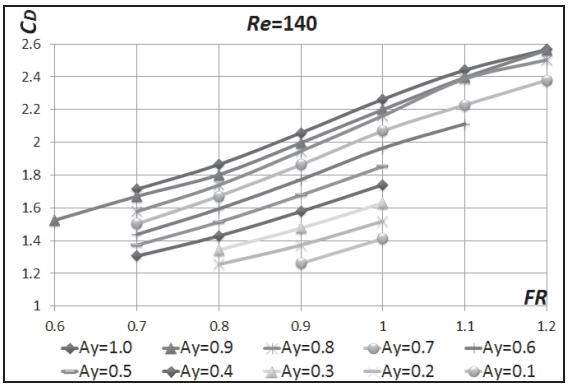

Figure 14. Drag coefficient against frequency ratio, *Re*=140

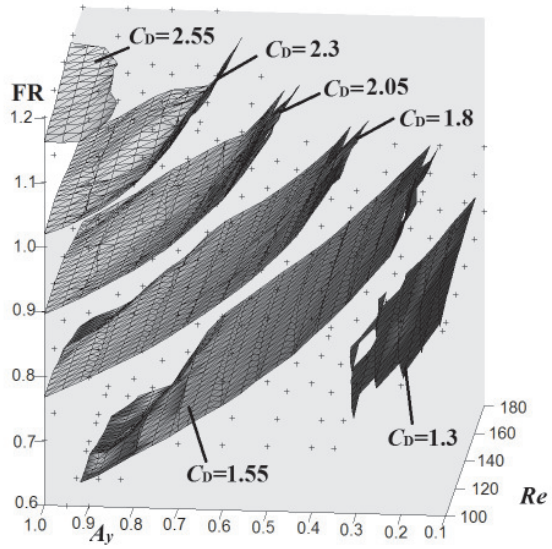

Figure 15. Isosurfaces of time-mean of drag

3.4. Fixed-body lift

The TM of lift was 0 for all cases computed, in accordance with earlier findings [6]. Figure 16 shows the rms of fixed-body lift $C_{Lfb,rms}$ against

frequency ratio for different oscillation amplitude values. It can be seen from the figure that $C_{\mathrm{Lfb,rms}}$ increases gradually with increasing FR and A_y.

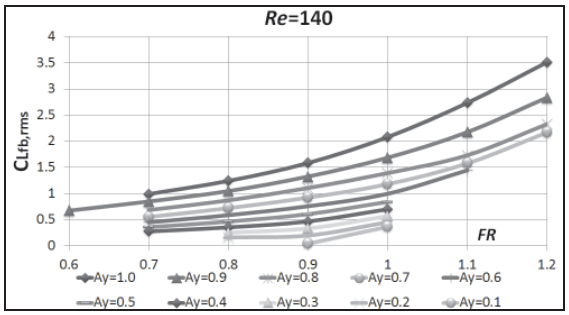

Figure 16. Rms of fixed-body lift against frequency ratio; *Re*=140

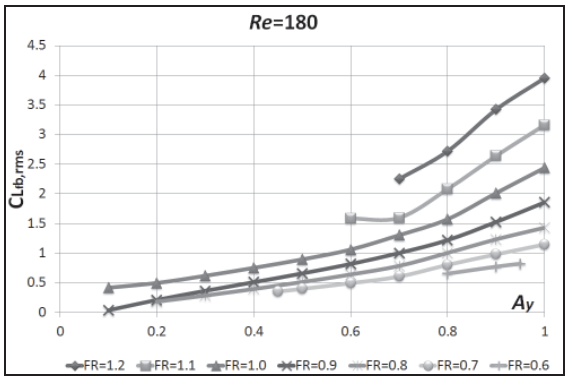

Figure 17. Rms of fixed-body lift against oscillation amplitude; *Re*=140

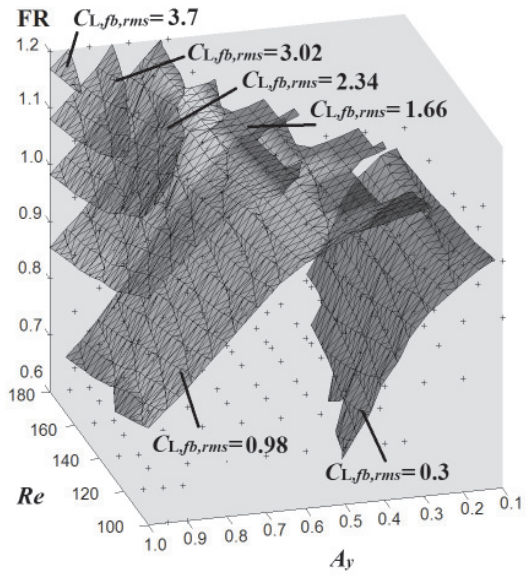

Figure 18. Isosurfaces of rms of fixed-body lift $C_{\mathrm{L,fb,rms}}$

Figure 17 shows $C_{\mathrm{Lfb,rms}}$ against A_y for different FR values. This representation of the function $C_{\mathrm{Lfb,rms}}(A_y, FR)$ basically conveys the same message: an increase in $C_{\mathrm{Lfb,rms}}$ with both A_y and FR. One exception is found for FR=1.1 in the range of A_y=0.6-0.7, where the curve is almost constant.

The isosurfaces of rms values of the fixed-body lift coefficient are plotted in Fig. 18, showing also the effect of Re, which appears to be minimal over much of the phase space.

3.4. Base pressure coefficient

The isosurfaces of base pressure coefficient C_{pb} are plotted in Fig. 19. Similarly to previous results, $-C_{\mathrm{pb}}$ (minus sign used for positive values) increases with the increase in the frequency and amplitude, while Reynolds number has only a weak effect on the coefficient over much of the phase space.

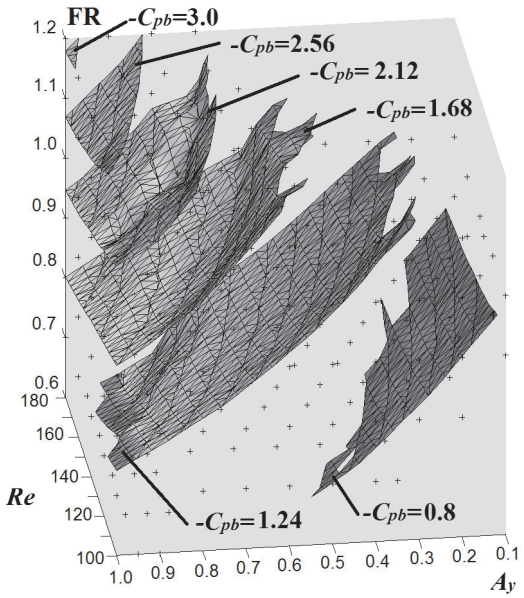

Figure 19. Isosurfaces of the base pressure coefficient

3.5. Vortex structure

Throughout the phase space vortex structure was identified as 2S, i.e., a single vortex is shed from each side in one cycle. A typical example can be seen in Fig. 20, where the grey colour indicates negative (clockwise rotation) vorticity values, while the black is positive (anti-clockwise).

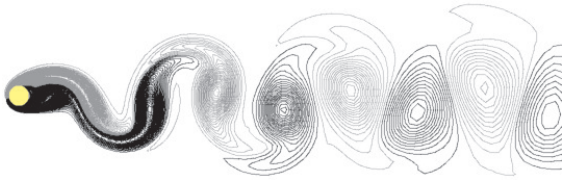

Figure 20. Vortex contours at *Re*=100, *FR*=0.8, A_y=0.5

4. CONCLUSIONS

Flow properties were investigated in the three-dimensional phase space (Re, A_y, f/St_0) under lock-in condition. The main emphasis was on the mechanical energy transfer E between the fluid and a cylinder mechanically oscillated transverse to the free stream.

In the largest part of the phase space, E was found to be negative, meaning that energy is extracted from the cylinder. Large-magnitude negative values were found at large oscillation amplitude A_y values. However, at $A_y < 0.6$, and at frequency ratios $f/St_0 = 0.8$-1.1, positive E values were found at all Reynolds numbers investigated (Re=100-180); this is near the upper boundary of the lock-in region.

The time-mean of drag and base pressure coefficients and the rms of the lift coefficient increased with both oscillation amplitude and frequency ratio, supporting previous findings.

For all parameters, including E, the effect of Reynolds number was found to be weak across most of the phase space.

Vortex structure was found to be 2S (one vortex is shed from the cylinder in each half cycle).

Further investigation might include the more accurate determination of lock-in boundaries and a more detailed investigation of positive mechanical energy transfer near the boundary of lock-in.

ACKNOWLEDGEMENTS

The support provided by the Hungarian Scientific Research Fund under contract No. OTKA K 76085 is gratefully acknowledged. The work was carried out as part of the TÁMOP-4.2.1.B-10/2/KONV-2010-0001 project in the framework of the New Hungarian Development Plan. The realization of this project is supported by the European Union, co-financed by the European Social Fund.

REFERENCES

[1] Newman, D.J., and Karniadakis, G.E., 1995, "Direct numerical simulation of flow over a flexible cable", Proc. *6th Int. Conference on Flow-Induced Vibration*, London, pp. 193-203.

[2] Williamson, C.H.K., and Roshko, A., 1988, "Vortex formation in the wake of an oscillating cylinder", *Journal of Fluids and Structures*, Vol. 2, pp. 355-381.

[3] Blackburn, H.M., and Henderson, R.D., 1999, "A study of two-dimensional flow past an oscillating cylinder", *Journal of Fluid Mechanics*, Vol. 385, pp. 255-286.

[4] Kaiktsis, L., Trantafyllou, G.S., and Özbas, N., 2007, "Excitation, inertia, and drag forces on a cylinder vibrating transversely to a steady flow", *Journal of Fluids and Structures*, Vol. 23, pp. 1-21.

[5] Lu, X.Y., and Dalton, C., 1996, "Calculation of the timing of vortex formation from an oscillating cylinder", *Journal of Fluids and Structures*, Vol. 10, pp. 527-541.

[6] Baranyi, L., 2009, "Sudden and gradual alteration of amplitude during the computation for flow around a cylinder oscillating in transverse or in-line direction", Proc. *ASME 2009 Pressure Vessels and Piping Conference*, *Symposium on Flow-Induced Vibration*. Prague, Paper No. PVP2009-77463

[7] Baranyi, L., 2008, "Effect of frequency ratio on the force coefficients of a cylinder oscillated in a uniform stream", Proc. *7th JSME-KSME Thermal and Fluids Engineering Conference*, Sapporo, Japan, Paper No. L132

[8] Bolló, B. and Baranyi, L., 2011, "Flow around an oscillating or orbiting cylinder – comparative numerical investigation", Proc. *11th Hungarian Conference on Theoretical and Applied Mechanics, HCTAM*, Miskolc, Hungary, Paper No. 84

[9] Baranyi, L., 2008, "Numerical simulation of flow around an orbiting cylinder at different ellipticity values", *Journal of Fluids and Structures*, Vol. 24, pp. 883-906.

[10] Baranyi, L., 2005, "Lift and drag evaluation in translating and rotating non-inertial systems", *Journal of Fluids and Structures*, Vol. 20(1), pp. 25-34.

[11] Posdziech, O., and Grundmann, R., 2007, "A systematic approach to the numerical calculation of fundamental quantities of the two-dimensional flow over a circular cylinder", *Journal of Fluids and Structures*, Vol. 23, pp. 479–499.

[12] Daróczy, L., and Baranyi, 2012, "Euler and second-order Runge-Kutta methods for computation of flow around a cylinder", Proc. *26th MicroCAD, International Scientific Conference,* Miskolc, Hungary, Section N, (accepted for publication)

[13] MathWorks, Matlab, "Triangulation and Interpolation of Scattered Data", http://www.mathworks.com/products/matlab/demos.html?file=/products/demos/shipping/matlab/qhulldemo.html (last accessed 18 Feb. 2012)

[14] Baranyi, L., and Shirakashi, M., 1999, "Numerical solution for laminar unsteady flow about fixed and oscillating cylinders", *Journal of Computer Assisted Mechanics and Engineering Sciences*, Vol. 6, pp. 263-277.

Conference on Modelling Fluid Flow (CMFF'12)
The 15th International Conference on Fluid Flow Technologies
Budapest, Hungary, September 4-7, 2012

Dynamic Mode Decomposition of PIV measurements for cylinder wake flow in turbulent regime

Gilles TISSOT[1], Laurent CORDIER [2], Bernd R. NOACK [3]

[1] Pprime Institut, 43 route de l'aérodrome, 86000 Poitiers, France, Tel.: +33549366047 E-mail: Gilles.Tissot@univ-poitiers.fr
[2] Pprime Institut, 43 route de l'aérodrome, 86000 Poitiers, France, Tel.: +33549366036 E-mail: Laurent.Cordier@univ-poitiers.fr
[3] Pprime Institut, 43 route de l'aérodrome, 86000 Poitiers, France, Tel.: +33549366015 E-mail: Bernd.Noack@univ-poitiers.fr

ABSTRACT

Dynamic Mode Decomposition (DMD) is a new post-processing technique that can extract from snapshots dynamic informations relevant for the flow. Without explicit knowledge of the dynamical operator, the DMD algorithm determines eigenvalues and eigenvectors of an approximate linear model. DMD can be viewed as a non linear generalization of global stability classically used for a linearized system. This algorithm can be used to determine the eigen-elements of the Koopman operator, an infinite dimensional linear operator associated with the nonlinear system. The ability of DMD to extract dynamically relevant features of the flow has been tested on an experimental PIV dataset of a turbulent cylinder wake flow.

Keywords : cylinder wake, dynamic mode decomposition, reduced-order model

NOMENCLATURE

$\mathcal{K}_N(A, \boldsymbol{v})$	$[-]$	Krylov subspace of order N generated by A from $\boldsymbol{v}$
A	$[-]$	time stepping operator
C	$[-]$	Companion matrix
D	$[m]$	Diameter of the cylinder
G	$[-]$	Gramian matrix of the DMD modes
Re	$[-]$	Reynolds number
T	$[-]$	Vandermonde matrix
U_∞	$[m.s^{-1}]$	velocity at infinity
V_1^N	$[-]$	matrix of snapshots
$\boldsymbol{v}_i$	$[-]$	i^{th} snapshot
$\boldsymbol{y}_i$	$[-]$	i^{th} eigenvector of C
$\boldsymbol{z}_i$	$[-]$	i^{th} eigenvector of C^H
Δt	$[s]$	time step
Φ	$[-]$	matrix $(\boldsymbol{\Phi}_1, \cdots, \boldsymbol{\Phi}_{N-1})$
$\widetilde{\Phi}$	$[-]$	matrix $(\widetilde{\boldsymbol{\Phi}}_1, \cdots, \widetilde{\boldsymbol{\Phi}}_{N-1})$
$\boldsymbol{\Phi}_i$	$[-]$	i^{th} Ritz eigenvector
$\widetilde{\boldsymbol{\Phi}}_i$	$[-]$	i^{th} DMD mode
$\boldsymbol{\Psi}_i$	$[-]$	i^{th} adjoint DMD mode
δ_{ij}	$[-]$	Kronecker symbol
λ_i	$[-]$	i^{th} Ritz eigenvalue
ν	$[-]$	matrix $(\boldsymbol{\nu}_1, \cdots, \boldsymbol{\nu}_N)$
$\boldsymbol{\nu}_k$	$[-]$	$(\nu_1(k), \cdots, \nu_{N-1}(k))^T$
$\nu_i(k)$	$[-]$	projection of the k^{th} snapshot on the i^{th} DMD mode
ν_{kin}	$[m^2.s^{-1}]$	kinematic viscosity
σ	$[s^{-1}]$	DMD growth rate
ω	$[rad.s^{-1}]$	DMD frequency

Subscripts and Superscripts

$\bar{}$	complex conjugate
H	Hermitian conjugate
T	transpose

1. INTRODUCTION

For a turbulent flow, the number of active degrees of freedom is so important that a preliminary step of *model reduction* is necessary for having a chance to understand the flow physics or to derive a control strategy. The general objective of model reduction is to extract, from physical insights or mathematical tools, the building blocks which play a dominant role in terms of modelling. In the case of flow control, this question of educing physically-relevant structures is even more difficult since by definition the flow dynamics will be fully modified by the introduction of the control. Reduced-order modelling is then more an art than a science and finding the appropriate basis for representing the flow in a low-dimensional space is strongly related to a given objective. Indeed, it is somewhat different for a flow to understand the instability mechanisms, to educe the coherent structures mainly responsible for the energy or to represent the non-linear dynamics.

In this communication, we are focusing on a procedure recently introduced by [1] called Dynamic Mode Decomposition (DMD). This

algorithm was proposed as a method that is able to extract dynamically relevant flow features from time-resolved experimental [2, 3, 4] or numerical [5, 6] data. Following [1], the DMD modes generalize the global stability modes since it is not necessary with this method to have an explicit knowledge of the dynamical operator to evaluate frequencies and growth rates associated to each DMD mode. Moreover, we will see that DMD can be used to determine the eigenvalues and eigenvectors of the Koopman operator [7], an infinite-dimensional linear operator associated with the full nonlinear system.

In section 2, Dynamic Mode decomposition is first discussed in terms of model reduction. Then, the DMD algorithm is described in broad outline as in [1]. Section 3 will give some specific properties: i) existence and uniqueness of DMD, ii) DMD for linear systems, iii) DMD for periodic solutions and iv) implications of mean subtraction. Section 4 will present practical considerations necessary to implement the DMD algorithm presented in section 2. Finally, in section 5, the DMD will be demonstrated on experimental data corresponding to a PIV dataset of a cylinder wake flow at Reynolds number 40000.

2. DYNAMIC MODE DECOMPOSITION

2.1. DMD and model reduction

Mathematically, model reduction can be described as a projection method where the dynamical process of interest is projected on an appropriate subspace of small size. For physical reasons or practical considerations, the spatio-temporal solution $\boldsymbol{u}(\boldsymbol{x}, t)$ where $\boldsymbol{x}$ corresponds to the spatial coordinate and t denotes time, is often searched as a separated representation

$$\boldsymbol{u}(\boldsymbol{x}, t) = \sum_{i=1}^{N_a} \nu_i(t)\boldsymbol{\Xi}_i(\boldsymbol{x}). \tag{1}$$

For a dynamical process of given complexity, the number N_a of modes in the expansion (1) depends exclusively on the choice of the spatial functions $\boldsymbol{\Xi}_i$. With an *a posteriori* model reduction technique, the spatial modes are first determined (section 2.2) and then used (section 4.2) to determine by projection the temporal coefficients ν_i. When the dynamics of the system is linear, the eigenvectors of the global stability problem, the so-called *global modes*, are often considered to derive a reduced-order model. This model is known to accurately describe the linearized dynamics of the system. When the dynamics becomes fully non linear, in the turbulent regime for instance, then the Proper Orthogonal Decomposition or POD [8] is the most well-known and used reduction approach. POD is widely used since it extracts from a sequence of data an orthonormal basis which captures optimally the flow energy. Unfortunately, energy level is not necessarily the correct criterion in terms of dynamical modelling and deriving a dynamical system based on POD modes leads sometimes to irrelevant models. Here, the DMD algorithm will be presented as a method useful to describe the dynamical behaviour of the system in the linear and non linear regime.

2.2. General description of the DMD algorithm

The data is represented in the form of a snapshot sequence, given by a matrix V_1^N defined as

$$V_1^N = (\boldsymbol{v}_1, \ldots, \boldsymbol{v}_N) \in \mathbb{R}^{N_x \times N} \tag{2}$$

where $\boldsymbol{v}_i$ is the i^{th} snapshot. In the previous definition, the subscript 1 denotes the first member of the sequence, while the superscript N denotes the last entry in the sequence. Moreover, in this temporal framework of DMD, we assume that the snapshots are separated by a constant sampling time Δt.

The DMD algorithm is built on two main assumptions. The first hypothesis is that there exists a linear operator $\mathcal{A}$ to step forward in time the snapshots. Since V_1^N is finite-dimensional, this operator is written as a matrix $A \in \mathbb{R}^{N_x \times N_x}$ such that

$$\boldsymbol{v}_{i+1} = A\boldsymbol{v}_i, \quad \text{for} \quad i = 1, \cdots, N-1. \tag{3}$$

It follows that the subspace spanned by the data set

$$V_1^N = \left(\boldsymbol{v}_1, A\boldsymbol{v}_1, \ldots, A^{N-1}\boldsymbol{v}_1\right) \tag{4}$$

corresponds to the N^{th} Krylov subspace $\mathcal{K}_N(A, \boldsymbol{v}_1)$ generated by A from $\boldsymbol{v}_1$ [9].

The goal of DMD is to determine the eigenvalues and eigenvectors of A but without first determining A. As such, DMD can be interpreted as an extension of the classical Arnoldi algorithm used to determine eigen-elements of large size problems [10]. In the Arnoldi algorithm, the knowledge of A is exploited to determine an orthonormal basis for the projection subspace of the Rayleigh-Ritz procedure. In the DMD algorithm, the orthonormal basis of the projection subspace is determined with a "matrix-free" point of view by considering that only snapshots obtained from a time-stepper are available. The matrix A is no more necessary but the price will be an ill-conditioning of the procedure (see section 4.1).

When the number of snapshots of the sequence V_1^N increased, it is reasonable to assume that, beyond a given number of snapshots, $\boldsymbol{v}_i$ becomes linearly dependent. The second hypothesis is then to consider that the N^{th} iterate writes as a linear combination of the previous iterates *i.e.*

$$\begin{aligned}\boldsymbol{v}_N &= c_1\boldsymbol{v}_1 + c_2\boldsymbol{v}_2 + \cdots + c_{N-1}\boldsymbol{v}_{N-1} + \boldsymbol{r} \\ &= V_1^{N-1}\boldsymbol{c} + \boldsymbol{r}\end{aligned} \tag{5}$$

where $\boldsymbol{c}^T = (c_1, c_2, \cdots, c_{N-1})^T$ and $\boldsymbol{r} \in \mathbb{R}^{N_x}$ is the residual vector. Following [11], we may write

$$AV_1^{N-1} = V_2^N = V_1^{N-1}C + \boldsymbol{r}\boldsymbol{e}_{\boldsymbol{N-1}}^T \tag{6}$$

where $\boldsymbol{e_i}$ is the i^{th} Euclidean unitary vector of length $(N-1)$ and C a Companion matrix defined as

$$C = \begin{pmatrix} 0 & 0 & \dots & 0 & c_1 \\ 1 & 0 & \dots & 0 & c_2 \\ 0 & 1 & \dots & 0 & c_3 \\ \vdots & \vdots & \vdots & \vdots & \vdots \\ 0 & 0 & \dots & 1 & c_{N-1} \end{pmatrix} \in \mathbb{R}^{(N-1)\times(N-1)}. \tag{7}$$

The Companion matrix C is uniquely defined by the coefficients c_i. The eigen-elements of C are then only dependent on c_i. Indeed, as soon as these coefficients are known, the characteristic polynomial of the transpose of C can be calculated:

$$P_{C^T}(\lambda) = \lambda^{N-1} - \sum_{i=1}^{N-1} c_i \lambda^{i-1}. \tag{8}$$

Moreover, since the eigenvalues of a matrix and its transpose are the same then the eigenvalues and eigenvectors of the Companion matrix C can be determined. We will see in section 4.2 the different ways for evaluating these coefficients.

Let $(\boldsymbol{y}_i, \lambda_i)$ be the i^{th} eigen-elements of C, it can be easily proved (see appendix 7.1) that $\left(\boldsymbol{\Phi}_i = V_1^{N-1}\boldsymbol{y}_i, \lambda_i\right)$ are approximated eigen-elements of A, the so-called Ritz eigenvectors and eigenvalues. The value of the residual $\boldsymbol{r}$ is a good measure of the approximation *i.e.* of the success of the DMD algorithm. We will see in section 3.2 that these Ritz eigenvalues can be used to determine the frequency and the growth rate of the linear process.

A few remarks are appropriate at this point. There is no normalization step in the algorithm. Then, the Ritz eigenvectors are known except for a scaling factor. We will see in section 2.3 that this scaling factor will be retrieved by exploiting some properties of the Companion matrix. Moreover, contrary to the POD modes, the Ritz eigenvectors are not orthonormal. The determination of the temporal coefficients $\nu_i(t)$ will thus require an extra effort. Different possible strategies will be presented in section 4.3.

2.3. Eigen-elements of the Companion matrix

Provided that the eigenvalues $\{\lambda_i\}_{i=1}^{N-1}$ of the Companion matrix are distinct, it can be demonstrated [7] that C can be diagonalized as $C = T^{-1}\Lambda T$ where T is the Vandermonde matrix defined by

$$T = \begin{pmatrix} 1 & \lambda_1 & \lambda_1^2 & \cdots & \lambda_1^{N-2} \\ 1 & \lambda_2 & \lambda_2^2 & \cdots & \lambda_2^{N-2} \\ \vdots & \vdots & \vdots & \vdots & \vdots \\ 1 & \lambda_{N-1} & \lambda_{N-1}^2 & \cdots & \lambda_{N-1}^{N-2} \end{pmatrix} \tag{9}$$

and $\Lambda = \operatorname{diag}(\lambda_1, \cdots, \lambda_{N-1})$. We then have an analytical expression for the eigenvectors of C that is based only on the eigenvalues λ_i. The matrix $\widetilde{\Phi} = (\widetilde{\boldsymbol{\Phi}}_1, \cdots, \widetilde{\boldsymbol{\Phi}}_{N-1})$ of the Ritz eigenvectors is given by

$$\widetilde{\Phi} = V_1^{N-1}T^{-1} \in \mathbb{R}^{N_x\times(N-1)}. \tag{10}$$

Since T is invertible, (10) writes $V_1^{N-1} = \widetilde{\Phi}T$ or

$$\boldsymbol{v}_k = \sum_{i=1}^{N-1} \lambda_i^{k-1}\widetilde{\boldsymbol{\Phi}}_i \quad k = 1, \cdots, N-1. \tag{11}$$

Moreover, we can deduce from $V_2^N = V_1^{N-1}C + \boldsymbol{r}\boldsymbol{e}_{\boldsymbol{N-1}}^T$ that

$$\boldsymbol{v}_N = \sum_{i=1}^{N-1} \lambda_i^{N-1}\widetilde{\boldsymbol{\Phi}}_i + \boldsymbol{r} \tag{12}$$

with $\boldsymbol{r} \perp \operatorname{span}(\boldsymbol{v}_1, \cdots, \boldsymbol{v}_{N-1})$.

In the DMD algorithm, the eigenvectors $\widetilde{\boldsymbol{\Phi}}_i$ are called the DMD modes and the eigenvalues λ_i, the DMD eigenvalues.

3. DMD PROPERTIES

In this section, we present some properties of DMD. We begin by reminding results on existence and uniqueness of DMD (section 3.1). In section 3.2, we illustrate the case of linear systems and show how the Ritz eigenvalues can be used to evaluate the frequency and growth rate of the DMD mode. In section 3.3, we discuss the case of periodic datasets. Finally, since in many applications, it is common to subtract the mean of the snapshots before performing a decomposition, we discuss this case in section 3.4.

3.1. Existence and uniqueness

The DMD algorithm presented in sections 2.2 and 2.3 proved by construction that for a set of data $\{\boldsymbol{v}_i\}_{i=1}^{N}$, there exist $\{\lambda_i\}_{i=1}^{N-1}$ and $\{\widetilde{\boldsymbol{\Phi}}_i\}_{i=1}^{N-1}$ such that (11) and (12) are satisfied, provided that $\{\lambda_i\}_{i=1}^{N-1}$ are distinct. In terms of Koopman analysis (see [7] for the definition of Koopman operator), λ_i and $\widetilde{\boldsymbol{\Phi}}_i$ are respectively the Koopman eigenvalues and modes of the dynamical process for the observable $\{\boldsymbol{v}_i\}_{i=1}^{N-1}$.

For the uniqueness result, it was proved recently in [12] that the choice of $\{\lambda_i\}_{i=1}^{N-1}$ and $\{\widetilde{\boldsymbol{\Phi}}_i\}_{i=1}^{N-1}$ in (11) and (12) is unique up to a reordering in i if and only if $\{\boldsymbol{v}_i\}_{i=1}^{N-1}$ are linearly independent and $\{\lambda_i\}_{i=1}^{N-1}$ are distinct.

3.2. Linear systems

A discretized version of the expansion (1) written at any time instant $k = 1, \cdots, N-1$ for the Ritz eigenvectors reads:

$$\boldsymbol{v}_k = \sum_{i=1}^{N-1} \boldsymbol{\Phi}_i \nu_i(k). \tag{13}$$

Using the first hypothesis (3), it can be immediately shown that

$$\boldsymbol{v}_{k+1} = A\boldsymbol{v}_k = \sum_{i=1}^{N-1} A\boldsymbol{\Phi}_i \nu_i(k) = \sum_{i=1}^{N-1} \lambda_i \boldsymbol{\Phi}_i \nu_i(k)$$
$$= A^k \boldsymbol{v}_1 = \sum_{i=1}^{N-1} \lambda_i^k \boldsymbol{\Phi}_i \nu_i(1). \quad (14)$$

The DMD eigenvalues $\{\lambda_i\}_{i=1}^{N-1}$ thus dictate the growth rate and frequency of each mode. Since in stability we are interested in the eigenvalues of the time-continuous matrix associated to the time-discrete matrix A of the linear map, it can be proved [10] that the growth rate σ_i and frequency ω_i are given by $\sigma_i = \ln(|\lambda_i|)/\Delta t$ and $\omega_i = \arg(\lambda_i)/\Delta t$.

We can deduce from this discussion that the most striking features between POD and DMD modes is that while a given DMD mode contains only a single frequency component, a POD mode contains in general a continuous spectrum. As a closing remark, we see that based on the Ritz eigenvalues and eigenvectors, (14) can be employed to reconstruct the snapshots as soon as $\nu_i(1)$ is known. This expression will be used in section 5 to reconstruct the data. Finally, by comparing (14) with (11), we can conclude that $\widetilde{\boldsymbol{\Phi}}_i = \boldsymbol{\Phi}_i \nu_i(1)$. $\nu_i(1)$ is then the scaling factor that links the eigenvectors of the Companion matrix C to the Ritz eigenvectors obtained by the DMD algorithm presented in section 2.2.

3.3. Periodic solutions

Now, suppose that we have a set of snapshots V_1^{N-1} that form a periodic solution of the dynamical system, such that $\boldsymbol{v}_{k+N-1} = \boldsymbol{v}_k$ for all k. In particular, we have $\boldsymbol{v}_N = \boldsymbol{v}_1$, suggesting that the coefficients of the Companion matrix C read $c_1 = 1$ and $c_i = 0$ for $i = 2, \cdots, N-1$.

From (8), we deduce immediately that $P_{C^T}(\lambda) = \lambda^{N-1} - 1$. The Ritz eigenvalues are then the $(N-1)^{\text{th}}$ roots of unity *i.e.* $\lambda_i = \exp(2\jmath\pi\frac{i-1}{N-1})$ with $i = 1, \cdots, N-1$.

These values are independent of the data. They can be determined as soon as N is known. Inserting this result into (11) and (12), we obtain for $k = 1, \cdots, N$

$$\boldsymbol{v}_k = \sum_{i=1}^{N-1} \exp\left(2\jmath\pi\frac{(i-1)(k-1)}{N-1}\right)\widetilde{\boldsymbol{\Phi}}_i.$$

This relation proves that for periodic solutions the DMD modes $\widetilde{\boldsymbol{\Phi}}_i$ correspond to the discrete Fourier transform of the data. In that case, the Vandermonde matrix (9) is exactly the Discrete Fourier Transform matrix.

3.4. Mean subtraction

As it is classically done in POD, we consider the case where DMD is applied to mean-subtracted data. For defining the mean, two possibilities exist. The first one consists of defining the mean as the ensemble average of the first $N-1$ snapshots contained in V_1^N. This choice leads to a rank deficient matrix [12] and by consequence (section 3.1) to a non unique DMD decomposition. The correct choice is then to define the data mean as $\langle \boldsymbol{v} \rangle = \frac{1}{N}\sum_{i=1}^{N} \boldsymbol{v}_i$.

At this point, a new data set $V'^N_1 = \left(\boldsymbol{v}'_1, \ldots, \boldsymbol{v}'_N\right)$ is introduced where $\boldsymbol{v}'_i = \boldsymbol{v}_i - \langle \boldsymbol{v} \rangle$ for $i = 1, \cdots, N$. It can be easily shown that if the matrix V_1^N is full-column rank than it is also the case for V'^N_1. Provided that the Ritz eigenvalues are distinct, the results of section (3.1) prove that the DMD decomposition exists and is unique.

By definition of the mean, we have $\boldsymbol{v}'_N = -\sum_{i=1}^{N-1} \boldsymbol{v}'_i$. This relation proves that the coefficients of the Companion matrix C are $c_i = -1$ for $i = 1, \cdots, N-1$.

From (8), the characteristic polynomial of C^T is now determined: $P_{C^T}(\lambda) = \sum_{i=0}^{N-1} \lambda^i = \frac{1-\lambda^N}{1-\lambda}$.

In that case, the Ritz eigenvalues are then the N^{th} roots of unity, excluding unity itself, *i.e.* $\lambda_i = \exp\left(2\jmath\pi\frac{i}{N}\right)$ with $i = 1, \cdots, N-1$.

Following the same approach as in section (3.3), we conclude that DMD is exactly equivalent to a temporal direct Fourier transform [12].

4. PRACTICAL CONSIDERATIONS

In this section, we will discuss practical considerations necessary to apply the DMD algorithm as described in section 2.2. Since DMD is a data-based analysis method, the characteristics of the dataset (value of time step, number of snapshots) are crucial. These points are discussed in section 4.1. Once the dataset is chosen, the next ingredient is the numerical method used to determine the coefficients of the Companion matrix C. Different approaches will be presented in section 4.2. Finally, when the DMD modes are known, we would like to reconstruct the original temporal dynamics. For this, we need to determine the temporal coefficients $\nu_i(t)$. Different oblique projection methods are discussed in sec. 4.3.

4.1. Choice of the dataset

In the original framework introduced by [1], DMD extracts dynamic modes which can be interpreted as a generalization of global stability modes when the flow is linearized and as a linear tangent approximation of the underlying dynamics for non linear flow. Whatever the flow regime considered, an important parameter is then the value of the constant time step Δt between successive snapshots. Obviously, in order for the DMD to extract pertinent flow processes, the flow must be sampled at a sufficiently high frequency. However, if this sampling frequency is too high then the snapshots will have a tendency to be correlated in time and the DMD modes will not be

unique following the results of section 3.1. The interpretation of Ritz eigenvalues and eigenvectors in terms of global stability is then subjected to an *a priori* good knowledge of the physical process under study in order to choose correctly the value of Δt.

The choice of the number N of snapshots contained in V_1^N is also a matter of discussion. Indeed, for the DMD to be unique, the first $N-1$ snapshots have to be linearly independent (section 3.1) and the N^{th} snapshot should be written as a linear combination of the previous ones (second DMD hypothesis, Eq. (5)). However, in most of the physical data, the end of the linear independence is not so sudden. One way of checking linear independence of the snapshots is to use the Gram-Schmidt process. In an intermediate step of this process, a sequence of vectors defined as $\boldsymbol{b}_j = \boldsymbol{v}_j - \sum_{l=1}^{j-1} \left(\boldsymbol{v}_j, \boldsymbol{b}_l\right) \boldsymbol{b}_l$ for $j = 1, \cdots, N$ is produced where $(\cdot,\cdot)$ stands for the Hermitian inner product *i.e.* $(\boldsymbol{w}_1, \boldsymbol{w}_2) = \boldsymbol{w}_1^H \boldsymbol{w}_2$. The variation with j of the ratio $\|\boldsymbol{b}_j\|/\|\boldsymbol{v}_j\|$ where $\|\boldsymbol{b}_j\|^2 = \left(\boldsymbol{b}_j, \boldsymbol{b}_j\right)$ gives a good indication of the loss of linear independence when new snapshots are added. Figure 1 corresponds to the case of the experimental data used in section 5. The decrease of $\|\boldsymbol{b}_j\|/\|\boldsymbol{v}_j\|$ is rather slow indicating that the choice of the number of snapshots to be processed by DMD is not obvious. As a consequence, the DMD algorithm will be probably ill-conditioned and the DMD modes may not be physically relevant. One way of checking the DMD procedure is to *a posteriori* determine the value of the residual $\boldsymbol{r}$ defined in (5).

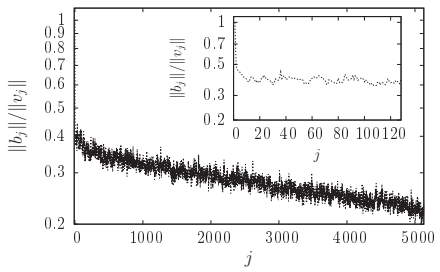

Figure 1. Variation of the normalized residual of the Gram-Schmidt process with the index of the snapshot.

4.2. Coefficients of Companion matrix

So far, the DMD algorithm was given (section 2.2) but without describing how the coefficients c_i of the Companion matrix C were found. The objective of this section is to present different methods that can be considered. It is possible in practice to:

1. Apply a QR factorization to V_1^{N-1} *i.e.*

$$\boldsymbol{v}_N = V_1^{N-1}\boldsymbol{c} = QR\boldsymbol{c} \quad \text{or} \quad \boldsymbol{c} = R^{-1}Q^H\boldsymbol{v}_N \tag{15}$$

where Q^H is the hermitian conjugate of Q.

2. Perform a SVD of V_1^{N-1} *i.e.*

$$\boldsymbol{v}_N = V_1^{N-1}\boldsymbol{c} = U_{\text{SVD}}\Sigma_{\text{SVD}}V_{\text{SVD}}^H\boldsymbol{c} \quad \text{or}$$
$$\boldsymbol{c} = V_{\text{SVD}}\Sigma_{\text{SVD}}^{-1}U_{\text{SVD}}^H\boldsymbol{v}_N. \tag{16}$$

3. Take the inner product of (5) with $\boldsymbol{v}_j$ for $j = 1, \cdots, N-1$. We obtain: $\left(\boldsymbol{v}_N, \boldsymbol{v}_j\right) = \sum_{i=1}^{N-1} \left(\boldsymbol{v}_i, \boldsymbol{v}_j\right) c_j$. If we now introduce the correlation matrix $K_{ij} = \left(\boldsymbol{v}_i, \boldsymbol{v}_j\right)$ and the vector $\boldsymbol{w} = (K_{N1}, \cdots, K_{NN-1})^T$, we arrive to the linear system of equations

$$\boldsymbol{c} = K^{-1}\boldsymbol{w}. \tag{17}$$

These three methods require a matrix inversion that can be done only if the snapshots $\{\boldsymbol{v}_i\}_{i=1}^{N-1}$ are linearly independent. So here we find with a numerical point of view the results of uniqueness given in section 3.1.

4.3. Determination of the coefficients $\nu_i(k)$

Equations (13) and (14) can be used to reconstruct the temporal dynamics of the snapshots from the Ritz eigenvalues and eigenvectors. However, the temporal coefficients $\nu_i(k)$ first need to be known at all the time instants $k = 1, \cdots, N$ or at the minimum at the first instant $k = 1$. Indeed, by identifying (13) and (14), it can be deduced immediately that

$$\nu_i(k+1) = \lambda_i^k \nu_i(1), \quad \text{for} \quad k = 1, \cdots, N-1. \tag{18}$$

Since the Ritz eigenfunctions are not orthonormal, two oblique projection methods are here proposed to determine $\nu_i(k)$.

4.3.1. Gramian matrix

A first idea is to use the Gramian matrix G of $\Phi = (\boldsymbol{\Phi}_1, \cdots, \boldsymbol{\Phi}_{N-1})$ whose entries are given by $G_{ij} = (\boldsymbol{\Phi}_i, \boldsymbol{\Phi}_j)$. Taking the inner product of (13) with $\boldsymbol{\Phi}_i$, $i = 1, \cdots, N-1$, we obtain the linear system of equations $G\boldsymbol{\nu}_k = \boldsymbol{z}_k$ for $k = 1, \cdots, N$ where $\boldsymbol{\nu}_k = (\nu_1(k), \cdots, \nu_{N-1}(k))^T$ and $\boldsymbol{z}_k = ((\boldsymbol{\Phi}_1, \boldsymbol{v}_k), \cdots, (\boldsymbol{\Phi}_{N-1}, \boldsymbol{v}_k))^T$. This relation can be written in matrix form as

$$\nu = G^{-1}\Phi^H V_1^N, \tag{19}$$

where ν is the matrix that contains the vectors $\boldsymbol{\nu}_k$. For using (19), the matrix G must be well conditioned.

4.3.2. Adjoint basis

Another solution is to search for adjoint modes $\boldsymbol{\Psi}_j$ of $\boldsymbol{\Phi}_i$. Indeed, if the adjoint modes are know then it is straightforward to determine the coefficients $\nu_j(k)$ as

$$\nu_j(k) = \sum_{i=1}^{N-1} \underbrace{\left(\boldsymbol{\Psi}_j, \boldsymbol{\Phi}_i\right)}_{\delta_{ij}} \nu_i(k) = \left(\boldsymbol{\Psi}_j, \boldsymbol{\nu}_k\right). \tag{20}$$

By definition, $\mathbf{\Psi}_i$ is solution of the adjoint eigenvalue problem

$$A^H \mathbf{\Psi}_i = \bar{\lambda}_i \mathbf{\Psi}_i. \tag{21}$$

It can be proved (see appendix 7.2) that $\left(\boldsymbol{z}_i = \left(V_1^{N-1}\right)^H \mathbf{\Psi}_i, \bar{\lambda}_i\right)$ are approximated eigen-elements of C^H. Since V_1^{N-1} is in general a non-square matrix, we can use the SVD decomposition of V_1^{N-1} (Moore-Penrose pseudoinverse) for finding that $\mathbf{\Psi}_i = U_{\text{SVD}} \Sigma_{\text{SVD}}^{-1} V_{\text{SVD}}^H \boldsymbol{z}_i$.

5. RESULTS

The DMD algorithm has been performed on data obtained by 2D-2C PIV measurements for a turbulent cylinder wake [13] corresponding to a sub-critical flow regime ($Re_D = DU_\infty/\nu_{\text{kin}} = 40000$ where $D = 40\,\text{mm}$ is the cylinder diameter and $U_\infty = 15.6\, m.s^{-1}$ is the free-stream velocity). The database contains $N_s = 5130$ snapshots taken at a sampling frequency $f_s = 1\,\text{kHz}$ over approximatively 400 periods of vortex shedding. Following the discussions in section 4.1, the DMD is applied on 128 snapshots (see Fig. 1) without subtracting the mean. Here, the coefficients $\boldsymbol{c}$ were calculated with (17) by inverting the correlation matrix K.

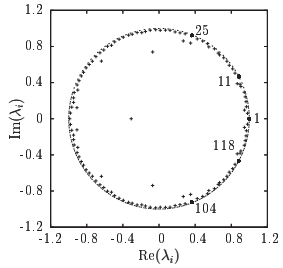

Figure 2. Empirical Ritz values λ_i.

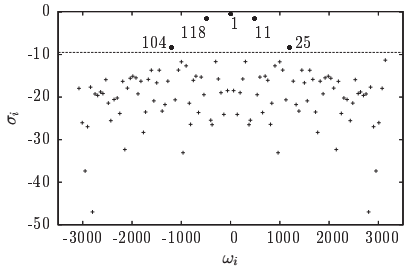

Figure 3. Time-continuous DMD spectrum of the cylinder wake flow.

Figure 2 shows that nearly all the Ritz values are on the unit circle indicating that the snapshots lie on or near an attracting set. The growth rate of each DMD mode σ_i is plotted versus its frequency ω_i in Figure 3. The spectrum appears symmetric with respect to the imaginary axis $\omega_i = 0$, which is a consequence of processing real-valued data. Indeed, in that particular case, the eigenvalues and associated eigenvectors are real or complex conjugate. At this point, the Ritz eigenvectors are available for the design of a reduced-order model. However, it remains to be decided which of the modes should be included in the reduction basis. One criterion that should be assessed is based on the damping rate of the DMD and employs the argument that modes with large decay rates are dynamically less relevant than modes that are only weakly damped. Figure 3 suggests that the mean flow and the two first pairs of modes should be sufficient to obtain a good description of the dynamics. The most amplified mode (mode 1) corresponds to the mean flow. The streamwise $\mathbf{\Phi}_1^u$ and vertical $\mathbf{\Phi}_1^v$ components of $\mathbf{\Phi}_1$ are plotted in Figures 7(a) and 7(b) (see appendix 7.3). The complex conjugates modes 11 and 118 oscillate at $St = 0.2$ (see figure 4) which is precisely the fundamental shedding frequency of the wake flow. Figures 7(c) to 7(j) represent the streamwise and vertical components of $\mathbf{\Phi}_{11}$ and $\mathbf{\Phi}_{25}$, respectively. The modes 118 and 104 are not represented for symmetry reasons.

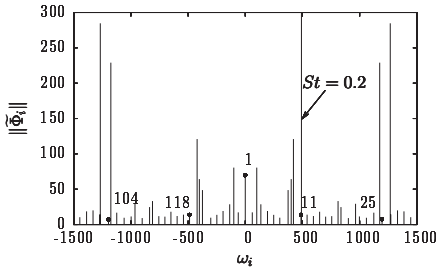

Figure 4. Magnitudes of the DMD modes at each frequency ω_i.

Figure 4 represents the amplitude of the DMD modes. Their amplitudes are not a criterion in itself of the dynamic relevance of these modes since even a mode with a very large amplitude can be strongly damped. For instance, the mode 11 corresponding dynamically to the vortex shedding ($St = 0.2$) has relatively low amplitude compared to other modes.

Concerning the temporal coefficients $\nu_i(k)$ of the Ritz eigenvectors, they are represented in Figure 5 for the two dominant modes: 11, and 25. For symmetry reasons, the temporal coefficients ν_{118} and ν_{104} are again not plotted. The three methods proposed in section 4.3 to determine the temporal coefficients, respectively with the Gramian matrix (19), the adjoint modes (20) and the multiplication of the Ritz eigenvalues by $\nu_i(1)$ (see Eq. (18)) have been compared and give exactly the same results. The amplitude of the mean flow (mode 1 no plotted) is real and approximatively constant over time. The oscillatory behaviour of the vortex shedding mode 11 is well captured and the mode 25 is clearly damped. Knowing $\nu_i(1)$, it was *a posteriori* checked that $\widetilde{\mathbf{\Phi}}_i = \mathbf{\Phi}_i \nu_i(1)$.

In order to assess the possibility of deriving an accurate reduced-order model based on some DMD

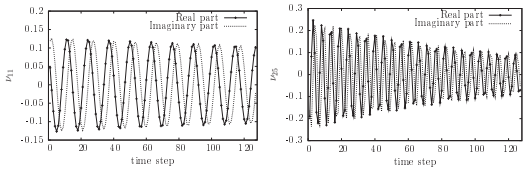

(a) $\mathrm{Re}\,(\nu_{11}(k))$, $\mathrm{Im}\,(\nu_{11}(k))$. (b) $\mathrm{Re}\,(\nu_{25}(k))$, $\mathrm{Im}\,(\nu_{25}(k))$.

Figure 5. Temporal coefficients of the DMD modes.

modes, different reconstructions of the snapshot $\boldsymbol{v}_5$ have been performed (see Figure 6). Figures 6(c) and 6(d) correspond to the reconstruction of the streamwise u and vertical v components of $\boldsymbol{v}_5$ using all the DMD modes. Compared to the original fields represented in Figures 6(a) and 6(b), respectively, a very good agreement is obtained. The error in L^2 norm is about 0.07%. If the number of DMD modes kept in the reconstruction is reduced, the tendency is to describe increasingly large space scales. When the modes 1, 11, 118, 25 and 104 are used for the reconstruction (Figures 6(e) and 6(f)), the L^2 error is 42.5%. When the modes in the reconstruction are still reduced to 1, 11 and 118 (Figures 6(g) and 6(h)), the L^2 error decreases up to 40.5%. Due to the non orthogonality of the DMD modes, the L^2 error is not monotonic with the number of modes as it is the case by definition for the POD modes. These reduced-order approximations may be on some circumstances (flow control for instance) sufficient good approximations of the physical phenomena.

6. CONCLUSION

DMD is a method that is able to extract dynamic information from empirical data obtained either numerically or in experiments. Without explicit knowledge of the underlying dynamical operator, it determines growth rates, frequencies and spatial structures of an approximate linear model. These modes can be viewed as a generalization of global stability modes obtained for a linearized system. The DMD algorithm was first presented in details and its potential use for finding Koopman modes discussed. In addition, the most important DMD properties were presented and in particular the link existing between DMD and Fourier modes when the mean-data is subtracted before the analysis. The DMD algorithm was applied on a PIV experimental dataset of a cylinder wake flow in turbulent regime. It was shown that a reduced-order model based on the three most unstable pairs of DMD modes can reproduce qualitatively well the original dynamics.

ACKNOWLEDGEMENTS

Nicolas BENARD (Electro-Fluido-Dynamic group of the Pprime institute) is warmly acknowledged for providing us with the PIV experimental database of the cylinder wake flow. This work has received support from the National Agency for Research on reference ANR-08-BLAN-0115-01.

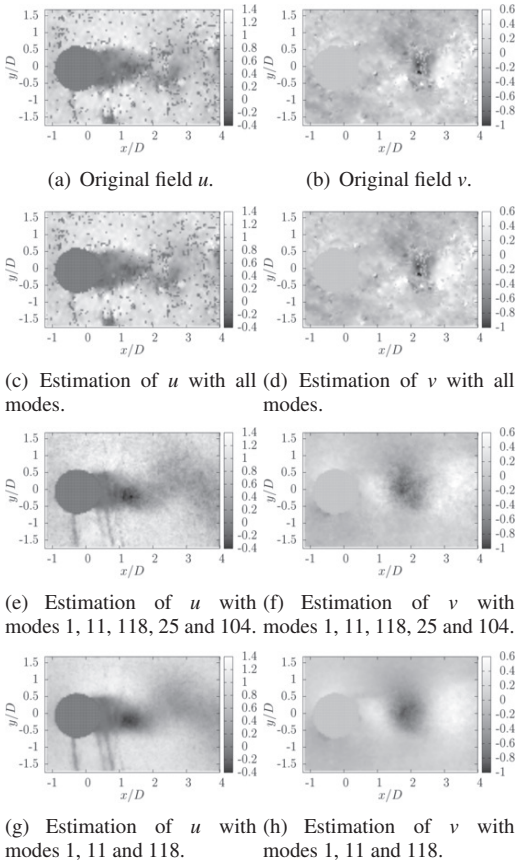

(a) Original field u. (b) Original field v.

(c) Estimation of u with all modes. (d) Estimation of v with all modes.

(e) Estimation of u with modes 1, 11, 118, 25 and 104. (f) Estimation of v with modes 1, 11, 118, 25 and 104.

(g) Estimation of u with modes 1, 11 and 118. (h) Estimation of v with modes 1, 11 and 118.

Figure 6. Reconstruction of the streamwise u and vertical v components of the snapshot $\boldsymbol{v}_5$.

7. APPENDIX

7.1. *Ritz eigenvectors and eigenvalues of* A

Let $(\boldsymbol{y}_i, \lambda_i)$ be the i^{th} eigen-elements of C, the objective is to prove that $\left(\boldsymbol{\Phi}_i = V_1^{N-1}\boldsymbol{y}_i, \lambda_i\right)$ are approximated eigen-elements of A. Proof:

$$\begin{aligned} A\boldsymbol{\Phi}_i - \lambda_i\boldsymbol{\Phi}_i &= AV_1^{N-1}\boldsymbol{y}_i - \lambda_i V_1^{N-1}\boldsymbol{y}_i \\ &= \left(AV_1^{N-1} - V_1^{N-1}C\right)\boldsymbol{y}_i \\ &= \boldsymbol{r}\boldsymbol{e}_{\boldsymbol{N-1}}^T\boldsymbol{y}_i \longrightarrow 0 \quad \text{if} \quad \|\boldsymbol{r}\| \longrightarrow 0. \end{aligned}$$

7.2. *Eigen-elements of* C^H

For $\|\boldsymbol{r}\| \to 0$, taking the Hermitian of (6) leads to:

$$\left(V_1^{N-1}\right)^H A^H = C^H\left(V^{N-1}\right)^H. \tag{22}$$

Multiplying (22) by $\boldsymbol{\Psi}_i$ and considering (21) reads

$$\begin{aligned} \left(V_1^{N-1}\right)^H A^H\boldsymbol{\Psi}_i &= C^H\left(V_1^{N-1}\right)^H\boldsymbol{\Psi}_i \\ &= \bar{\lambda}_i\left(V_1^{N-1}\right)^H\boldsymbol{\Psi}_i \end{aligned}$$

proving that $\left(z_i = \left(V_1^{N-1}\right)^H \boldsymbol{\Psi}_i, \bar{\lambda}_i\right)$ are approximated eigen-elements of C^H.

7.3. Ritz eigenvectors

The most amplified Ritz eigenvectors $\boldsymbol{\Phi}_i$ are represented in this appendix.

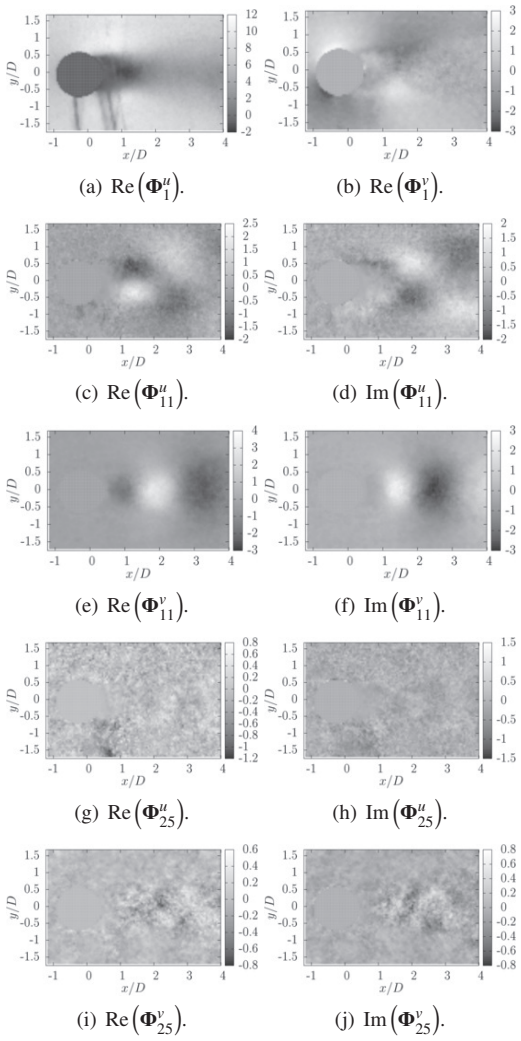

(a) $\mathrm{Re}\left(\boldsymbol{\Phi}_1^u\right)$. (b) $\mathrm{Re}\left(\boldsymbol{\Phi}_1^v\right)$.

(c) $\mathrm{Re}\left(\boldsymbol{\Phi}_{11}^u\right)$. (d) $\mathrm{Im}\left(\boldsymbol{\Phi}_{11}^u\right)$.

(e) $\mathrm{Re}\left(\boldsymbol{\Phi}_{11}^v\right)$. (f) $\mathrm{Im}\left(\boldsymbol{\Phi}_{11}^v\right)$.

(g) $\mathrm{Re}\left(\boldsymbol{\Phi}_{25}^u\right)$. (h) $\mathrm{Im}\left(\boldsymbol{\Phi}_{25}^u\right)$.

(i) $\mathrm{Re}\left(\boldsymbol{\Phi}_{25}^v\right)$. (j) $\mathrm{Im}\left(\boldsymbol{\Phi}_{25}^v\right)$.

Figure 7. Ritz eigenvectors 1, 11 and 25.

References

[1] Schmid, P. (2010) Dynamic mode decomposition of numerical and experimental data. *Journal of Fluid Mechanics*.

[2] Schmid, P. (2009) Dynamic mode decomposition of experimental data. *8th International Symposium on Particle Image Velocimetry*.

[3] Schmid, P., Meyer, K., and Pust, O. (2009) Dynamic mode decomposition and proper orthogonal decomposition of flow in a lid-driven cylindrical cavity. *8th International Symposium on Particle Image Velocimetry*.

[4] Schmid, P., Li, L., Juniper, M., and Pust, O. (2010) Applications of the dynamic mode decomposition. *Theoretical and Computational Fluid Dynamics*, pp. 1–11.

[5] Tu, J., Rowley, C., Aram, E., and Mittal, R. (2011) Koopman spectral analysis of separated flow over a finite-thickness flat plate with elliptical leading edge. *49th AIAA Aerospace Sciences Meeting including the New Horizons Forum and Aerospace Exposition 4-7 January 2011, Orlando, Florida*.

[6] Rowley, C., Mezić, I., Bagheri, S., Schlatter, P., and Henningson, D. (2009) Reduced-order models for flow control: balanced models and Koopman modes. *Seventh IUTAM Symposium on Laminar-Turbulent Transition*, pp. 43–50, Springer.

[7] Rowley, C., Mezić, I., Bagheri, S., Schlatter, P., and Henningson, D. (2009) Spectral analysis of nonlinear flows. *Journal of Fluid Mechanics*, **641**, 115–127.

[8] Aubry, N., Holmes, P., Lumley, J., and Stone, E. (1988) The dynamics of coherent structures in the wall region of a turbulent boundary layer. *Journal of Fluid Mechanics*, **192**, 173355.

[9] Ipsen, I. and Meyer, C. (1998) The idea behind Krylov methods. *American Mathematical Monthly*, **105**, 889–899.

[10] Bagheri, S. (2010) *Analysis and control of transitional shear flows using global modes*. Ph.D. thesis, Department of Mechanics Royal Institute of Technology SE-100 44 Stockholm, Sweden.

[11] Ruhe, A. (1984) Rational Krylov sequence methods for eigenvalue computation. *Lin. Alg. Appl.*, **58**, 391–405.

[12] Chen, K., Tu, J., and Rowley, C. (2011) Variants of dynamic mode decomposition: connections between Koopman and Fourier analyses. *Submitted of the Journal of Nonlinear Science*.

[13] Benard, N., Debien, A., David, L., and Moreau, E. (2010) Analyse par PIV rapide du sillage d'un cylindre manipulé par actionneurs plasmas. *Congrès Francophone de Techniques Laser*, Vandoeuvre-lès-Nancy 14-17 septembre.

Conference on Modelling Fluid Flow (CMFF'12)
The 15th International Conference on Fluid Flow Technologies
Budapest, Hungary, September 4-7, 2012

INFLUENCE OF HYSTERESIS EFFECTS ON THE CALIBRATION DATA OF A THREE-HOLE PRESSURE PROBE: EXPERIMENTAL, NUMERICAL AND ANALYTICAL INVESTIGATION

Reinhard WILLINGER

Institute for Energy Systems and Thermodynamics, Vienna University of Technology. Getreidemarkt 9 / 302, A-1060 Vienna, Austria.
Tel.: +43 1 58801 302403, Fax: +43 1 58801 302399, E-mail: reinhard.willlinger@tuwien.ac.at

ABSTRACT

This paper presents an investigation on the calibration of a three-hole pressure probe (cobra probe). Hysteresis effects have been documented by the probe manufacturer at increasing respectively degreasing free stream velocities for the probe nulled in yaw. Conventional calibration coefficients for a probe Reynolds number of about 7400 are obtained in a free jet wind tunnel at subsonic conditions. The experimental calibration is extended by computational as well as analytical results. The calibration coefficients are predicted by the streamline projection method, at least qualitatively. The method can also be used to describe the hysteresis effect as a result of laminar/turbulent transition at the probe head side holes. This fact is supported by unsteady computational fluid dynamics (CFD) calculations.

Keywords: CFD, hysteresis effect, laminar/turbulent transition, non-nulling experimental calibration, Reynolds number, three-hole pressure probe

NOMENCLATURE

Ma	[-]	Mach number
Re	[-]	Probe Reynolds number
Sr	[-]	Strouhal number
d	[mm]	probe width
f	[1/s]	frequency
k_d	[-]	dynamic pressure coefficient
k_i	[-]	hole coefficient
k_β	[-]	direction coefficient
k_s	[-]	static pressure coefficient
k_t	[-]	total pressure coefficient
p	[Pa]	static pressure
p_t	[Pa]	total pressure
w	[m/s]	velocity
Δt	[s]	time increment
$\Delta\beta$	[°]	yaw angle
δ	[°]	probe wedge angle
ν	[m^2/s]	kinematic viscosity
ρ	[kg/m^3]	density

Subscripts and Superscripts

i = 1, 2, 3	related to hole number

1. INTRODUCTION

Three-hole pressure probes are robust and reliable tools for flow measurement in turbomachinery components. They yield total as well as static pressure and direction of a two-dimensional steady flow field. An extension to the three-hole probe is the five-hole probe, which can be used for three-dimensional flow measurements. Due to space restrictions in turbomachinery applications, both probe types are used in the non-nulling mode and a calibration procedure prior to the measurement is required. Usually, a free jet wind tunnel is used for this task. According to Dominy and Hodson [1], the main factors influencing the calibration of five-hole pressure probes are: probe geometry, probe Reynolds number, Mach number, turbulence intensity. In contrast to the free jet, the flow field downstream of a turbomachinery blade row is dominated by blade wakes. When the three-hole probe is traversed in pitchwise direction through the wake, its head experiences a sequence of decreasing and increasing velocity. Maximum velocity corresponds to the undisturbed value at mid passage whereas minimum velocity appears in the centre of blade wake. The difference between maximum and minimum velocity increases when the axial distance of blade row trailing edge plane and measurement plane decreases. As a consequence, systematic errors of the measured flow quantities can occur.

The first effect, which is the so-called gradient effect, influences mainly the flow angle measurement [2]. The second effect is the Reynolds number effect due to the variation of velocity magnitude. Lee and Jun [3] investigated the influence of probe Reynolds number on the non-nulling calibration of a cone-type five-hole probe. For probe Reynolds numbers $6600 < Re < 31700$ they found that the sensitivity of calibration coefficients on Reynolds number depends on yaw and pitch angle. Dominy and Hodson [1] performed five-hole probe calibrations at a probe Reynolds number range $7000 < Re < 80000$. At relatively low Reynolds numbers, separation around the probe head affects the calibration while changes in the detailed structure of the flow around the sensing holes affects the calibration even when the probe is nulled. Following the literature, hysteresis effects, especially at external flow applications, can be observed when geometry and/or Reynolds number are changed continuously. Generally speaking, hysteresis is the dependence of a system not only on its current environment but also on its past environment. This dependence arises because the system can be in more than one internal state. Mittal and Saxena [4] present computational results of flow past an isolated NACA 0012 airfoil using Reynolds Averaged Navier Stokes equations with Baldwin-Lomax turbulence model. Hysteresis in the flow is observed for angles of attack close to the stall angle of the airfoil. The ability of the flow to remember its past history is responsible for its hysteretic behaviour. For the same angle of attack, the flow obtained with increasing angles results in an almost attached flow with higher lift and lower drag, whereas the one with decreasing angle of attack is associated with large unsteadiness, lower lift and higher drag. Schewe [5] reviews results of flow experiments carried out over a wide range of Reynolds numbers ($10^4 < Re < 10^7$) on three different two-dimensional sections of more-or-less bluff bodies: circular cylinder, trapezoidal-shaped bridge element, thick airfoil at high angle of attack. Reynolds number affects the location of laminar/turbulent transition of the boundary layer which in turn influences the topological structure of the flow. At distinct Reynolds numbers, hysteretic behaviour of lift, drag and vortex shedding frequency has been observed. Finally, Reneau et al. [6] performed an experimental investigation on the performance of straight, two-dimensional diffusers. At fixed nondimensional axial diffuser length and various area ratios, they observed different flow regimes. For very large area ratios, fully developed two-dimensional stall and jet flow can be found. These flow regimes correspond to distinct combinations of nondimensional axial diffuser lengths and area ratios. However, both flow regimes are overlapping in a hysteresis zone at certain combinations of axial diffuser length and area ratio.

To the author's knowledge, hysteresis effects associated with the calibration of pressure probes haven not been documented yet. Therefore, the present paper focuses on this topic, performing experimental, numerical and analytical investigations on a specific three-hole pressure probe.

2. PROBE GEOMETRY, HOLE AND CALIBRATION COEFFICIENTS

The three-hole pressure probe used for the present investigation is a cobra probe with a characteristic dimension $d = 3 \times 0.8 = 2.4$ *mm* and a wedge angle $\delta = 30°$. The pressure holes are forward faced with a diameter of 0.5 *mm* and are numbered "1", "2" and "3". Figure 1 shows the geometry, the numbering of the holes as well as the definition of the yaw angle $\Delta\beta$. This is the angle between the velocity vector w and the probe axis. The pressure p_i, sensed by the hole "i" differs from the static pressure p. Since the experiments are performed at Mach numbers $Ma < 0.2$, conditions are essentially incompressible and a hole coefficient can be defined according to

$$k_i = \frac{p_i - p}{(\rho/2)w^2}. \tag{1}$$

The hole coefficient k_i can be interpreted as a nondimensional pressure sensed by the hole "i".

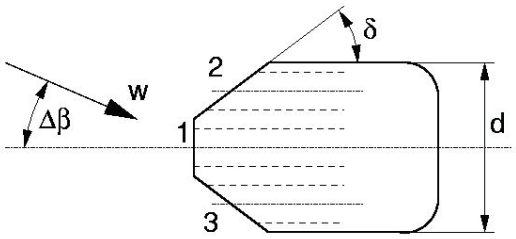

Figure 1. Probe geometry, hole numbering and definition of yaw angle $\Delta\beta$

The three-hole probe can be used to measure the direction of the flow as well as the total and the static pressure. The relationship between these quantities and the yaw angle $\Delta\beta$ is given by the nondimensional calibration coefficients. Various definitions of these calibration coefficients can be found in the literature. The present work uses the common definition of Treaster and Yocum [7] for direction coefficient k_β, total pressure coefficient k_t and static pressure coefficient k_s, adapted to the requirements of a three-hole probe:

$$k_\beta = \frac{p_2 - p_3}{p_1 - \overline{p}} = \frac{k_2 - k_3}{k_1 - \overline{k}}, \tag{2}$$

$$k_t = \frac{p_1 - p_t}{p_1 - \overline{p}} = \frac{k_1 - 1}{k_1 - \overline{k}}, \tag{3}$$

$$k_s = \frac{\overline{p} - p}{p_1 - \overline{p}} = \frac{\overline{k}}{k_1 - \overline{k}}. \quad (4)$$

The quantities

$$\overline{p} = \frac{p_2 + p_3}{2} \quad \text{and} \quad \overline{k} = \frac{k_2 + k_3}{2} \quad (5)$$

represent a mean pressure and a mean hole coefficient, respectively. As can be seen from Eqs. (2) to (5), the calibration coefficients are related directly to the three hole coefficients.

3. OBSERVATION OF PROBE CALIBRATION HYSTERESIS EFFECT

The three-hole pressure probe under investigation has been manufactured by SVUSS a.s., Prague, Czech Republic, in 1994. At this time, it was the objective of the institute to use the probe exclusively in nulling mode. Therefore, appropriate nulling mode calibration curves have been supplied by the probe manufacturer [8]. The calibration has been performed in a free jet wind tunnel, 92.5 *mm* downstream of a nozzle with diameter 75 *mm* in the velocity range 3 *m/s* < *w* < 87 *m/s*, corresponding to probe Reynolds numbers 800 < *Re* < 13500. Turbulence intensity of the free jet was not documented. For the probe nulled in yaw, Fig. 2 shows the distribution of the dynamic pressure coefficient

$$k_d = \frac{p_t - p}{p_1 - p_2} = \frac{1}{k_1 - k_2}. \quad (6)$$

This single calibration coefficient is sufficient for a three-hole probe used in nulling mode. It is used to get the static pressure, since total pressure is already known from the pressure at the probe centre hole.

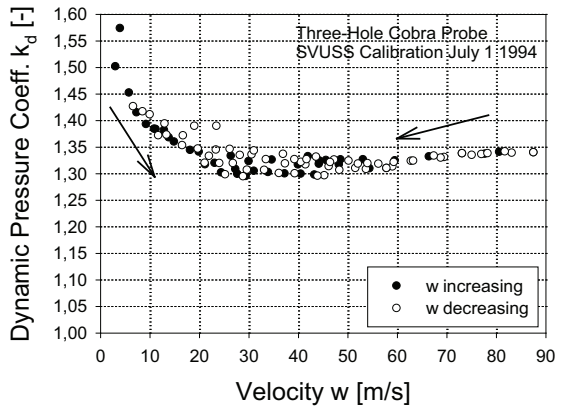

Figure 2. Dynamic pressure coefficient k_d according to manufacturers calibration [8]

As can be seen from Fig. 2, dynamic pressure coefficient decreases at increasing velocities up to about 20 *m/s*. At velocities higher than about 70 *m/s*, dynamic pressure coefficient is nearly constant. In the intermediate velocity range 20 *m/s* < *w* < 70 *m/s*, strong variations of dynamic pressure coefficient are visible. Furthermore, a hysteretic behaviour can be observed since dynamic pressure coefficients are different for increasing respectively decreasing velocity. Individual hole coefficients k_1 and k_2 have not been provided by the probe manufacturer. However, as will be explained later, the side hole coefficient k_2 is responsible for the behaviour of k_d versus flow velocity, since k_1 is rather independent of Reynolds number.

4. STREAMLINE PROJECTION METHOD

The streamline projection method is a simple analytical approach which is used in addition to the experimental as well as the computational investigations. This method is based on the assumption that the free stream velocity is projected on each of the three sensing holes. The velocity component normal to the probe head surface results in a "dynamic pressure" which is added to the free stream static pressure. Under the assumption of constant velocity magnitude *w*, the three hole coefficients obtained from the streamline projection method are

$$k_1 = \cos^2 \Delta\beta, \quad (7)$$

$$k_2 = \sin^2(\delta + \Delta\beta) \quad \text{and} \quad (8)$$

$$k_3 = \sin^2(\delta - \Delta\beta). \quad (9)$$

Corresponding calibration coefficients follow directly from Eqs. (2) to (5). For small yaw angles $\Delta\beta$, a Taylor series expansion of Eq. (2) provides

$$k_\beta = \Delta\beta \frac{\pi}{45°} \tan\delta. \quad (10)$$

Furthermore, the dynamic pressure coefficient from Eq. (6) gets for the nulled probe

$$k_d = \frac{1}{1 - \sin^2\delta} = \frac{1}{\cos^2\delta} = 1.33, \quad (11)$$

in good correspondence to the measured value at high flow velocities (Fig. 2).

5. EXPERIMENTAL CALIBRATION

A free jet wind tunnel is used for the probe calibration at various velocities and yaw angles. The probe is mounted in a support device to adjust different yaw angles. Throat diameter of the convergent nozzle is 120 *mm* and the probe head is positioned inside the potential core of the jet, 130 *mm* downstream of the nozzle exit plane. Air is supplied by a radial fan with variable rotational speed with a streamwise turbulence intensity of about 1%. Calibration is performed for different yaw angles in the range ±30° in steps of 2.5° at fixed probe Reynolds number

$$\mathrm{Re} = \frac{wd}{\nu} \approx 7400. \quad (11)$$

For a fixed probe geometry and fixed ambient temperature, variation of velocity is synonym for variation of probe Reynolds number. Furthermore,

free stream velocity is gradually increased to a maximum and then decreased to investigate hysteresis effects of the probe nulled in yaw. Velocity range is from 20 *m/s* to 80 *m/s* in steps of about 2.5 *m/s*. This velocity range corresponds to a probe Reynolds number range $4000 < Re < 15000$. Since the throat Mach number $Ma < 0.2$, conditions are essentially incompressible. At a fixed operating point, following measurement data are taken: three pressures sensed by the probe holes, total pressure and total temperature in the settling chamber, ambient pressure. 50 pressure readings are taken over a period of about 10 seconds. The ambient pressure is used as the free stream static pressure for subsequent calculation of hole and calibration coefficients. Temperature is measured using a Pt-100 resistor thermometer. All pressures are sensed by piezoresistive transducers (HONEYWELL). The HP 3852A data acquisition system is controlled by a personal computer using LabVIEW (NATIONAL INSTRUMENTS).

6. NUMERICAL INVESTIGATION

6.1. Numerical Method and Finite-Element Mesh

The numerical method is based on the governing equations for two-dimensional, incompressible, unsteady flow. The probe Reynolds number during the wind tunnel calibration is $4000 < Re < 15000$. Therefore, a laminar as well as a turbulent simulation is performed. Turbulent computation is based on a simple algebraic model assuming a constant mixing-length $0.1d$. The finite-element based CFD code FIDAP8.7.4 [9] is performed to solve the governing equations. A nondimensional time step

$$\Delta t \frac{w}{d} = 0.1 \qquad (12)$$

is used for the 2nd order implicit time integration. A single vortex shedding period is resolved by about 70 time steps. Periodic flow is established after about 500 time steps at Strouhal numbers

$$Sr = \frac{fd}{w} \approx 0.16. \qquad (13)$$

This Strouhal number value can be compared with $Sr = 0.134$ for the flow around a square cross-section cylinder [10]. The computational domain, plotted in Fig. 3, comprises a rectangle $38.5d$ by $25d$ with the inlet plane positioned $15d$ upstream of the probe. The finite-element mesh in the vicinity of probe head is plotted in Fig. 4. Total number of nodes of the structured mesh is about 24000. As can be seen from Fig. 4, the three pressure holes are taken into account in the finite-element model, since the hole diameter of 0.5 *mm* is relatively large in comparison to the probe width $d = 2.4$ *mm*. To check the grid sensitivity, computations with a finer mesh (about 56000 nodes) have been performed for the nulled probe at $Re = 7400$. Results indicate that there is no change in Strouhal numbers. Therefore, results from the computations with the coarser mesh are presented throughout.

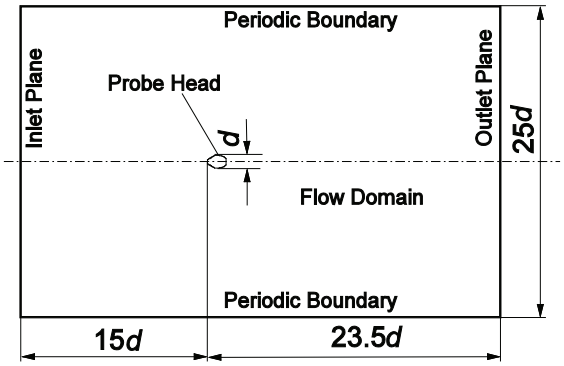

Figure 3. Computational domain

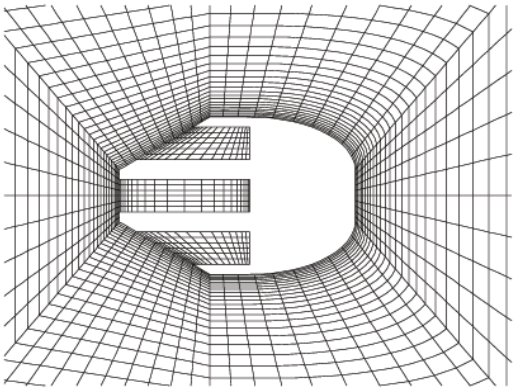

Figure 4. Finite-element mesh in the vicinity of probe head

6.2. Boundary Conditions

The applied boundary conditions can be explained with reference to Fig. 3. At the inlet plane velocity components are set according to the required velocity magnitude w and yaw angle $\Delta\beta$. Furthermore, no slip boundary conditions are applied to the surface of the probe head. At the outlet plane, the applied "traction-free" condition is equivalent to a constant static pressure distribution. Finally, periodic boundary conditions are applied to the bottom and the top boundary of the computational domain (Fig. 3).

7. RESULTS AND DISCUSSION

7.1. Variation of Yaw Angle Δβ at Fixed Probe Reynolds Number Re = 7400

The hole coefficients k_1, k_2 and k_3 versus the yaw angle $\Delta\beta$ are plotted for constant probe Reynolds number $Re = 7400$ in Fig. 5, Fig. 6 and Fig. 7, respectively.

Agreement between the measured hole coefficient k_1 and the results gained from the streamline projection method is acceptable. The measured distribution shows asymmetries for positive and negative yaw angles. These asymmetries are caused by manufacturing imperfections, since there is a small deviation of the front face with respect to the plane normal to the probe axis. The CFD simulation provides slightly lower values for k_1 at very high as well as very low yaw angles compared with measurement and streamline projection method. Difference between laminar and turbulent CFD results is negligible throughout the whole yaw angle range. This means that the pressure at the centre hole is not influenced by viscous effects.

Great discrepancies between measurement, streamline projection method and CFD simulation are in part observed for the hole coefficients k_2 and k_3. These are the nondimensional pressures, sensed by the side holes. The general agreement is acceptable for the "pressure side" hole coefficients. These are k_2 for $\Delta\beta > 0$ and k_3 for $\Delta\beta < 0$, respectively. Great discrepancies occur for the "suction side" hole coefficients. These are k_3 for $\Delta\beta > 0$ and k_2 for $\Delta\beta < 0$, respectively. Computed "pressure side" hole coefficients are nearly the same for laminar and turbulent flow and they are slightly higher than the measured values. On the other hand, computed "suction side" hole coefficients are considerably too low. The flow separates at the sharp corner and a large separation region is established. This separation region is larger for laminar flow since "suction side" k_2 and k_3 are lower for laminar than for turbulent computation. It is expected that the real flow undergoes a separated flow transition and reattaches as a turbulent boundary layer. The streamline projection method does not take into account any separation and, therefore, the hole coefficients k_2 and k_3 are positive throughout the entire yaw angle range.

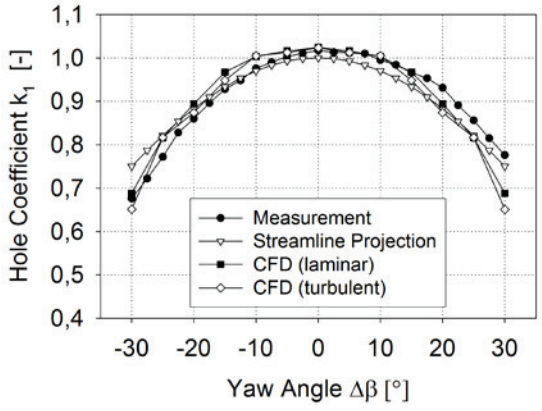

Figure 5. Hole coefficients k_1 for Re = 7400

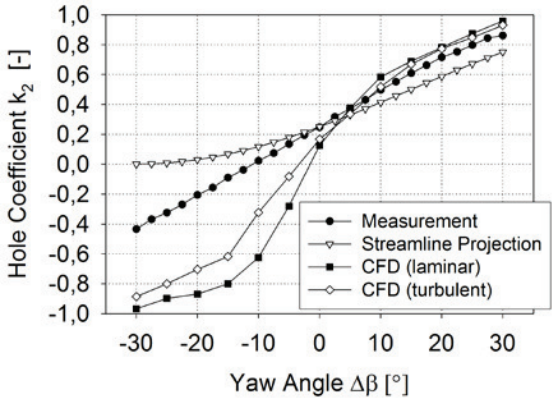

Figure 6. Hole coefficients k_2 for Re = 7400

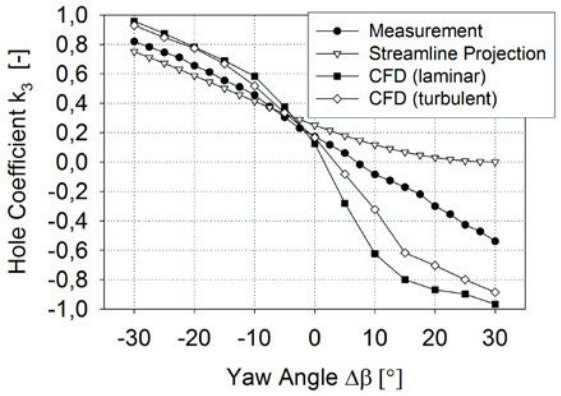

Figure 7. Hole coefficients k_3 for Re = 7400

The direction coefficient k_β, the total pressure coefficient k_t and the static pressure coefficient k_s versus the yaw angle $\Delta\beta$ at fixed probe Reynolds number Re = 7400 are plotted in Fig. 8, Fig. 9 and Fig. 10, respectively. These coefficients are of practical interest for the probe application to measure a distinct flow field.

Good agreement between measurement, streamline projection method and CFD simulation is achieved for the direction coefficient k_β as well as for the total pressure coefficient k_t. However, the yaw angle sensitivity of the direction coefficient at $\Delta\beta = 0°$ is somewhat underpredicted by the streamline projection method. On the other hand, it is overpredicted by the CFD results. Following Eq. (10), the sensitivity $k_\beta/\Delta\beta$ is proportional to the probe wedge angle δ. Due to the computed seperation at the side faces, the flow experiences a larger wegde angle and, therfore, a higher direction coefficient sensitivity. The slight asymmetry of the manufactured probe head with respect to the probe axis is reflected by the measured distribution of the total pressure coefficient k_t. Great discrepancies between measurement, computation and streamline projection method are observed for the static pressure coefficient k_s. According to Eq. (4), these

discrepancies are caused by the differences of "suction side" hole coefficients k_2 and k_3, respectively.

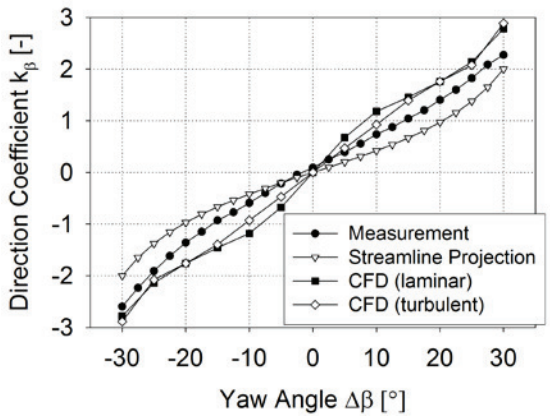

Figure 8. Direction coefficients k_β for Re = 7400

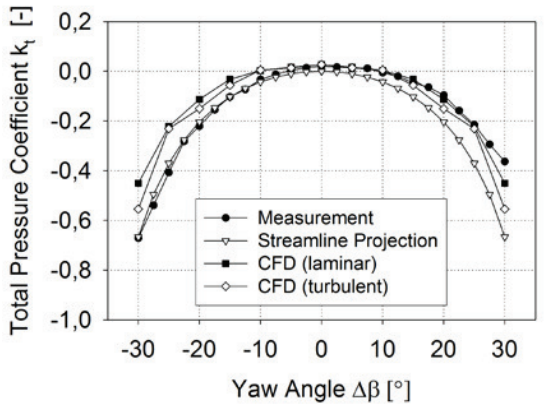

Figure 9. Total pressure coefficients k_t for Re = 7400

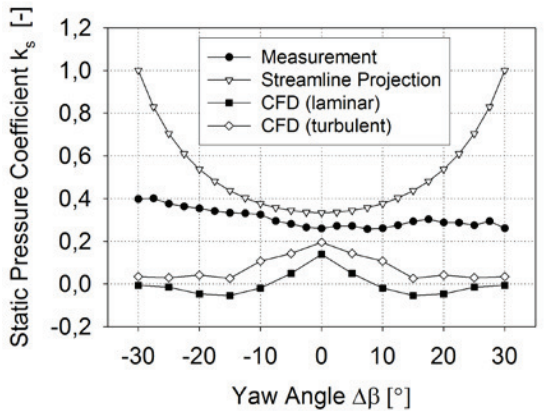

Figure 10. Static pressure coefficients k_s for Re = 7400

7.2. Variation of Reynolds Number for Nulled Probe

Figure 11 shows the distribution of the dynamic pressure coefficient k_d versus flow velocity. As can be seen from the error bars, measurement uncertainty is relatively high. Following Eq. (6), the dynamic pressure coefficient depends on k_1 and k_2. Measurement results indicate that the centre hole coefficient $k_1 \approx 1$, independent of probe Reynolds number. Therefore, the variation of k_d must be a result of variation of side hole pressure coefficient k_2. Indeed, this hole coefficient decreases with increasing Reynolds number [11]. In comparison to Fig. 2, the global trend of decreasing dynamic pressure coefficient for increasing velocity is the same. However, no hysteresis effect can be observed for increasing respectively decreasing velocity. A number of possible reasons may be responsible for this discrepancy: (1) Streamwise turbulence intensity in the present free jet wind tunnel is about 1%, whereas turbulence intensity in the probe manufacturer's wind tunnel is unknown. Onset of laminar/turbulent transition is influenced by different free stream turbulence intensities. (2) In the present experiments probe vibration may have an influence on the turbulence level experienced by the probe head. (3) The present calibration has been performed in 2008, whereas manufacturer's calibration dates back to 1994. This means that the probe has been in operation over a period of more than 14 years. Even a careful probe handling produces wear and sharp corners of the probe head get rounded off. (4) Finally, speed change of the blower is done manually by a potentiometer.

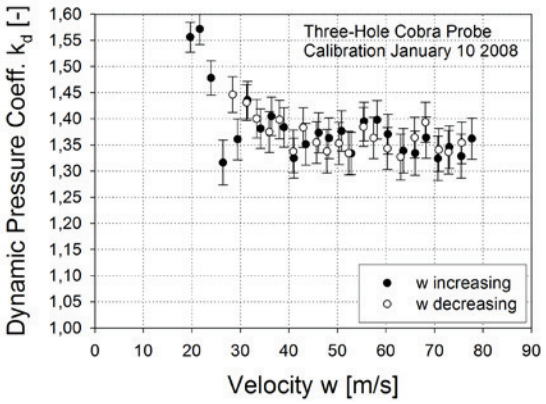

Figure 11. Dynamic pressure coefficient k_d

Figure 12 shows the computed distribution of the dynamic pressure coefficient k_d versus velocity. It can be seen that k_d decreases with increasing velocity and values are generally higher for turbulent flow computation than for laminar one. Starting from low velocities, it can be expected that the flow around the probe head is laminar. On the other hand, turbulent flow can be expected when

starting from high velocities. This fact is indicated by the two symbolic arrows in Fig. 12. Due to the laminar/turbulent transition of the flow, a hysteresis of k_2 and, therefore, of k_d can be expected at medium flow velocities. Finally it should be mentioned that Strouhal numbers according to Eq. (13) are the same for laminar and turbulent computation.

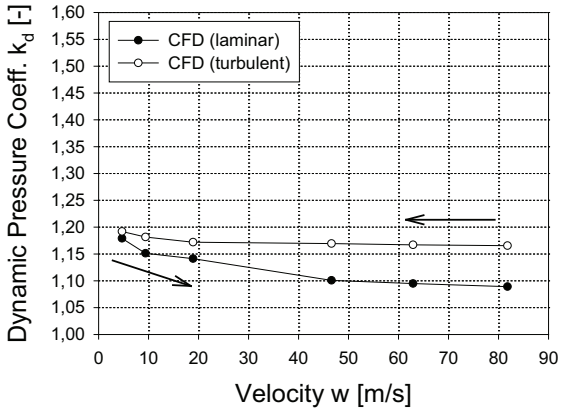

Figure 12. Dynamic pressure coefficient k_d according to CFD simulation

8. SUMMARY

The manufacturer of a three-hole pressure probe has observed hysteresis effects in the calibration results when the probe was nulled in yaw. The pressure measured at the probe head side face depends on whether flow velocity is increasing or decreasing. This will result in systematic errors when the probe is used for flow measurements in the wakes downstream of a turbomachinery blade row. Therefore, the three-hole cobra probe has been recalibrated in a free jet wind tunnel at Re = 7400 at different yaw angles in the range ±30° and at zero yaw angle at various velocities, respectively Reynolds numbers. The experimental results for the hole coefficients as well as the calibration coefficients are compared with data obtained from a simple streamline projection method. Furthermore, unsteady laminar and turbulent CFD simulations have been performed to predict the flow field as well as the hole and calibration coefficients.

Due to different wind tunnel operating conditions, the hysteresis effect could not be reproduced by the present experimental calibrations. However, an evaluation of the computational as well as the streamline projection method results indicate that laminar/turbulent transition at the probe head is responsible for the observed hysteresis effect. When velocity is increased, starting from low values, the flow at the probe head will stay laminar. On the other hand, turbulent flow can be expected when velocity from a high value starts to decrease. At medium velocities or Reynolds numbers, laminar as well as turbulent flow can occur. This results in different separation patterns and a hysteretic behaviour of the probe head side wall pressure.

REFERENCES

[1] Dominy, R. G., and Hodson, H.P., 1993, "An Investigation of Factors Influencing the Calibration of Five-Hole Pressure Probes for Three-Dimensional Flow", *ASME J Turbomachinery*, Vol. 115, pp. 513-519.

[2] Willinger, R., and Haselbacher, H., 2003, "A Three-Hole Pressure Probe Exposed to Velocity Gradient Effects – Experimental Calibration and Numerical Investigation", Proc. *Conference on Modelling Fluid Flow (CMFF'03)*, September 3 – 6, Budapest, Hungary, pp. 413 – 420.

[3] Lee, S.A., and Jun, S.B., 2003, "Effects of Reynolds Number on the Non-Nulling Calibration of a Cone-Type Five-Hole Probe", *ASME Paper GT2003-38147.*

[4] Mittal, S., and Saxena, P., 2000, "Prediction of Hysteresis Associated with the Static Stall of an Airfoil", *AIAA Journal,* Vol. 38, No. 5, pp. 933-935.

[5] Schewe, G., 2001, "Reynolds-number effects in flow around more-or-less bluff bodies", *Journal of Wind Engineering and Industrial Aerodynamics*, 89, pp. 1267-1289.

[6] Reneau, L.R., Johnston, J.P., and Kline S.J., 1967, "Performance and Design of Straight, Two-Dimensional Diffusers", *ASME J Basic Engineering*, pp. 141-150.

[7] Treaster, A.L., and Yocum, A.M., 1979, "The Calibration and Application of Five-Hole Probes", *ISA Transactions*, Vol. 18, No. 3, pp. 23 - 34.

[8] Konecny, G., 1994, „Eichungsprotokoll der Dreilochsonde 0,8 / 600 – 650", SVUSS a.s., Praha, Czech Republic.

[9] FLUENT, 1998, „FIDAP8 Users Manual", FLUENT Inc.

[10] Sakamoto, H., Haniu, H., and Kobayashi, Y., 1989, "Fluctuating Force Acting on Rectangular Cylinders in Uniform Flow (on Rectangular Cylinders with Fully Separated Flow)", *Transactions of the Japan Society of Mechanical Engineers*, Series B 55, No. 516, pp. 2310 – 2317.

[11] Cubi, R.G., 2008, "Investigation on the Effect of Reynolds Number on Pneumatic Three-Hole Pressure Probe Calibration", Diploma thesis, Vienna University of Technology.

Conference on Modelling Fluid Flow (CMFF'12)
The 15th International Conference on Fluid Flow Technologies
Budapest, Hungary, September 4-7, 2012

Numerical modeling of ice accretion on a wing section

Róbert-Zoltán SZÁSZ[1], László FUCHS[2]

[1] Corresponding Author. Department of Energy Sciences, Lund University, P.O.Box 118, 22100, Lund, Sweden. Tel.: +46 46 222 0480, Fax: +46 46 222 4717, E-mail: robert-zoltan.szasz@energy.lth.se
[2] Flow Linné Centre, Royal Institute of Technology, Stockholm, Sweden. E-mail: laszlo.fuchs@energy.lth.se

ABSTRACT

A combined approach is presented to model ice accretion on an airfoil. The flow is simulated by solving the incompressible Navier-Stokes equations using finite differences on a cartesian grid. The Immersed Boundary Method (IBM) is used to account for solid surfaces and Lagrangian Particle Tracking (LPT) for the transport of water droplets. The proposed method has larger flexibility compared to already existing methods. The approach is used to predict ice accretion measured in refrigerated wind tunnel experiments found in the literature. The predicted ice mass is of right order of magnitude and measures for further improvements of the model accuracy are suggested.

Keywords: icing, Immersed Boundary, LES, LPT, wind turbine

NOMENCLATURE

A	$[m^2]$	cross-sectional area
d	$[m]$	distance
d_{cr}	$[m]$	critical distance
f	$[-]$	model parameter
M	$[kg]$	accreted ice mass
S	$[m/s^2]$	momentum source
t	$[s]$	time
$\underline{u}$	$[m/s]$	velocity vector
$\alpha_{1...3}$	$[-]$	correction coefficients
Δ	$[m]$	cell size
ϕ	$[kg/m^3]$	mass concentration of particles

Subscripts and Superscripts

L	local
T	target

1. INTRODUCTION

Ice accretion on wind turbine blades is a major concern for wind power plants installed in areas with cold climate, i.e. in nordic regions and high altitudes. A recent review of the status of wind energy in cold climate is presented in [1].

The deposited ice has several negative impacts on the performance of the wind turbine. First, the ice layer changes the aerodynamic shape of the blade, resulting in non-optimal profiles and a decrease of the extracted energy. Second, the extra mass imbalances the rotor causing vibrations of the structure which lead to earlier fatigue and, in extreme cases, mechanical failures. A third concern is due to the fact that ice chunks may detach from the blades. Beside the sudden load changes on the solid structures, these chunks represent a danger for the persons or objects located in the turbines neighborhood.

Ice deposition is not specific to only the wind turbine industry, similar concerns occur in aircraft [2] or marine [3] applications. As result, there is an intensive research focusing on ice accretion. In a wind turbine context the major focus is on:

- Developing icing maps. Commonly climatological models are scaled down to forecast the probability of icing events in a certain area.
- Ice prevention mechanisms, which can involve active or passive measures to avoid the accretion of ice on the blades and instruments.
- Ice detection and measurement, to monitor the occurrence of ice and control the wind turbine to avoid damages.

Compared to the above mentioned areas, the modeling of ice accretion receives relatively low attention. Makkonen [4, 5] was among the first ones to characterize different kind of icing events and to create models for it. Based on thermodynamic considerations the following model was proposed to predict the rate of ice accretion:

$$\frac{dM}{dt} = \alpha_1 \alpha_2 \alpha_3 \phi \underline{u} A \tag{1}$$

where M is the mass of the ice, t the time, ϕ the mass concentration of particles, $\underline{u}$ the velocity of the particles relative to the object, A the cross sectional area of the object. α_1, α_2 and α_3 are correction factors having values between zero and one and account for the collision efficiency, sticking efficiency and accretion efficiency, respectively. For further details about the model the reader is referred e.g. to [5]. Eq. 1 is still the most widely used ice prediction model, often combined with other methods. As an example, Homola [6] used a two step approach to study the effect of ice accretion on the performance of wind turbine blades. First, the shape of the ice was predicted using TURBICE. In the second step the performance of the blade with the modified shape was compared to the unaltered case using CFD.

For more flexibility, it would be desired to account for the shape alteration due to the accreted ice online, thus avoiding the need for a 'guessed' ice shape. This work is a first step in this direction. The amount of ice deposited is modeled using a combined Eulerian-Lagrangian approach, opening the possibility of shape alterations in a longer term depending on the instantaneously deposited amount of ice.

Numerical models need to be validated. For this purpose experimental investigations are needed, preferably involving simplified cases and controlled conditions. Kollar et al. [7] for example investigated icing on an inclined cylinder for a series of different kind of icing conditions. Hochart et al. [8] carried out measurements on a NACA 63415 blade section in a refrigerated wind tunnel. The considered conditions were derived to mimic realistic parameters for a real wind turbine blade. Here, one of the cases presented in [8] is used to test the proposed modeling approach.

2. METHODS

A coupled Eulerian-Lagrangian method is used to model ice accretion. A simplified version of this approach was implemented in [9] where it was applied to predict ice accretion on a full wind turbine. Water droplets are released upstream the airfoil and transported using the LPT approach. For the time being the simplest accretion mechanism is modeled, i.e. the droplets freeze immediately after their impact on a solid surface.

2.1. Air flow

The air flow is simulated by solving the incompressible Navier-Stokes equations using the finite differences method. Since the temperature variations are considered to be small, the energy equation is not solved. Nevertheless, it can be included in a longer term, if stratification of the atmospheric boundary layer or heat transfer will be included. The geometry is discretized using a cartesian equidistant grid. Third order finite differences are used for the convective part, while the diffusive terms are discretized using forth order schemes. The high order approximation is achieved using the defect correction approach. Multigrid is employed to speed up convergence. For further speed-up, the solver is parallelized using the MPI library. Turbulence is accounted for by Large Eddy Simulations (LES) with no explicit subgrid-scale model, instead, the third order upwind scheme used for the convective terms adds extra dissipation to account for the effect of sub-grid scale vortices [10, 11].

Equidistant cartesian grids have the advantage of higher computational speed and easier implementation of higher order methods, compared to stretched or unstructured grids. One of the major drawbacks of using such grids is the difficulty to account for complicated surfaces. Here, the IBM is used for this purpose as it was implemented in [12]. For the IBM, an extra surface mesh is generated where the solid surfaces are situated. In the fluid cells located in the vicinity of the surface mesh(es) extra source terms are included in the momentum equations to force the local velocity, $\underline{u}_L$, to converge towards the desired target velocity, $\underline{u}_T$, see Eq. 2.

$$S_i = (u_{iT} - u_{iL}) e^{-C\,d^2} \tag{2}$$

where S_i is the source for the i^{th} momentum equation, d the distance from the cell center to the surface mesh and C is a large positive constant which is responsible to vanish the source term far from solid surfaces. The major advantage of the method is its flexibility, no remeshing of the fluid grid is needed when the solid surfaces are moving or deforming, thus rotating blades or changes in the blade profile due to ice accretion can be accounted for with relatively low effort.

2.2. Droplet transport

Since the liquid water content (LWC) and the median volume diameter (MVD) of the droplets are typically small in icing conditions LPT can be used to track droplet parcels having a predefined distribution of droplet sizes. In the present article the droplets have uniform size equal to the MVD. The effort needed for LPT being proportional to the number of transported parcels, measures have been taken to decrease this effort. First, the droplets are not injected at the inlet, but at a certain distance upstream the object, where the flow can still be considered uniform enough such that this simplification will not affect the results. Second, droplets propagated sufficiently far downstream (they have no chance to be recirculated and deposited on solid surfaces) are removed from the domain.

During the first attempts the parcels were released equidistantly. This approach, however, resulted in aliasing effects due to the lack of upstream turbulence fluctuations and the equidistant character of the grid. The aliasing was avoided by releasing

randomly distributed droplets in space. In time, the parcels are released periodically, the period being determined based on the average inter-parcel distance, resulting from the LWC.

After their release, it is considered that the droplets are far enough from each other to avoid interaction, thus they are transported as spherical individual droplets, subject to the drag force. The other forces typically occurring in a LPT context are estimated small enough to be neglected. When needed, the timestep used in LPT is smaller than the flow timestep to avoid unphysical particle transport when the droplets are subject to large accelerations.

2.3. Ice accretion

For the time being, it is assumed that all droplets freeze upon impact. This behavior is typical for rime-ice conditions, and the accreted ice layer has lower density than in glaze-ice conditions, due to the trapped air bubbles [8]. The distance to the nearest solid surface is estimated using the distance function d already needed for the IBM (see Eq. 2). This parameter being stored in cell centers, it needs to be interpolated first to the droplet position. A critical distance is then defined as function of the cell size, Δ, (see Eq. 3). All droplets situated at distances closer than d_{cr} to the airfoil surface are considered as frozen and the time instance and coordinates of the impact are logged for post processing purposes.

$$d_{cr} = f\Delta \tag{3}$$

This parameter turned out to have a major impact on the predicted accreted ice mass, and the sensitivity of the results to this parameter is discussed in Section 4.2.2.

3. Problem set-up

The 'In-fog icing event 2' presented in [8] has been selected as a testcase. This set-up was chosen because it corresponds to rime-ice formation conditions when all droplets impacting on the surface freeze instantaneously and is easier to model than glaze-ice conditions, when a fraction of the water runs along the profile. In [8] several cases have been tested, simulating different radial positions of a real wind turbine. Here, the case corresponding to the lowest radial position was chosen, its parameters being summarized in Table 1.

The sketch of the computational domain is shown in Figure 1. The flow solver being non-dimensional, all length have been normalized with the chord length (0.2 m). For the velocity scale the inlet velocity magnitude was chosen. The transversal cross section of the domain is smaller than in the experiments (WxH=1.5x2.5 instead of 2.5x3.0) to reduce the computational effort, however, is considered still large enough to consider the flow three-dimensional.

Table 1. Main parameters of the icing phenomenon

Profile	NACA 63415
Angle of attack	3^o
LWC	$0.37\ g/m^3$
MVD	$27.6\ \mu m$
Vrel	$18.7\ m/s$
Re	2.49×10^5
time	$10.6\ min$
Mass of accreted ice	$24 \pm 1.75\ g$

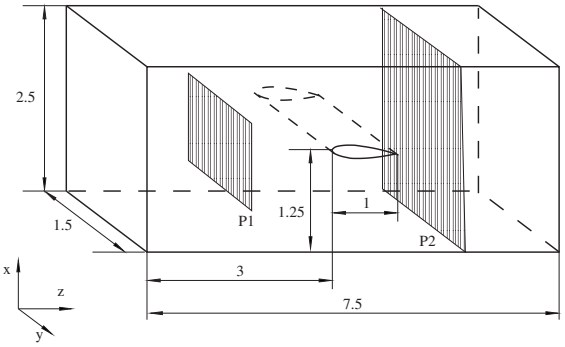

Figure 1. Sketch of the computational domain and the coordinate system

A constant, top-hat velocity profile is imposed at the inlet of the domain, while at the outlet flux-conserving zero gradient conditions are applied. Slip conditions are used on the side walls. The immersed boundary method forces no-slip conditions at the blade surface.

The droplets of equal size, matching the LWC and MVD listed in Table 1, are released upstream the blade, in the plane marked P1 in Figure 1. Those droplets which did not accrete on the blade surface are removed from the simulations when passing the axial position marked P2 in the figure.

Five different cases have been set up, the differences between the cases being summarized in Table 2. Beside the base case, two cases (denoted G1 and G2) have been ran to study the grid dependency of the solutions. The grid resolution is given in Table 2 and resulted in approximately 74.6e6, 18.6e6 and 4.2e6 cells, computed on eight cores. Cases F1 and F2 were set up to study the sensitivity of the results on the model parameter f (see Eq. 3).

Each case has been run at least twenty non-dimensional time units to develop the solution. After this initial start-up time, at least eleven time units were computed to collect statistics.

Figure 2 shows the time evolution of the accreted ice for case G1 as a histogram. The time interval of the accretion was divided in 100 bins and the number of depositing droplets in each bin was normalized with the total number of droplets. The increasing ramp at the left side of the plot (until

Table 2. Summary of the simulated cases

Case	f	Δ	Comment
B	1.0	7.81e-3	Base case
G1	1.0	1.25e-2	Coarse grid 1
G2	1.0	2.08e-2	Coarse grid 2
F1	0.75	7.81e-3	Distance parameter 1
F2	0.50	7.81e-3	Distance parameter 2

ca. t=15) corresponds to the time needed for the settling of the flow. After approximately 15 time units the ice accretion can be considered statistically stationary and no low frequency phenomena can be observed. Thus, even if the time used for collecting statistics is significantly lower than the one corresponding to the experiments, the logged results can be used to estimate the accreted ice mass if they are extrapolated to the right time interval. Of course, this extrapolation assumes that no significant changes in the blade profile occur.

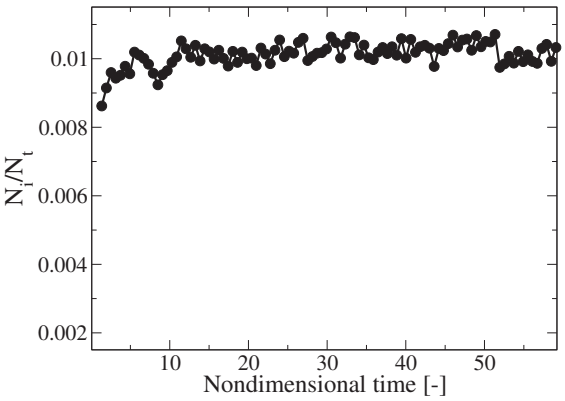

Figure 2. Time evolution of the ice accretion

4. Results

4.1. Flow

The main focus being on ice accretion, the air flow is described herein only shortly, describing the major features of the flow. The average axial velocity field for the base case is presented in a cross section in Figure 3. One can observe the acceleration of the flow when passing the airfoil. Also, a small recirculation is seen close to the trailing edge.

4.2. Icing

First the predicted ice mass will be presented for all cases, followed by a discussion of the spacial distribution of the accreted ice for the cases ran for the model sensitivity analysis.

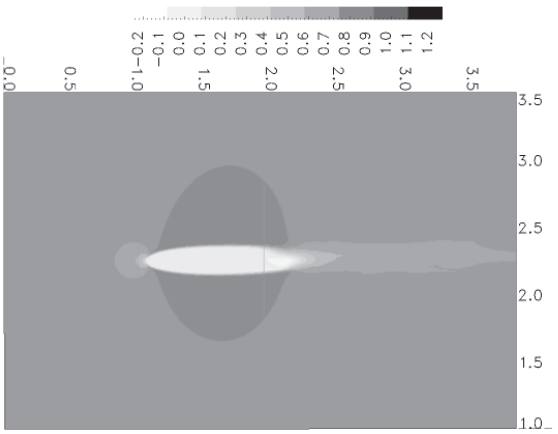

Figure 3. Average axial velocity component

4.2.1. Grid sensitivity

All droplets impacting on the airfoil are considered to freeze instantaneously and their position, as well as the time instance of the impact are logged. By post-processing the log-files one can deduce the number of accreted droplets within a certain time interval, which leads to the deposited ice mass. These results have to be corrected to account for the reduced size of the cross section in the computations compared to the experimental set-up, and for the longer sampling time of the experiments. Both effects are accounted for herein by linear extrapolation.

Figure 4 plots the predicted deposited ice mass for three grid resolutions. Furthermore, the experimentally measured average value is also shown, the error bars having the length of the measured rms of the ice mass. One should note, that even in the finest case, the size of the droplets (nondimensional diameter of 1.38e-4) is still significantly smaller than the cell size, thus the assumptions of using the LPT approach to model droplet transport are still valid.

The predicted deposited ice mass in the two coarser cases ($\Delta x = 0.0208$ and $\Delta x = 0.0125$) have approximately similar values and both underpredict the experimentally observed mass. Surprisingly, the amount of ice predicted in the finest case is significantly larger than in the previous two cases and overpredicts the measured value. Thus, one can conclude that the first two grid resolutions are too coarse for predictions.

4.2.2. Model sensitivity

An important model parameter is the constant f in Eq. 3 adjusting the critical distance within which it is considered that the droplet collides with the surface. Such a parameter is needed since an absolute 'zero distance' does not exist, one needs to allow a tolerance interval for numerical reasons. Furthermore, even in reality, the surfaces

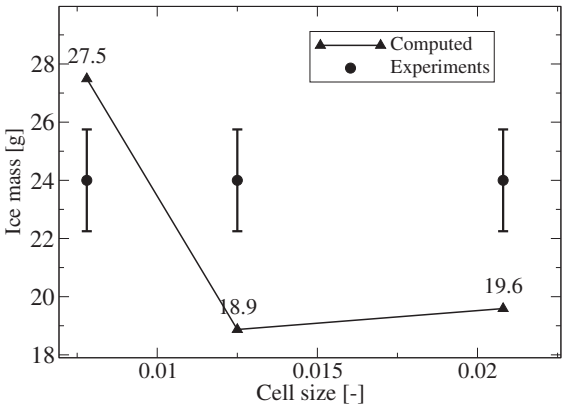

Figure 4. Predicted ice mass for several grid resolutions

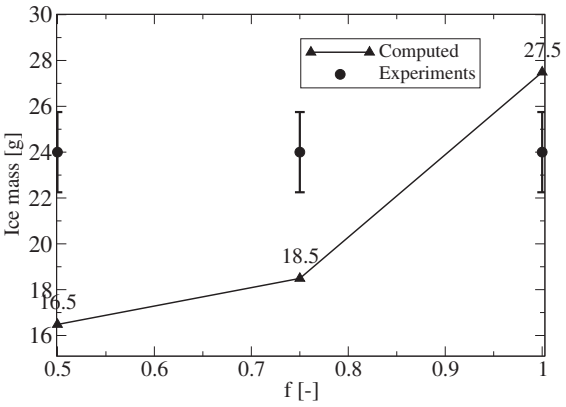

Figure 5. Predicted ice mass for several values of the model parameter

are probably not perfect, either due to imperfections or to the already accreted ice layer.

As it was mentioned in the method description, the droplet distance to the airfoil surface is computed from the distance function already used for the immersed boundary method. This approach was chosen for performance considerations, it is significantly faster to identify cells surrounding a droplet in the cartesian fluid mesh than on the possibly unstructured surface mesh.

Three cases have been compared, having values of the model parameter of 0.5, 0.75 and 1.0, respectively. Larger distances than one cell size would be reasonable eventually if one would like to account for already deposited ice layers, however the flow field would not be adjusted accordingly, thus it is recommended to adjust the distance function itself. Smaller values of the model parameter lead to significantly larger residence time of the droplets in the vicinity of the surface and in some cases might lead to droplets 'sneaking through' the surface.

The predicted ice mass for the three considered cases are shown in Figure 5. As it is expected, the number of accreted droplets increases with increasing critical distance to the surface since droplets from a larger volume are captured. The two lower values of the parameter ($f = 0.5$ and $f = 0.75$) under-predict, while the largest value ($f = 1.0$) over-predicts the deposited ice mass. Thus the order of magnitude of the deposited ice is right for the considered interval of the model parameter, however, the model is too sensitive to changes in the value of the model parameter. One possible explanation is the use of the faster, but less accurate method of computing the droplet distance to the surface. Another source of error is the fact, that the airfoil shape is not yet changed to account for deposited ice layers. In reality, with the increase of the ice layer the cross sectional area increases as well and so does the number of impacting droplets.

The spacial distribution of the accreted ice is shown in Figure 6, where the frequency of the impacting droplets are interpolated onto the airfoil surface, identified by an iso-contour of the distance function. The trailing edge part is missing from the figure because that region belonged to another block in the parallel computations. Since no droplets were deposited in that region it was considered unnecessary to occupy the extra space by including one more block in the post-processing. Also, the distribution being uniform in transversal direction, only half of the computed blade width is shown. Dark regions correspond to low, while light regions to large amount of accreted ice. The colormap was chosen to be nonlinear, to visualize all regions where ice deposits.

Two regions of ice can be observed. The first region is the leading edge of the airfoil where most of the ice is accumulated. The largest amount is accumulated on the leading edge and is decreasing with the distance from the leading edge. Approximately the same region was also found in the experiments of Hochart et al. [8]. A second region of ice is found also upstream the trailing edge, however, as it will be shown later, the amount of ice deposited here is very low. Between these two regions no depositing droplets were logged. The areas of both iced regions increase with increasing values of the critical distance (compare Figures 6(a) to 6(c)). The coarse grid results (Figure 6(d)) show reduced icing areas compared to the case with the same value of the model parameter (Figure 6(c)). When compared to the fine case with approximately the same amount of deposited ice (Figure 6(b)), the leading edge icing areas are approximately the same, whereas the downstream area is smaller in the coarse grid computations.

For a more quantitative evaluation, the three cases with different model parameters are compared in Figure 7. The histogram of impacting droplets versus axial position is shown, the origin of the coordinate system being the leading edge. Since the leading edge region is dominant, only the first 5% of the chord length is shown. The sampling times for

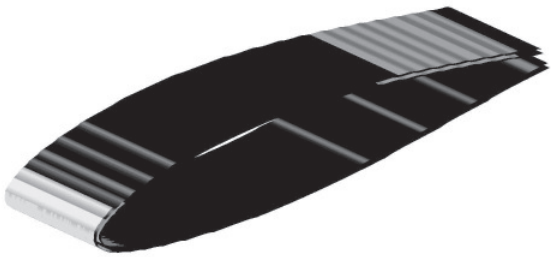

(a) Base

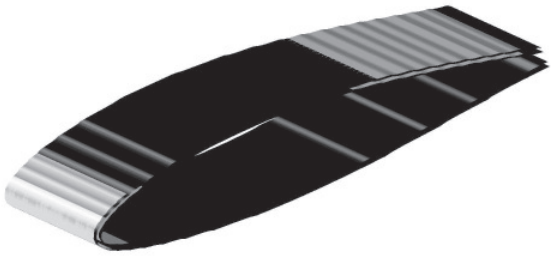

(b) F1

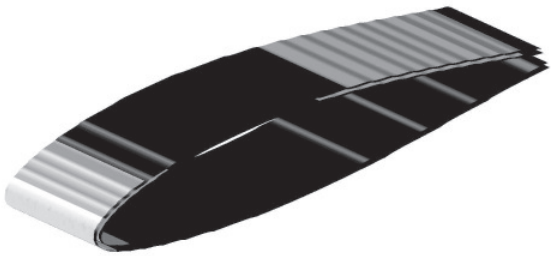

(c) F2

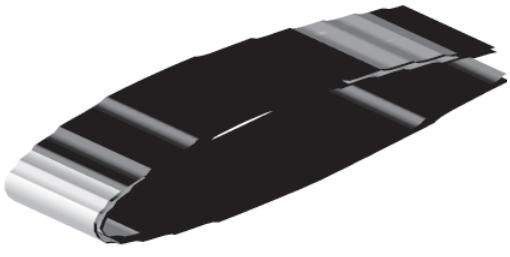

(d) G1

Figure 6. Distribution of the deposited ice droplets for four of the considered cases

the three cases not being perfectly equal, the numbers of droplets were normalized with the sampling time. Although the data is noisy, a clear tendency of increasing amount of deposited ice is observed for increasing values of the model parameter.

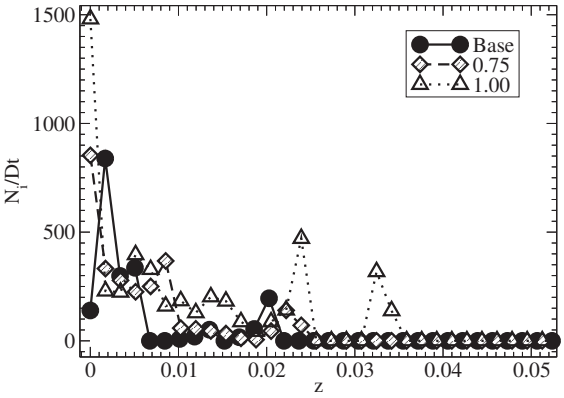

Figure 7. Number of droplets impacting normalized with sampling time, versus axial position normalized by the chord length

5. SUMMARY

Ice accretion on an airfoil has been simulated using a combined Eulerian-Lagrangian approach. Water droplets are tracked in an air flow using the LPT method. The air flow is simulated with finite differences and LES is used to account for turbulence. All droplets impacting on the surface are assumed to freeze instantaneously.

The chosen testcase matches the conditions of one of the experimentally studied set-ups presented in [8]. Rime-ice condition is simulated which is consistent with the assumption of direct frost of impacting droplets.

A grid sensitivity study has been carried out to evaluate grid effects on the simulations. The predicted ice mass was of the right order of magnitude in all three cases, the two coarser cases were under, while the finest case was over-predicting the experimentally measured value.

A sensitivity study of the model parameter was also performed. The predicted ice quantities were again of right order of magnitude, but varied significantly with the model parameter, when accreted ice mass was increasing with the critical distance.

To improve the predictions the followings are planned as future work. First, the droplet-surface distance will be computed using the surface mesh instead of the distance function stored on the fluid grid. This approach is computationally more expensive but more accurate and the comparison will reveal if it is worth sacrificing computational time for the increased accuracy. Second, the surface mesh will be reshaped to account for the increased cross-sectional area due to the already deposited ice layer. Since one case is not considered

sufficient to validate the model, further experimental configurations will be simulated.

ACKNOWLEDGEMENTS

The authors would like to acknowledge the financial support of the Swedish Research Council (VR). The computational time offered at the Center for Scientific and Technical Computing at Lund University (LUNARC) and at HPC2N (within the allocation program SNAC) is highly appreciated.

References

[1] Laakso, T., Baring-Gould, I., Durstewitz, M., Horbaty, R., Lacroix, A., Peltola, E., Ronsten, G., Tallhaug, L., and Wallenius, T. 2010 , "State-of-the-art of wind energy in cold climates".

[2] Gent, R. W., Dart, N. P., and Cansdale, J. T. 2000 "Aircraft icing". *Philosophical Transactions of the Royal Society A: Mathematical, Physical and Engineering Sciences*, **358**, 2873–2911, Vol. 358, No. 1776, pp. 2873–2911.

[3] Lozowski, E. P., Szilder, K., and Makkonen, L. 2000 "Computer simulation of marine ice accretion". *Philosophical Transactions of the Royal Society A: Mathematical, Physical and Engineering Sciences*, **358**, 2811–2845, Vol. 358, No. 1776, pp. 2811–2845.

[4] Makkonen, L. 1985 "Heat transfer and icing of a rough cylinder". *Cold Regions Science and Technology*, **10**, 105–116, Vol. 10, pp. 105–116.

[5] Makkonen, L. 2000 "Models for the growth of rime, glaze, icicles and wet snow on structures". *Philosophical Transactions of the Royal Society A: Mathematical, Physical and Engineering Sciences*, **358**, 2913–2939, Vol. 358, No. 1776, pp. 2913–2939.

[6] Homola, M. C., Virk, M. S., Wallenius, T., Nicklasson, P. J., and Sundsbø, P. A. 2010 "Effect of atmospheric temperature and droplet size variation on ice accretion of wind turbine blades". *Journal of Wind Engineering and Industrial Aerodynamics*, **98**, 724–729, Vol. 98, No. 12, pp. 724–729.

[7] Kollár, L. E. and Farzaneh, M. 2010 "Wind-tunnel investigation of icing of an inclined cylinder". *International Journal of Heat and Mass Transfer*, **53**, 849–861, Vol. 53, No. 5-6, pp. 849–861.

[8] Hochart, C., Fortin, G., Perron, J., and Ilinca, A. 2008 "Wind turbine performance under icing conditions". *Wind Energy*, **11**, 319–333, Vol. 11, No. 4, pp. 319–333.

[9] Fuchs, L. and Szasz, R. 2009 "Ice accretion on wind-turbines". *3th International Workshop on Atmospheric Icing of Structures, IWAIS XIII*, September 8-11.

[10] Olsson, M. and Fuchs, L. 1996 "Large Eddy Simulation of the Proximal Region of a Spatially Developing Circular Jet". *Phys. Fluids*, **8**, 2125–2137, Vol. 8, No. 8, pp. 2125–2137.

[11] Gullbrand, J., Bai, X.-S., and Fuchs, L. 2001 "High-order cartesian grid method for calculation of incompressible turbulent flows". *Int. J. Numerical Methods in Fluids*, **36**, 687–709, Vol. 36, pp. 687–709.

[12] Salewski, M., Duwig, C., Milosavljevic, V., and Fuchs, L. 2007 "LES of Spray Dispersion and Mixing in a Swirl Stabilized GT Combustor". *AIAA paper*, **AIAA-2007-0924**, Vol. AIAA-2007-0924.

Conference on Modelling Fluid Flow (CMFF'12)
The 15th International Conference on Fluid Flow Technologies
Budapest, Hungary, September 4-7, 2012

A STUDY ON MOMENTUM SOURCE MODELING OF MICRO VORTEX GENERATORS FOR NUMERICAL SIMULATIONS

Geon-Hong Kim[1], Younghwa Kim[2], Seung O Park[3]

[1] Department of Aerospace Engineering, Korea Advanced Institute of Science and Technology. E-mail: kgb3233@kaist.ac.kr
[2] Department of Aerospace Engineering, Korea Advanced Institute of Science and Technology. E-mail: movie425@kaist.ac.kr
[3] Corresponding Author. Department of Aerospace Engineering, Korea Advanced Institute of Science and Technology, 291 Daehak-ro, Yuseong-gu, Daejeon, Republic of Korea, Tel.:+82 42 350 3713, Fax: +82 42 350 3710, E-mail: sopark@kaist.ac.kr

ABSTRACT

Flow around a wing at a high angle of attack is quite likely to be separated resulting in various negative effects. A way to control flow separation is to employ micro vortex generator (MVG). To design a flow control system for preventing or delaying separation using MVG's, it is necessary to simulate a whole flow field for many different design parameters. For an accurate Navier-Stokes simulation of the whole flow field, the geometry of MVG's should be treated as solid boundary in the computational domain. This then requires a rather complex grid arrangements and a fairly large number of grid points. Therefore, numerical simulations for a parametric study including several design variables would be very time consuming. In the present study, we adopt a new momentum source modeling approach to model efficiently the flow around MVG's, that is, without solving the Navier-Stokes system around the MVG's to effectively simulate the whole flow field. The numerical simulation of a single MVG using the present momentum source modelling has been carried out. The results are found to be in good agreements to previous CFD results and experimental data.

Keywords : CFD, micro vortex generator, low-profile vortex generator, momentum source method

NOMENCLATURE

C_P	[-]	Pressure coefficient
C_l, C_d	[-]	lift, drag coefficients
c	[m]	chord
f	[-]	lift distribution function
L, D	[N]	lift, drag
s_i	[N/m^3]	source term per unit volume
V	[m/s]	velocity of flow
v	[m/s]	downwash velocity
α_e	[deg]	effective angle of attack
ϕ	[deg]	inflow angle
λ	[-]	relaxation factor
θ	[deg]	geometric angle of attack

Subscripts and Superscripts

T	tangential component
P	perpendicular component
n,t	normal, tangential directions
x,y,z	streamwise, vertical, and lateral (coordinates)
-	average value

1. INTRODUCTION

When an airplane flies at a high angle of attack or extends flaps during take-off or landing, flow over a wing or a flap might be separated. There have been numerous studies to delay or prevent such separated flows with the aid of flow control devices. One of those devices is a vortex generator (VG). Vortex generators are usually categorized into two groups according to their heights with respect to the local boundary layer thickness. Conventional vortex generators (VG) have heights greater than local boundary layer thickness, and the others called as low-profile or micro vortex generators (MVG) have heights smaller than the boundary layer thickness. The MVG's may provide similar performance to the conventional VG's with less drag penalty owing to their small wetted area. Therefore, MVG's can be much better flow control devices in some cases[1].

Lin et al. [2] fulfilled an experimental study on triangular and trapezoidal MVGs attached on a flap surface. They observed that the MVG increased the lift and lift-to-drag ratio of the wing with extended flap by about 10% and 100%, respectively; the drag was reduced by about 50% under a specific condition. Stillfried et al.[3] studied effects of VG on a multi-element airfoil numerically. In their

study, they pointed out that it took a long time to generate a grid to simulate VG's numerically, and proposed a statistical VG model by using the lifting line theory and adding the additional stress contributions from the vortices to the turbulence stresses in the flow. Bender et al.[4] developed the source term model which describes vortex generator modeling for Navier-Stokes codes. The basic methodology of the model is to introduce a side force that is normal to the local flow. The formulation includes a calibration coefficient which is used to scale the side force in the source term model.

Previous studies on VG's or MVG's mainly focused upon their effects on drag or lift of a wing, and physical characteristics of flow past them. For a specific application in practice, additional studies to determine design parameters for MVG are essential. Those parametric studies might be performed experimentally but it is too expensive and time consuming to test against various design parameters. A numerical parametric study is a good alternative but grid generation for simulating flows passing tiny fins over a wing surface is a rather cumbersome task. Furthermore, an MVG has height lower than the thickness of local boundary layer, thus the fin generates another boundary layer inside a boundary layer. To resolve the flows of this region properly, one should employ very dense meshes near an MVG, which definitely increases computational cost.

To alleviate such efforts on grid generation and decrease computational burden, we employ a momentum source method recently proposed by Kim and Park[5]. In this study, we demonstrate how to model MVG aerodynamics by the momentum source method and compare the simulation results with those of previous numerical studies and experimental data.

2. MODELING OF AN MVG

It is straightforward to construct geometry of MVG and allocate meshes around it for simulating flows around the MVG. As mentioned earlier, however, this is a cumbersome and time consuming task. Furthermore, we should prepare different grid sets corresponding to various design parameters such as fin heights, angles of attack, and shapes when the MVG geometry is directly dealt with as solid boundary. On the other hand, if a momentum source method is adopted, we do not need to worry about the MVG geometry as solid boundary. Instead of modeling the geometry of MVG, the momentum source method estimates the momentum source generated by the MVG which is added to the momentum equation as a source term. The momentum sources are computed based on the concept of blade element theory.

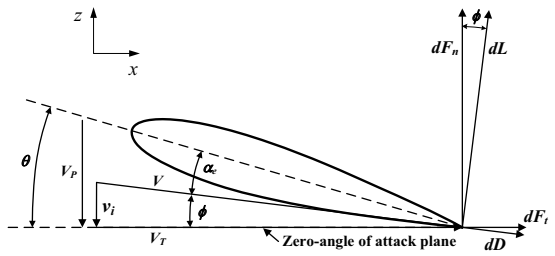

Figure 1. An aerodynamic geometry of a wing section.

2.1. Estimation of Momentum Sources

Incompressible Navier-Stokes equations with a source term can be written as below.

$$\frac{\partial u_j}{\partial x_j} = 0 \tag{1}$$

$$\rho \frac{\partial u_i}{\partial t} + \rho \frac{\partial \left(u_j u_i \right)}{\partial x_j} = -\frac{\partial p}{\partial x_i} + \frac{\partial \tau_{ij}}{\partial x_j} + s_i \tag{2}$$

where τ_{ij} is a stress tensor and s_i is the momentum source per unit volume in i direction. We employed the STAR-CD[6] and adopted SIMPLE algorithm to solve the governing equations with momentum source terms.

The momentum source terms at each fin or MVG section are computed by using blade element theory. Figure 1 shows airfoil section geometry. Previous momentum source approaches usually employ inflow and/or tip-loss models to determine local aerodynamic situation for momentum source evaluation. On the contrary, the present model does not need an additional inflow and tip loss model since the local aerodynamic information is obtained from the computed flow field where various three dimensional effects are naturally taken into account.

To evaluate the aerodynamic forces generated by an airfoil section of a wing (or a fin), we have to estimate the effective angle of attack α_e and the resultant velocity for the section. The effective angle of attack, α_e is given by

$$\alpha_e = \theta - \phi \tag{3}$$

where θ is the geometric angle of attack and ϕ is the inflow angle. To get the resultant velocity V and the effective angle of attack α_e for a specific airfoil section (or blade element), we need to determine V_T and ϕ from the flow field. For the case of a finite wing, freestream velocity can simply be used as V_T . However, the freestream velocity cannot be used for the case of MVG simulation since the MVG is immersed in a boundary layer. Instead of the freestream velocity, the local streamwise velocity at the corresponding location of

a boundary layer upstream of the MVG has been used as V_T in the present study. If V_T and the inflow angle ϕ are determined, the resultant velocity V can be estimated via

$$V = \sqrt{V_T^2 + \left(V_T \tan\phi\right)^2} \tag{4}$$

For a symmetric 2D airfoil at an angle of attack α, the well-known lift distribution of the airfoil informs us that the downwash velocity v is constant along the chord and related to α by $\alpha = \tan^{-1}\left(-v/V_\infty\right)$. Based on this idea, we introduce V_P which is defined as $V_P = V_T \tan^{-1}\theta$ as shown in figure 1. This V_P makes it easier to get the effective angle of attack. V_P can be estimated by integrating vertical velocity component (z-component velocity) along the chord as given below.

$$\overline{w} = \frac{1}{c - x'}\int_{x'}^{c} w dx_c \; and \qquad V_P = -\overline{w} \tag{5}$$

Note that leading edge region is excluded to avoid an irregular value which is likely to be caused by a singular behavior near the leading edge. In the present work, we set $x' = 0.2c$, where c is the chord length.

When the velocity components V_T and V_P are determined, one can get the effective angle of attack as follows.

$$\left(\alpha_e\right)_{new} = \lambda\left\{\left(\theta - \tan^{-1}\left(\frac{V_P}{V_T}\right)\right) + \left(\alpha_e\right)_{old}\right\} + (1-\lambda)\left(\alpha_e\right)_{old} \tag{6}$$

where λ is a relaxation factor. $\left(\alpha_e\right)_{old}$ represents an effective angle of attack which is previously used and $\left(\alpha_e\right)_{new}$ is newly updated effective angle of attack. Figure 2 shows the iterative procedure for estimating α_e and consequently the resultant velocity at all the spanwise wing sections.

Once an effective angle of attack is estimated, lift and drag coefficients of a wing section can be determined by using a look-up table or analytic solution for the sectional lift and drag forces. Finally we can estimate the lift and drag forces experienced by a wing section using following equations.

$$dL = \left(\frac{1}{2}\rho V^2 C_l c \Delta b\right)\left(\int_{x_{c1}}^{x_{c2}} f(x) dx_c\right) \tag{7}$$

$$dD = \left(\frac{1}{2}\rho V^2 C_d c \Delta b\right)\frac{\Delta x_c}{c} \tag{8}$$

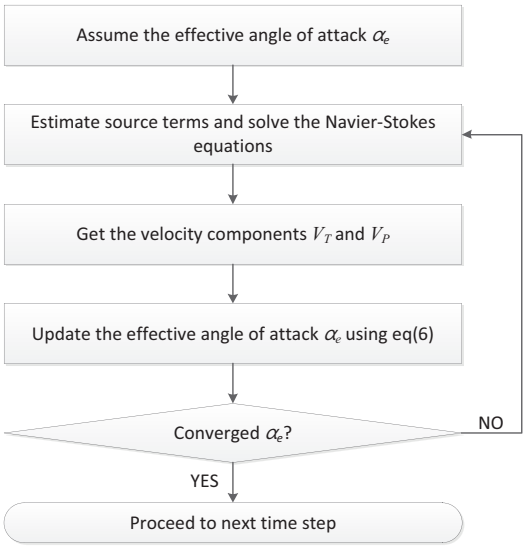

Figure 2. The procedure for estimation of α_e distribution

where Δb and Δx_c are spanwise width and chordwise length of a local grid cell, respectively. The function $f(x)$ of Eq (7) denotes a lift distribution function along the chord of a wing (see Figure 3a). We determine the lift distribution by adopting a chordwise pressure distribution from the thin airfoil theory. From the 2D thin symmetric airfoil theory based on the potential flow, the distribution of the difference of pressure coefficient ΔC_P is given by

$$\Delta C_P = 4\sqrt{\frac{c-x}{x}}\alpha \tag{9}$$

This distribution is known to induce a constant downwash along the chord as is well explained in typical aerodynamics text books[7]. We can easily obtain a chordwise lift distribution function by dividing Eq. (9) by $2\pi\alpha$,

$$f = \frac{2}{\pi}\sqrt{\frac{c-x}{x}} \tag{10}$$

From the NS simulation for an airfoil, the peak value of the lift distribution occurs at around 0.01c. To deal with the singularity of Eq.(10) at the leading edge, the linear approximation over 0~0.01c is combined to the pressure distribution of Eq.(10) as

$$f = \begin{cases} 63.34\dfrac{x}{c} & 0 \le x \le 0.01c \\ \dfrac{2}{\pi}\sqrt{\dfrac{c-x}{x}} & 0.01c \le x < c \end{cases} \tag{11}$$

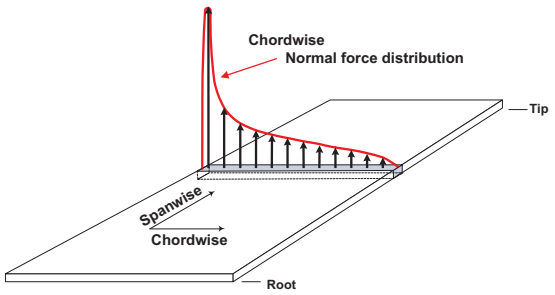

(a) Schematic diagram of chordwise normal force distribution over a wing

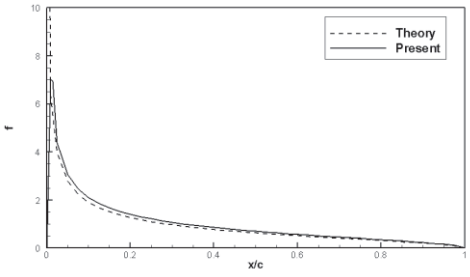

(b) Distribution of function *f*.

Figure 3. A lift distribution along a chord

In the case of present MVG analysis, the root of a MVG in figure 3a is attached to a flat plate and the free stream flows in the chordwise direction.

Figure 3b shows the chordwise lift distribution, $f(x/c)$. The total area of the graph is equal to 1. When this distribution is utilized to assign momentum source value for each cell, the downwash from the Navier-Stokes solution is found to be almost constant along the chordwise direction of a finite wing element except for the leading edge region.

Since the lift and drag forces are defined in the "wind-axis", the lift and drag are perpendicular and parallel to the resultant velocity vector, respectively. We should transform these forces into those corresponding to computational coordinate system. Usually, the streamwise coordinate is in line with the V_T plane, we have

$$F_n = dL\cos\phi - dD\sin\phi$$
$$F_t = dL\sin\phi + dD\cos\phi \qquad (12)$$

where subscript n and t denote normal and tangential directions to V_T plane, respectively. By dividing the volume of local grid cell $\forall$, we can evaluate the source terms direction and add the resultant source terms to the momentum equation. With the coordinate system of Figure 1, source terms in x and y directions at a given cell can be estimated as

$$s_x = -\frac{F_t}{\forall} \qquad and \qquad s_y = -\frac{F_n}{\forall} \qquad (13)$$

Note that negative sign (-) is added to forces since the forces estimated from Eq (12) represent the forces acting on the wing section.

In the present modeling, we consider the momentum sources as a primary contribution to disturbed flow fields due to a MVG, thus source term modeling for k and ω equations are excluded.

3. RESULTS

Kim and Park applied the method to simulate flows around a finite wing mounted on a wall and showed that resultant solutions are in good agreement with the experimental data and other CFD results. In this study, we apply the method to simulate flows around an MVG. The results are compared to experimental data and computational results which directly models MVG as a no-slip wall.

3.1 Computational Conditions

To validate current set up for numerical simulations, experimental data of Yao et al. is employed[8]. In their study, they attached a rectangular MVG and a conventional VG to a flat plate and measured various flow characteristics by using PIV. The experiments were fulfilled at NASA Langley 20x28 in. shear flow tunnel with free stream velocity of 34m/s and the height of the conventional VG and the MVG were 100% and 20% of the local boundary layer thickness, respectively. They were attached at 2.25m downstream distance from the leading edge where the local boundary layer thickness was measured to be 35mm. In this study, we simulate a specific case of $h/\delta = 0.2$ and $\alpha = 10°$. The computational domain and boundary conditions are shown in Figure 4. Sufficient number of grid points should be provided to resolve flows generated by an MVG if the MVG is modeled as a no-slip wall. In contrast, all we need is a portion of cells of the computational domain where momentum source is to be applied.

We select STAR-CD with SIMPLE algorithm to solve the incompressible Navier-Stokes equations with momentum source terms. 1st-order upwind scheme for both convection and diffusion terms are applied and the $k-\omega$ SST low Reynolds number model has been adopted as a turbulence model. The computational results are compared with experimental data of Yao et al. and results of previous numerical study using OpenFOAM fulfilled by Kim and Park[9].

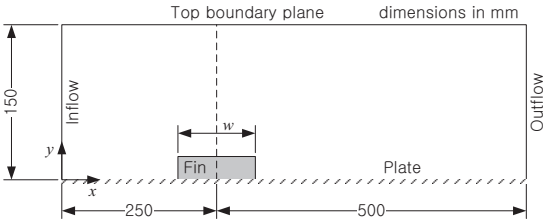

(a) Side view

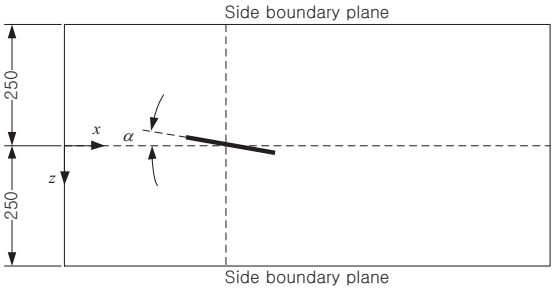

(b) Top-down view

Figure 4. Computational domain and boundary conditions for the numerical simulation of a single MVG on a flat plate.

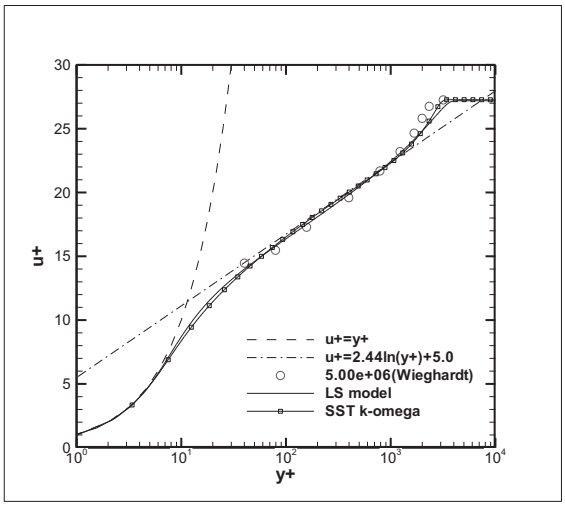

Figure 5. u-plus distribution of turbulent boundary layer at the inlet boundary.

For the inflow boundary condition, 2D boundary layer over a flat plate is simulated. The data corresponding to the Reynolds number of $\mathrm{Re}_x = 5.276 \times 10^6$ is specified as inflow condition. The u^+ distribution of inlet condition is shown in Figure 5 together with the experimental data of Wieghardt and Tillman[10]. The predicted boundary layer thickness at the point is 33.5mm which is close to the experimental result of 35mm.

Figure 6 shows grid arrangements for the two different computations: no-slip wall model and momentum source model. We can use uniformly distributed mesh along the chord for the case of momentum source modeling (see Figure 6a). The grid does not have to be fine meshed in lateral direction to resolve boundary layer due to MVG. On the other hand, the grid for no-slip wall modeling has to be fine meshed to compute properly the MVG boundary layer flow. It is worthwhile to note that the no-slip wall model has a skew angle (angle of attack) relative to the inflow while the momentum source modeling does require such skewness since the effect of the geometric angle is already included in the momentum source term. This makes it easy to test the effect of various angles of attack of MVG with a single grid arrangement which is very efficient in numerical parametric studies in the context of grid generation. 1.16 million cells were constructed to simulate flows around a MVG using the present momentum source modeling, while 4.32 million cells were employed for the no-slip wall model.

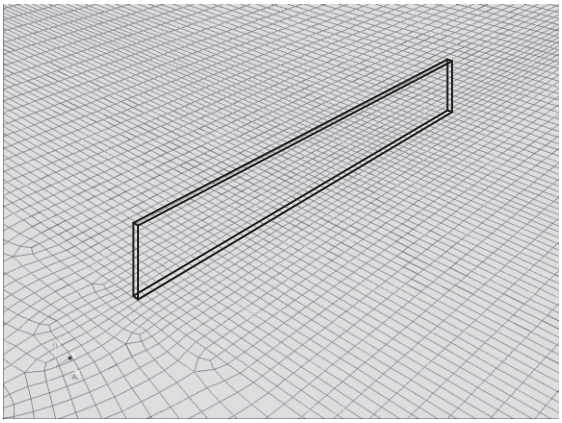

(a) Momentum source modelling

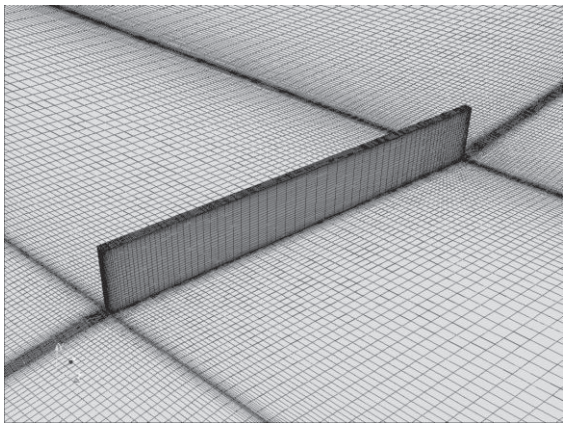

(b) No-slip wall modeling

Figure 6. Grid arrangements for numerical simulation using two different MVG modelings.

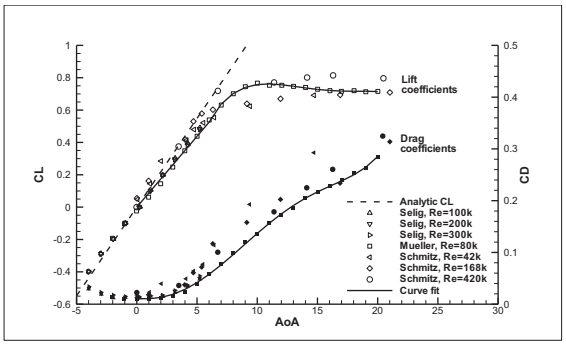

Figure 7. Aerodynamic coefficients of 2D flat plate.

To estimate the source terms, it is essential to get lift and drag coefficients corresponding to the effective angle of attack. The cross section of the MVG used in this study is a thin flat plate. We adopt aerodynamic data of 2D flat plate of previous experimental study of Pelletier and Mueller[11]. We used polynomial curve fitting to establish lift and drag coefficients as functions of an angle of attack. Figure 7 shows variation of lift and drag coefficients versus angle of attack with analytic lift coefficient ($C_L = 2\pi\alpha$) and curve fitting line of Pelletier and Mueller. Experimental data of 2D flat plate of Schmitz and Selig is plotted as well[12,13].

3.2 Computational Results

Figure 8 shows the mean streamwise velocity contour of computational results on y-z plane with the data of the PIV measurement. Though a thorough quantitative comparison of the data can hardly be made, we clearly see that the important flow features of the data compare very well with each other. In the near wake region ($\Delta x/h = 3$), present momentum source method seems to provide poor prediction of vortical flow structure relative to the no-slip wall computation. No-slip wall modeling of MVG blocks the flow and this generates a column-like low velocity structure. Momentum source modeling, meanwhile, blocks no flows passing through the fin region thus it cannot predict those column-like structures. At further downstream, the momentum source modeling predicts similar flow fields to the case of no-slip wall modeling. These trends can be found in the study of Waithe[14] and Dudek[15], and can be seen clearly when the peak vorticity distribution along the downstream is compared, as shown in Figure 9. Although the result with present momentum source modeling tends to under-predict the peak vorticity relative to the experimental data, it still shows that the present modeling provides solution close to other CFD results and reflects well the trend of vortex decay well.

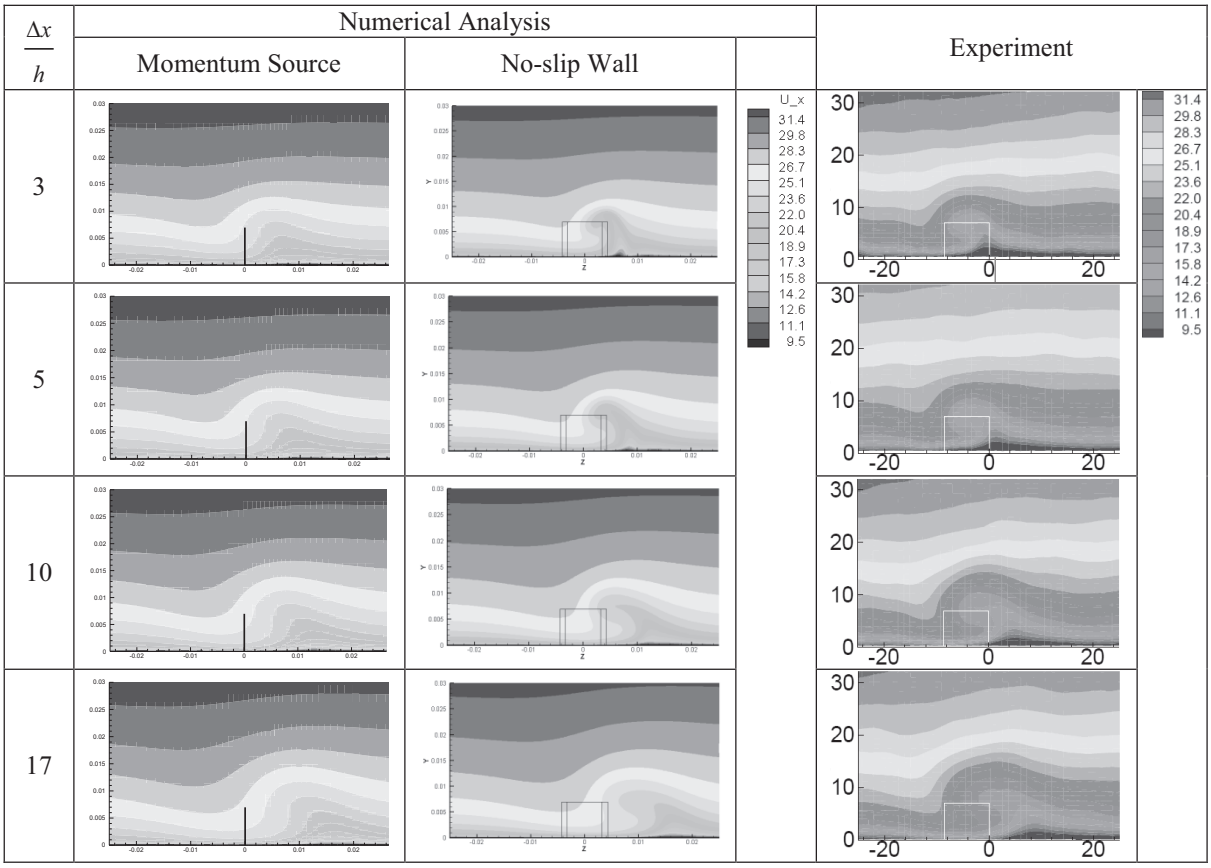

Figure 8. Streamwise velocity contours at various distances downstream from the MVG.

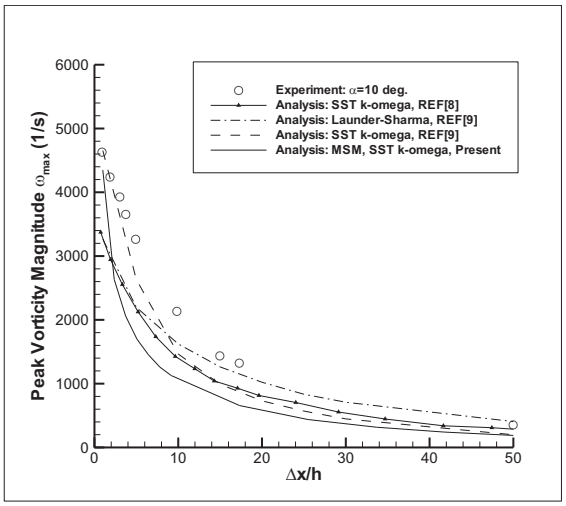

Figure 9. Distribution of the peak vorticity magnitude in downstream.

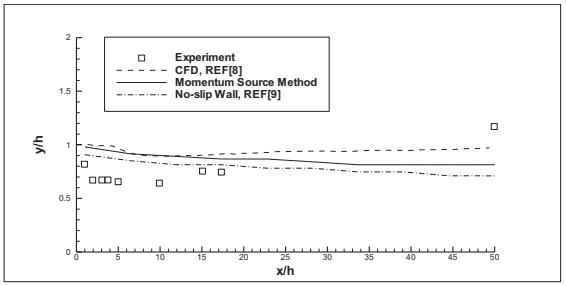

(a) Vertical path

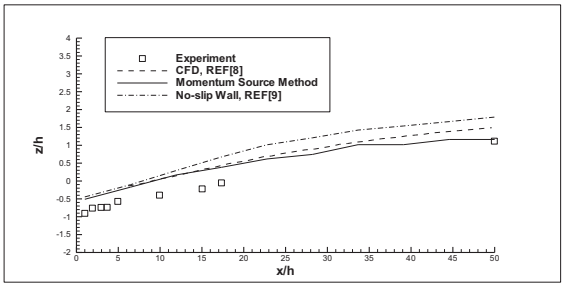

(b) Lateral path

Figure 10. Vortex paths nondimensionalized by device height

Figure 10 shows the vortex path as a function of downstream location in both lateral (z) and vertical (y) directions. The experimental data and predicted results show that the vertical path tends to stay roughly on the order of the device height. The results of the present model provide close to other CFD results. The present model also predicts the lateral path of the vortex core in good agreement to other CFD results and experimental data. Note that the lateral paths of no-slip wall and momentum source modeling results are shifted in z direction by $z/h = -0.6078$ from the original results since the center locations of the device of present analysis and the referred case are different to each other.

4. CONCLUSIONS

We applied a new momentum source method to simulate flows passing a single MVG on a flat plate. The new momentum source method uses velocity information of flow field to estimate the induced velocity without employing inflow model and/or tip loss model. A chordwise lift distribution function is determined by adopting a chordwise pressure distribution from the thin airfoil theory. The computational results are compared to experimental data and CFD results of Yao et al. as well as previous numerical studies which used no-slip wall model for the MVG. Although the present modeling seems to perform poorly in the near wake region, it still provides reasonably good solutions that are in good agreement with other CFD results in the downstream and reflects important flow features well such as vortex decay with much smaller number of grid cells. We expect that the present method is quite attractive for a parametric study since it demands a simple grid arrangement.

ACKNOWLEDGE

This work has been supported by Defense Acuisition Program Administration and Agency for Defense Development (UC100031JD).

REFERENCES

[1] Lin, J. C., 2002, "Review of research on low-profile vortex generators to control boundary-layer separation," *Progress in Aerospace Sciences*, Vol. 38, pp. 389-420.

[2] Lin, J. C., Robinson, S. K., McGhee, R. J., and Valarezo, W. O., 1994, "Separation Control on High-Lift Airfoils via Micro-Vortex Generators," *Journal of Aircraft*, Vol. 31, No. 6, pp. 1317-1323.

[3] Von Stillfried, E., Wallin, S., and Johansson, A. V., 2009, "Application of a Statistical Vortex Generator Model Approach on the Short-Chord Flap of a Three-Element Airfoil," *KATnet II conference on Key Aerodynamic Technologies*, Bremen, Germany.

[4] Bender, E. E., Anderson, B. H., and Yagle, P. J., 1999, "Vortex Generator Modeling for Navier-Stokes Codes," FEDSSM99-6919, *3rd Joint ASME/JSME Fluids Engineering Conference*, San Fransisco, CA.

[5] Kim, Y. H., and Park, S. O., "New Unsteady Momentum Source Method for Rotor Aerodynamic Simulation," in preparation.

[6] STAR-CD, CFD and CAE Software and Support, CD-adopco, http://www.cd-adapco.com.

[7] Katz, J., and Plotkin., A., 2001, *Low-speed Aerodynamics*, Cambridge University Press.

[8] Yao, C. S., Lin, J. C., and Allan, B. G., 2002, "Flow-field Measurement of Device-induced Embedded Streamwise Vortex on a Flat Plate," AIAA 2002-3162, *1st AIAA Flow Control Conference*, 24-27 June, St. Louis, MO.

[9] Kim, G. H., and Park, S. O., 2011, "Numerical Study on the Wake of Micro Vortex Generators with Various Design Parameters," *11th International Conference on Fluid Control, Measurements and Visualization 2011*, Paper No.126, Dec 5-9, Keelung, Taiwan.

[10] Wieghardt, K., and Tillman, W., 1951 "On the Turbulent Friction Layer for Rising Pressure," NACA TM-1314.

[11] Pelletier, A., and Mueller, T. J., 2000, "Low Reynolds Number Aerodynamics of Low-Aspect-Ratio, Thin/Flat/Cambered-Plate Wings," *Journal of Aircraft*, Vol. 37, No. 5, pp. 825-832.

[12] Selig, M. S., Donovan, J. F., and Fraser, D. B., 1989, *Airfoils at Low Speeds*, Stokely, Virginia Beach, VA.

[13] Schmitz, F. W., 1942, *Aerodynamik des Flugmodells*, C.J.E.Volckmann Nachf. E. Wette, Berlin-Charlottenburg.

[14] Waithe, K. A., 2003, "Source Term Model for an Array of Vortex Generator Vanes," NASA/CR-2003-212157.

[15] Dudek, J. C., 2011, "Modeling Vortex Generators in a Navier-Stokes Code," *AIAA Journal*, Vol. 49, No. 4, pp. 748-759.

Conference on Modelling Fluid Flow (CMFF'12)
The 15th International Conference on Fluid Flow Technologies
Budapest, Hungary, September 4-7, 2012

MECHANISM OF DRAG REDUCTION BY DIMPLE STRUCTURES OF A GOLF BALL

Katsumi AOKI[1], Hiroo OKANAGA[2]

[1] Corresponding Author. Department of Mechanical Engineering, School of Engineering, Tokai University, 4-1-1 Kitakaname, Hiratsuka-shi, Kanagawa 259-1292, Japan Tel.: +81 463 58 1211, Fax: +81 463 59 2207, E-mail: katumi@keyaki.cc.u-tokai.ac.jp
[2] Department of Mechanical Engineering, School of Engineering, Tokai University,4-1-1 Kitakaname, Hiratsuka-shi, Kanagawa 259-292, Japan. E-mail: okanaga@keyaki.cc.u-tokai.ac.jp

ABSTRACT

The purpose of the present study is to clarify the mechanism of drag reduction for a golf ball with arc type dimples. The golf ball has 328 dimples of different depths uniformly distributed on its surface. The present study measured the pressure and velocity distributions inside and between the dimples, and visualized the flow on the sphere surface by an oil film method. The results indicated that separation bubbles were generated inside the dimples and transformed a laminar boundary layer into a turbulent boundary layer. Compared to a smooth sphere, the critical Reynolds number decreased and the separation point shifted further downstream. Therefore, the drag coefficient of a test golf ball was smaller than that of a smooth sphere. The magnitude of the decrease in the critical Reynolds number was found to increase with dimple depth. However, the separation point shifted to the upstream side and the drag coefficient became larger in the super-critical Reynolds number region.

Keywords: Golf ball, Dimple structure, Drag coefficient, Pressure distribution, Velocity distribution, Flow Visualization

1. INTRODUCTION

A common goal in fluid mechanics is to decrease drag by controlling the boundary layer of a flow. If the drag can be decreased by altering the surface structure without altering the shape of the object, the practical design range for industrial applications can be extended. For a smooth sphere, the following general classification has been made for the drag coefficient in terms of Reynolds number[(1), (2)]. The sub-critical region is a region in which the drag coefficient has an almost constant value of approximately 0.45 to 0.5, independent of Reynolds number. The critical region is a region in which the drag coefficient decreases rapidly and becomes a minimum for Reynolds number of approximately 3.5×10^5. Regions beyond the critical region are classified as the super-critical and trans-critical regions, in which the drag coefficient gradually increases with Reynolds number. The sudden reduction of the drag coefficient in the critical region is caused by a boundary layer transition on the surface of the sphere. It has been reported that this boundary layer transition can be enhanced by the presence of roughness or dimples on the sphere surface as a golf ball. As a result, the drag coefficient of such a sphere decreases at low Reynolds number compared to that of a smooth sphere. Achenbach[(3)] reported that the critical Reynolds number became lower as the surface roughness increased. However, after the critical Reynolds number was reached, the drag coefficient immediately increased. Moreover, the drag coefficient in the super-critical region increased as the surface roughness increased. In contrast, Bearman and Hervey[(4)] reported that the drag coefficient of a dimpled sphere increased gradually in the super-critical region. The drag coefficient in the super-critical region of a dimpled sphere differs from that of a sphere with a rough surface. The present authors[(5),(6)] previously investigated a sphere covered with regular circular arc type dimples in an attempt to clarify the optimum surface structure for decreasing the drag, and examined the effect of the number of dimples on the drag characteristics. The critical Reynolds number was found to decrease as the number of dimples was increased, and the drag coefficient increased after the critical Reynolds number was reached. However, it has not been clarified how the flow mechanism is changed by the presence of surface roughness or dimples. Moreover, the influence of the surface structure on the drag coefficient is not known. The final goal of the present study is to clarify the optimum surface structure for decreasing the amount of drag on a golf ball.

In the present study, the pressure and flow velocity distributions inside and between dimples were measured for the test golf ball of circular arc

type dimples with three different depths. In addition, the surface flow on the test golf ball and the smooth balls were visualized by an oil film method and spark tracing method. From these results, the mechanism of the drag reduction by arc type dimple structure of the golf ball was clarified.

2. EXPERIMENTAL APPARATUS AND METHODS

2.1 Test golf ball

Figure 1 shows a schematic cross section of the dimples on the surface of the test ball. The test balls were made of vinyl chloride and had diameters (d) of 42.6 mm and 100 mm. In the present study, the dimples were in the form of circular arcs. The depth ratio of the dimples (k/d) (k: depth of dimple, d: diameter of ball) was varied from 0.0079 to 0.0188. The width ratio of the dimples (c/d) (c: width of dimple) was 0.0828. A total of 328 dimples were distributed uniformly over the test ball. A pressure tap having a diameter of 0.8 mm was positioned on the surface of the test ball (d = 100 mm). Two test balls, one having a pressure hole tap inside a dimple and the other having a pressure tap between dimples, were used in the pressure measurement. Table 1 shows the primary specifications of the test balls.

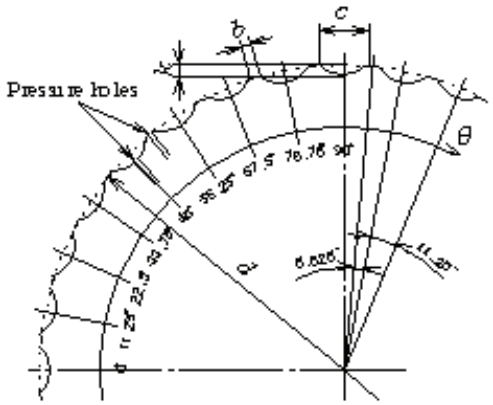

Figure 1. Equatorial section of test ball

Table1 Specifications of test ball surface

Type	*b/d*	*c/d*	*k/d*	*k/c*
Smooth	—	—	—	—
A	0.0152	0.0828	0.0079	0.0958
B			0.0151	0.1830
C			0.0188	0.2270

2.2 Wind tunnel

A blow-down type wind tunnel having a test section of 400 mm × 400 mm was used for aerodynamic measurements and flow visualization around the test ball. The free stream velocity (U) was varied from 10 to 50 m/s. The turbulence intensity in this velocity range is 0.3 %. The Reynolds number ($Re = Ud/v$, v: kinematic viscosity) based on the free stream velocity and the diameter of the test ball ranges from 0.4×10^5 to1.4×10^5. Figure 2 shows an outline of the equipment used to measure the drag (D). The dimensions of the frame were 500 mm × 500 mm, and the frame was placed 100 mm downstream from the outlet of the wind tunnel.

2.3 Measurement of drag and pressure

The test ball was fixed at the center of the frame using piano wire to provide tension at both fixed ends. The drag on the test balls were measured by a three-component load cell with a strain gauge attached below the frame. Based on the measured drag values, the drag coefficient (C_D) was calculated using Eq. (1). Measurement of the pressure (P) was placed 100 mm downstream from the outlet of the wind tunnel by means of a hollow shaft and a small pipe. One side of the pipe was connected to the pressure tap at the center of the test ball and the other side was connected to a semiconductor pressure transducer. For a ratio of the piano wire diameter to the ball diameter (d_P/d : dimensionless value) of 0.037 or less, the effect of the piano wire is assumed to be negligible[7]. In the present study, d_P/d was 0.037. Using the semiconductor pressure transducer, the pressure distribution over the test ball surface was measured at intervals of $\theta = 5.625°$ in the angular range $\theta = 0°$ (stagnation point) to $\theta = 180°$. From these values, the pressure coefficient(C_P) was calculated using Eq.(2).

2.4 Measurement of flow velocity and turbulence intensity

The flow velocity and turbulence intensity near the ball surface was measured using a hot-wire anemometer. In the flow velocity measurements, the probe was set at an angle of 30° to the flow direction in order to avoid disturbing the flow.

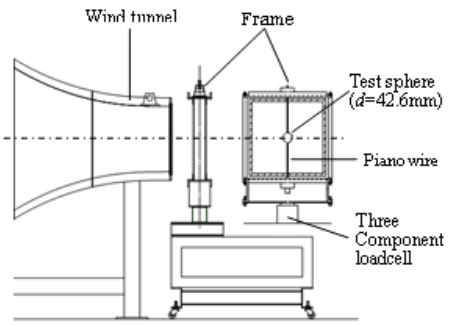

Drag measurement

Figure 2.Outlines of experimental apparatus

The flow velocity at the equator of the ball was measured in the angular range of θ = 78.75° ~ 129.375° inside the dimples and between them, with a step size of θ = 5.625°.

2.5 Flow Visualization by Spark Tracing Method

Figure 3 shows the outline of measurement equipment for the spark tracing method.

The principle of the spark tracing method makes an instaneous path of ionized air, when the electric spark travels in air. This path has a very low resistance for a very short period, during which detectable ionization exists. When a pair of electrodes is placed in the air flow to be measured and high-voltage pulses are applied to them, the first electric spark connects these electrodes through the shortest distance, making an ionized path. This ionized path moves together with the air flow, and the second electric spark travels along this moving path with very low electrical resistance. Subsequent electric sparks travel along the moving ionized path one after another, tracing the timelines of the air flow. Therefore, the movement of the ion is also disturbed, when the flow has been disturbed, and the velocity distribution in which the time line was also disturbed is shown. Two electrodes are set on the surface of the sphere at θ=±60deg and two needle electrodes set 30 mm away from the test golf ball. The high voltage and high frequency pulses are supplied from a pulse generator.

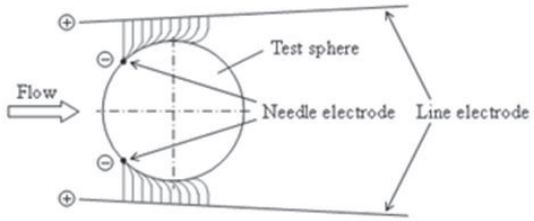

Figure 3. Outline of measurement equipment for spark tracing method

3. EXPERIMENTAL RESULTS AND CONSIDERATIONS

3.1 Drag coefficients for various Reynolds numbers

Figure 4 shows the drag coefficient for each test ball as a function of Reynolds number. The drag coefficient (C_D) was calculated using Eq. (1).

$$C_D = \frac{D}{A\rho U^2/2} \tag{1}$$

The C_D value for the smooth sphere is largely independent ($C_D \fallingdotseq 0.45$) of Reynolds number because this Reynolds number range represents the sub-critical region. On the other hand, the critical Reynolds number for the Type A is approximately 0.5×10^5, which is lower than that for the smooth sphere (approximately 3.5×10^5). Above the critical Reynolds number, the C_D value for the Type A increases gradually but remains smaller than that of the smooth sphere. For the Type B with deeper dimples, the critical Reynolds number shifts to an even lower value. In addition, for the Type C , even the lowest Reynolds number in the present study is already above the critical value. The rate of increase in C_D above the critical Reynolds number becomes larger as the dimples become deeper. Although the dimple number, width ratio (c/d) and dimple arrangement are different, the dependence of C_D on the depth ratio (k/d) is similar to that reported by Choi et al.[5] and Bearman and Hervey[4] in that the critical Reynolds number decreases with increasing dimple depth, and C_D tends to increase above the critical Reynolds number.

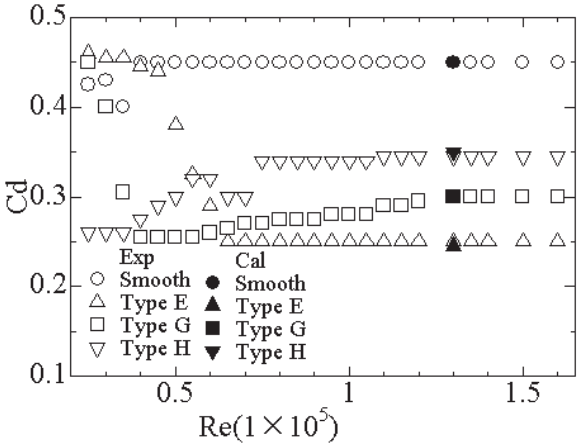

Figure 4. Drag coefficient to the Reynolds number in the test golf balls

3.2 Pressure distribution on test ball surface

Figure 5 shows the pressure distribution at the equator on the surface of the test balls at Re = 1.27×10^5. Here, θ indicates the angle measured from the stagnation point (θ = 0°), and the pressure coefficient C_P represents the average of the values inside and between dimples, and is calculated using Eq. (2).

$$C_P = \frac{P - P_0}{\rho U^2/2} \tag{2}$$

The continuous line in Fig. 5 shows the pressure distribution of a smooth sphere in an ideal fluid. The measured C_P values for the smooth sphere exhibit a minimum in the vicinity of θ = 72°, and become approximately constant at about θ = 80°, which is similar to the result reported by Achenbach[2]. Based on this result, the separation point for the smooth sphere is thought to be approximately θ = 80°. In contrast, although the C_P values for the Type A are similar to those for the

smooth sphere up to approximately $\theta = 11.25°$, they are lower in the range $\theta = 16.875° \sim 118.125°$. In other words, the flow velocity near the surface between dimples is higher than that inside the dimples. Since the golf ball surface is discontinuous, the flow separates in front of the dimple entrance, and then reattaches inside the dimple. Separation bubbles are formed in dimples due to such flow. This is thought to give rise to a pressure difference, since a circulating low-velocity flow is formed. The C_P between the dimples on the Type A is smaller than that for the smooth sphere at the same angle. In other words, the surface flow velocity between the dimples is higher than that on the smooth sphere. Therefore, the flow for the Type A overcomes the downstream adverse pressure gradient. As a result, the separation point (near $\theta = 118.125°$) for the Type A shifts downstream in comparison to that (near $\theta = 80°$) for the smooth sphere. Moreover, C_P inside the dimples becomes smaller in the range $\theta = 56.25° \sim 112.5°$ as the dimples become deeper. In the present study, the pressure in the dimple is measured at the center of the dimple. For the Type A, C_P is thought to be larger than that for the Type B and Type C because the flow for the Type A reattaches near the center of the dimple. Moreover, C_P between the dimples increases in the range $\theta = 61.875° \sim 118.125°$ as the dimples become deeper.

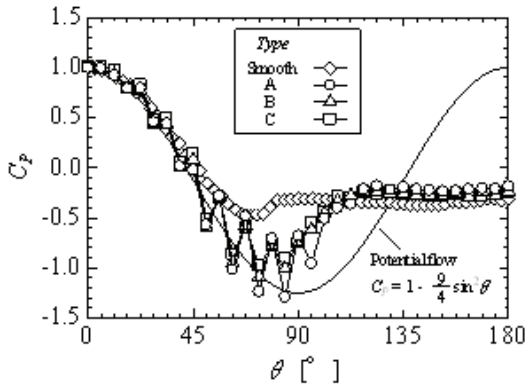

Figure 5. Pressure distributions on sphere surfaces

In other words, the surface flow velocity between the dimples decreases. Therefore, the flow cannot overcome the downstream adverse pressure gradient. As a result, the separation point shifts upstream for both the Type B and Type C near $\theta = 106.875°$. Moreover, the back pressures become smaller in the order of Type A, Type B, Type C, and the smooth sphere, which corresponds to the C_D relations shown in Fig. 4. Therefore, C_D changes even if the Reynolds numbers for the golf ball are equal, since the pressure distribution depends on the dimple depth. The C_P values between the dimples are smaller than that for an ideal fluid for a smooth sphere. This type of flow appears to give rise to the regression of the separation point.

3.3 Flow visualization over ball surface by oil film method and spark tracing method

The flow over the surface of the balls was next visualized using an oil film method. Figure 6 shows photographs of the sphere surfaces at the equator for Re = 1.27×105, and Fig. 7 shows sketches of the flow in equatorial cross sections. For the smooth sphere, this Reynolds number is in the sub-critical region. As seen in Fig. 6, the oil film on the smooth sphere is missing from the stagnation point to θ = 80°. Therefore, the flow moves along the surface to θ = 80°, and then separates. An oil film is missing in the dimples of the Type A from the stagnation point up to θ = 33.75°, indicating that a flow occurs along the surface in this region. However, the oil film is still remaining at the entrance of dimples in the range θ = 45° ~ 123.75°, with some streak-like regions also appearing in the center of dimples. This indicates that the separation bubbles are formed further upstream as the dimples become deeper. Moreover, the oil film in the Type B and located between the entrance and the center of the dimples moved in a direction opposite to that of the main flow. However, regions of oil located between the center and the exit of the dimples moved in the direction of the main flow. This is because circulating flow is formed by the separation bubbles, which are produced at the entrance of the dimples. Although the oil film is missing in the vicinity of θ = 118.125°, it is present in the vicinity of θ = 129.375°. Therefore, it is thought that the separation point is in the vicinity of θ = 118.125°. For the Type B and Type C an oil film is present in the dimples in the range θ = 22.5° ~ 112.5° and θ = 11.25° ~ 112.5° respectively. Although the oil film is missing in the vicinity of θ = 106.875°, it is present in the vicinity of θ = 118.125°. Therefore, it is thought that the separation points for the Type B and Type C are in the vicinity of $\theta = 106.875°$. Figure 8 show the flow visualization photographs by the spark tracing method. From the flow visualization results, the position of the separation point has moved to the downstream side, as the depth ratio of (k/d) is smaller. The arrow in the figure shows the position in the separation point. The separation point shifts to the upstream, as the value of (k/d) increases. And, the area of the wake is big, and the reverse flow also increases. Therefore, the behavior of this flow also consequentially in the drag coefficient. Therefore, the behavior of this flow also consequentially influence for the drag coefficient.

3.4 Velocity and turbulence intensity distributions near ball surface

Figure 9 shows the flow velocity at a height of 0.05 mm from the surface of the equator of the test golf balls ($r/d = 0.5$ in Fig. 9) for $Re = 1.27\times10^5$. Here, θ is the angle from the stagnation point ($\theta = 0°$),

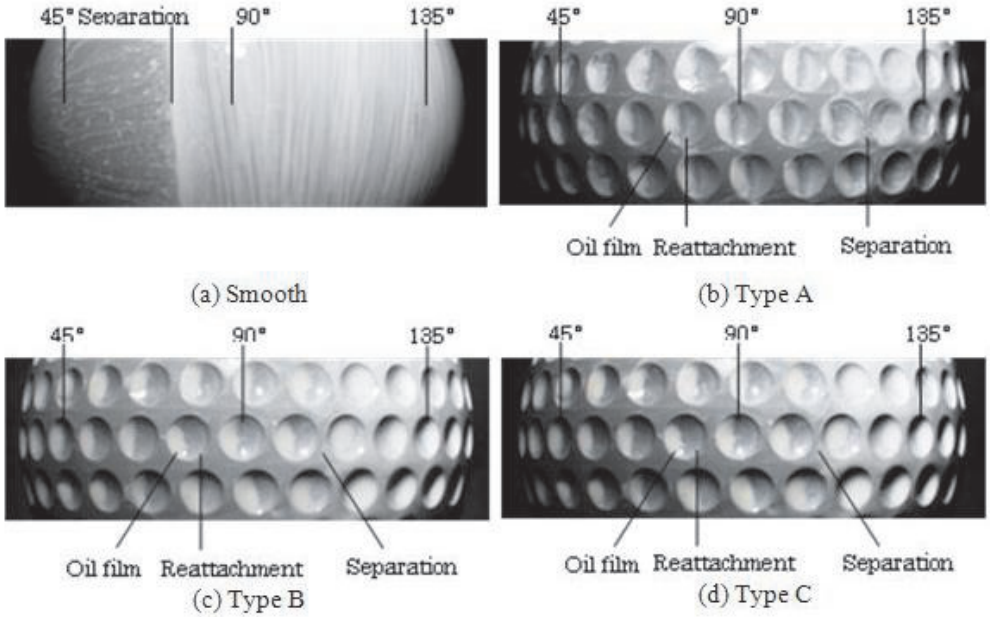

Figure 6. Flow visualization by oil film method

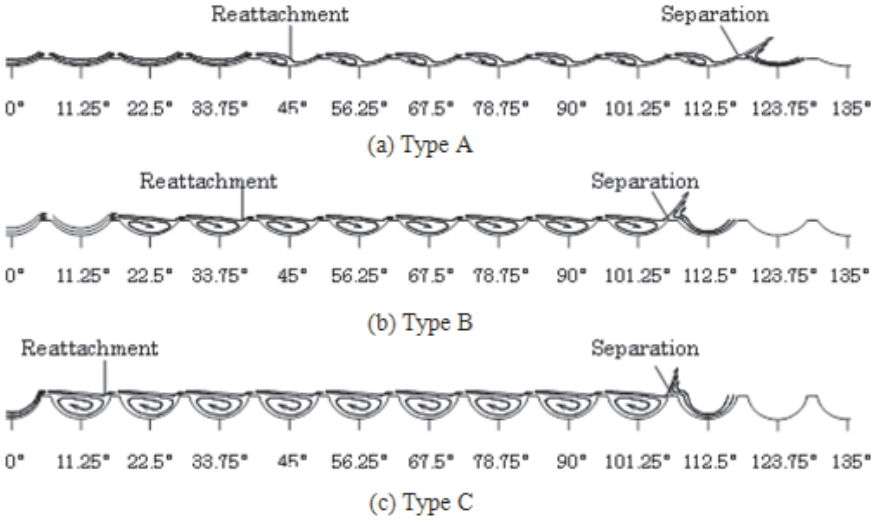

Figure 7. Sketches of flow patterns near sphere surface

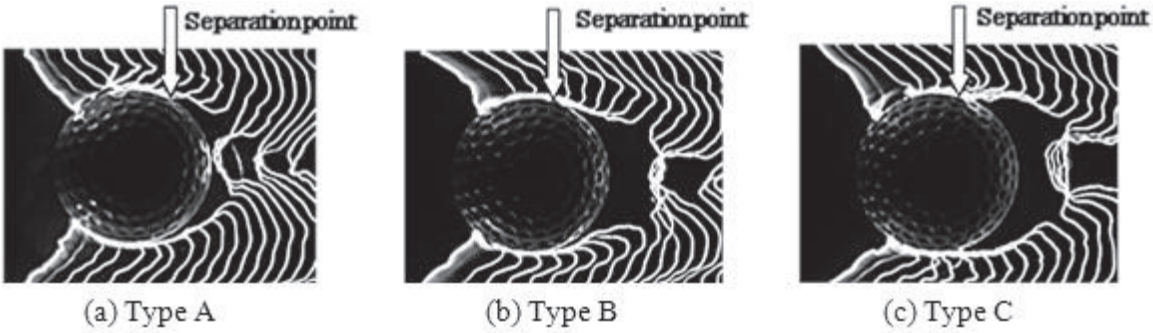

Figure 8. Flow visualization around test golf balls by Spark tracing method (Re=1.27×10^5)

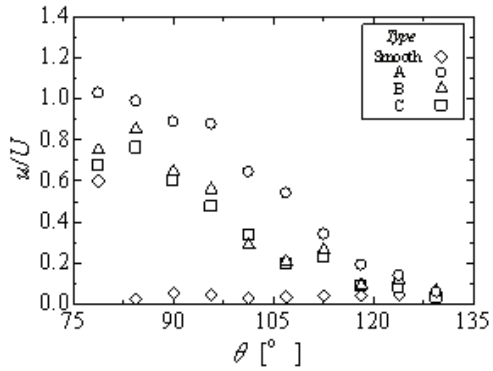

Figure 9. Velocity distributions near ball surface(*r/d*=0.5)

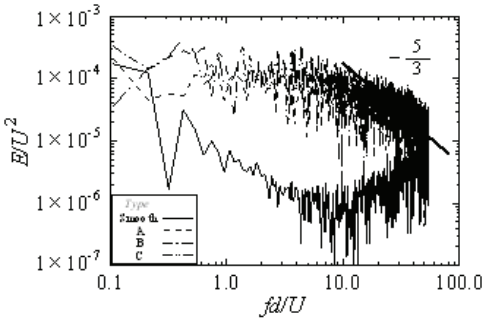

Figure 10. Spectra of velocity fluctuations (*r/d*=0.5)

and *u/U* indicates the dimensionless velocity, where *u* is the time averaged velocity, and *U* is the free stream velocity. In the case of the smooth sphere, the velocity decreases near θ = 80°. Therefore, it is thought that the flow separates in this vicinity. On the other hand, the velocity for the Type A is remarkably larger than that for the smooth sphere at θ = 80°, and this is thought to contribute to the regression of the separation point. Moreover, the velocity at the same angle becomes smaller as the dimples become deeper. Therefore, it is thought that the separation point shifts upstream. Figure 10 shows the results of a frequency analysis of the dimensionless velocity *u′/U*. Here, *u′* is the fluctuating velocity at *r/d* = 0.5 of θ = 78.75°, and *U* is the free stream velocity. The boundary layer formed near the surface of the smooth sphere is laminar at this Reynolds number, and the dimensionless frequency of vortex shedding is approximately 0.18[8]. The spectrum for the smooth sphere decreases at a dimensionless frequency of approximately 0.18. On the other hand, the spectra for the golf balls decrease at this point. Therefore, in the case of the dimpled spheres, it is thought that vortices are generated not only with laminar flow dimensionless frequency. Choi et al.[9] reported that a turbulent flow transition of the boundary layer is promoted by the formation of separation bubbles in the separation but also with various sizes.

The spectrum begins to gradually decrease as the frequency increases above about 20, and the slope of the decrease is approximately -5/3 times the dimensionless the dimples and that the spectrum decreases in the range 20 to 100 almost at the dimensionless frequency. The range in which the spectrum in the present study decreases agrees well with that reported by Choi et al.[9]. In the case of the dimpled balls, the laminar boundary layer is transformed into a turbulent boundary layer near the separation point for the smooth sphere. The spectrum does not decrease for such a flow field. Therefore, the dimples are considered to contribute to the regression of the separation point.. Figure 11 shows the velocity distributions at the equator for $Re = 1.27\times10^5$, and Fig.12 shows the turbulence intensity distributions. Here, *u′* is the fluctuating velocity. The surface of the smooth sphere is represented by *r/d*= 0.5 (the position at a height of 0.05 mm from the surface) and *r/d* values of 0.5 or less represent the dimples. In the case of the smooth sphere, the velocity near the surface decreases in the range θ = 78.75° ~ 84.375°. It is thought that the flow separates within this range. This agrees well with the separation point obtained from the results of the pressure distribution and the flow visualization. On the other hand, in the case of the Type A flow occurs in the dimple at θ = 78.75°, and the velocity at *r/d* = 0.5 is larger than that for the smooth sphere. In addition, the velocity near the surface between the dimples at θ = 84.375° is larger than that for the smooth sphere. The velocity near the surface for the Type A increases downstream, and the development of the boundary layer thickness is controlled in comparison with the smooth sphere. A turbulent flow transition of the boundary layer is promoted by the formation of separation bubbles in the dimples. The velocity near the surface becomes large so that a flow with large velocity enters near the surface. Therefore, the flow can overcome the adverse pressure gradient, and the development of the boundary layer thickness is controlled. The velocity near the surface for the Type A becomes small in the vicinity of θ = 118.125°. Therefore, it is thought that the flow separates in this region. This result agrees well with the separation point obtained from the results of the pressure distribution and the flow visualization. As the dimples become deeper, the velocity near the surface decreases at θ = 78.75°, and the boundary layer thickness increases. In addition, the velocity of the circulating flow in the dimple becomes smaller because the separation bubble is formed in the vicinity of *r/d* = 0.5. The flow at *r/d* = 0.5 is subjected to greater shear from the circulating flow in the dimple. As a result, the velocity at *r/d* = 0.5 decreases, and the turbulence intensity increases. Moreover, the reattachment point of the flow shifts to the vicinity of the dimple exit as the dimple becomes deeper. Therefore, it is thought that the velocity near the surface decreases as the pressure increases in the vicinity of the dimple exit.

The velocity near the surface between the dimples

(near θ = 84.375°) decreases because such a boundary layer occurs between the dimples, and the position at which the turbulence intensity increases moves away from the surface.

The flow near the surface cannot overcome the adverse pressure gradient, and the boundary layer thickness becomes larger. In the cases of the Type B and Type C, the velocity near the surface

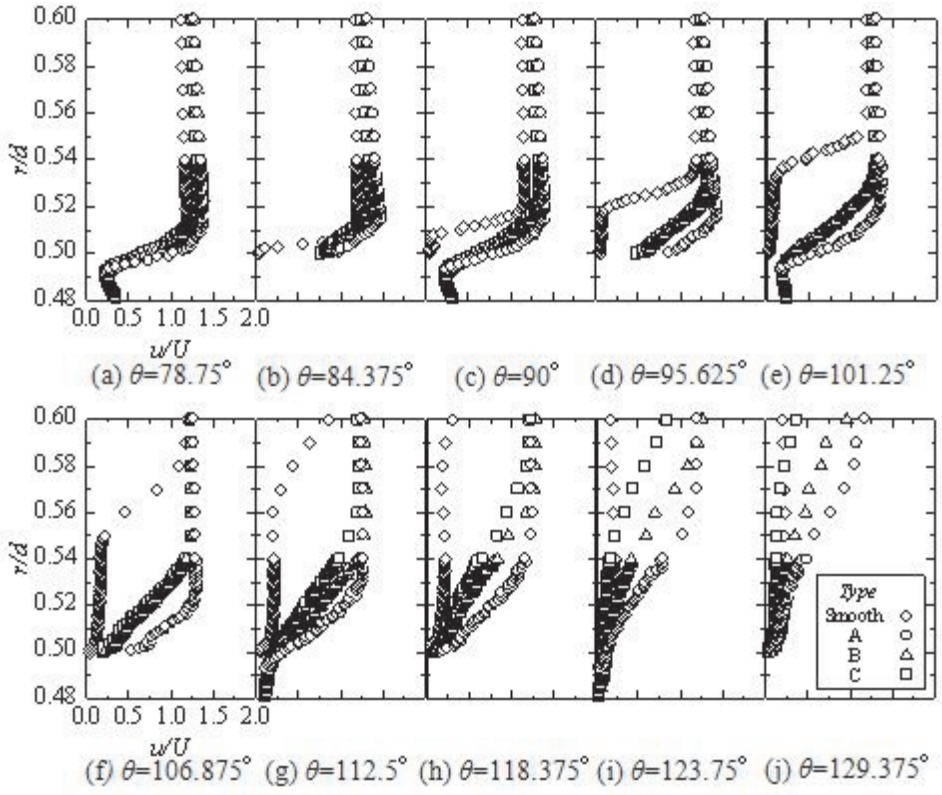

Figure 11. Velocity distributions

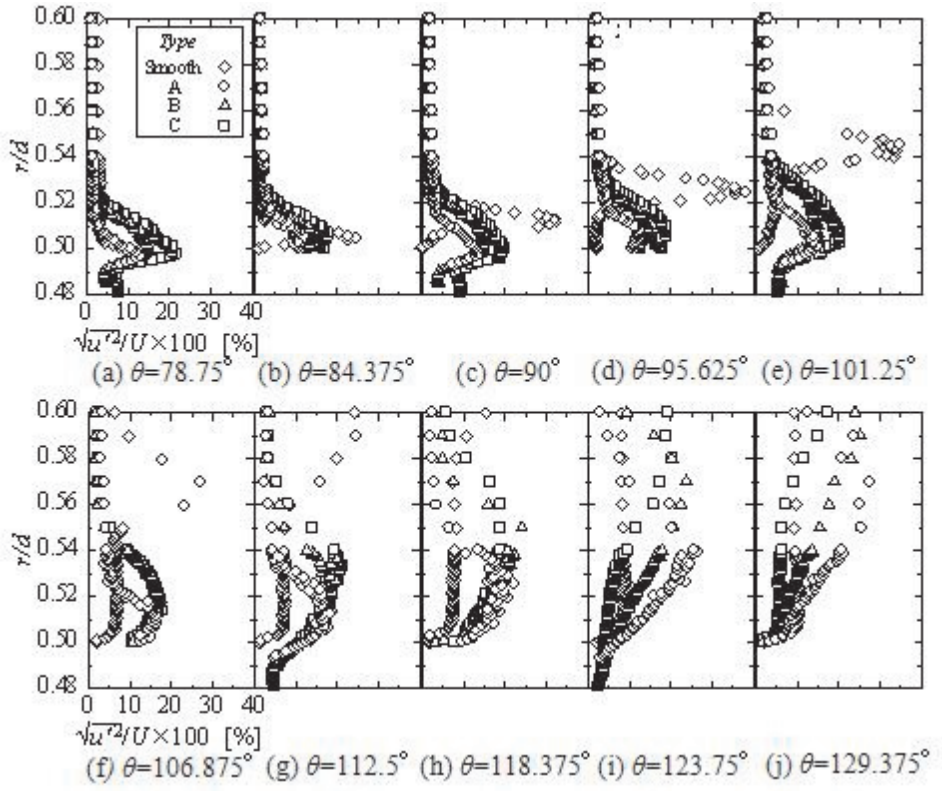

Figure 12. Turbulent intensity distributions

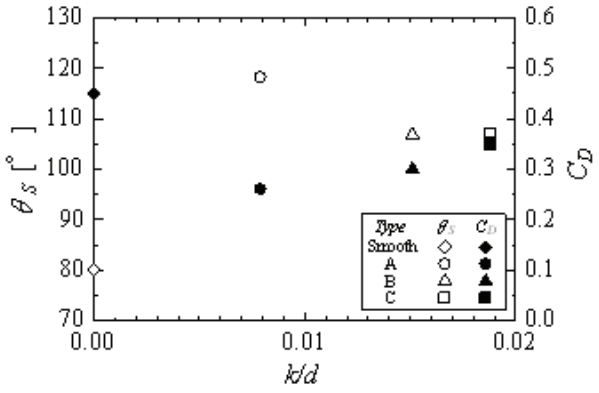

Figure 13. Separation points and drag coefficients (Re=1.27×10^5)

The flow near the surface cannot overcome the adverse pressure gradient, and the boundary layer thickness becomes larger. In the cases of the Type B and Type C, the velocity near the surface becomes small at around θ = 106.875°, and it is thought that the flow separates in this region. This agrees well with the separation point obtained from the results of the pressure distribution and the flow visualization. The separation point for the dimpled balls cannot be changed continuously like that for the smooth sphere because the dimples are arranged at equal intervals. The separation points for the Type B and Type C were the same because the separation point is influenced by the dimple arrangement. However, the velocity near the surface for the Type B is slightly larger than that for the Type C, and the boundary layer thickness is slightly smaller.

3.5 Separation point

Figure 12 shows the separation point angle (θ_S) and drag coefficient (C_D) as functions of the depth ratio (k/d) for Re = 1.27×10^5. For the smooth sphere, θ_S is at about 80°, whereas for the golf ball, it is shifted downstream. Moreover, θ_S shows a tendency to shift upstream as the dimples become deeper. Separation occurs for the smooth sphere with laminar flow, whereas it occurs for the golf ball with turbulent flow by controlling the boundary layer. The regression of the separation point appears to greatly affect the drag reduction of the golf ball.

4. CONCLUSIONS

In the present study, the pressure and flow velocity distributions were measured in order to clarify the mechanism of drag reduction for balls with circular arc type dimples of three different depths. Based on the experimental results, the following conclusions were reached.

(1) The critical Reynolds number decreases as the dimples become deeper. The drag coefficient above the critical Reynolds number also increases with dimple depth. In addition, the drag coefficient gradually increases with Reynolds number.

(2) When the flow along the surface of a test ball enters a dimple, a small separation bubble is formed in the dimple. This accelerates the flow between the dimples on the surface of the test ball, promoting a turbulent flow transition of the boundary layer. The boundary layer thickness can be controlled. Since the separation point shifts downstream compared to the case for a smooth ball, the drag coefficient is smaller for a ball with dimples. Moreover, a differential pressure is generated between the dimples because the velocity over the surface of the ball is higher than that in the dimples, so that the pressure between dimples is reduced.

(3) The separation bubbles are formed further upstream as the dimple depth increases, and the reattachment point of the flow shifts to the exit side of the dimple. The separation point shifts upstream as the dimple depth increases, and the drag coefficient increases.

REFERENCE

(1) Schlichting, H., Boundary Layer Theory, 6th edition, (1968), p.17, McGraw-Hill.

(2) Achenbach, E., Experiments on the Flow past Spheres at very High Reynolds Numbers, Journal of Fluid Mechanics, Vol.54, Part 3 (1972), pp.565-575.

(3) Achenbach, E., The Effects of Surface Roughness and Tunnel Blockage on the Flow past Spheres, Journal of Fluid Mechanics, Vol.65, Part 1 (1974), pp.113-125.

(4) Bearman, P. W. and Harvey, J. K., Golf Ball Aerodynamics, Aeronautical Quarterly, Vol.27 (1976), pp.112-122.

(5) Aoki,K.,Ohike,A.,Yamaguchi,K.andNakayama,Y, Flying Characteristics and Flow Pattern of a Sphere with Dimples, Journal of Visualization, Vol.6, No.1 (2003), pp.67-76.

(6) Aoki,K,Okanaga,H,andNakayama,Y.,Aerodynamic Behavior and Drag Characteristics for the Surface Structure of the Sphere with Dimples, The 13th International Symposium on Flow Visualization, (2008).

(7) Smits, A.J. and Smith, D.R., A New Aerodynamic Model of a Golf Ball in Flight, Science and Golf 2, (1994), pp.340-347.

(8) Achenbach, E., Voltex Shedding from Spheres, Journal of Fluid Mechanics, Vol.62, Part 2 (1974), pp.209-221.

(9) Choi, J., Jeon, W. P. and Choi, H., Mechanism of Drag Reduction by Dimples on a Sphere, Physics of Fluids, Vol.18, No.4 (2006), pp.0417021-0417024.

Conference on Modelling Fluid Flow (CMFF'12)
The 15th International Conference on Fluid Flow Technologies
Budapest, Hungary, September 4-7, 2012

4D-Variational Data assimilation using POD Reduced-Order Model

Gilles TISSOT[1], Laurent CORDIER [2], Bernd R. NOACK [3]

[1] Pprime Institut, 43 route de l'aérodrome, 86000 Poitiers, France, Tel.: +33549366047 E-mail: Gilles.Tissot@univ-poitiers.fr
[2] Pprime Institut, 43 route de l'aérodrome, 86000 Poitiers, France, Tel.: +33549366036 E-mail: Laurent.Cordier@univ-poitiers.fr
[3] Pprime Institut, 43 route de l'aérodrome, 86000 Poitiers, France, Tel.: +33549366015 E-mail: Bernd.Noack@univ-poitiers.fr

ABSTRACT

In flow control, reduced-order models based on Proper Orthogonal Decomposition (POD ROM) are often used as surrogate model for deriving a control law. However, these models are in general too fragile to be used in closed-loop control where the dynamics is strongly modified by the control. Here, a 4D-Variational data assimilation approach (4D-Var) as classically used in meteorology is used to estimate at best the state of the system from inhomogeneous sources of information coming from a model, noisy observations and a background solution. Two complementary strategies (strong constraint 4D-Var and weak constraint 4D-Var) are assessed in the case of a cylinder wake flow with data coming from numerical simulation and PIV experiments.

Keywords: cylinder, data assimilation, estimation, POD, reduced-order model

NOMENCLATURE

$\mathcal{B}$	[−]	covariance matrix of the initial condition
C	[−]	covariance matrix of the coefficients
$\mathcal{I}$	[−]	cost functional of the calibration
$\mathcal{L}$	[−]	Lagrangian of the 4D-Var
$\mathcal{R}$	[−]	covariance matrix of the observations
$\mathcal{W}$	[−]	covariance matrix of the noise
$\mathcal{Y}$	[−]	observations
$\mathbb{H}$	[−]	observation operator
$\mathbb{M}$	[−]	dynamical model
C	[−]	constant coefficients of the ROM
L	[−]	linear coefficients of the ROM
N_{gal}	[−]	number of modes kept
N_s	[−]	number of time steps
$\mathcal{J}$	[−]	cost functional of the 4D-Var
Q	[−]	quadratic coefficients of the ROM
T	$[s]$	temporal horizon
X	[−]	state variable
a_i	[−]	i^{th} POD coefficient
e	[−]	error
t	$[s]$	time
u	[−]	coefficients of the model $\mathbb{M}$
$\boldsymbol{v}$	[−]	snapshots
w	[−]	noise of the model $\mathbb{M}$
$\boldsymbol{\Phi}_i$	[−]	i^{th} POD mode
η	[−]	perturbation of the initial condition
λ	[−]	Lagrange multiplier associated to the model $\mathbb{M}$
μ	[−]	Lagrange multiplier associated to the initial condition

Subscripts and Superscripts

$*$	adjoint
0	initial condition
a	analysed solution
b	background solution
cal	calibration procedure
m	mean
i, j, k	modes indices
P	projection on the POD subspace
R	POD Reduced-Order Model
True	true state

1. INTRODUCTION

In turbulence, the number of active degrees of freedom is so important that a preliminary step of *model reduction* is compulsory for determining an efficient control strategy. The general objective of model reduction is to extract, from physical insights or mathematical tools, the building blocks which play a dominant role in terms of dynamical modelling. For historical reasons, Proper Orthogonal Decomposition (see [1] for an introduction) is the most used reduction approach in the turbulence community. POD is widely employed since it

extracts from a sequence of data an orthonormal basis which captures optimally the flow energy. In general, this basis is then used in a Galerkin approach to derive a POD Reduced-Order Model (POD ROM) of the flow by projecting the Navier-Stokes equations onto the POD modes. Unfortunately, this dynamical system is sometimes not sufficiently accurate to predict anything useful in terms of flow control, and identification methods [2] are then used to improve the prediction ability of the POD ROM. In this communication, an alternative procedure is proposed where identification methods are replaced by *data assimilation*.

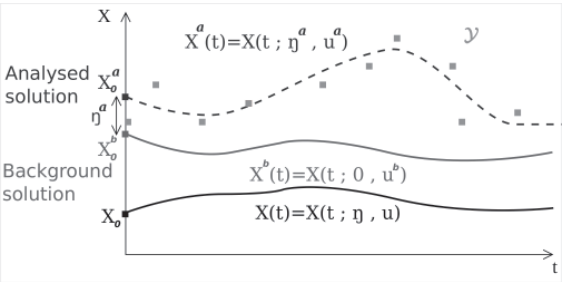

Figure 1. Schematic representation of 4D-Var.

Data assimilation is a generic methodology which combines heterogeneous observations with the underlying dynamical principles governing the system under observation to estimate at best physical quantities. Starting from a background solution and incoming imperfect informations, an optimal estimation of the true state of the system is determined (see Figure 1) which takes into account the respective statistical confidences of the different observations. By convention, this true state is often called *analysed solution*. Data assimilation is now routinely used in meteorology and oceanography to combine images coming from satellites, meteorological observations and a dynamical model in order to forecast the weather [3, 4]. Since numerical weather prediction is an initial value problem, the goal of assimilation is here to find the best initial condition of the numerical model that minimises the observations errors. In fluid mechanics, data assimilation was more recently introduced for estimating quantities [5] and predicting their time evolutions. There are two basic approaches in data assimilation: stochastic estimation that is based on probability considerations (Kalman filtering for instance), and variational data assimilation, which is used in this communication, where the estimation is found as a solution of an optimization problem. When the observations are distributed in time, this approach is referred as four-dimensional variational assimilation or 4D-Var.

If the dynamical model is assumed to be known perfectly then no extra uncertainty terms are included in the governing equations and the 4D-Var is said with *strong constraint* (see section 2). In that case, the solution of the model is considered to be only dependent on some unknown or imperfectly known parameters: initial condition and coefficients of the model. These values can then be used as control parameters in a minimization problem where the cost functional is built as a sum of an observation error, which measures the difference between the observations and the output of the identified model, and different background errors, which penalize the variation between the background states and the estimated values. In practice, these different terms can be weighted accordingly on the level of statistical confidence that can be evaluated from expert knowledge. Another strategy is to consider a *weak constraint assimilation* approach (see section 3) where the coefficients of the model are assumed to be known in advance, and where an uncertainty function is added to the dynamical model.

The solutions of these constrained optimization problems are computed through an iterative descent algorithm where the gradient of the cost functional with respect to the variation of the control parameters is found by solving an adjoint problem. Computing the solution of an optimality system is known to be computationnaly very expensive since the optimal solution is found iteratively by integrating backward in time the adjoint equation. However, here, the dynamical model corresponds to a POD ROM and then the computation is numerically tractable [6].

In this communication, two datasets of increasing dynamical complexity have been used: i) a DNS dataset of a cylinder wake flow at a Reynolds number of 200 (see section 5.1) to validate the algorithm with twin experiments, and ii) an experimental PIV dataset of a cylinder wake flow at a Reynolds number of 40000 (see section 5.2). In the two cases, a POD analysis has first been done and then a POD ROM derived by Galerkin projection of the Navier-Stokes equations onto the POD basis. In the 4D-Var setting, the POD temporal modes served as observations for the assimilation procedure. We will see in section 5 that a qualitative good prediction can be obtained for the two datasets and that relaxing the dynamical constraint can help in the PIV case to follow the observations.

2. STRONG CONSTRAINT 4D-VAR

Let X be the state variable and $\mathbb{M}$ be the non-linear operator relative to the dynamics, the evolution in time of X is given by the following dynamical system:

$$\begin{aligned} &\frac{\partial X}{\partial t}(t) + \mathbb{M}(X(t), u) = 0 \\ &X(0) = X_0^b + \eta \end{aligned} \tag{1}$$

where X_0^b is an *a priori* known initial condition of the system, η an initial condition perturbation and u a set of coefficients of the model.

Strong constraint assimilation consists of finding the solution $X(t)$ of the dynamical system (1) that is closest at the same time to the observations $\mathcal{Y}$

and to regularisation terms called *background* terms. The goal is then to find the control parameters (η, u) which minimize the cost functional $\mathcal{J}$ defined as:

$$\mathcal{J}(u,\eta) = \frac{1}{2}\int_0^T \|\mathcal{Y}(t) - \mathbb{H}(X(t;\eta,u))\|^2_{\mathcal{R}^{-1}} dt + \frac{1}{2}\|\eta\|^2_{\mathcal{B}^{-1}} + \frac{1}{2}\|u - u^b\|^2_{C^{-1}}. \quad (2)$$

The non-linear operator $\mathbb{H}$, called observation operator, goes from the state space to the observation space. $\mathcal{R}$, $\mathcal{B}$ and C are covariance tensors of the observation space, state space and control space. They are related respectively to the observations, the state variables' initial conditions and to the control variables. The norms $\|\cdot\|_{\mathcal{R}^{-1}}$, $\|\cdot\|_{\mathcal{B}^{-1}}$ and $\|\cdot\|_{C^{-1}}$ are induced norms of the inner products $\langle\mathcal{R}\cdot,\cdot\rangle$, $\langle\mathcal{B}\cdot,\cdot\rangle$ and $\langle C\cdot,\cdot\rangle$. The role of these covariance tensors is to give more or less confidence in the observations and background states. These tensors have a key influence for combining inhomogeneous sources of information in data assimilation. The covariance tensors may be chosen based on extra knowledge of the system. Here, they have been simply defined as diagonal tensor. The optimal control parameters (η^a, u^a) are called *analysed solutions* and the associated analysed dynamics $X^a(t)$ is the best estimation of the system's state, solution of (1) according to the criterion (2). The couple $(0, u^b)$ corresponds to the *background* solution of the problem. Data assimilation is described schematically in Fig. 1.

The minimization of $\mathcal{J}$ is done using the limited storage variant of the BFGS quasi-Newton algorithm [7]. For determining the descent directions, the gradients of the functional with respect to the two control variables η and u need first to be evaluated. The use of finite differences to determine the gradient of the cost functional is in practice unfeasible when the dimension of the state variables is too large. An elegant solution is to write an *adjoint formulation* of the problem. We will see soon that the determination of the gradient of $\mathcal{J}$ with respect to the control variables then corresponds to the forward integration of the dynamical system (1) followed by a backward integration of an adjoint dynamical model to be determined.

In variational data assimilation, the analysed dynamics is found as solution of the constrained minimization problem given by (2) and (1). A classical way for solving this type of constrained optimization problem [8] is by introducing a Lagrangian functional $\mathcal{L}$ defined by

$$\mathcal{L}(X(t), u, \eta, \lambda(t), \mu) = \mathcal{J}(u,\eta) - \int_0^T \langle \frac{\partial X(t)}{\partial t} + \mathbb{M}(X(t), u), \lambda(t)\rangle dt - \langle X(0) - X_0^b - \eta, \mu\rangle \quad (3)$$

where $\lambda(t)$ and μ are two Lagrange multipliers introduced to enforce the constraints given by (1). When the minimum of $\mathcal{J}$ is reached, $\nabla\mathcal{J} = \nabla\mathcal{L} = 0$.

Setting the first variation of $\mathcal{L}$ with respect to X to 0 leads to the adjoint equation

$$-\frac{\partial\lambda}{\partial t}(t) + \left(\frac{\partial\mathbb{M}}{\partial X}\right)^* \lambda(t) = \left(\frac{\partial\mathbb{H}}{\partial X}\right)^* \mathcal{R}^{-1}\left(\mathbb{H}(X(t)) - \mathcal{Y}(t)\right), \quad (4)$$

where $\frac{\partial\mathbb{M}}{\partial X}$ and $\frac{\partial\mathbb{H}}{\partial X}$ denote respectively the linear tangent operator[1] of $\mathbb{M}$ and $\mathbb{H}$, and $\left(\frac{\partial\mathbb{M}}{\partial X}\right)^*$ and $\left(\frac{\partial\mathbb{H}}{\partial X}\right)^*$ their adjoint operators[2]. The adjoint equation (4) is defined backward in time with the terminal condition $\lambda(T) = 0$.

Setting the first variation of $\mathcal{L}$ with respect to the control parameters u and η to 0 leads to the optimality conditions

$$\frac{\partial\mathcal{J}}{\partial u} = -\int_0^T \left(\frac{\partial\mathbb{M}}{\partial u}\right)^* \lambda(t)dt + C^{-1}(u - u^b)$$
$$\frac{\partial\mathcal{J}}{\partial\eta} = \lambda(0) + \mathcal{B}^{-1}\eta. \quad (5)$$

These optimality conditions can then be evaluated to determine the gradient of $\mathcal{J}$ as soon as the Lagrange multipliers are known, it means as soon as the adjoint equation (4) is integrated backward in time.

3. WEAK CONSTRAINT 4D-VAR

In the strong constraint 4D-Var context (see section 2), the coefficients u of the model were considered to be adjustable parameters that can be optimally determined to reproduce imperfect observations of the dynamical system. Here, this constraint is relaxed and we assume that the coefficients of the dynamical system are directly provided by the data. For taking into account errors of the model, the dynamical system is then defined up to an additive uncertainty function $w(t)$ considered as Gaussian white noise. In the weak constraint 4D-Var approach, the dynamical system becomes:

$$\frac{\partial X(t)}{\partial t} + \mathbb{M}(X(t)) = w(t),$$
$$X(0) = X_0^b + \eta. \quad (6)$$

In that case, the control parameters of the variational assimilation approach are $w(t)$ and η and

[1] The linear tangent of an operator A is the directional derivative operator or Gâteaux derivative of A defined as:

$$\frac{\partial A}{\partial X}(X)\delta X = \lim_{h\to 0}\frac{A(X + h\delta X) - A(X)}{h} \quad \forall\delta X.$$

[2] The adjoint A^* of a linear operator A on a space $\mathcal{D}$ is such that $\forall x, y \in \mathcal{D}, \langle Ax, y\rangle = \langle x, A^* y\rangle$.

the cost functional to be minimized is:

$$\mathcal{J}(w(t),\eta) = \frac{1}{2}\int_0^T \|\mathcal{Y}(t) - \mathbb{H}(X(t))\|^2_{\mathcal{R}^{-1}} dt + \frac{1}{2}\|\eta\|^2_{\mathcal{B}^{-1}} + \frac{1}{2}\int_0^T \|w(t)\|^2_{\mathcal{W}^{-1}} dt, \quad (7)$$

where $\mathcal{W}$ is the covariance matrix of $w(t)$. To solve the constrained optimization problem associated to this new formulation, the same procedure as the one described in section 2 is followed. A Lagrangian functional defined as

$$\mathcal{L}(X(t), w(t), \eta, \lambda(t), \mu) = \mathcal{J}(w(t),\eta) - \int_0^T \langle \frac{\partial X(t)}{\partial t} + \mathbb{M}(X(t)) - w(t), \lambda(t)\rangle dt - \langle X(0) - X_0^b - \eta, \mu\rangle, \quad (8)$$

is first introduced. The first variation of $\mathcal{L}$ with respect to $X(t)$ leads to the same adjoint equation as in the case of the strong constraint 4D-Var *i.e.*

$$-\frac{\partial \lambda}{\partial t}(t) + \left(\frac{\partial \mathbb{M}}{\partial X}\right)^* \lambda(t) = \left(\frac{\partial \mathbb{H}}{\partial X}\right)^* \mathcal{R}^{-1}\left(\mathbb{H}(X(t)) - \mathcal{Y}(t)\right), \quad (9)$$

with the terminal condition $\lambda(T) = 0$. Finally, the first variation of $\mathcal{L}$ with respect to the control parameters leads to the following optimality conditions:

$$\frac{\partial \mathcal{J}}{\partial w}(t) = \lambda(t) + \mathcal{W}^{-1} w(t) \quad \text{and} \quad \frac{\partial \mathcal{J}}{\partial \eta} = \lambda(0) + \mathcal{B}^{-1}\eta. \quad (10)$$

In this formulation, the uncertainty function $w(t)$ is part of the dynamical system. Then, since the optimal solution is found on a given time horizon T, it means that the weak constraint 4D-Var approach can not be used to predict the system's state after the end of the assimilation time interval.

4. POD REDUCED-ORDER MODEL

Given the high spatio-temporal complexity of turbulent flows, the attraction of adopting a model-based approach in flow control is extremely high. Indeed, difficult to imagine deriving an efficient control strategy in open-loop and even more, in closed-loop, if no dynamical model is used in the design process. A natural tendency would be to go towards models based on first principles. However, the number of active degrees of freedom in turbulence is so high that it will lead to high fidelity model of very large dimension. A way to cope with this difficulty is to employ surrogate models for developing the control strategy. Proper Orthogonal Decomposition [1] is often used for this purpose since it extracts, from snapshots, modes that are optimal to capture the energy of the system. Starting from a set of N_s snapshots of velocity fields $\boldsymbol{v}$ taken evenly over a time interval $[0, T_s]$, snapshot POD can be used to determine spatial modes $\boldsymbol{\Phi}_i$ and temporal coefficients $a_i^{\mathrm{P}}(t)$ such that:

$$\boldsymbol{v}(\boldsymbol{x}, t) = \boldsymbol{v}_m(\boldsymbol{x}) + \sum_{i=1}^{N_s} a_i^{\mathrm{P}}(t)\boldsymbol{\Phi}_i(\boldsymbol{x}), \quad (11)$$

where $\boldsymbol{v}_m$ corresponds to the average of the snapshots and where $\boldsymbol{x} \in \Omega$, the spatial domain of interest. Truncating the number of modes in (11) to N_{gal}, with $N_{\mathrm{gal}} \ll N_s$, this expansion is substituted into the Galerkin projection of the incompressible Navier-Stokes equations onto the spatial modes $\boldsymbol{\Phi}_i$ to obtain a POD Reduced-Order Model (POD ROM). After some algebraic manipulations [2], the following expression is found for the POD ROM:

$$\frac{da_i^{\mathrm{R}}(t)}{dt} = C_i + \sum_{k=1}^{N_{\mathrm{gal}}} L_{ik} a_k^{\mathrm{R}}(t) + \sum_{k=1}^{N_{\mathrm{gal}}}\sum_{j=1}^{N_{\mathrm{gal}}} Q_{ijk} a_j^{\mathrm{R}}(t) a_k^{\mathrm{R}}(t) \quad (12)$$

where $a_i^{\mathrm{R}}(0) = a_i^{\mathrm{P}}(0)$. The constant, linear and quadratic coefficients, C_i, L_{ik} and Q_{ijk} depend explicitly on $\boldsymbol{\Phi}_i$ and $\boldsymbol{v}_m$ and as such their values can be directly determined. However, it is well known [2] that for different reasons (structural instability of the Galerkin projection, truncation of the POD basis, inaccurate treatment of the boundary and pressure terms) the dynamical system (12) does not represent sufficiently well the correct dynamics. This problem is then perfectly matching the objectives of data assimilation as described in section 1. The temporal coefficients $a_i^{\mathrm{R}}(t)$ can be considered as state variables $X(t)$. The POD ROM (12) can serve as dynamical model $\mathbb{M}$ and the POD coefficients $a_i^{\mathrm{P}}(t)$ as observations $\mathcal{Y}(t)$. Finally, the coefficients C_i, L_{ik} and Q_{ijk} of (12) can be used as control parameters u in the strong constraint 4D-Var. Concerning the background solutions X_0^b and u^b, they can be determined from the temporal coefficients obtained directly by POD ($a_i^{\mathrm{P}}(t)$) for the initial condition, and from the values determined by Galerkin projection or identification [2] for the coefficients of the POD ROM. The two 4D-Var formulations described in sections 2 and 3 can then be easily applied.

As a final remark, let us comment on the differences between the approach followed in this communication and the reduced-order strategy often employed for 4D-Var data assimilation in meteorology [9, 10]. In flow control, a low-order dynamical system is often first developed and then an optimal control approach, or here a variational data assimilation procedure, is then applied. In meteorology, the steps of variational data assimilation and reduced-order modelling are reversed. A full dynamical model is first

considered for the data assimilation and since the analysed solution is searched iteratively by integrating forward/backward in time the direct/adjoint systems, the control space is then restricted to a low-dimensional space spanned by the first POD eigenfunctions. In the two strategies, the computational costs are highly decreased. However, the influence of the chosen strategy on the determination of the analysed solution is still not well determined.

5. RESULTS

In this section, the variational data assimilation approach will be tested in a simple flow configuration corresponding to the cylinder wake. Due to its simple geometry and its representative behaviour of separated flows [11], the viscous flow past a circular cylinder has been extensively used in the past decade as a test bed to develop control strategies [12]. Here, the first objective is to evaluate the ability of 4D-Var to improve the description of the dynamics within the time horizon where the observations are known. By definition (see section 1), this interpolatory requirement should be offered by 4D-Var. A second objective is to assess the predictive behaviour of the dynamical system obtained as solution of 4D-Var and to measure the influence of strong and weak constraint hypothesis on the analysed dynamics.

In a first time (see section 5.1), the 4D-Var approach will be applied on numerical data to test the method and evaluate the role of some numerical parameters. In particular, the assimilation procedure will be exercised with a convenient methodology, termed as twin experiments. In a second time (see section 5.2), an experimental dataset based on PIV data will be used to analyse this time the influence of the dynamical complexity of the observed dynamics on the analysed solution obtained by 4D-Var.

5.1. Numerical dataset

4D-Var The 4D-Var approach is here applied to a two-dimensional incompressible cylinder wake flow at $Re = 200$. The database was computed using a finite-element code (DNS code Icare, IMFT/university of Toulouse, see [13] for details) and contains $N_s = 200$ two-dimensional snapshots of the flow velocity, taken over a period $T_s = 12$ *i.e.* over more than two periods of vortex shedding ($T_{\text{vs}} = 5$). Since 4D-Var is applied on POD-ROM with observations corresponding to the POD temporal coefficients a_i^{P}, snapshot POD is first applied on the previous data. The first six POD modes are here sufficient to represent 99.9% of the flow energy (see [2] for more details on the procedure and on the POD results) indicating that $N_{\text{gal}} = 6$ should be sufficient for the order of the POD ROM (12).

The strong constraint 4D-Var, as described in section 2, is now applied. The background of the initial condition is given by $a_i^{\text{P}}(t = 0)$ and the background of the coefficients C_i, L_{ik} and Q_{ijk} of (12) are equal to zero. These background values are also used to initialize the coefficients of the dynamical system (12) at the beginning of the iterative procedure. Lastly, the covariant matrices are chosen as $\mathcal{R}^{-1} = \mathbb{I}$ and $\mathcal{B}^{-1} = \mathcal{C}^{-1} = \sigma^2\mathbb{I}$ where $\sigma = 10^{-3}$ and $\mathbb{I}$ denotes the identity matrix.

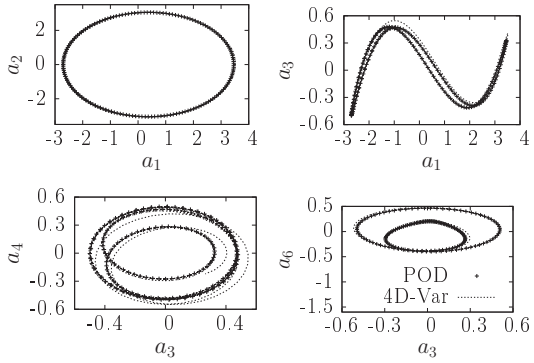

Figure 2. Results of 4D-Var for the DNS dataset (perfect observations).

Figure 2 represents the results of strong constraint 4D-Var for the DNS dataset when perfect observations are used. The 4D-Var approach has been first applied over the 200 time steps contained in the database (assimilation window). Then, the analysed dynamical model has been integrated in time over 400 time steps (forecast window) to conclude on the predictive character of the model. Very good agreements are obtained between the observations and the analysed dynamics. Moreover, the analysed model can predict correctly the dynamics over twice the assimilation period.

Twin experiments Twin experiments [4] consist of exercising the assimilation procedure with observations obtained artificially by integrating in time the same model that will be used after for the assimilation. If the assimilation with real data fails but the twin experiments are successful, then the observations and assimilation algorithms usually do not require improvements, but the constraints and the model do. The analysed dynamics obtained previously with perfect observations (see Fig. 2) is now considered as true state for the twin experiments. The previous observations $a_i^{\text{P}}(t)$ are modified by adding a Gaussian noise defined as $\mathcal{X}/\sigma_i$ where $\mathcal{X} \simeq \mathcal{N}(0, \sigma_t^2)$ with $\sigma_t = 0.2$ and $\sigma_i = 2[\frac{i+1}{2}]$ where $[x]$ returns the nearest integer to x. These noisy states are taken as observations for the twin experiments. The strong constraint 4D-Var approach is applied with the same numerical parameters as in the previous case.

Figure 3 represents the results of the twin experiments for the DNS dataset. Despite the noisy observations used in the 4D-Var approach, the analysed dynamics is in good agreement with the expected true state. Moreover, the forecast dynamics corresponds to the correct attractor of the system.

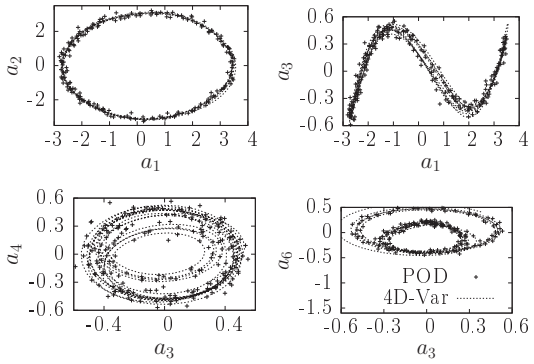

Figure 3. Results of 4D-Var twin experiments for the DNS dataset (noised observations).

The interest of the twin experiments framework is to fairly compare different assimilation procedures based on the values of the error $e(t)$ defined as

$$e(t) = \sqrt{\sum_{i=1}^{N_{\text{gal}}} \left(a_i(t) - a_i^{\text{True}}(t)\right)^2}, \tag{13}$$

where $a_i(t)$ corresponds to the i^{th} temporal coefficient of the POD expansion. Figure 4 represents the time evolution of (13) for the twin experiments. The minimum level of error that can be obtained corresponds to the case where perfect observations are used (Fig. 2). These reference values are represented in Fig. 4 for comparison with the case where the observations are noised. In addition, the time error for the analysed dynamics is also given in Fig. 4. As it can be expected from the 4D-Var approach, the value of error is systematically lower than for the noised observations over the assimilation time window. Moreover, this error does not increase in the forecast window meaning that the predictability of the analysed dynamical system is satisfactory.

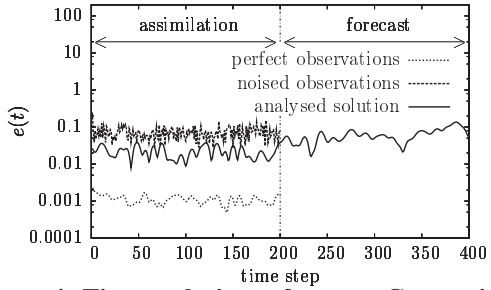

Figure 4. Time evolutions of errors. Comparison between the case of perfect observations and the case of twin experiments.

Sensitivity of the initial condition The role of the initial conditions for capturing correctly the long-term dynamics of the process is well recognized. Indeed, in numerical weather prediction and in many other fields of data assimilation, the control variables are usually the initial conditions of the dynamical system [3]. Here, we would like to see if the situation is the same in the strong constraint 4D-Var approach described in section 2. For the results corresponding to the perfect observations, it was found that the order of magnitude of the initial condition perturbation η was equal to 0.1% of the modes amplitudes. The question is then raised of knowing if these low amplitude modifications have an important influence on the dynamics. To respond, the coefficients C_i, L_{ik} and Q_{ijk} found in the strong constraint 4D-Var approach with perfect observations were used to integrate the dynamical model (12) with $\eta = 0$. The results of the time integration are represented in Figure 5. It can be shown (see Figure 6) that the dynamical system is not predictive any more. The error grows exponentially in the assimilation window, and continues to increase in the forecast window until the time step reaches 270 when the error saturates. As a conclusion, when $\eta = 0$, a lost of predictability of the dynamical system occurs.

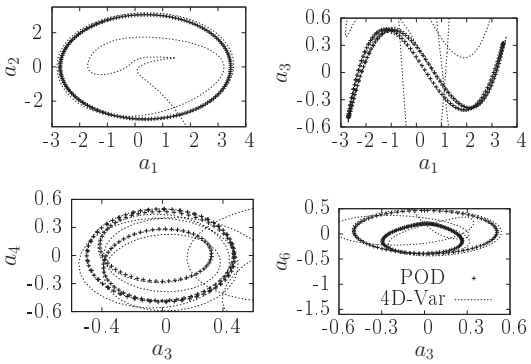

Figure 5. Results of 4D-Var forecast for the coefficients found by assimilation with perfect observations and $\eta = 0$.

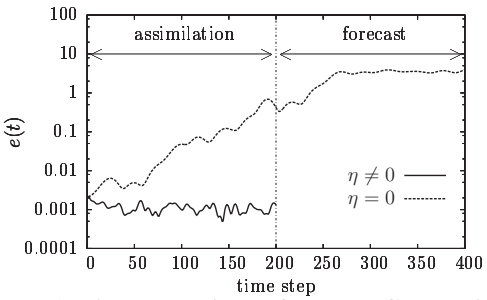

Figure 6. Time evolutions of errors. Comparison between the case of perfect observations with $\eta \neq 0$ and $\eta = 0$.

5.2. Experimental dataset

In section 5.1, the strong constraint 4D-Var approach has been applied successfully for a laminar cylinder wake obtained by numerical simulations. Here, data assimilation will be applied on data

obtained by 2D-2C PIV measurements for a turbulent cylinder wake [14] corresponding to a sub-critical flow regime ($Re_D = DU_\infty/\nu = 40000$ where $D = 40\,\text{mm}$ is the cylinder diameter and $U_\infty = 15.6\,m.s^{-1}$ is the free-stream velocity). The database contains $N_s = 5130$ snapshots taken at a sampling frequency $f_s = 1\,\text{kHz}$ over approximatively 400 periods of vortex shedding. First, a snapshot POD has been performed on this dataset. The first 16 POD modes capture 31% of the flow energy. It was found (see Figure 7) to be sufficient for describing the wake flow.

Strong constraint 4D-Var A strong constraint 4D-Var approach is now applied to the first 128 time steps contained in the database. Compared to the case of section 5.1, the dynamics is much more complex and the PIV data correspond to a 2D description of a pure 3D physical phenomenon. The observations are then noised and incomplete, a typical situation where data assimilation should help to reconstruct optimally the flow states. As previously, a POD ROM derived this time with $N_{\text{gal}} = 16$ served as dynamical model for the assimilation.

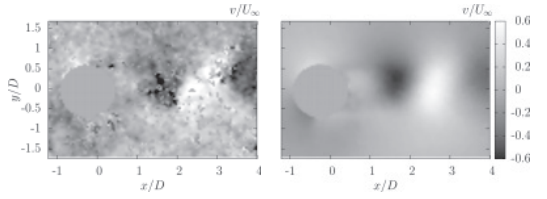

(a) *PIV measurement* (b) *16 POD modes approximation*

Figure 7. Vertical velocity of one snapshot issued from the PIV dataset. Comparison with the POD approximation.

Similarly to the case of the numerical database, the background of the initial condition is chosen as $a_i^{\text{P}}(t = 0)$. For the background of the coefficients of the model (12), the situation is different since the configuration is more complex. In the previous case, the coefficients were initialized to zero. Here, a preliminary identification is performed following the method described in [2]. The background coefficients C_i^b, L_{ik}^b and Q_{ijk}^b are searched as to minimize a quadratic cost functional $\mathcal{I}$ given by

$$\mathcal{I}(C_i, L_{ik}, Q_{ijk}) = \frac{1}{T_{\text{cal}}} \int_0^{T_{\text{cal}}} \left\| \frac{d\boldsymbol{a}^{\text{P}}}{dt}(t) - \mathbb{M}_{\text{gal}}(\boldsymbol{a}^{\text{P}}(t), C_i, L_{ik}, Q_{ijk}) \right\|^2 dt,$$

where $\mathbb{M}_{\text{gal}}$ corresponds to the right hand side of (12) and where $T_{\text{cal}} = 102.4\,\text{ms}$ is the length of the identification window. Finally, the same values as in section 5.1 are chosen for the covariant matrices.

The results of strong constraint 4D-Var are represented in Figure 8. For the first POD modes, the analysed dynamics is well reproduced and is smoother than the observations, especially for the modes 1 and 2 corresponding to the Von Kármán vortex shedding. For higher order modes, the estimation obtained by 4D-Var has a smaller amplitude than the observations. This difference of quality between the estimation of the large and fine scales can be explained by: i) POD truncation that neglects in the POD ROM the effect of the fine scales on the large scales of turbulence, ii) 2D observations used for describing a 3D phenomenon, and iii) signal-to-noise ratio that is lower for the fine scales. The objective of the next section is to see if the 4D-Var estimation can be improved by using a weak constraint 4D-Var approach.

Weak constraint 4D-Var Here, the dynamical constraint given by the POD ROM (12) is relaxed and the modelling error is considered to be represented globally with an additive Gaussian noise $w(t)$. The same background solutions $(0, C_i^b, L_{ik}^b, Q_{ijk}^b)$ as the ones used previously in the strong constraint 4D-Var approach is now employed for performing a weak constraint 4D-Var. In addition, the values of the covariance matrices are also the same as in the strong constraint 4D-Var. The analysed solution is shown in Fig. 8 for comparison with the solution obtained by strong 4D-Var.

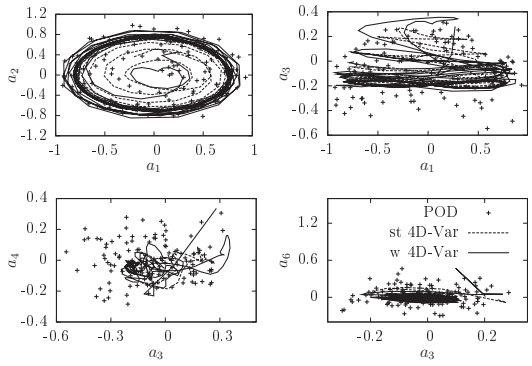

Figure 8. Results of 4D-Var for the PIV dataset. Comparison between strong (st) and weak constraint (w) 4D-Var. The horizontal and vertical axes are multiplied by a factor 1000.

The estimations obtained by weak constraint 4D-Var approach are qualitatively slightly better than those obtained by strong constraint 4D-Var. However, we have to keep in mind that the additive noise $w(t)$ is defined only over the assimilation window preventing the use of the analysed model for forecasting the flow dynamics.

6. CONCLUSION

4D-Var data assimilation is a well established method in meteorology and oceanography. Essentially, it combines different inhomogeneous sources of information (data, dynamical model) to estimate optimally the true state of the system and

to potentially predict its future dynamics. In this paper, this approach has been applied in a fluid mechanics context to a POD ROM of a cylinder wake flow. The control parameters were respectively the initial conditions and the coefficients of the POD ROM for the strong constraint 4D-Var and the initial conditions and an additive noise in the weak constraint 4D-Var.

The strong constraint 4D-Var procedure has first been tested on a numerical dataset corresponding to a low value of Reynolds number. The original dynamics was well reproduced in the case of the perfect observations and also in twin experiments. Moreover, a good predictability of the analysed dynamical model was found. For the experimental database and the strong constraint 4D-Var, only the dynamics of the higher POD modes is well reproduced. The dynamical constraint was then relaxed by considering a weak constraint 4D-Var. With this approach, the estimation was qualitatively improved over the assimilation window but no prediction is possible.

An important result of this study was to demonstrate numerically that the modification of the initial condition plays a crucial role for capturing the correct dynamics with a POD ROM. Finally, the success of the 4D-Var approach is deeply linked to the accurate estimation of the different covariance matrices used in the procedure. This point should be studied more carefully in the future.

ACKNOWLEDGEMENTS

Nicolas BENARD (Electro-Fluido-Dynamic group of the Pprime institute) is warmly acknowledged for providing us with the PIV experimental database of the cylinder wake flow. This work has received support from the National Agency for Research on reference ANR-08-BLAN-0115-01.

References

[1] Cordier, L. and Bergmann, M. (2008) Proper Orthogonal Decomposition: an overview. *Lecture series 2002-04, 2003-03 and 2008-01 on post-processing of experimental and numerical data*, Von Kármán Institute for Fluid Dynamics.

[2] Cordier, L., Abou El Majd, B., and Favier, J. (2010) Calibration of POD Reduced-Order Models using Tikhonov regularization. *International Journal for Numerical Methods in Fluids*, **63**.

[3] Navon, I. M. (2009) Data assimilation for numerical weather prediction : a review. *Data Assimilation for Atmospheric, Oceanic, and Hydrologic Applications*, Springer Book.

[4] Titaud, O., Vidard, A., Souopgui, I., and Le Dimet, F. (2010) Assimilation of image sequences in numerical models. *Tellus A*, **62**, 30–47.

[5] Papadakis, N. (2007) *Assimilation de données images : application au suivi de courbes et de champs de vecteurs*. Ph.D. thesis, Université de Rennes I.

[6] D'Adamo, J., Papadakis, N., Mémin, E., and Artana, G. (2007) Variational assimilation of POD low-order dynamical systems. *Journal of Turbulence*, **8**, 1–22.

[7] Gilbert, J. and Lemaréchal, C. (2009) The module M1QN3 – Version 3.3. *INRIA Rocquencourt & Rhone-Alpes*.

[8] Gunzburger, M. D. (1997) Introduction into mathematical aspects of flow control and optimization. *Lecture series 1997-05 on inverse design and optimization methods*, Von Kármán Institute for Fluid Dynamics.

[9] Robert, C., Durbiano, S., Blayo, E., Verron, J., Blum, J., and Le Dimet, F.-X. (2005) A reduced-order strategy for 4D-Var data assimilation. *Journal of Marine Systems*, **57**, 70–82.

[10] Daescu, D. and Navon, I. (2007) Efficiency of a POD-based reduced second-order adjoint model in 4D-Var data assimilation. *International Journal for Numerical Methods in Fluids*, **53**, 985–1004.

[11] Zdravkovich, M. (1997) *Flow Around Circular Cylinders, vol. 1. Fundamentals*. Oxford University Press.

[12] Bergmann, M., Cordier, L., and Brancher, J. (2005) Optimal rotary control of the cylinder wake using proper orthogonal decomposition reduced-order model. *Physics of Fluids*, **17**, 097101.

[13] Favier, J. (2007) *Contrôle d'écoulements : approche expérimentale et modélisation de dimension réduite*. Ph.D. thesis, Institut National Polytechnique de Toulouse.

[14] Benard, N., Debien, A., David, L., and Moreau, E. (2010) Analyse par PIV rapide du sillage d'un cylindre manipulé par actionneurs plasmas. *Congrès Francophone de Techniques Laser*, Vandoeuvre-lès-Nancy 14-17 septembre.

Conference on Modelling Fluid Flow (CMFF'12)
The 15th International Conference on Fluid Flow Technologies
Budapest, Hungary, September 4-7, 2012

TRANSPORT EQUATION FOR ROUGHNESS EFFECTS ON LAMINAR-TURBULENT TRANSITION

Patrick DASSLER[1,4], Dragan KOŽULOVIĆ[2], Andreas FIALA[3]

[1] Corresponding Author. Institute of Fluid Mechanics, Technische Universität Braunschweig, Bienroder Weg 3, Germany, 38106 Braunschweig,. Tel.: +49 531 2976, Fax: +49 531 5952. E-mail: p.dassler@tu-bs.de,
[2] Institute of Fluid Mechanics, Technische Universität Braunschweig. E-mail: d.kozulovic@tu-bs.de
[3] MTU Aero Engines GmbH, München, Germany. E-mail: andreas.fiala@mtu.de
[4] Author's address at date of conference: Dassler GmbH, Salzwiese 2, 37581 Bad Gandersheim, Germany, phone: +49 5382 2317, email: dassler.p@industrie-ventilatoren.de

ABSTRACT

An approach for modeling the roughness-induced laminar-turbulent transition has been developed, which is based on the γ - $Re_{\theta t}$ - transition model. That approach for incorporating roughness effects uses an additional transport equation for a new variable, called A_r. The values of A_r depend on the applied equivalent sand grain roughness height on solid walls and then are convected and dissipated through the flow field by the additional transport equation. Through interaction of A_r with the $Re_{\theta t}$ - transport equation, in a way $Re_{\theta t}$ is decreased, the transition is shifted upstream. The model has been implemented in a 3D RANS solver "TRACE" of the DLR (Deutsches Zentrum für Luft- und Raumfahrt). It is calibrated and validated by two test cases with increasing complexity. The first test case is a flat plate with different roughness heights and linear pressure gradients. Here transition onset locations, i.e. minima of the friction coefficients, are compared to experiments. As a more complex test case simulations of a highly loaded turbine cascade with three different roughness heights has been done. Comparisons of calculated and measured loss coefficients, pressure distributions and wake losses are presented. The result analysis shows the feasibility of this approach and a good agreement with experimental findings.

Keywords: CFD, roughness, transport equations, turbomachinery

NOMENCLATURE

A_r	[-]	amplification roughness variable
$AVDR$	[-]	axial velocity density ratio
H_{12}	[-]	form factor of boundary layer
P_θ	[-]	source term
PG	[-]	pressure gradient
PS	[-]	pressure side
R_a	[μm]	arithmetic average roughness height
Re	[-]	Reynolds number (based on axial location x or turbine chord l)
$\tilde{R}e_{\theta t}$	[-]	transition onset momentum thickness Reynolds number (obtained from transport equation)
SS	[-]	suction side
Tu	[%]	turbulence intensity
U	[m/s]	velocity
k	[μm]	roughness height
k_s	[μm]	equivalent sand grain roughness
l	[m]	chord length
p_t	[Pa]	total pressure
γ	[-]	intermittency
δ	[m]	boundary layer thickness
δ_1	[m]	displacement thickness
δ_2	[m]	momentum thickness
ζ	[-]	loss coefficient, $(p_{t1}-p_{t2})/(p_{t1}-p_2)$
θ	[m]	momentum thickness
μ	[$kg/m/s$]	dynamic viscosity
μ_t	[m^2/s]	eddy viscosity
ν	[m^2/s]	kinematic viscosity
ρ	[kg/m^3]	density
σ_{Ar}	[-]	diffusion coefficient
τ	[$kg/m/s^2$]	wall shear stress, $\rho\nu(\partial U/\partial y)_W$

Subscripts and Superscripts

W	wall values
ref	reference condition (Re_{2th}= 200,000; smooth wall; Tu= 6 %)
t	transition onset
x, y	axial (along the wind tunnel axis), transversal (coordinate)
θ	momentum thickness
1, 2	inlet, exit of the test section and turbine cascade

1. INTRODUCTION

It is known that surface roughness exerts different effects at the flow. In dependency of Reynolds number it increases the turbulent

fluctuations in the turbulent boundary layer and it shifts the laminar-turbulent transition at some upstream position. Both effects increase the boundary layer losses and hence the drag forces, as reported by Schlichting [1] and Feindt [2], correspondingly. In contrast, the losses can also be decreased if the separation length of a laminar/ turbulent bubble is reduced or even completely prevented by enhanced transition tendency. Considering the laminar-turbulent transition process, the surface roughness can be regarded as one of the transition influencing parameters, like turbulence intensity, pressure gradients and Reynolds number, just to state some of them.

At large Reynolds numbers, where the boundary layer is almost completely in the turbulent state, the loss increasing mechanisms will prevail. Depending on the roughness dimensions and topology, the flat plate losses can be more than doubled [1]. According to Hummel et al. [3], the loss coefficient ζ of a high Reynolds number turbine blade (Re = 1 200 000) is increased by 40 % by typical roughness structures, which usually occurs after comparably small amount of gas turbine operation time.

At low Reynolds numbers the loss decreasing effect can be the dominant one. In particular, this effect is of interest for the low pressure turbine blades of jet engines operating at low Reynolds numbers ($Re \approx$ 100 000) during the cruise flight. Usually, the surface of the turbine blades is hydraulically smooth after the manufacturing process, but is roughened during operation such as from the equivalent sand grain roughness $k^+ < 1$ for the smooth surface to $k^+ > 5$ for a transitional-rough surface. Due to the aforementioned positive effect at the laminar separation bubbles, some low pressure turbine blades show even better performance after some time in operation.

The aim of the present work is to accurately predict the roughness effects at the laminar-turbulent transition process, yielding a suitable tool for the estimation of roughness effects. The effects at fully turbulent boundary layers are also accounted for by the approach of Wilcox [4], and will not be subject of additional modelling improvements herein. Furthermore, the single roughness elements will not be considered. The focus of the paper is at the distributed roughness only.

Recent developments have been made on accounting roughness effects on boundary layer transition process. Stripf et al. [5], [6] published correlations for implementing in CFD codes based on data of a variety of authors. Elsner [7] implements these correlations into the γ - $Re_{\theta t}$ - transition model by Menter et al. [8]. In the given correlation there is the need to know the ratio between roughness height and displacement thickness. The latter makes an integration perpendicular to the wall along boundary layer necessary for obtaining the value of the displacement thickness. In turbomachinery three-dimensional flows occur near endwalls with complex shapes of the boundary layer edge, which in turn may make the integration fail.

In this work the authors decided to introduce a new variable which is transported by an additional transport equation and is set at the wall in dependency of sand grain roughness height. Without the need for integration along the boundary layer, the transition onset variable $Re_{\theta t}$ is reduced and thus the transition is shifted upstream.

In an earlier version [9] it was shown that the transport equation approach has an additional benefit by transporting roughness information. With that approach it is possible to model a laminar-turbulent transition which is located far downstream of the transition trigger mechanism. So experiments conducted by Pinson et al. [10] dealing with two-scale roughness heights and so creating a backward facing step can be modelled.

For this work the model firstly introduced in [9] has been improved. Thus a better mesh convergence is achieved.

2. MODEL FORMULATION

As mentioned earlier, instead of using boundary layer integral values, this model uses only local variables. With this approach the transition can be calculated without determining the boundary layer's edge and integral values. The transition model contains two transport equations, one for the intermittency, and one for the momentum thickness Reynolds number. The intermittency equation's source term depends on a local strain-rate Reynolds number. Based on Van Driest and Blumer's vorticity Reynolds number concept, cf. [11], a connection can be found that relates the local strain-rate Reynolds number to non-local empirical correlations for the transition onset Reynolds number.

For simulating roughness effects an additional transport equation for A_r has been formulated, cf. Eq. (1).

$$\frac{\partial(\rho A_r)}{\partial t} + \frac{\partial(\rho U_j A_r)}{\partial x_j} = \frac{\partial}{\partial x_j}\left[\sigma_{Ar}(\mu + \mu_t)\frac{\partial(A_r)}{\partial x_j}\right] \qquad (1)$$

$$with: \quad \sigma_{Ar} = 10.0$$

In this version discrete values of A_r are set depending on the non-dimensional equivalent sand grain roughness height, cf. Eq. (2).

$$A_{r,W} = 8.0 \cdot k_s^+ \quad with: \quad k_s^+ = \sqrt{\frac{\tau_W}{\rho_W}} \cdot \frac{k_s}{\nu} \tag{2}$$

The variable A_r then is transported through the flow field by the convective and dissipative terms of equation (1). Fig. 1 gives an introduction to the principle of A_r. The upper figure gives the k_s^+ distribution for a flat plate with zero pressure gradient. At two locations A_r-profiles within the boundary layer are given below in Fig. 1. Thus Eq. (2) is demonstrated.

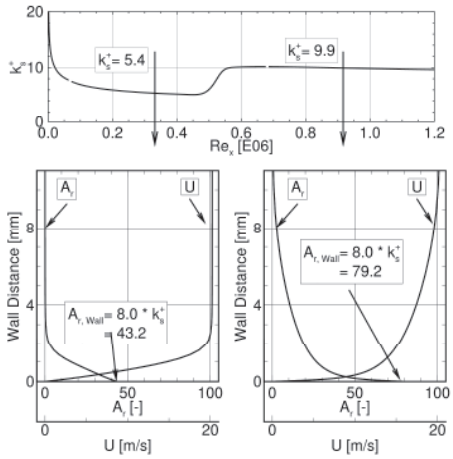

Figure 1. Principle of the A_r - transport equation

Finally A_r reduces the source term of the $Re_{\theta t}$ - transport equation. The source term of the $Re_{\theta t}$ - transport equation is defined for the original γ - $Re_{\theta t}$ - transition model by Eq. (3) , cf. Langtry et al. [8].

$$P_{\theta t} = c_{\theta t} \frac{\rho}{t} \left(\mathrm{Re}_{\theta t} - \tilde{\mathrm{R}}\mathrm{e}_{\theta t}\right)\left(1.0 - F_{\theta t}\right)$$
$$with: \quad t = \frac{500\mu}{\rho U^2} \tag{3}$$

In Eq. (3) t is a time scale for dimensional reasons. The factor $F_{\theta t}$ equals one in the boundary layer, thus turning off the source term. The $Re_{\theta t}$ - transport equation's source term $P_{\theta t}$ is defined by equation (4) including the roughness approach.

$$P_{\theta t} = \frac{\rho}{t}\left[c_{\theta t}\left(\mathrm{Re}_{\theta t} - \tilde{\mathrm{R}}\mathrm{e}_{\theta t}\right)\left(1.0 - F_{\theta t}\right) - Arg_r\right] \tag{4}$$

The reducing element Arg_r is a function of A_r. This function consists of two equations, starting with a cubic at low A_r-values ($A_r < A_{r,s}$) and continuing with a linear funtion at higher values ($A_r > A_{r,s}$) of A_r. Both the functions are matched at a certain point $A_{r,s}$ where the slope is same, cf. Fig. 2. Additionally Arg_r is multiplied by a factor b that reduces the impact of Arg_r with lower values for $\tilde{R}e_{\theta t}$. Is the value for $\tilde{R}e_{\theta t}$ big, b is near one, but if $\tilde{R}e_{\theta t}$ becomes a value near the initialised minimum ($\tilde{R}e_{\theta t} = 20.0$), b decreases to zero. This behaviour avoids unphysical overshoots of shear stress at test cases with high Reynolds numbers and high roughnesses.

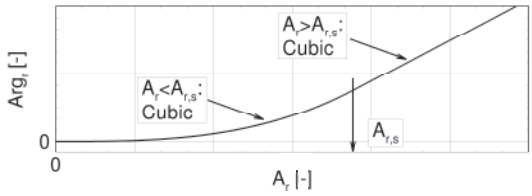

Figure 2. Function of Arg_r

Please notice that there has been no change to the original γ - $Re_{\theta t}$ model [8], i. e. when no roughness is applied A_r is zero and the $Re_{\theta t}$ source term is not affected.

3. NUMERICAL METHOD

The numerical simulations have been conducted with the DLR Cologne in-house solver TRACE, cf. Nürnberger [12] and Kügeler [13]. In these simulations the Reynolds averaged Navier-Stokes equations are solved using a finite volume technique, cf. Hirsch [14, 15]. The convective fluxes have been discretized by the 2nd order upwind scheme of Roe [16]. Furthermore, the diffusive fluxes have been discretized by a 2nd order central differencing scheme, where the mixed derivatives are also included ("Full Navier Stokes" approach). These derivatives appear when transforming from the curvilinear to the cartesian frame of reference, and their inclusion leads to accuracy improvement in three-dimensional flows, cf. Röber et al. [17]. Only steady simulations have been conducted, where an implicit predictor-corrector scheme of Mulder and van Leer [18] has been used for the time integration. With this scheme, the density residual has been decreased by at least three orders of magnitude for all investigated test cases. Furthermore, non-reflecting boundary conditions by Saxer and Giles [19] have been applied to the inlet and outlet boundaries.

The two equation turbulence model k-ω by Wilcox [20] has been used, together with a dimensionless wall distance of less than 1 for all simulated test cases. To capture roughness effects in turbulent boundary layers, the boundary condition of the ω-equation at Stokes walls (y = 0.0) has been corrected as supposed by Wilcox:

$$\varpi_{rough} = \frac{u_\tau^2 \cdot S_r}{\nu} \; with: u_\tau = \sqrt{\frac{\tau_W}{\rho_W}} \tag{5}$$

Parameter S_r depends on the surface roughness:

$$S_r = \left(\frac{50}{k_s^+}\right)^2 \qquad for: k_s^+ \le 25 \qquad (6)$$

$$S_r = \left(\frac{100}{k_s^+}\right) \qquad for: k_s^+ > 25 \qquad (7)$$

We notice that Eqs. (6) to (7) has changed slightly in Wilcox [21]. As compared to the smooth boundary condition at wall distance $y = 0.0\ m$:

$$\varpi_{smooth} = 10\frac{6\nu}{(\beta y)^2} \qquad with: \beta = \frac{3}{40} \qquad (8)$$

the roughness correction by Eq. (5) to (7) leads to larger turbulence production rates at the beginning of the log-layer, resulting in larger turbulence and viscous loss in the boundary layer. In this way, the roughness effects are reproduced by adjusting the turbulence model's boundary condition only.

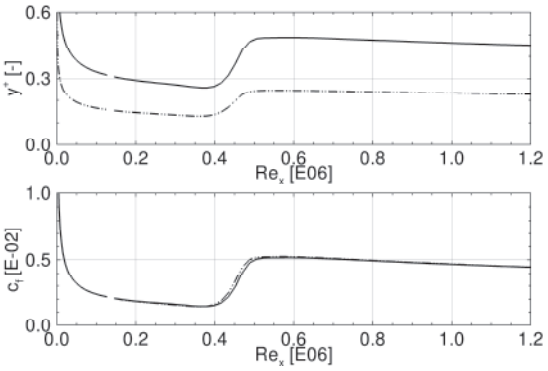

Figure 3. Transition Onset Location and Friction Coefficient for Two Dimensionless Wall Distances (PG1, Re_{ks}= 220)

In [22] it is reported that the Wilcox roughness boundary condition needs extremely low y^+ values $y^+(1) < 0.01$ for k_s^+<100 for mesh convergent values. It could be observed, that y^+ should be significantly lower than one. For a certain range of Reynolds numbers and roughness heights concerning the test cases in this work mesh convergence was achieved with y^+ values shown in Fig. 1. As it can be seen in Fig. 3 the friction coefficient values in both the laminar and turbulent state are not affected by a halved dimensionless wall distance at medium roughness heights. Furthermore even the transition onset location does not vary significantly.

4. FLAT PLATE TEST CASE

The roughness model has been validated on a flat plate test case with zero pressure gradient as reported by Feindt [2]. In Feindt's experiments the dependency of transition onset on the roughness height has been measured. With none, expanding and contracting geometries of the outer wall, different linear pressure gradients could be set up.

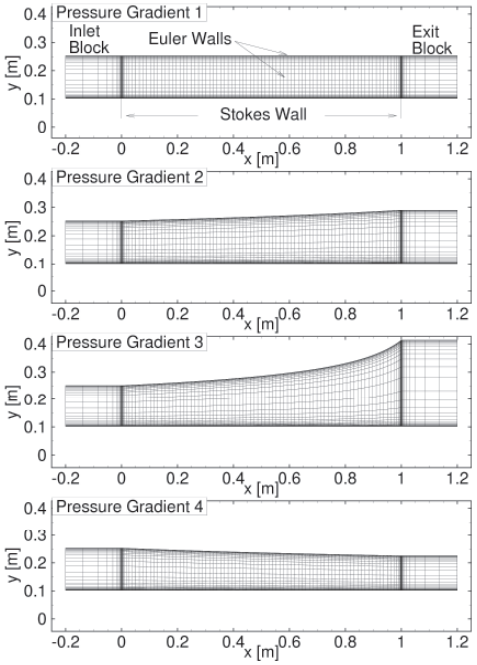

Figure 4. Grids with Every 2nd Node Displayed and Geometry of Flat Plate Test Case

Here, four grids have been generated for simulating the corresponding measurements, see Fig. 4. All grids have 20128 cells with an applied free stream velocity U_1= 20 *m/s* at the beginning of the flat plate.

$$r(x) = \sqrt{\frac{r_1^2}{\sqrt{1.0 - PG}}} \quad with: PG = \frac{p_2 - p_1}{q_1} \qquad (9)$$

The outer wall geometry for the non zero pressure gradients (*PG2*, *PG3* and *PG4*) is set by Eq. (9). Thus the outer geometry *r(x)* can be calculated for the linear pressure gradients, Fig. 5.

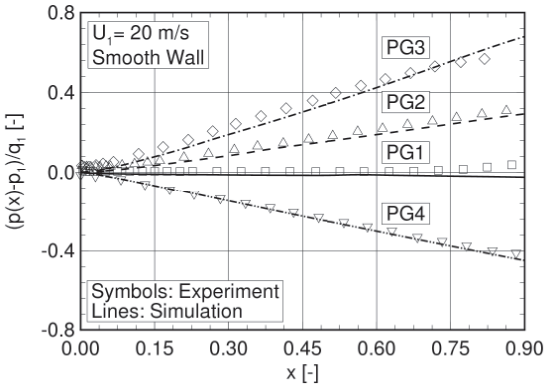

Figure 5. Linear Pressure Gradients of Feindt's Flat Plate Test Case

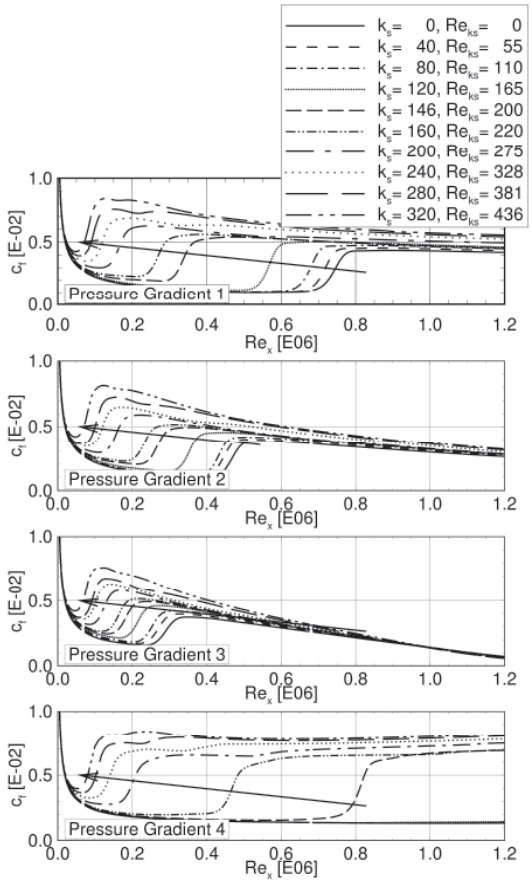

Figure 6. Friction Coefficients with Different Pressure Gradients

Different equivalent sand grain roughness heights have been applied to the flat as it is listed in Fig. 6. With $\nu = 14.96 \cdot 10^{-6}\ m^2/s$ as kinematic viscosity in all cases the same range for the equivalent sand grain roughness Reynolds number Re_{ks} is achieved like in Feindt's experiments. Because the turbulence intensity Tu is not given for the measurements, it was set up in a way that the simulated transition onset with smooth wall is the same as in the experiments.

Thus at the beginning of the flat plate the turbulence intensity of Tu = 1.8 % (PG1), 1.5 % (PG2 and PG3), and 1.0 % (PG4) has been prescribed. The eddy viscosity ratio μ_t/μ was below 200 in freestream for all cases.

The resulting friction coefficients are displayed in Fig. 6 for the three simulated pressure gradients. The plots show the curves for the skin friction c_f with positive (adverse) and negative (favourable) pressure gradients. It can be seen, that increasing pressure gradient moves the transition onset location upstream.

A transition shift does not occur for the smallest roughness heights, indicating a hydraulically smooth region. Furthermore this figure displays that in the turbulent region the skin friction is modulated due to Wilcox' roughness boundary condition.

The transition behaviour can be seen more clearly in Fig. 7. The transition onset location Re_{xt} is shown in dependency of roughness Re_{ks} and pressure gradients including experimental results. As Feindt stated, for $Re_{ks} < 120$ there is no transition shift due to roughness for all cases. Regarding Fig. 7 one can say a roughness correlation has been found, predictiong adequate results on flat plates.

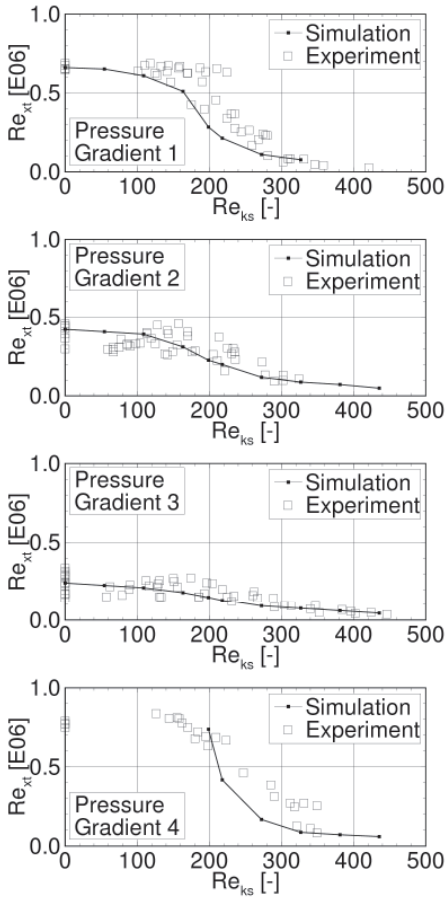

Figure 7. Transition Onsets Re_{xt} in Simulations and Experiments

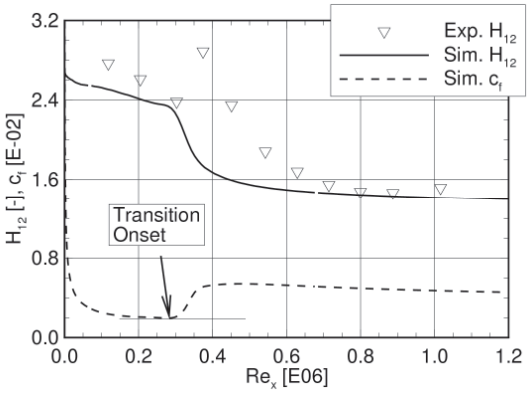

Figure 8. Boundary Layer Values (Re_{ks}= 200, PG1)

The transition onset location Re_{xt} was defined in this work as point of minimum friction coefficient c_f. An example for defining this point Fig. 8 is shown. In the laminar section the displacement and momentum thickness are proportional to $x^{½}$. At the minimum of the friction coefficient the curves of $Re_{\delta 1}$ and $Re_{\delta 2}$ change their shape. For this reason the shape factor H_{12} decreases rapidly and the transition onset is located at this point.

5. TURBINE CASCADE T106C

Experiments on a low pressure gas turbine airfoil, named T106C have been done. A comparison of the T106 blade is given by Hoheisel [23]. Montis et al. [24] investigated the effect of roughness applied to that blade. A Reynolds number range from 50000 to 700000, two turbulence intensities (3 % and 6 %) and three roughness heights have been investigated. Only one turbulence intensity (Tu= 6 %) is considered here. According to [24] for simulations the equivalent sand grain roughness heights (k_s= 5 μm, 39 μm and 187 μm) have been applied, belonging to (Ra/l= $0.8 \cdot 10^{-5}$, $5 \cdot 10^{-5}$ and $25 \cdot 10^{-5}$) as average roughness heights with chord length l= 0.1 m. A detailed view on roughness modeling in turbomachinery is given in [25].The outlet Mach number was fixed for all cases at Ma_2= 0.6.

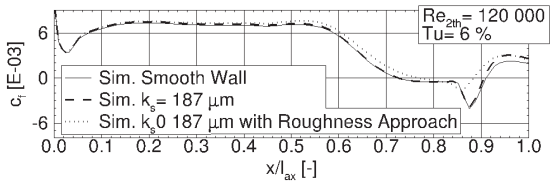

Figure 9. Skin Friction with and without new Roughness Approach

Fig. 9 gives skin friction c_f at Re_{2th}= 120000 with smooth and rough boundary conditions. At this Reynolds number the original γ-$Re_{\theta t}$ model does not show roughness effects. The simulations have been done with a structured quasi three-dimensional mesh. It consists of 42939 nodes, while y^+ is less 1.0 for all Reynolds numbers. For smooth and rough surfaces a doubling of nodes in I- and J-direction does not give more accurate results, see Fig. 10.

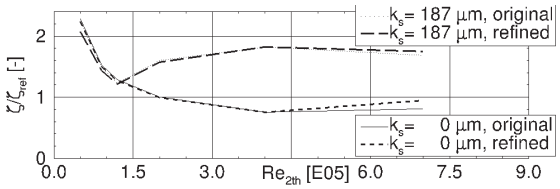

Figure 10. Study with Original and Refined Grid for Smooth and Rough Surfaces

The axial velocity density ratio has been hold constant and set to $AVDR$= 0.96. With this $AVDR$ value the γ - $Re_{\theta t}$ model predicts pressure dirstribution very well for smooth walls, cf. Fig. 11.

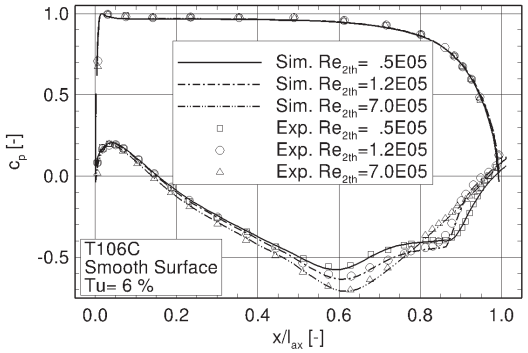

Figure 11. Pressure Distributions with γ-$Re_{\theta t}$ Model and Smooth Walls

The Fig. 12 gives aerodynamic losses for one turbulence intensity (Tu= 6 %). Both the roughness induced loss decrease at low Reynolds numbers and loss increase at large Reynolds numbers is reproduced by the simulation. However, contrary to the measurements, the loss coefficient at Re_{2th}= 400000 with highest roughness is slightly larger than at Re_{2th}= 700000. In both cases the transition takes place slightly downstream the leading edge. Hence, this is most likely a deficiency of the roughness modelling in the turbulence model. This issue is confirmed by fully turbulent simulations (not shown here).

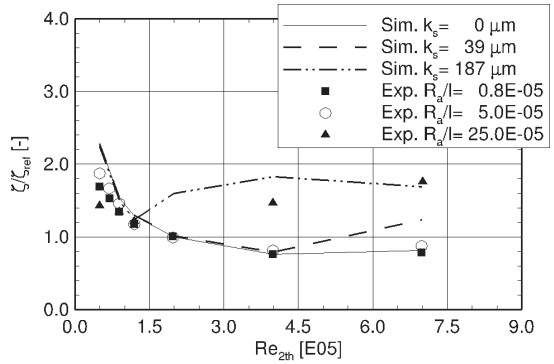

Figure 12. Reynolds Number Lapse Rates for Smooth and Rough Walls

Pressure distributions for highest Reynolds number are shown in Fig. 13. All cases do not exhibit a separation bubble. The simulations correctly predict that.

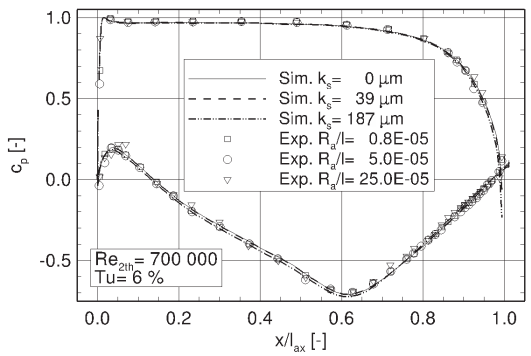

Figure 13. Pressure Distributions for Smooth and Rough Walls at Re_{2th}= 700000

For low Reynolds number one can clearly see the separation bubble, cf. Fig. 14.

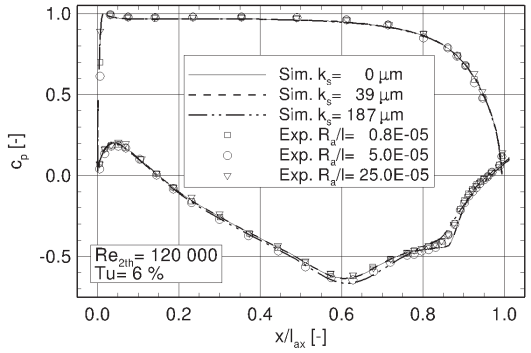

Figure 14. Pressure Distributions for Smooth and Rough Walls at Re_{2th}= 120000

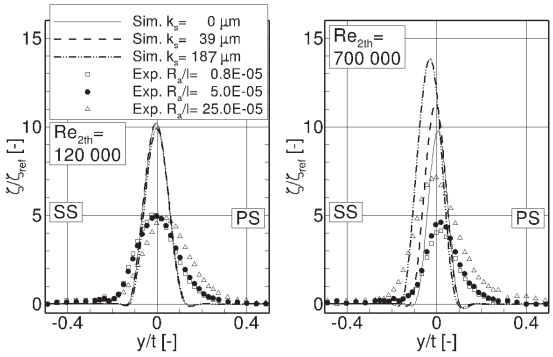

Figure 15. Wakes for Smooth and Rough Walls at Re_{2th}= 120000 and Re_{2th}= 700000

Fig. 15 presents wake losses. The wakes of the two Reynolds numbers mentioned above are shown. In both cases the wakes of the simulations are too sharp and maximum values are overestimated. The prediction of very sharp wakes has been observed for a while, but it still could not be sufficiently explained and fixed. Probably the spreading rate of the near wake downstream of a rounded trailing edge is considerably different than the rate of shear layer mixing used for turbulence modelling calibration.

Nevertheless the wakes shift due to roughness. With roughness for the small Reynolds number the wake shifts to pressure side, while at Re_{2th}= 700 000 the wake is shifted to suction side. At the small roughness this behaviour is weaker than in experiments, but can already be noticed.

6. SUMMARY

An approach for modeling the roughness induced transition with an additional transport equation is presented. Calibration for that model has been done on a flat plate test case with zero pressure gradient and various roughness heights. Verification on other test cases with increasing complexity clearly shows the feasibility and furthermore well predicted results for these test cases. The main conclusion are:

1) On flat plate test cases the roughness model accurately exhibits a hydraulically smooth region (Re_{ks}<120), wherein the transition does not shift upstream.

2) Simulations with smooth walls of the turbine cascade exhibits pressure distributions that accurately predict experimental findings except a too sharp wake.

3) With highest roughness at Re_{2th}= 120000 the maximum of wake losses shifts to pressure side, while at Re_{2th}= 700000 it shifts to suction side. This behaviour is more accurately predicted at higher Reynolds numbers.

4) Reynolds number lapse rate presents increase in losses for highest roughness and high Reynolds numbers, according to experiments.

ACKNOWLEDGEMENTS

The development work was conducted as a part of the joint research programme COORETEC-turbo in the frame of AG Turbo. The work was supported by the Bundesministerium für Wirtschaft und Technologie (BMWi) as per resolution of the German Federal Parliament under grant number 0327715H. The authors gratefully acknowledge AG Turbo and MTU Aero Engines for their support and permission to publish this paper. The responsibility for the content lies solely with its authors.

REFERENCES

[1] Schlichting, H., 1936, "Experimentelle Untersuchungen zum Rauhigkeitsproblem", Ingenieur-Archiv, VII. Band, 1. Heft, S. 1-34.

[2] Feindt, E. G., 1956, "Untersuchungen über die Abhängigkeit des Umschlages laminar-turbulent von der Oberflächenrauhigkeit und der Druckverteilung", *DFL Bericht*, 43, 1956.

[3] Hummel, F., Lötzerich, M., Cardamone, P., and Fottner, L., 2005, „Surface Roughness Effects

on Turbine Blade Aerodynamics“, *Journal of Turbomachinery*, Vol. 127.

[4] Wilcox, D. C., 1998, “Turbulence Modeling for CFD”, DCW Industries, 2nd edition, ISBN-10 0963605151.

[5] Stripf, M., Schulz, A. Bauer, H.-J., and Wittig, S., 2009, “Extended Models for Transitional Rough Wall Boundary Layers With Heat Transfer - Part I: Model Formulation”, *Journal of Turbomachinery*, Vol. 131, pp. 031016-1-10.

[6] Stripf, M., Schulz, A. Bauer, H.-J., and Wittig, S., 2009, “Extended Models for Transitional Rough Wall Boundary Layers With Heat Transfer - Part II: Model Validation and Benchmarking”, *Journal of Turbomachinery*, Vol. 131, pp. 031017-1-11.

[7] Elsner, W., and Warzecha, P., 2010, “Modeling of rough wall boundary layerswith intermittency transport model”, *TASK Quarterly*, Vol. 14, No. 3, pp. 271-282.

[8] Langtry, R. B., and Menter, F. R., 2009, “Correlation-Based Transition Modeling for Unstructured Parallelized Computational Fluid Dynamics Codes”, *AIAA Journal*, 47 (12), 2894-2906.

[9] Dassler, P., Kožulović, D., and Fiala, A., 2010, “Modelling of Roughness-Induced Transition Using Local Variables”, V European Conference on CFD, ECCOMAS CFD 2010.

[10] Pinson, M., W., and Wang, T., 2000, “Effect of Two-Scale Roughness on Boundary Layer Transition Over a Heated Flat Plate: Part 1 - Surface Heat Transfer”, *Journal of Turbomachinery*, Vol. 122, pp. 301-316.

[11] Van Driest, E. R., and Blumer, C. B., 1963, “Boundary Layer Transition: Freestream Turbulence and Pressure Gradient Effects”, AIAA Journal, Vol. 1, No. 6, pp. 1303–1306.

[12] Nürnberger, D., 2004, “Implizite Zeit-integration für die Simulation von Turbo-maschinenströmungen”, *DLR Forschungs-bericht*, 2004-27.

[13] Kügeler, E., 2005, “Numerisches Verfahren zur genauen Analyse der Kühleffektivität filmgekühlter Turbinenschaufeln”, DLR Forschungsbericht, 2005-11.

[14] Hirsch, C, 1988, “Numerical Computation of Internal and External Flows”, Volume 1: “Fundamentals and Numerical Discretization” John Wiley and Sons Ltd., Wiley series in numerical methods in engineering, ISBN-10 0471917621

[15] Hirsch, C, 1991, “Numerical Computation of Internal and External Flows”, Volume 2: “Computational Methods for Inviscid and Viscous Flows” John Wiley and Sons Ltd., Wiley series in numerical methods in engineering, ISBN-10 0471933516

[16] Roe P., 1981, “Approximate Riemann solvers, parameter vector and difference schemes”, *Journal of Computational Physics*, Vol. 34, pp. 357–372.

[17] Röber, T., Kožulovic, D., Kügeler, E., and Nürnberger, D., 2006, “Appropriate turbulence modelling for turbomachinery flows using a two-equation turbulence model”, in: *New Results in Numerical and Experimental Fluid Mechanics V*, pp. 446–454, Eds.: H. J. Rath et al., Springer, Berlin.

[18] Mulder W. A. and van Leer, B., 1983, “Implicit Upwind Methods for the Euler Equations”, AIAA Journal, No. 83-1930

[19] Saxer, A. and Giles, M. B., 1993, “Quasi-three-dimensional non-reflecting boundary conditions for Euler equation calculations”, AIAA Journal Prop. and Power, Vol. 128, pp. 263–271.

[20] Wilcox, D. C., 1988, “Reassessment of the scale-determining equation for advanced turbulence models”, *AIAA Journal*, Vol. 26, No. 11, pp. 1299–1310.

[21] Wilcox, D. C., 2006, “Turbulence Modeling for CFD”, DCW Industries, 3rd edition, ISBN-10 1928729088.

[22] Knopp, T., Eisfeld, B., and Calvo, J. B., 2009, “A new extension for k-ω turbulence models to account for wall roughness”, *International Journal of Heat and Fluid Flow*, 30, pp. 54-65.

[23] Hoheisel, H., 1990, “Test Case E/Ca-6: subsonic turbine cascade T106”, *AGARD-Ar-275: Test Cases for Computation of Internal Flows in Aero Engine Components*, pp. 112-123, Fottner, L. (Ed.), SPS, Loughton.

[24] Montis, M., Niehuis, R., and Fiala, A., 2011, “Effect of Surface Roughness on Loss Behaviour, Aerodynamic Loading and Boundary Layer Development of a Low-Pressure Gas Turbine Airfoil”, *Proc. of ASME Turbo Expo*, GT2011-23317, Glasgow.

[25] Fiala, A., Kügeler, E., 2011, “Roughness Modeling for Turbomachinery”, *Proc. of ASME Turbo Expo*, GT2011–45424, Vancouver.

[26] Dassler, P., Kožulović D., Fiala, A., 2012, “An Approach for Modelling the Roughness-Induced Boundary Layer Transition Using Transport Equations”, Europ. Congress on Comp. Methods in Appl. Sciences and Engineering, ECCOMAS 2012, Vienna.

Conference on Modelling Fluid Flow (CMFF'12)
The 15th International Conference on Fluid Flow Technologies
Budapest, Hungary, September 4-7, 2012

DIRECT NUMERICAL SIMULATION OF A NACA0012 IN FULL STALL

Ivette RODRIGUEZ[1], Aleix BAEZ [1] Oriol LEHMKUHL [1 2], Ricard BORRELL [1 2] Assensi OLIVA [1]

[1] Centre Tecnològic de Transferència de Calor (CTTC), Universitat Politècnica de Catalunya (UPC). ETSEIAT, Colom 11, 08222, Terrassa, Barcelona, Spain. cttc@cttc.upc.edu
[2] Termo Fluids, S.L., Avda. Jaquard, 97 1-E, 08222 Terrassa (Barcelona), Spain

ABSTRACT

This work aims at investigating the mechanisms of separation and the prediction of the transition to turbulence in the separated shear-layer while at the same time to gain insight into coherent structures formed in the separated zone at low-to-moderate Reynolds numbers. To do this, direct numerical simulations of the flow past a NACA 0012 airfoil at Reynolds numbers $Re = 50000$ (based on the free-stream velocity and the airfoil chord) at angles of attack $AOA = 9.25^\circ$ and $AOA = 12^\circ$ have been carried out. At low-to-moderate Reynolds numbers, NACA 0012 exhibits a leading-edge/trailing-edge stall which causes the massive separation of the flow on the suction side of the airfoil. The initially laminar shear layer undergoes transition to turbulence and vortices formed are shed forming a von Kármán like vortex street in the airfoil wake. The main characteristics of this flow together with its main features, including power spectra of a set of selected monitoring probes at different positions on the suction side and in the wake of the airfoil are described and discussed in detail.

Keywords: CFD , DNS, stall, coherent flow, vortex shedding

1 INTRODUCTION

Stall on airfoils is caused by massive separation of the flow leading to a sharp drop in the lift and an increase in the drag over the airfoil surface. NACA 0012 airfoil exhibits two types of stall. A trailing-edge stall at all Reynolds numbers and a combined leading-edge/trailing-edge stall at intermediate Reynolds number [1]. The latter shows the presence at stall of a turbulent boundary layer separation moving forward from the trailing-edge and a small laminar bubble in the leading-edge region failing to reattach which complete the flow breakdown. An oscillating situation is often noticed near stall angles (see for instance [2]).

The flow around airfoils in full stall is a problem of great interest in aerodynamics and specifically for the design of turbo-machines (turbines, propellers, wind turbines, etc.). However, mechanisms of quasi-periodic oscillation observed near stall and stall behaviour, which affect airfoil efficiency, remain still not fully understood. Thus, the study of the separation mechanism and the correct prediction of boundary layer transition are both key aspects for improving engineering designs.

The development of coherent structures and transition to turbulence in the separated shear-layer and wake of airfoils have been object of different studies. For instance, Huang & Lin [3] and Lee & Huang [4] studied the flow patterns and characteristics of the vortex shedding of a NACA 0012 airfoil identifying four different modes of vortex shedding. In addition, Huang & Lin [3] measured the vortex shedding frequency in the range of Reynolds numbers of 2.5×10^4 - 1.2×10^5 and observed that for angles of attack (AOA) larger than 15° this frequency gradually converges to a value of 0.12 as the AOA approaches to 90°. More recently, Yarusevych et. al. [5] studied experimentally the development of the coherent structures in the separated shear layer of a NACA 0025 at low-to-moderate Reynolds numbers in the range 5.5×10^4 - 2.1×10^5. They provided some insight into the structures formed and also measured both, the shear-layer instability and vortex shedding frequencies for low AOA. Although, some similarities can be observed with the flow past a NACA 0012, there are also important differences as the type of stall these airfoils experience is different than the observed in NACA 0012.

The advances in computational fluid dynamics together with the increasing capacity of parallel computers have made possible to tackle complex turbulent problems by using high-performance numerical techniques such as direct numerical simulation (DNS) [6, 7]. DNS has a key role for improving the understanding of the turbulence phenomena and for the simulation of transitional flows in complex geometries. In the present work DNS of the flow past a NACA0012 airfoil at low-to-moderate Reynolds numbers $Re = 5 \times 10^4$ and angles of attack of 9.25° and 12° (the last one correspond to a full-stall

situation) have been carried out. This work aims at investigating the mechanisms of separation and the prediction of the transition to turbulence in the separated shear-layer while at the same time to gain insight into coherent structures formed in the separated zone at low-to-moderate Reynolds numbers. The main features of the flow, including power spectra of a set of selected monitoring probes at different positions in the suction side and in the near-wake of the airfoil are discussed in detail.

2 MATHEMATICAL AND NUMERICAL METHOD

The Navier-Stokes and continuity equations can be written as

$$\mathsf{M}u = 0 \qquad (1)$$

$$\frac{\partial u}{\partial t} + \mathsf{C}(u)\,u + \nu \mathsf{D}u + \rho^{-1}\mathsf{G}p = 0 \qquad (2)$$

where u and p are the velocity vector and pressure, respectively; ν is the kinematic viscosity and ρ the density. Convective and diffusive terms in the momentum equation for the velocity field are given by $\mathsf{C}(u) = (u \cdot \nabla)$ and $\mathsf{D} = -\nabla^2$ respectively. Gradient and divergence (of a vector) operators are given by $\mathsf{G} = \nabla$ and $\mathsf{M} = \nabla\cdot$, respectively.

The governing equations have been discretised on a collocated unstructured grid arrangement by means of second-order spectro-consistent schemes [8]. Such schemes are conservative, i.e. they preserve the kinetic energy equation. These conservation properties are held if, and only if the discrete convective operator is skew-symmetric ($\mathsf{C}(u) = -\mathsf{C}^*(u)$), the negative conjugate transpose of the discrete gradient operator is exactly equal to the divergence operator ($-(\Omega\mathsf{G})^* = \mathsf{M}$) and the diffusive operator D, is symmetric and positive-definite. These properties ensure both, stability and conservation of the kinetic-energy balance even at high Reynolds numbers and with coarse grids.

For the temporal discretization of the momentum equation, a two-step linear explicit scheme on a fractional-step method has been used, while for the pressure-gradient term an explicit first-order scheme has been used.

The velocity-pressure coupling has been solved by means of a classical fractional step projection method,

$$u^p = u^{n+1} + \mathsf{G}\tilde{p} \qquad (3)$$

where $\tilde{p} = p^{n+1}\Delta t^n/\rho$ is the pseudo-pressure, u^p the predicted velocity, $n+1$ is the instant where the temporal variables are calculated, and Δt^n is the current time step ($\Delta t^n = t^{n+1} - t^n$). Taking the divergence of (3) and applying the incompressibility condition yields a discrete Poisson equation for $\tilde{p}$: $\mathsf{L}\,\tilde{p} = \mathsf{M}\,u^p$. The discrete laplacian operator $\mathsf{L} \in \mathbb{R}^{m\times m}$ is, by construction, a symmetric positive definite matrix ($\mathsf{L} \equiv \mathsf{M}\Omega^{-1}\mathsf{M}^*$). Once the solution of p^{n+1} is obtained, $\tilde{p}$ results from equation 3.

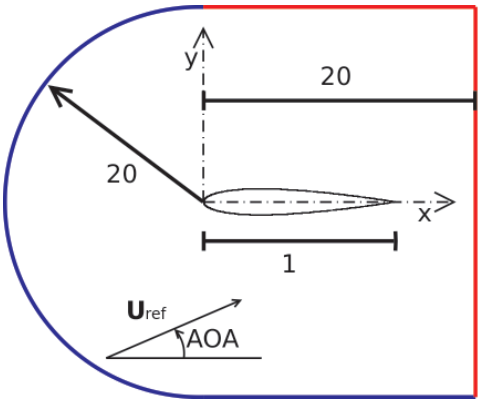

Figure 1: Computational domain. Blue boundary represents inflow conditions, with specified velocity and pressure. Red boundary represents outflow condition.

Finally the mass-conserving velocity at the faces ($\mathsf{M}_s u_s^{n+1} = 0$) is obtained from the correction,

$$u_s^{n+1} = u_s^p - \mathsf{G}_s\tilde{p} \qquad (4)$$

where G_s represents the discrete gradient operator at the CV faces. This approximation allows to conserve mass at the faces but it has several implications. If the conservative term is computed using u_s^{n+1}, in practice an additional term proportional to the third-order derivative of p^{n+1} is introduced. Thus, in many aspects, this approach is similar to the popular Rhie & Chow [9] interpolation method and eliminates checkerboard modes.

However, collocated meshes do not conserve the kinetic energy as have been shown by Morinishi et. al. [10] for finite-difference schemes and by Felten & Lund [11] for finite-volume schemes. When the fractional step method on a collocated arrangement is used, there are two sources of errors in the kinetic energy conservation: i) due to interpolation schemes and, ii) due to inconsistency in the pressure field in order to ensure mass conservation. While the first one can be eliminated through the use of conservative schemes such as those used in the present work, the latter equals to:

$$\varepsilon_{\mathbf{ke}} = (\tilde{p}_c)^*\mathsf{M}_c(\mathsf{G}_c - \mathsf{G}_s)\tilde{p}_c \qquad (5)$$

This contribution of the pressure gradient term to the evolution of the kinetic energy can not be eliminated. Felten & Lund [11] have conducted a study to determine its scaling order. They have shown that the spatial term of the pressure error scales as $O(\Delta x^2)$ and the temporal term scales as $O(\Delta t)$, i.e. pressure errors are of the order of $O(\Delta x^2\,\Delta t)$. However, in their work they have proven that pressure errors do not have a significant impact on the results at grid resolutions and time-steps used in LES and in DNS. The methodology used in this work have been proven to yield accurate results and have been previously used for solving the

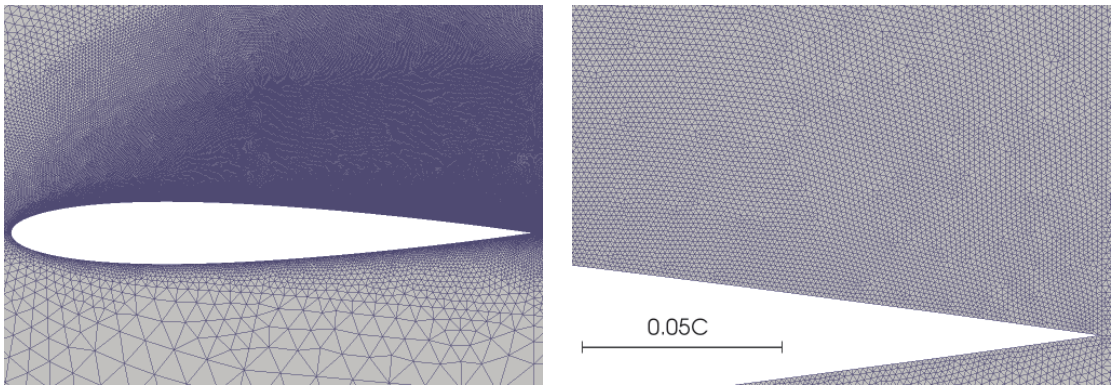

Figure 2: Detail of the 2D grid in the suction side and in the region near the airfoil surface

flow over bluff bodies with massive separation in [12] and [13].

In the parallel code used to perform the simulations presented in this paper, the algorithm followed at each time-step can be divided into two parts: i) an implicit part where the Poisson equation is solved to project the velocity field into a divergence-free space (this is usually the main bottleneck from the computational point of view), and ii) the rest of the calculations which are carried out in an explicit manner. The meshes used for solving the domain considered have been generated by a constant step extrusion of a two-dimensional (2D) unstructured grid. Under these conditions, the spanwise coupling of the discrete Poisson equation results into circulant sub-matrices that are diagonalizable in a Fourier space [14, 15]. This allows to solve the Poisson equation by means of a Fast Fourier Transform (FFT) method [16, 17]. The algorithm used is based on the explicit calculation and direct solution of a Schur Complement system for the independent 2D systems. Its main drawback is the requirement of a computationally demanding pre-processing stage and large memory resources. However, this additional pre-processing cost becomes almost negligible compared to the total time-integration cost. For the meshes used in this work, parallelisation strategies have considered partitions of 256 CPUs. For more details the reader is referred to [18].

3 DEFINITION OF THE CASE. COMPUTATIONAL GEOMETRY

All computed flows are around a NACA-0012 airfoil extended to include sharp trailing edge. All coordinates are referred to body axes unless remarked. The x axis is chord-wise, y is in the plane of the airfoil and z is spanwise direction. Solutions are obtained in a computational domain of dimensions $40C \times 40C \times 0.2C$ with the leading edge of the airfoil placed at $(0,0,0)$ (see figure 1). Distances from the profile to the domain boundaries have been chosen according to previous experiences and potential vortices notions. The boundary conditions at the inflow consist of a uniform velocity profile (u,v,w)=$(U_{ref}\cos AOA,\ U_{ref}\sin AOA, 0)$. As for the outflow boundary, a pressure-based condition is imposed. No-slip conditions on the airfoil surface are prescribed. Periodic boundary conditions are used in the spanwise direction.

For carrying out the computations at both AOA ($AOA = 9.25^\circ$ and $AOA = 12^\circ$) the same grid has been used. Flow around an airfoil is mostly laminar with the exception of a zone close to the surface of the airfoil (suction side) and in the wake of it. When performing DNS, it must be ensured that the grid size is enough to solve well the smallest flow scales in the turbulent zones. Furthermore, within laminar zones, boundary layer must also be well-solved. Taking into account that the accuracy of the results is highly grid dependent, specially in the region of the separated shear-layer where transition to turbulence occurs, care must be taken when the computational grid is constructed. Another critical region is the near wake of the airfoil, where a poor grid resolution may cause notable upstream flow distortions. With these criteria, more control volumes have been clustered in these zones, but even though the grid used is unstructured, it has been constructed as uniform as possible in the regions of interest. Thus, the results presented in the paper have been performed on a grid of about 46.6 million CVs (340526×128 planes) which covers the whole domain. The 2D grid and its refinement around the suction side of the airfoil is depicted in figure 2.

In *a-posteriori* analysis the grid resolution of the zones off the wall is assessed by comparing the grid size h ($h \equiv (\Delta x \times \Delta y \times \Delta z)^{1/3}$) to the Kolmogorov length scale η. Kolmogorov length scale has been obtained from the dissipation rate ε as,

$$\eta = (\nu^3/\varepsilon)^{1/4} \tag{6}$$

Note that the output obtained by using this criteria is only valid in the regions where the flow can be considered locally isotropic. Thus, it can not be applied to the region of the separated shear layer or in the near wall zone. Figure 3 shows the ratio h/η for the suction side of the airfoil for $AOA = 12^\circ$, which is the most challenging situation. As can be seen from the figure,

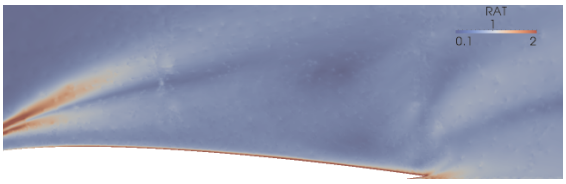

Figure 3: Ratio of the grid size to the Kolmogorov length scale in the suction side of the airfoil

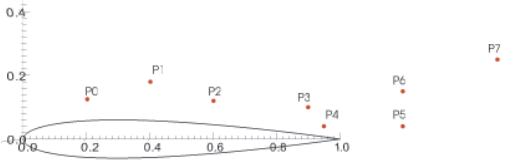

Figure 4: Location of the computational probes

in the suction side this ratio is on average $h/\eta \approx 0.52$. In the near wake, at a distance $1 < x/C < 1.5$, this ratio is about $h/\eta \approx 0.59$ and increases up to $h/\eta \approx 0.63$ in the wake zone between $1.5 < x/X < 3$. With these considerations, the grid density obtained should be fine enough to solve the smallest flow scales in the zone of interest at this Reynolds number.

Regarding the spanwise size of the domain, it has been fixed to 20% of the chord, similar to the values adopted by other investigations at comparable Reynolds numbers [19, 20]. However, in order to verify if this size is adequate, spanwise two-point correlations have been computed. These correlations give an indication of the size of the flow structures in this direction. Thus, the domain should be considered wide enough if their values tend to zero as they approach to the half-size of the domain. Two-point correlations are defined as,

$$\Re_{ii}(\mathbf{x}, \delta z) = \frac{< u_i'(\mathbf{x},t)\, u_i'(\mathbf{x}+\delta z,t) >}{< u_i'^2 >} \qquad (7)$$

where $\mathbf{x} \equiv (x,y,z)$ and $< \cdot >$ denotes averaging over time and space. In order to calculate two-point correlations at different locations, the time signals of different stations on the suction side have been recorded. The location of these probes are given in figure 4. The computed values for the streamwise velocity fluctuations (Re_{uu}) are given in figure 5. As can be observed, Re_{uu} at the different stations vanish at the half-width of the domain. In the figure can also be seen the average size of streamwise structures at the different locations, as the position of the minimum denotes the mean distance between a high and a low-speed flow structure. Thus, the size of these structures is twice this distance. Considering these results, the value of 20% of the chord is good enough for capturing the largest scales of the flow.

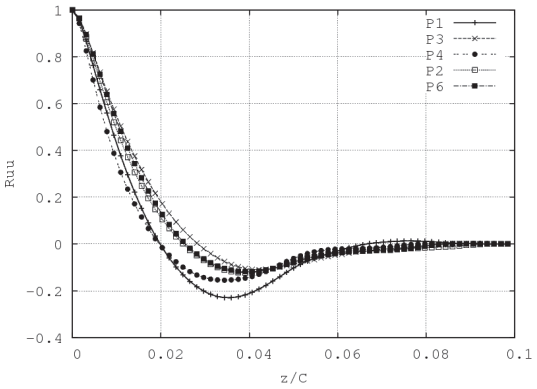

Figure 5: Spanwise two-point correlations of the streamwise velocity at different stations

4 RESULTS

For obtaining the numerical results presented, the simulations have been started from an initially homogeneous flow field which introduces some numerical disturbances as it is not the solution of the governing equations. These disturbances eventually cause the flow became three-dimensional and trigger the transition to turbulence. Then, simulation has been advanced in time until statistical stationary flow conditions have been achieved and the initial transient is completely washed out.

4.1 *Instantaneous flow structures*

In order to gain insight into the coherent structures developed in the separated zone, instantaneous stream- and spanwise vortical structures have been depicted in figure 6 for both AOA. A first inspection to the figure reveal the large quantity of small scales in the separated zone. In fact as the AOA increases one can note how this region is enlarged due to the increase of the adverse pressure gradient.

Furthermore, it can also be observed how the flow separates laminarly from the airfoil surface near the leading edge as can be inferred from the two-dimensional shear-layer developed. Vortex breakdown occurs at the end of the laminar shear-layer as a consequence of the instabilities developed by the action of a Kelvin-Helmholtz mechanism (see figure 7). These instabilities are high frequency fluctuations in the velocity field which grow in magnitude as the distance from the leading edge increases and eventually causes shear layer to roll-up and undergo transition to turbulent flow. For instance, if spanwise vorticity at $AOA = 12^\circ$ is inspected (see figure 6(b)), these instabilities can clearly be seen in the laminar shear-layer. Indeed, the increase in their amplitude until finally transition to turbulence occurs is also well capture in the figure. This mechanism of transition is similar to that observed in shear-layers developed in other bluff bodies such as the flow past a circular cylinder (see for instance [21]) or the flow past a sphere

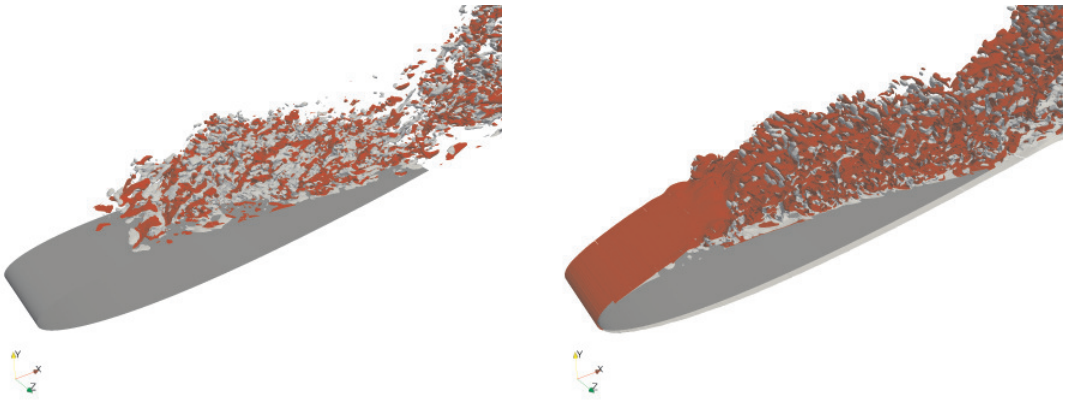

(a)

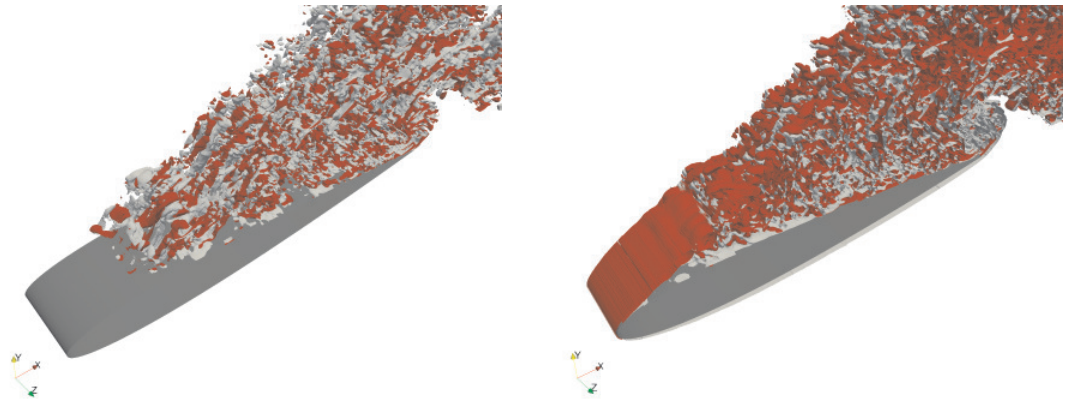

(b)

Figure 6: Vortical structures on the suction side of the airfoil a) $AOA = 9.25^{\circ}$; b)$AOA = 12^{\circ}$. (left) streamwise vorticity $\omega_x = \pm 25$. (right) spanwise vorticity $\omega_z = \pm 10$

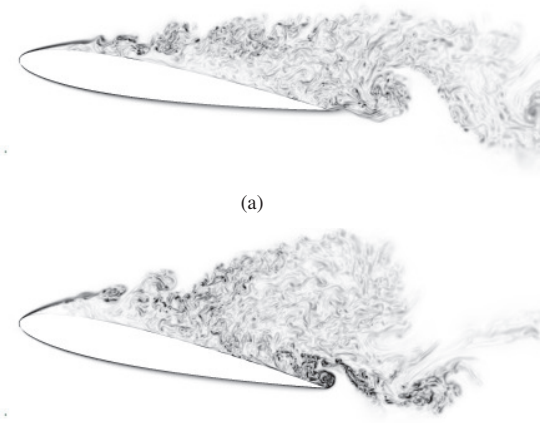

(a)

(b)

Figure 7: Instantaneous vorticity contours a) $AOA = 9.25°$; b)$AOA = 12°$

[13].

At the end of the two-dimensional shear layer, corrugated structures along the homogeneous direction, can also be observed. These corrugated structures are related with the formation of streamwise vortices (ribs) in the separated zone. After vortex breakdown, small-scale vortices are formed and accumulate into larger structures forming packets. The frequency at which these instabilities develop is much higher than that of the vortex shedding mechanism (see section 4.2). These turbulent vortical packets formed, eventually grow up as the flow moves downstream. A close-up to the developing flow structures in the separated shear-layer is shown in figure 7 by means of vorticity isocontours projected into a two-dimensional plane. For both *AOA* this phenomena can be seen in the figure. After transition, the vortices formed break into small-scale vortices, and by means of the pairing of vortices large scale structure are formed. These large-scale vortices evolve in the near wake with a pattern similar to a von Kármán like vortex street (not shown here), which resembles that formed behind a circular cylinder.

According to Huang & Lin [3] observations of the flow past a NACA 0012 airfoil at low-to-moderate Reynolds numbers, the way vortices are shed into the wake present four characteristics modes: laminar, subcritical, transitional and supercritical. At $AOA = 9.25°$, wake mode should corresponds with transitional, whereas at $AOA = 12°$ supercritical mode should be detected. In fact, from the inspection of time series at P5 station (placed at $x/C = 1.2$; $y/X = 0.04$), streamwise velocity exhibits a transitional mode characterised by the lost of coherence in the signal (see figure 8(a)). Furthermore, at $AOA = 12°$, the streamwise signal is highly coherent (the vortex shedding frequency can almost be calculated directly from the signal) which agrees well with Huang & Lin

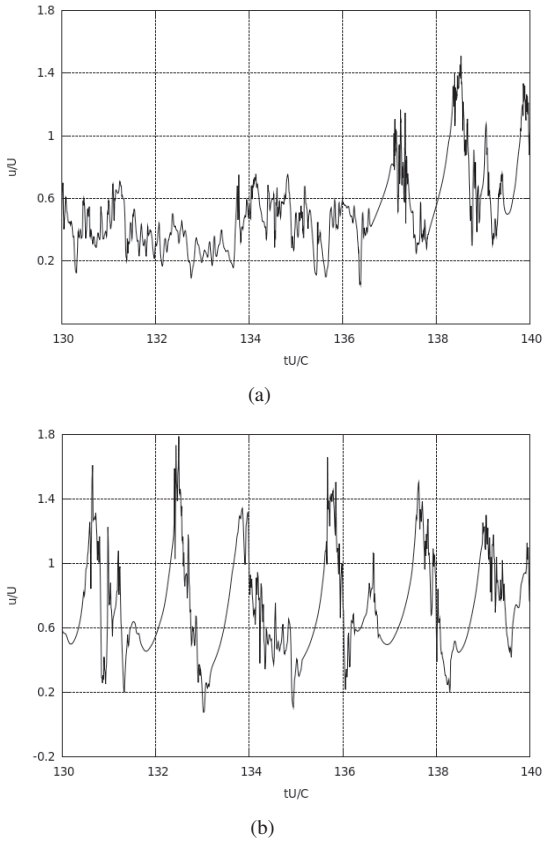

Figure 8: Streamwise velocity time series at P5 station. a) $AOA = 9.25°$; b)$AOA = 12°$

supercritical mode (see figure 8(b)). The signal of the streamwise velocity fluctuates due to the passing of large-scale vortices, but also the footprint of the small-scale shear layer fluctuations is superimposed.

It is important to point out, that $AOA = 9.25°$ corresponds to a near stall situation in which the flow oscillates between attached and detached states at a frequency much lower than that of the vortex shedding (see for instance Zaman et. al. studies [22]). This flow oscillation, which corresponds with a leading-edge/trailing-edge type of stall characteristic of the NACA 0012 at these Reynolds numbers, might interact with the process of vortex formation, and consequently produce the lost of coherence observed both, experimentally and numerically. This might also be the reason why Huang & Lin did not detect the presence of vortex shedding in the transitional mode. Unfortunately, currently the data series collected from DNS at $AOA = 9.25°$ is still insufficient to completely support this hypothesis, but from preliminary inspection to the energy spectra of short time series (not shown here), it seems that although not so coherent and weaker than in the supercritical regime, vortex shedding exists also at this angle of attack.

4.2 Energy spectra

As has been commented before, time series of velocity components and pressure have been recorded on different locations (see figure 4). The data have been collected over 123 time units (tU/C). The results presented correspond with $AOA = 12°$, as by the time this communication is written, the simulation for $AOA = 9.25°$ is still under-way. The energy spectra have been calculated by using the Lomb periodogram technique and the resulting spectra have also been averaged in the homogeneous direction.

For the sake of brevity, we are only presenting the results for streamwise velocity fluctuations as both spectra, i.e. for streamwise and cross-stream fluctuations, capture well the main frequencies of the flow. Figure 9 shows the resulting energy spectra for the streamwise velocity fluctuations. For clearness, the amplitude of each spectrum has been shifted and are represented for increasing x/C from bottom to top. The energy spectra exhibit different ranges and fundamental frequencies, from transition to turbulent flow observed in the bottom curve (corresponding with probe P0) to the regular decay of slope close to $-5/3$ as the flow approaches the airfoil aft and flows into the wake (probe P5). This is indicative of the presence of an inertial subrange for more than a decade of frequencies.

As for the significant frequencies, the spectrum for P0 shows a broadband peak at $f_{SL} = 9.74$ ($S_t = f\sin(AOA)C/U = 2.025$, here Strouhal is based on the airfoil projection on a cross-stream plane). This peak corresponds with the frequency of the shear-layer instabilities and disappears as the flow moves downstream and the separated shear layer becomes turbulent. Note that it has only been captured by the probe located at ($x/C = 0.2$; $y/C = 0.125$) which is close to the separated shear layer.

In addition, the energy spectra of all probes show a peak at the frequency $f_{vs} = 0.613$ ($S_t = 0.127$). This peak is associated with the vortex-shedding process and its energy content increases as the flow approaches the aifoil aft anf flows into the wake. Indeed, the signals of the stream-wise and cross-stream velocities gain coherence as the flows moves downstream into the wake.

5 CONCLUDING REMARKS AND FUTURE WORK

In the current work the mechanisms of transition at the separated shear-layer of a NACA0012 airfoil at AOA near stall and in full stall have been addressed. The study has been performed by means of the direct numerical simulation of the flow at a low-to-moderate Reynolds number of $Re = 50000$. To do this, a second-order spectro-consistent scheme on a collocated unstructured grid arrangement has been used for the discretization of the governing equations. All computations have been carried out on a 43.6 MCVs grid generated by the constant step extrusion in the homogeneous direction of a two-dimensional grid.

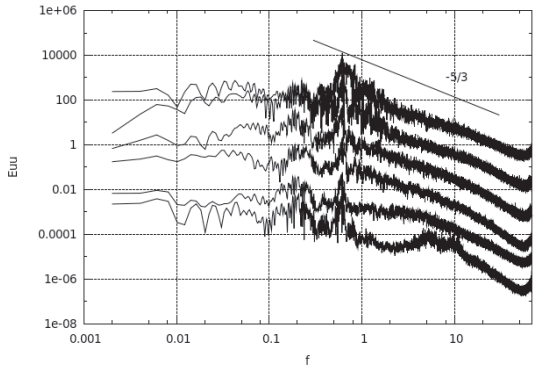

Figure 9: Energy spectra of the streamwise velocity fluctuations for $AOA = 12°$. From top to bottom, spectra correspond with stations P5, P4,P3, P2, P1, P0 (see figure 4 for details)

It has been observed that the separated flow at bot AOA is slightly different. Indeed, coherent structures identified have shown that in agreement with the experimental observations of Huang & Lin [3], the flow at $AOA = 12°$ is in the supercritical mode, characterised by the presence of a coherent vortex shedding. On the other hand, the flow at $AOA = 9.25°$ has been identified with the transitional mode. We suggest that the low level of coherence observed in the vortex shedding might be caused by the interaction with the low-frequency fluctuation observed near stall, which might change the way the vortices are shed. However, further studies will be necessary to completely support this hypothesis.

In addition, the main frequencies of the flow at $AOA = 12°$ have been detected by means of power spectra of several probes located on the suction side and in the near wake. In fact, the probe located near the shear-layer well captured the small-scale shear-layer instabilities frequency. These instabilities can be idenfied in the spectra as a broad-band peak centred at a frequency of $f_{SL} = 9.74$ ($S_t = f\sin(AOA)\,C/U = 2.025$). As a consequence of the growth of these instabilities the shear-layer roll-up and transition to turbulence occurs. The small vortices formed after transition are packet into large-scale streuctures dur to vortex pairing. Eventually, these vortices are shed at a frequency of $f_{vs} = 0.613$ ($S_t = 0.127$) which is observed at all probes.

Currently, simulations at $AOA = 9.25°$ are still underway and it is expected by means of the study of the instantaneous flow, to identify not only shear-layer instabilities and vortex shedding frequencies, but also the one corresponding with the fluctuation of the flow near stall angles.

ACKNOWLEDGEMENTS

This work has been by financially supported by the Ministerio de Educación y Ciencia, Secretaría de Estado de Universidades e Investigación, Spain (ref.

ENE2010-17801) and by the Collaboration Project between Universidad Politècnica de Catalunya and Termo Fluids S.L. (ref. C06650)

References

[1] W.J. McCroskey. A critical assessment of wind tunnel results for the NACA 0012 airfoil. Technical report, National Aeronautics and Space Administration, 1987.

[2] J.H. Almutairi, L.E. Jones, and N.D. Sandham. Intermittent bursting of a laminar separation bubble on an airfoil. *AIAA journal*, 48(2):414–426, 2010.

[3] R. F. Huang and C. H. Lin. Vortex shedding and shear-layer instability of wing at low-Reynolds numbers. *AIAA Journal*, 33(8):1398–1403, 1995.

[4] H. W. Lee and R. F. Huang. Frequency selection of wake flow behind a NACA 0012 wing. *Journal of Marine science and technology*, 1998.

[5] Serhiy Yarusevych, Pierre E. Sullivan, and John G. Kawall. On vortex shedding from an airfoil in low-Reynolds-number flows. *Journal of Fluid Mechanics*, 632:245, 2009.

[6] A Baez, Lehmkuhl O., I. Rodriguez, and C.D. Perez-Segarra. Direct Numerical Simulation of the turbulent flow around a NACA 0012 airfoil at different angles of attack. In *Parallel CFD 2011*, 2011.

[7] O. Lehmkuhl, A. Baez, I. Rodríguez, and C. D. Perez-Segarra. Direct numerical simulation and Large-Eddy simulations of the turbulent flow around a NACA-0012 airfoil. In *7th International Conference on Computational Heat and Mass Transfer*, pages 1–8, 2011.

[8] R. W. C. P. Verstappen and A. E. P. Veldman. Symmetry-Preserving Discretization of Turbulent Flow. *Journal of Computational Physics*, 187:343–368, May 2003.

[9] C. M. Rhie and W. L. Chow. Numerical study of the turbulent flow past an airfoil with trailing edge separation. *AIAA Journal*, 21:1525–1532, 1983.

[10] Y. Morinishi, T.S. Lund, O.V. Vasilyev, and P. Moin. Fully conservative higher order finite difference schemes for incompressible flow. *Journal of Computational Physics*, 143(1):90–124, 1998.

[11] F.N. Felten and T.S. Lund. Kinetic energy conservation issues associated with the collocated mesh scheme for incompressible flow. *Journal of Computational Physics*, 215(2):465–484, 2006.

[12] O. Lehmkuhl, R. Borrell, J. Chivas, and C.D. Perez-Segarra. Direct numerical simulations and symmetry-preserving regularization simulations of the flow over a circular cylinder at Reynolds number 3900. In *Turbulence, Heat and Mass Transfer*, 2009.

[13] I. Rodríguez, R. Borrell, O. Lehmkuhl, C.D. Pérez-Segarra, and A. Oliva. Direct Numerical Simulation of the Flow Over a Sphere at Re = 3700. *Journal of Fluids Mechanics*, 679:263–287, 2011.

[14] P. J. Davis. *Circulant Matrices*. Wiley-Interscience, New York, 1979.

[15] R. M. Gray. Toeplitz and circulant matrices: A review. *Foundations and Trends in Communications and Information Theory*, 2:155–239, 2006.

[16] P.N. Swarztrauber. The Methods of Cyclic Reduction, Fourier Analysis and the FACR Algorithm for the Discrete Solution of Poisson's Equation on a Rectangle. *SIAM Review*, 19:490–501, 1977.

[17] M. Soria, C.D. Pérez-Segarra, and A. Oliva. A direct parallel algorithm for the efficient solution of the pressure-correction equation of incompressible flow problems using loosely coupled computers. *Numerical Heat Transfer, Part B*, 41(2):117–138, 2002.

[18] R. Borrell, O. Lehmkuhl, F.X. Trias, and A. Oliva. Parallel direct poisson solver for discretisations with one fourier diagonalisable direction. *Computational Physics*, 230(12):4723–4741, 2011.

[19] Donghyun You, Frank Ham, and P. Moin. Discrete conservation principles in large-eddy simulation with application to separation control over an airfoil. *Physics of Fluids*, 20(10):101515, 2008.

[20] Ying Zhou and ZJ Wang. A Low-Frequency Instability/Oscillation near the Airfoil Leading-Edge at Low Reynolds Numbers and Moderate Incidences. In *20th AIAA Computational Fluid Dynamics Conference*, pages AIAA 2011–3548, 2011.

[21] A. Prasad and C.H.K. Williamson. The instability of the shear layer separating from a bluff body. *Journal of Fluid Mechanics*, pages 375–492, 1997.

[22] K. Zaman, DJ McKinzie, and CL Rumsey. A natural low-frequency oscilation for the flow over an airfoil near stalling conditions. *Journal of Fluid Mechanics*, 202:403–442, 1989.

Internal flows

Conference on Modelling Fluid Flow (CMFF'12)
The 15th International Conference on Fluid Flow Technologies
Budapest, Hungary, September 4-7, 2012

THE NUMERICAL AND EXPERIMENTAL ANALYSIS OF VELOCITY FIELDS AND TURBULENCE IN THE REVERSE CHAMBER

Robert KŁOSOWIAK[2], Jarosław BARTOSZEWICZ[3] Leon BOGUSŁAWSKI[1]

[1] Corresponding Author. Poznan University of Technology, Chair of Thermal Engineering, Piotrowo 3, PL-60965 Poznan, Poland
Tel.: +48 61 6652209, Fax: +48 61 6652281, E-mail: leon.boguslawski@put.poznan.pl
[2] Poznan University of Technology, Chair of Thermal Engineering. E-mail: robert.klosowiak@doctorate.put.poznan.pl
[3] Poznan University of Technology, Chair of Thermal Engineering. E-mail: jaroslaw.bartoszewicz@put.poznan.pl

ABSTRACT

The paper presents the results of numerical and experimental studies of a jet flowing through an axisymmetric reverse chamber. The test results have been presented in the form of distributions of components of axial and radial velocities and their fluctuations. The investigated cases of the phenomena include the flow with the interaction of the walls and therefore have characteristics of free- and confined flows. The numerical results have been compared with the experimental results. The numerical and experimental results have been presented in the form of normalized radial distributions for different velocities of the outlet of the inner tube against the bottom of the reverse chamber. The research aimed at demonstrating the similarities and differences between free and confined jets. For the numerical simulation of the turbulent flow in a cylindrical vessel the Phoenics program has been used. For the simulation of the turbulent flow the standard high-Reynolds-number form of the k-ε model or Reynolds stresses model has been used. The measurement of velocity and its fluctuation has been carried out with the use of the CTA anemometer. The standard X probe TSI-1241 to measure the two components of the velocity has been used. The position of the jet axis has been indicated by the laser beam. Probes were connected to the TSI-1050 constant temperature anemometer bridge. The auto trigger option has been selected. The recorded signal has been processed and analyzed by the same program.

Keywords: reverse chamber, cylindrical vessel, turbulent flow, turbulent model, impinging jet

NOMENCLATURE

D	– diameter of pipe inside the reverse chamber, [m]
r	– radius of the reverse chamber,[m]
U	– axial component of velocity, [m/s]
u'	– fluctuation of axial component of velocity, [m/s]
V	– radial component of velocity, [m/s]
v'	– fluctuation of radial component of velocity, [m/s]
y	– axial coordinate, [m]
z	– measurement cross-section, [m]

1. INTRODUCTION

A significant number of scientific papers that have appeared around the world are devoted to studies of free and impinging jets. These types of jets have a very wide application in engineering. The papers [1,2,3] provide the descriptions of the structure of the free jets. In subsequent years these papers were supplemented by studies of the processes occurring in the jets [4,5,6,7]. In recent years more complex phenomena occurring in the free and confined jets have been investigated. In paper [8] the authors analyzed the propagation of the jet flowing from the ventilation system in the vicinity of a vertical wall. In [9] the authors present the results of the effect of natural convection on the heat transfer on the impinging area. Another group of papers includes the descriptions of the processes of the transport between the free jet and the rotating surfaces, descriptions of the relations between the tensions on the impinged walls resulting from the impact of the jet (helpful at reducing the corrosion), the descriptions of the deformations of the free jet as a result of the interaction of the transverse jet at the nozzle outlet [10], deformation of the transverse flame under the external influence [11] and, finally, testing of the velocity distributions in the fluidized bed through which the gas jet flows [12]. The above shows a wide application range of free and impinging jets in technology. In most of the papers the authors show that the place of occurrence of the

jets is heat-flow machines. Such a type of flow belongs to a restricted class of flows. The previous work yielded information on the structure and shape of free jets. At present, one can point out two important scientific works that describe the effect of changes in the structure of the free jet due to externalities. The first one describes the changes in the structure of a jet, the length of the potential core and the size of the coherent structures resulting from the impact of the ring eccentrically located in the nozzle [13]. The second one examines the impact of the impinging jet on the porous surface [14] while the jet flows out of a rectangular nozzle in the presence or without the presence of the trailing wall. Despite the said reasons the authors of these and other works on geometrically limited jets, similar to free or impinging jets still use the present experimental data obtained for free jets.

This procedure can be considered acceptable only as the first approach to the considered problem of an organic nature.

Experimental research provides new information that is used as boundary conditions for numerical simulations. The results of numerical studies provide detailed information about the structure of the jet that flows into the reversing chamber and redistributions of the average values and turbulence. For turbulent flows, numerical Phoenics can solve equations that are time-averaged. It is presumed that the time over which the averaging is made is long as compared with the time scale of the turbulent motion. In non-stationary flows it must also be small as compared with the time scale of the mean flow. The k-ε turbulence model proposed by Harlow and Nakayama is, by far, the most widely used two-equation eddy-viscosity turbulence model, mainly because the ε does not require extra terms near the walls. This model is widely used because its effectiveness is well documented in the literature. Phoenics code provides the standard high-Reynolds-number form of the k-ε model, as presented by Launder and Spalding [15,16], with the inclusion of allowance for buoyancy effects for low Reynolds number flows.

The results of the numerical flow analysis are presented in the pictures for: distributions of components of axial and radial velocities and their fluctuations. The geometry of the analyzed cylindrical chamber is shown in Figure 1. A numerical calculation was carried out for the diameter of the nozzle $D=0.1m$, where this diameter is used as a characteristic dimension of the vessel. The distance between the nozzle and the impinging wall was $10D$ and the radius of the cylindrical vessel was $5D$. Because of many combinations of the dimensions only such a numerical simulation using numerical code, validated experimentally for a few dimensions, provides the possibility of predicting the flow and local shear stresses distributions.

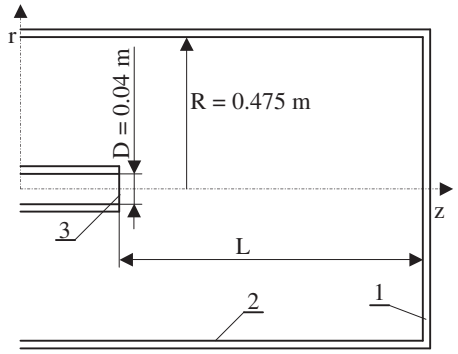

Figure. 1. The schematics of the reverse chamber 1 – impinging wall, 2 – side wall, 3 – outlet of pipe

2. NUMERICAL ANALYSIS

Phoenics provides solutions of discretized versions of sets of differential equations having the general form as follow:

$$\frac{d(\rho \cdot \varphi)}{dt} + div\left[\rho \cdot \vec{u} \cdot \varphi - G \cdot grad(\varphi)\right] = S \qquad (1)$$

where ρ stands for density, φ stands for any conserved property, such as enthalpy, momentum per unit mass, mass fraction of a chemical species, turbulence energy, etc., $\vec{u}$ stands for the velocity vector component, G represents the exchange coefficient of the entity φ and S stands for the source rate of φ. When time-averaged correlations of various quantities are not described precisely, as it happens commonly when turbulent flows are to be simulated, special expressions have to be introduced for G and S, accounting for the correlations between the velocity, density, φ, and other properties of the flow and of the fluid. Auxiliary variables are distinguished from dependent variables by being derived from algebraic equations rather than from differential ones. The examples of auxiliary variables are:

-molecular properties of the media such as laminar viscosity, diffusivity, Prandtl,

-thermodynamic properties such as density, saturation enthalpy, temperature (if not a dependent variable),

-quantities characterizing the state of the turbulence such as the length scale, the turbulent kinematic viscosity, the generation rate,

-inter-phase-transport parameters such as the rates of evaporation and condensation, the coefficient of inter-phase friction and heat transfer.

For high turbulent Reynolds numbers, the standard form of the k-ε model of turbulence may be summarized as follows:

$$\frac{\mathrm{d}(\rho k)}{\mathrm{d}t}+\frac{\mathrm{d}}{\mathrm{d}x}\left[\rho U k-\frac{\rho \nu_t}{Pr(k)}\frac{\mathrm{d}k}{\mathrm{d}x}\right]= \quad (2)$$
$$=\rho(P_k+G_b-\varepsilon),$$

$$\frac{\mathrm{d}(\rho \varepsilon)}{\mathrm{d}t}+\frac{\mathrm{d}}{\mathrm{d}x}\left[\rho U \varepsilon-\frac{\rho \nu_t}{Pr(\varepsilon)}\frac{\mathrm{d}\varepsilon}{\mathrm{d}x}\right]= \quad (3)$$
$$=\rho\frac{\varepsilon}{k}(C_1P_k+C_3G_b-C_2\varepsilon),$$

The following constants are normally used: $Pr(k) = 1.0$, $Pr(\varepsilon) = 1.314$, $C = 0.09$, $C_1 = 1.44$, $C_2 = 1.92$, $C_3 = 1.0$.

3. BOUNDARY CONDITIONS

The measurements were made in an axisymmetrical jet, not swirled and unstimulated, flowing out of the sharp-edged ring channel of *0.04 m* in diameter to the reverse chamber of *0.475 m* in diameter. The pipe outlet position in relation to the impinged surface, was varying from *z/D=10* to *z/D=2*. The boundary conditions used for the measurements comprised the air outflow velocity changes from the internal pipe of the reverse chamber. The measurements were made for three pipe outlet velocities: *10, 20* and *30 m/s*, which corresponded to the Reynolds numbers from 26000 to 78000 respectively. The air temperature was maintained on the level of 20^oC. The tests included measurements of average values in time: axial and radial component of velocity and their fluctuations.

The numerical calculations were based on the geometry of the actual property described in the boundary conditions for the experiment that was carried out. Numerical calculations were performed for many different variants of velocity and distances of the nozzle from the bottom of the reverse chamber. Pipe outlet velocities varied from *2* to 50 *m/s* and the turbulence intensity was *4%*.

4. EXPERIMENT RESULTS

Normalized radial profiles of the axial component of velocity and its fluctuation for three different flow velocities of the inner pipe have been presented in figures 2 (a) (b) c). The shape of the graph describing the jet flowing from the pipe is in line with the actual impinging jet [17]. With respect to the impinging jet the area under the positive part of the curve is slightly larger, which means that the flowing jet is rapidly spreading in the chamber. Unlike the free jets, where the core potential reaches a distance *r/D= 4* in the reverse chamber a decrease in the velocity between distances *r/D= 6-7* in the axis of the pipe is shown. A different situation occurs in the wall region of the wall flow where significant differences are visible in the velocity waveform profiles for different flow velocities. Between distances *z/D=7-10* radial velocity profiles are similar and the jet behaves in the same way. From a distance *r/D=6* a noticeable difference in the structure and character of the flow velocity of *10m/s* was observed.

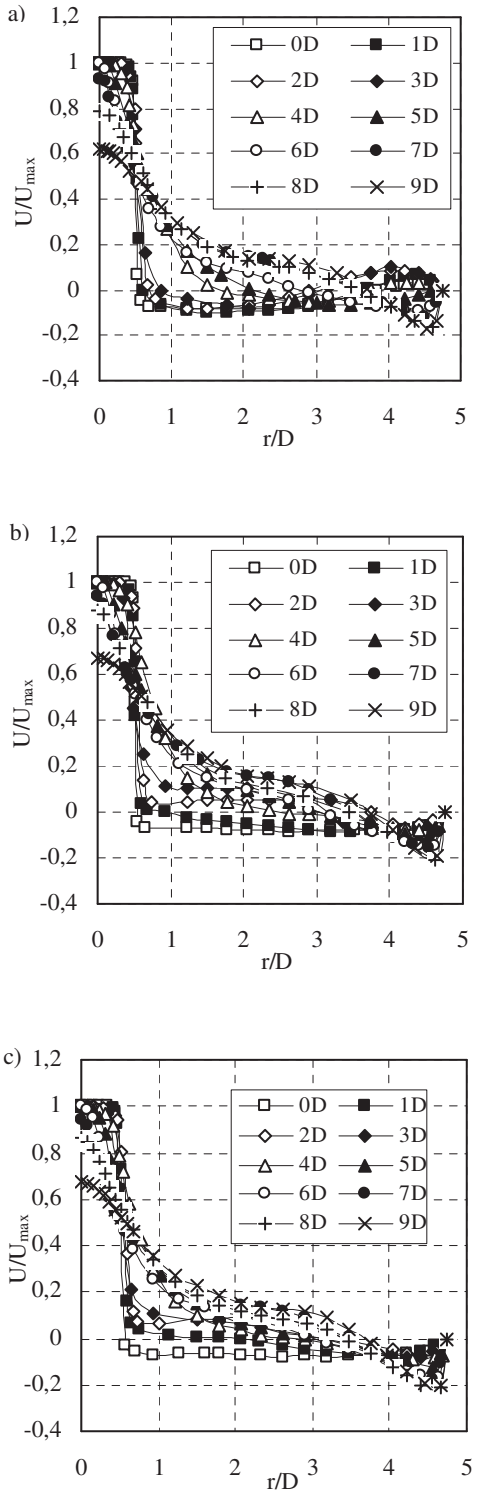

Figure 2. The distributions of axial component of velocity at: a – 10[m/s], b – 30[m/s], c – 50 [m/s]

At distance *r/D ≈ 5* a separation of the flow from the trailing wall occurs. The backward jet directs the central part of the chamber to the outlet. On the wall appears a jet towards the direction of the outflow pipe, which represents positive values of velocity in the figures. In the case of *30* and *50 m /s* the jet behaves as the boundary, moves towards the outlet and gradually increases towards a jet from the wall flow to the axis flow. We may observe a shift of the intersection of the x-axis profiles of about *r/D=3* and *y/D =2*. At cross section *r/D=0* the jet fills the whole cross-section of the reverse chamber between the inner pipe and the wall flow. For these two velocities in the middle of the reverse chamber a vortex lying at a distance *r/D≈2* is formed that represents the local maximums in the figures. In Figure 2a compared with figures 2b and 2c the differences are negligible in terms of the distribution for a velocity of *10 m/s*, which should be associated with the different nature of the flow at the wall flow.

Figures 3 (a, b, c) show the normalized distributions of the fluctuations of the axial component of velocity.

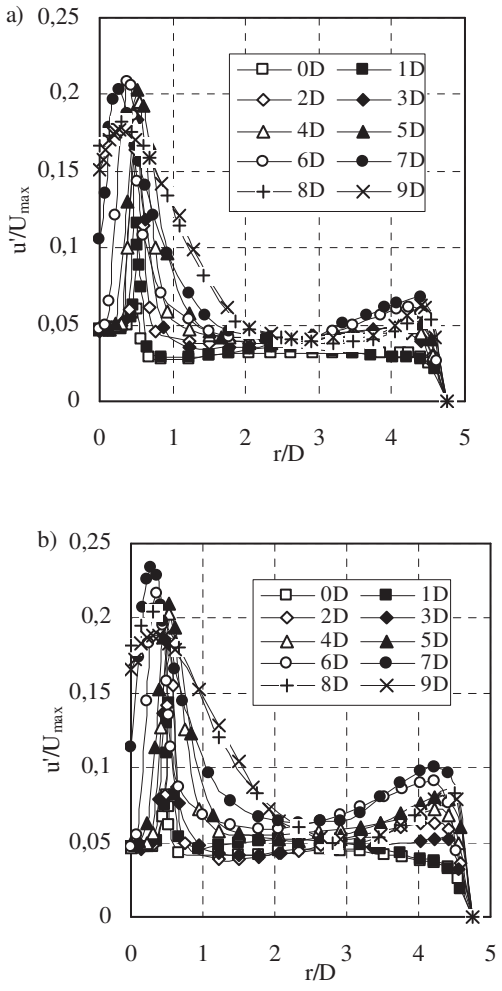

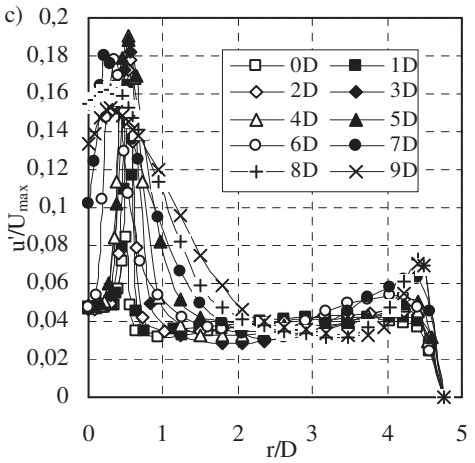

Figure 3. The distributions of fluctuations of axial component of velocity at: a – 10[m/s], b – 30[m/s], c – 50 [m/s]

Compared to the results for free jets the authors noticed a difference in the surroundings of the axis of the jet. The reason for this is the outflow from the pipe with a length of *30D*, which forms the characteristics of the flow in a straight channel and the turbulence profile with a value between *4* and *5%*. This high level of turbulence does not change the maximum values for the following radial profiles. These values are at similar level as in the free jets. This means no additional relevant phenomena occurring in the mixing zone of the jet lying in the jet flowing side. After changing the main flow direction and the flow distribution in the zone of the turbulence the levels are stable on the radius of a local maximum in the zone boundary wall of flow. It is a characteristic fact that starting from the distance *z/D=0* and ending at *z/D=9*, the maximum values were obtained for the velocity of *30m/s*. The dominance of this profile is not due to a significant changing of the nature of the turbulence in the jet, but only due to the fact that the maximum velocity for the highest values of fluctuations was recorded. Despite the apparent similarity of the radial distributions of the axial component of velocity fluctuations are different in the free and impinging jets. The maximum values in figures 3a and 3c gradually move away from the axis with an increasing distance of the outlet from the nozzle. In the case of the flow in the reverse chamber the maximum values of velocity do not displace and what is more, at distances *z/D=4* to *z/D=7* they get slightly closer to the axis. This is due to a limiting of the impact of the counter-jet mixing zone size on the jet flowing from the pipe.

Figure 4 shows the radial profiles of the radial component of velocity dimensionlessed by the maximum value of the velocity in the cross-section of the inner pipe outlet. Similar to the axial

components of velocity profiles we can see differences depending on the cross section flow.

The most significant effect occurs for the cross section *z/D=1*. Near the jet axis the analogous distribution of free jets is observed. The value of the radial component is zero in the potential core after the increase reaching positive values and then decreases reaching negative values in the mixing of the jet and the environment. Environment in the reverse chamber is stationary as in the free jet; hence the mixing zone occupies a smaller area. In the graphs at distance *z/D=7* we can see negative velocity values associated with the distribution of the radial component in the backward jet and not in the jet that flows from the inner pipe. This is clearly seen at all drawings at distance *r/D≈0.7* where we have a local maximum that results from the changes in the radial direction of the main jet. In the middle of the graph we may observe a spreading of the jet, depending on the measuring section. The biggest differences demonstrate the extreme sections of the *z/D=1* and *z/D =9*. The behavior of the jet is caused by the influence of the impinged wall. The jet is caused by the influence of the impinged wall.

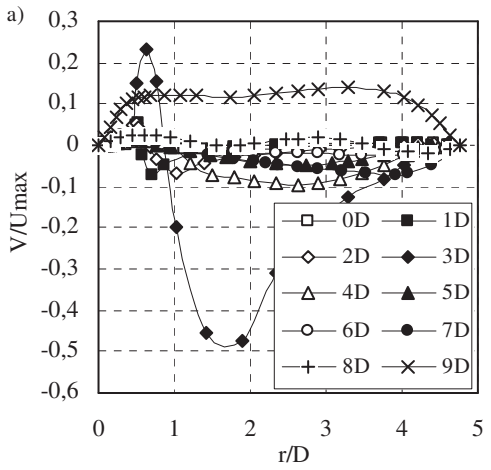

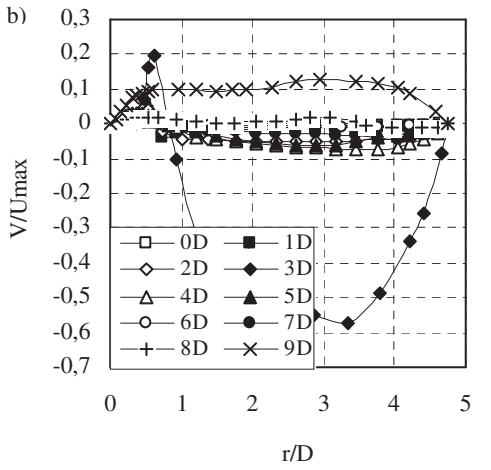

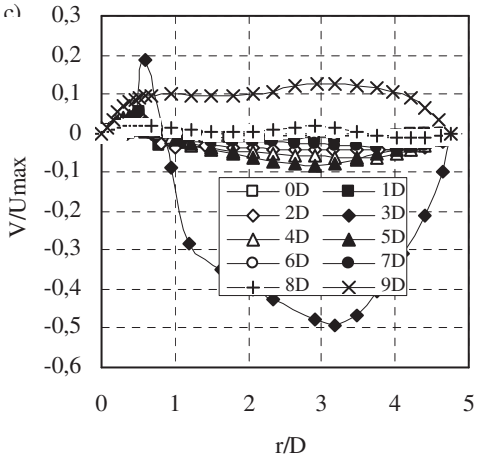

Figure 4. The distributions of the radial component of velocity at: a – 10[m/s], b – 30[m/s], c – 50 [m/s]

5. NUMERICAL RESULTS

The results of the numerical simulations are presented for *z/D=0, z/D=3, z/D=5, z/D=9* measurement cross-sections, so that the characteristic values for the velocity distributions can be read. The results of the numerical simulations are very close to the experimental results. Only in some cases are there clear discrepancies in the presented graphs. This proves the correctness of the performed experimental studies and numerical simulations.

Figures 5(a, b, c) show the normalized distributions of the axial component of velocity. Analyzing the distribution of the axial velocity component, the numerical trend is the same as for the experiment. For large distances *z/D=0, z/D=3, z/D=5* between the nozzle outlet and the head of the reverse chamber we can clearly see the existence of the core potential. In the mixing zone extreme values are obtained. First it is a minimum for *r/D=0.7* moving towards the trailing wall, depending on the measuring section. At small distances between the bottom of the reverse chamber and the outlet nozzle, the potential core fades, and the minimum value falls just before the impinged wall. Subsequently, it reaches the value of zero on the wall. On the impinged wall the conversion of the kinetic energy occurs. This phenomenon can be observed when recording the pressure on the wall.

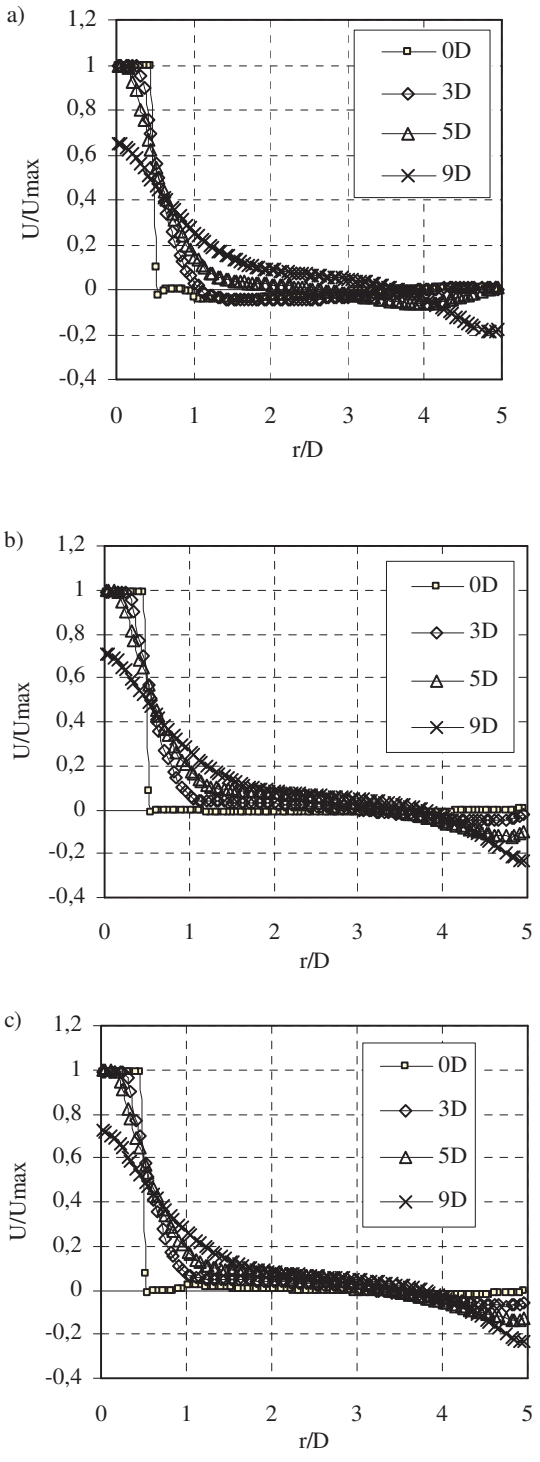

Figure 5. The axial distribution of velocity calculated numerically: a - 10[m/s], b - 30[m/s] c -50[m/s]

In figure 6 the normalized radial profiles of velocity are presented. In the case of the radial distribution we may observe similarities to the experimental data. The value of the radial component is zero in the potential core. Then the values increase towards positive, and then decrease reaching negative values in the mixing of the jet. Only in cross-section *z/D=9* we may observe positive values of the radial component of velocity, which means that the jet flows in this area along the impinged wall and it is a boundary flow. In contrast to the boundary jet, it quickly reaches the value of zero on the wall limiting radial diffusion.

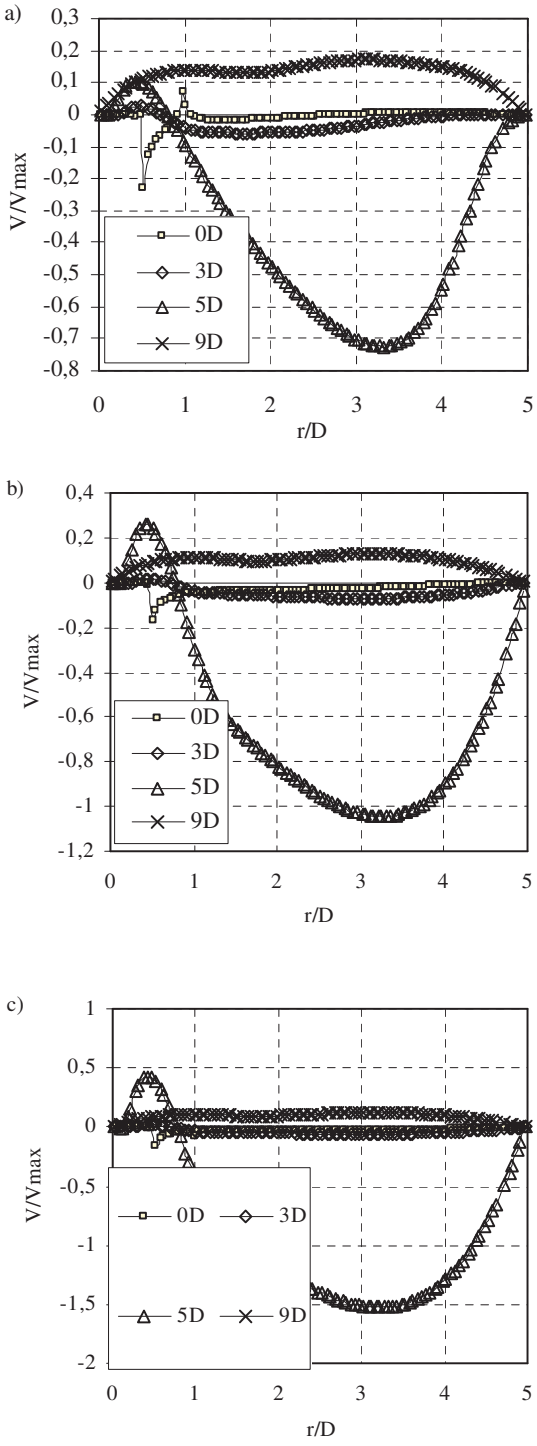

Figure 6. The radial distribution of velocity calculated numerically: a - 10[m/s], b - 30[m/s] c -50[m/s]

6. SUMMARY

The results of the numerical calculations present a very complicated structure of the flow inside the reverse chamber. Numerical and experimental studies have yielded important information about the nature of the flow inside the reverse chamber. Earlier experimental studies have greatly facilitated the possibility of simulating the flow inside the chamber, because the turbulent flow is extremely difficult to describe mathematically. The use of the numerical results could visualize complex structures occurring in the flow. Both, the experiment and the simulation have shown the impact of the distance from the outlet nozzle to the impinged wall on the formation of vortex structures. Changing the distance is affected by the phenomenon of mass and energy transport throughout the space of the reverse chamber. The velocity at the outlet of the nozzle changes the distribution of the avergae parameters as well. The presented comparisons show that the numerical results and experimental ones are convergent.

REFERENCES

[1] Crow S.C., Champagne F.M., Orderly structure in jet turbulence, Journal of Fluid Mechanics, 48, 547–591, 1970.

[2] Wygnanski I., Peterson R.A., Coherent motion in excited free shear flows, AIAA Journal, 25, 201–213, 1974.

[3] Gutmark E., Wygnanski I., The planar turbulent jet, Journal of Fluid Mechanics, 73, 465–495, 1976.

[4] Winant C.D., Browand F.K., Vortex pairing-the mechanism of turbulent mixing layer growth at moderate Reynolds number, Journal of Fluid Mechanics, 63, 237–255, 1974.

[5] Brown F.K., Roshko A., On the density effects and large structure in turbulent mixing layers, Journal of Fluid Mechanics, 64, 775–816, 1974.

[6] Popiel Cz.O., Buguslawski L., Mass or heat transfer in impinging single, round jets emitted by a bell-shaped nozzle and sharp-ended orifice, Proceeding of the 8th International Heat Transfer Conference, 3, 1187–1192, 1986.

[7] Cohen, J., Wygnanski, I., The evolution of instabilities in the axisymmetric jet. Part 1. The linear growth of disturbances near the nozzle. Journal of Fluid Mechanics 176, 191–219, 1987.

[8] Cho Y. et al. Theoretical and experimental investigation of wall confluent jets ventilation and comparison with wall displacement ventilation, Building and Environment, 43, 1091–1100, 2008.

[9] Koseoglu M.F., Baskaya S., Experimental and numerical investigation of natural convection effects on confined impinging jet heat transfer, International Journal of Heat and Mass Transfer, 52 1326–1336, 2009.

[10] Tamburello D.A., Amitay M., Active control of a free jet using a synthetic jet, International Journal of Heat and Fluid Flow, 29, 967–984,2008.

[11] Hourri A., AngersB., Be´nard P., Surface effects on flammable extent of hydrogen and methane jets, International Journal of Hydrogen Energy, 34, 1569-1577, 2009.

[12] Ounnar A. et al., Hydrodynamic behavior of upflowing jet in fluidized bed: Velocity profiles of sand particles, Chemical Engineering and Processing, 48, 617–622, 2009.

[13] Yeh Y.-L. et al., Vertical structure evolutions and spreading characteristics of a plane jet flow under anti-symmetric long-wave excitation, Experimental Thermal and Fluid Science, 33, 630–641, 2009.

[14] Deo R.C. et al. Comparison of turbulent jets issuing from rectangular nozzles with and without sidewalls, Experimental Thermal and Fluid Science, 32, 596–606, 2007.

[15] Launder, B. E., and Spalding, D.B., 1972, “Mathematical models of turbulence”, Academic Press.

[16] Launder, B. E., and Spalding, D.B., 1974, “The numerical computation of turbulent flows”, Comp. Meth. in Appl. Mech. & Eng., Vol. 3, pp. 269.

[17] Bartoszewicz J., Bogusławski L., The effectivity of two-equation turbulence model in an impinging jet in a short nozzle to surface distance, Journal of Theoretical and Applied Mechanics, 2009.

Conference on Modelling Fluid Flow (CMFF'12)
The 15th International Conference on Fluid Flow Technologies
Budapest, Hungary, September 4-7, 2012

Coupled CFD simulation of Heat Transfer in a Refinery Furnace

H. Zhao[1,2] , Abdallah S. Berrouk[2], Renbo Hu[1], Chao H. Yang[1]

[1] State Key Laboratory of Heavy Oil Processing, China University of Petroleum, Qingdao 266555, China
[2] Chemical Engineering Department, Petroleum Institute, Abu Dhabi 2533, United Arab Emirates

ABSTRACT

CFD simulations were performed to investigate heat transfer between flue gas and firebox tubes of a typical refinery furnace. Coupling fluids' motion on both sides of the tubes by using a 1D evaporation model, standard k-ε turbulent model, the non-premixed combustion model, and the discrete ordinate transfer radiation model proved successful in simulating such complex system. Detailed information about the flow field, temperature field, the furnace tube's circumferential, and axial distributions of the temperature and heat intensity are obtained and systematically analyzed. Results show that the high velocity of the bottom combustor's jet resulted in a large scale recirculation zone of flue gas. The latter plays an important role in uniformising the temperature of flue gas at the bottom of the furnace as well as the furnace tube's circumferential and axial distribution of the temperature and heat intensity. This leads to an increase of the lifecycle of the firebox tubes and a decrease in fuel consumption of the furnace. Accurate numerical results on temperature and heat flux of the tube skin are obtained and they compare very well with the measured and design data. The successful CFD model offer foundation to help design and improve atmospheric still.

Keywords: Furnace, Coupled simulation, Radiation

NOMENCLATURE

$C_{1\varepsilon}, C_{2\varepsilon}, C_{3\varepsilon}, \sigma_k, \sigma_\varepsilon$	[-]	k-ε model parameters ;
σ_t , C_g , C_d	[-]	model constant;
M	[-]	turbulent Mach number;
a	[*m/s*]	acoustic velocity;
I	[W/(m^2 ·s)]	radiation intensity,;
Pr_t	[-]	turbulent Prandtl number ;
g_i	[m/s^2]	gravity in the i direction ;
β	[-]	coefficient of thermal expansion;
$f^{'}$	[-]	mixing fraction;
$f^{'}$	[-]	mixing fraction variation, $f^{'} = f - \overline{f}$;
S_m	[-]	gas phase mass source term;
S_{user}	[-]	source term;
$\vec{r}$	[-]	coordinate vector;
$\vec{S}$	[-]	direction vector;
T	[*K*]	temperature;
α	[-]	absorb coefficient;
n	[-]	refraction coefficient ;
σ_s	[-]	scattering coefficient ;
$\Omega^{'}$	[-]	stereo-angle.

1. INTRODUCTION

Crude distillation is a basic petroleum refinery process to produce different types of engine fuel. Furnace is the main part of any crude distillation unit. The processed fluid flows through the tube suspended in the furnace chamber and is heated up and then evaporated by means of gas fired burners installed at the bottom of furnace. Heat requirement for this process is provided by several gas/oil fired burners installed at the bottom of the furnace. In

modern refineries, the energy consumption of a crude distillation unit (CDU) accounts for a large part of the refinery's total energy duty with the furnace contributing most to CDU energy consumption. Thus optimization of heat transfer within a CDU furnace can yield a substantial energy saving and thus efficient refinery operations. This can be achieved through an accurate simulation of the coupled heat transfer between the flue gas and the processed fluid on both sides of the furnace tube. Simulation results can then be used to help optimize the furnace design and operation.

In this work, an industrial-scale furnace firebox is modeled through coupling 1D evaporation model, standard k-ε turbulent model, the non-premixed combustion model, and the discrete ordinate transfer radiation model. The model is used to investigate flow and heat transfer in a furnace firebox. Influence of different turbulent models as well as radiation models on the simulation results have been thoroughly investigated in the literature [1-4]. The latter has guided the models' choice for the present investigation. Crude oil evaporation has also been taken into account for its significant influence on the temperature of tube surface and hence the radiative heat transfers within the furnace firebox.

2. FURNACE AND FEEDSTOCK CALCULATION

2.1 Flow model

The calculation of the three-dimensional turbulent flow field taking place in the furnace is greatly influenced by the used turbulent model[1]. In this work, the turbulent flow field is computed using RANS equations closed by the standard k-ε model[2]:

$$\frac{\partial}{\partial t}(\rho k)+\frac{\partial}{\partial x_i}(\rho u_i k) = \frac{\partial}{\partial x_j}\left[\left(\mu+\frac{\mu_t}{\sigma_k}\right)\frac{\partial k}{\partial x_j}\right]+G_k+G_b-\rho\varepsilon-Y_M+S_k \quad (1)$$

$$\frac{\partial}{\partial t}(\rho\varepsilon)+\frac{\partial}{\partial x_i}(\rho u_i \varepsilon) = \frac{\partial}{\partial x_j}\left[\left(\mu+\frac{\mu_t}{\sigma_\varepsilon}\right)\frac{\partial k}{\partial x_j}\right]+C_{1\varepsilon}\frac{\varepsilon}{k}\left(G_k+C_{3\varepsilon}G_b\right)-C_{2\varepsilon}\rho\frac{\varepsilon^2}{k}+S_\varepsilon \quad (2)$$

Where, G_b=0, Y_M=0, $C_{1\varepsilon}$=1.44, $C_{2\varepsilon}$=1.92, $C_{3\varepsilon}$=0.09, σ_k=1.0, σ_ε=1.3.

2.2 Combustion model

Under the assumption of equal diffusivities, the species concentration fields can be calculated by solving a single equation for the mixture fraction under an averaged form:

$$\frac{\partial}{\partial t}\left(\rho\overline{f}\right)+\nabla\cdot\left(\rho\overline{v}\,\overline{f}\right) = \nabla\cdot\left(\frac{\mu_t}{\sigma_t}\nabla\overline{f}\right)+S_m+S_{user} \quad (3)$$

$$\frac{\partial}{\partial t}\left(\rho\overline{f'^2}\right)+\nabla\cdot\left(\rho\overline{v}\,\overline{f'^2}\right) = \nabla\cdot\left(\frac{\mu_t}{\sigma_t}\nabla\overline{f'^2}\right)+C_g\mu_t\left(\nabla^2\overline{f}\right)-C_d\rho\frac{\varepsilon}{k}\overline{f'^2}+S_{user} \quad (4)$$

2.3 Radiation model

Due to the high temperature of the flue gas in the furnace chamber, radiation is the predominant mode of heat transfer in the furnace[3]. Thus, the selection of the radiation model plays an important role in obtaining accurate simulation results. Discrete ordinate method[4] is used to solve the radiation transfer equation:

$$\nabla\cdot\left(I\left(\vec{r},\vec{S}\right)\vec{S}\right)+\left(\alpha+\sigma_S\right)I\left(\vec{r},\vec{S}\right) = \alpha n^2\frac{\sigma T^4}{\pi}+\frac{\sigma_S}{4\pi}\int_0^{4\pi}I\left(\vec{r},\vec{S}\right)\phi\left(\vec{S},\vec{S}\right)d\Omega' \quad (5)$$

2.4 Coupled simulation

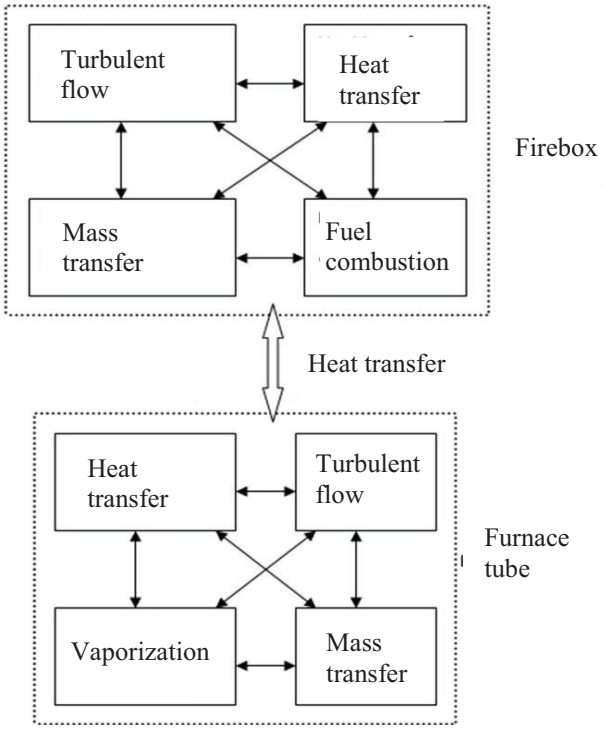

Figure 1. The complex physics taking place in the furnace

In the furnace chamber, the high-temperature flue gas that is generated from combustion of the fuel, will heat up and subsequently vaporize the processed fluid in the furnace tube through radiation and turbulent convection. The result is a complicated fluid system where fluid flow, mass transfer, and heat transfer are highly coupled. The different physics and their relationship are illustrated in Figure 1. Due to the complexity of the involved physics, simulation of a furnace is often highly complicated, in particular, the calculation of combustion and heat transfer mechanism across the furnace tube wall.

In this work, only the radiant section of the furnace is simulated. The mathematical model consists of a steady-state flow and heat transfer models to describe the behavior of flue gas and heat transfer to the outer tube surface and a 1-D steady-state model to describe vaporization of the processed fluid inside the tube. The computational domain is divided into two parts: an inner-tube domain occupied by the processed fluid and an outer-tube domain occupied by the flue gas. Continuity of temperature and heat flux at the tube surface has been ensured [5, 6]. Detailed thermal boundary conditions between the two domains are as follow:

(1) Heat flux calculated from the flue gas combustion and flow is used as an initial boundary condition for the 1-D simulation of the processed fluid inside the tube in order to get the temperature distribution on the tube surface.
(2) Simulations are performed by using the new tube surface temperature as a thermal boundary condition and hence heat flux is obtained.
(3) Steps 1 and 2 are repeated until the difference between heat fluxes obtained from the two steps is less than 5%.

3. SIMULATION SET-UP

3.1 Furnace geometry and operating conditions

A schematic representation of the simulated furnace is given in Fig. 2a. Assuming that the flow and heat transfer in the furnace are in general steady, and the furnace structure is a regular and symmetrical structure, only fourth (¼) of the firebox was simulated to reduce the computational expense to an affordable level. The dimension of the radiation section of this furnace firebox is 10.09m in length, 6.85m in width, and 20.35m in height. Eight flue gas burners are arranged in two lines at the bottom of radiation section. Four-way furnace tubes are arranged vertically on the furnace wall. Feedstock (processed fluid) is introduced into the furnace from the inlet arranged at the upper part of the furnace tube.

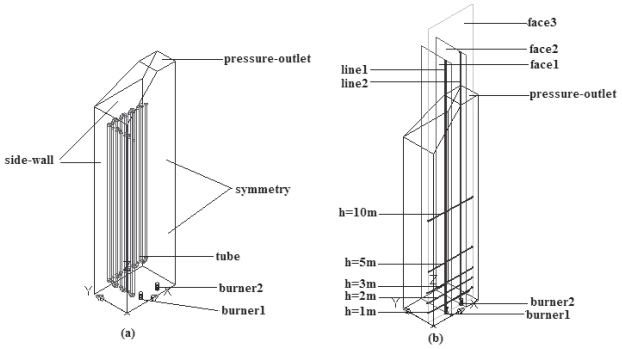

Figure 2. Geometry of the atmospheric still

Tetrahedral cells are used to discretize the physical region near burners and furnace tube surface. Hexahedral cells are used for the central region. Simulation of flue gas flow in furnace chamber (no coupling with the process fluid) is first performed to determine suitable grid number. Appropriate grid number is selected according to the comparison of simulation results from different grid configurations as explained in Section 4.1.

The composition of the fuel gas is listed in the first column of Tab. 1. The furnace operating conditions and other thermal boundary conditions are listed in the second column of Tab. 1.

Several reference lines and planes are defined at some appropriate locations in the furnace for the purpose of analysis as shown in Fig. 2b. Face 1 and face 2 are defined as faces perpendicular to the x-axis and through the center of the burner 1 and 2 respectively. Face 3 is defined as the face through two burner centers and perpendicular to the y-axis. Line 1 and Line 2 are defined as lines through the center of the burner 1 and 2 and perpendicular to the x-y plane.

Table 1. Fuel composition and Boundary conditions

Fuel gas composition	Volume fraction	Boundary conditions	Value
H_2	0.502	Mass flow rate of fuel gas	3671kg/h
CO_2	0.0141	Mass flow rate of air	42370kg/h
CO	0.00864	Inlet temperature of fuel gas	313K
CH_4	0.302	Inlet temperature of air	473K

C_2H_6	0.144	Outlet pressure	-50Pa (g)
C_2H_4	0.0143	Temperature of outlet	1000K
C_3H_8	0.00954	Temperature of the furnace wall	930-940K
C_3H_6	0.00542	Emissivity of the furnace wall	0.85
——	——	Temperature of tube skin	663-668K
——	——	Emissivity of tube skin	0.8

3.2 Boundary conditions

Basic simulation boundary conditions can be determined from furnace operation conditions as shown in Tab. 1. Fuel gas and air with specific mass flow rates and temperatures are introduced into the firebox through burners, which are modeled as a velocity inlet at the bottom of the furnace. The outlet boundary condition of the furnace is determined by the pressure outlet boundary, which is -50Pa in gage pressure. No-slip wall boundary conditions and standard wall functions are used for the furnace walls. The value of heat flux on the furnace walls is determined from the test run results of a similar industrial furnace. Zero fluxes of all quantities are assumed across all the symmetry boundaries.

4. RESULTS AND DISCUSSION

4.1 Grid dependency

Although tetrahedron grids are often recommended for furnace chamber simulation [7], different types of grids have been used to investigate their influence on the results of the numerical simulations. It is well known that temperature and velocity predicted profiles are very sensitive to the grid nature and distribution [8] in particular in the vicinity of burners. Furthermore, calculation of radiation heat transfer also needs sufficient grid resolution to achieve an acceptable accuracy. To ensure grid independent results, several different types of grids with different resolutions have been tested in this investigation as shown in Tab. 2.

Only small differences on the velocity profiles can be recognized for the across several different grid configurations as shown in Fig. 3. For the temperature profiles, very slight discrepancies are recorded between the different grids as shown in Fig. 4. Considering that the radiation heat transfer is predominant in the furnace chamber, temperature distribution is a more adequate grid-judging criterion than velocity distribution. In the light of these results, Grid1 was chosen to carry out the simulations.

Table 2. List of grid configurations

		Grid1	Grid2	Grid3	Grid4
burners	elements	Hex /wedge	Hex /wedge	Hex /wedge	Hex /wedge
	type	cooper	cooper	cooper	cooper
	interval size	0.02	0.02	0.01	0.01
Size function	type	fixed	fixed	fixed	fixed
	start size	0.02	0.02	0.01	0.01
	growth rate	1.1	1.1	1.1	1.1
	Max.size	0.5	0.3	0.5	0.3
Furnace chamber	elements	Tetra /hybrid	Tetra /hybrid	Tetra /hybrid	Tetra /hybrid
	type	tgrid	tgrid	tgrid	tgrid
	interval size	0.5	0.3	0.5	0.3
Grid number		257123	269607	415060	480076

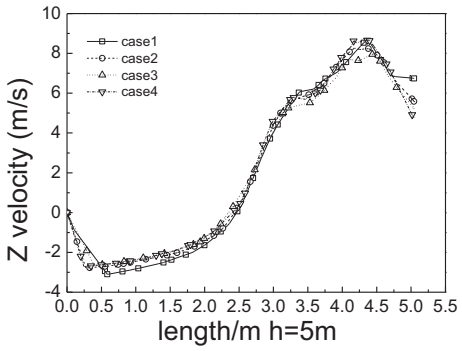

Fig.3. Z component of flue gas velocity distribution along the firebox length at 5m height

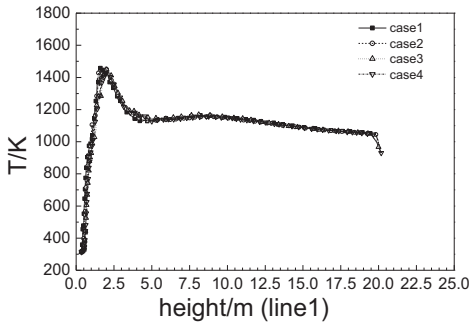

Fig.4. Flue gas temperature profile along the firebox length

4.2 Temperature profile in the furnace

Temperature profile in the firebox is one of the most important indicators used to evaluate the furnace performance. Often, the configurations and operation schemes of the burners arranged at the bottom of the furnace have a predominant influence on temperature profiles in the furnace. A combustion region can be easily recognized at the outlet of the burner nozzle. Intense combustion reaction of fuel gas occurred in this region and the typical temperature can be in the range of 1500k-1700K. As the flue gas raises through the furnace, its temperature decreases. Typically, the flue gas temperature decreases to about 1000K in the upper part of the furnace firebox. Figure 5 shows a snapshot of temperature distribution and flame shape in the vertical section plane. Figures 6a and 6b depict the same but in horizontal section planes at two different heights ((a) h=1.5m and (b) h=2.5m). Based on Fig. 5a, it is clear that the flame height of burner 1 is restrained compared to the one of burner 2. This is caused by the different environments surrounding burners 1 and 2. High velocity at the bottom combustor's jet yielded a large scale recirculation zone of flue gas as shown in Fig. 5b. A declining flame toward the central part of the furnace forms a semicircle-plate-shaped temperature profile in the x-y cross-section as shown in Fig. 6a (h = 1.5m) and 6b (h = 2.5m)

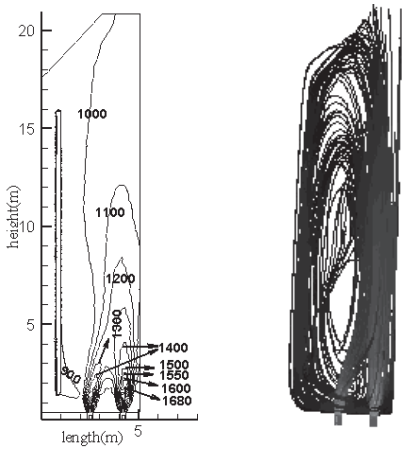

(a) (b)

Figure 5 Temperature distributions and flow pathline on face1

The temperature in the upper-middle part of the radiation section is 938K, according to the test run result of the real industrial furnace. The numerical results indicate an average temperature of about 950K in the region higher than 8m which is in good agreement with the test run results.

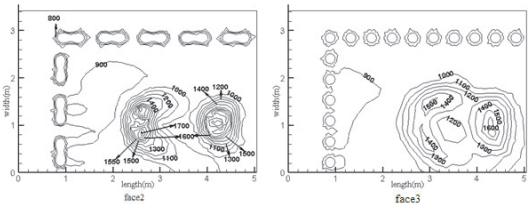

(a) (b)

Figure 6 Temperature distributions on face2 and face3

4.3 Temperature and heat flux distributions on tube surface

Temperature distribution along the length of the furnace tube is shown in Fig. 7. Temperature of the tube surface becomes higher with the increasing of the tube length. Surface temperature of 3rd to 6th tubes (36m to 56m in Fig. 7) are among the highest because these tubes are the nearest to the burners. For the same reason, significant high temperatures are recorded on the surface of 14th to 16th tube (182m to 224m in Fig. 7).

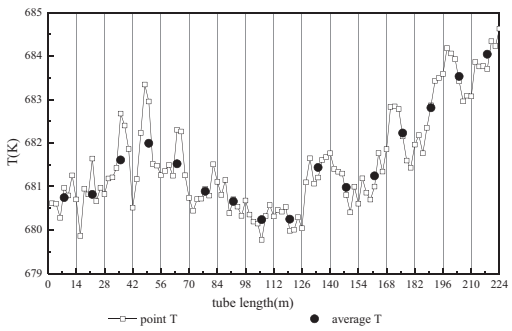

Figure 7 Profile of tube skin temperature along tube length

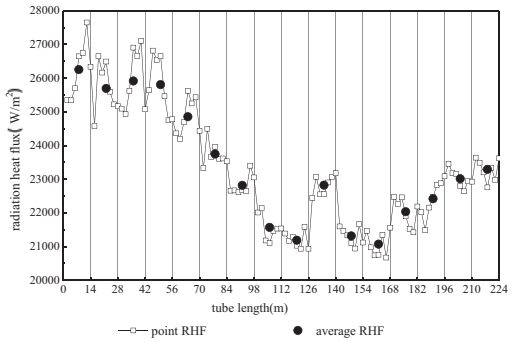

Figure 8 Profile of tube skin heat flux along tube length

Heat flux intensity of the furnace tube is another important parameter to monitor to ensure better furnace design and operation. Non-uniform distribution of heat flux over the tube surface caused by non-uniform distribution of temperature and flow field in a furnace chamber brings lots of difficulty to furnace optimization as it was explained earlier. Typical heat flux intensity along tube surface is shown in Fig. 8. Because the burners are present only at the bottom of the furnace chamber, heat flux intensity on the lower and middle parts of the tube is higher than the one on the upper part of the tube. The reason behind low heat flux in the region (98m to 126m) in Fig. 8 is the rectangle shape of the furnace chamber that causes the 8th and 9th tubes (in the corner of the firebox) to be far from the burner. Furthermore, heat flux intensity is influenced by the temperature difference between flue gas and the processed fluid. The heat flux intensity across the tube surface decreased with the increase of the processed fluid temperature.

Typical value of the averaged tube surface heat flux intensity for this real industrial furnace is 23450W/m^2 which is provided by the test run results. It is in a very good agreement with the numerical prediction of 23364W/m^2.

5. CONCLUSION

An industrial furnace is simulated using a CFD model where of a steady-state flow and heat transfer are coupled to give a detailed description of flow field and heat transfer. Good agreement is obtained between test run results and numerical predictions. A large scale recirculation zone of flue gas is identified in the furnace chamber due to the high velocity of the bottom combustors' jet flow. Obvious non-uniform distribution of temperature and heat flux existing over the surface of furnace tube is detected which can have an adverse impact on furnace operations. Because of its accuracy, the developed CFD model can be used in the future to optimize the design and operation of refinery furnaces.

6. ACKNOWLEDGEMENT

Financial support for this project provided by National Basic Research Program of China (2012CB215006), TAKREER (Abu Dhabi Oil Refining Company) operating company of the Abu Dhabi National Oil Company (ADNOC) and the Fundamental Research Funds for the Central Universities of China is gratefully acknowledged.

REFERENCES

[1]Karim, V., M., Bart, M., 2006, Application of two buoyancy-modified k-ε turbulence models to different types of buoyant plumes, Fire Safety Journal, vol. 41, pp.122-138.

[2]Launder, B.E., Spalding, D.B., 1972, Lectures in Mathematical Models of Turbulence, Academic Press, London.

[3]Carvalho, M.G., Farias, T.L., 1998, Modeling of Heat Transfer in Radiating and Combusting Systems. Institution of Chemical Engineers. Trans IchemE, 76(A):175-183.

[4]Habibi, A., Merci, B., Heynderickx, G.J., 2007 Impact of radiation model in CFD simulation of steam cracking furnaces. Computer and Chemical Engineering. Vol. 31, pp.1389-1406.

[5]Zhou, G.J., Mao, Y., Wang, J., 2007, Numerical simulation of flow combustion and heat transfer in delayed coker furnace. Acta Petrolei Sinica(Petroleum Processing). Vol. 23(1), pp.77-81.

[6]Han, Y.L., 2007, Numerical simulation and optimization of a cracking furnace. Nanjing: Southeast University of China.

[7]Oprins, A.J.M., Heynderickx, G.J., 2003, Calculation of three-dimensional flow and pressure fields in cracking furnace , Chemical Engineering Science. Vol. 58, pp.4883-4893

[8]Xin , Y., 2004, Assessment of Fire Dynamics Simulation for Engineering Applications : Grid and Domain Size Effects, In Proceedings of the Fire Suppression and Detection Research Application Symposium , Orlando , Florida. National Fire Protection Association, Quincy , Massachsetts.

Conference on Modelling Fluid Flow (CMFF'12)
The 15th International Conference on Fluid Flow Technologies
Budapest, Hungary, September 4-7, 2012

A NOVEL COMPUTATIONAL PROCESS FOR NUMERICAL SIMULATION AND OPTIMIZATION OF AIR DRYER CARTRIDGES

Árpád VERESS[1], Huba NÉMETH[2], László PALKOVICS[3]

[1] Corresponding Author. Department of Aircraft and Ships, Budapest University of Technology and Economics, H-1111 Budapest, Sztoczek u. 6. J. ép. 426, Hungary. Tel.: (+36 1) 463-1992, E-mail: averess@rht.bme.hu
[2] Department of Automobiles, Budapest University of Technology and Economics, H-1111 Budapest, Sztoczek u. 6. J. ép. 515, Hungary. Tel.: (+36 1) 463-1205, E-mail: nemeth.huba@auto.bme.hu
[3] Department of Automobiles, Budapest University of Technology and Economics, H-1111 Budapest, Sztoczek u. 6. J. ép. 504, Hungary. Tel.: (+36 1) 463-3914, E-mail: palko@auto.bme.hu

ABSTRACT

The main goal of the present investigation is to develop a computational tool for design and optimize air dryer cartridges.

A 3D computational procedure has been established, implemented and applied for modelling transient adsorption process and related fluid dynamics phenomena to provide central core for the optimization method.

The numerical model is based on the mass, momentum and energy conservation laws. Darcy's law has been implemented into the overall mass balance for describing flow physics in a porous media. Linear driving force model is used for computing mass fraction of the absorbed amount of water. The equilibrium loading of the desiccant is described by adsorption isotherms in the function of temperature and the partial vapour pressure. The non-linear system of the differential equations is coupled with ideal gas law to recover density distribution over the computational domain. The mathematical model is validated by experimental results.

Concerning the optimization, drying performance, pressure loss and filter efficiency are considered in the cost function to be minimized. The non-dimensional components of the objective function are weighted by the order of functionality relevancies. Nelder-Mead simplex method is used in the optimization algorithm. A new cartridge geometry has been proposed as an outcome of the optimization, which fulfils design conditions.

Keywords: adsorption, air dryer cartridge, CFD, filter efficiency, optimization, pressure drop

NOMENCLATURE

Variables (Latin)

Cc	[-]	Cunningham correction factor
c	$[mol/m^3]$	adsorbate concentration
c_{p_air}	$[J/kg/K]$	heat capacity of the air
c_{p_water}	$[J/kg/K]$	heat capacity of the adsorbed water
c_v	$[mol/m^3]$	the water concentration
$c_{Zeolite}$	$[J/kg/K]$	heat capacity of the zeolite
D, $\boldsymbol{D_1}$	$[m^2/s]$	diffusion coefficient, diameter
D_{eff}	$[m^2/s]$	the effective diffusivity
d	$[m]$	diameter
d_m	$[m]$	collision diameter of air molecules
$\boldsymbol{H_1}$	$[m]$	height
H^{st}_{H2O}	$[J/kg]$	isosteric heat of the water
K^{LDF}	$[1/s]$	mass-transfer coefficient
Kn	[-]	Knudsen number
K_u	[-]	Kuwabara hydrodynamic factor
k	$[J/K]$	Boltzmann constant
L	$[m]$	length of the filter
M_{H2O}	$[kg/mol]$	molecular mass of water
N_a	$[1/mol]$	Avogadro's number
P_e	[-]	Peclet number
R_M	$[J/mol/K]$	universal gas constant
R_p	$[m]$	the pellet radius
Stk	[-]	Stokes number
T	$[K]$	temperature
T_w	$[K]$	wall temperature
U_0	$[m/s]$	flow velocity
$\overline{V}$	$[m/s]$	superficial velocity vector
V	$[m^3]$	volume
X	$[kg/kg]$	loading
p	$[Pa]$	static pressure
Δp_c	$[Pa]$	pressure drop
Δp^*_c	$[Pa]$	pressure drop at orig. geom.
q_v	$[mol/kg]$	adsorbent amount of water
q_v^*	$[mol/kg]$	saturation limit of the water
t	$[s]$	time
t_B	$[s]$	the breakthrough time
t^*_B	$[s]$	breakthrough time at orig. geom.
y_v	$[mol/mol]$	molar fraction of water in air

Variables (Greek)

α	[-]	solidity
β	[$1/m^2$]	inverse factor of the permeability
ε	[-]	gas void fraction
ε_p	[-]	the particle void fraction
η	[-]	efficiency
η_f	[-]	filter efficiency
η_{f_*}	[-]	filter efficiency at orig. geom.
Θ	[$mol/kg/K^{3/4}/s$]	kinetic coefficient constant
κ	[m^2]	permeability coefficient
λ	[m]	mean free path of the molecules
λ_{eff}	[$W/m/K$]	effective thermal conductivity
μ	[Pas]	dynamic viscosity
ρ	[kg/m^3]	density
τ	[s]	relaxation time

Subscripts and Superscripts

D	diffusion
I	impaction
R	interception
f	fiber
in	incoming flow
out	outcoming flow
p	particle

1. INTRODUCTION

Air filter cartridge has been found in the air treatment of the pneumatic system of the commercial vehicles to clean and dry supplied air – delivered by the compressor – before entering into the further part of the system to prevent freeze-up and to protect the system from internal corrosion and blockage (see Figure 1.).

Until now, the most commonly used filter cartridge is the conventional type one focusing mostly on air drying with the main goal of keeping a predefined dew point margin in the reservoir.

Fulfilling the expectations arisen from low emission condition – especially for oil carryover, as a general requirement in automotive industry – and prevent air dryer material from pollutants, a new design strategy has been introduced. The oil separator cartridge has been developed to remove oil vapour, droplets, emulsion, soot and any other pollutants from the compressed air before it reaches the drying medium.

The container of the cartridge can be charged with adsorbent pellets as zeolite, activated alumina or silica gel desiccants. One of the most widespread amongst them is the zeolite due to the ability of adjusting the micro pores precisely in the pellets, which allows for molecules smaller than its pore diameter to be adsorbed whilst excluding larger molecules.

Several physical disciplines can be distinguished in the drying process of the desiccant bed. The air is unsteady, viscous and compressible, it contains water vapour while flowing through the porous medium, in which the adsorption is realised. The molecules of the absorbent and adsorbate become so close to each other that the cohesive attraction increases significantly and the pellet surface captures water molecules forming a thin liquid layer. Usually, the collision of the water molecules with the pellet surface is rigid and so the translation kinetic energy of the water is turned to heat. Hence, the heat transfer plays also an important role in the entire saturation process.

The overall performance of an adsorption process depends on both equilibrium and kinetic factors, but the relative importance of these contributions varies greatly for different systems.

Beside the filtering and the adsorption characteristics of the cartridge, the pressure drop over the assembly should be also considered in design and optimization processes of the cartridge to improve efficiency and fuel consumption.

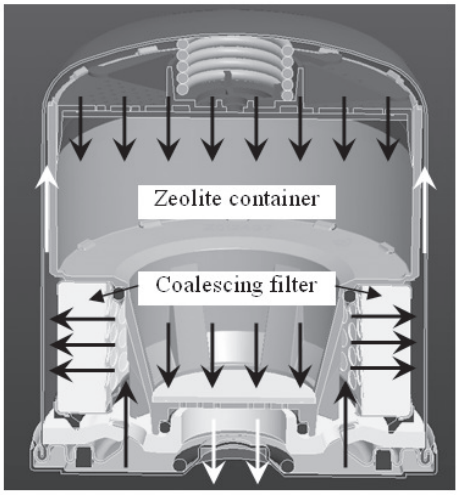

Figure 1. Cross sectional view of the air dryer cartridge with flow directions

2. MATHEMATICAL AND NUMERICAL MODEL

2.1. Governing Equations

One of the key point in case of air dryer cartridge is the drying performance via adsorption process. The mass transfer resistance between the fluid and porous adsorbent is essential to consider.

The adsorption kinetics is controlled mainly by intraparticle diffusion in the most adsorption mechanism, but the use of a diffusion equation to model the kinetics introduces an additional differential equation.

The linear driving force model has been used in adsorption modelling, by which the equilibrium and diffusion-controlled kinetics are satisfactorily represented. This approach is an accurate, simple and computationally cheap algorithm. The linear driving force model equation is shown in Eq. (1) [1].

$$\frac{\partial q_v}{\partial t} = K^{LDF}\left(q_v^* - q_v\right) \tag{1}$$

q_v describes the adsorbent amount of water, *t* is the time, K^{LDF} is the mass-transfer coefficient and q_v^* is the equilibrium loading from the adsorption isotherm and depends on the temperature and partial pressure of the water phase.

The individual mass transfer resistances for a spherical adsorbent are related to the mass transfer coefficient. An analytical expression, Eq. (2) has been used to count its dependency on water concentration, temperature and pressure [1].

$$\frac{1}{K^{LDF}} = \frac{R_p^2}{15\varepsilon_p D_{eff}} \rho_{bed} \frac{q_v^*}{c_v} \tag{2}$$

In Eq. (2), R_p is the pellet radius, ε_p is the particle void fraction, D_{eff} is the effective diffusivity, ρ_{bed} is the bed density, q_v^* is the equilibrium loading and c_v is the water concentration in the flow. Having the reference effective diffusivity and combining the invariant terms (pellet radius, bed density and bed void fraction) to one kinetic coefficient Θ finally, the mass transfer coefficient is given by Eq. (3) [1],

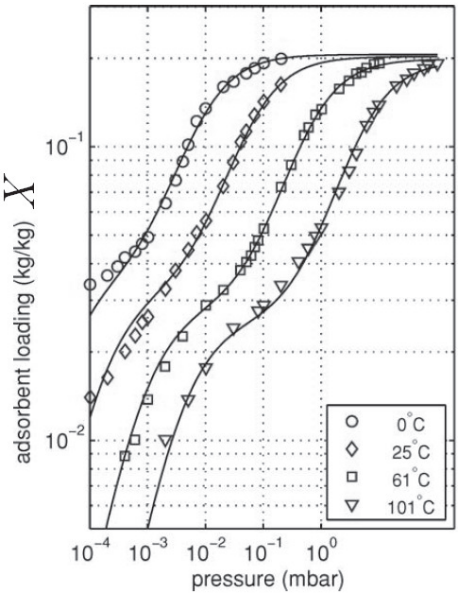

Figure 2. Equilibrium loading - adsorption isotherms as function of temperature and partial pressure of water [1]

$$K^{LDF}(y_v, p, T) = \Theta \frac{y_v T^{0.75}}{q_v^*(y_v, p, T)} \tag{3}$$

where $\Theta = 0.0345$ $\left[mol/kg/K^{3/4}/s\right]$ is the kinetic coefficient constant, y_v is the molar fraction of water in air, T is the temperature and p is the pressure. The equilibrium loading, $q_v^*(y_v, p, T)$ comes from the adsorption isotherms, which are found in Figure 2, together with Eq. (4) [1], where M_{H_2O} is the molar mass of water.

$$q_v^* = \frac{X}{M_{H_2O}} \tag{4}$$

Darcy's law has been used to describe the relation between the pressure and velocity field in porous media in Eq. (5), where κ is the permeability coefficient, μ is the dynamic viscosity and *p* is the pressure [2].

$$\bar{V} = -\frac{\kappa}{\mu}\nabla p \tag{5}$$

The overall mass balance for the gas phase is given by Eq. (6) and the mass balance for the water phase is described by Eq. (7), in which ε denotes the gas void fraction, ρ is the density of gas mixture, $\bar{V}$ is the bulk or superficial velocity vector, M_{H2O} is the molar mass of the water and ρ_{bed} is the adsorbent bed density [2]. q_v comes

$$\varepsilon\frac{\partial \rho}{\partial t} + \nabla\left(\bar{V}\rho\right) = -M_{H2O}\rho_{bed}\frac{\partial q_v}{\partial t} \tag{6}$$

from Eq. (1) and describes the amount of adsorbent water. c_v is the water concentration [2].

$$\varepsilon\frac{\partial c_v}{\partial t} + \nabla\left(c_v\bar{V}\right) = -\rho_{bed}\frac{\partial q_v}{\partial t} \tag{7}$$

The investigated adsorption is an exotherm process and the temperature has a strong effect not only for the equilibrium but the kinetics, hence the energy equation, Eq. (8) is used for determining temperature field in each time step [2].

$$\begin{aligned}&\left(\rho_{bed}c_{Zeolite} + \varepsilon\rho c_{p\_air} + \rho_{bed}c_{p\_water}q_v\right)\\ &\frac{\partial T}{\partial t} + \nabla\left(-\lambda_{eff}\nabla T + \rho c_{pAIR}\bar{V}T\right) =\\ &= H_{H2O}^{st}\rho_{bed}M_{H2O}\frac{\partial q_v}{\partial t} + \frac{4\alpha}{D}\left(T_w - T\right)\end{aligned} \tag{8}$$

The main outcome of solving the discretized forms of the above mentioned governing equations is the transient process of the saturation of the desiccant bed and the breakthrough.

In the aspect of the optimization, the key point is the breakthrough time of the cartridge, which

should be as high as possible in order to maximise drying performance beside minimising pressure drop, within the given bounding dimensions.

2.2. Filtering Efficiency

Due to the oil lubricant compressors, the supplied air can contain oil fractions, droplets, soot and emulsion, which are originated from the high speed dynamics, friction, high temperature, spraying and evaporation. These particles can dramatically reduce the absorbing capacity of the occlusive materials. Hence, a coalescing filter is placed upstream to the cartridge (see Figure 1.) and the filter efficiency is considered also in the objective function of the optimization.

Based on the single fiber theory, the filter efficiency of a mono-component filter can be calculated by Eq. (9) [3], in which c is the

$$\eta_f = \frac{c_{in} - c_{out}}{c_{in}} = 1 - e^{-\frac{4\alpha\eta_f L}{\pi d_f (1-\alpha)}}, \quad (9)$$

concentration of the particle (*in*: at incoming flow, *out*: at outcoming flow), α is the solidity and it is found in Eq. (10), L is the length of the filter, η_f is

$$\alpha = \frac{V_{solid}}{V_{solid} + V_{void}}, \quad (10)$$

the fiber efficiency and d_f is the fiber diameter. The fiber efficiency can be expressed in the function of different collection mechanism as interception [3], impaction [4] and diffusion [4] as it is shown in Eq. (11), meanwhile the effect of gravitational sedimentation and the electrical attraction are not considered.

$$\eta_f = 1 - (1-\eta_R)(1-\eta_I)(1-\eta_D) \quad (11)$$

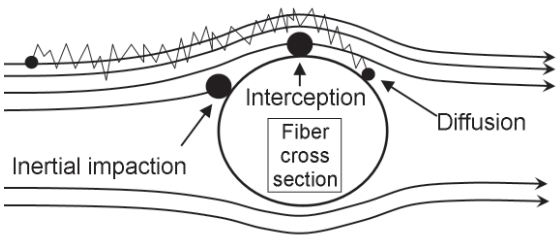

Figure 3. Illustration of considered particle collection mechanism on filter

The visual representation of the different capturing mechanism is found in Figure 3.
In case of interception, the particles follow the streamline on the radius of the fiber and adhere to it. It can be formulated by Eq. (12) [5], where the Kuwabara hydrodynamic factor is given by Eq. (13). d_p is the particle diameter in Eq. (14). η_R increases with increasing R and does not depend on flow velocity U_0.

$$\eta_R = \frac{1+R}{2K_u}\left(2\ln(1+R) - 1 + \alpha + \right. \\ \left. + \left(\frac{1}{1+R}\right)^2\left(1-\frac{\alpha}{2}\right) - \frac{\alpha}{2}(1+R)^2\right), \quad (12)$$

$$K_u = -(1/2)\ln\alpha - 3/4 + \alpha - \alpha^2/4 \quad (13)$$

$$R = \frac{d_p}{d_f} \quad (14)$$

Impaction represents that the larger particles are not able to avoid fibers due to their inertia and they are forced to embed them [6]. The impaction

$$\eta_I = \frac{Stk\ J(\alpha, R)}{2K_u^2(\alpha)}, \quad (15)$$

efficiency is shown in Eq. (15), in which the Stokes number:

$$Stk \equiv \frac{\tau U_0}{d_f} = \frac{\rho_p\, d_p^2\, Cc\, U_0}{18\mu_{air}\, d_f} \quad (16)$$

and if R<0.4:

$$J = \left(29.6 - 28\alpha^{0.62}\right)R^2 - 27.5R^{2.8} \quad (17)$$

else J=2. In the Cunningham correction factor, Eq.

$$Cc = 1 + Kn_p\left(1.257 + 0.4e^{-1.1/Kn_p}\right) \quad (18)$$

(18), Kn_p is the particle Knudsen number:

$$Kn_p = \frac{2\lambda}{d_p}, \quad (19)$$

λ is the mean free path of the molecules:

$$\lambda = \frac{R_M T}{2^{0.5} N_a \pi d_m^2 p} \quad (20)$$

and d_m is the collision diameter of air molecules:

$$d_m = 3.66E\text{-}10 \quad (21)$$

μ_{air} is the dynamic viscosity of air in Eq. (16). R_M, N_a, T and p are the universal gas constant, Avogadro's number, temperature and pressure respectively in Eq. (20). The contribution of the diffusion in the filter efficiency is more dominant for small particles. In this case the collision with the gas molecules has higher influence, they can retard

and delay the particle similar to the Brownian motion resulting higher probability that a particle will be stopped by interception or impaction. The effect of diffusion on filter efficiency can be expressed by Eq. (22) [7],

$$\eta_D = 2.6\left((1-\alpha)K_u\right)^{1/3} Pe^{-2/3} \quad (22)$$

where the Peclet number:

$$P_e = \frac{d_f U_0}{D} \quad (23)$$

and the diffusion coefficient:

$$D = \frac{kCcT}{3\pi\mu_{air} d_p} \quad (24)$$

The filter efficiency is shown in Figure 4. as function of the normalized particle diameter and the filter thickness, which is the highest contribution to the particle collection. The shape of the filter geometry is annular (see Figure 1.).

The filter efficiency is considered also in the optimization process and should be maximised.

Keeping the overall geometry of the cartridge unchanged, the compromise, governed by filter thickness, must be made between the filter efficiency and the earlier breakthrough due to the less zeolite. Furthermore, higher filter thickness and the reduced cartridge diameter can cause higher pressure drop.

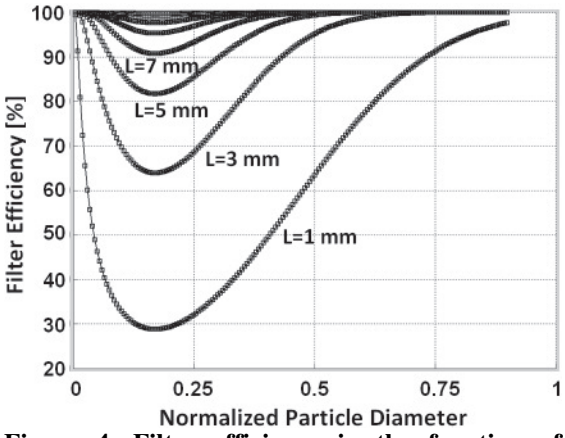

Figure 4. Filter efficiency in the function of normalized particle diameter and filter thickness L

2.3. Pressure Drop

The pressure drop has a considerable effect on compressor performance and so the fuel consumption, hence it is considered also in the objective function of the optimization.

The pressure field is available over the desiccant bed by using governing equations described in subchapter 2.1 and the pressure drop is identified. In case of the oil separator filter, the Forchheimer equation is used to determine pressure drop and to consider the nonlinearities caused by the relatively high flow velocity. The expression is shown in Eq. (25) [8], where μ is the dynamic viscosity of the air by Sutherland's law [9].

$$-\frac{\partial p}{\partial x} = \frac{\mu}{\kappa} V + \beta \rho V^2 \quad (25)$$

$$\mu_{air} = 1.82E-5\left(\frac{293.15+117}{T+117}\right)\left(\frac{T}{293.15}\right)^{3/2} \quad (26)$$

where T is the temperature and ρ is the density of the operational fluid. The β factor and the inverse of the permeability ($1/\kappa$) is derived by using the results of the measurements and computed by conventional way.

2.4. Numerical Set up

Finite element framework of the Comsol commercial software has been used for implementing, discretizing and solving the governing equations for adsorption and related fluid dynamics phenomena.

UMFPACK iterative direct solver is set up to evaluate the unknown parameters of the algebraic equations. Although the direct solvers with many degree of freedom need higher memory, they are more stable and have favourable convergence characteristics compared with iterative solvers.

Boundary and initial conditions play a significant role in the stability and convergence of the solution to have well posed problem. Velocity boundary condition at the inlet and pressure at the outlet has been imposed in case of overall mass balance with Darcy's law. Neumann boundary condition is implemented at the linear driving force model and the outlet of the water concentration and energy balance. Dirichlet type condition is imposed at the inlet for water concentration balance and energy equation. Static fluid dynamics calculation has been performed without adsorption to have initial condition for modelling entire saturation process.

3. VALIDATION

The breakthrough curve is a basic characteristic of an air dryer system and represents the water content of the air at the outlet of the cartridge in the function of time. Other quantitative results, such as velocity, concentration, temperature or adsorbent loading distribution provide deeper insight into the reason of the earlier or later breakthrough.

The measurement, which are used for validation, are come from the scientific literature in order to focus strictly on the adsorption process and to avoid the effects of any other fraction as oil particles, droplets, soot and emulsion, which are generally found in the vehicle industry based applications.

Four different test cases are considered to have wider operational range for the validation and to see the effect of boundary conditions on the breakthrough. The geometry of the desiccant container is a simple tube, which has a dimension of 0.797 m length and 0.01 m and it is filled with zeolite pellets.

Table 1. Boundary conditions for A, B, C and D validational test cases [1]

Experimental range	A	B	C	D
Molar fraction of water $y_{i,f}$ [ppm]	4594	4410	4603	4531
Volumetric feed rate [Nl/min]	1.84	1.998	2.00	1.98
Pressure p [bar]	5.0	2.0	2.0	2.0
Wall temperature T_W [C]	30	30	50	80

Due to the simple geometry, 1D version of the method is used. The boundary conditions for the test cases are found in Table 1. The validation of the computational procedure has been completed and the results are shown in Figure 5. The deviation between the measured and calculated results is less than 5 % at different test conditions, hence, the model can be used in further applications.

However, it must be considered that the ambient and entire conditions in the field tests and the real applications are different from the laboratory environment, so these effects must be considered in

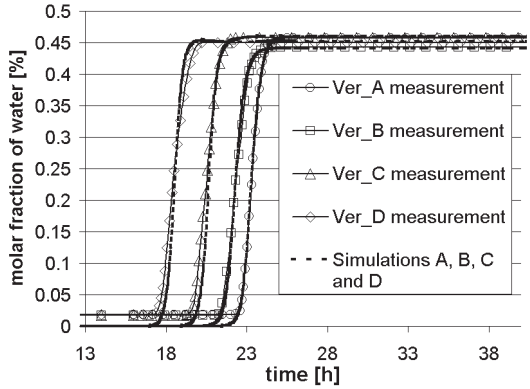

Figure 5. Breakthrough curves at different test cases; Version A, B, C and D. Continuous lines with symbols: measurements from [1], dashed line: corresponding results of the simulations

cartridge operation as a next step of the present work.

4. CARTRIDGE OPTIMIZATION

Normalized breakthrough time, filter efficiency and pressure drop are considered in the objective function to be minimized. The reference parameters are based on the initial geometry (see parameters in Eq. (27) denoted by * in superscript). The weight functions of the tree components are determined by the order of functional relevancies. It means that these parameters can be tuned by the developer based on the expected distribution and economical, physical and spatial constraints. The design variables of the optimization are the diameter D_1 of

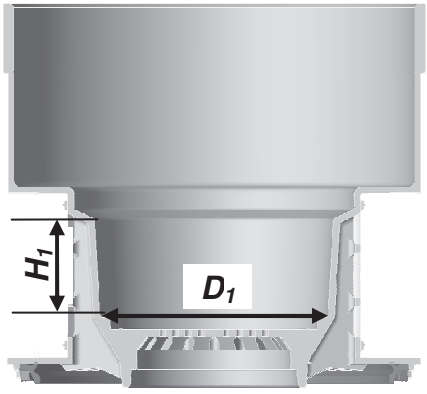

Figure 6. Geometry of the desiccant container with the design variables of the optimization

the lower part of the cartridge and the height of the downstream part of the container H_1 (see Figure 6). All other dimensions are expressed as a linear function of these two parameters and the overall geometry is constrained by the unchanged bounding size of the cartridge. The objective function of the optimization is given by Eq. (27).

$$C(D_1, H_1) = -0.25\left(\frac{t_B}{t_B^*}\right) - 0.25\left(\frac{\eta_f}{\eta_f^*}\right) + 0.5\left(\frac{\Delta p_c}{\Delta p_c^*}\right) \qquad (27)$$

t_B is the breakthrough time, η_f is the filter efficiency and Δp_c is the overall pressure drop of the cartridge. The sum of the weight functions is unit for simplicity. The breakthrough time and the pressure drop in container are calculated by Comsol in distributed parameter type manner and it is coupled with Matlab, in which filter efficiency and pressure drop of the coalescing filter – related with the actual geometry of the optimization – are determined.

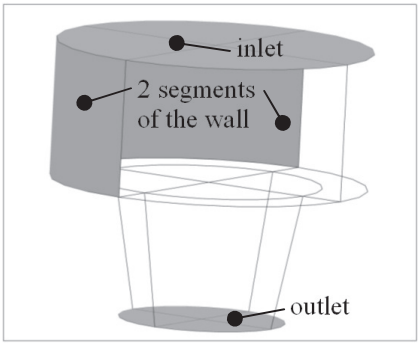

Figure 7. Location of the boundary conditions at the conical bed [10]

Fminsearch function of Matlab has been used for the optimization, in which Nelder-Mead simplex algorithm is implemented. This is a direct search method that does not use numerical or analytic gradients. If n is the length of x, a simplex in n-dimensional space is characterized by the $n+1$ distinct vectors that are its vertices. In two-space, a simplex is a triangle; in three-space, it is a pyramid. At each step of the search, a new point in or near the current simplex is generated. The function value

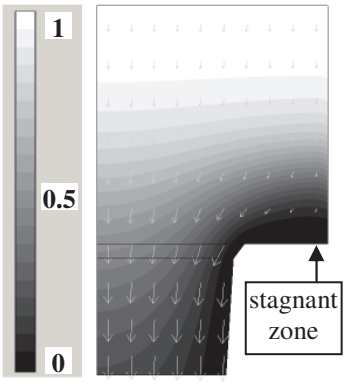

Figure 8. Velocity vectors and normalized water content (loading) along the centre plane of the conical bed at 1500 seconds

at the new point is compared with the function's values at the vertices of the simplex and, usually, one of the vertices is replaced by the new point, giving a new simplex. This step is repeated until the diameter of the simplex is less than the specified tolerance [11].

The boundary conditions of the optimization are based on the nominal operation, at which the upstream flow conditions are next. The relative humidity of the ambient air is 50% at 101325 *Pa* and 296.15 *K*. It is compressed till 12 *bar* in the reservoir (downstream of the cartridge) and has a temperature of 323.15 *K* before entering into the cartridge. The locations of the boundary conditions on the container are found in Figure 7. The streamlines with the magnitude of the velocity vectors and the normalized absorbent loading at 560 seconds are shown in Figure 8. The decrease of cross section at the middle part of the container causes contraction of the breakthrough front and stagnant zone is developed. The flow velocity is increased due to the smaller cross section, which has a negative effect on adsorption and pressure drop.

The result of the optimization is found in Figure 9. D_1, H_1 dimensions and the volume of the container are increased by 37, 45 and 5 % respectively. The last modification corresponds to the fact that higher amount of zeolite can be stored into the cartridge and so the saturation time is increased. Additionally, the shape of the cartridge is modified on such a way that the flow becomes more uniform and homogeneous. The intensity of sudden change of cross section at the mid-part of the container is decreased and the negative effect of the stagnant zone is also damped (see Figure 8 and 9). The higher diameter at the lower-part allows smaller flow velocity and less chocking, which improves breakthrough time and pressure drop. The increased D_1 has a negative effect of filter efficiency due to the less layer number, but it has a favourable effect on the pressure drop too.

The quantitative results of the optimization show that the breakthrough time is increased by 26 %, the filter efficiency is decreased by 17 % and the pressure drop over the coalescing filter and desiccant bed is also decreased by 91.7 % compared to the original configuration. Of course the results must satisfy the expected design condition for minimal filter efficiency and allows higher freedom for maximising saturation time.

The other consequences of the numerical investigation are the effects of several factors on breakthrough and it is shown in Table 2. The most straightforward and highest factor for later breakthrough is the volume of zeolite. The uniform

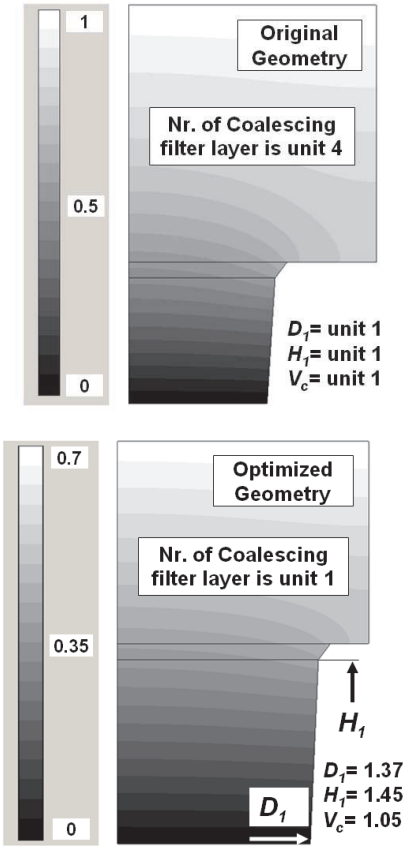

Figure 9. Original and the optimized geometry of the container with normalized characteristics and pressure distribution

and unchanged geometrical shape (e.g. cylindrical) with high cross section has also favourable effect on delaying saturation due to the homogeneous and low speed flow. The higher operational temperature and pressure can accelerate and decelerate the

breakthrough respectively due to the adsorption isotherms (see Figure 2.) and mass transfer coefficient (see Eq. (3)).

Table 2. Parameters and its effect on drying performance (breakthrough curve)

Parameter	Ascending characteristic	Weighted effectivity in terms of later breakthrough
Zeolite Volume	[m^3]	+++
Geometry	uniformity	++
Operational Pressure	[Pa]	+
Operational Temperature	[K]	-
Feed rate (velocity)	[Nl/min] [m/s]	--- (--)
Ambient Temperature and RH	[K] and [%]	--

5. CONCLUSIONS

A 3D computational procedure has been established, implemented and applied for modelling and optimizing air drying and filtering in the pneumatic system of the commercial vehicle.

The numerical model is based on the mass, momentum and energy conservation laws. Darcy's law has been implemented into the overall mass balance for describing flow physics in a porous media. Linear driving force model is used for computing mass fraction of the absorbed amount of water. The equilibrium loading of the desiccant is described by adsorption isotherms in the function of temperature and the partial steam pressure. The non-linear system of the differential equations is coupled with ideal gas law to recover density distribution over the computational domain. The mathematical model is validated by experimental results.

Concerning the optimization, drying performance, filter efficiency and pressure drop are considered in the objective function to be minimized. The non-dimensional components of the cost function are weighted by the order of functionality relevancies. Nelder-Mead simplex method is used in the optimization algorithm.

A new cartridge geometry has been proposed as result of the optimization by which the breakthrough time is increased by 26 %, the filter efficiency is decreased by 17 % and the pressure drop over the coalescing filter and the desiccant bed is also decreased by 91.7 %.

Beside the expected geometry, the other conclusion of the numerical investigation is the effect of several factors on later breakthrough. The most straightforward and highest influence is the volume of zeolite. The uniform and unchanged geometrical shape (e.g. cylindrical) with higher cross section has also favourable effect on delaying saturation due to the homogeneous and low speed flow. The higher operational temperature and pressure can accelerate and decelerate the impregnation respectively.

ACKNOWLEDGEMENTS

The work reported in the paper has been developed in the framework of the project „Talent care and cultivation in the scientific workshops of BME" project. This project is supported by the grant TÁMOP-4.2.2.B-10/1-2010-0009.

REFERENCES

[1] Gorbach, A., Stegmaier, M., and Eigenberger, G., 2004, "Measurement and Modelling of Water Vapor Adsorption on Zeolite 4A – Equilibria and Kinetics", *Chemistry and Material Science, Springer Netherlands*, Volume 10 Nr. 1, pp 29-46.

[2] Veress, Á., Danyi, A. and Palkovics, L., 2008, "Numerical Modelling and Simulation of Air Dryer Cartridges", *Comsol Multiphysics Conference*, Budapest, Hungary, pp 75-78. 24. November 2008.

[3] Hinds, W. C., 1982, "Aerosol Technology: Properties, Behaviour, and Measurement of Airborne Particles", *Wiley, Cop. New York,* ISBN-10: 0471087262.

[4] Strauss, W., 1975, "Industrial Cleaning", *Pergamon Press.*

[5] Kirsh, A. A. and Stechkina, I. B., 1978, "The Theory of Aerosol Filtration with Fibrous Filters" in Shaw, D. T. (Ed.), "Fundamentals of Aerosol Science", *John Wiley & Sons, New York.*

[6] Yeh, H. and Liu, B. Y. H., 1974, "Aerosol Filtration by Fibrous Filters - I Theoretical", *Journal of Aerosol Science,* 5, 191-204.

[7] Lee, K. W. and Liu, B. Y. H., 1982, "Theoretical Study of Aerosol Filtration by Fibrous Filters", Aerosol Science and Technology, Volume 1, Issue 2.

[8] Forchheimer, P., 1914, "Teaching and manual of hydraulics", *5 volumes*, 1914-16.

[9] Sutherland, W., 1893, "The viscosity of gases and molecular force", *Philosophical Magazine*, S. 5, 36, pp. 507-531.

[10] Danyi, A., 2007, "Numerical Simulation of Adsorption Process in Zeolite Molecular Sieves", *MSc Thesis, BME, Department of Hydrodynamic Systems.*

[11] http://www.mathworks.com/help/techdoc/ref/fminsearch.html

Conference on Modelling Fluid Flow (CMFF'12)
The 15th International Conference on Fluid Flow Technologies
Budapest, Hungary, September 4-7, 2012

Experimental Characterization of a Cost-Effective Semi-Active Grid for Turbulence Stimulation

Norbert SZASZÁK[1], Róbert BORDÁS[2], Zsolt MÁTRAI[3],
Szilárd SZABÓ[4], Dominique THÉVENIN[5]

[1] Corresponding Author. Department of Fluid and Heat Engineering, University of Miskolc. Miskolc-Egyetemváros, H-3515. Tel: +36 46 565 111/1251, E-mail: aramszn@uni-miskolc.hu
[2] Lab. of Fluid Dynamics & Technical Flows , University of Magdeburg "Otto von Guericke". E-mail: bordas@ovgu.de
[3] Department of Fluid and Heat Engineering, University of Miskolc. E-mail: arammzs@uni-miskolc.hu
[4] Department of Fluid and Heat Engineering, University of Miskolc. E-mail: aram2xsz@uni-miskolc.hu
[5] Lab. of Fluid Dynamics & Technical Flows , University of Magdeburg "Otto von Guericke". E-mail: thevenin@ovgu.de

ABSTRACT

The aim of the presented contribution is to experimentally characterize an innovative, semi-active system for turbulence generation. The main drawback of passive grids is that only moderate velocity fluctuations can typically be obtained in this manner. Higher turbulent intensities can be achieved by using actively controlled grids. Combined with stochastic geometries, these active systems are very efficient but extremely costly and not very robust.

As a possible cost-effective alternative, flexible tubes are fixed in the present project at the intersection points of a jet grid and set into motion by the exiting high-pressure air flow. Turbulence intensity, turbulent kinetic energy and its dissipation rate have been quantified using Particle Image Velocimetry (PIV). For comparison, passive and active experiments have been carried out. The PIV data were evaluated by the commercial software Dynamic Studio (Dantec Dynamics), before post-processing the resulting vector fields with MATLAB.

It has been shown that using the grid equipped with silicon tubes, turbulence intensity and turbulent kinetic energy may be considerably increased. The proposed system appears to work in a suitable manner and will be characterized in more details in future projects.

Keywords: active grid, grid generated turbulence, PIV, wind tunnel

1. INTRODUCTION

Controlled turbulence is required in most wind tunnel experiments, in order to define suitable boundary conditions according to running examinations. In this way it becomes possible to investigate e.g. wind turbines, airfoils, etc. with conditions close to that of real flows, also found in the nature.

Wind tunnels of normal laboratory size with conventional passive grid allow generating only relatively low Reynolds number turbulence [1]. The main reason is that the RMS velocity developing downstream of a passive grid is relatively low. As an alternative, several studies have focused on active grids. In contrast to passive grids they contain usually several flaps fixed on horizontal and vertical axes that can independently be driven by electrical drivers [2]. Fine mechanics and plenty of electric parts make this variant extremely costly. Therefore, innovative ideas have been followed to plan a reasonable, controlled grid for the generation

NOMENCLATURE

D	$[m]$	outer diameter
d	$[m]$	inner diameter
l	$[m]$	length
M	$[m]$	mesh spacing
k	$[m^2/s^2]$	specific turbulent kinetic energy
ε	$[m^2/s^3]$	specific energy dissipation rate
ν	$[m^2/s]$	kinematic viscosity
Tu	$[\%]$	turbulence intensity
I	$[-]$	isotropy ratio
η	$[m]$	Kolmogorov lengthscale
u	$[m/s]$	instantaneous velocity
U	$[m/s]$	mean velocity
u'	$[m/s]$	RMS velocity

Subscripts and Superscripts

passive	passive grid experiment
active	active grid experiment
x	horizontal (main flow) direction
y	vertical direction

of turbulence. Instead of stepper motors and fine mechanical parts, jets of compressed air and semi-rigid obstacles are considered.

The main task of this work is to characterize the turbulence properties of the flow, generated by this innovative grid, and to compare results with and without using the active flow control. Particle Image Velocimetry (PIV) seemed to be an effective method to investigate the flow field downstream of the grid, thus measurement have been carried out by means of this technique.

Inter alia the task was to experimentally determine the most suitable material and dimensions of the flexible active elements. The nearly uniform main flow was produced by an air ejector and its streamwise velocity downstream of the grid was set approximately to the same value in each case. The desired main velocity was in the range of $2.5-3\ m/s$. PIV data was evaluated by Dynamic Studio software (co. Dantec Dynamics). In each experimental case 500 image pairs were captured, and from them, the same number of velocity field was obtained.

During post-processing, these velocity vector fields were imported to the MATLAB software, where post-processing and presentation of the results occurred. In the followings, the comparison between the passive and the active grid flows will be presented.

2. EXPERIMENTAL SETUP

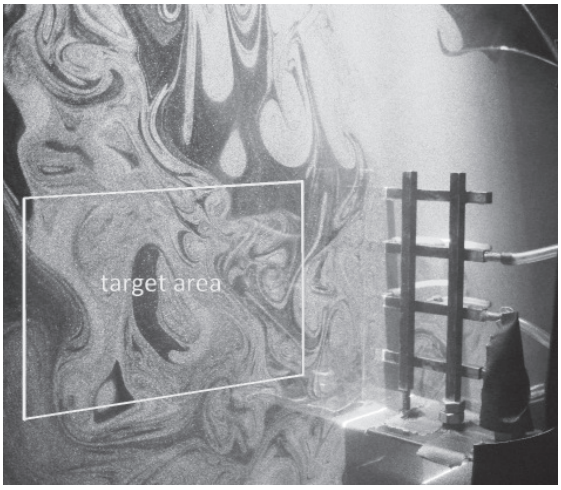

Figure 1. PIV target area marked with a rectangle downstream the grid.

For the proposed measurement, an experimental apparatus was assembled, consisting of an air ejector producing the inlet flow, the grid and the measurement technique (Fig. 1). PIV technique [3, 4] was employed for the measurements, in order to determine velocity vector fields and finally derive turbulence properties following the description in the scientific literature [5, 6]. The velocity field downstream the turbulence grid was directly measured and evaluated by a PIV-system consisting of

- a water cooled double pulse, frequency doubled Nd-YAG laser (co. New Wave), equipped by a laser mirror arm and a sheet optics,
- a HiSense Mk II double frame PIV/PLIF camera (co. Dantec Dynamics), mounted with a Nikon Micro Nikkor 60 *mm* objective,
- and a PC with a commercial PIV-software (Dynamic Studio v. 3.14) by the co. Dantec Dynamcis.

The flow was seeded by oil fog, produced by a high volume liquid seeding generator (model 10F03, co. Dantec Dynamics). This apparatus generated oil droplets with diameter of 3 μm according to the manufacturer. The intensity of the single laser beams was adjusted such way that the particles were illuminated homogeneously over the whole target area by approximately the same laser intensity.

The PIV camera was fixed to the bracket and was focused to the target area, without changing during the measurements. Therefore, all the vector fields, derived from the PIV data processing, belonged to the same coordinate system. This was an essential requirement for the comparison of the examined cases. The target area was located 4 *cm* downstream of the grid, mounted 10 *cm* behind the outlet of the ejector. The velocity of the main flow was adjusted by a pressure reducer. The pressure led through the silicon tubes of the active grid was set in the same manner in order to adjust the proper gauge pressure, assuring the chaotic movement of the tube exits.

2.1. Turbulence grid

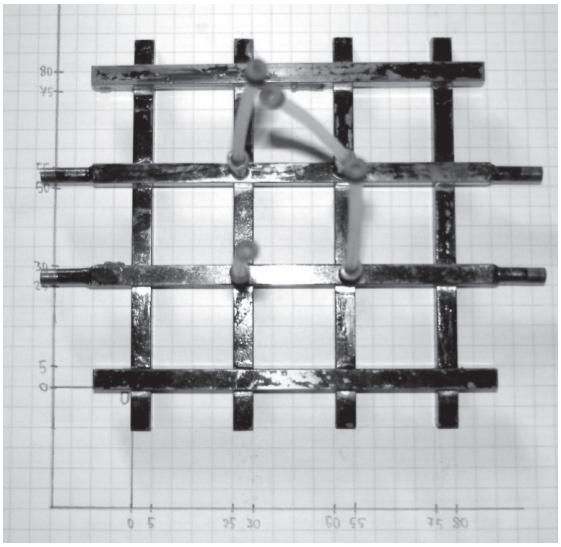

Figure 2. Experimental grid with silicon tubes mounted.

The applied grid (Figure 2) was prepared especially for the present test purposes and composed of 4×4 pieces of hollow rectangular copper bars with a length of $l_g = 100\ mm$ and a cross-section of $D_g = 5\ mm \times 5\ mm$. The mesh spacing of the grid was fixed to $M = 25\ mm$. The mesh Reynolds number was estimated from the mean flow velocity, the mesh spacing and the kinematic viscosity of air at ambient temperature, resulting in $\mathrm{Re}_M = 4\,400$.

As it can be seen (Fig. 2), two of the horizontal bars are longer than the others, since four pieces of tubes were soldered into their respective endings. PVC tubes conveying pressurized air were attached to these soldered tubes. At the four inner grid crossings, the copper profiles were drilled and copper pipes of diameter 3 *mm* and of length 28 *mm* were glued perpendicular to the plane of the bars. These pipes were needed to attach the flexible tubes to them with the objective to increase the turbulent kinetic energy of the flow. According to our experiments (detailed in section 2.2), the silicon tubes were the most appropriate active elements for the experimental grid. The copper pipes in the grid points with the attached tubes are shown in Figure 3.

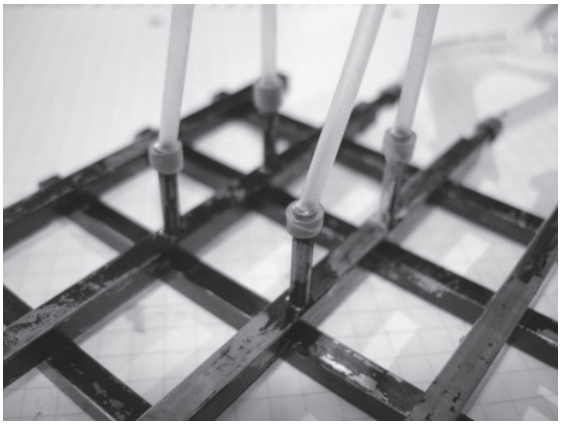

Figure 3. Copper pipes in the grid intersections with the attached silicon tubes.

To create active grid from the passive one, the flexible tubes were forced to make a chaotic motion using a suitable mass flow rate at their outlets. The minimal operating gauge pressure, which caused chaotic motion of the silicon tubes was different for each tube type, but for the case, selected as the best one, was about 1.5 *bar*. However, it was evident at this minimal pressure that this motion was rather oscillating than chaotic. The higher the gauge pressure was set, the more chaotic tube motion was achieved. Nevertheless, the increase of the gauge pressure over 3 *bar* resulted in the damage of the tubes. Therefore, during our active grid measurements the gauge pressure was finally limited to 2.5 *bar*.

2.2. Considered flexible tube types

Important aim of the present preparations was to find the most suitable material and the right tube dimensions in order to produce the desired chaotic motion. Therefore, several tubes of different materials and dimensions were considered. It was necessary to find such a hose, which were able to move with a high frequency even if it was relatively short and the gauge pressure was comparatively low. The length of the tube was one important property. It was obvious that shorter tubes should be preferred, since the excess of a specified tube length could lead to collisions so that the motion was stopped. Moreover, the force acting on the tube walls due to the increased inner surface would damage the tubes.

Another important property was the flexibility of the tubes. The objective was to find less rigid hoses, producing the most intensive motion for the same hose length. The rigidity depended on several quantities. For example it is a function of the material, wall thickness and diameter of the tube. The examined materials were the following: rubber, silicon, and PVC. The dimensions of these tubes are summarized in Table 1.

Table 1. Physical properties of the considered tube types

Material of the tube	Inner diameter d [mm]	Outer diameter D [mm]	Wall thickness t_w [mm]
PVC	1.5	2.5	0.5
Rubber	2.0	4.0	1.0
Silicon[1]	2.0	4.0	1.0
Silicon[2]	2.0	2.6	0.3

The best results were achieved by the silicon[2] type tube with dimensions $d = 2\ mm$, $D = 2.6\ mm$, $l = 58\ mm$. It was the most flexible variant. The active length, which is able to move was 55 *mm*, the remaining 3 *mm* was necessary to fix the tube onto the copper tube. Unfortunately, when the pressure was lead in the bare silicon tube it started to produce a very loud noise, due to the motion with an extremely high frequency. It was caused by its relatively low inertia and its low rigidity. In order to improve motility and to eliminate whistling of the tubes, some modifications were applied. The motion is caused by the high speed air stream out of the pipe. According to the momentum equation, the force that causes the motion of the tube is proportional to the speed of the stream flowing out, thus proportional to the mass flow rate of the air. The motion results from the sum of the momentum and of the inertia of the pipe.

Therefore, one of the ideas was to increase air speed at the jet outlets: small tube segments were fit additionally into the ending of each silicon tube

(Fig. 4, tube numbers 5-7) in order to decrease the outlet cross-section. Thus, higher outflow air speed was assured at the same gauge pressure. Nevertheless, the mass flow rate was decreased due to the narrowed outlet cross sections. In order to reach higher mass flow rates, the pressure had to be increased, damaging the attached flexible hoses.

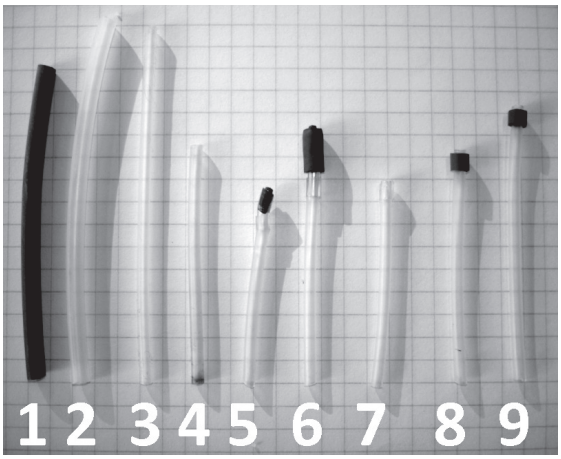

Figure 4. Assortment of the considered types of flexible tubes.

Another attempt was to fix a small piece of rubber tube onto the outer surface of the silicon pipes at the outlets. These variants are denoted by numbers 8 and 9 in Fig. 4. The best results were achieved following this method. Instead of increasing the outflow speed, the mass of the extra piece of tube caused the relocation of the center of gravity. Therefore, the unbalanced mass was increased, which started the motion at lower gauge pressures. By its beneficial properties the variant 9 was finally selected for the present experiments.

3. PIV EXPERIMENTS

After identifying the suitable active element, the measurements could be started. Before image recordings, the setup of the PIV system was carried out.

3.1. Geometric calibration

Firstly the calibration of the PIV camera was necessary, in order to get velocity vector lengths according to the world coordinate system in the real flow. Without calibration, the software could not account for the real displacement of the tracers. The calibration was carried out by DLT (Direct Linear Transformation). To get the transformation matrix, a calibration target was used with marker mapping (points with well defined distances and diameters). The selected calibration process in Dynamic Studio also includes the so called image dewarping, whereat image distortions due to off-axis camera position are eliminated.

3.2. Laser pulse and camera settings

After the geometrical calibration, the system was ready for image acquisition. The time between two frames (and laser pulse pairs) was set according to the rule of thumb that the tracer displacement between two frames is within the range of some pixels. This criterion resulted in a $\Delta t = 50\ \mu s$. The trigger rate of the laser equaled to the camera recording frequency. During the presented experiments it was set to the maximum of 6 Hz. To get sufficient number of vector fields for post-processing, the number of recorded image pairs was set to 500.

3.3. Spatial resolution

After dewarping image maps a standard cross-correlation was accomplished. Interrogation area (IA) was set to 32×32 pixels, with an overlap of 50%. The resulting vector map consisted of 83×63 vectors. An attempt to use an IA of size 16×16 pixels resulted in increased number (more than 10%) of rejected vectors. The reason for that was the insufficient number of tracer particles in the IAs. Furthermore, IA size of 64×64 pixels was tested as well. In this case the relative number of rejected vectors was far below 5%, but unfortunately the spatial resolution of the vector field was not satisfying, as described in the following subsection. For these reasons interrogation areas by 32×32 pixels were finally used .

It was important to determine the spatial resolution of the vector field, in order to compare with the Kolmogorov length scale. The spatial resolution of the vector field should ideally be smaller than the smallest scale that can be resolved in the flow. The width of the target area was 145 mm corresponding to 1346 pixels in a horizontal row of the CCD-chip. Thus, pixel resolution was equal to 0.108 mm/pixel. The velocity vector distance was 1.728 mm corresponding to an IA of 32×32 pixels with an overlap of 50%.

3.4. Vector validation

Vector length validation was also applied to reject evidently erroneous vectors, outside the valid region ($-10\ m/s$ to $2\ m/s$ in the main flow direction; $-6\ m/s$ to $6\ m/s$ in the perpendicular direction). Additional to the length validation, vector masking was also applied to ignore vectors outside of the examined volume downstream the turbulence grid. The height of the examined area was larger than the height of the grid, thus after masking, vectors below and above the grid were not taken into account.

After processing with the commercial PIV software (Dynamic Studio), the obtained information were exported in ASCII-format for post processing in MATLAB.

4. POST PROCESSING

After exporting velocity information from the PIV software the next step was data processing, in order to characterize flow turbulence behind the passively and actively controlled grid. For this task, the scientific software, MATLAB was used to program a script able to import, reconstruct and process measured quantities and finally get flow characteristics.

4.1. Derived flow properties

Due to the nature of the flow, isotropy was assumed in y- and z-directions, thus velocity fluctuation components in the transversal directions were assumed to be equal. Turbulence intensity is then defined by Eq. 1:

$$Tu = 100\% \sqrt{\frac{\frac{1}{3}(\overline{u_x'^2} + 2\overline{u_y'^2})}{U_x^2 + 2U_y^2}}, \tag{1}$$

and Eq. 2 was used to calculate the turbulent kinetic energy k per unit mass:

$$k = \frac{1}{2}(\overline{u_x'^2} + 2\overline{u_y'^2}). \tag{2}$$

Turbulent kinetic energy and its decay could be estimated in this way. The decay of turbulent kinetic energy is presented in the next section.

The isotropy ratio in Eq. 3 was defined as the ratio of the standard deviations of streamwise to transverse velocities:

$$I = \frac{\overline{u_x'}}{\overline{u_y'}}. \tag{3}$$

This value was more than one for all cases similar to the grid experiments presented in [7].

Following Hinze [8], the dissipation rate of the turbulent kinetic energy for the case of isotropic turbulence can be calculated using Eq. 4:

$$\varepsilon = 6\nu \left[\overline{\left(\frac{\partial u_x}{\partial x}\right)^2} + \overline{\left(\frac{\partial u_x}{\partial y}\right)^2} + \overline{\frac{\partial u_x}{\partial y}}\,\overline{\frac{\partial u_y}{\partial x}} \right] \tag{4}$$

To get a function corresponding to the dissipation rate as a function of the dimensionless grid distance, the values of the energy dissipation were computed for every vector columns by averaging the derivatives for each vertical profiles. The decay of turbulent kinetic energy and its dissipation rate was computed by fitting a curve on the single mean values using a MATLAB function (splinefit).

Finally, from the energy dissipation rate it was possible to calculate the Kolmogorov length scale using Eq. 5, derived from [8]:

$$\eta = \left(\frac{\nu^3}{\varepsilon}\right)^{1/4} \tag{5}$$

Using the decay of energy dissipation rate, a function could be created where the length scale was plotted as a function of the dimensionless distance from the grid. In addition the average value of the length scale was defined, which characterized the examined flow.

Using the previously described parameters, the characteristics of the examined flows could be compared. Measurements with passive and active grids will be presented and analyzed.

5. RESULTS AND ANALYSIS

Table 2. Statistical flow parameters of the examined cases

Quantity	Passive grid	Active grid	Ratio act./pass.
U_{mean} $[m/s]$	2.77	2.73	0.99
U_{median} $[m/s]$	2.75	2.70	0.98
U_{mode} $[m/s]$	2.43	2.39	0.98
Tu_{mean} $[\%]$	19.72	27.09	1.37
Tu_{median} $[\%]$	18.72	26.00	1.39
Tu_{mode} $[\%]$	13.98	19.91	1.42
k_{mean} $[m^2/s^2]$	0.46	0.79	1.72
k_{median} $[m^2/s^2]$	0.39	0.72	1.85
k_{mode} $[m^2/s^2]$	0.21	0.43	2.05

The objective of the present measurement series was to find the answer, whether the active control could increase the turbulent kinetic energy downstream the grid, since a significant increase is expected in case of the actively controlled grid. It was a necessary condition, to have nearly the same mean velocity for passive and active cases. The velocity of the air jet was controlled by the pressure reducer, as already described before. Obviously in case of the active grid, a higher pressure was required, since the active jet caused a higher pressure drop that had to be overridden. After setting the right gauge pressures of the ejector, the mean velocity magnitudes of both experiments were approximately in the same range: in case of the passive grid the mean velocity was 2.77 m/s, in the active grid experiment this value was found to be 2.73 m/s.

Turbulence intensities were different in the two examined cases, as expected. It was established that in the case of active grid turbulence intensity is remarkably greater than in the passive case. This effect demonstrates the advantage of the active grid. The moving silicone tubes randomly added perpendicular velocity components to the vectors of the air jet, so in the target area the standard deviation of the velocity fluctuations were increased. The values of the space averaged turbulence intensities can be found in Table 2.

The turbulent kinetic energy was primarily the quantity, which should be increased by actively controlling the grid. The decay of the turbulent

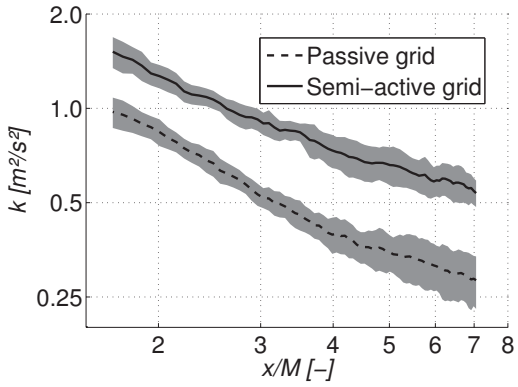

Figure 5. Decay of turbulent kinetic energy for both the active and the passive grids. Gray area means the uncertainty.

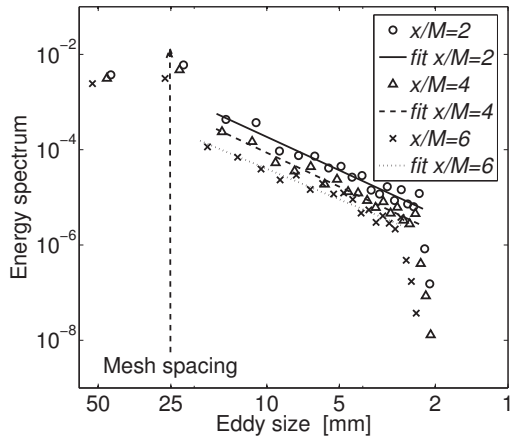

Figure 6. Energy spectra vs. eddy size at different dimensionless distances behind the active grid.

Table 3. Energy dissipation rates and Kolmogorov length scales at different distances downstream the grid.

x/M	Quantity	Passive grid	Active grid
2	$\varepsilon\ [m^2/s^3]$	2.95e-5	3.35e-5
	$\eta\ [mm]$	3.61	3.50
4	$\varepsilon\ [m^2/s^3]$	1.56e-5	1.73e-5
	$\eta\ [mm]$	4.23	4.13
6	$\varepsilon\ [m^2/s^3]$	1.55e-5	1.45e-5
	$\eta\ [mm]$	4.24	4.31

kinetic energy is compared for both cases in Figure 5. It can be established that the turbulent kinetic energy is significantly increased behind the active grid as expected and its decay corresponds to a typical log-log curve as usually presented in the literature [7].

By averaging the values of dissipation rates for different x/M positions, it was possible to determine the development of energy dissipation rate and the energy spectrum of the flow. The energy spectrum development of the active grid is presented in Figure 6. The values of the dissipation rates and the derived Kolmogorov length scales can be found in Table 3 for both experimental cases.

6. SUMMARY

A complete PIV measurement of passive and active grid generated turbulent flow has been presented in this article. The analysis of the experimental results in section 5 covers the comparison of the properties of passive and active grid measurements. It has been shown that by using flexible active elements as a companion to traditional jet grids, the intensity of the turbulence and the turbulent kinetic energy greatly increases, preserving the turbulent length scales. So the final conclusion is that this new type of active grid can be used for applications, where a significantly increased turbulent kinetic energy is required.

ACKNOWLEDGEMENTS

The authors are grateful to the Hungarian-German Intergovernmental S&T cooperation programs P-MÖB/386 for the financial support of this research. The work was carried out as part of the TÁMOP-4.2.1.B-10/2/KONV-2010-0001 project in the framework of the New Hungarian Development Plan. The realization of this project is supported by the European Union, co-financed by the European Social Fund.

REFERENCES

[1] Gad-el Hak, M. and Corrsin, S. 1974 “Measurements of the nearly isotropic turbulence behind a uniform jet grid”. *Journal of Fluid Mechanics*, Vol. 62, No. 1, pp. 115–143.

[2] Makita, H. 1991 “Realization of a large-scale turbulence field in a small wind tunnel”. *Fluid Dynamics Research*, Vol. 8, No. 1, pp. 53–64.

[3] Adrian, R. J. 2005 “Twenty years of particle image velocimetry”. *Experiments in Fluids*, Vol. 39, No. 2, pp. 159–169.

[4] Raffel, M., Willert, C., and Kompenhans, J. 2007 *Particle image velocimetry: a practical guide*. Springer Verlag, Berlin.

[5] Saarenrinne, P. and Piirto, M. 2000 “Turbulent kinetic energy dissipation rate estimation from PIV velocity vector fields”. *Experiments in Fluids*, Vol. 29, pp. 300–307.

[6] Tanaka, T. and Eaton, J. 2007 “A correction method for measuring turbulence kinetic energy dissipation rate by PIV”. *Experiments in Fluids*, Vol. 42, No. 6, pp. 893–902.

[7] Kang, H., Chester, S., and Meneveau, C. 2003 “Decaying turbulence in an active-grid-generated flow and comparisons with large-eddy simulation”. *Journal of Fluid Mechanics*, Vol. 480, pp. 129–160.

[8] Hinze, J. 1975 *Turbulence (2nd edn)*. McGraw-Hill, New York.

Conference on Modelling Fluid Flow (CMFF'12)
The 15th International Conference on Fluid Flow Technologies
Budapest, Hungary, September 4-7, 2012

COMPARISON OF DIFFERENT POD METHODS FOR TIME-RESOLVED MEASUREMENTS IN COMPLEX FLOWS

Patrícia ARÁNYI[1], Gábor JANIGA[2], Katharina ZÄHRINGER[3], Dominique THÉVENIN[4]

[1] Lab. of Fluid Dynamics & Technical Flows, Otto-von-Guericke-University Magdeburg.
E-mail: patricia.aranyi@gmail.com
[2] Corresponding Author. Lab. of Fluid Dynamics & Technical Flows, Otto-von-Guericke-University Magdeburg. Universitätsplatz 2, D-39106 Magdeburg, Germany. Tel.: +49 391 67 18196, Fax: +49 391 67 12840, E-mail: janiga@ovgu.de
[3] Lab. of Fluid Dynamics & Technical Flows, Otto-von-Guericke-University Magdeburg.
E-mail: Katharina.Zaehringer@ovgu.de
[4] Lab. of Fluid Dynamics & Technical Flows, Otto-von-Guericke-University Magdeburg. E-mail: thevenin@ovgu.de

ABSTRACT

Proper Orthogonal Decomposition (POD) is an effective tool in fluid dynamics for investigation of complex, transitional or turbulent flows. In POD the transient vector or scalar field (velocity, concentration, temperature...) is decomposed into a sum of spatial modes multiplied with time coefficients (Fourier-splitting method). However, these spatial modes and time coefficients can be obtained by different methods in practice. Even if the POD method has been used in numerous fluid dynamical studies (e.g., [1-4]), there are only few publications describing the relationship between the different methods and comparing the results [1]. In the present case the POD basis functions are calculated either by Singular Value Decomposition (SVD) or by the Snapshot-POD approach. The results are compared in order to understand better similarities and differences between the methods, as well as advantages and drawbacks. Comparisons between the obtained spatial modes, time coefficients, required computational effort, complexity of calculation are presented and discussed. The influence of the numerical settings is also investigated, in particular the impact of the number of snapshots on the results. Finally, the differences obtained when analysing a vector field globally or component-wise are discussed.

Keywords: Snapshot POD, SVD, TR-PIV

NOMENCLATURE

Latin symbols

a	$[m/s]$	temporal coefficients
A	$[m/s]$	Snapshot Data Matrix
C	$[m^2/s^2]$	Temporal Correlation Matrix
M	[-]	number of measurement points
N_t	[-]	number of time instants
r	$[m]$	spatial vector
R	$[m^2/s^2]$	two-point correlation tensor
u	$[m/s]$	velocity vector
$\tilde{u}$	$[m/s]$	approximated velocity vector
U	[-]	left singular vectors of A
v	[-]	eigenvectors of C
V	[-]	right singular vectors of A
W	[-]	eigenvectors of A^TA
x,y,z	$[m]$	spatial coordinates

Greek symbols

δ	[-]	Dirac delta function
λ	$[m^2/s^2]$	eigenvalues of C
Λ	$[m^2/s^2]$	eigenvalues of A^TA
Σ	$[m/s]$	singular values of A
Φ	[-]	spatial modes
Ψ	[-]	possible basis functions

Abbreviations

CFD	Computational Fluid Dynamics
FFT	Fast Fourier Transformation
I/O	Input/Output
PIV	Particle Image Velocimetry
POD	Proper Orthogonal Decomposition
SVD	Singular Value Decomposition
TCM	Temporal Correlation Matrix
TR-PIV	Time-Resolved PIV

1. INTRODUCTION

The Proper Orthogonal Decomposition (POD) is a well-known, advanced mathematical approach to analyze data in many fields of science. The present work focuses on its fluid dynamic application. By means of POD the coherent, dominant structures of even a complex flow field can be obtained without losing the time dependency

of the data. Furthermore, measurement errors can be filtered out, missing data can be reconstructed, or data can be compressed. The main idea of the method is somewhat similar to the Fourier Transformation (FT). The original flow field is decomposed into a linear combination of so-called spatial modes and time coefficients.

After decomposition different investigations can be carried out. For instance, Kapitza et al. [2,5] analysed the time coefficients by means of Fourier analysis in order to extract the dominant frequencies of the flow field. They used also the method for lower-order modelling approaches. The different spatial modes represent different energy levels: the first depicts the dominant mode of the flow field, while the others are following each other in decreasing order of importance. Depending on the complexity of the flow field, the first few spatial modes (for example 10-20) contain a considerable part of the whole energy content of the flow field (perhaps up to 95 %). If the flow field is reconstructed from these modes, then the main coherent structures of the flow can be investigated without losing the time dependency of the data [1].

This can also help to remove stochastic measurement errors from the measured flow fields, since these measurement errors belong to the higher-order spatial modes [5].

The original flow field used for the decomposition can be obtained from numerical calculations (Computational Fluid Dynamics, CFD), or from experimental results (e.g., Particle Image Velocimetry, PIV). In the present investigation, experimental measurement data (which consist of N_t time instants at M measurement points) obtained by Time-Resolved Particle Image Velocimetry (TR-PIV) measurements are used. They are described in more details next.

2. INVESTIGATED CASES

To improve generality, two different TR-PIV results obtained at the Lab. of Fluid Dynamic & Technical Flows in Magdeburg have been analyzed. In this section they are first briefly described.

2.1. Static mixer

In the first case simultaneous TR-PIV and Planar Laser-Induced Fluorescence (PLIF) measurements have been carried out behind a static mixer with high temporal and spatial resolution. The results of the measurements are discussed extensively in other publications by Lehwald et al. [6-7].

2.2. Centrifugal fan

In the second case an industrial centrifugal fan at part-load conditions is characterized by means of TR-PIV in 2D and 3D. More details about the measurements and results are given in [8].

3. THEORETICAL BACKGROUND

3.1. Main idea of the POD method

The present description mainly follows that of Cordier et al. [1].

In POD the original flow field ($r(x,y,z) \rightarrow u(r,t) \in \mathrm{D} = \Omega \times [0,T]$) is decomposed into a linear combination of spatial nodes ($\Phi^k(r) \in H^2$) and time coefficients ($a^k(t)$) by the well-known Fourier splitting method:

$$u(r,t) \cong \sum_{k=1}^{K} a^k(t) \cdot \Phi^k(r) \tag{1}$$

Similar to FT, if $K \rightarrow \infty$ then this series exactly describes the original flow field. Mathematically speaking this description is not unique; infinite sets of function combinations can satisfy it. If the POD modes are orthonormal to each other, then the temporal coefficients can be investigated separately. As a consequence, the temporal coefficients are orthogonal to each other as well:

$$\left(\Phi^{k1}(r), \Phi^{k2}(r)\right) = \delta_{k1,k2} \tag{2}$$

$$a^k(t) = \left(u(r,t), \Phi^k(r)\right) \tag{3}$$

where (.,.) denotes the inner product.

3.2. Determining POD basis modes

The approximation problem is equivalent to find an orthonormal basis in such a way, that the basis functions are projected onto the original flow field in every time instant [1]:

$$\min \sum_{i=1}^{Nt} \left\| u(r,t_i) - \tilde{u}(r,t_i) \right\|_2^2 \tag{4}$$

$$\tilde{u}(r,t_i) \cong \sum_{k=1}^{N_t} \left(u(r,t_i), \Phi^k(r)\right) \cdot \Phi^k(r) \tag{5}$$

where $\|.\|_2$ means the norm related to the L^2 inner product (.). In order to find an orthonormal basis different mathematical approaches can be used. In the present work the SVD and the Snapshot POD methods are described and compared in more details.

3.3. SVD method

In the SVD technique the data are arranged into a so-called Snapshot Data Matrix ($A \in M \times N_t$) in such a way that every column of the matrix ($A_{:,i}$) represents one time instant ($u(r,t_i)$). The SVD of A can be formulated by following definition [1]:

$$A = U \Sigma V^T \tag{6}$$

where $U \in M \times M$ and $V \in N_t \times N_t$ unitary matrices are the left and right singular vectors of A, respectively, while V^T represents the adjoint matrix of V and $\Sigma = diag(\sigma_1, \sigma_2, ...\sigma_n)$, where $\sigma_1 \geq \sigma_2 \geq ... \geq \sigma_n \geq 0$ are the singular values of A.
Now, the temporal coefficients of the POD can be obtained as a product of the right singular vectors and singular values of A:

$$a_i^k = \Sigma_k^k \cdot V_i^k \tag{7}$$

while the spatial modes can be obtained by using the left singular vectors of A :

$$\Phi^k = U^k \tag{8}$$

If the original data size is limited, it is then really easy and fast to use this method. However, for large-size data (for example when using high temporal or spatial resolution, or for long-time measurements) the usage of this method can lead to serious memory problems. In the first example associated with PLIF measurements [6], 512 Snapshots are recorded at high spatial resolution (approx. 1.5 millions of scalars for each snapshot). Trying to analyze all the measurement data with the Snapshot Data Matrix, an eigenvalue problem must be solved for a matrix consisting of 1.5 million elements in one direction and of 512 in the other... On the other hand, for small-size data, there is a built-in Matlab function for SVD calculations, easy to use and reasonably fast.

3.4. Snapshot POD method

In the Snapshot POD method, the basis functions are projected onto the original flow field in every time instant in order to find that deterministic function that is most similar to the members of u on average. Mathematically, it means trying to find the maximal value (Φ) of the possible functions (Ψ) [4]:

$$\max_{\Psi} \frac{\left\langle \left| (u, \Psi) \right|^2 \right\rangle}{(\Psi, \Psi)} = \frac{\left\langle \left| (u, \Phi) \right|^2 \right\rangle}{(\Phi, \Phi)} \tag{9}$$

where (.,.) means the inner product and $\langle \cdot \rangle$ is the average over space. Based on the calculus of variations Eq. (9) can be formulated also as a classical eigenvalue problem in the form of the so-called Fredholm Integral Equation [9]:

$$\int_{\Omega} \underbrace{\left[\frac{1}{N_t} \sum_{i=1}^{Nt} u(r, t_i) \otimes u(r', t_i) \right]}_{R(r,r')} \cdot \Phi(r') dr' = \lambda \cdot \Phi(r) \tag{10}$$

where Φ is the eigenfunction of the two-point correlation tensor $R(r, r')$. As described above the spatial modes are assumed to be orthonormal to each other. Hence, if the time coefficients are known, the spatial nodes can be determined in the following way:

$$\Phi^k(r) \cong \sum_{i=1}^{Nt} a_i^k \cdot u(r, t_i) \tag{11}$$

After mathematical substitution of Eq. (1) and Eq. (11) into Eq. (10) and simplification, the eigenvalue problem can be formulated in the following way [10]:

$$\sum_{k=1}^{Nt} \underbrace{\frac{1}{N_t} \left[(u(r, t_k), u(r, t_i)) \right]}_{C} \cdot a(t_k) = \lambda \cdot a(t_i) \tag{12}$$

After the eigenvalues (λ) and eigenvectors (v) of the Temporal Correlation Matrix (TCM, C) have been calculated, the normalised spatial modes (Φ) and time coefficients (a) can be obtained in the following way:

$$\Phi^k(r) \cong \frac{1}{\sqrt{N_t \lambda^k}} \sum_{i=1}^{Nt} v_i^k \cdot u(r, t_i) \tag{13}$$

$$a_i^k = v_i^k \cdot \sqrt{N_t \lambda^k} \tag{14}$$

These temporal coefficients are orthogonal to each other, while the eigenvectors of the TCM (v_i^k) are orthonormal to each other.
In practice, the determination of the TCM is the most critical part of the calculation for the Snapshot POD method.
In the simplest case all vector fields can be loaded into the memory in order to calculate the elements of the spatial correlation matrix. If the amount of data is relatively small, then this is an easy and fast way, as there is no need to spend too much time for the I/O operations. But, if the data set is too large, then memory problems similar to the SVD method can occur. In that case, it will usually be necessary to load only selected time instants into the memory, repeating sequentially the operation. Of course, the time spent with I/O operations will increase in this case. However, it is the only possibility to handle large data sets.

4. COMPARISON OF THE DIFFERENT METHODS

4.1. Connection between Snapshot POD and SVD

If the number of snapshots (N_t) are significantly smaller than the number of measurement points

(M), Snapshot-POD (SPOD) usually becomes more efficient than SVD [1]. For SPOD, the symmetrical eigenvalue problem of $A^T A$ is solved instead of calculating the sigular value decomposition of A (like in SVD). The concept can be explained in the following way. If $UU^T = I_M$ and $VV^T = I_{Nt}$ and $A^T A$ is a Hermitian matrix, then the following equation can be obtained:

$$A^T A = V\Sigma U^T U\Sigma V^T = V\Sigma^2 V^T = W\Lambda W^T \qquad (15)$$

where Λ contains the eigenvalues, while W describes the eigenvectors of $A^T A$. It can be seen from Eq. (15), that the eigenvectors (W) of $A^T A$ are identical to the right singular vectors of A (V).
Even if both the SVD and SPOD methods are based on the same concept, there can be differences between the finally calculated values. The reason for that lies in the different numerical formulations, as described in Subsection 3.2. For example in our case the TCM does not necessary equal to $A^T A$ exactly and the connection for the 2D case can be formulated in the following way:

$$C = \frac{1}{N_t} \cdot dA \cdot A^T A \qquad (16)$$

where dA denotes the cell size. In the following sections such differences and similarities are discussed in more details.

4.2. Temporal coefficients

First, the temporal coefficients of the different POD algorithms are presented for the TR-PIV measurements of the static mixer.
The calculation of the temporal coefficients leads to a classical eigenvalue problem in both cases. In the Snapshot POD method the temporal coefficients are calculated from the eigenvectors and eigenvalues of the TCM (Eq. 14), while in the SVD they are computed from the right singular vectors and the singular values of the Snapshot data matrix (Eq. 7). For both cases the results are $N_t \times N_t$ matrices, where each line represents the time coefficients of one time instant.
Even if the temporal coefficients are always based on the eigenvectors and right singular vectors, the exact values can be somewhat different because of the different numerical formulations, as described in Section 3. Due to such differences in the temporal coefficients, it is easier to compare the eigenvectors and the right singular vectors, as a constant multiplication factor could only change the eigenvalues. Comparing the eigenvectors to the right singular vectors is also useful because the temporal coefficients are often used for Fourier analysis in order to find the characteristic frequencies inside the flow [5]. In this case it is also enough to investigate the eigenvectors and the right singular vectors. In what follows some examples are presented.
Figure 1 shows the POD eigenvectors (marked with stars) and SVD right singular vectors (plotted as continuous line) corresponding to the second spatial mode. It can be seen that the results are identical. Possible differences are within the numerical uncertainty of Matlab. It can be also noticed, that the flow is highly periodic, which agrees with direct observations.
In Fig. 2 the POD eigenvectors (marked with dots) and the SVD right singular vectors (plotted as continuous line) corresponding to the third spatial mode can be seen. It is obvious from the figure, that they are mirrored around the horizontal axis.

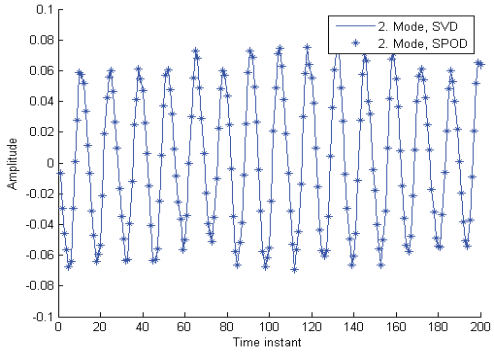

Figure 1. Comparison of the eigenvectors and right singular vectors of the second spatial mode

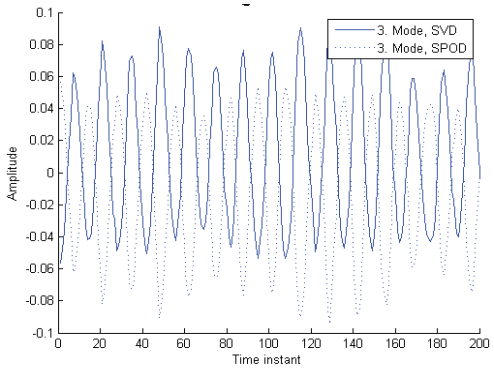

Figure 2. Comparison of the eigenvectors and the right singular vectors of the third spatial mode

This phenomenon can be explained if the properties of the eigenvalue calculation are taken into consideration. The eigenvectors and right singular vectors represent just directions, the sign is not significant. For example in a Cartesian system the only effect of the sign is to determine if the basis is left- or right-handed.

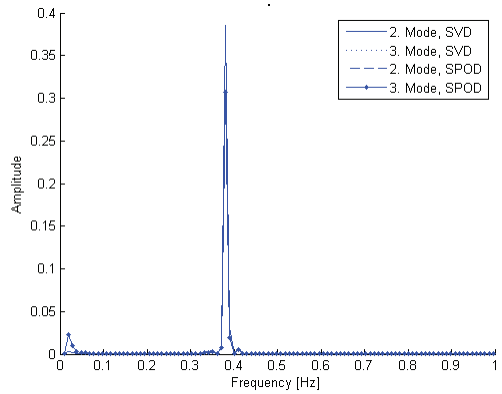

Figure 3. FFT analysis of the temporal coefficients

In Fig. 3 the FFT analysis of the flow field can be seen. The applied method is described in more details by Krause [11]. After analysing the temporal coefficients, the eigenvectors and right singular vectors, the same characteristic frequency (0.37 Hz) is obtained both from the TR-PIV and PLIF measurements [6].

4.3. Spatial modes

The structure of the first spatial mode should be always very similar to the average velocity field, while the others are flow-like structures, but not necessarily physical structures [3]. In what follows the spatial modes obtained from the different methods are presented and compared (TR-PIV measurements, static mixer). All modes have been normalised to facilitate visual comparison.

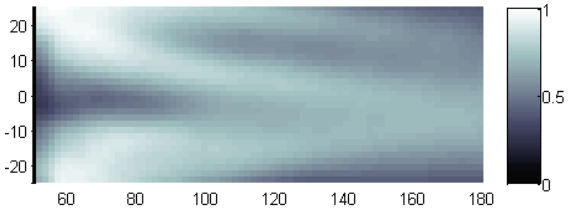

Figure 4. SPOD; 1. Mode; X-velocity component

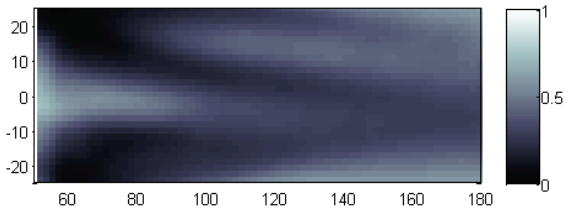

Figure 5. SVD; 1. Mode; X-velocity component

In Figs. 4 and 5 the first spatial mode associated with the *x*-velocity component can be seen. The structures are very similar, but the colours of the figures appear inverted. The reason for that is again based on the properties of the eigenvalue calculation. If the time coefficient has a negative sign, then the spatial mode also necessarily has one. As there is only one time coefficient for one spatial mode the *y*-velocity component is then also reversed (Figs. 6 and 7).

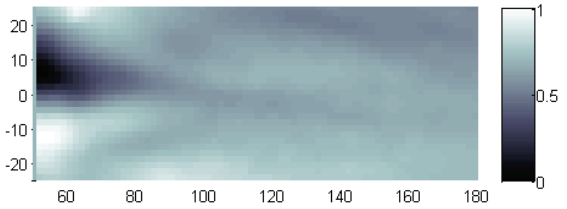

Figure 6. SPOD; 1. Mode; Y-velocity component

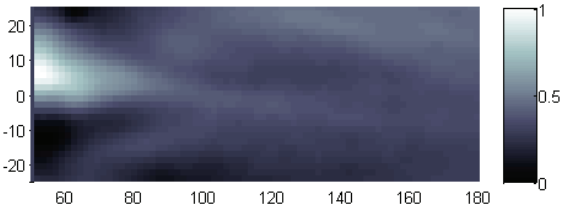

Figure 7. SVD; 1. Mode; Y-velocity component

As the sign of the temporal coefficients are the same for the second spatial mode, the normalised spatial modes also fit each other perfectly, as it is seen in Figs. 8 and 9.

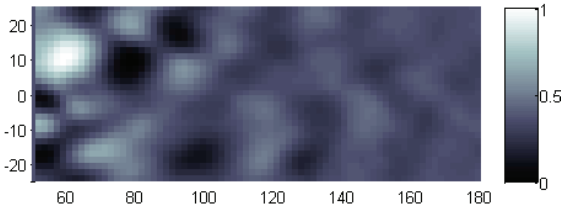

Figure 8. SPOD; 2. Mode; Y-velocity component

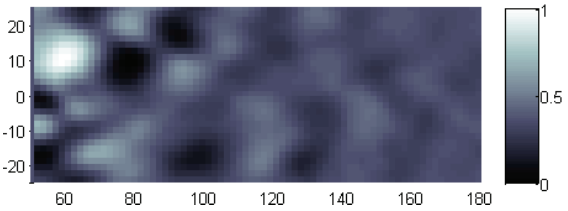

Figure 9. SVD; 2. Mode; Y-velocity component

The same phenomenon can be observed for the other spatial modes. Please note, that, even if the normalized structures are similar, significant differences in the absolute magnitudes may be found. The reason for that is the difference between the applied numerical methods.

4.4. Required computational effort

One of the most important differences between the two methods is the required computational effort

during the calculations. As mentioned before, for the SVD method all of the data are loaded into the memory, building a huge 2D Snapshot Data Matrix. Afterwards, the eigenvalue problem is solved. If the analyzed data is small, then the process is fast. For example, in case of the TR-PIV measurements of the static mixer (512 snapshots and 30 x 80 velocity vectors) the calculation takes only 2.5 seconds with a maximal memory usage of 1130 MB during the process on a standard PC. For the same computer and the same data the Snapshot POD calculation takes 97.1 seconds, but the maximal memory requirement is just 885 MB. The reason for that is that not all of the data is loaded into the memory at one time, but this significantly increases the time required for I/O processes. For the PLIF data of the static mixer (512 Snapshots, 453 x 1264 pixels) the SVD method reached the hardware limit – just 10 % of the data could be loaded into the memory (approximately 60 GB), while the Snapshot POD method was able to solve the problem in 1737 seconds by using just 3170 MB of memory.

5. INFLUENCE OF THE DIFFERENT NUMBER OF SNAPSHOTS

In the following some examples are presented to show how the different number of snapshots influences the structure of the obtained spatial modes (static mixer, TR-PIV, SPOD method).

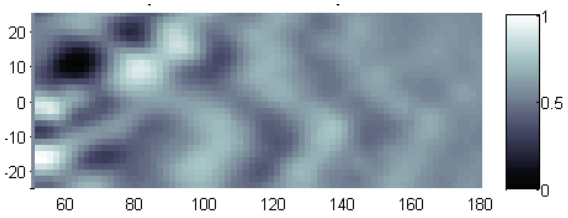

Figure 10. 2. Spatial mode, X-velocity comp., 256 Snapshots

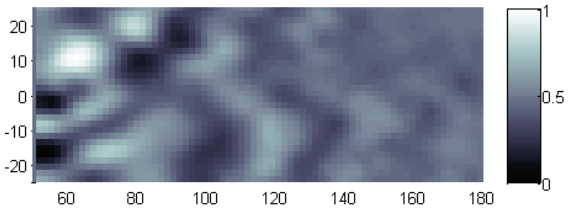

Figure 11. 2. Spatial mode, X-velocity comp., 128 Snapshots

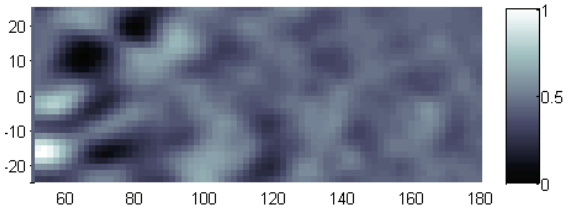

Figure 12. 2. Spatial mode, X-velocity comp., 64 Snapshots

Our tests show that the needed number of snapshots always depends on the complexity of the flow. If the flow is highly complex, such as for the static mixer, then more snapshots are necessary in order to obtain proper results. Based on our observations it can be stated, that changing the number of snapshots has less effect on the first modes, as demonstrated with the second spatial mode in Figs. 10-12. As it can be observed, the structure of this mode stays nearly constant (it is only spuriously inverted in Fig. 11). On the other hand, decreasing the number of applied snapshots will impact considerably the higher modes, as it can be seen in Figs. 13-15. The structure of this mode is completely changing as the number of snapshots is decreased.

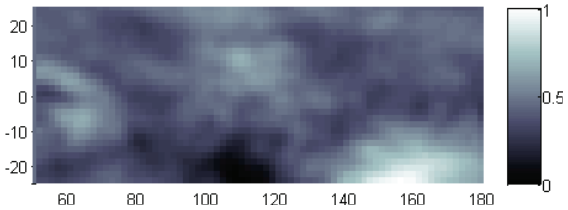

Figure 13. 4. Spatial mode, Y-velocity comp., 256 Snapshots

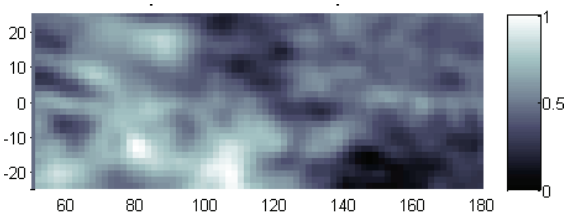

Figure 14. 4. Spatial mode, Y-velocity comp., 128 Snapshots

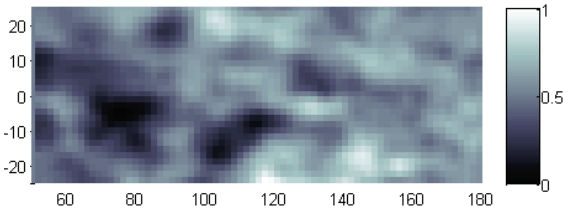

Figure 15. 4. Spatial mode, Y-velocity comp., 64 Snapshots

6. COMPARISON BETWEEN THE GLOBAL AND COMPONENT-WISE ANALYSIS

If the data to be decomposed consists of vector fields (for instance for velocity), then the POD decomposition can be calculated also in such a way, that the two different temporal correlation matrices

are calculated separately for the two different directions. In this case the connection between the two directions is lost. Different spatial modes are then calculated, and the different directions can be investigated separately. In this section the results of the global and component-wise methods are compared (for the centrifugal fan, part-load conditions, TR-PIV measurements).

6.1. Global analysis

A global analysis has been first carried out for all the presented cases in this paper. First, the second and third spatial modes obtained from the global Snapshot POD analysis of the centrifugal fan are presented in Figs. 16 and 17. They show clear and smooth vortex structures.

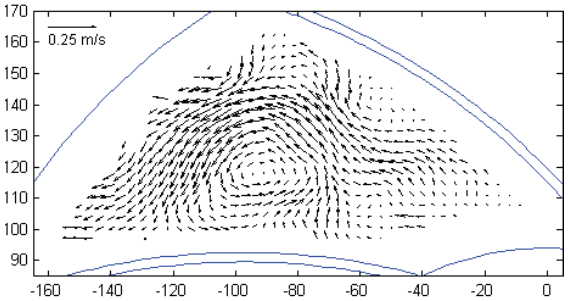

Figure 16. 2. Spatial mode, global analysis

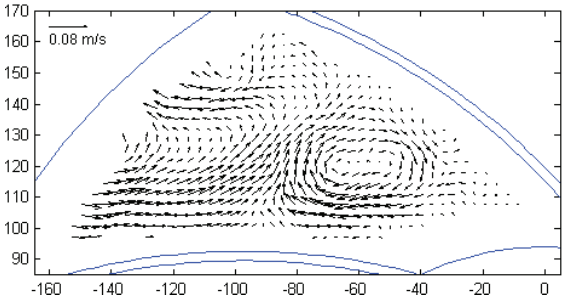

Figure 17. 3. Spatial mode, global analysis

For the calculation one TCM is defined, which takes into account the influence of both velocity vector components. After the eigenvalue calculation of the TCM the eigenvalues (λ_i) also represent energy levels, like the singular values in the SVD calculation: $\lambda_1 \geq \lambda_2 \geq \ldots \geq \lambda_n \geq 0$. After analysing this energy spectrum some observations can be done. The first spatial mode (which is practically the average flow field) contains approximately 65 % of the whole energy, while the other modes represent the transient processes. In Fig. 18, the energy distribution (in %) is presented.

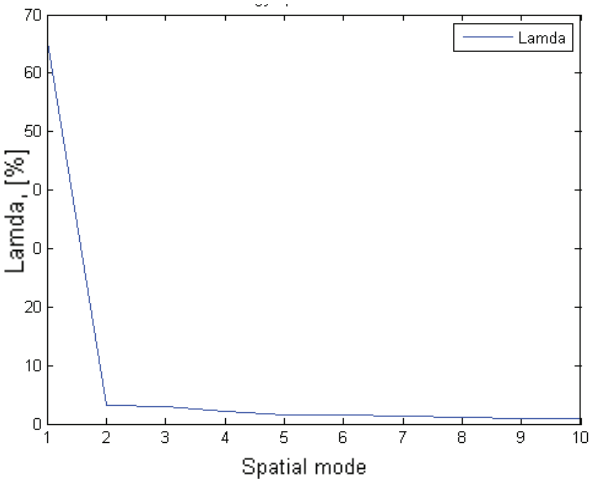

Figure 18. Energy spectrum, global analysis

6.2. Component – wise analysis

As it was mentioned before, Eq. (1) does not have a unique solution; an infinite number of different solutions can be found. Now, two TCM are calculated from the two velocity vector components in a separate manner.

In Figs. 19 and 20 the second and the third spatial modes are presented. The results are visualised together for both components in order to facilitate understanding.

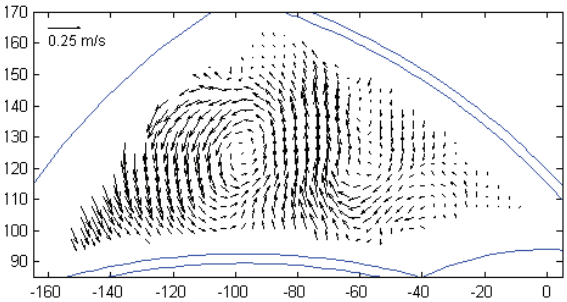

Figure 19. 2. Spatial mode, component - wise analysis

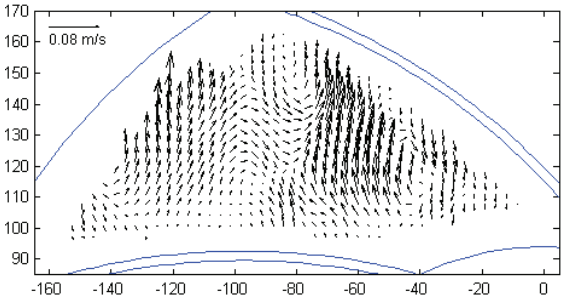

Figure 20. 3. Spatial mode, component - wise analysis

In Fig. 21 the energy spectrum of the different velocity vector components are presented (λ_{ui} for

the x direction and λ_{vi} for the y direction, both in %). It is interesting to see that there is a clear difference between the two directions. In the x-direction the first mode contains approximately 70% of the whole energy, while in y-direction this is just 50%. This means that the dominant flow direction is the x direction, while along y the effect of turbulent fluctuations is more significant.
If the aim is to reconstruct the vector field [5], then more spatial modes need to be used along the y-direction because of the turbulent fluctuations.

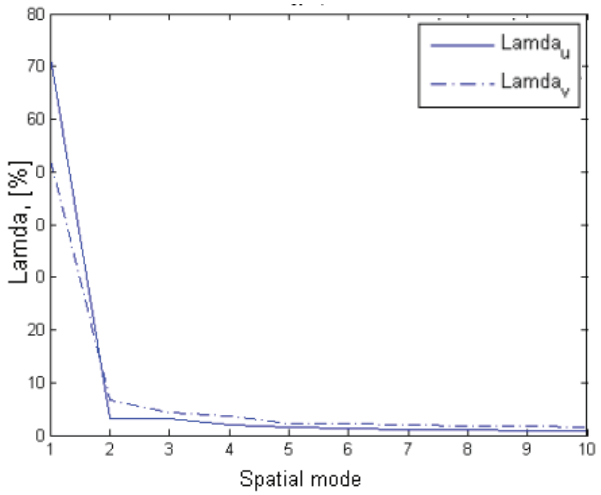

Figure 21. Energy spectrum, component – wise analysis

Comparing Figs.16-17 with Figs.19-20, it is clear that the obtained results differ strongly. Every time this is possible, a global analysis should be preferred.

7. SUMMARY

Two different POD methods have been implemented successfully and applied for analysing time-resolved experimental results. The mathematical properties of the employed algorithms have been discussed in details, highlighting similarities and differences. The results obtained by the different methods such as the spatial modes are compared, and the differences are extensively discussed. Advantages and disadvantages of the different methods have been also presented, especially regarding computational requirements. These results will hopefully facilitate the understanding of the differences between the POD algorithms and provide some guidelines for a selection of the most appropriate method.

ACKNOWLEDGEMENTS

Very helpful discussions with Dr. Lars Kapitza and Dr. Tamás Régert are gratefully acknowledged.

REFERENCES

[1] Cordier, L., and, Bergmann M., 2003, "Proper Orthogonal Decomposition: an overwiev", *Lecture series 2003-03 in VKI, Post-Processing of Experimental and Numerical Data*, Vol.2

[2] Kapitza, L., Imberdis, O., Bensler, H. P., Willand, J., Thévenin, D., 2010, "An experimental analysis of the turbulent structures generated by the intake port of DISI-engine", *Exp. Fluids,* Vol.48(2) pp. 265-280.

[3] Régert, T., Rambaud, P., Riethmuller, M.L., 2005, "Investigation of the Link between Physics and POD modes", In *Recent Developments in Non-Intrusive Measurement Technology for Military Application on Model- and Full-Scale Vehicles*, Meeting Proceedings Paper 4. Neuilly-sur-Seine, France

[4] Berkooz, G., Holmes, P., Lumley, J.L., 1993, "The proper orthogonal decomposition in the analysis of turbulent flows", *Annu. Rev. Fluid Mech.*, Vol. 25, pp. 539-75.

[5] Kapitza, L., 2010, "Experimentelle Analyse des transienten Verhaltens der einlasskanal-generierten Zylinderinnenströmung", *PhD Thesis*, Univ. of Magdeburg, Germany

[6] Lehwald, A., Leschka, S., Zähringer, K., Thévenin, D., 2008, "Fluid dynamics and mixing behaviour of a static mixer using simultaneously Particle Image Velocimetry and Planar Laser-Induced Fluorescence measurements", *14th Int. Symp on Applications of Laser Techniques to Fluid Mechanics,* Lisbon, Portugal

[7] Lehwald, A., Thévenin, D., Zähringer, K., 2010, "Quantifying macro-mixing and micro-mixing in a static mixer using two-tracer laser-induced fluorescence", *Exp. Fluids*, Vol. 48(5), pp. 823-836.

[8] Arányi, P., 2011, "Investigation of an industrial centrifugal fan by means of 3D Time Resolved PIV measurement technique", *Bachelor Thesis*, Budapest University of Technology and Economics, Budapest, Hungary

[9] Riesz, F., Sz.-Nagy, B., 1955, "Functional analysis", *Dover publications*, N.Y., USA

[10] Régert, T., 2004, "Experimental investigation of the effect of droplets on coherent structures in a flow over an open, rectangular cavity", *Von Karman Institute,* Project report 200416.

[11] Krause, N., 2008, "Untersuchung der Laufradströhmung einer Kreiselpumpe unter Teillastbediengungen mit Hilfe der zeitaufgelösten Particle Image Velocimetry", *PhD Thesis*, Univ. of Magdeburg, Germany, available online: http://www.ovgu.de/isut/LSS

Conference on Modelling Fluid Flow (CMFF'12)
The 15th International Conference on Fluid Flow Technologies
Budapest, Hungary, September 4-7, 2012

NUMERICAL STUDY OF VORTEX STRUCTURE GENERATION IN HYBRID ROCKET MOTORS

F. Stella[1], M. Giangi[2], F. Nardecchia[3] D. Barbagallo[4]

[1] Corresponding Author. Department of Mechanical and Aerospace Engineering, Italy University of Rome "La Sapienza", Via Eudossiana 18, 00184 Rome (Italy). Tel.: +39 0644585220, Fax: +39 06484854, E-mail: fulvio.stella@uniroma1.it
[2]Dep. of Mech. and Aerospace Eng., Italy University of Rome "La Sapienza". E-mail:mgiangi@stella.dma.uniroma1.it
[3]Dep. Of Mech. and Aerospace Eng., Italy University of Rome "La Sapienza". E-mail:fabio.nardecchia@stella.dma.uniroma1.it
[4] Consulant – ESA ESRIN Frascati (Roma – Italy). E-mail: daniele.barbagallo@hypotheses.it

ABSTRACT

Aim of the present work is to study the effects of vortex structures in the combustion chamber on propellant-oxidizer mixing in hybrid rocket motors. The proposed way for the production of these vorticity structures is the introduction in the combustion chamber of ad-hoc obstacles and localized oxidizer injection. For this reason a parametric study, by varying: the length of the combustion chamber, the height of an obstacle place in the combustion chamber and the possibility of side injection of oxidizer, has been conducted.

Results, obtained by means of CFD simulations, have shown that the values of mixing intensity are several times larger than the case of the motor without obstacle and injection. Therefore starting from this results, an improved solution with the proposed devices and a reduced length has been finally tested.

Keywords: CFD, combustion chamber, hybrid propulsion, vortex structures.

NOMENCLATURE

A	$[m^2]$	area
I	[-]	mixing indicator
$\dot{m}$	$[kg/s]$	secondary mass flow rate
$\dot{P}$	$[kg/s]$	principal mass flow rate
$\dot{Q}$	$[kg/s]$	mass flow rate of oxidizer
u_∞	$[m/s]$	free-stream velocity
v	$[m/s]$	velocity

Subscripts and Superscripts

r	radial
TOT	total

1. INTRODUCTION

Hybrid rocket propulsion represents a possible future alternative for civilian and military rocket vehicles propulsion [1-2]. A hybrid rocket motor represents a combination between a solid and a liquid rocket motor: uses a solid fuel and a liquid oxidizer (see Figure 1).

This configuration has several expected advantages, such as less security problems, smaller costs, etc.

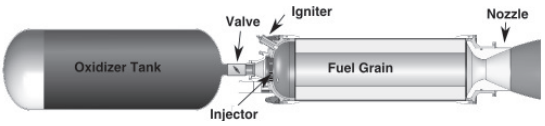

Figure 1. Hybrid rocket structure

On the other hand, main problem of this type of motors is the difficult mixing, inside the combustion chamber, between the solid propellant and the oxidizer. As consequence, combustion chamber usually results to be quite long or complex in order to respect time and mechanism of mixing between propellant and oxidizer.

Several different solutions have been proposed in the past to overcome this problem, going from complex design of the internal propellant grain to the addition of a post-combustion chamber.

In particular, a common solution is the use of a multi port design for solid fuel. Rhee et al. [3] and Lee et al. [4] adopted a multi-port configuration for an air lanched small rocket using HTPB as solid fuel. Main drawback of this approach is that, to avoid solid fuel breakage, part of the propellant has to be left maused, sensibly reducing overall performances.

Another adopted solution for mixing enanderent is the induction of swirl flow in the combustion chamber. This result is obtained or using an elicoidal configuration of the internal grain configuration [5] or using a swirled injection of the oxidizer [6-8]. Main disadvantage of this approach is the augmented pressure drop due to the swirl flow and the possible generation of roll torque.

Also the addition of a post-combustion chamber [9-10] has been adopted to increase mixing time between fuel and oxidizer. Main drawback of this approach is the obvious increase of weight of the launcher.

In a previous work [11] the authors have studied the presence of protrusions of thermal protections in a large solid rocket motor (e.g. ARIANE V - P230) because they are the reason for the production of large coherent vortex structures that are responsible of undesidered pressure oscillations. During that study by chance, it has been observed that these structures are also responsible for increased internal mixing with extraction of fluid from the propellant grain boundary layer. Therefore in the present work the possibility to improve internal mixing by means of obstacles of appropriate size placed in the combustion chamber will be discussed.

Another possible way to improve mixing is to introduce a localized distribution injection of oxidizer that could increase mixing. The introduction of such injection scheme with the main flow has not yet been studied. In particular this distributed injection strategy can be combined with the above discussed obstacles. The interaction between the two has obviously an even stronger effect on the presence of the intensity of vorticity structures.

Therefore as successive test a study of oxidizer injection with varying intensity will be also conducted.

Finally an improved solution will be presented.

2. PHYSICAL DOMAIN AND ADOPTED SET-UP

The physical domain is sketched in Figure 2 and can be described as a long duct with a submerged nozzle placed at one end. A principal axial flow is present with a mass flow rate equal to $\dot{P}$, laterally a secondary flow ($\dot{m}$), produced from the propellant phase change, is over-imposed. In addition a second localized, lateral injection of oxidizer ($\dot{Q}$) is introduced.

To keep consistency between the different cases studied, the overall mass flow rate laterally injected (i.e. $\dot{m}+\dot{Q}$) is maintained constant. Therefore the quantity $\dot{m}_{TOT}=\dot{m}+\dot{Q}$ is fixed in all cases presented.

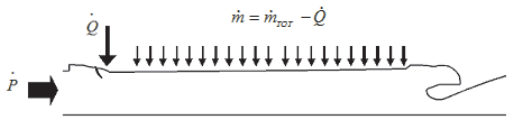

Figure 2. Physical problem

The mixing phenomenon under study is driven by the evolution of the various vortex structures released in the combustion chamber, therefore all the numerical simulations of the present work were performed using unsteady flow conditions. The grain geometry has been considered frozen at the time instant studied. Axi-symmetric flow conditions have been assumed in all the cases under study.

In the numerical simulations, adopted meshes are as much possible uniformly spaced along the whole motor, this to guarantee an uniform accuracy in the whole domain.

The commercial CFD code FLUENT has been used for all the simulations [12]. FLUENT uses a control-volume-based technique for discretization and numerical solution of field equations.

A pressure-based algorithm has been chosen to solve the conservation equations. Using this approach, the equations are solved sequentially, but since they are nonlinear and the phenomenon unsteady, several iterations of the solution loop must be performed before a converged solution is obtained for each time step. The convective terms in the equations for momentum and energy are discretized using a second-order upwind scheme. The PISO (Pressure Implicit with Splitting of Operators) algorithm has been used to achieve the pressure-velocity coupling and an implicit discretization of time derivatives has been also chosen. Further details of computational approach and numerical schemes adopted can be found in [12].

3. RESULTS AND DISCUSSION

As said, main goal of the present paper is to improve the internal mixing in hybrid motors. For this reason a parametric study, by varying: the length of the combustion chamber, the height of an obstacle place in the combustion chamber and the possibility of side injection of oxidizer, has been conducted, by means of CFD simulations.

Since the radial velocity (v_r), orthogonal to the horizontal propellant surface, seems to be the most responsible for increasing the internal mixing of the flows, this variable has been used as parameter, to evaluate the mixing intensity, during the numerical simulation.

Therefore a mixing indicator *I*, built using the radial velocity (v_r), has been introduced:

$$I = \frac{1}{u_\infty \cdot A} \int_A |V_r| dA \qquad (1)$$

Where *A* is the area of interest (see Figure 3), u_∞ is the free-stream velocity u_∞=38.05 *m/s* and v_r the velocity orthogonal to the propellant surface.

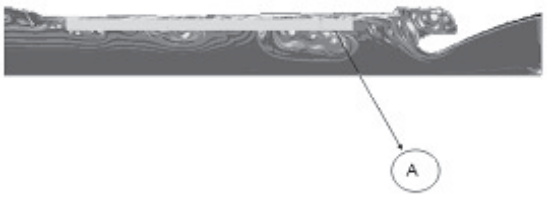

Figure 3. Surface A

Effects of obstacle size

The possibility to improve internal mixing by means of obstacles placed in the combustion chamber has been studied first (see Figure 4).

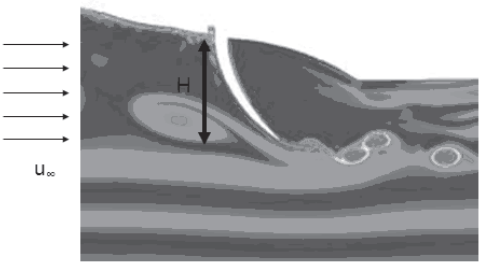

Figure 4. Obstacle in the combustion chamber

During the numerical simulations it has been observed that the presence of an obstacle, in the combustion chamber, with different height (*H*), increases the production of large coherent vortex structures (Figure 6).

In particular, from the parametric study of the obstacle height (*H*=0, *H/2*, ¾ *H*, *H*) appears that, in these conditions, there is a minimum height (*H/2*) of the obstacle to be truly effective (Figure 5).

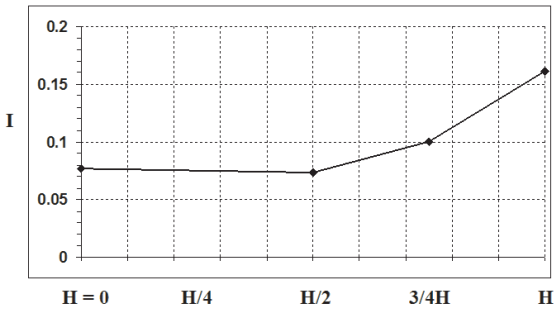

Figure 5. Parametric Study of the obstacle height: mixing indicator

It is worthy observing that the nominal case (full length of the motor without obstacle) presents a value for mixing indicator *I*=0.08, while the case *H*/2 presents a similar value. The analysis of CFD results presents a slightly more animated flow field but with a similar vorticity structure as it is also possible to guess from relative comparison in Figure 5. On the contrary looking cases 3/4*H* and *H* the enhanced mixing is clearly evident.

Effect of combustion chamber length

Generally long motors are constructed, so that the boundary layer has time to become thick and then, in some case, unstable. As observed above, the presence of an obstacle in the combustion chamber increases the vorticity intensity; therefore the possibility to reduce the combustion chamber length (*L*), with the presence of an obstacle, has been studied (see Figure 7).

From the parametric study conducted, appear as a reduction of the combustion chamber to *L*/4 gives a value of the mixing indicator *I*=0.05 (see Figure 8) that is slightly lower than the nominal case with combustion chamber length *L* and without obstacle (*I*=0.08). Therefore, from this study appear as the presence of an obstacle increases the mixing and may allow the reduction of the combustion length.

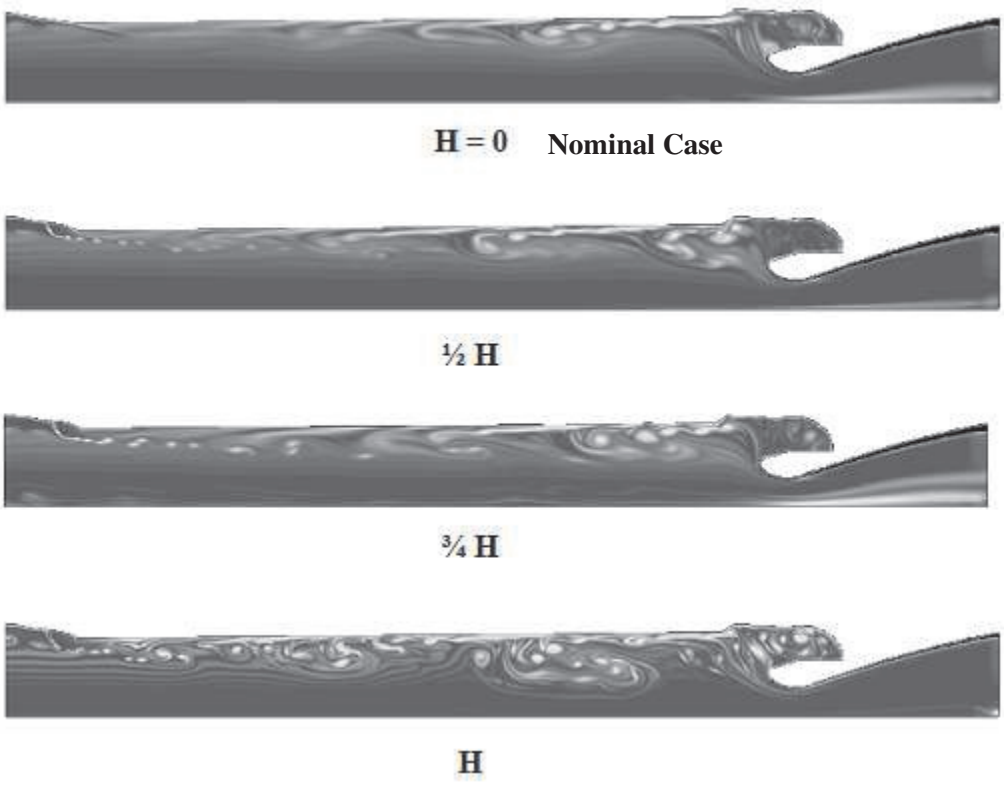

Figure 6. Parametric Study of the obstacle height: vortices evolution

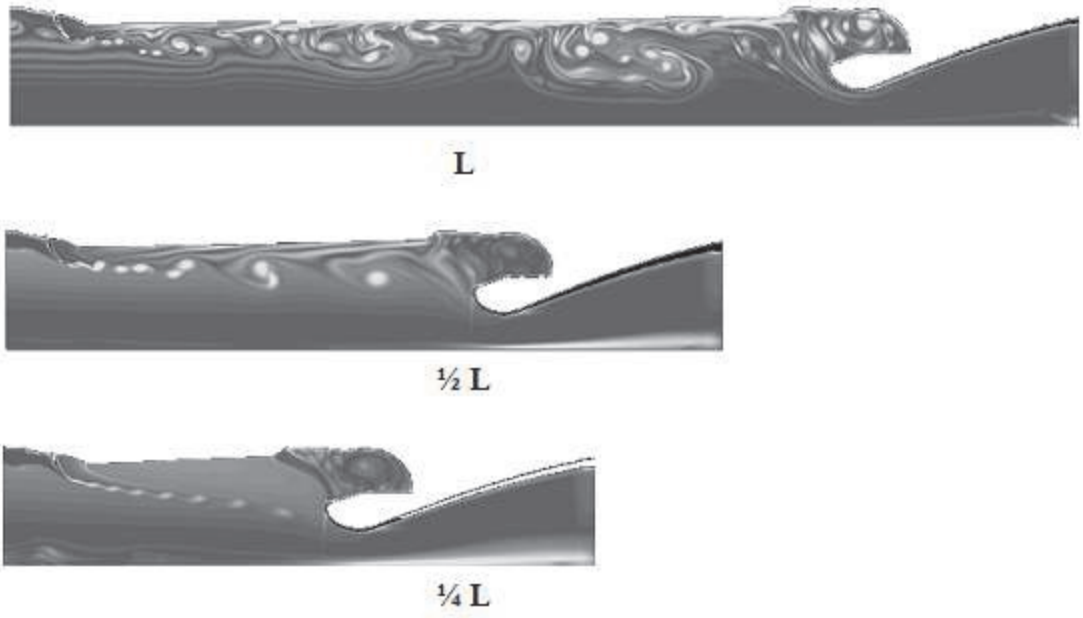

Figure 7. Parametric Study of the lengh of the combustion chamber: vortices evolution

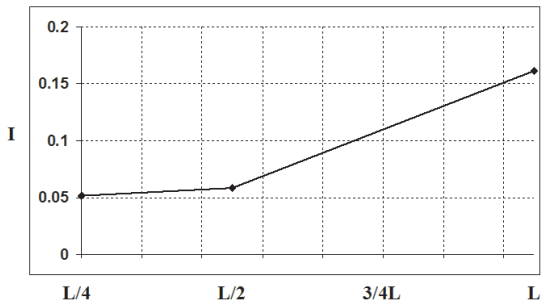

Figure 8. Parametric Study of the length of the combustion chamber: mixing indicator

Side injection of oxidizer

Another possibility studied is to substitute the presence of the solid obstacle with a sort of "fluid obstacle". This effect is obtained with a localized side injection of oxidizer (see Figure 9). Moreover, this solution has others appealing "incidental" advantages e.g.: allows the injection of oxidizer right in the place where it is required, maintains a more balanced O/F ratio and a more uniform temperature distribution.

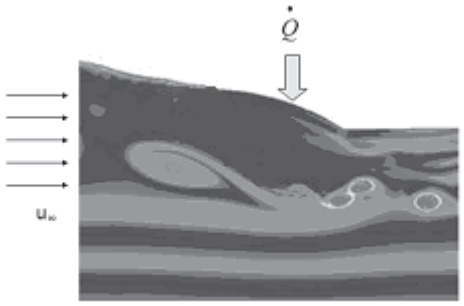

Figure 9. Side injection of oxidizer

From Figure 10 it is possible to observe that, even with a small fraction of side injection (e.g. 10%), the vorticity structure produced is very developed. Increasing more the injected fraction (e.g. 50%), effects on vorticity became impressive. These effects are also clearly visible on mixing indicator (*I*) in Figure 12. With a 10% of fraction injection a value of 0.17 is found, while with 50% a value of 0.36 is found.

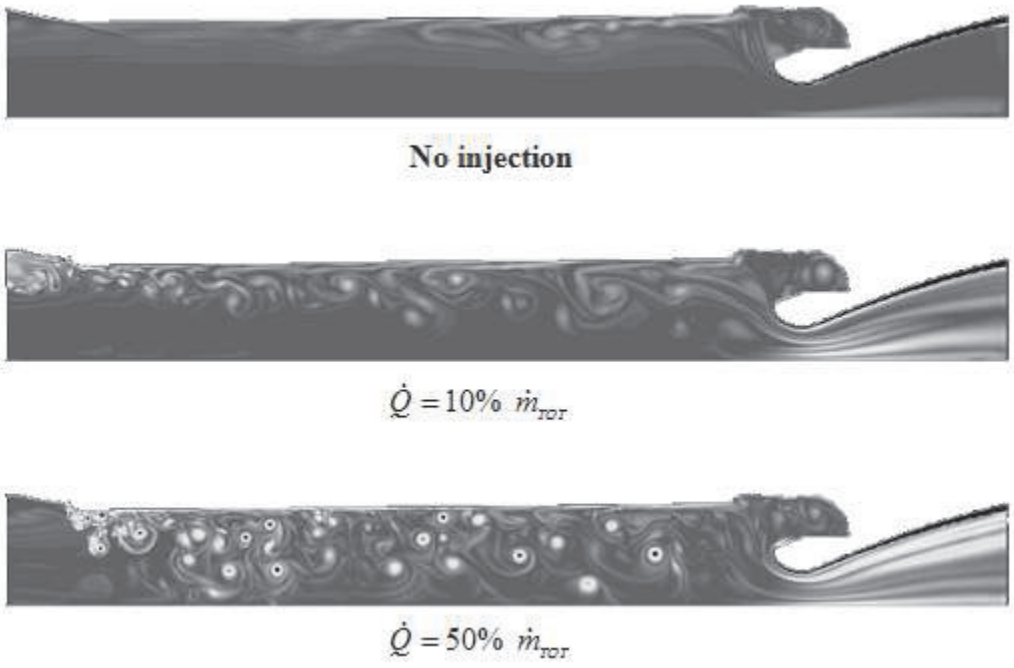

Figure 10. Different side injections without obstacle: vortices evolution

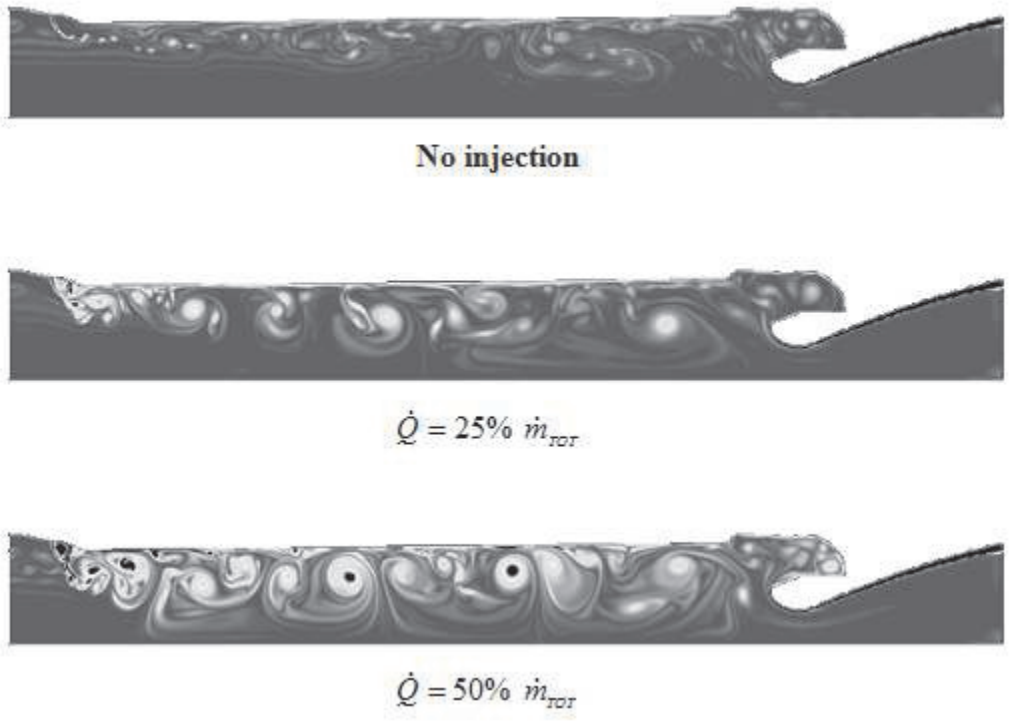

Figure 11. Different side injections with an obstacle: vortices evolution

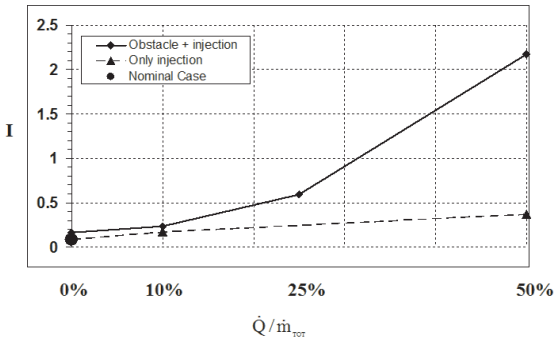

Figure 12. Comparison between obstacle with injection and only injection

Then a combination of this two effects has been obviously studied. From numerical simulations it is possible to observe that the global effects are more and more intense due to a mutual energization of these effects (see Figure 11). Results in terms of mixing intensity (see Figure 12) are very encouraging since values obtained are several times larger than nominal case.

Improved Design.
Finally, starting from the good results obtained so far it is possible to attempt an improvement in the design using a combination of all the effects. Therefore geometries with an obstacle (of height H), side injection ($\dot{Q} = 50\% \dot{m}_{TOT}$) and reduction of chamber length ($L/2$,$L/4$), have been studied.
From Figure 13 it is possible to observe, that in all the cases, the mixing indicator is higher than in the nominal case. Therefore is reasonable to consider the possibility of study an hybrid motor with a reduced length, when the two described mixing devises (obstacle and side injection) are used.

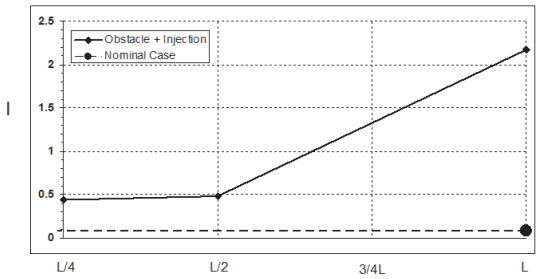

Figure 13. Improved Design: comparison between obstacle with injection and nominal case

5. CONCLUSIONS

In the present paper the possibility to improve internal mixing in hybrid rocket motor has been numerically studied. Two different individual solutions have been tested: the introduction of ad-hoc obstacles in the combustion chamber and the use of localized side injection of oxidizer. Numerical results found are quite encouraging

showing, for these two solutions, the presence of a significant increasing of oxidizer/propellant mixing.

Then, the combination of these two solutions has been tested as a third possibility. In this case, results in terms of mixing intensity have been shown that the values are several times larger than the nominal case of the motor without obstacle and injection.

Therefore starting from this results, an improved solution with the proposed devices and a reduced length has been finally tested.

REFERENCES

[1] Karabeyoglu A., 2008, "Hybrid Rocket Propulsion for Future Space Launch", *Aero/Astro 50th Year Anniversary*.

[2] Davydenko N.A., Gollender R.G., Gubertov A.M., Mironov V.V., Volkov N.N., 2007, "Hybrid rocket engines: The benefits and prospects", *Aero. Sci. and Tech.*, Vol.11, pp.55-60.

[3] Rhee, R., Lee, C., and Lee, Jae-Woo, 2008, "Optimal Design for Hybrid Rocket Engine for Air Launch Vehicle", *J. of Mech. Sci. and Tech*., Vol.22, pp.1576-1585.

[4] Lee, J.W., Noh, K.H., and Byun Y.H., 2007, "Preliminary Design of the Hybrid Air launching Rocket for Nanosat", *Fifth Intenational Comference on Computational Science and Applications*, pp. 290-295.

[5] Lee, C., Lee, J., Lee, Y.B.S., 2005, "Effect of Induced Swirl Flow on Regression Rate of Hybrid Rocket Fuel by Helical Grain Configuration Rocket", *EUCASS Conference.*

[6] Potapkin, A.V. and Lee, T.S., 2004, " Experimental Study of Thrust Performance of a Hybrid Rocket Motor with Various Methods of Oxidizer Injection", *Combustion Explosion and Shock Waves*, Vol.40, (4), pp.386-392.

[7] Yuasa S., Shimada O., Imamura T. Tamura T. and Yamamoto, K., 1999, "A Technique for Improving the Performance of Hybrid Rocket Engines", AIAA paper 99-2322, *35th AIAA/ASME/SAE/ASEE Joint Propulsion Conference & Exhibit*.

[8] Tamura, S., and Yusa, S., and Yamamoto, K., 1999, "Effect of Swirling Oxidizer Flow on Regression Rate of Hybrid Rocket", AIAA paper 99-2323, *35th AIAA/ASME/SAE/ASEE Joint Propulsion Conference & Exhibit*.

[9] Venugopal, S., Ramanujachar V., and Rajesh, K.K., 2011, "Combustion Experiments of HTPB/RFNA Mixed Hybrid Propellants", *Indian Journal of Science and Technology*", Vol. 4 (10), pp. 1267-1272.

[10] Tsohas, J., Appel, B., Rattenmainer, A., Walker, M., and Heiste, S.D., , 2009, "Development and Launch of the Purdue Hybrid Rocket Technology Demonstrator", AIAA 2009-4842, *45th AIAA/ASME/SAE/ASEE, Joint Propulsion Conference & Exhibit*.

[11] Stella F., Paglia F., 2009, "Pressure Oscillations In Solid Rocket Motors: Effect of Nozzle Cavity", *Aerotecnica Missili & Spazio*, Vol. 88 (1-2), pp.31-41.

[12] Fluent 6.3 user's manual.

Conference on Modelling Fluid Flow (CMFF'12)
The 15th International Conference on Fluid Flow Technologies
Budapest, Hungary, September 4-7, 2012

NUMERICAL SIMULATION OF THERMODYNAMIC PROCESSES IN THE WORKSPACE OF A STIRLING HEAT PUMP

Andrea HANDKI[1], Béla TOLVAJ[2]

[1] Corresponding Author. Department of Fluid and Heat Engineering, University of Miskolc, Miskolc - Egyetemváros, H-3515, Hungary. Tel.: +36 46 565-111, Fax: +36 46 565-471, E-mail: aramha@uni-miskolc.hu
[2] Department of Fluid and Heat Engineering, University of Miskolc, Miskolc - Egyetemváros, H-3515, Hungary. Tel.: +36 46 565-111, Fax: +36 46 565-471, E-mail: aramtb@uni-miskolc.hu

ABSTRACT

This paper presents a numerical method to calculate the thermodynamic processes in Stirling engines or heat pumps. The gas flow in the workspace is considered as one-dimensional, non-isentropic, unsteady flow. The cycle taking place in the Stirling machines is described with the partial differential equation system containing the equation of motion, equation of continuity and the energy equation. The partial differential equation system is solved by the method of characteristics. The boundary conditions, initial conditions necessary to solve the differential equation system and the connecting equations of the workspaces are presented in details. At the end of the article a concrete numerical example is solved and compared to a measurement result of a test machine.

Keywords: Alpha type Stirling machine, method of characteristics, numerical simulation

NOMENCLATURE

a	$[m/s]$	speed of sound
A	$[m^2]$	cross section of the pipe
$\underline{\underline{A}}$	[-]	coefficient matrix
$\vec{b}$	[-]	right-hand vector
BDC	[-]	bottom dead centre
c_p	$[J/kgK]$	specific heat at constant pressure
dx	$[m]$	elementary pipe length
$d\dot{Q}$	$[W]$	elementary heat convection
D	$[m]$	pipe diameter
k	$[W/m^2K]$	coefficient of heat transfer
L	$[m]$	pipe length
$p(x,t)$	$[Pa]$	pressure of gas
R	$[J/kgK]$	gas constant
s	$[J/kgK]$	specific entropy
t	$[s]$	time
$T(x,t)$	$[K]$	temperature of gas
T_a	$[K]$	ambient temperature
TDC	[-]	top dead centre
$v(x,t)$	$[m/s]$	velocity of gas
x	$[m]$	coordinate attached to the centre line of workspace
x_p	$[m]$	piston displacement
$\vec{x}$	[-]	vector of unknowns

Greek letters

λ	[-]	pipe friction factor
Δt	$[s]$	time step
Δx	$[m]$	grid step
κ	[-]	isentropic exponent
$\rho(x,t)$	$[kg/m^3]$	density of gas
τ	$[Pa/m^2]$	shear stress on the wall

Subscript

c	characteristic line
i	workspace element
p	piston
i,j,k	pipe element, grid point along x, grid point along t
E	enlarged

1. INTRODUCTION

The first Stirling engine was built in 1816 to displace the steam engine. As the internal combustion engines became widespread, the Stirling engines last the importance, but because of the incursion of the machines using alternative energy, the Stirling machines go to the centre of interest. Nowadays machines working on the Stirling cycle are available in the commerce.

The first model describing the operation of the engine was given by Schmidt in 1871. This model contained several assumptions and was only able to anticipate the power of an engine approximately. Since that several model came into birth. These are more and more detailed and can predict the characteristics of a Stirling machine more accurately.

The basic works of the literature are the books of Walker [1], Urieli-Berchowith [2] and Organ [3, 4]. These books beyond the Schmidt model summarize the basic types of Stirling machines, the processes taking place in the heat exchangers and the losses that occur during the operation.

Regarding the efficiency of the Stirling machines Curzon and Ahlborn [5] presented a new formula which gives a more accurate result compared to the measured value than the Carnot efficiency.

For the optimization of the power of Stirling refrigerators and heat pumps the method of finite time thermodynamics was applied successfully by Wu [6], Chen [7], Wu et al. [8, 9], Kaushik et al. [10], [11]. The control volume analysis was used by Ataer et al. [12], [13] to create a model to a V-type refrigerator.

In our previous work [14] the flow of the working gas was examined with the connection of unsteady, open thermodynamic systems. In this paper a numerical method is presented which is different from the previous work in that the thermodynamic processes in the cylinders, heat exchangers, and the regenerator are described as one dimensional, non isentropic, unsteady flow. During the modelling it is assumed that the value of the physical parameters is a function of time and a coordinate x associated with the centre line of the workspaces. An x-t coordinate system is coupled to each workspace and the value of the velocity, density, pressure, temperature and entropy of the flow are calculated in every grid point. Depending on the position of the pistons moving in the cylinders, the number of the grid points changes, which is taken into account in the determination of the boundary conditions. The connecting conditions of the coordinate systems are shown. The derivation of the partial differential equation system containing the equation of motion, equation of continuity and the energy equation is presented. The method of solution is demonstrated, which is the method of characteristics. The initial conditions and boundary conditions needed to solve the equation system are created.

Our goal is to validate the results of the model by comparison based on the measurements done on a Stirling test machine manufactured at the University of Miskolc. In this paper only a preliminary comparison is presented.

2. THE STIRLING TEST MACHINE

A Stirling test machine was built in cooperation of two departments at the University of Miskolc. The aim was to determine the behaviour of the machine in different working conditions and to provide experimental background for the validation of the numerical simulation. The main parameters of the test machine are included in Table 1.

Table 1. The main parameters of the test machine

Swept volume per cylinder	820 cm^3
Compression volume per cylinder	25 cm^3
Volume of connecting pipe	105 cm^3
Max. revolution of crank shaft	200 $1/min$
Max. temperature of cylinder	+150 $°C$
Min. temperature of cylinder	-10 $°C$
Max. pressure in cylinder	10 bar
Power of electric motor	9 kW

The test machine is an alpha type Stirling machine with two cylinders and can be assembled as a heat pump or as an engine. In first case the crank mechanism is driven by an electric motor and the temperature difference between the cylinders are measured. In the second case, one cylinder is heated, the other one is cooled and the provided power is measured. First the behaviour of the heat pump is investigated. The working gas is air in both cases. Hereafter in general case the expression of Stirling machine is used. The test machine assembled as a heat pump is presented in Figure 1.

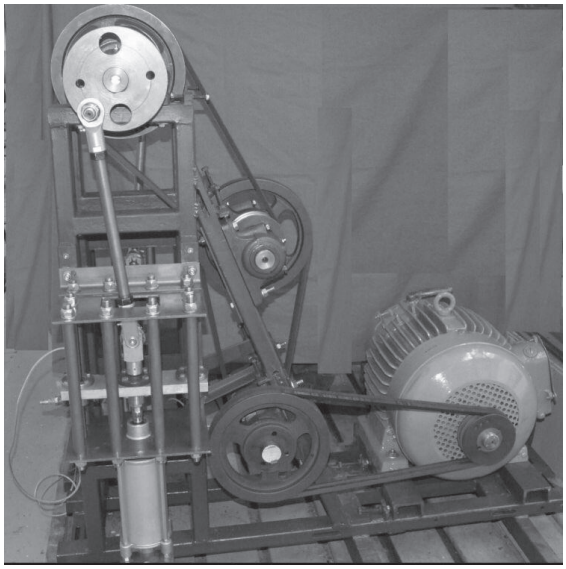

Figure 1. Stirling test machine as a heat pump

All components of the machine can be purchased commercially. To eliminate the leakage of the working gas, pneumatic cylinders were chosen. The crank mechanism is driven by an electric motor via gear-down mechanism, the rotational speed is regulated by frequency changer. During the measurements the temperature of the cylinders, the pressure in the workspace, the speed of revolution of the crank shaft and the power consumed by the electric motor are measured. Measurements can be done at different rotational speed and at different initial charging. The pressure sensor can be found in the middle of the pipe

connecting the cylinders. Accordingly the pressure difference between the cylinders cannot be determined with this apparatus. The built-in sensors and their accuracy class is collected in Table 2. To detect the sign of the sensors Spider 8 data collecting system is used. The real time results are visualised by Catman Easy software. The detailed description of the test machine, built in sensors and its data collecting system is presented in our previous work [18].

Table 2. The measurement sensors and their accuracy

Name	Type	Accuracy [%]
Pressure sensor	P8AP	0.3
Temperature sensor	K	1
Position sensor	PMIS4	0.01
Frequency converter	Frenic-Eco	0.2

3. THE APPLIED MODEL

The flow of the working gas in the cylinders, heat exchangers and connecting pipes is presented by the model shown in Figure 2. It is assumed that the gas flow is one-dimensional, the diameter of the pipe is constant in each workspace element, the velocity and characteristic values of the flow depend on time and a coordinate x fixed to the centre line of the pipe. The friction between the gas particles is neglected, but the shear stress slowing down the flow acts between the pipe wall and the working fluid. Throughout the pipe wall heat exchange is possible.

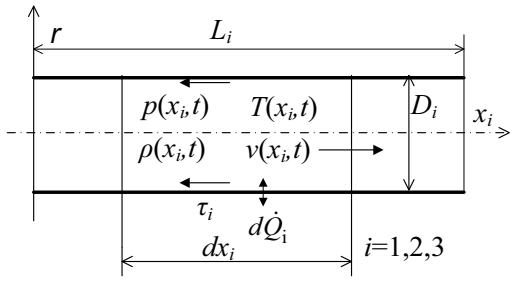

Figure 2. Elementary pipe length and related notations

The workspace of the Stirling machine is closed, the mass of the working fluid is constant. The workspace consists of three elements, among them the volume of cylinders are changing in time because of the moving pistons. At least three coordinate systems need to be coupled to the workspace of the Stirling machine. In our model the coordinate system x_1,t is coupled to cylinder 1., coordinate system x_2,t is coupled to cylinder 2., coordinate system x_3,t is coupled to the connecting pipe between the cylinders. In practice more complex compositions can be found. In the first two coordinate systems the number of grid points is changing in time because of the time dependent motion of the pistons.

The equation system describing the gas flow consists of three equations [15]. These are the equation of motion:

$$\frac{\partial v}{\partial t}+v\frac{\partial v}{\partial x}+\frac{1}{\rho}\frac{\partial p}{\partial x}+\frac{\lambda v|v|}{2D}=0\,, \tag{1}$$

the equation of continuity:

$$\frac{1}{\rho a^2}\left[\frac{\partial p}{\partial t}+v\frac{\partial p}{\partial x}\right]+\frac{\partial v}{\partial x}+v\frac{\partial\left(ln(A)\right)}{\partial x}=0\,, \tag{2}$$

and the energy equation:

$$\begin{aligned}\frac{ds}{dt}&=\left[\frac{\partial s}{\partial t}+v\frac{\partial s}{\partial x}\right]=\\&=\frac{\lambda}{2DT}v^2|v|-\frac{4}{D\rho T}k\left(T-T_a\right)\end{aligned}\,. \tag{3}$$

4. THE METHOD OF CHARACTERISTICS

The method of characteristics is suitable for the investigation of a gas flow if the partial differential equations describing the flow are hyperbolic. The characteristic line is a path along which a physical change of state spreads.

The characteristic lines are the $x_c(t)$ curves on the physical plane x,t along which the partial derivatives $\frac{\partial v}{\partial t}$, $\frac{\partial v}{\partial x}$, $\frac{\partial p}{\partial t}$, $\frac{\partial p}{\partial x}$, $\frac{\partial s}{\partial t}$, $\frac{\partial s}{\partial x}$ cannot be determined unambiguously.

The derivatives of the velocity, pressure and entropy (v, p, s) along the characteristic curves can be defined as:

$$\frac{dv}{dt}=\frac{\partial v}{\partial t}+\frac{dx_c}{dt}\frac{\partial v}{\partial x}, \tag{4}$$

$$\frac{dp}{dt}=\frac{\partial p}{\partial t}+\frac{dx_c}{dt}\frac{\partial p}{\partial x}, \tag{5}$$

$$\frac{ds}{dt}=\frac{\partial s}{\partial t}+\frac{dx_c}{dt}\frac{\partial s}{\partial x}. \tag{6}$$

Eqs. (1) to (6) can be written in the form of $\underline{\underline{A}}\cdot\vec{x}=\vec{b}$. From Eqs. (1) to (6) the six partial derivatives $\left(\frac{\partial v}{\partial t}, \frac{\partial v}{\partial x}, \frac{\partial p}{\partial t}, \frac{\partial p}{\partial x}, \frac{\partial s}{\partial t}, \frac{\partial s}{\partial x}\right)$ cannot be determined unambiguously if the determinant of the equation system or the enlarged

determinant of each unknown parameter is zero. From the condition of det($\underline{\underline{A}}$)=0 the equation of characteristic lines can be determined on the physical *x,t* plane:

$$\frac{dx_c}{dt} = v + a\,, \quad \frac{dx_c}{dt} = v - a\,, \quad \frac{dx_c}{dt} = v\,. \quad (7\text{-}9)$$

The enlarged matrix $\underline{\underline{A}}_E$ can be obtained if the right-hand vector is put into the appropriate column of matrix $\underline{\underline{A}}$. The determinant of matrix $\underline{\underline{A}}_E$ has to be zero for the reason that the unknowns from the equation systems cannot be determined unambiguously. From this condition the equations of characteristic lines on the phase planes can be obtained.
The first characteristic equation is:

$$\frac{dv}{dt} + \frac{1}{\rho a}\frac{dp}{dt} = -\frac{\lambda v|v|}{2D}\,, \quad (10)$$

if $\frac{dx_c}{dt} = v + a$.
The second is:

$$\frac{dv}{dt} - \frac{1}{\rho a}\frac{dp}{dt} = -\frac{\lambda v|v|}{2D}\,, \quad (11)$$

if $\frac{dx_c}{dt} = v - a$.
The third is:

$$\frac{ds}{dt} = \frac{\lambda}{2DT}v^2|v| - \frac{4}{D\rho T}k(T - T_a)\,, \quad (12)$$

if $\frac{dx_c}{dt} = v$.
The next step is the discretization of the Eqs. (10) to (12). A plane x_i,t (i=1,2,3) is assigned to both cylinders and to the connecting pipe. The x_i,t plane is covered by an equidistant mesh with spacing Δt. The workspace elements are denoted by subscript *i*, the number of grid points in each element is given by N_i. The grid points are determined by a triple subscripts of an *i,j,k*, where *i* identifies the pipe element, *j* refers to the grid point along *x* and *k* refers to the grid point along *t*.

The calculation was carried out with the interpolation of the grid points. The essence of the method is that on the x_i,t plane the conditions at a given point *M* are determined by the characteristic lines I., II., III. going into *M.* The derivation of the method is presented in our previous work [16], henceforth only the main equations are introduced.

First the position of points *P, R* and *Q* need to be found using linear approximation starting from the known values of row *k.* The three characteristic lines start from points *P, R, Q* and all go through point *M.* After that with the integration of equations (7-12) using linear approximation the value of velocity, pressure and entropy ($v_{i,j,k+1}$, $p_{i,j,k+1}$, and $s_{i,j,k+1}$) in point *M* can be determined. This method cannot be used at the ends of the pipe elements; therefore boundary conditions and connecting conditions are needed for each pipe element. The method is shown in Figure 3.

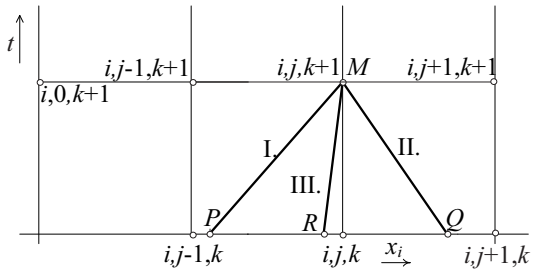

Figure 3. Mesh attached to pipe element *i*

The characteristic curves starting from points *P, R* and *Q* and going through point *M* (*i,j,k+1*) are obtained as follows:

$$v_{i,j,k+1} + \frac{1}{\rho_P a_P}p_{i,j,k+1} = B_{P_i}\,, \quad (13)$$

$$v_{i,j,k+1} - \frac{1}{\rho_Q a_Q}p_{i,j,k+1} = B_{Q_i}\,, \quad (14)$$

$$s_{i,j,k+1} = B_{R_i}\,. \quad (15)$$

The right side of the equations are expressed as follows:

$$B_{P_i} = v_P + \frac{p_P}{\rho_P a_P} - \lambda_i \frac{v_P|v_P|}{2D_i}\Delta t\,, \quad (16)$$

$$B_{Q_i} = v_Q - \frac{p_Q}{\rho_Q a_Q} - \lambda_i \frac{v_Q|v_Q|}{2D_i}\Delta t\,, \quad (17)$$

$$B_{R_i} = s_R + \frac{\lambda}{2DT_R}v^2|v| - \\ + \frac{4}{D\rho_R T_R}k(T_R - T_a)\,. \quad (18)$$

The characteristic values in point *M* (*i,j,k*+1) can be calculated as:

$$v_{i,j,k+1} = \frac{B_{P_i}\rho_P a_P + B_{Q_i}\rho_Q a_Q}{\rho_Q a_Q + \rho_P a_P}\,, \quad (19)$$

$$p_{i,j,k+1} = \left(B_{P_i} - B_{Q_i}\right)\left(\frac{1}{\rho_P a_P} + \frac{1}{\rho_Q a_Q}\right)^{-1}, \quad (20)$$

$$s_{i,j,k+1} = B_{R\,i} \ . \quad (21)$$

Accordingly, starting from values in row k, the values of $v_{i,j,k+1}$, $p_{i,j,k+1}$ and $s_{i,j,k+1}$ in the grid points of row (k+1) can be determined, except for the first and last grid points of each pipe ($j \neq 0, j \neq N_i$); where boundary conditions and connecting conditions need to be fulfilled.

The computation is convergent if the Courant – Friedrichs – Lewy stability and convergence condition [17] is satisfied for every pipe element:

$$T_i = \frac{\Delta t}{\Delta x_i} < \frac{1}{v_{max} + a_i}. \quad (22)$$

Beyond the values of $v_{i,j,k+1}$, $p_{i,j,k+1}$ and $s_{i,j,k+1}$ determined from the characteristic equations, the values of $T_{i,j,k+1}$, $\rho_{i,j,k+1}$ and $a_{i,j,k+1}$ are needed.
It is known that from the thermodynamics:

$$Tds = c_p dT - \frac{1}{\rho} dp \ , \quad (23)$$

and from the perfect gas law:

$$\frac{p}{\rho} = RT \ . \quad (24)$$

Substituting Eq. (24) into (23) yields:

$$s_{i,j,k+1} - s_R = c_p ln\frac{T_{i,j,k+1}}{T_R} - Rln\frac{p_{i,j,k+1}}{p_R} \ , \quad (25)$$

from which the required variables can be determined:

$$T_{i,j,k+1} = T_R e^{\frac{s_{i,j,k+1} - s_R}{c_p}} \left(\frac{p_{i,j,k+1}}{p_R}\right)^{\frac{\kappa-1}{\kappa}}, \quad (26)$$

$$\rho_{i,j,k+1} = \frac{p_{i,j,k+1}}{RT_{i,j,k+1}} \ , \quad (27)$$

$$a_{i,j,k+1} = \sqrt{\kappa R T_{i,j,k+1}} \ . \quad (28)$$

5. Boundary conditions

Figure 4 shows the coordinate systems coupled to the workspace elements. The horizontal axis represents the coordinate x_i, the vertical axis represents the time. For the reason that the boundary- and connecting conditions could be defined easily, the value of the time step Δt is the same in every coordinate system.

The value of grid scale Δx_i can be different in each coordinate system. The number of calculative points is given by N_i in each coordinate system.

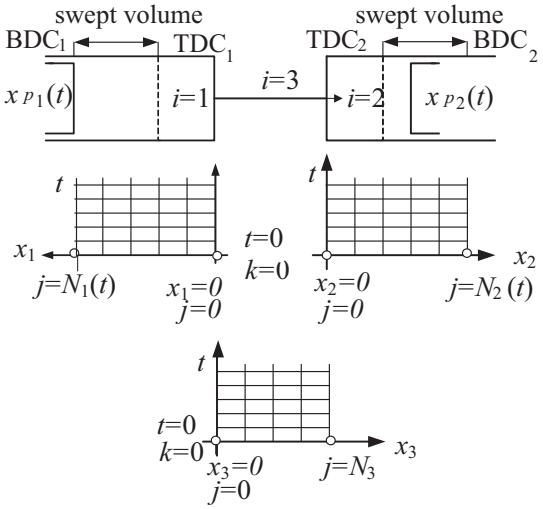

Figure 4. The coordinate systems coupled to the workspace elements

5.1. Boundary condition of the piston of cylinder 1.

The mesh coupled to cylinder 1 (i=1) can be seen in Figure 5. In the moment of t=0 (k=0) the piston can be anywhere between the dead centres, but its motion is determined by the function $x_{p1}(t)$. In the grid point (j=0…N_1(t), k=0) the value of $p_{i,j,k}$, $s_{i,j,k}$, and $v_{i,j,k}$ is known from the initial conditions. During Δt time step the piston moves $x_{p1}(t_{k+1})$ distance. In the moment t_{k+1} the value of $p_{i,j,k+1}$, $s_{i,j,k+1}$, and $v_{i,j,k+1}$ can be determined in the inner points using Eqs. (19) to (21).

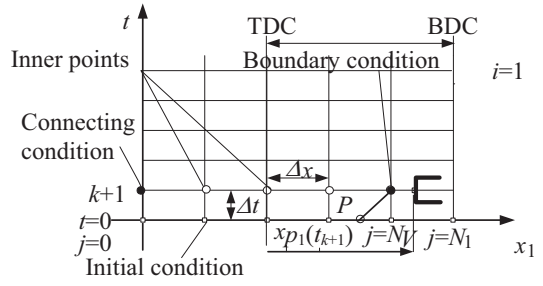

Figure 5. The mesh coupled to cylinder 1

The motion of the pistons $x_{p1}(t)$ thereby its velocity and acceleration are known. Substituting the value of t_{k+1} into t (t=t_{k+1}) the position, velocity and acceleration of piston 1 can be obtained in the moment of k+1:

$$x_{p1,k+1} = x_{p1}(t_{k+1}), \tag{29}$$

$$v_{p1,k+1} = v_{p1}(t_{k+1}), \tag{30}$$

$$a_{p1,k+1} = a_{p1}(t_{k+1}). \tag{31}$$

In point j=N_V the velocity can be determined using linear approximation:

$$v_{1,N_V,k+1} = v_{1,N_V-1,k+1} + \\ + \Delta x_1 \frac{v_{p1,k+1} - v_{1,N_V-1,k+1}}{\Delta x_1 + s_{V,k+1}}, \tag{32}$$

where:

$$N_V = int\left(\frac{x_{p1,k+1}}{\Delta x_1}\right), \tag{33}$$

$$s_{V,k+1} = x_{p1,k+1} - N_V \cdot \Delta x_1. \tag{34}$$

As the velocity is known, with the help of the the characteristic line between point P and 1,N_V,k+1:

$$v_{1,N_V,k+1} + \frac{1}{\rho_P a_P} p_{1,N_V,k+1} = B_P, \tag{35}$$

the pressure can be calculated:

$$p_{1,N_V,k+1} = \left(B_Q - v_{1,N_V,k+1}\right)\rho_P a_P. \tag{36}$$

In the point 1,N_V,k+1 the entropy can be obtained using the characteristic line III.:

$$s_{i,j,k+1} = B_{R_i}. \tag{37}$$

Finally from Eqs. (26) and (27) the temperature and density can be determined:

$$T_{1,N_V,k+1} = T_R e^{\frac{s_{i,j,k+1} - s_R}{c_p}} \left(\frac{p_{1,N_V,k+1}}{p_R}\right)^{\frac{\kappa-1}{\kappa}}, \tag{38}$$

$$\rho_{1,N_V,k+1} = \frac{p_{1,N_V,k+1}}{R T_{1,N_V,k+1}}. \tag{39}$$

The boundary conditions of piston 2 are identical with that of piston 1, but the value of index i has to be changed from 1 to 2.

5.2. Attachment of the cylinders and the connecting pipe

The schema of the boundary condition is presented in Figure 6.

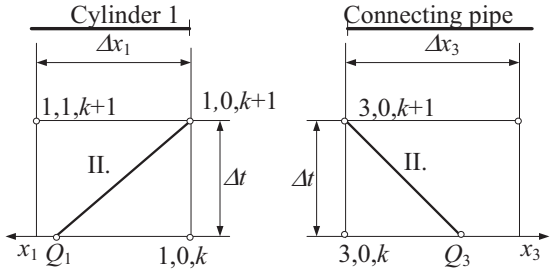

Figure 6. The attachement of cylinder 1 and the connecing

In the connection points six parameters have to be determined. These are: $p_{1,0,k+1}$, $\rho_{1,0,k+1}$, $v_{1,0,k+1}$, $p_{3,0,k+1}$, $\rho_{3,0,k+1}$, $v_{3,0,k+1}$. To do that six equations are required. These are:

$$v_{1,0,k+1} - \frac{1}{\rho_{Q1} a_{Q1}} p_{1,0,k+1} = B_{Q1}, \tag{40}$$

$$v_{3,0,k+1} - \frac{1}{\rho_{Q3} a_{Q3}} p_{3,0,k+1} = B_{Q3}, \tag{41}$$

$$\frac{p_{3,0,k+1}}{a_R^2} - \rho_{3,0,k+1} = B_{R3}, \tag{42}$$

$$v_{1,0,k+1} A_1 \rho_{1,0,k+1} = -v_{3,0,k+1} A_3 \rho_{3,0,k+1}, \tag{43}$$

$$p_{1,0,k+1} = p_{3,0,k+1}, \tag{44}$$

$$\rho_{1,0,k+1} = \rho_{3,0,k+1}. \tag{45}$$

From the six equations the six unknown parameters can be calculated:

$$v_{1,0,k+1} = \frac{B_{Q1} a_{Q1} \rho_{Q1} - B_{Q3} a_{Q3} \rho_{Q3}}{\rho_{Q1} a_{Q1} + \frac{A_1}{A_3} \rho_{Q3} a_{Q3}}, \tag{46}$$

$$v_{3,0,k+1} = \frac{v_{1,0,k+1} A_1 \rho_{1,0,k+1}}{A_3 \rho_{3,0,k+1}}, \tag{47}$$

$$p_{1,0,k+1} = \left(v_{1,0,k+1} - B_{Q1}\right) a_{Q1}\, \rho_{Q1} \quad , \tag{48}$$

$$p_{3,0,k+1} = \left(v_{3,0,k+1} - B_{Q3}\right) a_{Q3}\, \rho_{Q3} \quad , \tag{49}$$

$$s_{3,0,k+1} = B_{R3} \, . \tag{50}$$

From Eq. (50) the density can be obtained using Eqs. (38) and (39).

The connection of cylinder 2 and the connecting pipe is presented in Figure 7.

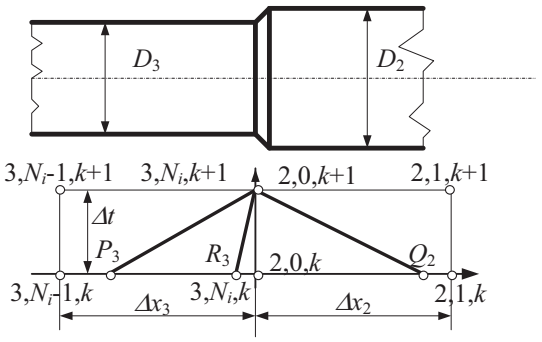

Figure 7. The connection between cylinder 2 and the connecting pipe

In the connection points the equation of continuity is satisfied, additionally the three characteristic lines can be obtained as:

$$v_{3,N3,k+1} A_3 \rho_{3,N3,k+1} = v_{2,0,k+1} A_2 \rho_{2,0,k+1} \, , \tag{51}$$

$$v_{3,N3,k+1} + \frac{p_{3,N3,k+1}}{a_{P3}\, \rho_{P3}} = B_{P3} \, , \tag{52}$$

$$v_{2,0,k+1} - \frac{p_{2,0,k+1}}{a_{Q2}\, \rho_{Q2}} = B_{Q2} \, , \tag{53}$$

$$s_{3,N3,k+1} = B_{R3} \quad . \tag{54}$$

In Eq. (51) A_i (i=2,3) is the cross section of the connecting pipe and the cylinder:

$$A_i = \frac{D_i^2 \pi}{4} \quad . \tag{55}$$

If it is assumed that the pressure and density of the gas is equal in the connection of cylinder 2 and connecting pipe:

$$p_{2,0,k+1} = p_{3,N3,k+1} \, , \tag{56}$$

$$\rho_{2,0,k+1} = \rho_{3,N3,k+1} \quad . \tag{57}$$

From Eqs. (51) to (54) and Eqs. (56) to (57) the six unknown parameters ($p_{2,0,k+1}$, $v_{2,0,k+1}$, $\rho_{2,0,k+1}$, $p_{3,N3,k+1}$, $v_{3,N3,k+1}$, $\rho_{3,N3,k+1}$) parameters can be determined as follows:

$$v_{3,N3,k+1} = \frac{B_{P3} a_{P3}\, \rho_{P3} + B_{Q2} a_{Q2}\, \rho_{Q2}}{\rho_{P3}\, a_{P3} + \dfrac{A_3}{A_2} \rho_{Q2}\, a_{Q2}} \, , \tag{58}$$

$$v_{2,0,k+1} = \frac{v_{3,N3,k+1}\, A_3\, \rho_{3,N3,k+1}}{A_2\, \rho_{2,0,k+1}} \, , \tag{59}$$

$$p_{3,N3,k+1} = p_{2,0,k+1} = \left(B_{P3} - \frac{B_{P3} a_{P3} + B_{Q2} a_{Q2}}{\rho_{P3}\, a_{P3} + \dfrac{\rho_{Q2}\, A_2\, a_{Q2}}{A_3}} \right) a_{P3}\, \rho_{P3} \quad . \tag{60}$$

The value of entropy in point M is calculated as:

$$s_{2,0,k+1} = s_{3,N3,k+1} = B_{R3} \quad . \tag{61}$$

6. RESULTS

Using the method presented above the pressure and temperature in the workspace of a Stirling machine, further the velocity, density and entropy of the working gas can be determined. The input parameters of the simulation are set according to the measurement previously done on the test machine. The basic settings are presented in Table 3.

Table 3. The basic settings of the measurements

Charging pressure	1 *bar*
Revolution of crankshaft	45 1/*min*
Ambient temperature	20 °*C*

For all measurements carried out, the initial charging is always the smallest pressure during the cycle. The measured and calculated pressures are compared in Figure 8. Good agreement can be observed between the pressures. The visualised period is 1 second. The pressure varies between 1 and 5 bars over a cycle.

The temperature of the hot and cold side cylinder provided by the model is not compared to the measured values, because the temperature sensors measure the temperature on the surface of the cylinders, while the model determines the temperature of the working gas inside the cylinder. The verification of the temperature is the way of our further research.

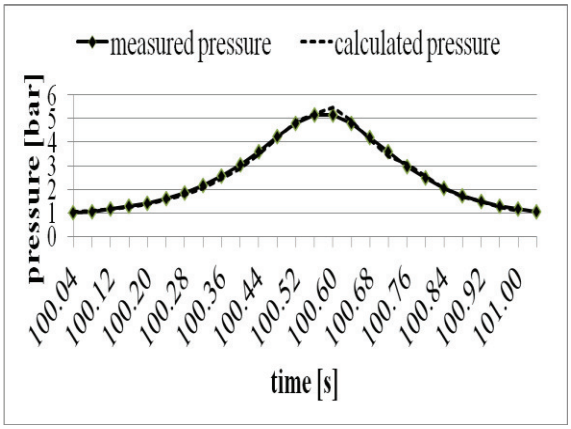

Figure 8. The comparison of the measured and calculated pressures

7. SUMMARY

In this paper a computational method is presented, which can predict the main characteristics of a Stirling engine or a heat pump by modelling the thermodynamic processes inside it. The equation system based on the governing equations and the mesh coupled to the workspace elements are presented. This work is a continuation of our previous work [16] containing the detailed derivation of the equations, and completed with the connecting- and boundary conditions of the workspace elements. Finally a particular computational result is presented and compared to a measurement results obtained using our Stirling test machine. The modification of the model based on experimental results has just begun, but the results obtained so far are promising.

ACKNOWLEDGEMENTS

The described work was carried out as part of the TÁMOP-4.2.1.B-10/2/KONV-2010-0001 project in the framework of the New Hungarian Development Plan. The realization of this project is supported by the European Union, co-financed by the European Social Fund.

REFERENCES

[1] Walker, G., 1980, *Stirling Engines*, Oxford University Press.

[2] Urieli, I., and Berchowitz, D.M., 1984, "Stirling cycle engine analysis, Adam Hilger Ltd.

[3] Organ, A.J., 1992, *Thermodynamics and gas dynamics of the Stirling cycle machine*, Cambridge University Press.

[4] Organ, A.J., 2007, *The air engine*, CRC Press.

[5] Curzon, F.L., and Ahlborn, B., 1975, "Efficiency of a Carnot engine at maximum power output", *AJP*, Vol. 43, pp. 22-24.

[6] Wu, C., 1995, "Maximum obtainable specific cooling load of a refrigerator", *Energy Convers. Mgmt.,* Vol. 36, pp. 7-10.

[7] Chen, J., 1998, "Minimum power input of irreversible Stirling refrigerator for given cooling rate", *Energy Convers. Mgmt*., Vol. 39, pp. 1255-1263.

[8] Wu, C., Chen, L., and Sun, F., 1998, "Cooling load versus COP characteristics for an irreversible air refrigeration cycle", *Energy Convers. Mgmt*., Vol. 39, pp. 117-125.

[9] Wu, C., Chen, L., and Sun, F., 1998, "Optimization of steady flow heat pumps" *Energy Convers. Mgmt.,* Vol. 39, pp. 445-453.

[10] Kaushik, S.C., Tíagi, S.K., Bose, S.K., and Singhal, M.K., 2002, "Performance evaluation of irreversible Stirling and Ericsson heat pump cycles*", Int. J. Therm. Sci*., Vol. 41, pp 193-200.

[11] Kaushik, S.C., Tyagi, S.K., and Singhal, M.K., 2002, "Parametric study of irreversible Stirling and Ericsson cryogenic refrigeration cycles", *Energy Convers. Mgmt*., Vol. 43, pp. 2297-2309.

[12] Ercan Ataer, Ö., and Karabulut, H., 2005, "Thermodynamic analysis of the V-type Stirling-cycle refrigerator", *Int. J. Refrigeration,* Vol. 28, pp. 183-189.

[13] Ercan Ataer, Ö., and Tekin, Y., 2010, "Performance of V-type Strling-cycle refrigerator for different working fluid", *Int. J. Refrigeration*, Vol. 33, pp. 12-18.

[14] Handki, A., and Tolvaj, B., 2010, "Thermodynamic model of Stirling machines", *Proc. 19th Polish National Fluid Dynamics Conference*, Poznan, Poland, published on CD. pp. 1-9.

[15] Seifert, H., 1962, *Instationäre Strömungsvorgänge in Rohrleitungen an Verbrennungskraftmaschinen*, Springer-Verlag.

[16] Handki, A., and Tolvaj, B., 2012, "Investigation of the processes in a Stirling machine with the method of characteristics", *Proc. MicroCad 2012,* Miskolc, Hungary, section N, article N8, published on CD. pp. 1-6.

[17] Kozák, M., 1977, *Calculation of non-permanent free surface water flow using digital computers* (in Hungarian), Akadémiai Press.

[18] Handki A., and Tolvaj B., 2012, "*Stirling test machine and its data collecting system*" (in Hungarian) *Proc. OGÉT 2012*. Kolozsvár, Romania, pp. 161-164.

Conference on Modelling Fluid Flow (CMFF'12)
The 15th International Conference on Fluid Flow Technologies
Budapest, Hungary, September 4-7, 2012

HEAT TRANSFER AND INTERNAL WAVES IN A RECIPROCATING COMPRESSOR

Thomas Müllner[1], Herbert Steinrück[2]

[1]Vienna University of Technology, Institute of Fluid Mechanics and Heat Transfer, Resselgasse 3, 1040 Vienna, Austria, E-mail: thomas.muellner@tuwien.ac.at
[2]Corresponding author. Vienna University of Technology, Institute of Fluid Mechanics and Heat Transfer, Resselgasse 3, 1040 Vienna, Austria, Tel.: +43 1 58801 32231, Fax +43 1 58801 32299, E-mail: herbert.steinrueck@tuwien.ac.at

ABSTRACT

The internal flow in a reciprocating compressor, its interaction with the valves, and the heat transfer from the compressed gas to the compressor housing are studied using different flow and heat transfer models. For simple compressors, having only one suction and one discharge valve it turns out that a one dimensional non-linear flow model is sufficient to describe the interaction of the internal pressure waves with the valves. For more complex geometries 2D- or 3D-flow models are required.

Although a one dimensional model seems insufficient to predict the heat transfer in the compressor, which depends on the internal flow structure, a method has been developed, how a reasonable approximation of the heat fluxes can be obtained by expressing the heat-fluxes as a weighted sum of four reference enthalpy fluxes resulting from the 1D-flow model. The weight factors can be interpreted as Stanton numbers and have to be determined a priory by 3D-CFD simulations. The gain of this approach is that these Stanton numbers have to be determined only once for a certain class of compressors and depend only weakly on the compressor data.

Keywords: reciprocating compressor, internal waves, heat transfer

NOMENCLATURE

A	area
$\dot{Q}$	heat flow
Z	distance cylinder head piston
St	Stanton number
c	speed of sound
c_p	specific isobaric heat capacity
c_v	specific isochoric heat capacity
d	diameter
e	specific internal energy
f	compressor speed
h	stroke
k_S	valve spring constant
$\dot{m}$	mass flow
m_V	mass valve plate
p	pressure
$\dot{q}$	heat flux density
s	specific entropy
t	time
u	gas velocity
$\underline{u}$	state vector
x	coordinate along diameter
y	coordinate perpendicular to diameter
z	coordinate in axial direction
z_V	valve lift
γ	ratio of specific heat capacities
φ	crank angle
λ	shock speed
ρ	gas density

1. INTRODUCTION

The cross section of a reciprocating compressor is shown in Figure 1. It consists of a cylindrical compression chamber closed at one end by the cylinder head and at the other end by a movable piston. During the expansion phase the volume in the compression chamber increases, and gas enters through the suction valve. After the piston has reached the position of maximal volume, it starts to compress the gas. If the pressure in the compression chamber exceeds the discharge pressure, the discharge valve opens, and the gas leaves the compressor through the discharge valves.

Until recently for the design of a compressor a quasi static description of the gas in the compressor has been sufficient [2]. However, due to the design of larger and faster compressors it turns out that internal waves cannot be neglected. They result in unwanted valve losses or in large oscillating moments on the piston rod [3].

The suction and discharge valves are usually

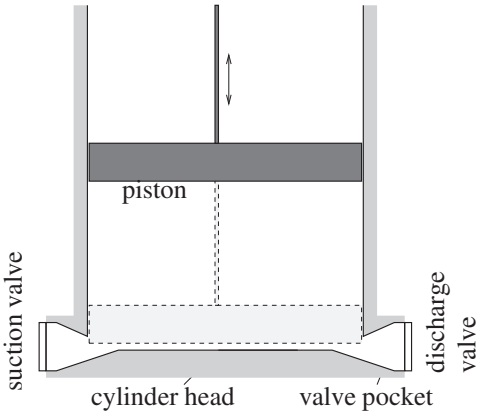

Figure 1: Reciprocating compressor

situated at the cylinder barrel near the cylinder head. They are connected to the cylinder by valve pockets (see Figure 1). The valves are passive. That means a valve opens if there is a sufficient positive pressure difference across it; otherwise it is closed. If the discharge valve opens, a rarefaction wave is initiated. It is reflected at the opposite side of the cylinder and thus interacts with the discharge valve. As a consequence, the discharge valve may open and close several times during discharge.

For the design of a compressor, the interaction of the internal waves with the valves is essential since the waves contribute to losses of efficiency.

A series of models has been developed (1D-, 2D-, and 3D) to describe the interaction of the valves with the internal waves and the fluid flow based on the Euler equations.

In the 1D-case the wave propagation between the suction and discharge valve is modeled by the quasi 1D-Euler equations, see Aigner [1]. Although, this model is very simple, reasonable qualitative agreement with experiments have been obtained. However, for compressors with more than one suction or discharge valve at least a 2D-flow model is necessary. A comparison of the wave propagation models (1D, 2D, 3D) and with experiments will be given.

For the design of a compressor the heat transfer of the gas to the surrounding compressor walls is also of interest. For internal combustion engines a relation for the instantaneous heat transfer coefficient was given by Woschni [6].

For the heat transfer analysis a 3D-flow simulation seems to be necessary. However, we have developed an approach to estimate the heat transfer by using the the 1D-flow model. The main idea is that the heat transfer is proportional to a weighted sum of enthalpy fluxes which can be determined by the 1D-flow model. The weights can be interpreted as Stanton numbers. Thus empirical relations for these Stanton numbers are needed. They can be obtained a priori on a data base generated by 3D-flow simulations.

Thus, a fast, reliable tool for the compressor design has been developed which is capable predicting internal waves, impact speed of the valve plate onto the valve seat and heat transfer.

The paper is organized as follows. In section 2 we review flow models, and compare their predictions with measurements. In section 3 we present a heat transfer model.

2. Flow models

Since, under normal operating conditions, the Reynolds number is very large, the flow field of the gas in the compressor is turbulent, and thus, the Reynolds Averaged Navier Stokes (RANS) equations can be used to describe the flow field. However, solving the RANS equations with a commercial code in a 3D domain is very much time consuming. Thus, there is a need for simplified flow models which will be described in the following.

2.1. 1D-Flow model

Let us consider a simple compressor with just one suction and one discharge valve sitting opposite to each other at the circumference of the compression chamber first. The following two observations justify a one dimensional approach:

- Internal waves are initiated when the discharge valves opens. Then the piston is sufficient close to the cylinder head, and the flow takes place in a narrow gap between the cylinder head and the piston.
- Waves travel mainly back and forth between the discharge and suction valve.

When the piston is not close to the cylinder head, the flow is three dimensional. However, usually during this stage waves have been already damped.

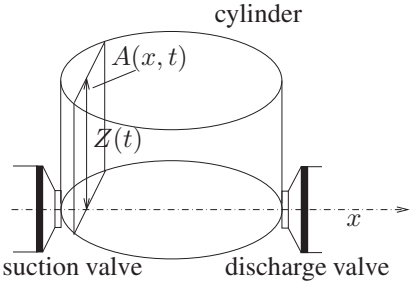

Figure 2: Cross section in 1D-flow model

Let x denote the spatial coordinate along the diameter between the valves. The state of the gas at a position x and time t is denoted by $\underline{u} = (\rho, \rho u, \rho e + \rho u^2/2)$, where u is the flow velocity in x-direction, ρ the density of the gas and e the specific inner energy. Furthermore, let $A(x,t)$ be the cross section of the compressor perpendicular to the x-axis, see Figure 2. It is of course a function of x and t. Assuming that all

flow quantities are functions of x and t, the mass- and momentum balance read:

$$(A\rho)_t + (A\rho u)_x = 0, \tag{1}$$

$$(A\rho u)_t + (A\rho u^2 + Ap)_x = pA_x. \tag{2}$$

$$\left(A\rho(e + \frac{u^2}{2})\right)_t + \left(A\rho u(e + \frac{p}{\rho} + \frac{u^2}{2})\right)_x = -A_t p, \tag{3}$$

where p is the pressure and $e = e(p, \rho)$ is the specific internal energy given by equation of state.

Instead of using the energy equation in [1] it is assumed that the flow is isentropic and smooth (no shocks). Thus (2) is replaced by

$$\rho_t + \left(\frac{u^2}{2} + \int_{\rho_0}^{\rho} \frac{c^2(\tilde{\rho}, s_0)}{\tilde{\rho}} \mathrm{d}\tilde{\rho}\right)_x = 0, \tag{4}$$

where c is the isentropic speed of sound, and s is the specific entropy.

2.1.1. Discontinuous cross section

At the connection of the valve pocket to the compression chamber the cross section A has a discontinuity. Thus, the 1D-flow model is there of limited accuracy since the flow is there locally three dimensional. However, we want to model this discontinuity in the frame work of a one dimensional Euler flow.

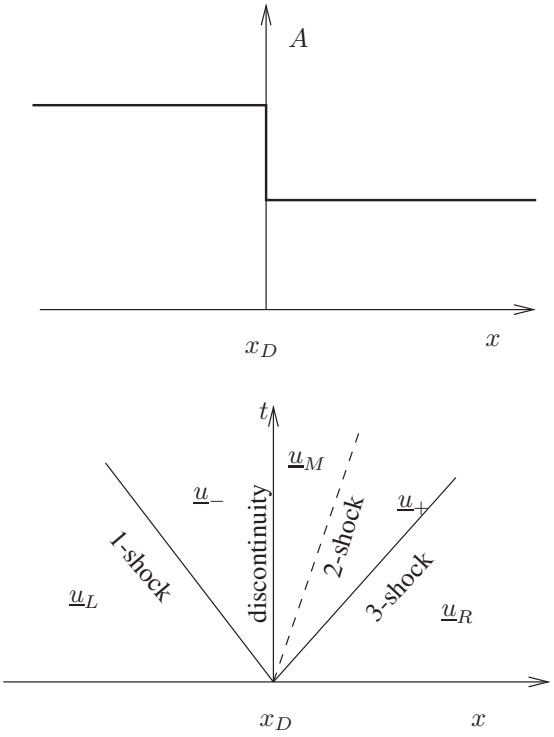

Figure 3: Riemann problem with discontinuity of cross section

Using a finite volume scheme for the discretization of the flow equation, we place the control volume such that there is a cell boundary at the discontinuity located at x_D. The basic idea is now to determine the numerical flux at both sides of this cell boundary. Since, the cross section A is discontinuous there, the flux is there also discontinuous. However, the mass and enthalpy fluxes are continuous. Only the momentum flux and the pressure are discontinuous. Now following the basic idea of Gudunov's method [5], we solve a Riemann problem where the initial data is discontinuous at the cell boundary. The solution structure for subsonic flow from left to right is depicted in Figure 3. The x, t-half-plane is divided by shocks, expansion fans or the discontinuity of the cross section into four regions, see Figure 3.

Across a shock the Rankine-Hugoniot conditions hold. For example for the 1-shock we have:

$$\rho_L u_L - \rho_- u_- = \lambda_1(\rho_L - \rho_-), \tag{5}$$

$$\rho_L u_L^2 + p_L - \rho_- u_-^2 - p_- = \lambda_1(\rho_L u_L - \rho_- u_-), \tag{6}$$

$$\begin{aligned} \rho_L u_L(h_L + \tfrac{u_L^2}{2}) - \rho_- u_-(h_- + \tfrac{u_-^2}{2}) = \\ \lambda_1(\rho_L(e_L + \tfrac{u_L^2}{2}) - \rho_-(e_- + \tfrac{u_-^2}{2})), \end{aligned} \tag{7}$$

where λ_1 is the speed of the 1-shock and $\underline{u}_L$ is the state vector left of the 1-shock and $\underline{U}_-$ is the vector right of the 1-shock. For the 3-shock the same conditions hold for the state vectors $\underline{u}_+$ and $\underline{u}_R$ left and right of the 3-shock and the shock speed λ_3. Across a 2-shock the pressure and flow velocity are continuous.

To obtain a relation between $\underline{u}_-$ and $\underline{u}_M$ we assume a stationary isentropic flow in case of a decrease of the flow cross section in flow direction. In case of a sudden increase of the cross section, we use the Borda-Carnot pressure loss.

In both cases a non-linear equation for the flow velocity u_- can be derived which has to be solved iteratively. Thus, the states $\underline{u}_-$ and $\underline{u}_M$ can be determined and the mass, momentum, and energy flow and the pressure on both sides of the discontinuity can be obtained and prescribed in the finite volume scheme.

Note that we have discussed only the simplest case of subsonic flow with $u_- > 0$. Depending on the sign of the shock speeds we have to distinguish several cases similar to Gudunov's method. However, here an additional case can occur, when in the $-$-region the flow is subsonic, but reaches critical flow conditions $\underline{u}_C$ after the restriction of the cross section at $x = x_D+$. In this case an expansion fan to supersonic flow follows, see Figure 4.

2.2. 2D-Flow model

Since, the waves are mainly initiated by the opening and closing of the discharge valves, wave phenomena are of primary interest, only when the distance between the piston and cylinder head is small compared to the diameter of the cylinder. Thus, during discharge the flow can be approximated by a 2D-dimensional flow parallel to the cylinder head.

Let $Z = Z_p(t) - z_H(x, y)$ be the distance between the cylinder head and the piston, where $Z_p(t)$ denotes

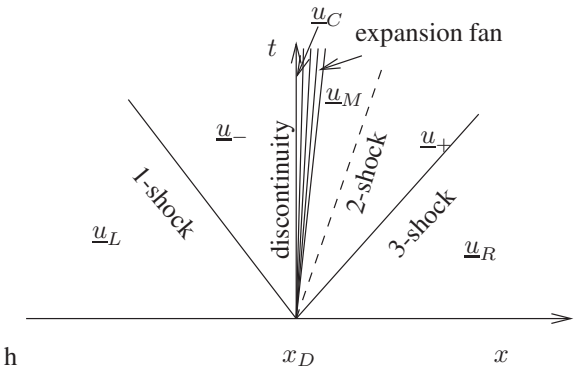

Figure 4: Riemann problem with critical flow conditions downstream of the discontinuity of the cross section

the actual position of the piston at time t and $z = z_H(x, y)$ is the surface of the cylinder head.

Assuming isotropic flow the governing equations are:

$$(\rho Z)_t + (\rho Z u)_x + (\rho Z v)_y = 0, \quad (8)$$

$$(\rho Z u)_t + (\rho Z u^2 + pZ)_x + (\rho Z u v)_y = pZ_x, \quad (9)$$

$$(\rho Z v)_t + (\rho Z u v)_x + (\rho Z v^2 + pZ)_y = pZ_y, \quad (10)$$

where ρ, u, v are the density and the velocity components in x and y direction, respectively. The pressure is given by the equation of state $p = p(\rho, s)$.

2.3. Valve model

2.3.1. Mass flow

In Figure 5 a plate valve is sketched. The valve plate is pressed to the valve seat by springs and by the pressure p_2 behind the valve acting on the effective area A_V. If the pressure p_1 in front of the valve exceeds the pressure p_2 and the spring force, the valve begins to open. The position z_V of the valve plate is governed by the equation of motion

$$m_V \ddot{z}_V = (p_1 - p_2)A_V - k_s(z_V + l_1), \quad (11)$$

where m_V is the mass of the valve plate, k_s the spring constant and, l_1 an initial deflection. The valve lift z_V is limited by 0 (closed valve) and the maximum valve lift $z_{V,\max}$ (valve completely open).

The mass flow through the valve is given by:

$$\dot{m} = \phi \rho_1 \left(\frac{p_2}{p_{t1}}\right)^{1/\gamma} \sqrt{\frac{2\gamma}{\gamma - 1}\frac{p_{t1}}{\rho_1}\left(1 - \left(\frac{p_2}{p_{t1}}\right)^{\frac{\gamma-1}{\gamma}}\right)}, \quad (12)$$

where p_{t1} is the total pressure in front of the valve and $\phi = \phi(z_V)$ is the effective flow cross section which is a function of the valve lift z_V only [2] .

2.3.2. Implementing the boundary condition

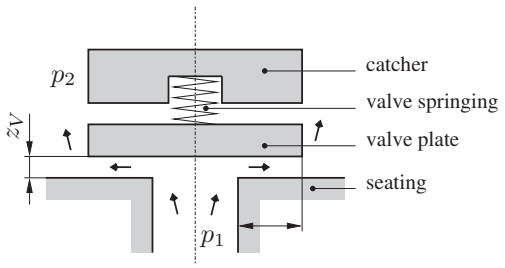

Figure 5: Scheme of a passive plate valve

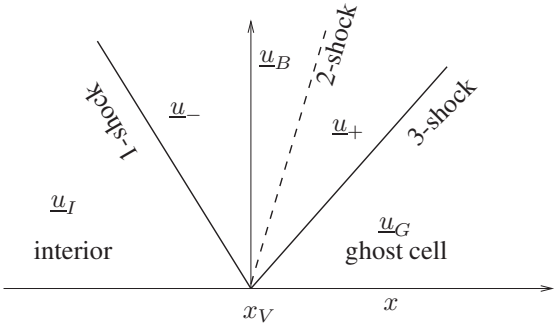

Figure 6: Prescribing boundary conditions

In order to prescribe the mass flow given by eq. (12) at the boundary of the computational domain $x = x_V$, we proceed as follows:

Inspired by Gudonov's method, we first extend the computational domain to a ghost cell adjacent to the boundary. Let $\underline{u}_I$ denote the state vector in the first interior cell, and and assume the state vector $\underline{u}_G$ in the ghost cell is known. Now solving the Riemann problem for the first interior cell and the ghost cell, we obtain the state values $\underline{u}_B$ at the boundary, and thus, the Euler flux $\underline{F}(\underline{u}_B)$. The solution of the Riemann problem is given by three shocks or expansion fans radiating from the discontinuity at the boundary with the speeds $\lambda_1 < \lambda_2 < \lambda_3$.

Let $\underline{u}_-$ and $\underline{u}_+$ the states between the 1- and 2-shock and between the 2- and 3- shock, respectively (see Figure 6).

In case of a 1-shock, the Rankine-Hugoniot conditions (5)-(7) hold by replacing $\underline{u}_L$ and $\underline{u}_-$ with $\underline{u}_I$ and $\underline{u}_-$.

Across the 2-shock the pressure and the flow velocity are constant $u_- = u_+$ and $p_- = p_+$. In case of outflow $\dot{m} > 0$, the boundary value is $\mathbf{u}_B = \mathbf{u}_-$. Thus, the Rankine-Hugoniot conditions are supplemented with the condition for the mass flow. In case of inflow $\dot{m} < 0$ the boundary value is $\underline{u}_B = \underline{u}_+$. Additionally to the mass flow a second boundary condition can be prescribed, e. g. the entropy of the gas $s_+ = s_B$ entering the compressor. Let $\rho(s, p)$ denote the density as a function of the entropy and pressure. Using that the pressure and the flow velocity are constant across the 2-shock the following condition to supplement the quasi 1D-Euler equations (1)-(3) is obtained.

$$\dot{m} = \begin{cases} A\rho_- u_-, & \dot{m} > 0, \\ A\rho(s_B, p_-)u_-, & \dot{m} < 0. \end{cases} \qquad (13)$$

An alternative way to implement the boundary condition is, to prescribe the total pressure $p_{t,G}$ and the entropy s_G in the ghost cell, and to determine the flow velocity in the ghost cell such, that when applying a finite volume scheme to the interior cell I and the ghost cell G, the numerical flux at the boundary yields the prescribed mass flow. A similar approach was used by [1]. The advantage of this method is that is can be applied to all finite volume schemes while the first method is essentially Gudonov's scheme, which is of first order.

2.4. Results

In order to evaluate the different flow models, a compressor with the main specifications given in table 1 has been chosen. For details, see [4]. The compressor has one suction and one discharge valve. Thus, the 1D-model can be applied (see figure 7). The pressure at the locations, shown in Fig. 4, has been measured at the test compressor and compared to the predictions given by the different numerical models.

Table 1: Specifications of the test compressor

diameter	d_p	0.2 m
stroke	h	90 mm
speed	f	16.3 1/s
suction press.	p_{suc}	1 bar
discharge press.	p_{dis}	5 bar
inlet Temp.	T_{in}	300 K
medium		air

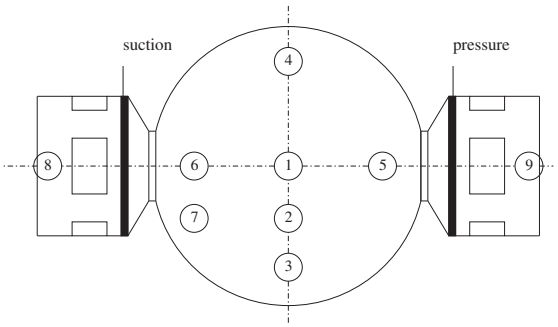

Figure 7: Location of pressure sensors in the cylinder

In Figure 8, the pressure difference between the sensors pc6 and pc5 computed with the 1D-, 2D-and 3D-flow model is shown. For the 1D-model 330 cell per diameter have been used, for the 2D-model 104 cells, and for the 3D-model (FLUENT) 70 cells per diameter. The computation time for two revolutions had been 2 minutes, 4 hours, and 2.5 days for the 1D-, 2D-, and 3D-simulation program, respectively.

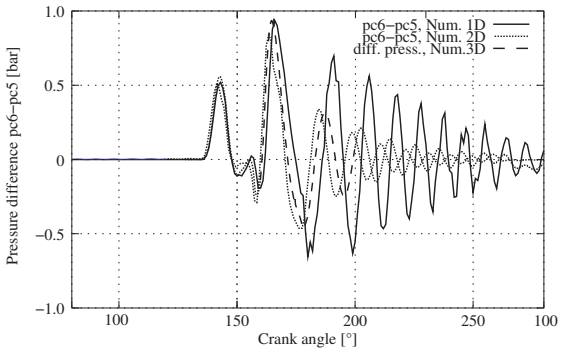

Figure 8: Internal pressure waves: comparison of different flow models for the pressure difference between suction and discharge side in the cylinder

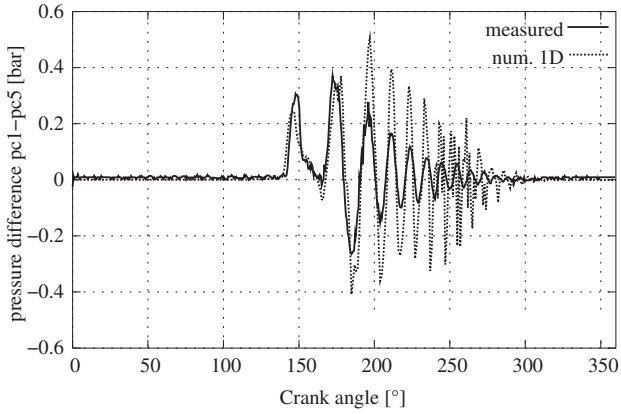

Figure 9: Internal pressure waves: comparison measurement and 1D-flow model for the pressure difference between suction side and center

The difference of the pressures at the positions pc6 and pc5 is an indicator of internal waves. The first peak in the pressure difference corresponds to the rarefaction wave due to the opening of the discharge valve at a crank angle of about 135°. The predictions of all three models agree up to a crank angle of about 160°, and differ only slightly up to 180°. The discharge valve closes, shortly after the piston has reached the dead point at a crank angle of 180°. During the beginning expansion phase, internal waves remain in the compression chamber. However, the results for the 2D-, and 3D-flow model agree reasonably well. The damping of the waves predicted by the 1D-model is much weaker.

In Figure 9, a comparison of the predictions of the 1D-model with measured data is given. There is a good agreement during the discharge phase. During expansion, waves, traveling back and forth, can be observed. Again, the damping of the waves, predicted by the 1D-model, is weaker than damping of the measured pressure waves. The damping rate of the predictions of the 2D- and 3D-model are approximately the same as the damping rate of the measured data. All signals have the same frequency which can be estimated by the speed of sound and the distance

between the two valves.

3. Heat Transfer

3.1. Heat transfer modeling

A disadvantage of the simple 1D-model is that it is not capable to calculate the heat transfer. Thus another strategy is adopted. The basic idea is to relate the wall heat flux density to a reference enthalpy flux density

$$\dot{q} = St \cdot \dot{h}_{\mathrm{ref}} = St \cdot c_p \Delta T_{\mathrm{ref}} \rho_{\mathrm{ref}} u_{\mathrm{ref}}, \qquad (14)$$

where St is a suitable Stanton number, and ΔT_{ref}, ρ_{ref}, u_{ref} are suitable reference values for the temperature difference, the gas density, and the flow velocity, respectively. The cycle of a compressor consists of four phases: inflow, compression, discharge, expansion.

3.1.1. Inflow

The gas enters through the suction valve. Thus a jet of cold gas emanating at the suction valve and impinges onto the piston rod or surfaces adjacent to the suction valve. The reference velocity from the inlet mass flow $\dot{m}_{\mathrm{in}}$ through the suction valve is given by:

$$u_{\mathrm{ref,in}} = \dot{m}_{\mathrm{in}} / \left(\rho_{\mathrm{in}} A_{\mathrm{cross}}(t)\right), \qquad (15)$$

where the $A_{\mathrm{cross}}(t) = d_p\, Z(t)$ is the cross section of the compression chamber along the piston rod and $Z(t)$ is the distance of the piston from the cylinder head. The reference density ρ_{ref} is taken from the values of the thermodynamic state of the gas at inflow, $\rho_{\mathrm{ref}} = \rho_{\mathrm{in}}$.

The heat transfer will be influenced after some retardation time t_0, since it takes some time for the cold gas to impinge at the surfaces of the compression chamber. Thus the associated heat flux through a surface of area $A(t)$ of the compression chamber is written as a function of the time t as:

$$\dot{Q}_{\mathrm{in}}(t) = St_{\mathrm{in}} c_p (T_w - T_{\mathrm{in}}) \frac{A(t)}{A_{\mathrm{cross}}(t)} \dot{m}_{\mathrm{in}}(t - t_0). \qquad (16)$$

The retardation time t_0, defined as the time the inflow jet with velocity u_{injet} needs to reach the center of the cylinder, is given by

$$t_0 = \frac{d}{2u_{\mathrm{injet}}}. \qquad (17)$$

The inflow velocity u_{injet} is estimated by

$$u_{\mathrm{injet}} = \frac{\dot{m}_{\mathrm{in}}}{\rho A_{\mathrm{eff}}}, \qquad (18)$$

where A_{eff} is the effective flow cross section of the inflow path. We approximate A_{eff} by the cross section A_{slot} of the opening between the cylinder and the valve pocket times an empirical factor f_{ret}, $A_{\mathrm{eff}} = A_{\mathrm{slot}} f_{\mathrm{ret}}$. We choose

$$f_{\mathrm{ret}} = \begin{cases} 2.5 & \text{piston, head, piston rod} \\ 5.0 & \text{cylinder barrel} \end{cases}. \qquad (19)$$

The main surfaces of the compression chamber are the piston, cylinder cap, piston rod and the cylinder barrel. Their areas are

$$\begin{aligned} A_{\mathrm{rod}} &= \pi d_{\mathrm{rod}} Z(t), \\ A_{\mathrm{pist}} &= A_{\mathrm{head}} = \pi d_p^2/4, \\ A_{\mathrm{side}} &= \pi d_p Z(t). \end{aligned} \qquad (20)$$

3.1.2. Outflow

During outflow, it is expected that the flow is dominated by the outflow of the gas. Similar to the inflow phase, the reference velocity

$$u_{\mathrm{ref,out}} = \dot{m}_{\mathrm{out}} / \left(\rho_{\mathrm{out}} A_{\mathrm{cross}}(t)\right) \qquad (21)$$

is used. The choice of a reference density is not of relevance since it does not appear in the formula for the heat flux density when expressing the heat flux density in terms of the mass flow.

Thus the local velocities will be proportional to the out going mass flow $|\dot{m}_{\mathrm{out}}|$. Thus the heat transfer related to the out going mass flow is

$$\dot{Q}_{\mathrm{out}}(t) = St_{\mathrm{out}} c_p \frac{A(t)}{A_{\mathrm{cross}}(t)} \dot{m}_{\mathrm{out}} (T_w - T_{\mathrm{gas}}). \qquad (22)$$

For the outflow phase, no retardation time is necessary since the information, that the valve is open, spreads with the speed of sound which is considerable larger than the actual flow velocity.

3.1.3. Compression and Expansion

In the compression phase a natural reference velocity is the actual velocity of the piston $u_p(t)$. However, at the turning points of the piston motion, it is zero, but the heat flux density will not vanish. Thus as a second reference velocity is chosen, $u_{\mathrm{m}} = h \cdot f$, which is $\frac{2}{\pi}$ times the average of the modulus of the piston speed. Thus, the heat transfer during compression and expansion is given by

$$\dot{Q}_{\mathrm{comp}} = \left(St_p \frac{u_p(t)}{u_m} + St_m \right) \rho_{\mathrm{isen}} u_m c_p \Delta T A(t). \qquad (23)$$

As reference density, the density ρ_{isen}, which results from an isentropic change of state from the inflow condition $(\rho_{\mathrm{in}}, T_{\mathrm{in}})$ to the actual gas temperature T in the compressor, is used.

Assume a constant isochoric heat capacity c_v of the ideal gas. Then the density ρ_{isen} is given by

$$\rho_{\mathrm{isen}}(T) = \rho_{\mathrm{in}} \left(\frac{T}{T_{\mathrm{in}}} \right)^{\frac{1}{\gamma - 1}} \qquad (24)$$

Summarizing the reconstructed heat flux $\dot{Q}_{\mathrm{rec}}(t)$ has the form

$$\dot{Q}_{\mathrm{rec}}(t) =$$

$$\left(St_{\mathrm{in}} \frac{\dot{m}_{\mathrm{in}}(t-t_0)}{A_{\mathrm{cross}}(t)} + St_{\mathrm{out}} \frac{\dot{m}_{\mathrm{out}}}{A_{\mathrm{cross}}(t)} \right.$$

$$\left. + St_p u_p(t) \rho_{\mathrm{isen}} + St_m \rho_{\mathrm{isen}} u_m \right) \qquad (25)$$

$$\cdot A(t) \bar{c}_p (T_w - T_{\mathrm{gas}}).$$

3.2. Results

First a commercial CFD program, FLUENT, is used to calculate the heat fluxes $\dot{Q}_{\mathrm{num}}$ through the faces of the compression chamber (piston, cylinder head, barrel, piston rod). Additionally to the compressor data given in Table 1 and the properties of the gas (air), the wall temperature $T_w = 400\,\mathrm{K}$ has been prescribed. The heat fluxes $\dot{Q}_{\mathrm{num}}$ calculated by FLUENT through the side wall and the cylinder head are shown in Figures 10 and 11 by the solid line as a function of the crank angle, respectively. Note, that the area of the side wall $A_{\mathrm{side}}(t)$ changes with time due to the piston motion, while A_{head} is constant.

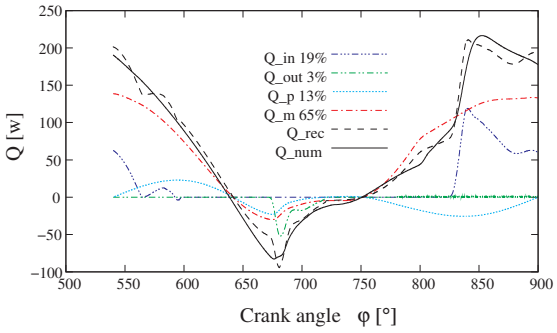

Figure 10: Components of the reconstructed heat flux through the side wall

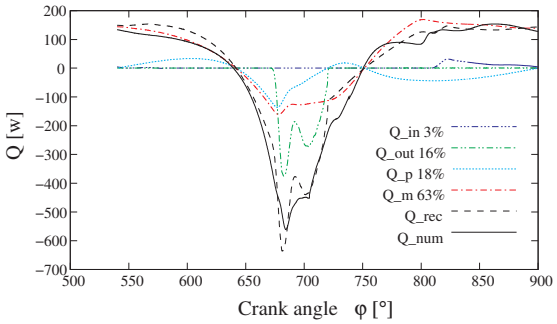

Figure 11: Components of the reconstructed heat flux through the cylinder head

At a crank angle angle of $540°$, the compression chamber has its maximal volume. The gas temperature is almost equal to the inlet temperature of $T_{\mathrm{in}} = 300\,\mathrm{K}$. Thus, the heat flow is directed into the compression chamber (positive sign). Then the compression starts, the temperature of the gas rises, and the heat flux decreases. At a crank angle of about $640°$, the gas temperature is equal to the wall temperature, and the direction of the heat flow is reversed.

At a crank angle of $680°$, the discharge valve opens, and the flow is dominated by the outflow which is strongly influenced by the valve motion. However, this valve motion causes rapid variations in the heat flux.

During expansion, the gas temperature decreases. In this stage, the heat flux is again dominated by the flow induced by the piston motion until the suction valves opens at about $830°$, resulting in a sharp increase of the heat flux through the side walls.

In order to reconstruct the heat fluxes from data available from a 1D-flow model, the Stanton numbers have to be known. They are determined such, that the reconstructed heat flux $\dot{Q}_{\mathrm{rec}}$ approximates the heat flux $\dot{Q}_{\mathrm{num}}$ determined by the CFD code best in the sense of least squares. The quadratic approximation error

$$\int_0^{t_p} (\dot{Q}_{\mathrm{num}}(t) - \dot{Q}_{\mathrm{rec}}(t))^2 \mathrm{d}t \to \min \qquad (26)$$

over a complete compression cycle with period t_p has to be minimized. The results for the Stanton numbers for the cylinder head and the side wall are listed in Table 2.

Table 2: Stanton numbers

	head	side wall
St_{in}	$1.01 \cdot 10^{-3}$	$4.3 \cdot 10^{-3}$
St_{out}	$-0.74 \cdot 10^{-3}$	$-0.47 \cdot 10^{-3}$
St_{p}	$-4.9 \cdot 10^{-3}$	$-3.1 \cdot 10^{-3}$
St_{m}	$51.8 \cdot 10^{-3}$	$-36.3 \cdot 10^{-3}$
rel. error	18%	10 %

The Stanton number St_{out} is negative since the out going mass flow $\dot{m}_{\mathrm{out}}$ is negative. The Stanton number St_p is a correction to the mean piston velocity, and thus, its sign has no direct physical interpretation.

The reconstructed heat flux for both faces is shown in the figures 10 and 11, respectively. The relative error is about 18% for the cylinder head and 10% for the side walls. The approximation of the heat flux through the side wall is better since the area of the side wall during the outflow is smaller. Additionally the contributions of the four components to the reconstructed heat flux are also indicated. Obviously the main component is associated with the heat flux due to the piston motion (about 80%). The heat flux associated with the outflow has a significant influence on the heat flux through the cylinder head but is negligible for the side wall. The heat flux associated with the inflow has a significant contribution to the heat flux through the side wall but almost no influence on the heat flux through the cylinder head.

4. CONCLUSIONS

Flow models have been discussed to predict internal waves and a heat transfer analysis of a reciprocating compressor. Although these quantities can be predicted by commercial codes, there is a need for fast easy to handle models using only a fraction of the computational effort. For internal waves, it has been shown, that, in case of a simple compressor, a 1D-flow model is sufficient. For the heat transfer analysis a 1D-flow model is also sufficient provided that a data base for dimensionless coefficients, Stanton numbers, for compressors under similar operation conditions is available.

ACKNOWLEDGMENTS

This work was funded by the EFRC, European Forum of Reciprocating Compressors.

REFERENCES

[1] Aigner, R., (2007), "Internal Flow and Valve Dynamics in a Reciprocating compressor", PhD-thesis TU Vienna, Institute of Fluid Mechanics and Heat Transfer.

[2] Costagliola, M, (1950), "The theory of spring loaded valves for reciprocating compressors", J. Appl. Mech. pp. 415-420.

[3] Machu, E., (1998), "Problems with high speed short stroke compression: Increased power requirements due to pocket losses, piston masking and gas inertia, eccentric loads on piston", Proc. of Gas Machinery Conference, USA.

[4] Steinrück, H., Aigner, R., and Machu, G., (2008), "Transversal waves in a reciprocating compressor", Acta Mech., Vol. 201, pp. 231-248.

[5] Toro, E., (1999), *Riemann solvers and Numerical methods for Fluid Dynamics*, Springer.

[6] Woschni, G., (1967), "A Universal Applicable Equation for the Instantaneous Heat Transfer Coefficient in the Internal Combustion Engine", SAE technical paper 670931.

Conference on Modelling Fluid Flow (CMFF'12)
The 15th International Conference on Fluid Flow Technologies
Budapest, Hungary, September 4-7, 2012

UPRATING STUDY OF LARGE HYDRO-GENERATOR BASED ON ANALYTICAL AND CFD APPROACH

Chaaban Mohamed, Hudon Claude, Morissette Jean-Francois,
Torriano Federico, Merkouf Arezki

Institut de Recherche d'Hydro-Québec (IREQ), 1800 Boul. Lionel Boulet, Varennes, Québec, Canada, J3X1S1, E-mail: chaaban.mohamed@ireq.ca

Abstract

An ideal hydro-generators model would solve the fluid Navier-Stokes equations and the electromagnetic Maxwell equations with a strong coupling with the energy equation. As this is still computationally too expensive, the work done at the research institute of Hydro-Québec (IREQ) uses a simpler approach by simulating each aspect (electromagnetic, thermal and fluid) separately and exchanging results from one field with others (weak coupling). The solution to Maxwell equations provides the magnetic losses in the teeth and yoke of the stator and the pole face and damper bars of the rotor. The electromagnetic model also provides a distribution of stray losses in the stator winding, the stator teeth and pole face. The CFD solution provides the necessary distribution of convection heat transfer coefficients and the distribution of the cooling fluid across the various components of the generator. The temperature field in the solid, where the hotspot is located, is calculated by solving independently the heat conduction partial differential equation using Finite element/Finite volume methods. In parallel with these simulations, on-site measurements of losses in generators are carried out at different loads during a heat run test. At the same time, the operating conditions and several critical temperatures are recorded during the test. The measurements are used to validate and calibrate the numerical model in order to extrapolate with greater confidence the potential increase in the maximum machine's output. This paper presents an example of the step by step procedures to analyse and up-rate an existing 123 MVA generator at Hydro-Québec.

Keywords: Hydro-generator, Stator, Rotor, CFD, Finite element

Nomenclature

T	[$°C$]	Temperature
Q	[W/m^3]	Volumetric heat source
X, Y, Z	[m]	Coordinates
C	[$J/kg°C$]	Specific heat
K	[$W/m°C$]	Thermal conductivity
ρ	[kg/m^3]	Density
τ	[s]	Time

Subscripts and Superscripts

x, y, z along the x, y and z coordinates

1. Introduction

Nowadays, utilities around the world, including Hydro-Québec, are looking to replace older and less efficient hydraulic turbines with new ones, more powerful and more efficient. When the generators (Figure 1), driven by these turbines, can be kept in place without any modifications and accommodate the increased load, the economic advantages are significant. One of the major obstacles to any generator uprating is the overheating that may result from the increased losses. At any load, the temperature field in the stator and in the rotor must be calculated by balancing these losses with the heat extracted by the cooling system via air-water heat exchangers.

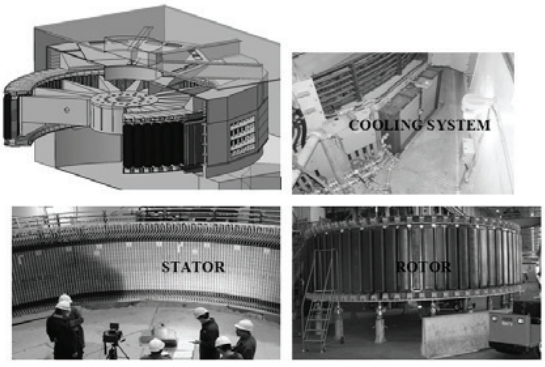

Figure 1. Hydro-generator components

The subject of this paper is rarely discussed among the scientific community. Mainly, generators' manufacturers are the ones who perform similar work but unfortunately, they do not communicate openly their results. This is why few references are outlined in this paper and this is also why we rely on great amount of expensive measurements on site to validate our assumptions in the model.

2. Numerical simulation

The procedures to analyze the thermal behaviour of a generator, at any given load, begin with the calculation of losses and their spatial distribution in the stator and in the rotor; namely the electromagnetic losses, the Joule losses, the windage losses and the stray losses. The electromagnetic and stray losses are calculated using in-house and commercial software based on 2D finite element methods. These losses are present in the damper bars, at the surface of the poles, in the teeth and yoke of the stator winding and to a lesser extent in other components such as the pressure fingers, the end plates, and the stator vent-ducts spacers. On-site measurement of some of these losses is also carried out at different power levels in order to validate the calculation results. The calculation of Joule losses is easy since the currents and the electrical resistances of the windings in both stator and rotor are well known for the generator under study, but must be corrected as a function of local temperatures following an iterative process. The evaluation of windage loss represents a greater challenge. The global windage loss can be obtained by on-site measurement at different cooling air temperature during, for instance, a calorimetric test. However, this does not provide any spatial distribution of this global loss in the different components.

The second step concerns the evaluation of the cooling air flow, induced by the rotor spiders and by the fans on the top and the bottom of the poles, and the calculation of the various convection heat transfer coefficients between the circulating air and the hot solid surfaces. CFD plays a major role in evaluating these parameters. A dedicated team at IREQ is using different commercial software (Numeca Hexpress, Ansys Fluent, ICEM-CFD, Ansys CFX) to calculate numerically the steady state induced air flow rate and its distribution among the various ducts and passages. The windage loss, its distribution and the various convection heat transfer coefficients are also calculated. In parallel, on-site measurements are conducted to evaluate some of these parameters for comparison purposes. For the study outlined in this paper, we are using in the thermal model the various heat transfer coefficients calculated by CFD in the air gap, along the pole faces and in the inter-pole regions. As discussed later, these coefficients are not uniform and their spatial distribution has a significant impact on the precision of the calculation.

The third step of the process is to characterize the performance of the cooling system normally composed of air-water heat exchangers. The temperature of the cooling water taken from the nearby dam has a direct impact on the permissible load. This is why a generator winter load at Hydro-Québec is about 15% higher compared to summer. The effect of clogging or fouling of the water tubes in the heat exchangers due to deposits of various kind, must not be neglected because this leads to lower exchanger efficiency and consequently to higher generator temperature. A dedicated computer program to analyze the performance of the exchangers was developed and integrated to the global generator model. The results of the model and the fouling factor can be verified by comparing the outlet air and water temperature to the measured one at various loads.

Finally, the last step consists of solving the 3D heat diffusion equation (Eq. 1) in the solid parts of the stator and rotor in order to find out the hotspots. The Finite Volume Method (FVM) is used to solve equation (1) in the stator and the Finite Element Method (FEM) in the rotor.

$$\left(K_x \frac{\partial^2 T}{\partial X^2} + K_y \frac{\partial^2 T}{\partial Y^2} + K_z \frac{\partial^2 T}{\partial Z^2}\right) + Q = \rho C \frac{\partial T}{\partial \tau} \qquad (1)$$

3. Real case study

The simulation procedures outlined in this paper were tested for a 122.6 MVA generator currently in service. This generator was identified as a candidate for potential up-rate because the turbine is scheduled to be replaced by a more efficient and powerful one. The recorded stator temperatures by the Resistive Temperature Detector (RTD), a sensor sandwiched between the top and bottom bars in twelve of the 504 slots, were much lower than the limit of 110°C at nominal load, which gave some potential margin for increase. On the rotor side, there are no permanent sensors to monitor the temperature. Only the average winding temperature is evaluated at the end of the heat run test by measuring the winding electrical resistance and compare this value to its known resistance at 25°C. Any increase in generator load may also lead to unacceptable temperature rise in the field winding and this need to be considered in the model.

As part of the up-rate study, a heat run test must be done at various loads until thermal stability.

Several dozens temperature sensors were installed at various critical locations in the stator, the rotor and across the cooling system and monitored throughout the course of the test. Temperature measurement at the rotor pole face, field winding and damper bars was a challenge because of the rotation. These sensors were fixed and anchored solidly together and the data acquisition system was mounted at the back of the rotor rim. The data was retrieved at the end of each test for subsequent analysis. Air flow rate and its radial velocities through the stator vents ducts were also measured at the back of the core. The test was conducted at open circuit, at 70% of the nominal load, 100% and 123%. Operation above summer rating was possible because tests were done in November and water temperature was of 6.2°C.

Table 1 and Figures 2-4 show the comparison between the measured and calculated temperatures at several locations. Currently the thermal model of the rotor only calculates temperature in a 2D slice located at mid-height of the pole, as illustrated in Figures 2-4. Table1 shows the hotspots in both the rotor and the stator. In order to maintain the integrity of the dielectric insulation material, the hotspot temperatures must not exceed some critical values. However, because the stator winding temperature cannot be directly measured and the field winding one is usually not measured, the temperature rise generally relies on sensor temperatures such as the RTD.

Power level	**70%**		**0 %**	
	Calc.	Meas.	Calc.	Meas.
T-air entering radiators	38.9	39.3	31.7	31.0
T-air exiting radiators	15.8	16.2	13.4	14.2
T-water exiting radiators	13.235	13.307	11.454	10.817
T-stator @RTD locations	48.3	45.7	34.5	32.8
Hotspot stator	**50.5**	**----**	**39.9**	----
Hotspot rotor	**67.2**	**----**	**48.1**	----

Power level	**123%**		**100 %**	
	Calc.	Meas.	Calc.	Meas.
T-air entering radiators	50.2	48.9	44.4	44.4
T-air exiting radiators	19.1	18.7	17.3	17.4
T-water exiting radiators	15.805	15.760	14.080	14.168
T-stator @RTD locations	70.5	67.1	60.4	58.0
Hotspot stator	**75.6**	**----**	**64.3**	----
Hotspot rotor	**101.4**	**----**	**84.7**	----

Table 1. Comparison between calculated and measured temperatures

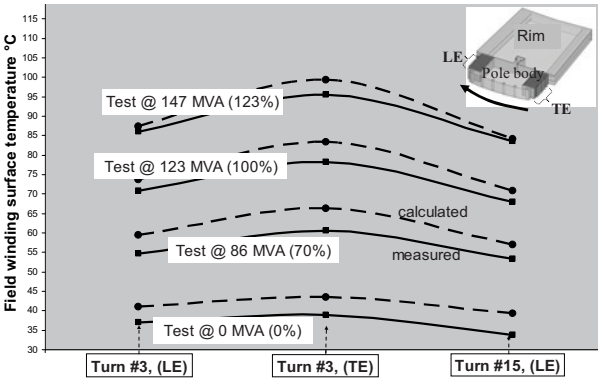

Figure 2. Comparison between calculated and measured temperature at the field winding surface (LE= leading edge, TE= trailing edge of the pole, turn #1 is on the air gap side)

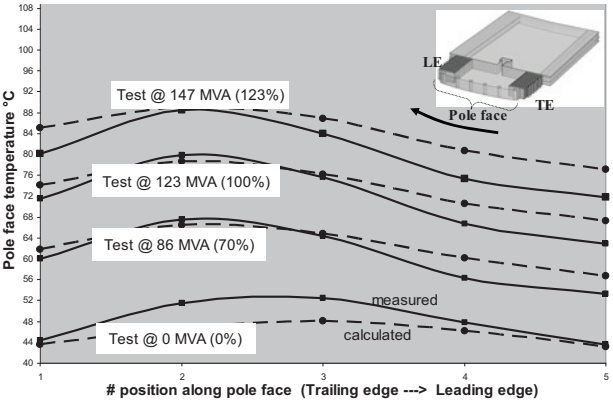

Figure 3. Comparison between calculated and measured temperatures at the pole face of the rotor (LE = leading edge, TE = trailing edge)

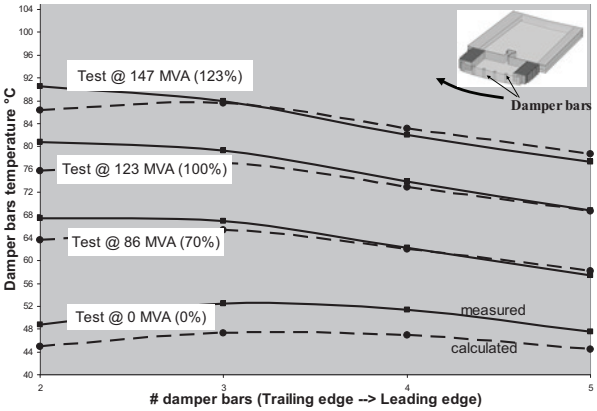

Figure 4. Comparison between calculated and measured temperature at the damper bars of the rotor (LE = leading edge, TE = trailing edge)

The difference between the calculated copper temperature and the RTD can in some cases reach more than 20°C, but here this difference in the stator is no more than 5°C. In this case it can be seen that the highest temperature is in the rotor. Although the calculated hotspot temperature is

below the maximum allowed on the rotor of this machine, it is clear that any power increase will be limited by the rotor which has much less margin than the stator.

The comparison of the measured and calculated temperatures for the cooling air, cooling water and RTD is quite acceptable as shown in Table 1. The comparison is somehow less satisfactory in the rotor where the calculated field winding temperatures were warmer than the measured ones by as much as 5°C. A similar spread was observed on the pole face and this was more pronounced on the trailing edge of the pole. The discrepancies can be attributed to several factors, such as the difficulties to measure the temperature of fast moving surfaces or potential errors introduced by inaccurate material thermal properties and convection coefficient calculated by the CFD.

The convection coefficient is highly dependent on the rotor tip velocity (V_{tip}) and on the axial and radial air flow rate entering the air gap. Several CFD studies in the literature use a constant value for the heat transfer coefficient along the pole face and inter-poles [1-3], but this is far from reality. By looking at the experimental data outlined in Figure 2, it is obvious that the convection coefficient cannot be uniform over the entire pole. For instance, at a load of 123% of the nominal rating, turn number 3 of the field winding is 12°C warmer on the trailing edge (TE) compared to the leading edge (LE), despite the fact that the current is the same everywhere. Similarly, the pole face temperature is highly non-uniform as shown in Figure 3, a behaviour that cannot be explained when using a uniform convection coefficient.

To obtain, among other information, the mean heat transfer coefficient distribution on generator components, a major steady state 3D flow simulation has been conducted, leading to insightful knowledge of the air flow over all the ventilation circuit of the machine. A first order spatial accuracy was used to solve the 3D problem. Moreover, a classical RANS k-ε turbulence model with wall function was used, in combination with a frozen rotor approach to take into account the relative motion between the rotor and the stator. Considering the complexity of the geometry, especially the high ratio in size between the generator components, the representation of the geometry with a reduced sector (18° in this case) leads to a very large mesh (100 M hexahedral elements partially shown on Fig. 5). The set of equations must be solved on a large cluster computer in parallel and it takes around three weeks of computational time. As we cannot afford CHT and unsteady simulations of this size, an unsteady 2D calculation was conducted to evaluate locally the heat transfer coefficient distributions around the pole and inter-pole regions.

The results of our CFD study (Figures 5 and 6) confirm that the convection coefficient is highly non-uniform as shown by the distributions in Figures 7 and 8. Figure 7 shows the radial distributions of the heat transfer coefficient in the inter-pole region for the trailing and leading edge. A sensitivity study was made with two air flow rate (22 and 46 kg/s) coming out of the rim into the inter-pole. It can be seen that the coefficient on the leading edge is about 35% larger than on the trailing edge. The tangential distribution of the heat transfer coefficient along the pole face, illustrated in Figure 8, shows that values are slightly larger on the trailing edge. The convection coefficient drops down to a minimum just off the center of the pole in the direction of the rotation because at this location the two air flows are opposed and cause a stall in air tangential velocities.

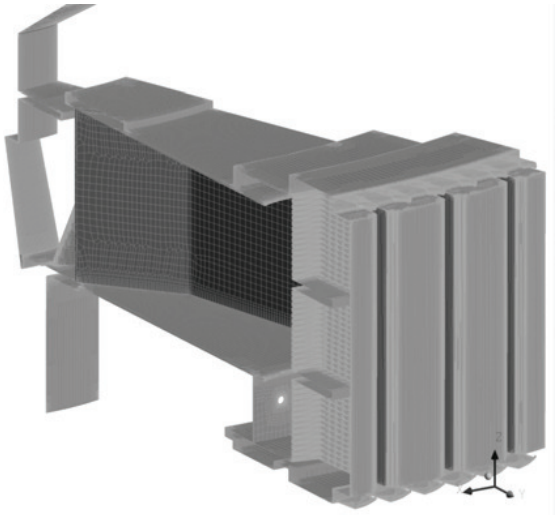

Figure 5. Mesh of the rotor

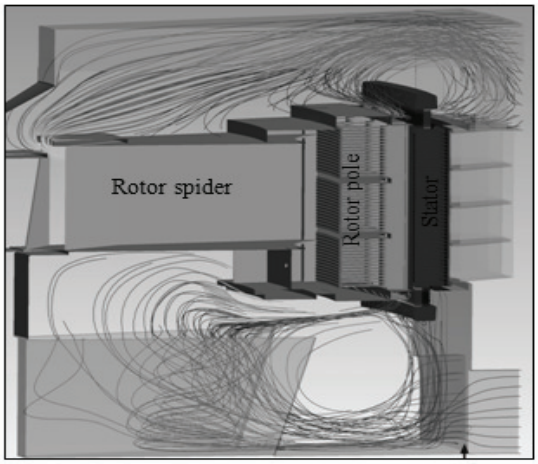

Figure 6. Stream lines of cooling air flow calculated by CFD

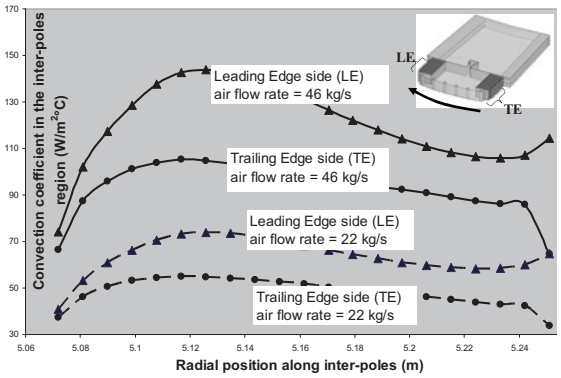

Figure 7. Heat transfer convection coefficient in the inter-poles region.

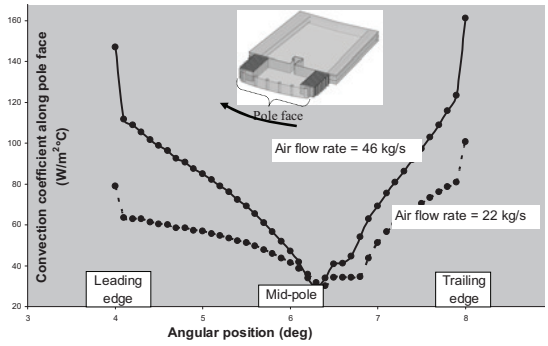

Figure 8. Heat transfer convection coefficient at pole face

The numerical simulation of heat diffusion in the solid components is based on the convective boundary conditions shown in Figures 7 and 8, with the air flow rate of 22 kg/s. Since these values were obtained from 2D CFD simulation at the middle of the rotor, they neglect the axial contribution. We are currently expanding our rotor model into full 3D to include all contributions of heat transfer coefficient (radial, tangential and axial) but for the time being the values of the 2D model are simply increased by 10% everywhere to correct for axial contributions. This value was used to fit as best as possible with the experimental results. However, it can be noticed that by using the shape of the calculated convection coefficient distribution in the thermal model, there was a good fit between the shape of measured and calculated temperature profiles along the pole face and at the inter-poles as shown in Figures 2 to 4.

4. Uprating study

Once the generator numerical model has been validated by measurement, it can be used to calculate an up-rate that would not exceed the temperature limits of neither the stator nor the rotor. The limits are imposed by the insulation class and for class F insulation system of the stator, this limit is 110°C at the RTD (at nominal voltage). The limit for the average field winding temperature is of 100°C. The calculation of a new maximum load is an iterative process that begins with a higher load than the test conditions and the evaluation of all losses and their distribution. Thereafter, the model calculates the hotspots temperatures in rotor and stator. The load is then increased or decreased depending if the hotspot temperatures fall under or above the limit. This is repeated until neither one of the 2 hotspots exceeds the maximum allowable temperature.

The results of this iterative process show that the load should be a little bit lower than the goal of 170 MVA in winter condition where the dam water temperature is 5°C. At this load, the electromagnetic simulations by MAXWELL give losses of 171 kW in the yoke of the stator, 216 kW in the teeth, 162 kW in the pole face, 54 kW in the damper bars and 111 kW for eddy and circulation losses in the stator bars. The distribution of these losses given in X, Y and Z coordinates of the electromagnetic model needs to be transposed to the thermal model mesh by an interpolation process to establish the local volumetric heat sources. The boundary conditions are set by the convection coefficients shown in Figures 7 and 8. For the stator air vents, analytical correlations are used [4-5].

At 170 MVA, the calculated stator temperature at RTD's locations is equal to 81°C which is far below the maximum limit of 110°C. However, in the rotor, the calculated average winding temperature reaches a value of 104.8°C which exceeds by a few degrees the permissible maximum of 100°C. It should be noted however that this average temperature is based on a slice in the middle of the rotor. Therefore, we neglect for now the cooling effects of air at both extremities. We believe that the impact of this additional cooling will lower the average winding temperature to a value equal or less than the limit of 100°C, but this remains to be validated. At 170 MVA, the hotspot temperatures reach the values of 87°C and 120°C for the stator and the rotor, respectively. Figures 9 and 10 show the temperature fields in the rotor and the stator at this load. The same load in summer conditions, where the dam water temperature is equal to 15°C, would leads to an unacceptable temperature rise in the rotor. We estimate the average winding temperature at 114°C in this case.

It should be noted that nothing has been said here about mechanical limits that also need to be evaluated through coupling of thermal, fluid, electromagnetic and mechanical interaction. This exceeds the scope of the current paper, but should not be neglected.

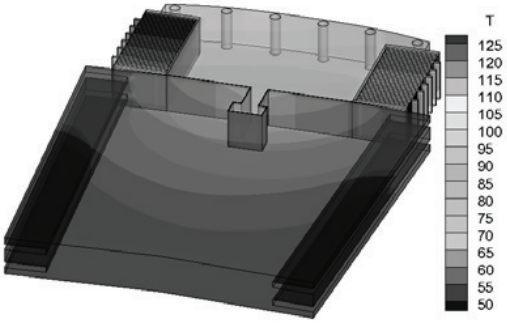

Figure 9. Calculated temperature (°C) distribution in the slice at the middle of the rotor at 170 MVA

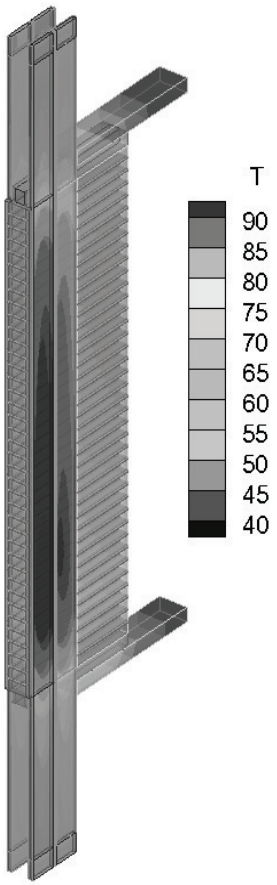

Figure 10. Calculated temperature (°C) distribution in the stator at 170 MVA

5. Conclusions

Although true multi-physics modeling is still years away, more manageable weakly coupled models can already be used thanks to the computational calculation capabilities available nowadays. It has been shown in the current paper that our approach of coupling CFD and electromagnetic simulation output with the diffusion heat transfer equation can provide a generator model with results comparable to measurement data. This model improves the accuracy of the estimation of the hotspot temperatures by including all physical phenomena (thermal, mechanical, electromagnetic and fluid) active in hydro-generators. The model still needs to evolve, for example by expanding the rotor model to include full 3D effects such as the contribution of axial ventilation. But this first version can already be used to estimate the effect of any power increase, with more confidence than traditional methods.

References

[1] W. Ondruska, E., Malousek, A., "Ventilace a chalazeni electrickych stroju tocivych", SNTL, Prague, 1985.

[2] W. Liebe, "Kühlung von Grossmaschnen", ETZ-A, vol87, No. 13, 1966, pp 434-442.

[3] M. Shanel, S.J. Pickering, D. Lampard, "Application of computational fluid dynamics to the cooling of salient pole electrical machines", ICEM, 2000, pp 338-342.

[4] Özisik, "Heat transfer, a basic approach", McGraw-Hill, 1985

[5] Rohsenow, Harnett and Ganic, "Handbook of heat transfer fundamentals", McGraw-Hill, 1985.

Conference on Modelling Fluid Flow (CMFF'12)
The 15th International Conference on Fluid Flow Technologies
Budapest, Hungary, September 4-7, 2012

STUDY OF HEAT TRANSFER CHARACTERISTICS FOR THE FUEL CELL SYSTEM OF THE HUMIDIFIER DUE TO ANALYSIS AND THE HOT TESTING

Seonhwa KIM[1], Yongmin OH[2], Jaesig KIM[3]

[1] Corresponding Author. Fuel Cell Division, POSCO Energy Inc. #13-9 Jukcheon-ri, Heunghae-eup, Buk-gu, Pohang-si, 791-941, Gyeongsangbuk-do, Korea Tel.: +82 10 4622 5110, E-mail: makgang11@gmail.com
[2] Fuel Cell Division, POSCO Energy Inc. #13-9 Jukcheon-ri, Heunghae-eup, Buk-gu, Pohang-si, 791-941, Gyeongsangbuk-do, Korea Tel.: +82 54 254 1431, E-mail: petri@poscopower.co.kr
[3] Fuel Cell Division, POSCO Energy Inc. #13-9 Jukcheon-ri, Heunghae-eup, Buk-gu, Pohang-si, 791-941, Gyeongsangbuk-do, Korea Tel.: +82 54 254 1432, E-mail: jaesig.kim@poscopower.co.kr

ABSTRACT

The Fuel Cell system of BOP (Balance of Plant) contains various mechanical equipments. Humidifier is one of the most important equipments of the heat exchangers which are highly related to have high efficiency and the cost. In MCFC system, several heat exchangers are used according to the application. Most typical heat exchanger is a humidifier which is the humidifier in BOP for the MCFC system; because it preheats the fuel and water so that a reactor will easily convert some of the incoming fuel to hydrogen. And then, the hot side fluid service will use the exhausted gas from the fuel cell and the cold side fluid service will have the fuel and water. The operation temperature range is about 25~500 Celsius Degree. [1] This heat exchanger has some problems of multiphase fluids and phase change heat transfer. So it is necessary to analyze the heat transfer characteristic and propose some reasonable design methodologies for the humidifier.

In this study, the thermal characteristic for the humidifier is estimated by using some commercial tools of heat exchanger design, rating and simulating. Also this study presents the results of the fabrocation test facility and the test.

Keywords: Humidifier, Fuel Cell, Balance of Plant

INTRODUCTION

In purpose of energy regeneration, heat exchanger is used widely in industry. Likewise, it is used in Molten Carbonate Fuel Cell (MCFC) System of Balance of Plant (BOP). The primary purpose of the heat exchanger is to supply suitable temperature for the fuel that can perform the reaction. Then, the hot side service is contained of exhaust gas from the fuel cell stack module. The cold side service uses fuel that will be reacting in the reforming vessel. So temperature of the cold side outlet is critical for the reaction. Also, it is necessary to install additional equipments or utility to meet the operation condition in fuel cell system. It is important feature in side of cost and design. So, In order to predict and submit the parameters to design is very efficient, for example, piping sizing, selections for materials, i.e.

This study presents some proper design methodologies for above problems at design step, and results from the real operation testing based on its thermal & hydraulic design.

2. APPROACH

The general method for the heat exchanger design is like following figure.

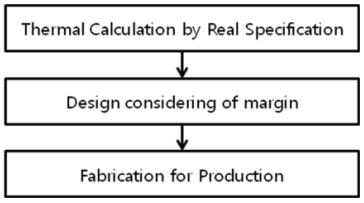

Figure1. General Method for Heat Exchanger Design

It is specified that the heat exchanger in plant engineering in design condition. At that time, the engineer performs the thermal calculation for rating. Then its type and several mechanical designs are assumed. After simulation of operation, it could predict the state of the operation. In most plants, the productions are fabricated without testing on hot testing facility due to cost and lack of need. Because, general plants are not required the severe condition for exchanging temperature. By adding the margin as safety factor, it could cover the problem.

On other side, the heat exchanger, which is presented in this study, is hard to meet the specification in the MCFC system. So it is necessary to test by using test facility and estimate the results before fabricating the production. The following figure is the procedure for this study.

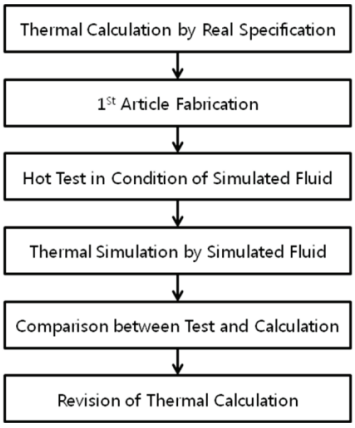

Figure2. Proposed Methodology

In this study, the thermal calculation is performed by two commercial S/W; ASPEN PLUS and ASPEN BJAC. ASPEN PLUS is used to simulate chemical reactions and ASPEN BJAC is used to design the heat exchanger.

3. THERMAL CALCULATION

3.1 REAL SPECIFICATION

In this chapter, it describes thermal and hydraulic designs for the heat exchanger. The design is performed by using the commercial S/W. The required performance is like as following table, which consists of 4 steps due to real operation condition in the fuel cell system. It is transient condition from the first step to the third step. Their cases of heat duty are lower than its normal operation condition. So the design is based on the case 4, but the hot test is performed in all cases.

Table1. Operation Condition for Design Specification

		Case1	Case2	Case3	Case4
Hot Inlet	Flow Rate (ft^3/min)	8,434	6,706	3,258	8,668
	Temperature (°F)	621	1062	935	1031
Cold Inlet, (G)	Flow Rate (ft^3/min)	12.0	27.2	158.8	374.9
	Temperature (°F)	74	74	74	74
Cold Inlet, (L)	Flow Rate (ft^3/min)	66.1	149.2	313.7	740.4
	Temperature (°F)	75	75	75	75
Hot Out	Flow Rate (ft^3/min)	8,434	6,706	3,258	8,668
	Temperature (°F)	597	988	653	705
	Pressure (IWC)	5.5	6.5	1.1	7.3
Cold Out	Flow Rate (ft^3/min)	78	176	473	1,115
	Temperature (°F)	611	790	790	710
	Pressure (psig)	1.8	2.4	1.2	5.4

The application heat exchanger model of type is economizer for using the S/W. The composition information is brought from MCFC design data to input the hot side fluid. Also it is important to secure the composition of natural gas from the NG supplier for exact calculation.

The thermal rating is performed after inputting the value for the thermal, mechanical and structural condition. At that time, the boundary condition is like following for the heat exchanger. Inlet temperature is fixed for both hot and cold services. And hot outlet temperature of condition is free, but cold side outlet condition is fixed at the rating mode. At that time, it can select proper design. The following table presents the design parameters.

Table2. Design Parameters

Parameter	Value
Tube Outer Diameter, inch	1.5
Tube Thickness, inch	0.079
Tube Material	SS310
Fin Pitch, #/inch	5
Fin Thickness	0.031
Fin height, inch	2.2
Fin Material	SS316
Tube Layout	Staggered
Longitudinal Pitch, inch	7.752
Transverse Pitch	2.697
Tube Rows	8
Tube Number	24

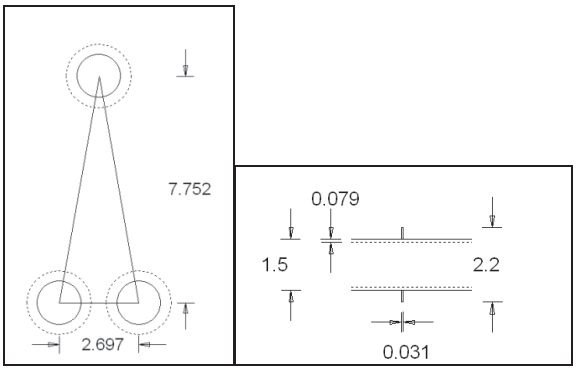

Figure3. Bundle Condition

3.2 THERMAL SIMULATION BY SIMULATED FLUID

The designed ASPEN BJAC model can simulate operation condition due to unsteadying from real fluid to simulated fluid for the hot testing. At this time, the calculation has to be fixed as simulation mode.

The thermal simulation performs after inputting value for the thermal, mechanical and structural condition. At that time, the mechanical and structural information is same with the thermal calculation as the real design specification. But the

boundary condition is different as following. Inlet temperature is fixed for both hot and cold service. Hot and cold outlet temperature of condition is free. The following table presents results of the simulation.

Table 3. Simulation Results

		Case1	Case2	Case3	Case4
Hot Inlet	Flow Rate (ft^3/min)	8,434	6,706	3,258	8,668
	Temperature (°F)	621	1062	935	1031
Cold Inlet, (G)	Flow Rate (ft^3/min)	12	27.2	158.8	374.9
	Temperature (°F)	74	74	74	74
Cold Inlet, (L)	Flow Rate (ft^3/min)	66.1	149.2	313.7	740.4
	Temperature (°F)	75	75	75	75
Hot Out	Flow Rate (ft^3/min)	8,434	6,706	3,258	8,668
	Temperature (°F)	597	988	653	700
Cold Out	Flow Rate (ft^3/min)	78	176	473	1,115
	Temperature (°F)	597	987	790	700

Also it can be known by the mechanical calculation results that the finned tube area is 1,568 square foot, bare tube

4. PROTOTYPE FABRICATION

After the thermal rating, the prototype of heat exchanger is fabricated in manufacture of the shop. Its outline shape is like followings.

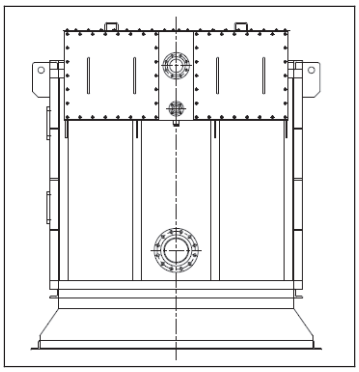

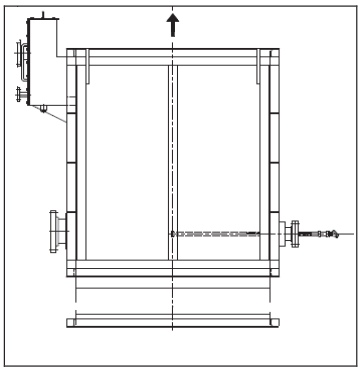

Figure 4. Prototype Heat Exchanger

In front view, there are 3 nozzles; NG inlet, DI water inlet and mixture outlet. The nozzle size is designed due to piping design of overall plant. In side view, the cold service is flowing in internal of the tube. The hot gas flow in outside of the tube from bottom to top. The insulation is fabricated for protecting heat transfer from atmosphere.

4. HOT TEST

The test process diagram is like the following schematic diagram. In the test facility, the treated water is supplied as cold side fluid service, at that time; the water flow is controlled by pump rotating speed. Also pump outlet opening area is controlled by control valve due to homogeneous flow control.

In order to simulate the NG supplying, the simulated air is compressed as about 80 psig by air compressor, and then regulated as 15~40 psig for proper control by pressure regulator. The back pressure is set as specific value for the proper control.

Figure5. Test Facility

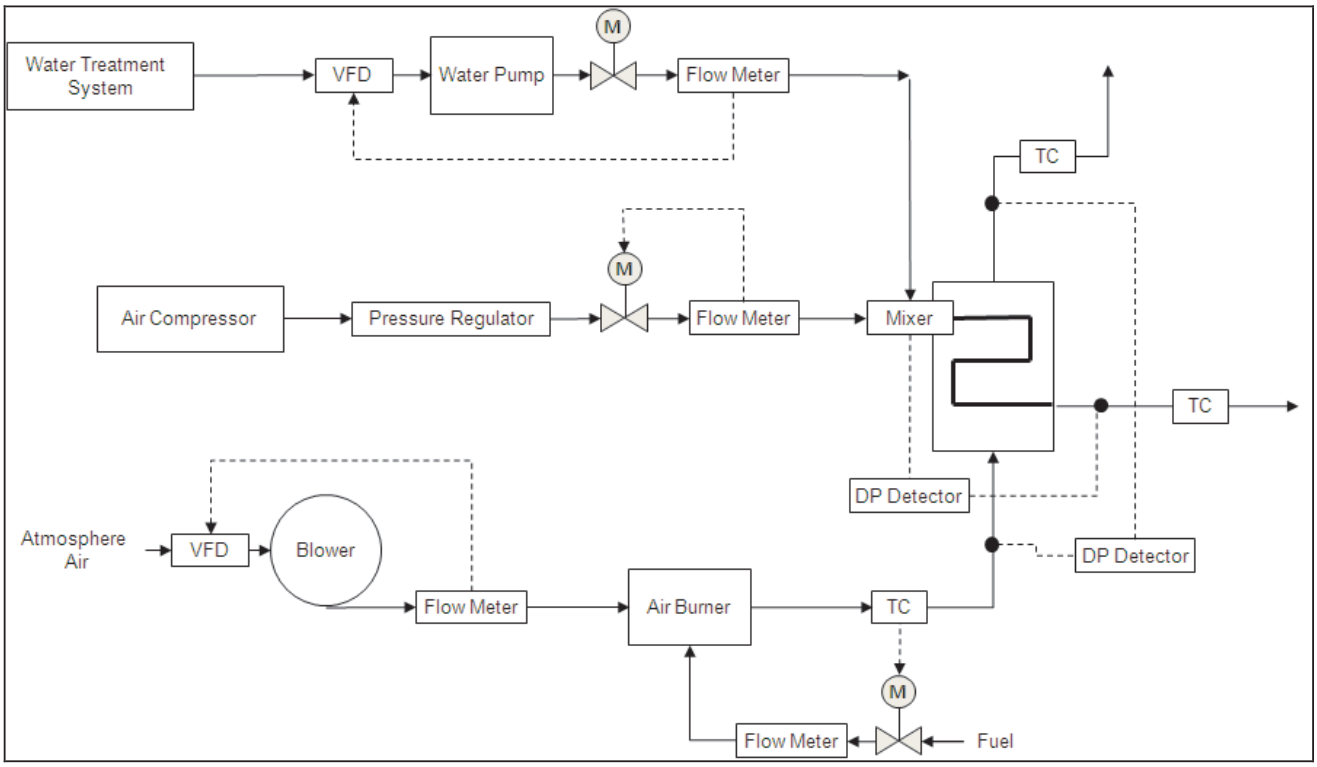

Figure6. Schematic Diagram for Test Facility

4.1 HOT INLET

Each of the components is following for hot gas supplying line in the test facility.

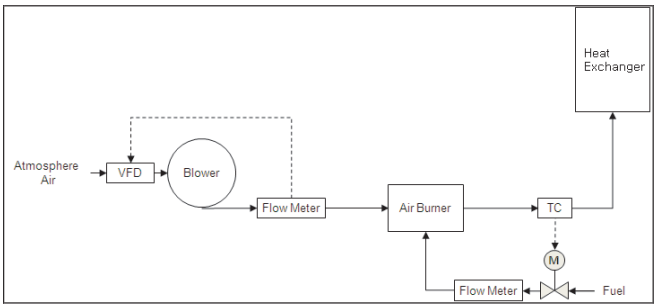

Figure7. Hot Gas Supplier

An air burner is one of them that supply proper hot gas to heat exchanger. It has the capacity of 10MMBtu/hr. Also there is an air blower, which is for supplying the fresh air from atmosphere into the air burner. Its capacity is at 250hp, and its performance is about 9000SCFM at 95iwc and 3600rpm.

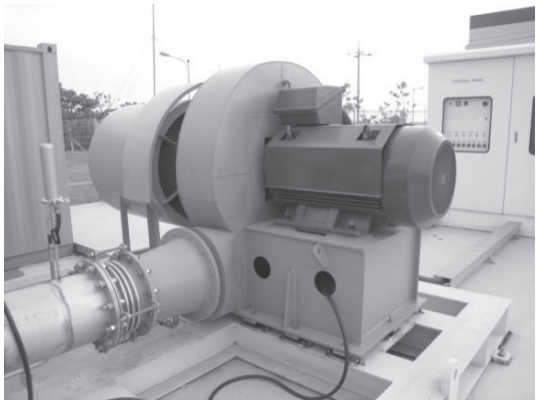

Figure8. Air Blower

The air blower is centrifugal type of the blower, which is manufactured to meet the flow rate of specification as 3000~9000 SCFM. That has to estimate by manufacture of performance curve or data and attach the VFD (Variable Frequency Driver) in order to supply the proper flow.

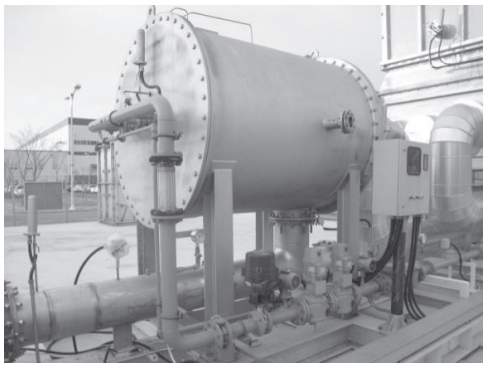

Figure9. Gas Burner

This test facility supplies the proper gas for hot side service by using the air burner. Thermocouple read the temperature which is placed in outlet of the air burner. To meet the required temperature and heat duty of the value, it can be controlled by control valve on the fuel train.

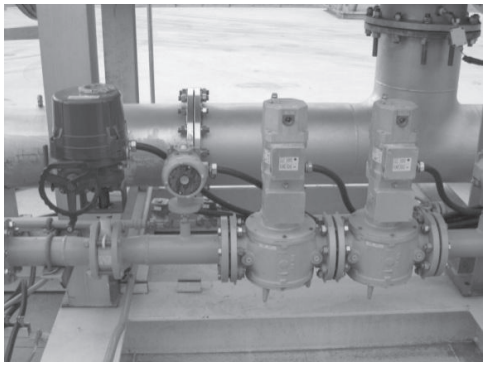

Figure10. Valve Train for Gas Burner Control

At this time, it is important to estimate the overall flow rate. Because the overall flow rate of the hot gas is consist of the fuel flow and air from the fresh air blower.

4.2 COLD INLET

In MCFC system, the fuel gas, that is the mixture for reforming react, is flowing in the cold line of the heat exchanger. As the fuel gas is combustible and clumsy for testing, substituted gas is used as the compressed air and DI water (Distilled water and de-ionized water) instead of the real fuel gas.

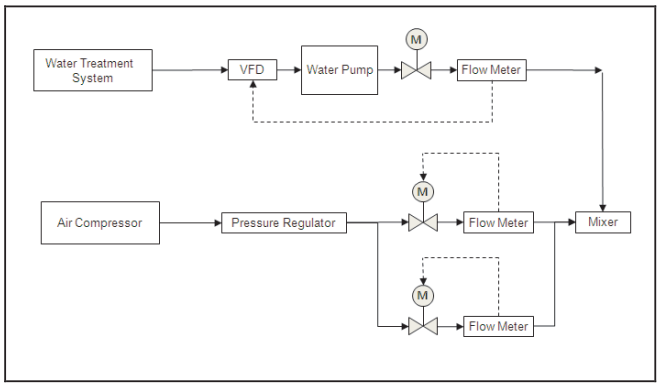

Figure 11. Cod Gas Supplier

The flow control is performed by using the flow meter and control valve. Especially, as the required flow rate is about 10~400 SCFM, it is necessary to efficient control ability for the valve. This facility uses the 2 kind of the valve in this study for the homogenous control.

Figure 12. Ion-Exchanger Resin

The ion-exchange resin is installed in order to supply the DI water on the water line. It is helpful to protect the scale in the tube inside at operation condition as high temperature. At that time, the flow of water is controlled by pump of rotating speed. The required flow is set in control system. At that time, the flow of water is controlled by pump of rotating speed.

4.3 DETECT DESIGN PARAMETERS

Several thermocouples and DP (pressure drop) detectors are installed in this test facility. It is important to measure them in order to estimate the design criteria. The temperature meters are placed on the hot side in/out and cold side out. DP detectors are installed using additional tubing on the hot side in/outlet and cold side in/outlet.

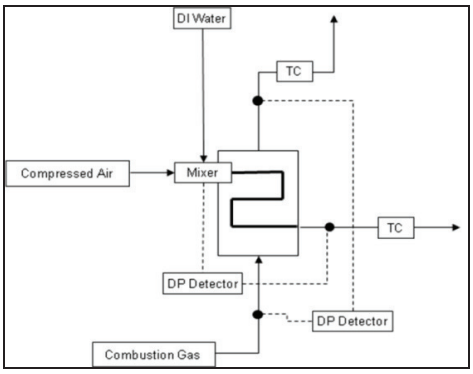

Figure 13. Major Parameter Detect Map

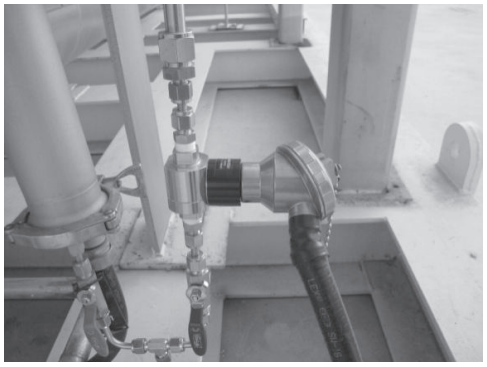

Figure 14. Cold Side Pressure Drop Detector

Figure15. Hot Side Pressure Drop Detector

4.3 REVISE OF THE DESIGN PARAMETERS

There are some assumptions in this testing. It is assumed that it has same heat capacity between exhaust gas of MCFC and simulated hot gas. As following figure, it can calculate the combusted gas of the composition ratio by ASPEN PLUS based on the real test condition.

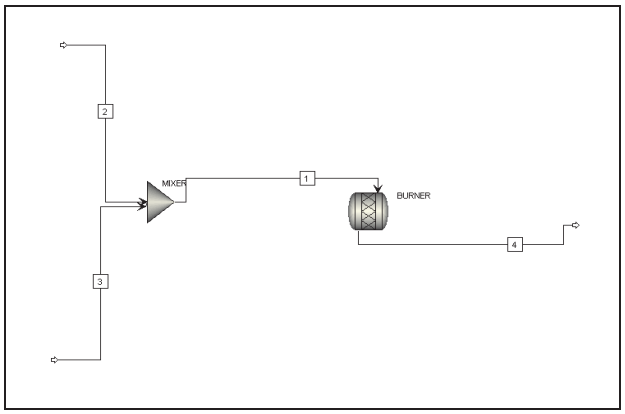

Figure 16. Energy Balance Calculation for Combustion

Table 4. The Composition for Hot Gas for Testing

	Case1	*Case2*	*Case3*	*Case4*
N_2	78%	78%	78%	78%
CO_2	1%	2%	2%	2%
H_2O	2%	4%	5%	3%
O_2	19%	17%	16%	17%

Also it can be revised the cold side outlet by using combined heat capacity for simulation air. The following table presents for the reference of the heat capacity based on the test cases in the operating temperature.

Table 5. Heat Capacity Comparison

Temperature (°F)	Case 1 & 2 (J/kmole-k)		Case 3 & 4 (J/kmole-k)	
	Simulated Fluid	Real Fluid	Simulated Fluid	Real Fluid
76	33,635	34,543	32,701	34,759
165	34,064	35,250	33,074	35,761
254	34,375	35,943	33,349	36,904
343	34,624	36,637	33,578	38,140
433	34,856	37,334	33,797	39,415
522	35,101	38,038	34,032	40,690
611	35,381	38,751	34,301	41,940
700	35,711	39,485	34,614	43,167
789	34,974	44,367	36,097	40,241
878	35,381	45,546	36,539	41,024
967	35,831	46,707	37,034	41,832
1,056	36,317	47,852	37,575	42,663
1,145	36,832	48,988	38,153	43,515
1,234	37,369	50,112	38,759	44,381
1,324	37,919	51,222	39,386	45,255
1,413	38,477	52,317	40,024	46,130

Table 6. Comparison between Test Results and Design Data for Hot Testing

		Case1		*Case2*		*Case3*		*Case4*	
		Design	Test	Design	Test	Design	Test	Design	Test
Hot Inlet	Flow Rate (ft^3/min)	8,434	8,419	6,706	6,670	3,258	3,256	8,668	8,642
	Temperature (°F)	621	629	1,062	1,069	935	945	1,031	1,039
Cold Inlet, NG	Flow Rate (ft^3/min)	12.0	12.6	27.2	27.2	158.8	158.8	374.9	374.5
	Temperature (°F)	74	74	74	74	74	74	74	74
Cold Inlet, Water	Flow Rate (ft^3/min)	66.1	65.0	149.2	148.5	313.7	315.5	740.4	742.4
	Temperature (°F)	75	75	75	75	75	75	75	75
Hot Out	Flow Rate (ft^3/min)	8,434	8,419	6,706	6,670	3,258	3,256	8,668	8,642
	Temperature (°F)	597	571	988	918	653	560	700	610
	Pressure Drop (IWC)	-	1.53	-	1.49	-	0.53	-	2.02
Cold Out	Flow Rate (ft^3/min)	78	77.56	176		473	474.26	1,115	1,117
	Temperature (°F)	597	508	987	790	790	888	700	862
	Revised Temperature, (°F)	597	467	987	901	790	791	700	664
	Pressure Drop, (psig)	-	0.001	-	0.027	-	0.116	-	0.452

5. CONCLUSIONS

This study has tried the hot testing for the heat exchanger. Before the test, it can be predicted and designed by using the commercial S/W. After the test, it can be comparable with the results of them.

According to the table 6, the predicted results are different with the specification. So this study presents the needs of design value for additional facility to maintain the homogeneous situation.

Also if the flow rate is short, it would be difficult to predict the performance. The other side, it is shown that it is available to predict the cold side outlet temperature by revising the temperature value based on the ratio of the heat capacity.

REFERENCES

[1] U.S. Department of Energy under Contract No. DE-AM26-99FT40575, 2004, “Fuel Cells Hand book”.

[2] J. M. Smith, H. C. Van Ness, M. M. Abbott, 2007, “Introduction to chemical engineering thermodynamics”, 7th ed., McGraw-Hill.

[3] R. W. Serth, 2007, Process Heat Transfer, Academic-Press

Conference on Modelling Fluid Flow (CMFF'12)
The 15th International Conference on Fluid Flow Technologies
Budapest, Hungary, September 4-7, 2012

COUPLED SIMULATION METHOD FOR INVESTIGATING EGR MIXERS IN TURBOCHARGED COMMERCIAL VEHICLE DIESEL ENGINE

Balázs KERESZTY[1], Marcell KISZELY[2], Huba NÉMETH[3]

[1] Corresponding Author. Department of Automobiles, Budapest University of Technology and Economics. Stoczek u. 6, H-1111 Budapest, Hungary. Tel.: +36 1 463 1615, Fax: +36 1 463 3978, E-mail: bkereszty@gmail.com
[2] The Regional University Knowledge Center (JRET), Széchenyi Istvan University, Győr. E-mail: kiszely.marcell@gmail.com
[3] Department of Automobiles, Budapest University of Technology and Economics. Stoczek u. 6, H-1111 Budapest, Hungary. Tel.: +36 1 463 1205, Fax: +36 1 463 3978, E-mail: nemeth.huba@auto.bme.hu

ABSTRACT

Strict emission regulations on heavy-duty (HD) commercial vehicle engines bear upon engineering society. The primary target of these legislations is the reduction of nitrogen-oxides (NO_x) and particulate matter (PM) emissions. By applying novel technical solutions to engine air management, industry keeps up with the challenge.

Initial engine development efforts were aiming to reduce emission by retarding the fuel injection process. As a side effect of this method, increased PM emission and/or brake specific fuel consumption (BSFC) is occurred. In order to avoid this symptom the manufacturers of HD diesel engines have introduced advanced features such as low swirl cylinder heads with four valves per cylinder and vertically positioned central injector. Shallow centrally located piston bowls; speed and load dependent injection timing control combined with ever-increasing pressure of fuel injection systems are all recently added features that improve emission. Exhaust gas recirculation (EGR) with Diesel Particulate Filter (DPF) or Selective Catalytic Reduction (SCR) are also getting into the focus of engine developers [2, 5].

EGR is a proven and effective way of decreasing NO_x emission. This work investigates the main factors of EGR mixers that contribute to cylinder exhaust gas distribution and overall mixture quality by utilizing both steady state and transient computational fluid dynamic (CFD) modeling of the high pressure intake path of the engine. According to the complex dependency of the intake and exhaust gas parameters of a turbocharged diesel engine, the transient boundary conditions are maintained by coupling 3D CFD code to a 1D engine model. The simulation settings and parameters that may also have effect on resulting exhaust-gas/air mixture quality such as different turbulence models, mass diffusivity and boundary layer resolution are also studied.

Keywords: coupled CFD, compression ignition engine, diesel, EGR mixer, emission, validation, wave action engine model

NOMENCLATURE

1D	[-]	one-dimensional
3D	[-]	three-dimensional
AIR	[-]	fresh air in the intake manifold
BSFC	[g/kWh]	brake specific fuel consumption
CA	[deg]	crankshaft angle
CFD	[-]	computational fluid dynamic
DPF	[-]	Diesel Particulate Filter
EB	[-]	exhaust brake
EGR_{rate}	[-]	ratio of EGR at the engine intake
ESC	[-]	European Stationary Cycle
HD	[-]	heavy-duty type of the commercial vehicle
LR	[-]	Long Route System of EGR methods
$m_{exhaust}$	[kg/s]	exhaust gas mass flow in the intake
$m_{freshair}$	[kg/s]	fresh air mass flow value
n	[1/rev]	revolution speed of engine
NO_x	[ppm]	nitrogen-oxids
PM	[ppm]	particulate matter
RPM	[-]	revolutions per minute
SCR	[-]	Selective Catalytic Reduction
SR	[-]	Short Route System of EGR methods
TC	[-]	Turbocharger
US	[-]	United States
VGT	[-]	Variable Geometric Turbocharger

1. INTRODUCTION

The benefit of diesel engines is the efficiency and a lower greenhouse effect due to their higher thermal efficiency over other heat engines. The

target of the increasingly stringent exhaust emission regulations for compression ignition engines, which are expected to come into force within the next couple of years, are the reduction of the emission of NO_x and PM, due to a major difficulty with the DI diesel engine is to control its emissions of these two components. For example, in Europe the diesel NO_x and PM limits are being cut by 90% in the Euro VI regulation compared to the Euro III level. In the US, the PM limits cutting are even more dramatic (See Fig. 1). These tightening regulations are having a dramatic effect on technology development.

Various strategies should be made to reduce NO_x and PM emissions levels, while maintaining acceptable fuel consumption levels. With these technologies commercial vehicle diesel engines could meet EURO V legislation even by 2008.

Due to the simultaneous reduction of NO_x and PM emissions are incompatible with the diesel engines the best possible alternative of the improvements is to combine the aftertreatment systems with combustion improvement techniques. These potential key new technologies have been identified and are summarized in Figure 2 [4].

First solutions improve the emissions trade-off by influencing only the engine physical parameters with the processes of fuel injection and air admission. From the start different solutions were identified in the current generation of HD diesel engines like EGR, DPF or SCR (See Fig. 3). The Re-optimized combustion method does not give enough rate of the emission decreasing. The EGR system is the biggest price-value ratio solution among the other methods with acceptable BSFC level. Thus the EGR is one of the most interesting candidate technologies for wide spread introduction in the next generation of HD diesel engines.

Preceding researches on EGR-technology for HD diesel engines has shown and confirmed that very low levels of NO_x and PM emissions can be achieved with appropriate hardware and a dedicated control strategy by lowering the local combustion temperature and the concentration of oxygen while maintaining competitive fuel economy and transient behavior [2, 3]. The cooled EGR is one of the new potential for achieving future NO_x emission levels by increased EGR volume. Without cooled EGR the heat release is affected in an unfavorable way. Reported effects on the heat release of EGR are increased ignition delay that increases the premixed combustion and a delay of the whole non premixed combustion event. The combination of a cooled EGR mixer and an appropriate pressure differential control (e.g. by VGT turbocharger) can give the best results for the very low NO_x levels with parallel the lowest PM increasing and fuel consumption penalty.

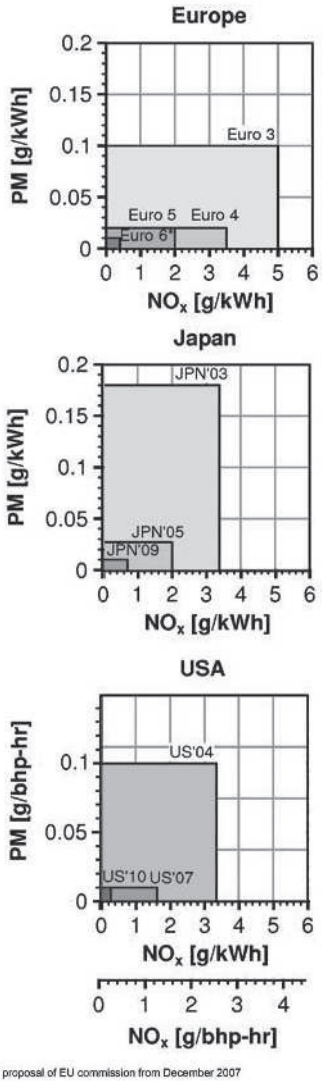

Figure 1. EU, US and Japan emission limits

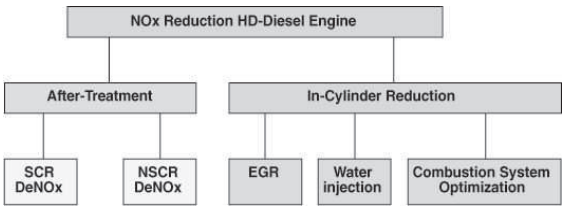

Figure 2. Different technologies for NO_x reduction

More homogeneous EGR gas and air mixture lowers NO_x levels due to evolved uniform cylinder-to-cylinder EGR rate distribution. The mixture homogeneity is an important parameter of the EGR mixer.

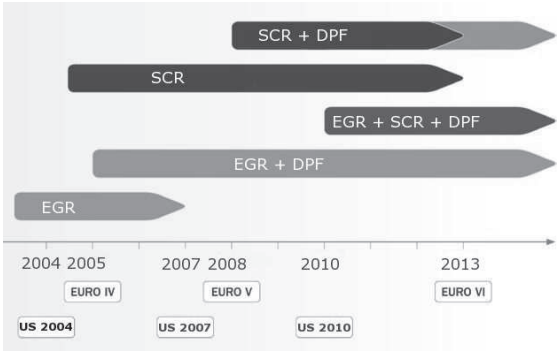

Figure 3. Additional solutions to reach emission regulations

2. THE ENGINE

The engine simulated and used for validation measurements, is a medium duty turbocharged and intercooled, commercial vehicle with common rail Diesel fuel injection system. The main parameters are given in Table 1.

Table 1. Engine parameters

Bore [mm]	102
Stroke [mm]	120
Number of cylinders	4
Engine displacement [cm^3]	3922
Number of valves	4/cyl.
Compression ratio	17.3:1
Rated effective torque [Nm]	600 (1200 to 1600 RPM)
Rated effective power [kW]	123 at 2500 RPM

There are two typical theoretical EGR methods, Long Route System (LR) – as low pressure method – (Figure 4.a) and Short Route System (SR) – as high pressure method – (Figure 4.b). In the LR-system the exhaust gas is taken downstream to the turbine and fed back to the intake system over an EGR valve and EGR cooler. In the SR-system the exhaust gas is taken away upstream to the turbine and fed back to engine intake manifold over an EGR valve and EGR cooler. Both of them have their own shortcomings.

In the LR concept the exhaust gas velocity creates a small stagnation pressure and it affects an increased pressure difference to accomplish EGR in any operation point of the engine. However PM and water condensate in the exhaust gas attacks the compressor and the after cooler and causes which influence to durability and intercooler clogging. Therefore, it is not practical in actual use. In the case of SR at the high-pressure side of turbocharger (TC) the intake air pressure could be higher than the exhaust gas pressure. Although recirculation is possible in the high load regions of the engine, but the air-fuel ratio can decrease and fuel consumption could increase remarkably. Other solutions to manage the shortcomings of the SR system are such as EGR pump, EGR check valve, a throttle valve downstream to the EGR mixer or an EGR-injector [4].

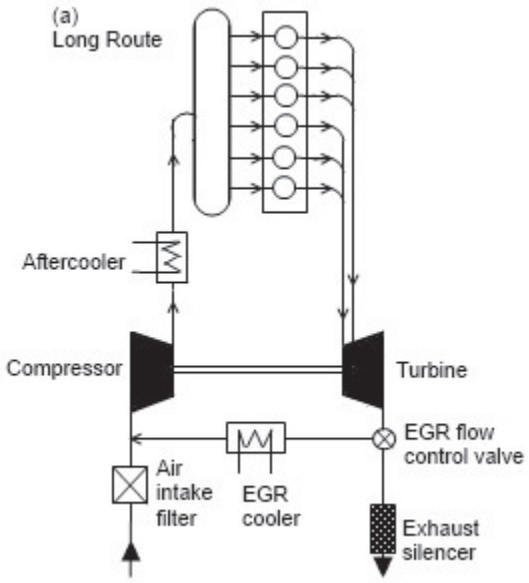

Figure 4. (a) Long Route (low pressure) EGR

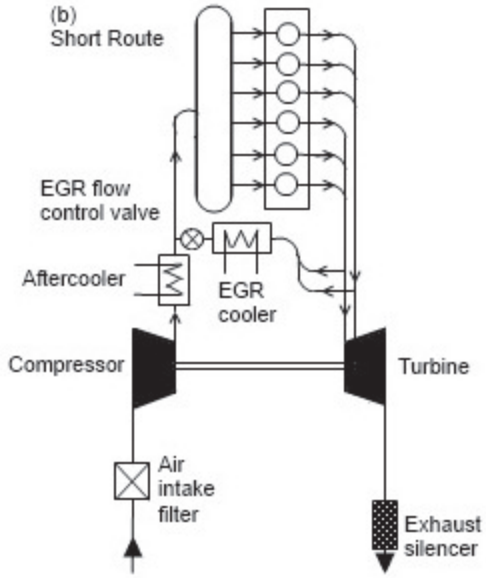

Figure 4. (b) Short Route (high pressure) EGR

The EGR system of the inspected engine is shown in Figure 5. Exhaust gas is taken from the exhaust side upstream of the turbine and fed to the intake system over an EGR valve and EGR cooler.

At fixed EGR valve position the EGR rate is commensurate with the pressure difference between the exhaust and the intake system. The pressure difference drives the exhaust gas into the intake system. This pressure difference is mainly depending on the applied turbocharger maps and the engine load.

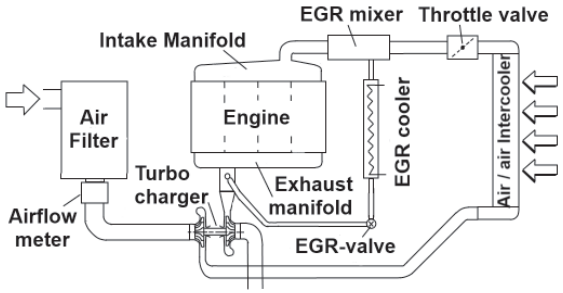

Figure 5. Cooled EGR layout of the inspected HD engine

At low loads, when the turbocharger does not supply high boost pressures, the pressure in the exhaust system is usually lower than the pressure in the intake system, thus a recirculation would not occur. To increase the EGR mass flow rates at small or negative pressure differences, pressure decrease is generated downstream to the EGR feed point in the intake system by an intake throttle valve. Another option is by generating back pressure downstream to the turbine by the exhaust brake (EB-valve).

The EGR rate is defined as the mass fraction of exhaust gas in the total intake charge as:

$$EGR_{rate} = \frac{m_{exhaust}}{m_{fresh\ air} + m_{exhaust}} \quad (1.)$$

The engine test bench is based on an eddy current brake dynamometer. The torque is measured by a load cell of the brake. The accelerator pedal position is actuated and measured by a linear motor. The fuel consumption is metered based on the gravimetric fuel mass meter [7].

3. SIMULATION METHOD AND MODELS

3.1. 1D–3D engine model description

The diesel engine model presented in [7] is used as a basis for coupling method. This validated 1D wave action GT-Suite engine model is modified by only applying the necessary components for making it capable of coupling to a 3D CFD code. To achieve high accuracy level of pre-cycles (simulated cycles before coupling starts), a detailed 1D intake manifold system is kept within the system. The investigated operation point of the engine is the A25 point of the European Stationary Cycle (ESC) test. Within this standard emission test, each operation point is determined by the engine speed along with engine load in percentage. The load at A25 point is 25% of the maximum torque, while the speed (A) is calculated with the following formula:

$$A = n_{lo} + 0.25\left(n_{hi} - n_{lo}\right) \quad (2.)$$

Where n_{hi} is the speed determined by calculating 70% of the declared maximum net power, and n_{lo} is the speed determined by calculating 50% of the declared maximum net power [9]. The selected operation point is at relatively low speed and load values that occur frequently in real life engine operation, hence making it representative in terms of EGR investigations. The GT-Suite model is coupled to a transient Fluent model. Each coupled simulation presented herein is coupled with the same GT-Suite model; changes are only affected to the Fluent part.

The CFD code utilizes a single-phase, homogeneous, multi-component flow. Mutual settings are applied such as pressure-based solver with species transport module, SIMPLE pressure-velocity coupling scheme, second-order upwind spatial discretization of Reynolds Averaged Navier-Stokes, turbulence, specific dissipation rate, continuity and energy equations and first order implicit transient formulation. The diversity of CFD models involves different numerical meshes, mass diffusion theories and modifications in turbulence modeling. The applied mixture template consists of O_2, N_2 as fresh air components, while species in the products of combustion (representing the EGR gas) is lumped to a single scalar species termed as *Burned* component [6]. The CFD model domain is similar to the models studied in [8]. It consists of charge air and exhaust gas recirculating domains, an intake throttle valve, an EGR mixer, an elbow and the intake manifold. The geometry with its boundaries can be seen in Fig. 6.

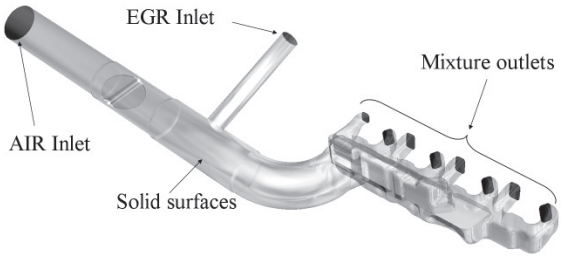

Figure 6. 3D CFD domain boundaries

3.2. Contribution of solver coupling

For simulating component mixing inside the intake manifold an accurate standalone transient 3D CFD calculation could not be set up, due to the complex time dependency of boundary condition parameters. Whereas a standalone 1D engine model has limited capabilities of modeling local discrepancies in lateral field variables. Consequently, the distribution of important time dependent variables such as EGR rate can only be mapped accurately with coupling the two solvers.

4. VALIDATION AND MESH SENSITIVITY

In order to check result sensitivity, three mesh variants were used for spatial discretization of the 3D CFD domain. Based on the experiences of former studies [8], the first type is a hybrid mesh

consisting of 1.1 million cells. Structured hexahedral elements are applied on constant diameter pipe sections, while unstructured tetra cells are used for more complex shapes (butterfly valve, mixer, manifold). The second type features the same resolution (overall cell count), but only tetra elements are used instead of the combination of tetrahedral and hexahedral cells. The third grid is again a full tetra type, but with higher resolution and a refined boundary layer on solid surfaces. Table 2 contains the main properties of the meshes.

Simulation results of both 1D and 3D models are analyzed in order to see any deviation. Test bench measurement data are also used as a reference for the validation of GT-Suite results (Table 3). EGR temperature is measured upstream to the EGR mixer (on the bench) and evaluated in the exhaust gas channel 150 mm downstream to the EGR inlet boundary (in the CFD domain). Brake torque and BSFC are both recorded on the Dyno.

Table 2. Mesh variants

Mesh Variant	Mesh Type	Element count (million cells)	Boundary layer
1.	Hybrid	1.1	No
2.	Tetra	1.1	No
3.	Tetra	2.9	Yes

Table 3. Validation of GT-Suite results

Mesh Variant	EGR Temp. [C]	Brake Torque [Nm]	BSFC [g/kWh]
Test bench data	72.0	142.90	268.42
1.	73.2	141.82	270.67
2.	73.6	141.84	270.64
3.	73.9	141.81	270.70

It is observed that applying different mesh types and element quantities have minor effect on coupled system performance. Consequently, it is the GT-Suite model accuracy that has higher importance in simulating an engine cycle. Increasing the resolution of CFD domain by this level does not affect accuracy of coupled simulation, whereas solver runtime is increased radically. The CFD domain resolution is still important although in terms of solver robustness. As engine RPM – and mass flow rate – is increasing, higher flow velocities at coupled boundaries require higher mesh resolution.

Indicated pressure in cylinders also show a good match to simulation results evaluated from GT-Suite model (See Fig. 7). As a conclusion, the first mesh variant was selected for use in further simulations (See Fig. 8).

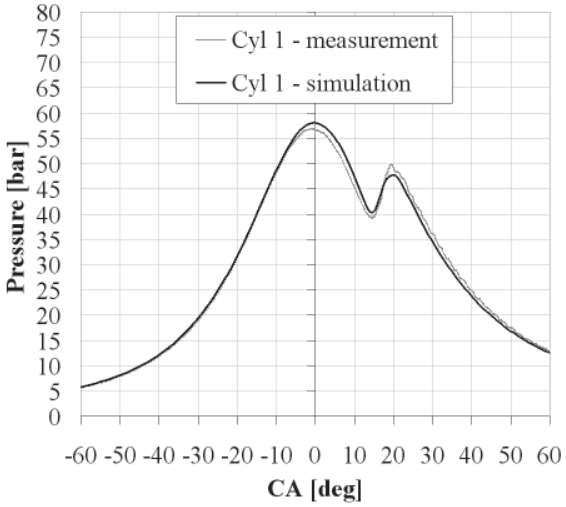

Figure 7. Indicated cylinder pressure comparison in Cyl 1 (1. mesh variant)

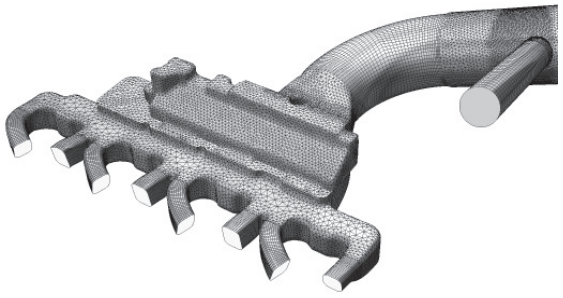

Figure 8. Selected mesh variant (Hybrid mesh of 1.1 million cells)

5. STANDALONE STEADY STATE SIMULATIONS

According to former studies [8], relatively fast steady state CFD simulations can give an insight on pressure losses of air and exhaust gas channels that set EGR rate within the mixer. In order to highlight the validity of this statement, four steady state calculations are also performed involving the upper described geometry and mesh. The composition of inlet flows are 23% of O_2 and 77% of N_2 at AIR inlet and 100% *Burned* at EGR inlet. This series of cases are modeling fluid flow through the intake manifold system with only one cylinder ports open at a time. The steady state result dataset of the case when cylinder 3 is open used for initialization of all coupled simulations. Standalone, non-coupled engine simulation in GT-suite is used for determining boundary conditions. Cycle averaged total pressure is applied for AIR and EGR inlets, while outflow is defined on currently open cylinder ports with the sum of average mass flow rates at inlets evenly split for the two ports. Resulting EGR rate at the valves are evaluated. See Table 4.

Table 4. Steady state EGR rates

valve	Cyl 1		Cyl 2		Cyl 3		Cyl 4		Ave
	1	2	1	2	1	2	1	2	
EGR rate	30.5	35.2	31.1	34.7	32.7	33.6	46.3	45.7	36.2

Various cylinder configurations result in different length of flow domain and hence pressure loss varies which affects the mass flow balance of exhaust gas and fresh air that can enter the mixer.

6. COUPLED SIMULATION RESULTS

The selected engine operation point is modeled with three CFD solver setting variants. The first mesh variant is applied to each model. Two model settings are being varied: turbulence model and mass diffusion. The baseline model (Sim I.) utilizes k-ω turbulence model and constant-dilute-approximation (also used for mesh sensitivity investigations), the second simulation (Sim II.) features k-ε RNG turbulence model with unchanged material properties, while the third simulation (Sim III.) involves k-ω SST turbulence model with modified material properties. The effect of changing mass diffusivity is investigated. Constant-dilute-approximation is changed to kinetic-theory along with its subsequent parameters. The Lennard-Jones parameters of each component are corrected according to the database of [1]. Each model simulates six engine cycles (6x720 CA) with 50 uncoupled pre-cycles to flush out initial transients. Turbocharger inertia in GT-Suite model is modified for faster response in order to gain equilibrium of the engine parameters. Figure 9 indicates the convergence history of EGR rate in cylinders (Sim I.).

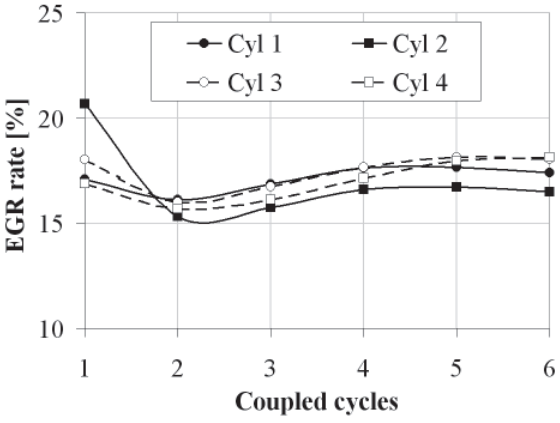

Figure 9. Coupled simulation convergence with cylinder EGR rate (Sim I., GT-Suite result)

The performance of the EGR mixer is investigated by mapping the component concentrations downstream to the mixer outlet. The evaluation planes can be seen in Fig. 10.

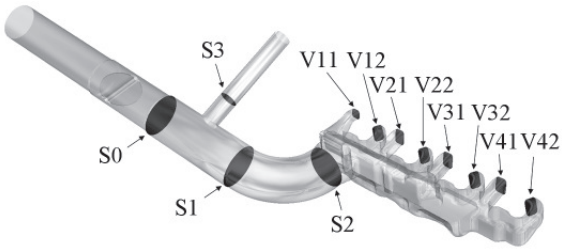

Figure 10. Evaluation planes

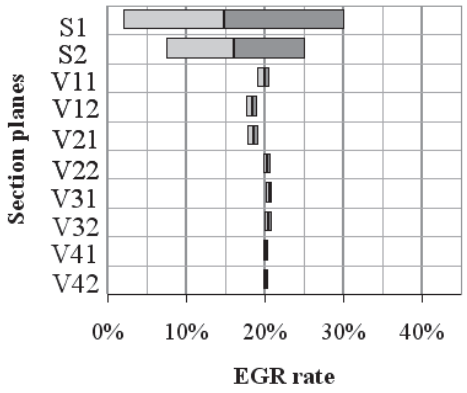

Figure 11. EGR rate fluctuations at various sections (Sim I., Fluent result)

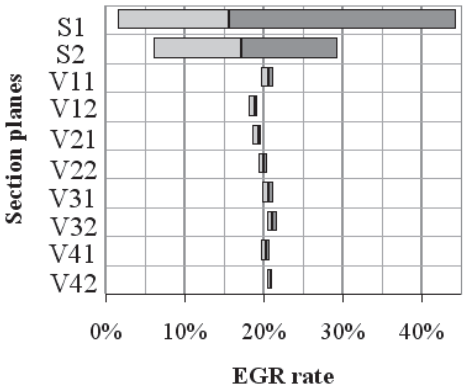

Figure 12. EGR rate fluctuations at various sections (Sim II., Fluent result)

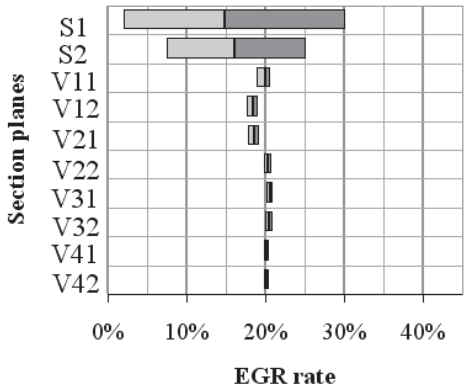

Figure 13. EGR rate fluctuations at various sections (Sim III., Fluent result)

The minimum, maximum and area-average of EGR rate of the each CFD solver model (Sim I., Sim II. and Sim III.) is evaluated downstream the EGR mixer at sections S1, S2 and V11-V42 for every time step within the 6th coupled cycle (see Figs. 11 - 13). These values are time-averaged for the last coupled cycle to get a single measure for each section. Thee graphs depict the change in EGR rate fluctuation from mixer towards the valves interpreted as cycle averages.

DISCUSSION

The investigation of the exhaust gas-fresh air mixture homogeneity was one target of the study (Figs. 11-13). Comparing the EGR rates of transient run and the upper described steady state CFD results indicates that steady simulations overestimate EGR rate by double, i.e. there is a significant influence of EGR operation to the engine and turbocharger operation. The biggest difference in the 3 simulation versions can be seen in the cross sections closer to the EGR mixer (S1, S2), the EGR rate deviation decreases going closer to the intake valve ports. The intake valve section average values and deviations are very similar in the 3 simulations and show influence of the intake manifold asymmetry. V12 and V21 channels get a quite direct path from the mixer with the shortest possible route and get consequently more fresh air and lower exhaust gas portion. Cylinder 3 and 4 ports (V31, V32 and V41, V42) get always a higher exhaust fraction because of the longer mixing path. One can conclude that the applied mixer had longer mixing route than the available common intake pipe length to the intake manifold and consequently the majority of the mixing occurred in the intake manifold.

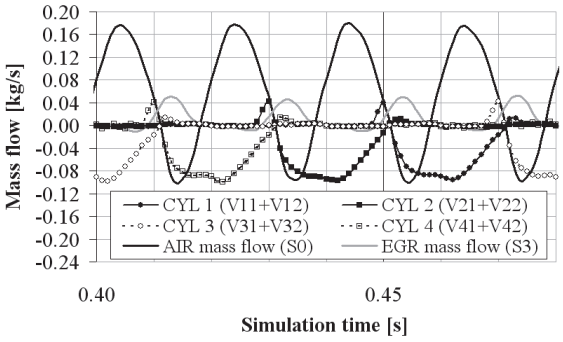

Figure 14. Transient mass flow profiles at various sections (Sim I., 6th coupled cycle, negative values refers to outflows from CFD domain)

The instantaneous mass flow profiles at the investigated interfaces are shown in Fig. 14. The reason why the average EGR rate of the coupled transient simulation differs to the steady state can be seen in this figure. The cause is a temporary back flow of the exhaust gas inside the EGR mixer in each cycle. Obviously a steady state simulation cannot reveal this effect and consequently does not provide enough accuracy level.

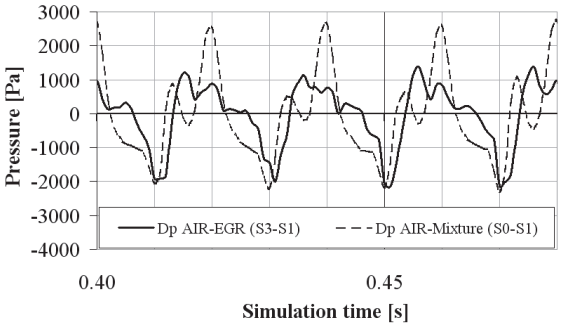

Figure 15. Transient pressure difference profiles inside the EGR mixer (Sim I., 6th coupled cycle)

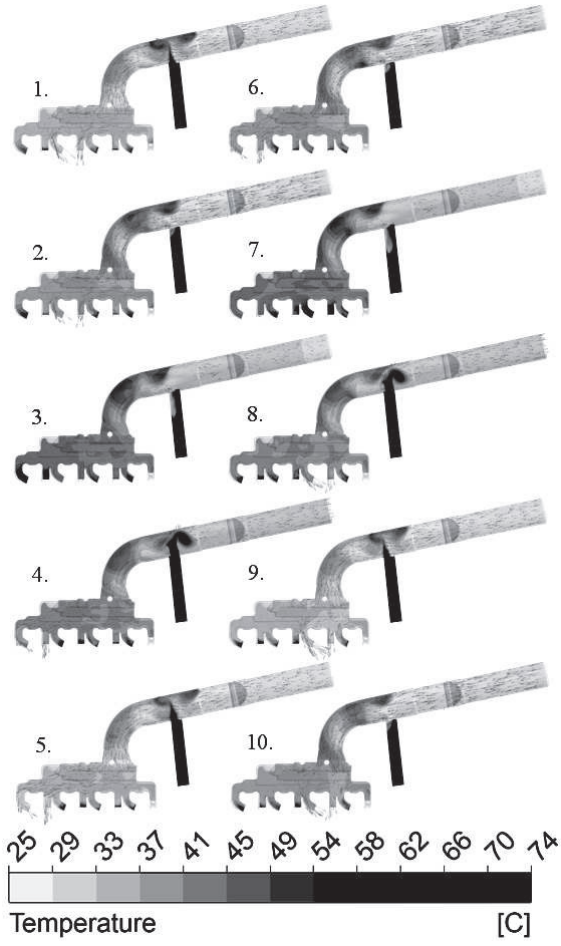

Figure 16. Transient temperature distribution in the inlet assembly (at 0.400-0.445s of 6th coupled cycle by 0.005s steps)

Based on the above symptoms the pressure differences between mixer interfaces can be used as a measure of the goodness of the mixer (see Figs. 15 and 16). Further studies have to be done to show

the correlation. The EGR rate realized by the investigated mixer and related engine performance could be derived in that case from the pressure amplitude levels.

The evaluation of the oxygen volumetric portion shows a good correlation to the EGR rates at each intake valve port (See Tab.5). Based on the results the instantaneous oxygen portion shows a negligible influence by the applied turbulence model (See Fig.17).

Table 5. Oxygen cycle average volumetric portions in % in 6th coupled cycle

	CYL 1	CYL 2	CYL 3	CYL 4
Sim I.	18.36	18.62	18.26	18.29
Sim II.	18.56	18.67	18.11	18.15
Sim III.	18.36	18.63	18.26	18.29

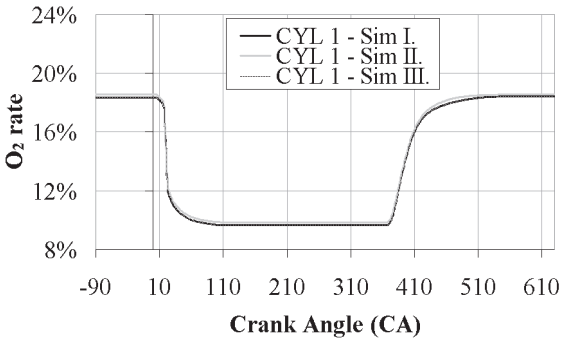

Figure 17. Average rate of oxygen in cylinder 1 (Sim I., II.,III.)

CONCLUSIONS

In earlier studies steady state simulation were used to evaluate the properties of EGR mixers. In this paper the EGR mixer domain was extended by a coupled engine model and calculation as transients to provide more accurate boundary conditions. It has been shown that the steady state results are acceptable with significant restrictions and the EGR loop and mixer influenced the coupled results significantly. The mixer behavior from the transient coupled simulations revealed that the difference is mainly caused by pressure fluctuations and the resulted backflow. Further studies should show the correlation between goodness of given EGR mixer design and the fluctuating values from the coupled simulation.

ACKNOWLEDGEMENTS

The presented work is connected to the scientific program of the "Development of quality-oriented and harmonized R+D+I strategy and functional model at BME" project. This project is supported by the New Széchenyi Plan (Project ID: TÁMOP-4.2.1/B-09/1/KMR-2010-0002).

REFERENCES

[1] Hirschfelder, J. O, Curtiss, C. F, Bird, R. B, John, 1954, "Molecular theory of gases and liquids", Wiley & Sons, inc., New York

[2] Baert, R. S. G, Beckman, D. E., and Verbeek, R. V., 1996, "New EGR technology retains HD diesel economy with 21st century emissions", *SAE Paper* 960848, Int. Congress & Exposition

[3] Baert, R. S. G., Beckman, D. E., and Veen, A., 1999, "Efficient EGR Technology for Future HD Diesel Engine Emission Targets", *SAE Paper* 1999-01-0837

[4] Kanesaka, H., Tanaka, T., and Sakai, H., 1999, "Reduction of Hyperbrid Diesel Engine Emission by EGR: [An Only Possible Method to Meet US Emission Standard of the Year 2004]", *SAE Paper* 1999-01-0971

[5] Gieshoff, J., Schäfer-Sindlinger, A., Spurk, P. C., van den Tillaart, J. A. A. and Garr, G., 2000, "Improved SCR Systems for Heavy Duty Applications", *SAE Paper* 2000-01-0189

[6] Gamma Technologies, 2010, "GT-Suite Fluent coupling manual and tutorials", *v7.0*, pp. 10.

[7] Bárdos, Á., Németh, H., 2011, "EGR Support Investigation on a Diesel Engine", *A Jövő Járműve 3\4*, Hungary, pp. 48-53.

[8] Kereszty, B., Kiszely, M., Németh, H., 2011, "CFD Analysis of EGR Mixers", *A Jövő Járműve 3\4*, Hungary, pp. 85-90.

[9] European Stationary Cycle (ESC) measurement cycle:http://www.dieselnet.com/standards/cycles/esc.php

Conference on Modelling Fluid Flow (CMFF'12)
The 15th International Conference on Fluid Flow Technologies
Budapest, Hungary, September 4-7, 2012

MATHEMATICAL AND PHYSICAL FLOWS MODELING IN ANGLE THROTTLE CONTROL VALVES

Zaryankin A.E.[1], Chernoshtan V.I.[2], Savin S.V.[3]

[1] Steam and Gas turbines Department, Moscow Power Engineering Institute (National Research University). E-mail: ZariankinAY@mpei.ru
[2] Joint-stock company "ARMEX". Avtozavodskaya str. 14/23, Moscow, Russia. Tel./ Fax: (495)234-76-25, E-mail: info@armex.org.ru
[3] Corresponding Author. Joint-stock company "ARMEX". Avtozavodskaya str. 14/23, Moscow, Russia. Tel./ Fax: (495)234-76-25, E-mail: savin@armex.org.ru

ABSTRACT

In presented data there are the results of mathematical and physical flows modeling in angle valves which allow to reveal the most problematical in terms of gas dynamics flows areas and develope effective control flow stabilization measures in the areas referred above.

Offered measures effectivenes is proved by testing data of mathematical and direct physical modeling on special experemental assemblies which allow to define flow rate, force, vibe and acoustic characteristics of angle valves.

Keywords: angle valve, energy valves, flow, hydraulic losses, mathematical modeling, throttle control valve.

NOMENCLATURE

D_1	[m]	minimal diameter of the seat cross-section
F_1	[m^2]	minimal area of the seat cross-section
M	[-]	dimensionless velocity
P_0	[Pa]	pressure in the valve body
P_2	[Pa]	pressure behind the valve
T_0	[K]	temperature in the valve body
h	[m]	absolute slide opening
$\bar{h}$	[-]	relative slide opening
m	[kg/s]	real flow rate through the valve
m_*	[kg/s]	theoretical critical flow rate through the valve
n	[-]	rate of expansion of the outlet diffuser
q	[-]	dimensionless flow rate
α	[^{o}]	angle of expansion of the outlet diffuser
ΔP	[Pa]	pressure losses in valve
Δh	[mm]	increment of the slide opening
ε_2	[-]	dimensionless pressure
λ_i	[-]	dimensionless local velocity

1. INTRODUCTION

Standard angle valves are mostly performed excluding a number of significant aerodynamic requirements. As a result all of valves details are under high dynamic loads and the whole valve unit brings in the pipeline system a very high disturbance causing an increase in acoustic emission and high vibration [1].

Noted shortcomings are due to the following constructional defects:

1. Cantilevered position of a slide on the rod at non-stationary flow of working medium abruptly increases probability of fatigue failure of the rod;

2. At small slides openings of existing forms and the absence of axial symmetry of the flow in the area of their location due to flow 90^o rotation, there are intensive oscillations very often [2];

3. In standard angle valves used with the standard system of rod counterbalancing because of axial forces at large slide openings the magnitude of a force, which presses the slide to the head of the rod, decline sharply. As a result if there are high pressure pulsations in the flow the slide easily loses the axial stability and it`s intensive vibrations begin within free stroke of the counterbalancing valve;

4. With ball, plate-shaped or conical shape of the slide in the angle valves there is no valve channel, which is able to form a relatively uniform velocity field through the valve seat, what causes the following increase of pressure pulsation in working medium flow.

In the following presented data there is a new one design of the angle counterbalance valve in which on basis of mathematical and physical flows modeling in its flowing channel there was able to eliminate denoted shortcomings and to design the angle throttle control valve which meets most of the requirements which exist in modern valves field.

2. NEW ANGLE THROTTLE CONTROL VALVES DESIGN FEATURES

Regardless of angle valves functionality it must satisfy certain general requirements among which are the following:

1. At maximum opening of the slide control valves must have a minimum flow resistance and the minimum extent of disturbing the working medium behind it;

2. When closed a working detail of valves (the slide) must safely shutdown the controlled channel of the working medium;

3. Throttle control valves design should allow a possibility of wide range changing of a force magnitude which is required for relocation of the slide;

4. In terms of gas dynamics the flow of working mediums in flowing channels of valves should not be accompanied by high pressure pulsations occurrence in a flow, what causes high dynamic loads on details of the valve, which causes outword appearance high vibration of the whole valve unit;

5. Acoustic emission of valves must not exceed the permissible sanitary standards.

Those requirements are substantially satisfied by new angle valves of «ZE» series. Counterbalance valve of that series is shown in Figure 1.

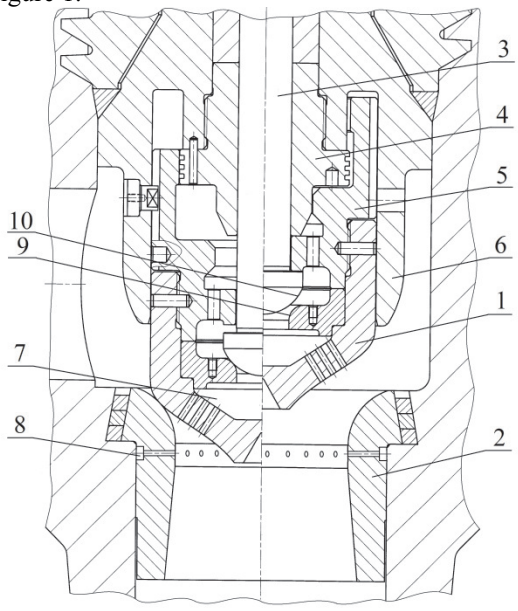

Figure 1. Counterbalance valve of ZE series.

It consists of a body, valve (the slide) 1, diffuser seat 2, a rod 3, box 4 and protective sleeve 6.

Towards control valves of well-known turbine construction firms a new one valve have a number of fundamental distinctions:

1. Streamlined part of a slide is profiled so that at its maximum opening with the inlet cross-section of a seat axisymmetric confuser channel forms which secures steam flow without separations in almost all the working positions of the slide;

2. To ensure the axial symmetry of the flow in valve channel at the asymmetric steam supply in valve body there are three hoops of perforations on the surface of the slide which are closed in a common damping chamber 7 (Figure 1) what reduces the level of dynamic loads transmitted to the valve rod;

3. Valve diffuser seat 2 after inlet confuser section has cylindrical section of flow stabilization with one hoop of perforations which is closed for a common annular chamber 8 (Figure 1).

To reduce the axial forces during its opening and the following moving special counterbalancing system is used.

The matter of fact is that the seat 9 of counterbalancing valve 10 is inside the slide and the stroke of counterbalancing valve 10 is set by means of special nut 5 external surface of which is extension of external surface of the slide.

At counterbalancing valve opening internal surface of the slide connects to the seat area 2 by means of three hoops of perforations on the streamlined surface of the slide.

In term of large slide openings 1 cylindrical part of the box 4 blocks access for steam to counterbalancing valve and load of main valve happens (the slide) by means of steam load in that area of stroke where axial force becomes unacceptably low.

Hydraulic resistance of pointed valve doesn`t exceed 2% of the initial steam pressure.

The maximum level of dynamics forces on the rod of as not counterbalanced as counterbalanced valves is about 1,5% of the static force magnitude which influence over the rod. Permissible in terms of reliability of operating process of control valves depth of counterbalance is 90%.

Noted design features of reported valve are a consequence of long-term studies of character of the flow in flowing channels of angle valves involving both mathematical and physical modeling.

The main consideration was given to the problem of the flow structure in annular channel formed by a streamlined surface of the slide 1 and diffuser seat inlet section 2 because exactly in that area direct contact of the working medium with the slide surface is. Accordingly the character of flow in noted channel influences not only the level of static and dynamic loads acting on the slide, but also it influences on hydraulic resistance of the valve which depends on the level of pressure recovery in the following diffuser part of the seat 2.

Profile of streamlined slide designed on basis of mathematical modeling creates a channel in which continuous acceleration of the flow up to narrow cross-section of the seat happens at maximum opening of the valve. The design of that channel

and velocity distribution along its surface are shown in Figure 2 [3]. Along valve surface from point 1 to point 5 at maximum opening of the valve continuous increase of dimensionless local velocity λ_i happens. Unfortunately that picture is disturbed when the valve is closed and at $\bar{h} = h/D_1 = 0{,}15$ there the area of diffuser flow on the valve bowl happens inevitably. At further shutting down of the valve the level of the stagnation of flow increases and it`s impossible to avoid a flow separation on its "spout". To exclude direct contact of valve surface with vortex flow when flow separation happening it`s reasonably to cut off valve output and on the formed front area to pierce conical recess with 60^o cone apex angle. Formed in such a way damper cavity protects the valve from direct contact its surface with its vortex trace behind it.

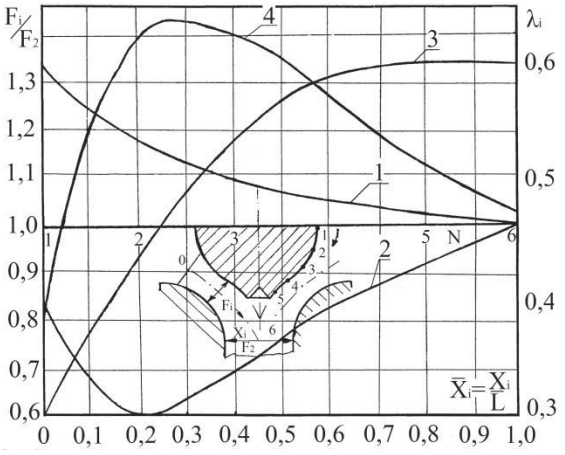

Figure 2. Distribution of dimensionless local velocity along profile surface of a slide.

Further leveling of flow characteristics occurs in a small cylindrical cross-section of the seat [3, 4, 5, 6, 7], which is currently used by both company "Siemens" and by company "General Electric". As a result in front of diffuser in terms of specified mentioned design it`s possible to get relatively uniform velocity field which provides effective energy conversion in the following cone diffuser. Final effect of such conversion primarily depends on the rate of expansion of diffuser n. The greater magnitude of n the higher expected effect. However at small angles of diffuser openings ($\alpha = 7 \div 8^o$) its structural length at expansion rates $n > 2{,}8 \div 3{,}0$ turns out very large and there are problems with both its accommodation and its secure fixing inside the valve body.

Before proceeding to review of the results of mathematical valves modeling which were designed for the specified principle it`s necessary to dwell on one more important issue.

At unidirectional side steam inlet with the following its rotation by 90^o it`s impossible to get axisymmetric flow in a profiled axisymmetric channel. That asymmetry increases at partial openings of the valve when flow separation is possible even in the profiled channel [8, 9].

Particular attention should be given to flow stabilization in a diffuser part of the seat which is normal cone diffuser. Great number of works are devoted to a study of such diffusers, but mostly they relate to a study of diffusers at virtually uniform inlet velocity field. If based on data of those studies it should be assumed that at high Reynolds numbers permissible from the standpoint of unseparated flow angle α of diffuser opening shouldn`t exceed $10 \div 12^o$ at $n < 2{,}5$. However in this case inlet velocity field depends on valve shape and in general cases it appears very problematical. The most nonuniformity of the flow at the inlet cross-section of the valve diffuser occurs at ball and plate shape of valve bowl. With the transition to profiled valves that nonuniformity is substantially reduced, but even here noticeable circular and radial nonuniformity of velocity field at the inlet of diffuser are.

To reduce the negative influence of that nonuniformity on the following flow in a conical diffuser as mentioned above it`s reasonable to bind confuser (inlet) part of the seat with cone diffuser cylindrical channel which provides the leveling of velocity field in front of the inlet cross-section of the diffuser [2, 5, 6]. With that the results of such valve studies showed that even in case of active influence on the flow with the help of cylindrical cross-sections of stabilization and additional hoops of perforations which are closed for a common damper cavity maximum angles of valve diffuser opening shouldn`t exceed 7^o.

3. MATHEMATICAL MODELING OF THE WORKING MEDIUM FLOWS IN FLOWING PART OF PROFILED ANGLE THROTTLE CONTROL VALVE.

The entire series of designed throttle control valves has similar flowing channels which are smooth annular axysimmetric channel before the inlet cross-section of the cone diffuser, which with small areas break due to front bowl cut, closes with the axysimmetric channel of diffuser part of a seat.

Theoretical calculation of such channels by using modern computer engineering provides a complete picture of velocity distribution and pressure across the flowing channel of the valve.

As an object to calculate specific valve (shown in Figure 1) was used.

The calculation was carried out in two-dimensional axysimmetric formulation for the various positions of the valve bowl (from maximum opening and further in increments of $\Delta h = 10$ *mm*). Relative pressure ε_2 ($\varepsilon_2 = P_2/P_o$, where P_2 – pressure behind the valve, and P_o – pressure in the valve body) was taken in accordance with working characteristic of the valve.

The results of calculation of pressure fields and velocities shown in Figure 3 were received at relative height of the valve opening for $\bar{h}$ = 0,361 and in terms of relative pressure ε_2 = 0,976 . That height of the valve opening is somewhat larger than calculated and accordingly the valve influence on velocity distribution in inlet diffuser cross-section is less.

Received distribution of parameters which determine steam flow pattern is rather predictable. In valve annular axysimmetric channel the pressure declines sharply (Figure 3 *a*) and the most intense pressure drops in the area of corbelled seat surface. As a result in the inlet cross-section of diffuser in its central part pressure is higher than near the sidewall of the diffuser. Then pressure gradually levels in the cross-sections. It increases near the sidewalls of the diffuser and in the central part it declines. Further for unseparated diffusers with uniform inlet velocity field the process of flow damping with pressure increase in the direction of working medium takes place.

The velocity distribution in described channel (Figure 3 *b*) is the opposite of the pressure distribution. Near corbelled seat sidewall velocities come up to almost 200 *m/s*, on the streamlined surface of the bowl – 100 *m/s* and then they decline to 30÷40 *m/s*. «Dead zone» in the front part of the valve with zero speed takes only cone cavity of the bowl. Along the whole length of the diffuser there are minimum velocities in its central part and in the relatively thin boundary layer near sidewall.

Despite the low rate of expansion of the diffuser ($n \approx 1{,}3$) the process of velocity decrease along diffuser channel is evidently visible.

Received flow velocity field indicates the unseparated streamline over surfaces which form flowing part of the valve.

Qualitatively examined picture changes a little also at decrease of the valve opening to the calculated value ($\bar{h}$ = 0,306). However absolute pressures and velocities in curvilinear valve channel significantly increase.

Serious changes in that picture of distribution of flow parameters in flowing channel of the valve take place at the decrease of relative pressure ε_2 = 0,948 and the height of the valve opening till $\bar{h}$ = 0,194 (Figure 4). With that the area of confuser flow reduced markedly (the area of decreased pressure in Figure 4 *a*) and the area of diffuser flow expanded where pressure increase takes place in the direction of main working medium which occupies the major part of the valve bowl. As a result from its surface flow separation occurred causing the «dead zone» with almost zero speeds formation in central part of the diffuser.

Within that zone behind front conical cavity closed area of circulating flow happened (Figure 4 *b*). On the surface of diffuser seat the unseparated flow remained. Maximum velocities in a narrow cross-section of the valve channel increased till 400 *m/s* (*M* = 0,75) and on relatively short area decreases till 120÷160 *m/s*. If exclude the central part of diffuser it`s possible to note the intensive decrease of the transverse nonuniformity of velocity field with the moving off the minimum cross-section of the channel at the same time with strong stagnation of the flow.

In the area of stagnation dimensionless velocities (numbers *M*) decreased from 0,6÷0,75 in narrow cross-section till 0,3 on the diffuser way out.

It's also possible to note the decrease of the area with zero speeds in the central part of the diffuser in direction of main steam flow and to note the expansion of buffer zone which is between «dead zone» and the rest of the flow.

Steam flow pattern in flowing channel becomes more difficult at supercritical pressure drops which occurs at the initial moment of the first valve opening (at nozzle steam distribution).

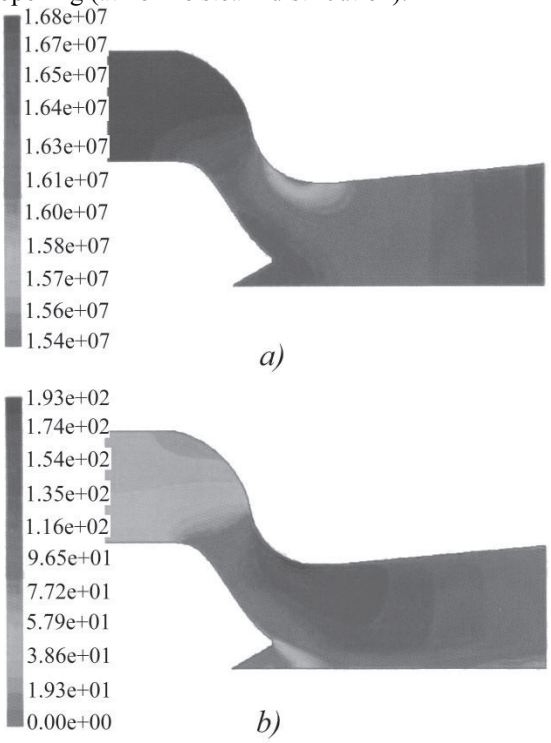

Figure 3. Pressure distribution a) and velocity distribution b) in flowing channel at $\bar{h}$ = 0,361 and ε_2 = 0,976.

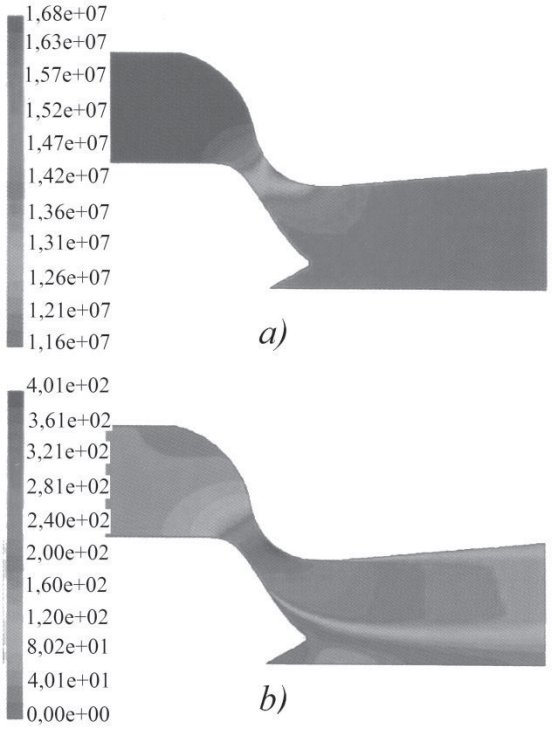

Figure 4. Pressure distribution a) and velocity distribution b) in flowing channel at $\bar{h}$ = 0,194 and ε_2 = 0,948.

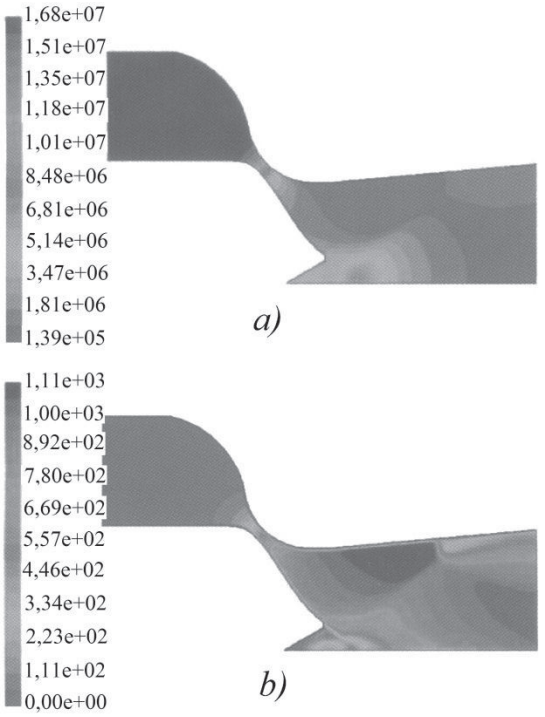

Figure 5. Pressure distribution a) and velocity distribution b) in flowing channel at $\bar{h}$ = 0,083 and ε_2 = 0,078.

That case is shown in Figure 5 (at ε_2 = 0,078 and $\bar{h}$ = 0,083). Here after the critical cross-section intensive pressure drop takes place till outlet diffuser cross-section and the pressure field behind the valve bowl is very heterogeneous that is typical for all supersonic flows (Figure 5 *a*).

Velocity field turns out such heterogeneous also (Figure 5 *b*). After critical cross-section the flow continues to accelerate and unseparated supersonic steam flow remains almost along the whole diffuser. Maximum velocities are near diffuser sidewall where dimensionless velocity reaches the great magnitude (M = 3,26). Such considerably flow overexpansion leads to wall direct compression shock which is clearly visible in Figure 5 *b*, behind it a small flow area with subsonic velocities is. Subsonic flow remains also behind bowl face. Throughout the rest of that part flow with great subsonic working medium (steam) velocities is.

The above calculations results show demonstrate the complexity of the problem of the design reliable control valves whose flow pattern constantly changes depending on current pressure drop and the valve position relative to the seat.

4. THE RESULTS OF THE PHYSICAL FLOWS MODELING IN A NEW ANGLE THROTTLE CONTROL VALVE

Despite of the obvious success of the modern computational aerodynamics in all cases that require guaranteed data about used equipment characteristics the results of the mathematical modeling are compared to the data of direct physical experiment either on the model or on the full-scale facilities. The majority of power valves is precisely that type of equipment.

The results of the model studies of mentioned valve were obtained at the air bench in gas dynamics laboratory of the Moscow Power Engineering Institute where it was possible to study throttle control valves at changing the relative pressure in that valves for ε_2 between ε_2 = 0,98 up to ε_2 = 0,44. All the studies were conducted in the field of self-similarity at Reynolds number.

Dimensionless functional dependence of the form $q = f(\varepsilon_2, \bar{h})$ was used as the metering characteristic. Here q – dimensionless flow rate which is equal to the ratio of the real (measured) flow rate through the valve m to theoretical critical flow rate m_* through minimum seat cross-section of the area $F_1 = \pi D_1^2/4$ (D_1 – diameter of the seat in that cross-section) at measured initial air parameters (P_o, T_o) in the valve body

$$q = m/m_* = mT/(0{,}0404 P_o F_1),$$

and a magnitude $\bar{h} = h/D_1$ – relative slide opening, where h – its absolute opening.

Shown in Figure 6 variables demonstrate how dimensionless flow rate q changes depending on dimensionless pressure ε_2 at maximum slide opening ($\bar{h}$ = 0,3) for the number of compared

valves which are used as control turbine units in the number of the largest turbine design firms.

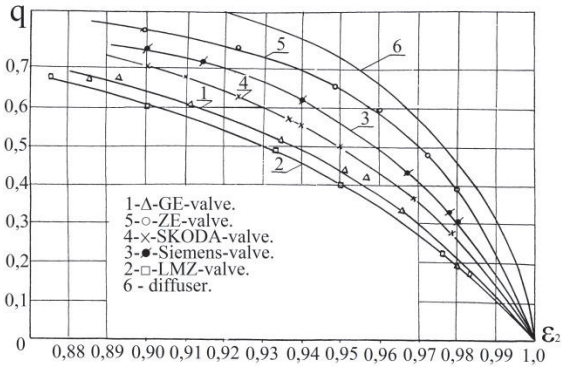

Figure 6. Dependence of dimensionless flow rate q on dimensionless pressure ε_2 at maximum slide opening.

It is clear that at fixed value of the magnitude q minimum relative resistance

$$((P_o-P_2)/P_o = \Delta P/P_o = 1-\varepsilon_2)$$

belongs to a new profiled angle valve with perforated surface of the slide.

The same valve has the minimum level of dynamic loads on the rod at a high level of pressure pulsations in the valve body.

To confirm the above in Figure 7 there are relevant pressure pulsations oscillograms and oscillograms of the forces on the rod of the studied valve at two diffuser seats with the opening angle α, which is equal to 7^o and 10^o.

At the angle $\alpha = 10^o$ (the upper part of Figure 7) pressure pulsations in the valve body and behind the diffuser seat were significantly higher than in the case of seat setting with the angle of 7^o. Nevertheless both in the first and in the second cases dynamic loads on the valve rod remained practically invariable.

That noted fact indicates high aerodynamics damping of external disturbances in the inner cavities of the perforated slide.

5. CONCLUSIONS

1. As a result of the conducted studies and constructive examination a new angle throttle control valve is designed that has low hydraulic resistance and extremely low level of dynamic loads perceived by the rod.

2. New design of internal counterbalancing system of throttle control valve was developed. Steam which flows through inner cavity that is behind counterbalancing system gets to the space behind the slide through three rows of perforations which are on the streamlined surface of that slide.

3. Usage of streamlined perforated surfaces which are closed for a common damping chamber allowed aligning circular nonuniformity of the flow and also it allowed eliminating virtually dynamic loads transmission on the valve rod.

4. Accepted constructive method of deactivation of the counterbalancing system at high openings of the slide totally excluded the possibility of the slide autooscillation at the open position.

5. All claimed valve characteristics are completely supported by the results of conducted mathematical and physical flow modeling in a flowing part of the valve which is under consideration.

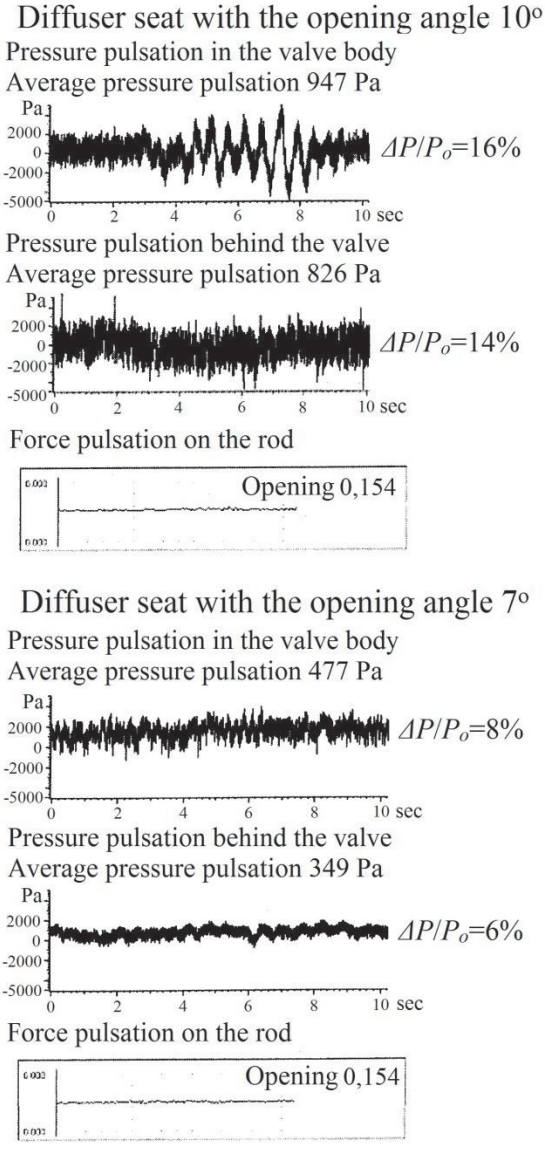

Figure 7. Oscillograms of pressure and forces pulsations on the rod of the studied valve at diffuser seats with different opening angles.

REFERENCES

[1] Kraft E.A., 1954, "Die Neuzeitliche Dampfturbine", Veb Verlag Technik, Berlin.

[2] Костюк А.Г., Куменко А.И., Некрасов А., Медведев С.В., 2000, “Экспериментальный анализ пульсаций давления в пароподводящих органах турбоагрегата”, Теплоэнергетика №6, стр. 50-57.

[3] Зарянкин А.Е., Симонов Б.П., 1995, “Новые регулирующие клапаны, их характеристики и опыт эксплуатации на энергетических турбинах”, Теплоэнергетика №1, стр. 40-44.

[4] Zariankin A.E., Simonov B.P., 1994, “New control valves, their Parameters and Service Experience the Tenth Conference of Steam and Gas Turbines”, Karlovy Vary Czech Republic, стр. 353-359.

[5] Зарянкин А.Е., 1973, “Исследования диффузоров и вопросы их использования в турбомашинах. Автореферат”, диссертация на соискание ученой степени доктора технических наук, Москва.

[6] Симонов Б.П., 2003, “Аэродинамические методы совершенствования элементов паровых турбин и их практическая реализация. Автореферат”, диссертация на соискание ученой степени доктора технических наук, Л.

[7] Этт В.В., 1975, “Исследование и аэродинамическое совершенствование регулирующих клапанов паровых турбин. Автореферат”, диссертация на соискание ученой степени кандидата технических наук, Москва.

[8] Tajc L., Bednar L., Stastny M., 2003, “Control valvaes for turbines of large output”, transactions of the institute of Fluid-Flow Machinery, Polish Academy of sciences, Gdansk.

[9] Tajc L., Bednar L., Makarov A., 2002, “Control valvaes with flat bottom and a muffler”, Prc. Of the Seminar on Topical problems of fluid mechanics, Praha.

Conference on Modelling Fluid Flow (CMFF'12)
The 15th International Conference on Fluid Flow Technologies
Budapest, Hungary, September 4-7, 2012

A CFD STUDY ON THE STABILITY OF A HYDRAULIC PRESSURE RELIEF VALVE

Csaba BAZSÓ,[1] Csaba HŐS, [2]

[1] Corresponding Author. Department of Hydrodynamic Systems, Budapest University of Technology and Economics. Műegyetem rkp. 1-3, H-1111 Budapest, Hungary. Tel.: +36 1 463 1680, Fax: +36 1 463 3091, E-mail: csaba.bazso@hds.bme.hu
[2] Department of Hydrodynamic Systems, Budapest University of Technology and Economics. E-mail: csaba.hos@hds.bme.hu

ABSTRACT

Poppet valves are widely used in industrial hydraulics, notably in pressure relief valves. These valves tend to self-oscillate even under steady-state conditions, often referred to as valve chatter. For developing reliable mathematical models it is important to estimate the unsteady flow forces, especially fluid damping. This paper presents a CFD-based analysis of valve dynamics; unsteady axisymmetric simulations including deforming mesh were performed for two inlet boundary conditions. In the first case the inlet pressure was suddenly changed and the damping coefficient was estimated with the help of the resulting free oscillations. In the second case an ODE was embedded to the solver modelling the pressure dynamics of the hydraulic system, whose capacity destabilizes the relief valve's operation giving rise to limit cycle oscillations. A qualitative and quantitative description of the variation of flow forces during the oscillation cycle is presented.

Keywords: CFD, Fluid damping, Pressure relief valve, Self-excited oscillation, Valve chatter

NOMENCLATURE

A	$[m^2]$	area
D	$[m]$	diameter
E	$[Pa]$	bulk modulus of the fluid
$\underline{F}$	$[N]$	force
$\underline{I}$	$[N]$	momentum flux of the fluid
$\mathbf{I}$		unit matrix
$\mathbf{J}$		linear coefficient matrix
$\underline{P}$	$[N]$	pressure force
$\underline{Q}$	$[m^3/s]$	flow rate
V	$[m^3]$	fluid volume
$a_{0,1,2}$		coefficients of characteristic polynomial
d	$[m]$	diameter of the upstream pipe
k	$[N/m]$	spring constant
m	$[kg]$	mass of the valve body
p	$[Pa]$	pressure
t	$[s]$	time
v	$[m/s]$	valve velocity
y	$[m]$	valve displacement
y_0	$[m]$	pre-compression of the spring
α	$[^\circ]$	half cone angle
λ		eigenvalue
ρ	$[kg/m^3]$	density of the fluid

Subscripts and Superscripts

amb	ambient
e	equilibrium
fl, mom, s, pr	force components: fluid, momentum, spring, pressure
in, out	inlet, outlet
old, new	variables at the old and new time level
st	steady
us	unsteady

1. INTRODUCTION

Hydraulic systems are commonly found in such industrial applications where large forces or torques are to be exerted with high stiffness and small response time. An essential component of such systems is the relief valve, which protects other system elements from overpressure peaks by reducing the excess pressure in a safe manner. However, it is known that relief valves intend to oscillate under certain conditions. Due to the complex fluid-structure interactions it is challenging to describe relief valve instability (called valve chatter).

Several studies are concerned with the analysis of the flow through conical valves both in steady and unsteady cases. Of main interest are the discharge coefficients, fluid forces and damping effect due to the flow. Daily [1] in 1955 pointed

out that under transient conditions in orifices the discharge coefficient C_d differs significantly from the static case. The unsteady flow produces different effects in the change of C_d depending on the flow pattern after the orifice and whether the flow is accelerating or decelerating. This was confirmed by McCloy et al. [2] for the case of poppet valve. Their experimental results showed that the discharge coefficient is affected by the pressure gradient. Positive pressure gradient resulted in the increase of C_d while negative pressure gradient caused decrease in C_d. Their results moreover revealed that the fluid force highly depends on the existing flow pattern in the seat region of the downstream chamber. The fluid–induced forces are effected by the change of the flow pattern. The bending jet through the gap induced small vortex in the seat region that resulted in high velocities and low pressure on the poppet face causing higher closing force. They suggest that the change of flow pattern during opening and closing and hysteresis effect of discharge may lead to oscillations. Stone [3] in 1960 studied experimentally the discharge coefficients and steady flow forces on the poppet valve. Takenaka [4] in 1964 studied the performance of several hydraulic control valves. He established dynamic equations for unsteady behaviour predictions, but unfortunately no experimental validation was given. He determined formulas for the discharge coefficient for several ranges of the Reynolds number based on his experiments. Urata [5] in 1969 performed experiments to study the static characteristics of the thrust of poppet valves under different conditions. The experimental results revealed his estimation for the thrust using the momentum theory and boundary layer theory. Vaughan et al. [6] in 1992 studied the developing flow pattern through poppet valve by finite volume Computational Fluid Dynamics (CFD) techniques and experiments. The results were compared and showed good agreement. Visualization of the flow pattern confirmed McCloy's results, namely in case of conical valve–body a jet is developed in the orifice and it travels at the angle of the poppet face, driving recirculation zones on either side of the jet. Mokhtarzadeh-Dehghan et al. [7] in 1997 described a finite element study of laminar flow of oil through a hydraulic pressure-relief valve of the differential–angle type used in a variable compression ratio piston of an internal combustion engine. The work presents fluid forces for steady case, the results showed considerable agreement with experimental results and analytical prediction.

Due to the development of CFD techniques many studies has been published in the dynamic flow analysis of the hydraulic valves. Shrikanth [8] in 2009 presents 2 dimensional (2D) flow analysis of a circuit breaker valve with moving grid, the work has been then extended by FSI simulation by Song et al. [9] in 2010. Viel [10] in 2011 reported the methodolgy of co–simulation between AMESim and CFD software for transient simulation of hydraulic components in their surrounding environment. Unfortunately neither experimental nor analytical validation by [8], [9] and [10] were not given.

The aim of this paper is to study the dynamical behaviour of a simple single–stage pressure relief valve with a special emphasis on the damping force due to the fluid. By performing unsteady CFX computation with deforming mesh, the overall fluid force is computed in the case of free oscillations, out of which the damping coefficient is extracted. Than, using this damping coefficient the valve dynamics is studied in tandem with the pressure dynamics of the pressure vessel the relief valve is mounted onto. Analytical stability computations are compared to the CFD results, showing reasonable qualitative agreement.

2. CFD MODEL

The test valve is a spring-loaded single-stage pressure relief valve with conical valve body of half cone angle of α and spring constant of k, see Figure 1. Many studies were concerned with the visualization

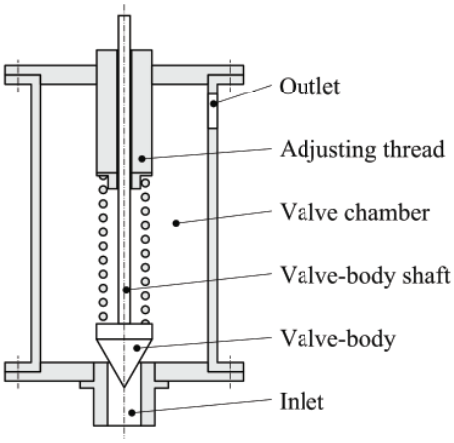

Figure 1. Sketch of the relief valve

of the arising flow pattern both with experiments and CFD simulation. These works revealed that the dominating effect on the flow pattern is the jet through the gap that drives usually small vortices in the chamber (see [2]) causing high velocities and low pressures on the poppet face. For this reason a much simpler geometry was used in the CFD modelling. With the assumption that the flow pattern and hence forces acting on the valve body are hardly effected by further elements of the valve (eg. spring, valve shaft) only the conical poppet was modelled but the mass of the omitted parts was included. Also, to accelerate the computations, axisymmetric geometry was used. The geometry is shown in Figure 2. To develop appropriate velocity profile in the seat region $10d$ long upstream section was used while to avoid recirculation at the outlet a relatively long

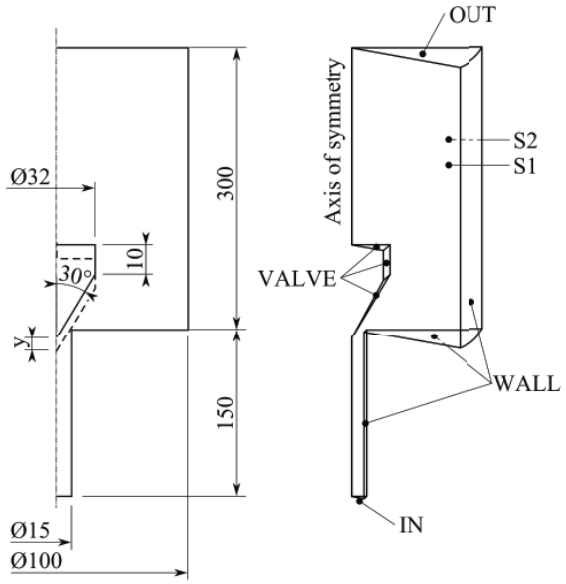

Figure 2. Geometry of modelled relief valve and the 2D axisyymetric fluid domain

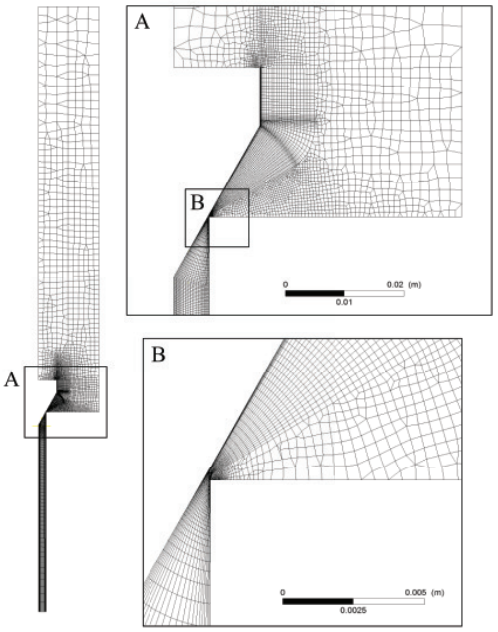

Figure 3. Meshing topology

7D downstream section was used. The axisymmetric model was built with angle of 10°.

2.1. Meshing

The meshing was designed to provide enough sensibility in the crucial region around the poppet, while the density of the mesh was reduced as the gradients of the flow variables are less. Structured mesh was employed in the critical regions while in the rest of the flow field unstructured but smooth meshing was employed. The initial grid is presented in Figure 3.

2.2. Boundary conditions

Inlet and Opening boundary conditions were employed with prescribed pressure at the inlet and outlet, respectively while on the walls and the valve body standard wall boundary condition was set.

2.3. Deforming mesh and pressure dynamics coupling

Both in the case of free oscillations and coupled simulations, the mesh deformation was computed by the standard algorithm of ANSYS CFX. Although it is possible to include the pressure vessel dynamics (see below) as User Function, it was found to be more straightforward and easy to use CFX in tandem with a Matlab code that takes care of the reservoir pressure update and drives the CFX computation.

3. SIMPLIFIED MATHEMATICAL MODEL

Figure 4 depicts the hydro-mechanical model of the system. The conical valve body is connected to a spring with spring constant s, m denotes the mass of the moving parts including the unmodelled bodies' mass (spring and shaft). The pre–compression of the spring will be denoted by y_0 while y stands for the displacement of the body. Only the capacity of the pressure transmission line will be modelled by its bulk modulus E and volume V. The spatially averaged pressure in the transmission line is denoted by p, the constant flow rate entering the transmission line is Q_{in}, while the outflow is Q_{out}, the latter depends both on the valve body displacement y and pressure p. The pressure p_0 in the downstream part of the valve is assumed to be the ambient pressure.

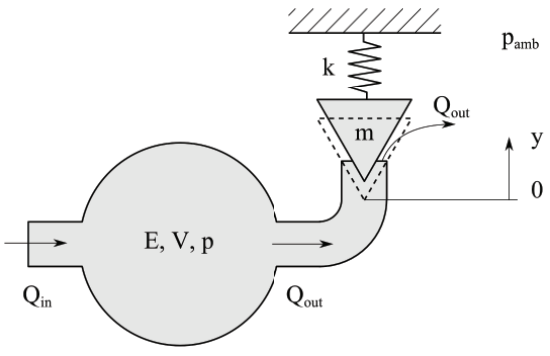

Figure 4. Hydro–mechanical model of the relief valve

The inertia, friction and internal (wave) dynamics of the fluid in the transmission line are neglected. By applying Newtons second law of motion on the valve body and considering the mass balance of the

transmission line the governing equations are

$$\begin{aligned}\dot{y} &= v \\ \dot{v} &= \frac{F_{fl}}{m} - \frac{k}{m}(y + y_0) \\ \dot{p} &= \frac{E}{V}(Q_{in} - Q_{out}(y, p)),\end{aligned} \tag{1}$$

where F_{fl} stands for the (overall) fluid force. Considering that the flow-through area for small displacement is $A(y) = D\pi \sin(\alpha)x = c_1 x$ (see [2]), the flow rate through the poppet valve is

$$\begin{aligned}Q_{out}(x, p) &= c_1 x C_d \sqrt{\frac{2}{\rho}p} = \gamma x \sqrt{p}, \\ \gamma &= c_1 C_d \sqrt{\frac{2}{\rho}}.\end{aligned} \tag{2}$$

In the following theoretical calculations and numerical simulations the discharge coefficient is considered to be constant, which is a common assumption in dynamic simulations (see e.g. [2]).

For the latter CFD computations, the temporal derivatives need to be discretized. As only the previous time step is available in CFX, the following simple explicit schemes will be used:

$$\ddot{y}(t) = \dot{v}(t) \approx \frac{v^{new} - v^{old}}{\Delta t} \tag{3}$$

$$v^{new} \approx \frac{y^{new} - y^{old}}{\Delta t} \tag{4}$$

$$\dot{p}(t) \approx \frac{p^{new} - p^{old}}{\Delta t} \quad . \tag{5}$$

Substituting Eqs. (3), (4) and (5) into Eq. (1) and expressing the displacement at the new time level we obtain

$$y^{new} = \frac{y^{old} + \Delta t\left(v^{old} + \frac{\Delta t}{m}\left(F_{fl} - k\, y_0\right)\right)}{\left(1 + \frac{\Delta t^2 k}{m}\right)} \tag{6}$$

$$p^{new} = p^{old} + \Delta t\left(\frac{E}{V}(Q_{in} - Q_{out})\right). \tag{7}$$

The parameter values of the simulations are listed in Table 1.

Table 1. System parameters used in the simulations

Parameter	Value
m	0.65 $[kg]$
s	15000 $[N/m]$
d	15 $[mm]$
ρ	870 $[kg/m^3]$
V	$2.75 \cdot 10^{-4}$ $[m^3]$
c_1	0.0236 $[m^2]$
E	870 $[MPa]$
y_0	15.5 $[mm]$
C_d	0.8 [–]

4. ESTIMATING THE FLUID DAMPING

The fidelity of a numerical model for such valves heavily depend on the discharge coefficient and the flow forces. Big deal of studies investigated them both for steady and unsteady cases, but very few works addressed the problem of finding the damping effect of the flow on oscillating valve body. Despite damping has great influence on dynamical behaviour of the poppet its value usually *is only* estimated and assumed to be constant because sensitivity of the flow through the valve and difficulties of the measurement set–up make it cumbersome to measure. Since CFD techniques provide this possibility, an attempt has therefore made to determine its characteristics. To do this we excite the valve body with various inlet pressure signals and, based on theoretical considerations, extract the damping force from the CFD results.

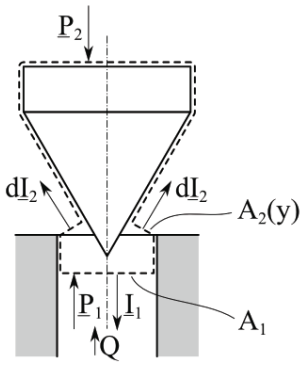

Figure 5. Applying the momentum theory on the valve body

Assuming *steady*, incompressible and frictionless flow, the momentum equations applied to the control volume shown in Figure 5 is

$$I_1 - I_2 = P_1 - P_2 - F_{fl,st}, \tag{8}$$

where P_1 and P_2 denotes the net force due pressure distribution at the inflow and outflow respectively, I_1 and I_2 are the momentum flux of the flow entering and leaving the control surface, while F_{fl} denotes the force on the poppet exerted by the fluid. Substituting $I_1 = \frac{Q^2\rho}{A_1}$ and $I_2 = \frac{Q^2\rho}{A_2(y)}\cos\alpha$ the fluid force becomes

$$F_{fl,st} = \underbrace{A(p_1 - p_2)}_{F_{pr}} + \underbrace{Q^2\rho\left(\frac{1}{A_1} - \frac{\cos\alpha}{A_2(y)}\right)}_{F_{mom}} \tag{9}$$

It is worth noting that as Eq. (9) shows for small displacement the upstream area of the control surface is much bigger than the downstream surface, thus for small displacements and high flow rate the momentum flux change results in negative thrust on the poppet valve.

In the unsteady case, we assume that the above equation must be augmented by an unsteady term $F_{fl,us}$, which is mainly due to the added mass effect and results in damping. Hence we have

$$F_{fl} = F_{fl,st} + F_{fl,us} = F_{pr} + F_{mom} + F_{damp} \tag{10}$$

The advantage of the above form is that the left-hand side can be extracted from CFD computations (as a function of flow rate, velocity and pressure), while an analytical approximation of the pressure and momentum force is available, which allows the estimation of the damping force.

Simulations were carried out to find the relation for the damping force as a function of valve–body velocity. The amplitude of the input pressure was set to 1 *bar*, 2 *bar* and 5 *bar* with 10 *Hz*, 20 *Hz* and 50 *Hz* excitation frequency, respectively, as it is represented in the top panel of Figure 6. To find the damping force from the resulting fluid force (F_{fl}) we subtract the calculated momentum force and the force derived from the pressure distribution. As the bottom panel of Figure 6 shows, the damping force is linearly proportional the valve–body velocity in the prescribed excitation range, with a coefficient of $k = 203.6\,Ns/m$.

5. SELF-EXCITED OSCILLATIONS

The work reported so far has been concerned with the dynamic response of the poppet due to pressure excitation. In this section we describe the dynamical behaviour of a pressure relief valve interacting with the upstream pipeline. It is well-known that pressure relief valves tend to self-oscillate for a wide parameter range, which is often referred to as valve chatter, see [4]. It is clear from these studies that fluid forces (notably fluid damping) play an important role. In this section, we present a linear stability analysis resulting in the critical transmission line volume that is needed to stabilize the valve motion. In the last chapter, we compare these results with direct numerical simulations on the ODE and CFD model.

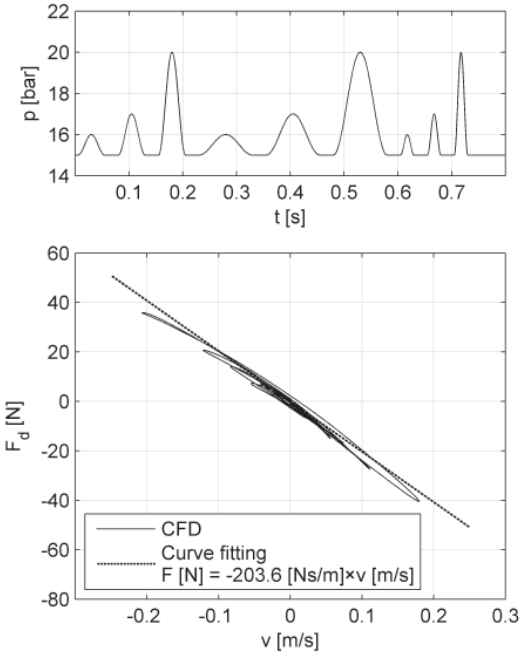

Figure 6. Top panel: Pressure excitation in function of time. Bottom panel: Damping force trajectory in function of valve–body velocity.

5.1. *Linear stability analysis*

The equilibrium of system Eq. (1) is given by $\dot{x}$=0, $\dot{v}$=0 and $\dot{p}$=0. For prescribed spring pre–compression and flow rate the equilibrium pressure and displacement are easy to be found. The aim of this analysis is to find those critical parameter values at which the system looses its stability. Close to the equilibrium, the dynamics is governed by the eigenvalues of the linear coefficient matrix given by

$$\mathbf{J} = \begin{pmatrix} 0 & 1 & 0 \\ -\frac{p_e\delta\gamma^2}{m} - \frac{s}{m} & -\frac{k}{m} & \frac{A - x_e\gamma^2\delta}{m} \\ -\frac{\sqrt{p_e}E\gamma}{V} & 0 & -\frac{x_eE\gamma}{2\sqrt{p_e}V} \end{pmatrix}. \tag{11}$$

The eigenvalues are the roots of the characteristic

polynomial

$$\det(\mathbf{J} - \lambda\mathbf{I}) = \lambda^3 + a_2\lambda^2 + a_1\lambda + a_0 = 0 \tag{12}$$

with

$$a_0 = -\frac{\sqrt{p}x_e E\delta\gamma^3}{2mV} + \frac{sx_e E\gamma}{2m\sqrt{p_e}V} + \frac{A\sqrt{p_e}E\gamma}{mV}, \tag{13}$$

$$a_1 = \frac{p_e\delta\gamma^2}{m} + \frac{kx_e E\gamma}{2m\sqrt{p_e}V} + \frac{s}{m}, \tag{14}$$

$$a_2 = \frac{k}{m} + \frac{x_e E\gamma}{2\sqrt{p_e}V}. \tag{15}$$

Oscillations are born in the system if we have purely imaginary eigenvalues (Hopf bifurcation) as explained e.g. in [11]. Inserting $\lambda = i\omega$ into Eq. (12) and forcing both the real and imaginary parts to vanish, we find that the necessary condition for stability loss and the frequency of the appearing oscillation is

$$a_0 = a_1 a_2, \quad \text{and} \quad \omega = \sqrt{a_1}. \tag{16}$$

We are interested in computing those critical fluid volume values at which the system losses its stability and self-excited oscillations are born. We set an initial fluid volume $V_0 = LD^2\pi/4$ (with $L = 3.5m$ and $D = 10mm$) and represent the results in terms of the multiplier of this initial volume C_V, i.e. $V = C_V V$. These critical values are presented in Table 2 for different flow rates. The valve oscillates for smaller volumes and operates in a safe manner for larger volumes. We also observe a slight decrease in the critical value as flow rate increases.

Table 2. Critical parameter values

Q_{in} [l/min]	V/V_0 [-]
10	49.651
20	47.839
30	46.038
40	44.244

5.2. Comparison with CFD results

A series of CFD simulations were carried out with constant Q_{in}=30[l/min] flow rate and with V/V_0=1, 10, 30, 50, 60 parameter values and based on the CFD results numerical simulation were performed with the above determined damping coefficient, i.e. Eq. (1) was solved by a standard Runge-Kutta solver. As it can be seen in Figure 7 the time signal shows qualitative agreement. In the case of V/V_0=1, 10, 30, the valve heavily oscillates and also hits the seat, beyond which the CFD computations could not be continued. in the case of V/V_0=50 and 60, the motion becomes stable for both types of computations, although the CFD results tend to exhibit higher damping. This correlates with the result of the linear stability analysis (see Table 2), namely at Q_{in}=30[l/min] the system becomes stable over the boundary of loss of stability.

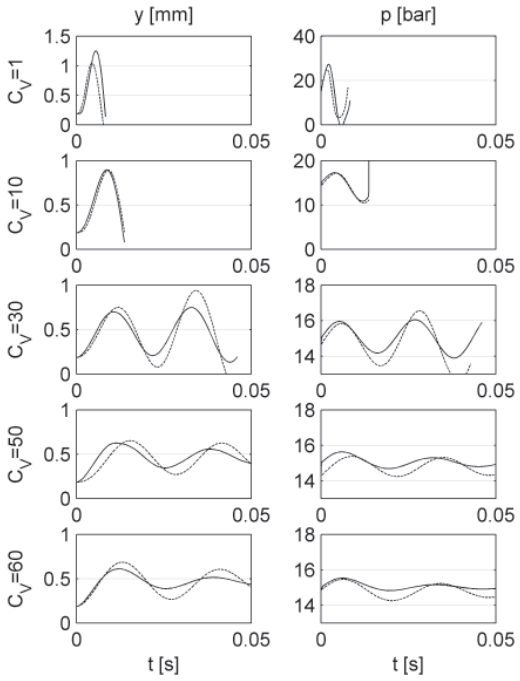

Figure 7. Comparison of the CFD (solid lines) and ODE (dashed lines) dynamics given by Eq. (1)**.**

6. SUMMARY

The dynamics and stability of a simple pressure relief valve was studied with the help of Computational Fluid Dynamics tools. By using deforming mesh and one-way coupling (rigid body simulation), the motion of the valve body was computed for two scenarios. First, by applying direct pressure excitation at the inlet the unsteady fluid force was computed, which turned out to be a linear function of the valve velocity (independently of the pressure), hence we refer this force to as classic viscous damping. The second set of computations took into account the averaged pressure dynamics of the transmission line (as a simple pressure vessel). The analytical stability boundaries and the CFD computations were compared showing reasonable

agreement. These results suggest that based on CFD computations, it is possible to develop low-order models of valve dynamics which can than be analysed with the help of the toolbox of non-linear dynamics.

ACKNOWLEDGEMENTS

This research was supported by grant OTKA PD 76478 of C. Hős.

References

[1] Daily, J. 1955 "Resistance coefficients for accelerated and decelerated flows through smooth tubes and orifices". Tech. rep., DTIC Document.

[2] McCloy, D. and McGuigan, R. 1964 "Some static and dynamic characteristics of poppet valves". *ARCHIVE: Proceedings of the Institution of Mechanical Engineers, Conference Proceedings 1964-1970 (vols 178-184), Various titles labelled Volumes A to S*, vol. 179, pp. 199–213, Prof Eng Publishing.

[3] Stone, J. 1960 "Discharge coefficients and steady-state flow forces for hydraulic poppet valves". *Journal of Basic Engineering*, Vol. 82, p. 144.

[4] TAKENAKA, T. 1964 "Performances of Oil Hydraulic Control Valves". *Bulletin of JSME*, Vol. 7, No. 27, pp. 566–576.

[5] Eizo, U. 1969-10 "Thrust of Poppet Valve". *Bulletin of JSME*, Vol. 12, No. 53, pp. 1099–1109.

[6] Vaughan, N. D., Johnston, D. N., and Edge, K. A. 1992 "Numerical simulation of fluid flow in poppet valves". *Proceedings of the Institution of Mechanical Engineers*, Vol. 206, pp. 119–127.

[7] Mokhtarzadeh-Dehghan, M., Ladommatos, N., and Brennan, T. 1997 "Finite element analysis of flow in a hydraulic pressure valve". *Applied Mathematical Modelling*, Vol. 21, No. 7, pp. 437 – 445.

[8] Srikanth, C. and Bhasker, C. 2009 "Flow analysis in valve with moving grids through CFD techniques". *Advances in Engineering Software*, Vol. 40, No. 3, pp. 193–201.

[9] Song, X., Jung, J., Lee, H., Kim, D., and Park, Y. 2010 "2-D dynamic analysis of a pressure relief valve by CFD". *Proceedings of the 9th WSEAS international conference on Applied computer and applied computational science*, pp. 136–140, World Scientific and Engineering Academy and Society (WSEAS).

[10] Viel, A. and Imagine, L. "Strong Coupling of Modelica System-Level Models with Detailed CFD Models for Transient Simulation of Hydraulic Components in their Surrounding Environment".

[11] Kuznetsov, I. 1998 *Elements of applied bifurcation theory*, vol. 112. Springer Verlag.

Conference on Modelling Fluid Flow (CMFF'12)
The 15th International Conference on Fluid Flow Technologies
Budapest, Hungary, September 4-7, 2012

NUMERICAL SOLUTION OF GENERALIZED NEWTONIAN AND GENERALIZED OLDROYD-B FLUIDS FLOW

Radka Keslerová,[1] Karel Kozel [2]

[1] Corresponding Author. Department of Technical Mathematics, Czech Technical University in Prague. Karlovo nm. 13, 121 35 Prague, Czech Republic. E-mail: keslerov@marian.fsik.cvut.cz
[2] Department of Technical Mathematics, Czech Technical University in Prague. E-mail: Karel.Kozel@fs.cvut.cz

ABSTRACT

This work deals with the numerical solution of laminar incompressible viscous and viscoelastic flow in 2D channel for generalized Newtonian and generalized Oldroyd-B fluids. The governing system of equations is based on the system of balance laws for mass and momentum. The generalized Newtonian fluids differ through choice of a viscosity function. A power-law model with different values of power-law index is used. Numerical solution of the described models is based on cell-centered finite volume method using explicit Runge–Kutta time integration. In the case of unsteady computation a dual-time stepping method is considered. The flow is modelled in a bounded computational domain. Numerical results obtained by this method are presented and compared.

Keywords: generalized Newtonian and Oldroyd-B fluids model, Navier–Stokes equatios, finite volume method, dual-time stepping method, Runge–Kutta method

NOMENCLATURE

$\underline{\mathsf{D}}$	[-]	symmetric part of velocity gradient
$\underline{F}, \underline{G}$	[-]	numerical fluxes
P	[-]	kinematic pressure
$\underline{R}, \underline{R_\beta}$	[-]	diagonal matrices
$\underline{\mathsf{T}}$	[-]	stress tensor
$\underline{\mathsf{T}_e}$	[-]	Newtonian part of stress tensor
$\underline{\mathsf{T}_s}$	[-]	elastic part of stress tensor
$\underline{\mathsf{W}}$	[-]	antisymmetric part of velocity gradient
$\underline{W}$	[-]	vector of conservative variables
f	[Hz]	frequency
p	[Pa]	pressure
r	[-]	power-law index
t	[s]	time
u, v	[m/s]	velocity components
$\underline{u}$	$[m.s^{-1}]$	velocity vector
x, y	[m]	Cartesian coordinates
α	[-]	Runge-Kutta coefficients
β	[-]	artificial compressibility coefficient
λ_1	[s]	relaxation time
λ_2	[s]	retardation time
μ	[-]	viscosity
ρ	$[kg.m^{-3}]$	density
τ	[s]	pseudo-time
ω	[-]	angular velocity

Subscripts and Superscripts

i, j	indices
r	power-law index
t	derivative over the time
x, y	derivatives over the coordinate variables
τ	derivative over the pseudo-time
c	convective part
n, ν	time index, pseudo-time index
v	viscous part
$*$	reference value

1 MATHEMATICAL MODEL

The governing system of equations is the system of balance laws of mass and momentum for incompressible fluids [7], [10]:

$$\text{div } \underline{u} = 0 \tag{1}$$

$$\rho \frac{\partial \underline{u}}{\partial t} + \rho(\underline{u}.\nabla)\underline{u} = -\nabla P + \text{div } \underline{\mathsf{T}} \tag{2}$$

where P is the pressure, ρ is the constant density, $\underline{u}$ is the velocity vector. The symbol $\underline{\mathsf{T}}$ represents the stress tensor.

1.1 Stress Tensor

In this work the different choices of the definition of the stress tensor are used.

a) Viscous fluids

The simple viscous model is *Newtonian model*:

$$\underline{\mathsf{T}} = 2\mu \underline{\mathsf{D}} \tag{3}$$

where μ is the dynamic viscosity and tensor $\underline{\mathsf{D}}$ is the symmetric part of the velocity gradient.

This model could be generalized by extending Newtonian model for shear thinning and thickening fluids flow. For this case the viscosity μ is no more constant, but is defined as the viscosity function by the power-law model [5]

$$\mu = \mu(\dot{\gamma}) = \mu_\epsilon \left(\sqrt{\mathrm{tr}\underline{\mathsf{D}}^2} \right)^r, \tag{4}$$

where μ_ϵ is a constant, e.g. the dynamic viscosity for Newtonian fluid. The symbol tr $\underline{\mathsf{D}}^2$ denotes the trace of the tensor $\underline{\mathsf{D}}^2$. The exponent r is the power-law index. This model includes Newtonian fluids as a special case ($r = 0$). For $r > 0$ the power-law fluid is shear thickening, while for $r < 0$ it is shear thinning.

b) Viscoelastic fluids

The behavior of the mixture of viscous and viscoelastic fluids can be described by *Oldroyd-B model* and it has the form

$$\underline{\mathsf{T}} + \lambda_1 \frac{\delta \underline{\mathsf{T}}}{\delta t} = 2\mu \left(\underline{\mathsf{D}} + \lambda_2 \frac{\delta \underline{\mathsf{D}}}{\delta t} \right). \tag{5}$$

The parameters λ_1, λ_2 are *relaxation* and *retardation time*.

The stress tensor $\underline{\mathsf{T}}$ is decomposed to the Newtonian part $\underline{\mathsf{T}}_s$ and viscoelastic part $\underline{\mathsf{T}}_e$ ($\underline{\mathsf{T}} = \underline{\mathsf{T}}_s + \underline{\mathsf{T}}_e$) and

$$\underline{\mathsf{T}}_s = 2\mu_s \underline{\mathsf{D}}, \qquad \underline{\mathsf{T}}_e + \lambda_1 \frac{\delta \underline{\mathsf{T}}_e}{\delta t} = 2\mu_e \underline{\mathsf{D}}, \tag{6}$$

where

$$\frac{\lambda_2}{\lambda_1} = \frac{\mu_s}{\mu_s + \mu_e}, \qquad \mu = \mu_s + \mu_e. \tag{7}$$

The *upper convected derivative* $\frac{\delta}{\delta t}$ is defined (for general tensor) by the relation (see [10])

$$\frac{\delta \underline{\mathsf{M}}}{\delta t} = \frac{\partial \underline{\mathsf{M}}}{\partial t} + (\underline{u}.\nabla)\underline{\mathsf{M}} - (\underline{\mathsf{W}}\underline{\mathsf{M}} - \underline{\mathsf{M}}\underline{\mathsf{W}}) - (\underline{\mathsf{D}}\underline{\mathsf{M}} + \underline{\mathsf{M}}\underline{\mathsf{D}}) \tag{8}$$

where $\underline{\mathsf{D}}$ is the symmetric part of the velocity gradient $\underline{\mathsf{D}} = \frac{1}{2}(\nabla \underline{u} + \nabla \underline{u}^T)$ and $\underline{\mathsf{W}}$ is the antisymmetric part of the velocity gradient $\underline{\mathsf{W}} = \frac{1}{2}(\nabla \underline{u} - \nabla \underline{u}^T)$.

The governing system (1), (2) of equations is completed by the equation for the viscoelastic part of the stress tensor

$$\frac{\partial \underline{\mathsf{T}}_e}{\partial t} + (\underline{u}.\nabla)\underline{\mathsf{T}}_e = \frac{2\mu_e}{\lambda_1}\underline{\mathsf{D}} - \frac{1}{\lambda_1}\underline{\mathsf{T}}_e + \\ + (\underline{\mathsf{W}}\underline{\mathsf{T}}_e - \underline{\mathsf{T}}_e\underline{\mathsf{W}}) + (\underline{\mathsf{D}}\underline{\mathsf{T}}_e + \underline{\mathsf{T}}_e\underline{\mathsf{D}}). \tag{9}$$

2 NUMERICAL SOLUTION

2.1 Steady Numerical Results

Numerical solution of the described models is based on cell-centered finite volume method using explicit Runge–Kutta time integration. The unsteady system of equations with steady boundary conditions is solved by finite volume method. Steady state solution is achieved for $t \to \infty$. In this case the artificial compressibility method can be applied. It means that the continuity equation is completed by the time derivative of the pressure in the form (for more details see e.g. [1]):

$$\frac{1}{\beta^2}\frac{\partial p}{\partial t} + \mathrm{div}\ \underline{u} = 0, \quad \beta \in \mathbb{R}^+. \tag{10}$$

The system of equations (including the modified continuity equation) could be rewritten in the vector form.

$$\tilde{R}_\beta W_t + F^c_x + G^c_y = F^v_x + G^v_y + S, \\ \tilde{R}_\beta = \mathrm{diag}(\frac{1}{\beta^2}, 1, 1, 1, 1, 1). \tag{11}$$

where W is the vector of unknowns, F^c, G^c are inviscid fluxes, F^v, G^v are viscous fluxes and the source term S.

The following special parameters are used:

Newtonian	$\mu(\dot{\gamma}) = \mu_s = const.$	$\underline{\mathsf{T}}_e \equiv 0$
Generalized Newtonian	$\mu(\dot{\gamma})$	$\underline{\mathsf{T}}_e \equiv 0$
Oldroyd-B	$\mu(\dot{\gamma}) = \mu_s = const.$	$\underline{\mathsf{T}}_e$
Generalized Oldroyd-B	$\mu(\dot{\gamma})$	$\underline{\mathsf{T}}_e$

The eq. (11) is discretized in space by the cell-centered finite volume method (see [6]) and the arising system of ODEs is integrated in time by the explicit multistage Runge–Kutta scheme (see [5], [4], [3]):

$$\begin{aligned} W_i^n &= W_i^{(0)} \\ W_i^{(s)} &= W_i^{(0)} - \alpha_{s-1}\Delta t \mathcal{R}(W)_i^{(s-1)} \\ W_i^{n+1} &= W_i^{(M)} \qquad s = 1, \ldots, M, \end{aligned} \tag{12}$$

where $M = 3$, $\alpha_0 = \alpha_1 = 0.5, \alpha_2 = 1.0$, the steady residual $\mathcal{R}(W)_i$ is defined by finite volume method as

$$\mathcal{R}(W)_i = \frac{1}{\sigma_i}\sum_{k=1}^{4}\Big[\left(\overline{F}^c_k - \overline{F}^v_k\right)\Delta y_k - \\ - \left(\overline{G}^c_k - \overline{G}^v_k\right)\Delta x_k\Big] + \overline{S}, \tag{13}$$

where σ_i is the volume of the cell, $\sigma_i = \int\int_{C_i} dx\ dy$. The symbols $\overline{F}^c_k, \overline{G}^c_k$ and $\overline{F}^v_k, \overline{G}^v_k$ denote the numerical approximation of the inviscid and viscous fluxes, for more details see [5], symbol $\overline{S}$ represents the numerical approximation of the source term with central approximation of derivatives. The multistage Runge–Kutta scheme (12) is conditionally stable.

2.1.1 Steady Boundary Conditions

The flow is modelled in a bounded computational domain where a boundary is divided into three mutually disjoint parts: a solid wall, an outlet and an inlet. At the inlet Dirichlet boundary condition for

velocity vector is used and for a pressure Neumann boundary condition is used. At the outlet the pressure value is given and for the velocity vector Neumann boundary condition is used. The homogenous Dirichlet boundary condition for the velocity vector is used on the wall. For the pressure Neumann boundary condition is considered.

Remark

The problem is to numerically solve Navier–Stokes equations for incompressible flows. Mathematical theory is possible to use for flow in one type of channel (steady) for one or more outputs where existence and unicity of the solution is proved (see [9]).

2.2 Unsteady Computation

For the numerical solution of unsteady flows the dual-time stepping method is used. The principle of dual-time stepping method is following. The artificial time τ is introduced and the artificial compressibility method in the artificial time is applied. The system of Navier-Stokes equations is extended to unsteady flows by adding artificial time derivatives $\partial W/\partial\tau$ to all equations, for more details see [8], [2]

$$\tilde{R}_\beta W_\tau + \tilde{R} W_t + F^c_x + G^c_y = F^v_x + G^v_y, \qquad (14)$$

$$\tilde{R} = \mathrm{diag}(0,1,1), \quad \tilde{R}_\beta = \mathrm{diag}(\frac{1}{\beta^2},1,1). \qquad (15)$$

The vector of the variables is denoted by W, F^c, G^c are the inviscid fluxes and F^v, G^v represent the viscous fluxes.

The derivatives with respect to the real time t are discretized using a three-point backward formula, it defines the form of unsteady residual

$$\tilde{R}_\beta \frac{W^{l+1}-W^l}{\Delta\tau} = -\tilde{R}\frac{3W^{l+1}-4W^n+W^{n-1}}{2\Delta t} - \\ -\mathrm{Res}(W)^l = -\overline{\mathrm{Res}}(W)^{l+1}, \qquad (16)$$

where $\Delta t = t^{n+1} - t^n$ and $\mathrm{Res}(W)$ is the steady residual defined as for steady computation, see (13). The symbol $\overline{\mathrm{Res}}(W)$ denotes unsteady residual. The superscript n denotes the real time index and the index l is associated with the pseudo-time. The integration in pseudo-time can be carried out by explicit multistage Runge–Kutta scheme. The dual-time step is limited so that $\Delta\tau \leq 2\Delta t/3$.

2.2.1 Unsteady Boundary Condition

The unsteady boundary conditions are defined as follows. In the inlet, in the solid wall and in one of the outlet part the steady boundary conditions are prescribed. In the second outlet part new boundary condition is defined. For the velocity Neumann boundary condition is used. The pressure value is prescribed by the function

$$p_{21} = \frac{1}{4}\left(1+\frac{1}{2}\sin(\omega t)\right), \qquad (17)$$

where ω is the angular velocity defined as $\omega = 2\pi f$, where f is a frequency.

3 NUMERICAL RESULTS

3.1 Steady Numerical Results

In this section the steady numerical results of two dimensional incompressible laminar viscous flows for generalized Newtonian fluids are presented. The different values of the power-law index were used. Reynolds number is 400.

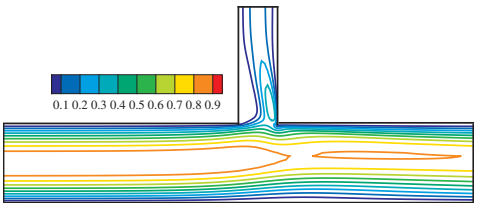

Figure 1: Velocity isolines of steady flows for Newtonian fluids ($r = 0.0$).

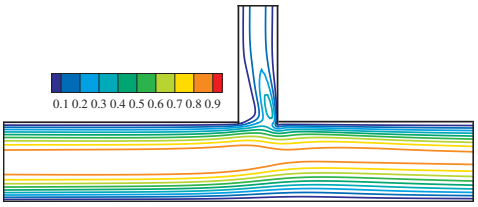

Figure 2: Velocity isolines of steady flows for shear thickening fluids ($r = 0.5$).

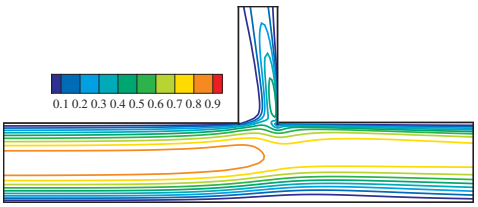

Figure 3: Velocity isolines of steady flows for shear thinning fluids ($r = -0.5$).

In Figures 1, 2, 3 velocity isolines for generalized Newtonian fluids flow are presented. In the Figure 4 the histories of the convergence are presented. One of the main differences between Newtonian and non-Newtonian fluids flow is in the size of the separation region. This is in the place where the channel is branched. From Figures 1, 2, 3, the separation region is the smallest for shear thickening fluids and the biggest separation region is for the shear thinning fluids.

In Figures 5, 6, 7 nondimensional axial velocity profile for steady fully developed flow of generalized

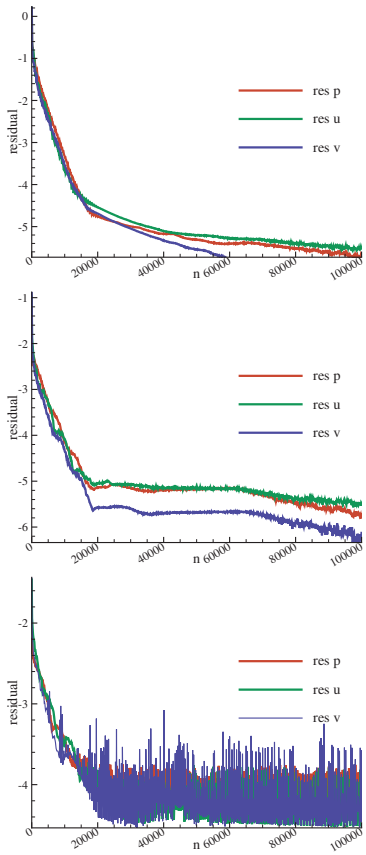

Figure 4: History of the convergence of steady flows for generalized Newtonian fluids.

Newtonian. In these figures the small channel is sketched. The line (inside the domain) marks the position where the cuts for the velocity profile were done.

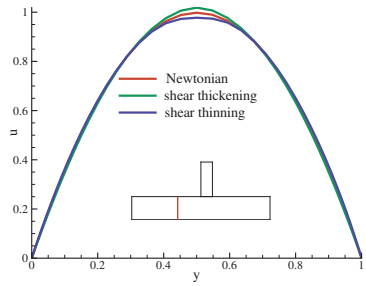

Figure 5: Nondimensional velocity profile for steady fully developed flow of generalized Newtonian fluids in the branching channel.

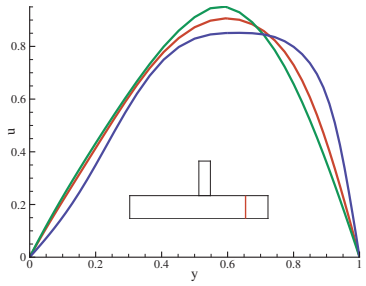

Figure 6: Nondimensional velocity profile for steady fully developed flow of generalized Newtonian fluids in the branching channel.

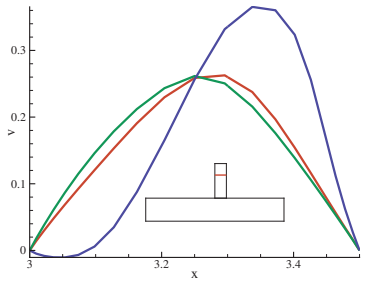

Figure 7: Nondimensional velocity profile for steady fully developed flow of generalized Newtonian fluids in the branching channel.

3.2 Unsteady Numerical Results

In this section two dimensional unsteady numerical results for generalized Newtonian flow through the branching channel are presented. The used unsteady method is the dual-time stepping method with artificial compressibility coefficient $\beta = 10$. In the branch (going up) the pressure is prescribed by pressure function (17) with two frequencies f, 2 and 20. As initial data the numerical solution of steady fully developed flow of generalized Newtonian fluid in the branching channel was used. Reynolds number is 400.

In Figures 8, 10 and 12 graphs of velocity as the function of time for generalized Newtonian fluids flow with frequency 2 are shown. In Figures 9, 11 and 13 the velocity distribution for tested fluids.

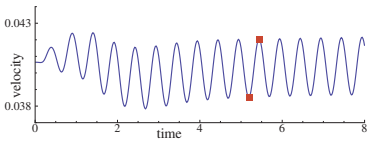

Figure 8: The graphs of the velocity as the function of the time, $f = 2$.

In Figures 8, 10 and 12 graphs of velocity as the function of time for generalized Newtonian fluids flow with frequency 2 are shown. In Figures 9, 11 and 13

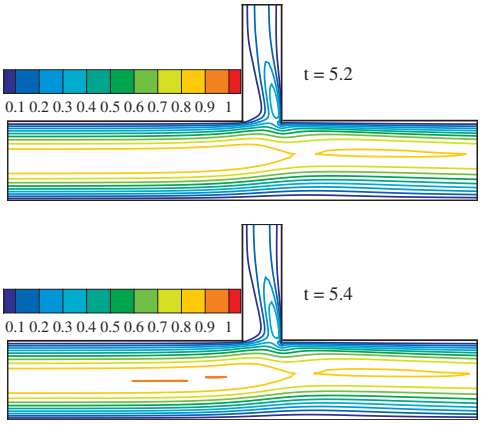

Figure 9: The unsteady numerical solution for Newtonian fluids ($r = 0.0$).

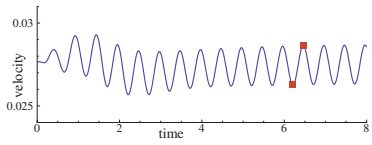

Figure 10: The graphs of the velocity as the function of the time, $f = 2$.

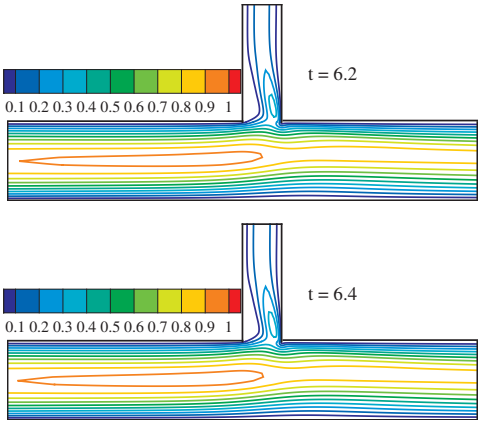

Figure 11: The unsteady numerical solution for shear thickening fluids ($r = 0.5$).

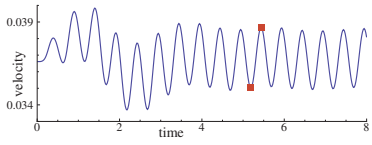

Figure 12: The graphs of the velocity as the function of the time, $f = 2$.

the velocity distribution for tested fluids.

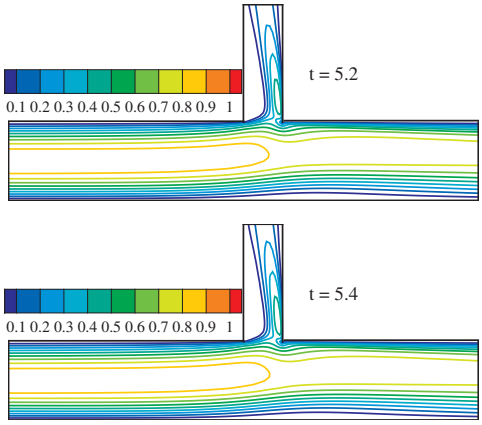

Figure 13: The unsteady numerical solution for shear thinning fluids ($r = -0.5$).

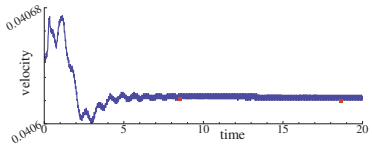

Figure 14: The graphs of the velocity as the function of the time, $f = 20$.

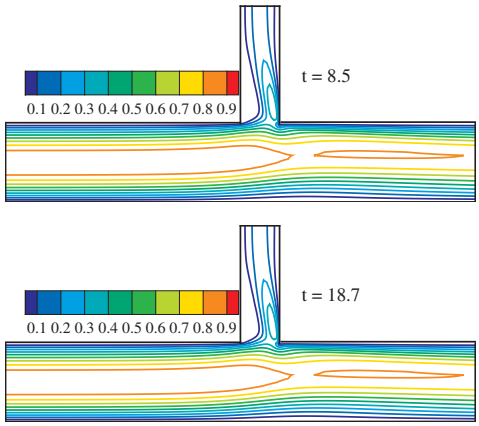

Figure 15: The unsteady numerical solution for Newtonian fluids ($r = 0.0$).

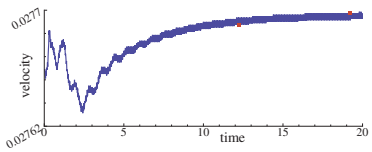

Figure 16: The graphs of the velocity as the function of the time, $f = 20$.

3.3 Newtonian and Oldroyd-B Numerical Results

The comparison of the numerical simulations of generalized Newtonian and generalized Oldroyd-B

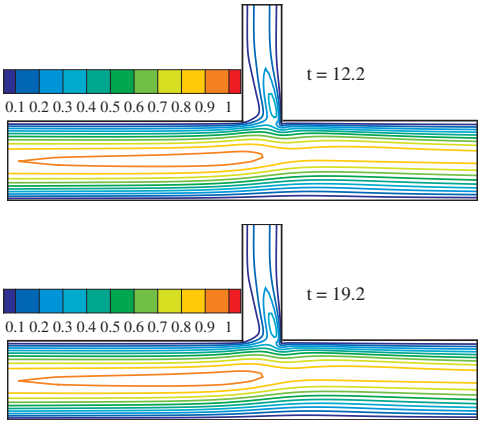

Figure 17: The unsteady numerical solution for shear thickening fluids ($r = 0.5$).

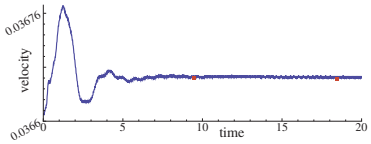

Figure 18: The graphs of the velocity as the function of the time, $f = 20$.

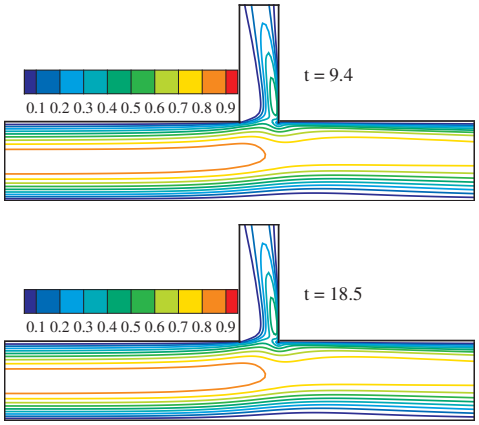

Figure 19: The unsteady numerical solution for shear thinning fluids ($r = -0.5$).

fluids flow is presented. Figure 20 shows the shape of the tested domain.

The following model parameters are:

$$\mu_e = 4.0 \cdot 10^{-4} Pa \cdot s \quad \mu_s = 3.6 \cdot 10^{-3} Pa \cdot s$$
$$\lambda_1 = 0.06s \quad \lambda_2 = 0.054s$$
$$U_0 = 0.0615m \cdot s^{-1} \quad L_0 = 2R = 0.0062m$$
$$\mu_0 = \mu = \mu_s + \mu_e \quad \rho = 1050kg \cdot m^{-3}.$$

Parabolic velocity profile (corresponding to Newtonian flow) is prescribed at the inlet. Outlet pressure is fixed to a constant. On the walls no-slip conditions are used for velocity and homogeneous

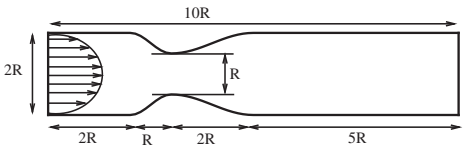

Figure 20: Structure of the computational domain

Neumann condition for the pressure. For Oldroyd-B model variables (T_e) there is zero kept at the inlet and homogeneous Neumann condition at the walls and at the outlet. The following sets of figures (21 and 22) shows comparison of pressure and axial velocity distribution in the narrowed channel for above described models:

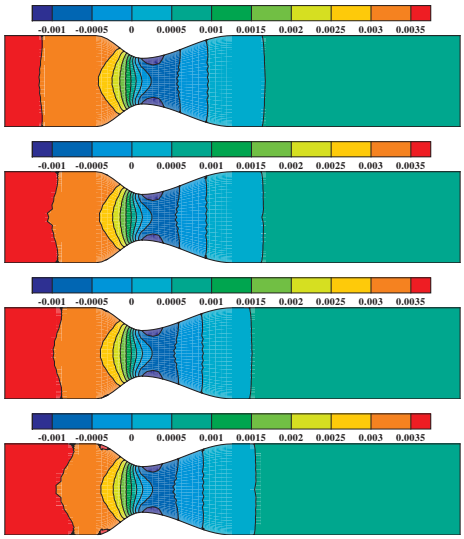

Figure 21: Comparison of pressure distribution in the narrowed channel

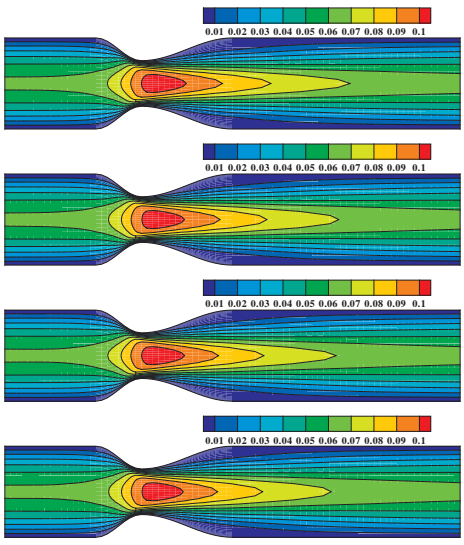

Figure 22: Comparison of axial velocity distribution in the narrowed channel

Pressure and axial velocity distribution along the axis for all tested fluids models is shown in the Fig. 23. By simple observation one can conclude that the main effect of the Oldroyd-B fluids behavior is visible mainly in the recirculation zone.

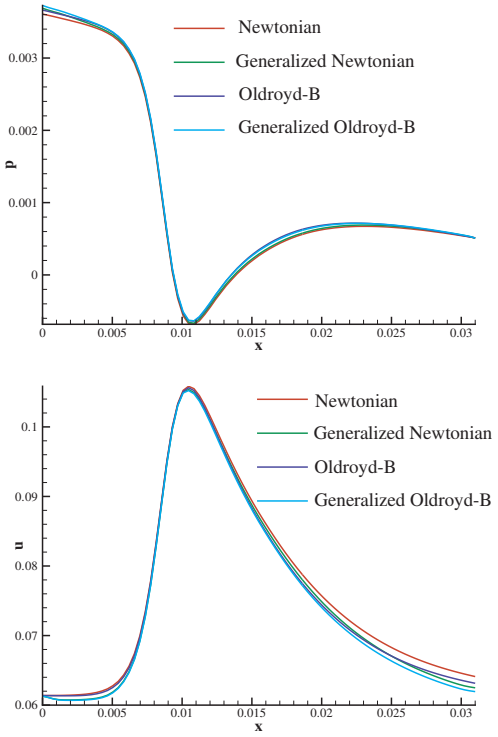

Figure 23: Pressure and axial velocity distribution along the axis

4 CONCLUSION

In this paper a finite volume solver for incompressible laminar viscous flows in the branching channel was described. Newtonian model was generalized for generalizing Newtonian fluids flow. Power-law model with different values of power-law index were tested. The convergence history confirms robustness of the applied method. The numerical results obtained by this method were presented and compared. The dual-time stepping method was considered for unsteady numerical computation. This method was tested for generalized Newtonian fluids with initial data obtained by steady numerical computation.

Newtonian and Oldroyd-B models with their generalized modification have been considered for numerical simulation of fluids flow in the idealized axisymmetric stenosis. The cell-centered finite volume solver for incompressible laminar viscous and viscoelastic fluids flow has been described. The numerical results obtained by this method were presented. For the generalizing of the models the viscosity function is computed by the cross model. In the idealized stenosis we tested the generalized Newtonian and generalized Oldroyd-B fluids models. Based on the above numerical results we can conclude that the difference between the viscous and viscoelastic fluids is visible in the recirculation zone.

ACKNOWLEDGEMENTS

This work was partly supported by the grant GACR 101/09/1539, GACR P201/ 11/1304 and GACR 201/09/0917.

References

[1] Chorin A.J. A numerical method for solving incompressible viscous flow problem. *Journal of Computational Physics*, 135:118–125, 1967.

[2] Gaitonde A.L. A dual-time method for two dimensional unsteady incompressible flow calculations. *International Journal for Numerical Methods in Engineering*, 41:1153–1166, 1998.

[3] Vimmr J. and Jonášová A. Non-newtonian effects of blood flow in complete coronary and femoral bypasses. *Mathematics and Computers in Simulation*, 80:1324–1336, 2010.

[4] Schmidt W. Jameson, A. and E. Turkel. Numerical solution of the euler equations by finite volume methods using runge-kutta time-stepping schemes. In *AIAA 14th Fluid and Plasma Dynamic Conference California*, 1981.

[5] R. Keslerová and K. Kozel. Numerical modelling of incompressible flows for newtonian and non-newtonian fluids. *Mathematics and Computers in Simulation*, 80:1783–1794, 2010.

[6] R. LeVeque. *Finite-Volume Methods for Hyperbolic Problems*. Cambridge University Press, 2004.

[7] Dvořák R. and Kozel K. *Mathematical modelling in aerodynamics (in Czech)*. CTU, Prague, Czech Republic, 1996.

[8] Honzátko R. *Numerical simulations of incompressible flows with dynamical and aeroelastic effects*. PhD thesis, Czech Technical University, Prague, Czech Republic, 2007.

[9] Kračmar S. and Neustupa J. Global existence of weak solutions of a nonsteady variational inequality of the navier–stokes type with mixed boundary conditions. In *Proc. of the International Symposium on Numerical Analysis, Charles University Prague*, pages 156–177, 1993.

[10] Bodnar T. and Sequeira A. Numerical study of the significance of the non-newtonian nature of blood in steady flow through s stenosed vessel. *Advances in Mathematical Fluid Mechanics*, pages 83–104, 2010.

Conference on Modelling Fluid Flow (CMFF'12)
The 15th International Conference on Fluid Flow Technologies
Budapest, Hungary, September 4-7, 2012

FLUID-STRUCTURE INTERACTION IN COMPLEX PIPING SYSTEMS

Stefan RIEDELMEIER,[1] Stefan BECKER, [2] Eberhard SCHLÜCKER [3]

[1] Corresponding Author. Institute of Process Machinery and Systems Engineering, Friedrich-Alexander University Erlangen-Nuremberg. Cauerstr. 4, 91058 Erlangen, Germany. Tel.: +49 9131 85 29596, Fax: +49 9131 85 29449, E-mail: rie@ipat.uni-erlangen.de
[2] Institute of Process Machinery and Systems Engineering, Friedrich-Alexander University Erlangen-Nuremberg. E-mail: sb@ipat.uni-erlangen.de
[3] Institute of Process Machinery and Systems Engineering, Friedrich-Alexander University Erlangen-Nuremberg. E-mail: sl@ipat.uni-erlangen.de

ABSTRACT

In order to examine the effects of fluid-structure interaction (FSI) in piping systems, a test facility was built at the Friedrich-Alexander University Erlangen-Nuremberg in cooperation with AREVA. The research objective is to identify the conditions under which FSI has to be taken into account for water hammer events and if there are special cases in which the consideration of FSI leads to increased loads.

Resonance experiments with movable bends in two piping system configurations were carried out. The transient forces on the structure were produced by water hammer. The displacement of the bend and the pressure inside the pipe were measured for various free oscillating lengths of the bend. As a consequence of changing the support position, the natural frequency of the bend alters. The results were displayed in resonance curves and frequency spectra for the different configurations. In both a correlation between the pressure and the displacement spectrum showed a transfer of momentum from the fluid to the structure, but only in one configuration a reaction of the fluid onto the structural movement could be observed. Frequency shifts of the pressure outside the resonance area and a splitting of the pressure peak inside the resonance area were obvious.

Keywords: bend, FSI, oscillation, piping system, resonance, water hammer

NOMENCLATURE

DN	$[mm]$	nominal diameter
H	$[m]$	pressure head
$\mathbb{N}$	[-]	natural numbers
PN	$[bar]$	nominal pressure
c	$[m/s]$	propagation velocity of the water hammer
d_i	$[mm]$	inner diameter
g	$[m/s^2]$	acceleration of free fall
f_f	$[Hz]$	fluid frequency
f_s	$[Hz]$	structural frequency
l	$[m]$	length of the piping system
n	[-]	mode number
p	$[bar]$	pressure
p_{max}	$[bar]$	maximum allowable pressure
x_{max}	$[mm]$	mean maximum displacement
y	$[mm]$	support position

1. INTRODUCTION

Water hammer analysis is a fundamental part in the design progress of piping systems. In most cases this calculation does not consider fluid-structure interaction (FSI). In the following FSI stands for a two-way interaction in contrast to an one-way interaction where there is only a load transmission from the fluid onto the structure. In the analysis of pipe oscillations the two-way FSI generally is not considered. There is no reaction from the fluid on the calculated results of the structure. If the piping system is rigidly anchored, the method is justified [1]. If not, the introduction of FSI can show an effect. As a consequence there could be changes in the amplitudes and the frequencies [2]. FSI comprises three different coupling types. Poisson coupling is related to the radial movement of the pipe wall and causes a variation of the speed of sound in the fluid. This is often integrated in the calculation of the fluid system by considering the mentioned reduction of the propagation velocity. Friction coupling is a result of the wall shear stresses. The last type is called junction coupling and occurs at movable bends or tees etc. [3] [4]. The general opinion is that a consideration of FSI has either no influence or leads to lower loads [5]. So the calculation of a piping system without FSI is conservative. If this statement is always valid should be investigated in detail.

2. TEST FACILITY

The test facility consists of a piping system and measurement equipment.

2.1. Piping System

The piping system for water hammer experiments is sketched in Figure 1. It consists of a water container,

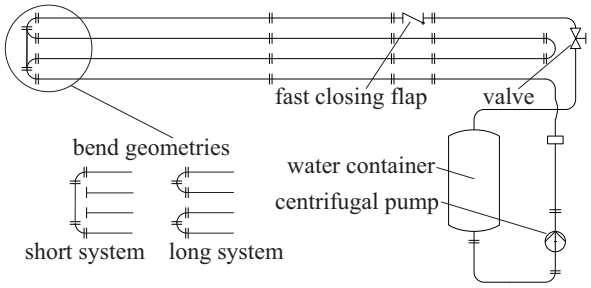

Figure 1: Flow diagram of the test facility

a centrifugal pump, a fast closing flap and a valve to regulate the flow rate. The pressure level is PN 63 ($p_{max} = 63\ bar$) and the diameter is DN 100 ($d_i = 106,3\ mm$). There are two configurations of the piping system. In the short system the distance between the container and the flap is $l = 35\ m$, in the long one the distance is $l = 63\ m$. Along with the variation of the pipe length the frequency of the water hammer oscillation changes. The water container has a volume of 5 m^3 (tap water). A frequency converter allows to regulate the pump frequency, which allows to change the pressure level. The maximum pressure head is $H = 150\ m$. The mean velocity in the piping system can be varied between 0 m/s and 4 m/s. The fast closing flap was constructed at the institute, produces water hammer and is optimized for short closing times.

In order to get an impression of the water hammer test facility, it is shown in Figure 2.

Figure 2: Water hammer test facility in Erlangen

2.2. Hydraulic modes

The length of the piping system, the propagation velocity of the water hammer and the boundary conditions at both ends fix the fluid frequency. At the flap the velocity of the fluid is zero (hydraulically closed) and at the water container the pressure is constant (hydraulically open). With these boundary conditions the fluid frequency f_f is calculated by equation (1) where n defines the mode number, l is the length of the piping system and c is the propagation velocity of the water hammer which is lower than the speed of sound of the fluid due to the elasticity of the pipe wall.

$$f_f = (2n-1) \cdot \frac{c}{4l} \quad , \quad n \in \mathbb{N} \tag{1}$$

The first eigenmodes of the piping system are sketched in Figure 3. For the calculation of the fluid frequencies

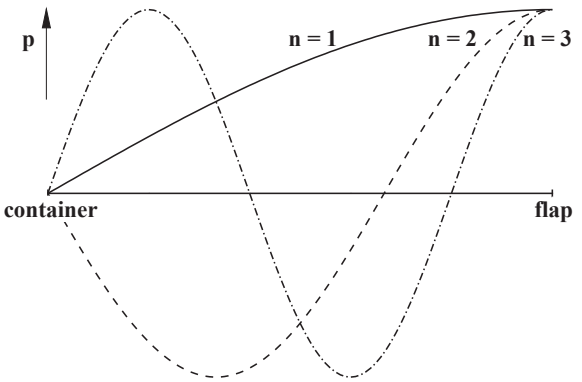

Figure 3: First three eigenmodes of the piping system

of both configurations it is necessary to measure the propagation velocity of the water hammer which is dependent of various parameters like temperature and solute gas such that the velocity varies. Previous investigations of water hammer at the piping system depicted in Section 2.1 identified a propagation velocity between 1276 m/s and 1325 m/s [6]. Given the length of the piping system it is possible to calculate the frequencies of the first eigenmodes analytically (Table 1).

Table 1: Frequencies of the eigenmodes for both configurations

mode	short system	long system
$n = 1$	9.1 Hz - 9.5 Hz	5.1 Hz - 5.3 Hz
$n = 2$	27.3 Hz - 28.4 Hz	15.2 Hz - 15.8 Hz
$n = 3$	45.6 Hz - 47.3 Hz	25.3 Hz - 26.3 Hz
$n = 4$	63.8 Hz - 66.3 Hz	35.4 Hz - 36.8 Hz

Measurements at the rigidly anchored system showed in both configurations that the base frequency of the water hammer oscillation ($n = 1$) is dominant (Figure 4). The excitation frequency of the short system is 8.3 Hz and of the long system 4.6 Hz. But also higher modes were excited. Comparing the analytically calculated frequencies with measured ones it is obvious that for the long system the frequencies fit well. For the short configuration differences in the frequencies occur.

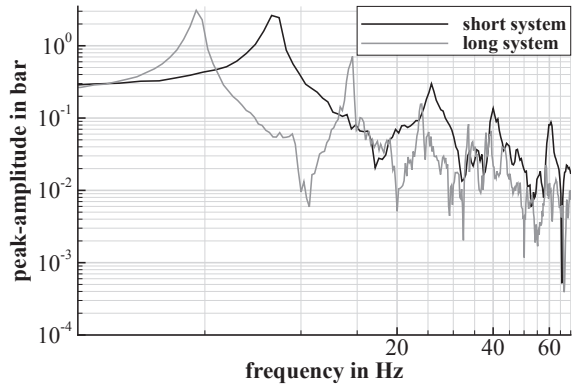

Figure 4: Frequency spectra of the pressure signal in front of the flap for both configurations when the piping system is rigidly anchored

2.3. Measurement Equipment

All over the piping system there are 25 positions where piezoresistive pressure sensors can be installed. There are six sensors with a measurement range of 200 bar (Kistler type 4043A200) and one with a range of 10 bar (Kistler type 4045A10). The latter is used in the suction side of the piping system. Additional piezocapacitive acceleration sensors measure the pipe vibration. There are six uniaxial sensors (Kistler type 8702B500M1T) and one triaxial sensor (Kistler type 8793A500). All of them have a measurement range of 500 g. A magnetic-inductive measurement system (Endres + Hauser Proline Promag 50W) determines the flow rate. The movement of a bend is measured by an inductive displacement transducer (HBM W10). Additionally rotary encoders (Leine Linde RSA 670/671 analog) determine the rotation angles of the pump and the fast closing flap.

3. EXPERIMENTAL PROCEDURE

Water hammer experiments with oscillating bends were carried out. The water hammer was produced with the fast closing flap. The whole piping system was rigidly anchored with the exception of a single bend. The geometry of this bend depends on the system configuration (Figure 1). The piping system was excited by a water hammer at a mean velocity of 0.5 m/s. Due to the fixed length of the hydraulic system, the frequency of the pressure oscillation respectively the excitation frequency was kept constant. The support position y of the movable bend and thus the natural frequency was varied (Figure 5). The

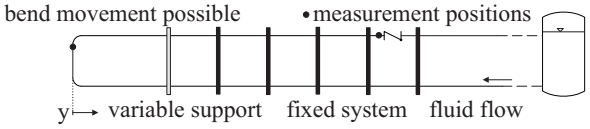

Figure 5: Support system shown at the bend of the short configuration

displacement of the bend, the pressure as well as the acceleration at various positions were recorded. At each support position the measurement was repeated five times.

4. RESULTS

The results are divided into resonance curves and frequency spectra.

4.1. Resonance Curves

The resonance curves show at which support position the system is in resonance.

For the determination of the structural frequency f_s or rather the bend frequency a Fourier transformation of the displacement signal was performed. In Figure 6 the mean maximum displacement of the bend x_{max} is depicted over the structural frequency f_s. The results show

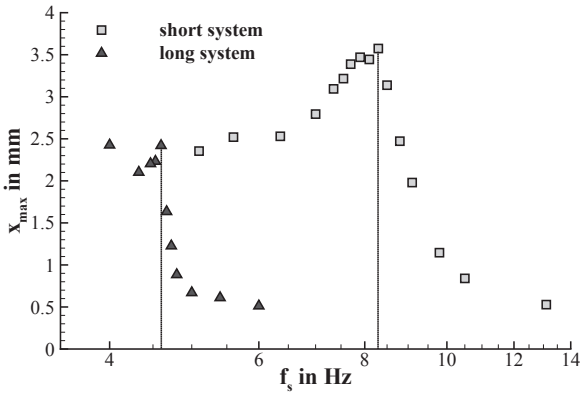

Figure 6: Mean maximum displacement x_{max} over the frequency of the structure f_s for the short and the long configuration

that the resonance point of each system is at the excitation frequency of the water hammer. For high frequencies the displacement of the bend is low, towards the resonance point the displacement rises, reaches a maximum and afterwards decreases. This characteristic is similar to the forced oscillation of a single mass or the free oscillation of two masses. The displacements of the bend of the short configuration are higher due to the higher excitation. In Figure 1 the bend geometries are illustrated. Owing to the longer vertical pipe section of the bend of the short configuration the excitation force produced by the water hammer affects the bend longer but the amplitude of the force is in both configurations the same.

4.2. Frequency Spectra

In order to examine the effects of FSI the signals were examined in the frequency domain.

For every support position y a Fourier transformation of the pressure signal in front of the flap and of the displacement signal of the bend was performed. The spectra were averaged over the five repeated measurements. Additionally to the pictured spectra in the following graphs the frequency spectrum

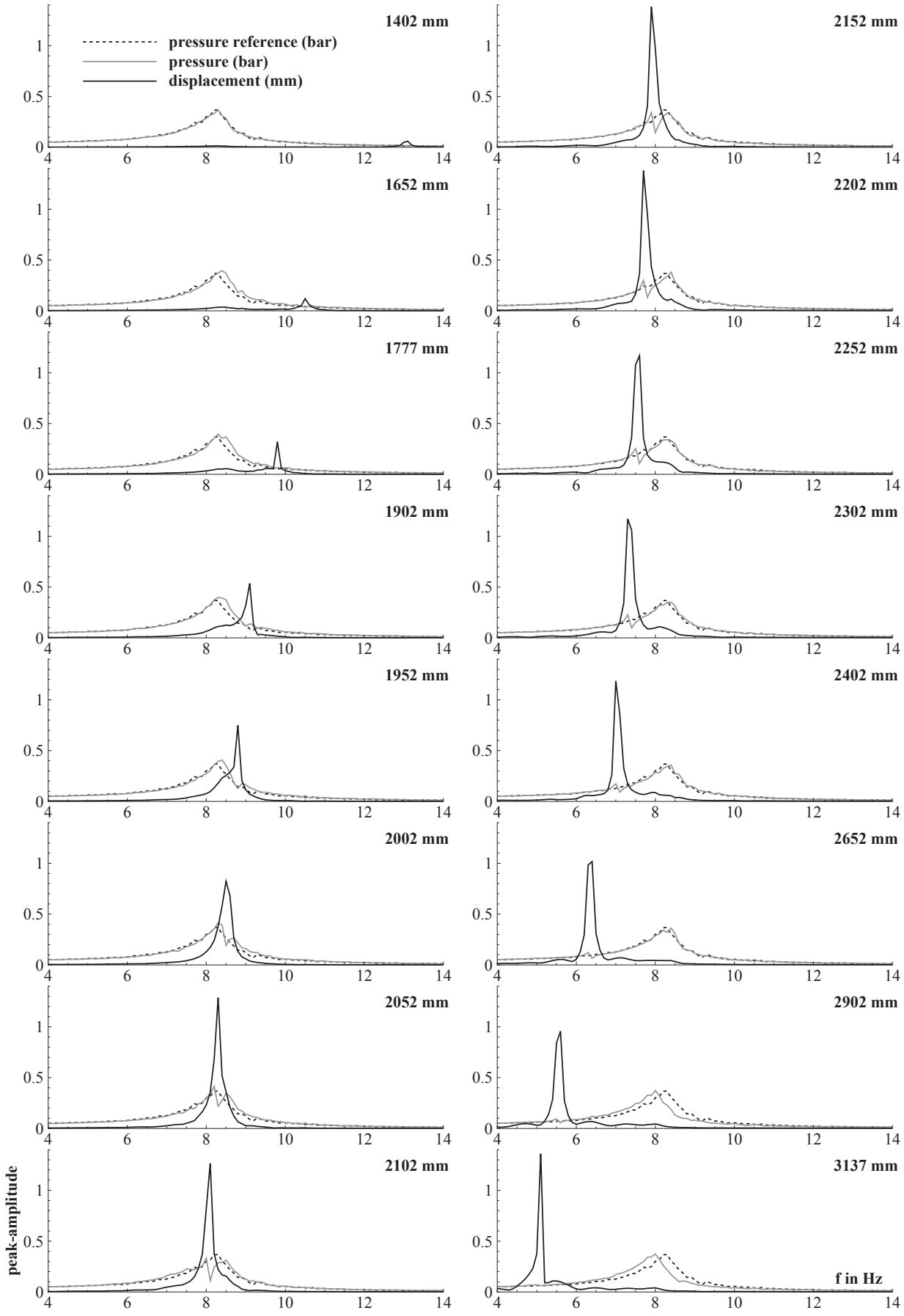

Figure 7: Averaged frequency spectra for various support positions of the short system

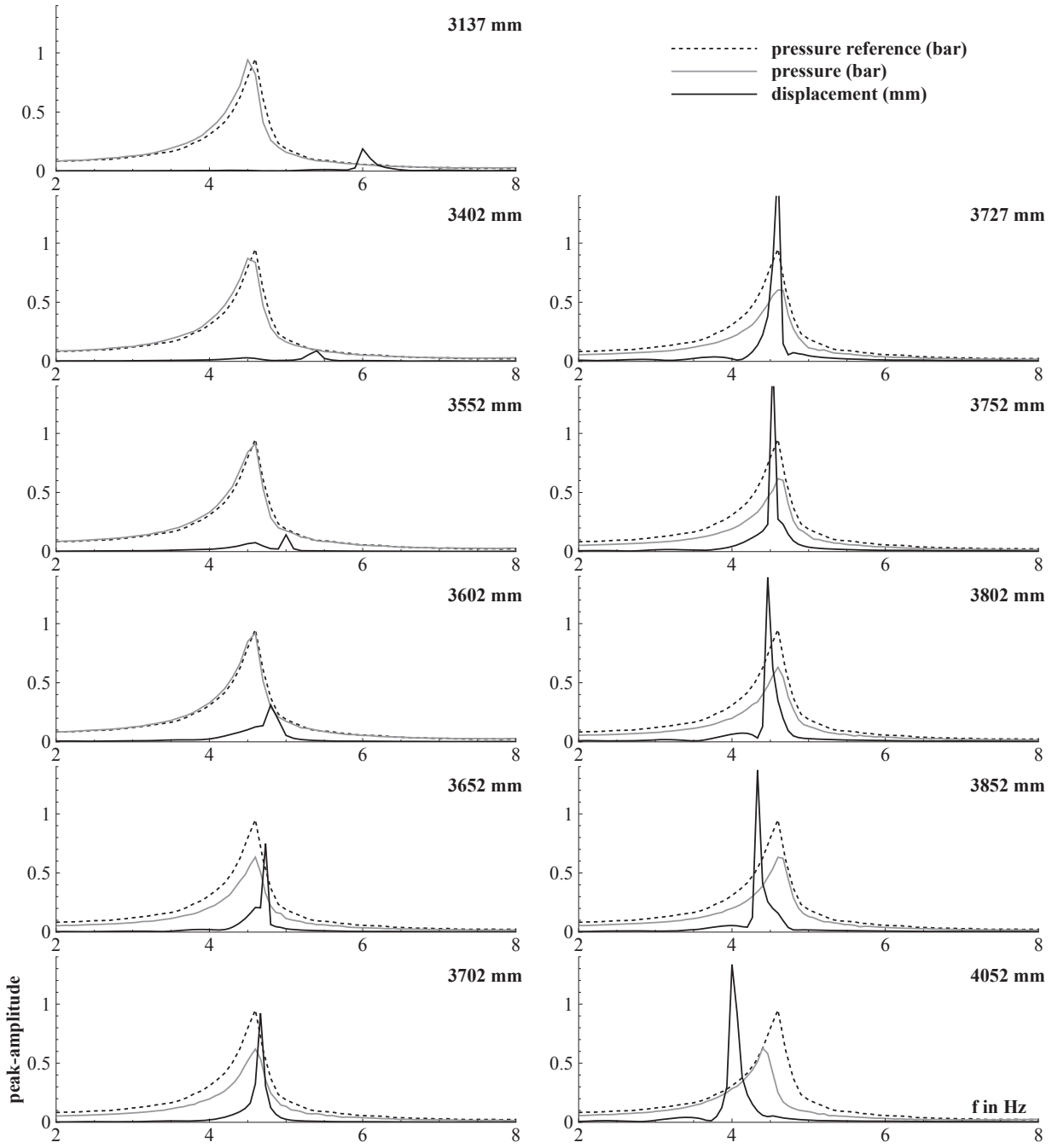

Figure 8: Averaged frequency spectra for various support positions of the long system

of the pressure in front of the flap for a rigidly anchored system is plotted as reference (*pressure reference*). This would be a result of an analysis without FSI respectively of an analysis with one-way interaction. For an oscillating bend differences in the pressure signal are expected because the movement of the pipe causes secondary pressure waves. The spectrum of the pressure for an oscillating bend is labelled with *pressure* and the corresponding spectrum of the displacement is labelled with *displacement*.

The diagrams in Figure 7 show the spectra for the short system for various support positions. The longer the free oscillating length of the bend respectively the more distant the support position the lower is the structural frequency of the bend. In the resonance area FSI is obvious. At the frequency of the displacement a local minimum in the spectrum of the pressure occurs. There is a transport of momentum from the fluid onto the structure. The reaction of the bend causes a minimum in the fluid spectrum. The peak of the pressure is split into two peaks. Moreover there are frequency shifts of the pressure outside of the resonance area (Figure 7 e.g. support positions 1652 mm, 1777 mm, 2902 mm and 3137 mm).

In Figure 8 the frequency spectra for the long system are depicted. In the resonance area no splitting

of the pressure peak appears. There is only a wide reduction in the amplitudes of the fluid peak and a rise of the amplitudes of the displacement. The transport of momentum is just one way. The movement of the bend has little effect on the fluid. Also no striking frequency shifts can be noticed.

In summary two different oscillation characteristics occur. This is a consequence of the unequal bend geometries (Figure 1). In the short system the bend has a long vertical pipe section, in the long one this section is small. The mass of fluid inside this vertical pipe section and the length itself are a measure for the coupling of the structure and the fluid. The longer this section the longer the excitation force acts on the bend. The greater the mass of the fluid the greater is the potential momentum of the fluid onto the structure.

Far from the resonance area the influence of the movement of the bend on the fluid is relatively small. Here no effect of the introduction of FSI would be expected. In the resonance area the above mentioned differences are obvious. It is remarkable that the spectra of the pressure do not always lie under the reference spectrum for a completely fixed system. That means that a one-way calculation is not conservative without exception. For example at a fluid resonance in small secondary pipelines under disadvantageous but very rare conditions it is possible that a movable pipeline causes higher loads than a fixed one.

4.3. Time Signals

The pressure in front of the flap and the displacement of the bend are plotted for both configurations. Each diagram includes the distributions for two support positions - in and out of the resonance between fluid and structure.

Figure 9 shows the graphs for the short system. The influence of fsi is obvious in form of a beat in the resonance case. Here in the first phase of the oscillation primarily there is a transfer of momentum from the fluid onto the structure. The amplitudes of the pressure decrease and those of the displacement increase. There is a little phase shift between the minimum of the pressure and the maximum of the structure which is caused by the distance between the measurement positions. Afterwards the amplitudes of the pressure increase and the distribution of the displacement shows a dent. This indicates a transport of momentum from the structure back to the fluid. Out of resonance there is a little transport of momentum from the fluid onto the structure, but no beat is apparent.

Figure 10 includes the distributions of the long system in and out of the resonance. No beats occur. The pressure signals in and out of the resonance are nearly identical. Only the distributions of the displacement illustrate the resonance state.

The results of the time signals coincide with the findings of the frequency spectra, that two different oscillation characteristics occur. A two-way interaction

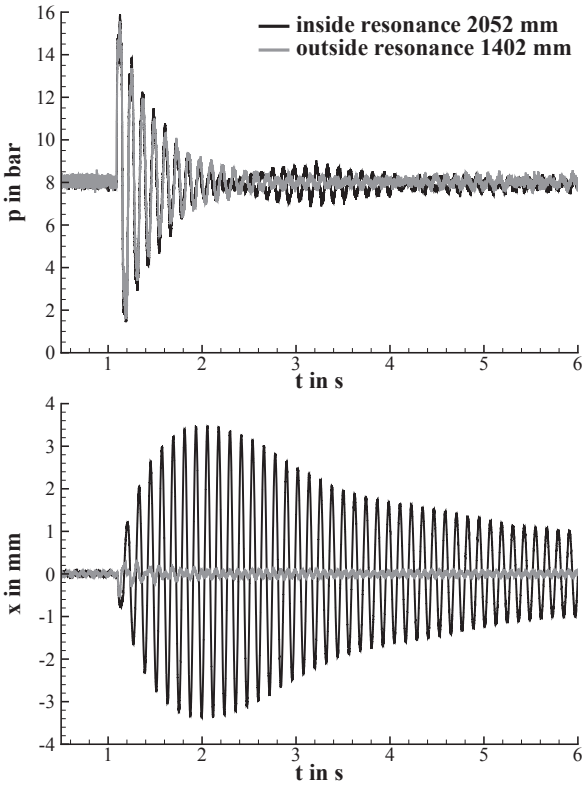

Figure 9: Pressure and displacement distribution for the short system and two support positions

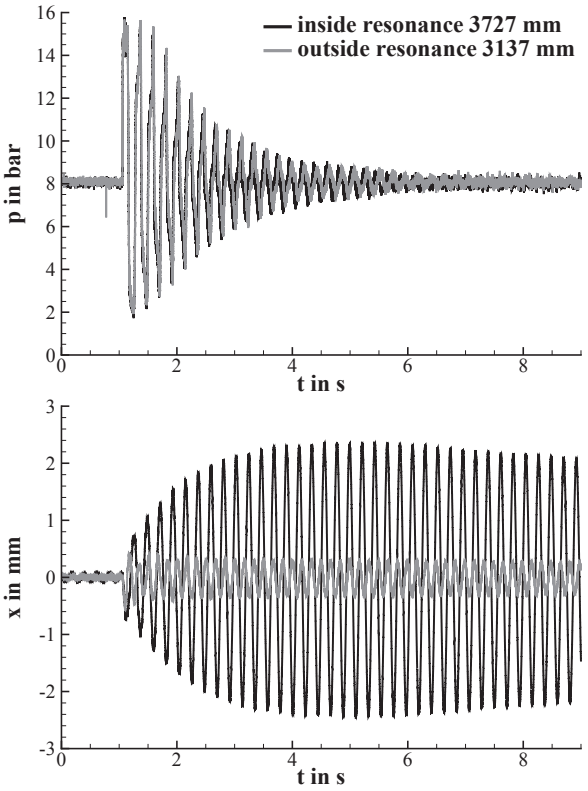

Figure 10: Pressure and displacement distribution for the long system and two support positions

can only be observed for the short system due to the different bend geometries.

5. CONCLUSION

In order to examine the effects of FSI water hammer experiments at bends near resonance were performed. Measurements at the rigidly anchored system identified the base frequencies to be dominant. Resonances of the different bends depending of the system configuration appeared at the base frequencies of the water hammer. For the long system the excitation of the bend was smaller due to the short vertical pipe section of the bend. The frequency spectra of the pressure in front of the flap and of the displacement of the bend identified differences in the oscillation characteristics. These are caused by the various bend geometries. The coupling between the structure and the fluid is dependent of the bend geometry. So the effects of FSI are more dominant in the short system, which also showed the time signals.

Outside of the resonance area FSI has little influence on the spectra. Here a two-way interaction wouldn't show an effect. Inside the resonance area the analysis identified frequency shifts and a splitting of the peak in the pressure spectrum. In some cases the spectrum of the pressure lies over the reference spectrum. That means a calculation with one-way interaction wouldn't be conservative in all cases. In some seldom and disadvantageous situations the consideration of FSI can lead to higher loads.

ACKNOWLEDGEMENTS

We would like to thank AREVA NP GmbH (section Fluid Dynamics PEPR-G Erlangen) for the long lasting cooperation and the funding. Additionally we are grateful for the expertise assistance and the possibility to benefit from decades of experience.

References

[1] C. S. W. Lavooij and A. S. Tijsseling, "Fluid-structure interaction in liquid-filled piping systems," *Journal of Fluids and Structures*, vol. 5, pp. 573–595, 1991.

[2] A. G. T. J. Heinsbroek and A. S. Tijsseling, "The influence of support rigidity on water hammer pressures and pipe stresses," in *2nd International Conference on Water Pipeline Systems*, 1994.

[3] A. S. Tijsseling, "Fluid-structure interaction in liquid-filled pipe systems: A review," *Journal of Fluids and Structures*, vol. 10, pp. 109–146, 1996.

[4] D. C. Wiggert and A. S. Tijsseling, "Fluid transients and fluid-structure interaction in flexible liquid-filled piping," *Applied Mechanics Reviews*, vol. 54, pp. 455–481, 2001.

[5] Verein Deutscher Ingenieure, "*VDI-Richtlinie 3842: Schwingungen in Rohrleitungssystemen (Vibrations in piping systems)*," July 2004.

[6] A. Ismaier, *Untersuchung der fluiddynamischen Wechselwirkung zwischen Druckstößen und Anlagenkomponenten in Kreiselpumpensystemen*. PhD thesis, Lehrstuhl für Prozessmaschinen und Anlagentechnik, Friedrich-Alexander Universität Erlangen-Nürnberg, 2011.

Conference on Modelling Fluid Flow (CMFF'12)
The 15th International Conference on Fluid Flow Technologies
Budapest, Hungary, September 4-7, 2012

FLOW ANALYSIS IN PIPE OF A MANIFOLD BLOCK

Osamu ABE[1], Tetsuhiro TSUKIJI[1], Takeshi HARA[1] Kazutoshi YASUNAGA[2],

[1] Faculty of Science and Technology, Sophia University. 7-1, Kioi-cho, Chiyoda-ku, Tokyo, Japan. E-mail: t-tukiji@sophia.ac.jp
[2] TOKYO KEIKI INC., 1-1, Sakae-cho, Sano-shi, Tochigi, Japan

ABSTRACT

Manifold blocks are recently used to connect hydraulic components in a hydraulic system, which has flow channels inside. They are useful for reducing the size and weight of hydraulic systems. This paper deals with solid manifold block and laminated manifold block. They are different from machining point of view. We investigate pressure drops of their pipe flow with computational fluid dynamics (CFD) and compare those of two types. And then, we conduct experiment, measuring pressure and visualization, to validate the results of CFD analysis. By using these results, we are intended to obtain guidelines for pipeline design in laminated manifold block.

Keywords: cavitation, CFD, manifold block, pipe flow, pressure drop, visualization

NOMENCLATURE

d	[mm]	pipe diameter
ρ	[kg/m^3]	density
v	[m^2/s]	kinematic viscosity
T	[K]	temperature
Q	[L/min]	volume flow rate
p	[Pa]	pressure
p_e	[Pa]	exit pressure
Re	[-]	Reynolds number
h	[mm]	groove height
w	[mm]	groove width
θ	[$degree$]	angle

1. INTRODUCTION

Hydraulic machines have many valves and piping parts. So there are problems that much space is needed and plumbing is more troublesome. Recently, as one of the methods to reduce the space and piping parts, manifold system is developed. This system is the method of connecting valves and actuators by using steel blocks that have pipelines inside. These blocks are called 'Manifold Block'. It is said that pressure drop of pipe flow in the block because it has many curved section.

Manifold block is generally classified into two types by way of machining. One is a solid manifold block (solid type) that has some holes by drilling as shown in Figure 1. The other is a laminated manifold block (laminated type) that is composed of some blocks grooved and drilled in advance. In solid type, design of pipeline is relatively simple since its pipeline only connects some holes, but it is impossible to design pipeline freely. On the other hand, in laminated type, it is possible to design pipeline freely because it has pipes of rectangular groove, but it is difficult to weld blocks. So it takes much time to manufacture laminated type.

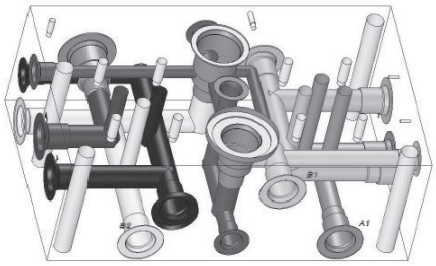

Figure 1. Solid manifold block

Generally, researches by the experiment and using CFD analysis about the pressure loss and the flow state in circular or rectangular pipes have been done for many years [1-4]. Those researches focus on flow characteristics or pressure loss in the simplified single bend part of a circular or rectangular pipe. Besides the researches on pressure loss in pipes with some ideal bends also have been done [5, 6]. However, the research on the pipeline flow in a manifold block has hardly been done, and pipelines in a manifold block have many bend parts and are subject to the influence of an upstream bend part. Especially, a laminated type has bend parts connected between a circular pipe and a rectangular one. Research on such a complicated pipe flow is not performed. Furthermore, it is found that cavitation generates at bend parts of a manifold block because of the complexity of the pipeline, but

the detailed information about the cavitation is not acquired now.

Then, the purpose of this research is to acquire the design guideline of the manifold block by estimating pressure loss of the complicated pipeline in the manifold block, and to reduce pressure loss of pipe flow in the manifold block, a solid type and a laminated type, with both CFD analysis and experiments. Furthermore the purpose of this study is also to find the design of the shape of the flow channel at corners to reduce cavitation.

In this paper, we deal with a manifold block as port converter in case of connecting ports shown in Figure 2 (a) to ports shown in Figure 2 (b) when we compare a solid type with a laminated type.

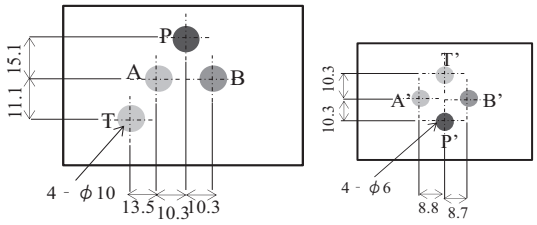

(a) Ports of one valve (b) Ports of another valve

Figure 2. Port standards of valves

2. COMPARISON OF TWO TYPES

2.1. CFD Analysis

Figure 3 shows a port converter of solid type. And Figures 4 (a), (b) show flow channels in the block connecting the port T with T' (solid-T) and P with P' (solid-P). These channels go around because they must avoid tapped holes for attachment and other channels. Pipe diameter is d=6mm, partially 10mm. Figure 5 (a) shows a port converter of laminated type (laminated 1). This is composed of three blocks as shown in Figure 5 (b). In the same, Figures 6 (a) and (b) show flow channels in the block (laminated 1-T and laminated 1-P, respectively). Unlike solid type, it is possible to connect ports by curved channel. To compare with solid type, we deal with flow channels that are the same length as solid type channel as shown in Figures 7 (a) and (b) (laminated 2-T and laminated 2-P, respectively). Cross section of groove is 6mm square. Analysis objects are the above six flow channels. In this paper, we use FLUENT12.0. Along the lines of the study in past times, SST k-ω model is used for turbulence model [7]. Inflow boundary condition is set to velocity inlet (uniform flow), and outflow boundary condition is set to pressure outlet (0Pa). Those flow channels contain tetrahedral and hexahedral cells. Properties of working fluid is ρ=870g/m^3, and v=3.2×10^{-5}m^2/s where T=317K (40 degrees Celsius).

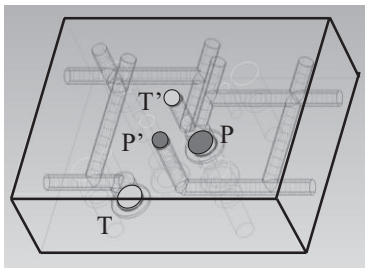

Figure 3. Port converter of solid manifold block

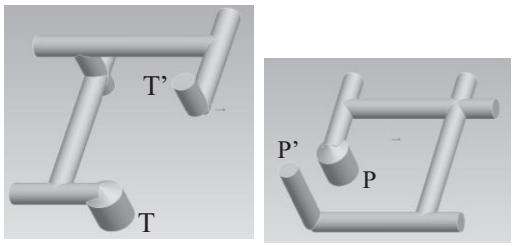

(a) Solid-T (b) Solid-P

Figure 4. Flow channels in solid manifold block

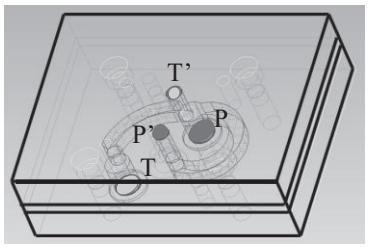

(a) Block after attached

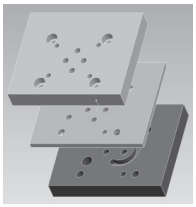

(b) Three blocks before attached

Figure 5. Port converter of laminated manifold block (laminated 1)

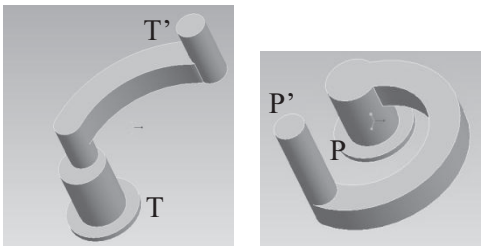

(a) Laminated 1-T (b) Laminated 1-P

Figure 6. Flow channels in laminated 1

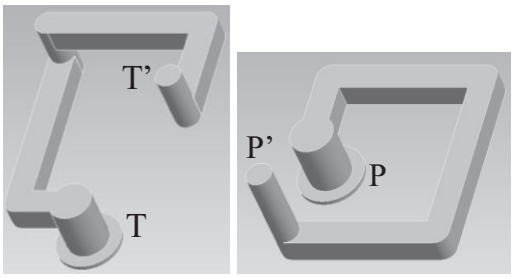

(a) Laminated 2-T (b) Laminated 2-P

Figure 7. Flow channels in laminated 2 (Like solid type)

2.2. Results of CFD Analysis

Figures 8 (a) and (b) show pressure on central axis of flow channel for Q=50L/min. The vertical axis shows the difference of pressure (p) on central axis and outlet pressure (pe). Central axis of solid type is shown in Figures 9 (a) and (b). Symbol a to f in Fig.8 show the corners in Fig.9. From these figures, pressure drop at corners is the majority of pressure drop of flow channel in all types. Pressure drop of solid type at corners is different from each other, so it is found that the distance to upstream corner and the bend angle of upstream corner affect pressure drop in solid type.

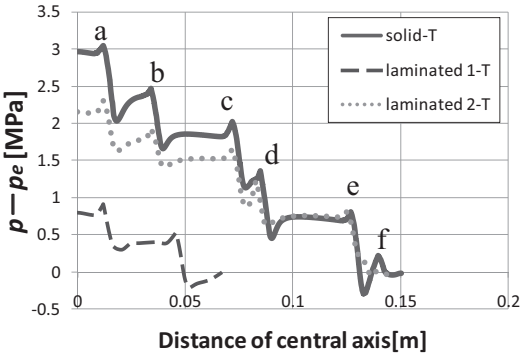

(a) Pressure of flow channels T

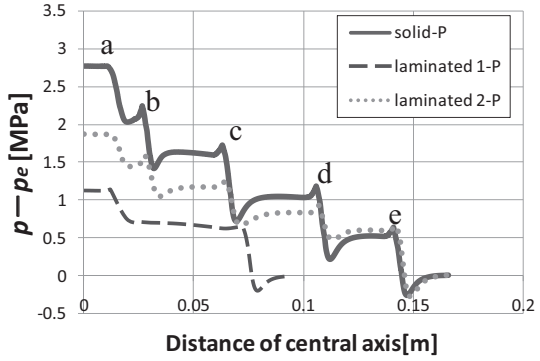

(b) Pressure of flow channels P

Figure 8. Pressure on central axis of flow channels

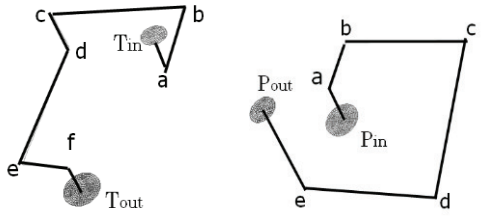

(a) solid-T (b) solid-P

Figure 9. Central axis of solid type

Laminated 1 and 2 have less pressure drop than solid type. When laminated 2 is compared with solid type, pressure drops of laminated 2 at corners are smaller than that of solid type. This is because laminated type has lager sectional area than solid type even if their flow channels have the same width. Figures 10 (a) and (b) show velocity vectors of entire flow channels of solid type for Q=50L/min. Figures 11 (a) and (b) show velocity vectors on cross sections of corner d and e in Fig. 10 (a). Figures 12 (a) and (b) also show velocity vectors on cross sections of corner b and d in Fig. 10 (b).

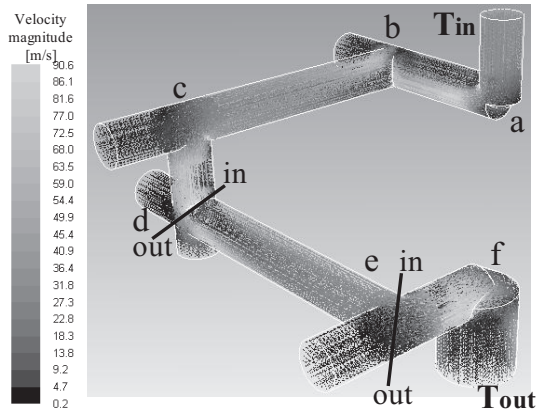

(a) Velocity vectors of solid-T

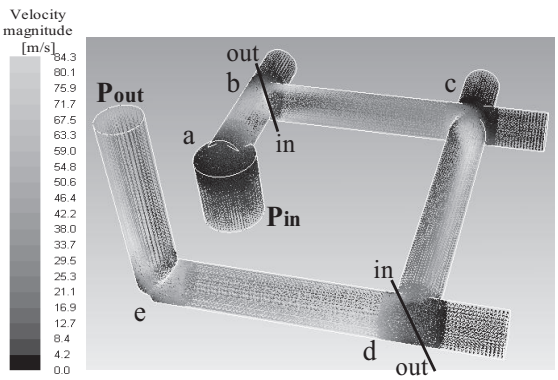

(b) Velocity vectors of solid-P

Figure 10. Velocity vectors of solid type

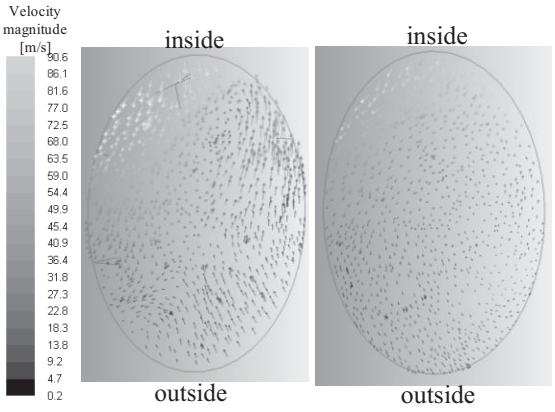

(a) Cross section d (b) Cross section e

Figure 11. Velocity vectors on cross section of solid-T

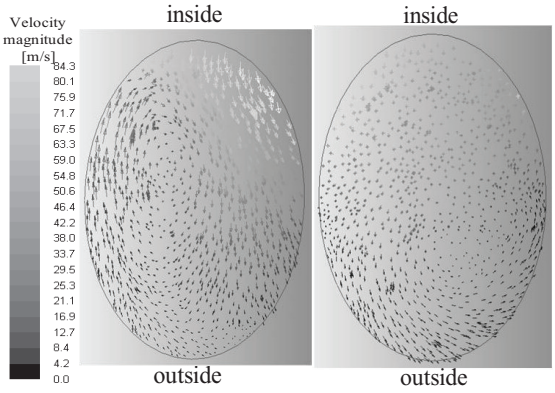

(a) Cross section b (b) Cross section d

Figure 12. Velocity vectors on cross section of solid-P

It is found that there are regions of large velocity (red regions in figures) downstream from Fig. 10, and vortex regions are seen in Fig. 11 (a) and Fig. 12 (a), but not seen in Fig. 11 (b) and Fig. 12 (b). This is because the distance from corner c to d is shorter than the distance from corner d to e in Solid-T, and the bend angle of upstream corner is different from each other in corners b and d of Solid-P.

3. EXPERIMENTS

3.1. Experimental Apparatus and Method

We manufacture port converter of manifold blocks (test piece) that have the same flow channel used in CFD analysis, and prepare experimental apparatus for measuring pressure shown in Figure 13. These manifold blocks are attached to blocks for connecting electronic pressure sensors, a block for returning oil flow from B' to T' or from P' to A', electronic pressure sensors, A/D converter, and 24V power supply.

Data of voltage are transmitted from pressure sensor to A/D converter and converted to pressure data. In this paper, pressure drop of each flow channel is defined as the pressure gap of upstream data and downstream data. By comparing with experimental results, we verify the validity of the CFD results. Temperature of working oil is about 40 degree Celsius to fit condition of CFD analysis.

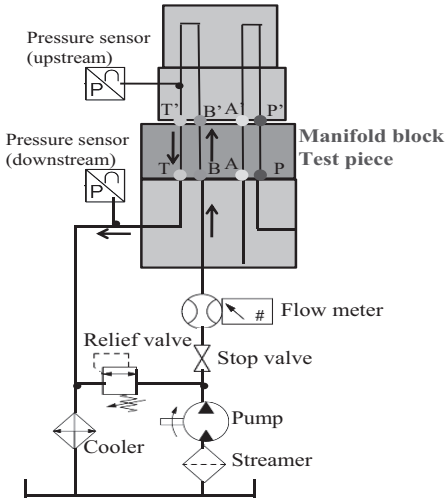

Fig. 13 Experimental apparatus for measuring pressure of port T

3.2. Comparison of CFD Results with Experimental Results

Figures 14 (a) and (b) show the relations between volume flow rate and pressure drop of solid type. Figures 14 (c) and (d) show the relations between flow rate and pressure drop of laminated type. The experimental error is about 5%. Reynolds number is defined by

$$\mathrm{Re} = \frac{ud}{\nu} \qquad (1)$$

In solid type, there is a tendency that experimental values are about 15 percent smaller than CFD results from Q=20L/min (Reynolds number is about 2,200) to Q=70L/min (Reynolds number is about 7,700). Reynolds number is based on pipe diameter, the mean velocity of flow, and kinematic viscosity. So it is found that it is possible to regard pipe flow in solid type as turbulent flow even if Reynolds number is small in case flow channel has many corners. In laminated type, experimental values show good agreement with CFD results except laminated 1-T. In laminated 1-T, the more the flow rate increase, the larger the error between experimental values and CFD results.

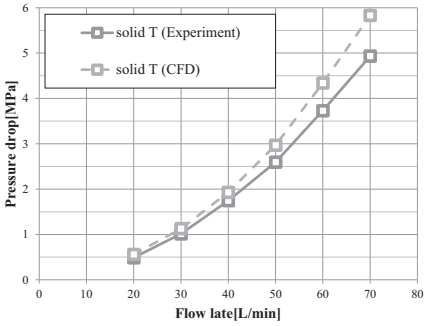

(a) Solid-T

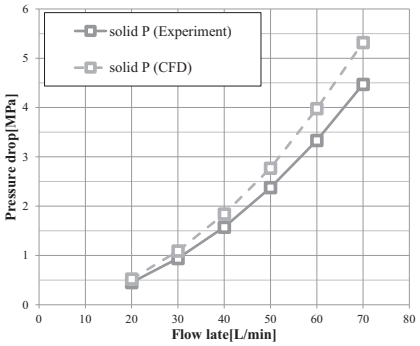

(b) Solid-P

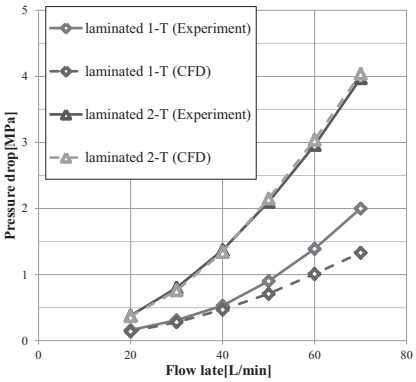

(c) Laminated 1-T and 2-T

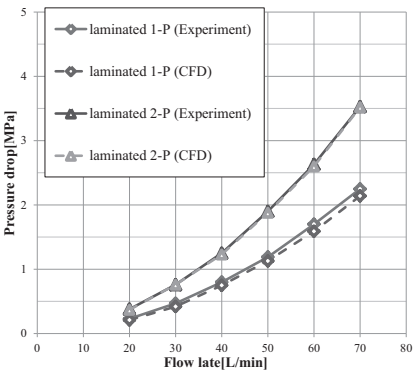

(d) Laminated 1-P and 2-P

Figure 14. Relations between flow rate and pressure drop

So when we manufacture an acrylic test piece of laminated 1 and observe oil flow in laminated 1 to investigate factors, luminescence by heavy cavitation [8] is seen at a red circle in Figures 15 (a) and (b) in case of more than Q=50L/min. This is the factor of the error. Fig. 15 (a) shows a direction for visualization of laminated 1-T. A picture of cavitation is shown in Fig. 15 (b).

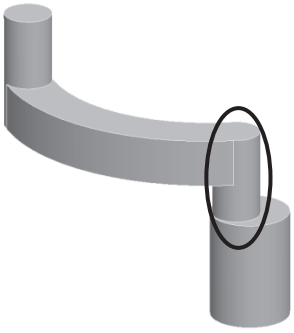

(a) Direction for visualization of laminated 1-T

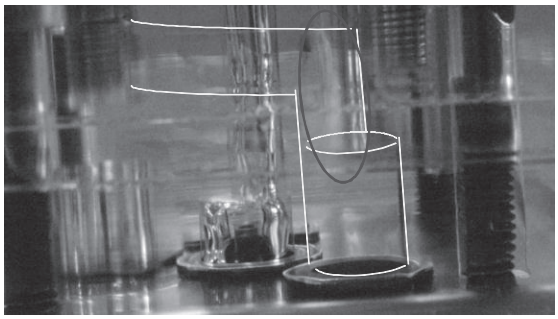

(b) Picture of cavitation

Figure 15. Luminescence by heavy cavitation

4. REDUCTION OF CAVITATION

4.1. Cavitation

According to Section 3.2, cavitation is observed at the corner of laminated type flow channel. Cavitation is the phenomenon of bubble generation. When flow velocity suddenly increase and static pressure rapidly decrease in fluid machinery, bubbles generate because of lower pressure than vapor pressure. In case of oil, bubbles also generate because of evaporation of air dissolved in oil. Cavitation causes many problems such as noise, oscillation, a decrease in efficiency, erosion, and so on. Therefore reduction of cavitation is required to make hydraulic machines smaller, faster and more efficient. Besides, evaluation method of oil cavitation with CFD analysis is not still established.

4.2. Simplified Flow Cannel and Groove at Corner

In previous study, it was proved that cavitation in solid type can be reduced by changing hole depth [7]. But laminated type has grooves as flow channel in addition to hole, so it is necessary to devise another method. Then we propose laminated block with simplified flow channel to evaluate cavitation easily as shown in Figure 16, and Figure 17 shows internal flow channel and its size.

As one of the method for reducing cavitation, we propose that a groove is machined to a corner near outlet in advance as shown in Figure 18. This groove prevents pressure to decrease rapidly. This method can apply laminated type which is composed of some blocks.

Then, we define groove height h[*mm*], groove width w[*mm*], and groove angle θ[*degree*] as parameter of design. In case of h=4.2, w=3, and θ=45, we call flow channel h4.2w3-45 in following section.

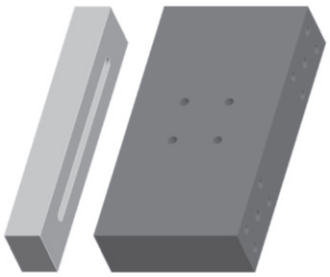

Figure 16. Laminated block for evaluating cavitation

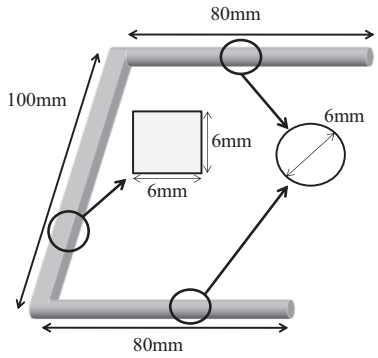

Figure 17. Internal flow channel and its size

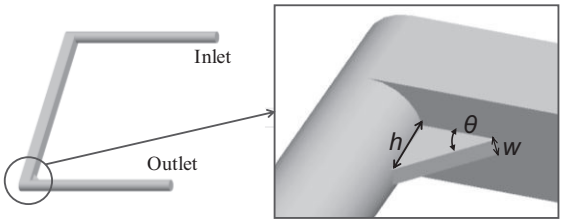

Figure 18. Laminated block with groove

4.3. Experiments

4.3.1. Visualization

We conduct visualization experiments to compare cavitation between without and with groove, and investigate influence of parameter. First, we show the pictures below. As you can see Figures 19 to 22, cavitation region is different from each other in spite of the same flow rate. Cavitation starts to generate about in Q=35*L/min* in case of no groove, but in Q=55*L/min* in case of h4.2w3-45. Therefore, it is proved that groove prevent cavitation in low flow rate. Besides, groove which has larger h and w can reduce cavitation. From Figures 22 and 23, there is not much difference in cavitation region between θ=45*degree* and θ=30*degree*.

Figure 19. Cavitation in 60L/min (no groove)

Figure 20. Cavitation in 60L/min (h1.4w3-45)

Figure 21. Cavitation in 60L/min (h4.2w1-45)

Figure 22. Cavitation in 60L/min (h4.2w3-45)

Figure 23. Cavitation in 60L/min (h4.2w3-30)

4.3.2. Pressure Measurement

Second, the relation between volume flow rate and pressure drop is shown in Figure24 and 25. In both case, it is proved that groove decreases pressure drop. Furthermore, pressure drop is smaller

when h, w and θ are larger, especially h is more influential than w. This is because sectional area at the corner changes smoothly in the flow direction due to the groove. In 30-70*L/min*, Reynolds number is about 3300-7700, so the flow is dominantly turbulent inside the manifold block because it is greater than critical Reynolds number.

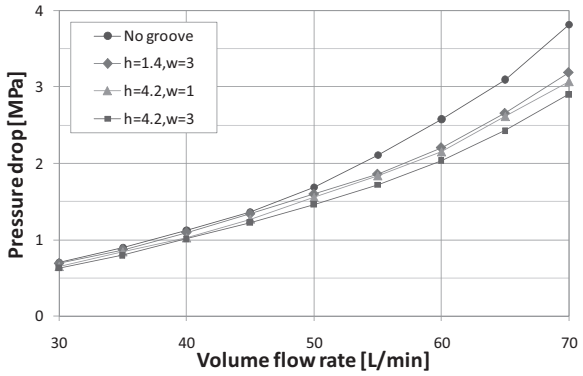

Figure 24. Relation between volume flow rate and pressure drop (θ=30 degree)

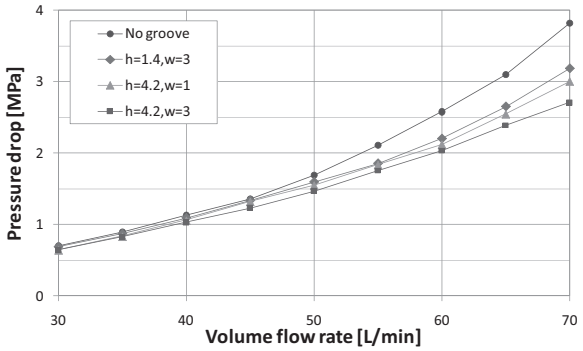

Figure 25 Relation between volume flow rate and pressure drop (θ=45 degree)

4.4. CFD Results and Comparison with Experimental Results

We analyze the flow channel as shown in Figures 17 and 18 with CFD. Analysis conditions are about the same as what we showed in Section 2.2. But we freshly introduce mixture model as multiphase model, and second phase is set to air. Furthermore we introduce Schenerr-Sauer model as cavitation model and vapor pressure of oil is set to 6.7*Pa* [9, 10].

Figures 26 and 27 show the comparison of experimental results and CFD results in pressure drop. Experimental values show agreement with CFD results to some extent in case of introducing cavitation model.

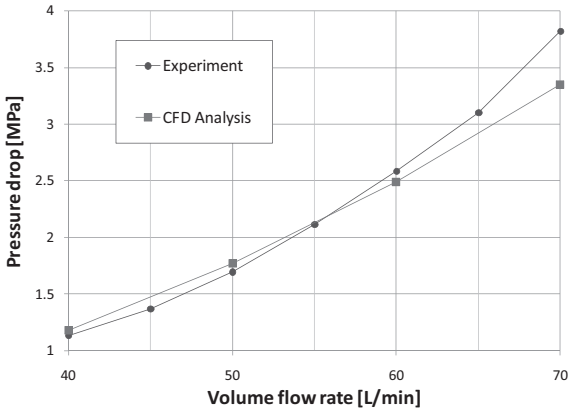

Fig. 26 Comparison of experiment with CFD analysis (no groove)

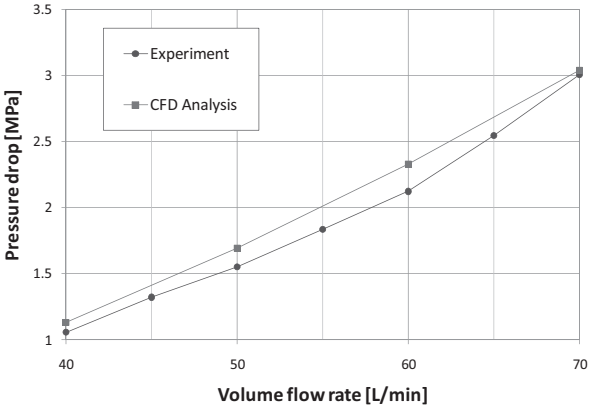

Fig. 27 Comparison of experiment and CFD analysis (h4.2w1-45)

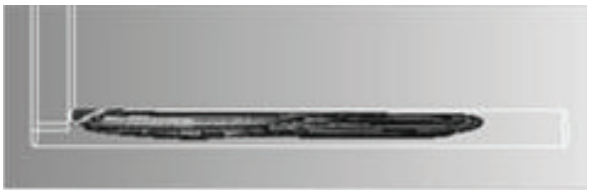

Figure 28. Cavitation by CFD analysis in 60L/min (no groove)

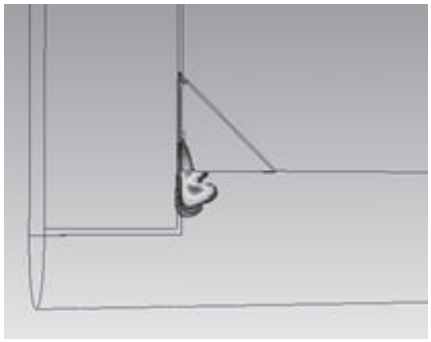

Figure 29. Cavitation by CFD analysis in 60L/min (h4.2w1-45)

Compared Fig. 19, cavitation region in Figure 28 is smaller. This is because noncondensable gas is not considered in calculation. The same is true of cavitation in Fig. 21 and Figure 29. Therefore it is necessary to calculate in consideration of noncondensable gas for the future.

But, cavitation of CFD analysis is very similar in generation region to that of high-speed video camera as shown in Figures 30 (a) and (b)

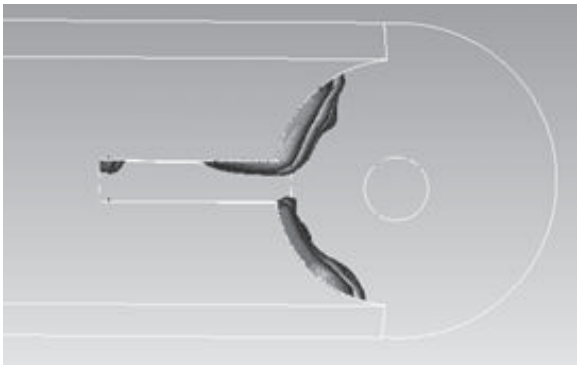

(a) Cavitation by CFD analysis in 60L/min from side view (h4.2w1-45)

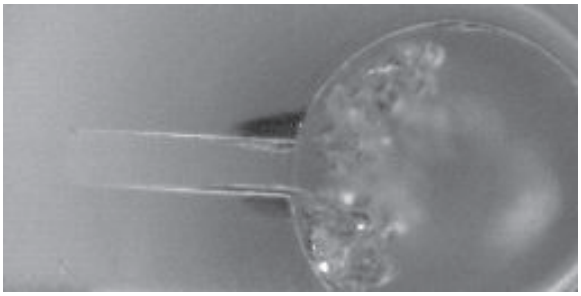

(b) Cavitation by high-speed video camera in 60L/min from side view (h4.2w1-45)

Figure 30. Cavitation comparison of CFD analysis with high-speed video camera from side view

5. CONCLUSIONS

This paper focuses on estimation of pressure drop of pipe flow in two types of manifold block with CFD analysis, verification of the validity of CFD results by comparison with experimental results, and obtainment of guidelines for pipeline design in a manifold block. The conclusions of this paper are as given below.

(1) Pressure drop at corners is the majority of pressure drop of pipe flow in manifold block.
(2) Pressure drop of laminated type is smaller than that of solid type because laminated type has lager sectional area than solid type even if their flow channels have the same width.
(3) In laminated type, groove makes it possible to reduce cavitation and pressure drop.
(4) Generation region of oil cavitation and pressure drop can be simulated with present cavitation model of CFD.

ACKNOWLEDGEMENTS

My heartfelt appreciation goes to Kenichi Watanabe of undergraduate student in Tsukiji laboratory whose enormous support was invaluable during the course of my study. Special thanks also go to Techno center of factory in Sophia University, whose cooperation has helped me very much throughout the production of this study.

REFERENCES

[1] Idelchik, I. E., 1986, "Handbook of hydraulic resistance", *Hemisphere Publishing Corporation*, pp. 265-328
[2] Hellstrom, L. H. O., Smits, A. J., 2012, "Turbulent Pipe Flow through a 90 degree Bend", *1000 Islands Fluid Mechanics Meeting*, pp. 1-3
[3] Tarek, A. M., Walid, A. A., Soubhi, A. H., Osama, H., 2011, "CFD Simulation of Dilute Gas-Solid Flow in 90° Square Bend", *Scientific Research*, pp. 246-252
[4] ROWE, M., 1970, "Measurements and Computations of Flow in Pipe Bends", *Journal of Fluid Mechanics*, pp. 771-783
[5] Quamrul, H. M., 2012, "CFD Analysis of Single and Multiphase Flow Chracteristics in Elbow", *Scientific Research*, pp. 210-214
[6] Murakami, M., Shimizu, Y., Shiragami, H., 1969, "Studies on Fluid Flow in Three-Dimensional Bend Conduits", *The Japan Society of Mechanical Engineers*, pp. 1369-1379
[7] Shimizu, Y., Sugino, K., Kuzahara, S., 1982, "Hydraulic Losses and Flow Patters in Bent Pipe: Comparison of the Results in Wavy Pipes and Quasi-coiled Ones", *The Japan Society of Mechanical Engineers*, pp. 24-31
[8] Hara, T., "Research on pipe flow in a manifold block", *The Proceedings on Spring Conference of Fluid Power System Society*, 2010, pp. 4-6.
[9] LEIGHTON, T. G., FARHAT, M., FIELD, J. E. and AVELLAN, F. " Cavitation luminescence from flow over a hydrofoil in a cavitation tunnel", *Journal of Fluid Mechanics*, No.480, pp.43-60, 2003
[10] Yamazaki, T., 1978, "Cavitation engineering", *Nikkan Kougyou Shinbun*, pp. 251
[11] Warring, R.H., Hydraulic fluids, *1st ed. Trade & Technical Press*, 1961, pp. 582

Conference on Modelling Fluid Flow (CMFF'12)
The 15th International Conference on Fluid Flow Technologies
Budapest, Hungary, September 4-7, 2012

Large eddy simulation of flow in smooth pipes and internally grooved heat exchanger tubes

Zoltán HERNÁDI[1], Gábor VARGA[2], Gergely KRISTÓF[3]

[1] Corresponding Author. Department of Fluid Mechanics, Budapest University of Technology and Economics. Bertalan Lajos u. 4 - 6, H-1111 Budapest, Hungary. Tel.: +36 1 463 2546, Fax: +36 1 463 3464, E-mail: hernadi@ara.bme.hu
[2] Department of Physics, Budapest University of Technology and Economics. E-mail: vargag@phy.bme.hu
[3] Department of Fluid Mechanics, Budapest University of Technology and Economics. E-mail: kristof@ara.bme.hu

ABSTRACT

Geometries of internally grooved tubes play a big role in the performance of heat exchangers. Although there are great databases of measurement data for some groove geometries, the empirical correlations based on these databases are often inaccurate for new groove patterns. While it is usually too expensive to manufacture a new groove geometry for optimization of heat exchangers, an accurate prediction model for the performance of non-existing groove geometries is of great importance.

A model based on large eddy simulation (LES) of turbulent pipe flow is proposed. Three-dimensional unsteady Navier-Stokes and mass continuity equations are solved in OpenFOAM, [1]. Equations are solved for streamwise periodic variables in order to investigate fully developed turbulence. Simulations are carried out for a smooth pipe and a helically grooved tube. Accuracy of different mesh resolutions and different sub-grid scale models are investigated. Great effort is done in minimizing computational costs while maintaining accuracy. Simulation results for the friction factor and the velocity profile of a smooth pipe are validated to literature data. Simulation results for the friction factor, velocity and turbulent kinetic energy profiles of a helically grooved tube in Re=5000...17000 range are compared to smooth pipe results.

Keywords: friction factor, helically grooved tube, large eddy simulation, microfin tube

NOMENCLATURE

CFL	$[-]$	Courant number, [2]
D	$[m]$	pipe diameter
L	$[m]$	pipe length
NL	$[-]$	mesh resolution, longitudinal
NO	$[-]$	mesh resolution, o-grid
NS	$[-]$	mesh resolution, square
R^+	$[-]$	dimensionless radial resolution
$(R\phi)^+$	$[-]$	dimensionless azimuthal res.
Re	$[-]$	Reynolds number
Re_τ	$[-]$	friction Reynolds number
U	$[m/s]$	velocity vector
Z^+	$[-]$	dimensionless axial resolution
d	$[m]$	wall-normal cell size
e_z	$[-]$	unit vector in z direction
k	$[m^2/s^2]$	turbulent kinetic energy
p	$[Pa]$	pressure
r	$[m]$	radial coordinate
u_ϕ	$[m/s]$	azimuthal velocity
u_z	$[m/s]$	axial velocity
$\langle u_z \rangle$	$[m/s]$	volume average axial velocity
u_*	$[m/s]$	friction velocity
t	$[s]$	time
z	$[m]$	axial coordinate
β	$[m/s^2]$	pressure gradient/density
λ	$[-]$	Darcy friction factor
ν	$[m^2/s]$	kinematic viscosity
τ_{SGS}	$[m^2/s^2]$	subgrid-scale stress/density

Superscripts

$*$	streamwise periodic value
$-$	grid-filtered value

1. INTRODUCTION

Geometries of internally grooved tubes are important in the performance of heat exchangers, as heat transfer can be enhanced by increased heat transfer surface and increased local heat transfer coefficient. On the other hand, a tube with grooved inner surface induces more friction than a smooth pipe, therefore using a grooved tube might have a disadvantage on the pressure drop. According to Dalkilic et al. [3], micro-fin tubes improve heat transfer in both single-phase and two-phase flows with relatively low pressure drop increases.

Although there are great databases of measurement data for some groove geometries, empirical correlations based on these databases are often inaccurate for new groove patterns, as shown by Wellsandt et al. [4] for evaporation or Zdaniuk

et al. [5] for single-phase flow. Manufacturing a new groove geometry for optimization of heat exchangers is usually too expensive, so an accurate prediction model for the performance of non-existing groove geometries is of great importance. The goal of this paper is to introduce a prediction model for single-phase friction factors of internally grooved tubes using a CFD method based on large eddy simulation (LES).

Section 2 describes the details of the LES technique. In section 3, the method is validated for smooth pipe including a mesh dependency study, a subgrid-scale model study and a Reynolds number dependency study. In section 4, the method is used for estimating friction factors in a grooved tube and velocity profiles are presented. Section 5 summarizes the main results.

2. Methodology

Large eddy simulation is performed for a single-phase incompressible flow by solving the three-dimensional unsteady Navier-Stokes equation, Eq. (1) and the continuity equation for mass, Eq. (2). Sub-grid scale stress is defined by Eq. (3).

$$\frac{\partial \bar{U}}{\partial t} + \nabla(\bar{U}\bar{U}) = \frac{-\nabla \bar{p}}{\rho} - \nabla \cdot \nu(\nabla \bar{U} + \nabla \bar{U}^T) - \nabla \cdot \tau_{\mathrm{SGS}}, \tag{1}$$

$$\nabla \cdot \bar{U} = 0, \tag{2}$$

$$\tau_{\mathrm{SGS}} = \overline{UU} - \bar{U}\bar{U}. \tag{3}$$

In order to establish an accurate simulation of fully developed turbulent flows with cyclic boundaries, pressure is decomposed into a streamwise periodic variable, $\bar{p}^*$ and a pressure gradient in streamwise direction (z) as shown in Eq. (4). β does not depend on spatial coordinates. Using this formula, Eq. (1) is rewritten into Eq. (5). For simulating fully developed flow, β is changed in time to keep the volume flow rate constant.

$$\frac{\bar{p}}{\rho} = \frac{\bar{p}^*}{\rho} - \beta \cdot z, \tag{4}$$

$$\frac{\partial \bar{U}}{\partial t} + \nabla(\bar{U}\bar{U}) = \frac{-\nabla \bar{p}^*}{\rho} - \nabla \cdot \nu(\nabla \bar{U} + \nabla \bar{U}^T) - \nabla \cdot \tau_{\mathrm{SGS}} + \beta \cdot e_z. \tag{5}$$

Equations are solved using channelFoam solver in OpenFOAM, [1].

3. Smooth pipe

Mesh dependency, subgrid-scale model dependency and Reynolds number dependency are crucial parts in LES methodology, as they can highly affect the accuracy and the computational costs. While a well-established method with a poor mesh or bad subgrid-scale model may be inaccurate at high Reynolds number, a refined mesh may result in a computationally ineffective simulation. In this section, these problems are investigated and the simulation methodology is validated for smooth pipe.

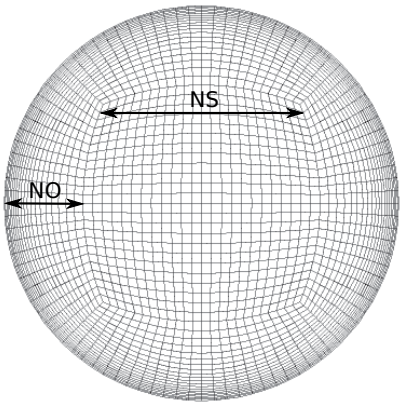

Figure 1. Smooth pipe mesh structure
A central square block (slightly deformed) with an o-grid. The number of cells in the central square is $\mathrm{NS} \cdot \mathrm{NS} \cdot \mathrm{NL}$**. The o-grid contains NO cells in radial direction.**

3.1. Mesh dependency study

Block-structured meshes are created using blockMesh. The number of cells is controlled by three parameters: NO, NS, and NL as shown in Figure 1. As near-wall resolution is very important in LES, increasing NO, NS and NL can improve near-wall mesh resolutions in radial (R), azimuthal (ϕ) and axial (z) directions. Total number of cells can be calculated as $(\mathrm{NS}^2 + 4 \cdot \mathrm{NS} \cdot \mathrm{NO}) \cdot \mathrm{NL}$.

In LES literature, e.g. [6], the required grid resolution for wall-resolved LES is expressed in wall units. These resolution requirements can be expressed using NO, NS and NL parameters and the definition of the friction Reynolds number, Re_τ, see Eqs. (6) to (9).

$$R^+ = \frac{2 \cdot d(\mathrm{NO})}{D} \cdot \mathrm{Re}_\tau, \tag{6}$$

$$(R\phi)^+ = \frac{\pi}{2 \cdot \mathrm{NS}} \cdot \mathrm{Re}_\tau, \tag{7}$$

$$Z^+ = \frac{2 \cdot L}{D \cdot \mathrm{NL}} \cdot \mathrm{Re}_\tau, \tag{8}$$

$$\mathrm{Re}_\tau = \frac{u_* \cdot D}{2 \cdot \nu}. \tag{9}$$

A base mesh with NS=48, NO=38, NL=100 (1st study, 960000 cells) is created for simulating single-phase turbulent flow of water in a smooth pipe with $L/D = 5$ and $\mathrm{Re} = 5310$. The

base mesh is systematically refined and coarsened in radial, azimuthal and axial directions. In the mesh dependency study, the dynamic Smagorinsky subgrid-scale model "dynamicSmagorinsky" is used, [7].

Simulations are performed with variable time steps of CFL $\leq$ 0.8 condition for 1.02 s (approximately 10 transmit times of full length) before time-averaging is started. To the authors' experience, this time is enough for the flow to become independent of the initial conditions. Then simulation is continued for another 1.02 s with fixed time step for averaging statistically enough data on the mean flow properties.

Simulation results for friction factors calculated from β are compared to literature reference value $\lambda = 0.03675$ of Colebrook-correlation, [8]. Difference from literature reference friction factor is shown in Figures 2 to 5. While most of the data points are within $\pm 5\%$ from the literature, it is important to note that refining in radial or azimuthal directions causes bigger errors (no grid-convergence). Increasing accuracy for increasing cell numbers (grid-convergence) is found only in axial direction. A possible explanation is that the numerical accuracy is sensitive to the maximum aspect ratio of near-wall cells. We conclude that, refinements make sense only if the maximum aspect ratio is not increased. Therefore the base mesh must be refined in axial direction. A new base mesh with NS=48, NO=38, NL=125 (2nd study, 1200000 cells) is created and systematically refined and coarsened in radial, azimuthal and axial directions, as shown in Figs. 2 to 5.

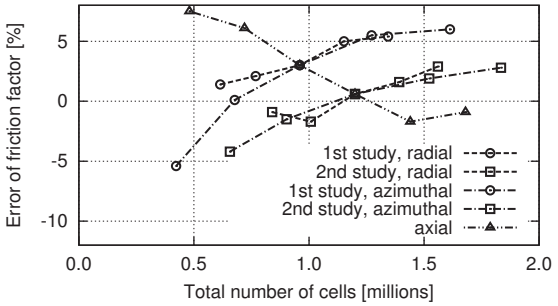

Figure 2. Comparison of mesh accuracies for smooth pipe Axial refining shows grid-convergence. Radial and azimuthal refining result in higher errors.

The conclusion of the mesh dependency study: Eqs. (10) to (12) should be satisfied for good enough accuracy.

$$R^+ \leq 1.1 \text{ (wall-normal)}, \tag{10}$$

$$(R\phi)^+ \leq 10 \text{ (spanwise)}, \tag{11}$$

$$Z^+ \leq 20 \text{ (streamwise)}. \tag{12}$$

We note that Eqs. (10) to (12) conditions are slightly different than Eqs. (13) to (15) available in literature, [6].

$$y^+ \leq 1 \text{ (wall-normal)}, \tag{13}$$

$$z^+ \leq 30 \text{ (spanwise)}, \tag{14}$$

$$x^+ \leq 100 \text{ (streamwise)}. \tag{15}$$

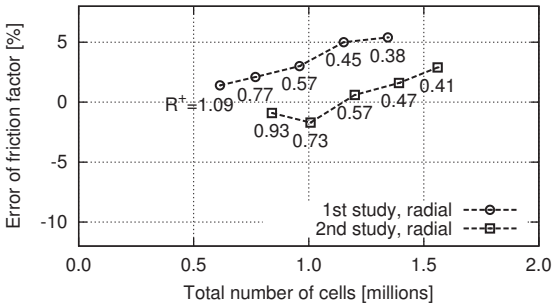

Figure 3. Radial refinement in smooth pipe $R^+ < 1.1$ can supply $\pm 5\%$ accurate results.

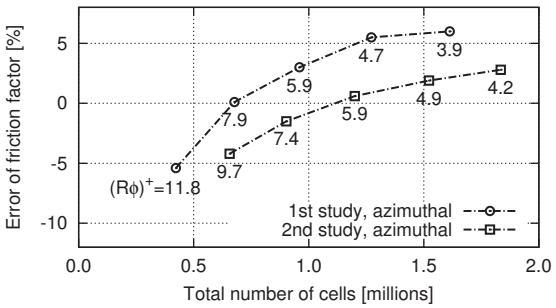

Figure 4. Azimuthal refinement in smooth pipe $(R\phi)^+ < 10$ can supply $\pm 5\%$ accurate results.

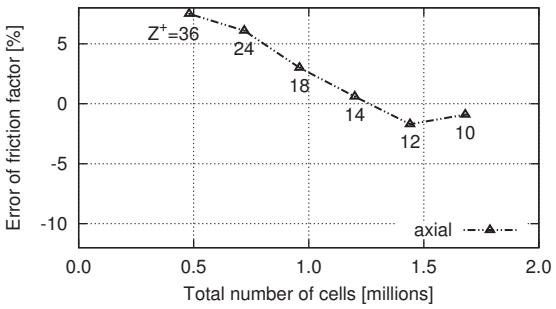

Figure 5. Axial refinement in smooth pipe $Z^+ < 20$ can supply $\pm 5\%$ accurate results.

3.2. Subgrid-scale model dependency study

NS=48, NO=38, NL=100 (960000 cells) mesh is used for testing different subgrid-scale models. Simulations are performed for 2.04 s, similar to the

Table 1. Comparison of subgrid-scale model accuracies for smooth pipe simulations Reference: $\lambda = 0.03675$ (Colebrook, [8]).

Subgrid-scale model	Simulated λ	Error of λ
laminar (no model)	0.03870	+5.3%
Smagorinsky	0.04372	+19.0%
dynSmagorinsky	0.03912	+6.4%
dynamicSmagorinsky	0.03784	+3.0%
oneEqEddy	0.04366	+18.8%
dynOneEqEddy	0.03919	+6.6%
locDynOneEqEddy	0.03788	+3.1%

mesh dependency study (first half of the time interval: initializing, second half: time-averaging). Model constants are set to default values in OpenFOAM 1.7. Comparison of simulation results are shown in Table 1.

The "dynamicSmagorinsky" subgrid-scale model results the best agreement with literature reference value $\lambda = 0.03675$ of Colebrook-correlation, [8]. Most subgrid-scale models do not improve the solution in comparison with the laminar (no SGS model) case at this Reynolds number.

3.3. Reynolds number dependency study

NS=48, NO=38, NL=100 (960000 cells) mesh with "dynamicSmagorinsky" subgrid-scale model is used for testing different Reynolds numbers. The transmit time in the full length of the simulation domain is different for different velocities. All simulations are performed for at least 10 transmit times for initializing fully developed turbulent flow and another 10 transmit times for time-averaging. As the mesh is the same for simulating different Reynolds numbers, the resolutions expressed in wall units are different, see Table 2. Eq. (10) and Eq. (11) are fulfilled for all Reynolds numbers, while Eq. (12) is fulfilled only for Re $\leq$ 6000. Comparison of simulation results are shown in Table 3.

All performed simulations slightly over-predict the friction factor, but the results are within 4% from the literature reference.

Table 2. Resolutions expressed in wall-units for smooth pipe for different Reynolds numbers using a mesh with NS=48, NO=38, NL=100 (960000 cells)

Re	Re_τ	R^+	$(R\phi)^+$	Z^+
5310	180	0.6	5.9	18
6000	203	0.6	6.7	20
7000	233	0.7	7.6	23
8000	260	0.8	8.5	26
9000	288	0.9	9.4	29
10000	315	1.0	10.3	31

Table 3. Dependency on Reynolds number for smooth pipe Reference value of λ is calculated using Colebrook-correlation, [8].

Re	Simulated λ	Reference λ	Error of λ
5310	0.03784	0.03675	+3.0%
6000	0.03679	0.03551	+3.6%
7000	0.03532	0.03401	+3.8%
8000	0.03380	0.03279	+3.1%
9000	0.03277	0.03176	+3.2%
10000	0.03167	0.03088	+2.5%

3.4. Validation

Simulation results for time-averaged velocity and the velocity fluctuation root-mean-square (RMS) profiles are shown for NS=48, NO=38, NL=100 (960000 cells) mesh with "dynamicSmagorinsky" subgrid-scale model in Figure 6 and in Figure 7. Profiles are compared to direct numerical simulation (DNS) available in literature [9] and very good agreement is found.

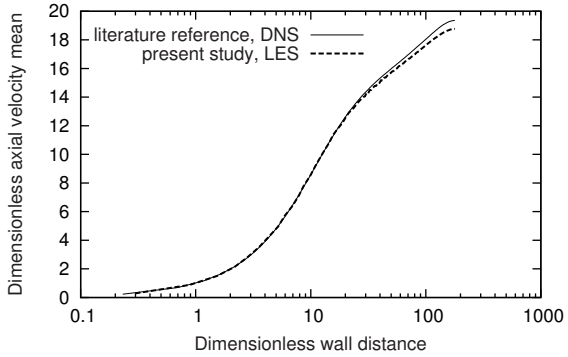

Figure 6. Comparison of axial mean velocity profile with DNS reference, [9]

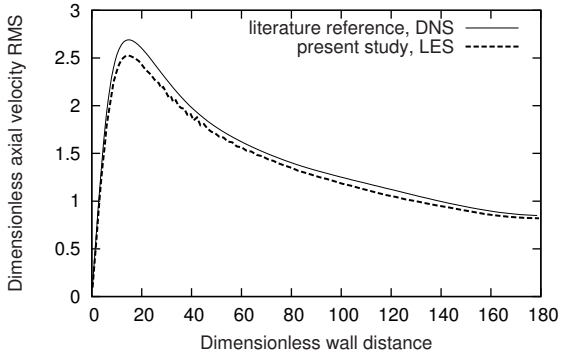

Figure 7. Comparison of axial velocity RMS profile with DNS reference, [9]

4. Grooved tube

In this section, the LES method is used for estimating friction factors in a grooved tube. A helically grooved heat exchanger tube with 9.3 *mm* diameter, 105 *mm* pitch length is studied. Helix angle is 16 °, the number of grooves is 60, groove depth is 0.18 *mm*. Groove depth-to-diameter ratio is 0.019. Simulations are performed with a mesh of 6444000 cells. Helical grooved mesh is generated in two steps: first a straight extruded mesh is created, then the points of the mesh are twisted around z axis. Mesh structure is shown in Figure 8.

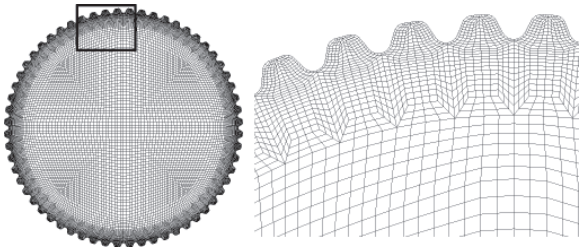

Figure 8. Grooved tube mesh structure 6444000 cells (all hexahedra) are generated using blockMesh. Number of cells on the inlet surface is 21480. In streamwise direction the mesh contains 300 cells.

Simulations are performed using "dynamicSmagorinsky" subgrid-scale model for 13 different Reynolds numbers. Eqs. (10) to (12) are fulfilled for all Reynolds numbers. Comparison of simulation results are shown in Figure 9 and in Table 4.

For Re < 12000, frictional losses in the grooved tube are similar to a smooth pipe, while for higher Reynolds numbers the grooved tube induces higher friction than a smooth pipe. The grooves does not effect the skin friction when the groove depth is so small, that the grooves are present only in the laminar sublayer. Increasing the Reynolds number, the groove depth reaches the turbulent boundary layer, so the skin friction is increased. These results are in accordance with literature, [10].

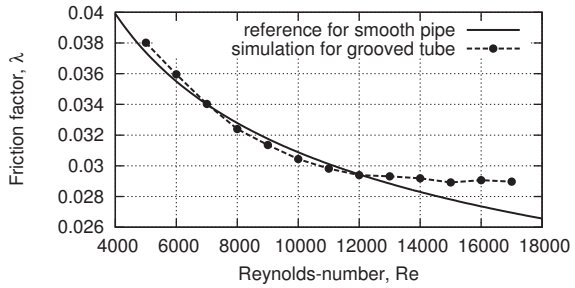

Figure 9. Friction factor simulation results for helically grooved tube are compared to Colebrook-correlation, [8] of smooth pipe

Table 4. Simulated friction factors for grooved tube

Re	Re_τ	R^+	$(R\phi)^+$	Z^+	Simulated λ
5000	90	0.4	0.6	7	0.03802
6000	103	0.5	0.7	8	0.03596
7000	118	0.5	0.8	9	0.03403
8000	133	0.6	1.0	10	0.03239
9000	144	0.6	1.0	11	0.03136
10000	159	0.7	1.1	12	0.03044
11000	174	0.8	1.2	13	0.02982
12000	189	0.8	1.4	14	0.02939
13000	204	0.9	1.5	15	0.02931
14000	219	0.9	1.6	16	0.02918
15000	236	1.0	1.7	18	0.02892
16000	250	1.1	1.8	19	0.02906
17000	264	1.1	1.9	20	0.02897

As a result of helical grooves, the velocity also changes near the wall. In the grooves, the flow is swirling, while there is almost no rotation near the centreline. This is shown in Figures 10 to 11. In Fig. 11, sharp peaks are observed near the groove depth ($2r/D = 0.962$).

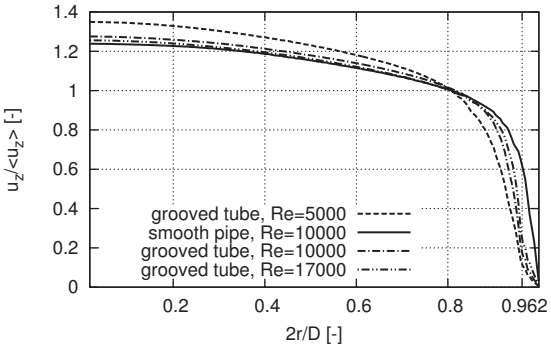

Figure 10. Axial velocity profiles for different Reynolds numbers Groove depth: $2r/D = 0.962$**.**

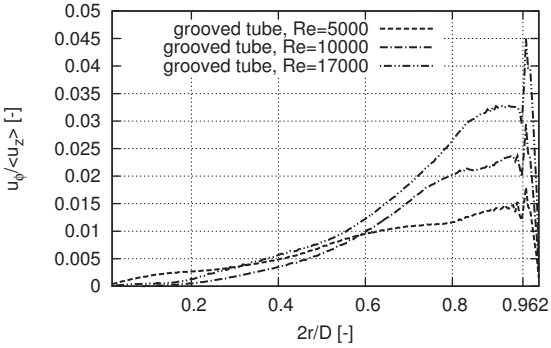

Figure 11. Azimuthal velocity profiles for different Reynolds numbers Groove depth: $2r/D = 0.962$**.**

The turbulent kinetic energy profile shows Reynolds number dependency as the turbulent kinetic energy peak shifts, see Figure 12.

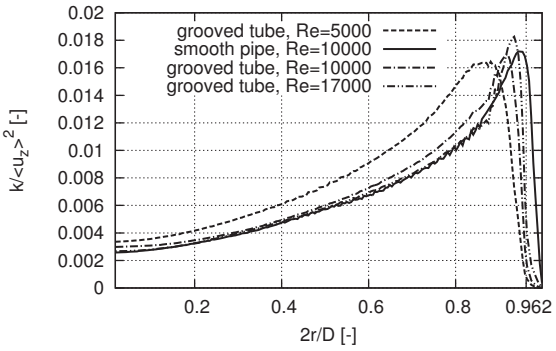

Figure 12. Turbulent kinetic energy profiles Groove depth: $2r/D = 0.962$**.**

5. SUMMARY

In this paper, a model based on large eddy simulation of turbulent flow is proposed for complex geometries like helically grooved heat exchanger tubes. Simulation methodology includes no empirical parameters (e.g. fitted model constants), therefore it is universal in predicting the performance of non-existing groove geometries. Simulation technique is validated using literature data. Less than 5% error is found in the calculated Darcy friction factors and velocity profiles are in very good agreement with direct numerical simulation database. Special interest is given to mesh dependency, subgrid-scale model dependency and Reynolds number dependency. New criteria are established for simulating Darcy friction factor in pipes for $R^+ \leq 1.1$ (wall-normal), $(R\phi)^+ \leq 10$ (spanwise) and $Z^+ \leq 20$ (streamwise) directions.

Simulation results for a helically grooved heat exchanger tube (60 grooves, 0.019 groove depth-to-diameter ratio and 16 helix angle) meshed with 6444000 cells are presented. For Re $<$ 12000, frictional losses in the grooved tube are similar to a smooth pipe. For Re $>$ 12000, the grooved tube induces higher friction than a smooth pipe.

Velocity profiles and turbulent kinetic energy profiles for helically grooved tubes with different Reynolds numbers are presented. These can help in understanding fluid flow phenomena. While one might expect that a flow in a helically grooved tube rotates as a rigid body, in Fig. 11 it is shown that near-wall region swirl is faster and centreline swirl is lower than a rigid body rotation.

In future, this result should be experimentally validated to have a better understanding of the flow and determine the accuracy of the presented model. If the model predictions become accurate for modern refrigerant media, this technique could help developing future geometries with maximum efficiencies.

ACKNOWLEDGEMENTS

We gratefully acknowledge financial support from Furukawa Electric Co. We further acknowledge the help of Furukawa Electric Yokohama R&D Laboratories, K. Shintomi and S. Yokoyama for their helpful remarks. Support from Furukawa Electric Institute of Technology, Gy. Besztercey and L. Romvári is also acknowledged. Help of Budapest University of Technology and Economics, Department of Fluid Mechanics community, especially M. Lohász, J. Vad and V. Józsa is highly appreciated.

References

[1] "OpenFOAM, The open source CFD toolbox". *http://www.openfoam.com*.

[2] Courant, R., Friedrichs, K., and Lewy, H. 1967 "On the Partial Difference Equations of Mathematical Physics". *IBM Journal of Research and Development*, Vol. 11, No. 2, pp. 215–234.

[3] Dalkilic, A. and Wongwises, S. 2009 "Intensive literature review of condensation inside smooth and enhanced tubes". *International Journal of Heat and Mass Transfer*, Vol. 52, pp. 3409–3426.

[4] Wellsandt, S. and Vamling, L. 2005 "Evaporation of R407C and R410A in a horizontal herringbone microfin tube: heat transfer and pressure drop". *International Journal of Refrigeration*, Vol. 28, pp. 901–911.

[5] Zdaniuk, G., Chamra, L., and Mago, P. 2008 "Experimental determination of heat transfer and friction in helically-finned tubes". *Experimental Thermal and Fluid Science*, Vol. 32, pp. 761–775.

[6] Davidson, L. 2009 "Large Eddy Simulations: How to evaluate resolution". *International Journal of Heat and Fluid Flow*, Vol. 30, No. 5, pp. 1016–1025.

[7] Lilly, D. K. 1992 "A proposed modification of the Germano subgrid-scale closure method". *Physics of Fluids A: Fluid Dynamics*, Vol. 4, No. 3, p. 633.

[8] Colebrook, C. and White, C. 1937 "Experiments with fluid friction in roughened pipes". *Proceedings of the Royal Society of London. Series A, Mathematical and Physical Sciences*, Vol. 161, No. 906, pp. 367–381.

[9] Fukagata, K. 2002 "Highly Energy-Conservative Finite Difference Method for the Cylindrical Coordinate System". *Journal of Computational Physics*, Vol. 181, No. 2, pp. 478–498.

[10] Nikuradse, J. 1950 "Laws of flow in rough pipes - Translation of Stromungsgesetze in rauhen Rohren, Nikuradse, Forschung auf dem Gebiete des Ingenieurwesens, 1933.". *NACA Technical Memorandum*, Vol. 1292.

Conference on Modelling Fluid Flow (CMFF'12)
The 15th International Conference on Fluid Flow Technologies
Budapest, Hungary, September 4-7, 2012

SKIN FRICTION REDUCTION BY MICRO BUBBLES IN PIPE FLOW

Erny AFIZA[1], Hiroo OKANAGA[2], Katsumi AOKI[3]

[1] Department of Mechanical Engineering, Tokai University 4-1-1 Kitakaname, Hiratsuka-shi, Kanagawa, 259-1291 Japan. Tel: +81 463 58 1211, Fax: +81 463 50 2479, E-mail: ernyafiza@yahoo.com
[2] Department of Mechanical Engineering, Tokai University 4-1-1 Kitakaname, Hiratsuka-shi, Kanagawa, 259-1291 Japan. Tel: +81 463 58 1211, Fax: +81 463 50 2479, E-mail: okanaga@tokai-u.jp
[3] Department of Mechanical Engineering, Tokai University 4-1-1 Kitakaname, Hiratsuka-shi, Kanagawa, 259-1291 Japan. Tel: +81 463 58 1211, Fax: +81 463 50 2479, E-mail: katumi@keyaki.cc.u-tokai.ac.jp

ABSTRACT

Recently, micro bubbles injection has emerged as a promising drag reduction device in ships due to their significant reduction in frictional drag, cost-effectiveness, environmental-friendly and easy to implement in an existing ship. Frictional drag reduces up to 80% by injecting micro bubbles to the boundary layer. However, the mechanism of drag reduction by micro bubbles is complicated and poorly understood. Therefore, the objective of this study is to clarify the mechanism of drag reduction by micro bubbles in the most basic flow condition. Several controllable factors associated with the efficiency of micro bubbles in drag reduction including pipe diameter, temperature and purity of water, micro bubbles size and distribution were investigated to identify the optimum condition for skin friction reduction by micro bubbles. As the results, a higher reduction rate was obtained with larger distribution area of attached micro bubbles at the tube wall in smaller Reynolds number. Moreover, the distribution area and size of micro bubbles at the tube wall increase with time and contributed a great effect in pipe friction loss. Flow pattern and the bubble's behaviour were observed by flow visualization. The ideal bubble size and distribution were evaluated by the measurement of skin friction.

Keywords: boundary layer, drag reduction, micro bubbles, pipe flow, Reynolds number

NOMENCLATURE

λ	[-]	friction factor
D	[m]	tube diameter
g	[m/s^2]	gravitational force
$\underline{v}$	[m/s]	fluid velocity

1. INTRODUCTION

Micro bubbles are defined as tiny bubbles with diameters of $10\sim50\text{x}10^{-6}$ m (μm). Due to its small size, they are characterized by having large surface area, high inner pressure, low buoyancy, and electrically charged. Therefore, they have been applied in many fields such as agriculture, aquaculture, medical treatment, and as a drag reduction device in ships. Micro bubbles injection has emerged as a promising drag reduction device in ships due to their significant reduction in frictional drag, cost-effectiveness, environmental-friendly and easy to implement in an existing ship. Many experimental studies have been carried out by injecting micro bubbles into the turbulent boundary layer for reduction of frictional drag.

This study pioneered by McCormick and Bhattharcharrya [1] has triggered a large number of investigations on the mechanism of skin friction reduction by micro bubbles. They reported that the drag force of fully-submerged body decreased up to 65% by using micro bubbles which were created by electrolysis. It is found that the reduction increased as gas flow rate increases.

Experimental results from several studies have been shown that drag reduction by micro bubbles is influenced by void fraction. Bogdevich [2] reported that the reduction rate positively correlated to void fraction in boundary layer. Later, an extensive study by Guin [3] has shown that the reduction efficiency is associated with near wall void fraction compared to overall void fraction.

The results by McCormick and Bhattharcharrya [1] and Kodama [4] have agreed on the effect of drag reduction by micro bubbles in different flow speed. The reduction rate declined in higher flow speed and improves with the increasing of air injection rate.

The bubbles size in comparison to turbulent boundary layer thickness is also one of the most

important factors that greatly affect drag reduction by micro bubbles as shown in several studies. Kodama and Kato [5] found that micro bubbles efficiency is declined because void fraction is reduced as smaller bubbles (diameter; $d<0.5\times10^{-3}$ *m*) dispersed faster than larger bubbles. By using 50 *m* flat plate, they also found that the reduction rate is independent in bubbles diameter between $0.5\sim2\times10^{-3}$ *m*.

However, micro-sized bubbles whose are widely known with its special characteristics also contribute a significant reduction in drag frictional. Besides the results reported by McCormick and Bhattharcharyya [1], related studies by Serizawa proposed that the two-phase flow is "laminarized" by injecting micro bubbles into the boundary layer [6]. For a single-phase in a pipe flow, the turbulent transient is known to take place when Reynolds number=2300. However, when micro bubbles are injected into the flow, this transient region initiated at the Reynolds number=10000~12000. Merkle and Deutsh [7] suggested that the ideal bubble size for an optimum efficiency was not fixed and strongly influenced with the flow characteristics.

In addition, properties of micro bubbles changed in different water quality as reported by Eric S. [8]. Because of the bubbles diameter generated in salt water and fresh water is different, the efficiency in drag reduction was also affected. Therefore, earlier studies in fresh water regarding the reduction efficiency in seawater may not precisely assume.

Based on previous research, a lot of possible explanations on the mechanism were proposed but several fundamental factors were being assumed and overlooked. Therefore, experiments were carried out in various conditions including pipe diameter, temperature and purity of water, micro bubbles size and distribution in order to comprehend the characteristics and its effects on the efficiency.

2. EXPERIMENTAL APPARATUS

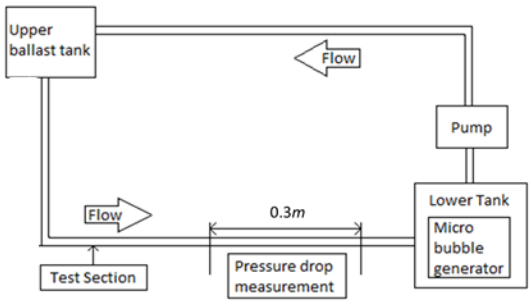

Figure 1. The closed-loop circulating water system (side view)

Experiments were carried out in a horizontal tube using a circulating water loop system that basically designed to measure pipe friction loss as shown in figure 1. First, water is pumped from the lower tank to ballast tank located at 2 *m* high above the ground. The water head in the ballast tank is maintained to ensure a constant flow. Then water flowed to the test tube by gravity and finally fed back to the lower tank. Flow rate is adjusted by controlling the valve placed between the tank and test section.

Micro bubbles are generated continuously in the tank throughout the experiment. The pressure drop is measured from manometer located at 1 *m* downstream from the valve. In order to observe the bubbly flow, photographs by using USB microscope were taken near the tube wall. Laser sheet is projected vertically through the tube cross-section and in the area where the pressure drop is measured. All experiments were carried out in basic conditions as follows; tap water, tube diameter: $20\text{x}10^{-3}$ *m*. However, in each experiment one of these conditions were changed and its affects in drag reduction were investigated.

2. METHODOLOGY

The following manipulative factors associated with the reduction rate were tested and evaluated;

(a) Micro bubbles size and distribution
(b) Water purity
(c) Water temperature
(d) Pipe diameter
(e) Temporal change

The friction factors in laminar and turbulent flows are determined from the following eqs. (1) to (2);

Laminar flow ($Re<2300$);

$$\lambda = 64/Re \tag{1}$$

Turbulent flow ($3\text{x}10^3<Re<10^5$):

$$\lambda = 0.3164\ Re^{-1/4} \tag{2}$$

Eq. 3 was used to determine the pressure head loss;

$$H = \frac{\lambda l v}{2Dg} \tag{3}$$

Where, H, l, v, d, g are head friction loss, the distance between two manometers, fluid velocity, pipe diameter, and gravitational force respectively.

3. RESULTS AND DISCUSSION

3.1. Effect micro bubbles size and distribution

Table 1. Types of micro bubbles generators

Company	M2-LM/PVC (NanoPlanet)	AS3 (ASUPU)
Generation rate (ℓ/min)	1	7-10
Generation method	Shear stress	decompression + Shear stress
Notation in paper	MB1	MB2

As shown in table 1, two types of micro bubbles generators were used. The bubbles size and quantity are different by the generator of MB1 and MB2. Figure 2 (a) and (b) show the density distribution of micro bubbles generated from each generator. MB2 produced larger numerical density of smaller bubbles compared to MB1.

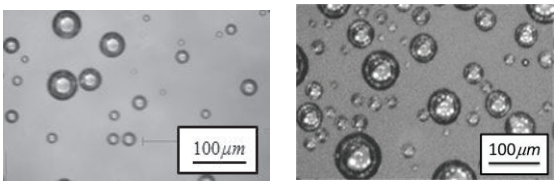

(b) MB1 (b) MB2

Figure 2. Micro bubbles density distribution

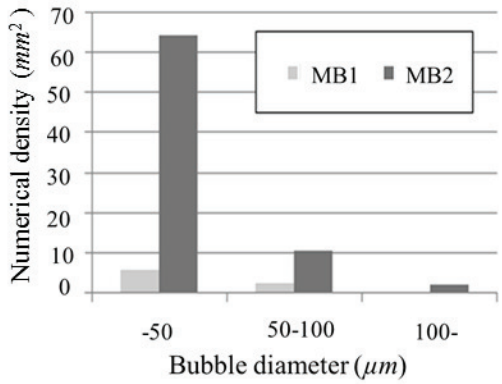

Figure 3. Numerical density of micro bubbles

The generated bubbles were compared and classified into three ranges of diameter within $1x10^{-3}$ *m* per mm^2 in figure 3. As shown in fig. 3, numerical density of micro bubbles generated by MB2 is also comparably higher in all range of bubble diameters, and especially is highest in bubbles diameter less than 50 μm ($d<50\ \mu m$).

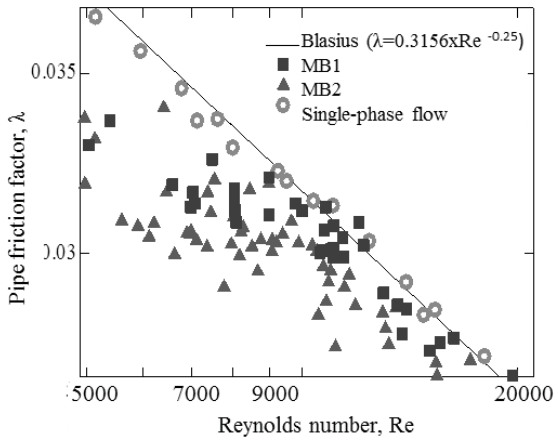

Figure 4. The friction reduction effect by micro bubbles (Micro bubbles size and distribution)

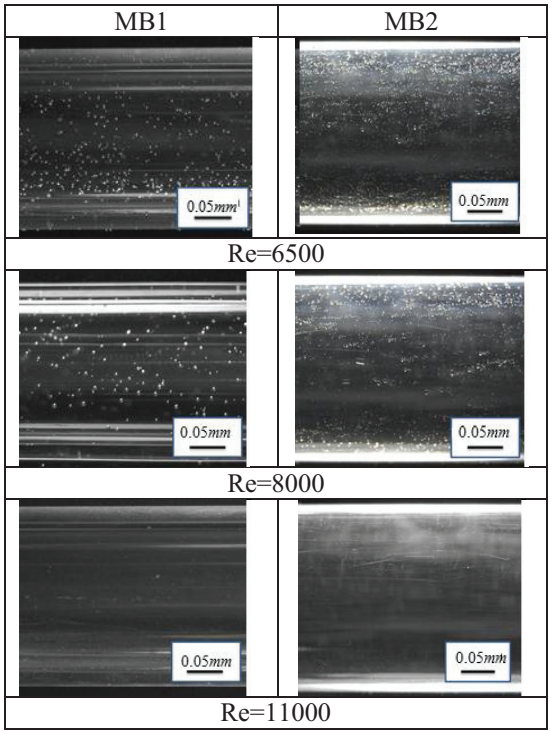

Figure 5. Tube's visualization of the attached bubbles (Micro bubbles size and distribution)

The results on the skin friction reduction effect of each generator were shown in figure 4. Horizontal axis represents Reynolds number and vertical axis represents pipe friction loss. The gradient line in the graph shows Blasius's value ($\lambda=0.13164\times Re^{-0.25}$). In this study, the pipe friction loss measurements were divided into two range of Reynolds numbers, $5000<Re<10000$ is when micro bubbles were attached to the tube wall, and $Re>10000$ is when the bubbles started to detach from the tube wall and flow freely due to higher speed flow.

In the case of MB1, at $5000<Re<10000$, average 10%, and maximum 16% of reduction in

skin friction were obtained. However, the efficiency is decreased at Re>10000 with up to 4% and average 2% of friction loss reduction. From the results MB2, at 5000<Re<10000, as much as 24% and average 10% of reduction were obtained. In Re>10000, almost no existence of adhered bubbles were observed at the tube wall, and the efficiency decreases with average 5%, the largest 8% of friction reduction.

Figure 5 shows the tube's visualization of the attached bubbles at the tube wall for each generator. The distribution area of the attached bubbles by MB2 is larger compared to MB1. However, both cases show a similar phenomenon where the distribution of the attached bubbles decreases at higher Reynolds number and almost no existence of the attached bubbles were observed at Re<10000.

3.2. Effect of water purity

The characteristics of micro bubbles and their efficiency in skin friction reduction were investigated by using two type of liquid; pure water and tap water. The PPM (parts per million) level for each type of water was measured by using water quality tester (Total Dissolved Solids meter, TDS). The PPM level for each tap water and pure water were between 60-90*ppm* and 2-6*ppm* respectively.

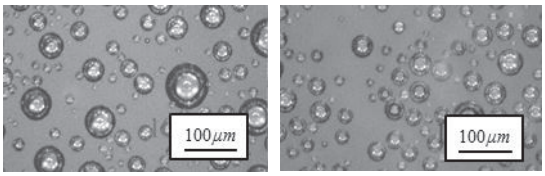

(a) Pure water (b) Tap water

Figure 6. Micro bubbles density distribution (Water purity)

Micro bubble is generated for 20 minutes in each type of liquid. Water with micro bubbles is observed by using microscope. Figure 6 (a) and (b) show the density distribution of micro bubbles generated in each type of water. Figure 7 shows the numerical density distribution of bubbles for certain range diameters. As the results, no significant difference can be seen in larger diameter bubbles (d>50 μm). However, density of smaller bubbles (d<50 μm) in pure water was 40% less than the density generated in tap water.

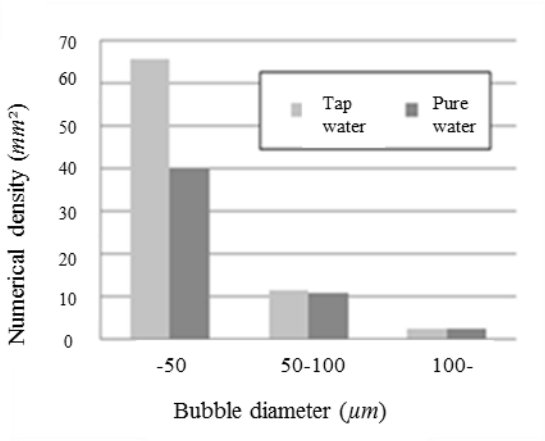

Figure 7. Numerical density of micro bubbles (Water purity)

Figure 8 shows the friction reduction effect by micro bubbles in different water purity. The reduction rate in tap water is comparably higher with average reduction of 8% larger than pure water, because the density of smaller bubbles (d<50 μm) of tap water is higher.

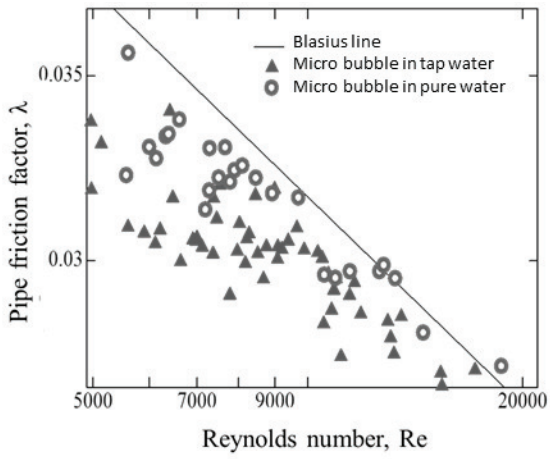

Figure 8. The friction reduction effect by micro bubbles (Water purity)

3.3. Effect of water temperature

Figure 9 shows the friction loss reduction effect by micro bubbles investigated at the water temperature; 20 °*c*, 25 °*c*, and 30 °*c*.

From fig 9, in range of 5000<Re<10000, up to 16% and average 10% of reduction were obtained by micro bubbles in 20 °*c* water. Meanwhile, in Re>10000, the largest 7% and average 4% of reduction was observed. In case of 25 °*c*, average 10% and maximum 15% in 5000<Re<10000, however in Re>10000 average 3% and largest 5% of reduction were confirmed. At 30 °*c* water, pipe friction loss decreased as much as 18% and average

11% in 5000<Re<10000, and up to 7% and average 3% in Re>10000.

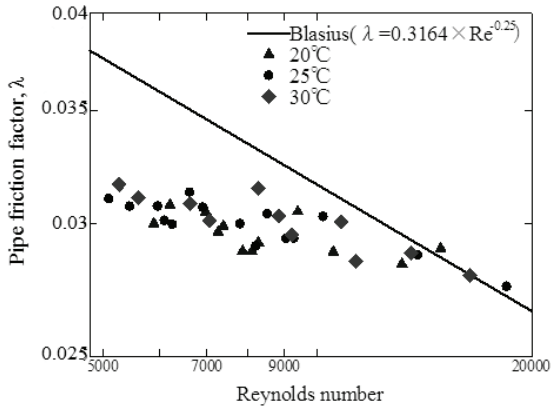

Figure 9. The friction reduction effect by micro bubbles (Water temperature)

As conclusion, there is no significant effect in micro bubbles efficiency in friction reduction as the water temperature changes.

3.4. Effect of pipe diameter

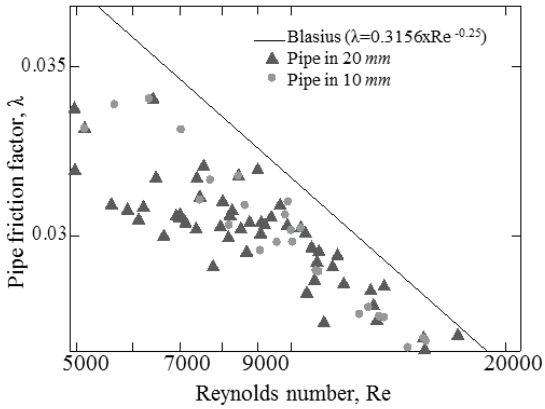

Figure 10. The friction reduction effect by micro bubbles (Pipe diameter)

In this experiment, besides Reynolds number, the relationship between micro bubbles efficiency in friction loss reduction and fluid velocity was investigated by using two different pipe diameters, D; 10×10^{-3} *m*, 20×10^{-3} *m*.

Figure 10 shows the effect of velocity rate on friction reduction by micro bubbles. By using pipe with 10×10^{-3} *m* in diameter maximum 18% and average 8% of reduction rate were obtained in lower Reynolds number (5000<Re<10000). As the Reynolds number increased (Re>10000), micro bubbles becomes less efficient as only maximum 8% and average 5% of reduction was observed. In case of 20×10^{-3} *m* pipe, the reduction rate is bigger with maximum 24% and average 10% of reduction in skin friction loss was obtained.

Figure 11 shows the visualization of micro bubbles distribution in both pipe diameters. In overall, the distribution of the attached bubbles at the tube wall decreased as the Reynolds number increases. By using 10×10^{-3} *m* pipe, only a small distribution of micro bubbles were observed attached at the tube wall. Almost no adhered bubbles at the tube's wall can be seen in higher Reynolds number (Re>8000). In case of 20×10^{-3} *m* pipe, the quantity of the attached bubbles appears to be larger than $10\text{x}10^{-3}$ *m* in diameter pipe. Micro bubbles become smaller as the Reynolds number increases. Micro bubbles were observed in Re=8000 in diameter 20×10^{-3} *m* pipe. The skin friction reduction by micro bubbles in 20×10^{-3} *m* in diameter pipe is bigger than the reduction in 10×10^{-3} *m* in diameter pipe.

As the tube diameter becomes smaller, fluid velocity becomes faster in the same Reynolds number. As the result, the quantity of the bubbles attached at the tube wall decrease. Therefore, micro bubbles efficiency in friction loss reduction decreases in smaller tubes.

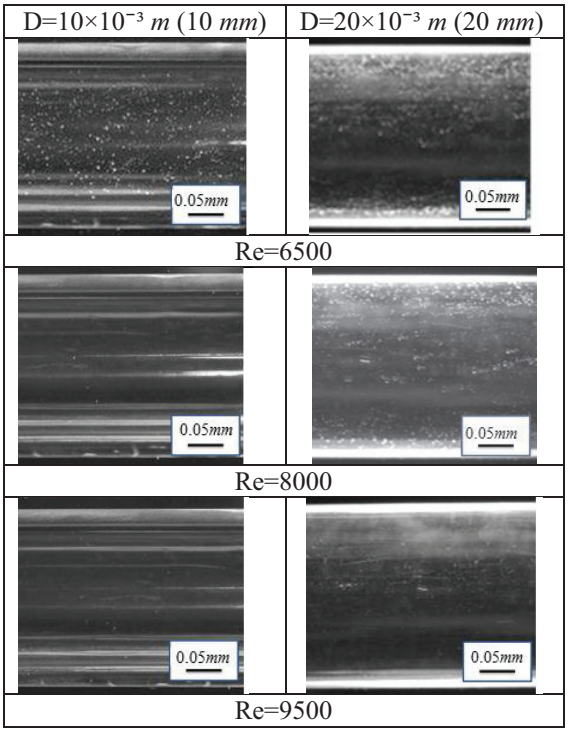

Figure 11. Tube's visualization of the attached bubbles (Tube diameter)

3.5. Effect of temporal change

In this experiment, the stability of frictional reduction by micro bubbles was studied at a constant fluid velocity for a period of time. As a consequence, the diameter and distribution of attached bubbles at the tube wall changes with time and greatly affect the pipe friction loss.

Figure 12 shows the distribution of micro bubbles at the tube wall during 1.5 minutes and 20 minutes at; Re=6500, Re=8000, and Re=13500. The lower photographs represent the enlarged view of the photographs above them. As time prolonged, the quantity of the attached bubbles on the surface of the tube wall increased with time when Re=6500, 8000. Bubble diameter also increased from about 10 *μm* to 2 *mm*. However, bubbles detached from the tube wall in higher Reynolds number and eventually no bubbles were observed at Re=13500, even after 20 minutes.

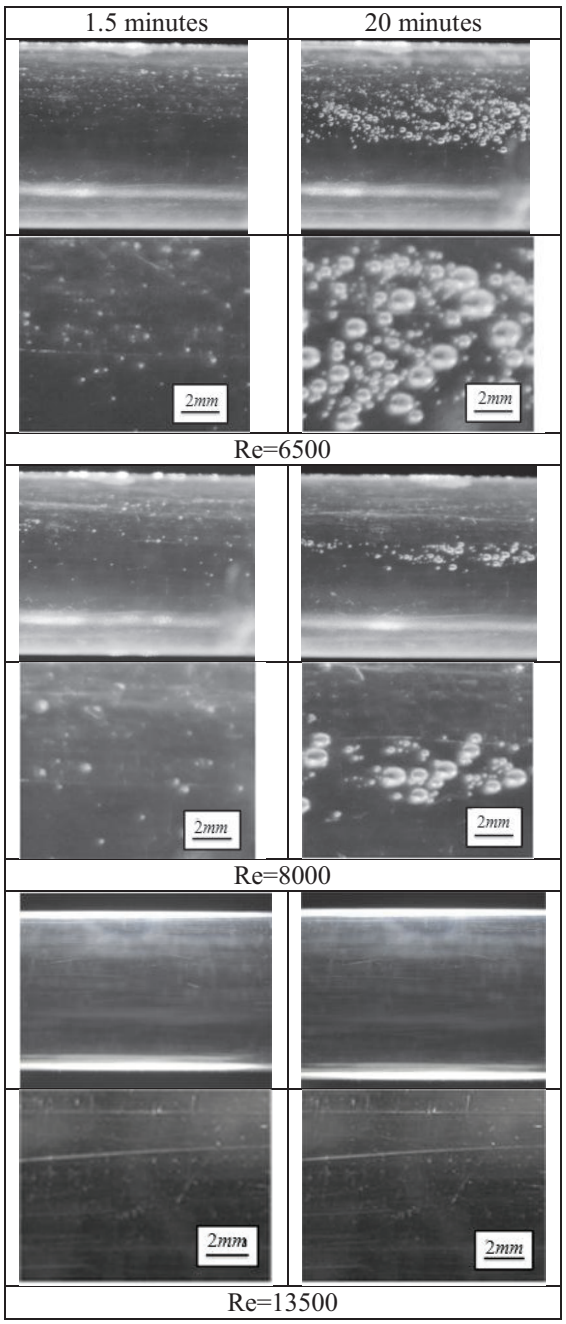

Figure 12. Tube's visualization of the attached bubbles (Temporal change)

Figure 13 shows the relation between Reynolds number and pipe friction loss at; t=1.5, 10, 20, 30 minutes. The gradient line in the graph shows Blasius's theoretical value of tap water. In the first 1.5 minutes the reduction rate at Re=4500 is up to 21%. However, the pipe friction loss increased with time as the diameter and quantity of the attached bubbles on the surface of the tube wall increased. After 10 minutes, at Re=4500, the reduction is 19%. Frictional resistance was increased about 34% after 10 minutes at Re=6500, 8000. After 20 minutes, 9% reduction is measured in Re=4500, but in Re=6500, 8000, up to 66% skin friction skin friction addition were observed. The pipe friction reduction by micro bubbles eventually increased at 20 minutes, then the pipe friction is not changed after 30 minutes. The change in time interval does not affect the pipe friction loss in Re=11500, 13500 and the reduction rate maintained 5% throughout the experiment. This phenomenon showed a smaller reduction was obtained even without the existence of the attached bubbles at the tube wall.

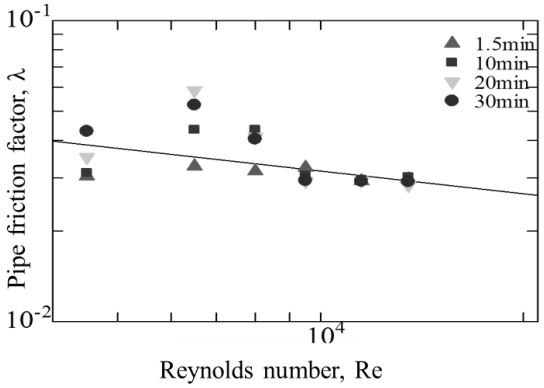

Figure 13. The friction reduction effect by micro bubbles (Temporal change)

Figure 14 shows tube's visualization taken in lower shutter speed at Re=8000. Large bubbles were adhered at the top of the tube wall because of the larger buoyancy forces, the smaller bubbles freely move along the flow.

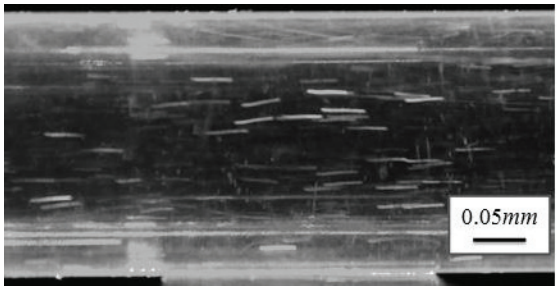

Figure 14. Tube's visualization in lower shutter speed (Re=8000)

It is assumed that ideal bubble size for a significant drag reduction depends on the thickness of the boundary layer. However, to obtain an optimum reduction in skin friction, whether the bubbles attached to the tube wall or freely move along the flow still remains unknown

4. CONCLUSIONS

The effects of skin friction reduction by micro bubbles in several conditions were studied experimentally.

(a) The reduction in skin friction loss at 5000<Re<10000 was larger than one at Re>10000.
(b) A bigger reduction in skin friction was obtained by using tap water compared to pure water at the same Reynolds number (5000<Re<10000).
(c) A bigger reduction in skin friction was obtained by using 10×10^{-3} *m* in diameter pipe compared to 20×10^{-3} *m* in diameter pipe at the same Reynolds number (5000<Re<10000).
(d) No significant difference in skin friction reduction rate was observed by using different water temperature.
(e) At 5000<Re<10000, micro bubbles tend to attach at the tube wall and getting bigger in time which leads to the increment in pipe friction loss. Meanwhile, at Re>10000 almost no existence of attached bubbles were observed resulted to a small change in reduction rate.

REFERENCES

[1] McCormick, M.E. and Bhattarcharrya,R.,"Drag Reduction of asubmersiblee Hull by Electrolysis", Naval Engineers Journal, Vol.85, No.2(1973),pp.11-16.

[2] Bogdevich, V. G., Evseev, A. R., "Effect of gas Saturation on wall turbulent in Investigation of Boundary Layer Control", Thermophysics Institute Publishing House, p.49, (1976)

[3] Guin M.M., Kato, H., Maeda, M., and Miyanaga, M., „Reduction of Skin Friction by microbubbles and Its Relation with Near-wall bubble concentration in a channel", J. Of the Society of Naval Architects of Japan, vol.182(1996), pp.1-8.

[4] Y. Kodama, et al.,:"Experimental study on microbubbles and their applicability to ships for skin friction reduction.",International Journal of Heat and Fluid Flow21(2000).

[5] Takafumi Kawamura, Akiko Fujiwara, Takahito Takahashi, et al.,"The Effects of the Bubble size on the Bubble Dispersion and Skin Friction Reduction", University of Tokyo, Japan, National Maritime Research Institute,Japan.

[6] Serizawa, A., Inui, T., Yahiro,T. and Kawara, Z., 2003, "Laminarization of micro bubbles containing milky bubbly flowing a pipe, Proc. Of the 3rd European-Japanese Two-Phase flow group Meeting, September 21-27(2004), Certosa di Pontignano.

[7] Merkle, C. and Deutsch, S. "Micro bubbles Drag Reduction". Frontiers in Experimental Fluid Mechanics. (ed. M. Gad-el-Hak) Lecture Notes in engineering, Vol. 46 (1989), p. 291. Springer.

[8] Eric S. Winkle, Steven L. Ceccio, David R. et al."Bubble-size distributions produced by wall injection of air into flowing freshwater, saltwater and surfactant solutions", Experiments in Fluids 27(2004) 802-810

Conference on Modelling Fluid Flow (CMFF'12)
The 15th International Conference on Fluid Flow Technologies
Budapest, Hungary, September 4-7, 2012

FLUID FLOW IN A COLLAPSIBLE TUBE WITH UNSTEADY EXTERNAL PRESSURE EXCITATION

Ádám ANGYAL[1], Gergely BÁRDOSSY[2]

[1] BSc Mechanical Engineer, Budapest University of Technology and Economics. E-mail: mail.adam.angyal@gmail.com
[2] Department of Hydrodynamic Systems, Budapest University of Technology and Economics. E-mail: bardossy@hds.bme.hu

ABSTRACT

The goal of our research work is the modeling of the venous muscle pump. Fluid-Structure Interaction (FSI) analysis was used for this purpose. The venous section was modeled as a thin-walled tube using a linear material model with low elasticity modulus. The muscle pump effect was taken into account as a time-dependent external load (pressure excitation).

After setting up the FSI analysis several calculations were carried out. However the structural part of the simulation caused convergence problems. Therefore the mechanical properties of the analysis were investigated. A variety of coarse and fine structural meshes were created and analyzed. Furthermore the results of the different solution methods were investigated.

The created FSI model of the venous muscle pump is similar to a simple volumetric pump. Thus the volume and mass flow rate as a function of time was investigated.

Keywords: Blood flow, Collapsing tubes, Fluid-Structure Interaction, Veins

NOMENCLATURE

d	$[m]$	inner diameter of the tube
p	$[Pa]$	pressure
p_0	$[Pa]$	pressure amplitude
T	$[s]$	period time
Re	[-]	Reynolds number
v_{max}	$[m/s]$	maximum velocity
μ	$[Pa\ s]$	dynamic viscosity
ν	$[m^2/s]$	kinematic viscosity
ρ	$[kg/m^3]$	density
$\underline{\omega}$	$[1/s]$	angular velocity

1. INTRODUCTION

1.1. Motivation

While in the arterial system continuous blood flow is guaranteed by the pressure difference generated by the heart, in the venous system the pressure difference driving the flow is established by other mechanisms. The periodically contracting and relaxing muscles that excite the venous vessel wall play a main role in the generation of venous blood flow (Monos [1]). This mechanism is in the focus of our investigation.

The muscle pump consists of the skeletal muscles and the arteries with strong elastic wall surrounding the thin-walled veins. When these muscles are used (e.g. during walking) and blood flows through the surrounding arteries they expand and make the veins collapse. Thus the blood is squeezed out of the vein section.

To avoid backflow the check valves (so called venous valves) guarantee that the blood flows in only one direction. Disease and inflammation can cause malfunction of the valves, therefore backflow may occur, which usually leads to varicose veins.

1.2. Overview of the literature

The role of the venous muscle pump is essential since in upright position the pressure difference generated by the heart is not sufficient to deliver blood back to the heart. The effect is called orthostatic intolerance according to Molnár et al. [2]. The authors state that the transmural pressure might reach 100 to 120 *mmHg* (approx. 13322 to 16000 *Pa*) in the ankles which can cause severe damage to the venous vessels. By moving the leg the muscle pump is activated and the transmural pressure is reduced to approx. 15 to 30 *mmHg* (approx. 2000 to 4000 *Pa*).

A measurement system for detecting muscle pump activity was developed by O'Donovan et al.

[3]. Two accelerometers with perpendicular alignment were used for this purpose. The measurement system was validated using electromyography (EMG). Literature and previous research work in the field of the venous muscle pump is limited. The muscle pump mechanism is based on the phenomenon of collapsible tubes. Knowlton and Starling [4] developed the so called Starling reservoir for investigating the behavior of collapsible tubes. The reservoir was further developed by Holt [5] and Conrad [6]. Conrad measured the pressure difference between the upstream and downstream ends of a collapsible tube while the outer pressure (and thus the transmural pressure) was held constant. The resulting pressure difference versus volumetric flow rate is fundamentally different than in case of a non-collapsible, rigid tube.

Measurements were carried out on collapsible tubes with variable outer pressure (Kamm and Shapiro [7], Jan et al. [8]), but these researches dealt mainly with analyzing the stability of the collapse.

The shape of collapsing tubes due to outer pressure was investigated by Kresch and Noordergraaf [9]. The authors set up a two-dimensional mathematical model for calculating the collapsed cross-shape of a tube section. Using this model they determine the cross section of the tube in case of negative transmural pressures.

Yang et al. [10] investigated a pulmonary arterial bifurcation using three-dimensional FSI simulations. Due to some diseases the transmural pressure can turn negative in these bifurcations, therefore the vessels collapse. The aim of the authors was to examine the effect of the collapse on the blood flow in the bifurcation. Deformation of the tube, velocity and pressure were calculated. The calculated results were compared with previously published data and the agreement was fairly good.

1.3. Aim of this study

The aim of the current study is the investigation of the venous muscle pump mechanism using three-dimensional fluid-structure interaction simulations. In the first step the venous valves are neglected, the main focus of the investigation is on the periodical collapse of the venous vessel. A simple straight tube geometry is set up, appropriate CFD and FEM meshes are created for the fluid and solid domains. The Ansys software package is used for the calculations - Ansys CFX and Ansys Mechanical respectively. A sinusoidal pressure waveform is defined as an outer boundary condition of the straight tube, which causes the tube to collapse periodically. The resulting pressure and velocity field inside the tube is examined.

2. THE MODEL

In the FSI analysis two models were defined which are coupled through a common boundary called fluid-solid interface.

The structure is a finite element model of a thin-walled tube consisting of shell elements. Using a linear material model the governing equation can be written as

$$\{\sigma\} = [D]\{\varepsilon^{el}\} \tag{1}$$

Where $\{\sigma\}$ is the stress vector, [D] is the elasticity or elastic stiffness matrix, $\{\varepsilon^{el}\}$ is the elastic strain vector.

Fixed node constraints were defined at the upstream and downstream ending edges, and an external time-dependent pressure load at the outer surface of the tube. The finite element model was created in ANSYS Mechanical APDL.

The fluid domain is the inner part of the tube. For the discretization a classical o-grid mesh was used. The mesh was created in ANSYS ICEM CFD. The governing equations are the continuity and the Navier-Stokes equations for incompressible flows neglecting body forces. In vector form these are the following

$$\nabla \cdot \underline{u} = 0 \tag{2}$$

$$\frac{D\underline{u}}{Dt} = -\frac{1}{\rho}\nabla \cdot p + \nu \cdot \nabla^2 \cdot \underline{u} \tag{3}$$

with $D/Dt = \partial/\partial t + \underline{u} \cdot \nabla$ the substantial derivative.

The preprocessing of the FSI calculation was performed with the preprocessor of ANSYS CFX.

The fluid-solid interface was the cylindrical surface where the structure and the fluid connect to each other. The FSI problem was solved using the ANSYS CFX Solver.

2.1. The geometry

The geometrical sizes of the model are in the range of larger veins. In order to avoid the perturbation of the constraints set at the upstream and downstream endings, a reasonably long tube was selected. Table 1 shows the main dimensions of the model.

Table 1. Dimensions

Dimension	Value [*mm*]
Inner diameter	3.5
Outer diameter	4.0
Length	50

2.2. The materials

According to Monos [1] the vein walls have viscoelastic properties. It means that the current state -e.g. stress-state- of the material depends on the previous states. Modelling this behaviour is challenging, therefore an elastic, isotropic linear material model was selected as the first approach of the problem. As a next step the usage of a viscoelastic material model will be considered. The parameters of the vessel wall are shown in Table 2.

Table 2. Parameters of the material model

Parameter	Value
Elasticity modulus	10^6 *Pa*
Poisson ratio	0.3

Blood is a non-Newtonian fluid, however this behavior plays important role only in small size range of veins (about 0.1 *mm* of diameter, Bojtár et al. [11]). The modeled venous section has a larger size, thus Newtonian fluid can be used for modeling blood. Therefore an incompressible fluid was selected with the density set to 1050 kg/m^3. The application of an incompressible fluid can easily lead to instabilities in the FSI calculations (Degroote et al. [12]). However during the current FSI calculations no instabilities occurred. It is still possible that in the future the method of artificial compressibility will have to be used.

2.3. Finite element model of the tube

As it was mentioned the finite element model consisted of shell elements. Shell elements are the simplest way to model a tube since we are not interested in the stress distribution inside the wall. The selected shell element type was SHELL 281, which has eight nodes with six degrees of freedom at each node. It is well-suited for both linear and nonlinear applications [13].

The mesh contained only quadrilateral elements. It was defined by two parameters: one is the element number on the circumference and the other the element number along the length.

Both ends of the tube were fixed, which means that all degrees of freedom were taken away.

The load was applied on two opposite quarters of the outer cylindrical area. It was the absolute value of a sinusoidal time-dependent pressure. The function is the following:

$$p(t) = abs(p_0 \cdot \sin(\omega \cdot t)) \qquad (4)$$

One period is defined as the range which starts at $i\pi/\omega$ *[s]* and ends at $(i+1)\pi/\omega$ *[s]*, where *i* is a positive integer. The amplitude was 800 *Pa* (approx. 6 *mmHg*) in all cases. This is an empirical value, which causes the appropriate collapse of the tube while the fluid mesh does not suffer excessive deformations. The frequency of the excitation was varied.

There are basically four ways to carry out an analysis in Mechanical APDL. We can take into account nonlinearities or not, and the calculation can be quasi-static or transient. These can be combined which means the four types of investigation. These were compared to each other in the following way. In case of a given tube with fixed pressure amplitude (800 *Pa*) and fixed load frequency (the angular velocity of the load $\omega = 10$ *1/s*) all of four modes were used. The maximum displacement was always calculated at T/4 time. The results are shown briefly in Table 3.

Table 3. Four modes of investigation

Maximum displacement [mm]	Linear calculation	Nonlinear calculation
Quasi-static calculation	0.768	1.628
Transient calculation	0.768	1.628

It can be seen that there is significant difference between the linear and nonlinear calculations. Furthermore in aspect of the results there is no difference between the transient and quasi-static calculations. Both of the statements agreed with our preliminary expectations. However, it is important to mention that quasi-static and transient calculations show differences during the simulations. These differences do not have an important role in case of pure finite element analysis, but they will have in the FSI analysis. It means that in case of transient case the time dependence causes oscillations during the calculation. These oscillations are not problem in pure finite element analysis, these have no significant effect to the result. However, in case of FSI calculations these oscillations are usually amplified and the simulation becomes instable.

A mesh-dependence investigation was carried out as well. The element number on the circumference was varied from 40 pcs to 100 pcs. The element number on the length was determined by the fact that the elements should be approximately square shaped. During the investigation the pressure amplitude and the frequency of the load were fixed as in case of the previous investigation. For comparison the maximum displacement was always calculated at a given time (0.15 *s*). The investigation was carried out for both the linear and nonlinear model. Analyzing the results showed that the solution is independent from the element number. Hence the case of the minimal element number was applied in the FSI simulations.

2.4. CFD and FSI model

As it was mentioned above the fluid was discretized using a structured o-grid mesh. Our

mesh, which was used for the calculation, is a coarse one with 93843 elements. The o-grid mesh is built up from the followings: the square in the middle of the o-grid consists of 10x10 elements, in the direction of the radius from the middle square to the edge of the domain there are 15 elements refined close to the edge and the length is divided to 150 elements. This grid is the result of a mesh independence test, when this mesh was compared to a finer one which consists of 304608 elements. The test showed that the selected pressure and total mesh displacement values differ from each other within 2%. The mesh was created and generated in ICEM CFD and it is shown in Figure 1.

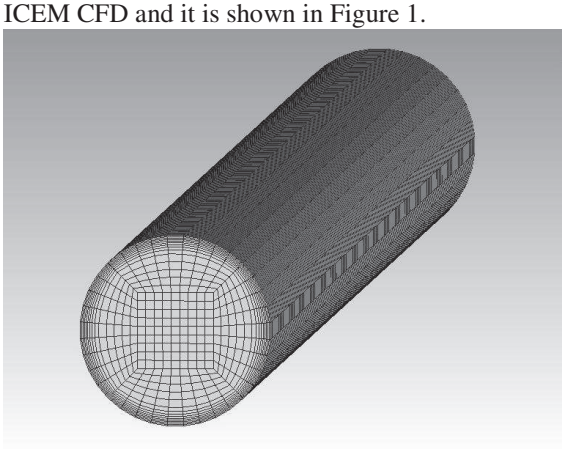

Figure 1. O-grid mesh of the fluid domain

During the first simulations the upstream and downstream surfaces were set to "Opening" boundary conditions, which means that the fluid can flow in both directions. The static pressure was set to zero at both endings. The third surface, the cylinder was defined as the fluid-solid interface with the specification that it gets the total mesh displacement information from the structural solver. Furthermore the wall-law was applied.

The flow is assumed to be laminar. The advection scheme was 'High resolution", the transient scheme was "Second order backward Euler". The convergence was defined by the maximum and minimum number of coefficient iteration and the convergence criteria. These parameters were the same in case of all simulations.

Table 4. Convergence properties

Maximum no. of iteration	10
Minimum no. of iteration	1
Convergence criteria	1e-5

Coupling and monitoring the solution was performed by the CFX-Solver Manager. The simulation time and the timestep were defined in the structural part. The solver got these data from the structural domain. Adaptive time stepping was not applied. The timestep size was selected to meet the CFL criterion. However during the simulations the timestep had to be varied - the cause of this is discussed below.

Furthermore the number of iterations in every timestep between the FE and CFD models was defined as it is shown in Table 5.

Table 5. Parameters of stagger iterations

Maximum no. of iteration	10
Minimum no. of iteration	1
Target number of iteration	5

3. RESULTS

As it was mentioned before, laminar flow was assumed inside the venous vessel. The evaluation of the results started with the calculation of the Reynolds number to strengthen or confute this assumption. With the maximum velocity of all the calculations, the main diameter of the tube and the properties of the water at $25°C$ the Reynolds number is around 985. The value is under the critical value of 2300, however this criterion is only valid for steady flow. Since the phenomenon is unsteady, turbulent regions might occur but in the current calculations this is neglected.

The detailed result is the case when excitation frequency was 2 *Hz*. This value comes from the fact that the frequency of the heart is between 1 and 2 *Hz* depending on the activity of the body. Furthermore as it was mentioned the pressure excitation of the veins is partly caused by the arteries which pulsate due to the periodical contraction of the heart. This excitation therefore has the same frequency as the heart. In the first calculation the simulation time was 0.5 *s*, the timestep 0.005 *s*.

The most important result of the calculations is the transport diagram which contains the volumetric or mass flow rate as a function of time. This shows whether the results of the FSI simulations are qualitatively appropriate. Furthermore these diagrams can show whether there exists a phase shift or if the excitation frequency is the same as the frequency of the outflow. In the transport diagram the outflow is indicated as negative values because the evaluation takes the normal direction of the surface into account.

Figure 2 shows the transport diagram of the case described above. The dashed curve is the exciting pressure acting on the tube wall. The continuous curve is the volume flow rate at the outlet.

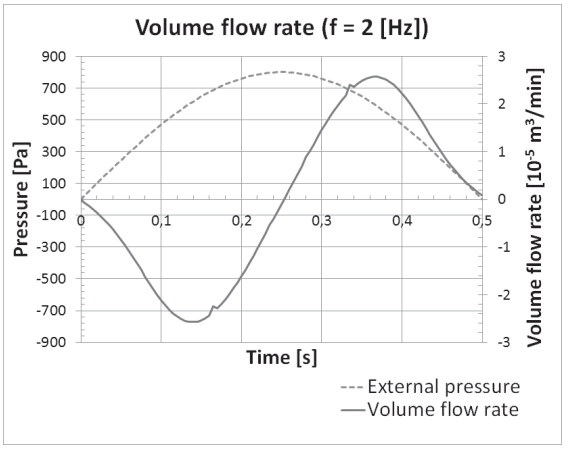

Figure 2. Flow rate versus time (dt = 0.005 *s*)

The shape of the volumetric flow rate curve matches the expectations: there is a sinusoid outflow while the tube is compressed and then there is a sinusoid inflow while the tube expands. It can be seen that there is no phase shift. The period of the load is considered according to (1). The period of the volume flow rate starts when fluid starts flowing out of the vessel, and it ends when the inflow stops. The frequencies of the load and the volume flow rate are the same.

Furthermore there are two small irregularities along the curve of the volume flow rate. These appeared in all cases of calculations and they seemed to be unavoidable. However, if the timestep was larger the irregularities were reduced. That is the explanation why the timestep of 5e-3 *s* was applied, in spite of the fact that the calculated one (according to the CFL criterion) is 7e-4 *s*. In case of smaller timesteps the irregularities showed up as an oscillation. Figure 3 shows the same simulation with timestep of 2e-3 *s*.

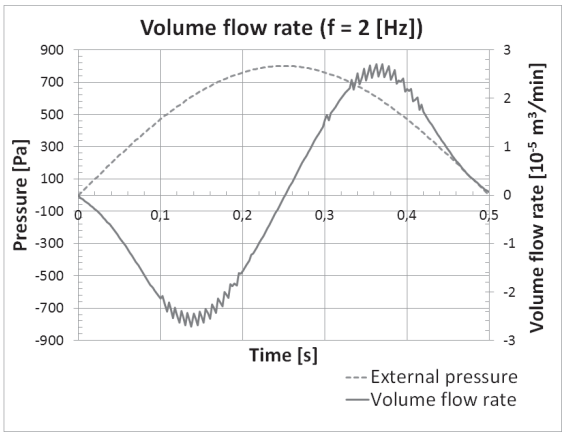

Figure 3. Flow rate versus time (dt = 0.002 *s*)

It can be seen that the same transport diagram has been calculated in which a strong oscillation has appeared. This oscillation can be smoothed with a smoothing algorithm (e.g. with the Gaussian window) to get back the transport diagram. Instead of applying an algorithm like this, the larger timestep (dt = 0.005 *s*) was applied.

The pressure distribution along the tube is theoretically very simple: in the first half of a period there is an increasing pressure in the middle of the tube caused by the increasing external pressure acting on the tube wall. The increasing pressure causes the water to flow out. In the second half the tube is expanding, hence there is a suction effect causing the water to flow inside the tube. In the calculation an important difference appears. Figure 4 shows the pressure distribution at 0.17 *s*. which is we expected.

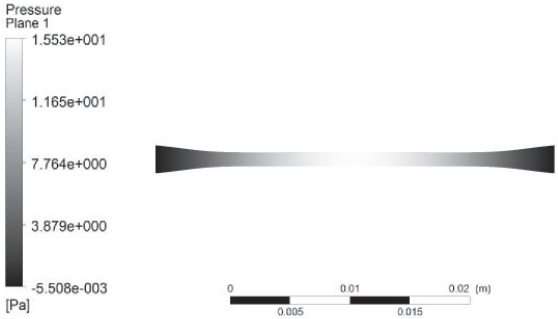

Figure 4. Pressure distribution at 0.17 *s*

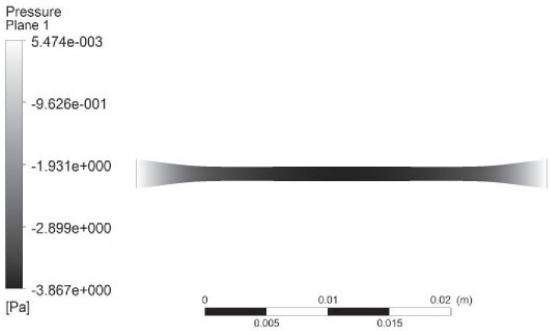

Figure 5. Pressure distribution at 0.175 *s*

However, Figure 5 shows the pressure distribution at 0.175 *s*. It can be seen that the pressure in the middle of the tube is less than at the upstream and downstream ends. Furthermore this pressure distribution remains like this while the calculation reaches the half of the whole period (0.25 *s*). It can be assumed that this phenomenon is caused by the inertia of the fluid. The fluid is accelerated in the first quarter of the period, while during the second quarter it is decelerated. Thus it can happen that the accelerated fluid causes a suction effect in the middle of the tube during the second quarter of the period due to its inertia. The same phenomenon

appears between the third and fourth quarter where the accelerated fluid causes an overpressure in the middle of the tube.

The simulation shows that velocity distribution creates also an interesting and important phenomenon during the period. Because of the fixed ends of the tube a diffusor is formed from a given point of the simulation. The shape of the "diffusor" is non-ideal, therefore a separation zone shows up. The presence of the separation zone means a recirculation near to the wall. Figure 6 shows the surface stream lines at the mid-plane of the half-tube.

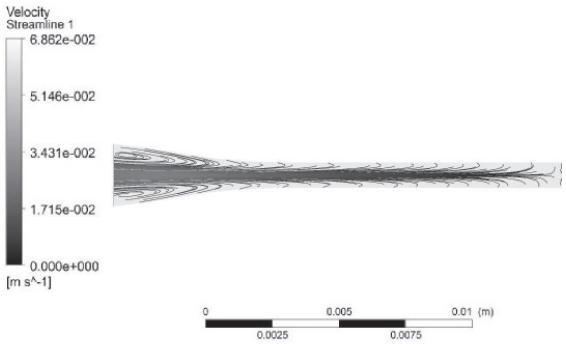

Figure 6. Separation zone

The frequency dependence of the flow was also investigated for three cases. The cases differ from each other in the frequency of the excitation. The angular velocities of the excitations were the following: 10, 20, 30 *1/s*. The corresponding transport diagrams are shown in Figure 7, 8, 9. The coupled time step was 0.002 *s* in every calculation.

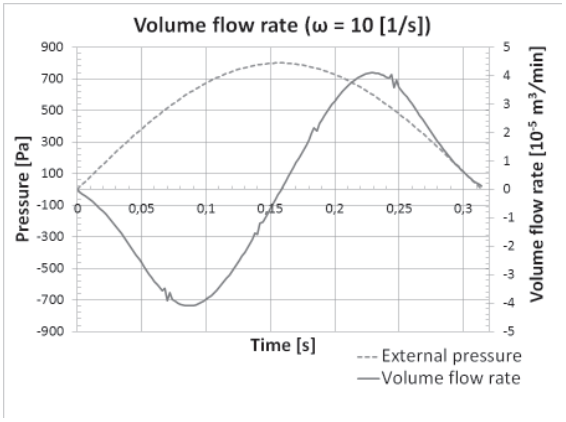

Figure 7. Transport diagram (ω=10 *1/s*)

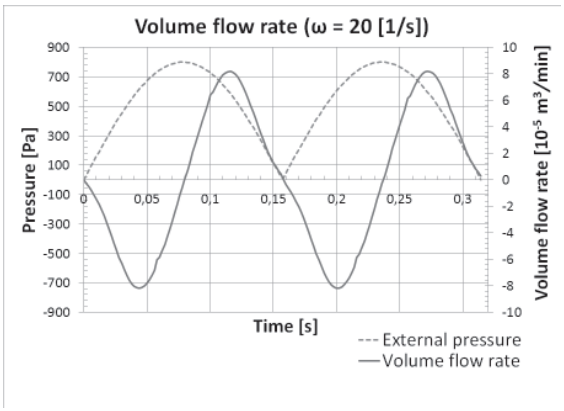

Figure 8. Transport diagram (ω=20 *1/s*)

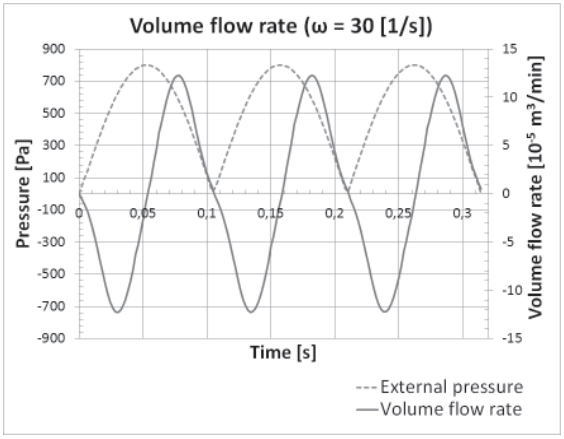

Figure 9. Transport diagram (ω=30 *1/s*)

It can be seen in the figures that the volume flow rate has the same frequency as the excitation in every case. There is no phase shift between the excitation and the outflow signal.

However, the irregularities mentioned above showed up again along the volumetric flow rate curves, especially in the case of ω = 10 *1/s* (in Fig. 7). At the same time it can be seen that in the case of ω = 20 *1/s* (in Fig. 8) the irregularities are less sharp, and in case of ω = 30 *1/s* (in Fig. 9) the irregularities simply disappear. This fact strengthens the statement that the larger timestep means less irregularities. To avoid confusions it should be repeated that the timestep was the same in every case, but the excitation frequency changed. It occurred that the number of timesteps contained in one period was less in case of higher frequencies.

A possible reason for these irregularities and oscillations detailed above is the phenomenon of the collapse. It means that there is a moment where the tube loses its stability and it is starting to collapse. If a large timestep is applied the solver goes through this problematic region more easily. This way it can happen that none of the irregularities show up at all in the transport diagram. See Fig 9. If a small timestep is applied, the solver has several timesteps to calculate in this region thus it can happen that an

oscillation starts as Fig. 3 shows. Between these two timestep sizes it can happen that the critical points appear, but the oscillation cannot start. This is the case of ω = 10 *1/s* shown in Fig. 9.

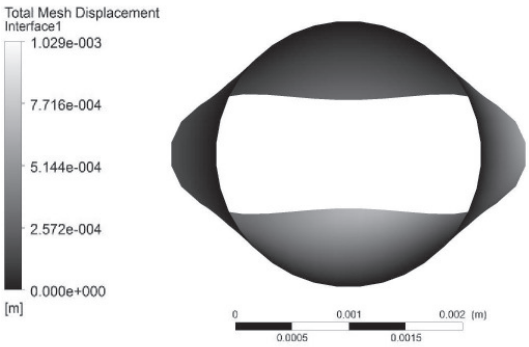

Figure 10. Deformation at maximum outer pressure

The amplitudes of the displacement are the same in all of the three cases, which is 1.028e-3 *m*. Obviously, the amplitudes of the volume flow rate are not the same, because the higher frequency means the shorter period time, hence the lower volume flow rate value. Figure 10 shows the deformed vessel section.

5. SUMMARY

In the current work the mechanism of the venous muscle pump was investigated using FSI methods. As a first step the effect of the venous valves was neglected, therefore a periodical flow with changing directions was expected inside the vessel. A simple straight tube geometry was created for the FSI analysis. A sinusoidal pressure excitation was applied to the outer surface of the tube. As a result the vessel section collapsed periodically. The resulting volumetric flow rate versus time diagrams were plotted and analyzed. The frequency of the excitation was changed stepwise and the resulting changes in volumetric flow rate were investigated. Pressure distribution and streamlines inside the vessel are presented.

In the future the most important development is the modeling the vein valves. There are two methods which can be followed. One is to choose an appropriate boundary condition at the beginning and at the end of the tube. It is the simplest way, but it can cause problems and instability in the calculation. The other way is to model geometrically the valves and carrying out another complete FSI simulation for them. If it is works the model of the tube and the valves can be connected. The latter is the most complicated solution, however, the geometry of the valves can be taken into account, which in fact has great advantages.

The other possibility to improve the model is applying a viscoelastic material model. There are some built-in material models in the ANSYS Mechanical APDL (e.g. Mooney-Rivlin model). These calculations probably will be able to show the importance of the viscoelastic effects in this size and load range.

ACKNOWLEDGEMENTS

This work is connected to the scientific program of the " Development of quality-oriented and harmonized R+D+I strategy and functional model at BME" project. This project is supported by the New Széchenyi Plan (Project ID: TÁMOP-4.2.1/B-09/1/KMR-2010-0002).

REFERENCES

[1] Monos, E, 1999, *Physiology of the venous system (in Hungarian)*, Semmelweis University, Centre of Training Research and Documentary

[2] Molnár, AÁ, Apor, A, Kiss, RG, Préda, I Monos, E, Bérczi, V and Nádasy, GL, 2008, "New results in the research of the venous system", *Weekly Medical Paper (in Hungarian),* Vol. 149, pp. 1801-1809.

[3] O'Donovan, KJ, O'Keeffe, DT, Grace, PA and Lyons, GM, 2005, "Accelerometer based calf muscle pump activity monitoring" *Medical Engineering & Physics,* Vol. 27(8), pp. 717-722.

[4] Knowlton, FP and Starling, EH, 1912, "The influence of variations in temperature and blood pressure on the performance of the isolated mammalian heart" *Journal of Physiology*, Vol. 44(3), pp. 206-219.

[5] Holt, JP, 1969, "Flow through collapsible tubes and through in situ veins", *IEEE Transactions on Biomedical Engineering,* Vol. 16(4), pp. 274-283.

[6] Conrad, WA, 1969, "Pressure-Flow Relationships in Collapsible Tube" *IEEE Transactions on Biomedical Engineering*, Vol. 16(4), pp. 284-295.

[7] Kamm, RD and Shapiro, AH, 1979, "Unsteady flow in a collapsible tube subjected to external pressure or body forces", *Journal of Fluid Mechanics,* Vol. 95, pp. 1-78.

[8] Jan, DL, Kamm, RD and Shapiro, AH, 1983, "Filling of partially collapsed compliant tubes", *Journal of Biomechanical Engineering,* Vol. 105, pp. 12-19.

[9] Kresch, E and Noordergraaf, A, 1972, "Cross-Sectional Shape of Collapsible Tubes" *Biophysical Journal,* Vol. 12(3), pp. 274-294.

[10] Yang, XL, Liu, Y and Yang, JM, 2007, “Fluid-structure interaction in a pulmonary arterial bifurcation” *Journal of Biomechanics,* Vol. 40, pp. 2694–2699.

[11] Bojtár, I, Pál, Gy, Tóth, B and Nasztanovics, F, 2007, *Numerical modeling of the vessel walls*, in *Gábor Halász: Modeling in biomechanics (in Hungarian),* Műegyetem Kiadó, pp. 179-228

[12] Degroote, J, Swillens, A, Bruggeman, P, Haelterman, R, Segers, P and Vierendeels, J, 2010, “Simulation of Fluid-structure interaction with the interface artificial compressibility method”, *International Journal for Numerical Methods in Biomedical Engineering* , Vol. 26(3-4), pp. 276-289.

[13] ANSYS Help 14. (Element Reference // I. Element Library // SHELL281)

Conference on Modelling Fluid Flow (CMFF'12)
The 15th International Conference on Fluid Flow Technologies
Budapest, Hungary, September 4-7, 2012

ON STREAMWISE STREAK GENERATION BY OBLIQUE WAVES IN A BENT CHANNEL

Donghun Park[1], Seung O Park[2]

[1] Department of Aerospace Engineering, KAIST, Daejeon, 305-701, Korea. E-mail: donghunpark7043@gmail.com
[2] Corresponding Author. Department of Aerospace Engineering, KAIST, Daejeon, 305-701, Korea. Tel.: +82 42 350 3713, Fax: +82 42 350 3710, E-mail: sopark@kaist.ac.kr

ABSTRACT

Generation and evolution of streamwise vortices and streaks in a bent channel are investigated by using Nonlinear Parabolized Stability Equations (NPSE). Mean flow for NPSE is obtained from the Navier-Stokes solution. A pair of oblique waves from linear stability analysis forms the initial disturbance. The pair of finite amplitude oblique waves acts to readily generate streamwise vortices and streamwise streaks by nonlinear mechanism. When the initial amplitude of the wave is not too high, the oblique wave decay exponentially exhibiting linear stability behavior while the streaks are nonlinearly generated and amplified. The streaks are eventually saturated and then decay very slowly with downstream distance. The amplitudes of various modes, instantaneous and stationary velocity and vorticity contours are examined. Effect of bent on the development characteristics of streaks is assessed. Parametric studies are also carried out to examine the effects of Reynolds number, radius of curvature, and bent angle.

Keywords : channel flow, bent channel, nonlinear parabolized stability equations, oblique transition, streamwise streaks

1. INTRODUCTION

The stability and transition in channel flows have been studied for a long time due to its practical importance. A number of experimental, theoretical, and numerical studies have been carried out. Although validity of linear stability theory (LST) for the evolution of two-dimensional disturbances in plane Poiseulle flow was confirmed by experimental study [1], many transition experiments found that the flow undergoes transition at a much lower Reynolds number than the critical Reynolds number predicted by LST (R_c=5770). Several transition scenarios were proposed to explain the transition at subcritical Reynolds numbers. Secondary instability theory [2] in conjunction with 2-D equilibrium state initiated by a finite-amplitude Tollmien-Schlichting (T-S) wave yielded better results that were in good agreement with observations from experiments in which T-S wave was introduced via vibrating ribbon. However, it can hardly predict well the natural transition in plane Poiseulle flow. Reddy et al. [3] examined the threshold energy required for transition for T-S wave, two-dimensional optimal (2DOPT), streamwise vortex (SV) and oblique wave (OW) scenarios. They found that SV and OW scenario showed much lower threshold energy than the other scenarios.

Transition initiated by a pair of oblique waves, hereinafter referred to as oblique transition, has received considerable research attention as a possible transition scenario after the first suggestion of Schmid and Henningson [4]. This transition scenario has been studied for subsonic [5] and supersonic boundary layers [6,7]. The oblique transition in a supersonic boundary layer gained much attention since oblique wave was found to be most unstable in supersonic boundary layers from LST. As already mentioned, oblique transition has been emerged as the most probable transition scenario in channel flows [3]. The oblique transition in plane Poiseulle flow was studied by many authors [4,8,9]. A typical process of oblique transition from previous studies is as follows. Streamwise vortices are first generated from a pair of oblique waves. The streamwise vortices are then developed into streamwise streaks. Secondary instability of the streamwise streak eventually leads to breakdown to turbulence.

Most of the previous studies on the stability and transition on a channel flow have dealt with two flow configurations: plane channel and curved channel. It is well known that concave curvature sustains the amplification of longitudinal vortices. The longitudinal vortices due to curvature are

named as Görtler vortices and Dean vortices for boundary layer and curved channel flows, respectively. The Dean vortices and its secondary instability are known to be typical characteristics of stability and transition in a curved channel [10,11].

To the author's knowledge, there is few studies on stability in a channel flow where the plane channel and the curved channel are combined. A bent channel is one of the simplest flow configuration of such flows. We thus intend to investigate generation and growth characteristics of streamwise streaks and streamwise vortices initiated by a pair of oblique waves in a bent channel in this study within the framework of non-linear parabolized stability equations (PSE). The laminar mean flow for non-linear PSE analysis is obtained by solving the Navier-Stokes equation. A pair of oblique waves obtained by linear stability analysis is prescribed as the initial condition. Non-linear PSE analysis is carried out to investigate the downstream evolution of stationary as well as non-stationary modes. The amplitudes of various modes, instantaneous and stationary velocity and vorticity contours are examined. The effect of bent on the development of streaks and vortices is assessed by comparison with the results for plane channel. Influence of the bent geometry on the streamwise vortices and streaks is studied through analyses for several parameter ranges.

2. METHOD OF ANALYSIS

2.1. Definition and Geometry

The geometry of the bent channel together with the coordinate system of the present study is schematically shown in Fig. 1. The bent channel consists of two straight sections and a curved section which connects them. U_0 and h represent respectively the centerline velocity of incoming Poiseulle flow for straight section and channel half width, which are used as the reference velocity and the reference length. Reynolds number, Re, is defined by U_0h/v. The origin of the general coordinate system, (x_1, x_2, x_3), is the center of the channel at the junction between the first straight and the curved section as shown in Fig. 1. The x_1 coordinate measures the distance along the centerline of the channel, and x_2 and x_3 are the normal and the spanwise coordinate, respectively. All velocities and coordinates are non-dimensionalized by reference values (U_0 and h).

Dean number, frequently used in curved channel flow, is defined as $De=U_{avg}d/v\times(d/r_i)^{1/2}$ where d is the channel width(=$2h$), r_i the inner radius(=r-h), and U_{avg} is the average velocity across the channel width. As is well known, U_{avg} is equal to $2/3U_0$. Then Dean number can be expressed as $De=4/3Re\times\{2h/(r-h)\}^{1/2}$. A non-dimensional measure of the channel curvature is the radius ratio given by $\eta=r_i/r_o=(r-h)/(r+h)$.

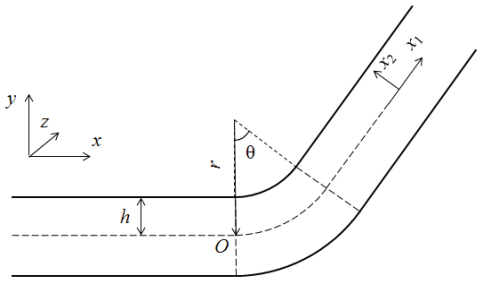

Figure 1. Geometry and coordinate system

2.2. Parabolized Stability Equations

In this study, non-linear parabolized stability equation (PSE) is used to calculate the generation and development of the streamwise vortices and streaks via non-linear evolution of the instability waves. In contrast to the linear stability theory (LST)[12], the PSE can deal with both linear and non-linear stability, can take into account of flow non-parallelism, and is also computationally more efficient than LST. Its validity has been proved by a number of studies on many stability problems. The details of PSE formulations and numerical methods can be found in many references [13,14]. We briefly summarize here the PSE formulation of the present study. The flow variables, viscosity, and conductivity in the non-dimensional governing equations are decomposed into a mean quantity and small disturbance. The disturbance equations in generalized coordinate system can be expressed as

$$\begin{aligned}&\bar{\Gamma}\frac{\partial\phi}{\partial t}+\bar{A}\frac{\partial\phi}{\partial x_1}+\bar{B}\frac{\partial\phi}{\partial x_2}+\bar{C}\frac{\partial\phi}{\partial x_3}+\bar{D}\phi\\&=\bar{V}_{11}\frac{\partial^2\phi}{\partial x_1^{\,2}}+\bar{V}_{22}\frac{\partial^2\phi}{\partial x_2^{\,2}}+\bar{V}_{33}\frac{\partial^2\phi}{\partial x_3^{\,2}}\\&+\bar{V}_{12}\frac{\partial^2\phi}{\partial x_1\partial x_2}+\bar{V}_{23}\frac{\partial^2\phi}{\partial x_2\partial x_3}+\bar{V}_{31}\frac{\partial^2\phi}{\partial x_3\partial x_1}+F^n\end{aligned}\qquad(1)$$

where $\varphi=(p',u',v',w',T')^T$. Matrices with over-bar in Eq. (1) are of size 5×5 whose elements correspond to linear part of the disturbance equations that are composed of mean flow data and fluid properties. F^n represents all the non-linear terms. For the mean flow which is independent of x_3 coordinate, the disturbance φ is assumed to be the sum of finite number of Fourier modes which are periodic in space and time as given below

$$\begin{aligned}&\phi(x_1,x_2,x_3,t)\\&=\sum_{m=-M}^{M}\sum_{n=-N}^{N}\left\{\begin{aligned}&\psi_{mn}(x_1,x_2)\exp\left[i\int_{x_{1,0}}^{x_1}\alpha_{mn}(\bar{x}_1)d\bar{x}_1\right]\\&\exp\left[i(n\beta x_3-m\omega t)\right]\end{aligned}\right\}\end{aligned}\qquad(2)$$

Here, β and ω are fundamental spanwise wave number and fundamental frequency, respectively. The subscripts m and n represent the temporal and spanwise mode number, respectively. The variable α_{mn} is the streamwise wave number for mode (m, n).

Since the spatial stability is considered, α_{mn} are complex numbers while β and ω are real. The shape function, $\psi_{mn}=(\ \hat{p}_{mn}\ ,\ \hat{u}_{mn}\ ,\ \hat{v}_{mn}\ ,\ \hat{w}_{mn}\ ,\ \hat{T}_{mn}\ )^T$, represents complex amplitude for mode (m, n). Eq. (2) is substituted into Eq. (1) and terms corresponding to the same exponent are collected to obtain the equations for ψ_{mn}. The decomposition of α_{mn} and ψ_{mm} in Eq. (2) is assumed to behave such that the change of shape function along the streamwise direction x_1 is of order $1/R_0$. Neglecting the terms of $O(1/R_0^2)$ and smaller, we get the PSE in the following form.

$$\hat{D}_{mn}\psi_{mn}+\hat{A}_{mn}\frac{\partial\psi_{mn}}{\partial x_1}+\hat{B}_{mn}\frac{\partial\psi_{mn}}{\partial x_2}=\hat{V}_{22,mn}\frac{\partial^2\psi_{mn}}{\partial x_2^{\,2}}+\frac{F_{mn}}{\mathrm{A}_{mn}}$$

where

$$\begin{aligned}\hat{D}_{mn}&=-i\omega\overline{\Gamma}+i\alpha_{mn}\overline{A}+in\beta\overline{C}+\overline{D}+\alpha_{mn}{}^2\overline{V}_{11}\\&\quad+n^2\beta^2\overline{V}_{33}+n\alpha_{mn}\beta\overline{V}_{31}-i\frac{d\alpha_{mn}}{dx_1}\overline{V}_{11}\\\hat{A}_{mn}&=\overline{A}-i2\alpha_{mn}\overline{V}_{11}-in\beta\overline{V}_{31}\\\hat{B}_{mn}&=\overline{B}-i\alpha_{mn}\overline{V}_{12}-in\beta\overline{V}_{23}\\\hat{V}_{22,mn}&=\overline{V}_{22}\qquad\mathrm{A}_{mn}=\exp\left[i\int_{x_{1,0}}^{x_1}\alpha_{mn}(\bar{x}_1)d\bar{x}_1\right]\end{aligned}\tag{3}$$

The nonlinear term is treated explicitly and in pseudo-spectral manner. F_{mn} represents the Fourier components of non-linear term F^n. Eq. (3) is subjected to the boundary conditions that the velocity and temperature disturbances vanish at the solid surface.

To deal with the ambiguity on the decomposition of streamwise wavenumber α_{mn} and shape function ψ_{mm} in Eq. (2), an additional condition, known as the normalization condition, is imposed to determine the unique combination of α_{mn} and ψ_{mn} which satisfy the basic assumptions of PSE. For this, marching procedure of PSE involves an iteration procedure to update α at each streamwise location. In this study, α is updated based on integrated disturbance kinetic energy as can be found in many references [14].

To initiate the marching procedure, initial condition which satisfies locally the stability equation is needed. The initial condition is obtained from LST. Since the spatial stability is concerned in the present study, the nonlinear eigenvalue problem is formulated and is solved as described in [15].

To solve Eq. (3), fourth-order central differencing scheme is used for all the derivatives except for the streamwise derivative of shape function for which second order backward difference scheme is adopted. To take care of the numerical instability in the marching procedure caused by the weak ellipticity of PSE, we follow Chang and Malik [6] and Chang [14] which suppress the term corresponding to the streamwise derivative of pressure shape function, i.e., $\partial\hat{p}/\partial x_1$ by weighting the factor in terms of local Mach number. The non-linear terms are simply treated as source term. At each iteration, the nonlinear term F^n is evaluated in the physical space and is then transformed back into spectral domain by using two dimensional FFT to extract F_{mn}. To avoid aliasing in the FFT results, the domain size is enlarged by larger than twice the number of mode of interest. For the mean flow which is uniform in spanwise direction, the mode symmetry condition can be derived from mathematical characteristics of PSE. The application of mode symmetry condition reduces the computational cost and required memory since only a quarter of the modes are needed to be kept and analyzed ($M\geq 0$, $N\geq 0$).

In this study, the mean flow data in the bent channel is obtained by solving the Navier-Stokes equations. Inflow for plane channel section is given by plane Poiseulle flow. The convective terms are discretized by the second-order upwind scheme while all the other terms are centrally differenced. The streamwise locations of inflow and outflow boundary are set to be at least 25h and 60h away from the upstream and downstream end of the curved section, respectively. In most of the calculations of this study, 201 grid points are equally distributed in the x_2-direction. The streamwise step size is usually taken to be $\Delta x_1=0.05h$. For outflow boundary condition, vanishing of the secondary derivatives is adopted.

3. RESULTS AND DISCUSSIONS

The non-linear evolution of a pair of oblique waves in a bent channel is analyzed by non-linear PSE analysis. The oblique wave in a plane Poiseulle flow obtained from LST is prescribed as initial condition in the first straight section of the bent channel. Among infinite number of discrete eigenvalues from LST for Poiseulle flow, it is known that there are several modes of interest as described in Zang and Krist [16]. In the present study, the eigenvalue corresponding to typical Tollmien-Schlichting (T-S) wave that is unstable for higher Reynolds numbers ($Re>Re_c$) is chosen as the initial condition. Zang and Krist [16] named this eigenvalue as the anti-symmetric wall Orr-Sommerfeld (O-S) mode. Figure 2 shows typical eigenfunction profiles. The eigenfunction of Fig. 2 corresponds to an oblique wave with β=1, F=0.3852, and Re=2000. The non-dimensional frequency is defined by $F=2\pi fh/U_0$. For this β and Re, the frequency of F=0.3852 results in the eigenvalue, α=1.00029+0.05715i, which represents an oblique wave with oblique angle of 45 degrees. The profiles of Fig. 2 are those non-dimensionalized by maximum value of streamwise velocity component. The maximum amplitude of streamwise velocity component is seen to occur at a position close to the

wall ($x_2 \approx \pm 0.74$). The real and imaginary parts of the eigenfunction corresponding to streamwise velocity are shown in Fig. 2b. We see from Fig. 2b that the eigenfunction is anti-symmetric with respect to the centerline signifying that upper and lower sides of the channel are out of phase.

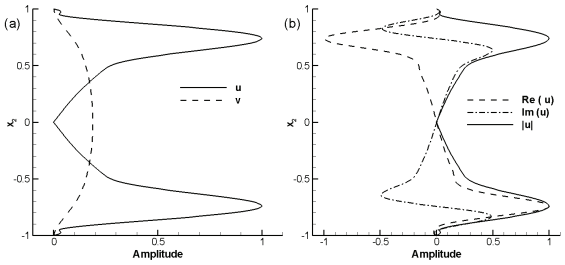

Figure 2. Profiles of eigenfunction for an oblique wave in plane Poiseulle flow

We first consider the case of a bent channel with Re=2000, r/h=40, and θ=30 degrees. The Dean number for the curved section is De=603.88 which is much higher than the critical Dean number, De_c of 35.92. The curved section extends from x_1=0 to x_1=20.94. A pair of oblique waves with F=0.3852 and β=±1 (Fig. 2) is imposed at x_1=-30 with the maximum rms amplitude of A_0=1%. Figure 3 shows the evolution of maximum amplitude of streamwise velocity for several modes. The present results for a plane Poiseulle flow are shown together. The results for plane channel are found to be in good qualitative agreement with those from previous studies of oblique transition [5,16]. The vertical dashed lines indicate the start and end location of the curved section. Within the framework of LST, the fundamental mode [(1,1)] would decay continuously with downstream distance since the Reynolds number is much smaller than the critical Reynolds number. We confirm this from Fig. 3. We also see that the decaying behavior of the fundamental mode for the bent channel deviates a little from that of LST for plane channel beyond the entrance region of the curved section.

The mode (0,2) represent the stationary mode whose spanwise wave length is the half of that of the fundamental mode. As well known from previous studies of boundary layer and plane channel, this mode corresponds to the streamwise vortices and streamwise streaks. For both the plane and the bent channel cases, we see from Fig. 3 that this mode is highly amplified while the fundamental mode decays. We note here that, in the straight section, the fundamental mode follows LST behavior while the (0,2) mode is generated via non-linear interaction of the fundamental modes. The amplitude of this mode overtakes that of the fundamental mode and becomes the mode of the highest amplitude. The amplitude of (0,2) mode starts to deviate from that of the plane channel case as it enters the curved section. It obtains much higher amplitude passing the curved section. Beyond the bent region, the amplitude saturates and decays very slowly. The saturated amplitude of (0,2) mode is around 20% while only 0.8% is reached for the case of plane channel. This implies that the curved section induces additional amplification of (0,2) mode. In addition to (0,2) mode, all the stationary modes such as mean flow distortion(MFD) [(0,0)] and (0,4) modes are also highly amplified due to the existence of the curved section.

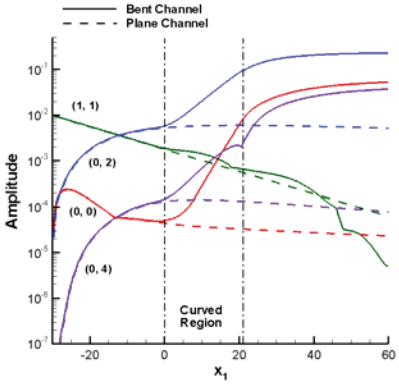

Figure 3. Variation of maximum amplitude velocity component for several modes

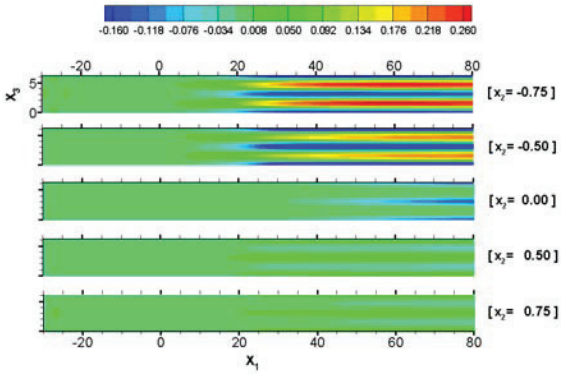

Figure 4. Contours of instantaneous streamwise velocity due to disturbances in x_1-x_3 plane

The contours of instantaneous streamwise velocity from all the disturbances are shown in Fig. 4 at several constant x_2-planes. Since mean flow is not included, the velocity contours in Fig. 4 represent the deviation from the mean flow. The x_3 coordinate of the figure covers one spanwise wave length λ which is 2π since β =1. The x_3-coordinate elongated much for better illustration in the figure. We clearly see that streaky structure is formed by disturbances and becomes apparent as proceed downstream. The streaky structure is established earlier and reaches much higher amplitude in the lower half region ($-1<x_2<0$). The lower half region is concave surface region. This structure can be observed also from the contours for cross-section plane (x_2-x_3 plane) at several streamwise locations

as shown in Fig. 5. We see again that the streaky structure is much pronounced at the side of concave surface. Compared to the results from the case of plane channel, the formation and amplification of the streaky structure is strengthened very much by the bent region.

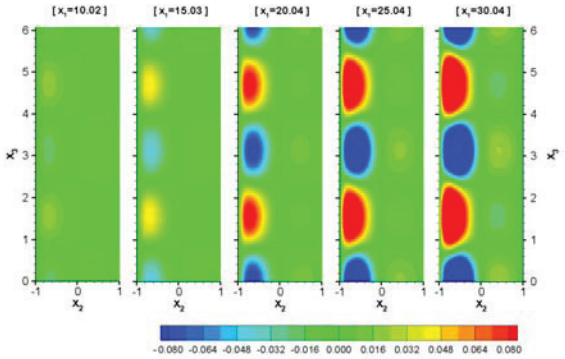

Figure 5. Contours of instantaneous streamwise velocity due to disturbances in x_2-x_3 plane

From Figs. 4 and 5, we see that the streaky structure contains two positive and two negative velocity regions appearing alternatively within one spanwise wave length of the fundamental mode. We have confirmed that contours of the stationary modes (time-independent) alone almost coincide with the contours of Figs. 4 and 5 where all the stationary and non-stationary modes are included. This implies that the stationary modes dominate the streaky structure and amplitudes of the non-stationary modes are relatively small. These two observations suggest that the streaky structure is a typical characteristic of (0,2) mode. This agrees with the dominance of (0,2) mode as shown in Fig. 3.

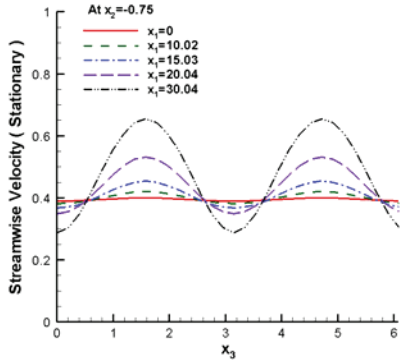

Figure 6. Profiles of total stationary streamwise velocity at x_2=-0.75

We expect that the mean flow modified by disturbances would exhibit regions of fast and slow streamwise velocity which appear periodically in spanwise direction. This will form a well-known structure named as streamwise streaks. Total stationary streamwise velocity which is the summation of the mean flow and all the stationary modes is evaluated. The profiles of stationary streamwise velocity at x_2=-0.75 for several streamwise locations are plotted in Fig. 6. We clearly see the formation and amplification of streamwise streaks which is much enhanced in the concave side. The streamwise streaks become apparent over the curved region and continuously strengthened with downstream distance in the region of straight section.

Figure 7 shows contours of streamwise vorticity due to the stationary modes at several streamwise locations. We readily see that the strong counter-rotating streamwise vortices are formed and considerably amplified in the concave side. For the case of plane channel flow, the strength of the vortices is very weak and decay continuously. Evidently, the vortices are amplified greatly in the curved region for the case of the bent channel. This might be mainly due to the fact that the Dean number of the curved section is much higher than the critical Dean number to enhance the Dean vortices by the centrifugal instability. Thus, the streamwise vortices of the figure are inferred to correspond to the Dean vortices of curved channel flows. This implies that centrifugal instability is properly taken into account in the present analysis.

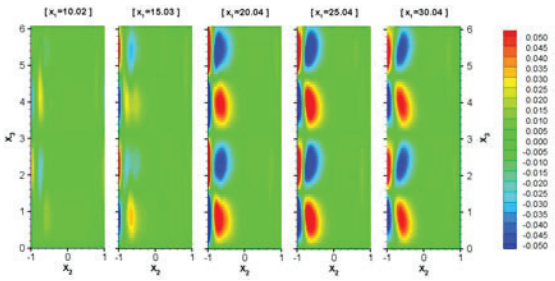

Figure 7. Contours of instantaneous streamwise vorticity due to disturbances in x_2-x_3 plane

The difference between the fastest and the slowest velocity in the stationary streamwise velocity profile (Fig. 6) may represent the strength of the streamwise streaks. This difference can be evaluated at each x_2 location and would vary with the location. We introduce the streak amplitude, A_{streak}, as the maximum difference of the streamwise velocity. The variations of the streak amplitude for both cases of the bent and plane channel are plotted in Fig. 8. In the case of bent channel, the streak amplitude starts to increase considerably as it enters the curved region. Even beyond the curved region (x_1>20.94), the steramwise streaks are continuously amplified until around x_1=60 at which the streaks reach almost saturated state. This means that the amplification of streamwise streaks is induced by the flow field not only in the curved region but also in the following straight section. The streak amplitude is seen to increase up to 0.53 for the case

of bent channel while that for the plane channel reaches the value of only 0.0122. The amplitude is increased by more than 43 times due to the influence of the bent channel. The maximum amplitude of streamwise vorticity, $A_{vortices}$, is also plotted in Fig. 8. We see that the streamwise vortices are strongly amplified in the bent region. However, it immediately starts to decay as it enters the straight section. This means that the streamwise vortices are amplified only in the curved region. Although the mean flow deviates considerably from that of the plane Poiseulle flow, the flow in the second straight section is not able to sustain the streamwise vortices as in plane channel. This confirms again that the amplification of the streamwise vortices is a direct consequence of the centrifugal instability. We see that the curved region acts as a strong amplifier of both streamwise streaks and vortices but the following straight section provides additional amplification only for the steamwise streaks, not vorticity.

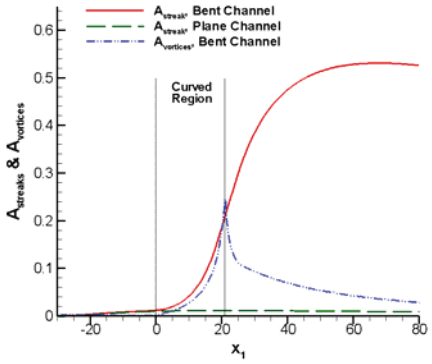

Figure 8. Variation of streak amplitude and maximum amplitude of streamwise vortices

It has to be noted that both the streamwise streaks and streamwise vortices yield considerable modification of the original mean flow (Fig. 6). It is well known from the crossflow vortices on the swept wing [18] and the Görtler vortices on concave surfaces [19] that the modified mean flow is susceptible to secondary instability which eventually leads to breakdown. For the case of secondary instability, the modification of mean flow serves as a primary mode. The large amplitude of primary mode, in general, results in higher growth rate of secondary instability. It seems natural that the bent region brings forth higher secondary instability via strong modification of mean flow.

Fig. 9 compares the amplitude variation curves when the location of initial disturbance application is changed (x_1=-30,-20,-10) while keeping other parameters unchanged. We see that as the initiation location moves upstream, (0,2) mode reaches higher amplitude while the fundamental mode becomes smaller at the entrance of the curved section. We also see that all the stationary modes reach higher amplitudes for the case of high amplitude of (0,2) mode at the entrance of the curved region. This suggests that the amplification of the stationary modes such as streamwise streaks and vortices in the bent channel depends directly on the amplitude of (0,2) mode itself.

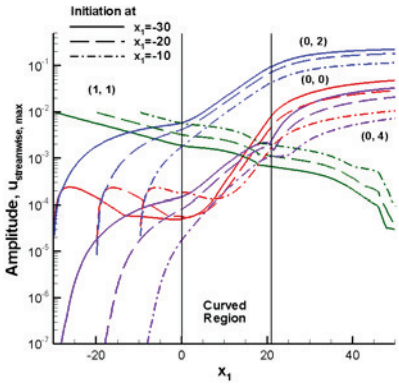

Figure 9. Maximum amplitudes of several modes with varying initiation location

Since the streamwise streaks and streamwise vortices are closely related to secondary instability, investigation on the behavior of their amplitudes is important in understanding and estimation of the breakdown phenomena. In this regard, we carry out analyses with various parameters such as θ, r/h, and Re.

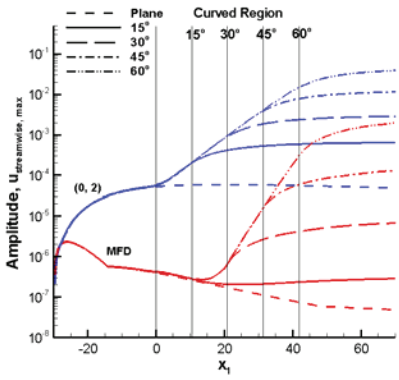

Figure 10. Evolution of maximum amplitude of (0,2) and MFD

To see the effect of bent angle, analysis has been carried out for the cases θ =15, 30, 45, and 60 degrees. Re and r/h are fixed at 2000 and 40, respectively. The end locations of the curved section for these four cases are x_1≈10.47, 20.94, 31.42, and 41.89. Initial condition is prescribed at x_1=-30 with amplitude of 0.1% for the oblique wave (α_r=β=1, F=3852). The amplitude variation of MFD and (0,2) mode are shown in Fig. 10. Although not shown in the figure, amplitudes of all the stationary modes as well as MFD and (0,2) mode increase with the bent angle as expected. The amplitudes of streamwise streaks and vortices also show the same behavior. We recall here that the larger bent angle

means the longer streamwise extent of the curved region.

The ratio of the maximum streak amplitude in a bent channel to that in a plane channel is evaluated as $\max[(A_{streak})_{bent}] / \max[(A_{streak})_{plane}]$. The maximum amplitude of streamwise vortices is also evaluated. We confirmed that the logarithmic values of them are linearly proportional to the bent angle. This implies that the streamwise streaks and vortices grow exponentially in curved region. We may expect that even a small elongation of the curved region can be critical to breakdown.

Analyses for the cases of r/h=30, 40, 50, and 60 when Re=2000 and θ=30 degrees have been carried out to examine the influence of radius of curvature. The corresponding Dean numbers for the curved section are 700.30, 603.88, 538.75, and 490.97 respectively. The locations of the end of the bent region are $x_1 \approx$15.71, 20.94, 26.17, and 31.42. The same initial condition is used. The results are shown in Fig. 11. We see from Fig. 11 that the growth rates of the stationary modes in the curved region are greater for smaller radius of curvature. This confirms the fact that the amplification in a curved region becomes greater as the Dean number increases. We note from Fig. 11 that the overall amplification is bigger when the radius is larger. This is simply due to the larger streamwise extent of the curved region. If the streamwise extent is set to be the same, total amplification would certainly be larger for the case of smaller radius. The same discussion can be applied to the amplitude of streamwise streaks and vortices.

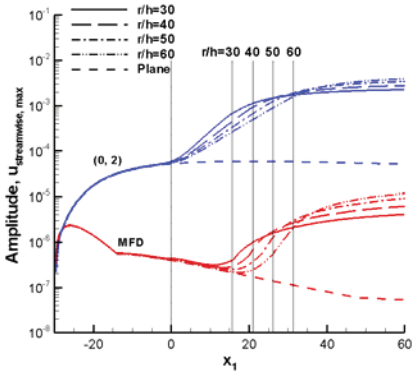

Figure 11. Evolution of maximum amplitude of (0,2) and MFD and varying radius

Influence of Reynolds number is examined by carrying out the analyses for several cases of Re when r/h =50 and θ=45 degrees. We note here that the same initial condition cannot be used for different Reynolds numbers since $\alpha=f(\beta,F,Re)$. If we intend to keep the oblique angle of fundamental wave to be 45 degrees, there are two possible choices for the wave frequency and wave number. We may vary non-dimensional frequency with Re by keeping the wave number at $\alpha_r=\beta$=1. Or we vary the wave number to make the non-dimensional frequency remain the same (F=0.3852). The cases of Re=1500, 1750, 2250, and 2500 are investigated.

The results of fixed wave number cases ($\alpha_r=\beta$=1) are shown in Fig. 12. As expected, the amplitude of streamwise streaks and vortices increases with Reynolds number. The results for fixed non-dimensional frequency (F=0.3852) cases also exhibit the same trend although not shown here. We see that the oblique wave induced streamwise streaks and vortices are strengthened very much even at very low Reynolds number (Re=1500). This suggests that this non-linear mechanism can be served as the first stage of breakdown to turbulence by modification of mean flow subject to secondary instability even at very low Reynolds number.

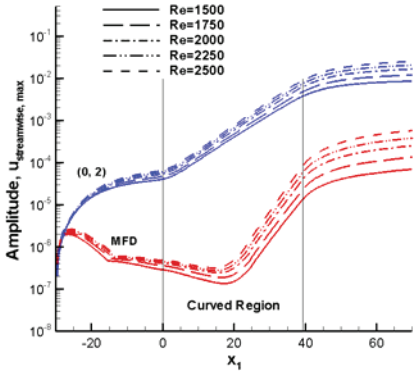

Figure 12. Evolution of $A_{streaks}$ and $A_{vortices}$ with varying Re

It has to be kept in mind that we have provided the results subjected to the initial condition of only specific oblique wave with chosen frequency and wave number. In practical situation, a number of instability waves would be present and mixed together. In such cases, the most unstable or frequencies of specific range would be amplified enough to dominate flow field.

4. CONCLUDING REMARKS

The generation and amplification of streamwise streaks and vortices in a bent channel initiated from a pair of oblique wave was investigated by using NPSE. The anti-symmetric wall O-S mode corresponding to T-S wave was obtained from LST and used as initial condition. The (0,2) mode which becomes the most dominant mode was found to be induced by the non-linear interaction of the oblique waves. All the stationary modes as well as (0,2) mode were much amplified over the region of the bent channel and the following strainght channel whereas the fundamental oblique wave continuously decayed. It was confirmed that both the streamwise streaks and vortices exhibit the characteristics of (0,2) mode. Both the streaks and vortices were considerably amplified as they entered the curved region. The amplification of

them was much pronounced in a concave side. Amplified vortices in concave side correspond to the Dean vortices in a curved channel flow due to the centrifugal instability. Amplitude of streamwise streaks exhibited much higher amplitude than that in a plane channel flow. The streaks continue to be amplified even beyond the curved region until the saturated state is reached while the vortices immediately start to decay in the straight channel beyond the curved region. This confirms again that the vortices are amplified via centrifugal instability just like the Dean vortices.

Influence of several parameters on the amplification of streamwise streaks and vortices was examined. Maximum amplitudes of both streaks and vortices were found to increase exponentially with the bent angle of the curved region. The amplification rate became larger as the radius of curvature decreased reflecting the increase of the centrifugal instability for small radius. For a fixed bent angle, total amplification increased with the radius since the total streamwise extent of the curved region increased. Total amplification also increased with the Reynolds number for both cases of fixed wave number and non-dimensional frequency.

ACKNOWLEDGEMENTS

This research was supported by Basic Science Research Program through the National Research Foundation of Korea (NRF) funded by the Ministry of Education, Science and Technology (2010-0012834)

REFERENCES

[1] Nishioka, M., Iida, S., and Ichikawa, Y., 1975, “An experimental investigation of the stability of plane Poiseuille flow,” J. Fluid Mech. Vol. 72, pp. 731-751.

[2] Herbert, T., 1988, "Secondary Instability of Boundary Layers," Annu. Rev. Fluid Mech., Vol.20, pp.487-526.

[3] Reddy, S. C., Schmid, P. J., Baggett, J. S., and Henningson, D. S., 1998, “On stability of streamwise streaks and transition thresholds in plane channel flows,” J. Fluid Mech. Vol. 365, pp. 269-303.

[4] Schmid, P. J. and Henningson, D. S., 1992, “A new mechanism for rapid transition involving a pair of oblique waves,” Phys. Fluids A Vol. 4, No. 9, pp. 1986-1989.

[5] Berlin, S., Wiegel, M., and Henningson, D. S., 1999, “Numerical and experimental investigations of oblique boundary layer transition,” J. Fluid Mech. Vol. 393, pp. 23-57.

[6] Chang, C.-L. and Malik, M.R., 1994, "Oblique-mode breakdown and secondary instability in supersonic boundary layers," J. Fluid Mechanics, Vol.273, pp.323-360.

[7] Mayer, C. S. J., Fasel, H. F., Choudhari, M., and Chang, C.-L., 2010, “Detailed Comparison of DNS with PSE for Oblique Breakdown at Mach 3,” AIAA 2010-4596.

[8] Schmid, P. J., Lundbladh, A., and Henningson, D. S., 1994, “Spatial evolution of disturbances in plane Poiseulle flow,” In Transition, Turbulence and Combustion, Volume I (ed. Hussaini, M. Y., Gatski, T. B., and Jackson, T. L.), pp. 287-297, Kluwer.

[9] Elofsson, P. A. and Alfredsson, P. H., 1998, “An experimental study of oblique transition in plane Poiseulle flow,” J. Fluid Mech. Vol. 358, pp. 177-202.

[10] Finlay, W. H., Keller, J. B., and Ferziger, J. H., 1988, “Instability and transition in curved channel flow,” J. Fluid Mech. Vol. 194, pp. 417-456.

[11] Matsson, O. J. E. and Alfredsson, P. H., 1993, “Secondary Instability and Breakdown to Turbulence in Curved Channel Flow,” Applied Scientific Research Vol. 51, pp. 9-14.

[12] Mack, L. M., 1984, “Boundary-Layer Linear Stability Theory,” AGARD CP-709, NATO, Belgium.

[13] Herbert, T., 1997, “Parabolized Stability Equations,” Annu. Rev. Fluid. Mech. Vol. 29, pp. 245-283.

[14] Chang, C.-L., 2004, “Langley Stability and Transition Analysis Code (LASTRAC) Version 1.2 User Manual,” NASA TM-2004-213233.

[15] Malik, M. R., 1990, "Numerical Methods for Hypersonic Boundary Layer Stability," Journal of Computational Physics, Vol.86, pp.376-413.

[16] Zang, T. A. and Krist, S. E., 1989, “Numerical Experiments on Stability and Transition in Plane Channel Flow,” Theoret. Comput. Fluid Dynamics Vol. 1, pp. 41-64.

[17] Elofsson, P. A. and Alfredsson, P. H., 1998, “An experimental study of oblique transition in plane Poiseulle flow,” J. Fluid Mech, Vol. 358, pp. 177-202.

[18] Malik, M. R., Li, F., Choudhari, M., and Chang, C.-L., 1999, “Secondary Instability of Crossflow Vortices and Swept-Wing Boundary-Layer Tranistion,” J. Flluid Mech. Vol. 399, pp.85-115.

[19] Yu, X. and Liu, J. T. C., 1994, “On the mechanism of sinous and varicose modes in three-dimensional viscous secondary instability of nonlinear Görtler rolls,” Phys. Fluids, Vol. 6, No.2, pp. 736-750.

Conference on Modelling Fluid Flow (CMFF'12)
The 15th International Conference on Fluid Flow Technologies
Budapest, Hungary, September 4-7, 2012

COMPARISON OF ADVANCED RANS MODELS AGAINST LARGE EDDY SIMULATION AND EXPERIMENTAL DATA IN INVESTIGATION OF RIBBED PASSAGES WITH HEAT TRANSFER

Amir KESHMIRI[1,2], Osman KARIM[2], Sofiane BENHAMADOUCHE[3,4]

[1] School of Engineering, Manchester Metropolitan University, Manchester M1 5GD, UK. E-mail: a.keshmiri@mmu.ac.uk
[2] School of Mechanical, Aerospace and Civil Engineering, The University of Manchester, Manchester M60 1QD, UK.
[3] Électricité de France R&D Division, Fluid Mechanics, Energy and Environment Department, 6 Quai Watier, 78401 Chatou Cedex, France. E-mail: sofiane.benhamadouche@edf.fr
[4] LaMSID, UMR EDF-CNRS-CEA 8193, Clamart, France.

ABSTRACT

The present paper reports simulations of the flow and heat transfer in a 2-dimensional rib-roughened passage using a number of advanced RANS turbulence models including Eddy-Viscosity Models (EVM) and a Reynolds Stress Model (RSM). Large Eddy Simulation (LES) is also conducted and results are compared against experimental measurements. The blockage ratio of the transversely-mounted rectangular ribs is 10% and the rib pitch-to-height ratio of 9 is selected. The Reynolds number, based on the channel bulk velocity and hydraulic diameter, is 30,000. The RANS-based turbulence models investigated here are the *k-ω-SST*, the v^2-*f*, the φ-*f* and the Elliptic Blending RSM. All computations are undertaken using the commercial and industrial CFD codes, 'STAR-CD' and '*Code_Saturne*', respectively.

Keywords: RANS, LES, *Code_Saturne*, STAR-CD, Rib-roughness, Turbulence Modelling.

NOMENCLATURE

A	Cross-sectional area of the channel
b	Rib width
c_f	Local friction coefficient
C_p	Pressure coefficient, $(p - p_{ref})/(0.5\rho U_b^2)$
D_e	Hydraulic diameter, $4A/P$
H	Channel height
k	Height of the rib or turbulent kinetic energy
L	Length scale or computational domain length
Nu	Nusselt number, $\dot{q}D_e/(\lambda(T_w - T_b))$
p	Pressure
P	Pitch or wetted perimeter
$\dot{q}$	Wall heat flux
Re	Reynolds number, $U_b D_e/v$
T,	Mean temperature
T_s	Turbulent timescale
U_i, u_i	Mean and fluctuating velocity components in Cartesian tensors
U_τ	Friction velocity, $(\lvert\tau_w\rvert/\rho)^{1/2}$
x,y	Streamwise and wall-normal coordinates
y^+	Dimensionless distance from the wall, yU_τ/v

Greek Symbols

ε	Dissipation rate of turbulent kinetic energy
λ	Thermal conductivity
μ	Dynamic viscosity
μ_t	Turbulent viscosity
v	Kinematic viscosity, μ/ρ
θ	Fluctuating temperature
ρ	Density
σ_{k1}	Coefficient in the SST model
σ_t	Turbulent Prandtl number
τ_w	Wall shear stress
ω	Dissipation rate per unit of kinetic energy, $\varepsilon/(C_\mu k)$

Subscripts

b	Bulk
ref	Reference
t	Turbulent
w	Wall

Additional symbols are defined in the text.

1. INTRODUCTION

For many years, rough surfaces have been one of the most common methods for convective heat transfer augmentation through increasing turbulence levels. The penalty associated with such roughening is an increase in pressure loss. Despite numerous studies on heat transfer, turbulence and turbulent boundary layer in rough surface problems, the

detailed physics of these flow problems are still a topic of research.

In this section, some of the previous numerical works carried out on rib-roughened channels are reviewed.

There have been numerous attempts to numerically simulate rib-roughened channels; the most widespread techniques adopted are based on solution of the Reynolds-Averaged Navier-Stokes (RANS) equations where the choice of turbulence model plays a critical role in determining the accuracy of the simulations. Some of the numerical investigations of rib-roughened surfaces using RANS were carried out by Iacovides and Raisee [1, 2], Manceau et al. [3], Bredberg et al. [4], Ooi et al. [5], Raisee et al. [6], Ryu et al. [7], Keshmiri et al. [8] and Keshmiri and Gotts [9], amongst others.

Iacovides and Raisee [1, 2] examined the capabilities of the low-Reynolds-number Launder and Sharma [10] model (LS) and second moment closures in predicting convective heat transfer in ribbed annular channels, pipes and plane channels. They showed that the most reliable results were obtained using the low-Reynolds-number second moment closures. The authors also obtained a more realistic variation of heat transfer levels in the separation region and by employing a differential form of the Yap length-scale correction term, originally introduced by [11], in ε-equation.

Manceau et al. [3] applied the v^2-f model to a number of test cases including a 2D periodic ribbed-channel. They concluded that the v^2-f model is a good compromise between simplicity and accuracy for simulating separated flows. They also showed that the v^2-f model is an accurate turbulence model especially in estimating the near-wall turbulence anisotropy which is essential for reproducing the correct levels of heat transfer.

Ooi et al. [5] carried out simulations of the flow and heat transfer in 3-dimensional rib-roughened ducts using the v^2-f and Spalart-Allmaras (S-A) turbulence models; they compared their results with the experimental data of Rau et al. [12] and the k-ε simulations of Chen and Patel [13]. Configurations with various geometrical parameters including pitch, rib height, and cavity depth were considered. It was shown that, while the k-ε model severely underestimates heat transfer levels, the S-A model gave results that were closer to the experimental data, but nonetheless the computed values of Nu were still far from the measured values. The authors reported that heat transfer results generated by the v^2-f model were closest to the experimental values of Rau et al. [12]. However, none of the above models could capture the secondary flow structure which consequently led to incorrect predictions of Nu on the heated side wall.

Bredberg et al. [4] modified the k-ω formulation in an attempt to improve its performance in recirculating flows. Comparison was made against the experimental data of Rau et al. [12] and three other EVMs including the k-ε model of Abe, Kondoh and Nagano [14], the k-ω model of Wilcox [15], and the v^2-f model of Lien and Kalitzin [16]. For the Nusselt number distribution, it was found that both their proposed model and the v^2-f model gave reasonable predictions, while the Wilcox k-ω model under-predicted the Nusselt number. Once again they confirmed that there exists a close connection between heat transfer and predicted turbulence level.

Recently, Ryu et al. [7] carried out a series of simulations using the k-ω model of Wilcox [17] to obtain the resistance coefficient and velocity profile for a turbulent flow in channels with 2D ribs and 3D blocks. Various rib configurations were tested including ribs with square, triangular, semi-circular, and wavy cross-sections over a range of rib pitch and Reynolds numbers. It was found that the k-ω model can successfully capture essential features of the flow.

More Recently, Keshmiri and Gotts [9] tested the effects of four geometrical factors on heat transfer and friction coefficient using two low Reynolds number turbulence models including the k-ω-SST [18] and a variant of Durbin's v^2-f formulations [19]. They concluded that the v^2-f model generally returns more accurate results than the k-ω-SST closure.

In the present work, the simulations are compared with the data of Rau et al. [12]. In that study, detailed flow and heat transfer measurements were made in a square channel with ribs presenting a blockage ratio of 10% (Figure 1). The results of the local measurements were discussed for three different P/k ratios (6, 9 and 12) in a one-side-ribbed channel ('1s'). Measurements for a two-side-ribbed ('2s') channel were reported for P/k = 9. Air was the working fluid, and the Reynolds number based on the bulk velocity and the hydraulic diameter was fixed at Re = 30,000.

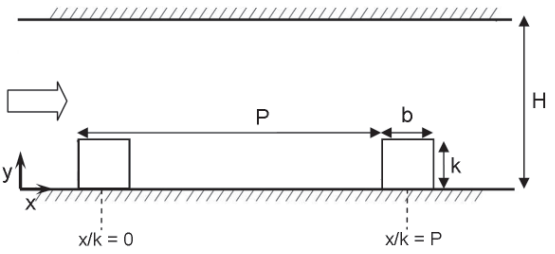

Figure 1. Schematic diagram of a rib-roughened surface.

In the present study, the performance of four refined RANS models and a Large Eddy Simulation are evaluated for a rib-roughened channel flow using a commercial and industrial CFD codes, 'STAR-CD' and '*Code_Saturne*', respectively.

Details of the configuration used in this work are given in Section 3.

2. COMPUTATIONAL CODES

2.1. Code_Saturne

Code_Saturne [20] is the Electricité de France (EDF) in-house CFD tool for incompressible flows. It is based on an unstructured collocated finite-volume approach for cells of any shape with Rhie and Chow interpolation and a SIMPLEC algorithm for pressure correction. While using LES, a fully centered scheme is applied for the velocity components and the temperature. For this latter, a slope test which switches to a 1st order upwind scheme is utilized to limit the overshoots. The time scheme is second order based on Crank-Nicolson/Adams Bashforth scheme (the diffusion is totally implicit whereas the convection is semi-implicit). While using RANS or URANS, a centered scheme with a slope test is used for the velocity components and the temperature and a 1st order upwind scheme for the turbulent quantities. The time scheme is first order Euler in this case.

2.2. STAR-CD

The second code to be used here is 'STAR-CD' [21], a commercial unstructured CFD package. In common with *Code_Saturne*, the program solves the governing equations using a finite volume approach. Similar to *Code_Saturne*, STAR-CD is a co-localized cell centred incompressible Navier-Stokes solver. In the present STAR-CD computations, the momentum and turbulence transport equations are discretized using second-order central differencing and first-order upwind differencing schemes, respectively. The energy equation is discretized using the 'Monotone Advection and Reconstruction Scheme' (MARS) [21]. The SIMPLE algorithm is adopted for pressure-velocity correction. The simulations are run at steady-state condition.

2.3. Turbulence Models

Brief descriptions of the turbulence models used here are as follows:

k-ω-SST Model (STAR-CD)

Advantages of both the k-ε and k-ω models are combined in the Shear Stress Transport (SST) model of Menter [18]. Through a blending function this model effectively uses the Low Reynolds Number (LRN) formulation of the k-ω model in the boundary layer and a version of the k-ε model (usually the 'standard k-ε model') in the free shear layer. This is based on the observations that the k-ε model is much less sensitive to the free-stream value of ε than the k-ω model is to ω. Apart from this unique feature, the main differences between the standard k-ω model and the SST model are the following:

- The SST model includes a damped cross-diffusion derivative term, as well as a blending function, in the ω-transport equation.
- The definition of the turbulent viscosity in the SST was modified to improve the prediction of the turbulent shear stress.
- The coefficients were modified to improve the overall performance of the model.

Note that the functions and coefficients of the *k-ω-SST* model may be found in several text books and are not included here for the sake of brevity. However, it is worth noting that the *k-ω-SST* models implemented in STAR-CD uses the original version of *k-ω-SST* model proposed by Menter [18] (except the value of σ_{k1} in STAR-CD is set to 0.85 instead of 0.5).

v^2-f Model (STAR-CD)

Another model to be considered here is the $\overline{v^2}-f$ model (or simply 'v^2-f') which was originally proposed by Durbin [22] and was designed to handle near-wall and non-local effects in turbulent boundary layers. In this model, the conventional ad-hoc damping functions are replaced with a third transport equation for $\overline{v^2}$, where v is the wall-normal component of the fluctuating velocity. The revised turbulent viscosity equation then becomes:

$$\nu_t = C_\mu \frac{v^2}{k} k T_s \tag{1}$$

where T_s is the time scale and is defined as

$$T_s = \max\left[\frac{k}{\varepsilon}, C_{kT}\left(\frac{\nu}{\varepsilon}\right)^{0.5}\right] \tag{2}$$

where C_{kT} is a constant. In addition, an elliptic equation for f_{22} (the redistribution term in the $\overline{v^2}$ equation) is also included to account for near-wall and non-local effects.

Note that there are currently several v^2-f formulations in the literature, however, the version implemented in STAR-CD is that given by Iaccarino [19]. Therefore, the interested reader is referred to [19, 21] for further details on the present formulation.

φ – f Model (Code_Saturne)

Laurence et al. [23] developed a robust formulation of the v^2-f model which was based on the original v^2-f model proposed by Durbin [22]. This formulation has been shown to be more stable than the original one and has been implemented in

Code_Saturne in order to be used in industrial studies. The idea behind this model is to solve an equation for the ratio of v^2 and k (named φ) which modifies the wall asymptotic behaviour and thus increases the stability of the system. The Simple Gradient Diffusion Hypothesis (SGDH) is used with a turbulent Prandtl number set to $\sigma_t = 1$. (Note that in all the present STAR-CD computations, the turbulent Prandtl number is set to a constant value, $\sigma_t = 0.9$.)

Elliptic Blending - Reynolds Stress Model (Code_Saturne)

As noted earlier by Iacovides and Raisee [1, 2], the use of a low Reynolds second order closure performed quite well on this test case. Manceau and Hanjalić [24] developed a new version of the second order turbulence model of Durbin [25]. They noticed that the six relaxation variables of Durbin's original model essentially account for geometrical effect to modify the pressure-strain process as the wall is approached. Hence, Manceau and Hanjalić proposed to define this transition by a single non-dimensional variable, solution of an elliptic equation (so called 'Elliptic Blending'). The blending factor is used to switch between high Reynolds and near-wall models for the scrambling term and the dissipation rate. The high Reynolds model is based on the SSG model (Speziale et al. [26]). The turbulent heat fluxes are solved using a transport equation which also uses the concept of elliptic blending (EB-DFM for Elliptic Bending – Differential Flux Model, see Dehoux et al. [27]).

Large Eddy Simulation (Code_Saturne)

The sub-grid scale tensor is modeled using the dynamic Smagorinsky model based on Germano [28] identity and Lilly [29] minimization.

For the present LES procedure, an implicit (grid) filter is assumed, whereas an explicit filter is applied only to compute the dynamic constant. The width of the explicit filter is based only on the immediate neighbors of every cell (cells sharing a common face). The widely used approach of averaging the constant in the homogeneous (span-wise) direction to add stability is not utilized in the present work. The constant is capped between values of 0 and its value for the channel flow simulations. The code has been validated on several academic (decaying isotropic turbulence and channel flow) and industrial (T-junctions, tube bundles, etc.) test cases – see Benhamadouche [30]. The temperature equation uses a turbulent Prandtl number set to $\sigma_t = 0.5$.

3. GEOMETRY AND GRID

The rib height to channel hydraulic diameter ratio in the present simulations is $k/D_e = 0.05$, and the blockage ratio (k/H) is 10%. The rib pitch-to-height ratio of $P/k = 9$ is selected for the present analysis. Ribs are also assumed to have square cross-sections (i.e. $k = b$). The Reynolds number based on the bulk velocity and the hydraulic diameter is fixed at $Re = 30{,}000$ and the Prandtl number is set to 0.71.

The geometry considered here consists of a 2-dimensional channel, the lower wall of which is roughened by square ribs of height k. In STAR-CD simulations, the computational domain is of length $2P$, i.e. it includes 2 ribs, while *Code_Saturne* uses a configuration with only 1 rib. Streamwise periodicity is assumed for all the computations. The domain is of height H and the thermal boundary condition at both the lower and upper walls is set as uniform wall heat flux for STAR-CD computations and with an insulated rib for *Code_Saturne* computations. (Note that the thermal boundary conditions of the ribs have previously been reported to have insignificant effects on the heat transfer results – see [31], for example.)

STAR-CD Computations

The mesh used for STAR-CD computations is a structured Cartesian grid with approximately 160,000 computational cells. Since low-Reynolds-number turbulence models are employed, the grids were generated so as to be very fine near the wall (the wall-adjacent cell typically extends only to $y^+ \leq 0.5$).

Code_Saturne Computations

RANS: The mesh used for *Code_Saturne* RANS computations is a structured Cartesian grid with approximately 54,000 computational cells. Several tests have been performed to ensure that the solution is mesh-independent. The y^+ distribution is below 1 everywhere along the boundary.

LES: The present LES is well-resolved and uses a mesh containing 33 Million cells (160 cells in the span-wise direction). The maximum Courant number does not exceed 1 and the averaging is performed in time and space (30 flow passes based on the bulk velocity are used for time averaging).

4. RESULTS AND DISCUSSION

Figure 2 compares heat transfer results of the *k-ω-SST*, v^2*-f* , φ*-f* and EB-RSM against the LES and the experimental data of Rau et al. [12]. Following Rau et al., all Nusselt number distributions for the ribbed duct calculations are normalized by the value associated with a smooth channel (the Dittus-Boelter equation):

$$Nu_0 = 0.023\, Re^{0.8}\, Pr^{0.4} \qquad (3)$$

In Figure 2 it can be seen that the results of the v^2*-f* model and LES are closest to the experimental data, while the *k-ω-SST* and EB-RSM under-predict

the rate of heat transfer especially in the recirculation area. In the figure, it is also evident that different models predict different shapes for the heat transfer distribution; while the φ-f and v^2-f formulations tend to predict a uniform profiles, the LES predicts a rather skewed distribution towards the first rib. The k-ω-*SST* and EB-RSM, however, predict a distribution which is rather skewed towards the second rib.

It is interesting to note that despite their contradicting predictions for the overall shape, LES and EB-RSM predict a sudden rise in heat transfer rate near the second rib. This abrupt rise in heat transfer corresponds to the secondary vortex (recirculating bubble) formed in the vicinity of the downstream rib (this point is discussed further below in connection with Figure 5). Therefore, one could argue that even though the EB-RSM fails to accurately predict the overall shape of the heat transfer distribution, it captures the *physics* of the flow more accurately in comparison to the two-equation models tested here. In fact improving the performance of the EB-RSM in detaching flows is still an active research topic in turbulence modelling.

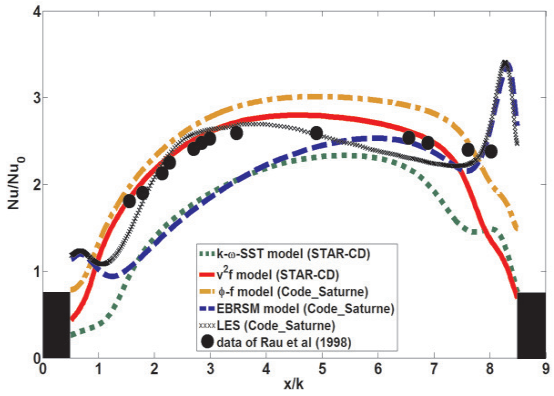

Figure 2. Heat transfer distributions.

It is also worth mentioning that due to measurement limitations, the experimental data of Rau et al. [12] do not extend all the way to the faces of the ribs and therefore the accuracy of the simulations in these regions cannot be assessed by direct comparison.

Streamlines obtained by all four RANS turbulence models as well as LES are shown in Figure 3. It can be seen that the k-ω-*SST* model and the LES/φ-f model return the largest and smallest separation bubbles, respectively. The former is probably due to a turbulent viscosity limiter that exists in the k-ω-*SST* model which limits the shear stress when the production of k exceeds its dissipation rate (by about an order of magnitude, for example). This limiter tends to eliminate the unrealistic build-up of eddy viscosity in the stagnation regions [18, 32]. Furthermore, in Figure 3 it is seen that the φ-f and v^2-f formulations return the smallest counter-rotating separation bubble near the second rib compared to the other models. Consequently, both models fail to capture the sudden increase of heat transfer which occurs in LES within $8 \leq x/k \leq 8.5$ – see Figure 2.

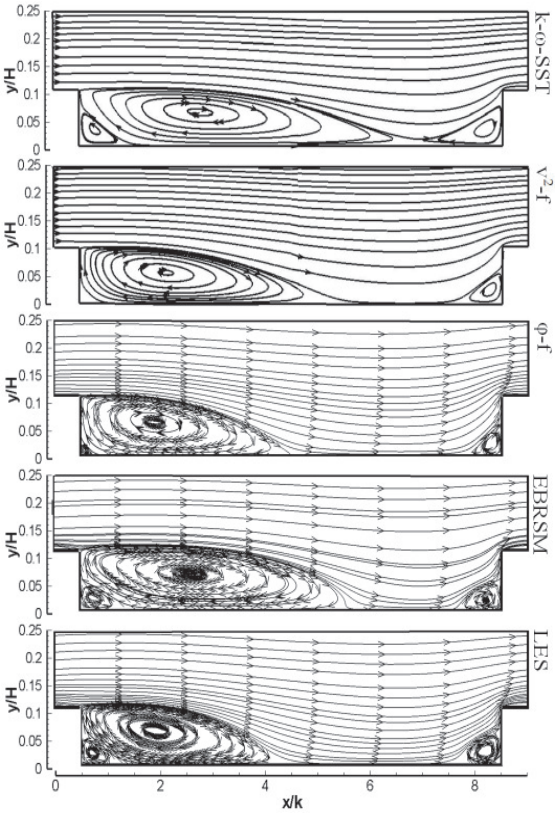

Figure 3. Comparison of streamlines and reattachment lengths for various models.

Figure 4 shows the normalized streamwise velocity distributions at one-tenth of the rib height. The profile predicted by the LES is the closest to the experimental data, while k-ω-*SST* has the worst prediction. In addition, all the RANS and LES models and the data clearly show a reattachment point (U/U_b = 0), except for the k-ω-*SST* model which indicates that the flow remains reversed at this elevation. The k-ω-*SST* model therefore fails to predict flow renewal in the inter-rib cavity which is partly responsible for the under-prediction of heat transfer rate seen in Figure 2. The reattachment lengths predicted by the LES and the φ-f model are the closest to that found by Rau et al. [12].

Results for the wall-normal velocity at rib height are presented in Figure 5. It can be seen that the results of the LES, v^2-f and φ-f models are in reasonably good agreement with the experimental data, with the LES being the closest. However, the EB-RSM and the k-ω-*SST* model generally under-predict the magnitude of the wall-directed velocity.

The poor performance of the EB-RSM and the *k-ω-SST* model in Figure 5 could also be anticipated from the streamlines shown in Figure 3, where these models returned the largest separation bubbles.

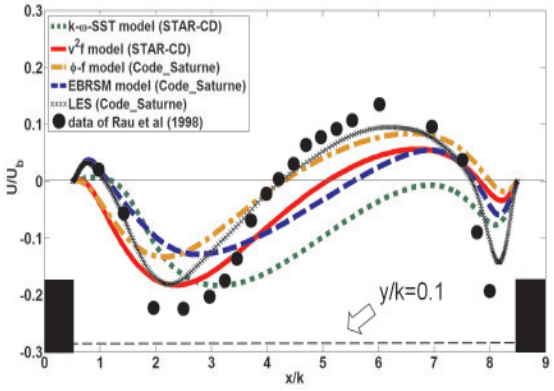

Figure 4. Streamwise velocity distributions at *y/k* = 0.1.

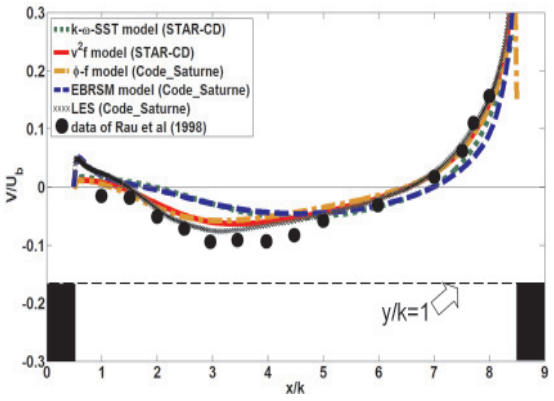

Figure 5. Wall-normal velocity distributions at *y/k* = 1.

Normalized streamwise velocity profiles at two wall-normal planes, namely over the rib-top (*x/k* = 0) and in the separation region (*x/k* = 4) are shown in Figure 6 and Figure 7, respectively. In Figure 6, it can be seen that all the models are in reasonable accord with the measurements. The *k-ω-SST* and v^2-*f* models generally over-predict the magnitude of the velocity, while the LES, *φ-f* and EB-RSM tend to predict smaller velocity magnitude.

At *x/k* = 4, Figure 7 shows that all the models generally under-predict the magnitude of the velocity. However, further away from the wall (*y/H* > 0.2), the predictions of the *k-ω-SST* and v^2-*f* models are in better agreement with the data.

The size of the separation bubble predicted by each model is illustrated more clearly in the inset of Figure 7. It is shown that all the models yield longer separation bubble compared to the data. The results shown in the inset of Figure 7 are also consistent with the magnitude of the streamwise velocity in Figure 4 at *x/k* = 4.

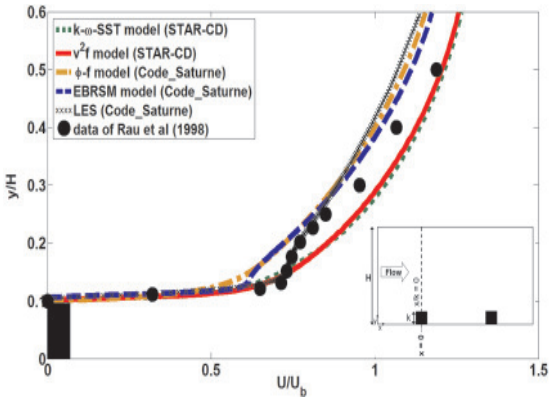

Figure 6. Streamwise velocity profiles on the rib-top (*x/k* = 0).

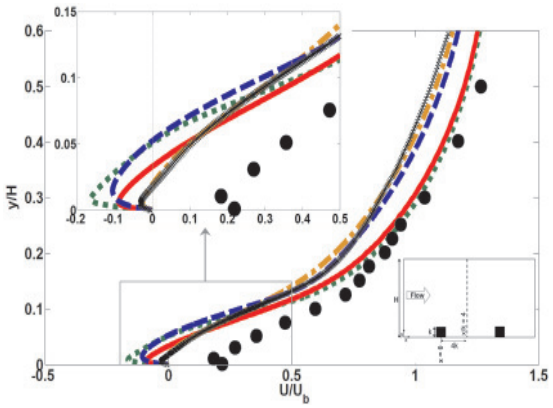

Figure 7. Streamwise velocity profiles at *x/k* = 4 plane.

Attention is turned next to the inter-rib pressure distribution.

Impingement on the upstream face of the rib leads to high static pressure, while there is a low pressure zone downstream of the rib. These effects can be seen in Figure 8, where the pressure coefficient distributions between the two ribs are plotted against *x/k*. Note that in this figure, C_p in all cases is offset to the experimental value at *x/k* = 4.5 (the centre of the inter-rib cavity). In Figure 8 the performance of the present numerical results can be assessed by splitting the inter-rib cavity into recirculation ($0.5 \leq x/k \leq 4.5$) and recovery ($4.5 \leq x/k \leq 8.5$) regions. Clearly most of the models (except the *φ-f* model) fail to return a correct level of pressure in the recirculation region which is directly linked to the predicted size of the recirculation bubble (Figure 3) e.g. the longer the separation bubble, the lower the pressure magnitude. The predictions of the models tend to improve within the recovery region but still only the LES, EB-RSM and v^2-*f* are in good agreement with the data.

A more detailed examination of the results shown in Figure 8 reveals that the LES and EB-RSM predict a sharp increase in the value of C_p

near the second rib, while the eddy-viscosity-based turbulence models (i.e. *k-ω-SST*, v^2*-f* and *φ-f*) return quasi-linear distributions. Similar findings were also emerged from the heat transfer results shown in Figure 2. These discrepancies clearly show the advantages of the LES and EB-RSM in simulating the counter-rotating recirculating flow ('secondary strain') near the second rib in comparison to linear eddy-viscosity models.

Furthermore, in the inset to Figure 8 the predicted pressure coefficient distributions are re-plotted but now C_p is offset to the experimental value at x/k = 0.5. The models return a wide range of pressure differences between x/k = 0.5 and x/k = 8.5, with the v^2*-f* and EB-RSM predicting the maximum and minimum, respectively. The pressure difference predicted by the LES is clearly in very good agreement with the data.

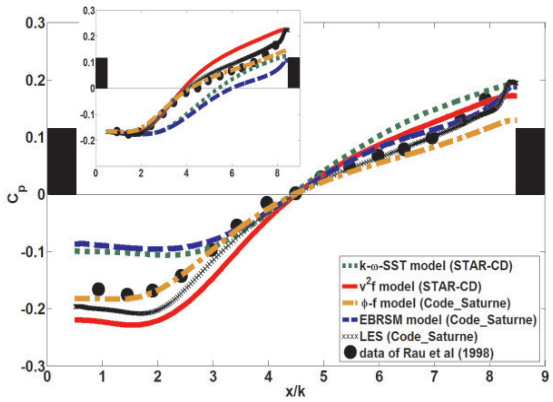

Figure 8. Pressure coefficient distribution.

5. CONCLUSIONS

Numerical simulations of the flow and heat transfer in a 2-dimensional rib-roughened passage have been performed using *k-ω-SST*, v^2*-f*, *φ-f*, Elliptic Blending Reynolds Stress Model (EB-RSM) and Large Eddy Simulation (LES). Comparison was made against the experimental data of Rau et al. [12]. All simulations were undertaken using the commercial and industrial CFD codes, 'STAR-CD' and '*Code_Saturne*', respectively.

Of all the models, the LES predictions were found to be in the best agreement with the dynamic and thermal field data of Rau et al., while the *k-ω-SST* and EB-RSM returned the least accurate results (although the EB-RSM was able to capture some of the physics of the flow more accurately). The v^2*-f* and *φ-f* models also returned acceptable predictions, especially the v^2*-f* model for the heat transfer.

It was also shown that the effects of some of the flow features such as the counter-rotating separation bubble near the second rib cannot be successfully simulated by linear eddy-viscosity models and were captured only by the LES and EB-RSM.

ACKNOWLEDGEMENTS

The authors are pleased to acknowledge the contribution of their colleagues in the School of Mechanical, Aerospace and Civil Engineering (MACE) at the University of Manchester, especially Dr. M.A. Cotton, Professor D. Laurence and Dr. I. Afgan. The travel grant provided by the school of engineering at Manchester Metropolitan University to the lead author is also acknowledged. Finally, the authors are grateful to EdF for allowing the use of its 'BlueGene P' supercomputer for the LES simulations.

REFERENCES

[1] Iacovides H., and Raisee M., 1999, "Recent progress in the computation of flow and heat transfer in internal cooling passages of turbine blade". *Int. J. Heat Fluid Flow*, Vol. 20, pp. 320-328

[2] Iacovides H., and Raisee M., 2001, "Computation of flow and heat transfer in two-dimensional rib-roughened passages, using low-Reynolds-number turbulence models". *Int. J. Numerical Methods for Heat and Fluid Flow*, Vol. 11, pp. 138-155

[3] Manceau R., Parneix S., and Laurence D., 2000, "Turbulent heat transfer predictions using the v^2-f model on unstructured meshes". *Int. J. Heat Fluid Flow*, Vol. 21, pp. 320-328

[4] Bredberg J., Peng S. H., and Davidson L., 2002, "An improved k-ω turbulence model applied to recirculating flows". *Int. J. Heat Fluid Flow*, Vol. 23, pp. 731-743

[5] Ooi A., Iaccarino G., Durbin P. A., and Behnia M., 2002, "Reynolds averaged simulation of flow and heat transfer in ribbed ducts". *Int. J. Heat Fluid Flow*, Vol. 23, pp. 750-757

[6] Raisee M., Noursadeghi A., and Iacovides H., 2004, "Application of a non-linear k-ε model in prediction of convective heat transfer through ribbed passages". *Int. J. Heat Fluid Flow*, Vol. 14, pp. 285-304

[7] Ryu D. N., Choi D. H., and Patel V. C., 2007, "Analysis of turbulent flow in channels roughened by two-dimensional ribs and three-dimensional blocks. Part I: Resistance". *Int. J. Heat Fluid Flow*, Vol. 28, pp. 1098-1111

[8] Keshmiri A., Cotton M. A., Addad Y., and Laurence D. R., 2009, "Thermal-hydraulic analysis of rib-roughened fuel pin performance in gas-cooled nuclear reactors". *Proc. 6th International Symposium on Turbulence, Heat and Mass Transfer*, *Rome, Italy*, pp. 1011-1014

[9] Keshmiri A., and Gotts J., 2011, "Thermal-hydraulic analysis of four geometrical design parameters in rib-roughened

channels". *J. Numerical Heat Transfer; Part A: Applications*, Vol. 60, pp. 305-327

[10] Launder B. E., and Sharma B. I., 1974, "Application of the energy dissipation model of turbulence to the calculation of flow near a spinning disc". *Lett. Heat Mass Transfer*, Vol. 1, pp. 131-138

[11] Yap C. R. 1987. *Turbulent heat and momentum transfer in recirculating and impinging flows*. Ph.D. Thesis, University of Manchester, UK

[12] Rau G., Çakan M., Moeller D., and Arts T., 1998, "The effect of periodic ribs on the local aerodynamic and heat transfer performance of a straight cooling channel". *ASME J. Turbomach.*, Vol. 120, pp. 368-375

[13] Chen H. C., and Patel V. C., 1988, "Near-wall turbulence models for complex flows including separation". *AIAA J.*, Vol. 26 (6), pp. 641-648

[14] Abe K., Kondoh T., and Nagano Y., 1994, "A new turbulence model for predicting fluid flow and heat transfer in separating and reattaching flows - I. Flow field calculations". *Int. J. Heat Mass Transfer*, Vol. 37, pp. 139-151

[15] Wilcox D. C., 1993, "Comparison of two-equation turbulence models for boundary layers with pressure gradient". *AIAA J.*, Vol. 31, pp. 1414-1421

[16] Lien F., and Kalitzin G., 2001, "Computations of transonic flow with the v^2-f turbulence model". *Int. J. Heat Fluid Flow*, Vol. 22, pp. 53-61

[17] Wilcox D. C. 1998. *Turbulence Modeling for CFD*. DCW Industries Inc., La Cañada.

[18] Menter F. R., 1994, "Two-equation eddy-viscosity turbulence models for engineering applications". *AIAA J.*, Vol. 32, pp. 1598-1605

[19] Iaccarino G., 2001, "Predictions of a turbulent separated flow using commercial CFD codes". *J. Fluids Eng.*, Vol. 123, pp. 819-828

[20] Archambeau F., Mechitoua N., and Sakiz M., 2004, "A finite volume method for the computation of turbulent incompressible flows – Industrial applications". *Int. J. on Finite Volumes, Electronic edition, ISSN 1634(0655)*, Vol. 1(1), pp. 1-62

[21] CD-Adapco. 2006. STAR-CD Methodology, Version 4.02.

[22] Durbin P. A., 1991, "Near-wall turbulence closure modeling without damping functions". *Theoret. Comput. Fluid Dynamics*, Vol. 3, pp. 1-13

[23] Laurence D. R., Uribe J. C., and Utyuzhnikov S. V., 2004, "A robust formulation of the v^{2}-f model". *Flow, Turbulence and Combustion*, Vol. 73, pp. 169-185

[24] Manceau R., and Hanjalić K., 2002, "Elliptic blending model: A new near-wall Reynolds-stress turbulence closure". *Phys. Fluids*, Vol. 14, pp. 744-754

[25] Durbin P., 1993, "A Reynolds-stress model for near-wall turbulence". *J. Fluid Mech.*, Vol. 249, pp. 465-498

[26] Speziale C. G., Sarkar S., and Gatski T. B., 1991, "Modelling the pressure-strain correlation of turbulence: an invariant dynamical system approach ". *J. Fluid Mech.*, Vol. 227, pp. 245-272

[27] Dehoux F., Lecocq Y., Benhamadouche S., Manceau R., and Brizzi L., 2012, "Algebraic Modeling of the Turbulent Heat Fluxes Using the Elliptic Blending Approach - Application to Forced and Mixed Convection Regimes". *Flow, Turbulence and Combustion*, Vol. 88, pp. 77-100

[28] Germano M., Piomelli U., Moin P., and Cabot W., 1991, "A dynamic subgridscale eddy viscosity model". *Phys. Fluids*, Vol. 3, pp. 1760-1766

[29] Lilly D., 1992, "A proposed modification of the Germano subgrid-scale closure method". *Phys. Fluids*, Vol. 4, pp. 633

[30] Benhamadouche S. 2006. *Large eddy simulation with the unstructured collocated arrangement*. Ph.D. Thesis, University of Manchester, UK

[31] Keshmiri A., 2012, "Numerical sensitivity analysis of 3- and 2-dimensional rib-roughened channels". *J. Heat Mass Transfer*, DOI 10.1007/s00231-012-0968-z, pp. 1-15

[32] Kral L. D., 1998, "Recent experience with different turbulence models applied to the calculation of flow over aircraft components". *Progress in Aerospace Sciences*, Vol. 34, pp. 481-541

Conference on Modelling Fluid Flow (CMFF'12)
The 15th International Conference on Fluid Flow Technologies
Budapest, Hungary, September 4-7, 2012

EXPERIMENTAL INVESTIGATION ON STREAMWISE DEVELOPMENT OF TURBULENT STRUCTURE OF DRAG-REDUCING CHANNEL FLOW WITH DOSED POLYMER SOLUTION FROM CHANNEL WALL

Takanobu SAWADA[1], Shota ISHITSUKA[1], Masaaki MOTOZAWA[2], Kaoru IWAMOTO[3], Hirotomo ANDO[4], Tetsuya SENDA[4], and Yasuo KAWAGUCHI[1]

[1] Department of Mechanical Engineering, Tokyo University of Science.
[2] Corresponding Author. Department of Mechanical Engineering, Tokyo University of Science. 2641 Yamazaki, Noda, Chiba 278-8510, Japan. Tel.: +81 4 7122 9589, Fax: +81 4 7123 9814, E-mail: motozawa@rs.noda.tus.ac.jp
[3] Department of Mechanical Systems Engineering, Tokyo University of Agriculture and Technology.
[4] National Maritime Research Institute.

ABSTRACT

Streamwise development of the turbulent structure of the drag-reducing channel flow using a dosed polymer solution from a wall was investigated experimentally. Particle image velocimetry (PIV) was employed to investigate the turbulent structure in the *x*-*y* plane and we carried out PIV measurements downstream at three positions: 250 *mm* (position 1), 800 *mm* (position 2), and 1350 *mm* (position 3) from the leading edge of the dosing wall. The Reynolds number based on the channel height and the bulk mean velocity was set to 40,000. The concentration of dosing polymer solution was 100 ppm. As a result of the experiments, Reynolds shear stress and root mean square (RMS) of the wall normal velocity fluctuation gradually decreased downstream. Corresponding to this decrement, the drag reduction rate developed downstream and drag reduction rate of about 63% was obtained at position 3. In addition, the results of the analyses by Galilean decomposition and swirling strength showed that the suppression of the ejection around the vortical core became stronger downstream. These changes of the turbulent structure in the streamwise direction led to the development of drag reduction downstream.

Keywords: drag reduction, PIV, polymer solution, wall dosing method, swirling strength.

NOMENCLATURE

u	[*m/s*]	streamwise velocity
v	[*m/s*]	wall normal velocity
τ	[Pa]	shear stress
p	[Pa]	total pressure
L	[*m*]	length between two pressuretaps
h	[*m*]	half of the channel height
U_c	[*m/s*]	processing velocity by Galilean decomposition
U_b	[*m/s*]	bulk mean velocity
λ_{ci}	[-]	swirling strength
ω_y	[1*/s*]	vorticity
Re	[-]	Reynolds number
x	[*m*]	streamwise coordinate
y	[*m*]	wall normal coordinate
z	[*m*]	spanwise coordinate

Subscripts and Superscripts

$^+$ normalized by kinetic viscosity and shear velocity

1. INTRODUCTION

Some kinds of high-molecular-weight polymer solutions significantly reduce the skin frictional drag in turbulent flow even at rather dilute concentrations of tens of parts per million (ppm). This phenomenon was first reported by Toms [1] in 1948 and thus came to be known as the Toms effect. This drag-reducing effect has the major benefit of reducing energy consumption in industrial applications such as district heating/cooling systems. In the case of such an internal flow, many researchers have investigated the drag-reducing effects of homogeneous polymer solutions experimentally [2, 3] or using numerical simulations [4, 5, 6]. In particular, the fundamental work for the drag-reducing effect in pipe flow was carried out by Virk [7, 8]. Virk pointed out that the drag reduction depends on the polymer characteristics and polymer concentration, but saturates beyond a certain value. This limitation of the drag reduction is called the maximum drag reduction (MDR) and Virk's asymptote was defined.

Recently, there has been a growing need for novel techniquesto achieve drag reduction for an external flow, such as the flow around ship hulls. Toward such a goal, we suggested a novel method for reducing the skin frictional drag by dosing polymer solution from the whole surface of the channel wall. We called this method "wall dosing method" [9].

In contrast, one of the most well-known methods for achieving drag reduction for an external flow is to inject polymer solution from a slot; we call this method "slot injection." There have also been a large number of studies on inhomogeneous drag reduction by slot injection. Tiederman et al. [10] found that large drag reduction occurred by injecting polymer directly into the buffer layer but this drag reduction rate decreased downstream.

Although several studies on the drag reduction by slot injection were performed as mentioned above, some disadvantages of slot injection were identified. For instance, polymer injected from a slot immediately diffuses downstream of the slot and drag reduction cannot be sustained over a large region. Moreover, Iwamoto et al. [11] simulated turbulent channel flow with damping of only the near-wall turbulence and reported that large drag reduction was obtained by controlling only the near-wall turbulence. Therefore, in the case of the wall dosing method, because polymer can be provided downstream continuously and dosed polymer solution would accumulate in the near-wall region, it is possible that the frictional drag can be reduced more effectively than with slot injection.

In our previous study [9], we obtained drag reduction effect of up to 20% comparede with that in the water flow by the wall dosing method. Moreover, we measured the instantaneous velocity u-v in the x-y plane by using PIV [12], and reported that streamwise turbulent intensity increases, but wall-normal turbulent intensity and Reynolds shear stress decrease. In order to discuss the near-wall turbulent structure of the drag-reducing flow by the blown polymer solution in more detail and to obtain new information about the drag reduction mechanism, we analyzed the PIV results with Galilean decomposition and swirling strength, and reported the characteristic coherent structure of the drag-reducing flow by the dosed polymer solution from the wall [13]. This turbulent structure should change gradually downstream from the leading edge of the dosing wall. In the case of slot injection, Hou et al. [14] investigated the streamwise development of the turbulent statistics in the turbulent boundary layer drag-reducing flow, and found that Reynolds shear stress was largely suppressed near the slot, but increased downstream from the slot. Therefore, we focused on the change of the turbulent structure in the streamwise direction for the drag-reducing channel flow by wall dosing method in this study.

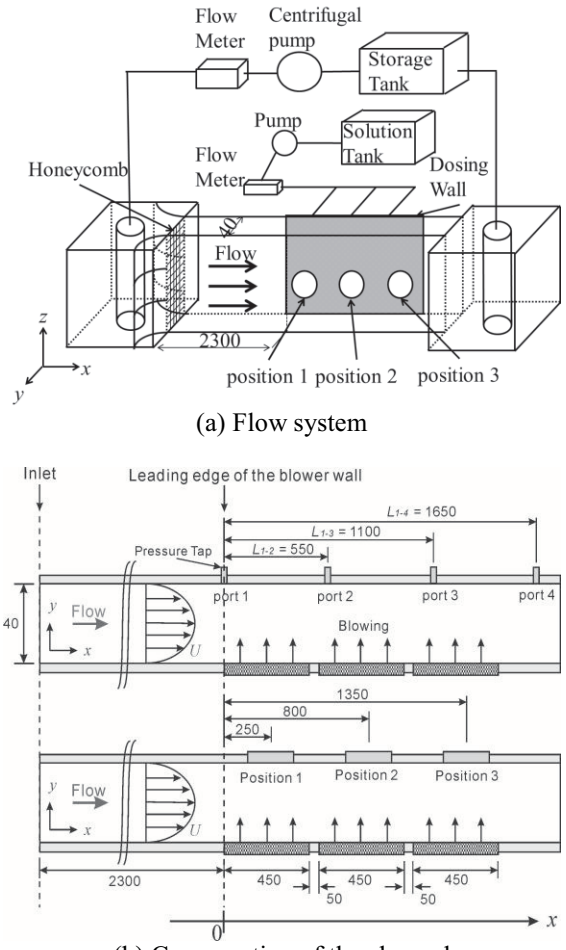

(a) Flow system

(b) Cross section of the channel

Figure 1. Experimental apparatus: (a) flow system and (b) cross section of the channel.

2. Experiment

2.1. Experimental apparatus

Figure 1 shows a schematic diagram of the experimental apparatus including (a) the flow system and (b) cross section of the channel with a dosing wall. The flow system consists of a closed-circuit water loop having a two dimensional channel with a dosing wall. The channel was made of transparent acrylic, with a length of 6000 *mm*, a width of 500 *mm*, and a height of 40 *mm* (2*h*). A honeycomb rectifier with a grating space of 10 *mm* was set at the channel entrance to remove large eddies. A storage tank was equipped with a heater and an agitator to adjust the fluid temperature. The temperature of the flowing fluid was kept stable at 25 ± 0.1°C duringthe experiments.

The wall for dosing of polymer solution was made of an SUS filter with a size of 450 *mm* × 450 *mm*. The pore size of this filter was 150 *μm*. Three dosing walls were attached to one side of the channel in a line. The leading edge of the dosing

wall was located 2300 *mm* downstream from the entrance of the channel. Polymer solution can be dosed into the channel flow from the whole surface of this dosing wall. The dosing rate of polymer solution can be adjusted by the pump and the flow meter, which are equipped with a dosing system.

We defined the position of the leading edge of the dosing wall as $x = 0$. There were four pressure taps at the opposite side of the dosing wall. These taps were located at $x = 0$ (port 1), $x = 550$ *mm* (port 2), $x = 1100$ *mm* (port 3) and $x = 1650$ *mm* (port 4) downstream from the leading edge. The static pressure gradient (Δp) between two taps can be measured. The wall shear stress upon dosing of polymer solution can be estimated by the pressure gradient and the force balance as follows:

$$\tau_{dosing} = 2 \cdot \frac{h}{L} \Delta p - \tau_{water} \quad (1)$$

where τ_{dosing} and τ_{water} are the wall shear stress with and without dosing of polymer solution at the same Reynolds number, respectively. In Eq. (1), the wall shear stress of the side wall opposite the dosing wall was estimated to be the same as the skin friction of the water flow (τ_{water}). In this experiment, because there are four pressure taps on the channel wall, we can calculate the drag reduction at various sections. The drag reduction rate is defined by the following equation:

$$DR = \frac{\tau_{water} - \tau_{dosing}}{\tau_{water}} \times 100(\%) \quad (2)$$

Reynolds number was defined on the basis of the channel height and the bulk mean velocity U_b as follows:

$$\mathrm{Re} = \frac{2hU_b}{\nu} \quad (3)$$

where ν is the kinematic viscosity of the solvent. In this study, the Reynolds number was set to 40,000.

2.2. PIV measurement

The PIV system consisted of a double-pulse laser, laser sheet optics, CCD camera with a resolution of 2048 × 2048 pixels, synchronizer and a computer with image processing software (Dantec Dynamics, Dynamic Studio ver.2.30). The double-pulse laser (New Wave Research Co., Ltd., Minilase-II/30Hz) was a combination of pair of Nd-YAG lasers, each having an output of 30 *mj/pulse* and a wavelength of 532 *nm* and the laser sheet thickness was set to 0.6 *mm*. The synchronizer, which generates pulses to control the double pulse laser, communicated with the CCD camera and the computer.

We used this PIV system to measure the instantaneous velocity field *u-v* in the *x-y* plane. To investigate the difference of the turbulent structure in the streamwise direction, PIV measurement was carried out at the following three positions downstream from the leading edge of the dosing wall: $x = 250$ *mm* (position 1), 800 *mm* (position 2), and 1350 *mm* (position 3). The PIV images were using the cross-correlation technique. The interrogation area was 64 × 64 pixels with cross-correlation with each interrogation area overlapping by 75%. Turbulent statistics were calculated using 62,500 vectors (125 vectors at each *y*-position in one velocity field × 500 velocity fields). We defined the dosing wall position as $y = 0$ in the PIV images. The flow was seeded with nylon particles as tracer particles with a mean diameter of 4.1 μm and specific gravity to water of 1.02.

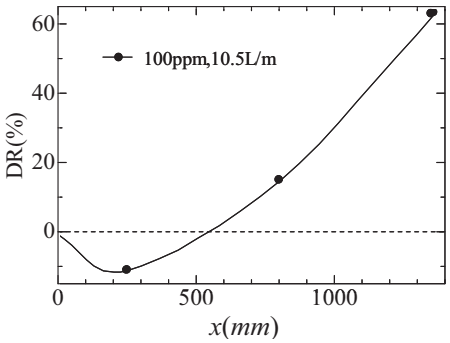

Figure 2. Streamwise development of the drag reduction.

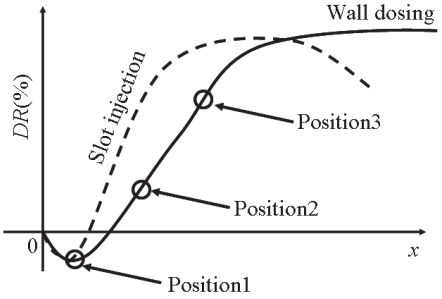

Figure 3. Conceptual model of streamwise development of the drag reduction.

2.3. Polymer solution

The polymer used in this experiment was PEO-18Z, produced by Sumitomo Seika Chemicals Co. Ltd. The major component of PEO-18Z is water-soluble poly (ethylene oxide) with a molecular weight of 4.3 million. We prepared polymer solution at 100 ppm uniform weight concentration. The dosing rate of polymer solution from the whole surface of the dosing wall was set to 10.5 L/min. In this condition, because the dosing velocity (wall-normal velocity) is much lower than the bulk mean velocity of the channel flow, the dosing flow does not influence the channel flow at all.

3. Results & Discussion

3.1. Drag reduction rate

Figure 2 shows the streamwise development of the local drag reduction rate downstream of the leading edge of the dosing wall. The drag reduction

rate was evaluated locally by the wall shear stress estimated using the pressure gradient between ports 1 and 2, ports 2 and 3, and ports 3 and 4. This figure indicates that the drag reduction rate develops downstream from the leading edge of the dosing wall. Maximum drag reduction of about 63% was obtained with wall dosing at position 3 under these experimental conditions, in which the length of the dosing wall was 1650 *mm*. In the wall dosing method, the polymer solution can be provided continuously to the buffer layer and the concentration boundary layer also develops downstream from the leading edge of the dosing wall. As a result, the drag-reducing effect also develops downstream.

Figure 3 shows a conceptual model to explain the streamwise development of the drag reduction, with a comparison between the slot injection and wall dosing. In the case of slot injection [14], the drag reduction rate develops within a short distance and is saturated downstream of the slot, but this drag reduction rate cannot be maintained at a constant level and gradually decreases. Moreover, to obtain a large drag reduction rate, it is necessary to inject a very high concentration of polymer solution (e.g. 1000 ppm or 500 ppm). According to Poreh and Hsu [15], the trend of the streamwise development of drag reduction can be categorized into the following three regimes in terms of the region downstream from the slot: (i) Development region: the drag reduction develops a maximum drag reduction rate downstream of this region; (ii) Steady region: the drag reduction rate is maintained at a constant level downstream in this region; and (iii) Depletion region: the drag reduction rate decreases downstream in this region. In contrast, in the case of the wall dosing method (this study), because the drag reduction rate continues to develop downstream as shown in Fig. 2, position 2 and position 3 correspond to the development region. If the dosing wall is longer, it seems that we can observe the steady region and the drag reduction rate should be saturated. Furthermore, this drag reduction rate can be kept at a constant level downstream of the dosing wall because the polymer solution is provided continuously into the flow downstream and the depletion region can not be observed. This ability of the wall dosing method is the most significant merit for achieving drag reduction for an external flow. If we can apply the wall dosing method to fairly long walls such as ship hulls, a large drag-reducing effect can be expected using a relatively small amount of polymer.

On the other hand, the skin frictional drag in the immediate vicinity of the leading edge of the dosing wall (i.e. position 1) increases by dosing polymer solution. This drag-increasing phenomenon was reported from an experimental study [10] and one using numerical simulation [16]. Tamano et al. [16] performed direct numerical simulation of zero

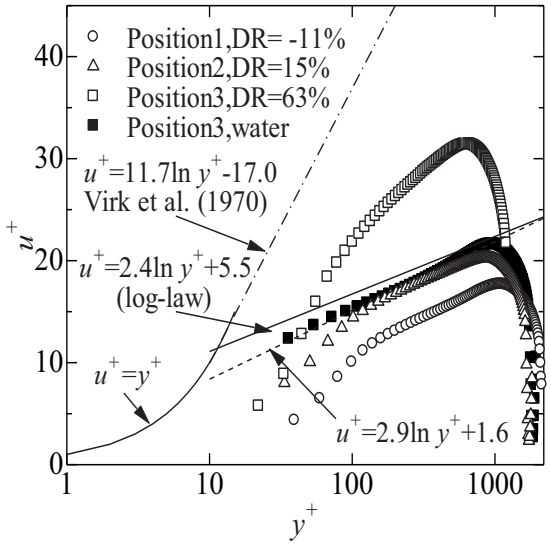

Figure 4. Mean velocity profiles.

of homogeneous viscoelastic fluids using the FINE-P model. They observed drag-increasing phenomenon at the inlet region and concluded that this occurred because the velocity field changed suddenly. In contrast, Tiederman et al. [10] measured the streamwise variation of the drag reduction from the slot in the drag-reducing channel flow by slot injection. In the case of slot injection, skin frictional drag also increases in the immediate vicinity of the slot. This is because the injected polymer solution does not mix well with the water flow and the viscosity increases locally. Almost the same phenomenon seems to occur in the wall dosing method.

3.2. Mean velocity profile

Figure 4 shows mean streamwise velocity profiles, u^+ *vs.* y^+, of water with and without dosing polymer solution at Re = 40,000. u^+ is defined as mean velocity normalized by frictional velocity u_τ and y^+ is defined as the position y normalized by u_τ/ν. The solid line in this figure represents the linear profile and log-law profile of streamwise velocity for Newtonian turbulent flow. The viscous sublayer is expressed as follows:

$$u^+ = y^+ \tag{4}$$

The buffer layer and the logarithmic layer are expressed in equation (5).

$$u^+ = 2.4 \ln y^+ + 5.5 \tag{5}$$

For comparison with our experiment, Virk's asymptote, which was obtained in the drag-reducing flow of homogeneous polymer solution by Virk [7].

$$u^+ = 11.7 \ln y^+ - 17 \tag{6}$$

is plotted with a dashed-dotted line in Fig. 4. In the water flow, the measured velocity profile slightly differs from the log-law profile of the turbulent flow of Newtonian fluid. The velocity profile obtained in our experiment was displaced below the

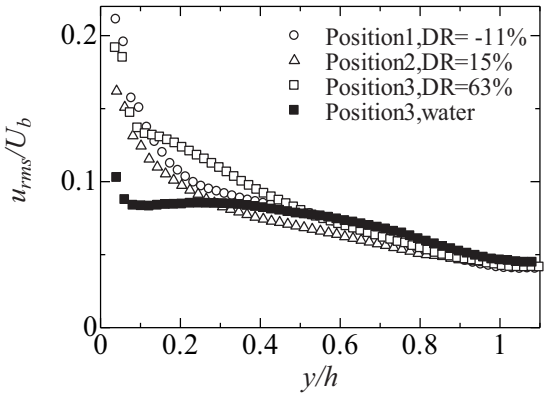

Figure 5. Distributions of RMS of streamwise velocity fluctuation.

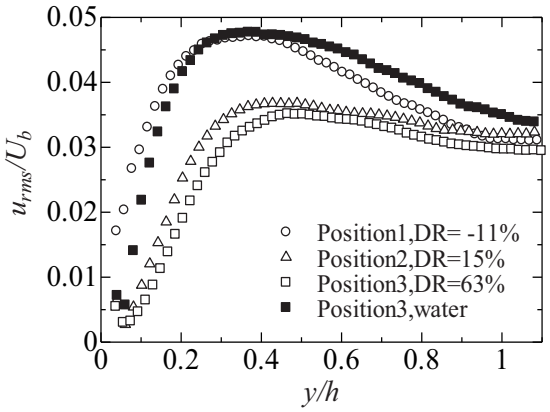

Figure 6. Distributions of RMS of wall-normal velocity fluctuation.

velocity profile of the water flow. This suggests that the roughness of the dosing wall affects the velocity profile. According to Suga et al. [17], the wall roughness influences the velocity profile of the turbulent flow and the slope of the log-law would thus change. The broken line in Fig. 4 represents the fitted line of the log-law profiles of our experiment. The logarithmic layer of our experiment is expressed as follows:

$$u^+ = 2.9 \ln y^+ + 1.6 \quad (7)$$

In the drag-reducing flow, because large drag reduction was obtained at position 3, the mean velocity profile of position 3 is upshifted in the log-law layer with a larger gradient than that of the water flow. In particular, the slope of this profile more closely resembles Virk's ultimate profile. However, since the skin frictional drag at position 1 is larger than that of water flow, the velocity profile at position1 is displaced less below the velocity profile of the water flow.

3.3. Turbulent statistics

Figure 5 shows the distribution of RMS of streamwise velocity fluctuations normalized by the bulk mean velocity. In the dosing method, because the polymer solution is only present near the dosing wall, the value of u_{rms}^+ increases near the dosing

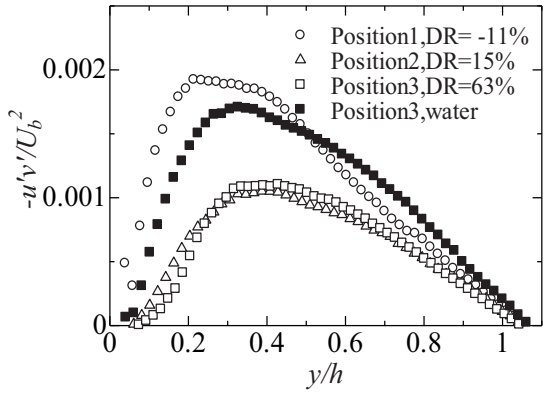

Figure 7. Distributions of Reynolds shear stress.

wall and remains almost unchanged away from the dosing wall. Ptansinski et al. [4] performed direct numerical simulation of turbulent channel flow using the FENE-P model and reported that the energy transfer from the streamwise component to the other component in the drag-reducing flow is much weaker than that of the water flow. Therefore, u_{rms}^+ near the dosing wall increases similar to the results of Ptansinski et al. In addition, from a comparison between position 2 and position 3, u_{rms}^+ increases with increasing drag reduction. This means that the polymer concentration boundary layer develops downstream from the leading edge of the dosing wall and the effect of the polymer solution on turbulence becomes greater further downstream.

Figure 6 shows the distributions of RMS of wall-normal velocity fluctuation normalized by the bulk mean velocity. In the cases of position 2 and position 3 (i.e. where drag reduction occurs), because the effect of the polymer solution becomes greater further downstream as mentioned above, the peak of v_{rms}^+ shifts away from the dosing wall and the value of the peak gradually decreases to downstream (i.e. increasing drag reduction). However, the result of position 1 is a special case. Because polymer solution does not mix well in this position, polymer cannot affect the turbulence sufficiently. Furthermore, polymer is dosed in the wall-normal direction. As a result, v_{rms}^+ slightly increases near the dosing wall.

Finally, the distribution of Reynolds shear stress is shown in Fig. 7. In the cases of position 2 and position 3, the Reynolds shear stress gradually decreases and the peak position of the Reynolds shear stress is displaced to the channel center with increaing drag reduction similar to the wall-nomal velocity fluctuation. This indicates that the dosed polymer solution directly interacts with the turbulent structures near the dosing wall and this interaction of the polymer solution becomes stronger downstream from the leading edge of the dosing wall because a polymer concentration boundary layer also develops downstream. However, the Reynolds shear stress of the drag-reducing flow is larger than that of the

water flow at position 1. Corresponding to this, skin frictional drag also increases at this position as shown in Fig. 2. This suggests that a special phenomenon, which is different from the phenomena at other positions, occurs at position 1. Because this position is in the immediate vicinity of the leading edge of the dosing wall, dosed polymer solution does not mix well and the amount of polymer provided from the wall is relatively low. Therefore, in the region near the leading edge of the dosing wall, because dosed polymer cannot act sufficiently to produce drag reduction, the skin frictional drag increases. More detailed experiments are needed to clarify this drag increasing phenomenon.

3.4. Turbulent structure

3.4.1. Analytical method

Galilean decomposition

Adrian et al. [18] proposed the Galilean decomposition which visualizes the uniform momentum zone in instantaneous velocity fields. This method can be used to deduce arbitrary velocity from the original velocity fields as per the following equation,

$$U_c = u - \alpha U_b \quad (8)$$

where U_c, u, α, and U_b are the processing velocity by Galilean decomposition, original velocity, proportional constant, and bulk velocity, respectively. In this paper, we give the proportional constant as $\alpha = 0.8$.

Swirling strength

Vorticity is a very useful method to visualize vortices in flow fields. However, because vorticity includes rotation and shear, we cannot extract only vortex cores. The using of swirling strength, proposed by Zhou et al. [19], is an effective method that can identify only vortex cores. The swirling strength, λ_{ci}, is defined as the magnitude of the imaginary part of the eigenvalue of the local velocity gradient tensor.

3.4.2. Streamwise change in turbulent structure

Figures 8-10 show the turbulent structures of water flow (Fig. 8), drag-reducing flow at position 1 (Fig. 9), and drag-reducing flow at position 3 (Fig. 10). In each figure group, the top figure (i) shows the contour of the Galilean decomposition and instantaneous velocity vectors, the middle figure (ii) shows the contour of the swirling strength, and the bottom figure (iii) shows the instantaneous Reynolds shear stress distribution. In addition to these figures, we describe the conceptual model as shown in Fig. 11 to aid understanding.

In the case of water flow, Fig. 8-(i) indicates that the individual group of the hairpin vortex in the same streamwise velocity, called a hairpin vortex packet, can be observed and that a velocity difference exists between each packet. The boundary on this velocity difference is called a shear layer, which is represented by the white line in Fig. 8-(i). The spanwise vortices that correspond to the hairpin vortex head can be seen on the shear layer by analysis of the swirling strength, as shown in Fig. 8-(ii). These vortex heads are denoted by white circles. Moreover, Fig. 8-(iii) indicates that strong negative Reynolds shear stress exists under the vortex cores. Therefore, Reynolds shear stress is produced under the head of a hairpin vortex. This turbulent structure of the water flow agrees with the hypothesis of Adrian et al. [18] and we define this structure as "water-like structure" in this paper.

In contrast, in the case of the drag-reducing flow at position 3, a characteristic structure was observed. Fig. 10-(i) indicates that the inclination angle of the shear layer becomes small compared with the water flow represented by the white broken line. It seems that this is because the ejection motions in the near-wall region are suppressed by the dosed polymer solution. In addition, the hairpin vortex cores along the shear layer are markedly diminished. However, the vortex core exists near the inclined shear layer, the same as in the water flow, and the group of clockwise vortex (CV) cores and the group of counterclockwise vortex (CCV) cores are arranged alternately bordering the shear layer, as shown in Fig. 10-(ii). Moreover, Fig. 10-(iii) indicates that there are strong interaction motions in the near-wall region. Examining the vectors carefully, these interaction motions are wall-ward interactions and can be confirmed under the shear layer. This characteristic behavior (i.e. decrease of ejection motions) leads to a decrease of the Reynolds shear stress and causes drag reduction. We define this characteristic structure as "polymer-affected structure" in this paper. We summarize the features of water-like structure and polymer-affected structure in Table 1.

Finally, we would like to consider the drag-reducing flow of position 1. As shown in Fig. 9-(i), the shear layer and hairpin vortex cores can be observed similarly to those in the water flow and the inclination angle of the shear layer is hardly changed. Therefore, a water-like structure is observed. However, in addition to this water-like structure, we can find the polymer-affected structure of the drag-reducing flow by dosed polymer solution. Focusing on the near-wall structure, the group of CV cores and the group of the CCV vortex cores are arranged alternately, but the scale of this structure at position 1 is smaller than that at position 3, as shown in Fig. 9-(iii). Therefore, there seems to be a common structure between the water-like structure and the polymer-affected structure in the drag-reducing flow by the wall dosing method at position 1. Therefore, in the region in the immediate vicinity of the leading edge of the dosing wall, the layer where the polymer

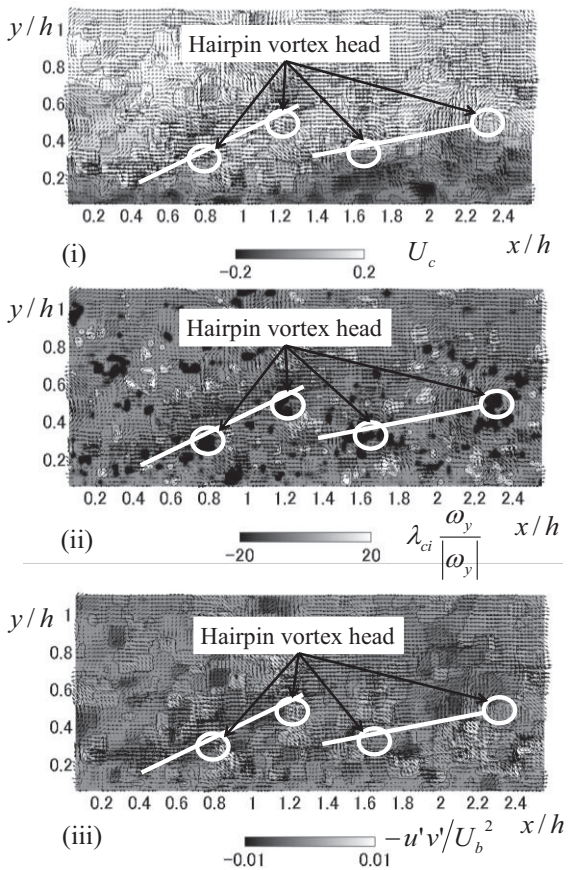

Figure 8.

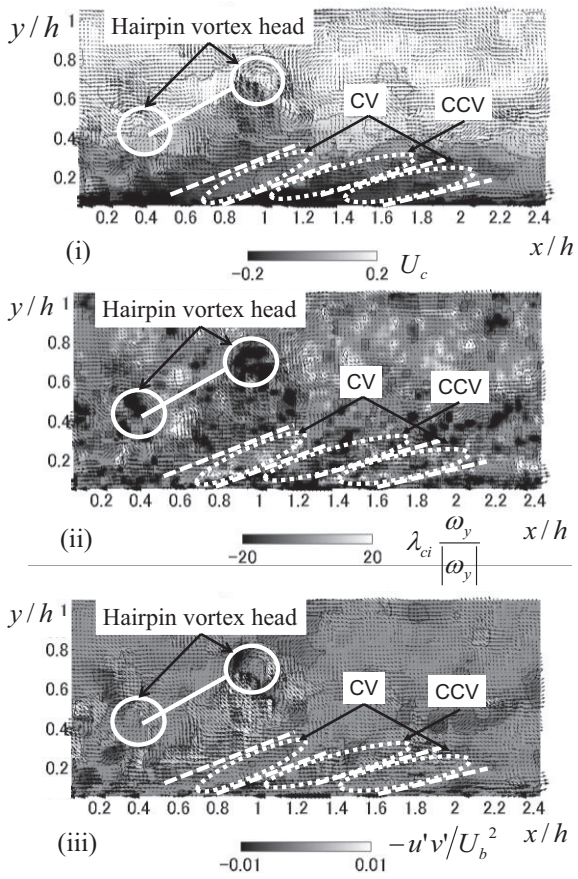

Figure 9.

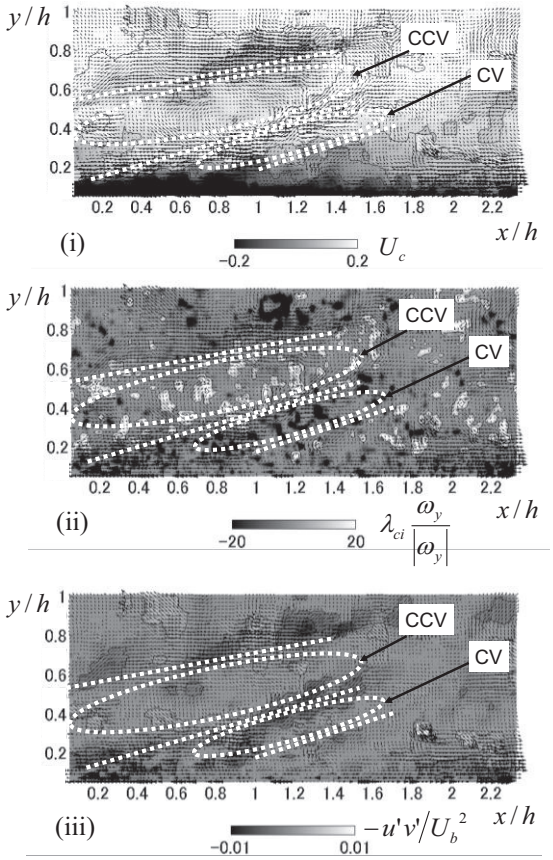

Figure 10.

Figure 8. Turbulent structure of water flow,. In these figures, top figure (i) by Galilean decomposition, middle figure (ii) by swirling strength, and bottom figure (iii) contour of instantaneous Reynolds shear stress

Figure 9. Same as Fig.8 for drag-reducing flow at position 1.

Figure 10. Same as Fig.8 for drag-reducing flow at position 3.

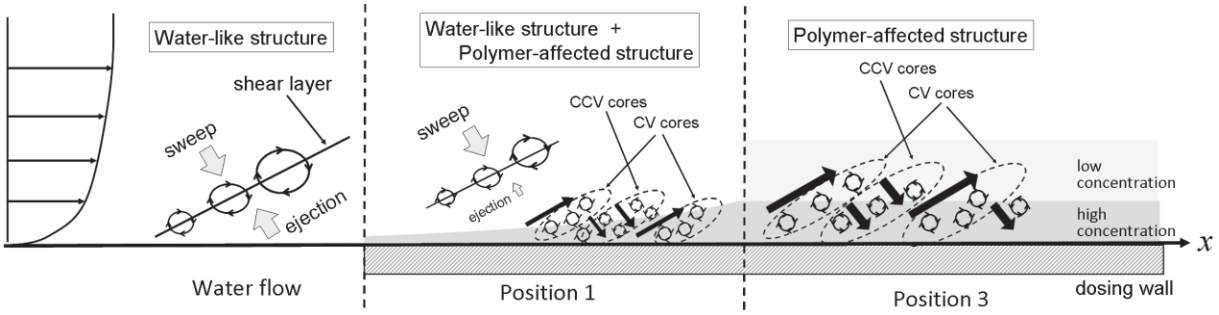

Figure 11. Conceptual model for the streamwise change of the turblent structure of the drag-reducing flow by dosed polymer solution.

Table 1. Feature of the water-like structure and polymer-affected structure.

	Water-like structure	Polymer-affected structure
Hairpin vortex packet	Develops	Hardly observed
Shear layer	Strong, Large inclination angle	Weak Small inclination angle
Coherent motion	Ejection Sweep	Sweep Wall-ward interaction
CV and CCV	Irregular	Zonal
Skin frictional drag	Large	Low

solution affects the turbulent structure is present near the dosing wall, and there is turbulence of Newtonian fluid away from this layer. This characteristic structure causes the increment of the skin frictional drag.

4. CONCLUSION

We measured the velocity field *u-v* in the *x-y* plane in drag-reducing flow with dosed polymer solution from the channel wall using a PIV system. The experiments showed that drag reduction developed downstream and that Reynolds shear stress and RMS of wall-normal velocity fluctuation gradually decreased downstream. However, drag reduction and Reynolds shear stress increased at a position near the leading edge of the dosing wall. In addition, characteristic turbulent structure was observed in the drag-reducing flow by dosed polymer solution. At position 3, the hairpin vortex cores along the shear layer were markedly diminished, but the vortex core existed near the inclined shear layer. The strong interaction motions could be observed in the near-wall region. In contrast, at position 1, which was near the leading edge of the dosing wall, the structure with which water-like structure and the characteristic structure in the drag-reducing flow was observed.

REFERENCES

[1] Toms, B. A., 1948, *Proc. 1st Int. Cong. Rheology*, Amsterdam, pp. 135-141.

[2] Warholic, M. D. et al., 2001, *Exp. Fluid*, 31, pp. 474-483

[3] White, C. M. et al., 2004, *Exp. Fluids*, 36, pp. 62-69.

[4] Ptasinski, P. K. et al., 2003, *J. Fluid Mech.*, 490, pp. 251-291.

[5] Spalart, P. and Allmaras, S., 1992, *Technical Report*, AIAA-92-0439.

[6] Den Toonder, J. M. J. et al., 1997, *J. Fluid Mech.*, 337, pp. 193-231.

[7] Virk, P. S., 1971, *J. Fluid Mech.*, 45, pp. 225-246.

[8] Virk, P. S., 1975, *AIChE J.*, 21, pp. 625-656.

[9] Motozawa, M. et al., 2009, *Proc. ExHFT-7*, Krakow, pp. 1025-1035

[10] Tiederman, W. G. et al., 1985, *J. Fluid Mech.*, 156, pp. 419- 437.

[11] Iwamoto, K. et al., 2005, *Phys.Fluids*, 17, 011702.

[12] Motozawa, M. et al., 2012, *Flow, Turbul. Comb.*, 88, pp. 121-141.

[13] Ishitsuka, S. et al., 2011, *J. Phys.: Conf. Series*, 318, 092017.

[14] Hou, Y. X. et al., 2008, *J. Fluid Mech.*, 597, pp. 31-66.

[15] Poreh, M. et al., 1972, *J. Hydronautics*, 6, pp. 27-33.

[16] Tamano, S. et al., 2011, *J. Fluid Mech.*, 686, pp. 352-377.

[17] Suga, K. et al., 2010, *Int. J. Heat and Fluid Flow*, 31, pp. 974-984.

[18] Adrian, R. J. et al., 2000, *J. Fluid Mech.*, 422, pp. 1-54

[19] Zhou, J. et al., 1999, J. Fluid Mech., 387, pp. 353-396.

Conference on Modelling Fluid Flow (CMFF'12)
The 15th International Conference on Fluid Flow Technologies
Budapest, Hungary, September 4-7, 2012

NUMERICAL SOLUTION OF TURBULENT FLOWS IN A CHANNEL WITH VARIOUS BACKWARD-FACING INCLINED STEPS

Petr LOUDA[1], Jaromír PŘÍHODA [2], Karel KOZEL [3], Petr SVÁČEK [3]

[1] Corresponding Author. Dept. of Technical Mathematics, Czech Technical University in Prague, Karlovo nám. 13, CZ-121 35 Prague 2, Czech Republic, E-mail: petr.louda@fs.cvut.cz
[2] Institute of Thermomechanics, Czech Academy of Sciences. E-mail: prihoda@it.cas.cz
[3]Dept. of Technical Mathematics, Czech Technical University in Prague. E-mail: karel.kozel@fs.cvut.cz

ABSTRACT

The work deals with the numerical solution of incompressible turbulent flow in a channel with the backward-facing step having various inclination angles. Also, the inclination of upper wall is considered. The mathematical model is based on Reynolds averaged Navier-Stokes equations. The governing equations are closed by the explicit algebraic Reynolds stress (EARSM) model according to Wallin (2000) and for comparison by linear eddy viscosity models (SST, TNT k-ω). The numerical solution is carried out partly by the implicit finite volume method based on the artificial compressibility and partly by the finite element method. Majority of results is obtained by 2D simulations, but the test simulation of 3D flow is considered too. The numerical results are compared with experimental data by Makiola (1992) and Driver and Seegmiller (1985). The computational results are compared with experiments in terms of friction coefficient, velocity profiles and recirculation length.

Keywords: backward facing step, EARSM turbulence model, one sided diffuser

NOMENCLATURE

a_{ij}	[1]	dimension-less anisotropy tensor
c_f	[1]	friction coefficient
H	$[m]$	step height
k	$[m^2/s^2]$	turbulent energy
ν	$[m^2/s]$	kinematic viscosity
Ω_{ij}	$[s^{-1}]$	rotation rate tensor
ω	$[s^{-1}]$	specific dissipation rate
p	$[m^2/s^2]$	static pressure divided by density
Re	[1]	Reynolds number
S_{ij}	$[s^{-1}]$	strain rate tensor
t	$[s]$	time
τ	$[s]$	turbulent time scale
τ_{ij}	$[m^2/s^2]$	Reynolds stress tensor
u_i	$[m/s]$	Cartesian velocity components
x_i	$[m]$	Cartesian coordinates

1. INTRODUCTION

In this work, different geometrical configurations of backward facing step flow are numerically simulated. The mathematical model is based on the Reynolds averaged Navier-Stokes equations. The turbulence models considered use eddy viscosity approximation or an explicit algebraic Reynolds stress (EARSM) constitutive relation. The models use very similar k-ω system of equations for turbulent scales, including so called cross-diffusion term.

The measurement of flow around basic, perpendicular backward facing step over wide range of Reynolds numbers from laminar to fully turbulent regimes is given by Armaly et al [1]. The step was very confined, since the expansion ratio was approximately 2 (height of the channel behind the step : height of the channel in front of the step). Measurements of less confined flow over perpendicular step, with expansion ratio 1:8, presented Driver and Seegmiller in their detailed study [3]. They also superimposed to the flow pressure gradients by deflecting upper wall of the channel. In this work, the simulations of cases with adverse pressure gradient are considered. Another generalization of the geometry was considered by Makiola [10] who measured steps with inclined wall. For smallest inclination angle, 10°, the geometry could better be labeled as one-sided diffuser than step.

The sensitivity of recirculation length to the artificial diffusion of numerical scheme can be large. In experiment, the point of reattachment is always unsteady. In steady simulations based on RANS equations there is small margin between early reattachment (too diffusive method) and very unsteady behavior of reattachment. The simulations in this work use either an implicit finite volume (FV) method or a finite element (FE) method. The implementation of the methods by the authors is independent. Their results are compared which enables to distinguish the influence of turbulence model from the influence of its numerical approximation. Also the "do-nothing"

boundary condition routinely used in FE methods was loosely transferred to FV method to improve its performance in cases with inclined upper wall.

In this paper, the cases of Driver-Seegmiller and Makiola are presented with emphasis on inclined geometries. The authors published simulations of perpendicular step in 2D and 3D e.g. also in papers [7, 6, 8].

2. Mathematical model

The flow is governed by the Reynolds-averaged Navier-Stokes equations (RANS) in Cartesian coordinates

$$\frac{\partial u_j}{\partial x_j} = 0,$$
$$\frac{\partial u_i}{\partial t} + \frac{\partial (u_i u_j + \delta_{ij} p)}{\partial x_j} = \frac{\partial (2\nu S_{ij} - \tau_{ij})}{\partial x_j}, \quad (1)$$

where x_i is Cartesian coordinate, u_i mean velocity vector, t time, p mean static pressure divided by constant density of fluid, δ_{ij} Kronecker delta, ν kinematic viscosity, $S_{ij} = \left(\partial u_i/\partial x_j + \partial u_j/\partial x_i\right)/2$ mean strain rate tensor, and τ_{ij} is Reynolds stress tensor.

Turbulence modelling

Two classes of closure for the Reynolds stress τ_{ij} are applied: the eddy viscosity model and an explicit algebraic Reynolds stress model (EARSM). Both classes of models use k-ωtwo-equation system for turbulent scales prediction. The eddy viscosity models considered are:

- SST model by Menter [11]
- TNT k-ω model by Kok [5]

The EARSM model considered here was proposed by Wallin and Johansson [13] and further optimized by Hellsten [4].

The models based on eddy viscosity use the constitutive relation for Reynolds stress in the form

$$\tau_{ij} = 2k\delta_{ij}/3 - 2\nu_t S_{ij}, \quad (2)$$

where $k = \tau_{ii}/2$ is turbulent energy. The EARSM closure in terms of dimensionless anisotropy tensor a_{ij} reads

$$\begin{aligned}\tau_{ij} &= a_{ij}k + \frac{2}{3}k\delta_{ij}, \quad (3)\\ a_{ij} &= \beta_1\tau S_{ij}\\ &\quad + \beta_3\tau^2(\Omega_{ik}\Omega_{kj} - II_\Omega\delta_{ij}/3)\\ &\quad + \beta_4\tau^2(S_{ik}\Omega_{kj} - \Omega_{ik}S_{kj})\\ &\quad + \beta_6\tau^3(S_{ik}\Omega_{kl}\Omega_{lj} + \Omega_{ik}\Omega_{kl}S_{lj} - 2IV\delta_{ij}/3)\\ &\quad + \beta_9\tau^4(\Omega_{ik}S_{kl}\Omega_{lm}\Omega_{mj} - \Omega_{ik}\Omega_{kl}S_{lm}\Omega_{mj}),\end{aligned}$$

where τ is turbulent time scale, $\Omega_{ij} = \left(\partial u_i/\partial x_j - \partial u_j/\partial x_i\right)/2$ is mean rotation rate tensor and II_Ω, IV are invariants formed from S_{ij}, Ω_{ij}. The coefficients β are given by Hellsten [4], who optimized original propositions of Wallin. In 2D mean flow, the only non-zero coefficients should be β_1 and β_4. However, due to the approximate explicit solution, the other coefficients are not exactly zero. In this work, the full 3D form (3) is used.

All the k-ω systems of equations employed in the above-mentioned models are very similar, including so-called cross-diffusion terms in the ω-equation. This makes possible to observe the influence of constitutive relation. For the form of the respective k-ω equations see the references.

3. NUMERICAL METHODS

A finite volume and finite element methods were used to solve the system of RANS equations.

3.1. *Finite volume method*

The artificial compressibility method [2] is used to obtain equation for pressure. It consists of adding a pressure time derivative term $a^{-2}\partial p/\partial t$ into the continuity equation, where a is selectable positive parameter, which should ensure fast convergence to a steady state solution. In this work it is chosen equal to the maximum inlet velocity. The discretization is done by a cell centered finite volume method (FVM) with hexahedral finite volumes:

$$\frac{dW_{i,j,k}}{dt}\Delta V_{i,j,k} + Rez(W)_{i,j,k}\Delta V_{i,j,k} = 0, \quad (4)$$

$$Rez(W)_{i,j,k} = \frac{1}{\Delta V_{i,j,k}}\sum_{\alpha=1}^{6}(F^I - F^V)_\alpha \Delta S_\alpha - Q_{i,j,k} \quad (5)$$

where the the unknown cell average $W_{i,j,k} = (p, u_1, u_2, u_3)_{i.j,k}$ and F^I, F^V are inviscid and viscous flux through boundaries of finite volume (i, j, k). The ΔV denotes size of the finite volume. The convective terms are discretized using third order van Leer upwind interpolation. The viscous terms are approximated using 2nd order central approximation on dual finite volume grid of octahedrons (quadrilaterals in 2D) constructed over each face of primary finite volume. The Eq. (4) is integrated in time by the backward Euler (implicit) scheme

$$\frac{W_{i,j}^{n+1} - W_{i,j}^{n}}{\Delta t} + Rez(W)_{i,j}^{n+1} = 0 \quad (6)$$

where the steady residual $Rez(W)_{i,j,k}^{n+1}$ is linearized by Newton method. The linear system of equations is solved by block relaxation method. For more details see [9]. The turbulence model equations are solved in the same manner however decoupled from the RANS equations.

3.2. *Finite element method*

The finite element method (FEM) is based on approximation of the weak formulation of the mathematical model. For the approximation of

RANS equations the so called "equal-order" choice of finite element pair on regular triangulation τ_h of the computational domain is used, i.e. continuous piecewise linear velocity and pressure approximations. In that case the method requires the use of an additional stabilization due to the violation of the Babuška-Brezi inf-sup condition as well as due to high Reynolds numbers. The following stabilization procedure based on the use of both the Streamline-Upwind/Petrov-Galerkin and Pressure Stabilizing/Petrov-Galerkin(SUPG/PSPG) method together with div-div stabilization is used, cf. [12]. Find the finite element approximations $U = (u_1, u_2, p)$ such that (u_1, u_2) satisfy approximately the Dirichlet boundary conditions, and

$$a(U;U,V) + \mathcal{L}_h(U;U,V) + \sum_{K\in\tau_h} \tau_K \Big(\nabla\cdot\mathbf{u}, \nabla\cdot\mathbf{N}\Big) = f(V) + \mathcal{F}_h(V) \quad (7)$$

holds for any $V = (N_1, N_2, q)$, such that N_1, N_2 are finite element functions being zero on the Dirichlet part of boundary and q is the finite element function from the pressure space. Further, the forms $a,\ f$ are the Galerkin terms arising from weak formulation of RANS equations, and the forms $\mathcal{L}_h(U;U,V),\ \mathcal{F}_h(V)$ are the SUPG/PSPG stabilization terms, for details see [12].

The k-ω turbulence model is time discretized by BDF2 formula, linearized, and approximated by the finite element method stabilized by the Streamline Upwind/Petrov-Galerkin(SUPG) method together with an additional nonlinear crosswind diffusion. For approximations of k and ω the space V_h of continuous piecewise linear functions on the regular triangulation τ_h are used. The nonlinear stabilized problem on each time step then reads: Find k and $\omega \in V_h$ such that

$$B_{SUPG}(k,\omega;\varphi_1,\varphi_2) + B_{ADC}(k,\omega;\varphi_1,\varphi_2) = L_{SUPG}(\varphi_1,\varphi_2) \quad (8)$$

holds for any test functions $\varphi_1, \varphi_2 \in V_h$. Here B_{SUPG} and L_{SUPG} are the linear forms arising from the SUPG formulation of equations for k and ω, and the form B_{ADC} is the additional crosswind dissipation suppressing the non-physical oscillations.

3.3. Boundary conditions

The boundary of the solution domains consists of inlet boundary, smooth walls and outlet boundary. The following boundary conditions are prescribed:

- inlet: developed turbulent flow
- walls: zero velocity and turbulent energy k, sufficiently large value of ω
- outlet: Neumann boundary condition for all velocity components, k and ω.

The used finite volume method requires the pressure to be specified on the boundaries. Generally it is extrapolated from the interior of the domain. However, the outlet boundary needs more attention since extrapolating pressure makes the solution strongly dependent on the length of the domain if the channel is diverging. As a remedy an approximation of the so called "do-nothing" condition, implicitly applied in FEM, was used in finite volume method. The pressure p in the outlet is computed using

$$\nu\frac{\partial u}{\partial x} - p = C \quad (9)$$

where ν is viscosity, u streamwise velocity, p pressure and C arbitrary constant (e.g. reference pressure).

4. NUMERICAL RESULTS

4.1. Step with inclined upper wall

First the step with inclined upper wall is considered according to measurements of Driver and Seegmiller at $Re_H = 37500$. The positive inclination angle up to 10° introduces an adverse pressure gradient to the flow. The step is perpendicular. The computed length of the recirculation zone behind the step is given in Fig. 1 for 3 turbulence models, in comparison with the measurement. The results are obtained by finite volume method. The next Fig. 2 shows the influence of numerical method on the same quantity.

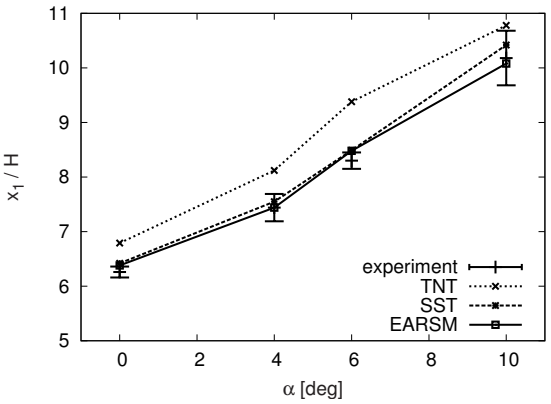

Figure 1. Recirculation length vs. upper wall deflection angle for Driver-Seegmiller case, comparison of turbulence models, FV method

The Fig. 3 shows computed friction coefficient on the bottom wall behind the step, again compared with Driver-Seegmiller [3].

These differences between FEM and FVM approach can be observed:

- FEM is slightly more viscous than FVM
- FVM needs longer domain for acceptable results than FEM, this is more remarkable with diverging channel. The length of channel for FEM was $35H$. For FVM and inclination angle of 10°, the length was $45H$. The sensitivity of TNT model to the

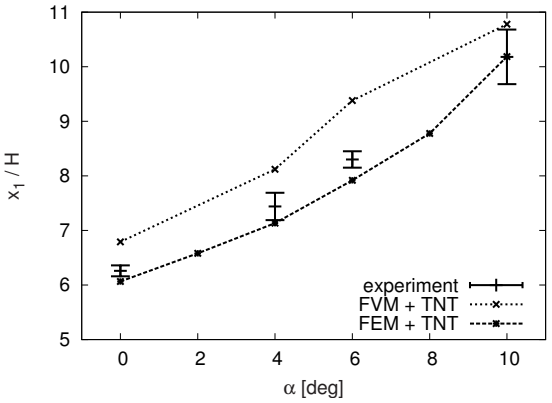

Figure 2. Recirculation length vs. upper wall deflection angle for Driver-Seegmiller case, comparison of FV and FE method, TNT turbulence model

length of domain is higher than that of SST or EARSM model.

4.2. Inclined step

Makiola measured [10] flow over perpendicular step as well over inclined steps. Here the cases with expansion ratio (channel height behind step : channel height in front of the step) 2 is considered. The length of separation is sensitive to the turbulent scales in the inlet. Makiola claims developed channel flow in front of the step, however the velocity profile at a distance $2H$ in front of the step is non-symmetric. In simulations, the developed channel flow was prescribed at this position. The length of the domain behind the step was only $16H$ in order to use same length for 2D and 3D simulation. The following results were achieved by finite volume method with EARSM turbulence model. The inclination angles of the step were $\beta = \{10, 25, 45, 90\}^\circ$.

The computed velocity profiles at different streamwise positions are compared with measurement in Fig. 4 for Reynolds number $Re = 15\,000$ and 4 inclination angles. The agreement with experiment for larger inclination angles is satisfactory. However for small inclination angle of 10°, the simulation does not capture well the flow above inclined wall. Due to this, the position of maximum velocity is shifted towards the upper wall. Downstream of the step, the velocity approaches the measured one. Similar observation holds for results at Reynolds number $Re = 64\,000$, shown in Fig. 5.

The next Figure 6 shows the flow-field in terms of streamlines. It is apparent that for large inclination angles, the main recirculation remains unaffected by the inclination.

The simulation has been carried out in 3D as well. The span of the channel was 16 H (vs. 40 H in measurement), whereas the length of the domain was same as in 2D. The comparison of velocity profiles in the center-plane with measurement is shown in Fig. 7.

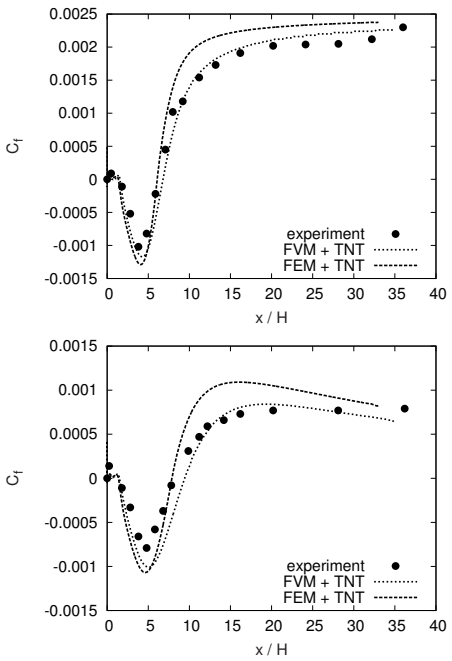

Figure 3. Friction coefficient for Driver-Seegmiller case, comparison of FV and FE methods, TNT turbulence model. Above: inclination angle $\alpha = 0^\circ$, below:$\alpha = 6^\circ$

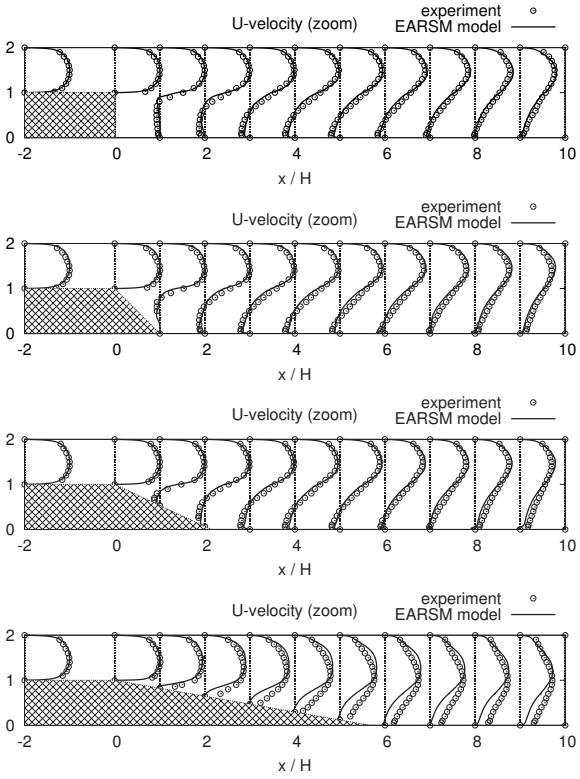

Figure 4. Velocity profiles of 2D simulation compared with experiment, $Re = 15\,000$

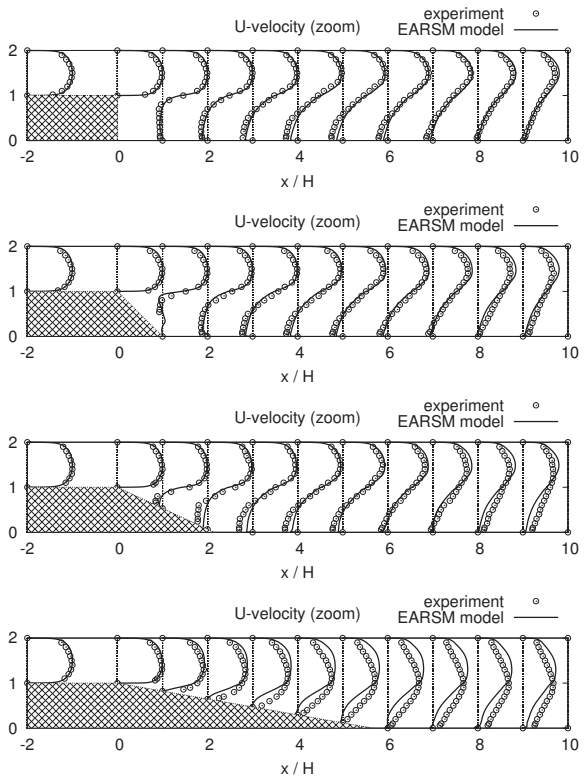

Figure 5. Velocity profiles of 2D simulation compared with experiment, $Re = 64000$

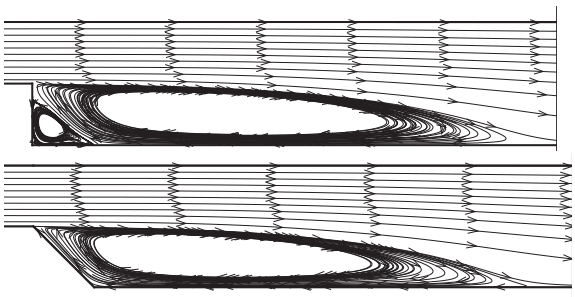

Figure 6. Computed streamlines for the Makiola case, $Re = 64\,000$

The agreement with experiment is same as in 2D, cf. Fig. 4.

The Fig. 8 shows secondary flow at different streamwise positions starting approximately at the edge of the step. Compared are channel with perpendicular step and with step inclined at $10°$. The secondary flow starts as developed channel flow, i.e. with 2 secondary vortices in each corner. After the perpendicular step, there appears a flow towards the center-plane and later large vortex in the lower corner develops which spreads to the center and gradually decays into flow towards center-plane and vertical vortex close to the side wall. With inclined wall, the flow towards center-plane is more strong and gradually a recirculation towards side walls near bottom wall appears.

The recirculation length measured from the edge of the step agrees well with measurement for higher

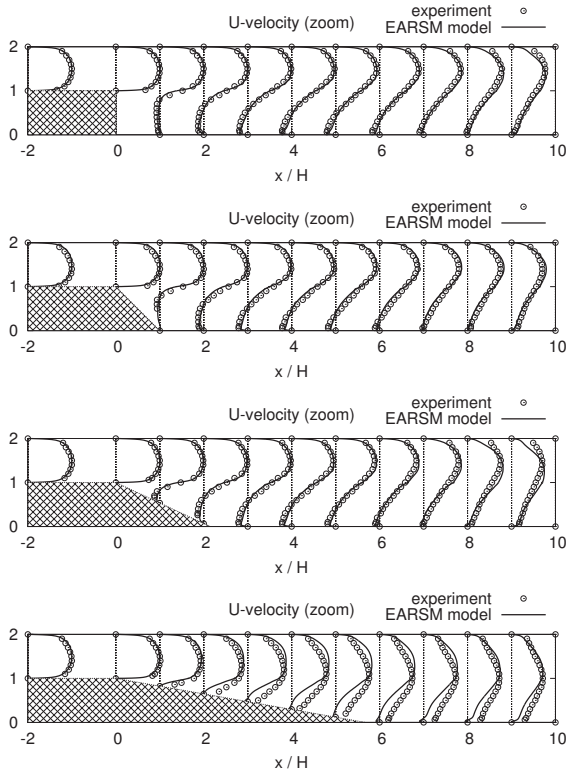

Figure 7. Comparison of 3D simulation with experiment, $Re = 15\,000$

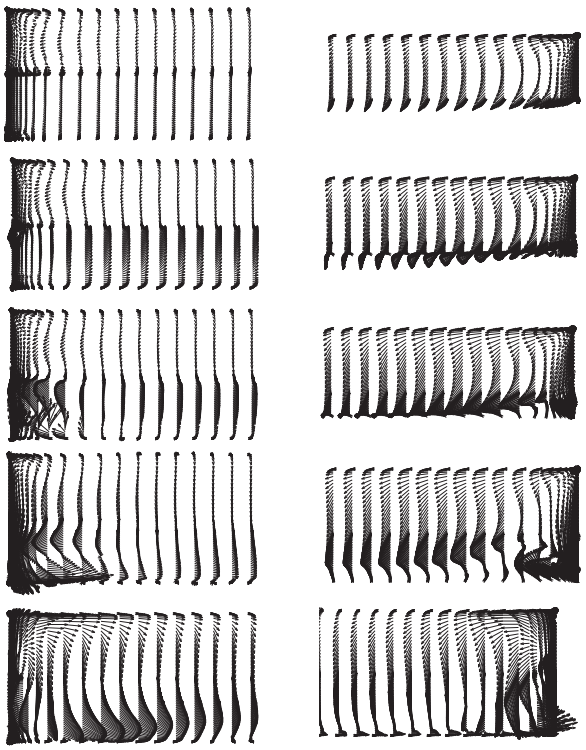

Figure 8. Velocity vectors at streamwise positions $x = \{0, 1, 2, 4, 8\}H$, $Re = 15000$. Left: perpendicular step, right: step inclined at $10°$. Only approx. 1/4 of the span shown

Reynolds numbers (33 000, 47 000, 64 000), however for $Re = 15\,000$ the predicted length is higher than measured (approx. $9H$ vs. $8.2H$ for perpendicular step). The trend of decreasing recirculation length with decreasing inclination angle is captured too for higher Re.

5. SUMMARY

Numerical simulations of incompressible flow over backward facing steps with various inclinations were presented. The cases of Driver-Seegmiller with inclined upper wall over perpendicular step were simulated by finite volume and finite element method with different eddy viscosity turbulence models and an EARSM turbulence model. The results agree well with experiments for all turbulence models. The used finite element method is more viscous than the finite volume method and its results are less sensitive to the length of the solution domain.

Next inclined step as measured by Makiola was considered. The simulation has been carried out by finite volume method with EARSM turbulence model. The agreement with experiment is satisfactory for lower inclination angles of the step and higher Reynolds numbers. For inclination of 10° the diffuser-like flow appears difficult to predict. The same behavior was observed with 2D as well as with corresponding 3D simulation.

ACKNOWLEDGMENTS

This work was partially supported by grants No.103/09/0977 and P101/10/1230 of Czech Science Foundation.

References

[1] B. F. Armaly, F. Durst, J. C. F. Pereira, and B. Schönung. Experimental and theoretical investigation of backward-facing step flow. *J. Fluid Mech.*, 127:473–496, 1983.

[2] A. J. Chorin. A numerical method for solving incompressible viscous flow problems. *J. of Computational Physics*, 2(1):12–26, 1967.

[3] D. M. Driver and H. L. Seegmiller. Features of a reattaching turbulent shear layer in divergent channel flow. *AIAA J.*, 23:163–171, 1985.

[4] A. Hellsten. New advanced k-ω turbulence model for high-lift aerodynamics. *AIAA J.*, 43:1857–1869, 2005.

[5] J. C. Kok. Resolving the dependence on free stream values for the k-omega turbulence model. Technical Report NLR-TP-99295, NLR, 1999.

[6] K. Kozel, P. Louda, and J. Příhoda. Numerical solution of 2D and 3D backward facing step flows. *PAMM*, 5(1):467–468, 2005.

[7] K. Kozel, P. Louda, and J. Příhoda. Numerical modelling of turbulent flow over three dimensional backward facing step. In T. Lajos and J. Vad, editors, *Conference on modelling fluid flow CMFF'06*, pages 448–455, Budapest, 2006. Budapest University of Technology and Economics. ISBN 963 420 872 X.

[8] Karel Kozel, Petr Louda, Petr Sváček, and Jaromír Příhoda. Finite volume and finite element methods applied to backward facing step flows. In D. T. Tsahalis, editor, *1st International conf. From scientific computing to computational engineering*, Patras, 2004. CD-ROM.

[9] P. Louda, K. Kozel, and J. Příhoda. Numerical solution of 2D and 3D viscous incompressible steady and unsteady flows using artificial compressibility method. *Int. J. for Numerical Methods in Fluids*, 56:1399–1407, 2008.

[10] B. Makiola. *Experimentelle Untersuchungen zur Stroemung ueber die schraege Stufe*. PhD thesis, Univ. Karlsruhe, 1992. (also ERCOFTAC Classic collection database, case C.53).

[11] F. R. Menter. Two-equation eddy-viscosity turbulence models for engineering applications. *AIAA Journal*, 32(8):1598–1605, 1994.

[12] P. Sváček, M. Feistauer, and J. Horáček. Numerical modelling of flow induced airfoil vibrations problem. In *Innovation and Integration in Aerospace Sciences*, Quenn's University Belfast, 2005.

[13] S. Wallin and A. V. Johansson. A complete explicit algebraic Reynolds stress model for incompressible and compressible turbulent flows. Technical Report FFA TN 1997-51, FFA, Stockholm, 1997.

Conference on Modelling Fluid Flow (CMFF'12)
The 15th International Conference on Fluid Flow Technologies
Budapest, Hungary, September 4-7, 2012

NUMERICAL STUDY OF A TURBULENT LID-DRIVEN CAVITY FLOW. MODELS ASSESSMENT

Julian E. JARAMILLO[1 2], Roel W.C.P. VERSTAPPEN [1]

[1] Johann Bernoulli Institute for Mathematics and Computing Science,
University of Groningen, P.O. Box 407, 9700 AK Groningen, The Netherlands, E-mail: r.w.c.p.verstappen@rug.nl
[2] Corresponding Author. School of Mechanical Engineering,
Universidad Industrial de Santander, Cra 27 calle 9, Bucaramanga, Colombia, Tel.: +57 7634 4000 ext 2816, E-mail: jejarami@uis.edu.co

ABSTRACT

The main objective of this paper is to study the predictive ability of various large eddy simulation and regularization models in a turbulent lid-driven cavity flow at a Reynolds number of $10,000$. They are compared with the results from a direct numerical simulation. This flow is treated as a three-dimensional, turbulent flow with periodic boundary conditions in the spanwise direction. The influence of the domain size, the total time integration, the grid and the number of planes in the spanwise direction is assessed. It is found that a second order symmetry-preserving regularization model produces good results even for very coarse grids.

Keywords: CFD, driven cavity, DNS, LES, regularization modelling, symmetry-preserving discretization

NOMENCLATURE

L	$[m]$	cavity length
Re	$[-]$	Reynolds number
$\bar{S}_{ij}$	$[s^{-1}]$	mean rate of strain tensor
U_o	$[m/s]$	lid velocity
p	$[Pa]$	pressure
t	$[s]$	time
t_{ref}	$[-]$	time unit:L/U_o
u_i	$[m/s]$	velocity
$\bar{u}_i$	$[m/s]$	filtered velocity
V	$[m]$	filter size: $(\Delta_x\Delta_y\Delta_z)^{1/3}$
x_i	$[m]$	Cartesian coordinate in the i-direction
Δ	$[m]$	filter width
δ_{ij}	$[-]$	Kronecker delta
μ	$[Pa \cdot s]$	dynamic viscosity
ν_{sgs}	$[m^2/s]$	kinematic subgrid viscosity
ρ	$[kg/m^3]$	density
τ_{ij}	$[s]$	subgrid stress tensor
τ_w	$[Pa]$	wall shear stress

Subscripts and Superscripts

i	i-direction
o	at the lid
sgs	subgrid
x, y, z	streamwise, transversal and spanwise coordinate
$\bar{\cdot}$	volume filtered
$\tilde{\cdot}$	regularised

1. INTRODUCTION

Lid-driven cavity flow is often selected as benchmark problem for testing numerical methods for laminar flow. A few numerical studies deal with this configuration in the turbulent regime [1, 2, 3, 4]. Its relevance relies in the simplicity of the geometry and boundary conditions, while preserving interesting flow properties that turbulence involves. At Reynolds number $Re = 10,000$ two-dimensional, laminar models are inadequate and eventually misleading [5]. Therefore we treat this flow as a three-dimensional, turbulent flow with periodic boundary conditions in the spanwise direction. Here it may be emphasised that the references mentioned above apply no-slip condition in the third direction (in case the simulation is $3D$). Up to the authors knowledge there are no studies that consider the turbulent case with periodic conditions. This work is intended to fill this gap. Therefore, we have performed a direct numerical simulation (DNS). Furthermore, the resulting DNS-data are used to asses the predictive ability of various large eddy simulation (LES) and regularization models. Comparison is done in terms of mean and root mean square (rms) velocities.

The influence of the size of the computational domain in the spanwise direction is analysed first. Thereafter, a verification study is carried out to check that the DNS predictions are grid independent. The grid is stretched towards the walls of the cavity and is taken it uniform in the spanwise direction. A second-order symmetry-preserving discretization is

applied [6]. This spatial discretization is well-suited for DNS, see for instance [2, 6, 7].

The large-eddy simulations are based on the same numerical technique. The grid for the large-eddy simulations consists of $40 \times 40 \times 64$ *nodes*, which is coarser than the LES-mesh that was used by Zang et al. [1]. Various LES-models are tested, among others recently proposed eddy viscosity models that are based on the invariants of the rate of strain tensor [8]. In addition, regularization models that have been applied successfully to a differentially-heated cavity [9] have also been applied here.

The work starts with a description of the studied case in Section 2. Afterwards, the mathematical modelling and numerical method are briefly explained in Section 3. In Section 4, DNS results of mean velocities and turbulent stresses are presented. Furthermore, the performance of LES and regularization models is assessed by means of a detailed comparison with the DNS solution. Finally, concluding remarks are outlined in Section 5.

2. DESCRIPTION OF STUDIED CASE

Although the turbulent lid-driven cavity flow geometry is simple, it presents complex flow physics. Most of the work found in the literature deals with the laminar situation or simulates relatively high Reynolds numbers using a two-dimensional configuration. For three-dimensional flow at $Re = 10,000$ literature is scarce. Experimental studies have been carried out by Koseff and Street [10] and Prasad and Koseff [11] using Laser Doppler Anemometry in order to elucidate flow structure. Regarding numerical studies, large eddy and direct numerical simulations have been addressed to fully three-dimensional configurations,e.g. Leriche and Gavrilakis [3] and Verstappen and Veldman [12] did a DNS simulation in a cubic cavity, whereas Zang et al. [1] and Bouffanais et al. [4] applied a LES model to study a fully $3D$ cavity with side walls. Up to the authors best knowledge, for this Re, there are no numerical studies that use periodic boundary conditions in the spanwise direction.

In this work, a turbulent square lid-driven cavity with a Reynolds number, $Re = U_0 L/\nu = 10,000$, with one homogeneous direction ($z-$coordinate) is studied. In this configuration the flow, initially at rest, is driven by the motion of the lid. At the beginning, most of the total kinetic energy and dissipation is concentrated near the lid. The motion in this flow is maintained by the continuous diffusion of kinetic energy from the moving wall, which is initially restricted to a thin boundary layer of fluid next to the moving wall.

The mean flow moves parallel to the lid until it impinges on the downstream wall, what induces a region of strong pressure in the upper corner of the downstream (right) wall. Afterwards, the flow moves vertically downwards. This mean flow separates from the wall and hits the bottom wall, creating two counter

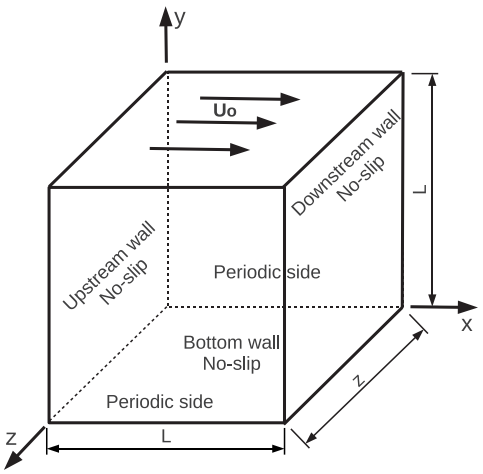

Figure 1: Sketch of the lid-driven cavity problem.

rotating eddies near both bottom corners, upstream and downstream. Then it moves upwards to generate a main vortex. For this Re a third eddy is observed near the upper corner of the upstream wall because of the underpressure generated by the lid displacement. For more details about flow physics see [3, 5].

The no-slip boundary condition is imposed for the velocity on downstream, upstream and bottom walls. On the driving boundary (top wall), a constant velocity function of the Re number is imposed, $U_0 = \nu Re/L$. In the $z-$direction, periodic boundary conditions are assumed, i.e. $\phi(x, y, 0) = \phi(x, y, L)$, (see Figure 1).

3. NUMERICAL SIMULATION

3.1. Mathematical formulation

The fluid in the cavity is assumed to be incompressible and Newtonian. Thermophysical properties are constant. Under these assumptions, the fluid flow motion is governed by the Navier-Stokes (NS) equations

$$\frac{\partial u_i}{\partial x_i} = 0 \tag{1}$$

$$\frac{\partial u_i}{\partial t} + u_j \frac{\partial u_i}{\partial x_j} = -\frac{1}{\rho}\frac{\partial p}{\partial x_i} + \nu \frac{\partial^2 u_i}{\partial x_j^2} \tag{2}$$

which are solved without further simplification when using DNS. However, in LES the effects of the smallest scales of motion are modelled, whereas the large three-dimensional unsteady turbulent motions are directly represented. In order to carry out this scales separation a volume filtering is applied by means of a spatial filter [13]. The volume-filtered Navier-Stokes equations of the fluid flow, used in LES simulations,

can be written as follows:

$$\frac{\partial \bar{u}_i}{\partial x_i} = 0 \tag{3}$$

$$\frac{\partial \bar{u}_i}{\partial t} + \bar{u}_j \frac{\partial \bar{u}_i}{\partial x_j} = -\frac{1}{\rho}\frac{\partial \bar{p}}{\partial x_i} + \frac{\partial}{\partial x_j}\left(2\nu \overline{S}_{ij} - \tau_{ij}\right) \tag{4}$$

where an overbar denotes filtered resolved quantities, τ_{ij} is the subgrid (unresolved) stress tensor that is generally modelled using the strain rate tensor of the resolved field $\overline{S}_{ij} = \frac{1}{2}\left(\frac{\partial \bar{u}_i}{\partial x_j} + \frac{\partial \bar{u}_j}{\partial x_i}\right)$, and the subgrid eddy viscosity, ν_{sgs}, as follows:

$$\tau_{ij} = \overline{u_i u_j} - \bar{u}_i \bar{u}_j \approx -2\nu_{sgs}\overline{S}_{ij} + \frac{1}{3}\tau_{kk}\delta_{ij} \tag{5}$$

Selected models, which are explained in subsection 3.2, are used to model the subgrid eddy viscosity.

In the regularization approach a smooth approximation of the nonlinear convective term is introduced to control its energetic exchanges. This method alters the convective term to reduce the production of small scales of motion [14]. In these kind of models the NS-equations are modified:

$$\frac{\partial v_i}{\partial x_i} = 0 \tag{6}$$

$$\frac{\partial v_i}{\partial t} + \widetilde{v_j \frac{\partial v_i}{\partial x_j}} = -\frac{1}{\rho}\frac{\partial p}{\partial x_i} + \nu \frac{\partial^2 v_i}{\partial x_j^2} \tag{7}$$

where the tilde in the convective term means it is regularised, and the velocity variable is changed from u_i to v_i to emphasise that the solution of (7) differs from that of (2). Details about regularization models considered are given in subsection 3.3.

3.2. Subgrid-scale LES models

For the models applied in this work the grid acts as an implicit filter in order to separate the low-frequency resolved modes and high-frequency unresolved (subgrid) modes. Therefore, a suitable approach for the subgrid eddy viscosity is needed to model turbulent scales which can not be resolved. The simplest model is the Smagorinsky model [15]. In Smagorinsky's model, subgrid viscosity is proportional to the subgrid characteristic length scale, Δ, and to a characteristic turbulent velocity.

$$\nu_{sgs} = (C_s\Delta)^2\sqrt{2\bar{S}_{ij}\bar{S}_{ij}} \equiv (C_s\Delta)^2|\bar{S}| \tag{8}$$

A shortcoming of this model is that the Smagorinsky coefficient, C_s, is a constant that must be tuned. Furthermore, this model needs a damping function to correct the near-wall behaviour of the subgrid viscosity. Therefore, in order to overcome these deficiencies several models are taken into account in this work. The first one, was presented by Nicoud and Ducros [16], who proposed a model known as wall adapting local eddy viscosity (WALE) model. This model accounts for the effects of both the strain and the rotation rate of the smallest resolved turbulent fluctuations. Moreover, it reproduces correctly the subgrid eddy viscosity behaviour near solid walls, and it does not require a second filtering operation to evaluate Smagorinsky coefficient. The second model, developed by Verstappen [17], uses two invariants q and r of the filtered strain tensor in order to correctly damp the small scales, without further phenomenological assumptions. The third model, was proposed by Vreman [18]. This model is constructed in such a way that its dissipation is relatively small in transitional and near-wall zones. The model does not requires explicit filtering, and is rotationally invariant for isotropic filter widths. Furthermore, it uses only first-order derivatives [18]. Finally, a recently developed model that is based on the analysis of the singular values of the resolved velocity gradient tensor is taken into account [19]. The authors show that the model satisfies three desirable properties,i.e. $\nu_{sgs} = 0$ in two-dimensional flows and in pure axisymmetric or isotropic contraction or expansion. Moreover, it varies with $O(y^3)$ near solid walls without further ad-hoc functions [19].

The WALE model reads [16]:

$$\nu_{sgs} = (C_w\Delta)^2\frac{(\bar{S}^d_{ij}\bar{S}^d_{ij})^{3/2}}{(\bar{S}_{ij}\bar{S}_{ij})^{5/2} + (\bar{S}^d_{ij}\bar{S}^d_{ij})^{5/4}} \tag{9}$$

$$\bar{S}^d_{ij} = \frac{1}{2}(g^2_{ij} + g^2_{ji}) - \frac{1}{3}\delta_{ij}g^2_{kk},$$

$$g_{ij} = \frac{\partial \bar{u}_i}{\partial x_j}, \qquad g^2_{ij} = g_{ik}g_{kj},$$

$$C_w = 0.33, \quad Pr_{sgs} = 0.4, \ \Delta = V^{1/3}$$

Verstappen's model [17] (VERS) can be summarised as:

$$\nu_{sgs} = c^2\Delta^2\frac{max[r,0]}{q} \tag{10}$$

$$r = -\frac{1}{3}(\bar{S}_{ij}\bar{S}_{jk}\bar{S}_{ki}), \ c = \frac{1}{\pi^2} + \frac{1}{24}$$

$$q = \frac{1}{2}(\bar{S}_{ij}\bar{S}_{ij}),$$

$$\Delta = \frac{3.0}{1/(\Delta x)^2 + 1/(\Delta y)^2 + 1/(\Delta z)^2}$$

The model proposed by Vreman [18] (VREM) is:

$$\nu_{sgs} = c\sqrt{\frac{B_\beta}{\alpha_{kl}\alpha_{kl}}} \tag{11}$$

$$\alpha_{ij} = \frac{\partial \overline{u}_j}{\partial x_i}, \ \beta_{ij} = \sum_{m=1}^{3}\Delta^2_m\alpha_{mi}\alpha_{mj}, \ c = 0.07$$

$$B_\beta = \beta_{11}\beta_{22} - \beta^2_{12} + \beta_{11}\beta_{33} - \beta^2_{13} + \beta_{22}\beta_{33} - \beta^2_{23}$$

where Δ_m is the grid-filter width in the $m-$direction.

The last model herein taken into account by Baya

Toda et al. [19] (BAYA) can be written as follows:

$$\nu_{sgs} = (C_\sigma \Delta)^2 D_\sigma \quad (12)$$
$$C_\sigma = 1.5\,,\ \Delta = V^{1/3}$$
$$D_\sigma = \frac{\sigma_3(\sigma_1-\sigma_2)(\sigma_2-\sigma_3)}{\sigma_1^2}$$

where σ_1, σ_2, σ_3 are the square root of the eigenvalues of the matrix $\mathbf{G}=\mathbf{g}^\mathbf{t}\mathbf{g}$, and $\mathbf{g} = g_{ij}$.

3.3. Regularization modelling

In this work the regularization models proposed by Verstappen [14] are taken into. In these kind of models nonlinear approximations that preserve the symmetry of the convective operator in the NS-equations are applied. Specifically, energy, enstrophy ($2D$) and helicity, in the absence of viscous dissipation, are conserved. Thus, the convective term can be approximated as follows.

$$\widetilde{v_j \frac{\partial v_i}{\partial x_j}}|_2 = \overline{\bar{u}_j \frac{\partial \bar{u}_i}{\partial x_j}} \quad (13)$$

$$\widetilde{v_j \frac{\partial v_i}{\partial x_j}}|_4 = \bar{u}_j \frac{\partial \bar{u}_i}{\partial x_j} + \overline{\bar{u}_j \frac{\partial u_i'}{\partial x_j}} + \overline{u_j' \frac{\partial \bar{u}_i}{\partial x_j}} \quad (14)$$

where $u' = u - \bar{u}$, $|_2$ and $|_4$ indicate the error order, i.e. 2 and 4, respectively. Finally, the overline denotes spatial filtering. Hereafter, these models are referred as REGUC2 and REGUC4, respectively.

The three dimensional explicit discrete filter selected here is constructed as a linear combination of one dimensional three-point Gaussian [20] filters.

$$\bar{\phi}_i = \frac{1}{24}\epsilon^2(\phi_{i-1}+\phi_{i+1}) + \frac{1}{12}(12-\epsilon^2)\phi_i \quad (15)$$

where $\epsilon = 2$ represents the ratio of the mesh size to the cut-off length scale of the targeted filter.

Furthermore, this filter can be expressed as $\bar{\phi}_i = \sum_{l=-N}^{N} a_l \phi_{i+l}$, where the coefficients a_l specify the filter. In this kind of filter each direction is filtered independently of the others, which can be written as [20]:

$$F^p = \frac{1}{p}\sum_{i=1}^{p} F^i \quad (16)$$

where F^i is the filter in the ith direction. In the three dimensional case $p = 3$, and the filter reads:

$$\bar{\phi}_{i,j,k} = \frac{1}{3}\sum_{l=-N}^{N} a_l(\phi_{i+l,j,k}+\phi_{i,j+l,k}+\phi_{i,j,k+l}) \quad (17)$$

Care must be taken of the characteristics of the filter in order to preserve symmetry properties of the discretized governing equations.

3.4. Numerical Method

The governing partial differential equations are discretized on a Cartesian staggered grid by means of the finite volume technique. Velocity and pressure fields coupling is solved by means of a classical fractional step projection method [21]. A central difference scheme is used for transient term, an implicit first-order Euler scheme is employed for the pressure gradient term and continuity equation, whereas a second-order Adams-Bashforth scheme is applied for convection and diffusion terms. Second order conservative spectrum-consistent scheme is applied for the spatial discretization. It preserves the symmetry properties of the underlying differential operators: the convective operator is represented by a skew-symmetric matrix and the diffusive operator by a symmetric positive-definite matrix [6]. For the solution of the pressure (Poisson) equation, a direct LU-Fourier decomposition is used. Taking into account the periodicity of the domain in the homogeneous direction, a Fourier diagonalisation is applied in this direction. It decomposes the $3D$ problem into a set of $2D$ independent ones, which are solved using a sparse LU direct solver.

3.5. Verification of code and numerical solutions

The code was verified using the Method of Manufactured Solutions [22], and tested in various benchmark cases, e.g. results by Albensoeder and Kuhlmann [23] for a laminar ($Re = 1000$) fully three dimensional cubic lid-driven cavity, and using periodic boundary conditions in the spanwise direction, have been reproduced. Good agreement was achieved.

For the turbulent configuration studied, mean quantities presented are averaged in time, and in the spanwise homogeneous direction. The simulation starts with the flow initially at rest until it reaches a statistically steady-state. The time integration is started after $400t_{ref}$, and mean variables are averaged over a time interval of $1200t_{ref}$. The time unit is $t_{ref} = L/U_0$. The period for averaging has been selected after a study of the influence of this time on variables for $800t_{ref}$, $1200t_{ref}$ and $1600t_{ref}$. Differences between the second and third intervals are hardly observable. Therefore, it has been considered that an integration interval of $1200t_{ref}$ is sufficient.

The number of control volumes of the grid is changed depending on the turbulence approach (DNS, LES, regularization) being applied. In general, the mesh is concentrated near the solid walls, and it is taken uniform in the spanwise $z-$direction. Grid concentration is accomplished by means of a piecewise $tanh$-like function. Close attention has been paid to placing an adequate number of nodes within the boundary layers. Table 1 shows the grids selected for each turbulent approach here considered.

Firstly, the size of the computational domain in the

Table 1: Grids applied for each turbulent methodology.

		Number of control volumes		
Mesh	Method	$x-$direction	$y-$direction	$z-$direction
1	DNS	20	20	64
2	DNS	40	40	64
3	DNS	60	60	64
4	DNS	80	80	64
5	DNS	40	40	128
6	DNS	60	60	128
7	DNS	40	40	256
8	LES	40	40	64
9	Reg.	20	20	32

spanwise homogeneous direction has been investigated using REGUC2 model. As it can be seen in Figure 2, it is necessary to increase the size of the computational domain in $z-$direction up to $z/L = \pi$ in order to avoid the effect of the periodic boundary conditions both in the mean and the fluctuating vertical velocities. However, by increasing domain size to $z/L = 2\pi$ differences are small enough as to select a domain of dimensions $x/L = 1,\ y/L = 1,\ z/L = \pi$.

Since grid refinement studies are meaningless in the case of LES and regularization methods, the grid independence study is carried out only for DNS. The verification process is carried out in two stages. In the first one, the grid is increased only in the $xy-$plane, while the number of planes in the spanwise direction is kept constant. Afterwards, for a given number of control volumes in the $xy-$plane, the number of planes is changed to test its influence on the DNS predictions. The variation of the vertical mean velocity component, at mid height of the cavity, when the grid is increased is plotted for grids 1, 2, 3 and 4 in Figure 3(a). Differences between results of grids 3 and 4 are almost imperceptible for the mean vertical velocity, and less than 5% for v_{rms} (not shown). Furthermore, the effect of the number of planes is shown in Figure 3(b) for the grids 2, 5 and 7. As it can be seen, differences are only important near the downstream wall ($x/l \geq 0.95$), when the number of control volumes (planes) in $z-$ direction is increased from 64 to 128 (see Figure 3(b)). Nevertheless, they are rather limited when the number of planes is changed from 128 to 256. Therefore, taking into account these results, numerical DNS predictions obtained using the mesh 6 can be considered credible. Moreover, this grid represents a good compromise in order to have reasonable computational costs using DNS, even though the smallest scales are under-resolved.

4. RESULTS AND DISCUSSION

In this section, numerical results of DNS, LES and regularization models are presented. Three-dimensional experimental data of a cubic cavity obtained by Prasad and Koseff [11] are also shown as reference.

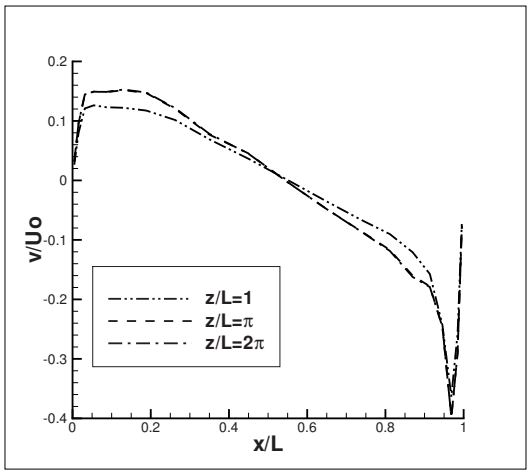

(a)

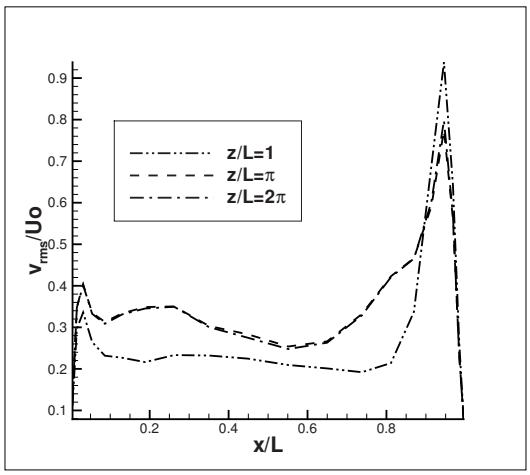

(b)

Figure 2: Influence of domain size in z−direction using REGUC2 model. (a) mean vertical velocity. (b) root mean square vertical velocity.

4.1. *Mean velocity field*

In this section the numerically predicted fluid-flow field is analysed in terms of mean velocities at mid vertical and horizontal planes. Results are presented in dimensionless form using U_o as characteristic velocity.

Figure 4 shows the distribution of the predicted mean velocity profiles at the cavity mid point ($z/L = \pi/2$). DNS, LES and REGUC2 models are plotted together with experimental data [11]. It is worth to highlight that the experimental data are obtained from a fully $3D$ square cavity with a spanwise aspect ratio $z/L = 1$. Therefore, the differences observed can be attributed to the confinement walls in the spanwise direction, which contributes to increasing the energy content of the higher frequency fluctuations [11]. For the DNS with periodic boundary conditions the peaks in both velocity profiles are slightly larger than those from the fully $3D$ experimental data. Moreover, a slope more pronounced of the velocity profile in the

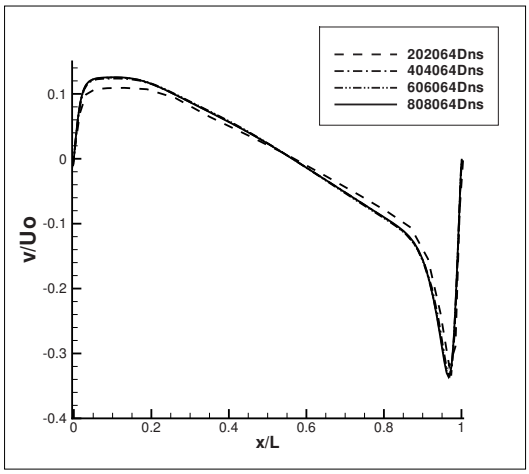

(a)

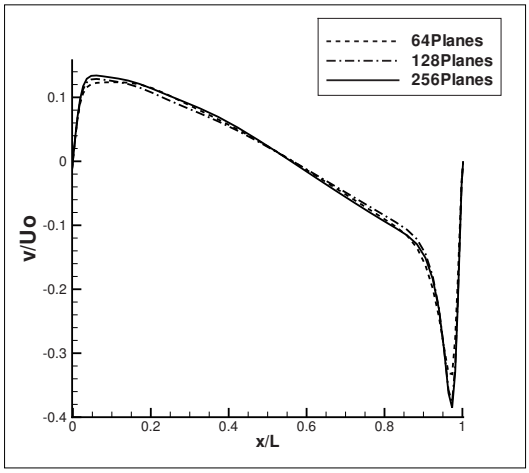

(b)

Figure 3: DNS grid refinement study. (a) control volumes $\mathbf{xy-}$plane. (b) Number of planes in $\mathbf{z-}$direction (spanwise).

intermediate zone is observed.

As indicated in Table 1, LES models have been simulated using the grid 8, whereas for the REGUC2 model the grid 9 has been selected. It is interesting to note in Fig. 4, the overall good agreement achieved using REGUC2 model with such a coarse grid ($20 \times 20 \times 32$ cvs). Even though all LES models perform well, BAYA model presents the most similar profiles to DNS results, followed by VERS and WALE models. VREM model exhibits the less accurate predictions.

The mean horizontal ($x-$direction) velocity component is shown in Figure 4(a). All LES models behave fairly well for this quantity, and only minor differences can be observed for the velocity peaks near the bottom wall and the cavity lid. Furthermore, it is difficult to distinguish the velocity predicted by each LES model. The REGUC2 model presents some deviations for this velocity component.

Figure 4(b) shows the mean velocity vertical ($y-$direction) profile. For this velocity component, LES models present more scattered predictions.

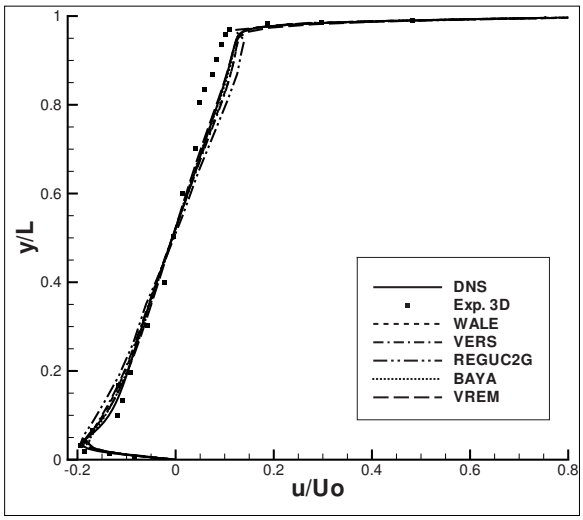

(a)

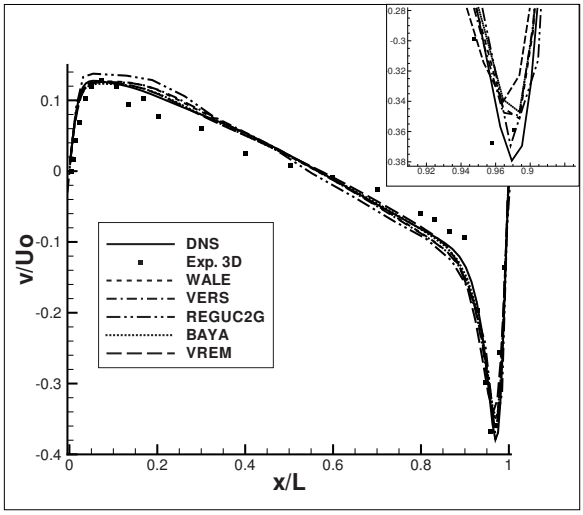

(b)

Figure 4: Models performance at the cavity mid planes at $\mathbf{z/L = \pi/2}$. (a) mean horizontal velocity at $\mathbf{x/L = 0.5}$. (b) mean vertical velocity at $\mathbf{y/L = 0.5}$.

Furthermore, they under-predict the velocity peak near the downstream wall ($x/L \geq 0.95$). Among them, BAYA model is the one that more adequately reproduces DNS results. VERS and WALE models exhibit similar results. VREM model predicts fairly well DNS results near the upstream wall, but its performance is degraded when it approaches the downstream wall. On the other hand, REGUC2 model reproduces correctly the vertical velocity near the downstream wall, even the velocity peak (see the upper-right corner in Fig. 4(b)), but over-predicts this velocity component near the upstream wall.

4.2. Reynolds stresses

Attention is now focussed on the higher order statistics namely, fluctuating velocities. Figure 5 shows the profiles of the non-dimensional velocity fluctuation

or root mean square (rms) horizontal u_{rms}/U_0, and vertical v_{rms}/U_0 components, for the case under study, and at $z/L = \pi/2$. At the Re studied, the high-frequency velocity fluctuations are responsible for the momentum transfer from the boundary layer to the core zone. Moreover, they reduce the presence of Taylor-Goertler vortices [11].

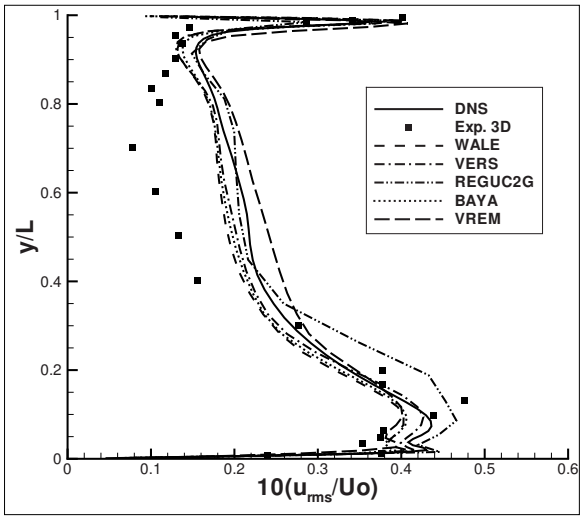

(a)

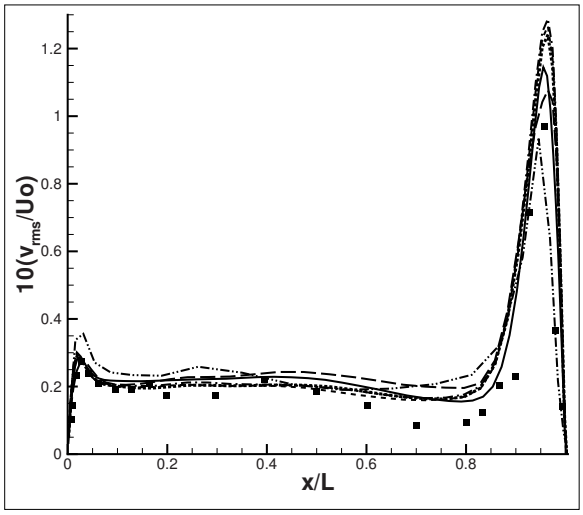

(b)

Figure 5: Models performance at the cavity mid planes $\mathbf{z/L = \pi/2}$. (a) rms $\mathbf{x-}$direction velocity component. (b) rms $\mathbf{y-}$direction velocity component.

In Figure 5(a) u_{rms}/U_o profile is shown. By comparing DNS results with experimental data by Prasad and Koseff [11], it can be observed that the u_{rms}/U_o peaks predicted by DNS are smaller. Furthermore, the values of the u_{rms}/U_o in the upper part of the central vortex are larger. Comparison of models performance is made against DNS results. Their results are also shown in Fig. 5(a). The behaviour of WALE, VERS and BAYA models is similar, however, VERS model reproduces more adequately u_{rms}/U_o maximums. Furthermore, REGUC2 model predicts correctly u_{rms}/U_o in the central region, but over-predicts the peak near the bottom wall, and under-predicts the maximum near the cavity lid.

The v_{rms}/U_o velocity is plotted in Figure 5(b). The influence of the end walls in the spanwise direction for this quantity is more notorious in the right region near the downstream wall, where DNS shows larger values than the experimental data [11]. Even though, WALE, VERS and BAYA models over-predict the v_{rms}/U_o maximum near the downstream wall, they adequately reproduces DNS results in the core and upstream zones. Nevertheless, VREM model over-predicts v_{rms}/U_o in the right part of the core region, and under-predicts the peak near the downstream wall. Regarding REGUC2 model, it presents larger v_{rms}/U_o values in the left zone and under-predicts the maximum near the downstream wall.

5. CONCLUSIONS

Direct numerical simulation using a second order symmetry preserving discretization has been carried out for the lid-driven cavity flow at $Re = 10,000$. First and second order velocity statistics have been obtained by time and spanwise averaging. Integrating time has been selected long enough to capture the long time scales of the flow. DNS results have been used to evaluate the performance of several turbulence models. The results obtained using LES and regularization models indicate that the averaged variables are well predicted by the large-scale quantities. WALE, VERS and BAYA models have presented a similar overall performance, whereas VREM model shows some limitations. Some discrepancies haven been observed using REGUC2 model. However, this is a useful approach given the coarse grid selected for the simulation. It would be interesting to test the REGUC4 model in conjunction with a fourth order symmetry preserving discretization. Furthermore, the influence of different test filters on the REGUC2 results should be assessed.

ACKNOWLEDGEMENTS

This research has been partially financed by a *Generalitat de Catalunya Beatriu de Pinós* postdoctoral fellowship (Ref. 2008 BP-A 00227)

References

[1] Zang, Y., Street, R., and Koseff, J.,1993, "A dynamic mixed subgrid-scale model and its application to turbulent recirculating flows", *Physics of Fluids*, Vol. 5, pp. 3186–3196.

[2] Verstappen, R. and Veldman, A., 1998, "Spectro-consistent discretization of navier-stokes: a challenge to RANS and LES", *Journal of Engineering Mathematics*, Vol. 34, pp. 163–179.

[3] Leriche, E. and Gavrilakis, S., 2000, "Direct numerical simulation of the flow in a lid-driven cubical cavity", *Physics of Fluids*, Vol. 12, pp. 1363–1376.

[4] Bouffanais, R., Deville, M., Fischer, P., Leriche, E., and Weill, D., 2006, "Large-Eddy simulation of the lid-driven cubic cavity flow by spectral method", *Journal of Scientific Computing*, Vol. 27, pp. 151–162.

[5] Shankar, P. and Deshpande, M., 2000, "Fluid mechanics in the driven cavity", *Annual Review of Fluid Mechanics*, Vol. 32, pp. 93–136.

[6] Verstappen, R. and Veldman, A., 2003, "Symmetry-preserving discretization of turbulent flow", *Journal of Computational Physics*, Vol. 187, pp. 343–368.

[7] Trias, F. X., Gorobets, A., Soria, M., and Oliva, A., 2010, "Direct numerical simulation of a differentially heated cavity of aspect ratio 4 with ra-number up to 10^{11} - part i: Numerical methods and time-averaged flow", *International Journal of Heat and Mass Transfer*, Vol. 53, pp. 665–673.

[8] Verstappen, R., Bose, S., Lee, J., Choi, H., and Moin, P., 2010, "A dynamic eddy-viscosity model based on the invariants of the rate-of-strain", *Proc. 2010 Summer Program, Center for Turbulence Research, Stanford*, pp. 183–192.

[9] Trias, F. X., Verstappen, R. W. C. P., Soria, M., and Oliva, A., 2010, "Parameter-free symmetry-preserving regularization modelling of turbulent differentially heated cavity". *Computer and Fluids*, Vol. 39, pp. 1815–1831.

[10] Koseff, J. and Street, R., 1984, "Visualization studies of shear driven three-dimensional recirculating flow", *Journal of Fluids Engineering*, Vol. 106, 21–27.

[11] Prasad, A. and Koseff, J., 1989, "Reynolds number and end wall effects on a lid-driven cavity flow". *Physics of Fluids*, Vol. 1, pp. 208–218.

[12] Verstappen, R. and Veldman, A., 1994 "Direct numerical simulation of a 3d turbulent flow in a driven cavity at Re=10000". *Proceedings of the 2nd Fluids Dynamics Conference, ECCOMAS*, pp. 558–570.

[13] Sagaut, P., 2001, *Large Eddy Simulation for Incompressible Flows*. Springer-Verlag.

[14] Verstappen, R., 2008, "On restraining the production of small scales of motion in a turbulent channel flow", *International Journal of Heat and Fluid Flow*, Vol. 37, pp. 887–897.

[15] Smagorinsky, J., 1963, "General circulation experiments with the primitive equations, part. I: the basic experiment", *Monthly Weather Rev.*, Vol. 91, pp. 99–164.

[16] Nicoud, F. and Ducros, F., 1999, "Subgrid-scale stress modeling based on the square of the velocity gradient tensor". *Flow, Turbulence and Combustion*, Vol. 62, pp. 183–200.

[17] Verstappen, R., 2010, "When does eddy viscosity restrict the dynamics to large eddies?", *Proceedings of the Fifth European Conference on Computational Fluid Dynamics ECCOMAS CFD 2010*, pp. 1–14.

[18] Vreman, A., 2004, "An eddy-viscosity subgrid-scale model for turbulent shear flow: Algebraic theory and applications", *Physics of Fluids*, Vol. 16, pp. 3670–3681.

[19] Baya Toda, H., Cabrit, O., Balarac, G., Bose, S., Lee, J., Choi, H., and Nicoud, F., 2010, "A subgrid-scale model based on singular values for les in complex geometries", *Proc. 2010 Summer Program, Center for Turbulence Research, Stanford*, pp. 193–202.

[20] Sagaut, P. and Grohens, R., 1999, "Discrete filters for large eddy simulation", *International Journal for Numerical Methods in Fluids*, Vol. 31, pp. 1195–1220.

[21] Yanenko, N., 1971, *The Method of Fractional Steps*. Springer-Verlag.

[22] Roache, P. J., 2002, "Code Verification by the Method of Manufactured Solutions", *Journal of Fluids Engineering*, Vol. 124, pp. 4–10.

[23] Albensoeder, S. and Kuhlmann, H., 2005, "Accurate three dimensional lid-driven cavity flow", *Journal of Computational Physics*, Vol. 206, pp. 536–558.

Conference on Modelling Fluid Flow (CMFF'12)
The 15th International Conference on Fluid Flow Technologies
Budapest, Hungary, September 4-7, 2012

NUMERICAL COMPARISON OF UNSTEADY COMPRESSIBLE FLOWS WITH LOW INLET VELOCITY IN CONVERGENT CHANNEL

Petra Pořízková[1], Karel Kozel [2], Jaromír Horáček [3]

[1] Corresponding Author. Department of Technical Mathematics, Faculty of Mechanical Engineering, Czech Technical University in Prague. Karlovo nám. 13, CZ 121 35 Prague, Czech Republic. Tel. +420 22435 7540, E-mail: puncocha@marian.fsik.cvut.cz
[2] Institute of Thermomechanics AS CR, Centre of Energetics, Dolejškova 5, CZ 182 00 Prague, E-mail: kozelk@fsik.cvut.cz
[3] Institute of Thermomechanics AS CR, Centre of Energetics, Dolejškova 5, CZ 182 00 Prague, E-mail: jaromirh@it.cas.cz

ABSTRACT

This study deals with a numerical solution of a 2D flows of a compressible viscous fluids in a convergent channel for low inlet airflow velocity. Three governing systems - *Full system, Adiabatic system, Iso-energetic system* based on the Navier-Stokes equations for laminar flow are tested. The numerical solution is realized by finite volume method and the predictor-corrector MacCormack scheme with Jameson artificial viscosity using a grid of quadrilateral cells. The unsteady grid of quadrilateral cells is considered in the form of conservation laws using Arbitrary Lagrangian-Eulerian method.

The numerical results, acquired from a developed program, are presented for inlet velocity $\hat{u}_\infty = 4.12\ m/s$ and Reynolds number Re = 4×10^3.

Keywords: CFD, compressible viscous fluid, Finite Volume Method, low Mach number, unsteady flow

NOMENCLATURE

D_1	$[-]$	computational domain
$D_{i,j}$	$[-]$	cell of domain
$\mathbf{F}, \mathbf{G}$	$[-]$	vectors of inviscid fluxes
H	$[-]$	width of channel
L	$[-]$	length of channel
L_r	$[m]$	length, reference variable
Pr	$[-]$	Prandtl number
Re	$[-]$	Reynolds number
$\mathbf{R}, \mathbf{S}$	$[-]$	vectors of viscous fluxes
T	$[-]$	temperature
$\mathbf{W}$	$[-]$	vector of conservative variables
$\hat{c}_\infty$	$[m/s]$	velocity of sound at the inlet
e	$[-]$	total energy per unite volume
f	$[-]$	frequency of the channel walls
$\hat{f}$	$[Hz]$	frequency of the channel walls
k	$[-]$	coefficient of thermal diffusivity
$\mathbf{n}$	$[-]$	outlet normal vector
p	$[-]$	static pressure
$\hat{p}$	$[Pa]$	static pressure
$\mathbf{s}$	$[-]$	vector of velocity of the edge of the cell
t	$[-]$	time
u, v	$[-]$	ratio velocity of the fluid
$\hat{u}$	$[m/s]$	velocity of the fluid
x, y	$[-]$	coordinates
η	$[-]$	dynamic viscosity
$\hat{\eta}_\infty$	$[Pa \cdot s]$	dynamic viscosity at the inlet
κ	$[-]$	adiabatic exponent
$\mu_{i,j}$	$[-]$	volume of cell
ρ	$[-]$	density
$\hat{\rho}$	$[kg/m^3]$	density

Subscripts and Superscripts

i, j	position of data in x-direction, y-direction
k	on cell edge
max, min	maximum, minimum of magnitude
n	time layer
wall	property of the channel wall
$\tilde{}$	numerical approximation of reality
∞	inflow variables
2	outflow variables

1 Introduction

A current challenging question is a mathematical and physical description of the mechanism for transforming the airflow energy in human vocal tract (convergent channel) into the acoustic energy representing the voice source in humans. The voice source signal travels from the glottis to the mouth, exciting the acoustic supraglottal spaces, and becomes modified by acoustic resonance properties of the vocal tract [1]. The airflow coming from the lungs causes self-oscillations of the vocal folds, and the glottis completely closes in normal phonation regimes, generating acoustic pressure fluctuations. In this study, the movement of the boundary channel is known, harmonically opening and nearly closing in

the narrowest cross-section of the channel, making the investigation of the airflow field in the glottal region possible. For phonation of vowels, the frequencies of the vocal folds oscillations are in the region from cc 82 Hz for bass up to cc 1170 Hz for soprano in singing voice, the airflow velocity in the trachea is approximately in the range of 0.3-5.2 m/s taking into account the tracheal diameter in humans in the range 14.5-17.6 mm [2].

Acoustic wave propagation in the vocal tract is usually modeled from incompressible flow models separately using linear acoustic perturbation theory, the wave equation for the potential flow [2] or the Light-hill approach on sound generated aerodynamically [3].

Goal of this work is numerical simulation of compressible viscous flow in 2D convergent channel which involves attributes of real flow causing acoustic perturbations as is "Coandă phenomenon" (the tendency of a fluid jet to be attracted to a nearby surface), vortex convection and diffusion, jet flapping etc. along with lower call on computer time, due to later extension in 3D channel flow.

2 Governing equations

The 2D system of Navier-Stokes equations has been used as mathematical model to describe the unsteady laminar flow of the compressible viscous fluid in a domain. The system of Navier-Stokes equations is expressed in non-dimensional conservative form [4]:

$$\frac{\partial \mathbf{W}}{\partial t} + \frac{\partial \mathbf{F}}{\partial x} + \frac{\partial \mathbf{G}}{\partial y} = \frac{1}{\mathrm{Re}} \left(\frac{\partial \mathbf{R}}{\partial x} + \frac{\partial \mathbf{S}}{\partial y} \right). \quad (1)$$

$\mathbf{W}$ is the vector of conservative variables $\mathbf{W} = [\rho, \rho u, \rho v, e]^T$ where ρ denotes density, u and v are the components of the velocity vector and e is the total energy per unit volume. $\mathbf{F}$ and $\mathbf{G}$ are the vectors of inviscid fluxes and $\mathbf{R}$, $\mathbf{S}$ are the vectors of viscous fluxes. The static pressure p in $\mathbf{F}$ and $\mathbf{G}$ is expressed by the state equation in the form

$$p = (\kappa - 1) \left[e - \frac{1}{2} \rho \left(u^2 + v^2 \right) \right], \quad (2)$$

where $\kappa = 1.4$ is the ratio of specific heats.

The transformation to the non-dimensional form uses inflow parameters (marked with the infinity subscript) as reference variables. Using state equation $\hat{p}/\hat{\rho} = \hat{R}\hat{T}$ and relation $\hat{c}_\infty^2 = \kappa \hat{R} \hat{T}_\infty$ inlet dimensionless boundary condition are enumerated. Reference variables: the speed of sound $\hat{c}_\infty = 343$ m/s, density $\hat{\rho}_\infty = 1.225$ kg/m^3, reference length $\hat{L}_r = 0.02$ m and dynamic viscosity $\hat{\eta}_\infty = 18 \cdot 10^{-6}$ $Pa \cdot s$.

General Reynolds number in (1) is computed from reference variables $\mathrm{Re} = \hat{\rho}_\infty \hat{c}_\infty \hat{L}_r / \hat{\eta}_\infty$. The non-dimensional dynamic viscosity in the dissipative terms is a function of temperature in the form $\eta = (T/T_\infty)^{3/4}$.

The system of equations (1) and (2) is so-called *Full system*. We present two other governing systems of equations based on the Navier-Stokes equations (1), depend on expression of state equation for static pressure p which is depend on energy flow condition in the system. The second governing system is so-called *Adiabatic system*

$$p = \frac{1}{\kappa} \rho^\kappa, \quad (3)$$

and third governing system is so-called *Iso-energetic system*

$$p = \frac{\rho}{\kappa} \left[1 + \frac{\kappa - 1}{2} \left(\frac{\hat{u}_\infty}{\hat{c}_\infty} \right)^2 - \frac{\kappa - 1}{2} (u^2 + v^2) \right]. \quad (4)$$

Both last systems have the pressure expression independent on variable e and the system (1) is reduced on the first three equations.

2.1 Computational domain and boundary conditions

The bounded computational domain D_1 used for the numerical solution of flow field in the channel is shown in Figure 1. The domain is symmetric channel, the shape of which is inspired by the shape of the trachea (inlet part), vocal folds, false vocal folds and supraglottal spaces (outlet part) in human vocal tract. The upper and the lower boundaries are the channel walls. A part of the walls changes its shape between the points A and B according to given harmonic function of time and axial coordinate (see [6]). The gap width is the narrowest part of the channel (in point C) and is oscillating between the minimum $g_{min} = 0.4$ mm and maximum $g_{max} = 2.8$ mm.

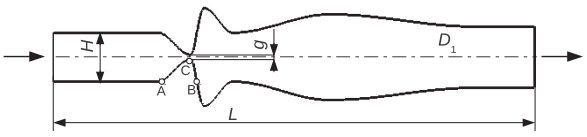

Figure 1: The computational domain D_1. $L = 8$ (160 mm), $H = 0.8$ (16 mm), $g = 0.08$ (1.6 mm) - middle position.

The boundary conditions are considered in the following formulation:

1. Upstream conditions: $u_\infty = \frac{\hat{u}_\infty}{\hat{c}_\infty}$; $v_\infty = 0$; $\rho_\infty = 1$; p_∞ is extrapolated from D_1.

2. Downstream conditions: $p_2 = 1/\kappa$; $(\rho, \rho u, \rho v)$ are extrapolated from D_1.

3. Flow on the wall: $(u, v) = (u_{\mathrm{wall}}, v_{\mathrm{wall}})$ and furthermore for *Full system* $\frac{\partial T}{\partial \vec{n}} = 0$. Vector $(u_{\mathrm{wall}}, v_{\mathrm{wall}})$ represents velocity of the channel walls and $T = \kappa p / \rho$ is the temperature.

The general Reynolds number in (1) is multiply with non-dimensional value $\frac{\hat{u}_\infty}{\hat{c}_\infty} H$ and for computation of the real problem inlet Reynolds number $\mathrm{Re}_\infty = \hat{\rho}_\infty \hat{c}_\infty \frac{\hat{u}_\infty}{\hat{c}_\infty} H \hat{L}_r / \hat{\eta}_\infty$ is used.

3 Numerical solution

The numerical solution uses finite volume method (FVM) in cell centered form on the grid of quadrilateral cells, see e.g. [4]. In the time-changing domain, the integral form of FVM is derived using Arbitrary Lagrangian-Eulerian (ALE) formulation. The ALE method defines homomorphic mapping of the reference domain $D_{t=0}$ at initial time $t = 0$ to a domain D_t at $t > 0$ [5]. The explicit predictor-corrector MacCormack (MC) scheme in the domain with a moving grid of quadrilateral cells is used. The scheme is 2nd order accurate in time and space [4]:

$$\begin{aligned}
\mathbf{W}_{i,j}^{n+\frac{1}{2}} &= \frac{\mu_{i,j}^n}{\mu_{i,j}^{n+1}} \mathbf{W}_{i,j}^n - \frac{\Delta t}{\mu_{i,j}^{n+1}} \sum_{k=1}^{4} \Big[\Big(\tilde{\mathbf{F}}_k^n - s_{1k} \mathbf{W}_k^n \\
&- \frac{1}{Re} \tilde{\mathbf{R}}_k^n \Big) \Delta y_k \\
&- \Big(\tilde{\mathbf{G}}_k^n - s_{2k} \mathbf{W}_k^n - \frac{1}{Re} \tilde{\mathbf{S}}_k^n \Big) \Delta x_k \Big], \\
\overline{\mathbf{W}}_{i,j}^{n+1} &= \frac{\mu_{i,j}^n}{\mu_{i,j}^{n+1}} \frac{1}{2} \Big(\mathbf{W}_{i,j}^n + \mathbf{W}_{i,j}^{n+\frac{1}{2}} \Big) \\
&- \frac{\Delta t}{2\mu_{i,j}^{n+1}} \sum_{k=1}^{4} \Big[\Big(\tilde{\mathbf{F}}_k^{n+\frac{1}{2}} - s_{1k} \mathbf{W}_k^{n+\frac{1}{2}} \\
&- \frac{1}{Re} \tilde{\mathbf{R}}_k^{n+\frac{1}{2}} \Big) \Delta y_k \\
&- \Big(\tilde{\mathbf{G}}_k^{n+\frac{1}{2}} - s_{2k} \mathbf{W}_k^{n+\frac{1}{2}} - \frac{1}{Re} \tilde{\mathbf{S}}_k^{n+\frac{1}{2}} \Big) \Delta x_k \Big] \qquad (5)
\end{aligned}$$

where $\Delta t = t^{n+1} - t^n$ is the time step, $\mu_{i,j} = \int\int_{D_{i,j}} dxdy$ is the volume of cell $D_{i,j}$, Δx and Δy are the steps of the grid in directions x and y, vector $\mathbf{s}_k = (s_1,\ s_2)_k$ represents the speed of edge k (see Figure 2). The physical fluxes $\mathbf{F}$, $\mathbf{G}$, $\mathbf{R}$, $\mathbf{S}$ on the edge k of the cell $D_{i,j}$ are replaced by numerical fluxes (marked with tilde) $\tilde{\mathbf{F}}$, $\tilde{\mathbf{G}}$, $\tilde{\mathbf{R}}$, $\tilde{\mathbf{S}}$ as approximations of the physical fluxes. The higher partial derivatives of velocity and temperature in $\tilde{\mathbf{R}}_k$, $\tilde{\mathbf{S}}_k$ are approximated using dual volumes V_k' (see [4]) as shown in Figure 2.

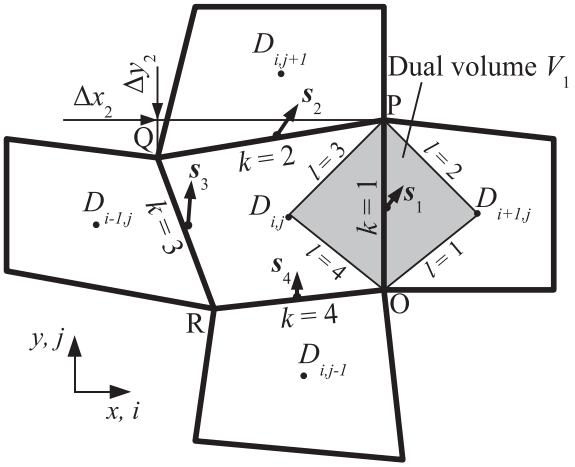

Figure 2: Finite volume $D_{i,j}$ and the dual volume V_k'

The last term used in the MC scheme is the Jameson artificial dissipation $AD(W_{i,j})^n$ [7], then the vector of conservative variables $\mathbf{W}$ can be computed at a new time level $\mathbf{W}_{i,j}^{n+1} = \overline{\mathbf{W}}_{i,j}^{n+1} + AD(W_{i,j})^n$.

The grid of the channel have successive refinement cells near the wall (see Figure 3). The minimum cell size in y - direction is $\Delta y_{min} \approx 1/\sqrt{\mathrm{Re}_\infty}$ to resolve capture boundary layer effects.

4 Numerical results

The numerical results were obtained (using a specifically developed program) for the following input data: uniform inflow ratio velocity $\frac{\hat{u}_\infty}{\hat{c}_\infty} = 0.012$ ($\hat{u}_\infty = 4.116\ m/s$), Reynolds number $\mathrm{Re}_\infty = 4481$ and atmospheric pressure $p_2 = 1/\kappa$ ($\hat{p}_2 = 102942$ Pa) at the outlet. The computational domain contained 450×100 cells. The detail of the mesh near the gap is shown in Figure 3.

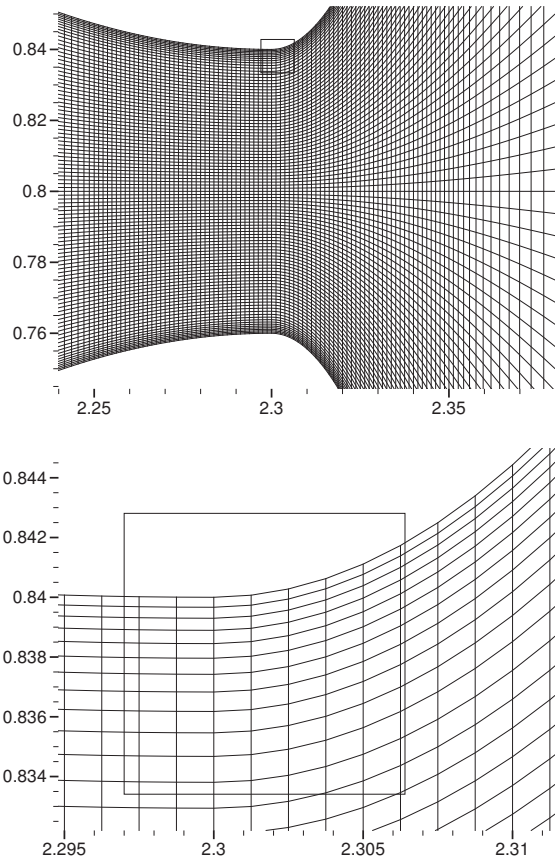

Figure 3: Mesh in domain D_1 - detail.

The computation has been carried out in two stages. First, a numerical solution is obtained, when the channel between points A and B has a rigid wall fixed in the middle position of the gap width (see Fig. 1). Then this solution is used as the initial condition for the unsteady simulation.

Figure 4 shows initial conditions of the flows in domain D_1 computed with the governing systems. The pictures display non-symmetric flow developed behind

the narrowest channel cross-section. Figure 5 shows

(a) *Full system*, $\frac{\hat{u}_{max}}{\hat{c}_\infty} = 0.177$

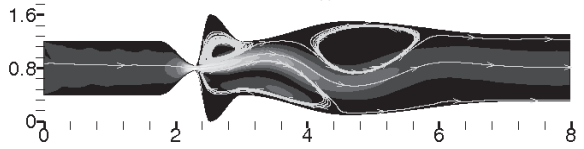

(b) *Adiabatic system*, $\frac{\hat{u}_{max}}{\hat{c}_\infty} = 0.166$

(c) *Iso-energetic system*, $\frac{\hat{u}_{max}}{\hat{c}_\infty} = 0.160$

Figure 4: Initial conditions in domain D_1 computed with the governing systems. $\frac{\hat{u}_\infty}{\hat{c}_\infty} = 0.012$, $\mathrm{Re}_\infty = 4481$, $p_2 = 1/\kappa$, mesh: 450×100. Results are mapped by iso-lines of ratio velocity and by streamlines.

the convergences to the steady state solution computed using the L_2 norm of momentum residuals (ρu). The convergence depends on coefficients of artificial dissipation $AD(W_{i,j})^n$ making strong or weak numerical viscosity of the scheme and on governing system. The graphs indicates the non-stationary solution which is caused probably by eddies separated behind gap and floating away. Numerical solution computed with *Iso-energetic system* has the worst residuals.

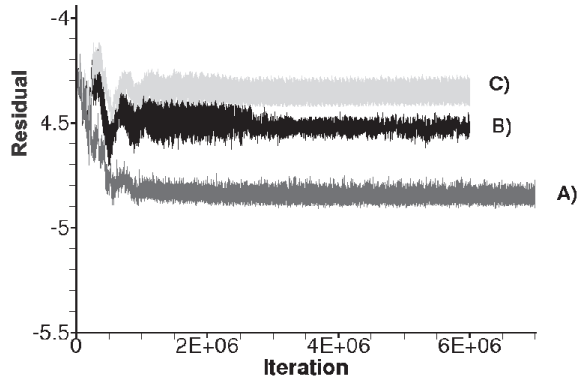

Figure 5: Convergence to the steady state solution. Computed in domain D_1 with: A) *Full system*, B) *Adiabatic system*, C) *Iso-energetic system*.

Figures 6, 7, 8 show the unsteady flow fields computed with the governing systems in domain D_1. Simulation is captured in five time instants during one vibration period (in the fourth cycle of the wall oscillation). The highest absolute maximum velocity ratio during one vibration period is computed with *Full system* (Fig. 6) where $\frac{\hat{u}_{max}}{\hat{c}_\infty} = 0.535$ ($\hat{u}_{max} = 183.5\ m/s$) at $g = 1.002\ mm$ (opening phase). *Adiabatic system* and *Iso-energetic system* (Figs. 7, 8) have same absolute maximum velocity ratio during one vibration period $\frac{\hat{u}_{max}}{\hat{c}_\infty} = 0.199$ ($\hat{u}_{max} = 68.2\ m/s$) at $g = 0.993\ mm$ and $g = 1.09\ mm$ respectively, during closing phase.

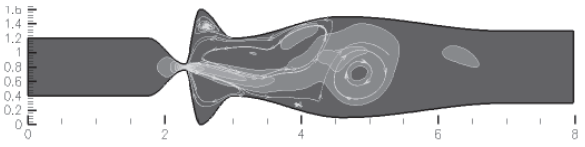

(a) $t = 30\ ms,\ g = 1.6\ mm,\ \frac{\hat{u}_{max}}{\hat{c}_\infty} = 0.162$ (55.6 m/s)

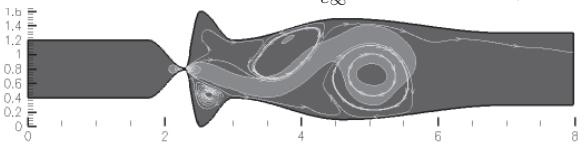

(b) $t = 32.5\ ms,\ g = 0.4\ mm,\ \frac{\hat{u}_{max}}{\hat{c}_\infty} = 0.236$ (80.9 m/s)

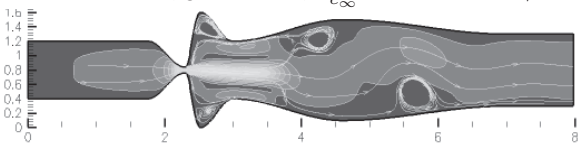

(c) $t = 35\ ms,\ g = 1.6\ mm,\ \frac{\hat{u}_{max}}{\hat{c}_\infty} = 0.370$ (126.9 m/s)

(d) $t = 37.5\ ms,\ g = 2.8\ mm,\ \frac{\hat{u}_{max}}{\hat{c}_\infty} = 0.097$ (33.3 m/s)

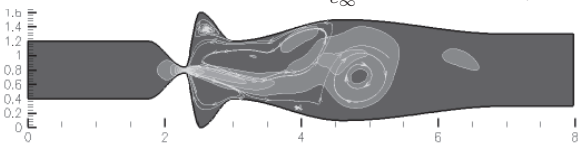

(e) $t = 40\ ms,\ g = 1.6\ mm,\ \frac{\hat{u}_{max}}{\hat{c}_\infty} = 0.162$ (55.6 m/s)

Figure 6: The unsteady numerical solution of the airflow in D_1 computed with *Full system* - $\hat{f} = 100\ Hz$, $\frac{\hat{u}_\infty}{\hat{c}_\infty} = 0.012$, $\mathrm{Re}_\infty = 4481$, $p_2 = 1/\kappa$, 450×100 cells. Data computed during the fourth oscillation cycle. Results are mapped by iso-lines of velocity ratio and by streamlines.

5 SUMMARY

Three governing systems for flow of viscous compressible fluid based on Navier-Stokes equations for laminar flow are tested. Numerical solutions showed similar pattern of the flow fields computed with *Full*, *Adiabatic* and *Iso-energetic systems*. In unsteady simulations was possible to detect a "Coandă phenomenon" and large-scale vortices in the flow field patterns. The direction of the jet is independent on the coarseness of mesh but depends on the geometry of the channel, on the type of mesh in the domain, on the computational scheme [9] and on the governing

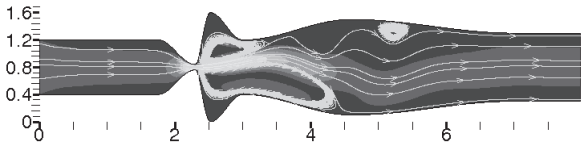

(a) $t = 30\ ms,\ g = 1.6\ mm,\ \frac{\hat{u}_{\max}}{\hat{c}_\infty} = 0.167\ (57.2\ m/s)$

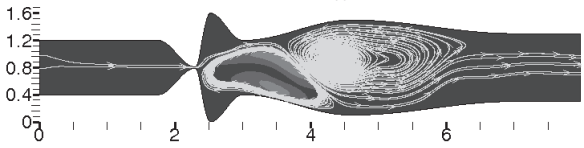

(b) $t = 32.5\ ms,\ g = 0.4\ mm,\ \frac{\hat{u}_{\max}}{\hat{c}_\infty} = 0.032\ (10.9\ m/s)$

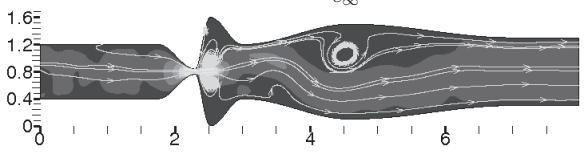

(c) $t = 35\ ms,\ g = 1.6\ mm,\ \frac{\hat{u}_{\max}}{\hat{c}_\infty} = 0.171\ (58.6\ m/s)$

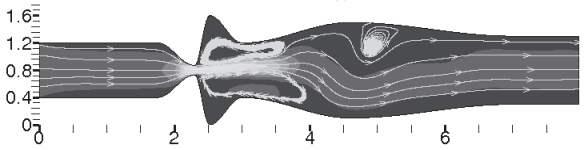

(d) $t = 37.5\ ms,\ g = 2.8\ mm,\ \frac{\hat{u}_{\max}}{\hat{c}_\infty} = 0.093\ (31.9\ m/s)$

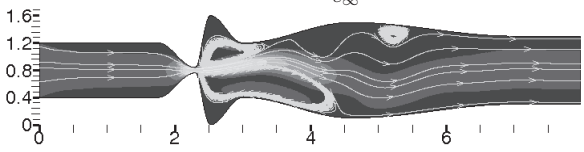

(e) $t = 40\ ms,\ g = 1.6\ mm,\ \frac{\hat{u}_{\max}}{\hat{c}_\infty} = 0.167\ (57.2\ m/s)$

Figure 7: The unsteady numerical solution of the airflow in D_1 computed with *Adiabatic system* - $\hat{f} = 100\ Hz$, $\frac{\hat{u}_\infty}{\hat{c}_\infty} = 0.012$, $\mathrm{Re}_\infty = 4481$, $p_2 = 1/\kappa$, 450×100 cells. Data computed during the fourth oscillation cycle. Results are mapped by iso-lines of velocity ratio and by streamlines.

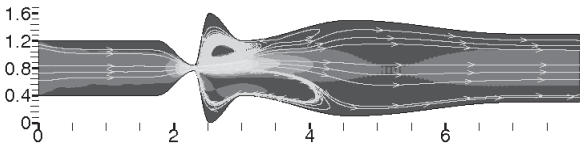

(a) $t = 30\ ms,\ g = 1.6\ mm,\ \frac{\hat{u}_{\max}}{\hat{c}_\infty} = 0.163\ (55.9\ m/s)$

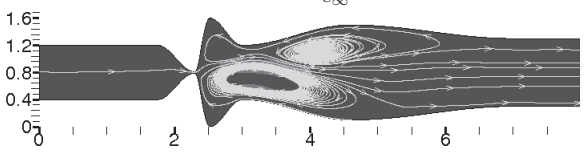

(b) $t = 32.5\ ms,\ g = 0.4\ mm,\ \frac{\hat{u}_{\max}}{\hat{c}_\infty} = 0.030\ (10.3\ m/s)$

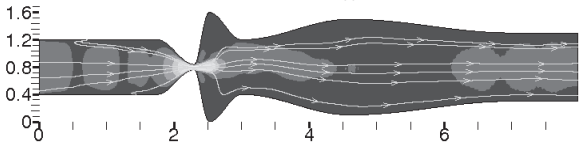

(c) $t = 35\ ms,\ g = 1.6\ mm,\ \frac{\hat{u}_{\max}}{\hat{c}_\infty} = 0.159\ (54.5\ m/s)$

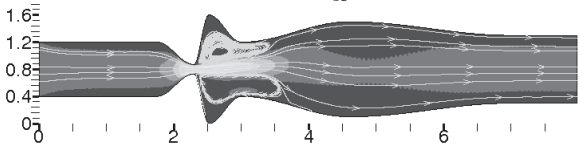

(d) $t = 37.5\ ms,\ g = 2.8\ mm,\ \frac{\hat{u}_{\max}}{\hat{c}_\infty} = 0.097\ (33.3\ m/s)$

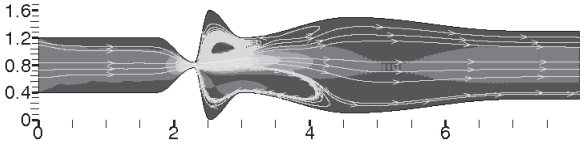

(e) $t = 40\ ms,\ g = 1.6\ mm,\ \frac{\hat{u}_{\max}}{\hat{c}_\infty} = 0.163\ (55.9\ m/s)$

Figure 8: The unsteady numerical solution of the airflow in D_1 computed with *Iso-energetic system* - $\hat{f} = 100\ Hz$, $\frac{\hat{u}_\infty}{\hat{c}_\infty} = 0.012$, $\mathrm{Re}_\infty = 4481$, $p_2 = 1/\kappa$, 450×100 cells. Data computed during the fourth oscillation cycle. Results are mapped by iso-lines of velocity ratio and by streamlines.

system of flow. A similar generation of large-scale vortices, vortex convection and diffusion, jet flapping, and general flow patterns were experimentally obtained in physical models of the vocal folds by using Particle Image Velocimetry method in [8].

In next time we consider analyze spectrum of acoustic pressure found near the outlet of domain D_1 and to compute the similar case by model of incompressible Navier-Stokes equations and to use extension to 3D case.

ACKNOWLEDGEMENTS

This contribution was partially supported by Research Plans MSM 6840770010, GAČR P101/11/0207, 201/08/0012 and P101/10/1329.

References

[1] Titze, I.R., Principles of Voice Production. National Center for Voice and Speech, Iowa City, 2000. ISBN 0-87414-122-2.

[2] Titze, I.R., The Myoelastic Aerodynamic Theory of Phonation. National Center for Voice and Speech, Iowa City, 2006. ISBN 0-87414-122-2.

[3] Zöner, S. and Kalteenbacher, M. and Mattheus, W. and Brücker, C., Human phonation analysis by 3d aero-acoustic computation. In: Proceedings of the International Conference on Acoustic NAG/DAGA 2009, 1730-1732, Rotterdam.

[4] Fürst, J., Janda, M., Kozel, K., Finite volume solution of 2D and 3D Euler and Navier-Stokes equations. J. Neustupa, P. Penel (Eds.), Mathematical fluid mechanics, 173-194, Berlin, 2001, ISBN 3-7643-6593-5.

[5] Honzátko, R., Horáček, J., Kozel, K., Solution of inviscid incompressible flow over a vibrating profile. In: M. Beneš & M. Kimura & T. Nataki (Eds.), COE Lecture notes, **3**: 26-32, Kyushu university, 2006. ISSN 1881-4042.

[6] Punčochářová - Pořízková, P., Horáček, J., Kozel, K., Fürst, J., Numerical simulation of unsteady compressible low Mach number flow in a channel, Engineering mechanics, **17**(2), 83-97, 2010.

[7] Jameson, A., Schmidt, W.,Turkel, E., Numerical solution of the Euler equations by the finite volume methods using Runge-Kutta time-stepping schemes, AIAA,81-125,1981.

[8] Horáček, J., Šidlof, P., Uruba, V., Veselý, J., Radolf, V., Bula, V., PIV Measurement of Flow-Patterns in Human Vocal Tract Model. In: Proceedings of the International Conference on Acoustic NAG/DAGA 2009, 1737-1740, Rotterdam, 2009.

[9] Pořízková, P., Kozel, K., Horáček, J., Numerical tests of flow in human vocal tract. In: Interaction of Dynamic Systems with Surroundings and Systems with Feedbacks. Prague: Institute of Thermomechanics, AS CR, v.v.i., 2010, p. 79-86. ISBN 978-80-87012-29-1.

Liquid applications, water pollution and treatment

Conference on Modelling Fluid Flow (CMFF'12)
The 15th International Conference on Fluid Flow Technologies
Budapest, Hungary, September 4-7, 2012

MODELLING POLLUTION TRANSPORT OF THE INDUSTRIAL WASTE UNDERGROUND

Mihail LUCA[1], Razvan-Paul BALAN[2], Andreea MANESCU[3] Alexandru Lucian LUCA[4]

[1] Corresponding Author: Department of Hydrotechnic and Environment Engineering, Technical University „Gh. Asachi". Mangeron Dumitru Str. 63, 770800, Jassy, Romania, Tel. +040 232 270804, Fax +040 232 270804, E-mail: mluca2004@yahoo.com
[2] National Agency „Romanian Water" Prut – Birlad Branch. E-mail: razvanpaul@yahoo.com
[3] Department of Hydrotechnic and Environment Engineering, Technical University „Gh. Asachi". E-mail: andreeamanescu@yahoo.com
[4] Department of Hydrotechnic and Environment Engineering, Technical University „Gh. Asachi". E-mail: lucian.luca@gmail.com

ABSTRACT

The paper presents the modelling of the pollution phenomenon of underground water in an industrial waste deposit area. The pollution phenomenon is analyzed in time, during the period of the deposit exploitation and conservation. We opted for a model of transport type, applicable to: 1° the flow processes through porous unsaturated/saturated media, in the stationary / transitory regimes; 2° the processes of miscible /non-miscible pollutants transport from porous unsaturated/saturated media, in transitory regime. The equations governing the flow consist of the equations of the fluid mass balance and moment equation, the famous Darcy's equation, generalized to non-saturated porous media. The numerical simulations achieved for different scenarios and for a certain period of time can appreciate the dispersion of a pollutant in a carrier of water. The mathematic model represents the flow and transport of pollutants from one layer of underground water from the analysis field. The numerical simulation used the FEFLOW program package. We successively treated a flow problem in four scenarios and two flow and transport problems (therefore, in total, 6 calculation variations). The simulation model through the FEFLOW program package has allowed the analysis and the methods of underground waters depollution for a certain determined period of time.

Keywords: flow, industrial waste, modelling, pollution, underground water.

NOMENCLATURE

A	$[m^2]$	area
C	$[mg/dm^3]$	pollutant concentration
g	$[m/s^2]$	gravidity acceleration
n	[%]	porosity
p	$[N/m^2]$	fluid pressure from the pores,
Q	$[m^3/s]$	discharge
Q_p	$[m^3/s]$	$Q_p = Q_p(x, y, t)$ the intensity of the distributed (punctiform) source of volume (specific debit) of fluid
T	$[^0C]$	temperature
t, t_0	[s]	moment in time
v	$[m/s]$	$v = v(x, y, z. t)$ the average speed vector of the fluid (water) through the pores of the porous medium
V	$[m^3]$	volume
$\underline{w}$	$[m/s]$	absolute velocity vector
ρ_s	$[kg/m^3]$	density of the solid phase,
η	$[kg/m\,s]$	the dynamic viscosity of water
ρ	$[kg/m^3]$	water density
Γ	frontier of analysis domain	
∇	$[m^{-1}]$- *nabla* differential operator	

Subscripts and Superscripts

I	initial moment
x, y, z	axial coordinate

1. INTRODUCTION

Waste products represent one of the most acute problems of environment protection in the current stage of economic and social development. In Romania, large quantities of waste products are generated because of the economic development, growth of production and consumption.

The inappropriate management of industrial waste and their deposits determine numerous cases of air, soil and underground pollution, with a negative impact on the environment and population health.

Of the total volume of waste produced in Romania, about 97.98 % are industrial and agricultural type and only 2.3 % of such waste.

Waste disposal on land is the main solution found for waste disposal industry in Romania. Over 80% of wastes generated in Romania are stored in each year. While accumulated a large amount of

waste in existing landfills. Currently in Romania there are 951 industrial warehouses occupy over 11,000 hectares [1].

Industrial landfills in the conservation and exploitation and to be designed or implemented new rules must comply with European legislation transposed into Romanian legislation.

The mass of deposited waste represents the main source of pollution of soil, underground waters and surface waters in certain cases, from the area of the placement of deposits and industrial waste stock-piles, both directly, by changing the use of the occupied land, and indirectly, through the contamination of neighbouring surfaces (Figure 1) [7].

Figure 1. Deposit of industrial wastes.

The soil is the most stable environment factor, which keeps the traces of pollution for a long period of time; the soil pollution implicitly leads to the pollution of the underground water.

2. THE PHYSICAL - MATHEMATIC MODEL OF POLLUTANTS TRANSPORT

Without ignoring the important role of the physical models, current practice in modelling pollutant dispersion in the underground is increasingly focusing on developing mathematical models as accurate.

Numerical simulation of the dispersion of pollutants in the landfill and adjacent aquifer consists of solving a 2D isothermal flow and transport in phase in an aquifer, the horizontal distribution of surface source of fluid and pollutant. Hypothesis implies that the aquifer water level does not exceed the upper surface to define the aquifer [1].

Pollutant (NH4 anion considered in the first stage of research) is soluble and neconservativ. Sorption processes are considered, but it neglects the reaction of production / degradation of substance. Aquifer level is free, and saturated porous medium is considered homogeneous and isotropic [1].

The mathematical model is customized according to the conceptual model and analysis is to specify the area and its border, the basic equations of flow and transport of substances. The mathematical model is consistent with the initial conditions and conditions outline the area of domain analysis considered (Figure 2) [1], [8].

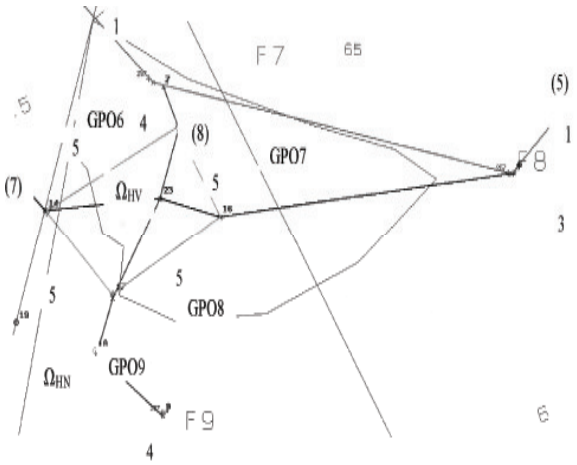

Figure 2. Domain of analysis - detail for the industrial waste (with subdomains ΩHV and ΩHN), with benchmarks: 11 out of 44 observation points, OP (7 ... 9, 14 ... 19, 23 and 24); 4 out of 5 profiles-section (1-1, 3-3, 4-4 and 5-5); 4 out of 9 groups of observation points, GPO (GPO 6, ..., GPO 9).

In order to apply the numerical model with EF, the domain was discretized in our EF = 12,247 triangular, thus obtaining a linear network presenting n_x = 6278 nodes (Figure 3 and 4) [1], [8], [5].

We opted for a model of transport type, applicable to: 1° the flow processes through porous unsaturated/saturated media, in the stationary / transitory regimes; 2° the processes of miscible /non-miscible pollutants transport from porous unsaturated/saturated media, in transitory regime [1], [8].

These mathematic models consisted in:

1° - non-governing equations (also called basic) of the flow and/or transport processes;

2° - contour conditions;

3° - initial conditions (only for the processes dependent of the time *t*).

The equations governing the flow consist of the equations of the fluid mass balance – named also the continuity equation and, respectively, moment equation, the famous Darcy's equation, generalized to non-saturated porous media; these

can be presented under the following general form [3], [11]:

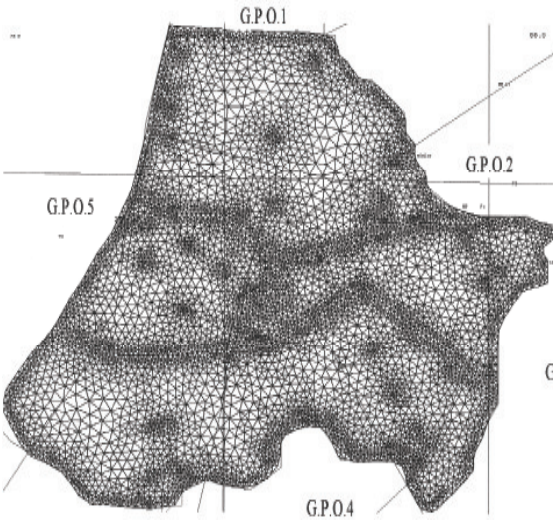

Figure 3. Meshing in finite element (FE) of the domain Ω (nE = 12 247, nX = 6278) with reference elements: 5 out of 9 groups of observation points, GPO, (GPO1 ... GPO5).

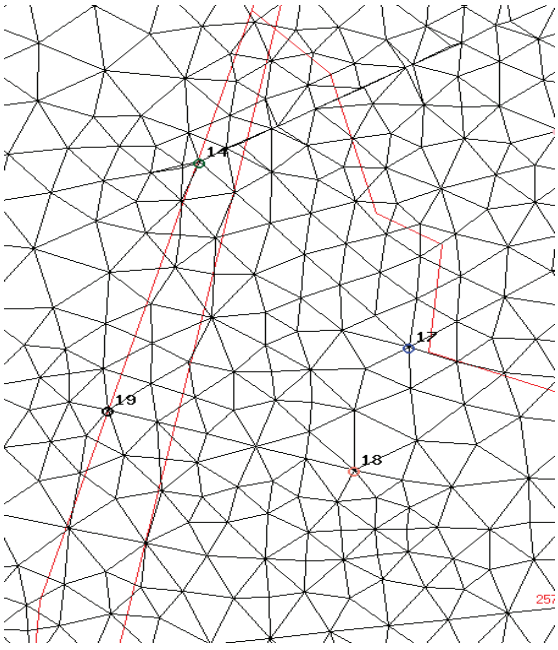

Figure 4. EF scheme in the study area waste industrial dump (partial scheme).

$$\frac{\partial(n\cdot S_w\cdot\rho)}{\partial t}=-\nabla\cdot(n\cdot S_w\cdot\rho\cdot\mathbf{v})+Q_p\rho \qquad (1)$$

$$\mathbf{v}=-\left(\frac{\mathbf{k}\cdot k_r}{n\cdot S_w\cdot\eta}\right)(\nabla p-\mathbf{g}\cdot\rho) \qquad (2)$$

where parameters used depend on space, time, temperature : $n = n\ (x,\ y,\ t)$, $\rho = \rho\ (T(x,\ y,\ z))$, $v = v\ (x,\ y,\ z)$, $Q_p = Q_p\ (x,\ y,\ t)$, $\eta = \eta(T(x,y,t))$, $p = p\ (x,\ y,\ t)$.

The equations governing the flow and transport of substances were derived introducing the relation (2.1)…(2.3) of [3] condition:

$$B=H-z_b,\ S=S_0(H-z_b)+n_e,\qquad \vartheta=0,\qquad \text{and}$$
$$K_{xx}=K_{yy}=K\ ; \qquad (3)$$

such expressions have the following particular result [1]:

- Darcy's equations

$$\bar{q}_x=-K(H-z_b)\frac{\partial H}{\partial x},\ \bar{q}_y=-K(H-z_b)\frac{\partial H}{\partial y} \qquad (4)$$

- the equation of continuity

$$S\frac{\partial H}{\partial t}+\frac{\partial\bar{q}_x}{\partial x}+\frac{\partial\bar{q}_y}{\partial y}=\bar{Q}_\rho, \qquad (5)$$

were customization in detail the analysis of the parameters is presented in [1].

Contour conditions were defined for the flow and pollutant transport. Relationships classical definition for each type of contour flow conditions are [1], [8]:

1º *type 1 contour conditions* (Dirichlet), where there are the values of the dependent H variable on the frontier,

$$H(x,y,t)=H_{\Gamma_1}(t),\ (x,y,t)\in\Gamma_1\times[t_I,t_F] \qquad (6)$$

2º *type 2 contour conditions* (von Neumann), where are given the values of the H size flow, according to the ***n*** direction of the normal to the Γ frontier, flow marked with $q_{n_H}(x,y,t)$:

$$-e_{ij}\cdot\frac{\partial H}{\partial x_j}\cdot n_i=q^R_{H\_\Gamma_2}(t),\ (x,y,t)\in\Gamma_2\times[t_I,t_F] \qquad (7)$$

where, according to the rule of mute indices, for $i,j\in\{x,y\}$,

$$e_{ij}\cdot\frac{\partial H}{\partial x_j}\cdot n_i=\left(e_{xx}\frac{\partial H}{\partial x}+e_{xy}\frac{\partial H}{\partial y}\right)n_x+\left(e_{yx}\frac{\partial H}{\partial x}+e_{yy}\frac{\partial H}{\partial y}\right)n_y \qquad (8)$$

when $q^R_{H\_\Gamma_2}(t)\equiv 0$, the conditions (4) are named *natural contour conditions*. In this case, the frontier is considered impermeable for the flow of H size.

3° *type 3 contour conditions* (Cauchy), when the values of the flow $q_{n_H}(x,y,t)$ depend also on the H variable, according to a law considered as linear:

$$-e_{ij}\cdot\frac{\partial H}{\partial x_j}\cdot n_i=-\Phi_{H\_\Gamma_3}\left[H^R_{\Gamma_3}(t)-H\right],\ (x,y,t)\in\Gamma_3\times[t_I,t_F] \tag{9}$$

where the function $H^R_{\Gamma_3}(t)$ generates the values for the H variable, imposed on the frontier Γ_3, and $\Phi_{H\_\Gamma_3}$ is the rate of the transfer (coefficient) which generally depends on the sense of the q_{n_H} flow.

$$\Phi_{H\_\Gamma_3}=\begin{cases}\Phi^{in}_{H\_\Gamma_3} & for\ H^R_{\Gamma_3}(t)\rangle H\\ \Phi^{out}_{H\_\Gamma_3} & for\ H^R_{\Gamma_3}(t)\le H\end{cases} \tag{10}$$

Outline conditions for contaminant transport refers to [1], [8]:

- the pollutant concentrations in the border area of domain analysis;
- hydrodynamic dispersion mass flow;
- Cauchy type conditions.

The initial conditions for the flow refers to piezometric H share knowledge baseline points (x, y) in the analysis domain.

$$H(x, y, t) = H_I(x, y) \text{ for } t = t_I \text{ and } (x, y) \in \Omega \tag{11}$$

The initial condition for the transport problem knowledge of baseline $t = t_I$ (usually $t_I = 0$) the value of the dependent variable C at any point (x, y) in the field and are of the form [1]:

$$C(x, y, t) = C_I(x, y) \text{ for } t = t_I \text{ and } (x, y) \in \Omega \tag{12}$$

The numerical simulations achieved for different scenarios and for a certain period of time can appreciate the dispersion of a pollutant in a carrier of water.

We used for the numerical simulation the FEFLOW program package [4].

3. EXPERIMENTAL RESULTS

We achieved a conceptual model for solving the proposed problems, for which we elaborated a mathematic model of pollutants transport. The mathematic model represents the flow and transport of pollutants from one layer of underground water from the analysis field considered. We used a complex of basic data in the analysis, specific to the case study. The data introduced in the calculation model come from systematic measurement in 13 observation wells positioned in the location of the industrial waste deposit.

The observation period regarding the underground water layer was between 2005…2009. In this period, we collected data regarding the pollution phenomenon parameters. For the prognosis, we considered a period of 10 years, respectively 2010…2019. The analysis carried out on the main pollutant substances indicated for the first prognosis stage the consideration of the anion from the NH_4 ammonium.

The climatic data was acquired from the meteorological station. In the analysis, we also used the data from two hydrometric stations placed on the nearby water flows. The basic data was processed with different frequencies: daily, monthly, quarterly, every semester etc.

The numerical simulation using the FEFLOW program package requires going through three distinctive stages [1]:

- pre-processing of the basic data,
- the effective processing of basic data,
- the post-processing of the resulted data.

We successively treated a flow problem in four scenarios and two flow and transport problems (therefore, in total, 6 calculation variations):

1. The flow problem for the study duration, $t \in [0, 1825]$ days (01.01.2005 – 31.12.2009) in four scenarios regarding the functioning of drillings from the area of the closed deposit (for establishing the optimal scenario):
   a) Scenario without pumping.
   b) Scenario with pumping from the drillings P1 (P.O. 14) and P2 (P.O. 15).
   c) Scenario with pumping from the drilling E2 (P.O. 23).
   d) Scenario with pumping from the drillings E1 (P.O. 24) and E2 (P.O. 24).

2. The flow and transport problem for the study duration, $t \in [0, 1825]$ days (01.01.2006-31.12.2009), in the scenario established as being optimal within the flow problem (for monitoring the pollution phenomenon in all the interest points from the domain Ω); taking into account the different periods for which we collected study data from the 13 observation drillings, the interval [0, 1825] days was divided in three adjacent disjoint sub-intervals:

$$[365,1825]=[365,775]\cup[775,956]\cup[956,1825]$$

It must be emphasized that on each of the three sub-intervals, we dispose of contour conditions of *I type,* with own forms.

3. The flow and transport problem in the perspective of the following decade, $t \in [0, 1825]$ days (01.01.2010-31.12.2019), in the scenario established as being optimal within the flow problem 1° and through the simulation of the contour conditions and variation of the material parameters (for the prognosis of the evolution of

the pollution phenomenon in all the interest points from the domain Ω).

It must be emphasized that on each of the three sub-intervals, we dispose of contour conditions of *I type,* with own forms.

The study data were pre-processed, regarding [1]:

1. The natural environment: topographic – the lay-out plan of the study area (Figure 5); climatic – precipitations and evapo-transpiration; hydrological – levels and debits in the hydrometric stations Bârlad and Râpa Albastră; hydro-geological – levels of the underground water and the depth of the basic layer, impermeable, of the carrier of water in the observation drillings and the material constants of the aquifer layer regarding the processes of mass flow and transport.

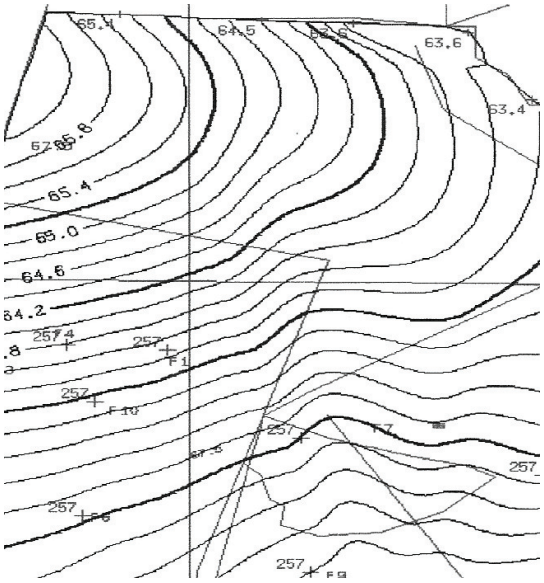

Figure 5. The altitude of the basic layer of the carrier of water represented through isohypses (the numbers in red colour represent the altitude of the support points).

2. The analyses regarding the qualitative indicators of the soil and underground water and from the rivers.

3. The quarterly rate of waste depositing (garbage, industrial non-recyclable wastes-emulsions, slime, ash, cinder etc.) and the monthly rate of sediment powders upon emission and their concentration in NH_4.

After pre-processing this study data, we determined the concrete numerical constants for the entry parameters and elaborated the input data files in the FEFLOW program package.

Post-processing of data files for scenario 1 resulted in a large series of graphics for the primary unknowns and derivatives. Graphics have enabled the correct interpretation, both qualitatively and quantitatively, the numerical simulation results (Figure 6 and 7).

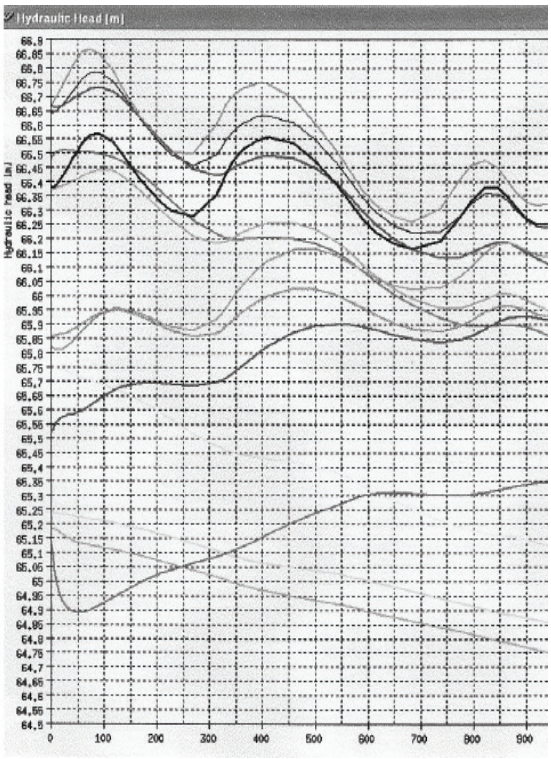

Figure 6. The variation of the hydraulic load in the observation drillings F1...F13 (P.O. 1...13) bottom-up 5, 11, 13, 3, 12, 6, 4, 10, 1, 9, 7, 8, 2 in the time interval [0, 1825] days.

Optimal operating scenario of closed landfill must minimize effect of water pollutants discharged from this underground environment containing water deposits.

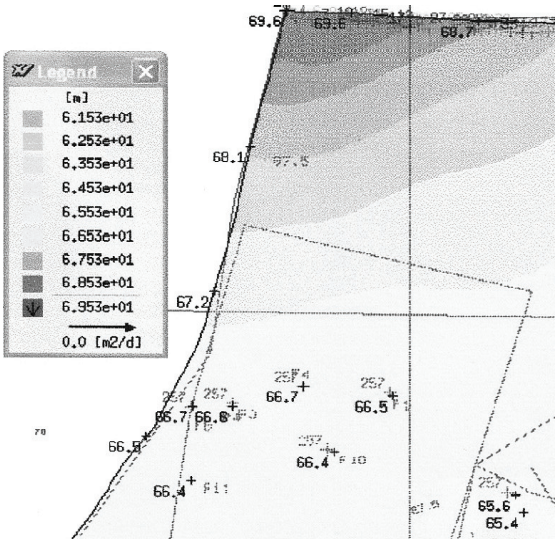

Figure 7. The initial pressure load field for the flow problem (t_1 = 0 days, on 01.01.2005) represented through the colour code (numbers in black colour represent the pressure load of the support points).

Data obtained and presented in figures allowed qualitative analysis compared the four scenarios to the operation of the landfill closed wells and power lines in the spectrum of the area. The analysis show that in scenario d) flow out of the store is closed the lower intensity.

Comparing data from Table 1, column 4, emerge as optimal scenario 1.d: the pumping of wells E1 and E2 [1].

Table 1. Fluid flows (water with dissolved polluants) entry into and exit from the closed landfill area at time t=1825 days

No.	Interval time simulation problem (days)	Inflow (m^3/d)	Outflow (m^3/d)	Balance (m^3/d)
1	2	3	4	5=3x4
1	**1°**a, [0.1825]	26.791	15.029	11.762
2	**1°**b, [0.1825]	45.744	4.954	40.790
3	**1°**c, [0.1825]	94.984	1.732	93.252
4	**1°**d, [0.1825]	104.025	1.078	102.947

For optimal scenario 1d were postprocessor data files computer program for the time period [0, 1825] and representative calculation times $t \in \{365, 956\}$. Numerical simulation results showed transport of pollutants in the analysis domain and the time considered (Figure 7, 8, 9, 10, 11 and 12).

A domain of the accidentally polluted water sources can be subject to a depollution process, of certain duration, in order to be reintroduced in the circuit of water supply for either industry, or population.

Through the analysis and prognosis model conceived, we attempted a response to this problem that has been affecting, lately, the underground medium, more and more stringently.

In order to determine the evolution of the pollution process in the entire interest field, we can only make interpolations on bi-dimensional fields, according to certain mathematic techniques accepted in this field.

The intensity of the evacuation process of a pollutant soluble in water (NH4, in the present study), through pumping, at a constant debit, decreases to the diminishment of its concentration in the carrier of water, and in order to obtain /maintain an acceptable intensity of this process, the pumped debit must be increased, or certain processes of the pollutant biotransformation be activated.

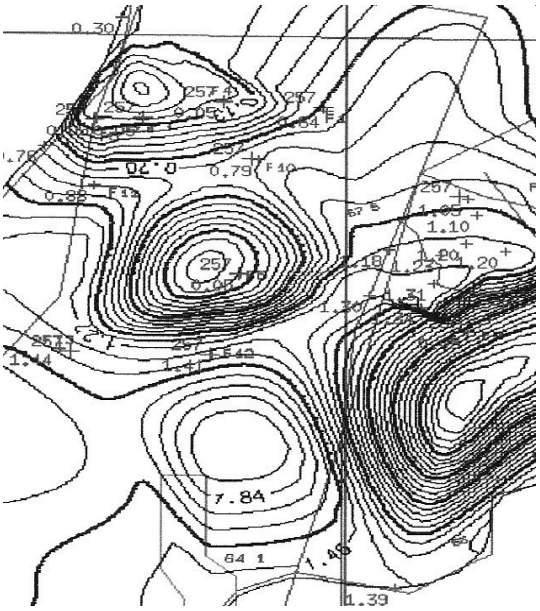

Figure 8. The NO_4 initial concentration (t = 365 days, on 01.01.2006) represented by isolines of equal concentration (partial scheme).

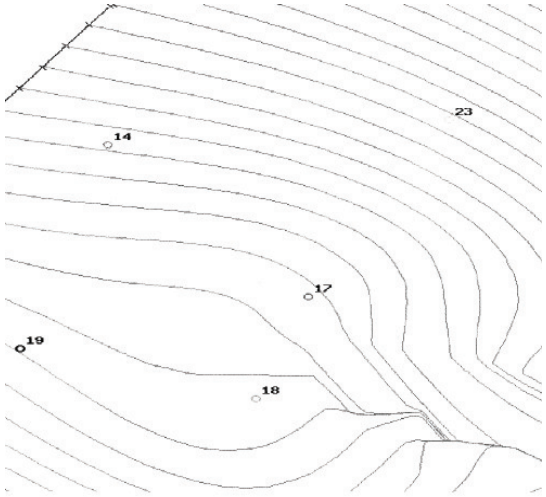

Figure 9. The power lines in the spectrum of closed landfill at the time t_F = 1825 days in a) scenario without pumping adjacent wells.

The analysis of data shows that the remediation process when considering anion NH4 as conservative pollutant is slow. To accelerate the remediation process, we must consider / chemical and biochemical processes activated by NH4 anion degradation.

Also, the process must be completed with additional pumping from wells located in areas with high concentrations for NH4 (eg drilling F9).

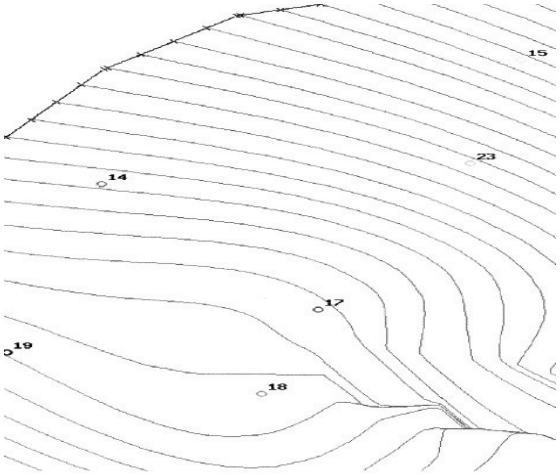

Figure 10. Power lines in the spectrum of closed landfill at the time tF = 1825 days in a) scenario pumping from wells adjacent to P1 and P2.

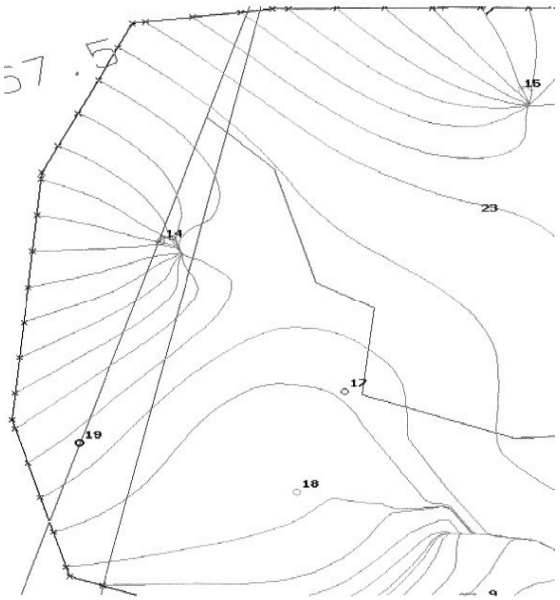

Figure 11. Power lines in the spectrum of closed landfill at the time tF = 1825 days in b) scenario pumping from wells adjacent to P1 and P2.

Similarly post processing was performed for flow and transport problems 2, 3 and 4. The obtained results revealed the best scenarios for each case analyzed.

Part of this research is applied to protect groundwater from industrial waste deposit area analyzed

Method of recovery of groundwater quality parameters (pumping wells) involves little investment. Remediation requires a minimum number of wells on the site.

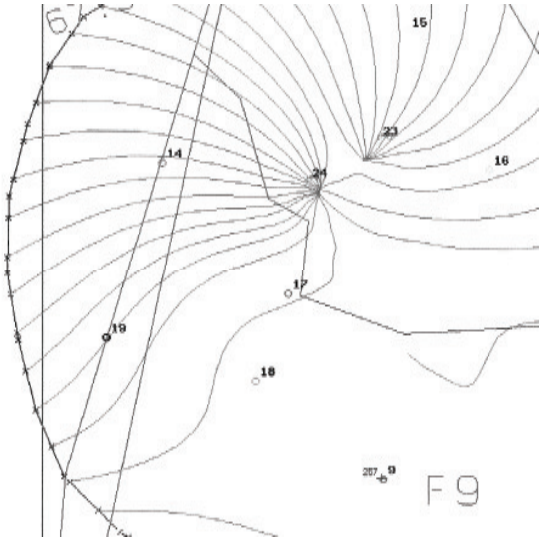

Figure 12. Power lines in the spectrum of closed landfill at the time tF = 1825 days in d) scenario pumping from wells adjacent to E1 and E2.

4. CONCLUSIONS

Studies and researches have enabled the following conclusions assertion:

1. The dangerous industrial waste deposits must be monitored to protect air, water and soil from the site area.

2. Modelling the transport of pollutants in the soil in the area of industrial waste deposits has a special importance for the protection of underground waters.

3. The simulation model elaborated allows the analysis of the pollutant transport in the area of underground waters by emphasizing the variation of concentrations in time and space.

4. The simulation model through the FEFLOW program package has allowed the analysis and the methods of underground waters depollution for a certain determined period of time.

5. Using the numerical simulation techniques, we can solve both the problems regarding the monitoring of the pollution process for the entire duration of the experimental measurements (approached problems, but insufficiently solved through the current monitoring techniques), but also the future evolution, on the extended periods, in different scenarios, of the pollution and/or depollution processes.

6. The simulation model can also be generalized for similar situations in the industrial waste deposits.

7. Groundwater remediation can be achieved by hydraulic methods (pumping wells) in a period of time.

REFERENCES

[1] Balan R., V., 2010, "Contributions to enhance safety in mining waste dumps has potential in reducing pollution", *PhD Thesis, Technical University of Iasi*.

[2] Charbeneau, R., J., 2000, „Groundwater Hydraulics and Pollution Transport" *Prentice Hall, New Jersey, SUA*.

[3] David, I., Şumălan, I., Beilici, E., 1998, "Influence of meshing in numerical modelling of pollutant transport in aquifers", *Bulet. Timişoara Politehnica University, Hidrotehnica serie, tom 43 (57), vol. I*, pp. 121-131.

[4], Diersch, H.J.G., 2002, "FEFLOW (Finite Element Subsurface Flow & Transport Simulation System) - Reference Manual", *WASY Institute, Berlin*.

[5] Hâncu, S., Marin, G., Vîrsta A., 2003, "Transport and dispersion of polluants", *BREN Publishing House*, Bucureşti, Romania.

[6] Kovarik K., 2000, „Numerical Models in Groundwater Pollution", *Ed. Springer-Verlag, Berlin*.

[7] Luca, M., Bălan, P., R.,, 2008. "Monitoring the exploitation of the industrial waste dumps", *Bulet. Iaşi Techn. University, Hidrotehnica serie, tom* LIV (LVIII) Fasc. 2, pp. 25 - 35.

[8] Luca, M., Bălan, P., R., 2010, "The modeling of pollution processes in the area of the industrial waste", *Scient. Bulet. "Politehnica" University of Timişoara,* tom 55 (68), Fasc. 1, 2, serie Hidrotehnica, pp. 61-66.

[9] Marinov, A., M., Poruţ, A., D., 2004, "Two-dimensional mathematical model, horizontal dispersion of a pollutant in groundwater", *Rev. Hidrotehnica, vol. 49, nr. 5-6, Bucureşti*, pp. 26-35.

[10] de Marsily G., 1994, „Hydrogéologie, comprendre et estimer les écoulements souterrains et le transport des polluants", *Écoles des Mines de Paris (Paris VI)*.

[11] Rasula, M., 1999, „Hydrogeological approach to design an active groundwater quality monitoring system", *Proceedings of the XXVIII IAHR Congress,* pp 50

[12] Splajt, T., 1999, "Investigating leachate migration case study: field anal ysis and modeling of a municipal landfill in Northern England", *Proceedings of the XXVIII IAHR Congress,*. pp. 7.

[13] Voss, C., I., 1984 "SUTRA. A F.E.M. Simulation Model for Saturated-Unsaturated, Fluid –Density - Dependent Ground - Water Flow with Energy & Chemically Single - Species Solute Transport", *U.S. Geological Survey, S.U.A*.

[14] Weber, O., Mohrolk, U., Jirka, G., H., 1999, „Mass transfer process in the saturated subsurface with a groundwater circulation flow field", *Proceedings of the XXVIII IAHR Congress, aug*. pp. 10.

Conference on Modelling Fluid Flow (CMFF'12)
The 15th International Conference on Fluid Flow Technologies
Budapest, Hungary, September 4-7, 2012

INVESTIGATION ON HOW TO OBTAIN RELIABLE EXPERIMENTAL DATA IN A BIOLOGICAL WASTE WATER PROCESS TANK

Morten Aa. Kristensen[1], Christian Brix Jacobsen[2], Bruno Kiilerich[3], Niels E. Linnemann Nielsen[4]

[1] Trainee, Structural and Fluid Mechanics, Global Research and Technology Grundfos Holding, Poul Due Jensens Vej 7, DK-8850 Bjerringbro Denmark. Tel.: +45 87506766, Fax +45 87501402, E-mail: maakristensen@grundfos.dk
[2] Manager, Structural and Fluid Mechanics, Global Research and Technology, Grundfos Holding, E-mail: cbjacobsen@grundfos.com
[3] Application Specialist, Water Utility - Treatment Plants, Business Development, Grundfos Holding, E-mail: bkiilerich@grundfos.com
[4]Development Engineer, Structural and Fluid Mechanics, Global Research and Technology, Grundfos Holding, E-mail: nelnielsen@grundfos.com

ABSTRACT

This paper addresses the complexity of measuring the flow field in a biological process tank of a waste water treatment plant (WWTP). A 3-D Acoustic Doppler Velocimeter (ADV) is applied, experiments are performed in both water and waste water which allows studies of the differences in flow field for both fluids.

The measurements are conducted in the aerobic process tank with and without the influence from aeration. The aeration, affects the fluid flow, by a vertical force and bubbles have an impact on the signal received by the ADV. Spikes occurs, standard deviation increases, subsequently the noise changes the mean velocity and at a specific point the value becomes opposite of the overall flow direction. This is investigated in field experiments at WWTP at Douchy Les Mines in France, creating a 6x6 array of 3-D velocities presented by a 3-D vector plot.

It is concluded that the ADV does not transmit reliable signals with air bubbles inside the sampling volume; hence an algorithm to filter data and determine the actual flow field is applied. A new velocity profile is hereby defined for the aerated case, removing corrupted data. The filtered date improves accuracy of measurements obtaining information of the flow and the applicability for validation of CFD simulations.

Keywords: 3-D ADV, aeration, data filtration flow field, multiphase flow, waste water.

NOMENCLATURE

K	$[N/m^2]$	Modulus of compression
$\underline{V}$	$[m/s]$	Absolute velocity vector
c	$[m/s]$	Speed of sound
f	$[1/s]$	Frequency
m	$[m]$	Meter
p_{abs}	$[Pa]$	Absolute pressure
u	$[m/s]$	Velocity
ε	[-]	Mass fraction of air in water
λ	$[m]$	Wave length
ρ	$[kg/m^3]$	Density
χ	[-]	Ratio of specific heat

1. INTRODUCTION

Waste water process tanks are designed differently from plant to plant. However the main objective of the biological process tanks is to reduce the carbonaceous, nitrogenous and phosphorus matter of the incoming wastewater. Operating the aerobic process zone includes addition of air to supply bacteria with oxygen used for their metabolic processes. In aerobic tanks where the aeration grid only covers part of the tank floor i.e. closed loop tanks, mechanical mixing are introduced to ensure that sedimentation does not occur and that bacterial flocs at all times are homogenous mixed with suspended and dissolved matter in the tank. [1]

The motivation for this article arises from the issue of obtaining reliable experimental data when measuring a 3-D velocity profile. Reliable data is necessary for characterizing the fluid flow and for comparison with CFD simulations of the process tank in the aerated and non-aerated case. The transients of experimental data allow comparison with transient CFD simulations. Using a valid CFD model introduce abilities to investigate aspects of mixing for a deeper understanding and a study of the performance of the tank design. Subsequently simulations provide information on performance of plant design and operating efficiency. Velocity measurements by [2] are completed for a squared

aerated tank over 60 minutes and demonstrate the transient behaviour of the velocity.

To analyse the flow field, velocities in a cross section of the tank are measured, depending on the size of the process tank, different numbers of data points are required. For the WWTP in Douchy Les Mines (DLM) i.e. a grid of 6x6 points is measured. Measurements in the cross section are performed twice for further understanding of the different dynamics between water and waste water. The amount of total suspended solids (TSS) in waste water are of interest since the suspended solids influence on the fluid properties as viscosity and hence the flow characteristics [3].

After construction the new process tank at DLM was filled with water and in March 2011 the first experiment was performed. For the same tank put into operation the experiment was repeated in November 2011.

To obtain information of the instantaneously velocity and the overall average velocities of the water measurements are required in the entire cross section of the tank.

Before the waste water enters the biological process tank it has been subjected to fine mechanical screening before it passes through a grit and grease removal. The fact that waste water still contains particles exclude the use of Pitot tubes as they are sensitive to particles introduced in the tube and have a low accuracy on fluctuation in the flow [4]. The visibility of the waste water is low and limits a technique as laser Doppler velocimetry (LDV) which otherwise would require a powerful laser to penetrate several meters into the waste water. Using an optical tool as particle image velocimetry (PIV) is likewise problematic because this technique uses a camera to visualize the tracing particles. This leaves the ADV as the best method to measure velocities in waste water for the reasons:

- The ADV is flexible and mobile for measurements submerged in water.
- The ADV uses acoustics which is applicable for turbid liquid as waste water.

2. ADV MEASUREMENTS

The Doppler Effect is the effect of frequency shift of sound reflected from a moving object. For a signal in a single medium the speed of sound is constant, defining a relation between frequency and wave length in (1).

$$c_f = f \cdot \lambda \tag{1}$$

If an acoustic signal is transmitted into a solid particle with a relative velocity to the source of the signal. The moving particle causes a shift in the transmitted frequency which allows the velocity of the particle to be calculated as in (2) [5].

$$v_{particle} = c \cdot \frac{f_{transmit}}{f_{received}} - c \tag{2}$$

The ADV calculates the x, y and z components of the 3-D velocity in a focus volume, placed 0.05 m below the ADV tip, see Figure 1. An acoustic signal is transmitted in the focus volume where particles reflect the signal. Four receivers obtain the reflected acoustic signal. Depending on the Doppler frequency shift, direction and magnitude of the x, y and z velocities are calculated. The sampling output rate is 25 *Hz* and the intern sampling rate is 10 *MHz* [6].

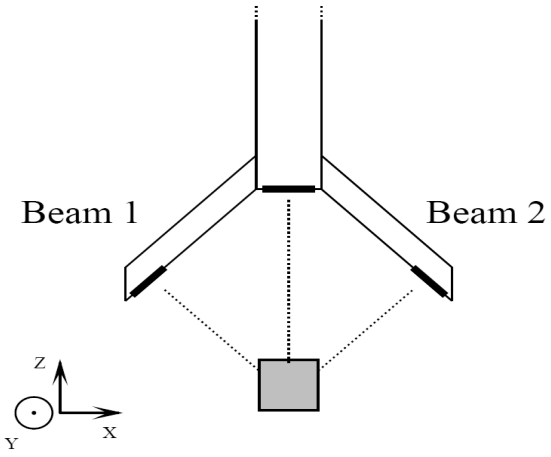

Figure 1. The position of the sampling volume of the ADV. For this setup a positive x velocity would decrease the frequency obtained in beam 1 and increased beam 2, no information is available on y-velocity from beam 1 and 2. The z-velocity affects both beams similar.

2.1. Limitations of ADV measurements

Studies have validated accurate ADV measurements compared to LDV [7]. The drawback using an ADV is the possible disturbance of the signal path or the focus area by contaminants. During field measurements the focus volume is not visible and it may contain matter i.e. air bubbles interfering the signal or hair twisted around receivers. Air is stuck on the ADV in Figure 4 upon a sampling of aerated water performed in lab. The interference of air is supported by the change in speed of sound in water as a function of mass fraction of air [8]:

$$c_W = \frac{1}{\sqrt{\frac{\rho_W}{K} + \frac{\varepsilon \cdot \rho}{x \cdot p_{abs}\left(\frac{\rho}{\rho_W} + \left[1 - \frac{\rho}{\rho_W}\right]\right)^2}}} \tag{3}$$

A section of the graph of equation (3) is illustrated in Figure 2. The change in speed of sound is remarkable even for small mass fractions of air which introduce disturbance of the signal.

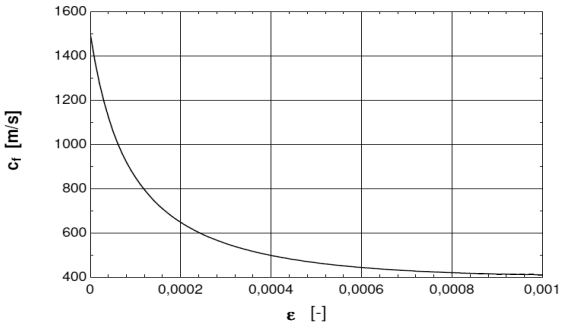

Figure 2. The influence of speed of sound, for a change in mass fraction of air

2.2. Compensation of ADV errors

The errors of the measured signal due to bubbles results in spikes. Earlier studies of spikes concentrate on the method to remove corrupted signals [9,10]. Studies by [10] assume spikes as turbulence velocities above the velocity range or pulse-to-pulse interference. It is determined that neither filters based on Signal to Noise Ratio (SNR) nor autocorrelation removes spikes sufficiently. Introducing the Phase-Space Tresholding Method (PSTM), where information on first and second order derivatives are calculated as in (4) and (5):

$$\Delta u_i = \frac{(u_{i+1} - u_{i-1})}{2} \tag{4}$$

$$\Delta^2 u_i = \frac{(\Delta u_{i+1} - \Delta u_{i-1})}{2} \tag{5}$$

The standard deviation and rotation angle are applied for further calculation. The method requires a dense mean. The filter is developed by [4] investigating the influence of why spikes are created. Concluding that large particles as bubbles interfere the signal path and the focus volume. [4] developed a new hybrid despiking filter which is an expansion of the PSTM that removes spikes. The hybrid filter includes a limitation on maximum acceleration and other requirements for standard deviation.

When a sufficient data series is calculated, the points conflicting with the filter are replaced with linear interpolation. An individual filtration is made for each velocity component x, y and z, increasing the performance since each data series are not affected to the same extend.

3 FIELD AND LABORATORY EXPERIMENTS

To study the properties of an ADV, laboratory tests are conducted with the purpose of describing the properties of the ADV and characterize the noise from bubbles to the possible extend. Field tests are performed to investigate the flow field in a biological process tank with and without the influence of aeration.

3.1 Laboratory experiments

In laboratory it is tested, how bubbly flow affects the signal of the ADV in calm water and swirling water. A noisy signal is generated when air enters the sampling volume and the data needs to be validated on behalf of the actual motion of the fluid. The ADV is tested in an aquarium in calm water and in a vessel with dynamic flow. As stated in [4]: The measurements in the aquarium show how the ADV cannot be used in demineralised water to measure velocities. The lack of particles generate a highly fluctuating signal, hence the data is corrupted. Yeast cells suspended in the water are suitable as reflecting particles in the water. Tap water requires attention on software settings and pulse to pulse interference to obtain a steady signal, however with the right settings it is possible to obtain a steady signal. As expected water with colloid particles added record a steady velocity around 0 *m/s* and an autocorrelation approaching 1 for calm water.

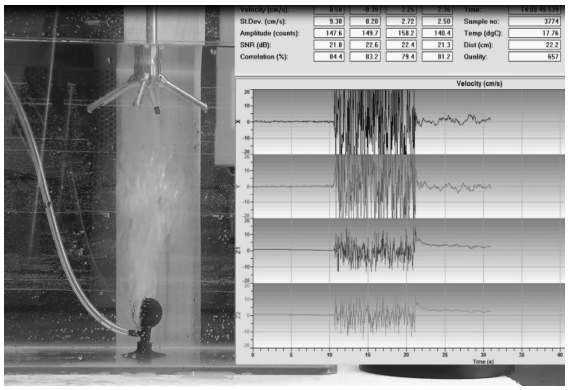

Figure 3. A snapshot shows setup for the calm water measurements before the bubbles enter the sampling volume. To the left: The test rig showing the actual bubble plume, from the bottom mounted bubble dispenser. To the right: The sampling of velocities in the Vectrino software, the axes from the top show: x, y, z0 and z1

For the aerated case the velocity is disturbed and autocorrelation is lowered by the air bubbles. For visualization of bubble disturbance, two videos are recorded: One with 10 sec. of on/off operation of the air pump applying a constant volume flow and another video with manual release of a single air bubble. For both measurements the velocity range is set to 0.30 *m/s*. In Figure 3 a snapshot from the video with influence from aeration is shown. It is revealed how the velocities are around zero

before aeration is turned on. When air is applied the signal becomes noisy with highly fluctuating velocities. When air supply afterwards is turned off the velocities show some smaller succeding fluctuations, untill the flow becomes calm again.

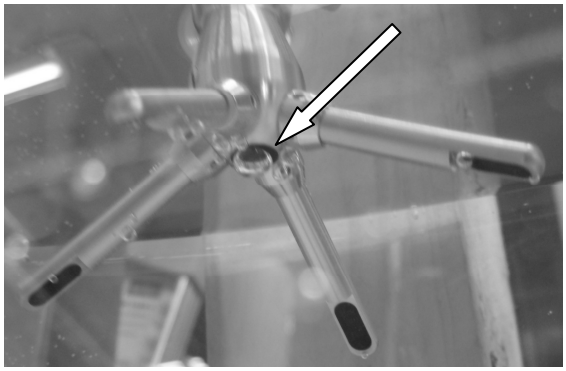

Figure 4. The ADV submerged in water. The transmitter is situated in the middle and the four receivers situated at the end of the ADV arms obtain the signal. Here a bubble is stuck on the transmitter.

3.2 Field experiments

Field experiments are made according to what is described in [11]. The specification defines the measures of an array as illustrated in Figure 5. The span is defined by the area of the cross section and for that reason the cross section of DLM is 6x6.

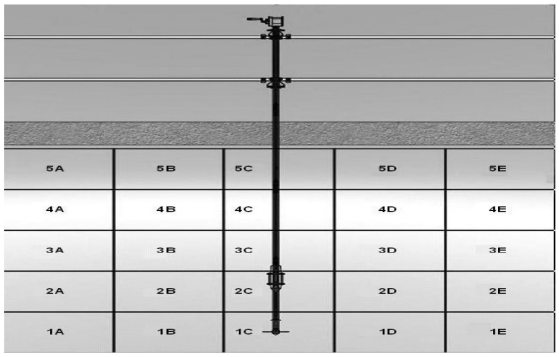

Figure 5. The positions of measured points. Here a section of the x-axis from A-E, and the y-axis is 1-5. A-serie is the outer points, and E-serie are inner.

In a process tank it is necessary to have a turbulent flow in the entire tank to create proper mixing. The flowmaker should however not create a jet flow as a too high velocity gradient implies a higher shear stress, which might result in breakup of bacterial flocs and thereby give problems with the subsequent clarification [12]. A turbulent flow with a uniform velocity profile and without any slow spots where sedimentation might occur is desired. The data provides information on the transient velocity and the turbulence in the fluid. This provides opportunities to compare measurements with a transient CFD simulation. In the tank the flow direction is counter clockwise, in relation to Figure 6. Thus measurements are performed upstream of the installed flowmakers.

3.2.1 Douchy Les Mines

The tank in DLM is of the annular type, see Figure 6. Liquid flow is created by 3 Grundfos AFG 24.180.39 illustrated as round disks. The experiment is conducted twice: The first measurements are performed with water in the process tank; obtaining data for a liquid with well known properties. The experiment was afterwards repeated with waste water and activated sludge, after the tank has been put into operation.

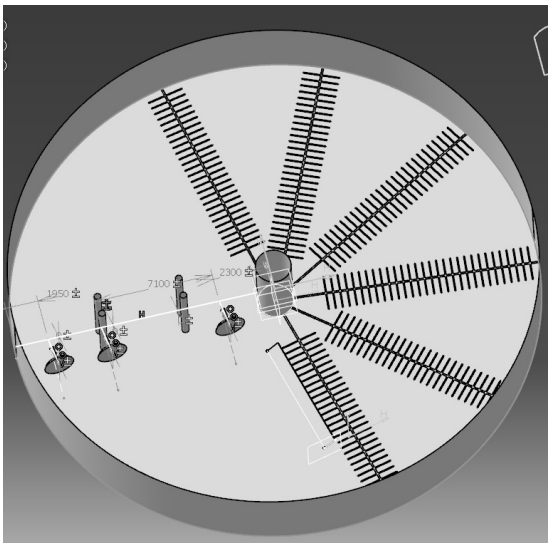

Figure 6. The tank in DLM. The outer diameter is 31.2 m, the inner diameter is 2.1 m and water debt is 4.1 m. The 3 discs placed in the left in the tank are flowmakers. The 6 pipelines are the aeration system, which is connected to a main pipe. The measurements are conducted upstream the flow makers.

At each measured point in the cross section, 200 seconds of data are recorded. The series are conducted both with and without the influence from aeration. The test rig is fixed in the horizontal position and adjustable in the vertical by a metal wire, the vertical position changes starting at 1C i.e. 1C, 2C… 6C. In A1 the horizontal distance to the wall is 0.5 *m* and the vertical distance is 0.14 *m*. The software settings for the ADV allow the user to measure at a specific velocity range, which should correspond to the expected range of measurements.

It is essential to notice that all measurements for water are conducted with the ADV velocity range of ±0.30 *m/s* the measurements in waste water are conducted with the range of ±1.00 *m/s* for. Measurements in waste water with the influence of aeration are measured with a velocity range of

±1.00 *m/s*. The software setting greatly changes the results of measurements. To display the difference in velocity measurements, point A3 under influence of aeration is shown in Figure 7 and 8 for each velocity ranges. It is clear that the lower velocity range of ±0.30 *m/s* is sensitive to aeration. Table 1 states the difference in terms of the velocities.

Table 1. Measured velocities for two velocity ranges in aerated waste water at point A3 at the cross section.

Velocity range [*m/s*]	Mean velocity [*m/s*]	Variance [-]
x ± 0.30	0.34	0.19
y ± 0.30	-0.091	0.15
z ± 0.30	-0.050	0.0071
x ±1.00	-0.30	0.0048
y ±1.00	0.049	0.0047
z ±1.00	-0.20	0.0036

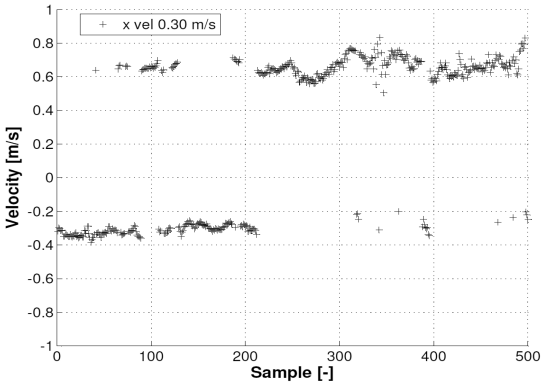

Figure 7. A snapshot of 500 samples for the measurements at A3 in waste water under influence of aeration using the velocity range of ± 0.30 *m/s*.

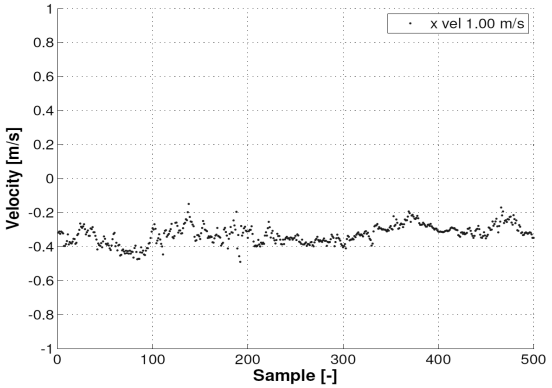

Figure 8. A snapshot of 500 samples for the measurements at A3 under the influence of aeration using the velocity range of ± 1.00 *m/s*

4 DATA PROCESING

For the sake of understanding only x velocities are shown in the following. As expected, data series with spikes are recorded, this is especially pronounced for measurements under influence of aeration performed with a velocity range of ±0.30 *m/s.* These measurements are subjected to the hybrid filter from [13] in MATLAB. The filter shows good performance in series with moderate spikes as shown in Figure 10 for the measurement in point F6 in water with aeration turned on, see Figure 9-10. For visualisation Figure 9 shows intervals with moderate noise as in sample point 1500-2000. In Figure 11 the noise is heavy and the filter is not applicable.

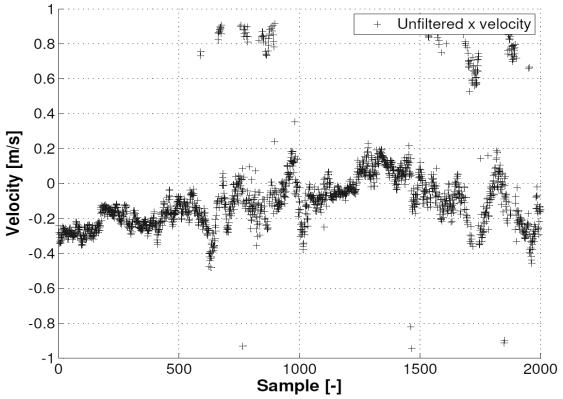

Figure 9. A plot of the unfiltered x velocity in point F6 performed in water with the influence of aeration.

The spiked data points from Figure 9 are filtered and shown in Figure 10. The use of the despiking filter applied show how spikes are removed, from a dense signal. The velocities are in the range of -0.4 to 0.2 *m/s.* The spiked velocities are around ±0.9 *m/s.* However a downside of the filter is illustrated with the linear interpolation of the x velocities from sample 1250 to 1400 where the slightly positive x velocities are regarded as noise, because the velocities are too far away from the mean, see Figure 10.

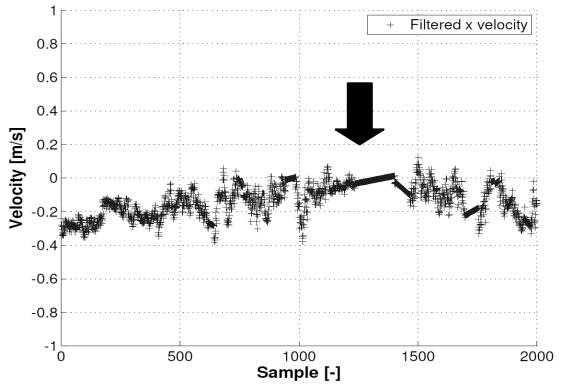

Figure 10. A plot of the filtered x velocity in point F6 performed in water under the influence of aeration.

The filter exhibits a limit for a too noisy data series, for A3/A4/A5 for aerated water. It is not beneficial to use the hybrid filter for despiking; only a few points in the x velocities are replaced in the

entire series. There is not a sufficient amount of dense and steady velocities to create a base for the signal processing. There are two dense areas around -0.3 and 0.6 *m/s*. The hybrid filter accepts the velocities around -0.3 and 0.6 *m/s* and removes the few values in between, which are around 0.2 *m/s*. Referring to Figure 7, the positive velocities have the same properties as the noise in Figure 11, and therefore the filtered data of Figure 11 should have characteristics as Figure 8 where the noise are reduced by changing software settings for the ADV. This must be kept in mind before accepting filtered measurements, without any knowledge of the actual tank flow; the positive mean flow of the tangential (x) velocities in Figure 11 may be accepted.
The instant values of x(i), y(i) and z(i) are used to calculate a velocity magnitude $\underline{V}$(i). Each of the four data series are averaged to a mean value which represents the averaged direction and length of the velocity vector.

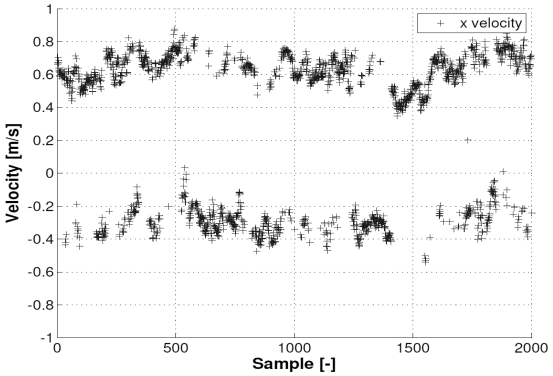

Figure 11. A plot of the velocity for A4 in water under the influence of where the filter is not applicable.

5 RESULTS FROM FIELD EXPERIMENTS

The approved or despiked x, y, z velocities and velocity magnitudes are implemented in a 3-D vector- and contour plot, see Figure 12-18. The figures show the average velocity of the flow field in a cross section, the greyscale in the figure indicates the mean velocity magnitude in a range from 0 to 0.5 *m/s* and the vectors show the direction of the mean tangential (x), radial (y) and axial (z) velocities for the measured period. For illustration of the direction the length of the vectors are scaled by a factor 10. The points of the y axis are replaced with the letters A-F presenting the radial position from -13.9 *m* to -0.5 *m*. The figures are listed in Table 2 in order to create an overview of the presented average velocities.

The filtered velocity profile of water without the influence of aeration is shown in Figure 12-13. The outer boundary of the cross section is to the left, and the center of the tank to the right. For Figure 12-14 the velocities is higher at the outer boundary, with mean values around 0.35-0.40 *m/s*. Where as the inner velocity is in the area of 0.1 *m/s.* The vector plots are averaged and do not inform about transients as turbulence intensity. Thus information regarding sedimentation and mixing cannot be interpreted directly.

Table 2. Overview of settings for Figure 12-18

Figure	WW	Water	Aeration on	Filter
12-13		x		x
14	x			
15		x	x	
16		x	x	x
17-18	x		x	

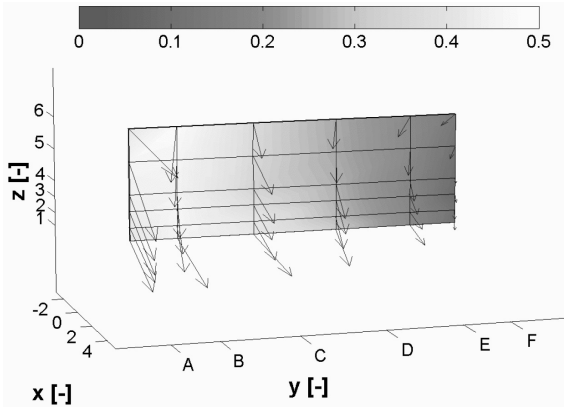

Figure 12. Vector plot of the average filtered 3-D velocities, for water without influence of aeration

Figure 13 shows the difference in velocity direction and magnitude as the position changes.

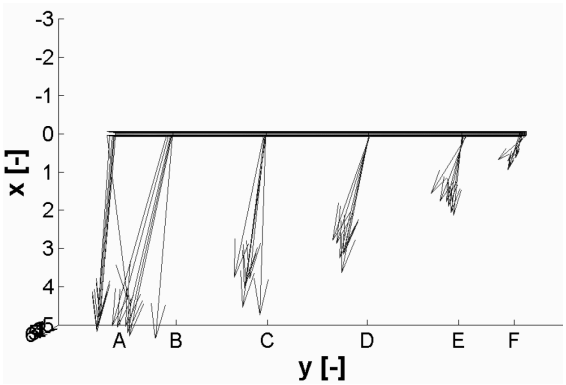

Figure 13. The top view of the velocity profile for water without the influence of aeration and with filtered data. Vectors are scaled.

The unfiltered velocity profile for waste water is shown in Figure 14. There is an increasing velocity from F to A. Measurements are similar to the water with filter in Figure 12. But the vectors of the A series are pointing away from the center and the B series is pointing towards the cente, as a change in the radial direction. A and B series points

towards each other in Figure 12 and away from each other for Figure 14.

Measurements with aeration turned on for water are showed with and without data filtered by the hybrid filter in Figure 15-16. For the measurements under influence of aeration the force acting on the water is increased by the air. The air increases the velocity magnitude for the inner points. At the bottom it influences as sink and in the top in influences as a source, forcing the velocity direction towards and away from the aeration zone.

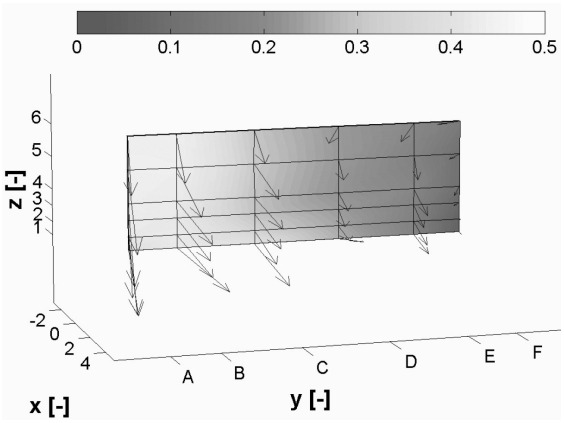

Figure 14. Vector plot of the average unfiltered 3-D velocity, for waste water without the influence of aeration.

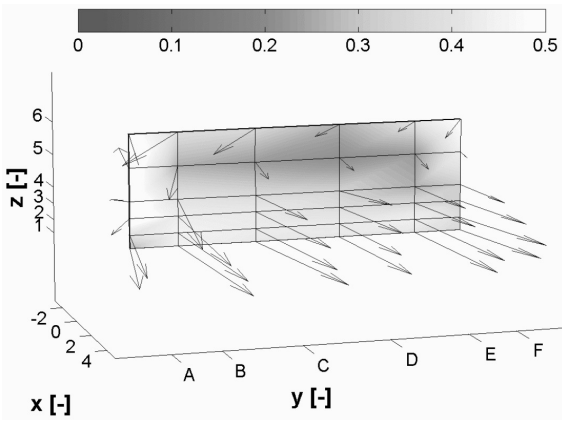

Figure 15. The velocity profile for water with the influence of aeration.

Figure 16 shows a higher velocity at the bottom; the velocity is decreasing non-uniformly from the bottom to the surface. The directions of the velocities are turned towards the center of the tank compared to the vector plots in Figure 12-14 which did not have the influence from aeration. The limitations of the filter are proven as it is unlikely that measurements in point A3, A4 and A5 experience a back flow compared to the general flow direction of the tank, simultaneous with the highest velocity magnitude of the cross section. The short vectors and high velocity magnitude in point F5 and F6 indicate high velocities in opposite direction.

The filtered data of the measurements in water with influence of aeration are shown in Figure 16. For comparison it is notable how the hybrid filter decreases the velocity magnitude, but increases the length in F5 and F6, by removing spiked velocities with opposite direction of the flow direction.

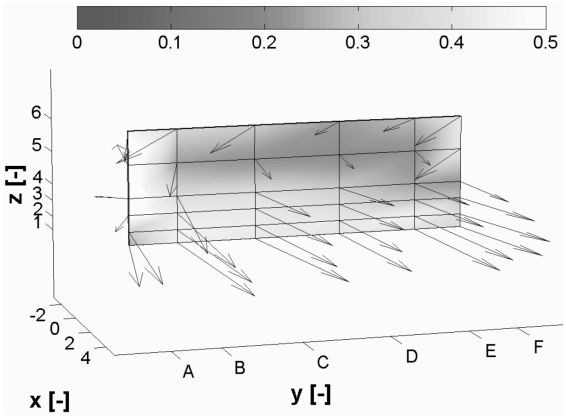

Figure 16. The filtered data showing the flow field in water with the influence of aeration.

For the velocity plot of the measurements in waste water with the influence of aeration in Figure 17 the velocity profile has an area with lower velocity in the upper center (B4-D6) and additional lower velocities in the D-series from D1-D4, indicating that the generated thrust of the flowmakers are not sufficient to penetrate the aeration zone. For the flow at the inner boundary, there is a change in direction from the bottom to the surface. In the bottom the flow is sucked towards the aeration system while at the upper points at the surface they are pushed away from the inner boundary. The directions of the flow indicate that a continuous vortex is formed Figure 18 shows the top view of wastewater under the influence of aeration and it is seen how the inner series F and E have velocities pointing in different direction.

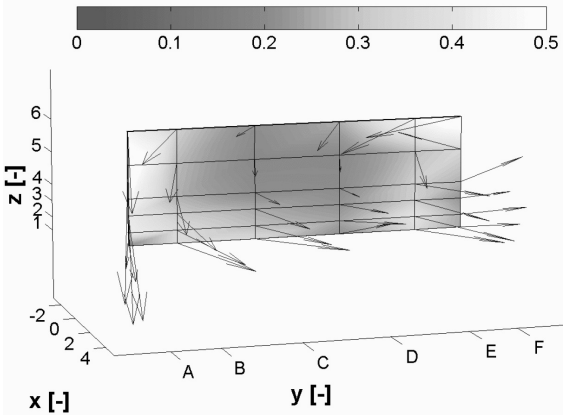

Figure 17. Velocity profile for waste water under the influence of aeration.

Looking solely into velocities with no aeration Figure 12-14, indicates a poor performance of the

process tank in the measured cross section. The poor hydraulic performance may be neglected as the tank under influence from aeration have higher velocities at the inner boundary. The results show how dominating the aeration is for the flow pattern in this tank with a relatively small inner diameter.

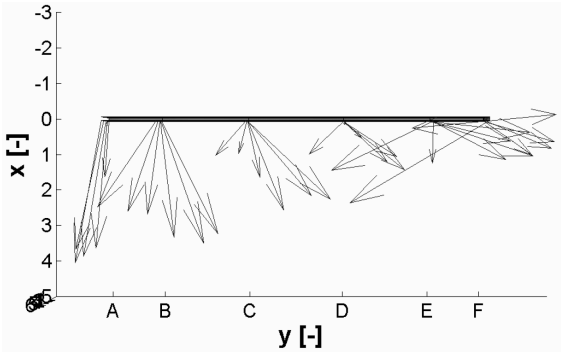

Figure 18. The top view of the waste water under influence of aeration.

6. CONCLUSION

Results are obtained for velocity measurements in laboratory and at a WWTP.

The velocity spikes generated by aeration cannot be identified nor characterized to an estimated value. The noise is a reaction of the transient speed of sound in water with air bubbles, influencing the focus volume, around the transmitter and the receivers. It is concluded that compensation is impossible. For this reason a filter is used to replace the corrupted data with linear interpolation between the nearest accepted data points.

Aerated water increases the complexity of acquiring a valid data set. Combining the correct software settings, positioning the ADV away from aeration fields and away from pulse-to-pulse interference; measurements can be obtained with a minimum of noise. Remaining noise can be successfully identified and removed by the hybrid filter. The filter thus exhibits limitation in very noisy flow fields as in Figure 11.

To illustrate the flow field, a 3-D vector and contour plot provides information on averaged velocity magnitude and direction. The plots show a small difference in the non-aerated flows in water and waste water. For aerated flow the difference is notable between water and waste water, Figure 16-17. The non-uniform velocity profile obtained for flows under the influence of aeration supports the complexity for further comparison with CFD.

ACKNOWLEDGEMENTS

The author would like to thank the support from the employees at the R&T division at Grundfos A/S for support, Philipp Egger and Nicholas Troffaes for providing help to conduct field experiments, Eau et Force for allowing measurements at Douchy Les Mines.

REFERENCES

[1] Tchobanoglous, G., and Burton, F., L., and Stensel, H., D., 2004, *Wastewater Engineering Treatment and Reuse,* Mc Graw Hill

[2] Gresh, M., Armbruster, M., Braun, D., and Gujer, W., 2010, "Effects of aeration patterns on the flowfield in wastewater aeration tanks", *Water Research,* Vol. 45 , pp 810-818

[3] Guibaud, G., and Dollet, P., and Tixier, N., and Dagot, C., and Baudu, M., 2003, "Characterisation of the evolution of activated sludges using rheological measurements", *Process Biochemestry*, Vol. 34, pp 1803-1810

[4] Birjandi, A. H., and Bibeau., E. L., 2011, "Improvement of Acoustic Doppler Velocimetry in bubbly flow measurements as applied to river characterization for kinetic turbines" , *I.J. of Multiphase Flow,* Vol. 37 , pp 919-929

[5] Rosen, J., and Gothard, L., Q., 2009, *Encyclopedia of Physical Science*, Fact on File

[6] Nortek, 2004, *Vectrino Velocimeter User Guide,* Nortek A/S Rev. C

[7] Lohrmann, A., Cabrera, R., and Kraus, M. N. C., "Acoutsic-Doppler Velocimeter (ADV) For Laboratory Use*", American Society of Civil Engineers (ASCE*), 1994

[8] Verein Deutscher Ingenieure, 1996, Geräusche bei Rohrleitungen ,VDI 3733, Publisher

[9] Mori, N., Takuma, S., and Shohachi, K., 2004, "Noise of Acoustic Doppler Velocimeter Data in Bubbly Flows*", ASCE*, Vol. 133

[10] Goring, D., G., and Nikora, V., L., 2002, „Despiing Acousting Doppler Velocimeter Data", *Journal of Hydraulic Engineering*, Vol, 128, pp 117-126

[11] VDMA, 2010, *Agitators in activated sludge tanks of wastewater treatment plants Information on planning, project design and construction*, Beuth Verlag GmbH

[12] Tang, H., and Li, T., and Zhu, Z., and Wang, D., and Yao, C., 2006, "Characterization of floc size strength and structure under various coagulation mechanisms", *Powder Technology*, Vol. 168, pp 104-110

[13] Birjandi, A. H., 2011, *River ADV measurement and hybrid filter*, URL: http://dx.doi.org/10.5203/ds_bib_3

Conference on Modelling Fluid Flow (CMFF'12)
The 15th International Conference on Fluid Flow Technologies
Budapest, Hungary, September 4-7, 2012

RESEARCH ON FILTRATION PROCESS THROUGH SORTED CRUSHED ROCK

Josif BARTHA [1], Nicolae MARCOIE [2], Daniel TOMA [3], Daniel TOACĂ [4], Victor GABOR [5], Aron Gabor MOLNAR [6], Adina LUPUSORU [7]

[1] Prof. PhD. Eng., "Gheorghe Asachi" Technical University of Iasi, Faculty of Hydrotechnical Engineering, Geodesy and Environmental Engineering, 65 Prof. dr. docent Dimitrie Mangeron Street, 700050, Iasi, Romania, phone number: +40232 270804, email: i_bartha@yahoo.com
[2] Assoc. Prof. PhD. Eng.,email: nmarcoie@yahoo.com
[3] Assist. Eng., email: daniel_10hid@yahoo.com
[4] PhD. Eng.,email: daniel.toaca@yahoo.com
[5] Lect. PhD. Eng.,email: vicgabor@yahoo.com
[6] PhD. Student, email: agmolnar@yahoo.com
[7] Master Student, email: nyxgl@yahoo.co.uk

ABSTRACT

The paper presents the experimental results of fluid flow through homogeneous permeable media – sorted crushed rock with four different diameters: 22.5, 10.0, 5.4 and 3.9 mm. Experiments for hydraulic gradients from 0.01 (corresponding to Darcy's law) up to 7.5 (post Darcy's movement) have been undertaken.

Using a capillary tube model of filtration, parameters of the movement have been determined: porosity, pores diameter, tortuosity, Forchheimer type quadratic relationship of hydraulic gradient, the dynamic and static specific area and friction factor law in function of pore diameter Reynolds number.

Keywords: Capillary tube model, Newtonian fluid, Post Darcy's filtration,

NOMENCLATURE

a	$[m^{-1}\cdot s^{1}]$	coefficient
b	$[m^{-2}\cdot s^{2}]$	coefficient
c	$[m^{-3}\cdot s^{3}]$	coefficient
d	$[m]$	pore tub equivalent diameter
d_p	$[m]$	gravel nominal diameter
f	[-]	friction factor
k_e	$[m]$	equivalent roughness
n	[-]	porosity
Δp	$[Pa]$	pressure drop
A_d, A_s	$[m^{-1}]$	dynamic and static specific area
D, Dn	$[m]$	infiltrometer diameter
L, L', ΔL	$[m]$	length
M, M^*	$[Pa\cdot s^2\cdot m^{-3}]$	coefficient
N, N^*	$[Pa\cdot s\cdot m^{-2}]$	coefficient
NM	[-]	number of experiments in a set
Re_d	[-]	pore diameter Reynolds number
V	$[m\cdot s^{-1}]$	mean pore velocity
V_0	$[m\cdot s^{-1}]$	superficial velocity
α	$[m^{-\beta}\cdot s^{\beta}]$	coefficient
β	[-]	coefficient
λ	[-]	Darcy-Weisbach coefficient
θ	$[^0C]$	temperature
μ	$[Pa\cdot s]$	dynamic viscosity
ρ	$[kg\cdot m^{-3}]$	density
τ	[-]	tortuosity
δQ	[-]	accuracy of discharge measurement

1. INTRODUCTION

The velocity of filtration through permeable medium, beginning with a certain limit may overpass the Darcy's linear filtration law.

This happens for Reynolds number computed on micro scale, for that $Re_d > 1$ [1, 2]. For higher values of Reynolds number the filtration is described by nonlinear laws, proposed by Forchheimer [3], in different forms, as:

- power relationship

$$\frac{\Delta p}{L} = \alpha \cdot V_0^{\beta} \tag{1}$$

- or polynomials of 2nd or 3rd order

$$\frac{\Delta p}{L} = a \cdot V_0 + b \cdot V_0^2 \tag{2}$$

$$\frac{\Delta p}{L} = a \cdot V_0 + b \cdot V_0^2 + c \cdot V_0^3 \tag{3}$$

These laws are widely commented until today [4, 5, 6]. They can be obtained using the relationships Navier-Stokes, applied for describing the movement within permeable mediums.

Post Darcy's filtration has many technical applications, as it follows: in the hydraulic of permeable bed rivers [7], in medicine [8], flows within permeable hydraulic structures [9], movement over permeable walls [10], fluid raw material extraction [11], dispersing polluting substances within built areas, oxygen and carbon dioxide exchanges in vegetation zones, forest fires propagation [12], in the drain and well filters, packed bed reactors computation [13], etc.

2. CAPILLARY TUB MODEL OF FILTRATION

Capillary tubes model of the permeable media considers that bed void is formed as a set of cylindrical small diameter equivalent curved tubes within which the loss of head occurs like in circular pipes, having equivalent roughness equal to the fictive tubes diameter (Fig. 1.) [1, 3, 4, 13, 14, 15].

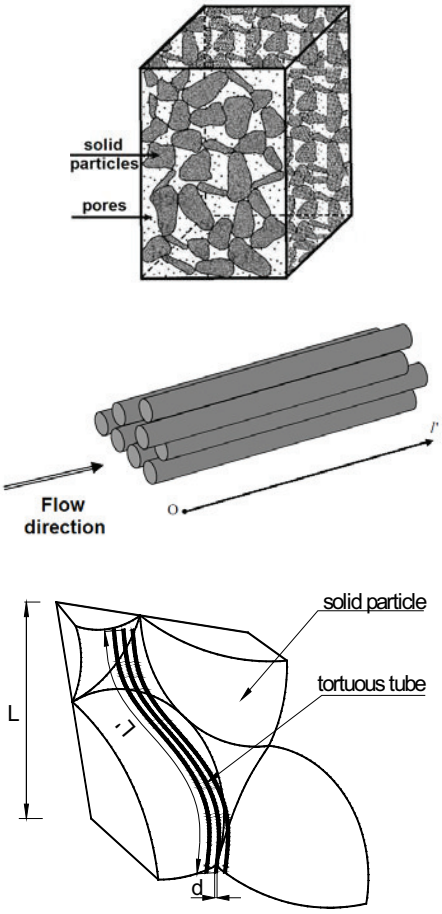

Figure 1. Scheme of the capillary tub model of permeable medium [3, 17]

The parameters of filtration on micro scale: real velocity - V, tortuosity - τ, the measure of fictive diameter of pores - d and the friction factor λ through macro scale experimental measurements are obtained. The macro scale pressure gradient - $\Delta p / L$, in function the superficial velocity V_0 on infiltrometer, together porosity - n is measured.

Considering the pressure drop due to viscous friction (after Poiseuille relationship) and due to the inertia through the tubes of the model, that are working in the rough pipe zone ($k_e = d$), relationship (2) can be brought to the form [4, 16]:

$$\frac{\Delta p}{LV_0} = 2 \cdot \tau^2 \mu A_d \frac{(1-n)^2}{n^3} + 0.0968 \cdot \tau^3 \rho A_d \frac{1-n}{n^3} \tag{4}$$

$$\frac{\Delta p}{LV_0} = N + M \cdot V_0 \tag{4'}$$

where $\Delta p / L$ is the hydraulic gradient, V_0 – the superficial velocity, τ – tortuosity, μ – the dynamic viscosity, A_d – the specific dynamic area, n – porosity and ρ – the liquid density.

The walls' effect on results have to be corrected [4].

In the neighborhood the infiltrometer wall the rougness of the tubes of the model is considered $k_e = d/2$, then resulting the corrected factors of equation (4):

$$N^* = 2\tau^2 \mu A_d \frac{(1-n)^2}{n^3} \left[1 + \frac{4}{A_d D (1-n)} \right]^2 \tag{5}$$

$$M^* = \left\{ 0.0413 \left[1 - \left(1 - \frac{d_p}{D} \right)^2 \right] + 0.0968 \left(1 - \frac{d_p}{D} \right)^2 \cdot \tau^3 \, A_d \, \rho \frac{1-n}{n^3} \right\} \tag{6}$$

where D is the infiltrometer's diameter. For acceptable accuracy results, $D/d_p > 10$ condition has to be satisfied [4].

After computation parameters A_d and τ, using equations (5) and (6), the diameter d of fictive tubes, the friction factor λ and the microscopic Reynolds number will be determined:

$$d = \frac{4n}{A_d (1-n)} \tag{7}$$

$$4f = \lambda = \frac{\Delta p}{L} \frac{n^3}{2\rho\tau^3 (1-n) A_d V_0^2} \tag{8}$$

$$Re_d = \frac{\rho V_0 d}{\mu} \frac{\tau}{n} \tag{9}$$

3. THE EXPERIMENTAL INSTALLATION

The experimental installation includes a vertical cylindrical infiltrometer, with upstream and downstream fixing permeable walls, with upwards

water circulation for continuous air evacuation (Photo 1., Fig. 2.) [18, 19, 20].

a) **b)**

Photo 1. Experimental installation with indirect manometers: a) general wiev; b) filtering column detail.

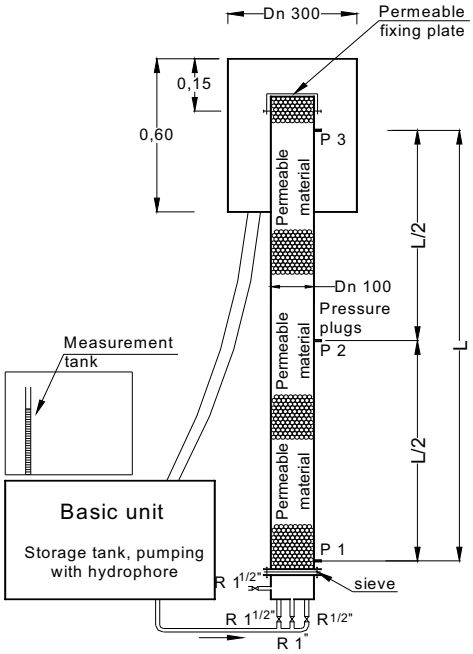

Figure 2. The experimental installation (vertical infiltrometer under pressure)

The infiltrometer has a nominal diameter D = 100 mm and a total length of 2.50 m; the distance between the extreme pressure intake port (PIR) being L = 2.00 m. The permeable packed bed is limited by two permeable walls that are fixing the granular material. All hydraulic parameters within this installation are controlled via three spherical valves, that are featuring decreasing diameters from 1 ½" to ½", in order to ensure a fine control of flows.

Flow measurement is volumetric, measurements' maximal relative errors being $\delta Q \leq 0.001$. The pressure drop is measured with inclined tube micro manometers with direct differential manometers and with indirect differential manometers with mercury.

Porosity and water temperature are controlled.

4. THE EXPERIMENTAL RESULTS

In experiments, as permeable solid material, crushed rock with four different diameters has been used. As regards the solids diameter, the average of hypotenuse and catheus of square sides sieves over that particles passed have been considered**.**

During experiments a stable layer of crushed rock has been assured. Aspects of the crushed rock used are shown in Photo 2.

The hydraulic slope and the superficial (apparent) velocity $(i,V_0)_i$ have been computed [20], the pairs of values being statistically processed, thus obtaining the M and N, than M^* and N^* parameters of equation (4). The values for the porosity n and the determination coefficient R, respectively the number of measurements NM, are listed in Table 1.

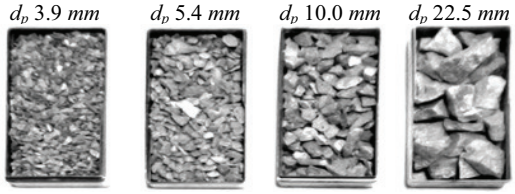

Photo 2. Crushed rock used in experiments

By means of equations (5) N^* and (6) M^* the specific dynamic area A_d and the tortuosity τ , have been computed, and, afterwards, with equation (7), the fictive diameter of the tortuous tubes d. The specific static area A_s with particles diameter d_p was computed. All these values are listed in Table 2.

Table 1. Experimental parameters through homogenous crushed rock

d_p (mm)	R	n	θ (^oC)	NM
3.9	0.999	0.3965	21.6	90
5.4	0.997	0.3841	21.4	123
10	0.999	0.3915	19.4	174
22.5	0.999	0.4219	22.6	187

Table 2. Computed micro scale parameters for homogeneous crushed rock

d_p (mm)	M ($s^2\ m^{-2}$)	N ($s^1\ m^{-1}$)	τ	A_d (m^{-1})	A_s (m^{-1})	$10^3 d$ (m)
3.9	789.509	20.725	1.410	1476	1538	0.89
5.4	520.199	9.193	1.359	1087	1111	1.29
10	238.828	4.152	1.154	581	600	1.66
22.5	80.231	0.768	1.061	252	267	3.30

The pairs of values $(i/V_0,\ V_0)_i$ can be observed in the corresponding graphs, which are in Fig. 3-6., for each diameter used in experiments.

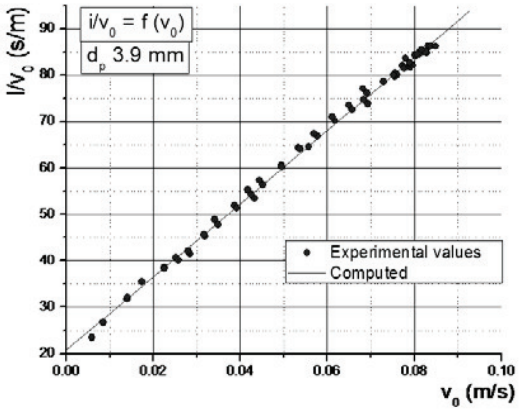

Figure 3. Experimental relative hydraulic gradient for d_p = 3.9 *mm* crushed rock

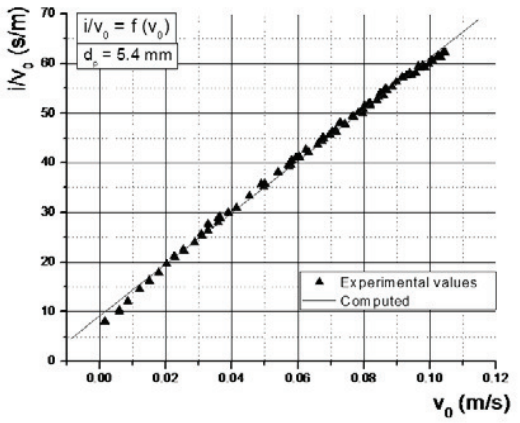

Figure 4. Experimental relative hydraulic gradient for d_p = 5.4 *mm* crushed rock

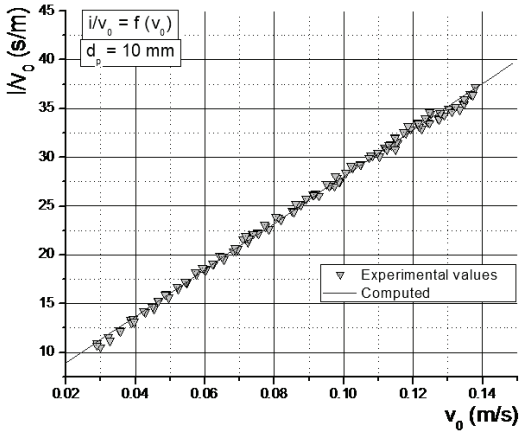

Figure 5. Experimental relative hydraulic gradient for d_p = 10.0 *mm* crushed rock

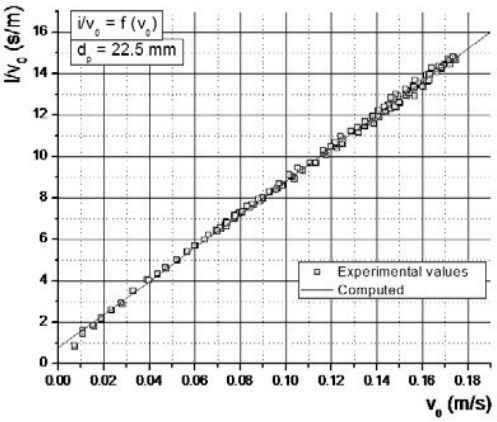

Figure 6. Experimental relative hydraulic gradient for d_p = 22.5 *mm* crushed rock

The hydraulic gradient i for the experimented permeable material with respect superficial velocity V_0 corresponds to Fig. 7.

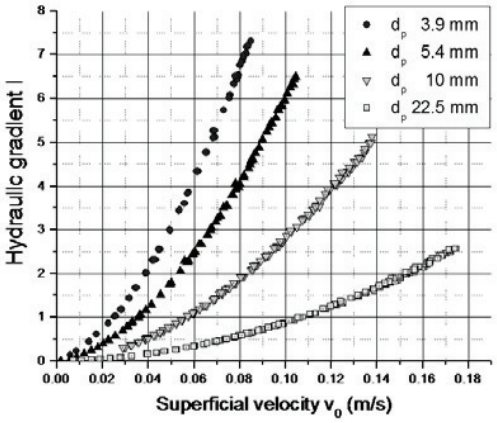

Figure 7. Hydraulic gradient in the superficial velocity function for crushed rock

After the calculation of pores' Reynolds number Re_d (9) and friction factor λ (8), the Fig. 8 graphically shows the values $(Re_d,\ f)_i$ for all experimental diameters.

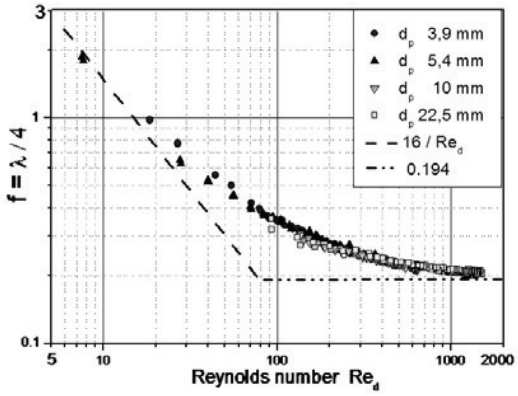

Figure 8. Pore friction versus pore Reynolds number

5. CONCLUSIONS

Relationship $f = \frac{16}{Re_d} + 0.194$ (10) describes the friction factor $f = \lambda / 4$ within the wide range of studied pore Reynolds numbers (Re_d = 7.5 - 1500) for crushed rock. The studied Reynolds number range joins weak and strong inertia and transition to turbulence of the movement.

In engineering practice Darcy's law could be accepted for $Re_d \leq 4.3$, errors due to kinetic losses being up to 5%. More pretentious works claim higher precision; for errors up to 1% the limit pore Reynolds number is $Re_d \leq 0.8$.

Figures 3 - 6 shows a slight curvature of experimental data, and the quadratic relationship (2), (10) are approximations of the phenomena. Corrections of Darcy's law for inertial and transition zones have to be polynomial [3, 7, 8], at least cubic.

ACKNOWLEDGMENTS

The paper on results of grant PN II, ID_2298, financed by UEFISCDI, contract 589/2009 CNCSIS-UTI and project PERFORM-ERA "Postdoctoral Performance for integration in the European Research Area (ID-57649), financed by the European Social Fund and the Romania Government are based.

REFERENCES

[1] Comiti, J., Sabiri, N.E., and Montillet, A., 2000, "Experimental characterization of flow regimes in various porous media – III: Limit of Darcy's or creeping flow regime for Newtonian and purely viscous non-Newtonian fluids", *Chem. Eng. Sci*., vol. 55, pp. 3057-3061;

[2] Bartha, I., Marcoie, N., Toacă, D., Toma, D., Gabor, V., Molnar, A. G., and Lupuşoru, A., 2010, "Post-Darcy Filtration Through Rigid Permeable Media", *Environmental Engineering and Management Journal*, vol. 9, No. 12, pp. 1727-1734;

[3] Forchheimer, P., 1914, "Hydraulik. Druck und Verlag von B.G. Teubner", *Leipzig und Berlin*;

[4] Comiti, J., and Renaud, M., 1989, "A new model for determining mean structure parameters of fixed beds from pressure drop measurements: application to bed packed with parallelepipedal particles", *Chem. Eng. Sci.,* vol. 44, No. 7, pp. 1539-1545;

[5] Firdaouss, M., Guermond, J.L., and Le Quéré, P., 1997, "Nonlinear corrections to Darcy's law at low Reynolds numbers", *Journal of Fluid Mechanics*, vol. 343, pp. 331-350;

[6] Balhoff, M., Mikelic, A., and Wheeler, M.F., 2009, "Polynomial filtration laws for low Reynolds number flows through porous media", *Research report, The University of Texas at Austin*;

[7] Klark, M., 2005, "Design of endoscopic 3D particle tracking velocimetry system and its application in flow measurements with a gravel layer", *PhD Theses, Ruperto Carola University, Heidelberg, Germany*;

[8] Feng, J., and Weinbaum, S., 2000, "Lubrification theory in highly compressible porous media: the mechanics of skiing, from red cells to humors", *J. Fluid Mech*., nr. 422, pp. 281-307;

[9] Martinet, Ph. G., 1998, "Flow and dogging mechanisms in porous media with applications to dams", *PhD Thesis, Stockholm, Sweden*;

[10] Dunn, L. S., 2001, "Wave setup in river entrens", *PhD Thesis, Brisbane, Australia*;

[11] Klow, T., 2000, "High velocity flow in fractures", *PhD Thesis, Trondheim*;

[12] Meroney, N. R., 2004, "Fires in porous media: Natural and urban canopies", *Colorado State University, Fort Collins, USA*

[13] Xu, Z., Woche, H., and Specht, E., 2009, "CFD flow simulation of structured packed bed reactors with injections", *Proceedings of the Conference on Modelling Fluid Flow*, vol. II, pp. 518-524, Budapest University of Technology and Economics, ISBN 978-963-420-986-7, Budapest;

[14] Seguin, D., Montillet, A., and Comiti, J., 1998, "Experimental characterization of flow regimes in various porous media – I: Limit of laminar flow regime", *Chem. Eng. Sci*., vol. 53, No. 21, pp. 3751-3761;

[15] Seguin, D., Montillet, A., Comiti, J., and Huet, F., 1998, "Experimental characterization of flow regimes in various porous media – II: Transition to turbulent regime", *Chem. Eng. Sci*., vol. 53, No. 22, pp. 3897-3909;

[16] Wahyudi, I., Montillet, A., and Khalifa, A.O.A., 2002, "Darcy and post-Darcy flows within different sands", *Journal of Hydraulic Research*, vol. 40, No.4, pp. 519-525;

[17] Bartha, I., and Marcoie, N., 2010, "Post-Darcy filtration through rigid permeable media and real situations in engineering practice", *Annals of the University "Ovidius" Constanţa, Construction Series*, XIII, pp. 155-164;

[18] Bartha, I., Marcoie, N., Toma, D., Gabor, V., and Toacă D., 2010, "Research of filtration through uniform geometry permeable material-glass spheres", *Annals of the University "Ovidius" Constanţa, Construction Series*, XIII, pp. 165-172;

[19] Bartha, I., Marcoie, N., Toma, D., Gabor, V., and Toacă, D., 2010, "Research of filtration through sorted river gravel", *Scientific Bulletin of the „Politehnica" University of Timisoara, Transactions on Hydrotechnics*, Tomul 55(69), Fascicola 1, 2, pp. 71-76;

[20] Bartha, J., Marcoie, N., Gabor, V., Toma, D., and Toacă, D., 2010, "Cercetări asupra curgerilor turbulente în medii poroase permeabile rigide", *Research report, UEFISCDI, ID_2298, Bucuresti*, www.idei-cdi.ro.

Conference on Modelling Fluid Flow (CMFF'12)
The 15th International Conference on Fluid Flow Technologies
Budapest, Hungary, September 4-7, 2012

LDV Measurements and CFD Simulations of the Swirling Flow in a Hydrodynamic Mixer

Péter CSIZMADIA[1], Csaba HŐS [2], Zoltán PANDULA [3],

[1] Corresponding Author, PhD student. Department of Hydrodynamic Systems (HDS), Budapest University of Technology and Economics (BME) H-1111 Budapest, Műegyetem rkp. 3, Hungary. Tel.: +36 1 463 2553, Fax: +36 1 463 3091, E-mail: csizmadia@hds.bme.hu
[2] BME HDS, E-mail: hos.csaba@hds.bme.hu
[3] BME HDS, E-mail: pandula@hds.bme.hu

ABSTRACT

The paper analyses the cyclone-like flow field inside a hydrodynamic mixer, in which two tangential fluid jets rotate the fluid body. The jets are located beneath the fluids surface. The emphasis is on studying the core rotating as a rigid body and the free vortex-like segment surrounding it. Steady-state, single-phase CFD simulations were performed with the help of Ansys CFX code. The importance of employing Reynolds-stress turbulence model is highlighted with the help of tangential and axial velocity distributions. Two-component LDV measurements were also performed allowing direct evaluation of the CFD computations.

Keywords: highly swirling flow, hydrodynamic mixer, LDV, Reynolds stress model

NOMENCLATURE

v	$[m/s]$	velocity
Q	$[l/min]$	flow rate
Δp	$[Pa]$	pressure drop
z	$[mm]$	vertical position
r	$[mm]$	radial position
n	$[-]$	model parameter

Subscripts and Superscripts

tan	tangential component
ax	axial component
max	maximal
mid	middle
min	minimal

Abbreviations

ORS	omega Reynolds stress (model)
SSGRS	SSG Reynolds stress (model)
M.V.	measuring volume

1. INTRODUCTION

1.1. Motivation

This paper presents the first studies on the flow field inside a cyclone-like hydrodynamic mixer with the help of CFD computations and LDV measurements. The actual industrial application is a dense slurry mixer that mixes dry bed ash and water to allow its pumping to the deposition site. Although the slurry is non-newtonian and the slurry level in the mixer gives rise to open-surface flow, this introductory study deals with water and fully filled tank. A scaled-down mixer was built in the laboratory of the Dept. of Hydrodynamic Systems with plexiglass walls allowing visual access to the flow for two-component (circumferential and axial) LDV measurements.

This paper is organized as follows. The rest of this section gives an overview of the corresponding literature. Section 2 describes the test rig and gives the details of the LDV measurements. Section 3 includes the details of the CFD computations while section 4 presents the results and their discussion. Finally, section 5 summarizes the work.

1.2. Literature overview

Highly swirling flows can be used both for mixing purposes (e.g. static mixers) or separation of contaminations (typically, some kind of powder) from gases. It is well-known (see e.g. [1] and the references therein) that the tangential flow field consists of two main regimes: close to the centreline, the flow behaves like a forced vortex or a rigid body (v_{tan}/r = const), while in the outer region, the profile is akin to a free vortex $v_{tan}\, r^n$ = const with the exponent n varying around 0.5-0.6 (a truly free vortex has $n = 1$).

As cyclones are simple and relatively inexpensive to manufacture and operate, much research has been made on their design and operation, see e.g. [2, 3]. The emerging non-invasive

measurement systems allow the acquisition of valuable pieces of information on the velocity field, as e.g. LDV techniques [4, 5, 6], which help in verifying such design techniques. Recently, Chang et al. in [7] employed positron emission particle tracking technique being capable of tracking the path of particles in the flow field. Yet it seems that there is no widely accepted methodology of designing such devices, which is mainly due to the fact that the velocity field is highly challenging to predict.

CFD techniques would be a natural choice to employ for such predictions. However, the highly anisotropic behaviour of the Reynolds stress and thus the inevitable use of advanced turbulence models make such computations time-consuming and challenging. The applied turbulence models range from augmented $k-\varepsilon$ models (see [8, 9, 10]) to classic Reynolds stress models and LES [1]. Moreover, usually unsteady simulations are needed due to the precessing motion of the vortex core (see e.g. [1]). Having said this, it has became clear that, with careful set-up, CFD techniques are able to give accurate predictions not only on the flow field itself but also on separation efficiency or e.g. wall deposition.

2. Experiments

The experimental set-up consists of a mixer tank (element 5 in Figure 1), in which the fluid is rotated by two tangential jets (4) which are driven by a centrifugal pump (6). The flow rate is set by a control valve (7), which is equipped with two pressure taps to measure the flow rate based on calibrated $\Delta p(Q)$ curves. The two-component LDV system (1) allows the measurement of the axial and circumferential velocity components. The LDV is positioned with the help of the traverse system (2) in three dimensions, with an accuracy of 0.1 mm. The data acquisition system (8) then transfers the data to the PC (9). To minimize the spatial error cased by the refraction due to the curved plexiglass wall, an additional tank with planar walls (3) was mounted to the mixer.

Figure 2 depicts a sketch and the main dimensions of the mixer. The flow rate is measured based on the pressure difference of the U-tube manometer (10). In what follows, we present measurement and CFD results for three flow rates: Q_{max} = 76.4 l/min, Q_{mid} = 48.7 l/min and Q_{min} = 33.1 l/min). During the measurements, the mixer was operated with constant flow rate.

A two-component TSI LDV system with 300 mW Ar-ion laser was operated in backscatter mode. A Bragg cell unit was used with an opto-electronic shift of 40 MHz, the downmix frequencies were set to 39.96 and 39.85 MHz for the circumferential and tangential velocity components, respectively. The front lens of the system has a focus length of 362.6 mm, this allowed to measure up to the half of the diameter inside the mixer tank. The

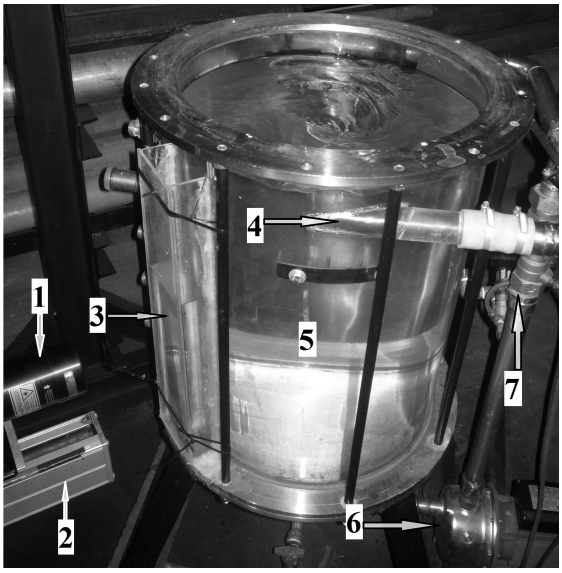

Figure 1. The experimental scaled-down mixer

scattered light was detected on photomultipliers, the signal was band-pass filtered and processed by a bust spectrum analyser. To reach better accuracy of the measurement in each measuring point 10000 bursts were collected, with a timeout of 300 seconds. To show the measurement quality, the standard deviations are also plotted for the measured values.

Four vertical positions were chosen to measure the velocity components along the radius: z=220, 300, 360 and 425 mm, measured downwards from the top of the mixer. As seeding for the LDV experiments, polymer spheres of diameter 50-100 μm were used (Spheriglass). The measurement radii are located at every 0.5 mm close to the wall, than 2 mm and finally 5 mm in the fluid body. As already mentioned, for radii smaller than approx. 120 mm we were unable to collect data of appropriate quality due to light refraction.

3. CFD setup

A fully structured grid was built with the help of ICEM CFD, consisting of 1.7M elements. 128, 284 and 152 elements were used in the radial, circumferential and axial direction, respectively. This spatial resolution was found to be suitable to obtain grid-independent solutions. Some details of the mesh are shown in Figures 3 and 4.

ANSYS CFX 13.0 was used as flow solver. Although it is well-known from the literature that the flow is inherently unsteady, steady-state computations were performed, not only to reduce the computational time but also to gain some experiences on the quality of such solutions. Single-phase (water) models was employed with two Reynolds Stress turbulence models: (a) an ε-based model (SSG) and (b) an ω-based model (ORS), for details see [11]. However, as it was found to be cumbersome

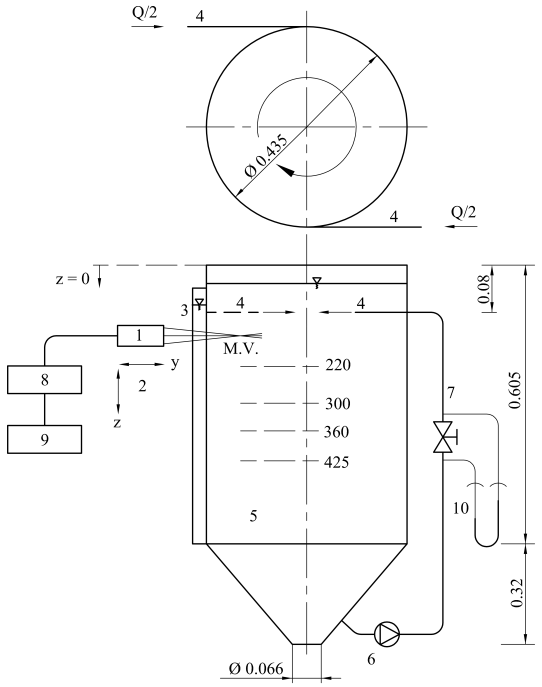

Figure 2. The sketch of scaled-down mixer

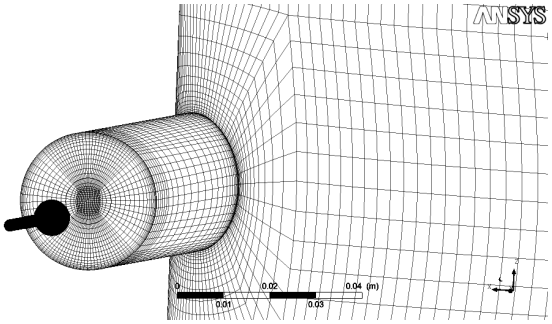

Figure 3. The computational mesh close to the inlet

to obtain converged solution with these models at once, typically $k-\varepsilon$ and SST pre-computations were performed to provide initial guess for the Reynolds stress models. High-resolution scheme was used [11] for all of the equations (including turbulence models). Simple inlet boundary condition with prescribed mass flow rate was set at the tangential jets and outlet at the pressure side of the pump, with prescribed pressure. Convergence was judged by monitoring the velocity at several locations in the flow field and the computation was stopped once all these components reached a quasi steady state. One computation typically needed approx. 5000 iteration steps and and about 45-50 hours on a standard desktop PC (4×3.4 GHz CPU, 8 Gb RAM).

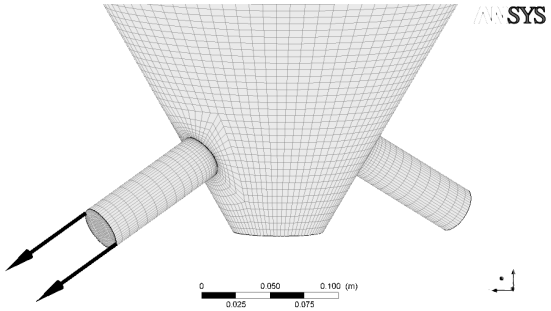

Figure 4. The computational mesh close to the outlet

Figure 5 depicts a typical convergence history in terms of the tangential velocity components at three monitor points. As it can be seen, the velocity values keep changing and a periodic fluctuation is observed, which did not change by varying the timescale control technique (e.g. physical timescale). The inherent unsteadiness of such flows is well-known, see e.g. Gronald et al. in [1]. In what follows, we present the mean values of the velocities. As it will be shown, even these results provide a fairly acceptable approximation of the flow field.

4. Results

Profiles of simulated and measured velocities can be seen in Figures 6 – 8. Generally speaking, we observe a fairly good agreement in the case of the tangential profiles between the measured values and the ORS model while a relatively weak agreement with any of the simulation results in the case of the axial velocity component.

4.1. Tangential velocity distributions

In the case of the tangential velocity profiles, in all three cases the ORS model provides significantly better solutions compared to the SSGRM model. In the case of the minimum flow rate (Figure 6), apart from the uppermost position (z = 220), the measured and simulated values coincide within the error range, for the two higher flow rates the maximum deviation is less than 20% (in the range were measurements are available). We also experience better coincidence as we move downwards, i.e. away from the jets. A high-impulse boundary layer due to the jets is present at the upper positions (z = 220 and z = 300), which is not experienced in the measurements. Both simulation models overestimate this layer, however, in the case of the SSGRS model the error is up to 100% while for the ORS model the largest deviation is approx. 20% (uppermost left panel in Figure 8).

It is interesting that both in the case of the measurements and simulations, the tangential velocity distributions differ from the classic cyclone–type distributions, which consists of a forced vortex-like distribution close to the centreline

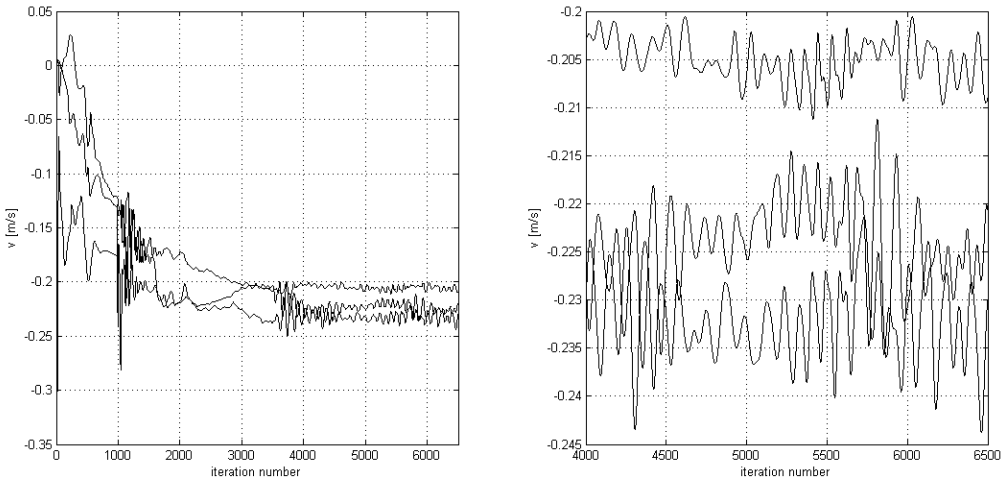

Figure 5. Typical convergence history in terms of velocity values

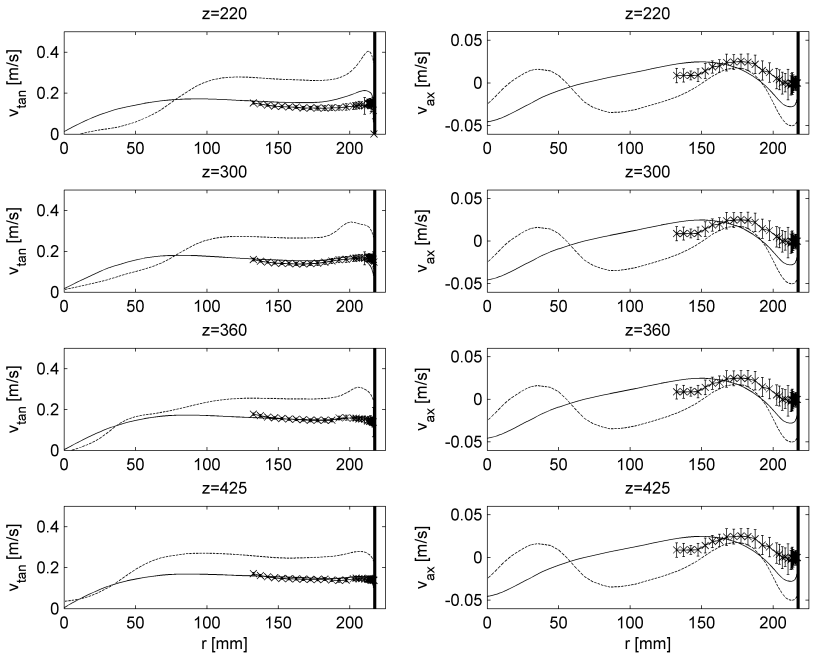

Figure 6. Velocity distributions with Q_{min}: measurements (crosses), CFD with ORS model (solid lines) and CFD with SSGRS model (dashed lines)

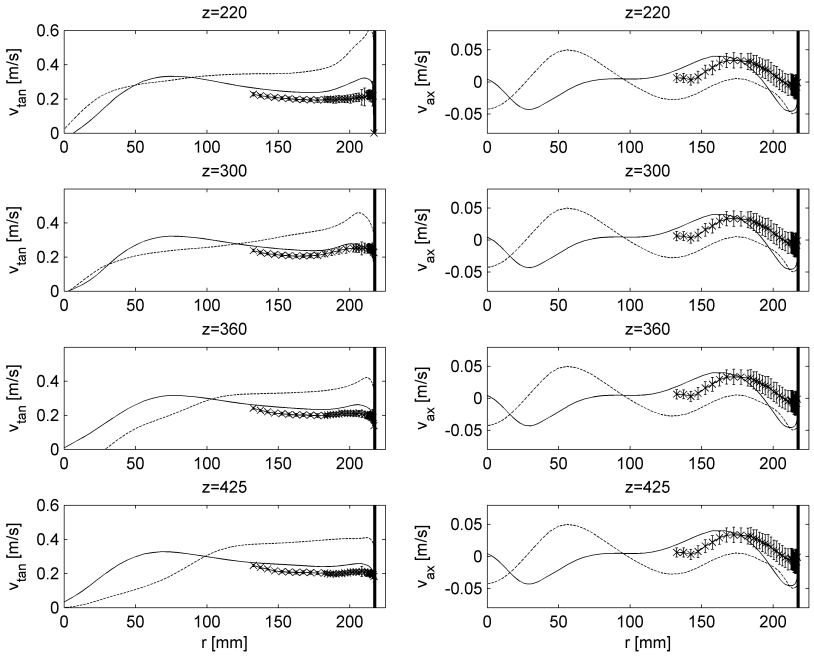

Figure 7. Velocity distributions with Q_{mid}: measurements (crosses), CFD with ORS model (solid lines) and CFD with SSGRS model (dashed lines)

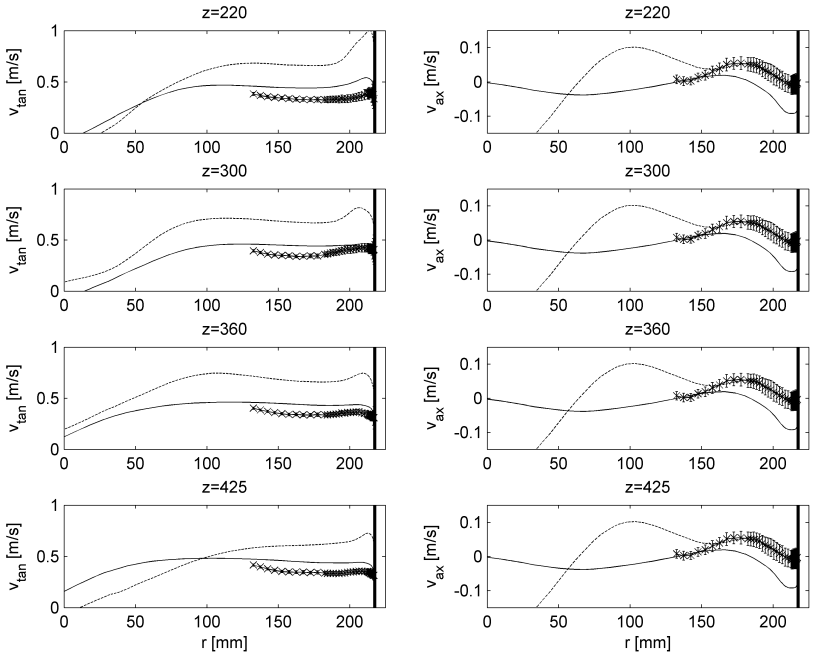

Figure 8. Velocity distributions with Q_{max}: measurements (crosses), CFD with ORS model (solid lines) and CFD with SSGRS model (dashed lines)

and a free-vortex regime beyond the vortex finder tube radius (see e.g. [1]). In our case, the tangential velocity distribution is relatively constant along the free-vortex regime and the peak in tangential velocity around the middle of the radius is also not present. In the case of the middle and maximum flow rates (Figures 7 and 8), one observes a slight increase in the measured tangential profiles, which might be the outer region of a classic cyclone-type distribution. This would mean that the ORS prediction (solid line) is poor. However, another possibility is that the distributions are close the ORS profiles and the tangential distribution differs from the classic one due to the lack of the upper (vortex finder tube) outlet. This issue needs further studies.

4.2. Axial velocity distributions

Generally speaking, we observe a larger deviation in the case of the axial velocity components. Note that these velocity values are one order of magnitude less than the tangential ones. Starting off with the smallest and middle flow rates (right panels of Figures 6 and 7), it is striking that close to the wall, both models highly overpredict the (negative) axial component. Similarly to the tangential velocities, the SSGRS model predicts about twice the magnitude of the ORS model. Moving towards the centreline, the magnitude of the maximum axial velocity is captured fairly well, however, its location is missed. Again we see that the SSGRS model gives unrealistic profiles.

In the case of the highest flow rate (Figure 8), an interesting phenomena appears: close to the wall, the SSGRS model gives good results, while away from the wall, the measurements seem to 'converge' to the ORS results. However, we cannot observe the same issue in the case of the tangential velocities. It is one of the authors' future plans to study this issue further and clarify if this is a coincidence or a robust observation present also under other circumstances. Nevertheless, the ORS profiles are in qualitative agreement with both the measurements and the literature (e.g. [5] and [1]); close to the wall, the fluid moves downwards, which is followed by an upper motion. In the centreline region, due to the missing upper outlet, in our case the fluid moves downwards again (contrary to the classic cyclones, where it moves upwards, towards the vortex finder tube).

5. Summary

A cyclone-like mixer was analysed by means of LDV measurements and steady state CFD computations; the axial and tangential velocity distributions were compared for three driving jet flow rates. Two Reynolds stress models were applied: an ε-based model (SSG Reynolds stress model) and an ω-based one (Omega Reynolds stress model). The latter was found to be more appropriate, it typically gave significantly better results, compared to the measurements. It was also found that although steady-state runs do not converge in the sense that a periodic fluctuation remains in the velocities, the results are acceptable, especially if computational time is an issue (which is typical in industrial applications). The velocity distributions computed with the omega Reynolds stress model were not only qualitatively proper but also were within 20% bound in the case of tangential velocities, while for the axial velocity components, the discrepancy was larger.

Acknowledgement

The work reported in the paper has been developed in the framework of the project Talent care and cultivation in the scientific workshops of BME" project. This project is supported by the grant TÁMOP-4.2.2.B-10/1–2010-0009.

References

[1] Gronald, G. and Derksen, J. 2011 "Simulating turbulent swirling flow in a gas cyclone: A comparison of various modeling approaches". *Powder Technology*, Vol. 205, No. 13, pp. 160 – 171.

[2] Veerapen, J. P., Lowry, B. J., and Couturier, M. F. 2005 "Design methodology for the swirl separator". *Aquacultural Engineering*, Vol. 33, No. 1, pp. 21 – 45.

[3] Kolbl, A., Kraut, M., and Wenka, A. 2011 "Design parameter studies on cyclone type mixers". *Chemical Engineering Journal*, Vol. 167, No. 23, pp. 444 – 454, special Issue - IMRET 11: 11th International Conference on Microreaction Technology.

[4] Obermair, S., Woisetschlager, J., and Staudinger, G. 2003 "Investigation of the flow pattern in different dust outlet geometries of a gas cyclone by laser Doppler anemometry". *Powder Technology*, Vol. 138, pp. 239 – 251.

[5] Liu, Z., Zheng, Y., Jia, L., and Zhang, Q. 2007 "An experimental method of examining three-dimensional swirling flows in gas cyclones by 2D-PIV". *Chemical Engineering Journal*, Vol. 133, No. 13, pp. 247 – 256.

[6] Marins, L., Duarte, D., Loureiro, J., Moraes, C., and Freire, A. S. 2010 "LDA and PIV characterization of the flow in a hydrocyclone without an air-core". *Journal of Petroleum Science and Engineering*, Vol. 70, No. 34, pp. 168 – 176.

[7] Chang, Y.-F., Ilea, C., Aasen, L., and Hoffmann, A. 2011 "Particle flow in a hydrocyclone investigated by positron emission particle tracking". *Chemical Engineering Science*, Vol. 66, No. 18, pp. 4203 – 4211.

[8] Meier, H. F. and Mori, M. 1999 “Anisotropic behavior of the Reynolds stress in gas and gassolid flows in cyclones”. *Powder Technology*, Vol. 101, No. 2, pp. 108 – 119.

[9] Saqr, K. M., Kassem, H. I., Aly, H. S., and Wahid, M. A. 2012 “Computational study of decaying annular vortex flow using the R_ε/k - ε turbulence model”. *Applied Mathematical Modelling*, Vol. 36, No. 10, pp. 4652 – 4664.

[10] Dai, G., Li, J., and Chen, W. 1999 “Numerical prediction of the liquid flow within a hydrocyclone”. *Chemical Engineering Journal*, Vol. 74, No. 3, pp. 217 – 223.

[11] ANSYS, Inc. *ANSYS CFX-Solver Theory Guide, Release 13.0.*

Conference on Modelling Fluid Flow (CMFF'12)
The 15th International Conference on Fluid Flow Technologies
Budapest, Hungary, September 4-7, 2012

BOUND-STATE FORMATION IN FALLING LIQUID FILMS

Phuc-Khanh NGUYEN,[1] Marc PRADAS, [2]
Serafim KALLIADASIS, [2] Vasilis BONTOZOGLOU [1]

[1] Department of Mechanical Engineering, University of Thessaly, Pedion Areos GR-38334, Volos, Greece.
E-mail: nguyen@mie.uth.gr; e-mail: bont@mie.uth.gr
[2] Department of Chemical Engineering, Imperial College London, London SW7 2AZ, United Kingdom.
E-mail: m.pradas-gene@imperial.ac.uk; e-mail: s.kalliadasis@imperial.ac.uk

ABSTRACT

Bound-state formation in falling liquid films is examined numerically by finite-element solutions of the Navier-Stokes equations subjected to wall and free-surface boundary conditions. It is shown that the interaction between solitary pulses may give rise to the formation of bound states, i.e. clusters of waves consisting of two or more pulses separated by well-defined distances, and travelling at the same velocity. A binary system is considered first to study the formation of bound states of two pulses (doublets). Seeking stationary-in-a-moving-frame solutions of the governing equations and associated boundary conditions, it is observed that for sufficiently separated pulses the steady pulse separation lengths are in excellent agreement with analytical predictions obtained from a weak interaction theory. When both pulses are closely spaced, strong interactions start to be more relevant and the theoretical predictions become less accurate. On the other hand, time-dependent simulations reveal that for short-to-moderate separation lengths all initial conditions lead to an oscillatory dynamics where the pulse separation oscillates around the analytically predicted steady distances. Bound states consisting of three pulses (triplets) are computed next. If the leading and trailing pulses are placed symmetrically with respect to the middle one, the equilibrium separation distances are similar to those theoretically predicted in a binary system. However, when the leading and trailing pulses are placed asymmetrically, the pair of pulses with the shortest separation length equilibrates with the remaining pulse at distances that may deviate significantly from those in the binary system.

Keywords: Bound-state formation, solitary wave interactions, thin film instabilities

1. INTRODUCTION

Falling liquid films can be encountered in many multiphase industrial applications, specially because wave formation on free surfaces has a strong affect on e.g. heat and mass transfer or the quality of coating processes. Falling liquid films have also been extensively studied theoretically. A falling film is an open-flow, long-wave hydrodynamic instability, exhibiting a rich spatio-temporal dynamics and a wide spectrum of wave forms and interactions, starting from nearly harmonic waves upstream to complex spatio-temporal highly nonlinear wave patterns downstream. Reviews of the dynamics of a falling film are given, amongst others, in [1, 2, 3, 4].

For low-to-moderate Reynolds numbers (the Reynolds number is typically defined as the ratio of flow rate per unit span to kinematic viscosity), the flow is primarily in the streamwise direction as it is stable to spanwise modulations [5]. As it has been observed in many experimental studies [6, 7, 8, 9] and theoretical works [10, 11], under these conditions, the film free surface appears to be randomly covered by localized coherent structures, each of which resembling infinite-domain solitary pulses. These pulses are a consequence of a secondary modulation instability of the primary wave field. They consist of a nonlinear hump preceded by damping ripples and can even appear at sufficiently small Reynolds numbers.

The organization of the free surface of falling liquid films into trains of coherent structures, has been numerically investigated by time-dependent finite-element simulations of the Navier-Stokes equations with free-surface boundary conditions [12], and analytically scrutinized in a recent coherent-structure theory based on weak interaction [13], by appropriately extending previous works on coherent-structure interaction of model equation such as the generalized Kuramoto-Sivashinsky (gKS) equation [14, 15, 16]. As far as the falling film problem is concerned, the study by Pradas *et al.* [13] was based on a low-dimensional model for the flow containing terms up to second order in the long-wave expansion parameter [17], and including the second-order viscous effects originating from the streamwise viscous

diffusion and the tangential stress balance. These terms have been ignored in previous pulse interaction theories for film flows [2, 10]. They prove to have a dispersive effect on the phase speed, the wave height, and the shape of the capillary ripples in front of a solitary hump.

The coherent-structure theory in [13] showed that the interaction between solitary pulses may give rise to the formation of bound states consisting of two or more pulses separated by well-defined distances and travelling at the same velocity. The dynamics around such bound states is actually very rich since different behaviours, such as repulsion, attraction or self-sustained oscillations may emerge depending on the separation length between pulses [18].

The present work aims to validate the results of the Pradas *et al.* study obtained from a low-dimensional model, through direct numerical simulation (DNS) of the full two-dimensional (2D) Navier-Stokes equations and associated boundary conditions. It confirms the results obtained in [13] on bound-state formation on a two-pulse system, and provides further insight concerning the oscillatory interaction. Moreover, a detailed numerical study of bound states on a system compound of three pulses is presented, thus offering insight into the interpretation of the wideband spectrum of separation distances predicted by dynamic simulations of the low-dimensional model used in [13] and involving many pulses.

Section II presents the Galerkin finite-element method and the technique to construct numerically initial guesses. The numerical results on stationary and non-stationary doublets, as well as stationary triplet interactions, are outlined in Sec. III. Finally, it closes with conclusions in Sec. IV.

2. COMPUTATIONAL METHOD

2.1. Governing equations and numerical methods

This study consider 2D solitary pulses in liquid films flowing down along an infinite, vertical and planar wall (see Fig. 1). The liquid is incompressible and Newtonian, with density ρ, dynamic viscosity μ, and surface tension σ. The free surface is taken as shear-free, i.e. the dynamic effect of a superposed gas phase is negligible.

The problem is formulated as two-dimensional in a Cartesian coordinate system, with the x-axis pointing towards the mean flow direction and the y-axis across the film. A frame moving with the velocity c of a solitary pulse is introduced to transform the laboratory frame coordinates as $t = \tau$, $x = \xi - c\,\tau$, and $y = \eta$, so

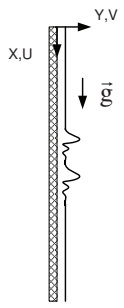

Figure 1: Bound-state formation in vertically falling liquid films

that:

$$\frac{\partial}{\partial \tau} = \frac{\partial}{\partial t}\frac{\partial t}{\partial \tau} + \frac{\partial}{\partial x}\frac{\partial x}{\partial \tau} = \frac{\partial}{\partial t} - c\,\frac{\partial}{\partial x},$$
$$\frac{\partial}{\partial \xi} = \frac{\partial}{\partial x}\frac{\partial x}{\partial \xi} = \frac{\partial}{\partial x},$$
$$\frac{\partial}{\partial \eta} = \frac{\partial}{\partial y}\frac{\partial y}{\partial \eta} = \frac{\partial}{\partial y}.$$

The primitive flow input is the volumetric flow rate per unit span, q, and the location of the free surface in the moving frame is denoted as $y = h(x)$.

The Navier-Stokes equations governing the 2D flow are non-dimensionalized using as characteristic scales the film thickness and the mean velocity of the undisturbed substrate far away from the main hump transporting the flow rate q along a planar wall,

$$h_S = \left(\frac{3\mu q}{\rho g \sin\alpha}\right)^{1/3}, \qquad u_S = \frac{g h_S^2 \rho \sin\alpha}{3\mu}, \quad (1)$$

respectively. g is gravity and α is the wall inclination angle which for simplicity is set to $\alpha = 90°$. The resulting stationary differential equations are formulated in the moving frame as follows:

$$\mathbb{C} = \underline{\nabla} \cdot \underline{U} = 0, \quad (2)$$
$$\mathbb{M} = -C\frac{\partial \underline{U}}{\partial X} + \underline{U} \cdot \underline{\nabla}\,\underline{U} + \underline{\nabla} P - \frac{1}{Re}\underline{\nabla}^2 \underline{U} - \frac{3}{Re \sin\alpha}\underline{g} = \underline{0}, \quad (3)$$

where capital letters indicate dimensionless variables; $\underline{U} = [U \quad V]^T$ is the velocity vector in the laboratory frame, P is the pressure, C is the dimensionless speed, and the scaled gravity vector is given as $\underline{g} = [\sin\alpha \quad -\cos\alpha]^T = [1 \quad 0]^T$. The above equations are coupled to the kinematic equation for free surface evolution:

$$\mathbb{K} = -C\frac{\partial H}{\partial X} + U\frac{\partial H}{\partial X} - V = 0. \quad (4)$$

Non-stationary states are also studied in the moving

frame by using the unsteady form of Eqs. (3) and (4):

$$\mathbb{M} = \frac{\partial \underline{U}}{\partial T} - C\frac{\partial \underline{U}}{\partial X} + \underline{U}\cdot\underline{\nabla}\,\underline{U} + \underline{\nabla}P - \frac{1}{Re}\underline{\nabla}^2\underline{U} - \frac{3}{Re\sin\alpha}\underline{g} = \underline{0}, \quad (5)$$

$$\mathbb{K} = \frac{\partial H}{\partial T} - C\frac{\partial H}{\partial X} + U\frac{\partial H}{\partial X} - V = 0, \quad (6)$$

where we have used $t_s = h_s/u_s$ as the characteristic time scale. Furthermore, we impose the no-slip and no-penetration boundary conditions on the wall,

$$U = V = 0, \quad (7)$$

and the dynamic boundary condition at the free surface,

$$\underline{n}\cdot\underline{\underline{T}} = \Delta P\,\underline{n} + 3^{1/3}\,Ka\,Re^{-5/3}\,K\,\underline{n}, \quad (8)$$

where $\underline{\underline{T}}$ is the stress tensor, $\underline{n}$ is the outward unit vector normal to the free surface and $K = \dfrac{H''}{(1+H'^2)^{3/2}}$ is the surface curvature. The dimensionless parameters Re and Ka appearing in Eqs. (5) and (8) correspond to the Reynolds and Kapitsa numbers, respectively, and will be defined and discussed in Sec. 2.3.

The case of a single travelling pulse serves as a basis for all subsequent investigations. Its computation involves six field variables: the two velocity components U and V, pressure P, free surface height H, pressure jump ΔP of a reference point in the liquid to the (uniform) gas pressure, and phase speed C. So far, we have four equations: one from (2), two from (3), and one from (4). The two additional equations needed to close the system are provided by (a) pinning the maximum of the hump at the middle of the flow domain (this eliminates a degeneracy without loss of generality),

$$H'(x = L/2) = 0, \quad (9)$$

and, (b) fixing the thickness of the undisturbed substrate far away from the main hump

$$H(x = 0) = 1. \quad (10)$$

By using the Galerkin finite element method on a structured mesh, the system of governing equations is integrally weighted with bi-linear $\Psi^i(\xi,\eta)$ (i = 1, 9), bi-quadratic $\Phi^i(\xi,\eta)$ (i = 1, 9), and quadratic basis functions $\Phi^i(\xi,\eta = 1)$ (i = 1, 3), to produce, respectively, the residuals of the continuity, momentum and kinematic equation:

$$\iint_V \mathbb{M}\,\Phi^i(\xi,\eta)\,dV = 0, \quad (11)$$

$$\iint_V \mathbb{C}\,\Psi^i(\xi,\eta)\,dV = 0, \quad (12)$$

$$\int_S \mathbb{K}\,\Phi^i(\xi,\eta = 1)\,dS = 0. \quad (13)$$

The flow field variables consisting of velocities U and V, pressure P, and free surface height H are also interpolated from nodal unknowns using the above bases:

$$\underline{U} = \sum_{i=1,9} \underline{U}_i\,\Phi^i(\xi,\eta),$$

$$P = \sum_{i=1,4} P_i\,\Psi^i(\xi,\eta),$$

$$H = \sum_{i=1,3} H_i\,\Phi^i(\xi,\eta = 1).$$

The elementwise integration of Eqs. (11), (12), and (13) is made by the nine, four, and three-point Gaussian quadratures, respectively. The time integration in unsteady computations is based on the Crank-Nicolson scheme. The resulting system of algebraic equations is solved by a Newton-Raphson iterative algorithm, coupled with a frontal technique.

2.2. Constructing initial guesses for two-pulse and three-pulse structures

To obtain converged solutions to the different bound-state doublets, an appropriate initial condition needs to be devised. This is illustrated for the case of doublets. First, a single-pulse solution is obtained on a periodic domain of length L_D, which is sufficiently long to approach the infinite domain solitary-wave solution properties. Two of such pulses are then assembled one next to the other along the streamwise direction, to set up a two-pulse structure. This initial structure, which in general is not a solution to the equations, is parametrized by the separation distance between the two humps. The structure is subsequently modified by removing a certain number of columns of elements in the film region joining the two pulses. Although the joining zone is no more continuous, this initial condition works very well: by fixing the location of one pulse [using Eq. (9)], and letting the other pulse relax to adjust to a new position, all the stable and unstable bound states predicted by weak interaction theory [13] are recovered.

This technique is particularly efficient to successfully construct initial guesses of bound states with very closely-spaced pulses where use of a naive superposition of the two single-pulse solutions would lead to unacceptably high film thickness between the pulses. It is also important to remark that the success on using such a technique is based on the exponentially fast decay of both the front and back tails of the solitary pulses, as it is confirmed in Figs. 2 and 3, which is in turn also responsible for the very accurate computation of single-pulse properties based on a long but finite flow domain with periodic boundary conditions. Likewise, the construction of an initial guess for a bound-state triplet is a straightforward extension of the above technique by joining a numerically converged doublet with a single pulse or vice versa. The location of the single pulse is then fixed while the other two are left to relax to equilibrium positions. It should be noted however,

that convergence to bound-states is numerically more tedious for triplets than for doublets.

2.3. Parameters and characteristic properties

The dimensionless parameters arising in the governing equation (3) are the Reynolds number, defined as the ratio of the mean flow rate per unit span to the kinematic viscosity,

$$Re = \frac{\rho\, q}{\mu} = \frac{\rho u_S h_S}{\mu}, \tag{14}$$

and the Kapitsa number appearing in Eq. (8) which depends only on the liquid properties as:

$$Ka = \left(\frac{l_c}{l_v}\right)^2, \tag{15}$$

involving the viscous length, $l_v = (\nu^2/(g\sin\alpha))^{1/3}$, and the capillary length, $l_c = (\sigma/(\rho g \sin\alpha))^{1/2}$.

Alternatively, three other dimensionless parameters, a reduced Reynolds number δ, a viscous dispersion number η, and a scaled inclination ζ are used often in falling film studies [3, 17], and are related to the above conventional parameters as follows:

$$\delta = (3Re)^{11/9} Ka^{-1/3} = \frac{h_s^{11/3}}{l_\nu^3 \quad l_c^{2/3}}, \tag{16}$$

$$\eta = (3Re)^{4/9} Ka^{-2/3}, \tag{17}$$

$$\zeta = \cot\alpha (3Re)^{2/9} Ka^{-1/3}. \tag{18}$$

To make a comparison between the results given by the low-dimensional models and the Navier-Stokes computations for $\alpha = 90^\circ$, only two parameters are varied independently, namely δ and Ka. Moreover, for solitary pulses in particular, the Shkadov scaling is appropriate, and it involves the compression factor $\kappa = \eta^{-1/2}$ followed by the transformation $X \to X\kappa^{-1}, T \to T\kappa^{-1}$.

The principal characteristics of a solitary pulse are: (a) wave height, H, which is measured at the peak of solitary wave and scaled with the thickness of the undisturbed substrate as:

$$H = \frac{h}{h_S};$$

(b) phase speed, C, of the steady travelling pulses, scaled as:

$$C = \frac{c}{3\, u_S};$$

and (c) separation between pulses, L_S, nondimensionalized with flat substrate thickness $L_S = l/h_S$, and followed with a stretching via the Shkadov factor κ as:

$$L = \frac{l}{h_S \kappa}.$$

3. NUMERICAL RESULTS

3.1. Steady doublets

Water is used as working liquid throughout the whole study with kinematic viscosity $\nu = 10^{-6}$ *m²/s*, density $\rho = 1000$ *kg/m³*, and surface tension $\sigma = 72.01$ *mN/m*, giving a Kapitsa number of $Ka = 3364$. At first, the bound-state formation of two-pulses structure is studied by considering two cases of flow rates that correspond to the values $\delta = 0.98$ and $\delta = 1.82$. Other parameters such as Re, η, and κ are also calculated for reference. The computation of a single pulse yields the phase speed, C, and the wave height, H, shown in Table 1. These pulses are used to construct initial guesses.

Table 1: Parameters and characteristics of the single solitary pulse in two study cases with water as working liquid

δ	Re	η	κ	C	H
0.98	3	0.0118	9.1932	1.1595	1.2040
1.82	5	0.0148	8.2146	2.3999	2.9280

The equilibrium separations between both pulses in bound-state doublets are shown in Table 2, and an example of a doublet profile for the low flow rate case, $\delta = 0.98$, is provided in Fig. 2. In the table, the dimensional separation distances l are obtained by rescaling with the substrate thickness $h_S = 0.097$ *mm*, and $L = L_S/\kappa$ is obtained after Shkadov scaling. The results presented in the fourth and fifth columns correspond to the analytical findings in [13]. Note that there is a tolerance of L less than 0.05 due to mesh resolution with $\Delta X = 0.0296$ and $\Delta X = 0.0420$ respectively for two cases $\delta = 0.98$ and $\delta = 1.82$.

Table 2: Bound-state separation lengths for $\delta = 0.98$

L_S	l [*mm*]	L	L by [13]	Stability [13]
135.29	13.12	14.72	13.9	stable
156.79	15.21	17.06	17.3	unstable
190.54	18.48	20.73	20.7	stable
220.76	21.41	24.01	24.1	unstable
252.33	24.48	27.45	27.5	stable
283.37	27.49	30.82	30.9	unstable
314.67	30.52	34.23	34.3	stable
345.97	33.56	37.63	37.7	unstable
377.28	36.60	41.04	41.1	stable
408.31	39.61	44.41	44.5	unstable

As the flow rate is increased, the amplitude of the solitary wave becomes larger and the wave steeper, and both the frequency and amplitude of the front-running capillary ripples increase (see Fig. 3). As a result,

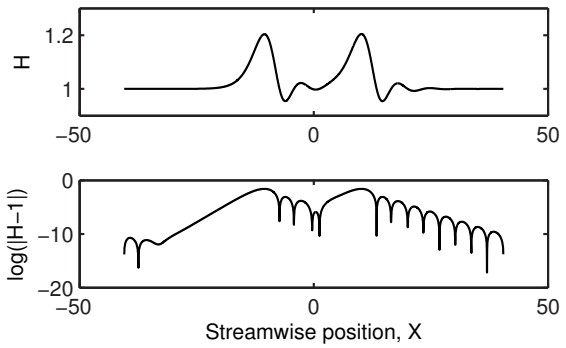

Figure 2: Free-surface profile and exponential representation of doublets for $\delta = 0.98$ for the bound-state separation $L = 20.73$

the number of bound states observed at moderate distances also increases. Indeed, Table 3 shows a range of consecutive stationary separations with shorter increment as compared to the low flow rate case. Here, the dimensional separation distances l are obtained by rescaling with the substrate thickness $h_S = 0.115$ *mm*, and $L = L_S/\kappa$ is obtained after Shkadov scaling. The results presented in the fourth and fifth columns correspond to the analytical findings in [13].

Remarkably, for both low and high flow rate cases (Table 2 and 3, respectively) there is an excellent agreement between the computed bound states at intermediate and large separations distances and the analytical predictions based on a low-dimensional model under the assumption of well-separated pulses (weak interaction) [13]. As expected, however, a deviation between theory and DNS appears for the shortest separation distances, where strong interactions between pulses start to play a prominent role.

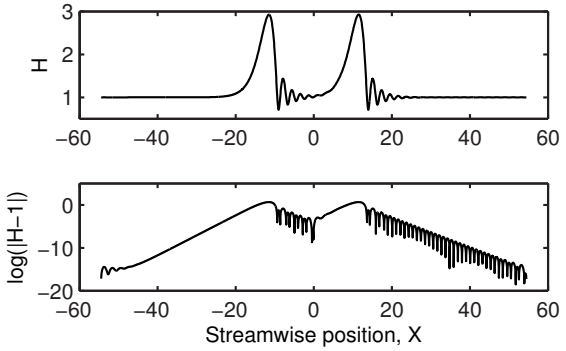

Figure 3: Free-surface profile and exponential representation of doublets for $\delta = 1.82$ for the bound-state separation $L = 22.97$

3.2. Unsteady doublets

Unsteady doublets are studied by setting $\delta = 1.82$ and $Ka = 3364$, and by choosing three different initial separation lengths (see Table 4).

Table 3: Bound-state separation lengths for $\delta = 1.82$

L_s	l [*mm*]	L	L by [13]	Stability [13]
156.23	17.97	19.02	18.81	stable
161.06	18.52	19.61	19.84	unstable
172.09	19.79	20.95	20.89	stable
178.99	20.58	21.79	21.93	unstable
188.65	21.69	22.97	22.98	stable
196.58	22.61	23.93	24.01	unstable
205.89	23.68	25.06	25.06	stable
213.83	24.59	26.03	26.09	unstable
222.79	25.62	27.12	27.14	stable
231.41	26.61	28.17	28.17	unstable
240.04	27.60	29.22	29.21	stable
248.66	28.60	30.27	30.25	unstable
257.28	29.59	31.32	31.29	stable
265.90	30.58	32.37	32.33	unstable
274.52	31.57	33.42	33.37	stable
283.15	32.56	34.47	34.41	unstable
291.77	33.55	35.52	35.45	stable
300.39	34.54	36.57	36.49	unstable
309.01	35.54	37.62	37.53	stable
317.63	36.53	38.67	38.56	unstable

Table 4: Table of initial guesses and the dynamic properties of the doublet

Case study	Attraction	Repulsion	Oscillation
Initial separation	37.95	37.28	25.06
Mean separation	37.62	37.62	27.12
Main frequency	0	0	0.082
Separation amplitude	0	0	0.75
Vert. ampl. of 1^{st} pulse	0	0	0.015
Vert. ampl. of 2^{nd} pulse	0	0	0.013

Following [13], the bound states given in Tables 2 and 3 have been classified alternatively as nominally stable and nominally unstable, according to the competition between weak attractive and repulsive forces when slightly displaced from equilibrium. Although it is expected that unstable states would not survive in time-dependent computations (pulses would shift towards stable positions), our computational results show that the actual behaviour is more complex and in fact intriguing. It is observed that stationary bound states emerge from time-dependent computations only when the initial pulse separation length is sufficiently large. An example is shown in Fig. 4, where initial separation distances of $L = 37.95$ and $L = 37.28$ of doublet approach monotonically the stable bound state $L = 37.62$ presented by the dashed dotted line, whereas the dotted lines depict unstable doublet separation distances. This weakly coupled pulse system may be viewed as an overdamped

oscillator, where any deviation from equilibrium will be damped in time.

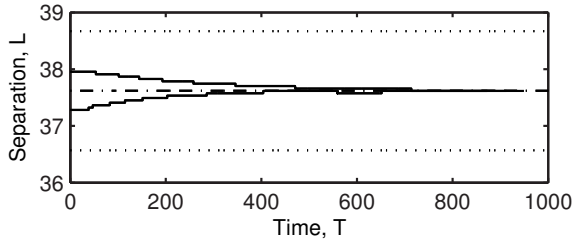

Figure 4: Monotonic attraction between two pulses when they are initially separated with $L = 37.95$, and monotonic repulsion when $L = 37.28$

On the other hand, when both pulses are initially placed closely enough, the structure may exhibit an oscillatory behaviour around its steady separation with a pronounced and non-decaying amplitude. An example is provided in Fig. 5, where the simulation is initially fed with a nominally stable separation solution, $L = 25.06$. The long-time behaviour consists of an oscillatory variation with the mean pulse separation around the value $L = 27.12$, which is similar to the steady separation $L = 27.12$ of a nominally stable bound state and it is in excellent agreement with the analytical prediction of $L = 27.14$ [13].

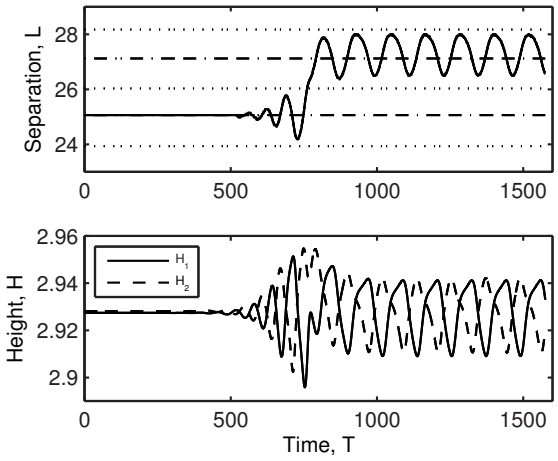

Figure 5: The dynamic oscillation of the separation length (top) and the pulse heights, H_1 and H_2, (bottom) of the unsteady doublet with mean separation $L = 27.12$

It is important to note that such an oscillatory behaviour is clearly harmonic with a well-defined frequency F, in this case of $F = 0.0082$, demonstrating a periodic attracting-repelling alternation under the gravity forcing. This behaviour is coupled to the mass exchange between pulses: the growing pulse accelerates and the shrinking pulse decelerates, and their overshoot leads to an oscillation. The maximum and the minimum of the pulse-to-pulse separation is apparently confined between two neighbouring unstable separations.

The complex nature of pulse-to-pulse interactions is reflected in Table 5. First, it is noted that different initial separation lengths ranging between $L = 22$ and $L = 28$ lead to the same oscillatory behaviour with mean separation around $L = 27.20$ (see also Fig. 6 for the separation time evolution when initially is $L = 22.97$). This means that the stable bound states, which were found at distances below $L \sim 28$ when computing steady solutions, turn out to be unstable when we consider time-dependent computations. Therefore, any initial separation length chosen in the range of $L \sim [22, 28]$ is attracted towards the oscillatory state.

On the other hand, it is also observed that both the amplitude and frequency of the final oscillatory state are independent of the initial condition, in particular, starting with either an initial separation of $L = 27.63$, which is slightly perturbed from the nominally stable state located around 27.12, or a strongly perturbed initial separation of $L = 22.97$, leads to a similar frequency and amplitude (cf. Table 5).

Table 5: Different initial conditions and dynamic properties of the doublet separation for $\delta = 1.82$

Initial L	Mean L	Main frequency	Amplitude
22.97	27.33	0.0085	0.75
25.06	27.12	0.0082	0.75
26.79	27.32	0.0085	0.74
27.63	27.33	0.0081	0.67

Finally, it is also observed that for even smaller initial separation lengths ($L < 22$, see Fig. 6), there is an initial strong repulsive interaction that brings both pulses to rapidly repel each other exhibiting a monotonic growth until the pulses get locked into a stable bound state located at much larger distances. From a physical point of view, this behaviour may be qualitatively explained by considering that, at short separations, pulse interactions do not only occur via the tails (weak theory), but also between the main humps and capillary ripples, giving rise to a more complex interaction. Therefore, the oscillatory solutions found around the stable bound state $L = 27.12$ demarcate the transition from, on one hand a monotonic approach to stable equilibrium at much larger separations, and on the other hand, strong repulsive growth at much shorter separations. In this sense, such oscillatory states may be viewed as metastable states, that could tentatively be attributed to a narrow strange attractor of film flow dynamics.

3.3. Steady triplets

The final question intended to address is the effect caused by the presence of a third pulse in the binary system studied in the previous sections. As starting

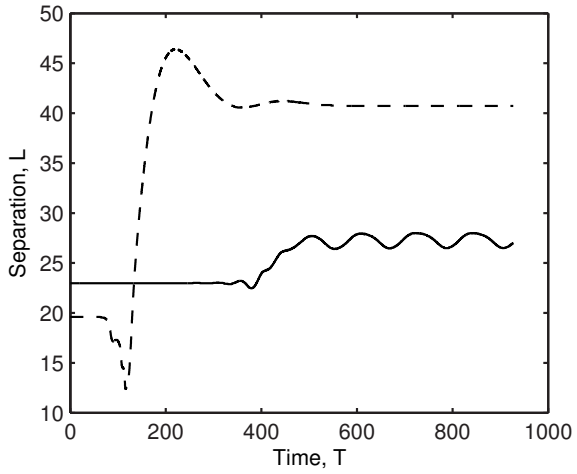

Figure 6: Time evolution of separation lengths for two different initial conditions: $L = 19.61$ (dashed line) and $L = 22.97$ (solid line)

point, and for the sake of simplicity, it is focused on the formation of stationary triplets. The numerical results for $\delta = 0.98$ and $Ka = 3364$ are given in Table 6 in terms of the separation length between the first and second pulses, L_{12}, and between the second and third, L_{23}. The equilibrium doublet separations are also provided for reference along the left column and the bottom row of the table.

Table 6: Pairs of $(L_{12}; L_{23})$ of the triplet bound-state formation for $\delta = 0.98$, $Ka = 3364$. The left column and the bottom row depict doublet separations for reference

34.23	-	-	20.73; 34.55	23.98; 34.29	27.45; 34.23	30.82; 34.23	34.23; 34.23
30.82	-	17.03; 30.32	20.73; 30.73	24.01; 30.79	27.45; 30.82	30.82; 30.82	34.23; 30.82
27.45	-	17.06; 27.68	20.73; 27.51	24.01; 27.45	27.45; 27.45	30.82; 27.45	34.23; 27.45
24.01	14.72; 23.57	17.03; 23.92	20.73; 23.98	23.98; 24.01	27.42; 24.01	30.82; 24.01	34.17; 24.01
20.73	14.72; 21.11	17.03; 20.76	20.73; 20.73	24.01; 20.73	27.39; 20.73	30.94; 20.73	33.96; 20.73
17.06	14.72; 17.06	17.06; 17.03	20.70; 17.06	24.07; 17.06	27.04; 17.06	31.59; 17.06	32.90; 17.06
14.72	14.72; 14.78	17.14; 14.63	20.52; 14.63	24.96; 14.63	25.91; 14.63	31.30; 14.95	32.27; 14.95
L_{12}; L_{23}	14.72	17.06	20.73	24.01	27.45	30.82	34.23

The question of whether the existence of a third pulse modifies the previously computed equilibrium distance of doublet bound states is addressed more conveniently in Fig. 7. Grid lines mark pulse separation of nominally stable (dot-dashed) and nominally unstable (dotted) doublets bound states, and solid circles correspond to the separations L_{12} and L_{23} of the triplets. Points along the diagonal indicate that, if the leading and trailing pulses are placed symmetrically with respect to the middle one, the equilibrium separation distances are similar to those obtained in a binary system. However, when the leading and trailing pulses are placed asymmetrically (points off the diagonal), the pair of pulses with the shortest separation length equilibrates with the remaining pulse at separation lengths that may deviate considerably from the binary system, especially at short distances (see points located around $L_{23} = 15$ and $L_{12} > 20$). It is also important to note that these results depend on whether the pair with shortest distance is located in front or behind the remaining pulse. This is consistent with the numerical observations in [13] using random initial conditions, the statistical analysis of which indicates that pulse separation may exhibit a broad distribution around specific mean distances.

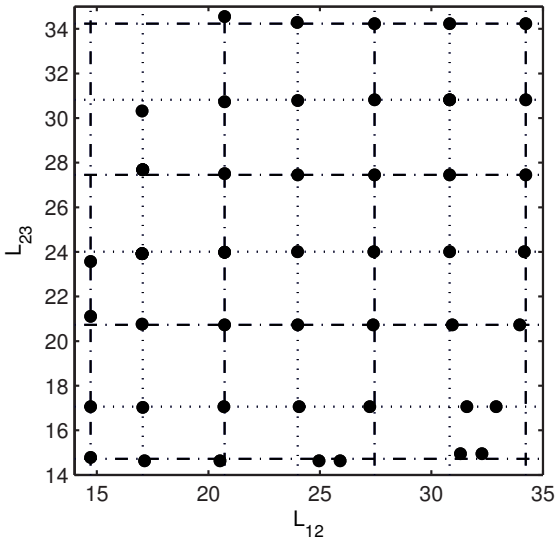

Figure 7: Map of the separation distances in a triplet for the same set of parameters in Table 6

4. CONCLUSION

It has been shown via DNS that the interaction between solitary pulses may give rise to the formation of bound states consisting of two or more pulses separated by well-defined distances and travelling at the same velocity. Two-pulse systems are studied first: stationary solutions of the governing equations are sought and the resulting equilibrium pulse separation lengths compare favourably to theoretical predictions at large-to-intermediate separations. The approach to these solutions from appropriately perturbed initial conditions is shown by time-dependent computations to be monotonic and straightforward.

When two pulses are closely spaced, strong interactions between the two start to be relevant and the theoretical predictions based on weak interaction

become less accurate. In addition, time-dependent simulations indicate that different initial conditions lead to an oscillatory dynamics with well-defined frequency and non-decaying amplitude. When the pulses are placed at very short separation lengths, strong repulsive interactions induce a rapid and monotonic growth of the pulse separation until a stable bound state is reached.

Stationary bound states consisting of three pulses were computed next, and pulse distances were compared to those obtained in the binary system. Deviations grow with the asymmetry in pulse location, indicating that multi-pulse systems are expected to exhibit broad distributions around the mean pulse separation distances.

ACKNOWLEDGEMENTS

The present work was partially supported by the EU under the FP7-Marie Curie Initial Training Network "MULTIFLOW" [PITN-GA-214919-2].

References

[1] Chang, H.-C. (1994) Wave evolution on a falling film. *Annu. Rev. Fluid Mech.*, **26**, 103.

[2] Chang, H.-C. and Demekhin, E. (2002) *Complex Wave Dynamics on Thin Films*. Springer, Amsterdam.

[3] Kalliadasis, S., Ruyer-Quil, C., Scheid, B., and Velarde, M. G. (2012) *Falling Liquid Films*. Springer Series on Applied Mathematical Sciences, Vol. 176.

[4] Kalliadasis, S. and Thiele, U. (2007) *Thin Films of Soft Matter*. Springer-Wien, New York.

[5] Demekhin, E. A., Kalaidin, E. N., Kalliadasis, S., and Vlaskin, S. Y. (2007) Three-dimensional localized coherent structures of surface turbulence. i. scenarios of two-dimensional three-dimensional transition. *Phys. Fluids*, **19**, 114103.

[6] Argyriadi, K., Serifi, K., and Bontozoglou, V. (2004) Nonlinear dynamics of inclined films under low-frequency forcing. *Phys. Fluids*, **16**, 2457.

[7] Liu, J. and Gollub, J. P. (1993) Onset of spatially chaotic waves on flowing films. *Phys. Rev. Lett.*, **70**, 2289.

[8] Liu, J., Paul, J. D., and Gollub, J. P. (1993) Measurements of the primary instabilities of film flows. *J. Fluid Mech.*, **250**, 69.

[9] Vlachogiannis, M. and Bontozoglou, V. (2001) Observations of solitary wave dynamics of film flows. *J. Fluid Mech.*, **435**, 191.

[10] Chang, H. C., Demekhin, E. A., and Kalaidin, E. N. (1995) Interaction dynamics of solitary waves on a falling film. *J. Fluid Mech.*, **294**, 123.

[11] Chang, H.-C., Demekhin, E. A., and Saprikin, S. S. (2002) Noise-driven wave transitions on a vertically falling film. *J. Fluid Mech.*, **462**, 255.

[12] Malamataris, N. A., Vlachogiannis, M., and Bontozoglou, V. (2002) Solitary waves on inclined films: Flow structure and binary interactions. *Phys. Fluids*, **14**, 1082.

[13] Pradas, M., Tseluiko, D., and Kalliadasis, S. (2011) Rigorous coherent-structure theory for falling liquid films: Viscous dispersion effects on bound-state formation and self-organization. *Phys. Fluids*, **23(1)**, 1070.

[14] Duprat, C., Giorgiutti-Dauphin, F., Tseluiko, D., Saprykin, S., and Kalliadasis, S. (2009) Liquid film coating a fiber as a model system for the formation of bound states in active dispersive dissipative nonlinear media. *Phys. Rev. Lett.*, **103**, 234501.

[15] Tseluiko, D., Saprykin, S., Duprat, C., Giorgiutti-Dauphin, F., and Kalliadasis, S. (2010) Pulse dynamics in low-reynolds-number interfacial hydrodynamics: Experiments and theory. *Physica D*, **239**, 2000.

[16] Tseluiko, D., Saprykin, S., and Kalliadasis, S. (2010) Interaction of solitary pulses in active dispersive-dissipative media. *Proc. Est. Acad. Sci., 59*, p. 139.

[17] Ruyer-Quil, C. and Manneville, P. (2000) Improved modeling of flows down inclined planes. *Eur. Phys. J. B*, **15**, 357–359.

[18] Pradas, M., Tseluiko, D., and Kalliadasis, S. (2011) Binary interactions in falling liquid films (submitted). *Proc. IMA Conference on Nonlinearity and Coherent Structures, Reading, UK*.

Multiple phases and components

Conference on Modelling Fluid Flow (CMFF'12)
The 15th International Conference on Fluid Flow Technologies
Budapest, Hungary, September 4-7, 2012

EFFECT OF PRESSURE-OSCILLATING ON CONTROLLING MOTION OF A BUBBLE IN BRANCH FLOW CHANNEL FILLED WITH VISCOELASTIC FLUID

Shuichi IWATA[1], Keisuke MURAKAMI and Hideki MORI

[1] Corresponding Author. Department of Material Science and Engineering, Nagoya Institute of Technology. Gokiso-cho, Showa-ku, Nagoya, 466-8555, Japan. Tel.: +81 52 735 5256, Fax: +81 52 735 5255, E-mail: iwa@nitech.ac.jp

ABSTRACT

In-line defoaming of highly viscous fluids is one of the remaining challenges that needs to be addressed for realizing their industrial use. To overcome the problem of air bubbles in such fluids, the pressure-oscillating defoaming for shear-thinning fluids has been developed. This method is performed by intentionally applying pressure oscillation to a fluid containing a bubble to produce a continuous and strong local flow around the alternately contracting/expanding bubble, where the shear viscosity has been lowered. On the basis of the success that we achieved using this technique for causing bubbles in a quartz cell to rise faster, we applied it to a branched-flow channel filled with a viscoelastic fluid with a zero-shear viscosity of 90 *Pa·s* for the purpose of developing an in-line defoaming system.

In this study, the motions of bubbles in a revised flow channel filled with a higher-viscosity liquid (220 *Pa·s*) were investigated experimentally. In addition, a small air cavity was introduced on the upper side of the flow channel to act as a bubble trap for improving the defoaming performance. We studied the effect of the trap position and volume of air in the trap on the defoaming performance.

Keywords defoaming process, pressure oscillation, shear-thinning fluid

NOMENCLATURE

D	$[m]$	bubble diameter
f	$[Hz]$	frequency
g	$[m/s^2]$	gravity acceleration
H	$[m]$	height of test section
N_1	$[Pa]$	Normal stress difference
P	$[Pa]$	pressure
q	$[m^3/s]$	flow rate
t	$[s]$	time
V	$[m^3]$	volume
v	$[m/s]$	velocity
ε	[-]	flow ratio (defined in Eq. (1))
η	$[Pa·s]$	viscosity
η_0	$[Pa·s]$	zero-shear viscosity
ρ	$[kg/m^3]$	density
ξ	[-]	height of the bubble centre
ζ	[-]	non-dimensional height (defined in Eq. (2))

Subscripts and Superscripts

A	at exit A
B	at exit B
in	feed
min	minimum
max	maximum
T	trap

1. INTRODUCTION

A high demand for in-line defoaming of highly viscous fluids continues in the industrial use. Currently, only few defoaming techniques are available. The typical defoaming techniques are as follows: leaving the target liquid for a long time in a settler or storage tank, heat defoaming, vacuum defoaming, centrifugal defoaming, and ultrasonic defoaming [1, 2]. Most of these techniques involve a batch process. This may entail handling, transportation, and cleaning for each batch. In the case of the centrifugal defoaming of a liquid containing volatile components stored at a high pressure and temperature, additional care and time are needed to prevent vaporization during cooling and depressurizing before transportation. To overcome these difficulties, an in-line defoaming technique is desired. Therefore, the goal of this study was to develop an in-line defoaming

technique for viscoelastic fluids of relatively high viscosity to process such fluids more efficiently.

Kurabo Co. Ltd. has introduced continuous centrifugal devices [3] that can be used as continuous defoaming devices. In these devices, when a fluid enters the centrifuge, bubbles move spontaneously into its axial section. The bubble-dense fluid can then be removed. In such a device, both the robust frame of the centrifugal rotor and the fluid inside it are heavy, such that the energy consumption required for their rotation is high. In addition, the temperature of the fluid may become high owing to the viscous dissipation of high shear between the stator and rotor sections. Therefore, the viscosity of the fluids treated by these devices is limited to 10 *Pa·s*.

Pressure-oscillating defoaming (POD) was proposed by Iwata et al. [4,5], and it is effective for enhancing the rising velocity of small air bubbles in a quartz cell filled with viscous shear-thinning fluids. The zero-shear viscosity of the test fluid was 90 *Pa·s*. The typical experimental results are shown in **Figure 1**. The left three images show the unassisted rise (i.e., without pressure oscillation). The rising velocity of the bubbles was very small. However, when pressure oscillation was applied, the rising velocity of the bubbles increased to about 100 times its natural value. It was shown that a strong shear flow was induced near the rising bubbles under an oscillating-pressure field [6].

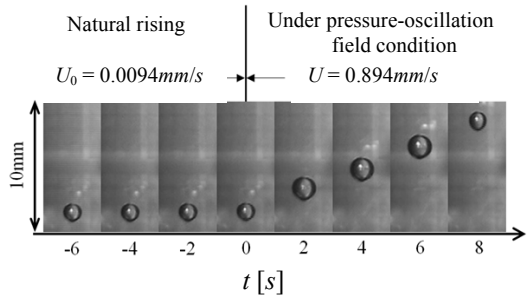

Figure 1. Experiment on quartz cell cited from our previous study (Iwata *et al.*[4])

This principle is applicable to a liquid flow. Iwata *et al*. [7] demonstrated that pressure oscillation in the flow section has the potential to control the motion of the bubbles in an in-line branched channel. The zero-shear viscosity of the test fluid was 150 *Pa·s*. The authors also found that the intentional placement of an additional air bubble on the top-wall surface improved the defoaming performance. However, the best position for the air trap for controlling the moving bubbles has not yet been clarified. In this study, we experimentally examined the effect of the trap position on the defoaming of a highly shear-thinning fluid.

2. EXPERIMENTS

2.1 Test fluid

0.8 *wt%* SPA (sodium polyacrylate; Wako Pure Chemical Industries, Ltd.; MW:22,000 – 70,000) was used as the test fluid. **Figure 2** shows the rheological behaviour of the test fluid measured by a Haake RS-600 system with a cone-plate flow geometry. The zero-shear viscosity of the test fluid was 220 *Pa·s*, which is higher than that in previous studies [4-6]

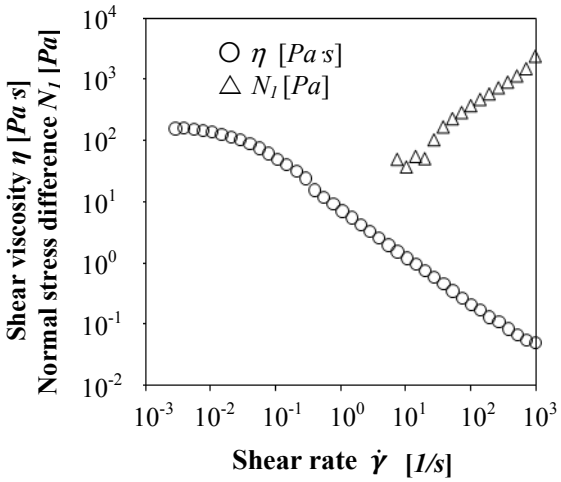

Figure 2. Rheological behavior of 0.8*wt%* Sodium polyacrylate (SPA)

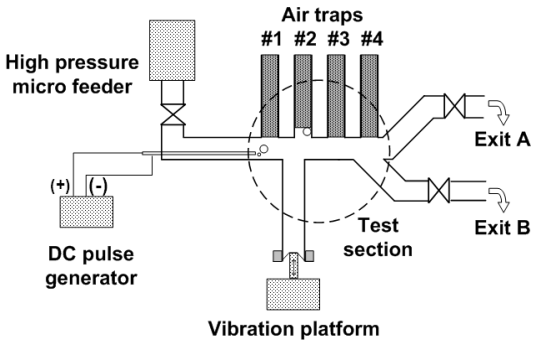

Figure 3. Experimental apparatus

2.2 Experimental apparatus

Figure 3 shows the experimental apparatus used in this study. The test fluid was supplied to the test channel by a high-pressure micro feeder (Furue Science Corp.). A pair of electrodes was inserted, which was used to generate and place the bubbles upstream of the test section. The bubbles were generated by turning introduced by turning on the electric pulse current at a prescribed time with a DC pulse generator (MN-305; Sugawara Laboratory). The cross section of the flow channel (SUS 304) was 7.0 *mm* (H)×7.0 *mm* (W), and the flow channel was split into two exits. Four cavities (air traps #1

to #4) were prepared by shifting one of the pins on the upper surface of the flow channel.

Needle valves (Swagelok Corp.) were inserted upstream and downstream of the test section. Two electronic balances (FX-300i; A&D Corp.) recorded the fluid weight at each of the exits. The measurement data were recorded by a PC through a LAN to calculate the flow rate at the exits. To ensure that the pressure oscillation had the desired effect, stainless steel pipes (SUS304; 8 *mm*ϕ) were used for all the piping.

The dashed circle in the middle of Fig. 3 indicates the sight glass used for monitoring the moving bubbles under a pressure-oscillating field. The pressure oscillation was applied at 300 *Hz* through a rubber sheet at the bottom of the test section. The movements of the generated bubbles under the pressure-oscillating field were monitored by a high-density CCD video camera (Sony Corp.) with the help of stroboscopic lighting at 301 *Hz* to capture changes in the bubble diameter, which were compared with the path of the convected bubbles under stable-pressure conditions.

2.3 Experimental conditions

2.3.1 Effect of trap position

The feed flow rate and open degree of the throttle valves were fixed throughout the experiments. The generated bubble diameters were almost identical (1.77–1.82 *mm*; 3 μL), and the ratio of the flow rate q_B (Exit B) to the channel flow rate $q_A + q_B$ was set constant:

$$\varepsilon = q_B/(q_A+q_B) = 0.79 \qquad (1)$$

The volume of the air cavity in all the experiments was 71 μL (5.5 *mm*ϕ × 3 *mm* in depth).

2.3.2 Performance curve

The effects of the ratio of flow rate (0.5–0.9) and the bubble diameter (0.8–1.8 *mm*) were examined for the following three cases: (i) without pressure oscillation, (ii) with applied pressure oscillation, and (iii) with applied pressure oscillation as well as an air trap placed at #2 (see Fig. 3).

To verify the defoaming performance, we defined the bubble exit height in front of the branching point as shown in **Figure 4**. The normalized bubble position ζ is defined as

$$\zeta = \xi / H \qquad (2)$$

where ξ and H are the bubble position and height of the test section, respectively, as shown in Fig. 4. A positive value for ζ indicates that defoaming is successful.

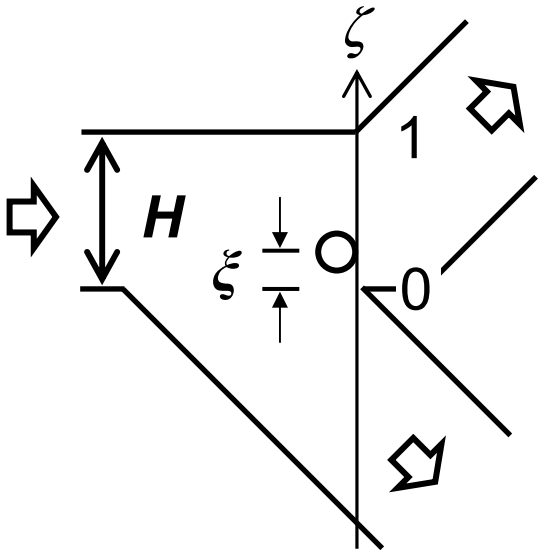

Figure 4. Bubble position at branched section

The residence time between the bubble-generating point and the branched section was recorded for all the experiments.

3. RESULTS AND DISCUSSION

3.1 Effect of trap position

Figures 5 (A) to (D) show the composite images of the experiments extracted from the video data. The arrows in the right-side images indicate the starting point of the pressure oscillation. The images on the left side are for the experiments without pressure oscillation. It is shown that all the bubbles moved into the lower exit (Exit B). As we suppose that the lower exit contains the defoamed product, all the left-side images show cases for failed defoaming.

The right-side images show pictures are the experimental conditions with pressure oscillation.

The dotted lines indicate the cavity positions. As seen from these images, all the bubbles moved into the upper exit, indicating successful defoaming. However, slight differences can be seen between the results.

To make quantitative comparisons, the values for bubble exit height ζ, exit flow ratio ε, and residence time are listed in **Table 1**. The flow ratios were successfully contolled at almost the same value, ε = 0.79. This implies that the flow profile in the channel section was almost the same for each case.

Table 1. Experimental results of defoaming performance

Trap	#1	#2	#3	#4
ζ [-]	0.13	0.33	0.24	0.21
ζ* [-]	0.130	0.275	0.227	0.204
ε [-]	0.796	0.788	0.789	0.787
Residence time [*s*]	105	126	111	108

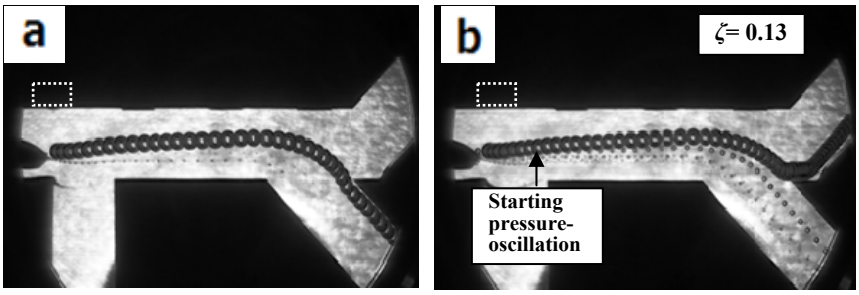

(A) Comparison of bubbles behaviour for #1,

(a) without and (b) with pressure oscillation

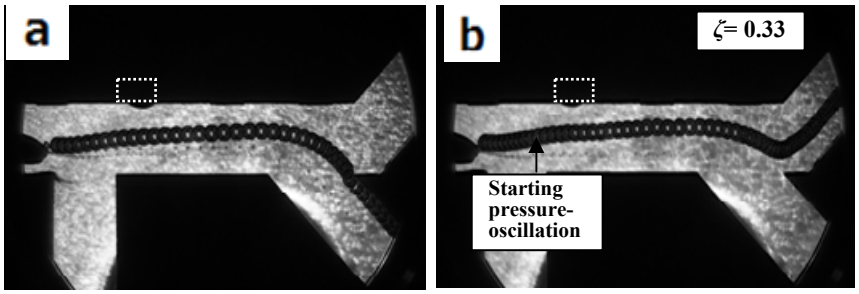

(B) Comparison of bubbles behaviour for #2,

(a) without and (b) with pressure oscillation

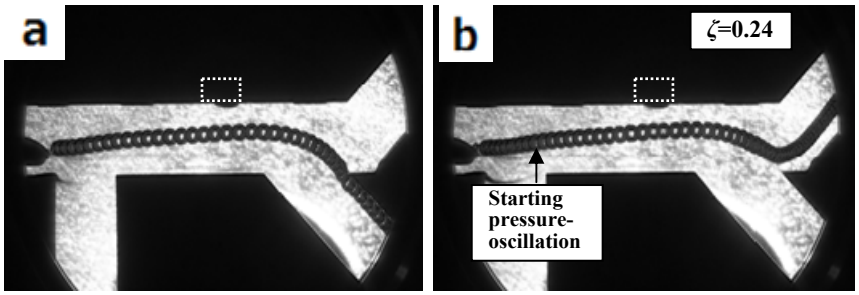

(C) Comparison of bubbles behaviour for #3,

(a) without and (b) with pressure oscillation

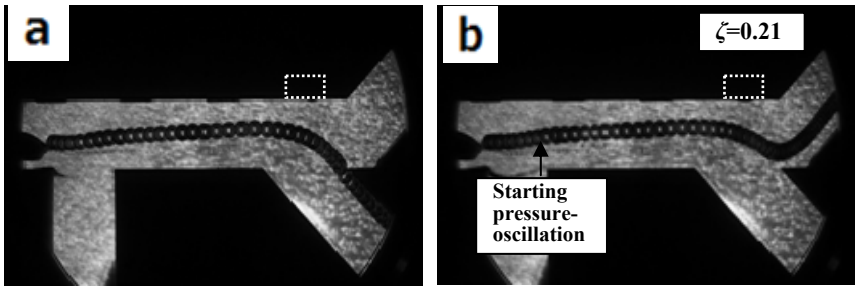

(D) Comparison of bubbles behaviour for #4,

(a) without and (b) with pressure oscillation

Figure 5. Superimposed images for each experiment

As shown in the table, the highest value of ζ was observed in the case of air trap #2.

It was also evident that the longer residence time for air trap #2 should increase the rise of the bubbles because the convected bubbles may be surrounded by a slower fluid near the wall. To compensate for this effect, we introduced a normalized exit height ζ^*, defined as the exit height ζ divided by the residence time normalized by the shortest residence time (air trap #1 in this case). On the basis of ζ^*values, air trap #2 still showed the highest performance.

Figure 6 shows the effect of pressure oscillation and air trap #2 on the movement of the bubble. The experimental bubble rose faster near the oscillating-pressure source point. In order to assess the effect of the air trap, we evaluated a dimensionless factor G_b. Iwata *et al*. [4,5] pointed out that the degree of non-dimensional acceleration, G_b, is related to the defoaming performance, which is defined by Eq. (3), where g is the gravitational acceleration, and D_{max} and D_{min} denote the maximum and minimum bubble diameters, respectively, as determined from the video frames.

$$G_b \equiv (D_{max} - D_{min})(2\pi f)^2 / 4g \qquad (3)$$

When the major-axis bubble diameter D_L was not equal to the minor-axis bubble diameter D_H a weighted logarithmic mean diameter D_m as defined by Eq. (4) was used instead of D_L and D_H.

$$D_m = \sqrt[3]{D_H^2 D_L} \qquad (4)$$

Figure 7 shows the effect of the air trap on G_b. In particular, higher G_b values were obtained upstream of the air trap. From another angle, higher G_b values were obtained between the pressure source point and air trap. In the case of applying pressure oscillation, the bubble was compressed non-uniformly near points where x/H = 0, as shown in

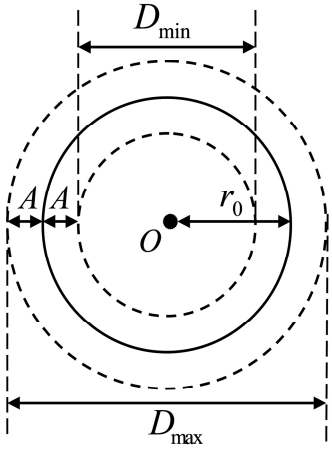

Figure 6. Contracting and expanding bubble with pressure-oscillation

Figure 9. At the same time, the air in the air trap was also compressed. From the point of view of material balance, a local oscillating flow arose from the pressure source point toward both the bubble and air trap, as shown by the arrows in Fig. 9. Therefore, placing the air cavity may play a role in producing a more complex flow around the bubble. As is obvious from its definition, the factor G_b represents the degree of oscillation intensity at the bubble surface. In the case of shear-thinning fluids as shown in Fig. 2, it is expected that the bubble may be a surrounded by a less viscous fluid because of the more complex flow.

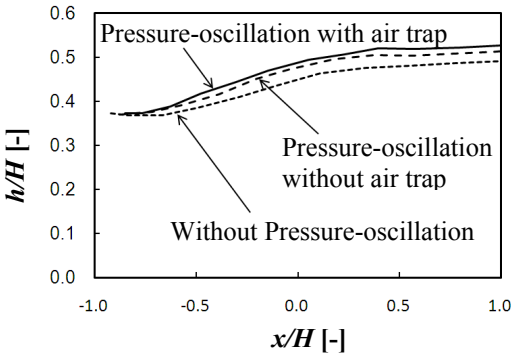

Figure 7. Effect of pressure oscillation and air trap #2 on motion of bubbles

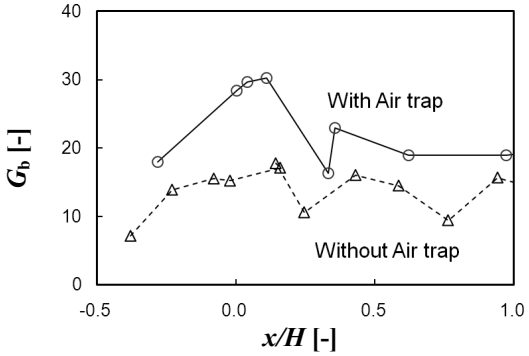

Figure 8. Effect of air trap #2 on normalized maximum acceleration of bubble surface G_b

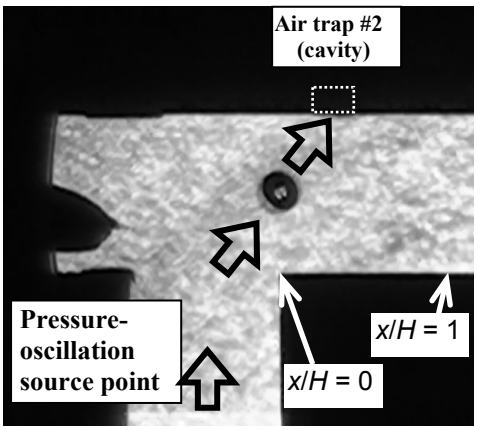

Figure 9. Snapshot of bubble and local flow (image) in pressurizing phase

Therefore, an increase in bubble rising is expected. However, it is hard to obtain the real-time local flow around the convected bubble. The study of hydrodynamic interactions arising from the oscillating local flow between air bubbles will comprise our future study.

3.2 Effect of trap air volume

In the previous section, introduction of the air trap enhanced the defoaming performance. However, an effect of air volume of the trap on defoaming performance has not been discussed. When the air was filled to the cavity, the air volume was 71μL (5.5 $mm\phi \times 3$ mm in depth). However, the volume of injected bubble to be defoamed was only about 3μL. The volume of air trap was much bigger than the injected bubble. In other words, most of the air in the flow channel was occupied by the trap air. The pressure oscillation may not be effectively applied to the target bubble to be defoamed. Therefore, an optimal volume of the air trap in which pressure oscillation can be applied to the target bubble effectively may be expected.

We studied an effect of the volume of air trap on defoaming performance. In this experiment, the air trap #2 was used, which gave the best performance in the previous section. Placed air in the trap was the same volume as the target bubble (2.7μL) through the experiments. Experiments were performed the following four cases: (a) without pressure-oscillation, (b) with applied pressure-oscillation, (c) with applied pressure oscillation and a bubble placed at air trap #2, and (d) with applied pressure-oscillation and two bubbles (2.7μL for each bubble) placed at air trap #2, respectively.

The zero-shear viscosity of the test fluid in this experiment was 191 $Pa \cdot s$. The rheological behaviour was similar to Fig. 2. To make quantitative comparisons, the values for bubble diameter D, exit flow ratio ε, feed flow rate q_A+q_B, $G_{b\,\max}$ and exit height ζ are listed in **Table 2**.

The value of the experimental result of each condition was summarized in **Figure 10**. When without pressure-oscillation (a), the generated

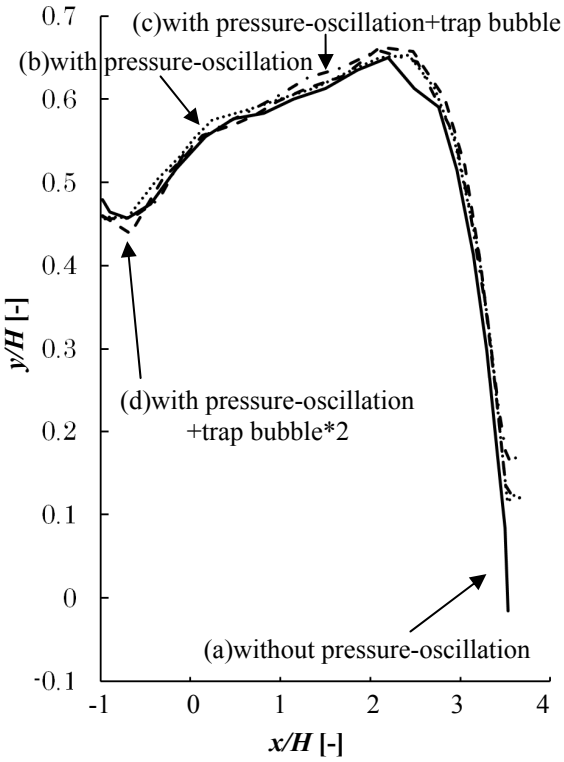

Figure 10. Effect of pressure-oscillation on the bubble position exit height

bubble moved into Exit B. The negative value at the branched section (x/H [-] = 3.5) means that the bubble moved into the Exit B. When applying pressure-oscillation (b), the bubble successfully moved into Exit A. The positive value at the branched section means that the bubble moved into the Exit A, in other words, the bubble was defoamed successfully. The calculated G_b was 23.6. In the case of without pressure-oscillation, the diameter of bubble is the larger than ones in the cases with pressure-oscillation. Deviations of the flow ratios were controlled successfully less than 1% through the experiments. Therefore, the defoaming performance corresponds to the exit height ζ. The case (c) gave the best defoaming performance. Aldo, the biggest G_b was obtained through the experiments. However, when the two bubbles were set in the cavity, the performance and G_b were relatively damped as shown in (d). Therefore, the proper choice of trap air volume

Table 2. Experimental results of defoaming performance

Experimental condition	Bubble diameter D [mm]	Flow ratio ε [-]	Feed flow rate q_A+q_B [g/min]	$G_{b\,max}$ [-]	The Exit Height ζ [-]
(a) without pressure-oscillation	1.8	0.81	1.98	–	–0.02
(b) pressure-oscillation	1.7	0.81	1.95	23.6	0.11
(c) pressure-oscillation and placement of a trap bubble	1.7	0.80	2.03	31.4	0.19
(d) pressure-oscillation and placement of two trap bubbles	1.7	0.80	1.99	22.6	0.11

improves the defoaming performance.

3.3 Performance curve

It is important to clarify the effect of the air trap on the performance curve for this process. **Figure 11** summarizes the experimental results for the three cases. When the size of the bubble is bigger or the ratio of the exit flow rate ε is smaller (i.e., most of the feed flows into the upper exit), the bubble moves spontaneously into the upper exit (Exit A) without any special effort. We call such a flow condition as Zone I. The symbol ''◆'' indicates the critical experimental results without pressure oscillation. With an increase in the flow ratio or a decrease in the bubble diameter, the bubble moves into the lower exit (Exit B).

Above Zone I lies Zone II, where the bubble requires pressure oscillation for successful defoaming; these results are plotted as "■."Above the dashed-dotted line lies Zone III, where the air trap as well as pressure oscillation are needed for successful defoaming as plotted by "▲." Zone IV, which is above Zone III, and is plotted by "×," indicates defoaming failure in which all the bubbles move into the lower exit.

Summing up the experimental results, the pressure-oscillating method enhanced the defoaming performance of 0.8 *wt%* SPA. With the help of an air trap, the performance was further improved.

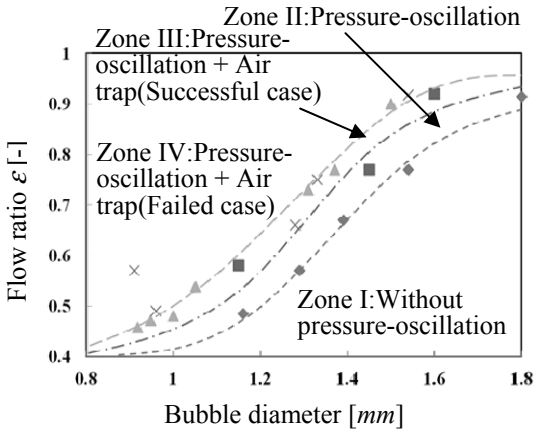

Figure 11. Performance curve

4.CONCLUSIONS

We succeeded in controlling the bubble motion in a branched-flow channel for a viscous shear-thinning fluid. The proper placement and volume of an air trap on the upper surface of the flow channel enhanced the defoaming performance.

It was also shown that upward bubble movement increased in the vicinity of the air trap.

ACKNOWLEDGEMENTS

Part of this work was supported by JST "Linking mechanism of research results to practical application" and JST "Accelerating Utilization of University Intellectual Property Program."

LITERATURE CITED

[1] Ishii, T., 2005, *Engineering of Air Bubbles, Concepts in Basic Bubble and Foam Engineering*, Techno System, pp. 205-219.

[2] Robert. H. P., CECIL H. C., *CHEMICAL ENGINEERS' HANDBOOK*, 5th EDITION, pp. 18.95-18.96.

[3] Taniguchi, T., Sonoda, K., Takahashi, K., Morioka, T. and Uehira, K., 2005, "Centrifugal Defoaming Machine," *Japanese Patent Disclosure* 2005-131600.

[4] Iwata, S., Uchida, S., Ishida, K. and Mori, H., 2007, "Pressure-Oscillatory Defoaming for Shear-thinning Fluids," *Kagaku Kogaku Ronbunshu*, **33**, pp. 294-299.

[5] Iwata, S., Yamada, Y., Takashima, T. and Mori, H., 2008, "Pressure-oscillation defoaming for viscoelastic fluid," *J Non-Newtonian Fluid Mech*, **151**, pp. 30-37.

[6] Iwata, S., Yamada, Y., Komori, S. and Mori, H., 2008, "Experimental Visualization of Local Flow of Shear-Thinning Fluid around a Small Bubble for Pressure-Oscillating Defoaming," *Kagaku Kougaku Ronbunshu*, **34**, pp. 417-423.

[7] Iwata, S., Obikane, T., Shibata, H. and Mori, H., 2010, "Motion of a Bubble in a Branch Flow Channel under a Pressure-Oscillating Field," *Kagaku Kogaku Ronbunshu*, **36**, pp. 366-370.

Conference on Modelling Fluid Flow (CMFF'12)
The 15th International Conference on Fluid Flow Technologies
Budapest, Hungary, September 4-7, 2012

NUMERICAL PREDICTION OF CAVITATION IN PUMPS

S. SALVADORI[1], A. CAPPELLETTI[2], F. MARTELLI[3],
A. NICCHIO[4], L. CARBONINO[5], A. PIVA[6]

[1] Corresponding Author. Energy Engineering Department "Sergio Stecco", University of Firenze, via di S. Marta, 3 – 50139, Firenze, Italy. Tel. +39 055 4796 330, Fax. +39 055 4796 342, E-mail: Simone.Salvadori@unifi.it
[2] Energy Engineering Department "Sergio Stecco", University of Firenze. E-mail: Alessandro.Cappelletti@unifi.it
[3] Energy Engineering Department "Sergio Stecco", University of Firenze. E-mail: Francesco.Martelli@unifi.it
[4] WEIR-Gabbioneta Srl. E-mail: Alessandro.Nicchio@weirgabbioneta.com
[5] WEIR-Gabbioneta Srl. E-mail: Luca.Carbonino@weirgabbioneta.com
[6] WEIR-Gabbioneta Srl. E-mail: Alberto.Piva@weirgabbioneta.com

ABSTRACT

Cavitation is a fundamental issue in pump design. This topic is usually approached through costly experimental tests. The aim of this work is to apply numerical methodologies to the evaluation of the required Net Positive Suction Head in centrifugal impellers.

An industrial pump from WEIR-Gabbioneta SRL has been experimentally analyzed to collect detailed information on the pump behaviour in cavitating conditions. The experimental apparatus has been also analyzed to individuate the pressure levels along the hydraulic circuit.

Numerical analyses were performed on a 2D test case representing the NACA 0009 profile using the ANSYS CFX® commercial code. The available cavitation model has been tested and tuned considering different values for the bubble number density, the vapour volume fraction and the bubble diameter. After comparison with the experimental data, the most accurate configuration has been used for the pump simulation.

Then, multiphase simulations have been performed using the tuned cavitation model. The computational domain includes several diameters of the hydraulic circuit before the pump and the impeller. The bubble cavitation phenomenon generated by the circuit characteristics as well as the flow pre-swirl at the impeller inlet section are individuated for the lowest flow rate.

Keywords: Cavitation, CFD, Multiphase, Pump

NOMENCLATURE

BD		Bubble Dynamics
BEP		Best Efficiency/Design Point
BT		BaroTropic
C	$[m]$	chord length
C_p	[-]	pressure coefficient
CFD		Computational Fluid Dynamics
g	$[m/s^2]$	gravity
y^+	[-]	non-dimensional wall distance
M	$[kg/s]$	mass-flow rate
H	$[m]$	hydraulic head
k	$[m^2/s^2]$	turbulent kinetic energy
n	[-]	bubble number density
NPSH	$[m]$	Net Positive Suction Head
p	$[Pa]$	pressure
Q	$[m^3/s]$	volume flow rate
R	$[m]$	radius
RANS		Reynolds Averaged Navier-Stokes
S	$[kg/m^3s]$	net phase change rate
TVC		Tip Vortex Cavitation
u	$[m/s]$	velocity
VoF		Volume of Fluid
x	$[m]$	axial coordinate
z	$[m]$	height

Subscripts and Superscripts

a	available
b	vapour bubble
c	concentrated (losses)
d	distributed (losses)
in	inlet
j	j-th component
l	liquid
p	pump
r	requested
ref	reference (main-flow/inlet value)
sat	saturation
v	vapour
x	relative to the "x" phase

Greek

α	[-]	vapour volume fraction
ρ	$[kg/m^3]$	density
σ	[-]	cavitation number
Ω	$[rad/s]$	rotating velocity
ω	$[1/s]$	specific dissipation rate

1. INTRODUCTION

Cavitation is a paramount issue for pump designers. Its development is responsible for noise production and damage of the impeller surfaces. Under certain working conditions, fluid pressure decreases under the saturation value and bubbles appear. Due to the density step between the two phases, steam volume is much higher than the corresponding water volume. Bubbles move toward the exit section driven by the positive pressure gradient. Then, implosion occurs and the surfaces are continuously subject to tough forces. This phenomenon is called "pitting" and is responsible for pump mechanical deterioration. Also the pump performances are affected by cavitation insurgence, since both head and efficiency decrease when bubbles appear.

A classification has been proposed by Brennen [1]. Considering an un-shrouded axial pump, the tip leakage vortex development generates low-pressure zones near the top end-wall and the tip vortex cavitation can occur near the blade leading edge. When considering an un-shrouded impeller, operating at a very low mass-flow rate, the tip leakage vortex can move upstream of the inlet section. If TVC occurs, bubbles could recirculation across the inlet section as well. In this case the phenomenon is called backflow cavitation. In an axial or centrifugal pump the water pressure level could reach the saturation value before the blade section. Then, bubbles appear before the inlet plane and bubble cavitation occurs. The most common cavitation insurgence is related to the flow acceleration on the blade suction side. This case is called blade cavitation and can be divided into two sub-categories. When bubbles collapse on the suction side surface a partial cavitation occurs. This is the most dangerous case due to the pitting occurrence. When bubbles are transported downstream of the blade trailing edge and collapse in the region before the volute supercavitation occurs. The main advantage of the latter case is that the pitting is neglected as well as the surface damage.

For all these reasons, predicting cavitation is a key aspect of pump design. This issue is usually approached through costly experimental tests. Nowadays, the available computational resources allow evaluating cavitation by also using numerical models implemented in state-of-the-art Computational Fluid Dynamics codes. According to the classification proposed by Tamura and Matsumoto [2], the numerical approaches can be divided into two main groups: the interface tracking methods, like Volume of Fluid (VoF) methods [3], and the continuum modelling, like the barotropic (BT) methods [4] and the bubble dynamics (BD) methods.

The VoF method is used when a large portion of the fluid is going to cavitation, e.g. in case of blade cavitation. Barotropic methods are able to resolve cases with small cavitating bubbles (e.g. TVC and backflow cavitation). A barotropic law is chosen to link steam/water density to the local pressure value. The slope of the curve between the two phases is defined as a function of the minimum sound speed in the mixture. With the bubble dynamics method both accumulation and collapse of the bubbles can be considered. For this reason these methods can be used in a wide range of cases, except for cases with very large void fractions. In fact, the main drawback of the BD methods is that bubble-bubble interactions are negligible and a large steam portion generates numerical instability.

Amongst the BD methods, the algorithms proposed by Singhal *et al.* [5], Schnerr and Sauer [6] and Zwart *et al*. [7] are the most interesting. A detailed description of the methods can be found in the cited papers while the main characteristics are listed below. All these methods use the same steam transport equation and the same bubble dynamics considerations. These methods differ in the definition of the vapour volume fraction α_v and of the net phase change rate $\dot{S}$. The key parameter for those methods is represented by the bubble number density n that represents the number of bubbles per unit volume. Through this number it is possible to evaluate the α_v parameter via the bubble radius R_b value. With this approach the evaluation of $\dot{S}$ can be performed numerically once the local values of density, pressure, α_v and R_b are available.

Nowadays, the application of the cited methods to real centrifugal pumps is limited by the entity of the necessary computational resources. In fact, a good estimation of the required Net Positive Suction Head ($NPSH_r$) can only be obtained using computational meshes with well discretized blade surfaces and CFD codes able to resolve unsteady cavitation. For these reasons, the authors decided to evaluate the reliability of cavitation models when studying an in-line centrifugal pump. The numerical campaign has been realized using the ANSYS CFX® code. In the present study the bubble dynamics methods have been considered due to their wide range of applications.

2. ANALYSIS OF THE TEST FACILITY

A 1D model of the test facility where the pump is installed was prepared using the Bernoulli equation:

$$(p + \rho\frac{\boldsymbol{u}^2}{2} + \rho g z)_1 - (p + \rho\frac{\boldsymbol{u}^2}{2} + \rho g z)_2 + \Delta p_p = \Delta p_d + \Delta p_c \quad (1)$$

The test facility was divided into 14 stations where the 1st represents the tank, the 8th is positioned in the vicinity of the first pressure tap, the 11th and the 12th at the pump's inlet and outlet, respectively, and the 14th near the last pressure

measurement point. The performance of the pump has been evaluated using the pressure variation between station 8 and station 14.

Figure 1 shows the test rig behaviour in terms of static pressure for an off-design condition of the pump of around 17% of the design flow rate. Focusing on the region of flow positioned before the pump (stations from 8 to 11), Figure 2 shows that the static pressure is lower than the saturation pressure in all the duct. In this situation there is the risk of inflow cavitation in the inlet pipe, which is the phenomenon that was observed during the experimental tests. Therefore, it is important to analyse the experimental apparatus with sophisticated 3D approaches to capture the typical torch occurring in those cases.

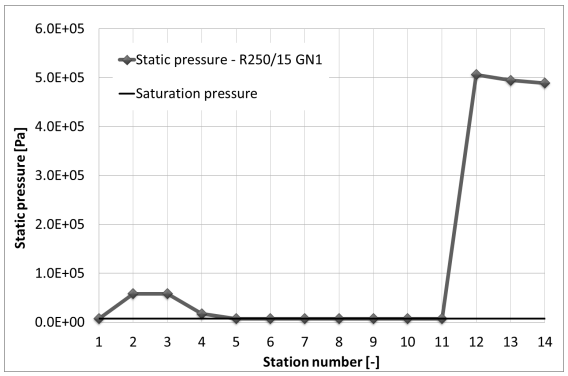

Figure 1. Static pressure in the test facility

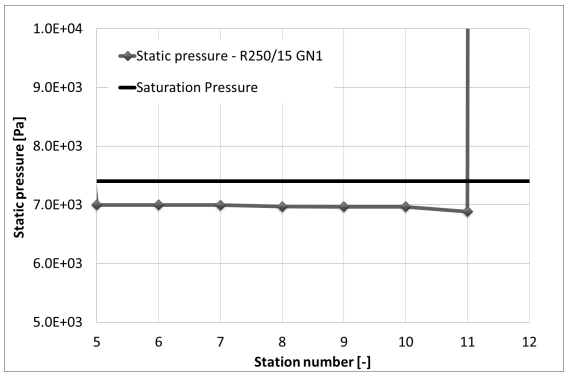

Figure 2. Detail of the static pressure behaviour in the channel positioned before the pump

3. CFD MODELLING

The accuracy of the ANSYS FLUENT® code in reproducing the cavitation phenomenon has been already analysed by Marini *et al.* [8]. For the present activity the ANSYS CFX® code has been chosen. It is a CFD code based on the unsteady Reynolds-Averaged Navier-Stokes equations in their conservative form [9], and has already been validated for many applications [10]. This study was based on a RANS approach and the *k-ω* turbulence closure has been used with the following inlet parameters:

- $k = 0.005$ m^2/s^2
- $\omega = 100$ 1/s

The choice of a steady analysis is based on the necessity to define an industrial-design-oriented method.

3.1. Cavitation model

In ANSYS CFX® the cavitation model is based on the conventional continuity and momentum equation plus simplified Rayleigh-Plesset equation [9], in particular the Bakir *et al.* implementation [11]. The vapour-liquid mixture is treated as an homogenous continuum without slip between phases. They share the same velocity field and a thermal equilibrium is considered. The transport equations of liquid or vapour fraction are the following:

$$\frac{\partial}{\partial t}\left(\rho_l(1-\alpha_v)\right) + \frac{\partial}{\partial x_j}\left(\rho_l(1-\alpha_v)u_j\right) = -\dot{S} \quad (2)$$

$$\frac{\partial}{\partial t}\left(\rho_v\alpha_v\right) + \frac{\partial}{\partial x_j}\left(\rho_v\alpha_v u_j\right) = \dot{S} \quad (3)$$

Where $\dot{S}$ is the source term that is modelled in different way for evaporation and condensation. Defining α_v as vapour volume fraction in Eq. (4), the definition of $\dot{S}$ is reported in Eq. (5):

$$\alpha_v = \frac{4}{3}\pi R^3 n \quad (4)$$

$$\dot{S} = F\frac{3\alpha_v\rho_v}{R}\sqrt{\frac{2}{3}\frac{|(p_v-p)|}{\rho_l}} \quad (5)$$

The value of F changes for evaporation and condensation as follows:

- $F = 50$ for evaporation
- $F = 0.01$ for condensation

Bubble number density is the key parameter for the selected model:

$$n = \frac{3}{4}\frac{\alpha_v}{\pi R_b^3} \quad (6)$$

This number is a representation of real number of bubbles. The default value of n, 10^{14}, is generally defined for high intensity cavitation phenomena [7][12]. On the contrary, the intensity for industrial interests is much lower, and thus a model tuning is necessary.

4. TUNING OF THE MODEL

For the tuning of the code the NACA 0009 Hydrofoil was considered, this type of geometry being a classical test case for cavitation occurrence. The experimental data comes from Dupont [13]. The analyses in cavitating conditions were conducted with a constant cavitation number σ,

defined in Eq. (6), of 0.81. The inlet pressure and velocity were selected as reference values.

$$\sigma = \frac{p_{ref} - p_{sat}}{\frac{1}{2}\rho_l u_{ref}^2} \quad (7)$$

The computational mesh is 2D (Figure 3) and is composed by two zones: a structured grid was realized using an in-house tool while the test section is modelled using the commercial grid generator Centaur [14]. The zones are joined using a grid interface: special attention was devoted to the dimension of the elements facing each other in the boundary layer and the free stream zones. The mesh has around 300k elements. Due to the pure 3D nature of ANSYS CFX® the mesh was converted with an extrusion of one element.

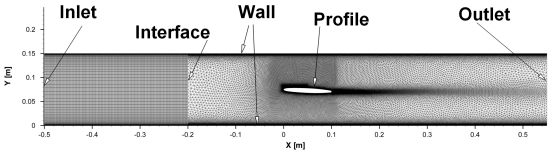

Figure 3: Test case's grid composed by a structured zone and a hybrid unstructured zone

4.1. Evaluation of the optimal parameters

Ansys CFX® doesn't allow a direct manipulation of the value of *n* while it is possible to operate on R_b and α_{vap}. The default values are $R_b = 10^{-6}$ *m* and $\alpha_{vap} = 0.0005$. The tuning points to the effects of their modification on the pressure distribution along the profile. These distributions are presented here in terms of pressure coefficient, defined as follows:

$$C_p = \frac{p - p_{ref}}{\frac{1}{2}\rho_l U_{ref}^2} \quad (8)$$

For these activities a series of simulations were performed with different combinations of R_b and α_{vap} to obtain values of *n* ranging from 10^{13} to 10^{17}. Table 1 reports six amongst the most interesting simulations plus the case without cavitation (named *0*). Case *1* represents the simulation performed using the default values for R_b and α_v.

Table 1. Test matrix

Simulation	*n*	R_b	α_v
0	no cavitation		
1	10^{14}	10^{-6}	$5*10^{-4}$
2	10^{13}	10^{-6}	$5*10^{-5}$
3	$9.55*10^{14}$	$0.5*10^{-6}$	$5*10^{-4}$
4	10^{15}	10^{-6}	$4*10^{-3}$
5	10^{17}	10^{-7}	$5*10^{-4}$
6	10^{17}	10^{-6}	$5*10^{-1}$

Figure 4 shows the comparison between cases *0* and *1*. The flat zone before the pressure recovery (*x/C* lower than 0.18 for the dash-dotted line) shows the area interested by the cavitation.

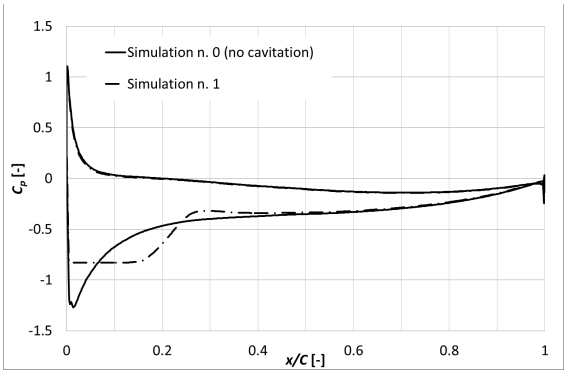

Figure 4. Comparison between the no cavitation case (0) and the baseline setup of the model (1)

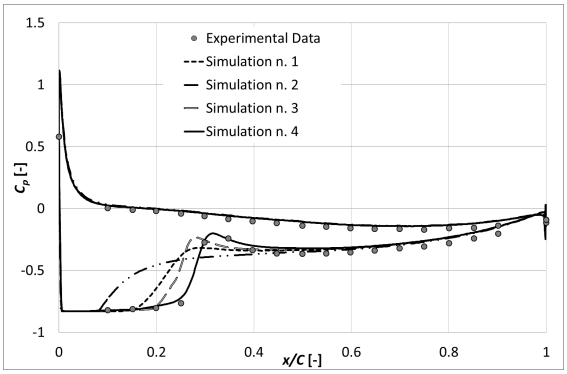

Figure 5. Sensitivity analysis on α_{vap} (case 1,2,3,4)

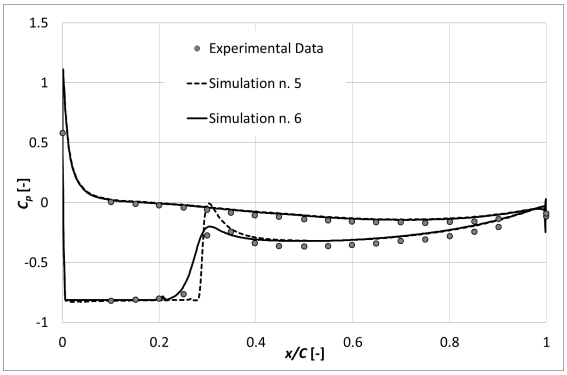

Figure 6. Sensitivity analysis on α_{vap} (case 5,6)

Figure 5 reports the analysis on the sensibility of the solution to the α_v modification. Experimental values are also reported. As shown, an increased vapour volume fraction induces a bigger cavitation area and a stronger pressure recovery, similar to the one suggested by the experimental data (Simulation *4*).

Figure 6 reports other tuning cases based on a value of 10^{17} for n. Simulation *6* shows a good agreement with the experimental data but the selected value of 10^{17} results to be non-physical. Therefore, the dataset relative to Simulation *4* has been chosen as the most promising for the pump analysis. In fact, Figure 7 shows a good agreement between numerical and experimental data using a soft tuning both for $R_b = 10^{-6}$ and $\alpha_v = 4*10^{-3}$.

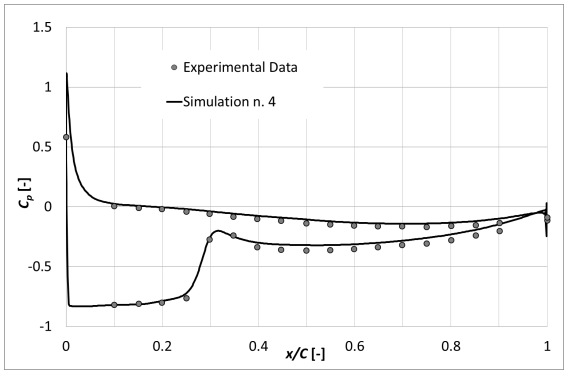

Figure 7. Best tuning (case 4)

5. ANALYSIS OF PUMP

The analysed single stage pump is the R250/15 GN1 model produced by WEIR-Gabbioneta SRL and installed in their test facilities. The fluid domain is composed by a first part of piping followed by the suction nozzle and the impeller (Figure 8). The other parts of the pumps after the impeller were removed to reduce the global volume and to focus on the initial part of impeller and the piping, where cavitation occurs.

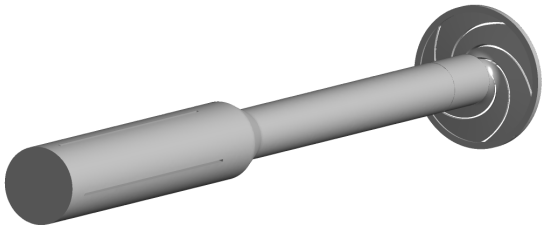

Figure 8. Full model of fluid domain

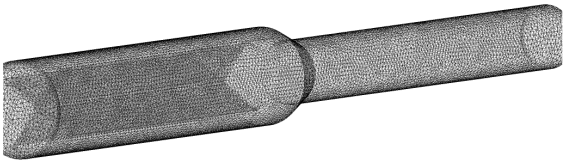

Figure 9. Pipe mesh, including internal walls

The unstructured computational grid was composed by three zones as the solid model. All volumes were meshed using ANSYS ICEM® [15] (Figure 9 and Figure 10). Pipe-impeller interface meshing has been carefully performed to better reproduce the local flow complexity. The complete computational grid counts 1,450k elements. The value of y^+ ranges from 0.3 to 24, in agreement with the k-ω model implementation [9].

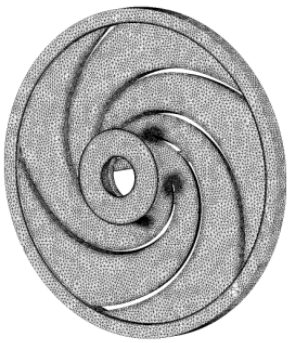

Figure 10. Inducer computational grid

5.1. CFD setup

The setup derived from the preliminary analysis performed on the NACA 0009 profile has been used. The impeller zone is rotating so the selected interface type is the "stage" one. This type uses circumferential average of the flow and it is able to consider an averaged interaction between the incoming flow and the impeller. Rotational velocity of the impeller is around 300 *rad/s*, which is the velocity imposed on the rotating parts in the stationary frame. The inlet turbulence level was set to 1%. An important parameter is the time scale, the default value is $0.2/\Omega$ [9], but for the cavitation simulation it was set to $0.1/\Omega$ to reduce the "Bouncing Convergence" effect [16].

5.2. Non-cavitating analysis

A preliminary analysis on the fluid domain shows an almost constant total pressure field in the pipe section, Figure 11, as already suggested by the 1D analysis.

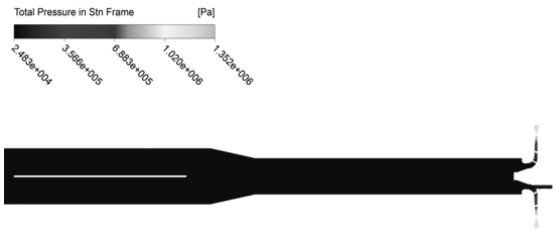

Figure 11. Total pressure field in the pipe

The performed analysis allowed defining the performance curve of the impeller, as shown in Figure 12. These curves are important to manage the simulation in cavitation mode. Four simulations

have been performed changing the flow rate, including the design condition, while the shut-off condition is extrapolated. The CFD curve shows a linear pattern, which is justified by the absence of the discharge volute.

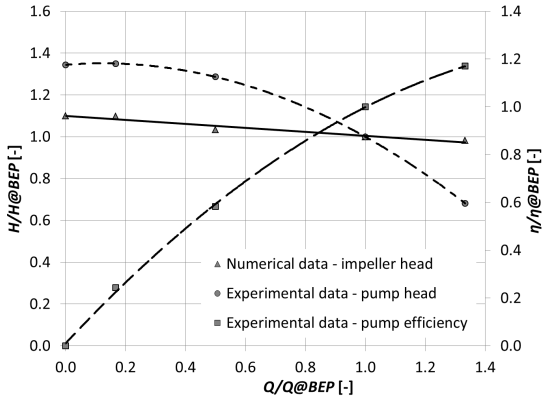

Figure 12. Pump's performances CFD Vs Exp

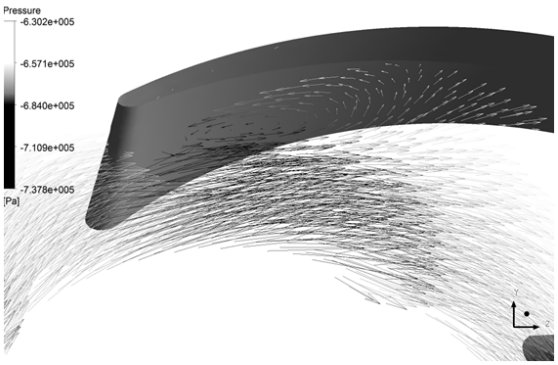

Figure 13. Velocity vector at leading edge

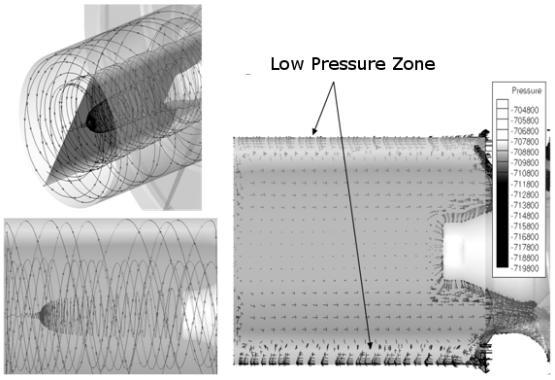

Figure 14. Flow in the inlet section

The simulations also showed the main-flow behaviour in the impeller inlet section. At low flow rates (*Q/Q@BEP* around 0.2) a recirculation zone appears on the suction side of the blade (Figure 13). This phenomenon is generated by the low value of the axial component of the velocity triangle occurring near the blade leading edge. Furthermore, a strong tangential component generated by the rotating walls is evidenced (Figure 14). In this zone a low pressure region induced by the tangential velocity generates the inflow cavitation torch that was observed by the experimental analysis.

5.3. Cavitating Analysis

The cavitating simulation was performed at a temperature of 315K: in that condition the saturation pressure is around 8,000 Pa. The target of this analysis is to evaluate the $NPSH_r$ value and the knee of the $NPSH_a$ curve for the selected impeller and for a specific mass flow rate. This is generally an experimental activity where a series of tests are performed in constant flow rate and the inlet static pressure decreased step by step. The $NPSH_r$ is individuated when the hydraulic head decreases by a factor of 3% with respect to the nominal value for the selected flow rate.

The best way to impose the boundary condition for this kind if simulation would be to use static pressure in the inlet section and mass flow rate in the outlet. Nevertheless, due to convergence stability issues, flow rate is imposed at the inlet section and static pressure at the outlet. To control the inlet static pressure the outlet value is set to $p_{in}+\Delta p$, which is the desired inlet pressure plus the differential pressure obtained from the non-cavitating simulation. The study is based on running several successive simulations where the pressure level was reduced step by step as in the experimental test.

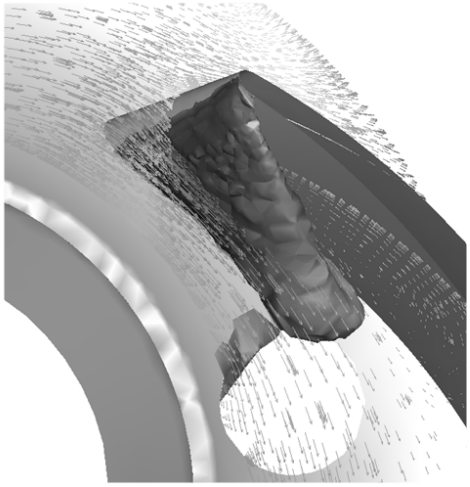

Figure 15. Flow field and cavitation bubble

5.4. Flow details in cavitating simulation

The angle of incidence, Figure 13, influences the region where the cavitation bubble is generated. Figure 15 reports vector field and iso-surface at 8,000 Pa for the case with inlet at 34,751 Pa. As expected, cavitation occurs on the suction side of blades near the leading edge and seems to be

enhanced by the increased angle of incidence. Figure 16 and Figure 17 report the iso-surfaces at 8,000 Pa: in the first image the inlet pressure is 34,571 Pa, which is a failsafe operating condition. The second image is for p_{in} of 13,761 Pa, which represents the 3% condition on the $NPSH_r$ graphic. The blocking effect of the bubble is visible for the latter working condition.

Figure 16. Iso-surface at 8,000 Pa, p_{in} = 34,571 Pa

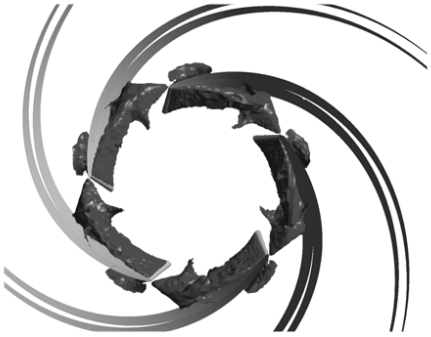

Figure 17. Iso-surface at 8,000 Pa, p_{in} = 13,761 Pa

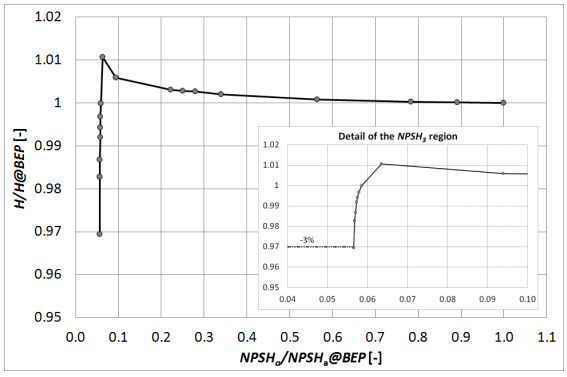

Figure 18. NPSHa curve

5.5. Evaluation of the NPSHr curve

Figure 18 reports the $NPSH_a$ curve calculated using the CFD approach. On that image the NPSHr is evaluated at 0.97 of *H/H@BEP*. This result is affected by the absence of the discharge volute and the -3% condition is based on a *H* value which is not the experimental one. Nevertheless, it presents physics congruity. To underline the *H/H@BEP* increase occurring at $NPSH_a/NPSH_a@BEP$ around 0.1, before the sudden decrease of performance reproducing a physical behaviour, which is always visible when the cavitation curve is experimentally evaluated. Furthermore, the inlet pressure step necessary to evaluate correctly the decreasing part of the curve is very small if compared with the impeller head, and can be quantified around 0.2% of *H*.

CONCLUSIONS

In this work a numerical approach for the evaluation of cavitation has been presented. The numerical model has been tuned using the experimental data obtained for the NACA 0009 profile. The values selected for the bubble radius R_b ($10^{-6}m$) and the vapour volume fraction α_v ($4*10^{-03}$) allow for an accurate prediction of the pressure coefficient.

The obtained set of parameters has been used to analyse a real pump, experimentally tested at WEIR-Gabbioneta SRL. The performed activity allowed to describe the physical phenomena occurring at the impeller inlet section, including negative incidence and pre-swirl responsible for torch cavitation in the pipes for an off-design condition. The selected approach also allowed reproducing the $NPSH_a$ curve for a selected flow rate with a simplified approach.

Further studies have to be performed on the complete geometry using an unsteady approach to visualize the time-dependent bubble generation and collapse, and the proposed set of parameters for the cavitation model.

REFERENCES

[1] Brennen, C.E., 1994, "Hydrodynamic of Pumps", Oxford University Press, New York, ISBN 0-19-856-442-2

[2] Tamura, Y., and Matsumoto, Y., 2009, "Improvement of Bubble Model for Cavitating Flow Simulations", Journal of Hydrodynamics, Ser. B, Vol. 21, n. 1, pp. 41-46

[3] Kunz, R.F., Boger, D.A., Stinebring, D.R., Chyczewski, T.S., Lindau, J.W., Gibeling, H.J., Venkateswaran, S., and Govindan T.R., 1999, "A Preconditioned Navier Stokes Method for Two-Phase Flows with Application to Cavitation Prediction", Computers and Fluids, Vol. 29, n. 8, pp. 849–875

[4] Delannoy, Y., and Kueny, J.L., 1990, "Two Phase Flow Approach in Unsteady Cavitation Modelling", Cavitation and Multiphase Flow Forum FED, Vol. 98, pp. 153-158

[5] Singhal, A.K., Athavale M.M., Li, H., and Jiang, Y., 2002, "Mathematical Basis and Validation of the Full Cavitation Model", Journal of Fluids Engineering, Vol. 124, n. 3, pp. 617-624

[6] Schnerr, G.H., and Sauer J., 2001, "Physical and Numerical Modeling of Unsteady Cavitation Dynamics", Proc. of 4th International Conference on Multiphase Flows, New Orleans, Louisiana, USA
[7] Zwart, P.J., Gerber, A.G., and Belamri T., 2004, "A Two-Phase Flow Model for Predicting Cavitation Dynamics", Proc. of the 5th International Conference on Multiphase Flows, May 30th – June 3rd, Yokohama, Japan, paper n. 152
[8] Marini, A., Salvadori, S., Bernardini, C., Insinna, M., Martelli, F., Nicchio, A., and Piva, A., 2009, "Numerical Prediction of Cavitation Inception in Centrifugal Impellers", Proc. of the 8th European Turbomachinery Conference, March 23rd – 27th, Graz, Austria
[9] ANSYS Inc., 2009, "ANSYS CFX-Solver Theory Guide"
[10] ANSYS Inc., 2011, "ANSYS Fluid Dynamics Verification Manual"
[11] Bakir, F., Rey, R., Gerber A.G., Belamri T., and Hutchinson, B., 2004, "Numerical and Experimental Investigations of the Cavitating Behavior of an Inducer", International Journal of Rotating Machinery, Vol. 10, n. 1, pp. 15-25
[12] Yuan W., 2001, "Modeling and Computation of Unsteady Cavitation Flows in Injection Nozzles", Mécanique & Industries, Vol. 2, n. 5, pp. 383-394
[13] Dupont, P., 1991, "Etude de la Dynamique d'une Poche de Cavitation Partielle en Vue de la Prediction de l'Erosion dans les Turbomachines Hydrauliques" Thèse de l'EPFL, Lausanne, no 931
[14] CentaurSoft, "Online User's Manual - CENTAUR™ v9.6.1", www.centaursoft.com
[15] ANSYS Inc., 2009, "ANSYS ICEM CFD User Guide"
[16] ANSYS Inc., 2010, "ANSYS CFX Tutorials"

Conference on Modelling Fluid Flow (CMFF'12)
The 15th International Conference on Fluid Flow Technologies
Budapest, Hungary, September 4-7, 2012

NEW METHOD TO DETERMINE SHEDDING/DISCHARGING FREQUENCY OF CAVITATION CLOUDS BASED ON COMPUTER TOMOGRAPHY

Ezddin A.F. HUTLI[2], Petar B. PETROVIC[3], Milos S. NEDELJKOVIC[1]

[2] PhD, Faculty of Mechanical Engineering University of Belgrade, Serbia (FMEUB), ezddinhutli@yahoo.com
[3] Prof., FMEUB, e-mail: pbpetrovic@gmail.com
[1] Prof., FMEUB, Kraljice Marije 16, 11120 Belgrade 35, Serbia, Tel/Fax: +381-11-337-0317, mnedeljkovic@mas.bg.ac.rs, corr.author

ABSTRACT

In order to study the jet structure and the behavior of cloud cavitation within time and space, visualization of highly submerged cavitating water jet has been done using high speed video camera. The obtained movies were submitted to analysis using new approach for cloud cavitation detection based on computer tomography. This included obligatory dynamic analysis of cavitation clouds and estimation of frequency of cloud based on computer image processing. The cloud life time, and the frequency of shedding/discharging were successfully obtained. The influencing hydro-dynamic and geometrical parameters were experim-entally proven to be very significant. The obtained results proved the validity of the proposed formula for shedding/discharging frequency of cavitation phenomenon which has been published by authors in a previous work.

Keywords: cavitation cloud, cavitating jets, computer tomography, frequency, image processing, shedding/discharging

NOMENCLATURE

CC	[-]	Cavitations cloud.
CCSF	[Hz]	Cavitation cloud shooting frequency.
mu_CCSF	[Hz]	Mean of cavitation cloud shooting frequency.
Sigma_CCSF	[Hz]	Standard deviation of cavitation cloud shooting frequency.
CCLC	[s]	Cavitation cloud lifecycle.
$f_{C.lifecycle}$	[Hz]	Frequency cloud life cycle.
$f_{C.shedding}$	[Hz]	Shedding frequency of cavitation cloud.
Ts	[μs]	Time series - Number of frames (20 μs /frame)

1. INTRODUCTION

Over the past few years, cavitating fluid jets have received considerable attention, primarily with laboratory experiments, in order to understand their behaviour and to determine the feasibility of their use in a variety of situations. If the unsteady behaviour and the jet structure (the unsteady behaviour of rapid fracture and break off of the cavitating jet, as well as the development and collapse of cavitation clouds on the impinging surface) are clarified in detail, expectedly, the jet working capacity may be drastically improved [1-3]. As it is well known, the cavitation clouds (cavitating jets) behave stochastically both in time and space, with a very rapid change within μs. However, the cavitation cloud shedding and breakdown of the cavitating jet cloud in water take place periodically with a certain frequency. This frequency depends on the injection pressure of the cavitating jet and/or the cavitation number, but does not depend on the nozzle geometry [1, 4-6]. The periodic shedding is dependent on the formation and coalescence of micro-vortex cavities on the separated shear layer and the re-entrant motion after shedding [3, 5, 6]. As a result of studied structure of the cavitating jet, the formulas for the dependence of the vortex ring cavitation frequency and cloud shedding and discharging frequencies in cavitating jet on upstream pressure and on other influencing parameters was proposed [5, 6].

In this paper an attempt is made to understand the behavior of severely erosive cavitation clouds by collecting visual information about a high speed submerged water jet using PHOTRON APX (high-speed video camera). More information about visulization protocol is presented in [6].

The images were extracted from video recording that was captured with high speed video camera that can capture maximum frame number of 100,000 f/s, whereas the degree of resolution is

dependent on the chosen frame rate [7]. That means that video was converted to a series of images in JPEG format using a commercial software (Photron Fastcam Viewer PFV Version 2.1) provided by camera manufacturer. These images were subjected to the image processing algorithm described in the following paragraphs. The aim of this work was to study the behavior of cavitation clouds and quantify the properties of the cloud shape and to correlate these properties with working conditions (geometrical and hydrodynamic conditions). These properties were calculated using pixel properties of the image as explained in the next section.

2. TRACES OF CC -DYNAMICS BASED ON COMPUTED TOMOGRAPHY METHOD

In this part the task is finding cloud cavitation (CC) traces peaks (core line of the trace) using Radon transform on filtered and histogram adapted time development profile images. Thus, identification (discovering/understanding) of CC dynamics is based on Computed Tomography Method. Here we will start to apply this method on the movie with a high frame rate 50,000 fps (convergent nozzle, P_1=105 bar) for the reason of better classified clouds in the extracted images from this movie. Further on this method will be used for other movies with a low frame rate. To represent an image, the Radon function takes multiple, parallel-beam projections of the image from different angles by rotating the source around the center of the image produced by aligning the profiles extracted from the frames (as in Fig.5 and Fig.8). The beams are spaced 1 pixel unit apart. Fig.1 shows a single projection at a specified rotation angle.

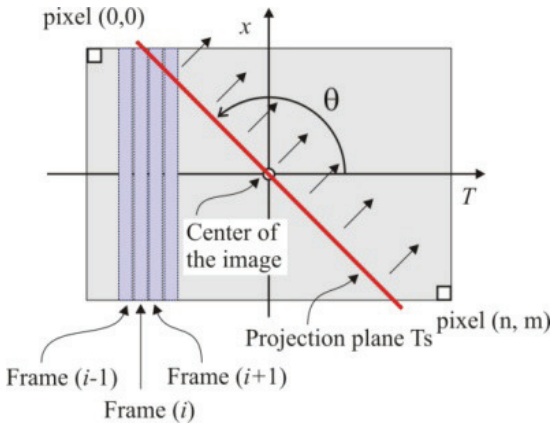

Figure 1. Projection plane moving with angle θ (n is Chamber length, m is Number of frames).

Roughly speaking, flow of a submerged cavitating jet belongs to the class of one-dimensional flows. Starting from that fact, it is possible to set up a new method for cavitation clouds identification and analysis of their behavior in time domain, that is significantly more reliable than the method based on recognition of two-dimensional contours in the binary map of each individual frame. Transferring a two-dimensional monochromatic map into a one-dimensional is achievable by using two procedures. First procedure is based on the projection of a three-dimensional surface that shows illumination intensity field, which is reduced to application of MAX operator over columns of the frame matrix. The profile thus obtained is a vector, containing maximum values of illumination intensities across transversal coordinate. Although computationally very simple, this procedure neglects the spatial content of cavitation cloud, i.e. its voluminosity, which exists even when we consider only the case of one-dimensional flow.

The other procedure is based on integration of illumination intensity field profile in transversal plane. Since the field is discrete, the integration function is reduced to summing the elements of frame matrix over columns. The obtained profile is a vector that contains sums of illumination intensity over transversal coordinate. The application of this procedure saves the voluminosity information of the cavitation cloud. Moreover, this procedure excludes the possibility of discontinuity, which is not the case for the projection method, where a possibility for appearance of discontinuity is realistic. This method is sensitive to background noise, and it cannot detect the reflected wave from cavitation cloud! In both cases the surface field is reduced to a line field, i.e. to intensity profile which is reduced to lateral plane (plane that contains the main axes of submerged cavitating jet flow – spatial coordinates). Both procedures were made after the steps presented in Fig.2.

The examples of the profiles generated by application of both procedures are given in Fig.3(a&b), and Fig.4.

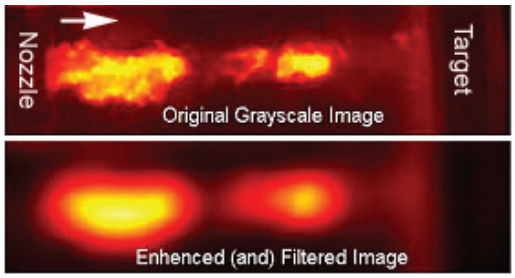

Figure 2. The steps done on the images before steps of measuring properties and statistical analysis.

3. PRIMARY RESULTS

For the further analysis of dynamics of cavitational flow, it is necessary to introduce a time coordinate. In this way, a 3D space is formed which has its spatial dimension (x coordinate of the

chamber), time dimension (which carries the information regarding timeline/development/ evolution of the process of cavitational flow and genesis of cavitation clouds) and the dimension of illumination intensity (through which it is possible to establish a relation to the process of cavitation). With the third parameter (dimension) we get the information on the intensity of generated micro-bubbles which comprise the cavitation cloud (greater concentration of micro-bubbles means higher intensity of illumination for local pixel, i.e. determination of discrete values of spatial coordinate for the chamber). Into a previously defined T-x-I space we write profiles of illumination intensity for each individual frame, so that two consecutive illumination profiles are placed on a time separation of T_s (sampling time), i.e. on each time interval of n*T_s we can locate the content that belongs to one frame. In this way we obtain a time series that transmits the

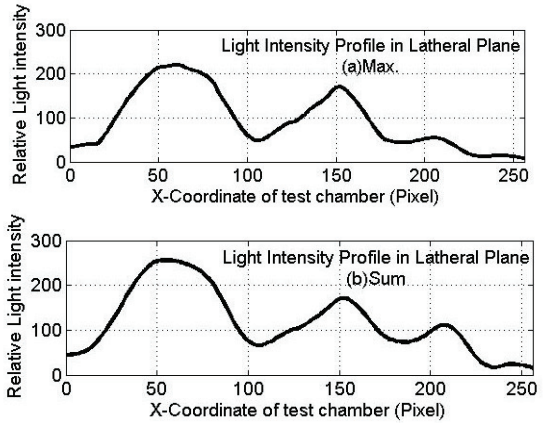

Figure 3. Lateral profile of illumination intensity generated with (a) MAX & (b) SUM procedure.

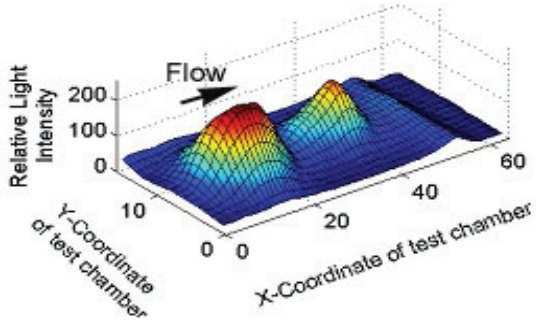

Figure 4. Cavitation cloud topology - 3D Surface plot.

information about the dynamics of the process of cavitation flow.

The image in Fig.5 shows the sample that was made of a time series of 8 profiles shown in 3D T-x-I space. For each of the aforementioned profiles we have shown the corresponding illumination field on the basis of which a profile is generated. Fig.6 represents the 3D images which were processed to extract the intensity profiles presented in Fig.5.

It can be seen, in the sequence shown, that there are two cavitation clouds, in the positions of first, second, third and fourth frame (time axis). The presence of two cavitation clouds can be seen, in traces, even in the next two frames. Cavitation cloud #1 is in its final developmental phase, while in this subsequence it can be seen that the cloud #2 is arising. Cavitation cloud #2 is present in the whole sample that consists of 8 frames (time axis). The very moment of cavitation cloud appearance and disappearance is not a part of this sequence. The time window of its genesis (appearance, development and disappearance) is larger than 8T_s. It can be seen that both cavitation clouds drift from the nozzle at the end of the chamber. Also, it can be seen that the size of cavitation clouds is gradually increasing, shifting its shape from circular to elliptical, with a saturation level in the central region. When the cloud approaches the end of the chamber, its size begins to shrink and it gradually disappears. The process of disappearance corresponds to the sequence [T_s, 5T_s] of cavitation cloud #1, with the terminal phase of this process being located at 5T_s. The position of 6T_s, which corresponds to the sixth frame, is seen as a moment just before the disappearance of the third cavitation cloud. The process of its genesis can be observed in time sequence [6T_s, 8T_s]. It can be seen that this cloud is developing and gradually growing, thus increasing its volume.

The described process of cavitation clouds genesis and movement is regular. This process strictly follows a unique pattern, which is distributed through a finite sequence of consecutive frames, starting from initial frame in which the cloud disappears, all the way through to the terminal frame in which cloud completely disappears.

The analysis of the process of generation of cavitation clouds can be realized by analyzing the time-series that has a greater scope than the one previously analyzed. Next image shows the orthogonal projection of three-dimensional T-x-I space. The illumination intensity is expressed with a color map. In this way, a 3D space is reduced to the equivalent color image representation, which can create the space for analyzing the process of generation of cavitation clouds by applying different techniques, which are developed for image analysis.

On the graphs (Fig.7) we note an obvious presence of regular straight-line segment pattern whose physical interpretation is that they represent trajectories of cavitation clouds, starting from the moment of appearance and concluding with the moment of disappearance. The length of these lines,

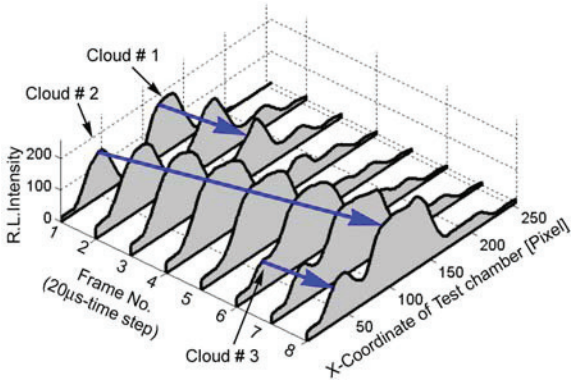

Figure 5. 3D T-x-I space - computer tomography (segmentation) of a time series profiles.

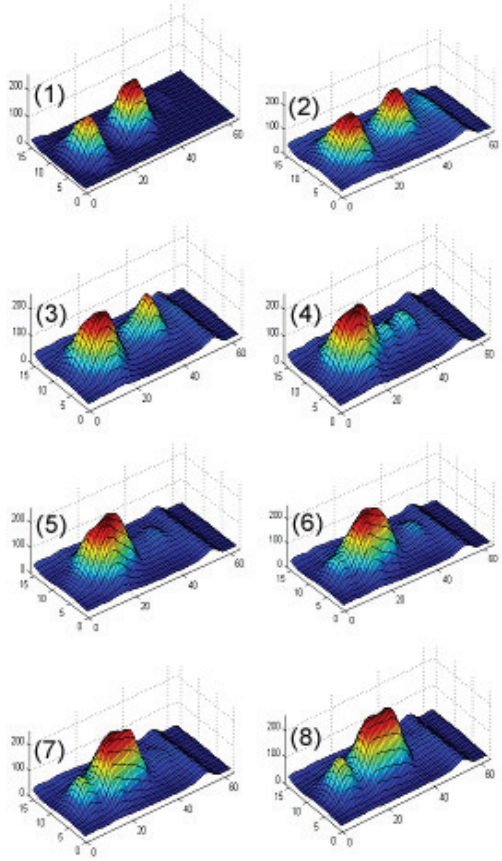

Figure 6. 3D cavitation clouds extracted from 8 consecutive frames, which were used to extract intensity profiles shown in 3D T-x-I space.

measured by coordinates given on horizontal axis – time axis, corresponds to the duration of cavitation cloud. The process of generating cavitation clouds in this concrete example is discrete, so that cavitation clouds could be observed as miniature projectiles originating from the nozzle. The trajectories of cavitation clouds are almost perfectly aligned, the difference being only in their intensity, which corresponds to the difference in size of cavitation clouds expressed through their volume (this is completely true if the line profile of illumination is derived by SUM procedure). The distance between these parallel trajectories has been expressed through time coordinate, and determines the time interval between "shooting" the projectiles. To conduct the appropriate quantification it is necessary to analyze a monochromatic 2D image with a method sensitive to straight line segments . A wide choice of image analysis and pattern recognition methods offers different tools that can be applied in this concrete example [9].

The identification/quantification of a line content in the generated image can be realized with Radon transform. Radon transform is a tool that projects the initial 2D image of illumination field to a plane which forms a predefined angle with the vertical axis as in schematic diagram Fig.1. The rotation of 2D monochromatic image (from the movie of 50,000 fps) is conducted around its central pixel (64, 128) with Fig.8 used. The projection is made by integrating the illumination field across the bundle of parallel beams which are orthogonal to current projection plane and are separated 1 pixel apart. The result is given in Fig.7.

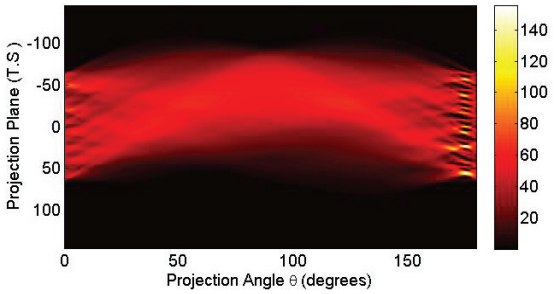

Figure 7. 2D map 128x256 and its Radon transform for interval of 0^o to 180^o, increment 0.1^o.

The Radon transform of previously mentioned 2D image within the interval of 0 to 180 degrees, with a 0.1 degree increment, is shown on the next image. The vertical axis represents the angle of projection (theta) while the horizontal axis represents the projection plane, which in this case ranges within +/- 142 pixels. The overview of the graph (Fig.7) shows the peaks (singular points in white color) on the location of 175.5 degrees, which points out that under this projection angle a content is located that has a dominant linear character. The positions of these points are defined by a value of vertical axis, which determines their spatial location along projected horizontal axis, which in this case has the dimension of time.

Further, we focus on projection plane under the angle of 175.5 degrees. The profile of Radon transform under this angle generates well concentrated peaks, which clearly points to existence of shapes that possess a clear linear character. This confirms the above statement that

the trajectories of cavitation clouds are linear and parallel among themselves. The distance between peaks is measured in discrete time intervals T_s, and their reciprocal value has a physical meaning of the frequency of cavitation clouds generation (this is a life frequency which includes shedding, growing, discharging, collapsing, oscillation, etc) (frequency of "shooting micro projectiles"). The accumulated intensity of illumination in this case corresponds to the size of cavitation cloud.

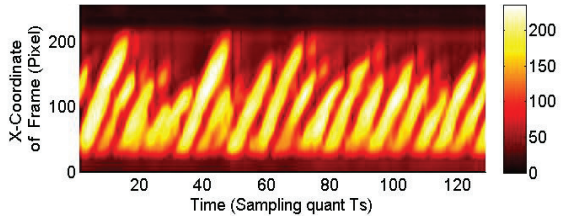

Figure 8. A series of 128 intensity profiles obtained by SUM procedure used in Radon transform process.

For further analysis it is important to determine the distance between the Radon transform peaks under the angle which corresponds to the main direction of cavitation clouds movement in space-time plane. The graph Fig.9 shows the locations of identified peaks and time distance between them. We have identified 26 peaks whose intensity is greater than 20 intensity units.

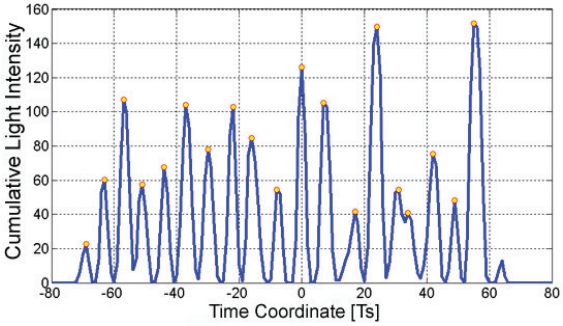

Figure 9. Locations of identified peaks and time distances between them.

4. STATISTICAL CHARACTERIZATION OF DYNAMICS OF CAVITATION CLOUDS GENERATION PROCESS

Since each cavitation cloud is recognized from its early stage of generation up to the moment when the cloud vanishes and no longer exists (CC lifecycle sequence), and this sequence is precisely located in time, it is possible to quantize this discrete process in dynamical sense.

The first what is to be done is the estimation of frequency of appearance of clouds, i.e. estimation of Cavitation Clouds Shooting Frequency (CCSF). This is done by measuring the time intervals between adjacent clouds, measured in sampling time quantum's (Ts). Statistical character of CCSF can be identified by fitting Gaussian (NORMAL) probability function to the set of calculated time intervals over the whole set of analyzed frames. The result is MEAN value of CCSF (mu_CCSF), standard deviation (sigma_CCSF) and confidence intervals for both parameters (mu_CCSF_ci and sigma_CCSF_ci). In this way the dynamic nature of cavitation clouds generation process is characterized in a statistical sense. This approach is much more realistic than categorical estimation of any kind of frequencies (cloud thickness variation, cloud area variation, and similar), since the true nature of cavitation clouds generation process is stochastic. However, this process is not completely random. It has its dominant frequency, as a point at the 'weighted' frequency axis, having maximum weight factor. Around this point other shooting frequencies exist but with lower weight factors. This behavior is expressed by appropriate probability density function.

Another dynamical property of cavitation clouds generation process can be lifecycle variation time. Identified traces of any single cloud show that some of them have short traces while the other ones have long traces. It means that the cavitation cloud lifecycle (CCLC) is not a constant but a variable quantity, which can be characterized statistically in the manner as it was made in case of CCSF.

Moreover, the dynamical characterization of the cavitation clouds generation process can be achieved by analyzing the size of projected intensity light profile. For this purpose the most convenient is SUM method since the intensity of each point of the light intensity profile is calculated by integration of the light intensity in the lateral plane of the chamber (frame). In this way the information related to the CC size is preserved. On the contrary, the MAX method does not take into account this information and consequently the cavitation cloud size, as a physical quantity, is completely lost and cannot be recovered. This dynamical property is not considered within this analysis. Robustness of this approach can be estimated by comparison of estimated CCSF and other statistical parameters among various sequences of frames taken from one single experiment, or by comparison of various experiments conducted under the same experimental conditions, excluding the parameters of acquisition process performed by high-speed camera.

Fig.10 contains 200 images gathered in time sampling, and we can see completely traced clouds, since their shedding and thier vanishing can be completely seen (complete cloud life). The jet trajectory is almost straight, which means that we can extract a straight line based on the pixel intensity. Fig.10 also shows the steps needed to

enhance the images before starting to work with this method. As the clouds are well defined in the frame the results are good. As we see later in Fig.11, the traces are good enough and we have a well defined cavitation clouds (the frameing time is compatible with cloud time behavior). The bottom part of image represents the nozzle exit and the top part of the image represents the target wall.

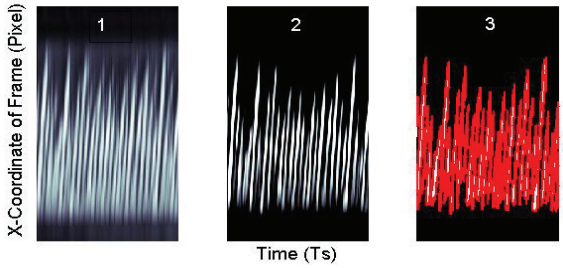

Figure 10. (1) Original image, (2) Smoothed image and Histogram adapted image, and (3) Identified traces of images of cavitation clouds.

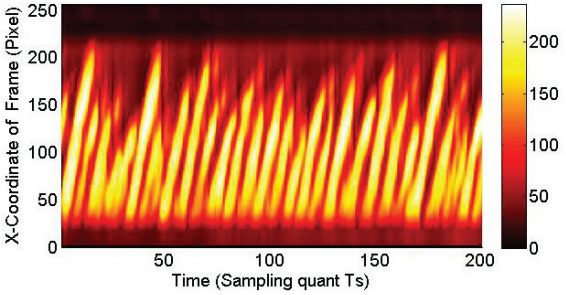

Figure 11. Traces of cavitation clouds generated in submerged cavitating water jet.

Fig.12 represents the profile after the Radon transform as a function of projection angle. The peaks appear at certain angle and the locations of strong peaks in the Radon transform matrix are shown. The locations of these peaks correspond to the locations of straight lines in the original image in Fig.10 and in Fig.11.

The strongest peaks in projection plane correspond to the angle θ=172.57^{o} while x = vary (-100 to +100) (number of processed frames = 200 frames). As it can be seen, the x positions of strong peaks are equal to the number of processed frames, which means that these straight lines could represent the jet projection path. In addition, we can see that these strong peaks are wider or thicker which means that the angle is not exactly 175.5, or this thickness of strong peaks could also be related to the fact that we did not have completely straight parallel lines. Notice that the other areas with less strong intensity also appear as colored area (yellow color). It means that in this angle of viwe of the plane projection ($\theta \cong 172.57^{o}$) we have only the vapour (full cavitation), while in other angles the jet has partial (less dense) cavitation or even discontnuity of the jet. In these other angles only portion of obscure area in the jet appears and this may be the area of collapsing or cloud vanshing (red area).

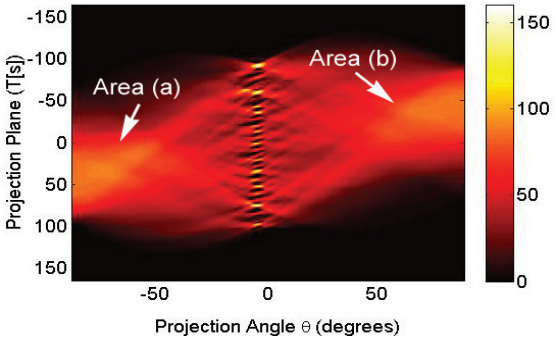

Figure 12. Profile Radon transform as a function of projection angle - images of cavitations clouds generated in submerged water jet

The existance of the two areas (a and b) in Fig.12 reveals that the jet is almost symmetric around the center of image in Fig.11 (transformation is symmetric), which means that the jet repeats itself and has a periodical behavior.

Fig.13 represents the cumalitive light intensity as a function of time or of the frame number. As we can see the intensities vary with time because the contents of the frame change with time, i.e. we have a dynamic process (micro and macro dynamice process). The distribution of the variation of the light intensity with time could be related to the frequencies of shedding, discharging and to the other processes during the cloud (jet) life stages. This variation can be used to estimate the frequncy, or as an indicator of periodic behavior of the cavitating jets.

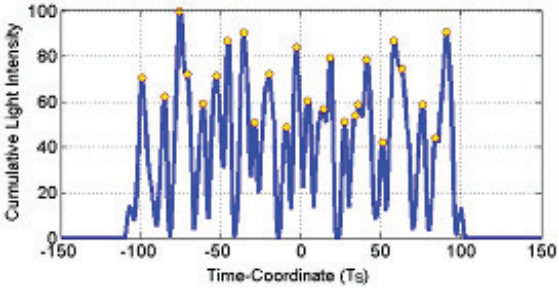

Figure 13. R_{175.5^{o}} Projection Plane (Pixels) shows the locations of identified peaks and time distance between them.

Fig.14 shows the time interval between adjacent clouds. As we can see the time is not constant because of the nature of the cavitating jet (chain process of periodically producing clouds). There is an acceleration and deacceleration phenomenon in the region (i.e test chamber) as a result of growing, shrinking and collapsing of the

clouds during thier life stages. In addition the jet may produce different cloud sizes. In this movie we have a good agreement with the results of frequency calculated using proposed formula in presented and in previous work. The frequency was $f_{C.shedding}$ = 6,335 and here is $f_{C.shedding}$ = 6,316, which is only 0.2% of difference. This is because the calculated frequency using this code represents the whole process of shedding and discharging (complete jet) and what we measured and calculated using the formula in priviouis work [6] was only shedding frequency of the clouds. Here, the code analyses 560 frames and the found frequency could be related to the breaking off of the jet because there are no time differences between the clouds, i.e. they are shedding and at the same time this represents the jet breaking off (cloud divided to two or more clouds), The distribution of the frequency is presented in Fig.15.

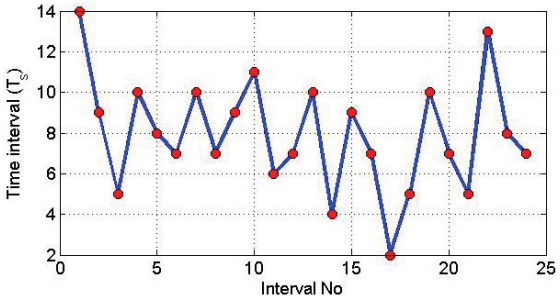

Figure 14. Time interval between adjacent clouds.

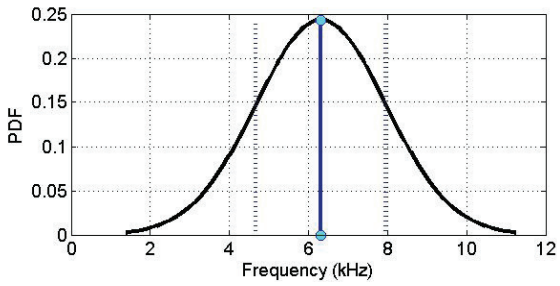

Figure 15. Gaussian probability distribution of estimated CC shooting frequency of cavitation clouds.

Fig.15 shows the life time of each cloud. As we can see, within this time of 200 frames, using the projection (or segmentation) method only 28 clouds are recognized as generated. The range of thier life is between 0.1 to 0.32 ms. This is a proof of two facts: first - that the pressure distribution is not the same throughout the time, so acceleration and deacceleration processes exist as a result of differences occuring during the cloud life cycle (growing, shrinking, rebounding and collapsing processes); and second - the cloud shedding frequency is not equal to the cloud life frequency. Here we calculated the frequency using the data from Fig.16 and as we have 28 clouds existing in 200 frames, and each frame is made after 20μs, it means that we needed 4000μs to get 28 clouds, i.e. each cloud needs 4000μs/28=143μs as a shedding time. So the shedding frequency is $f_{C.shedding}$ = 7,000 Hz and it is not equal to that one in Fig.15, since in Fig.15 the shooting frequency is in the range between 4,748 Hz and 8,000 Hz (confidence interval). The cloud average life time, as presented in Fig.17 (Gaussian distribution), or consequently the average frequency of cloud life cycle is $f_{C.lifecycle}$ = (1/0.00021) = 4,762 Hz. This means that the shedding time is a part of the life time. According to data in Fig.17, the cloud life frequency is in interval $f_{C.lifecycle}$ = 3,636 Hz to 7,142 Hz (confidence interval).

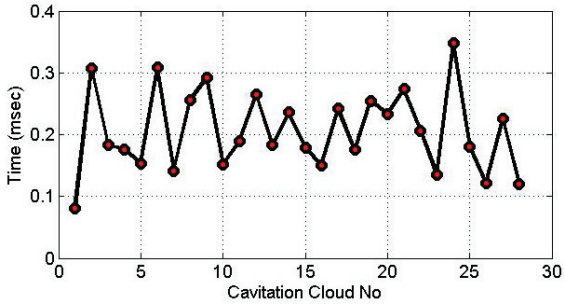

Figure 16. Cavitations Cloud Lifecycle.

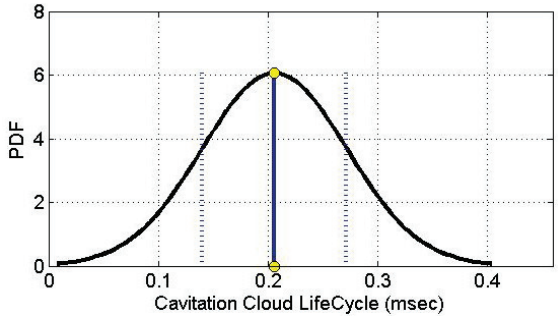

Figure 17. Gaussian probability distribution of estimated CC LIFECYCLE of cavitation clouds.

5. INFLUENCES OF HYDRODYNAMIC AND GEOMETRICAL CONDITIONS ON CAVITATION CLOUD BEHAVIOR

In this case five groups of images were processed and analysed. These groups of images were extracted from five movies for cavitating jets produced under different hydrodynamic and geometrical conditions. The obtained results were very sensitive to the projection angle, for example, the number of recognized cavitation clouds is very

sensitive to the θ^o, and this angle is the main parameter in Radon Transform. For this reason, the software was run many times in order to find the optimum angle. In general the obtained results show the dependency of behavior of cavitating jets and cavitation clouds on the parameters related to hydrodynamic and geometrical conditions. These results proved the validity of the proposed formula in previous work [6] (see Fig.18). The results are not presented here because of the space

6. COMPARISON BETWEEN THE FORMULA AND TRACES OF CC DYNAMICS BASED ON COMPUTED TOMOGRAPHY METHOD

The frequency of shedding/discharging of cavitation clouds produced by highly submeged cavitating water jets was calculated using computed tomography method and using the formula presented in previous work [6]. Fig.18 represents the frequencies calculated as a function of injection pressure and nozzle geometry based on traces of CC dynamics (computed tomography second method). Fig.18 shows good matching between the results obtained using the method based on traces of CC dynamics (computed tomography second method) and the one obtained using formula proposed in our previous work.

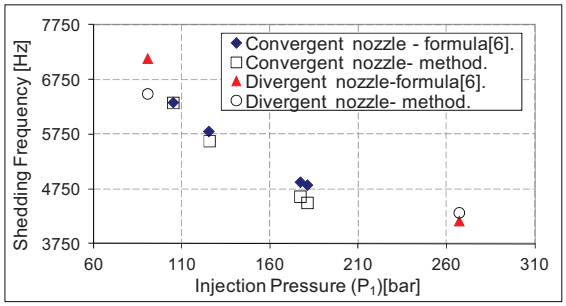

Figure 18. Influence of injection pressure (P_1) and nozzle geometry on the shedding frequency.

7. CONCLUSION

An experimental study was conducted to investigate the characteristics of cavitating water jet. It is clear that proposed approach (computerized tomography of cavitations clouds: Cavitations Clouds Dynamics Analysis based on cloud Computed Tomography approach – CCCT (Cavitations Clouds Computed Tomography) Method) brings radically new tool/platform for analysis of highly submerged cavitations jet.

The most important fact is that the series of isolated frames (captured by high speed camera) are now mathematically linked into a single variable which recovers lost information content. The obtained results show good matching with those established using proposed formula.

ACKNOWLEDGEMENT

Part of this work has been supported by the Serbian Ministry of Science and Technological Development under contract TR/35046.

REFERENCES

[1] Soyama H, et al, 1994, "High-Speed Cavitation-Cloud Observations Around High-Speed Submerged Water Jets", 2nd International Symposium on Cavitation, Tokyo Japan, pp. 225-230.

[2] Vijay MM, et al, 1991, "A Study of the Characteristics of Cavitating Water Jets by Photography and Erosion", Elsevier Science Publishers L td, Jet Cutting Technology, Proceedings of 10th International Conference, pp. 37-67.

[3] Ganippa LC, 2001, "Comparison of Cavitation Phenomena in Transparent Scaled-Up Single-Hole Diesel Nozzles, Fourth International Symposium on Cavitation, California Institute of Technology, Pasadena, CA USA ,CAV2001. http://cav2001.library.caltech.edu/162/00/Ganippa.pdf.

[4] Soyama H, et al, 1995, "High-Speed Cavitation-Cloud Observations Around High-Speed Submerged Water Jets", JSME International Journal, Series (B), Vol. 38, No. 2, pp. 245-251.

[5] Yamauchi Y, et al, 1996, "Formation of process of vortex ring cavitation in high-speed submerged water jet", Transactions of JSME (B), Vol. 62, pp. 72-78.

[6] Hutli E, Nedeljkovic M, 2008, "Frequency in Shedding/Discharging Cavitation Clouds Determined by Visualization of a Submerged Cavitating Jet", Journal of Fluids Engineering, Trans ASME, Vol. 130, pp. 561–568.

[7] Photron Apx Camera, http://www.photron.com/index.php

[8] Slice Reconstruction Radon Transform Informatics Homepages Server - University of Edinburgh.

[9] Otsu N, 1979, "A Threshold Selection Method from Gray-Level Histograms", IEEE Transactions on Systems, Man and Cybernetics, Vol. 9, pp. 62-66.

Conference on Modelling Fluid Flow (CMFF'12)
The 15th International Conference on Fluid Flow Technologies
Budapest, Hungary, September 4-7, 2012

NUMERICAL STUDY OF THE INCOMPRESSIBLE RICHTMYER-MESHKOV INSTABILITY. INTERFACE TRACKING METHODS ON GENERAL MESHES

Lluís JOFRE[1], Néstor BALCÁZAR [2], Oriol LEHMKUHL [2 3],
Jesús CASTRO [2], Assensi OLIVA [2]

[1] Corresponding Author. Heat and Mas Transfer Technological Center, Technical University of Catalonia, C/ Colom 11, 08222 Terrassa, Spain.
Tel.: (+34) 93 739 81 92, Fax: (+34) 93 739 89 20, E-mail: lluis@cttc.upc.edu
[2] Heat and Mas Transfer Technological Center, Technical University of Catalonia, C/ Colom 11, 08222 Terrassa, Spain.
Tel.: (+34) 93 739 81 92, Fax: (+34) 93 739 89 20, E-mail: cttc@cttc.upc.edu
[3] Termo Fluids S.L., Av. Jaquard 97 1-E, 08222 Terrassa, Spain.
Tel.: (+34) 93 783 61 13, E-mail: termofluids@termofluids.com

ABSTRACT

The numerical simulation of interfacial and free surface flows is a vast and interesting topic in the areas of engineering and fundamental physics, such as the study of liquid-gas interfaces, formation of droplets, bubbles and sprays, combustion problems with liquid and gas reagents, study of wave motion and others.

Many different methods for interface tracking exist, but Volume-of-Fluid and Level-Set methods are two of the most important. The Volume-of-Fluid preserves mass in a natural way but requires large computational resources. On the other hand, the Level-Set is not as accurate and mass conservative as the Volume-of-Fluid but is a faster way to track interfaces, representing them by the middle contour of a signed distance function.

The objective of this work is to analyze the advantatges and drawbacks of the Volume-of-Fluid and Level-Set methods by solving the incompressible two-liquid Richtmyer-Meshkov instability and to compare the results to experimental data.

Keywords: general mesh, interface tracking, multiphase flows, Richmyer-Meshkov instability

NOMENCLATURE

A	$[m^2]$	surface
C	$[-]$	volume fraction
$\underline{g}$	$[m/s^2]$	gravity
$\dot{m}$	$[kg/s]$	mass flux
$\underline{n}$	$[-]$	unit normal vector
p	$[Pa]$	pressure
t	$[s]$	time
$\underline{u}$	$[m/s]$	velocity vector
u	$[m/s]$	normal face velocity
V	$[m^3]$	volume
W	$[m]$	width
$\underline{x}$	$[m]$	position vector
μ	$[Pa \cdot s]$	dynamic viscosity
ρ	$[kg/m^3]$	density
$\underline{\omega}$	$[1/s]$	vorticity vector

Subscripts

c	cell
f	face
k	fluid
c_1, c_2	cells adjacent to face
P, F	nodes adjacent to face

Superscripts

CC	cell circumcenter
CG	cell center of gravity
f	face
n	discrete time level
$*$	predictor

1. INTRODUCTION

1.1. Richtmyer-Meshkov Instability

This work is focused on the study of the Richtmyer-Meshkov (RM) instability [1, 2]. Particularly, the RM instability of incompressible miscible liquids with two and three-dimensional (2D,3D) single-mode initial perturbations. The amplitude and velocity of the instability along time and vorticity is analyzed and compared to experimental data [3, 4]. The instability is solved using two different interface tracking methods: Volume-of-Fluid and Level-Set, and the momentum equation is discretizated by a staggered mesh scheme.

The RM instability occurs at a nearly planar interface separating two fluids that are impulsively accelerated in the direction normal to the interface, as a result of a impulsive body force or a passing shock wave. The initial development of the instability creates small amplitude perturbations which initially grow linearly with time. Followed by a nonlinear regime with bubbles appearing in the case of a light fluid penetrating a heavy fluid, and with spikes appearing in the case of a heavy fluid penetrating a light fluid.

The RM instabilities initiated with a single-mode 2D and 3D initial perturbations have been extensively studied and experimentally investigated beginning with the pioneering work of Richtmyer and Meshkov and lately by Niederhaus, Chapman and Jacobs. Experiments have verified the early time linear growth predicted by Richtmyer. However, no nonlinear solution capable of predicting the behavior from the early linear stages into the far nonlinear regime is available at the moment. Many researchers have developed nonlinear analyses [5], heuristic models [6] and analytical approaches [7] that capture some of the physics of the late-time asymptotic flow, but they all necessarily must incorporate empirical constants making them not general solutions.

1.2. Methods for interface tracking

The contact of different fluids or phases in motion, produces a thin region that separates them called interface. This kind of flows are named free surface or interfacial flows and are found in multiple fields such as engineering, fundamental physics, geophysics, etc. Typical examples of this phenomena are bubbles, drops, sprays, jets, waves, clouds and particularly the RM instability.

The numerical strategies used to track the motion of the interface between fluids are called interface tracking methods. There are many different methods, a general list classified in three main classes can be found in the literature by Scardovelli and Zaleski [8]. In particular, this work focuses in the Volume-of-Fluid (VOF) and Level-Set (LS) methods, since they are two of the most known and used.

The Volume-of-Fluid preserves mass in a natural way and presents no problem for reconnection or breakup of the interface but requires large computational resources. The first VOF implementations were presented in the 1970s for 2D cartesian meshes, being the method proposed by Hirt and Nichols [9] the reference one. In recent years, the method has been improved and adapted to 3D meshes, in a cartesian approach by Liovic et al. [10] and more generally to 3D cartesian and unstructured meshes by Jofre et al. [11].

On the other hand, the Level-Set is a fast way to track interfaces, representing them by the middle contour of a signed distance function, but its main drawback is the not conservation of mass. This method was first introduced in the 1980s by Osher and Sethian [12] for n-D general meshes but did not conserve mass. Recently, Olsson and Kreiss [13] have proposed a different approach for the method, based on previous works, in order to be mass conservative.

1.3. Discretizations of the Navier-Stokes equations

One of the main difficulties when solving the Navier-Stokes equations is the localization of the velocity grid points in order to avoid a checkerboard pressure field, due to the decoupling of the velocity and pressure fields present in the equations. This issue is more critical when high discontinuities are present in the domain, such as when multiphase flows or combustion problems are being solved. In order to solve this problem, there are two main mesh arrangements for the computation of the Navier-Stokes equations, the collocated and staggered schemes.

One of the first collocated schemes was presented by Rhie and Chow [14] for body-fitted meshes in the 1980s. In recent years, the scheme has been extended to unstructured meshes and improved to diminish the kinetic energy conservation error; i.g. changing the pressure gradient term by Mahesh et al. [15] and defining particular face mass fluxes that locally conserve mass by Lehmkuhl et al. [16]. The main characteristic of the scheme is that the velocity field is located at the same grid points as the pressure one, what can result in a checkerboard pressure problem when solving discontinuous flows like the RM instability.

In order to solve this problem, a staggered mesh arrangement is used in this work. This type of scheme is a numerical strategy where variables are located at different points within the mesh. Many different staggering schemes are possible. However, in this work we are interested in the scheme presented by Perot [17] since it is a generalization to unstructured meshes of the one originally presented by Harlow and Welch [18]. This scheme locates pressure at cell centers and normal velocity at cell faces. The main variable is the normal face velocity, then, velocity vectors at cell centers are interpolated from normal face velocities, in a particular form that conserves kinetic energy and momentum.

1.4. Objectives and novelty of the paper

The principal objective of this work is to demonstrate that computational fluid dynamics can be a good tool to study multiphase flows. In particular, the Richtmyer-Meshkov instability since no nonlinear solution capable of predicting the behavior at all stages has been found and the lack of generality of other heuristic models. On the other hand, it is an exigent test to check the performance of the self-developed implementations of the Volume-of-Fluid and Level-Set methods for 3D unstructured meshes, hence, allowing other more industry oriented problems to be afforded in the near future.

2. GOVERNING EQUATIONS

Interface tracking methods, such as Volume-of-Fluid and Level-Set, describe both fluids with one set of momentum equations and solve a volume fraction advection equation for the evolution of the interfaces between the two fluids.

The volume fraction color function $C_k(\underline{x})$ is defined as an identity function

$$C_k(\underline{x}) = \begin{cases} 1 & \text{if there is fluid k.} \\ 0 & \text{otherwise.} \end{cases} \quad (1)$$

Then, the discrete volume fraction of the kth fluid for a general volume is calculated as

$$C_k = \frac{\int C_k(\underline{x}) dV}{\int dV}, \quad (2)$$

it ranges from 0 to 1 and its sum over all k is unity.

If the flow is assumed to be incompressible and there is no surface tension between fluids, the volume fraction advection equation results in

$$\frac{\partial C_k}{\partial t} + \nabla \cdot (C_k \underline{u}) = 0 \quad (3)$$

and mass and momentum conservation are defined as

$$\nabla \cdot \underline{u} = 0, \quad (4)$$

$$\frac{\partial (\rho \underline{u})}{\partial t} + \nabla \cdot (\rho \underline{u}\underline{u}) = -\nabla p + \nabla \cdot (\mu(\nabla \underline{u} + \nabla \underline{u}^T)) + \rho \underline{g}, \quad (5)$$

where the fluid density and viscosity are evaluated as

$$\rho = \sum_k \rho_k C_k \quad \text{and} \quad \mu = \sum_k \mu_k C_k. \quad (6)$$

The solution of the momentum equation, Eq. (5), provides the velocity field used in the volume fraction advection equation, Eq. (3), to calculate the new volume fraction scalar field.

3. NUMERICAL MODEL

3.1. Volume fraction advection equation

The two interface tracking methods used in this work solve the volume fraction advection equation, Eq. (3), but they differ in the discretization and procedure followed to do so.

3.1.1. Volume-of-Fluid method

The VOF method discretizes the volume fraction advection equation, Eq. (3), for each cell as

$$C_k^{n+1} - C_k^n + \frac{1}{V_c} \sum_f \delta V_{k,f}^n = 0, \quad (7)$$

where the kth fluid volume flux across face f, $V_{k,f}^n$, is geometrically calculated from the total volume flux given by

$$\delta V_f = \underline{u}_f \cdot \underline{n}_f A_f \delta t = \sum_k \delta V_{k,f}. \quad (8)$$

Then, the volume fraction advection, Eq. (7), is solved for each fluid k in two steps: Interface Reconstruction and Advection. First, the interface is reconstructed by approximating its form to a geometric surface, this work reconstructs interfaces by planes using a Least Square Gradient (LSG) approach of the Youngs' method [19]. Once the interface is reconstructed, the advection step constructs volume fluxes at cell faces and cuts them by the reconstructed interface to compute the amount of fluid kth that is being fluxed through the face, this works uses a self-developed unstructured 3D unsplit advection algorithm. These two steps are explained in detail by Jofre et al. [11].

3.1.2. Level-Set method

The conservative LS method, proposed by Olsson and Kreiss [13], discretizes the volume fraction advection equation, Eq. (3), for each cell in a conservative form given by

$$C_k^{n+1} - C_k^n + \Delta t \sum_f C_{k,f}^n \underline{u}_f \cdot \underline{n}_f A_f = 0, \quad (9)$$

where $C_{k,f}$ is evaluated by a first-order upwind plus flux limiter (FUDFL) convective numerical scheme [20].

The solution of the discretizated volume fraction equation, Eq. (9), provides a non-uniform thickness interface due to numerical diffusion. Hence, an artificial compression of the interface is applied, in order to mantain the profile and thickness of the interface constant, by solving to steady state the reinitialization equation

$$\frac{\partial C_k}{\partial \tau} + \nabla \cdot C_k(1 - C_k)\underline{n} = \varepsilon \nabla \cdot \nabla C_k, \quad (10)$$

where $\underline{n} = \frac{\nabla C_k}{||\nabla C_k||^2}$, $C_k(1 - C_k)\underline{n}$ is a compressive flux evaluated by a central difference (CD) convective numerical scheme [21], τ is the reinitialization time and $\varepsilon \nabla \cdot \nabla C_k$ is an artificial diffusion term added to avoid discontinuities.

3.2. Multiphase momentum equation

Multiphase flows present high discontinuities in the domain due to the density difference between fluids. Therefore, in order to avoid possible spurious pressure modes, the momentum equation is discretizated following the unstructured staggered formulation by Perot [17]. This mesh scheme, instead of evaluating velocities at cell centers, evolves normal face velocities, $u = \underline{u} \cdot \underline{n}_f$, in time. The velocity-pressure coupling is solved by using a fractional step procedure [22] written as

$$\underline{u}^{n+1} - \underline{u}^* = -\frac{\Delta t}{\rho^{n+1}} \nabla p^{n+1}. \quad (11)$$

The predictor normal face velocity, $u^* = \underline{u}^* \cdot \underline{n}_f$, is evaluated for each face from

$$T + C = D + F, \quad (12)$$

$$T \equiv \frac{\rho_f^{n+1} u^* - \rho_f^n u^n}{\Delta t} W^f A_f,$$
$$C \equiv \underline{n}_f \cdot (W_{c_1}^f \underline{C}_{c_1}^n + W_{c_2}^f \underline{C}_{c_2}^n) A_f,$$
$$D \equiv \underline{n}_f \cdot (W_{c_1}^f \underline{D}_{c_1}^n + W_{c_2}^f \underline{D}_{c_2}^n) A_f,$$
$$F \equiv \underline{n}_f \cdot (W_{c_1}^f \underline{F}_{c_1}^n + W_{c_2}^f \underline{F}_{c_2}^n) A_f,$$

where geometric parameters are shown in Fig. 1, *T*, *C*, *D* and *F* stand for transient, convective, incompressible diffusive and body force cell-centered terms defined as

$$\underline{C}_c = \frac{1}{V_c} \sum_f \dot{m}_f \underline{u}_f, \tag{13}$$

$$\underline{D}_c = \frac{1}{V_c} \sum_f \mu_f \frac{\underline{u}_F - \underline{u}_P}{W^f} A_f, \tag{14}$$

$$\underline{F}_c = \rho_c \underline{g}, \tag{15}$$

and $\underline{u}_f$ is the convected face velocity evaluated by an upwind convective numerical scheme.

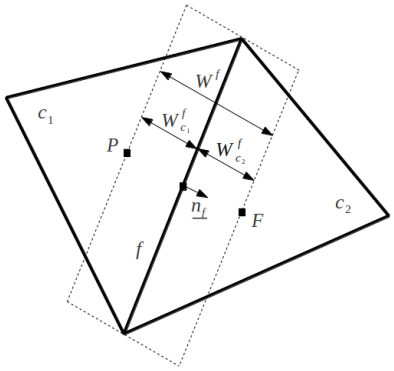

Figure 1. Notation for the unstructured staggered mesh scheme on a 2D unstructured mesh.

The pressure Poisson's equation, applying the divergence operator on both sides of Eq. 11, results in

$$\sum_f \hat{u}^* A_f = \frac{\Delta t}{\rho^{n+1}} \sum_f \frac{p_F^{n+1} - p_P^{n+1}}{W^f} A_f, \tag{16}$$

which is solved by a preconditioned conjugate gradient solver [23] giving the new pressure field. Then, new normal face velocity equals

$$u^{n+1} - u^* = -\frac{\Delta t}{\rho_f^{n+1}} \frac{p_F^{n+1} - p_P^{n+1}}{W^f}. \tag{17}$$

Finally, new cell centered velocity is interpolated from normal face velocities as

$$\underline{u}_c^{n+1} = \frac{1}{V_c} \sum_f (\underline{x}_f^{CG} - \underline{x}_c^{CC}) \hat{u}^{n+1} A_f. \tag{18}$$

4. RM INSTABILITY RESULTS

The instability simulations are based on the 2D and 3D experiments of Niederhaus and Jacobs [3] and Chapman and Jacobs [4], respectively. The 2D tank is 119.9 mm in width and 254.4 mm in height, on the other hand, the dimensions for the 3D case are 72.6 mm in width and depth and 250 mm in height. The lighter upper fluid and the heavier bottom fluid result in an Atwood number equal to $A = (\rho_2 - \rho_1)/(\rho_2 + \rho_1) = 0.1587$. At the beginning of the calculations a small periodical disturbance of the surface shape with 2D amplitude $a_0 = 0.23/k$ and wavelength $\lambda = 82.6$, and 3D amplitude $a_0 = 0.38/k$ and wavelength $\lambda = 48.4$, where $k = 2\pi/\lambda$, are incorporated to make the system unstable. Then, the initial disturbances are approximated as 2D $\eta = a_0 \cdot \sin(kx)$ and 3D $\eta = a_0[sin(kx) + sin(ky)]$. The experimental acceleration pulse imparted to the fluids is approximated as a triangular shape with a duration of 26 ms, a peak magnitude of 50g, and an integrated impulse ΔV of 6.4 m/s.

Variables used to compare numerical results to experimental ones are defined in Fig. 2. Where a, a_b and a_s stand for total, bubble and spike amplitudes and $\dot{a}$, $\dot{a}_b$ and $\dot{a}_s$ represent total, bubble and spike velocities.

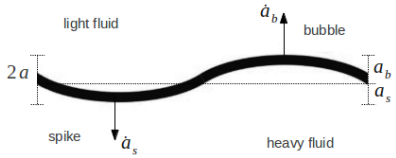

Figure 2. Schematics of the interface variables used to analyze the RM instability.

The two interface tracking methods previously presented, VOF and LS, are used to solve the instability and results are compared to experimental ones. The 2D and 3D cases are numerically solved using cartesian and unstructured meshes with average grid size of 0.0025; i.e. 4900 cells (2D test) and 84000 cells (3D test). A fixed time step of $5.0e^{-4}$ seconds is used to evolve discretized equations in time. The numerical conservation of kth fluid volume in relative value, defined as the amount of volume lost or gained respect to the initial one divided by the initial one, is approximately $1.0e^{-6}$ and $1.0e^{-4}$ when using VOF and LS in unstructured meshes, respectively.

Figures 3 and 4 are a sequence of images showing the evolution of the 2D and 3D instabilities using the two interface tracking methods, and compared to the Planar Laser-Induced Fluorescence (PLIF) images from experiments. The impulsive acceleration in these experiments is directed from the heavier fluid into the lighter one. Thus, the observed amplitude changes sign before growing. Immediately after inversion, the instability retains a sinusoidal shape. Though, with time, vortices begin to form producing the typical mushroom pattern of the RM instability.

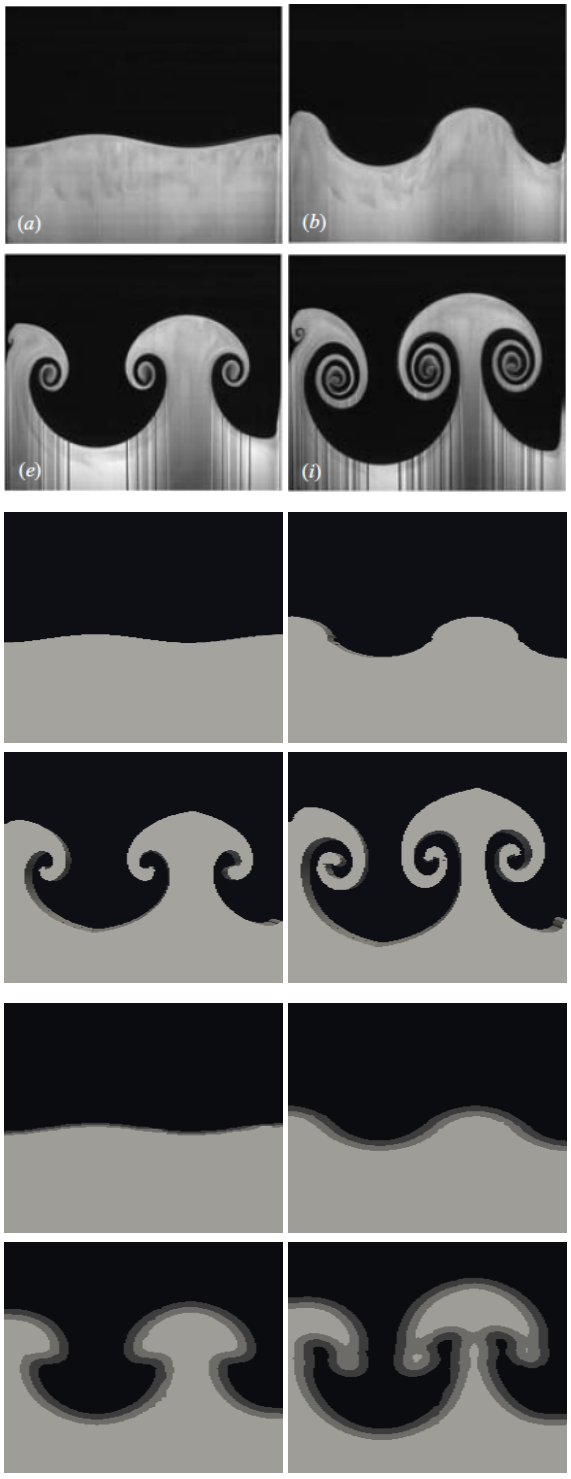

Figure 3. Three blocks of images showing the bottom fluid of the 2D RM instability tests.

Figure 3 contains three blocks of images showing the bottom fluid in the 2D RM instability tests. Blocks: (top) PLIF images from the Niederhaus and Jacobs [3] experiment, (center) interface reconstruction planes using cartesian mesh and VOF method and (bottom) volume fraction contours using cartesian mesh and LS method. Times are: (first) -14 ms, (second) 102 ms, (third) 353 ms and (fourth) 686 ms.

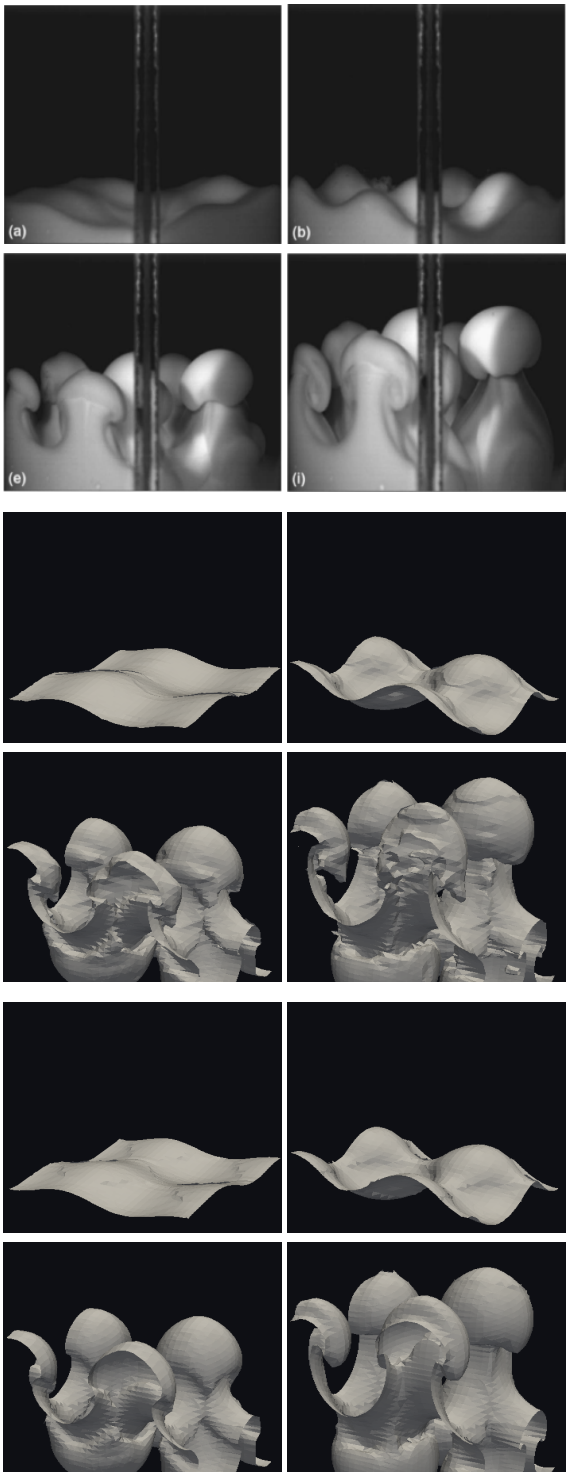

Figure 4. Three blocks of images showing the bottom fluid of the 3D RM instability tests.

Three blocks of images representing the bottom fluid in the 3D RM instability tests are shown in Figure 4. Blocks: (top) PLIF images from the Chapman and Jacobs [4] experiment, (center) 0.5 volume fraction contour using unstructured mesh and VOF and (bottom) 0.5 volume fraction contour using unstructured mesh and LS. Times are: (first) -33 ms, (second) 50 ms, (third) 300 ms and (fourth) 633 ms.

4.1. *Amplitude measurements*

Figures 5 and 6 show the 2D and 3D RM instability's amplitude along time for experimental and numerical results. These amplitude measurements are made dimensionless as done in the experiments of Niederhaus, Chapman and Jacobs [3, 4], by scaling amplitude with wave number k and time with wave number and theoretical initial growth rate $\dot{a}_0$.

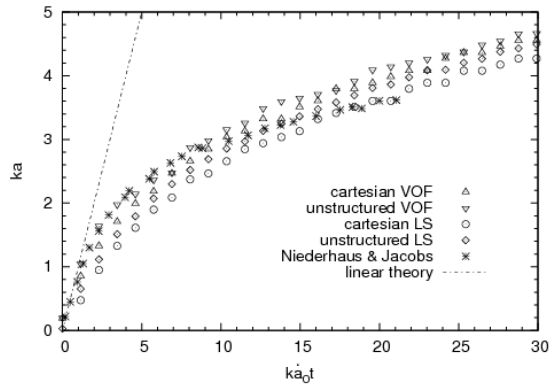

Figure 5. Plot of nondimensional amplitude versus nondimensional time for the 2D tests.

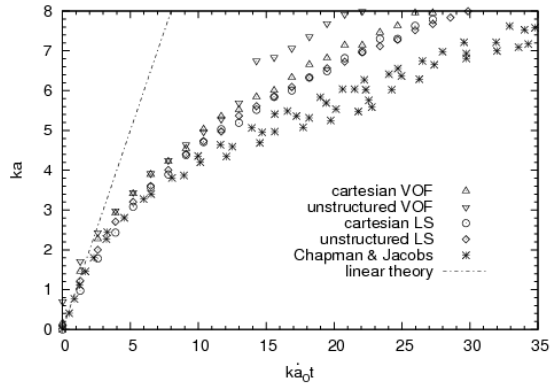

Figure 6. Plot of nondimensional amplitude versus nondimensional time for the 3D tests.

The linear theory that describes the early stages of the RM instability, developed by Richtmyer [1], is shown to be satisfied until nondimensional time 2 - 3 both by experimental results and numerical solutions from the interface tracking methods and mesh configurations used in this work. On the other hand, numerical results of the late time instability's amplitude follow the pattern of experimental ones but they are not accurate enough, though, it is believed that numerical results would merge with experimental ones if meshes are densified.

4.2. *Velocity measurements*

The velocity, defined as the average of bubble and spike velocities, for the 2D and 3D RM instability's experimental and numerical results is plotted along time in Figures 7 and 8. The velocity is non-dimensionalized dividing by theoretical initial growth rate $\dot{a}_0$.

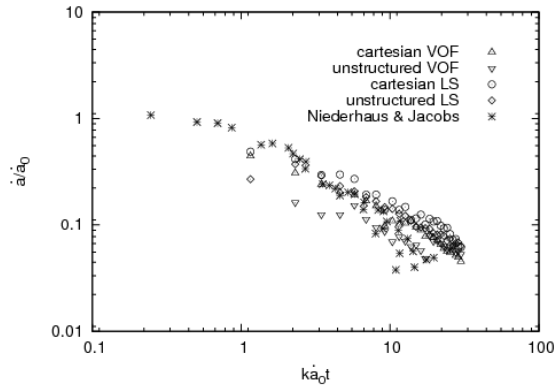

Figure 7. Plot of nondimensional velocity versus nondimensional time for the 2D tests

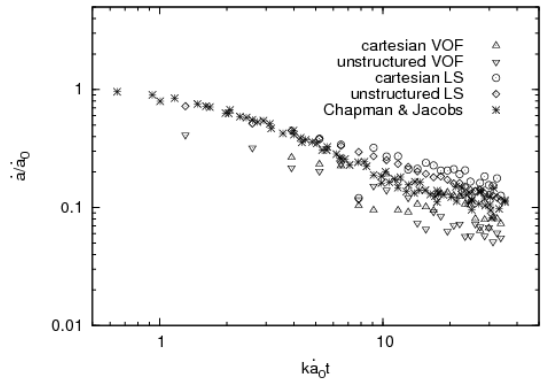

Figure 8. Plot of nondimensional velocity versus nondimensional time for the 3D tests.

It is observed, from experimental and numerical results, that 3D velocities present slightly faster nonlinear growth than the 2D ones. This 2D - 3D difference in velocity behaviour is due to the configurations of the vorticity fields: 2D vortexs are stationary while 3D vortex rings move alternately upward and downward as it is shown in Figures 9 and 10. As a result, 2D interface velocity decays with time as it is pushed away from the vortex centers. On the other hand, in the 3D flow the interface velocity is the sum of a decaying component similar to the 2D flow and the vortex ring velocity associated to the vortex stretching mechanism. Thus, with time, interface velocity approaches the vortex ring one.

4.3. *Vorticity*

The vorticity equation, simplified for incompressible flows of inviscid fluids and conservative body forces, is written as

$$\frac{D\underline{\omega}}{Dt} = (\underline{\omega} \cdot \nabla)\underline{u} + \frac{1}{\rho^2}\nabla\rho \times \nabla p, \tag{19}$$

where vorticity is defined as $\underline{\omega} = \nabla \times \underline{u}$, the term on the left-hand side is the material derivative of the vorticity

vector that describes the rate of change of angular acceleration of the fluid, first term on the right-hand side describes the stretching or tilting of vorticity due to velocity gradients and the second term is the baroclinic mechanism which accounts for changes in vorticity due to intersectioning of density and pressure isosurfaces.

In the RM instabilities studied in this work, vorticity is created during the impulsive acceleration by the baroclinic term of Eq. 19. In detail, the pressure gradient during the impulsive acceleration is hydrostatic and thus oriented in the direction of the acceleration while the density gradient is perpendicular to the fluid interface. In the 2D instability case the distribution of these gradients result in the formation of vortices oriented perpendicular to the viewing plane, which are shown in Fig. 9. The 3D case, however, results in the vorticity distribution of Fig. 10, which consists of an array of vortex rings.

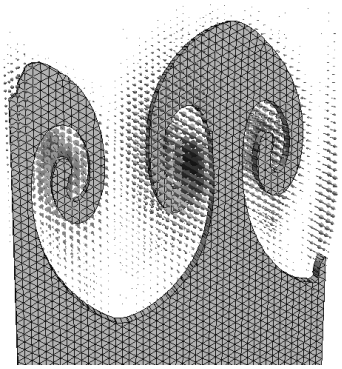

Figure 9. Vorticity vectors, VOF planes and mesh of the 2D RM instability test.

The difference between 2D and 3D velocity behaviour due to the vortex stretching mechanism, stated in Section 4.2, is explained by calculating the first term on the right-hand side of Eq. 19 using Figures 9 and 10. The 2D case results in a null vector space, since $\underline{\omega} = (0, 0, \omega_z)$ and the zth derivatives of the velocity tensor are equal to zero. However, the 3D case presents two main vectors with opposite senses at the crests of the bubbles and spikes, meaning that the interface of the instability is being stretched and its amplitude increased by the vortex stretching mechanism.

5. CONCLUSIONS

In this work an assesment of two different 3D interface tracking algorithms has been done. The VOF and LS interface tracking methods for 3D general meshes have been shown to correctly calculate the evolution of 2D and 3D RM instabilities initiated with single-mode perturbations. Hence, CFD for multiphase flow is proven to be an excellent tool to study RM instabilities. In particular, the self-developed interface tracking methods for 3D unstructured meshes present good results, encouraging the authors to test them against more industry oriented multiphase problems.

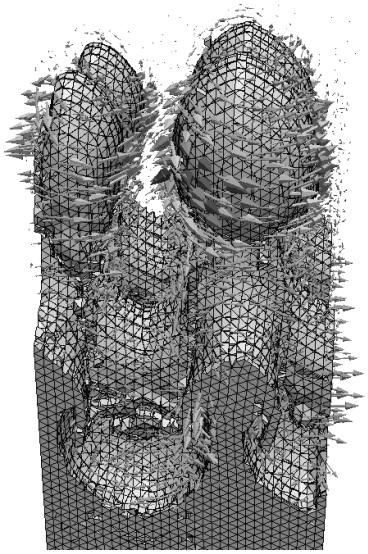

Figure 10. Vorticity vectors, VOF planes and mesh of the 3D RM instability test.

The two interface tracking methods present good overall results in cartesian and unstructured meshes, see Figures 3 and 4. In particular, numerical evolution in time of interface amplitude and velocity correspond to the experimental physical behavior, shown from Fig. 5 to 8. Results using the VOF method present better detail accuracy, specifically at vortex tips, but require large computational resources, while results from LS are able to accurately calculate the main pattern of the flow in a fast way.

Analysis of the vorticity distributions, applying the vorticity equation to the results obtained from the solution of the 2D and 3D RM instabilities, reveal a main physical difference between 2D and 3D cases. In the 2D case, the stretching term of the vorticity equation due to velocity gradients is zero, while in the 3D case, the term presents two main vectors with opposite senses at the crests of bubbles and spikes. As a result, the 2D interface velocity decays with time as it is pushed away from the vortex centers, however, in the 3D flow the interface velocity approaches that of the vortex ring associated to the vortex stretching mechanism.

ACKNOWLEDGEMENTS

This work has been financially supported by the Ministerio de Ciencia e Innovación, Spain (ENE-2010-17801), a FPU grant by the Ministerio de Educación, Spain (AP-2008-03843) and by Termo Fluids S.L.

The authors would like to acknowledge sincerely Jeffrey W. Jacobs, Journal of Fluid Mechanics and Physics of Fluids for their permission to partially reproduce some images, specifically the PLIF images of the 2D and 3D RM instability in Figures 3 and 4.

References

[1] Richtmyer, R.D., 1960, "Taylor Instability in Shock Acceleration of Compressible Fluids", *Communications on Pure and Applied Mathematics*, Vol. 13(2), pp. 297-319.

[2] Meshkov, E.E., 1969, "Instability of the Interface of Two Gases Accelerated by a Shock Wave", *Izv. Ross. Akad. Nauk, Mekh. Zhidk. Gaza*, Vol. 4(5), pp. 101-104.

[3] Niederhaus, C.E. and Jacobs, J.W., 2003, "Experimental Study of the Richtmyer-Meshkov Instability of Incompressible Fluids", *Journal of Fluid Mechanics*, Vol. 485, pp. 243-277.

[4] Chapman, P. R. and Jacobs, J. W., 2006, "Experiments on the Three-Dimensional Incompressible Richtmyer-Meshkov Instability", *Physics of Fluids*, Vol. 18(7).

[5] Zhang, Q. and Sohn, S., 1999, "Quantitative Theory of Richtmyer-Meshkov Instability in Three Dimensions", *ZAMP*, VOl. 50(1).

[6] Oron, D., Arazi, L., Kartoon, D., Rikanati, A., Alon, U. and Shvarts, D., 2001, "Dimensionality Dependence of the Rayleigh-Taylor and Richtmyer-Meshkov Instability Late-Time Scaling Laws", *Physics of Plasmas*, Vol. 8(6), pp. 2883-2890.

[7] Goncharov, V. N., 2002, "Analytical Model of Nonlinear, Single-Mode, Classical Rayleigh-Taylor Instability at Arbitrary Atwood Numbers", *Phys. Rev. Lett.*, Vol. 88(13), pp. 134502-134506.

[8] Scardovelli, R. and Zaleski, S., 1999, "Direct Numerical Simulation of Free-Surface and Interfacial Flow", *Annual Review of Fluid Mechanics*, Vol. 31(-), pp. 567-603.

[9] Hirt, C. W. and Nichols, B. D., 1981, "Volume of fluid (VOF) Method for the Dynamics of Free Boundaries", *Journal of Computational Physics*, Vol. 39(5), pp. 201-225.

[10] Liovic, P., Rudman, M., Liow, J.L., Lakehal, D. and Kothe, D., 2006, "A 3D Unsplit-Advection Volume Tracking Algorithm with Planarity-Preserving Interface Reconstruction", *Computers and Fluids*, Vol. 35(10), pp. 1011-1032.

[11] Jofre, L., Lehmkuhl, O., Castro, J. and Oliva A., 2010, "A PLIC-VOF Implementation on Parallel 3D Unstructured Meshes", Proc. *Fifth European Conference on Computational Fluid Dynamics*, pp. 1-15.

[12] Osher, S. and Sethian, J., 1988, "Fronts Propagating with Curvature Dependent Speed: Algorithms Based on Hamilton-Jacobi Formulations", *Journal of Computational Physics*, Vol. 79, pp. 12-49.

[13] Olsson, E. and Kreiss, G., 2005, "A conservative Level Set method for two phase Flow", *Journal Computational Physics*, Vol. 210, pp. 225-246.

[14] Rhie, C.M. and Chow, W.L., 1983, "Numerical Study of th Turbulent Flow Past an Airfol with Trailing Edge Separation", *AIAA Journal*, Vol. 21, pp. 1525-1532.

[15] Mahesh, K., Constantinescu, G. and Moin, P., 2004, "A Numerical Method for Large-Eddy Simulation in Complex Geometries", *Journal of Computational Physics*, Vol. 197, pp. 215-240.

[16] Lehmkuhl, O., Borrell, R., Pérez-Segarra, C.D. and Oliva, A., 2009, "Direct numerical simulations and symmetry-preserving regularization simulations of the flow over a circular cylinder at Reynolds number 3900", Proc *VI International Symposium on Turbulence, Heat and Mass Transfer*, pp. 325-328.

[17] Perot, B., 2000, "Conservation Properties of Unstructured Staggered Mesh Schemes", *Journal of Computational Physics*, Vol. 159, pp. 58-89.

[18] Harlow, F. H. and Welch, J. E., 1965, "Numerical Calculation of Time-Dependent Viscous Incompressible Flow of Fluid with Free Surface", *Physics of Fluids*, Vol. 8(12), pp. 2182-2189.

[19] Youngs, D.L., 1982, "Time-Dependent Multi-Material Flow with Large Fluid Distortion", Proc *Numerical Methods for Fluid Dynamics Conference*, pp. 273-285.

[20] Sweby, P.K., 1984, "High Resolution Schemes using Flux Limiters for Hyperbolic Conservation Laws", *SIAM Journal of Numerical Analysis*, Vol. 21(5), pp. 995-1011.

[21] Yeoh, G.H. and Tu, J., 2009, *Computational Techniques for Multiphase Flows*, Elsevier Science Publishing Co. Inc.

[22] Chorin, A.J., 1968, "Numerical Solution of the Navier-Stokes Equations", *Journal of Computational Physics*, Vol. 22, pp. 745-762.

[23] Shewchu,k J.R., 1994, "An Introduction to the Conjugate Gradient Method without the Agonizing Pain", *Technical Report* Carnegie Mellon University.

Conference on Modelling Fluid Flow (CMFF'12)
The 15th International Conference on Fluid Flow Technologies
Budapest, Hungary, September 4-7, 2012

NUMERICAL MODELLING OF SINGLE PARTICLE DRYING IN A STREAM OF HOT AIR

Robin SCHMIDT[1], Petr A. NIKRITYUK [2],

[1] Corresponding Author. CIC Virtuhcon Technische Universität Bergakademie Freiberg. Fuchsmühlenweg 9, 09596 Freiberg, Germany. Tel.: +49 3731 39-4273, Fax: +49 3731 39-4555, E-mail: robin.schmidt@vtc.tu-freiberg.de
[2] CIC Virtuhcon Technische Universität Bergakademie Freiberg E-mail: petr.nikrityuk@vtc.tu-freiberg.de

ABSTRACT

This work is devoted to the development of a CFD-based model and a so-called sub-grid model for the modelling of the convective drying of a single porous coal particle moving in a hot air atmosphere. The CFD-based model utilizes a continuum approach, where the mass, species, momentum and energy conservation equations are solved numerically for gas and solid phase using a fixed Eulerian grid. Based on the results of the numerical simulations a sub-grid model is developed. This model uses the so-called receding core assumption. The distinguished feature of the sub-grid model is its ability to take into account the effect of the Stefan flow on the mass transfer inside the particle. The validation of the sub-grid model against experimental data published recently (Zhang & You [1]) reveals good agreement.

Finally, we studied the influence of drying conditions such as the ambient temperature (413–1000 K) and particle velocity on the drying process using the CFD and the sub-grid model.

Keywords: Drying, Particles, Transient Heat and Mass Transfer

NOMENCLATURE

A	$[m^2]$	surface
D	$[m^2/s]$	diffusion coefficient
K	$[1/m^2]$	permeability
M	$[kg/mol]$	molar mass
$\dot{Q}$	$[J/s]$	heat flux
R	$[m]$	radius
S	[-]	saturation
T	$[K]$	temperature
V	$[m^3]$	volume
Y	$[kg/kg]$	mass fraction of vapour
X	$[kg/kg]$	dry base moisture content
c_p	$[J/(kg\,K)]$	heat capacity
$\underline{\dot{m}}$	$[kg/(m^2\,s)]$	mass flux
$\dot{m}_{\mathrm{v}}$	[kg/$(m^3\,s)$]	evaporating mass flux
p	$[Pa]$	pressure
t	$[s]$	time
$\underline{u}$	$[m/s]$	velocity
α	$[J/(K\,m)]$	heat transfer coefficient
$\Delta_{\mathrm{v}}h$	$[J/kg]$	enthalpy of evaporation
ϵ	[–]	volume fraction / extinction
λ	$[W/(K\,m)]$	heat conductivity
μ	$[Pa\,s]$	dynamic viscosity
ρ	$[kg/m^3]$	density
σ	$[N/m]$	surface tension

Subscripts

0	initial, base
amb	ambient
av	averaged
c	capillar
d	dry
diff	diffusive
eff	effective
eq	equilibrium
g	gas
in	inlet
l	liquid
m	mean
p	particle
rad	radiation
rel	relative
s	solid
ss	stair—step
v	evaporation; vapour
w	wet

1 INTRODUCTION

Solids are dried in many technological contexts. For example drying is employed in food processing, pharmaceutics and the building industry. But drying is not only important to produce the final good it, is also a step in industrial processes such as burning or the partial oxidation of coal or biomass. It is estimated that

12% of the total industrial energy consumption goes towards drying [2].

To understand the drying of porous materials it is necessary to describe the heat and mass transfer within the solid and in the boundary layer. For water transport in porous media three basics mechanisms are known, namely vapour diffusion, capillary flow and evaporation—condensation [3]. For a review of different mathematical models applied to drying we refer to the work [4]. Following this review the so-called semi-empirical coefficient for the effective liquid diffusivity was used to model the moisture transport to the particle surface, where the evaporation occurred. The pioneering works in this area were introduced by Lewis [5] and Sherwood [6] almost 90 years ago. Recently a similar method was utilized by Queiroz & Nebra to model the drying of bananas [7]. A model based on effective diffusivities was summarized by Chen & Pei [8].

The next generation of drying models was introduced by Whitaker [9], who utilized the volume averaging technique to describe drying processes using the continua conservation equations. The advantages of this model in comparison to the theory described by Luikov [10] is that the assumptions are very clear, the physics of the model is represented better and the parameters are all well defined. Adopting Whitaker's approach, recently, Zhang and You [1] investigated numerically the drying of large lignite coal particles using volume-averaged equations written in spherical coordinates. The results of the numerical simulations were validated against experiments at different drying conditions varying the particle size, ambient temperature, ambient air humidity and air velocity. Good agreement was achieved. Strictly speaking, the work of Zhang & You [1] demonstrated the benefits of volume-averaging methods applied to the modelling of different transport phenomena inside the porous media.

Finally it should be noted that in spite of significant progress in the numerical modelling of a moving single particle drying in a hot environment, there are few works about the modelling of many particles drying. This fact is explained by the computational expense of such simulations, which have a multiscale character. One of the most promising solutions to this problem is to use discrete particle models (UDPM)[11]. To overcome the multi-scale character of the problem and to reduce the computational time, the so-called *subgrid* models are used. In particular, the model used most often for drying is the *receding core* model; for detail see the works of Chen et al. [12, 11]. In this work we adopt the receding core model to describe the drying of a single coal particle at different ambient conditions. The distinguishing feature of the model we developed is its validations and tuning against a detailed CFD-model based on the volume-averaged conservation equations. Additionally we validated our subgrid model against experimental data published in the literature.

2 Problem Formulation

The general setup of the system is shown in Fig. 1. A wet particle with a radius R=2 mm is placed in a system with the dimensions $L_1 = 140\,R \times L_2 = 10\,R$. The centre of the particle is set to $r = 2/7\,L_1$ and $z = 0$. The convective flow is set in z-direction with the inlet velocity u_{in}. The ambient gas is mainly nitrogen with a small amount of vapour, $Y_{\mathrm{in}} = 1 \cdot 10^{-3}$.

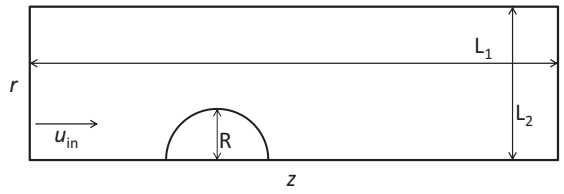

Figure 1. Sketch of the system for the convective drying of a single particle

The particle drying was investigated at inlet temperatures T_{in} in the range of 413.15 to 1000 K. To determine the effect of the heat transfer on the drying process, different inlet velocities u_{in} were used and the flow condition was described by the inlet Reynolds number $\mathrm{Re}_{\mathrm{in}} = \frac{u_{\mathrm{in}}\,\rho_{\mathrm{in}}\,2R}{\mu}$ with the inlet density ρ_{in}.

To proceed with the governing equations the following assumptions have been made. The flow is incompressible and Newtonian; the gas flow inside the pores is laminar; gas radiation is neglected; the evaporation energy is constant; the gas viscosity is constant; the continuum model is capable of describing the heat and mass flux inside the particle and the buoyancy is neglected.

3 Mathematical Models

3.1 CFD-Model

To model the evaporation inside the particle a continuum model is used. The big advantage of this model is that the evaporation and water transport inside the particle are considered, but the porous structure does not need to be resolved on the computational grid. The influence of the different phases on the properties were expressed using volume-weighted properties. Figure 2 provides a schematic view of the micro-structure of the particle.

The system consists of three phases, the stationary coal matrix (s), the liquid water inside the pores (l) and the gas phase (g) as a mixture of vapour and nitrogen. Bound water is not considered and all moisture is handled as liquid water inside the pores. The volume fractions of the different phases are defined as

$$\epsilon_{\mathrm{s}} = \frac{V_{\mathrm{s}}}{V_{\mathrm{av}}}; \quad \epsilon_{\mathrm{l}} = \frac{V_{\mathrm{l}}}{V_{\mathrm{av}}}; \quad \epsilon_{\mathrm{g}} = \frac{V_{\mathrm{g}}}{V_{\mathrm{av}}}; \quad \sum \epsilon_i = 1 \quad (1)$$

The intrinsic $\langle \phi_{\mathrm{i}} \rangle$ and spatial $\langle \phi_{\mathrm{i}} \rangle^{\mathrm{i}}$ average are correlated by the volume fraction ϵ_{i} of the phase i in

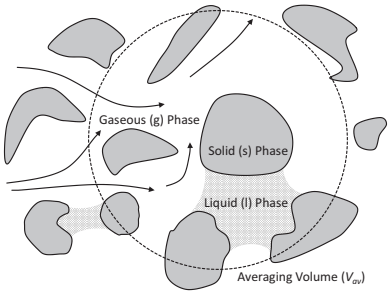

Figure 2. Microscopic structure of the wet porous body with the gas (g), solid (s) and liquid (l) phases, the averaging region is marked with a circle, adapted from [13, 1]

the following way:

$$\langle \phi_{\mathrm{i}} \rangle = \epsilon_{\mathrm{i}} \, \langle \phi_{\mathrm{i}} \rangle^{\mathrm{i}} \tag{2}$$

The governing equations for the porous particle and the surrounding gas phase, where $\dot{m}_{\mathrm{v}} = 0$ and $\epsilon_{\mathrm{g}} = 1$, are [13, 14]:

Continuity Equation:

$$\nabla \cdot \langle \vec{u}_{\mathrm{g}} \rangle = \dot{m}_{\mathrm{v}} \, (1/\rho_{\mathrm{g}} - 1/\rho_{\mathrm{l}}) \tag{3}$$

Impulse Conservation Equation:

$$\rho_{\mathrm{g}} \frac{\partial \langle \underline{u}_{\mathrm{g}} \rangle}{\partial t} + (\rho_{\mathrm{g}} \, \langle \underline{u}_{\mathrm{g}} \rangle \cdot \nabla) \langle \underline{u}_{\mathrm{g}} \rangle = - \nabla p + \mu \nabla^2 \langle \underline{u}_{\mathrm{g}} \rangle - \mu \langle \underline{u}_{\mathrm{g}} \rangle / K_g \tag{4}$$

The gas permeability of the porous body is the product of the base permeability ($K_{\mathrm{g},0} = 2 \cdot 10^{-12} \, m^2$ [1]) and the relative permeability ($K_{\mathrm{g,rel}}$): $K_{\mathrm{g}} = K_{\mathrm{g},0} \cdot K_{\mathrm{g,rel}}$ The relative permeability is a function of the pore saturation S which is the ratio of the liquid water volume to the total pore volume V_{pores}:

$$S = V_{\mathrm{l}} / V_{\mathrm{pores}} = \epsilon_{\mathrm{l}} / (1 - \epsilon_{\mathrm{s}}) \tag{5}$$

The relative permeability of the gaseous phase is then calculated as follows [15]:

$$K_{\mathrm{g,rel}} = (1 - S)^3 \tag{6}$$

The term $\mu \langle \underline{u}_{\mathrm{g}} \rangle / K_g$ of Eq. (4) is not considered in the gas phase around the particle.

To avoid numerical problems, which can arise from K_{g} being to low (see Eq. (4)), the permeability is calculated as follows:

$$K_{\mathrm{g}} = \mathrm{MAX} \left(\frac{(\Delta x)^2}{1 \cdot 10^4} ; \frac{(\Delta x)^2}{1 \cdot 10^2} \cdot K_{\mathrm{g,rel}} \right) \tag{7}$$

with Δx as the side length of the control volume inside the particle.

Energy Conservation Equation:

$$\begin{aligned} &(\rho c_p)_{\mathrm{eff}} \frac{\partial T}{\partial t} + (\rho \, c_p)_{\mathrm{g}} \nabla \cdot \left(\langle \underline{u}_g \rangle T \right) \\ &+ (\rho \, c_p)_{\mathrm{l}} \nabla \cdot \left(\langle \underline{u}_l \rangle T \right) \\ &= \nabla \cdot (\lambda_{\mathrm{eff}} \nabla T) - \dot{m}_{\mathrm{v}} \Delta_{\mathrm{v}} h + \dot{Q}_{\mathrm{rad}} \end{aligned} \tag{8}$$

The parameters ρ_{eff}, $c_{p,\mathrm{eff}}$, λ_{eff} are the effective density, heat capacity and thermal conductivity:

$$(\rho c_p)_{\mathrm{eff}} = \epsilon_{\mathrm{s}} \rho_{\mathrm{s}} c_{p,\mathrm{s}} + \epsilon_{\mathrm{l}} \rho_{\mathrm{l}} c_{p,\mathrm{l}} + \epsilon_{\mathrm{g}} \rho_{\mathrm{g}} c_{p,\mathrm{g}} \tag{9}$$

$$\lambda_{\mathrm{eff}} = \epsilon_{\mathrm{s}} \lambda_{\mathrm{s}} + \epsilon_{\mathrm{l}} \lambda_{\mathrm{l}} + \epsilon_{\mathrm{g}} \lambda_{\mathrm{g}} \tag{10}$$

$$\epsilon_s = 1 - \epsilon_{\mathrm{g,d}}; \;\; \epsilon_l = X_{\mathrm{l}} \rho_{\mathrm{s}} \epsilon_{\mathrm{s}} / \rho_{\mathrm{l}}; \;\; \epsilon_g = 1 - \epsilon_{\mathrm{s}} - \epsilon_{\mathrm{l}} \tag{11}$$

with $\epsilon_{\mathrm{g,d}}$ as the volume fraction of the dry media.

The radiative heat transfer $\dot{Q}_{\mathrm{rad}}$ is only activated in the surface cells of the particle:

$$\dot{Q}_{\mathrm{rad}} = A_{\mathrm{eff}} \epsilon_{\mathrm{rad}} \, \sigma \cdot (T_{\mathrm{amb}}^4 - T^4) \tag{12}$$

with the ambient temperature T_{amb} far away from the surface and the effective surface of the control volume A_{eff}. The utilisation of A_{efff} is governed by numerics. In particular, due to the stair step approximation of the particle surface, the real surface exceeds the theoretical value for a sphere.

$$A_{\mathrm{eff}} = A \cdot A_{\mathrm{p,ss}} / (4 \, \pi \, R_{\mathrm{p}}^2) \tag{13}$$

where $A_{\mathrm{p,ss}}$ is the total surface of the particle on the computational grid. The convective energy transport in the energy conservation equation (Eq. (8)) arises from the gas flow with the average velocity $\langle \vec{u}_{\mathrm{g}} \rangle$ and the flow of liquid water in the pores $\langle \vec{u}_{\mathrm{l}} \rangle$.

Species Conservation of Vapour:

$$\epsilon_{\mathrm{g}} \rho_g \frac{\partial Y}{\partial t} + \rho_g \, \nabla \cdot \left(\langle \underline{u}_g \rangle Y \right) = \nabla \cdot (\rho_g D_{\mathrm{v,eff}} \nabla Y) + \dot{m}_{\mathrm{v}} \tag{14}$$

The diffusion coefficient for the gas—gas diffusion is calculated from the assumption that the Lewis number (Le) is unity and $D_{\mathrm{v}} = \lambda_{\mathrm{g}} / (\mathrm{Le} \, c_{\mathrm{p,g}} \, \rho_{\mathrm{g}})$. In the pore system of the porous medium the gas diffusion is hindered. A simple but commonly used method is to correlate the diffusion coefficient with the porosity:

$$D_{\mathrm{v,eff}} = \begin{cases} D_{\mathrm{v}}, & \text{if } \epsilon_{\mathrm{g}} = 1 \\ D_{\mathrm{v}} \cdot \epsilon_{\mathrm{g}}^2, & \text{if } \epsilon_{\mathrm{g}} < 1 \end{cases} \tag{15}$$

Species Conservation of Liquid Water:

$$\epsilon_{\mathrm{s}} \rho_s \frac{\partial X_{\mathrm{l}}}{\partial t} = \underline{\dot{m}}_{\mathrm{l}} - \dot{m}_{\mathrm{v}} \tag{16}$$

where X is the liquid moisture content in the solid phase based on the mass of the dry solid. In the model the liquid water movement is described by Darcy's law. Thus the liquid water flux is [16, 17]:

$$\underline{\dot{m}}_{\mathrm{l}} = \langle \underline{u}_{\mathrm{l}} \rangle \rho_{\mathrm{l}} = \frac{K_{\mathrm{l}} K_{\mathrm{l,rel}}}{\mu_{\mathrm{l}}} \rho_{\mathrm{l}} \nabla p_{\mathrm{c}} \tag{17}$$

with the capillary pressure p_c, the permeability $K_{l,0} = 1 \cdot 10^{-19}\, m^2$ [18] and $K_{l,rel} = S^3$. The capillary pressure p_c is calculated using the Leveret J function. The Leveret J function is dimensionless and describes the capillary pressure of a porous system as a function of the saturation S. The capillary pressure is given by [18]:

$$p_c = J(S)\sigma(T)\sqrt{\epsilon/K_l} \tag{18}$$

with [1]:

$$\begin{aligned} J(S) =& 0.364[1 - \exp(-40[1 - S])] \\ &+ 0.221(1 - S) + 0.005/S \end{aligned} \tag{19}$$

and the surface tension σ is calculated according to the VDI Heat Atlas [19].

Evaporation Rate

The calculation of the evaporation rate $\dot{m}_v$ in the control volumes is based on the assumption that the water mass fraction in the gas phase Y is equal to the equilibrium mass fraction Y_{eq}. The equilibrium vapour mass fraction is calculated using the reduced water pressure p_v^*:

$$Y_{eq} = p_v^* \cdot \frac{M_{H_2O}}{p_v^* M_{H_2O} + (1 - p_v^*) M_g} \tag{20}$$

with the molar mass of water M_{H_2O} and an inert gas M_g. The reduced water pressure is calculated as follows:

$$p_v^* = p_v / p_{amb} \tag{21}$$

were p_{amb} is the bulk pressure, which is constant. In a porous body the vapour pressure is a function of the liquid saturation. The model takes this effect into account by using a correction factor $f_p(X)$ for the desorption of water from the porous particle. The vapour pressure in the porous particle is thus calculated according to:

$$p_v = p_{v,H_2O}(T) \cdot f_p(X) \tag{22}$$

where $p_{v,H_2O}(T)$ is the vapour pressure of pure water and $f_p(X)$ is calculated as follows [12]:

$$f_p(X) = 1 - \exp(-2.53(T - 273)^{0.47} X^{1.58}) \tag{23}$$

The vapour pressure $p_{v,H_2O}(T)$ is calculated according to the VDI Heat Atlas [19].

3.2 Subgrid Model

To take care of the transient and spatial water distribution inside the particle the subgrid model is based on the receding core assumption. Figure 3 shows the scheme of the model.

The particle consists of two shells: the dry outer shell and the wet inner one. The shells are characterised by their radius r_d, r_w, thermal conductivity λ_d, λ_w, heat capacity c_{pd}, c_pw and density ρ_d, ρ_w. The diffusion coefficient D_d is only defined for the dry phase. The properties of the wet shell are calculated as follows:

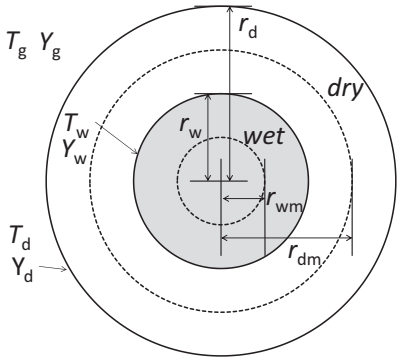

Figure 3. Scheme of the shrinking core model for the particle heating and drying, adapted from [20]

$$r_w = \left(\frac{m_l}{4/3\pi\rho_l\epsilon_l} \right)^{1/3} \tag{24}$$

$$\rho c_{p_{w,eff}} = \epsilon_s\rho_s c_{p,s} + \epsilon_l\rho_l c_{p,l} + \epsilon_{g,d}\rho_{g,d} c_{p,g,d} \tag{25}$$

$$\lambda_w = \epsilon_s\lambda_s + \epsilon_l\lambda_l + \epsilon_{g,w}\lambda_{g,d} \tag{26}$$

with the volume fraction of the solid matrix ϵ_s, the liquid ϵ_l and the gas phase ϵ_g. The mass of liquid water m_l depends on $\dot{m}_v$: $\frac{dm_l}{dt} = -\dot{m}_v$. In the dry shell the liquid water fraction ϵ_l is zero and the properties are calculated according to:

$$r_d = r_p - r_w\ ;\ \lambda_d = \epsilon_s\lambda_s + \epsilon_{g,w}\lambda_{g,d} \tag{27}$$

$$\rho c_{p_{d,eff}} = \epsilon_s\rho_s c_{p,s} + \epsilon_{g,d}\rho_{g,d} c_{p,g,d} \tag{28}$$

For both shells the influence of the gaseous phase is represented by the properties of the gas phase in the dry shell.

The temperature profile which is formed in reality is in the model reduced to one mean temperature for each shell T_w and T_d. For the calculation of the evaporation mass flux two concentrations were used, namely the gaseous water concentration on the wet-dry interface Y_w and the concentration at the particle surface Y_p. The corresponding quantities in the gas phase are marked with the subscript 'g', e.g. T_g.

The energy balance for the inner wet shell includes the conductive heat transport from the dry shell and the heat flux due to evaporation [20]:

$$m_w c_{p\mathrm{w}} \frac{dT_w}{dt} = \alpha_{wd}(T_d - T_w) - \dot{m}_v \Delta_v h \tag{29}$$

where α_{wd} is the heat transfer coefficient between the two shells, $\dot{m}_v$ is the evaporating mass flux and $\Delta_v h$ is the evaporation enthalpy. The heat transfer coefficient is calculated as series of the two different effective thermal conductivities of the shells [20]:

$$\alpha_{wd} = \frac{4\pi\lambda_w\lambda_d}{\lambda_w\left(\frac{1}{r_w} - \frac{1}{r_{dm}}\right) + \lambda_d\left(\frac{1}{r_{wm}} - \frac{1}{r_w}\right)} \tag{30}$$

with r_{wm} and r_{dm} as the half radius of the wet and dry shell:

$$r_{\mathrm{wm}} = 0.5\, r_{\mathrm{w}}\,;\; r_{\mathrm{dm}} = 0.5\, r_{\mathrm{d}} + r_{\mathrm{w}} \tag{31}$$

In the dry shell the energy balance includes the conductive heat flux to the wet shell, the convective heat transfer to the surrounding gas phase and the radiative heat exchange with a wall:

$$m_{\mathrm{d}} c_{pd} \frac{dT_d}{dt} = -\alpha_{\mathrm{wd}}(T_{\mathrm{d}} - T_{\mathrm{w}}) + \alpha_{\mathrm{dg}} A_{\mathrm{d}}(T_{\mathrm{g}} - T_{\mathrm{d}}) + \varepsilon\sigma A_{\mathrm{d}}(T_{\mathrm{g}}^4 - T_{\mathrm{d}}^4) \tag{32}$$

with the surface of the dry shell A_{d}, the heat transfer coefficient to the gas phase α_{dg}, the Stefan-Boltzmann constant σ and the emission coefficient ε which is assumed to be unity. Gas radiation is neglected.

$$\alpha_{\mathrm{dg}} = \frac{\mathrm{Nu}\,\lambda_{\mathrm{g}}}{2\, r_{\mathrm{d}}}\,;\; A_{\mathrm{d}} = 4\pi r_{\mathrm{d}}^2 \tag{33}$$

where the Nusselt number Nu is calculated using the Ranz & Marshall relation [21, 22].

For the calculation of $\dot{m}_{\mathrm{v}}$ the Stefan flow must be taken into account. For the mass flux at the wet—dry interface $\dot{m}_{\mathrm{v}}$ and the particle surface $\dot{m}_{\mathrm{p}}$ the following condition must be fulfilled for an incompressible flow:

$$\dot{m}_{\mathrm{v}} - \dot{m}_{\mathrm{p}} = 0 \tag{34}$$

using:

$$\dot{m}_{\mathrm{v}} = \frac{-4\pi\rho_{\mathrm{g,d}} D_{\mathrm{d}}}{\frac{1}{r_{\mathrm{w}}} - \frac{1}{r_{\mathrm{d}}}} \log\left(\frac{1 - Y_{\mathrm{w}}}{1 - Y_{\mathrm{d}}}\right) \tag{35}$$

$$\dot{m}_{\mathrm{p}} = \frac{-4\pi\rho_{\mathrm{g}} D_{\mathrm{d}}}{\frac{1}{r_{\mathrm{d}}} - \left(\frac{1}{\infty}\right)} \log\left(\frac{1 - Y_{\mathrm{d}}}{1 - Y_{\mathrm{g}}}\right) \frac{\mathrm{Sh}}{\mathrm{Sh}_{\mathrm{diff}}} \tag{36}$$

with the Sherwood number Sh and the Sherwood number at Re=0 $\mathrm{Sh}_{\mathrm{diff}}$.

The vapour concentration on the wet—dry interface depends on the temperature and on the liquid water content [20, 23]. The temperature of the wet—dry interface is calculated as follows [20]:

$$T_{\mathrm{v}} = f_T\, T_{\mathrm{d}} + (1 - f_T)\, T_{\mathrm{w}} \tag{37}$$

the blending factor f_{T} must be chosen according to the drying conditions. For example, if the ambient temperature is low e.g. $413\,K$ a factor of 0.5 works well. For higher ambient temperatures, especially when the wet core in the particle reaches the boiling point of free water, f_{t}=0 is used.

The liquid water concentration at the evaporation front is approximated by the mean moisture content of the whole particle X.

The properties of the gas phase in the boundary layer were calculated using the mean temperature T_{m} and mean water vapour concentration Y_{m}:

$$T_{\mathrm{m}} = 0.5\,(T_{\mathrm{d}} + T_{\mathrm{g}})\,;\; Y_{\mathrm{m}} = 0.5\,(Y_{\mathrm{d}} + Y_{\mathrm{g}}) \tag{38}$$

For the gas properties in the dry shell the mean temperature of the dry shell T_{d} and the mean water vapour concentration $Y_{\mathrm{m\,d}}$ is used:

$$Y_{\mathrm{m\,d}} = 0.5\,(Y_{\mathrm{w}} + Y_{\mathrm{d}}) \tag{39}$$

4 Numerics & Transport Properties

The transport equations in the CFD model has been discretized using a finite-volume based method. The SIMPLE algorithm with a collocated-variables arrangement was used to calculate the pressure and the velocities. The description of the code and basic numerical scheme can be found in [22].

The cylindrical coordinates r, Θ and z are used. Axisymmetricity is forced by cancelling the respective derivatives with respect to Θ. The system was meshed with a Cartesian grid with a total number of 43 050 control volumes (cv) which corresponds to 410 cv in the z-direction and 105 in the r-direction. The grid is locally refined to a resolution of 50 cv/R in the area of the particle.

The transport properties of the gas phase, except the viscosity, were calculated as a function of the temperature and mixture composition; for details see [24]. The coal properties are taken from Zhang & You [1] and describes a lignite coal. The parameter used in the simulations are given in Tab. 1.

Table 1. Parameters used in the simulations [1, 19]

param.	value	param.	value
p_0	$1 \cdot 10^5\, Pa$	$\epsilon_{\mathrm{g,d}}$	0.38
$\mu_{413\,K}$	$22.73\,\mu Pa\,s$	$c_{p,\mathrm{s}}$	$1000\; J/(kg\,K)$
$\mu_{500\,K}$	$25.96\,\mu Pa\,s$	$\langle\rho_{\mathrm{s}}\rangle^{\mathrm{s}}$	$1370\; kg/m^3$
$\mu_{800\,K}$	$35.87\,\mu Pa\,s$	λ_{s}	$0.19\; W/(m\,K)$
$\mu_{1000\,K}$	$48.76\,\mu Pa\,s$	$c_{p,\mathrm{l}}$	$4200\; J/(kg\,K)$
$\Delta_{\mathrm{v}} h$	$2.263\, MJ/kg$	$\langle\rho_{\mathrm{l}}\rangle^{\mathrm{l}}$	$1000\; kg/m^3$
		λ_{l}	$0.658\; W/(m\,K)$

5 Results

5.1 CFD Model

Next we present the results of CFD-based numerical simulations of the convective drying of a single coal particle.

To study the dynamics of the drying process we utilize the particle-averaged evaporation rate $\dot{m}_{\mathrm{v}}$ and the mean moisture content X averaged over the particle volume as follows:

$$X = 2\pi \frac{\int_0^{L_1}\int_0^{L_2} X_{\mathrm{local}}\,(\Phi)\;\cdot r \cdot dz\, dr}{V_{\mathrm{p}}} \tag{40}$$

$$\dot{m}_{\mathrm{v}} = 2\pi \frac{\int_0^{L_1}\int_0^{L_2} \dot{m}_{\mathrm{v,local}}\,\Phi\;\cdot r \cdot dz\, dr}{V_{\mathrm{p}}} \tag{41}$$

with the volume of the spherical particle V_{p} and the particle marker Φ which is unity in the particle and zero in the gas phase.

To illustrate the dynamics of the drying process Fig. 4 shows the time dependent spatial distribution of the moisture content X and the evaporation rate $\dot{m}_v$ in the particle. The drying process starts with evaporation from the surface, and inside the particle a moisture gradient is formed. After the particle surface is dried

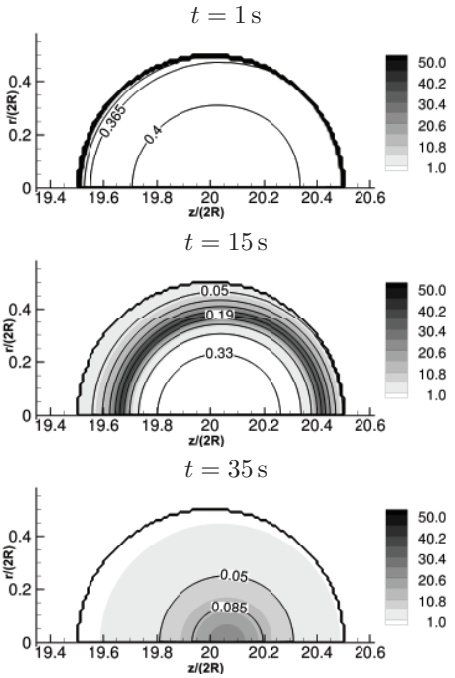

Figure 4. Contour plot of the evaporation rate $\dot{m}_{\mathrm{v}}$ in $kg/(s\,m^3)$ (see the legend to the right of each figure) and the moisture content X (lines) at $T_{\mathrm{in}} = 413.15\,K$ and $\mathrm{Re}_{\mathrm{in}} = 100$

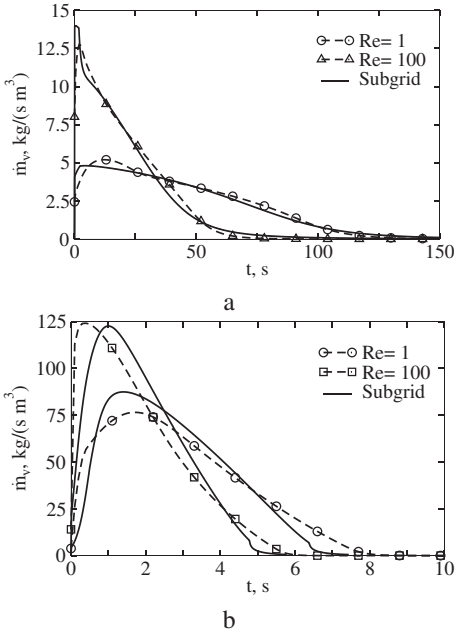

Figure 5. Time histories of the evaporation rate $\dot{m}_{\mathrm{v}}$ predicted using the CFD-based model and the subgrid model at different ambient temperatures $T_{\mathrm{in}} = 413.15\,K$ (a) and $T_{\mathrm{in}} = 1000\,K$, and different $\mathrm{Re}_{\mathrm{in}}$ numbers

a thin evaporation front is formed inside the particle, see Fig. 4. With on going drying the evaporation front radius decreases and its thickness increases until it disappears, see Fig. 4.

The time history of the particle-averaged evaporation mass flux is depicted in Fig. 5 calculated for the different ambient temperatures, namely $T_{\mathrm{in}} = 413.15\ K$ and $T_{\mathrm{in}} = 1000K$. It can be seen that the increase in T_{in} leads to a significant reduction of the drying time, which is logical. In particular, at $T_{\mathrm{in}} = 1000K$ the values of $\dot{m}_{\mathrm{v}}$ is increased by a factor of 10 in comparison to the case for $T_{\mathrm{in}} = 413.15K$. The increase in the particle Re number enhances the evaporation rates. This effect is more noticeable at lower values of T_{in}. An analysis of the $\dot{m}_{\mathrm{v}}$-curves shows that at the beginning of drying $\dot{m}_{\mathrm{v}}$ reaches its maximum value in both cases. *The initial increase in the evaporation rate arises from the increasing vapour pressure when the surface temperature increases*. We found out that the maximum in $\dot{m}_{\mathrm{v}}$ predicted for $T_{\mathrm{in}} = 413.15K$ corresponds to the the time when the drying changes from the surface to the volume drying. However, the maximum in $\dot{m}_{\mathrm{v}}$ predicted for $T_{\mathrm{in}} = 1000K$ is related to the case when the evaporation front is located inside the particle. This fact is explained by the large temperature gradient occurring between the particle surface, which is heated rapidly due to the radiation, and the evaporation front, which is at boiling temperature.

This effect can also be seen on analysing Fig. 6, which shows the time histories of the minimum temperature T_{min}[1] inside the particle. It can be seen that increasing the ambient temperature from 413.15 to $1000\,K$ changes the heat transfer inside the particle. In particular, the major difference to the drying at $T_{\mathrm{in}} = 413.15K$ is that the water inside the particle starts to boil at $T_{\mathrm{in}} = 1000K$, see Fig. 6b. It can be seen that independently of the Reynolds number the minimum temperature T_{min} reaches the boiling point of the water 372.8 K after approximately 2.5 s. As time progresses the minimum temperature increases when at the end of drying the vapour pressure is determined by the sorption isotherm.

5.2 Subgrid Model

In this section the results of the subgrid model are presented and compared with the results of the CFD-based model and experimental results obtained by Zhang and You [1].

The initial conditions for the subgrid model are identical to the CFD-based simulations. The subgrid model uses an explicit time integration scheme and the time steps were varied with the ambient temperature; for T_{in}=413.15 and $1000\,K$ was $\Delta t = 1 \cdot 10^{-4}$ and $5 \cdot 10^{-6}\,s$ respectively. To validate the subgrid model against the experimental data by Zhang and You [1] we used a coarse lignite particle with a diameter R=15 mm and an ambient temperature $T_{\mathrm{in}} = 413.15K$. The

[1] The minimum temperature T_{min} is defined as temperature of the coldest control volume of the particle.

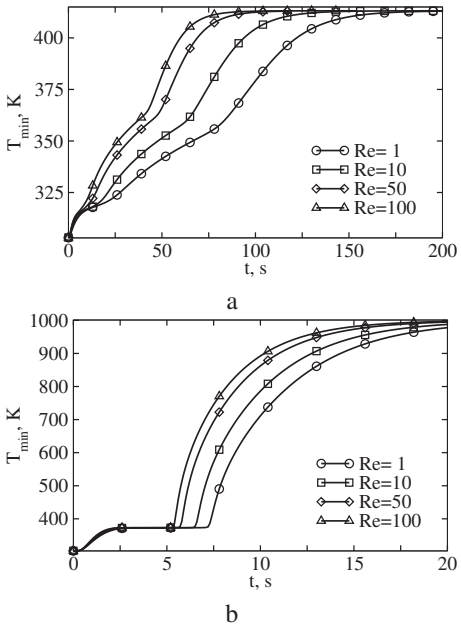

Figure 6. Time history of the minimum temperature T_{min} predicted using CFD-based model for different ambient temperatures $T_{\mathrm{in}} = 413.15\,K$ (a) and $T_{\mathrm{in}} = 1000\,K$ (b)

Reynolds number was set to 310 and 660. The initial moisture content was set to 0.42 and the time step in the subgrid model was $2 \cdot 10^{-3}\,s$. Figure 7 shows an comparison of the time histories of the moisture content X in the experiments and the developed subgrid model.

Good agreement between the experimental and the

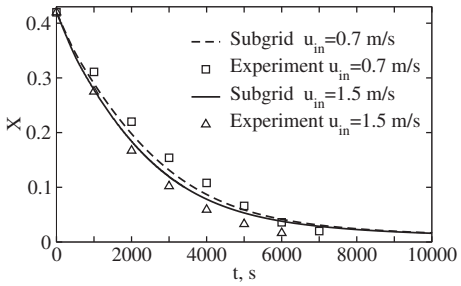

Figure 7. Comparison of experimental [1] and simulated time histories of the moisture content

numerical results is obtained.

Fig. 8 shows the comparison between the results obtained using CFD-based simulations and the subgrid model. It can be seen that the subgrid model reproduces the time-histories of the moisture content very close to the profiles predicted by the CFD-based model. It should be noted that the agreement between the subgrid and CFD-based model is better for $T_{\mathrm{in}} = 413.15\,K$ in comparison to the case with $T_{\mathrm{in}} = 1000\,K$.

Figure 5 shows that the evaporation rates are also well reproduced by the subgrid model. Only at the

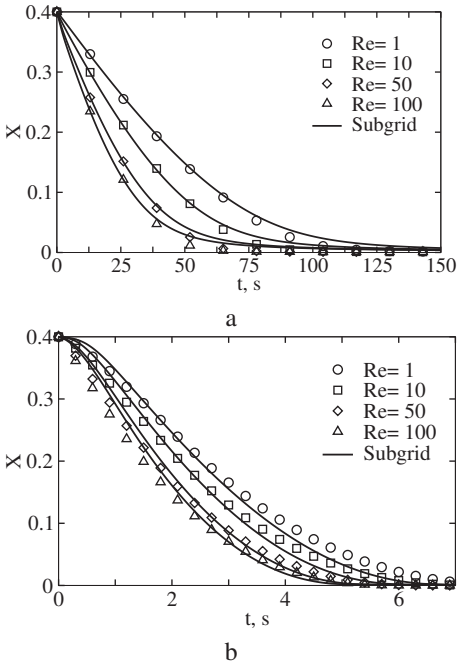

Figure 8.
Time histories of the moisture content X predicted using CFD-based (symbols) and subgrid models (lines) for different ambient temperatures $T_{\mathrm{in}} = 413.15\,K$ (a) and $T_{\mathrm{in}} = 1000\,K$ (b) and $\mathrm{Re}_{\mathrm{in}}$

beginning can a greater difference be seen between the two models. In the subgrid model the maximum evaporation rate is approximately 10% higher than in the CFD simulations, at $\mathrm{Re}_{\mathrm{in}}$=100 and at $\mathrm{Re}_{\mathrm{in}}$=1 it is approximately 7% lower .

Finally we note that the factor f_T was introduced to take into account the effect of water boiling in the subgrid model. The factor describes the blending between T_{d} and T_{w}, see Fig. 3 and Eq. (37). In particular for $T_{\mathrm{in}} = 413.15$ K f_T was set to 0.5, and for $T_{\mathrm{in}} > 500$ K f_T was set to zero.

6 SUMMARY

The drying of a single coal particle was the subject of the work. The drying was modelled using a detailed CFD model based on a continuum approach for porous materials which takes into account the gas and fluid flow inside the particle. A second model was a subgrid model using a receding core assumption. In this model the flow of liquid water was neglected but the Stefan flow was taken into account for the gas flow in the dry shell.

The results using the CFD model showed that inside the particle a drying front is formed. The change from surface to volume evaporation takes place when the flow of liquid water from the inner particle is too low to keep the surface wet.

The comparison of the results of the CFD model with the subgrid model showed a good agreement. The

subgrid model was able to reproduce the characteristic form of the evaporation rate at low temperatures as well as for high temperature where the water boils inside the particle.

ACKNOWLEDGEMENTS

The authors appreciate the financial support of the Government of Saxony and the Federal Ministry of Education and Science of the Federal Republic of Germany as a part of the Centre of Innovation Competence VIRTHUCON.

References

[1] Zhang, K., and You, C., 2010, "Experimental and Numerical Investigation of Convective Drying of Single Coarse Lignite Particles", *Energy & Fuels*, Vol. 24(12), pp. 6428-6436.

[2] Strumillo, C., Jones, P.L., and Romuald Z., 1995, "Energy Aspects of Drying", *in: A.S. Mujumdar (Ed.), Handbook of Industrial Drying, 2nd ed.*, pp. 1241-1276.

[3] Huang, C.L.D., 1979, "Multi-Phase Moisture Transfer in Porous Media Subjected to Temperature Gradient", *Int. J. Heat Mass Transfer*, Vol. 22(9), pp. 1295-1307.

[4] Waananen, K.M., Litchfield, J.B., and Okos, M.R., 1993, "Classification of Drying Models for Porous Solids", *Drying Technol.*, Vol. 11(1), pp. 1–40.

[5] Lewis, W. K., 1921, "The Rate of Drying of Solid Materials", *J. Ind. Eng. Chem.*, Vol. 13(5), pp. 427-432.

[6] Sherwood, T.K., 1929, "The Drying of Solids", *J. Ind. Eng. Chem.*, Vol. 21, pp. 12-16.

[7] Queiroz, M. R., and Nebra, S. A., 2001, "Theoretical and Experimental Analysis of the Drying Kinetics of Bananas", *J. Food Eng.*, Vol. 47(2), pp. 127-132.

[8] Peishi, C., and Pei, D.C.T., 1989, "A Mathematical Model of Drying Processes", *Int. J. Heat Mass Transfer*, Vol. 32(2), pp. 297-310.

[9] Whitaker, S., 1977, "Simultaneous Heat, Mass, and Momentum Transfer in Porous Media: A Theory of Drying", *Advances in Heat Transfer*, Vol. 13, pp. 119 – 203, Elsevier.

[10] Luikov, A.V., 1975, "Systems of Differential Equations of Heat and Mass Transfer in Capillary-Porous Bodies (Review)", *Int. J. Heat Mass Transfer*, Vol. 18(1), pp. 1-14.

[11] Chen, Z., Agarwal, P. K., and Agnew, J. B., 2001, "Steam Drying of Coal. Part 2. Modeling the Operation of a Fluidized Bed Drying Unit", *Fuel*, Vol. 80(2), pp. 209-223.

[12] Chen, Z., Wu, W., and Agarwal, P. K., 2000, "Steam-Drying of Coal. Part 1. Modeling the Behavior of a Single Particle", *Fuel*, Vol. 79(8), pp. 961-974, 2000.

[13] Quintard, M., and Whitaker, S., 2000, "Theoretical Analysis of Transport in Porous Media", *in: K. Vafai (Ed.), Handbook of Porous Media*, pp. 1–52.

[14] Whitaker, S., 1996, "The Forchheimer Equation: A Theoretical Development", *Transp. Porous Media*, Vol. 25, pp. 27-61.

[15] Plumb, O.A., 2000, "Transport Phenomena in Porous Media: Modeling the Drying Process", *in: K. Vafai (Ed.), Handbook of Porous Media*, pp. 755–785.

[16] Nasrallah, S.B., and Perre, P., 1988, "Detailed Study of a Model of Heat and Mass Transfer During Convective Drying of Porous Media", *Int. J. Heat Mass Transfer*, Vol. 31(5), pp. 957-967.

[17] Prat M, 2002, "Recent Advances in Pore-Scale Models for Drying of Porous Media", *Chem. Eng. J.*, Vol. 86(1-2), pp. 153-164.

[18] Wang, Z.H., and Chen, G., 1999, "Heat and Mass Transfer During Low Intensity Convection Drying", *Chem. Eng. Sci.*, Vol. 54(17), pp. 3899-3908.

[19] VDI Gesellschaft Verfahrenstechnik und Chemieingenieurwesen, 2010, *VDI Heat Atlas*, VDI-Buch, Springer.

[20] Bluhm-Drenhaus, T., Simsek, E., Wirtz, S., and Scherer, V., 2010, "A Coupled Fluid Dynamic-Discrete Element Simulation of Heat and Mass Transfer in a Lime Shaft Kiln", *Chem. Eng. Sci.*, Vol. 65(9), pp. 2821-2834.

[21] Ranz, W.E., and Marshall, W.R. Jr., 1952, "Evaporation from Drops", *Chem. Eng. Prog.*, Vol. 48, pp. 141-146.

[22] Schmidt, R., and Nikrityuk, P.A., 2011, "Numerical Simulation of the Transient Temperature Distribution Inside Moving Particles", *Can. J. Chem. Eng.*, Vol. 90, pp. 246-262.

[23] Allardice, D.J., and Evans, D.G., 1971, "The Brown Coal/Water System: Part 2. Water Sorption Isotherms on Bed-Moist Ysallourn Brown Coal", *Fuel*, Vol. 50(3), pp. 236-253.

[24] Bride, B.J., Gordon, S., and Reno, M.A., 1993, Coefficients for Calculating Thermodynamic and Transport Properties of Individual Species, *Technical report, NASA*.

Conference on Modelling Fluid Flow (CMFF'12)
The 15th International Conference on Fluid Flow Technologies
Budapest, Hungary, September 4-7, 2012

LARGE EDDY SIMULATION OF A PNEUMATICALLY POWERED ABRADING SPHERE

Kristofer LEACH[1], Rodion GROLL[2], Hans J. RATH[3]

[1] Kristofer Leach. Center of Applied Space Technology and Microgravity, University of Bremen. Am Fallturm, D-28359 Bremen, Germany. Tel.: +49 421 218 57845, Fax: +49 421 218 9857845, E-mail: kristofer.leach@zarm.uni-bremen.de
[2] Center of Applied Space Technology and Microgravity, University of Bremen. E-mail: rodion.groll@zarm.uni-bremen.de
[3] Center of Applied Space Technology and Microgravity, University of Bremen. E-mail: hans.rath@zarm.uni-bremen.de

ABSTRACT

This paper describes the design of a new kind of miniature abrading sphere, which is magnetically mounted inside a spherical gap and set in rotation pneumatically with air.

Large Eddy Simulation is performed in conjunction with the compressible Smagorinsky model according to Fureby [1]. Minimal temperature variation allows for the assumption of adiabatic walls. Fluid-solid interaction is modelled using the law of the wall for compressible turbulent flow [2].

A parametric study is done to determine optimal geometric layout while taking physical restrictions into account. The resulting optimal configuration is then examined in detail in order to determine demands to be met by the computerised control of the magnetic bearing as well as to quantify the force available to the abrasion process. Finally, a mathematical relation is given that determines available abrasion force depending on standard volumetric flow rate and rotation frequency.

The findings presented here provide a basis for further development of smaller versions of the tool.

Keywords: CFD, compressible Large Eddy Simulation, miniature grinding tools, OpenFOAM

NOMENCLATURE

C	$[-]$	constant
C_k	$[-]$	Smagorinsky constant
$\underline{\mathbf{F}}$	$[N]$	force
$\underline{\mathbf{M}}$	$[Nm]$	moment
Pr_sgs	$[-]$	subgrid scale Prandtl number
R	$[m^2/s^2K]$	specific gas constant
$\underline{\underline{\mathbf{S}}}$	$[1/s]$	symmetric velocity gradient
T	$[K]$	temperature
T_S	$[K]$	Sutherland constant
$\dot{V}_\mathrm{N}$	$[m^3/s]$	standard volumetric flow rate
f	$[1/s]$	rotation frequency
h	$[m^2/s^2]$	enthalpy per unit mass
h	$[m]$	height
k_sgs	$[m^2/s^2]$	subgrid scale kinetic energy
$\underline{\mathbf{n}}$	$[m^2]$	surface normal vector
p	$[N/m^2]$	pressure
r	$[m]$	radius
t	$[s]$	time
$\underline{\mathbf{u}}$	$[m/s]$	velocity vector
u^*	$[-]$	dimensionless velocity
u_τ	$[m/s]$	shear velocity
x, y, z	$[-]$	cartesian coordinates
y^*	$[-]$	dimensionless wall distance
Δ	$[m]$	characteristic cell length
α	$[kg/ms]$	thermal diffusivity
δ_{ij}	$[-]$	Kronecker delta
κ	$[-]$	Von Kármán constant
μ	$[kg/ms]$	dynamic viscosity
ν	$[m^2/s]$	kinematic viscosity
ψ	$[-]$	arbitrary property
ρ	$[kg/m^3]$	density
σ	$[-]$	standard deviation
τ_w	$[kg/ms^2]$	wall shear stress

Subscripts and Superscripts

0	idle value, reference value
GB	GrindBall
N	at standard conditions
d	duct
fluid	exerted by the fluid
g	gap
magnet	exerted by the magnets
o	offset
p	pressure related
sgs	subgrid scale
x, y, z	vector components
μ	viscosity related
$\sim$	Favre filtered
$-$	average
$'$	fluctuation
$*$	dimensionless quantity

1 INTRODUCTION

Project *GrindBall* is an applied research project sponsored by the German Research Foundation (DFG) as part of the work-group *Small Machine Tools* (SPP 1476) involving simulation, electro-magnetic control, and manufacture of a miniature abrading device. The workload in this project is hence distributed on to three institutes: computational simulation is conducted at the *Center of Applied Space Technology and Microgravity* (ZARM), the electro-magnetic control element is developed at the *Institute for Electrical Drives, Power Electronics and Devices* (IALB), and manufacture of the tool itself is undertaken by the *Laboratory for Precision Machining* (LFM).

1.1 Motivation

Miniaturisation is of great importance in many fields such as mechatronics, optics, or medicine as it enables new functionality or makes processes more economical. While increasing precision has made it possible to produce smaller and smaller workpieces, the tools used to work on them have for the most part remained constant in size. The skewed ratio of tool size to workpiece size creates a growing ecological, economical and technical inefficiency regarding respective processes. Until now, miniaturising existing tools was performed in order to combat this skewed ratio. This approach is, however, reaching its limits regarding technical feasibility and usefulness. For this reason, new innovative concepts and tools need to be developed in order to advance in the field of miniaturisation.

Since the ratio of surface to volume increases dramatically with increasing miniaturisation, one has, proportionally, far more functional surface to work with as volume decreases. This effect is extremely useful for abrasive tools, as the control dynamics improve with deceasing tool size, thus also improving the tools ability to adapt to particular machining conditions. Most abrasive tools used to create micro cavities suffer from the following problem: since the axis of rotation and its orientation to the workpiece are crucial in ensuring positive grinding results, aligning the axis of rotation is key when grinding a cavity. A grinding pencil, for instance, has its theoretical maximum effectiveness when the axis of rotation is parallel to the work piece. This, however, is not always practical since the grinding pencil's mounting apparatus could touch down on to the workpiece. Furthermore, should the axis of rotation be perpendicular to the workpiece, the grinding pencil's abrasion would tend to zero. This problem can be countered by tilting the apparatus slightly, however, this still delivers mediocre results at best. Figure 1 depicts the problems stated along with a theoretical solution in which the axis of rotation is parallel to the workpiece at all times, thereby maximising the tool's effectiveness. It is the goal of project *GrindBall* to develop such a tool, which, in addition, combines propulsion and control into one single element.

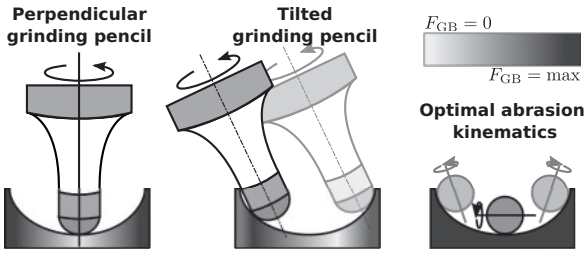

Figure 1. Grinding speed depending on axis orientation (picture courtesy of LFM)

1.2 Basic setup

To achieve the objectives stated above, fluid driven propulsion is used in conjunction with a ferro-magnetic sphere covered with an abrasive coating. The repelling force $\underline{\mathbf{F}}_{\text{fluid}}$ is compensated by an adjustable opposing force $\underline{\mathbf{F}}_{\text{magnet}}$, so that the sphere is held in a predefined position relative to the shaft at all times (see Fig. 2). A magnetic bearing is used to control the tool by preventing any unwanted movement of the sphere while at the same time defining an axis of rotation in combination with the flow. The first prototype utilises

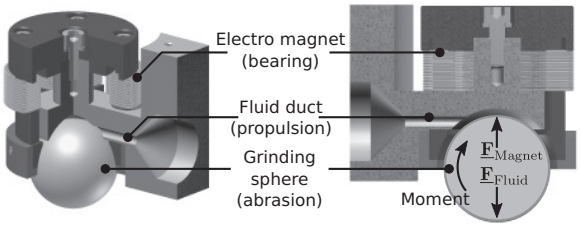

Figure 2. *GrindBall* - basic setup

a sphere with a diameter of 40 *mm*. Throughout the duration of the project, this diameter is to be gradually scaled down to 1 *mm*, with surrounding elements shrinking in proportion. The force necessary to achieve abrasion is applied by the fluid flow. Due to the sphere having little mass and the resulting low moment of inertia, high rotational frequencies and an extremely high control dynamic are to be expected. Planning and construction of the *GrindBall* requires interdisciplinary cooperation between production technology, electrical engineering, and fluid mechanics.

1.3 Goals

This paper begins by introducing the equations governing computational simulations used in the scope of this project. A parametric study is performed to determine optimal configuration of the tool for the case of a 40 *mm* sphere. Once found, the optimal layout is subjected to a variety of simulations which ascertain the *GrindBall*'s possibilities and limitations. This includes identifying conditions for stable and efficient

operation of the tool, quantification of acting forces, and derivation of a mathematical relation governing the force available to the abrasion process. In addition, the results presented here are intended to serve as a basis for future development of the *GrindBall*, i.e. step-by-step miniaturisation.

2 SIMULATION FRAMEWORK

2.1 Governing equations

The following introduces the equations and models governing the simulations conducted for the *GrindBall*.

2.1.1 Large Eddy Simulation

The basic principle in Large Eddy Simulation (LES) is to differentiate between resolved scales and subgrid scales. The former are those which are directly calculated by the governing equations while the latter are included by means of a statistical model. A generic property ψ is split into two separate components

$$\psi = \overline{\psi} + \psi', \tag{1}$$

where the overbar denotes a filtered quantity and the prime denotes a fluctuation. Additionally, density-weighted Favre filtering [3] is used for compressible flow

$$\widetilde{\psi} = \frac{\overline{\rho\psi}}{\overline{\rho}}, \tag{2}$$

which prevents having to model additional terms.

In practise, ψ is unknown and hence cannot be filtered. Instead, the filtered quantity $\overline{\psi}$ is taken as a result obtained on a finite computational grid cell. The information ψ' which is lost as it is too fine to be captured by the grid cell is subsequently modelled to compensate.

2.1.2 Transport equations

The Favre-filtered continuity equation is given by

$$\frac{\partial\overline{\rho}}{\partial t} + \frac{\partial\overline{\rho}\widetilde{u_i}}{\partial x_i} = 0. \tag{3}$$

Conservation of momentum is governed by

$$\frac{\partial\overline{\rho}\widetilde{u_i}}{\partial t} + \frac{\partial\overline{\rho}\widetilde{u_j}\widetilde{u_i}}{\partial x_j} = -\frac{\partial\overline{p}}{\partial x_i} + 2\left(\mu + \mu_{\mathrm{sgs}}\right)\frac{\partial\widetilde{S}_{ij}}{\partial x_j}, \tag{4}$$

with

$$\widetilde{S} = \frac{1}{2}\left(\frac{\partial\widetilde{u_i}}{\partial x_j} + \frac{\partial\widetilde{u_j}}{\partial x_i}\right) - \frac{1}{3}\frac{\partial\widetilde{u_k}}{\partial x_k}\delta_{ij}. \tag{5}$$

Conservation of energy in terms of enthalpy is given by

$$\frac{\partial\overline{\rho}\widetilde{h}}{\partial t} + \frac{\partial\overline{\rho}\widetilde{u_j}\widetilde{h}}{\partial x_j} = \frac{\mathrm{D}\overline{p}}{\mathrm{D}t} + \frac{\partial}{\partial x_j}\frac{\partial}{\partial x_j}\left(\left(\alpha + \alpha_{\mathrm{sgs}}\right)\widetilde{h}\right). \tag{6}$$

2.1.3 Ideal gas law

Pressure and density are linked using the ideal gas law (cp. [2]):

$$p = \rho RT. \tag{7}$$

2.1.4 Sutherland's viscosity model

The viscosity's temperature dependence is determined using Sutherland's viscosity model stated in [2]:

$$\mu = \mu_0\left(\frac{T}{T_0}\right)^{\frac{3}{2}}\frac{T_0 + T_{\mathrm{S}}}{T + T_{\mathrm{S}}}, \tag{8}$$

where $\mu_0 = 1.8325 \cdot 10^{-5}\,kg\,m^{-1}s^{-1}$ is the reference viscosity of air measured at a reference temperature of $T_0 = 296.15\,K$ and $T_{\mathrm{S}} = 120\,K$ is the Sutherland constant for air (see [4]).

2.1.5 Smagorinsky subgrid scale model

Modelling of subgrid scales is done using the compressible Samgorinsky model according to [1]:

$$\mu_{\mathrm{sgs}} = C_{\mathrm{k}}\rho\Delta\sqrt{k_{\mathrm{sgs}}}, \tag{9}$$

where k_{sgs} represents the modelled turbulent kinetic energy and $C_{\mathrm{k}} = 0.02$. Modelled thermal conductivity is proportional to the modelled viscosity:

$$\alpha_{\mathrm{sgs}} = \frac{\mu_{\mathrm{sgs}}}{Pr_{\mathrm{sgs}}}, \tag{10}$$

where Pr_{sgs} is the subgrid scale Prandtl number, here taken to be 0.8.

2.1.6 Law of the Wall

The Law of the Wall discussed in [2] states that the mean velocity at a given point in a turbulent flow is proportional to the logarithm of the distance between the point in question and the nearest wall or boundary layer:

$$u^* = \frac{1}{\kappa}ln(y^*) + C, \tag{11}$$

where $u^* = u/u_\tau$ is a dimensionless velocity, $u_\tau = \sqrt{\tau_w/\rho}$ is the shear velocity and τ_w is the wall shear stress. Furthermore, $y^* = yu_\tau/\nu$ is a dimensionless distance from the wall where y is the actual wall distance, made dimensionless by u_τ and the kinematic viscosity ν. C is a constant of integration and κ is the Von Kármán constant equal to 0.41. This holds for $y^* \geq 30$. Adjacent to the wall, i.e. for $y^* \leq 5$, the velocity is given by $u^* = y^*$. For $5 < y^* < 30$ the law relies on an approximation that smoothly combines the two regions.

2.2 Simulation setup

Two sets of simulations are performed using the pressure-based compressible finite volume method (FVM) solver `rhoPimpleFoam` which is part of the open source CFD package OpenFOAM-2.0.1. The first is a parametric study which aims to determine the optimum geometric layout of the tool. The second investigates the optimum geometry and attempts to quantify forces acting on the grinding sphere and the force available to the abrasion process.

Rough walls are neglected pending an experimental comparison between smooth and coated grinding spheres.

2.2.1 Computational grid

Simulations are conducted on a single mesh consisting of approx. 1 million cells for the parametric study and on two meshes (one coarse with approx. 1.8 million cells and one fine with approx. 5 million cells) for the analysis of the optimal geometry. The reason for conducting the second part on two meshes is to save computational cost while still achieving accurate results. The computation is first run on a coarse mesh until an equilibrium is reached. The results are then mapped on to the finer grid where the simulation is continued. The fine mesh is based on the coarse mesh, but with each cell inside the spherical gap refined once in each direction, thus increasing the number of cells inside the gap by a factor of 8. Also note that since the simulations involve turbulence modelling, equilibrium does not refer to a steady state, but fluctuation about a steady mean.

2.2.2 Discretisation methods

Spacial discretisation is performed using the central differencing scheme (CDS) and temporal discretisation is done using the Euler method. Both methods are described in [5]. Furthermore, pressure correction is performed with the PIMPLE method, which is an amalgamation of the SIMPLE and PISO methods also discussed in [5].

2.2.3 Boundary conditions

At the inlet, velocity is calculated based on a given mass flow rate. Pressure adheres to a zero gradient condition. Temperature is set to room temperature at 293.15 K. μ_{sgs} and α_{sgs} are calculated directly based on available data.

Boundary conditions at the outlet are zero gradient for flow exiting the system as well as for pressure and temperature. Flow entering the system is at room temperature and obtains its velocity based on mass flow rate. Again, μ_{sgs} and α_{sgs} are calculated directly.

Static walls ensure a no-slip condition by enforcing a velocity of zero. Pressure and temperature are set to zero gradient. μ_{sgs} and α_{sgs} are determined using wall functions which ensure that the law of the wall is applied.

The grinding sphere is a special case. As it is rotating, surface velocity is calculated based on a given rotation speed about the axis of rotation. All other variables adhere to the same conditions as for static walls.

2.2.4 Forces

The main criterion in this analysis are forces and moments acting on the sphere.

Pressure p is calculated in each cell adjacent to the sphere and multiplied by the surface normal belonging to the corresponding cell face making up part of the sphere's surface. The sum of the resulting vectors yields the total pressure force acting on the sphere:

$$\underline{\mathbf{F}}_p = \sum_{i=1}^{n} p_i \underline{\mathbf{n}}_i, \tag{12}$$

where $\underline{\mathbf{n}}_i$ is the surface normal vector of the individual sphere boundary face i, and n is the total number of cell faces on the sphere. This is the discrete equivalent of integrating pressure over the entire surface.

Viscous forces are calculated using the part of stress tensor $\underline{\underline{\widetilde{\mathbf{S}}}}$ defined in Eqn. 5 that acts on the cell face i:

$$\underline{\mathbf{F}}_\mu = \sum_{i=1}^{n} \underline{\mathbf{n}}_i \cdot 2\left[\mu + \mu_{\text{sgs}}\right]_i \underline{\underline{\widetilde{\mathbf{S}}}}_i. \tag{13}$$

Viscous moment is calculated by taking the cross product of the vector $\underline{\mathbf{r}}_i$, which points from the centre of the sphere to the centre of the cell face, with the viscous force:

$$\underline{\mathbf{M}}_\mu = \sum_{i=1}^{n} \underline{\mathbf{r}}_i \times \left(\underline{\mathbf{n}}_i \cdot 2\left[\mu + \mu_{\text{sgs}}\right]_i \underline{\underline{\widetilde{\mathbf{S}}}}_i\right). \tag{14}$$

Henceforth, total forces acting on the sphere, i.e. $\underline{\mathbf{F}}_p + \underline{\mathbf{F}}_\mu$ are referred to as $\underline{\mathbf{F}}$ and the force available to the abrasion force is given by

$$F_{\text{GB}} = \frac{M_{\mu,y}}{r}, \tag{15}$$

where $r = 0.02\,m$ is the radius of the sphere and $M_{\mu,y}$ is the y-component of $\underline{\mathbf{M}}_\mu$, i.e. the moment acting about the axis of rotation y.

2.2.5 Time averaging

Results are averaged over time, beginning from a point at which the simulation has reached equilibrium, according to

$$\overline{\psi} = \frac{1}{t_{\text{n}} - t_1} \sum_{i=1}^{n-1} \frac{1}{2} \left(\psi_i + \psi_{i+1}\right)\left(t_{i+1} - t_i\right), \tag{16}$$

where n is the number of time steps in the interval.

3 RESULTS

The previously discussed principles are now applied to a particular case, namely a pneumatically powered abrading sphere, the *GrindBall*. First, a parametric study is conducted in order to identify an optimal geometric configuration for the tool. The resulting optimal setup is subsequently simulated and analysed in detail to determine the demands to be met by the magnetic bearing and the force effectively available to the abrasion process. Furthermore, a mathematical relation governing the behaviour of the available abrasion force is derived.

3.1 Parametric study

The goal of this parametric study is to make the *GrindBall* as efficient as possible while abiding to certain practical and physical restrictions. The sphere's radius of 40 *mm* is considered fixed and will not be varied here. Furthermore, air is the only considered medium of pneumatic propulsion.

An important physical restriction is the fact that the height of the spherical gap should not exceed 3 *mm* as the resulting heat transfer of the magnetic bearing on to its surroundings would impair prolonged use of the tool. Momentum transfer on to the sphere should be maximised under these conditions while also maintaining acceptable pressure forces which can be easily countered by the magnetic control element. It should furthermore be noted that the magnetic bearing consists of five individual magnets, four of which can exert force on the sphere horizontally, and one of which can exert force in an upward direction (see Fig. 3). Hence, the bearing relies on the weight

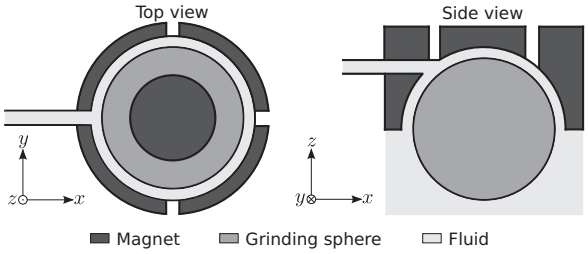

Figure 3. Magnetic bearing aligned around the grinding sphere

of the sphere itself should the sphere be required to lower its position. The grinding sphere exerts a force approximately equal to 2.5 *N* in a downward direction due to its own weight. This force should not be overcome by any upward force resulting from effects the flow might have. Mass flow rate at the inlet is chosen such that the mean velocity inside the duct is approx. 230 $m\,s^{-1}$. Also, a rotating sphere will not be considered during the parametric study as it is not a necessary factor when comparing individual geometries.

3.1.6 Variable parameters

There are essentially three main variable factors considered here. These are the height of the spherical gap h_g in which the abrading sphere is mounted and where most of the momentum transfer on to the sphere takes place, the diameter of the duct h_d which is responsible for introducing the pneumatic propulsion medium into the spherical gap, as well as the offset h_o of the duct relative to the top of the spherical gap. See Fig. 4 for a graphic overview.

Gap heights of 2 *mm*, 3 *mm*, and 4 *mm* are examined with duct diameters also ranging from 2 *mm* to 4 *mm*. Offset is taken to equal to gap height for this first run. Neglecting cases in which duct diameter is

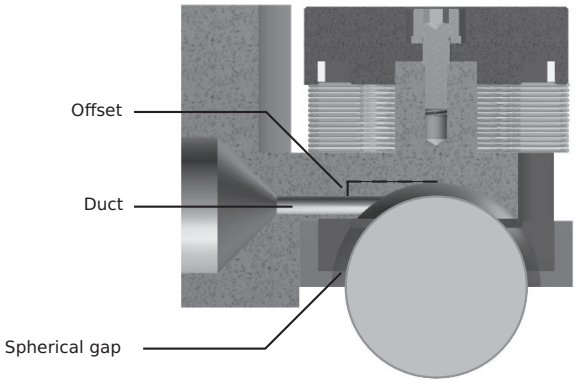

Figure 4. Variable parameters for the parametric study

less than the height of the gap results in 6 individual cases to be considered (see Table 1). The 4 *mm* gap height case is considered here purely as a means of comparison since the maximum practical gap height is 3 *mm* as stated previously.

Table 1. Cases considered while examining duct diameter and spherical gap height

	2 *mm* duct	3 *mm* duct	4 *mm* duct
2 *mm* gap	√	√	√
3 *mm* gap		√	√
4 *mm* gap			√

Offset of the duct relative to the top of the spherical gap is then examined using the optimum configuration obtained from the first run for the following values: 50%, 75%, 125%, 150%, 175%, and 200%, where the percentage refers to the offset's value relative to gap height.

3.1.7 Simulation results

The results from the first part of the parametric study can be seen in Fig. 5.

Clearly the case with a 2 *mm* gap and a 4 *mm* duct delivers the best results in terms of momentum transfer. The 3/4 *mm* case follows, with 4/4 *mm* and 2/3 *mm* closely behind. 3/3 *mm* and 2/2 *mm* deliver a rather poor performance by comparison. Forces in x-direction all display a similar average ranging from 0.06 *N* to 0.13 *N*. What is more interesting here are the large differences among standard deviations. From here on, only the top three cases are considered remembering that the 4/4 *mm* case is not practically feasible. The 3/4 mm case's $\sigma(F_x)$ is approximately half of that seen in the cases 2/4 *mm* and 2/3 *mm*. This means that the former would deliver a much smoother performance as the force exerted does not oscillate as heavily about its mean. Similar observations can be made for F_y and F_z. Forces F_y all display an extremely low average as is to be expected since the geometry is symmetric about $y = 0$ and the main flow direction is perpendicular to

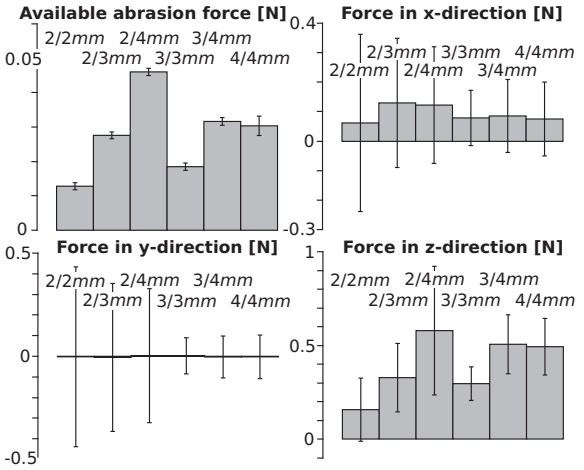

Figure 5. Results from part one of the parametric study: abrasion force F_{GB} and exerted forces F_x, F_y, and F_z (error bars denote standard deviation)

the y-axis. Standard deviations again display varying results. Here the cases $2/3\,mm$ and $2/4\,mm$ both deliver a $\sigma(F_y)$ more than 3 times as large as the $0.1\,N$ seen in the $3/4\,mm$ case.

The force F_z is not quite in keeping with F_x and F_y: $2/3\,mm$ delivers the best result with the lowest upward force of $F_z = 0.33\,N$ and a standard deviation of $\sigma(F_z) = 0.18\,N$. $3/4\,mm$ and $2/4\,mm$ both show values around $0.5\,N$ for F_z. The standard deviation, however, of $0.34\,N$ for $2/4\,mm$ is more than double the deviation of $0.16\,N$ seen in the $3/4\,mm$ case.

Despite having the largest available abrasion force, the $2/4\,mm$ case displays such high standard deviations that is not a practical choice. The high upward force F_z combined with a corresponding large standard deviation $\sigma(F_z)$ make this configuration particularly problematic.

Comparing $2/3\,mm$ and $3/4\,mm$ sees $3/4\,mm$ as the far better choice. While $2/3\,mm$ shows a lower F_z with similar values for $\sigma(F_z)$, the standard deviations of F_x and F_y are simply too high by comparison. Such highly fluctuating forces could cause strong vibrations which would in turn cause the magnetic bearing to emit more heat while trying to compensate. This may impair prolonged use of the tool.

Generally it can be said that the forces F_{GB}, F_x, and F_z increase with increasing gap height for the cases in which duct diameter is equal to gap height. Furthermore, these forces increase with increasing duct diameter for constant gap height. Standard deviations of F_{GB} show very little difference across all cases. Forces F_x, F_y, and F_z, however, display great variations in their standard deviations. The standard deviations seen for all cases using $2\,mm$ gap height are far greater that those seen using a $3\,mm$ or $4\,mm$ gap. Gap heights of $3\,mm$ and $4\,mm$ are similar regarding $\sigma(\underline{\mathbf{F}})$. A smaller gap, thus seems to promote heavier vibration of the sphere while a larger gap enables smoother operation. Varying the duct diameter at constant gap height shows similar results for standard deviations in all cases.

The optimum case from the first part of the study with a $3\,mm$ gap height h_g and a $4\,mm$ duct diameter h_d is now subjected to a second study with varying offset. The offset h_o is given as a percentage of h_g and is measured as the vertical distance between the top of the gap and the highest point of the duct (see Fig. 4). Cases investigated are for $h_o \in \{50\%, 75\%, 100\%, 125\%, 150\%, 175\%, 200\%\}$. An offset higher than 200% cannot be considered since the hose would penetrate the outlet basin, making multiple grid cells occupy the same space. Again, the goal here is to maximise F_{GB} while maintaining acceptable values for $\underline{\mathbf{F}}$ and $\sigma(\underline{\mathbf{F}})$.

Fig. 6 shows results of the study. Standard deviations for the individual forces are relatively uniform across all cases compared to the first study. Hence, the absolute values of the forces and how they compare across cases is the focus of this second study.

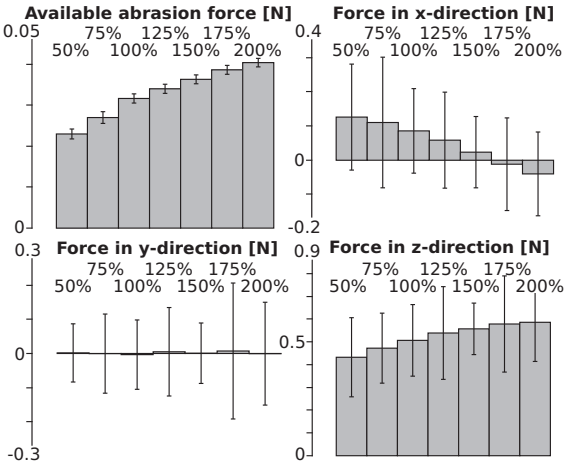

Figure 6. Results from part two of the parametric study: abrasion force F_{GB} and exerted forces F_x, F_y, and F_z (error bars denote standard deviation)

It is easily seen that the abrasion force F_{GB} increases with higher offsets. This can be explained by the fact that the angle at flow's point of impact on the sphere between the flow's main direction and the surface of the sphere becomes larger as the offset increases. Greater viscous forces are a direct consequence of this. Although a maximum offset of 200% cannot be exceeded, it is clear that there must exist an optimum offset beyond which abrasion force starts to drop. Should the afore mentioned angle become perpendicular, viscous forces vanish, cancelling each other out as they are distributed uniformly in all directions. This is supported by inspecting the abrasion force in Fig. 6. Regarding F_{GB} as a function of offset h_o, there is a clear decrease in the slope of the function as offset increases. Assuming $F_{GB} \approx 0$ for $h_o = 23\,mm$, the slope must become negative somewhere between $h_o = 2h_g$ and $h_o = 23\,mm$. This can be further investigated in the future

for different geometries that allow for higher offsets.

Forces F_x in x-direction clearly display a reduction with increasing offset. Forces are minimal for $h_o = 1.5h_g$ and $h_o = 2h_g$. Forces F_y are similar across all cases while F_z shows increasing upward force with increasing offset. Forces F_z, nonetheless, only vary between $0.43\,N$ and $0.58\,N$. Based on this data, the optimal value for the offset is $h_o = 1.5h_g = 4.5\,mm$. While only in third place for abrasion force, it delivers the lowest standard deviation across all directional forces F_x, F_y, and F_z. Furthermore, the force F_x is comparatively small. Hence, the sphere is subjected to the least amount of vibration with this setup, causing the magnetic bearing to emit less heat.

Unfortunately, a tight manufacturing schedule did not permit for the second study to reach completion on time. Consequently, only results from the first parametric study could be considered which is why the following deals with a setup consisting of $h_g = 3\,mm$, $h_d = 4\,mm$, and $h_o = 3\,mm$.

3.2 GrindBall Prototype

The optimum configuration determined previously is now simulated using a variety of rotation frequencies and mass flow rates (see Table 2). Forces F_x, F_y, and F_z

Table 2. Case configurations simulated for the *GrindBall* prototype

Flow rates $[m^3h^{-1}]$	1	2	3	4	5
Frequencies $[Hz]$	0	0	0	0	0
	50	75	25	50	75
			100	100	150
Flow rates $[m^3h^{-1}]$	6	7	8	9	10
Frequencies $[Hz]$	0	0	0	0	0
	50	50	50	50	200
	100	100	100	100	400
	200	250	300	350	

as well as abrasion force F_{GB} are investigated. Finally, a relation is established which states the dependency of abrasion force F_{GB} on rotation frequency f and on standard volumetric flow rate $\dot{V}_N$. Note that $\dot{V}_N = \dot{m}/\rho_N$, where $\rho_N = 1.293\,kg\,m^{-3}$ is the standard density of air at $273.15\,K$ and atmospheric pressure. This representation is preferred over the mass flow rate $\dot{m}$ as it is a more common quantification and is also the unit employed by the flow meter used in practise.

3.2.1 Pressure and viscous forces

Fig. 7 shows forces averaged over each constant $\dot{V}_N$ with error bars denoting average standard deviation. While magnitudes of $\overline{F_x}$ are similar for all flow rates, their standard deviations increase severely with increasing $\dot{V}_N$. A similar observation can be made for $\overline{F_z}$ regarding standard deviation, however, magnitudes of $\overline{F_z}$ also increase with rising flow rate. Use of the tool is not impaired by upward force for high flow rates as even with $max\left(\overline{F_z} + \sigma\left(\overline{F_z}\right)\right) \approx 0.8\,N$, the sphere still

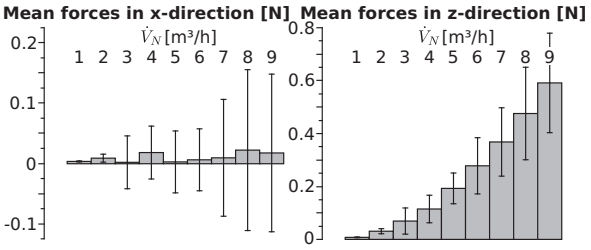

Figure 7. Exerted mean forces $\overline{F_x}$, $\overline{F_y}$, and $\overline{F_z}$ averaged over constant volumetric flow rates $\dot{V}_N$

has $1.7\,N$ of downward force resulting from its own weight at its disposal.

3.2.2 Analysis of available abrasion force

As seen in Fig. 8, abrasion force F_{GB} displays a linear dependency on rotation rate f for constant standard volumetric flow rates $\dot{V}_N$. This allows for a linear regression line to be fitted to each constant $\dot{V}_N$ which gives a mathematical approximation for the dependency of F_{GB} on f. As is to be expected,

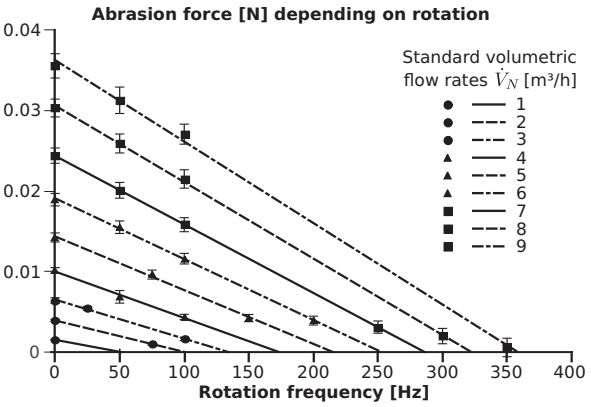

Figure 8. Abrasion force with fitted regression curves for each standard volumetric flow rate

the slope of each regression line is negative since the velocity gradients (and thus the viscous forces) between the sphere's surface and the flow impacting the sphere become lower as rotation frequency increases. The intercept of each regression line corresponds to the momentum transfer for a stationary sphere $F_{GB,0}$, i.e. the abrasion force for $f = 0$. Each null point can be interpreted as the idle rotation frequency f_0 for the corresponding flow rate due to the fact that if $F_{GB} = 0$, the sphere can neither accelerate nor decelerate. Fig. 9 shows $F_{GB,0}$ and f_0.

To avoid dimensioned coefficients, the parameters F_{GB}, f, and $\dot{V}_N$ are made dimensionless using the radius of the sphere $r = 0.02\,m$, the standard kinematic viscosity of air $\nu_N = 1.33 \cdot 10^{-5}\,m^2s^{-1}$, and the standard density of air $\rho_N = 1.293\,kg\,m^{-3}$. The resulting dimensionless variables are: $F^*_{GB} = F_{GB}/\nu_N^2\rho_N$, $f^* = f/\nu_N r^{-2}$, and $\dot{V}^*_N = \dot{V}_N\nu_N r$. A dimensionless relation for momentum transfer on to a stationary sphere is thus

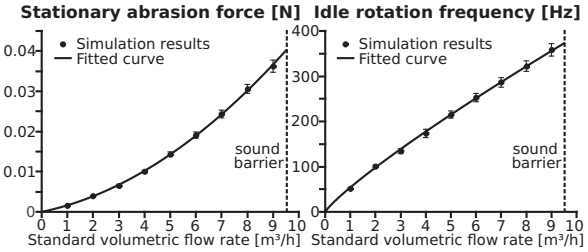

Figure 9. Force transfer for a stationary sphere (left) and idle rotation frequency (right)

given by:

$$F^*_{\mathrm{GB},0} = 1.2198\dot{V}^{*2}_{\mathrm{N}} + 5597.4383\dot{V}^*_{\mathrm{N}}. \tag{17}$$

A similar analysis can be done for idle rotation frequencies which are extrapolated from the null points of the individual linear equations for constant standard volumetric flow rates:

$$f^*_0 = 4.2086\dot{V}^{*\frac{6}{7}}_{\mathrm{N}}. \tag{18}$$

3.2.3 Abrasion force dependency

The relation between abrasion force F^*_{GB} and rotation frequency f^* is linear for constant volumetric flow rates $\dot{V}^*_{\mathrm{N}}$. Furthermore, the 2D relations between $F^*_{\mathrm{GB},0}$ and $\dot{V}^*_{\mathrm{N}}$ for $f^* = 0$ and between f^*_0 and $\dot{V}^*_{\mathrm{N}}$ for $F^*_{\mathrm{GB}} = 0$ are known. A single equation relating all three variables to one another can hence be obtained using $F^*_{\mathrm{GB},0}$ as intercept, the ratio of $F^*_{\mathrm{GB},0}$ to f^*_0 as the slope, and f^* as the dependant variable:

$$F^*_{\mathrm{GB}} = F^*_{\mathrm{GB},0} - \frac{F^*_{\mathrm{GB},0}}{f^*_0} f = F^*_{\mathrm{GB},0}\left(1 - \frac{f^*}{f^*_0}\right). \tag{19}$$

Hence, available abrasion force F^*_{GB} is governed by

$$F^*_{\mathrm{GB}} = (1.22\dot{V}^{*2}_{\mathrm{N}} + 5597.44\dot{V}^*_{\mathrm{N}})\left(1 - 0.24 f^* \dot{V}^{*-\frac{6}{7}}_{\mathrm{N}}\right). \tag{20}$$

Eqn. 20 is of particular interest for the use of the *GrindBall*, as prior knowledge of the abrasion force and its behaviour is required before commencing operation. Typically, particular materials require a certain amount of force. This required force can simply be plugged into Eqn. 20, resulting in a 2D equation governing flow rate vs. rotation frequency. Thus, the flow rate can then be chosen to achieve a certain frequency for a given amount of force.

4 CONCLUSION

Having found a viable geometry and performed an extensive analysis of forces acting on the sphere, as well as having determined the force available for abrasion mathematically, the *GrindBall* is now ready for construction and subsequent operation. It remains to validate the results presented in this paper with experimental data.

Examination of this first prototype shows that air is not a viable propulsion medium as the resulting abrasion force is simply too low for industrial use. Hence, a fluid with a high viscosity such as oil may prove to be a possible future alternative since it can transfer far more momentum through viscous stress.

The next step of development is an 8 *mm* sphere which will build upon this first prototype and employ improvements inspired by the results presented here. Two supplemental ducts will be introduced vertically from the top in order to create enough downward force to enable the sphere to penetrate into a workpiece. Pneumatic propulsion will be replaced by hydraulic propulsion to increase momentum transfer. Also, the main duct will receive a larger offset pending a further parametric study with the new propulsion medium.

Upon completion of the 8 *mm GrindBall*, further miniaturisation will be performed, most likely beginning with 4 *mm* and then 2 *mm*. Should there still be room for further reduction, a 1 *mm* grinding sphere could also be developed. This gradual miniaturisation process will not only aid in making the *GrindBall* viable for industrial use, but also produce a unique and highly effective tool in the field of "micro-grinding".

Hopefully this project will inspire others to develop new miniature tools and thus help the scientific community in finding new and innovative possibilities for machining small workpieces. Furthermore, it would be pleasing to see this and other such projects encouraging research on the general topic of miniaturisation.

ACKNOWLEDGEMENTS

The authors wish to thank Ralf Gläbe (LFM), Carla Brandao (LFM) and Alexander Norbach (IALB) for their cooperation on this project. Furthermore, thanks are due to the German Reseach Foundation (DFG) for sponsoring project *GrindBall* and the North-German Supercomputing Alliance (HLRN) for providing access to their super-computing facilities.

REFERENCES

[1] Fureby, C., 1996, "On subgrid scale modelling in large eddy simulations of compressible fluid flow", *Physics of Fluids*, Vol. 8, pp. 1301-1311.

[2] White, F.M., 1991, *Viscous Fluid Flow*, McGraw-Hill.

[3] Favre, A., 1983, "Turbulence: space-time statistical properties and behaviour in supersonic flows", *Physics of Fluids*, Vol. 26, pp. 2851-2863.

[4] Montgomery, R.B., 1947, "Viscosity and thermal conductivity of air and diffusivity of water vapor in air", *Journal of Atmospheric Sciences*, Vol. 4, pp. 193-196.

[5] Ferzinger, J.H., and Perić, M., 1996, *Computational methods for Fluid Dynamics*, Springer Verlag.

Conference on Modelling Fluid Flow (CMFF'12)
The 15th International Conference on Fluid Flow Technologies
Budapest, Hungary, September 4-7, 2012

HEAT TRANSFER EFFECTS ON PARTICLE MOTION UNDER RAREFIED CONDITIONS

Henrik STRÖM[1], Srdjan SASIC[2]

[1] Corresponding Author. Department of Applied Mechanics, Division of Fluid Dynamics, Chalmers University of Technology, SE-412 96 Göteborg, Sweden. Tel.: +46 31 772 13 60, E-mail: henrik.strom@chalmers.se
[2] Department of Applied Mechanics, Division of Fluid Dynamics, Chalmers University of Technology. E-mail: srdjan@chalmers.se

ABSTRACT

It is currently not well established how particle motion and filtration are affected by non-isothermal conditions at the micro- or nano-scales. Furthermore, when the particle size is comparable to the mean free path of the gas, rarefaction effects become important. In the present work, we investigate the effects of heat transfer and non-isothermal conditions on the motion of small particles in rarefied flow. A suitable framework for that purpose is developed here by extending a previously validated generic multiphase DNS method for rarefied flows. The resulting model is valid for low particle Reynolds number flows, irrespective of the Biot number, and for particle Knudsen numbers up to unity in unbounded flow. Using the new model, we show that the settling behavior of particles with an internal heat source is different when the carrier gas is rarefied compared to the continuum case. The difference is reflected in the fact that the chances for thermal levitation and/or lifting up of the particle due to buoyancy effects are significantly reduced.

Keywords: gas-solid flow, heat transfer, rarefied flow

NOMENCLATURE

A	[m^2]	surface area
C_c	[-]	Cunningham correction
E	[J/kg]	specific enthalpy
$\underline{F}_\sigma$	[N]	fictitious surface tension force
Gr	[-]	Grashof number
Kn	[-]	Knudsen number
Nu	[-]	Nusselt number
P	[Pa]	pressure
Pr	[-]	Prandtl number
Q	[-]	dimensionless heat source
Re	[-]	Reynolds number
T	[K]	temperature
U	[m/s]	characteristic velocity
c_p	[$J/kg,K$]	heat capacity
d	[m]	diameter
$\underline{g}$	[m/s^2]	gravitational acceleration vector
h	[$W/m^2,K$]	heat transfer coefficient
k	[$W/m,K$]	thermal conductivity
r	[m]	radial position
t	[s]	time
u	[m/s]	relative velocity
$\underline{u}$	[m/s]	absolute velocity vector
y	[m]	wall-normal coordinate direction
α	[m^2/s]	thermal diffusivity
α_t	[-]	thermal accommodation coeff.
β	[$1/K$]	thermal expansion coeff.
χ	[-]	ratio of specific heats
γ	[-]	volume fraction in cell
κ	[-]	viscosity ratio
λ	[m]	mean free path of the gas
μ	[Pa,s]	viscosity
ρ	[kg/m^3]	density

Subscripts

Kn	Knudsen layer
T	terminal
f	fluid
i	phase index
p	particle
ptf	particle-to-fluid ratio
r	radial position
ref	reference
s	surface
0	initial
∞	infinity (ambient conditions)

Superscripts

*	adjusted

1. INTRODUCTION

1.1 Background

Filtration of fine solid particles is important in many industrial processes, for example in the removal of particulate matter from exhaust gases. In such systems, the events governing the overall

performance of the device are occurring on micro- or nano-scales. It is not yet well established how particle motion and filtration are affected by non-isothermal conditions at these small spatial scales. In addition, when the particle size is comparable to the mean free path of the gas, rarefaction effects become important.

As an example, the pore diameters of a diesel particulate filter are of the order of 2-20 μm, whereas the particle sizes range from a few nanometers up to 1 μm. The mean free path is 100-200 nm. Oxidation of the particulate matter creates temperature gradients on the micro-scale, as well as gradients in concentration of the oxidizing species [1]. This can in turn yield gradients in the reaction rate over the particles, which may alter their diffusive properties and hence affect their motion [2]. Furthermore, heat transfer effects influence the particle settling velocities, since natural convection in the boundary layer around the particles gives rise to a force that may counterbalance, equate or even exceed the buoyancy force [3]. The special case of zero terminal velocity is known as "thermal levitation" [4].

In the present work, we investigate the effects of heat transfer and non-isothermal conditions on the motion of small solid particles in rarefied gas flow. A suitable framework for this investigation is developed by extending a previously validated generic multiphase DNS method for rarefied flows [5]. The resulting model is valid for low particle Reynolds number flows, irrespective of the Biot number, and for particle Knudsen numbers of up to unity in unbounded flow. Using the new model we show that, under rarefied conditions, the heat transfer effects on a settling particle with an internal heat source are smaller than in the continuum case.

1.2 Rarefied flow

The degree of rarefaction in the flow around a particle of diameter d_p is characterized by the Knudsen number, $Kn_p = 2\lambda/d_p$, where λ is the mean free path of the gas that may be determined from [6]:

$$\lambda = \frac{\mu}{0.499\rho_f\left(\frac{8P}{\pi\rho_f}\right)^{1/2}} \qquad (1)$$

Rarefaction effects become apparent for values of Kn_p above 0.015 [7]. Particles affected at atmospheric pressure are therefore typically very small (d_p < 1 μm). They also have short response times and typically low relative velocities to the carrier fluid. As a consequence, the particle Reynolds number ($Re_p = \rho_f d_p u/\mu$) is very small and the particles remain within the (rarefied) Stokes flow regime.

In order to fully characterize the flow around a particle at non-isothermal conditions, knowledge about the Peclet number is also necessary. The Peclet number represents the importance of heat transport by convection to that by diffusion, and is equal to the product of the Reynolds number and the Prandtl number. Since $Pr \sim O(1)$ for gases at normal temperatures and $Re_p \ll 1$ for small solid particles in a rarefied gas, the assumption that the Peclet number remains small is generally valid.

It is also of interest to discuss briefly the meaning of the Biot number, defined as the ratio of the internal (conductive) to the external (convective) resistance to heat transfer. A common assumption in the case of multiphase DNS methods for non-isothermal particulate flows is that the Biot number is very small or practically zero [8]. In such a case, the external heat transfer resistance dominates and the particle temperature will always be uniform. This assumption therefore leads to a situation where the temperature fields inside the particles do not have to be resolved. In the present work however, no such restriction on the value of the Biot number is made.

1.3 Rarefaction effects on heat transfer

In the continuum regime, the boundary condition for temperature at the interface between the particle and the surrounding fluid is that the temperature is continuous across the interface. However, at rarefied conditions, the surface of the solid particle will no longer be in thermal equilibrium with the adjacent gas. As a consequence, the heat transfer between a suspended particle and its surroundings is impeded. Already at a Knudsen number of unity, the reduction in the heat transfer rate may be as high as 70% [9].

In the limit of a low Reynolds number, conduction is a totally dominant heat transfer mechanism. The Nusselt number for a spherical particle in rarefied flow under these conditions has been well described by:

$$Nu = \frac{2}{1+\frac{15}{4}\alpha_t^{-1}Kn_p} \qquad (2)$$

Equation (2) has been obtained from several different investigations [10-12]. Mikami et al. [10] showed that it was in good agreement with experimental data that spanned $0.016 \le Kn_p \le 0.8$ using various mixtures of hydrogen, helium and nitrogen. Interestingly, Eq. (2) is also identical to the harmonic mean of the continuum regime heat transfer rate and the free molecular regime heat transfer rate [12]. The derivation of Eq. (2) is typically based on the assumption of a small temperature difference (i.e. that the temperature difference between the particle and the gas is small

in relation to the absolute temperature of the gas) [11], but it has been shown that it provides a fair approximation of the impeded heat transfer in the transition regime even if the assumption of small temperature difference is not appropriate [13].

Since the relation provided by Eq. (2) has been proven to be valid over a large range of Knudsen numbers and for fairly large temperature differences, it is used as the basis for the current work. It should also be noted here that the factor 15/4 in Eq. (2) is valid for a monoatomic gas, whereas it changes to 19/6 for a diatomic gas [12].

Using a correlation such as Eq. (2) for the heat transfer coefficient also avoids the introduction of altered boundary conditions as a means to extend the validity of continuum fluid dynamics. It has, for example, been suggested to use a "temperature jump" boundary condition at solid surfaces [14], much in the vein of the slip boundary condition approach for velocity [cf. 15]. In the temperature jump boundary condition approach, the equality $T_f = T_p$ at the particle surface is exchanged for:

$$T_f = \frac{2-\alpha_t}{\alpha_t}\frac{2\chi}{\chi+1}\frac{\lambda}{Pr}\frac{\partial T_f}{\partial y} + T_p \qquad (3)$$

However, just as with the slip velocity boundary condition, the temperature jump boundary condition is only theoretically valid if $Kn_p \ll 1$. Springer and Tsai [9] showed that, when compared to experimental data, the temperature jump boundary condition underpredicts the reduction in the heat transfer with approximately 5% already at very low Knudsen numbers and that this discrepancy then grows with increasing the Knudsen number.

In addition to the reduction in heat transfer that stems from the occurrence of the "temperature jump", there is an additional effect on heat transfer from the velocity slip. The temperature jump decreases the magnitude of the temperature gradient in the fluid outside the particle, so that heat transfer is impeded. On the other hand, the velocity slip increases the convective heat transfer along the surface. For low Peclet numbers, however, the effect of the velocity slip can be neglected compared to that of the temperature jump [16].

2. MODELLING

In multiphase direct numerical simulation (DNS), the Navier-Stokes equations are solved directly together with a method for taking the presence of particles into account. Since rarefaction effects are molecular to their nature, they must be modeled. In this work, a Volume of Fluid (VOF)-based model for solid particles in rarefied flow will be used to consider in detail the heat transfer phenomena taking place on the particle scale. A thorough derivation and validation of this model for simulations of isothermal systems of solid particles under rarefied conditions was provided by Ström et al. [5].

2.1 Momentum balance

A shared set of equations is used for both the continuous phase and the solid particles. The volume fraction of particulate phase in each cell is designated γ_p. The volume fraction of gaseous phase is then given by $\gamma_f = 1 - \gamma_p$.

The velocity field is determined from the shared continuity and momentum equations, assuming that the flow is incompressible and that the velocity of the two phases is continuous across the interface:

$$\nabla \cdot \underline{u} = 0 \qquad (4)$$

$$\begin{aligned} \rho\frac{\partial \underline{u}}{\partial t} + \rho\nabla\cdot(\underline{u}\underline{u}) = \\ -\nabla P + \nabla\cdot\left[\mu\left(\nabla\underline{u} + \nabla\underline{u}^T\right)\right] \\ +\left[1-\beta(T-T_0)\right]\gamma_f\rho_{f,0}\underline{g} \\ +\gamma_p\rho^*\underline{g} + \underline{F}_\sigma \end{aligned} \qquad (5)$$

where the density and viscosity without subscripts in Eq. (5) are determined locally using:

$$\rho = \gamma_f\rho_f + \gamma_p\rho^* \qquad (6)$$

$$\mu = \mu_f\left(\gamma_f + \gamma_p\kappa\right) \qquad (7)$$

As seen from the third term on the right hand side of Eq. (5), the Boussinesq model [17] is employed to describe the variation of the buoyancy force with temperature. Consequently, the only effect of temperature on the fluid properties is via the thermal expansion coefficient, β. The primary reason for choosing this approach, instead of a more comprehensive treatment (in which all properties are allowed to vary as functions of temperature), is that this approximation is used in the literature studies to which we will compare our work [3, 8, 18]. It should be stressed that the limitations of the Boussinesq model are therefore not built into the proposed framework. In its current formulation, however, the approach presented here is primarily intended for situations in which the temperature difference between a particle and the surrounding fluid is not excessively large, since the validity of the Boussinesq model for the buoyancy term in Eq. (5) requires that $\beta(T-T_0)$ is smaller than unity.

In theory, κ in Eq. (7) should approach infinity in the regions occupied by solid particles; here a sufficiently high numerical value is used instead [5]. The term $\underline{F}_\sigma$ represents a force designed to ensure that the particle retains its spherical shape

[5]. In the current work, we have extended the earlier approach so that the current value of $\underline{F}_\sigma$ is updated globally in every time step based on the restriction that the maximal local Capillary number for the solid particle remains below 0.05.

The effects of rarefication come in via the adjusted density ρ^* in Eq. (5) and (6). The adjusted density is calculated as [5]:

$$\rho^* = \rho_\mathrm{p} C_\mathrm{c} = \rho_\mathrm{p} \cdot \left(1 + Kn_\mathrm{p} \left[1.155 + 0.471 \exp\left(-\frac{0.596}{Kn_\mathrm{p}} \right) \right] \right) \quad (8)$$

In the continuum limit, Kn_p goes to zero and ρ^* becomes equal to the particle density ρ_p, meaning that the conventional continuum version of the VOF-model is recovered.

The interface between the particle and the gas is tracked by solving a continuity equation for the particulate phase:

$$\frac{\partial \gamma_\mathrm{p}}{\partial t} + \nabla \cdot \left(\gamma_\mathrm{p} \underline{u} \right) = 0 \quad (9)$$

2.2 Energy balance

Temperature is solved for using an energy transport equation:

$$\frac{\partial (\rho E)}{\partial t} + \nabla \cdot \left[\underline{u} (\rho E + P) \right] = \nabla \cdot (k \nabla T) \quad (10)$$

where

$$E = \frac{\gamma_\mathrm{p} \rho^* E_\mathrm{p} + (1 - \gamma_\mathrm{p}) \rho_\mathrm{f} E_\mathrm{f}}{\rho} \quad (11)$$

and

$$E_\mathrm{i} = \int_{T_{ref}}^{T} c_{p,\mathrm{i}} dT + \frac{\underline{u}^2}{2} \quad (12)$$

The local value of the thermal conductivity, k, is calculated as:

$$k = \gamma_\mathrm{p} k_\mathrm{p} + \gamma_\mathrm{f} k_\mathrm{f} \quad (13)$$

2.3 Temperature effects on the adjusted density

The effects of rarefication on the motion of a solid particle is in the current work addressed using the concept of the adjusted density [5]. Since the adjusted density is a function of the particle Knudsen number (which is proportional to the mean free path of the gas), the adjusted density must also be a function of temperature. In non-isothermal simulations, a method for choosing the appropriate temperature for the determination of the adjusted density is therefore needed.

Since the adjusted density is used to describe the particle motion (that is, the change in momentum transfer to the particle due to rarefication), it should be evaluated from the properties of the gas that are directly involved in this momentum transfer. The current degree of rarefication is then characterized by the size of the mean free path in the fluid layer closest to the particle surface, i.e. the Knudsen layer, which is of the order of the the mean free path. The adjusted density is thus calculated as:

$$\rho^* = \rho_\mathrm{p}(T_\mathrm{p}) C_c(T_{\mathrm{f,Kn}}) \quad (14)$$

Consequently, the true particle density is determined as a function of the mass-weighted mean temperature of the particle itself, T_p, whereas the Cunningham correction factor is determined as a function of the volume-weighted mean temperature of the Knudsen layer. The reason for using the volume-weighted, rather than the mass-weighted, mean temperature of the Knudsen layer is that the the Cunningham correction is direction-independent and thus characterized by the whole environment surrounding the particle.

In order to avoid iterations and subgrid-scale interpolation in the determination of the current value of λ, it is assumed that the cell layer adjacent to the outer surface of the particle provides a relevant measure of λ irrespective of the current λ-to-grid-spacing ratio. The error in the value of λ obtained from this procedure is smaller than 0.2%, since the use of the Boussinesq model already puts a restriction on the tolerable variation of the fluid temperature in the boundary layer surrounding the particle.

2.4 The adjusted heat capacity

For the inclusion of heat transfer effects in the rarefied flow regime we propose the following approach, which is based on the analysis of a single particle of uniform temperature T_p suspended in an unbounded fluid of temperature T_∞. If when $r \to \infty$ then $T_\mathrm{r} \to T_\infty$, then the following energy balance is valid at the particle surface in a multiphase DNS framework:

$$\rho^* c_p^* \frac{dT_\mathrm{p,s}}{dt} = hA_\mathrm{p}(T_\infty - T_\mathrm{p,s}) = \pi k d_\mathrm{p} Nu (T_\infty - T_\mathrm{p,s}) \quad (15)$$

First, the particle heat capacity must be compensated for the adjusted density (in order not to overestimate the thermal mass of the particle):

$$c_p^* = \frac{c_{p,\mathrm{p}}}{C_\mathrm{c}} \tag{16}$$

Since the particle heat capacity already needs modification within the current framework, it is an ideal candidate to also take into account the effects of impeded heat transfer. Eq. (15) then becomes:

$$\rho^* c_p^* \frac{dT_{\mathrm{p,s}}}{dt} = \frac{2\pi k d_\mathrm{p}\left(T_\infty - T_{\mathrm{p,s}}\right)}{1+\frac{15}{4}\alpha_\mathrm{t}^{-1} Kn_\mathrm{p}} \tag{17}$$

so that c_p^* must be defined as:

$$c_p^* = \frac{c_{p,\mathrm{p}}\left(1+\frac{15}{4}\alpha_\mathrm{t}^{-1} Kn_\mathrm{p}\right)}{C_\mathrm{c}} \tag{18}$$

Figure 1 illustrates the concept of the adjusted heat capacity of a spherical particle as a function of the particle Knudsen number for five different thermal accomodation coefficients.

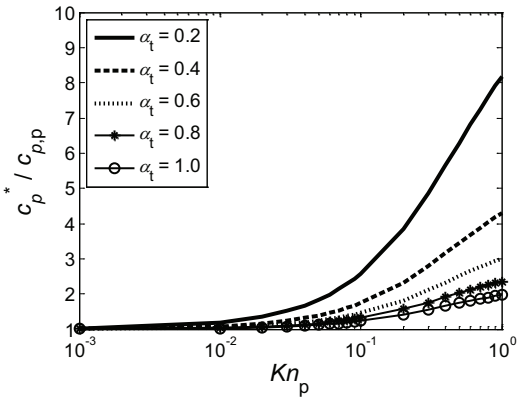

Figure 1. The normalized adjusted heat capacity versus the particle Knudsen number.

In summary, this derivation implies that we may use the adjusted density and the adjusted heat capacity to simulate the heat and momentum transfer to a solid spherical particle under rarefied conditions in a multiphase DNS framework.

3. RESULTS

We first perform a simulation of conduction from a stationary cylinder in a square enclosure. This allows us to validate the implementation of the energy balance within the current framework. Then, we perform a simulation of a settling particle with an internal heat source in a rectangular enclosure. Similar cases have been considered previously in the literature, which allows us to carry out a qualitative comparison. Finally, we investigate the settling of a particle with an internal heat source in rarefied flow.

3.1 Circular cylinder placed eccentrically in a square enclosure

This case is used for validation of the current model against the numerical results of Yu et al. [3], Feng and Michaelides [8], Pacheco et al. [19] and Demirdzic et al. [20], who all used different DNS methods to solve the same problem and whose results all agree well.

The domain is a two-dimensional square box and the particle is represented by a circular cylinder placed eccentrically in the enclosure. The cylinder is kept stationary and at a constant temperature, which is higher than that of the surrounding fluid. The walls to the left and the right are kept at the initial temperature of the fluid, whereas the top and bottom walls are adiabatic. The steady-state solution for the natural convection around the fluid is obtained and compared to the previous studies. The mesh is 100x100 as in the simulations of Feng and Michaelides [8]. The properties of the fluid and the temperature boundary conditions are chosen so that Pr = 10 and the Grashof number $Gr = \beta|g|\rho_\mathrm{f}^2 d_\mathrm{p}^3 \Delta T/\mu^2 = 10^5$.

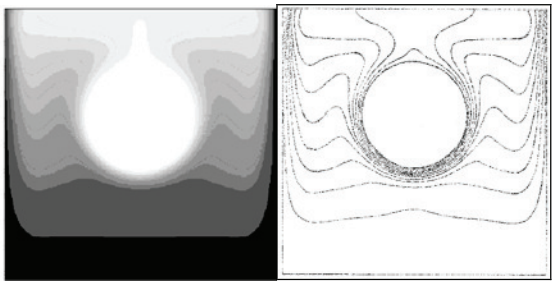

Figure 2. Hot cylinder in square enclosure. Left: Current work. Right: Feng and Michaelides [8].

The result is shown in Figure 2, where iso-contours of temperature are depicted for a hot cylinder in a square enclosure. The contour levels to the left represent 0.1 units of normalized temperature on the interval 0.1-0.9 (cold = black, hot = white), whereas the right contour lines represent 0.1 units on the interval 0.05-0.95. The isotherms obtained by the proposed method agree very well with the results of Feng and Michaelides [8], and hence also with the other previous investigations [3, 19, 20].

3.2 Settling velocity of non-isothermal particle

Here, we consider the settling of a particle in an adiabatic enclosure ($8d_\mathrm{p}$ x $16d_\mathrm{p}$) under the influence

of gravity and heat transfer effects. The particle and the surrounding fluid are initially of the same temperature. There is however a uniform heat source inside the particle that increases the temperature of the particle (and eventually also its surroundings). The evolution of the particle velocity in the vertical direction is monitored as a function of time. The velocity is made dimensionless by a characteristic velocity $U = d_{\mathrm{p}}^{\,2}\left(\rho_{\mathrm{p}} - \rho_{\mathrm{f}}\right)\underline{g}\big/16\mu$ that is representative of the terminal velocity [21], position by the particle diameter and time by the characteristic time scale $t = d_{\mathrm{p}}/U$. The set of governing dimensionless parameters used is ($Re_{\mathrm{p,T}}$, ρ_{ptf}, k_{ptf}, $c_{p,\mathrm{ptf}}$, Gr, β_{ptf}, Pr, Q, Kn_{p}) = (0.06, 2, 5, 1, 1000, 0, 0.7, 1, 0). This choice of parameters ensures that the particle motion always remains within the Stokes regime, which is desirable for the continuum case and the rarefied cases to be comparable.

The result is shown in Figure 3, where the velocity history of an identical particle settling in isothermal flow is also plotted as a reference. A close-up of the initial evolution of the velocities is embedded in the graph.

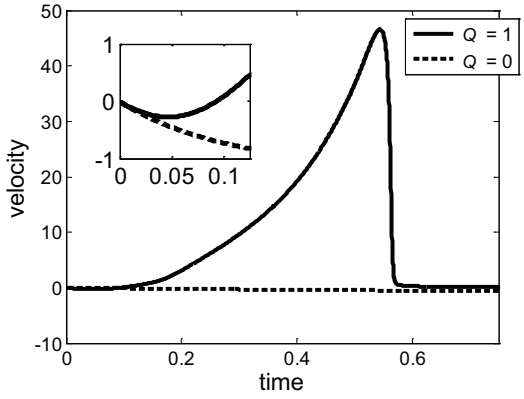

Figure 3. Settling velocity of a particle with an internal heat source in continuum flow.

The simulation predicts that the particle initially falls towards the bottom of the enclosure. However, it does not take long before the heating of the boundary layer around the particle gives rise to the buoyancy force that first counterbalances and then overcomes the gravitational acceleration of the particle. The particle therefore starts to move upwards, until the effects of the upper wall become apparent and the particle motion is slowed down because of the aerodynamic resistance. The results obtained in the present work are in good qualitative agreement with the results obtained by other authors [3, 8, 18] for the same problem with varying choices of the governing dimensionless parameters.

It should be stressed here that, even if there is a high particle velocity observed in Figure 3 (due to the particle being lifted up by natural convection of the surrounding fluid), the relative velocity to the continuous phase is still low and the flow around the particle remains within the Stokes regime.

3.3 Settling velocity of non-isothermal particle in rarefied flow

We next consider the same case of a settling particle with an internal heat source when the flow around it is rarefied. Two different particle Knudsen numbers, $Kn_{\mathrm{p}} = 0.1$ and $Kn_{\mathrm{p}} = 1$, are investigated. In order not to change any of the other parameters in the set of dimensionless numbers, the mean free path is scaled to obtain the desired particle Knudsen number (this is the only way in which a straightforward comparison can be made, since changing the particle diameter would affect also $Re_{\mathrm{p,T}}$ and Gr).

In the non-isothermal rarefied flow regime, a value of the thermal accommodation coefficient (α_{t}) is needed in order for the efficiency of energy transfer between the gas and the solid particle to be fully characterized. A comprehensive discussion about the dependence of α_{t} on the material properties and temperatures involved is beyond the scope of the current work, but we may note that for graphite (a major constituent of diesel soot) at 273 K, α_{t} varies from 0.36 to 0.96 depending on the incoming gas phase molecule [22]. The value chosen for the current investigation is $\alpha_{\mathrm{t}} = 0.5$.

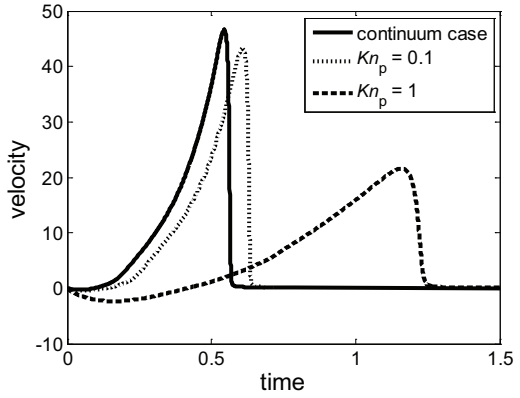

Figure 4. Settling velocities of particles with an internal heat source in rarefied flow.

As can be seen in Figure 4, the particle motion history is similar but delayed (slower) when the surrounding fluid is rarefied compared to the continuum case. Firstly, the rarefied fluid surrounding the particle cannot resist the initial particle acceleration due to gravity as in the continuum case. In both rarefied cases, the particle therefore falls farther than in the continuum case. Secondly, the impeded heat transfer from the particle to the fluid delays the growth of the buoyancy force. Consequently, the particle attains a

larger downward velocity before changing direction with increasing Kn_p.

Although the main effect of the rarefication is to delay the growth of a sufficiently large buoyancy force for the particle downward acceleration to be fully outweighed, the net result is not limited to merely slowing down of the same process that occurs in the continuum regime. Since thermal levitation and/or lifting up of the particle can only occur if there is sufficient available space for the natural convection streams underneath the particle to fully develop [18], the delay observed in the rarefied regime may actually prevent the upward motion of the particle altogether by shifting the heating-up of the fluid to a later point in time when the space underneath the particle may have become too small. This phenomenon is illustrated by the particle vertical trajectories plotted in Figure 5 for (ρ_{ptf} = 20, Q = 1), where the particle eventually moves upward in the continuum case but falls to the bottom of the enclosure for (Kn_p = 0.5, α_t = 1).

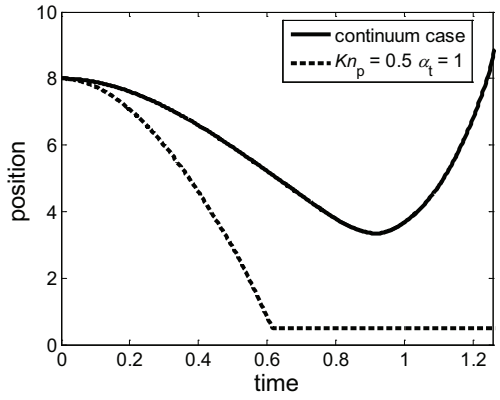

Figure 5. Particle vertical position versus time in continuum and rarefied flow (ρ_{ptf} = 20, Q = 1).

4. DISCUSSSION

In the present work, it is assumed that the temperature difference between the particle and its surroundings does not give rise to any significant thermophoresis. For small particles in a rarefied gas, the molecules impinging obliquely on the particle surface coming from a hotter region of the gas will transfer more momentum to the particle than molecules from the colder region. This phenomenon is known as thermophoresis when discussing the induced motion of a particle that takes place in the opposite direction of the gas phase temperature gradient. On the other hand, one speaks about thermal creep when discussing the induced motion of the gas adjacent to the particle surface. In slip boundary condition approaches, the thermal creep is typically accounted for by the addition of a thermal slip term to the expression for the velocity slip [23, 24]. However, since the slip boundary condition approach is only applicable for very small values of the particle Knudsen number [15, 23], a more practical solution to deal with the effects of thermal creep is to implement them into the current framework as an external (thermophoretic) force [5]. The magnitude of this force, when estimated using the relation derived by Talbot et al. [23], remains at least two orders of magnitude smaller than the force on the particle due to gravity throughout the simulations performed in the current work. Hence, neglecting the effects of thermophoresis in this study is justified.

In theory, the constants in the Cunningham correction could be affected by a change in temperature, if it produces an alteration of the degree of momentum accommodation of the gas molecules on the particle surface. However, Willeke [25] has shown that the maximum deviation in the correction from this effect is below 3%, and it has therefore been neglected.

5. CONCLUSIONS

In this paper, we present a multiphase DNS method that can be applied to resolve the motion of solid particles in rarefied flow with heat transfer effects. The model agrees well with the available data for the continuum regime [3, 8, 18, 19, 20], and is used to investigate particles with internal heat sources settling in confined, rarefied flow.

It is shown that the impeded heat transfer in the rarefied flow regime results in a delay of the fluid response to the heat generation inside the particle. Consequently, the chances for thermal levitation and/or lifting up of small, heat releasing particles are significantly reduced as the particle size becomes comparable to the mean free path of its carrier gas.

REFERENCES

[1] Koci, P., Stepanek, F., Kubicek, M., and Marek, M., 2007, „Modelling of micro/nano-scale concentration and temperature gradients in porous supported catalysts", *Chem. Eng. Sci.*, Vol. 62, pp. 5380-5385.

[2] Zia, R. N., and Brady, J. F., 2010, „Single-particle motion in colloids: force-induced diffusion", *J. Fluid Mech.*, Vol. 658, pp. 188-210.

[3] Yu, Z., Shao, X., and Wachs, A., 2006, „A fictitious domain method for particulate flows with heat transfer", *J. Comput. Phys.*, Vol. 217, pp. 424-452.

[4] Mandujano, F., Rechtman, R., 2008, „Thermal levitation", *J. Fluid Mech.*, Vol. 606, pp. 105-114.

[5] Ström, H., Sasic, S., and Andersson, B., 2011, „A novel multiphase DNS approach for

handling solid particles in a rarefied gas", *Int. J. Multiphase Flow*, Vol. 37, pp. 906-918.

[6] Maxwell, J. C., 1860, „Illustrations of the dynamical theory of gases", *Phil. Mag.*, Vol. 19, pp. 19-32.

[7] Cercignani, C., 2000, *Rarefied gas dynamics: From basic concepts to actual calculations*, Cambridge University Press.

[8] Feng, Z.-G., and Michaelides, E. E., 2009, „Heat transfer in particulate flows with Direct Numerical Simulation (DNS)", *Int. J. Heat Mass Transfer*, Vol. 52, pp. 777-786.

[9] Springer, G. S., and Tsai, S. W., 1965, „Method for Calculating Heat Conduction from Spheres in Rarefied Gases", *Phys. Fluids*, Vol. 8, pp. 1561-1563.

[10] Mikami, H., Endo, Y., and Takashima, Y., 1966, „Heat transfer from a sphere to rarefied gas mixtures", *Int. J. Heat Mass Transfer*, Vol. 9, pp. 1435-1448.

[11] Springer, G. S., and Wan, S. F., 1966, „Note on the Application of a Moment Method to Heat Conduction in Rarefied Gases between Concentric Spheres", *AIAA J.*, Vol. 4, pp. 1441-1443.

[12] Liu, F., Daun, K. J., Snelling, D. R., and Smallwood, G. J., 2006, „Heat conduction from a spherical nano-particle: status of modeling heat conduction in laser-induced incandescence", *Appl. Phys. B*, Vol. 83, pp. 355-382.

[13] Sherman, F. S., 1963, „A survey of experimental results and methods for the transition regime of rarefied gas dynamics", in: *Rarefied Gas Dynamics*, ed. J. A. Lauermann, Academic Press, New York.

[14] Smoluchowski, von M., 1898, „Ueber Wärmeleitung in verdünnten Gasen", *Ann. Der Phys. Chem.*, Vol. 64, pp. 101-130.

[15] Bailey, C. L., Barber, R. W., Emerson, D. R., Lockerby, A., and Reese, J. M., 2005, „A critical review of the drag force on a sphere in the transition flow regime", Proc. *Rarefied Gas Dynamics: 24th International Symposium*, American Institute of Physics.

[16] Taylor, T. D., 1963, „Heat Transfer from Single Spheres in a Low Reynolds Number Slip Flow", *Phys. Fluids*, Vol. 6, pp. 987-992.

[17] Boussinesq, J., 1903, *Théorie analytique de la chaleur*, Paris: Gathier-Villars, Vol. 2.

[18] Wachs, A., 2011, „Rising of 3D catalyst particles in a natural convection dominated flow by a parallel DNS method", *Computers Chem. Eng.*, Vol. 35, pp. 2169-2185.

[19] Pacheco, J. R., Pacheco-Vega, A., Rodic, T., and Peck, R. E., 2005, „Numerical simulations of heat transfer and fluid problems using an immersed-boundary finite-volume method on non-staggered grids", *Numer. Heat Transfer B*, Vol. 48, pp. 1-24.

[20] Demirdzic, I., Lilek, Z., and Peric, M., 1992, „Fluid flow and heat transfer test problems for non-orthogonal grids: bench-mark solutions", *Int. J. Numer. Meth. Fluids*, Vol. 15, pp. 329-354.

[21] Yu, Z., Phan-Thien, N., Fan, Y., Tanner, R. I., 2002, „Viscoelastic mobility problem of a system of particles", *J. Non-Newtonian Fluid Mech.*, Vol. 104, pp. 87-124.

[22] Day, K. L., 1973, „The Thermal Accommodation Coefficient of Graphite", IAU Symp. No. 52 – Interstellar Dust and Related Topics, Greenberg & Van de Hults (eds), 311-315.

[23] Talbot, L., Cheng, R. K., Schefer, R. W., and Willis, D. R., 1980, „Thermophoresis of particles in a heated boundary layer", *J. Fluid Mech.*, Vol. 101, pp. 737-758.

[24] Sone, Y., 2000, „Flows induced by temperature fields in a rarefied gas and their ghost effect on the behavior of a gas in the continuum limit", *Ann. Rev. Fluid Mech.*, Vol. 32, pp. 779-811.

[25] Willeke, K., 1976, „Temperature Dependence Of Particle Slip In A Gaseous Medium", *J. Aerosol Sci.*, Vol. 7, pp. 381-387.

Conference on Modelling Fluid Flow (CMFF'12)
The 15th International Conference on Fluid Flow Technologies
Budapest, Hungary, September 4-7, 2012

PARTICLE SEPARATION USING HIGH-GRADIENT MAGNETIC FIELD IN WASTEWATER TREATMENT

Tamás KARCHES[1]

[1] Corresponding Author. Department of Sanitary and Environmental Engineering, Budapest University of Technology and Economics. Muegyetem rkp. 3., H-1111 Budapest, Hungary. Tel.: +36 1 463 4260, E-mail: karches@vkkt.bme.hu

ABSTRACT

Separation of flock size particles in wastewater treatment is essential to ensure the appropriate effluent water quality. Gravitational settling may be insufficient (time- and money consuming) in many cases. Eliminating this problem, magnetite dispersion was stirred to the sludge and static magnetic field induced by permanent magnets was applied, which accelerated the settling-thickening process. The aim of this paper is to establish a novel model system, which couples the magnetostatics and fluid flow in order to describe the magnetic separation of the wastewater sludge. This coupling is achievable by calculating the magnetic force on particles. The model system was calibrated by the laboratory experiments. The magnetic susceptibility of the magnetite dispersion was determined using Langevin function. The model results pointed out the differences in the flow field of gravitational and magnetic settling. For evaluation of the settling phenomenon Lagrangian particle tracking was used.

Keywords: CFD, magnetic separation, thickening, wastewater treatment

NOMENCLATURE

$\underline{A}$	[*Wb/m*]	magnetic vector potential
$\underline{B_r}$	[*A/m*]	remanent magnetic flux
D	[-]	demagnetisation factor
$\underline{F_m}$	[*N*]	magnetic force
$\underline{\underline{I}}$	[-]	unit tensor
L	[-]	Langevin function
M	[*A/m*]	ferrofluid magnetisation
M_d	[*A/m*]	magnetisation of ferrimagnet
T	[*K*]	temperature
X_{ff}	[-]	ferrofluid mass fraction
d	[*m*]	diameter of magnetite particle
d_s	[*m*]	equivalent diameter of sludge
k	[J/K]	Boltzmann constant
g	[m^2/s]	gravitational acceleration
p	[*Pa*]	pressure
t	[*s*]	time
$\underline{v}$	[*m/s*]	velocity of fluid
α	[-]	Langevin function parameter
χ	[-]	susceptibility
χ_e	[-]	susceptibility in external field
η	[*kg/ms*]	dynamic viscosity
μ_0	[H/m]	magnetic permeability of vacuum
μ_r	[*H/m*]	relative magnetic permeability
ρ	[kg/m^3]	density of the fluid
ρ_w	[kg/m^3]	density of water
ρ_{ff}	[kg/m^3]	density of ferrofluid
ρ_s	[kg/m^3]	density of sludge
ψ_v	[-]	magnetic volume fraction

Subscripts and Superscripts

x, y, z	Cartesian coordinates
Nd	neodymium magnet

1. INTRODUCTION

Wastewater treatment using activated sludge is a popular technology, which has to fulfil the requirements of strict regulations [1] on effluent water quality. Numerous innovations have been developed in recent years, e.g. [2, 3] and computational fluid dynamics (CFD) has also a major role in design, operation [4] and upgrading of the treatment processes. The latter means that the effluent water quality can be improved with e.g. nitrification process, chemical phosphorous removal [5] in the existing systems or by new construction of the tanks. CFD is an efficient tool to analyze new technologies at the design phase, and it reduces the required laboratory and field experiments.

In this paper a novel approach is presented to separate the flock size particles (sludge) in wastewater treatment process, which are the scapegoat of bad effluent quality in many cases [6]. Due to their size the gravitational force is not enough for an appropriate separation, therefore an external field is applied. Magnetic force have influence on the magnetised particles, therefore magnetite dispersion (multicomponent mixture) was

stirred to the sludge and imposed to an externally induced magnetic field. Sakai et al. [7] realized 92 % carbon removal at high, 15.3 g/l mixed liquor suspended solid (MLSS) concentration applying magnetic separation in wastewater treatment, Hattori et al. [8] improved the settling charachteristics by stirring Fe(III)-chloride in a concentration of 0.1 % w/v to an aeration vessel, but no one establish a model system, which could describe this magnetic separation phenomena. Our previous results [9] also showed that the flow of the particles could be manipulated and the settling-thickening process was accelerated.

The main design parameters of the magnetic separation like magnetic field strength, iron concentration and sludge volume index were investigated with the tool of factorial analysis in order to determine the importance of the different parameters. The outcome was that the magnetic remanent flux has a major impact on settling efficiency. A magnet with at least $\underline{B_r}$ = 0.5 T have to be applied. Using the neodymium magnet and dosing 70-80 mg iron to 1 litre sludge, the dry solid content doubled compared to gravitational settling/thickening.

Magnetite dispersion can be produced by simple reactions described in the literature [10]. Figure 1 shows the connections of the different kind of particles used in this experiment.

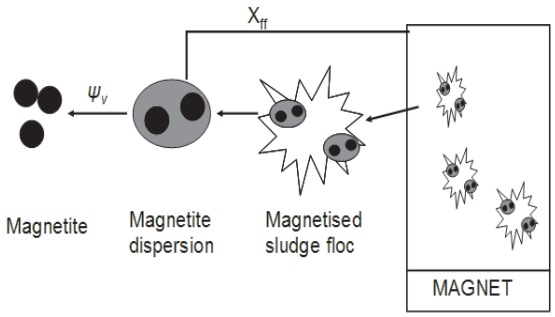

Figure 1. Magnetic separation of sludge using different kind of particles

The aim of this paper is to build a model system, which is able to simulate the magnetic separation of the sludge and to have a better understanding about the phenomena in order to design a full scale industrial application. The model system was calibrated by measurements and has two main elements. One is the magnetostatic-fluid flow coupled system for the magnetite dispersion and the second is a Lagrangian method, which is used for the magnetised sludge flocks. Laboratory measurements described in section 2 are required to calibrate the numerical model (magnetic properties of ferrofluid and sludge properties). Section 3 presents the modelling concept in detail and the results.

2. LABORATORY EXPERIMENTS

2.1 Magnetite dispersion

Magnetite dispersion was produced from $FeCl_2$ and $FeCl_3$ in alkaline environment as in [9] is described. The 500 ml dispersion has 168 mg magnetisable (iron) content, therefore the dispersion gains magnetic behaviour, when external magnetic field is applied. This can be quantified with Langevin function [11] as follows:

$$\frac{M}{\psi_v M_d} = L(\alpha) = \coth(\alpha) - \frac{1}{\alpha} \qquad (1)$$

Using the low field limit of the function the slope of the linear part of the magnetisation curve can be calculated. The slope equals to the magnetic susceptibility of the fluid as Eq. 2. describes:

$$\chi_e = \frac{\pi}{18} \cdot \frac{\mu_0}{k \cdot T} \cdot \psi_v \cdot M_d^2 \cdot d^3 \qquad (2)$$

This susceptibility should be modified with the demagnetisation factor (D) – which takes into account the effect of external field - as Eq. 3. shows. For the demagnetisation factor D=0.211 was applied according to the literature [11]:

$$\chi = \frac{\chi_e}{1 - \chi_e \cdot D} \qquad (3)$$

As Eq. 1. reflects, the diameter of magnetic particles is an important factor to determine the susceptibility. The microscopical analysis revealed that the value of "d" was in the range of 4-5.3 μm, and the susceptibility was in the range of 0.68-1.96.

2.2 Settling-thickening efficiency

Magnetite dispersion was stirred to the sludge and a permanent magnet was put to the bottom of the settling column. The level of the sludge blanket was observed in the course of time and the result was compared to the settling in absence of the magnets, see Figure 2. In the applied magnetite dispersion the iron content was 20 mg. The initial sludge blanket level was 15 cm, the dry solid content of the sludge was 4.3 g/l. After 30 minutes the dry solid content reached 12 mg/l with in presence of the magnetic field, while it was 7.1 mg/l without magnets.

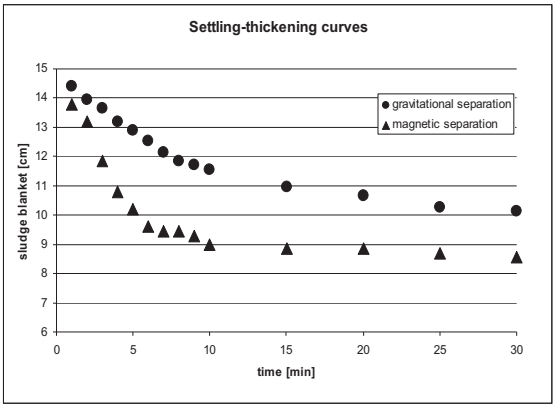

Figure 2. Settling-thickening curves in presence and absence of magnetic field.

As Fig. 2 shows, the linear part of the curve (discrete settling, the particles do not hinder the movement of each other) is till 10 minutes using only the gravitational force, 5 minutes using magnets. From the slope of the linear part the average discrete settling velocity can be calculated, which is $5.7 \cdot 10^{-5}$ m/s in the first case and $1.7 \cdot 10^{-4}$ m/s in the second. The Reynolds number of the particle settling is 0.2, therefore it is considered to be laminar.

3. NUMERICAL MODELLING

3.1 Modelling concept

The applied model system can be seen on Figure 3, where the rectangles are the numerical model elements and circles demonstrate the experiments. First the geometry of the experimental setup was created (as it was described in the previous section) and that was followed by the spatial discretisation. Three domains were separated as the Table 1 shows:

Table 1. Domains used in the magnetostatic model

Domain	Material	Number of elements (tetra)	Elements size [m]
1.Magnet	Nd	810	0.005
2.Settling column	Water	1837	0.005
3.Outer region	Air	7577	0.02

For the magnetostatic simulation all the three domains were active, whereas for CFD simulation only the settling column was used. It was assumed that there is only one-way coupling between the magnetostatics and CFD; only the magnetic field has influence on fluid flow, the velocity field does not reflect back to the magnetic field. That could have been done, because the external magnetic field induced by permanent magnets is stronger than the magnetic field induced by the ferrofluid.

The force acting on the particles of the magnetite dispersion due to the magnets can be calculated if the volume fraction of magnetite dispersion is known. The result of the CFD calculation is the velocity field induced by magnetic field. According to Newton II. law, the settling of the sludge particles can be determined from the force balance. The physical properties of the sludge flocks can be derived from the experimental results.

As the sludge goes through the settling-thickening process, the sludge blanket level decreases and gets denser in the course of time, which means the volume fraction of the magnetite gets higher near the magnet and lower at the top. Therefore the domain 2 has to be separated according to sludge blanket level. The changes in the velocity field and the settling characteristics are observed at different "snapshots".

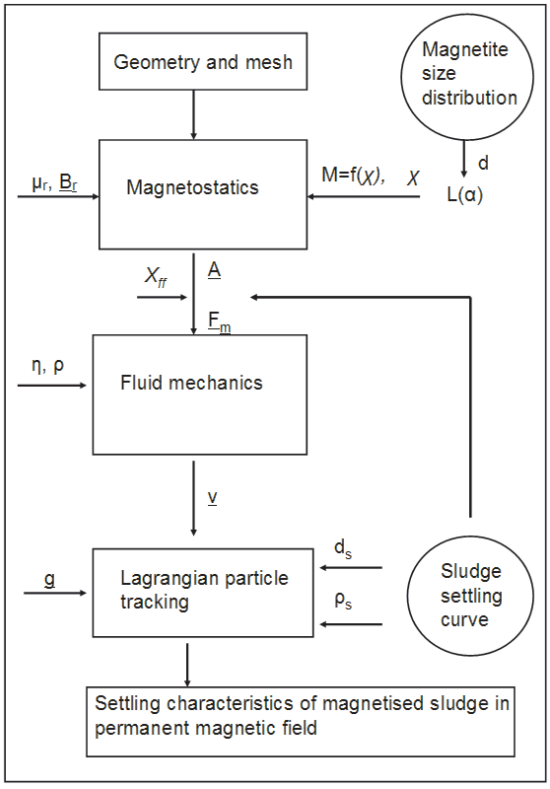

Figure 3. The applied model system

3.2 Magnetostatics

Depending on the different materials presented in the model, different equations have to be used in order to describe the magnetic field induced by permanent magnets. Introducing magnetic vector potential is a convenient method for the numerical solution [12]. For static magnetic field without any electric current the following equations are solved for the domain, which contains magnet:

$$\nabla \times \left(\frac{1}{\mu_0 \mu_r} \left(\nabla \times \underline{A} - \underline{B_r} \right) \right) = 0 \tag{4}$$

For the outer region:

$$\nabla \times \left(\frac{1}{\mu_0 \mu_r} \left(\nabla \times \underline{A} \right) \right) = 0 \tag{5}$$

For the ferrofluid:

$$\nabla \times \left(\frac{1}{\mu_0} \left(\nabla \times \underline{A} - \underline{M} \right) \right) = 0 \tag{6}$$

3.3 Magnetohydrodynamic model

CFD calculations were performed assuming laminar flow and laminar sedimentation as the experimental results revealed. The continuity (Eq. 7.) and momentum (in the form of Eq. 8) equations [13] are solved after the result of magnetostatic calculation is stored.

$$\nabla \cdot \underline{v} = 0 \tag{7}$$

$$\rho \underline{v} \cdot \nabla \underline{v} = \nabla \left[-p\underline{\underline{I}} + \eta \left(\nabla \underline{v} + \left(\nabla \underline{v} \right)^T \right) \right] + \underline{F} \tag{8}$$

The density of the flow can be calculated as follows:

$$\frac{1}{\rho} = \frac{1 - X_{ff}}{\rho_w} + \frac{X_{ff}}{\rho_{ff}} \tag{9}$$

It could be noted that there is no significant difference between the pure water density and the magnetite dispersion, because the magnetite volume fraction was low. The calculation of the force acting on the particles due to the magnetic field uses the magnetic susceptibility, permeability, vector potential and volume fraction data as these are described in [11 and 14]:

$$F_x = \frac{\chi}{\mu_0 \mu_r^2} \left(\frac{\partial A_z}{\partial x} \frac{\partial^2 A_z}{\partial x^2} + \frac{\partial A_z}{\partial y} \frac{\partial^2 A_z}{\partial x \partial y} \right) \cdot X_{ff} \tag{10}$$

$$F_y = \frac{\chi}{\mu_0 \mu_r^2} \left(\frac{\partial A_z}{\partial x} \frac{\partial^2 A_z}{\partial x \partial y} + \frac{\partial A_z}{\partial y} \frac{\partial^2 A_z}{\partial y^2} \right) \cdot X_{ff} \tag{11}$$

3.4 Model results

Results of the magnetostatic calculation can be seen on Figure 4, where the magnetic potential is drawn as contour lines. It is evident that the lines are denser around the magnet, due to the high gradients of the field. As a consequence, the magnetic force acts on the particle differently with function of their location within the settling column, making the settling uneven and producing swirl in the system. Furthermore, the speciality of the magnetic field is that the coverage radius is small and therefore the geometry of the traditional settling tanks should be reconsidered.

On Fig. 4 the velocity field can be seen as surface plot. The lighter is the area, the higher are thevelocities. The velocity magnitude is around 0.13 mm/s in the immediate vicinity of the magnet. Comparing this value to the experimental results (0.17 mm/s), it is lower, but not significantly. The reason is that the gravitational force is not built in the model, only the magnetised ferrofluid movement is calculated, which has a higher proportion of the total force balance.

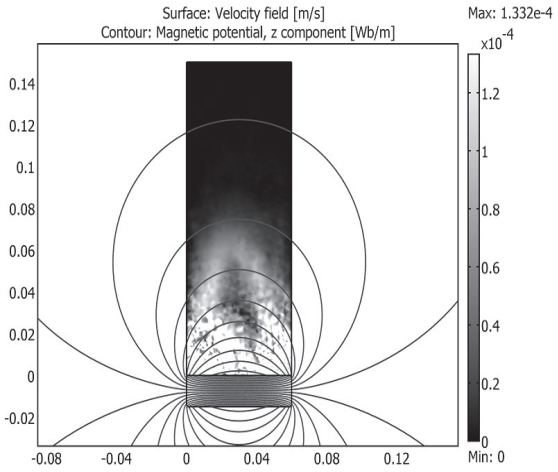

Figure 4. Velocity field induced by permanent magnet and contours of magnetic flux

The sludge blanket level is decreasing with time, therefore domain 2 has to be separated into two sub-domains due to the blanket level. Both are fluid domains, but the upper can not gain magnetisation, because there are not any magnetite particles connected to the sludge flocks. The lower sub-domain has an increased number of magnetite particles, therefore its volume fraction and the magnetic force becomes higher. As a result, the velocity field changes with time. Three "snapshots" were investigated; at the first, 5th and 10th minutes. The velocity streamlines can be seen on the Figure 5.

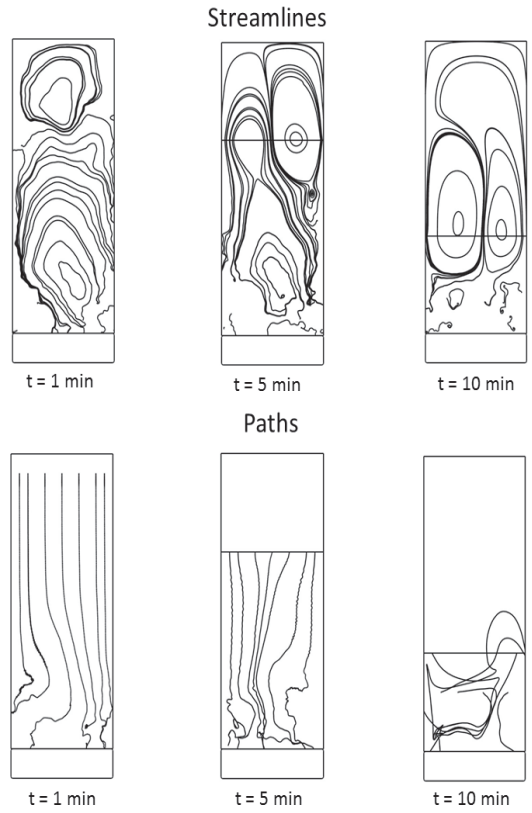

Figure 5. Streamlines and pathlines at different time

At the beginning two parts can be separated. The first is situated near the lower part of the settling column, where the velocity streamlines follow the contour of the magnetic potential. The second part has a much smaller extension, where the magnetic field does not have effect. With time they rearrange their situation as Fig. 5 presents.

Lagrangian approach was used to model the separation of magnetised sludge. Sludge flocks (with density of 1070 kg/m^3 [15]) are released at different point of the fluid domain as Fig. 5 shows. The particles released from the upper zone settle straightforward at the beginning, but as the distance from the magnet decreases the magnetic field divert the paths.

Particles released at the lower zone after the tenth minute show other kind of pattern. According to the laboratory experiments the settling is hindered here with the consequence that the inner particle effects can not be neglected. The applied model does not take into account the thickening and compression effect, therefore the experimental results are necessary to assign the limitation of the model.

4. CONCLUSIONS

In this paper a new model system was introduced, which is able to show certain patterns of magnetic separation of flock sized particles in wastewater treatment. The magnetostatic-fluid dynamic coupled system is calibrated by experimental data (particle size distribution of magnetite, gravitational settling curve of sludge) as well as verified (magnetic separation curve). The velocity field induced by magnets was calculated using Eulerian approach, while the settling phenomenon of sludge flocks used Lagrangian particle tracking based on the body force acting on the flocks.

The velocity field induced by permanent magnets has an uneven character and high gradients appear near the magnet, therefore the drive force of the process is much higher (due to magnetic field) compared to the traditional gravitational settling. In addition the flow patterns were studied at different sludge blanket level, which were effectuated by applying varying magnetic susceptibility.

To be concluded, the effect of different design parameters, as sludge characteristics, applied magnetic field and magnetite concentration can be analysed with this method. It is helpful in the future in order to reduce the number of the necessary experiments. The next step in improving this model system is to work out an elaborate method for describing the sludge characteristics in the hindered settling zone.

ACKNOWLEDGEMENTS

This work is connected to the scientific program of the “Development of quality-oriented and harmonized R+D+I strategy and functional model at BME” project. This project is supported by the New Széchenyi Plan (Project ID: TÁMOP-4.2.1/B-09/1/KMR-2010-0002). The work has also been supported by the project “ Talent care and cultivation in the scientific workshops BME”. This is in connection by the grant TÁMOP- 4.2.2.B-10/1—2010-0009.

REFERENCES

[1] Council Directive 91/271/EEC concerning urban waste-water treatment, 1991., Brussels.

[2] Fleit, E., Melicz, Z., Zrínyi M., Filipcsei G., László K., Dékány I., and Király Z., 2007, “IASON-Intelligent Activated Sludge Operated by Nanotechnology”, 9th Conference on Colloid Chemistry, Siófok, Hungary.

[3] Judd, S., 2006, The MBR book. Principles and applications of membrane bioreactors in water and wastewater treatment, Elsevier, Oxford.

[4] Brouckaert, C.J., and Buckley, C.A, 1999, “The use of Computational Fluid Dynamics for Improving the design and operation of water and wastewater treatment plants”, *Water*

Science and Technology, Vol. 4., No. 4-5., pp. 81-90.

[5] Vacker, D., Connell, C.H., and Wells, N.W., 1967, "Phosphate Removal through Municipial Wastewater Treatment at San Antonio, Texas", *Journal Water Pollution Control Federation,* Vol. 39., No. 5., pp. 750-771.

[6] Swope, G.H., 1930, "Correlation between B.O.D. and Suspended Solids of Activated Sludge Effluent", *Sewage Works Journal*, Vol. 2., No. 4., pp. 500-503.

[7] Sakai, Y., Terakado, T., and Takahashi, F., 1994, "A Sewage Treatment Process Using Highly Condensed Activated Sludge with an Apparatus for Magnetic Separation", *Journal of Fermentation and Bioengineering*, Vol. 78., No. 1., pp. 120-122.

[8] Hattori, S., Watanabe, M., Endo, T., Togii, H., and Sasaki, K., "Effects of an External Magnetic Field on the Sedimentation of Activated Sludge", *World Journal of Microbiology and Biotechnology*, 17, 279-285.

[9] Buzás, K., and Karches, T., 2011, „Separation of flock-size particles using magnetic field" (In Hungarian), *Építőmérnöki Kar a Műegyetemért,* pp. 103-108.

[10] Hajdú, A., 2010, „Synthesis and stabilization of magnetic fluids under physiological conditions with the view of biomedical applications" (In Hungarian), *PhD Dissertation, University of Szeged, Department of Physical Chemistry and Material Science.*

[11] Rosenweig, R.E., 1997, *Ferrohydrodynamics*, Dover Publications, Inc. Mineola, New York.

[12] Simonyi, K., and Zombory, 2000, Theoretical Electrotechnics (In Hungarian), Műszaki Könyvkiadó, Budapest, pp. 284-287.

[13] Temam, R., 1977, *Navier-Stokes Equations, Theory and Numerical Analysis*, North-Holland Pub. Com., Amsterdam, New York, Oxford.

[14] Rinaldi, C., 2001, Body vs. Surface forces in continuum mechanics: Is the Maxwell stress tensor a physically objecctive Cauchy stress? Thesis, Massachusetts Institute of Technology.

[15] Hribersek, M., Zajdela, B., Hribernik, A., and Zadravec, M., 2011, "Experimental and numerical investigations of sedimentation of porous wastewater sludge flocs", *Water Research,* Vol. 45., pp. 1729-1735.

Conference on Modelling Fluid Flow (CMFF'12)
The 15th International Conference on Fluid Flow Technologies
Budapest, Hungary, September 4-7, 2012

THE FREE LEVEL POST-DARCY FILTRATION THROUGH HOMOGENOUS MEDIA

Josif BARTHA [1], Nicolae MARCOIE [2], Daniel TOMA [3], Daniel TOACĂ [4], Victor GABOR [5], Aron Gabor MOLNAR [6], Adina LUPUSORU [7]

[1] Prof. PhD. Eng., "Gheorghe Asachi" Technical University of Iasi, Faculty of Hydrotechnical Engineering, Geodesy and Environmental Engineering, 65 Prof. dr. docent Dimitrie Mangeron Street, 700050, Iasi, Romania, phone number: +40232 270804, email: i_bartha@yahoo.com
[2] Assoc. Prof. PhD. Eng.,email: nmarcoie@yahoo.com
[3] Assist. Eng., email: daniel_10hid@yahoo.com
[4] PhD. Eng.,email: daniel.toaca@yahoo.com
[5] Lect. PhD. Eng.,email: vicgabor@yahoo.com
[6] PhD. Student, email: agmolnar@yahoo.com
[7] Master Student, email: nyxgl@yahoo.co.uk

ABSTRACT

This paper refers to the post-Darcy free level permanent filtration. The capillary tube model is applied to this movement. The theoretical filtration coefficient and Chézy coefficient are computed and also experimentally verified for a homogeneous and isotropic material, made of glass spheres, river gravel and crushed rock.

The typical features for the free-level post-Darcy filtration (depending on slope) are the lower, critical and higher stages of the flow.

Gradually accelerated and retarded post-Darcy's flows within permeable media are theoretically studied and results experimentally checked.

Keywords: Capillary tube model, free level flows, hydraulic parameters, post-Darcy's filtration.

NOMENCLATURE

d	$[m]$	pore tub equivalent diameter
d_p	$[m]$	particles nominal diameter
g	$[m \cdot s^{-2}]$	gravity acceleration
$h, h_0', h_1, h_2, h_{cr}, h_{sp}, dh, \Delta h$	$[m]$	depth
i, i_p, i_e, i',	[-]	slopes
l, l', l_{exp}, l_t	$[m]$	distances
k_{pD}, k_t	$[m \cdot s^{-1}]$	filtration coefficient
m	[-]	channel side slope
n	[-]	porosity
p	[-]	parabola's parameter
q	$[m^3 \cdot s^{-1}]$	specific flow
x	$[m]$	length
y	[-]	hydraulic exponent of the bed
$A, A_0, A_0', A_m, A_{cr}$	$[m^2]$	cross sections
A_d,	$[m^{-1}]$	dynamic specific area
B	$[m]$	channel width at water level
C_{pD}, C_f	$[m^{0.5} \cdot s^{-1}]$	Chézy coefficient
$H, H_1, H_2, dH, \Delta H$	$[m]$	depth
Re_d	[-]	pore diameter Reynolds number
Q	$[m^3 \cdot s^{-1}]$	volumetric flow rate
V	$[m \cdot s^{-1}]$	mean pore velocity
V_0	$[m \cdot s^{-1}]$	superficial (apparent) velocity
α	[-]	Coriolis coefficient
θ	[^{o}]	angle
ζ, η	[-]	relative depth
λ	[-]	Darcy-Weisbach coefficient
μ	$[Pa \cdot s]$	dynamic viscosity
τ	[-]	tortuosity
δl	[-]	relative error
ρ	$[kg \cdot m^{-3}]$	density

1. INTRODUCTION

Engineering practice is frequently using filtering structures and materials including voids in which the motion of free level liquids overruns the Darcy's law volubility domain which is acceptable for laminar flows and weak inertia ($Re_d < 4$).

Such flows correspond to the Forchheimer zone of high inertia ($Re_d = 4 \ldots 180$), to the transition zone ($Re_d = 180 \ldots 900$) and to the turbulent zone ($Re_d > 900$) [1]. These flows occur through filtering dams, bridges [2], flows within mobile river beds [3], in debris, gullies, permeable marine dams, drains and wells filters, air change and pollution in crops, built up areas, etc.

The post-Darcy free level uniform filtration takes place for hydraulic gradients $i > 1$ and means that there is need to take into account the inertial losses, not only the viscous ones [4].

For describing the motion the capillary tubes model is used. [5].

For post-Darcy motions, with viscous and inertial energy losses, the λ coefficient has the next form [6, 7, 8, 9, 10]:

$$\lambda = \frac{64}{Re_d} + 0.7743 \tag{1}$$

where Re_d is the Reynolds number computed for the pores' fictive diameter d, and velocity in pores V.

$$Re_d = \frac{\rho \cdot V \cdot d}{\mu} \tag{2}$$

To define the diameter of the fictive capillaries is used the model of thin tubes [5]:

$$d = \frac{4n}{(1-n)A_d} \tag{3}$$

where A_d is the specific dynamic area [5, 6].

For post-Darcy free level filtration the superficial (apparent) velocity is expressed under the form given by Chézy, proposed by Izbas C. V. [2]:

$$V_0 = C_f \cdot n\sqrt{d_p \cdot i} = k_t \cdot \sqrt{i} \tag{4}$$

where: n is the porosity, d_p – the solid particles diameter of the permeable medium; C_f – the Chézy coefficient and i – the bed slope. The empirical formulae are given for Chézy coefficient.

The equivalent diameter of solid particles is uncertain; in literature there exist different definition for it [12].

The post-Darcy, uniform filtration with free level has the energy gradient, piezometric gradient and slope of the bed the same:

$$i = i_p = i_e \tag{5}$$

Its characteristic equation is:

$$Q = V_0 A_0 = A_0 C_{pD} \frac{n}{\tau}\sqrt{d \cdot i} = A_0 k_{pD} \frac{n}{\tau}\sqrt{i} \tag{6}$$

with: V_0 the supperficial velocity; A_0 –the apparent cross section of the filtering column; n – the porosity; τ – the tortuosity; d – the fictiv diameter of the model tubes; C_{pD} – the Chézy's coefficient and k_{pD} – the filtration coefficient for post-Darcy movement. The elements are defined in [2, 5, 6, 7].

The velocity distribution for filtration currents is almost uniform on the cross section and due to this the Coriolis coefficient can by considered $\alpha = 1$.

The filtration post-Darcy, with free level admits alternate stages for the motion of liquids [2,6], defined by:

$$\frac{\tau^2 Q^2}{n^2 g} = \frac{A_0^3(h_{cr})}{B(h_{cr})} \tag{7}$$

2. GRADUALLY ACCELERATED OR RETARDED FLOW

The filtering channel can have different shapes along the movement: trapezoidal (marine dikes, groins, filtering bridges, culverts), rectangular (riprap cofferdams, debris channels) as it is shown in Fig. 1. Geometrical slope of the bottom may be positive, negative or null.

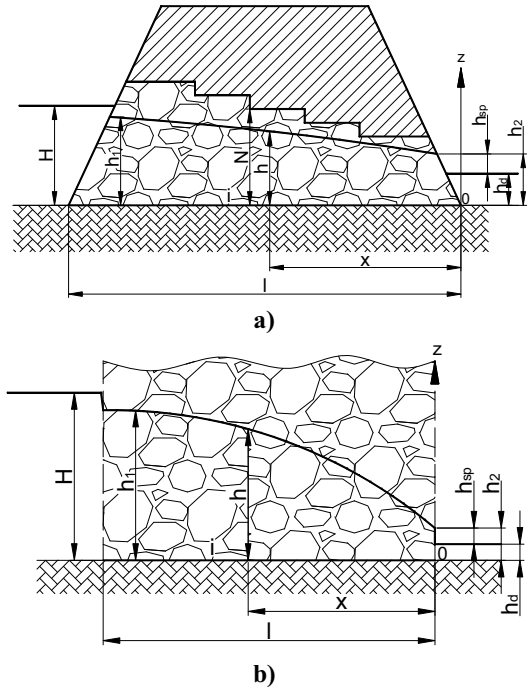

Figure 1. Post-Darcy non-uniform filtration a) rock fill culvert; b) coffer dam

a) The differential equation of the movement

The steady, non-uniform, post-Darcy filtration is characterized by water depth changing along the flow (Fig. 2).

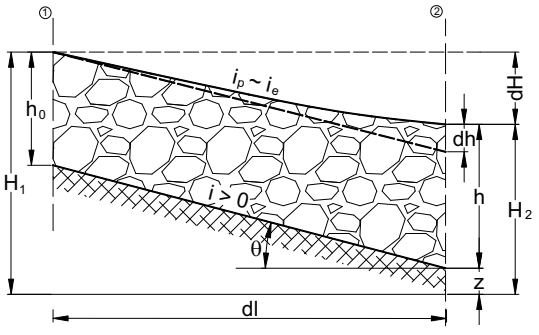

Figure 2. Steady, non-uniform, post-Darcy flow on positive bed slope

The filtration water free surface slope is defined as:

$$i_e = -\frac{dH}{dl} = \sin\theta - \frac{dh}{dl} \approx tg\theta - \frac{dh}{dl} = i - \frac{dh}{dl} \tag{8}$$

The conservation of mass, together apparent velocity defines the flow, as:

$$Q = A \cdot V_0 = A \cdot k_{pD} \frac{n}{\tau} \sqrt{i - \frac{dh}{dl}} \tag{9}$$

For positive slope $i > 0$, equalize of the equation (9) with a virtually uniform flow (5), the free level current depth variation will be defined (Fig. 2), as:

$$\frac{dh}{dl} = i\left(1 - \frac{A_0^2}{A^2}\right) \tag{10}$$

For horizontal bed (Fig. 3), $i = 0$, from (9) it results:

$$\frac{dh}{dl} = -\frac{Q^2}{A^2 k_{pD}^2} \frac{\tau^2}{n^2} \tag{11}$$

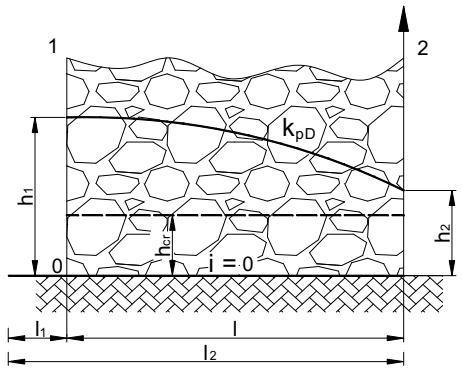

Figure 3. Steady, non-uniform, post-Darcy flow on horizontal bed

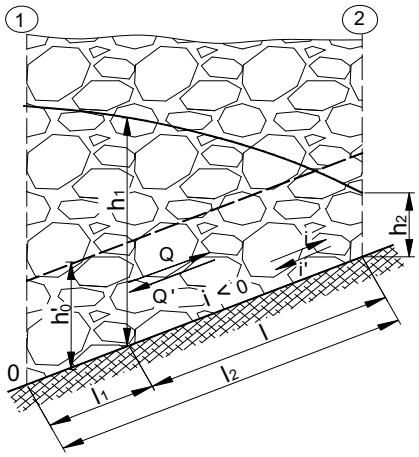

Figure 4. Steady, non-uniform, post-Darcy flow on negative slope bed

For negative bed slope (Fig. 4), $i < 0$, the depth variation along the flow is obtained by replacing $|i| = -i'$ and equalizing the flow (9) with a virtually uniform one on reversed movement, that is:

$$\frac{dh}{dl} = -i'\left(1 + \frac{A_0'^2}{A^2}\right) \tag{12}$$

where A_0' is the cross section for the normal depth h_0' of the reversed current.

Qualitative analysis of the flow, based on equation (10) for $i > 0$, (11) for $i = 0$ and (12) for $i < 0$ corresponds to Table 1.

Table 1. Steady, non-uniform, post-Darcy filtration

Nr.	*i*	*h*	$\frac{dh}{dl}$	Flow type
1	$i > 0$	$h > h_0$	> 0	retarded
		$h < h_0$	< 0	accelerated
2	$i = 0$	-	< 0	accelerated
3	$i < 0$	-	< 0	accelerated

There are possibilities for analytical and numerical solutions of the differential equations of the motion.

b) Hydraulic exponent of the bed

Analytical resolution of differential equations uses the hydraulic exponent of the bed, defined by the relationship [11]:

$$\left(\frac{A_2}{A_1}\right)^2 = \left(\frac{h_2}{h_1}\right)^y \tag{13}$$

where A_1 and A_2 are the apparent cross sections of the flow (corresponding to depth h_1 and h_2).

After logarithmation of the equation (13) the hydraulic exponent of the bed for a certain cross section will be obtained:

$$y = \frac{2\lg\left(A_2 / A_1\right)}{\lg\left(h_2 / h_1\right)} \tag{14}$$

For particular cross sections the following values are valid: rectangular $y = 2$; parabolic $y = 3$; triangular $y = 4$.

c) Analytical solutions of the differential equations

Integration of the differential equation of the flow for positive and negative bed slope of the rectangular cross section channel is possible.

- *For positive bed slope* ($i > 0$), by noting $A / A_0 = h / h_0 = \eta$, respectively $dh = h_0 \cdot d\eta$ the integrate form of equation (10) is:

$$\frac{i}{h_0} l = \eta_2 - \eta_1 + \varphi(\eta_2, y) - \varphi(\eta_1, y) \qquad (15)$$

where η is the relative depth with respect to the normal one, and

$$\varphi(\eta, y) = \int \frac{d\eta}{\eta^y - 1} \qquad (16)$$

- *For negative bed slope* (i < 0), by noting $A / A_0' = h / h_0' = \zeta$; respectively $dh = h_0' \cdot d\zeta$ the integrate form of equation (12) becomes:

$$\frac{i'}{h_0'} l = -(\zeta_2 - \zeta_1) + \varphi(\zeta_2, y) - \varphi(\zeta_1, y) \qquad (17)$$

where ζ is the relative depth with respect to the reversed normal current depth h_0', and

$$\varphi(\zeta, y) = \int \frac{d\zeta}{\zeta^y + 1} \qquad (18)$$

Functions $\varphi(\eta, y)$ and $\varphi(\zeta, y)$ are computed by performing a development in Taylor series.

- *For horizontal bed* (i = 0), the differential equation (11) has solutions for particular cross sections where relationships for $A(h)$ exist, as below:

- rectangular, $A = h \cdot b$, and

$$l = \frac{n^2 k_{pD}^2 b^2}{3\tau^2 Q^2} \left(h_1^3 - h_2^3\right) \qquad (19)$$

- parabolic, $A = \frac{4}{3}\sqrt{p} \cdot h^{3/2}$ (p – parabola's parameter), and

$$l = \frac{4}{9} \frac{n^2 k_{pD}^2 p}{\tau^2 Q^2} \left(h_1^4 - h_2^4\right) \qquad (20)$$

- triangular, $A = m \cdot h^2$ ($m = \mathrm{ctg}\theta$, the channel slide slope with respect horizontal), and

$$l = \frac{n^2 k_{pD}^2 m^2}{5\tau^2 Q^2} \left(h_1^5 - h_2^5\right) \qquad (21)$$

d) Numerical possibility of solving the differential equations

Equations (10), (11) and (12) have to be written in finite differences instead of dh / dl , the finite difference ratio $\Delta h / \Delta l$ will be used. Overall, the cross section $A(h)$ will be the average $A_m = \frac{A(h_1) + A(h_2)}{2}$ of sections corresponding to depth h_1 and h_2 respectively $\Delta h = h_1 - h_2$.

3. EXPERIMENTAL CHECKING OF STEADY, FREE LEVEL, POST-DARCY FILTRATION

In laboratory, physical models for checking theoretic results of steady, free level, post-Darcy filtration have been developed.

a) The hydraulic installation

As permeable media glass spheres, river gravel and crushed rock with three diameters for each have used. Sorting particles on round slot sieves diameter d_p results.

The installation consists in a glass-sided, variable slope canal, on which the experimental section is limited by permeable walls, this section being filled with solid permeable media (Fig. 5, Photo 1 and 2):

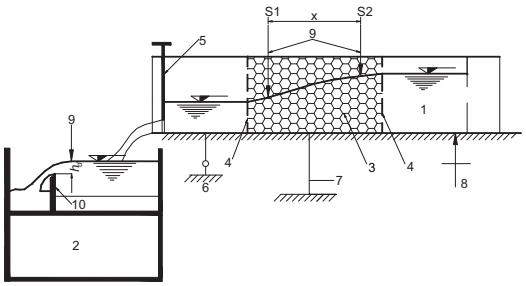

Legend:
1. glass side channel; 2. supplying base unit; 3. permeable porous wall; 4. support sieve wall; 5. adjusting weir; 6. free bearing; 7. joint support; 8. channel slope adjustment; 9. hook gauge; 10. overflow.

Figure 5. The experimental channel [12]

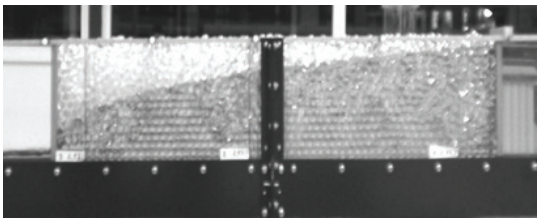

Photo 1. Experiments for steady, non-uniform flow, glass spheres [12]

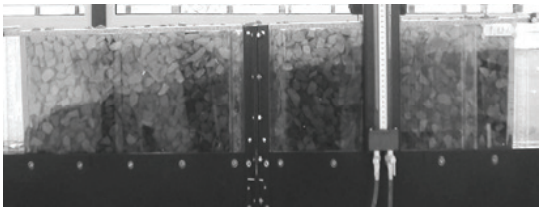

Photo 2. Experiments for steady, non-uniform flow, crushed rock [12]

The granular materials used in experiments are shown in Photo 3.

Experimental conditions ensured the required accuracy of the measurements**.**

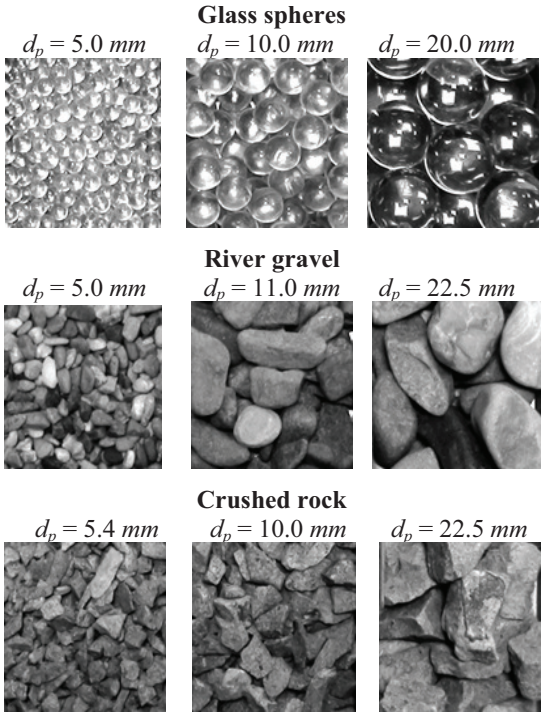

Photo 3. The experimental permeable materials [12]

b) Results of measurements for steady, non-uniform, free level, post-Darcy filtration

Measurements on steady, non-uniform, free level, post-Darcy flow on the experimental canal with a packed bed section have been undertaken.

Measurement cross sections are placed far enough from the limiting permeable walls in order to make sure that results are not influenced.

Table 2. Relative deviations of measured and computed length

Filtering material	d_p **(*mm*)**	**Number of experimental slopes and depth pairs**	$\delta l = \frac{l_{\exp} - l_t}{l_{\exp}}$	
			+	-
Glass spheres	20.0	5 / 15	-	-0.013
	10.0	5 / 15	-	-0.028
	5.0	5 / 15	0.031	-0.046
River gravel	22.5	3 / 6	0.036	-0.026
	10.0	3 / 6	0.011	-0.024
	5.4	3 / 6	0.016	-0.031
Crushed rock	22.5	3 / 6	0.007	-0.008
	11.0	3 / 6	0.010	-0.004
	5.4	3 / 6	0.001	-0.021

For different bed slope i, unit flow q, and permeable bed the depths h_1 and h_2 placed at the distance l_{exp} have been registered. Based on equation (15), (17) and (19) the theoretic length l_t of the liquid current for the measured depth was computed. The relative deviations of measured and computed length are characterizing the accuracy of theoretical equations. Results correspond to values from Table 2.

4. CONCLUSIONS

The physical simulation of the steady non-uniform, free level, post-Darcy filtration through homogeneous, rigid packed bed, made up by using glass spheres, sorted river gravel and crushed rock with different diameters have carried out.

The capillary tube models of filtration have been used for developing a theory for uniform and non-uniform steady flow.

Post-Darcy filtration coefficient and Chézy coefficient for packed bed have been defined and non-uniform, steady flow equations have been developed.

Experimental measurements have certified the validity of the theoretic determined equations.

High sensibility the studied flows present with respect porosity and bed slope. Knowledge of these characteristics with good accuracy is important.

In granular packed bed, having particles diameter less than 4 mm, for the free level filtration Darcy's law is valid (Re_d < 4). The free level filtration longitudinal slope does not permit high velocities.

ACKNOWLEDGMENTS

The paper on results of grant PN II, ID_2298, financed by UEFISCDI, contract 589/2009 CNCSIS-UTI and project PERFORM-ERA "Postdoctoral Performance for integration in the European Research Area (ID-57649), financed by the European Social Fund and the Romania Government are based.

REFERENCES

[1] Comiti, J., Sabiri, N.E., and Montillet, A., 2000, "Experimental characterization of flow regimes in various porous media – III: Limit of Darcy's or creeping flow regime for Newtonian and purely viscous non-Newtonian fluids", *Chem. Eng. Sci*., vol. 55, pp. 3057-3061;

[2] Богомолов, А. N., and Константинов, Н. М., 1962, Примеры гидравлических расчетов (Exemples of hydraulic calculations), *Научно техническое издателство, Москва*;

[3] Klark, M., 2005, "Design of endoscopic 3D particle tracking velocimetry system and its application in flow measurements with a gravel layer", *PhD Theses, Ruperto Carola University, Heidelberg, Germany*;

[4] Montillet, A., Akkari, E., and Comiti, J., 2006, "About a correlating equation for predicting pressure drops through packed beds of spheres in a large range of Reynolds numbers", *Chemical Engineering and Processing*, CEP-5147, www.sciencedirect.com, www.elsevier.com?locate/cep;

[5] Comiti, J., and Renaud, M., 1989, "A new model for determining mean structure parameters of fixed beds from pressure drop measurements: application to bed packed with parallelepipedal particles", *Chem. Eng. Sci*., vol. 44, No. 7, pp. 1539-1545;

[6] Bartha, I., Marcoie, N., Toacă, D., Toma, D., Gabor, V., Molnar, A. G., and Lupuşoru, A., 2011, "The free level uniform post-Darcy filtration through a sphere-made homogenous medium", *Environmental Engineering and Management Journal*, vol.10, No. 12, pp. 1959-1966;

[7] Bartha, I., Marcoie, N., Toacă, D., Toma, D., Gabor, V., Molnar, A. G., and Lupuşoru, A., 2010, "Post-Darcy Filtration Through Rigid Permeable Media", *Environmental Engineering and Management Journal*, vol. 9, No. 12, pp. 1727-1734;

[8] Bartha, I., Marcoie, N., Toma, D., Gabor, V., and Toacă, D., 2010, "Research of filtration through uniform geometry permeable material-glass spheres", *Anals of the University "Ovidius" Constanţa, Construction Series*, XIII, pp. 165-172;

[9] Montillet, A., 2004, "Flow through a Finite Packed Bed of Spheres: A Note on the limit of Applicability of the Forchheimer Type Equation", *ASME, Journal of Fluids Engineering*, **126**, pp. 1-5;

[10] Wahyudi, I., Montillet, A., and Kalifa, A.O.A., 2002, "Darcy and post-Darcy flows within different sands", *Journal of the Hydraulic Research*, **40**, pp. 519-525;

[11] Михайлов, К. А., and Богомолов, А. N., 1950, Гидравлика, гидрология и гидрометрия, (Hydraulics, hydrology and hydrometry) *Дориздат, Москва*;

[12] Bartha, J., Marcoie, N., Gabor, V., Toma, D., and Toacă D., 2010, "Cercetări asupra curgerilor turbulente în medii poroase permeabile rigide", *Research report, UEFISCDI, ID_2298, Bucuresti*, www.idei-cdi.ro.

Conference on Modelling Fluid Flow (CMFF'12)
The 15th International Conference on Fluid Flow Technologies
Budapest, Hungary, September 4-7, 2012

THE FEATURES OF GRAVITATIONAL CONVECTION CAUSED BY MECHANICAL EQUILIBRIUM OF ISOTHERMAL TERNARY GAS SYSTEMS WITH EQUAL MOLAR MASS OF COMPONENTS

Vladimir KOSSOV[1], Dusembek KUL'ZHANOV[2], Serik NURBAEV[3], Olga FEDORENKO[4], Venera MUKAMEDENKYZY[5]

[1] Corresponding Author. Kazakh National Pedagogical University. Dostyk 13, 050100 Almaty, Kazakhstan. Tel.: + 7 727 291 83 82, Fax: + 7 727 291 90 12, E-mail: kosov_vlad_nik@list.ru
[2] Atyray University of oil and gas. E-mail: D.u.kulzhanov@mail.ru
[3] Kazakh National Pedagogical University. E-mail: serik.i25k@mail.ru
[4] Department of Thermal Physics and Technical Physics, Al-Farabi Kazakh National University. E-mail: fedor23.04@mail.ru
[5] Department of Thermal Physics and Technical Physics, Al-Farabi Kazakh National University. E-mail: mukameden@inbox.ru

ABSTRACT

Instability of mechanical equilibrium (diffusion instability) in ternary gas system 0.220 C_3H_8 + 0.780 CO_2 – N_2O with equal molar mass components is studied experimentally. The nonlinear dependence of propane concentration on pressure is observed in the given results, that denotes the unstable behaviour of the diffusion process. Within the linear theory of stability, the macroscopic flow of the isothermal ternary gas mixture with zero density gradient is described. The possibility of the convective regime changing is shown at various perturbation modes.

Keywords: convection, diffusion, gases with equal molar masses, instability of mechanical equilibrium

NOMENCLATURE

A_i	[-]	dimensionless concentration gradient
A	[-]	arbitrary constant
B	[-]	arbitrary constant
C	[-]	arbitrary constant
D	[-]	arbitrary constant
D_{ij}	$[m^2/s]$	interdiffusion coefficients
D_{ij}^*	$[m^2/s]$	"practical" coefficients of three-component diffusion
K_i	[-]	dimensionless parameter
L	$[m]$	length
P_{ii}	[-]	Prandtl diffusion number
R_i	[-]	Rayleigh partial number
T	$[K]$	temperature
V_l	$[m^3]$	volume of the lower flask
V_u	$[m^3]$	volume of the upper flask
c_i	[-]	i-th component concentration
d	$[m]$	diameter
$\underline{j}_i$	$[m/s]$	diffusion flux
$\underline{g}$	$[m/s^2]$	free-fall acceleration vector
g	$[m/s^2]$	free-fall acceleration scalar
m_i	$[kg]$	mass
n	$[m^{-3}]$	number density
n	[-]	mode of disturbances
p	$[Pa]$	pressure
r	$[m]$	radius
t	$[s]$	time
$\underline{u}$	$[m/s]$	weight-average velocity vector
u	$[m/s]$	weight-average velocity scalar
x	[-]	abscissa axis
z	[-]	applicate
β_i	$[m/K]$	coefficient of thermal expansion
$\underline{\gamma}$	[-]	unit vector
γ	[-]	characteristic equation root
η	$[Pa \cdot s]$	shear viscosity
λ	$[s^{-1}]$	damping decrement
$\underline{v}$	$[m/s]$	average velocity vector
v	$[m/s]$	average velocity scalar
ν	$[m^2/s]$	kinetic viscosity
ξ	$[Pa \cdot s]$	bulk viscosity
ρ	$[kg/m^3]$	density
τ_{ij}	[-]	denotes the parameters, which determine relationship between the "practical" diffusion coefficients

Subscripts and Superscripts

i, j	numbering of components in multicomponent system
l, u	lower, upper

1. INTRODUCTION

A study of sustainability issues on the border line between two media, for example, liquid - liquid, liquid - porous media is relevant both in practical and theoretical aspects [1-3]. One of the

reasons that lead to the loss of stability in these systems is the existence of two thermodynamic forces, such as the concentration gradient and temperature gradient [4-6].

Under certain conditions of isothermal diffusion in some multicomponent gas mixtures, the areas stratified by the density form, and cause the occurrence of convection in the field of gravity [7-9]. In this case, the emergence of convective instability is due to the presence of two independent partial concentration gradients. Experimental study of the instability of mechanical equilibrium in isothermal gas mixtures has shown [10, 11] that the change of «the diffusion and a gravitational convection» regime is possible at the thermodynamic parameters (pressure, temperature, concentration) and the geometry of the diffusion channel (characteristic dimension, length, form). The theoretical description of mechanical balance instability has shown the satisfactory fit with experimental results [12, 13]. All results obtained in [7, 10, 12] have been studied for the systems with a various density gradient direction. In this paper, we study the change of regimes of mass transfer at different pressures for mixtures whose components have the same molar mass, i.e. for the case of zero density gradient.

1.1. Experimental Study

To carry out the research we chose the gas system consisting of gases, the densities of which are almost the same under normal conditions. The binary mixture C_3H_8 + CO_2 was in the upper flask of apparatus, while the pure N_2O was placed in the lower flask. One of the conditions influencing on the appearance of the instability of mechanical equilibrium, i.e. diffusive instability, is the difference between the interdiffusion coefficients of components [11]. The interdiffusion coefficients ($D_{C_3H_8-CO_2} = 0.0863 \cdot 10^{-4}$ m^2/s, $D_{C_3H_8-N_2O} = 0.0860 \cdot 10^{-4}$ m^2/s and $D_{N_2O-CO_2} = 0.1170 \cdot 10^{-4}$ m^2/s), as we see, are close to each other in the magnitude. Therefore, only diffusion process may occur in the system. However, these gases have difference in the density behaviour subject to pressure that is shown in Figure 1.

As it is seen in Fig. 1, the carbon dioxide is the lightest component in three component gas system $C_3H_8 - CO_2 - N_2O$ up to the pressure $p = 1.6$ *MPa*. The heaviest component up to $p = 0.65$ *MPa* is the nitrogen protoxide. But as the pressure exceeds this value the heavy component is the propane which transits from the gas phase to the liquid one at a room temperature and a pressure $p = 0.9$ *MPa*. Such behaviour of the density denotes the most complex nature of the convection occurrence in the systems consisting of real components.

To research the diffusive instability, we used a two-flask method [10, 14] where the analysis of gas mixtures before and after diffusion was carried out by the interferometric and chromatographic methods.

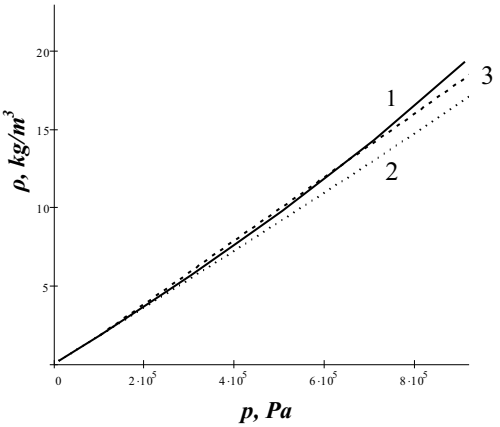

Figure 1. ρ vs. p. The full line (1) represents the data for C_3H_8. The dotted line (2) represents the data for CO_2. The dashed line (3) represents the data for N_2O

Experiments were carried out within the range of pressure from 0.2 to 2.0 *MPa* at a temperature of 298.0 *K* on the experimental setup, as shown schematically in Figure 2. Under the upper limit of the pressure, the propane still was in the gas phase; under the lower limit of pressure, it was possible to take several samples for the analysis.

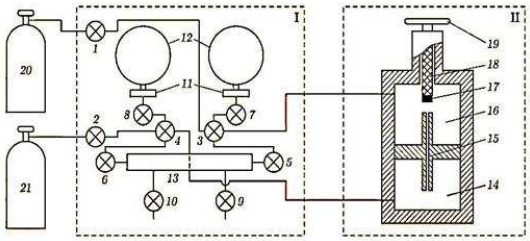

Figure 2. Block diagram of the installation of the two-flask method. The gas preparation block and the two-flask diffusion setup are indicated by I and II, respectively; valves (1-8); valve connected to the backing vacuum pump (9); valve connected to the interferometer or chromatograph (10); membrane dividers (11); reference pressure gages (12); equalizing tank (13); bottom flask (14); diffusion channel (15); top flask (16); fluoroplastic pellet (17); rod (18); handwheel (19); gas holders (20) and (21)

The experimental setup consisted of two parts (see Fig. 2). The first one was a gas preparation unit. It consists of two pressure gages (12) to measure the pressure in the flasks, a tank (13) to equalize the pressure in the flasks of the diffusion apparatus, and a set of the needle valves (stopcocks)

(1-10) to fill the setup flasks with appropriate gas mixtures from the cylinders (20) and (21). The pressure gages were supplied with the specially prepared membrane dividers (11).

The second part of the setup was the diffusion apparatus with the upper and lower flasks of volume $V_u=2.268\cdot10^{-4}$ m^3 and $V_l=2.145\cdot10^{-4}$ m^3, respectively. The flasks were connected through a slotted diffusion channel of geometrical sizes $(0.17 \times 0.05 \times 0.006)\cdot10^{-6}$ m^3. The choice of the slotted form of the diffusion channel is determined by the smaller values of the critical parameters (particularly, the pressure) under the change of the diffusion process towards the convective mass transfer.

The experiments lasted 20 min that made it possible to obtain the full information about the character of the examined mass transfer.

While filling, and for monitoring the pressure during the experiments there have been used in the reference pressure gauges to the corresponding measurement range to an accuracy class of 0.4.

The diffusion apparatus was placed directly in the thermostatic bath by means of which the temperature could be held constant to an accuracy of ± 0.1 *K*.

The experiments were carried out using a method proposed in works [15-17].

The experimental procedure on the installation was as following. As soon as the upper flask (16) and the lower one (14) of the apparatus were washed by the gases studied from the cylinders (20) and (21), the both flasks were filled with the gas up to the experimental pressure. The fluoroplastic pellet (17) ensured leakproofness while filling the flasks. The diffusion channel (15) was opened by upraising a rod (18) using a handwheel (19), and simultaneously the time corresponding to the mixing process beginning was registered. After the experiment, the channel was closed and the gas mixture in both flasks was analyzed by a chromatograph. The errors of concentration analysis were in the range of 0.3 – 0.5 %.

The results of experimental study for the system 0.220 C_3H_8 + 0.780 CO_2 - N_2O are shown in Figure 3 as the dependence of propane quantity (molar concentration of component) diffused from the upper flask of apparatus to the lower one on the pressure of the experiment.

As it is seen in Fig. 3, for the examined system the concentration of propane in the lower flask of the apparatus increases non-monotonically when growing the common pressure. The intensive growth of C_3H_8 up to the pressure 0.68 *MPa* occurs and the maximum of the propane concentration are observed.

The further pressure increase up to 0.98 *MPa* leads to the decrease of the passed propane concentration and to the process stabilization. Such system behaviour denotes the unstable behaviour of the diffusion process.

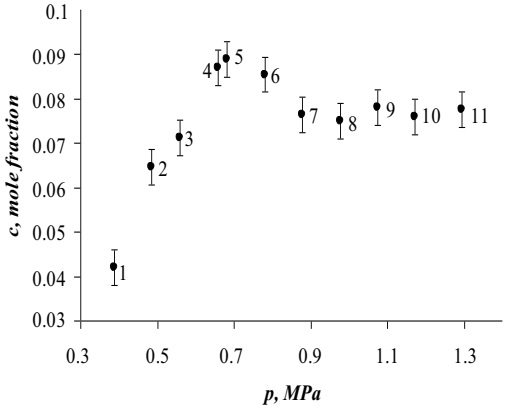

Figure 3. Quantity of the diffused propane vs. the pressure. Numbers of points - the pressure at which the regime change of mixing: 1 - 0.38; 2 – 0,49; 3 – 0.56; 4 – 0.66; 5 - 0.68; 6 – 0.78; 7 – 0.88; 8 – 0.98; 9 - 1.07; 10 – 1.17; 11 – 1.29 *MPa*

These results suggest that the concentration separation of the components of binary mixture is possible in the systems with zero density gradient, as described in [18]. This effect can be used for rectification of the natural gas mixture from the heavy fractions. This is an actual problem to be solved by the modern oil and gas industry.

1.2. Mathematical model of diffusion instability

To explain these results, we use the theory of stability, as described in [19, 20].

The macroscopic flow of the isothermal triple gas mixture is described by the general system of hydrodynamic equations that includes the Navier – Stokes equations, equations for conservation of the number of particles in the mixture and the components. With allowance for the conditions of independent diffusion for which the equalities $\sum_{i=1}^{3}\vec{j}_i=0$ and $\sum_{i=1}^{3}c_i=1$ hold, the system of equation takes the form [12, 13, 19]:

$$\rho\left[\frac{\partial \underline{u}}{\partial t}+\left(\underline{u}\nabla\underline{u}\right)\right]= \tag{1}$$

$$-\nabla p+\eta\nabla^2\underline{u}+\left(\frac{\eta}{3}+\xi\right)\nabla\mathrm{div}\underline{u}+\rho\underline{g},$$

$$\frac{\partial n}{\partial t}+\mathrm{div}\left(n\underline{v}\right)=0,$$

$$\frac{\partial c_i}{\partial t}+\underline{v}\nabla c_i=-div\,\underline{j}_i,$$

$$\underline{j}_1 = -\left(D_{11}^* \nabla c_1 + D_{12}^* \nabla c_2\right),$$
$$\underline{j}_2 = -\left(D_{21}^* \nabla c_1 + D_{22}^* \nabla c_2\right),$$

where D_{ij}^* are the "practical" coefficients of three-component diffusion.

The equations (1) are supplemented by the environmental state equation

$$\rho = \rho\left(c_1, c_{2,} p\right), \quad T = const,$$

relating the thermodynamic parameters entering Eq. (1).

The method of small perturbations is used for solution of the system of Eq. (1). Taking into account that at $L \gg r$ (L, r are the length and the radius of diffusion channel, respectively) the differences in the perturbations of the average $\underline{v}$ and the weight-average $\underline{u}$ velocities in the Navier – Stokes equations is negligible. Then the final system of equations of gravitational concentration convection, which is written in terms of the perturbed dimensionless parameters, takes the following form [13]:

$$\begin{aligned}
&P_{22}\frac{\partial c_1}{\partial t} - \left(\underline{u}\underline{\gamma}\right) = \tau_{11}\nabla^2 c_1 + \frac{A_2}{A_1}\tau_{12}\nabla^2 c_2, \\
&P_{22}\frac{\partial c_2}{\partial t} - \left(\underline{u}\underline{\gamma}\right) = \frac{A_1}{A_2}\tau_{21}\nabla^2 c_1 + \nabla^2 c_2, \\
&\frac{\partial \underline{u}}{\partial t} = -\nabla p + \nabla^2 \underline{u} + \left(R_1\tau_{11}c_1 + R_2 c_2\right)\underline{\gamma}, \\
&\mathrm{div}\underline{v} = 0,
\end{aligned} \tag{2}$$

where $P_{ii} = \nu / D_{ii}^*$ is the Prandtl diffusion number, $R_i = g\beta_i A_i d^4 / \nu D_{ii}^*$ is the Rayleigh partial number, $\tau_{ij} = D_{ij}^* / D_{22}^*$ denotes the parameters, which determine the relationship between the "practical" diffusion coefficients.

The equation system (2) for the indicated problem is solved by the method given in [19].

We consider the instability problem of diffusion mixing in a plane vertical slot when the perturbations of the velocity and the flow of matter vanish at the vertical planes that enclose the gas mixture:

$$u = 0, \frac{\partial c_1}{\partial x} = 0, \frac{\partial c_2}{\partial x} = 0, x = \pm 1. \tag{3}$$

The system of equations will be sought in the form of:

$$u(x,t) = u(x)\exp[-\lambda t],$$

where λ is a damping decrement.

With this in mind, we write the system of equations for the amplitudes:

$$\begin{aligned}
&-\lambda P_{22}c_1 - u = \tau_{11}\frac{\partial^2 c_1}{\partial x^2} + \frac{A_2}{A_1}\tau_{12}\frac{\partial^2 c_2}{\partial x^2}, \\
&-\lambda P_{22}c_2 - u = \frac{A_1}{A_2}\tau_{21}\frac{\partial^2 c_1}{\partial x^2} + \frac{\partial^2 c_2}{\partial x^2}, \\
&-\lambda u = \frac{\partial^2 u}{\partial x^2} + R_1\tau_{11}c_1 + R_2 c_2.
\end{aligned} \tag{4}$$

The regime change occurs under the condition $\lambda = 0$, and then the system of Eq. 4 can be written as:

$$\begin{aligned}
&\tau_{11}\frac{\partial^2 c_1}{\partial x^2} + \frac{A_2}{A_1}\tau_{12}\frac{\partial^2 c_2}{\partial x^2} + u = 0, \\
&\frac{A_1}{A_2}\tau_{21}\frac{\partial^2 c_1}{\partial x^2} + \frac{\partial^2 c_2}{\partial x^2} + u = 0, \\
&\frac{\partial^2 u}{\partial x^2} + R_1\tau_{11}c_1 + R_2 c_2 = 0.
\end{aligned} \tag{5}$$

From the first two expressions of Eq. 5, we can find the equation for the components concentrations:

$$\begin{aligned}
&\frac{\partial^2 c_i}{\partial x^2} = -uK_i, \\
&i = 1,2
\end{aligned}$$

where

$$K_1 = \frac{\left(1 - \frac{A_2}{A_1}\tau_{12}\right)}{\left(\tau_{11} - \tau_{12}\tau_{21}\right)}, K_2 = \frac{\left(\tau_{11} - \frac{A_1}{A_2}\tau_{21}\right)}{\left(\tau_{11} - \tau_{12}\tau_{21}\right)}. \tag{6}$$

Twice differentiating the third equation of Eq. 5 and taking into account Eq. 6, we obtain the equation containing only velocity:

$$\begin{aligned}
&u^{IV} - \gamma^4 u = 0, \\
&\text{где } \gamma^4 = K_1 R_1 \tau_{11} + K_2 R_2.
\end{aligned} \tag{7}$$

The common solution of Eq. 7 has the form:

$$u = A\mathrm{ch}\gamma x + B\mathrm{sh}\gamma x + C\cos\gamma x + D\sin\gamma x. \tag{8}$$

The examined problem has the even and the odd solutions relative to x. We consider the solution of odd type, and then the expression for the velocity can be written as:

$$u = B\mathrm{sh}\gamma x + D\sin\gamma x, \tag{9}$$

where B and D are the arbitrary constants.

Substituting Eq. 9 into the Eq. 6, we obtain:

$$c_i = -\frac{K_i}{\gamma^4}(B\mathrm{sh}\gamma x - D\sin\gamma x)\,. \tag{10}$$

Taking into account the boundary conditions (3), we can obtain the system of homogeneous equations for the determination of B and D. From the solvability condition of this system, we have the following characteristic relation:

$$\mathrm{cth}\gamma = -\mathrm{ctg}\gamma\,, \tag{11}$$

but eigenfunction (5) u and c_i have form:

$$\begin{aligned} u &= \frac{\mathrm{sh}\gamma x}{\mathrm{sh}\gamma} - \frac{\sin\gamma x}{\sin\gamma}\,, \\ c_i &= -\frac{K_i}{\gamma^4}\left(\frac{\mathrm{sh}\gamma x}{\mathrm{sh}\gamma} + \frac{\sin\gamma x}{\sin\gamma}\right)\,. \end{aligned} \tag{12}$$

Thus, the critical Rayleigh numbers spectrum for the odd solutions is found from Eq. 11 and we have:

$$\begin{aligned} &\gamma_1 = 2{,}365;\ \gamma_3 = 5{,}498;\ \gamma_5 = 8{,}639;\ldots \\ &R_1 = 31{,}29;\ R_3 = 931{,}8;\ R_5 = 5570;\ldots \end{aligned} \tag{13}$$

If the value of the Rayleigh number in the system exceeds the critical Rayleigh number (13) for the first, the most dangerous mode of disturbances, within the system might occurs a critical current, appropriate for this Rayleigh number [12]. Critical movements corresponding to the Rayleigh numbers for the higher modes are unavailable while the system will not create conditions that impede the development of the first critical motion.

The line of monotonous instability MM on the Rayleigh number plane can be found:

$$\begin{aligned} &\tau_{11}\left(1 - \frac{A_2}{A_1}\tau_{12}\right)R_1 + \left(\tau_{11} - \frac{A_1}{A_2}\tau_{21}\right)R_2 \\ &= [\gamma]^4(\tau_{11} - \tau_{12}\tau_{21}), \end{aligned} \tag{14}$$

where n = 1, 3, 5 ... are odd modes of the perturbations.

Eq. 14 was obtained according to analogy with the solution of stability problem for the plane vertical slot in the presence of mass transfer through its walls [5].

This equation gives a straight line MM on the plane (R_1, R_2), dividing the area of damping (diffusion) and growing (convection) of monotonic disturbances. The location of the neutral line of monotonic instability for n = 1, 3, 5, is shown in Figure 4. The area that lies below the line M_1M_1 corresponds to diffusion.

1.3. Comparison of the experimental data with the theoretical calculation results

To compare the theory with the experimental data is shown in Fig. 3, we represent them in the form of partial Rayleigh numbers. The partial Rayleigh numbers in accordance with (2) applied to the slotted diffusion channel, which is written as follows:

$$\begin{aligned} R_1 &= \frac{gnr^4\Delta m_1}{\rho\nu D_{11}^*}\cdot\frac{\partial c_1}{\partial z}\,, \\ R_2 &= \frac{gnr^4\Delta m_2}{\rho\nu D_{22}^*}\cdot\frac{\partial c_2}{\partial z}\,, \end{aligned} \tag{15}$$

where $\Delta c_1 = c_{1u} - c_{1l}$, $\Delta c_2 = c_{2u} - c_{2l}$, $\Delta m_1 = m_1 - m_2$, $\Delta m_2 = m_2 - m_3$, m_i is the mass of a molecule of i-th component. If conditions of the experiment are known (pressure, temperature, composition of mixtures in each of the flasks, the size of the diffusion channel), then according to Eq. (15) can be found R_1, R_2 and thus determine the point representing this experience on the plane (R_1, R_2). From experiment, we know what the regime (diffusion or convection) occurs under the given conditions.

In Fig. 4 shows the experimental data in terms of the Rayleigh numbers for the system 0.220 0.780 C_3H_8 + CO_2 - N_2O, obtained by varying the pressure. In Fig. 4 the lines of stability was obtained for the case of the plane vertical channel (14) in the absence of mass transfer through its walls, but the symbols displaying the experiment results correspond to the local Rayleigh numbers taking into account the nonlinear distribution of concentration along the diffusion channel length (12). The line M_1M_1 separates the Rayleigh number plane into the diffusion area and the mechanical equilibrium instability one. The lines M_2M_2, M_3M_3 are drawn for second and third modes of the disturbances characterizing the change of convective mass transfer type.

As it is seen from the experimental data in Fig. 3, the change of the passed propane concentration subject to the pressure is the curve with the maximum. If we suppose that the areas connecting with the abrupt changes of the process intensity correspond to the transfer mode change, then the experimental partial Rayleigh numbers determining at pressures of the intensity jump should be near the critical Rayleigh numbers fitting with the change of disturbances modes n.

The comparison of results shown in Figs. 3 to 4 points to that first regime change happens at the pressure $p \approx 0.38$ *MPa*. For the mode $n = 1$ the experimental critical Rayleigh number is $R_1 = 32.33$, i.e. the change of one flow typical for the diffusion process on the flow and the counterflow characterizing the convection one and running along the channel half-bat, for example along one of them up but along other down is happened.

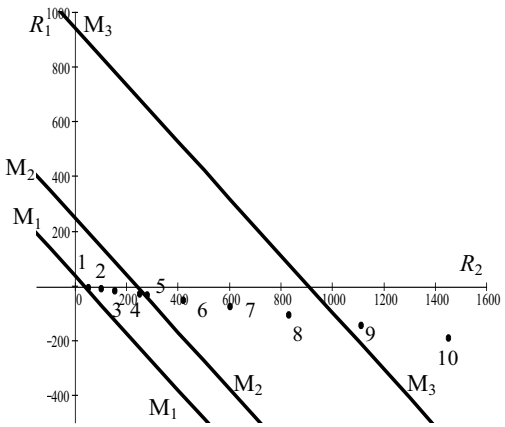

Figure 4. Regions of stable and unstable diffusion for the system 0.220 C_3H_8 + 0.780 CO_2 - N_2O. Symbols • correspond to data that determine unstable state. The calculation is carried out at the pressure values: 1 - 0.38; 2 – 0,49; 3 – 0.56; 4 – 0.66; 5 - 0.68; 6 – 0.78; 7 – 0.88; 8 – 0.98; 9 - 1.07; 10 – 1.17 *MPa*. M_1M_1 is the neutral line of monotone perturbations for $n = 1$, M_2M_2 is the neutral line of monotone perturbations for $n = 2$, M_3M_3 is the neutral line of monotone perturbations for $n = 3$

At the pressure $p \approx 0.66$ *MPa* the change of the disturbance scale to the formed flow regime occurs and the next convective regime corresponding to the critical Rayleigh number $R_2 = 244.92$ calculated for $n = 2$ arises. The line M_3M_3 corresponds to the critical Rayleigh number $R_3 = 937.99$, i.e. the area of stable convective flow characterized by the motion along four channels (two flows and two counterflows) is located behind this line. The experimental point obtained at the pressure 1.07 *MPa* is situated near this line.

5. SUMMARY

The conducted researches have shown that in ternary gas systems with equal molar mass components the «diffusion – convection» regimes' changing is possible. It is shown that the intensity of convective mixing at the pressure increase changes nonlinear. Comparison of the experimental data with the results of numerical modeling demonstrates good agreement.

ACKNOWLEDGEMENTS

This work has been supported by the Fund of Science of the Ministry of Education and Science of Republic of Kazakhstan (the project number: 0112PK00953).

REFERENCES

[1] Turner, J.S., 1973, *Buoyancy Effects in Fluids,* Cambridge University Press, Cambridge.

[2] Grandjean, E., and Monkewitz, P.A., 2009, "Experimental Investigation into Localized Instabilities of Mixed Rayleigh-Bénard-Poiseuille Convection", *J. Fluid Mech.,* Vol. 640, pp. 401-419.

[3] Pakara, S., Pawar, R.J., Stauffer, P.H., Zhang, D., and Chen, S., 2009, "Onset of Convection over a Transient Base-State in Anisotropic and Layered Porous Media", *J. Fluid Mech.*, Vol. 641, pp. 227-244.

[4] Kötter, K., Schmick, M., and Markus, M., 2000, "Self-confinement into a Plane and Stability Enhancement of Double-Diffusive Fingering", *Nonlinear Phenomena in Complex Systems,* Vol. 4, No. 4, pp. 322-332.

[5] Jasmin, S., and Prud'homme, M., 2004, "An Inverse Solution for Heat Source Profile in Porous Medium with Chemical Species Diffusion", Proc. *European Congress on Computational Methods in Applied Sciences and Engineering,* Jyväskylä, pp. 1-12.

[6] Bratsun, D.A., and Wit, A.De., 2004, "On Marangoni Convective Patterns driven by an Exothermic Chemical Reaction in Two-Layers Systems", *Physics of Fluids,* Vol. 16, No. 4, pp. 1082-1096.

[7] Zhavrin, Yu.I., Kosov, V.N., and Seleznev, V.D., 2000, "Anomalous Gravitational Instability of Mechanical Equilibrium During Diffusion Mixing in Isothermal Three-component Gas Mixtures", *Fluid Dynamics*, Vol. 35, No. 3, pp. 464-470.

[8] Miller, L., and Mason, E.A., 1966, "Oscillating instabilities in multicomponent diffusion", *Phys. Fluids*, Vol. 9, No. 4, pp. 711-721.

[9] Ruev, G.A., Fedorov, A.V., and Fomin, V.M., 2006, "Development of the Rayleigh-Taylor instability due to Interaction of a Diffusion Mixing Layer of Two Gases with Compression Waves", *Shock Waves*, Vol. 16, No. 1, pp. 65-74.

[10] Ankusheva, N.B., Kosov, V.N., and Seleznev, V.D., 2010, "Effect of Diffusion Channel Inclination on Stability of Mechanical Equilibrium in Isothermal Binary Gas

Mixtures", *Journal of Applied Mechanics and Technical Physics*, Vol. 51, No. 1, pp. 62-64.

[11]Zhavrin, Yu.I., Kosov, N.D., Belov, S.M., and Tarasov, S.B., 1996, "Some Features of Convective Heat and Mass Transfer in Multicomponent Gaseous Mixtures", *J. of Engineering Physics and Thermophysics*, V. 69, No. 6, pp. 977-981.

[12]Ankusheva, N.B., Kosov, V.N., and Zhavrin, Yu.I., 2008, "Convective Regimes of Mixing in Binary Systems With the Mechanical Equilibrium Instability of a Gas Mixture", *J. of Engineering Physics and Thermophysics*, Vol. 84, No. 3, pp. 525-531.

[13]Akylbekova, G., Kosov, V.N., Poyarkov, I.V., and Zhavrin, Yu.I., 2010, "Diffusion in Isothermal Ternary Gas Mixtures", *International Review of Chemical Engineering (I.Re.Ch.E.)*, Vol. 2, No. 1, pp. 174-177.

[14] Dunlop, P., and Bignell, C.M., 1987, "Diffusion and Thermal Diffusion in Binary Mixtures of Hydrogen with Noble Gases", *J. Chem. Phys.,* Vol. 86, pp. 2922-2926.

[15]Zhavrin, Yu.I., Mukamedenkyzy, M., and Poyarkov, I.V., 2007, "Diffusive and Convective Mixing of a Propane-Carbon Dioxide Binary Mixture with Pure Nitrogen Protoxide", *Technical Physics,* Vol. 52, No. 7, pp. 947-949.

[16] Zhavrin, Yu.I., and Kosov, V.N., 1988, "Effect of Temperature on Diffusional Instability", *Journal of Engineering Physics*, Vol. 55, No. 1, pp. 774-778.

[17] Zhavrin, Yu.I., Aitkozhaev, A.Z., Kosov, V.N., and Krasikov, S.A., 1995, "The Effect of Viscosity on the Stability of Mass transport by Diffusion in an Isothermal Three-component Gas Mixtures", *Technical Physics Letters*, Vol. 21, No. 3, pp. 206-207.

[18] Kosov, V.N., Seleznev, V.D., and Zhavrin Yu.I., 1997, "Separation of Components during Isothermal Mixing of Ternary Gas Systems under Free-Convective conditions", *Technical Physics,* Vol. 42, No. 10, pp. 1236-1237.

[19] Gershuni, G.Z., and Zhukhovitskii, E.M., 1976, *Convective Stability of Incompressible Fluids,* Keter, Jerusalem.

[20]Ingel, L.Kh., 2009, "Convective Instability Mechanism for a Binary Mixture at a Vertical Surface", *Technical Physics,* Vol. 54, No. 2, pp. 204-209.

Conference on Modelling Fluid Flow (CMFF'12)
The 15th International Conference on Fluid Flow Technologies
Budapest, Hungary, September 4-7, 2012

NUMERICAL SIMULATION OF MICRO PARTICLES MOVEMENT IN TURBULENT FLOW AND STUDY OF THEIR DISPOSITION IN RIBBED CHANNEL

Kianoosh SAMIMI[1], Helia Sharafi[2], Seyed Amir BAHRANI[3]

[1]Imen Rah consulting Engineers.Research and development service, Tehran, IRAN.E-mail: kianooshsamimi@imenrah.com
[2]School of Civil Engineering, University of Shiraz, Shiraz, IRAN
[3]Corresponding Author.LaSIE, FRE-CNRS 3474, La Rochelle University.Avenue Michel Crépeau, 17000 La Rochelle, FRANCE. Tel: +33 5 46 45 83 42, Fax: +335 46 45 86 16, E-mail: seyed_amir.bahrani@univ-lr.fr

ABSTRACT

In the design of air conditioning systems, it's important to study the indoor air quality because the human are mostly in the indoor areas. The indoor air comes from the out after passing through transforming channels. The outdoor pollution is majorly caused by aerosols smaller than 10 µm. It's favorable to remove these aerosols from indoor air or make their quantity minimum. The most common way, is installing absorption filters at inlet of air flow, although this method consumes energy. If the particle deposition enhances, the effective filtration augments as well. Moreover particle depositions can be increased by roughening the channel surface.

The air is modeled as incompressible flow in a ribbed channel. The existence of ribs on channel surface causes the turbulence in flow, therefore we must solve the turbulence equations. There are previous experimentally investigations on turbulence flow in ribbed channels. In this article, the results of numerical simulation are compared with experimental results and the effectiveness of k-ε model in solving the problem of micro-particle deposition with Lagrangian model is studied because of complexities of turbulent flow, the problem is modeled both 2- and 3-dimensionally. After solving the fluid domain, the particle equations of motion are solved separately and finally the particle deposition on channel surface is calculated.

For solving fluid domain with simulation software FLUENT, grid independent results with k-ε model are obtained for different wall conditions. Considering the physic and complications of turbulent flows, the results of 2-D simulation are different with experimental results, despite of 3-D results, which are in complete accordance with experimental results.

Keywords: aerosol deposition, ribbed channel, turbulence k-ε model.

NOMENCLATURE

A	$[m^2]$	area
C_∞	$[particle/m^3]$	aerosol concentration
d_p	$[m]$	particle diameter
D_e	$[m]$	hydraulic mean diameter
f	[-]	friction factor
J	$[particle/m^2s]$	deposited aerosol flux
k	$[m^2/s^2]$	turbulence kinetic energy
ΔL	$[m]$	distance
M	$[g]$	particle mass detected
p	$[m/s]$	static pressure
ΔP	$[Pa]$	differential pressure loss
Q	$[m^3]$	volumetric flow rate through the air filter samplers
Re	[-]	Reynolds number
t	$[sec]$	sampling time
u	$[m/s]$	phase velocity
u_p	$[m/s]$	particle velocity
U	$[m/s]$	bulk mean velocity
V_d	$[m/s]$	mass transfer coefficient

Greek Symbols

ε	$[m^2/s^3]$	turbulencedissipation rate
δ	$[m]$	half of channel height
μ	$[Pa.s]$	fluid viscosity
μ_t	$[Pa.s]$	turbulent eddy viscosity
ρ	$[kg/m^3]$	fluid density
ρ_p	$[kg/m^3]$	particle density
$\bar{\bar{\tau}}$	$[Pa]$	stress tensor

Subscripts and Superscripts

acetate	acetate
filter	air filter

1. INTRODUCTION

Aerosols transfer and deposition in turbulent channels are always important and widely used in

engineering projects [1, 2]. Considering the human spend most of their time in indoor areas, it is very important to check indoor air pollution for air conditioning projects. The air pollution mostly cause by aerosols smaller than 10 μm [2] and aerosol concentration in the air vary locally. Epidemiological evidence suggests a positive correlation between outdoor PM_{10} (particular matter less than 10μm in diameter) concentrations and mortality in urban areas. Therefore it is desirable to remove these particles from air conditioning systems. The most common way is installation the absorption filter at air flow inlet, obviously this method needs energy [3] and it is not very effective [4].

If aerosols deposition augmented in ventilation channel, the effective filtration will be enhanced. The enhancement of small particle deposition along the length of ventilation duct may present an effective alternative to filtration. The aerosol deposition augment by the use of roughen the internal area of channel. Also, particle deposition can be increased by heat transfer. The later method is used in turbine blades and nuclear reactor cooling [3]. One way of roughen channel area is adding the ribs on channel surface.

Although there are a few investigations on numerical simulation of particle deposition in ribbed channels, but the turbulent flow in ribbed channels is surveyed widely by researcher. In the year 2006, Liu and his colleagues used two turbulence model ''LES'' and '' RANS'' in order to simulate numerically the turbulent flow in electrical devices [5]. Also in the same year, Viswanthan and Tafti [6] modeled a turbulent flow in a channel which has ribs on both bed and ceiling of channel, they used Detached Eddy Simulation "DES" model. They compared the numerical results with experimental data [7]. In the year 2007, Ahn et al., [8] modeled fluid flow with ribs on both bed and ceiling of channel by use of LES. They assumed that rotating channel is a model of cooling flow on turbine blades. Tian and Ahmadi [9] compared the results of different numerical turbulence models for a simple channel and confirmed the results of k-ε model which is used by fluent software, can show an acceptable prediction for particle deposition. More investigations upon ribbed channels are carried out recently. In 2010, Ahn and Lee [10] worked on large eddy simulation (LES) of turbulent flow and heat transfer in a channel with both detached and attached rib array.

In recent investigation, by use of fluid domain solution the micro particle equation of motion is solved independently in fluent software. For solving fluid domain by fluent, the grid independent results for *k-ε* model with different wall conditions are obtained. By use of same channel geometry with Lai's experimental work, the results of numerical work are compared with experimental data. This comparison shows the numerical simulation capability in modeling aerosol filtering problems in ventilation channels.

2. PHYSICAL MODEL AND SOLVING METHOD:

2.1. Geometry of experimental model

For physical simulation the geometry of Lai's experiment is used [1]. In Figure 1 the experimental apparatus and the ribs on its bed is shown. Channel cross section is 150 mm × 150mm. The channel is consisted of ten galvanized section. The length of each section is 500 mm. Channel hydraulic diameter is 150 mm. Each galvanized rib has 6mm height and the pitch length between two successive ribs is 60mm.

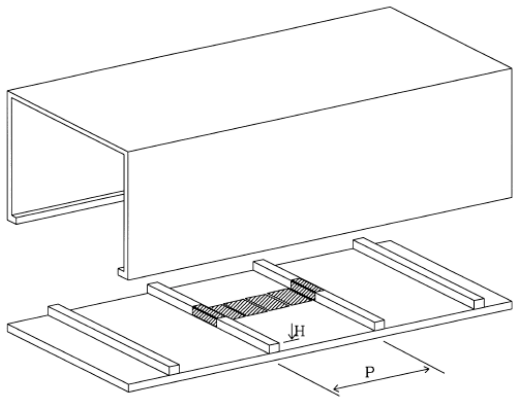

Figure 1. Ribbed channel schematic. The dashed area is test section [1]

The test section was located at the 10th galvanized channel. There for the inlet flow to this area is fully turbulent flow. As shown in the Figure 1, the test section is placed in the middle of channel and particle deposition is measured in this section although the particle deposition in depth is neglected. Hence, for flow simulation, first a 2-dimensional model is used. Despite of the simplicity of geometry, the fluid flow has its complexities, which need a great number of grid cells to be modeled. This grid slows the solving process in order to achieve a convergent solution. In the second step, 3-dimensional modeling is carried out. The comparison between 2D and 3D results shows the importance of third dimension in this problem.

In Lai's experiment, there are 14 ribs before test section and it is insisted the inlet flow, before first rib, is in fully developed turbulent regime. In Lai's experiments, the friction factor *f*, for both smooth and ribbed surface was calculated by measuring the

pressure difference across two Perspex channels and can be written as:

$$f = \frac{D_e/4}{\frac{1}{2}U^2}\frac{\Delta P}{\Delta L} \quad (1)$$

Where U [m/s], is the bulk mean velocity, D_e [m], is the hydraulic mean diameter and $\Delta P/\Delta L$ [Pa/m], is the pressure loss across the length by which two pitot tubes are separated. For this experiment, air velocity is 4.4[m/s] and Reynolds number is 4.4×10^4. Considering Blasius equation, friction factor for the channel is equal to;

$$f = \frac{0.0791}{\mathrm{Re}^{0.25}} \xrightarrow{if\ \mathrm{Re}=4.4\times10^4} f = 5.46\times10^{-3} \quad (2)$$

With use of friction factor, the experimental value of pressure drop per channel length can be calculated.

This quantity is equal $\Delta P/\Delta L$=7.4437 [Pa/m] from experimental data. This parameter is used as a criterion to check the accuracy of converged results.

2.2. Governing Equations (for fluid)

The air governing equation is Navier-Stokes equation for incompressible fluid without heat transfer and constant viscosity. The continuity or mass conversation equation is defined as;

$$\frac{\partial\rho}{\partial t} + \nabla.\left(\rho\vec{v}\right) = 0 \quad (3)$$

The momentum equation for inertial or non-accelerating coordinate is;

$$\frac{\partial}{\partial t}\left(\rho\vec{v}\right) + \nabla.\left(\rho\vec{v}\vec{v}\right) = -\nabla p + \nabla.\left(\bar{\bar{\tau}}\right) + \rho\vec{g} + \vec{F} \quad (4)$$

In the above equation, p is static pressure, $\bar{\bar{\tau}}$ is stress tensor [Pa], ρg and F are gravitational and external body force, respectively. The definition of stress tensor is as following;

$$\bar{\bar{\tau}} = \mu\left[\left(\nabla\vec{v} + \nabla\vec{v}^T\right) - \frac{2}{3}\nabla\vec{v}I\right] \quad (5)$$

Where μ is molecular viscosity [$Pa.s$] and I is unit tensor. The second term in above equation is volume dilatation effect.

The turbulence model which is used in this investigation is k-ε 2-equational model. Standard k-ε model is a semi-experimental model based on the transport equation of turbulence kinetic energy (k) and dissipation rate (ε). The transport relation for k is extracted from exact equation and ε-transport model is obtained from physical reasons which have small similarities with exact mathematical solution.

The transport equations for standard k-ε model are;

$$\frac{\partial}{\partial t}(\rho k) - \frac{\partial}{\partial x_i}(\rho k u_i) = \frac{\partial}{\partial x_i}\left[\left(\mu + \frac{\mu_t}{\sigma_k}\right)\frac{\partial k}{\partial x_i}\right] + G_k + G_b - \rho\varepsilon - Y_M + S_k \quad (6)$$

$$\frac{\partial}{\partial t}(\rho\varepsilon) + \frac{\partial}{\partial x_i}(\rho\varepsilon u_i) = \frac{\partial}{\partial x_i}\left[\left(\mu + \frac{\mu_t}{\sigma_\varepsilon}\right)\frac{\partial\varepsilon}{\partial x_i}\right] + C_{1\varepsilon}\frac{\varepsilon}{k}\left(G_k + C_{3\varepsilon}G_b\right) - C_{2\varepsilon}\rho\frac{\varepsilon^2}{k} + S_\varepsilon \quad (7)$$

G_k is turbulence energy generation due to mean velocity gradient. G_b is turbulence energy generation due to buoyancy. Y_m is related to dilatation is compressible turbulence $C_{1\epsilon}$, $C_{2\epsilon}$, $C_{3\epsilon}$are constant. σ_k, σ_ϵ are turbulence Prandtl numbers for k and ε, respectively. S_k, S_ϵ are source terms which can be added to equations in certain problems for k-ε model, turbulent eddy viscosity μ_t [$Pa.s$] is defined as;

$$\mu_t = \rho C_\mu\frac{k^2}{\varepsilon} \quad (8)$$

In the above equation C_μ is constant. The constants in this model are obtained by experiments on air water as follow;

$$C_{1\varepsilon} = 1.44, C_{2\varepsilon} = 1.92, C_\mu = 0.09,$$
$$\sigma_k = 1.0, \sigma_\varepsilon = 1.3$$

After solving fluid turbulent flow, the micro particles are added to flow. The particle motion equation or discrete phase is studied in Lagrangian view point. This equation which is basically the force balance for particle is written as below for x-direction in Cartesian coordinate.

$$\frac{du_p}{dt} = F_D\left(u - u_p\right) + \frac{g_x\left(\rho_p - \rho\right)}{\rho_p} + F_x \quad (9)$$

F_x is external acceleration term (force divided by unit particle mass) and $F_D(u-u_p)$ is drag per unite particle mass.

$$F_D = \frac{18\mu}{\rho_p d_p^2}\frac{C_D\,\mathrm{Re}}{24} \quad (10)$$

u is phase velocity[m/s], u_p is particle velocity [m/s], μ is fluid viscosity[$Pa.s$], ρ is fluid density [kg/m^3], ρ_p is particle density [kg/m^3] and d_p is particle diameter [m]. The relative Reynolds number is defined as;

$$\mathrm{Re} \equiv \frac{\rho d_p \left| u_p - u \right|}{\mu} \tag{11}$$

2.3. Grid generation

For geometrical simulation two models are created separately in Gambit software. Figure 2 shows both of these two models.

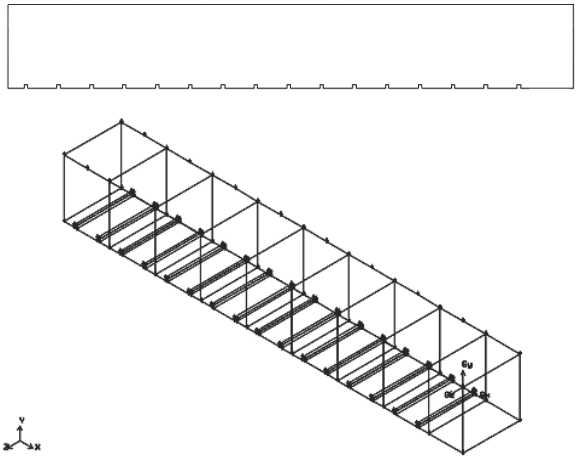

Figure 2. Geometry of 2D and 3D models

As shown in the Figure, at the channel end, the added zone is considered in order of avoiding recirculated flow. For 2-dimensional model, structured grid with 132800 elements is created. The grid quality is acceptable with maximum equei-angle skew 0.07 and maximum aspect ratio 4.32 finally; the results grid independency is proved by comparing the results with results associated to two different grids (one with 309600 elements and other with 218016 elements). Figure 3 shows structured grid for 2D model. It is obvious that grid lines are more compressed near the walls and it is because of flow complexities after the ribs.

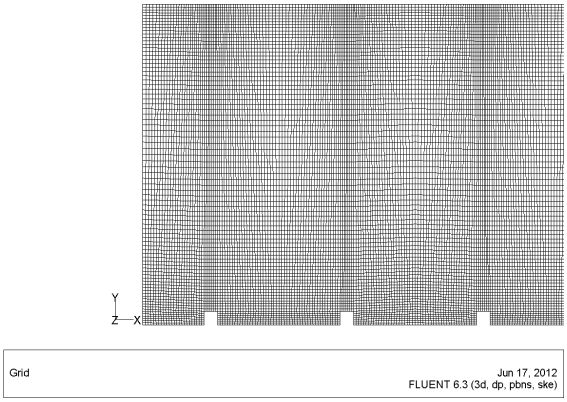

Figure 3. Generated grid for 2D model

The grid of 3-dimensional model is like the 2D model in grid quality and grid lines density. 3D grid has 3280640 3D-rectangular elements. 98.63% of elements have the acceptable aspect ratio (between 1 and 5). The maximum aspect ratio is 6 because of grid span in depth direction.

The velocity condition at inlet is defined by use of UDF (User Defined Function) by use of this code the fully turbulent developed flow is defined as [11];

$$u = U \times \left(\frac{y}{\delta} \right)^{1/7} \tag{12}$$

The flow is fully turbulent when δ is equal to half of channel height. Also the equation for k and ε associated for fully turbulent flow are defined by this UDF. The outlet boundary condition is pressure outlet condition.

In the flowing, the grid independent results for both 2D and 3D models are presented and particle deposition results are compared with experimental results.

3. RESULTS

3.1. Fluid domain

In the first step, the fluid domain is solved. Convergence criterion for each case is iteration independency. The outlet relative pressure for all cases is considered to be zero. According to experimental results, the pressure drop per unit length is 7.4437 Pa/m, therefore by using channel length, the pressure at the inlet boundary is determined. To obtain the inlet pressure in numerical results, the area weighted average of static pressure is calculated. Note that the outlet static pressure is zero; hence the calculated quantity is the total pressure drop in modeled channel.

It is logical to model this problem 2-dimensionally because the problem parameters do

not vary considerably with depth direction. But there are main differences between 2D and 3D flows. For example, in 2D problem the effect of two lateral walls, the corner effect at inlet and . . . are neglected. As a result, it is expected that the 2D calculated pressure drop is less of the 3D problem result.

For k-ε turbulence model, the Enhancement Wall Treatment is chosen. This model is the best one for the y^+ associated to generated grid ($0< y^+<50$). For 2D model, the pressure drop per unit length is 5.5329 Pa/m for RNG k-ε model. Moreover the recirculation length after the rib is important for this problem. In the following, the velocity contours are shown for the range of stream function 0-2.0. In Figure 4 the end part of the grid or test section is draw. From 2D results the length of recirculation zone after the rib is 4.52 times of rib height.

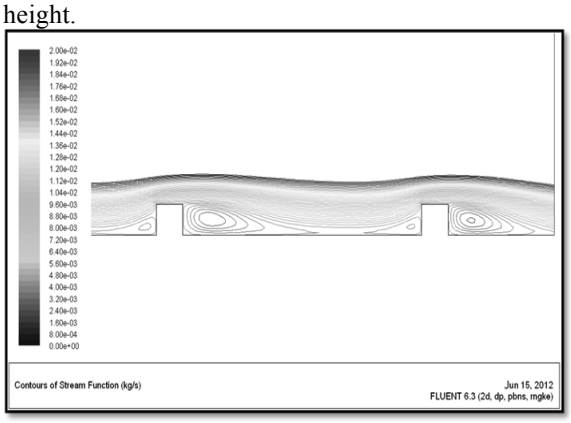

Figure 4. Streamlines in test section for 2D model

For 3D model with standard k-ε turbulence model, also the Enhancement Wall Treatment is selected ($0< y^+<50$). For grid independent solution, the pressure drop per unit length is 7.1566 Pa/m. The pressure contours and velocity vectors on middle plane in depth direction is shown in the figure 5 & 6. The length of recirculation zone after the rib is 5.38 times of rib height.

As it was expected, the 3D model not only calculate greater pressure drop than 2D model, but also the calculated length of recirculation zone is much greater for 3D model.

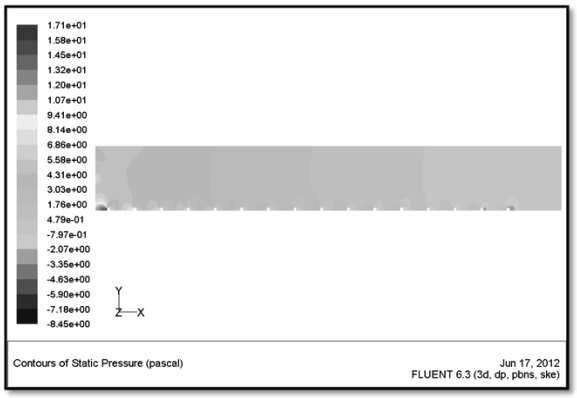

Figure 5. Contours of static pressure on the middle surface in depth direction for 3D model

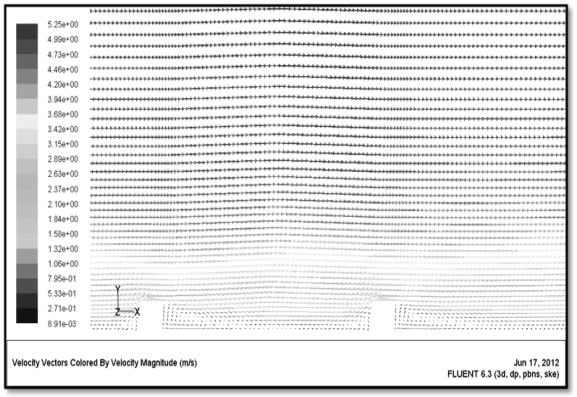

Figure 6. Velocity vectors on the middle surface in depth direction for 3D model

3.2. Aerosol deposition

Because the flow is turbulent, we need a model to exert the turbulence diffusion effect to the problem. In this investigation, Stochastic Tracking model is used. Stochastic Tracking model (Random Walk) contains the turbulence instantaneous velocity fluctuation effect on the particle trajectory by use of stochastic model. For solving particle motion in Lagrangian viewpoint, the Saffman lift is active and Stokes-Cunningham drag law is selected.

Mass transfer coefficient (deposition velocity) V_d [m/s], is the key parameter to be determined. Aerosol deposition velocity is as follow [11];

$$V_d = \frac{J}{C_\infty} \tag{13}$$

In the channel, J [$particle/m^2s$],is deposited aerosol flux on channel area and C_∞ [$particle/m^3$], is aerosol concentration in free stream air, were evaluated from

$$J = \frac{M_{acetate}}{A_{acetate} t} \tag{14}$$

$$C_{\infty} = \frac{M_{filter}}{Q} \tag{15}$$

Where $M_{acetate}$, M_{filter} are the particle mass detected on the acetate and air filter paper samples respectively, t is sampling time[s], $A_{acetate}$ is the area of the acetate simple [m^2] and Q [m^3], is the volumetric flow rate through the air filter samplers [12].

In Figure 7, the numerical results of 2D models are compared with Lai's experimental results for particle with 4.5 μm diameter and Figure 8 show the same results for 3D model.

4. DISCUSSIONS AND CONCLUSION

In this investigation, the importance of third dimension in numerical simulation of turbulent flow in channel is reviewed. However the turbulence models can be exerted to 2D problems in commercial software, but because of 3-dimensional nature of turbulence, the 3-dimensional modeling can give better results. The difference of results for two models is 22% in the length recirculation zone after the rib. This recirculated length is measured experimentally 6±0.7of rib height [5]. The 3-dimensional model with k-ε turbulence model predicts this length in the range of experimental data. On the other hands the pressure drop per unit length is 7.1566 Pa/m for 3D model and 5.5329 pa/m for 2D model. From Lai's experimental results this parameter is 7.4437 Pa/m. Therefore 3D model result has 3.85% error and 2D model result has 25.67% error.

Also with comparing Figures 6 and 7, the 3D model has better prediction in aerosol deposition rather than 2D model. The greatest error in deposition velocity is 3.85% for 3D model and 25.67% error for 2D model.

At least we can conclude the 2D model results have grater error than 3D model, because the span of channel is finite. Although 2D model is preferred for study the physics of flow because it takes less time to execute the calculations. With use of suitable boundary condition the k-ε model can results in accurate answers for turbulent flow in ribbed channel and also for particle deposition in these flows.

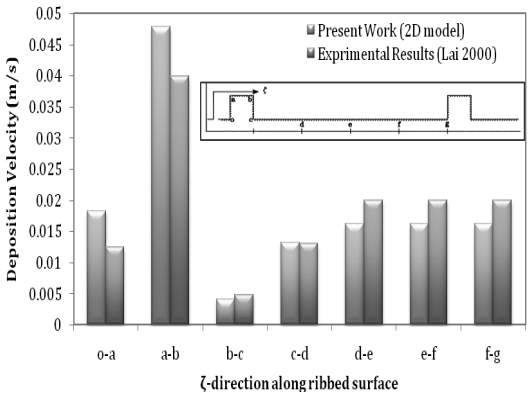

Figure 7. Aerosol deposition velocity in ribbed channel for 2D model

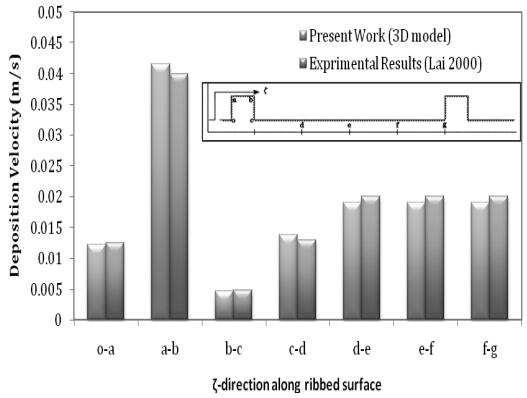

Figure 8. Aerosol deposition velocity in ribbed channel for 2D model

REFERENCES

[1] Lai, Alvin C.K., Byrne, Miriam A. and Goddard, Anthony J.H., 2001, "Aerosol deposition in turbulent channel flow on a regulararray of three-dimensional roughness elements.", *Journal of Aerosol Science*, Vol. 3, pp. 121-137.

[2] Lai, Alvin C.K., Byrne, Miriam A. and Goddard, Anthony J.H., 2000, "Enhanced particle loss in ventilation duct with ribbed surface.", *Building and Environment*, Vol. 35, pp. 425-432.

[3] Labbé, O. Ryan, J. and Sagaut, P., 1997, "Direct numerical simulation of flow in ribbed channel." , International symposium on advances in computational heat transfer, Cesme, Turkey.

[4] Lai, A.C.K, 2003, ''particale deposition indoors: a review'', Indoor Air, ISSN 0905-6947, Denmark.

[3] Hinds, W. C., 1999,"Aerosol Technology.", New York : John Wiley & Sons Inc.

[4] Hanley, J.T., Ensor D.S., Smith D.D., Sparks L. E., 1994, "Fractional Aerosol Filtration Efficiency of In-Duct Ventilation Air Cleaners.", *Indoor Air*, Vol. 4, pp. 169-178.

[5] Liu, Yan., Tucker, Paul G., and Iacono, G.Lo., 2006, "Comparison of zonal RANS and LES for a non-isothermal ribbed channel flow.", *International Journal of Heat and Fluid Flow*, Vol. 27, pp. 391-401.

[6] Viswanathan, Aroon K., and Tafti, Danesh K., 2006, "Detached eddy simulation of flow and heat transfer in fully developed.", *International Journal of Heat and Fluid Flow*, Vol. 27, pp. 351-370.

[7] Sewall, Evan A., Tafti Danesh K., Gvaham Andrew B., Thole Karan A., 2006, "Experimental validation of large eddy simulations of flow and heat transfer in a stationary ribbed duct.", *International Journal of Heat and Fluid Flow*, Vol. 27, pp. 243-258.

[8] Ahn, J., Choi, H., and Lee, J.S., 2007, "Large eddy simulation of flow and heat transfer in a rotating ribbed channel.", *International Journal of Heat and Mass Transfer*, Vol. 50, pp. 4937-4947.

[9] Tian, L., and Ahmadi, G., 2007, "Particle deposition in turbulent duct flows-comparisons of different model predictions.", *Aerosol Science*, Vol. 38, pp. 377-397.

[10] Ahn, Joon and Lee, J.S., 2010, "large eddy simulation of flow and heat transfer is a channel with a detected rib array", International journal of heat and mass transfer, vol.53, pp. 445-452.

[11] Streeter, Victor L., Wylie, E. Benjamin and Bedford, Keith W., 2002, "Fluid Mechanics." New York : McGraw-Hill.

[12] Lai, Alvin C.K., Byrne, Miriam A. and Goddard, Anthony J.H., 1999, "Measured deposition of aerosol particles on a two-dimentional ribbed surface in a turbulent duct flow.", *Journal of Aerosol Science*, Vol. 30, pp. 1201-1214.

Conference on Modelling Fluid Flow (CMFF'12)
The 15th International Conference on Fluid Flow Technologies
Budapest, Hungary, September 4-7, 2012

INFLUENCE OF DIFFERENT GAS MODELS ON THE NUMERICAL RESULTS OF HIGH-VELOCITY CONDENSATION

Sebastian SCHUSTER[1], Friedrich-Karl BENRA[2], Hans Josef DOHMEN[3], Sven KOENIG[4], Uwe MARTENS[5]

[1] Corresponding Author. Department of Mechanical Engineering, University Duisburg-Essen. Lotharstr. 1, 47048 Duisburg, Germany. Tel.: +49 203 379 7069, Fax: +49 203 379 3038, E-mail: sebastian.schuster@stud.uni-due.de
[2] Department of Mechanical Engineering, University Duisburg-Essen. E-mail: friedrich.benra@uni-due.de
[3] Department of Mechanical Engineering, University Duisburg-Essen. E-mail: hans-josef.dohmen@uni-due.de
[4] Energy Sector Oil and Gas Division, Siemens AG, Duisburg. E-mail: koenig.sven@siemens.com
[5] Energy Sector Oil and Gas Division, Siemens AG, Duisburg. E-mail: uwe.martens@siemens.com

ABSTRACT

High-velocity condensation has attracted considerable research interest since the last century, and several experimental, theoretical, and numerical investigations have been carried out. In the literature, there exist about five different nucleation models with up to two correction factors and about three heat transfer models with various modifications. By comparing experimental and numerical results, correction factors have been found by various authors to achieve the experimental results. It is important to note that these results are dependent on the gas law (perfect–ideal–real). In the current paper, a Lagrange approach is used to determine the dispersed droplet phase. Three different experimental test cases were selected from the literature. In the first one the pressure rise, in the second one the droplet diameter over time and in the last one the Wilson-Line is investigated. The working fluid in all three cases is water steam. Starting with a nucleation model that fits the experimental results best, the influence of different gas laws on the result of the numerical simulation is shown in detail. The investigations are divided into two parts. The first part takes into account the influence of different gas models on the transport equations. The second part deals with the influence of the gas properties on the nucleation model equations.

Keywords: condensation, gas law, nucleation, numerical, two-phase flow

NOMENCLATURE

A	$[m^2]$	cross-sectional area
U	$[m/s]$	velocity vector
F	$[N]$	force
ΔG	$[J]$	change in Gibbs free energy
Δh	$[kJ/kg]$	heat of evaporation
k	$[W/mK]$	conductivity
κ	[-]	isentropic exponent
ρ	$[kg/m^3]$	density
r	$[m]$	radius
d	$[m]$	diameter
R	$[J/kgK]$	gas constant
σ	$[N/m]$	surface tension
S	[-]	source term
T	$[K]$	temperature
m	$[kg]$	mass
m_{H2O}	$[kg]$	mass of one water molecule
k_B	$[J/K]$	Boltzmann constant
ϕ	[-]	general variable

Subscripts and Superscripts

d	droplets
g	gas phase
sat	saturation conditions
sc	subcooling
tot	total conditions

1. INTRODUCTION

High-velocity condensation occurs in a wide range of technical applications. One of them is the area of turbo machinery. The aim of a turbine is the relaxation of a fluid to the lowest possible pressure. Often, the static pressure is then below the saturation pressure. Different processes have to be understood before designing a turbine, which works in the two-phase flow regime. These processes can

be divided roughly into wall films, erosion, and efficiency reduction. Information on water accumulation can be found in Schuster et al. [1]; on erosion rates, in Khan and Wang [2]; and on efficiency reduction, in Schuster et al. [3].

Starting with Baumann's [4] and Gyarmathy's [5] work, the topic of condensation in turbines has now been studied for a century. Investigations are mainly based on numerical calculation approaches that are validated with experimental data from simplified test rigs. Over a long period of time, various models have been published with a variety of empirical correction factors, and each model has been validated with various experimental studies. The idea behind the investigations presented in this paper is the assessment of the influence of the equation of state (EOS), which constitutes one major source of modelling uncertainty. As soon as the influence is understood, it is possible to compare the results of different numerical investigations. In a second step, model constants, which were defined with a less accurate EOS, can be corrected, in order to use them with an EOS of higher accuracy.

Condensing flows can be characterized by three parameters: the maximum sub cooling, pressure rise at the nucleation point, and droplet diameter over time. Measurement of these parameters under laboratory conditions is mostly performed in cascades of steam turbine blades and Laval nozzles. Unfortunately, no experiments are known in which all three parameters have been investigated in the same geometry. For this reason, three different geometries were chosen from the literature for the investigations presented in this paper.

The mathematical model is based on the Euler-Lagrange method that is implemented in the commercial CFD Code Ansys CFX. With the help of Fortran User Routines, a nucleation model is added to the code based on classical nucleation theory.

The discussion of the gas model means the dependency of the state variables pressure and temperature in the transport equations. In the case of nucleation, there are additional equations that depend on the steam properties. In order to distinguish between the influence of the gas model on the transport equations and on the equations of the nucleation model, the investigations were divided into two parts. In the first part, only the state variables in the transport equations are calculated based on different gas models. In the second part, the state variables and material properties in the nucleation model are calculated taking into account different model assumptions.

2. MATHEMATICAL MODEL

2.1. Euler-Lagrange Solver

As already mentioned in the first chapter, the mathematical model is based on an Euler-Lagrange framework wherein the gas phase is solved in the meaning of the Euler approach and the liquid droplets are solved using the Lagrange approach.

The general transport equations Eq. (1) for mass, momentum, and energy are solved using a finite volume approach. S_i represents source terms due to interphase interaction.

$$\frac{\partial \rho \phi}{\partial t} + \nabla \rho U \phi = S_\phi + S_i \tag{1}$$

The liquid phase droplets are tracked through the domain, and their motion is influenced by the gas phase. The motion of the particle is computed using an ordinary differential equation (ODE), as given below by Eq. (2).

$$m_d \frac{dU}{dt} = \sum F_i \tag{2}$$

At the domain inlet, only pure water steam is present; during the expansion, the water steam sub cools. This means that the static temperature falls below the saturation temperature. At a certain amount of sub cooling, droplets begin to form. Sub cooling is defined as the difference between static temperature and saturation temperature at static pressure, as given below by Eq. (3).

$$\Delta T_{sc} = T_g - T_{sat}\left(p_g\right) \tag{3}$$

A complete description of the complex processes involved in the condensation is not within the scope of this article, information on this can be found in the literature, e.g. in Abraham [6], Vehkamäki [7], or Gerber [8]. At this point, it should suffice to know that a large number of small initial droplets is needed to start the condensation process. The number of initial droplets and their size given by Eq. (5), are calculated at the location of the local maximum in the change of Gibbs free energy, given by Eq. (4), as a function of the droplet radius.

The nucleation rate, given by Eq. (6), is calculated in each node of the computational grid. A correction of the nucleation rate has been omitted here; this correction factor q_c in Eq. (6) normally has a value between 0.1 and 1.0. In addition, there are some investigations where values below 0.1 are used to obtain agreement between the experimental and the numerical results.

If the nucleation rate is above a predetermined value of 1.0E+15 [1/(m³ s)], a representative

particle with the diameter calculated using Eq. (5) is injected at the node position into the domain. The droplet is then tracked using Eq. (2) until it reaches the outlet.

$$\Delta G = -\frac{4}{3}\pi r_d^3 \rho_d R T_g \ln\left(\frac{p_g}{p_{sat}\left(T_g\right)}\right) + 4\pi r_d^2 \sigma \tag{4}$$

$$r_d = \frac{2\sigma}{\rho_d R T_g \ln\left(\frac{p_g}{p_{sat}\left(T_g\right)}\right)} \tag{5}$$

$$J = \frac{q_c}{1+\nu}\frac{\rho_g^2}{\rho_d}\left(\frac{2\sigma}{\pi m_{H2O}^3}\right)^{0.5} \cdot \exp\left(-\frac{4}{3}\frac{\pi r_d^2 \sigma}{k_B T_g}\right) \tag{6}$$

$$\nu = 2.0\frac{\kappa-1}{\kappa+1}\frac{\Delta h}{R T_g}\left(\frac{\Delta h}{R T_g}-\frac{1}{2}\right), \quad q_c = 1 \tag{7}$$

For each integration step, in addition to the new velocity and position, the interaction terms for mass, momentum, and energy are also calculated. The mass transfer is related to the heat transfer, and it is calculated using Eq. (8). In the literature, this model is also called the thermal phase change model.

$$m_{gd} = \frac{q_g}{\Delta h_{gd}} \tag{8}$$

The heat transfer is calculated using Eq. (9) by taking into account the Nusselt number correction for small Knudsen numbers, given by Eq. (11), as done by several authors. In these investigations, the Nusselt number is calculated using Eq. (10). This formulation can be found in Gerber [8]. In the presented investigations a slightly modified coefficient c is used.

$$q_g = \frac{k_g Nu}{2 r_d} A_d \left[T_g - T_{sat}\left(p_g\right)\right] \tag{9}$$

$$Nu = \frac{2}{1+cKn} \qquad c = 3.88 \tag{10}$$

$$Kn = 1.5\frac{\eta_g \sqrt{T_g R}}{p_g d_d} \tag{11}$$

The drag acting on a particle is calculated using the Schiller-Naumann [9] correlation, which is applicable for small particle Reynolds numbers, as they occur in condensing flows.

2.2. Equation of state (EOS)

For all cases, pure water steam is the working fluid.

2.2.1. Perfect Gas (PG)

A perfect gas (PG) is defined as a material whose density can be calculated based on the ideal gas law, given by Eq. (12), having a constant specific heat capacity c_p. The material properties used here are listed in Table 1.

$$\rho = \frac{p}{R \cdot T} \tag{12}$$

Table 1. Perfect Gas

Molar Mass M	18.02	kg/kmol
Gas constant R	461.0	J/(kg K)
Density	Eq. (12)	kg/m³
Dynamic Visc.	9.4E-06	kg/(m s)
Thermal Cond.	193E-04	W/(m K)
c_p	2000.0	J/(kg K)

2.2.2. Ideal Gas (IG)

Like the perfect gas, the density of the ideal gas (IG) is by definition calculated using the ideal gas law. The specific heat c_p is a function of temperature. In these studies, c_p is calculated using the NASA format polynomial expression, given by Eq. (13), with the coefficients a_i listed in Table 2. All other material properties are listed in Table 3.

$$c_p = R\sum_{i=1}^{5} a_i T_g^{i-1} \tag{13}$$

Table 2. Coefficients Eq. (13)

R	461.0	J/(kg K)
a_1	0.03386842E+02	-
a_2	0.03474982E-01	1/K
a_3	-0.06354696E-04	$1/K^2$
a_4	0.06968581E-07	$1/K^3$
a_5	-0.02506588E-10	$1/K^4$

Table 3. Ideal Gas

Molar Mass M	18.02	kg/kmol
Gas constant R	461.0	J/(kg K)
Density	Eq. (12)	kg/m³
Dynamic Visc.	9.4E-06	kg/(m s)
Thermal Cond.	193E-04	W/(m K)
c_p	Eq. 13	J/(kg K)

2.2.3. Real Gas (RG)

As a real gas (RG), a fluid is understood as one whose properties are dependent on pressure and temperature. A usual formulation for the real gas properties of water consists of the IAPWS equations. The release IAPWS 97 is used. All equations and coefficients can be found in the available literature [10].

2.2.4. Properties in Eqs. 4–10

In addition to the gas properties, which are needed to calculate the fluid motion, several properties are required to compute Eqs. (4)–(10). These are the heat of evaporation, Gibbs free energy, and surface tension. It is anticipated that these three properties will greatly influence the results. A distinction is made between constant properties for heat of evaporation/surface tension and Gibbs free energy by taking into account the real gas behaviour.

In the presented investigation, the constant properties are calculated based on the IAPWS equations at ISO conditions (p = 101.3 kPa, T = 288.15 K). Later on, this is referred to as constant properties (CP).

The Gibbs free energy as a function of pressure and temperature is calculated based on the IAPWS equations. The critical radius of the droplets is then calculated using Eq. (14). Later on, this is referred to as the Gibbs free energy of a real gas (GRG).

$$r_d = \frac{2\sigma}{\rho_d R T_g \Delta G} \tag{14}$$

3. INVESTIGATIONS

The objective of this work is to present the influence of the gas models on the main characteristic parameters of condensing flows, which includes the location of maximum sub cooling, pressure rise, and droplet diameter. For each of these parameters, an experimental investigation is selected from the literature. The present investigations deal with the condensation at low pressure as it occurs in low-pressure steam turbines or single-stage turbines. Hence, experiments were chosen that have an inlet pressure below 2.0 bar. The geometry is described briefly. Then, the differences between the equations of state are presented. Table 4 provides an overview of the various investigations carried out.

Table 4. Overview of calculation

#	Geometry	EOS	Δh	ΔG	σ
1	Bakhtar	PG	f(p,T)	PG	f(T)
2	Dorey A	PG	f(p,T)	PG	f(T)
3	Dorey B	PG	f(p,T)	PG	f(T)
4	White	PG	f(p,T)	PG	f(T)
5	Bakhtar	IG	f(p,T)	PG	f(T)
6	Dorey A	IG	f(p,T)	PG	f(T)
7	Dorey B	IG	f(p,T)	PG	f(T)
8	White	IG	f(p,T)	PG	f(T)
9	Bakhtar	RG	f(p,T)	PG	f(T)
10	Dorey A	RG	f(p,T)	PG	f(T)
11	Dorey B	RG	f(p,T)	PG	f(T)
12	White	RG	f(p,T)	PG	f(T)
13	Bakhtar	RG	f(p,T)	RG	f(T)
14	Dorey A	RG	f(p,T)	RG	f(T)
15	Dorey B	RG	f(p,T)	RG	f(T)
16	White	RG	f(p,T)	RG	f(T)
17	Bakhtar	PG	cons.	PG	cons.
18	Dorey A	PG	cons.	PG	cons.
19	Dorey B	PG	cons.	PG	cons.
20	White	PG	cons.	PG	cons.

3.1. Experiments from Literature

Figure 1 shows a schematic illustration of the turbine cascade from the experiments of Bakhtar et al. [11] together with the boundary conditions used in the numerical simulation. The surface pressure was measured, so that with these experiments, the pressure rise can be compared between the experimental and the numerical solutions.

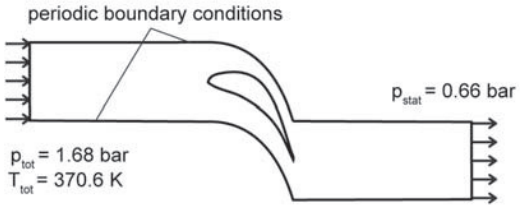

Figure 1. Illustration of Bakhtar Cascade

Dorey et al. [12] focused their investigations on a Laval nozzle of three different scales. For the presented investigations, Nozzle A (scale factor 1) and Nozzle B (scale factor 0.5) were chosen. A schematic illustration of the geometry together with the boundary conditions is shown in Figure 2. Both nozzles A and B are only different in terms of the scale factor.

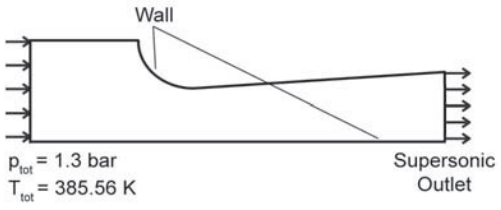

Figure 2. Illustration of Dorey Nozzle

White et al. [13] also investigate a turbine cascade, which is schematically illustrated in Figure 3. As before, the boundary conditions for the numerical simulation are also shown. From the experiments, the Wilson-Line was obtained.

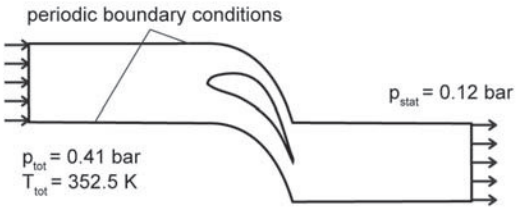

Figure 3. Illustration of White Cascade

3.2. Validation of the numerical code

The three experimental investigations presented in chapter 3.1 are used to validate the numerical code. The equation of state is that for a real gas; Δh and σ are functions of pressure and temperature, respectively; and the Gibbs free energy is calculated under the perfect gas assumption. The surface pressure, which was measured by Bakhtar, is compared with the numerical results in Figure 4. It can be seen that the measured pressure rise at the beginning of nucleation is higher than that predicted by the numerical code, but the starting point is calculated at the right position along the axial chord.

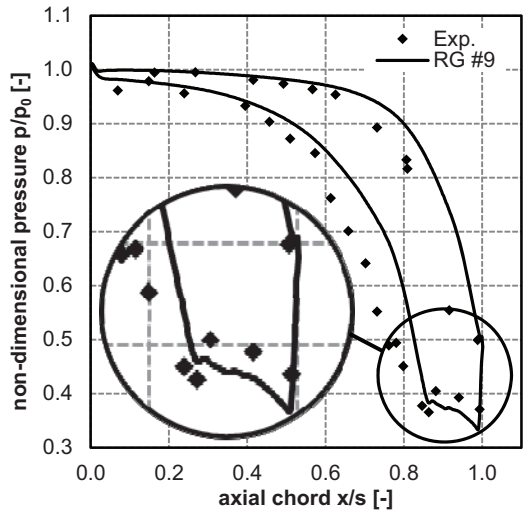

Figure 4. Bakhtar exp. [11] vs. num. results #9

Figure 5 shows the calculated droplet diameter over the axial axis of the nozzle. The experimental results, which were obtained by Dorey, are indicated by black diamonds. For one nozzle, the diameter is smaller than that predicted, and for the other, it is larger than that predicted. Such results were achieved in many other investigations.

It was predicted by many authors that the droplet diameter at any point on the nozzle axis changes nearly in proportion to the expansion rate. Where Nozzle A has an expansion rate of 4000 s^{-1} and nozzle B, 8000 s^{-1}, in the experiment, the droplet diameter at the measurement point in Nozzle A is twice that at the measurement point in Nozzle B. The numerical results show a factor of 2.4.

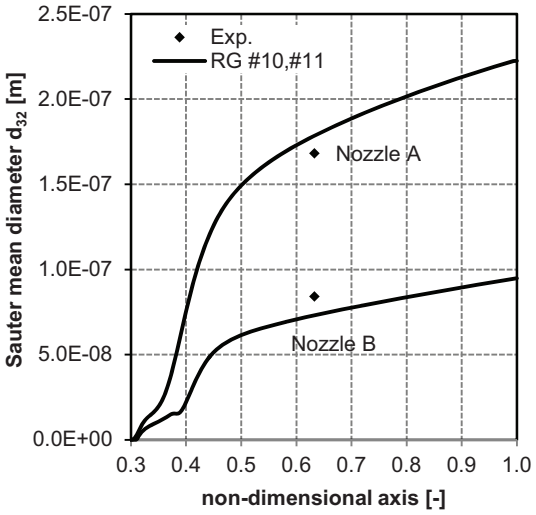

Figure 5. Dorey exp. [12] vs. num. res. #10, #11

Considering the mathematical model, it can be determined that the nucleation model must have a great influence on the position of the Wilson-Point with respective to the point of nucleation. Therefore, White's experiments are used for additional code validation. In Figure 6, the experimental results obtained by White are shown on the left-hand side, and the numerical results are shown on the right-hand side. As already shown by the studies of the Bakhtar cascade, in the White cascade, the starting point of nucleation is also well predicted with the numerical model.

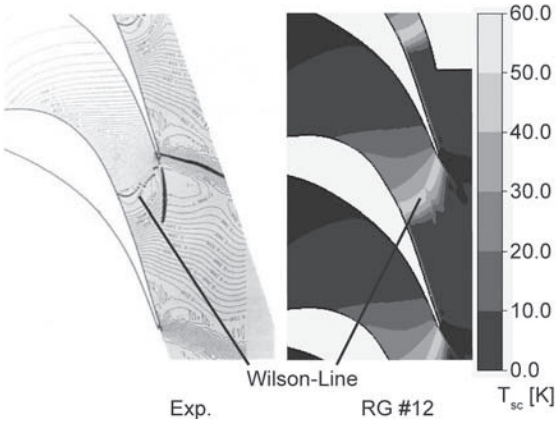

Figure 6. White exp. [13] vs. num. results #12

3.3. Comparison of the three gas models

In the following section, the numerical results obtained with the various gas models are compared

with each other. In Figure 7, the surface pressure obtained with the numerical model is shown for the three different gas models PG/IG/RG. The difference between RG and IG/PG is evident. Whereas with RG the calculated pressure rise is lower than that measured, the one calculated with IG/PG is higher than the measured one.

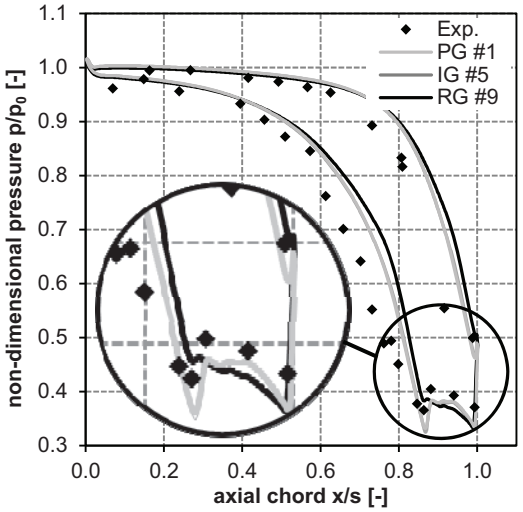

Figure 7. Bakhtar exp. [11] vs. num. results #1, #5, #9

The droplet diameter calculated with the PG/IG gas model is approximately 50% smaller than that calculated with the RG gas model. There is only a small difference between the PG and the IG values. In addition, the droplet diameter course along the nozzle axis differs between RG and PG/IG, as can be seen in Figure 8 for Nozzle A and Figure 9 for Nozzle B. Between axis position 0.5 and the outlet 1.0, the droplet growth rate has a factor of 1.5 for RG and 1.2 for PG. The rate is nearly the same for nozzle B, with a factor of 1.5 for RG and 1.3 for PG.

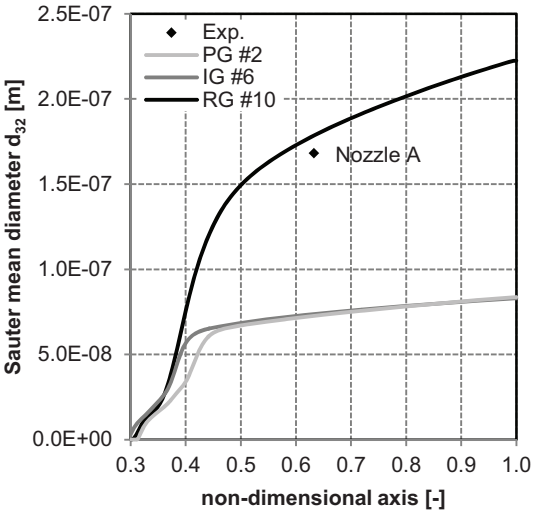

Figure 8. Dorey A exp. [12] vs. num. results #2, #6, #10

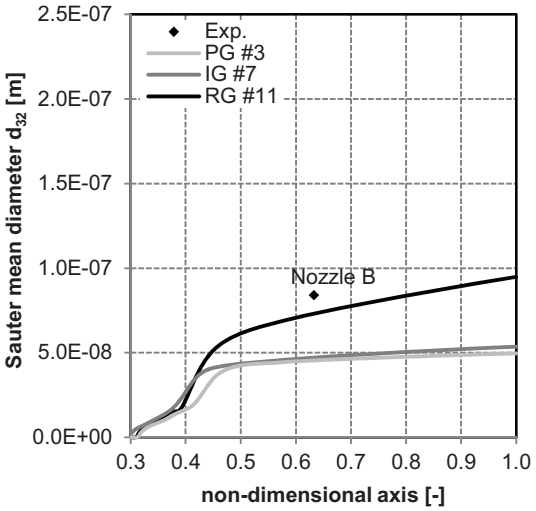

Figure 9. Dorey B exp. [12] vs. num. results #3, #7, #11

The ratio of the droplet diameter between the two nozzles at the measurement point is greater than the measured one if calculated with RG. The calculation with PG/IG shows a ratio lower than the measured value. The droplet diameters and the ratio at the axis point 0.63 are shown in Table 5.

Table 5. Droplet Diameter [m] at 0.63

	PG	IG	RG
Nozzle A	8.96E-08	9.69E-08	1.78E-07
Nozzle B	5.35E-08	5.67E-08	7.30E-08
Ratio	1.7	1.7	2.4

The sub cooling that is calculated in the White cascade (Figure 10) shows only a small difference for the three gas models. For the RG model, the temperature increases faster after the Wilson-Line.

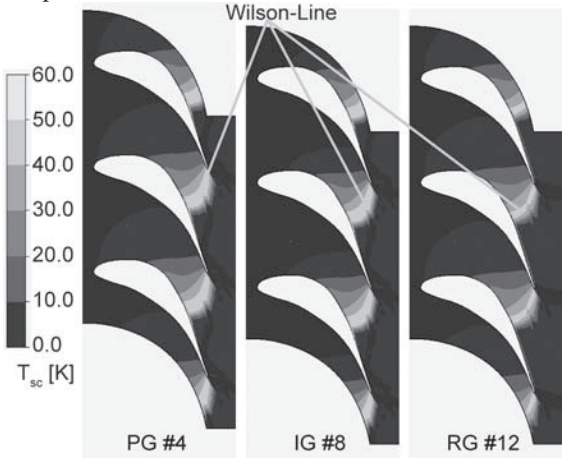

Figure 10. White exp. [13] vs. num. results #4, #8, #12

3.4. Influence of gas properties in the nucleation model equation

The nucleation behaviour is greatly dependent on the surface tension; for high-pressure flows, depending on the reference point at which the surface tension is calculated, the pressure rise might be significantly different if calculated with surface tension, depending on the temperature. In the investigated case, such a difference is not visible, as seen from Figure 11. In contrast, it can be seen that if the Gibbs free energy is computed with the IAPWS equations, the location of the pressure rise is shifted upstream. The pressure rise on the suction side is in a range comparable to that calculated with PG/IG/CP; however, on the pressure side, the pressure rise is three times higher than that computed with the other models.

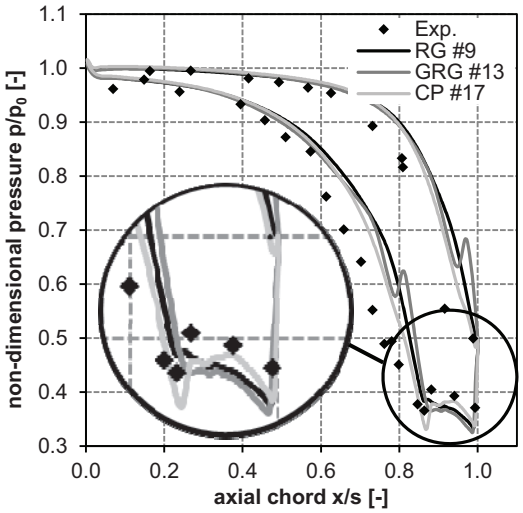

Figure 11. Bakhtar exp. [11] vs. num. results #9, #13, #17

There are two reasons for different droplet diameters in the calculations 10/11, 14/15, and 18/19. One reason is the surface tension, which might lead to a shift in the nucleation point. The other reason is the enthalpy difference of evaporation because from Eq. (8), it is clear that the droplet growth is a function of this enthalpy difference.

In Figures 12 and 13, it is depicted that for the CP case, the droplet diameter fits for Nozzle B but is much lower for Nozzle A. The calculated ratio between the droplet diameters at the measurement point between the two nozzles is 1.6.

In contrast to the CP calculations, the GRG calculations show a much better result. Although the calculated droplet diameters are lower than the measured ones, the ratio between Nozzle A and B is 1.8, close to the measured value of 2.0. Considering that the diameter ratio is near the experimental ratio, a slight modification of the coefficient c would give numerical results that are very close to the experimental data.

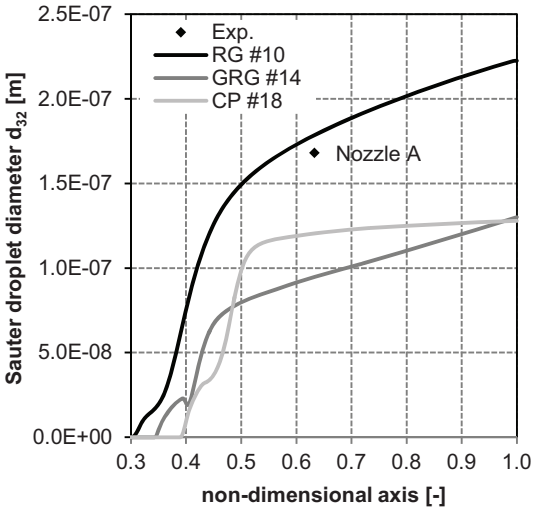

Figure 12. Dorey A exp. [12] vs. num. results #10, #14, #18

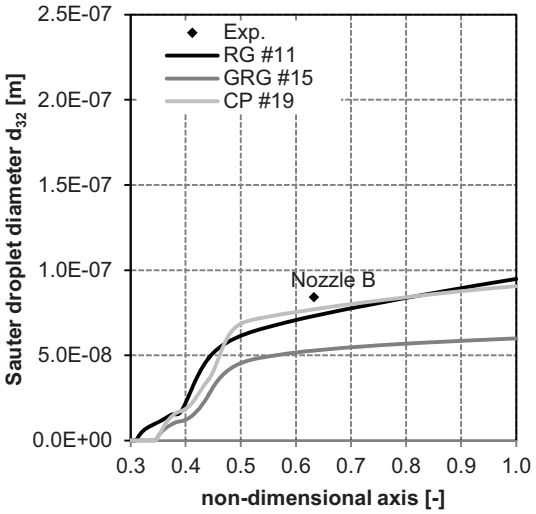

Figure 13. Dorey B exp. [12] vs. num. results #11, #15, #19

Figure 14 shows that the temperature increases in the GRG calculations in a narrower region than in the RG calculations. The Wilson-Line is at the same position as calculated with the other models. Figure 14 also shows that there is no difference between the Wilson-Line calculated with RG and with CP.

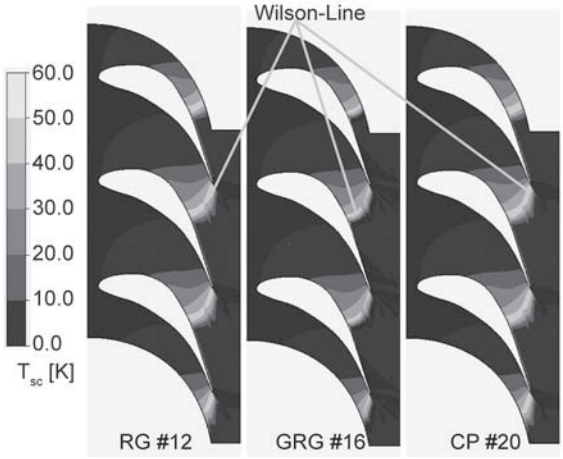

Figure 14. White exp. [13] vs. num. results #12, #16, #20

4. CONCLUSIONS

This paper aimed to show the differences in the numerical results of high-velocity steam condensation using different gas models. A large difference was found between the IAPWS real gas model and the perfect/ideal gas law. The droplet diameter calculated with the real gas model is greater than that calculated with the perfect/ideal gas model. Exactly the opposite is true for the pressure rise at the onset of nucleation; here, the pressure calculated with the perfect/ideal gas model is greater.

In terms of pressure rise and the Wilson-Line, the difference between taking Δh and σ as constant values or real gas values is negligible, but the results for the droplet diameter are unsatisfactory.

In contrast, the computation of the Gibbs free energy with the IAPWS equations has a great influence on the results. The ratio between the droplet diameters is closer to the experimental results. The location of pressure rise is shifted upstream. It is found that the prediction of the Wilson-Line is as good as with the other models.

All conducted calculations were performed with the same constants in the nucleation model. A modification of coefficients c and q_c might bring the numerical results for the perfect/ideal gas models and for the real gas formulation of Gibbs free energy in good agreement with the experimental results.

Finally, it can be stated that the gas model has a strong influence on the results of condensation calculations. With the presented results, a qualitative comparison of different numerical calculation procedures is possible. For the next step, the results of these calculations can be converted qualitatively to the same gas model. This will help to determine which condensation model fits the experimental results best.

REFERENCES

[1] Schuster, S., Benra, F. -K. and Dohmen, H. J., 2010, "Application of Euler-Euler Model for Numerical Simulation of a Radial Turbine Working in the Two-Phase Flow Regime", *WSEAS Transactions on Fluid Mechanics*, Vol. 5, pp. 276-286.

[2] Khan, J. and Wang, T., 2011, "Three-Dimensional Modeling for Wet Compression in a Single Stage Compressor Including Liquid Particle Erosion Analysis", *Journal of Engineering for Gas Turbines and Power*, Vol. 133, pp. 012001-1 - 012001-13.

[3] Schuster, S., Benra, F. -K. and Dohmen, H. J., 2011, "Investigation of nucleation influence on the efficiency of radial turbines", *12th International Conference on Multiphase Flow in Industrial Plants*, MFIP12, Ischia, Italy.

[4] Baumann, K., 1921, "Some recent Developments in Large Steam Turbine Practice", *I.E.E. Journal*, Vol. 59, No. 302.

[5] Gyarmathy, G., 1962, "Grundlagen der Theorie einer Naßdampfturbine", Diss., ETH Zürich.

[6] Abraham, F. F., 1974, "Homogeneous Nucleation Theory", New York, Academic Press.

[7] Vehkamäki, H., 2005, "Classical Nucleation Theory in Multicomponent Systems", Helsinki, Springer, pp. 3-540-29213-6.

[8] Gerber, A. G., 2008, "Inhomogeneous Multifield Model for Prediction of Nonequilibrium Phase Transition and Droplet Dynamics", *Journal of Fluids Engineering*, Vol. 130.

[9] Schiller, L. and Naumann, A., 1933, "Über die grundlegende Berechnung bei der Schwerkraftaufbereitung". Zeitschrift des Vereins Deutscher Ingenieure, Band 77 Nr.12.

[10] Wagner, W. and Kretzschmar, H. -J. 2007, "International Steam Tables", Berlin, Springer.

[11] Bakhtar, F., et al., 1993, "An Investigation of Nucleation Flows of Steam in a Cascade of Turbine Blading", *Journal of Fluids Engineering*, Vol. 115, pp. 128-134.

[12] Dorey, J.-M. et al., 2010, "Steam Condensation Experiments in three homothetic Nozzles", *Proceedings of the 9th European Turbomachinery Conference*, Istanbul, Turkey.

[13] White, A. J., Young, J. B. and Walters, P. T., 1996, "Experimental Validation of Condensing Flow Theory for a Stationary Cascade of Steam Turbine Blades", *Philosophical Transactions Mathematical, Physical and Engineering Sciences*, Vol. 354, pp. 59-88.

Conference on Modelling Fluid Flow (CMFF'12)
The 15th International Conference on Fluid Flow Technologies
Budapest, Hungary, September 4-7, 2012

EULERIAN MODELLING OF THE FORMATION AND FLOW OF AGGREGATES IN DISSOLVED AIR FLOTATION

Mia BONDELIND[1], Henrik STRÖM[2], Srdjan SASIC[2], Lars BERGDAHL[3]

[1] Corresponding Author. Department of Water Environment Technology, Chalmers University of Technology, 412 96 Göteborg, Sweden. Tel: +46 (0) 31 772 21 51, Fax: +46 (0) 31 772 21 28, E-mail: mia.bondelind@chalmers.se
[2] Department of Applied Mechanics, Chalmers University of Technology. henrik.strom@chalmers.se
[3] Department of Applied Mechanics, Chalmers University of Technology. srdjan@chalmers.se
[4] Department of Water Environment Technology, Chalmers University of Technology. lars.bergdahl@chalmers.se

ABSTRACT

Dissolved Air Flotation (DAF) is a well-established process within the drinking water treatment community. The process is driven by density differences caused by injection of air bubbles into the main water flow. Particulate matter in the water is flocculated into larger particles (termed flocs). The water, together with flocs, is thereafter mixed with the injected air bubbles. Buoyant aggregates are formed by adhesion of bubbles to the flocs. The aggregates rise to the surface of the unit where they are removed from the water phase. The objective of this paper is to conduct simulations of fluid dynamics of a DAF unit, with a specific aim to capture the formation and flow of aggregates. For that purpose, a model has been developed that explains the mechanisms that lead to creation of aggregates and results in estimation of their size. Details on the implementation of the aggregation model into an Eulerian framework are given in the paper. We show in the paper that the modelling framework can describe the dynamics of flotation by capturing the formation, change in size and movements of the aggregates through the contact zone of a pilot DAF unit as a function of the properties of the flocs.

Keywords: aggregate model, air bubble, Dissolved Air Flotation (DAF), Eulerian model, floc, water treatment

NOMENCLATURE

A	$[J]$	Hamaker coefficient
α	[-]	fraction of phase
D	[-]	fractal dimension
d	$[m]$	diameter
E	[-]	dielectric constant
ε_0	$[C^2/Jm]$	permittivity of vacuum
$\underline{F}$	$[N]$	force
g	$[m/s^2]$	gravity
h	$[m]$	distance: floc and bubble
K	$[mN/m]$	force constant
κ	$[1/m]$	Debye constant
λ	$[nm]$	decay length
P	$[N/m^2]$	pressure
ρ_f	$[kg/m^3]$	density floc
ρ_b	$[kg/m^3]$	density air bubble
ρ_w	$[kg/m^3]$	density water
u_f	$[m/s]$	floc velocity
U	$[m/s]$	velocity
v	$[m/s]$	velocity
ς_f	$[mV]$	zeta potential
ς_b	$[mV]$	zeta potential

Subscripts and Superscripts

agg	aggregate
B	buoyancy force
b	air bubble
dis	dispersion
E	electrostatic force
f	floc
H	hydrophobic force
HR	hydrodynamic repulsion force
in	inlet
k	phase index
w	water
W	van der Waals force

1. INTRODUCTION

Dissolved Air Flotation (DAF) has for a long time been a well-established process within the drinking water treatment community [1]. The DAF process has proven to efficiently remove low density particles and operate well for low temperature waters in comparison to sedimentation [2]. In addition, operational advantages of DAF are a short start-up time and a more compact sludge [3]. The particulate matter to be removed from the raw water is flocculated into larger particles (termed

flocs) in a pre-treatment step, Figure 1. The flocculation step can be either stirred hydraulically by walls inserted in the flocculation chamber or stirred by paddles (shown in the figure). The main water with the flocs is thereafter led into the flotation unit. The flotation process is driven by density differences caused by the injection of air bubbles into the main water flow. At the lower part of the contact zone the water is mixed with the dispersion flow injected from needle valves or nozzles. The dispersion flow has been saturated with air under high pressure and at the sudden drop in pressure at the injection point microscopic air bubbles are formed. Flocs and air bubbles are mixed and the bubbles attach to the flocs, forming aggregates. The aggregates, having lower density than the water, rise to the surface of the flotation unit where they are removed. The clear water is withdrawn from the lower part of the flotation unit. A fraction of the clear water is recycled and saturated with air and injected into the contact zone.

Experimental investigations have shown that the flotation process mostly depends on the type of raw water to be treated, successful coagulation and flocculation, and the flow pattern in the unit [2, 4, 5]. The surface properties of the flocs will affect the probability of attachment of bubbles to flocs, while, for example, the strength of a floc will prevent undesired shearing of the floc when entering the flotation unit. The optimal flow pattern in the unit should promote formation of aggregates and their upward movement to the surface of the unit, while air bubbles should be prevented from escaping through the outlets for clear water. Although extensive experimental work exists on this subject [5], the flotation process still proves challenging to examine. For example, there are reports that show that air bubbles considerably disturb the probe used for measuring the velocity in a flotation unit [6].

To avoid difficulties of experimental work, there are now attempts to numerically model the flotation process. A numerical model can be an efficient tool to investigate problems with a malfunctioning DAF unit [7] or to evaluate the optimal geometry for a new unit to be installed [8]. It is expected that numerical simulations will, in the future, provide developers and water treatment personnel with an efficient design and decision tool [9]. However, to reach such a goal, further research is still needed.

Historically, the least complex numerical models of flotation have only accounted for the flow of water (termed “one-phase flow” in the water treatment community) through a tank [10]. Over the years and due to continual developments in computer capacity, numerical models have significantly evolved and several publications are now available modelling the flow including both water and air bubbles [11, 12]. The multiphase flow of water and air bubbles, referred to as the “two-phase flow”, can be modelled in either the Eulerian-Lagrangian or the Eulerian-Eulerian framework. In the former framework, air bubbles are tracked individually through the flow domain, whereas in the latter framework, the water and air phases are treated as interpenetrating continua. In the present work, we will employ the Eulerian-Eulerian framework (for brevity, hereafter termed the “Eulerian model”).

To correctly evaluate the removal efficiency of the flocs by the flotation process, not only water and air bubbles have to be present in the modelling framework, but also flocs and aggregates have to be included. Inclusion of two new phases (flocs and aggregates) to the modelling framework already consisting of water and air bubbles, will exceptionally increase the complexity of the Eulerian model. In such a case, the model will have to account for a number of phenomena taking place at a great range of length and time scales. Namely, a study of the general flow pattern in a flotation unit belongs to modelling on a macroscopic level, whereas interaction between flocs and air bubbles and the formation of the aggregates necessitates studies involving significantly smaller scales. This wide range of scales poses a problem when modelling the process within a numerical framework. It would become a challenging task to resolve the flow around each floc and air bubble or to model individual formation of each aggregate in a full scale DAF unit. Additionally, it would be far from trivial to properly resolve within the Eulerian model the momentum exchange between multiple individual phases. Consequently, to reduce the complexity of the modelling, one or several phases need to be excluded and/or the interaction between some of the phases neglected. One example of such reduction of complexity has been proposed by Ta et al. [13], where the flocs and the subsequently formed aggregates do not have an impact on the flow in the unit when they rise through the domain. In a model presented by Kostoglou et al. [14], the capture of a floc by a bubble is accounted for by an additional model included in the numerical

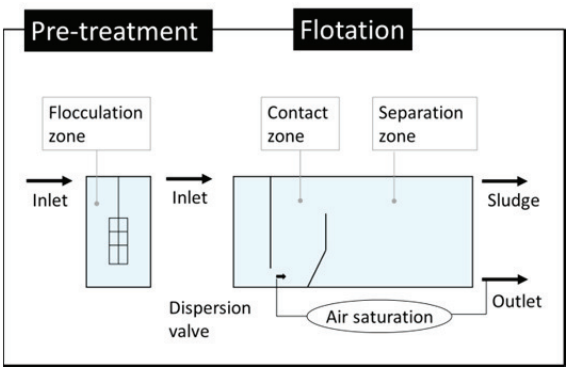

Figure 1. The pre-treatment and the flotation step.

framework. In their model, the probability of a successful attachment is dependent on the movement of the floc and the bubble due to buoyancy, gravity and turbulence in the flotation unit. Due to small floc sizes used in the simulations (3-10 μm) in comparison to those of air bubbles (100-1000 μm), the formed aggregates were not included in the modelling framework.

The objective of this paper is to conduct Eulerian simulations of fluid dynamics of a DAF unit, with a specific aim to capture the formation and flow of aggregates. For that purpose, a model has been developed that explains the mechanisms that lead to creation of aggregates and results in estimation of their size [15]. In this paper the benefits of the aggregate model and its first implementation into a comprehensive Computational Fluid Dynamics (CFD) framework will be demonstrated. As such, this study represents the proof of concept, rather than a full-detailed investigation of all possible aspects of the flow field.

2. MODELLING FRAMEWORK

To simulate the formation of aggregates in a DAF geometry, the aggregate model [15] is coupled to the Eulerian-Eulerian framework. Two phases are present in the unit: the first phase is water and the second phase represents the aggregates. The aggregate phase consists of flocs and air bubbles, where the size of the aggregates is determined by surface properties of the flocs and the bubbles and by the flow pattern in the unit. The modelling concept will be evaluated in the contact zone of a flotation unit, Fig. 1. Further elaboration on the implementation and the geometry of the DAF unit are given below.

2.1 Eulerian model

The water and aggregate phases are treated here as interpenetrating continua. The equations describing the continuity and momentum conservation for each phase are derived by volume or ensemble averaging of the Navier-Stokes equations [16].

$$\frac{\partial}{\partial x_i}\left(\alpha_k \rho_k U_{i,k}\right) = 0 \tag{1}$$

$$\frac{\partial}{\partial t}\left(\alpha_k \rho_k U_{i,k}\right) + \frac{\partial}{\partial x_j}\left(\alpha_k \rho_k U_{i,k} U_{j,k}\right) = -\alpha_k \frac{\partial P}{\partial x_i} + \frac{\partial \tau_{ji,k}}{\partial x_j} + \alpha_k \rho_k g_i + F_{i,k} \tag{2}$$

In Eq. (1) and (2) k is the phase index, $\tau_{ji,k}$ is the stress tensor of the respective phases and $F_{i,k}$ is the momentum interaction between the phases. The momentum interaction is a function of the size of the aggregates, which is determined locally by the aggregate model.

2.2 The aggregate model

The process of formation of aggregates in the contact zone of a DAF unit can be conceived to consist of two sub-processes: gravity settling and interception. In essence, air bubbles in the contact zone act as collectors of flocs.

We propose here a model that estimates the size of the aggregates formed in the contact zone. In general, the capture of flocs suspended in aqueous medium by rising air bubbles implicates the existence of a broad range of phenomena (both hydrodynamic and physicochemical). Our work focuses on the local behaviour of flocs when approaching and attaching to air bubbles. In reality, during the approach of a floc towards a bubble, a thin film of liquid forms between them [17]. For this film to rupture and in order for an aggregate to be formed, a net attractive force is required between the flocs and bubbles. We hypothesize in this work that the formation of aggregates in a DAF unit is a complex outcome of the equilibrium between the hydrodynamic and physicochemical phenomena. We include in the model, among other effects, the energy that is required for drainage of the intervening film between bubbles and flocs. In other words, we calculate the resistance to the thinning of the water layer between bubbles and flocs.

There are two options on how to devise an aggregation model. The first one is to express it in terms of the energies involved in the process. Alternatively, it is possible to formulate the model using the relevant forces acting on flocs and bubbles and leading to creation of agglomerates. The latter approach is chosen in our work and it is thus needed that a proper description of these forces is obtained. However, before examining the forces constituting the model, there are a number of general assumptions that have to be clearly stated. First, the bubbles are assumed to have a constant size in the contact zone. Thus, the possible bubble growth that can be either due to air uptake from the water or from coalescence of bubbles is neglected. Second, bubbles are assumed to rise as rigid spheres. This assumption is valid for bubbles smaller than several hundreds of μm [18], and the bubbles of that size and smaller are clearly present in DAF units. Third, the main mechanism of mixing of the suspended entities (bubbles and flocs) is assumed to be by fluid shear (the so-called turbulent flocculation), i.e. that Brownian diffusion is neglected as a mixing mechanism. In summary, the forces that constitute our aggregate model are: the long-range attractive hydrophobic interaction ($\underline{F}_H$), the hydrodynamic repulsion force ($\underline{F}_{RP}$), the van der Waals force ($\underline{F}_W$), the electrostatic force ($\underline{F}_E$) and, finally, the buoyancy force ($\underline{F}_B$). The identified forces satisfy the following force balance (the

assumption of equilibrium) formulated from the perspective of a floc, Eq. (3).

$$\underline{0} = \underline{F}_B + \underline{F}_{HR} + \underline{F}_W + \underline{F}_E + \underline{F}_H \quad (3)$$

Note that this equation cannot be satisfied by either the floc or the bubble diameter. Hence a new diameter, i.e. the aggregate diameter, has to be calculated in order to satisfy the balance. Also, this approach by no means implies that the aggregates consist of a single bubble and a single floc. Additionally, in this work it is assumed that there is a clear separation of time scales between the process of creating aggregates and their mean advection through the flotation unit. In other words, the model assumes that aggregates are formed considerably faster compared to their mean vertical movement through the unit. Under such conditions, we can neglect inertia in Eq. (3).

The properties of the flocs and the air bubbles are presented in Table 1. On the whole, the formation of an aggregate is promoted by the hydrophobicity of the floc and the air bubble while the attachment is counteracted by the negative zeta potential of both the floc and the air bubble. In this work, the following expressions, Eqs. (4-8) are used for the forces mentioned in Eq. (3):

The van der Waals force [19]:

$$\underline{F}_w = \frac{A}{12h^2}\frac{d_f d_b}{(d_f + d_b)} \quad (4)$$

where d_f and d_b are the floc and bubble diameters respectively, h is the distance between the floc and the bubble and A is the Hamaker coefficient.

The electrostatic force [20]:

$$\underline{F}_E = \varepsilon\varepsilon_0\kappa\frac{\pi d_f d_b}{d_f + d_b}\frac{2\varsigma_f\varsigma_b\exp(\kappa h) + \varsigma_f^2 + \varsigma_b^2}{\exp(2\kappa h) - 1} \quad (5)$$

Here, ε is the dielectric constant, ε_0 is the permittivity of vacuum, κ is the Debye constant and ς_f and ς_b are the floc and bubble surface zeta potentials, respectively. Typically, there is negative charge between bubbles and bubbles and flocs, thus making the electrostatic force repulsive in nature.

The hydrophobic force [20]:

$$\underline{F}_H = \frac{K}{2}\frac{d_f d_b}{d_f + d_b}\exp\left(-\frac{h}{\lambda}\right) \quad (6)$$

Where K is a force constant and λ is the decay length. This force is the primary force behind attachment of hydrophobic flocs to air bubbles. The origin of this force is not fully understood. A possible explanation [21] is that bubbles favour hydrophobic surfaces relative to the water, i.e. that the bubbles being in water tend to actively seek any hydrophobic surface (a floc in this case).

Table 1. Experimental data used when calculating the aggregate size.

Parameter		Unit	Value	Ref.
Hamaker coefficient	A	$[J]$	$3.54\cdot10^{-20}$	[22]
Dielectric constant	ε	[-]	80.36	[22]
Permittivity of vacuum	ε_0	$[C^2/Jm]$	$8.854\cdot10^{-12}$	[22]
Force constant	K	$[mN/m]$	1.5	[20]
Decay length	λ	$[nm]$	5	[20]
Density floc	ρ_f	$[kg/m^3]$	1050	[23]
Density air	ρ_b	$[kg/m^3]$	1.225	
Density water	ρ_w	$[kg/m^3]$	998	
Floc velocity (D=1.79)	u_f	$[m/s]$	$u_f = 1.14\cdot d_f + 1.1\cdot10^{-5}$	[23]
Floc velocity (D=2.25)	u_f	$[m/s]$	$u_f = 1.33\cdot d_f - 5.3\cdot10^{-5}$	[23]
Debye constant	κ	$[1/m]$	$2.6\cdot10^{8}$	[22]
Zeta potential	ς_f	$[mV]$	-4	[22]
Zeta potential	ς_b	$[mV]$	-25	[22]

The hydrodynamic repulsive force [23, 24]: This force is repulsive in nature – it inhibits both bubble coalescence and bubble-floc attachment. Its existence implies that energy is required for draining (i.e. displacing) the intervening liquid film between bubbles or bubbles and flocs. Here, this force is modelled as a hydrodynamic drag force with a correction due to existence of micro-hydrodynamic interactions at short distances.

$$\underline{F}_D = \frac{\rho_w\pi}{8}C_D u_f^2 d_f^2 \quad (7)$$

where ρ_w is the density of water. Also, we use a modified drag coefficient, C_D, for settling flocs determined experimentally by Johnson et al. [23] to account for phenomena such as the irregularity in shape and the porosity of the floc.

The buoyancy force:

$$\underline{F}_g = \frac{\pi}{6}(\rho_f - \rho_w)d_f^3 g \quad (8)$$

where ρ_f is the density of the floc and g is the gravitational acceleration.

The roots of Eq. (3) are found numerically employing the Secant method. The advantage with this method is that it does not require the derivative

of the equation to be evaluated, in comparison to a faster converging Newton-Raphson method [25].

2.3 Implementation

In this paper our interest is to argue for the necessity to introduce an aggregation model to study DAF and then to implement it into a CFD framework. In the process, we use a relatively simple turbulence model (the standard k-epsilon model), neglect the possible necessity for a detailed representation of the stresses of the aggregate phase, keep the density of the formed aggregates constant and conduct a steady state solving procedure. A comprehensive refinement of the overall numerical model will be a subject of further study. The simulations in this paper are carried out using ANSYS Fluent™ [26]. The size of the formed aggregates depends on the relative velocity between flocs and water. The velocity is modelled here as a sum of two contributions: the settling velocity of a floc and a local turbulent velocity fluctuation.

The settling velocity is estimated using the results by Johnson et al. [23]. The turbulent fluctuation is related to the Kolmogorov velocity scale, but adjusted to account for the short acceleration period of a floc in relation to the lifetime of a turbulent eddy.

The density of aggregates, ρ_{agg}, used in our simulations is based on experimental observations of the number of bubbles that attach to a floc of a certain size [27]. An aggregate is assumed to consist of one floc, air bubbles and water. Then, by knowing the size of the aggregate and the number of bubbles and flocs within the aggregate the density of the aggregate has been estimated by

$$\rho_{agg} = \frac{V_b\rho_b + V_f\rho_f + V_w\rho_w}{V_{agg}} \quad (9)$$

where ρ represents the density and V the volume of each phase. The results are presented in Figure 2 where the density variation for estimated aggregates consisting of a floc of size d_f with a fractal dimension of D = 1.79 and D = 2.25 is shown. Since only minor density differences are observed, a constant mean density has been used in this first implementation of the numerical model. The density variation is dependent on the number of bubbles attached to the floc.

2.4 Case study

The numerical framework derived above is evaluated in the contact zone of a flotation unit, Fig. 1. The geometry of the contact zone is taken from a pilot DAF unit previously investigated [11]. With the aim of demonstrating the implementation and applicability of the derived modelling framework, the geometry is limited to a two-dimensional representation of the contact zone.

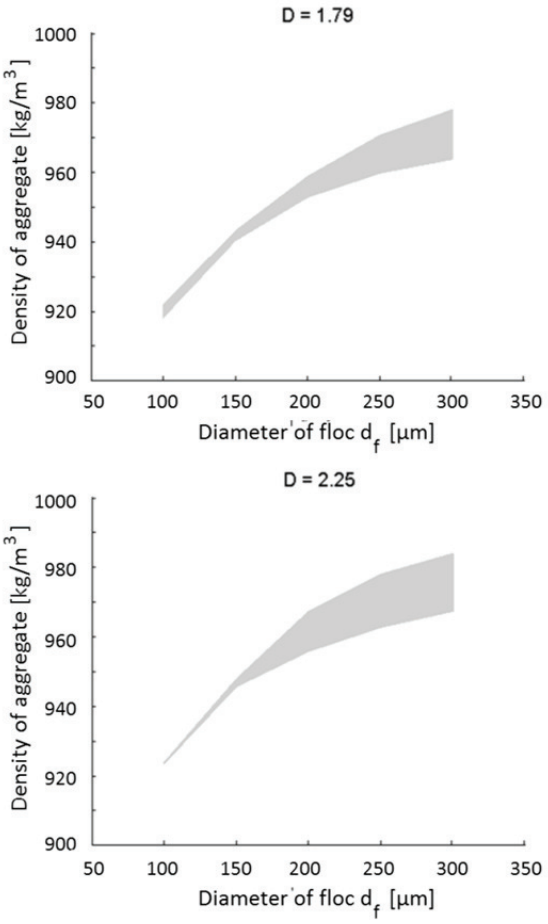

Figure 2. The density variation for estimated aggregates consisting of a floc of size d_f.

The initial conditions used in the simulations are shown in Table 2. Both inlets are modelled as velocity inlets and the outlet as a pressure outlet. Previous research [11] has shown that a two-dimensional geometry will overestimate the flow close to the bottom of the contact zone, causing a circulating motion if the velocity from the dispersion valve is not reduced. To prevent this circulation, the velocity from the dispersion valve is decreased and modelled in accordance to suggestions given by Giumet et al. [28].

Eqs. (1) and (2) are solved in a finite volume framework using a pressure-based, segregated solver on a co-located grid. The grid used in the simulations presented here consists of 4,450 quadrilateral cells, with cell side lengths of approximately 5 *mm*. In comparison, the contact zone measures 0.25x0.89 *m* and the dispersed phases are more than one order of magnitude smaller than the cell size. The minimum orthogonal quality of the grid is 0.96 and the maximum aspect ratio is 2.5, indicating that the grid is of very high quality. Grid convergence is ensured by performing a reference simulation on successively finer grids and choosing a final grid resolution that yields spatially converged results.

Table 2. Initial conditions used in the simulations.

Parameter		Unit	Value
Inlet velocity	v_{in}	[*m/s*]	0.043
Dispersion valve velocity	v_{dis}	[*m/s*]	0.078
Aggregate fraction	α_{agg}	[-]	0.058

3. RESULTS AND DISCUSSION

The results of the simulations are presented in Figures 3 and 4. The formed aggregates in the contact zone are presented as a function of the fractal dimension, D, and the size of the flocs, d_f. The simulated aggregate sizes in the contact zone for a fractal dimension of D = 2.25 are shown in Fig. 3 for a floc size of 100 μm (Fig. 3A) and a floc size of 200 μm (Fig. 3B). The simulated aggregate sizes for a fractal dimension of D = 1.79 are shown in Fig 4 for a floc size of 100 μm (Fig. 4C) and a floc size of 200 μm (Fig. 4D). The aggregate model has previously been experimentally validated [15] and the predicted aggregate sizes in the CFD simulations are in accordance with these results.

A relatively narrow distribution of aggregate sizes in the contact zone and a similar distribution pattern for all the simulated cases can partly be attributed to the two-dimensional geometry and the neglected variation in density for the aggregates. The two-dimensional framework neglects the three-dimensional movements caused by the injected flow from the dispersion valves. Consequently, the flow pattern will be very similar for the simulated cases. The density of the aggregate is not varied within the simulation. If, for example, the increased size of the aggregate is caused by the attachment of more air bubbles the buoyancy of the aggregates should increase. The larger aggregates formed along the wall of the unit and close to the dispersion valve inlet are a consequence of the definition of the relative velocity between the floc and the water. The largest diameters closest to the dispersion valve are not included in Figs. 3 and 4.

The formation of aggregates predominantly takes place in the contact zone, although it has been reported that the phenomenon also occurs in the separation zone [1]. The geometry of the contact zone has been modelled in two-dimensions to further reduce the complexity of the model. Previous research [11] has however shown that the contact zone is better represented by a three-dimensional model. Consequently, future development of the modelling framework should account for a three-dimensional geometry. In addition, the separation zone should be included into the framework due to the reported continued formation of aggregates in this zone. An interesting potential with the current modelling concept is that, since the aggregates are included, the formation of the sludge layer can be investigated if a complete DAF geometry is modelled.

The number of phases included in a numerical flotation model has been addressed above in the paper. The selection of phases to be included in the modelling is not trivial and should be based on the aim of the simulations. It is clear that, by assuming that flocs and bubbles are continuously forming aggregates within the unit, neither free flocs nor air bubbles will be present in the modelling framework. This assumption implies that all attachments necessarily lead to a successful formation of aggregates. The fraction of formed aggregates is here assumed to be the same as the fraction of the air phase. This assumption may overestimate the amount of aggregates formed in the unit and will be addressed in future work.

Another interesting aspect of future research is to address is the variation of the density as the aggregates increase in size. This density variation can for example be accounted for by assuming a factor that increases the number of bubbles attached to a floc for an increased aggregate size. The

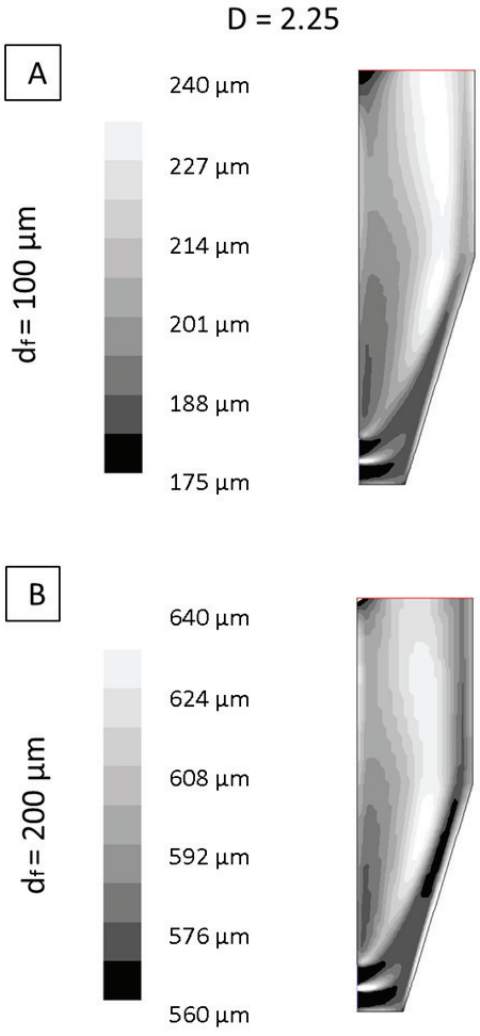

Figure 3. The simulated aggregate sizes in the contact zone for a fractal dimension of D = 2.25.

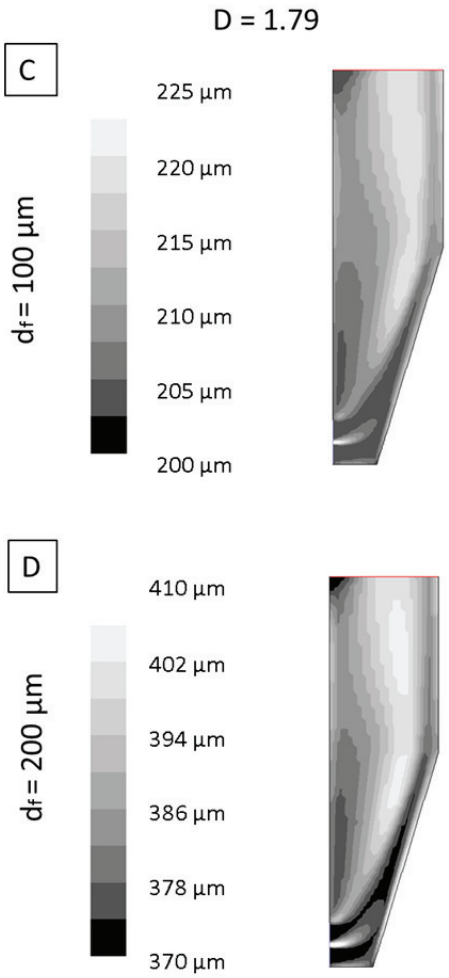

Figure 4. The simulated aggregate sizes in the contact zone for a fractal dimension of D = 1.79.

density will have a direct effect on the buoyancy of the aggregates and consequently on their movement through the DAF unit. Currently, the implementation of the aggregation model can only account for one floc size and one air bubble size. In a future refinement of the model, this issue will be addressed in order to evaluate the effect of several sizes simultaneously. In summary, although several improvements of the modelling framework can be identified, the derived concept demonstrates a promising approach to account for the formation and flow of aggregates within a DAF unit.

4. SUMMARY

In this paper we propose a model that estimates the size of the aggregates formed in a DAF unit, and then implement it into an Eulerian simulation setup. The entire framework demonstrates the formation and movements of the aggregates through the contact zone of a pilot DAF unit depending on the diameter of the flocs and their fractal dimension. The investigation also identifies several issues that need to be addressed for further improvements of the modelling framework.

ACKNOWLEDGEMENTS

Financial support from the Swedish Research Council for Environment, Agricultural Sciences and Spatial Planning (FORMAS), The Swedish Water & Wastewater Association through Dricks and, finally, TECHNEAU, funded by the European Commission, are gratefully acknowledged.

REFERENCES

[1] Haarhoff, J. 2008 "Dissolved air flotation: Progress and prospects for drinking water treatment," *Journal of Water Supply: Research and Technology - AQUA*, vol. 57, pp. 555-567.

[2] Valade, M.T., Becker, W.C. and Edzwald, J.K., 2009, "Treatment selection guidelines for particle and NOM removal," *Journal of Water Supply: Research and Technology - AQUA*, vol. 58, pp. 424-432.

[3] Crossley, I.A. and Valade, M.T., 2006, "A review of the technological developments of dissolved air flotation," *Journal of Water Supply: Research and Technology - AQUA*, vol. 55, pp. 479-491.

[4] Yan, M.Q., Wang, D.S., Shi, B.Y., Wei, Q.S., Qu, J.H. and Tang, H.X., 2007, "Transformations of particles, metal elements and natural organic matter in different water treatment processes," *Journal of Environmental Sciences*, vol. 19, pp. 271-277.

[5] Lundh, M., Jönsson, L. and Dahlquist, J., 2001, "The flow structure in the separation zone of a DAF pilot plant and the relation with bubble concentration," *Water Science and Technology*, vol. 43, pp. 185-194.

[6] Lundh, M., 2002, "Effects of flow structure on particle separation in dissolved air flotation", *Thesis*, Department of Water and Environmental Engineering, Lund University, Lund, Sweden.

[7] Emmanouil, V., Skaperdas, E.P., Karapantsios, T.D. and Matis, K.A., 2007, "Two-phase simulations of an off-nominally operating dissolved-air flotation tank," *International Journal of Environment and Pollution*, vol. 30, pp. 213-230.

[8] Amato, T. and Wicks, J., 2009, "The practical application of computational fluid dynamics to dissolved air flotation, water treatment plant operation, design and development," *Journal of Water Supply: Research and Technology - AQUA*, vol. 58, pp. 65-73.

[9] Speight, V. and Via, S., 2011, "Recent research every utility manager needs to know about," *American Water Works Association Journal* vol. 103, pp. 48-59.

[10] Hague, J., Ta, C.T., Biggs, M.J. and Sattary, J.A., 2001, "Small scale model for CFD validation in DAF application", *Water Science and Technology*, vol. 43, pp. 167-173.

[11] Bondelind, M., Sasic, S., Kostoglou, M., Bergdahl, L. and Pettersson, T.J.R., 2010, "Single- and two-phase numerical models of Dissolved Air Flotation: Comparison of 2D and 3D simulations", *Colloids and Surfaces A: Physicochemical and Engineering Aspects*, vol. 365, pp. 137-144.

[12] Kwon, S.B., Park, N.S., Lee, S.J., Ahn, H.W. and Wang, C.K., 2006, "Examining the effect of length/width ratio on the hydro-dynamic behaviour in a DAF system using CFD and ADV techniques," *Water Science and Technology*, vol. 53, pp. 141-149.

[13] Ta, C.T., Beckley, J. and Eades, A. 2001, "A multiphase CFD model of DAF process," *Water Science and Technology*, vol. 43, pp. 153-157.

[14] Kostoglou, M., Karapantsios, T.D., and Matis, K.A., 2007, "CFD model for the design of large scale flotation tanks for water and wastewater treatment," *Industrial and Engineering Chemistry Research*, vol. 46, pp. 6590-6599.

[15] Bondelind, M., 2011, "Dissolved Air Flotation, a numerical investigation of the flotation process", *Thesis*, Chalmers, Göteborg.

[16] Ishii, M., 1975,*Thermo-fluid dynamic theory of two-phase flow*. Paris: Eyrolles.

[17] Derjaguin, B.V. and Dukhin, S.S., 1993, "Theory of flotation of small and medium-size particles," *Progress in Surface Science*, vol. 43, pp. 241-266.

[18] Clift, R., Grace, J.R. and Weber, M.E., 1978 *Bubbles, Drops and Particles*: Academic Press.

[19] Israelachvili, J.N., 2011, Intermolecular and surface forces, 3 ed. Santa Barbara, USA: Elsevier Inc.

[20] Nguyen, A.V., 2007, "One-step analysis of bubble-particle capture interaction in dissolved-air flotation," *International Journal of Environment and Pollution*, vol. 30, pp. 231-253.

[21] Ducker, W.A., Xu, Z. and Isrealachvili, J.N., 1994, "Measurements of hydrophobic and DLVO forces in bubble-surface interactions in aqueous solutions," *Langmuir*, vol. 10, pp. 3279-3289.

[22] Okada, K., Akagi, Y., Kogure, M. and Yoshioka, N., 1990, "Effect on surface charges of bubbles and fine particles on air flotation process," *Canadian Journal of Chemical Engineering*, vol. 68, pp. 393-399.

[23] Johnson, C.P., Li, X. and Logan, B.E., 1996, "Settling velocities of fractal aggregates," *Environmental Science and Technology*, vol. 30, pp. 1911-1918.

[24] Adamczyk, Z., Adamczyk, M. and van de Ven, T.G.M., 1983, "Resistance coefficient of a solid sphere approaching plane and curved boundaries," *Journal of Colloid and Interface Science*, vol. 96, pp. 204-213.

[25] Press, W., Flannery, B.P., Teykolsky, S.A. and Vetterling, W.T. Eds., 1986, *Numerical recipies*. The art of scientific computing. Camebridge University Press.

[26] Fluent, 2010, *ANSYS FLUENT Theory guide: Release 13.0*, Ansys Inc., Southpointe 275 Technology Drive Canonsburg, PA 15317.

[27] Fukushi, K., Matsui, Y. and Tambo, N., 1998, "Dissolved air flotation: experiments and kinetic analysis," *Journal of Water Supply: Research and Technology – Aqua*, vol. 47, pp. 76-86.

[28] Guimet, V., Broutin, C., Vion, P. and Glucina, K., 2007, "CFD modeling of high-rate dissolved air flotation," in *Proceedings of The 5th International Conference on Flotation in Water and Wastewater Systems*, Seoul South Korea, Seoul, South Korea, pp. 113-119.

Conference on Modelling Fluid Flow (CMFF'12)
The 15th International Conference on Fluid Flow Technologies
Budapest, Hungary, September 4-7, 2012

SURFACE TENSION MEASUREMENT FOR WATER SURFACTANT SOLUTIONS USING A SMALL DROPLET ON A VERTICALLY VIBRATING PLATE

Shuichi IWATA[1], Fumihiko NAKAMURA and Hideki MORI

[1] Corresponding Author. Department of Material Science and Engineering, Nagoya Institute of Technology. Gokiso-cho, Showa-ku, Nagoya, 466-8555, Japan. Tel.: +81 52 735 5256, Fax: +81 52 735 5255, E-mail: iwa@nitech.ac.jp

ABSTRACT

The effect of the frequency of a vibrating plate on the surface tension of a small droplet of surfactant present on it was studied. Assuming a static droplet at the lowest position of the vibrating plate, the theoretical droplet shape could be rigorously determined by numerical analysis that takes into account the force balance equation on the droplet surface and the momentum equation. The surface tension was determined by optimizing four parameters until the theoretical droplet shape agreed well with the experimental droplet shape when the vibrating plate was at its lowest position. The four parameters were the surface tension, the height of the droplet, the radius of the three-phase contact circle, and the horizontal shift of the origin in the experimental droplet coordinates.

The accuracy and repeatability of the proposed method were confirmed using distilled water. In this case, the vibration frequency plate had no influence on the surface tension. However, for aqueous solutions of surfactants, the surface tension was found to gradually increase with frequency. A stronger frequency dependence was observed for a low surfactant concentration near the critical micelle concentration.

Keywords : dynamic surface tension, numerical analysis, high-speed camera, droplet

NOMENCLATURE

$\underline{e_r}$	[-]	radial vector
p	[Pa]	pressure
ρ	[kg/m^3]	density
p_G	[Pa]	pressure of gas phase
$\underline{n}$	[N]	normal force vector
$\underline{\tau}$	[Pa]	deviatoric stress
$2H$	[m^{-1}]	mean curvature
σ	[N/m]	surface tension
f	[m]	radial distance
g	[m/s^2]	gravitational acceleration
S	[m]	horizontal origin shift
ω	[rad/s]	angular velocity
A	[m]	amplitude of vibration platform
a	[m]	radius of three-phase contact circle
b	[m]	height of liquid droplet
τ	[s]	surface age

Subscripts and Superscripts

G	Gas phase
H	Highest position
L	Lowest position
U	Upper side
L	Lower side

1. INTRODUCTION

Surface tension is one of the most important physical properties affecting the performance of products such as coating agents, pesticides, inks, cosmetics and surfactants. In processes where mass transfer of surfactants occurs, interface phenomena are affected by the dynamic surface tension due to a non-uniform distribution of surfactants at the gas-liquid interface. There are several methods available for measuring the dynamic surface tension: for example, the maximum bubble pressure method [1, 2], the pendant-drop method [3-5] and the jet reaction method [6]. However, there are some difficulties with these methods. In the case of the maximum bubble pressure technique, the system can be relatively expensive, because the pressure sensor in the bubbling system should have a high sensitivity and time resolution. The pendant-drop method uses a capillary and special care is required to keep it clean throughout the measurements, especially for the case of viscous liquids. In addition, a correction factor is required in order to calculate the maximum volume at the critical condition. These conventional methods are difficult to apply to highly viscous fluids. In addition, they

require at least a few hundred milliliters. They are not suitable for measuring precious samples such as synthesized derivatives, because a large amount of starting materials may be needed if the yield of the reaction is poor. Therefore, it is desirable to develop a dynamic surface tension measurement method that uses only a small amount of sample.

In this study, we observed droplets placed on a vertically vibrating flat smooth horizontal plate using a high-speed video camera. The shape of the droplet could be calculated numerically given certain assumptions. The dynamic surface tension could be determined by optimizing the parameters used in the analysis until the calculated droplet shape agreed well with the experimentally observed shape. One advantage of this method is that only a small amount of sample solution is needed. For a single measurement, this amounts to only 1 or 2 μL. The effect of inertial forces can be neglected due to the tiny size of the droplet. In this paper, we applied this technique to study the effect of vibration frequency on the dynamic surface tension of aqueous surfactants.

2. MATERIALS AND CALCULATION METHODS

2.1 Materials

Three types of surfactants were used in this study, sodium dodecyl sulfate (SDS, MW = 288.3, cmc. = 8.67 *mM*), cetyl trimethyl ammonium bromide (CTAB, MW = 364.5, cmc. = 0.9 *mM*) and Triton X-100 (MW = 625, cmc. = 0.321 *mM*) from Wako Industries (Japan). The surfactants have different molecular weights, and their relevant physical properties at a room temperature of 23°*C* are listed in Table 1. Distilled water was used as the reference system. The surfactant was placed in distilled water, stirred for 24 hours, and then left for an additional 24 hours.

2.2 Calculation methods

The mathematical analysis uses a spherical polar coordinate system (r, θ, ϕ) as shown in Figure 1. The origin is defined as the center of the three-phase contact circle. The radial distance f is a function of the zenith angle θ. The contact angle is defined as γ. Assuming quasi steady-state conditions, the equation of motion can be written as:

Table. 1 Physical properties of surfactant

Surfactant	Ionic nature	MW [-]	cmc. [*mM*]
SDS	Anionic	288.3	~8.67
CTAB	Cationic	364.5	~1.01
Triton X-100	Nonionic	624(av.)	~0.321

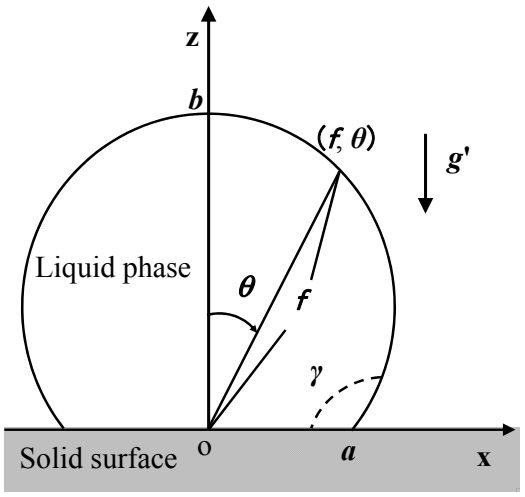

Figure 1. Droplet model and coordinate system for numerical analysis

$$\nabla p = \rho \underline{g}', \tag{1}$$

where p is the pressure, ρ is the density of the droplet, ∇ is the gradient operator, and g' is the acceleration acting on the droplet, expressed by

$$\underline{g}' \equiv \underline{g} - A\omega^2 \sin \omega t \, \underline{e}_z . \tag{2}$$

The dynamic boundary condition at the liquid-gas interface is given by the force balance

$$\underline{n}\left(p - p_G\right) + \underline{n} \cdot \left(\underline{\tau}_G - \underline{\tau}\right) + 2H\sigma \underline{n} = \underline{0}, \tag{3}$$

where $\underline{n}$ is a normal vector pointing outward, and $2H$ indicates the mean curvature.

From Eqs. (1) to (3), the following third-order ordinary differential equation can be derived:

$$\frac{d}{d\theta}\left[\frac{\left\{\left(f^2 + 2f_\theta^2 - ff_{\theta\theta}\right) + \left(f^2 + f_\theta^2\right)\left(1 - \frac{f_\theta}{f}\cot\theta\right)\right\}}{\left(f^2 + f_\theta^2\right)^{\frac{3}{2}}}\right] \tag{4}$$
$$= \left(\rho g a^2 / \sigma\right)\left(f\sin\theta - f_\theta \cos\theta\right)$$

Here, f_θ represents the differential of f with respect to θ. The same notation is used in the following sections. Equation (4) can be transformed into the standard form of Eqs. (5) to (7) for numerical calculation. Ψ in Eq. (7) indicates a kind of mean curvature, which is equivalent to the square brackets in Eq. (4). F is defined as $f \equiv f / f_\theta$.

$$\frac{df}{d\theta} = fF \tag{5}$$

$$\frac{dF}{d\theta} = (1+F^2)(2-F\cot\theta) - \Psi(1+F^2)^{\frac{1}{2}} \tag{6}$$

$$\frac{d\Psi}{d\theta} = (\frac{\rho g' a^2}{\sigma})(f\sin\theta - F\cos\theta) + \Psi F \tag{7}$$

The following boundary conditions are applied.

$$\begin{cases} f = b \text{ at } \theta = 0 \\ F = 0 \text{ at } \theta = 0 \\ \Psi = \Psi_0 \text{ (Assumed) at } \theta = 0 \\ f = a \text{ at } \theta = \pi/2 \end{cases} \tag{8}$$

These equations can be solved by the Runge-Kutta-Gill method. The calculation starts from (f, F, Ψ) = (b, 0, Ψ_0) at θ = 0 under the given parameters (a, b, σ). If a suitable Ψ_0 is provided, the final value of f becomes the same as the radius of the contact circle a at $\theta = \pi/2$. However, the assumed value usually contains a certain level of error. Therefore, the starting value Ψ_0 should be numerically corrected by the shooting method until the third boundary condition ($f = a$) is satisfied at $\theta = \pi/2$. The Regula-Falsi method is used in the correction process.

Once the shooting method is accomplished, the objective function defined in Eq. (9) can be evaluated, which is a summation of the root mean square of the relative errors in droplet shape, expressed as the difference between the experimentally obtained radial distance $(f_{exp})_n$ and the simulation result $(f)_n$ at the same zenith angle θ_n. The experimental droplet coordinates are manually extracted from the video images and may thus contain a certain level of error. Therefore, we introduced an additional parameter S, referred to as the shift factor. All of the droplet coordinates are shifted from (x^i, y^i) to (x^i+S, y^i) in order to minimize the horizontal errors in the droplet coordinate data. The shift factor is determined using the Simplex method.

In this study, the Simplex method is also used for minimizing the object function E. Figure 2 shows a flow chart of the calculation procedure. The optimization process continues until the objective function is well satisfied within a given tolerance. After the optimization process, the dynamic surface tension can be determined.

$$E(a, b, \sigma, S) \equiv \sqrt{\frac{1}{N}\sum\left[\frac{(f_{exp})_n - (f)_n}{(f_{exp})_n}\right]^2} \tag{9}$$

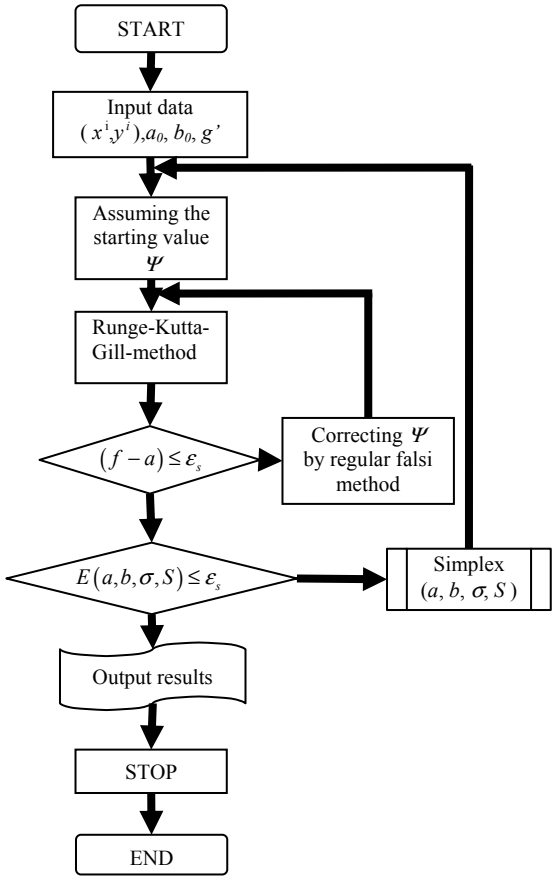

Figure 2. Calculation flow chart

3. EXPERIMENTAL PROCEDURE AND APPARATUS

Figure 3 shows a schematic view of the experimental apparatus. The sample liquid was placed on an acrylic substrate, which was connected to a vibrating platform (Wave Maker 05, Asahi Factory Corp.). A cylinder of thin PVC film (2 *mm* in diameter) was placed on the vibrating plate to hold the circle contact line. The amplitude and frequency of the sinusoidally vibrating plate were controlled by a feedback control system inside the vibrating platform. The substrate was well cleaned with distilled water and ethanol, and then allowed to dry completely before each of the experiments. The entire system was placed in a N_2 vessel.

The volume of the droplet was 2 μL. Its shape was captured by a high-speed video camera system (VW-6000 system, Keyence Co., Ltd.) with a 50× close-up lens. The camera, substrate and vibrating platform were aligned horizontally.The light source was placed behind the droplet so as to obtain a clear and sharp image. The frame rate of the high-speed camera was set at 500 *fps* with a shutter speed of 1/30000 *s*. A set of images of the droplet was

caputured for several vibration cycles. The droplet image at the bottom of the vibration cycle was extracted from the video data for use in the numerical analysis described in the previous section.

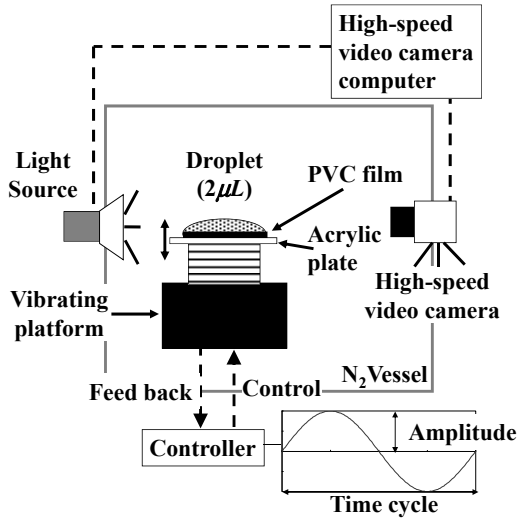

Figure 3. Experimental apparatus

4. RESULTS AND DISCUSSION

To evaluate the accuracy of the numerical simulation, we used a droplet of mercury on a ZrO_2 plate under static conditions. Figure 4 shows a comparison of the numerical results and droplet image. The coordinates used in the numerical prediction are plotted as closed squares. The solid line indicates the numerical results. It is clear from the figure that they agree well with the experimental results. The calculated surface tension was 482.46 *mN/m*, which is in good agreement with the literature value of 482.1 *mN/m*.

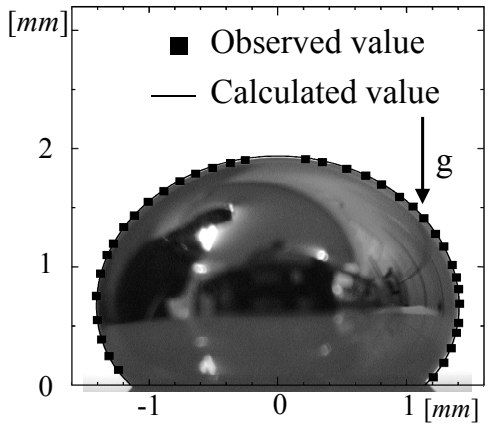

Figure 4. Comparison of observed droplet profile and predicted profile (Mercury/ZrO_2 system; 24.0 °*C*) cited from Iwata *et al.*[7]

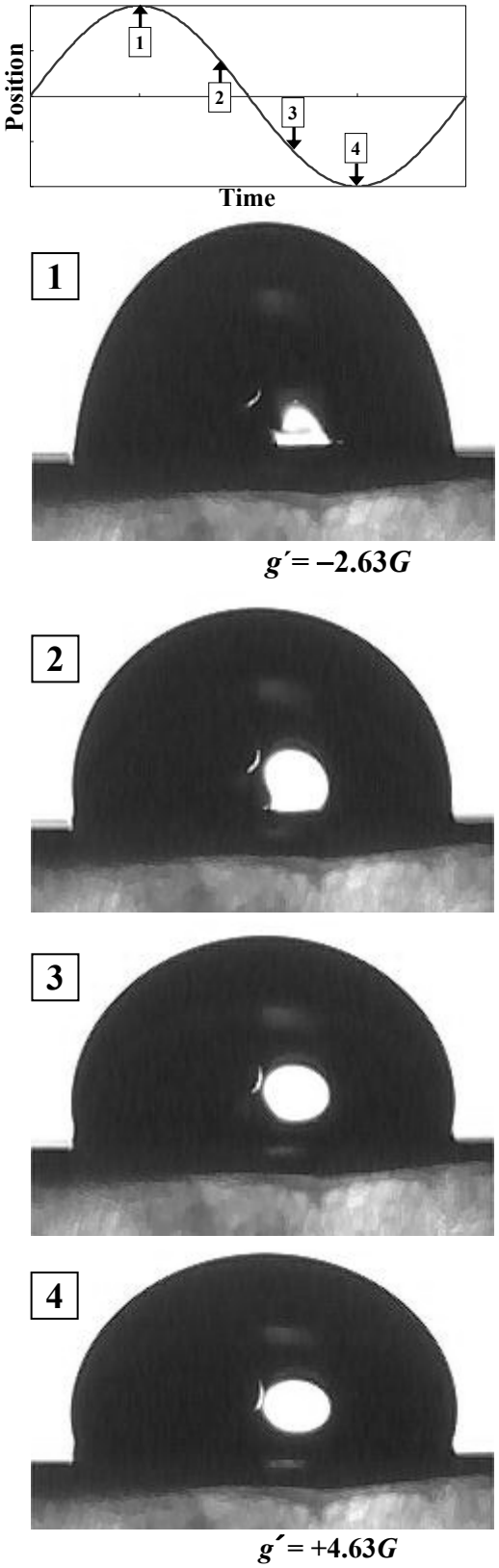

Figure 5. Periodic change in droplet shape during a single cycle for 1-*mM* CTAB aq. under a vibration field (*f* = 30 *Hz*)

After the successful experiment under static conditions, we measured a droplet on the vibrating plate. The vibration amplitude of the plate was set at 1 *mm* and the frequency was varied from 5 to 35 *Hz*. Figure 5 shows the periodic change in the droplet shape during a single cycle for 8.67-*mM* SDS *aq*. under a vibration field (f = 30 *Hz*). The numbers in the open squares indicate the phase in the cycle. As can be seen from the images, although the droplet shape changed substantially due to the apparent gravity, the contact line did not move during the cycle. In addition, the maximum relative error between the optimized value of a and the experimental value was less than 0.5%. Figure 6 shows a composite of two droplet images recorded at the highest and lowest positions of the plate. The blue and red areas correspond to the droplet image at the top and bottom position of the vibration cycle, respectively. The black area indicates where the blue and red areas are overlapped. The surface of the droplet can be divided into upper and lower regions, as indicated by the dotted line (c)-(c)'. It is clear from the figure that above and below this line, bulging of the surface occurs during opposite half cycles. Assuming axial symmetry about the vertical direction, the areas of the upper and lower surfaces can be directly calculated from the images, and the results are summarized in Table 2. As the plate moved from its highest to its lowest position, the lower surface area increased by 5% and the upper surface area decreased by 9%. However, the overall surface area of the droplet S_U+S_L remained almost constant. Such a sudden local increase in surface area may disrupt the uniform adsorption of surfactants on the droplet surface. Therefore, the surface tension may depend on the ability of surfactants to become adsorbed on the droplet surface. The largest change in the mean curvature of the droplet surface occurred at the lowest plate position. Therefore, in the present analysis, the dynamic surface tension was evaluated when the droplet was at its lowest position and had momentarily entered a stationary state.

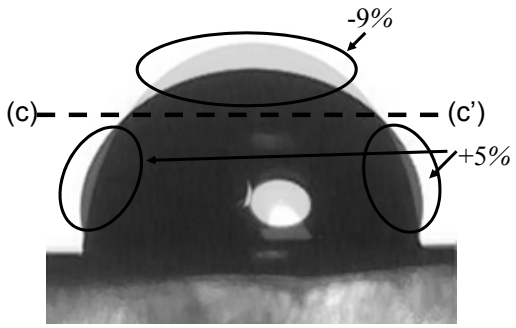

Figure 6. Composite image of droplet at highest and lowest plate position

Table 2. Surface areas at highest and lowest plate position

	Upper surface area S_U [mm^2]	Lower surface area S_L [mm^2]	Total S_U+S_L [mm^2]
Highest Position	S_{HU} 2.02	S_{HL} 7.49	S_H 9.51
Lowest Position	S_{LU} 1.83	S_{LL} 7.83	S_L 9.66
Ratio S_L/S_H	S_{LU}/S_{HU} 0.91	S_{LL}/S_{HL} 1.05	S_L/S_H 1.02

Figure 7 shows the effect of the CTAB concentration on the dynamic surface tension. For the distilled water reference sample, the calculated surface tension was independent of vibration frequency and was close to the value of 71.5 *mN/m* reported in the literature. This is because the droplet surface is almost completely made up of water molecules.

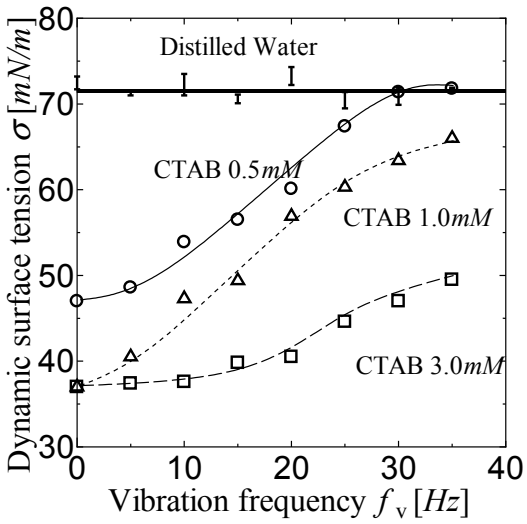

Figure 7. Effect of vibration frequency on dynamic surface tension of CTAB aqueous solutions and distilled water

However, in the presence of CTAB, the situation entirely changed. Under static conditions, *i.e.*, f = 0 *Hz*, the surface tension for a CTAB concentration of 0.5 *mM* was higher than that for 1.0 and 3.0 *mM*. The surface tension depended on the amount of CTAB absorbed on the droplet surface, and decreased up to the critical micelle concentration (cmc.) of 0.96 *mM*. In addition, for all of the CTAB solutions, the surface tension increased gradually with vibration frequency. For the case of 0.5 *mM*, the surface tension reached the same level as that for distilled water. For a CTAB concentration of 3.0 *mM*, which is higher than the cmc., a flat region was observed at low frequencies, but this was not the case for 1.0-*mM* CTAB. When a sufficient amount of surfactant is present, it is

generally easier for full adsorption to occur on the surface. However, at higher vibration frequencies, the adsorption of surfactants is limited by their diffusion rate, thus leading to an increase in surface tension.

Figure 8 shows the effect of the molecular weight of the surfactant on the dynamic surface tension. The concentration of the three different aqueous surfactants was adjusted to be close to the cmc. The concentrations of CTAB, SDS and Triton X-100 were 1.0, 8.67 and 0.34 *mM*, respectively. Although the surface tension increased with frequency in each case, the slopes were different due to differences in the mobility of the surfactant, which depends on its molecular weight. In general, surfactants with higher molecular weights diffuse more slowly [7]. In summary, the proposed method was effective for measuring the dynamic surface tension, which was closely related to the ability of the surfactant to be adsorbed on the surface.

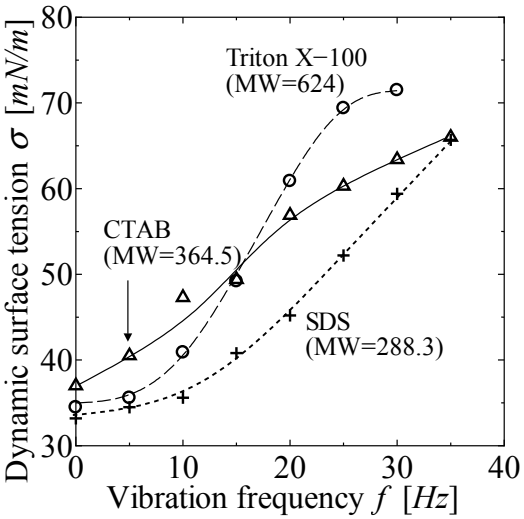

Figure 8. Effect of molecular weight of surfactants on dynamic surface tension

Figure 9 shows the vertical movement of the vibrating plate during a single cycle with a period of *T*. As shown in Figure 6, the bulging of the surface occurs during opposite half cycles. We therefore chose half the oscillation period (0.5*T*) as a characteristic time. Figure 10 shows a comparison between this characteristic time and the surface age parameter τ measured by Gatne *et al.*[8], which yielded the same results for surface tension. The surface age is defined as the inverse of the rate of bubble generation in the maximum bubble pressure technique. As can be seen, the data are well correlated for the case of CTAB, and a linear dependence is obtained for all surfactants. The slope is largest in the case of Triton X-100, which may reflect its ability to be adsorbed on the surface and its diffusion rate in the bulk liquid. These results indicate that the vibration half period is almost equivalent to the surface age measured by the maximum bubble pressure method.

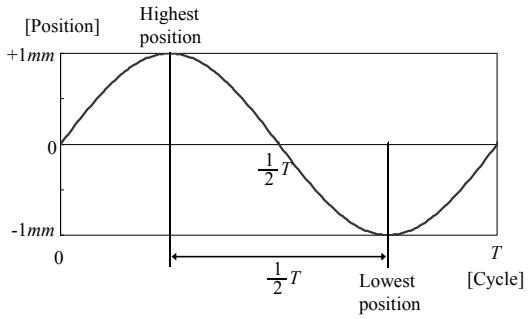

Figure 9. Vertical motion of vibrating plate

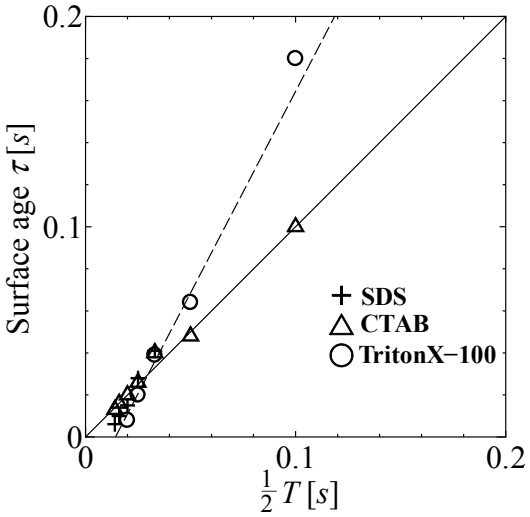

Figure 10. Relation between half the vibration period and surface age (Gatne *et al.*)

5. CONCLUSIONS

We successfully developed a method of measuring the dynamic surface tension of aqueous surfactant solutions. In this approach, parameter optimization was carried out until the theoretical droplet shape agreed well with the experimentally observed shape when the vibrating plate was at its lowest position. This technique requires only about 2 μL of the sample solution.

Measurements were carried out for CTAB, SDS and Triton X-100 aqueous solutions, and the frequency dependence of the surface tension was determined. The proposed method was effective for measuring the dynamic surface tension. The effect of the surfactant concentration was also investigated for a CTAB aqueous solution. In addition, the influence of the surfactant molecular weight on the surface tension was clarified; it was found to be closely related to the ability of the surfactant to be

adsorbed on the surface and its diffusion rate in the bulk liquid. It was also found that half the vibration period is almost equivalent to the surface age measured by the maximum bubble pressure method.

REFERENCES

[1] Sugden, S., 1922, "XCVII.-The Determination of Surface Tension from the Maximum Pressure in Bubbles," *J. Chem. Soc.*, Vol. 121, pp. 858-866.

[2] Mysels, K. J., 1990, "The Maximum Bubble Pressure Method of Measuring Surface Tension, Revisited," *Colloids and Surfaces*, Vol. 43, pp. 241-262.

[3] Ferguson, A., 1923, "On the measurement of the surface tension of a small quantity of liquid," *Proceedings of the Physical Society of London*, Vol. 36, pp. 37-44.

[4] Garanet, J. P., Vinet, B. and Gros, P., 1994, "Considerations on the Pendant Drop Method: A New Look at Tate's Law and Harkins' Correction Factor," *J. Colloid and Interface Sci.*, Vol. 165, pp. 351-354.

[5] del Rio, O., I. and Neumann, A. W., 1997 "Axisymmetric Drop Shape Analysis: Computational Methods for the Measurement of Interfacial Properties from the Shape and Dimensions of Pendant and Sessile Drops," *J. Colloid and Interface Sci.*, Vol. 196, pp. 136-147.

[6] Hasegawa, T., Asama, H. and Narumi, T., 2003, "A Simple Method for Measuring Elastic Stresses by Jet Thrust and Some Characteristics of Tube Flows," *J. Soc. Rheology, Japan*, Vol. 31(4), pp. 243-252.

[7] Iwata, S., Suzuki, H. and Mori, H., 2010, "Measurement of Surface Tension and Contact Angle by Analysis of Force Balance along a Bubble/Droplet Surface," *Kagaku Kogaku Ronbunshu*, Vol. 36(5), pp. 441–448.

[8] Gatne, K.P., Jog, M.A. and Manglik, R.M., 2009, "Surfactant-Induced Modification of Low Weber Number Droplet Impact Dynamics," *Langmuir*, Vol. 25(14), pp. 8122-8130.

Conference on Modelling Fluid Flow (CMFF'12)
The 15th International Conference on Fluid Flow Technologies
Budapest, Hungary, September 4-7, 2012

NUMERICAL SIMULATION OF INCOMPRESSIBLE TWO PHASE FLOWS BY CONSERVATIVE LEVEL SET METHOD

N. BALCAZAR[1], L. JOFRE [1], O. LEHMKHUL [1 2], J. RIGOLA [1], J. CASTRO [1]

[1] Centre Tecnològic de Transferència de Calor (CTTC). Universitat Politècnica de Catalunya (UPC). ETSEIAT. Colom 11, 08222, Terrassa, Barcelona, Spain. Fax: +3493 739 89 20, E-mail: cttc@upc.edu
[2] Termo Fluids, S.L. Av. Jacquard, 97 1-E, 08222 Terrassa (Barcelona), Spain. E-mail: termofluids@termofluids.com

ABSTRACT

A numerical formulation for the Conservative Level-Set Method of Olsson and Kreiss [1, 2] is implemented using the finite volume approach. Both convective term of the interface advection equation and compression term of the reinitialization equation are discretized by the first order upwind plus flux limiter scheme [3]. Time integration is solved by the TVD Third Order Runge Kutta method [4], whereas gradients are computed by the linear Least-Squares approach. The method is tested computing moving interfaces with external velocity fields on unstructured meshes.

Additionally, Level-Set method was coupled to a variable density Navier-Stokes solver for incompressible flow TERMOFLUIDS [5]. Physical properties are assumed to vary smoothly in a narrow band around the interface to avoid numerical instabilities. Pressure velocity coupling is solved using a two step projection method where in the first step the convection, diffusion and source terms are computed explicitily using the Adams-Bashforth time integration. In the second step the velocity is corrected by adding the gradient of the pressure variable. Numerical solution of pressure Poisson equation is calculated with an efficient preconditioned conjugate gradient solver. Mass conservation and convergence properties of the model are investigated for cases with large density and viscosity ratios. For the purpose of validation, numerical results are compared with numerical and experimental data for standard benchmark problems [6, 7].

Keywords: conservative level set method, least square method, unstructured meshes, upwind plus flux limiter scheme, TVD Runge Kutta time integration.

NOMENCLATURE

M	$[kg]$	mass
V	$[m^3]$	volume
$\underline{g}$	$[m/s^2]$	gravitational acceleration vector
$\underline{i}, \underline{j}, \underline{k}$		unit vector
p	$[Pa]$	pressure
t	$[s]$	time
$\underline{v}$	$[m/s]$	absolute velocity vector
Γ		general diffusion coefficient
ε		artificial diffusion coefficient
ρ	$[kg/m^3]$	mass density
κ	$[m^{-1}]$	curvature
ϕ		level set function, general variable
σ	$[N/m]$	surface tension coefficient
μ	$[Pa \cdot s]$	dynamic viscosity

Subscripts and Superscripts

P, C, D	actual, upwind or downwind cells-nodes
f	face node
k	phase index
p	projected node
$*$	non dimensional or auxiliar variable
0	at initial condition

1 INTRODUCTION

There is a large choice of methods that can be used for modelling of flows with inter-phase boundaries, for instance: the Volume-of-Fluid (VOF) method, the Level-Set (LS) method and the Phase-Field method.

Many authors treat the two-phase flow using some kind of LS method [8, 9, 10, 11, 12, 13, 1, 2, 14, 15]. In the standard LS method, the moving interface is implicitly represented by a smooth distance function. Interface propagation is frequently implemented by two steps: interface advection and reinitialization step. An important advantage of LS method is straightforward calculation of geometric properties of the interface. On the other hand, sometimes

undesirable properties are reported when LS method is applied to problems of two-phase flows. A loss of mass conservation is found, the fact that the volume is not conserved during the calculations, and numerical instabilities in the calculations of the curvature.

The Conservative LS method of Olsson and Kreiss [1, 2] improves some of the properties of the standard LS method. Mass conservation is assured if conservative schemes are employed for the interface advection. The reinitialization step keep the shape and width of the interface constant. Last property is important when surface tension is used for modelling two-phase flows.

2 GOVERNING EQUATIONS

In this section the general equation of level set function and the one fluid formulation of the two-phase Navier Stokes equations are presented.

2.1 Level Set Equation

The conservative LS method was proposed by Olsson and Kreiss (2005). In this method a regularized indicator function denoted by $\phi(\underline{x},t)$ is used in place of the distance function $d(\underline{x})$ defined for the standard LS method. The LS function is initialized as

$$\phi(\underline{x},0) = \frac{1}{1+e^{d(\underline{x})/\varepsilon}} \tag{1}$$

The interface is defined as the 0.5 level set of the indicator function

$$\Lambda = \{\underline{x} \mid \phi(\underline{x},t) = 0.5\} \tag{2}$$

The evolution of ϕ in a free divergence velocity field is given by the advection equation as follows,

$$\frac{\partial \phi}{\partial t} + \nabla \cdot \phi \underline{v} = 0 \tag{3}$$

Artificial compression of the interface (Reinitialization equation) is added in order to mantain the profile and thickness of the interface constant,

$$\frac{\partial \phi}{\partial \tau} + \nabla \cdot \phi(1-\phi)\underline{n} = \varepsilon \nabla \cdot \nabla \phi \tag{4}$$

$$\underline{n} = \frac{\nabla \phi}{||\nabla \phi||_2} \tag{5}$$

where $\phi(1-\phi)\underline{n}$ is a compressive flux and τ is the reinitialization time. The artificial diffusion term $\varepsilon \nabla \cdot \nabla \phi$ is added to avoid discontinuities. By solving this equation to steady state the interface thickness will remain constant and proportional to ε [1].

2.2 Incompressible Two-Phase Flow: One fluid formulation.

Let a domain Ω ocupied by two incompressible fluids at the sub-domains Ω_1 and Ω_2 respectively and separated by the interface Λ. The Navier Stokes equations for incompressible two-phase flow are written in conservative form as,

$$\frac{\partial}{\partial t}(\rho_k \underline{v}_k) + \nabla \cdot (\rho_k \underline{v}_k \underline{v}_k) = \nabla \cdot \underline{\underline{S}}_k + \rho_k \underline{g} \qquad \underline{x} \in \Omega_k \tag{6}$$

where

$$\underline{\underline{S}}_k = -p_k \underline{\underline{I}} + \mu_k \left(\nabla \underline{v}_k + (\nabla \underline{v}_k)^T \right) \tag{7}$$

$$\nabla \cdot \underline{v}_k = 0 \tag{8}$$

Navier-Stokes equations are coupled by the interface boundary conditions,

$$\underline{v}_1 = \underline{v}_2 \qquad \underline{x} \in \Lambda \tag{9}$$

$$(\underline{\underline{S}}_1 - \underline{\underline{S}}_2) \cdot \underline{n} = \sigma \kappa \underline{n} \qquad \underline{x} \in \Lambda \tag{10}$$

where $\underline{n}$ is the unit normal vector outward $\partial\Omega_1$, κ is the mean curvature of Λ and σ is the surface tension factor. This dynamic boundary condition (Laplace-Young equation) represents the jump in the normal stress at the free surface balanced by the surface tension. If the surface tension is treated as a body force [16], the one fluid formulation of the Navier-Stokes equations for incompressible, Newtonian flows with sharp interface is given by

$$\frac{\partial}{\partial t}(\rho \underline{v}) + \nabla \cdot (\rho \underline{v}\underline{v}) = -\nabla p + \nabla \cdot \mu \nabla \underline{v} + \nabla \cdot \mu (\nabla \underline{v})^T + \sigma \kappa \underline{n} \delta(\Gamma) + \rho \underline{g} \tag{11}$$

$$\nabla \cdot \underline{v} = 0 \tag{12}$$

where the density and viscosity are regularized by the phase field indicator function ϕ,

$$\rho = \rho_1 \phi + \rho_2 (1-\phi) \tag{13}$$

$$\mu = \mu_1 \phi + \mu_2 (1-\phi) \tag{14}$$

The term $\underline{n}\delta(\Gamma)$ is smoothed over a finite thickness using the continuum surface force model (CSF) of Brackbill [16].

$$\sigma \kappa \underline{n} \delta(\Gamma) = \sigma \kappa \nabla \phi \tag{15}$$

whereas the curvature κ is given by

$$\kappa = \nabla \cdot \left(\frac{\nabla \phi}{||\nabla \phi||_2} \right) \tag{16}$$

3 NUMERICAL METHOD

The finite volume integration of a general convection-diffusion equation yields the following expression

$$\int_\Omega \frac{\partial}{\partial t}(\rho \phi) dV = -\int_\Omega \nabla \cdot (\rho \mathbf{v} \phi)\, dV + \int_\Omega \nabla \cdot (\Gamma \nabla \phi)\, dV + \int_\Omega S_\phi dV \tag{17}$$

where Ω is a finite volume enclosed in a surface $\partial\Omega$, Γ is the diffusion coefficient, ρ is the density, S_ϕ is a source term and ϕ represents any conservative variable on a per unit mass basis ($\underline{v}$, 1, etc.). The spatial terms are approximated acoording to the following discretization,

$$\frac{\partial}{\partial t}(\rho\phi)_P V_P = -\sum_f (\phi\rho\underline{v})_f \cdot \underline{n}_f A_f + \sum_f (\Gamma\nabla\phi)_f \cdot \underline{n}_f A_f + (S_\phi)_P V_P \quad (18)$$

where P is a reference to the actual cell and f is a reference to the cell faces.

3.1 Convective Transport Terms

Discretization of the convective terms is based in the Godunov's monotonicity concept [17]. The face value ϕ_f in a total variation diminishing scheme (TVD) can be written as the sum of a first order upwind part plus a high resolution term,

$$\phi_f = \phi_{C_p} + \frac{1}{2}\psi(\theta_f)(\phi_{D_p} - \phi_{C_p}) \quad (19)$$

$$\theta_f = \frac{\phi_{C_p} - \phi_{U_p}}{\phi_{D_p} - \phi_{C_p}} \quad (20)$$

$$\phi_{C_p} = \phi_C + \Delta\underline{x}_{CCp} \cdot (\nabla\phi)_C \quad (21)$$

$$\phi_{D_p} = \phi_D + \Delta\underline{x}_{DDp} \cdot (\nabla\phi)_D \quad (22)$$

$$\phi_{U_p} = \phi_U + \Delta\underline{x}_{UUp} \cdot (\nabla\phi)_U \quad (23)$$

where the function $\psi(\theta)$ is the *flux limiter function*, and C and D are denoted as the upwind and downwind nodes around the face f of cell C, and the node U is the upwind node of C.

Gradients at cell centroids are computed using the linear Least Squares Approach, such that it reconstructs the solution in the neighborhood of the cell (Perez-Segarra et. al. [18]).

There are a number of limiters that satisfy the Sweby's requirement [3], which include van Leer, MINMOD and SUPERBEE schemes. These methods approximate conservation laws without introducing oscillations near discontinuities. The Superbee limiter is the least diffusive.

$$\psi(\theta) = max(0, min(2\theta, 1), min(2, \theta)) \quad (24)$$

The generalized upwind-biased expression conforms to the first order upwind scheme (FUD) and second order central difference scheme (CD) [19] when

$$\psi(\theta) = 0 \quad \text{FUD}$$
$$\psi(\theta) = \theta \quad \text{CD}$$

The convective flux at the face f is given by

$$(\phi\underline{v})_f \cdot \underline{n}_f A_f = F_f^- \phi_{D_p} + F_f^+ \phi_{C_p} + \frac{1}{2} F_f \psi(\theta_f)\left(\phi_{D_p} - \phi_{C_p}\right) \quad (25)$$

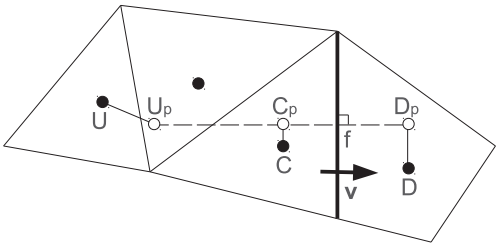

Figure 1: Advection Node Stencil

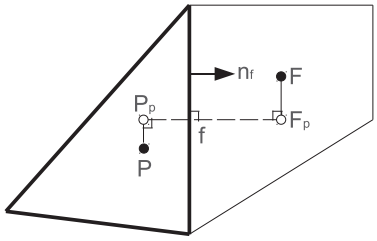

Figure 2: Diffusion Node Stencil

where

$$F_f = \underline{v}_f \cdot \underline{n}_f A_f \quad (26)$$

$$F_f^+ = max(F_f, 0) \quad (27)$$

$$F_f^- = min(F_f, 0) \quad (28)$$

3.2 Diffusive Transport Terms

The diffusive term of fluid transport equations at the face f is calculated as

$$-(\Gamma_f \nabla\phi)_f \cdot \underline{n}_f A_f = -\Gamma_f A_f \frac{\phi_{F_p} - \phi_{P_p}}{\|\Delta\underline{x}_{P_p F_p}\|_2} \quad (29)$$

$$\phi_{P_p} = \phi_P + \Delta\underline{x}_{PP_p}(\nabla\phi)_P \quad (30)$$

$$\phi_{F_p} = \phi_F + \Delta\underline{x}_{FF_p}(\nabla\phi)_F \quad (31)$$

where gradients are computed using the linear least square method.

3.3 Solver for Two-Phase Flow

Based on a semi-discrete formulation (discretized in time only) of the governing equations for two-phase incompressible flow, the projection steps defining the solution algorithm are as follows:

1. Physical properties $\rho(\phi^n)$, $\mu(\phi^n)$ and curvature $\kappa(\phi^n)$ are updated.

2. Intermediate velocity is solved by the explicit *Adam-Bashforth* time integration.

$$\underline{R}_P^n = \int_\Omega -\nabla\cdot(\rho\underline{v}\underline{v})^n + \nabla\cdot(\mu\nabla\underline{v})^n + \nabla\cdot\left(\mu(\nabla\underline{v})^T\right)^n + \rho^n\underline{g} + \sigma\left(\kappa\nabla\phi\right)^n dV \quad (32)$$

$$\int_\Omega \frac{\rho^n\underline{v}^* - \rho^n\underline{v}^n}{\Delta t} dV = \frac{3}{2}\underline{R}_P^n - \frac{1}{2}\underline{R}_P^{n-1} \quad (33)$$

3. The Poisson equation for the pressure variable is solved using a preconditioned conjugate gradient solver (PCG),

$$\int_\Omega \nabla \cdot \underline{v}^* dV = \Delta t \int_\Omega \nabla \cdot \frac{1}{\rho^n} \nabla p^{n+1} dV \quad (34)$$

4. Divergence free velocity field is updated using the pressure variable and intermediate velocity.

$$\int_\Omega \frac{\rho^n \underline{v}^{n+1} - \rho^n \underline{v}^*}{\Delta t} dV = -\int_\Omega \nabla p^{n+1} dV \quad (35)$$

5. Phase indicator ϕ is solved using the conservative LS method.

3.4 Numerical method for LS function

Using a semi-discrete formulation, the steps defining the solution algorithm are sketched as follows:

1. A free divergence velocity field is updated.

2. The interface is advected with the explicit TVD Third Order Runge-Kutta (RK3) method.

$$R_P^n = -\int_\Omega \nabla \cdot (\underline{v}\phi)^n \, dV \quad (36)$$

$$\int_\Omega \frac{\phi^{**} - \phi^n}{\Delta t} dV = R_P^n \quad (37)$$

$$\int_\Omega \frac{\phi^* - \frac{3}{4}\phi^n - \frac{1}{4}\phi^{**}}{\Delta t} dV = \frac{1}{4} R_P^{**} \quad (38)$$

$$\int_\Omega \frac{\phi^{n+1} - \frac{1}{3}\phi^n - \frac{2}{3}\phi^*}{\Delta t} dV = \frac{2}{3} R_P^* \quad (39)$$

3. A vector field of normals to the LS phase indicator is computed,

$$\underline{n} = \frac{\nabla \phi}{\|\nabla \phi\|_2} \quad (40)$$

RK3 time integration is used to solve for steady state the reinitialization equation,

$$\frac{\partial}{\partial \tau} \int_\Omega \phi dV = \int_\Omega -\nabla \cdot \underline{n}\phi(1-\phi) dV + \int_\Omega \nabla \cdot \varepsilon \nabla \phi dV \quad (41)$$

Since an explicit method is used, there is an stability restriction on $\Delta\tau$,

$$\Delta\tau \leq C \frac{(V_P)^{2/3}}{\varepsilon} \quad (42)$$

where C is a numerical parameter selected to keep the numerical stability and V_P is the volume of the actual cell. The parameter ε determines the interface thickness to depend of the grid size

$$\varepsilon = \frac{(V_P)^{(1-d)/3}}{2} \quad (43)$$

with d as a numerical parameter associated to the resolution of the smooth interface profile.

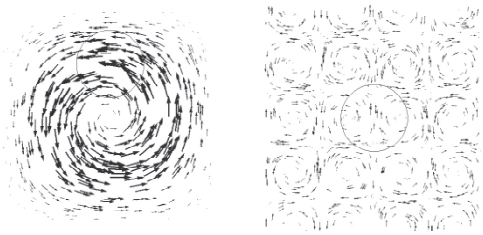

a. b.

Figure 3: Numerical experiments with external velocity field. (**a**.) Circular interface in single vortex field. (**b**.) Circular interface in time-reversed deformation field

3.5 Boundary conditions.

Considering a cell P with the face b at the boundary, the Dirichlet boundary conditions are fixed as

$$\phi_b = \phi_{given} \quad (44)$$

For Newman boundary conditions, the gradient is fixed at the node b as

$$-(\nabla\phi)_b \cdot \underline{n}_b = 0 \quad (45)$$

or equivalently

$$(\phi_{P_p} - \phi_b) = 0 \quad (46)$$

$$\phi_{P_p} = \phi_P + \Delta \underline{x}_{PP_p} (\nabla\phi)_P \quad (47)$$

Or, for most good quality meshes

$$\phi_b = \phi_P \quad (48)$$

4 Numerical Experiments

There are a set of test cases that we have considered. Stringent test problems having flows that change the topology of the interface are useful to measure the strength and weaknesses relevant to the present numerical formulation.

In our computations, we define the total mass (M) and the total volume (V) as

$$M = \sum_k \phi_k V_k \quad (49)$$

$$V = \sum_k \phi_k V_k \quad \text{if } \phi_k \geq 0.5 \quad (50)$$

where k is an index associated to the cells and V_k is the volume of the actual cell. The details of the tests are described below.

4.1 Circular interface in single vortex field.

A circular interface of radius 0.15 is placed with its center initially positioned at $(x, y) = (0.5, 0.75)$. The flow is prescribed with a solenoidal velocity field,

$$u(x,y) = -\sin^2(\pi x)\sin(2\pi y) \quad (51)$$

$$v(x,y) = \sin^2(\pi y)\sin(2\pi x) \quad (52)$$

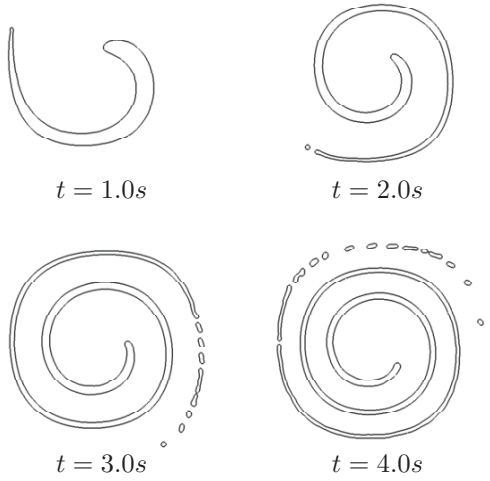

Figure 4: Circular interface in single vortex field. 300×300 triangular mesh.

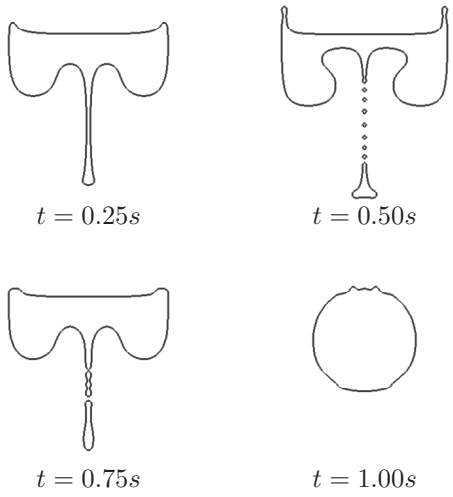

Figure 5: Circular interface in time-reversed deformation field. 300×300 triangular mesh.

The resulting vortex field streching the circular interface into a very long filament that spirals around the center of the domain. The time step was fixed in $\Delta t = 1.0 \times 10^{-3}$.

Figures displays the shape of the interface at different times. This test measure the ability of the schemes to mantain thin and elongated filaments for longer times.

4.2 Circular interface in time-reversed deformation field

This test is even more stringent than the single vortex test. The problem was proposed by Smolarkiewicz (1982). It consists of a circular interface in a deformation field with 16 vortices . The periodic velocity field for this complex problem is defined in the domain $\Omega = [0, 1] \times [0, 1]$,

$$u(x, y, t) = \sin(4\pi(x + 1/2)) \sin(4\pi(y + 1/2)) \cos(\pi t/T) \quad (53)$$

$$u(x, y, t) = \cos(4\pi(x + 1/2)) \cos(4\pi(y + 1/2)) \cos(\pi t/T) \quad (54)$$

This velocity field has the ability to deform the circular interface of radius $r = 0.15$ positionated at $(x, y) = (0.5, 0.5)$ to produce extreme topological changes by a period of time of $T = 1s$. The time step was fixed to $\Delta t = 1.0 \times 10^{-3}$.

4.3 Dam breaking

The dam break problem of Martin and Moyce [6] is analyzed. In our simulations, the spatial domain Ω_1 is a rectangular column of water of size $a = 0.057m$ width and $h = a$ heigh, whereas Ω_2 is filled by air. The computational domain Ω is a rectangular region of $L = 5a$ and $H = 1.25a$. Non-slip boundary condition

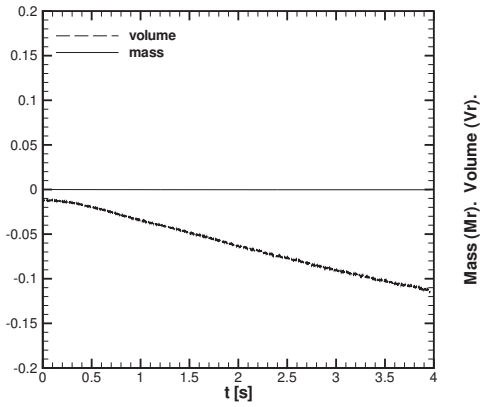

a

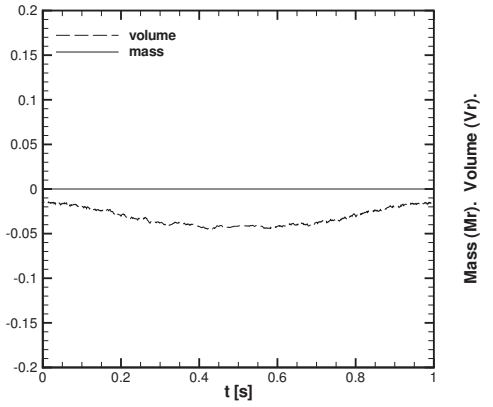

b

Figure 6: Mass and volume conservation. $M_r = \frac{M-M_0}{M_0}$, $V_r = \frac{V-V_0}{V_0}$. (**a**.) Circular interface in single vortex field. (**b**.) Circular interface in time-reversed deformation field.

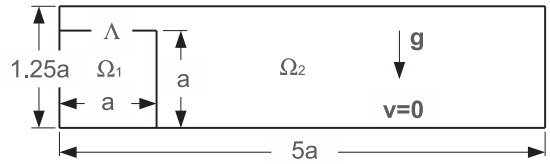

Figure 7: Dam Break Problem

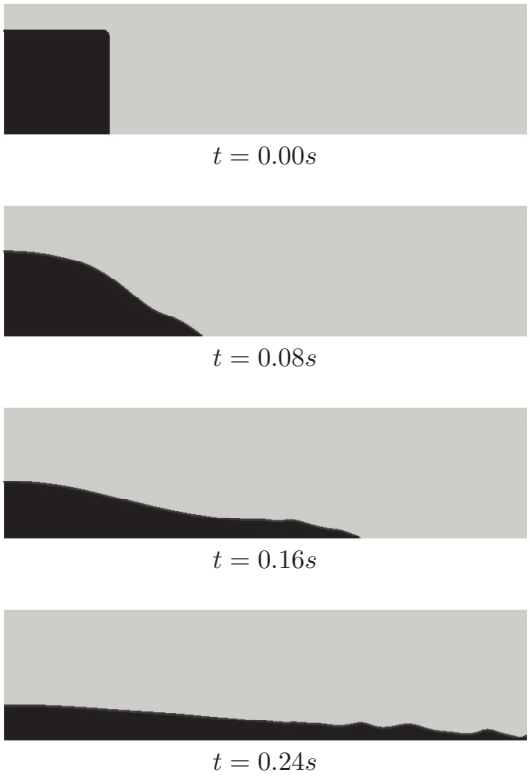

Figure 8: Figures shows the evolution of a 2D rissing bubble in a gravitational field. 200×50 rectangular mesh.

is applied at bottom, right and left boundaries of Ω, and Neumann boundary condition is fixed for the top boundary. The following physical properties are used: $\rho_1 = 1000$, $\rho_2 = 1$, $\mu_1 = 1 \times 10^{-3}$, $\mu_2 = 1 \times 10^{-5}$ and $\sigma = 0$. Under the effect of the gravity $\underline{g} = 0\underline{i} - 9.81\underline{j} + 0\underline{k}$, the column collapses. Gravitational acceleration represents the main driving force, wich cause the water column to fall. Inertial forces dominate at the early stages with the viscous effect increasing rapidly as the time advance. The non-dimensional height of the collapsing water column is plotted as a function of the non-dimensional time. Numerical calculations predicted the heigh of the collapsing water column to be in good agreement with the experimental data presented by Martin and Moyce [6]. The non-dimensional position of the leading edge is also plotted as a function of the non-dimensional time. We can observe a good agreement with experimental data.

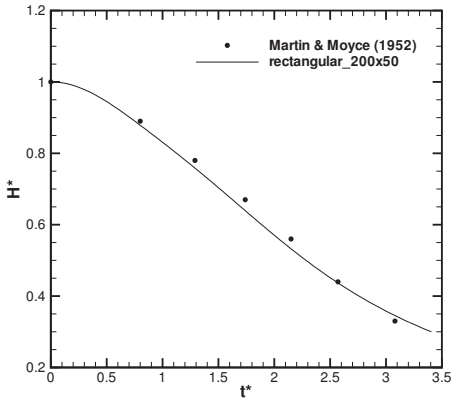

a

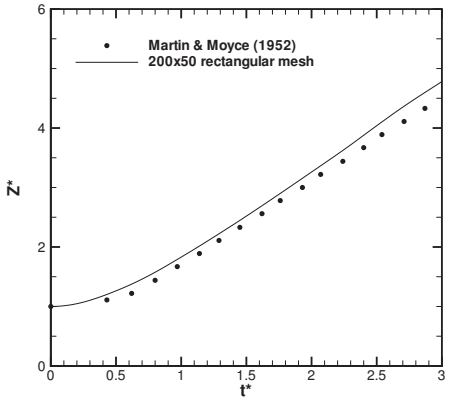

b

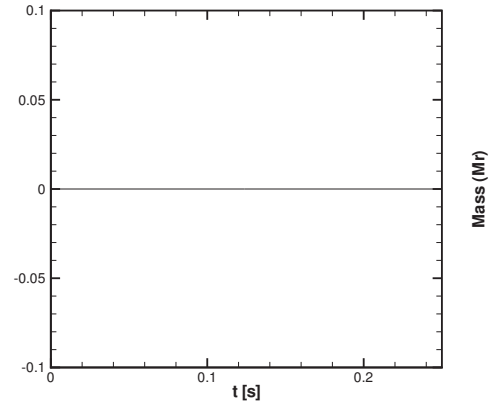

c

Figure 9: Dam break problem. Mass conservation and comparison between numerical solution and experimental data of Martin and Moyce [6]. (**a**.) Height of the column $H^* = y/(2a)$ vs. dimensionless time $t^* = t\,(g/a)^{1/2}$. (**b**.) Front position $Z^* = x/a$ vs. dimensionless time $t^* = t\,(2g/a)^{1/2}$. (**c**.) Mass conservation $M_r = \frac{M - M_0}{M_0}$.

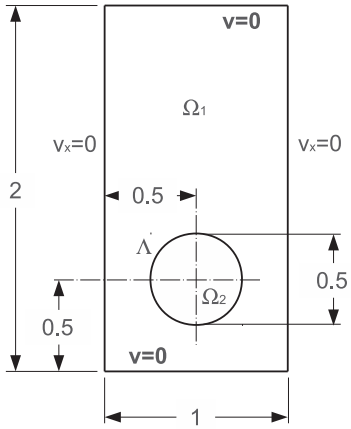

Figure 10: Rising Bubble Problem.

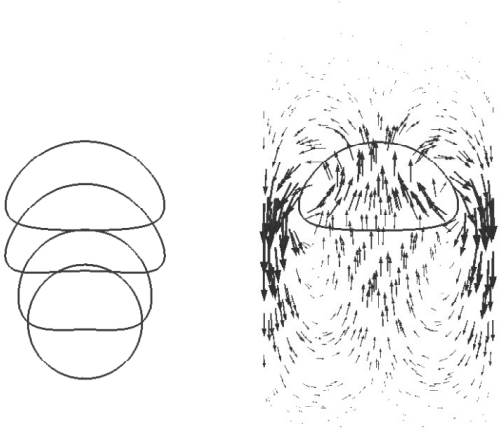

a b

Figure 11: Figures shows the evolution of a 2D rising bubble in a gravitational field. As initial condition, the bubble is a cylinder with circular cross section. (**a**.) Snapshots of 2D rising bubble: $t = 0.0s$,$t = 1.0s$,$t = 2.0s$ and $t = 3.0s$. (**b**.) Velocity field: $t = 3.0s$

4.4 Rising bubble

The rise and the deformation of a two dimensional bubble is computed including surface tension force. In experiments, the following parameters are used: ρ_1 = 1000, ρ_2 = 100, μ_1 = 10, $\mu_2 = 1$, $\underline{g} = 0\underline{i} - 0.98\underline{j} + 0\underline{k}$ and $\sigma = 24.5$.

Rise velocity and centroid of the bubble are used as benchmark quantities. The mean velocity is defined as

$$\underline{v}_{bubble} = \frac{\int_{\Omega_2} \underline{v} dV}{\int_{\Omega_2} dV} \tag{55}$$

Center of mass is used to track the translation of the bubble,

$$\underline{x}_{bubble} = \frac{\int_{\Omega_2} \underline{x} dV}{\int_{\Omega_2} dV} \tag{56}$$

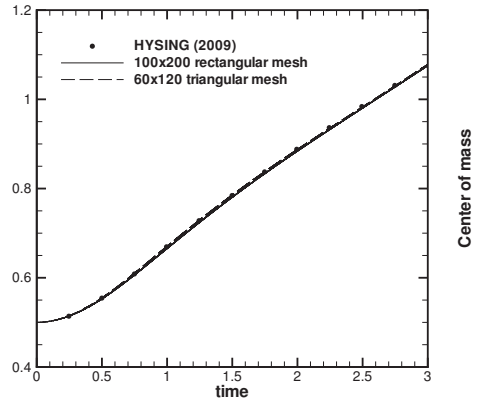

a

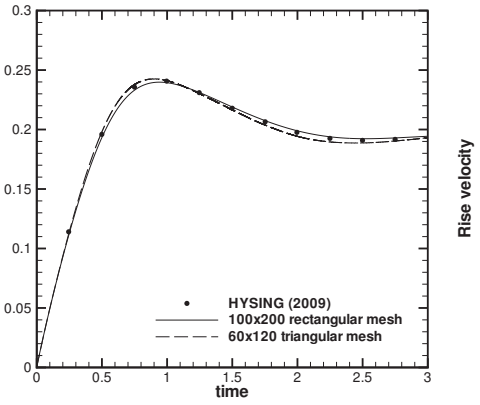

b

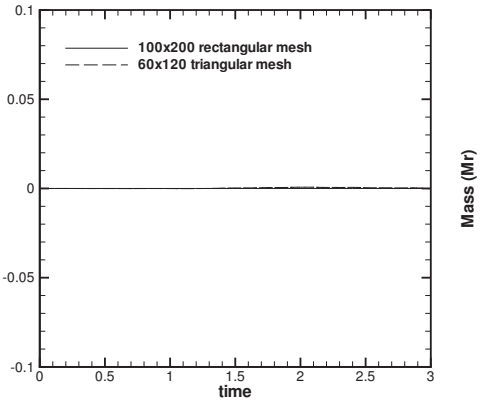

c

Figure 12: Comparison between our numerical solution and reference data of Hysing et al. [7]. Center of mass and rise velocity. (**a**.) Center of mass. (**b**.) Rise velocity. (**c**.) Mass conservation.

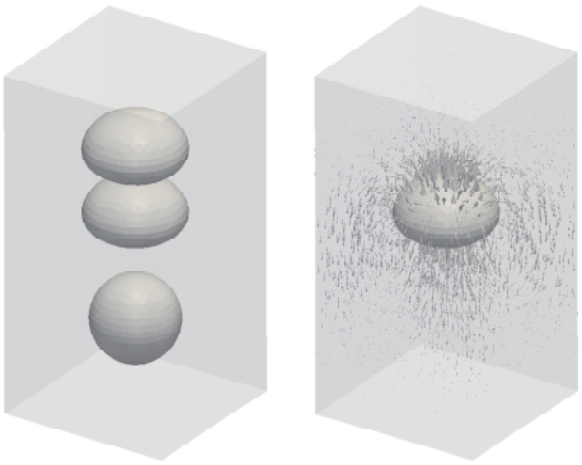

a b

Figure 13: Figures shows the evolution of a 3D rising bubble in a gravitational field. As initial condition, the bubble is an sphere. (**a**.) Snapshot of 3D rissing bubble: $t = 0.0s$, $t = 2.0s$ and $t = 3.0s$. (**b**.) Velocity field $t = 2.0s$.

For three dimensional simulation, the domain is a rectangular box $\Omega = [0, 1] \times [0, 2] \times [0, 1]$. A spherical bubble of $r = 0.25$ radius is at the initial position $\underline{x} = (0.5, 0.5, 0.5)$. The calculations are performed on a $30 \times 60 \times 30$ rectangular mesh.

5 SUMMARY

The conservative level set method of Olsson and Kreiss has been implemented on unstructured meshes using the finite volume approach. The numerical method is conservative. The thickness of the diffusive interface is kept constant. Since mass conservation is an important property, we have quantified the variation of mass for different tests. For external velocity fields the emphasis was given on how the shape and integrity of interfaces is mantained.

Incompressible Navier-Stokes solver for two-phase flows was coupled to LS method. Dam break and Rising bubble problems were analyzed. Our scheme employs a three step projection method on unstructured collocated meshes. We compared our results to experimental and numerical data. A very good agreement was observed.

Model calculations have shown that LS method discretized with high-resolution scheme on colocated unstructured meshes is able to predict the dynamics of free surface and bubble flows including surface tension forces. The future work will be focus on evaluating two-phase flows on complex geometries, coupling of two fluid model and LS method, and direct numerical simulation of bubble flows.

ACKNOWLEDGEMENTS

This work has been supported by the Ministerio de Educación y Ciencia, Spain (Project: Development of high performance parallel codes for the optimal design of thermal equipments, reference ENE2010-17801), Termo Fluids S.L. and Ministerio de Asuntos Exteriores y Agencia Española de Cooperación Internacional para el Desarrollo (MAEC-AECID Scholarship).

References

[1] Olsson E., Kreiss G., 2005, "A conservative level set method for two phase flow ". *Journal of computational physics*, Vol. 210, pp. 225-246.

[2] Olsson E., Kreiss G., 2007, "A conservative level set method for two phase flow II ". *Journal of computational physics*, Vol. 210, pp. 225-246.

[3] Sweby P.K., 1984, "High Resolution Using Flux Limiters for Hyperbolic Conservation Laws ". *SIAM Journal on Numerical Analysis*, Vol. 21, pp. 995-1011.

[4] Gottlieb S., Chi-Wang S., 1998, "Total Variation Dimishing Runge-Kutta Schemes". *Mathematics of Computations*, Vol.67, pp.73-85.

[5] Lehmkuhl O., Perez-Segarra C.D., Soria M., Oliva A., 2007, "A new Parallel unstructured CFD code for the simulation of turbulent industrial problems on low cost PC cluster ". *Proceedings of the Parallel CFD 2007 Conference*, pp.1-8.

[6] Martin J.C., Moyce J., 1952, "An experimental study of the collapse of liquid columns on a rigid horizontal plane". *Philosophical Transactions of the Royal Society of London. Series A. Mathematical and Physical Sciences*, Vol.244, pp.312-324.

[7] Hysing S., Turet S., Kuzmin D., Parolini N., Burman E., Ganesan S., Tobiska L., 2009, "Quantitative benchmark computations of two-dimensional bubble dynamics ". *International Journal for Numerical Methods in Fluids*, Vol.60, pp.1259-1288.

[8] Osher S., Sethian J.A., 1988, "Fronts propagating with curvature-dependent speed: Algorithms based on Hamilton-Jacobi formulations ". *Journal of Computational Physics*, Vol.79, pp.175-210.

[9] Sussman M., Smereka P., Osher S., 1994, "A Level Set Approach for Computing Solutions to Incompressible Two-Phase Flow ". *Journal of Computational Physics*, Vol.144, pp.146-159.

[10] Sussman M., Fatemi E., Smereka P., 1998, "An Improved Level Set Method for Incompressible Two-Phase Flows ". *Journal of Computers and Fluids*, Vol.27, pp.663-680.

[11] Sussman M., Fatemi E., 1999, "An efficient interface-preserving level set redistancing algorithm and its application to interfacial incompressible fluid flow ". *SIAM J. Sci. Comput.*, Vol.20,pp.1165-1191.

[12] Sussman M., 2000, “A Coupled Level Set and Volume-of-Fluid Method for Computing 3D and Axisymmetric Incompressible Two-Phase Flows ”. *Journal of Computational Physics*, Vol.162, pp.301-337.

[13] Tornberg A., Engquist B., 2000, “A Finite element based level set method for multiphase flow applications ”. *Computing and Visualization in Science*, Vol.3,pp.93-101.

[14] Marchandise E., Geuzaine P., Chevaugeon N., 2006, “A Quadrature free discontinuous Galerkin method for the level set equation ”. *Journal of Computational Physics*, Vol.212, pp.338-357.

[15] Marchandise E., Geuzaine P., Chevaugeon N., Remacle J., 2007, “A stabilized finite element method using a discontinuous level set approach for the computation of bubble dynamics ”. *Journal of Computational Physics*, Vol.225, pp.949-974.

[16] Brackbill J., kothe B., Zemach C., 1992, “A Continuum Method for Modeling Surface Tension. ”. *Journal of Compuational Physics*, Vol.100,pp.35-354.

[17] Leveque R., Finite volume methods for hyperbolic problems. Cambridge University Press, 2002.

[18] Perez-Segarra C.D., Farre C., Cadafalch J., Oliva A., 2006, “Analysis of diferent numerical schemes for the resolution of convection-difusion equations using finite-volume methods on three dimensional unstructured grids. Part I: Discretization Schemes ”., *Numerical Heat Transfer, Part B* , vol.49, pp.333-350.

[19] Guan Heng Yeoh, Jiyuan Tu, Computational Techniques for Multi-Phase Flows. ELSEVIER, Oxford, 2010.

[20] Jakobsen Hugo, Chemical Reactor Modeling: Multiphase Reactive Flows. Springer, Oxford, 1 edition, 2008.

Reactive flows

Conference on Modelling Fluid Flow (CMFF'12)
The 15th International Conference on Fluid Flow Technologies
Budapest, Hungary, September 4-7, 2012

DNS-based Investigation of the Flow Field of a Lifted Strongly Buoyant Jet Flame

Christian WALCHSHOFER,[2] Helfried STEINER, [1]

[1] Corresponding Author. Institute of Fluid Mechanics and Heat Transfer, Graz University of Technology. Inffeldgasse 25F, 8010 Graz, Austria. Tel.: +43 316 873 7344, Fax: +43 316 873 7356, E-mail: helfried.steiner@tugraz.at
[2] Institute of Fluid Mechanics and Heat Transfer, Graz University of Technology. E-mail: floaty@gmx.at

ABSTRACT

The present work performs a Direct Numerical Simulation (DNS) of a non-premixed turbulent reacting jet at low Reynolds and Froude numbers to investigate the dynamical interaction between the flow field and the embedded flame, with a special focus on the mechanism of flame stabilization. The results unveil a weak, essentially impeding effect of the flame on the non-burning flow region upstream. A significant effect is seen in the large-scale motion, which is generated by the periodic formation, growth, and departure of large bulb-shaped low-density structures at the flame base, as it is also seen in experiments. The analysis of the dominant stabilization mechanism of the lifted flame essentially supports the concept of edge-flame propagation. In addition, the buoyancy-driven large-scale flow structures temporarily produce a further strongly destabilizing scenario, where large circumferential sections of the flame base recede deeply downstream, which is shown to be associated with high local values of the scalar dissipation rate. Showing this particular scenario the present work does not only highlight an important stabilization mechanism governed by large three-dimensional ("out-of-the-plane") structures, it also demonstrates the possible strong relevance of the scalar dissipation rate being even far below the extiction limit.

Keywords: buoyancy, flame stability, non-premixed combustion

NOMENCLATURE

Latin symbols		
A_R	$[m, mol, s]$	pre-exponential factor
D	$[m]$	nozzle diameter
D_i	$[m/s^2]$	mass diffusion coefficient
Fr	$[-]$	Froude number, $U_J/\sqrt{gD}$
$\underline{\underline{I}}$	$[-]$	unit tensor
N_i, N_R	$[-]$	number of species, reactions
Re	$[-]$	Reynolds number, $\rho_J\, U_J\, D/\mu_J$
R_m	$[J/kmolK]$	molar gas constant
$\underline{\underline{S}}$	$[1/s]$	strain tensor
T	$[K]$	temperature
$T_{0,R}$	$[K]$	activation temperature
W_i	$[kg/kmol]$	molecular weight
W_0	$[kg/kmol]$	unity mol. reference weight
U_J	$[m/s]$	nozzle exit bulk velocity
Y_i	$[-]$	mass fraction
Z	$[-]$	mixture fraction
c_p	$[J/kgK]$	isobaric specific heat
$\underline{g}$	$[m/s^2]$	gravitational acceleration
$h_{0,i}$	$[J/kg]$	enthalpy of formation
p	$[Pa]$	pressure
s	$[m/s]$	flame propagation speed
t	$[s]$	time
u	$[m/s]$	streamwise velocity
$\underline{v}$	$[m/s]$	velocity vector
x	$[m]$	streamwise distance
y	$[m]$	cross-stream distance
Greek and Caligraphic symbols		
Γ	$[-]$	boundary surface
λ	$[W/mK]$	thermal conductivity
μ	$[Pas]$	dynamic viscosity
ν'_{iR}, ν''_{iR}	$[-]$	stoichiometric coefficients
$\dot{\omega}_R$	$[kmol/kg\ s]$	elementary reaction rate
Ω_i	$[1/s]$	reactive source term
ρ	$[kg/m^3]$	density
χ	$[1/s]$	scalar dissipation rate
$\mathcal{V}$	$[m^3]$	computational volume
$\mathcal{W}$	$[1/s]$	vorticity
Subscripts, superscripts, and operators		
J		nozzle exit
R		index of elementary reaction
$c,\ 0.5$		jet centerline, half-width
fb		flame base
i		index of species
$*$		non-dimensionalized
∇		nabla operator
$\overline{\ }$, $\langle\ \rangle$		statistical average

1. INTRODUCTION

A major challenge in the development of modern combustion devices is to satisfy the often competing requirements of high efficiency, low pollutant emission, save and reliable operation. The latter is of special concern to the stabilization of turbulent lifted flames in non-premixed combustion. During the last decades much progress has been made in the experimental as well as computational research to better understand the complex interactions between the chemistry, the instantaneous flow and mixing conditions. Most of the studies carried out on lifted turbulent diffusion flames contend that the flame stabilization is dominated by the premixed flame propagation mechanism. Based on their early measurements Vanquickenborne and van Tiggelen [1] and Kalghatgi [2] claim that the flame base propagates into a fully premixed region ahead faster than with the laminar flame speed. They attributed the increased propagation velocity to turbulence, so that the flame can effectively stabilize in regions, where the velocities exceed the laminar flame speed. Later measurements by Muñiz and Mungal [3] report the same behavior, in that the flame counters oncoming flow velocities up to three times higher than the laminar flame speed. However, they do not observe any significant influence of the turbulence level as suggested by Kalghatgi [2]. As it was later also confirmed by Mansour [4] and Upatnieks et al. [5], they rather suggested a laminar flame propagation mode, where volumetric dilatation leads to diverging stream lines ahead of the flame base, so that the reaction zone effectively encounters a reduced oncoming velocity being close to the laminar flame speed. The effect of the heat release on the flame propagation was computationally investigated by Ruetsch et al. [6], who found the increase in the propagation velocity to be dependent on the density ratio of the unburnt to the burned gas up- and downstream of the flame, respectively. Su et al. [7] deduced from their experiments a stabilization model depending on the large-scale mixing field. Their suggested mechanism basically falls into the Large-Eddy concept, which assumes that the flame stabilizes migrating from one large-scale structure to a neighbouring one seeking most favourable velocity and mixing conditions. There is still considerable doubt, if large-scale structures effectively determine the lift-off height, or, if they rather disturb only temporarily the position of the flame. A further debated issue is the effect of unmixedness, which can be basically parameterized by the scalar dissipation rate. Peters and Williams [8] argue that premixing does not reach any significant level ahead of the flame. Consequently, the leading edge of the flame burns in the non-premixed regime, and it stabilizes at a position, where the local scalar dissipation rate falls below the quenching limit. In the strict sense, this hypothesis was not confirmed by experiments, where the dissipation rates near the flame base were generally found to be well below the quenching limits obtained from studies on counterflow diffusion flames [9, 7]. However, the scalar dissipation rate exhibits strong turbulent fluctuations in time and space, so that it may reach sufficiently high instantaneous local values to exert a significant effect on the flame propagation.

Although the studies mentioned above were dealing in part with fairly moderate Reynolds and Froude numbers, the effect of buoyancy is therein mostly not addressed. Upstream effects of the flame on the non-burning near field of the jet have been mostly discarded either, or considered as insignificant. The present work puts the focus on these particular aspects investigating the case of a highly buoyant non-premixed methane-air jet flame using Direct Numerical Simulation (DNS). A nitrogen-diluted fuel feed is assumed to provide highly sensitive burning conditions, which helps to clearly identify the most relevant mechanisms for the stabilization of the considered flame. As for the relevance of upstream effects of the flame on the non-reacting near field, the spreading and decaying behaviour of the fuel jet is of particular interest. It is investigated, to which extent this behavior resembles to that of the non-reacting case, as claimed by most previous studies (e.g., Su et al. [7]), considering a reacting turbulent jet at fairly low Reynolds and Froude numbers. Due to the latter, much attention is spent on the effects of the buoyancy-driven large-scale motion on the temporal evolution of the flow field. Being essentially generated by the reactive heat release the investigated large-scale structures are strongly coupled with the behaviour of the flame, so that a significant influence on the flame stabilization is expected. Experimental reference data for the considered flame are available from the measurements by Köberl et al. [10].

2. Mathematical formulation and numerical solution

The present DNS solves the low Mach number conservation equations for mass, momentum, species and energy, which are written as

$$\frac{\partial \rho}{\partial t} + \boldsymbol{\nabla} \cdot \left(\rho \, \underline{v} \right) = 0 \tag{1}$$

$$\frac{\partial \rho \, \underline{v}}{\partial t} + \boldsymbol{\nabla} \cdot \left(\rho \, \underline{v} \, \underline{v} \right) = -\boldsymbol{\nabla} p + \boldsymbol{\nabla} \cdot \left[2 \mu \left(\underline{\underline{S}} - \frac{1}{3} \underline{\underline{I}} \, \boldsymbol{\nabla} \cdot \underline{v} \right) \right] + \rho \, \underline{g} \tag{2}$$

$$\frac{\partial \rho \, Y_i}{\partial t} + \boldsymbol{\nabla} \cdot \left(\rho \, \underline{v} \, Y_i \right) = \boldsymbol{\nabla} \cdot \left(\rho D \, \boldsymbol{\nabla} Y_i \right) + \rho \Omega_i \tag{3}$$

$$\frac{\partial \rho \, T}{\partial t} + \boldsymbol{\nabla} \cdot \left(\rho \, \underline{v} \, T \right) = \frac{1}{c_p} \boldsymbol{\nabla} \cdot \left(\lambda \boldsymbol{\nabla} T \right) + \frac{\rho}{c_p} \sum_{i=1}^{N_i} \Omega_i h_{0,i} \, , \tag{4}$$

respectively, with the density dependent on the temperature and chemical composition

$$\rho = p_0 \Big/ \Big(R_m T \sum_{i=1}^{N_i} \frac{Y_i}{W_i} \Big). \tag{5}$$

The chemical source terms for the reactive species Y_i read

$$\Omega_i = W_i \sum_{R=1}^{N_R} (\nu''_{iR} - \nu'_{iR})\, \dot{\omega}_R, \tag{6}$$

where the elementary reactions are generally given by Arrhenius-type expressions

$$\dot{\omega}_R = A_R \prod_{i=1}^{N_i} \left(\frac{\rho Y_i}{W_i} \right)^{\nu'_{iR}} T^{b_R}\ exp\left(-\frac{T_{0,R}}{T} \right). \tag{7}$$

A reduced two-step mechanism proposed by Williams [11] was applied for the methane-air chemistry. It involves two elementary reactions ($N_R = 2$), a fuel breakup, and a successive oxidation step, which are specified by

$$\begin{aligned} \dot{\omega}_I : &\quad CH_4 + O_2 \rightarrow INT + PRO \\ \dot{\omega}_{II} : &\quad INT + O_2 \rightarrow 2\,PRO\,, \end{aligned}$$

respectively. The mechanism carries in total four ($N_i = 4$) reactive species, $Y_{CH_4}, Y_{O_2}, Y_{PRO}, Y_{INT}$, where the intermediate and product species are (molar) composed as

$$\begin{aligned} INT &= \frac{2}{3} CO + \frac{4}{3} H_2 \\ PRO &= \frac{2}{3} H_2O + \frac{1}{3} CO_2 \end{aligned}$$

The governing set of equations was numerically solved second-order accurate in time and space on a spherical grid schematically shown in Figure 1 with a resolution of 512 × 150 × 128 cells in the radial, cross-stream, and azimutal directions, respectively. A fuel jet of methane diluted with 50% nitrogen by mass issuing into still air is imposed at the inlet boundary. The inlet temperature of both the fuel and oxidizer is $T_J = 298\,[K]$, the stoichimetric mixture fraction is $Z_{st} = 0.104$. The Reynolds and Froude numbers based on the fuel nozzle exit conditions are Re=2750 and Fr=57, respectively. The variable-density simulations are carried out with mixture- and temperature-dependent transfer coefficients. A dynamically thickened flame approach as proposed by Legier et al. [12] is used to resolve the very thin reactive layers. The reacting flow field was initialized imposing a uniform laminar flamelet solution, obtained from a precursor one-dimensional flame analysis. A non-reacting jet was simulated as well for use as a reference case to single out possible upstream effects of the flame on the flow field.

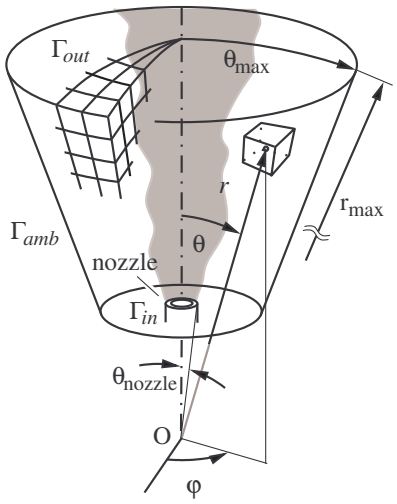

Figure 1. Computational domain

3. Results and discussion

3.1. *Reacting flow and mixing field - effect of buoyancy*

The effect of the flame on the turbulent motion is most apparent in the far field of the jet, as it is qualitatively shown in Figure 2 by the contours of the vorticity norm, non-dimensionalized with the ratio of the jet half-width to the centerline velocity $\overline{y_{0.5,u}}/\overline{u_c}$. Downstream of the flame base located around $x/D = 20$ the increased viscosity in the hot product gases together with the volumetric dilatation dampen predominantly the small-scale structures in the radially outer region as compared to the non-reacting reference case. The vorticity remains higher only near the centerline, where cold rich fuel gas penetrates deeply into the flame base, forming a turbulent non-burning core region.

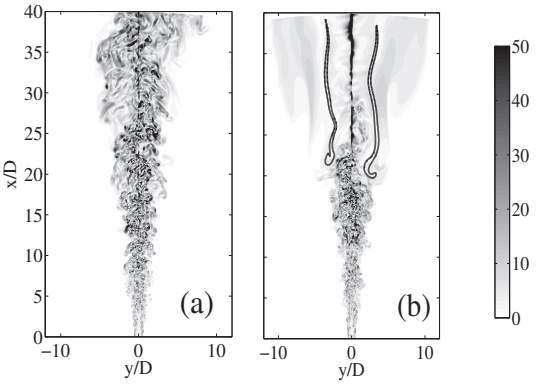

Figure 2. Contours of the non-dimensional norm of the vorticity $\mathcal{W}^* = \| \nabla \times \underline{v} \| \overline{y_{0.5,u}}/\overline{u_c}$ for (a) the inert, (b) reacting jet, position of flame marked by thick solid line.

Less pronounced, but notable upstream effects of the flame become evident in the spreading and decaying behaviour of the fuel jet, as shown in

Figure 3. The half-widths of the velocity and the mixture fraction, and consistently, the inverses of the respective centerline values, increase somewhat faster in the reacting case. The flame evidently impedes the oncoming jet flow. In fact, the flame acts dynamically similar to a potential point source located in a parallel free stream, as it also was concluded by Upatnieks et al. [5] from their experimental observations. In the burning region, i.e., downstream of $x/D = 20$, the half-widths are significantly increased. This almost step-like change to a higher level as well as the slower increase, or even decrease, of the inverses of the centerline values have to be attributed to the effects of volumetric dilatation and buoyancy-driven re-acceleration, respectively.

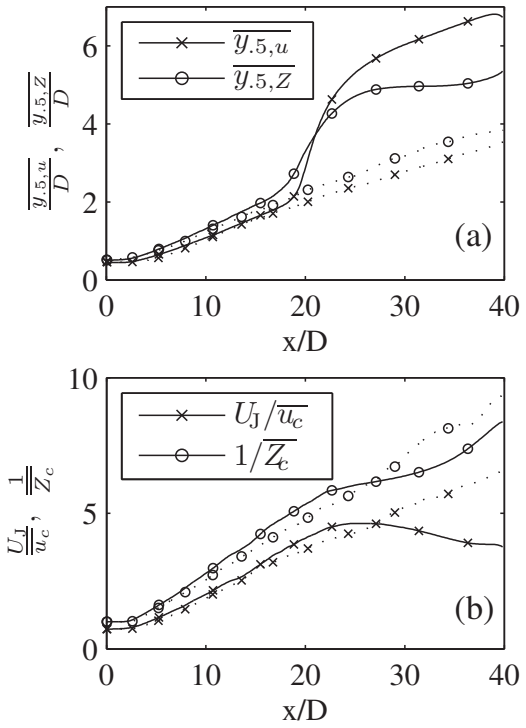

Figure 3. (a) Spread rate of the mean half-widths for the velocity profile, $\overline{y_{0.5,u}}$ and mixture fraction $\overline{y_{0.5,Z}}$, (b) decay of the mean centerline velocity $\overline{u_c}$ and the mixture fraction $\overline{Z_c}$; — reacting jet, ···· inert jet

The most pronounced influence of the buoyant forces is manifested in the large-scale motion. The reactive heat release and volumetric dilatation periodically generate large bulb-shaped structures with low-density, as seen from Figure 4, where the evolution of the shape and extension of the low-density (hot) region is displayed in terms of a temperature iso-surface. The low-density region keeps growing until buoyancy induces its lift-off from the flame base ($t^* = 1440$) and its further convection downstream towards the exit ($t^* = 1510$). The lift-off leads to a strong temporal acceleration

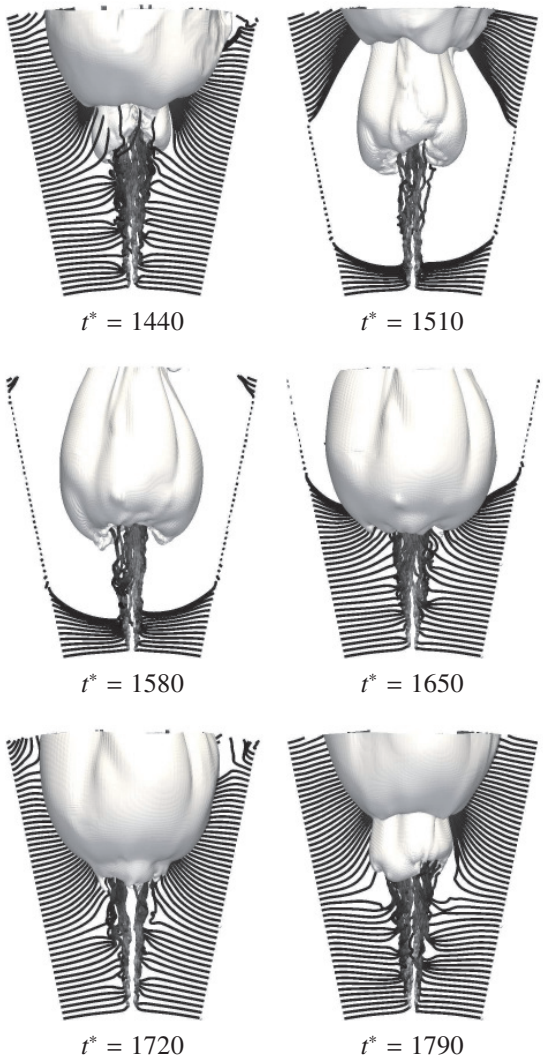

Figure 4. Instantaneous non-dimensional temperature iso-surfaces at $T/T_J = 1.1$ at different times $t^* = t\,U_J/D$, and incoming streamlines starting from the lateral boundary.

of the flow as seen from the converging streamlines approaching the neckline between the ascending bulb and the flame base at $t^* = 1440$. The large region void of incoming streamlines seen at $t^* = 1510$ and 1580 indicates a strong lateral displacement of the oncoming flow. After a further period of growth the low-density bulb finally separates from the flame $t^* = 1790$ base, which completes the shown cycle.
The buoyancy-induced periodic large-scale perturbations of the flow translate into strong oscillations of the total mass, momentum, and reactive conversion rate inside the domain as seen from the corresponding volumetric averages over the computational domain in Figure 5. Periods of lowest total momentum shown in subfigure 5(b) are associated with phases of most intense reactive conversion, so that the total reactive heat reaches a maximum. During these phases the large bulb-shaped low-density structures are generated

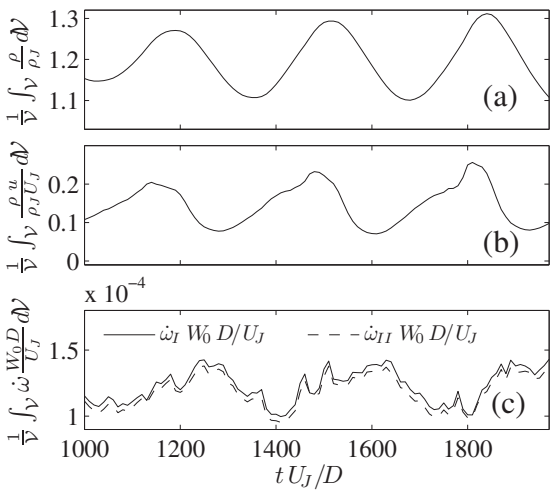

Figure 5. Temporal evolution of non-dimensional domain volumetric averages: (a) mass, (b) streamwise momentum , (c) rates of elementary reactions.

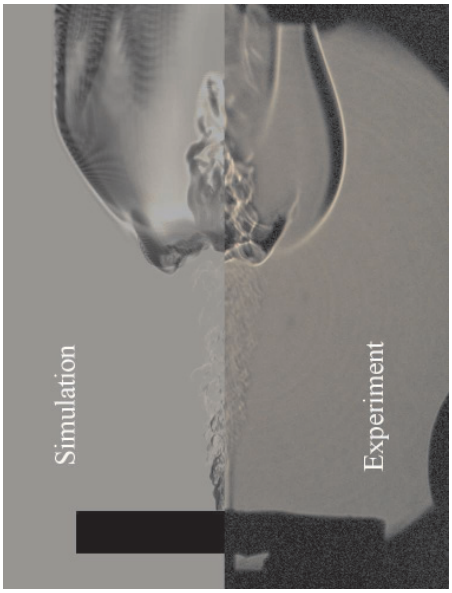

Figure 6. Computational vs. experimental schlieren visualizations [10]

and strongly growing in size, as already discussed in Figure 4. On the other hand, the periodic lift-off of the low-density structures from the flame base increases temporarily the axial momentum significantly, which leads to a strong entrainment of heavier (cold) ambient gas from the lateral boundaries. Consequently, the total mass reaches a maximum and chemical conversion falls to a minimum. The time lag observed between the maxima of the total mass and the maxima of the conversion rates reflects the time which is needed until the entrained fresh oxidizer has become sufficiently mixed with the inner fuel stream and preheated to provide a well burnable mixture.

The periodically generated large-scale structures are consistent with the experimental observations as shown in Figure 6, where schlieren visualizations from measurements of Köberl et al. [10] are compared against their numerically obtained counterparts. The density field is evidently reproduced very well by the simulation. The buoyancy-induced large-scale motion is of high relevance for the flame stabilization as will be shown in the following section.

3.2. Flame stabilization

The DNS results provide a highly accurate comprehensive description of the flow and mixing conditions immediately upstream of the flame base, which allows for a detailed analysis of the flame stabilization process. The present analysis follows a reaction based method for flame localization, where the streamwise position of the flame base x_{fb} is identified by the instantaneous leading edge of the iso-surface of the non-dimensional fuel-breakup reaction rate associated with a certain threshold value being here $\dot{\omega}_I W_0 D/U_J = 0.004$. The statistical distributions of the key flow and mixing quantities obtained at the flame base x_{fb} can be seen from the normalized histograms in Figure 7. The histogram of the mixture fraction in Figure 7(a) makes evident that flame is stabilized close to the surface stoichiometric mixing conditions, predominantly on the lean side. This indicates that, although the laminar burning velocity is basically fastest on the rich side, the flame preferably burns towards the lean side, where it counters smaller oncoming velocities occurring in the radially outer region of the jet. The histogram of the streamwise velocity shown in 7(b) are associated with a mean $\langle u/U_J \rangle_{x_{fb}} = 0.080$, which exceeds the laminar flame speed s_L by a factor of 2.9. This relative excess can be attributed to the flow accelerating effect of the volumetric dilation, whose highest possible extent is marked by the right vertical dashed line representing the velocity in the burnt gas at adiabatic flame temperature downstream of a planar premixed flame. The obtained ratio $\langle u \rangle_{x_{fb}}/s_L = 2.9$ agrees very well with the measurements of Watson et al. [13], who applied as well a reaction rate based method for flame localization yielding a ratio $\langle u \rangle_{x_{fb}}/s_L = 2.7$. The histogram of the scalar dissipation rate displayed in 7(c) shows a typically log-normal distribution which covers a range well below the extinction limit, $\chi_{st,q} = 22\,[1/s]$, as it is obtained from a one-dimensional solution of a counterflow reference flame. The flame does evidently not stabilize at a position, where the local scalar dissipation rate falls below the corresponding extinction limit. This clearly contradicts the stabilization concept which assumes the quenching of non-premixed flames as determining mechanism, and, hence, it confirms the findings of various experimental studies [9, 7].

However, the instantaneous values of scalar dissipation still have a significant influence on the local propagation of the flame base relative to the oncoming flow. This can be seen from Figure 8 displaying a scatter plot of the Lagrangian flame propagation speed

$$s_E = u|_{x_{fb}} - \frac{dx_{fb}}{dt} \tag{8}$$

versus the mixture fraction obtained at the flame base x_{fb}. The solid line representing the conditional average $\langle s_E/U_J|Z\rangle_{x_{fb}}$ reaches a maximum on the rich side, $Z > Z_{st} = 0.104$, which indicates that the flame propagates fastest into a rich oncoming mixture, which is typically featured by premixed planar flames. Approaching the rich and the lean limits the conditionally averaged velocity decreases as the mixing state increasingly deviates from stoichiometric condition. The drop is apparently faster on the rich side, which can be attributed to the increased scalar dissipation rate as seen from the gray level of the scatter points on the rich side. Although being well below the exinction limit, the increased instantaneous scalar dissipation rates occurring preferentially in the fuel-rich inner region evidently affect the rich-side behavior of the edge flame, which otherwise stabilizes along the principles of premixed flame propagation. The perturbations associated with a locally increased scalar dissipation rate may temporarily even lead to a highly critical scenario of flame destabilization as will be shown in the following section.

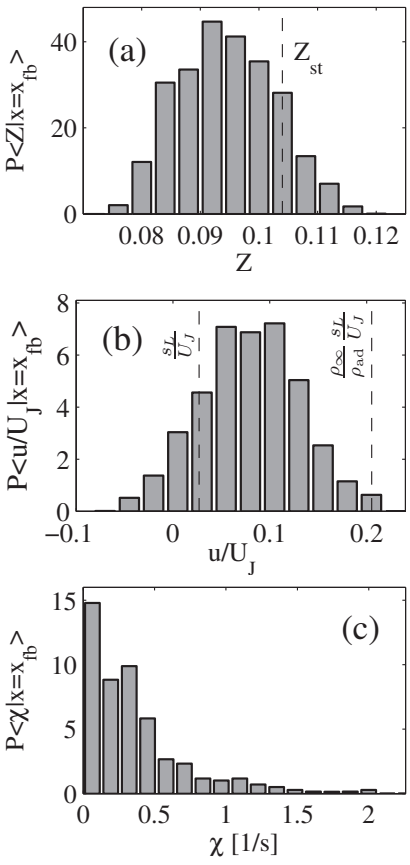

Figure 7. Normalized histograms at the flame base x_{fb}: (a) mixture fraction, (b) streamwise velocity, (c) scalar dissipation rate.

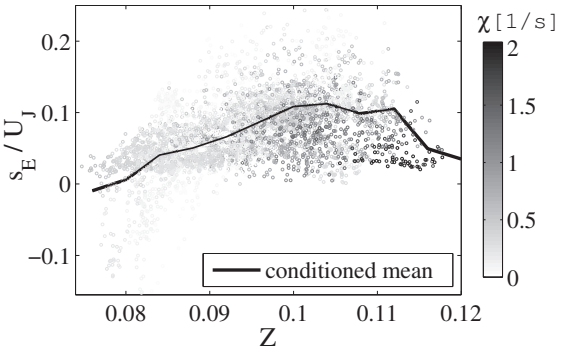

Figure 8. Scatter plot of Lagrangian flame propagation speed vs. mixture fraction at the flame base x_{fb}. Gray-scale indicates magnitude of scalar dissipation rate

3.3. Three-dimensional large-scale effects

The statistical analysis of the present DNS results discussed above essentially confirmed the established consensus that the stabilization is mainly determined by the mechanism of premixed flame propagation. However, the strong temporal acceleration observed during the phase of low-density bulb separation shown in Figures 4 and 5 repeatedly introduces highly destabilizing perturbations of the flame. Figure 9 exemplarily illustrates three highly critical burning conditions, each following a low-density bulb separation. The shown iso-surfaces of the fuel-breakup reaction exhibit deep, notch-like recessions, which indicates that considerable sections of the flame base have moved deeply downstream. The observed partial receding can be explained by looking on a series of iso-surfaces of the fuel-breakup reaction rate shown in Figure 10. The iso-surfaces above the horizontal line refer to different stages of a critical scenario associated with strong partial receding of the flame base. For comparison, the row below the line displays an uncritical later state, where the flame base has fully recovered its almost cylindrically symmetric shape. The iso-surfaces in the left, center and right columns are gray-shaded with the mixture fraction, streamwise velocity, and scalar dissipation rate, respectively, in order to display their spatial variation particularly near the flame base, and hence, to illustrate their possible influence on the local flame propagation. The mixture fraction as well as the streamwise velocity do not vary significantly at the flame base. Both quantities show fairly uniform distributions along the entire edge of the flame

without significant differences to the uncritical state. In contrast, the scalar dissipation rate exhibits local maxima especially in the receding parts of the flame edge. The partial receding is evidently associated with a strong local increase of the scalar dissipation rates. Although the flame stabilization can not be explained on the grounds of a typical non-premixed flame close to extinction (the extinction limit χ_{ext} is practically never reached near the flame, as seen from Figure 7(c)), the local scalar dissipation rate plays a key role for the periodically occurring partial blow-off of the flame exemplarily shown in Figure 9. A total blow-out of the flame still does not occur owing to the non-axisymmetric nature of the perturbations. As such, they make the scalar dissipation rate strongly increase only along some sections of the edge flame, so that there always remain some parts with a relatively low scalar dissipation rate, which do not recede. This gives the flame the chance to remain essentially anchored at the non-receding parts, from where the deep notches in the flame surface are laterally closed. This closing process is promoted by the relatively low dissipation rates seen on the lateral rims of the notches in Figure 10, and the continuous supply of heat from the burning sections. The present results unveil that buoyancy can produce a very particular scenario of flame stabilization characterized by large three-dimensional perturbations of the flame base. These perturbations have already been addressed as out-of-the-plane effects in experimental studies [14, 15], which can be hardly described by the mostly two-dimensional, planar measurements, and have therefore often been discarded. The here observed particular scenario highlights the possible relevance of these effects for the flame stabilization. It also emphasizes the significant role of the scalar dissipation rate, which is otherwise mostly assumed of minor importance by today's generally accepted theories on flame stabilization.

4. SUMMARY

A nitrogen-diluted methane-air jet flame at moderate Reynolds and Froude numbers is computationally investigated using Direct Numerical Simulation (DNS).

The comparison against the DNS results computed for a non-reacting reference jets shows

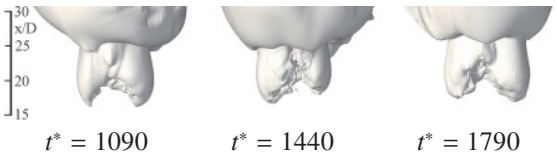

Figure 9. Iso-surfaces of non-dimensional temperature at $T/T_J = 1.2$, spaced in time by one buoyancy-induced oscillation period $\Delta t\, U_J/D = 350$ respectively.

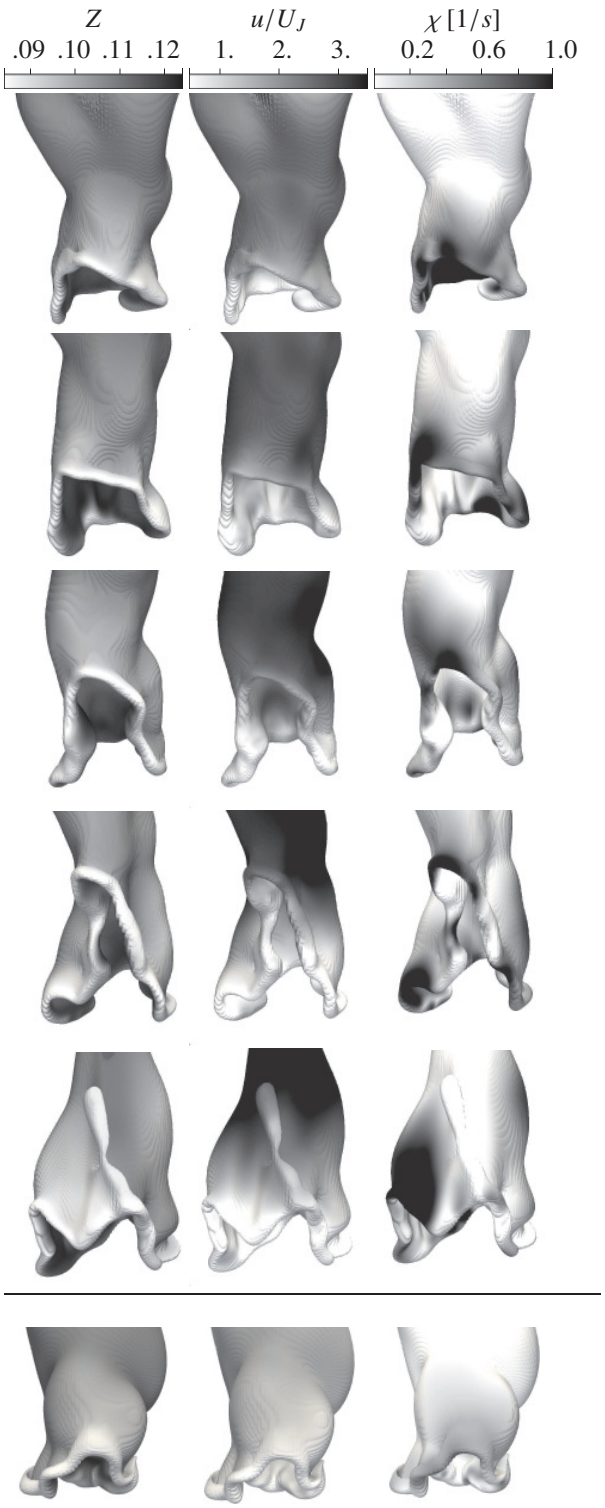

Figure 10. Instantaneous non-dimensional iso-surfaces of $\omega_I W_0 D/U_J = 0.004$, gray-shaded with mixture fraction (left column), streamwise velocity (center column), and scalar dissipation rate (right column).

that the increased viscosity and the volumetric dilatation in the hot product gases significantly reduce the turbulence intensity as expected. High turbulence levels are retained in the non-reacting core

region. The decay of the centerline velocity and the spreading of the jet are weakly increased, which indicates a flow impeding effect of the flame.

The intermittent action of buoyancy-induced acceleration, entrainment and reactive heat release generates an oscillatory large-scale motion involving the periodic formation, growth and lift-off of bulb-shaped low-density structures, which are also observed in experiments.

The statistical analysis of the flow and mixing conditions at the flame base essentially confirms the generally accepted theory of flame stabilization, which assumes the propagation of an edge flame into a partially premixed region countering a velocity field altered by the heat release. The observed average values of the velocity at the flame base agree well with experimentally obtained data from literature.

The potential influence of three-dimensional, out-of-the-plane effects on the flame stabilization process is demonstrated as well. In the present flame these effects are associated with the buoyancy-induced acceleration leading to a strong temporal destabilization of the flame, where considerable azimuthal sections of the flame front are receding deeply downstream. It is shown that the local scalar dissipation rate plays an important role in this particular scenario of partial flame blow-off. Despite the marked receding of large parts of the flame base, the flame is not blown-out completely, but is stabilized again from the non-receding parts, from where the notch-like deep recessions in the flame surface are laterally closed.

ACKNOWLEDGEMENTS

This work was conducted within the framework of the Doctoral School Numerical Simulations in Technical Sciences, funded by the Austrian Science Fund (FWF). Financial support is gratefully acknowledged.

References

[1] L. Vanquickenborne and A. van Tiggelen, "The stabilization mechanism of lifted diffusion flames," *Combustion and Flame*, vol. 10, no. 1, pp. 59–69, 1966.

[2] G. T. Kalghatgi, "Blow-out stability of gaseous jet diffusion flames. part i: In still air," *Combustion Science and Technology*, vol. 26, no. 5, pp. 233–239, 1981.

[3] L. Muñiz and M. G. Mungal, "Instantaneous flame-stabilization velocities in lifted-jet diffusion flames," *Combustion and Flame*, vol. 111, no. 1-2, pp. 16–30, 1997.

[4] M. S. Mansour, "Stability characteristics of lifted turbulent partially premixed jet flames," *Combustion and Flame*, vol. 133, no. 3, pp. 263–274, 2003.

[5] A. Upatnieks, J. F. Driscoll, C. C. Rasmussen, and S. L. Ceccio, "Liftoff of turbulent jet flames–assessment of edge flame and other concepts using cinema-piv," *Combustion and Flame*, vol. 138, no. 3, pp. 259–272, 2004.

[6] G. R. Ruetsch, L. Vervisch, and A. Lin, "Effects of heat release on triple flames," *Physics of Fluids*, vol. 7, no. 6, pp. 1447–1454, 1995.

[7] L. Su, O. Sun, and M. Mungal, "Experimental investigation of stabilization mechanisms in turbulent, lifted jet diffusion flames," *Combustion and Flame*, vol. 144, no. 3, pp. 494–512, 2006.

[8] N. Peters and F. A. Williams, "Liftoff characteristics of turbulent jet diffusion flames," *AIAA Journal*, vol. 21, no. 3, pp. 423–429, 1983.

[9] K. Watson, K. Lyons, J. Donbar, and C. Carter, "On scalar dissipation and partially premixed flame propagation," *Combustion Science and Technology*, vol. 175, pp. 649–664, 2003.

[10] S. Köberl, F. Fontaneto, F. Giuliani, and J. Woisetschläger, "Frequency-resolved interferometric measurement of local density fluctuations for turbulent combustion analysis," *Measurement Science and Technology*, vol. 21, no. 3, p. 035302, 2010.

[11] F. A. Williams, "Overview of asymptotics for methane flames," in *Reduced Kinetic Mechanisms and Asymptotic Approximations for Methane-Air Flames* (M. D. Smooke, ed.), ch. 4, pp. 68–85, Springer, New York, 1991.

[12] J. P. Legier, T. Poinsot, and D. Veynante, "Dynamically thickened flame les model for premixed and non-premixed turbulent combustion," *Center for Turbulence Research Summer Program*, pp. 157–168, 2000.

[13] K. Watson, K. Lyons, J. Donbar, and C. Carter, "Scalar and velocity field measurements in a lifted ch4-air diffusion flame," *Combustion and Flame*, vol. 117, no. 1-2, pp. 257–271, 1999.

[14] R. Schefer, M. Namazian, and J. Kelly, "Three-dimensional structure of lifted turbulent-jet flames," *Combustion Science and Technology*, vol. 125, pp. 371 – 394, 1997.

[15] R. Schefer, "Flame sheet imaging usinh ch-chemiluminescence," *Combustion Science and Technology*, vol. 126, pp. 255 – 270, 1997.

Conference on Modelling Fluid Flow (CMFF'12)
The 15th International Conference on Fluid Flow Technologies
Budapest, Hungary, September 4-7, 2012

APPLICATION OF OPENFOAM LIBRARY TO SIMULATIONS OF PREMIXED TURBULENT COMBUSTION USING FLAME SPEED CLOSURE MODEL

Ehsan Yasari[1], Andrei Lipatnikov[2]

[1] Combustion Division, Department of Applied Mechanics, Chalmers University of Technology, E-mail: yasari@chalmers.se
[2] Corresponding Author. Combustion Division, Department of Applied Mechanics, Chalmers University of Technology, SE-41275, Gothenburg, Sweden. Tel.: +46 31 772 13 86, Fax: +46 31 18 09 76, E-mail: lipatn@chalmers.se

ABSTRACT

Over the past few years, an open-source code called Open-FOAM has been becoming a promising CFD tool for multi-dimensional numerical simulations of various turbulent flows, but applications of the code to RANS modeling of turbulent flames are still very rare. The goals of the present work are to implement the well-known and thoroughly validated TFC and FSC models of premixed turbulent combustion into the code and to test the extended code by simulating an oblique confined preheated lean methane-air turbulent flame experimentally investigated by Moreau (1977). Results computed using the two combustion models are compared with each other and with the experimental data. The comparison shows that premixed turbulent flame development plays a role even in the statistically stationary combustion process addressed in the paper. Results obtained using the TFC and FSC models agree reasonably well with the experimental data without tuning the combustion model, but such a validation requires tuning of the inflow mean rate of dissipation of turbulent kinetic energy and turbulent Prandtl number.

Keywords: FSC model, OpenFOAM, premixed turbulent combustion, RANS, TFC model

NOMENCLATURE

A	[-]	constant of TFC and FSC models
a	$[m^2/s]$	heat diffusivity
C_μ	[-]	constant
c	[-]	combustion progress variable
D	$[m^2/s]$	diffusivity
Da	[-]	Damköhler number
k	$[m^2/s^2]$	turbulent kinetic energy
L	$[m]$	integral turbulent length scale
P_q	[-]	quenching probability
Pr_T	[-]	turbulent Prandtl number
Q	$[1/s]$	source term
Re_T	[-]	turbulent Reynolds number
S_L	$[m/s]$	laminar flame speed
$\dot{s}$	$[1/s]$	stretch rate
t	$[s]$	time
U_T	$[m/s]$	turbulent burning velocity
$\underline{u}$	$[m/s]$	velocity vector
u'	$[m/s]$	rms turbulent velocity
$\overline{W}$	$[kg/(m^3 s)]$	mean rate of product creation
$\underline{x}$	$[m]$	coordinate vector
ε	$[m^2/s^3]$	dissipation rate
η	$[m]$	Kolmogorov length scale
ϑ	$[s]$	flame-development time
ρ	$[kg/m^3]$	density
σ	[-]	density ratio
τ	$[s]$	time scale

Subscripts and Superscripts

b	burned
c	chemical
L	laminar or Lagrangian
q	quenching
T	turbulent
u	unburned
∞	fully-developed
–	ensemble mean
~	Favre (mass-weighted) mean

1. INTRODUCTION

To satisfy stringent requirements for ultra-low emission and highly efficient energy production and to secure the sustainable growth of the postindustrial society under the conditions of the increasing instability of the oil market, new solutions are strongly required in the field of internal combustion engines. To find such new solutions and, in particular, to develop clean and

efficient combustion technologies, industry and academy need both advanced experimental investigations and unsteady multi-dimensional numerical simulations.

Although several mature commercial Computational Fluid Dynamics (CFD) codes have been elaborated and are widely used for such simulations, industrial companies are keen to adopt less expensive software, while researchers from academy are strongly interested in access to source codes in order to develop and implement new models and to easily exchange knowledge with each other. For these reasons, Open Field Operation and Manipulation (OpenFOAM) library, which is a free, open source CFD software package available at www.openfoam.com, has attracted increasing amounts of attention from both commercial and academic organizations since its first release in 2004. However, although the number of problems relevant to internal combustion engines that have been studied with OpenFOAM continues to grow, there are still a great many such problems that have not yet been addressed with this code. Consequently, many more studies will be required in order to properly assess its utility in the automotive and gas turbine industry.

Accordingly, one goal of the present work is to assess the potential of the code (and further develop it if necessary) for multi-dimensional Reynolds-Averaged Navier-Stokes (RANS) simulations of premixed turbulent combustion.

Moreover, besides an efficient CFD code, a predictive model of the influence of turbulence on a premixed flame is necessary in order to investigate burning in such devices as Spark Ignition (SI) reciprocating engines, Lean Premixed Prevaporized (LPP) gas turbine combustors, and aero-engine afterburners.

Although a number of premixed turbulent combustion models reviewed elsewhere [1] are available, the vast majority of them strongly need straightforward and wide target-directed validation. Straightforward validation means that if an experiment is selected to test a model, then, simulated flame and post-processing of numerical data (e.g. evaluation of turbulent burning velocity U_T) should be close to the experimental techniques and flame geometry as much as possible. For instance, certain recent models were tested [2-7] by quantitatively comparing an expression for U_T that resulted from the model in the statistically planar, one-dimensional, and stationary case with measured speeds of curved and developing laboratory flames, e.g. expanding spherical ones. Such a test cannot be considered to be straightforward validation, because turbulent flame speed is well known to be sensitive to the method of measuring it [8,9]. For instance, the speed of a typical statistically spherical premixed turbulent flame that expands in a fan-stirred bomb after spark ignition is reduced by a factor of about three due to the flame development and curvature of the mean flame brush [10].

Wide target-directed validation means that a model is tested against a representative set of experimental data obtained in well defined simple cases under substantially different conditions, with the same model constants being used in all tests. The vast majority of premixed turbulent combustion models have been validated either against a few experimental data obtained from simple laboratory flames or against data measured in internal combustion engines. A recent paper by Chauduri et al. [7] is an example of the former (narrow) validation. In the cited paper, a new model that yielded the following scaling $U_\mathrm{T} \propto S_\mathrm{L}\,\mathrm{Re}_\mathrm{T}^{1/2}$ was claimed to be validated using experimental data obtained by a single research group from a single class of flames [11,12]. Here, S_L is the laminar flame speed, $\mathrm{Re}_\mathrm{T} = u'L/\nu_\mathrm{u}$ is the turbulent Reynolds number, u' is the rms turbulent velocity, L is an integral length scale of turbulence, and ν_u is the kinematic viscosity of unburned mixture. However, exactly the same scaling was obtained in the pioneering paper by Damköhler [13] more than sixty years ago and, since that, the scaling was already contradicted by numerous experiments.

As regards, testing a model against data obtained from internal combustion engines, such a validation is neither target-directed nor solid. Due to complexity of combustion in an engine, which involves not only burning itself, but also injection, evaporation, turbulent mixing, heat losses, etc., and due to the shortage of a typical experimental data set, which often includes only pressure curves, testing a model of turbulent combustion in engine simulations offers wide opportunities for tuning. Such tests are necessary, but they seem to be valuable only after straightforward validation of the model against a wide set of experimental data obtained in well-defined simple cases.

Among various models for RANS simulations of premixed turbulent combustion, only two groups of models have straightforwardly been applied to a wide set of laboratory flames. These are (i) the Eddy-Break-Up model by Spalding [14] and the model by Magnussen and Hjertager [15], with both yielding the following scaling $\overline{W} \propto \tau_T^{-1}$ for the mean rate of product creation, where $\tau_\mathrm{T} = L/u'$ is a turbulent time scale, and (ii) the so-called Turbulent Flame Closure (TFC) model by Zimont and Lipatnikov [16]. When applying the former models to different flames, the key model constant was substantially varied in order to get agreement with experimental data obtained from each particular flame. To the contrary, the constant A of the TFC model, which involves the following expression

$$U_{\mathrm{T},\infty} = Au'\mathrm{Da}^{1/4}\left(1-P_\mathrm{q}\right), \qquad (1)$$

retained the same value 0.5 when testing the model against experimental data obtained from laboratory flames. Here, $\mathrm{Da} = \tau_\mathrm{T}/\tau_\mathrm{c}$ is the Damköhler number, $\tau_\mathrm{c} = a_\mathrm{u}/S_\mathrm{L}^2$ is a chemical time scale, a_u is the heat diffusivity of unburned mixture, and the probability P_q of local combustion quenching by turbulent stretching will be discussed later.

For instance, the TFC model with $A = 0.5$ was validated (i) by Zimont and Lipatnikov [16] against experimental data obtained from expanding statistically spherical premixed turbulent flames in a wide range of u' and mixture composition, (ii) by Zimont et al. [17] and by Ghirelli [18] against experimental data obtained from a statistically stationary oblique confined flame, (iii) by Dinkelacker and Hölzler [19], by Moreau [20], and by Ghirelli [18] against experimental data obtained from V-shaped flames, (iv) by Muppala and Dinkelacker [21] against experimental data obtained from Bunsen flames.

Lipatnikov and Chomiak [22] extended the TFC model in order (i) to simulate weakly turbulent combustion, (ii) to address early stage of flame development, characterized by well documented linear growth of the mean flame brush thickness with flame-development time, (iii) to facilitate setting boundary conditions, etc. The so-extended TFC model is called Flame Speed Closure (FSC) model and it was straightforwardly validated against a wide set of experimental data obtained by different research groups from various expanding statistically spherical premixed turbulent flames [22]. However, the present authors are aware of a single application of the FSC model to RANS simulations of a statistically stationary premixed turbulent flame, i.e. an oblique confined flame stabilized behind a bluff body [23]. Therefore, the FSC model needs more validation against experimental data obtained from statistically stationary premixed turbulent flames. In particular, it is of interest to study whether or not extensions of the TFC model introduced into the FSC one play a substantial role in stationary flames.

Accordingly, another goal of the present project is to implement the FSC model into OpenFOAM and to straightforwardly test it against experimental data obtained from different statistically stationary premixed turbulent flames. In the present paper, first results obtained from a single statistically stationary premixed turbulent flame are reported.

In Section 2, the TFC and FSC models are discussed. In Section 3, experiment used to test the models is briefly described and a numerical model of the experiment is reported, with particular emphasis being placed on uncertainties associated with testing any model of premixed turbulent combustion against experimental data obtained from statistically stationary flames. Test results are discussed in Section 4 followed by conclusions.

2. TFC AND FSC MODELS

Both the TFC and FSC models characterize the state of the mixture in a flame using a single combustion progress variable c and deal with the following closed balance equation

$$\begin{aligned}&\overline{\rho}\frac{\partial\widetilde{c}}{\partial t} + \overline{\rho}\widetilde{u}_k\frac{\partial\widetilde{c}}{\partial x_k}\\ &= \frac{\partial}{\partial x_k}\left(\overline{\rho}D_\mathrm{T}\frac{\partial\widetilde{c}}{\partial x_k}\right) + \rho_\mathrm{u}U_\mathrm{T}\left|\nabla\widetilde{c}\right| + \rho_\mathrm{u}Q,\end{aligned} \tag{2}$$

where t is time, x_k and u_k are the spatial coordinates and components of the flow velocity vector, respectively, $\widetilde{q} \equiv \overline{\rho q}/\overline{\rho}$ is the Favre-averaged value of a quantity q, the mean density

$$\overline{\rho} = \rho_\mathrm{u}/\left[1 + (\sigma - 1)\widetilde{c}\right] \tag{3}$$

is calculated invoking the Bray-Moss-Libby (BML) approach [24], $\sigma = \rho_\mathrm{u}/\rho_\mathrm{b}$ is the density ratio, subscripts u and b designate unburned and burned mixture, respectively, and the summation convention applies for the repeated index k.

Within the framework of the TFC model [16], in Eq. (2), (i) the turbulent diffusivity D_T is evaluated using the $k-\varepsilon$ turbulence model [25]

$$D_\mathrm{T} = D_{\mathrm{T},\infty} = \frac{C_\mu}{\mathrm{Pr}_\mathrm{T}}\frac{\widetilde{k}^2}{\widetilde{\varepsilon}} \tag{4}$$

where $C_\mu = 0.09$ and Pr_T are constants, k and ε are turbulent kinetic energy and its dissipation rate, respectively, (ii) U_T is equal to $U_{\mathrm{T},\infty}$ given by Eq. (1), and (iii) $Q = 0$. Moreover, folowing Bray [26], the probability P_q is equal to

$$P_\mathrm{q} = 1 - \frac{1}{2}\mathrm{erfc}\left\{\frac{1}{\sqrt{2}\sigma_L}\left[\ln\left(\frac{\varepsilon_\mathrm{q}}{\widetilde{\varepsilon}}\right) + \frac{\sigma_L^2}{2}\right]\right\}, \tag{5}$$

where $\sigma_L^2 = 0.26\ln(L/\eta)$, η is the Kolmogorov length scale, $\varepsilon_\mathrm{q} = 15\nu_\mathrm{u}\dot{s}_\mathrm{q}^2$, and $\dot{s}_\mathrm{q}$ is a critical stretch rate associated with quenching of the counterpart laminar flame. Because the critical stretch rate is poorly known and depends on mixture composition, $\dot{s}_\mathrm{q}$ in Eq. (5) is in fact a tuning parameter. However, because P_q is substantial only in sufficiently intense turbulence, the TFC model involves a single constant A in less intense turbulence, and most tests of the model cited in Introduction were done with $A = 0.5$ and $P_\mathrm{q} = 0$

Within the framework of the FSC model [22],

$$D_{\mathrm{T}} = D_{\mathrm{T},\infty}\left[1-\exp\left(-\frac{\vartheta}{\tau_{\mathrm{L}}}\right)\right], \quad (6)$$

$$U_{\mathrm{T}} = U_{\mathrm{T},\infty}\left\{1+\frac{\tau_{\mathrm{L}}}{\vartheta}\left[\exp\left(-\frac{\vartheta}{\tau_{\mathrm{L}}}\right)-1\right]\right\}^{1/2}, \quad (7)$$

where ϑ is flame-development time and

$$\tau_{\mathrm{L}} = \frac{D_{\mathrm{T},\infty}}{u'^2} \quad (8)$$

is the Lagrangian time scale. Equation (6) is based on the Taylor theory of turbulent diffusion [27] and Eq. (7) was derived [22] using Eq. (6). To the best of the present authors' knowledge, the probability $P_{\mathrm{q}} = 0$ in all previous applications of the FSC models and we also set $P_{\mathrm{q}} = 0$.

Moreover, the FSC model invokes a submodel for the second source term $Q > 0$ in order for Eq. (2) to yield the laminar flame speed in the limit case of $u' \to 0$. However, this submodel is not discussed here, because a role played by this source term is reduced by u'/S_{L} and it affected weakly results of the present simulations performed under conditions of sufficiently intense turbulence

If $u' >> S_{\mathrm{L}}$ and $\vartheta >> \tau_{\mathrm{L}}$, then, the FSC model reduces to the TFC model. However, the former model offers an opportunity to simulate weakly turbulent flames thanks to $Q > 0$ and allows us to address an early stage of premixed turbulent flame development thanks to Eqs. (6)-(8). The latter extension of the TFC model was shown to be of substantial importance for expanding statistically spherical flames [22], while the goal of the present work is to access the importance of this extension for staistically stationary flames.

Moreover, as already noted above, the predictive capabilities of the TFC model are substantially devaluated by tuning $\dot{s}_{\mathrm{q}}$ if $P_{\mathrm{q}} > 0$. The use of the quenching probability in Eq. (1) reduces turbulent burning velocity, while the time-dependent term in Eq. (7) acts in the same direction. Therefore, one might assume that the use of Eq. (7), which does not involve turning parameters, could allow us to skip term $\left(1-P_{\mathrm{q}}\right)$, which contains a tuning parameter. Accordingly, one more goal of the present work is to test this assumption.

3. NUMERICAL SIMULATIONS

3.1. Simulated Test Case

In the present paper, we report results of RANS simulations of an experiment by Moreau [28] who investigated an oblique confined preheated lean methane-air flame stabilized by a hot pilot flow of products in a planar combustion chamber, which had $100 \times 100\ mm$ square cross section and was 1300 mm long, see Fig. 1. The bottom (in Fig. 1) flow of hot products and the flow of unburned mixture were separated by a splitter which was sufficiently thin in order to avoid recirculation behind it. The product flow inlet was 20 mm high and the cold flow inlet was 80 mm high. The mean flow velocities were equal to 120 and 60 *m/s* in the two inlets, respectively. In the unburned mixture, the temperature and equivalence ratio were equal to 600 K and 0.8, respectively.

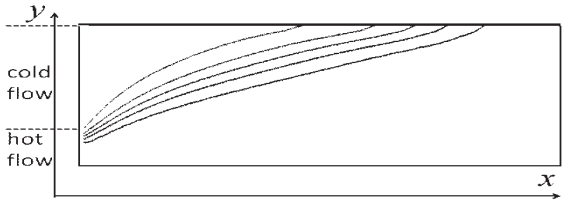

Figure 1. Schematic of the test case

3.2. Numerical Setup

To simulate the above experiment, the TFC and FSC models were implemented into OpenFOAM 1.7.x. Moreover, because the mean density computed by the original code differed notably from the mean density yielded by Eq. (3), the method of evaluating $\overline{\rho}$ based on Eq. (3) was also implemented, as discussed in detail elsewhere [29]. The standard $k-\varepsilon$ model [25] was invoked to simulate turbulence. When using the FSC model, the flame development time in Eqs. (6)-(7) was equal to a ratio of the distance *x* from the splitter to the mean inflow velocity of unburned mixture.

Simulations were 2D and unsteady until a stationary solution was reached. The results reported in the following were obtained using uniform 325×25 mesh. Basically similar results were computed using a finer mesh and various numerical schemes implemented into OpenFOAM. Moreover, a single test 3D run yielded results the same as obtained in the 2D case, with all other things being equal.

Table 1. Inflow boundary conditions

	T(K)	*k*(m^2/s^2)	*c*	*U(m/s)*	*ρ*(kg/m^3)
cold flow	600	100	0	60	0.5603
pilot flow	2199	793	1	120	0.1524

The inflow boundary conditions are specified in Table 1. The inflow values of the mean turbulent kinetic energy were taken from Ref. [17]. The inflow values of the mean dissipation rate will be discussed in the next subsection. Wall function and

outflow boundary conditions were set at other boundaries. The laminar flame speed $S_L = 1.1$ *m/s* of the lean preheated methane-air mixture was calculated running Premix code [30] and invoking GRI 3.0 chemical mechanism [31].

3.3. Validation and Tuning

The FSC model tested in the present paper consists of Eqs. (1)-(4), (6)-(8), and $Q = 0$. These equations all together involve a single model constant A. In the previous tests of the present version of the FSC model, the constant was set equal to 0.5 [23].

The TFC model consists of Eqs. (1)-(5) and involves a single constant $A = 0.5$ and an unknonw critical stretch rate $\dot{s}_q$, which affects computed results if $P_q > 0$. However, if $P_q = 0$, the model involves no tuning parameters.

Nevertheless, testing the TFC or FSC model against experimental data obtained from statistically stationary premixed turbulent flames is not free from tuning even if the constant A is not adjusted in such a test. The point is that we have to simulate turbulent flow in order to test a model of premixed turbulent combustion. Accordingly, computed flame characteristics are affected not only by the combustion models, which were not tuned in the present work, but also by turbulence model, its constants and boundary conditions. In particular, two uncertainities associated with turbulence modeling in RANS simulations are of importance for tesing any model of turbulent combustion.

First, to model a turbulent flow, the value of the dissipation rate $\bar{\varepsilon}$ at the inflow boundary is required, at least if the $k-\varepsilon$ model is invoked. This value is not specified in a typical paper that reports experimental data obtained from a premixed flame. In the best case, such a paper provides an integral length scale of turbulence, but does not define it (whether it is longitudinal or transversal). Such experimental data are definitely insufficient in order to evaluate the inflow value of $\bar{\varepsilon}$, not only because the longitudinal and transversal length scales are substantially different, but also because a ratio of $\bar{\varepsilon}L/u'^3$ depends on the Reynolds number and "details of forcing at low wavenumbers" [32]. This problem could be overcome by tuning the inflow value of $\bar{\varepsilon}$ using experimental data obtained from the same burner without combustion. However, such data are not reported in many papers that discuss measurements in flames.

Second, available data on the turbulent Prandtl number Pr_T are controversial. In CFD papers, it is commonly equal to 0.7 or 0.9. However, these numbers correspond to the fully-developed turbulent diffusivity given by Eq. (4) and reached at $\vartheta >> \tau_L$. Because a typical turbulent premixed flame is associated with $\vartheta/\tau_L = \mathrm{O}(1)$, a lower Pr_T should be used in conjunction with Eqs. (6) and (8) in order for these equations to yield diffusivity equal to the diffusivity resulted from Eq. (4) with $\mathrm{Pr}_T = 0.7$. For instance, Bilger et al. [33] obtained $\mathrm{Pr}_T = 0.35$ by experimentally studying reaction in a scalar mixing layer in grid-generated turbulence. Yeung [34] has reported that a ratio

$$\widetilde{C}_0 = \frac{4}{3}\frac{\bar{k}/\bar{\varepsilon}}{\tau_L} \tag{9}$$

tends to 6.4 at large Reynolds numbers, but may be substantially (by a factor of about two) lower at lower Re_T, which is associated with conditions in many laboratory premixed turbulent flames. Because Eqs. (4), (8), and (9) yield $\mathrm{Pr}_T = 0.65$ if $\widetilde{C}_0 = 6.4$, as low Pr_T as 0.3 are admissible in non-reacting turbulent flows.

Due to the above uncertainities in the inflow value of $\bar{\varepsilon}$ and in the turbulent Prandtl number, tuning of them is permissible and we did so. The length scale L in Eq. (1) was calculated as follows

$$L = \frac{C_\mu^{3/4}\bar{k}^{3/2}}{\bar{\varepsilon}} \approx 0.3\frac{u'^3}{\bar{\varepsilon}} \tag{10}$$

and it is directly affected by tuning of $\bar{\varepsilon}$.

Table 2. Inflow values of the mean dissipation rate (m^2/s^3)

	case I	case II	case III	case IV
Cold flow	6.85e3	2.64e4	3.7e4	7.4e4
Pilot flow	6.12e5	1.64e6	2.8e6	5.6e6

Inflow values of the mean dissipation rate used in our simulations are reported in Table 2. In case I, the mean dissipation rate has been calculated using Eq. (10) and the values of *L*=24 and 6 *mm* that are reported in Ref. [17]. In cases II and III, the values of $\bar{\varepsilon}$ are based on the inflow boundary conditions set by Ghirelli [18] and ny Maciocco and Zimont [35], respectively. In case IV, $\bar{\varepsilon}$ is increased by a factor of two as compared with case III.

4. RESULTS AND DISCUSSION

Shown in Figs 2 is the influence of the turbulent Prandtl number on the transverse profiles of $\widetilde{c}(y)$, computed using the (a) TFC and (b) FSC models in case III at x=322 *mm*. An increase in Pr_T results in increasing the slope of the computed curves, i.e. decreasing mean flame brush thickness. Moreover, when using the FSC model, an increase in Pr_T results in increasing the mass of burned fluid. The point is that the Lagrangian time scale

evaluated using Eq. (8) is decreased when $\mathrm{Pr_T}$ is increased. Accordingly, a ratio of $\vartheta/\tau_{\mathrm{L}}$ and, hence, the turbulent burning velocity calculated using Eq. (7) is increased by $\mathrm{Pr_T}$.

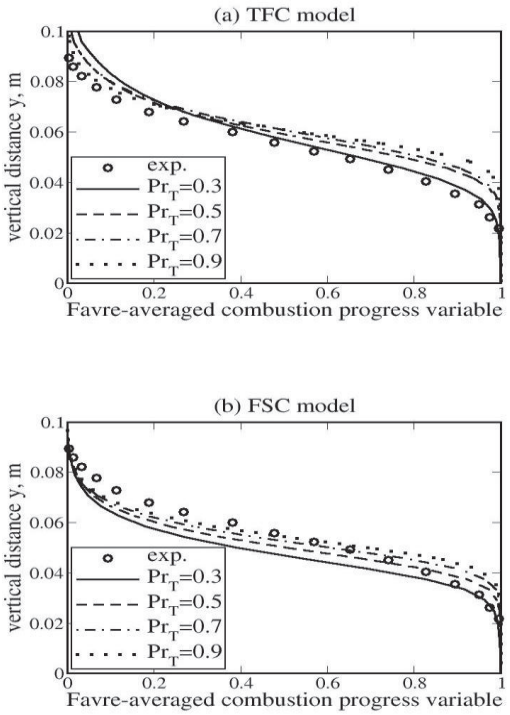

Figure 2. Effect of turbulent Prandtl number on computed transverse profiles of $\widetilde{c}$.

Effect of the inlet value of the mean dissipation rate on the profiles $\widetilde{c}(y)$, computed using the (a) TFC or (b) FSC models and $\mathrm{Pr_T}=0.3$ at x=322 *mm*, is shown in Fig. 3. An increase in the dissipation rate is associated with a decrease in the burning rate due to a decrease in the length scale L in Eq. (1), which is calculated using Eq. (10). Moreover, an increase in $\bar{\varepsilon}$ reduces turbulent diffusivity evaluated using Eq. (4) and, therefore, reduces the mean flame brush thickness similarly to an increase in the turbulent Prandtl number.

The effect of $\bar{\varepsilon}$ on $\widetilde{c}(y)$ is less pronounced when using the FSC model as compared with the TFC model. The point is that, in the former case, a decrease in the dissipation rate not only increases turbulent burning velocity due to an increase in the length scale L in Eq. (1), but also decreases U_T due to a decrease in $\vartheta/\tau_{\mathrm{L}}$ in Eq. (7), because τ_{L} evaluated using Eqs. (4) and (8) is increased.

Comparison of solid curves in Figs. 3a and 3b, computed using the TFC and FSC models, with all other things being equal, indicates that flame development modelled by Eqs. (6)-(8) plays a role in the considered statistically stationary flame. The former model, which does not address the effect, yields higher burning rate and thicker flame brush.

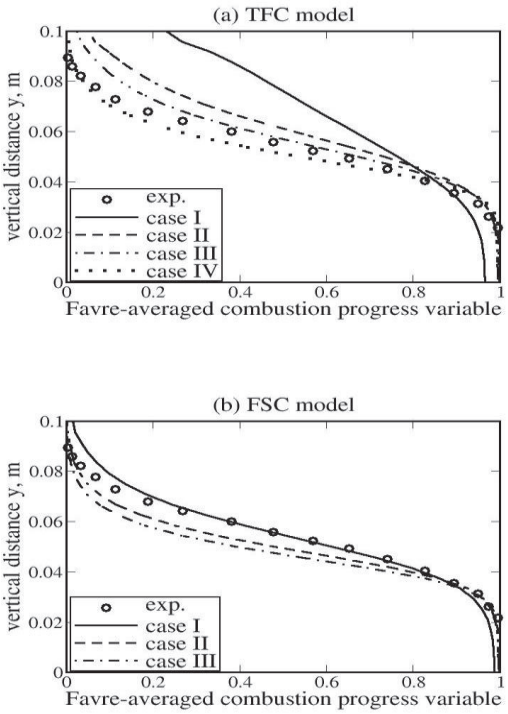

Figure 3. Effect of inlet dissipation rate on computed transverse profiles of $\widetilde{c}$.

Analysis of numerical results computed in different cases (different $\mathrm{Pr_T}$ and $\bar{\varepsilon}$) has shown that the TFC and FSC models yield the best agreement with the experimental data in cases III and I, respectively, with the optimum value of $\mathrm{Pr_T}$ being equal to 0.3 for both models. It is of interest to note that the same value of $\mathrm{Pr_T}=0.3$ was found by Sathiah and Lipatnikov [23] who applied the FSC model to simulating lean propane-air flames stabilized by a bluff body in a channel.

At x=122 *mm*, both models slightly overestimate burning rate (cf. solid and dashed curves with symbols in Fig. 4a), but the effect is less pronounced for the FSC model and $\widetilde{c}<0.4$. The overestimation may be reduced by tuning ε_{q} in Eq. (5), as Zimont et al. [17] did. Such tuning may weakly affect results computed at x=322 and 522 *mm*, because, due to a decrease in $\bar{\varepsilon}$ with x, the probability P_{q} may be much less at x=322 and 522 *mm* than at x=122 *mm*. Nevertheless, Fig. 4a implies that the overestimation not only may be associated with local combustion quenching, but also may be attributed to premixed turbulent flame development.

At x=322 and 522 *mm*, the two models agree well with the experimental data provided that different inflow values of $\bar{\varepsilon}$ are set for the TFC and FSC models.

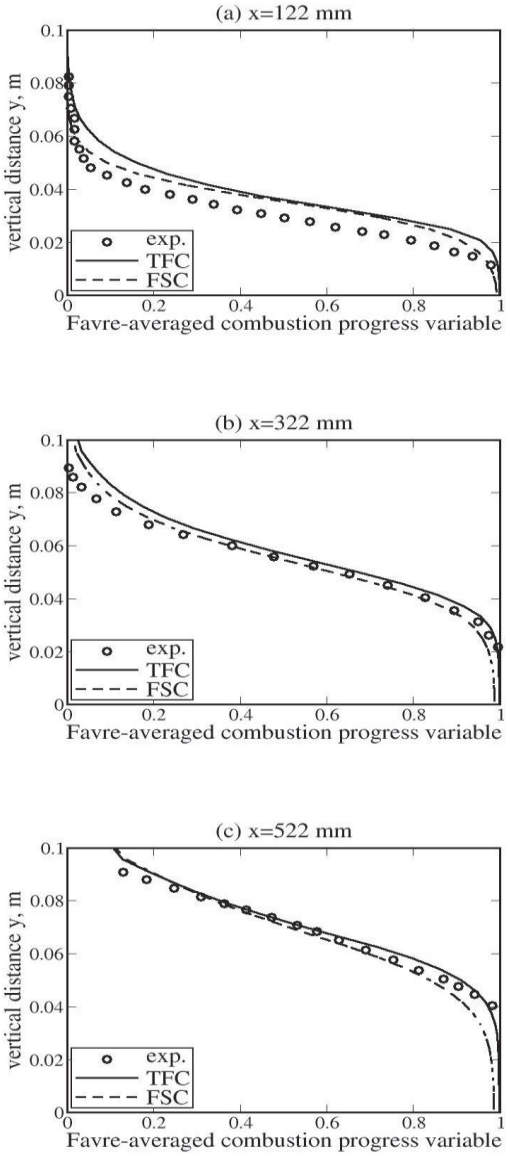

Figure 4. Transverse profiles of $\widetilde{c}$ computed using the TFC (solid curves) and FSC (dashed curves) models in cases III and I, respectively.

5. CONCLUSIONS

The TFC and FSC models of premixed turbulent combustion were implemented into OpenFOAM and applied to simulating experiments by Moreau [28] with oblique preheated lean methane-air flame stabilized in a highly intense turbulent flow by a hot product flow in a channel.

Comparison of results computed using the two models, with all other things being equal, indicates that premixed turbulent flame development plays a role by reducing the burning rate and mean flame brush thickness in the considered case.

The reasonable agreement between experimental and numerical data indicates the feasibility of the two models, but should not be considered to be a solid validation of their predictive capabilities, because computed results are sensitive to the inflow boundary condition for the mean dissipation rate, with the sensitivity being less pronounced for the FSC model.

ACKNOWLEDGEMENTS

This work has been supported by the Swedish Energy Agency. The computations were performed on C3SE computing resources. The authors are grateful to Dr. Ghirelli for help in implementation of the TFC model into OpenFOAM.

REFERENCES

[1] Veynante, D., and Vervisch, L., 2002, "Turbulent Combustion Modeling", *Prog. Energy Combust. Sci.*, Vol. 28, pp. 193-266.

[2] Duclos, J.M., Veynante, D., and Poinsot, T., 1993, "A Comparison of Flamelet Models for Premixed Turbulent Combustion", *Combust. Flame*, Vol. 95, pp. 101-117.

[3] Peters, N., 1999, "The Turbulent Burning Velocity for Large-Scale and Small-Scale Turbulence", *J. Fluid Mech.*, Vol. 384, pp. 107-132.

[4] Bychkov, V., 2003, "Importance of the Darrieus-Landau Instability for Strongly Corrugated Turbulent Flames", *Phys. Rev. E*, Vol. 68, paper 066304.

[5] Kolla, H., Rogerson, J.W., and Swaminathan, N., 2010, "Validation of a Turbulent Flame Speed Model Across Combustion Regimes", *Combust. Sci. and Tech.*, Vol. 182, pp. 284-308.

[6] Lindstedt, R.P., Milosavljevic, V.D., and Persson, M., 2011, "Turbulent Burning Velocity Predictions Using Transported PDF Methods", *Proc. Combust. Inst.,* Vol. 33, pp. 1277-1284.

[7] Chaudhuri, S., Akkerman, V., and Law, C.K., 2011, "Spectral Formulation of Turbulent Flame Speed with Consideration of Hydrodynamic Instability", *Phys. Rev. E*, Vol. 84, paper 026322.

[8] Driscoll, J.F., 2008, "Turbulent Premixed Combustion: Flamelet Structure and Its Effect on Turbulent Burning Velocities", *Prog. Energy Combust. Sci.*, Vol. 34, pp. 91-134.

[9] Lipatnikov, A.N., and Chomiak, J., 2010, "Effects of Premixed Flames on Turbulence and Turbulent Scalar Transport", *Prog. Energy Combust. Sci.*, Vol. 36, pp. 1-102.

[10] Lipatnikov, A.N., and Chomiak, J., 2007, "Global Stretch Effects in Premixed Turbulent Combustion", *Proc. Combust. Inst.*, Vol. 31, pp. 1361-1368.

[11]Kobayashi, H., Tamura, T., Maruta, K., Niioka, T., and Williams, F.A., 1996, "Burning Velocity of Turbulent Premixed Flames in a High-Pressure Environment", *Proc. Combust. Inst.*, Vol. 26, pp. 389-396.

[12]Kobayashi, H., Seyama, K., Hagiwara, H., and Ogami, Y., 2005, "Burning Velocity Correlation of Methane/Air Turbulent Premixed Flames at High Pressure and High Temperature", *Proc. Combust. Inst*., Vol. 30, pp. 827-834.

[13]Damköhler, G., 1940, "Der Einfuss der Turbulenz auf die Flammengeschwindigkeit in Gasgemischen", *Zs. Electrochemie*, Vol. 6, pp. 601-626.

[14]Spalding, D.B., 1971, "Mixing and Chemical Reaction in Steady Confined Turbulent Flame", *Proc. Combust. Inst*., Vol. 13, pp. 649-657.

[15]Magnussen, B.F., and Hjertager, B.H., 1976, "On Mathematical Modeling of Turbulent Combustion with Special Emphasis on Soot Formation and Combustion", *Proc. Combust. Inst.*, Vol. 16, pp. 719-729.

[16]Zimont, V.L., and Lipatnikov, A.N., 1995, "A Numerical Model of Premixed Turbulent Combustion", *Chem. Phys. Reports*, Vol. 14, pp. 993-1025.

[17]Zimont, V.L., Biagioli, F., and Syed, K., 2001, "Modelling Turbulent Premixed Combustion in the Intermediate Steady Propagation Regime", *Prog. Comput. Fluid Dyn.*, Vol. 1, pp. 14-28.

[18]Ghirelli, F., 2011, "Turbulent Premixed Flame Model Based on a Recent Dispersion Model", *Comput. Fluids,* Vol. 44, pp. 369-376.

[19]Dinkelacker, F., and Hölzler, S., 2000, "Investigation of a Turbulent Flame Speed Closure Approach for Premixed Flame Calculations", *Combust. Sci. and Tech.,* Vol. 158, pp. 321-340.

[20]Moreau, V., 2009, "A Self-Similar Premixed Turbulent Flame Model", *Appl. Math. Model.,* Vol. 33, pp. 835-851.

[21]Muppala, S.R.P., and Dinkelacker, F., 2004, "Numerical Modelling of the Pressure Dependent Reaction Source Term for Turbulent Premixed Methane-Air Flames", *Prog. Comput. Fluid Dyn.,* Vol. 4, pp. 328-333.

[22]Lipatnikov, A.N., and Chomiak, J., 2002, "Turbulent Flame Speed and Thickness: Phenomenology, Evaluation, and Application in Multi-Dimensional Simulations", *Prog. Energy Combust. Sci*., Vol. 28, pp. 1-74.

[23]Sathiah, P., and Lipatnikov, A.N., 2007, "Effects of Flame Development on Stationary Premixed Turbulent Combustion", *Proc. Combust. Inst.*, Vol. 31, pp. 3115-3122.

[24]Bray, K.N.C., Libby, P.A., and Moss. J.B., 1985, "Unified Modeling Approach for Premixed Turbulent Combustion - Part I: General Formulation", *Combust. Flame*, Vol. 61, pp. 87-102.

[25]Launder, B.E., and Spalding, D.B., 1972, *Mathematical Models of Turbulence,* Academic Press.

[26]Bray, K.N.C, 1987, "Methods of Including Realistic Chemical Reaction Mechanisms in Turbulent Combustion Models", In *Complex Chemical Reaction Systems. Mathematical Modelling and Simulation*, Ed. Warnatz, J., and Jager, W., Springer, pp. 356-375.

[27]Taylor, G.I., 1935, "Statistical Theory of Turbulence. IV. Diffusion in a Turbulent Air Stream", *Proc. R. Soc. London* A, Vol. 151, pp. 421-478.

[28]Moreau, P., 1977, "Turbulent Flame Development in a High Velocity Premixed Flow", *AIAA Paper* 77/49.

[29]Yasari, E., 2011, "Modification of the Temperature Calculation Library for Premixed Turbulent Combustion Simulation", Proc. *6th OpenFOAM Workshop*, Pennsylvania, USA.

[30]Kee, R.J., Grcar, J.F., Smooke, M.D., Miller, J.A., 1985, "PREMIX: A Fortran Program for Modeling Steady Laminar One-Dimensional Premixed Flames", Sandia National Lab., *Technical Report* SAND85-8240, 1985.

[31]Smith, G.P., Golden, M.D., Frenklach, M., Moriarty, N.W., Eiteneer, B., Goldenberg, M., Bowman, C.T., Hanson, R.K., Song, S., Gardiner, W.C.Jr., Lissianski, V.V., and Qin, Z., http://www.me.berkeley.edu/gri_mech/

[32]Sreenivasan, K.R., 1998, "An Update on Energy Dissipation Rate in Isotropic Turbulence", *Phys. Fluids*, Vol.10, pp.528-529.

[33]Bilger, R.W., Saetran, L.R., and Krishnamoorthy, L.V., 1991, "Reaction in a Scalar Mixing Layer", *J. Fluid Mech*., Vol. 233, pp. 211-242.

[34]Yeung, P.K., 2002, "Lagrangian Investigations of Turbulence", *Annu. Rev. Fluid. Mech*., Vol. 34, pp.115-142.

[35]Maciocco, L., and Zimont, V.L., 1997, "Test of the TFC Combustion Model on High Velocity Premixed CH_4-Air Combustion in a Channel", Proc. *20-th Annual Meeting of the Italian Section of the Combustion Institute "Frantic97"*, Cagliari, Italy, pp.X-2.1-2.4..

Conference on Modelling Fluid Flow (CMFF'12)
The 15th International Conference on Fluid Flow Technologies
Budapest, Hungary, September 4-7, 2012

Detailed numerical simulation of forced planar premixed hydrocarbon flames

Zoltan JOZEFIK,[1] Carmen JIMÉNEZ, [2] Heiko SCHMIDT [1]

[1] Corresponding Author. BTU Cottbus, Siemens-Halske-Ring 14, 03046, Cottbus Germany. Tel.:+49 355 694874, E-mail: jozefik@tu-cottbus.de
[2] CIEMAT, Avenida Complutense, 22, 28040, Madrid, Spain. E-mail: carmen.jimenez@ciemat.es

ABSTRACT

In this work we present numerical simulations of the response of a planar premixed propane flame to acoustic perturbations. We use detailed chemical kinetics including chemical mechanisms to account for OH* formation and de-excitation via collisional quenching and light emission. The computed oscillating response of the OH* chemiluminescence emission rate to acoustic pressure waves for the range of frequencies below and above the inverse of the flame transit time is compared to experimental measurements of OH* chemiluminescence. Our previous work on methane and hydrogen flames had cast doubt on the validity of using OH* chemiluminescence in combustion experiments as an indicator of heat release. In this work we further assess the link between OH* luminescence and heat release and also compare propane results to those of hydrogen and methane flames from our previous work. Our simulations predict an important phase shift between the OH* light signal and the forcing pressure for low frequencies, very close to what was found in the experiments. This high phase shift, which is not observed in the heat release rate response, shows that the OH* signal is not always correlated to the heat release signal.

Keywords: Acoustic-flame interaction, OH* chemiluminescence, thermo-acoustic instability

NOMENCLATURE

D_{th}	$[m^2/s]$	thermal diffusion
E_A	$[kJ/mol]$	activation energy
$\dot{Q}$	$[J/m^2 s]$	heat release rate
R	$[J/molK]$	gas constant
S_L	$[m/s]$	laminar flame velocity
T	$[K]$	temperature
c	$[m/s]$	speed of sound
f	$[Hz]$	frequency
p	$[Pa]$	acoustic pressure
t	$[s]$	time
γ	$[-]$	ratio of specific heats, c_p/c_v
δ_f	$[m]$	flame thickness
ρ	$[kg/m^3]$	density
τ_f	$[s]$	flame transit time, D_{th}/S_L^2
ω	$[Hz]$	angular frequency

Subscripts

u	unburnt gas
b	burnt gas

1. INTRODUCTION

A key issue for the design of enclosed combustion devices, e.g., low emission gas turbines, industrial boilers, and household burners is that fluctuating heat release may interact with resonant modes of the combustion chamber leading to unstable combustion [1, 2]. Unstable combustion refers to self-sustained combustion oscillations at or near the acoustic frequency of the combustion chamber, which are the result of the closed-loop coupling between unsteady heat release and pressure fluctuations.

As an estimate of the heat release rate, chemiluminescence of excited radicals has been a widely used diagnosis tool for combustion studies. Chemiluminescence is the radiative emission from electronically excited species formed by chemical reactions. The intensity of the chemiluminescence emission is directly related to the concentration of the electronically excited species, which is determined by the competition between the chemical reactions that produce the excited species and collisional quenching reactions. The strongest chemiluminescence emission in lean hydrocarbon flames is that due to CH*, OH* and CO_2* (the asterisk indicates an excited species) [3]. The detection of the naturally emitted light from excited radicals has been used to identify the reaction zone, as a measure of the equivalence ratio or to estimate the heat release rate [3, 4, 5, 6, 7]. There is, however, evidence that the relation between

the measured chemiluminescence and heat release could be pressure dependent and could also change locally with curvature and strain rate in unsteady flames [3, 4]. These results cast some doubt about the assumption of proportionality between the heat release rate and the chemiluminescence intensity under general conditions, in which other parameters can vary along the measured flames.

In Wangher et al. [8] and Wangher's Ph.D. thesis [9] the first attempt to measure the direct effect of acoustic pressure fluctuations in a flame was undertaken. They measured the chemiluminescence of the radical OH* in lean propane and methane flames, excited by low amplitude acoustic waves of frequencies close to the characteristic flame time, with the assumption that the OH* measured signal was proportional to heat release. In our previous work on methane and hydrogen flames [10] we compared our numerical results with the measurements and showed that OH* chemiluminescence does not always provide a reliable measure of heat release rate in the presence of a pressure driven interaction.

In this paper we extend our previous results and provide new numerical results of the unsteady pressure response of propane flames and compare them to the experiments. The paper is organized as follows: In section 2, we summarize our numerical model. In section 3, we discuss the chemistry mechanisms used. Section 4 shows the results obtained with the incompressible ansatz for propane and compare them to the experiments and previous results for methane and hydrogen. Finally, we finish with some concluding remarks.

2. Numerical set up

We use numerical experiments to investigate 1-D premixed flames interacting with acoustic waves that have characteristic times of similar order and wavelengths much longer than the flame width. The studied problem is presented in Figure 1.

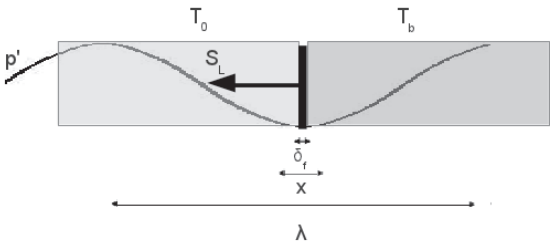

Figure 1. Sketch of the studied problem

A planar steady propane/air flame with equivalence ratio $\phi = 0.625$, inflow temperature $T_u = 300\ K$ at atmospheric pressure, corresponding to a flame speed S_L of 0.171 m/s and a flame width $\delta_f \approx 1\ mm$ is first established. We use 1000 grid points on a 7 mm domain. Standing acoustic waves are then imposed with an amplitude $p' = 500\ Pa$ and frequencies f ranging from 1 to 5000 Hz, corresponding to reduced frequencies $\omega \cdot \tau_f = 0.0047$ to 23.64, where $\tau_f = D_{th}/S_L^2$ is the flame transit time and $\omega = 2\pi f$.

The pressure waves have wavelengths much longer than the flame thickness when the flame speed is small compared to the speed of sound. Therefore, in this problem, the pressure seen by the flame is time-fluctuating but spatially uniform on the scale of the flame thickness.

The numerical code used is an incompressible zero-Mach-number solver, which uses implicit finite differencing, and for which the pressure waves are represented by time fluctuations of the background pressure $p(t)$, see e.g. [11, 12]. While the pressure is changing in time, the flame location is kept constant by stabilizing it on a velocity node. This represents very closely the experimental setup in [8].

2.1. *Incompressible solver*

We solve the variable density zero-Mach-number equations in one spatial dimension on a fixed grid. The balance equations for species mass fractions and temperature are

$$\rho \frac{\partial Y_s}{\partial t} + \rho u \frac{\partial Y_s}{\partial x} = -\frac{\partial j_s}{\partial x} + M_s \dot{\omega}_s \tag{1}$$

$$\rho c_p \frac{\partial T}{\partial t} + \rho u c_p \frac{\partial T}{\partial x} = \frac{\partial p}{\partial t} - \frac{\partial q}{\partial x} - \sum_s j_s \frac{\partial h_s}{\partial x} - \sum_s h_s M_s \dot{\omega}_s \tag{2}$$

with $s = 1, ..., n_s$ and n_s is the number of different species in the gas mixture. Here, ρ is the density, Y_s the mass fraction of species s, u is the velocity, j_s the species diffusive flux, M_s the molecular weight of species s, $\dot{\omega}_s$ the chemical source term of species s, c_p the heat capacity of the mixture at constant pressure, p the pressure, q the heat flux, and h_s the enthalpy of species s including the heats of formation. For the equation of state of a mixture of ideal gases we have

$$p = \rho T \sum_s Y_s R_s \tag{3}$$

with R_s denoting the gas constant of species s.

In the zero-Mach-number limit the thermodynamic pressure p is spatially constant. In this case, a divergence constraint on the velocity can be derived from the energy equation [11]:

$$\frac{\partial u}{\partial x} = -\frac{1}{\gamma p}\frac{dp}{dt} + \Psi \tag{4}$$

where γ is the ratio of specific heats and Ψ is given by Eq. (5) as

$$\Psi = -\frac{1}{\rho c_p T}\left(\frac{\partial q}{\partial x} + \sum_s j_s \frac{\partial h_s}{\partial x}\right) - \frac{1}{\rho}\sum_s \left(\frac{M}{M_s}\frac{\partial j_s}{\partial x}\right) + \frac{1}{\rho}\sum_s \left(\frac{M}{M_s} - \frac{h_s}{c_p T}\right) M_s \dot{\omega}_s. \quad (5)$$

Here M denotes the mean molecular weight of the mixture.

Integrating Eq. (4) over the whole domain from $x = x_1$ to $x = x_1 + L$ gives a relation between the global pressure change and inflow and outflow velocities, u_1 and u_2,

$$\frac{dp}{dt} = \frac{\gamma p}{L}\left(\int_{x_1}^{x_1+L} \Psi dx - (u_1 - u_2)\right). \quad (6)$$

Note that the acoustic pressure, similar to the thermodynamic pressure, is only a function of time when the wave length is much larger than the domain considered. This enables us to explicitly prescribe the lhs of Eq. (6) via Eq. (7),

$$\frac{dp}{dt} = p'\omega cos(\omega t) \quad (7)$$

where p' is the amplitude of the pressure fluctuation.

The velocity u in Eqs. (1), (2) and (4) represents the flow velocity induced by dilatational effects due to compression, diffusion, and chemical reactions as given by (4).

The inflow boundary condition u_1 is continuously adapted so as to keep the flame structure inside the domain. Note that u_1 can be chosen arbitrarily since the problem is Galilean invariant. The outflow condition u_2 then is uniquely determined using Eq. (6).

The zero-Mach-number equations are solved numerically using standard second-order finite-difference discretization. The time integration of the stiff set of equations is performed using the most recent version of the DAE solver IDA of the SUNDIALS package [13].

Thermodynamic and transport properties as well as reaction rates are calculated using the C++ interface of the CANTERA software package [14].

3. Chemistry mechanism

In this study we use a propane-air combustion mechanism proposed in [15], that contains 177 reactions and 37 species. In order to study the correlation between OH* chemiluminescence and heat release, we add a description of the formation of the excited radical OH* and its de-excitation into OH, by collision with other molecules (quenching) and by spontaneous light emission (chemiluminescence). We combine the propane-air combustion mechanism with the OH* mechanism proposed by Hall and Petersen [16], then for comparison with the mechanism proposed by Kathrotia [17]. For convenience, we name the resulting chemical schemes PropaneAir-H and PropaneAir-K, respectively. The two mechanisms differ only in the OH* formation paths, and will be shown to give identical results for the OH* de-excitation by chemiluminescence. In both cases we used the thermodynamical and transport properties of OH for the radical OH*, except for the formation enthalpy, which we make equal to the formation enthalpy of a molecule of OH, plus the energy of a photon with wavelength $\lambda = 307\ nm$ ($h^0_{OH^*} - h^0_{OH} = 93.5\ kcal/mol$).

4. Results

We first present the results of the numerical simulations for propane, discuss our validation of the numerical results and compare them to experimental measurements. Then later in section 4.4 and 4.5 we recapitulate important results from [10] for methane and hydrogen flames respectively. Finally in section 4.6 we give an overall comparison of the behavior of the three kinds of flames.

4.1. Propane numerical results

As a preliminary test, in Figure 2 we compare normalized heat release rate and OH* chemiluminescence response to static adiabatic pressure variations. Here we show the evolution of the heat release rate and OH* chemiluminescence obtained when a stationary planar lean propane flame ($\phi = 0.625$, $p = 1\ atm$, $T_u = 300\ K$) is submitted to static adiabatic compression. Note that the plotted results are normalized by their values at 1 atm. We find that the heat release rate increases with pressure, that is, it is in phase with pressure, while the OH* chemiluminescence intensity decreases with pressure, that is, it is out of phase with pressure. This test should correspond to the zero frequency limit of the unsteady response; accordingly the phase shift for heat release in the limit $\omega\tau_f = 0$ should tend to zero, while for OH* it should tend towards π, phase opposition.

Next, several simulations of a propane/air planar premixed flame oscillating under acoustic waves were conducted. A visualization of the oscillating flame response for two simulations, corresponding to frequencies 100 Hz and 1000 Hz is presented in Figures 3 through 5. In the figures the total, spatially integrated, OH* chemiluminescence emission rate and the heat release rate oscillations are plotted. Also included are the pressure fluctuations at the domain inlet (equivalent to the pressure fluctuations at the flame position, as the pressure is constant in the computational domain). Figures 3 and 4 are plotted for the PropaneAir-H mechanism while Figure 5 is plotted for the PropaneAir-K mechanism.

From the figures we see that the heat release and the OH* chemiluminescence emission rates have similar responses in amplitude to perturbation

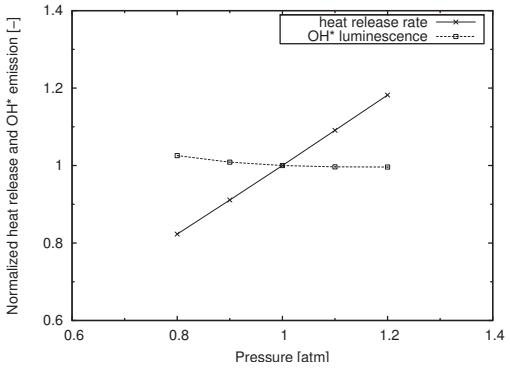

Figure 2. Heat release rate and OH* chemiluminescence, normalized by their values at $p = 1\ atm$, of a lean propane flame for adiabatic changes in static pressure. Flames are computed using the PropaneAir-H chemical mechanism.

and that with increasing frequency the amplitudes increase. For acoustic waves of frequency 100 Hz, the chemiluminescence response is in advance of the heat release rate and both are well in advance of the forcing pressure signal. For the acoustic waves of frequency 1000 Hz, the heat release rate and the chemiluminescence response signals are approximately in phase; with the chemiluminescence response slightly in advance of the forcing pressure signal, while the heat release is in slight delay of the forcing pressure signal.

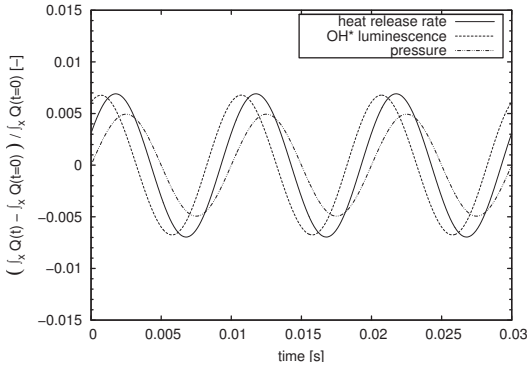

Figure 3. Integrated heat release rate and OH* chemiluminescence intensity oscillations compared to the forcing pressure at frequency 100 Hz. Mechanism used is PropaneAir-H.

This behavior can be observed for the full range of forcing frequencies. In Figure 6 we plotted the amplitude gain and in Figure 7 the phase shift corresponding to the total heat release rate and the total OH* chemiluminescence emission rate for forcing frequencies from 10 to 5000 Hz. The amplitude gain and phase shift are extracted

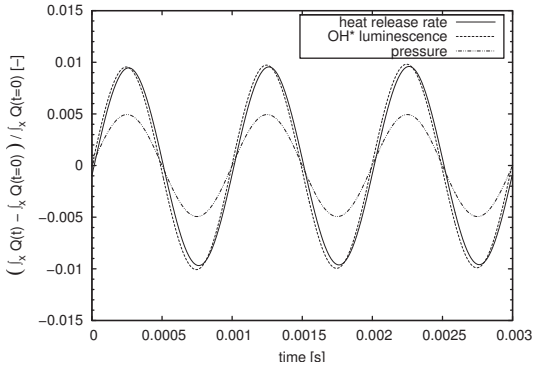

Figure 4. Integrated heat release rate and OH* chemiluminescence intensity oscillations compared to the forcing pressure at frequency 1000 Hz. Mechanism used is PropaneAir-H.

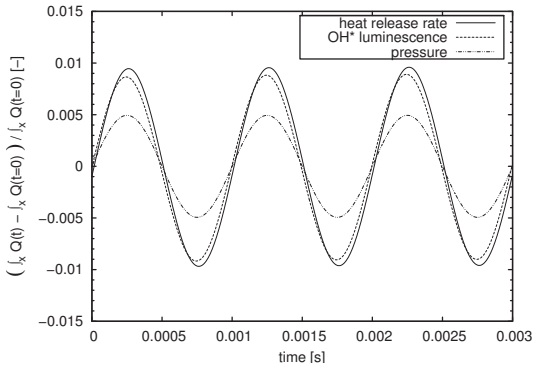

Figure 5. Integrated heat release rate and OH* chemiluminescence intensity oscillations compared to the forcing pressure at frequency 1000 Hz. Mechanism used is PropaneAir-K.

from the spatially integrated heat release (or OH* chemiluminescence reaction rate) signals Q' or light intensity I'. The amplitudes are normalized with respect to their mean values Q_{mean} and I_{mean} and then also with the amplitude of pressure fluctuations measured with ρc^2, to reproduce the normalization in [10]. The phase shift is measured as the advance or delay with respect to the pressure forcing and is given in units of π. Positive values indicate phase advance, and a value of 1 corresponds to phase opposition. Also included in the plot are the experimental measurements of [10].

4.2. Propane numerical results validation

4.2.1. Laminar flame speed

Solutions start from a converged stationary laminar lean ($\phi = 0.625$) propane flame structure at pressure 1 atm. For this configuration, the laminar flame speed obtained was 0.171 m/s. This flame speed is confirmed by experiments to within 7

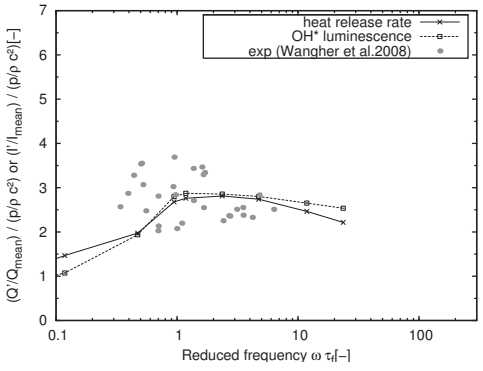

Figure 6. Amplitude gain for the integral of the heat release rate and OH* emission oscillations compared to the forcing acoustic waves pressure for a lean propane flame.

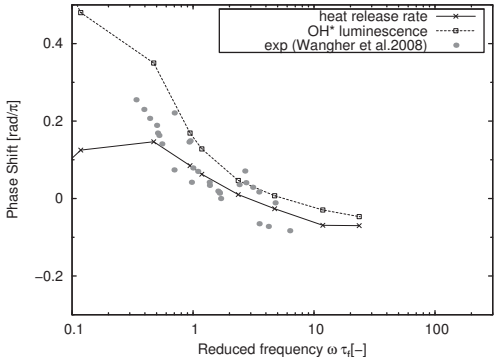

Figure 7. Phase change for the heat release rate and OH* emission compared to the forcing acoustic waves pressure for a lean propane flame.

percent in [18] and [19].

4.2.2. OH* mechanisms: Hall vs. Kathrotia

Comparing the PropaneAir-H and PropaneAir-K mechanism for the frequency presented in Figure 4 and 5 respectively, we see that the results are similar for amplitude and identical for phase shift. The OH* chemiluminescence emission rate of PropaneAir-K is slightly smaller with respect to that of PropaneAir-H. For simplicity, in Figure 6 and 7 only the results of the PropaneAir-H mechanism are plotted, but throughout the frequency range there is a close agreement between the PropaneAir-H and PropaneAir-K mechanisms.

4.3. Propane numerical results vs. experimental results

In Figure 6 the amplitudes of the heat release rate and OH* chemiluminescence intensity are plotted and are compared to the experimental measurements for OH* emission. We see that the OH* signal is in close agreement with the heat release rate response and both are in good agreement with the experimentally measured OH* chemiluminescence.

Figure 7 presents results for the phase shift of the heat release rate and the OH* chemiluminescence response, compared to experimental measurements. We see that the phase shift for both heat release rate and OH* chemiluminescence emission rate in the medium reduced frequency range of 1.0 to 10.0 are in close agreement with each other and also with the experimental results. The computed phase shift changes for both signals from positive values at low frequencies to negative values at higher frequencies. This is also the general trend in the experimental data, and the change occurs at similar values of the reduced frequency. At high frequencies, the phase of the heat release rate and OH* chemiluminescence seem to remain constant with increasing frequency. At low frequencies the heat release rate and OH* chemiluminescence diverge from each other. We expect the heat release rate to converge to 0 and the OH* chemiluminescence to converge to 1 at the limit of $\omega\tau_f = 0$ as per our test in Figure 2. The phase shift at low and high frequencies are not validated by experiments, as they do not cover this frequency range.

4.4. Methane flame results

We now recapitulate important results for the lean methane flame ($\phi = 0.625$, $p = 1\ atm$, $T_u = 300\ K$) presented in [10], simulated using the well establisehd GRI3.0 mechanism [20], with 53 reacting species and 325 reactions.

In Figure 8 we show the normalized heat release rate and OH* chemiluminescence response to static adiabatic pressure variations. We find that the heat release rate increases with pressure and temperature, while the OH* chemiluminescence intensity decreases. It is anticipated that this opposed behavior of the heat release and OH* signals will be recovered in the low frequency limit in the study of the unsteady response to adiabatic pressure waves.

In Figure 9, the amplitudes of the heat release rate and OH* chemiluminescence intensity obtained in the simulations are compared to experiments, and it is shown that both are comparable in magnitude to measurements.

As shown in Figure 10, the computed phase shift changes for both signals from positive values at low frequencies to negative values at higher frequencies. This is also the general trend in the experimental data, and the change occurs at similar values of the reduced frequency. In the low frequency range however the heat release and the OH* signal diverge from each other, the heat release signal showing a maximum phase shift of about $\pi/10$ and the OH* signal a maximum value close to 0.4π. The phase shift of the computed OH* signal follows more closely the slope of the experimental values.

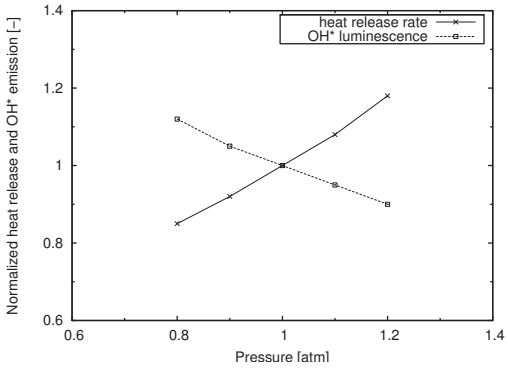

Figure 8. Heat release rate and OH* chemiluminescence, normalized by their values at $p = 1$ *atm*, of a lean methane flame for adiabatic changes in static pressure.

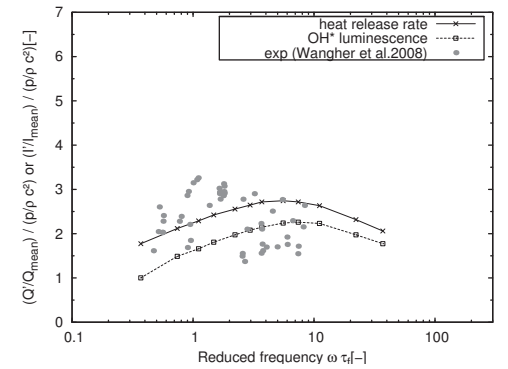

Figure 9. Amplitude gain for the integral of the heat release rate and OH* emission oscillations compared to the forcing acoustic waves pressure for a lean methane flame.

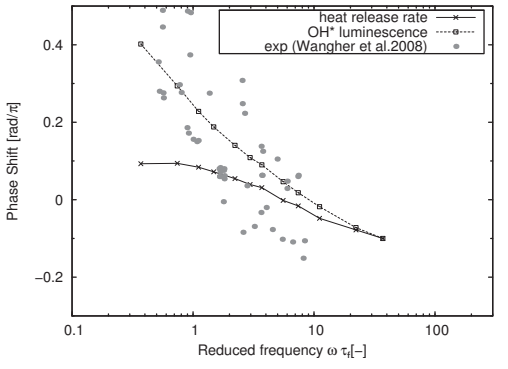

Figure 10. Phase change for the heat release rate and OH* emission compared to the forcing acoustic waves pressure for a lean methane flame.

4.5. Hydrogen flame results

Next we show results for the rich diluted hydrogen flame ($\phi = 1.15$, $p = 1$ *atm*, $T_u = 300$ *K*) presented in [10], simulated using the San Diego scheme with 21 reactions, publised by Saxena and Williams in 2006 [21].

In Figure 11 we show the normalized heat release rate and OH* chemiluminescence response to static adiabatic pressure variations. The figure shows that in the zero frequency limit of the unsteady response, the heat release rate and OH* chemiluminescence rate increase with pressure.

The amplitudes of the responses given by the simulations are of the order of magnitude of the experimental measurements, as shown in Figure 10. However, the OH* emission signal is stronger than the heat release signal, with a predicted amplitude closer to experimental measurements.

The phase response of the heat release and chemiluminescence signals are similar, and close to the experimental measurements of OH*, with a positive phase shift at low frequencies and a negative shift at high frequencies. Only at reduced frequencies below 1 does there seem to be a divergence between the heat release rate the the OH* signal. However, as per our test in Figure 11 we expect the two signals to converge at the limit $\omega\tau_f = 0$.

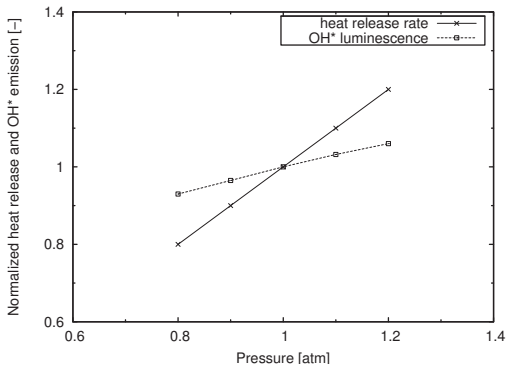

Figure 11. Heat release rate and OH* chemiluminescence, normalized by their values at $p = 1$ *atm*, of a rich hydrogen flame for adiabatic changes in static pressure.

4.6. Hydrogen, methane, and propane results compared

In this section we compare important simulation results for the behavior of the heat release rate and OH* chemiluminescence. In the static adiabatic pressure test, we saw that for propane and methane the two signals are out of phase, while for hydrogen it is in phase. In this simple test we see already a different behavior of the OH* chemiluminescence and heat release for different flames.

For all three flames the OH* chemiluminescence is in good agreement with experimental results, however OH* does not always correlate well to heat

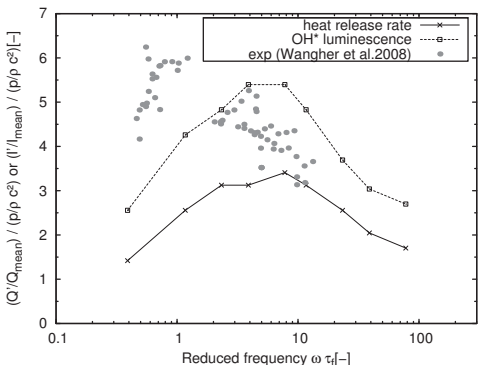

Figure 12. Amplitude gain for the integral of the heat release rate and OH* emission oscillations compared to the forcing acoustic waves pressure for a rich hydrogen flame.

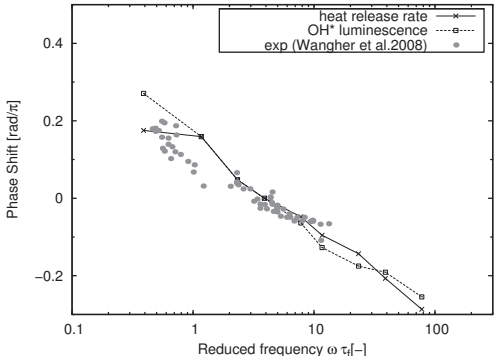

Figure 13. Phase change for the heat release rate and OH* emission compared to the forcing acoustic waves pressure for a rich hydrogen flame.

release. For propane, the correlation is best, with heat release overlapping the OH* chemiluminescence in the medium reduced frequencies range of 1 to 10. For methane, heat release is larger than the OH* chemiluminescence. And for hydrogen, heat release is less than the OH* chemiluminescence.

For phase shift, in the medium reduced frequency range of 1 to 10, the correlation between heat release rate, OH* chemiluminescence and experimental measurements for all three flames is quite good. However, for propane and methane, out of this frequency range the correlation tends to weaken. In the case of hydrogen, heat release rate and OH* chemiluminescence are in strong agreement through out the frequency range simulated.

5. Conclusions

In order to study the correlation between heat release and OH* chemiluminescence, simulations for propane, methane, and hydrogen flames were conducted and compared to experimental measurements of OH* light emission. Two different chemical models for OH* formation and de-excitation rates were used [16, 17], together with well validated chemical kinetic models for hydrogen [21], propane [15], and methane chemistry [20]. There is a relatively good agreement between experiments and numerical simulations, and the differences between heat release and OH* chemiluminescence fluctuations are highlighted.

For propane flames, the chemiluminescence amplitude response of the OH* radical is in accordance with experimental measurements and with the heat release response at acoustic forcing frequencies. For phase response, in the middle frequency range, $1 \lesssim \omega\tau_f \lesssim 10$, the agreement between experiments, OH* radicals and heat release is quite good. However, in the low frequency range, the phase of the heat release tends towards zero, while the phase of the OH* radicals tends towards phase opposition.

Concerning methane flames, the chemiluminescence response of the OH* radical tends to underestimate the heat release response at acoustic forcing frequencies. The phase response of OH* emission from methane flames is radically different from the heat release response at low frequency. The latter is in phase with pressure at low frequency, becomes slightly positive for $\omega\tau_f \lesssim 1$ and negative for $\omega\tau_f \gtrsim 1$. The phase of chemiluminescence follows the heat release for $\omega\tau_f \gtrsim 1$ but tends to phase opposition at low frequency.

The response of the OH* radical in hydrogen flames is stronger than the heat release response, in accordance with experimental measurements, and the phase responses differ only in the low frequency range. This implies, contrary to the methane flame, that the use of the OH* emission as a diagnostic tool would overestimate the source term in investigations of thermo acoustic instability of hydrogen combustion when the pressure driven interaction is dominant. However, the phase information is quite reliable over the whole frequency range.

The results suggest that the OH* chemiluminescence intensity cannot be granted to be directly proportional to the unsteady heat release rate, at least when only the direct pressure effects are involved. Both numerical simulations and experimental measurements confirm this behavior, the numerical simulation appearing as a useful tool for determining the relation between OH* chemiluminescence and heat release rate.

References

[1] Candel, S. 2002 “Combustion dynamics and control: Progress and challenges”. *Proc. Combust. Inst.*, Vol. 29, pp. 1–28.

[2] Wu, X., Wang, M., Moin, P., and Peters, N. 2003 “Combustion instability due to the nonlinear interaction between sound and flame”. *J. Fluid Mech.*, Vol. 497, pp. 23–53.

[3] Higgins, B., McQuay, M. Q., Lacas, F., Rolon, J., Darabiha, N., and Candel, S. 2001 “Systematic measurements of OH chemiluminescence for fuel-lean, high-pressure, premixed, laminar flames”. *Fuel*, Vol. 80, pp. 67–74.

[4] Docquier, N., Belhalfaoui, S., Lacas, F., Darabiha, N., and Rolon, C. 2000 “Experimental and numerical study of chemiluminescence in methane/air high-pressure flames for active control applications”. *Proc. Combust. Inst.*, Vol. 28, pp. 1765–1774.

[5] Hardalupas, Y. and Orain, M. 2004 “Local measurements of the time-dependent heat release rate and equivalence ratio using chemiluminescent emission from a flame”. *Combust. Flame*, Vol. 139, pp. 188–207.

[6] Kojima, J., Ikeda, Y., and Nakajima, T. 2000 *Proc. Combust. Inst.*, Vol. 28, pp. 1757–1764.

[7] Lee, J. and Santavicca, D. 2003 “Experimental Diagnostics for the study of Combustion Instabilities in Lean Premixed Combustors”. *J. Propulsion and Power*, Vol. 19, pp. 735–750.

[8] Wangher, A., Searby, G., and Quinard, J. 2008 “Experimental investigation of the unsteady pressure response of premixed flame fronts to acoustic pressure waves”. *Combust. Flame*, Vol. 154, pp. 310–318.

[9] Wangher, A. 2009 “Réponse de flammes de prémélange á des oscillations de pression”. Ph.D. thesis, University of Aix-Marseille.

[10] Jiménez, C., Quinard, J., Graña Otero, J., Schmidt, H., and Searby, G. 2012 “Unsteady response of hydrogen and methane flames to pressure waves”. *Combust. Flame*, Vol. 159, pp. 1894–1908.

[11] Klein, R. 1995 “Semi-implicit extension of a godunov-type scheme based on low mach number asymptotics I: One dimensional flow”. *J. Comput. Phys.*, Vol. 121, pp. 213–237.

[12] Oevermann, M., Schmidt, H., and Kerstein, A. 2008 “Investigation of autoignition under thermal stratification using linear eddy modeling”. *Combust. Flame*, Vol. 155, pp. 370–379.

[13] Hindmarsch, A. 2004 “Sundials: Suite of Nonlinear and Differential/algebraic Equation Solvers”. *Technial Report*, Vol. UCRL-JRNL-200037, Lawrence Livermore National Laboratory.

[14] Godwin, D. “http://www.cantera.org”.

[15] Petrova, M. and Williams, F. 2006 “A small detailed chemical-kinetic mechanism for hydrocarbon combustion”. *Combust. Flame*, Vol. 144, pp. 526–544.

[16] Hall, J. and Petersen, E. 2006 *Int. J. Chem. Kin*, Vol. 38, pp. 714–724.

[17] Kathrotia, T., Riedel, U., and Warnatz, J. 2009 *Proc. Eur. Combust. Meet.*.

[18] Jomaas, G., Zehng, X., Zhu, D., and Law, C. 2005 “Esperimental determination of counterflow ignition temperatures and laminar flame speeds of C2-C3 hydrocarbons at atmospheric and elevated pressures.”. *Proc. Combust. Inst.*, Vol. 30, pp. 193–200.

[19] Lowry, W., Vries, J., Krejci, M., Petersen, E., Serinyel, Z., Metcalfe, W., Curran, H., and Bourque, G. 2011 “Laminar Flame speed measurements and Modeling of Pure Alkanes and Alkane Blends at Elevated Pressues”. *J. Eng. Gas Turbines Power*, Vol. 133, p. 091501.

[20] Smith, S., et al. 2000 “http://www.me.berkeley.edu/gri-mech/version30 /text30.html”.

[21] University of California at San Diego, C. R. G. 2011 “http://web.eng.ucsd.edu/mae/groups/combustion/ mechanism.html”. *San Diego Mechanism*.

Conference on Modelling Fluid Flow (CMFF'12)
The 15th International Conference on Fluid Flow Technologies
Budapest, Hungary, September 4-9, 2012

NUMERICAL SIMULATION OF HTPB HYBRID ROCKET COMBUSTION WITH REDUCED-ORDER KINETICS AND REGRESSION MODELLING

José Antonio MORÍÑIGO[1], José HERMIDA-QUESADA[2]

[1] Department of Space Programmes, National Institute for Aerospace Technology, email: morignigoja@inta.es
[2] Department of Aerodynamics and Propulsion, National Institute for Aerospace Technology
Ctra. Ajalvir km.4, Torrejón de Ardoz, 28850 Madrid, Spain

ABSTRACT

The present work summarizes the unsteady Reynolds Averaged Navier-Stokes reacting flow axisymmetric simulations conducted with the solver Fluent and simplified two-step finite-rate kinetics for three thermal pyrolysis models with regression modelling of solid-fuel Hydroxyl Terminated PolyButadiene (HTPB). The fuel burns in a gaseous oxidizer stream at conditions corresponding to the small hybrid rocket motor manufactured for testing in the rocket test-stand at INTA and which comprises the igniter-chamber-nozzle assembly. The pyrolysis models take into account the effects of fuel regression rate upon the flowfield, set as a local boundary condition at the HTPB grain surface in the motor chamber. A description of the models and comparison of the numerical results obtained using the reduced-order kinetic mechanism in the three cases considered is addressed.

Keywords: HTPB pyrolysis, hybrid rocket motors, reduced-order kinetics.

NOMENCLATURE

C_p	[*J/kg-K-mol*]	heat capacity
E_a	[*J/kg-K-mol*]	activation energy
K	[s^{-1}]	Arrhenius
k	[*w/m-K*]	thermal conductivity
p	[*Pa*]	pressure
R_i	[-]	chemical reaction index
r_b	[*m/s*]	regression rate
t	[*s*]	time
T	[*K*]	temperature
x,n	[*m*]	axial, normal direction
x_i	[gr/cm^3]	mass fraction of species *i*
ρ	[kg/m^3]	density

Subscripts and Superscripts

f	adiabatic flame
g	gas side
i	index of chemical species
in	inlet, stagnation
f,b	forward, backward
p	fuel (solid propellant) side
s	surface
$-\infty$	far from surface

Acronyms

$1,3C_4H_6$	1,3-Butadiene
1,2,3D	one, two, three-dimensional
CD	computational domain
GOX	gaseous oxygen
GH2	gaseous hydrogen
HTPB	Hydroxyl Terminated Poly-Butadiene
RANS	Reynolds Averaged Navier-Stokes
SRM	Solid Rocket Motor

1. INTRODUCTION

Simplicity, lower demanding cost, shorter testing and design, ease of scalability and robustness inherent to hybrid rocket propulsion systems constitute essential factors that boost the interest of this technology in tactical and space applications, like sounding rockets and mini and micro-launcher vehicles. A test-stand for hot fire testing of small hybrid rocket motors operating with gaseous oxygen and hydrogen during the ignition phase has been developed in the recent years at INTA [1] for the experimental characterization and assessment of hybrid rocket propellant combustion, flow transients and motor performance for different candidates of solid-fuel, with the main focus on the commonly used fuels Hydroxyl Terminated Poly-Butadiene (HTPB), Glycidyle Azide Polymer and paraffin-based liquefying fuels [2,3,4]. A small hybrid motor filled with HTPB-based fuel, which provides a moderate fuel regression rate, has been manufactured and instrumented for the intended initial tests [1] (see Figure 1). In addition, to guide the tests and perform numerical characterization, 2D and 3D non-steady CFD simulations of reacting flow are being conducted for the igniter-chamber-nozzle assembly of the manufactured specimen. The present work summarizes some of the 2D results corresponding to the modelling of the HTPB-fuel

pyrolysis and regression with hot oxidizer stream passing through the motor fuel port, heating its surface. The paper is organized as follows: section 2 describes the numerical approach. The reduced-order kinetics is presented in section 3; the description of HTPB-fuel regression modelling and boundary conditions prescribed at the HTPB-fuel is detailed. Section 4 addresses the comparison of flowfields obtained with the three pyrolysis models considered. Finally some conclusions are given.

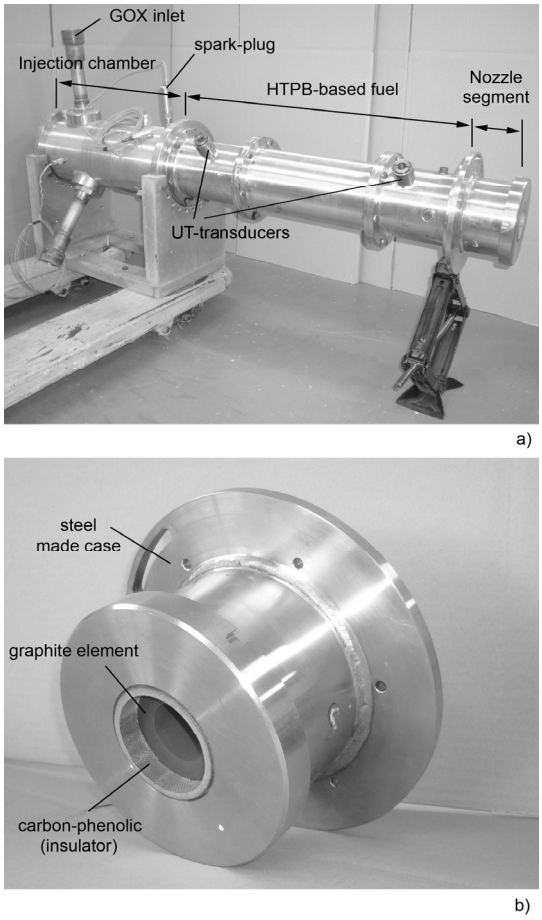

Figure 1. Hybrid motor developed at INTA: a) assembled elements and b) detail of the graphite-made nozzle segment

2. NUMERICAL APPROACH

2.1. Solver

Non-steady RANS axisymmetric simulations with the governing equations implemented in Fluent solver [5] coupled with the additional transport equations for combustion species and turbulence in the gas-phase zone have been carried out. A simplified finite-rate (reduced-order) kinetics mechanism involving two reaction steps for the HTPB combustion, which treats 1,3-Butadiene as the main product of the HTPB pyrolysis, is used to simulate the combustion of gaseous products.

Description of the chemical submodel and its selection is detailed in the next section. The solver follows a coupled density-based formulation with dual-time stepping time-accurate integration of the non-steady RANS equations with upwind 2nd-order AUSM-type scheme for inviscid fluxes and central differences for viscous terms. Turbulence effects are modelled with the two-equation Shear Stress Transport k-ω closure. Reaction modelling is based on the generalized finite-rate formulation with the eddy dissipation concept model, which incorporates multi-step Arrhenius-type kinetics into turbulent flows and it is suitable for both premixed and non-premixed combustion. It assumes different chemical rates controlled by dissipative proceses (turbulent mixing, difussion), then hydrocarbons dominant kinetics can be accounted for with reasonable computational cost in 3D simulations.

2.2. Computational Domain

Grid independence numerical results have been obtained and the adequate grid density identified. In the present study, two grids tailored for corresponding computational domains have been built: CD1 of 128,897cells, which comprises the entire region of the motor assembly (depicted in Figure 2). The grid cells along the wall are sized stretched to fulfill the turbulence model constrain $y^+<\sim 1$. Domain CD1 has been used for axisymmetric non-steady RANS simulations of the combustion of an oxygen-hydrogen lean-mixture introduced in the injection chamber and modelled with a seven-step reduced-order chemistry [6].

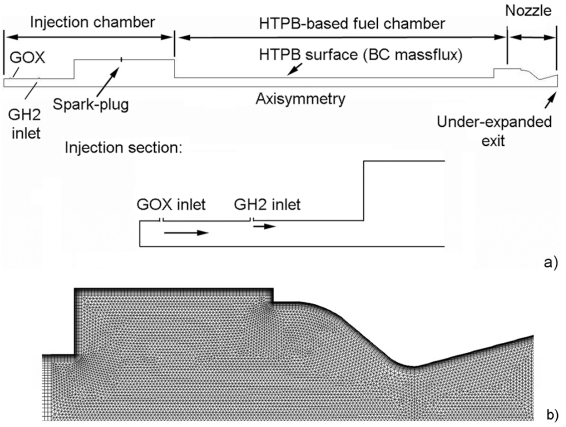

Figure 2. Layout of a) computational domain (CD1) assumed axisymmetric and b) grid at the aft-end of the HTPB-fuel chamber and nozzle region, for O_2 molar fraction characterization

The ignition and subsequent combustion process which results, increases the temperature of the oxygen-rich inflow gases entering the HTPB-fuel chamber, thus provoking the initial ignition of the solid-fuel and flame propagation along the port. Simulation results obtained for various reduced-

order oxygen-hydrogen kinetics, control of mixture ratio at injection and spark-plug ignition-induced models are detailed in [6] and have served to estimate the oxygen excess available in the gasflow arriving at the HTPB port.

And domain CD2 of 78,755 cells and $y^+ <\sim 1$, shown in Figure 3: shortened computational domain (injection chamber removed) for the development and testing of the pyrolysis and regression rate BCs prescribed at the HTPB-fuel surface. Combustion simulations for HTPB-GOX have been conducted prescribing a steady stream of gaseous products (hot GOX BC-inlet) with O_2 mass fraction estimated out of the steady state computed in the H_2-O_2 simulations in CD1. The geometrical modification visible at the fore-end of the HTPB-fuel chamber in CD2 is intended to avoid the appearance of recirculating flow near the hot oxygen inlet in the simulations. HTPB-fuel surface modelling and formulation of the BCs is presented in more detail in subsection 3.3. The results obtained with CD2 are summarized in section 4.

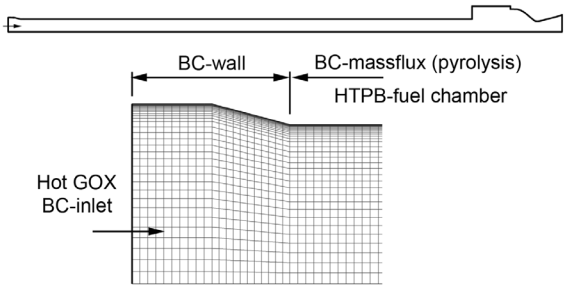

Figure 3. Schematic of the HTPB combustion chamber & nozzle computational domain (CD2) with HTPB fore-end detail (pyrolysis massflux and GOX inlet BCs indicated) for HTPB-fuel BC modelling

3. REACTIVE FLOW MODELLING

3.1. Chemical Kinetics Modelling

Detailed 1,3-Butadiene (C_4H_6) kinetics is described by a complex mechanism typically comprising more than 50 chemical species and over 600 elementary reactions for the gas phase according to [8], clearly too demanding for engineering CFD simulations, hence fewer steps are needed. A reasonable simplified reduced chemistry is proposed and investigated for HTPB-GOX combustion to carry out approximate non-steady numerical simulations.

Experimental characterization of gaseous composition of HTPB-fuel pyrolysis, that is solid-to-gas phase change accompanied by a chemical change in the in-depth near-surface region, shows that product concentrations depend strongly on temperature and there exists two main pyrolysis regimes, each with a dominant species dependent of a threshold temperature T_s at the HTPB grain [9]:

- $T_s < 770K$: 1,3-Butadiene (C_4H_6) appears as major product of pyrolysis plus small concentrations of other light hydrocarbons.
- $T_s > 1170K$: Ethene (C_2H_4) is the major product of pyrolysis plus small concentrations of other light hydrocarbons (only 2% turns to be C_4H_6).

Table 1 summarizes the major species of HTPB pyrolysis as a function of the solid-fuel surface temperature.

In addition to the major species concentration driven by T_s, judgement about which simplified reduced-order kinetics is set in the simulations results from CFD comparison of both 1,3-Butadiene and Ethene mechanisms with a reference kinetic. Because one-step (global reaction) mechanisms for the HTPB-fuel pyrolysis overestimate by far the adiabatic flame temperature, providing too inaccurate results for any realistic application, two-step mechanisms have been assessed and their prediction compared for premixed combustion against a detailed kinetic mechanism of C_4H_6 solved with the SENKIN (CHEMKIN®) code [10] for GOX concentrations in the range of interest (stoichoimetric and lean) [7] to mimic the interval of lean fuel conditions, typical of hybrid SRMs.

Table 1. **Major species in the HTPB pyrolysis, molar concentrations (Chiaverini *et al.*, [3]) at various temperatures.**

	Temperature (ºC):			
Species:	500	600	700	800
Ethene, C_2H_4	–	12.6	14.5	29.9
Propene, C_3H_6	–	4.56	7.38	11.9
1,3-Butadiene, C_4H_6	78.7	53.4	44.7	11.1
3-Pentene-1-Yne	–	11.3	18.4	14.3
Cyclopentene, C_5H_8	–	3.92	–	–
Benzene, C_6H_6	–	4.89	10.4	13.6
Toluene, C_7H_8	–	–	4.66	5.22
4-VynilCyclohexene	21.3	9.33	–	–
Styrene, C_8H_8	–	–	–	2.49
Indene, C_9H_8	–	–	–	6.04
Naphthalene, $C_{10}H_8$	–	–	–	5.43

Both simplified chemical-kinetic mechanisms involve five chemical species, namely: the major product of pyrolysis (1,3-C_4H_6 or C_4H_6, depending on the case), O_2, CO, CO_2 and H_2O. The mechanisms correspond to the quasi-global kinetic proposed in [11] according to the following two overall reactions:

- HTPB pyrolysed as 1,3-Butadiene mechanism:

R1: $1,3\text{-}C_4H_6 + 3.5O_2 \rightarrow 4CO + 3H_2O$

R2: $CO + 1/2O_2 \leftrightarrow CO_2$

Table 2 Reduced-order two-step rate parameters of Butadiene combustion.

$K = AT^n exp\{-E_a/R_uT\}[Fuel]^a[Oxidizer]^b$							
	A_f (1)	$E_{a,f}$	A_k	$E_{a,k}$	n	a	b
R1	1.35e10	30	0	0	0	1	1
R2	2.0e6	1.2e3	8.1e7	7.72e4	0	1	0.5

(1) $A,[m,kmole,s];E_a,kcal/kmole,R_u$:1.987$kcal/mole\text{-}K$
f: forward reaction, k: backward reaction.

where the empirical parameters of the Arrhenius-type rates are taken from [2] with the criteria established in [11]. Data for the formation reaction of CO_2 are taken from the recent investigation [12]. Rate parameters for reverse steps are to be obtained from those of the forward steps by application of chemical-equilibrium results, built by the solver. Imposition a=b=1 depart from the original values (a=0.1, b=1.65) in the used formulation to mitigate the numerical instability that may be caused by too high butadiene reaction rate in the flow regions with small fuel concentration.

- HTPB pyrolysed as Ethene mechanism:

R3: $C_2H_4 + 2O_2 \rightarrow 2CO + 2H_2O$

R4: $CO + 1/2O_2 \leftrightarrow CO_2$

Table 3 Reduced-order two-step rate parameter of Ethene combustion.

$K = AT^n exp\{-E_a/R_uT\}[Fuel]^a[Oxidizer]^b$							
	A_f (1)	$E_{a,f}$	A_k	$E_{a,k}$	n	a	b
R3	1.09e9	30	0	0	0	1	1
R4	2.0e6	1.2e3	8.1e7	7.72e4	0	1	0.5

(1) $A,[m,kmole,s];E_a,kcal/kmole,R_u$:1.987$kcal/mole\text{-}K$
f: forward reaction, k: backward reaction.

(empirical parameters taken from [9]). Analogous to the butadiene case, a=b=1; the pre-factor A_f in R3 has been lowered from 2.0e12 to 1.09e9. This recalibration of A_f according to [9] yields the same reaction rate as predicted in [11] over the range of fuel and oxidizer of concern. From the comparison against detailed kinetic data, the first two-step mechanism (Table 2) provides a closer estimation of the adiabatic wall temperature for fuel-lean conditions, hence it is the one prefered and used in the CFD simulations.

3.2. HTPB Pyrolysis and Regression

Data available from lab-scale hybrid motors testing have been used to determine a local, instantaneous, average regression rate law of the HTPB – GOX burning as a function of the local, instantaneous surface fuel grain temperature T_s [13], which is a more accurate approach than simply using average regression rates based on correlating global averages of fuel regression rate versus flowing mass flux inside the motor (which are more sensitive to scaling effects, port geometry or the appearance of recirculation regions driven by the GOX inflow, impingement on the HTPB grain, or significant radiation heat flux, and tend to produce large errors in the predictions). The regression rate is modelled in a semi-empirical fashion with a local Arrhenius form fitted with data of hybrid motor tests [9], plotted in Figure 4 versus the reciprocal surface temperature $1/T_s$ (in K^{-1}) and corresponds to the equation:

$$r_b = A\, exp\{-E_a/R_u/T_s\} \quad (1)$$

The Arrhenius parameters resulting of curve fitting are indicated in the Figure 4. Two regions are identified:

- Surface temperature above 722K results to be: E_a=4.91$kcal/mole$, A=11.04mm/s.
- At surface temperature below 722K the trend changes to: E_a=13.35$kcal/mole$, A=3960mm/s.

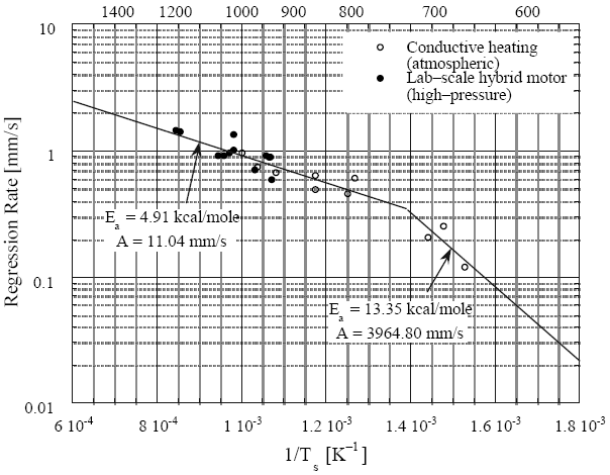

Figure 4. Regression rate of pure HTPB fuel (no additives) as function of surface temperature T_s

The experiments reported in [13] revel no significant effect of chamber pressure on the Arrhenius law parameters for the temperature interval swept in the tests, which includes the expected range of practical application for hybrid motors. The local T_s at each point of the grain surface results from the energy flux balance at the solid-fuel, being the total wall heat flux the sum of three contributions: convective heat flux, thermal radia-tion from the gas-phase combustion products and radiant heat flux from soot. The present study follows an incremental framework in the simulation complexity and in any case it does not include the

contribution of thermal radiation into the energy flux balance and regression process. Radiation can be seen as an ignition augmentation mechanism and a justification for not taking it into account in the present study is that radiative fluxes are rather independent of the flow rate and their effect may only be significant in motor operation with low convective heat fluxes (as at steady low flow rate firings or in the early stages of ignition). Furthermore, the medium to high operation pressure of the cases analyzed, in addition to the decreasing volume-to-surface ratio of the scale-down specimen (radiative fluxes are volumetric in nature), suggests a moderate to low contribution of radiation to the total wall heat flux.

3.3. Pyrolysis Boundary Condition

Three HTPB-fuel surface models consisting on an instantaneous, local pyrolysis regression (burning) rate law and surface temperature have been implemented at the gas-solid interface in the simulations. Figure 5 depicts a meridian section of the flame front over the HTPB grain in the chamber portion of the hybrid SRM, where the incoming stream with significant oxygen fraction and pyrolysis blowing rate $\rho_p r_b$ sustain the chemical reactions. One indirect effect of the gas blowing at the solid-gas interface is to block the convective heat transfer of the bulk flame; from the numerical standpoint, this increases the mechanical-thermal coupling near the grain surface in the simulations.

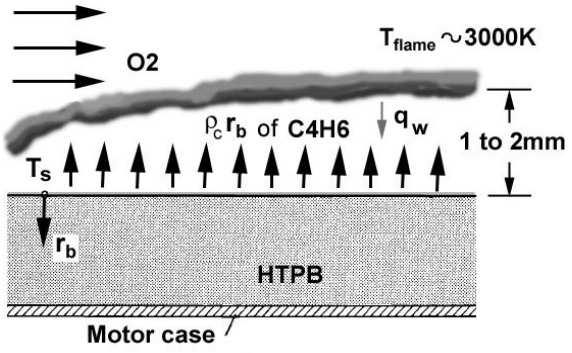

Figure 5. Layout of flow structure and flame front over the HTPB fuel grain and pyrolysis model notation

Three physical models at the solid-gas interface have been compared. They have been implemented as a set of boundary conditions which impose the local, instantaneous grain surface temperature T_s (efflux temperature) and massflux $\rho_p r_b$ following an Arrhenius-like pyrolysis relationship of the local, instantaneous regression rate Eqn. (1). Thus, the gas blowing of pyrolysed fuel is evaluated coupled with the local surface temperature modelled in three different ways:

1) Grain surface assumed adiabatic, hence $T_s = T_{cell\text{-}center}$ is imposed.

2) Assuming heat loss across the fuel grain (non-adiabatic, wall blowing) and considering the effect of wall blowing: pyrolysis massflux blocks the convective heat transfer to the grain. The model assumes 1D-heating, so it yields for the temperature profile

$$T(n) = T_{-\infty} + (T_s - T_{-\infty}) \exp\{-r_b n / D_p\} \quad (2)$$

where $T_{-\infty}$ refers to the conditions deep within the solid-fuel, $D_p = k_p/\rho_p C_p$ is the thermal diffusivity of the fuel slab, and n is the normal distance from the surface. Heat balance at the solid-gas interface leads to write the heat influx q_s at the gas phase as

$$q_s = -k_g \partial T/\partial n\big|_s = k_p/\delta_p (T_s - T_{-\infty}) \quad (3)$$

then

$$T_s = q_s \delta_p / k_p + T_{-\infty} = q_s / \rho_p r_p C_p + T_{-\infty} \quad (4)$$

being δ_p the thermal penetration depth (thickness of the preheat zone) in the condensed phase, which decreases as the burning rate increases, hence massflux $\rho_p r_p$ imparts a drop in T_s. Eqn. (4) provides the interfacial boundary condition for the surface temperature. The efflux of 1,3-Butadiene at the surface corresponds to a value of stagnation temperature $T_{in} \approx T_s$.

3) Solving the 1D non-steady heat conduction equation under the hypothesis of quasi-similarity of solution. The methodology follows the one reported in [14] by the Center for Simulation of Advanced Rockets (CSAR) of Illinois University, which permits to analyze transient and steady flows with solid-gas coupling in SRMs of 3D complex configurations. In this formulation 1D heat conduction into the solid-fuel is analogous to the preceeding method, that is

$$\frac{\partial T}{\partial t} = D_p \frac{\partial^2 T}{\partial n^2}, \; -\infty < n < 0, \; t > 0 \quad (5)$$

with the boundary and initial conditions

$$T(-\infty, t) = T_{-\infty}, \; k_p \partial T/\partial n(0, t) = -q_s(t)$$
$$T(0, t) = T_{-\infty} \quad (6)$$

The grain surface temperature is updated given the heat influx of gas heat convection solely at the gas phase. The model accounts for the time-delay of heating with its explicit time dependence according to the quasi-similarity expression proposed

$$T = T_{-\infty} + \sqrt{t}\, f(n/\sqrt{t}) \quad (7)$$

which assumes constant heat flux at n=0 (with n pointing into the gas) in strict sense, but it seems a reasonable approximation if the heat flux does not change too rapidly over time. From Eqns. (5) and (6) it reads

$$T = T_{-\infty} + C\eta\sqrt{t}\int_{-\infty}^{\eta} \frac{exp(-\eta^2/4D_p)}{\eta^2} d\eta \qquad (8)$$

where $\eta = n/\sqrt{t}$ and C is a constant determined from the flux condition at η=0. The heat flux is evaluated on the gas side at the solid-gas interface with

$$q_s = k_g \partial T/\partial n\big|_s \qquad (9)$$

And the wall temperature finally computed as

$$T_s(t) = T_{-\infty} + \frac{2q_s(t)}{k_p\sqrt{\pi/D_P}}\sqrt{t - t_0} \qquad (10)$$

where t_0 is an origin of time which controls the heat transfer to the propellant surface and which is set independently at each boundary cell using the criterion of reaching auto-ignition temperature (equal to 560K in the simulations with HTPB): each cell element is assumed to be instantaneously ignited once the auto-ignition temperature is locally surpassed and computed with Eqn. (10), thus more and more solid-fuel surface is heated up over time and flame spreading occurs.

The three methodologies deal with local BCs at the boundary cells, therefore a kind of combustion ignition and flame spreading is captured as the hot gas flows along the solid-fuel port. None of these models explicitly accounts for pressure effects which are only important at high mass fluxes.

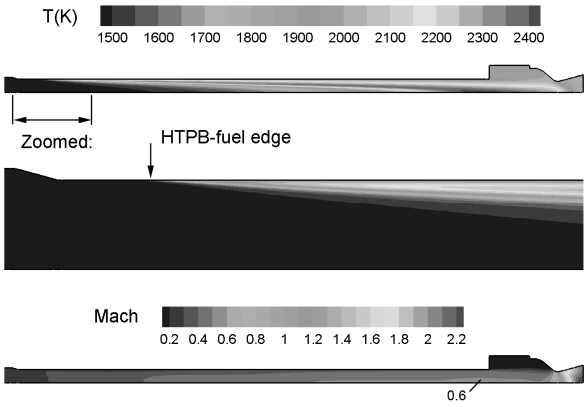

Figure 6. Temperature and Mach number map in the HTPB-fuel chamber after 200ms

4. RESULTS

The results summarize the assessment of the three BCs pyrolysis models set at the HTPB-fuel surface for the simulation of a reference burning transient of 200ms lasting with a uniform gas stream entering the fuel port, corresponding to the CD2 and gasflow conditions: $p_{t,in}$=3.71bar, $T_{t,in}$=1500K, x_{O2}=0.28, turbulence intensity of 10%. Monitorization of kinetic and thermal quantities reveals that quasi-steady state is attained after the initial ~20ms of transient time. Estimation of flame propagation time through the HTPB-fuel port ranges less than 6ms. The propagation of the flame core up to the nozzle throat points out to modify the geometry of the settle zone in the nozzle segment of future prototypes. This can be achieved by enlarging the subsonic portion of the nozzle segment, to drop the high heat-flux in the vicinity of the throat wall. It should be noted that the numerical setup of a rocket nozzle of this class enforces sub-expanded gas conditions (entirely supersonic flow at its exit section) to appear during the flow startup, which uncouple the development of the combustion process from the outside ambient in the simulations.

High subsonic Mach number develops near the rear-end of the HTPB-fuel chamber (see Fig. 6) caused by the slender fuel port and progressive incorporation of pyrolysis massflux to the stream of combustion gases.

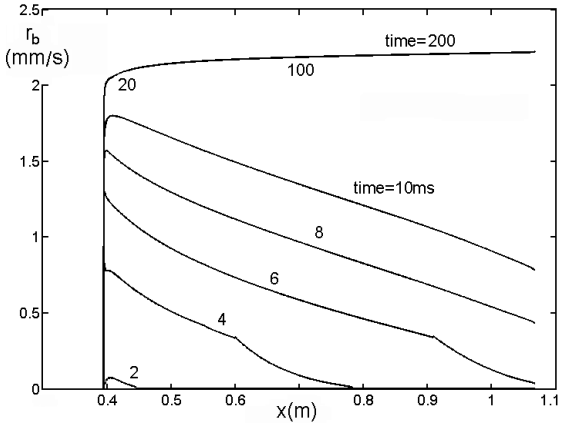

Figure 7. Time-evolving HTPB-fuel regression rate with 1D heat-conduction modelling

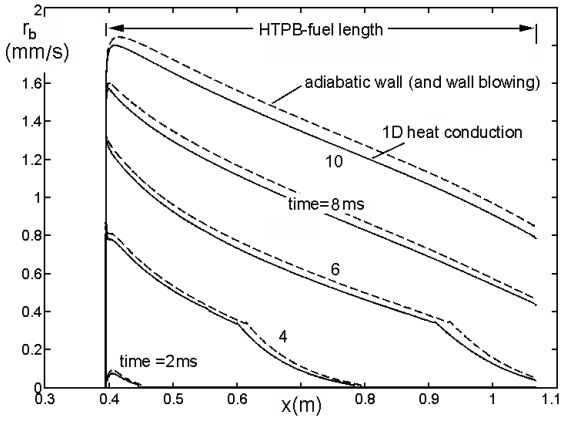

Figure 8. Regression rate at the initial instants of combustion, computed with three pyrolysis BCs

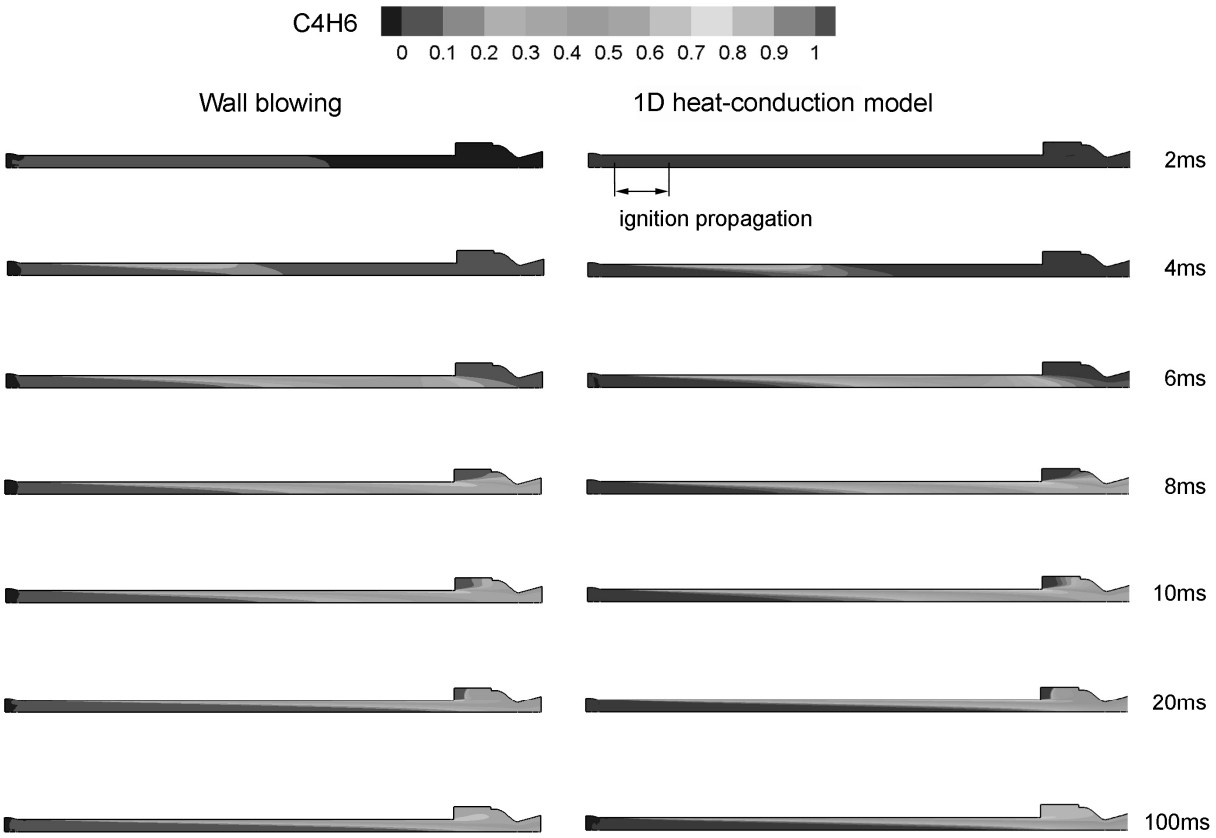

Figure 9. Time sequence of 1,3-Butadiene mass fraction for two BCs pyrolysis models

This behaviour also points out to some room of improvement of this part of the nozzle segment, hence to minimize the pressure losses due to the excess of velocity. Nevertheless, the gas acceleration enhances the convective heat-flux to the fuel surface, increasing the recession rate velocity with the axial station, which is a desirable property in hybrid motors.

This effect is visible in the quasi-steady state plots of r_b given in Figure 7, where differences over 10% in regression rate values are obtained between fore and rear ends of the HTPB-fuel block. During initial and intermediate combustion stages, the progressive flame spreading over the HTPB-fuel surface yields decreasing r_b profiles (see Figure 8). The inclusion of an explicit time-delay term in the 1D heat-conduction model makes the flame propagation rate slower over the fuel surface compared with the flame propagation provided by the other two pyrolysis models, as expected and here quantified. This delay is visible in the 1,3-Butadiene mass fraction sequence of snapshots given in Figure 9, where wall-blowing and 1D heat-conduction model pyrolysis models are compared side-by-side. Differences in the advancing front length of pyrolyzed mass fraction are discernible for the very first instants of the transient, corresponding to the hot stream with excess of oxygen passing through the fuel port Interestingly, comparison of wall-blowing model against adiabatic-wall pyrolysis model has revealed that the indirect blocking of gas blowing at the solid-gas interface onto the convective heat transfer of the bulk flame parts has a negligible effect with the inflow conditions considered in this study (hence only wall-blowing results are included in Figure 9). Albeit the simulation with the 1D heat-conduction pyrolysis model exhibits a slower transient increase of T_s in presence of the hot stream and flame spreading along the port, steady-state results reveal a very similar flowfield with the three pyrolysis models. This is explained because of the inclusion of a limiter to the maximum reachable T_s at the HTPB-fuel surface (set to 1400*K*) to avoid its rise over unphysical levels. It should be noticed that experimental values of T_s for HTPB-GOX combustion are typically bounded within the 900-1100*K* interval, well below the computed one. One cause of mismatch in the prediction may be atributted to the overestimation of the adiabatic temperature provided by the reduced-order kinetics model formulated for the 1,3-C_4H_6 gas products of the gaseous combustion. In particular and from the authors´ numerical comparison [7] using detailed kinetic models, an overestimation of temperatures within 15-20% may occur in the stoichiometric region of the flame in computations performed with the reduced-order modelling. That implies a higher

overall heat-flux to the wall, accordingly a net increase in T_s has sense.

5. CONCLUSIONS

Three approaches to hybrid motor pyrolysis and regression rate BCs modelling with application to non-steady RANS simulations of reactive flow with reduced-order kinetics, have been addressed and compared following an incremental methodology, and focusing the guidance of small hybrid motors design and tests. A preliminary assessment of their predictive capability and limitations is gathered in the current study prior to the short-term, more detailed comparison against experimental data from the manufactured specimens. Some guidelines to improve the next small-scale motors design are suggested from the simulations accomplished.

REFERENCES

[1] "Investigation of Hybrid Rocket Motors Applications", Report EIB/PLN/0463/022/INTA/96, 1996, ESTEC Contract: 1138/94/NL/FG.

[2] Chiaverini, M.J., 2007, "Review of Solid-fuel Regression", in *Fundamentals of Hybrid Rocket Combustion and Propulsion*, Progress in Astronautics and Aeronautics, AIAA, pp. 37-116.

[3] Chiaverini, M.J., Hartling, G.C., Lu, Y.C., Kuo, K.K., Peretz, A., Jones, H.S., Wygle, B.S., Arves, J.P., 1999, "Pyrolysis Behavior of Hybrid-Rocket Solid Fuels Under Rapid Heating Conditions", *J. Propulsion and Power*, Vol.15, Nº6, pp. 888-895.

[4] Evans, E., Boyer, E., Kuo K.K., Risha, G., Chiaverini, M., 2009, "Hybrid Rocket Investigations at Penn State University´s High Pressure Combustion Laboratory: Overview and Recent Results", *AIAA-2009-5349*.

[5] Fluent Inc., 2006, Fluent 6.3 User Guide, Fluent Inc., Lebanon, USA.

[6] Moríñigo, J.A., Hermida, J., 2010, "Modelling and Simulation with Finite Rate Reduced-order Kinetics of a Hybrid Rocket Motor Ignition Transient", Report AP-RPT-4430004-INTA-10, 90pag. (in Spanish).

[7] Moríñigo, J.A., Hermida, J., 2011, "Assessment of Two Finite Rate Reduced-order Kinetics of the Oxidation of HTPB in Hybrid Rocket Motors", Report AP-RPT-4430001-INTA-01, 22pag. (in Spanish).

[8] Laskin, A., Wang, H., Law, C.K., 2000, "Detailed Kinetic Modeling of 1,3-Butadiene Oxidation at High Temperatures", *J. Chemical Kinetics*, Vol.32, pp. 589-614.

[9] Cai, W., Thakre, P., Yang V., 2008, "A Model of AP/HPTB Composite Propellant Combustion in Rocket-Motor Environments", *Combustion Science & Technology*, Vol.180, pp.2143-2169.

[10] Kee R.J. et al., 2004, CHEMKIN Release 4.0, Reaction Design Inc., San Diego, USA.

[11] Westbrook, Ch.K., Dryer, F.L., 1981, "Simplified Reaction Mechanisms for the Oxidation of Hydrocarbon Fuels in Flames", *Combustion Science & Technology*, Vol.27, pp. 31-41.

[12] Bibrzycki J., Poinsot T., 2010, "Reduced Chemical Kinetic Mechanisms for Methane Combustion in O_2/N_2 & O_2/CO_2 Atmosphere", ECCOMETWN/CFD/10/17, CERFACS.

[13] Evans, B., Boyer, E., Kuo, K.K., Risha, G., Chiaverini, M., 2009, "Hybrid Rocket Investigations at Penn State University´s High Pressure Combustion Laboratory: Overview and Recent Results", *AIAA-2009-5349*.

[14] Alavilli, P., Buckmaster, J., Jackson, T.L., Short, M., 2000, "Ignition Transient Modeling for Solid Propellant Rocket Motors", *AIAA-2000-3567*.

[15] Beckstead M.W., Puduppakkam K., Thakre P., Yang, V., 2007, "Modeling of Combustion and Ignition of Solid-propellant Ingredients", *Progress in Energy and Combustion Science*, Vol.33, pp. 497-551.

[16] Sankaran V., 2007, "Computational Fluid Dynamics Modeling of Hybrid Rocket Flowfields", in *Fundamentals of Hybrid Rocket Combustion and Propulsion*, Progress in Astronautics and Aeronautics, AIAA, pp. 323-349.

Conference on Modelling Fluid Flow (CMFF'12)
The 15th International Conference on Fluid Flow Technologies
Budapest, Hungary, September 4-7, 2012

NUMERICAL MODELLING OF CO_2 ABSORPTION

Dariusz ASENDRYCH[1], Paweł NIEGODAJEW[2], Stanisław DROBNIAK[3]

[1] Corresponding Author. Department of Thermal Machinery, Częstochowa University of Technology. al. Armii Krajowej 19c, Częstochowa, Poland. Tel./Fax: +48 34 32-50-507, E-mail: darek@imc.pcz.czest.pl
[2] Department of Thermal Machinery, Częstochowa University of Technology. E-mail: niegodajew@imc.pcz.czest.pl
[3] Department of Thermal Machinery, Częstochowa University of Technology. E-mail: drobniak@imc.pcz.czest.pl

ABSTRACT

The paper deals with the numerical modelling of carbon dioxide capture from flue gases in the post combustion method, the most preferred option among the carbon capture and storage (CCS) technologies. The process is performed by means of a chemical absorption of CO_2 by aqueous solution of monoethanolamine in the absorber column filled in with the porous material ensuring the enlarged contact area between fluids.

The complex flow system including multi-phase countercurrent streams with chemical reaction and heat transfer is considered to resolve the CO_2 capture. The Euler-Euler model was applied to treat the gas-liquid system and the simplified chemistry has been adopted to describe the CO_2 absorption.

The absorber model follows the small-scale pilot CO_2 capture installation being ready for tests at the Institute for Chemical Processing of Coal, Zabrze. The model developed has been used to conduct a series of test simulations both for non-reacting and reacting conditions. The results obtained have shown the realistic behaviour of the system in terms of its hydrodynamics as well as CO_2 absorption.

Keywords: CO_2 capture, chemical absorption, multiphase flow, countercurrent flow, porous region.

NOMENCLATURE

C	$[kmol/m^3]$	molar concentration
D_m	$[s^{-1}]$	mass diffusion coefficient
D_T	$[kg/(m^2 \cdot s)]$	thermal diffusion coefficient
J	$[kg/(m^3 \cdot s)]$	stream of species diffused
M	$[kg/kmol]$	molecular weight
Q	$[W/m^3]$	heat flux exchanged between phases
R	$[kg/(m^3 \cdot s)]$	heterogeneous reaction rate
R	$[N/m^3]$	phase interaction force
Re	[-]	Reynolds number
S	$[kg/(m^3 \cdot s)]$	mass source term
S_e	$[W/m^3]$	enthalpy source term
S_m	$[N/m^3]$	momentum source term due to chemical reaction
S_{pz}	$[N/m^3]$	momentum sink term in porous zone
T	$[K]$	temperature
Y	[-]	mass fraction
h	$[J/kg]$	specific enthalpy
k_f	$[m^3/(kmol \cdot s)]$	forward reaction rate constant
p	$[Pa]$	static pressure
r	$[m]$	radial coordinate
t	$[s]$	time
u	$[m/s]$	velocity
y	$[m]$	axial coordinate
α	[-]	volume fraction
λ	$[W/(m \cdot K)]$	thermal conductivity
μ	$[Pa \cdot s]$	dynamic viscosity
ρ	$[kg/m^3]$	density

Subscripts and Superscripts

CO2	denotes carbon dioxide
MEA	denotes monoethanolamine
in	denotes inlet to the absorber
out	denotes outlet from the absorber

1. INTRODUCTION

Continuously growing CO_2 emission is one of the most important threats of today's power industry. Three technologies are currently available for carbon capture and storage (CCS), namely:

- pre-combustion capture - removal the CO_2 from decarbonised and gasified fuel (heating value transferred to hydrogen),
- oxy-fuel combustion - burning of fuel in oxygen atmosphere with CO_2 and water vapour as easily separable combustion products [1],
- post-combustion - removal of CO_2 from flue gases [2].

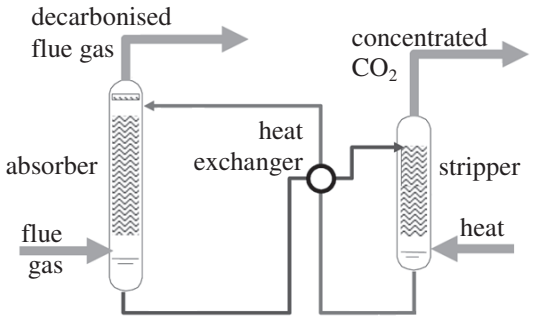

Figure 1. The general process flow diagram for amine absorption

With post-combustion approach, being at present the preferred option of CO_2 capture, the flue gases are sent through the absorber where carbon dioxide is separated by chemical absorption with the use of aqueous amine solution flowing countercurrently. The general process flow diagram for amine absorption is presented in Figure 1. Here the flue gas enters the absorber at the bottom whereas the solvent is released at the top of the column. Both phases pass through the packed bed where the most of the chemical reaction occurs due to the enlarged contact area between phases. The solution with CO_2 is pre-heated before entering the stripper where, through the addition of heat, the reaction is reversed. Desorbed CO_2 is then compressed and transported to the storage location. The recycled solvent is then pumped back to the absorber completing the process cycle. The monoethanolamine (MEA) is the most common choice of chemical solvent used for these purposes mainly due to its high reactivity [3] and the existing comprehensive data base of its physical and chemical properties [4,5]. Most of the present research of CCS technology is being performed in two ways:

- experimentally with the use of laboratory small-scale CC installations,
- simulating the process by means of 0D commercial codes, mainly ASPEN [e.g. 3, 4] and gPROMS [2,6] or 1D rate based models (e.g. [7]).

Although continuous progress in CCS technology is observed in recent decade, it still becomes extremely expensive as decreasing overall efficiency of the power cycle by appr. 30 %. In order to make carbon capture commercially attractive further significant progress should be achieved. It is believed that CFD modelling would provide the sufficient insight into the absorption process allowing for its further optimisation and noticeable reduction of costs.

The present paper deals with the numerical modelling of CO_2 capture process, the complex phenomenon including hydrodynamics of gas-liquid two-phase flow in porous region, chemical reaction and thermal effects due to its exothermic character. The simulation work is a part of a larger project, including also the experimental investigations. For that purpose a small-scale pilot installation has been designed and made operational at the Institute of Chemical Coal Processing (IChPW) in Zabrze. The results of experimental trials will be available for testing and validating the numerical model of carbon dioxide capture being developed.

2. NUMERICAL MODEL

The present numerical study is focused on the simulation of CO_2 absorption process, i.e. the first stage of CCS technology.

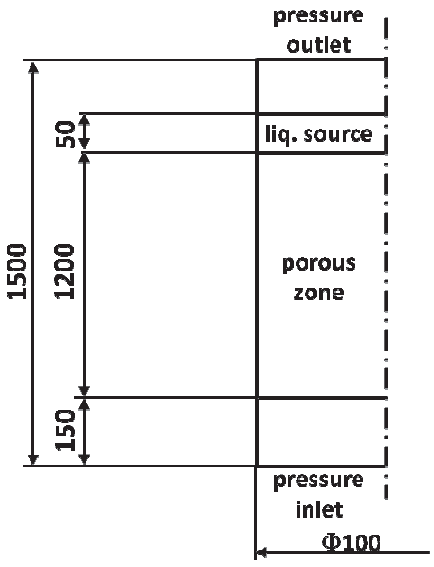

Figure 2. Geometry of the absorber column (not to scale) and boundary conditions applied in the numerical model

The model absorber column (following the geometry and dimensions of a pilot CCS installation at IChPW - see Figure 2) is of cylindrical shape with a diameter of 0.1 *m* and height of 1.5 *m*. A working absorber section filled with packing elements, 1.2 *m* high, is placed in the centre of the column. Standard Raschig rings 6*mm* were used as a packing material with void fraction 0.76 and surface area 789 m^2/m^3. The nominal fluxes of media in the column are: 5 m^3/h and 0.05 m^3/h of flue gas and MEA, respectively. Such a flow intensity of gaseous phase (dominating one) results in the Reynolds number about Re=1400 besides the porous region and appr. Re=50 in the porous region. Such a flow corresponds to the inertial-laminar flow regime [8]. The operational parameters of the column are collected in Table 1.

The model of the absorber column was developed as a 2-dimensional axi-symmetric, laminar and unsteady multiphase gas-liquid flow.

The Eulerian/Eulerian approach was implemented to describe the two-phase countercurrent flow.

Table 1. Working parameters of absorber column

gas phase:	
p_{in}	6 *kPa*
T_{in}	300 *K*
volumetric flux	5 m^3/h
Y_{CO2}	0.10
liquid phase:	
T_{in}	298 *K*
volumetric flux	0.05 m^3/h
Y_{MEA}	0.15

The boundary conditions of model are presented in Figure 2. The pressure inlet and outlet boundaries were chosen at the bottom and the top of the column, respectively, to drive the flow and allowing the phases to freely leave the domain. The gas phase was released from the mass source placed at the bottom of the column while the liquid from the mass source located just above the porous region. These types of boundary conditions have been found to ensure the convergence of the solution. The boundary conditions of the 2-dimensional axis-symmetric model are presented in Figure 2. The pressure inlet and pressure outlet boundaries were assigned suitably to the bottom and the top of the column. Such setup allows the phases freely leave the domain. The flue gas enters the column at its bottom and the aqueous solution of MEA is released from the source located above the porous region. These types of boundary conditions have been found to ensure the convergence of the solution [9].

In the Euler-Euler multiphase approach the fluid phases are treated as the interpenetrating continua. In order to describe the coexistence of different phases in the flow the concept of volumetric fraction is introduced. The volume fractions for all the phases have to sum up to unity

$$\sum \alpha_k = 1 . \tag{1}$$

Conservation equations are formed for each phase separately. The equation of mass conservation for k^{th} phase takes the form

$$\frac{\partial}{\partial t}(\alpha_k \rho_k) + \nabla(\alpha_k \rho_k \underline{u}_k) = S_k \tag{2}$$

where u_k is the velocity vector, ρ_k phase density and S_k is a mass source term corresponding to species production/destruction due to chemical reaction.

The momentum equation for k^{th} phase with respect to the Eulerian multiphase model (assuming flow incompressibility) has the following form:

$$\begin{aligned} &\frac{\partial}{\partial t}(\alpha_k \rho_k \underline{u}_k) + \nabla(\alpha_k \rho_k \underline{u}_k \underline{u}_k) = \\ &= -\alpha_k \nabla p + \nabla^2(\alpha_k \mu_k \underline{u}_k) + \alpha_k \rho_k \underline{g}_k + \\ &+ \underline{R}_k + S_m + S_{pz,k} \end{aligned} \tag{3}$$

where p is the static pressure shared by all phases, μ_k stands for dynamic viscosity, g_k is the gravity vector and R_k describes an interaction force between phases. In the porous region, being the most important absorber column section, the additional flow resistance $S_{pz,k}$ occurs

$$S_{pz,k} = \frac{\mu_k}{\varsigma_k}\underline{u}_k + C_k \frac{1}{2}\rho_k \underline{u}_k^2 \tag{4}$$

where the first term on the right hand side is the viscous loss term, while the second one corresponds to the inertial momentum loss. The values of the coefficients were determined in experimental way for the air flow.

The phase interaction force $\underline{R}_k$ appearing in Eq. (3), has been defined with the use of Schiller-Naumann formula [10], which adequately describes the interactions of dispersed phases (i.e. droplets or bubbly flows). By adjusting model parameters it was possible to obtain realistic flow behaviour of countercurrent streams, however, it is planned to adopt from the literature (e.g. [11]) more relevant mechanism, specific for gas-liquid film system. The interphase force is related to phase relative velocity $\Delta\underline{u}$ accordingly:

$$\underline{R}_k = K_k \Delta \underline{u} \tag{5}$$

where K_k is the interphase momentum exchange coefficient given by:

$$K_k = \frac{\rho_k f}{\tau_k}\prod_i \alpha_i \tag{6}$$

where relaxation time τ_k is defined as:

$$\tau_k = \frac{\rho_k d_k^2}{18\mu_k} \tag{7}$$

Characteristic dimension d_k appearing in Eq. (7) represents a diameter of a droplet or a thickness of a liquid film, while quantity f in Eq. (6) is a drag function described as:

$$f = \frac{c_D \,\mathrm{Re}}{24} \tag{8}$$

For the reacting system the additional governing equations have to be included in the model. General transport equation of i^{th} species in multiphase flow can be written as

$$\frac{\partial}{\partial t}(\alpha_k \rho_k Y_{i,k}) + \nabla(\alpha_k \rho_k \underline{u}_k Y_{i,k}) = \\ = -\nabla \alpha_k \underline{J}_{i,k} + R_i \quad (9)$$

where $Y_{i,k}$ is the mass fraction, R_i is the heterogeneous reaction rate. $J_{i,k}$ is a stream of the i^{th} species due to diffusion. In laminar flow the diffused flux can be described by the Fick's law

$$\underline{J}_{i,k} = \alpha_k \rho_k D_{i,M} \nabla Y_{i,k} - D_{i,T} \frac{\nabla T}{T} \quad (10)$$

where $D_{i,m}$ and $D_{i,T}$ are mass and thermal diffusion coefficients of the i^{th} species in the mixture, respectively.

To describe the energy transfer in Eulerian model, a separate enthalpy equation is solved for k^{th} phase

$$\frac{\partial}{\partial t}(\alpha_k \rho_k h_k) + \nabla(\alpha_k \rho_k \underline{u}_k h_k) = \\ = \alpha_k \frac{\partial p}{\partial t} + \nabla(\lambda_k \nabla T_k) + Q_k + S_{e,k} \quad (11)$$

where h_k is the specific enthalpy, λ_k stands for conductivity, Q_k is the intensity of heat exchange between phases and $S_{e,k}$ is enthalpy source term due to chemical reaction.

The chemistry of CO_2 absorption by aqueous monoethanolamine solution is usually described by the system of several equilibrium reversible reactions. However, for the typical operating conditions of absorber columns the process may be regarded as a non-reversible and approximated by the 2-step reaction mechanism [12,13]. At first the so-called zwitterion is formed by absorption CO_2 by amine molecule

$$CO_2 + RNH_2 \rightarrow RNH_2^+ COO^- \quad (12a)$$

and then it undergoes deprotonation by second amine molecule

$$RNH_2^+ COO^- + RNH_2 \rightarrow RNHCOO^- + RNH_3^+ \quad (12b)$$

resulting in carbamate formation. In above reactions R represents an alcanol group $(CH_2)_2OH^-$. The expression (12) neglects the presence of the ions (like H_30^+, OH^-, CO_3^{2-}) as their content for CCS installations working on fossil fuels is very small. The mass rate of i^{th} chemical species produced due to the heterogeneous second-order reaction is given by:

$$R_i = M_i \cdot k_f \cdot C_{MEA} \cdot C_{CO2} \quad (13)$$

where M_i is the molecular weight of species i, k_f is a forward reaction rate constant and C_{MEA} and C_{CO2} stand for molar concentrations of reacting media, i.e. MEA and carbon dioxide, respectively. According to the experimental studies presented in [14] reaction constant may be approximated by the following expression:

$$\log(k_f) = 10.99 - 2152/T \quad (14)$$

The model of the absorber column was developed in ANSYS FLUENT 13, a commercial CFD code. The Eulerian/Eulerian approach was implemented to describe the two-phase counter-current flow. The geometry and numerical grid was created in Gambit - Fluent's preprocessor.

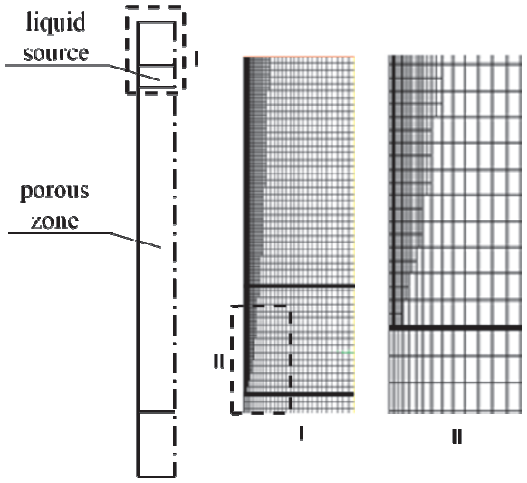

Figure 3. Numerical mesh

Numerous variants of meshing strategies as well as several grid sizes were investigated in order to determine the most optimal mesh allowing minimised numerical diffusion. In order to satisfy different requirements of particular column sections the 2-step procedure was applied. First, the structured mesh was created for entire geometry with adequate cell density in the near-wall regions. After that the mesh was conditionally refined in the sections outside the porous zone in the flow regions of high velocity gradients (see Figure 3). A series of test calculations has shown that the mesh size of appr. 13,000 cells provided the best compromise between high accuracy and computational speed.

3. HYDRODYNAMICS OF NON-REACTING FLOW

As a first step of model development the hydrodynamics of the 2-phase countercurrent flow of non-reacting fluids was implemented and tested. Water and air material properties were used as the

first approximation. Figure 4 shows sample results of the flow-field in the form of contour maps. Three parameters are presented, volume fraction of liquid phase (a), the velocity magnitude of liquid (b) and the static pressure (c). From the volume fraction (VF) distribution it is seen that the liquid is released from the source and enters the porous region (above the source water does not appear) driven by gravity. Inside the porous region the VF is constant at appr. level of 1%, so the flow is dominated by the gas phase with liquid films created on elements of porous zone. Just below the porous region the liquid content dramatically drops down as a result of its acceleration due to reduced flow resistance (see the whitish region in Figure 4b). The static pressure distribution inside the domain shows clearly that the pressure drops practically only in porous region, and beyond that zone pressure changes are negligible.

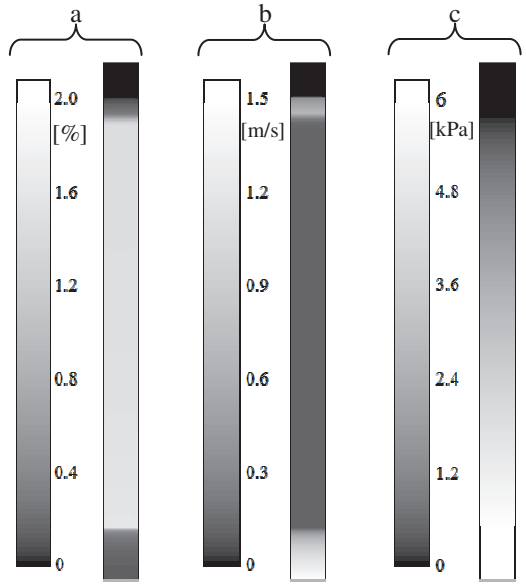

Figure 4. Contours of liquid VF (a), liquid velocity magnitude (b) and static pressure (c)

The flow in a absorber column has been tested for varying flow conditions, in particular for varying gas pressure at column inlet p_{in}. The results of selected flow parameters, namely liquid volume fraction and velocity magnitudes of both phases inside the porous zone as a function of p_{in} are shown in Figure 5. For the increasing pressure gas velocity is growing which in turn leads to the increased flow resistance of liquid phase. As a result liquid slows down and its content (volume fraction) inside the porous zone is growing. The results of are fully consistent with the available literature data devoted to the packed towers (e.g. [11]).

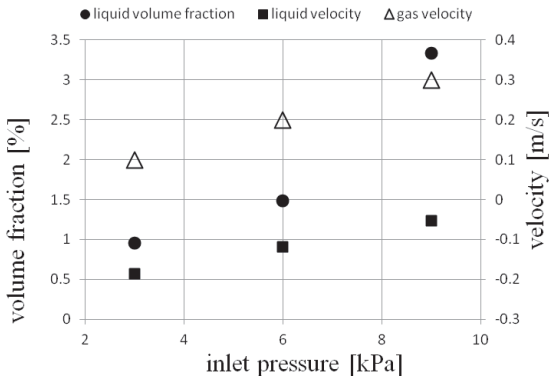

Figure 5. Influence of inlet pressure on liquid volume fraction (solid circles), gas (empty triangles) and liquid (solid squares) velocity magnitudes at the column centreline in the porous zone

4. SIMULATION OF REACTING FLOW

The model developed within the present work has been then employed to conduct the simulation of the CO_2 capture process. Thus, the flow hydrodynamics has been complemented by remaining phenomena, i.e. chemical reaction with accompanying heat release, heat transfer and the species transport. In order to test the model the test simulations has been performed for the typical operational parameters of the column (see Table 1). It should be noted that in this case the flue gas was composed of the mixture of nitrogen and carbon dioxide (of 10 % mass content), as a solvent aqueous amine solution with 15 % content of MEA was used. Moreover, the actual material properties of media were implemented, in particular dynamic viscosity of monoethanolamine (according to [15]) varying significantly with temperature, CO_2 loading

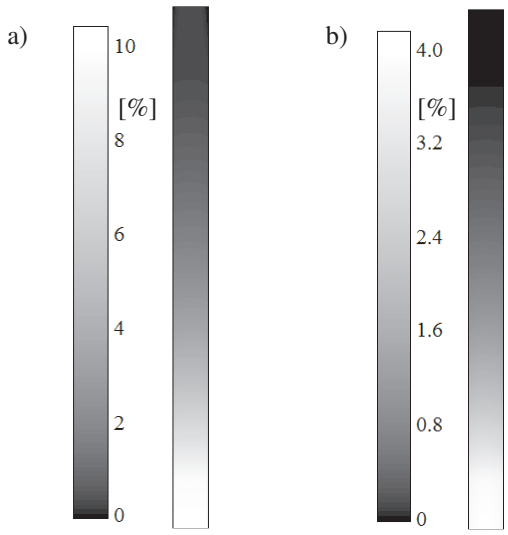

Figure 6. Contours of CO_2 mass fraction in a gas mixture (a) and loaded MEA mass fraction in a liquid mixture (b)

(number of moles of CO_2 per mole of MEA) and mass MEA content in liquid mixture.

The presentation of simulation results is started in Figure 6 from the contour maps presenting the mass content of carbon dioxide (see Fig. 6a) and loaded MEA (solvent with CO_2 absorbed - Fig. 6b). When interpreting the results it should be noted that carbon dioxide is a vanishing species, while loaded MEA is being formed, and the fluids flow countercurrently. One may easily notice the gradual decrease of CO_2 mass fraction (see Fig. 6a) with vertical position when passing through the porous zone, as well as the accompanying change of loaded MEA content (Fig. 6b). For the set of parameters applied, the capture efficiency reaches 95 %, as the inlet CO_2 content was 10 % of flue gases, while at the outlet it fell down to 0.5 %.

As the reaction of CO_2 absorption by MEA is an exothermic process, it is of great importance to control the temperature field in the column. Its distributions are shown in Figure 7 for both phases, i.e. for gas (Fig. 7a) and liquid (Fig.7b). Liquid temperature varies in much wider range due to the heat release taking place in it. The heat transfer between phases allows to warm up the gas to 302 *K* while liquid temperature reaches 308 *K*.

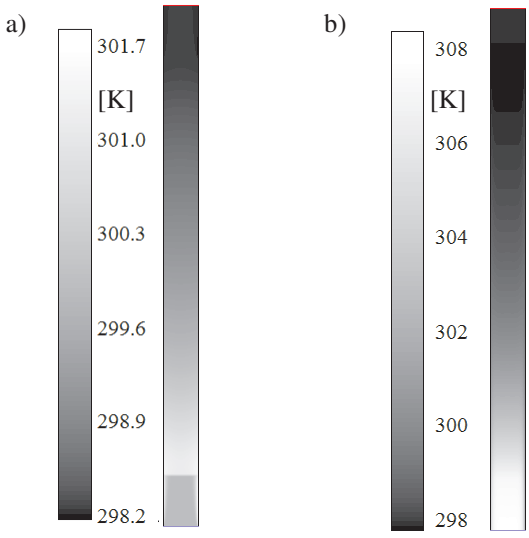

Figure 7. Contours of temperature of the gas mixture (a) and temperature of the liquid mixture (b)

As the results presented in Figs. (6) and (7) have mainly qualitative character, thus in order to have a more detailed insight into the absorption process the axial distributions of key parameters at the column centreline were analysed.

As it may be seen from the data collected in Figure 8 the variation of species content along the absorber column axis is highly nonlinear. Flue gas before entering the porous zone (i.e. in the bottom part of the column) reacts with amine solvent rather weakly, which is reflected by minor changes of mass fractions of loaded MEA and CO_2. Much larger contact area between phases in the porous zone, as well as longer residence times (due to increased flow resistance) lead to significant acceleration of CO_2 absorption, which is manifested in an abrupt decrease of its mass fraction (solid line in Fig. 8). Flowing further up flue gas contains less and less CO_2 but the process intensity continuously

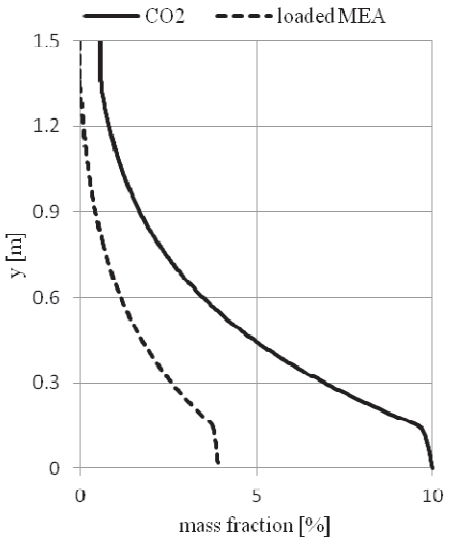

Figure 8. Centreline mass fraction distributions of CO_2 in gaseous phase (solid line) and loaded MEA in liquid mixture (dashed line)

falls down reaching asymptotically level of appr. 0.5 % above the MEA source. The distribution of loaded solvent (dashed line in Fig. 8) is qualitatively identical to the CO_2 profile, which should be expected for the system of countercurrently flowing streams. The MEA stream enters porous zone from the top and then starts to

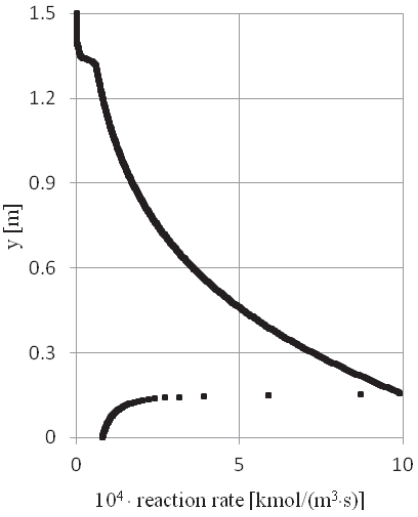

Figure 9. Reaction rate distribution in liquid mixture along the axis of the column

react with carbon dioxide. The mass fraction of loaded MEA increases gradually reaching the outlet level of about 4 %.

The changes in species production (or destruction) intensity are fully consistent with the reaction rate distribution shown in Figure 9. As mentioned before outside the porous zone the reaction either does not take place (the region above the MEA source where solvent does not enter) or proceeds weakly. The most of reaction takes place just downstream the gas entrance to the porous region. At this location reaction rate reaches its maximum and, similarly like species mass fraction profiles (see Fig. 8), decreases gradually while moving up. Such a behaviour may be explained in twofold:

- reaction rate constant, being actually a function of temperature (see Eq. 14), increases with T which holds its maximum at this location,
- reaction rate is proportional to molar concentrations of reacting species (see Eq. 13) - and the product of C_{CO2} and C_{MEA} is the highest at the bottom of porous zone ($Y_{CO2} \approx 10$ % and $Y_{MEA} \approx 11$ %) and then decreases to the ($Y_{CO2} \approx 0.5$ % and $Y_{MEA} = 15$ %).

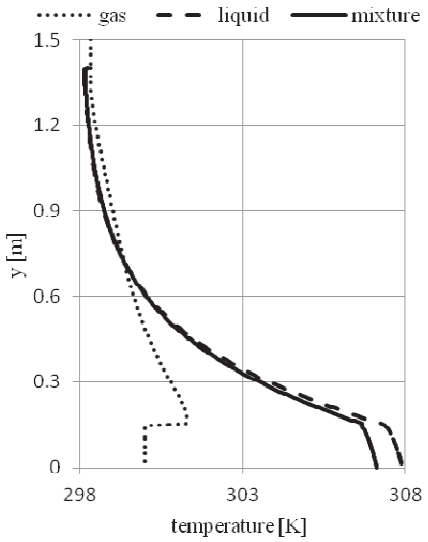

Figure 10. Temperature distributions of gaseous and liquid phases as well as their mixture along absorber centreline

As a supplement to the already presented results the temperature profiles along the absorber axis are shown in Figure 10 for both fluids and additionally for the mixture. One may easily notice the qualitative similarity to the distributions of the reaction rate and the mass fractions. And they directly results from the mutual relations these parameters have. It is worth to note the quite significant discrepancies between temperatures of liquid and gaseous phases in the bottom part of the column. That is because the heat due to chemical reaction is released in the liquid phase and the interphase heat exchange mechanism is not able to increase gas temperature along such a short distance. The mixture temperature is nearly the same as of liquid phase, which may be explained with largely differing thermal capacities of phases. Although volume fraction of liquid oscillates around 1%, its mass content in the mixture reaches 90 %, thus it mostly contributes to the overall mixture temperature. Temperature profile of liquid phase shown in Fig. 10 has a shape typical for absorber columns (see e.g. [6]) which may prove model relevance.

5. SUMMARY

The CFD Euler-Euler multiphase model has been developed in order to simulate the CO_2 capture from flue gases by chemical absorption in porous zone. The complex flow system including the countercurrent gas-liquid streams, chemical reaction and the heat transfer has been successfully adopted and tested in the typical operational conditions of absorber column. The preliminary simulations showed the realistic behaviour of the model both in terms of flow hydrodynamics as well as chemical absorption of CO_2 by the amine solvent, proving model relevance.

The model will be further validated with the use of the experimental data from the pilot installation of the same geometry and operational conditions. This will enable to tune the model and further apply for the parametric study of CO_2 capture process aimed at its optimisation.

ACKNOWLEDGEMENTS

The results presented in this paper were obtained from research work co-financed by the National Centre of Research and Development in the framework of Contract SP/E/1/67484/10 - Strategic Research Programme - Advanced technologies for energy generation: Development of a technology for highly efficient zero-emission coal-fired power units integrated with CO_2 capture.

REFERENCES

[1] Zhao C.S., Duan L.B., Chen X.P. Liang C., 2010, "Latest Evolution of Oxy-Fuel Combustion Technology in Circulating Fluidized Bed", Proc. *20th Int. Conference on Fluidized Bed Combustion*, V.2009, Xian, China, 49-58.

[2] Lawal, A., Wang, M., Stephenson, P., Koumpouras, G., Yeung, H., 2010, "Dynamic modelling and analysis of post-combustion CO2 chemical absorption process for coal-fired power plants", *Fuel* 89, 2791-2801.

[3] Alie, C.F., 2004, "CO_2 Cature with MEA: Integrating the Absorption Process and Steam

Cycle of an Existing Coal-Fired Power Plant", *MSc thesis, University of Waterloo*, Waterloo, Ontario, Canada, 2004.

[4] Kothandaraman A, Nord L., Bolland O., Herzog H.J., McRae G.J., 2009, "Comparison of solvents for post-combustion capture of CO_2 by chemical absorption", *Energy Procedia* 1, 1373-1380.

[5] Moser P., Schmidt S., Sieder G., Garcia H., Stoffregen T., 2011, "Performance of MEA in long-term test at the post-combustion capture pilot plant in Niederaussem", *Int. J. of Greenhouse Gas Control* 5, 620-627.

[6] Harun N., Douglas P.L., Ricardez-Sandoval L., Croiset E., 2011, "Dynamic Simulation of MEA Absorption Processes for CO_2 Capture from Fossil Fuel Power Plant", *Energy Procedia* 4, 1478-1485.

[7] Simon L.L., Elias Y., Puxty G., Artanto Y., Hungerbuhler K., 2011, "Rate based modeling and validation of a carbon-dioxide pilot plant absorbtion column operating on monoethanolamine", *Chemical Engineering Research and Design*, Vol. 89, Issue 9, 1684-1692.

[8] Crespy, A., Bolève, A., Revil, A., 2007, "Influence of the Dukhin and Reynolds numbers on the apparent zeta potential of granular porous media", *Journal of Colloid and Interface Science* 305 (2007) 188-1.

[9] Xu, Y., Paschke, S., Repke, J.-U., Yuan, J., Wozny, G., 2008, "Portraying the Countercurrent Flow on Packings by Three-Dimensional Computational Fluid Dynamics Simulations", *Chem. Eng. Technol*. 31, No. 10, 1445-1452.

[10] Schiller, L., Naumann, Z., Z., 1935, "A drag coefficient correlation", *Ver. Deutsch. Ing.*, 77-318.

[11] Billet, R., 1995, "Packed Towers in Processing and Environmental Technology", *VCH Verlagsgesellschaft mbH, Weinheim.*

[12] Astarita, G., Savage, D. W., Bisio, A., 1983, "Gas Treating with Chemical Solvents", *Wiley: New York.*

[13] Vaidya P.D., Kenig E.Y., 2007, "CO_2-Alkanolamine Reaction Kinetics: A Review of Recent Studies", *Chem. Eng. Technol.* 30, No 11, 1467-1474.

[14] Faiz, R., Al-Marzouqi, M., 2009, "Mathematical modeling for the simultaneous absorption of CO_2 and H_2S using MEA in hollow fiber membrane contractors", *Journal of Membrane Science* 324, 269-278.

[15] Weiland, R.H., Dingman, J.C., Cronin, D.B., Browning, G.J., 1998, "Density and Viscosity of Some Partially Carbonated Aqueous Alkanolamine Solutions and Their Blends", *J. Chem. Eng. Data* 43, 378-382.

Turbomachinery

Conference on Modelling Fluid Flow (CMFF'12)
The 15th International Conference on Fluid Flow Technologies
Budapest, Hungary, September 4-7, 2012

ASSESSMENT OF TURBULENCE MODELS FOR PREDICTING COAXIAL JETS RELEVANT TO TURBOFAN ENGINES

Mihai MIHAESCU[1], Bernhard SEMLITSCH[2], Laszlo FUCHS[3], Ephraim GUTMARK[4]

[1] Corresponding Author. Linné FLOW Centre, Department of Mechanics, Royal Institute of Technology (KTH). Osquars Backe 18, SE-100 44 Stockholm, Sweden. Tel.: +46 (0)8 790 7572, Fax: +46 (0)8 790 7577, E-mail: mihai@mech.kth.se
[2] Linné FLOW Centre, Department of Mechanics, Royal Institute of Technology (KTH), Sweden. E-mail: bernhard@mech.kth.se
[3] Linné FLOW Centre, Department of Mechanics, Royal Institute of Technology (KTH), Sweden. E-mail: lf@mech.kth.se
[4] School of Aerospace Systems, University of Cincinnati, USA. E-mail: ephraim.gutmark@uc.edu

ABSTRACT

A numerical study is carried out for analyzing the compressible, non-isothermal flow associated with a separate-flow exhaust nozzle system with conic plug. Within the steady-state Reynolds-averaged Navier-Stokes (*RANS*) framework three two-equation turbulence models are considered. These are the standard *k-ε*, the standard *k-ω*, and the Shear-Stress Transport (*SST*) *k-ω* models. Additionally, the unsteady Large Eddy Simulation (*LES*) approach is employed. The results are compared with experimental Particle Imaging Velocimetry (*PIV*) flow data, in terms of time-averaged axial velocity and turbulence kinetic energy levels.

The *k-ω* turbulence model performed worst, overpredicting by large margins the length of the potential core region of the jet. The same model computed significantly lower turbulence kinetic energy levels, corresponding to a slower mixing rate, in the shear-layer between the secondary flow (i.e. the fan-stream) and the ambient air. A fair agreement was found between the *PIV* data and the predictions obtained with the *LES* approach, the standard *k-ε*, and the *SST k-ω* turbulence model, respectively. The largest differences were found at the location of eight equivalent diameters downstream distance from the tip of the center-body, probably due to a larger air entrainment in the experiment.

Keywords: coaxial jet nozzle, LES, RANS, validation

NOMENCLATURE

BPR	[-]	bypass ratio
CB		center-body
D_{eq}	[*m*]	nozzle equivalent diameter
LES		Large Eddy Simulation
NITA		Non-Iterative Time Advancement
NPR	[-]	nozzle pressure ratio
P0 to P3		monitoring points
PIV		Particle Imaging Velocimetry
PISO		Pressure Implicit with Splitting of Operators
PSD		Power Spectral Density
RANS		Reynolds-averaged Navier-Stokes
SGS		subgrid-scale
SST		shear-stress transport
TKE	[m^2/s^2]	turbulence kinetic energy
U_o	[*m/s*]	velocity at the throat
dt	[*s*]	time step
ε	[m^2/s^3]	dissipation rate of turbulence kinetic energy
k	[m^2/s^2]	turbulence kinetic energy
ske		standard *k-ε*
skw		standard *k-ω*
y+	[-]	dimensionless distance to the wall
ω	[*1/s*]	specific dissipation rate

1. INTRODUCTION

Today the Reynolds-averaged Navier-Stokes (*RANS*) formulations with the correspondent turbulence closures are the preferred methods in particular by industry for analysis of compressible turbulent jet flows [1 - 6]. Within this framework, the two-equation turbulence models are used the most. Evaluating turbulence models against reliable experimental data is a necessary step in the solver validation process, in assessing their potential and limitations [7 - 9]. Moreover, often the obtained flow data are used further on for post-processing, e.g. aeroacoustics calculations that are frequently performed on turbulent jets exhausting nozzles without [e.g. 1, 2, 8] or with noise suppression devices [e.g. 10, 11]. Any result of such analysis is highly dependent on the quality of the initial data (i.e. the previously obtained flow field solution).

While the more expensive Large Eddy Simulation (*LES*) approach offers promising for the future by directly calculating large scale turbulence structures and the dynamics of the flow, the *RANS* techniques are very useful in particular for "fast-screening" of a large number of cases or set-ups. This is a necessary process within any nozzle design optimization process, or to identify trends in the flow behaviour when performing a parameter study. Typically, only the most promising or thought-provoking set-ups are then analysed with the more time-consuming but more accurate and more reliable *LES*.

In this paper the capabilities of three different turbulence models within the steady-state *RANS* formulation for predicting a high subsonic, coaxial heated jet issued from a bypass ratio of five (*BPR5*) turbofan engine model are assessed. Further, a *LES* calculation of the same flow field is carried out. The numerical data are contrasted against existent experimental measurements performed using Particle Image Velocimetry (*PIV*) at the Aeroacoustics Test Facility, University of Cincinnati [12, 13].

2. TURBULENCE MODELING

Three two-equation turbulence models (i.e. the standard k-ε, standard k-ω, and *SST* k-ω) and the LES approach are used for investigating the flow associated with a coaxial axisymmetric nozzle system.

Probably the most popular two-equation model, the standard k-ε model [14] is robust, fast and gives a reasonable accuracy for a wide range of turbulent flows. It allows determination of the turbulence length and time scales by solving two transport equations for the turbulence kinetic energy (k) and the dissipation rate of turbulence kinetic energy (ε). The k-ε model used here considered the pressure gradient effects at the near-wall region.

The standard k-ω turbulence model is based on Wilcox's k-ω model [9] with two transport equations for k and the specific dissipation rate (ω) and incorporates modifications for compressibility and shear flow spreading effects. One of the weak points of the model is the sensitivity of the solutions to k and ω values outside the shear layer, which gives poor accuracy when predicting free-shear flows.

An improved two-equation turbulence model is the *SST* k-ω model [15] with compressibility effects. The modified turbulent viscosity to account for the transport of the principal turbulent shear-stress gives it an advantage in terms of performance over both the standard k-ω and k-ε formulations. It behaves as a k-ω model in the inner region of the boundary layers and as a k-ε model in the outer region of the boundary layers, in the free-stream zones. No changes were performed to any of the *RANS* models in terms of their closure coefficients.

The *LES* approach uses the dynamic Smagorinsky-Lilly subgrid-scale (*SGS*) model [16], where the model's constant is dynamically computed based on the information provided by the resolved scales.

3. PROBLEM DESCRIPTION

The compressible jet associated with the BPR5 separate flow exhaust nozzle configuration is simulated using the Fluent® (ANSYS, Inc.) commercial software program.

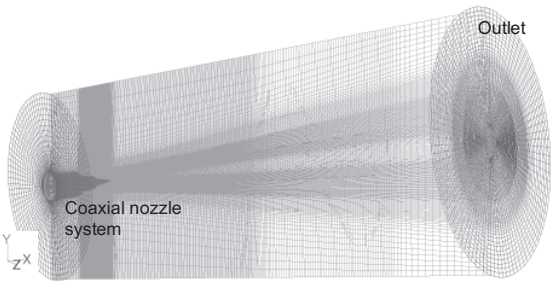

Figure 1. Computational domain and the generated mesh surrounding the nozzle system.

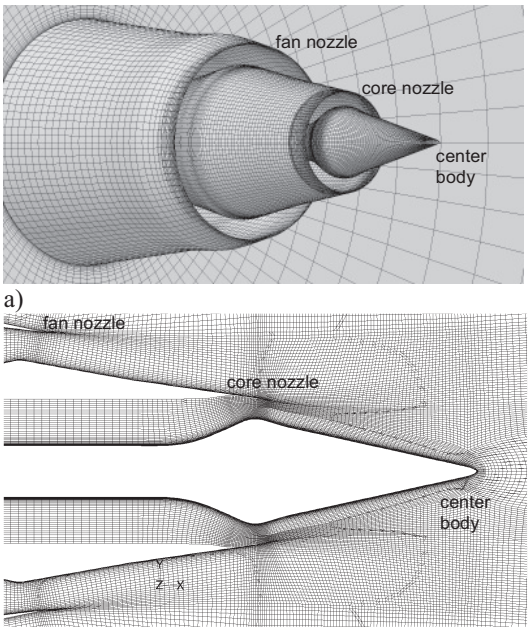

Figure 2. Details of the computational grid: a) the *BPR5* coaxial nozzle system and the generated mesh; b) cut through the hexahedral computational mesh in the nozzle's mid-longitudinal *x-y* plane.

3.1. Geometry and Computational Mesh

The nozzle system includes a center-body (*CB*), a core-stream nozzle, and a fan-stream nozzle. Its geometrical characteristics are based on those of a

BPR5 coaxial nozzle model existent in the Aeroacoustics Test Facility at the University of Cincinnati [12]. The ratio between the equivalent cross-sectional exit areas for the core and the fan nozzles is approxiately of *0.3*.

A conical computational domain, with a *7* degrees half angle to follow the development and the spreading of the jet in the radial direction is generated. Figure 1 shows the computational mesh surrounding the *BPR5* nozzle. It has a total length of about thirty equivalent diameters (D_{eq}) in the stream-wise flow direction (x) and a radius of about $8.0D_{eq}$ at the exit plane of the domain. The equivalent diameter is estimated based on the total nozzle exit area obtained by summating the core and the fan-streams exit areas.

Details of the generated block-structured hexahedral mesh which contains approximately five million hexahedral mesh volumes are presented in Fig. 2. Three regions are distinguished with the built grid: one defining the geometry, where the criterion of wall attached cells size ($y+$) used in wall functions is considered, another designed to capture jet's development, and a third defining the entrainment zone.

3.2. Methods and Boundary Conditions

The compressible flow simulations are carried out by using a pressure-based solver. Sutherland's viscosity formula with three coefficients is utilized.

For the *RANS* simulations, the pressure-velocity coupling is achieved through the *Coupled* scheme, which provides superior performance compared with the segregated scheme for steady-state flows. Second-order upwind finite volume schemes are employed for the spatial discretization of the terms in the *RANS* equations.

For the unsteady *LES* calculations, bounded central differencing schemes are used when discretizing the momentum and energy equations to ensure low numerical diffusion. A second order implicit temporal discretization using the Non-Iterative Time Advancement (*NITA*) scheme is selected for the time marching algorithm. The *PISO* scheme is used for pressure-velocity coupling. The time step imposed with the *LES* calculations was of *dt = 5.5e-7s* and the simulations were run for about *55.0e4* time steps.

The calculations are performed for a take-off set-point condition without considering the forward-flight effect. Pressure and temperature boundary conditions are imposed at the core and fan inlet ports of the computational domain. These are corresponding to existent upstream measured values for the core and the fan streams [12]. Thus, the core-stream jet temperature is considered to be *400K*, while the fan-stream temperature is the same as the ambient air temperature (*300K*).

The ratio between the core and the fan-stream static pressures is *1.38* and turbulent intensity levels of *5%* are enforced at the inlet ports.

At the outlet and on the surrounding boundaries of the computational domain, atmospheric conditions are considered. No-slip boundary conditions for velocity are imposed at the nozzle's solid surfaces.

4. RESULTS AND DISCUSSION

The overall characteristics of the axisymmetric non-isothermal jet exhausting the *BPR5* coaxial nozzle system are exposed in Fig. 3. For this purpose the data obtained with the *SST k-ω* model are used. The contours of mean axial velocity, total temperature, and turbulent kinetic energy (*TKE*) are presented in cross-sectional planes located at *1*, *2*, *4*, *6*, *8*, and $10D_{eq}$ downstream distances from the tip of the center-body (*CB*), which is positioned at $x = 0.0D_{eq}$.

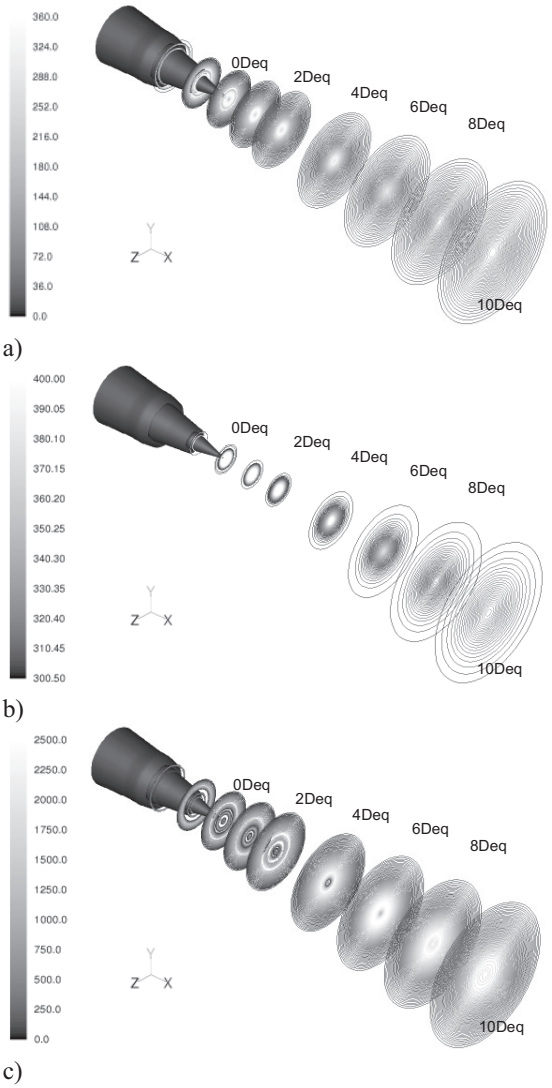

Figure 3. Mean flow variables of the coaxial jet as calculated by *RANS* (*SST k-ω*): a) Axial velocity (*m/s*); b) Total temperature (*K*); c) turbulence kinetic energy (m^2/s^2).

The primary heated jet is accelerated at the throat of the nozzle close to sonic conditions. It surrounds the conic plug and forms a wake downstream of it, which is visible in Fig. 3a along the jet center-line. The temperature distribution (Fig. 3b) follows the high velocity core-stream. Strong shear-layers are formed between the core-stream jet and the higher mass flow, lower velocity fan-stream, as well as between the secondary flow (i.e. fan-stream) and the ambient surrounding air. The highest interaction between the shear layers is found between *4* to $8D_{eq}$ downstream distance from the *CB*'s tip as exposed by the larger *TKE* levels found in this region as shown in Fig. 3c.

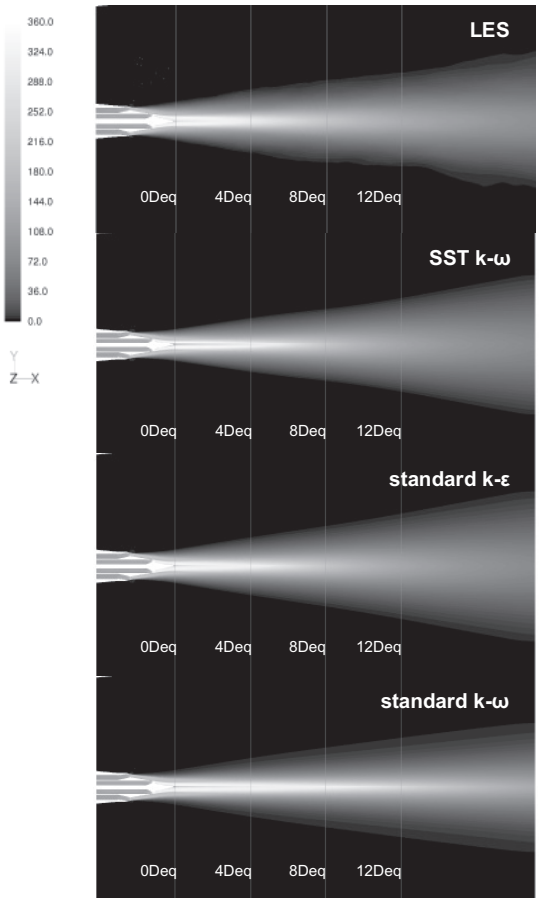

Figure 4. Mean axial velocity (*m/s*) contours in the longitudinal *x-y* mid-plane of the jet as calculated with the *LES* approach and the three different *RANS* turbulence models.

Figures 4 and 5 present a qualitative comparison between the data predicted by the four different formulations in terms of mean axial velocity and *TKE* distributions, respectively. The results are depicted in the longitudinal *x-y* mid-plane of the nozzle. Among all the *RANS* models the standard *k-ω* predicts the longest potential core region for the coaxial jet. Differences are also visible between the results obtained with the *LES* approach, the standard *k-ε*, and the *SST k-ω* model in terms of length and strength of the wake formed downstream of the conic plug and the *TKE* levels. One can observe larger *TKE* levels predicted by *LES* (as compared with *RANS* data) in the initial development of the fan-ambient shear layer, downstream of the fan nozzle trailing edge ($x < 1.0D_{eq}$).

The numerical predictions of mean axial velocity and *TKE* levels are compared against experimental *PIV* measurements in Figs. 6 and 7. The data are normalized by the velocity of the primary jet at the core nozzle's throat (U_o) and plotted along radial-lines positioned at several locations in the stream-wise direction (x) downstream from the nozzle. These are *CB*'s tip location ($x = 0.0D_{eq}$) and *1*, *2*, *4*, *6*, *8*, *12*, and $14D_{eq}$ downstream of it, respectively. The distance in the radial direction (r) is normalized by the equivalent diameter. The measurements are available along radial lines at the axial locations of $x = 1$, *2*, *4*, and $8D_{eq}$. In addition, details of both normalized axial velocity and *TKE* distributions in the wake of the conic plug along jet's center-line are presented in Figs. 8a and 8b, respectively.

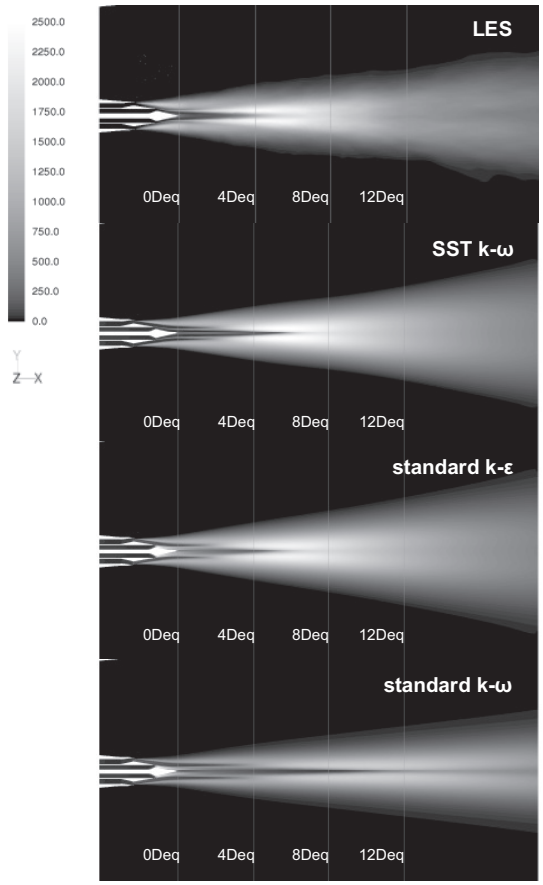

Figure 5. *TKE* (m^2/s^2) distributions in the longitudinal *x-y* mid-plane of the jet as calculated with the *LES* approach and the three different *RANS* turbulence models.

The low velocity region in the wake of the conic plug ($r/D_{eq} = 0.0$) is captured by all the simulations. It is the most prominent for the standard k-ω (i.e. *skw*) and the *SST* k-ω models as can be seen in Figs. 4, 6, and 8a.

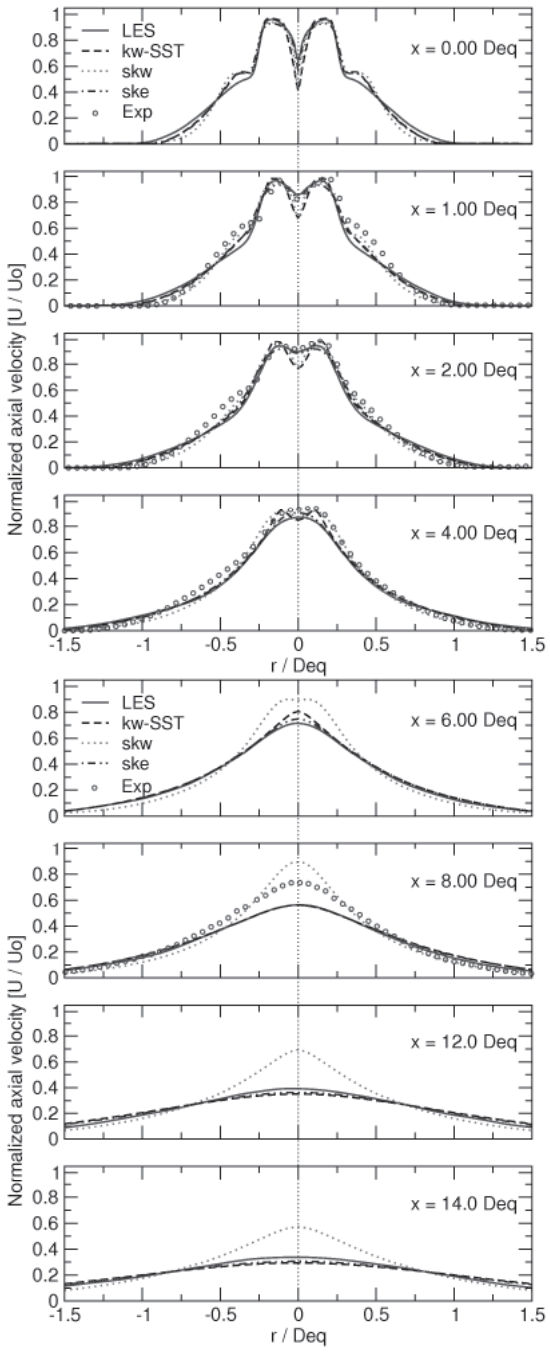

Figure 6. *LES* vs. *RANS* vs. experimental *PIV* data (o). Normalized mean axial velocity profiles along radial-lines located at several downstream positions from the nozzle.

As compared with the experimental *PIV* data, the simulations capture the overall trend of the mean axial velocity profiles within the first four equivalent nozzle diameters downstream from the center-body's tip. It has to be noted that the center-line velocity starts to decay after the downstream location of $x \sim 8.0$ to $10.0D_{eq}$ from the *CB*'s tip in the solution obtained with the standard k-ω model, as compared with the axial location of $x \sim 4$ to $6D_{eq}$ for the other two *RANS* models and the *LES* approach (Fig. 8a).

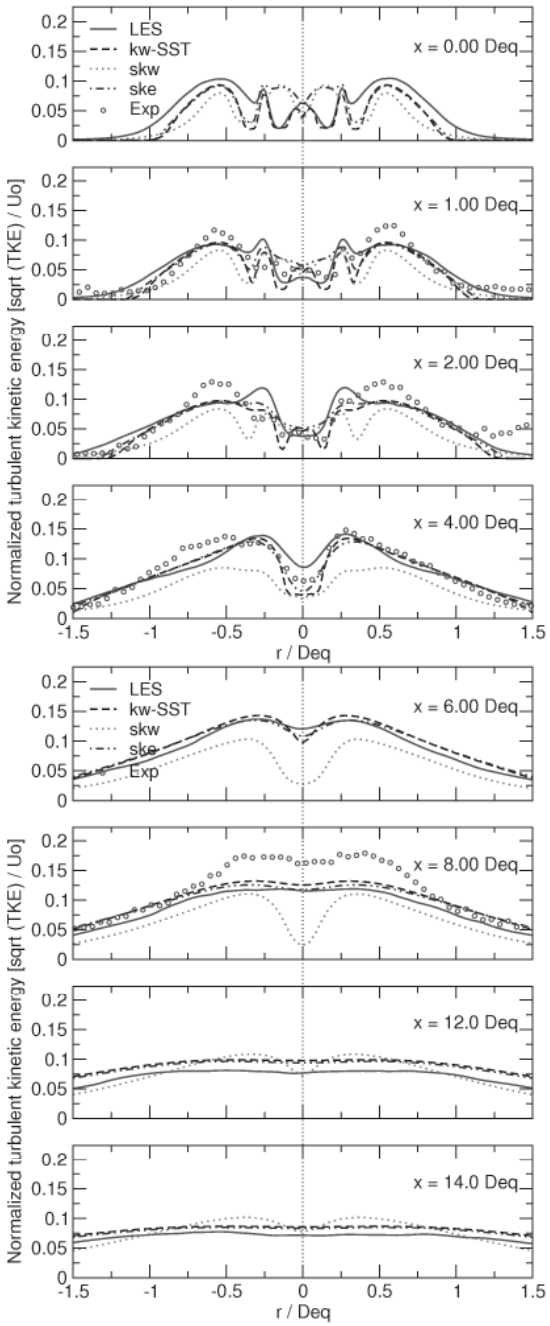

Figure 7. *LES* vs. *RANS* vs. experimental *PIV* data (o). Normalized TKE profiles along radial-lines located at several downstream positions from the nozzle.

The core-fan and fan-ambient shear-layers of the jet are still visible in the *TKE* plots at the axial

distance of $x = 2.0D_{eq}$ (Fig. 7). There is a complete merge between the primary and the secondary streams of the jet at the axial location of $x = 4.0D_{eq}$.

In the region just downstream of the nozzle system there are some differences between the *TKE* levels calculated with the different *RANS* models. However, after the downstream distance of $x \sim 6.0D_{eq}$ excluding the data obtained with the standard k-ω model, these differences are minimal. This is because the *SST* model behaves as a *k-ε* model in the far-downstream zone of the jet, away from the solid boundaries (Figs. 7 and 8b). The standard *k-ω* behaves reasonably in the near nozzle region, but gives very poor agreement with the other models in the far-field region of the jet.

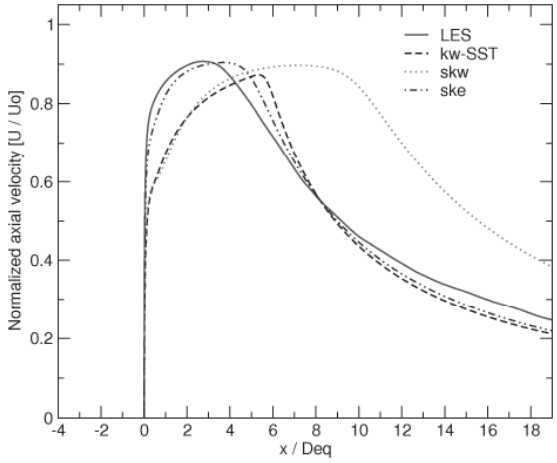

a)

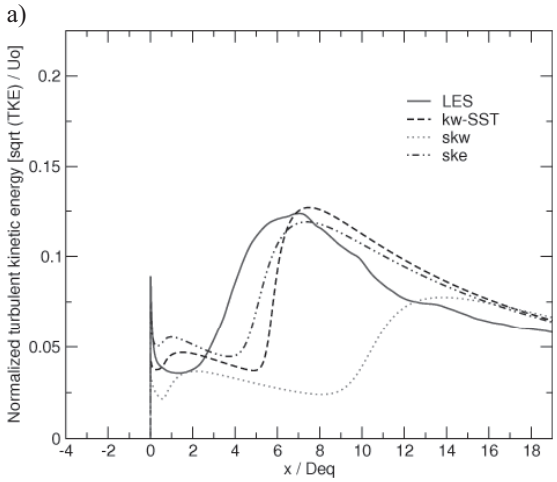

b)

Figure 8. *LES* vs. *RANS*: a) normalized axial velocity along center-line of the jet; b) normalized *TKE* along center-line of the jet; $x/D_{eq} = 0.0$ represents the *CB*'s tip location.

The *LES* calculations show larger *TKE* values as compared with RANS simulations within the potential-core region of the jet. Up to *25%* larger turbulence production associated with the core-fan shear layer ($r \sim \pm 0.25D_{eq}$) is predicted by *LES*. These values are closer to the peak values found by the *PIV*. As compared with the *SST k-ω* and the standard *k-ε* results, a slower decay of the center-line axial velocity is found with *LES* at distances greater than $x \sim 8.0D_{eq}$ downstream of the CB's tip.

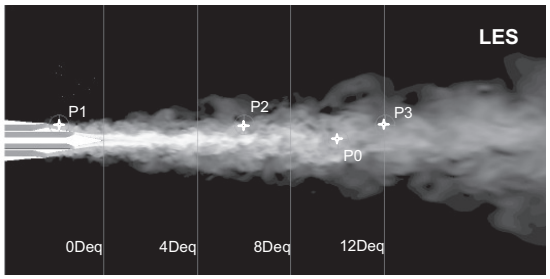

a)

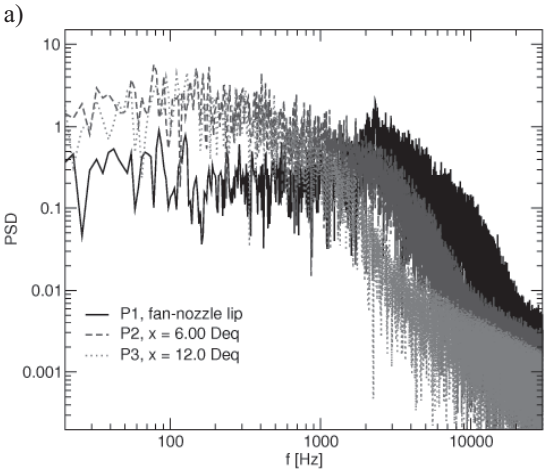

b)

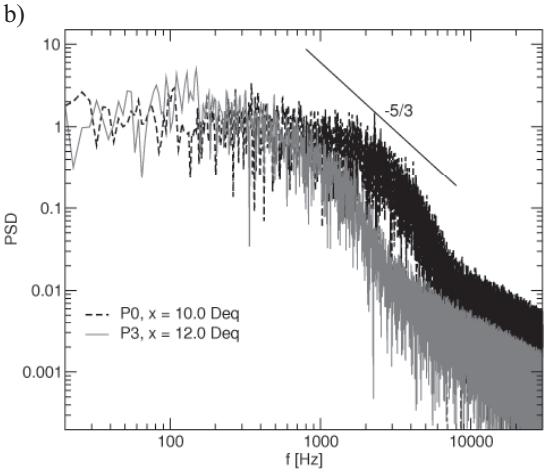

c)

Figure 9. Power Spectral Density (*PSD*) plots calculated at several locations in the flow field from time-history of axial velocity *LES* data: a) the locations of the monitoring points overlapping the instantaneous axial velocity contours in the mid-longitudinal *x-y* plane; b) spectra at *P1*, *P2*, and *P3* locations; c) spectra at *P0* and *P3* locations.

The lower turbulent kinetic energy levels associated with *RANS* may correspond to a slower mixing rate associated with the used turbulence model, a characteristic feature for most of the two-

equation models when applied to jet flows [1, 8, 17]. However, the larger differences between the data obtained with the standard k-ω and the other data sets shown here may be attributed to k-ω model's sensitivity to the free-stream turbulence properties.

Discrepancies were expected between the computational and the experimental data due to the unavoidable mismatch between the inlet boundary conditions used in the simulations (e.g. inlet turbulence intensity levels, flow profiles) and the conditions under which the experimental tests were performed at University of Cincinnati. The differences observed at the larger downstream distances from the nozzle ($x > 8.0D_{eq}$) may be also due to a possible larger air entrainment associated with the experiment.

Power Spectral Density (*PSD*) plots obtained from the LES data are depicted in Fig. 9. Time-history data of axial velocity component were stored at several locations in the flow field. The positions of the monitoring points (*P0* to *P3*) are presented in Fig. 9a. As it is shown in Fig. 9b, there is a frequency shift in the fan-ambient shear-layer of the jet from larger frequencies of about *2.4kHz* found just downstream of the trailing edge of the fan-nozzle to about *80-160Hz* in the area located downstream of the end of potential core region of the jet. Figure 9c shows the spectra obtained at the locations *P0* and *P3* of $10D_{eq}$ and $12D_{eq}$ downstream distances from the *CB*'s tip of the nozzle. Both spectra follow the *-5/3* line for about an order of magnitude.

4. CONCLUSIONS

Within the framework of the commercial solver Fluent® (ANSYS, Inc.) the steady-state *RANS* formulation with three different turbulence closures and then *LES* approach are used to analyze a turbulent jet exhausting a coaxial nozzle system. This nozzle system is a model for the exhaust of a medium bypass ratio turbofan engine.

It is well known that *RANS* turbulence models, although robust and economic, may have limitations in accurately predicting three-dimensional compressible jets with large velocity and temperature gradients. Moreover, the more expensive *LES* approach is highly dependent on the quality of the computational grid as well as on the boundary conditions used, which are supposed to replicate into detail the experimental conditions.

In the present paper the differences between the results obtained using the standard k-ε, the standard k-ω, the *SST* k-ω turbulence models, and the *LES* approach were quantified and the numerical data were compared against *PIV* flow measurements. The comparisons were performed in terms of mean axial velocity component and turbulence kinetic energy levels.

Among all the numerical formulations used in this study, the k-ω turbulence model performed the worst, overpredicting the length of the potential core region of the jet by roughly $4D_{eq}$. The same model predicted significantly lower turbulence kinetic energy levels (up to *70%* lower than the other models) in the shear-layer between the secondary fan-stream and the ambient air.

Within the potential core region of the jet, an overall good agreement was observed between the *PIV* data and the results predicted by the standard k-ε, the *SST* k-ω models, and the *LES* approach. The relatively large differences observed between the numerical and the experimental data at the downstream location of $8D_{eq}$ were attributed to the possible larger air entrainment associated with the experiment.

ACKNOWLEDGEMENTS

This work was supported in part by an allocation of computing time from the Ohio Supercomputer Center (OSC).

REFERENCES

[1] Koch, L.D., Bridges, J.E., and Khavaran, A., 2002, "Flowfield Comparisons from Three Navier-Stokes Solvers for an Axisymmetric Separate Flow Jet", *AIAA paper*, AIAA-2002-0672.

[2] Page, G.J., McGuirk, J.J., Hossain, M., Self, R., and Bassetti, A., 2003, "A CFD Coupled Acoustic Approach for Coaxial Jet Noise", *AIAA paper*, AIAA-2003-3286.

[3] Georgiadis, N.J., Yoder, D.A., and Engblom, W.A., 2006, "Evaluation of Modified Two-Equation Turbulence Models for Jet Flow Predictions", *AIAA paper*, AIAA-2006-0490.

[4] Pao, S.P., Abdol-Hamid, K.S., Campbell, R. L., Hunter, C.A., Massey S. J., and Elmiligui A. A., 2006, "Unstructured CFD and Noise Prediction Methods for Propulsion Airframe Aeroacoustics", *AIAA paper*, AIAA 2006-2597.

[5] Mihaescu, M., Kastner, J.F., and Gutmark, E.J., 2012, "Tertiary Flow Effects on a Co-axial Ducted Jet", *AIAA paper*, AIAA-2012-0064.

[6] Mihaescu, M., Semlitsch, B., Fuchs, L., and Gutmark, E.J., 2012, "Airframe Installation Effects on the Jet Exhausting a Coaxial Nozzle System of a Gas Turbine Engine", *ASME paper*, GT2012-69631.

[7] Hirsch, C. and Tartinville, B., 2009, "Reynolds Averaged Navier-Stokes Modelling for Industrial Applications and some Challenging Issues", *Int Journal of Computational Fluid Dynamics*, Vol. 23, pp. 295-303.

[8] Georgiadis, N.J. and DeBonis, J.R., 2006, "Navier-Stokes Analysis Methods for Turbulent Jet Flows with Application to Aircraft Exhaust Nozzles", *Progress in Aerospace Sciences*, Vol. 42, pp. 377-418.

[9] Wilcox, D.C., 1998, *Turbulence Modeling for CFD*, DCW Industries, Inc., La Canada, CA.

[10] Koch, L.D., Bridges, J., Khavaran, A., 2004, "Mean Flow and Noise Prediction for a Separate Flow Jet with Chevron Mixers", *AIAA paper*, AIAA 2004-0189.

[11] Dippold, V., III, 2008, "CFD Analyses and Jet-Noise Predictions of Chevron Nozzles With Vortex Stabilization", *AIAA paper*, AIAA 2008-0037.

[12] Callender, B., Gutmark, E.J., and DiMicco, R., 2002, "Design and Validation of a Coaxial Nozzle Acoustic Test Facility", *AIAA paper*, AIAA 2002-0369.

[13] Callender, B., Gutmark, E.J., and Martens, S., 2010, "Flow Field Characterization of Coaxial Conical and Serrated (chevron) Nozzles", *Experiments in Fluids*, Vol. 48, pp. 637-649.

[14] Launder, B.E., and Spalding, D.B., 1972, *Lectures in Mathematical Models of Turbulence*, Academic Press, London.

[15] Menter, F.R., 1994, "Two-Equation Eddy-Viscosity Turbulence Models for Engineering Applications", *AIAA Journal*, Vol. 32 (8), pp. 1598-1605.

[16] Lilly, D.K., 1992, "A Proposed Modification of the Germano Subgrid-Scale Closure Model", *Physics of Fluids*, Vol. 4, pp. 633-635.

[17] Engblom, W.A., Khavaran, A., and Bridges, J.E., 2004, "Numerical Prediction of Chevron Nozzle Noise using Wind-MGBK Methodology", *AIAA paper*, AIAA 2004-2979.

Conference on Modelling Fluid Flow (CMFF'12)
The 15th International Conference on Fluid Flow Technologies
Budapest, Hungary, September 4-7, 2012

DEVELOPMENT OF A NEW DESIGN APPROACH FOR HIGH EFFICIENCY LOW PRESSURE AXIAL FANS WITH SMALL HUB RATIO

Thore Bastian LINDEMANN[1], Jens FRIEDRICHS[2], Günter KOSYNA[3]

[1] Corresponding Author. Institute of Jet Propulsion and Turbomachinery, Technical University Braunschweig, Hermann-Blenk-Straße 37, 38108 Braunschweig, Germany. Tel.: +49 531 391 94212, Fax: +49 531 391 94222, E-mail: t.lindemann@ifas.tu-bs.de
[2] Institute of Jet Propulsion and Turbomachinery, Technical University Braunschweig. E-mail: j.friedrichs@ifas.tu-bs.de
[3] Institute of Jet Propulsion and Turbomachinery, Technical University Braunschweig. E-mail: g.kosyna@ifas.tu-bs.de

ABSTRACT

This paper presents the results of an experimental survey on low pressure axial fans. Based on these experimental results a new design program for low pressure axial fans with non-profiled blades was developed and tested. One focus of the new design program was the reduction of the dead water zone in the hub region. Typical low pressure axial fans often have dead water extending up to 50% hub ratio. By using the Strscheletzky criterion [1] in the design process, dead water can be reduced nearly completely.

Designing a low pressure axial fan, prediction of the axial flow velocity is not possible using a standard approach like the extended radial equilibrium. This required using a new assumption for the axial flow velocity. This paper describes the results of scientific researches which show that it is possible to design thin non profiled blades with the computational procedure from Weinig [2] even by changing the stagger angel of the blades.

Based on the new design program three new fans with a different flow and pressure coefficients combined with different hub ratios were designed and measured. The efficiency of the new fan was increased by 8%, keeping all other characteristics similar to conventional fans.

Keywords: axial velocity, dead water, design approach, low pressure axial fan, non-profiled blades

NOMENCLATURE

C	[m/s]	absolute velocity
$\overline{C_x}$	[m/s]	average absolute axial velocity
$const$	[-]	constant variable
d	[m]	diameter
f	[m]	blade camber
$f_{1C\Theta}$	[-]	constant variable for design
$f_{2C\Theta}$	[-]	constant variable for design
f/l	[-]	blade camber ratio
g_{St}	[-]	Strscheletzky criterion
n	[$1/min$]	number of resolutions
l	[m]	chord length
M_W	[Nm]	input torque
P_W	[W]	input power
p	[Pa]	pressure
Δp_{ts}	[Pa]	total to static pressure change
Q	[m^3/s]	volume flow rate
Re	[-]	Reynolds number
r	[m]	radius
s	[mm]	blade thickness
t	[m]	solidity
U	[m/s]	circumferential speed
W	[m/s]	relative velocity
W_U	[m^2/s^2]	weighted Euler work
z	[-]	blade number
α	[°]	absolute angle
β	[°]	relative angle
β'	[°]	modified relative angle
η	[-]	efficiency
λ	[°]	stagger angle
$\Delta\lambda$	[°]	stagger angle variation
ν	[-]	hub to tip ratio
ρ	[kg/m^3]	density
φ	[-]	flow coefficient
ψ	[-]	pressure coefficient

Subscripts and Superscripts

design	design
C	Cone
H	hub
max	maximum
r	radial direction
T	tip
ts	total to static
x	axial direction
Θ	circumferential direction
1,2	inlet, outlet

1. INTRODUCTION

Low pressure axial fans are used in many different fields of application. Due to the low pressure rise of these fans, a stator is not needed and the rotor has only a low blade count. To obtain a larger flow rate, low pressure axial fans are often built with a small hub to tip ratio. Mostly those fans were built with non-profiled blades, made of thin sheet metal plates. Even by larger fans, the blades were designed without twist [3,4]. For critical Reynolds numbers, which are less than $Re \approx 10^5$ in a cascade, a non-profiled blade has obvious advantages over profiled blades [5]. One reason for these advantages is the different behavior of the boundary layers between profiled and non-profiled blades. At a profiled blade the laminar boundary layer breaks up into turbulence and reattaches to the surface. For thick airfoils like profiled blades the separation of the turbulent boundary layer is at the rear of the airfoil. The separation bubbles of this type are normally very short but they hardly affect the lift on the airfoil. Non-profiled or thin airfoils have also separation bubbles, but of a different type. For thin blades the bubbles are at the leading edge. The length of these bubbles tends to decrease with increasing stagger until the bubbles break down [6,7]. For decreasing Reynolds numbers thin blades have the advantage that the separation bubbles increase slowly and due of that the characteristic declines slowly [8]. The disadvantage of non-profiled blades is that only a smaller inlet angle range can be used.

Typical of those fans is the occurrence of separated flow in the hub area and a non-uniform axial flow velocity, which complicates the design of low pressure axial fans. Also the solidity ratio varies highly from hub to tip, and the Reynolds numbers often change from laminar, in the hub region to turbulent at the tip. These complicated flow conditions and the low pressure rise of these fans are perhaps the main reasons that a simple and reliable approach for low pressure axial fans with non-profiled blades and high efficiency does not exist. In consideration of the new European Energy Related Products (ErP) directive there is an increasing interest from the industry for such a design approach. For the first step of developing the new design approach the blade angle calculation according to Weinig [2] were tested for a static blade row [9]. This project was financed by the Forschungsvereinigung für Luft- und Trocknungstechnik e.V. (FLT) from own resources. As a next step, a new design approach for non-swept low pressure axial fans with non-profiled blades was developed. This project was financed by FLT and the Federation of Industrial Research Associations (AIF) and financed within the budget of the Federal Ministry of Economics and Technology Germany (BMWi).

2. MEASUREMENT TECHNOLOGY BASIC PARAMETER

2.1. Test Rig and Measurements

All measurements mentioned in this paper were conducted at a suction side chamber test rig for low pressure axial fans with a maximal diameter of 720 mm, according to the DIN EN ISO 5801 and DIN 24163. All fans were tested and installed on the measuring chamber at free air intake and exhaust (installation category A, according to DIN EN ISO 5801) with constant rotational speed at each operating point.

For measurement the input power of the fan a torque meter with a range of ± 5Nm and an overall accuracy of 1% of full scale was used. An incremental shaft encoder could detect the rotating frequency and the position of the disc. The position of the fan is required for conducting time averaged Partical Image Velocimetry (PIV) measurements for each blade position. In order to evaluate the flow conditions of the different fans a 2D2C PIV system was used. Furthermore the fan was tested with five hole and hot wire probes at the in- and outlet.

With a 2D2C PIV system only two velocity components of an air flow could be measured. To analyze the 3D air flow, two 2D2C PIV measurements were necessary. The outlet flow of a low pressure axial fan has a high turbulence. Therefore the average air speed of a blade position was calculated of the mean values of 100 PIV measurements. As source for the PIV measurements a haze generator was used. This generator produces continually a constant volume of haze, by using a fluid based on propylene glycol. The haze is sucked in at the inlet cone and mixed by the flow straightener of the test rig.

Pneumatic five hole probes were used to measure the inlet and outlet angles along the radius of the fan. With a Five hole probe it is only possible to measure time averaged values. The probe was 5 mm in front or behind the closest position of the blade to the probe.

A hot wire probe was used to define the turbulence of the flow. To analyze the turbulence the probe was placed in different positions behind the fan.

2.2. Equations and Definitions

To compare different low pressure axial fans, dimensionless values are used. The dimensionless flow coefficient is defined as:

$$\varphi = \frac{Q}{\frac{\pi}{4}\left(d_T^2 - d_H^2\right) \cdot U_T} \qquad (1)$$

The dimensionless pressure rate total to static is

$$\psi_{ts} = \frac{\Delta p_{ts}}{\rho \frac{U_T^2}{2}} \quad (2)$$

The efficiency total to static is defined as

$$\eta_{ts} = \frac{Q \cdot \Delta p_{ts}}{P_W} \quad (3)$$

with

$$P_W = 2 \cdot \pi \cdot n \cdot M_W \quad (4)$$

The hub to tip ratio is

$$\nu = \frac{d_H}{d_T} \quad (5)$$

One important aspect for the design was to minimize the separated flow in the hub region. To estimate if there is a risk of separated flow for the design, the Strscheletzky criterion is helpful. The Strscheletzky criterion is defined as

$$g_{St} = \frac{C_{2x}}{C_{2\Theta}} \geq 0.8 \quad (6)$$

The definition of flow velocities and angles are shown in Figure 1.

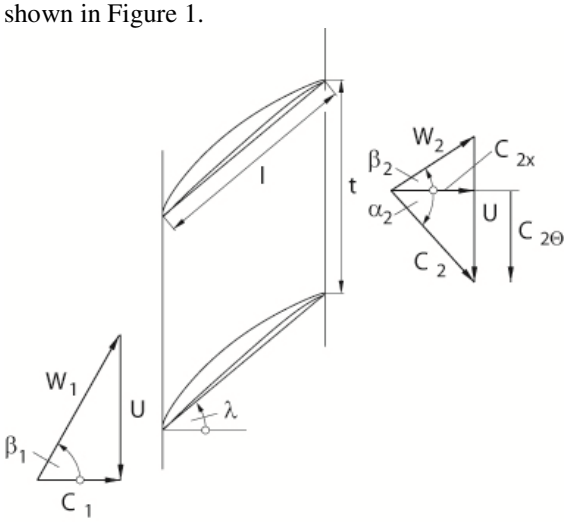

Figure 1. Definition of flow velocities and angles

The stagger angle for the blade design from Weinig is defined as

$$\lambda = \frac{\beta_1 + \beta_2}{2} \quad (7)$$

To estimate the local workload of the blade the weighted Euler work was used

$$W_U(r) = U \cdot C_{2\Theta}(r) \cdot \frac{C_x(r)}{\overline{C_x}} \quad (8)$$

2.3. Design parameters

To evaluate the new design approach three different low pressure axial fans were designed and built. Before designing the first new fan a reference fan with swept blades was tested. All new designed fans have the following specifications

- No stator
- Rotor diameter d_T= 497mm
- Cone diameter d_C = 503mm
- Non-profiled blades with constant thickness of s = 2mm
- Maximal available space for the hub in axial direction 80mm
- Variable chord length
- Maximal chord length l = 190mm
- Blade number z = 5
- No sweep or dihedral on the blade
- Reynolds numbers in critical region

All designed fans have an external diameter of 497mm. The minimal inner diameter of the cone is 503mm. The cone was a standard full nozzle covering the full axial length.

The design parameters of the developed new fans are:

Table 1. Design parameters of new fans

	ψ_{ts} [-]	φ [-]	ν [-]	n [1/min]
Reference	0.22	0.23	0.3	1350
Fan 1	0.22	0.23	0.3	1350
Fan 2	0.15	0.25	0.2	1350
Fan 3	0.20	0.25	0.3	1350

Each newly designed fan was able to change the stagger angle λ continuously by turning the whole blade.

3. DESIGN APPROACH

Low pressure axial fans have in general a small hub to tip ratio. Due to this small hub ratio, low pressure axial fans often have hub dead water up to 50% of the diameter in the design point. This means that only the outer blade area produces the required workload. Also the large tip clearance of the fan causes separation in this area. These two dead water areas are one reason why the axial flow velocities of these fans are inhomogeneous and make the design of low pressure axial fans difficult.

Aim of this project was to develop a simple approach which can design low pressure axial fans

with minimized hub dead water and maximized total to static efficiency. As reference a fan of serial production with a maximum static efficiency of 43.9% and a hub dead water of around 50% was chosen. The serially produced fan had swept blades.

3.1. Circumferential component of absolute velocity

The reference measurements show that even if the camber of the blade does not produce a constant circumferential component of the absolute velocity $C_{2\Theta}$, the circumferential velocity behind the fan is nearly constant. Only at the tip region as a cause of the large tip clearance of this blade and at the hub because of the dead water, the circumferential component differs. Due to the high turbulence, there is an intensive mixing effect on the flow cause of interaction between the wakes of the blades and the passage flow combined with diagonal characters of the radial flow. Because of this mixing effect the average circumferential velocity becomes nearly constant. In some cases the circumferential velocity decreases from hub to tip around 10% of the highest circumferential velocity when measured in radial direction.

For the design of fluid machines there are several different classic design methods. One classic existing approach is the Free Vortex design. By a Free Vortex Design the circumferential velocity is defined as

$$C_\Theta = \frac{const}{r} \tag{9}$$

The highest circumferential components are at the hub. For a low pressure axial fan with a small hub ratio this would increase the risk of getting hub dead water and decrease the usable blade area. Because of that a Free Vortex Design could not be used for these fans.

The second classic design, the Solid Body Design has great advantages for reducing the hub dead water [10]. For a Solid Body Design the circumferential component is defined as

$$C_\Theta = const \cdot r \tag{10}$$

In this case C_{x1h} is larger than C_{x2h}. To reach the required circumferential component of the absolute velocity $C_{2\Theta}$ for a Solid Body Design a pre-swirl is therefore necessary. To produce a pre-swirl a stator would be needed. Due to the fact that this design approach should work without stator, the Solid Body Design couldn't be used.

As consequence only a nearly constant circumferential component of the absolute velocity $C_{2\Theta}$ in radial direction seems to be reasonable. For the approach the "Eq. (11)" was used for $C_{2\Theta}$

$$C_\Theta = f_{1C\Theta} \cdot r \quad + f_{2C\Theta} \tag{11}$$

This circumferential function is comparable to a design concept of Lewis [11], but Lewis has combined the Free Vortex and the Solid body Design. For the new design the circumferential component is split in two parts. The constant variable $f_{2C\Theta}$ generates a constant circumferential component; the constant variable $f_{1C\Theta}$ gives the possibility to increase or decrease the circumferential component in the tip region. In "Fig. 2" the gray line is an example for the circumferential velocity designed with "Eq. 11". The design process starts with a constant circumferential component ($f_{2C\Theta}$). For designing a fan with a high workload a positive $f_{1C\Theta}$ value is chosen to reduce dead water in the hub region. If the workload of the fan is low, the risk of getting hub dead water is low as well. For these fans it is advantageous using a negative $f_{1C\Theta}$ to reduce the losses at the tip region.

To evaluate the estimated dead water in hub region the Strscheletzky criterion, shown in "Eq. (6)" can be used. The boundary value of 0.8 is originally for a single stage machine in free vortex design [1, 12 - 13]. Different studies at the IFAS show that this value is also reasonable for low pressure axial fans even when they are not designed with free vortex workload. For some designs g_{st} – values of 0.42 were possible without getting a hub dead water. For this case the axial velocities were already pretty low. By Strscheletzky it is possible to avoid hub dead water by using solid body design [10]. As already mentioned above, for a low pressure axial fan the Solid Body Design could not be used. Strscheletzky has also considered different design combinations in one cylindrical pipe [14-16].

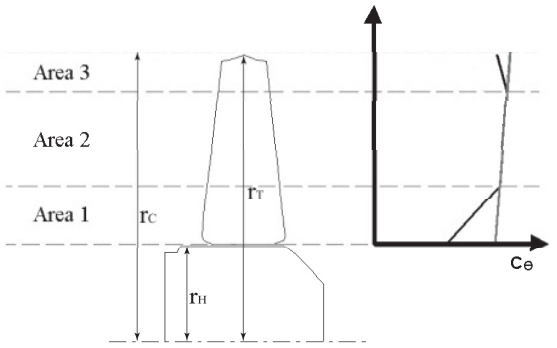

Figure 2. Schematic design of the circumferential velocity for low pressure axial fans

To decrease hub dead water the swirl in the hub region must be reduced to a minimum. The simplest way to minimize the swirl is to increase the stagger angle or/and to decrease the camber of the blade. For stability reasons the blade must have a minimum camber. With the camber, the stagger angle, the rotary speed and the maximal hub space

the circumferential velocity can be calculated according to the axial velocity.

Because of the high losses at the tip of the blade due to the large tip clearance it is positive for efficiency to reduce the pressure gradient from pressure to section side of the blade. To reduce the deflection of the blade has to be decreased. By decreasing the deflection the circumferential velocity gets lower. Combining these three conditions to a design strategy, the fan has the following principle circumferential velocity characteristic from hub to tip (Figure 2).

In the hub region the design starts with a minimum blade camber for a non-profiled blade designed by the method from Weinig [2]. Than the circumferential velocity increases up to the radius were Strscheletzky criterion is fulfilled. For designing a g_{st} – value of 0.8 was used. After reaching the Strscheletzky point a nearly constant circumferential velocity was used, depending on the pressure rise the fan should produce. For a low pressure rise a decreasing circumferential velocity is good for the efficiency, for greater pressure raises an increasing circumferential velocity is useful. To avoid losses in the tip region the circumferential velocity at the blade tip should be reduced as shown in "Fig. 2".

3.2. Axial velocity

The second important part for the design is the computation of the axial velocity for a given circumferential velocity. Aim of the project was to develop a simple design approach for low pressure axial fans. As the design approach should be simple and easy to handle the computation of the axial velocity with a computational fluid dynamics (CFD) program would be too complex during design.

It is impossible to use the simple radial equilibrium as for these the radial components of the flow have to be small. Due to the flow separations in the hub and tip region, low pressure axial fans have large radial flow velocities. Therefore the simple radial equilibrium could not be used for computation.

In order to use the extended radial equilibrium different parameter conditions have to be known. The fan works with a free air intake and a free exhaust. Due to that it is impossible to assume boundary conditions in front or behind the cone. Assuming boundary conditions in the cone is not possible, cause of the flow separations at the hub and the tip. Often there is also backflow in the tip region. Without these boundary conditions it is not possible to solve the extended radial equilibrium.

Comparing different axial velocity measurements and CFD calculations it becomes apparent that the dimensionless axial velocity distribution along blade height is nearly the same for each proved low pressure axial fan. In "Fig. 3" different axial velocities for the aforesaid fans in "Tab. 1" are shown. Only the size of the hub dead water is different for each fan. For Fan 1, two different axial velocities are shown. The measurement of Fan 1 is the axial velocity for this fan without changing the stagger angle. "Fan 1 -7°" means, the stagger angle was reduced by 7° deviant to the stagger angle for a shock less inlet defined by Weinig ("Eq. (7)"). Based on these experimental results an equation for the axial velocity was designed. Using this function in combination with the design for the circumferential velocity it is possible to design a low pressure axial fan.

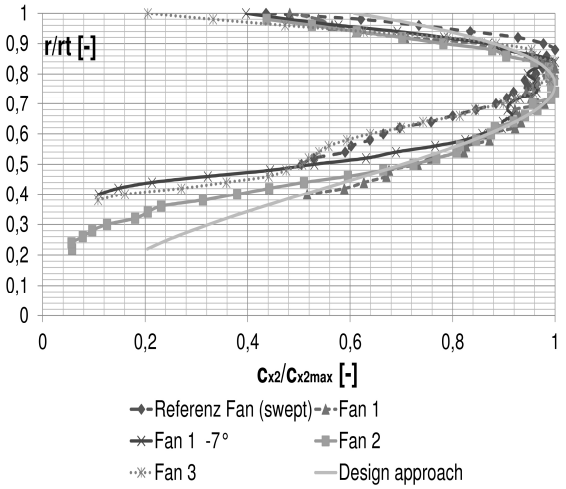

Figure 3. Axial velocity distributions for tested fans

3.3. Blade design

Following the above contemplated axial and circumferential velocity the outlet angle for the blade can be calculated. The circumferential velocity is at the inlet zero, so for the inlet angle only the axial velocity is needed. The inlet axial velocity distribution in this design case increases a little from hub to tip. For the full nozzle used in the test rig the inlet axial velocity at the tip is around 30% higher than at the hub. With the continuity equation (conservation of mass) the inlet axial velocity and therefore the inlet angle could be calculated.

With the flow angles the blade angles can be calculated with the method from Weinig [2]. In the literature by Eckart and Schnell [17] it is possible to use Weinig up to camber angles of 50°, this equates a camber ratio of f/l = 0.125. In a work from Scholz [18] the maximum camber angle for non-profiled thin sheet blades is 36°. In the FLT research project from Schrapp [9] a maximum camber ratio of *f/l* = 0.09 was tested. Schrapp also studied how the outlet angle reacts by changing the stagger angle.

While changing the stagger angle the outlet angle changes as well. For the tested fans, changing the stagger angle in a moderate range, the outlet

flow angle changes according to the change of the stagger angle.

$$\beta_2' \approx \beta_2 + \Delta\lambda \qquad (12)$$

For a moderate stagger angle change the efficiency of the fan does not change much. The range for the maximum possible change of the stagger angle depends on the camber of the blade. A highly curved blade has already a high workload, so the diffusion factor is high. By decreasing the stagger angle, the load of the blade increases additionally and the flow separates earlier. Because of that the stagger angle for a less loaded blade could be decreased more than at an already high loaded blade.

4. MEASUREMENTS AND RESULTS

The three fans shown in "Tab. 1" have been designed and measured. The first built fan "Fan 1" has a maximum camber of $f/l \approx 0.08$. The camber at the hub was around $f/l \approx 0.045$, at the tip f/l ≈ 0.06. To reach the design parameters the stagger angle has to decrease 7°. The fan reaches a maximum efficiency of 52.7% without changing λ with a modified stagger angle of -7° the efficiency decrease marginal to 52.2%. By decreasing λ about 10° the efficiency decrease 2%, for λ = - 15° the efficiency goes down about 7%. The dead water in the hub region goes up to a radius $r/r_t = 0.45$. The fan version without changed stagger angle had no dead water in the hub region, but only a low workload. Compared to the reference fan with the same design parameters of "Fan 1 -7°" the efficiency could increases by more than 8%, also the dead water in the hub region could be reduced. "Fig. 4" shows the efficiency for the different fans.

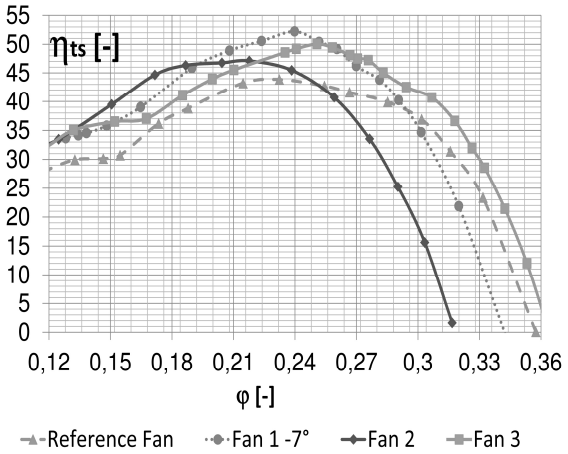

Figure 4. Efficiency of the measured fans

On "Fan 1" the blade design method from Weinig with modifying the stagger angle was used to design a low pressure axial fan for the first time. Before this Weinig was only used in a cascade at the IFAS. With "Fan 1" it could be verified that Weinig is useable for the blade design of these fans.

"Fig. 5" shows a 2D PIV measurement of "Fan 1 -7°" working at the design point. The white area indicates the cone and the hub of the fan. Behind the hub there is the lowest axial velocity of around -4 m/s which leads to backflow. With increasing distance to the fan the dead water increases as well. The axial velocity at a diameter around r = 200 mm is not constant. The velocity alternates according to the blade position.

The following fan built was designed with a higher camber ratio. "Fan 2" has a maximum camber of $f/l \approx 0.12$. With this high camber it is possible to reach the required workload without decreasing the stagger angle. Aim of this design was to design a low pressure fan which reaches the design point without having hub dead water. Especially for a hub to tip ratio of $\nu = 0.2$ it is hard to prevent a dead water in design point.

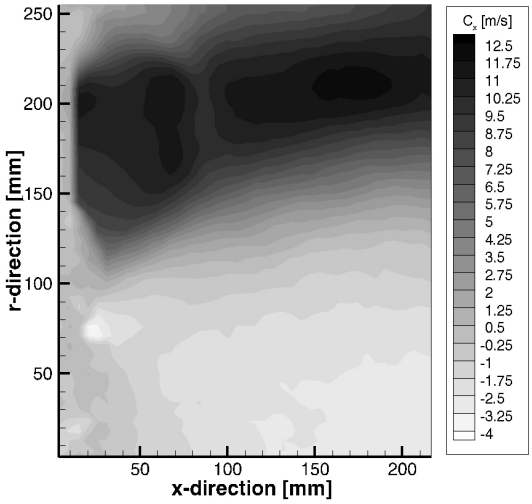

Figure 5. 2D PIV measurement "Fan 1 -7°" Axial velocity at design point

"Fan 2" reaches the design point without modifying the stagger angle. In spite of the small hub to tip ratio "Fan 2" has no hub dead water at the design point. Due to the high camber and the smaller hub to tip ratio the maximum efficiency of the fan is only 47.1%. By increasing the stagger angle about 5° the efficiency rose up to 0.5%, by decreasing the stagger the efficiency lowered by 1.8%. To compare the efficiency of "Fan 1" and "Fan 2" the hub diameter of "Fan 2" had been increased up to $\nu = 0.3$. With this new hub diameter "Fan 2" reaches a maximum efficiency of 48.2%.

"Fig. 6" shows the results of a five hole probe measurement behind "Fan 2", working at design point. The points in the diagrams are the measurement points. The design velocities $C_{x,design}$ and $C_{\Theta,design}$ are drawn in this figure. The measured circumferential component in the middle area is a

little lower as designed. Due to that the axial velocity in this area is higher than expected.

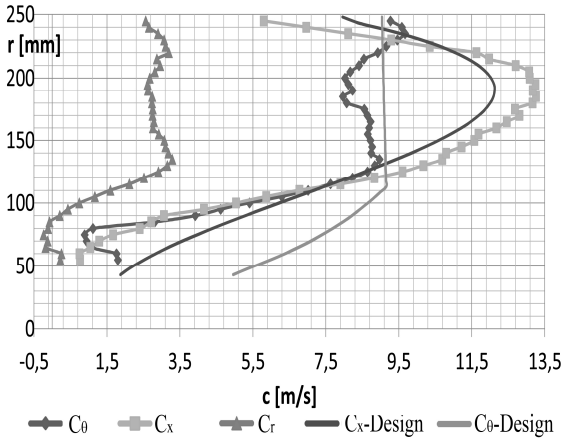

Figure 6. Velocities "Fan 2" at design point, compare design and measurement

The designed weighted Euler work at middle blade height, shown in "Fig. 7", could be achieved. Due to the tip clearance the axial velocity at the tip is lower than designed. In hub region due to the incipient dead water, the axial and circumferential component is lower than designed. By checking the Strscheletzky criterion in the design process hub dead water was expected in the region. At the hub up to $\nu = 0.24$ g_{St} is around 0.42. For a higher hub ratio g_{St} is around 1 and higher. At the tip ($\nu = 0.96$ to 1) g_{St} is again below 0.8.

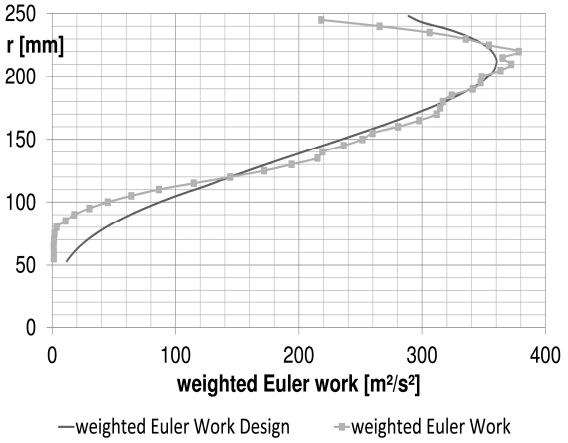

Figure 7. Weighted Euler work "Fan 2" at design point, compare design and measurement

"Fig. 8" shows a 2D PIV measurement of "Fan 2" working at design point. Directly behind the hub is a small "dead water" because of the wake of the hub. With increasing distance to the fan the dead water decreases. The axial velocity at the middle diameter is not constant either. Due to the higher flow coefficient of "Fan 2" the axial velocities are higher than for "Fan 1".

The last fan built "Fan 3" was designed and measured to verify if the design approach works reliable. The camber of the blades was limited during design on $f/l = 0.08$. By exceeding the maximum camber the design program decreases the stagger angle automatically and starts the calculation process again. The fan reaches the design point almost exactly. The maximum efficiency of the fan is 50.1%. The dead water at the hub region goes up to a hub to tip ratio of $\nu = 0.4$. The design works automatically by using MATLAB. From starting the design process until complete CAD – model it takes around 15min for an experienced user. Due to this the user is able to design customized fans according to given requirements.

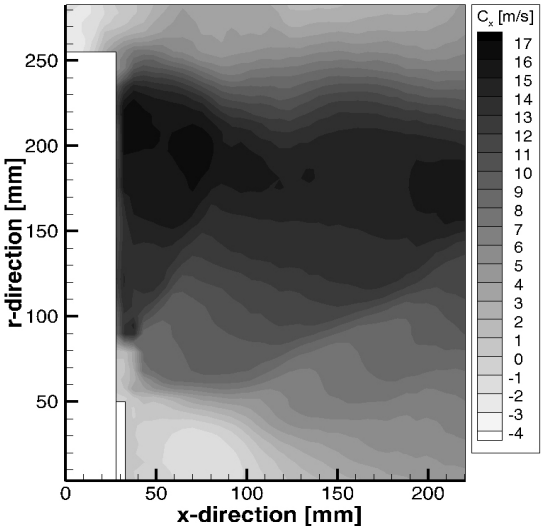

Figure 8. 2D PIV measurement "Fan 2" Axial velocity at design point

5. SUMMARY

This paper describes a new design approach for high efficiency low pressure axial fans with non-profiled blades and a small hub ratio. Due to the small hub ratio these fans often have a large separation area in the hub region. By reducing the circumferential velocity in the hub region it is possible to avoid or reduce the dead water. To reduce dead water the camber ratio of the blade should be minimized in the hub region. A little camber is needed for stability reasons. To estimate the occurrence of hub dead water the Strscheltzky criterion can be used. Decreasing the stagger angle increases the risk of hub dead water.

The optimal circumferential dispersion for low pressure axial fans should be split in three areas. In the hub area the circumferential velocity should, as mentioned above, be reduced to a minimum. In the middle area a nearly constant circumferential velocity should be used. A Solid Body Design in this area is impossible. A stator would be necessary. Due to the small hub ratio a Free Vortex Design is also impossible, because the circumferential velocity in the hub region would be too high. A

combination of small circumferential velocities from area 1 at the hub and high velocity in area 2 will not match. The third area is the tip region. Because of the high tip losses due to the large tip clearance of these fans, the circumferential velocity should be reduced in the region as well.

For a low pressure axial fan the simple and the extended radial equilibrium could provide a simple and usable solution. To complete the design process an assumption for the axial velocity is needed. The dimensionless axial velocity distribution along blade height is nearly the same for each proved low pressure axial fan. Due to that it is possible to assume the axial velocity by using an estimated function derived from measurement results.

With the blade design method for thin blades of Weinig it is possible to calculate the required blade angles. According to the maximum camber ratio of the blade the workload can by increased by decreasing the stagger angle. A moderate modification of the stagger angle has only a small effect on the efficiency. For efficiency reasons a camber ratio greater than f/l = 0.09 should be avoided. On the opposite if the hub dead water needs to be reduced, this can be reached by using a larger camber ratio, in order to get a lower efficiency.

The design approach is limited for non-swept blades. In a new FLT research project the design approach will be enhanced to design swept low pressure axial fans. Swept blades are used to reduce the noise of the fans.

ACKNOWLEDGEMENTS

We would like to thank the research association, Forschungsvereinigung für Luft- und Trocknungstechnik (FLT) e.V. for financial support of the research project AiF-Nr.: 14958 N/1. This project was carried out under the auspices of Federation of Industrial Research Associations (AIF) and financed within the budget of the Federal Ministry of Economics and Technology Germany (BMWi).

REFERENCES

[1] Horlock, J. H. 1967, „Axialkompressoren“, *Verlag G. Braun, Karlsruhe.*

[2] Weinig, F., 1935, „Die Strömung um die Schaufeln von Turbomaschinen“, *Verlag von Johann Ambrosius, Leipzig.*

[3] Beyer, B., 2001, „Beitrag zur Auslegung von Kühllüftern für Nutzfahrzeuge“, *Diss. Univ. Hannover.*

[4] Stangl, M., Weinhold, K., 1998, „Zur Auslegung von Breitschaufel-Axialventilatoren“, *Luft und Kältetechnik*, 25 3, pp. 121 – 124.

[5] Eck, B., 1972, „Ventilatoren, 5th edition”, *Springer Berlin.*

[6] Berg, B van den, 1969, „Renolds number and Mach number effects on the maximum lift and the stalling characteristics of wings at low speeds”, *NLR* TR 69025 U.

[7] Walraevens, R. E., Cumpsty, N.A., 1995 „Leading Edge Separations Bubble on Turbomachinery Blades”, *Journal of Turbomachinery* , Vol 117 ,pp.115-125.

[8] Sunada, S., Skaguchi, A., Kawachi, K., 1997, „Airfoil Section Characteristics at Low Reynolds Number*”, Journal of Turbomachinery*, Vol 119, pp.129-135.

[9] Schrapp, H., Stark, U., 2006, „Gitter-untersuchungen an Kreisbogenprofilen konstanter Dicke bei kleinen Reynoldszahlen“, *FLT,* Heft L208, Frankfurt am Main.

[10] Strscheletzky, M., 1962, „Gleichgewichts-formen einer aus zwei Teilströmungen bestehenden inkompressiblen Drallströmung in geraden, langen, zylindrischen Rotations-hohlräumen. 1. Mitteilung*“, Voith Forschung und Konstruktion*, Heft 9, Article 3.

[11] Lewis, R. I., 1996, „Turbomachinery Performance Analysis”*, Arnold Great Britain.*

[12] Schlünkes F., 1959, „Messungen an Luft-strömungen mit konstantem Drall im geraden Kreisrohr*“, Voith Forschung und Konstruktion*, Heft 5, Article 2.

[13] Marcinowski, H.., 1959 „Optimalprobleme bei Axialventilatoren*“, Voith Forschung und Konstruktion*, Heft 5, Article 3.

[14] Strscheletzky, M., 1964, „Gleichgewichts-formen einer aus zwei Teilströmungen bestehenden inkompressiblen Drallströmung in geraden, langen, zylindrischen Rotations-hohlräumen. 2. Mitteilung“*, Voith Forschung und Konstruktion*, Heft 12, Article 4.

[15] Strscheletzky, M. 1959, „Gleichgewichts-formen der rotationssymmetrischen Strö-mungen mit konstantem Drall in geraden zylindrischen Rotationshohlräumen“, *Voith Forschung und Konstruktion*, Heft 5, Article 1.

[16] Strscheletzky, M., 1962, „Zur Berechnung der Gleichgewichtsformen von rotations-symmetrischen Strömungen mit konstantem Drall in langen zylindrischen Rotations-hohlräumen“, *Voith Forschung und Konstruktion*, Heft 8, Article 7.

[17] Eckert, B., Schnell, E., 1961, „Axial- und Radialkompressoren“*, Springer Verlag Berlin.*

[18] Scholz, N., 1965, „Aerodynamik der Schaufelgitter“, *Verlag G. Brauns*, Karlsruhe.

Conference on Modelling Fluid Flow (CMFF'12)
The 15th International Conference on Fluid Flow Technologies
Budapest, Hungary, September 4-7, 2012

Prediction of the Flow Characteristics of an Axial Fan at Off Design

Matthias SEMEL[1], Philipp EPPLE[2], Oliver LITFIN[3], Bettina WILLINGER[4], Antonio DELGADO[5],

[1] Corresponding Author. Institute of Fluid Mechanics, Friedrich Alexander University Erlangen/Nuremberg. Cauerstr.4, 91058 Erlangen, Germany. Tel.: +49 09131 85 29486, E-mail: matthias.semel@lstm.uni-erlangen.de
[2] Department of Mechanical Engineering, University of applied sciences Coburg. E-mail: philipp.epple@hs-coburg.de
[3] Institute of Fluid Mechanics, Friedrich Alexander University Erlangen/Nuremberg. E-mail: oliver.litfin@lstm.uni-erlangen.de
[4] Institute of Fluid Mechanics, Friedrich Alexander University Erlangen/Nuremberg. E-mail: bettina.willinger@lstm.uni-erlangen.de
[5] Institute of Fluid Mechanics, Friedrich Alexander University Erlangen/Nuremberg. E-mail: antonio.delgado@lstm.uni-erlangen.de

ABSTRACT

Axial fans are classically designed with the mean line theory based on the Euler turbo machinery equation. In order to design a machine, a span wise vortex distribution is chosen for a specific rotation speed. The result of this design process is a blade geometry with well-defined blade angles. With this theory the flow characteristics at the design point, such as the pressure and velocity distribution are known. However the interaction between the blade geometry and the flow at off-design regimes is analytically unknown, i.e. the design of a fan and its optimization is restricted to the design point. Solving the simplified equation of radial equilibrium (SRE) considering the specified blade geometry for the off-design domain, enables the analytical calculation of the velocity and the pressure distribution at each flow rate. This ideal flow calculation enables the designer to predict the whole hydraulic characteristic of an axial impeller. At the same time a deeper understanding of the flow process at off-design regimes is gained. In the present work the described approach of solving the SRE for defined blade geometry was analyzed and theoretical equations for the flow characteristics at off-design points were developed. The gained equations were validated by comparing the ideal flow predictions with flow data obtained by RANS CFD calculations of a designed fan.

Keywords: axial flow turbomachinery, forced vortex model, free vortex model, off-design characteristic, SRE

NOMENCLATURE

C	$[-]$	constant
K	$[m^2/s]$	angular momentum
$\underline{Q}$	$[m^3/s]$	flow rate
T	$[K]$	temperature
$\underline{c}$	$[m/s]$	absolute velocity
f	[-]	maximum camber
g	[-]	position of max. camber
k	[-]	ratio of active flow rate to design flow rate
l	$[m]$	length
m	[-]	hub to tip ratio
n	$[rev/min]$	rotation speed
p	$[Pa]$	pressure
$r \cdot c_u$	$[m^2/s]$	angular momentum
t	[-]	thickness
$\underline{u}$	$[m/s]$	rotational velocity
$\underline{w}$	$[m/s]$	relative velocity
z	$[-]$	blade number
ω	$[1/s]$	angular velocity
β	$[^\circ]$	blade angle
ψ	$[-]$	local head coefficient
ϕ	$[-]$	local flow coefficient
ρ	$[kg/m^3]$	density
γ	$[^\circ]$	segmented angle

Subscripts and Superscripts

0	design point
1	section before the blade entry
2	section behind the blade exit
f	fluid
imp	impeller
l	lift
s	static
sc	section
t-s	total-to-static
t	total
ti	tip

m	meridional direction
max	maximal flow rate
u	circumferential direction

1. INTRODUCTION

Analytic design methods known from the literature, e.g. Carolus [1], Eck [2] and Lakshminarayana [3], predict the performance characteristics of an axial impeller at the design point. There the classical mean line theory based on the Euler turbo machinery equation is used for calculating the flow. A constant meridional velocity distribution is assumed at the entry and at the exit of the blade. There are also two dimensional design approaches taking into account the span wise mass flow distribution at the blade exit by the help of the simplified radial equilibrium equation (SRE). In this theory the equations for a inviscid fluid are solved at the design point in order to obtain the three dimensional energy transfer and flow pattern in axial fans at the exit of the blade. An investigation concerning the validity of this approach and the resulting flow field behind the fan is given by Vad [4]. A possible approach for predicting the off design characteristics is neglecting the change in the mass flow distribution due to different flow rates over the span and to calculate the flow pattern at off design with fixed blade angles. This approach for radial and axial fans was elaborated and investigated by measurements and CFD-calculations by Epple [5, 6]. Assuming the validity of the SRE at any flow rate leads to a different solution of the problem. Here the interaction between the spanwise mass flow distribution and the corresponding spanwise angular momentum distribution at the blade exit is modeled at each flow rate. This approach postulates cylindrical stream surfaces or slightly conical stream surfaces at the blade exit at any flow rate. The aim of the presented work is to show the influence of the trailing edge angle distribution β_2 of the impeller onto the ideal flow at any operational point. In order to obtain flow pattern in the fan, CFD computations have been performed. This work includes an analysis and validation of a free vortex design. First the equations for the calculation of variable meridional velocity and the angular momentum at any flow rate will be derived. The total-to-static pressure for the full flow rate range will be obtained. Finally The new distributions and the resulting performance characteristics will be shown in detail together with a validation with CFD computations.

2. ANALYTICAL DERIVATION

2.1. The simplified equation of radial equilibrium

The simplified equation of radial equilibrium is given by Lakshminarayana [3]:

$$2 \cdot \pi \cdot n \frac{d\left(r \cdot c_{u2}\right)}{dr} = \frac{c_{u2}}{r} \frac{d\left(r \cdot c_{u2}\right)}{dr} + c_{m2} \frac{dc_{m2}}{dr} \quad (1)$$

n is the number of revolutions per minute, r is the radius, $r \cdot c_{u2}$ being the angular momentum and $c_{m,2}$ is the meridional velocity of the fluid at the exit of the blade. The SRE bases upon the assumption that the radial component of the velocity is negligible before the flow enters and after the flow exits the blade [1], rearranging the terms and interpreting the velocity c_u as the angular velocity of the fluid relative to the rotational axis of the impeller $\omega_f = \frac{c_u}{r}$ the following equation

$$\left(\omega_{imp} - \omega_f\right) \cdot \frac{d\left(r^2 \cdot \omega_f\right)}{dr} = c_{m2} \frac{dc_{m2}}{dr} \quad (2)$$

is obtained,where ω_{imp} is the angular velocity of the impeller. This approach has proven useful in treating the simplified equation of radial equilibrium mathematically. The angular velocity of the fluid is related to the angular velocity of the impeller through the local head coefficient, i.e.

$$\psi\left(r\right) = \frac{\omega_{f,0}}{\omega_{imp}} \quad (3)$$

$$\phi\left(r\right) = \frac{c_{m2,0}}{r \cdot \omega_{imp}} \quad (4)$$

Equation (2) is a first order ordinary differential equation and can be solved either for any given angular momentum distribution $\omega_f \cdot r^2$ or for any meridional velocity distribution. When an angular momentum is chosen the solution is the corresponding meridional velocity. In the literature, e.g. [1], [3], two different concepts of designs are defined. In case of an constant angular momentum distribution over the radius the design is called free vortex design. When the angular momentum is assumed as being a function of the radius, the design is named free vortex. Hence, there is only one possible free vortex design but a wide variety of forced vortex designs.

2.2. Extended mean line theory

Having designed a blade at a specific design point the spanwise distribution of the outflow blade angle β_2 is fixed. Two different configurations can be described assuming a strictly blade congruent flow: The reference configuration at the design point 0 and the active configuration at any other flow rate. The angular velocity of the fluid can be described in both configurations:

$$\frac{\omega_{f,0} - \omega_{imp}}{c_{m2,0}} = \frac{1}{r \tan\beta_{2,0}} \quad (5)$$

$$\frac{\omega_f - \omega_{imp}}{c_{m2}} = \frac{1}{r \tan\beta_{2,0}} \quad (6)$$

So the active angular velocity ω_f of the fluid can be described as a function of the active meridional velocity (active flow rate), the reference meridional velocity(index:0) and the reference angular velocity of the fluid :

$$\omega_f = \omega_{imp} - \frac{c_{m2}}{c_{m2,0}} \cdot \left(\omega_{imp} - \omega_{f,0}\right) \quad (7)$$

The derivation of the active angular velocity of the fluid ω_f is given by:

$$\frac{d\omega_f}{dr} = \left[\frac{c_{m2}}{c_{m2,0}^2}\cdot\frac{dc_{m,0}}{dr} - \frac{1}{c_{m2,0}}\cdot\frac{dc_{m2}}{dr}\right] \cdot \left(\omega_{imp} - \omega_{f,0}\right) + \frac{c_{m2}}{c_{m2,0}}\cdot\frac{d\omega_{f,0}}{dr} \tag{8}$$

Rewriting Eq. (7) and combining it with the SRE (Eq. (2)) leads to :

$$\frac{\omega_{imp} - \omega_{f,0}}{c_{m2,0}}\frac{dr^2\omega_f}{dr} = \frac{dc_{m,2}}{dr} \tag{9}$$

Substituting the derivation into the equation of radial equilibrium, rearranging the terms, and using the definitions of the head coefficient and the flow coefficient (Eqs. (3) and (4)), the following equation results:

$$\frac{dc_m}{dr} + p(r)\cdot c_m = s(r) \tag{10}$$

with

$$p(r) = -\frac{1}{\varphi\cdot r\cdot\omega_{imp}}\cdot\frac{dc_{m2,0}}{dr} + \underbrace{\frac{2\cdot(1-\psi)}{r\cdot\left(\varphi^2+(1-\psi)^2\right)}}_{p_2} \tag{11}$$

$$s(r) = 2\frac{\omega_{imp}\cdot(1-\psi)\cdot\varphi}{\left(\varphi^2+(1-\psi)^2\right)} \tag{12}$$

The general solution of this first order ordinary differential equation is given as:

$$c_m = e^{-\int p(r)dr}\cdot\left[s(r)\cdot e^{\int p(r)dr}\int dr + C\right] \tag{13}$$

The constant C can be calculated by using the definition for the flow rate Q:

$$Q = 2\pi\cdot\int_{m\cdot r_{ti}}^{r_{ti}} r\cdot c_m dr \tag{14}$$

Here m is the hub to tip ratio and r_{ti} is the shroud radius. After some manipulation the general solution is obtained:

$$c_{m2} = c_{m2,0}\cdot\left[1 + C(k)\cdot e^{-\int p_2(r)dr}\right] \tag{15}$$

$$C(k) = \frac{Q_0\cdot(k-1)}{2\cdot\pi\int r\cdot e^{-\int p_2 dr}dr} \tag{16}$$

In the equation is k the ratio between the active flow rate Q and the design flow rate Q_0.

$$k = \frac{Q}{Q_0} \tag{17}$$

The presented equations enable the designer to compute an ideal head-flow characteristic of an axial impeller considering also the change in the angular momentum and the meridional velocity.

2.3. Hydraulic characteristics

Following the extended mean line design theory, the static pressure rise $\Delta p_{s,sc}$ at a specific radius section of an axial fan is given by

$$\Delta p_{s,sc} = \frac{\rho}{2}\cdot\left(\underline{w}_1^2 - \underline{w}_2^2\right) \tag{18}$$

In this equation is $\underline{w}_1$ and $\underline{w}_2$ the relative velocity at blade entry and blade exit and ρ the density of the fluid. The total-to-static pressure rise at a specific blade section sc $\Delta p_{t-s,sc}$ is defined as:

$$\Delta p_{t-s,sc} = \Delta p_s - \frac{\rho}{2}c_1^2 \tag{19}$$

Considering the no pre-swirl flow entry at the blade entry,the relative velocity $\underline{w}_1$ can be expressed as the sum of the rotational velocity $\underline{u}_1$ and the absolute velocity $\underline{c}_1$:

$$\underline{w}_1^2 = \underline{u}^2 + \underline{c}_1^2 \tag{20}$$

Inserting this equation into Eq. (19) leads to

$$\Delta p_{t-s,sc} = \frac{\rho}{2}\left[u^2 - \left(1 + \frac{1}{\tan^2\beta_2}\right)\cdot c_{m2}^2\right] \tag{21}$$

Combining Eq. (21) with Eq. (6) the total-to-static pressure rise can be given for any flow rate as:

$$\Delta p_{t-s,sc} = \frac{\rho}{2}\cdot\left[2\cdot\frac{1}{\rho}\Delta p_{t,sc} - c_m^2 - c_u^2\right] \tag{22}$$

In order to get the physical pressure rise of the whole axial fan the mass flow averaged pressure increase over the complete impeller surface has to be taken:

$$\Delta p_{t-s} = \frac{2\pi}{Q_0\cdot k}\int_{m\cdot r_{ti}}^{r_{ti}} r\cdot\Delta p_{t-s,sc}\cdot c_{m2}dr \tag{23}$$

3. CASE STUDY

The meridional velocity distribution, the angular momentum distribution and the pressure distribution were computed with the presented method for an exemplary design case. For the validation of the method CFD computations were performed. The computation was done for an impeller with 17 blades. The blade shape was derived by inverse calculation of a NACA 4 digit airfoil camber line. First the method for inversely calculating the camber line will be presented and then the configuration of the simulation will be shown.

3.1. Exemplary design case

A free vortex design was chosen in order to illustrate the effect of the extended mean line theory onto the ideal characteristics of the fan. For the reference configuration the following equations are valid:

$$c_{m2,0} = \frac{Q}{r_{ti}^2\cdot(1-m^2)\cdot\pi} = const. \tag{24}$$

$$\omega_{f,0} = \frac{K}{r^2} \tag{25}$$

Table 1. Reference configuration

Parameter	Variable	Value
rotation speed	n	3000 rev/min
hub to tip ratio	m	0.5
shroud radius	r_{ti}	0.28 m
design flow rate	Q	6 m^3/s
design angular momentum	K	5.85 m^2/s

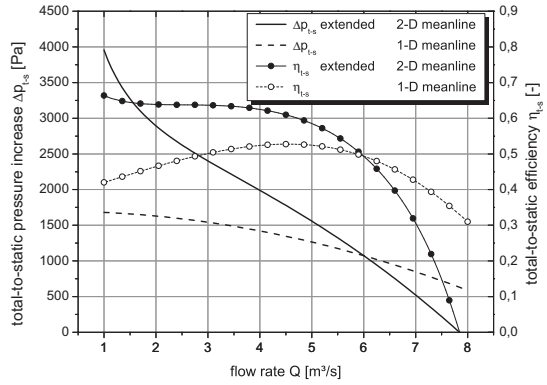

Figure 1. Ideal hydraulic characteristics

The design flow rate and the basic geometric dimensions are shown in table 1. Based on the given parameters, the ideal efficiency and t-s pressure increase characteristic can be calculated using the assumption of a constant meridional velocity profile at every flow rate (1-D mean line assumption) or the derived extended mean line approach considering the SRE. Both calculated graphs are depicted in Figure 1 The extended mean line t-s pressure characteristic shows high values at low flow rates decreasing nearly linear towards higher flow rates. The 1-D mean line solution however shows a parabolic behavior. This parabolic curve is open downwards with its maximum at zero flow rate. The whole characteristic is below the extended mean line solution up to the design flow rate of $Q_0 = 6\ m^3/s$. Behind the design point the 1-D mean line solution lies above the extended mean line solution. The maximum flow rate of the extended solution is reached at $Q_{max} = 7.8\ m^3/s$ while the 1-D solution does not posses a root in the investigated interval. The t-s efficiency of the extended mean line shows a parabolic rise from the maximum flow rate until a flow rate of $Q = 3\ m^3/s$. Beyond this point the efficiency is nearly constant. The 1-D mean line solution has a parabolic graph with its maximum efficiency at a flow rate of $Q = 4.5\ m^3/s$. Both curves differ significantly from each other. The reason for this difference in the characteristics appears due to different meridional velocity distributions at off design. Figure 2(a) shows the change in the meridional velocity due to

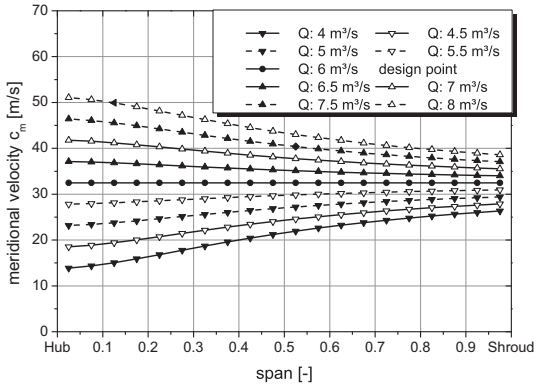

(a) meridional velocity

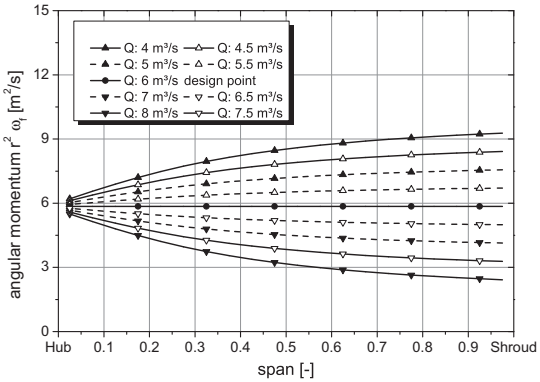

(b) angular momentum

Figure 2. Spanwise meridional and angular momentum distribution at different flow rates

different flow rates. For the design case (Fig. 2(a) $Q = 6\ m^3/s$) the meridional velocity is constant. If the impeller works at higher flow rates (Fig. 2(a) $Q > 6\ m^3/s$), it is in the *overload* regime and hence, the meridional velocity will change from a constant meridional velocity to a variable velocity with lower velocities at the hub and higher velocities at the shroud. For increasing flow rates this behavior becomes more significant. For an impeller working in *partial load* the whole behavior is reversed (Fig. 2(a) $Q < 6\ m^3/s$). Higher velocities can be found at the shroud and lower velocities at the hub (Fig.2(a)). The alterations in the meridional velocity results also in a variation of the angular momentum distribution. Figure 2(b) depicts the change in the angular momentum distribution due to different flow rates. For the design case the angular momentum is again constant (Fig. 2(b) Q = 6 m^3/s). In the overload regime the angular momentum drops slightly from hub to shroud (Fig. 2(b) $Q > 6\ m^3/s$). The drop of the angular momentum from hub to shroud is higher with increased flow rate. For partial load the whole behavior is reversed at the design point distribution. The higher the flow rate the higher is the angular momentum (Fig. 2(b) $Q < 6\ m^3/s$). It is worth mentioning that the design angular momentum

distributions are symmetric with reference to the horizontal angular momentum characteristic at the design point.

3.2. Calculation of the spanwise blade shape

For the blade geometry the camber line of a NACA4 airfoil was used. The three parameters that are necessary for the complete definition of such a camber line are the maximum camber f, the position of maximum camber g and the thickness t.As the CFD simulation should illustrate the flow behavior of a thin airfoil, the thickness t was kept constant at a relative low value of $t = 0.025 \cdot l$. The blade was rounded at the leading edge in order to avoid flow separations. f and g have to be calculated inversely depending on the desired inlet and outlet blade angles β_1, β_2, while the thickness can be given independently. According to Lakshminarayana [3] the blade turning angle is defined as

$$\Delta\beta = \beta_2 - \beta_1 \quad . \tag{26}$$

It is segmented into γ_1 and γ_2 (see Fig. 3) by means of a balancing factor *bal* that has to be chosen between 0 and 1.

$$\gamma_1 = bal \cdot \Delta\beta \tag{27}$$

$$\gamma_2 = (1 - bal) \cdot \Delta\beta \quad . \tag{28}$$

With this equation, it is possible to get f and g using

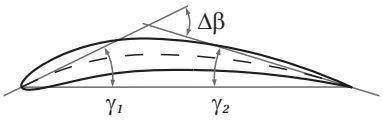

Figure 3. Parameters for the inverse definition of a NACA4 profile

a set of two linear equations.

$$f = \frac{\tan\gamma_2}{\tan\gamma_1 + \tan\gamma_2} \tag{29}$$

$$g = \frac{1}{2} \cdot \frac{\tan\gamma_1 \cdot \tan\gamma_2}{\tan\gamma_1 + \tan\gamma_2} \tag{30}$$

The camber lines were generated with a balancing factor of $bal = 0.65$. With the known balancing factor, γ_1 and consequently the stagger angle λ can be calculated as:

$$\lambda = \beta_1 - \gamma_1 \quad . \tag{31}$$

The spanwise distribution of the lift coefficient c_l of the chosen blade geometry was calculated analytically using the *thin airfoil theory* for the given blade angle distribution (Figure 4) in order to choose the correct blade number. With this c_l-distribution the number of 17 blades seems to be in good agreement to the suggestions in textbooks (e.g. Carolus [1], Eckert and Schnell [7]).

$$z = \frac{4 \cdot \pi \cdot r \cdot c_u}{\left|\underline{w}_\infty\right| \cdot l \cdot c_l} \tag{32}$$

A blade number between 10 at the hub and 22 at the shroud are suggested by this formula. $\underline{w}_\infty$ is the relative velocity

$$\underline{w}_\infty = \frac{1}{2} \cdot \left(\underline{w}_1 - \underline{w}_2\right) \tag{33}$$

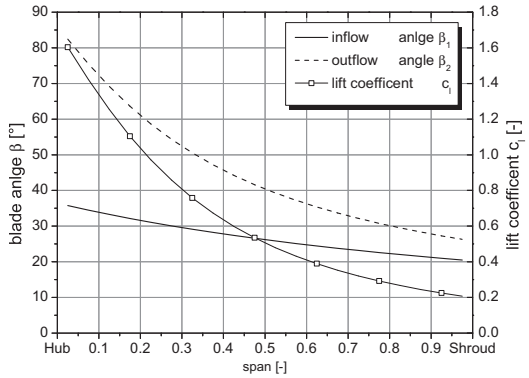

Figure 4. Spanwise blade angle and lift coefficient distribution

3.3. Computional fluid dynamics (CFD)-simulation setup

The 3D CFD simulations are performed on high performance computers (HPC) with ANSYS CFX®13. To reduce complexity, the hub and shroud radii are kept constant from inlet to outlet and a tip gap is not modeled. The 3D CFD simulations are performed with a single passage using a rotational periodicity interface and a constant pitch of $21,17°$ according to the blade number of $z = 17$. The simulation is composed of three domains

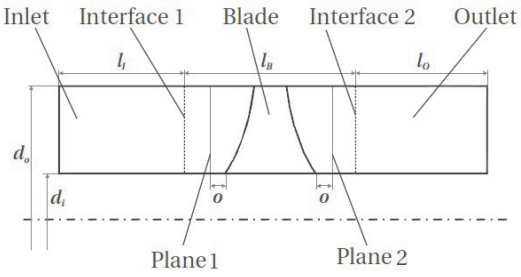

Figure 5. Simulation setup

– inlet, blade and outlet (see Fig. 5). The basic dimensions can be found in tab.2. The domains are connected by means of a *Frozen Rotor* interface. The mass-flow-rate and pressure increase at the interfaces

Table 2. Basic dimensions of the simulation setup

Parameter	Variable	Value
Inlet axial length	l_I	$0.65m$
Blade axial length	l_B	$0.2m$
Outlet axial length	l_O	$0.65m$
Axial offset	o	$0.02m$

as well as at the inlet and outlet were monitored in the solver during the simulation. The simulations reached the convergence criteria after approximately 1h with a RMS of less than 10^{-5}. A grid study was performed to ensure the independence of the solution from the number of elements. The grid consists of 318600 hexa-elements. For the inlet and outlet region the same mesh is used with 37500 Elements. For the blade channel 243600 Elements are used. A block-structured hexahedral grid is used for all three domains including an O-Grid around the blade. The mesh density is increased in the near-wall regions of the blade,hub and shroud (see. Fig.6). The flow behavior of the geometry was calculated

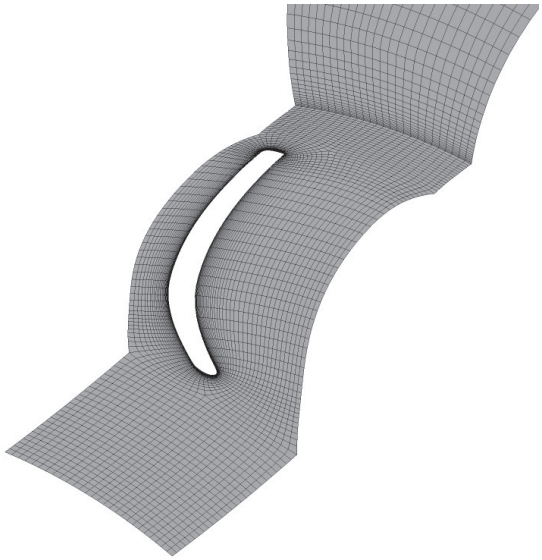

Figure 6. grid at the hub

for two different boundary conditions (BC). For a quasi potential flow a free-slip BC was applied at the walls and a no-slip-BC was used to simulate a viscous flow. The inlet boundary condition is set to a mass flow according to the flow rate and a reference density of $\rho = 1.184 kg/m^3$. A reference pressure of $p = 101325\ pa$ is chosen at the outlet together with a static temperature of $T = 25°C$. All CFD simulations were performed using the *Shear Stress Transport* turbulence model (Menter [8]).

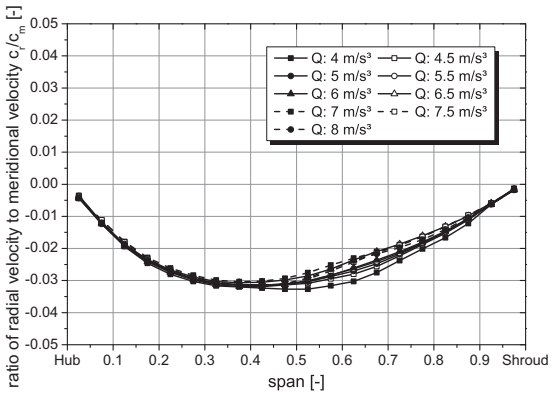

(a) potential flow

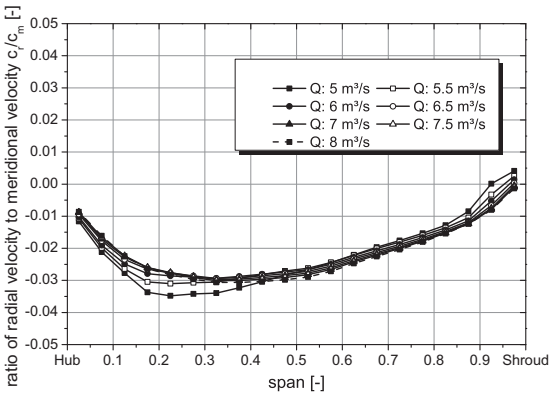

(b) viscous flow

Figure 7. Ratio c_r/c_m at plane 2 for different flow rates

3.4. Results

The derived equations are valid for the condition of negligible radial velocities before entering and after exiting the impeller. To verify this condition the radial velocity distribution was investigated at the plane "2" (Fig.5) for different flow rates and flow boundary conditions. Figure 7 shows the ratio of the radial velocity to the meridional velocity c_r/c_m for different flow rates. For the potential flow calculation is ratio very low at every flow rate (Fig. 7(a)). For the viscous flow solution is the ratio slightly higher, but it is still on a low level(Fig. 7(b)). The results demonstrates that the assumption of negligible radial velocities is in good agreement with the flow data for both investigated flow boundary condition. So the constrains for the derived equations are fulfilled. Figure 8(b) displays the calculated t-s efficiency and t-s pressure increase characteristics of the potential as well as the viscous flow calculation. The pressure increase of the potential flow calculation possess a maximum flow rate of $Q_{max} = 7.5\ m^3/s$. The value is lower than the one of the calculated extended mean line solution. For lower flow rates the t-s pressure increase of the potential flow is rising qualitatively similar to the extended 2-D mean line solution until a flow rate of $Q = 4\ m^3/s$ is reached. For lower

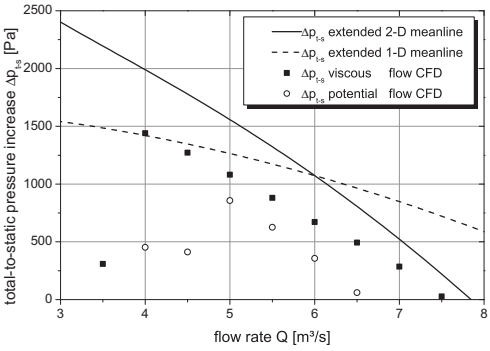

(a) t-s pressure increase

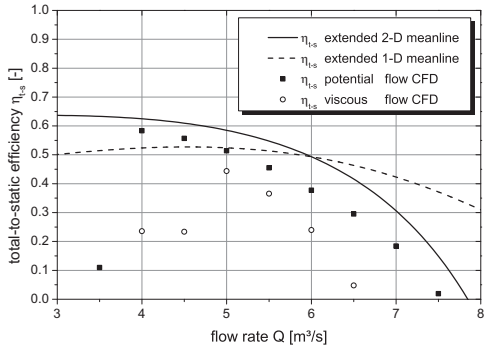

(b) t-s efficiency

Figure 8. Hydraulic characteristic

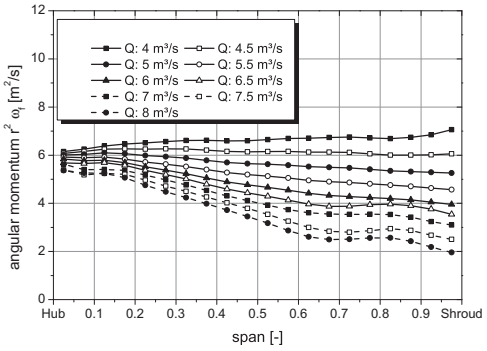

(a) potential flow

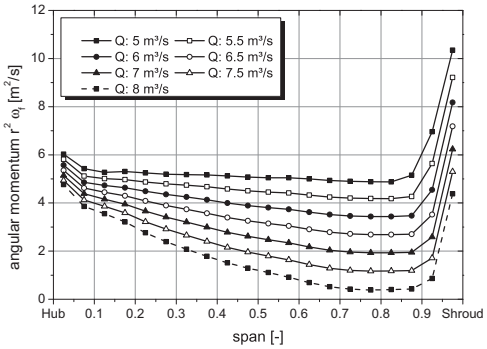

(b) viscous flow

Figure 9. Spanwise angular momentum distribution at different flow rates

flow rates the pressure drops to a lower level. The impeller is at stall. The pressure characteristic of the viscous flow calculation shows a qualitatively matching to the extended mean line approach. Here the viscous drag in the tube and at the blade leads to pressure losses. This results into a lower pressure characteristic of the viscous flow. The starting point of the stall behavior of the impeller migrates towards a higher flow rate of $Q = 5\ m^3/s$. The maximum flow rate also decreases towards $Q_{max} = 6.8\ m^3/s$. The difference in the slope of the potential flow as well as the viscous flow pressure increase and the mean line solutions are linked with the finite blade number and the deviation angle between the flow angle and the prescribed blade angle. As the calculated graphs of the mean line solutions are based on the fixed blade angles a different characteristic is likely to occur. However the characteristics should show a qualitatively matching as it is visible here. The t-s efficiency of the potential flow solution as well as the viscous flow solution shows a qualitatively good conformity to the extended 2-D mean line prediction. A similarity to the characteristic of the 1-D mean line solution cannot be observed for the potential flow solution as well as to the viscous flow solution.

Figure 9 depicts the dependency of the angular momentum distribution at different flow rates for the potential flow and the viscous flow analysis. All angular momentum distributions of the potential flow simulation possess qualitatively the same shape: High values at the hub reducing toward the shroud. The difference of the angular momentum between hub and shroud gets more pronounced at higher flow rates. Only for a flow rate of $Q = 4\ m^3/s$ the flow shows opposite behavior: Low values at the hub increasing slightly toward the shroud. The design goal of a constant angular momentum distribution at $Q = 6\ m^3/s$ was not achieved. This prescribed condition is shifted to a flow rate between $Q = 4.0\ m^3/s$ and $Q = 4.5\ m^3/s$. Moreover the constant angular momentum level at $Q = 4\ m^3/s$ posses a higher value than the design goal($K_0 = 5.85\ m^2/s$, $K = 6.2\ m^2/s$). The results of the CFD calculations for the angular momentum as well as the meridional velocity at flow rates between $Q = 4.5\ m^3/s$ and $Q = 8\ m^3/s$ can be interpreted as the flow behavior at *overload regime*. Comparing the design curves (Fig.2(b)) with the corresponding potential flow curves it is visible that all simulation curves behave qualitatively like the design curves at overload. Consequently the curves between $Q = 4.5\ m^3/s$ to $Q = 8.0\ m^3/s$ in Fig.9 should qualitatively match with the design distributions at overload. While the angular momentum distribution of the flow rate $Q = 4.0\ m^3/s$ has to comply with the *partial load regime* of the design distributions. These requirements are all fulfilled, and a qualitatively match between the extended mean line distribution and the potential flow distribution is visible. The angular momentum

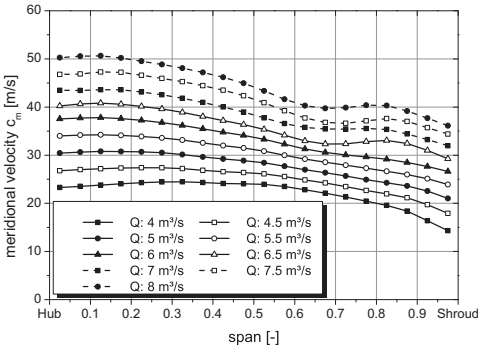

(a) potential flow

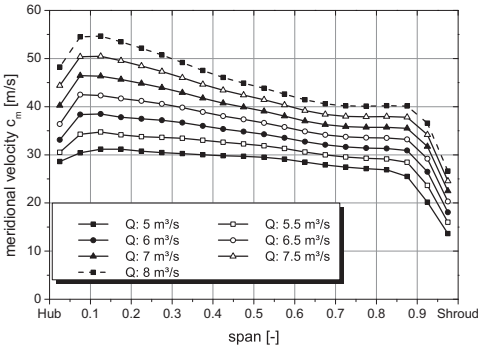

(b) viscous flow

Figure 10. Spanwise meridional velocity distribution at different flow rates

distribution of the viscous flow simulation behave predominantly analog to the potential flow solutions. Only at the region near to the shroud and the hub differences are visible. At the shroud the angular momentum is slightly higher, while at the hub a strong increase in the angular momentum is visible for each flow rate. Considering the undisturbed part of the spanwise distribution a similar result to the potential flow analysis is visible. The design goal of a constant angular momentum distribution is not reached at any flow rate. Analog to the potential flow simulations all distributions can be interpreted as the flow behavior at *overload regime*. So except the differences at the near wall region, all viscous flow distribution show a qualitative match to the extended mean line prediction. All the meridional velocity distributions of the viscous flow as well as the potential flow simulation possess qualitatively the same shape: High values at the hub reducing toward the shroud (Fig.2(a)). The difference of the meridional velocity between hub and shroud gets more pronounced at higher flow rates. The analysis of the angular momentum distribution has demonstrated, that the CFD-distributions have to be interpreted as distributions in *overload regime*. Consequently the curves in Fig.10 should qualitatively match with the design distributions at overload. All the CFD-distributions comply with this requirement. They all have qualitatively the same shape as the design distributions at overload. The comparison of both distributions, meridional velocity and angular momentum, indicate a good qualitative consistence between the design prediction and the CFD-simulations. The only additional effect that is visible for the viscous flow solutions is a meridional velocity reduction at near wall regions. This effect can be explained with wall friction effects.

4. SUMMARY

In the presented work a prediction method for the ideal flow field of an axial fan for each flow rate was introduced. This method is based on the SRE and the assumption of a strict blade congruent flow even in the off design domain. Global parameters such as the pressure increase or the t-s efficiency can be calculated for every flow rate as well as the ideal three dimensional flow pattern. With this method the designer is no longer limited by optimizing the design point as the whole characteristic can now be modeled. Moreover by comparing ideal flow data with results of a CFD-calculation noticeable problems in the real flow can be detected, and analyzed. The validation of the design prediction with CFD computations have shown that this prediction method provides a good qualitative estimation of the off-design behavior of the fan. The way in which the angular momentum distribution and the meridional velocity distribution is changing for different flow rates are consistent with the presented CFD results. The presented method provides just an ideal flow prediction, the designer is not able to skip real flow calculations and give a precise assumption of the real flow characteristics, however a qualitative estimation is possible.

References

[1] Carolus, T. 2009 *Ventilatoren*. Vieweg+Teubner, 2^{th} edn.

[2] Eck, B. 1972 *Ventilatoren*. Springer-Verlag, 4^{th} edn.

[3] Lakshminarayana, B. 1996 *Fluid Dynamics and Heat Transfer of Turbomachinery*. John Wiley & Sons, Inc.

[4] Vad, J. and Bencze, F. 1998 "Three-Dimensional Flow in Axial Flow Fans of Non-Free Vortex Design". *Int J Heat Fluid Flow*, Vol. 19, pp. 601–607.

[5] Epple, P., Karic, B., Illic, C., Becker, S., Durst, F., and Delgado, A. 2009 "Design of radial impellers: a combined extended analytical and numerical method". *Proceedings of the Institution of Mechanical Engineers, Part C: Journal of Mechanical Engineering Science*, Vol. 223, pp. 901–917.

[6] Epple, P., Miclea, M., Luschmann, C., and Delgado, A. 2009 "An extended analytical and

numerical design method with applications of radial fans". *Proceedings of the ASME 2009 International Mechanical Engineering Congress & Exposition*, Lake Buena Vista, Florida, USA, November, ASME.

[7] Eckert, B. and Schnell, E. 1980 *Axial- und Radialkompressoren*. Springer-Verlag, 2^{th} edn.

[8] Menter, F. 1994 "Two-Equation Eddy-Viscosity Turbulence Models for Engineering Applications". *AIAA Journal*, Vol. 32, No. 8, pp. 1598–1605.

Conference on Modelling Fluid Flow (CMFF'12)
The 15th International Conference on Fluid Flow Technologies
Budapest, Hungary, September 4-7, 2012

INVESTIGATION OF THE INFLUENCE OF SKEW ON THE AERODYNAMIC AND ACOUSTIC BEHAVIOUR OF AXIAL FANS FOR AUTOMOTIVE COOLING SYSTEMS

Mohamed ZAYANI[1], Şaban ÇAĞLAR, Martin GABI

[1]Corresponding Author. Institute of Fluid Machinery (FSM), Karlsruhe Institute of Technology (KIT). Engelbert Arnold Straße 12, 76131 Karlsruhe. Tel.: +49 721 608 43624, Fax: +49 721 608 43529, E-mail: zayani@kit.edu

ABSTRACT

The noise emission of axial fans for automotive cooling systems has considerable contribution to the sound emission of the vehicle. The target of many investigations is to find measures to reduce the noise of the fan. For this purpose, an understanding of the different noise generating mechanisms is essential. To analyze the influence of important characteristic parameters, time equivalent measurements of the noise propagation were carried out. The main focus is the change of the geometry while keeping the blade loading constant. The scope of this project is to investigate the influence of skewed blades to the aerodynamic and acoustic behaviour of axial fans. Therefore axial fans with different skewed geometries were built and measured. The variations include unskewed, backward and forward skewed blades. The strength of the skew is also varied and includes different forms for forward skewed axial fans. To explain the lower efficiency in the case of the forward skewed axial fan and the best result in the noise propagation, numerical investigations were carried out. For more details about the influence of the hub flow on the acoustic of the axial fans, two more axial fans were built and measured. These comprise additionally the skew of the near hub part of the blade.

Automotive cooling system, Axial fan, Gap flow, Noise emission, Skew variation

NOMENCLATURE

l	$[m]$	Chord length
t	$[m]$	spacing
s	$[m]$	Gap width
D_a	$[m]$	Outer diameter
n	$[min^{-1}]$	Rotational speed
Q	$[m^3/s]$	Volume flow rate
u	$[m/s]$	Circumferential velocity
P_W	$[W]$	Shaft power
Lp	$[dB]$	Sound pressure level
BPF	$[Hz]$	Blade passing frequency

Greek symbols

Δp_{fa}	$[Pa]$	Fan static pressure
φ	[-]	Volume flow coefficient
η	[%]	System efficiency
ψ	[-]	Pressure coefficient

1. INTRODUCTION

The aerodynamic noise generated by axial fans is usually an addition of tonal and broadband components. The noise in axial fans at lower Mach numbers is mainly attributed to the blade forces. These forces can be separated into steady and unsteady forces, the first ones resulting from the function of the fan and can not be avoided (so-called Gutin noise). The unsteady blade forces generate the largest part of the total noise [1, 2]. Possible mechanisms for these are: Interaction of turbulent inflow to the fan with the rotating blades, the flow separation at the fan blades, the interaction of the turbulent boundary layer with the blade trailing edge and the gap flow.

A widely used technique to reduce noise from axial fans in disturbed environment, like the case in the car installation situation, is to skew the axial fan. Former investigations about the influence of the skew to the aerodynamic and therefore the acoustic behaviour are not entirely clear. They are examined in this work in more detail. The main focus of this work is the investigation of the influence of different skewed axial fans on the acoustic behaviour, while keeping the aerodynamic load constant.

2. CONFIGURATION AND FAN GEOMETRY

The test rig at the Institute of Fluid Machinery (FSM) of the Karlsruhe Institute of Technology (KIT) allows simultaneous measurements of the aerodynamic (ISO 5801) and acoustic (ISO 3741) parameters (see Figure.1).

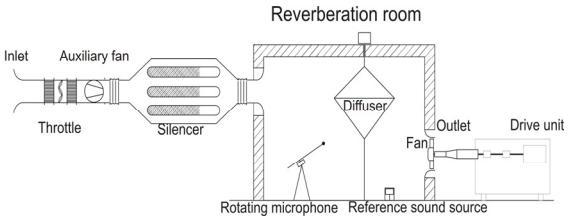

Figure 1. Aero-Acoustic test rig

The fan is installed at the outlet of the test rig and blows the air from the reverberation room out in the laboratory hall. The characteristic parameters are: Volume rate, pressure increase, rotational speed and torque at the drive unit and even the sound pressure fluctuation are measured simultaneously. For the calculation of the flow rate the velocity and the area of the inlet-nozzle is needed. The velocity is determined by measuring the pressure difference between nozzle and atmosphere. For the measurement of the pressure rise of the fan Betz-Manometer are used. For the measurement of the rotational speed a pulse counter was used and a torque flange for the torque measurement of the fan. The equipment used for this measurement has an uncertainty in the range of 1%. For the measurement of sound pressure fluctuation a rotating microphone is used. An unsymmetrical diffuser rotates in the middle of the room to homogenize the diffuse field. In the reverberation room a reference sound source is installed to calculate the sound power level by using the comparative method.

The instrumentation for noise measurement consisted of a Brüel & Kjaer diffuse-field microphone of 1/2" diameter type 4943, digital 2-Channel Front End (BEQII). Recording and analyzing was done by the software Head Recorder and Artemis from HEADacoustics®.

The used axial fans for this purpose have mostly a ring at the blade tips and so a special gap shape. The selected shape is similar to a labyrinth seal and should minimize the gap flow and thus the leakage losses (see Figure 2).

Figure 2. Gap shape (meridian cut)

General geometric dimensions and operating conditions are shown in Table 1.

Table 1. General Dimensions of the fans

Hub-tip ratio	υ	-	0.42
Solidity at D_a	l/t	-	0.476
Gap ratio	$2*s/D_a$	-	0.017
Rotational speed	n	min^{-1}	3000

The study includes a variation of the skew at a fan with 7 blades. The skew angle of the different axial fans related to the spacing is presented in Figure 3. One backward and three forward skewed fans were built. The forward skew includes three stages, one weak skewed fan (FSK_W), one middle skewed fan (FSK_M) and one strong skewed fan (FSK_S). The backward skewed fan is weak skewed and so called: BSK_W. To complete the naming the unskewed fan is called: USK. The skew angle of the different axial fans related to the spacing is presented in Figure 3.

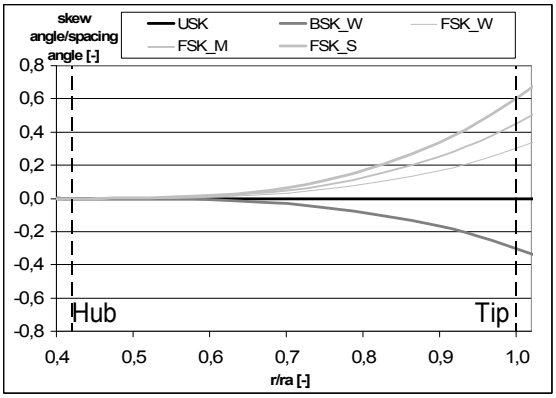

Figure 3. Skew distribution of the different axial fans

All of these fans have similar blade shape based on NACA 65-series and has been designed as an evolution of the original USK concept. The vortex design of all the fans is identical and is reduced at the hub and at the tip. The axial velocity at the inlet of the fan is assumed to be constant.

To reach the aim of constant loading by changing the blade skew corrections are required. The design of the skewed fans was realized under consideration of the corrections for Beiler [3, 4] and blade adjustment.

The characteristic curves are given by dimensionless ratios. The volume flow coefficient (based on the area the flow passes through), the pressure coefficient (system: blowing out pressure difference), the efficiency (system) and the circumferential speed at the outer diameter are defined as follows:

$$\varphi = \frac{Q}{\left[\frac{\pi}{4} D_a^2 \left(1 - \upsilon^2\right) u\right]} \quad (1)$$

$$\psi = \frac{\Delta p_{fa}}{\left(\frac{\rho}{2} u^2\right)} \quad (2)$$

$$\eta = \frac{Q \, \Delta p_{fa}}{P_W} \quad (3)$$

$$u = \pi \, n \, D_a \quad (4)$$

3. EXPERIMENTAL INVESTIGATIONS - RESULTS

The configuration for the measurement was without any component neither in the upstream nor the downstream flow, so free in- and outflow.

Figure 4 shows the characteristic curves of the studied fans. The comparison of the different characteristic curves shows very small difference especially in the range of best point ($\varphi \approx 0.14$) and when considering a given system curve.

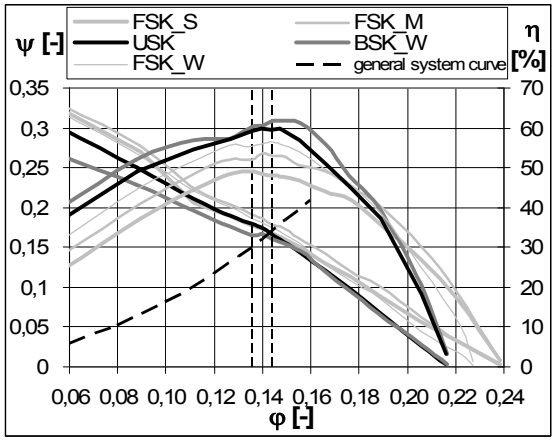

Figure 4. Characteristic curves

The following remarks about the consideration of the characteristic curves are carried out from the higher to the lower volume flow coefficient. The characteristic curve of the backward skewed fan starts, with decreasing volume flow rate, to become instable at $\varphi \approx 0.15$ and deviate from the curve of the unskewed fan. Nevertheless the curve of the backward skewed fan is in the range of best point almost identical with the unskewed fan. The curves of the forward skewed fans are almost identical and very close to the characteristic curve of the unskewed fan. The curves of the forward skewed fans are characterized by the fact that they hardly show instable range even in the partial load (this fits with [5]). Hereby the goal of this study, to skew fans by retention of the similar loading, was reached. The comparison of the efficiency shows an increase of the efficiency (1-2%) by the backward skewed fan in comparison to the unskewed fan and the small displacement of the best point to higher volume flow coefficient ($\varphi \approx 0.15$). In the case of forward skewed fans the efficiency becomes, depending on the strength of the skew, more and more lower and move to lower volume flow coefficient ($\varphi \approx 0.13$). The decrease of the efficiency is of 3% by the weak skewed fan, 7% by the middle strong skewed fan and 12% in case of the strongest skewed axial fan. This reduction of the efficiency is also due to the increase of the shaft power as in Figure 5 presented.

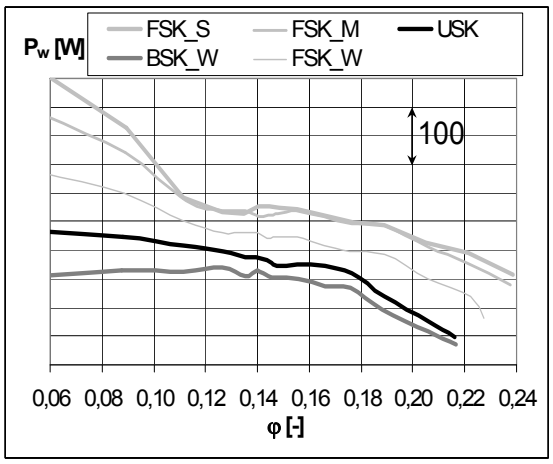

Figure 5. Shaft power curves

The deterioration of the efficiency at the case with forward skewed fans was mentioned in previous works [6]. In Figure 6 the acoustic curves of all axial fans in this study are presented. In the range of best point the sound pressure level of FSK_W is almost identical to the unskewed USK. The FSK_M and the BSK_W are about 1.5 *dB* less than the unskewed axial fan. The best result was reached by the FSK_S where the sound pressure level is almost 6 *dB* less than that of unskewed fan USK.

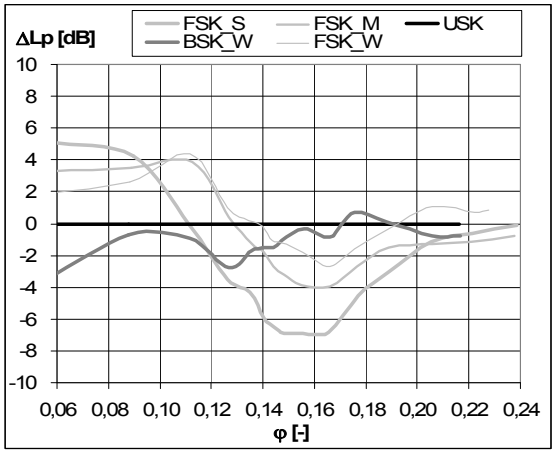

Figure 6. Sound pressure level

In Figure 7 the frequency spectra of all the axial fans from this study are presented. These consist of broadband, tonal components but also narrow-band enhancement next to the blade passing frequency (BPF) and its harmonics. A previous study [9] demonstrated that by avoiding the gap flow this narrow-band enhancement decrease immensely.

The main difference between the different axial fans is located in the range of 250 *Hz* to 4000 *Hz* so broadband noise in medium frequencies. A really important part here is the sharp decline of the narrow-band enhancement next to the BPF (about 300 *Hz* and its harmonics) for the case of strong skewed fan. This disappears completely around the frequencies 550 *Hz*, 850 *Hz* and 1150 *Hz*. Possible explanation for this purpose is the limitation of the leakage losses due to the forward skew [5] and the diminution of the noise propagation due to the interaction of the gap flow with the fan.

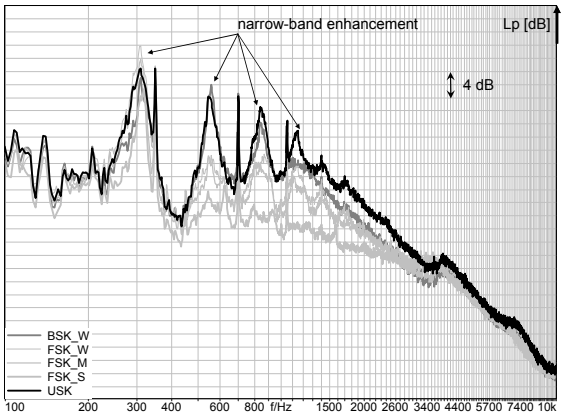

Figure 7. Frequency spectra at $\varphi \approx 0.14$, $\Delta f = 2.7$ *Hz*

4. FURTHER EXPERIMENTAL INVESTIGATIONS

For more details about the influence of the skew of the hub part on the aerodynamic and acoustic of the axial fans, two more axial fans were built and measured. These comprise additionally the skew of the near hub part of the blade (which was maintained unskewed for the previous research). Here is a combination of a backward skew in the outer part of the blade with a forward skew of the near hub part of the blade and vice versa by maintaining the loading constant and measuring the acoustic and the aerodynamic. For the better comparison of the two "new" fans the skew distribution of the different axial fans is presented in Figure 8 and compared with the variants BSK_W and FSK_S. It is obvious that in the outer part of the blade the skew of the variants BSK_W and HFSK even so FSK_S and HBSK are similar.

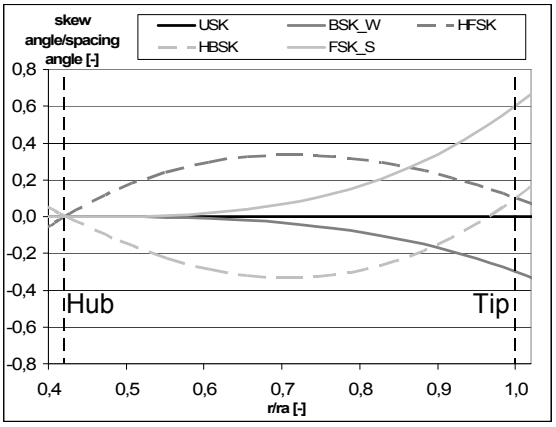

Figure 8. Skew distribution of the fans USK, FSK_S, HBSK, HFSK and BSK_W

The characteristic curves of the different variants are presented in Figure 9. The goal of this study was the retention of the loading and it was reached in the range of best point. It is obvious that by changing the skew of the near hub part for both cases, HFSK and HBSK, the efficiency increases slightly (1% for HFSK and 2% for HBSK in the range of $\varphi \approx 0.14$).

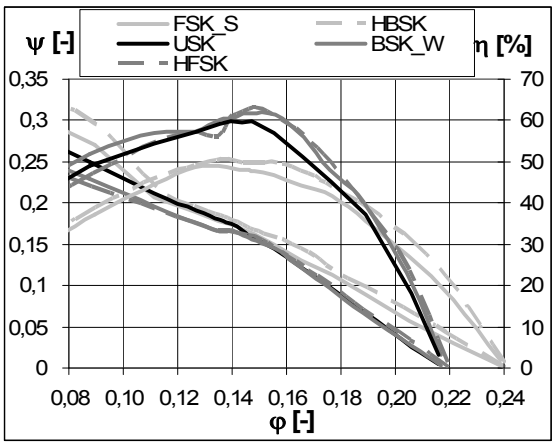

Figure 9. Characteristic graph

The comparison of the sound pressure levels in Figure 10 also shows the increase of the values of both variants HFSK and HBSK in the range of best point (at $\varphi \approx 0.14$) in comparison to the variants FSK_S and BSK_W. At $\varphi \approx 0.14$ the increase of HBSK is about 3.5 *dB* in comparison to FSK_S. The increase of the sound pressure level for HFSK is about 1 *dB* in comparison to BSK_W.

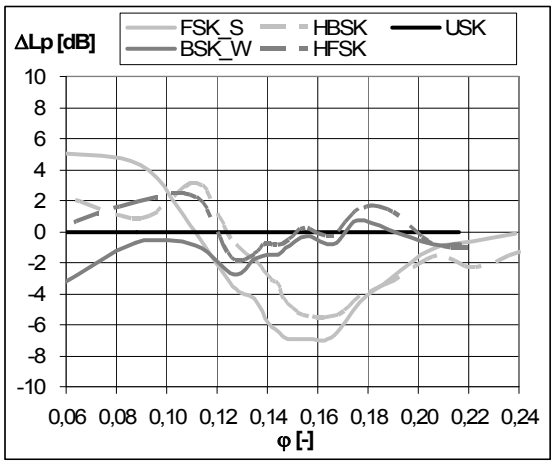

Figure 10. Sound pressure level

The observation of the frequency spectra of all variants in Figure 11 show similar characteristics for FSK_S and HBSK. The narrow-band enhancement disappears in both spectra. The biggest increase of the sound level of the variant HBSK in comparison to the variant FSK_S is in the range of 250 *Hz* - 4000 *Hz*.

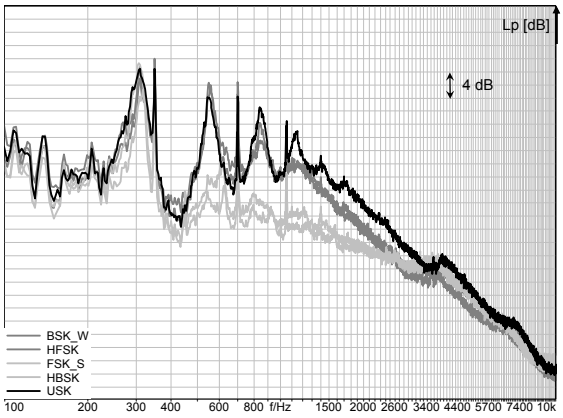

Figure 11. Frequency spectra at φ≈0.14, Δf=2.7 *Hz*

4. NUMERICAL INVESTIGATIONS - PROCEDURE

For the computational analysis the commercial code ANSYS®-CFX 12.1 was used. Because of the low Mach number the fluid can be considered as incompressible. Turbulence is modeled by the k-ω-SST model which has proven its reliability for adverse pressure gradient aerodynamic flows [7, 8]. The geometry is discretised by a 3-D-blockstructered mesh. The geometry and mesh was built with an in-house code. For more details about the grid quality 3 meshes with a different number of nodes were used. Mesh1 has about 650000 cells, Mesh2 around 900000 cells and Mesh3 1200000 cells. Wall function approach is used near the walls. The advantage of the wall function approach is that the high gradient shear layers near the wall can be modeled with relatively coarse meshes. All calculations presented in this work have mean $y+$ values between 30 and 120. The whole domain was divided into a rotor- and stator-domain. The rotor-domain includes the blade, hub and the ring and is defined as a rotating domain with fixed grid, whereas the rest of the fluid-domain is defined stationary as the stator-domain (see Figure 12). The interface between the rotor and the stator is defined as a frozen-rotor-interface. The specified boundary conditions in this problem are shown in Figure 12 and consist of a constant mass flow rate at the inlet and a constant static pressure of 0 Pa at the outlet. Reference pressure is 1 *atm*. The distance from inlet or outlet to the fan is many times larger than the fan-diameter ($7*D_a$). At the mesh generation care was taken to reach a (3x3)-determinant of the hexahedron-elements above 0.3.

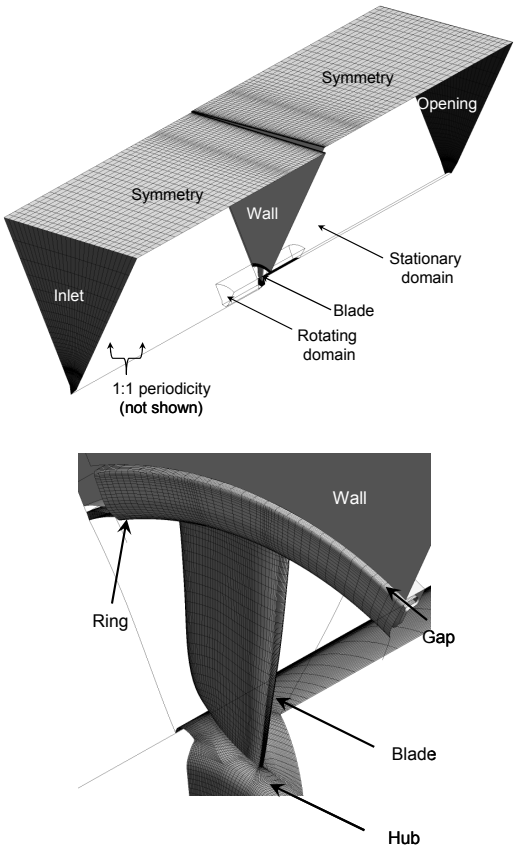

Figure 12. Fluid-domain and boundary conditions used

5. NUMERICAL INVESTIGATIONS - RESULTS

The results of the simulations of the Variants FSK_S and BSK_W were discussed in [10] and could be saved in this work. Figure 13 shows the comparison between the characteristic curves of the experimental measurement of the variant HFSK compared to the results of the numerical investigations. These numerical investigations contain the results of the three different meshes. It shows that the agreement between the experimental and the numerical results is very satisfying. Especially in the range of best point, $\varphi \approx 0.14$, the agreement is very acceptable. The results of the numerical investigations don't depend from the mesh used; because the three different meshes deliver quiet similar results (see Figure 13).

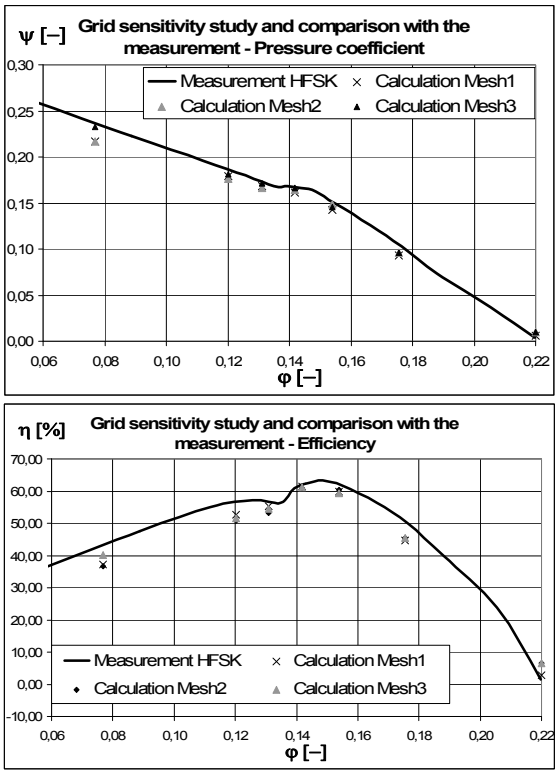

Figure 13. Grid sensitivity and comparison of the experimental and numerical characteristic curves for the variant HFSK

The comparison of the characteristic curves for the variants USK, HFSK and HBSK is presented in Figure 14. Also these curves show a good agreement between the experimental measurement and the numerical investigations. Especially in the range of best point the agreement is satisfying. The biggest difference between the experimental and numerical results is made with the variant HBSK and is in the range of 6 efficiency points difference. The reason for this difference could be the strong skewed geometry of the blade at the outer diameter and so the cells in this region.

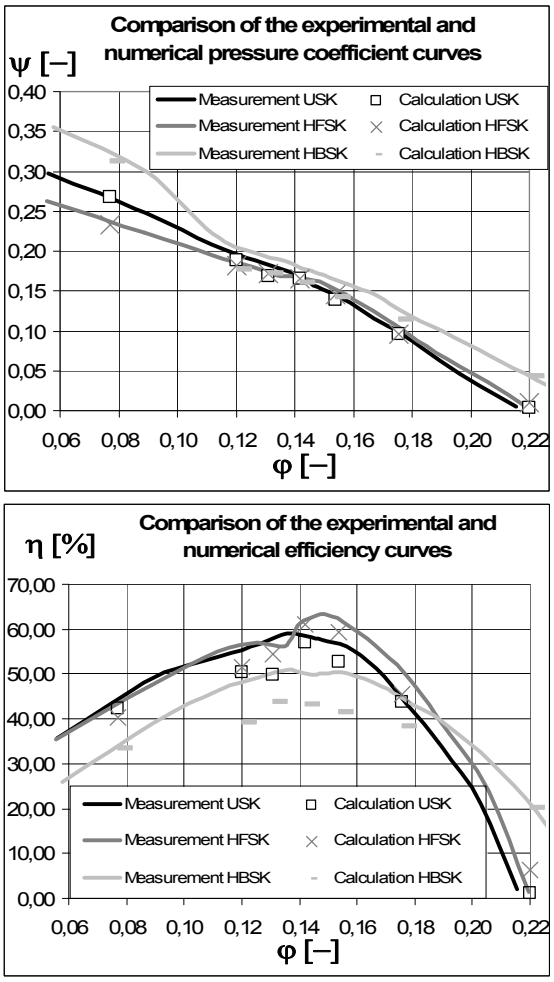

Figure 14. Comparison of the experimental and numerical characteristic curves for the variants USK, HFSK and HBSK

The analysis of the streamlines in three different surfaces around the blade situated at 52%, 77% and 99% of the outer diameter is presented in Figure 15. The analysis of these streamlines shows an amelioration of the flow situation around the blade in this blade section for the case HFSK in comparison to the unskewed axial fan. In contrast to that is the analysis of the streamlines for the variant HBSK, which shows the deterioration of the inflow to the blade and therefore the increase of the shock losses in this case. This comparison can be the explanation for the decrease of the efficiency curve for the case of HBSK or FSK_S (about 12% in the experiment) in comparison to USK. With a better inflow to the blade for HFSK and so BSK_W the shock losses can be diminished which explain the increase of the efficiency here (2-3% in the experiment). The increase in the measured efficiency (around 1-2%) of the cases HFSK and HBSK in comparison respectively to BSK_W and FSK_S is due to the improvement of the flow

conditions around the blade in all the three sections (see Figure 15 and [10]).

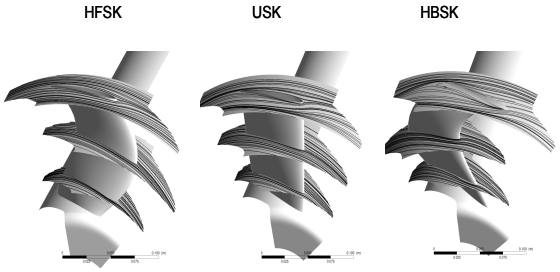

Figure 15. streamlines around the blade (blade section at 52%, 77% and 99% of the outer diameter)

Figure 16 shows the surface streamlines on the blades of the variants HFSK, USK and HBSK. Similar to the findings from [10] it can be observed that the flow in the case of HBSK goes towards the hub and stabilize the hub flow because of the forward skewed fan at the outer part of the blade. The flow for the variant HFSK goes towards the casing because of the backward skew at the outer part of the blade (see Figure 16).

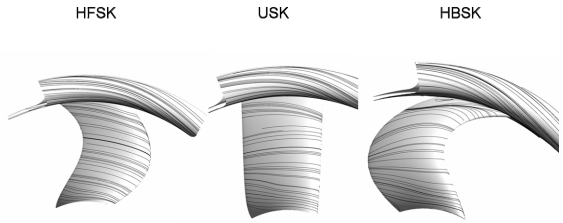

Figure 16. Surface streamline at blade (front view)

If the surface streamlines of the variants BSK_W and HFSK are now shown, in Figure 17, it can be observed that the forward skew of the hub region stabilizes the flow in the hub and leads to less separation in the near hub region.

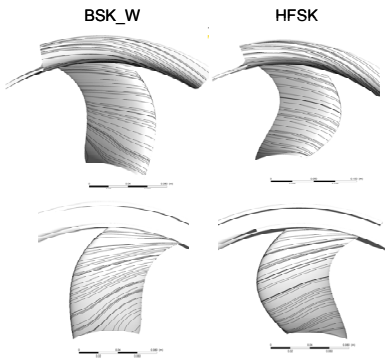

Figure 17. Surface streamlines at blade and ring (top: front view; bottom: rear view)

The comparison of the gap flow for the different variants HFSK, USK and HBSK is presented in Figure 18. This comparison shows the difference in the gap flow for these variants. For the variants USK and HFSK, where the narrow-band enhancement is developed (see Figure 11), is more present and has more displacement in the circumferential direction than the variant HBSK and so FSK_S, where the narrowband enhancement completely disappears.

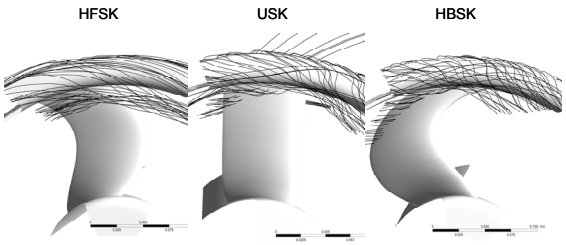

Figure 18. Comparison of the streamlines from the gap flow for the variants HFSK, USK and HBSK

6. CONCLUSION AND OUTLOOK

The skew of the blades plays an important role on the aerodynamic as well as on the acoustic behaviour of the fan. The comparison of the efficiency shows an increase for the backward skewed fan in comparison to the unskewed fan, and the small displacement of the best point to higher volume flows. In the case of forward skewed fans the efficiency decreases and moves to smaller volume flow. The amount of decrease depends on the strength of the skew and it is respectively 3%, 7% and 12% for the strongest forward skewed axial fan. The comparison of the acoustic graphs shows the best result for the strong forward skewed axial fan and the noise is about 6 *dB* less than the unskewed fan. This difference relates to the broadband noise and it is mainly in the range between 250 *Hz* and 4000 *Hz*. An important advantage for the strong skewed fan is the decline of the narrow-band enhancement next to the blade passing frequency. This phenomenon observed in the spectra disappears completely for the strongest forward skewed fan.

The skew of the near hub region shows a change in the aerodynamic graph. For this purpose two more axial fans were built, measured and compared with the variants BSK_W and FSK_S. These two variants are similar skewed in the outer part of the blade and can be used to prove the influence of the near hub region on the aerodynamic and acoustic of this type of fans. The comparison shows a small improvement in the efficiency in both cases of around 1-2% efficiency points without a significant increase in the noise emission. The numerical investigations show that a skew in the hub region can influence the flow.

In order to find out the reasons for these observations, more information about the influence of skewed blades on the gap flow and the related narrow-band enhancement or the main flow and the related broadband noise are required. Research on these topics is currently taken place.

More investigations about the interaction of the different skewed fans with the heat exchanger upstream or the retaining struts downstream are realized and have to be evaluated. The evaluation considers the influence of the skew on tonal and broadband components.

REFERENCES

[1] Gutin, L., 1948, "On the Sound Field of a Rotating Propeller", *NACA Tech. Memor. No. 1195.*

[2] Lowson, M. V., 1965, "The Sound Field for Singularities in Motion", *Proc. Roy. Soc., A 286 (559-572), London.*

[3] Beiler, M., 1996, "Untersuchung der drei¬dimensionalen Strömung durch Axial¬ventilatoren mit gekrümmten Schaufeln", *VDI-Fortschrittsberichte Nr. 298, Reihe 7: Strömungstechnik.*

[4] Carolus, T., 2009, "Ventilatoren - Aerodynamischer Entwurf, Schallvorhersage, Konstruktion", *2. Auflage, Vieweg+Teubner Verlag.*

[5] Corsini, A., Rispoli, F., 2004, "Using sweep to extend the stall free operational range in axial fan rotors", *IMechE , Part A: J. Power and Energy, 218, 129-139.*

[6] Meixner, H. U., 1995, "Vergleichende LDA-Messungen an ungesichelten und gesichelten Axialventilatoren", *Dissertation Universität Karlsruhe, VDI-Verlag, Reihe 7: Strömungstechnik, No. 266.*

[7] Menter, F. R., 1993, "Zonal two equations k-ω turbulence models for aerodynamic flows", *AIAA paper 93-2906.*

[8] Bardina, J. E., Huang, T. J., Coakly, T. J., 1997, "Turbulence modeling, validation, testing and development", *NASA Technical Memorandum 110446.*

[9] Zayani, M., Caglar, S., Gabi, M., 2010, "Strömungsakustische Untersuchungen an Axialventilatoren zur Motorkühlung", *Ventilatoren-Tagung, Braunschweig, Germany.*

[10] Zayani, M., Caglar, S., Gabi, M., 2012, "Aeroacoustical Investigations on Axial Fans for Automotive Cooling Systems", *Fan 2012, International Conference of Fan Noise - Technology and Numerical Methods, Senlis, France.*

Conference on Modelling Fluid Flow (CMFF'12)
The 15th International Conference on Fluid Flow Technologies
Budapest, Hungary, September 4-7, 2012

TURBULENT SWIRL FLOW CHARACTERISTICS AND VORTEX CORE DYNAMICS BEHIND AXIAL FAN IN A CIRCULAR PIPE

Đorđe ČANTRAK[1], Miloš NEDELJKOVIĆ[2], Novica JANKOVIĆ[3]

[1] Corresponding Author. Hydraulic Machinery and Energy Systems Department, Faculty of Mechanical Engineering, University of Belgrade. Kraljice Marije 16, 11120 Belgrade, Serbia. Tel.: +381 11 3302 363, Fax: +381 11 3370 364, E-mail: djcantrak@mas.bg.ac.rs
[2] Hydraulic Machinery and Energy Systems Department, Faculty of Mechanical Engineering, University of Belgrade. E-mail: mnedeljkovic@mas.bg.ac.rs
[3] Hydraulic Machinery and Energy Systems Department, Faculty of Mechanical Engineering, University of Belgrade. E-mail: njankovic@mas.bg.ac.rs

ABSTRACT

Turbulent swirl flow field in a circular pipe behind the axial fan of specified geometry has been investigated in this paper. The length of the test rig is 27.74D, where D=0.4 *m* is the average inner pipe diameter. Laser-based measuring techniques, such as stereo particle image velocimetry (SPIV) and laser Doppler anemometry (LDA) were applied in this investigation. Experiments were performed in two sections, behind the axial fan at the position 3.35D from the test rig inlet and downstream at the position 26.31D. The SPIV measurements were performed in the specified cross-sections of the region size of 200x90 *mm* with the center in the pipe axis and vertical meridian sections of 140x85 *mm* in size with the center in the pipe axis. Anisotropy of the turbulent velocity field, with the focus on the vortex core region and shear layer, was related to the mean velocity fields. Complex mechanisms in this fluid flow were investigated on the basis of turbulence statistical properties. Vortex core dynamics was investigated using the criterion of minimum total velocity. The turbulent swirl decay law was proved based on the integral flow characteristics, such as swirl parameter and average circulation. These results will help in constituting more reliable theoretical and numerical models for the turbulent swirl flow.

Keywords: LDA, stereo PIV, swirl, turbulence

NOMENCLATURE

D	[m]	inner pipe diameter
D_i	[m]	hub diameter
D_a	[m]	impeller diameter
F	[-]	flatness factor
Q	[m^3/s]	volumetric flow meter
N	[-]	number of samples
R	[m]	inner pipe radius
Re	[-]	Reynolds number
S	[-]	skewness factor
T	[-]	turbulence intensity
U	[m/s]	mean axial velocity
V	[m/s]	mean radial velocity
W	[m/s]	mean circumferential velocity
X,Y	[mm]	target coordinate system
n	[rpm]	fan shaft rotational speed
r	[m]	radial coordinate
t	[s]	transit time
u	[m/s]	fluctuating axial velocity
v	[m/s]	fluctuating radial velocity
w	[m/s]	fluctuating circumferential vel.
x	[m]	axial coordinate along a pipe axis
Γ	[m^2/s]	average circulation
Ω	[-]	swirl flow parameter
β_a	[º]	blade angle at impeller diameter
η	[-]	weighting factor
σ	[m/s]	root-mean-square of the turbulent velocity fluctuations
φ	[º]	coordinate of the polar cylindrical coordinate system (x,r,φ)

Subscripts and Superscripts

c	center
m	mean in volume

1. INTRODUCTION

Turbulent swirl flow behind the axial fan has been investigated in this paper. Turbulent swirl flow was studied by various experimental techniques [1-8]. The distribution of total and static pressures along a vertical diameter is obtained using the original classical probes [1,5,8]. Circumferential and axial velocity fields were derived from them. In this case, the velocity field was treated as two-dimensional, as the radial component was neglected. Turbulence statistics for the results obtained by using the hot-wire anemometry, together with the stereo particle image velocimetry

(SPIV), has shown very specific phenomena and transport processes in the core region and turbulent shear flow in the pipe swirl flow [3,4,6,7].

In this paper, the SPIV technique and one-component laser Doppler anemometer (LDA) were employed in two sections. On the basis of the results obtained the following integral statistical characteristics of the turbulent swirl flow were calculated: volume flow rate (Q), averaged axial velocity (U_m), average circulation (Γ), swirl flow number (Ω) and Reynolds number (Re). The average circulation decay was proved. The vortex core dynamics was presented on the basis of the position of total velocity minimum.

2. EXPERIMENTAL SETUP AND METHODS

2.1. Test Rig and Swirl Generator

The test rig is presented in Figure 1. It is 27.74D long, where D=0.4 m is the average inner pipe diameter. An axial fan is positioned inside the first acrylic glass section, 3.75D long, followed by the plastic non-transparent ducts, and one additional acrylic glass section, 3.45D long at the end. The SPIV and LDA measurements were performed in sections 1 (x/D=3.35) and 2 (x/D=26.31), where x is measured from the test rig inlet.

Figure 1 Experimental test rig: 1 -DC motor, 2-profiled free bell-mouth inlet, 3-axial fan, 4 and 5 LDA and SPIV measuring sections, 6-Nd:Yag laser

The fan rotation speed was regulated by a fully automated thyristor bridge with error up to ±0.5 *rpm*, originally designed and made by Stojiljković. In this paper results are presented for fan rotational speed n=1000 *rpm*.

The swirl generator is a variable pitch axial fan designed by Protić[†]. This axial fan has nine blades and has been designed after the rW=const. law. The impeller diameter is D_a=0.399 m. The dimensionless hub ratio is D_i/D_a=0.5. The blade angle at impeller diameter was adjusted to β_a=30º. Ambient conditions have been recorded.

2.2. LDA Measurements

The LDA measurements were performed subsequently for all three components using the one-component LDA system along the vertical diameter at the points, at a 10-*mm* distance each, in specified sections. The LDA system is a model of the Flow Explorer Mini LDA, Dantec, with the BSA F30 signal processor model. The measurement distance is 285 *mm*, power 35 *mW*, wavelength 660 *nm*, the measurement volume diameter is 0.1mm, the measurement volume length is 1mm and possible maximum velocity is 27 *m/s*. It works in a backscattered mode. The velocity was measured with uncertainty lower than 0.1%. Transit time was used as the weighting factor. Recording time of 10 *s* was set up as the stop criteria for all measurements. Data frequency varied along the vertical diameter, depending of the measured velocity component. Data validation during the test was, on average, 85%. Sensitivity was adjusted to the values 1200-1400 *V*.

The acquisition and a part of data processing were done in the BSA software. The major part of data processing was done by the self-made programs in MatLAB. The flow was seeded by the Antari Z3000II fog machine with liquid EFOG, Density Fluid, Invision. It was naturally sucked in the test rig by the fan. In this way, enough seeding was obtained.

2.3. SPIV Measurements

The SPIV measurements were performed in specified sections in the cross-section and vertical meridian section defined in Figure 2: Analogue SPIV setup in section x/D=26.31.

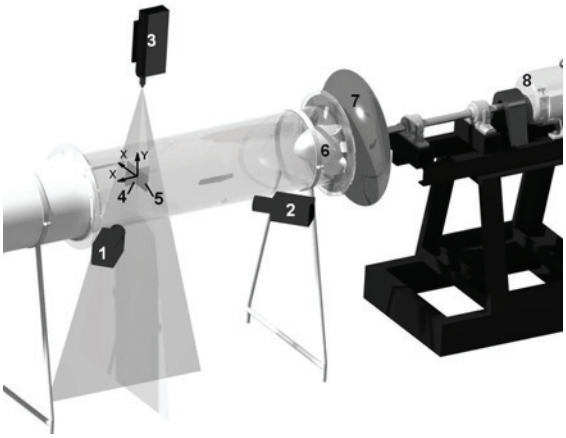

Figure 2 SPIV setup in section x/D=3.35: 1-left camera, 2-right camera, 3-Nd:Yag laser, 4-vertical meridian plane, 5-cross-section, 6-axial fan, 7-free bell-mouth inlet, 8-drive unit

The orientation of the target coordinate system is given in Figure 2 for both planes: vertical meridian (pos. 4) and cross-section (pos. 5). The x-axis is oriented opposite the TSI nomenclature for the first case. A dual head Nd:Yag laser (max power: 30mJ/pulse, wavelength 532 *nm*, 15 *Hz*), was used for flow illumination. Two 12-bit CCD cameras with the resolution of 1660x1200 pixels and 32 *fps* were in Scheimpflug setup. The INSIGHT 3G TSI software was used for data acquisition and processing. The post-processing

was performed in Tecplot and in-house programs written in Matlab. The number of pictures taken was 400 with the frequency of 2 *Hz* and 99 with 7 *Hz*. Image processing was performed using the central difference image correction (CDIC) deformation algorithm combined with the FFT correlator [9,10]. This four-pass method employed an interrogation region of 32x32 px^2. The vector fields were validated using standard velocity range criteria and a 3x3 local median filter. Any missing vectors were interpolated using a 3x3 local mean technique. The number of interpolated vectors was, on average, around 5%. The seeding was produced by the same fog machine and liquid like in the case of LDA measurements.

3. EXPERIMENTAL RESULTS AND ANALYSIS

3.1. LDA Experimental Results and Analysis

3.1.1. Integral Characteristics of Turbulent Flow

The distribution of all three velocities in both measuring sections is given in Figure 3. The angle φ=90º denotes the upper part (above-pipe axis) of the vertical diameter, while φ=270º the lower part (under-pipe axis).

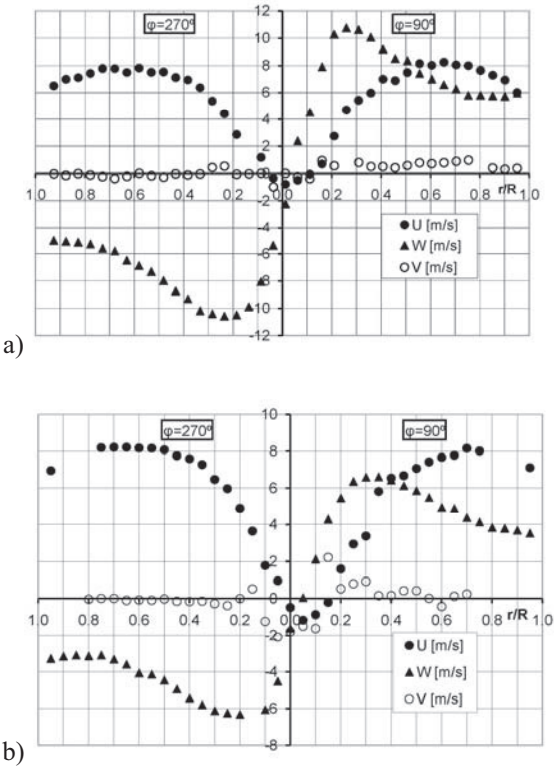

Figure 3 Distribution of the time averaged velocities in measuring section a) 1 and b) 2

The Rankine vortex structure is obvious in Figure 3. The minimum of axial velocity and zero value of circumferential velocity, which characterizes swirl core, is at the same point *r/R*=0.02 in section 1 (Figure 3a), while at *r/R*=0.05 in section 2 (Figure 3b). The distribution of circumferential and axial velocity is almost symmetric with respect to these positions. The reverse flow is evident in a central zone.

The vortex core or "solid body" region is detected with almost linear increase of the circumferential velocity up to *r/R*=0.2 in section 1, while up to *r/R*=0.15 in section 2.

The maximum axial velocity is almost the same in both measuring sections in the sound flow region.

Circumferential velocity decreases from the value W_{max}=10.74 *m/s* in the measuring section 1 up to W_{max}=6.6 *m/s* in the measuring section 2.

Radial velocity reaches its absolute maximum value in the vortex core region, 0.99m/s in the measuring section 1 and 2.09 *m/s* in the measuring section 2. The volume flow rate and axial average velocity are calculated as follows:

$$Q = 2\pi R^2 \int_0^1 kU \, \mathrm{d}k, \quad U_m = \frac{Q}{R^2 \pi}, \tag{1}$$

where $k=r/R$ is the dimensionless radius. The volumetric flow rate calculated in section 1 is Q=0.861 m^3/s, while in section 2 Q=0.837 m^3/s. Relative difference is 2.9%. Averaged axial velocities are $U_{m,1}$=6.69 *m/s* and $U_{m,2}$=6.66 *m/s*. The obtained Reynolds number is approximately $Re \approx 1.9 \cdot 10^5$. Average circulation is calculated on the basis of the axial and circumferential velocities as follows:

$$\Gamma = \frac{4\pi^2 R^3}{Q} \int_0^1 k^2 UW dk \tag{2}$$

Average circulation is calculated for both sections and following values are obtained Γ_1=5.62 m^2/s and Γ_2=3.79 m^2/s. In this way, the circulation decay process is again proved. The swirl flow parameter is obtained as follows:

$$\Omega = \frac{Q}{R\,\Gamma}. \tag{3}$$

The obtained values are Ω_1=0.76 and Ω_2=1.1 for appropriate measuring sections.

3.1.2. Statistics of Turbulence

Reynolds normal stresses are calculated as follows:

$$\overline{u_i^2} = \sum_{j=0}^{N-1} \eta_j \left(u_i^2\right)_j, \quad \eta_j = \frac{t_j}{\sum_{k=0}^{N-1} t_k}, \tag{4}$$

where t_j is transit time of the j-th particle crossing the measuring volume and u_i=u,v,w. Turbulence intensity is calculated in the following way:

$$T_i = \frac{\sigma_i}{U_i} = \frac{\sqrt{\overline{u_i^2}}}{U_i}, \tag{5}$$

where U_i=U,V,W. Figure 4 presents root-mean-square of the turbulent velocity fluctuations (RMS), i.e. σ_i, and turbulence intensity in both measuring sections for all three components.

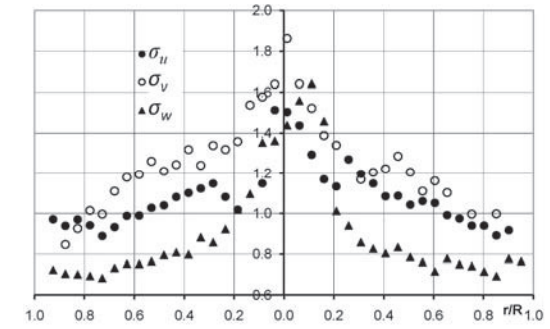

a)

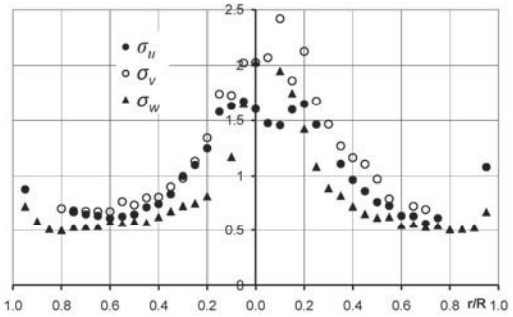

b)

Figure 4 Distribution of RMS in measuring section a) 1 and b) 2

Maximum values are reached in the vortex core region tending to increase in the wall region. The distribution in section 1 (Figure 4a) proved anisotropy and non-homogeneity. This physical behaviour is lesser but still significant in the measuring section 2 (Figure 4b). Turbulence intensity in section 1 is given in Figure 5.

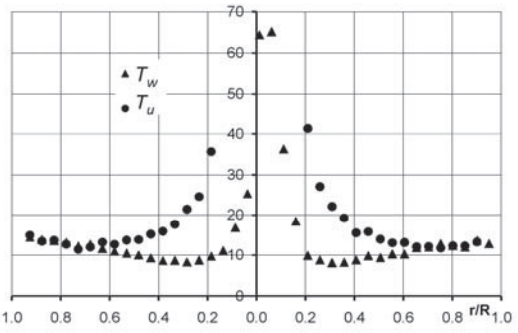

Figure 5 Turbulence intensity in section 1

Turbulence intensity of 10%, and even smaller, for the circumferential component is present in the sound flow region (Figure 5). It increases in the shear layer and reaches its maximum of 70% for circumferential velocity and is even higher for axial velocity in the vortex core region.

The values of the normalized central moments for all three velocity components of the third S_i (skewness), and the fourth order F_i (flatness), where u_i= u,v,w, are calculated as follows by introducing the weighting factor (η_j):

$$S_i = \overline{u_i^3} / \sigma_i^3, \quad F_{u_i} = \overline{u_i^4} / \sigma_i^4. \tag{6}$$

Skewness and flatness factors for axial and circumferential velocities are presented in Figure 6 and Figure 7, respectively.

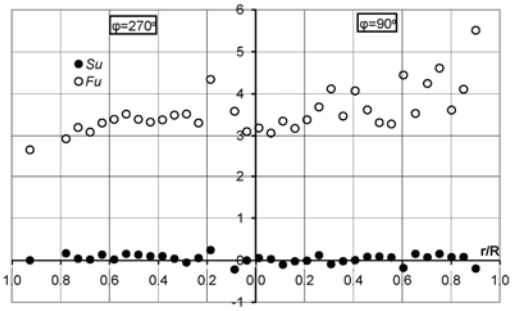

a)

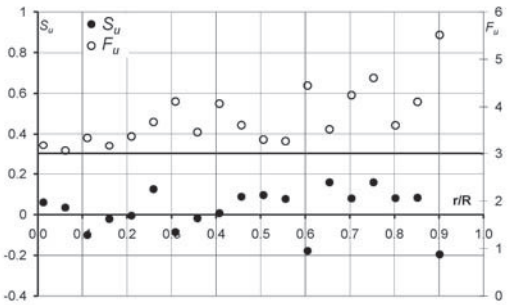

b)

Figure 6 Skewness and flatness factors in measuring section 1 for: a) axial velocity (whole section) and b) axial velocity (φ=90º)

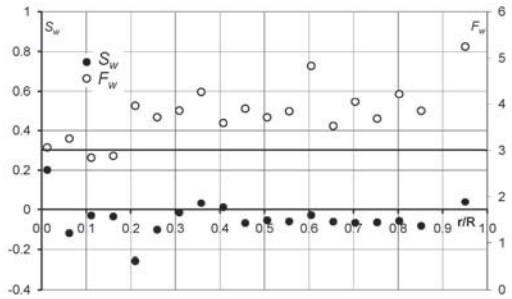

Figure 7 Skewness and flatness factors in measuring section 1 for circumferential velocity (φ=90º)

It can be noted that all skewness and flatness factors differ from the values for normal distribution S_i=0 and F_i=3. Negative skewness factors (S_i<0) indicate that large velocity fluctuations are negative, which is the case with circumferential velocity (Figure 7). This is not such a frequent case with an axial velocity (Figures 6a and b). The values of flatness factors F_i>3, in both cases, indicate great probability of small fluctuations. All this reveals the swirl flow nature [6].

3.2. SPIV Experimental Results and Analysis

3.2.1. Time Averaged Velocity Distributions

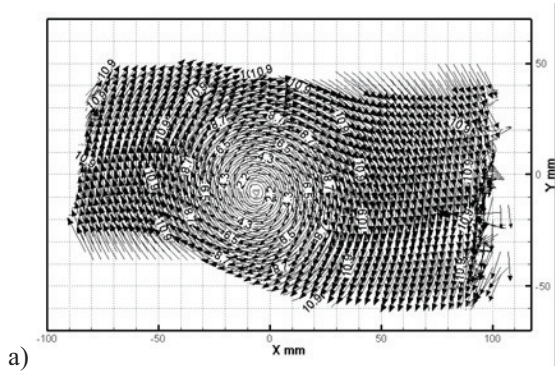

a)

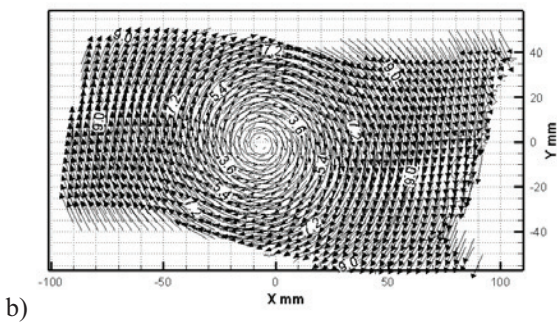

b)

Figure 8 Velocity vectors and magnitude in cross-sections in sections: a) 1 and b) 2

Measurements in both sections have been performed in a cross-section, i.e. the target plane X-Y of size 200x90 *mm* (Figure 8). The target origin is on the pipe axis. Velocity vectors and their intensities in the obtained vortex core region for measuring sections 1 and 2 are given in Figure 8a and b, respectively. These results are obtained on the basis of averaging 400 pictures taken with 2 *Hz*. Averaged velocity fields with 99 pictures taken with 7 *Hz* show the same intensity and character. It is noticeable that velocity intensity is greater in section 1 (Figures 8a and b). Maximum velocity is still not reached and this presents the vortex core region. In both cases the vortex core centre is not on the pipe axis, which will be shown.

Velocity components have been recalculated to the polar-cylindrical coordinate system. In Figure 9 are presented the axial velocity distributions in both sections. It is also shown here, like in LDA measurements, that axial velocity intensity is slightly decreased, but the character is not changed.

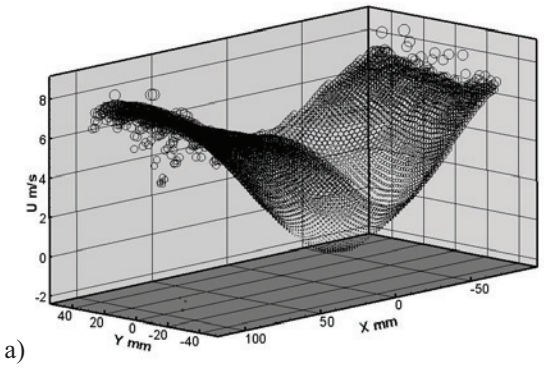

a)

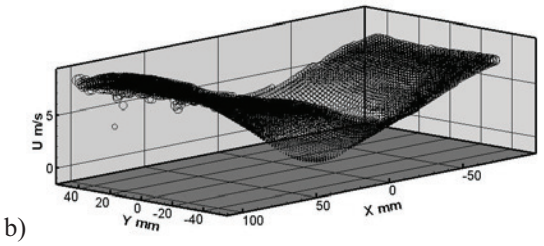

b)

Figure 9 Axial velocities in sections: a) 1 and b) 2

Figures 9a and b show the presence of reverse flow, which was also obtained by the LDA measurements. Circumferential velocity distributions in sections 1 and 2 are presented in Figures 10a and b, respectively, as a "tornado in a pipe". Solid body behavior in the vortex core region is visible in both cases. It is shown that the circumferential velocity intensity is decreased along the pipe, but the character remains the same, like in the case of LDA measurements [6]. Radial velocity distribution is given in Figure 10.

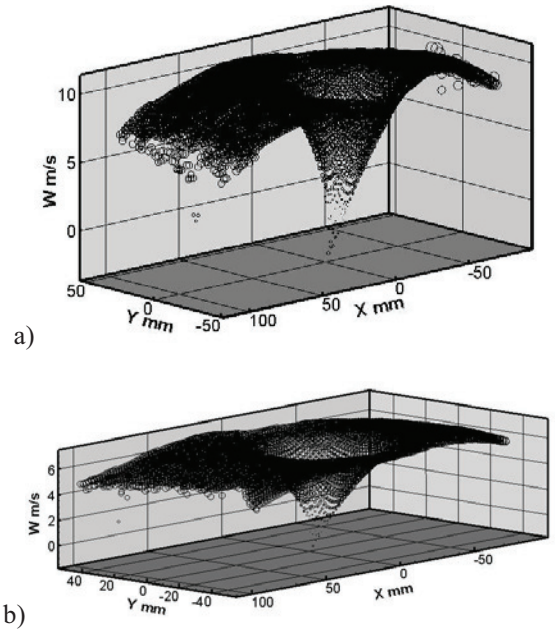

a)

b)

Figure 10 Circumferential velocities in sections: a) 1 and b) 2

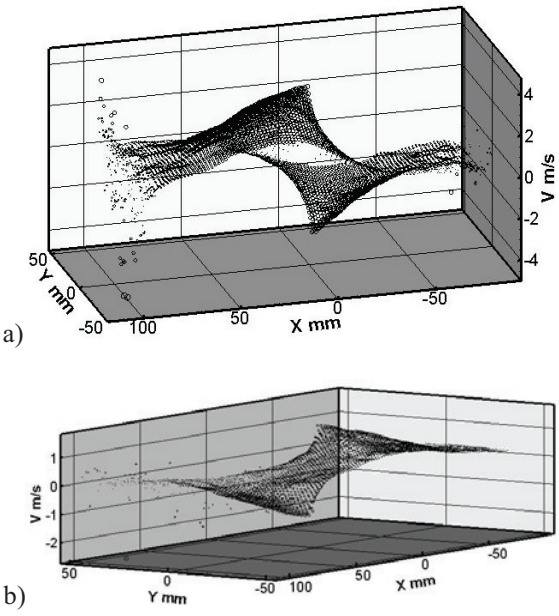

a)

b)

Figure 11 Radial velocities in sections: a) 1 and b) 2

It is shown that the radial velocity intensity is not great, but has final values in the vortex core region as it was the case with LDA measurements (Figure 11). Radial velocity has higher values in section 1 (Figure 11a).

In the specified measuring sections 1 and 2, the measurements have also been performed in the vertical meridian section with the target axis X positioned on the pipe axis and Y axis aligned with the vertical diameter in sections *x/D*=3.35 and 26.31. Axial and circumferential velocities in section 1 are presented in Figure 12.

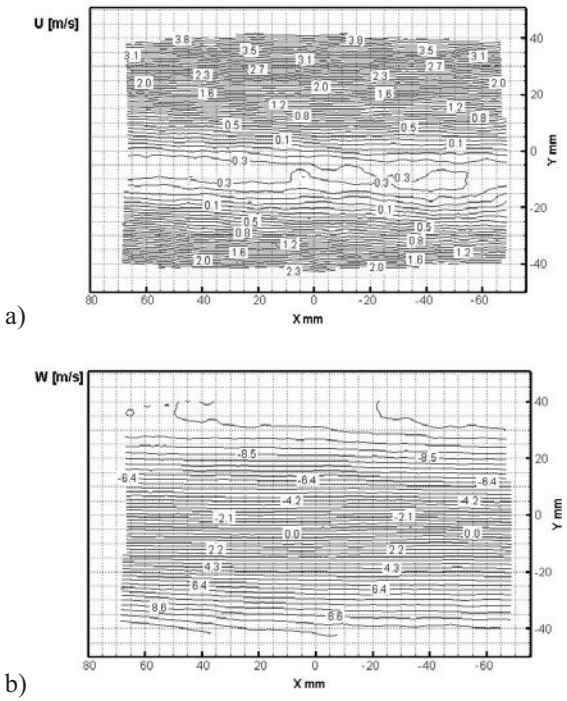

a)

b)

Figure 12 a) Axial and b) circumferential velocities in vertical meridian section 1

It was possible to extract data in the region of 140x85 *mm* in size. Velocity fields were obtained on the basis of averaging 400 pictures taken with 2 *Hz* frequency. Axial velocity reveals again the region of reverse flow (Figure 12a). Circumferential velocity clearly shows that the vortex core centre, i.e. the position of zero value, is approx. 8mm under the pipe axis (Figure 12b). Both diagrams show symmetry to this position, but not axisymmetry.

Vertical meridian section shows the velocity profile development along the pipe axis, but only the vortex core region as the circumferential velocity is linearly distributed. In the measuring section 2 the character is the same, but values are smaller as above shown with LDA and measurements in the cross-section.

3.2.2. Vortex Core Dynamics

Positions of the minimum total velocities for 400 pictures in both measuring sections are given in Figure 13. These minimums correspond to the vortex core center. The geometrical centre of all 400 positions is marked with a black cross, while the minimum of the average total velocity is marked with a grey cross that has the position X_{min}=-5.55mm, Y_{min}=-8.08mm in section 1 (Figure 13a), which is in accordance with the position read in the meridian plane. In the second section, these two crosses overlap almost totally (Figure 13b).

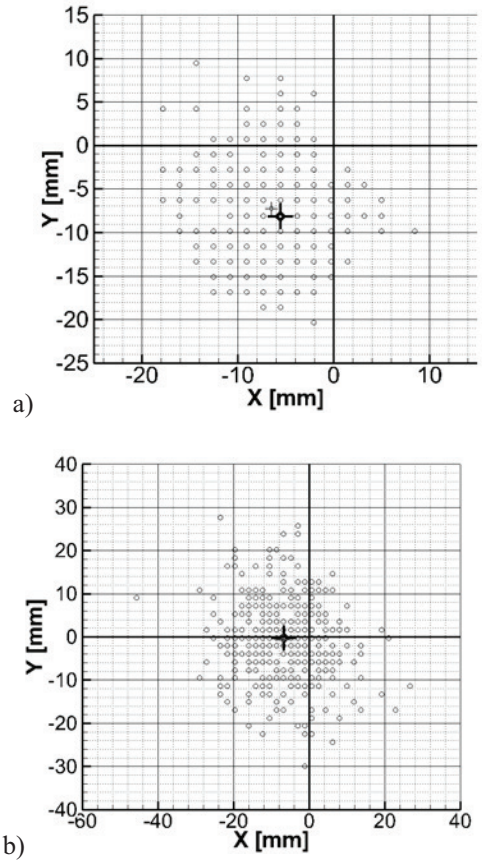

Figure 13 Positions of the total velocity minimum in cross-sections: a) 1 and b) 2

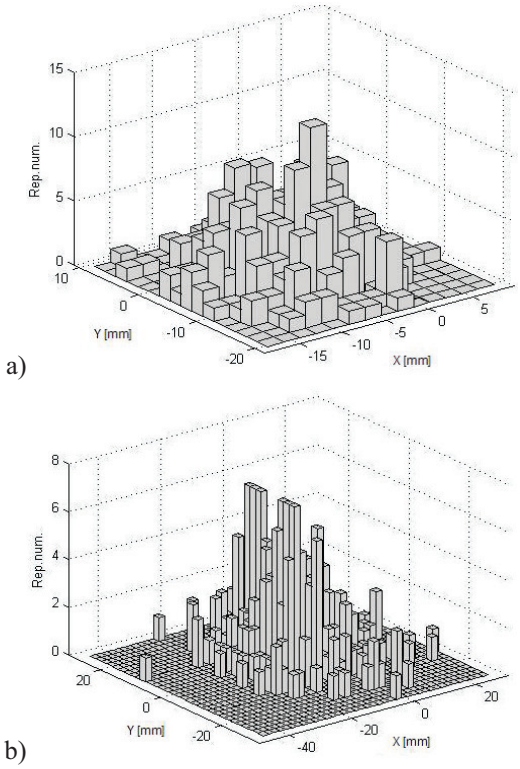

Figure 14 3D histograms of the velocity minimum repetitions in sections: a) 1 and b) 2

Not all 400 minimums are visible as some of them are repeated in one point. In section 1 only 10% of the points are unique, while in section 2 only 36% of the points. Some points are multiple-repeated, which is shown in Figure 14. It can be concluded that the points with the repetition are widely distributed in section 1 (Figure 14a). The coordinates of the point with the maximum repetition rate can be precisely determined for this section. It is the point with the coordinates [-5.55 *mm*, -9.83 *mm*]. The repetition rate is 13. In section 2 (Figure 14b) the points with the repetition are more concentrated, but there is not only one point with the max. repetition number.

In Figure 15 is presented the vortex core centre coordinates time dependence for section 1. The 400 pictures were taken during the time period of 200 *s* (Figure 15a), while 99 pictures in approx. 14 *s* (Figure 15b).

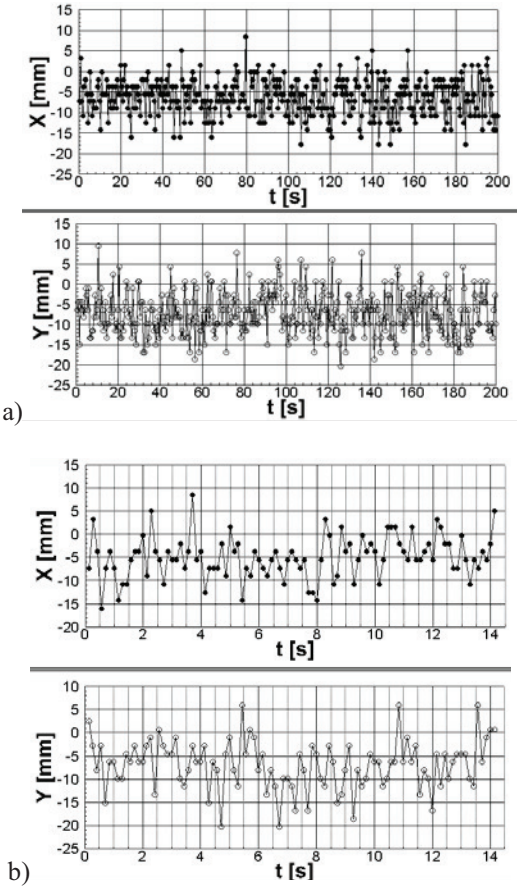

Figure 15 Vortex core centre coordinates time dependence in measuring section 1: a) 400 pictures with 2 *Hz* and b) 99 pictures with 7 *Hz*

From this interpretation the center coordinates can be found at any instant of time. As fan rotation speed is n=1000 *rpm*, which corresponds to the frequency of 16.67 *Hz*, it can be seen that even faster regime is not adequate for capturing the center moving frequency.

4. CONCLUSIONS

The performed LDA and SPIV measurements in two measuring sections proved the complexity of the turbulent swirl flow field behind axial fans. The Rankine vortex structure is detected at the axial fan outlet and is kept till the end of the setup. It is shown that only the intensity but not the character of velocities has been changed under the influence of the inner and wall friction, which was also concluded in [8]. The vortex core region is smaller downstream, however, not significantly. The maximum axial velocity is almost the same, while the circumferential velocity maximum decreases by almost 40%, under the influence of friction. Average circulation is, as expected, decreased downstream. Non-axisymmetry is proved in both ways, using the LDA and SPIV measurements.

Turbulence statistics proved non-homogeneity and anisotropy of the investigated flow, which is significantly demonstrated in section 1. Turbulence intensity is great and reaches its maximum in the vortex core region. Skewness and flatness differ from normal distribution values.

The vortex core region is measured in both planes with SPIV. These results proved non-axisymmetry and the Rankine vortex type velocities distribution, especially linear distribution of the circumferential velocity in the vortex core. Also, radial velocity existence has been documented.

The vortex core dynamics was observed by locating the total velocity minimum in the cross-section. It was shown that in the downstream section the points with the repetition are more grouped around the center, but there are more points having the same repetition rate. There is only one point with the maximum repetition rate in the section closer to the axial fan. Only 10% of points are unique in section 1, while 36% in section 2.

Correlation between fan operating regime and the level of generated turbulence behind axial fan has been treated, by use of HWA, in paper [11]. It is expected that precise correlations of these values will be established on the basis of future investigations.

ACKNOWLEDGEMENTS

We are grateful for scientific, engineering and personal support we have had from Prof. Dr.-Ing. Zoran Protić† (1922-2010). Prof. Zoran Stojiljković, PhD designed and built a very precise original fan rotation speed regulator. This work was supported by the Ministry of Education and Science, Republic of Serbia Project No. TR 35046.

REFERENCES

[1] Protić, M., Nedeljković, M., Čantrak, Đ., and Janković, N., 2010, "Novel Methods for Axial Fan Impeller Geometry Analysis and Experimental Investigations of the Generated Swirl Turbulent Flow", *Thermal Science*, Vol. 14, pp. S125-S139.

[2] Ilić, J., Čantrak, Đ., and Srećković, M., 2007, "Laser Sheet Scattering and the Cameras' Positions in Particle Image Velocimetry", *Acta Physica Polonica A*, Vol. 112, No 5., pp. 1113-1118.

[3] Čantrak, S., Benišek, M., and Nedeljković, M., 2001, "Problems of Non-Local Turbulent Transfer Modelling", *ZAMM*, Vol. 81, S4, pp. 913-914.

[4] Čantrak, Đ., Ilić, J., Hyde, M., Čantrak, S., Ćoćić, A., and Lečić, M., 2008, "PIV Measurements and Statistical Analysis of the Turbulent Swirl Flow", Proc. *International Symposium on Flow Visualization, FLUVISU 12 – 12th French Congress on Visualization in Fluid Mechanics*, Nice, France, CD-ROM, ID 183-0804203.

[5] Benišek, M., Lečić, M., Ilić, D., and Čantrak, Đ., 2010, "Aplication of New Classical Probes in Swirl Fluid Flow Measurements", *Experimental Techniques*, Vol. 34, Issue 3, pp. 74-81.

[6] Čantrak, S., 1981, "Experimentelle Untersuchungen statistischer Eigenschaften turbulenter drallbehafteter Rohr- und Diffusorströmungen", *Dissertation Universität Karlsruhe (TH), Institut für Strömungslehre und Strömungsmaschinen*.

[7] Čantrak, S., and Benišek, M., 2001, "Characteristic Magnitudes Determined from Mean Velocity Distributions of Turbulent Swirling Flow in Pipes", *ZAMM*, Vol. 62, Issue 4, pp. 201-203.

[8] Protić, Z., Benišek, M., and Manasijević, M., 1991, "Swirling Flow in the Circular Pipes – the Characteristic Values and Flow-patterns Specifics", *ZAMM*, Vol. 71, Issue 5, pp. T456-T459.

[9] Adrian, R., 1997, "Dynamic Ranges of Velocity and Spatial Resolution of Particle Image Velocimery", *Measurement Science and Technology*, Vol. 8, pp. 1393-1398.

[10] Wereley, S., and Gui, L., 2003, "A Correlation-based Central Difference Image Correction (CDIC) Method and Application in a Four-roll Mill Flow PIV Measurement", *Experiments in Fluids*, Vol. 34, pp. 42-51.

[11] Oro, J.M.F., Ballesteros-Tajadura, R., Marigorta, E.B., Díaz, K.M.A., Morros, C.S., 2008, "Turbulence and Secondary Flows in an Axial Flow Fan with Variable Pitch Blades", *J. of Fluids Eng*., Vol. 130, pp. 041101-1-11.

Conference on Modelling Fluid Flow (CMFF'12)
The 15th International Conference on Fluid Flow Technologies
Budapest, Hungary, September 4-7, 2012

CFD MODELLING FOR PERFORMANCE PREDICTIONS OF A HYDRAULIC TURBINE DRAFT TUBE: THE EFFECT OF INLET BOUNDARY CONDITIONS FOR TWO-EQUATION TURBULENCE MODELS

Anton B. KORSAKOV[1], Evgueni M. SMIRNOV[1], Valery D. GORYACHEV[2]

[1] Department of Aerodynamics, St.-Petersburg State Polytechnic University. E-mail: aero@phmf.spbstu.ru
[2] Corresponding Author. Department of Mathematics, Tver State Technical University. 170026, Tver, Russia. Tel.: +7 4822 311510, E-mail: valery@tversu.ru

ABSTRACT

Turbulent flow in an elbow draft tube of an axial turbine is calculated with an in-house CFD-code on the base of the RANS approach. The focus is to study sensitivity of the predicted pressure recovery and outlet energy non-uniformity to wide variations in the inlet boundary conditions for transported turbulence quantities used in popular turbulence models, such as the standard k-ε model, the Wilcox k-ω model and the Menter SST model. This information is important for appropriate CFD-based optimization. The steady-state computations at the inlet Reynolds number of about $6 \cdot 10^5$ were performed for a draft tube with two outlet channels tested several decades ago at an air test rig in combination with a runner. At the computations, inlet distributions of three velocity components were fixed and defined by experimental profiles. It has been established that in case of the k-ε and the k-ω model the engineering quantities characterizing the draft tube performance change dramatically when the inlet turbulent-to-molecular viscosity ratio are gradually increased from 100 to 10,000, with the inlet turbulence intensity varied from 5% to 10%. The SST model shows a considerably weaker sensitivity despite it produces a more complicated flow field. A comparison with the measurement data is given.

Keywords: CFD, draft tube flow, axial hydraulic turbine, turbulence modelling

NOMENCLATURE

A	$[m^2]$	cross section area
D	$[m]$	diameter
K	[-]	non-uniformity factor of the outlet dynamic pressure
Q	$[m^3/s]$	flow rate
R	$[m]$	radial distance from the runner axis
Re	[-]	Reynolds number
S	$[1/s]$	strain tensor magnitude
Tu	[-]	inlet turbulence intensity
U	$[m/s]$	bulk velocity
$\underline{V}$	$[m/s]$	velocity vector
V_n	$[m/s]$	normal velocity at a cross section
V_z, V_r, V_t	$[m/s]$	axial, radial and circumferential velocity components
Y^+	[-]	normalized distance to the wall of the first calculation point
X, Y, Z	$[m]$	Cartesian coordinates
k	$[m^2/s^2]$	turbulent kinetic energy
p	$[Pa]$	pressure
q	$[Pa]$	mass-averaged dynamic pressure
ε	$[m^2/s^3]$	dissipation rate of turbulent kinetic energy
η	[-]	pressure recovery factor
ν	$[m^2/s]$	molecular kinematic viscosity
ν_t	$[m^2/s]$	turbulent viscosity
ρ	$[kg/m^3]$	density
ω	$[1/s]$	turbulence eddy frequency

Subscripts and Superscripts

in	at the inlet of the draft tube
out	at the outlet of the draft tube
t	turbulent

1. INTRODUCTION

The task of a hydraulic draft tube is to convert the kinetic energy of the fluid leaving the turbine runner to a static pressure rise. Consequently, minimizing the energy losses is a challenge in the design of draft tubes. The relative importance of the losses depends on the water head. Particularly in case of the low head power plants, the losses in the draft tubes become relatively large and the design or redesign of existing draft tubes prove to be a critical issue.

In essence, the draft tube is a diffuser that typically has a complicated form, especially in the

elbow draft tube case. The diffuser nature of the draft tube flow predefines a strong influence of the inlet conditions, depending in turn on the regime of runner operation. Generally, the flow entering the draft tube can be characterized as three dimensional, turbulent and swirling.

Many Computational Fluid Dynamics (CFD) studies are dealing with the complex flow in the elbow draft tubes. A great deal of effort has been made in 1999-2005 by numerous participants of the ERCOFTAC Turbine-99 Workshops [1,2] at test computations of the flow in the sharp-heel draft tube of a Kaplan hydraulic turbine model studied at the Alvkarleby laboratory in Sweden. The computations were performed on the base of steady-state or unsteady problem formulation with various commercial and in-house CFD-codes using a number of turbulence models for closing the Reynolds-averaged Navies-Stokes (RANS) equations. Attempts of Large Eddy Simulation (LES) were presented at the 3rd Workshop as well. As an important result of these test calculations, it was stated that apart from discretization errors and specifics of a particular turbulence model the flow structure and the pressure field, as well as the engineering quantities predicted, are rather sensitive both to the inlet distributions of mean velocity components and to values prescribed at the draft tube inlet for transported turbulence quantities (see, for instance, [3]).

A straight way to overcome this issue is to simulate the flow through a whole rotor/stator configuration including stay vanes, guide vanes, a runner and a draft tube. Such kind of time and resource consuming computations are performed for models of the Francis turbines, with the aim to predict unsteady flow phenomena responsible for arising high pressure pulsations, first of all due to formation of the known vortex rope during partial load operation of the turbine [4-6]. However, adequate prediction of turbulence at the runner exit of a Kaplan turbine potentially can be achieved only at very costly unsteady rotor/stator calculations that would be able to resolve the vane wakes (interacting with the runner) and the runner blade wakes. Consequently, this "straight-way" approach hardly might be applied for engineering purposes in the near future, including a desire (see, for instance, [7-8]) to get tools for automatic shape optimization of draft tubes for low head hydraulic turbines.

Recently De Henau et al. [9] reported an investigation of methodologies to improve the reliability of CFD RANS-based analysis of axial turbine draft tubes. The study was performed with the ANSYS CFX 12.0 software using the SST turbulence model [10]. A steady-state rotor/stator solution (obtained with the mixing-plane approximation) and a draft tube only solution are presented. Particularly it has been established that in case of the draft tube only simulation prescribing a circumferential average value of the turbulent kinetic energy together with an average turbulent length scale as turbulence inlet conditions for the SST model equations is a proper technique as long as these averages are coherent with the rotor/stator steady solution. Nevertheless, comparisons of simulation results with the experimental data highlight some discrepancies between the predicted draft tube flow and the experimental observations.

All the above mentioned gives a motivation to study sensitivity of prediction results for the draft tube performance to wide variations in the inlet boundary conditions for transported turbulence quantities used in RANS turbulence models. The present contribution covers results of such a study for three two-equation turbulence models. The computations were performed for the axial turbine draft tube model examined many years ago at a large-scale air test rig that was under extensive operation at the Department of Aerodynamics of the Leningrad Polytechnic Institute (LPI, currently the St.-Petersburg State Polytechnic University) in the fifties of the last century.

2. TEST CASE

2.1. Experimental configuration

Figure 1 shows a scheme of the LPI aero test rig that was assembled in the middle of the last century to examine models of axial turbines. This rig was extensively used for many years to provide experimental data for performance of turbines designed for several hydro power plants in Russia.

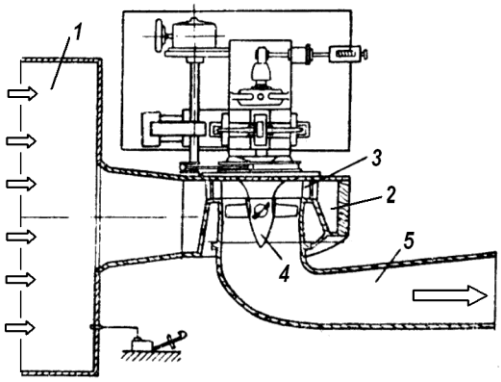

Figure 1. Scheme of the LPI aero test rig: (1) delivery duct, (2) spiral chamber, (3) guide vanes, (4) runner, (5) draft tube

The particular case selected for the present study is one of the variants of the draft tube design for the Kuibyshev hydroplant. Generally, this test case is described in [11], additional details were taken from available internal reports.

The draft tube under consideration consists of a short conical diffuser followed by a strongly curved 90º elbow of a varying cross section (circular to

rectangular) and then by two outlet channels separated by a pier (Figures 2,3). The outer diameter of the draft tube inlet section, D_{in}, is 434 mm. The outlet-to-inlet expansion ratio of the draft tube is of 4.88. Other dimensions characterizing the draft tube geometry are given in Fig.2.

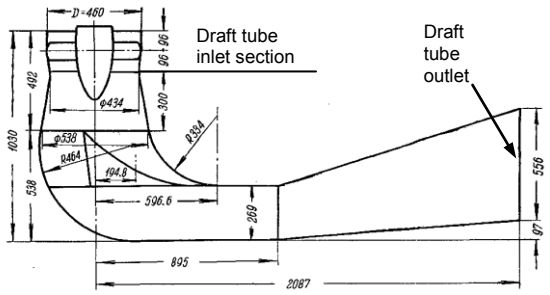

Figure 2. Dimensions of the test draft tube

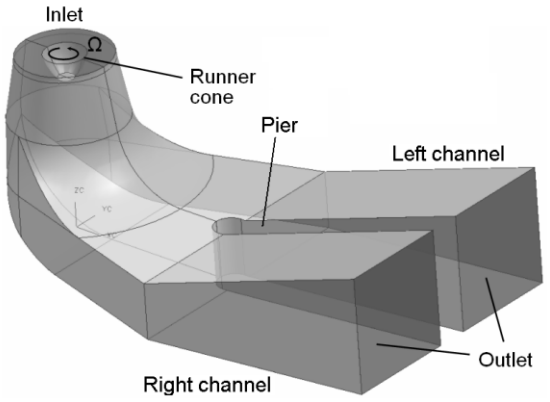

Figure 3. 3D model of the test draft tube

At the selected measurements of the draft tube flow, the runner, 460 mm diameter, with the blade angle of incidence of 15°, rotated with the angular speed of 2553 revolution per minute. The flow rate was kept at 2.64 m^3/s, that gave the inlet Reynolds number, $Re=U_{in}\cdot D_{in}/\nu$, of about $6\cdot10^5$. The draft tube outlet was open directly to atmosphere.

2.2. Measurement data

Three components of the velocity and the local static pressure were measured at the inlet and outlet sections of the draft tube using a spherical five-hole probe. The inlet velocity profiles were measured along one radial direction. The results given in [11] for the inlet section are reproduced in Figure 4.

For evaluation of the draft tube performance, two engineering quantities were calculated via integration of the measured velocity and pressure distributions over the inlet and outlet sections. The first one is the pressure recovery factor

$$\eta = <\Delta p> / q_{in} \qquad (1)$$

where the mass-averaged pressure rise, $<\Delta p>$, and the inlet dynamic pressure, q_{in}, are defined by

$$<\Delta p> = Q^{-1} \int_{A_{in}} (p_{out} - p_{in}) V_n dA \qquad (2)$$

$$q_{in} = Q^{-1} \int_{A_{in}} \frac{\rho V^2}{2} V_n dA \qquad (3)$$

In Eq.(2) the outlet static pressure, p_{out}, was treated in as a constant equal to the atmospheric one.

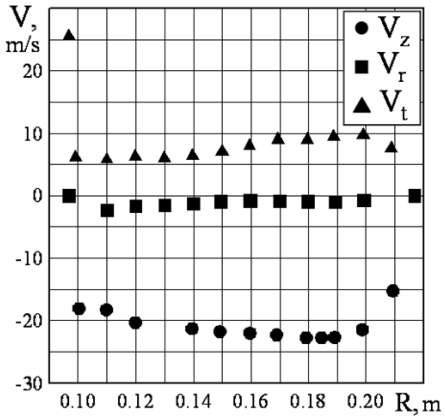

Figure 4. Experimental velocity component profiles at the draft tube inlet

The second integral quantity, K, is the non-uniformity factor of the outlet dynamic pressure. It is evaluated as

$$K = \left(Q \frac{\rho U_{out}^2}{2} \right)^{-1} \int_{A_{out}} \frac{\rho V^2}{2} V_n dA \qquad (4)$$

As reported in [11], for the test case selected, η=0.60, and K=4.07.

3. COMPUTATIONAL ASPECTS

3.1. Mathematical formulation

The present computations are performed on the base of the incompressible fluid Reynolds-averaged Navier-Stokes equations written for the case of steady-state mean flow. To close the RANS equations, two-equation turbulence models based on the isotropic turbulent viscosity assumption are used in combination with techniques of enhanced wall function. Among the wide variety of models of this family, the following three have been chosen due to their popularity in the CFD community: the standard k-ε model (written with the Kato-Launder modification [12]), the Wilcox k-ω model [13] and

the Menter SST model. The latter is applied in the formulation given in [10].

In case of the k-ε model, enhanced wall functions suggested and validated in [14] are used. These functions produce good quality results for the near wall layer even if Y^+ for the computational grid used is as low as 3-4. For the Wilcox k-ω model and the SST model, an approach similar to that suggested in [15] for the 'automatic wall treatment' is applied.

3.2. Boundary conditions

Boundary conditions are specified at the inlet, outlet and solid wall boundaries of the draft tube model. Inflow boundary conditions are prescribed at the start of the conical diffuser using interpolation of the measured mean axial, circumferential and radial velocity profiles (shown in Fig. 4). Due to lack of more detailed data, the calculations were carried out assuming that the inlet flow is axisymmetric.

The inlet turbulence is specified by prescribing turbulence intensity, Tu, and the turbulent-to-molecular viscosity ratio, $(\nu_t/\nu)_{\text{in}}$. To define inlet values of the transported turbulence quantities the following relations are used

$$k_{in} = \frac{3}{2}\left(Tu \cdot U_{in}\right)^2 \tag{5}$$

$$\varepsilon_{in} = \left(C_\mu k_{in}^2/\nu\right)/\left(\nu_t/\nu\right)_{in} \tag{6}$$

$$\omega_{in} = \left(k_{in}/\nu\right)/\left(\nu_t/\nu\right)_{in} \tag{7}$$

where C_μ=0.09 is an empirical constant of the k-ε model. At the calculations, the inlet turbulence intensity was set to 5%, 7.5%, or 10%, while the inlet viscosity ratio was varied from 100 to 10,000.

For pressure, the homogeneous Neumann boundary condition was used everywhere except at the outlet, where the area-averaged pressure is set to zero. Recirculating flow allowed at the outlet, with the homogeneous Neumann boundary condition where the flow was directed outward, and constant values of the turbulence transported quantities (coherent with the inlet values) where recirculation occurred.

3.3. Computational grid

A block-structured grid of about 150 K nodes was generated for the calculations. The grid is symmetrical with respect to the middle plane. Half of the grid is illustrated in Figure 5. The solutions presented below yielded first-computational-point wall distances of $5 < Y^+ < 80$ with an appropriate average of Y^+=30.

Sure, today such a grid may be treated as a relatively coarse one. However, this choice was motivated by the following considerations. First, it is no much sense to perform refined CFD modeling under conditions of existing experimental uncertainties related to the mean velocity distributions over the inlet, when there is no information about variations of the inlet velocity along the circumferential direction, and resolution of the near wall layers is pure. Second, it is well known that using a refined grid might result in problems of getting a steady-state solution for such a complicated three-dimensional flows, and the need to perform time-consuming unsteady computations is extremely undesirable for extensive parametric computations.

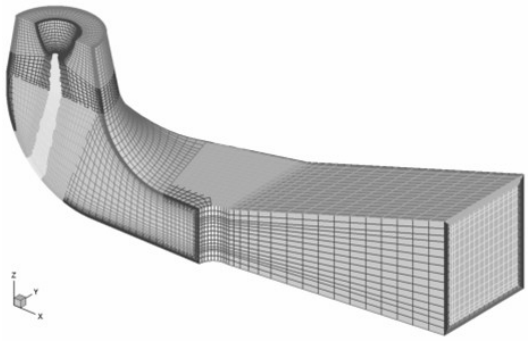

Figure 5. Half of the computational grid

3.4. CFD code

The calculations were performed with the in-house code SINF being under long-time development at the Department of Aerodynamics of the St.-Petersburg State Polytechnic University. This 3D incompressible/compressible Navier-Stokes code is based on the second-order finite-volume spatial discretization using the cell-centered variable arrangement and body-fitted block-structured grids. A general description of the code capabilities is given by Smirnov and Zajtsev [16]. One of the examples of refined simulations of 3D turbulent flows performed with this code and comparisons with the ANSYS CFX software results are given in [17].

4. RESULTS

4.1. Flow visualization

Figure 6 illustrates typical flow patterns computed for the draft tube under consideration with three different turbulence models. One can see that the k-ε model and the Wilcox model yield very similar results for global flow structure, with a relatively low intensity of the vortex forming in the elbow region and entering then into the left outlet channel. Contrary to that, the SST model produces a rather intensive vortex in the left outlet channel, and a pronounced swirl in the right channel as well. From a detailed flow analysis one can conclude that

a more complicated structure of the flow predicted with the SST model is due to a several times lower level of the flow core turbulent viscosity, as compared with the fields predicted by the other two turbulence models. Obviously, this reduction of the flow core turbulent viscosity is a result of the limitation introduced by Menter into the expression defining this quantity,

$$\nu_t = \frac{0.31k}{max\left(0.31\omega, SF_2\right)}, \qquad (8)$$

where S is the mean flow strain rate, and F_2 is one of the empirical functions of the SST model [10].

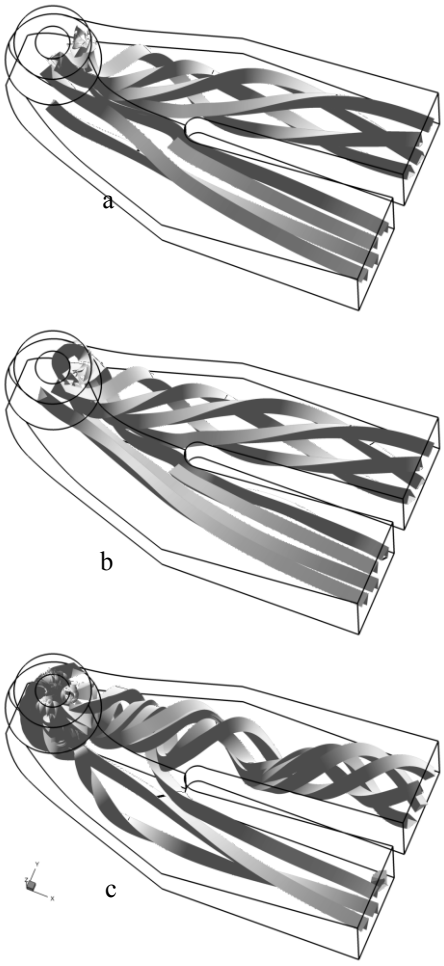

Figure 6. Streamline patterns computed with (a) *k-ε* , (b) *k-ω*, and (c) SST turbulence model

Figure 7 presents an example of streamwise velocity distributions over the outlet section, Tu=5%, $(\nu_t/\nu)_{in}=10^3$. One can see a pronounced unbalance of flows leaving the draft tube through the right and the left channels. From the other side, for all the tubulence models used, the right channel flow (more intensive) is highly non-uniform, with a maximum shifted to the side-bottom corner. Most distictions between the patterns obtained for different turbulence models are observed at the outlet of the left channel. For instance, a local minimum in the flow core is seen in the SST model case whereas for two other models the velocity varies steadily from the bottom to the top.

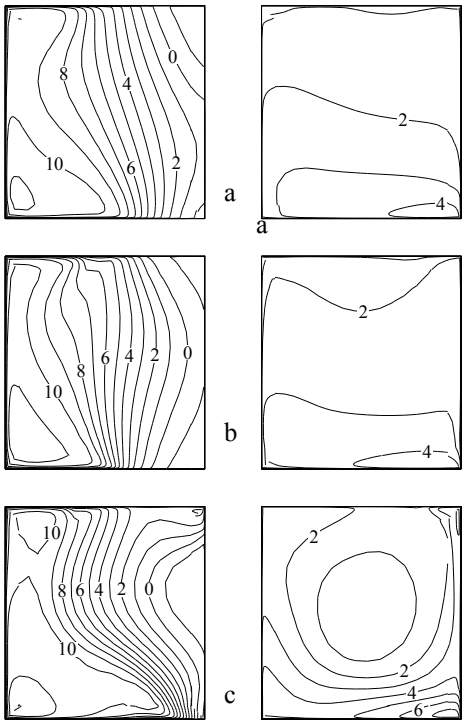

Figure 7. Outlet streamwise velocity distributions computed at Tu=5% and $(\nu_t/\nu)_{in}=10^3$ with (a) *k-ε* , (b) *k-ω*, and (c) SST turbulence model

4.2. Engineering quantities

Effect of wide variations in the inlet turbulence parameters on the predicted pressure recovery and outlet energy non-uniformity is illustrated in Figures 8, 9. It is clearly seen that in case of the *k-ε* and the Wilcox *k-ω* model the engineering quantities characterizing the draft tube performance change strongly over the whole range of the inlet viscosity ratio variations. The effect of an inlet turbulence intensity increase is more pronounced in the *k-ε* case. When comparing the prediction results with the experimental data one can conclude that the Wilcox *k-ω* model data match the experiments at $(\nu_t/\nu)_{in}$ of about 10^3. However this result should be treated as a casual one.

The SST turbulence model shows a weaker sensitivity to variations in the viscosity ratio especially for the outlet energy non-uniformity factor, the predicted value of which is in a surprisingly well agreement with the experimental data. The pressure recovery factor yielded by the SST model turns to be more sensitive to the inlet turbulence intensity variations, and it is typically under-predicted as compared with the measurements. However, for the highest value of Tu

and $(\nu_t/\nu)_{in}>10^3$ the calculation and the experimental data are in a satisfactory agreement.

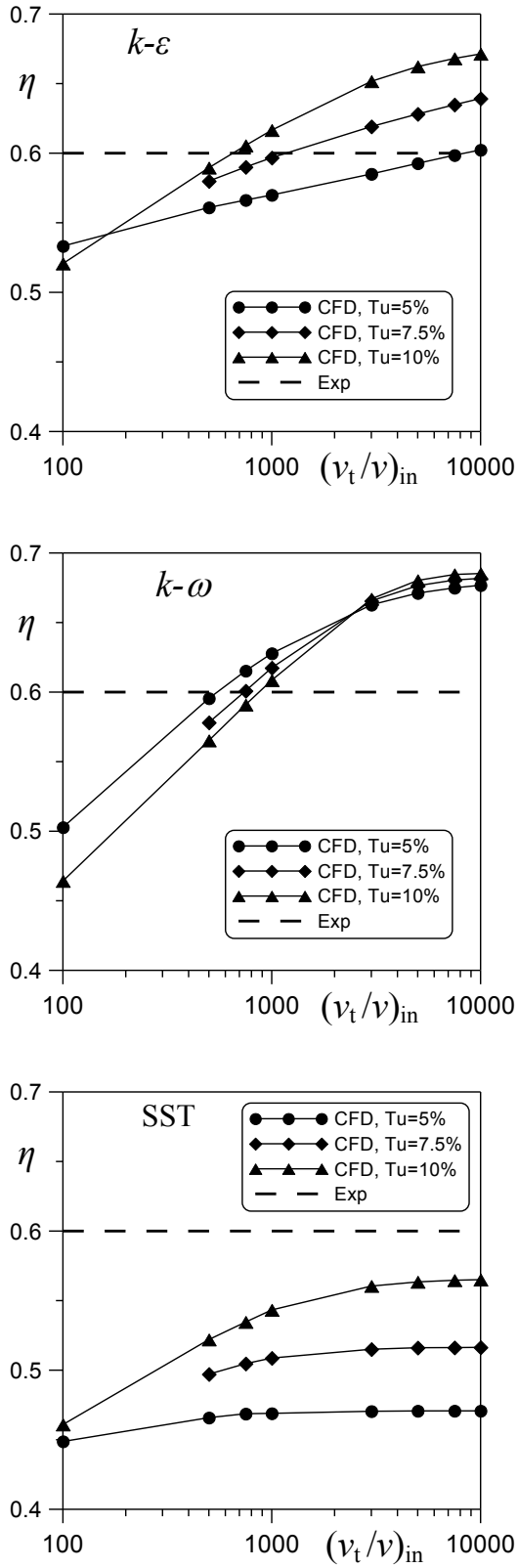

Figure 8. Effect of turbulence inlet boundary conditions on the pressure recovery factor computed with (top) *k-ε* , (middle) *k-ω*, and (bottom) SST turbulence model

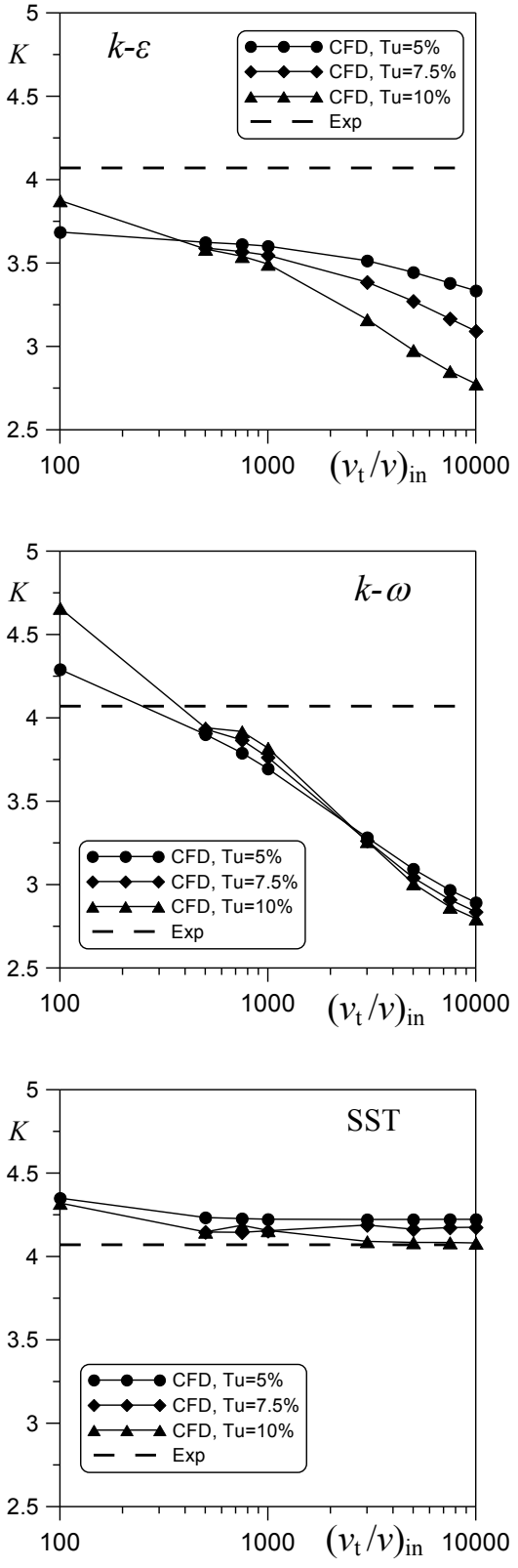

Figure 9. Effect of turbulence inlet boundary conditions on the outlet dynamic pressure non-uniformity factor computed with (top) *k-ε* , (middle) *k-ω*, and (bottom) SST turbulence model

5. SUMMARY

Systematic RANS-based computations have been performed for an axial turbine elbow draft tube using fixed prescribed profiles of the inlet velocity components and widely varied inlet values of turbulence quantities. The inlet turbulence intensity was in the 5% to 10% range while the inlet turbulent-to-molecular viscosity ratio was varied from 100 to 10,000. The standard k-ε turbulence model and the Wilcox k-ω model predict the engineering quantities, which change dramatically with inlet turbulence variations. Generally, the SST model shows a weaker sensitivity despite it produces a more complicated flow field as compared with the two other models. It should be treated as an attractive feature of the SST model having in mind developments of tools for automatic CFD-based shape optimization of the draft tubes, at least for low head hydraulic turbines.

REFERENCES

[1] Engström T.F., Gustavsson H., Karlsson R. I., 2002, "Turbine-99 – Workshop 2 on Draft Tube Flow", Proc. *21st IAHR Symposium on Hydraulic Machinery and Systems,* Laussane, Switzerland.

[2] Cervantes M. J., Engström T. F., Gustavsson L. H., 2005, "Turbine-99 III", Proc. *3rd IAHR/ERCOFTAC Workshop on Draft Tube Flow,* Porjus, Sweden.

[3] Page, M., Giroux, A.-M., Nicolle, J., "Steady and unsteady computations of Turbine 99 draft tube", Proc. *3rd IAHR/ERCOFTAC workshop on Draft Tube Flow, Turbine99-III*, Porjus, Sweden, Paper No. 9

[4] Ruprecht, A., Maihöfer, M., Heitele, M., and Helmrich, T., 2002, "Massively parallel computation of the flow in hydro turbines," Proc. *21st IAHR Symposium on Hydraulic Machinery and Systems*, Lausanne, Switzerland, pp. 199–206.

[5] Ciocan, D., Iliescu, M.,S., Vu, T.,C., Nennemann, B., Avellan, F., 2007, "Experimental study and numerical simelation of the FLINDT draft tube rotating vortex", *ASME J Fluid Eng*., Vol.129, pp.146-158.

[6] Magnoli, M. V., Schilling, R., 2008, "Vortex shedding in Francis runners trailing edges", Proc. *24th IAHR Symposium,* Foz do Iguaçu, Brazil.

[7] Eisinger, R., Ruprecht, A., 2005, "Automatic shape optimization of hydro turbine components based on CFD", Proc. *Workshop on Turbomachinery Hydrodynamics*, Timisoara, Romania.

[8] Marjavaara, B.D, Lundström, T. S, 2006, "Redesign of a sharp heel draft tube by a validated CFD-optimization", *Int. J Numer. Meth. Fluids,* Vol. 50, pp. 911-924.

[9] De Henau, V., Payette, F.-A, Sabourin, M., Gagnon, J-M., Gouin, P., Deschênes, C., 2010, "Computational study of a low head draft tube and validation with experimental data", Proc. *25th IAHR Symposium on Hydraulic Machinery and Systems,* Timisoara, Romania.

[10] Menter, F.R., Langtry R., Kuntz M., 2003, "Ten years of industrial experience with the SST turbulence model", *Turbulence, Heat and Mass Transfer 4 (CD-ROM Proceedings).* Begell House, Inc.

[11] Nevsky, D.Y., Sinochkina, L.A., 1955, "Study of the draft tube of a hydraulic turbine model for the Kuibyshev hydroplant", *Trans. Leningrad Polytechnic Institute*, No. 176, pp. 76-91 (in Russian).

[12] Kato, M., Launder, B.E., 1993, "The modelling of turbulent flow around stationary and vibrating square cylinders", Proc. *9th Symposium on Turbulent Shear Flows,* Kyoto, Japan, pp. 1041-1046.

[13] Wilcox, D., 1988, "Reassessment of the scale-determining equation for advanced turbulence models", *AIAA Journal*, Vol. 26, pp. 1299-1310.

[14] Kirillov, A.I., Ris, V.V., Smirnov, E.M., Zajtsev, D.K., 2001, "Numerical simulation of local heat transfer in rotating two-pass square channels", *Heat Transfer in Gas Turbine Systems. Annals of the New York Academy of Sciences*, Vol. 934, pp.456-463.

[15] Menter, F., Ferreira, J. C., Esch, T., Konno, B., 2003, "The SST turbulence model with improved wall treatment for heat transfer predictions in gas turbines", Proc. *Int. Gas Turbine Congress*, Tokyo, Japan, IGTC2003-TS-059.

[16] Smirnov, E.M., Zajtsev, D.K., 2004, "The finite-volume method in application to complex-geometry fluid dynamics and heat transfer problems", *Scientific-Technical Bulletin of the St.-Petersburg State Technical University*, No 2(36), pp. 70-81 (in Russian).

[17] Levchenya, A.M., Smirnov, E.M., Goryachev, V.D., 2010, "RANS-based numerical simulation and visualization of the horseshoe vortex system in the leading edge endwall region of a symmetric body", *Int. J Heat Fluid Flow*, Vol.31, pp. 1107-1112.

Conference on Modelling Fluid Flow (CMFF'12)
The 15th International Conference on Fluid Flow Technologies
Budapest, Hungary, September 4-7, 2012

SELF-INDUCED UNSTEADINESS OF THE GAMM FRANCIS TURBINE DRAFT TUBE AT PARTIAL DISCHARGE

Tiberiu CIOCAN[1], Sebastian MUNTEAN[2], Romeo F. SUSAN-RESIGA[3]

[1] Corresponding Author. Department of Hydraulic Machinery, Politehnica University of Timisoara. Mechanical Engineering Faculty Bvd. Mihai Viteazu 1, Timisoara, Romania. Tel.: + 40 256 403692, Fax: + 40 256 403700, E-mail: ciocan@mh.mec.upt.ro
[2] Center for Advanced Research in Engineering Science, Romanian Academy – Timisoara Branch. E-mail: seby@acad-tim.tm.edu.ro
[3] Department of Hydraulic Machinery, Politehnica University of Timisoara. E-mail: resiga@mh.mec.upt.ro

ABSTRACT

The paper aim is understanding the flow physics in order to enhance the knowledge to design/optimize a turbine runner for an existing draft tube [1]. As a result, the paper is focused on the three-dimensional numerical investigations of the unsteady swirling flow at partial discharge with vortex rope in a Francis turbine draft tube. The inflow conditions are defined with a novel mathematical model for computing the swirling flow over a wide range of operating regimes, developed by Resiga et al. [2]. The 3D turbulent numerical simulation is performed using the FLUENT commercial code. Mesh refinements are analyzed within the draft tube cone in order to assess the numerical results. The unsteady pressure pulsations acquired on the draft tube cone at part load operating point are examined using a Fourier analysis in order to determine the fundamental frequency and it amplitude associated to the vortex rope. Further, the numerical results are validated against experimental data [3] in order to assess the accuracy of the numerical methodology.

Keywords: draft tube, numerical simulation, unsteady swirling flow, pressure pulsations

NOMENCLATURE

F	$[W]$	net flux of specific mechanical energy
P, $\overline{P}$	$[Pa]$	pressure, averaged pressure
R	$[mm]$	radius
S	$[mm]$	section
$\overline{U}$	$[m/s]$	averaged velocity
U, V, W	$[m/s]$	velocity components (axial, radial, tangential)
f	[-]	dimensionless draft tube hydraulic power loss
k	$[m^2/s^2]$	turbulent kinetic energy
u, v, w	$[m/s]$	dimensionless mean velocity components (axial, radial, tangential)
v_{sf}	[-]	dimensionless swirl-free velocity
ν	$[m^2/s]$	kinematic viscosity
ρ	$[kg/m^3]$	density
τ_{ij}	$[Pa]$	Reynolds stress tensor
φ	[-]	discharge coefficient
ψ	[-]	dimensionless turbine head
ω	$[rad/s]$	angular speed

Subscripts and Superscripts

in, out	inlet and outlet of the draft tube
ref	reference
r, z	radial and axial direction
tot	total
wl	wall

1. INTRODUCTION

Modern hydraulic turbines meet new challenges associated with the variable demand on the energy market. As a result, quite often turbines tend to be operated over an extended range of regimes far from the best efficiency point. When hydraulic turbines operate at partial load a high level of residual swirl in the draft tube results as a consequence of mismatch between the angular momentum generated by the wicket gates (guidevanes) and extracted by the turbine runner. As a result, the vortex breakdown associated with this high level swirl is developed. Particularly, the helical vortex breakdown is seen as a source of the self induced unsteadiness. Consequently, the fixed pitch runner (e.g. Francis turbines) exhibits an abrupt decrease in efficiency and severe pressure fluctuations at off-design operating regimes.

The swirling flow generated downstream the hydraulic turbine runner has been extensively investigated both experimentally [4] and theoretically [5-7] in order to elucidate the physics of the phenomena. The swirling flow at runner

outlet measured in the first phase of the FLINDT project has been analyzed by Susan-Resiga et al. [8] who discovered that the axial and circumferential velocity profiles can be simultaneously represented as a superposition of three vortices: (i) a rigid body rotation with constant axial velocity, (ii) a counter-rotating Batchelor vortex with large characteristic radius, and (iii) a co-rotating Batchelor vortex with small characteristic radius. The last vortex is associated with the wake of the runner hub (also called crown), while the other two vortices are the direct outcome of the runner design.

It was clear from these investigations that the swirling flow ingested by the draft tube is the key issue in both minimizing the draft tube losses and avoiding unexpected hydrodynamic effects, respectively. While successful in analyzing the swirling flow at runner outlet [8], the approach further extended for the draft tube cone [9], lacks the capability of predicting the swirl configuration over a wide operating range. In particular, at low discharge conditions investigated in the second phase of the FLINDT project, where a precessing helical vortex is developed in the draft tube cone as a result of the self-induced swirl instability, also called helical vortex breakdown [10], the three-vortex model from [8] fails to predict the circumferentially-averaged annular swirling flow with central quasi-stagnant region. However, we were able to compute this particular swirling flow in the draft tube cone [11], using axisymmetric turbulent swirling flow models, in good agreement with experimental data. Predicting and understanding the swirling flow particularities at the runner outlet/draft tube inlet is also the key in developing novel flow control techniques aimed at mitigating the unwanted flow instabilities at partial discharge. Susan-Resiga et al. [12] propose a water injection through the runner crown, along the machine axis. It is shown that this method successfully mitigates the precessing helical vortex and the associated pressure fluctuations.

Experimentally the global behaviour of the draft tube is determined but hydrodynamic details are hardly distinguished. Therefore, the numerical simulation helps to analyse the draft tube flow in order to deeply understand the physics of the phenomena. However, computing the real flow (3D, unsteady and turbulent) through the whole hydraulic turbine requires large computer memory and CPU, even for the present day computers. As a result, a simplified simulation technique must be employed to obtain useful results for turbine draft tube analysis, using currently available computing resources. The key of this strategy is the inflow conditions imposed on the inlet section of the draft tube computational domain. The draft tube inflow conditions can be obtained from experimental investigations. However, it is employed a surrogate model [2] that replace the turbine runner, for computing the swirling flow at the draft tube inlet.

This investigation extends the work began in [4] by addressing the decelerated swirling flow in the GAMM Francis draft tube for a part-load operating regime in order to better understand the physics of the phenomena. Section 2 presents the problem setup for numerical analysis, including the computational domain, equations and boundary conditions, as well as the grid refinement study. Section 3 briefly reviews the problem set-up for the 3D unsteady simulation using FLUENT [13] and the instantaneous numerical results. Further, the numerical results are validated against experimental data. Then the conclusions are summarized in the last section.

The paper presents the numerical investigation of the swirling flow with precessing vortex rope into a hydraulic turbine draft tube. The main goal is to elucidate the occurrence of the stagnant region with a vortex rope wrapped around it at part load operating regime. This self-induced instability is generated due to the swirling flow configuration at the runner outlet, not by the viscous effects in the boundary layer developed on the crown and band surfaces.

2. PROBLEM SET-UP

2.1. 3D Computational domain

The cross-section of the GAMM Francis turbine draft tube [14] is shown in Fig. 1. Within the draft tube cone, one survey section, S_{survey}, located at $R_{wl\_survey} = 218.38\ mm$, has been used to measure the radial profiles of the velocity components. The geometry for the three-dimensional computational domain is given in Fig. 2 and it was reconstructed in the pre-processor GAMBIT [15]. The model draft tube inlet section has a wall radius of $R_{wl\_inlet} = 201\ mm$. The GAMM draft tube has an inlet conical diffuser with half cone angle of 6.6 degree, a 90 degree bend of circular cross section with the constant area, and an outlet conical diffuser with half cone angle of 5.0 degree. The outlet to inlet area ratio is 3.227.

The draft tube hydrodynamics is very complex, because the inflow includes both discharge and rotation velocity components, and the flow in the outlet survey section is highly non-uniform. Generally, the flow in the draft tube is decelerated while continuously changing both the direction and shape of the cross section from geometrical point of view.

Consequently, the numerical investigations have been performed in order to find a correlation with the flow instability at off-design turbine operation conditions [16].

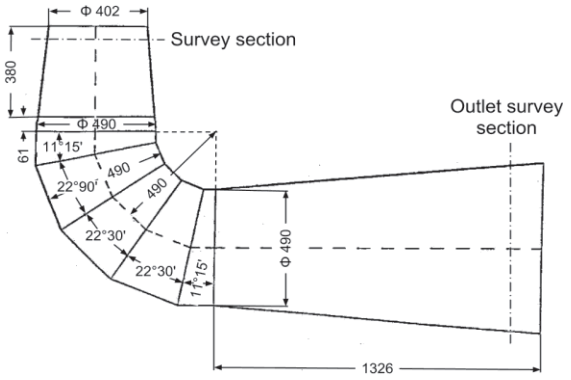

Figure 1. Draft tube cross section of the GAMM Francis turbine [14]

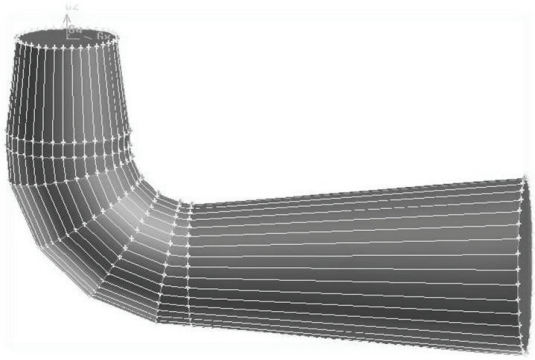

Figure 2. 3D computational domain of the GAMM Francis turbine draft tube

2.2. Equations and Boundary Conditions

In this investigation an incompressible fluid is considered. The governing equations describing, viscous and unsteady flows are the Navier-Stokes equations. Its express the conservation of mass and momentum. For engineering applications the solution of the RANS equations (1) and (2), allows predicting the flow in fairly complex configurations.

$$\frac{\partial \overline{U_i}}{\partial t} + \overline{U_j}\frac{\partial \overline{U_i}}{\partial x_j} = -\frac{\partial \overline{P}}{\partial x_i} + \nu\nabla^2\overline{U_i} - \frac{\partial \tau_{ij}}{\partial x_j} \tag{1}$$

$$\frac{\partial \overline{U_i}}{\partial x_i} = 0 \tag{2}$$

where τ_{ij} the Reynolds stress tensor is an unknown and has to be modelled. The τ_{ij} cannot be expressed exactly as a function of the mean flow variables and must be related to known quantities using a turbulence model. A wide range of models for the Reynolds stress is available, ranging from simple algebraic models, *k-ε* models to full algebraic Reynolds-stress closures.

The two-equation models are the more popular since they offer a good compromise between versatility and computing effort. The typical model examples are the *k-ε* model [17] and *k-ω* model [18], developed approximately twenty years lately.

In the ongoing work the *k-ω* model is used for computing the 3D unsteady swirling flow, because is more accurate than the *k-ε* model in the near wall layers, and has therefore been successful for flows with moderate adverse pressure gradients. The popular *k-ε* model is not able to capture the proper behaviour of turbulent boundary layers up to flow separation [19]. In addition the *ω*-equation shows a strong sensitivity to the values of *ω* in the main flow outside the boundary layer [20].

For more accurate prediction of the flow with strong adverse pressure gradients and separation, like in Francis turbines draft tube operated at part-load operating regimes, we use the Menter shear stress model [21]. The shear stress transport model, denoted further with the acronym SST, is a two-layer model which employs the *k-ω* model in the inner region of boundary layers and switches to a *k-ε* model for the main flow far away from the walls. The *k-ε* model from the main flow is transformed to provide a second set of *k-ω* equations with a blending function F_1 (F_1 is equal to zero away from the wall, the *k-ε* model is employed, and switches to one inside the boundary layer, then the *k-ω* model is employed), used to transition between the two sets of equations.

The complete formulation of the SST model is given below, in the following equations:

$$\frac{\partial(\rho k)}{\partial t} + \frac{\partial(\rho \overline{U_i} k)}{\partial x_j} = \frac{\partial}{\partial x_i}\left[\underbrace{(\mu + \sigma_\omega \mu_t)}_{\Gamma_k}\frac{\partial k}{\partial x_i}\right] + \widetilde{P}_k - \underbrace{\beta^* \rho k \omega}_{Y_k} \tag{3}$$

$$\frac{\partial(\rho \omega)}{\partial t} + \frac{\partial(\rho \overline{U_i} \omega)}{\partial x_j} = \frac{\partial}{\partial x_i}\left[\underbrace{(\mu + \sigma_\omega \mu_t)}_{\Gamma_\omega}\frac{\partial \omega}{\partial x_i}\right] + \alpha\rho S^2 - \underbrace{\beta\rho\omega}_{Y_\omega} + \underbrace{2(1-F_1)\rho\sigma_{w2}\frac{1}{\omega}\frac{\partial k}{\partial x_i}\frac{\partial \omega}{\partial x_i}}_{D_\omega} \tag{4}$$

In these equations, $\widetilde{P}_k$ is a production limiter used in the SST model to prevent the build-up of turbulence in stagnation regions, Γ_k and Γ_ω represent the effective diffusivity of k and ω, respectively, Y_k and Y_ω represent the dissipation of k and ω due to turbulence, D_ω represents the cross-diffusion term and S is the invariant measure of the strain rate. The SST model has been found to provide good predictions of the flow in the Francis turbine water passages [22].

Boundary conditions have an important effect on the numerical results. Consequently, an inappropriate boundary conditions lead to the wrong results. On the inlet surface of the turbine

draft tube, the radial profiles of the velocity components are prescribed while the pressure is imposed on the outlet section. The inflow conditions imposed on the inlet surface of the draft tube are discussed in the next section.

2.3. Inflow Conditions

The velocity profiles from the draft tube inlet are computed using the theory presented in [2] and validated with experimental data in [23].

In this theory the velocity field from Fig. 3 is computed with a mathematical model for computing the swirling flow that requires 3 parameters. The first two parameters are the integral quantities that characterized the swirling flow, i.e. the dimensionless discharge φ and the flux of moment of momentum downstream the runner m_2. In addition the swirling flow must satisfies the kinematic constraints corresponding to the runner blade at the trailing edge, described by the swirl-free velocity v_{sf}, which is the third parameter. This simplified flow model assumes a columnar flow, i.e. a flow with vanishing radial velocity. However the inlet section, shown in Fig. 1, is followed by the discharge cone, and obviously the radial velocity cannot be negligible at least in the wall neighbourhood. Moreover, neglecting the radial velocity leads to spurious flow detachment at the wall and alters the results in the discharge cone. In consequence, we will take in consideration also the radial velocity component at the draft tube inlet. Besides the axial and circumferential velocity component, computed with the flow model [2], the radial velocity will be computed in dimensionless form based on the axial velocity and the wall slope, as follows:

$$v(r) \cong u(r) \cdot \overbrace{\frac{r}{r_{wl}}}^{\substack{normalized \\ radius}} \cdot \overbrace{\frac{dr_{wl}}{dz}}^{\substack{wall \\ slope}} \qquad (5)$$

Eq. (5) provides a simple but rigorous expression for the radial velocity component. This is proportional with the axial velocity component and two constrains are satisfied: 1) it vanishes at the axis and 2) the flow tangency condition on the wall, respectively.

Figs. 3 shows the maps of the axial and circumferential velocity components versus the dimensionless radius for overall discharge coefficient domain $\varphi = 0.16..0.40$, in the survey section. One can be easily observed the development of the central stagnant region when the discharge coefficient goes down to the value $\varphi = 0.28$. Fig. 3b shows the development of a counter-rotation flow when the discharge coefficent goes up to the value $\varphi = 0.308$. That means, the positive values indicate co-rotating flow with respect to the runner.

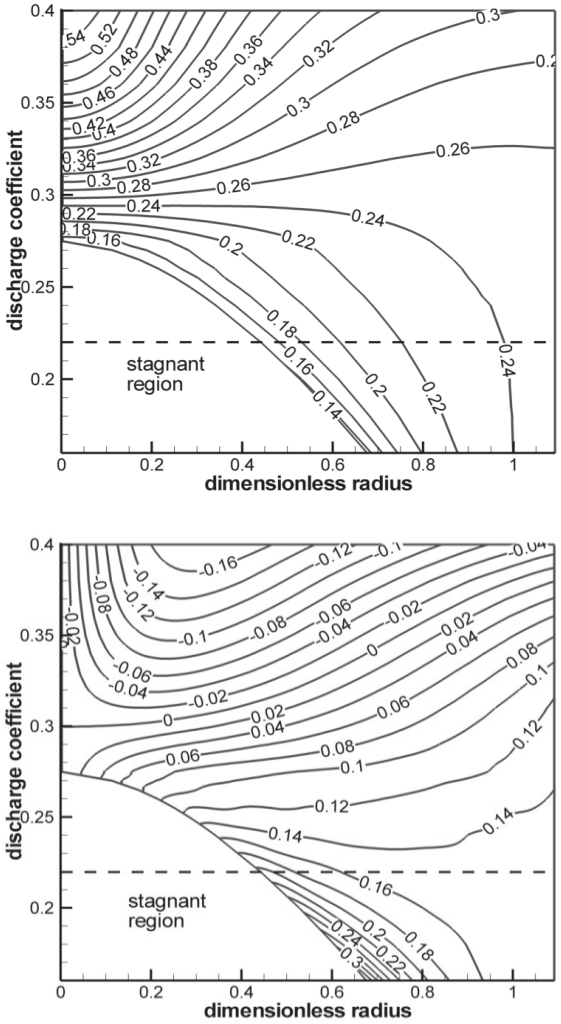

Figure 3. Axial (up) and circumferential (down) velocity components maps for variable discharge coefficient at constant head [23] in the draft tube survey section

The radial profiles of the velocity components associated to different discharge values corresponds to horizontal slices. The part-load operating regime investigated in this paper is marked with dashed line in Figs. 3. Consequently, one can observe a quite good agreement between the analytical velocity profiles with the experimental data in Fig. 4. It was proved that this velocity jump in both axial and circumferential velocity components at the stagnant region boundary with a corresponding vortex sheet [24, 10] is the one which triggers the self-induced instabilities of the swirling flow and the development of the helical precessing vortex [11].

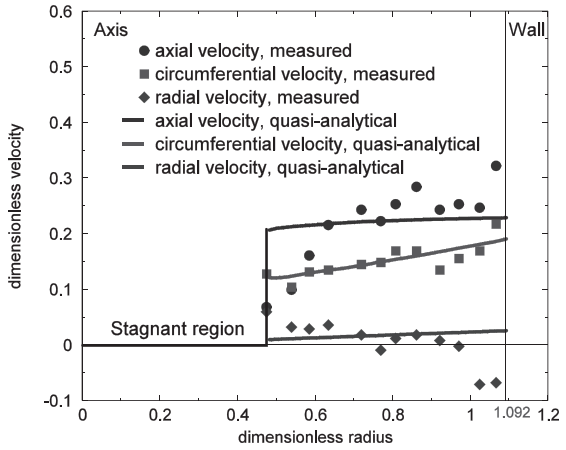

Figure 4. Axial and circumferential velocity components at part-load operating regime $\varphi = 0.22$ at the draft tube survey section

The swirl-free velocity v_{sf} was computed for the survey section where measurements for velocity components were available. In consequence, the swirl-free velocity was scaled-up with $R^2_{wl\_surwey} / R^2_{wl\_inlet}$ in order to compute the radial velocity profiles at the draft tube inlet.

Note that the estimated velocity profiles do not require a runner computation.

2.4. Mesh refinement

A hexahedral structured grid is used to discretize the computational domain, see Fig. 5.

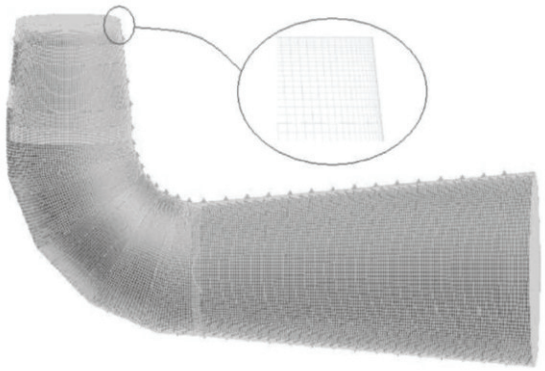

Figure 5. Spatial discretization of the three-dimensional computational domain of GAMM Francis turbine draft tube

Three structured grids with 337288 cells (denoted with 0.34M), 834344 cells (0.83M) and 1800000 cells (1.8M) are considered. The course grid with 0.34M cells corresponds to a uniform distribution along to the draft tube while 0.83M grid is generated based on the course grid with refinement in the draft tube cone region, respectively. The grid with 1.8M cells corresponds to a uniform distribution along to the draft tube using the same procedure like the course grid.

The draft tube head loss is computed according to Eq. (6) with respect to the turbine head $\psi = 1.07$, along to the curvilinear coordinate of the GAMM Francis draft tube in order to assess the accuracy of the grids. It is more intuitive to express the draft tube head loss as percent of the turbine head.

$$100 \times \frac{h_{DT}}{\psi} = \frac{draft\ tube\ head\ loss}{turbine\ head}\ [\%] \tag{6}$$

where,

$$h_{DT} = \frac{f}{\varphi}, \tag{7}$$

$$f = \frac{F}{\frac{\pi}{2}\rho\omega^3 R^3_{ref} R^2_{ref}} \tag{8}$$

and

$$F = F^{in} - F^{out} = \int_{S_{in}} P_{tot}\vec{V}\cdot\vec{n}dS - \int_{S_{out}} P_{tot}\vec{V}\cdot\vec{n}dS \tag{9}$$

Fig. 6 shows the draft tube relative head loss versus the dimensionless curvilinear coordinate along to the GAMM draft tube at discharge coefficient $\varphi = 0.22$ where the vortex rope is well developed. It can be seen that in the draft tube cone and elbow, the grid does not have a significant influence on the draft tube relative head loss, the differences between the grids occur only in the diffuser.

In the draft tube diffuser the discrepancies between the grids occur because at the elbow outlet we have flow detachment and the 0.34M grid tends to overestimate the draft tube relative head loss, while the 0.83M grid underestimates the losses in the first part of the diffuser.

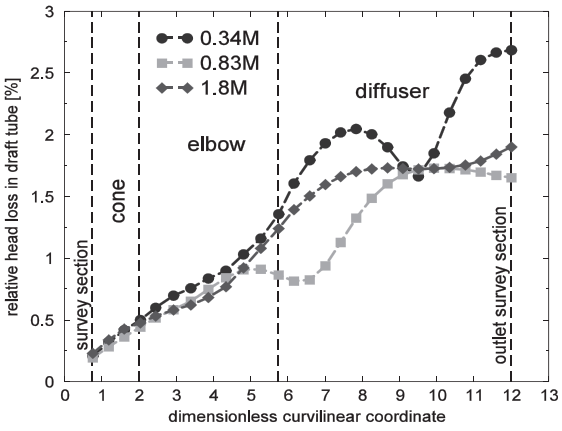

Figure 6. Draft tube relative head loss versus dimensionless curvilinear coordinate along to the GAMM draft tube at the discharge coefficient $\varphi = 0.22$

It can be clearly seen that all grids taken in consideration only the finest one (1.8M cells) provides the best result. However, the largest CPU time was required in order to obtain the results.

Since, it is numerically investigated the self-induced instabilities of the swirling flow, which occurs in the draft tube cone, in the numerical investigation it will be used the 0.83M grid. This grid is generated based on the course grid with refinement in the draft tube cone region, in order to capture accurately the flow unsteadiness and to maintain a good balance between the amount of time and CPU usage, when we perform a three-dimensional unsteady numerical simulation.

3. 3D UNSTEADY NUMERICAL SIMULATION

3.1. Numerical set-up

The 3D unsteady turbulent flow simulations are performed with the FLUENT commercial code [13], using the mesh generated with GAMBIT [15].

The numerical simulation solve the unsteady Reynolds averaged Navier-Stokes equations with a two-equation turbulence model closure as described in section 2.2, and the inlet condition used are specified in section 2.3.

In the numerical investigation the following solver parameters are selected: the time-advancing scheme is 1st-order implicit; the momentum equation, turbulent kinetic energy and the specific dissipation rate are discretized with a 3rd-order MUSCL scheme; the pressure discretization uses a Standard scheme, with the *Semi-Implicit Method for Pressure-Linked Equations* (SIMPLE) algorithm, which uses a relationship between velocity and pressure corrections to enforce mass conservation and to obtain the pressure field. The time step of $5x10^{-4}$ *s* was considered in this numerical simulation.

3.2. Instantaneous results

In Fig. 7 can be seen that the numerical simulation performed reproduces the well - known precessing vortex rope.

The vortex rope is visualized using a snap-shot of an iso-surface of constant pressure (-2.5 *kPa*) and the meridian cross-section is mapped by the static pressure. This three-dimensional precessing helical vortex induces an unsteady pressure field.

Four pressure monitors are located on the wall into the survey section ($R_{wl\_survey} = 218.38\ mm$) over the whole circumference of the cone at 90 degrees from each other, in order to acquire the unsteady pressure field.

Note that the outlet static pressure is set to zero in the simulation. That means the recirculation region can be developed from one time step to another.

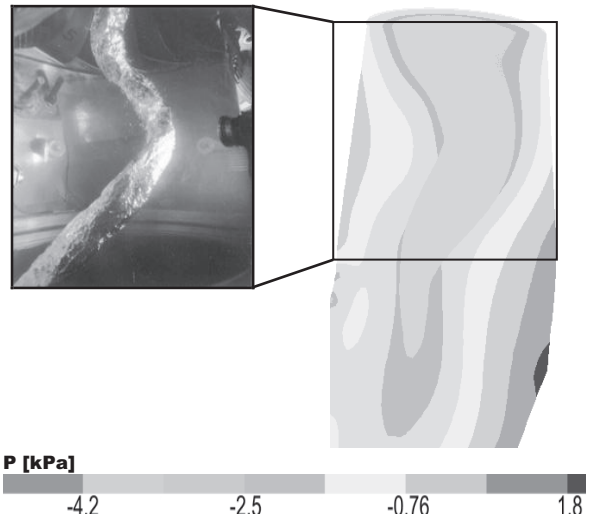

Figure 7. The precessing vortex rope visualized in the GAMM Francis draft tube cone (left) [3], and in the snap-shot obtained from the numerical simulation (right)

4. NUMERICAL RESULTS

The acquired unsteady pressure signals on the wall survey section are examined using a Fourier analysis [25]. The amplitudes are averaged and represented as a single amplitude of the precessing vortex rope from the numerical simulation.

The numerical results are validated against experimental data. Consequently, the Fourier spectra for pressure fluctuations are presented against experimental data are presented in Fig. 8.

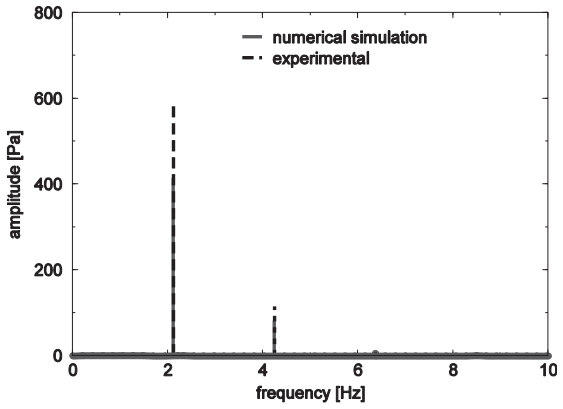

Figure 8. Frequency spectra from unsteady numerical simulation (line) versus experimental data (long dashed line)

In Fig. 8 it can be seen that the harmonics amplitude are underestimated relative to the experimental data. This occurs in the numerical simulation of the swirling flow, because the numerical diffusion dissipates much faster the precessing vortex rope. Consequently, the vortex rope is well developed and more compact in the

experimental investigations than the numerical simulation. The vortex rope frequency is 2.12 *Hz*, corresponding to a Strouhal number of 0.376.

Nevertheless, the Fourier spectra obtained in the three-dimensional turbulent simulation with inflow conditions computed based on inviscid model [2], extended in §2.3, correlates quite well with the experimental spectra obtained by Jacob [3].

5. CONCLUSIONS

The unsteady three-dimensional numerical investigation of the unsteady swirling flow in a turbine draft tube with a precessing vortex rope is performed, in order to analyze the self induced instability. The precessing vortex rope is computed using *k-ω* SST model from FLUENT code, with a swirling flow configuration computed with an inviscid flow model, and imposed at the draft tube inlet. The fundamental frequency and the higher harmonics are captured. The stagnant region with a vortex rope wrapped around it, is due to the swirling flow configuration at the runner outlet, actually to be more precisely that thin vortex sheet is the one which triggers the self-induced instabilities of the swirling flow and the development of the helical precessing vortex.

In order to optimize a turbine runner for an existing draft tube the key is to minimize the stagnant region (Fig. 3) and to reduce the pressure pulsations by controlling the swirl-free velocity v_{sf} (which describes the runner geometry at the trailing edge), such that we have a more favourable swirl configuration at the runner outlet/draft tube inlet.

ACKNOWLEDGEMENTS

This work was partially supported by the strategic grant POSDRU 107/1.5/S/77265 (2010) of the Ministry of Labor, Family and Social Protection, Romania, co-financed by the European Social Fund – Investing in people. Dr. Sebastian Muntean and Prof. Romeo Susan-Resiga were supported by the Romanian Academy program "Swirling flow analysis and instabilities control in the turbomachineries".

REFERENCES

[1] Kubota, T., Han, F., and Avellan, F., 1996, "Performance Analysis of Draft Tube for GAMM Francis Turbine", Proc. *XVIIIth IAHR Symposium on Hydraulic Machinery and Cavitation*, Valencia, Spain, pp. 130 - 138.

[2] Susan-Resiga, R. F., Muntean, S., Avellan, F., and Anton, I., 2011, "Mathematical Modelling of Swirling Flow in Hydraulic Turbines for the Full Operating Range", *Applied Mathematical Modelling*, Vol. 35(10), pp. 4759-4773.

[3] Jacob, T., 1993, "Evaluation sur modele reduit et prediction de la stabilite de functionnement des turbines Francis", *Phd Thesis Nr. 1146, Ecole Polytechinique Federale de Lausanne.* (in French)

[4] Muntean, S., Nilsson, H., Susan-Resiga, R. F., 2009, "3D Numerical Analysis of the Unsteady Turbulent Swirling Flow In A Conical Diffuser Using FLUENT and OpenFOAM", Proc. of the *3rd IAHR Meeting of the Workgroup on Cavitation and Dynamics Problems in Hydraulic Machinery and Systems*, Brno, Czech Republic, pp. 155-164.

[5] Muntean, S., Ruprecht, A., and Susan-Resiga, R. F., 2005, "A Numerical Investigation of the 3D Swirling flow in a Pipe with Constant Diameter Part 1 : Inviscid Computation", Proc. on the Workshop on *Vortex Dominated Flows. Achievements And Open Problems*, Timisoara, Romania, pp. 77-86.

[6] Muntean, S., Buntic, I., Ruprecht, A., and Susan-Resiga, R. F., 2005, "A Numerical Investigation of the 3D Swirling flow in a Pipe with Constant Diameter Part 2 : Turbulent Computation", Proc. of the Workshop on *Vortex Dominated Flows. Achievements And Open Problems*, Timisoara, Romania, pp. 87-96.

[7] Susan-Resiga, R. F., Avellan, F., Ciocan, G. D., Muntean, S., and Anton, I., 2005, "Mathematical and Numerical Modelling of Swirling Flow in Francis Turbine Draft Tube Cone", Proc. on the Workshop on *Vortex Dominated Flows. Achievements And Open Problems*, Timisoara, Romania, pp. 1-16.

[8] Susan-Resiga, R., Ciocan, G.D., Anton, I., and Avellan, F., 2006, „Analysis of the swirling flow downstream a Francis turbine runner", *J. Fluids Eng. – Trans. ASME*, Vol. 128, pp.177–189.

[9] Susan-Resiga, R., Muntean, S., Hasmaţuchi, V., Anton, I., and Avellan, F., 2010, „Analysis and prevention of vortex breakdown in the simplified discharge cone of a Francis turbine", *J. Fluid Eng. – Trans. ASME*, Vol. 132, Paper 051102 (15 pp).

[10] Kuibin, P.A., Okulov, V.L., Susan-Resiga, R. and Muntean, S., 2010, "Validation of analytical formulae for predicting the vortex rope rotating frequency", Proc. *25th IAHR Symposium on Hydraulic Machinery and Systems*, vol. 12, Earth and Environmental Science of Institute of Physics Conference Series, IoP, Paper 012051 (10 pp).

[11] Susan-Resiga, R., Muntean, S., Stein, P. and Avellan, F., 2009, „Axisymmetric swirling flow simulation of the draft tube vortex in Francis turbines at partial discharge", *Int. J. Fluid Machimery and Systems*, Vol. 2, pp. 295–302.

[12] Susan-Resiga, R. F., Vu, T. C., Muntean, S., Ciocan, G. D., and Nennemann, B., 2006 Jet control of the draft tube vortex rope in francis turbines at partial discharge, in: Proc. *of the XXIII*rd *IAHR Symposium on Hydraulic Machinery and Systems*, Yokohama, Japan. Paper F192 (on CD-ROM).

[13] Fluent Inc., 2006, Fluent 6.3 User's Guide, Lebanon, New Hampshire.

[14] Sottas, G., and Ryhming, I.L., 1993, "3D – Computation of Incompressible Internal Flows", Proc. of the *GAMM Workshop*, Notes Numerical Fluid Mechanics (NNFM) 39, Braunschweig, Germany.

[15] Fluent Inc., 2006, Gambit 2.4 User's Guide, Lebanon, New Hampshire.

[16] Thicke, R. H., 1981, "Practical Solutions for Draft Tube Instability," *Water Power & Dam Construction*, Vol. 33(2), pp. 31-37.

[17] Launder, B.E., and Spalding, D. B., 1974, "The numerical computation of turbulent flows", *Int J. of Computations Methods in Applied Mechanics and Engineering*, Vol. 31 (8), pp. 1414-1421.

[18] Wilcox, D.C., 1988, "Reassessment of the Scale-Determining Equation for Advanced Turbulence Models", *AIAA Journal*, Vol. 26, No. 11, pp. 1299-1310.

[19] Menter, F.R., 1993, "Zonal two-equation k-ω turbulence model for aerodynamic flows", *AIAA Journal,* pp. 1993-2906.

[20] Menter, F.R., 1992, "Influence of free stream values on k-ω turbulence model predictions", *AIAA Journal*, Vol. 30, No. 6.

[21] Menter, F.R., 1994, "Two-Equation Eddy-Viscosity Turbulence Models for Engineering Applications", *AIAA Journal*, Vol. 32, No. 8, pp. 1598-1605.

[22] Maruzewski, P., Hayashi, H., Munch, C., Yamaishi, K., Hashii, T., Mombelli, H. P., Sugow, Y., and Avellan, F., 2010, "Turbulence modeling for Francis turbine water passages simulation", Proc. *XV*th *IAHR Symposium on Hydraulic Machinery and Cavitation*, Timisoara, Romania, Vol. 2, pp. 554-561.

[23] Ciocan, T., Susan-Resiga, R. F., and Muntean, S., 2011, "Analysis of the swirling flow at GAMM Francis runner outlet for different values of the discharge", Proc. of the *XXXIII*rd *Caius-Iacob Conference On Fluid Mechanics and Its Technical Applications 2011*, Bucharest, Romania, pp: 33-41.

[24] Nishi, M., Matsunaga, S., Okamoto, M., Uno, M. and Nishitani, K., 1988, „Measurement of three-dimensional periodic flow in a conical draft tube at surging condition". In Rohatgi U.S. (ed.), *Flows in Non-Rotating Turbomachinery Components*, FED, vol. 69, ASME, pp. 81–88.

[25] Riley, K., Hobson, M., and Bence, S., 1997, "Mathematical methods for physics and engineering", *Cambridge University Press.*

Conference on Modelling Fluid Flow (CMFF'12)
The 15th International Conference on Fluid Flow Technologies
Budapest, Hungary, September 4-7, 2012

NUMERICAL INVESTIGATIONS OF THE REFEEDING CHANNEL OF A MULTISTAGE HIGH-HEAD PUMP-TURBINE

Eduard DOUJAK[1], Philipp UNTERBERGER[2], Mark-Michael WELTZL[3], Christian BAUER[4]

[1] Corresponding Author. Institute for Energy Systems and Thermodynamics, Department of Fluid Machinery, Vienna University of Technology. Getreidemarkt 9/E302, A-1060 Vienna, Austria. Tel.: +43 1 58801 302404, Fax: +43 1 58801 302399, E-mail: eduard.doujak@tuwien.ac.a, [2] philipp.unterberger@tuwien.ac.at, [3] mmweltzl@gmail.com [4] cbauer@tuwien.ac.at

ABSTRACT

The purpose of this study was to investigate the influence of two different geometries on the flow conditions in the refeeding channel of a multistage reversible pump-turbine. This paper presents basic information on the calculation and selection of the main dimensions, and describes two methods for the design: first, an unvaned cross over- duct connecting diffuser and de-swirl channels and second, diffuser and de-swirl duct that form a single continuous channel (vaned cross-over).

In a CFD study the different designs are investigated in pump- and turbine direction and compared by suitable coefficients: the static pressure coefficient C_p, the total pressure loss coefficient ω and the Swirl Number S_N. The investigations show that just by simply connecting diffuser- and de-swirl vane in the cross-over area, the performance of the refeeding channel can be improved.

Keywords: CFD, de-swirl vane, multistage pump-turbine, refeeding-channel, return channel, vaned diffuser

NOMENCLATURE

b	$[m]$	channel height
c	$[m/s]$	absolute velocity vector
C_p	[-]	static pressure coefficient
D, D_a	$[m]$	diameter, outher diameter
D_S	$[m]$	inner diameter of suction nozzle
H	$[m]$	head per stage
i	[-]	number of stages
L_U	$[m]$	meridional length
$\dot{m}$	$[kg/s]$	mass flow rate
n	$[min^{-1}]$	rotating speed
n_q,	$[min^{-1}]$	specific speed
p_{tot}, p_{stat}	$[Pa]$	total pressure, static pressure
Q	$[m^3/s]$	discharge
r, r_U	$[m]$	radius, curvature radius
R_a	$[m]$	outer radius
R_R	$[m]$	circular arc vane base radius
s	$[mm]$	vane thickness
S_N	[-]	Swirl Number
t	$[mm]$	vane pitch
Y_{kin}	$[J/kg]$	specific kinetic energy
z	[-]	number of vanes
α	[°]	vane angle
β	[°]	flow angle
λ_U	[-]	friction coefficient
μ	[-]	experience number
ρ, ρ_R	$[kg/m^3]$	density, circular arc vane radius
τ	[-]	vane factor
ω_1, ω_2	[-]	total pressure loss coefficient in pump mode, turbine mode

Subscripts

a, r	axial, radial
id	ideal, loss free
IN	at the inlet of the domain
OUT	at the outlet of the domain
u, m	circumferential, meridional
ST	per stage
S	suction side of the impeller
2, 3	runner outlet with/without vane influence
4, 5	diffuser LE with/without vane influence
6, 7	diffuser TE with/without vane influence
8, 9	de-swirl LE with/without vane influence
10, 11	de-swirl TE with/without vane influence
12	refeeding channel outlet in pump mode

1. INTRODUCTION

Hydraulic Machines are built with several stages if the specific speed n_q drops under a certain limit. This is the case for radial machines working at high heads H and very low discharge Q. In this case the efficiency is reduced by losses due to disk friction and gap flow in the spaces between impeller and casing [1]. They increase strongly when n_q is reduced [2]. By using several stages i, the specific

speed per stage $n_{q,ST}$ (1) can be raised to a range with higher efficiencies.

$$n_{q,ST} = n\frac{\sqrt{Q}}{(H/i)^{0.75}} \quad (1)$$

Refeeding channels are used in multistage systems to guide the flow leaving the impeller, to the inlet of the subsequent stage. According to [3-4] the refeeding channel task is manifold and depending on the operation mode:
In pump direction, the flow has to be turned from radial outwards to radial inwards and then again turned to axial direction. The second task is to lead the flow leaving the impeller and thereby ensure the maximum conversion of kinetic energy into static pressure rise with minimum total pressure loss. And last but not least the strongly swirling flow leaving the diffuser elements has to be guided to the inlet of the subsequent impeller, which it should enter with zero or nearly zero inlet swirl. In turbine operation the flow has to be turned from axial to radial outwards and again to radial inwards. Additional tasks are: lead the flow to the runner and ensure the conversion of potential energy into kinetic energy and create the needed pre rotation for the following runner.

Since the decelerated flow in pump direction is generally very sensitive to separation, the design and calculation process is mainly influenced from the flow conditions in pump direction. Therefore the focus for the following remarks is put on pump direction. Nevertheless the turbine direction has been investigated too.

2. GENERAL ASPECTS

When talking about refeeding channels of multistage systems, some general aspects have to be considered according the literature. The calculation of collector such as vaned and vaneless diffuser on the basis of potential flow is well proven and considered in literature [5, 6]. Investigations of Wesche [7] have shown that the flow in vaned diffusers behaves in the same way than ideal fluids. In a vaneless casing the flow follows the law of conservation of the angular momentum $c_u \times r = const.$ (apart from friction effects). Therefore the diffuser elements have to be designed that the flow field is compatible with the conservation of angular momentum. This results in a rotational symmetry around the impeller and thereby interaction between the flow in the collector and impeller is minimized [8].

Only a part of the energy transferred from the blades to the water in a pump impeller is transformed into pressure rise. The rest is converted in velocity increase. Since the main goal in pump direction is the pressure rise, this kinetic energy has to be transformed after the impeller [9]. A good efficiency can consequently only be achieved if the kinetic energy available for pressure recovery

$$Y_{kin} = (c_3^2 - c_S^2)/2 \quad (2)$$

is effectively decelerated in the diffusion elements. Therefore a diffuser is installed in multistage systems.

Two zones must be distinguished for the pressure rise in the diffuser as shown in Figure 1: The triangular inlet section and the actual diffusing channel. The triangular inlet section is the part of the guide vanes where the diffusing channel is not yet formed because it is opened on one side. After the entrance area the closed diffusing channel is formed. Measurements of Schrader [10] on vaned diffusers have shown that the major part of pressure rise in the diffuser is happening in the triangular section. According to Güllich [11], the role in off-design operation changes. He reports that measurement of the static pressure difference between P_2 and P_3 (Fig. 1) reveal an important pressure recovery in the triangular section at the diffuser inlet. It increases with falling discharge until the flow separates. In contrast the pressure recovery in the diffusing channel from P_3 to P_4 rises with increasing discharge. Downstream to the diffusing channel the cross-over section and the de-swirl vane section is connected as shown in Figure 2. In this area almost no energy conversion is happening.

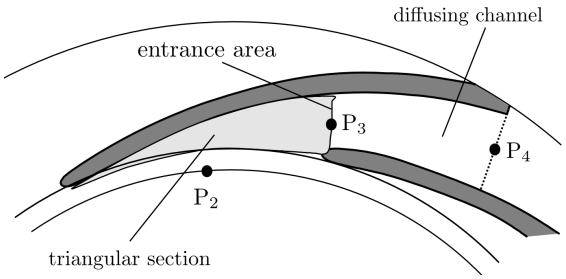

Figure 1. Schematic view of diffuser vanes with geometry definitions [11]

The task of the cross-over section is to deflect the flow by 180° to the radial inward direction. In literature some optimization approaches can be found. Pazzi et al. [12] concluded that increasing values of the cross-over curvature radius r_U and increasing the diameter D_6 at the cross-over inlet, tend to lower the loss coefficient. Hildebrandt [13] made a 2D U-turn optimization using genetic algorithms. He implements a pinch at the end of the diffuser which helps to reduce the risk of flow separation at the outer shroud contour. His results show that the optimum shroud contour depends on the inlet velocity profiles applied.

A design method for vaned cross-over sections is presented from Goto et al. in [14]. They use a 3-D

inverse design method for the cross-over section that connects the diffuser channel section with the de-swirl vane section, forming a continuous refeeding channel passage.

Veress and Braembussche [15] compare an optimized design of a vaneless diffuser and cross-over, with an optimized 3D vane design of the return vanes with Leading Edge (LE) upstream of the cross-over. They observe a positive influence on the loss coefficient when using a vaned cross-over section by avoiding flow separation inside and downstream of the cross-over. Additionally a positive effect of vane leaning is described: Optimum vane leaning contributes to a performance increase by reducing the vorticity resulting from secondary flows.

3. GEOMETRICAL DESCRIPTION

A refeeding channel system as shown in Figure 2, can be divided into four parts: the radially outward passage which is conventionally called the diffuser (4-7), the cross- over or U-turn bend passage (7-8), the radially inward or de-swirl passage (8-11) and the L-turn passage (11-12). In this section the design parameters are described and the calculation of the vane angles is presented. Furthermore the difference of the two design methods investigated in section 6 are described.

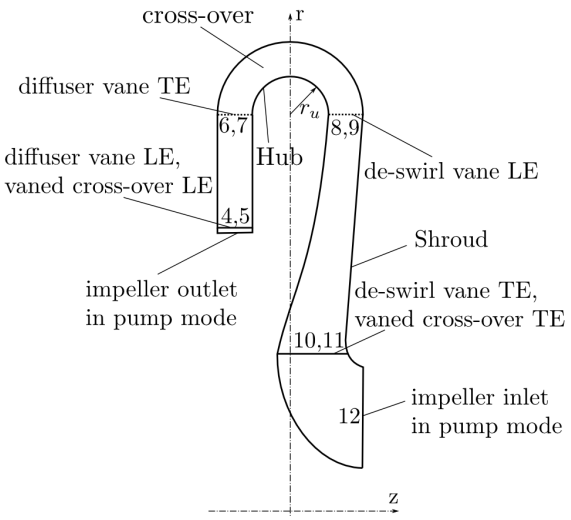

Figure 2. Schematic view of the meridional shape with geometry definitions of the refeeding channel

The refeeding channel device is designed for a discharge of $Q = 1.607\ m^3/s$ and no leakage flow is taken into consideration. Depending on the runner diameter $D_2 = 1.23\ m$, the inlet diameter is chosen to $D_5 = 1.24\ m$. The channel height $b_5 = 65\ mm$ is the same as at the runner outlet and constant for the whole diffuser, $b_6 = b_5$. The diameter $D_6 = 1.66\ m$ is chosen according to recommendation for D_6/D_5 found in [16].

At the triangular inlet section the vane angle is hold constant and equal to the flow angle, to guarantee no influence on the flow. The vane geometry for the diffusing channel vanes uses a point-wise convergence design with a vane angle defined by the following, general equation.

$$\alpha = \arcsin\left(\frac{s}{t} + \frac{Q}{c \cdot z \cdot b \cdot t}\right) \tag{3}$$

Thereby a constant vane thickness of $s = 20\ mm$, was chosen. The number of vanes is $z = 10$. In this equation t is the vane pitch for each calculated point and c the velocity. As can be seen from equation (3), the development of the vane angle is depending on the velocity distribution $\alpha = \alpha(c)$. In this paper the influence of different vane angles at the diffuser vane Trailing Edge (TE) should be investigated. Therefore three different TE velocities c_6 are chosen. As shown in Table 1 and Figure 3, this results in different vane angles α_6.

According to Sigloch [17] the de-swirl vane LE angle α_9 can be estimated with

$$\tan\alpha_9 = \mu \cdot \tau_9 \cdot \left(\frac{c_{m,7}}{c_{u,7}} + \frac{L_U \cdot \lambda_U}{4 \cdot b}\right) \tag{4}$$

where $\mu = 1.2$ is an experience number, τ_9 is considering the influence of the vane thickness and the vane pitch, L_U is the meridional length of the cross-over and $\lambda_U = 0.04$ is the friction coefficient. In this equation the circumferential velocity $c_{u7} = c_{u7}(\alpha_6)$, is a function of the chosen TE angle of the diffuser vanes (details can be found for example in [17]). Varying α_6 as described above results in different de-swirl vane LE angles α_9, consequently influencing the geometry of the vanes as shown in Table 1 and Figure 3.

Table 1. Diffuser vane TE velocities c_6 and resulting vane angles α_6 and α_9

c_6	14.69 *m/s*	9.86 *m/s*	7.6 *m/s*
α_6 eq.(3)	20°	30°	40°
α_9 eq.(4)	22°	24°	27°

To guarantee a smooth deflection the cross-over radius of $r_U = 70\ mm$ is chosen. The de-swirl vanes are designed as circular arc vanes with radius ρ_R (Fig.3).

$$\rho_R = \frac{r_9^{\,2} - r_{10}^{\,2}}{2 \cdot \left(r_9 \cdot \cos\alpha_9 - r_{10} \cdot \cos\alpha_{10}\right)} \tag{5}$$

The centre of the arc is positioned on the radius R_R.

$$R_R = \sqrt{r_9^2 + \rho_R^2 - 2 \cdot r_9 \cdot \rho_R \cdot \cos\alpha_9} \qquad (6)$$

To obtain the desired deflection at the outlet a slight angle exaggeration of 10° is chosen. This results in a vane TE angle of $\alpha_{10} = 100°$.

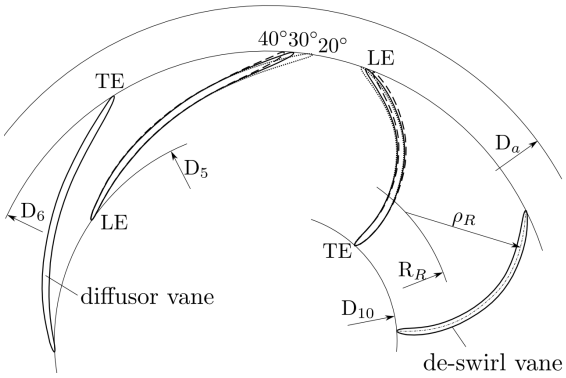

Figure 3. Vaneless cross-over: sketch of the vane geometries with modifications of α_6

The second investigated geometry is the vaned cross-over section. The design is obtain by simply connecting the diffuser vanes with the de-swirl vanes leading to a 3D vane geometry at the cross-over. To obtain a defined position in circumferential direction the same wrap angle ε is used for the three different designs investigated. The vaned cross-over geometry is shown in Figure 4.

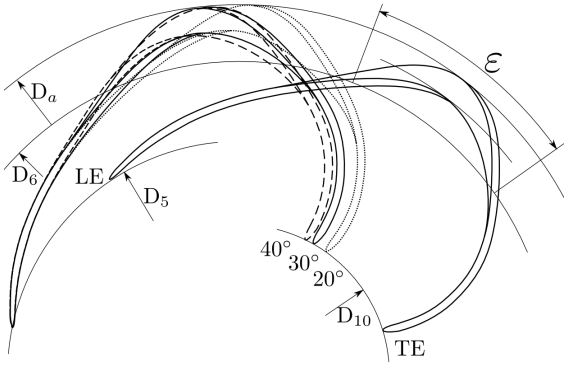

Figure 4. Vaned cross-over: sketch of the vane geometries with modifications of α_6

4. CHOICE OF PERFORMANCE INDICIES

Swirl Number S_N: According to Gupta et al. [18] the degree of swirl is usually characterized by the Swirl Number S_N. It is a nondimensional number representing axial flux of swirl momentum divided by axial flux of axial momentum times the outer radius R_a and defined as follow.

$$S_N = \frac{\int \rho c_a c_u r dA_{12}}{R_{a,12} \int \rho c_a^2 dA_{12}} \qquad (7)$$

The circumferential velocity component at the inlet of the subsequent runner directly affects the pump head of the stage. Therefore in pump mode the Swirl Number is used to characterize the performance of the refeeding channel system. In this context a smaller S_N means better performance.

The *static pressure recovery* C_p is defined as the static pressure rise between inlet and outlet normalized by the inlet dynamic pressure. It can be used to characterize how much of the kinetic energy at the outlet of the runner is transformed in static pressure rise.

$$C_P = \frac{p_{stat,OUT} - p_{stat,IN}}{p_{dyn,IN}} = \frac{p_{stat\_12} - p_{stat\_4}}{p_{tot\_4} - p_{stat\_4}} \qquad (8)$$

Total pressure loss Coefficient ω: The loss coefficient is defined as the total pressure drop between inlet and exit normalized by the inlet dynamic pressure.

$$\omega_1 = \frac{p_{tot,IN} - p_{tot,OUT}}{p_{dyn,IN}} = \frac{p_{tot,4} - p_{tot,12}}{p_{tot,4} - p_{stat,4}} \qquad (9)$$

This coefficient quantifies for a given geometry how much of the possible static pressure rise is not achieved because of total pressure losses. This gets clearer by looking at the following expression, where $C_{P,\mathrm{id}}$ is the pressure recovery factor in the ideal, loss free case.

$$C_P + \omega_1 = 1 - \frac{p_{tot,12} - p_{stat,12}}{p_{tot,4} - p_{stat,4}} = C_{P,id} \qquad (10)$$

For the rating of the performance in turbine direction the total pressure loss coefficient should be denominated as ω_2. It normalizes the total pressure drop by the dynamic pressure at the outlet. As seen from equation (11) the difference in the definition is because of the change of inlet and outlet for turbine mode. The balance sections are still the same.

$$\omega_2 = \frac{p_{tot,IN} - p_{tot,OUT}}{p_{dyn,OUT}} = \frac{p_{tot,12} - p_{tot,4}}{p_{tot,4} - p_{stat,4}} \qquad (11)$$

In the equations presented in this chapter, all values for p_{tot} are mass averaged and all values for p_{stat} are area averaged values.

5. TOOLS FOR THE ANALYSIS

All calculations have been performed by means of the commercial solver ANSYS®-CFX 5. This solver is well established in the field of fluid machinery to predict flow phenomena and

performance of hydraulic components. CFX-BladeGen is used for the parametrical construction of the vane geometry and channel shape and CFX-TurboGrid is used to generate the 3D grids. Computed results are evaluated by using the post processor software CFD-Post.

Preliminary tests have been carried out to study the grid dependence of the solutions and to guarantee an accurate and grid independent solution. In Figure 5 the trend of S_N, C_p and ω is shown over the number of grid elements. A mesh with 1 *Mio* to 1.5 *Mio* has been found to satisfy the requirement for the present comparison. One can observe that the critical mesh size for the C_P and ω values converge rather fast with low number of grid elements while the Swirl Number S_N was found to need a higher amount of grid elements for being independent.

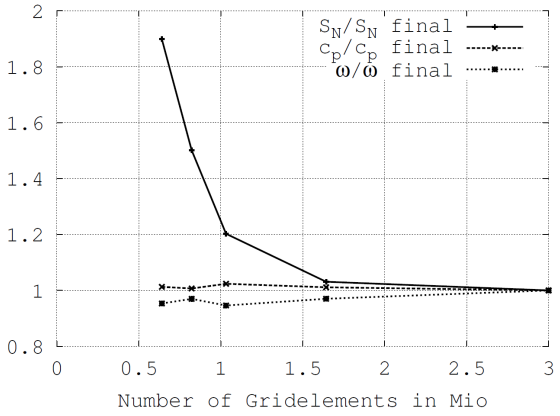

Figure 5. Results of the grid independency study

All calculations where performed with the Shear stress transport model *(SST)* which is a two equation turbulence model. According to Menter [19] the *SST* model is an attempt to combine the best elements of existing eddy viscosity models. It is based on a blending of the *k-ω*-model near walls with the *k-ε* model away from the surface. He investigated the behaviour of different turbulence models for special test cases. The results show good agreement between the simulation and experimental data for an adverse pressure gradient flow with separation, due to the calibration of the *SST* model for these flows.

A structured hexahedral grid was generated using ATM Optimized topology set in TurboGrid. From Hub to Shroud at TE and LE 40 elements are used whit refined layer next to the wall. Around the vane an O-Grid mesh is applied with a proportional boundary layer refinement factor. The whole passage mesh consists of about 1.2 *Mio* elements. For inlet domain and outlet domain the H-Grid mesh type is used. Inlet uses 5 Elements in radial direction, outlet 8 elements in axial direction.

Figure 6. Meshes for vaned and unvaned cross-over duct used for the CFD study.

As shown in Figure 6 the vaneless cross-over geometry uses two different domains for the diffuser and the de-swirl vane. These mesh domains were connected in CFX-Pre using a General Grid Interface (GGI). Since no boundary layer refinement in the cross-over section is needed for the unvaned geometry, in this case the element number is reduced to 1 *Mio*.

The boundary conditions for inlet and outlet used for the CFD simulation are listed in Table 2. Since a higher discharge is needed for a pump used in turbine mode as shown in a former work of the authors [20] a higher mass flow is used in the calculations for the turbine direction.

Table 2. Boundary conditions

	Pump Direction	Turbine Direction
INLET	c_a = 0 *m/s* c_r = 6.905 *m/s* c_u = -37.743 *m/s*	$\dot{m}$ =170.015 *kg/s* Flow Direction: Normal to Boundary
	Turbulence Intensity 5%	
OUTLET	Average Static Pressure 0 *Pa* (Average over whole outlet)	

6. CFD RESULTS

In the following section a description of results is given. First the refeeding channel with vaneless cross-over is investigated and afterwards the results of the refeeding channel with vaned cross-over are shown. The performed CFD simulations are analyzed in terms of effect on changes of geometrical parameters on the performance indices.

6.1 Vaneless cross-over

The first analyzed group is characterized by variation of α_6 describing the angle at diffuser vane TE. The value has been varied in 10° increments from 20° to 40° as shown in Figure 3. The de-swirl vanes have been adapted according the method described in section 3. The obtained results are listed in Table 3. Figure 7 shows the trend of the performance indices after modification of the vane angle.

Table 3. Comparison of performance indices for the vaneless cross-over

α_6	20°	30°	40°
Pump mode			
S_N	-0.355	-0.351	-0.341
ω_1	0.297	0.277	0.281
C_p	0.630	0.651	0.648
Turbine mode			
ω_2	0.228	0.183	0.166

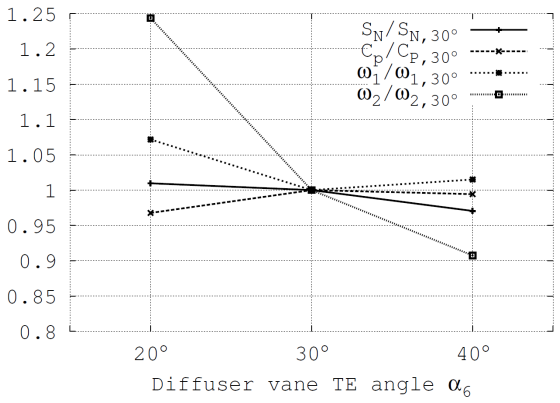

Figure 7. Vaneless cross-over: Trends of Swirl-Number S_N, pressure recovery C_p and loss coefficients ω_1 and ω_2 after changing the diffuser TE angle α_6

A small impact on the Swirl Number S_N can be seen. For higher vane angles S_N decreases which is equivalent to a better deflection of the flow to the following runner as already mentioned. A possible reason for that could maybe be found in the lower deflection of the flow in circumferential direction before entering the cross-over.

In pump mode the losses for the 20° vane are higher by more than 5% in reference to the 30° and the 40° vane resulting in a lower C_p value. This can be a result of the longer flow path for the smaller exit angle. The losses in turbine mode decrease for higher vane angle. The influence is higher than in pump mode. The 20° geometry has almost 25% higher losses than the reference geometry and the 40° geometry about 10% smaller losses.

When turbine- and pump operation are compared it gets clear that the losses in turbine mode are about 20% to 40% smaller than in pump direction. This is because of the decelerated flow in pump mode which is generally more affected to separation.

The shortcomings of the vaneless cross-over geometry are best illustrated in the blade to blade view of the de-swirl vanes for pump operation shown in Figure 8. As a consequence of the strong deflection a separation of the flow can be observed. This situation is caused mainly by the deceleration of the flow at the exit of the cross-over section in combination with incidence problems. Due to the strong recirculation on the suction side, the vane-row is not able to ensure the needed deflection and to guaranty a swirlless outflow. This results in high values for the Swirl Number and loss coefficients. Similar observations were made by Prager et al. [21] and Veress et al. [22].

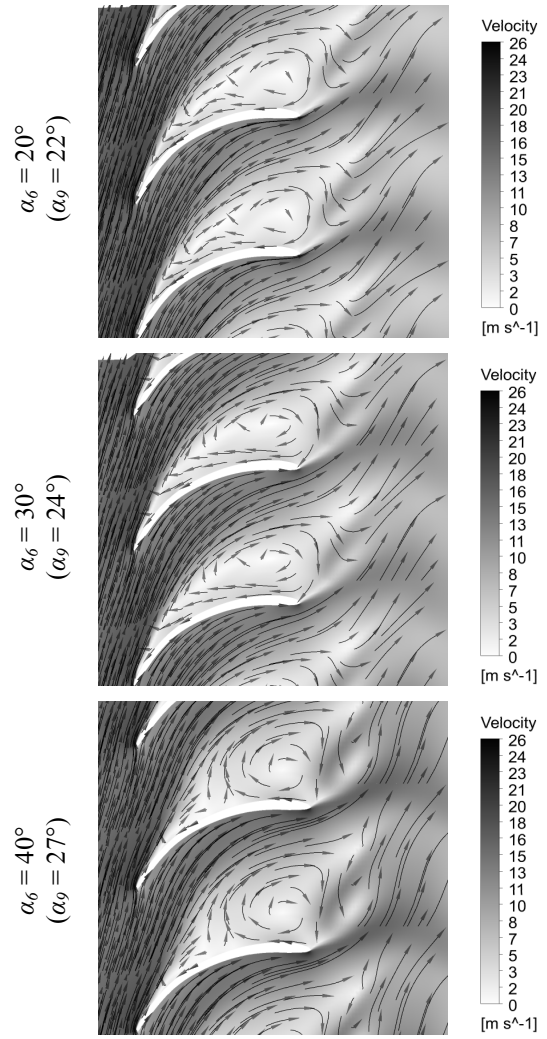

Figure 8. De-swirl Vane: Velocity vectors in blade to blade view at 50 % span location for the unvaned cross-over section.

6.2 Vaned cross-over

This section analyses the results of the *CFD* study for the vaned cross-over duct (Fig.4). The obtained results are listed in Table 4. Figure 9 shows the trend of the performance indices after modification of the vane angle α_6.

The trend for the Swirl Number S_N shows better performance for the lower angles. For 20° vane the S_N is about 15 % smaller than for the 40° vane.

Table 4. Comparison of the performance indices for the vaned cross-over.

α_6	20°	30°	40°
Pump mode			
S_N	-0.279	-0.294	-0.322
ω_1	0.245	0.286	0.281
C_p	0.696	0.651	0.647
Turbine mode			
ω_2	0.150	0.134	0.130

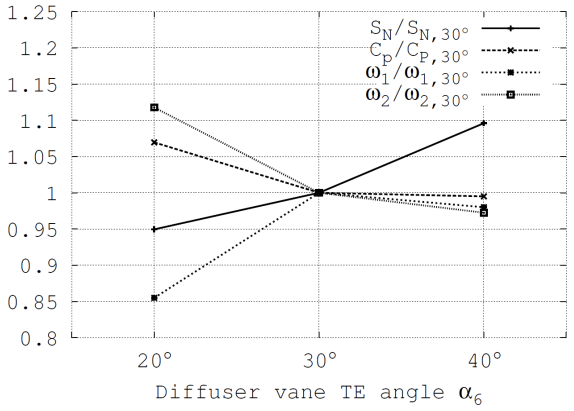

Figure 9. Vaned cross-over: Trends of Swirl-Number S_N, pressure recovery C_p and loss coefficients ω_1 and ω_2 after changing the diffuser TE angle α_6

The change from 30° to 40° has almost no influence on the losses in both operation modes. In pump mode the 20° geometry has lower losses than the others of about 15% and therefore a higher pressure recovery factor. The things change in turbine operation, the smallest angle has the highest losses, about 12% higher than the two other geometries.

As in the last chapter, the shortcomings of the vaned cross-over geometries are best illustrated in the blade to blade view for pump operation shown in Figure 10. By vaning the cross-over duct, the exchange of fluid and the compensation of pressure between suction and pressure side after the diffuser vane is disabled. This results in a large separation region at the inlet of the cross-over. Again the deceleration of the flow at the exit of the cross-over leads to recirculation on the suction side of the return vanes. Furthermore secondary flows in circumferential direction can be observed. This situation is caused by the changing of the vane loading in stream wise direction. The diffuser vane suction side becomes the de-swirl vane pressure side. This gets clear when looking at Fig. 10 and is the reason for the separation regions that are on the left channel side in the diffuser area and on the right side in the return vane section, when looking in stream wise direction.

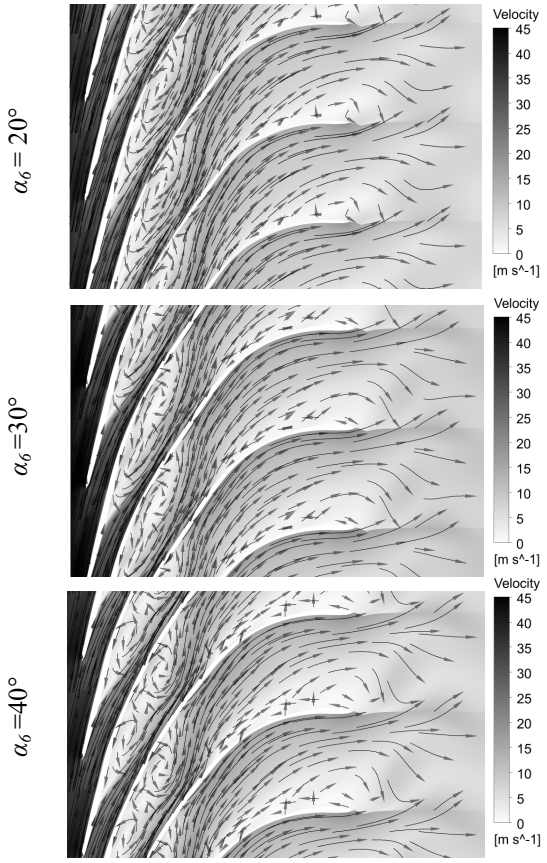

Figure 10. Vaned cross-over: velocity vectors in blade to blade view at 50 % span Location.

6.3 Comparison

When comparing the vaneless and the vaned cross-over the following observations can be made (see Table 3 and Table 4). In turbine operation the vaned solution has better performance with about 20% to 35% less losses. In pump operation the Swirl Number can be reduced for about 5% to 15 % by vaning the cross-over and better efficiency for the following runner can be expected. The losses and pressure recovery show similar values, only the 20° geometry has significant better values for the vaned solution. When comparing the blade to blade views in Fig. 8 and Fig. 10, one can see that the deflection towards the following runner is better for the vaned geometry because the separation region in the de-swirl area is smaller.

7. CONCLUSION

As a consequence of the strong deflection and the short radial extension of the return vanes in this multistage pump-turbine, large separation regions can be observed for the vaneless- and the vaned cross-over geometry in pump mode. This results in high losses and less deflection in circumferential direction at the outlet and therefore a lower efficiency in the following runner has to be expected.

When comparing the two geometries it gets clear that by simply connecting the diffuser vanes with the de-swirling vanes a better performance can be achieved. In pump operation lower swirl-number can be realized expecting better performance of the following runner. The losses and pressure recovery factors are similar. In turbine mode the vaned solution has significant lower losses.

ACKNOWLEDGEMENTS

This work has been supported from the *Klima und Energiefonds* and was performed within the framework of the program "NEUE ENERGIEN 2020".

REFERENCES

[1] Roclawski H., Hellmann D. H., 2006 "Rotor-Stator-Interaction of a Radial Centrifugal Pump Stage with Minimum Stage Diameter", *Proceedings of the 4th WSEAS International Conference on Fluid Mechanics and Aerodynamics,* Greece, pp 301-308.

[2] Osterwalder J., Hippe L., 1984, "Guidelines for efficiency scaling processes of Hydraulic Turbomachines with different technical roughness of flow passages, *Journal of Hydraulic Research*, Col. 22, pp 77-102.

[3] Oh, J.M., Engeda, A, and Chung, M. K. 2005, "A numerical study of the U-turn bend in return channel systems for multistage centrifugal compressors", *Proc. IMechE Part C: J. Mechanical Engineering Science*, Vol. 219, pp 749-756.

[4] Wesche W., 2011, Radiale Kreiselpumpen – Berechnung und Konstruktion der hydrodynamischen Komponenten, Springer

[5] Pfleiderer C., Peterman H., 2005 *Strömungsmaschinen*, Springer Berlin.

[6] Eckert B., Schnell E., 1961, *Axial- und Radialkompressoren* Springer Berlin.

[7] Wesche, W., 1989, "Experimentelle Untersuchungen am Leitrad einer radialen Kreiselpumpe", *Dissertation Technische Universität Braunschweig, Fakultät für Maschinenbau und Elektrotechnik*.

[8] Gülich, J.F., 2004, *Kreiselpumpen – Handbuch für Entwicklung, Anlagenplanung und Betrieb*, Springer Berlin.

[9] Schulz, H., 1977, *Die Pumpen- Arbeitsweise Berechnung Konstruktion*, Springer Berlin.

[10] Schrader, H. 1939, "Messungen an Leitschaufeln von Kreiselpumpen", *Dissertation Technische Hochschule zu Braunschweig*.

[11] Gülich, J.F., 2010, *Centrifugal Pumps,* Springer Berlin.

[12] Pazzi, S., Martelli F., 2002, "The use of artificial Neural networks for performance prediction of Return Channels for industrial Centrifugal Compressors", *Proceedings of ASME TURBO EXPO 2002*, Amsterdam, The Netherlands.

[13] Hildebrandt A., 2011, "Aerodynamic Optimisation of a Centrifugal Compressor Return Channel and U-turn with Genetic Algorithms", *Proceedings of ASME Turbo Expo2011*, Vancouver, Canada.

[14] Goto A., Nohmi M. Sakura T. Sogawa Y., 2002, "Hydrodynamic Design System for Pumps Based on 3-D CAD, CFD and Inverse Design Method", *ASME J Fluids Engineering*, Vol. 124, pp. 329-335.

[15] Veress Á., Braembussche R., 2002 "Inverse Design and Optimization of a Return Channel for a Multistage Centrifugal Compressor", *ASME J Fluids Engineering*, Vol. 126, pp. 799-806.

[16] Bohl W., 2004, *Strömungsmaschinen 2- Berechnung und Kalkulation*, Vogel, Würzburg

[17] Sigloch H., 2009, *Strömungsmaschinen – Grundlagen und Anwendung*, Hanser, München

[18] Gupta A.K., Lilley D.G., Syred N., 1984, *Swirl flows*, Abacus Press.

[19] Menter, F. R., 1996, "A Comparison of Some Recent Eddy-Viscosity Turbulence Models", *ASME J Fluids Engineering*, Vol. 118, pp. 514-519.

[20] Doujak E., Unterberger P., Bauer C., Samonig M.A. 2012, "Modular concept for decentraliced pump storage systems – A small hydro approach" *ISROMAC-14*, Honolulu, HI, USA.

[21] Prager, R., Hensel, G. 1989, "Einfluss der Rückführbeschaufelung auf die Energie-übertragung mehrstufiger Kreiselpumpen" *Information Pumpen und Verdichter* Vol. 2/1989, pp 5-9.

[22] Veress Á. and Braembusche, R.: 2003 "New approach to radial compressor return channel design", *Conference on Modelling Fluid Flow,* Budapest, Hungary.

Conference on Modelling Fluid Flow (CMFF'12)
The 15th International Conference on Fluid Flow Technologies
Budapest, Hungary, September 4-7, 2012

NUMERICAL ANALYSIS OF A SWIRLING FLOW GENERATED AT LOWER RUNNER SPEEDS

Alin I. BOSIOC[1], Constantin TANASA[2], Romeo F. SUSAN-RESIGA[3], Sebastian MUNTEAN[4], Ladislau VÉKÁS[5]

[1] Corresponding Author, PhD Eng., Romanian Academy – Timisoara Branch, Center for Fundamental and Advanced Technical Research, Bv. Mihai Viteazu 24, 300223, Timisoara, ROMANIA, Phone/Fax: +40256403692 , E-mail: alin@mh.mec.upt.ro
[2] PhD Student, Politehnica University of Timisoara, Department of Hydraulic Machinery, Bv. Mihai Viteazu 1, 300222, Timisoara, ROMANIA, Phone/Fax: +40256403692 ,E-mail: costel@mh.mec.upt.ro
[3] PhD Eng, Professor, Politehnica University of Timisoara, Department of Hydraulic Machinery, Bv. Mihai Viteazu 1, 300222, Timisoara, ROMANIA, Phone/Fax: +40256403692 ,E-mail: resiga@mh.mec.upt.ro
[4] PhD Eng., Senior Researcher, Romanian Academy – Timisoara Branch, Center for Fundamental and Advanced Technical Research, Bv. Mihai Viteazu 24, 300223, Timisoara, ROMANIA, Phone/Fax: +40256403692, E-mail: seby@acad-tim.tm.edu.ro
[5] PhD Phys., Senior Researcher, Romanian Academy – Timisoara Branch, Center for Fundamental and Advanced Technical Research, Bv. Mihai Viteazu 24, 300223, Timisoara, ROMANIA, Phone/Fax: +40256403700 , E-mail: vekas.ladislau@gmail.com

ABSTRACT

The paper focuses on numerical evaluation of energetic and hydrodynamic behaviour downstream to the runner of the swirling apparatus for lower runner speeds. The energetic behaviour of the runner consists in the analysis of the torque and mechanical power, while from the hydrodynamic behaviour is analysed the velocity field configuration downstream to it. Firstly, three-dimensional steady turbulent flow is performed along to the swirl apparatus geometry. The mixing interface method is used in order to couple the non-rotating three-dimensional domain with three-dimensional runner computational domain. As a result, only one guide vane channel and one runner interblade channel it is selected. Secondly, the computation of the runner at different speeds is performed. Then, the hydrodynamic behaviour of velocity profiles (circumferential and meridian components) it is analysed in order to evaluate the swirl configuration and correlate with a theory which help the optimisation of swirling flow ingested by the turbine's draft tube before designing the runner.

Keywords: lower runner speeds, numerical simulation, swirl generator.

NOMENCLATURE

P	$[W]$	mechanical power
M	$[Nm]$	torque
n	$[rpm]$	runner speed
η	$[\%]$	hydraulic efficiency
ρ	$[kg/m^3]$	density
V_{1r}, V_{2z}	$[m/s]$	axial velocity component upstream and downstream the runner
$V_{1\theta}$, $V_{2\theta}$	$[m/s]$	circumferential velocity component upstream and downstream the runner
φ	[-]	discharge coefficient
m_2	[-]	flux of moment of momentum coefficient
R_{ref}	$[m]$	reference radius (the radius from the shroud of the free runner)
v_{sf}	[-]	swirl-free velocity component

Subscripts and Superscripts

ref	reference
sf	swirl free

1. INTRODUCTION

When the hydraulic turbines (especially, turbines with fixed blades for example the Francis turbines) operate at partial discharge, the decelerated swirling flow downstream the runner becomes highly unstable. Consequently, a spiral vortex breakdown (also known as pressing vortex rope in the engineering literature) is developed. The flow unsteadiness from the draft tube cone leads to severe pressure fluctuations that hinder the turbine operation.

Based on the large experience accumulated over the decades of the design process, the hydraulic losses are smaller along to the upstream hydraulic passage of the hydraulic turbines (from the spiral casing to the runner) with respect to the draft tube. However, the hydraulic losses still exhibit large variations during the full operating range. The major energy losses are located in the draft tube according to Vu and Retieb [1]. Also, this is reflected by the Francis turbine hill chart, when the turbine is operated far from best efficiency point, its losses increase sharply with a corresponding decrease in overall efficiency. This is the reason why researchers concentrate their efforts to improve the draft tube cone flow.

An experimental test rig was developed in our laboratory in order to investigate the decelerated swirling flow unsteadiness in the draft tube cone [2]. The test rig is used to determine the parameters of the swirling flow with vortex rope. Also, different methods to control the vortex rope are evaluated in order to mitigate the pressure fluctuations, [3], [4]. The main component of the test rig is the swirl apparatus with two parts: the swirl generator and the test section similar with the draft tube cone. The swirl generator from our test rig has two blade rows. The upstream non-rotating blades (guide vanes) produce a free-vortex tangential component, while keeping the axial velocity practically constant. The second row of rotating blades (free runner) is used to create a specific energy deficit near the hub with a corresponding excess near the shroud [3]. The runner spins at the runaway speed, acting as a turbine near the hub and as a pump near the shroud, with vanishing overall torque, [5].

The main purpose of the paper it is to analyse numerically a swirl generator at different lower speeds in order to act as a Francis turbine model at different regimes. By reducing the speed of the runner of the swirling apparatus, it is obtained a similar velocity field with a Francis turbine runner operated at constant guide vane opening (with different discharges and heads). Secondly, based on numerical results is analysed a new mathematical theory which help the optimisation of swirling flow ingested by the turbine's draft tube before designing the runner.

2. SWIRLING FLOW GENERATOR AND EXPERIMENTAL TEST RIG

Two different methods are usually employed to generate a swirling flow in the laboratory conditions: using a turbine model or a swirl generator. Using a turbine model is quite expensive. Alternatively, a swirl generator it is a simpler solution allowing physical phenomena investigation. For producing a swirling flow, Kurokawa et al. [6] uses an axial flow impeller at about 3.3*d* upstream of the diffuser inlet, where *d(=156 mm)* it is the inlet pipe diameter. Kurokawa's rig employs an additional blower arranged at far upstream of the divergent channel to widely change the discharge. Another method to generate a swirling flow in a conical diffuser was proposed by Kirschner et al. [7]. The swirl generator with adjustable guide vanes it is installed instead of the turbine model in order to investigate different swirling flow configurations into a straight draft tube, [7].

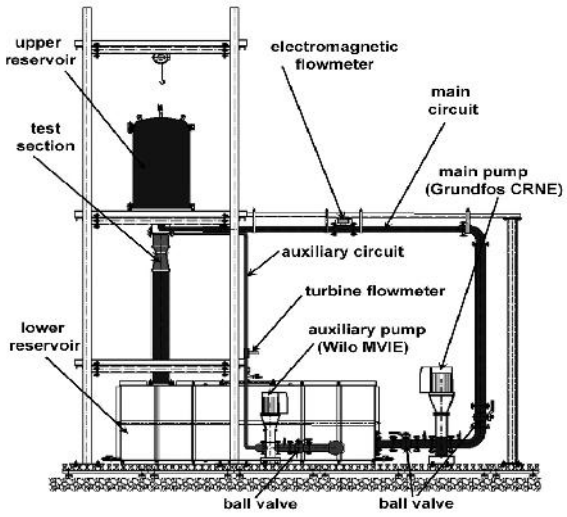

Figure 1. Experimental test rig for decelerated swirling flow, sketch (up) and picture (down).

The experimental test rig was developed to analyze the decelerated swirling flow in a conical diffuser and to evaluate the new water-injection control method [9]. The main purpose of the rig is to reproduce the hydrodynamic phenomena taking place in a conical diffuser with a decelerated swirling flow and the development of the vortex rope. The test rig, it is composed by the following main elements: (*i*) the main hydraulic circuit used to generate the decelerated swirling flow in the conical diffuser; (*ii*) the auxiliary hydraulic circuit needed to supply water for the jet control method. The main hydraulic circuit (showed in Figure 1 - up, with blue colour) is employed to generate the main flow while the auxiliary circuit (showed in Figure 1- up with red colour) help to inject water in the conical diffuser's inlet through a nozzle.

The main part of the experimental facility it is the swirl apparatus. The swirl apparatus serve to generate a swirling flow similar with the flow from a Francis turbine outlet operating at partial discharge.

The swirl generator ends with a nozzle which allows to supply with water the jet at the inlet in the conical diffuser.

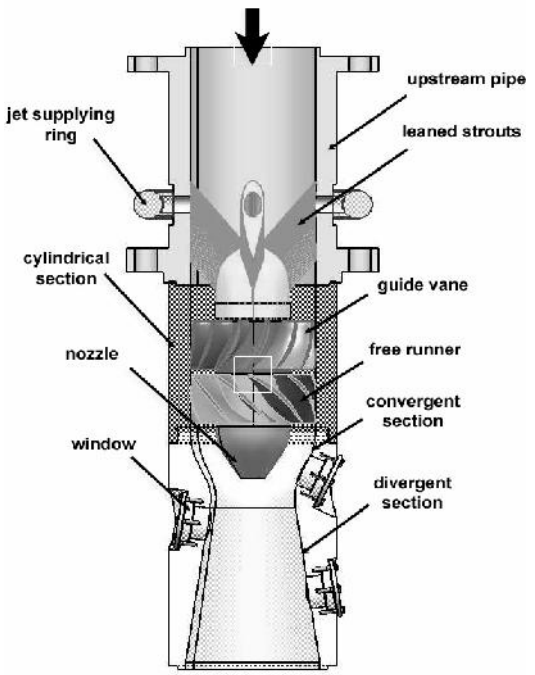

Figure 2. Sketch of the swirl apparatus with swirling flow generator and convergent-divergent test section

The test section retains only the draft tube cone from the draft tube of hydraulic turbines. Our test section was design to have a convergent part (where the flow it is accelerated) and a divergent part (where the flow it is decelerated) similar with the draft tube cone, having the same cone angle.

3. NUMERICAL SIMULATIONS

In order to compute the swirl apparatus we respect the following order presented in Figure 3.

Mixing interface method for coupling velocity and turbulence fields from consecutive components it is used. In the mixing plane approach, each fluid zone it is treated as a steady-state problem. Flow-field data from adjacent zones are passed as boundary conditions that are spatially averaged or "mixed" at the mixing plane interface. This mixing removes any unsteadiness that would arise due to circumferential variations, thus yielding a steady-state result. Despite the simplifications inherent in the mixing plane model, the resulting solution can provide reasonable approximation of the time-averaged flow field. For each domain in our computation we considered the following boundary conditions presented in Table 1.

For numerical simulation, the ogive domain was divided into 8 symmetrical domains; being investigated only a part. The 3D numerical domain for the ogive has a structured grid with 40.000 hexahedral cells. In all investigated domains the imposed fluid it is water. The guide vane has 13 fixed blades, and was investigated only an interblade channel. For domain meshing was used a structured grid with 284.000 hexahedral cells.

Table 1. Boundary conditions imposed for the computational domains:

Surface	Boundary condition
inlet	Turbulence quantity and velocity components
outlet	Pressure outlet
solid	Wall
periodic	Periodicity for all quantities

The runner has 10 blades, and for numerical simulation as in the previous cases only one interblade channel it is calculated. For numerical domain of the runner we used a structured mesh with 533.000 hexahedral cells. In order to simulate the lower speeds we calculate 7 regimes.

Table 2. Speed regimes for simulation of the runner:

No.	Speed of the runner [rpm]
1.	870 (design speed of the runner)
2.	800 (simulation at lower speeds)
3.	700 (simulation at lower speeds)
4.	600 (simulation at lower speeds)
5.	500 (simulation at lower speeds)
6.	400 (simulation at lower speeds)
7.	300 (simulation at lower speeds)

First regime as shown in Table 2, it is for design speed of the runner (870 rpm), and 6 regimes simulate the brake of the runner. 6 regimes were taken from 100 to 100 rpm, 300 rpm being the minimum speed which was calculated.

A dimensionless parameter was used for analysing the grid depending by the flow in the area of pressure side and suction side of the runner blade. The dimensionless wall distance (y^+) can be defined in the following equation:

$$y^+ = \frac{u_* \cdot y}{\upsilon} \qquad (1)$$

where u_* it is the friction velocity at the nearest wall, y represent the distance to the nearest wall and υ represent the local kinematic viscosity of the fluid. In our case, for the design speed of the runner the dimensionless wall distances it is 55, which it is in a good agreement for numerical simulations in hydraulic machinery.

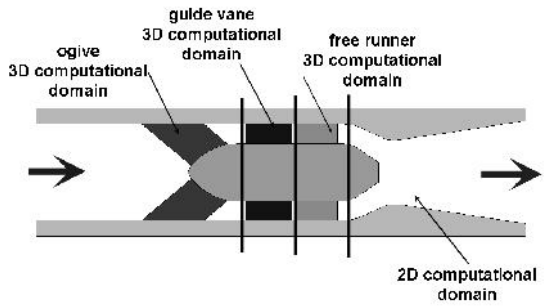

Figure 3. 3D computational domains for ogive, guide vane and free runner and 2D computational domain for the test section

The test section domain it is identical with a transversal section to the real test section from the experimental test rig. The entire domain was meshed with 30.898 hexahedral cells. Also close to the wall of the convergent divergent test section, we used a refinement of the grid. For three-dimensional domains of the swirl generator is used Detached Eddy Simulation model (DES). The reason for choosing the Detached Eddy Simulation model is that on the runner blades especially at lower speeds we have flow detaches. According with Travin et al. [10], the DES model functions as a sub grid scale model in regions where the grid density is fine enough for a large eddy simulation and as a Reynolds- averaged model in regions where it is not.

From numerical simulation of the ogive, velocity profiles from the outlet of the domain were mounted as inlet conditions for the guide vane and velocity profiles from the outlet of the guide vane were mounted as inlet conditions for the runner. For the runner were imposed identical inlet conditions, and were calculated 7 regimes at different speeds as mentioned above in Table 2.

4. NUMERICAL RESULTS

From numerical simulation of the ogive, at the outlet we have the velocity distribution presented in Figure 4.

Knowing that the ogive has the role to sustain the swirl generator, the ogive domain will affect only the axial velocity distribution. As is observed in Figure 4, the influence of the leaned strouts, is observed close to the hub (corresponding to a radial coordinate by r=0.045 m), and close to the shroud (corresponding to a radial coordinate by r=0.075 m). A small influence of the strouts is observed in tangential velocity. This influence is observed close to the hub, at the shroud the tangential component being equal with 0.

If it is analysed the velocity distribution at the exit from the guide vane (Figure 5), the flow have also a tangential component. The tangential component it is given deliberately in order to offer the acquired flow at the exit from the swirl generator. Having calculated the velocity profiles at the outlet from the guide vane, it is calculated the runner.

The runner was design that at the optimum speed (in our case 870 rpm), to operate as a Francis turbine at 70% discharge, [3],[5]. Was selected this operating point because the vortex rope which it is formed downstream in the draft tube cone it is well developed, and the pressure fluctuations generated by the vortex rope are the highest, [11].

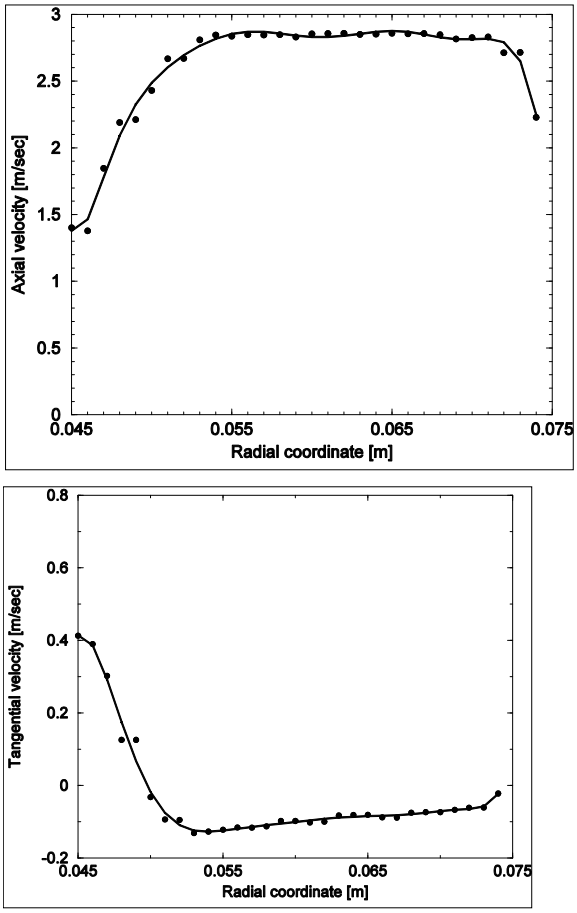

Figure 4. Axial (above) and tangential velocity (down) component distribution at the outlet from the ogive

According with Figure 6 (up) in the case of numerical simulation for the runner, the axial component at the exit has approximately a constant velocity for all 7 cases. A velocity deficit it is observed close to the hub and a velocity excess it is observed close to the shroud. If we analyse the tangential component at the outlet from the runner, the velocity profiles at different lower speeds are changed dramatically. If at the optimum speed (870 rpm), we have a velocity deficit close to the hub, and a velocity excess close to the shroud with a mean velocity by 1.8 m/sec, when the speed of the runner it is reduced, the mean velocity start to

decrease. The runner reaches that at a speed of 600 rpm, the mean tangential velocity is equal with 0.

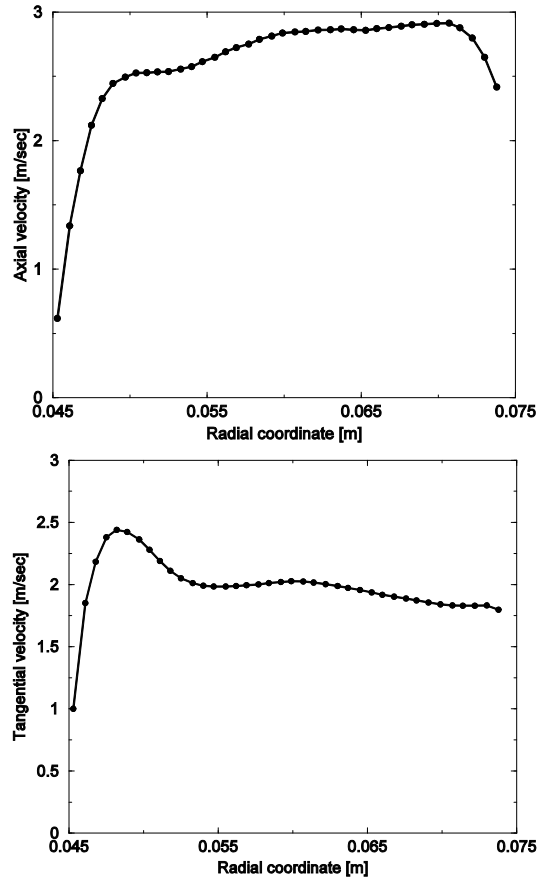

Figure 5. Velocity distribution at the outlet from the guide vane (axial and tangential velocity)

If the speed of the runner it is reduced more, the tangential component will have the mean velocity negative. More clearly if the speed of the runner it is reduced we reach that a certain speed to have zero mean velocity, and if the speed of the runner it is reduced more we reach to have at the exit an opposite velocity than the case with optimum speed.

If we analyse the radial velocity component at the exit from the runner it is observed that once what the speed it is reduced, the velocity distribution changes. We have this modification even the radial velocity distribution at a model Francis runner it is insignificant [12]. The reason for radial velocity modification in our case may be produced by the blade detaches of the runner.

Another analysis of the runner it is to calculate the mechanical power generated at the shaft. The runner was design that at the optimum speed to don't produce power, but when the runner will operate at lower speeds, at the shaft it is produced mechanical power. The mechanical power was calculated with the following formula:

$$P = M \cdot \omega [W], \ \omega = \frac{\pi \cdot n}{60} [rad / \sec] \qquad (2)$$

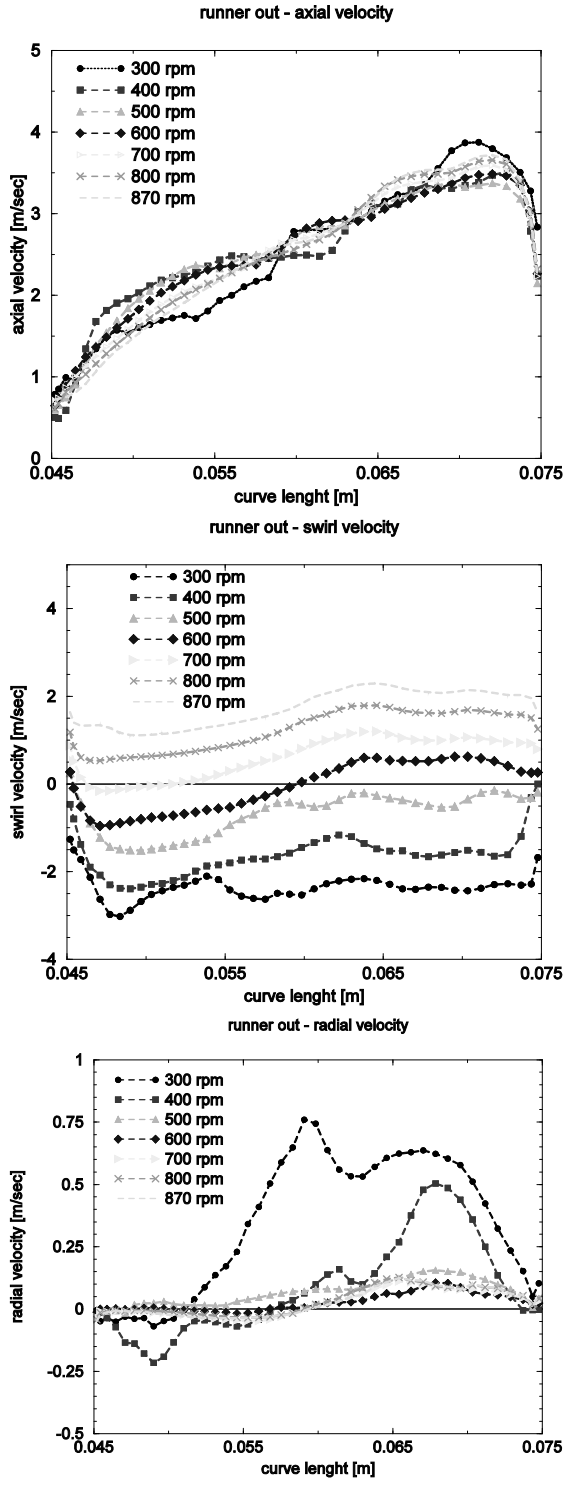

Figure 6. Axial (up), tangential (middle) and radial velocity (down) distribution at the outlet from the runner at lower speeds

Where M is the torque calculated from Fluent code between the pressure side and suction side of the blade and n it is the speed of the runner. The power was calculated for each investigated regime and it is presented in Figure 7.

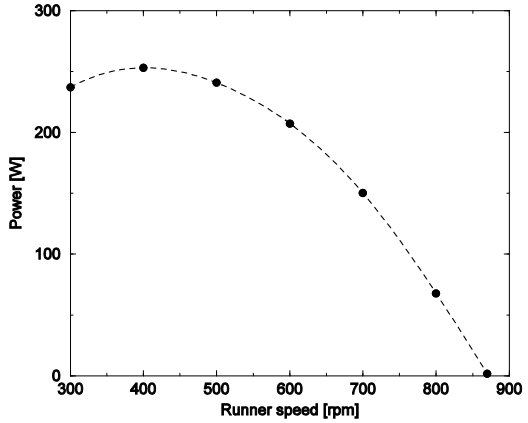

Figure 7. Power generated by the runner vs. speed

According with Figure 7, at optimum design speed, the runner does not produce power. When the speed of the runner is reduced, the mechanical power starts to increase, reaching at a maximum value by 250W at a corresponding speed by 400 rpm. If the speed of the runner it is reduced over this value, the power starts to decrease. Also this decrease of the power it is associated with the blade detaches.

5. DISCUSSION

In the last section, it is validated a mathematical theory proposed by Resiga et al.[13]. According with this theory the so called swirl-free velocity profile at the outlet from the runner which takes into account the axial and circumferential velocity component have approximately a similar velocity profile within the full operating range. This mathematical model is suitable for early optimisation of the runner design, as it provides the swirling flow configuration at runner outlet without actually computing the runner. By optimising the parameterized swirl-free velocity profile one can achieve through the inverse design approaches the most suitable runner blades configuration at the trailing edge.

The main hypothesis concerning the swirl-free velocity profile introduced above as an alternative to the relative flow angle at runner outlet is that $v_{sf}(r)$ is practically unchanged as the operating regime spans the whole operating range of the turbine.

Having the computed velocity profiles at the outlet of the runner, we will calculate this parameter in order to determine if the theory it is validated on our swirl generator.

The analysis of the swirl generator starts with the fundamental equation of turbomachines, written for a hydraulic turbine as:

$$\eta(\rho Q)(gH) = \\ = \int_{S_1} \overbrace{(\omega R V_\theta)}^{M_1} \rho V_r dS_1 - \int_{S_2} \overbrace{(\omega R V_\theta)}^{M_2} \rho V_z dS_2 \qquad (3)$$

In the left-hand side we have the hydraulic power written as the product of the mass flow rate ρQ and specific energy gH, multiplied by the hydraulic efficiency η. In the right hand side we have the rate at which the fluid does work on the runner, which by Newton's second law applied to the moment of forces is equal to the difference in the flux of moment of momentum between cross-sections upstream the free runner S_1, and downstream the runner S_2, respectively. Obviously, when computing the flux of moment of momentum upstream and downstream the runner respectively, M_1 and M_2, we use the axial velocity V_{1r} and V_{2z} respectively. The circumferential velocity upstream the runner is $V_{1\theta}$, while downstream the runner we have $V_{2\theta}$. The above equation can be written in dimensionless form by introducing the following coefficients:

$$\phi = \frac{\rho Q}{\rho\left(\omega R_{ref}\right)\pi R_{ref}^2} \qquad (4)$$

where ϕ is defined as discharge coefficient, having R_{ref} shroud radius from the swirl generator.

$$m_2 = \frac{M}{\rho\left(\omega R_{ref}\right)^3 \pi R_{ref}^2} \qquad (5)$$

where, m_2 is defined as the flux of moment of momentum coefficient at the outlet from the runner. From numerical simulation of the runner from the swirl apparatus at lower speeds we have the variation of flux of moment of momentum coefficient presented in Figure 8.

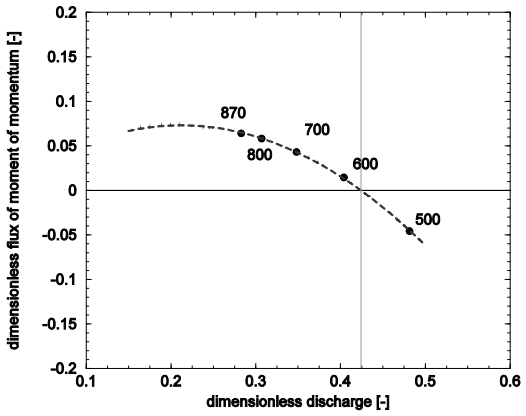

Figure 8. Dimensionless flux of moment of momentum downstream the runner depending by the discharge coefficient

This coefficient is directly related to discharge and circumferential velocity downstream the runner. We observe that at the optimum design speed, 800, 700 and 600 rpm, the circumferential velocity at the exit of the runner has a positive value and if we continue to reduce the speed of the runner, the circumferential velocity will have a negative value and the swirl counter-rotates with respect to the runner. Also from this graph it is possible to notice the speed of the runner where the flux of moment of momentum coefficient vanishes. At this operating point the circumferential velocity profile will have the mean value equal with zero, at the outlet of the runner being only the axial component.

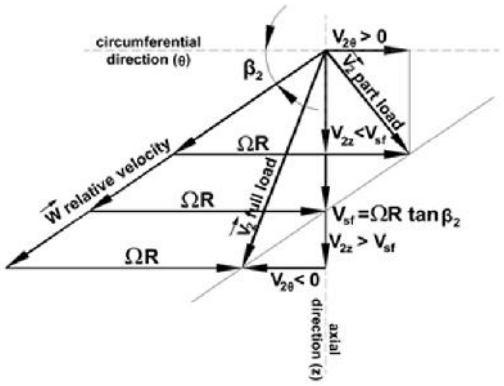

Figure 9. Velocity triangle downstream the runner, for variable operating regimes.

For turbine runners with fixed pitch blades, the swirling flow at the runner outlet must satisfy the kinematic constraints given by the runner blades geometry. Accordingly with Figure 9, the velocity triangle provides the kinematic constraint corresponding to the relative flow angle β_2. This angle is changing along the radius, corresponding to the blade geometry from hub to shroud. Figure 9 shows three particular configurations of the velocity triangle, with the relative velocity kept on the same direction given by β_2. Also the transport velocity ωR remains the same for all three cases. The absolute circumferential velocity $V_{2\theta}$ has the same direction as the transport velocity at low discharge and is in opposite direction with the transport velocity, and the swirl counter rotates with respect to the runner at large discharge case. In-between we can always identify a regime where the absolute circumferential velocity vanishes, $V_{2\theta}=0$.

The swirl-free velocity component is directly related to the relative flow angle, $V_{sf} = \omega R tan\beta_2 \Rightarrow tan\beta_2 = V_{sf} / \omega R$. For an arbitrary operating regime we have:

$$\frac{V_{2z}}{\omega R - V_{2\theta}} = \tan\beta_2 = \frac{V_{sf}}{\omega R} \qquad (6)$$

Thus the swirl-free velocity can be written as:

$$V_{sf} = \frac{\omega R V_{2z}}{\omega R - V_{2\theta}} \qquad (7)$$

Eq. 6, written in dimensionless form:

$$v_{sf} = \frac{r v_{2z}}{r - v_{2\theta}} \qquad (8)$$

Figure 10 shows the variation of swirl-free velocity component for all investigated regimes of the runner from our swirl apparatus. It can be seen that the swirl-free velocity is reasonably similar for all regimes. The exception it is for speeds of the runner by 300 and 400 rpm where the velocity is different. For these regimes we have detaches of the flow from the blade, and also this it is reflected in swirl-free velocity.

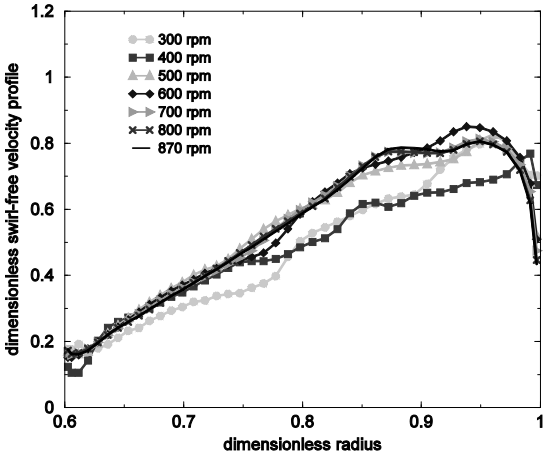

Figure 10. The swirl-free velocity profile at the runner outlet at lower speeds

From Figure 10 it is concluded that the theory proposed by Resiga et al. [13], for the computation of the swirling flow at the Francis runner outlet with swirl-free velocity is correct, the velocity v_{sf} remaining constant at all investigated regimes.

6. CONCLUSIONS

The paper presented a numerical analysis of a swirling flow generator at lower speeds. The main goal was to analyse the velocity profiles at the outlet. The swirl generator contains a free runner and was numerically investigated at the design speed and at 6 lower speeds. From the velocity profiles was observed that the axial component of the velocity at the exit from the runner remain constant. The major modification when the runner works at lower speeds is observed in tangential velocity component. Once the runner speed decrease, the tangential velocity also decrease. So the runner reach that a lower speed to have at the outlet only the axial component, the circumferential

velocity vanishing. At the end of the paper, is validated a mathematical theory proposed by Resiga et al.[13]. According with this theory the so called swirl-free velocity profile at the outlet from the runner which takes into account the axial and circumferential velocity component have approximately a similar profile for all operating regimes. The theory was validated also on our swirl generator, the swirl-free velocity having a similar profile for all investigated regimes. Knowing the axial and circumferential velocity profile from the outlet of the runner (therefore the swirl-free velocity), the proposed theory will help at the optimisation of swirling flow ingested by the turbine's draft tube before designing the runner. The theory connects the swirl from the inlet in the draft tube cone with the swirl from the hydraulic turbine, knowing that the efficiency hill-chart is actually driven by the hydraulic losses in the draft tube.

ACKNOWLEDGEMENTS

This work was supported by a grant of the Romanian National Authority For Scientific Research, CNCS – UEFISCDI, project number PN-II-RU-PD-2011-3-0165.

REFERENCES

[1] Vu, T.C. and Retieb, S., 2002, "Accuracy assessment of current CFD tools to predict hydraulic turbine efficiency hill chart", *Proceedings of the XXIst IAHR Symposium on Hydraulic Machinery and Systems,* Laussane, Switzerland, pp. 1-6.

[2] Susan-Resiga, R., Muntean, S., Bosioc, A., Stuparu, A., Milos, T., Baya, A., Bernad, S., Anton L.E., 2007, "Swirling flow apparatus and test rig for flow control in hydraulic turbines discharge cone", *Proceedings of 2nd IAHR International Meeting of the Workgroup on Cavitation and Dynamic Problems in Hydraulic Machinery and Systems*, Tom 52(66), Fascicola 6, pp. 203-207. Scientific Bulletin of the Politehnica University of Timisoara, Transactions on Mechanics.

[3] Susan-Resiga, R., Muntean, S., Tanasa, C., Bosioc, A.I., 2008, "Hydrodynamic design and analysis of a swirling flow generator", *4th German-Romanian Workshop of Vortex Dynamics in Hydraulic Machinery*, Stuttgart, Germany, pp. 1-16.

[4] Susan-Resiga, R., Vu, T., Muntean, S., Ciocan, G., and Nennemann, B., 2006, Jet control of the draft tube vortex rope in Francis turbines at partial discharge. *Proceedings of the 23rd IAHR Symposium on Hydraulic Machinery and Systems*, Yokohama, Japan, (p. 192).

[5] Susan-Resiga, R., Muntean, S., 2008, "Decelerated Swirling Flow Control in the Discharge Cone of Francis Turbines" *Proceedings of the Fourth Symposium on Fluid Machinery and Fluid Engineering*, Beijing, China, Springer, pp. 89-96.

[6] Kurokawa, J., Kajigaya, A., Matusi, J., and Imamura, H., 2000, "Suppression of Swirl in a Conical Diffuser by Use of J-Groove," *Proceedings of the 20th IAHR Symposium on Hydraulic Machinery and Systems*, Charlotte, North Carolina, Paper DY-01.

[7] Kirschner, O., Schmidt, H., Ruprecht, A., Mader, R., and Meusburger, P., 2010, "Experimental investigation of vortex control with an axial jet in the draft tube of a model pump-turbine", *Proceedings of the 25th IAHR Symposium on Hydraulic Machinery and Systems in IOP Conf. Series: Earth and Environmental Science*, Timisoara, Romania, Vol. 12, p. 012092.

[8] Avellan, F., 2000, "Flow investigation in a Francis draft tube: the FLINDT project", *Proceedings of the 20th IAHR Symposium on Hydraulic Machinery and Systems*, Charlote, USA, pp. DES-11.

[9] Bosioc, A.I., Tanasa, C., Muntean, S., Susan-Resiga, R., 2010, "Pressure recovery improvement in a conical diffuser with swirling flow using water jet injection", *Publishing House of the Romanian Academy, Proceedings of the Romanian Academy, Series A: Mathematics, Physics, Technical Sciences, Informational Science*, Vol. 11, Number 3, pp. 245-252.

[10] Travin, A., Shur, M., Strelets, M., Spalart, P.R., 2000, „Detached-eddy simulations past a circular cylinder", *Flow, Turbulence and Combustion,* Vol. 63, pp. 293–313

[11] Jacob, T., 1993, "Evaluation sur modele reduit et prediction de la stabilite de fonctionnement des turbines Francis", *Phd thesis*, Ecole Politehnique de Lausanne, Switzerland.

[12] Tridon, S., Barre, S., Ciocan, G.D., Tomas, L., 2010, "Experimental analysis of the swirling flow in a Francis turbine draft tube: Focus on radial velocity component determination", *European Journal of Mechanics B/Fluids*, Vol. 29, pp. 321-335.

[13] Susan-Resiga, R., Muntean, S., Avellan, F., Anton, I., 2011, "Mathematical modelling of swirling flow in hydraulic turbines for the full operating regime", *Applied Mathematical Modelling*, Vol. 35, pp. 4759-4773.

Conference on Modelling Fluid Flow (CMFF'12)
The 15th International Conference on Fluid Flow Technologies
Budapest, Hungary, September 4-7, 2012

INVESTIGATION OF DEFORMATION AND STRESS IN IMPELLERS OF MULTISTAGE PUMPS BY MEANS OF FLUID-STRUCTURE INTERACTION CALCULATIONS

Andreas Schneider[1], Björn-Christian Will[2], Martin Böhle[3]

[1] Corresponding Author. Faculty of Mechanical and Process Engineering, Institute of Fluid Mechanics and Fluid Machinery, Technical University Kaiserslautern, Gottlieb-Daimler-Str., 67663 Kaiserslautern, Germany. Tel.: +49 631 205 2115, Fax: +49 631 205 3909, E-mail: andreas.schneider@mv.uni-kl.de
[2] KSB AG, Johann-Klein-Str. 9, 67227 Frankenthal. E-mail: bjoern-christian.will@ksb.com
[3] Faculty of Mechanical and Process Engineering, Institute of Fluid Mechanics and Fluid Machinery, Technical University Kaiserslautern. E-mail: martin.boehle@mv.uni-kl.de

ABSTRACT

This contribution focuses on the deformations and stresses in impellers of a multistage centrifugal pump with a specific speed of n_q=30. The loads acting on the impeller under operating conditions can be subdivided into a structural component (i.e. centrifugal forces and constraints) and a hydrodynamic component (i.e. pressure loads), which are considered by means of one-way coupled fluid-structure interaction (FSI) simulations. The hydrodynamic pressure loads are derived from the CFD solution for a single stage of the pump. These pressure loads are imposed on the impeller in the structural part of the simulation. In order to determine the resulting deformations and stresses of the impeller, static structural analyses with linear material behaviour are performed. Two operating points are considered, namely at design flow rate and at part load. Furthermore, the influence of structural impeller design parameters on the resulting deformations and stresses is investigated in detail. More precisely, the thickness of the impeller shrouds as well as the fillet radii between the blades and the rear shroud as well as between the blades and the front shroud are examined.

Keywords: Centrifugal Pump, CFD, Fluid-Structure Interaction, Impeller Modification, Stress, Structural Analysis

NOMENCLATURE

D	[m]	diameter
H	[m]	hydraulic head
c	[m/s]	velocity
d	[m]	displacement
g	[m/s^2]	gravity acceleration
n_q	[-]	specific speed
u	[m/s]	circumferential velocity
Φ	[-]	flow coefficient
Ψ	[-]	work coefficient
ρ	[kg/m^3]	density
ν	[m^2/s]	kinematic viscosity
σ	[Pa]	stress

Subscripts and Superscripts

2	impeller outlet
BEP	best efficiency point
eqv	equivalent
m	meridian component
n	non-dimensional
sum	vector sum (i.e. absolute value)

1. INTRODUCTION

In the structural design process of pumps and other turbomachinery, the knowledge of deformations and stresses in the different components is crucial. Insufficient structural design might result in a collapse of the machine and, under some circumstances, in a breakdown of the underlying process. On the other hand, a too conservative structural design causes unnecessarily high production costs. The stationary pump parts, such as stator or casing, are only loaded by the fluid pressure, whereas the rotation of the impeller causes additional centrifugal forces. These forces lead to complicated deformations and stresses in the machine parts. Especially the superposition of loads acting on the impeller leads to a complex deformation of the structure.

From a physical point of view, this reaction is the result of fluid-structure interaction (FSI). Such effects occur in everyday life. Examples are the waving of trees, bridges or skyscrapers in the wind.

An increasing number of publications dealing with FSI in turbomachinery can be found recently. Benra [1-3] investigated the oscillation of a sewage

water pump's single-blade impeller by means of FSI. Hübner [4] applied FSI to calculate the dynamic behaviour of water turbine components. Campbell [5] used fluid-structure interaction on turbomachinery for biomedical applications.

The present paper is structured as follows: Section 2 gives a short overview of the numerical treatment of fluid-structure interaction problems. Section 3 introduces the investigated pump and the numerical setup. Furthermore, this section describes the analysed impeller modifications. The obtained results are presented in section 4.

2. FLUID-STRUCTURE INTERACTION

The coupled system of equations, describing a fluid-structure problem in the simplest case, can be expressed as [4, 6]:

$$\begin{bmatrix} \underline{\underline{K_{SS}}} & \underline{\underline{K_{SF}}} \\ \underline{\underline{K_{FS}}} & \underline{\underline{K_{FF}}} \end{bmatrix} \cdot \begin{bmatrix} \underline{x_S} \\ \underline{x_F} \end{bmatrix} = \begin{bmatrix} \underline{f_S} \\ \underline{f_F} \end{bmatrix} \tag{1}$$

The diagonal submatrices $\underline{\underline{K_{ii}}}$ represent the system matrices for fluid and structure (subscript F indicates fluid and S structure). Off-diagonal submatrices $\underline{\underline{K_{ij}}}$ describe the coupling between the continua. $\underline{x}$ describes the vector of unknown variables in the respective system. The right-hand side $\underline{f}$ expresses the boundary conditions of each system.

To solve the system of Eq. (1), there are three different methods known in literature [7].

2.1 Field Elimination Method

The equations of the part systems (i.e. fluid and structure) are substituted into each other. This is only possible if linear equations hold for the physical description of the systems. As a result, one obtains complicated formulations, which are difficult to solve numerically.

2.2 Monolithic Methods

The system of Eq. (1) is solved as a whole with a single solver. Figure 1 schematically depicts this strategy. In a single iteration loop (ellipses) the set of equations for fluid and structure is solved (the rectangle represents an iteration step) and the mesh is updated according to the solution. After convergence is achieved, this time step is finished and the simulation moves to the next time step. This ensures a simultaneous solution of all variables (fluid and structure) and has great advantages, if the interaction between the different domains is strongly non-linear.

2.3 Partitioned Methods

The solution of the fluid and the structure problem is segregated. So, different and highly specialised solvers for each subtask can be used.

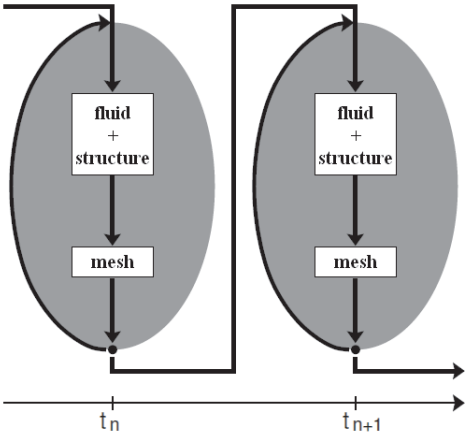

Figure 1. Monolithic approach [7]

The interaction between the different physical domains is incorporated in the boundary conditions of the domains. This can be derived from Eq. (1) by [4]:

$$\begin{aligned} \underline{\underline{K_{SS}}} \cdot \underline{x_S^i} &= \underline{f_S} - \underline{\underline{K_{SF}}} \cdot \underline{x_F^{i-1}} \\ \underline{\underline{K_{FF}}} \cdot \underline{x_F^i} &= \underline{f_F} - \underline{\underline{K_{FS}}} \cdot \underline{x_S^i} \end{aligned} \tag{2}$$

A distinction can be made between loose and strong coupling. When loose coupling is applied, every equation of the system is solved once per time step (denoted by *i* in Eq. (2)), as pictured in Figure 2. For strong coupling the equations are solved several times by an iteration scheme until a convergence criterion is achieved, which is shown schematically in Figure 3.

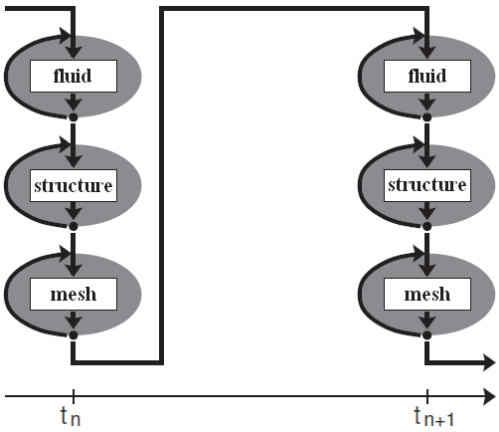

Figure 2. Partitioned approach (loose coupling) [7]

Neglecting of the interaction between one domain (e.g. structure) and the other (e.g. fluid) is called one-way coupling. Non-neglecting of this interaction is referred to as two-way coupling.

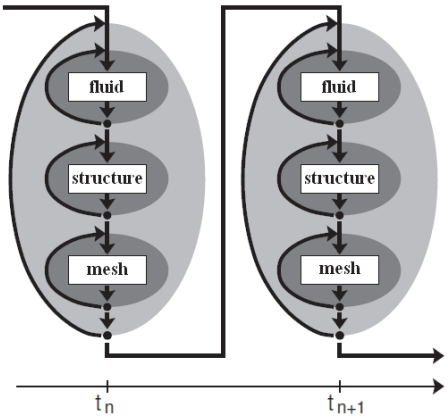

Figure 3. Partitioned approach (strong coupling) [7]

3. NUMERICAL INVESTIGATIONS

In the numerical analysis a centrifugal multistage pump with a specific speed n_q=30 was investigated. Since the pump is built of repeating stages, only one complete stage is explored in detail. The stage is schematically shown in sectional view in Figure 4. The stage characteristics at best efficiency point (BEP) are: flow coefficient Φ_{BEP}=0.1068 and work coefficient Ψ_{BEP}=0.4959.

The definitions of Ψ and Φ are:

$$\Psi = \frac{g \cdot H}{u_2^2}; \quad \Phi = \frac{c_{m,2}}{u_2} \tag{3}$$

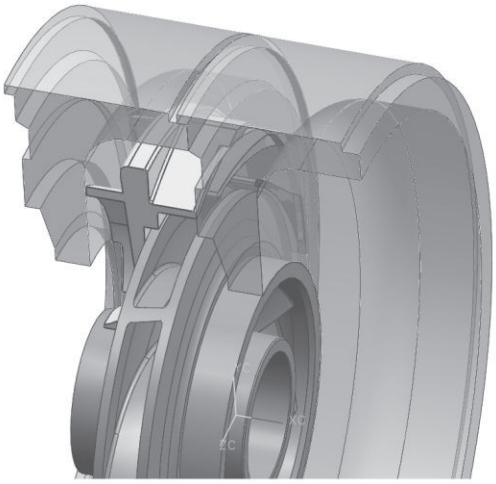

Figure 4. 3D model of the pump stage

The stage has a shrouded impeller with 7 blades. For deceleration of the flow, a radial vaned diffuser with 11 guide vanes is used. The flow is guided by a crossover section and 9 return channels to the next stage.

Deformation and stress analyses of the impeller were carried out using one-way coupled fluid-structure interaction calculations. According to section 2, this numerical treatment is a partitioned approach with loose coupling. The limitation to one-way coupling originated from the assumption of small impeller deformation and thus a negligible influence on the flow.

Two-way FSI calculations for a single-stage centrifugal pump [8] show only a marginal influence of the impeller deformation on the pressure field in the stage and of the radial force on the impeller. On the other hand, the results for a sewage water pump's single-blade impeller [3] are clearly dependent on the impeller deformation. In conclusion, the decision whether the case can be reduced to a one-way FSI strongly depends on the specific problem. A major advantage of one-way FSI, compared to two-way FSI, is the smaller amount of computation time.

All numerical calculations were carried out using Ansys CFX 12 for the fluid part and Ansys Mechanical for the solid part. The coupling between these tools was performed by Ansys CFX Post.

3.1 CFD Setup

The 3D flow field in the stage was calculated numerically by a transient RANS approach. The fluid domain of the stage consisted of a full 360 degree model, including both impeller side clearances and all sealing gaps. Since it was assumed that the impact of the impeller's surrounding flow field on the stress and deformation is of crucial importance, the flow field had to be modelled as good as possible. The domain was extended to 5·*D* (suction diameter) at inlet and outlet of the stage to obtain developed boundary profiles. The final mesh is shown in Figure 5, some facts about the mesh characteristics are listed in Table 1.

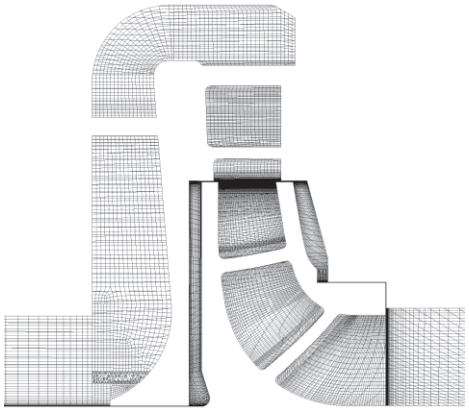

Figure 5. Mesh of the CFD-model

To account for a change of the reference frame, the transient rotor-stator model was applied. The time step was chosen to correlate to an impeller rotation of 1 degree. For time discretisation a second order backward Euler scheme and for spatial discretisation the high-resolution scheme was used.

Table 1. Mesh characteristics

Domain	*Number of cells*
Impeller (total)	About 1e6, hexahedral cells
Stationary parts (total)	About 5e6, mainly hexahedral cells
Impeller side clearances	25 cells in axial direction
Sealing gaps	15 cells in radial direction

The employed boundary conditions are listed in Table 2, the inflow and outflow conditions are used at the inlet and outlet of the domain respectively. Turbulence was modelled with the SST model implemented in CFX.

Table 2. Boundary conditions

Boundary	*Condition*
Inflow	Velocity, according to desired flow rate
Outflow	Static pressure
Walls	Smooth walls, no slip
Interfaces	Transient rotor stator
Fluid	Water, at 20°C

To check convergence and periodicity of the transient solution, residuals and physical properties, e.g. pressure, were monitored. The transient calculations were initialised with stationary frozen rotor solutions for the resulting flow rate.

The flow field in the pump stage was calculated for two operating points, namely the BEP and part load with a flow coefficient of $\Phi=0.3\cdot\Phi_{BEP}$.

3.2 Structural Setup

The impeller structure was simulated by static analyses with linear material behaviour. A 360 degree model of the impeller solid was used for the calculations and contained all impeller details except for the hub keyway. The impeller was modelled with isotropic material behaviour, and appropriate specific values were used as impeller material, which is stainless steel in this application.

The mesh contained about 2.5e6 quadratic tetrahedral elements and is shown as a cross section in Figure 6. During mesh creation, special attention was paid to the fillet radii, which were resolved by a minimum of 8 elements along the radius.

Constraints were applied to the impeller hub. The cylindrical hub surface was locked against radial and tangential movements. The hub front and end surfaces were locked against axial moving, as demonstrated in Figure 7. All other surfaces were loaded with the fluid pressure calculated in the CFD analyses. Since static structural analyses were performed, multiple results of the transient CFD analyses (at different points of time) were employed as pressure loading.

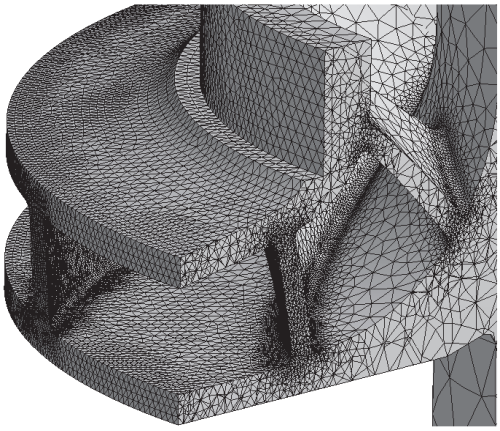

Figure 6. Mesh of the structural model

This was done to capture the effects of the varying pressure field on the deformation and stress of the impeller due to the rotor-stator interaction. The pressure loads were interpolated to the nodes of the structural mesh by means of a nearest neighbour interpolation method. This interpolation was provided by a CFX Post module. The centrifugal force due to the impeller rotation was applied as a further load.

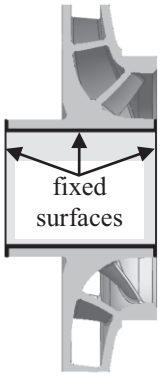

Figure 7. Impeller constraints

3.3 Impeller Design Parameters

The influence of two structural impeller design parameters on the distribution of deformation and stress was analysed. More precisely, the thickness of the impeller shrouds as well as the fillet radii between the blades and the rear shroud as well as between the blades and the front shroud were examined. These investigations were done for either one of the aforementioned operating points.

More precisely, the study on the impeller shroud thicknesses was done for part load operation, and the study on the fillet radii for the best efficiency point. Both analyses were performed only for the structural part of the FSI. This means that the influence of impeller shroud thicknesses as well as of the variation of fillet radii on the flow field was neglected. The modified impellers were

loaded in the structural analysis with the pressure derived from the flow field of the initial geometry.

To emphasise the influence of the shroud thicknesses, three impeller modifications were investigated and compared to the initial geometry. Variant one, called “thick front”, was equipped with a 50 percent thicker front shroud. The second variant, “thick rear”, had a 1.5 times thicker rear shroud. And the last modification “thick rear+front” possessed a 50 percent thicker front and rear shroud. The internal geometry of the impeller remained unchanged for all variants; the shroud thickness was increased into the direction of the impeller side clearances.

To investigate the influence of the fillet radii, also three different impeller variants were considered. At variant one, the original fillet radii were doubled; variant two had three times bigger fillet radii, and the fillet radii of variant three were even four times the radii of the initial geometry.

4. RESULTS

4.1 CFD Calculations

Since the emphasis of this work is on structural investigations, the CFD results are presented briefly here.

The accuracy of CFD was evaluated by a comparison of the calculated work coefficient to measured values. Figure 8 plots the work coefficient Ψ over the flow coefficient Φ.

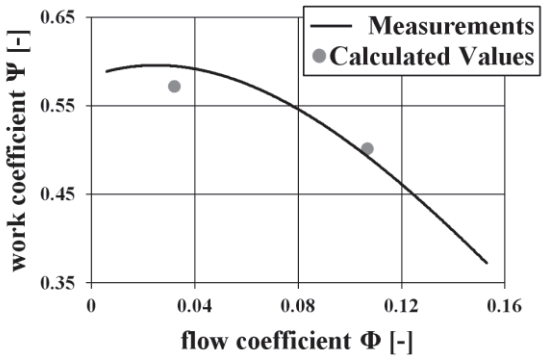

Figure 8. Work coefficient

The deviation between both values is -4.8 percent at part load and 1.2 percent at BEP. These simulated values are averaged values of a complete impeller revolution after obtaining a periodical solution. The results show quite a good accuracy of the CFD model.

The pressure loading for the following structural analyses was derived, for simplicity, from a single CFD result at a certain point of time. This point of time correlated to equal moments during an impeller revolution for both operating points.

4.2 Structural Analyses

Figure 9 shows the impeller deformation for the two investigated flow rates by means of a non-dimensional displacement sum $d_{n,sum}$, compare Eq. (4). On the left-hand side the deformation is shown as viewed on the suction eye of the impeller, and on the right as viewed on the rear shroud.

$$d_{n,sum} = \frac{d_{sum}}{D_2} \tag{4}$$

Qualitatively seen, the displacement fields are similar: The displacement grows from the hub to the outer diameter, and each blade passage has a local maximum on the rear shroud and front shroud. However, in a detailed analysis, the fields differ a lot. While at Φ_{BEP} the maximum displacement occurs on the front shroud, for $0.3 \cdot \Phi_{BEP}$ it occurs on the rear shroud. This is due to the different loading configuration. At part load operation, the pressure in and around the impeller (especially in the rear impeller side clearance) is much higher than at design point operation. Since the centrifugal force originating from the impeller rotation remains constant for both operating conditions, the relative influence of the pressure on the deformation decreases with increasing flow rate.

Quantitatively, the maximum deformations at the design point are about 7 percent smaller than at part load.

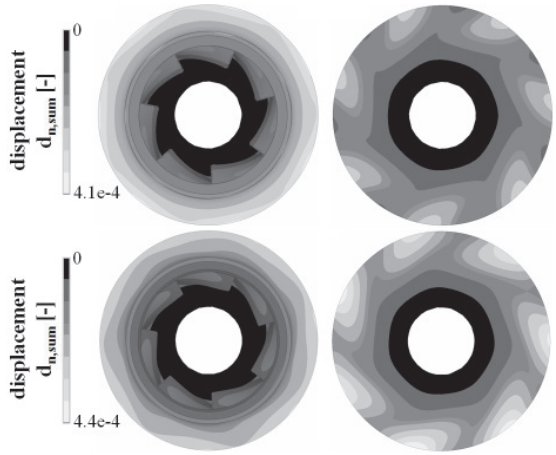

Figure 9. Dimensionless displacement: top $\Phi = \Phi_{BEP}$, bottom $\Phi = 0.3 \cdot \Phi_{BEP}$

A qualitative investigation of impeller stresses indicated that the critical regions of high stress were the fillet radii between the blades and the shrouds. Paths were defined to study the stress distribution in each fillet. These paths extended on the impeller surface from leading edge to trailing edge at a mean fillet radius. Figure 10 depicts the paths and notation used (ps expresses pressure side, whereas ss indicates the suction side of the blade).

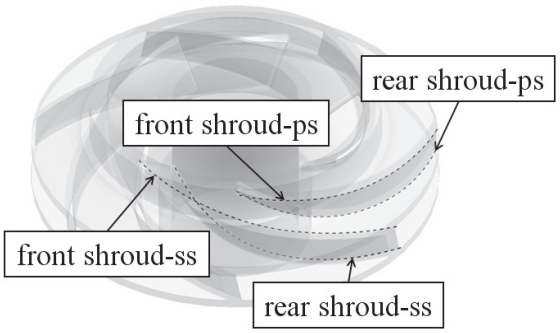

Figure 10. Investigated paths in the fillet radii

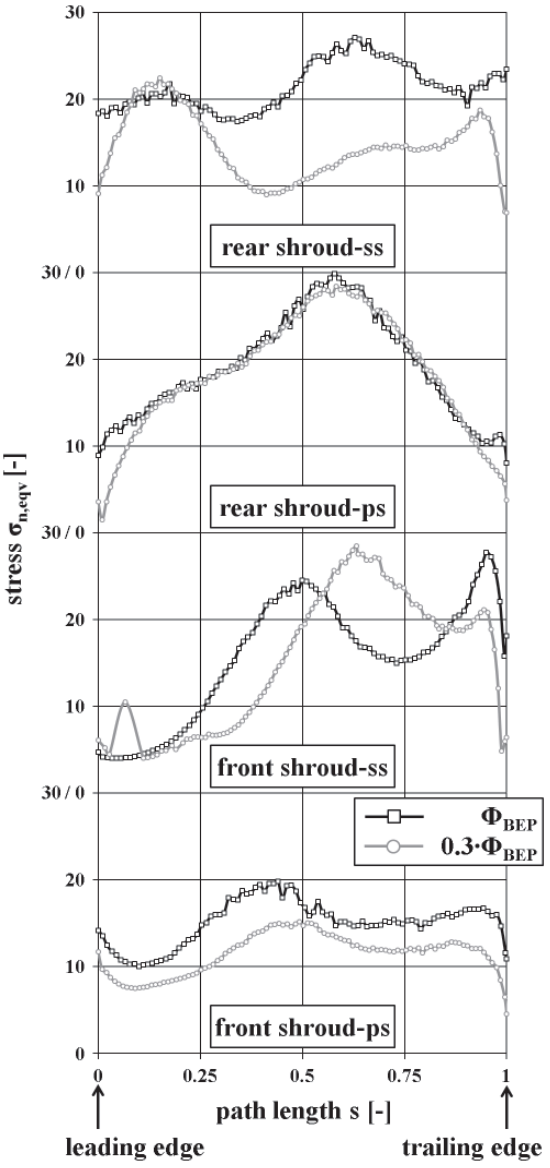

Figure 11. Comparison of equivalent stress in the fillet radii paths

The stress distribution along the above-stated paths is drawn in Figure 11. Stress is plotted as a non-dimensional value, built with von Mises stress (eqv) according to Eq. (5) over the path length, starting at the leading edge and ending at the trailing edge.

$$\sigma_{n,eqv} = \frac{\sigma_{eqv}}{0.5 \cdot \rho \cdot u_2^2} \tag{5}$$

Comparing the stress distributions for the different operating points reveals that there is an obvious dependence on the operating point, except for the path between the rear shroud and the pressure side. The distributions along this path are very similar and hold the highest stress values at approximately half blade length.

The shape of the distributions shows, that not only the amount of stress changes with the flow rate, but also the location of high-stress areas. A correlation between stress and corresponding flow phenomena will be part of future investigations.

Except for the path front shroud-ss, stresses higher than for $0.3 \cdot \Phi_{BEP}$ appear for Φ_{BEP}. This reveals that the stress is in principle not decreasing if the head (i.e. pressure load) is reduced. An explanation for this may be partial compensation of pressure and centrifugal forces in certain regions of the impeller. As mentioned before, there will be an influence of the flow structure on the stress distributions. The strong deviation in the shape of the stress distributions on the suction side paths may be induced by flow separation, which occurs on the suction side at part load.

In addition, other operating points need to be analysed to find the most critical flow rate and the flow structures associated to this. For example, the investigations of an axial flow pump [9] showed that the highest stress in the impeller occurred for a flow rate of 70 percent of the design flow rate.

4.3 Impeller Design Parameters

4.3.1 Impeller Shroud Thickness

The influence of the shroud thicknesses on the impeller deformation and the stress was investigated for a flow rate of $0.3 \cdot \Phi_{BEP}$. Since the shape of the displacement field remained qualitatively unchanged, the focus in this section is on quantitative results. Figure 12 compares the evolution of the maximum non-dimensional displacement on the rear shroud and front shroud for the different impeller shroud thicknesses introduced in section 3.3.

Merely increasing the front shroud thickness leads to a reduced deformation of the rear shroud, but, surprisingly, to a higher deformation of the front shroud. An increase of rear shroud thickness reduces the deformation of both rear and front shroud. A thicker rear and front shroud results in the lowest deformation of the front shroud. In contrast, the value of rear shroud displacement remains nearly constant, compared to the “thick

rear" model. Furthermore, with a thicker rear shroud, the global maximum deformation switches to the front shroud.

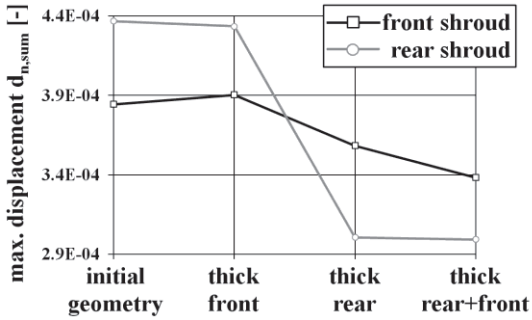

Figure 12. Maximum displacement $d_{n,sum}$ for impeller shroud modification

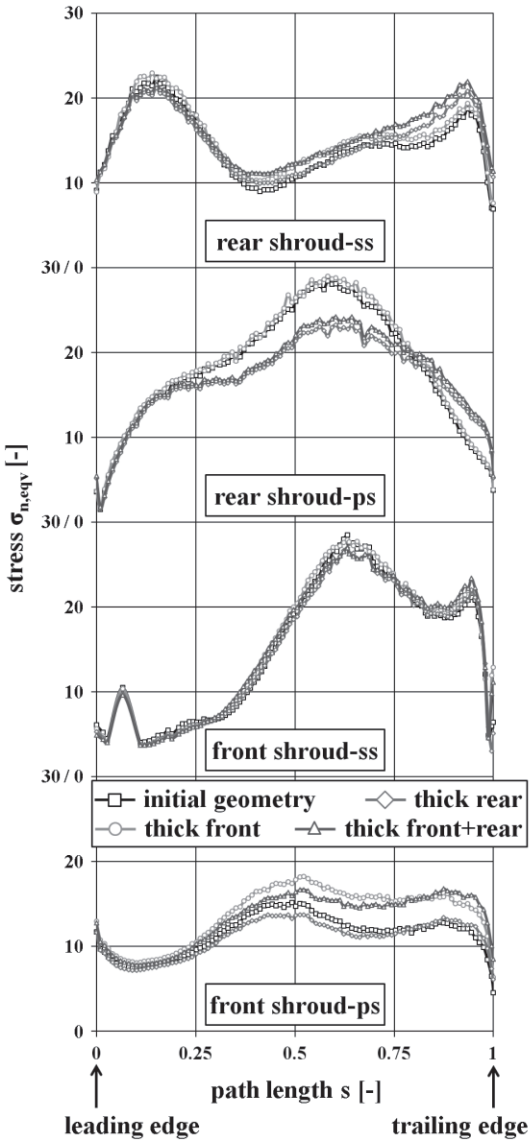

Figure 13. Impeller shroud impact on stress distributions in the fillet radii paths

The influence of the impeller shroud modifications on the impeller stress was analysed in the fillet radii by means of the paths of Figure 10. The results, plotted in Figure 13, illustrate that the stresses are almost independent of the shroud thickness, except for the path rear shroud-ps. Both modifications of the rear shroud thickness cause a reduction in the area of the highest stress.

4.3.2 Fillet Radii

The impact of fillet radii variation on characteristic structural values was investigated at Φ_{BEP}. The evolution of maximum rear shroud and front shroud displacement is pictured in Figure 14. The notation is as follows: fillet i expresses a radius of i-times the initial radius.

The maximum displacement of the rear shroud and the front shroud is reduced significantly with increasing fillet radii. For the front shroud a nearly linear relationship can be identified.

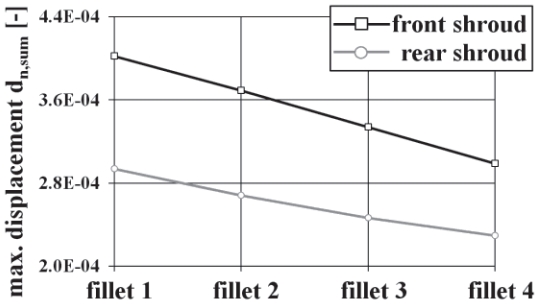

Figure 14. Maximum displacement $d_{n,sum}$ for fillet modification

A similar behaviour can be recognised for the impeller stress, which was again analysed in the aforementioned paths. For the modified impellers the paths were adjusted to meet the changed mean fillet radius.

The stress distributions are plotted in Figure 15. The shape of the stress distributions along the different paths remains similar for all models. In contrast, the maximum observable stress on all paths decreases dramatically with increasing fillet radius.

5. SUMMARY

Under operating conditions, both hydrodynamic and structural loads act on the wetted pump parts. Especially the deformation and the stress fields of the impeller, which is loaded by a complex fluid pressure field, centrifugal forces and constraints, cannot be described analytically. In order to achieve a structural design process, the knowledge of these fields, in particular the areas of maximum stress and deformation, is crucial.

In the present paper, the deformations and stresses of a multistage centrifugal pump's impeller

are calculated by one-way coupled fluid-structure interaction. The structural analyses consist of static simulations with linear material behaviour. The fluid flow field is derived from the numerical solution of transient RANS equations in a single stage of the pump.

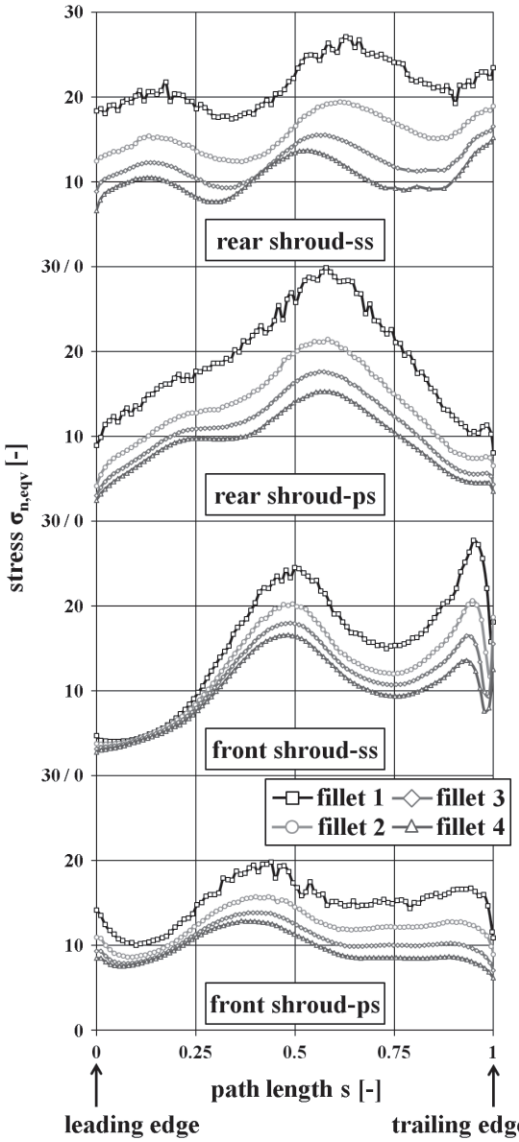

Figure 15. Impact of fillet radii on the stress distributions

From the results of this procedure for two different operating points, namely design flow rate and part load, it can be seen that the deformation and the stress distributions vary significantly with the operating point. In addition, the results emphasise the complex interaction of the different impeller loads. With increasing flow rate, the pressure rise in the impeller and thus the pressure loading are reduced. This leads to a change in the impeller stress distribution, but the maximum stress even increases in this case.

Additionally, the influence of structural design parameters on the structural behaviour of the impeller is investigated. The impeller shroud thicknesses show only a small influence on the impeller stress. The impact on the deformations turns out to be non-intuitive to some extent. A major influential design parameter is found in the fillet radii between the blades and the impeller shrouds. By increasing the fillet radii, deformation as well as stress can be reduced significantly.

REFERENCES

[1] Benra, F.-K., 2006, "Numerical and Experimental Investigation of Flow Induced Oscillations of a Single-Blade Pump Impeller", *ASME Journal of Fluids Engineering*, Vol. 128, pp. 783-793

[2] Benra, F.-K.; Dohmen, H.J.; Bo, W., 2006, "Determination of Pump Impeller Deflections: Comparison of FSI-Simulations to Measurements", *Proceedings of ASME FEDSM*, Miami, USA

[3] Benra, F.-K., 2007, "Application of Fluid/ Structure Interaction Methods to Determine the Impeller Orbit Curves of a Centrifugal Pump", *Proceedings of the 5th IASME/WSEAS International Conference on Fluid Mechanics and Aerodynamics, Athens, Greece,* pp. 169-174

[4] Hübner, B.; Seidel, U.; Roth, S.; 2009, "Application of fluid-structure coupling to predict dynamic behavior of turbine components", *Proceedings of the 25th IAHR Symposium on Hydraulic Machinery and Systems*.

[5] Campbell, R.L.; Paterson, E.G., 2011, "Fluid-structure interaction analysis of flexible turbomachinery", *Journal of Fluids and Structure,* Vol. 27, pp. 1376-1391

[6] Löhner, R.; Baum, J.D.; Soto, O.A., 2008, "On Some Open Problems in Fluid-Structure Interaction", Fluid-Structure Interaction: Theory, Numerics and Application, Kassel University Press, pp.179-188

[7] Hübner, B., 2003, "Simultane Analyse von Bauwerk-Wind-Wechselwirkungen", *Dissertation Technische Universität Braunschweig, Institut für Statik (in German)*

[8] Shouqi, Y.; Pei, J.; Jianping, Y., 2011, "Numerical Investigation on Fluid Structure Interaction Considering Rotor Deformation for a Centrifugal Pump", *Chinese Journal of Mechanical Engineering,* Vol. 24

[9] Kobayashi, K.; et al., 2010, "Numerical Analysis of Stress on Pump Blade by One-Way Coupled Fluid-Structure Simulation", *Journal of Fluid Science and Technology*, Vol. 5, No.2, pp. 219-234

Conference on Modelling Fluid Flow (CMFF'12)
The 15th International Conference on Fluid Flow Technologies
Budapest, Hungary, September 4-7, 2012

NUMERICAL SIMULATION OF CAVITATING FLOW FOR MARINE PROPULSORS ON UNSTRUCTURED MESHES

Sang Joon Ahn[1], Oh Joon Kwon[2]

[1] Department of Aerospace Engineering, Korea Advanced Institute of Science and Technology. E-mail: sjan177@kaist.ac.kr
[2] Corresponding Author, Department of Aerospace Engineering, Korea Advanced Institute of Science and Technology. Daejeon, 305-701, Korea, Tel.: +82 42 350 3720, Fax: +82 42 350 3710, E-mail: ojkwon@kaist.ac.kr

ABSTRACT

In the present study, the cavitating flows around marine propulsors have been numerically investigated by using a multi-phase RANS flow solver based on pseudo-compressibility and a homogeneous mixture model. The mass transfer rate between liquid and vapor phases was determined by Merkle's cavitation model based on the difference between the local and vapor pressure. An unstructured overset mesh technique was adopted to treat the relative motion between the rotating rotor and the stator. The predicted results for thrust, headrise and power coefficients were validated by comparing with experiment. Cavity shape was also compared with experiment. Calculations were made for the P4381 marine propeller with different cavitation numbers at several advancing ratios. The vapor structure, such as cavity size and shape, was well captured at cavitating flow conditions. Reasonable agreements were obtained between the present results and the experiment for the integrated blade loadings, such as thrust and torque. The observation of the cavitation breakdown behavior was also made. Calculations were also made for a water-jet pump configuration at several flow conditions.

Keywords: cavitation, loading breakdown, marine propulsor, RANS, unstructured meshes

NOMENCLATURE

C_p	[-]	pressure coefficient $\equiv (p-p_\infty)/(1/2\rho_l U_\infty^2)$
C_{prod}	[-]	condensation constant
C_{dset}	[-]	evaporation constant
H^*	[-]	head-rise coefficient $\equiv (p_{out}-p_{in})/(\rho n^2 D^2)$
J	[-]	advancing ratio $\equiv U_\infty/nD$
K_Q	[-]	torque coefficient $\equiv Q/\rho_l n^2 D^5$
K_T	[-]	thrust coefficient $\equiv T/\rho_l n^2 D^4$
Q^*	[-]	non-dimensional flow rate $\equiv Q/(nD^3)$
R	[m]	propeller radius
T	[N]	thrust
α	[-]	volume fraction
σ	[-]	cavitation number $\equiv (p_\infty-p_v)/(1/2\rho_l U_\infty^2)$

Subscripts and Superscripts

0	single-phase flow
in, out	inlet, outlet
l, m, v	liquid, mixture, vapor
s	single blade
∞	freestream value

1. INTRODUCTION

Cavitation on marine propulsors is an undesirable phenomenon that causes asymmetric load, performance breakdown, vibration, noise and erosion. Therefore, the prediction of cavitating flows is very important in efficiently designing the marine propulsors with high performance. Many researchers have made experimental [1, 2] and numerical [3-5] efforts to physically understand the cavitating flow phenomena and also to reduce the effects of cavitation on the marine propulsors.

For the past few decades, several methods for computational modelling of cavitation have been developed. The numerical methods can be classified into two categories depending on the treatment of the interface between liquid and vapour phases.

The first category is the interface tracking method [6, 7]. In this method, local pressure at the vapor region is assumed to be constant cavity pressure. The interface between liquid and vapor is explicitly updated by monitoring the local pressure, and the mesh is regenerated at each time step. However, its applications are limited to simple problems, such as the well-defined sheet cavitation.

The second category is the homogeneous mixture model which is based on a single-fluid approach. In this model, the interface and the interaction between the phases, and the bubble dynamics are neglected, and all fluids and phases are treated as a homogeneously mixed single-fluid. This model has a drawback of empirically determining the model constant, but because it can

be applied to various cavitation problems and considers non-condensable gas, the model is widely used to numerically simulate the cavitating flows [8-12]. The mass transfer rate between the liquid and vapour phases is simply determined by the cavitation model.

In present study, an attempt was made to numerically predict the cavitating flow around marine propulsors using an incompressible multi-phase Navier-Stokes flow solver on unstructured meshes. The cavitation model developed by Merkle, Feng, and Buelow [8] was employed to evaluate the mass transfer rate between the liquid and vapour phases. For validation, calculations were made for the P4381 marine propeller with different cavitation numbers at several advancing ratios. The vapor structure, such as cavity size and shape, was analyzed for different flow conditions. The integrated blade loadings, such as thrust and torque, were compared with experiment. Additional calculations were also made for a water-jet pump named the AxWJ-2 at several flow conditions. The predicted results for cavity shape, headrise, thrust and torque coefficient were compared with experiment.

2. GOVERNING EQUATIONS

In the present study, an unstructured mesh multi-phase RANS flow solver has been developed to simulate the time-accurate unsteady cavitating flow around the marine propulsors. The fluid motion is modeled by using the incompressible Reynolds averaged Navier-Stokes equations in conjunction with an artificial compressibility method [13] and a homogeneous mixture model. The equations may be written in an integral form for arbitrary computational domain V with boundary ∂V as

$$\Gamma \frac{\partial}{\partial \tau}\int_V \vec{Q}dV + \Gamma_e \frac{\partial}{\partial t}\int_V \vec{Q}dV + \oint_{dV} \vec{F}(Q)\cdot\vec{n}dS = \oint_{dV} \vec{G}(Q)\cdot\vec{n}dS + \int_V S(Q)dV \quad (1)$$

$$\vec{Q} = \begin{bmatrix} p & u & v & w & \alpha_l \end{bmatrix}^T \quad (2)$$

$$\Gamma = \begin{bmatrix} \frac{1}{\rho_m \beta} & 0 & 0 & 0 & 0 \\ 0 & \rho_m & 0 & 0 & u\Delta\rho \\ 0 & 0 & \rho_m & 0 & v\Delta\rho \\ 0 & 0 & 0 & \rho_m & w\Delta\rho \\ \frac{\alpha_l}{\rho_m \beta} & 0 & 0 & 0 & 1 \end{bmatrix} \quad (3)$$

$$\Gamma_e = \begin{bmatrix} 0 & 0 & 0 & 0 & 0 \\ 0 & \rho_m & 0 & 0 & u\Delta\rho \\ 0 & 0 & \rho_m & 0 & v\Delta\rho \\ 0 & 0 & 0 & \rho_m & w\Delta\rho \\ 0 & 0 & 0 & 0 & 1 \end{bmatrix}$$

where $\vec{Q}$ is the vector of the primitive variables, and $\vec{n}$ is outward normal vector on the control surface. t is the physical time for unsteady calculations, and τ is the pseudo time for steady calculations. $\vec{F}(Q)$ and $\vec{G}(Q)$ are the inviscid and viscous fluxes of these variables, respectively.

The density and the viscosity of the mixture are calculated by

$$\begin{aligned} \rho_m &= \rho_l \alpha_l + \rho_v (1-\alpha_l) \\ \mu_m &= \mu_l \alpha_l + \mu_v (1-\alpha_l) \\ \Delta\rho &= \rho_l - \rho_v \end{aligned} \quad (4)$$

$S(Q)$ is the source term to consider the phase change over the interface between liquid and vapor.

$$S(Q) = \begin{pmatrix} \left(\dot{m}^+ + \dot{m}^-\right)\left(\frac{1}{\rho_l} + \frac{1}{\rho_v}\right) \\ 0 \\ 0 \\ 0 \\ \left(\dot{m}^+ + \dot{m}^-\right)\frac{1}{\rho_l} \end{pmatrix} \quad (5)$$

Here, $\dot{m}^+$ and $\dot{m}^-$ denote the condensation and the evaporation rates. The cavitation model by Merkle, Feng, and Buelow [8] was adopted to evaluate transfer rates as follows:

$$\begin{aligned} \dot{m}^+ &= \frac{C_{prod}(1-\alpha_l)\rho_v \max\left[0, p_\infty - p_v\right]}{t_\infty\left(\frac{1}{2}\rho_l U_\infty^2\right)} \\ \dot{m}^- &= \frac{C_{dset}\alpha_l \rho_l \min\left[0, p_\infty - p_v\right]}{t_\infty\left(\frac{1}{2}\rho_l U_\infty^2\right)} \end{aligned} \quad (6)$$

where C_{prod} and C_{dset} are empirical constant, and in the present study 100 and 100 were used. p_∞ is the freestream pressure, and p_v is the vapor pressure. t_∞ is the characteristic time of the problem.

3. NUMERICAL METHOD

The governing equations were discretized using a vertex-centered finite-volume method. The inviscid flux terms are computed using Roe's flux-difference splitting scheme [14], whilst the viscous flux terms are computed by adopting a modified central difference method. Implicit time integration is performed using a linearized Euler backward difference scheme of second order. The Spalart-Allmaras one-equation turbulence model [15] is used to estimate the eddy viscosity, and the flow is assumed to be fully turbulent. To reduce the large

computational time, a parallel algorithm based on a domain decomposition strategy was adopted. The load balancing between processors was achieved by partitioning the global computational domain into local subdomains using the MeTiS libraries. The Message Passing Interface was used to transfer the flow variables across the subdomain boundaries. All calculations were performed on PC-based Linux clusters. An unstructured overset mesh technique was adopted for simulating the unsteady flows around the multiple bodies in relative motion.

4. RESULTS AND DISCUSSION

4.1. P4381 Propeller

The cavitation performance test for the P4381 propeller was carried out to investigate appreciable benefits from the use of blade skew by Boswell [1]. The experimental data contain forward and backward open-water characteristics, cavitation inception on the propellers, and thrust and torque breakdown due to cavitation with consideration of blade skew. P4381 is a five-bladed and right-handed marine propeller without rake and skew. The key properties of P4381 are summarized in Table 1.

Table 1. Geometry of the propeller [1]

Rotation	Right hand (toward upstream)
Number of blades	5
Hub-diameter ratio	0.2
Skew, Rake	None
Section geometry	NACA66 with NSRDC modified
Design J	0.889

The computational meshes were generated for the P4381 propeller as shown Fig. 1. The far-field boundaries are located at 20 rotor radii upstream, and at a distance of 15 rotor radii from the axis of rotation in the radial direction. To resolve the boundary layer on the surface of the propeller, prismatic cells of 20 layers were constructed. The grid spacing of the first layer was selected such that y+ value is about unity. The remainder of the computational domain was populated by using tetrahedral elements. The mesh consisted of 19.9 million cells and 5.6 milion nodes. At the solid wall, the no slip condition was applied for viscous flows. The characteristic and extrapolation conditions were employed at the far-feild and at the downstream of the propeller. The grid velocity due to the rotation of the propeller was considered for the entire compurational domain.

The calculations were made for both non-cavitating flows and cavitating flows at several advancing ratios from J=0.5 to J=1.28. The Reynols number based on the radius and the tip velocity of the propeller blade is 1.134×10^6. For the cavitating flows, the cavitation numbers were 0.6, 2.0 and 5.0. The parallel computations were made by using 80 processors.

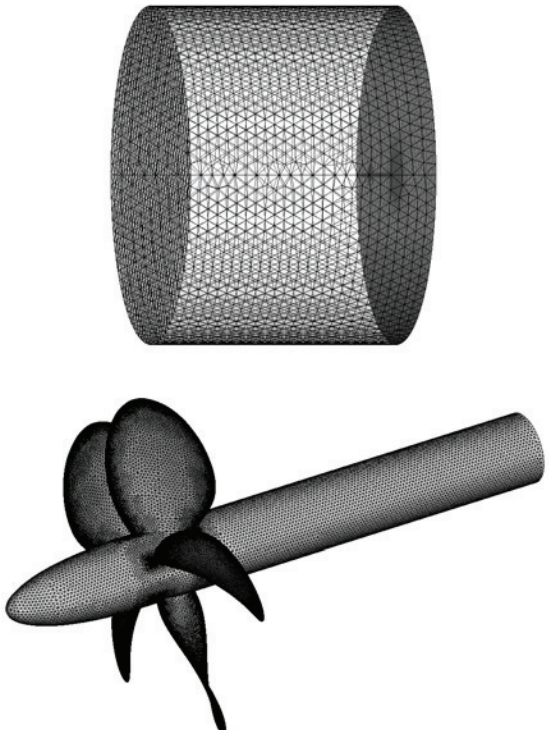

Figure 1. Computational mesh for the P4381 propeller

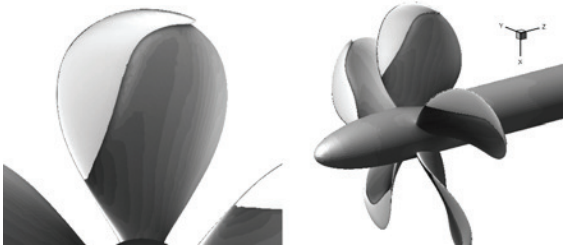

(a) Present calculation

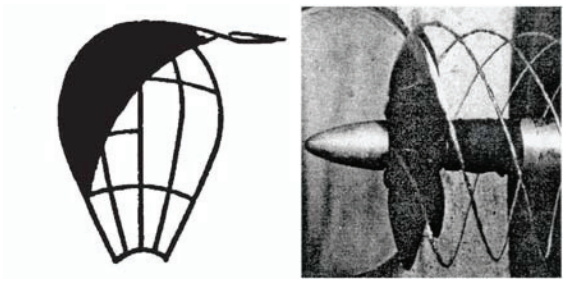

(b) Experiment

Figure 2. Cavity shape around the propeller at σ=3.5 and J=0.7

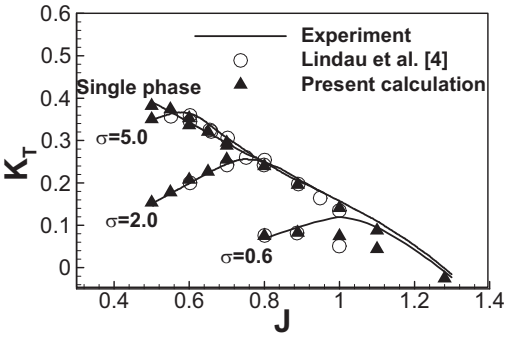

Figure 3. Thrust coefficient at different advancing ratios and cavitation numbers

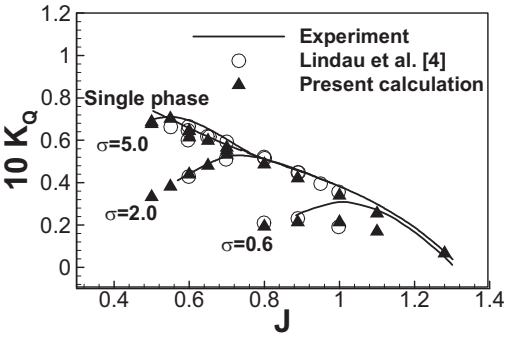

Figure 4. Torque coefficient at different advancing ratios and cavitation numbers

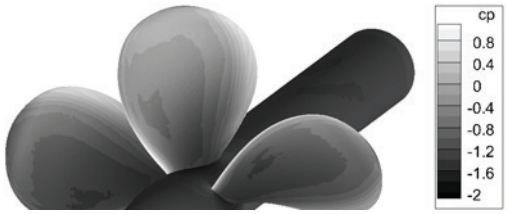

(a) Single-phase

(b) σ = 1.0

(c) σ = 0.6

Figure 5. Cavity structure at *J*=0.889

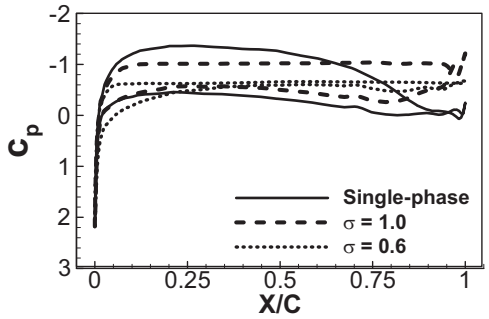

(a) r/R = 0.3

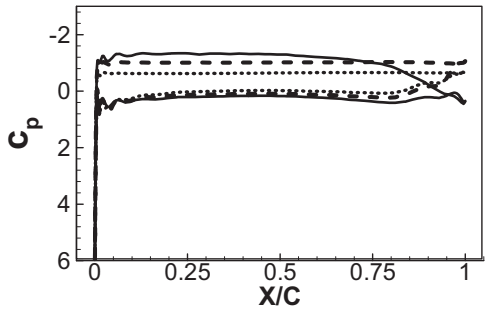

(b) r/R = 0.7

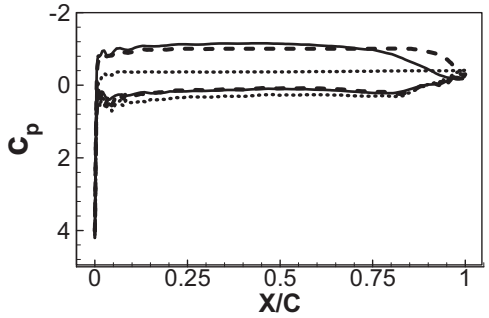

(c) r/R = 0.9

Figure 6. Static pressure distribution along blade chord at *J*=0.889

The calculated iso-surface of the vapor volume fraction of 0.5 at *J*=0.5 and σ=3.5 is compared with the experiment in Fig. 2. The covered area by cavity on the blade is reasonabley well predicted. However, the tip vortex-induced cavitation is terminated behind the the inception region, which may require better grid resolution in resolving the tip vortex induced cavitation.

Figure 3 presents the thrust coefficients at several advancing ratios with different cavitation numbers. The experimental data are represented with the lines, and the predicted results are represented with open symbols. Although the propeller loading is usually degraded by cavitation, however, at the high load region in the range of the

advancing ratio from 0.55 to 0.7, the cavity on the blades increases the integrated loading at σ=5.0. This phenomenon is also well observed in the computed results. The agreement between the prediction and experiment is very good, and the thrust breakdown behaviour is well predicted at all ranges of the advancing ratio.

In Fig. 4, the torque coefficients are presented. Although the torque coefficients for the non-cavitating flows are slightly underpredicted in the computed results, the overall agreement between the prediction and the experiment is still good.

Figure 5 presents the predicted iso-surface of the vapor volum fraction of 0.5 and the pressure distribution on the propeller surface for two cavitation numbers, σ=1.0 and σ=0.6, at the design condition of *J*=0.889. The minimum pressure is observed at the slightly downstream of the leading edge for the non-cavitating condition, and the cavitation is initially developed in this region at those cavitating conditions. At σ=1.0, the developed cavity covers the region from the inception to the trailing edge. At σ=0.6, the cavity covers the entire blade suction side, except the leading edge, and is also convected downdtream of the trailing edge.

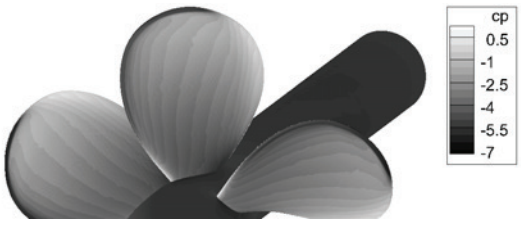

(a) Single-phase

(b) σ = 5.0

(c) σ = 2.0

Figure 7. Cavity structure at *J*=0.6

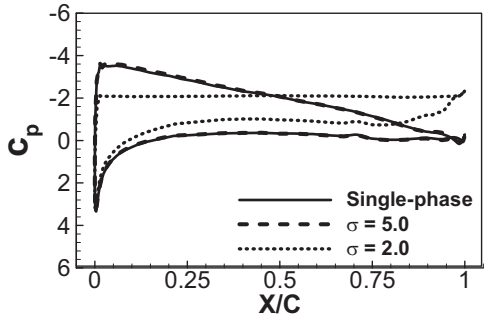

(a) r/R = 0.3

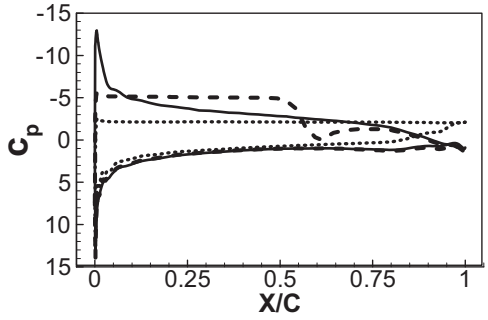

(b) r/R = 0.7

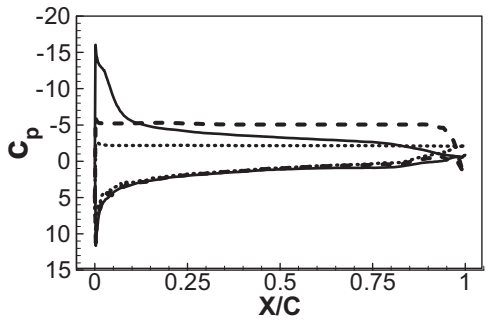

(c) r/R = 0.9

Figure 8. Static pressure distribution along blade chord at *J*=0.6

Figure 6 shows the static pressure coefficient at the sectional positions of 0.3, 0.7 and 0.9R on the blade surface at the same conditions. In the case of cavitating flow, the minimum pressure on the suction side corresponds to the negative of the cavitation number at the region covered with the cavity. This confirms the mechanism that cavity growth degrades the propeller loading.

For the highly loaded condition of *J*=0.6, the predicted iso-surface of the vapor volum fraction of 0.5 and the pressure distribution on the propeller surface is shown in Fig. 7. The minimum pressure at the non-cavitating condition is observed at the leading edge of the suction side, and the cavitation is initially developed near the leading edge at the cavitating conditions. The developed cavity patially covers the suction side of the blades at σ=5.0. At

σ=2.0, the cavity covers the entire suction side of the blades, and is convected to downdtream of the trailing edge.

The static pressure coefficient distributions at the sectional positions of 0.3, 0.7 and 0.9R of the blade surface are shown in Fig. 8. In the case of σ=5.0, the vapor pressure is observed in the region covered with the cavity at r/R=0.7 and 0.9, and the loading increses in that region.

The radial distributions of the thrust coefficient on the propeller blade are shown for the design condition of *J*=0.889 and the highly loaded condition of *J*=0.6 in Fig. 9. The sectional thrust was integrated along the chord at the each radial position. Figure 9(a) presents the thrust distribution for the non-cavitating flow and the cavitating flow at *J*=0.889. the maximun thrust at the non-cavitating condition is generated at about 0.7R. For the cavitating flow, the thrust is degrated at all radial positions except the region partially covered with the cavity near the blade tip. Figure 9(b) shows the thrust distribution at *J*=0.6. For the non-cavitating flow, the maximun thrust is observed at about 0.8R, and the thrust is incresed by the strong tip vortex at the tip. In the case of σ=5.0, the thrust on the raidial positions from about 0.6R to 0.95R increases due to the cavity partially covering the blade suction side. At σ=2.0, the cavity covers the entire surface of the blade suction side, and the thrust is decreased at all raidial positions.

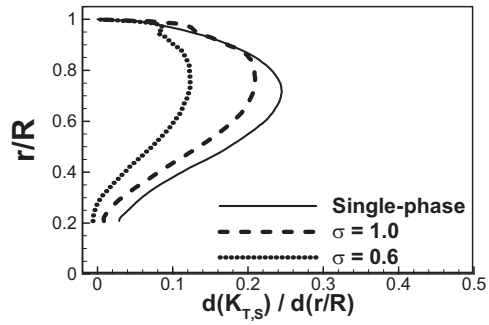

(a) *J*=0.889

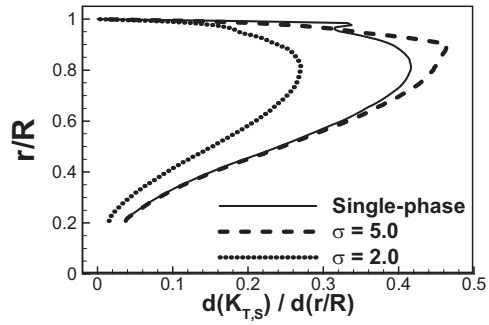

(b) *J*=0.6

Figure 9. Sectional thrust distributions along blade span

4.2. AxWJ-2 Pump

The AxWJ-2 pump experiment was conducted for a rotor-stator configuration by Chesnakas et al. [2]. The geometry of the AxWJ-2 pump is shown in Fig. 10. This water-jet pump consists of rows of 6 rotor blades and 8 sator blades. The gap clearance between the casing endwall and the rotor blade tip is 0.33% of the inlet radius.

The computational mesh was generated for the AxWJ-2 pump as shown in Fig. 11. To handle the relative motion between the stator and the rotor, an unstructured overset mesh technique was adopted. In this scheme, the mesh topology is composed of multiple independent mesh blocks. The main block mesh represents the complete computational domain, and contains the stator. The sub block mesh covers the rotating rotor. On the surface of the stator, the casing endwall, and the rotor, prismatic cells of 30 layers were constructed to capture the viscous shear layer. y+ value of the first layer is about unity. The remainder of the computational domain was populated using tetrahedral elements. The main block mesh contains 4.5 million nodes and 12.3 million cells, and the sub block mesh contains 2.7 million nodes and 8.3 million cells.

On the solid wall, the no slip boundary condition is used for viscous flows. At the inlet boundary plane, the velocity components are specified, and the static pressure is extrapolated from the interior. At the outlet boundary plane, the static pressure is specified and the velocity components are extrapolated from the interior.

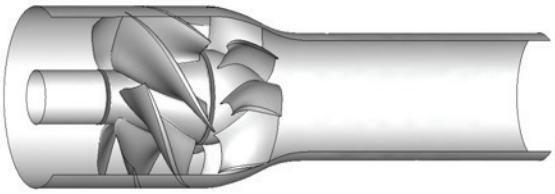

Figure 10. Geometry of AxWJ-2 pump

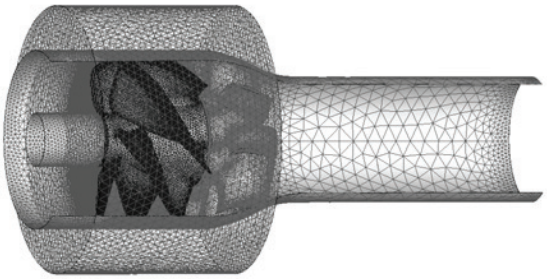

Figure 11. Computational mesh for AxWJ-2 pump

The calculations were made for the non-cavitating and the cavitating flow at the non-dimensional flow rate of Q^* =0.83. The Reynols number based on the radius and the tip velocity of the rotor blade is 3.4 x 10^6. For the cavitating flows, cavitation numbers are 1.86 and 0.56. 160 processors were used for the parallel computation.

Figure 12 presents the headrise and the torque coefficients over the flow rates for the non-cavitating flow. The predicted headrise is in good agreement with the experiment, and the torque coefficient is slightly underpredicted by about 4%.

In Fig. 13, the effect of cavitation breakdown is presented for the thrust. In the calculated results, the thrust breakdown is well captured with the decreasing cavitation numbers, and the agreement with the experiment is reasonable.

Figure 14 shows the computed iso-surface of the vapor volume fraction of 0.5 and the experimental results from Chesnakas et al. [2]. It shows that the agreement between the predicted and the measured cavity shapes is quite good.

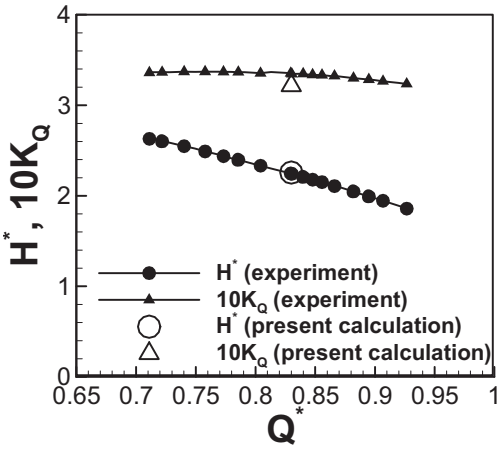

Figure 12. Pump head and thrust coefficient for non-cavitating flow

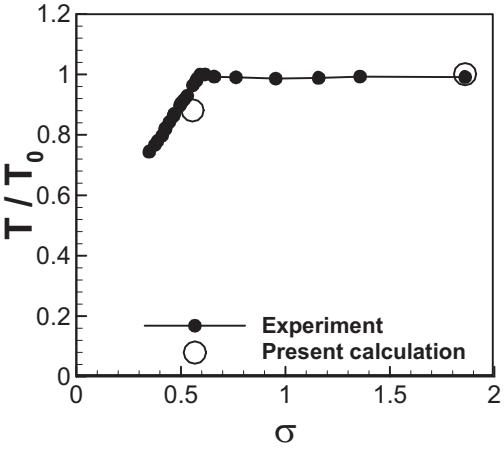

Figure 13. Thrust breakdown at two cavitation numbers

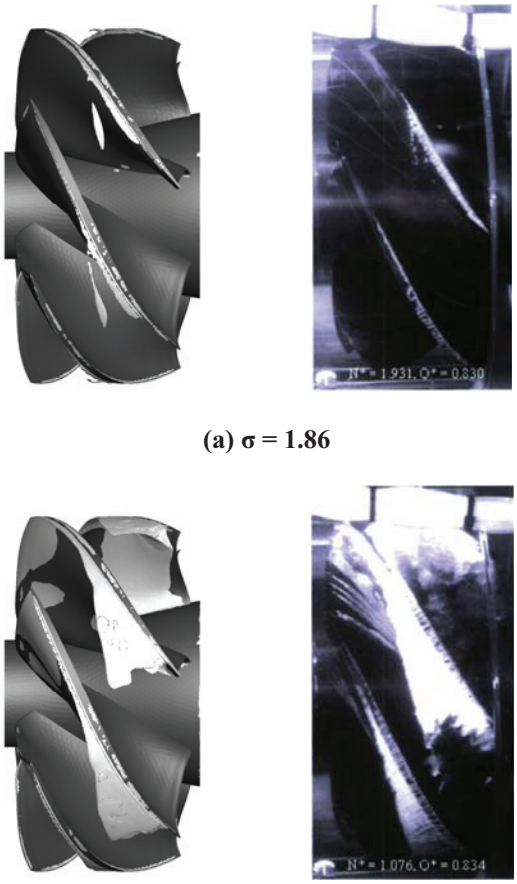

(a) σ = 1.86

(b) σ = 0.56

Figure 14. Tip gap leakage cavitation shape (left : present calculation, right : experiment)

5. CONCLUDING REMARKS

In the present study, numerical simulations were carried out to investigate the cavitating flow around the marine propulsors by using an incompressible multi-phase Navier-Stokes flow solver on unstructured meshes.

The calculations were made for the P4381 marine propeller with different cavitation numbers at several advancing ratios. For validation of the predicted results, the thrust and torque coefficients were compared with experiment. Good agreement was obtained between the two results. The cavity shape, pressure coefficient on the blade, and the radial thrust distribution were also analyzed to investigate the mechanism of loading breakdown of the propeller.

Additional calculations were also made for the AxWj-2 water-jet pump configuration, and the predicted results were compared with the experiment. The tip leakage cavitation was well captured under several cavitating flow conditions. The agreement between the prediction and the experiment was reasonable for the thrust breakdown rate.

ACKNOWLEDGEMENTS

This study was supported by the research grant from the Underwater Vehicle Research Center of the Agency for Defense Development, Korea and the National Research Foundation of Korea(NRF) grant No.20090083510 funded by the Korean government(MEST) through Multi-phenomena CFD Engineering Research Center. The financial support is gratefully acknowledged.

REFERENCES

[1] Boswell, R. J., 1971, "Design, Cavitation Performance and Open-Water Performance of a Series of Research Skewed Propellers," *Naval Ship Research and Development Center*, Washington, D.C., Report No. 3339.

[2] Chesnakas, C. J., Donnelly, M. J., Pfitsch, D. W., Becnel, A. J., and Schroeder, S. D., 2009, "Performance Evaluation of the ONR Axial Waterjet 2 (AxWJ-2)," *Hydromechanics Department Report*, Carderock Division, Naval Surface Warfare Center.

[3] Rhee, S. H., Kawamura, T., and Li, H., 2005, "Propeller Cavitation Study using an Unstructured Grid Based Navier-Stokes Solver," *Journal of Fluids Engineering*, Vol. 127, No. 5, pp. 986-994.

[4] Lindau, J. W., Boger, D. A., Medvitz, R. B., and Kunz, R. F., 2005, "Propeller Cavitation Breakdown Analysis," *Journal of Fluids Engineering*, Vol. 127, No. 5, pp. 995-1002.

[5] Lindau, J. W., Pena, C., Baker, W. J., Dreyer, B. J., Moody, W. L., Kunz, R. F., and Paterson, E. G., 2011, "Modeling of Cavitating Flow through Waterjet Propulsors," *Second International Symposium on Marine Propulsion*, Hamburg, Germany.

[6] Chen, Y., and Heister, S. D., 1996, "Modeling Hydrodynamic Non-equilibrium in Cavitation Flows," *Journal of Fluids Engineering*, Vol. 118, No. 1, pp. 172-178.

[7] Deshpande, M., Feng. J. Z., and Merkle, C. L., 1997, "Numerical Modeling of the Thermodynamic Effects of Cavitation," *Journal of Fluids Engineering*, Vol. 119, No. 2, pp. 420-427.

[8] Merkle, C. L., Feng, J. Z., and Buelow, P. E. O., 1998, "Computational Modeling of the Dynamics of Sheet Cavitation," Proc. *the 3rd International Symposium on Cavitation*, Grenoble, France.

[9] Iga, Y., Nohmi, M., Goto, A., Shin, B. R., and Ikohagi, T., 2003, "Numerical Study of Sheet Breakoff Phenomenon on a Cascade Hydrofoil," *Journal of Fluids Engineering*, Vol. 125, No. 4, pp. 643-651.

[10] Kunz, R. F., Boger, D. A., Stinebring, D. R., Chyczewski, T. S., Lingdau, J. W., Gibeling, H. J., Venkateswaran, S., and Govindan, T. R., 2000, "A preoconditioned Navier-Stokes method for two-phase flows with application to cavitation prediction, " *Computers and Fluids*, Vol. 29, No. 8, pp. 849-875.

[11] Senocak, I., and Shyy, W. A., 2002, "A Pressure-based Method for Turbulent Cavitating Flow Computations," *Journal of Computational Physics*, Vol. 176, No. 2, pp. 363-383.

[12] Singhal, A. K., and Athavale, M. M., Li, H., and Jiang, Y., 2002, "Mathmatical Basis and Validation of the Full Cavitation Model, " *Journal of Fluids Engineering*, Vol. 124, No. 3, pp. 617-624

[13] Chorin, A. J., 1967, "A Numerical Method for Solving Incompressible Viscous Flow Problems," *Journal of Computational Physics*, Vol. 2, No. 1, pp. 12-26.

[14] Roe, P. L., 1981, "Approximate Riemann Solvers, Parameter Vectors and Difference Scheme," *Journal of Computational Physics*, Vol. 43, No. 2, pp. 357-372.

[15] Spalart, P.R. and Allmaras, S.R., 1992, "A One-Equation Turbulence Model for Aerodynamic Flows," AIAA Paper 92-0439, Jan.

Conference on Modelling Fluid Flow (CMFF'12)
The 15th International Conference on Fluid Flow Technologies
Budapest, Hungary, September 4-7, 2012

3D NUMERICAL FLOW ANALYSIS AND EXPERIMENTAL VALIDATION INTO A MODEL IMPELLER OF A STORAGE PUMP

Gheorghiță GÎNGA[1], Ion Rareş STANCIU[2], Sebastian MUNTEAN[3], Alexandru BAYA[4], Liviu Eugen ANTON[4]

[1] Corresponding Author, PhD Student., Department of Hydraulic Machinery, Politehnica University of Timisoara, Bv. Mihai Viteazu 1, 300222, Timisoara, ROMANIA, Phone/Fax: +40256403692, E-mail: puiuginga@mh.mec.upt.ro
[2] PhD Eng., Researcher, Department of Hydraulic Machinery, Politehnica University of Timisoara, Bv. Mihai Viteazu 1, 300222, Timisoara, ROMANIA, Phone/Fax: +40256403692, E-mail: rares.stanciu@mh.mec.upt.ro
[3] PhD Eng., Senior Researcher, Romanian Academy – Timisoara Branch, Center for Fundamental and Advanced Technical Research, Bv. Mihai Viteazu 24, 300223, Timisoara, ROMANIA, Phone/Fax: +40256403692, E-mail: seby@acad-tim.tm.edu.ro
[4] PhD Eng, Professor, Department of Hydraulic Machinery, Politehnica University of Timisoara, Bv. Mihai Viteazu 1, 300222, Timisoara, ROMANIA, Phone/Fax: +40256403692, E-mail alexandru_baya@yahoo.com, liviu.anton@tiriacauto.ro

ABSTRACT

The paper aims to evaluate numerically and experimentally the hydrodynamic performance of a storage pump impeller model. In this case the pump presents a symmetric elbow-shaped suction chamber which induces a non-uniform flow at the inlet of the impeller. Additionally, two counter-rotating vortices were noticed by Van den Braembusche [7] and Gînga et al [8]. As a result, the cavitation phenomenon develops at the leading edge of the blade.

Storage pump model impeller and suction elbow were manufactured and installed on the test rig at Politehnica University of Timisoara. Experimental measurements were performed in order to determine the energetic curve ψ=f(φ) and cavitation performance ψ=f(σ).

The three-dimensional (3D) hydraulic passage geometry of the test rig's pump was reconstructed. 3D numerical simulation was performed in order to compute the flow into the suction elbow, impeller interblade channel and volute domains. The mixing interface method is used in order to couple the steady absolute flow with steady relative flow, Muntean et al [5]. The 3D turbulent flow with k-ω SST model is employed using the CFD software [6]. Numerical analysis was performed for five operating points: 0.8, 0.9, 1.0, 1.1 and 1.2 of the nominal discharge, Q_n. Consequently, the numerical results are validated against experimental data.

Keywords: energetic and cavitational performances, mixing interface algorithm, storage pump.

NOMENCLATURE

H	[m]	head
I1-I6	[-]	mixing interface loop number
NPSH	[m]	Net Positive Suction Head
Pt1, Pt2	[-]	inlet/ outlet pressure transducers
P_M	[W]	absorbed power
Q	[m^3/s]	discharge
Q_n	[m^3/s]	nominal discharge
R_{ref}	[m]	reference radius
cp	[-]	pressure coefficient
g	[m/s^2]	gravitational acceleration
n	[rpm]	revolution speed
n_q	[-]	characteristic speed
p_S	[Pa]	static pressure
p_D	[Pa]	dynamic pressure
v	[m/s]	velocity
z	[m]	linear dimension between pressure transducers axis
Δp	[Pa]	pressure drop/rise
ψ	[-]	energy coefficient
φ	[-]	flow coefficient
$\Sigma hp_{1\text{-}2}$	[m]	sum of longitudinal (hp_{long}) and local (hp_{loc}) hydraulic losses from Pt1 to Pt2
ω	[rad/s]	angular velocity
ρ	[kg/m^3]	water density
σ	[-]	Thoma cavitation number
η_H	[-]	hydraulic efficiency
ε	[%]	uncertainty

1. INTRODUCTION

Today, a total of 25% of the produced energy is used by pumping activities. Consequently, the interest for pumps development is increasing. State

of the art and tendencies in this field are outlined in Gopalakrishnan [1] and Hergt [2].

Besides electricity-producing plants, the hydropower systems use pumping stations. The investigated storage pump belongs to the largest hydropower system in Romania, located on the Lotru River. Their purpose is to pump water from dams into storage lakes. Almost 75% of hydro power plant Lotru turbine discharge is ensured by a number of pumping plants equipped with this type of pump. The pumping plants are operating at night, when the electricity is cheaper, with a consumption of only 10% of the electric energy produced by the hydro power plant. Usually, these pumps reach high flow rate values and high efficiency with an acceptable development of cavitation phenomena.

Several differences are to be noted between regular pumps and those installed at Lotru in order to insure higher flow rate: a) a symmetric elbow-shaped suction elbow crossed by the shaft; b) a double suction impeller. Consequently, the complex shape of the suction elbow generates a non-uniform flow which is ingested by the impeller. Several investigations of the flow upstream the impeller have underlined the non-uniform flow generated by the suction elbow and shaft, Sallaberger et al [3]. As a result, the cavitational performance of the pump diminishes and unsteady phenomena are generated. These units were designed in the 60s. At that time the unsteady flow phenomena were not taken into account. Consequently, during operation, several impellers were destroyed due to the cavitational erosion. A technical evaluation and rehabilitation process was developed a few years ago since the units are rapidly reaching their lifetime limit.

This paper presents experimental and numerical 3D steady flow investigations on the model storage pump (suction elbow, impeller and volute). The geometrical scaled-down model (1:5.7) is used for experimental investigations. These are performed in order to determine the energetic and cavitational performances of the model impeller. Because the pump has a double suction impeller (symmetric to a vertical plane), only half of the hydraulic passage of the storage pump is taken into account in our investigations. Numerical results are compared against experimental ones, in order to assess the simulation methodology. Conclusions are drawn in the last section of the paper.

2. EXPERIMENTAL INVESTIGATION

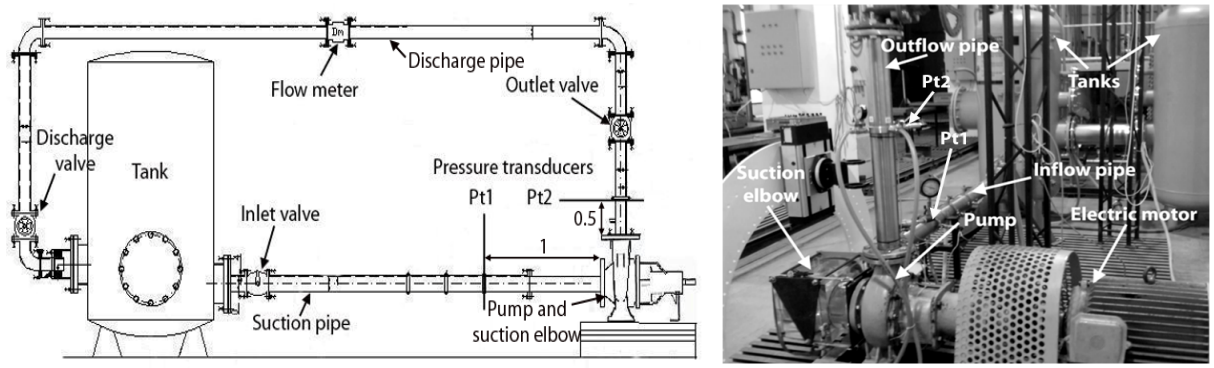

Fig. 1: The test rig: schematic (left) and photo (right)

2.1. Experimental facility

A new test rig was designed and installed at Politehnica University of Timisoara, Figure 1. It consists of two tanks of 1 m^3 each, a set of pipes and vanes, which form a closed hydraulic circuit, and a pump actuated by an induction motor. The inlet and outlet pipes diameters are 0.11m and 0.08m, respectively. Pump parameters are presented in Table 1.

Table 1. Pump parameters.

Parameter	Values
Nominal head H_n [m]	44.5
Nominal discharge Q_n [m^3/s]	0.0335
Mechanical power P_M [KW]	20
Efficiency [%]	72
Nominal speed n [rpm]	3000
Specific speed n_s [-]	116

$$n_s = 3.65 \cdot n_q = 3.65 \cdot n \frac{Q^{1/2}}{H^{3/4}} \quad (1)$$

The test rig is equipped with a real time acquisition data system. To acquire pressure at the inlet and outlet sections of the pump the rig is equipped with two pressure transducers: a vacuum gauge, located on the inlet pipe and labeled Pt1 as well as a manometer placed on the outlet pipe and labeled Pt2. Both transducers use stainless steel casing. The pressure ranges for inlet and outlet sensors is -1 - 2 *bar* and 0 - 6 *bar*, respectively. The output signal is 4 - 20 *mA* for both of them, with an accuracy reported to be ±0.25%. An electro-magnetic flow meter is installed on the rig`s top pipe in order to measure the discharge. Its domain is 0 - 45 *l/sec* with an accuracy reported to be ±0.4%.

For testing purpose, important are the inlet and the outlet pressure values, the motor's revolution speed, the mechanical power absorbed by pump, the discharge, and the water temperature. Real time data acquisition system ensures proper sensor biasing and serial PC communication. Built as a distinct module, it has 32 channels with voltage/current differential inputs, 12-*bit* resolution and an input range of ±10*V*/±25 *mA*/4 - 20 *mA*. The maximum acquisition frequency is 100*kb/sec*. A total memory of 512*k* sample is available. The data acquisition system communicates with the PC using the RS232 standard and the COM2 port, Figure 2.

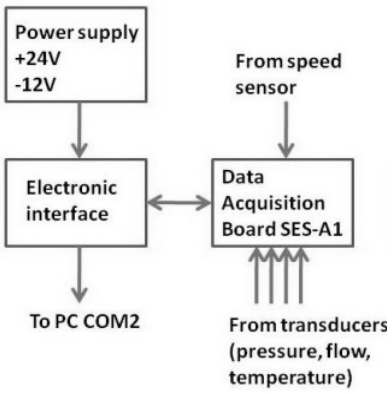

Fig 2: The data acquisition system

The 37 KW/3000 *rpm* induction motor set for this test rig is powered through an electronic inverter which eliminates electrical and mechanical starting shocks. The main motor data can be seen in Table 2. An adjustable thermal circuit breaker is used to protect the motor.

Table 2. - The electric motor's parameters

Parameter (nominal)	Values
Power (at shaft) [W]	37000
Voltage [V]	400
Current [A]	66.58
Efficiency [%]	89.64
Power Factor	0.895
Speed [rpm]	2958
Torque [Nm]	119.56
Slip [%]	1.4

For testing purpose, the speed is maintained constant by the inverter. The accuracy is reported to be 0.16% of the nominal speed. The mechanical power's accuracy is 4%.

2.2. Experimental results

Determination of measuring uncertainties was done taking into account the error propagation after Gauss's law Eq. (2). Measurements uncertainty quantities are 0.354% for head and 4.051% for total efficiency.

$$\varepsilon = \sqrt{\left(\frac{\delta f}{\delta x_1}\right)^2 \cdot \varepsilon_1^2 + \left(\frac{\delta f}{\delta x_2}\right)^2 \cdot \varepsilon_2^2 + \left(\frac{\delta f}{\delta x_3}\right)^2 \cdot \varepsilon_3^2} \qquad (2)$$

Experimental measurements were performed on the entire pump operating domain at 3000 *rpm*. Pump's total pressure Eq. (3) is presented in Table 3.

$$\Delta p_{T\text{-}Exp} = \Delta p_S + \Delta p_D + \rho g \times (z - \Sigma hp_{1\text{-}2}) \qquad (3)$$

$$\text{where: } \Delta p_S = (p_{S\_out} - p_{S\_in}) \qquad (4)$$

$$\Delta p_D = \rho/2 \times (v_{out}^2 - v_{in}^2) \text{ and } z = 0.9m \qquad (5)$$

$$\Sigma hp_{1\text{-}2} = (hp_{long} + hp_{loc})_{Pt1\text{-}Pt2} \qquad (6)$$

Table 3. –Experimental data – total pressure

Qx10^{-3} [m^3/s]	Δp_S [kPa]	Δp_D [kPa]	$\Sigma hp_{1\text{-}2}$ [kPa]	$\Delta p_{T\text{-}Exp}$ [kPa]
0	525.4	0.0	0.0	525.4
1.7	523.6	1.6	0.01	525.2
7.2	517.4	6.6	0.1	523.9
13	512.2	11.9	0.4	523.8
20.1	498.2	18.4	0.9	515.7
26.8	460.7	24.6	1.6	483.7
32.1	420.7	29.5	2.3	447.8
36.6	381.3	33.6	3.0	411.9
39.9	350.4	36.6	3.6	383.4
42.6	318.3	39.1	4.1	353.3
44.8	294.7	41.1	4.5	331.3

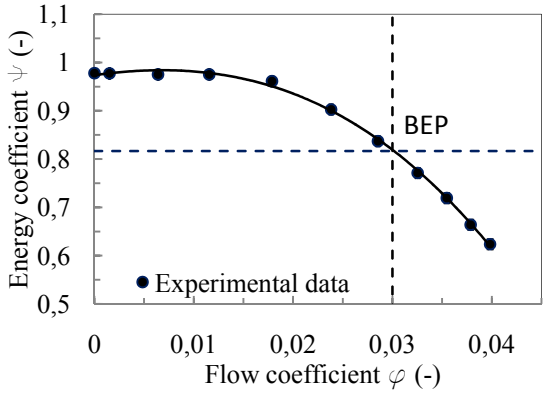

Figure 3. Energy coefficient ψ versus flow coefficient φ – measurements

Also, energy coefficient ψ Eq. (7) versus flow coefficient φ Eq. (8) is plotted in Figure 3. It can be seen that at BEP, where the nominal discharge coefficient is φ_n=0.03 the energy coefficient is ψ=0.815.

$$\psi = \frac{2gH}{\omega^2 R_{ref}^2}, \text{ where:} \quad (7)$$

$$H = \frac{\Delta p_{T\text{-}(Exp,Num)}}{\rho g} = \frac{p_{T\_out} - p_{T\_in}}{\rho g} \quad (8)$$

$$\varphi = \frac{Q}{\pi \omega R_{ref}^3} \quad (9)$$

Pumps head was determinate experimentally for seven values of discharge when operating in cavitating regimes. Also pumps Net Positive Suction Head Required *NPSHr* was evaluated. Energy coefficient ψ is plotted versus Thoma cavitation number σ Eq. (10) and $\sigma 3$ Eq. (12) shows when the pump is operating in developed cavitation, Figure 4.

$$\sigma = \frac{NPSH}{H}, \text{ where:} \quad (10)$$

$$NPSH = \frac{p_{S\_in}}{\rho g} + \frac{v_{in}^2}{2g} - \frac{p_{vap}}{\rho g} + z \quad (11)$$

$$\sigma 3 = \frac{NPSHr3\%}{H3\%} \quad (12)$$

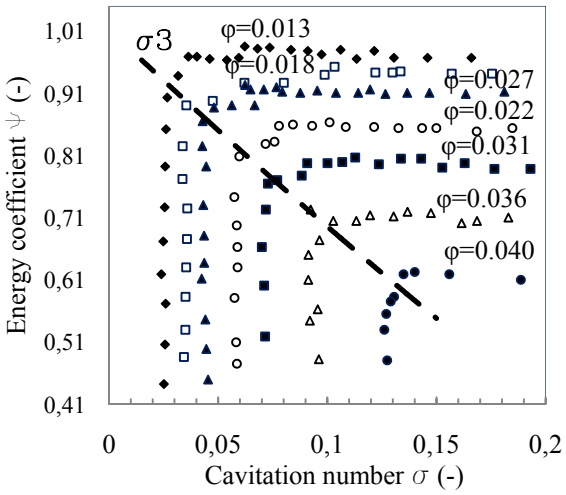

Figure 4. Energy coefficient ψ versus Thoma cavitation number σ – measurements

3. NUMERICAL ANALYSIS

3.1. 3D computational domains. Boundary conditions

The three-dimensional hydraulic passage was reconstructed considering the test rig passage, from Pt1 to Pt2 using Gambit [4].

The 3D computational domains of test rig's hydraulic passage with boundary conditions are presented below. Figure 5 shows the 3D computational domain of the model suction elbow from pressure transducer Pt1 to the inlet section of the pump, see Figure 1. Suction elbow domain is meshed with more than 2 million cells. The mesh is refined near to the outlet surface in order cu capture as accurate as possible the non-uniform flow.

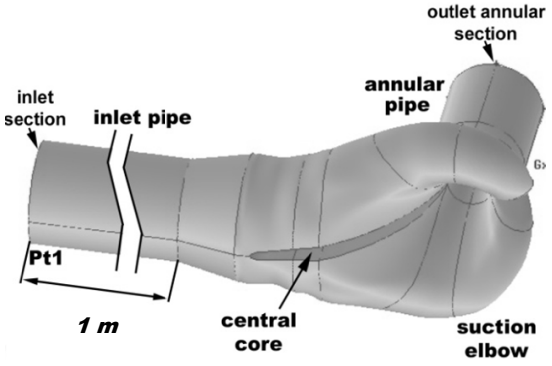

Figure 5. 3D computational domain of suction elbow

The 3D computational domain of one interblade channel of the impeller is presented in Figure 6, meshed with 362630 hexahedral cells.

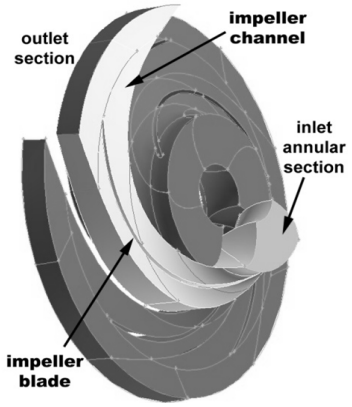

Figure 6. Impellers 3D computational domain. One interblade channel is selected

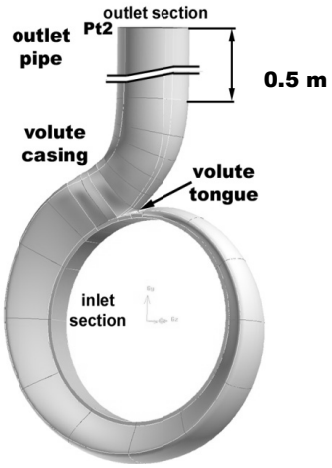

Figure 7. Volute 3D computational domain

Also, the 3D computational domain of the volute was reconstructed, Figure 7. The domain is extended up to pressure transducer Pt2, see Figure 1. A structural mesh with 599500 hexahedral cells was performed on the 3D computational domain of volute.

3.2. The Mixing Interface Algorithm

The 3D computational domains investigated correspond to the suction elbow, the interblade channel and the pump's volute. In this paper, a mixing technique algorithm is used in order to couple the steady absolute flow field with the steady relative flow, Muntean et al [5]. This algorithm is applied between suction elbow and impeller as well as between impeller and volute. This algorithm removes the circumferential variation of velocity components, pressure and turbulence quantities using a piecewise polynomial least squares algorithm. For this particular case the mixing interface algorithm is presented in Figure 8.

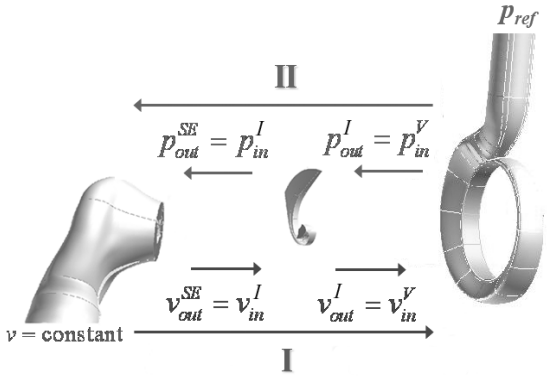

Figure 8. The mixing interface algorithm

Velocity field and turbulence quantities are computed on the inflow section for suction elbow, impeller and volute domains. The uniform velocity prescribed on the inlet section of the suction elbow corresponds to a certain discharge value. The 2% turbulence intensity and a 0.1 length scale are imposed on the suction elbow inlet section. A constant pressure is considered on the outlet section of suction elbow and on the outlet surface of the impeller's interblade channel as first guess in order to initialize the iterative process. Periodic conditions are imposed on the boundaries of the impeller. The wall condition is imposed for suction elbow walls, as well for the impeller hub, shroud and blade. Also, a constant pressure is imposed on the outlet suction of the volute. Water is considered as working fluid.

Firstly, the velocity profile and turbulent quantities on the suction elbow outlet section are imposed on the impeller inlet section using the mixing algorithm. Also, the velocity profile and turbulent quantities are passed from the impeller outlet section to the volute inlet section using mixing algorithm (Step I Figure 8).

Secondly, the static pressure profile on the inlet section of the volute is imposed on the impeller outlet section.

Finally, the mixed pressure profile on impeller inlet section is imposed on the outlet section of the suction-elbow outlet section (Step II Figure 8).

Iterative procedure is performed, until the solution remains unchanged from iteration to another. The 3D turbulent flow is computed using FLUENT code [6].

Figure 9 shows the mixed static pressure coefficient Eq. (13) distribution on the annular mixing interface between the suction elbow and the impeller after the iterative process converged at $1.2Q_n$. The loop (Step I and Step II) was performed six times (I1-I6) and it can be seen that the last three pressure profiles have the same radial distribution (I4, I5 and I6).

$$cp = \frac{p_S - p_{S\_in}}{\frac{1}{2}\rho U^2}, \text{ where } U = \omega R_{ref} \qquad (13)$$

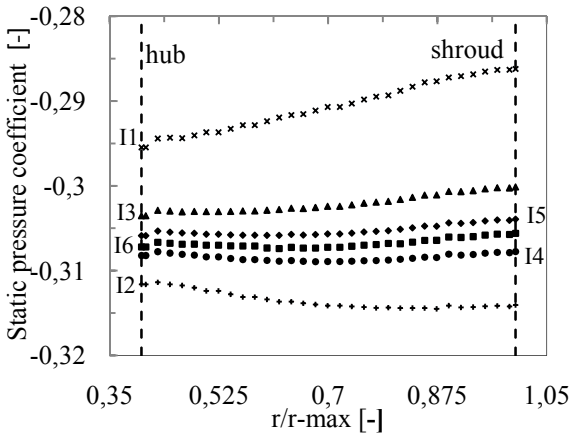

Figure 9. The static pressure coefficient distribution on the annular mixing interface between suction elbow and impeller

The distributions of points for each component of the velocity represent the numerical data obtained on the outlet annular section of the elbow (radial and axial components in Figure 10 and tangential component in Figure 12). A circumferential average distribution is obtained by applying the mixing algorithm for each velocity component. The average values are imposed as inflow condition on the impeller inlet. The points are displayed using rhombus, squares (Figure 10) and circles (Figure 12) respectively. That is equivalent to the full mixing of the wakes (or any other circumferential non uniformity).

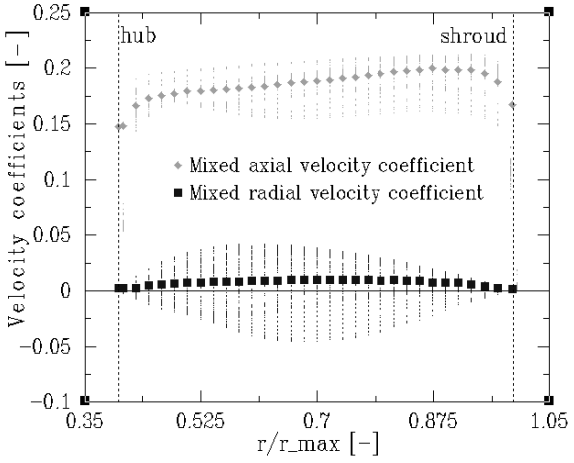

Figure 10. Velocity profile and average values obtained with the mixing interface algorithm – axial and radial velocity coefficients

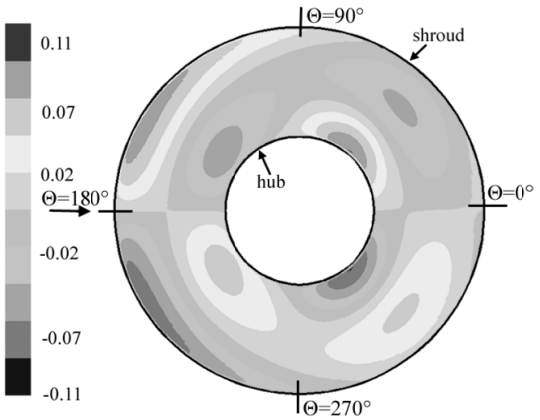

Figure 11. Tangential velocity coefficient map on the outlet section of the suction elbow

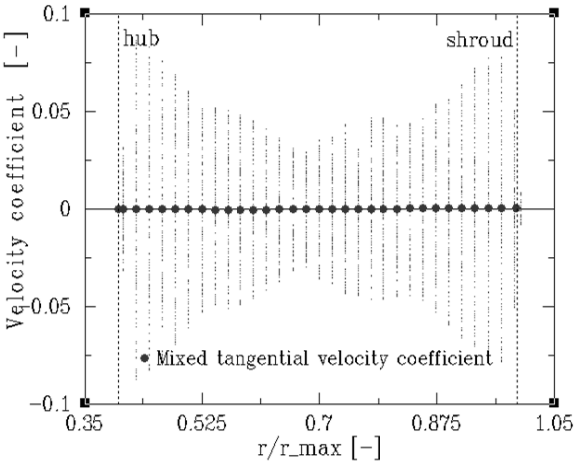

Figure 12. Velocity profile and average values obtained with the mixing interface algorithm – tangential velocity coefficient

The velocity component which presents the highest non uniformity is the tangential velocity one (Figure 12). Qualitatively, the tangential velocity map on the outlet section of the suction elbow is shown in Figure 11. In this towards-impeller view, the flow approaches the shaft at 180°. There are several flow vortices to be noted in Figure 11, due to the 3D suction elbow geometry. The vortices have the same values and opposite directions, and are represented with dark grey.

3.3. Numerical results

Numerical analysis was performed for five operating points: 0.8, 0.9, 1, 1.1 and 1.2 of nominal discharge Q_n. Table 4 presents the values of the numerically investigated points.

Table 4. Numerically investigated points

OP	1	2	3	4	5
Q	$0.8Q_n$	$0.9Q_n$	Q_n	$1.1Q_n$	$1.2Q_n$
Q 10^{-3} [m^3/s]	26.8	30.15	33.5	36.85	40.2
φ [-]	0.024	0.027	0.03	0.033	0.036

Total pressure drop on the suction elbow ($\Delta p_{T\text{-}SE}$) and volute ($\Delta p_{T\text{-}V}$) domains, total pressure rise on the impeller ($\Delta p_{T\text{-}I}$) domain and total pressure on the entire hydraulic passage ($\Delta p_{T\text{-}Num}$) Eq. (14) are presented in Table 5.

$$\Delta p_{T\text{-}Num} = \Delta p_{T\text{-}SE} + \Delta p_{T\text{-}I} + \Delta p_{T\text{-}V} \tag{14}$$

Table 5. Numerical results-total pressure

OP	$\Delta p_{T\text{-}SE}$ [kPa]	$\Delta p_{T\text{-}I}$ [kPa]	$\Delta p_{T\text{-}V}$ [kPa]	$\Delta p_{T\text{-}Num}$ [kPa]
1	-1.7	626.9	-57.3	567.9
2	-2.1	593.8	-47.3	544.4
3	-2.6	571.6	-40.9	528.0
4	-3.1	530.4	-30.2	497.1
5	-3.6	499.9	-31.7	464.6

4. EXPERIMENTAL DATA AGAINST NUMERICAL RESULTS

In order to assess the accuracy of the numerical method the results are compared against the experimental data.

Firstly, the total pressure obtained experimentally and numerically is compared in order to evaluate the errors, Table 6.

Table 6. Total pressure values: experimental data and numerical results

OP	1	2	3	4	5
$\Delta p_{T\text{-}Exp}$ [kPa]	483.6	462.1	440.6	413.8	381.5
$\Delta p_{T\text{-}Num}$ [kPa]	567.9	544.4	528	497.1	464.6
ε [%]	14.8	15.1	16.6	16.8	17.9

Secondly, the energy coefficients ψ versus flow coefficient φ is compared in the same manner

(Figure 13). It can be seen that the energy coefficient computed from numerical analysis has higher values than the one obtained from experimental measurements. The average difference (about 16%) is caused primarily by the mixing interface algorithm which computes a circumferential average of the velocity components on the two interfaces between the suction elbow and the impeller, and the impeller interblade channel and the volute, respectively.

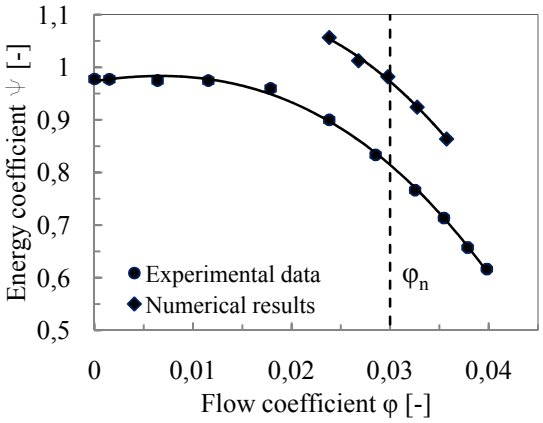

Figure 13. Energy coefficient ψ versus flow coefficient φ

The real flow structure on the outlet section of the suction elbow has a complex shape, presenting two counter rotating vortices behind the shaft, Van den Braembusche [7]. Naturally, the tangential velocity component has a circumferential asymmetric distribution. This provides a circumferential distribution of the relative flow angle β at the leading edge of the blade, which causes an unsteady loading, Ginga et al [8]. Any circumferential non uniformity of the velocity components are removed due to the mixing algorithm. As a result, the flow becomes steady and the flow angle β has a mean circumferential value. Accordingly, the associated hydraulic losses are diminished and the resulted total pressure $\Delta p_{T\text{-}Num}$ and energy coefficient are over estimated. This numerical algorithm is a compromise between the computation time and accuracy.

Next, the hydraulic efficiency η_H (numerically- $\eta_{H\text{-}Num}$ in Eq. (15) and experimentally- $\eta_{H\text{-}Exp}$ in eq. 16) curves versus flow coefficient φ are compared in Figure 14. Only the hydraulic efficiency $\eta_{H\text{-}Num}$ can be determined from numerical analysis. In experimental investigations, the volumetric and the mechanical efficiency (η_V and η_M) were estimated using statistical formulas (equations 18 and 19), Miloş [9].

$$\eta_{H-Num} = \frac{\rho g Q H}{P_M} \tag{15}$$

$$\eta_{H-Exp} = \frac{\eta_T}{\eta_M \cdot \eta_V} \tag{16}$$

where: $\eta_T = \eta_M \cdot \eta_V \cdot \eta_H$ is the total efficiency obtained experimentally; (17)

$$\eta_M = \frac{1}{1+\frac{820}{n_s^2}} = 0.94 \quad \text{mechanical efficiency;} \tag{18}$$

$$\eta_V = \frac{1}{1+\frac{0.68}{n_s^{2/3}}} = 0.97 \quad \text{volumetric efficiency.} \tag{19}$$

Figure 14 reveals that the highest value of the hydraulic efficiency is experimentally obtained at overload, $\varphi=0.036>\varphi_n$. The numerically hydraulic efficiency is about 5% higher compared to the experimental case. The difference occurs due to the overestimated total pressure in the numerical analysis and the underestimated hydraulic losses.

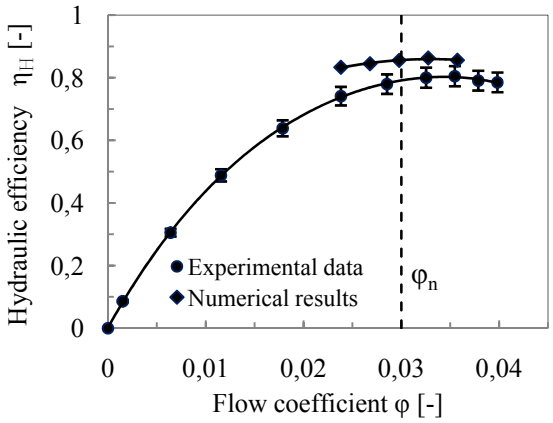

Figure 14. Hydraulic efficiency η_H versus flow coefficient φ

In equation 15, $P_M = M \cdot \omega$ is the impeller's mechanical power computed in the numerical analysis. Here, the total torque M is given by Eq. (20).

$$M = \left(\left(\int_S \left(\vec{r} \times \left(\bar{\bar{\tau}} \times \hat{n} \right) \right) dS \right) \times \hat{a} \right) \times Z_{Blade} \tag{20}$$

where: Z_{Blade}=5 – blades number;
S – the surface comprising all rotating parts;
$\bar{\bar{\tau}}$ – the total stress tensor (pressure and viscosity stresses);
$\hat{n}$ – the unit vector normal to the surface;
$\vec{r}$ – the position of the vector;
$\hat{a}$ – the unit vector parallel to the axis of rotation.

5. CONCLUSIONS

This paper presents experimental and numerical investigations for a scaled-down (1:5.7) hydraulic passage of a storage pump. The model passage consists of the suction elbow, one interblade channel of the impeller and the volute.

The total pressure $\Delta p_{T\text{-}Exp}$ is computed for the entire pump operating domain using the static pressure measured values. Consequently, the energy coefficient is plotted versus the flow coefficient.

Energetic and cavitational pump performances are determined through experiments. Energetically, the efficiency is plotted versus the flow coefficient. The maximum of hydraulic efficiency, $\eta_{H\text{-}Exp}$=0.81, is reached at higher discharge than the nominal one, φ=0.33. From cavitational point of view, the energy coefficient versus Thoma cavitation number is obtained for different discharge values. As expected, the cavitational risks increase when operating at overload.

The numerical flow analysis was performed for five operating point on the 3D hydraulic passage of the test rig. A mixing technique was employed to couple the steady absolute flow with the steady relative flow fields. The total pressure difference between the inlet and outlet sections $\Delta p_{T\text{-}Num}$ was computed versus the flow coefficient φ. All numerical results are greater than experimental data in entire operation domain due to the mixing interface algorithm. The numerically computed total pressure $\Delta p_{T\text{-}Num}$ is greater than the experimentally obtained total pressure $\Delta p_{T\text{-}Exp}$ with an average of about 16%. This discrepancy is the result of the circumferential average values of the velocity components on the two interfaces between the suction elbow and the impeller, and the impeller channel and the volute, respectively.

Also, the hydraulic efficiency $\eta_{H\text{-}Exp}$ was plotted versus the flow coefficient φ. The numerically computed hydraulic efficiency $\eta_{H\text{-}Num}$ is greater than the experimentally evaluated hydraulic efficiency $\eta_{H\text{-}Exp}$ with an average of about 5%. This difference occurs due to the overestimated total pressure in the numerical analysis and the underestimated hydraulic losses.

The mixing algorithm is a compromise between the computation time and the accuracy. However, more accurate algorithms (full unsteady flow) can be further employed for numerical analysis at the computation time expense.

ACKNOWLEDGEMENTS

This work was partially supported by the strategic grant POSDRU 2009 project ID 50783 of the Ministry of Labor, Family and Social Protection, Romania, co-financed by the European Social Fund – Investing in People. Dr. I.R. Stanciu was supported by the project "Development and support for multidisciplinary postdoctoral programs in major technical areas of national strategy for Research – Development – Innovation" 4D-POSTDOC, contract nr. POSDRU/89/1.5/S/52603, project co-funded by the European Social Fund through Sectorial Operational Program Human Resources Development 2007-2013. Dr. S. Muntean was supported by the Romanian Academy program.

REFERENCES

[1] Gopalakrishnan, S., 1999, "Pump research and developement: past, present, and future – an American perspective", *Journal of Fluids Engineering*, *Transactions of the ASME*, Vol. 121, pp. 237-247.

[2] Hergt, P.H., 1999, "Pump research and development: past, present and future", *Journal of Fluid Engineering, Transaction of the ASME*, Vol. 121, pp. 248-253.

[3] Sallaberger, M., Sebestyen, A., Mannschreck, E., Pinkas, W., 1999, "Modern pump impeller design with consideration of non-uniform inlet flow fields", *Proc. of the 28th IAHR Congress Hydraulic Engineering for Sustainable Water Resources Management*, Graz, Austria.

[4] Gambit 2. User's Guide, 2001, *Fluent Incorporated*, Lebanon, New Hampshire.

[5] Muntean, S., Resiga, R., Anton, I., 2004, "Mixing interface algorithm for 3D turbulent flow of the GAMM Francis turbine", *Modelling Fluid Flow - The State of the Art, Vad, J., Lajos, T., Schilling, R. (Eds),* Springer-Verlag, pp. 359-372.

[6] FLUENT 6. User's Guide, 2011, *Fluent Incorporated*, Lebanon, New Hampshire.

[7] Van den Braembussche, R.A., 2006, "Flow and loss mechanisms of centrifugal pumps", *Design and analysis of high speed pumps, Educational Notes RTO-EN-AVT*, Neuilly-sur-Seine, France, Paper 12, pp. 1-26.

[8] Ginga, G., Stuparu, A., Bosioc, A., Anton, L.E., Muntean, S., 2011, "3D Numerical simulation of the flow into the suction elbow and impeller of a storage pump", *Proc. of the 4th International Meeting on Cavitation and Dynamic Problems in Hydraulic Machinery and Systems,* Belgrade, Serbia, pp. 151-160.

[9] Miloş, T., 2009, "Pompe şi ventilatoare centrifuge şi axiale", Timişoara, Romania.

[10] Gülich, J.F., 2008, "Centrifugal Pumps, Springer", 1st edition, Berlin, Germany.

[11] International Electrotehnical Commission, 1999, *Hydraulic turbines, storage pumps and pumps-turbines-Model acceptance tests*, Second Edition, IEC 60193.

Conference on Modelling Fluid Flow (CMFF'12)
The 15th International Conference on Fluid Flow Technologies
Budapest, Hungary, September 4-7, 2012

INVERSE DESIGN AND 3D NUMERICAL ANALYSIS OF THE INDUCER FOR STORAGE PUMP IMPELLER

Irina G. MOISA[1], Gheorghita GINGA[1], Sebastian MUNTEAN[2], Romeo F. SUSAN-RESIGA[3]

[1] Corresponding Author. Department of Hydraulic Machinery, "Politehnica" University of Timisoara, Bv. Mihai Viteazu 1, 300222, Timisoara, ROMANIA, E-mail: irina.moisa@mh.mec.upt.ro, puiuginga@mh.mec.upt.ro
2 PhD Eng., Senior Researcher, Romanian Academy – Timisoara Branch, Center for Fundamental and Advanced Technical Research, Bv. Mihai Viteazu 24, 300223, Timisoara, ROMANIA, Phone/Fax: +40256403692, E-mail: seby@acad-tim.tm.edu.ro
[3] PhD Eng., Professor, Department of Hydraulic Machinery, Politehnica University of Timisoara, Bv. Mihai Viteazu 1, 300222, Timisoara, ROMANIA, Phone/Fax: +40256403692, E-mail: resiga@mh.mec.upt.ro

ABSTRACT

This paper presents the design and CFD (Computational Fluid Dynamic) analysis of an inducer for a storage pump model, in order to improve its suction performances. The storage pump has an elbow shaped inlet chamber which generates a non-uniform flow at the inlet section of the impeller, due to two secondary counter-rotating vortices [1]. This provides a non-uniform circumferential distribution of the angle of attack, consequently leading to a non-uniform blade loading, unsteady flow and cavitation phenomena.

By using the inducer, the objectives are: i) to raise the static pressure level in impeller inlet section; ii) to provide a more favorable, average angle of attack at the blade's leading edge; iii) to mitigate the flow's non-uniformities generated by the suction elbow.

A 3D inverse design method was used in this case. The inverse design method was developed by Zangeneh (1991) [2]. In [3], Ashihara & Goto (1999) used the inverse method for inducers design. In this paper, the design was realized for a model inducer at a scale of 1:5.7. The design's flow rate was increased by 20%, with respect to the pump's nominal flow rate.

A 3D numerical flow analysis of the designed inducer and impeller domains was performed using CFD. In order to reproduce the non-uniformity generated by the suction elbow, the tangential component of the velocity, 25% of the axial component of the velocity, was computed at the inducer's inlet section. K-omega SST turbulence model was used. The numerical analysis was performed for several values of the flow rate. These values were different percentages of the nominal flow rate of the model impeller.

The results of the numerical analysis show that the inducer's design objectives have been achieved.

Keywords: inducer, inverse design, storage pump.

NOMENCLATURE

P^+	*[Pa]*	upper blade surface pressure
P^-	*[Pa]*	lower blade surface pressure
N	*[-]*	number of blade
W_{mbl}	*[m/s]*	relative meridional blade surface velocity
$r\bar{v}_\theta$	*[-]*	kinetic momentum
S	*[m]*	meridional length
s	*[-]*	meridional length normalize
ρ	*[kg/m^3]*	water density
$\partial\left(R\bar{V}_\theta\right)/\partial S$	*[m/s]*	loading distribution along blade
θ	*[°]*	tangential coordinate of a cylindrical polar coordinate system
V_{ref}	*[m/s]*	reference velocity for impeller
U_{ref}	*[m/s]*	reference velocity for inducer
V_{ax}	*[m/s]*	axial velocity
R_{ref}	*[m]*	reference radius at the outlet inducer
r	*[-]*	dimensionless current radius
Ω	*[min^{-1}]*	rotational speed
P	*[Pa]*	static pressure
P_{in}	*[Pa]*	static pres. of inlet domain
R_{out_p}	*[m]*	outlet storage pump radius
β	*[°]*	relative flow angle

R_{in_p}	*[m]*	inlet storage pump radius
c	*[-]*	velocity coefficient

Subscripts and Superscripts

ref	reference value
mbl	meridional blade
LE	the value at leading edge
TE	the value at trailing edge
nom	nominal value
ax	axial component of the velocity
m	tangential component of the velocity
u	circumferential direction
out_p	outlet storage pump
in_p	inlet storage pump
+	upper side
-	lower side
$\bar{}$	medium value

1. INTRODUCTION

The presence of the cavitations phenomena in hydraulic installations has negative effects on the impeller's performance. If operating in cavitating conditions, blade cracks and ruptures can occur. In order to find the appropriate solutions to improve the suction behavior of the storage pump impeller and to enlarge the period of the operation it is necessary to first evaluate the suction performances of the impeller.

This paper studies a centrifugal pump with double flux. The pump is equipped with a suction elbow which generates a severe non-uniformity in the flow at the impellers inlet [1]. Moreover, the presence of the shaft in the suction elbow is also a source of the flow's non-uniformity. The non-uniform flow generated by the suction elbow is described by Van den Braembussche [4] and it manifests circumferential, leading to a significant variation of the incident angle. This variation causes areas of stagnation, with low pressure, on the suction side of the impeller's blades, in the vicinity of the leading edge [5]. The result is an over development of the cavitations phenomena with the mentioned consequences, Figure 1.

Considering the above mentioned observations, the need to level the non-uniformity of the flow and to increase the static pressure at the impeller inlet is emerging. The proposed solution is to use an inducer. The use of an inducer upstream the main impeller of a storage pump is a new approach, compared to already existing technologies, where the uniform of the flow was done by using an inlet cavity with deflection vanes (or an inlet volute) [4]. In [6], it is numerically and experimentally proven that a uniform flow upstream of the impeller inlet is important for an improved cavitations performance.

The designed inducer objectives are: i) to raise the pressure level at the pump's impeller inlet; ii) to provide a more favorable average angle of attack at the blades' leading edge; iii) to minimize the flow's non-uniformities generated by the suction elbow.

The inducer is designed using the 3D inverse design method. This inverse design method was proposed for the first time by Hawthorne et al.[7] which developed a 2D theory. The extension of the latter method, for incompressible radial-inflow turbines was realized by Borges [8] and for compressible mixed and radial flow turbomachines by Zangeneh [9].

The rotational speed of the inducer and the storage pump impeller model are the same. According to Japiske [10], the inducers are generally designed with one up to four blades. In this work, three blades were considered.

The design by Ashihara & Goto [3] has L/D=0.75, same as the inducer design by Kang et al [11] while the inducer analyzed by Bakir et al [12] has L/D=1. Particularly in this case the main constraint of the inducer's design is the small ratio between length and diameter, L/D=0.5. Also according to Japikse [10], to design stable inducers, attention must be given to several guidelines.

The numerical analysis was performed using Fluent, commercially available software in order to evaluate the cavitations behavior of the designed inducer and model impeller.

Because the inverse design method presumes a quasi 3D flow, with radial equilibrium, the first step is to perform an inviscid numerical analysis considering the interaction between the fluid layers. The results were compared with those obtained with the design software. In order to identify the zones with low pressure, where cavitations phenomena may occur, a 3D numerical simulation of the viscous flow using shear-stress transport (SST) k-ω turbulence model was performed. Three operating points were investigated: $0.8*Q_{nom}$ – part load, Q_{nom} - nominal flow rate, $1.2*Q_{nom}$ - overload.

Figure 1. Cavitation phenomena on the blade pump

2. THE 3D INVERSE DESIGN METHOD FOR INDUCER

2.1. Inverse design method

The 3D inverse design method computes the blade geometry for a specified distribution of the blade's load. The method uses a one-dimensional estimate of the meridional velocity, which was obtained from the specified mass flow rate, and the meridional geometry. These two, together with the specified mean tangential velocity, were used in order to compute an initial blade shape

[**13**]. In this case, the blade shape was computed using the inviscid slip condition. The flow must be aligned with the blade surfaces.

In the quasi-3D inverse design method, the blades are represented by sheets of vortices whose strength is determined by a specified distribution of circumferentially averaged swirl velocity ($R\bar{V}_\theta$) [**14**]. In this case $R\bar{V}_\theta$ is defined in Eq. (1):

$$R\bar{V}_\theta = \frac{N}{2\pi}\int_0^{2\pi/N} RV_\theta d\theta \qquad (1)$$

The blade load is in a direct relationship with the pressure distribution. For incompressible flow, the pressure loading on the blade is related with the meridional derivative of the kinetic momentum (or blade loading), Eq. (2):

$$P^+ - P^- = \frac{2\pi}{N}\rho \cdot W_{mbl}\frac{\partial\left(R\bar{V}_\theta\right)}{\partial S} \qquad (2)$$

In this method, the flow field is decomposed into tangentially mean and periodic components.

2.2. Impeller design

The inputs of this method are: 1) meridional geometry; 2) rotational speed; 3) blades thickness; 4) blockage factor; 5) number of blades; 6) flow rate; 7) inlet velocity; 8) blade loading; 9) stacking condition. The most important are meridional geometry and loading distribution on the blades. The impeller was designed using conventional techniques involving the use of curve fits to connect the blades' angles smoothly between the leading and trailing edges.

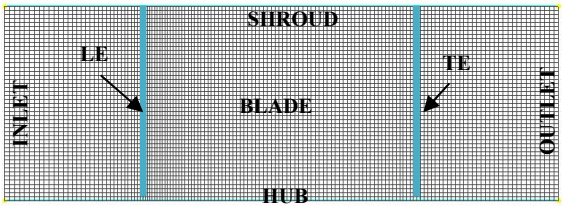

Figure 2. Inducers meridional geometry

In the meridional plane, the inducer has a simple axis-symmetric geometry. The computational mesh that was used is represented in Figure 2, the grid consists of 7105 cells.

The blade loading distribution depends on the three parameters presented in Table 1.

Table 1. Loading parameters

	s_{LE}	s_{TE}	slope
hub	0.14	0.14	0.0
shroud	0.215	0.523	0.0

Figure 3 shows the streamline loading distribution, from the hub to shroud. At the trailing edge, the blade loading distribution must be zero in order to satisfy the Kutta conditions.

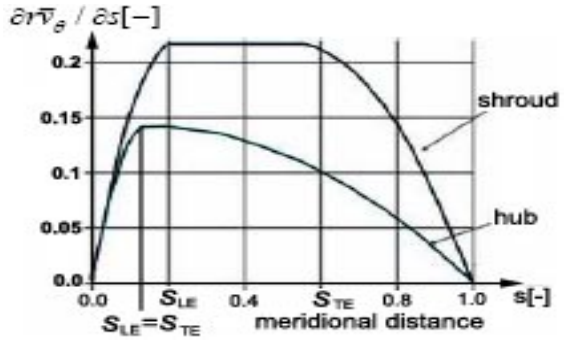

Figure 3. Streamwise blade loading distribution $\partial\left(r^*\bar{v}_\theta\right)/\partial s$ along meridional distance

From hub to shroud, the blade loading distribution was obtained by a linear interpolation between dimensionless loading values. In this case, for the leading edge (LE), a linear loading was chosen and for the trailing edge (TE) a parabolic loading one (

Figure **4**). $R\bar{V}_\theta$ values for leading and trailing edges were obtained using Euler's equation. The dimensionless value of $R\bar{V}_\theta$ is calculated using Eq. (3).

$$r\bar{v}_\theta = \frac{R\bar{V}_\theta}{R_{ref}\cdot U_{ref}} \qquad (3)$$

where: $R_{ref} = 104.5mm$ represents inducers reference radius;

$U_{ref} = \Omega \cdot R_{ref}$ represents the inducers reference velocity.

Axial flow is considered when designing the inducer and the loading at leading edge has a dimensionless value of $r\bar{v}_\theta = 0$. At trailing edge the loading was set to a value of 0.092 for hub, 0.136 at middle and 0.162 for tip.

Figure **4** present the dimensionless $r\overline{v}_\theta$ along blades normalized span-wise position.

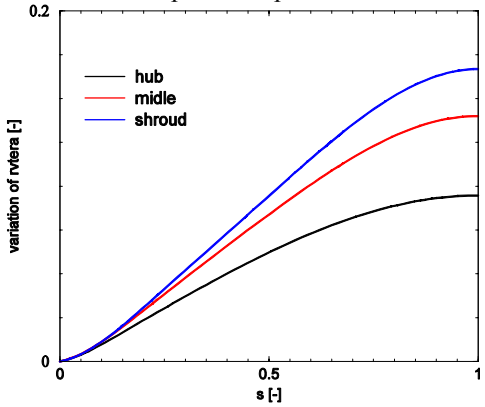

Figure 4. r^*v_θ **distribution on the blade along meridional distance**

The specifications for the inducer's design are presented in Table 2.

Table 2. Inducer design specification

Rotating speed	[rpm]	2900
Design flow rate	[m^3/s]	0.0402
Hub diameter	[m]	0.040
Tip diameter	[m]	0.103
Length inducer	[m]	0.100
Blade number	[-]	3
Thickness blades	[mm]	3

The 3D geometry of the inducer obtained with inverse design method is presented in Figure 5.

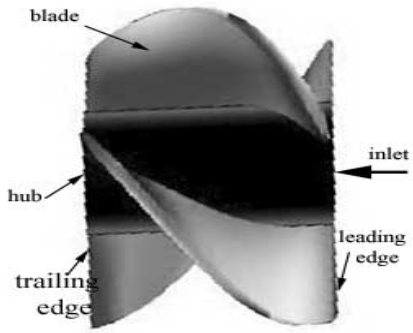

Figure 5. 3D inducers geometry

3. NUMERICAL ANALYSIS

3.1. Equations

The CFD software that was used for the flow's 3D analysis uses a series of equations such as: 1) equations which solve the primary quantities that govern the flow (the velocity and the pressure); 2) equations for the viscosity model.

The flow equations are composed of motion and continuity equations that solve the primary quantities.

The continuity equation for incompressible flow is:

$$\nabla \cdot \overline{v} = 0 \tag{4}$$

The equation of motion that describes the flow and solves its primary component, the velocity, is described by Eq. (5), where $\rho \cdot \vec{g}$ represents the gravitational body force:

$$\frac{\partial}{\partial t}(\rho\vec{v}) + \nabla \cdot (\rho\vec{v}\vec{v}) = -\nabla \cdot p + \nabla \cdot \overline{\overline{T}} + \rho \cdot \vec{g} \tag{5}$$

where $\overline{\overline{T}}$ is the stress tensor defined by Eq. (5):

$$\overline{\overline{T}} = \mu\left[\left(\nabla\vec{v} + (\nabla\vec{v})^T\right) - \frac{2}{3}(\nabla \cdot \vec{v})\overline{\overline{I}}\right] \tag{6}$$

where $\overline{\overline{I}}$ is the unit tensor and μ represents the molecular viscosity.

To close this system of equations, composed by continuity and Navier-Stokes equations, closed equation for k-ω SST model were used. The closed equations are given by Eq. (7) and Eq. (8):

$$\frac{\partial}{\partial t}(\rho k) + \frac{\partial}{\partial x_i}(\rho k u_i) = \frac{\partial}{\partial x_j}\left(\Gamma_k \frac{\partial k}{\partial x_j}\right) + G_k - Y_k \tag{7}$$

and

$$\frac{\partial}{\partial t}(\rho\omega) + \frac{\partial}{\partial x_i}(\rho\omega u_i) = \frac{\partial}{\partial x_j}\left(\Gamma_k \frac{\partial \omega}{\partial x_j}\right) + G_\omega - Y_\omega + D_\omega \tag{8}$$

where: - G_k represents the generation of turbulence kinetic energy due to mean velocity gradients;

- G_ω represents the generation of ω;

- Γ_k and Γ_ω represent the effective diffusivity of k and ω;

- Y_k and Y_ω represent the dissipation of k and ω due to turbulence;

- D_ω represents the cross-diffusion term.

3.2. Analysis domain

The quasi-3D (Q-3D) inverse design method assumes potential flow. In this case, the radial variation of the velocity is not taken into consideration Zangeneh [2]. So that the numerical analysis emulates the real phenomenon, it is necessary to analyze the impeller geometry for a viscous flow. When working with a viscous flow, the friction between the layers is taken into account. The viscous property of the real flow provides more accurate conclusions could be evaluated by applying Computation Fluid Dynamic (CFD). For the present study, FLUENT, a commercially available software, was used for solves the full three-dimensional

Navier-Stokes equations in turbomachinery evoked to predict the viscous effects.

The inducer 3D domain is meshed with 510 000 cells while the impeller domain with 560 000 cells.

Assuming periodicity, the flow was computed through one interblade channel of each domain. The Navier-Stocks equations and k-ω turbulence model were used.

Stuparu [5] discovered that the tangential velocity at the inlet section of the impeller is aprox. 25% less than the axial velocity.

In this paper, three cases were investigated, regarding the inlet boundary condition of the inducer:

1) a constant value of the axial velocity;

2) a velocity profile, composed by axial velocity component and negative tangential velocity component $V_u = -0.25V_{ax}$;

3) a velocity profile, composed by axial velocity component and positive tangential velocity component $V_u = +0.25V_{ax}$.

On impeller's inlet section, the velocity profile obtained on the outlet section of the inducer was set as a boundary condition. Radial equilibrium conditions were specified at the outlet for both domains. Inducer's hub and blade surfaces, impeller's hub, shroud and blade surfaces were set like moving walls with a rotational speed of 2900 *rpm*. The inducer's casing is a stationary wall.

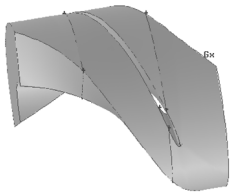

Figure 6. The 3D computational inducer domain

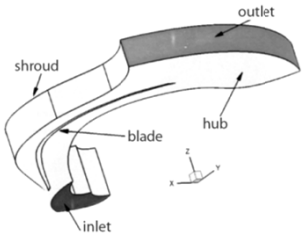

Figure7. 3D computational pump domain

4. RESULTS

Moisa et al in

[**13**] presents the pressure coefficient along two sections of the inducer's meridional blade length (near the hub and near the casing) for three operating points: $0.8*Q_{nom}$, $1.2*Q_{nom}$ and $1.35*Q_{nom}$.

The current paper presents the results of a numerical analysis for the pressure variation along the inducer's and impeller's blades in three points: $0.8*Q_{nom}$, Q_{nom} and $1.2*Q_{nom}$. The pressure coefficient distribution along the inducer's and impeller's blades meridional length are plotted for three sections between the hub and tip of the inducer and between the hub and shroud in the case of the impeller (R = 10% near the hub, R = 50% at the middle and R = 90% near inducers tip/impellers shroud).

$$c_p = \frac{P - P_{in}}{\rho \cdot \frac{\left(V_{ref}\right)^2}{2}} \qquad (9)$$

where: $V_{ref} = \Omega \cdot R_{out\_p}$ represents the impeller's reference velocity and $R_{out\_p} = 104.5mm$ represents the impeller's outlet radius.

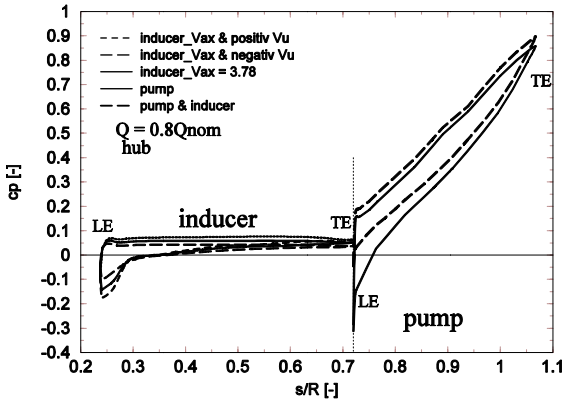

Figure 8. Pressure coefficient variation for Q = 0.8*Qnom, at radius R = 10%

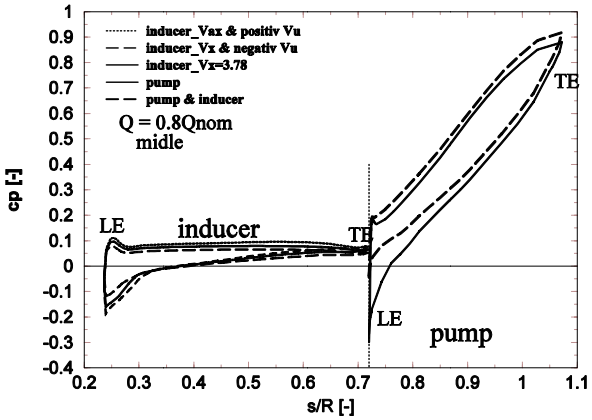

Figure 9. Variation of pressure coefficient for flow rate Q = 0.8*Qnom, at radius R = 35*mm*

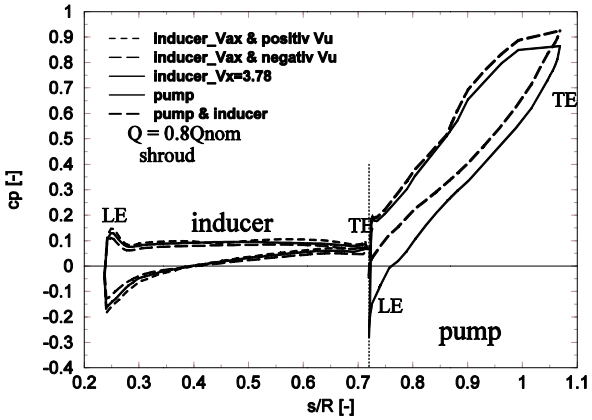

Figure 10. Variation of pressure coefficient for flow rate Q = 0.8*Qnom, at radius R = 45*mm*

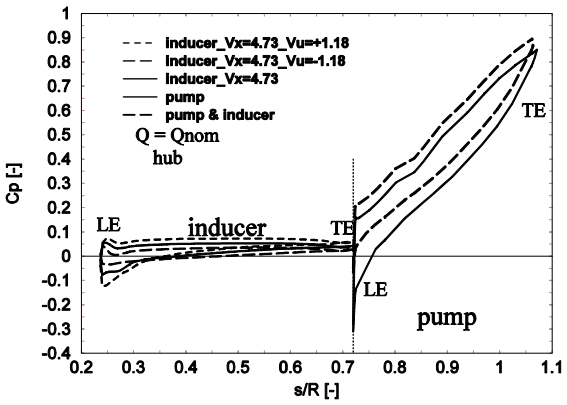

Figure 11. Variation of pressure coefficient for flow rate Q = Qnom, at radius R = 25*mm*

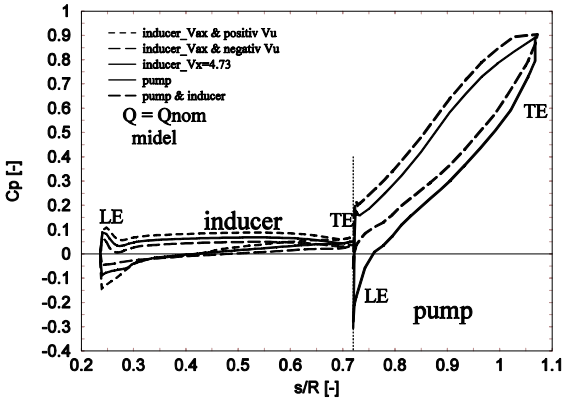

Figure 12. Variation of pressure coefficient for flow rate Q = Qnom, at radius R = 35*mm*

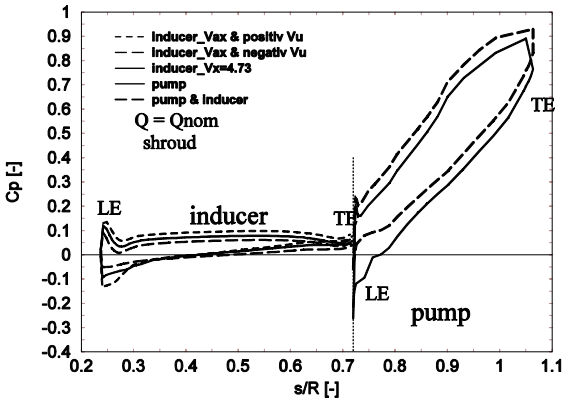

Figure 13. Variation of pressure coefficient for flow rate Q = Qnom, at radius R = 45*mm*

In Figure 8 – 10 a variation of the pressure coefficient along the inducer and impeller blades for $Q = 0.8*Q_{nom}$ along three streamlines can be observed. Here, when operating with positive tangential velocity at inducer inlet, the pressure coefficient (dotted line for inducer) is the lowest one for all operating points.

When operating with an inducer upstream the main impeller (dashed line for pump), it can be seen that the pressure coefficient values are higher than when operating without an inducer. The pressure coefficient drops to -0.32 when operating without inducer, while when operating with an inducer it increases to -0.05. The lowest value of the pressure coefficient is located on the impeller's blade near the hub, as well.

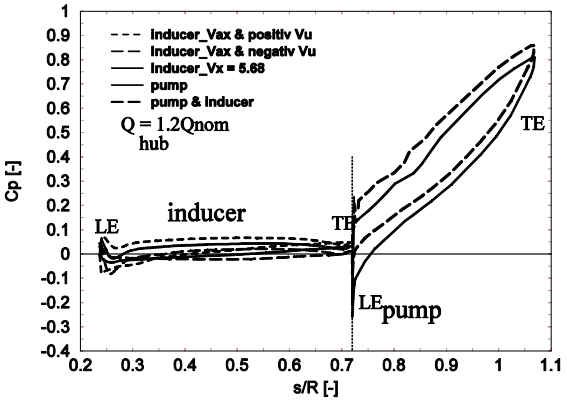

Figure 14. Variation of pressure coefficient for flow rate Q = 1.2*Qnom, at radius R = 25*mm*

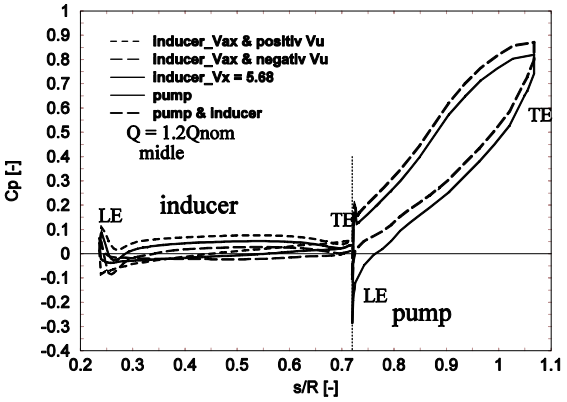

Figure 15. Variation of pressure coefficient for flow rate Q = 1.2*Q_{nom}, at radius R = 35*mm*

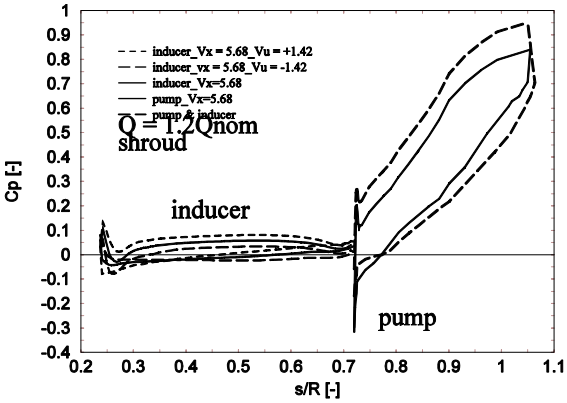

Figure 16. Variation of pressure coefficient for flow rate Q = 1.2*Q_{nom}, at radius R = 45*mm*

In Figure 11 -Figure **13** it can be observed that when operating at Q_{nom}, the pressure coefficient has low values on the leading edge of the inducer's blade. When operating with a velocity profile composed out of the axial velocity and positive tangential velocity, the values for c_p are the lower

compared to the case when the tangential velocity is negative. The inducer increases the pressure coefficient at the inlet of the impeller from -0.26 to -0.06 (near the tip) and from -0.32 to -0.07 (near the hub). The inducer increases the values of the pressure coefficient with approximately 80%. Overall when operating at Q_{nom} the pressure coefficient distribution on the inducer's and impeller's blades have the same shape as when operating at 0.8*Q_{nom}.

Increasing the flow rate at 1.2*Q_{nom} the incidence point at the inducer's blades leading edge creates a low pressure area on the pressure side, near the leading edge; see Figure 14 – 16. In this case one can observe a better incidence on the impeller's blades near the hub and in the middle. One can notice also an increase of the pressure coefficient value with 60% near the hub and with 50% near the shroud when operating with an inducer.

Ginga et al [1] investigated the non-uniform flow generated by the suction elbow, at the exit of the elbow. Stuparu [5] showed that the impeller presents highly unstationary character when operating at overload.

In this paper the authors demonstrate that the worst cavitational behavior of this model impeller is when operating at overload, at 1.2*Q_{nom}. Taking into account the variation of the relative flow angle on the impeller's inlet section and its significance for the non-uniformity that it causes, two situations can be distinguished. In the first case of the impeller without the inducer, the tangential velocity profile was observed to display non-uniformity (Figure 17). In the second case, when the inducer is located upstream the main impeller, a uniform flow field can be observed at the inlet of the impeller (Figure 18).

The relative velocity flow angle β is:

$$\beta = 90 - \arctan\left(\frac{c_t - c_m}{c_{ax}}\right) \qquad (10)$$

Where:

$c_t = \frac{\Omega R_{out\_p}}{\sqrt{2gH}}$ - reference velocity coefficient

$c_m = \frac{V_m}{\sqrt{2gH}}$ - tangential velocity coefficient

$c_{ax} = \frac{V_{ax}}{\sqrt{2gH}}$ - axial velocity coefficient

and H is pump head and for Q = 1.2*Qnom , H = 63.5 [m].

From Figure 17, it is noticeable that when operating without the inducer, the circumferential distribution of relative velocity flow angle is very non-uniform, it varies between -285° to 90°.

Figure 18 shows that when operating with the inducer upstream the main impeller, the circumferential distribution of relative velocity flow angle is quite uniform. One can observe two main areas where the relative velocity flow angle has constant values of 23° (from hub to middle) and 64° (from middle to tip). This shows that the inducer provides a quite uniform flow field upstream the main impeller. Consequently the energetic and most important, suction behavior of the impeller are to be improved.

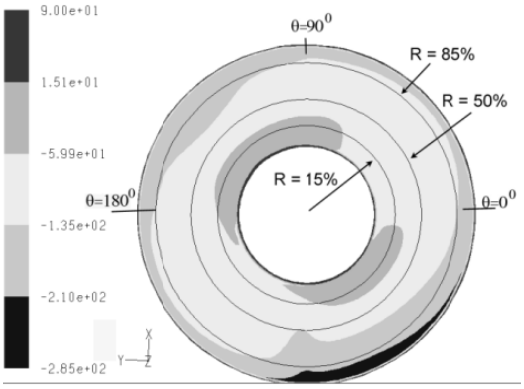

Figure 17. Distribution of relative velocity angle at the pump inlet without inducer, at Q = 1.2*Q_{nom}

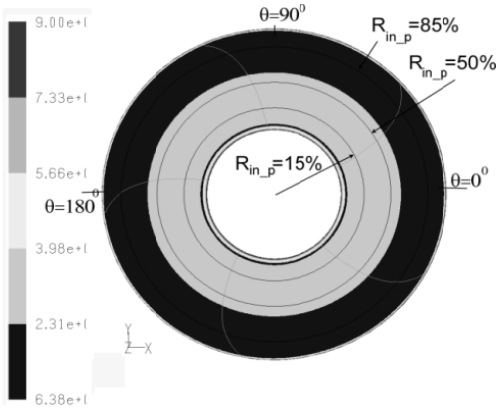

Figure 18. Distribution of relative velocity angle at the pump inlet with inducer, at Q = 1.2*Qnom

5. CONCLUSIONS

In this case the storage pump has an elbow shaped suction chamber that generates a non-uniform flow at the inlet section of the impeller. Consequently the energetic and cavitational performances of the impeller are diminished.

In order to improve the cavitational performances of the storage pump impeller model, an inducer was designed using the 3D inverse method.

The influence of the impeller upstream the main impeller was evaluated using 3D steady numerical analysis for three operating points.

One can observe that when operating with inducer, it manages to raise the static pressure at the inlet section of the main impeller. When operating at overload, where $1.2*Q_{nom}$, the static pressure is raised with aprox. 50%. At nominal flow rate and at partial load, at Q_{nom} and $0.8*Q_{nom}$, the inducer raises the static pressure with aprox. 80%.

Also, the inducer manages to improve the circumferential distribution of the relative flow angle at the inlet section of the impeller. Consequently, raising the static pressure and diminishing the non-uniformities generated by the suction elbow, the inducer is improving the hydrodynamic field; therefore the main impeller cavitational performances are to be improved.

ACKNOWLEDGEMENTS

This work was partially supported by the strategic grant POSDRU 2009 project ID 50783 of the Ministry of Labor, Family and Social Protection, Romania, co-financed by the European Social Fund – Investing in People.

Dr. Sebastian Muntean was supported by the Romanian Academy program "Hydrodynamics Optimization and Flow Control of the Hydraulic Turbomachinery in order to improve the Energetic and Cavitational Performances".

REFERENCES

[1] Ginga, G., Stuparu, A., Bosioc, A., Anton, L.E., Muntean, S., 2011, "3D Numerical simulation of the flow into the suction elbow and impeller of a storage pump", *Proc. of the 4th International Meeting on Cavitation and Dynamic Problems in Hydraulic Machinery and Systems*, pp.151-160, Belgrade, Serbia.

[2] Zangeneh, M., 1991, "A compressible three-dimensional design method for radial and mixed flow turbomachinery blades", *International Journal of Numerical Methods in Fluids*, Vol.13, pp. 599-624.

[3] Ashihara, K., and Goto, A., 1999, "Improvements of pump suction performance using 3D inverse design method", *Proc. of the 3rd ASME/JSME Joint Fluids Engineering Conference*, San Francisco, California.

[4] Van den Braembussche, R.A., 2006, "Flow and Loss Mechanisms in Volutes of Centrifugal Pumps", North Atlantic Trealy Organization, pp. 12-1 – 12-28, Belgium.

[5] Stuparu, A., 2009, "Modelarea numerica si experimentala a curgerii in pompele centrifuge", pp. 119-136, ed. "Politehnica", Timisoara, Romania.

[6] Luo, X., Zhang, Y., Peng, J., Xu, H. & Yu, W., 2008, "Impeller inlet geometry effect on performance improvement for centrifugal pumps", *J. of Mechanical Science and Technology*, No. 22.

[7] Hawthorne, W.R., Tan, C.S., Wang, C., and McCune, J.E., 1984, "Theory of Blade Design for Large Deflections: Part I – Two Dimensional Cascades", ASME *J. of Engineering for Gas Turbines and Power*, Vol. 106, pp. 346-353.

[8] Borges, J.E., 1990, „A Three-Dimensional Inverse Design Method in Turbomachinery: Part1 – Theory", *ASME Journal of Tourbomachinery*, Vol. 112, pp.346-354.

[9] Zangeneh, M., Goto, A. and Takemura, T., 1996, "Suppression of Secondary Flows in a Mixed-Flow Pump Impeller by Application of Three-Dimensional Inverse Design Method: Part1-Design and Numerical Validation", *J. of Turbomachinery*, Vol.118, pp. 536-43.

[10] Japikse D., 2002, "Overview of commercial pump inducer design", *The 9th International symposium on Transport Phenomena and Dynamics of Rotating Machinery*, Honolulu, Hawaii.

[11] Kang, D., Watanabe, T., Yonezawa, K., Horiguchi, H., Kawata, Y., and Tsujimoto, Y., 2009, "Inducer design to Avoid Cavitational Instabilities", *J. of Fluid Machinery and Systems*, Vol.2, No. 4.

[12] Bakir, F., Rey, R., Gerber, A.G., Belamri, T., and Hutchinson, B., 2004, "Numerical and experimental investigations of the cavitating behavior of an inducer", *International Journal of Rotating Machinery*.

[13] Moisa, I. G., Stuparu, A., Resiga-Susan, R., and Muntean, S., 2011, "Inverse design of a pump inducer and performance evaluation with 3d flow simulation", *Proc. of the 4th International Meeting on Cavitational and Systems*, pp. 171-177, Belgrade, Serbia.

[14] Zangeneh, M., Goto, A. and Harada, H., 1999, "On the role of three-dimensional inverse design methods in turbomachinery shape optimization", *Proc. of Mechanical Engineers,* Vol.213, Part C, pp. 27-42.

[15] Fluent Inc., 2005, *GAMBIT 2.2.30 User's Guide*, Fluent Incorporated, Lebanon, New Hampshire.

[16] Fluent Inc., (2001). *FLUENT 6.3 User's Guide*, Fluent Incorporated, Lebanon.

Conference on Modelling Fluid Flow (CMFF'12)
The 15th International Conference on Fluid Flow Technologies
Budapest, Hungary, September 4-7, 2012

EXPERIMENTAL STUDY OF PROPELLER-RUDDER INTERACTION USING PARTICLE IMAGE VELOCIMETRY

Tommi MIKKOLA[1], Keijo HANHIROVA[2], Raimo HÄMÄLÄINEN[3]

[1] Corresponding Author. Department of Applied Mechanics, School of Engineering, Aalto University. P.O.Box 15300, FI-00076 AALTO, Finland. Tel.: +358 9 4702 4170, Fax: +358 9 4702 3493, E-mail: tommi.mikkola@aalto.fi
[2] Department of Applied Mechanics, School of Engineering, Aalto University. E-mail: keijo.hanhirova@aalto.fi
[3] STX Finland, Turku, Finland. E-mail: raimo.hamalainen@stxeurope.com

ABSTRACT

The presented research focuses on the hydrodynamics of the propeller-rudder interaction. The paper presents the results of stereoscopic Particle Image Velocimetry (PIV) model test experiments for a twin screw ship with and without a rudder. The influence of the propeller-rudder interaction on the flow field has been studied by measuring the flow field aft of the propeller at several planes. The purpose of the measurements was to study the flow field induced by rotating propeller, to reveal interaction effects between the propeller and the rudder located in the propeller slipstream and to study the capabilities and limitations of such PIV-measurements. The measurements have been performed with the ship model and the measurement system fixed to a moving carriage. In the paper the measurement setup will be described. Time-averaged and phase-averaged results of the flow field (six blade positions) will be presented. The relevant differences in the flow field with and without the rudder are discussed and the main interaction effects are identified. It is observed that the rudder has a significant upstream influence and affects the operation of the propeller. The results are also discussed from the point of view of practical ship design.

Keywords: propeller-rudder interaction, stereoscopic PIV

NOMENCLATURE

D	[mm]	propeller diameter
J	[-]	advance number $J=V/(nD)$
V	[m/s]	model velocity
d	[mm]	propeller hub diameter
$\underline{u}$	[m/s]	flow velocity
x, y, z	[mm]	coordinate components
λ	[-]	model scale

Subscripts and Superscripts

x, t	axial, tangential vector components

1. INTRODUCTION

The ship designers and builders are facing new challenges with increasing requirements for the performance of ships. One example of this is the growing attention on passenger comfort particularly with cruise ferries and ships. The comfort in this context is related to the noise and vibration levels on board. Ship propeller is a major source of noise and vibration. A rudder is usually set in the propeller wash to maximise manoeuvring capabilities and efficiencies. Propeller-rudder interaction (PRI) has often been considered from the point of view of propulsive efficiency, but it has also influence on the comfort characteristics of the ship. It is therefore believed that improved understanding on the flow phenomena facilitate the design of ships with superior comfort characteristics.

Due to the practical importance of PRI effects they have been studied extensively in the past (see [1] and the references therein). A large part of the studies has focused on the global quantities such as the influence of PRI on the thrust, torque and components of propulsive efficiency. The advances in measurement techniques in the recent years have enabled more detailed studies on the flow phenomena associated with propulsion interaction effects. Various techniques and configurations have been used in the studies. [2] The evolution of the vortical structures and the wake of a propeller have been studied with propellers in open-water [3, 4]. The interaction of the vortical structures with the rudder and the influence of the rudder on mean flow direction have been studied mainly with propeller-rudder configurations without a hull [5, 6], whereas the influence of the hull on the propeller inflow has been studied with simulated wake [7] or with hull-propeller combinations without a rudder [8]. Studies

for fully appended configurations [9, 10] are limited.

The purpose of the presented research was to study the flow field induced by a rotating propeller for an actual design case and to reveal PRI effects using a towed stereo PIV system. Previous studies have focused on isolated propeller, propeller-rudder and propeller-hull configurations or single-screw ships, whereas here the studied case is a fully appended twin screw ship with an open shaft line arrangement. Furthermore, most of the published PRI studies have been performed in circulating water channels. Thus one aim of the work was to study the capabilities and limitations of the towed measurement system for the investigation of PRI effects. The study was also part of a larger campaign, where it was supporting cavitation and full scale observations.

The paper is organised as follows. First the main characteristics of the test case, the measurement setup and the system are described. After this results without and with the rudder are presented and compared. The paper concludes with a discussion and summary of the results.

2. EXPERIMENTAL SETUP

2.1. Description of the Test Case

The model tests were performed in a 130 *m* long, 11 *m* wide and 5.5 *m* deep towing tank at Aalto University. The test case is a twin screw cruise ferry built by STX Finland/Turku. The stern arrangement of the ship is shown in Figure 1.

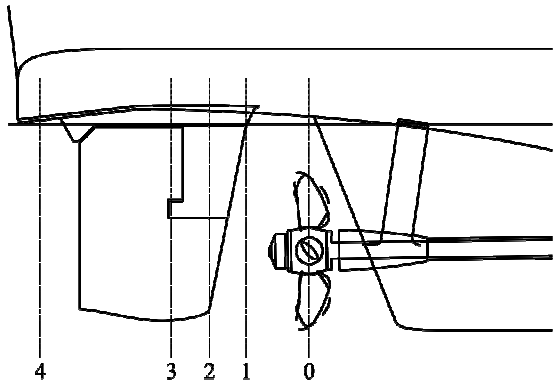

Figure 1. The stern arrangement of the test case, the propeller plane (0) and the measurement planes (1-4)

The ship has an open shaft line arrangement and a centre line skeg. The propellers are inwards rotating, four bladed, controllable pitch propellers (CPP). There is a horn type rudder behind each propeller. The rudders and the head-boxes are set toe-in relative to the centre line. The leading edge of the rudder is twisted over a short distance around the junction of the horn and the rudder blade, in order to reduce the loading and the cavitation risk of the rudder. The main particulars of the test case are given in Table 1.

Table 1. The main particulars of the test case.

		Model		Ship	
Model scale	λ	22.713	-	-	-
Velocity	*V*	2.447	*m/s*	22.7	*kn*
Prop. diam.	*D*	229	*mm*	5.20	*m*
Hub. diam.	*d*	63	*mm*	1.44	*m*
Rot. rate	*n*	10.803	*1/s*	136	*rpm*
Adv. num.	*J*	0.989	-	0.989	-

The flow field on the port side (left when viewed from aft) was measured at four cross sections behind the propeller plane with and without the rudder (see Fig. 1). The non-dimensional distances of the cross sections from the propeller plane are given in Table 2.

Table 2. The distance of the measurement cross sections from the propeller plane

No.	*x/D*
1	0.384
2	0.624
3	0.856
4	1.686

The measurements were synchronised to the propeller blade angle. For each cross section measurements were performed for six blade angles, i.e. 0, 15, 30, 45, 60 and 75 degrees. The 0 angle was defined as an angle, where the root of the blade at the 12 o'clock position was horizontal.

2.2. Underwater Stereoscopic PIV System

The measurement system consists of several components. The main components are a Nd:YAG double pulse laser, optics for generating a sheet from a unidirectional laser beam, two double frame Imagerpro 4M cameras (2048 x 2048 pixels), two camera control units, a framegrabber, a programmable timing unit (PTU) and a control computer. The setup is shown in Figure 2.

The cameras and the sheet optics are located in an underwater housing (see Fig. 2) supported to the towing carriage with three stainless steel tubes and aluminium profiles. The tubes are equipped with streamlined profiles to prevent vibrations related to vortex shedding. The profiles are not fixed to the tubes, but are free to rotate around them following the mean local flow field.

The cameras are located in the leading and the trailing sections of the housing. The laser is located above the underwater housing and the laser beam is directed into the sheet optics down the middle tube. The laser sheet is then directed to the measurement

area through an opening on the side of the middle section of the housing. The timing of the image acquisition and the laser pulses is controlled by the PTU located in the measurement computer.

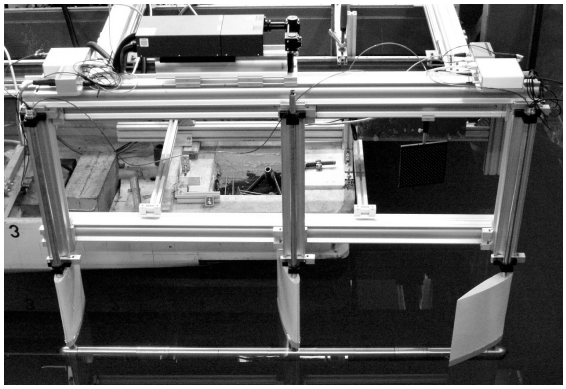

Figure 2. The underwater PIV system in the towing carriage

The system was equipped with two 50 *mm* f/1.4 Canon fixed focal length lenses connected to a remote focus ring inside the camera section. The cameras face towards the centre of the housing and have a view of the measurement plane through water filled sections with mirrors and plane windows. The useable measurement area is increased by using Scheimpflug correction, i.e. the cameras are rotated around the vertical axis of the image plane so that the extensions of the image plane, the lens plane and the object plane coincide in space. This ensures images that are in-focus over the whole image area despite the non-orthogonal viewing angle.

2.3. Model Setup

The model and the underwater PIV system were fixed to the adjustable measurement rig of the towing carriage. The possible problems related to the relative motion of the model and the PIV-system were minimised by fixing the stern of the model to the measurement rig as well as to the vertical supports of the underwater housing with aluminium profiles (see Fig. 2).

The model was towed first with free sinkage and trim. The sinkage of the stern was then fixed to the value measured in the free run. The measurement plane was changed by moving the model with respect to the measurement rig and the PIV system. The orientation of the model with respect to the towing direction was kept unchanged by two longitudinal guide rods close to the bow and stern of the model.

In order to maximise the contrast of the captured images the stern of the model, the propellers and the rudders were painted with a matte black paint.

2.4. Seeding

In order to get images of the flow, particles reflecting the laser light are required. This is done by seeding the flow with particles which are suitable for the purpose. In this case hollow glass spheres with a diameter of 8-10 μm and almost neutral buoyancy were used. They were mixed with water using a volumetric ratio of roughly 1:100. The seeding system located ahead of the model consisted of two streamlined aluminium profiles. The mixture was fed through small holes on both sides of the profiles. The exact location of the seeding system, the spacing and the immersion depth of the profiles were determined experimentally. Several test measurements were performed and the system was adjusted between each run until a satisfactory seeding for the measurement area was achieved.

2.5. System Calibration

The calibration of the system was done using a dedicated calibration plate. In these measurements a standard 20 by 20 *cm* calibration plate of Type 20 from Lavision was used. Images of the calibration plate are taken with both cameras. The system then generates a mapping function between the image world and the real world through a point search. The search uses user provided reference marks and known properties of the calibration plate. The resulting mapping is called the calibration.

The quality of the calibration can be assessed by comparing the locations of the marks in a mapped image of the plate with the theoretical locations of the marks for a perfect mapping. The rms of the deviations was below 0.3 pixels. The system manufacturer rates this as an excellent calibration. This indicates that the mapping of the particle locations from the captured images into actual physical locations for the PIV-analysis is sufficiently accurate and does not introduce significant error in the analysis.

Additional calibration was performed for the axial velocity by running the carriage without the model at a velocity corresponding to the test case and by comparing the average of the resulting axial velocity field with the set velocity. Because the seeding in this case did not cover the whole measurement plane, only the area with sufficient seeding was used in the averaging. As a result a calibration factor of 1.064 was used for the axial velocity component. For the in-plane components the calibration factor was assumed to be one.

2.4. Data Acquisition and Analysis

The analysis and the measurements were performed with DaVis 7.1 imaging software. The measurements were synchronised with the rotation of the propeller. A Hall sensor fixed to the shaft line sent a trigger signal to the PTU. The measurements

could be synchronised with different blade angles via the PIV control software with a user-defined time delay between the input trigger signal and the output acquisition signal. The delay for the 0 blade angle was determined experimentally by running the model and by adjusting the delay until the desired angle was reached. This was checked visually from the captured images. The additional delay (257 μs/*deg*) for the other blade angles was evaluated based on the rotation rate of the propeller. For each blade position and cross section three runs were performed. This resulted in around 120 double-frames for each blade position.

The analysis process consists of several steps. First the average of all images of the same measurement run was subtracted from the individual images. This minimises the influence of the background noise and visible parts of the model on the PIV-routine. Next each image was processed with the stereo-PIV cross-correlation routine. In the analysis a multi-pass routine was used. The window size in the first pass was 128 pixels with 50 percent overlap. In the second pass a window of 64 pixels with no overlap was used. Single pass was performed for both window sizes. A phase-averaged velocity field for each cross section was evaluated by taking the average of the instantaneous velocity fields for a blade position. A time-averaged field was obtained by taking the average of the phase-averaged fields.

3. RESULTS

In the following results are shown separately for the axial and in-plane velocity fields. The axial velocity, which is shown as contour plots, is the component parallel to the ship velocity. The in-plane velocity shown as vector plots is defined to be the component in the measurement plane. For the PRI the flow field around the plane of the rudder is of greatest interest. Therefore, axial and tangential velocity components are studied separately on the longitudinal plane intersecting the centre of propeller plane. The tangential component is defined in a cylindrical coordinate system, which has its axis through the centre of the propeller plane. It is positive in the counter-clockwise direction. Due to limited space full velocity fields are shown only for sections 1 and 4 and for a blade angle of 60 degrees. These are selected to show the most salient features of the flow field and its development. All of the results are presented for the port side viewed from the stern.

3.1. Results without the Rudder

The phase-averaged velocity field at cross-section 4 for the 60 degrees blade angle is shown in Figure 3. The tip vortices created by the propeller are clearly visible at 5, 8 and 11 o'clock positions. The vortex cores in the propeller wash form helix shaped paths, which rotate with the propeller. The strength of the vortex depends on the loading of the blade. This is influenced by the wake. The loading of the blade changes as it rotates through a non-homogenous upward directed wake caused by the hull shape, the hull boundary layer and the wake of the bossing and the shaft line.

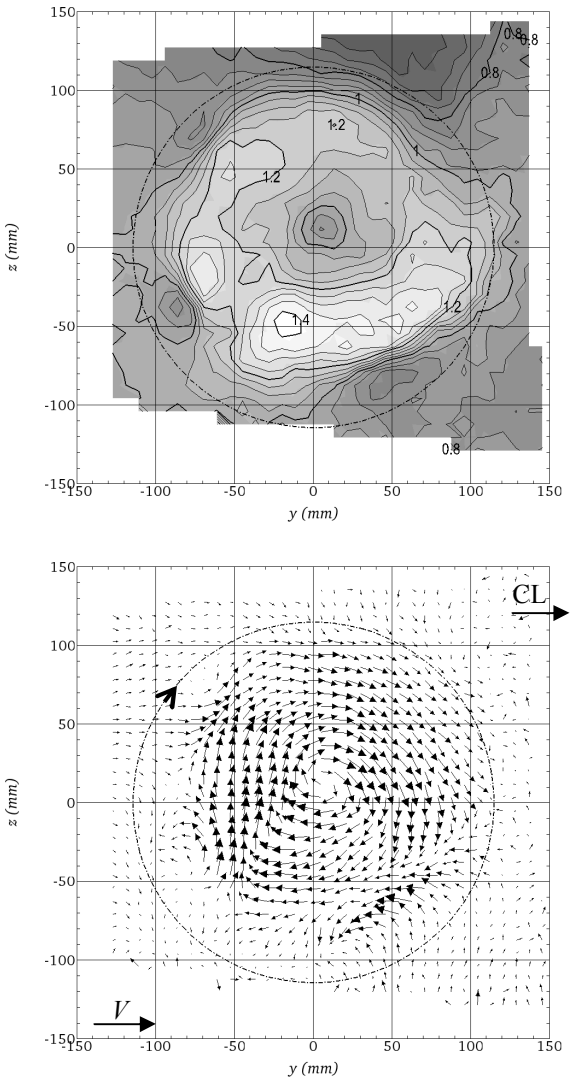

Figure 3. The phase-averaged non-dimensional velocity $\underline{u}/V$ without the rudder at the measurement plane 4 and 60 degrees blade angle. The axial and in-plane components are shown with contour and velocity plots respectively. The propeller plane is shown with a dashed line

The time-averaged velocity fields at sections 1 and 4 are shown in Figures 4 and 5. For the first cross section the propeller blade on the outside is blocking the view of the front camera, which results in the white area around the 3 o'clock position.

The axial velocity is largest at the lower part of the propeller wash and is significantly smaller in the upper part. The area of decelerated flow at the top of the measurement area is caused by the

combination of the hull boundary layer and the wake of the shaft line and the bossing.

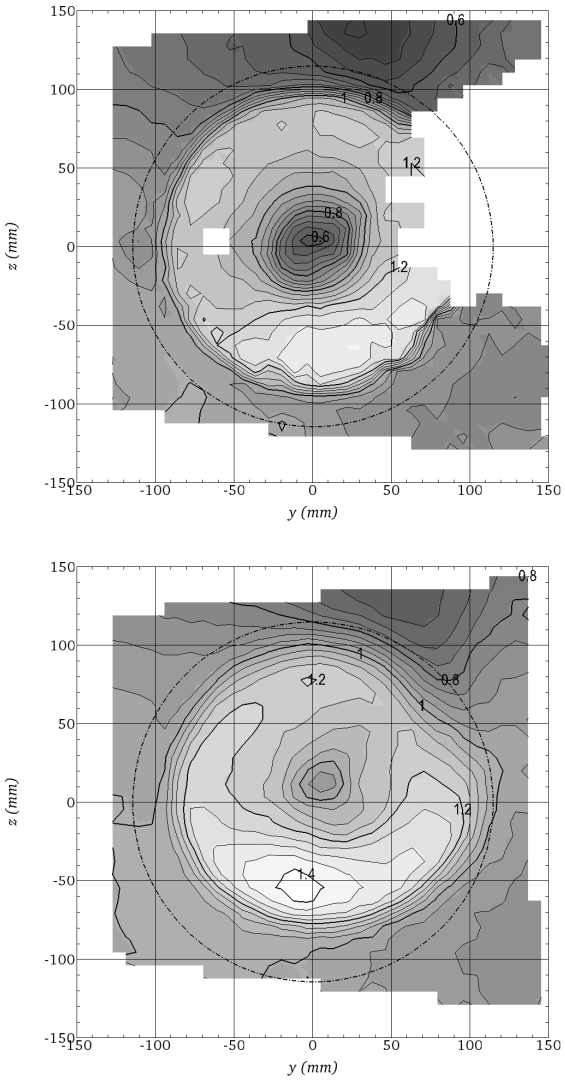

Figure 4. The time-averaged non-dimensional axial velocity u_x/V without the rudder at the measurement planes 1 and 4

The development of the axial field can be studied by comparing the fields at the two sections in Fig. 4. The transfer of axial momentum with the rotating velocity field is obvious and results in slow rotation of the wash peak. The area of large axial velocity is also stretched when moving downstream. The in-plane velocities are larger on the outside, because of the interaction of the upward hull flow and the propeller wash. The area of decelerated flow is also transferred with the rotating field down and towards the centre line. This momentum transfer also changes the distribution of the axial momentum in the propeller wash which is most obvious at section 4 around the 2 o'clock position.

Another interesting feature in the flow field is the deep wake of the hub. As the propellers are of CPP type, the diameter of the hub compared to the propeller diameter is quite large. Due to the large velocity gradients in the hub wake, it is rapidly diffused, as can be seen from the results at section 4.

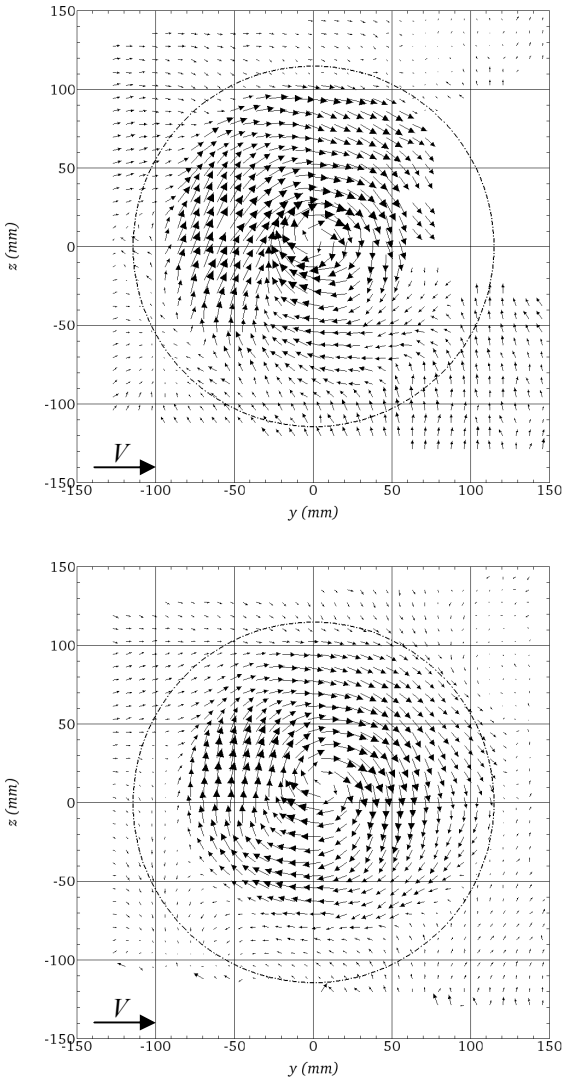

Figure 5. The time-averaged in-plane velocity without the rudder at the measurement planes 1 and 4

The in-plane velocities (see Fig. 5) are largest close to the centre of the plane particularly at cross sections close to the propeller plane. It is believed that there are two reasons for this. Firstly, the propellers of the test case have quite lightly loaded tips in order to reduce the size of the tip vortex. Reducing the loading of the tips increases the loading of the inner sections of the blade, which leads to larger induced velocities from these sections. Secondly, as has already been seen, the large and blunt hub creates a strong wake behind it. The associated low pressure just behind the hub may increase the tangential velocities outside the hub wake.

Another striking feature in the in-plane velocity fields is the rapid change of flow direction around the 5 o'clock position. This is also caused by the interaction of the upward flow, resulting from the hull shape, and the propeller induced velocities. Due to large velocity gradients the rapid variations in the in-plane velocity magnitudes and in the flow directions are diffused when moving downstream.

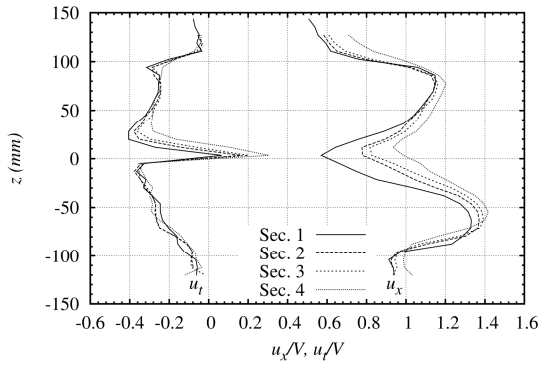

Figure 6. The non-dimensional axial and transversal velocity components without the rudder at different cross sections on the longitudinal plane y=0

The axial and the transversal velocity components on the longitudinal plane y=0 are shown in Figure 6. The distributions of transversal velocity component above and below the centre of the propeller plane are quite different. A linear reduction of tangential velocity is observed below the centre, whereas above the centre high values of tangential velocity are observed from the root to almost the tip of the propeller. These observations apply for all of the measured sections. The lower tangential component below the centre of the plane combined with the larger axial component results in smaller angle of attack relative to the y=0 plane. Thus the lower part of a rudder set in this slipstream is more lightly loaded.

3.2. Results with the rudder

The measured velocity fields with the rudder are shown in Figures 7 and 8. The results are shown only ahead and aft of the rudder. Reflection from the rudder surface causes strong saturation in the captured image. Because of this the PIV analysis fails close to the rudder surface. From the included figures it is also seen that because of the camera arrangement and the blocking effect of the rudder the captured area is slightly smaller than without the rudder. An additional side effect of this is large erroneous in-plane velocities at the edge of the blocked area.

The results show that the rudder has a strong influence on the flow field. The downstream influence is of course very large, but there is a clear upstream influence as well. The loading of the rudder, which is caused by the propeller induced velocities and the installation angle of the rudder, creates additional induced velocities. The resulting up-wash of the rudder is clearly visible. The most prominent effect of the rudder on the wake ahead of it is the considerable decrease of the axial velocity in front of the leading edge. At the same time the tangential component of the velocity in this area increases. The latter effect seems to centre around the suction sides of the rudder whereas the effect on the axial wake is larger on the pressure sides. This can be seen very clearly above the propeller slipstream, where the area of decelerated flow has shifted towards the pressure side of the rudder. The wake of the hub is also deeper compared to the case without rudder (see Fig. 4).

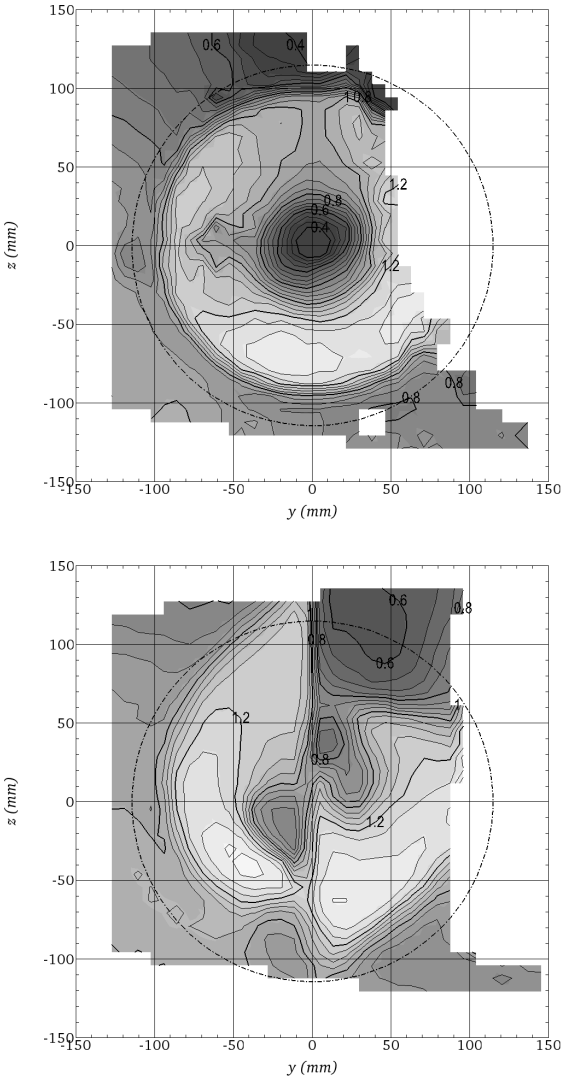

Figure 7. The time-averaged non-dimensional axial velocity u_x/V with the rudder at the measurement planes 1 and 4

It can also be seen that in general the influence of the rudder on the wake ahead of it increases

when moving up. There are two reasons for this. Firstly, due to the inclined leading edge of the rudder the distance from the leading edge to the measurement plane decreases when moving up, and the effect of the rudder up-wash in the measurement plane is thus stronger. Secondly, as the distance between the propeller plane and the leading edge decreases the interaction between the propeller and the rudder increases.

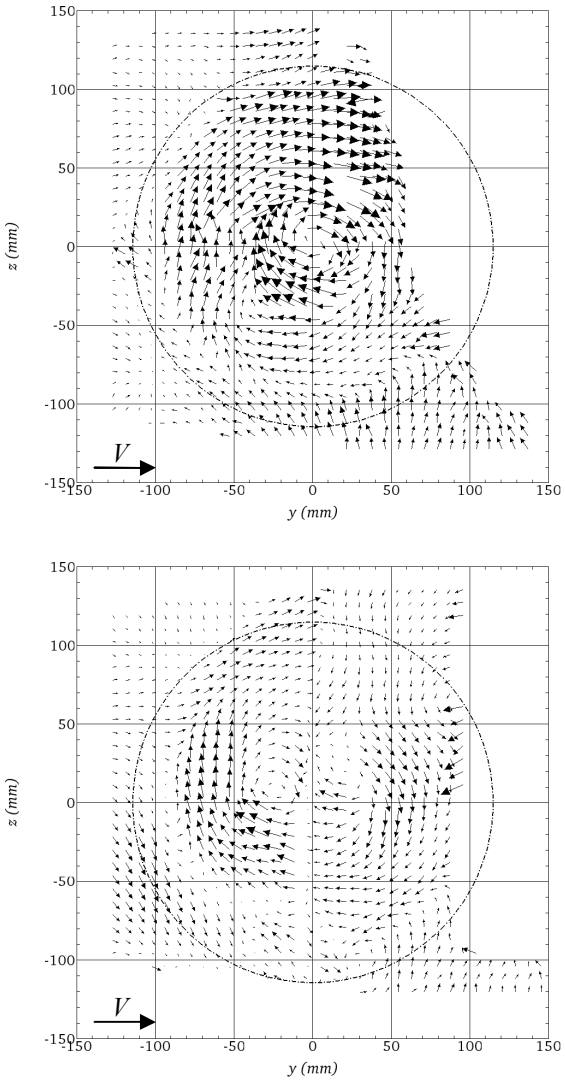

Figure 8. The time-averaged in-plane velocity with the rudder at the measurement planes 1 and 4

The influence of the rudder has also been studied by comparing the axial and transversal velocities with and without the rudder on the plane y=0 in front of the rudder leading edge in Figure 9. It can be seen that the inclusion of rudder affects mostly the flow above the shaft line. The tangential velocity below the shaft line is practically the same as without the rudder and there is only a slight decrease in the axial velocity.

At the downstream section the rudder has cut the flow into two parts. There is a vortex core on both sides of the rudder centre line. The upper part of the wake on the outside and the lower part on the inside correspond to the unobstructed part of the propeller wash which has passed ahead of the rudder leading edge. On the outside this area is larger and reaches closer to the rudder centre line, as the chord of the rudder decreases from root to tip. On the extension of the rudder centre line the unobstructed propeller wash collides with the part of the wash straightened by the rudder. This can be seen clearly as a rapid change in the axial velocity over the collision line. It can also be seen that as a result the rotational wake is spread out which transfers axial momentum up and down along the rudder centre line. It seems that the wake collision and the resulting velocities along the collision line push the vortex core down on the outside and up on the inside.

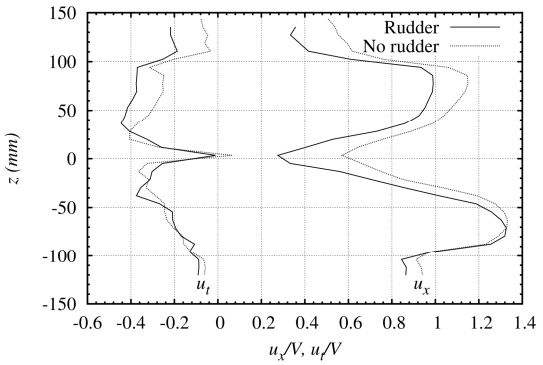

Figure 9. The non-dimensional axial and tangential velocity components with and without the rudder at the section 1 on the longitudinal plane y=0

The flow around the upper part of the rudder is very complicated as there are two distinctly different areas there. The part of the rudder above the propeller wash is almost parallel to the flow, whereas the part of the rudder just beneath experiences very high angles of attack due to the wash. The high angles of attack caused by the wash induce significantly lower pressure on the suction side than the pressure in the corresponding part above the slipstream. This pressure difference modifies the flow field above the wash and creates a downward directed flow in the upper part of the suction side.

4. DISCUSSION AND SUMMARY

The obtained results have shown that there is a clear upstream influence of the rudder. The loading of the rudder induces velocities which reduce the total axial velocities and increase the tangential velocities ahead of the rudder. At the same time, the

rudder creates a complex wake by dividing the propeller wash into two parts. A dominant phenomenon aft of the rudder is the strong interaction between the parts of the propeller wash passing ahead of the rudder and straightened by the rudder.

The rudder induced tangential velocities ahead of the rudder are interesting from the point of view of the comfort level. A typical feature of an open shaft line stern arrangement is a peak in the tangential wake above the shaft line. The upward directed flow following the hull contour has to flow around the bossing and the shaft line. The resulting wake affects the loading of the propeller. If the tangential components are against the rotation of the propeller, the blade loading will increase.

Full-scale observations and cavitation tank experiments of the same test case have shown that the rudder up-wash can be used to modify the wake above the shaft line and to reduce the strength of the blade tip vortex. This is based on the reduced loading of the blade, which results from the rudder induced tangential velocities in the direction of the propeller rotation. As the tip vortex cavitation is mostly responsible for the wide banded noise, the reduction of the strength of the vortex has a direct influence on the noise level.

The strength of the effect can be adjusted with the angle of the rudder. There is however an optimum for this effect if the noise is considered. It should be noted that the rudder up-wash has also an influence on the axial wake ahead of it. If the rudder angle is too large, the loading of the blade may increase resulting in stronger tip vortex. Furthermore, too large angles may result in excessive loading of the rudder. This in turn may result in rudder cavitation and erosion or flow separation and increased resistance of the rudder.

The study has provided knowledge on the applicability of towed PIV systems for a case at hand. The results have been encouraging. The problems have mainly been related to vibrations of the system, blockage of the field of view and reflections from the model, which were or can be solved with additional supports, alternative camera arrangements and with the use of fluorescent seeding particles. The study has demonstrated that towed PIV-measurements can be used to gain fundamental understanding on the physical effects related to propeller rudder interaction. The measurement results can also be used as an input data for other studies. For example, the obtained results have been combined with a lifting line model in order to study the loading and the induced resistance of the rudder.

ACKNOWLEDGEMENTS

The authors wish to thank STX Finland for the financial support of the study. The assistance of the technical staff of Aalto University Marine technology laboratory, particular that of Mr. Pentti Tukia, is also greatly appreciated.

REFERENCES

[1] Molland, A.F., and Turnock, S.R., 2007, *Marine Rudders and Control Surfaces.* Butterworth-Heinemann.

[2] Kim, J. (chairman), Fu, T.C. (secretary), Bugalski, T., Hinatsu, M., and Di Felice, F., 2008, "The Specialist Committee on Wake Fields", *Proceedings of the 25th International Towing Tank Conference*, Vol. II, pp. 535-562.

[3] Felli, M., Di Felice, F., Guj, G., and Camussi, R., 2006, "Analysis of the Propeller Wake Evolution by Pressure and Velocity Phase Measurements", *Experiments in Fluids*, Vol. 41, pp 441-451.

[4] Paik, B.G., Kim, J., Park, Y.H., Kim, K.S., and Yu, K.K., 2007, "Analysis of Wake Behind a Rotating Propeller Using PIV Technique in a Cavitation Tunnel", *Ocean Engineering*, Vol. 34, pp 594-604.

[5] Felli, M., and Falchi, M., 2011, "Propeller Tip and Hub Vortex Dynamics in the Interaction with a Rudder", *Experiments in Fluids*, Vol. 51, pp. 1385-1402.

[6] Paik, B.G., Kim, G.D., Kim, K.S., Kim, K.Y., and Suh, S.B., 2012, "Measurements of the Rudder Inflow Affecting the Rudder Cavitation", *Ocean Engineering*, Vol. 48, pp 1-9.

[7] Paik, B.G., Kim, K.Y., Lee, J.Y., and Lee, S.J., 2010, "Analysis of Unstable Vortical Structure in a Propeller Wake Affected by Simulated Hull Wake", *Experiments in Fluids*, Vol. 48, pp 1121-1133.

[8] Felli, M., and Di Felice, F., 2005, "Propeller Wake Analysis in Non-Uniform Inflow by LDV Phase Sampling Techniques", *Journal of Marine Science and Technology*, Vol. 10, pp 159-172.

[9] Van, S.H., Kim, W.J., Yoon, H.S., and Lee, Y.Y., Park, I.R., 2006, "Flow Measurements around a Model Ship with Propeller and Rudder", *Experiments in Fluids*, Vol. 40, pp 533-545.

[10] Muscari, R., Felli, M., and Di Mascio, A., 2011, "Analysis of the Flow Past a Fully Appended Hull with Propellers by Computational and Experimental Fluid Dynamics", *Journal of Fluid Mechanics*, Vol. 133, pp 061104/1-16.

Conference on Modelling Fluid Flow (CMFF'12)
The 15th International Conference on Fluid Flow Technologies
Budapest, Hungary, September 4-7, 2012

$NPSH_r$ CHARACTERISTICS AT EXTREME HIGH FLOW RATES DEPENDING ON ROTOR SPEED AND DIAMETER

Zoltán PANDULA[1], László KULLMANN[2]

[1] Corresponding Author. Department of Hydrodynamic Systems, Budapest University of Technology and Economics. Műegyetem rkp. 3., H-1111 Budapest, Hungary. Tel.: +36 1 463 2216, Fax: +36 1 463 3091, E-mail: pandula.zoltan@hds.bme.hu
[2] Department of Hydrodynamic Systems, Budapest University of Technology and Economics. E-mail: kullmann@hds.bme.hu

ABSTRACT

Series pumps of two worldwide known pump manufacturers have been tested to get information on the $NPSH_r$ values at extremely high flow rates (up to 1.4-1.6 times the flow rate of the best efficiency point - BEP) required e.g. for sprinkler application. As there are hardly any information available on the dependence of $NPSH_r$ on impeller diameter of turned rotors and change of rotor speed a series of laboratory tests have been performed and evaluated to receive empirical formulae based on theoretical considerations.

The aim of a series of experiments was to extend $NPSH_r$ characteristic curves of centrifugal pumps for high flow rates and estimate the maximal motor power for safe operation at high flow rates belonging to an extremely high $NPSH_r$ value to fulfil the prescription of the standard EN 12845:2004 for sprinkler systems.

Keywords: flow rate over optimal operation point, $NPSH_r$ characteristics

NOMENCLATURE

c	$[m/s]$	average flow velocity
d	$[m]$	impeller diameter
e_s	$[m]$	geometrical datum of pump
g	$[m/s^2]$	gravity
H	$[m]$	head
H_{sg}	$[m]$	suction head
h'_s	$[m]$	head loss of the suction pipe
n	$[1/min]$	rotor speed (r.p.m.)
$NPSH$	$[m]$	net positive suction head
$NPSH_a$	$[m]$	NPSH available
$NPSH_r$	$[m]$	NPSH required
p	$[Pa]$	pressure
p_{ref}	$[Pa]$	reference pressure
p_v	$[Pa]$	vapour pressure
Q	$[m^3/s]$	flow rate
t	$[°C]$	temperature
ρ	$[kg/m^3]$	fluid density

Subscripts and Superscripts

1	original operation state
2	changed diameter, rotor speed
s	suction side of the pump
d	discharge side of the pump
sa	turning point of the $NPSH_r$ characteristics

1. INTRODUCTION

Recently the prescriptions for sprinkler systems have been changed as the standard EN 12845:2004 [1] was introduced. This new standard prescribes that the motor power should be high enough to operate safely to an extremely high flow rate point, where the required net positive suction head of the pump is 16 m. Our industrial partners at the beginning of the investigations had only the measured $NPSH_r$ characteristics for the normal operation region of pumps, therefore the idea has presented itself to extend the characteristics by calculations on theoretical basis. As there is hardly any information available in the literature on high flow rate cavitation behaviour, measurements were performed on pump families and also dependency of the $NPSH_r$ characteristics on the impeller diameter reduction and rotor speed variation was studied.

2. CAVITATION AND $NPSH_r$ CHARACTERISTICS

In liquid delivering systems the phenomenon of cavitation may occur in a number of places. It is generated where the local pressure drops below the saturated vapour pressure. In piping systems cavitation takes place at various locations: in pumps, in throttling valves, in regulating pressure reduction valves, etc. In most cases cavitation is dangerous and detrimental.

Cavitation affects the environment through noise and vibration apart from causing physical damage (erosion) of the solid boundary surfaces of the flow. In modern light construction buildings the vibrations may easily diffuse and this may also damage the machines and the equipment inside. Considering cavitation in hydraulic systems pumps are critical elements since damage may appear in the pump at its inlet side.

The $NPSH_r$ characteristics of the pump can be obtained using measurements indirectly. The $NPSH_r$ curve is the function of the flow rate and defines the limit in operation to avoid harmful cavitation. During measurements the systems net positive suction head can be obtained. Such characteristics are shown in the Figure 1 where the shaft power and $NPSH_r$ of a pump with different impeller diameters for constant rotor speed is presented.

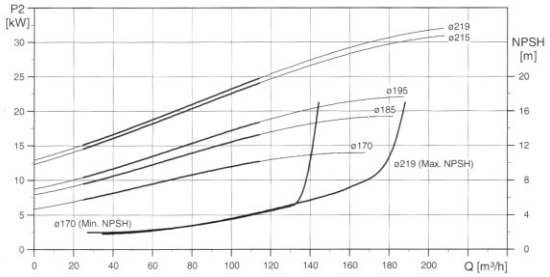

Figure 1. Measured catalogue $NPSH_r$ characteristics of a pump with different impeller diameters [2], nq≈25 (slightly depending on impeller diameter)

The available $NPSH_a$ in a given system can be calculated using a measured reference pressure in the tank p_{ref}, vapour pressure p_v at the actual liquid temperature t, the suction head H_{sg}, pressure loss in the suction pipe h'_s and a geometrical datum e_s of the pump by the following formula (see e.g. [3]):

$$NPSH_a = \frac{p_{ref} - p_v(t)}{g \cdot \rho} - H_{sg} - e_s - h'_s(Q) \qquad (1)$$

The negative signs are resulted because of the definition of the geometric parameters: the suction head H_{sg} is positive, if the reservoir level is below the pump's suction flange level (in the case of horizontal pumps flange axis level), the geometrical datum e_s is defined as the vertical distance of the highest point of the impeller suction side from the flange level referenced in the definition of H_{sg}. This point is the minimum pressure point of the suction side of the impeller; this is the most dangerous from the point of cavitation. The safe operation condition is that the available net positive suction head is higher than (or equal to) the pump's required $NPSH_r$ value for the actual operating point:

$$NPSH_r \le NPSH_a \qquad (2)$$

As the beginning of cavitation – the formation of the first vapour bubbles called incipient cavitation – is hard to determine, because there is no change in hydraulic parameters, the $NPSH_r$ is given in pump catalogues usually as the $NPSH_a$ value when the head drops by 3% [4]. To surely prevent the system from cavitation $NPSH_a$ should be higher than the pumps $NPSH_r$. In practical use when installing a pump in a given system or planning a suction pipe, the $NPSH_a$ should be at least 1-2 m higher than $NPSH_r$ (this can still result in bubble formation), higher value is reassuring.

$NPSH_r$ is obtained from suction experiments performed at constant flow rates. The $NPSH_a$ is reduced as long as cavitation is detected in the system through measurable head drop. In order to reduce $NPSH_a$ the resistance of the suction pipe should be increased, this may happen by closing a valve at the suction side. At the same time, to keep the operation point constant, the resistance of the overall pipe (suction and discharge pipe) should be kept unchanged; therefore a valve in the discharge pipe should be opened appropriately. The $NPSH_r$ for the set volume flow rate can be obtained as the abscissa of the 3% head drop in the head–$NPSH_a$ graph (Fig 2.).

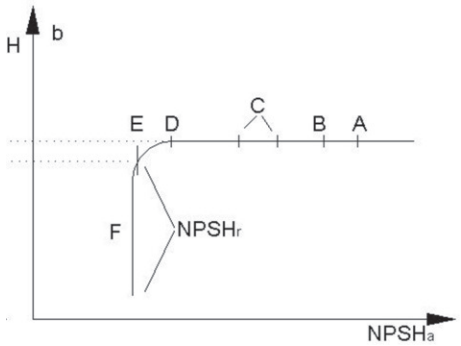

Figure 2. Result of the suction measurement. Points A, B: no cavitation; C: first bubbles (incipient cavitation); D: cavitation zone near the leading edge of impeller blades; E: fully developed cavitation in the blade channels, F: supercavitation

According to Fig. 2 the $NPSH_r$ at this flow rate is at point E. The change in hydraulic quantities begins already at D (start of the technical cavitation) but the first bubbles form earlier (points C, start of physical cavitation). The beginning of bubble forming can only be determined by using experimental pumps with transparent pump casing wall or with vibration measurements (e.g. [5], [6], [7], [8])

Such suction experiments should be repeated at several (6-8) flow rates to determine the pumps

$NPSH_r(Q)$ characteristics. Because of the difficulty to keep the flow rate constant the complete measurement of such a suction curve is cumbersome and a time expensive task.

According to Yedidiah [9] the $NPSH_r$ characteristics can be described for usual operating flow rates region by the following equation:

$$NPSH_r = k \cdot Q^2 + L \tag{3}$$

where k and L are constants.

The aim of our investigation was the extension of the $NPSH_r(Q)$ curve to high flow rates up to 1.4-1.6 times the flow rate of the BEP. According to Gülich [3], there is a turning point Q_{sa} (steep ascent) at which the $NPSH_r$ characteristics begin to rise quite rapidly. However this steeply increasing part of the characteristics is not properly estimated in the literature. Gülich defines it in the form given in Fig. 3, the power x is said to be in the range 2-3 and is increasing with the flow rate ratio Q/Q_{sa} [3].

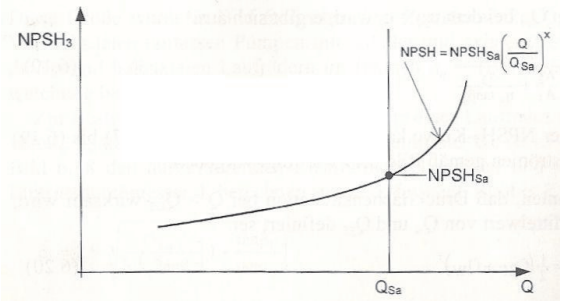

Figure 3. Theoretical extension of $NPSH_r$ = $NPSH_3$ (3% head drop) characteristics for high flow rates (Gülich [3])

Another question of our investigation is the transformation of the $NPSH_r$ characteristics when turning down the impeller diameter. According to the Hydraulic Institute [10], for some pumps, impeller trimming increases the pump's required net positive suction head. In the Reference Guide [11] an example is shown about how $NPSH_r$ increases. There are different linear to quadratic transformation theories concerning the change of $NPSH_r$ with the diameter ratio [4] depending on the type of the pump.

Our investigations have also concerned on the influence of the rotor speed change and impeller diameter trimming. The mostly used formula in literature is that the $NPSH_r$ in the normal operating region is changing with the square of the revolution speed and diameter ratio (e.g. [3], [4], [12], [13]):

$$\frac{NPSH_{r1}}{NPSH_{r2}} = \left(\frac{n_1 \cdot d_1}{n_2 \cdot d_2} \right)^2 \tag{4}$$

As neither the high flow rate behaviour of the pump nor the influence of both impeller diameter trimming and rotor speed is well known in this high flow rate region, a test rig was built up in the Laboratory of the Department of Hydrodynamic Systems, Budapest University of Technology and Economics to achieve more information about this region

3. MEASUREMENTS IN THE HIGH FLOW RATE REGION

The aim of our experiments is to study the suction capacity of the pump for extremely high flow rates. The $NPSH_r$ is over *10 m* at these flow rates which means overpressure at the suction side, while usual system pumps never operate at working conditions where the $NPSH_r$ is over *5-6 m*. Therefore either an upper reservoir or a booster pump is needed.

The $NPSH_r(Q)$ characteristics is determined from suction experiments from $NPSH_a$ values for 3% head drop. The standard testing procedure is described by ASME, ISO, Hydraulic Institute, etc [14]. Our test rig is presented in Fig. 4. A booster pump feeds the water from the underground reservoir of the laboratory into the pump test section beginning at the suction side valve T2 and ending at pressure side valve T3.

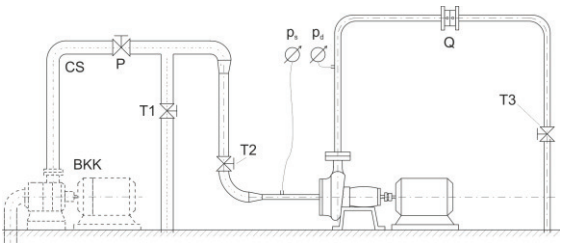

Figure 4. Laboratory test rig for high flow rate suction experiments with booster pump (BKK: booster pump, T2 and T3 gate valves, Q: volume flow rate measuring device)

In the experiments the static pressure at the pump suction (p_s) and discharge (p_d) side pressure points and the flow rate (Q) with an inductive flow meter were measured. From these measured values the available net positive suction head can be calculated by the following formula:

$$NPSH_a = \frac{p_s - p_v(t)}{\rho g} - h_s'(Q) + \frac{c_s^2}{2g} \tag{5}$$

According to Fig. 4. p_s is the pressure measured at the suction side, c_s the average flow velocity in the suction pipe calculated from the flow rate and h'_s the pressure loss between the suction side pressure tapping and pump inlet.

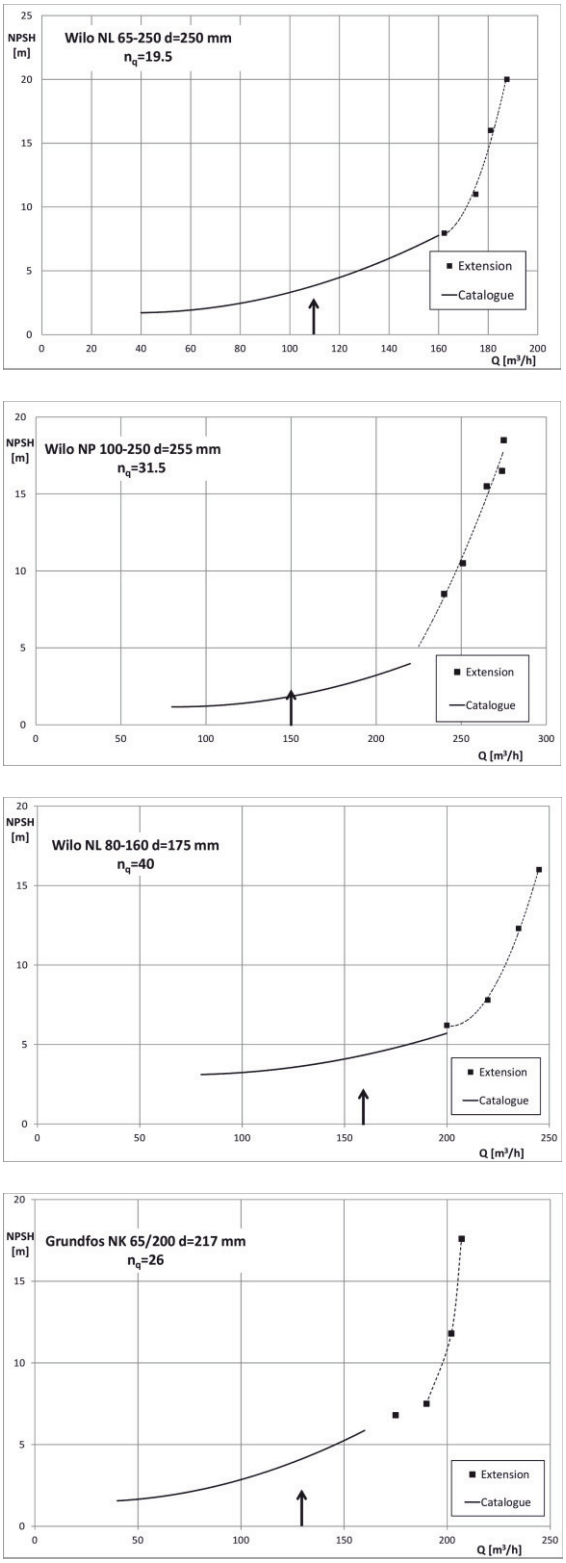

Figure 5. Measurement results (Pumps 1-4) with marked best efficiency points

The head of the pump can be calculated as the pressure and specific kinetic energy difference between suction and discharge side:

$$H = \frac{p_d - p_s}{\rho g} + \frac{c_d^2 - c_s^2}{2g} + h_s'(Q) + h_d'(Q) \qquad (6)$$

The $NPSH_a$ will decrease with increasing the resistance of the suction pipe through closing the valve T2 at the suction side. To keep the volume flow rate constant the pressure side valve T3 must also be operated. Simultaneous measurement of $NPSH_a$ and head allows to detect the $NPSH_r$ for the given flow rate, where the head begins to drop (Fig. 2, point E).

In this test rig the high flow rate suction capacity of four norm-pumps of two worldwide known manufacturers were measured. The results of these measurements are shown in the diagrams of Fig. 5. The pumps of Manufacturer 1 are the Pump 1-3 (Wilo NL 65-250, Wilo NP 100-250, Wilo NL 80-160) and Pump 4 (Grundfos NK 650-200) is produced by Manufacturer 2. The specific speeds of these pumps are: 19.5, 31.5, 40 and 26, respectively. In the diagrams the flow rate of the best efficiency point is marked by an arrow). For all four pumps a rapid increasing part over a turning point in the $NPSH_r$ characteristics can be observed according Fig. 2. [3]. The uncertainty of the measurement of the *NPSH* values was no higher than *0.2 m*.

In the case of Pump 3 and Pump 4 impeller diameter trimming has also been investigated. In Figures 6 and 7 the influence of diameter trimming can be seen showing similarity to the graphs in Fig. 1 presented by the manufacturer for impeller diameter trimming. The pump's specific speed is increasing with the reduction of the impeller diameter. These test were performed with direct driven 2900 rpm pumps. The meridional view of a trimmed impeller is shown in Fig. 8. Both the front and back shrouds of the impeller are trimmed down as well as the impeller blades.

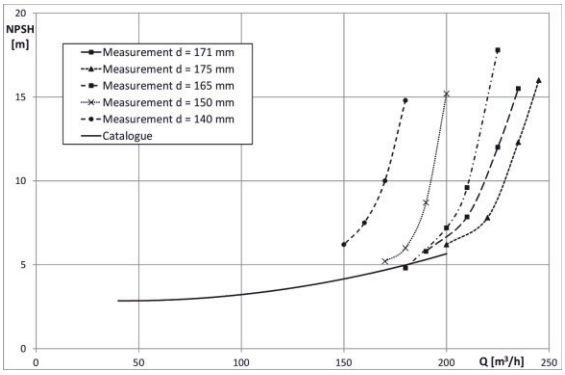

Figure 6. Diameter trimming on Pump 3

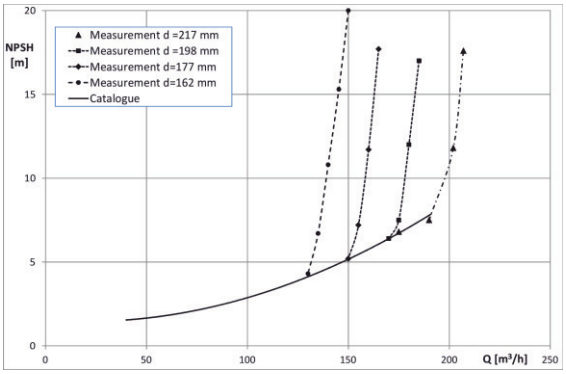

Figure 7. Diameter trimming on Pump 4

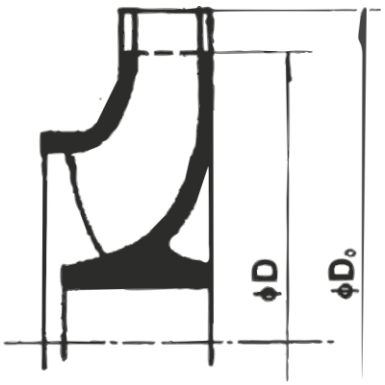

Figure 8. Impeller trimming

During the measurements on the Pump 4 (Manufacturer 2.) the influence of rotor speed change was tested too at the minimum impeller diameter. Fig. 9 presents the results of this measurement set. The pump's specific speed doesn't depend on the revolution speed.

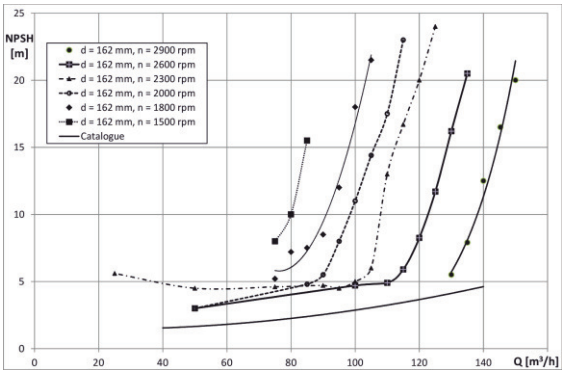

Figure 9. Influence of rotor speed change on Pump 4

4. RESULTS

First, the extension of the $NPSH_r$ characteristics was performed. Our results partly correspond to the formula of Gülich [3] Staring at a turning flow rate (Q_{sa}) the $NPSH_r$ is increasing rapidly, the $NPSH_r(Q)$ dependence according to Fig. 3 can be described with the following equation:

$$NPSH = NPSH_{sa}\left(\frac{Q}{Q_{sa}}\right)^{x} \tag{7}$$

where according to our measured data presented in Fig. 5 the power x depends on the Q/Q_{sa} ratio itself. According Gülich [3] x is in the range of 2-3 and increases with the flow rate. With the increase of this ratio the power increases rapidly, too. In our tests the power x for both pump manufacturer's products can be defined by the following formula:

$$x = a \cdot \left(\frac{Q}{Q_{sa}}\right)^{b} \tag{8}$$

where a and b are parameters depending on the pump type. For the measured pumps the parameters are summarised in the Table 1.

Table 1. Parameters for the measured pumps

Pump	a	b
Pump 1-3	1.8	4.8
Pump 4	4	10

In the next step the influence of turning down the impeller diameter was studied (pump 3 and 4). The rise of the rapidly increasing part for trimmed diameters is higher than for the original one. According to our experiments the Q_{sa} point is shifted nearly linearly by the diameter ratio (d_2/d_1):

$$\frac{Q_{sa_2}}{Q_{sa1}} \approx c \cdot \frac{d_2}{d_1} \tag{9}$$

By analysing the measured data the rapidly increasing part of the $NPSH_r$ characteristics can be calculated using formula (9) too. In Fig. 10 the calculated pump $NPSH_r$ characteristics of the Pump 3 is presented. The measured points for different impeller diameters are also plotted into the diagram.

Finally the influence of the rotor speed change was tested. The turning point and the increasing part of the characteristics are transformed according to our measurements (Fig. 9.) by the following formula:

$$\frac{Q_{sa_2}}{Q_{sa1}} \approx \left(\frac{n_2}{n_1}\right)^{n} \tag{10}$$

where the power of the rotor speed ratio is near to 1.

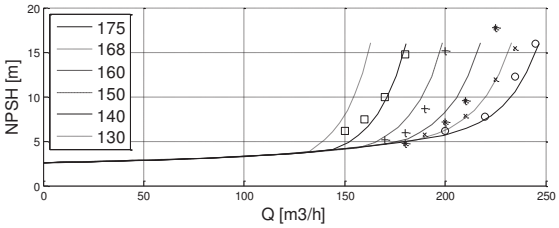

Figure 10. Calculated and measured characteristics of Pump 3

5. CONCLUSIONS

In this paper the results of the measurements on required net positive suction head of centrifugal pumps (n_q=19.5 – 40) is presented. In our study the effect of extremely high flow rates ($Q \leq 1.6\ Q_{BEP}$) on the $NPSH_r$ of the pump are investigated. The results show a rapid increase of the $NPSH_r$ characteristics over a turning point partly corresponding to the literature.

In the second part of the investigation the effects of impeller trimming and rotor speed are studied. Impeller trimming increases the $NPSH_r$, which results in considerable changes of the characteristics at high flow rates. The turning point is shifted to reduced flow rates; the rapid increase begins earlier. The rotor speed change too shifts the turning point to lower flow rates.

The results were applied to extend the characteristics of pumps in sprinkler systems to fulfil the EN 12845:2004 standard.

ACKNOWLEDGEMENTS

This work is connected to the scientific program of the " Development of quality-oriented and harmonized R+D+I strategy and functional model at BME" project. This project is supported by the New Hungary Development Plan (Project ID: TÁMOP-4.2.1/B-09/1/KMR-2010-0002), by the National Funding System (project number: GVOP-3.2.1-2004-04-0053/3.0) and by the Hungarian National Fund for Science and Research under contract number OTKA 61460.

REFERENCES

[1] EN 12845:2004+A2:2009, Fixed firefighting systems. Automatic sprinkler systems. Design, installation and maintenance, 2004.

[2] Grundfos Data Booklet, Fire NKF Grundfos fire systems, *Grundfos*, pp. 30.

[3] Gülich, J. F., 2010, *Kreiselpumpen: Handbuch für Entwicklung, Anlagenplanung und Betrieb*, Springer-Verlag GmbH,

[4] Schiavello, B., Visser, F.C., 2009, "Pump Cavitation – Various NPSHR Criteria, NPSHA Margins, and Impeller Life Expectancy", *Proceedings of the Twenty-Fifth International Pump Users Symposium*, pp. 113-144.

[5] Gülich, J. F., 1992, „Diagnosis of Cavitation in Centrifugal Pumps", *World Pumps*, pp. 13-20.

[6] McNulty P.J., Pearsall I.S, 1982, "Cavitation inception in pumps," *Journal of Fluids Engineering*, ASME, Vol. 104, pp. 99-104.

[7] Fáy A., Sebestyén G., Varga J. 1969, "Detection of Cavitation by Acoustic and Vibration Measurement Methods" *La Houille Blanche* n. 2

[8] Farkas, I., Pandula, Z., 2006, "Problems with conventional vibration measurements by detection of cavitation operating of centrifugal pumps", *Proceedings of the SPIE*, Vol. 6345, Paper 63450Z

[9] Yedidiah, S., 1996, *Centrifugal Pump User's Guidebook - Problems and Solutions*, Chapman Hall

[10] U.S. Department of Energy's Industrial Technologies Program - Hydraulic Institute, 1999, *Improving Pumping System Performance: A Sourcebook for Industry*

[11] European Association for Pump Manufacturers, 1999, *NPSH for rotodynamic pumps: a reference guide*, Elsevier Advanced Technology

[12] Folk, M. W., 2005, *Pump Characteristics and Applications*, Taylor&Francis

[13] Lawrence Pumps Inc, 2007, *Laurence Pumps Newsletter*, Vol 4, Issue 3, 03/2007

[14] Tuzson, J., 2000, *Centrifugal Pump Design*, John Wiley and Sons

Conference on Modelling Fluid Flow (CMFF'12)
The 15th International Conference on Fluid Flow Technologies
Budapest, Hungary, September 4-7, 2012

NUMERICAL SIMULATION AND EXPERIMENTAL SET UP OF A MULTIPHASE PUMP APPLICATION

Helmut BENIGNI[1], Helmut JABERG[2], Ludwig MICHAL[3]

[1] Corresponding Author. Institute for Hydraulic Fluidmachinery, Graz University of Technology, Kopernikusgasse 24, A-8010 Graz, Austria, Tel.: +43 316 873 7578, Fax: +43 316 873 107578, e-mail: helmut.benigni@tugraz.at
[2] Institute for Hydraulic Fluidmachinery, Graz University of Technology, e-mail: helmut.jaberg@tugraz.at
[3] Andritz AG, Stattegger Strasse 18, A-8045 Graz, Austria, e-mail: ludwig.michal@andritz.com

ABSTRACT

Medium consistency (MC) pulp is a three-phase fluid including dissolved and unresolved air, fibres as solid matter and water as the liquid phase. The medium – though of relatively high consistency as compared to normal liquid pumping – can easily provoke blockage effects as the water fibre mixture can be modelled as a kind of Bingham fluid. A new way of efficient and reliable stock pumping in modern fibre lines without vacuum pumps – and thus claims to change the rules for MC-pumping by setting new standards for efficiency, maintenance and usability of medium-consistency pulp up to 15 % – had to be developed. Normal process pumps are not able to pump such a strong non-Newtonian multiphase fluid with air.

A CFD-calculation gives detailed information on the degassing process, the fluidization of the pulp into the standpipe and the efficiency improvement potential for the whole pump configuration. Furthermore, a MC-pump test rig equipped with online air content measurement as well as other measurement systems was used to carry out a series of more than 1000 test trials for the experimental part of the development process. Thus, systematic variations of different elements were verified.

Keywords: air separation, CFD, multiphase, pulp, simulation

NOMENCLATURE

Specific speed:

$$n_q = n \cdot \frac{\sqrt{Q}}{H_{Def}^{0.75}} \quad (1)$$

Pressure number:

$$\psi = \frac{2 \cdot g \cdot H}{u^2} = \frac{2 \cdot g \cdot H}{\pi^2 \cdot n^2 \cdot D_3^{\,2}} \quad (2)$$

1. INTRODUCTION

In the last decades, marked by environmental and energy conservation concerns, the trend in pulping operations moved more and more from low to middle consistency pulp applications. Continuous pulping, diffusor washing, chlorination and/or displacement bleaching are typical examples for this trend [1]. Wood pulp fibres are hollow tubes having a typical average length of 1 to 3 *mm* and a diameter of 15 to 30 micro metres [2]. Kerekes et al. [2] classified pulp into 3 types of consistencies: low consistency (C_m=0%-8%), medium consistency C_m=8%-20% (compare also [3]) and high consistency C_m=20%-40%.

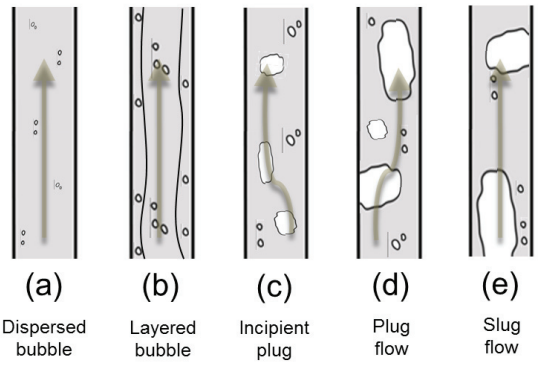

Figure 1. Schematic presentation of flow regimes (based on [1] and [4])

The medium, although of relatively high consistency – as compared to normal liquid pumping – can easily provoke blockage effects as the water fibre mixture can be modelled as a kind of Bingham fluid. Furthermore, the eventually high gas contents require the usage of an additional vacuum pump both for pumping as for system purposes. Possible flow regimes in pipe networks are dispersed bubble flow (a), layered bubble flow

(b), incipient plug flow (c), plug flow (d) and slug flow (e) [4].

When pulp is pumped with normal process pumps, cycle drop downs of the head and the flow rate could be detected. In Figure 3, the measurement of a regular process pump with a low consistency pulp (C_m=5.5%) is lined out for more than 10 minutes of operation. Those long time pulsations (approx. 15 seconds) are not directly corresponding to pulp concentration but are mostly caused by the air in the pulp. A self-deairiation in a regular pump is not possible. The air proportion is affected by the pulp raw material and the process, the pulp level in the standpipe, the consistency, the shear stresses in the impeller and the flow conditions in the suction pipe.

The operation range of such a process pump is limited by the drop of the pump‘s characteristic curve. A minimum pressure gradient towards the suction side of the pump is absolutely necessary for supplying middle consistency pulp to the pump.

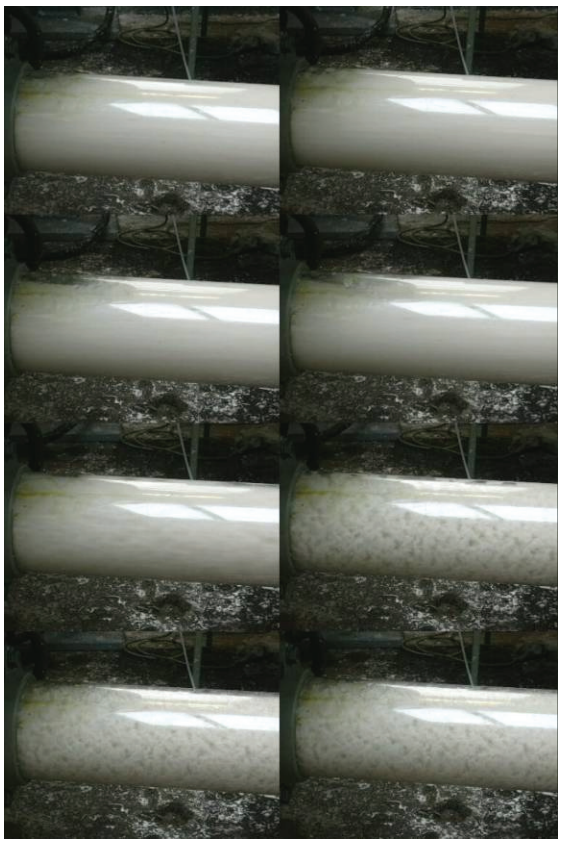

Figure 2. Air accumulation in a pipe section after a bend in the suction pipe of a process pump while pulp is being pumped [5]

Though friction forces help to maintain the pulp flow in the “liquid” phase, the decreasing pressure tends to dissolve the air resolved beforehand, which collects for example in the upper region of the suction pipe, causing – if the volume of the accumulated air bubble is big enough and enters the pump – the drop of the pump head curve and even the failure of the pumping process, not to mention the risk of dry running mechanical seals (Figure 4).

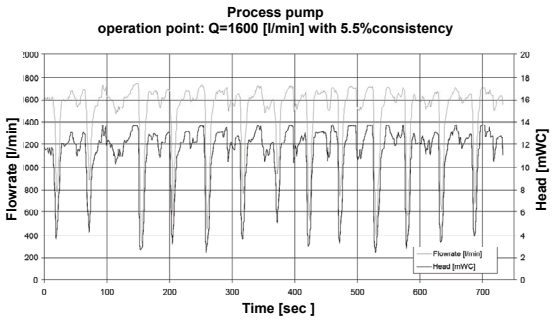

Figure 3. Head and flowrate pulsations for a regular process pump while pulp is being pumped [6]

The highest possible air content starts at a pulp consistency of 5% at a volume of 5% and grows up to a pulp consistency of 20% at a volume of 55%, the line depicted showing a slight S-shape in the characteristic. All values depend on the basic wood types [7]. Most bubbles were found to have a diameter of 0.5 to 1.5 *mm*, however, some were as large as about 5 *mm* [8].

1.1. Fibre damage

It is a fact, that fluidization (which describes a state of pulp suspensions in which elements of a suspension move relatively to one another so that the suspension adopts properties of a fluid [9]) and the removal of the air are a must for MC-pulp pumping. However, the higher the fluidization the more important is the power loss. Fluidization shall break the fibre network without damaging fibres, in order to allow the pulp to flow. The fluidized condition breaks down within a few 1/10 seconds (approx. 0,2 *s* – 0,4 *s*), when no shear stresses apply to the pulp. Fluidization occurs at two levels, whereas floc level fluidization is sufficient for pumping [10]. In a fluidized state the fibres in the pulp suspension are straightened. In a non-fluidized state of the pulp, the fibres are curly and kinked.

In recirculation areas of a machine fluidization gets bended and curled again, whereas in the normal flow field of a centrifugal pump the fibres are fluidized and therefore straightened. It has not been proven yet that the straightening effect of a fluidized flow field is stable after fluidization. But it seems that the pumps in a fibre line are not so harmful to the fibres because of the very short time fibres are exposed to the pump blade forces.

In general, the effects of refining, curling, kinking and bending of fibres in pulp suspensions decrease with decreasing consistencies. Additionally, it has to be mentioned that these effects only occur in soft wood fibres widely spread. For hard wood fibres these effects are not as

important because these fibres are already very short (see also [11]). Commonly, lower consistencies are more suitable with regard to fibre damages.

1.2. Pulp

Medium consistency pulp is a three-phase mixture consisting mainly of water, of pulp fibres for the solid component as well as solved and dissolved air as gaseous component (Figure 2). Pulp can be regarded a Bingham medium which behaves like a solid body unless the shear stress exceeds a certain level, depending on the pulp consistency which requires a certain fluidization process in the suction side drop leg in front of the pump. For high shear stresses the pulp flow approaches the behaviour of a Newtonian fluid behaving similar to a water flow. This flow characteristic changes according to the species of pulp, the air content, the consistency and the fibre shape.

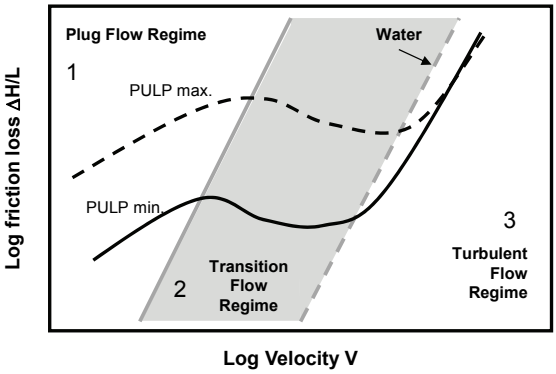

Figure 4. Friction loss curve based on [9] ,[12] and [13]

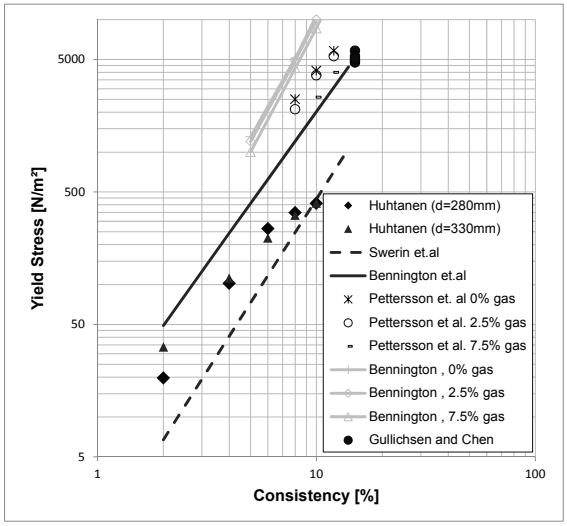

Figure 5. Overview of values for yield stress of pulp with different consistencies

Any moving liquid is characterized by decreasing pressure due to friction forces in the flow direction. For pulp, three flow regimes were identified, which occur with higher flow velocity. The friction loss (dH/L) is lined out over the velocity (v) in Figure 4 and follows a characteristic for pulp in a S-shape. In case of medium consistency this figure for lower consistencies changes to a permanent virtual plug flow and to a compressible flow because of the higher air content.

Figure 5 gives an overview of different references to Bennington et al. [14], Chen [15], Gullichsen [1][16], Pettersson [8], Swerin [17] and Huhtanen [18][19] regarding measured and calculated yield stresses for pulp of different consistencies.

$$S_w = \left(\frac{\tau_d}{0.178 \cdot C^{3.3}} \right)^4 \qquad (1)$$

The shear velocity gradient could be estimated by means of equation (1) using the values from Figure 5 based on a formula by Duffy.

1.3. Pump development: make it simpler – better – more reliable.

The high consistency of fibres in middle consistency pulp MAY cause failure of free suspension movement (especially in pipes). Different possibilities to pump such three-phase medium consistency pulp exist. E.g., a fluidizer can be installed in the dropleg in front of the pipe to exert the necessary shear stress and to fluidize – as mentioned above – the beforehand solid pulp. Also, a vacuum pump can be installed in parallel to the main pump extracting the air accumulating in or in front of the pump.

A comprehensive investigation with pump users and plant makers throughout the European pulp industry provided the necessity that a pump had to be developed that shall

- extract the air from the pump and from the pulp without the use of a vacuum pump over the whole operational flow rate,
- have an increased efficiency satisfying legal requirements for reduced power consumption,
- have fewer components and parts to increase reliability and to decrease maintenance costs.

These requirements resulted in a multiple function of the pump components. The fluidizer is not only a turbulence generator – the air separation starts there and continues in the runner, where separation works at different stages. These additional functions of the components are the key to the success of the developments and patents (WO 2008/116239 A1, WO 2009/082775 A1, a.o.).

In total, a series of 7 different sizes is actually available, starting from a 300 *adtm/d* up to a 5000 *adtm/d* daily production fibre line. The smallest size

is a low flow (high head) pump with a specific speed from 15.1 *rpm* up to 27.5 *rpm*. The flow rate for the smallest size is around 0.08 *m³/s* in the optimum and rises to more than 0.5 *m³/s* for the largest size. A stable head curve down to the minimum flow is guaranteed as well as good performance up to 16% consistencies. The impeller is with an optimized shape a patented inducer in front.

2. MACHINERY CONCEPT

A single shaft unit with a fluidizer in front of the impeller was chosen and a vacuum pump was fully omitted, however, the air had to be reliably removed from the flow. The idea behind the solution concept is explained in Figure 6. It was presumed, that it would be possible to separate the air from the rest of the solid-liquid pulp mixture in front of the pump and to design the fluidizer (1) in a way that besides the desired fluidization effect also a certain pressure head is created – all this well in front of the pump impeller (2). Thus, the pump impeller would be charged on its suction side with a certain pressure and with a flow regime where the gaseous flow component flows along the inner portion of the impeller and – due to the already higher pressure created by the fluidizer – is pressed through holes in the bottom of the impeller to the impeller backspace. There, a second separation at the back vanes (3) takes place and the gaseous flow goes through holes (4) in the pump bearing unit to the environment or to special degassing lines. The main flow from the impeller (2) and from the back vane side (3) leaves the pump via the volute (5).

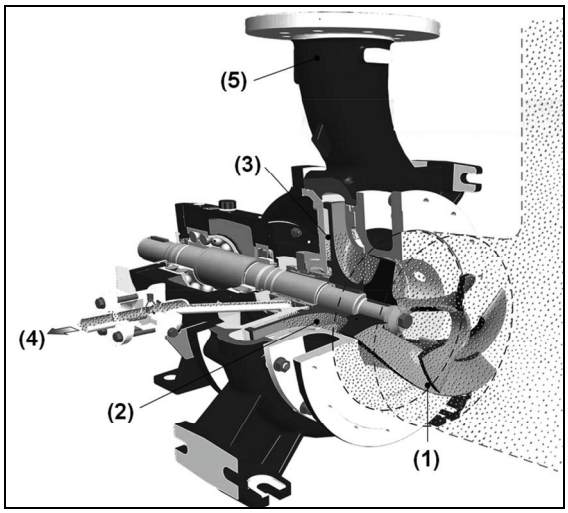

Figure 6. Cross-sectional view

The flow approaches the pump arrangement from the dropleg and enters the system through the fluidizer, which also creates the pressure used to press the air out of the pump. The main flow, now consisting only of water and fibres, enters the runner ((2) in Figure 6) where the pressure head is created in a conventional way. The separated air is pressed through holes in the impeller back shroud; it is modelled as a throttle between point 1 and point 2 in Figure 7.

First of all, the back vanes adjust the pressure and thus reduce the axial thrust in a conventional way. As an additional function, the back vanes work as a separator and transport the heavier pulp to the pump discharge like a radial pump. The now fully separated air is pressed to the holes in the pump bearing and through the degassing line.

3. EXPERIMENTAL SETUP

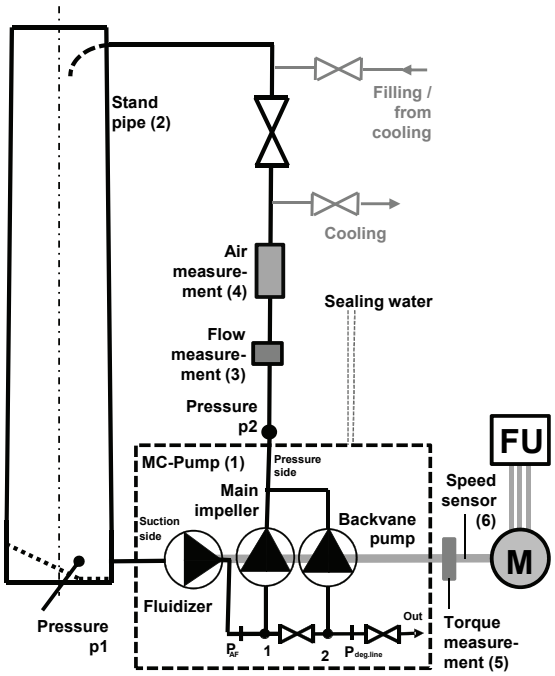

Figure 7. Test rig scheme with a hydraulic detail of the MC-pump

The main test rig consists of a 10m (height) conical stand pipe (2) with a top diameter of 1m. The MC pump (1) is connected to the stand pipe (2). The head is measured between pressure p1 in the standpipe and the pressure at the pressure side of the MC pump p2. The torque is measured with a torque measurement flange (5), the speed is measured with a speed sensor (6). The different motors (for the different sizes) are frequency controlled with a nominal power up to 630 *kW*. The inductive flow measurement (3) is located on the pressure side, just before the place where an online clamp-on air measurement device (4) is mounted. The options for cooling and modification of the consistency are given by a bypass.

4. NUMERICAL SETUP

The CFD-model consists of the lowest section of a stand pipe including the connection pipe to the MC pump, a 360 degree model of different fluidizer geometries, a 360 degree model of the runner including the rear side of the runner with the back vanes and the area of the 2nd stage air removal, which is connected with holes to the main portion of the runner. Finally, the fluid is collected by a volute, enlarged with a pipe on the pressure side. Due to the high number of geometry variations and the complex geometry, the runner and the fluidizer were meshed unstructured with CFX buildt®, whereas the geometry and the structured mesh of the volute were generated by means of an in-house-tool. The total mesh size is about 2.1 mio. nodes at 8.1 mio. elements. For the numerical simulation of the pump the commercial CFD-software package ANSYS CFX was applied. The SST-turbulence-model by Menter [20] was used for the stationary calculations with automatic wall functions.

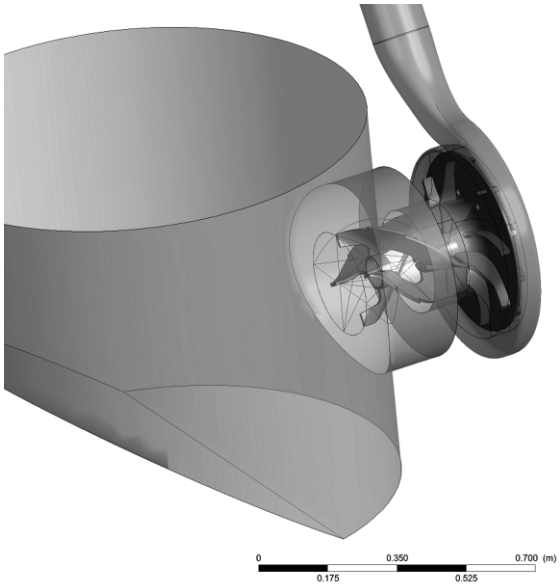

Figure 8. CFD model of the pump configuration

Different models and setups were used. The CFD-code uses a cell-centred control volume with identical nodes for velocity and pressure. A blending factor is computed locally, which is used for the spatial discretisation method of the convective terms implemented with a hybrid scheme. This results in a 2nd order accurate scheme.

In a first step, the simulations should help to understand the air separation and fluidization processes of the different components in the pump and the additional components. The calculation started with modified pure substances (A), followed by Bingham media (B) and ended with a pulp model (C), always with air as additional phase.

The density of the pulp and the modified pure substance were set to be 1.052 *kg/m³* [21] and the shear stress rate started from 500 to 5000 *N/m²* (A)(B). The dynamic viscosity for the pulp model (C) was calculated by:

$$\mu_{\text{pulp}} = 1.6 \cdot \frac{C^{1.87}}{S^{0.6}} \left[\frac{kg}{m \cdot s} \right] \qquad (4)$$

whereas the minimum shear strain rate of the pulp is evaluated for every time step. For the calculations as Bingham fluid the model in the software with a the viscosity consistency index k=0.001 *Pa.s* for water was used (compare also [22]). For the yield stress 5000 *N/m²* was used (see from Figure 5).

5. RESULTS

From the beginning of the development consequent thinking in a morphological box was used for all components of the pump and provided a lot of geometry variations.

5.1. Example for geometry variations – reinforcement of the fluidizer

For all components a series of geometry variations was processed – by CFD and numerical methods as well as experimental methods. A series of modifications of the front of the fluidizer in the geometry development phase is depicted. Due to the high forces acting on the fluidizer, an additional mechanical provision - is necessary - allowing high operational speeds

5.2. Understanding of air separation and fluidization

The air separation starts already in the fluidizer area, where the air is separated out of the pulp and at the same time the pulp is fed to the pump.

The track of the separated air bubbles to the second-stage air separation leads also to the rear side of the impeller. There, again, centrifugal forces split the air bubbles from the pulp.

Figure 9 and Figure 10 illustrates the comparison of the air content on the rear impeller side of the numerical simulation with the test rig results. The left picture shows different iso-volumes – coloured in grey – with a constant air content (Air.Vol.-Fraction) whereas the light grey at the lowest radius represents the highest air content. The same situation is presented in the right picture, where a Plexiglas window is mounted at the back vane area. The radius of the separation zone is exactly on the same radius as in the numerical simulation.

An indirect conclusion based on Figure 9 an Figure 10 could be, that the back vanes of the pump impeller work as reliable separators whereas we still

have got a mixture of air and pulp in the outer region – as can clearly be seen from the window photographs.

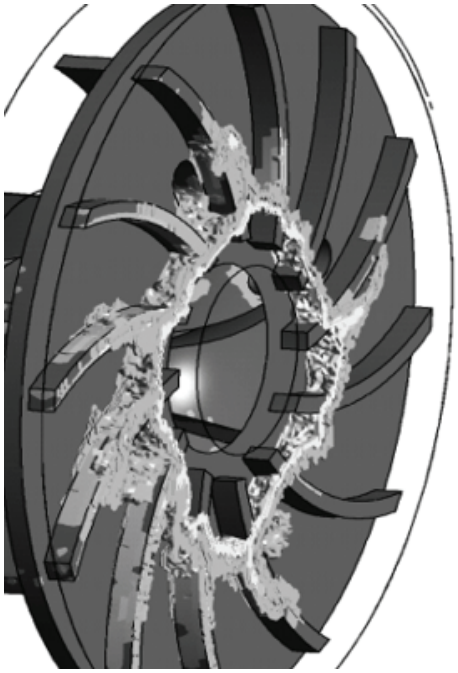

Figure 9. Air separation at the rear side of the pump, top – CFD calculation

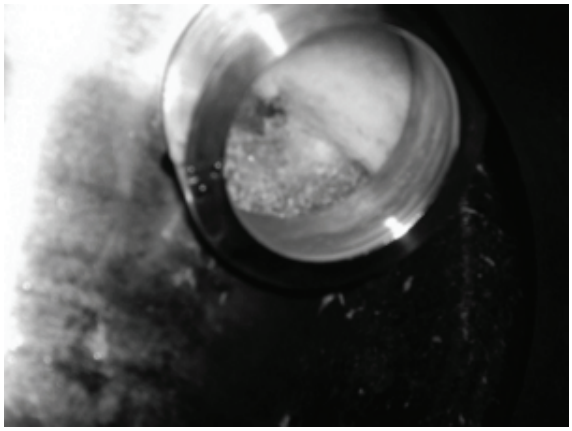

Figure 10. Air separation at the rear side of the pump – test rig

In Figure 11, a vector plot on a radius of 50% fluidizer blade height shows a homogenous velocity distribution. On the same plane the pulp shear strain rate is figured out in different grey colours. The highest rate can be found around the blades, especially in front of the fluidizer blades. This visualisation is from an intermediate development status.

The influence into the standpipe is visualized in Figure 12 where the turbulence kinetic energy is plotted on two main planes. The effect of the fluidizer clearly is predominant in front of the fluidizer itself but also extends deeply into the stand pipe.

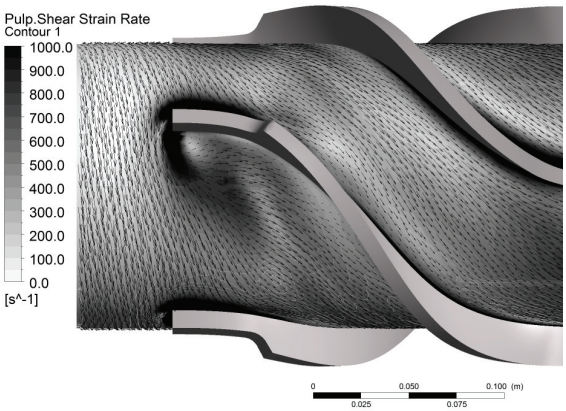

Figure 11. Fluidizer mode of operation (geometry development phase)

It is very critical to create the right pressure in front of the pump impeller [23][16]. If the pressure in front of the pump increases below the critical level, the pump head curves drop as then the air is not removed reliably.

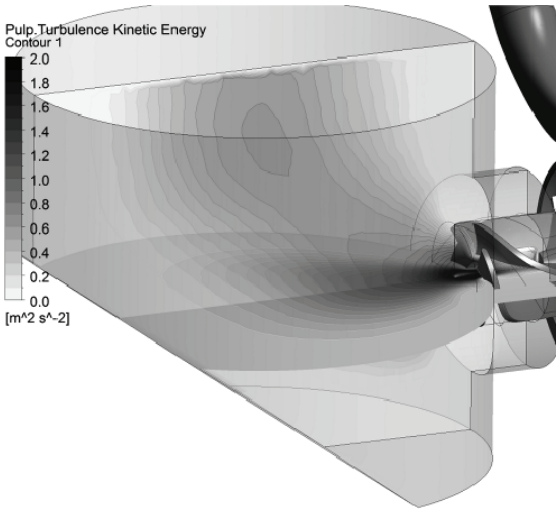

Figure 12. Turbulent kinetic energy in the fluidizer and standpipe area (geometry development phase)

5.3. CFD results with pulp model in comparison to test rig results

The hydraulic design was based on water basics and adapted according to experiences with different developments of the last decades. The usage of a pulp model in CFD calculation is new. The pulp model we used still overpredicts losses in the pump itself, and consistency has too much impact on the head curve. In Figure 13, test rig and CFD values are compared for the purpose of an intermediate version in the geometry development phase. Clearly visible is an almost stable head curve of the test rig configuration reaching the design point, however, still not having enough resources in overload. An

improved geometry and its head curve is shown in [23].

The CFD results are below the test rig results, with remarkable differences for different consistencies (8%, 10% and 12 %). The air content was set to the same level as the one measured on the test rig.

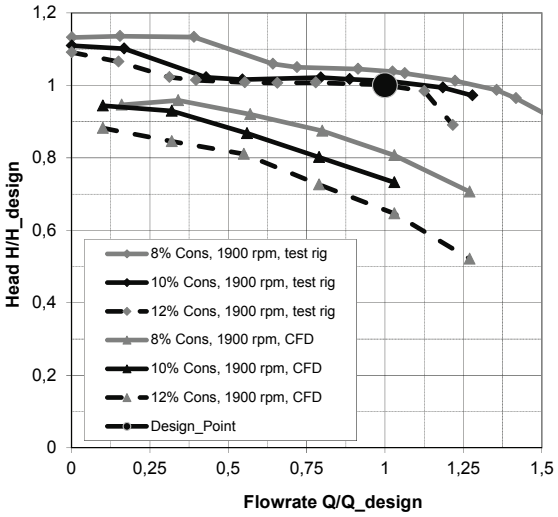

Figure 13. Head curve for different consistencies, CFD and test rig result

5. CONCLUSIONS AND OUTLOOK

During the past 20 years, the oxygen delignification process and new bleaching sequences have been developed, new chemicals have been introduced and temperature and pressure requirements have been increased . Simultaneously, pulp mill capacities and demands for single-line solutions have grown to exceed to 5000 *adtm/d* fibre lines. The requirement for efficient degassing in these positions is crucial as air or residual gases from the reactor have an effect on the capacity and washing efficiency of the washer and – consequently – on the chemical consumption of bleaching [24].

In a pulp mill pumps are still the main power consumers. The recently developed new generation of pumps further improves the overall pumping efficiency to more than 70%. These new pumps do not need a vacuum pump and still reliably remove the air from medium consistency pulp.

During the development phase, we simulated the flow distribution through the whole pump configuration. It is pleasant to see, how well the numerical simulation corresponds to what can be observed in reality. The regions with separated air can clearly be seen both in the numerical results as in the photographs. Furthermore, it can also be seen in the CFD flow field how the air moves through the degassing holes in the pump impeller disk to the backspace, where the air concentrates mainly in an area close to the shaft.

The CFD results regarding the hydraulic characteristics in cases of pulp model applications are still inferior and have to improve with the usage of other models.

REFERENCES

[1] Gullichsen, J., and Härkönnen, E., 1981, "Medium consistency technology", *Tappi Vol. 64 (6)*, pp. 69-72.

[2] Kerekes, R.J., et al., 1985, "The flocculation of pulp fibres", *Proceedings of the 8th Fundamental Research Symposium, Mechanical Engineering Publications, Oxford, United Kingdom*, pp. 265–310.

[3] Kuoppamäki, R., et al., 1992, "New high-intensity MC® Mixer – direct measurement of mixing efficiency", *Proceedings of 4th international conference on pulp and paper maintenance, New Available Techniques and Current Trends*, Bologna, Italy

[4] Xie, T., et al., 2003, "Flow regimes and gas holdup in paper pulp–water–gas three-phase slurry flow", *Chemical Engineering Science 58*, pp. 1417 – 1430.

[5] Penninger, G., Krisper, A., 2003, "Bericht über das kurzzeitige Abreissverhalten bei Stoffpumpen", *Internal measurement report for Andritz AG, Institute for Hydraulic Fluidmachinery, Graz, University of Technology*.

[6] Meusburger, P.L., 2002, "Hermetisch dichte Pumpen in der Papierindustrie", *Diploma thesis, Graz, University of Technology*.

[7] Meinl, K., Haapanen, P., 2002, "Verbesserungen der Prozesse bei der Zellstoff- und Papierherstellung durch geeignete Pumpensysteme", *Vortrag Aussteller-Seminar der Zellcheming*.

[8] Pettersson, J., and Rasmuson, A., 2004, "The Yield Stress of Gas/Liquid/Fibre Suspensions", *The Canadian Journal of Chemical engineering, Volume 82*, pp. 1313-1318.

[9] Derakhshandeh, B., et al., 2011, "Rheology of pulp fibre suspensions: A critical review", *Chemical Engineering Science 66 (2011)*, pp. 3460–3470.

[10] Hietaniemi, J., and Gullichsen, J., 1996, "Flow properties of medium consistency fibre suspensions", *Journal of Pulp and Paper Science 22 (12)*, pp. 469–474.

[11] Rauvanto, I., et al., 2006, “Fibre damage in unbleached reinforcement pulp : The phenomena in industrial softwood kraft pulps”, *Paperi ja puu, vol. 88, no. 4,* pp. 239-246, ISSN 0031-1243.

[12] Duffy, G., 1995, “Flow of medium consistency wood pulp fibre suspensions”, *Appita journal ISSN 1038-6807, vol. 48, no. 1,* pp. 51-55.

[13] Hemström, G., et al., 1976, “Boundary Layer Studies in Pulp Suspension Flow”, *Tappi, 1976, 59(8)*, pp. 115-118.

[14] Bennington, C.P.J., et al., 1995, “The Yield Stress of Medium- and High-Consistency Mechanical“ Pulp Suspensions at High Gas Contents”, *J. Pulp Pap. Sci. 21(4), J111–J118 (1995)*.

[15] Chen, K., 1994, “Technology and Equipment of Medium-High-Consistency Pulp”, *Guangzhou: South China University of Technology Press*.

[16] Gullichsen, J., and Härkönnen, E., 1981, “Medium consistency technology II. Storage dischargers and centrifugal pumps”, *Tappi Vol. 64 (9)*, pp. 113-116.

[17] Swerin, A., et al., 1992, “Linear and Nonlinear Dynamic Visco-elasticity of Pulp Fibre Suspensions”, *Nord. Pulp Pap. Res. J.,7 (3)*, pp. 126-132.

[18] Huhtanen, J.-P., 1994, “None-Newtonian flows in paper making”, *Dissertation Tampere University of Technology, UDC 532.5, report 137*.

[19] Huhtanen, J.-P., 2004, “Modelling of fibre suspension flows in refiner and other paper making processes by combining non-Newtonian fluid dynamics and turbulents”, *Tampere University of Technology, Publication 4097*, Tampere.

[20] Menter, F. R., 1994, “Two-equation eddy-viscosity turbulence models for engineering applications”. *AIAA-Journal, 32*, pp. 1598–1605.

[21] Tappi, 1999, “Viscosity of pulp (capillary viscometer method)”, T 230 om-99, Suggested standard.

[22] Bohle, M., et. al, 2009, „Characterization of Axial Flow Impellers in Fibre Suspensions”, *13th European Conference on Mixing, London, Chest, Volume: 87, Issue: April,* pp. 14-17

[23] Jaberg, H., Benigni, H., 2008, “Three Phase Pumping of Viscous Fluids – New Ways in Medium Consistency Pumping”, *International Rotating Equipment Conference, Düsseldorf*, pp. 490-499.

[24] Pikka, O., et al., 2009, “New MC™ equipment and concepts for the fiberline to improve process efficiency”, *O Papel (Brazil), Volume 70, Issue 2,* pp. 37-48.

Conference on Modelling Fluid Flow (CMFF'12)
The 15th International Conference on Fluid Flow Technologies
Budapest, Hungary, September 4-7, 2012

CFD-CALCULATION OF THE FLUID FLOW IN A ROTARY LOBE PUMP – EVALUATION OF A NUMERICAL MODEL BASED ON MEASUREMENT RESULTS

Jürgen SCHIFFER[1], Stephan KLOMBERG[2]

[1] Corresponding Author. Institute of Hydraulic Fluidmachinery, Graz University of Technology. Kopernikusgasse 14/IV, A-8010 Graz, Austria. Tel.: +43 316 873 7573, Fax: +43 316 873 7577, E-mail: juergen.schiffer@tugraz.at
[2] Institute for Fundamentals and Theory in Electrical Engineering, Graz University of Technology. E-mail: stephan.klomberg@tugraz.at

ABSTRACT

Rotary lobe pumps have been successfully used in the sewage water, the chemical and the agricultural industry for many decades. The pump design for different applications is usually carried out by means of 1D-/2D-calculation methods and experimental investigations.

Although Computational Fluid Dynamics (CFD) are a very important tool in the field of hydraulic machines today, the numerical simulation of the fluid flow in rotating displacement pumps is still a less discovered topic. Complex geometries and flow phenomena as well as the transient behaviour of the flow and continuously changing fluid fields complicate a reliable and realistic numerical simulation and emphasize the challenge of numerical investigations.

This paper is a contribution to numerical simulation studies of rotary displacement pumps illustrated by the example of a rotary lobe pump, using the recently developed "immersed solid method" implemented in the commercial CFD-software package ANSYS-CFX-12.1. Comprehensive transient calculations were carried out in order to compare CFD-results with measurement results gained in the course of experimental investigations on a test-rig.

On the one hand, a sensitivity analysis including the variation of grid size, the variation of face-, tip- and center-clearance as well as the variation of the angular resolution per time step, led to an optimized CFD-setup which was used to calculate transient CFD-results. On the other hand a comprehensive set of measurement data gained by experimental investigations carried out on a pump test-rig allows for a direct comparison between experimental and numerical results.

The comparison shows that the results of both approaches match well, however, it also identifies the limitations of the numerical model. Finally, a more detailed look into the CFD-results establishes the reasons for the deviations between the measurements and the numerical simulation.

Keywords:
CFD, Comparison of measurement and simulation, Immersed Solid Method, Rotary Lobe Pump, Transient Calculations;

NOMENCLATURE

$m_{p\text{-}in(t)}$	$[kg/s]$	Mass Flow Rate at Inlet
$m_{p\text{-}out(t)}$	$[kg/s]$	Mass Flow Rate at Outlet
$p_{in(t)}$	$[Pa]$	Static Pressure at Inlet
$p_{out(t)}$	$[Pa]$	Static Pressure at Outlet
$T_{z(t)Lobe1}$	$[Nm]$	Torque on Lobe No.1
$T_{z(t)Lobe2}$	$[Nm]$	Torque on Lobe No.2
Δp	$[bar]$	Differential Pressure
Q	$[l/min]$	Volumetric Flowrate
P_{mech}	$[W]$	Mechanical Power
P_{hydr}	$[W]$	Hydraulic Power
η_{Tot}	$[\%]$	Total Pump Efficiency
t_{Sim}	$[s]$	Simulation Time
D	$[m]$	Pipe Diameter

Subscripts and Superscripts

in	at the inlet of the CFD-model
out	at the outlet of the CFD-model
z	referring to the z-Axis
(t)	time-dependent
–	temporal mean

1. INTRODUCTION

Rotary Lobe Pumps, being the object of investigation in this paper, are usually equipped with two-vane- or three-vane-lobes and preferably provided with rubber lining to improve the abrasion resistance for the use in highly solid contaminated suspensions. The preferred areas of application are basically pumping systems for agricultural suspensions, pumping systems for sewage slurries and high viscosity industrial fluids and mobile

pumping systems. The flow in Rotary Lobe Pumps is dominated by highly transient effects. The rotating lobes generate pressure pulsations in the connected pipes due to acceleration and deceleration. The more teeth on a lobe, the faster the acceleration and deceleration phases alternate and the higher the frequencies are. The pressure peaks at constant speed decrease almost linearly with the number of teeth [1].

In addition to the rotor-angle dependent displacement, the pulsations are influenced by the internal leakage which varies with the rotor position. This effect becomes increasingly important with higher differential pressure, lower viscosity and unfavourable gap geometries [2].

In preparation of this study a Rotary Lobe Pump with straight 2-vane-lobes, helical 2-vane-lobes and helical 3-vane lobes was experimentally investigated on a closed pump test-rig. In parallel to the experimental work the Rotary Lobe Pump with the 2-vane lobe-design was modelled and meshed in order to carry out comprehensive numerical simulations. A comparison of results as well as the derived conclusions is presented within this paper.

2. EXPERIMENTAL FACILTIY

As a reference for the CFD-calculations a rotary lobe pump was investigated on a purpose-built test-rig where the pump characteristics and the pressure pulsations at different operation points were measured. During one measurement series the pump speed n was kept at a constant level while the discharge was regulated using a manually actuated control valve. The Δp-/Q-characteristics were measured within a speed range of n=100-600rpm. While the differential pressure Δp was kept between 0bar and 7bar, the discharge Q was kept within a range of Q=0-1000l/min. Additionally the speed-dependent efficiency curves were calculated and plotted above the discharge in a separate diagram. Particular attention was paid to the pressure pulsation measurements which were carried out at specific operation points at a differential pressure of Δp=1.5bar and Δp=3.0bar and at a pump speed of n=100, n=300 and n=600rpm. The pressure pulsation measurements were carried out on the suction- and pressure-side of the rotary lobe pump at a distance of 4*D away from the inlet and outlet of the pump.

3. A REVIEW OF CFD-STUDIES FOR ROTARY DISPLACEMENT PUMPS

Concerning the numerical simulation of rotating displacement pumps there is a trend of continuous development of different methods to solve the problems connected to complex fluid flow in such kind of pumps. While CFD-codes have been independently developed by several authors around one century ago, commercial CFD software-packages nowadays offer several approaches to investigate rotating displacement pumps.

In general there are two main techniques for the CFD-simulation of rotating displacement pumps.

The most commonly used technique is the Arbitrary Lagrangian Eulerian (ALE) Method. The Lagrange-Algorithm is widely spread in the field of structural mechanics. In course of an externally induced motion each individual node of the mesh follows the appropriate fluid particle. For strong deformation this method is not practical. The Euler-Algorithm is based on a fixed mesh and the fluid particles move related to this fixed mesh. The Euler-Algorithm can be used for strong deformations and is widely spread in the field of fluid mechanics. The ALE-description combines these two methods and was successfully used for the numerical simulation of rotating displacement pumps by several authors. [3]

Riemslagh et al [4] used the ALE-Method for the numerical simulation of 3-vane rotary lobe pump and a gear pump. He used an unstructured triangular mesh which is continuously deformed while the rotating parts move through the fluid regions. In case of strong deformations single nodes are added to or deleted from the actually used mesh. He investigated cavitation phenomena and the shear stress development within the pump. Both have a great influence on the pumped fluid and have to be minimized especially in the food industry.

A similar approach was implemented in the commercial CFD software-package FLUENT. Panta [5] used the “Moving Dynamic Mesh”-Option for the 2D numerical simulation of a gear pump conveying engine oil and investigated pressure-contours and velocity-vectors as well as regions of re-circulations and cavitation.

An extended ALE-formulation was used by Houzeaux et al [6]. For each time-step a separate mesh is used and the flow equations are solved. After each time-step the solutions for the previously used mesh are interpolated onto the new one.

A completely different approach for the numerical simulation of rotating displacement pumps is used by the Fictitious Domain (FD) Methods. In general there are four different methods belonging to the fictitious domain methods which are extensively discussed and described by Vande Voorde et al [7]. All the different techniques have in common that a solid mesh moves inside a fluid mesh, while the real solid geometry is not defined as boundary condition. In order to model the displacement effect executed by the rotating solid parts source terms are added to the Navier-Stokes-Equations describing the fluid flow within the pump. Vande Voorde et al [7] used the commercial fluid dynamics code FLUENT for the numerical simulation of a 2D lobe pump where he achieved good results despite using quite rough meshes. The numerical simulation of a 3D toothed

compressor working with a compressible medium was not successful.

A direct comparison between the simulation results achieved with the ALE- and FD-Method was carried out by Fuchs [8] and Schwotzer [9] who used a 2D rotary lobe pump as an example. Both studies relate to the Immersed-Solid-Method (ISM) and the Moving-Mesh-Method (MMM) implemented in ANSYS-CFX.

An alternative to the previously described ALE- and FD-Methods is the method of Smoothed Particle Hydrodynamics (SPH). SPH is a Lagrangian method for modelling fluid flows and heat transfer. Materials are approximated by particles that are free to move around rather than by fixed grids or meshes. SPH-simulations of a Rotary Lobe Pump were carried out by Prakash et al [10] who investigated variations in shear stress and efficiency by varying the gap size between rotating lobes and the fixed pump housing.

Most of the authors dealing with the numerical simulation of rotating displacement pumps offer a comprehensive description of their numerical models but do not compare the achieved results with experimental data. Additionally the previously mentioned studies mainly relate to 2D-approaches where especially the gaps existing in a rotating displacement pump are not fully resolved. Particularly these topics are a main focus of this paper.

4. CFD CALCULATION OF A ROTARY LOBE PUMP USING AN "IMMERSED SOLID METHOD"

4.1. The "Immersed Solid Method"

Based on its promising advantages and its convenient operability it was decided to use the Immersed Solid Method (ISM) for the numerical simulation of the previously mentioned Rotary Lobe Pump. ANSYS-CFX-Workbench, Release 12.1 was used to model, mesh and carry out the CFD-simulations presented in the following sub-chapters. ISM is a new option to more easily capture the effect of complex geometry motion on fluid flow – like in the case of a Rotary Displacement Pump. The model involves the use of an immersed solid domain (like the two lobes of a rotary lobe pump) that is placed inside a fluid domain. As a simulation proceeds, the solver applies a source of momentum to the fluid inside the immersed solid domain in order to force the flow to move with the solid. The immersed solid is represented as a source term in the fluid equations that drives the fluid velocity to match the solid velocity. The size of the source term is controlled by the "Momentum Source Scaling Factor"-setting [11]. While the IMS-model does not involve complex and time-consuming re-meshing and is convenient to use it has the drawback that the viscous contribution of forces and torques on an immersed solid is typically under-estimated [11]. This has several effects on the hereby presented CFD-results which will be discussed in chapter 5.

4.2. The geometric pump model

In course of the CFD-calculations a full 3D-pump-model was created in order to reproduce the real 3D-contour of the pump housing and its rotating lobes including the face- and tip-clearance as well as the center-clearance between the mating lobes. In course of the CFD-simulation of the rotary lobe pump a straight two-vane lobe design (see Figure 1) was used.

4.3. Description of the CFD-grids

The fluid region of the pump and the rotating lobes were meshed fully unstructured with tetrahedron-elements in the main fluid regions and prism-layers in the regions near walls. While the mesh inside the immersed solid may be arbitrarily coarse (except for the boundaries where it should be sufficiently fine to resolve the shape of the boundary surface), the mesh within the fluid regions has a great influence on the quality of the CFD-results. Therefore a main focus of attention was on the investigation of the influence of different mesh qualities on the results of simulations. Three different mesh sizes were created using a total number of approximately 500.000, 720.000 and 1.500.000 nodes for the fluid regions of the CFD-model. Additionally the number of thin prism layers at the walls of the housing and within the gaps between fixed and moving parts was varied between 5 and 15. Some details of the used meshes and detailed sections of important mesh-regions are shown with Figure 1. Because of the fact that the fluid-meshes do not change during one transient CFD-calculation the meshing-effort is kept at a minimum compared to similar simulation technologies already presented in chapter 3.

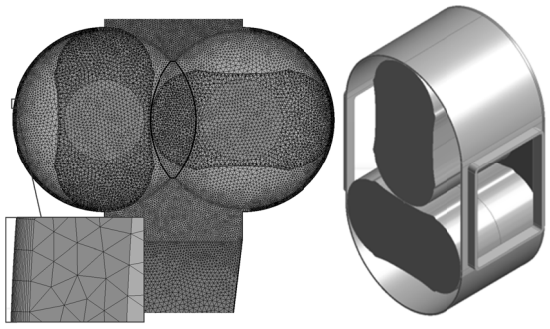

Figure 1. CFD-grid and housing of the Rotary Lobe Pump with its investigated lobe-geometry

4.4. Description of the CFD-model

The previously described CFD-grids were assembled using ANSYS-CFX-Pre V12.1, where

also the boundary conditions and the CFX-Solver-settings need to be defined. The transient CFD-calculations of the rotary lobe pump were carried out using a stationary fluid domain containing the sub-domains "Suction Pipe", "Pump Housing" and "Pressure Pipe". Additionally the fluid domain contains the boundary conditions for inlet and outlet as well as "no-slip-wall"-conditions for all boundaries of the fluid-region. For the inlet-boundary-condition the static pressure was fixed at a constant mean value of 1bar. Depending on the actually investigated operation point of the pump, the mass-flow-rate was fixed at a constant value for the outlet. This enables the evaluation of pressure pulsations at the outlet of the pump, which were recorded in course of the reference measurements on the test-rig. The only moving parts within the CFD-model of the Rotary Lobe Pump are the two counter-rotating lobes which need to be defined as immersed-solid-domains with a user-defined speed. All the domain information including the required boundary conditions and the used turbulence models are summed up with Table1.

As initially mentioned comprehensive transient CFD-calculations were carried out to investigate the rotary lobe pump in a numerical way. As advection scheme the "High Resolution" method was chosen for the simulations presented in this paper. Furthermore the "Second Order Backward Euler" approach was used as transient scheme. The number of iterations between the single time-steps was fixed between 5 and 20 coefficient loops. The convergence criteria was fixed at a RMS-target of 10^-5. For the "Momentum Source Scaling Factor", which controls the size of the source terms of the Immersed Solid, the default value of "10" was chosen. The simulation time for the transient simulations was chosen in a way to calculate at least 3 full rotations of the rotating lobes. All simulations were carried out on "HP Compaq dc7900"-workstations with following hardware setup:

Processors: Intel Core 2 Quad CPU 3.00GHz
Memory: 8.00 GB RAM
System: Windows Vista Business 64Bit

Table 1. Domain data and boundary conditions

Domain-Type	Options	Chosen Settings
Fluid	Domain Motion	Stationary
	Inlet	Const. Static Pressure
	Outlet	Const. Mass Flow Rate
	Walls	No-Slip-Walls (Hydraulically smooth)
	Turbulence Model	k-ε (recommended for IMS [11]) / SST
	Wall Functions	Scalable / Automatic
Immersed Solid	Domain Motion	Rotating
	Angular velocity	+/- 300rpm

4.5. Evaluation of results

For every time-step (or angularity of the lobes) the physical quantities $m_{p\text{-}in}(t)$, $m_{p\text{-}out}(t)$, $p_{in}(t)$, $p_{out}(t)$, $M_{z(t)Lobe1}$ and $M_{z(t)Lobe2}$ were evaluated. With the help of these physical quantities the main characteristic pump data (Differential Pressure Δp, Mechanical Power P_{mech}, Hydraulic Power P_{hydr} and Total Pump Efficiency η_{Tot}) were computed and finally compared to the measured data.

$$\Delta\overline{p} = \frac{\sum_{t=0}^{t_{Sim}} \left(p_{out(t)} - p_{in(t)}\right)}{t_{Sim}} \quad \dots \ [Pa] \tag{1}$$

$$\overline{P}_{mech} = \frac{\sum_{t=0}^{t_{Sim}} \left(M_{z(t),Lobe1} + M_{z(t),Lobe2}\right)}{t_{Sim}} \cdot \frac{n \cdot \pi}{30} \quad \dots \ [W] \tag{2}$$

$$\overline{P}_{hydr} = \Delta\overline{p} \cdot \frac{\dot{m}_{out}}{\rho} = \Delta\overline{p} \cdot \dot{Q}_{out} \quad \dots \ [W] \tag{3}$$

$$\overline{\eta}_{tot} = \frac{\overline{P}_{hydr}}{\overline{P}_{mech}} \cdot 100 \quad \dots \ [\%] \tag{4}$$

Another focus was on the comparison of measured and simulated pressure pulsations at the inlet and outlet of the pump. Additionally the fluid flow in the regions of the gaps was investigated in more detail which will be presented in chapter 5.

4.6. Sensitivity analysis

After a first set of CFD-simulations, where a medium sized grid with approximately 720.000 nodes, a constant tip-clearance of s=0.6mm and an angular resolution of 4 degrees per calculated time-step was used, it turned out that the differential-pressure dependent volumetric losses were unexpected high and the achieved results therefore quite far from reality. Furthermore it became evident that the grid size, the grid-resolution around regions of clearances between fixed and rotating parts and the chosen time-step have a different influence on the quality of results. Based on these findings a sensitivity analysis was carried out in order to find out the ideal setup for the CFD-simulation of the rotary lobe pump.

5. ANALYSIS OF CFD-RESULTS AND COMPARISON WITH MEASUREMENTS

5.1. Results of the sensitivity analysis

In course of the sensitivity analysis the Δp-/Q-characteristics calculated with the help of the numerical simulation were compared to the characteristics measured on the test-rig which are marked with a thick dotted line in following figures. Figure 2 shows a comparison of CFD- and measurement-results for a variation of the general grid size between 500.000 and 1.350.000 nodes. For the simulation a constant speed of n=300rpm, an angular resolution of 4 degrees per calculated time-step, a tip-clearance of s=0.6mm and 5 prism-layers

within the gaps were used. As a simplification the face-clearance was completely neglected.

It turns out that a refinement of the CFD-grid leads to a more realistic reproduction of the fluid field and to an improved quality of results. The finer the grid the smaller is the difference between the measured and simulated characteristic lines.

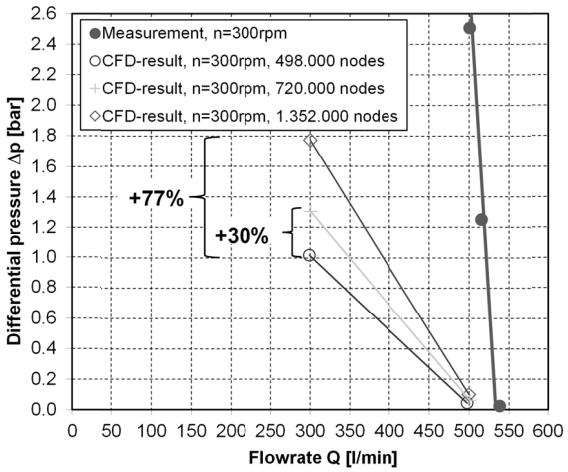

Figure 2. Results of the sensitivity analysis regarding the variation of mesh size

Furthermore the results show, that the maximum discharge (at Δp=0bar) is lower than measured on the test-rig. This is explained by the fact, that the pump-housing and the lobes were modelled based on basic sketches and the geometry therefore may not be exactly equal to the pump-geometry investigated in course of the experimental investigations. Additionally the clearance between moving and fixed parts of the CFD-model is adjusted by scaling of the lobes which leads to a reduction of the effective displacement volume. The deviation between the calculated and measured maximum discharge is therefore apparent in all other characteristic lines presented in this paper.

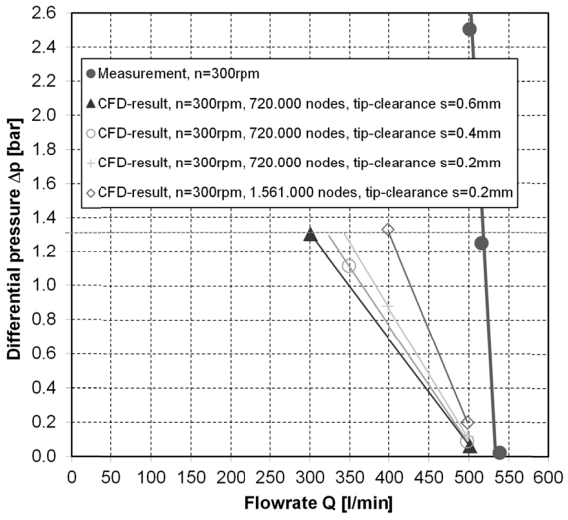

Figure 3. Results of the sensitivity analysis regarding the variation of tip clearance

Another set of CFD-simulations, using a medium sized mesh with 720.000 nodes, show the influence of the tip-clearance which varies from s=0.6mm to s=0.2mm for the thin marked Δp-/Q-characteristics shown in Figure 3. Additionally the CFD-simulation with a tip-clearance of s=0.2mm was recalculated with a refined mesh using a global mesh size of 1.500.000 nodes. Although the simulation results get closer to reality, the difference between measured and simulated characteristic lines is still unacceptable high.

The influence of the angular resolution per calculated time-step is shown with the results presented with Figure 4.

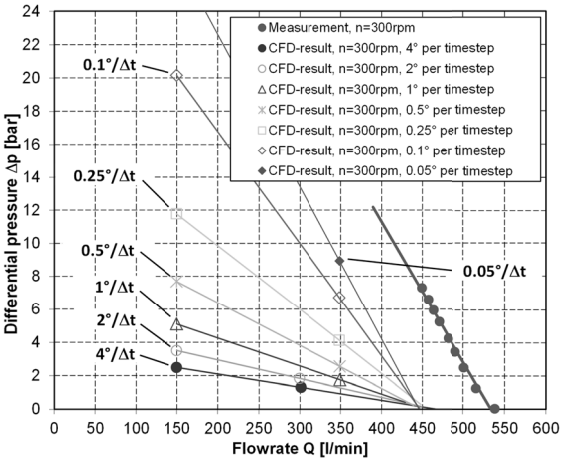

Figure 4. CFD-results regarding the variation of the angular resolution per time-step

Using the medium sized mesh with 720.000 nodes and a tip-clearance of s=0.6mm the angular resolution was reduced step by step from 4° per time-step (time-step=2.22*10-3s) to 0.05° per time-step (time-step=2.78*10-5s).

It turns out that the angular resolution has the strongest influence on the quality of results. The smaller the time-step chosen for the transient calculation, the longer the simulation time but the better the accordance between CFD- and measurement-results.

A more detailed look into the results shows that the refinement of the angular resolution leads to a more realistic development of the pressure pulsations at the outlet of the pump which is shown with Figure 5, where the pressure pulsations for an angular resolution of 1° (huge time-step, curve marked with crosses) and 0.02° (small time-step, curve marked with rhombuses) are compared to the lobe-angle-dependent center-clearance between the two mating lobes. As shown in Figure 5 the lobe-angle-dependent center-clearance varies between s=0mm and s=1.2mm which was determined on the geometric pump model with the help of an appropriate CAD-tool. The position numbers relate to lobe-positions shown in Figure 6.

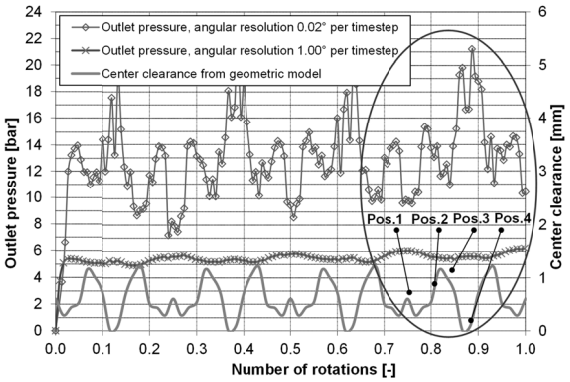

Figure 5. Influence of the center-clearance on the calculated outlet-pressure pulsations

The smaller the center-clearance in the real pump the lower the leakage losses and the higher the absolute pressure reached at the outlet of the pump. Figure 5 shows that the simulation with a resolution of 0.02° per time-step realistically relates to the lobe-angle-dependent center-clearance-curve while the simulation with a resolution of 1° per time-step seems to be unaffected by the continuously opening and closing clearance between the two mating lobes. Using an angular resolution of 0.02° the peak-values of pressure are reached when the centre clearance is perfectly closed (see also Figure 6).

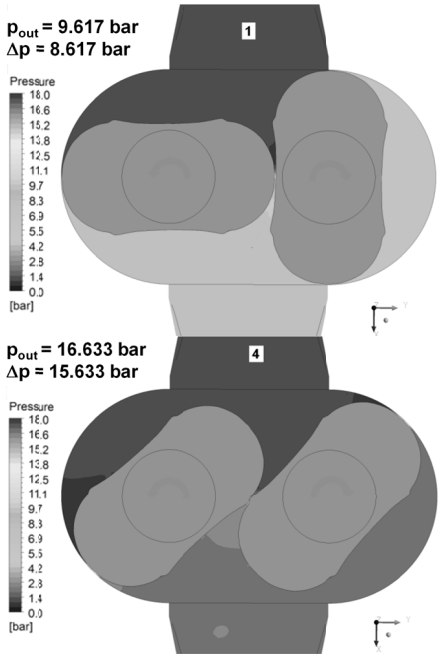

Figure 6. CFD-pressure-contours for different lobe positions

This was also discovered by VOGELSANG [1], who mentions that the maximum outlet pressure is reached and the pump delivers least, when the lobes contact at point S of the line of action (see Figure 7 and "Pos.4" in Figure 6). Conversely, the maximum delivery and minimum outlet pressure is reached, when the lobes contact at pitch point W (see also Figure 7 and "Pos.1" in Figure 6).

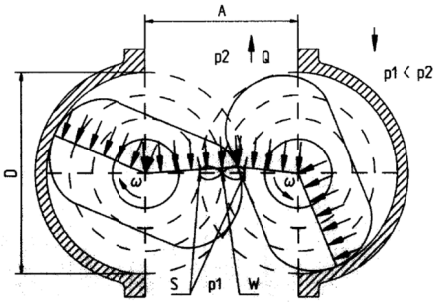

Figure 7. Contact points - Rotary Lobe Pump [1]

5.2. The optimized CFD-setup

Based on the conclusions drawn from the sensitivity analysis an optimized CFD-setup was defined. The settings for the optimized CFD-setup, which are a kind of trade-off between acceptable computing time and acceptable quality of results, are summed up as follows:

Number of nodes:	1.200.000
Prism-layers within the gaps:	z_{Prism}=7
Angular resolution / time-steps:	0.1°/5.56*10-5s
Constant speed:	n=300rpm

Tip- and face-clearance-measurements on the test-rig led to the conclusion that the average clearance accounts for s=0.1-0.2mm for completely new lobes which were used in course of the measurements. Depending on the total operation time of the pump and the abrasiveness of the pumped medium the clearance may even be larger in comparable pumps.

In order to carry out numerical simulations of rotary lobe pumps with such small clearances a large number of appropriate small elements have to be placed in the regions of the clearances. This leads to huge meshes and unacceptable long computation times. Therefore the minimum clearance was fixed with s=0.2mm=const. for the CFD-calculations.

In course of CFD-calculations three different operation points of the pump were calculated considering 3 full revolutions of the rotating lobes. A comparison of the CFD-results with the measurement-results is shown with Figure 8, where the characteristic curves of simulations with a clearance of s=0.4mm and s=0.2mm are compared with the measured values.

It turns out that a decreasing clearance in the CFD-model leads to a better approach of the measurement results. The gradient of the measured and simulated Δp-/Q-characteristic and therefore also the volumetric efficiency at s=0.2mm is even equal and thus points out the good quality of the CFD-calculations.

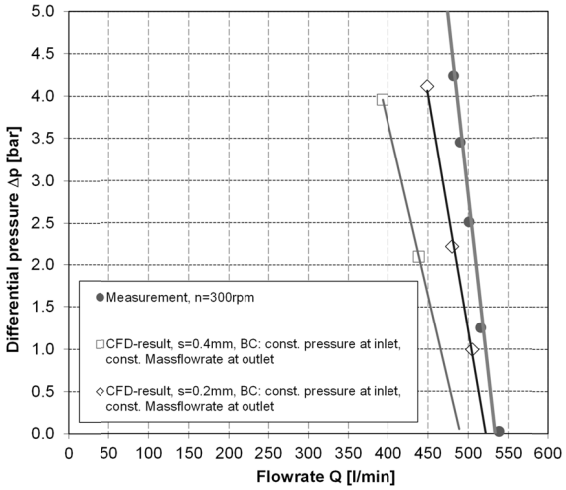

Figure 8. Characteristic lines calculated with the optimized CFD-setup

The main deviation between measurement and simulation appears at a differential pressure of 0bar. As previously mentioned this deviation is mainly based on the fact, that the tip-, center- and face-clearances was adjusted by scaling the two rotary lobes which consequently reduces the volumetric displacement of the pump.

On the other hand the application of an IMS-model leads to an underestimation of the viscous contribution of forces and torques on an immersed solid [11], which results in an over-prediction of the internal leakage which additionally decreases the volumetric efficiency of the investigated pump.

This underestimation of viscous forces does not only influence the volumetric efficiency but also the total efficiency of the pump. The under-estimation of viscous forces consequently leads to an under-estimation of the torque which finally results in an over-prediction of the total pump efficiency. This is shown with Figure 9 where the measured and simulated pump efficiency values are compared.

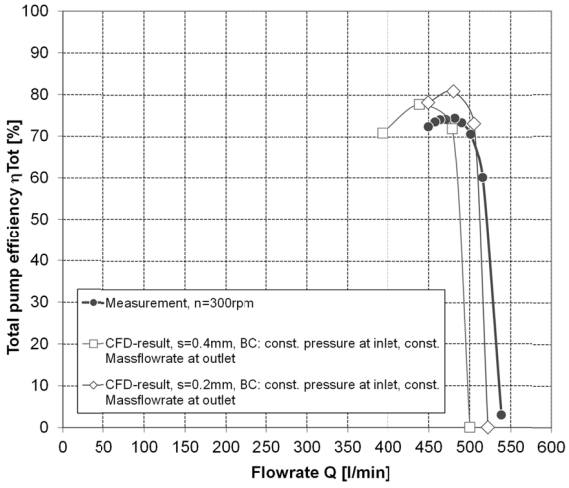

Figure 9. Efficiency lines calculated with the optimized CFD-setup

In order to account for the friction losses caused by the bearings, sealings and the gear box of the real pump a mechanical efficiency of 95% was incorporated in the calculation of the total pump efficiency of the CFD-results.

It turns out that the CFD-calculation leads to a total pump efficiency which is – considering a constant clearance of s=0.2mm - approximately 5 percentage points higher than the total pump efficiency detected on the test-rig.

A more detailed view into the results is given with Figure 10 which shows the velocity contours and the velocity-vectors within the tip-clearance between rotating lobe and the housing. The three detailed views a, b, c represent the three operation points for s=0.4mm shown in Figure 8. The conveying effect of the rotating lobe is strongly developed at a differential pressure of Δp=0.096bar (see detail "c"), and is getting lost at Δp=1.067bar (see detail "b").

It shows that the IMS-model is basically capable to calculate the velocity distribution in the gaps physically correct, although a no-slip-condition cannot be applied on the surface of the rotating lobes. Instead of the no-slip-condition the conveying effect of the moving lobe surfaces can be influenced by the variation of the "momentum source scaling factor" which was not done in course of this study but was investigated by Schwotzer [9] and Fuchs [8].

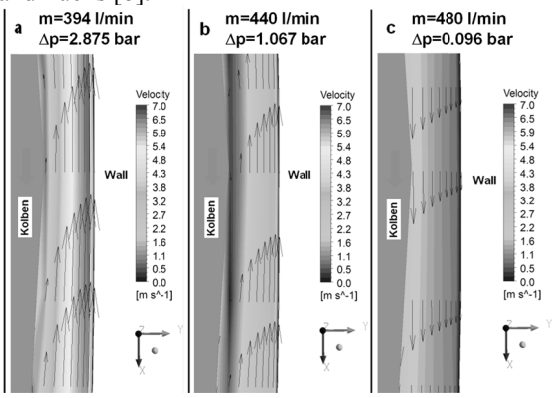

Figure 10. Analysis of gap flows at three different operation points

Figure 11 shows a comparison of measured and calculated pressure pulsations at a differential pressure of Δp=3.5bar. Based on the fact that a constant static pressure of 1bar was used as boundary condition for the inlet of the pump, no pressure pulsations at the inlet could be detected in the course of the CFD-calculations. The pressure pulsations calculated for the outlet of the pump show a quite good accordance with the measured data. The over-prediction of pressure pulsations in course of the CFD-calculations are based on the fact that the mass flow rate was kept at a constant value at the outlet of the pump.

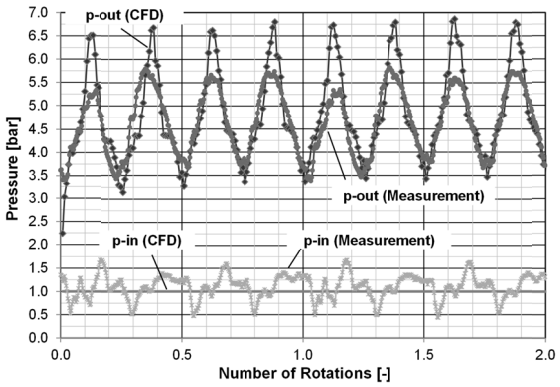

Figure 11. Comparison of pressure pulsations at the outlet of the pump

6. CONCLUSIONS

The results presented in this paper show that the Immersed-Solid-Method was successfully applied on the challenging numerical simulation of a Rotating Displacement Pump. The existence of comprehensive measurement-data led to a continuous improvement of the CFD-setup and finally suitable CFD-results were achieved within an acceptable range of computing-time. The CFD-results achieved by using an optimized CFD-setup basically show good accordance with the measurement-results achieved on the test-rig and come close to reality. Although there is a slight over-prediction of leakage flow the characteristic lines calculated in course of the CFD-simulations are close to the characteristics measured on the test-rig. Also the pressure pulsations detected at the outlet of the pump housing are well comparable.

More precise CFD-results may be achieved by more realistic boundary conditions for inlet and outlet considering transient flow conditions, which would have gone beyond the scope of this study.

Additional room for improvement was detected for the Immersed-Solid-Method itself which seems to be not fully developed yet. One deficiency is the inadequate wall-treatment of the immersed-solid-surface. The solid surfaces of an immersed solid are not explicitly resolved by the mesh. In addition a wall function cannot be applied to the boundary of the immersed solid. As a consequence, the quality of simulation results may be lower than can be obtained using mesh deformation or moving meshes that support the use of wall boundaries to directly resolve the solid surfaces. Nevertheless the achieved results are close to reality and basically display the physical flow phenomena known from theoretical studies [see Figure 11]. Further developments may be necessary for the turbulence-models available for the immersed-solid-method. The CFD-results presented in this paper were achieved by using the k-epsilon turbulence-model which is recommended for the immersed-solid-method by ANSYS-CFX [11]. A detailed look into the results led to the conclusion that the Reynolds-Number of the leakage flow in the tight gaps ranges between Re=800 and Re=2000 depending on the investigated operation point and the adjusted clearance. This shows that an adequate transition-model considering the transition between laminar flow in the tight gaps and turbulent flow in the main fluid region may lead to more accurate results.

Additionally the Immersed-Solid-Method does not enable the investigation of multi-phase-flows including cavitation phenomena, which are inherent in Rotating Displacement Pumps. The implementation of cavitation models is a matter of interest and may help to investigate the fluid-flow in the Rotary Lobe Pump in more detail.

REFERENCES

[1] Vogelsang H., Verhülsdonk B., Türk M., Hörnig G., 1999, „Pulsation problems in rotary lobe pumps", World Pumps.

[2] Vetter G., Kozmiensky R., 1999, „Pulsation and NPSHA in rotary positive displacement pumps", World Pumps.

[3] Klomberg S., 2011, „Numerische Simulation von rotierenden Verdrängermaschinen", Diploma Thesis, Graz University of Technology.

[4] Riemslagh K., Vierendeels J., Dick E., 2000, „An arbitrary Lagrangian–Eulerian finite-volume method for the simulation of rotary displacement pump flow", Applied Numerical Mathematics, Vol. 32, pp. 419–433.

[5] Yogendra M Panta, 2004, „Numerical Flow Analysis of Gear Pump", Master Thesis, Youngstown State University.

[6] Houzeaux G, Codina R., 2007, „A finite element method for the solution of rotary pumps", Computers & Fluids, Vol. 36, pp. 667-679.

[7] Vande Voorde J., Vierendeels J. Dick E., 2004, „Flow simulations in rotary volumetric pumps and compressors with the fictitious domain method", Journal of Computational and Applied Mathematics, Vol. 168, pp. 491ff.

[8] Fuchs M., 2010, „Numerische Simulation der instationären Strömung in einer Drehkolbenpumpe", Bachelor Thesis, Berlin University of Technology.

[9] Schwotzer T., 2009, „Simulation einer Drehkolbenpumpe mit der Immersed-Solid-Methode", Bachelor Thesis, Berlin Universtiy of Technology.

[10] Prakash M., Stokes N., Bertolini J, Tatford O., Gomme P., 2003, „SPH simulations of a lobe pump: Predition of protein shear stress at different pump efficiencies", 3rd International Conference on CFD in the Minerals and Process Industries, Melbourne, Australia.

[11] ANSYS Inc, 2009, „ANSYS CFX-Solver Modeling Guide", Release 12.1., Canonsburg.

Conference on Modelling Fluid Flow (CMFF'12)
The 15th International Conference on Fluid Flow Technologies
Budapest, Hungary, September 4-7, 2012

EXPERIMENTAL INVESTIGATIONS OF ROTATING INSTABILITIES IN A STEADY TURBINE GRID WITH HIGH SPEED PARTICLE IMAGE VELOCIMETRY

Robert SORGE[1], Paul Uwe THAMSEN[2]

[1] Corresponding Author. Department of Fluid System Dynamics, Berlin Institute of Technology. Straße des 17.Juni 135, D-10623 Berlin, Germany. Tel.: +49 30 31424024, Fax: +49 30 31421472, E-mail: robert.sorge@fsd.tu-berlin.de
[2] Department of Fluid System Dynamics, Berlin Institute of Technology. E-mail: paul-uwe.thamsen@tu-berlin.de

ABSTRACT

This paper discusses the experimental research of velocity fields in a high velocity circlet grid wind channel with time resolved, non-contact laser optical measurement method: High-Speed Particle Image Velocimetry (HS-PIV).

This research results in measured data that characterizes the complex fluid flow in the wake of the acceleration grid and the flow inside the compressor grid.

Using axial sections of the velocity distribution in the compressor grid starting at half-length of the blade's chord line the unsteady separation bubble can be observed at the suction side that developes into a circumferential-directed vortex. In the lower third of the compressor grid a massive blockage is presumed due to a massive gap of the hub vortex which highly influences the placement of seeding in the according measuring planes.

In contrast, the upper two-thirds in the compressor grid show pulsing accelerations that travel downstream.

Keywords: axial flow turbomachinery, HS-PIV, prismatic shaped controlled diffusion airfoil, rotating instability, velocity distribution

1. INTRODUCTION

Axial turbo machinery is structurally dependent on a radial clearance gap between the impeller and the casing. Depending on the clearance gap and the differential pressure of the impeller blades pressure and suction sides a clearance flow forms. Though interaction between clearance flow and the casing boundary layer a radial clearance vortex develops[1]. As long as the radial clearance vortex reduces corner separation, it can increase the compressor stages' efficiency. But if the blade loading increases to much, the radial clearance vortex grows into the compressor passage, blocks it and can be superposed by a circumferentially directed periodical disturbance, called Rotating Instability (RI). This RI travels opposite to the direction of rotating from compressor passage to compressor passage and shows a characteristic frequency pattern shorty before reaching the stability line. [2] [3] [4]. This broadband amplitude super elevation with a comb structure and a stable difference frequency Δf of peaks, as well as a linear phase transition for the frequency range of the comb structure for circumferentially distributed sensors are distinctive characteristics for RI. Ulbricht [5] and Weidenfeller et. al [6] [7] were independently able to verify RI in a steady turbine grid. Weidenfeller et. al [7] regarded an acoustic coupling of vortex separation at the tip clearance with an acoustic circumferential mode of the test rig as a cause for RI. Schrapp [8] [9] on the other hand sees the RI caused by the breakdown of the tip clearance vortex. In this process exactly the compressor passage is blocked in which the vortex breaks down. This causes the mainstream to be diverted into next the passage and a circumferentially coupled instability develops that travels with half of the circumferential speed.

2. TEST RIG

The Department of Aviation Drives at the Technical University of Berlin is operating the high velocity circlet grid wind channel for this research. The test rig was specially designed to produce unsteady flow phenomena in a static compressor grid at operating points near stall conditions [5] [10]. The required flow rate to obtain *Ma=0,4* and *Re=300.000* is provided by three centrifugal compressors. The adjustment control of the flow rate is realized by a throttle valve downstream of the compressor grid. The setting of this operating point is adjusted by changing the incidence angle of the accelerating grid. The parameters of

accelerating grid and compressor grid are shown in "Table 1".

Table 1. Parameters of accelerating grid and compressor grid

parameter	accelerating grid	compressor blades
airfoil	prismatic shaped controlled diffusion airfoil (CDA)	
chord length	*34mm*	*34mm*
aspect ratio	*1*	*1*
thickness	max. *3mm*	max. *2,7mm*
hub clearance gap	*3%*	*3%*
stagger angle	*50°*	*25°*
blades	*20*	*20*

A Quantronix Darwin PIV-100 laser with a wavelength of λ=*527nm* and a repetition rate up to $f_{rep} = 10kHz$, a Photron Fastcam SA1.1 with *1.024x1024 pixel* at *5.400 fps* and a synchronizer from ILA GmbH are used for the HS-PIV mesurments. The DEHS-Seeding, which is necessary to visualize the flow, is added into the settling chamber of the test rig. The light sheet is coupled with a downstream positioned strut made of acrylic glass with an Eppler 474 profile and an integrated enhanced aluminum mirror. The arrangement of the compressor grid, strut, mirror and light sheet is shown in Figure 1.

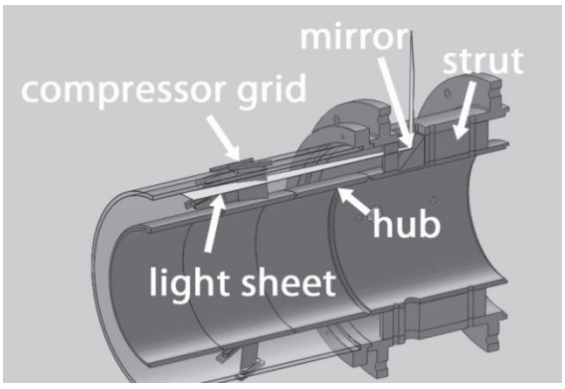

Figure 1. Arrangement of compressor grid, strut, mirror and light sheet

The light sheet thickness in the measuring plane is thinner than 1mm and adjusted to the measuring plane by a cross beam out of the test rig.

To calibrate the camera to the measuring plane and to adjust the light sheet, it is necessary to disassemble all test rig segments after the strut segment and to install a calibration target. The calibration target is inserted from the backside of the strut segment until it contacts the compressor grid.

To adjust the calibrating target to the measuring radius, it is initially arranged tangential to the hub and then traversed to the exact center of the blade section by a rotary table and linearly traversed to the right radius.

To adjust the light sheet to the calibration target during the laser operation mode, 3 fluorescing protusions are fitted to the target. This measure allows an exact control of adjustment and parallelism of the laser light sheet to the target during operation, even while wearing laser protection goggles.

After this procedure the camera can be arranged orthogonal to the target and a calibration picture can be taken. This enables conversion of the pixel coordinates to the global test rig coordinates. In Figure 2, the arrangement of the calibrating target is shown.

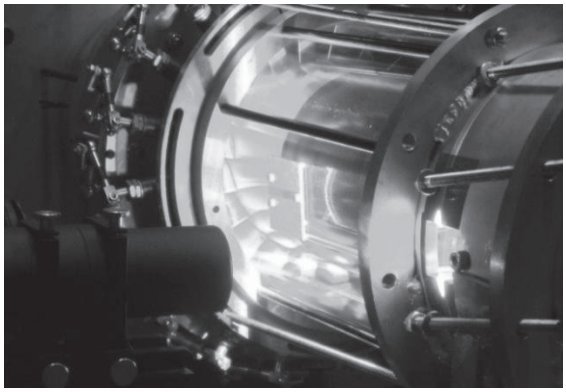

Figure 2. Arrangement of the light sheet to the calibration target

Since the first PIV-measurements are planned to be conducted directly within the compressor grid and also the near wall velocity distribution is to be visualized, it is necessary to minimize the reflection of the light sheet at the wall. This is realized by an anodic treatment of the aluminum blade and a subsequent coating with Rhodamin B endowed clear coat. Rhodamin B is a mineral which is absorbing a bigger part of the light with λ=*527* and emits the absorbed energy in another wavelength. The emission and absorption intensity of Rhodamin B is shown in Figure 3.

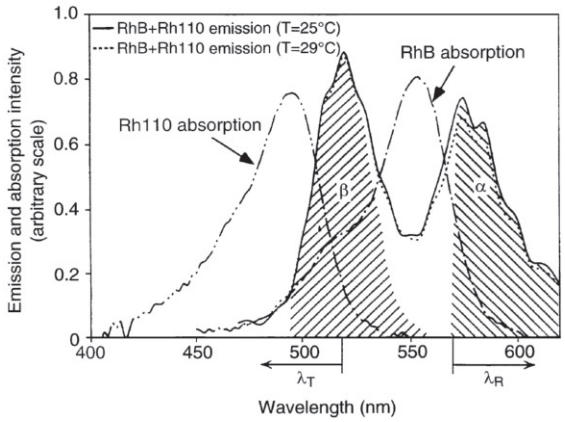

Figure 3. Emission and absorption intensity of Rhodamin B

The same procedure is exercised for the hub, therewith the reflection of hub does not overexpose the picture and the reflection of the seeding can be detected more clearly. To avoid detection of light with the shifted wavelength emitted by the Rhodamin B layer a band pass filter with a *transmission rate >85%* at λ*=532±2nm* is used. During operation temperatures within the compressor grid reach *T=50°C*. This requires preceding pilot testing to evaluate the wavelength shifting induced by the Rhodamin B layer in relation to temperature changes. The pilot tests were conducted on the basis of [11] on plates coated with Rhodamin B.

These measurements ensure that the coating features the required characteristics over the whole range of operation.

Figure 4 shows the test rig from the stilling chamber to the throttle valve and the edgewise arranged Fastcam and light sheet optic.

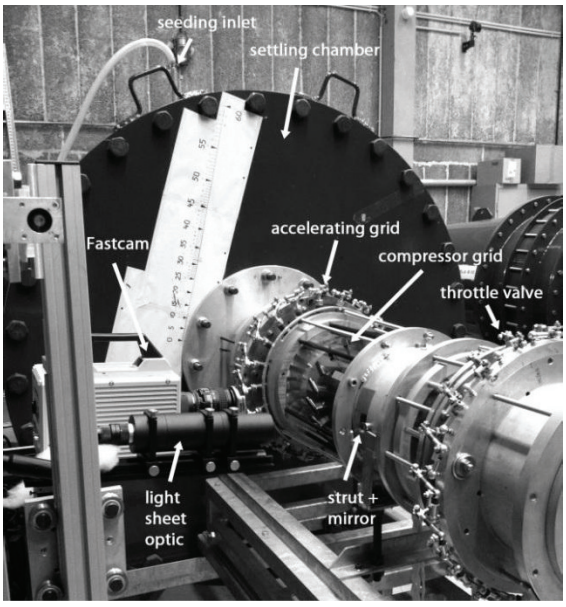

Figure 4. Test rig

3. RESULTS

For measuring the incident flow conditions to the compressor blades, the compressor grid is completely removed and exchanged for a cylinder segment of acrylic glass. This is necessary to provide optical access for the laser-light-sheet into this area. According to this modification it must be accepted that the upstream effect of the blades can not be evaluated in the results.

The incident flow velocities were measured at five different radial levels and the with a repetition rate of $f_{rep} = 3kHz$. The axial position is shown in Figure 5.

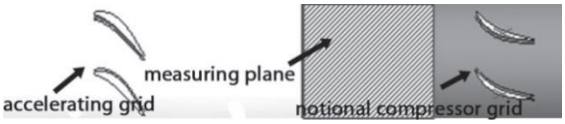

Figure 5. Position of the measuring plane between the acceleration and compressor grid

The incident flow conditions at the compressor blades, the swirl angles and the velocities are mean frames of *500* single frames and are shown in Figure 8. The measurements were conducted in 5 tangential planes with a distance of *5mm* to *25mm* to the hub. In the single frames no large scale structures can be observed. This indicates that the incident flow contains only small scale dissipating vortices. The mean frames are illustrating that the wake of the accelerating grid is very nonhomogeneous and is merging slowly with growing distance. Regarding the swirl angle and the velocity over the radial positions, it can be perceived, that both decrease with increasing radius. Likewise good identifiable are wake dents that are assumed to be caused by delamination at the accelerating grid. The incident flow conditions were additionally measured by the associate partner with 5-hole probes [12]. The head diameter of the probe is *3mm* and took away *10%* of the channel height. The measurements were conducted in one axial section of one blade section including part of the neighboring blade sections at different circumferential and radial positions. The mean values of *150.000* measurements are shown in Figure 6. The axial position of the five hole probe was *65mm* ahead the axis of the compressor blades. To make the comparison of the HS-PIV measurements and the five hole probe measurements easier, the HS-PIV measurements are converted to the same coordinates Figure 7. It would be advised that the measurement plane is rotated *90°*. However, the comparison shows that both measurement methods identify a major swirl angle in the hub section. They are scaling down with growing radius. Anymore both methods show a local increasing of swirl angle in the upper half. The division of the swirl angle is a little bit greater

than the blade division. So the incident flow conditions are not symmetric in circumferential direction. The differences in absolute values and the difference in the position of the local increasing can be ascribed with blocking of the five hole probe, the missing compressor grid during the PIV measurements and of the *90°* rotated measuring window.

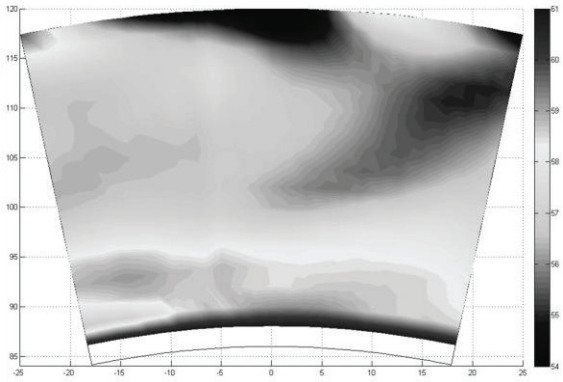

Figure 6. Swirl angle of the inflow at position *x=461mm* measured with a five hole probe

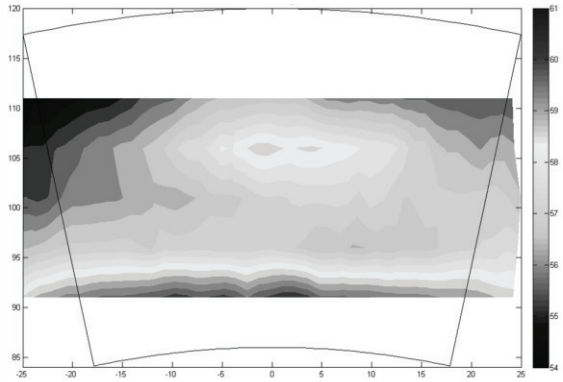

Figure 7. Swirl angle of the inflow at position *x=461mm* measured with HS-PIV

Figure 9 shows the velocity fields of the compressor grid measured with a repetition rate of $f_{rep} = 5kHz$ and averaged over *0,1* seconds. Based on the mount of the compressor blades there are some areas, where no velocity can be measured. An additional challenge within the measurements was to get the seeding in every measuring plane. Due the seeding inlet is upstream in the stilling chamber and due the gab vortex, there is too little seeding in lower levels [8].

Anyhow, there are a lot of informations in the mean values. In plane *z=21mm* and *z=19mm* the suctions side flow separation can be found at half chord length. On the pressure side a decrease of velocity in direction of the wall can be assessed. Furthermore, on the pressure side at the trailing edge a local increase of velocity can be observed. In plane *z=18mm* is until the half chord length more than half of the compressor blade passage blocked and downstream the mainstream at the pressure side is increasing again. In plane *z=17mm* the mainstream decreases more and more on the pressure side. From plane *z=16mm* to *z=10mm* there is forming a local velocity maximum between the leading edges of the blades that cannot cross the compressor passage. This is a hint for a three dimensional flow transverse to the measuring planes, that cannot be detected with two dimensional HS-PIV under this view angle. Another hint for blocking the passage is the back flow area at the trailing edge of the suction side in planes *z=14mm* until *z=10mm*.

The fact, that in plane *z=6mm* and *z=4mm* is no seeding and therefore no velocity information is available, supports the thesis, that the hub gab vortex is blocking the mainstream increase. Schrapp et al. describe an equivalent phenomenon in [8], [9]. In contrast to the averaged velocities, the time resolved measurements give a hint how the unsteady flow behaviours are growing. Figure 10 shows exemplary the velocities in plane *z=21mm* with a time interval of *dt=0,2ms*. The already described flow separation on the suction side is not fixed along the chord length, but rather slipping as a function of mainstream velocity. Once an area of higher velocity passes the middle chord length, the separation point is shifting upstream and the area of the separation area increase to the middle of the blade section. Furthermore, the areas of higher velocities shift from suction to pressure side while passing the blade section. By observing the wake of the compressor blades, it can be seen that the pulsing velocity field rotates.

4. CONCLUSIONS

The unsteady flow behaviours in an axial compressor grid as well as the incident flow conditions are measured with time resolved, non-contact, laser optical measurement method: High-Speed Particle Image Velocimetry. The investigations in incident flow conditions show, that the compressor grid is loaded with unsymmetrical conditions. The measurements in the compressor blade section and in the wake show the suction side separation of flow in the upper half blade section. In the lower half of the blade section the back flow on the suction side increases with decreasing hub distance. The lower third of the passage is almost blocked and the reason is assumed by brake down of the hub gab vortex. Further measurements will be identifying the reason for the blocked areas and locate the source of the pressure measured rotating instability.

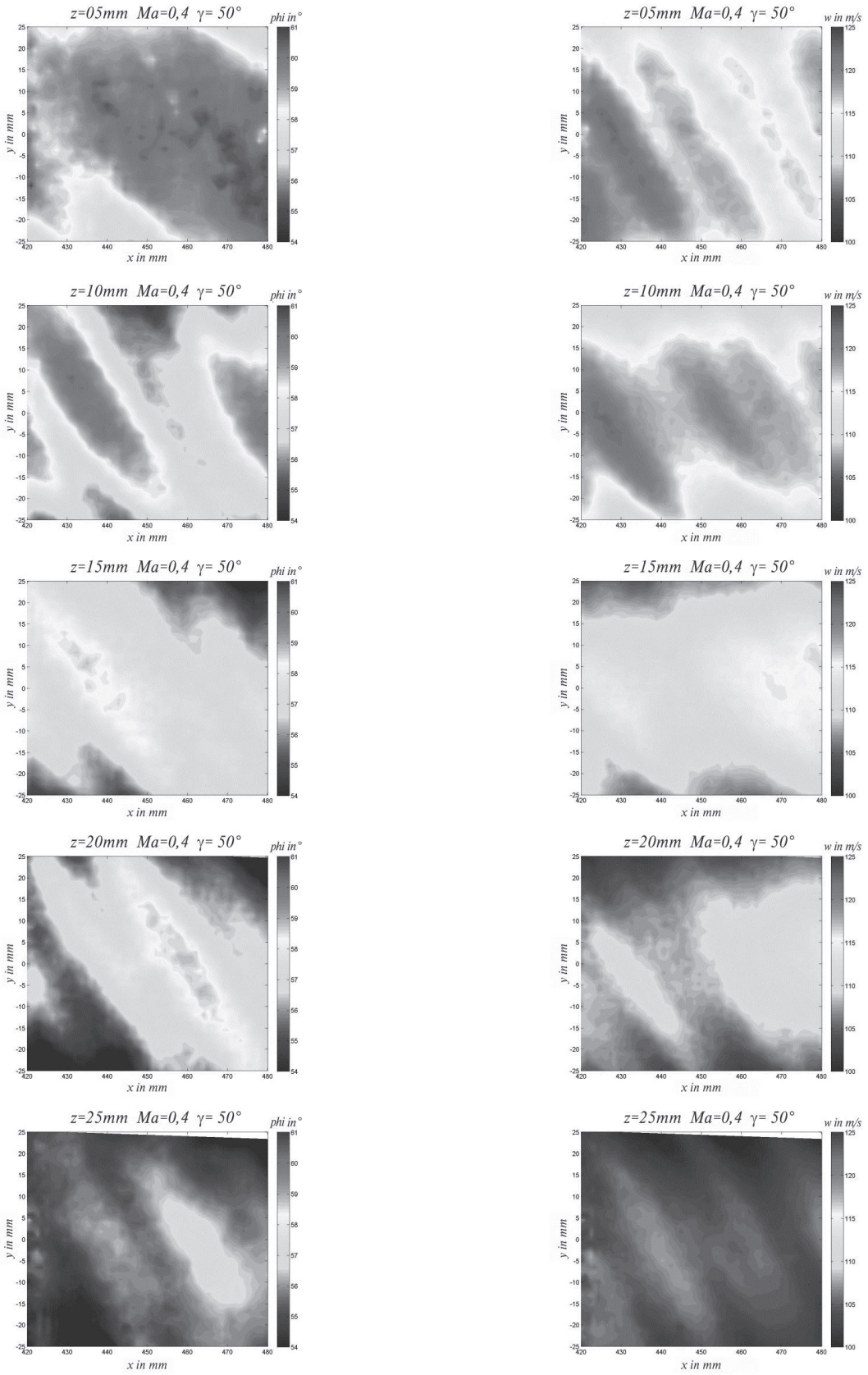

Figure 8. Inflow conditions to the compressor blades, (left) swirl angles (right) velocities

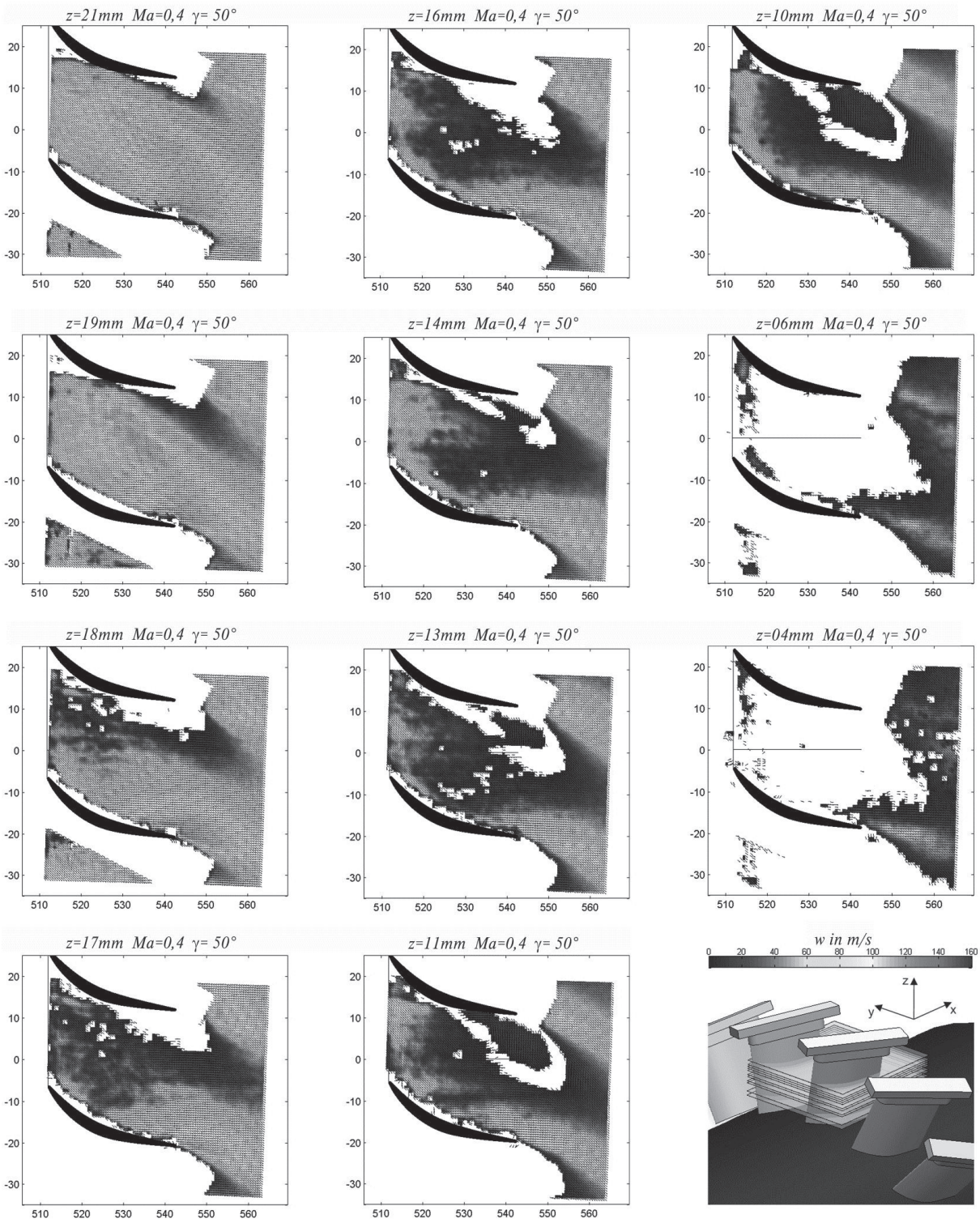

Figure 9. Mean values of the velocities of the compressor grid section at radial positions between *z=4mm* and *z=21mm*

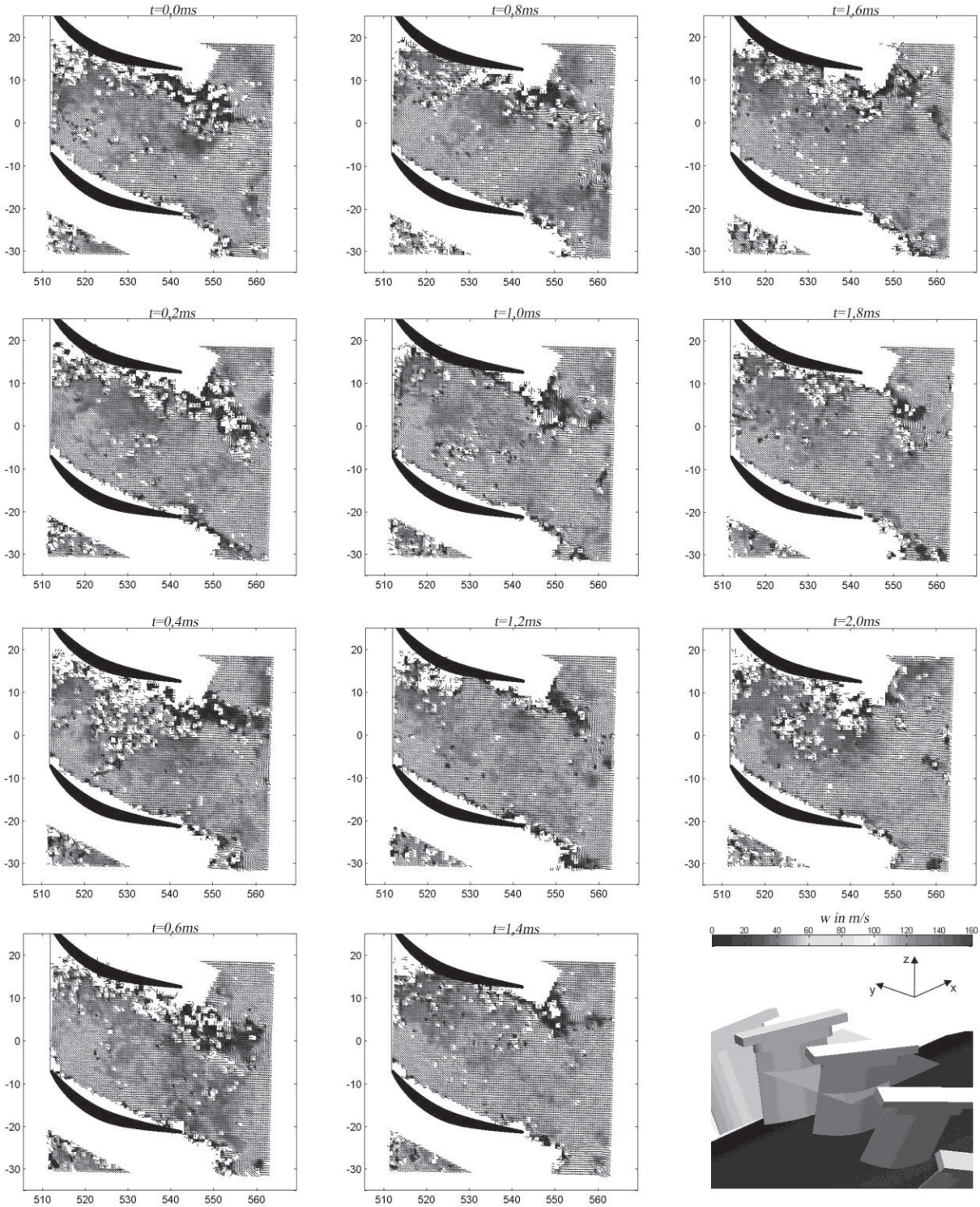

Figure 10. Velocities of the compressor blade section at a radial position of *z=21mm* with a time distance of *dt=0,2ms*

ACKNOWLEDGEMENTS

The presented results have been produced within the project "Flow induced acoustics in turbo machinery" funded by the German Research Foudation (DFG).

The author thanks everybody who made this paper possible.

REFERECES

[1] Cumpsty, N. A., 2004, „Compressor Aerodynamics", *Krieger Puplishing Company*

[2] Kameier, F., 1993, „Experimentelle Untersuchung zur Entstehung und Minderung des Blattspitzen-Wirbellärms axialer Strömungsmaschinen", *Dissertation Technische Universität Berlin*

[3] Kameier, F., Neise, W., 1997, „Experimental study of tip clearance losses and noise in axial turbomachines and their reduction", *Journal of Turbomachinery,* Vol. 119, pp. 460-471

[4] Mailach, R., , F., Neise, W., 2001, „Rotating Instabilities in an Axial Compressor Originating From the Fluctuating Blade Tip Vortex", *Journal of Turbomachinery*, Vol. 123, pp. 453-463

[5] Ulbricht, I., 2001, „Stabilität des stehenden Ringgitter", *Dissertation Technische Universität Berlin*

[6] Weidenfeller, J., 2001, „Experimentelle Untersuchung der stationären und instationären Strömung eines Axialverdichtergitters", *Dissertation Universität Kassel*

[7] Weidenfeller, J., Lawerenz, M., 2001, „Experimentelle Untersuchung zeitabhängiger Vorgänge in einem axialen Verzögerungsgitter", *Dissertation Universität Kassel*

[8] Schrapp, H., 2008, „Experimentelle Untersuchungen zum Aufplatzen des Spaltwirbels in Axialverdichtern", *Dissertation Technische Universität Braunschweig*

[9] Schrapp, H., Stark, U., Saathoff, H., 2008, „Breakdown of the tip clearance vortex in a rotor equivalent cascade and in a single-stage low-speed compressor", *ASME Coference Proceedings 2008,* pp.115-129

[10] Ulbricht, I., Hourmouziadis, J, 1999, „Stabilität des stehenden Ringgitters", *AG Turbo Turbotech II annual report*

[11] Sakakibara, J., Adrian, R. J., 1999, „Whole field measurement of temperature in water using two-color laser induced fluorescence", *Experiments in Fluids 26, Springer-Verlag*

[12] Beselt, Ch., Peitsch, D., Pardowitz B., Enghardt, L., 2011, „Strömungsinduzierter Schall in Turbomaschinen – Die Rotierende Instabilität", *Deutscher Luft- und Raumfahrtkongress 2011*

[13] Raffel, M., Willert, C.E., Wereley, S.T., Kompenhans, J, 2007, „Particle Image Velocimetry", *Springer-Verlag*

[14] Schröder, A., Willert, C.E., „Particle Image Velocimetry-New Developments and Recent Applications" *, Springer-Verlag*

Conference on Modelling Fluid Flow (CMFF'12)
The 15th International Conference on Fluid Flow Technologies
Budapest, Hungary, September 4-7, 2012

EVALUATION AND ANALYSIS OF THE STOCHASTIC UNSTEADINESS IN THE LAST STAGE OF A COUNTER-ROTATING TWO-SPOOL TURBINE RIG

Davide LENGANI,[1] Cornelia SANTNER, [2] Emil GÖTTLICH [3]

[1]Corresponding author, Inst. f. Thermal Turbomachinery and Machine Dynamics, Graz University of Technology, Inffeldgasse 25/A, 8010 Graz, Austria. Tel.: +433168737739, Fax: +43316873107739, E-mail: davide.lengani@tugraz.at
[2]Inst. f. Thermal Turbomachinery and Machine Dynamics, Graz University of Technology, E-mail: cornelia.santner@tugraz.at
[3]Inst. f. Thermal Turbomachinery and Machine Dynamics, Graz University of Technology, E-mail: emil.goettlich@tugraz.at

ABSTRACT

This paper describes the results of an extensive measurement campaign carried out in the counter-rotating two-spool transonic turbine rig at Graz University of Technology. The test setup consists of a high pressure (HP) stage, a diffusing mid turbine frame with turning struts and a shrouded low pressure (LP) rotor and it is operated at aerodynamic conditions relevant for current aero-engines.

A fast response aerodynamic pressure probe has been employed to provide time resolved aerodynamic area traverses inside the facility. The paper presents a method for evaluating the stochastic unsteadiness based on Fourier filtering. The stochastic fluctuating component of the total pressure is strictly correlated to the turbulence intensity. Hence, its determination allows the discussion of the interaction processes on the last stage of the turbine. The unsteadiness of the HP rotor influences considerably the aerodynamics of the intermediate duct. However, the losses upstream of the LP rotor are strictly correlated to the steady evolution of the flow that diffuses in the duct. Downstream of the LP rotor, the turbulent fluctuations are instead induced by the vortical structures of the turning struts and their unsteady interaction with the rotor blade.

Keywords: Counter rotating turbine, Fast response pressure probe, Unsteady interactions, Stochastic fluctuations

NOMENCLATURE

2S-FRAPP		2 sensor fast response aerodynamic pressure probe
BPF	$[Hz]$	Blade passing frequency
H	[-]	Relative channel height
HP, LP		High, low pressure
M	[-]	Mach number
PS, SS		Pressure, suction side
TMTF		Turning mid turbine frame
p_t	$[Pa]$	Total pressure
t	$[s]$	Time
v	$[m/s]$	Absolute velocity
θ	$[deg]$	Circumferential coordinate
ρ	$[kg/m^3]$	Density
$< ... >$		Deterministic periodic component

Subscripts and Superscripts

MAX	Maximum value, in the local plane
RMS	Root mean square
$\bar{}$	Time averaged properties
$\sim$	Ensemble-averaged properties
$'$	Stochastic fluctuating component

1 INTRODUCTION

The accuracy of the computational models available to aero-engine designers depends on their ability to account for deterministic and stochastic unsteadiness. For this reason, since the beginning of the 90s, a very large amount of time resolved measurements performed in test rigs with engine-relevant conditions has been provided in the open literature (e.g., [1, 2, 3, 4]). In the last years, among other components of the aero-engine, the designers and then the researchers have focused their attention on the intermediate turbine diffuser, which connects the high pressure (HP) with the low pressure (LP) turbine stages. The current design trend of this component leads to very high radial offsets between the HP and LP frames. Hence, this diffusing duct may face the problem of flow separation and therefore it is critical for the aerodynamic performances.

The review paper of Göttlich [5] summarizes the large amount of research performed in the last years on intermediate turbine diffusers. It has been shown that the unsteadiness of the HP stage, particularly the vortices shed by the HP rotor, helps the duct boundary layer to better withstand the adverse pressure gradient. Further, this unsteadiness influences the secondary flows of the turning vanes embedded in the diffuser and hence its outlet flow. However, the amount of works that could present the impact on the aerodynamic performance of the diffusing duct together with up-and downstream components is still limited.

The present paper includes time resolved aerodynamic area traverses performed on a recently developed test setup for turning mid turbine frames

(TMTF) with up- and downstream turbine stages operated at engine-relevant conditions [6]. A two sensor fast response aerodynamic pressure probe (2S-FRAPP) in a four-sensor virtual mode is used to provide the unsteady flow field in the last stage of this test turbine. The paper focuses on the isolation of the deterministic and stochastic fluctuations. In particular, the two rotors interact and the deterministic fluctuations may be identified at frequencies that correspond to the linear combinations of the two blade passing frequencies, as it has been shown in Lengani et al. [7]. The method proposed by Camp and Shin [8] and Oro et al. [9] to determine the stochastic component of the signal is used and extended to the case of a two shaft facility. The stochastic component of the signal is obtained filtering out, in the frequency domain, the sources of deterministic unsteadiness.

The first part of the paper discuss in details the method and the post processing procedure. Then, results in two measurement planes up- and downstream of the LP rotor of the facility are analyzed in terms of time resolved velocity and stochastic fluctuations of total pressure.

2 TEST FACILITY

The Institute for Thermal Turbomachinery and Machine Dynamics at Graz University of Technology operates a 3 MW compressor station to supply a couple of test facilities with pressurized air. Experiments were carried out on the continuously operating cold-flow counter-rotating test turbine facility. A full description of the test facility is provided by Hubinka et al. [6].

The test turbine facility (Fig. 1) consists of a transonic HP stage and a counter-rotating LP stage, where an S-shaped turning mid turbine frame guides the flow from the unshrouded HP rotor to the LP rotor. The HP turbine consists of 24 vanes and 36 blades. For the LP stage, a blade count of 16 turning struts and 72 blades was chosen in order to minimize the risk of excitation of the LP rotor.

This unique configuration allows the testing of rig inserts under aerodynamic conditions relevant for modern aero-engines, the operating condition was provided by MTU Aero Engines. The investigated aero design has an overall pressure ratio of 4. The total pressure ratio is 3 for the HP turbine and 1.3 for the LP turbine. The HP vanes are operating under choked conditions. The absolute Mach number at the TMTF inlet is 0.5. This is representative for realistic duct inlet conditions of modern jet engines with a single stage HP turbine at cruise operating point. More details on the operating condition of the facility may be found in Santner et al. [10].

3 MEASURING TECHNIQUE

3.1 *Fast response pressure probe*

Unsteady flow measurements were performed by means of a 2-sensor fast response aerodynamic probe (2S-FRAPP) [11], operated as a virtual four sensor probe for 3D aerodynamic measurements. Flow parameters

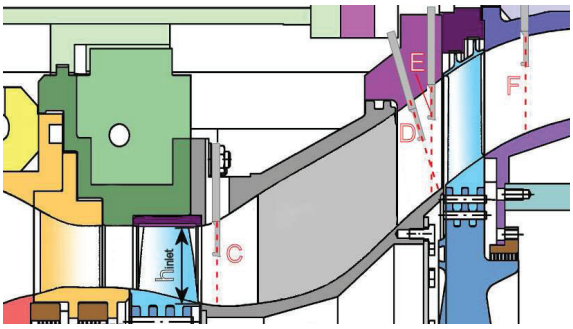

Figure 1. Schematic meridional section of the test facility with probe measurement planes (C, D, E, F), the results presented in the paper refer to planes D and F

including total and static pressure, flow angles and velocity components are derived from three rotations of the probe and a set of calibration coefficients (see for example Porreca et al. [12]). This probe is a modified version of the conventional cylindrical single sensor probe: the sensor sensible to the yaw angle is classically mounted on the cylindrical part and the second sensor, sensible to pitch angle, is mounted on the shaped probe head. The dimensions of each piezoresistive sensor are 0.4×0.8 mm, the distance between the two sensors is approximately 2.2 mm and the tip diameter of the probe is 1.8 mm. This concludes that the sensing area of the probe is in the order of 3.9 mm^2. The absolute uncertainties of the used probe techniques are equal to ± 0.3 deg for the flow angles, and $\pm 0.4\%$ for the Mach number. The uncertainty on the absolute value of the total pressure is ± 300 Pa when the uncertainty of the multi channel pressure transducers, employed to operate the facility, is also considered.

The present paper describes the results obtained by the probe in annular sectors in planes D and F (marked in Fig. 1). Plane D is a plane inclined by 110 deg to the horizontal direction and, at midspan, its distance from the vane trailing edge is 14% of the TMTF axial chord; whereas, plane F is perpendicular to the horizontal direction and is located at 77% of the rotor chord downstream of the blade trailing edge. Area traverses were performed over one strut pitch (22.5 deg). The measurement grid consists of 21 positions along the span and of 46 positions over the pitch for both planes (D and F).

The yaw sensor of the 2S-FRAPP measures directly the total pressure within a certain insensitivity to the flow angles (± 11 deg in the present case to both pitch and yaw angles). This is a typical characteristic of cylindrical pressure probes and it was verified during the calibration. Instantaneous total pressure fluctuations may be then derived if the instantaneous flow angle fluctuation remains inside the insensitivity range, where the pressure measured by the sensor is the instantaneous total pressure [13]. To obtain this condition, the central rotation of the probe was positioned along the time mean

flow direction, which was obtained from a preliminary measurement campaign with a five hole probe [10]. In the present case, in the measurements plane D, the maximum, time resolved, variation of the yaw angle with respect to the time mean direction does not exceed ± 10 deg. Whereas, the range of insensibility to the pitch angle variation is exceeded in a region of the plane, as it will be shown in the result section. It has to be noted that in this region not even the pitch sensor allows a direct reading of the instantaneous total pressure. Similar considerations may be formulated for plane F, for which the yaw angle deterministic fluctuations were shown in Lengani et al [14].

3.2 Data reduction method

Data is acquired at 200 kHz for 2 seconds, it corresponds to more than 100 revolutions of the LP turbine and more than 350 of the HP turbine. The determination of the flow properties is made possible after phase averaging: the periodic fluctuations of velocity, pressures and flow angles are determined at each phase from the phase averaged values of the three rotations of the probe [12].

The 2S-FRAPP signals, and the two shaft encoders were acquired simultaneously, in order to provide the frequencies of rotation of the two shafts. Such measurement allows the decomposition of the flow with respect to the phase of one of the two rotors, hence, the effects of the two rotors on the flow may be observed separately. Furthermore, it allows also the reconstruction of a phase that takes into account the relative rotor-rotor positions (see Lengani et al. [7]).

Phase averaging may be commonly performed triggering the flow with one of the 2 shaft encoders according to the triple decomposition procedure [15], for a generic variable q:

$$q(t) = \overline{q} + < q(t) > + q'(t) \tag{1}$$

where $< q(t) >$ is the purely periodic component associated with a coherent periodic structure and $q'(t)$ is the random fluctuation associated mainly with turbulence. This decomposition is used to characterize a single source of periodic unsteadiness and, in the present case, allows isolating the effects of each rotor. However, considering the presence of two rotors at uncorrelated frequencies the following decomposition is valid [7]:

$$\begin{aligned} q(t) \;\; = \;\; & \overline{q} + < q(t) >_{HP} + < q(t) >_{LP} + \\ & + < q(t) >_{HP,LP} + q'(t) \end{aligned} \tag{2}$$

Where the 2 distinct purely periodic components $< q(t) >_{HP}, < q(t) >_{LP}$, namely the coherent structures due to the HP and LP rotor respectively, have their own period and frequency. The term $< q(t) >_{HP,LP}$ indicates the rotor-rotor interactions which generate energy content at the frequencies of the linear combination $i \cdot BPF_{LP} + k \cdot BPF_{HP}$ (with i and k integer and not zero), which are observed in two shaft facilities (e.g., [7, 16]).

Classically, considering eq. 1, the stochastic fluctuating component is computed subtracting from the instantaneous value $q(t)$ the phase averaged value $\tilde{q} = \overline{q} + < q(t) >$. When two rotors are interacting, eq. 2 should be considered and hence the stochastic fluctuating component $q'(t)$ is obtained as:

$$\begin{aligned} q'(t) \;\; = \;\; & q(t) - (\overline{q} + < q(t) >_{HP} + \\ & + < q(t) >_{LP} + < q(t) >_{HP,LP}) \end{aligned} \tag{3}$$

This requires a particular phase averaging procedure, rotor synchronic averaging (RSA) as introduced in Lengani et al. [7], which takes into account for the relative positions of the two rotors in an absolute reference system. In particular it has been shown that the overall unsteadiness may be resolved creating a new trigger from coincidence positions of the blade passing periods interpolated from the shaft encoder.

In order to avoid such particular phase averaging procedure, Fourier filtering has been adopted here to determine the stochastic fluctuating component. Figure 2 schematically represents the post processing procedure, extending the method of previous works (e.g., [8, 9, 17]). Considering this figure, the fluctuating part of a variable directly measured from a probe, total pressure in the present case, may be determined with the following steps:

1) FFTs are performed over sufficiently large blocks of samples in order to have a good frequency resolution;

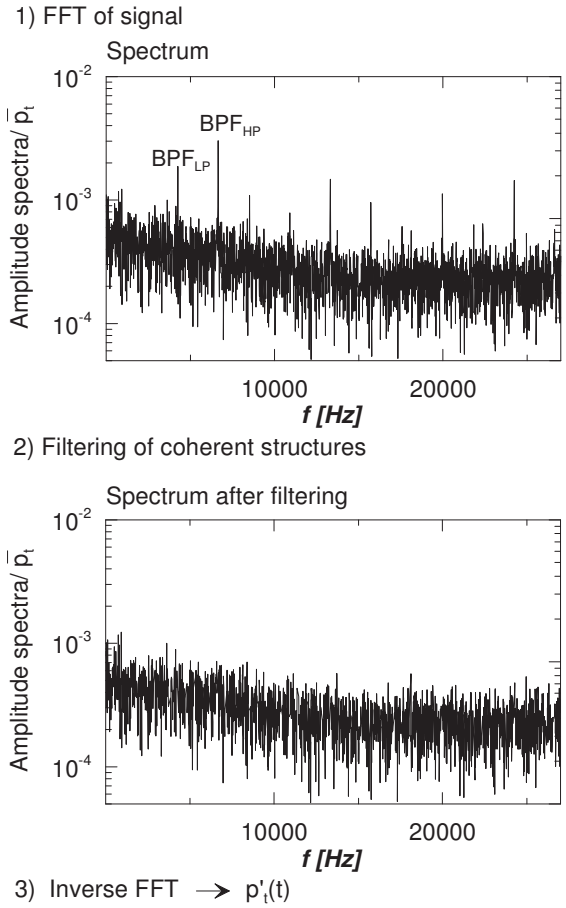

Figure 2. Schematic representation of the post-processing procedure

2) the amplitude of the deterministic periodic components is digitally filtered out setting it to zero (the sources of the deterministic fluctuations will be defined in the followings);
3) the "chopped" spectrum is transformed back into the time domain to directly provide the random fluctuating signal.

The deterministic unsteadiness contributions may be identified (top of Fig. 2) at the linear combinations of the blade passing frequencies of the two rotors ($i \cdot BPF_{LP} + k \cdot BPF_{HP}$). In the "chopped" spectrum (bottom of Fig. 2) the amplitude of these frequencies is set to zero. Furthermore, the energy content at the rotational speed of the HP and LP rotor and its multiple has also been set to zero. This procedure is done in order to remove from the stochastic fluctuating components any possible contribution due to deterministic stresses of the two rotors. In fact, even the smallest geometrical asymmetries of the rotor blades may generate energy content at the multiple of the rotational speed of the rotors (see Lengani et al. [7, 17, 18]). In the present facility the rotors were manufactured with very high geometrical precision. Particularly, the energy content at the rotational speed of the LP rotor is negligible. Whereas, the HP stage is characterized by strong shock waves, which enhance the generation of unsteadiness at low frequencies even for very small geometrical asymmetries of the blades (see for example McAlpine and Fisher [19]).

To better identify these contributions in the frequency domain, the steps "1, 2, 3" are performed twice [18]. At first, the FFT block length is set to be as close as possible to a multiple of the revolution period of the HP rotor. By this operation, the frequency resolution is about a divisor of the rotational speed of the HP rotor. The second time the FFT block length is set to be proportional to the LP rotor revolution period (this operation requires the resampling of the signal, see Lengani et al. [17, 18] for more details). In the first step the amplitude of the frequencies at the multiple of the BPF_{HP} and of the revolution period of the HP rotor are removed. Whereas, in the second step the amplitude of the coherent frequencies generated by the LP rotor and the linear combinations $i \cdot BPF_{LP} + k \cdot BPF_{HP}$ (with i, k non zero) are removed.

The final result of the post-processing procedure is the time resolved evolution of $p'_t(t)$. This data is further post-processed in order to provide the root mean square value $p'_{t,RMS}$ of its time or phase average. The time average is performed over ≈ 250000 samples, while the phase average is performed over ≈ 8500 samples (these numbers include the reduction of the original samples due to the resampling procedures).

4 RESULTS AND DISCUSSION

This section provides time resolved and time averaged results in the measurement planes D and F. The results are presented in Fig. 3, 4 and 5. These aerodynamic area traverse plots are views in the downstream direction on a sector covering one pitch of the TMTF. Consequently, the pictures cover 4 and 1/2 LP rotor blades and 2 and 1/4 blades of the HP rotor. In the plots the LP rotor has a clockwise sense of rotation while it is the opposite for the HP rotor.

Contour plots of the absolute Mach number and the stochastic fluctuations of total pressure in the absolute (stationary) reference frame are depicted in the figures. These quantities are plotted as non-dimensional coefficients. The Mach number is shown in terms of M/M_{MAX}, where M_{MAX} is the maximum value of the time averaged Mach number in the local measurement plane. Whereas, the stochastic fluctuations of total pressure $p'_{t,RMS}$ are made non-dimensional by ρv^2_{MAX}, where the term maximum is always referred to the time averaged value in the local measurement plane.

The term $p'_{t,RMS}$ is computed as the root mean square of the stochastic fluctuations according to the filtering procedure described in the previous section and considering the instantaneous measured pressure from the yaw sensor of the probe. As mentioned in section 3.1, this sensor measures directly the instantaneous total pressure except for regions where the flow exceeds the pitch angle insensitivity range. In these regions the uncertainty on the phase averaged stochastic fluctuations can go up to 20% otherwise it remains within 8%. The areas with the highest uncertainty may be identified in Fig. 3 and 4 inside the contour defined with white dotted lines (white arrows help understanding in which portion of the plane). It has to be noted that in these particular zones, the fluctuating part, because of the filtering procedure, may just underestimate the value of the stochastic fluctuations. In fact, there, the probe measures a pressure lower than the total pressure.

The terms M/M_{MAX} and $p'_{t,RMS}/\rho v^2_{MAX}$ are applied to both time averaged quantities (Fig. 3) and time resolved, phase locked averaged, quantities (Fig. 4). The first term is adopted to preserve the original distributions of the Mach number. The second definition ($p'_{t,RMS}/\rho v^2_{MAX}$) is used to provide a quantity as close as possible to the turbulence intensity. Recently, different authors have proposed different methods for computing the turbulence intensity from FRAPP in incompressible [12] and compressible [13, 17, 20] flows. To provide this, some hypotheses on the static pressure stochastic fluctuations must be done. These methods have been proved successfully, for example Paradiso et al. [20] validated FRAPP turbulent kinetic energy measurement by means of LDV in a transonic facility. However, in the present facility the necessary hypotheses are not verified, and hence no further conversion of total pressure to velocity stochastic fluctuations is proposed. On the other hand, the term $p'_{t,RMS}/\rho v^2_{MAX}$ is directly proportional to the turbulence intensity (see for example [12, 21]) and it helps, indeed, identifying the causes of loss generation.

To account for the relative stochastic unsteadiness directly induced by the two rotors a further term is introduced. The term $(\Delta p'_t)_{RMS}$ is computed as the root mean square of the difference between the time resolved and the time mean stochastic fluctuations. In plane

D it has been computed with respect to the unsteady stochastic fluctuations induced by the HP rotor, while in plane F it has been computed for both rotors. In Fig. 3 and 5 the term is made non-dimensional by the time mean value of $p'_{t,RMS}$.

4.1 Time averaged flow field, TMTF outlet

Detailed discussions of the flow in plane D were provided by Santner et al. [10] and Paradiso et al. [22]. A brief summary of their main findings is reported here and the discussion of the time mean results is extended considering the stochastic fluctuations of total pressure (Fig. 3).

High velocity gradients characterize the mean flow in both radial and circumferential directions (Fig. 3a): the radial gradients of velocity are due to the diffusing channel and to the endwall boundary layers, while the gradients in the circumferential direction are due to the turning of the flow evoked by the struts. The regions with lower momentum may be identified in the TMTF wake (marked over the picture). The lowest velocity is measured at the tip on the vane wake suction side (marked as S.S. on the plot).

Furthermore, secondary velocity vectors are superimposed to the plot, such vectors are defined as the difference between the local velocity vector and a reference flow direction (e.g., [23]). In the present case the reference flow vector has been determined subtracting from the local values the averages of the circumferential and radial velocity components in the radial and the circumferential directions, respectively (see Lengani et al. [14]). Two vortices are superimposed to the wake region at the tip and at the hub. A third relevant vortical structure that covers the lower side of the span may be instead identified as the passage vortex.

The term $p'_{t,RMS}/\rho v^2_{MAX}$ (Fig. 3b) shows high values in the proximity of these vortical structures. The highest stochastic fluctuations are measured in the wake region. In particular, losses are generated in the shear layer of the pressure side branch of the wake, this position is in fact characterized by the steepest circumferential velocity gradients. Similarly, losses are generated in the shear layers caused by the shed vortices at the tip and at the hub in the suction side of the wake. Furthermore, the region of the large passage vortex shows high values of $p'_{t,RMS}/\rho v^2_{MAX}$ with the maximum value in the proximity of the vortex center.

These regions of high stochastic fluctuations are correlated to the mean flow structures of the TMTF exit flow. To underline this aspect and provide the relative extent of stochastic fluctuations induced by the HP rotor unsteadiness, the term $(\Delta p'_{t,HP})_{RMS}$ is shown in Fig. 3c. The value of this term is quite low, in particular, the contribution to stochastic fluctuations in the region of the passage vortex is below 1%. The largest impact of the HP rotor unsteadiness on the generation of losses may be observed in the wake region for the hub shed vortex. However, the impact of the HP rotor remains quite small, around 10% of the time mean unsteadiness. Namely, in this regions the time resolved stochastic unsteadiness fluctuates at the frequency of the HP rotor but the main cause of loss generation has to be attributed to the TMTF vortical structures and shear layers but not to the HP rotor.

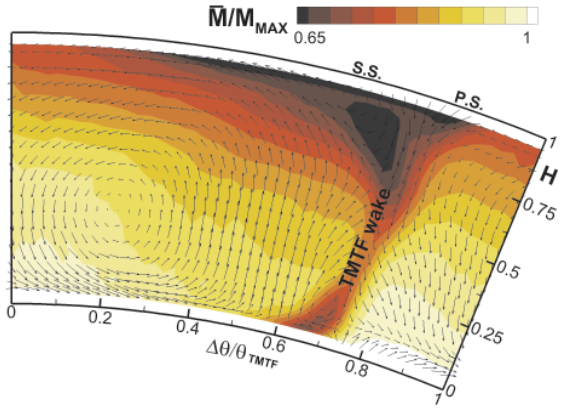

(a) Mach number

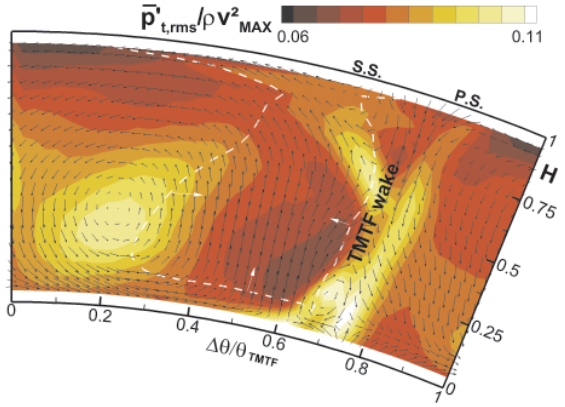

(b) Non-dimensional stochastic fluctuations of total pressure, the white dotted lines and corresponding arrows indicate the regions with higher measurement error

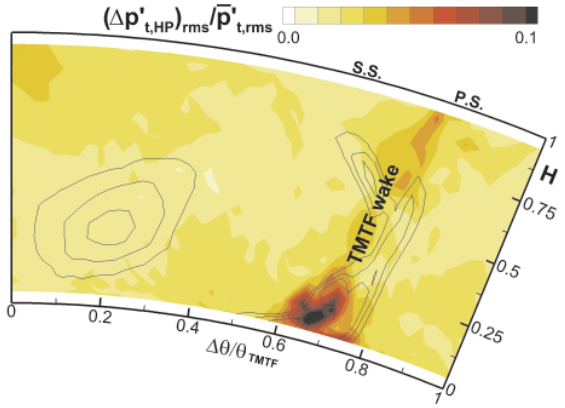

(c) Relative stochastic fluctuations induced by the HP rotor unsteadiness, and isocountour lines of the stochastic fluctuations

Figure 3. Contour plots of Mach number and stochastic fluctuations, time averaged values, plane D

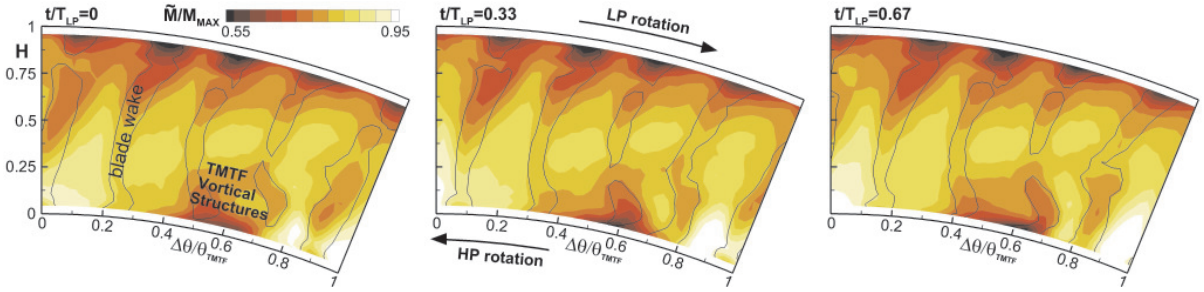

(a) Mach number

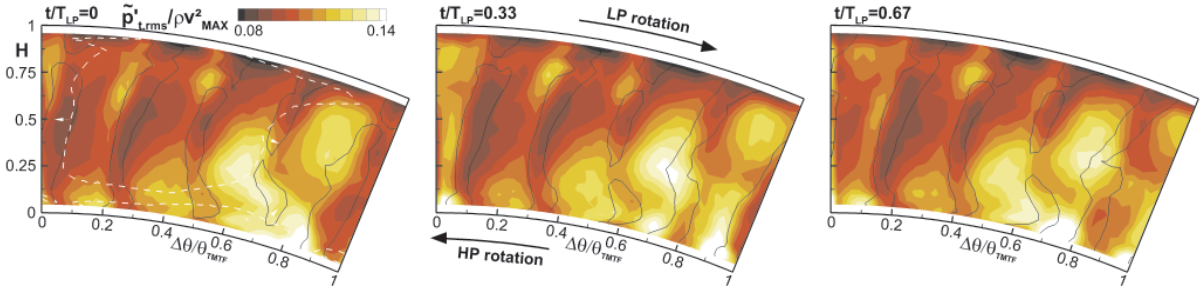

(b) Non-dimensional stochastic fluctuations of total pressure, the white dotted lines and corresponding arrows (displayed just for the first time step) indicate the region with higher measurement error

Figure 4. Contour plots of Mach number and stochastic fluctuations, phase averaged values considering the LP rotor induced unsteadiness, plane F

4.2 Time resolved flow field, LP rotor outlet

The flow downstream of the LP rotor is characterized by multiple sources of unsteadiness (see eq. 2). In order to simplify the analysis of such complex flow, the time resolved results are discussed at first considering the phase average based on the LP rotor. However, as discussed in Lengani et al. [14], velocity deterministic fluctuations downstream of the LP rotor are mainly caused by the LP rotor unsteadiness. For this reason, stochastic fluctuations are also mainly correlated to the LP rotor structures, as it will be discussed in the following.

Three time snapshots are extracted from one blade passing period of the LP rotor in order to show the time evolution of the Mach number and of the stochastic fluctuations of total pressure (Fig. 4). To allow the identification of the blade wake positions the iso-contour lines of the periodic fluctuations of the Mach number ($< M >= \tilde{M} - \overline{M}$) are superimposed on both plots of Fig. 4. The position of one of the rotor wake is marked over the experimental results (Fig. 4a) and it is enclosed by the iso-contour lines of $< M > /M_{MAX} = -2\%$, and, similarly, the other blade wakes may be identified enclosed within the iso-contour lines.

The clear trace of the 4 and 1/2 blades of the LP rotor, which is moving in the clockwise direction, may be observed in Fig. 4a. The velocity at the outer casing is low because of the radial pressure gradient generated by the duct curvature (see Fig. 1). At the same time, each blade generates a tip passage vortex which characterizes the velocity distribution in the region close to the tip. These flow structures slightly change with the relative circumferential position of blade and struts (compare the different time steps of Fig. 4a).

At the hub, the time resolved distribution is characterized by the trace of the TMTF flow structures (see the range $0.4 < \Delta\theta/\theta_{TMTF} < 0.7$). Due to this structure it is hard to identify the trace of the blade passage vortex which is also pushed towards the inner casing by the radial pressure gradient. However, the trace of the blade wake may be still observed from the iso-contour line of $< M >$. The wake is bowed and becomes thicker while the blade is passing through the remains of the TMTF flow structure: for example, in the last time step, at $\Delta\theta/\theta_{TMTF} \cong 0.75$ the blade passage seems then thinner, leading to the large gradients of velocity in circumferential direction and in time.

Figure 4b shows the non-dimensional stochastic fluctuations of total pressure. The largest values may be observed where such high gradients of velocity are identified (e.g., $0.5 < \Delta\theta/\theta_{TMTF} < 0.8$ in the first time step). The shapes of the structures at high $p'_{t,RMS}/\rho v^2_{MAX}$ are bowed and stretched and follow the contour of the periodic fluctuations of Mach number $< M >$ on suction and pressure side. From the first to the last time step the region at higher random fluctuations seems to lift up being generated by the interaction of the LP blade and the TMTF vortical structures and being transported with the rotor motion (clockwise direction).

In the region within the range $0.0 < \Delta\theta/\theta_{TMTF} < 0.4$, the distribution of $p'_{t,RMS}/\rho v^2_{MAX}$ still follows the contour of $< M >$. Here, the largest values are shown close to the hub, characterizing the region with relative height H <0.25, while the region between 0.25< H <0.6 is characterized by the lowest values

of stochastic fluctuations. At the tip, $p'_{t,RMS}/\rho v^2_{MAX}$ assumes again high values because of the formation of steep shear layers due to the tip secondary flows.

It has to be noted that, since the measurement plane is quite far downstream of the LP rotor trailing edge (77% of the blade chord) the generation of random fluctuations appears mostly on the pressure side, where the steepest shear layer start to dissipate energy. Nonetheless, the region with the highest values of $p'_{t,RMS}/\rho v^2_{MAX}$ ($0.5 < \Delta\theta/\theta_{TMTF} < 0.8$ at the hub) shows large values independently on suction or pressure side. Furthermore, the measured values are quite large, almost twice, when compared to classical results in 1 or 1 and 1/2 stage turbines (see for example [21]). However, it has to be noted that these measurements are performed downstream of a second stage and downstream of a diffusing duct. Unfortunately, at least to the knowledge of the authors, the presented configuration is quite unique and at the moment there is no similar data to compare these results to.

There is a very strict correlation between the LP rotor motion and the generation of losses. As presented in the previous section, the relative extent of stochastic fluctuations induced by the LP rotor unsteadiness is evaluated with the term $(\Delta p'_{t,LP})_{RMS}$ shown in Fig. 5. Clearly, in this measurement plane the impact of the unsteadiness of the LP rotor is larger than what previously observed for the HP rotor and plane D (Fig. 3c). The unsteadiness induced by the LP rotor contributes up to 35% of the mean stochastic fluctuations of total pressure. Whereas, in plane F, the stochastic fluctuations at the unsteadiness of the HP rotor are below 3% of mean value, hence they are not shown in the paper.

In particular, the largest contribution of $(\Delta p'_{t,LP})_{RMS}$ is observed for the skewed region that may be identified as the remains of the TMTF wake [14] (as marked over the plot). The contribution of the LP unsteadiness in the region influenced by the TMTF vortical structures (as marked in the picture) is instead less relevant. As previously observed, at any blade passage there is already a large amplitude of the stochastic fluctuations. They follow the local velocity gradients generated by the LP blade and lift up. However, their mean value is just slightly influenced by the LP rotor motion, while it is mostly due to the large lack of momentum due to the stationary flow structures induced by the TMTF.

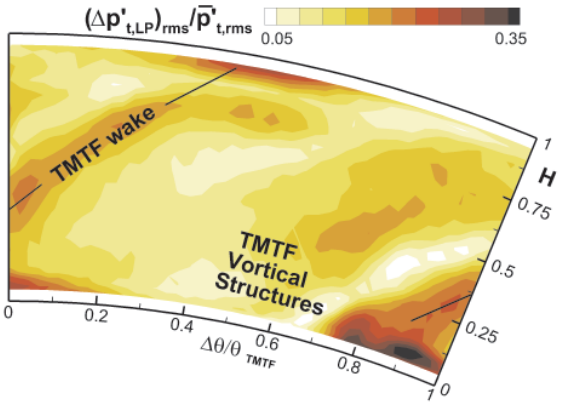

Figure 5. Relative stochastic fluctuations induced by the LP rotor unsteadiness, plane F

5 CONCLUSION

The development of the unsteady flow in the last stage of a two-stage counter-rotating turbine has been reported in the paper. The paper has analyzed the complexity of the unsteady flow features. In order to simplify the problem, a method for the determination of stochastic fluctuations of total pressure has been developed and discussed in details. All the contribution to the time signal due to deterministic fluctuations has been removed by means of Fourier filtering. By the inverse Fourier transform the stochastic fluctuating part of the time signal is reconstructed and then phase averaged and time averaged.

It has been shown that the largest random fluctuations downstream of the turning struts embedded in the diffusing duct are due to the vortical structures induced by the vane itself. Even though the unsteadiness of the HP rotor has a strong impact on the development of the mean flow within the duct it influences the generation of losses at the outlet section of the duct just in small part. In fact, the stochastic fluctuations directly induced by the HP rotor, and hence fluctuating at its frequency, are just up to 10% of the time mean value and confined in a small region. At the outlet of the second stage, two main phenomena are responsible for the random fluctuations and, therefore, for the loss generation. The first cause may be identified in the mixing out of the large vortical structures of the TMTF. The second cause is the unsteady interaction of TMTF with the LP rotor, which shows the largest impact on loss generation in the region of the remains of TMTF wake.

ACKNOWLEDGEMENTS

The research leading to these results has received funding from the European Union Framework Programme (FP7/2007-2013) under grant agreement n° 211861 as well as from the Austrian Ministry for Science and Research. MTU Aero Engines is acknowledged for allowing us to publish the data.

References

[1] Arndt, N., 1993, "Blade Row Interaction in a Multistage Low-Pressure Turbine". *ASME Journal of Turbomachinery,* Vol. 115, January, pp. 137–146.

[2] Sharma, O. P., Pickett, G. F., and Ni, R. H., 1992, "Assessment of Unsteady Flows in Turbines". *ASME Journal of Turbomachinery,* Vol. 114, January, pp. 79–90.

[3] Walraevens, R. E., and Gallus, H. E., 1995, "Stator-Rotor-Stator Interaction in an Axial Flow Turbine and its Influence on Loss Mechanisms". Proc. *In AGARD PEP- 85th Meeting on Loss Mechanisms and Unsteady Flows in Turbomachinery,* Derby, UK, May, Paper 39.

[4] Zaccaria, M. A., and Lakshminarayana, B., 1997, "Unsteady Flow Field due to Nozzle Wake Interaction with the Rotor in an Axial Flow Turbine: Part 1 – Rotor Passage Flow Field". *ASME Journal of Turbomachinery*, Vol. 119, April, pp. 201–213.

[5] Göttlich, E., 2011, "Research on the Aerodynamics of Intermediate Turbine Diffusers". *Prog Aerospace Sci,* Vol. 47 (4), pp. 249–279.

[6] Hubinka, J., Paradiso, B., Santner, C., Göttlich, E., and Heitmeir, F., 2011, "Design and Operation of a Two Spool High Pressure Test Turbine Facility". Proc. 9^{th} *European Turbomachinery Conference, March 21-25,* Istanbul, Turkey, Paper No. 112.

[7] Lengani, D., Santner, C., Spataro, R., and Göttlich, E., 2012, "Analysis Tools For the Unsteady Interactions in a Counter-Rotating Two-Spool Turbine Rig". *Experimental thermal fluid science,* doi: 10.1016/j.expthermflusci.2012.05.010.

[8] Camp, T. R., and Shin, H.-W., 1995, "Turbulence Intensity and Length Scale Measurements in Multistage Compressors". *ASME Journal of Turbomachinery,* Vol. 117, January, pp. 38–46.

[9] Oro, J. M. F., Díaz, K. M. A., Morros, C. S., and Marigorta, E. B., 2007, "On the Structure of Turbulence in a Low-Speed Axial Fan with Inlet Guide Vanes". *Experimental Thermal and Fluid Science,* Vol. 32, pp. 316–331.

[10] Santner, C., Paradiso, B., Malzacher, F., Hoeger, M., Hubinka, J., and Göttlich, E., 2011, "Evolution of the Flow Through a Turning Mid Turbine Frame Applied Between a Transonic HP Turbine Stage and a Counter-Rotating LP Turbine". Proc. 9^{th} *European Turbomachinery Conference, March 21-25,* Istanbul, Turkey, Paper No. 110.

[11] Kupferschmied, P., Köppel, O., Gizzi, W. P., and Gyarmathy, G., 2000, "Time Resolved Flow Measurements with Fast Response Aerodynamic Probes in Turbomachinery". *Measurement Science and Technology,* Vol. 11 (7), pp. 1036–1054.

[12] Porreca, L., Hollenstein, M., Kalfas, A. I., and Abhari, R. S., 2007, "Turbulence Measurements and Analysis in a Multistage Axial Turbine". *Journal of Propulsion and Power,* Vol. 23 (1), pp. 227–234.

[13] Persico, G., Gaetani, P., and Paradiso, B., 2008, "Estimation of Turbulence by Single-Sensor Pressure Probes". Proc. *XIX Biannual Symposium on Measuring Techniques in Turbomachinery*.

[14] Lengani, D., Santner, C., Spataro, R., Paradiso, B., and Göttlich, E., 2012, "Experimental Investigation of the Unsteady Flow Field Downstream of a Counter-Rotating Two-Spool Turbine Rig". Proc. *ASME Turbo Expo 2012, June 11-15,* Copenhagen, Denmark, ASME Paper No. GT2012-68583.

[15] Hussain, A., and Reynolds, W., 1970, "The Mechanics of an Organized Wave in Turbulent Shear Flow". *Journal of Fluid Mechanics,* Vol. 41, pp. 241–258.

[16] Peters, A., and Spakovszky, Z. S., 2012, "Rotor Interaction Noise in Counter-Rotating Propfan Propulsion Systems". *J Turbomach,* Vol. 134, January, p. 011002 (12 pages).

[17] Lengani, D., Paradiso, B., and Marn, A., 2012, "A Method for the Determination of Turbulence Intensity by Means of a Fast Response Pressure Probe and its Application in a LP Turbine". *Journal of Thermal Science,* Vol. 21, pp. 21–31.

[18] Lengani, D., Spataro, R., and Göttlich, E., 2012, "Comparison of Proper Orthogonal Decomposition and Fourier Filtering for the Determination of the Stochastic Unsteadiness in Time Signals". Proc. 9^{th} *International ERCOFTAC Symposium, ETMM*.

[19] McAlpine, A., and Fisher, M. J., 2001, "On the Prediction of "Buzz-Saw" Noise in Aero-Engine Inlet Ducts". *J Sound Vibrat,* Vol. 248 (1), pp. 123–149.

[20] Paradiso, B., Persico, G., Gaetani, P., Schennach, O., Pecnik, R., and Woisetschläger, J., 2008, "Blade Row Interactio in a One and a Half Stage Transonic Turbine Focusing on Three Dimensional Effects-Part 1: Stator-Rotor Interaction". Proc. *ASME Turbo Expo 2008, June 9-13,* Berlin, Germany, ASME Paper No. GT2008-50291.

[21] Schüpbach, P., Abhari, R. S., Rose, M. G., Germain, T., Raab, I., and Gier, J., 2010, "Improving Efficiency of a High Work Turbine Using Nonaxisymmetric Endwalls-Part II: Time-Resolved Flow Physics". *J Turbomach,* Vol. 132, April, pp. 021008–1–10.

[22] Paradiso, B., Santner, C., Hubinka, J., Göttlich, E., and Hoeger, M., 2011, "Turning Mid Turbine Frame Behavior for Different HP Turbine Outflow Conditions". Proc. *ASME Turbo Expo 2011, June 6-10,* Vancouver, Canada, ASME Paper No. GT2011-46506.

[23] Persico, G., Gaetani, P., Dossena, V., D'Ippolito, G., and Osnaghi, C., 2009, "On the Definition of the Secondary Flow in Three-Dimensional Cascades". *I MECH E Journal of Power and Energy,* Vol. 223, pp. 667–676.

Conference on Modelling Fluid Flow (CMFF'12)
The 15th International Conference on Fluid Flow Technologies
Budapest, Hungary, September 4-7, 2012

AERODYNAMIC INFLUENCE OF STREAMWISE SURFACE CORRUGATION ON AXIAL COMPRESSOR BLADES

Jörg Hartmann[1], Katharina Winter[2], Peter Jeschke[2]

[1] Corresponding Author. Institute of Jet Propulsion and Turbomachinery, RWTH Aachen University, Templergraben 55, D-52062 Aachen, Germany. E-mail: Hartmann@ist.rwth-aachen.de
[2] Institute of Jet Propulsion and Turbomachinery, RWTH Aachen University, D-52062 Aachen, Germany.

ABSTRACT

In this paper, a CFD study is presented by which the aerodynamic influence of compressor blade surface imperfections in the form of single sinusoidal bulges or hollows can be conveniently assessed. Corrugation with a small height to length ratio, typical for manufacturing malfunction, is applied to an open literature compressor profile. A sensitivity analysis is performed for the three parameters wave length, height, and position. In summary, this paper gives elementary insight into the loss production mechanism of compressor profiles that suffer from manufacturing imperfections.

The investigation approach itself includes three steps. First, the effects of waviness are discussed theoretically. Second, the influence of the waviness on a flat plate as a simple generic geometry is investigated. Finally, using the previous results, geometry configurations are selected and placed on the chosen compressor profile. As a result two possible main effects responsible for higher losses due to surface waviness are identified: a shift of the transition point and the development of local areas of increased Mach numbers.

Keywords: axial flow turbo machinery, compressor, CFD, manufacturing, surface waviness

NOMENCLATURE

B	[m]	corrugation height
Ma	[-]	Mach number
Re	[-]	Reynolds number
Tu	[-]	turbulence level
T_t	[K]	total temperature
c_p	[-]	static pressure coefficient
h	[m]	corrugation width
p_t	[Pa]	total pressure
ω	[-]	loss coefficient
η	[m]	wall distance

Subscripts and Superscripts

1, 2	at the inlet and outlet of the test section
cor	geometry with placed corrugation
i	isentropic
l	chord length
nom	nominal geometry
t	transition point
x, y, z	axial, transversal, spanwise (coordinate)

1. INTRODUCTION

In the development of turbo engines an integrated optimisation of contradictory requirements is necessary for each component. A balance has to be achieved between the participating disciplines such as aerodynamics, structural dynamics, and manufacturing. One important point in this context is the presence of local surface irregularities created by the manufacturing process. Due to short development cycles and often limited availability or insufficient knowledge about the influence of these small geometry deviations, the full optimisation potential cannot be exploited. Especially for modern manufacturing techniques and parts like integral components, for example "blisk" ("blade integrated disk"), which integrate many blades into one single component, this will lead to high production costs. The reason is that many restrictions evolve from traditional single blade manufacturing processes and are therefore characterised by past experiences. To give an example, a typical compressor blisk consists of up to 100 single blades. Based on the criteria mentioned above, a typical scrap rate for a single blade lies in the order of 1–3% and is no significant problem. For a blisk consisting of 100 blades, however, it leads to a scrap rate of 100%. As a consequence in practice an extremely cautious and cost intensive "zero scrap" manufacturing strategy is pursued. Especially in the context of evaluating aerodynamic parts it therefore makes sense to enlarge the fundamental knowledge of the sensitivities to manufacturing imperfections. One restricted imperfection existing in practical problems is waviness with a small height to length ratio. It is addressed here in the form of a single surface corrugation.

2. THEORY AND LITERATURE

The chosen geometry deviation in the form of a corrugation is a typical 2D case and from this perspective it is studied in this paper. This means that the bulge or hollow is parallel to the span direction of the blade and its span-wise extent is assumed to be infinite, neglecting end wall effects.

To quantify the induced loss of such a corrugation it is necessary to know what kinds of losses and mechanisms of loss exist as well as which of these play a major role in the present case. Denton [1] thoroughly analysed compressor losses and their physical causes in the past years and came to the conclusion that the most relevant losses result from viscous boundary layer effects, viscous mixing processes, shocks, and heat transfer. Due to an adiabatic system, the mechanisms of loss can be reduced to the first three points.

To predict the influence of a 2D surface waviness, empirical criteria have been proposed for many years. More recently at least part of the phenomena occurring on and around the surface imperfections have been modelled and more advanced prediction methods have been developed. Both aspects are now briefly discussed. The earliest research on the effects of a span wise corrugation on the boundary layer transition goes back to Fage [2], who carried out wind tunnel experiments to identify the transition point of a bulge and a hollow installed on a flat plate. Based on empirical data Fage derived a regression model. It can be divided into the following two sub-formulas.

$$\frac{h}{x_t} = 9 \cdot 10^6 \left(\frac{U_e x_t}{\nu} \right)^{-3/2} \left(\frac{B}{x_t} \right)^{1/2} \quad (1)$$

$$\frac{h}{B} = 9 \cdot 10^6 \left(\frac{U_e x_t}{\nu} \right)^{-3/2} \left(\frac{x_t}{B} \right)^{1/2} \quad (2)$$

B and h represent the corrugation width and the corrugation height, respectively, and x_t is the surface length to transition. U_e represents the boundary layer edge velocity at the location of the centre of the waviness for the undistorted surface.

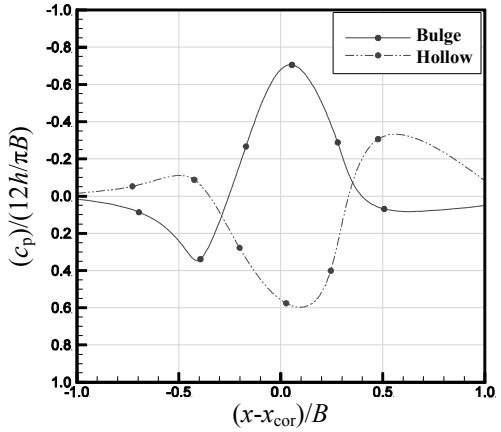

Figure 1. Experimental results for a bulge and a hollow, corresponding to Fage [2]

In Figure 1 Fage's measurements for a bulge and a hollow are plotted. For several Mach numbers and very short or very long corrugations Smith [3] performed calculations based upon a triple-deck structure. He showed how the presence of a hump generates an interaction between the inviscous region just outside the boundary layer and the viscous region near the hump. In the course of time the approach to the transition problem changed from experimental to numerical research. The linear stability theory (LST), which analyses the growth of sinuous disturbances of small amplitude, and the interacting boundary layer (IBL) method for calculating separated flows play important roles here. Authors who have used these methods to characterise the effects of 2D surface imperfections on transition include, for instance, Lesson and Gangwani [4], Nayfeh et al. [5], Cebeci and Egan [6], Masad and Iyer [6], Wie and Malik [7] and more recently Wörner et al. [8]. Nayfeh et al. [5] were able to verify the results obtained by Fage, whereby a separation bubble can follow a corrugation, and Wie and Malik [7] validated the Fage criterion for the transition point in areas with marginal or no pressure gradient. Furthermore, in conformity with Fage's experiments, their results show the effect of waviness scales as h^2/B. Masad [6] also compared his results with Fage's regression model and was able to verify those for. As an example, Figure 2 shows a comparison between the c_p-profile calculated by Masad, Fage's experimental data, and Fage's results calculated by the *Karman-Pohl-hausen* relation, all for a bulge of the same size.

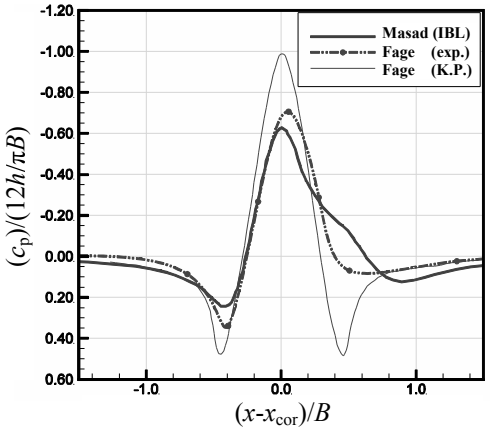

Figure 2. Comparison between Fage's [2] and Masad's numerical results [6]

As the graph shows, for all three results there is an area with a positive pressure gradient prior to the wave followed by a small area with strongly decreasing pressure in which the flow is stabilised. The pressure then increases again behind the wave. The strength of this pressure increase also depends on whether or not a separation occurs. This also explains the difference in this area between the results calculated by IBL (Masad) and the *Karman-Pohlhausen* relation (Fage). It is clear that both

positive pressure gradients support disturbances and so the flow tends toward transition and separation. In addition, Masad performed a parameter study of wave length and wave height and their effect on the transition point (Figure 3). As expected and as already shown by Fage's results, the transition point moves upstream with increasing wave height and decreasing wave length (smaller values of $(Re_x)_{N=9}$). By using direct numerical simulations Wörner et al. [8] investigated the influence of humps and steps on the stability characteristics of a 2D laminar boundary layer with great numerical effort and drew comparisons with water channel measurements.

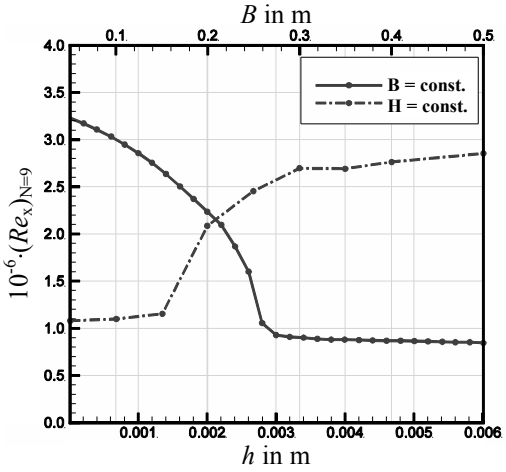

Figure 3. Calculated transition point shift with varying hump height and width by Masad [6]

Finally, at the end of this section, it should be mentioned that no work investigating the influence of the mentioned corrugation on turbomachinery blades is known to the author. Summarising the literature mentioned, possible surface corrugations have two impacts which are able to influence the profile losses. They create local pressure gradients and areas of de- and increased velocities. These effects amplify the unstable waves in the boundary layer responsible for the transition process.

3. COMPRESSOR TEST CASE

As a basis for the following numerical investigation the compressor cascade V103-220 consisting of three blades and experimentally investigated by Hilgenfeld [9] was chosen. The profile is a 48° circular arc with a superimposed NACA 65 thickness distribution which represents the hub section of a stator blade in a highly loaded axial compressor. The blade chord length is 220 mm. The geometrical definitions of the cascade, the angles, and the distances are displayed in Figure 4. The test conditions with an inlet Mach number of 0.75 and a Reynolds number based on the blade chord length of 450,000 lead to a fully subsonic cascade flow with, however, a peak Mach number close to 1.0. Furthermore the profile shows a transition process over a laminar separation bubble of between 25% and 50% of the chord length on the suction side. The design data are listed in Table 1.

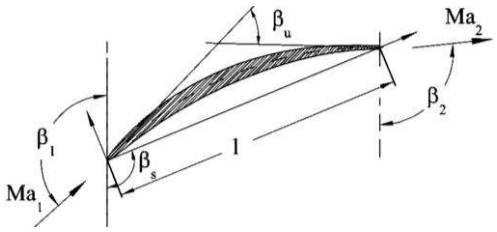

Figure 4. Profile definitions by Hilgenfeld [9]

Table 1. Data for cascade V103-220

t/l =	0.55	β_1 =	132°
d_{MAX}/l =	0.055	β_2 =	96°
β_U =	48°	β_S =	112.5°
Ma_1 =	0.75	Re_1 =	450,000
AVDR =	1.058	T_t =	313 K
Tu =	3.5%	Tu_x =	1.4%

As comparative data the following measurements are available: The main flow condition is provided by the Mach and Reynolds number as well as the total temperature in the inlet plane, hot-wire measurements upstream of the cascade inlet give the turbulence level, and for the instrumented centre blade the loading is available in the form of static pressure tappings on both the suction and the pressure side. A local total pressure traverse in the outlet plane provides the total pressure profile of the wake region. The boundary layer profiles have been measured by a laser-two-focus system through a glass window mounted on the sidewall of the cascade and with hot-wire probes.

3.1 Numerical setup

As a time-accurate and parallelised solver specialised for turbomachinery, TRACE is used as the fluid dynamics solver. TRACE has been developed by the German Aerospace Center especially to calculate flows in turbomachinery. As TRACE is optimised for multi-block structured grids the mesh used for the following calculations is also a structured O-C-H topology mesh. To resolve the geometry and influence of very small surface corrugations compared to the blade dimensions, it is necessary to use a high mesh resolution as illustrated in Figure 5. A mesh sensitivity study has been carried out but is not shown here.

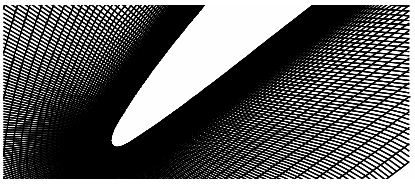

Figure 5. Generated numerical mesh near the leading edge

The chosen mesh consists of roughly 100,000 elements in its S2M-plane, while in the span wise direction the mesh consists of just one element. The stream wise contraction as an effect of the increasing boundary layer along the side walls is modelled by contracting the mesh itself. For this reason the mesh height is linearly decreased from the leading edge to the trailing edge by means of the measured axial velocity density ratio (AVDR) of 1.058. The mesh resolution near the blade surface of $y^+ \approx 1$ allows a low Reynolds wall treatment.

In order to simulate the turbulent effects, the Wilcox *k-ω* turbulence model in combination with a multimode transition model is used. It allows transition types encountered to be simulated, for example separation-induced transition, which is particularly important for the present case. Further details about the transition modelling approach are presented in [10]. The boundary data are chosen corresponding to Table 1 with the exception of the turbulence level. This is set to a value of 2.2%, which lies between the experimental values of Tu and Tu_x.

3.2 Numerical setup validation

To validate the numerical setup the calculated results should be compared to the earlier mentioned measurements of Hilgenfeld [9]. For the total pressure loss coefficient and some additional global parameters the comparison is shown in Table 3, which shows a very good match for all parameters.

Table 3. Cascade data for V103-220

	Experiment	Numeric
ω	0.03721	0.03728
β_2	96°	95.28°
$Ma_{i,max}$	0.99	0.994

The Mach number profile is displayed in Figure 6. By comparing the numerical and experimental curve characteristics it can be seen that there is an excellent conformity, especially on the suction side.

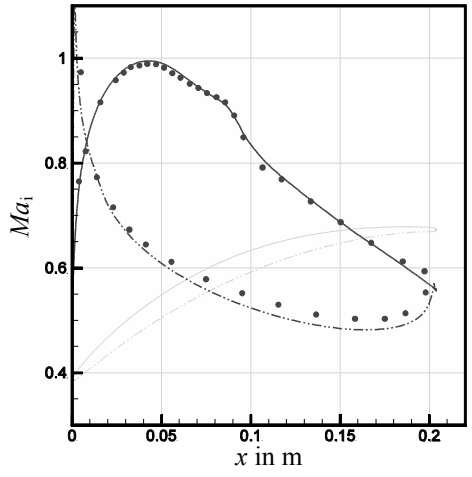

Figure 6. Comparison of the measured (dots) and calculated isentropic Mach number profiles

The minor shift at the rear end of the pressure side is caused by a slightly inadequate periodicity in the experiments. This effect has already been identified and discussed by Hilgenfeld [9]. The reason for this imperfect periodicity is that the experimental cascade consists of only three blades, which is a relatively low number. Nevertheless the maximum Mach number at approximately 20% of the axial chord, the separation process over a laminar separation bubble between 30% and 50% of the axial chord, and the diffusion process on the suction side are reproduced very well. The separation and transition could also be clearly observed by plotting the form parameter of the boundary layer and the calculated intermittency gradient (see Figure 7). The plot shows an increasing intermittency from 0 to 1 and a significant increasing shape parameter above the typical level of 2.5 for a laminar boundary layer in the appropriate axial position on the suction side.

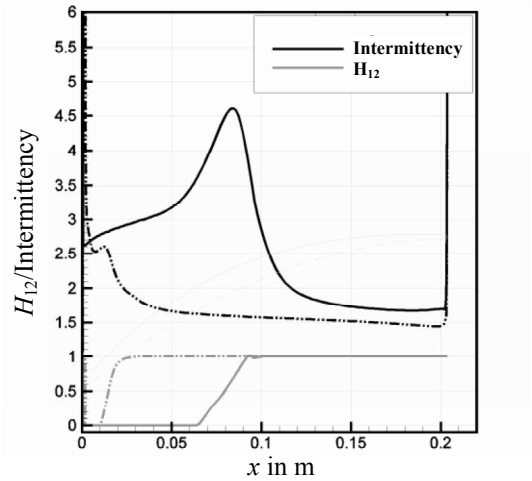

Figure 7. Shape parameter and intermittency level for the profile suction (solid line) and pressure side (dashed dotted line)

These two parameters are also used to evaluate the influence of the transition point for the waviness calculation which is yet to be carried out. To estimate or rather to fix the transition process to one location the point where the intermittency first reaches a value of 0.5 should be defined as a transition point. For the nominal unchanged blade, that is the case at an axial position of 40% of the axial chord on the suction side.

Another helpful parameter to estimate the quality of the numeric calculation is the measured boundary layer profiles. The corresponding comparison between experiment and numeric is plotted in Figure 8 for six axial positions on the suction side. Just like for the isentropic Mach number profile there is a good conformity between the data for all axial positions. However the velocities are slightly over predicted in the lower regions of the profile. It can also be seen how the profile shape changes from a laminar to a turbulent profile.

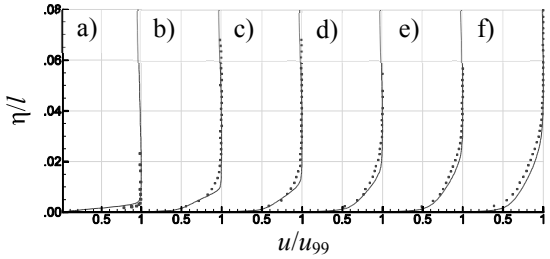

Figure 8. Comparison between measured (dots) and calculated boundary layer profiles at a) $x/l_x = 0.2$, b) $x/l_x = 0.5$, c) $x/l_x = 0.55$, d) $x/l_x = 0.65$, e) $x/l_x = 0.75$, and f) $x/l_x = 0.85$

4. CORRUGATION CALCULATIONS

This section of the paper deals with the results of the different calculated geometry deviations and is divided into two main subsections. In the first one a flat plate with six different corrugations placed in two positions is discussed as a first test case. It is used to explain briefly the geometry generation and to evaluate the suitability of the applied numerical tools. For that reason all boundary conditions given in section 3.1 are kept constant and equivalent to the given compressor test case.

In the second subsection the corrugation is impressed on the compressor test case itself. By using the maximum profile Mach number and the transition point location the effects of several bulges and hollows on the loss production are discussed.

4.1. Flat plate

The corrugation is placed on the plate by superimposing half of a full sinusoidal wave on the contour. The basic shape is defined by the half wave length eyuivalent to the corrugation width B and the height h (see Figure 9). In addition the beginning and ending of the waviness on the suction respectivly pressure side are specified. At the beginning and ending of the waviness they will be superimposed with a damping function, each until the first and from the last inflexion point. This ensures a continuous curvature progression between the original profile and impressed waviness.

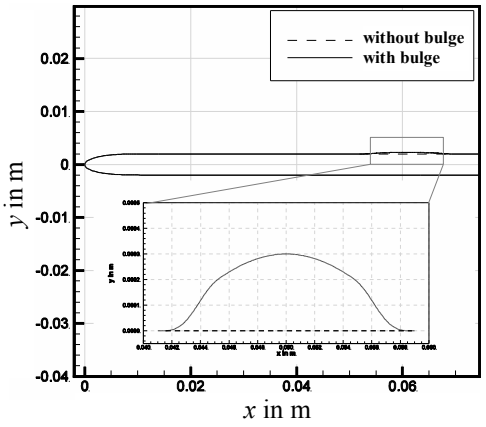

Figure 9. Plate and bulge sinusoidal geometry with superimposed attenuation function

In this way about twelve corrugations were defined and calculated (six heights h=-0.6…0.6mm; 2 axial positions, const. width).For a bulge respectively a hollow of 18mm width and ±0.3mm height on two axial positions, once in the laminar and once in the turbulent region of the boundary layer, the results can be seen in Figure 10. By comparing them with Fage's results the same characteristics as described in Section 2 can be identified. Thereby the calculated gradient in which the corrugation was placed in the turbulent zone (a) was found to be a little more suitable than the one in the laminar zone (b). However, by analysing the remaining calculations the tendencies of Fage regarding the transition shift could be verified.

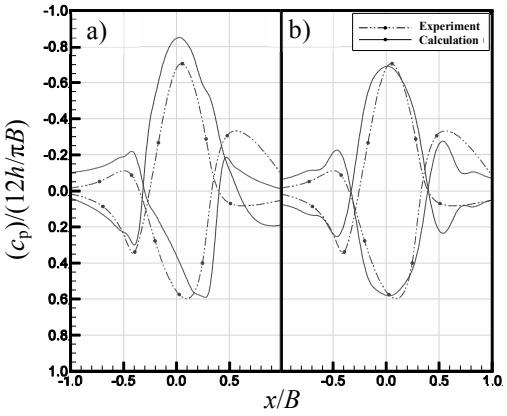

Figure 10. Comparison between the experimental results of Fage and the flat plate calculations with a bulge and hollow placed (a) upstream and (b) downstream of the transition

4.2. Compressor profile

Based on the results of Section 4.1 a total of 1,288 surface corrugations have been defined consisting of 23 different heights, 8 lengths, and 7 axial positions. The parameters are given in Table 4.

Table 4. Varied corrugation parameters

	Start	End	Step width
h	-0.6mm	-0.08mm	0.08mm
h	0.04mm	0.6mm	0.04mm
B	6mm	48mm	6mm
x_{cor}/l_{SS}	10%	40%	10%
x_{cor}/l_{SS}	50%	90%	20%

All corrugations have been exclusively placed on the suction side of the profile because a higher influence on the profile losses can be expected here. Reasons for this are the higher Mach numbers, the occurrence of the transition further downstream, and the higher diffusion in comparison to the pressure side. The accuracy of this assumption for the present case and the working point given by the experiments was confirmed by further calculations. However, this is not the subject of this paper. In Figure 11, four contours for the axial chord posi-

tions of 20%, 30%, 40%, and 70% are displayed. As could be expected, as a first result the additional loss production rises with increasing wave heights in both negative and positive directions. On the other hand it seems that the wave length *B* has a smaller influence on the additional loss production.

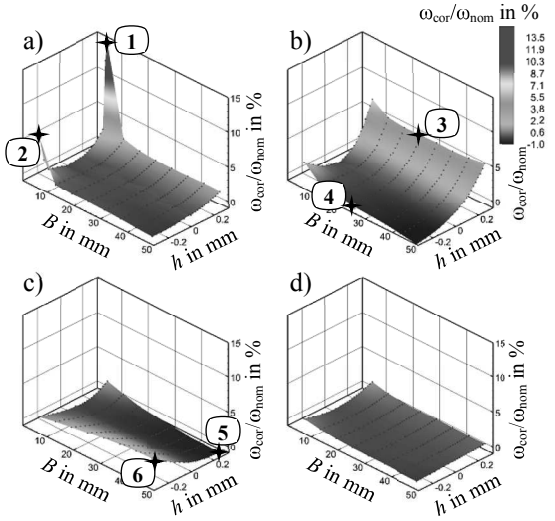

Figure 11. Relative loss increase for four axial positions at a) 20%, b) 30%, c) 50%, and d) 70% over *h* and *B*

To estimate the effects occurring in more detail for each of the first three contours and corresponding axial positions of the corrugation, two specific points should be compared to each other. The corresponding points are numbered 1 to 6 in Figure 11. The isentropic Mach number profile, the shape parameter, and intermittency level were chosen to compare the individual points. Figure 12 shows the graphs for the first two points (h=±0.3mm, B=6mm) for the position of 20% of the axial chord. It can be seen that the effect on the transition process is approximately the same for both cases, the bulge and the hollow. As a result of the placed corrugation the transition point moves upstream and the laminar separation bubble disappears. Nevertheless, the growth of the loss produced is different for the two cases.

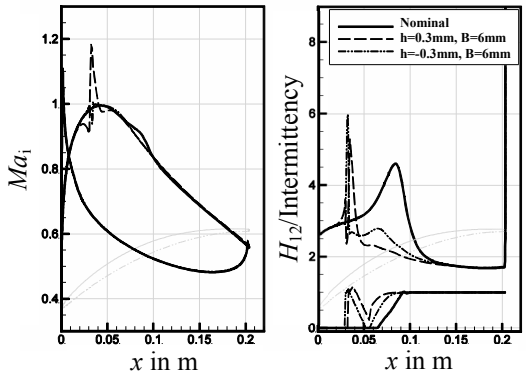

Figure 12. Mach number, intermittency, and shape factor change for point 1 and 2 (Figure 11)

Unlike the hollow, the bulge additionally causes a local area of a highly increased Mach number. As the Mach number is already relatively high (Ma_i≈1 on the suction side near 20% of the axial chord) this causes a shock and the additional profile losses are more than doubled. Towards higher wavelengths, in contrast, the loss drops abruptly.

Crucial for this effect is the accelerating flow in the front region of the blade, which has a stabilising effect on the boundary layer and hence reduces the impact of the introduced disturbances. This is why only the corrugations that have a high *h*/*B* ratio are able to cause a significant effect. Moving closer to the beginning of the diffusive part of the blade even the smaller corrugations, or rather corrugations with a smaller *h*/*B* ratio, are able to trigger the transition process. This can be clearly seen from the nearly constant increase in loss for varying wavelengths for an axial position of 30% of the chord. However, it has to be said that this statement is accurate for bulges in particular. Comparison of points 3 and 4 (h=±0.3mm, B=24mm) as shown in Figure 13 shows the reason for this consideration.

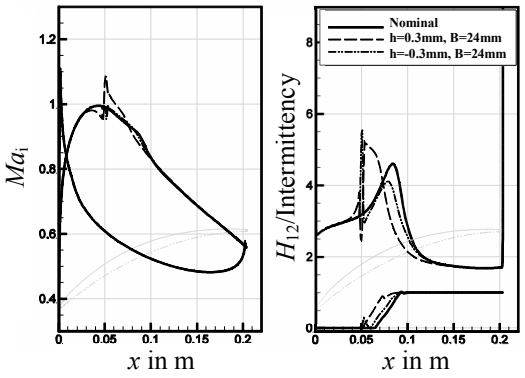

Figure 13. Mach number, intermittency, and shape factor change for point 2 and 3 (Figure 11)

For the placed bulge with its increased velocity the separation point of the boundary layer is shifting upstream directly to the corrugation end because of the higher positive pressure gradient in this region. This, in turn, accelerates the transition process significantly. Due to the lack of an increasing pressure gradient subsequent to the hollow an additional or earlier separation cannot be triggered. Because the separation marks the beginning of the transition, however, the hollow is not able to accelerate the transition process. The opposite effect, in terms of the additional losses, can be seen for the third axial position at 50% of the axial chord and points 5 and 6 (h=±0.3mm, B=48 mm). Here the hollow shows a higher loss than the bulge. Nevertheless, the causes are similar. Compared to the previous case the hollow now intensifies the separation and thereby shortens the transition process. But it has to be mentioned that the potential increase in loss resulting from the occurrence of the transition is rather small.

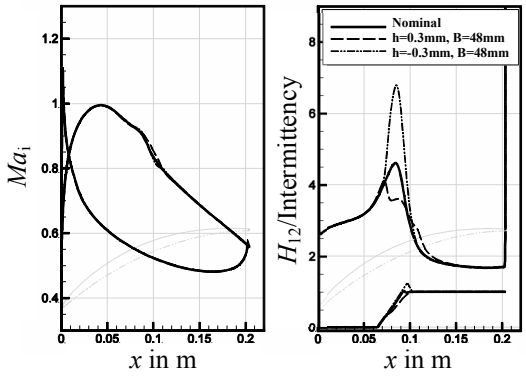

Figure 14. Mach number, intermittency, and shape factor change for point 2 and 3 (Figure 11)

As a provisional summary it can be noted that two main effects are able to cause an increase in the profile loss due to a single surface corrugation: first and foremost, an upstream movement of the transition point as a result of the instabilities introduced, and second, local areas of highly increased Mach numbers due to the flow acceleration across a bulge. The second effect may trigger the first one, if the Mach number reaches a value higher than one and shocks occur. The dependence on varying parameters *h, B,* and x_{cor} should now be given a closer look.

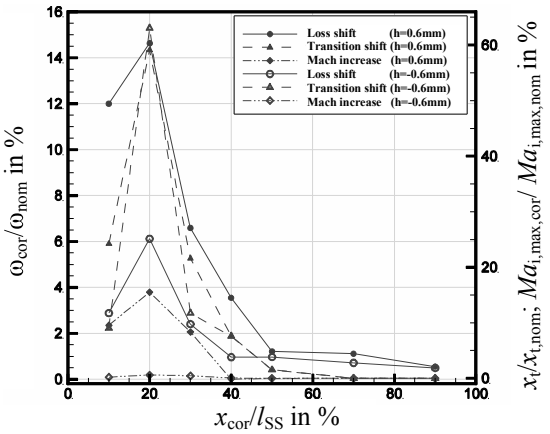

Figure 15. Relative shift of ω, x_t, and $Ma_{i,max}$ over a varying axial position x_{cor}/l_{SS} and a constant corrugation width *B* of 6 mm

For this purpose the Mach number increase and transition point shift were chosen for comparison in addition to the loss value. These parameters are plotted in Figure 15 depending on the axial position of the corrugation. It can be seen that there is a good correlation between the transition shift and the additional loss production for both the chosen bulge and the hollow (h=±0.6 mm, B=6mm). Although the transition point movement for both the bulge and the hollow is nearly the same at all points, the loss increase for the bulge is twice as high as for the hollow. The difference and a probable explanation is the Mach number increase. A significant shift in the maximum Mach number can be observed for the bulge, which shows a good relation to the variation of the loss increase. It can be concluded that the increased Mach number is responsible for the higher losses. This is also confirmed by considering the loss, transition, and maximum Mach number increase for varying widths, as pictured in Figure 16. An axial position of 30% of the chord and a height of ±0.3 mm were again chosen for comparison.

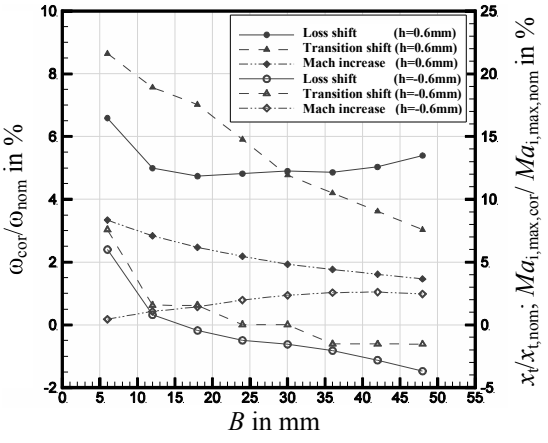

Figure 16. Relative shift of ω, x_t and $Ma_{i,max}$ over a varying corrugation width *B* of 6 mm with a constant axial positon of x_{cor}/l_{SS} = 30%

The hollow once more reveals a correlation close to 1:1 between the shift of the transition point and the additionally produced profile losses. The bulge shows, just like the changing corrugation height did, a loss production that is more than twice as high. In contrast to the previous case, however, the transition point also shifts further upstream. As already discussed in relation to Figure 13 this is due to a separation occurring earlier as a result of the positive pressure gradient at the bulge's rear side and causes a constant additional loss over the increasing wavelength. For very short widths this will additionally be intensified by a small shock at the end of the bulge so that the profile loss is highest here. In Figure 17 the three parameters Ma_i, x_t, and ω are plotted over the corrugation height h for the final comparison.

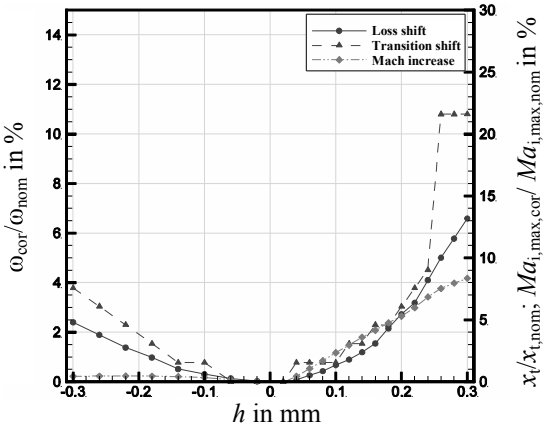

Figure 17. Relative shift of ω, x_t, and $Ma_{i,max}$ over a varying height *h* and a constant width *B* of 6 mm and an axial position x_{cor}/l_{SS} of 30%

Again as expected, the losses increase with rising wave height. They are, however, significantly higher in the case of the bulge. This correlates with the increasing maximum Mach. Figure 18 provides the proof that this is indeed the reason for the additional losses in comparison to the hollow. The same graph that was already used in the pilot survey is used again here for the flat plate. It is shown that the hollow and the bulge cause exactly the same additional loss if Mach numbers greater than Ma = 1 do not exist locally.

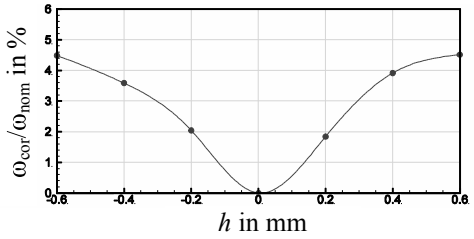

Figure 18. Shift of ω over a varying height *h* and a constant *B* of 18mm (flat plate Section 4.1)

Also interesting is that the transition point for the compressor profile jumps to a constant level once a specific wave height is reached. Here the transition is moved as far as possible upstream to the shock position at the end of the bulge.

5. SUMMARY

The importance of the subject of small scaled geometry irregularities in compressor profiles and the need for research in this field was explained in the introduction. In the following sections it was shown that a single surface corrugation has a significant influence on the profile losses for the given compressor profile. The corrugation height plays a more important role than the corrugation width here. With regard to the possible loss mechanism, overall three conclusions can be derived:

First, it is necessary to check whether the deviation takes place prior to the transition point and whether it is strong enough to influence the transition. The Fage criterion can be used for this purpose. In the case of the transition process moving upstream, the viscous losses in the boundary layer increase significantly. By estimating the influence according to Fage it is necessary to keep in mind that a possible flow diffusion or acceleration can intensify or attenuate the influence caused by the corrugation. A corrugation placed in a decelerated flow is therefore considered more detrimental.

Second, it is necessary to check whether the deviation in relation to the present profile Mach number is strong enough to produce areas of supersonic velocities which can cause considerable shock losses. An upper estimate, for example, can be given using the potential theory. Through the occurrence of small shocks and disturbances due to an interaction with the boundary layer, the transition process can be additionally accelerated.

Last, although it is unlikely for a small corrugation with a high width to height ratio, it is necessary to check whether areas of separation can be caused downstream of the corrugation or whether already existing separations are possibly intensified. For the laminar separation an interlinking with the first conclusion exists again. In addition to the losses the separation is able to accelerate the transition.

ACKNOWLEDGEMENTS

The investigations were partially conducted as part of the aeronautical research programme LuFo IV. The work was supported by the Bundesministerium für Wirtschaft und Technologie (BMWi) per resolution of the German Federal Parliament.

REFERENCES

[1] Denton, J., 1993, "Loss mechanism in turbomachines", Journal of Turbomachinery, Vol. 115, Issue 4, 621

[2] Fage, A., 1943, "The smallest size of spanwise surface corrugation which affects boundary layer transition on an airfoil", R&M N° 2120, A.R.C. Technical Report

[3] Smith, F., 1973, "Laminar flow over a small hump on a flat plate", Journal of Fluid Mechanics, Vol. 57, pp. 803-824

[4] Lessen, M., and Gangwani, S., 1976, "Effect of small amplitude wall waviness upon the stability of the laminar boundary layer", The Physics of Fluids, Vol. 31

[5] Nayfeh, A.H., Ragab, S.A., and Al-Maaitah, A.A., 1988, "Effect of bulges on the stability of boundary layers", Phys. Fluids, Vol. 31(4)

[6] Masad, J.A., and Iyer, V., 1994, "Transition prediction and control in subsonic flow over a hump", Phys. Fluids, Vol. 6

[7] Wie, Y., and Malik, M.R., 1998, "Effect of surface hardness on boundary layer transition in two-dimensional flow", Computers & Fluids, Vol 27(2), pp. 157-181

[8] Wörner, A., Rist, U., and Wagner, S., 2002, "Influence of humps and steps on the stability characteristics of a 2D laminar boundary layer", AIAA Paper 2002-0139

[9] Hilgenfeld, L., 2007, "Turbulenzstrukturen in hochbelasteten Transsonik-Verdichtergittern unter besonderer Berücksichtigung der Verdichtungsstoß-Grenzschicht-Interferenz", VDI Fortschritt-Berichte 487

[10] Kožulovic´, D., Röber, T., and Nürnberger, D., 2007, "Application of a Multimode Transition Model to Turbomachinery Flows", Proceedings of the Seventh European Turbomachinery Conference, Athens, Greece, pp. 1369–1378

Vibration, acoustics

Conference on Modelling Fluid Flow (CMFF'12)
The 15th International Conference on Fluid Flow Technologies
Budapest, Hungary, September 4-7, 2012

NOISE MODELLING AND ANALYSIS OF AIRCRAFT ENGINES WITH CONTRA-ROTATING OPEN ROTOR FANS

Leonidas SIOZOS-ROUSSOULIS[1], Anestis I. KALFAS[2], Kosmas KRITIKOS[3], Emidio GIORDANO[4], Nicolas TANTOT[5]

[1] Corresponding Author. Aristotle University of Thessaloniki, Department of Mechanical Engineering, Thessaloniki, Greece. Mitropolitou Iosif Avenue 15, 54622, Thessaloniki, Greece. Tel.: +302310262679, E-mail: leonidassr@windowslive.com
[2] Aristotle University of Thessaloniki, Department of Mechanical Engineering, Thessaloniki, Greece. E-mail: akalfas@auth.gr
[3] Aristotle University of Thessaloniki, Department of Mechanical Engineering, Thessaloniki, Greece. E-mail: kkritikos@gmail.com
[4] Aristotle University of Thessaloniki, Department of Mechanical Engineering, Thessaloniki, Greece. E-mail: email@emidiogiordano.com
[5] Snecma, Safran Group, Centre de Villaroche, Moissy-Cramayel, France. E-mail: nicolas.tantot@snecma.fr

ABSTRACT

Contra-rotating open rotors (CROR) seem to fulfill the task of adequately reducing emissions and fuel consumption of contemporary aircraft engines. On the other hand, extensive noise generation appears to be a clear drawback of CROR and thus, engines bearing these rotors have lately been the subject of constant research. This paper presents an audio simulation and analysis of sound generated by CROR engines, based on a synthesis of noise signals derived from noise level prediction models.

The original data files comprise of sound pressure level versus frequency results for measurements realized during three stages of flight. The discrete frequencies were simulated by sinusoidal tones which were edited in a Digital Audio Workstation software, according to the initial data. Consequently, a digital audio file was created for each stage of flight. Finally, a spectrum analysis of the audio signal was obtained, throughout the time domain. Blade Passing Frequencies, their harmonics and interaction tones were calculated and additionally located via the spectrum analysis, while overall Effective Perceived Noise Level directivity was also investigated.

The final simulated sounds can be utilized for the assessment of the perception of noise generated by innovative aircraft engines, without the need for experimental measurements. In addition, they can provide comparison between numerical data and the actual effect of aircraft noise on human hearing.

Keywords: aircraft engine, audio simulation, contra rotating open rotor fan, noise modelling, sound propagation, audio visualization

NOMENCLATURE

B_1	[-]	number of blades of rotor 1
B_2	[-]	number of blades of rotor 2
L_i	[*dB*]	SPL or EPNL of i-th noise source
L_p	[*dB*]	combined SPL or EPNL
N_1	[*rad/s*]	rotation speed of rotor 1
N_2	[*rad/s*]	rotation speed of rotor 2
f_1	[*Hz*]	harmonic frequency of rotor 1
f_2	[*Hz*]	harmonic frequency of rotor 2
f_{12}	[*Hz*]	interaction tone between the rotors
m	[-]	circumferential mode of tone
n_1	[-]	positive integer
n_2	[-]	positive integer
r_1	[*m*]	distance from noise source
r_2	[*m*]	distance from noise source
$\Phi(\theta)$	[*dB*]	overall SPL directivity
$\Phi'(\theta)$	[*dB*]	overall EPNL directivity
α	[-]	constant
θ	[deg]	engine noise emission angle
φ	[rad]	angle of climb or descent

Acronyms

2BPF	First Harmonic
BPF	Blade Passing Frequency
CROR	Contra-Rotating Open Rotor
DAW	Digital Audio Workstation
EPNL	Effective Perceived Noise Level
SPL	Sound Pressure Level
VST	Virtual Studio Technology

1. INTRODUCTION

In recent years, growing interest has been noted on aircraft engines capable of providing significant reduction of emissions and fuel consumption. This alteration of market demands is due to the late tendency towards environmentally friendlier means of transport, as well as the rising cost of jet fuel. As a result, research on innovative aircraft propulsion

systems has been initiated. Aircraft engines bearing Contra-rotating Open Rotors (Figure 1) seem to meet the aforementioned standards, because of their high propulsive efficiency, and have thus been the subject of extensive study and research. Besides the qualities of the jet engines stated above, a clear disadvantage is the reduced cruise Mach number as well as the greater than usual noise generation, due to the location of the fan's rotors outside the nacelle. The task of controlling sound propagation has evolved into a particularly serious matter, as regulations regarding noise levels near airfields have become notably severe during the past decade. Therefore, recent work has concentrated on the optimization of noise emissions, in order to overcome the drawbacks of the open rotor. The outcome of the aforementioned investigations was the basis for this paper and aided the development of audio files which simulate accurately the noise generated by CROR.

The generation and propagation of noise emanating from CROR has been lately studied by a number of research groups. Thus, several numerical methods have been introduced in order to achieve accurate modeling of tonal and broadband engine noise. Recently, Kritikos et al. [1] developed a numerical tool which allows fast estimation of noise emissions generated by CROR fans. The emissions were calculated for an adequately wide frequency range, throughout the time domain. The calculative results provided sufficient data, in order to create an elaborate audio simulation of the engine's noise.

The current paper presents the development of audio files which model the noise generated by a CROR aircraft engine, during three stages of flight. Furthermore, a spectrum analysis of the final audio signal was obtained and was employed in order to create a comprehensible visualization of the audio simulation. Additional analysis of the tonal components of the engine's noise and its overall directivity, provided further information regarding the rotors themselves, while proving the correctness of the method utilized to obtain the final results.

2. INPUT DATA ANALYSIS

In order to achieve accurate simulation of aircraft engine noise, data files containing the calculated sound emissions of a CROR aircraft engine, were derived from earlier research work [1].

The investigation providing the required results dealt with modeling and optimizing the noise generated by the two CROR of an innovative aircraft engine. A number of cases of engine operation were processed and investigated, each differing in operating conditions and structural specifications of said rotors. Data originating from one of these cases was adequate for developing the desired sound simulation. Airframe noise was not taken into account, while the aircraft incidence was determined to be 0 degrees during the investigated case.

The data files resulting from [1] comprise of EPNL versus frequency results, for calculative measurements realized during three different stages of flight (approach, sideline and takeoff). The computational data was theoretically extracted by three microphones stationed at three fixed positions on an airfield, according to the ICAO certification regulations [2]. Therefore, each microphone supposedly measured the noise emitted during one stage of flight, as depicted in Figure 2.

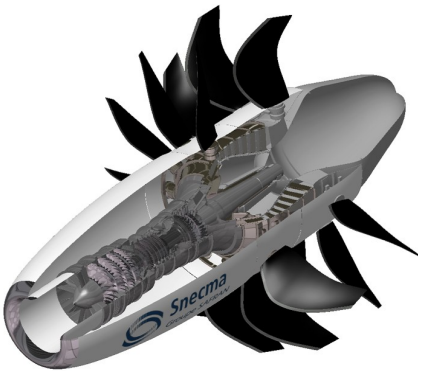

Figure 1. Contra-Rotating Open Rotor aircraft engine [1]

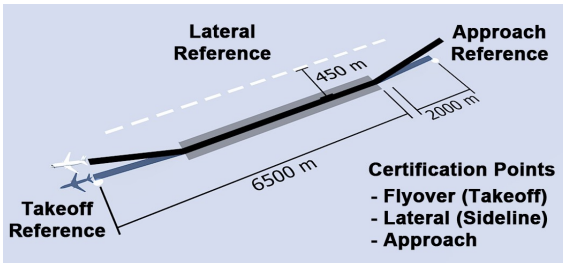

Figure 2. Microphone location according to ICAO certification regulations [2]

For each one of the stages of flight 41 computational reference points were investigated, thus summing up to a total of 123 reference points (named “observers”), throughout the time domain. The time interval between consecutive observers in the time domain was set to 0.5 seconds. Due to the number of observers (41) and the time step between them (0.5 seconds), the final time length of the audio file simulating each stage of flight would subsequently be 20.5 seconds. The microphones supposedly recorded the generated sound throughout the time domain and the reference data was then transferred into the frequency domain, via a Fast Fourier Transformation (FFT).

Each temporal observer provided an instantaneous spectrum analysis of the emitted noise. The frequency range stretched from 19.69 Hz

to 5039.37 Hz, while the frequency step was set to 19.69 Hz. Thus, the data file corresponding to each observer consisted of 256 discrete tones, all differing in EPNL. The upper limit of the frequency range was considered to be sufficiently high.

3. SOUND GENERATION AND PROCESSING

The creation of the final audio files required generating the 256 discrete tones in a computing software [3] and editing them in a sequencer and DAW software [4] thereafter.

3.1. Discrete Tone Generation and Input Data Re-arrangement

Initially, 256 sinusoidal sound waves of equal amplitude were generated. Each sound wave's frequency corresponded to the frequency of each one of the discrete tones, mentioned above, while the time length of every audio file was set to 20.5 seconds. The sound waves were finally exported as WAV digital audio files, thus lossless and uncompressed audio format. The sampling rate chosen during the encoding process was 96000 Hz, which is the standard for professional audio applications. In order to import the data into the DAW software, the original files were sorted and edited with the aid of a spreadsheet application. During this procedure the input data was grouped into three files, one for each of the stages of flight. The highest EPNL value was located in every stage of flight and was then deducted from all the measured levels of that stage. Therefore, the original data was converted, resulting in files containing EPNL values ranging from zero to lower negative values. Due to the logarithmic nature of sound pressure levels, the subtraction process is acceptable, as the general sense of EPNL is not altered.

3.2. Final Audio Processing

This format was finally suitable for editing, via the DAW software, since the gain of audio being processed by the software cannot exceed +20 dB. Additionally, extremely high gains could lead to digital distortion. On the other hand, gains can be reduced without the risk of distortion, while the software permits negative gain alteration ranging from zero to -60 dB. Consequently, only EPNL values ranging from zero to -50 dB were worth investigating, as values lower than -50 dB were considered negligible, compared to the highest EPNL value. All levels lower than -50 dB were treated as -60 dB in the sound editing process.

Eventually, the data was grouped into three files, which were processed separately, yet in the same manner. Each file corresponded to one of the three stages of flight and apparently led to the generation of one digital audio file.

A basic feature of every DAW software is the capability of simultaneously processing and editing, a practically infinite amount of audio tracks. The only actual limitation is the available computational power, as audio rendering can be considerably strenuous for a personal computer.

All 256 audio files generated earlier, were arranged in the software's workspace, each ranging from zero to 20.5 seconds. Thus, a 20.5 second long cluster of sounds of different frequency was created. The gain of all audio tracks was adjusted to -60 dB and each track was severed into 41 parts, each being 0.5 seconds long. Consequently, the outcome of the above process was a total of 10496 (41x256) audio clips, organized into 41 observers throughout the time domain and 256 discrete tones throughout the frequency domain. The numbers defining each of the 41 temporal observers were aligned along the horizontal axis, whereas the vertical axis defined the frequency domain. Apparently, clips located on the same row comprised of audio of the same frequency.

Once the audio files in the DAW software were organized in order similar to the input data's, the gain of each audio clip was altered manually according to the original computational data. Meanwhile, the gain of audio clips of EPNL below -50 dB, was not altered. This same process was repeatedly carried out for all three stages of flight.

Finally, after having altered the gain of all clips precisely according to the input data, the cluster of audio clips could be rendered and exported as one digital audio file. The final outcome was one 20.5 second long audio file, encoded as uncompressed WAV format. Likewise, this same process was carried out for all three stages of flight, resulting in three digital audio files.

4. SPECTRUM ANALYSIS AND VISUALIZATION

Having completed the audio simulation of all three stages of flight, a visual representation of the results was considered necessary. A spectrum analysis software [5] was selected in order to attain visualization of the final audio signal, during each stage of flight, throughout the time domain.The spectrum analyser was utilized as a VST plug-in, alongside the DAW software. Practically, 41 still frames were captured during the processing of the audio files by the spectrum analyser. Each of the still frames corresponded to each one of the temporal observers, as expected.

Achieving complete and comprehensible visual representation of the audio output required the creation of a time dependent series consisting of the 41 still frames. The still frames were merged into a real-time sequence, lasting 20.5 seconds and were

combined with a timer and an indicator of the observer corresponding to each time interval.

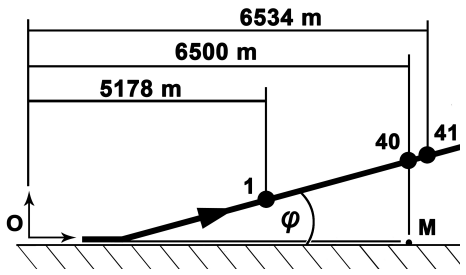

Figure 3. Theoretical Takeoff Measurement Procedure [1]

The synchronisation of audio files and still frames was realized via a video editing software [6] and was exported as a digital video file (AVI format). This same process was reiterated for all three stages of flight.

The theoretical measurement procedure and location of the microphone are described in Figure 3. Figures 4 and 5 typify the spectrum analysis of all 41 reference points of the takeoff stage. The spectrum analysis graphically illustrates the computed effective perceived noise levels in respect to the 256 discrete tones which constitute the frequency spectrum. Each separate curve represents the spectrum analysis of one temporal observer and therefore Figs. 4 and 5 depict the overall fluctuation

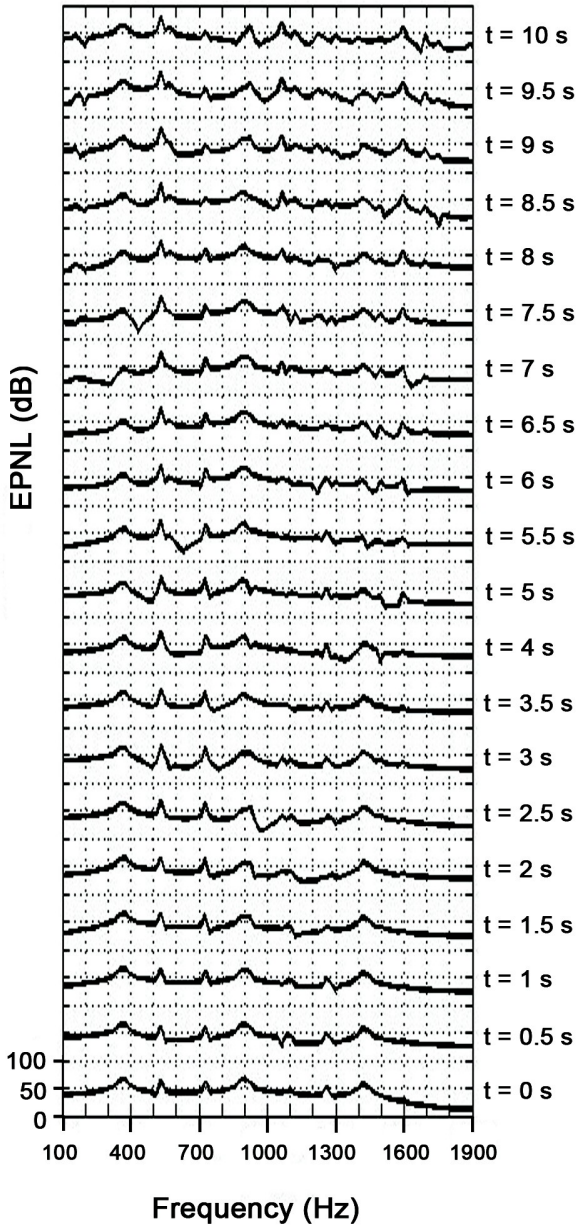

Figure 4. Spectrum Analysis of Temporal Observers 1 to 20, During the Takeoff Stage

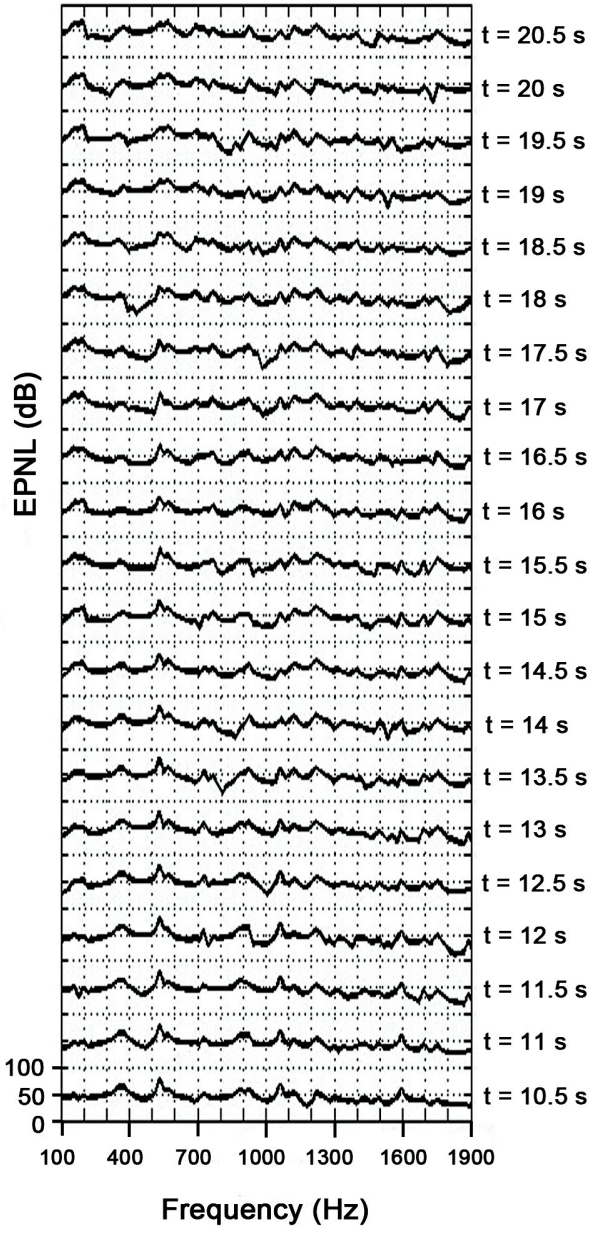

Figure 5. Spectrum Analysis of Temporal Observers 21 to 40, During the Takeoff Stage

of noise levels throughout the time and frequency domain.

During the takeoff stage the microphone "M" was theoretically stationed at a distance of 6500m away from the origin "O". This distance also corresponded to the fourtieth observer located in the time domain, while the aircraft was supposedly directly above the microphone. The computational process was initiated when the aircraft had reached a horizontal distance of 5178m from the origin and therefore, this reference value was assigned to the first temporal observer. Accordingly, the computational procedure ended when the aircraft reached a distance of 6534m from the origin and, consequently, this reference value was considered to be the last temporal observer. The angle φ represents the angle of climb which was equal to 4.3 degrees, during the entire takeoff stage [1]. Each one of the observers can be defined either temporally or spatially, as all 41 observers correspond to specific points on the aircraft's path which are determined by the already known [1] aircraft's takeoff speed and angle of climb.

A thorough examination of Figs. 4 and 5 can lead to certain conclusions regarding tone noise generation as will be cited in the following section of the paper. In addition, high frequencies tend to be absorbed more effectively by air. Thus, noise levels remain low for frequencies above 1500 Hz, during the first temporal observers, while the aircraft is supposedly located a significant distance away from the microphone. Sound transmission loss is mainly affected by atmospheric humidity, temperature and pressure, parameters which were defined by the original numerical model [1].

5. TONE NOISE CALCULATION

In CROR aircraft engines a very important amount of both tone and broadband noise originates from the fan. The aerodynamic interaction between the neighboring blade rows of the fan's rotors is the principal mechanism of tone noise generation. The sound spectrum is dominated by the harmonics of each rotor's BPF and by the interaction tones between the two rotors.

The tones which constitute the noise spectra were calculated in order to be compared to the tones located during the graphical analysis of the simulated audio. Concurrence of the outcome of the aforementioned processes would provide validation of the method followed during the modelling and simulation procedure.

5.1. Tone Noise Calculation

The BPFs of rotors 1 and 2 are derived from Eqs. (1) and (2) [7] :

$$f_1 = n_1 B_1 N_1 \quad \text{in Hz,} \tag{1}$$

$$f_2 = n_2 B_2 N_2 \quad \text{in Hz,} \tag{2}$$

The frequencies of the interaction tones between the two rotors are derived from Eq. (3) [7], while the circumferential mode of a tone f_{12} is calculated from Eq. (4) [7] :

$$f_{12} = | n_1 B_1 N_1 + n_2 B_2 N_2 | \quad \text{in Hz,} \tag{3}$$

$$m = n_2 B_2 - n_1 B_1 \tag{4}$$

In the above equations, N_1 and N_2 are the rotation speeds of each rotor, while n_1 and n_2 are positive integers. In addition, B_1 and B_2 are the number of blades in each rotor. The second row of blades is taken as reference for the rotation direction for the sign of m [7]. These variables were determined by Kritikos et al. [1] and thus, the interaction tones could be calculated accurately.

The results of the calculation of the interaction tones are presented in Table 1. The fundamental frequencies of the two rotors are stated as BPF_1 and BPF_2, while their first harmonics are named $2BPF_1$ and $2BPF_2$, respectively.

Table 1. Tone Frequency Calculation

n_1	n_2	f_{12}	mode	
0	1	165.78	10	BPF_2
1	0	198.94	-12	BPF_1
0	2	331.56	20	$2BPF_2$
1	1	364.72	-2	
2	0	397.88	-24	$2BPF_1$
0	3	497.34	30	$3BPF_2$
1	2	530.5	8	
2	1	563.66	-14	
3	0	596.82	-36	$3BPF_1$
0	4	663.12	40	$4BPF_2$
2	2	729.44	-4	
4	0	795.76	-48	$4BPF_1$
2	3	895.22	6	
3	2	928.38	-16	
3	3	1094.16	-6	
3	4	1259.94	4	
4	3	1293.1	-18	
4	4	1458.88	-8	
4	5	1624.84	2	
5	4	1658	-20	

5.2. Comparison of Graphical and Numerical Data

The grey-shaded areas of Table 1 demonstrate frequencies coinciding with significant tonal noise, indicated by the graphical visualization of the audio signal, as depicted in Figures 6 and 7. The graphs represent the spectrum analysis of the audio signal, simulating the engine's noise during the approach and sideline stage, respectively, throughout the time domain. The color gradient aids the identification of

sound pressure levels, ranging from minimum (lighter) to maximum (darker) levels.

Despite some slight divergences, mostly caused by the different computational measurement procedures applied during each flight stage, both graphs display undisputed similarities. The tones at frequencies BPF_1, BPF_2, f_{11}, f_{12}, f_{22}, f_{23}, f_{33}, f_{34} and f_{45} dominate the noise spectrum and their effect is clearly depicted by the continuous high levels observed in Figs. 6 and 7. A definite pattern governs the generation of dominant tones in respect to the circumferential modes, the origin of which, however, cannot yet be defined, thus dictating future investigation on tone generation and propagation. Similar conclusions can be drawn by comparing Figs. 6 and 7 to Figs. 4 and 5, as they all depict the correlation of noise levels, time and frequency.

The outcome of the aforementioned comparison of theoretically expected and numerical data, provided additional verification of the procedure followed and its results thus far.

It is worth noting that high frequency components appear attenuated throughout the approach stage. This is due to the significant differentiation of settings applied to the engine during the approach stage, as opposed to the sideline and takeoff stage.

6. OVERALL SOUND PRESSURE LEVELS AND DIRECTIVITY

The directivity of the overall measured EPNL was computed and compared to the theoretical data, which govern the propagation of noise emitted by CROR fans. Coincidence of the outcome of the above would provide further validation of each phase of the investigation. Furthermore, overall EPNL directivity patterns lead to a better understanding of noise generation and its variations throughout the time domain, for each stage of flight.

6.1. Theoretical Directivity of Overall Sound Pressure Level

Recent investigations [7] have proven that overall directivity of sound pressure can be approximated by a parabola, defined by Eq. (5) :

$$\Phi(\theta) = -\alpha[\,\theta\,(\theta - 180) + 90^2\,] \quad \text{in dB,} \qquad (5)$$

Where θ is the radiation angle in degrees, in the horizontal plane ($\theta = 0$ on the upstream axis), while α is a constant which can be estimated to be approximately $\alpha \approx 0.002$ [7]. Directivity of overall EPNL can be determined via Eq. (6) [7] :

$$\Phi'(\theta) = \Phi(\theta) + 20\log_{10}(\sin\theta) \quad \text{in dB,} \qquad (6)$$

The maximum value of $\Phi(\theta)$ and $\Phi'(\theta)$ is 0 dB, at $\theta = 0$ deg., as is depicted in Figure 8.

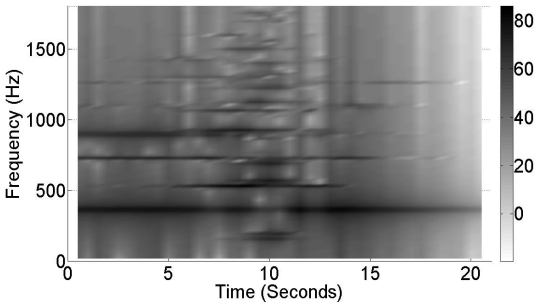

Figure 6. Spectrum Analysis of All Temporal Observers During the Approach Stage

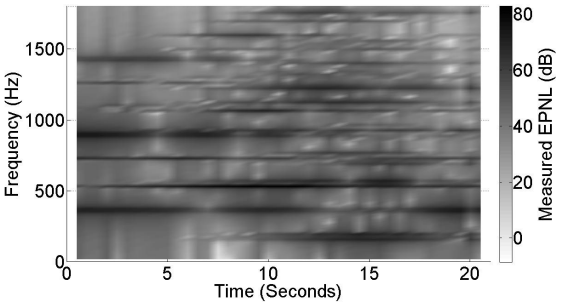

Figure 7. Spectrum Analysis of All Temporal Observers During the Sideline Stage

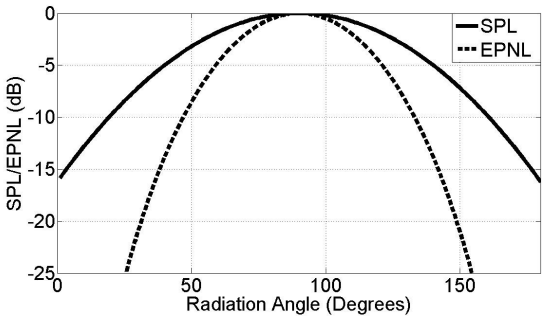

Figure 8. Theoretical Overall Sound Pressure Directivity

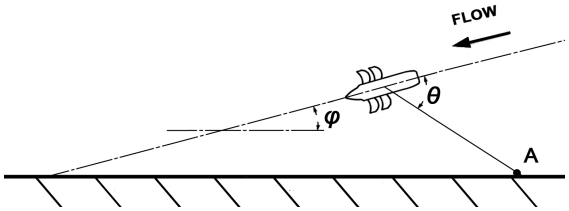

Figure 9. Emission Angle and Microphone Position, During the Takeoff Measurement Stage

6.2. Actual Emission Angle Determination

The emission angle of the radiated engine noise corresponding to each one of the 41 observers, of one stage of flight, can accurately be determined, as

the microphone retained a fixed position during all 41 reference points (Figure 9). The coordinates and the angle φ were predefined in [1], therefore, 41 radiation angles were derived for each stage of flight.

6.3. Effective Perceived Noise Level Combination

The combined sound pressure level, L_p, of n audio sources can be computed by Eq. (7) [8] :

$$L_p = 10\log_{10}\sum_{i=1}^{n}10^{L_i/10} \quad \text{in dB,} \qquad (7)$$

Where L_i is the SPL or EPNL of each noise source.

The actual combined overall EPNL values of the aircraft engine during all stages of flight was determined accordingly, for each one of the observers. Thus, the computation of combined EPNL during one flight stage required 41 separate calculations, one for each of the observers. It is apparent, that for each one of the 41 calculations realized, n = 256 (equal to the overall number of discrete frequencies throughout the frequency spectrum).

Apparently, the combined EPNL corresponded to each one of the observers and, thus, to each one of the 41 angles, calculated above.

6.4. Effective Perceived Noise Level Distance Correction

The theoretical results regarding overall EPNL directivity refer to successive measurements realized circumferentially of the engine, at equal distances from the upstream axis. On the contrary, the EPNL computed in [1] correspond to random distances from the sound source, as the microphone was considered to retain its position, during measurements, while the aircraft was in motion. A correction was thus required, when handling the combined EPNL, in order to compensate for the sound attenuation imposed by increased distance.

Firstly, the smallest distance between the path of the aircraft and the microphone was arbitrarily defined as a reference distance. The EPNL corresponding to this distance was not altered, whereas, noise levels of all other observers were considered to be attenuated due to the increased distance from the source (in respect to the reference value). The space surrounding the engine was assumed to approximate a free field, where the sound attenuation is governed solely by the inverse square law.

The impact of distance on sound pressure levels is indicated by Eq. (8) [8], where L_2 and L_1, indicate the sound levels, while r_2 and r_1 stand for the respective distances from the noise source.

$$L_2 = L_1 - 20\log_{10}(r_2/r_1) \quad \text{in dB,} \qquad (8)$$

The aforementioned assumption approximates adequately the actual correlation between sound transmission loss and distance, without however taking into consideration significant parameters, such as atmospheric pressure, temperature and humidity.

6.5. Comparison of Theoretical and Actual Overall Noise Level Directivity

The actual combined overall EPNL for each of the temporal observers were determined in accordance to the above. The outcome was then plotted against the emission angle as is depicted in Figure 10, in order to investigate overall noise level directivity.

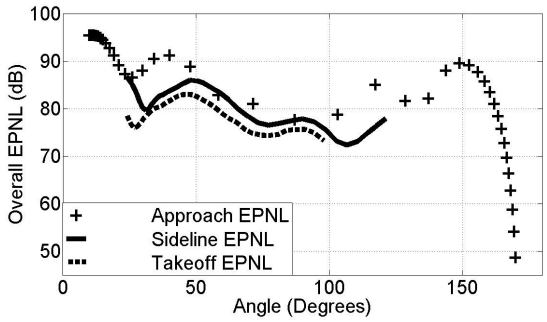

Figure 10. Overall Sound Level Directivity of Approach, Sideline and Takeoff Noise

In Fig. 10, noise levels of all three stages of flight were plotted. It is evident that the noise level values extracted during the approach stage covered a great range of angles, in contrast to the takeoff and sideline data. The placement of the microphone and the overall theoretical measurement procedure were liable for this differentiation.

The curves tend to follow the general curvature implied by the theoretical data. However, some divergence is clear, especially at very small angles, where all three curves display no decline, while at 90 degrees, they should reach their maximum values. On the other hand, higher angle values at the approach stage well duplicate the theoretical data.

Despite some overall convergence to the theoretically expected results, further study and analysis is required, as the atmospheric conditions were not taken into account when applying the correction equations, limiting thus the accuracy of the final outcome. An alternative method has to be investigated in order to compensate for sound transmission loss imposed by distance.

7. CONCLUSIONS

In this paper, the audio simulation of noise generated by the fan rotors of a CROR aircraft engine was presented. A spectrum analysis of the final audio signal was obtained, in order to provide

accurate visualization of the audio files and to aid further analysis. The spectrum analysis of each flight stage was studied and the contribution of tone noise to overall noise was investigated, while dominant tones, as well as their modes, were computed. The calculated tones were proven to coincide with the graphical results of the spectrum analysis, thus validating the process. Furthermore, the actual overall EPNL directivity was derived from the numerical data and the outcome underwent comparison to the theoretically expected results. The overall directivity patterns compared well to the theoretically defined data, however future work could include further research on tone noise directivity patterns and their impact on the propagation of engine noise.

In conclusion, three digital audio files were generated and are now available for calibration and research procedures related to CROR aircraft engine noise. These files can significantly enhance the acoustic perception of noise generated by CROR aircraft engines, particularly when combined with a visual display of the audio signal, throughout the time domain. The aforementioned combination of audio and visual elements is the key to intuitive understanding and perception of numerical data which represent noise levels, as well as their actual effect on human hearing. These audio files originate from research on aircraft engines of innovative design, still in early stages of development and could form a useful vehicle for future research endeavours.

ACKNOWLEDGEMENTS

The authors would like to acknowledge SNECMA, for the kind permission to publish this paper, and particularly Dr. Rasika Fernando, for providing his expert advice. The paper was realized within the frame of the European wide DREAM project (valiDation of Radical Engine Architecture systeMs).

REFERENCES

[1] Kritikos, K., Giordano, E., Kalfas, A. I., and Tantot, N., 2012, "Prediction of Certification Noise Levels Generated by Contra-Rotating Open Rotor Engines", *ASME Turbo Expo 2012, GT2012-69232*.

[2] ICAO, 2005, "Annex 16, Environmental Protection: Volume 1, Aircraft Noise". *International Civil Aviation Organization*.

[3] Mathworks Matlab User's Guide, http://www.mathworks.com/help/techdoc/matlab_product_page.html, *Mathworks*.

[4] Ableton Live 8 User's Manual: http://www.ableton.com/pages/downloads/manuals, *Ableton.*

[5] Bluecat FreqAnalyst Pro, http://www.bluecataudio.com/Products/Product_FreqAnalystPro/, *Blue Cat Audio.*

[6] Adobe Premiere CS4 User's Guide, http://help.adobe.com/en_US/PremierePro/4.0/premierepro_cs4_help.pdf, *Adobe.*

[7] Lewy, S., 2010, "Semi-Empirical Prediction of Tone Noise Due to Counter-Rotating Open Rotors", *20th International Congress on Acoustics, ICA 2010*.

[8] Everest, F. A., and Pohlmann, K. C., 2009, "Master Handbook of Acoustics, Fifth Edition", *McGraw-Hill*.

[9] Deconick, T., Hoffer, P. A., Hirsch, C., De Meulenaere, A., Bonaccorsi, J. C., and Ghorbaniasl, G., 2010, "Prediction of Near-Field and Far-Field Noise Generated by Contra-Rotating Open Rotors", *16th AIAA/CEAS Aeroacoustics Conference, AIAA 2010-3794*.

[10] ICAO, 2008, "Doc 9829 AN/451: Guidance on the Balanced Approach to Aircraft Noise Management (2nd Edition)", *International Civil Aviation Organization*.

[11] ICAO, 2007, "Doc 9501 AN/929: Environmental technical manual on the use of procedures in the noise certification of aircraft". *International Civil Aviation Organization.*

[12] ACARE, 2001, "European Aeronautics: A Vision for 2020", *European Communities*.

[13] Rhodes, D. D. P., 2005, "Document 29 3rd edition: Report on standard method of computing noise contours around civil airports". *ECAC.CEAC, Vol. 1: Applications Guide*.

[14] Rhodes, D. D. P., 2005, "Document 29 3rd edition: Report on standard method of computing noise contours around civil airports". *ECAC.CEAC, Vol. 2: Technical Guide*.

[15] Beranek, L., 1993, "Acoustics", *Acoustical Society of America*.

[16] Pinelli, L., Poli, F., Marconcini, M., Arnone, A., Spano, E., and Torzo, D., 2011, "A Linearized Method for Tone Noise Generation and Propagation in a Multistage Contra-Rotating Turbine", *9th European Turbomachinery Conference, ETC9 2011*.

[17] Brouwer, H., 2010, "Analytic Description of the Noise Radiation from Single- and Contra Rotating Propellers", *20th International Congress of the Aeronautical Sciences, ICAS 2010*.

Conference on Modelling Fluid Flow (CMFF'12)
The 15th International Conference on Fluid Flow Technologies
Budapest, Hungary, September 4-7, 2012

ROBUSTNESS OF VIVS FOR PERIODIC EXTERNAL FORCE

Masahiro Kamijo[1], Ryota Iiyoshi[2], Tsutomu Takahashi[3], Shuichi Yamada[4], Masataka Shirakashi[5], Mizuyasu Koide[6]

[1] Corresponding Author. Department of Mechanical Engineering, Nagaoka University of Technology. 1603-1 Kamitomioka, Nagaoka, Niigata, Japan. Tel.: +81-258-47-9728, Fax: +81-258-47-9770 , E-mail: kmasa@stn.nagaokaut.ac.jp
[2] Department of Mechanical Engineering, Nagaoka University of Technology. E-mail: iiyoshi@ stn.nagaokaut.ac.jp
[3] Department of Mechanical Engineering, Nagaoka University of Technology. E-mail: ttaka@ nagaokaut.ac.jp
[4] Department of Mechanical Engineering, Nagaoka University of Technology. E-mail: yamasyu@ stn.nagaokaut.ac.jp
[5] Department of Mechanical Engineering, Nagaoka University of Technology. E-mail: suikikusai@major.ocn.ne.jp
[6] Department of Economics, Niigata Sangyo University. E-mail: mkoide@ind.nsu.ac.jp

ABSTRACT

The charactoristics of the vortex-induced vibrations, VIVs, with applying periodical external force is investigated. A circular cylinder is supported by plate springs on a setting stage and it can vibrate only to the cross-flow direction. An electric-magnetic oscillator is attached on the stage and can apply a sinusoidal force with certain friquency and amplitude to the cylinder. Both the electric signal to the oscillator and the displacement of the vibrating cylinder are measured simultaneously. A water tunnel instrument is used in this experiment. Three kinds of VIVs, Karman VIV, Necklace VIV and Trailing VIV, are examined. The latter two VIVs are induced by longitudinal vortices when a wake plate is set as a cruciform to the cylinder.

When a periodic force that has a slightly different frequency from the VIV's is applied, the frequency of the cylinder vibration keeps the same frequency at lower magnitude of the external force. On the other hand, the vortex shedding is synchronaized with the external force frequency when the magnitude of the external force exceeds a critical value. The critical condition is one of the indices to evaluate the stability of the VIVs for the external disturbanse and it is named the robustness of stability. The maps of the critical condition on the external frequency – the vibration amplityde plot are drawn for each VIV and the characterristics of each VIV are compared.

Keywords: Cruciform cylinders, electro-magnetic force, longitudinal vortex, robustness of stability, vortex induced vibrations (VIVs)

NOMENCLATURE

A_R	[-]	aspect ratio (=L/d)
B	[Wb/m^2]	magnetic flux density
c	[kg/s]	structural damping factor
c_c	[kg/s]	critical damping factor ($=2\sqrt{m_e k}$)
c_e	[kg/s]	effective damping factor
c_G	[kg/s]	damping factor by generator
c_{total}	[kg/s]	total damping factor ($c_e + c_G$)
d	[m]	diameter of upstream circular cylinder
e	[V]	voltage through entire circuit
e_c	[V]	voltage through coil
e_r	[V]	voltage through load resister
F	[N]	magnitude of electromagnetic force (=$e_r Bl/R_L$)
F_{rms}**	[-]	non-dimensional external force (=$F_{\mathrm{rms}}/F_{\mathrm{vrms}}\|_{F=0}$)
F_v	[N]	exciting force caused by vortex shedding
f_e	[Hz]	external force frequency
f_e**	[-]	non-dimensional external force frequency ($f_e/f_Z\|_{F=0}$)
f_n	[Hz]	natural frequency
f_v	[Hz]	vortex shedding frequency
f_Z	[Hz]	vibration frequency
f_ζ	[-]	amplitude magnification factor (Eq. 9)
i	[A]	electric current
k	[N/m]	constant of spring
l	[m]	lead length in magnetic field
L	[m]	length of upstream circular cylinder
m_e	[kg]	effective mass (=$k/(4\pi^2 f_n^2)$)
m_e*	[-]	mass ratio (=$4m_e/(\rho\pi d^2 L)$)
n	[-]	coil turns
O-xyz	[-]	coordinate system
R	[Ω]	total resistance (= $r + R_L$)
R_L	[Ω]	load resistance
r	[Ω]	internal resistance of coil

Sc	[-]	Scruton number ($=2\delta_e m_e^*$)
s	[m]	gap between upstream circular cylinder and downstream object
S_Z	[-]	spectrum intensity
t	[s]	time
U	[m/s]	free stream velocity
U^*	[-]	non-dimensional flow velocity ($=U/(f_n d)$)
w	[m]	strip-plate width
Z	[m]	displacement of upstream circular cylinder
Z_{rms}^*	[-]	non-dimensional vibration amplitude of upstream circular cylinder ($=Z_{\mathrm{rms}}/d$)
Z_{rms}^{**}	[-]	non-dimensional vibration amplitude of upstream circular cylinder ($=Z_{\mathrm{rms}}/Z_{\mathrm{rms}}\|_{F=0}$)
δ_e	[-]	effective logarithmic damping factor ($=2\pi c_e/c_c$)
δ_G	[-]	logarithmic damping factor of electricity generation ($=2\pi c_G/c_c$)
δ_{total}	[-]	total logarithmic damping factor ($=\delta_e+\delta_G$)
ζ_{total}	[-]	total damping ratio ($=c_e/c_c+c_G/c_c$)
ρ	[kg/m^3]	density of water
φ	[rad]	phase difference between Z and F_v
ω_n	[Hz]	natural angular frequency ($=2\pi f_n$)
ω_v	[Hz]	angular frequency of vortex shedding ($=2\pi f_v$)
ω_v^*	[-]	non-dimensional angular frequency ($=\omega_v/\omega_n$)

Subscript

A	amplitude
F=0	without external force condition
rms	root mean square value

1. INTRODUCTION

The periodic shedding of vortices from a cylindrical body perpendicular to uniform flow causes fluctuating force to the body. When it is elastically supported, vibration is induced, e.g. Karman vortex induces vibration, KVIV. A lot of theoretical, numerical and experimental investigations about KVIV have been reported. The frequency of the vortex shedding from the vibrating cylinder is synchronized with the cylinder motion even if the flow velocity is different from the resonant condition estimated from the natural frequency of the cylinder. It is called the synchronization phenomenon or the lock-in phenomenon. By this phenomenon, KVIV occurs over a wide range of flow conditions compared with a prediction calculated by the linear oscillation model. The velocity range of the synchronization phenomenon and the amplitude of the cylinder vibration is affected by the mass ration m_e^* and the dumping factor c [1]. Therefore, theoretical prediction of KVIV is still difficult.

In case of a cruciform arrangement of two circular cylinders, two kinds of VIVs are induced by the longitudinal vortices. One is caused by the trailing vortex shedding from the cross sectional region and the other is by the necklace vortex, as shown in Fig.1 (a) and (b), respectively [2-4]. They are named the trailing vortex induced vibration TVIV and the necklace vortex induced vibration NVIV. Occurrence of TVIV and NVIV depends on the gap between the cylinders and their diameter. When the gap between them denotes s and the diameter of the front circular cylinder d, TVIV occurs in the range of $0<s/d \leqq 0.25$ and NVIV occurs in $0.25<s/d<0.5$.

When the downstream cylinder is replaced into a strip plate that has the same frontal projected area of the circular cylinder, the vibration amplitude and the synchronized velocity range become significantly large in both TVIV and NVIV [5,6]. These VIVs show the synchronization phenomenon as same as KVIV and then the characteristics of these VIVs are also unclear.

In this study, we observe the characteristics of VIVs by applying a periodical external force generated by an electro-magnetic oscillator. The purpose of this experiment is an evaluation of the robustness of the vortex shedding in each VIVs for disturbance caused by the external force. The frequency and the magnitude of the external force are controlled by the electro-magnetic oscillator. The frequency and average amplitude of the vibration with the periodic external force are compared with the original VIV behaviour without the external force and the robustness of stability of VIVs is examined by these comparisons.

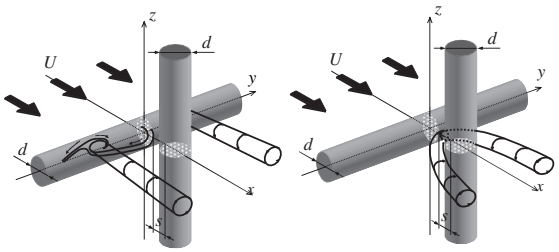

(a) Trailing vortex ($0 \leq s/d \leq 0.25$) (b) Necklace vortex ($0.25 \leq s/d \leq 0.5$)

Figure 1. Longitudinal vortices shedding from criss-cross circular cylinders[2].

2. EXPERIMENTAL APPARATUS AND PROCEDURE

The experimental apparatus arrangement for water tunnel experiments is shown in Fig.2. The experiments are carried out in a circulating water tunnel with a measuring section of 100(H) x 100(W) x 360(L) *mm*. The maximum velocity is 5 *m/s*, and the free flow velocity is obtained from the

flow rate measured by an electromagnetic flow meter.

The upstream cylinder is set horizontally and perpendicularly to the free stream supported by two cantilever plate springs to make the cylinder vibrate in the vertical direction (z-direction). The downstream strip-plate is set rigidly, and its x-directional position is adjustable precisely. A laser displacement sensor is used to measure the upstream cylinder displacement Z, and its RMS value Z_{rms} is used as a representative value to express the vibration amplitude.

The electricity-magnetic oscillator unit is composed of two sets of a coil and a magnet. The coils are mounted on both ends of the support arm of the upstream cylinder and vibrate with the upstream cylinder. The magnets are fixed on an external supporter, and the coils are sandwiched between the magnets with a certain gap. The load resistors are connected to the coils.

A part of the coil is set in a direction perpendicular magnetic field lines between the magnets. A periodic magnetic force is generated when a sinusoidal electric current is appled by using a function generator. The function generator can supply an arbitrary frequency and magnitude of voltage to the coils. The block diagram of the electric circuit is shown in Fig. 3. The RMS values of the supplied voltage e_{rms}, the load registor voltage e_r and the coil voltage e_c are measured.

The natural frequency f_n and the effective logarithmic damping factor δ_e are determined by a free damping oscillation in water at rest with open circuit, i.e. total resistance R=∞. The total logarithmic damping factor δ_{total} is determined by a free damping oscillation in water at rest with closed circuit for each load resister, and the logarithmic damping factor of electricity generation is obtained by subtracting δ_e from δ_{total}. The effective mass m_e is calculated from f_n and the spring constant k. Conditions for water tunnel experiments, coils and magnets are summarized in Table 1.

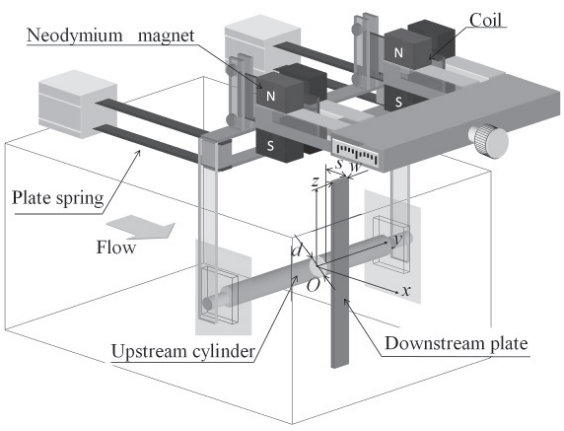

Figure 2. Experimental apparatus for water tunnel experiments.

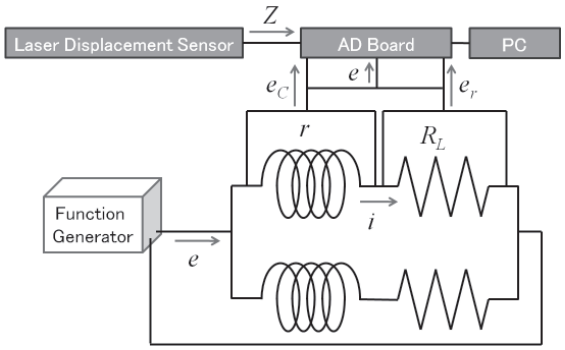

Figure 3. Block diagram of electric circuit and measurement system.

Table 1. Eperimental condisions.

Vortex	Karman	Trailing	Necklace
Measuring Section H x W x L [*mm*]	100 x 100 x 360		
Cylinder diameter d [*m*]	0.01		
Cylinder length L [*m*]	0.098		
Aspect ratio A_R (=L/d) [-]	9.8		
Strip-plate width w [*m*]	-	0.01	0.005
Gap-to-diameter ratio s/d [-]	-	0.22	0.35
Natural frequency f_n [*Hz*]	5.0	4.6	5.1
Spring constant k [*N/m*]	141	143	158
Effective mass m_e [*kg*]	0.143	0.172	0.157
Effective logarithmic damping factor δ_e [-]	0.326	0.264	0.264
Mass ratio m_e* [-]	18.6	22.4	20.0
Scruton number Sc (=$2m_e*\delta_e$) [-]	12.1	11.8	10.6
Coil turns n[-]	200		
Magnetic flux density B[Wb/m^2]	0.38		
Lead length l[*m*]	0.02		
Load resistance R_L[Ω]	30		

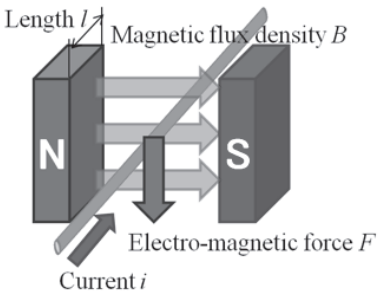

Figure 4. Generation of electro-magnetic force.

3. SIMPLE ESTIMATION OF EXCITING FORCE BY VORTEX SHEDDING AND ELECTRO-MAGNETIC FORCE [7, 8]

3.1. Estimation of fluid force in VIV

In order to examine the influence of the external force on the VIV, we need to compare it with the force F_v caused by the vortex shedding. It is not easy to measure the force F_v acting on the vibrating cylinder directly so that we try to estimate it based on the linear oscillatory model. When F_v oscillates sinusoidally with a frequency f_v, the cylinder vibrates sinusoidally with the same frequency. Hence, the displacement Z and F_v are given by

$$Z = Z_A \sin \omega_v t \tag{1}$$

$$F_v = F_{vA} \sin(\omega_v t + \phi) \tag{2}$$

where $\omega_v=2\pi f_v$.
If F_{vA} and f_v were independent of the cylinder motion, the equation of the cylinder motion would lead to the solution for the vibration amplitude as

$$Z_A = \frac{F_{vA}}{k} \cdot f_\zeta(\zeta_{total}, \omega_v^*) \tag{3}$$

Here, k is a spring constant, ζ_{total} is a damping ratio for c_{total}, ω_v* is a non-dimensional angular frequency and f_ζ is an amplitude magnification factor given by the next equation.

$$f_\zeta(\zeta_{total}, \omega_v^*) = 1 \Big/ \sqrt{\left\{1-(\omega_v^*)^2\right\}^2 + \left\{2\zeta_{total}(\omega_v^*)\right\}^2} \tag{4}$$

If $Z_A=Z_{rms}$, F_{vrms} can be estimated from the vibration amplitude Z_{rms}, which is measured at the no external force condition, by substituting in Eq.(5).

$$F_{vrms} = Z_{rms} k \sqrt{\left\{1-(\omega_v^*)^2\right\}^2 + \left\{2\zeta_{total}(\omega_v^*)\right\}^2} \tag{5}$$

F_{vrms} calculated by Eq.(5) will be used as a reference magnitude of the force to normalize the magnitude of the applying periodic external force.

3.2. Estimation of electro-magnetic force

The periodic external force is generated by the electromagnetic oscillator. When a current i is applied to the coil, the magunitude of the electromagnetic force F can be calculated by Eq.(6) with an assmption that the magnetic flux density B is constant between the magnets.

$$F = iBl = \frac{e_r}{R_L} Bl \tag{6}$$

Here, e_r is the voltage of a load resister, R_L is its regstance, and l is an effective length of the electric wire in the magnetic field. The coils are oscillated by appling a sinusoidal current but the oscillation induces a current by the electromagnetic effect. Terefore, the voltege e_r, not e which is the voltage generated by the function generator, is used in Eq.(6) to evaluate the magnitude of the electro-magnetic force.

4. EXPERIMENTAL RESULTS

4.1. KVIV experiments

A vibration behavior of the single circular cylinder in KVIV with applying the external periodic force is observed. Figure 5 shows the influence that the periodic external force causes for relationship between flow velocity and the vibration. In case of no external force, KVIV is induced a certain velocity range and the frequency of the vibration in KVIV is changed by the flow velocity. In the out of the KVIV range, vibration is not induced. When the periodic external frequency which has the same frequency to the natural frequency is applied, the vibration is induced in all range of the flow velocity and the average amplitude of the vibration increases with increasing the magnitude of the force F. When the external force has a different frequency from the natural frequency, the distinct vibration is induced in KVIV range only. In the KVIV range, the vibration frequency is changed by the flow velocity as same as the KVIV behavior without the external force.

The displacement signal of the cylinder is analyzed by FFT. Two patterns are found in the frequency spectrums. The first pattern exhibits the two peaks in the spectrum as seen in Fig.6(a). One is the frequency of the external force and the other is related with the vibration frequency of KVIV. It is named A-vibration pattern. The second pattern is shown in Fig.6(b). The only one peak which is the same to the frequency of the external force appears. There are two cases for appearing this spectrum pattern. When the external force is stopped to supply, the peak disappears or keeps the similar one peak state. If the peak disappears, the external force dominates to generate the vibration and it is the same as forced oscillation. On the other hand, the KVIV is synchronized with the frequency of the external force if the peak does not disappear. We focus on the latter case because our purpose is the investigation of the interaction effect of the VIVs and the periodic external force. We call the latter case the B-vibration.

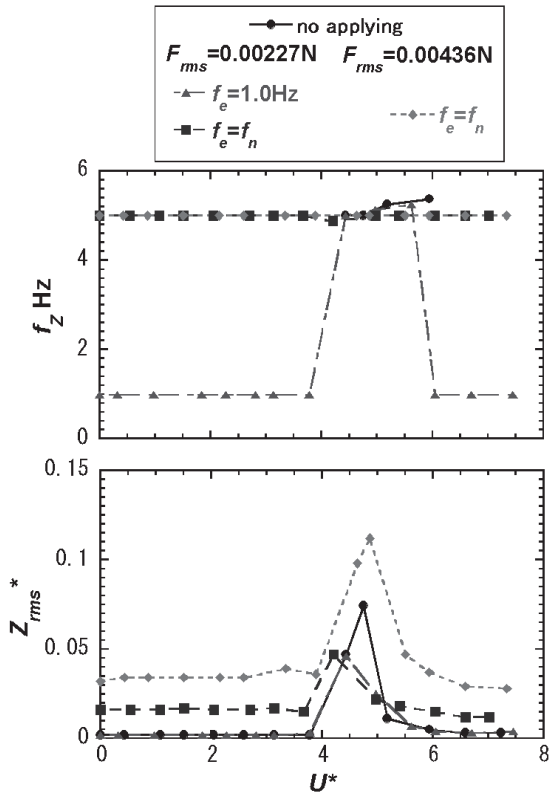

Figure 5. Comparison of vibration behavior of KVIV with or without external force.

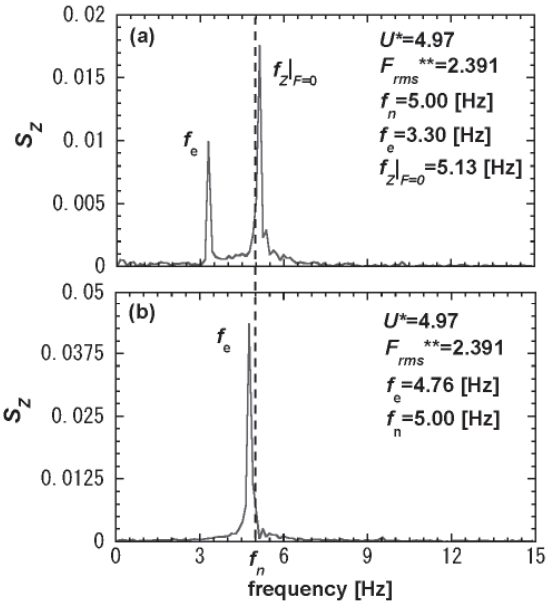

Figure 6. Spectrum of vibration motion with external force in frequency f_e . (a) A-vibration: $f_Z|_{F=0}$ is vibration frequency without external force. (b)B-vibration: vibration coinsides with f_e.

Figure 7 shows the non-dimensional average amplitude Z_{rms}^{**} caused by the external force which has the non-dimensional magnitude F_{rms}^{**}. Z_{rms}^{**} is the RMS value of the cylinder displacement Z normalized by the Z_{rms} without the external force at the same flow condition. F_{rms}^{**} is the magnitude of the external force nomalized by the magnitude of the vibration force $F_{v\mathrm{rms}}$ by the vortex shedding without the external force. $F_{v\mathrm{rms}}$ is evaluated from the VIV amplitude by Eq.(5). The open and filled symbols in Fig.7 denote the vibration pattern becomes the A- and B-vibration, respectively. In case of f_e^{**} =1.00, that is the frequency of the external force coinsides with the natural frequency, Z_{rms}^{**} increases linearly with increasing F_{rms}^{**}. This behavior is similar to the forced vibraion in a linear oscillation sisytem. When the external force frequency is different from the natural frequency, the vibration amplitude keeps the same value of KVIV without the external force until a critical magnitude of F_{rms}^{**}. In this state, the vibration pattern is the A-vibration shown in Fig.6(a). Z_{rms}^{**} increases linearly with increasing F_{rms}^{**} after F_{rms}^{**} exceeds the critical value. The vibration pattern changes to the B-vibration in this state.

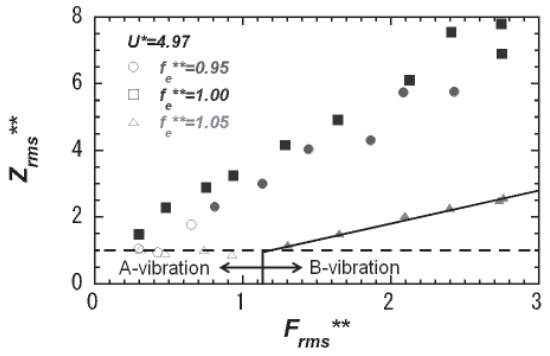

Figure 7. Amplitude and spectrum pattern of vibration as a function of external force F_{rms}.

Figure 8 shows influence of the magnitude of the external force on the amplitude of the vibration. The open and filled symbols denote the vibration pattern as same as Fig.7. When the external force frequency is close to the natural frequency, the B-vibration pattern appears and Z_{rms}^{**} increases with increasing the magnitude of the external force F_{rms}^{**}.

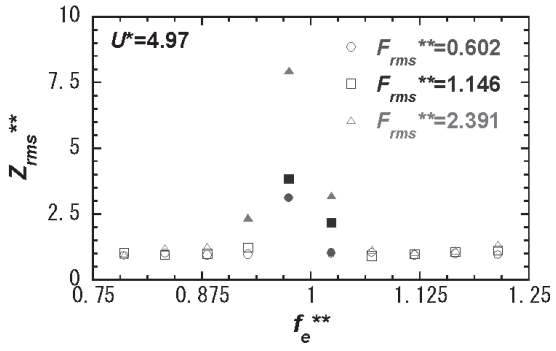

Figure 8. Influence of magnitude of external force on vibration amplitude of KVIV.

Figure 9 shows influence of the flow velocity on the relationship between Z_{rms}^{**} and f_e^{**}. The B-vibration pattern appears around the natural frequency as seen in Fig.8. In this state, the vibration amplitude significantly increases at the non-dimensional flow velocity U^*=4.97 but keeps similar amplitude of KVIV in U^*=4.54. The velocity difference between them is small but the influence to the amplitude is large. The interaction of the periodic external force for KVIV is sensitive for the flow velocity.

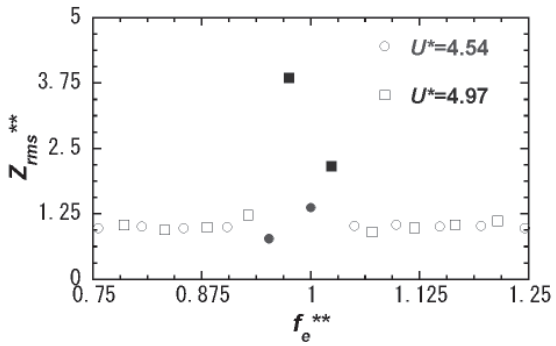

Figure 9. Influence of flow velocity on vibration amplitude of KVIV.

4.2. TVIV experiments

Figure 10 shows the comparison of the vibration amplitude and frequency induced by TVIV with and without the periodical external force. The influence of the frequency of the external force are compared with the vibration in the no-external force. In this case, the natural frequency f_n is 4.6. In the cases of f_e =1.0 and 10 *Hz*, that is considerably different from f_n, both the frequency and the amplitude conside with the case of the no-external force in the wide range of U^*. On the other hand, the vibration frequency keeps it same as the external force freqency until higher flow velocity when f_e is close to f_n. The vibration amplitude becomes large in this case.

Figure 11 shows the frequency dependance of the vibration amplitude in TVIV. The B-vibration pattern appears and the amplitude is changed around f_e^{**}=1.0 as same as KVIV shown in Fig. 9. However, increase of the amplitude induced by the external force is not so large compared with the case of KVIV.

4.3. NVIV experiments

Figure 12 shows the comparison of the vibration amplitude and frequency induced by NVIV with and without the periodic external force. When the applied external force has the frequency that is different from the natural frequency greatly, the amplitude of NVIV is not affected so much by it as same as the other VIVs. When the frequency of the external force is the same or close to the natural frequency, the vibration amplitude becomes large in the range of the low flow velocity and it coincides with the vibration amplitude without the external force in the high velocity range.

Figure 13 shows the influence of the external force frequency on the vibration amplitude of NVIV. In the NVIV state, the B-vibration pattern appears around f_e^{**}=1 as same as the other VIVs, but the B-vibration region is extended to high velocity side. Increase of the amplitude is not large.

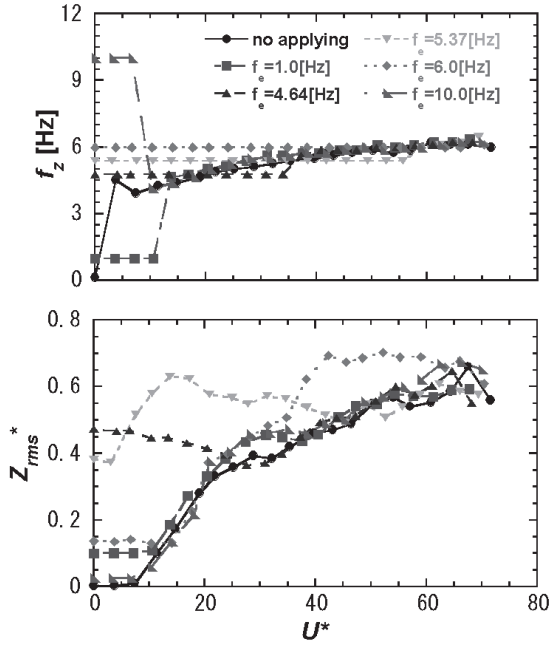

Figure 10. Influence of external force frequency on vibration amplitude and frequency of TVIV. (Magnitude of external force F_{rms}=0.144*N*)

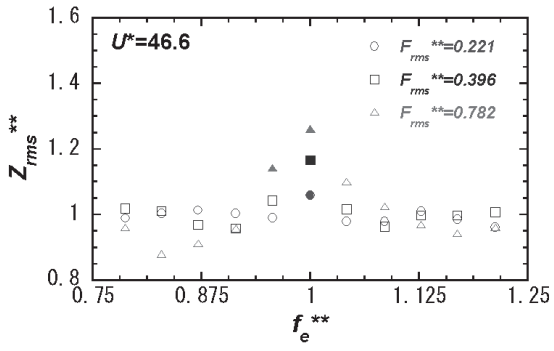

Figure 11. Influence of magnitude of external force on vibration amplitude of TVIV at U^*=46.6.

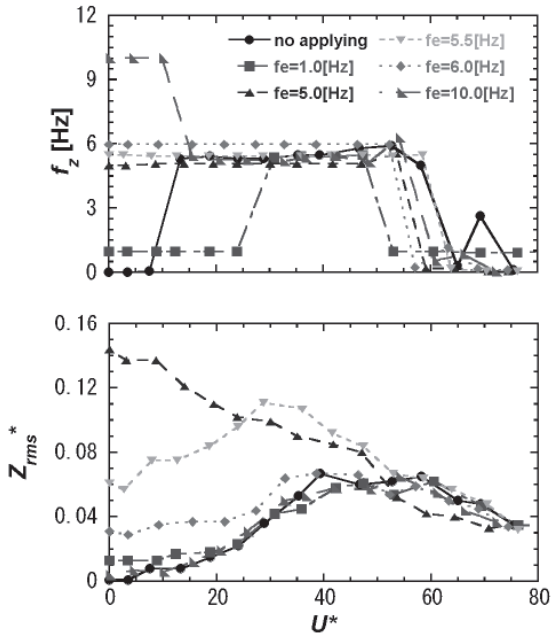

Figure 12. Influence of external force frequency on vibration amplitude and frequency of NVIV.

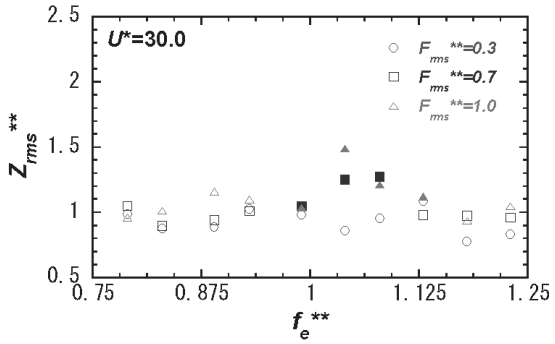

Figure 13. Influence of magnitude of external force on vibration amplitude of NVIV at U^*=30.0.

4.4. Comparison of B-vibration range in VIVs

We observed which vibration pattern, the A- or B-vibration, occurred when the periodic external force of various conditions was applied to each VIV. The results are plotted into the f_e^{**} - F_{rms}^{**} graph, as shown in Figs. 14, 15 and 16. In each graph, the colored area shows a region where the B-vibration pattern is dominant. In this region, the vortex shedding is synchronized with the external force frequency and the amplitude of the vibration is affected by the magnitude of the force. In other words, the VIV behavior is influenced and controlled by the periodic external force in this regime. In the outside of this region, the VIVs keep their original frequency against the external force. Therefore, the boundary of this regime has a meaning of a critical value that is the robustness of stability of each VIV in each condition. The robustness of stability is expected to be one of the indices to evaluate the stability of VIVs for the external disturbance. As comparing Figs.14, 15 and 16, it is found each VIV has a different property for the robustness of stability. The B-vibration regime in KVIV shown in Fig.14 is narrower than the others. It might be related that the lock-in condition of KVIV is narrower compared with TVIV and NVIV. KVIV occurs in a narrow range of the flow velocity, that is, KVIV can keep the original frequency caused by the vortex shedding against the external disturbance. On the other hand, the B-vibration region in NVIV shown in Fig.16 is widely extended to the high frequency side. The shedding of the necklase vortices can be changed by the external conditions and can synchronize with the cylinder vibration easier than KVIV. Therefore, the robustness of stability in NVIV is low and it is easily affected by the external force.

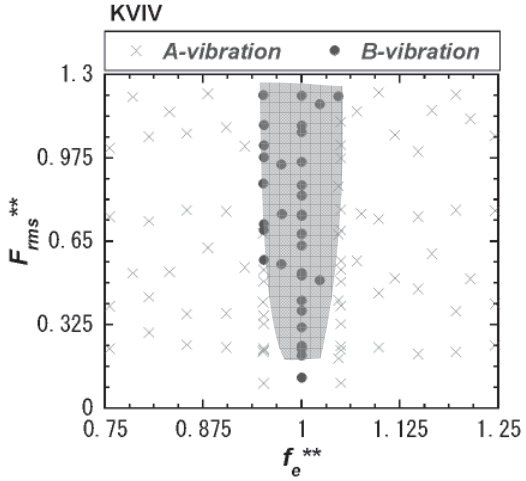

Figure 14. Vibration pattern map of KVIV on f_e^{**} - F_{rms}^{**} plot.

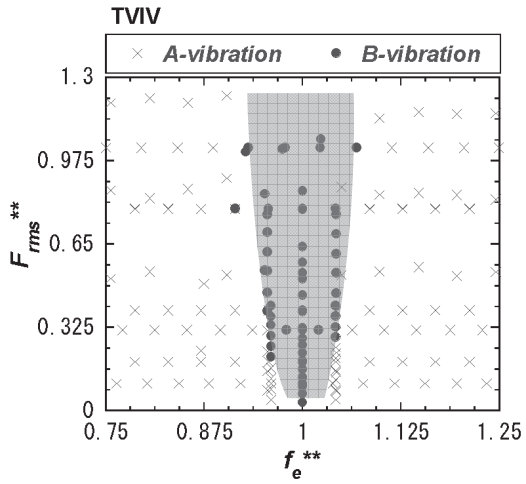

Figure 15. Vibration pattern map of TVIV on f_e^{**} - F_{rms}^{**} plot.

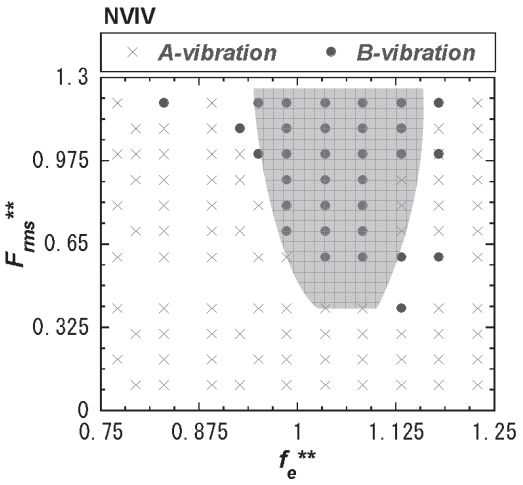

Figure 16. Vibration pattern map of NVIV on f_e^{**} - F_{rms}^{**} plot.

5. CONCLUDING REMARKS

Influence of applying the periodic external force on the vibration behavior of the VIVs was experimentally examined. When the periodic external force is applied to the circular cylinder vibrating by vortex shedding, two vibration patterns are observed in all three VIVs, that is KVIV, TVIV and NVIV. The A-vibration pattern has two spectrum peaks in the cylinder motion. One is the original frequency of VIV and the other is the external force frequency. In this vibration state, the average amplitude of the vibration is not changed so much by the external force. The latter pattern, which is named the B-vibration pattern, has only one peak in the frequency spectrum of the vibration. This peak is corresponding to the external force frequency and the vortex shedding is synchronized with the external force. In this state, the average amplitude of the vibration is linearly related with the magnitude of the external force.

When a pattern map of the A-vibration and B-vibration is plotted on a external force frequency vs the vibration amplitude graph, the boundary of the two vibration patterns expresses a critical condition of change of the vortex shedding frequency. It has a meaning of robustness of vortex shedding for the external disturbance and is named the robustness of stability. The condition of the robustness of stability depends on the type of VIVs and it should be one of the indices of the VIV stability for the external disturbance.

REFERENCES

[1] T. Nguyen, I. Kudo, M. Koide, S. Yamada, T. Takahashi, And M. Shirakashi, 2009, "Influence of mass ratio and damping factor on vivs of a circular cylinder in uniform flow", *Proceedings of CMFF'09*, pp. 658-665.

[2] M. Shirakashi, H. M. Bae, M. Sano, and T. Takahashi, 1994, "Characteristics of periodic vortex shedding from two cylinders in cruciform arrangement", *Journal of Fluid and Structures*, Vol. **8**, pp. 239-256.

[3] T. Takahashi, L. Baranyi, and M. Shirakashi, 1999, "Configuration and frequency of longitudinal vortices shedding from two circular cylinders in cruciform arrangement", *Journal of Visualization*, Vol. **19**, No. 75, pp. 328-336.

[4] M. Shirakashi, T. Takahashi, I. Kumagai, and T. Matsumoto, 2001, "Vortex induced vibration of the upstream cylinder of a two-cylinder system in cruciform arrangement", *Journal of Computational and Applied Mechanics*, Vol. **2**, No. 1, pp. 103-122.

[5] Naoto Kato, Mizuyasu Koide, Tsutomu Takahashi, and Masataka Shirakashi, 2007, "Vibration Control for a Circular Cylinder by a Strip-plate Set Downstream in Cruciform Arrangement (1st Report, Influence of a Downstream Strip-plate on the Shedding of Longitudinal Vortices from Fixed System)", *Bulletin of the Japan Society of Mechanical Engineering*, Series B, Vol. **73**, No. 728, pp. 957-964. (in Japanese)

[6] Naoto Kato, Mizuyasu Koide, Tsutomu Takahashi, and Masataka Shirakashi, 2009, "Vibration Control for a Circular Cylinder by a Strip-plate Set Downstream in Cruciform Arrangement (2nd Report, Generation and Suppression of Vortex Excitation on Elastically supported Cylinder)", *Bulletin of the Japan Society of Mechanical Engineering*, Series B, Vol. **75**, No. 752. (in Japanese)

[7] Mizuyasu Koide, Takahiro Sekizaki, Syuichi Yamada, Tsutomu Takahashi, and Masataka Shirakashi, 2009, "A NOVEL TECHNIQUE FOR HYDROELECTRICITY UTILIZING VORTEX INDUCED VIBRATION", Proceedings of PVP2009, ASME, pp. 1-10, PVP2009-77487.

[8] Tsutomu Takahashi, and Shirakashi Masataka, 2010, "Review on Electricity Generation utilizing Flow Induced Vibrations", *Function & Materials*, Vol. 30, No. 10, pp. 35-41.

Conference on Modelling Fluid Flow (CMFF'12)
The 15th International Conference on Fluid Flow Technologies
Budapest, Hungary, September 4-7, 2012

Direct Numerical Simulation of Flow over a Foward-Facing Step - Flow Structure and Aeroacoustic Source Regions

Christoph SCHEIT,[1] Ali ESMAEILI, [2] Stefan BECKER [2]

[1] Corresponding Author. Institute of Process Machinery and Systems Engineering, University of Erlangen-Nuremberg. Cauerstrae 4, D-91058 Erlangen, Germany. Tel.: +49 9131 85 29464, Fax: +49 9131 85 29449, E-mail: sh@ipat.uni-erlangen.de
[2] Institute of Process Machinery and Systems Engineering. E-mail: sb@ipat.uni-erlangen.de

ABSTRACT

Aeroacousticaly generated sound is a common phenomenon in engineering applications. Examples range from noise generated by turbo machinery over automotive aerodynamically noise to sound production in pipe systems. Numerical simulation can help to provide a deeper understanding of the physics involved. Today a wide range of numerical approaches exists to simulate turbulent flows and the propagation of sound. Especially in low Mach-number flows, hybrid approaches are very often used to compute the flow in a first step. Based on the flow information aeroacoustic source terms are calculated. In a second step the propagation of the sound is computed based on acoustic analogies or linearised transport equations. Since the acoustic calculation can be seen as a post-processing step within this hybrid approach, the quality of the flow field and the aeroacoustic source terms is crucial to the process. In this work a direct numerical simulation of the flow over a forward-facing step with a Reynolds number of 8000 based on the step height is presented. Calculations have been performed using second order finite volume discretisation in space on co-located meshes. The simulation results are used as a basis for the validation of different discretisation schemes and simulation approaches for the calculation of sound using a hybrid approach. Turbulent statistics are presented along with acoustic source regions. Also the data management for this simulation on a highly parallel system is explained together with the hybrid calculation approach based on Lighthills acoustic analogy implemented in a finite element framework. In summary, the investigations deliver a data basis for the assessment of the quality of simulated flow induced acoustic sources.

Keywords: DNS, forward facing step, Lighthills acoustic analogy, source term calculation

NOMENCLATURE

u_i	$[m/s]$	velocity vector
p	$[Pa]$	pressure
ρ	$[kg/m^3]$	density
τ_{ij}	$[kg/m^3]$	vsicous stress tensor
$\hat{T}_{ij}$	$[Pa]$	Lighthill Tensor
c	$[m/s]$	speed of sound
$\vec{x}$	$[m]$	spatial coordinates
t	$[s]$	time
w_h	$[-]$	test function
Ω_h	$[m^3]$	discretised spatial domain
H	$[m]$	step size
τ_c	$[s]$	characteristic time

Subscripts and Superscripts

0	ambient/free stream conditions
c	characteristic quantity
$+$	viscous/wall units

1. INTRODUCTION

In nature as well as in engineering exists an overhelming amount of examples for flow induced sound. To mention just a few of them, one can think about wind whistling through the trees, human phonation, helicopters or cars passing by. If the sound is unwanted or even annoying it is usually called noise. In this case one would like to totally avoid or at least reduce it. If it is wanted, the question about it's physical origin might still be of interest. This led during the past to the development of analytical, experimental, and numerical methods aiming at the investigation of flow-induced sound. A well-known example for aeroacoustic noise is the flow around a cylinder, which led to tonal component according to the vortex shedding frequency [1]. Another kind of flow is the flow over steps, like the flow over a backward facing step as investigated by Le et al. [2] or Schäfer

et al. [3] using direct numerical simulation (DNS). While backward-facing step flow is an established flow configuration for numerical benchmarking, the flow over a forward-facing step is still not as much considered in literature. Experimental work on forward-facing step flow has been done by Largeau and Moriniere [4] which investigated the flow topology and wall pressure fluctuations for different step heights and free stream velocities. Investigations of the acoustics of different forward facing step models including microphone array measurements and correlation between wall pressure fluctuations and acoustic have been performed by Hahn [5], and Becker et al. [6]. They identified the region directly in front of and shortly above the step as the main regime of acoustic sources. The laminar separation on forward facings steps has been investigated by Stür et al. [7] using hydrogen bubble technique to visualize the flow structures. They investigated step flows up to a Reynolds number of 2500 based on the step height and identified a dynamical flow with release of the entrained fluid in front of the step in longitudinal streaks. Numerical investigations on the forward facing step-flow including acoustics have been carried out by Ali et al. [8] using linearised Euler equations for the sound propagation and large eddy simulation (LES) in order to calculate the incompressible flow field. The geometry used for this work is identical to the one used by Ali, except that the domain in streamwise and spanwise direction is smaller here. Very recently, Ji and Wang [9] investigated the aeroacoustics of turbulent boundary layer flow over forward and backward facing steps. They performed incompressible LES and acoustic calculations by means of Lighthills acoustic analogy using a tailord greens function. They also used the same geometry like in this work, but turbulent boundary layers with a boundary layer thickness significantly larger than the step height. The work presented here is showing intermediate results of an ongoing research using DNS in order to examine the flow topology of the forward facing step flow. DNS is used to highly resolve acoustic sources and to avoid the influence of a turbulence model on the acoustic source terms. The acoustic sources are calculated based on Lighthills [10] acoustic analogy. A fine grid in streamwise direction has been used in order to avoid numerical oscillations as far as possible, since they introduce numerical noise which might mask the physical sound sources. On the other hand, using other than central differencing scheme for the convective term, numerical diffusion is introduced which might smooth velocity gradients. For this work, a step flow with a laminar inflow boundary layer profile is used, but in a second simulation also the case of turbulent inflow should be investigated. Data acquired by the simulations is intended to be used in order to compare different simulation and discretisation approaches for the calculation of aeroacoustic sound at low Mach numbers.

2. HYBRID ACOUSTIC SIMULATION

For the calculation of flow-induced sound exists several approaches in literature, ranging from DNS of flow and sound based on the compressible Navier-Stokes equations to hybrid approaches [8] treating flow and acoustic simulation separately. In case of a hybrid approach, the flow field is computed first. In a second step, acoustic source terms are calculated and the propagation of the sound waves is computed. Input data for the acoustics can be an compressible or incompressible flow field, depending on the kind of flow. For low Mach-number flows, such as considered in this work, an incompressible flow field can be used. The advantage is, that usually a larger time step can be used since convection velocity is much smaller than the speed of sound. Also, the acoustic calculation can be carried out on a grid tailord to capture acoustic propagation whith much larger cell sizes and extending to the acoustic far field, which is usually not possible in DNS calculation of sound.

2.1. DIRECT NUMERICAL SIMULATION

In a first step, the flow over the forward facing step is simulated. The equations being solved are the incompressible Navier-Stokes equations:

$$\frac{\partial u_i}{\partial x_i} = 0 \tag{1}$$

$$\rho_0 \left(\frac{\partial u_j}{\partial t} + u_i \frac{\partial u_j}{\partial x_i} \right) = -\frac{\partial p}{\partial x_j} - \frac{\partial \tau_{ij}}{\partial x_i} \tag{2}$$

In Eqs. (1) and (2), ρ is the density, u_i is the velocity vector, p the pressure, and τ_{ij} the viscous stress tensor. Gravitational forces are neglected. The software employed is a second order finite volume solver described by Durst and Schäfer [11]. Time advancement has been done using a third-order runge-kutta scheme. The grid is a co-located mesh, which is graded in streamwise and wall normal direction in order to save grid points in regions far off the step. The simulation has been carried out on 60 nodes of the compute cluster *lima* at the local center for information technology (RRZE). The residual has been fixed to $1 \cdot 10^{-11}$. A sketch of the domain used for the simulation including boundary conditions is shown in Figure 1. Lengths are made dimensionless by the step height H of 12 *mm*. The inlet profile for the presented simulation is based on Blasius solution for laminar boundary layer flow with a boundary layer thickness of 4 mm and was chosen according to measurements performed by Hahn et al. [12] at the same position in front of the step. The free-stream velocity was $U_0 = 10$ *m/s*. A convective exit boundary condition was applied at the outlet. While the presented results are based on purely laminar inflow, a second simulation is planed using a turbulent inflow profile using a precursor simulation in order to generate the inflow data. To make sure that the DNS is performed on an appropriate mesh,

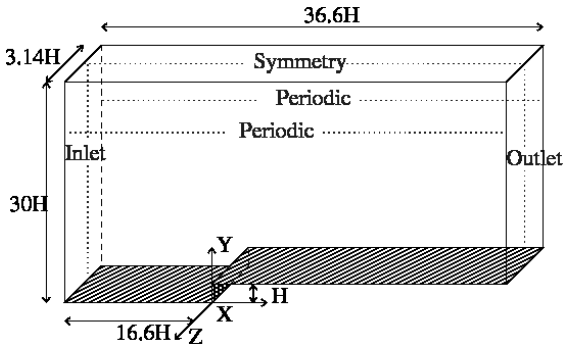

Figure 1. Domain and boundary conditions of flow simulation.

a grid study was performed as a first step, refining the mesh until an adequate resolution was obtained in terms of y^+, x^+ and z^+-values, where y denotes wall normal direction, z spanwise direction, and x streamwise direction. The final mesh consisted of $2.8 \cdot 10^8$ control volumina. A line plot of the wall coordinates above the step is presented in Figure 2. As can be seen, the maximum of y^+ is around 0.2, x^+ exceeds only at the end of the domain a value of 5 and the maximum of z^+ is around 3. Compared to the grid resolutions tested by Volkert [13], who compared different grids for turbulent channel flow using the same code, the resolution is quite high especially in streamwise and spanwise directions. Since for detached flow wall units are not a sufficient quality measure, also spanwise correlations have been checked using a total of 64 monitor points along a line. In Figure 3 one can see that about 30 grid points cover the range of two-point correlation values down to 0.2. Also one can see that the correlations go down to zero after about 50 to 60 grid points. This indicates that the spanwise extend of the domain is large enough. Above the step, at position 2, c.f. Figure 4, the turbulent structures are smallest, and here only about 12 to 18 points cover the correlated structures. This is still enough to resolve the energy containing scales. Downstream of this locations again larger flow structures are present which are highly resolved, see Figure 5. The timestep size δt was set to $4.5 \cdot 10^{-7}$ s resulting in a Courant-Friedrichs-Lewy (CFL) number of about 0.45.

2.2. SOURCE TERM CALCULATION

After obtaining the flow solution, source terms were extracted based on Lighthills acoustic analogy [10]. Since the amount of data is huge, source terms are calculated directly after a timestep is finished on the fine grid. Then source terms are transfered to a coarser grid, and finally data is stored in binary files using parallel IO. Lighthills equation in a simplified form for incompressible fluid writes

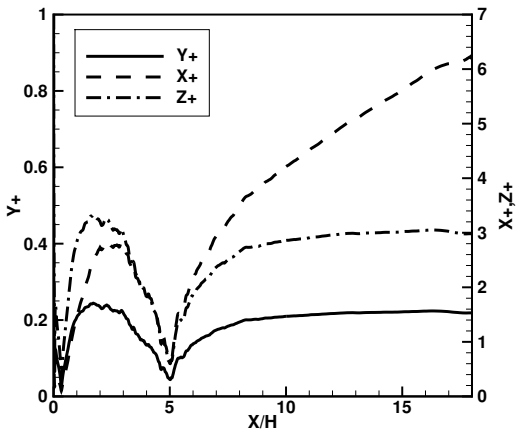

Figure 2. Grid resolution in wall coordinates above the step.

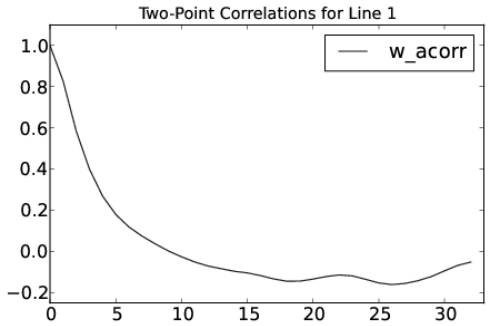

Figure 3. Spanwise correlation in foot vortex in front of step, one unit corresponds to 6 grid points.

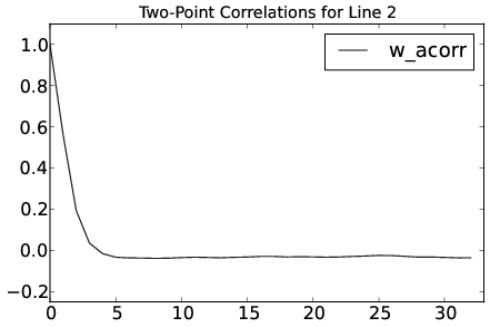

Figure 4. Spanwise correlation in top vortex in front of step, one unit corresponds to 6 grid points.

as

$$\frac{1}{c_0^2}\frac{\partial^2 p}{\partial t^2} - \nabla^2 p = \frac{\partial^2 \hat{T}_{ij}}{\partial x_i \partial x_j} \quad \text{with} \tag{3}$$

$$\hat{T}_{ij} = \rho_0 u_i u_j. \tag{4}$$

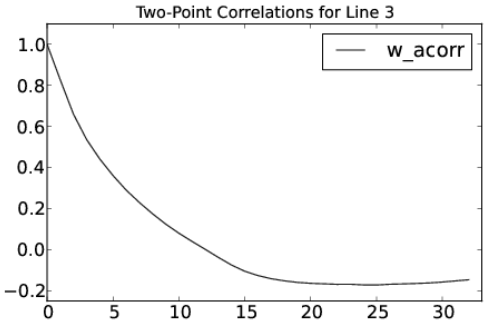

Figure 5. Spanwise correlation in foot vortex in front of step, one unit corresponds to 6 grid points.

In Eqs. (3) and (4), c is the speed of sound and subscript 0 defines ambient conditions. The tensor T_{ij} is the so-called *Lighthill Tensor* and is written here in the approximated form as used throughout this work. While Eq. (3) is the so-called strong formulation, the source term for later work will be calculated based on the weak formulation as introduced for instance by Kaltenbacher [14] and Escobar [15]. Using weak formulation, the source term of Eq. (3) reads

$$f(\vec{x},t) = -\int_{\Omega_h} \left(\nabla \cdot \hat{T}_{ij}\right) \cdot \nabla w_h \mathrm{d}\Omega \tag{5}$$

with f being the right hand side vector, Ω the acoustic source domain (i.e. the computational domain) and w_h a linear shape function.

One should note, that in the original work of Lighthill the solution was presented in terms of integration using Green's function for free field radiation. In this form, no solid bodies are allowed in the source domain. For flows interacting with solid bodies, the acoustic analogy of Curle [16] extends Lighthills acoustic analogy and takes the effect of the solid body on sound generation into account by introducing an additional surface integral. In case of low Mach number flows, the surface sources are dominating. However, discretizing Lighthills acoustic analogy and calculating numericaly the solution to the partial differential equation, the interaction of the acoustic sources with solid bodies is explicitly taken into account by the boundary conditions in the acoustic formulation. The interaction of the quadrupole-like source with the boundary will lead to a dipole-like sound radiation. No explicit knowledge of the Greens function is required, since it is computed by solving the partial differential equation. Since the presented work is still an ongoing process, only sources based on the strong formulation are presented.

3. RESULTS

Since a huge amount of data has to be analyzed for the simulation, a pre-selection has to be done and a co-visualization module developed by Schäfer and Breuer [17], [18] is used in order to generate particle trace data on the fly. For the purpose of analyzing wall-pressure fluctuations in a future step, the pressure distribution of the flow field on the step surface is stored for every tenth time step. Averaging of velocities and Reynolds-Stresses in spanwise direction and time has been switched on after 167 dimensionless time units based on the characteristic time $\tau_c = H/U_0$ with U_0 being the free stream inlet velocity. Averaging is performed every time step. In order to monitor the solution and to compute temporal and cross-correlations a set of monitor points is defined which is shown in Figure 6. According to the wall data, every tenth time step data for each monitor point is written to file system. Those monitor point positions in Figure 6, which are distributed along a line are listed in Table 1.

Table 1. Positions for monitor points along lines used for spatial correlations

x/H	y/H	Number of points
-0.25H	-0.25H	64
0.125H	1.125H	64
1H	1.125H	64
1H	1.25H	64
4H	1.125H	64

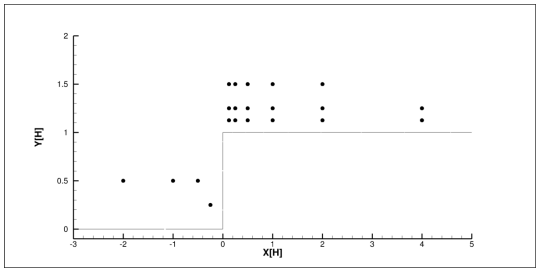

Figure 6. Monitor points used for DNS.

To get an impression of the instantaneous flow field, a snapshot of the instantaneous pressure and the instantaneous velocity is provided in Figures 9 to 11. One can clearly see the small structures in the shear layer above the step in the pressure in Figures 9 and 14. From Figure 11 it can also be seen, that the flow before the step is already turbulent, but with relatively low root mean square values of the velocity components and pressure. Taking a look on the averaged velocity component in x-direction and the streamlines based on the averaged velocity components in Figure 8, one can see that, a shear layer is formed with a sharp velocity gradient while the flow passes above the step. Before the step, a small recirculation zone is formed with extension of $H/2$ in negative x-direction and y-direction. A

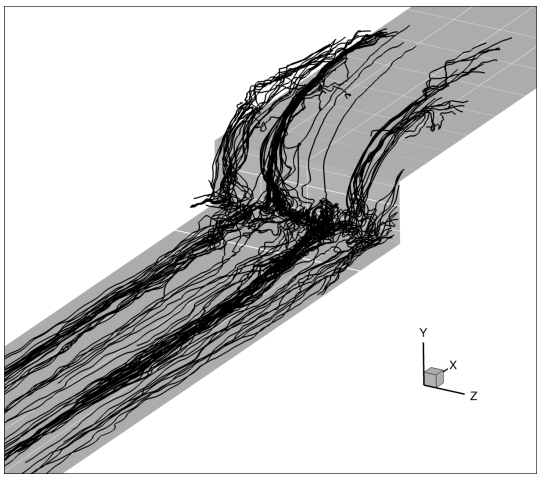

Figure 7. Streamtrace for flow over forward facing step.

second, larger recirculation zone is formed above the step, with a height of about $0.5H$ and length of about $4.5H$, which is in the range reported in literature, for example by Sherry et al. [19]. It has to be mentioned, that most of the experimental and numerical work published is based on turbulent inflow data. From literature it can also be seen, that recirculation lengths are strongly depending on inflow conditions, the ratio of the boundary layer thickness to the step height and on the ratio of step height to channel height, if measurements are performed in a closed channel. Also it can be difficult to assure that the angle of attack is exactly $0°$ in an experimental setup, see Becker [20].

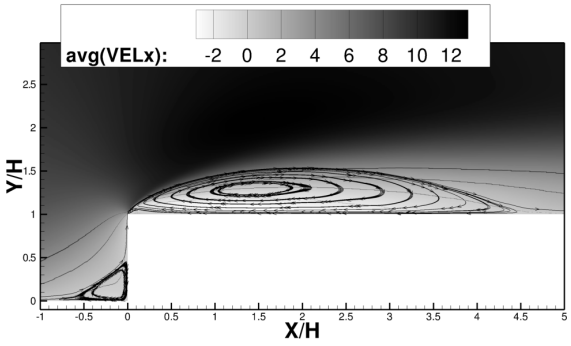

Figure 8. Time and spanwise averaged velocity component in x-direction, streamlines based on averaged velocity field

Based on the averaged turbulence statistics, the distribution of the turbulent kinetic energy is plotted in Figure 12. As one would expect, highest levels for the turbulent kinetic energy are obtained in the shear layer. Figure 13 shows the distribution of the acoustic source term in Eq. (3). Similar to the kinetic energy, highest values are located in the turbulent shear layer. Numerical oszillations, often

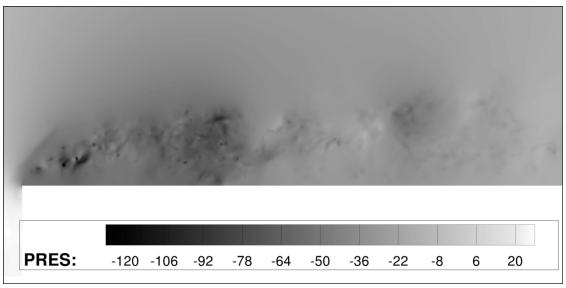

Figure 9. Snapshot of instantaneous pressure field, taken at the middle slice of the domain ($z = z_{max}/2$)

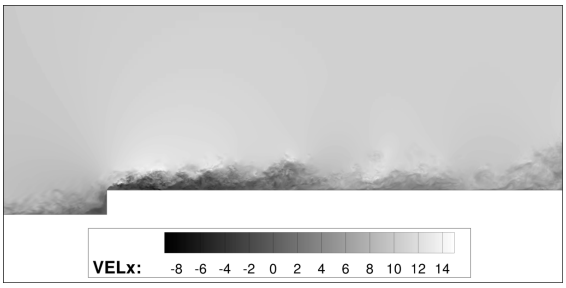

Figure 10. Snapshot of instantaneous velocity component in streamwise direction, taken at the middle slice of the domain ($z = z_{max}/2$)

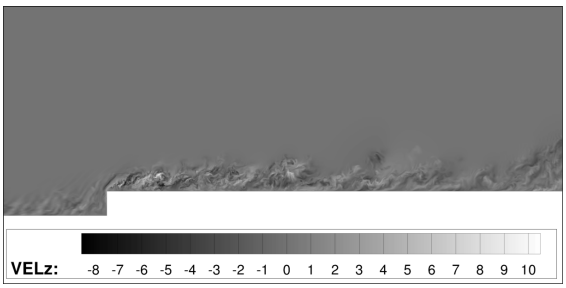

Figure 11. Snapshot of instantaneous velocity component in spanwise direction, taken at the middle slice of the domain ($z = z_{max}/2$)

called *wiggles* are generating no or only very small acoustic sources at a comparative low level, which was one of the aims of this work. From the two-point correlations in Figures 3 to 5 it can be seen, that the flow structures before the step are of relatively large size. Slighthly above the step, where a strong shear layer starts, small structures are genarated by the flow inside the shear layer, see Fig. (4). These structures are later on again larger in size for monitor points inside the recirculation zone or after the recirculation bubble. The same effect can be seen in Figures 15 to 19. One unit of the x-axis corresponds to 10 timesteps. Figure 15 shows the normalized autocorrelation function for the monitor point in the middle of monitor point line 1. One can see a

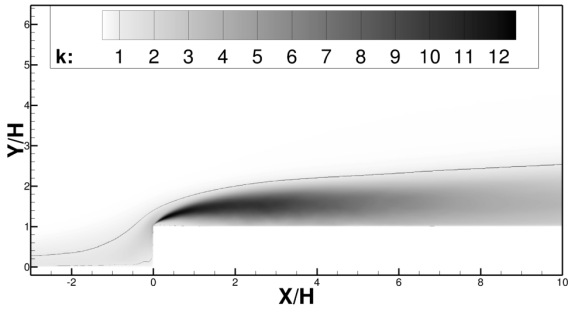

Figure 12. Time and spanwise-averaged turbulent kinetic energy ($z = z_{max}/2$)

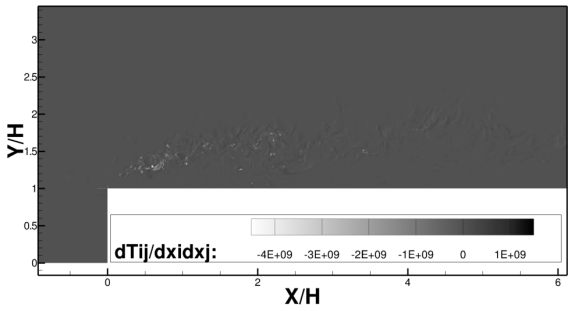

Figure 13. Snapshot of instantaneous acoustic source term, taken at the middle slice of the domain ($z = z_{max}/2$)

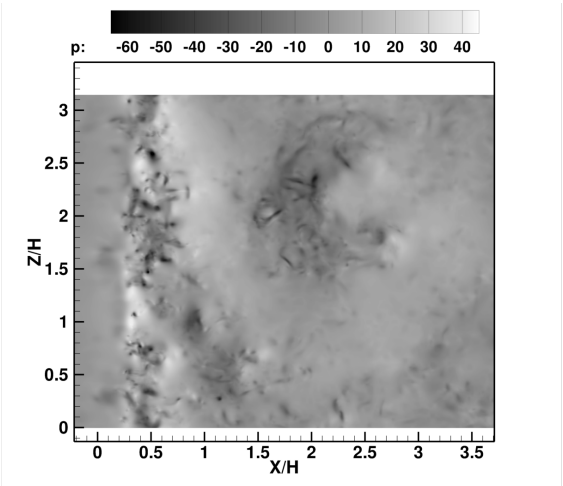

Figure 14. Snapshot of instantaneous turbulent pressure, ($y = 1.25H$)

relatively organized structure with large correlation in time. Moving on to the monitor point in the middle of line 2 (Figures 16 and 17), these organized structure does not exist anymore. Instead a relatively small region of correlation can be found. For the middle of monitor point line 3, which is located inside the recirculation zone above the step, again larger flow structures in space and time are forming, resulting in larger correlations in space as shown in Figure 5 and 18. In Figure 19 is the same x-axis range as in Figure 17 shown, which allows to clearly identify the difference in autocorrelation for both positions. Figures 20 to 22 show the coherence of

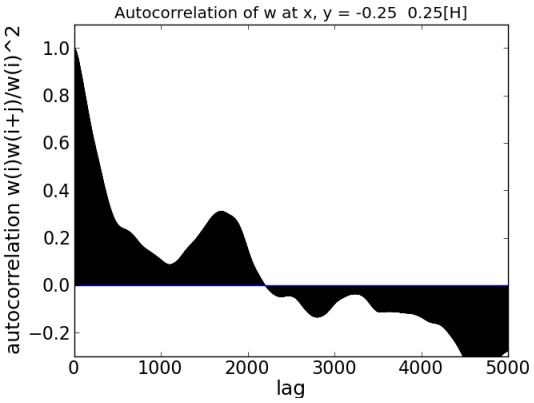

Figure 15. Autocorrelation at middle of line 1

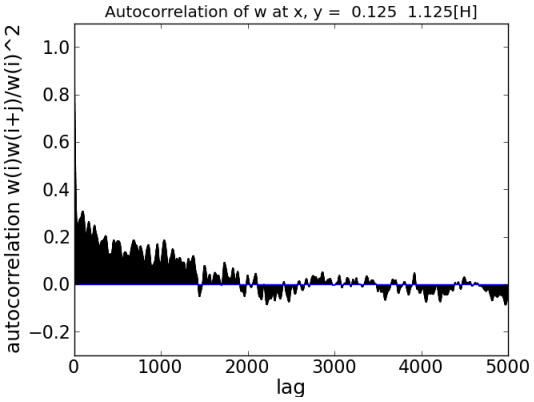

Figure 16. Autocorrelation at middle of line 2

the pressure fluctuations between different monitor points. Calculating the coherence between two different monitor points, it can be recognized that the flow structures in front of the step and in the shear layer above the step are not connected to each other. Figure. 20 shows that the coherence between those different flow regions is below 10% for the complete frequency range. In contrast to this, computing the coherence between two consecutive points in the shear layer, there is a small coherence for frequencies below 4000 Hz, see Fig 21. This correlation might be due to the formation and convective transport of vortex structures in the shear layer leading to pressure fluctuation of alternating signs. Taking two monitor points in the shear layer separated in vertical direction only (see Fig. 22), also a peak in

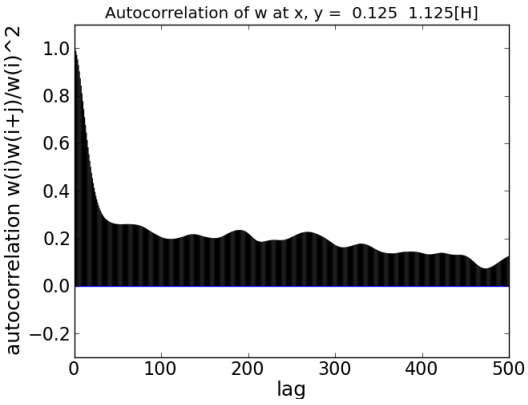

Figure 17. Autocorrelation at middle of line 2 - zoom

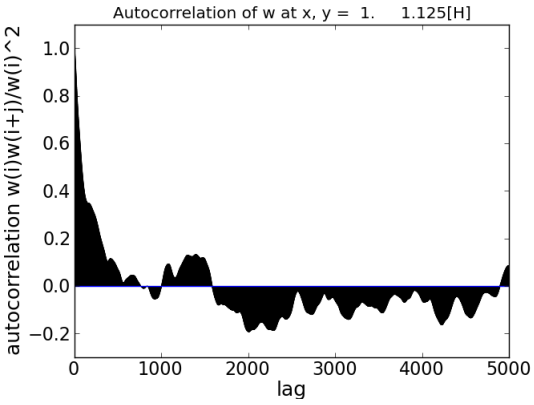

Figure 18. Autocorrelation at middle of line 3

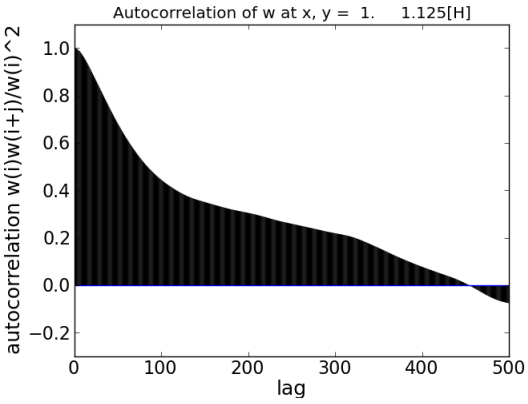

Figure 19. Autocorrelation at middle of line 3 - zoom

the frequency spectra can be observed at the same frequency of approximately 1900 Hz as in Fig. 21 with slightly higher coherence. For all evaluated monitor points, no coherence at higher frequencies could be observed.

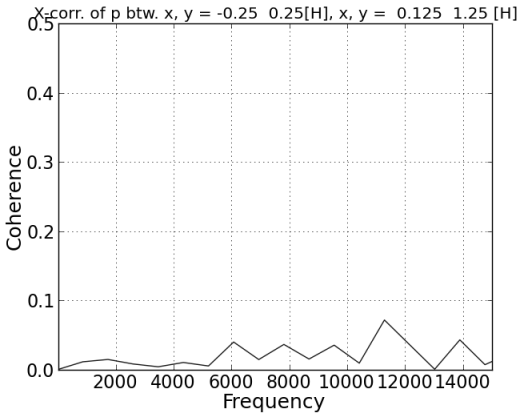

Figure 20. Coherence between pressure of monitor points in foot vortex and in the shear layer

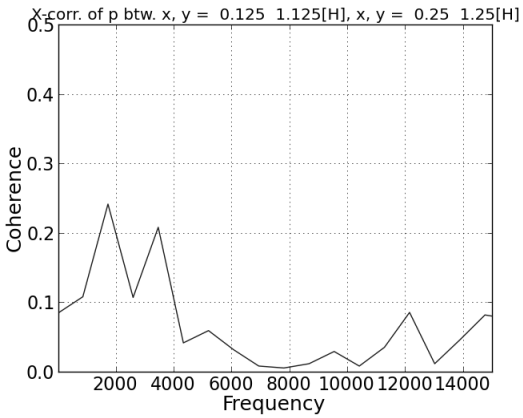

Figure 21. Coherence between pressure of consecutive monitor points in the shear layer

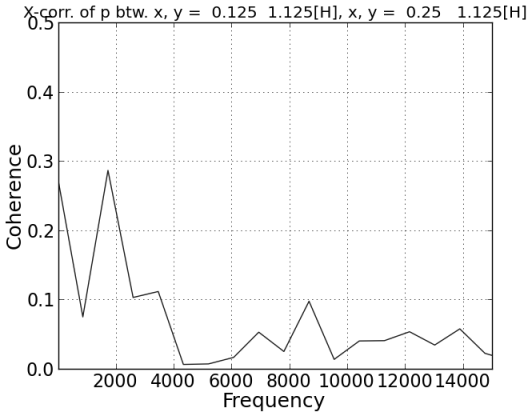

Figure 22. Coherence between pressure of consecutive monitor points in the shear layer

4. SUMMARY

Transitional boundary layer flow over a forward facing step was presented. Results are intended to

be used in order to validate aeroacoustic calculations based on hybrid approaches such as Lighthills acoustic analogy. A grid study and different techniques for the evaluation of the grid resolution had been performed. They indicate, that the grid is fine enough to capture the relevant scales of the flow. Flow features known from literature could be captured with the simulation, like the recirculation zone in front of and above the step, or the release of fluid from the recirculation zone in front of the step in streaks. A first impression of the acoustic source terms has also been presented. As expected, they are located mainly in the shear layer. In a next step, based on the weak form of Lighthills acoustic analogy, the sound generated by the sources will be calculated and a second simulation will be performed using a turbulent boundary layer for the inflow.

References

[1] Hahn, C., Kaltenbacher, M., Lerch, R., and Becker, S. 2007 "Impact of Geometry Changes on Noise Radiated by a Square Cylinder in Cross Flow". *13th AIAA/CEAS Aeroacoustic Conference*, no. 2007-3430.

[2] Le, H., Moin, P., and Kim, J. 1997 "Direct Numerical Simulation of Turbulent Flow over a backward-facing Step". *J. Fluid Mech.*, Vol. 330, pp. 349–374.

[3] Schäfer, F., Breuer, M., and Durst, F. 2009 "The Dynamics of the Transitional Flow over a Backward-Facing Step". *J. Fluid Mech.*, Vol. 623, pp. 85–119.

[4] Largeau, J. F. and Moriniere, V. 2007 "Wall Pressure Fluctuations and Topology in Separated Flows over a Forward–Facing Step". *Exp. Fluids*, Vol. 42, pp. 21–40.

[5] Hahn, C. 2007 "Experimentelle Analyse und Reduktion Aeroakustischer Schallquellen an Einfachen Modellstrukturen". Ph.D. thesis,

[6] Becker, S., Escobar, M., Hahn, M., Ali, I., Kaltenbacher, M., Basel, B., and Grünewald, M. 2005 "Experimental and Numerical Investigation of the Flow Induced Noise from a Forward Facing Step". *11th AIAA/CEAS Aeroacoustics Conference*, no. 2005-3006.

[7] Stür, H., Gyr, A., and Kinzelbach, W. 1999 "Laminar Separation on a Forward Facing Step". *Eur. J. Mech. B/Fluids*, Vol. 18, pp. 675–692.

[8] Ali, I., Escobar, M., Kaltenbacher, M., and Becker, S. 2008 "Time Domain Computation of Flow Induced Sound". *Comput. Fluids*, Vol. 37, No. 4, pp. 349–359.

[9] Ji, M. and Wang, M. 2010 "Sound Generation by Turbulent Boundary-Layer Flow over Small Step". *J. Fluid Mech.*, Vol. 654, pp. 161–193.

[10] Lighthill, J. M. 1952 "On Sound Generated Aerodynamically I. General Theory". *Proc. Roy. Soc.*, Vol. 211, No. 1107, pp. 564–587.

[11] Durst, F. and Schäfer, M. 1996 "A Parallel Block-Structured Multigrid Method for the Prediction of Incompressible Flows". *Int. J. Num. Methods Fluids*, Vol. 22, pp. 549–565.

[12] Hahn, C., Becker, S., Ali, I., Escobar, M., and Kaltenbacher, M. 2007 *New Results in Numerical and Experimental Fluid Mechanics VI*, vol. 96 of *Notes on Numerical Fluid Mechanics and Multidisciplinary Design*, chap. Investigation of Flow Induced Sound Radiated by a Forward Facing Step, pp. 438–445. Springer.

[13] Volkert, R. 2006 "Bestimmung von statistischen Turbulenzgrößen auf der Basis von direkten numerischen Simulationen der turbulenten Kanalströmung". Ph.D. thesis,

[14] Kaltenbacher, M., Escobar, M., Hahn, C., Ali, I., and Becker, I. 2006 "CAA as a Postprocessing-Step within CFD-Computations". *Proceedings of the ISMA 2006*, Leuven, 18 Sep., pp. 633–639.

[15] Escobar, M. 2007 "Finite Element Simulation of Flow-Induced Noise using Lighthill's Acoustic Analogy". Ph.D. thesis,

[16] Curle, N. 1955 "The Influence of Solid Boundaries upon Aerodynamic Sound". *Proc. Roy. Soc.*, Vol. 231, No. A, pp. 505–514.

[17] Schäfer, F. 2007 "Zeitlich hochaufgelöste Visualisierung und Analyse dreidimensionaler Simulationsdaten turbulenter Strömungen". Ph.D. thesis,

[18] Schäfer, F. and Breuer, M. 2002 "Comparison of C–Space and P–Space Particle Tracing Schemes on High–Performance Computers: Accuracy and Performance". *Int. J. for Numerical Methods in Fluids*, Vol. 39, pp. 277–299.

[19] Sherry, M. J., Lo Jcono, D., Sheridan, J., Mathis, R., and Marusic, I. 2009 "Flow Separation Characterisation of a Forward Facing Step Imersed in a Turbulent Boundary Layer". *Sixth Interational Symposium on Turbulence and Shear Flow Phenomena*, 22 Jun.

[20] Becker, S. 2009 , "Lokale Messverfahren und deren Anwendung zur Bestimmung der Strömungs- und Turbulenzeigenschaften wandgebundener Strömungen". Habilitationsschrift,

Conference on Modelling Fluid Flow (CMFF'12)
The 15th International Conference on Fluid Flow Technologies
Budapest, Hungary, September 4-7, 2012

HIGH-RESOLUTION CHARACTERISTICS-BASED GODUNOV-TYPE METHOD FOR MODELLING ACOUSTIC WAVES IN CONJUNCTION WITH INCOMPRESSIBLE MICRO-SCALE LAMINAR FLOW

László KÖNÖZSY[1], Nikolaos ASPROULIS[2], Dimitris DRIKAKIS[3]

[1] Corresponding Author. Department of Fluid Mechanics and Computational Science, Cranfield University. MK43 0AL Cranfield, Bedfordshire, United Kingdom. Tel.: +44 1234 758 236, Fax: +44 1234 758 205, E-mail: laszlo.konozsy@cranfield.ac.uk
[2] Department of Fluid Mechanics and Computational Science, Cranfield University. E-mail: n.asproulis@cranfield.ac.uk
[3] Department of Fluid Mechanics and Computational Science, Cranfield University. E-mail: d.drikakis@cranfield.ac.uk

ABSTRACT

This paper focuses on acoustic wave modelling in conjunction with high-resolution characteristics-based Godunov-type method for solving unsteady, incompressible, micro-scale laminar flow problem. A simplified acoustic wave model has been adopted and further developed to investigate the effects of acoustic waves on the Newtonian fluid flow pattern under the continuum hypothesis. In the last two decades, researchers devoted attention to surface acoustic waves. The reason for this interest is that these waves can cause changes in the material properties, and impact the pressure and velocity fields. The adopted acoustic wave model appears as the acoustic pressure gradient in the Navier-Stokes equations. The acoustic wave equation has been solved for the acoustic pressure; and the artificial compressibility method has been used for solving the governing equations. The proposed acoustic source term model is a closer approach to Poesio and Ooms theory rather than to Lighthill's theory, or to the theory of perturbation. In the present numerical study, the acoustic waves interact with DNA strands that have been released in a microfluidic T-channel, and are modelled through a coupled Eulerian-Lagrangian dynamics. A possible outcome of this study might be of great importance in the design process of highly selective micro- and nanofluidic sensors for DNA detection.

Keywords: acoustic wave modelling, artificial compressibility method, DNA flow meta-modelling, high-resolution characteristics-based Godunov-type method, incompressible flows, microfluidic applications

NOMENCLATURE

Main Latin and Greek Symbols

c_s	$[m/s]$	speed of sound in the medium
$\mathbf{f}$	$[N]$	external force field
$\mathbf{F}$	[-]	dimensionless external force field
$\mathbf{g}$	$[m/s^2]$	gravity vector
h	$[m]$	height or reference length
$\mathbf{i}_s$	$[W/m^2]$	acoustic intensity
$\mathbf{I}_s$	[-]	dimensionless acoustic intensity
Ma	[-]	Mach number
p	$[Pa]$	pressure field
P	[-]	dimensionless pressure field
p_s	$[Pa]$	acoustic pressure
P_s	[-]	dimensionless acoustic pressure
Re	[-]	Reynolds number
s	[-]	artificial speed of sound
t	$[s]$	physical time
t^*	[-]	dimensionless time
$\mathbf{u}$	$[m/s]$	velocity vector
u_a	$[m/s]$	magnitude of average velocity
$\mathbf{U}$	[-]	dimensionless velocity vector
β	[-]	artificial compressibility factor
ρ	$[kg/m^3]$	fluid density
τ	[-]	pseudo-time

Subscripts and Superscripts

L	left hand side intercell flux value
R	right hand side intercell flux value
s	sound in the medium
∞	reference physical quantity (constant)

Main abbreviations

AW	Acoustic Wave(s)
DNA	Deoxyribonucleic Acid
dsDNA	double-stranded DNA
ssDNA	single-stranded DNA
SAW	Surface Acoustic Wave(s)
WENO	Weighted Essentially Non-Oscillatory

1. INTRODUCTION

In the last two decades, researchers devoted significant attention to surface acoustic waves (SAW) in the fields of micro- and nanofluidics. The reason for this emerging interest that it is possible to transfer acoustic waves (AW) in the fluid flow that can dynamically cause changes in the material properties as density and viscosity, and impact the pressure and velocity fields. SAW were discovered and explained by Lord Rayleigh in 1885 [1,2], therefore, these are also called as Rayleigh waves nowadays. Rayleigh discussed the mode of wave propagation and described the properties of these waves that consist of longitudinal and vertical shear components. These Rayleigh wave components can also be coupled with any kind of medium on the surface giving the idea of SAW devices [2].

Rocha-Gaso et al. [1] published a review paper on Surface Generated Acoustic Wave (SGAW) technology considering technological and scientific improvements in the last 40 years. According to their classification [1], three groups of AW devices exist upon the AW guiding process; such as Bulk Acoustic Wave (BAW), SAW and Acoustic Plate Mode (APM) devices [1]. These devices operate with AW propagation in different ways. Wave can propagate as a) "unguided through the volume of substrate" (BAW device), b) "guided or unguided along a single surface of substrate" (SAW device), and c) "guided by reflection from multiple surface of the substrate" (APM device) [1, p. 5742]. SAW and APM biosensors can potentially be considered for DNA detection reported recently in [1-3]. These devices were further developed in the last two decades, therefore, SAW and APM type devices can work in liquid media [1-3] as well for biosensing applications. Furthermore, these devices are capable of detecting pathogen agents such as bacteria and viruses reported by Rocha-Gaso et al. [1].

Modelling of physical phenomena in the SAW devices is indispensable in order to further improve the sensor design [1-3]. Mathematical models and Finite Element Method (FEM) based simulations in SAW devices can be found in the literature [4,5]. These physical phenomena are essentially complex multiphysics problems, because the AW appears as acoustic pressure in the flow field, which can cause significant changes in the flow behaviour; therefore, these changes can lead to physical instabilities in the flow pattern. Multiphysics problems related to fluid dynamics in small-scale microfluidic devices are substantially different from physical problems in macro-scale systems. In terms of AW, the density and pressure changes due to the presence of AW is much smaller than the changes due to the fluid flow in macro-scale systems [1-5]; therefore, the AW model can be separated from the fluid flow model, or there are cases, when AW can be neglected [6]. In small-scale devices, the AW model has to be taken into account coupled with the fluid flow.

A simplified AW model has been adopted [7] and further developed to investigate the effects of AW on the Newtonian fluid flow pattern under the continuum hypothesis. For incompressible flows, the adopted AW model appears as the acoustic pressure gradient in the Navier-Stokes equations. The AW equation has been solved for the acoustic pressure; and the artificial compressibility method has been used for solving the governing equations. The AW equation for the acoustic pressure can be derived from the continuity, momentum and energy equations of compressible fluid using perturbation decomposition [6,8]. A theoretical description of acoustic sources was developed by Lighthill [9] relying on the acoustic analogy. Lighthill gave a tensor description of acoustic source terms [9], which may become too complicated for complex flow cases; therefore, Lilley [10] further developed Lighthill's theory in order to take into account the convection and refraction on AW in the fluid flow.

Different theoretical and practical applications can be found for AW modelling in the literature. Governing equations of acoustic perturbation was used by Shi [8] modelling structural-acoustic interaction relying on the Euler equation. For low-speed, unsteady, compressible flow, Wang et al. [11] derived a system of acoustic perturbation equations investigating two-dimensional automobile door cavity in turbulent flow. Poesio and Ooms [7] proposed a relatively simple acoustic source term model for high-frequency AW on the liquid flow through porous material; and they compared their theoretical approach with experimental data. Chu [12] investigated SAW on the laminar micro-scale flow stability using the fourth-order streamfunction equation eliminating the pressure term from the Navier-Stokes equations; and coupled the system of equations with Orr-Sommerfeld equation [12].

As a matter of fact, many authors dealt with the perturbation theory or simplified acoustic source models for solving flow problems including flow instability investigations [4,5,8,11,12]. Although, the mathematical and physical background of AW are often investigated related to SAW devices, but one can find small amount of literature relying on high-resolution characteristics-based Godunov-type method for modelling AW in conjunction with selective microfluidic sensors for DNA detection. High-resolution Godunov-type methods are reliable mathematical tools for solving hyperbolic system of equations with discontinuous solutions [13,14]; therefore, this paper focuses on AW modelling for unsteady, incompressible, micro-scale laminar flow in a microfluidic T-channel test geometry. In this study, AW interacts with DNA strands that have been released in the T-channel, and are modelled through a coupled Eulerian-Lagrangian dynamics. A possible outcome of the current study might be of great importance in the design process of highly selective microfluidic sensors for DNA detection.

2. MODELLING AND METHODOLOGY

High-resolution methods, which are developed for shock capturing in conjunction with non-linear hyperbolic conservation laws [13,14], are used in different fields of engineering sciences such as e.g. gas dynamics, astrophysics, and defense. LeVeque developed a high-resolution Godunov-type wave propagation method for solving multidimensional hyperbolic systems [13]; which was further tested to different acoustics problems by Fogarty et al. [14]. Since, these methods are proven to be reliable mathematical tools for AW capturing, therefore, the acoustic source term model of Poesio and Ooms [7] has been adopted and further developed in the framework of high-resolution characteristics-based (CB) Godunov-type method in this chapter. The Navier-Stokes equations have been solved by using explicit high-order Godunov-type discretization technique in the concept of artificial compressibility (AC) method [15-21]. The classical AC method for solving the Navier-Stokes equations was originally developed by Chorin in 1967 [15,16]. Eberle proposed a characteristic flux averaging approach for solving the Euler equations [17], which was further extended to the Navier-Stokes equations by Drikakis [18]. In this chapter, the solution algorithm and methodology of AW modelling with DNA flow have been described briefly in order to couple the Poesio and Ooms [7] simplified acoustic source term model with the acoustic wave equation. More technical details can be found about high-resolution Godunov-type numerical methods in [13-21].

For solving unsteady, incompressible, micro-scale laminar flow problem with the presence of acoustic wave and DNA strands in the Newtonian fluid flow, the conservation of mass and momentum equations may be written in a vector form as

$$\nabla \cdot \mathbf{u} = 0\,, \tag{1}$$

$$\frac{D\mathbf{u}}{Dt} = \mathbf{g} - \frac{1}{\rho}\nabla p + \upsilon \nabla^2 \mathbf{u} + \frac{1}{\rho c_s}\mathbf{u}\cdot\nabla p_s + \mathbf{f}_{DNA}\,, \tag{2}$$

where D/Dt is the substantial (total) derivative, $\mathbf{u}$ is the velocity vector, t is the physical time, $\mathbf{g}$ is the gravity vector, p is the hydrodynamic pressure, ρ is the fluid density, υ is the kinematic viscosity of the fluid, c_s is the speed of sound in the medium, and p_s is the acoustic pressure in the medium.

In order to determine the acoustic pressure gradient in the momentum Eq. (2), the hyperbolic-type second-order partial differential equation has been solved for the acoustic pressure as

$$\frac{1}{c_s^2}\frac{\partial^2 p_s}{\partial t^2} = \nabla^2 p_s\,, \tag{3}$$

which is called "acoustic wave equation" [6]. The last term of Eq. (2) $\mathbf{f}_{DNA}$ represents an external force field modelling the dsDNA or ssDNA molecule motion. The meta-model of DNA strands, used in the present paper, including Brownian-motion and Eulerian-Lagrangian coupling of fluid flow motion, was developed by Benke et al. [22,23].

The acoustic intensity (sound intensity in the medium) is defined as the product of the acoustic pressure p_s and the particle velocity using Eulerian-description of the fluid flow motion [6,7] as

$$\mathbf{i}_s = p_s\mathbf{u}\,, \tag{4}$$

and the divergence of the acoustic intensity can be expressed in a vector form as

$$\nabla\cdot\mathbf{i}_s = \nabla\cdot(p_s\mathbf{u}) = \mathbf{u}\cdot\nabla p_s + p_s(\nabla\cdot\mathbf{u})\,, \tag{5}$$

which is reduced to be the product of the particle velocity and the acoustic pressure gradient ($\mathbf{u}\cdot\nabla p_s$) for incompressible flows in Eq. (2); because the second term of Eq. (5) is vanished taking into account the continuity Eq. (1). Poesio and Ooms [7] characterized the acoustic field with the intensities of fast and slow AW including their damping coefficients by an explicit expression. In this paper, the acoustic pressure wave Eq. (3) has been employed for computing the acoustic pressure gradient in the momentum Eq. (2) in order to generalize the Poesio and Ooms [7] model. The initial value Riemann problem for Eqs. (1) to (3) is given by piecewise constant data [13,14,20] using high-resolution Godunov-type method.

In order to non-dimensionalize the governing equations (1) to (3), the following

$$t^* = \frac{tu_\infty}{h},\quad X = \frac{x}{h},\quad Y = \frac{y}{h},\quad Z = \frac{z}{h},$$
$$U = \frac{u}{u_\infty},\quad V = \frac{v}{u_\infty},\quad W = \frac{w}{u_\infty},\quad \mathbf{g}^* = \frac{h}{u_\infty^2}\mathbf{g},$$
$$P = \frac{p}{\rho_\infty u_\infty^2},\quad P_s = \frac{p_s}{\rho_\infty u_\infty^2},\quad Re = \frac{2hu_\infty}{\upsilon},$$
$$Ma = \frac{u_\infty}{c_s},\quad \mathbf{F} = \frac{h}{u_\infty^2}\mathbf{f},$$

dimensionless quantities have been introduced for time, spatial coordinates, velocity components, gravity field, hydrodynamic pressure field, acoustic pressure in the medium, and for external force field; where h, u_∞, ρ_∞ are constant reference quantities. The reference density is equal to the fluid density ρ; and the average velocity magnitude u_a is considered as the characteristic speed of the flow. By using dimensionless quantities and neglecting the gravity field $\mathbf{g}^*$, the governing equations relying on the artificial compressibility method can be written as

$$\frac{1}{\beta}\frac{\partial P}{\partial \tau} + \nabla\cdot\mathbf{U} = 0\,, \tag{6}$$

which is the perturbed continuity equation [20], and

$$\frac{\partial \mathbf{U}}{\partial \tau} = -\frac{\partial \mathbf{U}}{\partial t^*} - \nabla \cdot \left(\tilde{\mathbf{U}} \otimes \tilde{\mathbf{U}}\right) - \nabla P + \\ + \frac{2}{Re}\nabla^2 \mathbf{U} + Ma\mathbf{u} \cdot \nabla P_s + \mathbf{F}_{DNA} \qquad (7)$$

is the equation of fluid motion for unsteady, incompressible Newtonian fluid flow using dual-time stepping procedure; where β is the AC factor to ensure convergence, and τ is the pseudo-time step, which is computed in each control cell [19]. The convective flux term in the momentum Eq. (7) has been discretized and computed by applying conservative characteristics-based scheme derived by Shapiro and Drikakis [19]. Since, the system of governing equations (6) to (7) is hyperbolic-type, therefore, the Riemann method can be applied to determine the intercell flux values [19] as

$$\tilde{\mathbf{U}} = \begin{bmatrix} U_0 + \dfrac{\tilde{X}}{s}R \\ V_0 + \dfrac{\tilde{Y}}{s}R \\ W_0 + \dfrac{\tilde{Z}}{s}R \end{bmatrix}, \qquad (8)$$

where $\tilde{X} = k_X / L_k$, $\tilde{Y} = k_Y / L_k$, and $\tilde{Z} = k_Z / L_k$ are the coefficients of the governing equations; where k_X, k_Y, k_Z, (k=ξ,η,ζ) are the derivatives of the curvilinear coordinates according to the Cartesian (X,Y,Z) coordinates. The notation L_k applies to the Lamé metric coefficients appearing due to the coordinate transformation. The eigenvalues of the characteristic equations are $\lambda_0 = U\tilde{X} + V\tilde{Y} + W\tilde{Z}$, $\lambda_1 = 0.5(\lambda_0 + s)$, and $\lambda_2 = 0.5(\lambda_0 - s)$, where "1" and "2" subscripts correspond to the right and left hand side intercell eigenvalues; and $s = \sqrt{\lambda_0^2 + 4\beta}$ is the artificial speed of sound. For the sake of the compact way of writing, an auxiliary function has been introduced in the vector Eq. (8) as

$$R = P_L - P_R + \lambda_2\gamma_2 - \lambda_1\gamma_1, \qquad (9)$$

where "L" and "R" subscripts denote the "Left" and "Right" hand side intercell flux values containing

$$\gamma_1 = \tilde{X}(U_0 - U_L) + \tilde{Y}(V_0 - V_L) + \tilde{Z}(W_0 - W_L) \qquad (10)$$

auxiliary function related to eigenvalue λ_1 and

$$\gamma_2 = \tilde{X}(U_0 - U_R) + \tilde{Y}(V_0 - V_R) + \tilde{Z}(W_0 - W_R) \qquad (11)$$

auxiliary function related to eigenvalue λ_2. For computing the non-linear convective flux terms in conservative form relying on Eq. (8) in the momentum Eq. (7), Godunov-type discretization is employed to determine the velocity components U_0,V_0,W_0 corresponding to the eigenvalue λ_0 as

$$\mathbf{U}_0 = \frac{1}{2}\begin{bmatrix} U_L + U_R + sign(\lambda_0)(U_L - U_R) \\ V_L + V_R + sign(\lambda_0)(V_L - V_R) \\ W_L + W_R + sign(\lambda_0)(W_L - W_R) \end{bmatrix}, \qquad (12)$$

where $sign(\lambda_0)$ = -1 when ($\lambda_0 > 0$), and $sign(\lambda_0)$ = 1 when ($\lambda_0 < 0$). The Godunov procedure consists of three steps [20] relating to the high accurate convective flux computation. The first step is to use a high-order interpolation to approximate the "Left" and "Right" hand side intercell characteristic flux variables. The second step is the determination of intercell velocity components based on Eq. (8). In the third step, the non-linear convective fluxes are computed in the cell-centres by using FVM based discretization strategy. In this paper, to achieve high-order of accuracy, ninth-order WENO scheme [24] has been employed to approximate the intercell convective flux quantities in order to capture the AW in the Newtonian fluid flow field coupled with Eulerian-Lagrangian meta-modelling of the motion of DNA strands. The viscous term has been discretized by employing second-order central difference approximations. After performing a high accurate flow field computation, the following

$$\frac{1}{\beta^2}\frac{\partial^2 P_s}{\partial \tau^2} = \frac{1}{Ma^2}\nabla^2 P_s \qquad (13)$$

dimensionless AW equation has been solved for the acoustic pressure in order to compute the acoustic pressure gradient term in the momentum Eq. (7). The pseudo-time stepping procedure is advanced by using a fourth-order explicit Runge-Kutta scheme. The stopping criterions are defined by the absolute value of the difference between two pseudo-time level within a very small ε tolerance value for the pressure, velocity and acoustic pressure fields.

The presented numerical method may be used for either defense and/or environmental protection related industrial applications. These application areas are industrially sensitive, thus, experimental data for public engineering purpose are often protected by the industrial companies. Furthermore, it is difficult to perform accurate and trustable measurements, because of the small physical scales and geometrical sizes of micro- and nanofluidic devices. Therefore, it is reasonable and necessary to develop sophisticated mathematical models and set up simulation test cases to investigate the physical phenomena operating at these small-scales. The aim of the current numerical study is to provide information to those researchers and engineers who design highly selective micro- and/or nanofluidic sensors for DNA detection. More details can be found about practical applications in [25].

3. RESULTS AND DISCUSSION

In the present numerical study, longitudinal AW interacts with ssDNA chains aiming to investigate the effects of AW on the ssDNA motion. The current numerical study may essentially be important to determine the optimum location of a sensor within a DNA detection device. The ssDNA motion takes place within a three-dimensional microfluidic T-channel and is modelled through a coupled Eulerian-Lagrangian scheme [22,23]. The sketch of the three-dimensional microfluidic T-channel can be seen in Figure 1 along with the corresponding notations of geometrical sizes.

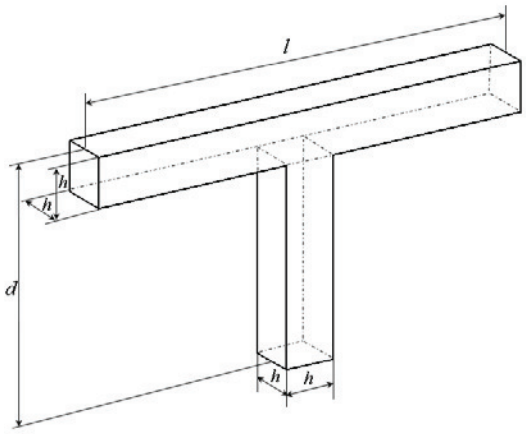

Figure 1. Sketch of the 3D T-channel geometry

The dimensions of the microfluidic T-channel (l,h,d) corresponding to the length, height and depth have been summarized in Table 1. The non-dimensionalization of the spatial coordinates has been carried out based on the height of the inlet sections h. The domain is rectangular, therefore, the three-dimensional grid is orthogonal (90° aspect ratio) everywhere on the computational domain.

Table 1. Geometrical sizes of the 3D T-channel

	Microfluidic T-channel	
Sizes	μm	dimensionless
l	110	11
h	10	1
d	60	6

The left hand side and bottom rectangular cross sections have been considered as inlet sections with the same volume flow rates ($Q_1 = Q_2$). The propagation of longitudinal AW has been modelled from the left hand side inlet to the right hand side outlet sections. The longitudinal waves appear as pressure waves travelling through the liquid; and relying on the model of Poesio and Ooms [7], these waves are proportional to the acoustic pressure gradient in the momentum Eqs. (2) and (7). The inlet velocity profiles are parabolic surfaces related to volume flow rate, and the normal derivatives of velocity components are vanished at the right hand side outlet cross section of the T-channel. For the acoustic pressure, Dirichlet boundary conditions have been prescribed in the inlet and outlet sections representing the dimensionless acoustic pressure difference between 0 and 1. In this numerical study, the longitudinal wave, travelling through the liquid, has only been taken into account; and any other acoustic sources are neglected on the boundaries.

The continuum model is limited at small physical scales [26]. A criterion exists to determine the validity of continuum hypothesis. According to Heller [26], the characteristic length scale of the atomistic scale of a fluid and the typical length scale of the investigated microfluidic device have to be compared. The average interatomic space [26] is

$$\lambda_A = \left(\frac{M_A}{\rho N_A} \right)^{1/3}, \tag{14}$$

where M_A is the molar mass of the fluid, and $N_A = 6.022 \cdot 10^{23}\ mol^{-1}$ is the Avogadro number. The criterion of the validity of continuum hypothes is the characteristic length scale of the investigated small-scale device/system has to be a bigger value than the average interatomic space λ_A in Eq. (14) [26]. In the present numerical study, the working fluid is water, therefore, the interatomic space of water can be expressed as $\lambda_W = 0.3 \cdot 10^{-9}\ m$, where $\rho_W = 1000\ kg \cdot m^{-3}$ is the density of water, and $M_W = 18.0153 \cdot 10^{-3}\ kg \cdot mol^{-1}$ is the molar mass of water. The biggest characteristic length of the three-dimensional microfluidic T-channel test geometry (see Table 1) is $110 \cdot 10^{-6}\ m$ (110 *micron*), which is much greater than $0.3 \cdot 10^{-9}\ m$ (0.3 *nanometer*); consequently, the continuum model is valid for the present numerical test case.

Simulations have been performed to investigate the pathlines of ssDNA with longitudinal AW in the macroscopic flow field at $Re = 10$ and at $Ma = 3.4 \cdot 10^{-6}$; where the speed of sound in the water has been taken as $c_s = 1497\ m/s$. The longitudinal wave length $\lambda_l = 4.25 \cdot 10^{-6}\ m$, which is smaller than the length of the microfluidic T-channel. The DNA sensing area has been assumed to be located in the upper wall close to the T-shape junction. Although, the Mach number is very small due to the small velocity components in each flow direction; but the acoustic pressure gradient has apparent impact the velocity field in the small-scale physics.

The importance of the simulations presented in this chapter is that the presence of AW in the flow field can induce flow instabilities that may also cause DNA-breaking, which should be avoided in detection device. In the simulation, longitudinal AW have been modelled by travelling through the water medium with ssDNA molecule chain in the microfluidic T-channel numerical test case.

Table 2. Results of grid convergence study

	T-channel Test Case		
	$N = 20$	$N = 50$	$N = 100$
$\left\|\Delta P_{error}^{relative}\right\|_{\infty}$	0.00485	0.00007	0.00006
$\left\|\Delta U_{error}^{relative}\right\|_{\infty}$	0.00168	0.00050	0.00048
$\left\|\Delta V_{error}^{relative}\right\|_{\infty}$	0.00137	0.00045	0.00041
$\left\|\Delta W_{error}^{relative}\right\|_{\infty}$	0.00116	0.00032	0.00029

A systematic grid convergence study has been performed to investigate the grid-independency of the numerical model. The left hand and bottom side located inlet sections have been divided into N parts (N = 10,20,40,50,100,…,200); which means that the grid density has been increased proportional to N. The maximum norm of the relative errors of pressure field and velocity components has been investigated. The results show that the relative errors are decreased when N is increased. The relative error of primitive variables does not change significantly above N = 50 (see Table 2); thus, reliable results can be obtained for the pressure and velocity fields above 25 000 control cells [21].

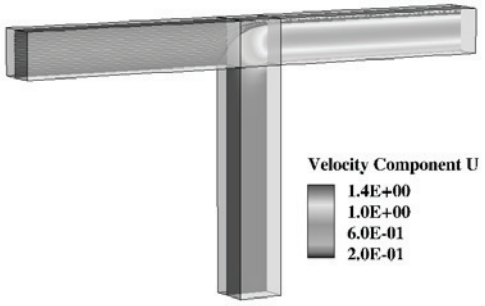

Figure 2. Velocity component *U* and ssDNA pathlines without the presence of AW

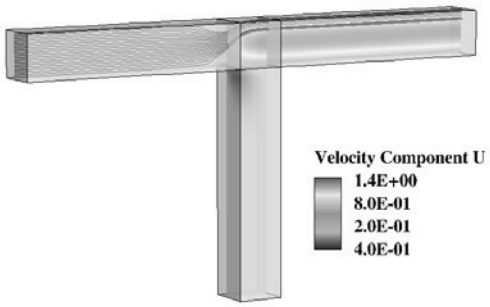

Figure 3. Velocity component *U* and ssDNA pathlines with the presence of AW

The AW model takes into account the longitudinal propagation of AW as the acoustic pressure gradient in the right hand side of the momentum Eq. (7); therefore, the velocity field is influenced via this source term. The acoustic pressure gradient is connected to the hyperbolic-type second-order acoustic wave Eq. (13).

The dimensionless velocity component U and ssDNA pathlines without and with the presence of longitudinal AW are shown in Figs. (2) to (3). Simulation result shows that the presence of AW has mainly influence on the dimensionless velocity component U. The direction of the flow approaches the sensor area from the left hand side upper inlet, and the flow becomes fully developed in the right hand side outlet section, see in Fig. (3). The distribution of velocity component V with the presence of AW has been observed slightly different than the distribution without the presence of AW. Higher velocity components can be observed close to the ssDNA sensing area (see in Fig. (3)) than in the simulation case without taking into account the presence of AW in the flow field (see in Figs. (2) and (4)). These simulation results suggest that the presence of AW in the macroscopic flow field has significant influence on the pathlines of ssDNA flow without breaking the molecule chain. The results also show that the ssDNA chain flows towards the upper wall effectively without the presence of longitudinal AW in the flow field.

It is important to mention that the ssDNA chain has been released when the fluid flow becomes fully developed in the microfluidic T-channel; thus, the criterion of a possible DNA-breaking remains unknown. In order to gain deeper understanding of the presence of AW in a DNA detection device, an acoustic source should be located in the opposite side of the DNA sensing area. The effect of the location of an acoustic source has to be further investigated, because the current results suggest that the presence of an acoustic source near the DNA sensing area could be advantageous to force the ssDNA chain to reach the sensor. The acoustic source generator on the geometry surface could be chosen in different ways, such as using microphone, piezoelectric crystal, or a magnetrostriction device could be attached to T-channel boundary.

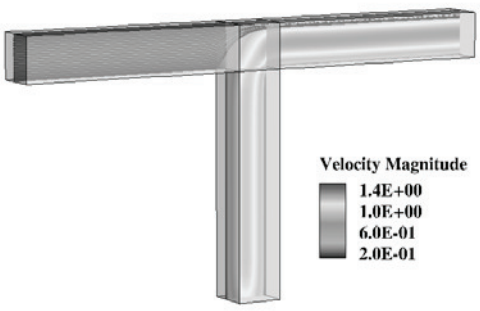

Figure 4. Velocity magnitude and ssDNA pathlines without the presence of AW

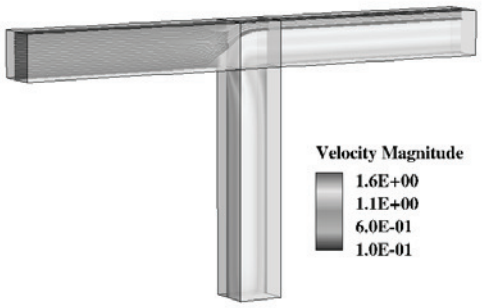

Figure 5. Velocity magnitude and ssDNA pathlines with the presence of AW

The velocity magnitude and ssDNA pathlines without and with the presence of longitudinal AW are shown in Figs. (4) to (5), respectively. Although the velocity magnitudes are similar to each other, the ssDNA flow stream (continuous black lines) shows small differences as shown in Figs. (2) to (5). This is due to the the wave length of longitudinal AW present in the flow field, and because of the ssDNA chain mainly follow the path of the flow streamlines. For modelling ssDNA flow, the number of particles is 206 with number of bead-rod structure 20; the relative particle radius is $4.56 \cdot 10^{-5}$ *m*, the relative particle density is $8.005 \cdot 10^{-15}$ $kg \cdot m^{-3}$, and the rod length of chain elements is $9.15 \cdot 10^{-5}$ *m* in the ssDNA meta-modelling approach. The number of cells has been chosen to be 288 000 on the fine grid in order to provide the characteristic length 10^{-4} *m* for the coupled Eulerian-Lagrangian simulation of ssDNA flow (see more details in [22,23]). In order to ensure converged solution of the pseudo-time stepping procedure, the artificial compressibility factor β has been chosen to be 20. Note that difficulty may arise to obtain converged numerical solution within small (e.g. 10^{-8}) tolerance values of ε. The reason for this difficulty is the acoustic pressure gradient in the right hand side of the momentum Eq. (7); because the velocity field might change rapidly due to the presence of longitudinal AW in the microfluidic T-channel. In order to overcome this numerical problem, the ssDNA meta-modelling approach has been performed after the flow field becomes fully developed; then, the ssDNA chain has been released in the upper inlet section. Consequently, the strong gradients of the acoustic pressure may cause numerical instability in the Eulerian-Lagrangian simulation of ssDNA flow. Furthermore, in consequence of the grid density and the small time-step size in each domain cell will increase the computational time compared to case when the longitudinal AW with ssDNA chain are not present in the macroscopic flow field. In order to decrease the computational cost, an alternative solution is that the fully developed flow field has been computed with the presence of AW, but without meta-modelling of the ssDNA flow. When the flow field becomes nearly fully developed with the presence of AW propagation, the ssDNA chain has been released in the microfluidic T-channel to avoid numerical instabilites in the flow field.

4. CONCLUSIONS

This paper focused on acoustic wave modelling in conjunction with high-resolution characteristics-based Godunov-type method for solving unsteady, incompressible, laminar flow problem in a three-dimensional microfluidic T-channel. A simplified acoustic wave model [7] has been adopted and further developed to investigate the effects of AW on the Newtonian fluid flow pattern. According to this AW model, the longitudinal AW propagation is proportional to the acoustic pressure gradient represented in the momentum Eqs. (2) and (7) as a source term. The system of governing equations has been solved by employing artificial compressibility method for incompressible flow [15-21]. In the present paper, the AW interacted with DNA strands that have been released in the three-dimensional microfluidic T-channel, and have been modelled through a coupled Eulerian-Lagrangian dynamics [22,23]. The following main conclusions might be drawn: a) the presence of AW in the flow field has influence on the pathlines of ssDNA flow without breaking the molecule chain; b) the ssDNA chain flows towards the upper wall effectively without the presence of AW in the flow field; c) the ssDNA chain has been released when the fluid flow becomes fully developed, thus, the criterion of a possible DNA-breaking remains unknown. Overall, the numerical results presented in this paper suggest that the presence of acoustic source near the sensing area could be advantangeous, because the ssDNA chain might reach the sensing area faster than without the presence of an acoustic source.

ACKNOWLEDGEMENTS

The authors would like to acknowledge Dr. Mátyás Benke and Dr. Evgeniy Shapiro for their co-operation in conjunction with the development and implementation of the DNA flow meta-model.

REFERENCES

[1] Rocha-Gaso, M.-I., March-Iborra, C., Montoya-Baides, Á. and Arnau-Vives, A., 2009, "Surface Generated Acoustic Wave Biosensors for the Detection of Pathogens: A Review", *Sensors*, Vol. 9, pp. 5740-5769.

[2] Ballantine, D. S., White, R. M., Martin, S. J., Ricco, A. J., Frye, G. C., Zellers, E. T. and Wohltjen, H., 1997, "Acoustic Wave Sensors, Theory, Design, and Physico-Chemical Applications", *Academic Press*, San Diego.

[3] Andle, J. C., Weaver, J. T., Vetelino, J. F. and McAllister, D. J., 1995, "Selective Acoustic Plate Mode DNA Sensor", *Sensors and Actuators B*, Vol. 24, pp. 129-133.

[4] Ippolito, S. J., Kalantar-Zadeh, K., Powell, D. A. and Wlodarski, W., 2003, "A 3-Dimensional Finite Element Approach for Simulating Acoustic Wave Propagation in Layered Saw Devices", *IEEE Ultrason. Symp.*, pp. 303-306.

[5] Abdollahi, A., Jiang, A. and Arabshahi, S. A., 2007, "Evaluation on Mass Sensitivity of Saw Sensors for Different Piezoelectric Materials Using Finite-Element Analyisis", *IEEE Trans. Ultrason. Ferroelectr. Freq. Cont.*, Vol. 54, pp. 2446-2455.

[6] Dowling, A. P. and Williams, J. E. Ffowcs, 1983, "Sound and Sources of Sound", *Ellis Horwood Limited*, *John Wiley and Sons*, New York.

[7] Poesio, P., and Ooms, G., 2005, "Influence of High-Frequency Acoustic Waves on the Flow of a Liquid Through Porous Material", *IUTAM Proc. Physicochemical and Electromechanical Interactions in Porous Media*, *Jacques M. Huyghe et al. (Eds.)*, Springer, Printed in the Netherlands, pp. 61-66.

[8] Shi, Y., 1996, "The Modeling of Structural-Acoustic Interaction Using Coupled FE/BE Method and Control of Interior Acoustic Pressure Using Piezoelectric Actuators", *Ph.D. thesis*, *Faculty of Old Dominion University*.

[9] Lighthill, J. M., 1952, "On Sound Generated Aerodynamically, I Generally Theory", *Proc. Royal Soc.*, Vol. 211, pp. 564 - 584.

[10] Lilley, G. M., 1974, "On the Noise from Jets", *AGARD CP-131*, pp. 13.1-13.12.

[11] Wang, Z.-K., Djambazov, G., Lai, C.-H. and Pericleous, K., 2007, "Numerical Simulation of Flow-Induced Cavity Noise in Self-Sustained Oscillations", *Comput. Visual. Sci.*, Vol. 10, pp. 123-134.

[12] Chu, R. K.-H., 2007, "Effects of Slip Velocity and Surface Acoustic Wave on the Laminar Flow Stability", *Meccanica*, Vol. 42, pp. 1-7.

[13] LeVeque, R. J., 1997, "Wave Propagation Algorithms for Multidimensional Hyperbolic Systems", *J. Comput. Phys.*, Vol. 131, pp. 327-353.

[14] Fogarty, T. R. and LeVeque, R. J., 1999, "High-Resolution Finite-Volume Methods for Acoustic Waves in Periodic and Random Media", *J. Acoust. Soc. Am.*, Vol. 106, No. 1, pp. 17-28.

[15] Chorin, A. J., 1967, "A Numerical Method for Solving Incompressible Viscous Flow Problems", *J. Comput. Phys.*, Vol. 2, pp. 12-26.

[16] Peyret, R. and Taylor, T., 1983, "Computational Methods for Fluid Flow", *Springer-Verlag*, *Berlin*, pp. 144-159.

[17] Eberle, A., 1987, "Characteristic Flux Averaging Approach to the Solution of Euler's Equation", *VKI Lecture Series*, *Computational Fluid Dynamics*.

[18] Drikakis, D., 1996, "A Parallel Multiblock Characteristic-Based Method for Three-Dimensional Incompressible Flows", *Advances in Engineering Software*, Vol. 26, pp. 111-119.

[19] Shapiro, E., and Drikakis, D., 2005, "Artificial Compressibility, Characteristics-based Schemes for Variable Density, Incompressible, Multi-species Flows. Part I. Derivation of Different Formulations and Constant Density Limit", *J. Comput. Phys.*, Vol. 210, pp. 584-607.

[20] Drikakis, D. and Rider, W., 2005, "High-resolution Methods for Incompressible and Low-Speed Flows", *Springer*, Berlin.

[21] Könözsy, L., 2012, "Multiphysics CFD Modelling of Incompressible Flows", *Ph.D. thesis*, *Cranfield University*, *Department of Fluid Mechanics and Computational Science*, *United Kingdom*.

[22] Benke, M., Shapiro, E., and Drikakis, D., 2008, "An Efficient Multi-Scale Modelling Approach for ssDNA Motion in Fluid Flow", *Journal of Bionic Engineering*, Vol. 5, pp. 299-307.

[23] Benke, M., 2010, "Mesoscale Modelling and Simulation of Macromolecule Transport in Microfluidic Channels", *Ph.D. thesis*, *Cranfield University*, *Department of Fluid Mechanics and Computational Science*, *United Kingdom.*

[24] Balsara, D. S., and Shu, C.-W., 2000, "Monotonicity Preserving Weighted Essentially Non-Oscillatory Schemes with Increasingly High Order of Accuracy", *J. Comput. Phys.*, Vol. 160, pp. 405-452.

[25] Mantzalis, D., Karantonis, K., Asproulis, N., Könözsy, L. and Drikakis, D., 2012, "Computational Modelling of Aqueous Environments in Micro and Nanochannels", Book Chapter on "Detection of Pathogens in Water using Micro and Nano-Techonology", *G. Zuccheri and N. Asproulis (Eds.)*, *IWA Publishing*. (in press)

[26] Heller, M., 2005, "Dynamics of Finite-sized particles in microfluidic systems", *M.Sc. thesis*, *Department of Micro- and Nanotechnology*, *Technical University of Denmark*, p. 8.

Conference on Modelling Fluid Flow (CMFF'12)
The 15th International Conference on Fluid Flow Technologies
Budapest, Hungary, September 4-7, 2012

BLOCK-STRUCTURED FINITE DIFFERENCE METHOD FOR THE SIMULATION OF HYDROACOUSTICS IN ARBITRARY DOMAINS

Sascha Seidl,[1] Rudolf Schilling, [2]

[1] Corresponding Author. Department of Fluid Mechanics, Technische Universität München. Boltzmannstrae 15, D-85748 Garching, Germany. Tel.: +49 89 289 16293, Fax: +49 89 289 16297, E-mail: seidl@flm.mw.tum.de
[2] Department of Fluid Mechanics, Technische Universität München. E-mail: schilling@flm.mw.tum.de

ABSTRACT

This paper describes the development of a block-structured finite difference method for the numerical simulation of pure acoustics as well as flow-induced acoustics in arbitrary domains. The developed CHA-method (Computational Hydro Acoustics) is based on the linearized Euler equations, which have been proven to determine acoustic behavior quite well.
Within the CHA-module the spatial discretization for the finite-difference framework is outlined via the DRP-scheme (Dispersion-Relation-Preserving scheme) after TAM & WEBB, whereas for the time discretization an optimized $2N$-storage low dissipation and dispersion Runge-Kutta scheme of fourth order by BERLAND has been developed. In combination with an appropriate filtering method, the developed CHA-solver performs in a quite efficient and numerically stable way. At the boundaries of the geometry, different sound-reflecting as well as non-reflecting boundary conditions can be imposed.
The domain is discretized using block-structured curvilinear meshes for arbitrary domains. Due to the design of the spatial discretization schemes of higher order, usually only rectangular meshes can be adopted for acoustic simulations. By transforming the physical curvilinear space into a computation space with cartesian coordinates, the same operations can be used as in the original rectangular case. To ensure accuracy, the metric coefficients for the coordinate transformation have to be computed numerically with the same interpolation schemes as the actual spatial approximations. Therefore the same discretization schemes are used.
First of all the results of the CHA-module will be compared to analytical solutions. Then, simplified test cases from real-life applications will be considered and discussed.

Keywords: Computational Hydro Acoustics, Curvilinear Meshes, Finite Difference Method

NOMENCLATURE

$A,\ B,\ C$	[–]	characteristic matrices of the LEE
$\tilde{A}_T,\ \tilde{B}_T,\ \tilde{C}_T$	[–]	transformed characteristic matrices
c_∞	[–]	speed of sound
D	[–]	filter term
d_j	[–]	filter coefficients
E	[–]	integration error
H	[–]	flow field inhomogeneities vector
M	[–]	Mach number
ω	[–]	exact wave number
$\bar{\omega}$	[–]	modified wave number
p_0	[–]	mean pressure
p'	[–]	fluctuating pressure
ρ_0	[–]	mean density
ρ'	[–]	fluctuating density
S	[–]	source vector
σ	[–]	damping coefficient
$\mathbf{U}$	[–]	vector containing the acoustic variables
$u_{0,i}$	[–]	mean velocity in i-direction
u_i'	[–]	fluctuating velocity in i-direction
$x,\ y,\ z$	[–]	coordinates of physical domain
$\xi,\ \eta,\ \zeta$	[–]	coordinates of computational domain

1. INTRODUCTION

At the Institute of Fluid Mechanics of the Technische Universität München (FLM) an Integrated Design System is being developed for several years. This system contains modules for the initial design process, the numerical simulation process as well as the post-processing of the calculated results for

problems located in a turbomachinery context, see GANTNER[12]. The simulation module involves a Finite Volume solver for structured as well as unstructured grid data for the numerical calculation of flow problems, see FLURL [10].
Furthermore, this system shall be enhanced by a software module for simulating acoustic and flow-induced acoustic problems, which is summarized under the term Computational Aero-Acoustics (CAA) or Computational Hydro Acoustics (CHA). For this reason, a Finite Difference based CHA solver for structured grids on the basis of the linearized Euler equations has been developed. By utilizing a block-structured multi-domain strategy, the developed solver will be adapted to real-life applications.
The paper presents the numerical fundamentals of the developed CHA-code as well as the validation of the implementation on the basis of several academic test cases and simple examples.

2. GOVERNING EQUATIONS

Both hydrodynamic and acoustic problems can be described by the full Navier-Stokes equations. Therefore, a direct computation of both the fluid flow field and the flow-induced acoustic field would make sense, however, because of high discrepancies between the length- and energy scales, such a Direct Numerical Simulation cannot be accomplished in an efficient way, especially with regard to the limited computing power of todays personal computers.
For this reason, a common way to overcome this problem is the usage of hybrid methods. It is supposed that the flow field may be decomposed into a mean flow part, which is assumed to be known at every point, and into time-dependent fluctuating terms for acoustics. The basis for each hybrid method is such a perturbation approach presented in (1):

$$\begin{aligned} \rho &= \rho_0 + \rho', \\ p &= p_0 + p', \\ u_i &= u_{0,i} + u_i'. \end{aligned} \tag{1}$$

Here the decomposition is presented by temporal constant mean values, denoted by the subscript "0", and the corresponding fluctuation values. The fluctuating values are much smaller in magnitude than the flow values, which make the perturbation method in (1) reasonable.
In this work, the three-dimensional linearized Euler equations (LEE) will be used for describing flow-induced acoustic phenomena, which are presented in matrix notation as the following system of equations:

$$\frac{\partial U}{\partial t} + \frac{\partial E}{\partial x} + \frac{\partial F}{\partial y} + \frac{\partial G}{\partial z} + H = S. \tag{2}$$

The conservation vector U of (2) contains the acoustic fluctuation variables ρ', u_i' and p'. Furthermore the vectors E, F and G have the following form:

$$U = \begin{pmatrix} \rho' \\ u' \\ v' \\ w' \\ p' \end{pmatrix}, \; E = \begin{pmatrix} \rho' u_0 + \rho_0 u' \\ u_0 u' + \frac{p'}{\rho_0} \\ u_0 v' \\ u_0 w' \\ u_0 p' + \gamma p_0 u' \end{pmatrix},$$

$$F = \begin{pmatrix} \rho' v_0 + \rho_0 v' \\ v_0 u' \\ v_0 v' + \frac{p'}{\rho_0} \\ v_0 w' \\ v_0 p' + \gamma p_0 v' \end{pmatrix}, \; G = \begin{pmatrix} \rho' w_0 + \rho_0 w' \\ w_0 u' \\ w_0 v' \\ w_0 w' + \frac{p'}{\rho_0} \\ w_0 p' + \gamma p_0 w' \end{pmatrix}$$

The vector H includes all inhomogeneities of the flow field. The source term S on the right hand side provides the flow information necessary for coupling the flow field with the acoustic field. It can be chosen after DJAMBAZOV [7] in the following manner:

$$S = \begin{pmatrix} 0 \\ 0 \\ 0 \\ 0 \\ \frac{\partial p_0}{\partial t} \end{pmatrix} \approx \begin{pmatrix} 0 \\ 0 \\ 0 \\ 0 \\ \frac{\left(p_0 - p_0^{old}\right)}{(\triangle t)_{fluid}} \end{pmatrix}. \tag{3}$$

Several other formulations for S can be found in DEROECK [6].
Furthermore, the equation system (2) can be rewritten in characteristic form, which reads:

$$\frac{\partial \mathbf{U}}{\partial t} + A\frac{\partial \mathbf{U}}{\partial x} + B\frac{\partial \mathbf{U}}{\partial y} + C\frac{\partial \mathbf{U}}{\partial z} + H = S, \tag{4}$$

with appropriate coefficient matrices A, B and C.

3. NUMERICAL SETUP

3.1. Spatial discretization

The acoustic propagation equations described in (4) have been discretized in space by different Finite Difference methods (FD), which can be written as

$$\left(\frac{\partial U}{\partial x}\right)_i \approx \frac{1}{\triangle x} \sum_{j=-N}^{M} a_j U_{i+j}. \tag{5}$$

As acoustic waves propagate over long distances, the employed numerical schemes must provide a low dispersion and low dissipation behavior. Therefore, TAM & WEBB [16] proposed a method, where the coefficients a_j in (5) are chosen by an optimization procedure in order to minimize the dispersion error. This is achieved by minimizing the integration error E of the difference between the actual and the modified wavenumber over a certain wavenumber range $[(\omega\triangle x)_l, (\omega\triangle x)_r]$:

$$E = \int_{(\omega\triangle x)_l}^{(\omega\triangle x)_r} |\omega\triangle x - \bar{\omega}\triangle x|^2 \, \mathrm{d}(\omega\triangle x). \tag{6}$$

At the expense of order reduction, TAM & WEBB achieved to construct a 4th order 7-point stencil scheme, which is well known as the Dispersion-Relation-Preserving Scheme (DRP). In order to achieve DRP-optimized schemes with up to 13-point stencils (FDo7p up to FDo13p), BOGEY & BAILLY [5] adopted the presented procedure and improved it by using the relative difference in (6) instead of the absolute difference, resulting in:

$$E = \int_{(\omega\triangle x)_l}^{(\omega\triangle x)_r} \frac{|\omega\triangle x - \bar{\omega}\triangle x|}{\omega\triangle x} \mathrm{d}(\omega\triangle x). \tag{7}$$

Figure 1 shows the comparison between the actual and the modified wavenumber of different Finite Difference Schemes. As can be seen, $\bar{\omega}$ of the optimized schemes gives a better approximation for the exact wavenumber for long waves than it is the case for the standard FD scheme.

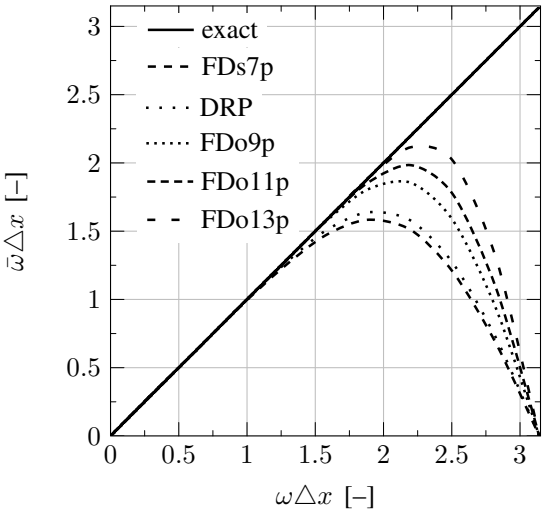

Figure 1. Modified wave numbers of standard and optimized Finite Difference schemes.

Furthermore, by utilizing the presented optimization technique, BOGEY & BAILLY constructed optimized one-sided FD schemes, which can be used near the numerical boundaries of the computational domain. In contrast, by using only centered FD schemes, additional grid layers at the boundaries would become necessary and would complicate the numerical solving procedure unnecessarily.
It shall be noted that in terms of the numerical efficiency the 7-point stencil DRP scheme of TAM & WEBB and the 11-point stencil scheme of BOGEY & BAILLY have been proven to be the dedicated discretisation schemes.

3.2. Temporal discretization

For the time discretization of a semi-discretised initial value problem of the following form

$$\frac{\partial U}{\partial t} = F\big(t, U(t)\big), \quad U(t_0) = U_0, \tag{8}$$

an explicit 6 stage low-dissipation and low-dispersion Runge-Kutta scheme after BERLAND ET AL. (LDDRK46) of fourth order is adopted, see BERLAND [3]. The operator $F(U)$ in equation (8) contains all the spatial derivatives in discretized form. This method is optimized according to its dispersion and dissipation behavior in an equivalent manner as it was achieved for the spatial discretization schemes. The inherent $2N$-storage implementation of the time-discretization scheme results in a truncation error of fourth order and shows a reduced numerical error in comparison to the non-optimized schemes of the same stage number. Its formulation was first conducted by WILLIAMSON [20] and has the following form:

$$w_i = \alpha_i w_{i-1} + \triangle t F(t_{i-1}, u_{i-1}), \tag{9a}$$
$$u_i = u_{i-1} + \beta_i w_i, \qquad i = 1, \dots s, \tag{9b}$$

where $u_0 = u^n$ represents the solution of the previous time step, $u_s = u^{n+1}$ the solution for the new time step and w_i interim solutions of the different Runge-Kutta steps. The new coefficients of the LDDRK46 method must be attained from the original Runge-Kutta coefficients. Advantages of this formulation are, next to the low computational storage requirements, a compact implementation due to the $2N$-storage implementation. Furthermore this method is also applicable for the application to non-linear problems.

3.3. Selective filtering

The selective filtering technique allows for filtering out the parasite waves with short wave length, whereas the underlying conservation equations remain the same. By applying a low-pass filter, the parasite portion of the acoustic waves can be removed from the numerical solution. The filter function works equivalent to the spatial discretization technique and is applied to the acoustic solution vector U, which reads

$$\bar{U}_i = U_i - D, \qquad \text{and} \tag{10a}$$
$$D = \sigma \sum_{j=-N}^{M} d_j U_{i+j}. \tag{10b}$$

The value of σ is chosen to lie between 0 and 1. The filter coefficients d_j can be determined by an optimization strategy similar to the DRP-approach in order to filter out the parasite wave portions of high frequency and keep the long-wave parts unchanged. Therefore, an optimized 11-point filter is gained and has been successfully adapted throughout this whole work. For further information, the reader is referred to BERLAND [4].

3.4. Application to complex geometries

Due to their definition in the Finite Difference context, the above mentioned numerical methods

for discretising the underlying linearized Euler equations are only valid for cartesian computational grids. Thus, without the correct treatment of curvilinear meshes, an unnatural distortion along the curved index lines can be observed, see Figure 2.

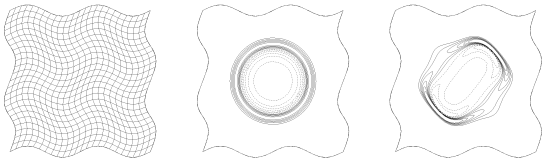

Figure 2. Contour lines of acoustic pressure pulse with and without correct treatment of curvilinear coordinates.

As the cartesian grid type is of low importance for complex geometries in real life applications, the authors suggest the usage of curvilinear grids. By using such curvilinear non-orthogonal computational grids with curved coordinates, easy setting of boundary conditions and flexible meshing is possible. However, the numerical solution of the governed differential equations becomes very difficult. Thus, a coordinate transformation (CT) has to be performed prior to the numerical solution. Here the curvilinear body-fitted mesh of the physical domain in terms of (x, y, z) is transformed into the cartesian computational domain (ξ, η, ζ). Therefore, the solution of the differential equations in the physical domain has to be expressed by the independent variables of the computational domain. The variables of the physical domain are related to the variables of the computational domain and vice versa in the following manner:

$$\xi = \xi(x, y, z), \qquad x = x(\xi, \eta, \zeta), \tag{11a}$$
$$\eta = \eta(x, y, z), \qquad y = y(\xi, \eta, \zeta), \tag{11b}$$
$$\zeta = \zeta(x, y, z), \qquad z = z(\xi, \eta, \zeta). \tag{11c}$$

By using the functional relationship (11a) to (11c) and adapting the chain rule, a transformation of the derivatives can be achieved:

$$\frac{\partial}{\partial x} = \frac{\partial}{\partial \xi}\left(\frac{\partial \xi}{\partial x}\right) + \frac{\partial}{\partial \eta}\left(\frac{\partial \eta}{\partial x}\right) + \frac{\partial}{\partial \zeta}\left(\frac{\partial \zeta}{\partial x}\right),$$
$$\frac{\partial}{\partial y} = \frac{\partial}{\partial \xi}\left(\frac{\partial \xi}{\partial y}\right) + \frac{\partial}{\partial \eta}\left(\frac{\partial \eta}{\partial y}\right) + \frac{\partial}{\partial \zeta}\left(\frac{\partial \zeta}{\partial y}\right),$$
$$\frac{\partial}{\partial z} = \frac{\partial}{\partial \xi}\left(\frac{\partial \xi}{\partial z}\right) + \frac{\partial}{\partial \eta}\left(\frac{\partial \eta}{\partial z}\right) + \frac{\partial}{\partial \zeta}\left(\frac{\partial \zeta}{\partial z}\right).$$

The derivatives in brackets are called metric components. If an analytical relation between the physical and the computational domain exists, the metric components can be determined in an exact manner. As in most other cases the transformation parameters have to be numerically computed. Typically, to ensure accuracy, the same discretization techniques are used as for discretising the spatial derivatives. By applying the coordinate transformation to the governing equations in (3), the transformed form of the LEE can be achieved, see EMMERT [8]:

$$\frac{\partial \mathbf{U}}{\partial t} + A_T \frac{\partial \mathbf{U}}{\partial \xi} + B_T \frac{\partial \mathbf{U}}{\partial \eta} + C_T \frac{\partial \mathbf{U}}{\partial \zeta} + H = S. \tag{12}$$

Furthermore, to obtain the strong conservative form of the transformed LEE, equation (12) is divided by $|J|$. Otherwise, an unnatural dilution of the numerical obtained amplitude towards smaller cell volumes can be observed. Thus, equation (12) takes the following form:

$$\frac{1}{|J|}\frac{\partial \mathbf{U}}{\partial t} + \tilde{A}_T \frac{\partial \mathbf{U}}{\partial x} + \tilde{B}_T \frac{\partial \mathbf{U}}{\partial y} + \tilde{C}_T \frac{\partial \mathbf{U}}{\partial z} + \frac{1}{|J|} H = S. \tag{13}$$

The matrices $\tilde{A}_T$, $\tilde{B}_T$ and $\tilde{C}_T$ are the transformed coefficient matrices and differ at each grid point because of different transformation parameters according to the form of the curved grid. Therefore, these matrices have to be determined for each grid point and have to be stored for further computation steps.

One important condition for a stable and therefore successful coordinate transformation between the physical and the computational domain is the partition of the grid points of the curvilinear grid, which should preferably be smooth. This is achieved by using an almost equidistant grid point arrangement whenever possible and at the same time avoiding volatile changes of the grid spacing. Thus, compared to the generation of the fluid mesh, the grid generation for the acoustic mesh underlies absolutely different criteria and almost needs the same effort and attention.

3.5. Multi-block strategy

Because simulating aero-acoustic problems on complex geometries with a single-block code is difficult and in most cases nearly impossible, a multi-block implementation was chosen in the presented CHA-code. The advantage of a block-structuring is that the numerical solution can be computed independently in each block domain at every time step. Here, individual boundary conditions can be attached to each single block and the numerical calculation is carried out as in a single-block computation. At adjacent interfaces an exchange of acoustic data has to be conducted via finite-size overlapping grid layers. This exchange procedure takes place after each Runge-Kutta step. GAITONDE & VISBAL [11] recommend that the exchange routine must also be carried out after each application of the filter procedure. Figure 3

illustrates the data transfer between two adjacent blocks in detail: The values at the points 0 and 1 in block 2 are set to be equal to the points $nx-5$ and $nx-4$ in block 1. In the same manner the values at the points $nx-2$ and $nx-1$ are set to be equal to the values at the points 3 and 4. GAITONDE & VISBAL [11] showed that stable and accurate simulations with numerical methods of high-order can be best achieved by a 5-point overlap region on curvilinear meshes and with a viscous flow. In terms of accuracy and computational speed and efficiency a 3-point overlap region represents the best choice.

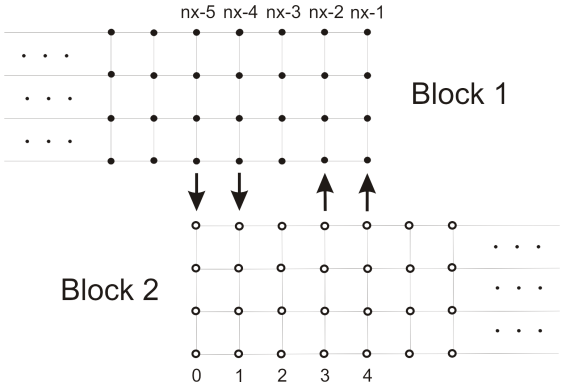

Figure 3. Illustration of exchange proceeding with 5-point mesh overlap.

Another possibility to handle adjacent block interfaces shall be presented here: By utilizing one-sided finite difference schemes it is possible to just exchange the acoustic values in the boundary grid cells . The advantage of this procedure is that no auxiliary grid layers for data exchange are needed. The disadvantages of this method are that also at block interfaces nonreflecting boundary conditions have to be attached. Furthermore, in order to suppress parasite numerical reflections which can lead to divergence of the numerical solution, a stronger filtering technique is necessary. A stable computational run can therefore be achieved by adopting a 7-point Artificial Selective Damping (ASD) technique, which has been presented by TAM& DONG [17]. This ASD is executed after a certain number of timesteps, whereas in the intermediate timesteps, the presented selective filtering technique by BERLAND is applied.

3.6. Boundary conditions

Characteristic Boundary Conditions

The numerical boundaries of the computational domain have to be treated in an appropriate manner for acoustic simulations. At boundaries, where outgoing acoustic waves are present, special non-reflecting boundary conditions (NRBC) have to be adapted. In addition, sound-reflecting boundaries like walls are also necessary. For this reason, THOMPSON [18, 19] derived NRBC on the basis of a one-dimensional characteristic analysis of the Euler equations, achieving the so called Characteristic Boundary Conditions (Char. BC): The equations to be solved are brought into characteristic form. Thus, the determined eigenvalues and eigenvectors describe the propagation behavior of the different waves. At the boundaries, the equations are rearranged in such a way that the solution only depends on values inside the computational domain. Therefore, numerical reflections can be diminished. By applying the characteristic analysis on the governing equations, boundary conditions for open boundaries, which form the non-reflecting boundary conditions, as well as for sound-reflecting wall boundaries can be obtained. Due to their simple handling, the characteristic non-reflecting conditions and wall boundary conditions can be selected for both cartesian and curvilinear mesh types.

Perfectly Matched Layer

Beside the characteristic approach, also a Perfectly Matched Layer (PML) has been implemented. The PML is part of the so called damping layer techniques, where a certain number of additional layers as boundary layers is added to the actual computational domain. Inside these layers, the numerical flow is dissipated by additional artificial dissipation terms which are added to the original propagation equations. This principle has been proposed by BÉRENGER [2] and has been adapted to aero-acoustic applications by HU [13]. Adding auxiliary layers to the boundaries requires additional computational effort. Furthermore, the method of attaching several boundary layers to an existing curvilinear mesh in a multi-block framework is a demanding task for itself and therefore it has not been carried out in the presented block-structured CHA-code. Nevertheless, for rectangular cartesian grids the PML is an adequate and promising equivalent boundary condition to the Char. BC.

4. RESULTS

A common way to validate new CHA-codes is the investigation of the propagation of sound waves resulting from acoustic pole sources. A distinction is made between initial pressure pulses, acoustic monopole, dipole and quadrupole sources. In this work, mainly pressure pulses and monopole sources will be investigated.

Wave propagation in an uniform mean flow

In a first test case the 2D radiation of a monopole source in a uniform mean flow shall be investigated. The computational domain denotes 201×201 grid points on a $[-1,1] \times [-1,1]$ domain. By identifying the source vector S of equation (4) with the following expression:

$$S = f(x,y) \cdot \sin(\omega t) \begin{pmatrix} 1 & 0 & 0 & 0 & 1 \end{pmatrix}^T, \tag{14}$$

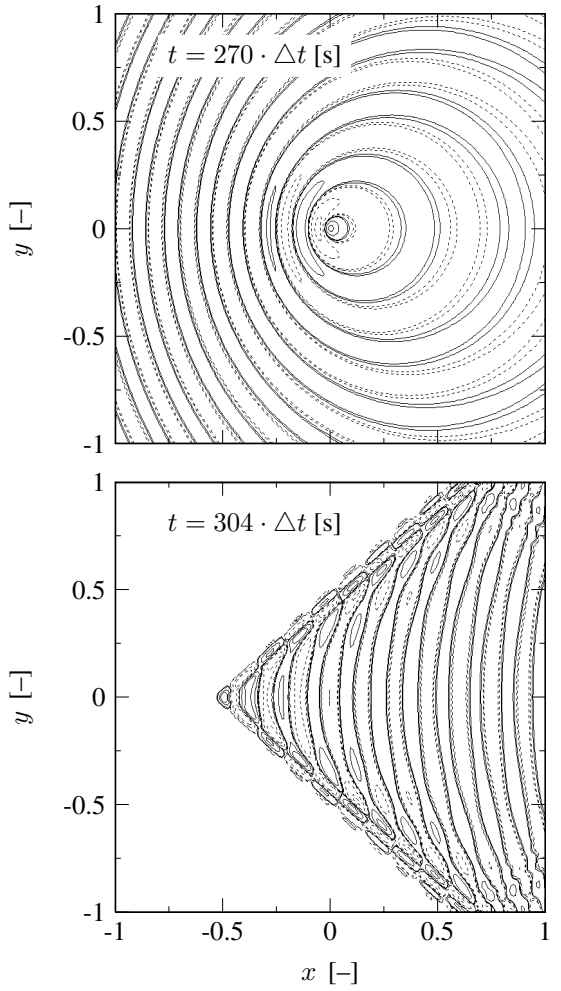

Figure 4. Acoustic Monopole source, *top:* **subsonic mean flow with** $M = 0.5$ **and** *bottom:* **supersonic mean flow with** $M = 1.5$ **in positive x-direction.**

a monopole source is introduced to the developed CHA-code, where $f(x, y) = \epsilon \mathrm{e}^{-\alpha[(x-x_c)^2+(y-y_c)^2]}$. The source is located at the center $(x_c, y_c) = (0, 0)$ of the domain. Furthermore, the amplitude is given by $\epsilon = 0.5$, the width of the monopole source is $\alpha = {}^{\ln(2)}/_{2}$ and the angular frequency is given by $\omega = {}^{2\pi}/_{30}$. First, the subsonic case will be investigated by setting the Mach number $M = 0.5$. Figure 4 shows the contour lines of the acoustic pressure p' at time $t = 270$ $[s]$. Furthermore, a good agreement between the numerical solution and the reference solution given by BAILLY ET AL. [1] along the line $x = y$ can be observed in Figure 5. Although a PML of 10 layer thickness at the East-side of the computational domain was used, a slight discrepancy in the downwind direction between numerical and reference solution cannot be neglected.

For the supersonic case a Mach number of $M = 1.5$ with $(x_c, y_c) = (-50, 0)$ has been chosen. The resulting contour lines for the time $t = 304$ $[s]$ can also be seen in Figure 4. Here, the numerical solution fails to reproduce the analytical solution right at the center of the monopole source, which is shown in Figure 5. Nevertheless, the achieved numerical solution is in good agreement with the numerical solution provided by BAILLY ET AL. Furthermore, the mentioned authors claim that the described error is due to an incorrect calculation of the convolution in the analytical solution.

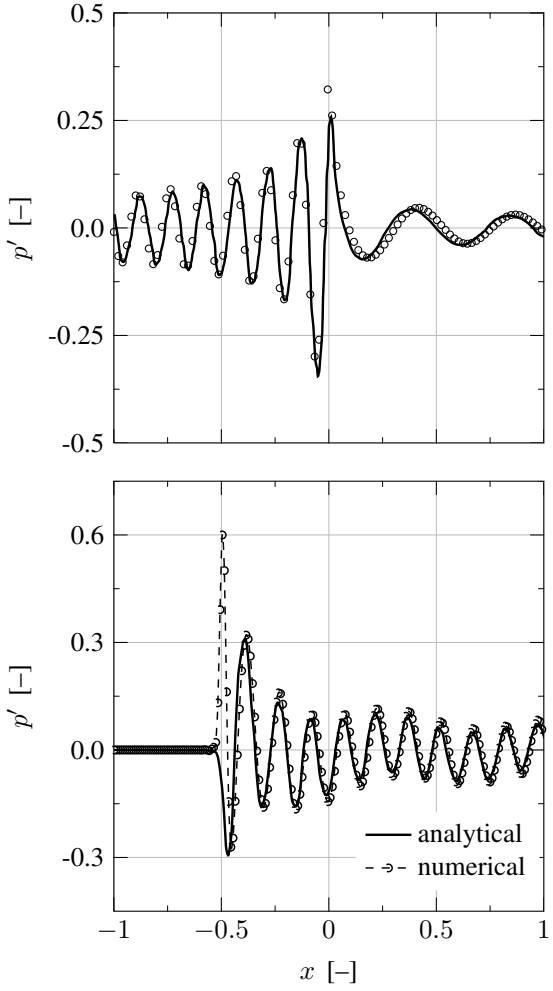

Figure 5. Comparison between analytical and numerical solution for a monopole source with subsonic and supersonic mean flow.

Wave propagation in a non-uniform mean flow

The second test case investigates the 2D wave propagation in a non-uniform sheared mean flow with velocity distribution given as follows:

$$u_0(x, y) = 0.5 c_\infty \cdot \tanh({}^{2y}/_{\delta_w}), \tag{15}$$

where the shear-layer thickness is denoted by the parameter δ_w which is either $\delta_w = 50$ or respectively $\delta_w = 10$. Since the thickness of the shear layer remains constant, no instability waves are excited in

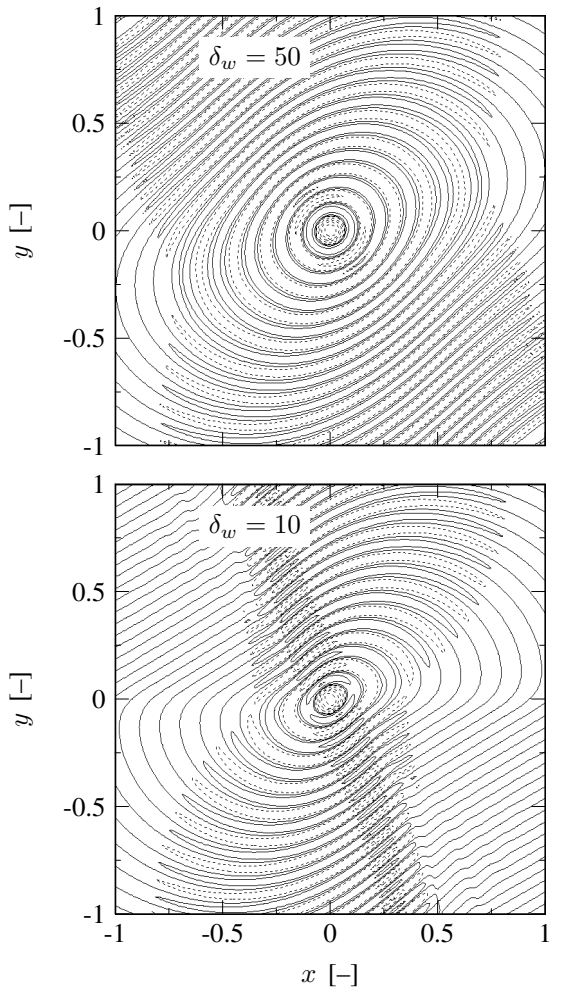

Figure 6. Contour lines of acoustic pressure with sheared mean flow at time $t = 180\,s$.

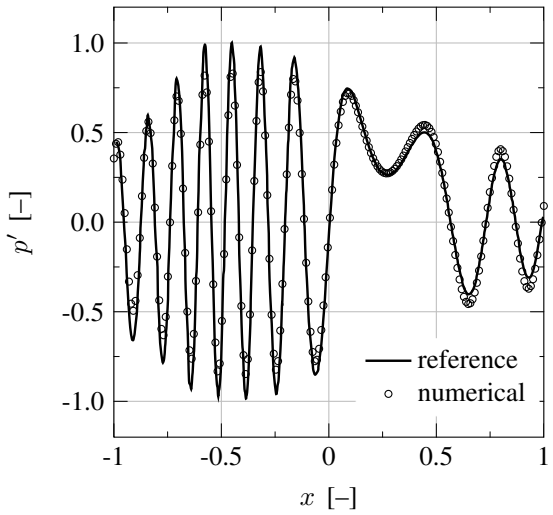

Figure 7. Comparison of sound pressure distribution at $y = 0.7$ and $t = 180\,s$ for $\delta_w = 50$.

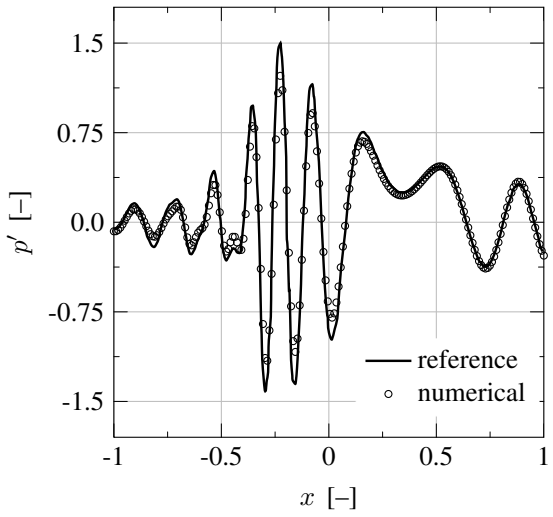

Figure 8. Comparison of sound pressure distribution at $y = 0.7$ and $t = 180\,s$ for $\delta_w = 10$.

the LEE and the acoustic computation shall proceed in a stable manner, see EWERT & SCHRÖDER [9]. Furthermore, the mean density is held to be constant to the value $\rho_0 = 1$ throughout the simulation. The computational domain comprises again 201×201 grid points, covering the domain from $[-1, 1] \times [-1, 1]$. The LEE are excited by an acoustic monopole source of the form presented in equation (14). Here, the parameters are given by $\epsilon = 1$, $\alpha = {}^{\ln(2)}/_{3^2}$ and the source is located in the origin of the domain at $(0, 0)$. Figure 6 shows snapshots of the acoustic pressure p' at time $t = 180$ $[s]$ for the examined shear-layer thicknesses. Figure 7 and 8 show the comparison between the reference solution, reported by EWERT & SCHRÖDER and the numerical solution. Although the tendency of the reference solution is gathered quite satisfactorily, the numerical solution underestimates the reference one in a slightly manner. Even though different mesh resolutions as well as different damping coefficients σ have been tested, it could not be clarified adequately, where the discrepancies come from.

Acoustic scattering from a circular cylinder

The next example demonstrates the accuracy of the implemented discretization schemes in a multi-domain framework, considering a 2D acoustic scattering problem from the Second CAA workshop on benchmark problems [15]. This problem models the sound field, generated by an propeller, and scattered off the fuselage of an aircraft. The fuselage is idealized by a circular cylinder with radius $r = 0.5$. The propeller is described by a pressure pulse with initial conditions

$$p_0(x, y)|_{t=0} = \mathrm{e}^{-\ln(2)(x-x_c)^2+(y-y_c)^2/(0.2)^2}, \tag{16}$$

at the center $(x_c, y_c) = (4, 0)$. As computational domain, a radial area extending from $r = 0.5$ to $r = 10.5$ with 202×302 grid points has been

chosen. Different boundary condition types have been selected: on the cylinder at $r = 0.5$ a wall boundary condition has been attached, whereas at the outer boundary at $r = 10.5$ a Char. BC can be found. Two numerical setups will be investigated: the first setup includes a single-block domain and the second one consists of a multi-block domain with a total of three blocks. Figure 9 shows contour lines of the acoustic pressure p' at different times. In the upper half of figure 9 the single-block simulation results can be observed, the lower half shows the multi-block simulations.

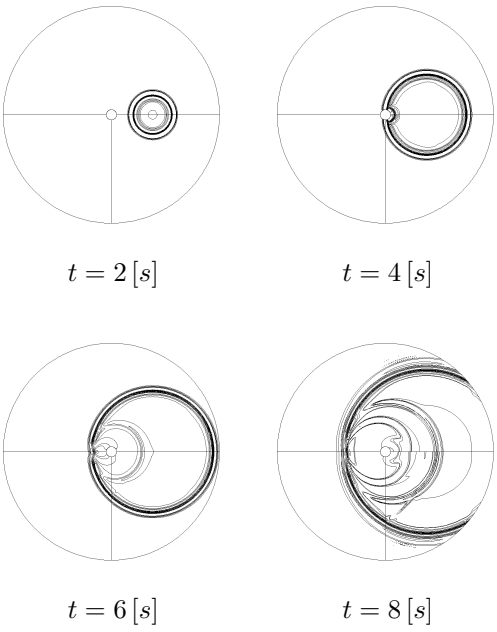

Figure 9. Contour lines of an acoustic pressure pulse at different times.

Overall, the simulation results in figure 9 show a good agreement with the reference results. Furthermore, the multi-block strategy produces similar results to the single-block simulation and seems to work well. At time $t = 8\ [s]$ small discrepancies can be observed, which is due to the number of overlapping grid layers used in the multi-block approach. As mentioned above, a 3-point overlap has been used throughout this work. An improvement can absolutely be achieved by increasing its number.

In addition, the unsteady pressure time history at four different points $A\big(x = 2, y = 0\big)$, $B\big(x = 2, y = 2\big)$, $C\big(x = 0, y = 2\big)$ and $D\big(x = -2, y = 0\big)$ can be investigated. The time series in Figure 10 are in good agreement in comparison to the reference solution, presented by SEO & MITTAL [14]. Little differences between single-block and multi-block simulation can be noticed.

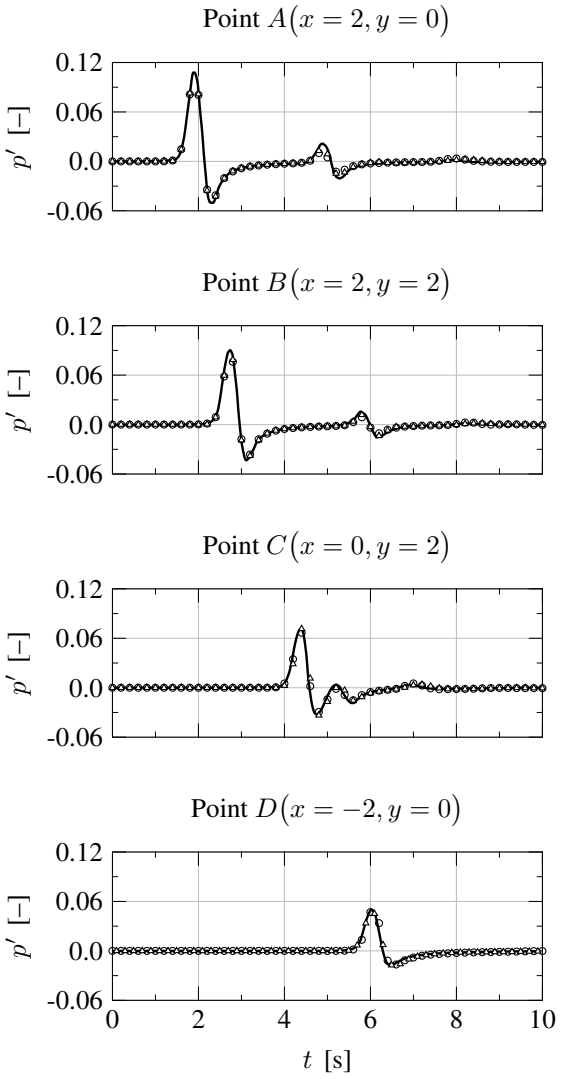

Figure 10. Time series of acoustic pressure at different observation points (—— reference solution, ◦ numerical solution on single-block domain, ▵ numerical solution on multi-block domain).

5. SUMMARY

A stable and consistent optimized low dissipation and low dispersion FD-solver for the numerical computation of acoustic phenomena in complex geometries has been presented. To ensure accuracy, all appearing terms of first order derivatives have been discretized by the same discretization method, achieved by a special optimization technique, for the first time introduced by TAM & WEBB. Also the coefficients for the temporal discretization scheme as well as the filter coefficients of the selective filter method were derived according to this optimization procedure. Furthermore, the developed solver is expanded by appropriate boundary conditions for walls and open boundaries. A block-structuring allows the usage of the developed solver on complex

geometries, which emerge in real-life applications. Due to the enhanced discretization stencils of the utilized numerical methods for spatial discretization, special treatment for data exchange at adjacent grid blocks is necessary. This can either be achieved by an overlapping grid technique or by utilizing optimized non-centered one-sided FD-schemes.
The implemented code is in good agreement with analytical and reference solutions. The presented examples demonstrate the ability to simulate accurate acoustic results in uniform and non-uniform mean flows. The considered results show very good agreement with the analytical reference solutions.
Finally, the applicability of the discussed coordinate transformation, simulating the acoustic propagation of an initial acoustic pressure pulse in the vicinity of a sound-reflecting cylinder using a cylindrical curvilinear mesh could be shown. The time plots show the assumed propagation behavior.

ACKNOWLEDGEMENTS

The authors of this paper would like to thank all co-workers at the FLM who supported this work by help and advice.

References

[1] C. Bailly and D. Juve. Numerical solution of acoustic propagation problems using linearized euler equations. *AIAA journal*, 38(1):22–29, 2000.

[2] J.P. Bérenger. A perfectly matched layer for the absorption of electromagnetic waves. *Journal of computational physics*, 114(2):185–200, 1994.

[3] J. Berland, C. Bogey, and C. Bailly. Optimized explicit schemes: matching and boundary schemes and 4th-order runge-kutta algorithm. *AIAA Pap*, 2814, 2004.

[4] J. Berland, C. Bogey, O. Marsden, and C. Bailly. High-order, low dispersive and low dissipative explicit schemes for multiple-scale and boundary problems. *Journal of Computational Physics*, 224(2):637–662, 2007.

[5] C. Bogey and C. Bailly. A family of low dispersive and low dissipative explicit schemes for flow and noise computations. *Journal of Computational Physics*, 194(1):194–214, 2004.

[6] W. De Roeck, W. Desmet, M. Baelmans, and P. Sas. On the prediction of near-field cavity flow noise using dif-ferent caa techniques. In *Proc. ISMA*, pages 369–388, 2004.

[7] GS Djambazov, CH Lai, and KA Pericleous. Staggered-mesh computation for aerodynamic sound. *AIAA journal*, 38(1):16–21, 2000.

[8] T. Emmert. *Development of a multidomain high-order algorithm for computational aeroacoustics: application to subsonic and transonic confined flows*. PhD thesis, École Centrale de Lyon, 2007.

[9] R. Ewert and W. Schröder. Acoustic perturbation equations based on flow decomposition via source filtering. *Journal of Computational Physics*, 188(2):365–398, 2003.

[10] B. Flurl. *Ein modulares Verfahren zur Simulation von Mehrfeldproblemen in Strömungsmaschinen*. PhD thesis, Technische Universität München, 2011.

[11] D.V. Gaitonde and M.R. Visbal. Padé-type higher-order boundary filters for the navier-stokes equations. *AIAA journal*, 38(11):2103–2112, 2000.

[12] A. Gantner. Optimization of radial turbomachinery runners using a genetic algorithm. In *The Fourteenth International Symposium on Transport Phenomena and Dynamics of Rotating Machinery (ISROMAC-14)*, 2012.

[13] F.Q. Hu. A stable, perfectly matched layer for linearized euler equations in unsplit physical variables. *Journal of Computational Physics*, 173(2):455–480, 2001.

[14] J.H. Seo and R. Mittal. A high-order immersed boundary method for acoustic wave scattering and low-mach number flow-induced sound in complex geometries. *Journal of Computational Physics*, 230(4):1000–1019, 2011.

[15] C.K.W. Tam and JC Hardin. Second computational aeroacoustics (caa) workshop on benchmark problems. 1997.

[16] C.K.W. Tam and J.C. Webb. Dispersion-relation-preserving finite difference schemes for computational acoustics. *Journal of Computational Physics*, 107:262–281, 1993.

[17] C.K.W. Tam, J.C. Webb, and Z. Dong. A study of the short wave components in computational acoustics. *Journal of Computational Acoustics*, 1(1):1–30, 1993.

[18] K.W. Thompson. Time dependent boundary conditions for hyperbolic systems. *Journal of Computational Physics*, 68(1):1–24, 1987.

[19] K.W. Thompson. Time-dependent boundary conditions for hyperbolic systems, ii. *Journal of Computational Physics*, 89(2):439–461, 1990.

[20] J.H. Williamson. Low-storage runge-kutta schemes. *Journal of Computational Physics*, 35(1):48–56, 1980.

Wall-bounded flows

Conference on Modelling Fluid Flow (CMFF'12)
The 15th International Conference on Fluid Flow Technologies
Budapest, Hungary, September 4-7, 2012

Development of a Model-Free Linear-Stability Analysis by a Time-Stepping Algorithm for Closed Geometries

Markus HAMIK[1], Hendrik C. KUHLMANN[2]

[1] Corresponding Author. Institute of Fluid Mechanics and Heat Transfer, Vienna University of Technology. Resselgasse 3, A-1040 Wien, Austria, Tel.: +43(1)58801-322 13, Fax: +43(1)58801-322 98, E-mail: markus.hamik@tuwien.ac.at
[2] Institute of Fluid Mechanics and Heat Transfer, Vienna University of Technology. E-mail: hendrik.kuhlmann@tuwien.ac.at

ABSTRACT

The aim of this investigation is a linear-stability analysis using a time-stepping algorithm. The current research phase focuses on comparison and validation of literature results based on examples of the lid-driven cavity flow with one-sided driving. For this system the basic flow is two-dimensional. Two- and three-dimensional test cases are considered, assuming periodic boundary conditions in spanwise direction. The critical mode can be either oscillatory or stationary depending on the aspect ratio of the cross-section of the cavity. To determine the critical Reynolds number the neutral Reynolds number must be minimised with respect to the wave number k.

To detect the neutral mode a variant of the dynamic mode decomposition (DMD) is used which is data-based and, therefore, model-free. The DMD is a variant of the Arnoldi method where the linearity of the method results from the definition of the Koopman operator, but not from an explicit linearisation. The present work is among the first investigations to compute the linear-stability from numerical simulation data by means of DMD. The present strategy can directly be applied to complex geometries as well. In the majority of cases considered the neutral modes of the lid-driven cavity computed compare very well with literature results.

Keywords: dynamic mode decomposition, Koopman modes, lid-driven cavity, linear-stability analysis, model-free approach, time-stepping algorithm

NOMENCLATURE

$\underline{\underline{C}}$	[−]	companion matrix
$\underline{\underline{\hat{C}}}$	[−]	least square system matrix
$\underline{\underline{D}}$	[−]	dissipation term
d	[−]	unit length
E	[−]	energy
I'	[−]	streamwise energy component
$\underline{\underline{K}}$	[−]	coefficient vector
$\underline{\underline{K}}^*$	[−]	index shifted coefficient vector
M	[−]	mesh number
M	[−]	Koopman operator
P	[−]	transport term
Re	[−]	Reynolds number
St	[−]	Strouhal number
$\underline{\underline{T}}$	[−]	Vandermonde matrix
$\underline{\underline{V}}$	[−]	linear combination vector matrix
$\underline{\underline{\hat{V}}}$	[−]	least square eigenvector matrix
c	[−]	coefficient for last snapshot
$\underline{c}$	[−]	coefficient vector for last snapshot
$\underline{e}$	[−]	unity vector
g	[−]	scalar observable
$\underline{g}$	[−]	vector observable
k	[−]	wave number
p	[−]	total flow pressure
$\underline{r}$	[−]	residual
t	[−]	time
Δt	[−]	time-step size
u	[−]	unit velocity magnitude
$\underline{u}$	[−]	total flow velocity vector
$\underline{v}$	[−]	linear combination vectors
Γ	[−]	aspect ratio
Δ	[−]	deviation
$\underline{\underline{\Lambda}}$	[−]	diagonal matrix of eigenvalues
ϕ	[−]	eigenfunction
λ	[−]	complex growth factor, eigenvalue
σ	[−]	growth rate
ω	[−]	oscillation frequency
$\underline{\xi}$	[−]	complete dynamical system
2D	[−]	two-dimensional
3D	[−]	three-dimensional

Subscripts and Superscripts

0	base flow, initial time-step
$\perp$	normal to streamline
$\parallel$	parallel to streamline
c	critical

e exponential definition
i row index
j column index, counting index
k snapshot counting index
n neutral
m number of snapshot time-steps
t time derivation
$\sim$ perturbation flow

1. INTRODUCTION

Traditional strategies of a global linear-stability analysis are difficult to parallelise and typically require a very large amount of working memory. Therefore, the size of the system (number of unknowns) that can be treated is comparatively small. This may lead to difficulties in resolving boundary layers or if the basic flow is complex. Moreover, conventional numerical linear-stability analyses have been carried out mainly using Cartesian or other fundamental geometries and the amount of work to adapt the problem to more general geometries was comparatively high.

It is the goal of this work to overcome these limitations. To that end a linear-stability method is developed which allows to analyse the flow in complex geometries and to treat large problems involving a large number of unknowns. Another goal is a certain flexibility and independence in code development. As a further step, it would be of advantage to be able to use the same algorithms for numeric and for experimental data analysis. As far as validation strategies are concerned the approach should allow using different computational fluid dynamics (CFD) codes (open source and commercial) to generate the data which are to be stability analysed.

In the present work a time-stepping approach provided by OpenFOAM [1] is adopted to obtain the numerical data. Integration is carried out through a transient phase up to a quasi-stationary or periodically oscillating flow state, whose flow data are then analysed regarding the stability of the reference flow state. Here the method is presented and applied to several test cases. In particular, the benchmark of a lid-driven cavity [2] is considered.

There exist quite a range of data-based methods for stability analysis. A short overview can be found in Schmid [3] who describes proper orthogonal decomposition (POD) and principal oscillation patterns (POP) or principal interaction patterns (PIP) as well as bi-orthogonal decomposition (BOD).

In Rowley et al. [4] Koopman modes and eigenvalues are discussed for linear and nonlinear flows with specialisations regarding periodic solutions and snapshot-based data-sets. Furthermore, the possibilities of DMD are demonstrated by application to a numerical example of a jet in crossflow. DMD results are compared to POD, direct numerical simulation (DNS) and linear global modes linearised about a steady-state solution, showing very good agreement with DNS.

In Schmid et al. [5] the principle of DMD is motivated and applied to experimental data of a helium jet. In a further step, several types of external forcing are applied to the jet by a loudspeaker and the corresponding DMD-spectra are analysed.

2. METHODS OF SOLUTION

The solution method is demonstrated employing the lid-driven cavity-flow system. In this section the theoretical concept of the stability analysis is explained in general, followed by a detailed description of the DMD method. Thereafter, the stability analysis is formulated. Finally, the evaluation of the kinetic energy budget is presented which is later used for a comparison of the stability results.

2.1. Data Generation

As a test the lid-driven cavity problem [2] is considered which is governed by the Navier-Stokes and continuity equations for an incompressible Newtonian flow in an infinite slab of rectangular cross section according to Eq. (1).

$$\underline{u}_t + \underline{u} \cdot \nabla \underline{u} = -\nabla p + Re^{-1} \Delta \underline{u} \qquad \nabla \cdot \underline{u} = 0 \quad (1)$$

The fluid motion is driven by a tangentially moving wall. In the present scaling the wall velocity and the length of the moving wall are unity. The cross-section of the plane in which the lid moves is characterised by the aspect ratio Γ, i.e. the depth of the cavity to the length of the moving wall. In spanwise direction periodic boundary conditions with period $2\pi/k$ are considered. For the pressure zero gradient boundary conditions are used at the solid walls.

The goal is the linear stability of a certain reference solution, here the steady two-dimensional flow. For typical initial conditions of the full temporal problem from Eq. (1) the early transient phase is not well-suited for the stability analysis, because the spectrum contains too many stable modes with large amplitude which decay rapidly. Best results are achieved by analysing a temporal period in which the amplitudes of the deviations from the reference state are slowly varying in time.

For the present calculations a variable time-step has been used with a constant maximum Courant number of 0.5. This was changed to a constant time-step as soon as the strong transients have decayed. From that instant, typically 200 equally-spaced snapshots of the velocity field (which may correspond to approximately five oscillation cycles in the case of a non-monotonic response) are recorded.

2.2. Stability

For the stability analysis the total flow $\underline{u}$ is decomposed into a steady basic flow $\underline{u}_0$ and a

perturbation flow $\underline{\tilde{u}}$ according to Eq. (2).

$$\underline{u} = \underline{u}_0 + \underline{\tilde{u}} \qquad p = p_0 + \tilde{p} \quad (2)$$

The steady basic flow satisfies Eq. (3) while the linearised equations for the perturbation flow $\underline{\tilde{u}}$ are according to Eq. (4) with suitable boundary conditions.

$$\underline{u}_0 \cdot \nabla \underline{u}_0 = -\nabla p_0 + Re^{-1} \Delta \underline{u}_0 \qquad \nabla \cdot \underline{u}_0 = 0 \quad (3)$$

$$\underline{\tilde{u}}_t + \underline{u}_0 \cdot \nabla \underline{\tilde{u}} + \underline{\tilde{u}} \cdot \nabla \underline{u}_0 = -\nabla \tilde{p} + Re^{-1} \Delta \underline{\tilde{u}} \qquad \nabla \cdot \underline{\tilde{u}} = 0 \quad (4)$$

In the traditional linear stability analysis the perturbation flow is expressed as a superposition of temporal normal modes given at Eq. (5).

$$\underline{\tilde{u}}(t) = e^{\lambda_e t} \underline{\tilde{u}}(t_0) \quad (5)$$

Here λ_e represents a complex growth factor whose real part is the growth rate and the imaginary part is the oscillation frequency. For a neutral mode the growth rate becomes zero. The complex growth factors λ_e are functions of the Reynolds number Re which is considered the control parameter and, in the three-dimensional case, also of the wave number k. Additional parameters are suppressed in the following as shown in Eq. (6).

$$\lambda_e = \sigma_e + i\omega_e = f(Re, k) \quad (6)$$

The critical Reynolds number is the minimum of all discrete neutral Reynolds numbers minimised with respect to k. The aim of the current work is the detection of critical states.

2.3. Dynamic Mode Decomposition

Here the DMD (Schmid [3], Rowley et al. [4]) is used. According to Rowley et al. [4] one can start with a general nonlinear dynamical system according to Eq. (7).

$$\underline{\xi}_{k+1} = \underline{f}\left(\underline{\xi}_k\right) \quad (7)$$

Here $\underline{f}$ describes the evolution of the system between two time-steps as $k \rightarrow k+1$. The evolution of any scalar observable g can be described by Eq. (8) where M is called the Koopman operator. Its eigenfunctions ϕ_j and eigenvalues λ_j satisfy Eq. (9).

$$Mg\left(\underline{\xi}\right) = g\left[\underline{f}\left(\underline{\xi}\right)\right] \quad (8)$$

$$M\phi_j\left(\underline{\xi}\right) = \lambda_j \phi_j\left(\underline{\xi}\right) \qquad j = 1, 2, \ldots \quad (9)$$

In the dynamical system Eq. (7) $\underline{\xi}$ is the total amount of data necessary to describe the flow field. A general vector valued observable $\underline{g}$, like e.g. the velocity vector field, can be written as a linear combination of eigenfunctions ϕ_j weighted by vectors $\underline{v}_j$ according to Eq. (10).

$$\underline{g}\left(\underline{\xi}\right) = \sum_{j=1}^{\infty} \phi_j\left(\underline{\xi}\right) \underline{v}_j \quad (10)$$

Owing to the eigenfunction representation of $\underline{g}$ a single time-step corresponds to an eigenvalue multiplication. Thus $\underline{g}\left(\underline{\xi}_k\right)$ at time k can be expressed through the first time-step $k = 0$ leading to Eq. (11).

$$\underline{g}\left(\underline{\xi}_k\right) = \sum_{j=1}^{\infty} \lambda_j^k \phi_j\left(\underline{\xi}_0\right) \underline{v}_j \quad (11)$$

Now $\underline{g} = \underline{u}$ is identified as the velocity vector and ϕ_j is incorporated into $\underline{v}_j$ by defining $\underline{v}'_j = \phi_j \underline{v}_j$. For a finite system, truncated at $j = m$, Eq. (12) is obtained, after dropping the prime.

$$\underline{u}_k = \sum_{j=1}^{m} \lambda_j^k \underline{v}_j \qquad k = 0, \ldots, m-1 \quad (12)$$

As there are m linear combination vectors $\underline{v}$ to fit $m+1$ velocity vectors, only m velocity vectors can be constructed exactly using the basis of the $\underline{v}_j$. Since the last velocity vector in Eq. (13) has a residual directed outward the dimension space spanned by $\underline{v}_j$, it is as small as possible.

$$\underline{u}_m = \sum_{j=1}^{m} \lambda_j^m \underline{v}_j + \underline{r} \qquad \underline{r} \perp \operatorname{span}\left(\underline{u}_0, \ldots, \underline{u}_{m-1}\right) \quad (13)$$

With the definition of a snapshot basis $\underline{\underline{K}} = \left[\underline{u}_0 \ldots \underline{u}_{m-1}\right]$ and a coefficient vector $\underline{c} = [c_0 \ \ldots \ c_{m-1}]^T$ for the last snapshot one can write the last velocity vector as follows in Eq. (14).

$$\underline{u}_m = \underline{\underline{K}}\underline{c} + \underline{r} \qquad \underline{r} \perp \operatorname{span}\left(\underline{u}_0, \ldots, \underline{u}_{m-1}\right) \quad (14)$$

From the coefficient vector $\underline{c}$ a companion matrix as in Eq. (15) can be constructed. The companion matrix $\underline{\underline{C}}$ can be diagonalised by a Vandermonde matrix $\underline{\underline{T}}$ and a diagonal matrix $\underline{\underline{\Lambda}}$ with eigenvalues λ of $\underline{\underline{C}}$ on its diagonal as defined in Eq. (16).

$$\underline{\underline{C}} = \begin{bmatrix} 0 & 0 & \cdots & 0 & c_0 \\ 1 & 0 & \cdots & 0 & c_1 \\ 0 & 1 & & 0 & c_2 \\ \vdots & & \ddots & & \vdots \\ 0 & 0 & & 1 & c_{m-1} \end{bmatrix} \quad (15)$$

$$\underline{\underline{T}}_{ij} = \lambda_i^{j-1} \qquad \underline{\underline{\Lambda}} = \operatorname{diag}(\lambda_1, \ldots, \lambda_m) \quad (16)$$

With the definition of $\underline{\underline{V}} = \left[\underline{v}_1 \ldots \underline{v}_m\right]$ as a Ritz vector matrix, calculated from the companion matrix

$\underline{\underline{C}}$, an index shifted matrix $\underline{\underline{K}}_* = \left[\underline{u}_1 \ldots \underline{u}_m\right]$ and the unit vector $\underline{e} = [0 \ldots 0 \;\; 1]^{\mathrm{T}}$, Eq. (17) is obtained.

$$\underline{\underline{K}}_* = \underline{\underline{KC}} + \underline{re}^T = \underline{\underline{KT}}^{-1}\underline{\underline{\Lambda T}} + \underline{re}^{\mathrm{T}} \tag{17}$$

From Eq. (12) one obtains Eq. (18).

$$\underline{\underline{K}} = \underline{\underline{VT}} \tag{18}$$

Eq. (18) enables to write the problem as in Eq. (19).

$$\underline{\underline{K}}_* = \underline{\underline{V\Lambda T}} + \underline{re}^{\mathrm{T}} \tag{19}$$

2.4. Implementation

The formulation presented above is mathematically correct. It could be implemented if the eigenvalues λ_j in Eq. (12) are non-degenerate and the coefficient vector $\underline{c}$ could be computed using a pseudo-inverse where the column vectors of $\underline{\underline{K}}$ need to be linearly independent. Unfortunately, this formulation is numerically ill-conditioned. Several strategies have been suggested to circumvent this problem. Among these are the singular-value-decomposition approach of Schmid [3] and the optimised DMD approach of Chen et al. [6]. Within the present formulation Eq. (20) is solved for $\underline{\underline{\hat{C}}}$ in a least square sense.

$$\underline{\underline{K\hat{C}}} = \underline{\underline{K}}_* \tag{20}$$

Defining $\underline{\underline{\hat{V}}}$ as the eigenvector matrix of $\underline{\underline{\hat{C}}}$ the eigenvectors of the original system can be calculated according to Eq. (21) in order to get the right size of the vector set.

$$\underline{\underline{V}} = \underline{\underline{K\hat{V}}} \tag{21}$$

The eigenvalues λ_j of $\underline{\underline{\hat{C}}}$ satisfy Eq. (22).

$$\underline{\tilde{u}}(t) = \lambda^{t/\Delta t}\underline{\tilde{u}}(t_0) \tag{22}$$

They are equivalent to the eigenvalues of the original system from Eq. (12). The definition of the eigenvalues differs here from the definition of the complex grow factors in Eq. (5). By comparison one gets Eq. (23).

$$\lambda_{\mathrm{e}} = \frac{\ln \lambda}{\Delta t} \tag{23}$$

This expression is used to determine the growth rates and the oscillation frequencies. To detect the dominant perturbation mode the complex modes are ranked according to their energy content. The first mode in this list represents the base flow as a time averaged mean, the second mode is identified as the dominant perturbation mode. The linear-stability analysis is implemented using the finite volume CFD code OpenFOAM [1] and the MKL library [7]. The point of neutral stability is approximated using bisection. The interval endpoint with smaller growth rate magnitude is used as the neutral state.

2.5. Energy Budget

The energy analysis is introduced here for the purpose of comparison only. By left-multiplication of the Navier-Stokes equation Eq. (4) and application of Gauss' theorem one obtains the Reynolds-Orr equation in Eq. (24).

$$\frac{dE\left(\underline{\tilde{u}}\right)}{dt} = P\left(\underline{\tilde{u}}\right) - Re^{-1}D\left(\underline{\tilde{u}}\right) \tag{24}$$

D is the viscous dissipation while the energy production P is the amount of energy being transferred between the basic and the perturbation flow. It is useful to formulate the energy production terms in a local coordinate system which is aligned with the flow. To that end the perturbation velocity is decomposed as in Eq. (25), where $\underline{\tilde{u}}_{\parallel}$ is the projection of the velocity vector onto the streamline and $\underline{\tilde{u}}_{\perp}$ the velocity component normal to it.

$$\underline{\tilde{u}}_{\parallel} = \frac{\left(\underline{\tilde{u}} \cdot \underline{u}_0\right)\underline{u}_0}{\underline{u}_0^2} \qquad \underline{\tilde{u}}_{\perp} = \underline{\tilde{u}} - \underline{\tilde{u}}_{\parallel} \tag{25}$$

Using this notation, the Reynolds-Orr equation can be written as in Eq. (26).

$$\begin{aligned} \frac{Re}{D\left(\underline{\tilde{u}}\right)}\frac{dE\left(\underline{\tilde{u}}\right)}{dt} &= -1 + I_1' + I_2' + I_3' + I_4' = \\ &= -1 - \Big[\underline{\tilde{u}}_{\perp}\left(\underline{\tilde{u}}_{\perp} \cdot \nabla \underline{u}_0\right) + \underline{\tilde{u}}_{\parallel}\left(\underline{\tilde{u}}_{\perp} \cdot \nabla \underline{u}_0\right) + \\ &+ \underline{\tilde{u}}_{\perp}\left(\underline{\tilde{u}}_{\parallel} \cdot \nabla \underline{u}_0\right) + \underline{\tilde{u}}_{\parallel}\left(\underline{\tilde{u}}_{\parallel} \cdot \nabla \underline{u}_0\right)\Big]\frac{Re}{D\left(\underline{\tilde{u}}\right)} \end{aligned} \tag{26}$$

Albensoeder [8] has shown that the production term I_2' plays a dominant role in the one-sided lid-driven cavity. Therefore, it may be considered separately from the sum of the energy transfer rates.

3. CODE VERIFICATION

In order to validate the present method three cases are considered: (I) The 2D lid-driven square cavity, (II) the 3D lid-driven square cavity and (III) the 3D lid-driven cavity with aspect ratio $\Gamma = 0.5$. It is aimed at detecting a neutral mode and the associated neutral Re for a fixed wave number.

3.1. 2D Lid-Driven Square Cavity

The problem is solved on a grid with 128^2 cells which are refined towards the boundaries. The initial velocity and pressure conditions are zero-fields except for the velocity-component in direction of the moving wall where a value of 10^{-4} is used. Figure 1 shows the growth factor eigenvalues $\lambda = \sigma + \mathrm{i}\omega$ according to Eq. (22) and for $Re = 8067$. The eigenvalues approximate a unit circle. The size of the symbols is correlated to energy content of the respective eigenmodes with the largest symbols corresponding to the most energetic modes. If $|\lambda| \leq 1$ the mode is decaying and basic state is considered

stable with respect to this mode. The eigenvalue corresponding to the base flow is located at $\lambda = 1+0\mathrm{i}$. Its linear-stability is determined by the second largest circle in Fig. 1 being located either inside (stable) or outside (unstable) the unit circle.

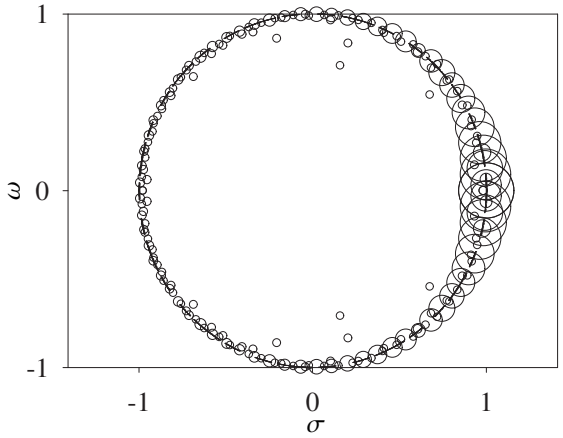

Figure 1. Spectrum of λ for $\Gamma = 1$, $Re = 8067$, 2D case

Figure 2 displays the modal energies on a logarithmic scale as function of the scaled frequency, i.e. the Strouhal number defined in Eq. (27).

$$St = \frac{\omega_e d}{u} \tag{27}$$

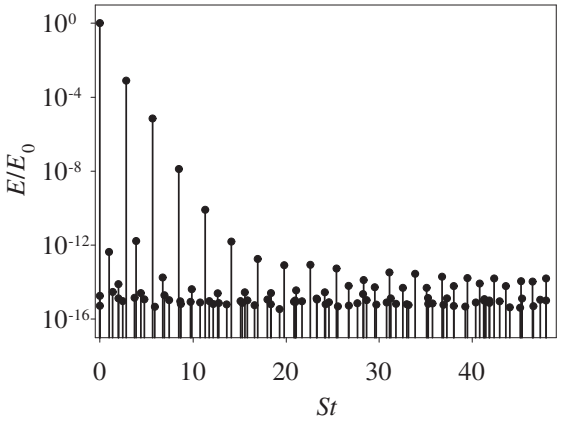

Figure 2. Modal energies as function of St for $\Gamma = 1$, $Re = 8067$, 2D case

The energies are normalised by the energy of the base flow E_0. For the present test case a good signal-to-noise ratio is found as the noise level is about 10^{-14} and the normalised energy content of the critical mode is 10^{-3}. Streamlines of the most unstable mode are shown in Figure 3. They compare very well with those obtained by Poliashenko and Aidun [9] which are reproduced in Figure 4.

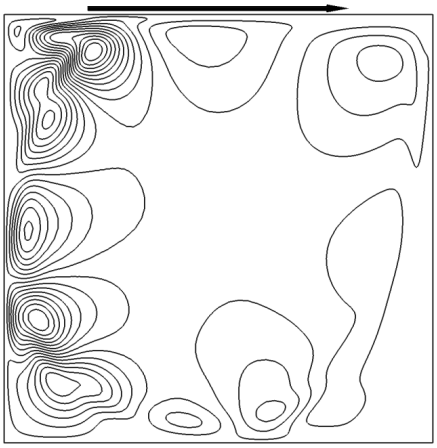

Figure 3. Streamlines of $\tilde{\underline{u}}$ for $\Gamma = 1$, $Re = 8067$, 2D case. The arrow indicates the lid motion.

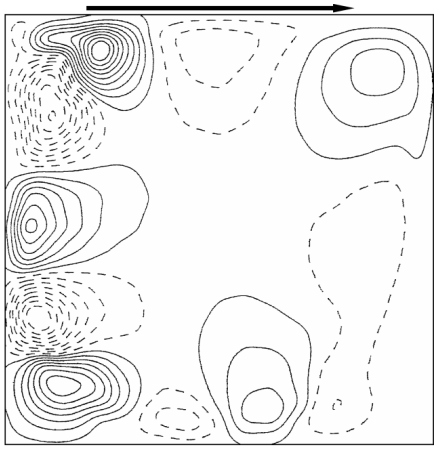

Figure 4. Streamlines of $\tilde{\underline{u}}$ after [9] for $\Gamma = 1$, $Re = 7763$, 2D case. The arrow indicates the lid motion. Dashed lines correspond to negative values of the perturbation stream function.

By variation of Re a critical Reynolds number of $Re_c = 8067$ is found in the present work. A comparison of the critical Reynolds numbers and oscillation frequencies found by other investigators along with the respective deviations is made in Table 1. The maximum deviation among all data is less than 6% and the present data are well within the range of the literature data. The relative uncertainty in Re due to the bisection algorithm is less than 0.02% and the neutral growth rate is of order 10^{-5}.

3.2. 3D Lid-Driven Square Cavity

For the 3D square cavity a grid with 64^2 cells in the cross-section defined by the lid motion is employed and 40 cells in spanwise direction in which periodic boundary conditions are assumed with period $2\pi/k$ where k is the wave number.

Table 1. Critical data for the 2D square-cavity flow compared with literature data. M1 to M3 indicate different grids.

Author	Re_c	$\omega_{e,c}$	ΔRe_c	$\Delta\omega_{e,c}$
[9] M2	7615	2.896	5.6%	2.5%
[9] M3	7763	2.863	3.8%	1.3%
[10]	7819		3.1%	
[11]	8000	2.836	0.8%	0.4%
[12]	8045		0.3%	
Present	8067	2.825		
[13] M3	8070	2.825	0.0%	0.0%
[13] M2	8109	2.826	0.5%	0.0%
[9] M1	8196	2.925	1.6%	3.5%
[13] M1	8245	2.832	2.2%	0.2%

The initial velocity and pressure conditions are zero-fields except for the velocity-component in periodic direction where a value of 10^{-4} is used. In Figure 5 the eigenvalues are shown for $Re = 803$ and $k = 15.4$. They line-up along the unit circle as in the 2D case. The corresponding neutral mode is stationary.

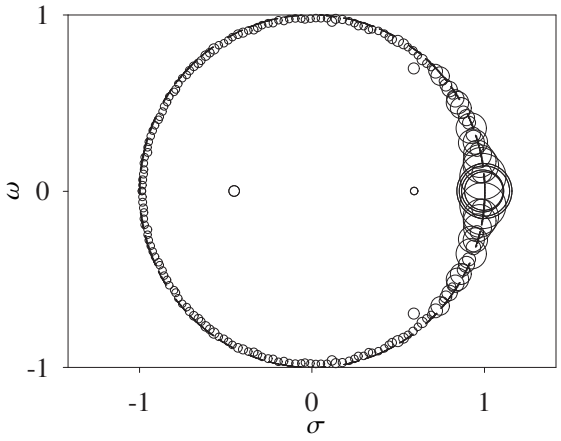

Figure 5. Spectrum of λ for $\Gamma = 1$, $Re = 803$, 3D case

Many modes with higher energy content can be found near $\lambda = 1 + 0\mathrm{i}$. The low energy modes near $\lambda = -1 + 0\mathrm{i}$ represent oscillations with period $2\Delta t$ and thus indicate numerical oscillations which are unphysical. Again, the signal-to-noise ratio is quite large as can be seen in Figure 6. The noise has an order of magnitude near 10^{-23} while the energy content of the neutral mode is of order 10^{-13}. The energy content of the dominant numerically oscillating mode is eleven orders of magnitude smaller than the one of the neutral mode.

Figure 7 shows perturbation flow velocity vectors of the neutral mode at the centre of the cavity in a plane parallel to the moving wall. The greyscale

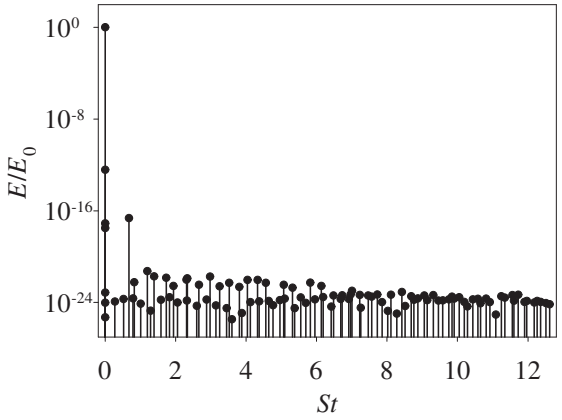

Figure 6. Modal energies as function of St for $\Gamma = 1$, $Re = 803$, 3D case

indicates the value of the energy production term I_2'. For comparison, the corresponding result of Albensoeder [8] is reproduced in Figure 8.

Figure 7. Velocity field $\tilde{\underline{u}}$ and I_2' (greyscale) for $\Gamma = 1$, $Re = 803$, 3D case

Figure 8. Velocity field $\tilde{\underline{u}}$ after [8] and I_2' (greyscale) for $\Gamma = 1$, $Re = 786$, 3D case

The main vortical structures on the right side are well reproduced by the present method as are the weak vortices on the left. An isosurface of the energy production rate I_2' and the corresponding surface obtained by [8] are shown in Figures 9 and 10, respectively. Both the major banana-like hypersurfaces and the flat hypersurfaces attached to the moving wall on the left are well reproduced. The cylindrical structure in Fig. 10 represents an isosurface of the basic flow not included in Fig. 9.

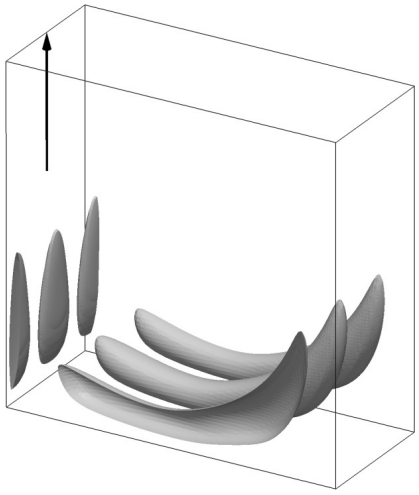

Figure 9. Isosurface of I_2' for $\Gamma = 1$, $Re = 803$, 3D case. The arrow indicates the lid motion.

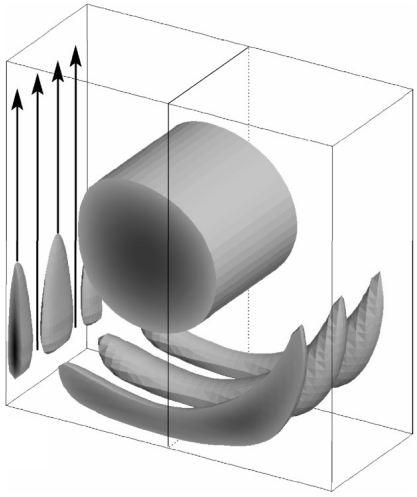

Figure 10. Isosurface of I_2' after [8] for $\Gamma = 1$, $Re = 786$, 3D case. The arrow indicates the lid motion.

Table 2 provides a comparison of the critical Reynolds numbers. They deviate less than 3% from each other. The critical mode is stationary in all cases. Here Re_c has not been minimised with respect to k, k_c was rather adopted from [8].

Table 2. Critical data for the 3D square-cavity flow compared with literature data

Author	Re_c	$\omega_{e,c}$	k_c	ΔRe_c	$\Delta\omega_{e,c}$
[12]	784	0.0	15.5	2.4%	0.0%
[8]	786	0.0	15.4	2.1%	0.0%
Present	803	0.0	15.4		

3.3. 3D Lid-Driven Cavity with $\Gamma = 0.5$

For $\Gamma = 0.5$ the 3D critical mode is oscillatory. The number of grid points used was 96^2 cells in the cross-section defined by the lid motion and 60 cells in spanwise direction. The initial velocity and pressure conditions are zero-fields except for the velocity-component in periodic direction where a value of 10^{-4} is used. The data acquisition for the stability analysis was initiated after approximately 100 rotation times for all cases considered. The eigenvalues at neutral conditions for $Re = 721$ and $k = 10.6$ are shown in Figure 11.

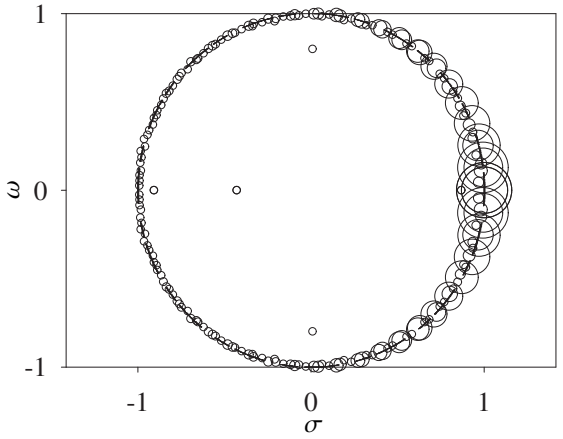

Figure 11. Spectrum of λ, $\Gamma = 0.5$, $Re = 721$, 3D case

The distribution of the eigenvalues is similar to the 2D case shown in Fig. 1. The neutral mode is even easier to identify from Figure 12, since the relative amplitude of order 10^{-6} is well above the noise level which is of the order of 10^{-15}.

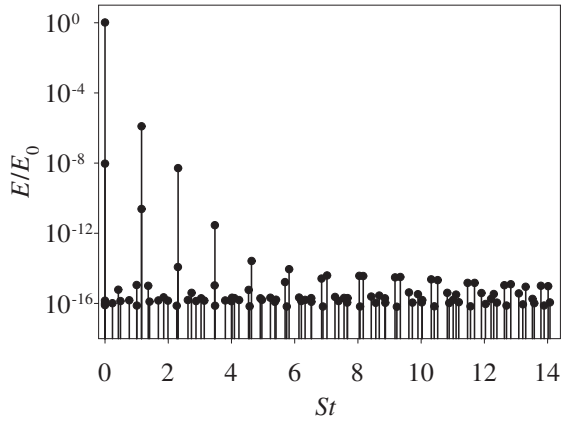

Figure 12. Modal energies as function of St for $\Gamma = 0.5$, $Re = 721$, 3D case

An isosurface of the velocity magnitude of the neutral mode is shown in Figure 13. The neutral

mode is organised around the basic vortex, which is located in half of the cavity downstream of the moving lid, and extends into the upstream half of the cavity in the form of fingers.

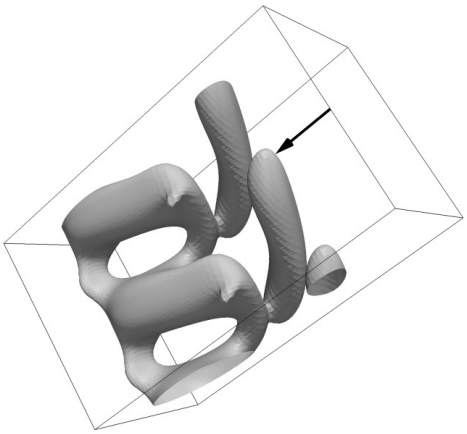

Figure 13. Isosurface of $\left\|\tilde{\underline{u}}\right\|$ for $\Gamma = 0.5$, $Re = 721$, 3D case. The arrow indicates the lid motion.

A comparison with the critical data of [8] shown in Table 3 indicates a good agreement. The deviation of the present neutral data from the critical Reynolds number and oscillation frequency is less than 2.5% and 0.5%, respectively. The length of the interval used for the bisection of the Reynolds number has been selected smaller than 0.8% of the Reynolds number and the residual growth rate is of order 10^{-3} for both 3D cases considered, $\Gamma = 1$ and 0.5.

Table 3. Critical data for the 3D cavity flow for $\Gamma = 0.5$ compared with literature data

Author	Re_c	$\omega_{e,c}$	k_c	ΔRe_c	$\Delta\omega_{e,c}$
[8]	706	1.161	10.6	2.1%	0.3%
Present	721	1.158	10.6		

4. CONCLUSIONS

The dynamic mode decomposition is a competitive method for the detection of dominant and coherent flow structures from experimental or numerical data-sets. A successful application requires a proper conditioning/selection of the time-series data. Some difficulties are caused by numerical oscillations of high frequency to get smoother time dependence. Despite of these difficulties, neutral stability data have been obtained which compare very well with previously reported results. This holds true, at least qualitatively, also for the comparison of the neutral/critical flow pattern and corresponding energy transfer rates. An important advantage of the present approach is the ease of application to flows in more complex domains, as the computations can be based on existing and general purpose computer codes.

References

[1] OpenCFD Ltd. 2010 *OpenFOAM User Guide Version 1.7.1*.

[2] Albensoeder, S., Kuhlmann, H., and Rath, H. 2001 "Three-dimensional centrifugal-flow instabilities in the lid-driven cavity problem". *Phys Fluid*, Vol. 13, pp. 121–135.

[3] Schmid, P. 2010 "Dynamic mode decomposition of numerical and experimental data". *J Fluid Mech*, Vol. 656, pp. 5–28.

[4] Rowley, C., Mezic, I., Bagheri, S., Schlatter, P., and Henningson, D. 2009 "Spectral analysis of nonlinear flows". *J Fluid Mech*, Vol. 641, pp. 115–127.

[5] Schmid, P., Li, L., Juniper, M., and Pust, O. 2011 "Applications of the dynamic mode decomposition". *Theor Comp Fluid Dyn*, Vol. 25, pp. 249–259.

[6] Chen, K., Tu, J., and Rowley, C. 2012 "Variants of dynamic mode decomposition: boundary condition, Koopman, and Fourier analyses". *J Nonlinear Sci*, p. 29, doi 10.1007/s00332-012-9130-9.

[7] Intel Inc. 2011 *Intel Math Kernel Library for Linux OS User's Guide, Version 10.3*.

[8] Albensoeder, S. 2004 "Lineare und nichtlineare Stabilität inkompressibler Strömungen im zweiseitig angetriebenen Rechteckbehälter". Ph.D. thesis, Universität Bremen, Fachbereich Produktionstechnik.

[9] Poliashenko, M. and Aidun, C. 1995 "A direct method for computation of simple bifurcations". *J Comput Phys*, Vol. 121, pp. 246–260.

[10] Cazemier, W., Verstappen, R., and Veldman, A. 1998 "Proper orthogonal decomposition and low-dimensional models for driven cavity flows". *Phys Fluid*, Vol. 10, pp. 1685–1699.

[11] Fortin, A., Jardak, M., Gervais, J., and Pierre, R. 1997 "Localization of Hopf bifurcations in fluid flow problems". *Int J Numer Meth Fluid*, Vol. 24, pp. 1185–1210.

[12] Non, E., Pierre, R., and Gervais, J. 2006 "Linear stability of the three-dimensional lid-driven cavity". *Phys Fluid*, Vol. 18, 084103.

[13] Sahin, M. and Owens, R. 2003 "A novel fully-implicit finite volume method applied to the lid-driven cavity problem. Part II. Linear stability analysis". *Int J Numer Meth Fluid*, Vol. 42, pp. 79–88.

Conference on Modelling Fluid Flow (CMFF'12)
The 15th International Conference on Fluid Flow Technologies
Budapest, Hungary, September 4-7, 2012

Bead-spring and bead-rod models for dsDNA mechanics in fluid flow

Mátyás BENKE,[1] Evgeniy SHAPIRO, [2] Dimitris DRIKAKIS [3]

[1] BHR Group, The Fluid Engineering Centre, Cranfield, UK. E-mail: mbenke@bhrgroup.co.uk
[2] Corresponding Author. Ricardo Software, Ricardo UK Limited, ShorehambySea, West Sussex, BN43 5FG, UK. E-mail: evgeniy.shapiro@ricardo.com
[3] Department of Fluid Mechanics and Computational Science, School of Engineering, Cranfield University, Cranfield, UK. E-mail: d.drikakis@cranfield.ac.uk

ABSTRACT

Due to their unique biological function, double-stranded DNA (dsDNA) molecules have received significant scientific attention in comparison with other biopolymers. An aspect of particular interest in a number of applications, including biosensors, molecular manufacturing and protein recognition techniques, is the dynamic behaviour of dsDNA molecules in fluid flow. The paper presents a new mesoscale modelling approach to the investigation of dsDNA molecules motion in fluid flow. The proposed method is based on the coupling of the Computational Fluid Dynamics (CFD) with the mechanical bead-spring model for dsDNA. It includes the effects of inertia and is capable of capturing accurately dsDNA mechanical properties in the relaxation and stretching processes. The accuracy of the proposed method is explored through comparisons with the published experimental data.

Keywords : DNA mechanics, modeling of DNA

1. INTRODUCTION

The range of applications of micro- and nanofluidic technology is rapidly expanding, driven by the increasing demand for high-precision medical and pharmaceutical devices [1]. Systems capable of operating with single macromolecules or dilute solutions of macromolecules are of particular interest in biological and medical applications, such as protein crystallisation [2] and bio-detection [3]. Physical processes occuring in these liquid-based systems cover a wide range of time and length scales (e.g. [4, 5]). Biochemical interactions, such as DNA-protein binding, occur on atomistic time and length scales [6, 7], whereas the transport of macromolecules is mainly governed by the flow field of the carrier liquid at the continuum scale [8, 9]. Furthermore, the motion and deformation of individual macromolecules occurs at mesoscopic scales [10, 11, 12], which are especially important when considering manipulation techniques, separators and focusing devices (e.g. [12, 8]).

The mesoscopic processes present a significant

NOMENCLATURE

$\boldsymbol{F}_n$	$[N/m^3]$	volume force acting on the fluid
$\boldsymbol{R}_{x,n}$	$[-]$	random displacement vector
$\boldsymbol{R}_{v,n}$	$[-]$	random velocity vector
T	$[K]$	temperature
a	$[m]$	segment length
b_n	$[m]$	bead radius
$\boldsymbol{f}_n$	$[N]$	total force acting on bead
k_B	$[J/K]$	Boltzmann constant
m_n	$[kg]$	bead mass
$\boldsymbol{n}$	$[-]$	unit vector
$\boldsymbol{r}_n$	$[m]$	bead position
t	$[s]$	time
$\boldsymbol{u}$	$[m/s]$	fluid velocity
$\boldsymbol{v}_n$	$[m/s]$	bead velocity
γ_n	$[1/s]$	phenomenological relaxation time
η	$[Pas]$	dynamic viscosity
$\boldsymbol{\omega}_n$	$[N]$	hydrodynamic force
$\boldsymbol{\phi}_n$	$[N]$	non-hydrodynamic force
$\boldsymbol{\varphi}_n$	$[N]$	Brownian force
∇p	$[Pa/m]$	pressure gradient
δ	$[-]$	Dirac operator
δ_ϵ	$[1/m^3]$	Smoothed Dirac function
λ_p	$[m]$	persistence length of the DNA
$\hat{x}$	$[-]$	fractional chain extension
σ	$[kgm/\sqrt{s^3}]$	amplitude of fluctuation
χ	$[-]$	number of persistence lengths represented by a spring

Subscripts and Superscripts

n	particle index
imp	indicator of impact

challenge from the modelling perspective due to the coupling of a wide range of length and timescales. While not impossible theoretically, the direct resolution of smallest scales involved in mesoscopic processes is not feasible when the computational resource requirements are considered. An alternative approach can be suggested based on a conceptual representation of the macromolecule as a mechanical structure with prescribed properties. This approach has been sucessfully employed in polymer science in order to model bulk properties of polymer solutions (e.g. [13]). The same idea is employed in the Brownian Dynamics (BD) methods (e.g. [14] which have been extensively used to determine macroscopic properties of solutions [15, 16], model the dynamics of DNA molecules [17, 18, 19] and investigate the migration of large molecules [20]. However BD methods rely on a negligible inertial force, which restricts the applications of BD methods to solvent flows without significant gradients and temporal variations of the velocity field.

In order to address these issues, a mesoscale modelling approach has been proposed based on the complete equations of motion for flexible macromolecules (e.g. [21, 22, 23, 24]). The technique has been explored qualitatitevely in these studies and the associated numerical methods have been verified against an analytical solution by Benke et al. [24], however no detailed experimental validation for flexible macromolecules has been reported to date.

In the present paper the validation of the mesoscale model developed for flexible molecules is reported based on experiments of Stein et al. [9]. The model is then modified to account for the elastic properties of dsDNA. The modified model is verified using an analytic solution and validated using experimental data of Perkins et al. [10].

2. MODEL FORMULATION

The modeling method is based on an individual treatment of large solute molecules, which can be coupled with the cumulative ensemble description of the solvent molecules on the continuum scale. Each macromolecule is represented by a mechanical structure incorporating a set of beads connected with freely rotating, non-extensible rods or elastic springs. The type of the connecting element depends on the elastic properties of the macromolecule in question. The beads act as centers for the external and internal forces and the connecting elements provide a method to control the structure and the elastic properties of the molecule. The motion of each bead n with the mass m_n is described by the Langevin equation written as

$$m_n \frac{d^2 \boldsymbol{r}_n}{dt^2} = \boldsymbol{f}_n \,, \tag{1}$$

where $\boldsymbol{f}_n$ represents the total force acting on the n_{th} bead. The force acting on the bead in a dilute solution can be decomposed as follows

$$\boldsymbol{f}_n(t) = \boldsymbol{\omega}_n(t) + \boldsymbol{\phi}_n(t) + \boldsymbol{\varphi}_n(t), \tag{2}$$

where $\boldsymbol{\omega}$, $\boldsymbol{\phi}$ and $\boldsymbol{\varphi}$ denote the hydrodynamic forces, the non-hydrodynamic forces and the random Brownian force respectively. The major contributor to the hydrodynamic forces acting on the macromolecule is the drag force which can be written as

$$\boldsymbol{\omega}_n(t) = m_n \gamma_n \left(\boldsymbol{u}(\boldsymbol{r}_n, t) - \boldsymbol{v}_n(t) \right). \tag{3}$$

Here, $\boldsymbol{u}(\boldsymbol{r}_n)$ is the fluid velocity at the bead position $\boldsymbol{r}_n$ and $\boldsymbol{v}_n$ denotes the velocity of the bead. The Reynolds number based on an individual bead radius is typically very small and assuming the Stokes experssion for the drag force in the equation (3), the friction coefficient can be expanded as

$$m_n \gamma_n = 6\pi\eta b_n \tag{4}$$

where b_n is the hydrodynamic equivalent radius of the bead and η is the dynamic viscosity of the carrier liquid.

The random Brownian force represents the effect of the solvent molecules stochastically colliding with the beads and exchanging momentum. This force possesses Gaussian distribution with the mean and correlaton given by (e.g. [13])

$$< \boldsymbol{\varphi}_n(t) >= 0 \tag{5}$$

and

$$< \boldsymbol{\varphi}_n(t) \boldsymbol{\varphi}_n(t') >= 2\, m_n \gamma_n\, k_B T\, \delta(t - t') \tag{6}$$

respectively. The resulting system of equations has to be solved together with a set of constraints for flexible macromolecules (see [25]) or a an appropriate definition of non-hydrodynamic forces for elastic macromolecules. The coupling with the carrier liquid can be implemented through the carrier liquid velocity in the equation (3). Alternatively, a two-way coupling can be implemented by considering the volumetric force exerted on the carrier liquid by macromolecule.This force can be written as

$$\boldsymbol{F}(\boldsymbol{r}) = -\sum_n \boldsymbol{f}_n\, \delta_\epsilon(\boldsymbol{r} - \boldsymbol{r}_n) \tag{7}$$

where δ_ϵ is the smoothed Dirac function of ϵ length scale. The function incorporates the division with the unit volume, and therefore transforms the point-like force $\boldsymbol{f}_n$ into a volumetric force field which can be added to the momentum conservation equation of the carrier liquid. The carrier liquid flow can then be modelled with an appropriate incompressible flow solver. The test cases presented in this paper are based on the one-way coupling with the frozen fluid flow provided by an analytic solution, therefore the discussion of the carrier fluid flow solver is omitted. The details of the implementation of the two-way coupling can be found in [25].

2.1. Modeling dsDNA

Behaviour of macromolecules with a strong secondary structure, such as double-stranded DNA, is highly influenced by the inter-molecular forces arising from changes of molecular configuration. Double-stranded DNA molecules consist of two long polymer chains held together by the Watson-Crick base pairs (A-T) and (C-G). In their natural form, strand pairs form a helical secondary structure. In the absence of the external forces, the configuration of the helical structure is similar to a self-avoiding random-walk for a given end-to-end distance of the molecule [13, 26, 27, 28]. When a moderate stretching force is applied to the ends of the molecule, the natural configurational space is bounded, therefore limiting the number of possible configurations. This results in entropic changes, giving a rise to restoring forces observed as the elastic response of the molecule on the macroscopic level [27].

In order to account for the distribution of the elastic force between multiple spring connectors, Underhill and Doyle [27] proposed the polymer ensemble transformation (PET) method to determine equivalent spring force laws, taking into account the coarse-graining level of each spring. Based on this transformation, the elastic force for a single spring connector can be expressed as [29]

$$f = \frac{k_B T}{\lambda_p}\left\{\frac{\hat{x}}{(1-\hat{x}^2)^2} - \frac{7\hat{x}}{\chi(1-\hat{x}^2)} + \right. \\ + \left(\frac{3}{32} - \frac{3}{4\chi} - \frac{6}{\chi^2}\right)\hat{x} + \\ + \left(\frac{(13/32) + (0.8172/\chi) - (14.79/\chi^2)}{1 - (4.225/\chi) + (4.78/\chi^2)}\right)\cdot \\ \left.\hat{x}(1-\hat{x}^2)\right\}, \quad (8)$$

where k_B is the Boltzmann's constant, T is the temperature, λ_p is the persistence length, $\hat{x} = x/l$ is the fractional extension and χ is the number of persistence lengths the spring connector represents.

Taking the effect of the elastic forces into account, the analytical integration of the equation (1) results in the following solution for the velocity

$$\boldsymbol{v}_n(t+\Delta t) = \boldsymbol{u}(\boldsymbol{r}_n) + \frac{\boldsymbol{\phi}_n}{\gamma_n m_n} + \frac{\sigma}{m_n}\boldsymbol{R}_{v,n}(\Delta t) + \\ + \left(\boldsymbol{v}_n(t) - \boldsymbol{u}(\boldsymbol{r}_n) - \frac{\boldsymbol{\phi}_n}{\gamma_n m_n}\right)\cdot \exp(-\gamma_n \Delta t). \quad (9)$$

The positions of the beads are then obtained from the analytical integration of the equation (9) leading to

$$\boldsymbol{r}_n(t+\Delta t) = \boldsymbol{r}_n(t) + \left(\boldsymbol{u}(\boldsymbol{r}_n) + \frac{\boldsymbol{\phi}_n}{\gamma_n m_n}\right)\Delta t + \\ + \frac{\sigma}{\gamma_n m_n}\boldsymbol{R}_{x,n}(\Delta t) + \left(\boldsymbol{v}_n(t) - \boldsymbol{u}(\boldsymbol{r}_n) - \frac{\boldsymbol{\phi}_n}{\gamma_n m_n}\right)\cdot \\ \frac{(1-\exp(-\gamma_n \Delta t))}{\gamma_n}, \quad (10)$$

where $\sigma = \sqrt{2 m_n \gamma_n k_B T}$. $\boldsymbol{R}_{v,n}(\Delta t)$ and $\boldsymbol{R}_{x,n}(\Delta t)$ are the vectors of independent random numbers drawn from Gaussian distributions with zero mean and variances

$$\langle R_{v,n}(\Delta t)^2 \rangle = \frac{1}{2\gamma_n}(1 - \exp(-2\gamma_n \Delta t)) \quad (11)$$

$$\langle R_{x,n}(\Delta t)^2 \rangle = \frac{1}{2\gamma_n}(2\gamma_n \Delta t - \exp(-2\gamma_n \Delta t) \\ + 4\exp(-\gamma_n \Delta t) - 3) \quad (12)$$

In equation Eq. 9 and Eq. 10, $\boldsymbol{\phi}_n$ is the non-hydrodynamic force representing the effect of entropic elastic forces acting on bead n. The total elastic force $\boldsymbol{\phi}_n$ acting on the bead n is comprises contributions of the connectors $n-1$ and n corresponding to bead pairs $(n-1, n)$ and $(n, n+1)$ respectively. This force is treated explicitly leading to the following expression

$$\boldsymbol{\phi}_n = -f(\boldsymbol{r}_{n-1}(t), \boldsymbol{r}_n(t)) \cdot \boldsymbol{n}(t)_{n-1,n} + \\ + f(\boldsymbol{r}_n(t), \boldsymbol{r}_{n+1}(t)) \cdot \boldsymbol{n}(t)_{n,n+1} \quad (13)$$

where $\boldsymbol{n}(t)_{n-1,n}$ and $\boldsymbol{n}(t)_{n,n+1}$ denote the unit direction vectors of the connectors $n-1$ and n respectively.

2.2. Wall treatment

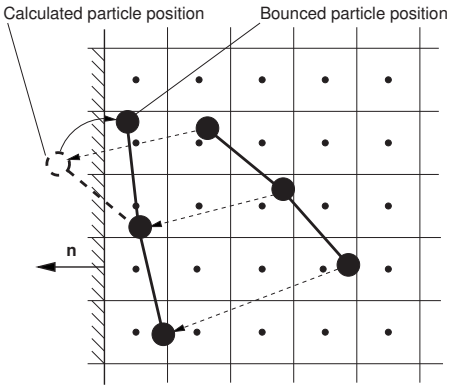

Figure 1. Schematic of the wall treatment

In microfluidic and nano-fluidic applications, the contour length of macromolecules can be comparable to the hydraulic diameter of the channel, therefore it is important to consider the behaviour of beads colliding with a solid wall. In order to address this issue, a perfectly elastic particle-wall collision model was adopted. The calculated particle trajectories were continuosly monitored and when a collision was forecasted, the impact position $\boldsymbol{r}_{n\,\mathrm{imp}}$ and the collision time Δt_{imp} was calculated. The post-collision particle velocity and position were then calculated as follows:

$$\boldsymbol{v}_n(t+\Delta t) = \boldsymbol{v}_n - 2\,(\boldsymbol{n}\cdot\boldsymbol{v}_n)\cdot\boldsymbol{n} \quad (14)$$

$$\boldsymbol{r}_n(t+\Delta t) = \boldsymbol{r}_{n\,\mathrm{imp}} + (\Delta t - \Delta t_{\mathrm{imp}})\cdot\boldsymbol{v}_n(t+\Delta t) \quad (15)$$

where $\boldsymbol{n}$ is the unit wall normal vector pointing outwards from the computational domain. Figure 1 demonstrates the schematic of the elastic collision correction. For a flexible molecule represented by the bead-rod model, the reflected particle position normally does not satisfy the length constraints, hence the particle correction algorithm was applied after each wall-bounce event (see [25], [24]).

3. RESULTS

3.1. Bead-rod model

The results presented in this section are based on the experiments of Stein et al. [9], who have carried out a detailed study of the dsDNA transport in pressure driven microflows. In this study, λ-DNA molecules were labelled with fluorescent dyes and the motion of individual molecules was traced using epifluorescence microscopy. Trajectories of the molecule's centre-of-mass were reconstructed by tracking the labeled dsDNA over a series of images. The experimental data was recorded with 5 Hz frequency, resulting in data points at 0.2 s interval. Ensemble average velocity of a small number of molecules was then calculated.

The pressure driven carrier liquid flow used in the experimental study was implemented in a high aspect ratio rectangular microchannel resulting in a steady two-dimensional Poisseuille flow in a crossection. The carrier liquid was an aqueous buffer with a dynamic viscosity of $\eta = 1.05 \times 10^{-3}$ Pas and density of $\rho = 10^3\,\mathrm{kg/m^3}$. The pressure gradient of $\nabla p = 1.44\,\mu\mathrm{Pa/m}$ used in the experiment corresponded to the parabolic velocity profile with a maximum velocity $u_{max} = 10.7\,\mu$m/s. The Reynolds number based on the maximum velocity u_{max} and the channel height h_c was equal to 2.54×10^{-6}.

The experiments have been carried out using 48.5 kbp λ-DNA molecules, with a contour length of $L_c = 22\,\mu$m. The configuration of the observed DNA molecules resembled a random coil with the equilibrium coil size of $R_g = 0.73\,\mu$m. The resulting Weissenberg number was below 5, which is the critical value for the molecular elongation. In the experiments, the steady state Poiseulle flow did not lead to a noticeable stretching of the transported molecules [9]. Therefore, no entropic elastic behaviour of the dsDNA molecules was expected. Based on the channel height of $h_c = 0.25\,\mu$m, the investigated DNA molecules have been strongly confined ($h_c < R_g$). Due to the confinement and the absence of strong velocity gradients, the conformational changes of the macromolecules were negligible over the duration of the convectional transport process [9].

Since no elastic behaviour was observed experimentally, the bead-rod model was chosen for the dsDNA molecules in the present study. The parameters of the bead-rod structure were determined from the experimental data. The rod length was specified based on the persistence length

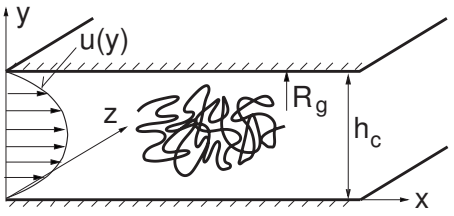

Figure 2. Schematic of the microchannel and the confined λ-DNA

λ_p of a stained dsDNA molecule, resulting in a segment length of $a = 2\lambda_p = 134.3$ nm. This approach resulted in a model comprising 165 beads. The radius of the beads was determined from the total drag coefficient of a coiled molecule, calculated from the Einstein relation (see [13, 30]), leading to the bead radius $b = 10.225$ nm. The mass of the complete 48.5 kbp λ-DNA was taken to be equal to 5.81×10^{-20} kg following [31]. This mass was distributed equally between the beads, resulting in a bead mass $m = 3.52 \times 10^{-22}$ kg.

The numerical calculations were carried out for a single dsDNA molecule in the three-dimensional channel geometry with a fixed parabolic velocity profile of the carrier liquid. Taking into account the preferred position of macromolecules in pressure driven flows [9], the dsDNA structure was injected at the centre of the channel height in the wall-normal direction in a random coil conformation. The computations were carried out with the time step $\Delta t = 2.33\,\mu$s selected based on the time step sensitivity tests.

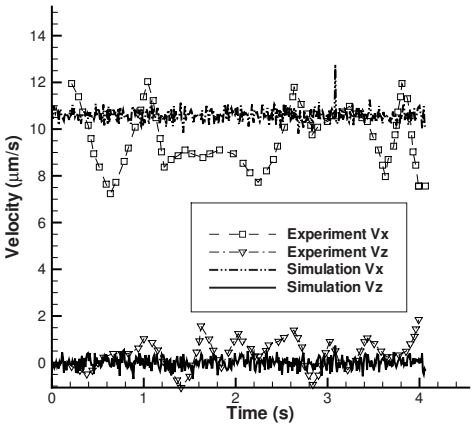

Figure 3. Experimental and numerical results for the dsDNA velocity

As the bead-rod structure was convected towards the channel outlet, it stayed in the middle of the channel height in the wall-normal direction in agreement with the experimental

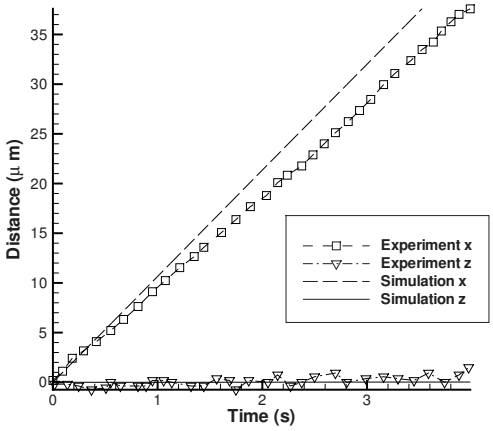

Figure 4. Experimental and numerical results for the dsDNA distance from the inlet

observations of Stein et al. [9]. Figure 3 and 4 illustrates the comparison between the experimentally observed and calculated velocity components and displacements of the dsDNA molecule. Here x and z denote the streamwise and spanwise directions respectively. Vx and Vz denote corresponding velocity components. The averaged velocity components are in a good agreement with the experimental data. However the streamwise velocity component is slightly over-predicted and the effect of the Brownian force is weaker in the calculated velocity components in comparison with the experiment. This leads to a slight over-prediction of the streamwise x displacement of the centre-of-mass of the dsDNA. The spanwise coordinate of the centre-of-mass is very close to zero in both cases. However the experimental data features stronger fluctuations in the spanwise drift.

The slight discrepancy in the streamwise velocity can be understood when one takes into account the dsDNA-wall collisions. According to Stein et al. [9], the majority of the molecules favours the middle region of the channel however a small number of molecules may drift away from the channel mid-plane and interact with the channel wall. It is difficult to quantify this effect in the experiment since the position of the dsDNA molecules in the wall-normal direction was not registered. However in the numerical simulation, a substantial number of collisions with the wall was observed. The absolutely elastic collision implemented in the numerical model corresponds to the tangential momentum accommodation coefficient of 0. The experiments of Stein et al. were conducted in a silica fluidic channel. There is no information available regarding the accommodation coefficients for the dsDNA collision with a silicon wall, however it is reasonable to assume that the collision is not perfectly elastic. The lower streamwise velocity observed in the experiments can then be attributed to the momentum loss in the dsDNA-wall interactions.

3.2. Bead-spring model

Perkins et al. [10] performed a set of detailed measurements for the relaxation of stretched DNA molecules. In this study, optically trapped stained DNA molecules were stretched to a full extension by fluid flow and then allowed to relax in the resting fluid. The process was recorded using video-enhanced fluorescence microscopy and the visible length of the molecules was measured for every frame. The experiments were carried out for long and medium macromolecules with the contour length L_c of 39.1 μm and 21.1 μm respectively.

A mechanical bead-spring model for this process was costructed incorporating 38 and 21 beads for long and medium DNA molecules, respectively based on 10 Kuhn steps per elastic connector. The mass of the beads was determined by uniformly distributing the mass of the DNA between the beads resulting in the bead mass m of 3.61×10^{-21} kg and 3.52×10^{-21} kg for the long and medium DNA models respectively. The bead radius were calculated using the Batchelor formula [32], resulting in the radius values of 3.47×10^{-2} μm and 3.61×10^{-2} μm for the long and medium DNA models respectively.

In the first instance, the accuracy of the solver was evaluated using the analytical solution which can be readily obtained if only two beads are considered with a constant spring coefficient (e.g. [33]). The parameters of the medium DNA model were used for this case and the constant spring coefficient was chosen to be equal to 5×10^{-7} N/m. The initial condition corresponded to the fractional extension of $\hat{x} = 1.0$ with spring length of $l_0 = 1\,\mu$m. The choice of the spring coeffient was based on the average value over the simulation timescales for the actual model of the medium DNA. The simulation was run with a time step of $\Delta t = 10^{-5}$ s typical for the simulations of the actual DNA molecules. The results are presented in Figure 5 and 6 which illustrates the position and velocity of one bead obtained from the analytical and numerical solutions. Excellent agreement is achieved with the relative velocity difference between the analytical and numerical solutions not exceeeding 1.3% over the duration of the simulation.

Following the verification based on the analytical solution, simulations were conducted for the model of the DNA relaxation experiment [10]. The simulations were conducted under no-flow conditions with a time step of 10^{-5} s. The time step was chosen based on the sensitivity tests.

Figure 7 illustrates the experimental and computational results for the DNA end-to-end distance as a function of time. The results obtained from the simulations are within the statistical spread of the experimental data for all cases (see [10]). The agreement is improved with the increase of the DNA

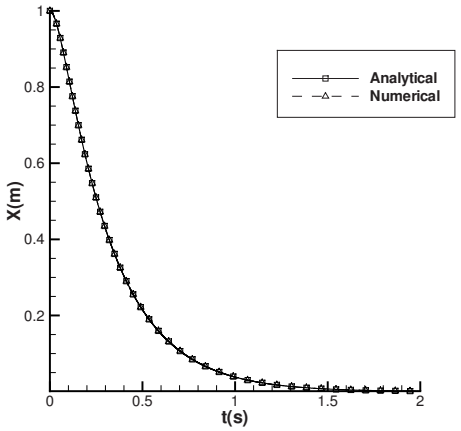

Figure 5. Position of the end of a single dsDNA segment, analytical and numerical solution

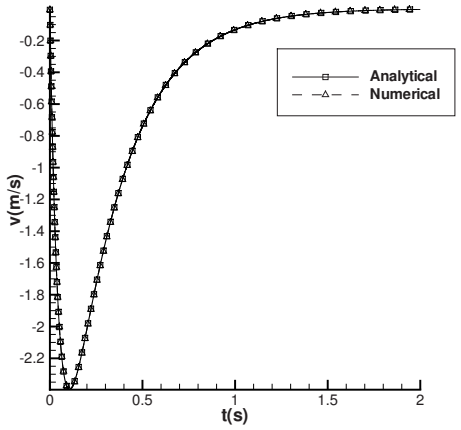

Figure 6. Velocity of the end of a single dsDNA segment, analytical and numerical solution

length, however it should be noted that the statistical uncertainty of the experiment is also increased with the decrease of the DNA segment length.

4. CONCLUSIONS

A mesoscale modelling approach has been presented capable of capturing the dynamic behaviour of flexible and elastic macromolecules. The approach is based on a mechanical representation of the macromolecule with the model parameters derived from the physical properties of the macromolecule in question. Flexible macro molecules with negligible elastic response are modelled using bead-rod mechanical structures whereas macromolecules exhibiting elastic response are represented by bead-spring structures. The simulations presented for the dsDNA transport

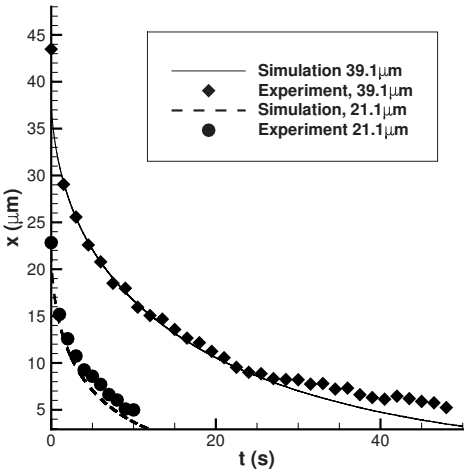

Figure 7. Length of a 39.1 μm dsDNA and 21.1 μm dsDNA - experimental and simulated results

and relaxation processes and comparisons with the experimental data demonstrate the applicability and accuracy of the proposed approach.

The modelling approach presented in this paper can be easily modified to incorporate additional physical effects through the modification of the forcing mechanisms.

ACKNOWLEDGEMENTS

This work has been supported in part by the European Commission under the 6th Framework Program (Project: DINAMICS, NMP4-CT-2007-026804).

References

[1] Whitesides, G. 2006 “The origins and the future of microfluidics”. *Nature*, Vol. 442, pp. 368–373.

[2] Hansen, L., C., Skordalakes, E., Berger, M., J., and Quake, R., S. 2002 “A robust and scalable microfluidic metering method that allows protein crystal growth by free interface diffusion”. *Proc Natl Acad Sci U S A*, Vol. 99 (26), pp. 16531–6.

[3] Bashir, R. 2004 “BioMEMS: state-of-the-art in detection, opportunities and prospects”. *Advanced Drog Delivery Reviews*, Vol. 56(11), pp. 1565–1586.

[4] el Hak, M. G. 2005 “Liquids: The holy grail of microfluidic modeling”. *Phys. Fluids*, Vol. 17(10), p. 100612.

[5] Squires, T. M. and Quake, S. R. 2005 “Microfluidics: Fluid physics at the nanoliter

scale". *Reviews of Modern Physics*, Vol. 77, No. 3, pp. 977–1026.

[6] Cheatham, T. E. 2004 "Simulation and modeling of nucleic acid structure, dynamics and interactions". *Current Opinion in Structural Biology*, Vol. 14, No. 3, pp. 360–367, cited By (since 1996): 41.

[7] Orozco, M., Noy, A., and Prez, A. 2008 "Recent advances in the study of nucleic acid flexibility by molecular dynamics". *Current Opinion in Structural Biology*, Vol. 18, pp. 185–193.

[8] Wong, P. K., Lee, Y. K., and Ho, C. M. 2003 "Deformation of DNA molecules by hydrodynamic focusing". *Journal of Fluid Mechanics*, Vol. 497, No. 497, pp. 55–65, cited By (since 1996): 20.

[9] Stein, D., van der Heyden, F. H. J., Koopmans, W. J. A., and Dekker, C. 2006 "Pressure-driven transport of confined DNA polymers in fluididc channels". *PNAS*, Vol. 103, pp. 15853–15858.

[10] Perkins, T. T., Quake, S. R., Smith, D. E., and Chu, S. 1994 "Relaxation of a single DNA molecule observed by optical microscopy". *Science*, Vol. 264, pp. 822–826.

[11] Perkins, T. T., Smith, D. E., Larson, R. G., and Chu, S. 1995 "Stretching of a single tethered polymer in a uniform flow". *Science*, Vol. 268, pp. 83–86.

[12] Perkins, T. T., Smith, D. E., and Chu, S. 1997 "Single polymer dynamics in an elongational flow". *Science*, Vol. 276, pp. 2016–2021.

[13] Doi, M. and Edwards, S. 1986 *The theory of polymer dynamics*. Oxford: Clarendon.

[14] Doyle, P. S. and Underhill, P. T. 2005 *Handbook of Materials Modeling, Brownian Dynamics Simulations of Polymers and Soft Matter*. Springer.

[15] Doyle, P. S., Shaqfeh, E. S. G., and Gast, A. P. 1997 "Dynamic simulation of freely draining flexible polymers in steady linear flows". *Journal of Fluid Mechanics*, Vol. 334, pp. 251–291.

[16] Doyle, P. S., Shaqfeh, E. S. G., McKinley, G. H., and Spiegelberg, S. H. 1998 "Relaxation of dilute polymer solutions following extensional flow". *Journal of Non-Newtonian Fluid Mechanics*, Vol. 76, pp. 79–110.

[17] Hur, J., Shaqfeh, E., and Larson, R. 2000 "Brownian dynamics simulations of single DNA molecules in shear flow". *Journal of Rheology*, Vol. 44, No. 4, pp. 713–742.

[18] Hur, J. S. and Shaqfeh, E. S. G. 2001 "Dynamics of dilute and semidilute DNA solutions in the start-up of shear flow". *Journal of Rheology*, Vol. 45, pp. 421–450.

[19] Jendrejack, R. M., de Pablo, J. J., and Graham, M. D. 2002 "Stochastic simulations of DNA in flow: Dynamics and the effects of hydrodynamic interactions". *Journal of Chemical Physics*, Vol. 116, pp. 7752–7759.

[20] Jendrejack, R. M., Schwartz, D. C., de Pablo, J. J., and Graham, M. 2004 "Shear-induced migration in flowing polymer solutions: Simulation of long-chain DNA molecules". *Journal of Chemical Physics*, Vol. 120, pp. 2513–2529.

[21] Trebotich, D., Miller, G. H., Colella, P., Graves, D. T., Martin, D. F., and Schwartz, P. O. 2005 "A tightly coupled particle-fluid model for DNA-laden flows in complex microscale geometries". *Computational Fluid and Solid Mechanics 2005*, pp. 1018–1022.

[22] Trebotich, D., Miller, G., and Bybee, M. 2007 "A hard constraint algorithm to model particle interactions in DNA-laden flows". *Nanoscale and Microscale Thermophysical Engineering,*, Vol. 11, pp. 121–128.

[23] Miller, G. H. and Trebotich, D. 2007 "Toward a Mesoscale Model for the Dynamics of Polymer Solutions". *Journal of Computational and Theoretical Nanoscience*, Vol. 4, pp. 1–5.

[24] Benke, M., Shapiro, E., and Drikakis, D. 2008 "An efficient multi-scale model approach for ssDNA motion in fluid flow". *Journal of Bionic Engineering*, Vol. 5, pp. 299–307.

[25] Benke, M. 2010 "Numerical Simulation of Macromolecules". Ph.D. thesis,

[26] Bao, G. 2002 "Mechanics of biomolecules". *Journal of Mechanics and Physics of Solids*, Vol. 50, pp. 2237–2274.

[27] Underhill, P. T. and Doyle, P. S. 2004 "On the coarse-graining of polymers into bead-spring chains". *Journal of Non-Newtonian Fluid Mechanics*, Vol. 122, pp. 3–31.

[28] Shaqfeh, E. S. G. 2005 "The dynamics of single-molecule DNA in flow". *Journal of Non-Newtonian Fluid Mechanics*, Vol. 130, pp. 1–28.

[29] Underhill, P. T. and Doyle, P. S. 2007 "Accuracy of bead-spring chains in strong flows". *Journal of Non-Newtonian Fluid Mechanics*, Vol. 145, pp. 109–123.

[30] Zimm, B. H. 1956 “Dynamics of polymer molecules in dilute solution: viscoelasticity, flow birefringence and dielectric loss”. *The Journal of Chemical Physics*, Vol. 24, pp. 269–278.

[31] Lukacs, G., P.Haggie, Seksek, O., Lechardeur, D., Freedman, N., and Verkman, A. 2000 “Size-dependent DNA mobility in Cytoplasm and Nucleus”. *J. Biol. Chem.*, Vol. 275, No. 3, pp. 1625–1629.

[32] Batchelor, G. K. 1971 “The stress generated in a non-dilute suspension of elongated parcles by pure straining motion”. *Journal of Fluid Mechanics*, Vol. 46, pp. 813–829.

[33] Braun, M. 1975 *Differential equations and their applications*. Springer-Verlag.

Conference on Modelling Fluid Flow (CMFF'12)
The 15th International Conference on Fluid Flow Technologies
Budapest, Hungary, September 4-7, 2012

INVERSE METHOD FOR 2D VISCOUS FLOW DESIGN PROBLEM USING STREAM-FUNCTION COORDINATES FOR AXISYMMETRIC MODEL

Michał Butterweck[1] , Jacek Pozorski [2]

[1] Corresponding Author, Hydrodynamics nad Multiphase Flow Department, Institute of Fluid-Flow Machinery, Polish Academoy of Sciences in Gdańsk, Email: mbutterweck@gmail.com
[2] Hydrodynamics nad Multiphase Flow Department, Institute of Fluid-Flow Machinery, Polish Academoy of Sciences in Gdańsk, Email: jp@imp.gda.pl

ABSTRACT

A new, inverse method for viscous 2D, laminar duct flows will be presented. The method is based on incompressible Navier-Stokes equations transformed to the stream function coordinate system (von Mises coordinates). Then the design problem with appropriate boundary conditions is solved numerically in stream-function coordinates domain. Next, the geometrical shape of the boundary walls is obtained through the integration along streamlines. The singularity problem at the wall and its special treatment are considered. The method formulation is described for axisymmetric model. The numerical implementation of the model with finite differences is prescribed. The validation of the inverse method with several analytical and numerical test cases is presented. The discretisation errors and convergency of the flow solver are discussed in details. Potential applications to design problem of fluid-flow machines are considered and developments towards 3D method are prescribed.

Keywords: design method, inverse problem, stream function coordinates

NOMENCLATURE

J	Jacobian of the transformation
R	radial reference length scale
Re	Reynolds number
Z	axial reference length scale
U_r	radial reference velocity scale
U_z	axial reference velocity scale
c	series expansion constant
p	pressure
r	radial and axial coordinate
u	velocity component
z	axial coordinate
β	artificial compressibility coefficient
ϵ	estimated error of the method
ψ	stream function, stream function coordinate
τ	pseudo-time in marching technique

Subscripts and Superscripts

in	at the inlet of the domain
num	numerically obtained geometry
out	at the inlet of the domain
r	radial direction
th	analytically designed geometry
w	at the wall boundary
z	axial direction
Ω	the solution domain
$\partial\Omega$	the boundary of solution domain
$'$	component in stream function coordinates

1. INTRODUCTION

Many engineering problems involve design of a geometrical shape (e.g., the nozzle wall or blading system) which should satisfy prescribed conditions (Figure 1). Some of these conditions may not refer directly to geometric quantities, but to some flow parameters (for example: the pressure distribution along wall). Yet, since the geometry is not known at this stage, the design process is brought to the field of inverse methods. Many of such methods in fluid dynamics rely on some model simplifications, which affects accuracy. Inverse methods were developed using such concepts as 2D blade-to-blade or through-flow models [1, 2]. Mixed direct-inverse techniques of moving boundary/transpiration concepts have been proposed even for viscous flows [3, 4] in recent years. However, those methods need to handle time-consuming remeshing. With the growth of computer power, the optimisation techniques [5, 6] (in general, less restrictive methods) have gained attention. However, performing full optimisation process on a daily basis is still prohibitive for most

applications. Consequently, there is a need of inverse methods to circumvent those limitations.

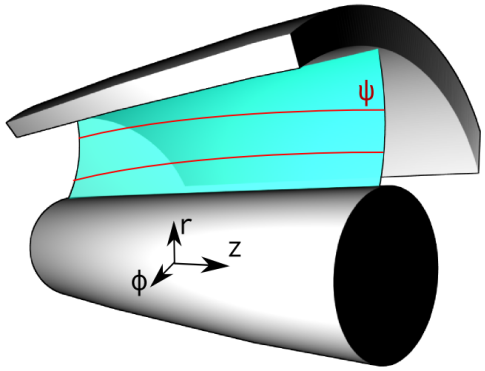

Figure 1. An axisymmetric channel design problem.

The history of stream function coordinates (SFC, also known as von Mises coordinates) goes back to the boundary layer analysis in von Mises work [7] in 1927. For direct (analysis) problems, the SFC method was used for potential and viscous flows in curved geometries [8, 9, 10, 11] and even for multiphase flows [12]. Up to nowadays, the SFC technique has been adapted also to inverse methods of various 2D and 3D design problems [8, 10, 13, 14, 15, 16, 17]. However, mostly inviscid flows were the subject of the inverse design with stream function coordinates, due to singularity of transformation along no-slip walls. Keller [16] presented an inverse method with possible application to 3D viscous flows. However, Scascighini [17] proved that such an approach is applicable only to the lamellar flows. This is due to the use of natural coordinates [18] which exist if and only if the velocity field satisfies the condition:

$$\mathbf{u} \cdot (\nabla \times \mathbf{u}) = 0, \tag{1}$$

where $\mathbf{u}$ is the velocity vector. Yet, the assumption about the flow being lamellar is quite restrictive. It is fully satisfied for 2D flows or irrotational 3D flows. Also, much of work was done in the matter of approximate treatment of viscous effects in 2D and quasi-3D flows [17, 19] using the Integral Boundary Layer approach, suitable for inertia-dominated (high Reynolds number) flows.

A new, fully inverse method (no solution of direct problem in the design domain) for 2D incompressible viscous flows, without explicit remeshing, is presented in the paper. In the direct problem (flow analysis), the system of governing equations is solved to obtain fields of flow variables (velocity, pressure, etc.) for a given shape of the boundary, initial and boundary conditions (e.g., no-slip wall, inlet, outlet, etc.) Yet, in inverse problems at least a part of geometry is unknown. One can replace some of geometrical variables by a fluid flow variable. That will affect the boundary condition which must be changed, too. One of the possibilities is the replacement through the transformation of equations to the stream function coordinates. The transformation gives the ability to eliminate one geometrical variable (here, r) by use of a flow variable (here, the stream function ψ). The essence of the approach and details of mathematical model are described in Section 2.

In Section 3, implementation details are presented. The solution algorithm based on pseudo-time marching technique was applied. The artificial compressibility method was used to obtain pressure. The discretisation scheme are described for each of the model equations. The influence of wall singularity problem on numerical solution is considered in detail.

The numerical results of axisymmetric model are presented in Section 4. The design of straight pipe was used as a validation case. The analytical solution of this problem (Hagen-Poiseuille flow) is compared with that numerically obtained by the stream function inverse method. The convergence of the solution process is analysed. Next, a more sophisticated nozzle design problem is considered. The obtained curved channel geometry is analysed with a commercial flow solver to check the fulfilment of the design conditions.

Next, various extensions of the method are discussed. The blade-to-blade approach and the application to turbulent flows are considered (in the meaning of the Reynolds-averaged Navier-Stokes equations with corresponding turbulence model) .

2. MODEL

2.1. Axisymmetric incompressible flow

Let us consider the channel flow as in Fig. 1. The axisymmetric flow with assumption of no tangential velocity in non-dimensional form is governed by:

$$\frac{1}{r}\frac{\partial r u_r}{\partial r} + \frac{\partial u_z}{\partial z} = 0, \tag{2}$$

$$u_r \frac{\partial u_r}{\partial r} + u_z \frac{\partial u_r}{\partial z} = -\frac{\partial p}{\partial r} + \frac{1}{Re}\left(\frac{1}{r}\frac{\partial}{\partial r} r \frac{\partial u_r}{\partial r} + \frac{\partial^2 u_r}{\partial z^2} - \frac{u_r}{r^2}\right), \tag{3}$$

$$u_r \frac{\partial u_z}{\partial r} + u_z \frac{\partial u_z}{\partial z} = -\frac{\partial p}{\partial z} + \frac{1}{Re}\left(\frac{1}{r}\frac{\partial}{\partial r} r \frac{\partial u_z}{\partial r} + \frac{\partial^2 u_z}{\partial z^2}\right). \tag{4}$$

However, in typical channel flow cases one of the flow directions is dominant. Assuming that length scales satisfy $R \ll Z$ and velocity scales behave as

$U_R \ll U_Z$, the momentum Eq. (3) and (4) can be reduced to:

$$u_r \frac{\partial u_r}{\partial r} + u_z \frac{\partial u_r}{\partial z} = -\frac{\partial p}{\partial r} + \\ + \frac{1}{Re}\left(\frac{1}{r}\frac{\partial}{\partial r} r \frac{\partial u_r}{\partial r} - \frac{u_r}{r^2}\right), \quad (5)$$

$$u_r \frac{\partial u_z}{\partial r} + u_z \frac{\partial u_z}{\partial z} = -\frac{\partial p}{\partial z} + \\ + \frac{1}{Re}\left(\frac{1}{r}\frac{\partial}{\partial r} r \frac{\partial u_z}{\partial r}\right). \quad (6)$$

Performing this step is not necessary to solve the inverse problem, however it simplifies the implementation of the method. The accuracy of the solution is not affected significantly as stated in [20].

2.2. Transformation

The stream function ψ in axisymmetric coordinates is defined as:

$$r u_r = -\frac{\partial \psi}{\partial z}, \quad (7)$$

$$r u_z = \frac{\partial \psi}{\partial r}. \quad (8)$$

Let us consider the following coordinate transformation:

$$(r, z) \rightarrow (\psi, z') \quad (9)$$

where z' has the same direction vector as z. To transform derivatives to stream function coordinates one may use the chain rule:

$$\frac{\partial}{\partial r} = \frac{\partial \psi}{\partial r}\frac{\partial}{\partial \psi} + \frac{\partial z'}{\partial r}\frac{\partial}{\partial z'}, \quad (10)$$

$$\frac{\partial}{\partial z} = \frac{\partial \psi}{\partial z}\frac{\partial}{\partial \psi} + \frac{\partial z'}{\partial z}\frac{\partial}{\partial z'}. \quad (11)$$

This lead us to the formula:

$$\frac{\partial}{\partial r} = r u_z \frac{\partial}{\partial \psi}, \quad (12)$$

$$\frac{\partial}{\partial z} = \frac{\partial}{\partial z'} - r u_r \frac{\partial}{\partial \psi}. \quad (13)$$

Please note that the new coordinate system is dependent on r coordinate implicitly via velocity u_r and u_z. This implies that $\partial z'/\partial z = 1$ and z is independent of r direction, that is $\partial z'/\partial r = 0$. The Jacobian determinant of the transformation from cylindrical coordinates to stream unction coordinates is:

$$J(r, z) = \begin{bmatrix} \frac{\partial \psi}{\partial r} & \frac{\partial \psi}{\partial z} \\ \frac{\partial z'}{\partial r} & \frac{\partial z'}{\partial z} \end{bmatrix} = \begin{bmatrix} r u_z & -r u_r \\ 0 & 1 \end{bmatrix} = r u_z. \quad (14)$$

Please note that the transformation is not directly invertible when $r u_z = 0$. The back transformation may be obtained from the stream function definition:

$$\frac{dr}{dz} = \frac{u_r}{u_z}. \quad (15)$$

Then we can obtain stream line shape through integration from inlet to outlet. However, both velocity components u_r and u_z vanish at the wall due to the no-slip and no-transpiration boundary conditions. This leads to indeterminate form $0/0$. To overcome this issue we propose to use in the near boundary wall region the formula derived from Eq. (3):

$$\int_{r_{\Delta\psi}}^{r_w} r\, dr = \int_{\Delta\psi}^{0} \frac{d\psi}{u_z} \quad (16)$$

then we have:

$$r_w = \sqrt{2\int_{\Delta\psi}^{0} \frac{d\psi}{u_z} + r_{\Delta\psi}^2}. \quad (17)$$

The above integral (17) does not behave well at the wall, either. Nonetheless, the integration of functions with boundary singularity is well established. It may be integrated easily down to the wall (here $\psi = \psi_w = 0$) from the nearest available stream line $\psi = \Delta\psi$ (which was obtained through equation (15)).

2.3. Transformed flow equations

The mass Eq. (2) and momentum conservation Eqs. (5), (6) may now be transformed to the stream function coordinates using formulas (12) and (13):

$$u_z \frac{\partial r u_r}{\partial \psi} + \frac{\partial u_z}{\partial z'} - r u_r \frac{\partial u_z}{\partial \psi} = 0, \quad (18)$$

$$u_z \frac{\partial u_r}{\partial z'} = -r u_z \frac{\partial p}{\partial \psi} + \\ + \frac{1}{Re}\left(u_z \frac{\partial}{\partial \psi} r^2 u_z \frac{\partial u_r}{\partial \psi} - \frac{u_r}{r^2}\right), \quad (19)$$

$$u_z \frac{\partial u_z}{\partial z'} = -\frac{\partial p}{\partial z} + r u_r \frac{\partial p}{\partial \psi} \\ + \frac{1}{Re}\left(u_z \frac{\partial}{\partial \psi} r^2 u_z \frac{\partial u_z}{\partial \psi}\right), \quad (20)$$

which are coupled with Eqs. (15) and (17) for evaluation of r.

Please note that the convective term was reduced in stream functions coordinates. However, the diffusive part is more complicated. It would be even more if we would used the full Navier-Stokes model i.e. Eqs. (3) and (4).

A standard Navier-Stokes boundary conditions are applicable to the equation system. At the inlet one may set:

$$u_r(z' = z'_{in}, \psi) = u_{r,in}(z'), \tag{21}$$

$$u_z(z' = z'_{in}, \psi) = u_{z,in}(z'), \tag{22}$$

$$p(z', \psi = \psi_w) = p_{in}(z'), \tag{23}$$

and for outlet:

$$\frac{\partial u_r(z' = z'_{out}, \psi}{\partial z'} = 0, \tag{24}$$

$$\frac{\partial u_z(z' = z'_{out}, \psi)}{\partial z'} = 0. \tag{25}$$

$$p(z' = z'_{out}, \psi) = p_{out}(z'). \tag{26}$$

At the wall no-slip and no traspiration boundary conditions are applicable. However, to solve inverse problem one need to apply Dirichlet pressure distribution. So, along the designed channel wall there is:

$$u_r(z', \psi = \psi_w) = 0, \tag{27}$$

$$u_z(z', \psi = \psi_w) = 0, \tag{28}$$

$$p(z', \psi = \psi_w) = p_w(z'). \tag{29}$$

3. NUMERICAL DISCRETISATION

The resulting equation system is highly non-linear with the structure similar to the original Navier-Stokes equations. For the sake of simplicity, the finite difference approach was adopted here for discretisation in space and the pseudo-time marching technique was used to obtain steady state solution. The artificial compressibility method was chosen to satisfy the continuity equation by adding an additional term to (18):

$$\frac{1}{\beta}\frac{\partial p}{\partial \tau} + u_z\frac{\partial r u_r}{\partial \psi} + \frac{\partial u_z}{\partial z'} - r u_r\frac{\partial u_z}{\partial \psi} = 0, \tag{30}$$

Consequently, Eqs. (19) and (20) were extended with pseudo-time derivative for u_r and u_z. Additionally, the diffusive terms are expanded:

$$\begin{aligned}\frac{\partial u_r}{\partial \tau} + u_z\frac{\partial u_r}{\partial z'} = -r u_z\frac{\partial p}{\partial \psi} + \\ + \frac{1}{Re}\left(u_z\frac{\partial u_r}{\partial \psi} + r u_z\frac{\partial r u_z}{\partial \psi}\frac{\partial u_r}{\partial \psi}\right) + \\ + \frac{1}{Re}\left(r^2u_z^2\frac{\partial^2 u_r}{\partial \psi^2} - \frac{u_r}{r^2}\right),\end{aligned} \tag{31}$$

$$\begin{aligned}\frac{\partial u_z}{\partial \tau} + u_z\frac{\partial u_z}{\partial z'} = -\frac{\partial p}{\partial z} + r u_r\frac{\partial p}{\partial \psi} \\ + \frac{1}{Re}\left(u_z\frac{\partial u_z}{\partial \psi} + r u_z\frac{\partial r u_z}{\partial \psi}\frac{\partial u_z}{\partial \psi}\right) + \\ + \frac{1}{Re}\left(r^2u_z^2\frac{\partial^2 u_z}{\partial \psi^2}\right).\end{aligned} \tag{32}$$

This brings us to a problem of three time-dependent equations coupled with Eqs. (15) and (17) for evaluation of r. The equations are integrated numerically, until a steady state is reached. The convergence criterion is used that:

$$max\left(\frac{\partial u_r}{\partial \tau}, \frac{\partial u_z}{\partial \tau}, \frac{\partial p}{\partial \tau}\right)|_\Omega < \epsilon \tag{33}$$

The explicit Euler scheme was used for integration in time. The second order central scheme was used for discretisation of derivatives in space. The uniform grid was used for the sake of simplicity. The continuity equation is discretised as follows:

$$\begin{aligned}-\frac{1}{\beta}\frac{p^{\tau+\Delta\tau}_{z',\psi} - p^{\tau}_{z',\psi}}{\Delta\tau} = \\ = (u_z)^{\tau}_{z',\psi}\frac{(ru_r)^{\tau}_{z',\psi+\Delta\psi} - (ru_r)^{\tau}_{z',\psi-\Delta\psi}}{2\Delta\psi} + \\ + \frac{(u_z)^{\tau}_{z'+\Delta z',\psi} - (u_z)^{\tau}_{z'-\Delta z',\psi}}{2\Delta z'} + \\ - (ru_r)^{\tau}_{z',\psi}\frac{(u_z)^{\tau}_{z',\psi+\Delta\psi} - (u_z)^{\tau}_{z',\psi-\Delta\psi}}{2\Delta\psi}\end{aligned} \tag{34}$$

The second order upwind scheme was used for convective terms in momentum equations. So, Eqs. (31) and (32) are discretised:

$$\begin{aligned}\frac{(u_r)^{\tau+\Delta\tau}_{z',\psi} - (u_r)^{\tau}_{z',\psi}}{\Delta\tau} + \\ + (u_z)^{\tau}_{z',\psi}\frac{3(u_r)^{\tau}_{z',\psi} - 2(u_r)^{\tau}_{z'-\Delta z',\psi} + (u_r)^{\tau}_{z'-2\Delta z',\psi}}{2\Delta z'} \\ = -(ru_r)^{\tau}_{z',\psi}\frac{p^{\tau}_{z',\psi+\Delta\psi} - p^{\tau}_{z',\psi-\Delta\psi}}{2\Delta\psi} \\ + \frac{1}{Re}(u_z)^{\tau}_{z',\psi}\frac{(u_r)^{\tau}_{z',\psi+\Delta\psi} - (u_r)^{\tau}_{z',\psi-\Delta\psi}}{2\Delta\psi} + \\ + \frac{1}{Re}(ru_z)^{\tau}_{z',\psi}\frac{(ru_z)^{\tau}_{z',\psi+\Delta\psi} - (ru_z)^{\tau}_{z',\psi-\Delta\psi}}{2\Delta\psi}\cdot \\ \cdot\frac{(u_r)^{\tau}_{z',\psi+\Delta\psi} - (u_r)^{\tau}_{z',\psi-\Delta\psi}}{2\Delta\psi} + \\ + \frac{1}{Re}(r^2u_z^2)^{\tau}_{z',\psi}\frac{(u_r)^{\tau}_{z',\psi+\Delta\psi} - 2(u_r)^{\tau}_{z',\psi} + (u_r)^{\tau}_{z',\psi-\Delta\psi}}{\Delta\psi^2} + \\ - \frac{1}{Re}\left(\frac{u_r}{r^2}\right)^{\tau}_{z',\psi},\end{aligned} \tag{35}$$

and:

$$\frac{(u_z)^{\tau+\Delta\tau}_{z',\psi} - (u_z)^{\tau}_{z',\psi}}{\Delta\tau} +$$
$$+ (u_z)^{\tau}_{z',\psi} \frac{3(u_z)^{\tau}_{z',\psi} - 2(u_z)^{\tau}_{z'-\Delta z',\psi} + (u_z)^{\tau}_{z'-2\Delta z',\psi}}{2\Delta z'}$$
$$= -\frac{p^{\tau}_{z'+\Delta z',\psi} - p^{\tau}_{z'-\Delta z',\psi}}{2\Delta z'} +$$
$$+ (ru_r)^{\tau}_{z',\psi} \frac{p^{\tau}_{z',\psi+\Delta\psi} - p^{\tau}_{z',\psi-\Delta\psi}}{2\Delta\psi}$$
$$+ \frac{1}{Re}(u_z)^{\tau}_{z',\psi} \frac{(u_z)^{\tau}_{z',\psi+\Delta\psi} - (u_z)^{\tau}_{z',\psi-\Delta\psi}}{2\Delta\psi} +$$
$$+ \frac{1}{Re}(ru_z)^{\tau}_{z',\psi} \frac{(ru_z)^{\tau}_{z',\psi+\Delta\psi} - (ru_z)^{\tau}_{z',\psi-\Delta\psi}}{2\Delta\psi} \cdot$$
$$\cdot \frac{(u_z)^{\tau}_{z',\psi+\Delta\psi} - (u_z)^{\tau}_{z',\psi-\Delta\psi}}{2\Delta\psi} +$$
$$+ \frac{1}{Re}(r^2u_z^2)^{\tau}_{z',\psi} \frac{(u_z)^{\tau}_{z',\psi+\Delta\psi} - 2(u_z)^{\tau}_{z',\psi} + (u_z)^{\tau}_{z',\psi-\Delta\psi}}{\Delta\psi^2}. \quad (36)$$

Eq. (15) is approximated with simple first order accurate formula:

$$\frac{r^{\tau}_{z'+\Delta z',\psi} - r^{\tau}_{z',\psi}}{\Delta z} = \frac{(u_r)^{\tau}_{z',\psi}}{(u_z)^{\tau}_{z',\psi}}. \quad (37)$$

To integrate Eq. (17) one must approximate u_z function near the wall. One way is to expand velocity profile in the standard way. In Cartesian coordinates the velocity profile along the wall may be expanded into polynomial series:

$$u_z(r) = c_0 + c_1 r + c_2 r^2 + ... \quad (38)$$

However, the most significant term near the wall r_w is the linear part $c_0 + c_1 r$. We may transform monomial $u_z(r) = cr$ to the stream function coordinates using formula:

$$\psi = \int r u_z dr \quad (39)$$

which after some algebraic manipulations will lead to:

$$u(\psi) = c' \sqrt{\psi} \quad (40)$$

On the other hand expanding binomial $u_z(r) = c_0 + c_1 r + c_2 r^2$ will bring us to the function with following (Puiseux) expansion series:

$$u(\psi) = c'_1 \sqrt{\psi} + c'_2 \psi + c'_3 \psi \sqrt{\psi} + ... \quad (41)$$

On this basis, one may state that it is convenient to expand the velocity profile near the wall in the same manner for a better accuracy. Such an approach was firstly proposed by Richard von Mises, in the first work on the stream function coordinates [7]. In our implementation we cut the expansion (41) after the second term. This brings the approximation of Eq. (17) to the form:

$$r_w = \sqrt{2\int_{\Delta\psi}^{0} \frac{d\psi}{c'_1\sqrt{\psi} + c'_2\psi} + r^2_{\Delta\psi}} =$$
$$= \sqrt{4\left(\frac{\log\left(c'_1 + c'_2\sqrt{\psi}\right)}{c'_2}\right)\Big|^{0}_{\Delta\psi} + r^2_{\Delta\psi}}. \quad (42)$$

So, we have demonstrated how to avoid the near-wall singularity, which was one of the concerns in the paper of Dulikravich [14].

4. RESULTS

4.1. Hagen-Poiseuille flow design

A steady laminar flow through a straight axisymmetric pipe section was chosen as a first test case. Its analytical solution is well known so one can easily estimate the error of the method.

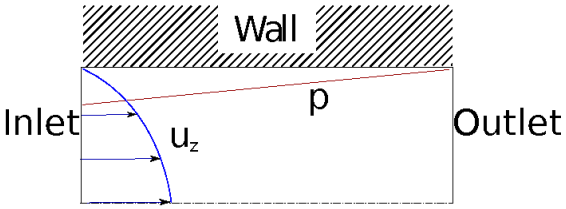

Figure 2. *Boundary conditions for design of the Hagen-Poiseuille channel flow.*

For pipe flow, the steady Navier-Stokes equations reduce to the following viscous relation (no convective terms) in the stream function coordinates:

$$\frac{\partial p}{\partial z'} = \frac{1}{Re}\left(u_z \frac{\partial}{\partial\psi} r^2 u_z \frac{\partial u_z}{\partial\psi}\right). \quad (43)$$

Let us assume that the walls be at the stream function $\psi_w = \pm 1/4$ and the rotation axis of the pipe will be at $\psi = 0$. Then one may find solution in the form of velocity distribution:

$$\begin{aligned} u_z(\psi) &= 2\sqrt{\psi_w - \psi}, \\ u_r(\psi) &= 0, \end{aligned} \quad (44)$$

for a constant pressure gradient along z' direction. So the pressure distribution along the walls is linear:

$$p(z') = p_{in} - \frac{4}{Re} z. \quad (45)$$

The corresponding stream lines will be straight and parallel to each other as:

$$r(\psi) = 1 - 2\sqrt{\psi_w - \psi}, \quad (46)$$

$$\frac{dr}{dz} = \frac{u_r}{u_z} = 0. \qquad (47)$$

The analytical solutions (44) and (45) will be respectively used as inlet and wall boundary conditions for inverse design problem of straight channel (see Fig. 2).

The Hagen-Poiseuille flow pipe was designed following the methodology just presented. The velocity and pressure fields were obtained.

Table 1. The inverse problem for Hagen-Poiseuille flow: estimated error ϵ, Eq. (48), as a function of the number N of grid nodes in ψ direction.

N	ϵ
32	0.0212
64	0.0149
128	0.0109
256	0.0084

From the analytical solution (47) it is known that the channel walls should be parallel to z direction. The difference between known (theoretical) and numerically designed shape represents an error of the inverse method:

$$\epsilon = \int_{z_{in}}^{z_{out}} \left| r_{w,th}(z) - r_{w,num}(z) \right| dz. \qquad (48)$$

As seen in Table 1, the total error of inverse method decreases with increasing grid density. The character of the convergence is slightly below linear. Possible reason is that, the total error of the method is the sum of the error originating from Eq. (37) and Eq. (42). Amplitude of both constituent errors may change non-linearly as the node nearest to the wall $\psi = \pm 1/4 \mp \Delta\psi$ will move with the grid density change. However, the maximum estimated error is satisfactorily small. Note that the Poiseuille flow is dominated by diffusion, and a possible error in the convective part is not estimated in this case. Nonetheless, the test case confirms that the method is applicable to the viscous flows.

4.2. Nozzle flow design

The pressure drop in Hagen-Poiseuille flow (cf. Sec. 4.1) is connected to viscous stress. If the pressure change along the wall is different from the one in the pipe flow (for a given inlet velocity profile), the convective term will participate in it. These possibilities bring us to a problem of curvilinear channel flow design. This test case is an example of such a design issue.

We slightly changed the pipe flow case by increasing pressure drop along the wall. The velocity profile at the inlet was left the same (quadratic in r). The sketch of the nozzle design problem is shown on Fig. (3).

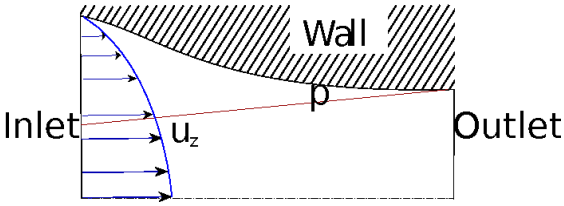

Figure 3. *Boundary conditions for design of the curved nozzle flow.*

In a such nozzle design outflow velocity should be much more uniform than that at the inlet. The geometry was obtained with the method. Next, it was an subject of the flow analysis with external solver. On the Fig. (4) velocity map of obtained geometry is shown. The resulted outflow velocity is more uniform, as predicted.

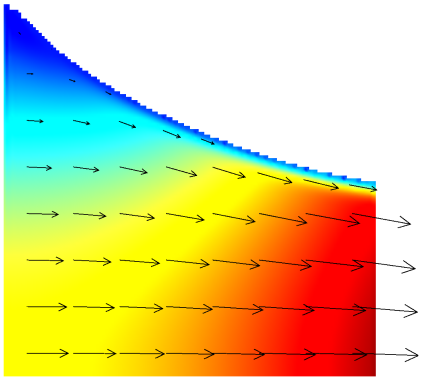

Figure 4. *Velocity vectors of the flow through the channel.*

5. Conclusions

The new inverse method for 2D viscous flow design was formulated and implemented. The method of curvilinear stream function coordinates was used. We excluded recirculating flow regions (normally, reflecting a bad design) and situations where the streamwise velocity component u_x is zero. However, for the unavoidable treatment of walls (where, obviously, both velocity components are zero) we have proposed a technique to deal with the indeterminacy of backward transformation at the domain boundary as described in Section 2.

The simple pseudo-time stepping technique was adopted. The second order numerical scheme for space discretisation was implemented, however with a caveat of a slow-down convergence in certain cases (Sec. 4.1). It has been demonstrated that the overall error of the method is linked to the limit behaviour

of flow velocity at the wall. The usage of Puiseux series $\sum c_i \psi^{i/2}$ for velocity function expansion near the wall was proposed as a solution to this problem. Comparisons with analytically-known case of the Poiseuille channel and the numerical nozzle flow design case have served to validate the approach. The total error of the method is kept at an acceptable level. Convergence of the solution process may be seen indirectly as a proof of existence of the inverse problem solution. Tests of the method show its applicability to prescribed pressure design problems such as nozzles.

One may use the RANS turbulence model with conjunction with eddy viscosity concept. Such a method for Cartesian model was studied by the authors [21].

An extension of the method to a compressible flow problems is straightforward. In such a case we need to change the stream function formulation. The stream function depends not only on the velocity field but also on the mass density ρ and its reference level ρ_0:

$$\rho r u_r = \rho_0 \frac{\partial \psi}{\partial z}, \quad \rho r u_z = -\rho_0 \frac{\partial \psi}{\partial r}. \tag{49}$$

Additionally, one may derive similar method for blade-to-blade flow design problem. The full, three-dimensional extension of the method is the subject of current work of the authors. However, in three dimensional space a second stream function must be prescribed [13, 1]. So, the approach can be extended to 3D in a straightforward way with the methodology similar to [15, 16].

The method has shown its flexibility and other extensions may be attempted as well. Though, the method is unable to solve the inverse problem with reverse flow regions (like boundary layer separation) which may be seen as a disadvantage. In engineering one does not want to design such a geometry, which (due to reverse flow) will imply additional losses, usually to be avoided. Therefore, a variety of geometries which may be designed with the method may encourage to implement a general purpose, inverse solver of the Reynolds-averaged Navier-Stokes equations in the same manner as direct problem solvers appear in modern Computational Fluid Dynamics.

The authors hope that the proposed approach (with further developments) may be useful as a fast tool in turbomachinery design process, specially for the preliminary design where state-of-the-art optimisation methods are still quite expensive.

6. ACKNOWLEDGEMENTS

The work was supported by National Science Committee under grant N 6694/B/T02/2011/40 for IFFM Polish Academy of Sciences in Gdańsk.

References

[1] R. Puzyrewski, *14 Lectures on theory of rotor machine stage - two-dimensional model (2D)* (in Polish), Wydawnictwo PG, Gdansk 1998.

[2] S. Rosa Taddei, F. Larocca, F. Bertini, E. Spano, *Euler inverse throughflow model based on an implicit upwind time marching technique*, 26th International Congress of the Aeronautical Sciences, 2008.

[3] M. Ferlauto, R. Marsilio, *A viscous inverse method for aerodynamic design*, Computers & Fluids, **35**, 304-325, 2006.

[4] R. Ramamurthy, B. Roidl, W. Ghaly, *A viscous inverse design method for internal and external flow over airfoils using CFD techniques* V European Conference on Computational Fluid Dynamics ECCOMAS CFD 2010.

[5] G.S. Dulikravich, *Shape inverse design and optimization for three dimensional aerodynamics*, AIAA Paper, **95-0695**, 1995.

[6] S. Takahashi, S. Obayashi, K. Nakahashi, *Inverse optimization of transonic wing shape for mid-size regional aircraft*, AIAA Paper, **98-0601**, 1998.

[7] R. von Mises, *Bemerkungen zur Hydrodynamik*, *Comments on hydrodynamics*, Zeitschrift für Angewandte Mathematik und Mechanik, **7**, 425-431, 1927.

[8] J.D. Stanitz, *Design of two-dimensional channels with prescribed velocity distribution along the channel walls*, NACA TN, **2595**, 1952.

[9] M.H. Martin, *The Flow of a Viscous Fluid*, Archives for Rational Mechanics and Analysis, **41**, 266-286, 1971.

[10] C.Y. Huang, G.S. Dulikravich, *Stream function and stream function coordinate (SFC) formulation for inviscid flow field calculation*, Computer Methods in Applied Mechanics and Engineering, **59**, 1986.

[11] A.M. Latypov, *Streamline-aligned orthogonal coordinates*, IMA Preprint Series,**1182**, 1993.

[12] M.H. Hamdan, *Recent developments in the von Mises transformation and its applications in the computational sciences*, 11th WSEAS Int. Conf. on Mathematical Methods, Computational Techniques and Intelligent Systems, 2009.

[13] M. Shen, Q. Liu, Z. Zhang, *Calculation of three dimensional transonic flow in turbomachinery with generalized von Mises coordinate system*, Science in China (Series A), **39**, 10, 1996.

[14] G.S. Dulikravich, *Aerodynamic shape design using stream-function-coordinate (SFC) formulation*, AIAA Paper, **91-0189**, 1991.

[15] J.J. Keller, *Inverse Euler equations*, Zeitschrift fur Angewandte Mathematik und Physik, **49**, 363-383, 1998.

[16] J.J. Keller *Inverse equations*, Physics of Fluids, **11**, 513-520, 1999.

[17] A. Scascighini, A. Troxler, R. Jeltsch, *A numerical method for inverse design based on the inverse Euler equations*, International Journal for Numerical Methods in Fluids, **41**, 339-355, 2003.

[18] L. Zannetti, *A natural formulation for the solution of two-dimensional or axis-symmetric inverse problems*, International Journal for Numerical Methods in Engineering, **22**, 451-463, 1986.

[19] M.B. Giles, M., M Drela, *Two dimensional transonic aerodynamic design method*, AIAA Journal, **25(9)**, 1199-1205, 1987.

[20] M. Butterweck, *Dimensional analysis of inverse problem model in stream function coordinates* (in Polish), Współczesne technologie konwersji energii, Wydawnictwo PG, Gdansk 2011.

[21] M. Butterweck, J. Pozorski, *Inverse method for viscous flow design using stream-function coordinates*, presented at the XIX Polish National Fluid Mechanics Conference, Submitted to Archives of Mechanics, 2010.

Conference on Modelling Fluid Flow (CMFF'12)
The 15th International Conference on Fluid Flow Technologies
Budapest, Hungary, September 4-7, 2012

ACCELERATING UNSTRUCTURED FINITE VOLUME SOLUTION OF 2-D EULER EQUATIONS ON FPGAS

Zoltán NAGY[1,3], Csaba NEMES[3], Antal HIBA[3], András KISS[2,3], Árpád CSÍK[4], Péter SZOLGAY[2,3]

[1] Corresponding Author. Computer and Automation Research Institute, Hungarian Academy of Sciences, Kende u. 13-17, H-1111, Budapest, Hungary. Tel.: +36 1 279 6286, Fax: +36 1 209 5264, E-mail: nagyz@sztaki.hu
[2] Computer and Automation Research Institute, Hungarian Academy of Sciences. E-mail: szolgay@sztaki.hu, kissa@sztaki.hu
[3] Faculty of Information Technology, Pázmány Péter Catholic University. E-mail: nemcs@digitus.itk.ppke.hu, hiban@digitus.itk.ppke.hu
[4] Széchenyi István University, Department of Mathematics and Computer Science. E-mail: dr.arpad.csik@gmail.com

ABSTRACT

Numerical simulation of complex computational fluid dynamics problems evolving in time plays an important role in scientific and engineering applications. Accurate behavior of dynamical systems can be understood using large scale simulations which traditionally requires expensive supercomputing facilities. In the paper a Field Programmable Gate Array (FPGA) based framework is described to accelerate simulation of complex physical spatio-temporal phenomena. Simulating complicated geometries requires unstructured spatial discretization which results in irregular memory access patterns severely limiting computing performance. Data locality is improved by mesh node renumbering technique which results in predictable memory access pattern. Additionally storing a small window of cell centered state values in the on-chip memory of the FPGA can increase data reuse and decrease memory bandwidth requirements. Generation of the floating-point data path and control structure of the arithmetic unit containing dozens of operators is a very challenging task when the goal is high operating frequency. Efficiency and use of the framework is described by a case study solving the Euler equations on an unstructured mesh using finite volume technique. On the currently available largest FPGA the generated architecture contains three processing elements working in parallel providing 90 times speedup compared to a high performance microprocessor.

Keywords: Field Programmable Gate Arrays, finite volume method, simulation acceleration, unstructured mesh

NOMENCLATURE

E	$[-]$	total energy density
F	$[-]$	flux vector
U	$[-]$	conservative state vector
c	$[m/s]$	local speed of sound
p	$[Pa]$	pressure
t	$[s]$	time
v	$[m/s]$	velocity vector
γ	$[-]$	ratio of specific heats
ρ	$[kg/m^3]$	density

1. INTRODUCTION

The number of transistors integrated into a single integrated circuit doubles in every 18 months according to Moore's Law. On the recent devices around 4 billion transistors can be implemented. Since the early 2000's the operating frequency of the conventional high-performance microprocessors is stopped in the 3-4GHz range due to power consumption limitations. As the number of transistors is increased significantly the main question is how to use them efficiently to create high performance computing systems. One possible solution is to integrate several conventional processors into the same chip creating a multi-core processor. Another way is to use the general purpose computing power of Graphics Processing Units (GPU), where hundreds of simpler processing elements can work in parallel. A more efficient way to increase computing power might be to design an application specific accelerator and implement it on a Field Programmable Gate Array (FPGA). Due to increased transistor density around one hundred double precision floating-point adders and multipliers can be implemented on the recent devices. Several previous studies proved the efficiency of field programmable logic devices in numerical simulation of various physical phenomena such as electromagnetic [1], transient wave [2] [3] and computational fluid dynamics [4] [5] simulations.

The most obvious way to solve complex spatio-temporal problems is numerical approximation over a regular mesh structure. Practical applications usually contains complex boundaries which can be handled by unstructured meshes more efficiently. The resolution of the mesh can be increased near rapid changes in the dynamics or shape of the problem. Unfortunately conventional microprocessors has around 10% utilization during unstructured mesh computations [6] due to the irregular memory access pattern of grid data.

To accelerate the computation irregular memory access patterns should be hidden by temporally storing the relevant grid points in the on-chip memory of the FPGA. Mesh points have to be properly ordered to minimize the size of this temporary memory. This optimization task is equivalent to the Matrix Bandwidth Minimization problem when the mesh is treated as an undirected graph and the bandwidth of the adjacency matrix of the graph is minimized.

When an explicit finite volume method is used during the solution of a PDE a complex mathematical expression must be computed on the neighborhood of each node. The complexity of the resulting arithmetic unit is determined by the governing equations and the discretization method used. Usually the arithmetic unit is constructed using dozens of floating-point units which makes manual design very tedious and error-prone. Therefore an automatic tool was developed to generate the arithmetic unit using the discretized governing equations.

2. FIELD PROGRAMMABLE GATE ARRAYS

The term programmable logic device (PLD) is used referring to any type of integrated circuit that can be configured by the end user for a special design implementation. If the device is programmed ”in the field” by the end user it is also called field programmable logic device.

FPGAs are usually built of coarse-grained blocks called configurable logic block (CLB). The CLB usually contains a logic function generator and a storage element pair, but it can be a dedicated resource such as multiplier, memory or even a complete microprocessor. The configurable logic blocks are arranged on a 2 dimensional grid which is surrounded by I/O cells as shown in Figure 1. The logic blocks are connected via a programmable routing architecture, which allows arbitrary interconnection between the logic blocks. The routing architecture contains vertical routing channels between the columns of logic blocks and horizontal routing channels between the rows. The routing channels provide a net of programmable wires for direct connections between the adjacent logic blocks, variable length general-purpose interconnections and long lines, which span the entire width or height of the chip.

The basic building block of a Xilinx Virtex CLB

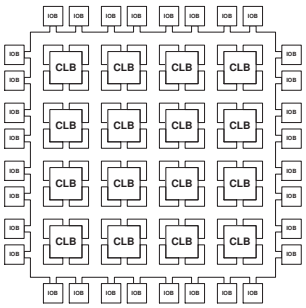

Figure 1. Symmetrical FPGA architecture

[7] is the slice shown in Figure 2. Each slice contains four 6-input function generators, four storage elements and four carry generators. The CLB is built form two slices. The function generator in the slice can implement any 6-input logic function. In addition to operating as function generator each LUT can be configured as 64×1 bit synchronous RAM. The LUTs also can be configured as a 32-bit shift register, which can be very efficient in deeply pipelined architectures.

The Virtex FPGAs has hierarchical memory system along with the RAM resources in the CLBs, dedicated on-chip memory elements (BRAM) are also implemented. Each memory element is a synchronous dual-ported 36kbit RAM with independent control signals and independently configurable data widths. These memories can be very efficiently used to store temporary data on the FPGA.

Another dedicated configurable element on the Xilinx FPGAs is the DSP slice which is designed to improve the performance in digital signal processing applications. The most common operations in these applications are multiplication and addition. Therefore each DPS slice contains a 25bit by 18bit multiplier and a 48bit wide adder/accumulator. These DSP slices can be efficiently used to create floating-point adder

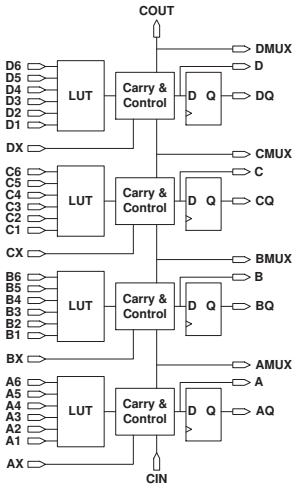

Figure 2. Structure of a Virtex-5 slice

and multiplier units. On the largest Xilinx Virtex-6 FPGA device 74,400 Slices, 2,016 DSP48E1 Slices and 1,064 36kbit BRAMs implemented. The huge amount of configurable resources makes these devices ideal candidate to implement high performance computing applications.

During the implementation of an application on an FPGA the algorithm should be rewritten in a Hardware Description Language such as VHDL or Verilog. These descriptions are then synthesized to digital circuits and a configuration bitstream is generated which can be used to program the device.

3. RELATED WORK

Several papers were published in the early 2000s [8, 9] dealing with the acceleration of Partial Differential Equations (PDE) on unstructured meshes. Most of them were focused on accelerating Finite Element Methods (FEM) where the global stiffness matrix is given and the resulting large linear system of equations are solved usually by the iterative Conjugate Gradient (CG) method. The most time consuming operation of this method is a sparse matrix vector multiplication therefore most of the papers try to accelerate this part. Though our architecture is designed for explicit unstructured finite volume calculations, examination of these architectures is helpful because similar problems arising in our case. For example the adjacency matrix of the mesh is sparse and elements of the state vector are accessed in a random order.

Elkurdi et al. [10] proposed a process where the finite element sparse matrix was reorganized into a banded form in the first step. Then the matrix vector multiplication was calculated along special pipelineable diagonal stripes, where two successive elements could be processed by a pipelined architecture. Performance of the architecture was determined by the available memory bandwidth and the sparsity of the matrix, however utilization of the processing elements was varying in a very wide range between $17.74 - 86.24\%$.

Recently Nagar et al. [11] proposed an architecture using an optimized Streaming Multiply-Accumulator with separate cache memories for matrix and vector data. The implementation platform they used has special memory architecture providing high 20GB/s peak memory bandwidth. Performance of the system with four FPGAs is in the $1.17 - 3.94$GFLOPs range outperforming a Tesla 1070 GPU. However utilization of the PEs is around 50% similarly to the previous architectures and increasing the number of PEs to occupy the entire FPGA still runs into a memory bandwidth limit.

The surveyed architectures provide general solutions to accelerate FEM calculations on FPGAs but suffer from the inherent high memory bandwidth requirement and small communication to computation ratio of sparse matrix vector multiplication. On the other hand utilization of the execution units depends on the structure of the sparse matrix.

Irregular memory access pattern and high memory bandwidth requirement can be eliminated by storing a small part of the grid on-chip and reordering its nodes. Right hand side of the discretized equations should be computed for each volume in every timestep, which requires several floating-point operations, resulting in better communication to computation ratio and higher utilization of FPGA resources.

4. FLUID FLOWS

A wide range of industrial processes and scientific phenomena involve gas or fluids flows over complex obstacles, e.g. air flow around vehicles and buildings, the flow of water in the oceans or liquid in BioMEMS. In such applications the temporal evolution of non-ideal, compressible fluids is quite often modelled by the system of Navier-Stokes equations. The model is based on the fundamental laws of mass-, momentum- and energy conservation, including the dissipative effects of viscosity, diffusion and heat conduction. By neglecting all non-ideal processes and assuming adiabatic variations, we obtain the Euler equations [12, 13], describing the dynamics of dissipation-free, inviscid, compressible fluids. They are a coupled set of nonlinear hyperbolic partial differential equations, in conservative form expressed as

$$\frac{\partial \rho}{\partial t} + \nabla \cdot (\rho \mathbf{v}) = 0 \tag{1a}$$

$$\frac{\partial (\rho \mathbf{v})}{\partial t} + \nabla \cdot \left(\rho \mathbf{v}\mathbf{v} + \hat{I}p \right) = 0 \tag{1b}$$

$$\frac{\partial E}{\partial t} + \nabla \cdot ((E+p)\mathbf{v}) = 0 \tag{1c}$$

$$E = \frac{p}{\gamma - 1} + \frac{1}{2}\rho \mathbf{v} \cdot \mathbf{v}. \tag{1d}$$

In equation (1d) the value of the ratio of specific heats is taken to be $\gamma = 1.4$. For later use we introduce the conservative state vector $\mathbf{U} = [\rho, \rho u, \rho v, E]^T$, the set of primitive variables $\mathbf{P} = [\rho, u, v, p]^T$ and the speed of sound $c = \sqrt{\gamma p/\rho}$. It is also convenient to merge (1a), (1b) and (1c) into hyperbolic conservation law form in terms of U and the flux tensor

$$\mathbf{F} = \begin{pmatrix} \rho \mathbf{v} \\ \rho \mathbf{v}\mathbf{v} + Ip \\ (E+p)\mathbf{v} \end{pmatrix} \tag{2}$$

as:

$$\frac{\partial U}{\partial t} + \nabla \cdot \mathbf{F} = 0. \tag{3}$$

5. DISCRETIZATION OF THE GOVERNING EQUATIONS

Logically structured arrangement of data is a convenient choice for the efficient operation of the FPGA based implementations [5]. However, structured

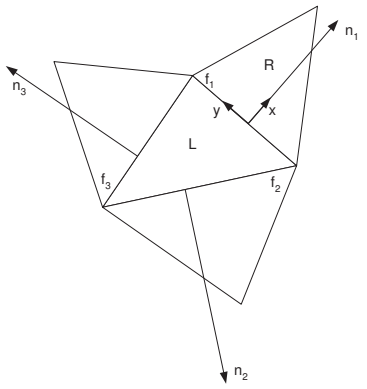

Figure 3. Interface with the normal vector and the cells required in the computation

data representation is not flexible for the spatial discretization of complex geometries. As one of the main innovative contributions of this paper, here we consider an unstructured, cell-centered representation of physical quantities. In the following paragraphs we describe the mesh geometry, the update scheme, and the main features of the numerical algorithm.

5.1. The geometry of the mesh

The computational domain Ω is composed of non-overlapping triangles. The i-th face of triangle $\mathcal{T}$ is labelled by f_i. The normal vector of f_i pointing outward $\mathcal{T}$ that is scaled by the length of the face is $\mathbf{n_i}$. The volume of triangle $\mathcal{T}$ is $V_\mathcal{T}$. Following the finite volume methodology, all components of the volume averaged quantities are stored at the mass center of the triangles.

5.2. The Discretization Scheme

Application of the cell centered finite volume discretization method leads to the following semi-discrete form of governing equations (3)

$$\frac{dU_\mathcal{T}}{dt} = -\frac{1}{V_\mathcal{T}} \sum_f \mathbf{F}_f \cdot \mathbf{n}_f, \tag{4}$$

where the summation is meant for all three faces of cell $\mathcal{T}$, and $\mathbf{F}_f$ is the flux tensor evaluated at face f. Let us consider face f in a coordinate frame attached to the face, such, that its x-axes is normal to f (see Fig. 3). Face f separates triangle L (left) and triangle R (right). In this case the $\mathbf{F}_f \cdot \mathbf{n}_f$ scalar product equals to the x-component of $\mathbf{F}$ (i.e. F_x) multiplied by the area of the face. In order to stabilize the solution procedure, artificial dissipation has to be introduced into the scheme. According to the standard procedure, this is achieved by replacing the physical flux tensor by the numerical flux function F^N containing the dissipative stabilization term. A finite volume scheme is characterized by the evaluation of F^N, which is the function of both U_L and U_R. In this paper we employ the simple and robust Lax-Friedrichs numerical flux function defined as

$$F^N = \frac{F_L + F_R}{2} - (|\bar{u}| + \bar{c}) \frac{U_R - U_L}{2}. \tag{5}$$

In the last equation F_L=$\mathrm{F}_x(\mathrm{U}_L)$ and F_R=$\mathrm{F}_x(\mathrm{U}_R)$ and notations $|\bar{u}|$ and $|\bar{c}|$ represent the average value of the u velocity component and the speed of sound at an interface, respectively. The temporal derivative is dicretized by the first-order forward Euler method:

$$\frac{dU_\mathcal{T}}{dt} = \frac{U_\mathcal{T}^{n+1} - U_\mathcal{T}^n}{\Delta t}, \tag{6}$$

where $U_\mathcal{T}^n$ is the known value of the state vector at time level n, $U_\mathcal{T}^{n+1}$ is the unknown value of the state vector at time level $n+1$, and Δt is the time step.

By working out the algebra described so far, leads to the discrete form of the governing equations to compute the numerical flux term F.

$$U_\mathcal{T}^{n+1} = U_\mathcal{T}^n - \frac{\Delta t}{V_\mathcal{T}} \sum_f \hat{\mathcal{R}}_{\mathbf{n_f}} F_f |\mathbf{n_f}|, \tag{7}$$

where $\hat{\mathcal{R}}_{\mathbf{n_f}}$ is the rotation tensor describing the transformation from the normal-parallel coordinate frame of face f to the $x-y$ frame. Quantity F_f is defined in a coordinate frame attached to face f, with such an orientation that state left is identical to the state of the update triangle $\mathcal{T}$ while state right corresponds to the state of the triangle situated at the opposite side of the face. With these conventions, the normal component of the numerical flux function is given by

$$\begin{aligned}
F_f^\rho &= \frac{\rho_L u_L + \rho_R u_R}{2} \\
&\quad + (|\bar{u}| + \bar{c}) \frac{\rho_R - \rho_L}{2} && \text{(8a)} \\
F_f^{\rho u} &= \frac{\left(\rho_L u_L^2 + p_L\right) + \left(\rho_R u_R^2 + p_R\right)}{2} \\
&\quad + (|\bar{u}| + \bar{c}) \frac{\rho_R u_R - \rho_L u_L}{2} && \text{(8b)} \\
F_f^{\rho v} &= \frac{\rho_L u_L v_L + \rho_R u_R v_R}{2} \\
&\quad + (|\bar{u}| + \bar{c}) \frac{\rho_R v_R - \rho_L v_L}{2} && \text{(8c)} \\
F_f^E &= \frac{\left(E_L + p_L\right) u_L + \left(E_R + p_R\right) u_R}{2} \\
&\quad + (|\bar{u}| + \bar{c}) \frac{E_R - E_L}{2} && \text{(8d)}
\end{aligned}$$

The arithmetic unit for the computation of (8a) to (8d) is generated and partitioned using the algorithm described in [14]. Block diagram of the resulting arithmetic unit is shown in Figure 4. Additionally a simple arithmetic unit is required to compute u, v, p, c values for each cell. The two arithmetic units contain 31 adders/subtractors and 38 multipliers, one reciprocal and one square root unit. Multiplication and division by powers of two is implemented by modifying the

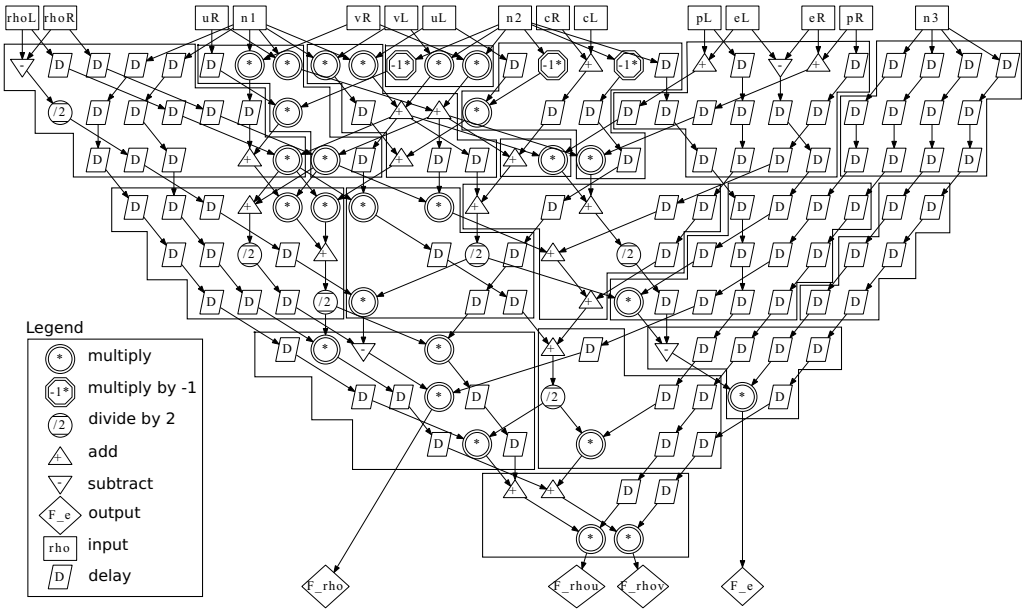

Figure 4. The partitioned arithmetic unit generated from equations (8a) to (8d)

exponent of the floating point numbers. A new interface value can be computed in each clock cycle therefore three clock cycles are required for updating each cell.

6. ARCHITECTURE

For practical applications the number of cells is far exceeding the available on-chip memory of recent FPGAs therefore cell centered state and constant values must be stored and loaded from an off-chip memory. Overlapping input data sets can be utilized to reduce the number of memory accesses and save memory bandwidth by storing all cells which required during the following computations into a local memory on the FPGA.

In case of structured grids neighbors of each cell can be determined by its array index. For unstructured grids connected cells can be described by a sparse adjacency matrix. Processing order of the cells and the memory access pattern is determined by the numbering of the volumes. The numbering produced by the mesh generator is not appropriate for the FPGA implementation because nonzero elements of the adjacency matrix are usually distributed randomly. To avoid nonuniform off-chip memory access all cell centered state values must be stored on-chip which severely limits the number of volumes. Therefore the cells should be reordered to get a banded adjacency matrix with bandwidth BW using a matrix bandwidth reduction algorithm [15]. When the i^{th} cell is processed only volumes in the $[i-BW, i+BW]$ index range must be stored on-chip. After the i^{th} cell is updated the center of the window is moved to the next cell. The oldest $(i-BW)^{th}$ cell can be discarded and the new $(i+1+BW)^{th}$ cell must be loaded.

Main parts of the proposed processor architecture are the Memory unit, the Neighborhood memory unit and the Arithmetic unit as shown in Figure 5. The Memory unit is built from dual ported on-chip BRAM memories and store a small part of cell centered state values. The minimal size of the on-chip memory is determined by the bandwidth of the adjacency matrix of the mesh. Computation of the updated cell value is carried out in an element by element order by the arithmetic unit. Therefore the new state value can be computed in 3 or 4 cycles in the case of 2D and 3D cell centered discretization, respectively.

Computation is started by loading serial sequence of state values into the Memory unit until it is half filled. In this phase value of the first cell is loaded to the Current node register and the Neighborhood memory is filled by its neighbors using the incoming connectivity descriptors. When all neighbors are loaded valid stencil data can be send to the arithmetic unit in each clock

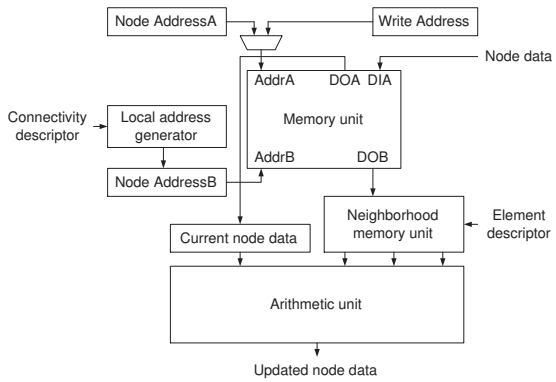

Figure 5. Block diagram of the proposed processor architecture

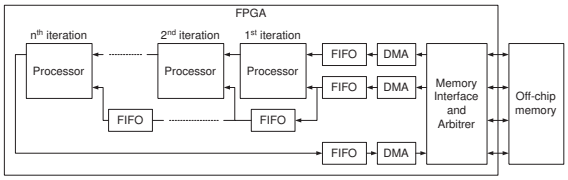

Figure 6. Block diagram of the proposed architecture

Table 1. Area requirements of the arithmetic unit

		Double		
	Number	DSP	LUT	FF
Mult	38	418	10,260	15,998
Add/Sub	31	93	21,948	29,295
Sqrt	1	0	1,957	3,243
Rec	1	14	378	536
Total		525	34,543	49,072
XC6VSX475T usage		26.04%	11.61%	8.24%

cycle. After computing all faces of the cell Node addressA register is incremented and the second cell is loaded into the Current node register. During this clock cycle new cell centered state value can be written into the Memory unit and computation of the second cell is started. After an initial latency of the arithmetic unit the updated state values are written back to the off-chip memory in the same sequential order as they are loaded.

Another advantage of the sequential load and store of state values is the straightforward utilization of task level parallelism between iteration steps of the explicit time integration. High-level block diagram of the proposed multi core architecture is shown in Figure 6. The memory interface provides the physical interface for the off-chip memory and arbitration between the DMA engines competing for the memory. The reordered state values and descriptor data can be loaded into the input FIFOs in long sequential bursts by the DMA engines. Computed new state values are stored in an output FIFO and can be written back to the off-chip memory in long sequential bursts.

State of the system is usually saved after computing hundreds of explicit timesteps during the computation. The results of the first iteration can be feed into a second processor element directly. This processor must wait until its Memory unit is half filled to start computation of the second iteration. The results of the second iteration can be either saved into the off-chip memory or feed into another processor. In this case a large FIFO is required to store the previously loaded connectivity and element descriptors between the two computation stages. The length of the pipeline chain is only limited by the available logic and memory resources on the FPGA. After a short initial startup latency, which is negligible compared to the number of cells, the pipelined chain of processors can work in parallel providing linear speedup without increasing memory bandwidth requirements.

The main advantage of the proposed architecture is the sequential off-chip memory access pattern when reading cell centered state value and descriptor arrays and writing updated state values. Each array is stored in a FIFO buffer therefore data can be moved by using an optimal burst length and penalties of random memory read and write patterns can be eliminated. Maximum size of the mesh is limited by the bandwidth of the adjacency matrix. Using today large, high performance FPGAs even 40,000-80,000 cells can be stored on-chip, which is usually enough for practical 2D applications.

7. RESULTS, PERFORMANCE

The generated arithmetic unit is implemented on our AlphaData ADM-XRC-6T1 reconfigurable development system [16] equipped with a Xilinx Virtex-6 XC6VSX475T FPGA [7] and 2Gbyte on-board DRAM in four 32bit wide banks running on $800MHz$ providing $12.8Gbyte/s$ peak theoretical bandwidth. During implementation the memory interface of the the AlphaData SDK and the standard Xilinx floating-point cores are used.

In our test case the cell centered approach is used therefore each triangle is represented by a volume and each volume has 3 neighbors except at the boundaries where ghost volumes are used to implement inflow, outflow or wall boundary conditions. For simplicity size and normal vector of all faces are precomputed which results in higher memory bandwidth requirement, but the arithmetic unit will be simpler. Therefore the actual connectivity descriptor structure has 4 fields: the 16 bit wide index of the neighboring volume, the x and y coordinates of the normal vector of the face and its length. The width of each descriptor is 26 byte.

The volume data structure contains four time dependent variables $[\rho, \rho u, \rho v, E]$ and the area of the triangle as a constant. Additionally pressure p and local speed of sound c which is computed on the FPGA for each volume also should be stored. When all BRAMs are allocated for the Memory unit 83,456 volumes can be stored on the FPGA which is usually more than enough for practical 2D meshes. When multiple processors are used in a pipeline to speed up computation connectivity descriptors should be saved into a FIFO as shown in Figure 6. Therefore the number of volumes stored in the Memory units altogether is reduced to 34,816 in a multiprocessor configuration.

Area requirements of the implemented double precision arithmetic unit and the utilization of the Virtex-6 SX475T FPGA on our prototyping board are summarized on Table 1.

Utilization of the FPGA shows that the most limiting factor of the implementation is the number of DSP48E slices and the number of implementable processors is three when computing with double

precision. The maximum bandwidth of the adjacency matrix of the mesh which can be handled by the three processors connected into a pipeline is 11,264 volumes.

Performance of our architecture is determined using the result of the post place and route static timing analysis which is indicated 390MHz operating frequency in the double precision case. Three clock cycles are required to update the state of one triangle therefore performance of one processor is 130million triangle update/s. Computation of one triangle requires 213 floating point operations therefore performance of our architecture is 27.69$GFLOPs$. On the Virtex-6 XC6VSX475T FPGA three arithmetic units can be implemented and connected in a pipeline resulting in 83.07$GFLOPs$ cumulative computing performance.

We tried to use performance data reported in previous works, but fair comparison is hard because different CFD models, discretization schemes and FPGA architectures are used during the implementations. Smith and Schnore [17] published an FPGA based CFD solver, but they used 3D model and smaller neighborhood during the computation. Additionally their architecture was implemented on several FPGAs. In the solution of the Euler equations they reported 24.6$GFlops$ sustained performance on four Virtex-II 6000 FPGAs. Sano et al. [4] used 2D systolic array to solve 2D flow problems and reported 11.5$GFlops$ peak performance on an ALTERA Stratix II FPGA.

Performance of our architecture is compared to a high performance Intel Xeon E5620 microprocessor running on 2.4GHz clock frequency. During a comparison various mesh sizes are used with 7,063 to 394,277 triangles. The measured performance of the microprocessor is 4.22million triangle update/s or equivalently 898.86$MFLOPs$.

According to our measurements performance of our architecture does not depend on the size of the mesh in the test cases. Comparison of the performance of the two architectures shows that a single processor implemented on the FPGA can outperform the Intel Xeon processor by computing 30 times faster. By connecting three processors into a pipeline on a single FPGA linear speedup can be achieved and 90 times more computing power can be provided than a microprocessor.

7.1. Test setup

To show the efficiency of our solution a complex test case was used, in which a Mach 3 flow over a forward facing step was computed. The simulated region is a two dimensional cut of a pipe which has closed at the upper and lower boundaries, while the left and right boundaries are open. The direction of the flow is from left to right and the speed of the flow at the left boundary is 3 times the speed of sound constantly. The solution contains shock waves reflecting from the closed boundaries.

Unstructured mesh for the domain is generated by the freely available Gmsh mesh generator [18]. Several meshes are generated using different characteristic length between $1/30 - 1/200$ and the characteristic length of the elements near the corner of the step is divided by 12.5. The number of triangles in the resulting meshes is ranging in the 7,063-394,277 interval. An example mesh generated by using $1/40$ characteristic length and containing 12,297 triangles is shown in Figure 7.

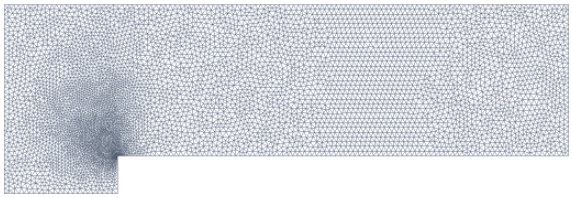

Figure 7. Coarse resolution mesh for the forward facing step test case

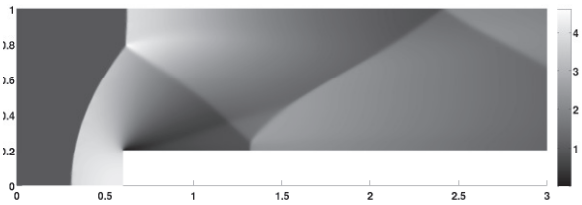

Figure 8. First-order solution of the Mach 3 flow after 4s of simulation time on a 394,277 triangle mesh

Result of the computation on the largest simulated grid after 4s of simulation time is shown in Figure 8. The required timestep is 56.81ms and 70,400 iterations are computed to get the result. Reference solution for the previous problem computed by the more accurate residual distribution upwind scheme can be found in [19]. Using double precision numbers 12.6Mbyte memory should be allocated for the initial state of the simulation and 30.7Mbyte for the connectivity descriptors. Communication time to download initial state and connectivity descriptors into the on-board memory from the host memory is 69.61ms and the result can be read in 20.25ms via the x8 PCI-Express interface of the board. Computation of the result using three arithmetic units is performed in 71.1s therefore communication between the host and the FPGA can be neglected. The same computation requires 1 hour 50 minutes on the Intel Xeon microprocessor.

8. CONCLUSIONS

A framework for accelerating the solution of the 2D Euler equations using explicit unstructured finite volume discretization is presented. Efficient use of the on-chip memory is provided by a node reordering algorithm. Irregular memory access patterns can be eliminated by using the proposed memory structure which results in higher available memory bandwidth

and full utilization of the arithmetic unit. The discretized state equations are automatically translated to a synthesizable VHDL description using Xilinx floating-point IP cores.

Performance comparison of the architecture using a single processor running on $390MHz$ showed that 30 times speedup can be achieved compared to a high performance microprocessor. Computing performance can be further improved by implementing three processors on one FPGA reaching 90 times speedup.

Currently the size of the mesh is limited by the bandwidth of its adjacency matrix which must be smaller than 80,000. The architecture should be improved to efficiently handle multiple partitions and extended to use multiple FPGAs during computation.

ACKNOWLEDGMENTS

This research project supported by the János Bolyai Research Scholarship of the Hungarian Academy of Sciences. The support of the grants TÁMOP-4.2.1.B-11/2/KMR-2011-0002, TÁMOP-4.2.2/B-10/1-2010-0014, OTKA Grant No. K84267 and in part by OTKA Grant No. K68322 is gratefully acknowledged.

References

[1] J. P. Durbano, F. E. Ortiz, J. R. Humphrey, P. F. Curt, and D. W. Prather. FPGA-Based Acceleration of the 3D Finite-Difference Time-Domain Method. In *Field-Programmable Custom Computing Machines, Annual IEEE Symposium on*, pages 156–163, 2004.

[2] C. He, W. Zhao, and M. Lu. Time Domain Numerical Simulation for Transient Waves on Reconfigurable Coprocessor Platform. In *Field-Programmable Custom Computing Machines, Annual IEEE Symposium on*, pages 127–136, 2005.

[3] P. Sonkoly, I. No, J. M. Carcione, Z. Nagy, and P. Szolgay. CNN-UM based transversely isotropic elastic wave propagation simulation. In *Proc. of 18th European Conference on Circuit Theory and Design*, pages 284–287, 2007.

[4] K. Sano, T. Iizuka, and S. Yamamoto. Systolic Architecture for Computational Fluid Dynamics on FPGAs. In *Proc. of the 15^{th} IEEE Symposium on Field-Programmable Custom Computing Machines (FCCM 2007)*, pages 107–116, 2007.

[5] S. Kocsárdi, Z. Nagy, Á. Csík, and P. Szolgay. Simulation of 2D inviscid, adiabatic, compressible flows on emulated digital CNN-UM. *International Journal on Circuit Theory and Applications*, 37(4):569–585, 2009.

[6] David A. Bader. *Petascale computing algorithms and applications*. Chapman and Hall/CRC, 2007.

[7] Xilinx Inc. http://www.xilinx.com/, 2011.

[8] M. T. Jones and K. Ramachandran. Unstructured mesh computations on CCMs. *Advances in Engineering Software*, 31:571–580, 2000.

[9] M. deLorimier and A. DeHon. Floating-Point Sparse Matrix-Vector Multiply for FPGAs. In *Proceedings of the International Symposium on Field Programmable Gate Arrays*, pages 75–85, 2005.

[10] Y. Elkurdi, D. Fernndez, E. Souleimanov, D. Giannacopoulos, and W. J. Gross. FPGA architecture and implementation of sparse matrixvector multiplication for the finite element method. *Computer Physics Communications*, 178:558–570, 2008.

[11] K. K. Nagar and J. D. Bakos. A Sparse Matrix Personality for the Convey HC-1. In *Field-Programmable Custom Computing Machines (FCCM), 2011 IEEE 19th Annual International Symposium on*, pages 1–8, may 2011.

[12] J. D. Anderson. *Computational Fluid Dynamics - The Basics with Applications*. McGraw Hill, 1995.

[13] T. J. Chung. *Computational Fluid Dynamics*. Cambridge University Press, 2002.

[14] C. Nemes, Z. Nagy, and P. Szolgay. Efficient Mapping of Mathematical Expressions to FPGAs: Exploring Different Design Methodologies. In *Proceedings of the 20th European Conference onCircuit Theory and Design*, pages 750–753, 2011.

[15] E. Cuthill and J. McKee. Reducing the bandwidth of sparse symmetric matrices. In *Proceedings of the ACM National Conference, Association for Computing Machinery, New York*, pages 157–172, 1969.

[16] Alpha Data Inc. http://www.alpha-data.com/, 2011.

[17] W. D. Smith and A. R. Schnore. Towards an RCC-Based Accelerator for Computational Fluid Dynamics Applications. *Journal of Supercomputing*, 30(3):239–261, 2004.

[18] C. Geuzaine and J.-F. Remacle. Gmsh: a three-dimensional finite element mesh generator with built-in pre- and post-processing facilities. *International Journal for Numerical Methods in Engineering*, 79:1309–1331, 2009.

[19] Á. Csík and H. Deconinck. Space-time residual distribution schemes for hyperbolic conservation laws on unstructured linear finite elements. *International Journal for Numerical Methods in Fluids*, 40:573–581, 2002.

Conference on Modelling Fluid Flow (CMFF'12)
The 15th International Conference on Fluid Flow Technologies
Budapest, Hungary, September 4-7, 2012

EFFECT OF THE INSTANTANEOUS LARGE-SCALE FLOW STRUCTURES ON THE TURBULENT DISPERSION OF PARTICLES IN A NATURAL CONVECTION BOUNDARY LAYER

Jordi PALLARES[1], Francesc X. GRAU[2]

[1] Corresponding Author. Department of Mechanical Engineering, University Rovira i Virgili. Av. Països Catalans 26, 43007-Tarragona, Spain. Tel.: +34 977 559 682, Fax: +34 977 559 691, E-mail: jordi.pallares@urv.cat
[2] Department of Mechanical Engineering, University Rovira i Virgili. E-mail: francescxavier.grau@urv.cat

ABSTRACT

We analyzed numerically the effect of the instantaneous flow structures in a turbulent natural convection flow on the instantaneous particle distribution near the wall. We performed a direct numerical simulation of the flow in a vertical plane channel and we tracked inertial particles until the flow and the particle distribution were statistically in steady state. Under these conditions we generated a database that contains the temperature, the velocities and the location of the particles during $0.2 \cdot H^2/\alpha$. The analysis of the database using a conditional sampling technique shows that the flow structures responsible for the large positive fluctuations of the wall heat transfer rate produce a localized instantaneous reduction of the particle concentration near the wall of about 50%. On the other hand, the structures that produce extreme negative values of the heat transfer rate are associated with an increase of the instantaneous particle concentration near the wall of about 30%.

Keywords: channel flow, conditional sampling, direct numerical simulation, natural convection, particles, turbulence

NOMENCLATURE

C	[*particles* m^{-3}]	particle concentration
C_d	[-]	drag coefficient
d	[m]	diameter
g	[$m\ s^{-2}$]	gravity
H	[m]	channel width
Pr	[-]	Prandtl number
Ra	[-]	Rayleigh number
St	[-]	Stokes number; $St=t_p/t_f$
T	[K]	temperature
t	[s]	time
t_f	[s]	flow time scale; $t_f=(\nu/u_\tau^2)$
t_p	[s]	particle time scale; $t_p=d_p^2\rho_p/18\mu$
u,v,w	[$m\ s^{-1}$]	velocity components
u_τ	[$m\ s^{-1}$]	friction velocity; $u_\tau=(\tau_w/\rho)^{1/2}$
x,y,z	[m]	Cartesian coordinates

Greek letters

Δ	[-]	increment
α	[$m^2\ s^{-1}$]	thermal diffusivity
β	[K^{-1}]	coefficient of thermal expansion
δ_{ij}	[-]	Kronecker's delta
μ	[$Pa\ s$]	dynamic viscosity
ν	[$m^2\ s^{-1}$]	kinematic viscosity
ρ	[$kg\ m^{-3}$]	density
τ	[Pa]	shear stress

Subscripts and Superscripts

$*$	non-dimensional quantity
c	cold
f	fluid
h	hot
p	particle
w	wall

Special symbols

$\langle\ \rangle$	time-averaged quantity

1. INTRODUCTION

Flows that transport small particles, bubbles or drops can be found in many engineering, industrial and environmental situations. The determination of the rates and the mechanisms responsible for the dispersion and deposition on solid surfaces of the dispersed phase has been the topic of many studies because they have important implications in practical problems. Reviews on the topic can be found elsewhere [1, 2]. The analyses of particulate flows in natural convection are scarce in the literature. The deposition of aerosol particles in laminar natural convection boundary layer was considered by Nazaroff and Cass [3] and Tsai [4] and by Akbar et al. [5] in laminar free convection in a square enclosure. However, the dispersion and

deposition of aerosol and small particles in turbulent natural convection flows have implications, for example, in the air indoor quality and in the fouling of art pieces in museums and exhibitions.

It is known that particles in wall-bounded turbulent flows tend to accumulate near the wall. This phenomenon, often refereed as "turbophoresis" [1], is produced by the larger turbulence intensity far from the wall than near the wall region. The accumulation of particles near the walls can be also understood considering that the particle fluxes towards the wall are more efficient than the particle fluxes away from the wall.

The determination and analyses of the time-averaged quantities near the wall in turbulent flows provide quantitative information useful for design purposes and to understand the overall interaction of the flow with the wall. The study of the statistics and the dynamics of the instantaneous fluctuations of the wall transfer rates or, for example, of the particle concentration in particulate flows can be considered a step forward in the understanding of the interaction between the flow and the wall. Particularly, it is interesting to detect and to describe the dynamics of the near wall flow structures since they are responsible for the instantaneous fluctuations of the wall transfer rates and of the particle concentrations in particulate flows. Knowing how these structures evolve and interact with the wall provide information that can be used to develop efficient techniques to manipulate the flow in order to obtain a desired modification of the wall transfer rates or of the particle concentration near the wall.

In this study, direct numerical simulations (DNS) of particle dispersion in the turbulent natural convection flow between two vertical walls kept at constant but different temperatures are reported. It is assumed that the particles do not affect the flow (i.e. the dilute phase approximation is adopted). The effects of the instantaneous large-scale flow structures on the particle distribution near the wall are analyzed using a conditional sampling technique.

2. PHYSICAL MODEL

Figure 1 shows the coordinate system and the computational domain, which models an infinite channel in the x and z directions. The natural convection flow, driven by the temperature difference imposed at the walls of the channel, is assumed to be hydrodynamically and thermally fully developed. The two walls of the channel located at y=-H/2 and y=H/2 are rigid, smooth and they are kept at constant but different temperatures. All physical properties of the fluid, with a Prandtl number (Pr=ν/α) of 0.7, are considered constant except for the linear variation of the density with temperature which is considered only in the buoyancy term according to the Boussinesq approximation. The viscous dissipation and the radiation heat transfer are neglected.

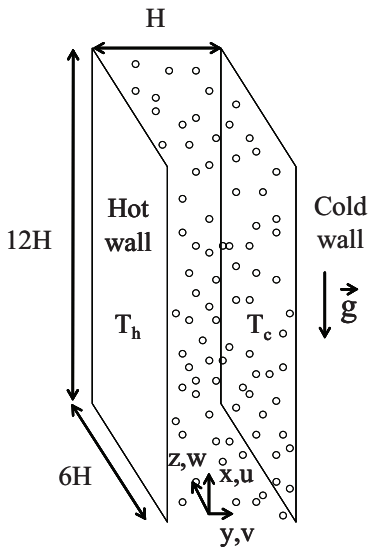

Figure 1. Physical model and coordinate system

The particles are assumed to be spherical and the heat and/or mass transfer between the fluid and the particles are neglected. The collisions between the particles are not considered. It is assumed that the particles do not affect the flow and the fluid properties. The only force considered acting in the particles is the hydrodynamic drag force. The gravity force acting on the particles, the pressure gradient force, the Basset force, the virtual mass force, the Brownian force, the Saffman's lift force and the thermophoretic force are neglected. Table 1 shows the different sizes of the particles and the non-dimensional parameters considered for the simulations. The value of the non-dimensional friction velocity, $u_\tau^*=u_\tau H/\alpha=(Pr\cdot dU^*/dy^*|_w)$, which is used to compute the Stokes number is included in Table 1.

Table 1. Non-dimensional parameters

Ra	Pr	$u_\tau^*=u_\tau H/\alpha$	ρ_{fp}^*	St	dp^*
$5.4\ 10^5$	0.7	88.56	$1.30\cdot10^{-3}$	0.843	$1.11\ 10^{-3}$
				1.75	$1.60\ 10^{-3}$
				8.38	$3.50\ 10^{-3}$
				17.45	$5.05\ 10^{-3}$

Considering the properties of air at ambient temperature, a possible set of dimensional parameters that corresponds to the non-dimensional values of Table 1 are, H=0.0662 m, ρ_p=1000 kg/m^3 and ΔT=20 K. Accordingly, the particle diameter

ranges from 73.5 μm (St=0.843) to 335 μm (St=17.45). Under these physical conditions the thermophoresis force produced by the temperature gradient imposed to the fluid is, on average, about two orders of magnitude lower than the drag force for the smallest particles considered.

3. MATHEMATICAL MODEL

The non-dimensional continuity, Navier-Stokes and thermal energy equations, that govern the momentum and thermal energy of the fluid, are

$$\frac{\partial u_i^*}{\partial x_i^*} = 0 \,, \tag{1}$$

$$\frac{\partial u_i^*}{\partial t^*} + \frac{\partial u_j^* u_i^*}{\partial x_j^*} = -\frac{\partial p^*}{\partial x_i^*} + Pr\frac{\partial^2 u_i^*}{\partial x_j^{*2}} + \delta_{i1} Ra\, Pr\, T^* \tag{2}$$

and

$$\frac{\partial T^*}{\partial t^*} + \frac{\partial u_i^* T^*}{\partial x_i^*} = \frac{\partial^2 T^*}{\partial x_i^{*2}} \,, \tag{3}$$

respectively.

The scales used to obtain the non-dimensional variables are the channel width (H) and the thermal diffusion time (H^2/α). The non-dimensional temperature is defined as $T^*=(T-T_o)/(T_h-T_c)$ where T_h and T_c are the temperatures of the hot and cold wall, respectively, $T_o=(T_h+T_c)/2$ is the mean temperature and $\Delta T=T_h-T_c$ is the temperature increment. The last term on the right-hand side of Eq. (2) corresponds to the non-dimensional buoyancy acceleration along the x-direction. In Eq. (2) Ra is the Rayleigh number ($Ra=g\beta\Delta TH^3/\nu\alpha$), which has been set to $5.4\cdot10^5$ to obtain a turbulent flow [6]. Periodic boundary conditions for velocities and temperature are applied along the homogeneous x and z directions. The non-slip condition is imposed at the walls. The thermal boundary conditions are T^*=0.5 and T^*=-0.5 at the hot and cold wall, respectively.

Under the hypotheses indicated above, the position and the velocity of the particles are governed by

$$\frac{d\left(x_p^*\right)_i}{dt^*} = \left(u_p^*\right)_i \tag{4}$$

$$\frac{d\left(u_p^*\right)_i}{dt^*} = -\frac{3}{4}\frac{\rho_{fp}^*}{d_p^*} C_d \left|u_p^* - u^*\right| \left[\left(u_p^*\right)_i - \left(u^*\right)_i\right] \tag{5}$$

The term on the right hand side of Eq. (5) is the hydrodynamic drag force. In Eq. (5) $d_p^*=d_p/H$ and $\rho_{fp}^*=\rho_f/\rho_p$. See Table 1 for the values used for the simulations. The drag coefficient is computed as,

$$C_d = \frac{24}{Re_p}\left(1 + 0.15\, Re_p^{0.687}\right) \tag{6}$$

and the particle Reynolds number is

$$Re_p = \frac{d_p\left|u_p - u\right|}{\nu} = \frac{d_p^*\left|u_p^* - u^*\right|}{Pr} \tag{7}$$

Equation (6) is valid for Re_p<800 [1]

The governing transport equations for the fluid, Eqs. (1 to 3), together with the corresponding boundary conditions are solved numerically with the 3DINAMICS code. This second-order accuracy finite volume code uses central differencing of the diffusive and convective terms on a staggered grid. The use of centred schemes is preferred for DNSs to avoid the uncontrolled numerical diffusion introduced by the upwind discretisations. The Crank-Nicolson scheme is used for the temporal discretisation of the convection and diffusion terms while the buoyancy term in the vertical momentum equation is discretised with a second order Adams-Bashford explicit scheme. The Poisson equation resulting from the coupling between the velocity and pressure fields is solved with an efficient parallel multigrid solver.

The computational domain, with dimensions L_x=12.5·H, L_y=H, L_z=6.3·H, is divided into 121x100x121 grid nodes. They are uniformly distributed along the streamwise and spanwise homogeneous directions ($\Delta x\approx0.1\cdot H$ and $\Delta z\approx0.05\cdot H$) in which periodic boundary conditions are imposed, while hyperbolic tangent distributions are used to stretch the nodes near the walls ($\Delta y_{min}\approx1.7\cdot10^{-3}\cdot H$ and $\Delta y_{max}\approx2.2\cdot10^{-2}\cdot$Ḥ) where the no-slip condition is applied. The time step used to integrate numerically the transport equations is $\Delta t=10^{-5}\cdot H^2/\alpha$ The time-averaged velocity and temperature profiles, as well as, the fluctuation intensities predicted with 3DINAMICS are compared successfully with the DNS of the literature in Pallares et al. [7] where the interested reader can be found more information about the validation. The characteristics of the turbulent flow analyzed in this study are described elsewhere [6-11]

To track the particles, the velocities of the fluid are computed in an Eulerian grid using the 3DINAMICS code and they are interpolated to the positions of the particle using fourth order Lagrange polynomials. Initially, 10^5 particles are distributed randomly in the computational domain and their positions and velocities are calculated using Equations (4) and (5), which are integrated in time with a fourth order Runge-Kutta method with the same time step as for the time marching of the equations for the fluid. The particles that leave the computational domain through the periodic boundaries are reintroduced accordingly. Perfectly-elastic collisions are assumed when the particle

center is at a distance from the wall lower than the particle radius.

The particle tracking method has been validated by simulating the dispersion of particles in a plane turbulent channel flow for which results can be found in the literature. Details about this validation can be found in Pallares and Grau [12].

4. RESULTS AND DISCUSSION

In this section we analyze the instantaneous particle distributions of the largest particle considered (St=17.45). This value of the Stokes number indicates that the inertia of the particles is important and, consequently, the particle response is limited to the large flow fluctuations.

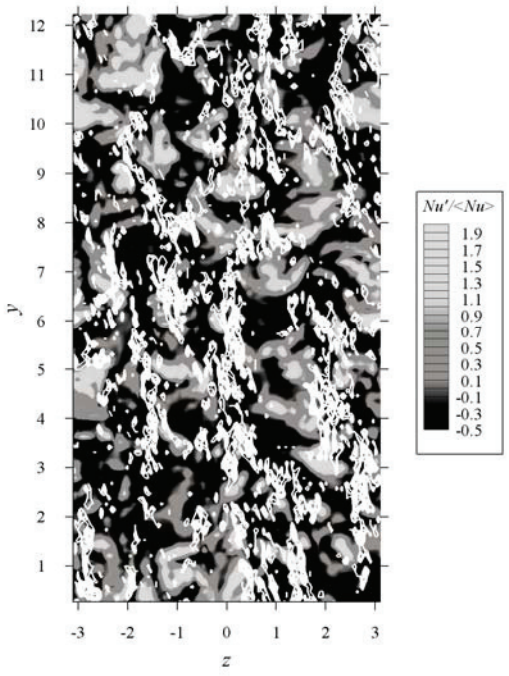

Figure 2. Fluctuations of the wall heat transfer rate on the hot wall. The line contours indicate regions near the wall where the concentration is high.

Figure 2 shows, as an example, an instantaneous visualization of the distribution of particles with St=17.45 near the hot wall. The white line contours correspond to regions were the concentration of particles is high while the colour contours correspond to the fluctuations of the non-dimensional wall heat transfer rate, Nu', scaled with the averaged value, $\langle Nu \rangle$. It can be seen that the large positive fluctuations ($Nu'/\langle Nu \rangle > 1$) are indicated with light gray; the moderate positive fluctuations ($1 > Nu'/\langle Nu \rangle > 0$) are depicted in dark gray and the negative fluctuations ($Nu'/\langle Nu \rangle > 0$) in black. Figure 2 indicates that the regions where the large positive fluctuations of the wall heat transfer rate occurs the instantaneous concentration of the particles does not attain large values. This suggests that the flow structures responsible for the large positive fluctuations of the heat transfer rate produce an instantaneous reduction of the concentration of particles near the wall. We applied a conditional sampling technique to verify this hypothesis and to analyze the effect on the instantaneous concentration of particles of the flow structures responsible for the negative fluctuations of the wall heat transfer rate.

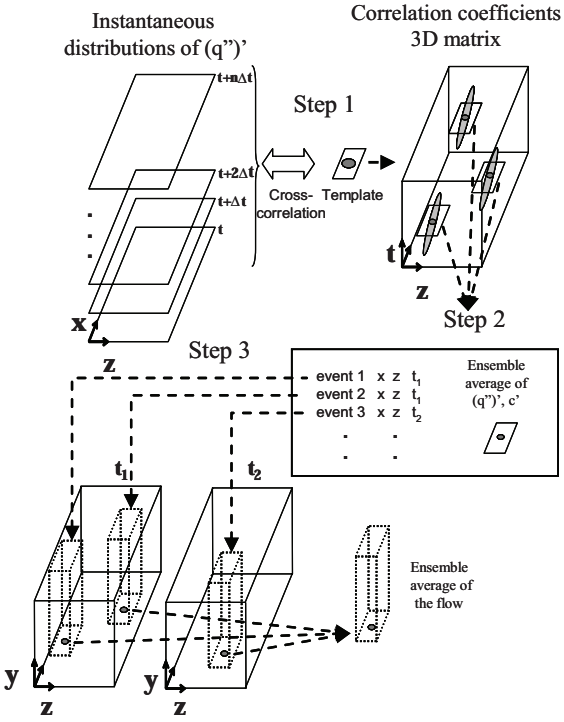

Figure 3. Steps of the conditional sampling procedure.

4.1. Conditional sampling technique

The conditional pattern recognition technique used is based on the detection of extreme values of the fluctuations of the local wall heat transfer rate in the instantaneous distributions of q'' on the walls of the channel. This technique has been previously applied to educe the flow structures responsible for large fluctuations of wall transfer rate in forced [13], mixed [14] and natural [7] convection turbulent channel flows. In what follows we summarize and describe the main steps of the procedure.

Figure 3 illustrates the main steps of the pattern recognition technique. As indicated in Step 1 of Figure 3, the cross-correlation coefficients, between the instantaneous distributions of $(q'')'$ and a template, are stored in a three-dimensional matrix (i.e. a two-dimensional matrix for each time step). As an example, Figure 2 shows an instantaneous distribution of the fluctuations of the heat transfer rate on the hot wall. It can be seen that the regions with large positive fluctuations, indicated in light

gray, have different shapes and sizes and they coexist with regions of extreme negative fluctuations, indicated in black. On the hot wall these regions with extreme fluctuations appear, evolve and disappear while are advected, mainly, along the positive streamwise direction, but also along the spanwise direction. The template used to detect the large positive fluctuations is a positive lobe with a diameter of, approximately, H.

As sketched in Figure 3, the time evolution of the spatial distributions of the fluctuations produces that the regions where the maxima of the correlation coefficients appear as elongated volumes in the 3D-matrix of the correlation coefficients according to the fact that the extreme values of the wall heat transfer rate move along the streamwise and spanwise directions. Within these volumes, which correspond to the detected events, only the region of the plane of time where the absolute maximum of correlation occurs is selected to obtain the ensemble average of the wall event (see Step 2 in Figure 3). This procedure prevents the selection of the different stages of the same event at different times. The positions and the time at which the selected events occur are stored in a file (see Step 2 in Figure 3). This information is used to obtain the conditional ensemble average of the flow and the concentration of particles near the wall when and where the selected wall events occur (see Step 3 in Figure 3).

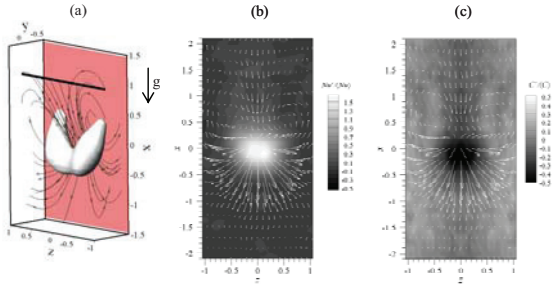

Figure 4. Flow structures producing large positive fluctuations of the heat transfer rate.

4.2. Conditional sampled flow structures and concentrations

Figure 4 shows the conditionally averaged flow structure responsible for the large positive fluctuations of the heat transfer rate on the hot wall. The isosurface corresponds to a negative value of the second largest eigenvalue of the velocity gradient tensor (λ_2). A quantity proposed by Jeong and Hussain [15] to detect the occurrence of vortex cores. The fluid particle paths in Figure 4.a are released from the line x=-1, y=-0.2 and they follow the conditionally averaged flow field. Figure 4.b shows the contours of the fluctuation of the heat transfer rate superimposed to the vector field of the fluctuations of the wall shear stress. The fluctuation of the concentration of particles with St=17.45 are shown in Figure 4.c. It can be seen that the flow structure has a hairpin-shaped topology. The legs of the hairpin are two counter-rotating vortices. The vortices of the legs advect cold fluid towards the hot wall and they produce a maximum of the wall heat transfer rate in the region between them, as shown in Figure 4.b. The injection of cold fluid towards the hot wall caused by the legs of the hairpin vortices produces a descending flow near the hot wall, where the flow, on average is ascending. The equivalent flow structure near the cold wall can be obtained by mirroring the flow structure near the hot wall, shown in Figure 4.a, firstly, with respect to the plane x=0 and secondly, with respect to the plane y=0. The fluctuation of the particle concentration for St=17.45 near the hot wall is shown in Figure 4.c. It can be seen that the reduction of the concentration of about 50% occurs where the maximum of heat transfer rate is located. The imprint is produced by the injection of relatively cold fluid with a low concentration of particles from the center of the channel towards the hot wall.

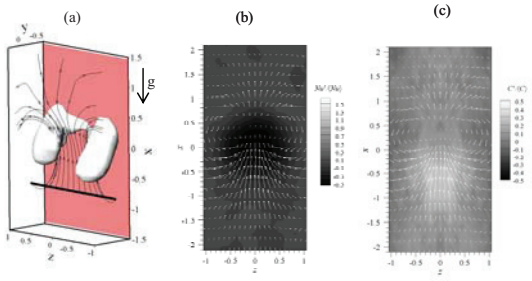

Figure 5. Flow structures producing extreme negative fluctuations of the heat transfer rate.

The conditional averaged flow structure obtained from the events associated with negative fluctuations of the heat transfer rate on the hot wall is shown in Figure 5. This flow structure consists in two counter-rotating vortices that convect fluid from the region between them towards the external part of the vortices, as shown in Figure 5.a. The vortices produce an ejection of fluid from the wall, which has associated the imprint of the fluctuation of heat transfer rate depicted in Figure 5.b. It can be seen in Figure 5.b that the induced negative fluctuations of the heat transfer rate are located between the legs of the vortices, which accelerate hot fluid near the hot wall along the positive streamwise direction. The flow structure responsible for the extreme negative fluctuations of the heat transfer rate on the cold wall can be obtained by mirroring the flow structure near the hot wall, shown in Figure 5.a, firstly, with respect to the plane x=0 and secondly, with respect to the plane y=0. The corresponding fluctuations of the particle concentration near the hot wall are depicted in Figure 5.c for particles with St=17.45. Note that, according to the conditional averaging procedure, the increase of the concentration of particles is, on

average, about 30% in the location where the minimum heat transfer rate occurs.

5. CONCLUSIONS

We performed direct numerical simulations of the particle dispersion in a turbulent natural convection flow in a vertical channel. It has been found that the large positive fluctuations of the wall heat transfer rate are associated with an instantaneous reduction of the particle concentration near the wall. This agrees with the fact that the flow structure responsible for the local increase of the heat transfer rate convects fluid, with a low concentration of particles, from the centre of the channel towards the wall. On the other hand, the extreme negative fluctuations of the heat transfer rate produce an accumulation of particles near the wall. This accumulation is produced below the flow ejection that is associated with these the extreme negative fluctuations of the heat transfer rate.

ACKNOWLEDGEMENTS

This study was financially supported by the Spanish Ministry of Science of Technology and FEDER under project DPI2010-17212.

REFERENCES

[1] Michaelides, E.E., 2006, *Particles, bubbles and drops – Their motion, heat and mass transfer*, World Scientific Publishing, Singapore.

[2] Guha, A., 2008, "Transport and deposition of particles in turbulent and laminar flow", *Annual Review of Fluid Mechanics*, Vol. 40, pp. 311-341.

[3] Nazaroff, W. and Cass, G.R., 1987, "Particle deposition from a natural convection flow onto a vertical isothermal flat plate", *Journal of Aerosol Science*, Vol. 18, pp. 445-455.

[4] Tsai, R., 2001, "Aerosol particle transport in a natural convection flow onto a vertical flat plate", *International Journal of Heat and Mass Transfer*, Vol. 44, pp. 867-870.

[5] Akbar, M. K., Rahman, M. & Ghiaasiaan, S. M. 2009, "Particle transport in a small square enclosure in laminar natural convection" *Journal of Aerosol Science*, Vol. 40, pp. 747-761.

[6] Versteegh, T. A. M. and Nieuwstadt, F. T. M. 1999, "A direct numerical simulation of natural convection between two infinite vertical differentially heated walls: scaling laws and wall functions", *International Journal of Heat and Mass Transfer,* Vol. 42, pp. 3673-3693.

[7] Pallares, J. Vernet A., Ferre, J.A. and Grau, F.X., 2010, "Turbulent large-scale structures in natural convection vertical channel flow" *International Journal of Heat and Mass Transfer*, Vol. 53, pp. 4168-4175.

[8] Philips, J. R., 1996, "Direct simulations of turbulent unstratified natural convection in a vertical slot for Pr=0.71", *International Journal of Heat and Mass Transfer,* Vol. 39, pp. 2485-2494.

[9] Boudjemadi, R., Maupu, V., Laurence, D. and Le Quéré, P. 1997, "Budgets of turbulent stresses and fluxes in a vertical slot natural convection flow at Rayleigh Ra=10^5 and $5.4 \cdot 10^5$", *International Journal of Heat and Fluid Flow*, Vol. 18, pp. 70-79.

[10] Versteegh, T. A. M. and Nieuwstadt, F. T. M., 1998, "Turbulent budgets of natural convection in an infinite, differentially heated, vertical channel", *International Journal of Heat and Fluid Flow,* Vol. 19, pp. 135-149.

[11] Tsujimoto, K., Ohya, N., Shakouchi, T. and Ando, T., 2006, "Analysis of turbulent structures of natural convection in vertical channel using DNS", In *Turbulence, Heat and Mass Transfer 5, (Edited by K. Hanjalic, Y. Nagano and S. Jakirlic)*.

[12] Pallares, J. and Grau, F.X., 2012, "Particle dispersion in a turbulent natural convection channel flow", *Journal of Aerosol Science*, Vol. 43, pp. 45-56.

[13] Pallares, J., Vernet, A., Ferre, J.A. and Grau, F.X., 2007, "Eduction of near-wall flow structures responsible for large deviations of the momentum-heat transfer analogy and fluctuations of wall transfer rates in turbulent channel flow", *Computers and Fluids,* Vol. 35, pp 1327-1334.

[14] Fabregat A., Pallares J., Vernet A., Cuesta I., Ferre, J.A., Grau, F.X., 2010, "Identification of near-wall flow structures producing large wall transfer rates in turbulent mixed convection channel flow" *Computers and Fluids*, Vol. 39, pp. 15-24.

[15] Jeong, J. and Hussain, F., 1995, "On the identification of a vortex", *Journal of Fluid Mechanics*, Vol. 285, pp. 69-80.

Conference on Modelling Fluid Flow (CMFF'12)
The 15th International Conference on Fluid Flow Technologies
Budapest, Hungary, September 4-7, 2012

SAS-SST MODEL ASSESSMENT AND IMPROVEMENT

Farid BENYOUCEF[1], Hervé BEZARD[2], Bertrand AUPOIX[3], Bertrand MICHEL[4]

[1] Corresponding Author. ONERA - The French Aerospace Lab. 2, avenue Edouard Belin, F-31055 Toulouse, France. Tel.: +33 5 6225 2437, Fax: +33 5 6225 2583, E-mail: farid.benyoucef@onera.fr
[2] ONERA - The French Aerospace Lab. E-mail: herve.bezard@onera.fr
[3] ONERA - The French Aerospace Lab. E-mail: bertrand.aupoix@onera.fr
[4] ONERA - The French Aerospace Lab. E-mail: bertrand.michel@onera.fr

ABSTRACT

This paper is devoted to a better understanding of the SAS approach. First, the SAS-SST model is reminded and an improvement is suggested. Then two testcases are analysed. First, a cylinder in a crossflow at a high Reynolds number is deeply investigated. The space discretisation scheme effect is analysed and comparisons to wall-modelled LES and experimental databases are carried out. Then a backward-facing step flow is investigated since the classical SAS model is unable to predict an unsteady solution while the solution computed with the improved version of the SAS model contains unsteadiness.

Keywords: backward-facing step, cylinder, Scale-Adaptive Simulation, Scale-Resolving Behavior, SST, upgraded URANS

NOMENCLATURE

BL	$[-]$	boundary layer
C	$[-]$	constant in SAS-SST model
C_{K}	$[-]$	Kolmogorov's constant
C_p	$[-]$	static pressure coefficient
CFL	$[-]$	Courant-Friedrichs-Lewy number
D	$[m]$	cylinder diameter
EVM	$[-]$	Eddy Viscosity Model
F_1	$[-]$	blending function involved in the BSL correction
H	$[m]$	backward-facing step height
k	$[m^2.s^{-2}]$	kinetic energy of turbulence
KH	$[-]$	Kelvin-Helmholtz
L	$[m]$	turbulence length scale
L_{vK}	$[m]$	von Kármán length scale
P_k	$[m^2.s^{-3}]$	Production rate of the kinetic energy of turbulence
PSD	$[m^2.s^{-1}]$	Power Spectral Density
Q	$[s^{-2}]$	$\frac{1}{2}\left(S^2-\Omega^2\right)$
Q_{SAS}	$[N.m^{-4}]$	SAS term in ω equation
Re	$[-]$	Reynolds number
SAS	$[-]$	Scale Adaptive Simulation
SST	$[-]$	Shear Stress Transport
S	$[s^{-1}]$	Strain rate tensor modulus
$\underline{U}$	$[m/s]$	velocity vector
U	$[m/s]$	streamwise velocity
β, β^*, γ	$[-]$	constants in the $k-\omega$ model
δ	$[m]$	boundary layer thickness
ε	$[m^2.s^{-3}]$	dissipation rate of the kinetic energy of turbulence
ζ_2	$[-]$	constant in the SST model
η	$[m^{-1}]$	wave number
κ	$[-]$	von Kármán's constant
ν	$[m^2/s]$	kinematic viscosity
ν_t	$[m^2/s]$	eddy viscosity
σ	$[-]$	Prandtl-Schmidt number
σ_ϕ	$[-]$	constant in the SAS model
ω	$[s^{-1}]$	specific dissipation
Ω	$[s^{-1}]$	vorticity tensor modulus

Subscripts and Superscripts

D, L	drag, lift
x, y, z	axial, vertical, spanwise (coordinate)

1. INTRODUCTION

Massively separated flows are computationally and physically challenging to tackle at practical Reynolds numbers. The application of LES approach to engineering systems such as airplane is unaffordable due to the presence of thin near-wall turbulent boundary-layers populated with small attached eddies which require a very high level of grid refinement that is hardly reachable with current computer resources. In addition, it is now commonly accepted that conventional RANS models are unable to reach engineering accuracy on massively detached flows since the dominant detached eddies are highly geometry-specific and have not the same behavior than universal eddies that exist in thin shear layers that are usually considered to calibrate RANS models. Hybrids

methods (DES [1]...) and upgraded URANS models (SAS [2]...) are designed to bridge this gap as they are able to model the boundary layer and to resolve (at least partially) the detached areas. This paper is dedicated to the Scale-Adaptive Simulation (SAS) approach.

2. SAS-SST model description and improvement

2.1. Standard SAS-SST model

SAS approach was proposed by Menter and Egorov [2] from an analysis of Rotta's [3] $k-kL$ model. kL transport equation contains two source terms. Rotta's assumptions lead him to model one of them using a third-order velocity derivative which makes this model physically interesting but numerically challenging. Menter and Egorov model this term with a second-order velocity derivative. Then they transform the kL form of this term into a $k-\omega$ one ($\omega = k^{\frac{3}{2}}/kL$) which results in the addition of a source term in the ω-transport equation of the SST [4] model. The SAS-SST model equations read:

$$\begin{aligned}
\frac{D(\rho k)}{Dt} &= P_k - \rho\beta^* k\omega \qquad (1)\\
&+ \text{div}\left[(\mu+\sigma_k\mu_t)\,\underline{\text{grad}}\,(k)\right]\\
\frac{D(\rho\omega)}{Dt} &= \frac{\gamma}{\nu_t}P_k + \boxed{Q_{\text{SAS}}} - \rho\beta\omega^2\\
&+ \text{div}\left[(\mu+\sigma_\omega\mu_t)\,\underline{\text{grad}}\,(\omega)\right] \qquad (2)\\
&+ (1-F_1)\,\sigma_{\omega 2}\frac{2\rho}{\omega}\underline{\text{grad}}(k).\underline{\text{grad}}(\omega)
\end{aligned}$$

The boxed Q_{SAS} term involved in equation (2) is the only difference with the classical SST model. It reads:

$$\begin{aligned}
Q_{\text{SAS}} &= \max\left(T_1 - T_2; 0\right)\\
T_1 &= \rho\zeta_2\kappa S^2\left(\frac{L}{L_{\text{vK}}}\right)^2 \qquad (3)\\
T_2 &= C\frac{2\rho k}{\sigma_\phi}\max\left(\frac{||\underline{\text{grad}}(k)||^2}{k^2}, \frac{||\underline{\text{grad}}(\omega)||^2}{\omega^2}\right)
\end{aligned}$$

where $L_{\text{vK}} = \dfrac{\kappa S}{||\Delta\underline{U}||}$, $\zeta_2 = 3.51$ and $C = 2$. L_{vK} stands for a 3D-generalization of the von Kármán length scale and $\Delta\underline{U}$ denotes the Laplacian of the velocity vector.

2.2. Classical SAS-SST model behavior

When using eddy viscosity models (EVM), unsteadiness increases velocity gradients which are responsible for the rise of the kinetic energy of turbulence which increases ν_t, thus damping the local unsteadiness. The Q_{SAS} term (equation (3)) allows a different behavior, thoroughly detailed by Menter et al. [2], and reminded here. When using the SAS model, local unsteadiness creates velocity gradients that are responsible for the decrease of the von Kármán length scale. Hence, the Q_{SAS} term becomes positive and ω raises so that ν_t decreases. The reduction of ν_t allows the unsteadiness to stay alive and even grow. The cutting down of ν_t as a reaction to local unsteadiness is the main advantage of the SAS model against EVM.

2.3. Classical SAS-SST model limits and possible improvement

Even if the SAS-SST model evidences many satisfactory results, it is unable to predict an unsteady solution on the backward-facing step (BFS) configuration despite the presence of the Kelvin-Helmoltz (KH) instability [5]. This leads to look for an improvement of the model.

In a mixing-layer, L_{vK} reduces to $\kappa\dfrac{\partial U}{\partial y}/\dfrac{\partial^2 U}{\partial y^2}$. Hence, at the velocity profile inflexion point, the denominator of L_{vK} is null, therefore L_{vK} tends toward infinity and Q_{SAS} tends toward zero. As a result, the SAS model reduces to the SST one which is not desirable since it delays the scale-resolving behavior and can damp the unsteadiness because of the persistence of too high level of eddy viscosity.

Hence, bounding the L_{vK} value by αL is suggested where α is a constant and L is the turbulence length scale. However, L_{vK} limiter must remain inactive in the boundary-layer (BL). In this way, it is suggested to keep standard version in the BL and to switch to the bounded version outside. This procedure is done thanks to the blending function F_1 proposed by Menter when introducing BSL model [4]. This function allows detecting the external zone of the boundary layer. Finally, in the present formulation, standard L_{vK} expression is replaced by the following one:

$$\widetilde{L_{\text{vK}}} = \min(L_{\text{vK}}, F_1 L_{\text{vK}} + (1-F_1)\alpha L) \qquad (4)$$

In the boundary layer, $F_1 \approx 1$ so $\widetilde{L_{\text{vK}}}$ is equal to L_{vK} and the standard version, which protects the boundary layer, is retrieved. Outside the boundary layer, $F_1 \approx 0$ and $\widetilde{L_{\text{vK}}}$ is equal to $\min(L_{\text{vK}}, \alpha L)$ which avoids infinite value at inflexion point.

Now, a brief description of the α constant calibration is given. Following Lilly [6], the constant α may be obtained by assuming that the cut-off wave number η_c lies within a $\eta^{-5/3}$ cascade for the energy spectrum $E(\eta) = C_{\text{K}}\varepsilon^{2/3}\eta^{-5/3}$ where C_{K} stands for the Kolmogorov constant equal to 1.4, η the wave number and ε the dissipation rate. It gives :

$$L_{\text{vK}}{}^2 = \kappa^2\frac{S^2}{||\Delta\underline{U}^2||} \approx \kappa^2\frac{\int_0^{\eta_c}\eta^2 E(\eta)d\eta}{\int_0^{\eta_c}\eta^4 E(\eta)d\eta} \qquad (5)$$

As a consequence, L_{vK} may be estimated as follow :

$$L_{\text{vK}} \approx \kappa\sqrt{5/2}\eta_c^{-1} \qquad (6)$$

The well-known relationships can be written

$$L = \frac{\sqrt{k}}{\beta^\star \omega} \quad ; \quad \varepsilon = \beta^\star k\omega \quad \text{to get} \quad L \approx \nu_t^{3/4}\varepsilon^{-1/4} \tag{7}$$

and the energy flux accross the cutoff may be assumed to be equal to the dissipation :

$$\varepsilon = \int_0^{\eta_c} 2\nu_t \eta^2 E(\eta) d\eta \tag{8}$$

that yields : $\nu_t = 2/(3C_{\mathrm{K}})\varepsilon^{1/3}\eta_c^{-1/4}$. So that :

$$L \approx (2/(3C_{\mathrm{K}}))^{3/4}\eta_c^{-1} \tag{9}$$

To avoid the activation of the limiter in the whole flow (except at the inflexion point), the $\alpha L > L_{\mathrm{vK}}$ condition must be satisfied. As a result, α constant must satisfy the following criterion :

$$\alpha > L_{\mathrm{vK}}/L = \frac{\kappa\sqrt{5/2}}{(2/(3C_K))^{3/4}} \approx 1.13 \tag{10}$$

However, as this rationale is based on statistical considerations, a higher value must be chosen. For safety, the hereafter revised model referred as SAS-αL has been tested with an α constant set to 2.5.

3. ONERA Navier-Stokes solver: elsA

3.1. General description

elsA [7] is a CFD software developped at ONERA and CERFACS. It is based on a cell-centered finite volume approach. For this study requirements, both SAS and SAS-αL models were implemented. The time-discretisation scheme considered here is the backward Euler one. Implicit methods would have been better-suited. However, to the authors knowledge, it does not exist any theoretical criterion to set the number of sub-iterations which may lead either to a lack of convergence or to too much time consumption. Furthermore, the dual-time-stepping approach was tested without noticeable differences. To analyse the space-discretisation scheme influence: centered Jameson's [8], upwind Roe's [9], and higher-order space discretisation schemes namely AUSM(+)-up [10] were tested.

4. APPLICATIONS

4.1. Cylinder in a crossflow at high Reynolds number

4.1.1. Computational patterns

In the present work, the simulation was performed at $\mathrm{Re}_D = 3.7 \times 10^6$ (super-critical regime) which ensures that the boundary-layer is fully turbulent at separation. However there are not so many experimental or numerical databases for this Reynolds number range. The computational domain features are: $20D$ height, $30D$ length ($10D$ upstream the center of cylinder and $20D$ downstream), $3D$ in the spanwise direction. Farfield conditions were prescribed at the top and bottom of the computational domain as at the inlet. Pressure was stipulated at the domain outlet. Periodic conditions were set on the side walls. The boundary layer was resolved (no wall-law is used) with a first normal to the wall cell dimension equal to 1 (in wall units). The mesh contains about 3.5 million points. As the scale-resolving behavior is expected in the cylinder wake, particular attention was paid to mesh this area with cubic cells following Spalart [11] recommendations. Furthermore, a one-half point per direction mesh was extracted to investigate the mesh effect. A global time step equal to $5\mu s$ was set to satisfy the $CFL < 1$ condition in each cell. In order to assess the space-discretisation influence, several simulations were performed using the centered second-order accurate Jameson scheme combined with a low value of the scalar artificial viscosity, the upwind second-order accurate Roe scheme combined with superbee limiter and 3^{rd} and 5^{th} order extended versions of AUSM(+)-up scheme. SST, SAS and SAS-αL models were tested. Simulations were carried out for about 700 non-dimensionnal time steps (tD/U_0). Transient phase was estimated using *meancalc*© software developed by Mockett et al. [12], which lead to discard 40 non-dimensional time steps to compute the mean drag coefficient and the lift coefficient root-mean-square.

4.1.2. Results discussion

SST and SAS models were used in this configuration on the coarse grid and it was observed (not shown) that the SAS model is able to compute a 3D solution, contrary to SST which computes a 2D solution due to a too high level of eddy viscosity. The same configuration was investigated on the standard mesh, using SST, SAS and SAS-αL models and the results are hereafter discussed.

As evidenced by figures 1 to 3, both SAS and SAS-αL allow resolving a wide range of turbulent structures while SST models predicts only quasi-2D rolls whose size is comparable to D. It is noticeable that SAS-αL solution shows rolls as soon as separation occurs on the contrary to SAS solution (figures 2 and 3). This behavior is consistent with a faster instability detection thanks to the new formulation. Furthermore, SAS-αL computes a solution which contains a wider range of turbulent length scales than SAS due to a lower eddy viscosity level. This observation is consistent with a faster activation of the scale-resolving behavior thanks to the SAS-αL model.

In order to compare the proportion of the kinetic energy of turbulence resolved by each model, time-averaged (10 000 samples) modelled and resolved kinetic energy of turbulence were computed in the streamwise plane. Time-averaged modelled kinetic energy of turbulence level is lower with SAS and SAS-αL models than with SST one (figures 4 to 6). This behavior is consistent with a higher part of

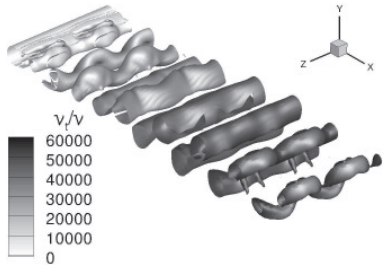

Figure 1: Iso-surfaces of Q-criterion colored by ν_t/ν ($Q = -250s^{-2}$) - SST

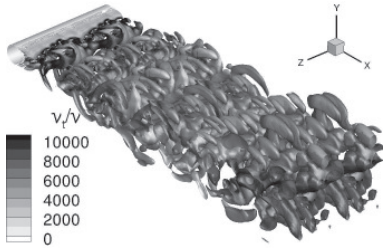

Figure 2: Iso-surfaces of Q-criterion colored by ν_t/ν ($Q = -250s^{-2}$) - SAS

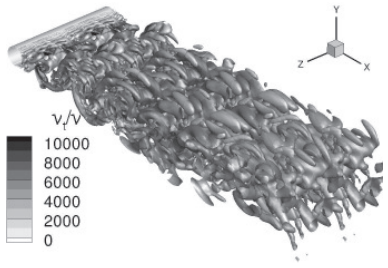

Figure 3: Iso-surfaces of Q-criterion colored by ν_t/ν ($Q = -250s^{-2}$) - SAS-αL

resolved kinetic energy of turbulence with SAS and SAS-αL models than with SST one. Hence, SAS is an intermediate strategy that lays between LES and URANS. Furthermore, modelled kinetic energy of turbulence, just after separation, is lower in the SAS-αL solution than in the SAS one. This observation shows that the scale-resolving behavior is faster activated with the SAS-αL model.

Velocity components were recorded at two probes, P1(0.7;0.15;0) and P2(1.7;0.15;0) (shown by crosses in figures 4 to 6), located in the cylinder near wake during about 350 non-dimensionnal time-steps. Power Spectra Densities (PSD) of each velocity component were estimated thanks to Welch's periodogram algorithm [13].

Figures 7 and 8 illustrate the PSD of the vertical component of the velocity computed with SST and SAS models. They reveal that SST PSD is harmonic, consistently with the 2D von Kármán streets, while SAS (and SAS-αL not shown) PSD

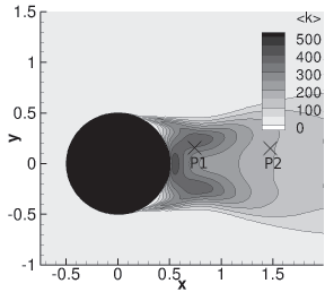

Figure 4: Time-averaged modelled kinetic energy of turbulence - SST

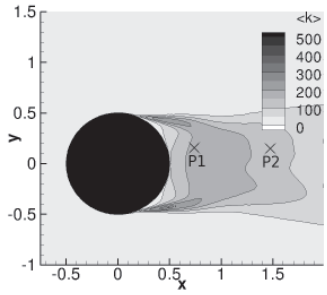

Figure 5: Time-averaged modelled kinetic energy of turbulence - SAS

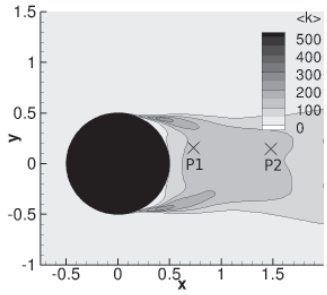

Figure 6: Time-averaged modelled kinetic energy of turbulence - SAS-αL

is continuous, consistently with a three-dimensional turbulent structures break-up. Furthermore, each spectrum exhibits a peak at a Strouhal number close to 0.3 which corresponds to the vortex shedding frequency at this range of Reynolds number. The streamwise and vertical velocity profiles at $x/D = 0.75$ and $x/D = 1.5$ were computed with each model and compared to a Wall-Modelled LES (WMLES) performed by Catalano et al. [14] at $Re = 10^6$. Pressure coefficient predictions are compared to experimental data of Achenbach [15] and DES data of Travin et al. [16].

First, it is noticeable that the SST predictions are in good agreement with WMLES data (figure 9). This

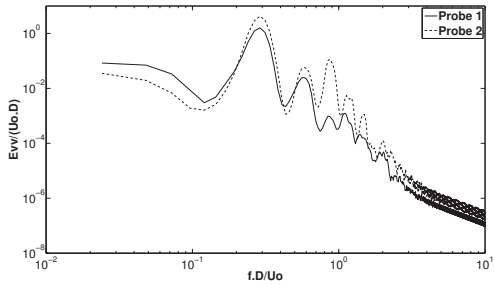

Figure 7: PSD of vertical velocity component at P1 and P2 - SST

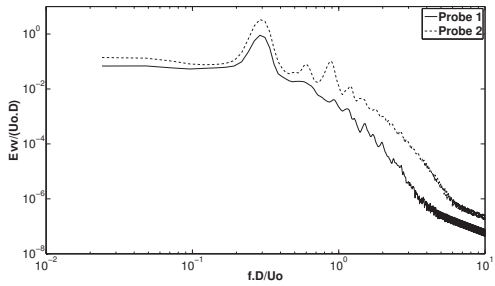

Figure 8: PSD of vertical velocity component at P1 and P2 - SAS

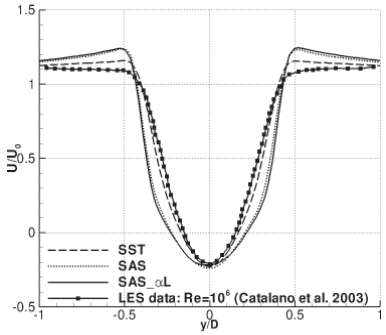

Figure 9: Comparison of streamwise velocity profile at $x/D = 0.75$ - Jameson's scheme

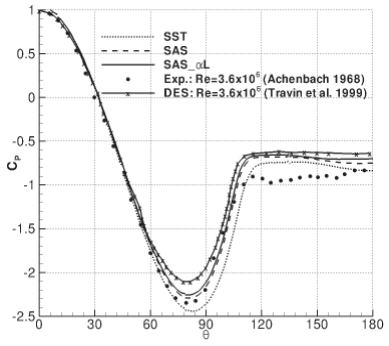

Figure 10: Time-averaged pressure coefficient prediction - Jameson's scheme

observation is consistent with the well-known good abilities of the SST model. The same conclusion may be drawn on pressure coefficients (figure 10). A comparison between Roe and Jameson scheme simulations (not shown here) showed a weak influence of the space-discretisation scheme on the SST solution while Roe's scheme is overly dissipative to allow accurate predictions with both SAS formulations. Hence, just as in DES or LES approaches, SAS approach requires to take care to the numerical methods. Second-order accurate simulations, using Jameson's scheme, show that pressure coefficient is better predicted with both SAS formulations than with SST or even DES. The poor predictions obtained thanks to DES may be due to an "under-resolved" simulation performed more than ten years ago.

Considering the weak influence of the space-discretisation scheme on the SST solution and the high computational cost of such simulations, only the SAS and SAS-αL were tested with higher-order space discretisation schemes. Their use obviously improve SAS predictions (figures 11 and 12).

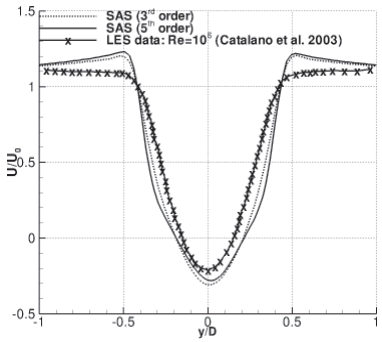

Figure 11: Comparison of streamwise velocity profile at $x/D = 0.75$ - AUSM(+)-up - SAS

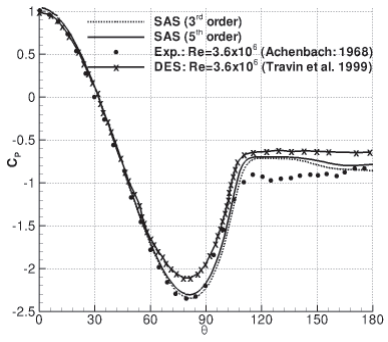

Figure 12: Time-averaged prediction with AUSM(+)-up schemes - SAS

So upwind schemes are not to be banned for such simulation but they have to be accurate enough to ensure reliable predictions. Nevertheless, 5^{th}-order space-discretisation scheme gives worse predictions than 3^{rd}-order ones when considering the velocity profiles (figure 13).

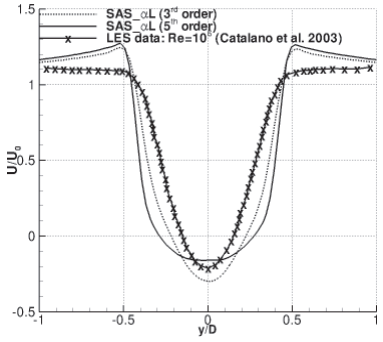

Figure 13: Comparison of streamwise velocity profile at $x/D = 0.75$ - AUSM(+)-up - SAS-αL

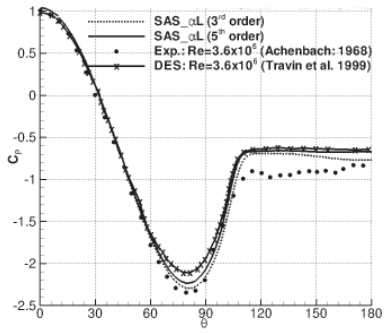

Figure 14: Time-averaged prediction with AUSM(+)-up schemes - SAS-αL

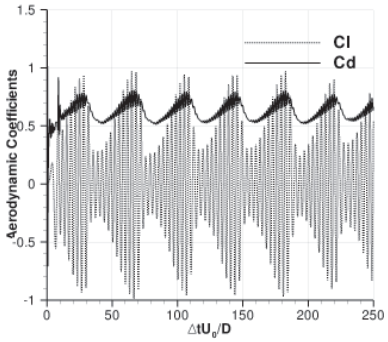

Figure 15: Drag (upper curve) and lift (lower curve) signal - SST - Jameson scheme

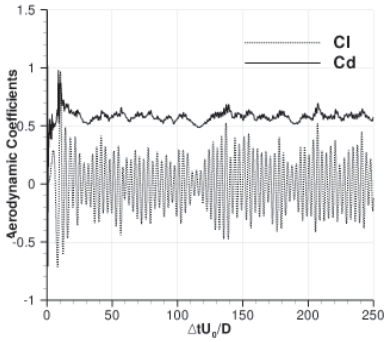

Figure 16: Drag (upper curve) and lift (lower curve) signal - SAS-αL - Jameson scheme

The time-averaged drag coefficients (C_{D}) as well as the lift coefficients root-mean-square (C'_{Lrms}) are summarized in table 1.

This investigation illustrates two kinds of behavior encountered at such range of Reynolds number corresponding to the upper-transition from supercritical regime to transcritical regime. In supercritical regime, the vortex shedding is weak leading to weak values of C_{D} and C'_{Lrms} while in transcritical regime a strong vortex shedding appears again (as observed by Roshko [17]) and C_{D} raises as C'_{Lrms}. This different kind of behavior is striking when considering the time-record of C_{D} and C_{L} plotted in figures 15 and 16. SST model exhibits a transcritical-likely behavior with high modulations of drag and lift time records while SAS-αL is in better agreement with supercritical-likely behavior. At such range of Re, a high sensitivity of C_{D} to Re is observed. In the early supercritical regime ($Re \approx 10^6$), C_{D} values lay between 0.17 and 0.4 [18] as predicted by WMLES [14] ($C_{\mathrm{D}} = 0.31$) or even 2D-RANS [19] ($C_{\mathrm{D}} = 0.34$). At the end of the supercritical regime ($Re \approx 3.5 \times 10^6$), C_{D} values are close to 0.52 as measured by Schewe [20] or predicted by Travin et al. [16] ($C_{\mathrm{D}} = 0.51$). It may be inferred that a transcritical-likely behavior is related to a C_{D} value close to 0.7 as measured by Roshko [17] on the contrary to the supercritical-behavior which may be related to a C_{D} value close to 0.52. Hence, it appears that SST computes a transcritical-likely solution while SAS-αL and DES compute a supercritical-likely solution. Conventional SAS model lays in between. This classification is consistent with "turbulent structures resolution" behavior in the sense that the more the turbulent structures are resolved, the better the supercritical-likely behavior is predicted.

Table 1: Drag and lift coefficients survey.

model	scheme (order)	C_{D}	error %	C'_{Lrms}
expe [20]	-	0.52	-	-
DES [16]	-	0.51	2	-
SST	Roe (2)	0.67	29	0.48
SST	Jameson (2)	0.67	29	0.44
SAS	Roe (2)	0.58	13	0.13
SAS	Jameson (2)	0.59	14	0.27
SAS	AUSM(+) (3)	0.64	23	0.37
SAS	AUSM(+) (5)	0.6	15	0.27
SAS-αL	Roe (2)	0.58	12	0.13
SAS-αL	Jameson (2)	0.57	10	0.20
SAS-αL	AUSM(+) (3)	0.55	6	0.16
SAS-αL	AUSM(+) (5)	0.55	6	0.16

According to Schewe [20], the many successive phases of instability until the transcritical regime is reached may be responsible for the multivaluedness of measured quantities. As a consequence, it may be stated that the different models as well as the space-discretisation scheme have the same kind of behavior than some variations of experimental parameters leading to different physical states.

4.2. Backward-facing step flow

4.2.1. Physical patterns

The second testcase investigated is the Driver and Seegmiller [21] backward facing-step flow. At the step lip, a Kelvin-Helmoltz (KH) instability occurs that results in quasi-2D rolls which pair and are convected downstream then they give Λ vortices whose legs are progressively elongated (figure 17). Despite the presence of a KH instability on this configuration, classical SAS model fails to predict an unsteady solution and is unable to capture the previously described turbulent structures [5].

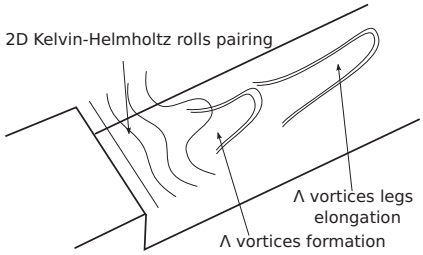

Figure 17: Turbulent structures creation on a backward-facing step configuration [22]

4.2.2. Computational patterns

The backward-facing step height is noted H and the computational domain considered here has $34H$ length ($4H$ upstream the step and $30H$ downstream), $10H$ height (including step height), and $4H$ spanwise dimension. A symmetric steady profile was injected at the inlet with the same characteristics than the experimental boundary layer ($\delta/H \approx 1.5$), the top and the bottom wall were considered as adiabatic, a massflow condition was prescribed at the outlet and periodic conditions were stipulated on the sides. A five million points mesh was designed in which both boundary layers are resolved (top and bottom). Particular attention was paid to the meshing of the mixing layer which is the critical area where the KH instability is encountered. A global time step equal to 0.7μs was set to satisfy the $CFL < 1$ condition.

4.2.3. Results discussion

Different space-discretisation schemes have been tested namely the second-order accurate Jameson one combined with a low scalar artificial viscosity level and the third-order, fifth-order and seventh-order AUSM(+)-up schemes. The second-order simulation reveals that SAS gives a steady solution as observed by Menter et al. [5]. On the other hand, third-order, fifth-order and seventh-order accurate AUSM(+)-up schemes give unsteady solutions. Furthermore, these solutions reveal some of the previously described turbulent structures as the 2D Kelvin-Helmoltz rolls and the Λ vortices which are gradually elongated (figure 18).

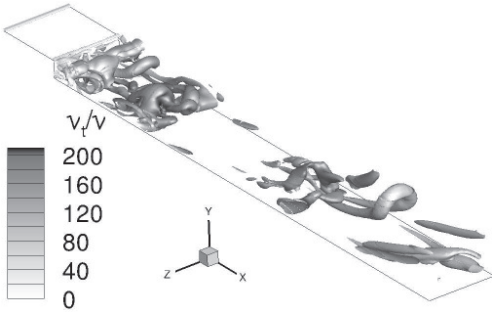

Figure 18: Iso-surfaces of Q-criterion colored by ν_t/ν - Seventh-order (AUSM(+)-up) computation - SAS

The unsteady feature of the high-order solution may be due to a better KH instability capture. In fact, the high boundary layer thickness ($\delta/H \approx 1.5$) suggests that a "true" massive separation does not occur. Hence, an accurate scheme is required here to capture this weak instability which is possible by the use of high-order space-discretisation schemes.

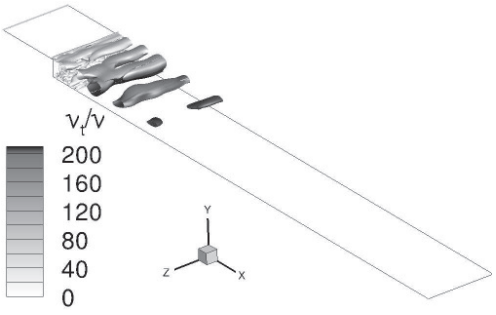

Figure 19: Iso-surfaces of Q-criterion colored by ν_t/ν - Second-order (Jameson) computation - SAS-αL

Then, the SAS-αL model has been tested, but at this time, only the second-order accurate simulation has been performed. SAS-αL is able to capture the 2D Kelvin-Helmoltz rolls (figure 19) on the contrary to SAS model. However, it is unable to capture the Λ vortices. Simulations that combine both SAS-αL and high-order space-discretisations are under progress.

5. CONCLUSION

This paper illustrates the high potential of the SAS model and the relevance of the proposed correction. Furthermore, it stresses the numerical

parameters influence as in hybrid RANS/LES methods. Eventually, these investigations evidenced that a unsteady solution should be computed by the SAS approach (if necessary with the SAS-αL version) providing that the numerical parameters are sufficiently well-suited to capture the instability that exists in the flow. Then, the scale-resolving behavior allowed by both SAS models makes possible the instability to grow toward turbulence. Nevertheless, the sooner the eddy-viscosity level is adapted the more likely a unsteady solution is to be computed. From this standpoint, the SAS-αL should be more reliable.

References

[1] Spalart, P. R. 2000 "Strategies for Turbulence Modelling and Simulations". *Int. J Heat and Fluid Flow*, Vol. 21, No. 3, pp. 252–263.

[2] Menter, F. and Egorov, Y. 2010 "The Scale-Adaptive Simulation Method for Unsteady Turbulent Flow Predictions. Part 1: Theory and Model Description". *Flow Turbulence Combustion*, Vol. 85, pp. 113–138.

[3] Rotta, J. C. 1951 "Statistische Theorie nicht-homogener Turbulenz I". *Zeitschrift für Physik*, Vol. 129, pp. 547–572.

[4] Menter, F. 1994 "Two-Equation Eddy-Viscosity Turbulence Models for Engineering Applications". *AIAA Journal*, Vol. 32, No. 8, pp. 1598–1605.

[5] Menter, F., Garbaruk, A., Smirnov, P., Cokljat, D., and Mathey, F. 2009 "Scale-Adaptative Simulation with Artificial Forcing". *Third Symposium on Hybrid RANS-LES Methods*, June.

[6] Lilly, D. K. 1966 "On the Application of the Eddy Viscosity Concept in the Inertial Sub-Range of Turbulence". Tech. Rep. NCAR 123, National Center of Atmospheric Research.

[7] Cambier, L. and Gazaix, M. 2002 "*elsA*: An Efficient Object-Oriented Solution to CFD Complexity". *AIAA 2002-0108*, 40$^{\text{th}}$ AIAA Aerospace Sciences Meeting and Exhibit, July.

[8] Jameson, A., Schmidt, W., and Turkel, E. 1987 "Numerical Solutions of the Euler Equations by Finite Volume Methods Using Runge-Kutta Time-Stepping". *AIAA Journal*, paper 81–1259.

[9] Roe, P. 1985 "Some Contributions to the Modelling of Discontinuous Flows". *Proceedings of 1985 AMS-SIAM Summer Seminar on Large Scale Computing in Fluid Mechanics*, pp. 163–193, Springer-Verlag, New-York.

[10] Liou, M. S. 2006 "A Sequel to AUSM, PART II: AUSM(+)-up for all Speeds". *J Computational Physics*, Vol. 214, pp. 137–170.

[11] Spalart, P. R. 2001 "Young-Person's Guide to Detached-Eddy Simulation Grids". Tech. Rep. NASA/CR-2001-211032, NASA.

[12] Mockett, C., Knacke, T., and Thiele, F. 2010 "Detection of Initial and Estimation of Statistical Error in Time-Resolved Turbulent Flow Data". *ETMM 8*, Marseille, France, June.

[13] Welch, P. 1967 "The use of Fast Fourier Transform for the Estimation of Power Spectra: a Method Based on Time-Averaging over Short, Modified Periodograms". *IEEE Trans. on Audio and Electroac.*, Vol. 15, No. 2, pp. 70–73.

[14] Catalano, P., Wang, M., Iaccarino, G., and Moin, P. 2003 "Numerical Simulation of the Flow around a Circular Cylinder at High Reynolds Numbers". *Int J Heat and Fluid Flow*, Vol. 24, pp. 463–469.

[15] Achenbach, E. 1968 "Distribution of Local Pressure and Skin Friction around a Circular Cylinder in Cross-Flow up to $Re = 5 \times 10^6$". *J Fluid Mechanics*, Vol. 34, No. 4, pp. 625–639.

[16] Travin, A., Shur, M., Strelets, M., and Spalart, P. 1999 "Detached-Eddy Simulations Past a Circular Cylinder". *Flow Turbulence and Combustion*, Vol. 63, pp. 293–313.

[17] Roshko, A. 1961 "Experiments of the Flow past a Circular Cylinder at very High Reynolds Number". *J Fluid Mechanics*, Vol. 10, pp. 345–356.

[18] Zdravkovich, M. M. 1997 *Flow around Circular Cylinders, Fundamentals, volume I*. Oxford University Press.

[19] Karabelas, S. J., Koumroglu, B. C., Argyropoulos, C. D., and Markatos, N. C. 2012 "High Reynolds Number Turbulent Flow past a Rotating Cylinder". *Applied Mathematical Modelling*, Vol. 36, pp. 379–398.

[20] Schewe, G. 1983 "On the Force Fluctuations Acting on a Circular Cylinder in Crossflow from Subcritical up to Transcritical Reynolds Numbers". *J Fluid Mechanics*, Vol. 133, pp. 265–285.

[21] Driver, D. M. and Seegmiller, H. L. 1985 "Features of a Reattaching Turbulent Shear Layer in Divergent Channel Flow". *AIAA Journal*, Vol. 23, No. 2, pp. 163–171.

[22] Delcayre, F. 1999 "Etude par Simulation des Grandes Echelles d'un Ecoulement Décollé : la Marche Descendante". Ph.D. thesis,

Conference on Modelling Fluid Flow (CMFF'12)
The 15th International Conference on Fluid Flow Technologies
Budapest, Hungary, September 4-7, 2012

CONDITIONAL ANALYSIS OF THE INSTANTANEOUS WALL FRICTION DURING BY-PASS TRANSITION OF ROUGH WALL BOUNDARY LAYER

Ondřej HLADÍK[2], Pavel JONÁŠ[1], Oton MAZUR[2], Václav URUBA[2]

[1]Corresponding Author. Institute of Thermomechanics, Academy of Sciences of the Czech Republic, v.v.i., Dolejškova 5, 182 00 Praha 8 Tel.: +420°266052025, Fax: +420286584695, E-mail: jonas@it.cas.cz
[2] Institute of Thermomechanics, AS CR.v.v.i. E-mail: hladik@it.cas.cz, mazur@it.cas.cz, uruba@it.cas.cz

ABSTRACT

The transitional intermittency was investigated in zero pressure gradient boundary layers developing on plate covered with sand paper (grits 60). The free stream mean velocity was about 5 *m/s* and the free stream turbulence level was either natural 0.3 percent or the FST was risen up to 3 percent by means of one from the two different square mesh plane grids generating the dissipation length parameter 3.8 *mm* or 33.4 *mm* respectively in the leading edge plane. The indicator function used for the determination of the transitional intermittency factor γ was employed for the digital conditional analysis of the wall friction measured by the single wire probe placed in the close proximity at the surface. The indicator function allows distinguish the time intervals in those with turbulent structure ($I = 1$) and those with laminar/nonturbulent structure ($I = 0$). The results received in rough wall layer are compared with the results received in the smooth wall boundary layer at similar boundary conditions.

Keywords: by-pass transition, conditional analysis of the wall friction, CTA, rough wall boundary layer, transitional intermittency factor

NOMENCLATURE:

C_f	[-]	skin friction coefficient
F	[-]	function for intermittency Eq. (9)I
	[-]	indicator function
Iu	[-]	turbulence intensity
L_e	[m]	dissipation length parameter (x=0)
$N(q)$	[-]	count of data points at the vicinity of the point q
L.E.	[-]	leading edge of the plate
Re_x	[-]	Reynolds number ($U_e x/\nu$)
Re_1	[-]	displacement thickness Reynolds number
Re_2	[-]	momentum thickness Re-number
Tu	[-]	turbulence level
U_e	[m/s]	free stream velocity
n	[$1/m/s$]	spot production rate
$n^*\sigma$	[–]	dimensionless spot production rate
u	[m/s]	fluctuating component of streamwise velocity
x	[m]	streamwise coordinate
y	[m]	normal to the plate's surface
(x, y, z)	[-]	orthogonal coordinate system
Δt	[s]	duration of an event
γ	[-]	intermittency factor
μ	[$kg/m/s$]	viscosity
ν	[m^2/s]	kinematic viscosity
ζ	[-]	variable Eq.(10)
ρ	[kg/m^3]	density
σ	[-]	Emmons propagation parameter

Subscripts

L	label of non-turbulent zone averages
T	label of turbulent zone averages
e	value of a quantity in the plain x = 0

1. INTRODUCTION

Theoretical considerations as well as experimental experiences give evidence that the alternation of "laminar" and "turbulent" pieces of the instantaneous velocity records and the turbulent spots (i.e. spatially localized regions of turbulent behaviour) arise as the consequence of the temporal amplitude modulation of the initial instability wave e.g. Kachanov [1] and Mayle [2]. This modulation occurs in "natural" flow conditions (aeronautics) and likewise in the "turbulized" outer stream (turbo machinery). The onset of the spot production probably affects the local transitional process and momentary position of the spatial *transition point*. Spots appear irregularly in time and at arbitrary locations of the boundary layer. Spots are an essential feature of transition to turbulence; they

appear as the building blocks of boundary layer turbulence, they control the length of the transition region etc. [3-10]. The calmed region arises behind a spot. The velocity profile within the calmed region relaxes from that more stable – fuller profile back towards the laminar profile. This happens in the consequence with the near-wall dynamics and the viscous instability mechanism. Ramesh and Hodson [7] derived that the near-wall unsteady effect is the key factor responsible for the existence of the calmed region and further they derived an expression for the time variation of the skin friction τ_w, which implies that the skin friction at a location decays exponentially to the laminar value after the passage of a turbulent spot. This knowledge bears out the experience that the distinctive periods of the boundary layer transition process are well pronounced from the distribution of the skin friction coefficient. So it appears, that the analysis of some statistical characteristics of the wall friction can add to the knowledge on the flow structure, in particular the turbulent spots generation, during the transition process.

Emmons [11] first reported spots as isolated regions of strong fluctuations that are stream-wise carried, growing in size and coalescing with neighbours. The turbulent spots followed by calmed regions are defined structures that dominate the last stage of transition. Spots production affects the length of transition region e.g. Narasimha [12]. The spot creation rate, growth characteristics and the merger of turbulent spots lead to fully developed turbulent flow.

The effect of free stream turbulence (FST) intensity *Iu* on boundary layer transition is known and investigated more than seventy years [13]. Later the effect of FST length scale *Le* has been also proved [14 – 17]. Several attempts were done to find causal connections of the free stream turbulence scales effect on by-pass transition of boundary layers on smooth surfaces. But a clear physical insight into the by-pass transition problem has not been achieved yet. The investigation of the transitional intermittency character of flow and turbulent spots behaviour during bypass transition can contribute to the problem explanation. Thus some investigations were accomplished on the propagation and the creation rate of turbulent spots in boundary layers on smooth surfaces under FST e.g. [18 – 24]. Received knowledge encouraged to apply the conditional analysis of the wall friction in the research of the joint action of surface roughness and FST on boundary layer laminar- turbulent transition.

2. EXPERIMENTAL FACILITY

Experiments were performed in the closed circuit wind tunnel IT AS CR, Prague with the working section cross section (0.5 x 0.9) m^2 and length 2.7 *m*; scheme in Figure 1.

Investigated boundary layers were developing either on the smooth flat plate (0.9 *m* wide and 2.75 *m* in length) or on the rough flat plate (7 *mm* thick) attached to the smooth one. Trailing parts of the plates, 1.15 *m* in length, were situated on entering the diffuser. The rough surface was made from sand paper grits 60 having the greatest sand grains $s = (0.43_5 \pm 0.01_4)$ *mm* high.

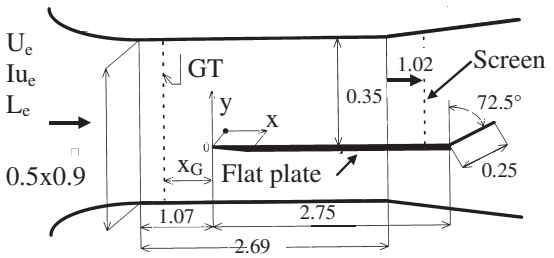

Figure 1. Working section of the wind tunnel

Free stream velocity was U_e = (5.0 ± 0.1) *m/s* with the natural turbulence level *Iu* = 0.3 percent. Measurements were also done with FST amplified by means of square mesh plane grids tightened across the working section upstream from the plane of plate leading edge (x = 0). Three turbulence generators of different geometry labelled as GT1, GT5 and GT8B were utilized all producing homogeneous close to isotropy turbulence

$$Tu = \sqrt{\overline{u_i u_i}/3U_e^2} \simeq Iu = \sqrt{\overline{u_e^2}}\Big/U_e$$
$$L_e = -\left(\overline{u_e^2}\right)^{3/2}\Big/U_e\left(d\left(\overline{u_e^2}\right)\Big/dx\right) \qquad (1)$$

Grids were placed in selected sections as to produce *Iu* = 0.03 and different turbulence length scales in the leading edge plane x = 0: L_e = 3.8 *mm* (GT8B); 5.9 *mm* (GT1) and 33.4 *mm* (GT5) respectively. The more detailed description of the set up with the smooth plate was given in [15] and a more extensiveness data on the FST control by passive devices were presented in [25]. The set up modifications caused by the replacement of smooth plate by rough plate were negligible.

3. MEASUREMENT METHODS AND EVALUATION PROCEDURES

The employed CTA measuring method with refined hot wire calibration and measurement corrections allowed determine statistical characteristics of the instantaneous velocity and wall friction. This method was the main tool during

investigations of boundary layers on the smooth wall. Details were described in [21, 22].

The above-mentioned method was supplemented with pressure measurements of the mean flow characteristics during investigation of rough wall layers. The reasons for this decision were the easy breakability of hot-wire probes by the spikes of roughness grains and the increased dustness near sandpaper. The couple of the thin flattened Pitot probe (nose: 0.18 *mm* x 2.95 *mm*) and round nosed static pressure probe (diameter = 1.8 *mm*) connected with the precise pressure transducer (max 1 *kPa*; error ±0.02% of readings above 20 *Pa*) was used for the measurements of the mean values of local total pressure and the static (ouside the layer) one.

The basic measurement of the instantaneous wall friction series, regardless of the surface roughness, was carried out by means of a hot wire probe step-wise moving in the stream wise direction at the distance $y_0 \sim 0.3$ *mm* from the surface. The heated wire coordinate y_0 was determined from the distance between the wire image and its reflection in the smooth surface, measured by the cathetometer with the precision ±0.01 *mm*. This procedure was not applicable in a rough boundary layer as the reflection in surface is missing. Thus the probe (calibrated in advance) was attached at the prescribed distance y_0 to the three wheels truck towed by the traversing system. The measurement proceeded regardless of the surface features. The probe was working in the CTA mode. The output voltage was digitalized and recorded (25 *kHz*, 750000 samples, 16 bit). The records were digitally transformed into the records of the local nominal instantaneous velocity using calibration parameters. Then the correction of the wall proximity effect [21] on hot wire cooling was applied. The linear regression of the mean velocity close to the wall was received together with the correction

$$\bar{U}^*(y) = y\left(\partial\bar{U}/\partial y\right)_w \tag{2}$$

Then the evaluation of the instantaneous wall-friction fluctuations τ_w' from the velocity records would be apparent from the following relations:

$$\begin{aligned} &\left(\tau_w'\right)_i = \left(\tau_w\right)_i - \bar{\tau}_w; \quad i = 1,2,...n, \\ &\left(\tau_w\right)_i = \left[\mu\left(\frac{\partial U}{\partial y}\right)_w\right]_i \cong \mu K_D \frac{U_i(y_1)}{y_1}, \\ &\bar{\tau}_w = \mu K_D \frac{\bar{U}(y_1)}{y_1}; K_D = \frac{\bar{U}^*(y_1)}{\bar{U}(y_1)} \end{aligned} \tag{3}$$

where n denotes the number of samples and K_D is empirical coefficient. The indicated measuring method and evaluation procedures [21] allow determining the instantaneous wall friction time series to be subjected to the relevant statistical analyses.

The applied method of the transitional intermittency analysis was so called TERA-method (Turbulent Energy Recognition Algorithm-Method) and the procedure of analysis was very similar to that described in [19, 26, 27]. The method consists of several consecutive steps. At the first, the obtained records of the instantaneous values of wall friction fluctuations τ_w' are filtered by Butterworth filter with low pass frequency 1 *kHz* to eliminate noise from the signal. At the second step, the detector function $D(t)$ is derived as to emphasize the differences of the signal time behaviour during turbulent and non-turbulent periods. The detector function is computed after the formula:

$$D(t) = \left|\tau_w' \cdot \partial^2\tau_w'/\partial t^2\right| \tag{4}$$

Then the detector function is smoothed to eliminate the scales much smaller than those to be recognized, thus the criterion function $K(t)$ is created. The criterion function *K(t),* the threshold *Th* and the indicator function *I(t)* are evaluated successively. Finally the transitional intermittency factor $\gamma(x)$ is calculated, details e.g. [28].

$$\begin{aligned} &I(t_i) = 1 \text{ if } K(t_i) > Th \text{ (turbulent)} \\ &I(t_i) = 0 \text{ if } K(t_i) \le Th \text{ (non/turbulent)} \\ &\gamma = \frac{1}{n}\sum_{i=1}^{i=n} I(t_i); n = 750000 \end{aligned} \tag{5}$$

According to Narasimha [12] the turbulent spot production rate can be derived from the transitional intermittency factor $\gamma(x)$ distribution in a smooth wall boundary layer.

Further, having determined the time behaviour of indicator function *I(t),* the record of the instantaneous wall friction $(\tau_w(t_i))$ is possible resolve in individual non-turbulent/laminar events and turbulent events. Every uninterrupted segment $I(t_i)$ = constant is understood as an event

$$\begin{aligned} &I(t_i) = 0; \ i = j, j+1,...j+L_j; 0 < L_j \\ &I(t_i) = 1; \ i = j, j+1,...j+T_j; 0 < T_j \end{aligned} \tag{6}$$

Next the total record $(\tau_w(t_i))$ can be divided in the non-turbulent/laminar part and the turbulent one

$$\begin{aligned}&(\tau_w(t_i)),\ i=1,2,..n=750000\\&(\tau_w(t_i))_L=(1-I(t_i))\tau_w(t_i)\\&(\tau_w(t_i))_T=I(t_i)\tau_w(t_i)\end{aligned}\qquad(7)$$

Apparently any kind of the statistical analysis of every record could be done as customary at every experimental set up and in each cross section x e.g. N_L and N_T numbers of events in the total record (number of samples 750000), the mean time of duration of events $(\Delta t)_L, (\Delta t)_T$ and the mean values of wall friction $(\tau_w)_L$ and $(\tau_w)_T$ can be evaluated.

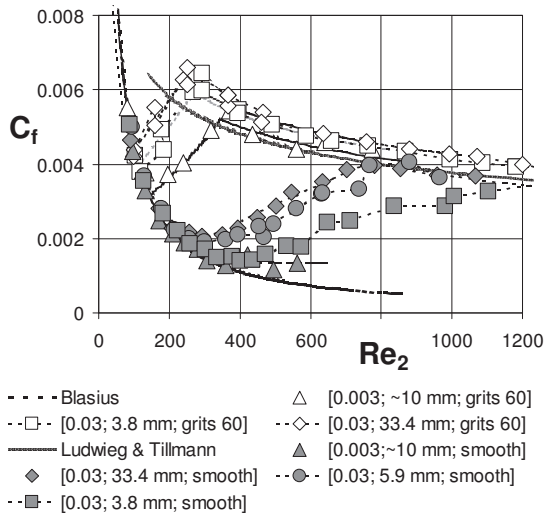

Figure 2. Skin friction coefficient on smooth and rough flat plate

4. RESULTS

The skin friction coefficient distributions C_f versus the momentum thickness Reynolds number Re_2, shown in the Figure 2, demonstrate dramatic effect of the surface roughness together with the effect of the free stream turbulence intensity *Iu* and length scale L_e. The boundary conditions are described in square brackets in the caption:

[*Iu; Le*; type of surface].

Other experimental conditions were kept identical during performed experiments.

The C_f distributions in boundary layers on the smooth flat plate ($grad\ p = 0$) calculated after Blasius solution (laminar boundary layer) and after Ludwieg and Tillman formulae (turbulent layer e.g. [8]) are drawn by solid lines in Figure 1. Crude estimates on the transition region can be derived from the measured C_f distribution: the beginning at the receding from Blasius solution and the termination at the approaching to the Ludwieg and Tillman distribution. But more accurate delimitation of transition region is possible by the transitional intermittency analysis.

4.1 Transitional intermittency

In accord with Narasimha [12] the shape of the transitional intermittency factor γ can be expressed in the form

$$\begin{aligned}&\gamma(\mathrm{Re}_x)=1-\exp\left[-(\mathrm{Re}_x-\mathrm{Re}_s)^2\, n^*\sigma\right]\\&\mathrm{Re}_x=xU_e/\nu;\quad n^*\sigma=n\sigma\nu^2/U_e^3\end{aligned}\qquad(8)$$

where the spot production rate n (the number of spots occurring per unit time and space distance) and the Emmons [11] dimensionless propagation parameter σ (including both the stream wise and lateral spot growth - effect of drift) are introduced. The substitution of the function $F(\gamma)$ into Eq. (8)

$$\begin{aligned}&F(\gamma)=\sqrt{-\ln(1-\gamma)}=\\&=\sqrt{n^*\sigma}\,(\mathrm{Re}_x-\mathrm{Re}_s);\ \mathrm{Re}_s=x_sU_e/\nu\end{aligned}\qquad(9)$$

brings relation suitable for the statistical estimates of the transition start x_s ($\gamma = 0$) and of the dimensionless spot production parameter $n^*\sigma$. The linear interpolations of function F are shown in Figure 3.

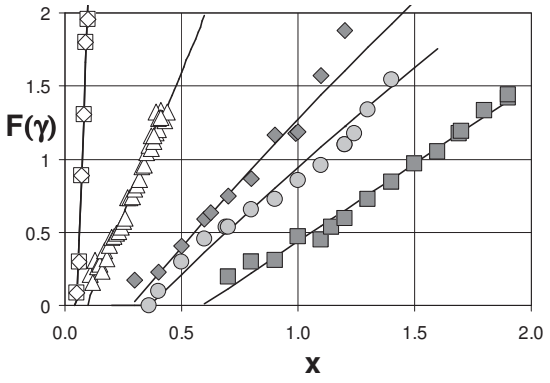

Figure 3. Linear interpolations of the function $F(\gamma)$ (symbols as in Fig.2)

Obviously both the FST and WR affect the start of transition ($\gamma = 0$) and change the turbulent spot production $n^*\sigma$. The intermittency factor distributions can be expressed in the universal form in smooth wall layers [12] after introducing a new variable ζ

$$\begin{aligned}&\zeta=(\mathrm{Re}_x-\mathrm{Re}_{tr})/\Delta\mathrm{Re}_{tr};\quad \mathrm{Re}_{tr}=\mathrm{Re}_x(\gamma=0.5)\\&\Delta\mathrm{Re}_{tr}=\mathrm{Re}_x(\gamma=0.9)-\mathrm{Re}_x(\gamma=0.1)\end{aligned}\qquad(10)$$

Diagram γ versus ζ presented in Figure 4 demonstrates that distributions γ measured in rough wall layers are compatible with measurements in

smooth wall layers [22] and with models of universal intermittency proposed by Narasimha [12] and Johnson and Fashifar [30]. The relations between the dimensionless turbulent spot production rate and the length of the transition region derived from measurements in rough wall layers are shown in Figure 5

$$n^{*}\sigma = 1.42/\Delta \mathrm{Re}_{tr}^{2} \qquad (11)$$

They confirm once more the validity of Narasimha intermittency concept in rough wall boundary layers.

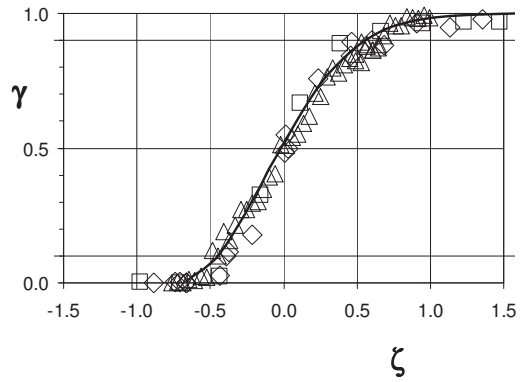

Figure 4. Universal intermittency function (symbols as in Fig. 2)

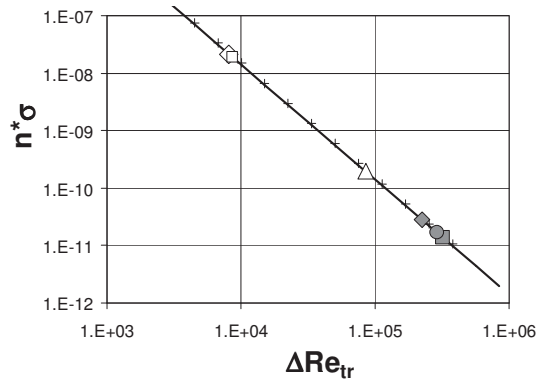

Figure 5. Dimensionless spot production rate versus transition length Re-number (symbols as in Fig. 2)

4.2 Conditional analysis

The beginning of the wall friction analysis with histograms of records is meaningful because they clearly physically depict behaviour of the wall friction with progress of transition. The analysed wall friction records (750 thousands samples) were made at the same boundary conditions as the measurements plotted in the Figure 2. Histograms N_L and N_T derived from measurements in the rough wall boundary layer under free stream turbulence [*Iu*=0.03; *Le* = 33.4 *mm*] are shown in Figure 6 as an example. As to avoid bad transparency of Figure 6, only histograms in sections x (γ), γ = 0, 0.1, 0.5, 0.9 and 1.0 are plotted in 3D-diagrams.

The mean durations of the wall friction stay in non-turbulent condition $(\Delta t)_L$ (white symbols, $I(t)$=0) and turbulent condition $(\Delta t)_T$ (smaller black symbols, $I(t)$=1) are plotted for rough wall boundary layers in Figure 7.

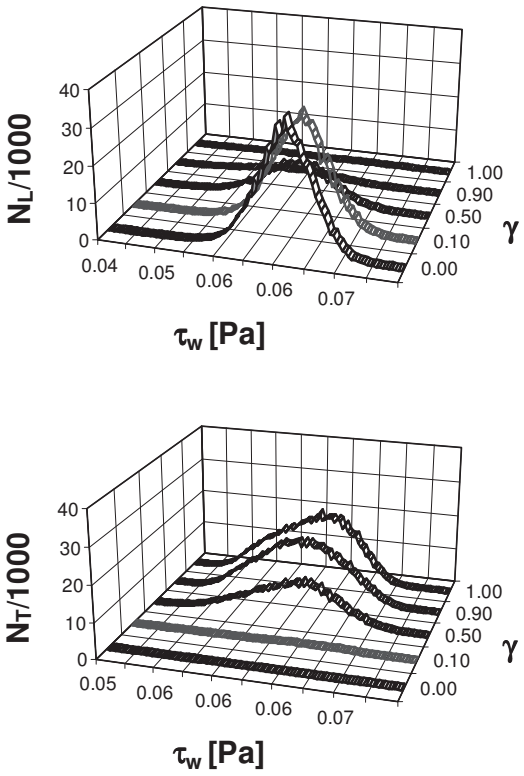

Figure 6. Example of the wall friction histograms

It is evident that periods $(\Delta t)_L$ are of orders longer then the turbulent periods $(\Delta t)_T$ at the start of transition x_S and vice versa at the end of transition. Similar courses can be found in smooth wall boundary layers but at that time the events durations are roughly of order longer. This is evident from the comparison of the Figure 7 with Figure 8 (see e.g. [23, 24]). This can be attributed to the effect of many flow disturbances generated by wakes of individual sand grains on rough surface however a definit physical explanations of this phenomenon is not available yet.

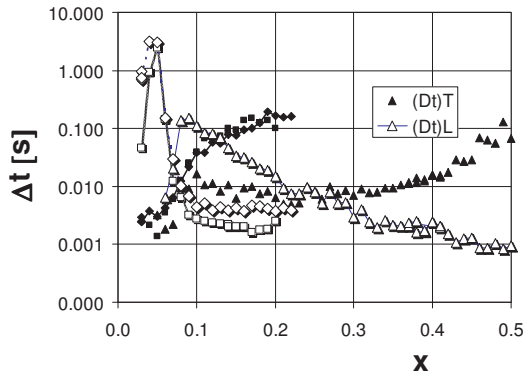

Figure 7. Mean time of the laminar- turbulent events duration; rough wall layers (symbols as in Fig. 2)

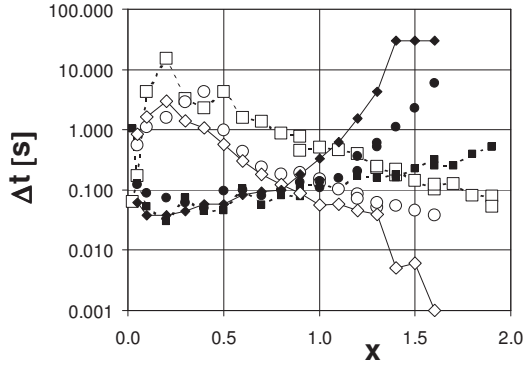

Figure 8. Mean time of the laminar- turbulent events duration; smooth wall layers (symbols as in Fig. 7)

The distributions of the conditional mean wall friction in boundary layers on the rough plate under free stream turbulence are shown in Figure 9 versus the displacement thickness Re-number. Distributions after Blasius solution (full line) and after Ludwieg and Tillmann formulae(dashed line) are also plotted in the Figure 9.

The non-turbulent/laminar means $(\tau_w)_L$ follow the Blasius distribution up to the location where the intermittency factor becomes positive. Afterwards the values $(\tau_w)_L$ start to grow. The increase continues little beyond the end of transition region $\gamma = 1$ and then possibly the decrease follows (unfortunately measurements were closed early after reaching locations $\gamma \approx 1$).

Behaviour of the wall friction $(\tau_w)_T$ during turbulent events ($I(t)$ = 1) is similar to the above discussed with only small differences.

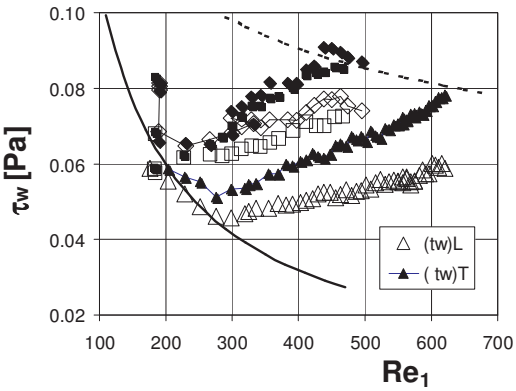

Figure 9. Conditional wall friction in rough wall layers (symbols as in Fig. 2)

They are namely: the diversion from the Blasius distribution comes sooner – about in the section where the displacement Re-number reaches value 200; the grows is steeper and finished at reaching the distribution computed by Ludwieg and Tillmann [20] empirical formulae (L.T.) with the use of correct values of the shape factor and the momentum thickness Re-number (dashed line). The distributions determined in rough wall layers are similar to the relevant ones in smooth wall layers in the earlier departures of turbulent means $(\tau_w)_T$ then the departures of laminar means $(\tau_w)_L$ from the Blasius distribution and that the turbulent means $(\tau_w)_T$ are joining the Ludwieg and Tillmann curve at last. However the courses of $(\tau_w)_T$ between „departure" and „joining" are different. The conditional means of turbulent events remain about on constant level in smooth wall boundary layer transition region.

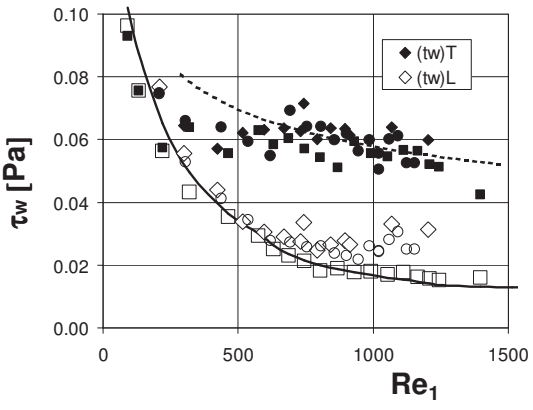

Figure 10. Conditional wall friction in smooth wall layers (symbols as in Fig. 2)

5. CONCLUSIONS

Surface roughness, though near the limit of admissible roughness, affects the boundary layer development more dramatically than the free stream turbulence intensity and the effect of the FST length scale on the boundary layer by-pass transition is somewhat suppressed.

The procedures of intermittency analysis and the conditional analysis of instantaneous wall friction records that were developed for studies of boundary layers on smooth surface proved successfully also in investigations of boundary layers on moderately rough surface.

Presented results are compatible with the Narasimha concept of intermittency.

Apparently the wakes of roughness grains constitute small flow disturbances that reduce the duration of the laminar events and the turbulent ones.

ACKNOWLEDGEMENTS

This work was supported by the Grant Agency of the Czech Republic, project GAP 101/12/1271 and with institutional support, project AV0Z20760514.

REFERENCES

[1] Kachanov, Y.S., 1994, „Physical mechanisms of laminar-boundary layer transition." *Ann. Rev. Fluid Mech.,* 26, pp. 411-482.

[2] Mayle, R.E., 1998, „A theory for predicting the turbulent-spot production rate." *ASME Paper* 98-GT-256, 7 p.

[3] Gostelow, J.P., Walker, G.J., Solomon, W.J., Hong, G. and Melwani, N., 1997, „Investigation of the calmed region behind a turbulent spot." *Journal of Turbomachinery ASME,* 1997, 119, pp. 802-809.

[4] Johnson, M.W., 2001, „On the flow structure within a turbulent spot". *Int. J. of Heat and Fluid Flow*, 22 , pp. 409-416.

[5] Koyabu, E., Funazaki, K. & Kimura, M., 2005, „Experimental studies on wake induced by-pass transition of flat-plate boundary layers under favourable and adverse pressure gradients". *JSME International Journal*, Series B, 48, 3, pp. 579-588.

[6] Matsubara, M., & Alfredsson, P.H., 2001, „Disturbance growth in boundary layers subjected to free-stream turbulence". *J. Fluid Mech.*, 430, pp. 149-168.

[7] Ramesh O. N., Hodson H. P., 2002, „On the dynamics of the calmed region behind a turbulent spot". In: *Proc. Minnowbrook III 2000 Workshop on boundary layer transition and unsteady aspects of turbomachinery flows* (Eds. J.E. LaGraff, D.E. Ashpis), NASA/CP-2001-210888, pp. 177-189.

[8] Schlichting H. and Gersten K., 2000, *Boundary-Layer Theory*. Springer, Berlin.

[9] Vinod, N. & Rama Govindarajan, 2004, *„Pattern of Breakdown of Laminar Flow into Turbulent Spots"*. Physical Review Letters, 93, 11, 114501-1.

[10] Volino, R.J., 2005, „An investigation of the scales in transitional boundary layers under high free-stream turbulence conditions". *Experiments in Fluids*, 38, pp. 516–533.

[11] Emmons, H., 1951, „The laminar-turbulent transition in a boundary layer – Part 1." *J. Aeronaut. Sci.*, 18, pp. 490-498.

[12] Narasimha, R., 1985, „The laminar-turbulent transition zone in the boundary layer". *Prog. Aerospace Sci.*, 22, pp. 29-80.

[13] Schubauer G.B. and Skramstad H.K,.1943-48, „Laminar boundary layer oscillations and transition on a flat plate". *National Bureau of Standards Research Paper 1772*. Reprint of a confidental NACA report from 1943 (citation adopted from [8]).

[14] Jonas P., 1997, „On the role of the length scale in the by-pass transition", *ZAMM - Z. angew. Math. Mech.* 77, pp. S145-S146.

[15] Jonas P., Mazur O. and Uruba V., 2000, „On the receptivity of the by-pass transition to the length scale of the outer stream turbulence". Eur.J.Mech. B 19, pp. 707-722.

[16] Roach P.E. and Brierley D.H., 2000, „Bypass transition modeling: a new method which accounts for free-stream turbulence intensity and length scale". *ASME Paper 2000-GT-0278.*

[17] Brandt L., Schlatter P. and Henningson D.S., 2004, „Transition in boundary layers subject to free stream turbulence". *J. Fluid Mech.* 517, pp. 167-198.

[18] Clark J.P., Jones T.V. and LaGraff J.E., 1994, „On the propagation of naturally occuring turbulent spots". *Journal of Engineering Mathematics*, 28, pp. 1-19.

[19] Elsner W., Wysocki M. and Drobniak S., 2006, "Determination of production rate of turbulent spots using wavelet analysis". *Chemical and Process Engineering*, 27, pp. 935-950.

[20] Fransson J.H.M., Matsubara M. and Alfredsson P.H., 2005, "Transition induced

by free-stream turbulence". *J. Fluid Mech.* 527, pp. 1-25.

[21] Jonas P., Mazur O. and Uruba V., 1999, "Statistical characteristics of the wall friction in a flat plate boundary layer through by-pass transition". *Z. Angew. Math. Mech*. 79, pp. S691-S692.

[22] Jonáš P., Elsner W., Mazur O., Uruba V. and Wysocki M., 2009, "Turbulent spots detection during boundary layer by-pass transition". *ERCOFTAC Bulletin 80*, pp. 16-19.

[23] Jonas P., Mazur O. and Uruba V., 2004, "Some results of the conditional analysis of the skin friction in transitional boundary layers", *Proc. Advances in Turbulence X*, CIMNE, Barcelona, Spain, pp. 811.

[24] Jonas P., Mazur O. and Uruba V., 2006, "Experimental study of the wall-friction development during boundary layer by-pass transition", *Proc. Colloquium Fluid Dynamics 2006*, IT AS CR, Praha, pp. 67-70.

[25] Jonáš P., 1989, "Control of free stream turbulence by means of passive devices. In *Proc. Int. Sem. Problems of Simulations in Wind Tunnels* Pt.2, ITPM SO AN SSSR, Novosibirsk, pp. 160-174.

[26] Zhang D.H., Chew Y.T. and Winoto S.H., 1996, "Investigation of intermittency measurement methods for transitional boundary". *Exp. Thermal and Fluid Sci.,* 12, pp. 433-443.

[27] Hendley T.B. and Keffer J.F., 1974, "Turbulent/non-turbulent decision in an intermittent flow". *J. Fluid Mech.* 64, pp. 625-644.

[28] Hladík O. and Uruba V., 2009, "Analysis of intermittent signal". *Mechanical Engineering J.*, 2009, ISSN 1335-2938, pp. 69–70.

[29] Johnson M.W. and Fashifar A., 1994, „Statistical propertiesof turbulent bursts in transitional boundary layers". *Int. J. Heat Fluid Flow* **15**, pp. 283-290.

Conference on Modelling Fluid Flow (CMFF'12)
The 15th International Conference on Fluid Flow Technologies
Budapest, Hungary, September 4-7, 2012

LATTICE-BOLTZMANN SIMULATIONS OF FLUID FLOWS AT FINITE KNUDSEN NUMBERS

Calin DAN[1], Sudhir SRIVASTAVA [2], Jens HARTING [3 4], Federico TOSCHI [5], Laurens VAN BOKHOVEN [6], Marco BARAGONA [7]

[1] Department of Applied Physics, Eindhoven University of Technology, Den Dolech 2, NL-5600MB Eindhoven, The Netherlands. Tel.: +31 40 247 5140 , Fax: +31 40 243 8272, E-mail: cdan@icp.uni-stuttgart.de
[2] Department of Applied Physics, Eindhoven University of Technology, Den Dolech 2, NL-5600MB Eindhoven, The Netherlands. E-mail: s.srivastava@tue.nl
[3] Department of Applied Physics, Eindhoven University of Technology, Den Dolech 2, NL-5600MB Eindhoven, The Netherlands. E-mail: j.d.r.harting@tue.nl
[4] Institute for Computational Physics, University of Stuttgart, Pfaffenwaldring 27, D-70569 Stuttgart, Germany. E-mail: jens@icp.uni-stuttgart.de
[5] Department of Applied Physics, Eindhoven University of Technology, Den Dolech 2, NL-5600MB Eindhoven, The Netherlands. E-mail: f.toschi@tue.nl
[6] Research Immersion, ASML Netherlands B.V., De Run 6501, 5504 DR Veldhoven, The Netherlands. E-mail: laurens.van.bokhoven@asml.com
[7] Product & Process Modeling, Philips Research, HTC-7 4.B.005, 5656 AE Eindhoven, The Netherlands. E-mail: marco.baragona@philips.com

ABSTRACT

The lattice-Boltzmann method is a possible alternative to standard computational fluid dynamics (CFD) or direct simulation Monte Carlo (DSMC) simulations of fluid flows in continuum, slip and transition regimes. We evaluate the accuracy of the lattice-Boltzmann (LB) method for the simulation of microchannel fluid flows at finite Knudsen numbers. A novel modeling of the adaptive Knudsen number as a function of fluid density is proposed in the lattice-Boltzmann model. Specific boundary conditions are used to represent the slippage at the wall and for the simulation of open flows. We compare our simulation results with DSMC data.

Keywords: DSMC, equilibrium boundary conditions, finite Knudsen number, lattice-Boltzmann, relaxation time correction

NOMENCLATURE

NOTE: In this article, we are using two unit systems: SI units and lattice-Boltzmann (abbreviated LB) units. In the nomenclature section, if a quantity is defined using both SI and LB units system, we indicate the SI units.

H	$[m]$	characteristic length / channel height
Kn	$[-]$	Knudsen number
L	$[m]$	channel length
Ma	$[-]$	Mach number
N	$[-]$	number of lattice sites
P	$[Pa]$	pressure
W	$[-]$	weight coefficient
c_s	$[m/s]$	speed of sound
$\underline{e}$	$[-]$	discrete velocity vector
f	$[-]$	distribution function
k_B	$[m^2kg/s^2]$	Boltzmann constant
$\underline{\dot{m}}$	$[kg/s]$	mass flow rate
t	$[tu]$	time
$\underline{u}$	$[m/s]$	velocity vector
$\underline{x}$	$[lu]$	lattice site position
λ	$[m]$	mean free path
ν	$[m^2/s]$	kinematic viscosity
π	$[-]$	constant 3.14
ρ	$[kg/m^3]$	density
σ	$[m]$	particle hard shell diameter
τ	$[-]$	relaxation time

Subscripts and Superscripts

c	copied quantity
calc	calculated quantity
d	desired (imposed) quantity
i	discrete direction
eq	equilibrium distribution
ref	reference quantity
*	quantity in SI units

1 INTRODUCTION

Direct simulation Monte-Carlo (DSMC) is standard method to simulate finite Knudsen number fluid flows, but its drawback is the large computational time required for each simulation. In this situation,

alternative numerical methods are required for simulation of finite Knudsen number flows at lower computational cost, but still maintaining reasonable accuracy. Due to its particulate nature and local dynamics, the lattice-Boltzmann (LB) method is a reliable candidate for the simulation of finite Knudsen number flows. Different models have been proposed in the literature to enhance the accuracy of the standard LB method for simulation of the finite Knudsen number flows: different slip boundary conditions at the walls, local relaxation time [1, 2] or higher order LB models [3]. Examples of slip boundary conditions for finite Knudsen number flows are the diffusive reflection boundary conditions with local accommodation coefficients [4] or the virtual wall collision mechanism [5]. However, these LB models do not represent accurately the heat transfer between the fluid and walls or temperature variation in the fluid. To simulate high Knudsen number thermal flows, we propose a coupled fluid flow and thermal solver, with the temperature field resolved using a passive-scalar approach. The first step of this thermal coupling approach is to develop a LB solver for fluid flow at high Knudsen number with boundary conditions that can be easily coupled with the temperature field solver. In this respect, the walls are represented using the equilibrium boundary conditions proposed by Ansumali and Karlin [6], which can be defined in both fluid flow and thermal solvers. Moreover, different boundary conditions to impose a mass flow rate at the inlet of a channel are evaluated and a model to account for the variation of the Knudsen number along the channel length is introduced.

In the following section we introduce the lattice-Boltzmann model. The LB simulation results are compared against DSMC data for microchannel flow at low and intermediate Knudsen numbers. For the sake of simplicity, only a two dimensional solver has been implemented, but the implementation and parallelization of the LB solver for three-dimensional geometries is straightforward. The purpose of the fluid flow simulations at low Knudsen number is to validate the implementation of specific boundary conditions and models in the LB solver. Finally, simulations of the fluid flow at Knudsen numbers around 2 are performed to evaluate the limits and accuracy of our LB solver.

2 LATTICE-BOLTZMANN MODEL

The Lattice-Boltzmann (LB) method is a powerful tool for simulating weakly compressible fluid flows [7, 8]. It considers solving the discretized Boltzmann equation

$$f_i(\underline{x}+\underline{e}_i, t+1) - f_i(\underline{x}, t) = - \frac{1}{\tau}\left[f_i(\underline{x}, t) - f_i^{eq}(\underline{x}, t)\right] , \quad (1)$$

where f represents the distribution function for the velocity component i at position $\underline{x}$ and time t. In the LB method, the physical domain is divided in square (in 2D) or cubic (in 3D) voxels with the lattice constant Δx, and the time is discretized with the timestep Δt. On each lattice site, the velocity vector is discretized into a finite set of directions $\underline{e}_i$, $i = 1 \dots N$. In this article, we consider only the two-dimensional D2Q9 lattice, *i.e.* $N = 9$ velocities for the two-dimensional domain. All physical quantities in this section are assumed in LB units, unless a different unit system is explicitly stated. The left hand side of Eq. (1) represents the propagation (streaming) of the fluid motion. The right hand side of Eq. (1) is a simple formulation of the collision operator using a single relaxation time with the time constant τ. This formulation of the collision part is called the Bhatnagar-Gross-Krook (BGK) scheme [9], and it assumes that the equilibrium distribution function is given by [10]

$$f_i^{eq}(\underline{x}, t) = W_i\, \rho\, [1+ \frac{\underline{e}_i \cdot \underline{u}^{eq}}{c_s^2} + \frac{(\underline{e}_i \cdot \underline{u}^{eq})^2}{2\, c_s^4} - \frac{|\underline{u}^{eq}|^2}{2\, c_s^2}\Bigg] , \quad (2)$$

where the weights W_i for the D2Q9 lattice site are given by

$$W_i = \left\{\frac{4}{9}, \frac{1}{9}, \frac{1}{9}, \frac{1}{9}, \frac{1}{9}, \frac{1}{36}, \frac{1}{36}, \frac{1}{36}, \frac{1}{36}\right\} . \quad (3)$$

The density and bulk velocity in absence of any external acceleration acting in the fluid are given as

$$\rho = \sum_i f_i(\underline{x}, t) , \quad (4)$$

$$\underline{u} = \sum_i f_i(\underline{x}, t) \cdot \underline{e}_i . \quad (5)$$

In absence of any external force, the equilibrium velocity $\underline{u}^{eq}$ equals the bulk velocity $\underline{u}$. The speed of sound in LB is a lattice-dependent quantity, which takes the value [7]

$$c_s = \frac{1}{\sqrt{3}} , \quad (6)$$

which can be employed in the equation of state for pressure as

$$P = c_s^2\, \rho . \quad (7)$$

The kinematic viscosity (ν) of the fluid is represented in the LB model by the relaxation time τ according to

$$\nu = c_s^2 \left(\tau - \frac{1}{2}\right) . \quad (8)$$

As the speed of sound is a fixed value in LB units (Eq. (6)), the relaxation time as function of kinematic viscosity is given as

$$\tau = 3\nu + 0.5 . \quad (9)$$

The computational domain is extended with two layers of halo lattice sites in all directions. The halo

sites are needed to implement some of the boundary conditions, *e.g.* free-slip, periodic, bounce-back, equilibrium at wall. The collision operator is applied only to the fluid lattice sites, while the streaming is applied in all sites (including the halo).

2.1 Finite Knudsen flow simulation

The Knudsen number can be defined using the quantities in LB units as

$$Kn = \frac{\nu}{c_s\, N}\,, \tag{10}$$

where the kinematic viscosity ν is defined by Eq. (8), N is the number of lattice sites representing the characteristic length (channel height, in this case) and the speed of sound c_s is defined by Eq. (6). In our simulations, the Knudsen number is introduced in the model through the relaxation time, using Eqs. (8) and (10):

$$\tau = \frac{Kn\, N}{c_s} + 0.5\,. \tag{11}$$

On the other hand, the Knudsen number defined using quantities in SI units is given by

$$Kn = \frac{\lambda^*}{H^*} = \frac{k_B^* T^*}{\sqrt{2}\pi(\sigma^*)^2\, P^*\, H^*}\,, \tag{12}$$

where λ^* is the mean free path, H^* is a characteristic length, k_B^* is the Boltzmann constant and σ^* is the particle hard shell diameter. In this formula, the superscript * indicates that the physical quantities are considered in SI units. Considering the isothermal fluid flow lattice-Boltzmann, one observes that the right hand side of the Eq. (12) is constant except for the pressure. Based on this observation and using the ideal gas equation of state assumed in the LB model (Eq. (7)), we consider that Kn ρ^* = constant. Furthermore, replacing in this constant relation the definition of the Knudsen number in LB units (Eq. (10)) and the relation between the relaxation time and viscosity (Eq. (8)), we found the following correction for the relaxation time:

$$\tau = 0.5 + \frac{(\tau^{\mathrm{ref}} - 0.5)\rho^{\mathrm{ref}}}{\rho}\,. \tag{13}$$

For the testcase considered in this project, density at the outlet is imposed and the Knudsen number at the outlet is known. Therefore, we choose the reference values for density ρ^{ref} and relaxation time τ^{ref} as the values at the outlet.

2.2 Boundary conditions

The walls are represented in our model using the boundary conditions proposed by Ansumali and Karlin [6]. Such boundary conditions are implemented by imposing on the halo lattice sites an equilibrium distribution with zero value of the normal component of velocity and the tangential velocity is the opposite tangential velocity in the neighboring fluid lattice site. With this approach, the wall is positioned at the half distance between halo and neighboring fluid lattice site. Moreover, the distributions going to the fluid nodes (unknown distributions) are re-scaled such that mass coming from the fluid nodes is conserved. According to Toschi and Succi [5], this boundary condition is significantly improving the accuracy and stability of the LB simulations at high Knudsen numbers with respect to the bounce-back boundary condition. Bounce-back boundary conditions are standard LB conditions to represent the walls, which are implemented by reversing the direction of the distribution function in the lattice sites situated next to the wall.

To represent open flows, *i.e.* to impose a desired density, velocity, or mass flow, two types of boundary conditions are implemented:

- Zou-He boundary conditions (abbreviated BC-ZH), documented in [11, 12], are derived assuming that the bounce-back condition holds in the direction normal to the boundary. These boundary conditions are applied on the fluid lattice sites closest to the inlet/outlet (not in the halo lattice) after the streaming step.

- equilibrium boundary conditions following the approach of Ansumali and Karlin [6] (abbreviated BC-AK). They are applied on the halo sites, before streaming, by imposing the equilibrium distributions calculated using the desired quantity and values copied from the closest lattice site in the fluid domain. For instance, if we impose a density ρ_d at the inlet using these conditions, one copies the velocity from the neighboring fluid site $\underline{u}_c$ and calculate the equilibrium distribution on the halo site $f_i^{eq}(\rho_d, \underline{u}_c)$. If the mass flow rate $\underline{\dot{m}}$ is imposed with this condition, the density is copied from the neighboring fluid site ρ_c and velocity is calculated from the mass flow rate $\underline{u}_{calc} = \underline{\dot{m}}/\rho_c$

3 SIMULATION RESULTS

The simulation results for finite Knudsen flows obtained using the LB code are compared to DSMC simulations. For comparison, we consider a two dimensional hydrogen gas flow through a parallel plate channel of 150mm×7mm (see Figure 1). For this testcase, the mass flow rate is imposed at the inlet and the pressure at the outlet. In the LB model, the pressure is proportional to density (Eq. (7)) and the density will be imposed at the outlet. We compare LB and DSMC results for two Knudsen numbers measured at the outlet: low Knudsen number simulations ($Kn \approx 0.07$) to validate the implementation of the LB model, and intermediate Knudsen number simulations ($Kn \approx 1.7$) to evaluate the limits and accuracy of our LB model. In this section, both SI and LB unit system are used. The quantities of DSMC simulations are given in SI units. The LB simulations are performed using

quantities in LB units, but the simulation results are converted in SI units for comparison with the DSMC data. The unit system of quantity is explicitly stated for each particular situation.

All DSMC calculations are done with G.A. Bird's DS2V code v4.5.06 [13, 14]. At the inlet we adopt a 'flow entry' boundary condition. It requires a number density and average inlet velocity. At the exit we specify a number density and a static gas temperature. This temperature is fixed at 295 K in all our runs. The gas-wall interaction is modeled by the Cercignani-Lampis-Lord scattering kernel. This kernel contains several parameters, called accommodation coefficients. When these coefficients are all set to unity, one retrieves the fully diffuse scattering kernel of Maxwell. We expect this kernel to reproduce the bounce-back boundary condition of the LB model at the the larger scale. The desired mass flow rate at the desired static outlet pressure is realized by tuning the two parameters at the flow entry together with the number density at the outlet. This iterative procedure was done manually.

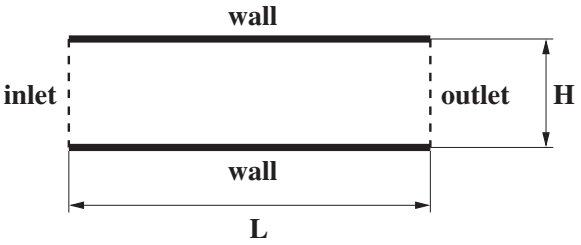

Figure 1. Parallel plate channel

In order to convert the quantities and dimensions considered in the DSMC simulations from SI to LB units, we choose the number of lattice sites on the channel height, the density at the outlet and calculate the relaxation time τ from the Knudsen number measured at the outlet of the DSMC simulations (see Eq. (11)). By fixing these quantities, one can determine the space, time and mass unity, which are further employed to convert the SI to LB units and vice-versa. Following this approach, the parallel plate channel is represented by 450×21 lattice sites and the relaxation time and density are calculated/chosen for each testcase. In the following simulations, maximum 10^5 iterations of the LB solver, *i.e.* about 15 minutes of single core computation time, are required to obtain the steady-state solution for both density and velocity fields.

3.1 Simulation of fluid flow at low Knudsen number

We consider DSMC simulations with the inlet mass flow rate $\dot{m} = 31.8 \cdot 10^{-6}$ kg/s and the outlet pressure $P = 20$ Pa. In the LB model, the density imposed at the outlet is chosen as 0.1 and the inlet mass flow rate determined from unit conversion is 0.0155. The relaxation time for Knudsen number 0.076 at the outlet is calculated as $\tau = 3.26$.

The fluid flow results are presented in Figures 2 and 3. We compare the DSMC data (solid lines) against the LB simulations in two situations: dashed lines are results obtained by correcting the fluid flow relaxation time with density (Eq. (13)) and the dotted lines are the results obtained for constant fluid flow relaxation time (τ = constant).

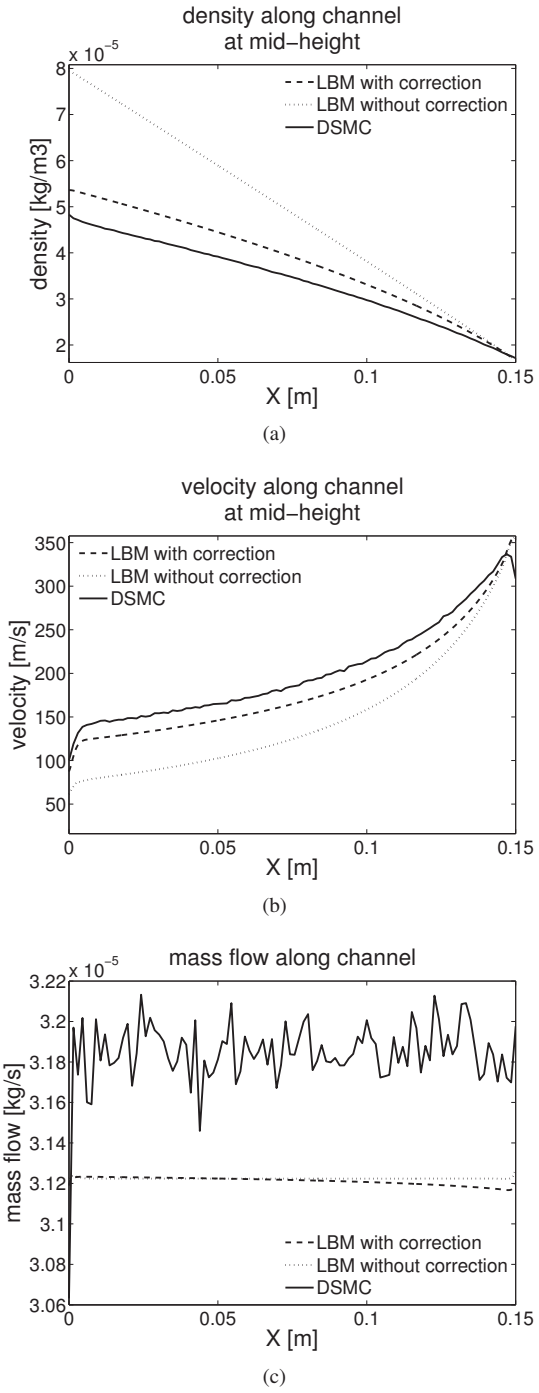

Figure 2. Comparison of density (a), velocity (b) and mass flow rate (c) along the channel at low Knudsen number (Kn = 0.076) .

In Fig. 2, we present the profiles of density and velocity along the channel length (u_x), at the middle of

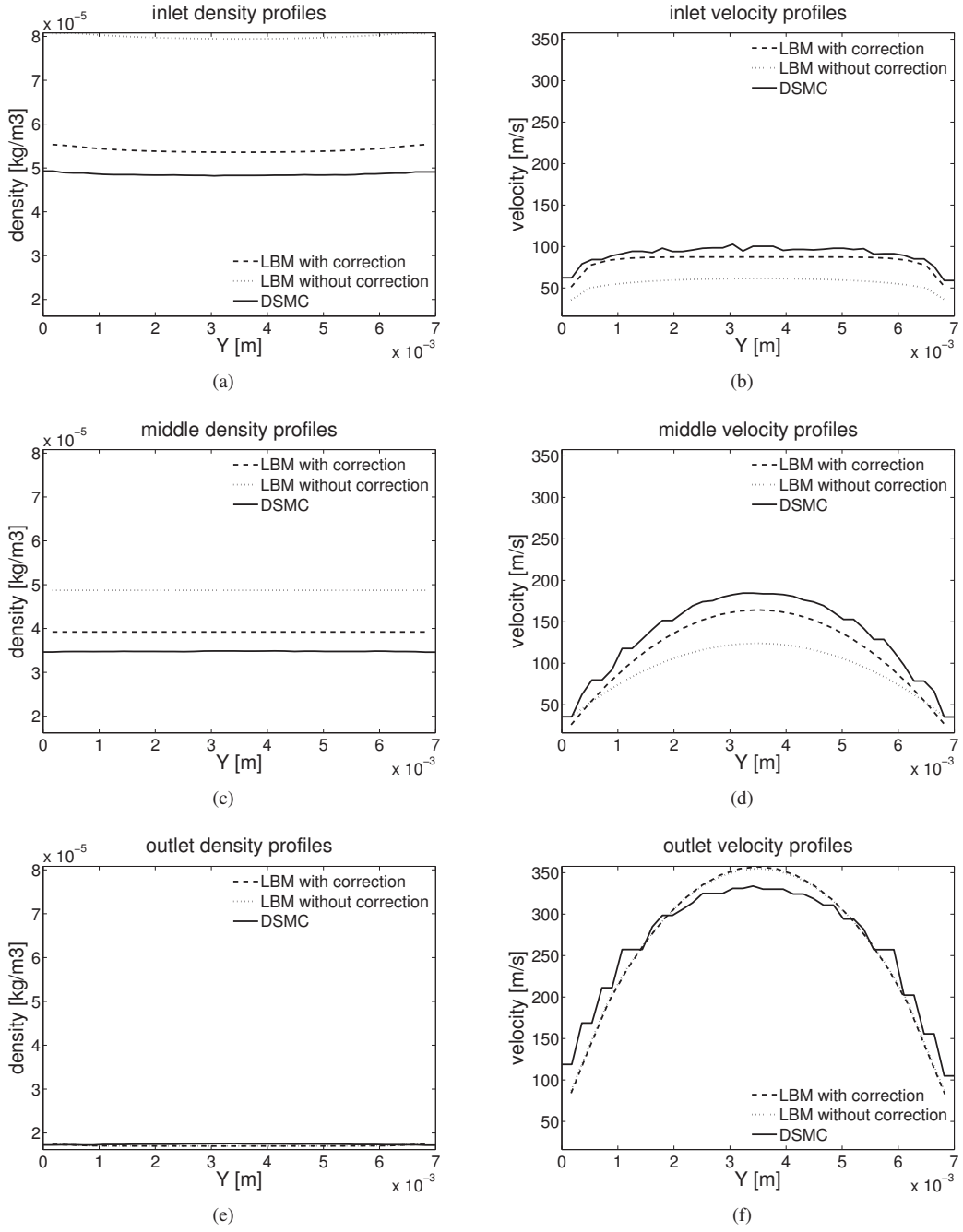

Figure 3. Density (left) and velocity (right) profiles obtained from cross-sections on the channel height at three positions along the channel: inlet, middle, and outlet.

the channel height. In Fig. 3, we present a cross-section of density and velocity on the channel height at three positions along the channel: at the inlet, in the middle of channel length and at the outlet. One observes that although the mass flow rate is similar in both LB simulations (Fig. 2(c)), a dramatic improvement of the density (Fig. 2(a)) and velocity profiles (Fig. 2(b)) in respect with the DSMC simulations is obtained by using the correction Eq. (13). The improvement is obvious when looking at the density profile at the inlet (Figs. 2(a) and 3(b)). Therefore, we apply the correction Eq. (13) in the following LB simulations of the finite Knudsen flows.

3.2 Simulation of fluid flow at intermediate Knudsen number

We consider the DSMC simulations with the inlet mass flow rate $\dot{m} = 3.66 \cdot 10^{-6}$ kg/s and the outlet pressure $P = 0.8$ Pa. In the LB model, the density imposed at the outlet is chosen as 0.1 and the inlet mass flow rate determined from the unit conversion is 0.04. The relaxation time for Knudsen number 1.71 at the outlet is calculated as $\tau = 62.7$. In Figure 4, we compare the DSMC data (solid lines) against the LB simulations (dashed lines). One notices differences in the density value at the inlet of the channel when comparing the DSMC and LB simulation results. To explain these differences, one can argue that we consider isothermal LB model, while temperature variation is integrated in the DSMC model. But these differences cannot be explained by the lack of coupling with the thermal field because, in these DSMC simulations, the temperature has small variations in the range $290 \ldots 295$ K over the domain. Furthermore, we run LB simulations with different profiles (constant or Poiseuille) of the mass flow rate profile, but we observed a change only on the velocity profile at the inlet and not a significant change of the density value along the channel.

3.3 Discussion of the simulation results

Furthermore, we investigate the influence of the Mach number on the variation of density along the channel in the LB simulations. It is known that following the SI to LB unit conversion, the speed of sound is not accurately represented in the LB simulations. Moreover, with the LB model considered in this work, one can not choose independently Mach and Knudsen numbers. If the speed of sound is not accurately represented in the LB simulations, one can expect errors in the density profile. As a rule of thumb, the LB method is expected to be accurate for Mach numbers up to values around 0.15. Regarding the value of Mach number in the DSMC simulations, we found a maximum value Ma = 0.34 for the low Knudsen number flow (section 3.1) and Ma = 0.55 for the high Knudsen number flow (section 3.2). Looking at the LB simulation results, we found the maximum value of velocity in LB units is 0.2 (Ma = 0.34) for the low

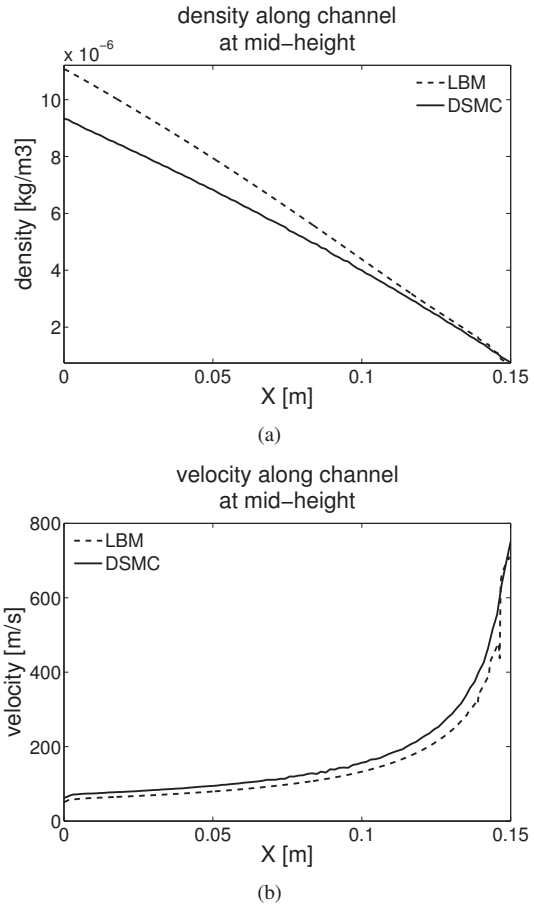

Figure 4. Comparison of density (a) and velocity (b) along the channel at intermediate Knudsen number (Kn = 2) .

Knudsen number flow (section 3.1) and the maximum value of velocity in LB units is 0.4 (Ma = 0.7) for the high Knudsen number flow (section 3.2). For this reason, we considered another DSMC simulation of fluid flow at high Knudsen number 2.04, which has the maximum Mach number Ma = 0.13. In the DSMC simulation, the inlet mass flow rate is $\dot{m} = 0.83 \cdot 10^{-6}$ kg/s and the outlet pressure $P = 0.8$ Pa. The density imposed at the outlet is chosen as 0.1 and the inlet mass flow rate is determined as 0.011. The relaxation times for Knudsen number 2.04 at the outlet obtained from unit conversion are $\tau = 75.1$. The fluid flow relaxation time τ corresponds to a Knudsen number at the outlet of 2.

The comparison of LB and DSMC simulation results for the fluid flow are presented in the Figure 5. In these LB simulations, we impose the mass flow rate at the inlet using different types of boundary conditions: equilibrium boundary conditions, *i.e.* BC-AK (dashed lines) and Zou-He boundary conditions, *i.e.* BC-ZH with constant (dotted lines) or Poiseuille profile (dash-dot lines). In these simulations, the maximum value of velocity is relatively small 0.16 (Ma = 0.27) and one notices a better match of velocity and density profiles.

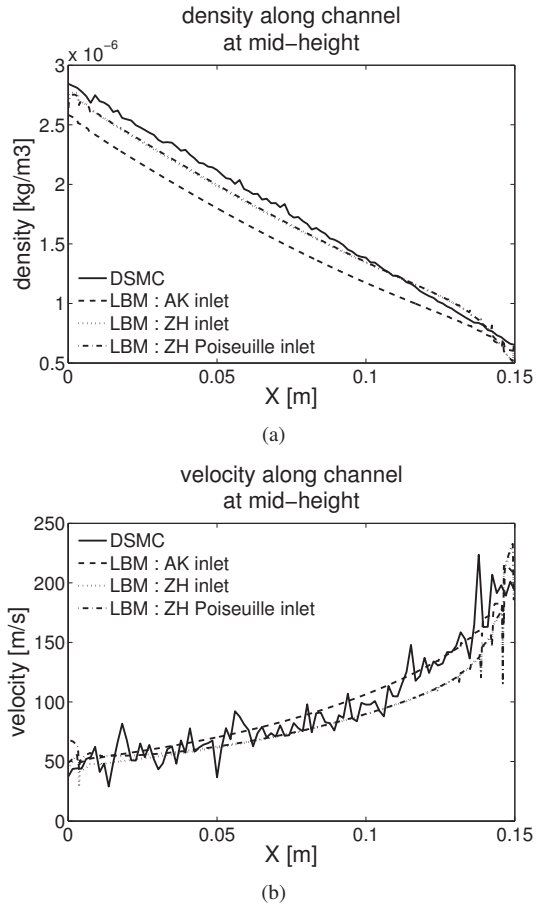

Figure 5. Comparison of density (a) and velocity (b) along the channel at intermediate Knudsen number and moderate Mach number for different type of inlet boundary conditions

Nevertheless, we can not explain the dependency on the type of boundary condition used to impose the mass flow rate at the inlet: the equilibrium boundary conditions BC-AK is better matching the DSMC density profile, while the Zou-He boundary conditions BC-ZH is matching the velocity profiles. This observation can help understanding the background of large deviations observed in the density profiles of the other LB simulations, but further investigations are required.

4 CONCLUSION

We implemented and validated a lattice-Boltzmann solver for simulation of the fluid flow at finite Knudsen numbers. Equilibrium boundary conditions are considered at the wall and two different methods to impose the mass flow rate at the inlet are presented. We introduced a correction of the relaxation time with density $\tau(\rho)$, which is critical to reproduce the physics of fluid flows at finite Knudsen numbers. We found good agreement between DSMC and LB simulation results of fluid flow at small Knudsen numbers. The LB simulation results at Knudsen number around 2 shown a qualitative agreement with the DSMC results, but the density at the inlet of the channel is different. We explain this difference by comparing the Mach number in different LB simulations. As outlook, a consistent approach for coupling the momentum and thermal fields in the LB model is expected to improve the accuracy of the LB simulations of fluid flow at finite Knudsen numbers. Further investigation on the boundary conditions to impose the desired mass flow rate at the inlet is required.

ACKNOWLEDGMENTS

The authors are thankful to Nico ten Kate, Ramin Badie (ASML) and Sergei Shulepov (Philips Research) for the fruitful suggestions and supporting our research.

References

[1] X. Nie, G. Doolen, and S. Chen, 2002, "Lattice-Boltzmann simulations of fluid flows in MEMS," *J Stat Phys*, Vol. 107, No. 1-2, pp. 279–289.

[2] G. Tang, W. Tao, and Y. He, 2005, "Gas slippage effect on microscale porous flow using the lattice Boltzmann method," *Phys Rev E*, Vol. 72, p. 056301.

[3] X. Shan, X.-F. Yuan, and H. Chen, 2006, "Kinetic theory representation of hydrodynamics: a way beyond the Navier-Stokes equation," *J Fluid Mech*, Vol. 550, pp. 413–441.

[4] Y. Zhang, R. Qin, and D. Emerson, 2005, "Lattice Boltzmann simulation of rarefied gas flows in microchannels," *Phys Rev E*, Vol. 71, p. 047702.

[5] F. Toschi and S. Succi, 2005, "Lattice Boltzmann method at finite-Knudsen numbers," *Europhys Lett*, Vol. 69, No. 4, pp. 549–555.

[6] S. Ansumali and I. Karlin, 2002, "Kinetic boundary conditions in the lattice Boltzmann method," *Phys Rev E*, Vol. 66, p. 026311.

[7] S. Succi, 2001, *The lattice Boltzmann equation for fluid dynamics and beyond*. Oxford University Press.

[8] M. C. Sukop and D. T. Thorne, 2007, *Lattice Boltzmann Modelling - An introduction for geoscientists and engineers*. Springer Berlin Heidelberg.

[9] P. L. Bhatnagar, E. P. Gross, and M. Krook, 1954, "Model for collision processes in gases. I. Small amplitude processes in charged and neutral one-component systems," *Phys Rev*, Vol. 94, No. 3, p. 511.

[10] S. Chen, H. Chen, D. Martínez, and W. H. Matthaeus, 1991, "Lattice Boltzmann model for simulation of magnetohydrodynamics," *Phys Rev Lett*, Vol. 67, No. 27, p. 3776.

[11] Q. Zou and X. He, 1997, "On pressure and velocity boundary conditions for the lattice Boltzmann BGK model," *Phys Fluids*, Vol. 9, pp. 1591–1598.

[12] M. Hecht and J. Harting, 2010, "Implementation of on-site velocity boundary conditions for D3Q19 lattice Boltzmann," *J Stat Mech*, Vol. 1, p. 1018.

[13] G. A. Bird, 1963, "Approach to translational equilbrium in a rigid sphere gas," *Phys Fluids*, Vol. 6, p. 1518.

[14] G. A. Bird, 1994, *Molecular Gas Dynamics and the Direct Simulation of Gas Flows*. Oxford University Press.

Conference on Modelling Fluid Flow (CMFF'12)
The 15th International Conference on Fluid Flow Technologies
Budapest, Hungary, September 4-7, 2012

Low Mach Navier-Stokes equations on unstructured meshes.

Jordi VENTOSA,[1,2] Jordi CHIVA, [2] Oriol LEHMKUHL, [2,3] Carlos-David PÉREZ-SEGARRA, [2] Assensi OLIVA [2]

[1] Corresponding Author. E-mail: jordivm@cttc.upc.edu
[2] Centre Tecnològic de Transferència de Calor (CTTC),Universitat Politècnica de Catalunya (UPC),ETSEIAT, Colom 11, 08222, Terrassa, Barcelona, Spain, Fax: +34 93 739 89 20 E-mail: cttc@cttc.upc.edu
[3] Termo Fluids, S.L. Magí Colet, 8, 08204 Sabadell (Barcelona), Spain E-mail: termofluids@termofluids.com

ABSTRACT

Numerical methods for fluxes with strong density variations but with speeds much lower than the sound speed, known as low Mach flows, present some particularities with respect to incompressible formulations. Despite having similar application ranges, incompressible formulations using the Boussinesq approximation with constant fluid properties cannot correctly describe fluxes with high density variations. According to Gray and Giorgini [1], use of the Boussinesq approximation can be considered valid for variations of the density up to 10% with respect to the mean value, so when strong density variations are present, variable density formulations are required. In the low Mach number Navier-Stokes equations the velocity divergence is not zero and acoustic waves are not considered. Also, the pressure is split into a dynamic pressure and a thermodynamic part. The latter is used to evaluate the density, by means of the ideal gas state law.
Here will be presented an extension of an incompressible pressure projection-type algorithm (fractional-step) to simulate low Mach fluxes, using a Runge-Kutta/Crank-Nicolson time integration scheme, similar to the one presented by Najm et al. [2] and Nicoud in [3]. The use of a predictor-corrector substeps is related to the instabilities introduced by the density time derivative into the constant coefficient Poisson equation, as reported in [2, 3]. The spatial discretisation is performed by means of an unstructured finite volume technique, using both the collocated formulation by Felten [4] and the staggered formulation by Perot [5]. Finally, the algorithm is tested against benchmark test cases, such as the differentially heated cavity with large temperature differences and cases with reactive fluxes.

Keywords: CFD, Low Mach Navier-Stokes equations, Runge-Kutta/Crank-Nicolson time integration, unstructured, combustion

NOMENCLATURE

Symbols not listed here correspond to their usual definition stated in the Journal of Heat Transfer, Vol 121, No. 4, pp. 770-773, November 1999.

A_f	$[m^2]$	Face area
D_i	$[m^2/s]$	diffusion coeficient of the *ith* specie
M_o	$[kg]$	initial mass in an enclosed cavity
N	$[-]$	number of species
P_o	$[Pa]$	thermodynamic part of the pressure
R_i	$[J/(kg\,K)]$	ith specie gas constant
V	$[m^3]$	volume
Y_i	$[-]$	*ith* specie mass fraction
h	$[J/kg]$	specific enthalpy (includes sensible and chemical)
h_s	$[J/kg]$	sensible enthalpy
$\underline{n}_f$	$[-]$	face normal vector
p	$[Pa]$	hydrodynamic part of the pressure
$\underline{u}_c$, $\underline{u}_f$	$[m/s]$	cell and face centred velocity
γ	$[-]$	heat capacity ratio
$\Delta h^o_{i,f}$	$[J/kg]$	standard enthalpy of formation of the *ith* specie
δt, Δt	$[s]$	time step
ϵ	$[-]$	temperature difference ratio
τ_{ij}	$[kg/(m\,s^2)]$	viscous stress tensor
$\dot{w}_i$	$[kg/(m^3\,s)]$	reaction rate of *ith* specie

Subscripts and Superscripts

c	cold wall of the differentially heated cavity
cv	current control volume
h	hot wall of the differentially heated cavity
n	current time step
nb	neighbour control volume
0	indicates reference value
$*$	predictor step quantities

1. INTRODUCTION

Compressible formulations of the Navier Stokes Equations are required to study flows with strong density variations, but the standard compressible algorithms are not suitable due to stability issues resulting in strong time step limitations. Neither are suitable incompressible formulations using the Boussinesq approximation, due to its limited application range [1]. Both incompressible formulations and Low Mach number formulations yield the same results when the Boussinesq approximation is valid, but as the temperature, the density and the physical properties, variations become higher, so become the differences between both formulations. Low Mach compressible formulations are able to deal with flows presenting high density variations under the influence of a low velocity field. This formulation results from the removal of the high order dependencies of the Mach number of the Navier Stokes equations. Therefore, Navier Stokes equations are expanded in power series of the Mach number and these high order terms are then removed, thus obtaining a formulation whose time step is not any more subject to Mach number limitations.

Most of the work found in the literature related to Low-Mach algorithms is for cartesian/structured grids [2, 3, 6, 7]. When faced against industrial applications such discretisations are not very well fitted due to the complexity of the geometry. yielding a more efficient way to approximate the simulation domain. The formulation to be used is an extension of the one presented by Najm et al. [2] and Nicoud in [3], which has a constant coefficient Poisson equation, on unstructured grids using both collocated [4] and staggered [5] formulations. The numerical algorithm will be validated against a non-reacting and a reacting test case. Use of a Runge-Kutta/Crank-Nicholson scheme is motivated by the reported instabilities introduced by the density time derivative, as shown by [2, 3].

The first case of study will be a differentially heated square cavity (of side $L = 1$) under a large temperature difference ($\Delta T = 720K$) filled with air, as presented by Vierendeels et al. [8].

A second case of study will be a chemically reacting laminar flow, as described in [9], which corresponds to a perforated plate burner with a premixed flame. This case is simplified to a two-dimensional case when the hole diameter and hole separation is small enough. A four step skeletal mechanism [10] is used to simulate the reaction of methane with air.

The aforementioned authors ([2],[3] and [8]) performed their tests using structured meshes, so the purpose of the present work is to study the modellization of the Low-Mach Navier-Stokes equations in unstructured meshes in cases where temperature and density variations are high, and clearly the Boussinesq approximation is not valid, with non-constant physical properties.

2. LOW-MACH NUMBER EQUATIONS

2.1. Flow equations

In order to obtain the low-Mach Number approximation of the Navier Stokes Equations, these equations are taken in its compressible formulation and the Mach dependant variables are expanded in power series of the Mach number, as shown by Papalexandris [11]. As flows presenting a low Mach number are considered, only the lowest order terms of this expansion are kept. The low-Mach Number equations for non reacting flows are

$$\frac{\partial \rho}{\partial t} + \frac{\partial \rho u_j}{\partial x_j} = 0 \tag{1}$$

$$\frac{\partial \rho u_i}{\partial t} = -\frac{\partial \rho u_j u_i}{\partial x_j} - \frac{\partial p}{\partial x_i} + \frac{\partial \tau_{ij}}{\partial x_j} + \rho g_i \tag{2}$$

$$\rho \frac{\partial h}{\partial t} = -\rho u_j \frac{\partial h}{\partial x_j} + \frac{dP_o}{dt} - \frac{\partial \dot{q}_j}{\partial x_j} \tag{3}$$

where $\tau_{i,j} = \mu(\frac{\partial u_i}{\partial x_j} + \frac{\partial u_j}{\partial x_i} + \frac{2}{3}\delta_{ij}\frac{\partial u_k}{\partial x_k})$ and $\dot{q}_j = -\kappa\frac{\partial T}{\partial x_j}$. P may be interpreted as the hydrodynamic pressure and P_o the thermodynamic pressure, which is considered spatially uniform. Here, due to the low-Mach approximation, the viscous heating term $\tau_{ij}\frac{\partial u_i}{\partial x_j}$, the term $u_i\frac{\partial p}{\partial x_i}$ are neglected, and the term $\frac{2}{3}\delta_{ij}\frac{\partial u_k}{\partial x_k}$ of the viscous stress tensor is considered to be negligible.The enthalpy used for non-reacting flows is equal to the sensible enthalpy

$$h_s = \int_{T_0}^{T} c_p dT \tag{4}$$

Using Eq. (4) the temperature, at each control volume after each iteration, can be recovered. The equation of state is as follows

$$P_o = \rho R_i T \tag{5}$$

If the system is considered open, this thermodynamic pressure is set at ambient pressure or the case reference pressure. If the system is closed, a mass conservation is invoked, and the pressure at a given time can be obtained through the total mass in the enclosure and the temperature field

$$M_o = \frac{P_o}{R_i}\int_V \frac{1}{T} dV \tag{6}$$

$$P_o(t) = \frac{M_o R_i}{\int_V \frac{1}{T} dV} \tag{7}$$

It should be noted that the transport equations of the scalars are formulated in non-conservative form, as shown in [11, 12]. The need for this formulation will be clearly shown when the temporal integration algorithm is presented. The thermophysical properties of the fluid are a function of the temperature and of the thermodynamic pressure, where it applies.

2.2. Chemistry model

When a chemically reacting flow is considered, the distribution of the different species composing the flow must also be tracked, which introduces N more equations. The transport equation of the *ith* species mass fraction Y_i in non-conservative form, and assuming Fickian diffusion

$$\rho\frac{\partial Y_i}{\partial t} = -\rho u_j\frac{\partial Y_i}{\partial x_j} + \frac{1}{\partial x_j}\left(\rho D_i\frac{\partial Y_i}{\partial x_j}\right) + \dot{w}_i \tag{8}$$

Due to the use of the Fickian diffusion approximation, and to ensure global mass conservation, the mass fraction of the last specie is computed as $Y_N = 1 - \sum_{i=1}^{N-1} Y_i$. The term $\dot{w}_i$ represents the chemical reaction. The energy equation is solved in its enthalpy form, as shown in Eq. (3). For chemically reacting cases this enthalpy is equal to the sum of the chemical enthalpy plus the sensible enthalpy as defined in Eq. (4), resulting in

$$h = \int_{T_0}^{T} c_p dT + \sum_{i=1}^{N}\Delta h^o_{f,i}Y_i \tag{9}$$

In these cases the temperature will be recovered using Eq. (9). The heat transfer flux for these cases becomes $\dot{q}_j = -\kappa\frac{\partial T}{\partial x_j} - \sum_{i=1}^{N}\rho D_i h_i \nabla Y_i$. Both Soret and Duffour effects are considered to be negligible, and thus no additional term needs to be introduced to the energy equation, because the enthalpy here considered represents both chemical and sensible enthalpy. In the chemically reacting cases here considered, the domain will be open, so the thermodynamic pressure will be considered constant and its time derivative in the energy equation taken as zero.

3. NUMERICAL ALGORITHM

The general purpose unstructured and parallel object-oriented CFD code TermoFluids [13] is used in this work. A variant of the Predictor-Corrector scheme shown by Najm et al.[2] is proposed here to solve the set of equations Eqs.(1) to (3) and Eq. (5). When chemically reacting flows are considered, Eq. (8) is added. The pressure-velocity coupling is solved by a fractional step as described by Nicoud [3] where a constant coefficient Poisson results. This fractional stepping is discretised using both collocated [4] and staggered [5] formulations. In the Predictor step a second-order Adams-Bashforth time integration scheme is used to calculate the intermediate scalar fields and the velocity and it incorporates a pressure correction step to satisfy the continuity equation. The Corrector step uses a Crank-Nicolson integration to advance the scalar fields, and it also involves a pressure correction step. In both cases the pressure correction step requires the resolution of a pressure Poisson equation, which is solved using a Direct Schur Decomposition [14, 15]. Use of the non-conservative form of the scalars transport equations is caused by the use of an explicit time integration because until the equations of species and energy are advanced, the density at the current time cannot be computed. The algorithm scheme is as follows (solution of the species equation Eq. (8) applies only to multicomponent fluxes)

3.1. Predictor

1. Evaluate species transport Eq. (8)

$$\rho^n\frac{Y_i^* - Y_i^n}{\Delta t} = \frac{3}{2}\left(\rho^n\frac{\partial Y_i}{\partial t}\Big|^n\right) - \frac{1}{2}\left(\rho^{n-1}\frac{\partial Y_i}{\partial t}\Big|^{n-1}\right) \tag{10}$$

2. Evaluate energy transport Eq. (3)

$$\rho^n\frac{h^* - h^n}{\Delta t} = \frac{3}{2}\left(\rho^n\frac{\partial h}{\partial t}\Big|^n\right) - \frac{1}{2}\left(\rho^{n-1}\frac{\partial h}{\partial t}\Big|^{n-1}\right) \tag{11}$$

   where n denotes the current time step.

3. Evaluate the thermodynamical pressure P_o from Eq. (7), if it is not constant.

4. Evaluate the density from the equation of state Eq. (5)

$$\rho^* = \frac{P_o}{R_i T^*} \tag{12}$$

5. Pressure corrector step. Compute the predictor velocities

   (a) Calculate the pseudo velocities using Eq. (2)

$$\frac{\rho^*\hat{u}_i - \rho^n u_i^n}{\Delta t} = \frac{3}{2}\left(\rho^n\frac{\partial u_i}{\partial t}\Big|^n\right) - \frac{1}{2}\left(\rho^{n-1}\frac{\partial u_i}{\partial t}\Big|^{n-1}\right) \tag{13}$$

(b) Solve the Poisson equation.

$$\nabla^2 p^* = \frac{1}{\Delta t}\left[\nabla\cdot(\rho^*\hat{u}_i) - \nabla\cdot(\rho^* u_i^*)\right] \quad (14)$$

where, using the continuity equation Eq. (1)

$$\nabla\cdot(\rho^* u_i^*) = -\left.\frac{\partial\rho}{\partial t}\right|^*$$

and the time derivative is approximated by

$$\left.\frac{\partial\rho}{\partial t}\right|^* = \frac{1}{2\Delta t}(3\rho^* - 4\rho^n + \rho^{n-1}) \quad (15)$$

(c) Calculate the predictor velocities

$$\frac{\rho^* u_i^* - \rho^*\hat{u}_i}{\Delta t} = -\frac{\partial p^*}{\partial x_i} \quad (16)$$

3.2. Corrector

1. With the values computed at the Predictor step, using equation Eq. (3) the time derivative of the predictor enthalpy ($\rho^*\frac{\partial h}{\partial t}|^{**}$) and using Eq. (8) the time derivative of the predictor mass fraction ($\rho^*\frac{\partial Y_i}{\partial t}|^{**}$) are computed. Then the time derivative at the next time is evaluated using a Crank-Nicolson scheme

$$\rho^n\frac{Y_i^{n+1} - Y_i^n}{\Delta t} = \frac{1}{2}\left(\rho^n\left.\frac{\partial Y_i}{\partial t}\right|^n + \rho^*\left.\frac{\partial h}{\partial t}\right|^{**}\right) \quad (17)$$

$$\rho^n\frac{h^{n+1} - h^n}{\Delta t} = \frac{1}{2}\left(\rho^n\left.\frac{\partial h}{\partial t}\right|^n + \rho^*\left.\frac{\partial h}{\partial t}\right|^{**}\right) \quad (18)$$

2. Evaluate the thermodynamical pressure P_o from Eq. (7), if it is not constant.
3. Using the ideal gas law Eq. (5), the density field at the next time step is computed.
4. Next the pressure corrector step, to compute the velocity field.

(a) Calculate the pseudo velocities using Eq. (2)

$$\frac{\rho^{n+1}u_i' - \rho^n u_i^n}{\Delta t} = \frac{3}{2}\left(\rho^n\left.\frac{\partial u_i}{\partial t}\right|^n\right) - \frac{1}{2}\left(\rho^{n-1}\left.\frac{\partial u_i}{\partial t}\right|^{n-1}\right) \quad (19)$$

(b) Solve the Poisson equation.

$$\nabla^2 p^{n+1} = \frac{1}{\Delta t}\left[\nabla\cdot(\rho^{n+1}u_i') - \nabla\cdot(\rho^{n+1}u_i^{n+1})\right] \quad (20)$$

where, using the continuity equation Eq. (1)

$$\nabla\cdot(\rho^{n+1}u_i^{n+1}) = -\left.\frac{\partial\rho}{\partial t}\right|^{n+1}$$

and the time derivative is approximated by

$$\left.\frac{\partial\rho}{\partial t}\right|^{n+1} = \frac{1}{2\Delta t}(3\rho^{n+1} - 4\rho^n + \rho^{n-1}) \quad (21)$$

(c) Calculate the velocities at the next time step

$$\frac{\rho^{n+1}u_i^{n+1} - \rho^{n+1}u_i'}{\Delta t} = -\frac{\partial p^{n+1}}{\partial x_i} \quad (22)$$

This Predictor-Corrector scheme was proposed for low-Mach number flows due to the numerical instabilities seen in tests when a fully explicit time integration scheme was used [2] for cases with strong temperature variations.

3.3. Time Step

Due to the use of a dual stepping the computational cost per iteration is increased, as a Poisson equation has to be solved in each sub-step. On the other hand the Courant-Friedrich-Lewy like condition for the time step can be relaxed, allowing to increase the time step.Tests where the time step was multiplied by a factor showed that it was feasible. It has been seen that multipliers higher than ten were not stable. It must be stated that the specific value for this multiplier has been found to be case dependant.

4. UNSTRUCTURED DISCRETITZATION

To discretise the momentum equation Eq. (2) and avoid numerical problems two formulations are used, the staggered formulation of Perot [5] and the collocated one of Felten [4]. A brief resume is shown here, a more detailed description is shown in [16].

4.1. Collocated discretisation

As shown by Felten [4], the computation of the convective term requires that the mass fluxes at the control volume faces and the cell centred velocity be corrected in order to conserve the kinetic energy. The reason of these corrections is that the solution variables of the problem are located at the centre of the control volume while the mass fluxes are interpolated at the faces. The pressure field obtained through the resolution of the Poisson equation ensures mass conservation at the faces, but to assure that the cell centred velocity remains solenoidal a pressure correction is necessary.

4.2. Staggered discretisation

An staggered formulation does not require corrections similar to those required for the collocated discretisation as it is fully conservative. But in unstructured meshes its formulation is more complex and special care must be taken in how it is formulated. Defining W_f as the width of the displaced control volume, and computed as $W_f = W_f^{C_{cv}} + W_f^{C_{nb}}$ where W_f^{Ci} is the distance from the face circumcentre to the i cell circumcentre, the volume of the displaced control volume is $V_{cv\text{displaced}} = W_f A_f$. Then, the values of the different terms of the equations, such as the convective and diffusive terms, are a weighted sum of their values computed as if considering a collocated formulation, but as said, no pressure corrections are required to conserve kinetic energy.

4.3. Spatial discretisation

The convective terms of the momentum equations are discretised using a second order Symmetry Preserving scheme (SP). Convective terms of the scalars equations have been discretised using either the Upwind differencing scheme (UDS), the Symmetry Preserving scheme or the QUICK scheme. Diffusive terms of all the equations are discretised using a second order central difference scheme (CDS).

5. TEST CASES

5.1. Differentially heated cavity with large temperature difference

The first benchmark case will be a differentially heated square cavity (DHC) of side $L = 1$ under a large temperature difference ($\Delta T = 720K$), as presented by Vierendeels et al. [8]. The cavity left wall is at a high temperature (T_h) and the right wall is at a low temperature (T_c). These temperatures are related to the temperature difference by $\epsilon = \frac{T_h - T_c}{2T_0}$. Here a value of $\epsilon = 0.6$ has been taken, in order to match the benchmark case. The top and bottom walls are considered adiabatic. The fluid filling the cavity is air with constant Prandtl number (and equal to 0.71) and constant specific heat capacity ($c_p = \gamma R_i/(\gamma - 1)$ where $R_i = 287$ J/(kg K) and $\gamma = 1.4$). Its dynamic viscosity and thermal diffusivity follow Sutherland's law (where the reference temperature has been taken as $T^* = 273$K and the reference viscosity $\mu^* = 1.68 \cdot 10^{-5}$kg/(m s)).

$$\frac{\mu(T)}{\mu^*} = \left(\frac{T}{T^*}\right)^{3/2} \frac{T^* + S}{T + S} \tag{23}$$

$$\kappa(T) = \frac{\mu(T) c_p}{Pr} \tag{24}$$

with S=110.5K. The ideal gas law Eq. (5) will be used to calculate the density. The Rayleigh number $\left(Ra = Pr\, g \rho_o^2 \Delta T L^3/(T_o \mu_o^2)\right)$ considered falls under the laminar regime ($Ra = 10^6$). The reference conditions to define the case are ($P_0 = 101325\, Pa$, $T_0 = 600\, K$ and $\rho_0 = P_0/(R_i T_0)$).

5.1.1. Results

Table 1 and Table 2 show the results for the DHC at $Ra = 10^6$ using two meshes of 64x64 control volumes, one being an structured mesh and the other an unstructured mesh, using for both meshes both staggered and collocated formulations. The control volumes of both meshes were stretched near the hot and cold walls using an hyperbolic bunching law with a spacings near the hot and cold walls of $\Delta x = 0.0046L$ and growing factors of 1.2. For the unstructured mesh two different discretisations of the convective term have been used, the Symmetry Preserving scheme (SP) and the QUICK scheme. The tables show the Nusselt number at each wall, its mean, maximum and minimum, as well as the ratio between the thermodynamic pressure P_o in stationary conditions and the initial thermodynamic pressure P_0. The last column of Table 1 shows the reference solutions of [8].

The last row of the table shows the difference between the Nusselt numbers at the hot and cold walls, in relative terms with respect to the benchmark solutions. This imbalance between walls heat fluxes arises from the use of the non-conservative form of the energy equation, as shown by Knikker [12]. This conservation error is triggered by the incompatibility of computing the density through the ideal gas state law and follow the continuity equation (Eq. (1)).

Comparing the results of the unstructured meshes, it can be seen that the QUICK scheme performs poorer than the Symmetry Preserving scheme, which is caused by the need in the QUICK scheme to approximate the nodal point values to the

line normal to the face, and being this approximation of first order, causes this deterioration of the solution.

Table 1. Collocated discretisation results for the DHC with Ra = 10^6

Case	Struct.	Unstruct.		Ref. [8]
Scheme	SP	SP	QUICK	-
$mean\,Nu_h$	8.73807	8.816	8.681	8.687
$mean\,Nu_c$	8.73819	8.829	8.496	8.687
$Nu_{h,max}$	20.974	22.443	21.947	20.270
$Nu_{h,min}$	1.078	1.000	0.992	1.067
$Nu_{c,max}$	16.252	16.179	16.288	15.519
$Nu_{c,min}$	0.831	0.700	0.788	0.758
P_o/P_0	0.9236	0.9188	0.928	0.9245
$Nu_h - Nu_c$	0.00138%	0.15%	2.13%	-

Table 2. Staggered discretisation results for the DHC with Ra = 10^6

Case	Struct.	Unstruct.	
Scheme	SP	SP	QUICK
$mean\,Nu_h$	8.74635	8.206	8.095
$mean\,Nu_c$	8.74646	8.218	7.944
$Nu_{h,max}$	21.125	21.102	20.681
$Nu_{h,min}$	1.080	0.957	0.951
$Nu_{c,max}$	16.228	15.457	15.551
$Nu_{c,min}$	0.832	0.560	0.632
P_o/P_0	0.9238	0.9161	0.9241
$Nu_h - Nu_c$	0.0013%	0.138%	1.738%

It can be seen from Table 1 and Table 2 that the results for both staggered and collocated discretisations are in good agreement with reference solutions although using a coarser mesh than those reported in [8]. The results of the unstructured meshes using the staggered discretisation can be seen to be in less agreement with the reference results. The reason for this behaviour is the use of a first order reconstruction of the cell centred velocity, as shown in [16]. When higher order reconstruction polynomials are used, as reported in [17], higher accuracy can be achieved at the cost of extra computing time. Structured meshes do not suffer from this deterioration of the solution due to their inherent geometric properties.

A mesh refinement study has also been performed in order to verify the independence of the results with respect to the grid. Structured meshes of $128x128$ and $256x256$ control volumes, concentrated near the vertical walls were also used. The spacings near the vertical walls for each mesh were $\Delta x = 0.0023L$ and $\Delta x = 0.0015L$, respectively. The error on the hot wall mean Nusselt number decreased from 0.587% for the mesh of $64x64$, to 0.170% for the mesh of $128x128$ an to 0.055% for the mesh of $256x256$. The cold wall mean Nusselt showed a similar behaviour being the errors 0.589%, 0.173% and 0.079%, respectively. Finally the pressure ratio P_o/P_0 was underpredicted for the mesh of $64x64$ with an error of -0.0973%, but it was correctly predicted for the other two more refined meshes.

Regarding the time step, several multipliers have been applied to the Courant-Friedrich-Lewy (CFL) like condition. Up to multipliers of around 6, the algorithm remained stable, and the computed scalar fields and the postprocessing variables, such as Nusselt numbers, variations remained under $10^{-2}\%$ of the reference value.

5.2. Premixed methane/air flat flame

The algorithm has also been verified against a case with a reactive flux, a laminar premixed flame. The geometry of the case is a perforated plate burner as defined in [9, 18], where choosing a small enough diameter and a small enough pitch, the three-dimensional behaviour of the flame is reduced notably. Neglecting the effects of the burner rim, the combustion phenomena can be modelled adopting a 2D computational domain enclosed within two symmetry planes. Figure 1 shows the geometry considered, where $L = 4mm$, $d = 1mm$ and $p = 3/2\,d$. In the references this case is referred as "wide flame".

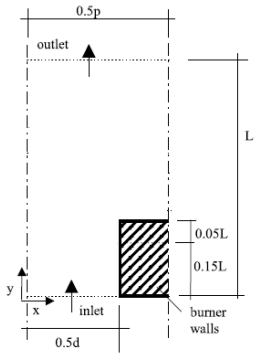

Figure 1. Premixed flame geometry

At the inlet, a parabolic velocity profile is assumed with $v(0,0) = 0.7875$, the mixture is premixed at stoichiometric condition with $Y_{CH_4} = 0.05$ and $Y_{O_2} = 0.225$ and the inlet temperature is $298.2K$. At the outlet the pressure is imposed. The vertical boundaries have symmetry boundaries. The burner walls are assumed to be isothermal with a temperature equal to the inlet temperature. Results for the stationary state are compared against the results from computations of this case using a SIMPLE-like algorithm as shown in [18, 19].

A four-step skeletal mechanism for methane-air flames as described by [10] has been used. This mechanism comprises 4 reactions and 7 species ($CH_4, O_2, CO, H_2, CO_2, H_2O$ and N_2 as an inert specie).

Transport and thermophysical properties have been evaluated using CHEMKIN's database.

5.2.1. Results

Figures 2 to 4 show the steady state computations of the present algorithm compared against the reference ones. They show the methane, temperature and velocity distribution along a vertical line passing through the $(0., 0.)$ coordinate, that is, a line through the centre of a hole of the plate.

The results here presented correspond to a simulation on an unstructured mesh using a collocated discretisation, using around 5500 control volumes, where a higher concentration is put around the flame front. Either Symmetry Preserving, Upwind Differencing scheme and QUICK scheme have been used, and in each case yielding the same steady state results.

It can be seen that the results are in good agreement with the reference values, thus reproducing correctly the flame position and fuel consumption. It can be seen that the velocity increase is at the same position where the methane is consumed and the temperature rises from the cold value to the hot value. After the flame front the different scalar fields do not change because the fluxe cannot loose energy to the surroundings, due to the flame configuration. In Figure 5 it is shown the temperature distribution and chemical energy released.

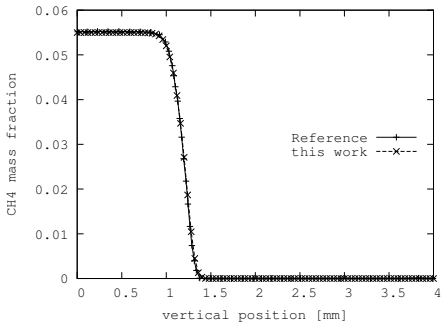

Figure 2. Methane distribution

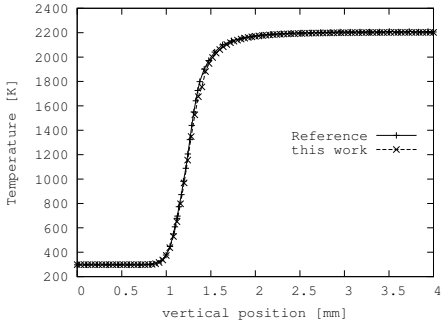

Figure 3. Temperature distribution

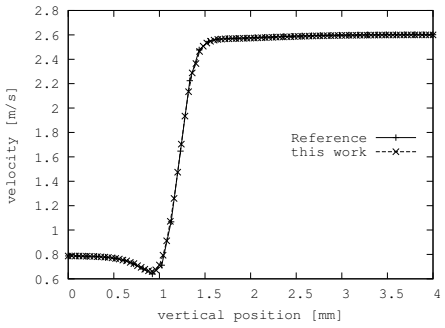

Figure 4. Velocity distribution

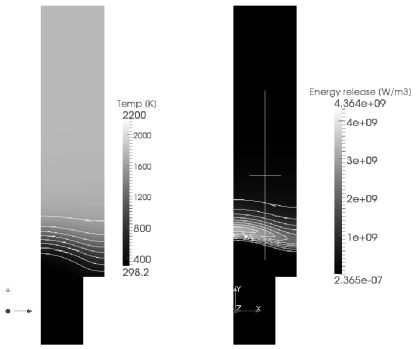

Figure 5. Temperature and chemical energy release $-\sum_{i=1}^{N} \dot{w}_i h_i$

6. CONCLUSIONS

The low-Mach number approximation of the Navier-Stokes equations has been presented and an algorithm for its resolution has been shown, which is suitable for both reacting and non-reacting flows. This algorithm consists of a dual stepping, predictor-corrector, in order to avoid the numerical instabilities seen in tests when a fully explicit time integration scheme was used.

A time step increase due to this dual stepping has been taken into consideration, and it has been seen that the CFL like condition can be relaxed without stability problems.

It has been shown that the algorithm is suitable for both collocated and staggered formulations of the pressure-velocity coupling for both structured and unstructures meshes.

The algorithm has been tested against the benchmark results of Vierendeels et al. [8]. Results for both structured and unstructured meshes have been presented and shown to be in good agreement with the reference, being the differences due to mesh resolution, as here coarser grids have been used. Also, use of low order interpolation schemes could be a source of inaccuracies.

The algorithm has also been tested in a case with a reactive flux and shown to provide accurate results. With this case it has been seen that the SP, the UDS

and QUICK discretisation schemes were suitable for both structured and unstructured meshes. A time step relaxation has also been possible with reactive fluxes.

ACKNOWLEDGEMENTS

This work has been financially supported by the *Ministerio de Educación y Ciencia*, Spain,(Project:"Development of high performance parallel codes for the optimal design of thermal equipments",reference ENE2010-17801) and with the support of the *Departament d'Innovació, Universitat y Empresa and Comissionat per a Universitats i Recerca de la Generalitat de Catalunya* and the European Social Fund.

References

[1] Gray, D. and Giorgini, A., 1976, "The validity of boussinesq approximation for liquids and gases", *Int. J. Heat Mass Transfer*, Vol. 19, pp. 545–551.

[2] Najm, H. N., Wyckoff, P. S., and Knio, O. M., 1998, "A semi-implicit numerical scheme for reacting flow", *Journal of Computational Physics*, Vol. 143, pp. 381–402.

[3] Nicoud, F., 2000, "Conservative high-order finite difference schemes for low-mach number flows", *Journal of Computational Physics*, Vol. 158, pp. 71–97.

[4] Felten, F. and Lund, T., 2006, "Kinetic energy conservation issues associated with the collocated mesh scheme for incompressible", *Journal of Computational Physics*, Vol. 215, pp. 465–484.

[5] Perot, B., 2000, "Conservation properties of unstructured staggered mesh schemes", *Journal of Computational Physics*, Vol. 159, pp. 58–89.

[6] Vierendeels, J., Merci, J., and Dick, E., 2001, "Numerical study of natural convective heat transfer with large temperature difference", *International Journal of Numerical Methods for Heat and Fluid Flow*, Vol. 11, No. 4, pp. 329–341.

[7] Munz, C.-D., Roller, S., Klein, R., and Geratz, K., 2003, "The extension of incompressible flow solvers to the weakly compressible regime", *Computers and Fluids*, Vol. 32, pp. 173–196.

[8] Vierendeels, J., Merci, B., and Dick, E., 2003, "Benchmark solutions for the natural convective heat transfer problem in a square cavity with large horizontal temperature differences", *International Journal of Numerical Methods for Heat and Fluid Flow*, Vol. 13(8), pp. 1057–1078.

[9] Somers, B., 1994, *The simulation of flat flames with detailed and reduced chemical models*, PhD thesis, Eindhoven University of Technology.

[10] Jones and Lindstedt, R., 1988, "Global reaction schemes for hydrocarbon combustion", *Combustion and Flame*, Vol. 73, pp. 233–249.

[11] Lessani, B. and Papalexandris, M., 2006, "Time-accurate calculation of variable density flows with strong temperature gradients and combustion", *Journal of Computational Physics*, Vol. 212, pp. 218–246.

[12] Knikker, R., 2011, "A comparative study of high-order variable -property segregated algorithms for unsteady low mach number flows", *Int. J. Numer. Meth. Fluids*, Vol. 66, pp. 403–427.

[13] Lehmkuhl, O., Pérez Segarra, C., Borrell, R., Soria, M., and Oliva, A., 2007, "Termofluids: A new parallel unstructured cfd code for the simulation of turbulent industrial problems on low cost pc cluster", *Proceedings of the Parallel CFD 2007 Conference*, pp. 1–8.

[14] Trias, F., Soria, M., Pérez Segarra, C., and Oliva, A., 2006, "A direct schur-fourier decomposition for the efficient solution of high-order poisson equations on loosely coupled parallel computers.", *Numerical Linear Algebra with Applications*, Vol. 13(4), pp. 303–326.

[15] Borrell, R., Lehmkuhl, O., Soria, M., and Oliva, A., 2007, "Schur complement methods for the solution of poisson equation with unstructured meshes", *Proceedings of the Parallel CFD 2007 Conference*, pp. 1–8.

[16] Chiva, J., Ventosa, J., Lehmkuhl, O., and Pérez-Segarra, C., 2011, "Modelization of the low-mach navier stokes equations in unstructured meshes.", In *Proceedings of the 7th International conference on computational heat and mass transfer*.

[17] Vidović, D., 2009, "Polynomial reconstruction of staggered unstructured vector fields", *Theoret. Appl. Mech.*, Vol. 36:2, pp. 85–99.

[18] Còsul, R., 2002, *Development of Numerical Codes for the Evaluation of Combustion Processes. Detailed Numerical Simulations of Laminar Flames*, PhD thesis, Polytechnic University of Catalonia.

[19] Còsul, R., Pérez-Segarra, C., Claramunt, K., Cadafalch, J., and Oliva, A., 2003, "Detailed numerical simulation of laminar flames by a parallel multiblock algorithm using loosely coupled computers", *Combust. Theory Modelling*, Vol. 7, pp. 525–544.

Conference on Modelling Fluid Flow (CMFF'12)
The 15th International Conference on Fluid Flow Technologies
Budapest, Hungary, September 4-7, 2012

A FILTERED KINETIC ENERGY PRESERVING FINITE VOLUMES SCHEME FOR COMPRESSIBLE FLOWS

A. BAEZ-VIDAL ,[1] O. LEHMKUHL, [2] C.D. PEREZ-SEGARRA, [1] A. OLIVA [1]

[1] Corresponding Author. Centre Tecnològic de transferència de Calor (CTTC), Universitat Politècnica de Catalunya (UPC).
ETSEIAT ,Colom 11, 08222 Terrassa (Barcelona) , Spain. Tel: (+34) 93 739 81 92 Fax: (+34) 93 739 89 20 E-mail: aleix@cttc.upc.edu
[2] TermoFluids S.L. Av. Jaquard, 97 1-E, 08222 Terrassa (Barcelona), Spain E-mail: termofluids@termofluids.com

ABSTRACT

The Kinetic Energy Preserving Scheme (KEP) for compressible flows has been shown to solve 1-D shock waves without smearing them. The method does not add numerical diffusion to solutions but, as a counterpart, it needs very dense meshes in order to be Local Variations Diminishing (LVD) and stable. For 2-D and 3-D geometries, the method needs unaffordable meshes. A Filtered Kinetic Energy Preserving Method (FKEP) that partially solves this issue is presented in this document. The method filters the solution obtained by a KEP at each time step. It is shown that the use of filters does not significantly change the low frequencies of the motion while it enables the use of much coarser meshes.FKEP is tested on the 1-D shock tube.

Compressible Flow, Finite Volumes, Kinetic Energy Preserving, CFD

NOMENCLATURE

E_t	Total Energy
K	Kinetic energy of the whole domain
L	Characteristic Length of the whole domain
M	Mach number
Pr	Prandtl Number
$\underline{R}$	Numerical Residue of an explicit time scheme
Re	Reynolds Number
$\underline{S}$	Surface
T	Temperature
a	Speed of sound
$\underline{b}_o$	Dependent fluid variables
c_p	Specific heat coefficient at constant pressure
$\underline{f}$	Numerical flux
$\underline{g}$	Convective part of numerical flux
$\underline{h}$	Diffusive and pressure part of numerical flux
h_t	Total enthalpy
k	Kinetic energy of a control volume
p	Pressure
$\underline{q}$	Heat conduction flux
$\underline{r}$	Residue of system of equations
t	Time
$\underline{u}$	Conservative fluid variables
u	x component of velocity
v	y component of velocity
w	z component of velocity
x	Space coordinate
Ω	Volume of a cell
α	Time scheme main variables coefficients
β	Time scheme residues coefficients
η	Characteristic length of a cell
δ	Kronecker Delta
γ	Specific heat ratio
λ	Volumetric viscosity coefficient
μ	Viscosity coefficient
ξ	Filter Ratio of a filter
ϕ	Scalar fluid magnitude
ρ	Density
$\underline{\underline{\sigma}}$	Viscous Stresses
ω	Averaging weight

Subscripts:

a	Relative to the speed of sound
o, p	Volumes identities
op	Interface between volumes o and p
$glob$	Relative to the whole domain
Kol	According to Kolmogorov scale cascade theory
LC	According to cell-length and characteristic waves based Reynolds

Superscripts:

i, j, k	Space coordinate
q	Time scheme dummy index
n	Time step

Upper symbols

$\overline{\phi}$	Filtered ϕ field
$\hat{\phi}_{op}$	$\frac{\phi_o+\phi_p}{2}$
$\tilde{\phi}$	Result of a weighted sum

1 INTRODUCTION

Wind Turbine blades usually operate in stall or near-stall angles of attack. When modeling the flow around them, numerical methods performing well on turbulence are needed. For finite volumes and incompressible flows it has been recently shown by Lehmkuhl et al. [1] that a good choice are the kinetic energy preserving methods [2] because they do not add artificial viscosity to the flow. This allows, as it has been shown by Rodríguez et al. [3], the numerical development of flow patterns that are usually damped by artificial viscosity when simulated.

On Wind Turbine offshore applications, as the blade length increases, so does the blade tip speed and the incompressibility hypothesis does not hold. On on-shore applications, one of the limits to the Wind Turbines operation is aerodynamic noise. It is necessary to improve compressible flow methods on turbulence and transition situations.

In compressible flows modeling with finite volumes, the most of the methods have been deduced from the 1-D hyperbolic equation [4]. Hence, most of them interpolate variables at interfaces giving more importance to the values on one side of it than the values on the other, adding artificial viscosity [5] to the simulated flow. Jameson [6] deduced a Kinetic Energy Preserving Scheme (KEP) for compressible flows which was not of the upwind kind and which did not take into consideration the characteristic lines when interpolating flow variables. This method gave good results on the Sod shock tube and has also been successfully tested on other flow situations at low Reynolds ($\sim$ 100) numbers by Allaneau [7]. The drawback of the KEP is that it requires unaffordable meshes.

In this work the Jameson KEP flux scheme is used and combined with a filter on the variables after each time step. This has allowed to keep the KEP good properties on extremely coarser meshes than those demanded by the local Reynolds number stability condition. The formulation used is developed and detailed in section 2, numerical results on 1D cases are shown in section 3 . Finally conclusions and future efforts directions are given in section 4.

2 FORMULATION

2.1 Jameson's Kinetic Energy Preserving scheme

Equations (1) and (2) are the basic conservative formulation of a finite volumes discretization of the Navier-Stokes is:

$$\Omega_o \frac{d\underline{u}_o}{dt} + \underline{r}_o = \underline{0}$$
$$\underline{r}_o = \underline{f}^j_{op} S^j_{op} \tag{1}$$

$$\underline{u}_o = \begin{pmatrix} \rho \\ \rho u \\ \rho v \\ \rho w \\ \rho E_t \end{pmatrix}_o \qquad \underline{b}_o = \begin{Bmatrix} p \\ h_t \\ T \\ \mu \\ \underline{\underline{\sigma}} \\ \underline{q} \end{Bmatrix}_o$$
$$\underline{f}^j_{op} = \begin{pmatrix} \rho v^j \\ \rho v^1 v^j - p\delta^{1j} + \sigma^{1j} \\ \rho v^2 v^j - p\delta^{2j} + \sigma^{2j} \\ \rho v^3 v^j - p\delta^{3j} + \sigma^{3j} \\ \rho h_t - \sigma^{jk} v^k - q^j \end{pmatrix}_{op} \tag{2}$$

For ideal air, Equations (3) apply. For dry air, $\mu_0 = 1.461 \cdot 10^{-6} Pa \cdot s$ but, as will be later commented, the value used in the present work is greater.

$$p = (\gamma - 1)\rho(E_t - \frac{v^i v^i}{2}) \qquad h_t = E_t + \frac{p}{\rho}$$
$$\sigma^{ij} = \mu\left(\frac{\partial v^i}{\partial x^j} + \frac{\partial v^j}{\partial x^i}\right) + \lambda\delta^{ij}\frac{\partial v^k}{\partial x^k} \qquad \lambda = \frac{-2}{3}\mu$$
$$T = \frac{h_t - \frac{v^k v^k}{2}}{c_p} \qquad q^j = -\frac{\mu \cdot c_p}{Pr}\frac{\partial T}{\partial x^j}$$
$$\mu = \mu_0 \frac{T^{\frac{2}{3}}}{T + 110.3} \tag{3}$$

The main unknowns are the conservative variables of compressible fluids $\underline{u}_o$.

Taking this in mind and defining the total numerical kinetic energy as is shown in Eq.(4),

$$K = \sum_o \Omega_o \kappa_o = \sum_o \Omega_o \left(\frac{(\rho v^j)(\rho v^j)}{2\rho}\right)_o \tag{4}$$

Jameson[6] deduced the KEP proceeding as in Eq.(5) and avoiding any contribution of the convective part of fluxes to change the kinetic energy Eq.(6).

$$\frac{dK}{dt} = \sum_o \frac{dK}{d\kappa_o}\frac{d\kappa_o}{d\underline{u}_o}\frac{d\underline{u}_o}{dt} = \sum_o \Omega_o \frac{d\kappa_o}{d\underline{u}_o}\frac{-\underline{r}_o}{\Omega_o}$$
$$\frac{dK}{d\kappa_o} = \Omega_o \qquad \frac{d\kappa_o}{d\underline{u}_o} = \begin{Bmatrix} \frac{-\kappa}{2\rho} \\ \frac{(\rho v^1)}{\rho} \\ \frac{(\rho v^2)}{\rho} \\ \frac{(\rho v^3)}{\rho} \\ 0 \end{Bmatrix}_o$$
$$\underline{f}^j_{op} = \underline{g}^j_{op} + \underline{h}^j_{op} \quad \underline{g}^j_{op} = \begin{pmatrix} \rho v^j \\ \rho v^1 v^j \\ \rho v^2 v^j \\ \rho v^3 v^j \\ \rho h_t \end{pmatrix}_{op} \tag{5}$$

$$\sum_o \frac{dK}{d\underline{u}_o}^T \underline{g}^j_{op} S^j_{op} = o \tag{6}$$

Jameson also forced the contribution of $\underline{h}^j_{op}$ to K to be according to the Kinetic Energy Equation applied to the whole volume. Then, resulting interface fluxes are restricted to accomplish Equation (7).

$$(\rho v^i v^j)_{op} = (\rho v^i)_{op} \hat{v}^j_{op} \tag{7}$$

The Eq.(7) can be got with the equalities in Eq.(8).

$$\begin{aligned} &(\rho v^i_{op}) = \hat{\rho}_{op} \hat{v}^i_{op} && p_{op} = \hat{p}_{op} \\ &\sigma^{ij}_{op} = \hat{\sigma}^{ij}_{op} && \\ &h_{top} = \hat{h}_{top} && q^i_{op} = \hat{q}^i_{op} \end{aligned} \tag{8}$$

It is not clear how to correctly compute $\underline{\underline{\sigma}}_o$ and in practice the viscous stresses are computed by means of the usual centered on interfaces derivatives of velocity. The h_{top} and q^i_{op} interface values are suggested to be computed as shown only for consistency with the other quantities reasons.

The main process for computing is, supposed known $\underline{u}_o(t)\ \forall o$:

1. Compute $(\underline{f}^j_{op})^n\ \forall op, \forall j$ according to Eqs.(8) and (2).
2. Compute $(\underline{r}_o)^n\ \forall o$, with (1).
3. Apply an explicit time integration scheme:

$$\begin{aligned} \underline{u}^{n+1}_o = \Psi(&\underline{u}^n_o, \underline{u}^{n-1}_o, ..., \underline{u}^{n+1-N}_o \\ &, \underline{r}^{n+1}_o, \underline{r}^n_o, ..., \underline{r}^{n+1-M}_o; \Delta t) = 0 \end{aligned} \tag{9}$$

4. Compute $(\underline{b}_o)^{n+1}$ from $(\underline{u}_o)^{n+1}$

Some tests with this scheme can be seen on Jameson [6]. In few words, tests on the Sod case show that the KEP scheme is the best on following a shock wave without dissipation.

The main problem of KEP is the need of very dense meshes that maintain the finite volume and maximum eigenvalue based Reynolds number under 2. This is the Local Cell-Based Reynolds Number Condition (LCBRC). Else, the method is not Local Variations Diminishing (LVD) and it diverges.

2.2 The Filtered Kinetic Energy Preserving scheme

This section contains the main discussion that lead to the proposal of the FKEP and the corresponding formulation.

2.2.1 KEP limits

After a power spectrum analysis on the 1-D shocktube resolved by a sub-LCBRC mesh[1], it was noticed that the cause of the KEP instability is the amplification of small wavelength scales of the flow, this producing instable oscillations of the fluid variables. Once small wavelengths amplified, the oscillation propagates to larger wavelengths as it grows. Finally, these oscillations instabilize computations, and can lead to divergence. In Figures 1 and 2 it can be seen that with the Total Variations Diminishing (TVD) 3 stages Runge-Kutta time scheme, the oscillations maximum amplitude is limited enough to permit an analysis of the divergence nature. Notice that the oscillated solution is just the sum of the correct solution of the case and oscillations[2]. This behavior suggests that if the amplitude growth of the small wavelengths was eliminated without affecting on the large wavelengths, the KEP method could be used on much coarser meshes.

The idea of damping small wavelengths oscillations is sustained by the fact that these oscillations have characteristic sizes of the mesh cells, which are would be set through Eq.(10) by the LCBRC.

$$\eta_{LC} \sim \sqrt[3]{\Omega}_o \leq \left(\frac{2\mu}{\rho a (1+M)} \right)_o = \frac{2L}{Re + Re_a} \quad \forall o \quad \forall t. \tag{10}$$

The ratio between the requested Direct Numerical Simulation (DNS) mesh size by the Kolmogorov scale criterion based on $\underline{v}$ and η_{LC} is provided in Eq.(11). It shows that LCBRC requests a finer than DNS mesh. This gives more power to the idea of eliminating the scales of flow causing the oscillations of KEP. However, for compressible flows with shock waves and contact discontinuities the Kolmogorov criterion could not be restrictive enough because these phenomena have a characteristic thickness proportional to the viscosity coefficient. In any case, LCBRC is too restrictive for the state of the art computing technology.

$$\frac{\eta_{Kol}}{\eta_{LC}} = \frac{L(Re)^{-3/4}}{2L \cdot (Re + Re_a)^{-1}} > \frac{Re^{1/4}}{2} \tag{11}$$

[1] A mesh too coarse to accomplish the LCBRC condition.

[2] This is not totally true as fluid dynamics equations are not linear.

2.2.2 FKEP Formulation

It is proposed to filter the discrete equation of an explicit an linear[3] time scheme on a KEP spatial discretization in order to eliminate the mentioned oscillations. The problem is formulated in Eq.(12), where the parameters defined in Eq.(13) are used and $\mathcal{F}$, which is a filter function, remains undetermined.

$$\mathcal{F}\left(\underline{u}_o^{n+1} = \underline{\tilde{u}_o}^n + \underline{R}_o^n\right) \tag{12}$$

$$\underline{\tilde{u}_o}^n = \sum_{q=1}^{q=N} \alpha_q \underline{u}_o^{n+1-q}$$
$$\underline{R}_o^n = \Delta t \Psi \left(\frac{\underline{r}_o^n}{\Omega_o}, \frac{\underline{r}_o^{n-1}}{\Omega_o}, ..., \frac{\underline{r}_o^{n+1-N}}{\Omega_o} \right) \tag{13}$$

The filtering function must be linear[4] and can depend or not on the fluid variables. For more information on filters, consult Pope [8] or Sagaut [9] . In this work, the filtering function was controlled, for Flow Depending Filters (FDF) through the filter ratio ξ. This parameter remains constant for Constant Filters (CF) . Filtered variables were in practice computed as in Eq.(14).

$$\mathcal{F}(\underline{u}_o^n) = \overline{\underline{u}_o}^n = \omega_{op} \underline{u}_p \tag{14}$$

After these comments, supposed known $\underline{u}_o^n$ and all variables and residues of previous time steps that may be needed by the actual time scheme, the FKEP algorithm reads, for a given time integration scheme:

1. Compute $\left(\underline{f}_{op}^j \left(\underline{u}_o^n, \underline{u}_p^n, \underline{b}_o^n, \underline{b}_p^n\right)\right)^n \quad \forall op, \forall j$ with Eqs.(8) and (2).
2. Compute $\underline{r}_o^n \quad \forall o$ as in Eq.(2) and $\underline{R}_o^n$ using Eq.(13).
3. Calculate $\underline{\tilde{u}_o}^n \quad \forall o$ according to Eq.(13).
4. Compute $\xi_o^n(\underline{\tilde{u}_o}^n) \quad \forall o$ and the filter function weights $\omega_{o,\,p}^n(\xi_o^n) \quad \forall o,\, p$
5. Compute $\overline{\underline{\tilde{u}_o}}^n = \omega_{o,\,p}^n \underline{\tilde{u}}_p^n \quad \forall o$
6. Apply the explicit N steps time integration scheme:

$$\underline{u}_o^{n+1} = \overline{\underline{\tilde{u}_o}}^n + \underline{R}_o^n \tag{15}$$

7. Compute $\underline{b}_o^{n+1}(\underline{u}_o^{n+1}) \quad \forall o$

In some points, FKEP formulation is not absolutely consistent. In FKEP, it must be accepted that $\underline{u}_o^{n+1}$ is properly computed as it is shown in Eq.(15). In this equation, the unfiltered value of independent variables is computed from filtered variables of previous time steps and the unfiltered time scheme residue of the actual time step. Consequently the value of $\underline{u}_o^{n+1}$ is not independent of filters and Eq.(15) does not exactly correspond to Eq.(12), mainly because $\overline{\underline{r}_o(\underline{u}_o)} \neq \overline{\underline{r}_o(\overline{\underline{u}_o})}$. The necessity of computing $\underline{u}_o^{n+1}$ comes from the fact that if $\underline{r}_o(\overline{\underline{u}_o})$ were used instead of $\underline{r}_o(\underline{u}_o)$, Jameson's deductions would not hold anymore and the method would lose it's KEP property. Nevertheless Another negative point is that , as it is deduced from Eq.(16) the method is not well suited for all time schemes when FDF are used.

$$\mathcal{F} \text{ depends on } \underline{u}_o(t) \Rightarrow \mathcal{F}\left(\int \frac{d\underline{u}_o(t)}{dt} + \frac{\underline{r}_o(t)}{\Omega_o}\, dt\right) \neq \int \mathcal{F}\left(\frac{d\underline{u}_o(t)}{dt} + \frac{\underline{r}_o(t)}{\Omega_o}\right) dt \tag{16}$$

3 NUMERICAL EXPERIMENTS

In this section experiences regarding the FKEP and KEP are presented. The test case is the 1D shock tube (Sod. [10]) . It has been resolved with various numerical parameters. Some computations were performed before stabilizing in order to identify the divergence of KEP causes and others were performed with the aim of analyzing the FKEP dependence on filtering functions and meshes.

The test case consists of a 1D $x \in [0, 1]$ domain with open boundaries with a gas inside. At $t < 0$ the gas is in two different states, one to the left and the other to the right of $x = 0.5$. The lefter state is at a greater pressure and density. At $t = 0$ the imaginary membrane separating the sub-domains is removed and, consequently, a shock wave travels to the right while an expansion wave travels to the left. Initial states of the gas are in Table 1. Unless specified, the presented results correspond to the state of gas at $t = 7e-4s$.The studied cases are summarized in Table 2.

In this document, the employed gas is ideal air with Sutherland's law for viscosity. However, the viscosity constant used in Sutherland's equation was 100 times greater than the air value. This allowed to reduce the local Re without increasing the mesh density.

For filtered cases with FDF, filter ratios take values that can be equal or greater than zero, taking zero only in the case that ϕ_o is not a local extremum. Tests were performed computing filter ratios in two manners: using binary values for ξ_o or using continuous values.

[3] respect to the problem variables

[4] $\mathcal{F}(a_1\phi_1 + a_2\phi_2) = a_1\mathcal{F}(\phi_1) + a_2\mathcal{F}(\phi_2)$

Table 1: Sod case gas at $t = 0$, the values for both states are gas constants.

Magnitude	left	right
p [Pa]	101325	10132.5
$\rho\,[kg/m^3]$	1	0.125
T [K]	344.32	275.46
cp [J/kgK]	1012	
γ	1.41	
Pr	0.71	
μ_0[Pas]	$1.461 \cdot 10^{-4}$	

Table 2: kCV's thousands of control volumes of the mesh .TS Time Scheme: Runge-Kutta 3 (RK3) or explicit Euler (Euler). Filters can be Constant "C", in which case the filter ratio ξ is specified or variable "V".

Name	kCV's	TS	Filter (ξ)
RK-40	40	RK-3	none
RK-15	15	RK-3	none
RK-15C	15	RK-3	C Box 1.5
RK-15V	15	RK-3	V Box
RK-4	4	RK-3	none
RK-4C	4	RK-3	C Box 2
RK-4V	4	RK-3	V Box
RK-1C1.5	1	RK-3	C Box 1.5
RK-1C5	1	RK-3	C Box 5
RK-1C	1	RK-3	C Box 2
RK-1V	1	RK-3	V Box
RK-1	1	RK-3	none
E-1C	1	Euler	C Box 2
E-1V	1	Euler	V Box
RK-0.3	0.333	RK-3	none

If $pr(\phi_o)$ is the prominence[5] of ϕ_o. On the binary values case $\xi_o = 0$ if $pr(\phi_o) = 0$ and ξ_o takes a value that makes the filter weight equally all the neighbor nodes and the studied node. On the other case, the value of ξ_o is a strictly increasing function of $pr(\phi_o)$. In this work are presented results from binary filter ratios functions only. Concretely, if the prominence was different to zero, the filter ratio was set to be great enough to make the filter act at it's maximum. The filtered used for all cases is the Box filter.

3.1 Spectral Analysis

With not LCBRC meshes KEP gives oscillations, which are greater for coarser meshes. This can be seen on Figures 1 and 2. Despite the oscillations, which seem to be caused by the great pressure variations within th shock wave, the basic shape of solutions is maintained although sub-LCBRC meshes are used. This was only possible with Runge Kutta TVD schemes, Euler schemes diverged. The only LCBRC case is RK-40.

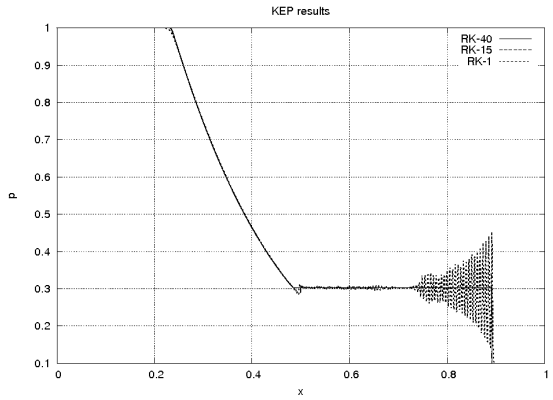

Figure 1: Results of KEP

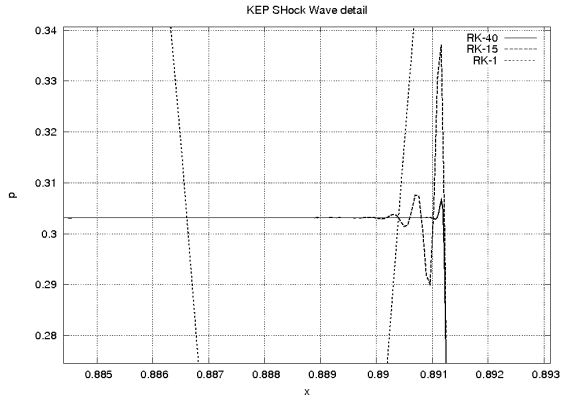

Figure 2: Detail of KEP results

The idea that the oscillations correspond to small wavelengths and that it's nature is numerical is held by Figures 3 and 4. Sub-LCBRC cases are similar to RK-40 on the low-frequency-large-wavelength range, but they differ as frequency rises. Each computed mesh has a frequency range with unphysical amplitudes, the range depending on the case. Since this instable frequencies depend on meshes, it can be set that their nature is numerical. This fact gives the idea that eliminating such unwanted phenomenon can be done by controlling the these frequencies amplitudes. Fig.4 shows that KEP can correctly resolve the relative-to-mesh low frequencies properly. Thus, once high frequencies amplitudes controlled, KEP could be stable for sub-LCBRC meshes.

3.2 Filter Influence

When putting to practice the filtering idea the most mathematically correct option would have been to compute a power spectrum of the solution after each time step, filter the instable frequency range from the

[5]Measure of the difference between an extremum of a set and the extremum of the previous set minus the former extremum element e. g. Let $S = \{1, 4, 5\}$ be a set. Then $pr(max(S)) = 1$ and $pr(min(S) = 3)$.

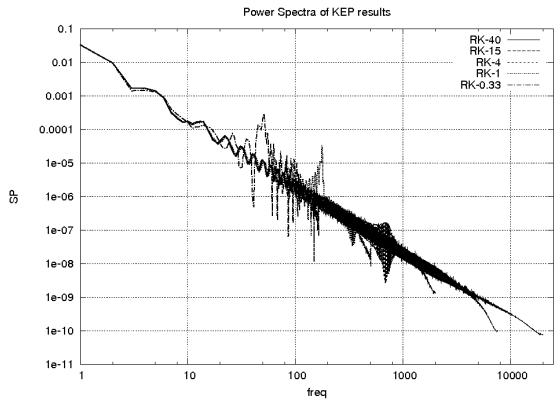

Figure 3: Power spectrum of KEP solution.RK-15, RK-4 and RK-1 are to RK-40 at low frequencies.

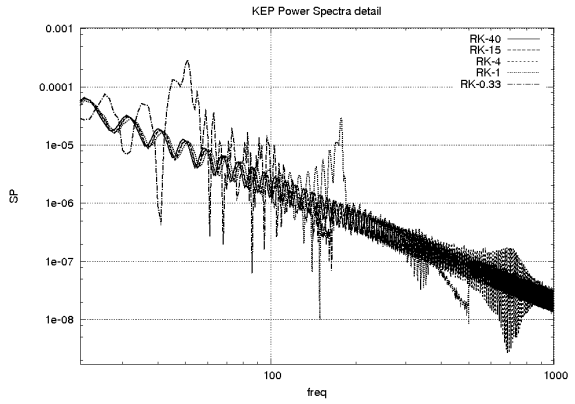

Figure 4: Detail of the power spectrum of P computed with KEP

power spectrum, and go back to physical dimensions with an anti-transform operation. In LES methods this procedure is not popular as it is too computationally costly. For the 1D shock tube cases presented, although power spectrum filterings could have been performed, filters have been applied on physical space variables. The most appropriate filters are be those corresponding to a low frequency-pass filter in the frequency space but only Box filters on space coordinates have been used.

As was expected, Figure 5 shows that using FKEP enables the control of the aforementioned unstable frequencies. The counterpart of this depends on the kind of filter used. For CF the flow is well resolved except for the addition of diffusion in all the domain, as it can be seen on Figure 6. Furthermore, the greater the filter ratio is, more diffusion is added.

The variable filter was tested in order to reduce the diffusion. It accomplished it's finality but it delayed the shock wave and slightly changed the intermediate state pressure level (Figure 7). The first hypothesis about the cause of the shock wave delay are the weakness of the formulation , already pointed in Eq.(16), or some bad filter property.

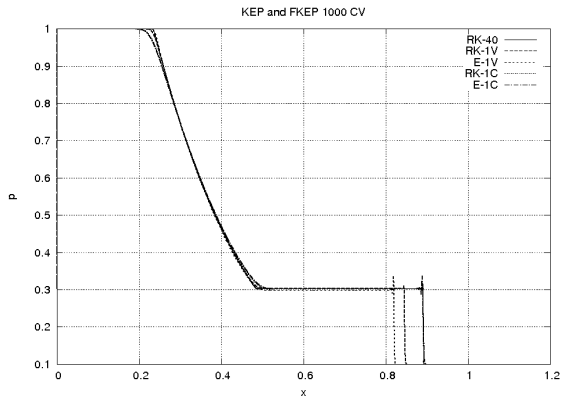

Figure 5: Results of FKEP on a 1000 CV mesh.

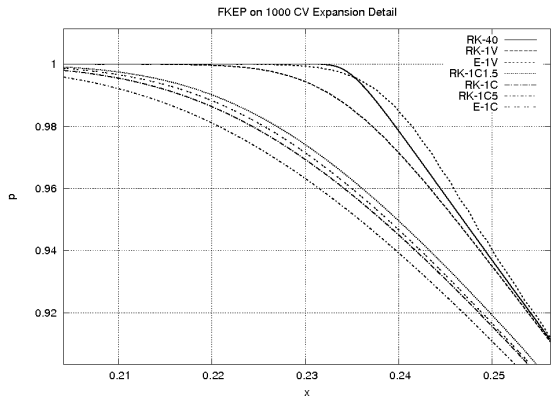

Figure 6: Constant filters are diffusive at the expansion.

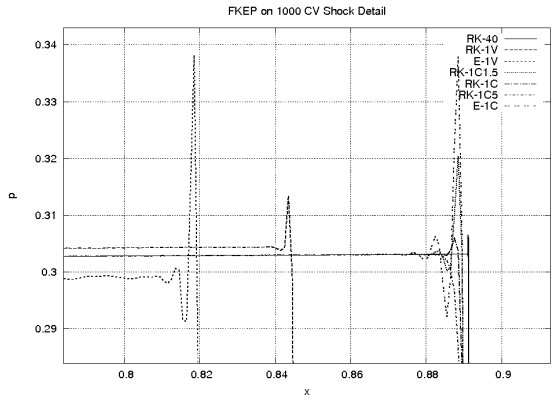

Figure 7: Variable filters do not reproduce well the shock wave.

It can be stated that FKEP eliminates the KEP instabilizes while it resolves well the low frequencies. This is shown in Figure 8.

When KEP was first envisaged by Jameson one of his main goals was to capture, without smearing, shock waves. This would be a very good property for FKEP because it would beat the Upwind-based methods. For Figure 9 a case was launched with Runge-Kutta 3

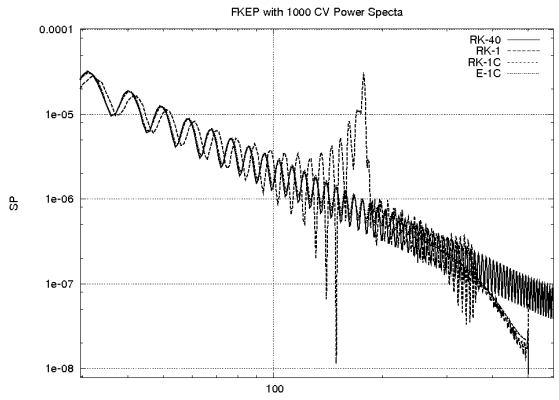

Figure 8: Constant Filter FKEP methods avoided instable growth of small wavelength's amplitude while reproduced long wavelengths well.

time integration , and $\xi = 2$ constant filter ratio on a 10000 CV mesh with a length of 10 m, resulting the same mesh density and filter as for RK-1C. Various instantaneous pressure fields corresponding to different times were saved. They show the evolution of the shock tube. These results were later represented joining all the shock waves in order to see the shock wave evolution in time. Figure 10 shows that no relevant smearing of the shock wave was produced (the shock waves are parallel).

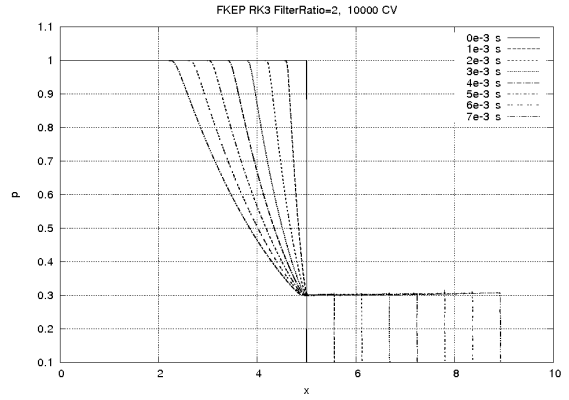

Figure 9: Time evolution of a shock wave with length 10 resolved with FKEP.

3.3 Mesh dependence

For a numerical method it is a must to improve it's performance when the used mesh is more dense. Figures 11 and 12 show that an increase on the number of CV leads to a better resolution in both sides of the domain.

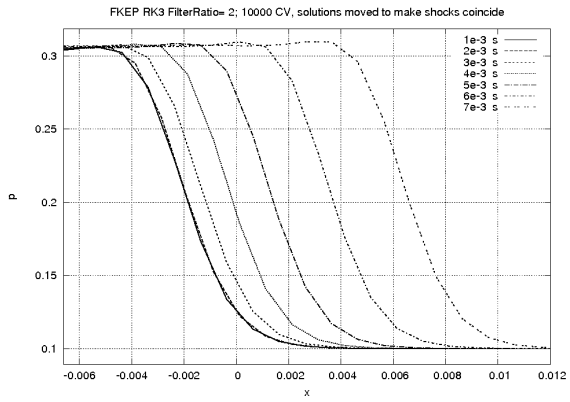

Figure 10: Moved shock waves with FKEP. They are all parallel.

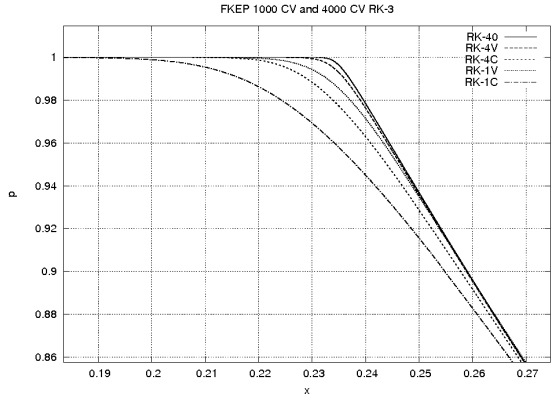

Figure 11: Detail of FKEP computed with different meshes. More CV, better results at the shock wave.

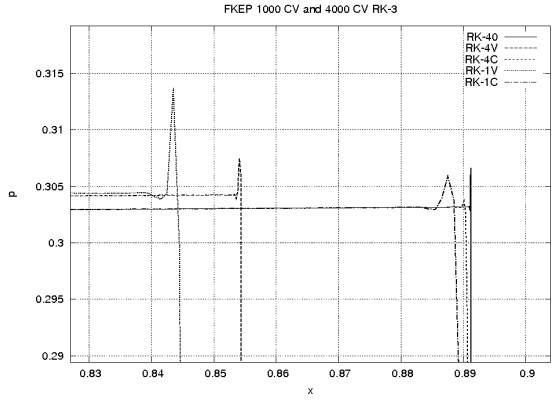

Figure 12: Detail of FKEP computed with different meshes. More CV, better results at the shock wave.

4 CONCLUSIONS AND FUTURE WORKS

In compressible flows, the common characteristic of all of the traditionally used numerical fluxes used is that they are of the upwind kind in a more or less

dramatic manner. Then, they are always dissipative for all the motion scales of any flow. Moreover, the less dissipative fluxes are all based in Finite Differences (as the bast majority of methods for compressible fluxes) and they do not clearly admit unstructured meshes.

The Jameson's KEP scheme is well formulated for unstructured meshes and has shown to have the best behavior when capturing shock waves. In tho other hand, it requires such large meshes that nowadays it can not be pretended to use on engineering real problems. Jameson has demonstrated that his scheme, contrary to the traditional ones, does not add diffusion to the numerical fluxes.

Furthermore, the idea of conserving kinetic energy has been shown to give the best results in incompressible flows (Lehmkuhl et al.[1] and Rodrguez et al. [3]) .Hence, it is expected that FKEP will work well when resolving turbulence.

The FKEP scheme has shown to hold the good features of the KEP referring to the shock wave and avoided some of its bad characteristics related with the sub-LCBRC meshes. Although a very rude filter has been used, the low frequencies of the Sod case were correctly resolved. Simulations with CF have resolved well the zone of the domain under the influence of the shock wave while those with FDF have performed better on the expansion zone.

The sub-lying idea of FKEP is that instead of eliminating the instability via upwinding, it could be left as part of the method and eliminate it every time it appears. A great variety of LVD discretization methods without the LCBRC restriction can be envisaged from this starting point.

At this moment, no mathematical proof of the consistency of FKEP has been attempted, neither conservation tests have been performed. Future work must include some proof that FKEP conserves the fluid conservative variables and the kinetic energy. Such theoretical study could impose restrictions to the suitable filters and clarify the shock wave's filter dependence. Another issue to study is if FKEP is well adaptable to variable-sized meshes. Finally, although the generalization of FKEP to 2D and 3D is straightforward in terms of formulation (in fact all computations presented have been performed with a 3D code), it may lead to filter anisotropy problems and incompatibility with the usual boundary conditions.

In Conclusion, FKEP is an incipient promising option for the resolution of the compressible Navier-Stokes set of equations. With it, the expansion affected sub domain of the shock-tube problem has been resolved with almost any diffusion added (FDF). However, there still remain many unresolved questions about the it.

ACKNOWLEDGEMENTS

Ministerio de Ciencia e Innovación BES-2010-032414 grant related to the ENE2009-07689 project. Collaboration Project between Universidad Politècnica de Catalunya and Termo Fluids S.L. (ref. C06650)

References

[1] O. Lehmkuhl, A. Baez, I. Rodrguez, and C. D. Prez Segarra. Direct numerical simulation and Large-Eddy simulations of the turbulent flow around a NACA-0012 airfoil. In *Proceedings of the 7th International Conference on Computational Heat and Mass Transfer*, pages 1–8, 2011.

[2] R. W. C. P. Verstappen and A. E. P. Veldman. Symmetry-preserving discretization of turbulent flow. *Journal of Computational Physics*, 187(1):343–368, 2003.

[3] I. Rodrguez, R. Borrell, O. Lehmkuhl, , C. D. Prez-Segarra, and A. Oliva. Direct numerical simulation of the flow over a sphere at $Re = 3700$. *Journal of Fluid Mechanics*, 25(25):263–283, 2011.

[4] A. Harten, Peter D. Lax, and Bram Van Leer. On upstream differencing and Godunov-type schemes for hyperbolic conservation laws. *SIAM Review*, 25(1):35–61, 1983.

[5] Bram Van Leer. Upwind and High-Resolution Methods for Compressible Flow: From Donor Cell to Residual- Distribution Schemes. *Communications in Computational Physics*, 1(2):192–206, 2006.

[6] A. Jameson. Formulation of Kinetic Energy Preserving Conservative Schemes for Gas Dynamics and Direct Numerical Simulation of One-Dimensional Viscous Compressible Flow in a Shock Tube Using Entropy and Kinetic Energy Preserving Schemes. *Journal of Scientific Computing*, 34(34):188–208, 2008.

[7] Y. Allaneau and A. Jameson. Direct Numerical Simulations of Plunging Airfoils. In *48th AIAA Aerospace Sciences Meeting Including the New Horizons Forum and Aerospace Exposition*, pages 1–12, 1984.

[8] S.B. Pope. *Turbulent Flows*. Cambridge University Press, 2000.

[9] P. Sagaut. *Large Eddy Simulation for Incompressible Flows*. Springer-Verlag, 2001.

[10] Gary A. Sod. A survey of several finite difference methods for systems of nonlinear hyperbolic conservation laws. *Journal of Computational Physics*, 27(1):1–31, 1978.

Modelling related to wind engineering, aerodynamics and meteorology

Conference on Modelling Fluid Flow (CMFF'12)
The 15th International Conference on Fluid Flow Technologies
Budapest, Hungary, September 4-7, 2012

INTERACTION BETWEEN AN INCOMPRESSIBLE FLOW AND ELASTIC CANTILEVERS OF CIRCULAR CROSS-SECTION

Johan REVSTEDT,[1]

[1] Corresponding Author. Department of Energy Sciences, LTH, Lund University. P.O.Box 118, 221 00 Lund, Sweden, Tel.: +46 46 222 4302, Fax: +46 46 222 4717, E-mail: johan.revstedt@energy.lth.se

ABSTRACT

The purpose of this work is to study the deformation of elastic cantilevers due to hydrodynamic forces by coupled fluid-structure interaction simulations. The cantilever is placed in a rectangular channel and the Reynolds number based on bulk velocity and cantilever diameter is 400. The reduced velocity the range $\pi/2$ to 2π are studied, which covers both un-synchronised motion and the initial branch of synchronisation. The cantilever surface is represented by a virtual boundary method which replaces a solid object in flow by additional force distribution to satisfy local boundary condition. The flow field is solved using a Cartesian finite difference code and the for the deformation of the cylinder a finite element approach using one-dimensional beam elements is used.

Keywords: deformation, FSI, immersed boundary

NOMENCLATURE

A	$[m^2]$	cross-sectional area
$\mathcal{A}$	$[-]$	normalised cross-sectional area
$\mathbf{C}$	$[-]$	damping matrix in the FE formulation
D	$[m]$	cantilever diameter
E	$[N/m^2]$	Young's modulus
$\mathcal{E}$	$[-]$	normalised Young's modulus
F	$[-]$	force per unit volume on boundary surface
$\mathcal{F}$	$[-]$	discrete force vector in the FE formulation
I	$[m^4]$	second moment of inertia
$\mathcal{I}$	$[-]$	normalised second moment of inertia
$\mathbf{K}$	$[-]$	stiffness matrix in the FE formulation
L	$[m]$	cantilever length
$\mathbf{M}$	$[-]$	mass matrix in the FE formulation
P	$[N/m]$	distributed external force
U	$[m/s]$	bulk inflow velocity
U_R	$[-]$	reduced velocity
c	$[-]$	force coefficient
d	$[-]$	distribution function
k	$[-]$	load case factor
p	$[-]$	normalised pressure
t	$[s]$	time
u	$[-]$	normalised velocity
w	$[m]$	deformation
x	$[m]$	spatial coordinate
Φ	$[-]$	source term in the momentum equation
Δt	$[-]$	time step
α	$[-]$	coefficient related to the damping
β	$[-]$	coefficient related to the damping
η	$[-]$	normalised coordinate
ϖ	$[-]$	normalised deformation
ρ	$[kg/m^3]$	density
ϱ	$[-]$	density ratio
σ_{ij}	$[N/m^2]$	stress tensor
τ	$[-]$	normalised time
ξ	$[-]$	normalised spatial coordinate

Subscripts and Superscripts

N	*in vacuo* eigenfrequency
f	fluid
b	boundary
s	solid
i, j, l	tensor indices
x, y, z	coordinate directions

1 INTRODUCTION

In recent years the combination of flow simulations and structural analysis has become increasingly popular in solving engineering problems that contain hydro- or aerodynamical loading on solid structures. Fluid-structure interaction (FSI) simulations can be

performed using different strategies. One may sort these strategies into the subgroups monolithic, segregated and one-way interaction. The choice of strategy will depend on parameters such as flow situation, density ratio, size of deformation etc. In one-way coupled strategies, as the name indicates there is no feed back from the structural deformation to the fluid flow. Hence, these methods can only be used for stationary cases with very small structural deformations and they are therefore unsuitable for most engineering applications, especially for rotating machinery studies. At the other end of the spectrum one finds the monolithic methods. Here all the discretised governing equations are solved in one equation system. The advantage of this is that one will avoid handling of the information transfer on the interface between fluid and solid. On the other hand it might be difficult to generate a grid with sufficient quality for both the fluid and the solid. Also, it might be difficult or inefficient to use if the time scales of the flow and the solid deformation are differing much, which is not uncommon in engineering applications. Finite element based monolithic approaches for the interaction between incompressible flow and elastic structures have been developed by for example Jog and Pal [1] and by Gee et al [2] who applied these to the study of flow in human arteries. A monolithic method for compressible flows applied was developed by Blom [3]. In segregated approaches two separate solvers are used for handling the deformation and the fluid flow. Information is the exchanged on the interface between the fluid and the solid. For this type of strategy one differentiates between strong and weak coupled strategies, the difference being that in the weak coupled approach information is only exchanged between the two solvers once per time step.

Flow around non-deforming cantilevers has been studied experimentally by Park and Lee [4] as well as numerically by Afgan et al [5]. Both these studies notes the strong three-dimensionality of the wake which is mainly caused by the counter-rotating vortices generated at the free end. This also causes the wake flow to be much more complex than for a cylinder of infinite length. Fujarra et al [6] performed an experimental investigation of vortex-induced vibrations of a elastic cantilever. They found a similar response as for elastically mounted non-deforming cylinders although the flexible cantilever showed larger amplitudes in the synchronisation range. The onset of the initial branch was found at a reduced velocity of about 3 and thereafter a rapid increase in amplitude with a maximum amplitude of around $1D$ at $U_R = 6$. Concerning the frequency, the cantilever was reported to oscillate with the shedding frequency of a stiff cantilever up to $U_R \approx 6$ and thereafter with a frequency related to the eigenfrequency of the structure. Similar findings can be seen in the numerical work by Yamamoto et al. [7].

The purpose of this work is to study the deformation of elastic cantilevers due to hydrodynamic forces by coupled fluid-structure interaction simulations. Also, to investigate the effects on the wake structure by the cantilever vibration.

2 MATHEMATICAL AND NUMERICAL FORMULATION

2.1 Governing Equations of the Fluid

The equations governing isothermal, incompressible flow of a Newtonian fluid can in non-dimensional form be written as

$$\frac{\partial u_i}{\partial \xi_i} = 0 \tag{1}$$

$$\frac{\partial u_i}{\partial \tau} + u_j \frac{\partial u_i}{\partial \xi_j} = -\frac{\partial p}{\partial \xi_i} + \frac{1}{Re}\frac{\partial}{\partial \xi_j}\frac{\partial u_i}{\partial \xi_j} + \Phi_i \tag{2}$$

where Φ_i is a source term.

Consider a boundary in the form of a closed surface Γ in a domain Ω with the parameterisation of the surface given by $X_i(s_i, \tau)$, then the force in the flow field can be written as

$$\Phi_i(\xi_j, \tau) = \iiint_\Omega F_i(s_j, \tau)\, \delta(\xi_j - X_j)\, d\xi_1 d\xi_2 d\xi_3 \tag{3}$$

where F_i is the force per unit volume on the surface and δ is the three dimensional Dirac function. Hence, the source terms will only be non-zero at the location of the boundary. However, discretising the computational domain using a Cartesian grid will in the general case lead to that the nodes on the grid will not coincide with the location of the surface of a body of arbitrary shape. The presence of the boundary must therefore be represented by source terms in positions away from the actual boundary location. This can be achieved in different ways, for example by approximating the Dirac function by a normalised Gaussian distribution [8] or by assuming a certain distribution of the velocity field normal to the boundary [9]. In this work we employ the following expression for the discretised source terms:

$$\overline{\Phi_i} = C_1 \frac{u_i^b - u_i^f}{\Delta t} e^{-C_2 d^2} \tag{4}$$

where C_1 and C_2 are positive constants, u_i^b is the target velocity of the solid surface and d is a positive function which should increase rapidly with increasing distance from the solid boundary. Hence, inside the body d will be set to zero and far away from the body it will have a large positive value, typically 10^6. Several strategies for setting the d-function may be considered. However, the one used in the present work is a step function, i.e.

$$d = \begin{cases} 0 \text{ if inside} \\ 10^6 \text{ if outside} \end{cases} \tag{5}$$

The source terms Φ_i are introduced to represent solid boundaries, i.e. they replace the boundary conditions on the solid body surface. In this case the sources Φ_i are computed so as to satisfy the local boundary conditions. Thus, Φ_i do not vanish only in certain parts of the volume.

2.2 Flow solver

The system of incompressible Navier-Stokes equations (1) and (2) is discretised on a Cartesian grid. The variables, velocity and pressure, are defined on a staggered grid. The velocity components are computed on the faces of control volumes, the pressure is computed at the centre of the control volume. In this situation the boundary condition for pressure is not needed. For discretisation the finite differences approach is used. The time integration is done by an implicit second-order accurate scheme. To combine numerical efficiency with higher order accuracy, we introduce the higher order terms as a "single-step" defect correction [10]. One can show that for smooth problems this procedure is adequate to maintain the theoretical accuracy of the high-order scheme. Hence, we obtain third-order accuracy for convective terms and fourth-order for other terms. At each time step the system of equations is solved by using a Multi-grid solver. To reduce the number of cells, locally refined Cartesian grids are used in addition to uniform global grids, as shown by [11] The relaxation procedure involves the point-wise relaxation of the momentum equations coupled with point-wise smoothing of the continuity equation. Then both the velocity vector and pressure are corrected to satisfy the continuity equation while residuals of the momentum equations are not changed.

2.3 Governing Equations of the Solid

In deriving the equation for the beam it is assumed that the it is slender (i.e. it has a well defined principal axis) and has a constant and symmetric cross-section. Furthermore, the material is assumed to be linear elastic and that the local deformation angles are small. Also neglecting the deformation due to shear and rotation one will find the Euler-Bernoulli beam equation, which in non-dimensional form can be written as (temporarily omitting the damping term)

$$\varrho\mathcal{A}\frac{\partial^2\varpi_i}{\partial\tau^2}+\mathcal{E}\mathcal{I}\frac{\partial^4\varpi_i}{\partial\eta^4}=c_i\left(\eta,\tau\right) \tag{6}$$

The normalisation of density (ϱ), cross-sectional area ($\mathcal{A}$), Young's modulus ($\mathcal{E}$), displacement (ϖ_i), time (τ), the coordinate along the principal axis (η), the second moment of inertia $\mathcal{I}$ and the force coefficient per unit length (c_i) has been performed according to

$$\varrho=\frac{\rho_s}{\rho_f},\ \mathcal{A}=\frac{A}{D^2},\ \mathcal{E}=\frac{E}{\rho_f U^2},$$
$$\varpi_i=\frac{w_i}{D},\ \eta=\frac{y}{D},\ c_i=\frac{P_i\left(y,t\right)}{\rho_f U^2 D}$$
$$\mathcal{I}=\frac{I}{D^4},\tau=t\frac{U}{D}$$

where ρ_s is the density of the solid, ρ_f is the density of the fluid, D is the beam diameter, U is the inlet bulk velocity and P is the hydrodynamic force per unit length.

The eigenfrequency of the first bending mode is determined from:

$$f_N=\frac{k}{2\pi L^2}\sqrt{\frac{EI}{\rho_s A}} \tag{7}$$

where L is the beam length and k is a constant dependent on the load case. For a cantilever $k=3.52$. Introducing the Strouhal number $St=\frac{fD}{U}$ one finds that the non-dimensional eigenfrequency can, in the case of a circular cross-section, be expressed as

$$St_N=\frac{kD^2}{8\pi L^2}\sqrt{\frac{\mathcal{E}}{\varrho}} \tag{8}$$

The reduced velocity is defined as

$$U_R=\frac{U}{f_N D} \tag{9}$$

hence, it is the inverse of the non-dimensional eigenfrequency.

2.4 Solid Solver

The governing equation for the beam motion can on matrix form be expressed as

$$\mathbf{M}\ddot{\varpi}_i+\mathbf{C}\dot{\varpi}_i+\mathbf{K}\varpi_i=\mathcal{F}_i \tag{10}$$

where $\mathbf{M}$, $\mathbf{C}$ and $\mathbf{K}$ are the global mass, damping and stiffness matrices,respectively. These are constructed using the element mass and stiffness matrices.

The damping matrix $\mathbf{C}$ represented in a simplified manner as a linear combination of the mass and stiffness matrices, e.g. Rao [12].

$$\mathbf{C}=\alpha\mathbf{M}+\beta\mathbf{K} \tag{11}$$

The coefficients α and β are related to the damping coefficients of each eigenmode. Assuming a constant damping ratio between each eigenmode one may set $\alpha=0$, which is used in this work.

The discretised equation for the deformation of the solid, equation (10), is solved using the Gauss-Seidel approach with a first order backward temporal discretisation.

3 Computational Set-up

Cantilevers of length $L = 5D$ and $L = 10D$ are mounted on the wall of a rectangular channel at $6D$ from the inlet. The cross-sectional size of the channel is (B,H)=(12D,16D) and it has a length of $20D$. The flow is in the z-direction and the cylinder axis is oriented in the y-direction. The flow is solved on a Cartesian grid using a multi-grid method, as is outlined above, and the number of grid points in each direction in the channel is $64, 48, 80$. However, to improve the resolution around the cantilever the grid is refined using several local multi-grid levels (see Figure 1), yielding a grid resolution of $D/32$ on the finest grid level.

At the inlet a uniform velocity distribution with a Reynolds number based on cantilever diameter of 400 is specified. At the outlet Neumann conditions adjusted fulfil global mass conservation are used and on the channel walls no-slip conditions are used. The number of nodes on the cantilever is 10 and 19 for the short and long cantilevers respectively which corresponds to an element length of $0.556D$. The normalised Young's modulus is varied such that the reduced velocity is in the range $\pi/4 \leq U_r \leq 2\pi$, the density ratio, ϱ, is 20 and the damping factor β is set to 0.1.

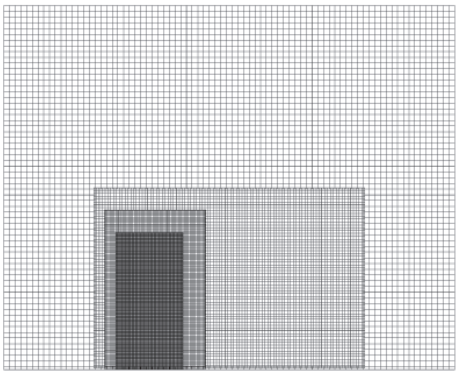

Figure 1: Computational domain and grid structure showing the regions of local refinement.

4 RESULTS

4.1 Stiff Cantilever

The mean flow around a non-deforming cylindrical cantilever resembles that of a finite length cylinder. Differences are of course introduced by the presence of the wall. Instantaneous flow field in the channel centre plane for a cantilever with $L/D = 5$ is shown in Figure 2. The flow will separate both from cantilever surface (as for any cylindrical surface) and from the free end of the cantilever. This will create a fairly complex three dimensional vortex shedding downstream of the cantilever. In figure 3 the wake structures are depicted using the λ_2 method of Jeoung and Hussain [13]. Closest to the wall the classical horse-shoe vortex is formed on the upstream side of the cantilever. At the lower part of the cantilever the vortex shedding resembles that of an infinitely long cylinder. Over the outer edge of the cantilever a vortex oriented in the x-direction is formed along with a counter rotating vortex pair oriented in the z-direction. These vortices are fairly constant over time. Further downstream in the wake a combination of stream-wise and span-wise vortices is observed. The stream-wise vortices are also deformed due to the span-wise vortices shed from the cantilever body. The shedding frequency, determined from the time history of the lift force, corresponds to a Strouhal number of 0.16, i.e. somewhat lower than for a infinitely long cylinder. However, if instead the spectral content of the cross-stream velocity is studied two distinct peaks corresponding to Strouhal numbers of 0.165 and 0.195 are found. Comparing to the work by Afgan et al [5], they found only the lower of these at $St = 0.167$ for the cantilever length $L = 10D$. Also, they found that the shedding frequency varied with cantilever length, a phenomenon not found in the present work. The lower of the two frequencies seen in Figure 4 originates from shedding at the cantilever tip and the higher from the "normal" vortex shedding from the cantilever body. Hence, the frequency content in the wake is a combination of the two shedding phenomena whilst the force loading is totally dominated by the tip shedding. A reasonable explanation is that the shedding with $St = 0.195$ is dominating only close to the wall, i.e. its contribution to the force fluctuations therefore only minor. As for any other finite length cylinder the average recirculation zone length will vary over the span. For the short cantilever, close to the wall the recirculating flow is directed against the stream-wise direction. However, for distances beyond $0.5D$ the recirculation is dominated by the large vortex oriented in the cross-stream direction, as can be seen in Figure 5. For the longer cylinder, the upper cross-stream vortex is less pronounced. However, the longer distance between the wall and the cantilever tip allows for the presence of a second counter-rotating cross-stream vortex in the region close to the wall, Figure 6.

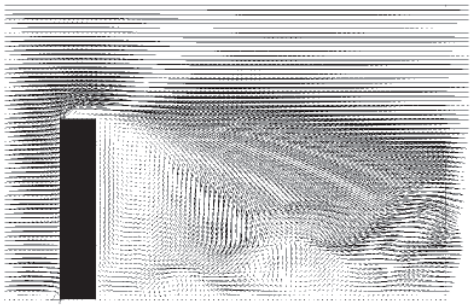

Figure 2: Instantaneous velocity at the centre plane normal to the x-direction.

Comparing cylinders of length $5D$ and $10D$ only

Figure 3: Visualisation of the wake vortices using a λ_2 iso-surface.

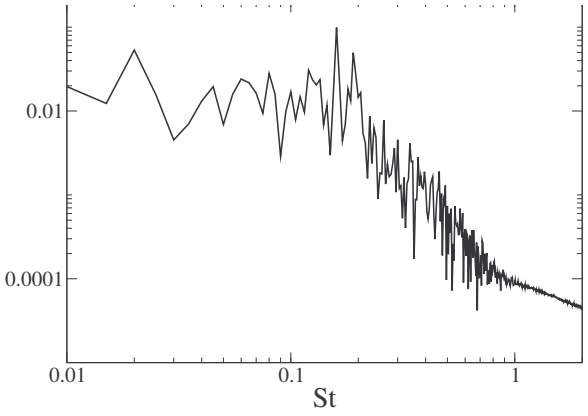

Figure 4: Frequency content in the wake at $(\mathbf{x}, \mathbf{y}, \mathbf{z}) = (\mathbf{0}, \mathbf{3D}, \mathbf{4D})$ for a non-deforming cantilever with $\mathbf{L/D = 10}$.

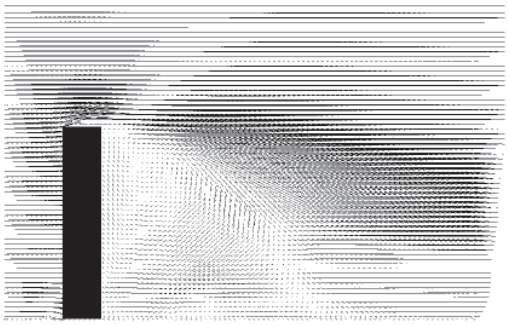

Figure 5: Time average velocity at the centre plane normal to the x-direction.

minor differences are found in the time averaged wake velocity. Figure 7 shows the average stream-wise velocity as a function of the span-wise distance normalised with the cantilever length at four positions in the wake, $z = 1.5D$, $z = 3.9D$, $z = 6.3D$ and $z = 8.7D$. The only major difference is found at the first position close to the wall, where the velocity

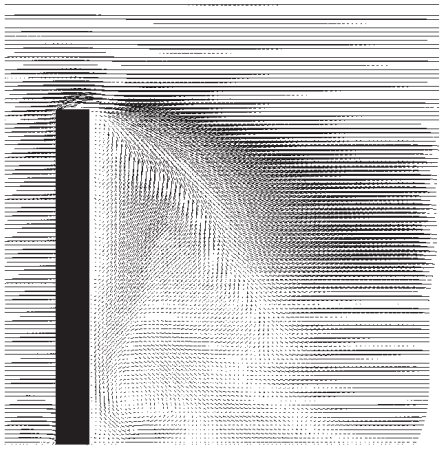

Figure 6: Time average velocity at the centre plane normal to the x-direction for a cantilever length $\mathbf{L/D = 10}$.

is positive for the case $L/D = 10$. On closer inspection one finds that this is caused by a secondary vortex formed close to the wall as is seen in Figure 6. The reason this vortex is not present in the short cantilever case is probably due to the proximity to the wall. Considering the rms. values of the stream-wise velocity fluctuations in Figure 8 significant differences are found. The velocity fluctuations of the longer cantilever are at some position more than twice larger than for the shorter one. At the position closest to the cantilever two maxima of the fluctuation are observed for the shorter cantilever. The upper maximum is related to the shedding from the cantilever free end and the lower is caused by the increasing influence of the vortex shedding from the cantilever body as the wall is approached. However, for the long cantilever a different pattern is observed. The vortex oriented in the y-z plane, which is situated just down-stream of the cantilever is much less pronounced for the long cantilever and alos does not cover the whole span of it. This might explain the higher fluctuation levels of the longer cantilever since the shedding from the cantilever body can develop with less influence from the tip.

4.2 Elastic Cantilever

The studies by Fujarra et al. [6] and by Yamamoto et al [7] show that the lock-in behaviour of an elastic cantilever is very similar to that of an elastically mounted non-deforming cylinder. At a certain reduced velocity the amplitude of the deformation will increase rapidly from a very low value and the remain at a large almost constant value in the lock-in region, where after the amplitude again drops of rapidly for large values of reduced velocity. Similar results are seen in the present work although the accuracy of the structural deformation is decreased at large deflections due to the element type used in the FEM calculations. This

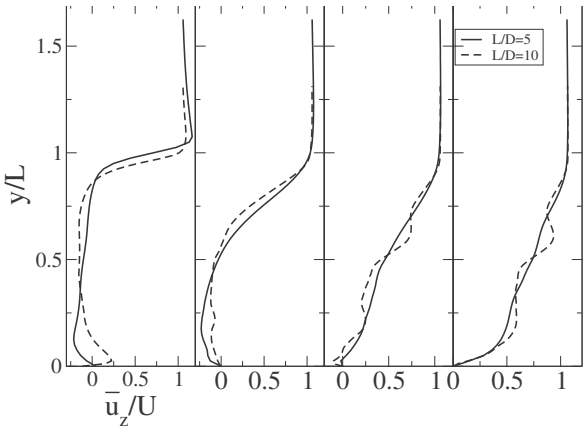

Figure 7: Average velocity profiles at four positions in the cantilever wake. For $\mathbf{L/D = 5}$ and $\mathbf{L/D = 10}$.

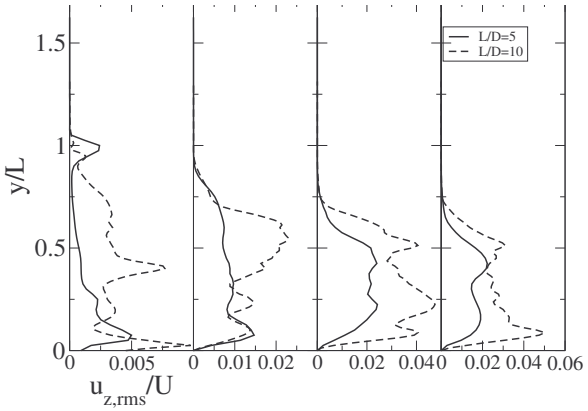

Figure 8: Profiles of rms of velocity fluctuations at four positions in the cantilever wake. For $\mathbf{L/D = 5}$ and $\mathbf{L/D = 10}$.

is probably why the end of the lock-in range cannot be predicted in Figure 9. Another reason may be that both Fujarra et al. [6] and Yamamoto et al [7] vary the flow rate and hence the Reynolds number in order to vary the reduced velocity, whilst in the present work the Reynolds number is kept constant and the variation is achieved by varying the Young's modulus of the cantilever. Despite this, the maximum amplitude and the onset of the initial branch are fairy well predicted in the present work. In the remainder of this study the upper limit of reduced velocity has therefore been set to 2π in order to avoid the large deformation range. Figure 10 shows the amplitude of the deformation of the tip of the cantilever in the cross-stream direction. At low values of reduced velocity (i.e. large Young's modulus) the amplitude is very low. As the reduced velocity is increased one will for the longer cantilever observe a monotonic increase in the deformation amplitude, which is expected since according to the theory for a linear elastic material the deformation should increase with reduced velocity squared, see equations (8) and (9). For the shorter cantilever the increase in amplitude occurs at a lower reduced velocity also a local minimum in amplitude is observed around $U_r = 3\pi/2$. This behaviour is is neither observed for higher Reynolds numbers nor for larger aspect ratios and it needs to be further investigated before it is fully understood. The frequency of the motion differs significantly for the two cantilever lengths. For the short cantilever the frequency is locked to the eigenfrequency of the first mode for low values of reduces velocity and at the reduced velocity where the amplitude starts to increase the shedding frequency changes to that of a stiff cantilever. For the longer cantilever on the other hand the frequency coincides with the tip shedding frequency of a stiff cantilever over the whole range of reduced velocities considered. The latter behaviour is more similar to what was found by Fujarra et al. [6].

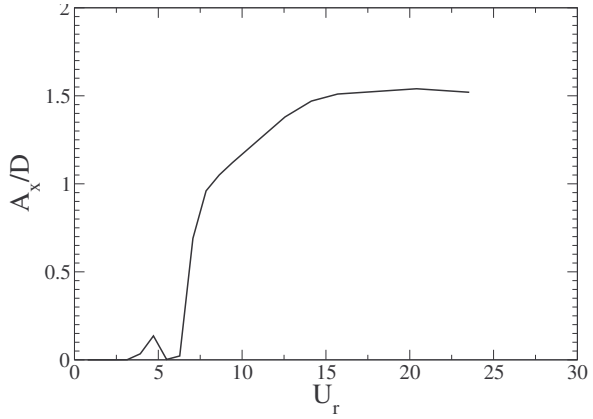

Figure 9: Maximum deflection in the cross-stream direction of the cantilever tip for $\mathbf{L/D = 5}$.

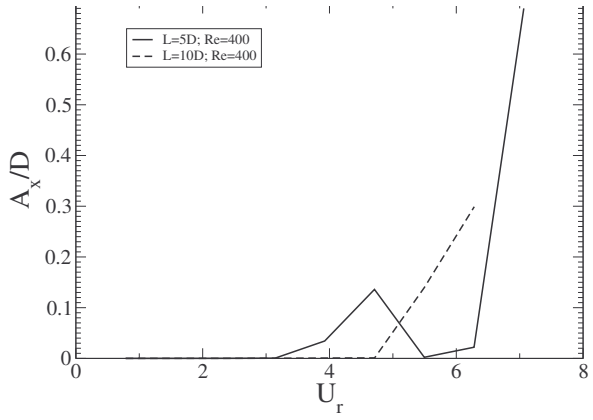

Figure 10: Maximum deflection in the cross-stream direction of the cantilever tip over the range of reduced velocities considered.

Considering the wake flow in more detail one finds that the average flow velocity in the wake centre plane is only marginally different to that of

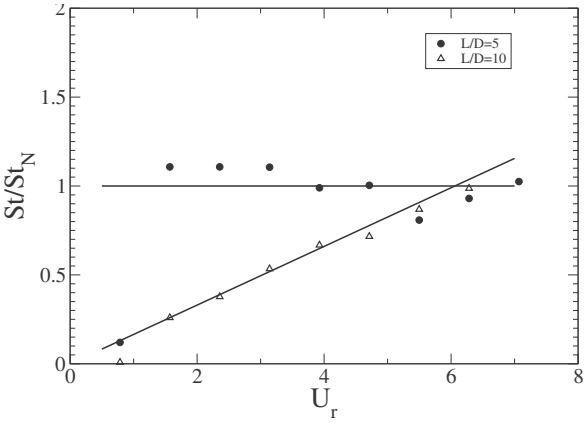

Figure 11: Frequency of the cantilever tip motion over the range of reduced velocities considered.

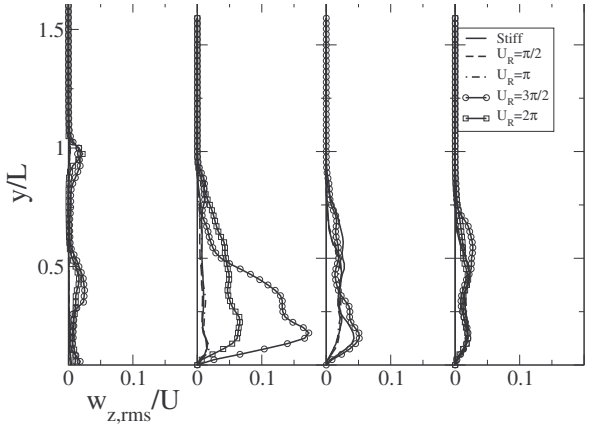

Figure 12: Profiles of rms of stream-wise velocity fluctuations at four positions in the cantilever wake and for four values of reduced velocity.

a stiff cantilever at positions close to the cantilever. However, further downstream in the wake there is a distinct difference between cases with high and low deformation amplitude. For $U_R = 3\pi/2$ (i.e. at the onset of the synchronisation range) and larger the recirculation region is shorter. The differences are even more pronounced concerning the wake fluctuations. In the upstream part of the wake the rms of stream-wise fluctuations can be up to a factor 5 to 10 larger for the cases with high reduced velocity as can be seen in Figure 12. This is of course expected due to the large deformation of the cantilever at the high end of the reduced velocity range. Also the vortex structure in the wake is different once the synchronisation range is reached. As can be seen in Figure 13 the tip vortex pair is no longer present. Instead a single vortex is shed from the tip and it is also spread in the cross-stream direction due to the tip motion. This together with the more pronounced vortex shedding from the cantilever body, with which the tip vortex strongly interacts, generates a completely different wake structure as compared to the lower reduced velocity and stiff cantilevers. Studying the frequency content in the wake (Figures 14 and 15) one can see that for the whole range of reduced velocities the wake motion is totally dominated by the frequency of motion of the cantilever and for the case of high reduced velocities also several of the harmonics of this frequency.

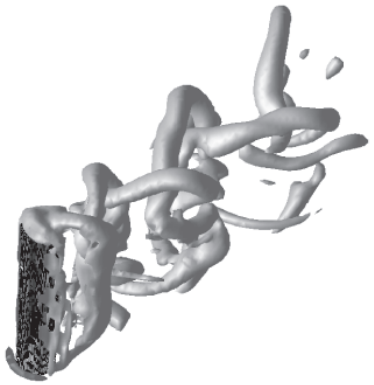

Figure 13: Visualisation of the wake vortices using a λ_2 iso-surface for $\mathbf{U_R = 2\pi}$.

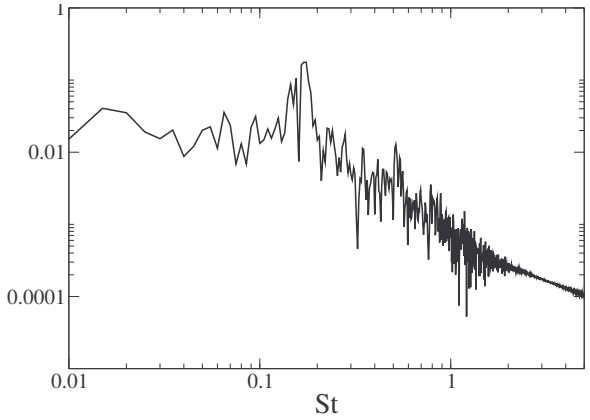

Figure 14: Frequency content in the wake at $(\mathbf{x, y, z}) = (\mathbf{0, 3D, 4D})$ for a deforming cantilever with $\mathbf{L/D = 10}$ at $\mathbf{U_R = \pi/2}$.

5 CONCLUDING REMARKS

Simulations of the fluid-structure interaction between a incompressible flow and a linear elastic cantilever has been performed using a weakly coupled solution strategy. From this study one may conclude that

- The results agree fairly well, at least qualitatively, with previous studies. However, the present strategy for simulating the cantilever deformation is not well suited for large deformations.
- In the de-synchronised regime (low reduced velocities) the cantilever motion has only a marginal influence on the wake structure.

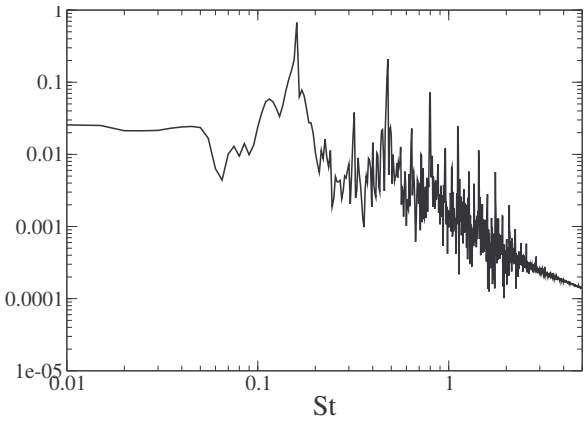

Figure 15: Frequency content in the wake at $(\mathbf{x}, \mathbf{y}, \mathbf{z}) = (\mathbf{0}, \mathbf{3D}, \mathbf{4D})$ for a deforming cantilever with $\mathbf{L/D = 10}$ at $\mathbf{U_R = 2\pi}$.

However, in the initial branch of synchronisation the influence on average flow field, frequency content and vortex structures is significant.

- Comparing cantilevers of aspect ratio 5 and 10 it seems that synchronisation is delayed to higher reduced velocity for the longer cantilever. One also observes differences in the vibrational frequencies in the de-synchronised regime. This might be caused by relatively large differences in average wake flow between the long and the short cantilever, where the presence of the wall will have a greater impact on the shorter one. Investigations at even larger aspect ratios should be performed to clarify this.

6 ACKNOWLEDGEMENTS

This work was financially supported by the Swedish Research Council (VR), grant no. 621-2007-5267. The the computational resources provided by the centre for scientific computing at Lund University, LUNARC, and the Swedish National Infrastructure for Computing (SNIC), is also greatfully acknowledged.

References

[1] C.S. Jog and R.K. Pal. A monolithic strategy for fluid-structure interaction problems. *Int. J Numerical Methods in Engineering*, 85:429–460, 2011.

[2] M.W. Gee, U. Küttler, and W.A. Wall. Truly monolithic algebraic multigrid for fluid structure interaction. *Int. J Numerical Methods in Engineering*, 85:987–1016, 2011.

[3] F.J. Blom. A monolithic fluid-structure interaction algorithm applied to the piston problem. *Computer Methods in Applied Mechanics and Engineering*, 167:369–391, 1998.

[4] C.W. Park and S.J. Lee. Effects of free-end corner shape on flow structure around a finite cylinder. *J. Fluids and Structures*, 19:141–158, 2004.

[5] I. Afgan, C. Moulinec, R. Prosser, and D. Laurence. large eddy simulation of turbulent flow for wall mounted cantilever cylinders of aspectratio 6 and 10. *int. J. Heat and Fluid Flow*, 28:561–574, 2007.

[6] A.L.C. Fujarra, C.P. Pesce, F. Flemming, and C.H.K. Williamson. Vortex-induced vibration of a flexible cantilever. *J. Fluids and Structures*, 15:651–658, 2001.

[7] C.T. Yamamoto, J.R. Meneghini, F. Saltara, R.A. Fregonesi, and J.A. Ferrai Jr. Numerical simulations of vortex-induced vibration on flexible cylinders. *J. Fluids and Structures*, 19:467–489, 2004.

[8] J. Revstedt. A virtual boundary method with improved computational efficiency using a multi-grid method. *int. J. Num. Meth. Fluids*, 45(7):775–795, 2004.

[9] E.A. Fadlun, R. Verzicco, P. Orlandi, and J. Modh-Yusof. Combined immersed-boundary finite-difference methods for three-dimensinal complex flow situations. *J. Comput. Phys.*, 161:35–60, 2000.

[10] J. Gullbrand, X-S. Bai, and L. Fuchs. High-order cartesian grid method for calculation of incompressible turbulent flow. *int. J. Num. Meth. Fluids*, 36:539–555, 2001.

[11] L. Fuchs and H-S. Zhao. Solution of three-dimensional viscous incompressible flows by a multi-grid method. *int. J. Num. Meth. Fluids*, 4:539–555, 1984.

[12] S.S. Rao. *The finite element method in engineering*. Pergamon Press, Oxford, 1989.

[13] J. Jeong and F. Hussain. On the identification of a vortex. *J. Fluid Mech.*, 285:69–94, 1995.

Conference on Modelling Fluid Flow (CMFF'12)
The 15th International Conference on Fluid Flow Technologies
Budapest, Hungary, September 4-7, 2012

DYNAMICS OF REDUCED ORDER MODELS OF THE FORCED KARMAN CYLINDER WAKE

Njuki MUREITHI[1], László BARANYI[2], Kenny HUYNH[3]

[1] Corresponding Author. BWC/AECL/NSERC Chair of Fluid-Structure Interaction, Department of Mechanical Engineering, Ecole Polytechnique, 2900 Boul. Edouard Montpetit, Montreal, Canada. Tel.: +1 514 340 4711, E-mail: njuki.mureithi@polymtl.ca
[2] Department of Fluid and Heat Engineering, University of Miskolc, Miskolc, Hungary. Email: arambl@uni-miskolc.hu
[3] Bombardier Aerospace, Montreal, Canada. E-mail: kenny.huynh@aero.bombardier.com

ABSTRACT

Employing symmetry-group equivariant bifurcation theory discrete reduced order models for the dynamics of the forced Karman wake have been developed. It turns out that the bifurcation behaviour of the complex forced wake flow can be approximately described by these simple models.

Although the symmetry approach is highly convenient when deriving the reduced order models, the general form of the resulting model requires the extra step of determination of the model coefficients for a given physical flow. In addition, an important assumption of the approach above is that symmetry holds exactly over the complete flow domain (and to infinity). In reality this is not the case – particularly for flow assumed to have translational symmetry.

The present paper addresses these two concerns. In a first attempt to obtain a physical interpretation of the reduced order model coefficients, the POD modes are employed in a Galerkin reduction of the complex Ginzburg-Landau (CGL) equation. The latter equation is a well known approximate model for spatio-temporal flow dynamics. To account for imperfect flow field symmetry, POD modes are derived directly from experimental PIV measurements.

An analysis of the CGL-based reduced order model yields the key bifurcations of the symmetrically forced Karman wake. Most importantly the model confirms the saddle-node bifurcation, supporting the findings based on the symmetry-based approach.

Keywords: bifurcation theory, Ginzburg-Landau equation, PIV, POD, Poincare map, saddle-node bifurcation, symmetry equivariance, von Karman wake.

NOMENCLATURE

a_i	$[-]$	CGL equation mode amplitude
C_L	$[-]$	lift coefficient
D	$[m]$	reference cylinder diameter
K_n	$[-]$	Karman mode amplitude
S_n	$[-]$	forcing mode amplitude
u	$[ms^{-1}]$	in-flow perturbation velocity
U	$[ms^{-1}]$	average flow velocity
v	$[ms^{-1}]$	transverse perturbation flow velocity
β	$[-]$	diffusion parameter in CGL equation
ϕ_n	$[-]$	POD mode
Γ_K	$[-]$	Karman mode symmetry
Γ_S	$[-]$	forcing mode symmetry
ν_1, ν_2	$[-]$	convection coefficients
σ	$[-]$	linear stability parameter in CGL equation

1. INTRODUCTION

The Karman wake is an ideal fluid system for the study of the dynamics, stability and control of fluid flow phenomena. Following the onset of vortex shedding at the critical velocity (near Re=45) via a Hopf bifurcation the Karman wake behaves, dynamically, as a well-defined spatio-temporal oscillator which can be described in terms of a finite number of orthogonal modes.

Recent work aimed at developing controllers for the Karman wake has taken the low order model approach. Low order modelling involves reduction of the effective number of degree-of-freedom of the

fluid system to a small finite number while still retaining the essential features of the dynamical behaviour.

Low order models may be derived by direct numerical reduction of the NS equations (e.g. via Galerkin projections) or by a phenomenological approach based on physical and geometrical arguments. An example of the latter is the symmetry-equivariance based approach which exploits the 'known' symmetries of the dominant modes to derive low order models which are equivariant under the action of the chosen base flow symmetries. This method has led Mureithi et al. [1] and Rodriguez [2] to develop simple discrete models for the forced Karman wake.

A pair of simple low order equations describing the nonlinear interaction of the Karman and reflection-symmetric modes was derived in the Poincare space [1,3]. An analysis of the model showed that a number of standard bifurcations of the forced Karman mode could be obtained as the amplitude of the reflection-symmetric mode was varied. Possible changes in the wake, induced by increased forcing, such as period-doubling or symmetry breaking in the case of stream-wise harmonic forcing were correctly predicted.

One of the challenges in exploiting the symmetry-equivariance based model is the determination of model parameters and their correct (physical) interpretation. This is because the model is only limited by symmetry hence may represent any physical phenomenon having the correct symmetry – this being the universality property of the symmetry based approach. It is the model parameters (or coefficients) which map the model to a specific physical phenomenon.

An alternative approach to using symmetry-equivariance is derivation of reduced-order models using the Galerkin projection of either the full Navier-Stokes (NS) equations or simpler equations capturing the basic flow features. The advantage of the Galerkin projection is the fact that, in principle, no external parameters need to be determined. As a first step we propose to use the complex Ginzburg Landau (CGL) equation as a spatio-temporal model for the Karman wake flow in the subcritical and super critical regimes. The CGL equation has been successfully used to model key spatio-temporal instabilities and limit cycle behaviour in fluid systems (see, for instance, the excellent review by Aranson and Kramer [4] and references therein). The CGL equation has the advantage of being simpler than the NS equations making it easier to interpret the predicted dynamical phenomena.

Galerkin projection of the CGL equations yields discrete model coefficients which can be directly related to the CGL parameters e.g. the convective velocity of spatial perturbations, and the diffusion parameter. Other parameters include the modal stability parameter and the limit cycle amplitude (nonlinear damping) parameter.

2. REDUCED ORDER MODELS

In this section a brief summary of the derivation of the low order models is presented. The key assumptions and derivations are outlined in order to clearly highlight the strengths and limitations of each approach. Reduced order models are based on the idea of the existence of fundamental coherent structures (modes) in the flow, [5]. The coherent structures may be described by their symmetries [6] which also govern their nonlinear dynamics. For the symmetry based approach, the detailed derivation may be found in Mureithi et al. [1]. An example of the CGL based model reduction may be found in Ilak et al. [7].

2.1. Symmetry based Model

Experimental measurements show that the Karman wake is dominated by two key modes. These modes correspond to the alternate shedding mode (***K***) and the symmetrical shedding mode (***S***). As detailed in Mureithi et al. [1,3], The spatial symmetries of these modes are, respectively, $\Gamma_K = Z_2(\kappa,\pi)$, and $\Gamma_S = D_2(\kappa,\pi)$. Starting with the symmetries Γ_K and Γ_S, Mureithi et al. [3] employed equivariant bifurcation theory, [8,9], to derive the general form of the amplitude equations governing the interactions between modes ***K*** and ***S***.

Representing the complex mode amplitude by *K* and *S,* respectively, the discrete form of the mode amplitude interaction equations to third order is (Mureithi et al. [1,3])

$$\begin{aligned} K_{n+1} &= \left(1+\alpha_0+\gamma_{11}|S_n|^2+\alpha_2|K_n|^2\right)K_n+\delta_{01}S_n^2\bar{K}_n \\ S_{n+1} &= \left(1+\beta_0+\beta_2|S_n|^2+\gamma_{21}|K_n|^2\right)S_n+\mu_{01}\bar{S}_nK_n^2 \end{aligned} \tag{1}$$

The map resulting when the mode ***S*** is considered "constant" (or the externally controlled parameter) has $Z_2(\kappa,\pi)$ symmetry. The map and its complex conjugate are:

$$\begin{aligned} K_{n+1} &= \left(\mu+\alpha_2|K_n|^2\right)K_n+\delta\bar{K}_n \\ \bar{K}_{n+1} &= \left(\bar{\mu}+\bar{\alpha}_2|K_n|^2\right)\bar{K}_n+\delta K_n \end{aligned}; \tag{2}$$

$$\mu = 1+\alpha_0+\gamma_{11}|S|^2$$

$$\delta = \delta_{01}S^2$$

$\alpha_0, \gamma_{11}, \alpha_2, \beta_0, \delta_{01}$.... are empirical constants.

2.2. CGL based Model

The CGL equation is a convection-diffusion partial differential equation. To take into account

amplitude limitation of unstable oscillations due to a Hopf bifurcation a nonlinear term of third order is incorporated which can be justified by a normal form analysis. The scaled CGL equation, which will be used in this study, has the form:

$$\partial_t u(x,y,t) = \begin{bmatrix} -\{\nu_1 \partial_x + \nu_2 \partial_y\} + \\ \beta\{\partial_{xx} + \partial_{yy}\} + (\sigma - c_1^2) \end{bmatrix} u(x,y,t) + g(u(x,y,t))$$

$$g(u(x,y,t)) = -\gamma |u(x,y,t)|^2 u(x,y,t) \tag{3}$$

The parameters $\nu_1 = U + 2ic_1$ and $\nu_2 = 2ic_1$ are the convection coefficients in the flow direction (i.e. convective velocity) and the transverse direction, respectively, U being the average inflow propagation velocity. The parameter β models the diffusion process while σ is the linear stability parameter for local perturbations. In equation (3) $u(x,y,t)$ is the (x-) direction velocity fluctuations about the mean velocity $\overline{u} = U$.

The CGL equation (3) is discretized via Galerkin projection using POD modes of the flow velocity field $u(x,y,t)$. The velocity field is decomposed as

$$u(x,y,t) = \sum_{n=1}^{N} \phi_n(x,y) a_n(t), \tag{4}$$

where $\phi_n(x,y)$ are the POD modes of the wake flow. Substituting (4) into (3) and performing a two mode (N=2) Galerkin projection we obtain the following pair of differential equations for the complex mode amplitudes

$$\dot{a}_1(t) = \left[\sigma_1 + \gamma_{12}|a_2(t)|^2\right] a_1(t) + \gamma_{11}|a_1(t)|^2 a_1(t) + ..$$
$$\dot{a}_2(t) = \left[\sigma_2 + \gamma_{21}|a_1(t)|^2\right] a_2(t) + \gamma_{22}|a_2(t)|^2 a_2(t) + .. \tag{5}$$

In equation (5) the coefficients $\sigma_i, \gamma_{ij}, ...$ must be determined from experimental or numerical data. These coefficients represent integrals of the POD modes and their spatial derivatives, e.g.,

$$\sigma_i = \int \left[-\{\nu_1 \phi_{ix} + \nu_2 \phi_{iy}\} + \beta\{\phi_{ixx} + \phi_{iyy}\} + \sigma\right] \phi_i dxdy$$
$$\gamma_{ij} = -\gamma \iint \phi_i^2 \phi_j dxdy. \tag{6}$$

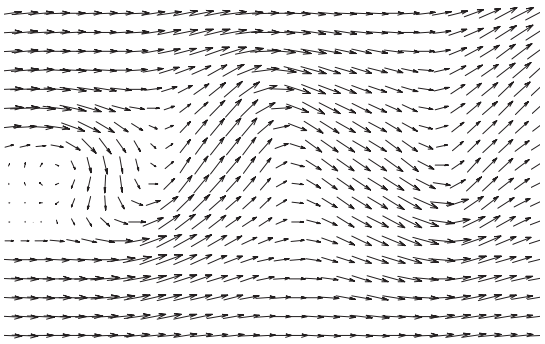

Figure 1. Velocity field in the wake of the cylinder for *Re*=200

3. EXPERIMENTAL MEASUREMENTS AND POD MODE COMPUTATION

To determine the POD wake modes, experimental tests have been conducted for a Reynolds number *Re*=200. The tests were conducted in a low-speed wind tunnel of test section dimensions 60 *cm* x 60 *cm*. The temperature controlled recirculating wind tunnel has a maximum empty test section speed of 90 *m/s* and turbulence intensity below 0.5%. The 76.2 *mm* diameter test cylinders spanned the test section eliminating unwanted 3D end effects. The flow field in the cylinder wake was measured using particle image velocimetry (PIV) and the resulting data analyzed using Dantec Dynamics's flow manager software. An in-house code was then used to determine the spatial (x,y) and spatial-temporal (x,t) POD modes of the measured wake flow. Further experimental details may be found in [10].

Figure 1 shows an image of the measured wake flow field for *Re*=200. The measurement area extends over a distance of approximately 5D (D being the cylinder diameter) downstream of the test cylinder. From this flow field the spatio-temporal POD modes are computed by using the transverse velocity data $v(x=D,y,t)$ at a location 1D downstream of the cylinder. Figure 2(a) shows a contour representation of the time varying transverse velocity profile $v(x=D,y,t)$; transverse position is given in cylinder diameters, y/D. At this location immediately downstream of the cylinder the flow is highly symmetrical as confirmed by the time invariance of the contours. The first two spatio-temporal modes are shown in Figs. 2(b-c). The first two modes are clearly highly structured and temporally 'stable'. The third mode (not shown) showed significant time variation (or

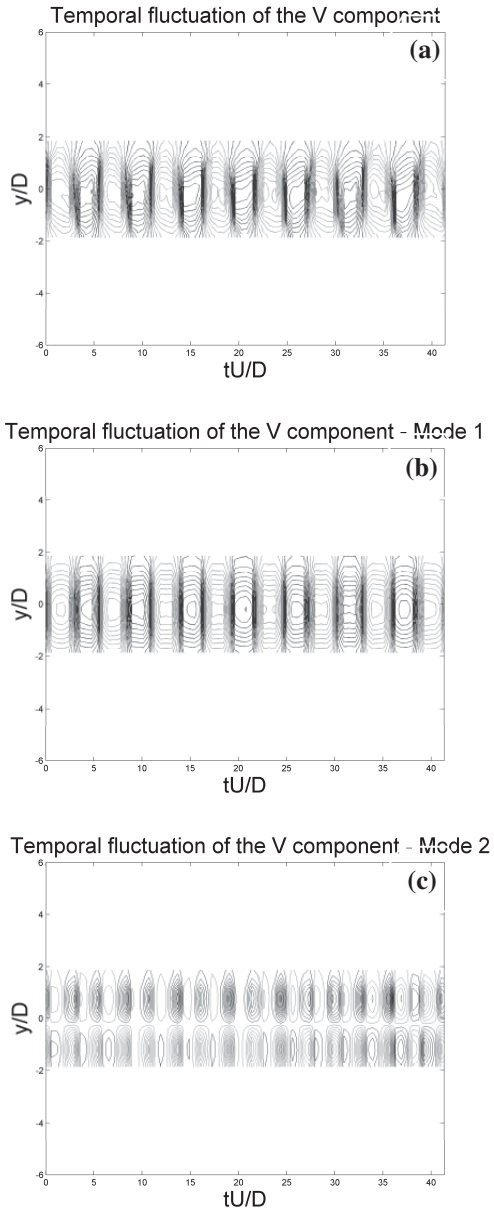

Figure 2. (a) Transverse velocity (*v*) contours, (b) POD mode 1, (c) POD mode 2 based on the velocity (*v*) at an *x*-location 1D downstream of the cylinder

'defects') suggesting the appearance of significant 3D effects. POD modes are obtained in Matlab.

The inflow velocity profile $u(x,y,t)$ and corresponding spatio-temporal modes (1 and 2) are presented in Figs. 3(a-c). Once again the strongly symmetrical nature of the first two modes is clearly evident. For reduced order modelling it is important to determine the minimal number of modes that can be expected to capture the dynamics of the infinite-dimensional system. An estimate can be obtained by looking at the energy distribution between the modes. In the POD analysis the singular values provide a measure of the energy contained in a given mode.

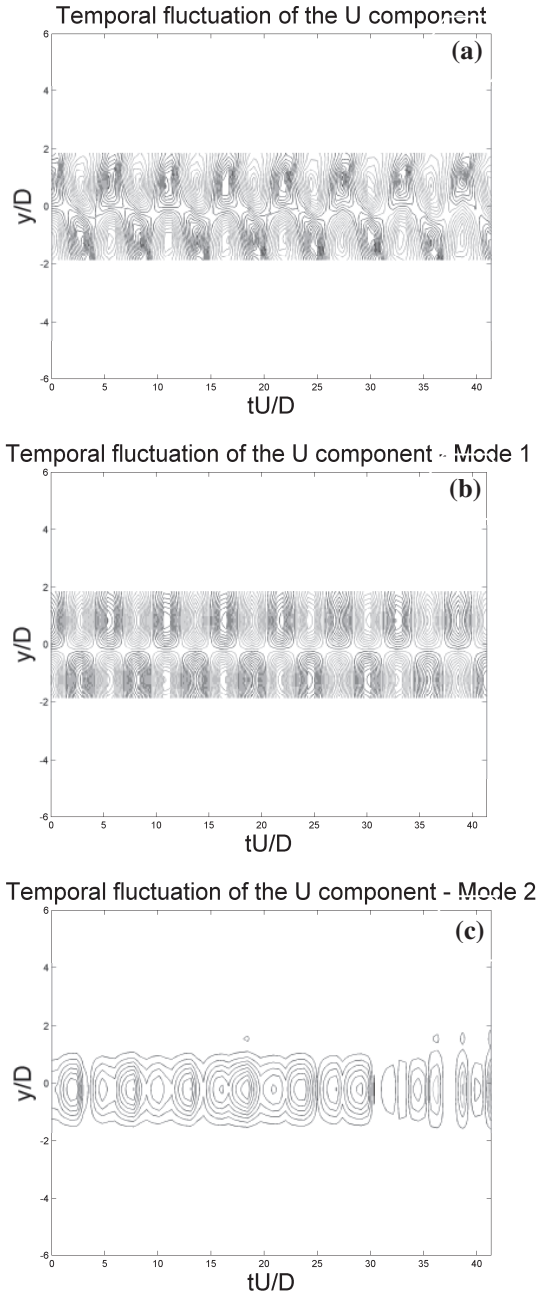

Figure 3. (a) Inflow velocity (*u*) contours, (b) POD mode 1, (c) POD mode 2

Figure 4 shows the energy distribution between the POD modes for *v*-velocity modes (Fig. 4(a)) and the u-velocity modes in Fig. 4(b). In both cases it is found that the first mode contains close to 85% of the flow energy. The second mode, on the other hand carries roughly 9% while the third mode carries 3% of the energy. The first mode is therefore clearly predominant as expected for this low Reynolds number and can therefore be expected to provide reasonable single mode approximation of the wake flow. The first two modes contain over 90% of the flow 'energy' and are therefore

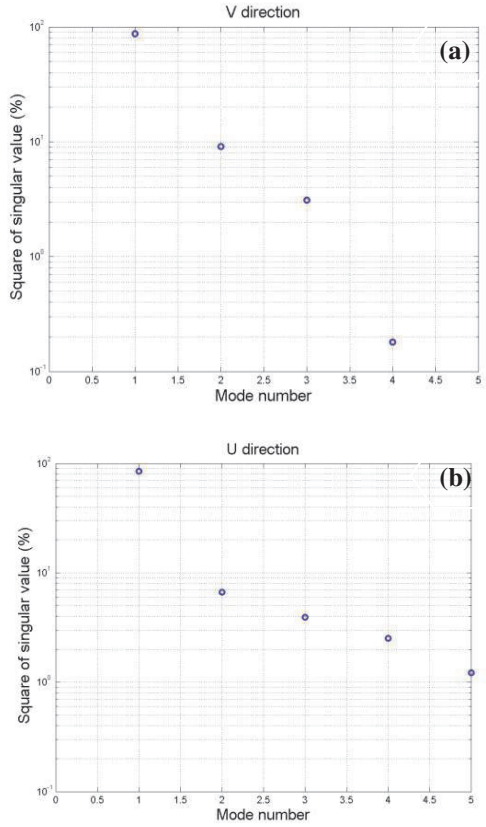

Figure 4. POD mode energy distributions for (a) transverse velocity (*v*) modes and (b) inflow velocity (*u*) modes

sufficient for a low order representation of the flow with a higher accuracy than the single mode case.

The spatio-temporal POD modes presented above contain the implicit assumption of perfect translation symmetry of the flow (along the flow direction -*x*). Indeed it is this assumption that makes it possible to derive the symmetry-equivariance based low order model in equations (1-2). Figure 5(a) presents an example of a contour representation of the instantaneous transverse velocity field (*v*) in the cylinder wake. The first two modes obtained from a POD analysis of this flow velocity field are presented in Figs. 5(b-c). Due to the spatial development of the flow as it propagates downstream, it is evident that perfect translation symmetry cannot be conserved. However, the flow does remain nearly or approximately translation symmetric. This is an encouraging result for the symmetry-equivariance based model. The first spatial and spatio-temporal modes have very similar features as confirmed by comparing Fig. 2(b) and Fig. 5(b). The comparison is less clear for modes 2 and 3. For the present measurements the mode order is reversed relative to the spatio-temporal case in Fig. 3. The singular values show that the second and third spatial modes have nearly equal energy levels

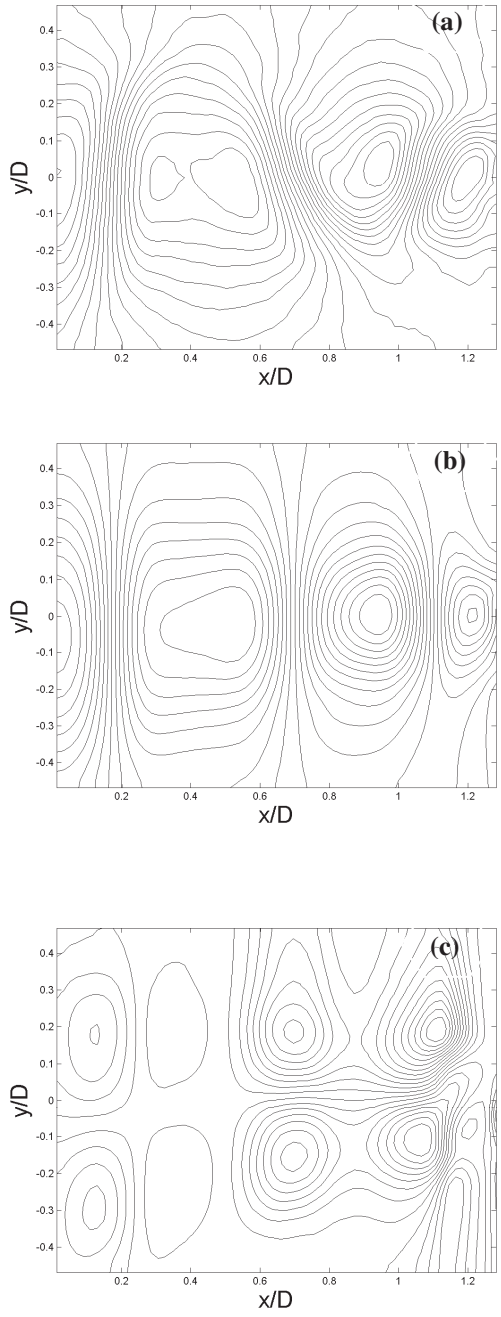

Figure 5. (a) Spatial transverse velocity (*v*) contours and (b) POD spatial mode 1, and (c) POD spatial mode 2, based on transverse velocity *v*

with the result that a mode order switching occurs.

It is interesting to note that the experimental spatial modes are closely similar to spatial modes obtained from a 2D CFD simulation for *Re*=200. Figure 6 shows the transverse velocity contours and the corresponding first POD mode. Comparison with Figs. 5(a, b) shows that the 2D simulation does capture the key modal features. This result is particularly relevant for the symmetry based reduced order model.

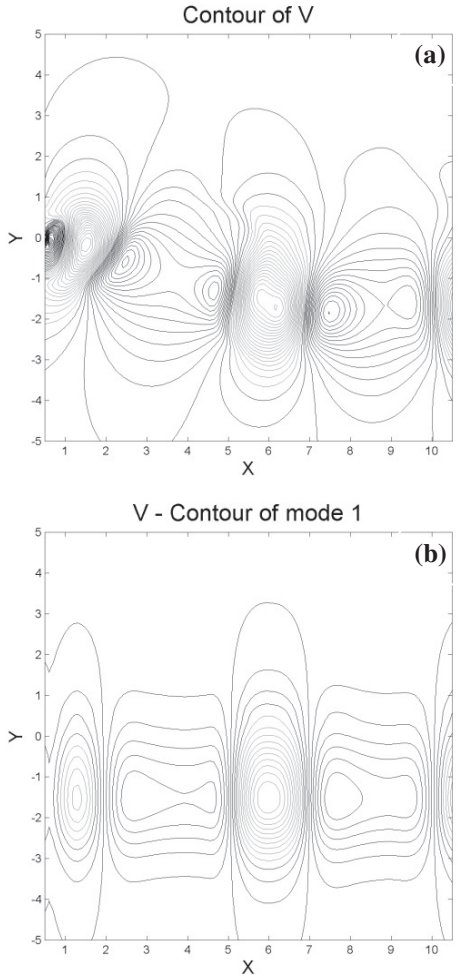

Figure 6. 2D CFD computation based (a) spatial transverse velocity (v) contours and (b) POD spatial mode 1

4. REDUCED ORDER MODEL DYNAMICS

We investigate next the dynamic interaction between the reflection-symmetric mode and the Karman mode. This corresponds to equation (2) for the symmetry based model with mode 2 amplitude (*S*) considered as a 'controlled' forcing parameter. For the CGL based model, the amplitude $a_2(t)$ is the controlled forcing parameter. The dynamic behaviour of mode 1 when forced by mode 2 is investigated. Experimentally, or in CFD simulations, mode 2 is 'generated' at a chosen frequency (here the vortex shedding frequency) by periodically forcing the cylinder in the flow direction.

Figure 7(a) shows a Poincare map of the lift coefficient obtained from CFD simulations (using CFX, [1]) for the fixed cylinder and *Re*=200. The symmetry based reduced order model prediction is shown in Fig. 7(b).

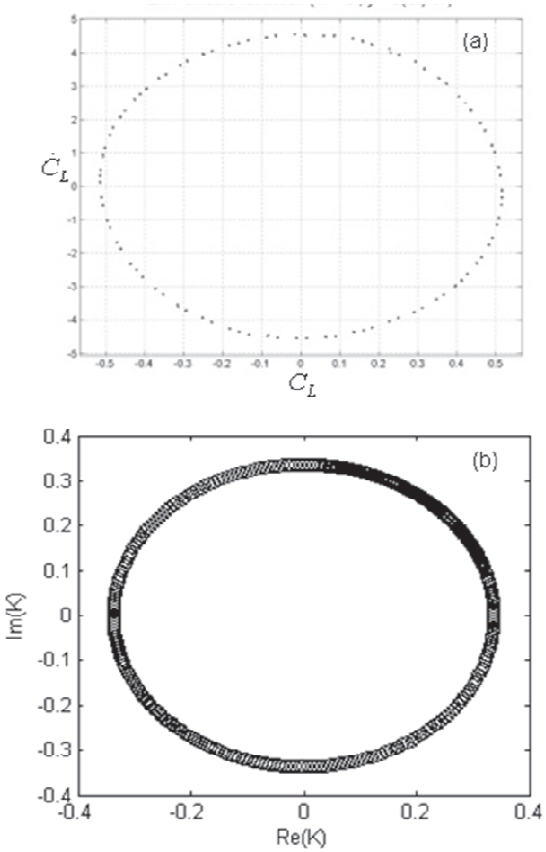

Figure 7. Low order model prediction relative to CFD simulations showing (a) computed and (b) predicted limit-cycles

The model (as expected) correctly reproduces the limit cycle in Fig. 7 (see [1] for details). For a higher forcing amplitude *A*/*D*=0.35 CFD simulations show that wake undergoes a saddle-node bifurcation. The Poincare map shows a series of saddle-node pairs (S, N) pairs as indicated in Fig. 8(a). As discussed in [1] the nodes appear to be unstable likely due to the effects of higher (unmodelled) modes. The symmetry based reduced order model correctly predicts the saddle-node bifurcation as shown in Fig. 8(b). Here two saddle-node pairs are predicted due to the low order of the model.

Simulations carried out with the CGL based model yield particularly interesting results. The spatial POD based model attempts to make the link between the observed bifurcations and the model parameters, particularly the stability parameter σ and the dissipation γ. Figure 9 shows the complex amplitude variation for increasing values of the effective stability parameter $\bar{\mu}$ containing the effect of mode 2 on mode 1, ($\bar{\mu} = \alpha\mu_0 - c_i^2$) where α is the parameter adjusted to study the dynamics (by simulating increasing mode 2 excitation). For

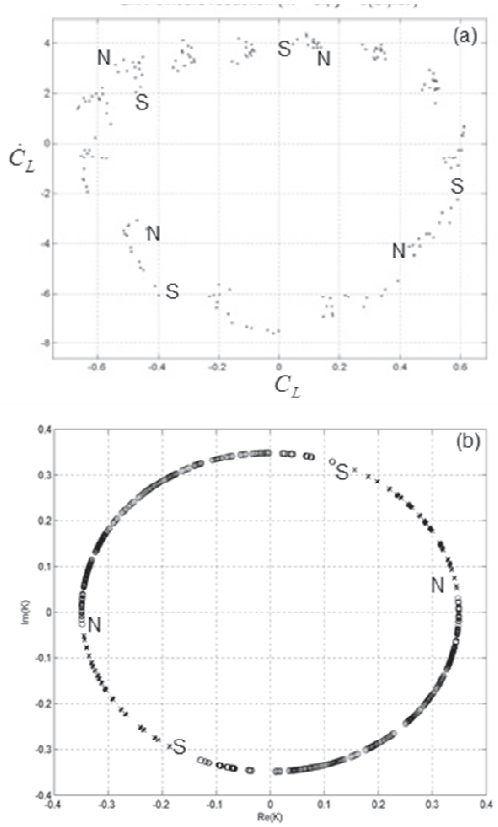

Figure 8. Low order model prediction relative to CFD simulations showing (a) computed and (b) predicted saddle-node bifurcation

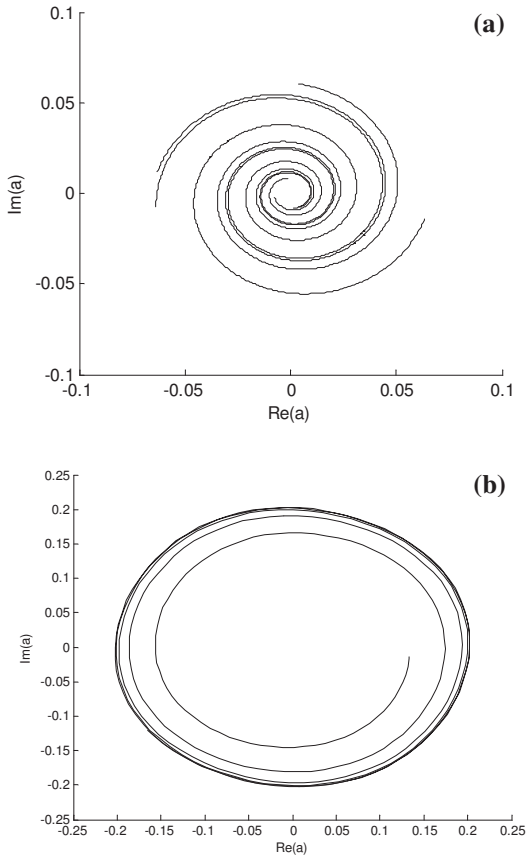

Figure 9. (a) stable fixed point and (b) limit cycle following a Hopf bifurcation

low $\bar{\mu}(\approx 0.017)$ the zero amplitude state is stable, (see Fig. 9(a)) corresponding to laminar flow with no vortex shedding; (to justify the validity of employing the POD modes in this state, we note the observation of Baranyi [11] showing the Karman mode, for instance, appears when the steady flow is perturbed below the vortex-shedding critical Reynolds number). As $\bar{\mu}$ is increased a Hopf bifurcation occurs resulting in limit cycle oscillations, Fig. 9(b). The limit cycle amplitude increase with $\bar{\mu}$ (Fig. 10(a)) while, more importantly, it deforms revealing four preferred points which become increasingly locally stable (at the same time limit cycle period becomes increasingly long, approaching infinity at the bifurcation point). For $\bar{\mu} \approx 0.078$, the limit cycle bifurcates into four saddle-node pairs as shown in Fig. 10(b). The latter figure shows the mode 1 amplitude evolution for different initial conditions. The four stable nodes are clearly identifiable by the convergence of orbits. The saddle points can be identified by observing the approach along the stable manifolds followed by sudden divergence at the saddle point. The results confirm the suspected saddle-nodes in the numerical computations of Mureithi et al. [1], Fig. 8(a).

5. CONCLUSIONS

The CGL equation has been employed to derive a reduced order model for the forced wake dynamics behind a circular cylinder. The model was found to predict the most important bifurcations including the Hopf bifurcation leading to vortex shedding and, more importantly, the saddle-node bifurcation of the Karman wake observed in CFD computations for *Re*=200.

The CGL based reduced order model provides a useful and simple tool for the study of the dynamics of the Karman wake which retains the key aspects of spatial-temporal energy propagation and dissipation effects. Most importantly the model provides an alternative confirmation of the validity of the symmetry-based reduced order models. The CGL model has the particularly important advantage that model coefficients can be related directly to physical quantities in the flow.

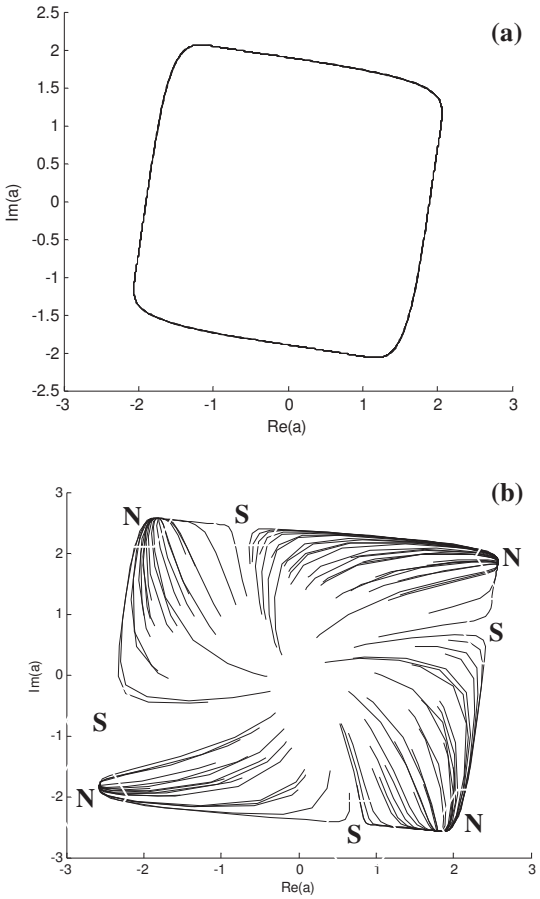

Figure 10. CGL low order model (a) limit cycle near bifurcation point ($\bar{\mu} \approx 0.055$) and (b) stationary states following a saddle-node bifurcation, $\bar{\mu} \approx 0.078$

ACKNOWLEDGEMENTS

The first author gratefully acknowledges the financial support of NSERC Canada.

The second author gratefully acknowledges the support of the Hungarian National Fund for Science and Research under Project No. OTKA K 76085. The work was carried out as part of the TÁMOP-4.2.1.B-10/2/KONV-2010-0001 project in the framework of the New Hungarian Development Plan. The realization of this project is supported by the European Union, co-financed by the European Social Fund.

REFERENCES

[1] Mureithi, N.W., Huynh, K., Rodriguez, M. and Pham, A., 2010, "A simple discrete model of the forced Karman wake", *International Journal of Mechanical Sciences*, Vol. 52, pp. 1522-1534.

[2] Rodriguez, M., 2006, "Simulation et analyse numérique de la trainée en aval d'un cylindre soumis à des oscillations forcées", *MSc. Thesis*, University of Montreal, Montreal Canada

[3] Mureithi, N.W., Kanki, H., Goda, S., Nakamura, T., and Kashikura, T., 2002, "Symmetry breaking and mode interaction in vortex-structure interaction", Paper IMECE 2002-32512, *ASME Int'l Mech. Engrg. Congress & Exhibition, New Orleans, Louisiana, USA.*

[4] Aranson, I.S., and Kramer, L., 2002, "The world of the complex Ginzburg-Landau equation", Review of Modern Physics, Vol. 74, pp. 99-143.

[5] Holmes, P., Lumley, J.L., and Berkooz, G., 1998, Turbulence, coherent structures, dynamical systems and symmetry, Cambridge University Press

[6] Crawford, J.D., and Knobloch, E., 1991, "Symmetry and symmetry-breaking bifurcations in fluid dynamics", *Annual Review* of Fluid Mechanics. Vol. 23, pp. 341-387.

[7] Ilak, M., Bagheri, S., Brandt, L., Rowley, C.W., and Henningson, D.S., 2010, "Model reduction of the nonlinear complex Ginzburg-Landau equation", SIAM Journal of Applied Dynamical Systems, Vol. 9, pp. 1284-1302.

[8] Golubitsky, M., Stewart, I. and Schaeffer, D.G., 1988, *Singularities and groups in bifurcation theory*, Vol. II, Springer, New York.

[9] Guckenheimer, J. and Holmes, P., 1987, Nonlinear oscillations, dynamical systems and bifurcations of vector fields, Springer-Verlag, New York.

[10] Mureithi, N.W., Rodriguez, M., Versailles, P., Pham, A., and Vo, H.D., 2008, "A POD based analysis of the 2D cylinder wake mode interactions", Proc. Flow Induced Vibration, Zolotarev & Horacek eds., Prague.

[11] Baranyi, L., 2009, "Triggering of vortex shedding by cylinder oscillation for Reynolds numbers under 47", Proc. ASME 2009 Pressure Vessels and Piping Conference, Symposium on Flow-Induced Vibration. Prague, on CD ROM, pp. 1-8, Paper No. PVP2009-77611.

Conference on Modelling Fluid Flow (CMFF'12)
The 15th International Conference on Fluid Flow Technologies
Budapest, Hungary, September 4-7, 2012

COMPUTATION OF AEROELASTICS OF FLEXIBLE BRIDGES BY THE DISCRETE VORTEX METHOD

Allan Larsen[1]

[1] Corresponding Author. Bridge Department 1702. COWI Consulting Engineers. Parallelvej 2, 2800 Kgs. Lyngby, Denmark,

ABSTRACT

The present paper outlines the basic equations and salient features of a two dimensional discrete vortex code developed with the objective of facilitating assessment of the aeroelastic performance of cable supported bridges. The flutter assessment can be performed in two modes, either by computing section flutter coefficients by means of the discrete vortex code and then combining these coefficients with structural properties in a classical flutter routine as is common place in aeronautics. Alternatively flutter instability can be assessed directly from flow simulations about the elastically suspended cross section a method which is also utilized for assessment of vortex shedding response. The application of the code in bridge design is illustrated through three examples of long span suspension bridges and results obtained are compared to scale model wind tunnel test results. Good correspondence is demonstrated.

2D flow simulation, discrete vortex method, aeroelasticity, flutter computation, vortex shedding response of flexible bridges.

NOMENCLATURE

$\overline{\overline{A}}$	[m^{-1}]	panel influence matrix
$A^*_{1..4}$	[-]	flutter coefficients, rotary DOF
a_s	[m/s^2]	body acceleration
B	[m]	body cord, deck width
$\overline{b}$	[m/s]	induced velocity vector
$C_{L,M}$	[-]	lift and moment coefficient
$\overline{e}$	[-]	unit vector
f	[Hz]	frequency
$H^*_{1..4}$	[-]	flutter coefficients, vertical DOF
h	[m]	vertical body displacement
i	[-]	complex unit
I	[kgm^2/m]	mass mom of inertia / unit length
K	[-]	non-dimensional frequency
k	[N/m]	structural stiffness
m	[kg/m]	mass / unit length
$\overline{n}$	[-]	body normal vector
p	[Pa]	pressure
s	[m]	distance along body perimeter
$\overline{s}$	[-]	body tangential vector
t	[s]	time
δt	[s]	time increment
$\overline{U}$	[m/s]	onset velocity vector
$\overline{u}$	[m/s]	perturbation velocity vector
$\overline{x}$	[m]	vector in plane
α	[rad]	body rotation
γ	[m/s]	sheet vorticity
ρ	[kg/m^3]	fluid density
ω	[m/s]	vorticity
ω	[s^{-1}]	circular frequency
ν	[m^2/s]	kinematic viscosity
Γ	[m^2/s]	vortex strength, circulation
Δ	[m]	distance
Ω	[rad/s]	angular body velocity
ζ	[-]	structural damping, rel-to-crit.
φ	[rad]	phase angle

Subscripts and Superscripts

B	body
F	fluid
L, M	lift, moment
0	reference point
p, q	point indices

1. INTRODUCTION

Flutter and vortex shedding excitation are very important factors for consideration during design of long span cable supported bridges. Traditionally assessment of the critical wind speed for onset of flutter for new long span bridge designs has been carried out by means of wind tunnel tests. Wind tunnel testing is costly and time consuming and thus often on the critical path of the design process. 15 years ago, the present author and co-workers started to consider the applicability of various numerical methods for computing aerodynamic response

considering practical bridge deck cross section shapes. In order to be of value in practical design situations the resulting aerodynamics code should fulfil the following requirements:

- Be applicable to external flows, i.e. satisfy the "free field" boundary condition at infinity.
- Be applicable to flows about two dimensional "bluff" sections as practical bridge girders are built from long lengths of identical cross sections shaped as sharp edged polygons.
- Allow flow for simulation of flow about moving boundaries as problems related to flutter stability and vortex shedding excitation involves cross sections in oscillatory motion.
- Allow easy modelling of cross sections and dynamic characteristics.

A survey of computational fluid dynamics techniques revealed that the two dimensional discrete vortex method pioneered by I.R. Lewis [1] in the field of turbo machinery, was likely to fulfil the above requirements.

2. THE VORTEX FORMULATION

2.1 Basic governing equations

The kinematics of an incompressible fluid having kinematic viscosity ν and density ρ flowing in a two dimensional domain $\boldsymbol{F}$ about a body $\boldsymbol{B}$ is governed by the Navier Stokes Equations:

$$\frac{\partial \bar{u}}{\partial t} + \left(\bar{u} \cdot \bar{\nabla}\right) \cdot \bar{u} = -\frac{1}{\rho} \bar{\nabla} p + \nu \bar{\nabla}^2 \bar{u} \quad \text{in } \boldsymbol{F} \tag{1}$$

$$\bar{\nabla} \cdot \bar{u} = 0 \qquad \text{in } \boldsymbol{F} \tag{2}$$

$$\bar{u} = \bar{u}_{\mathbf{B}} \qquad \text{on } \boldsymbol{F} \tag{3}$$

The dependent variables being the velocity vector $\bar{u}$ and pressure p. $\bar{u}_{\mathbf{B}}$ is the surface velocity on $\boldsymbol{B}$. (1) and (2) constitute the equations solved in traditional computational fluid dynamics codes. In a 2D formulation the number of unknowns is three corresponding to two velocity components and one pressure. The solution procedure taken here is to subdivide $\boldsymbol{F}$ in a computational mesh and then solve (1) and (2) in a finite difference or finite element formulation. In doing so it becomes necessary to design a computational mesh which is dense in the regions close to $\boldsymbol{B}$ where large velocity gradients are expected to develop (boundary layers and wakes) and less dense away from $\boldsymbol{B}$. The mesh generation process is often tedious and may have a direct influence on the accuracy of the results.

2.2 Vorticity formulation

Taking the curl of (1) recasts the 2D Navier-Stokes equations into a transport equation for vorticity, $\bar{\omega} = \omega \cdot \bar{e}$ which in 2D may be considered a scalar quantity ($\bar{e}$ is the unit vector normal to $\boldsymbol{F}$):

$$\frac{\partial \omega}{\partial t} + \left(\bar{u} \cdot \bar{\nabla}\right) \cdot \omega = \nu \bar{\nabla}^2 \omega \tag{4}$$

Which constitute a simplification (1). For solution equation (4) is split into an advection part (Euler equation) and a diffusion part (diffusion equation):

$$\frac{\partial \omega}{\partial t} + \left(\bar{u} \cdot \bar{\nabla}\right) \cdot \omega = 0 \tag{5}$$

$$\frac{\partial \omega}{\partial t} = \nu \bar{\nabla}^2 \omega \tag{6}$$

The velocity $\bar{u}$ is related to the vorticity ω by the Cauchy-Riemann equations: $\bar{\omega} = \bar{\nabla} \times \bar{u}$, $\bar{\nabla} \cdot \bar{u} = 0$ or the Biot-Savart relation:

$$u(\bar{x},t) = \bar{U} - \frac{1}{2\pi} \int_F \frac{\bar{\omega}_0 \times (\bar{x}_0 - \bar{x})}{\left|\bar{x}_0 - \bar{x}\right|^2} d\bar{x} + \frac{1}{2\pi} \oint_B \frac{(\bar{x}_0 \cdot \bar{n}) \cdot (\bar{x}_0 - \bar{x}) - (\bar{u}_0 \times \bar{n}) \times (\bar{x}_0 - \bar{x})}{\left|\bar{x}_0 - \bar{x}\right|^2} d\bar{x} \tag{7}$$

Where $\bar{U}$ is the irrotational onset flow velocity, $\left|\bar{x}_0 - \bar{x}\right|$ is the distance from a patch of vorticity $\bar{\omega} = \omega \cdot \bar{e}$ located at $\bar{x}_0$ to a field point $\bar{x}$. $\bar{n}$ is the unit vector normal to the boy surface $\boldsymbol{B}$.

The vorticity at the body surface is obtained via the Biot-Savart relation (7) in which the value of the integrals over $\boldsymbol{F}$ and $\boldsymbol{B}$ are known except for the contribution of the surface velocity. Introducing a surface vortex sheet γ defined by:

$$\frac{\partial \gamma}{\partial \bar{n}} = \omega \tag{8}$$

Allows the unknown surface vortex sheet γ to be defined by a Fredholm type integral equation:

$$\int_B \frac{\bar{\gamma}_0 \times (\bar{x}_0 - \bar{x}_B)}{\left|\bar{x}_0 - \bar{x}_B\right|} d\bar{x}_B = I(\bar{x}_B) + 2\pi(\bar{U} - \bar{u}(\bar{x}_B)) \tag{9}$$

Where $\left|\bar{x}_0 - \bar{x}_B\right|$ is the distance from a vortex patch $\bar{\gamma}_0$ situated at $\bar{x}_{0B}$ on $\boldsymbol{B}$ to another point $\bar{x}_B$ located on the contour $\boldsymbol{B}$. The vector $I(\bar{x}_B)$ represents the induced velocity from the vorticity in the fluid. The solution of (9) in the unknown surface vorticity distribution $\bar{\gamma}_0$ is unique up to a constant, i.e. an infinite number of solutions exist.

The solution is made unique by evoking the Kelvin circulation theorem which states that the rate of change of the total vorticity in both body ***B*** and fluid ***F*** is zero:

$$\frac{\partial}{\partial t}\int_{F+B}\omega dl(F+B)=0 \tag{10}$$

Thus if the total vorticity is zero at $t=0$ it remains zero for $t>0$.

3. DISCRETE VORTEX METHOD

The vorticity formulation of the flow equations is solved by taking a Lagrangian or particle approach progressing in time. The solution procedure follows 5 major actions in each time step:

1. Determination of the surface vortex sheet $\gamma(\bar{x}_B)$ on ***B*** to satisfy the non-penetration boundary condition.
2. Diffusion of vortex sheets by transformation of the vortex sheet into vortex "blobs" or particles of strength Γ_p and subsequently diffusing them into the flow by random walks.
3. Advection of discrete vortex particles allowing for mutual interaction.
4. Diffusion of vortex particles allowing for the effect of viscosity.
5. Computation of aerodynamic pressure and forces acting on ***B***.

3.1 Surface vortex distribution

The vortex distribution on ***B*** is obtained by subdividing the contour of ***B*** into *M* line segments assuming a spatial linear variation of $\bar{\gamma}_0$ along each segment or panel. Equation (9) is then approximated by a set of *M+1* linear equations:

$$\overline{\overline{A}}\cdot\bar{\gamma}=\bar{b} \tag{11}$$

Where the matrix $\overline{\overline{A}}$ contain the induced normal velocity at the *i*'th panel from the *j*'th panel, as well as the individual panel lengths.

The right hand side vector $\bar{b}$ contains the induced velocity at the *i*'th panel from the vortices in the flow and the total vorticity in the system. The latter is required to render the solution unique in accordance with Kelvin's theorem. The detailed structure of (11) is somewhat involved, but can be found in standard text books on potential flow panel methods, [2]. The system of linear equations is solved in the least squares sense.

The specific vortex distribution determined from (11) is then assigned to nascent vortices which are placed on ***B***. Nascent vortices are diffused into the flow applying a one-sided random walk method which satisfies (6). A Gaussian probability density function is applied:

$$p(w)=\frac{1}{\sqrt{\pi\nu\delta t}}\exp\left(\frac{-w^2}{4\nu\delta t}\right) \tag{12}$$

Where $w > 0$ and δt is the time step length. Once introduced in the flow, the individual vortex particles are assigned a radial symmetric Gaussian strength distribution:

$$\omega(\vec{x},t)=\sum_p^N\Gamma_p\frac{1}{2\pi\sigma^2}\exp\left(\frac{-((\bar{x}-\bar{x}_p(t))^2}{2\sigma^2}\right) \tag{13}$$

where σ is a vortex core radius, with *N* being the total number of particles in the flow.

3.2 Vortex advection and diffusion

The Lagrangian solution to (5) and (6) involves tracking of vortex particles $(\bar{x}_p,\Gamma_p)$ according to the following differential equations:

$$\frac{d\bar{x}_p}{dt}=\bar{u}(\bar{x}_p,t) \tag{14}$$

$$\frac{d\omega}{dt}=\nu\overline{\nabla}^2\omega \tag{15}$$

An equation for tracking vortex positions $\bar{x}$ in ***F*** is obtained by combining (5) and (14):

$$\frac{d\bar{x}_p}{dt}=\overline{U}-\sum_{q=1,p\neq q}^{N}\left(1-\exp\left(\frac{-\Delta_{pq}{}^2}{\sigma^2}\right)\right)\frac{\hat{\Delta}_{pq}\Gamma_p}{2\pi\Delta_{pq}{}^2} \tag{16}$$

Where $\Delta_{pq}=\left|\bar{x}_p-\bar{x}_q\right|$ is the distance between vortex particles *p* and q.

Equation (16) is solved numerically by ordinary differential equation methods. The diffusion equation (16) is again approximated by random walks to simulate the effect of viscosity. The combined solution to (15) and (16) using Euler integration is:

$$\bar{x}_p^{k+1}=\bar{x}_p^k+\bar{u}(\bar{x}_p^k)\delta t+\bar{\eta}_p \tag{17}$$

Where $\bar{x}_p^k$ is the position of the *p'*th vortex particle at the *k'*th time step and $\bar{\eta}_p$ is a random number with zero mean and variance $2\nu\delta t$.

3.3 Aerodynamic forces

The main objective of flow simulations in flutter investigations is to obtain time traces of the aerodynamic forces acting on the body ***B***. In case of bluff bodies the major contribution to the forces originates from the pressure distribution. Only an insignificant fraction may be ascribed to fluid shear stress along the body contour. By observing the no

slip boundary condition $\bar{u} = \bar{u}_B$, the Navier-Stokes equations reduce to:

$$\frac{1}{\rho}\frac{\partial p}{\partial \bar{s}} = -\nu\frac{\partial \omega}{\partial \bar{n}} - a_s \tag{18}$$

Where a_s is the tangential acceleration of the body boundary and $\bar{n}, \bar{s}$ are the unit normal and tangential vectors to ***B***. Neglecting now the stream wise at ***B*** the vorticity transport equation (4) now reads:

$$\frac{\partial \omega}{\partial t} = \nu\frac{\partial^2 \omega}{\partial \bar{n}^2} \tag{19}$$

Which, in combination with (8) yields:

$$\left(\frac{\partial \gamma}{\partial t}\right) = -\frac{\partial \gamma}{\partial t} - a_s \tag{20}$$

The flux of circulation of the *i*'th boundary panel of ***B*** is given by:

$$\left(\frac{\partial \gamma}{\partial t}\right)_i \approx \frac{\gamma_i^{k+1} - \gamma_i^k}{\delta t} \tag{21}$$

Equation (21) is thus integrated using the discrete circulation flux along the solid boundary:

$$\frac{1}{\rho}\oint_B \frac{\partial p}{\partial \bar{s}} = -\sum_i \frac{\gamma_i^{k+1} - \gamma_i^k}{\delta t}\Delta S_i - 2S\frac{\Omega^{k+1} - \Omega^k}{\delta t} \tag{22}$$

Where S is the body surface area and Ω^k is the body angular velocity at time step *k*.

4. NUMERICAL IMPLEMENTATION

Observation of (17) indicates that a naïve solution involves a large number of arithmetic unit operations per time step, proportional to the number of vortices squared S. This solution strategy have proven prohibitive for practical applications involving *N* = 30000 - 60000 vortices. This computational problem is overcome by adapting the fast multipole algorithm [3] which reduces the number of operations to roughly $O(N)$.

Also to limit the number of computational operations, vortices in the body wake are pooled when sufficiently downstream of the body, here $\bar{x}_p > 6$. Two vortices are pooled provided they satisfy the following relation:

$$\left|\frac{\Gamma_p\Gamma_q}{\Gamma_p + \Gamma_q}\left|\bar{x}_p - \bar{x}_q\right|^2\right| < \varepsilon \tag{23}$$

Where ε is a small number, $\varepsilon < 10^{-6}$ typically.

5. PRE AND POST PROCESSING

The input to discrete vortex simulations is a vortex panel model of a typical cross section of the bridge deck in a plane perpendicular to the bridge axis. Thus a number of polygons simulate the cross sections of the main girder and various deck furniture such as railings, crash barriers and wind screens. Typically the main girder cross section will be composed of approximately 200 - 400 line segments (panels) where as the smaller items each will be modelled from 20 - 50 panels. For flutter computations, the deck section may either be driven in prescribed crosswind or rotary oscillatory motion for computation of flutter coefficients or be assigned inertia and linear spring stiffness for simulation of flutter motion.

The output of the discrete vortex simulations is diction forces and flow induced displacements which must be analysed to identify the flutter condition.

5.1. Linear flutter analysis

Following aeronautic tradition, flutter of a bridge deck section is modelled as a 2DOF mass spring system subjected to motion dependent aerodynamic loads [4]:

$$m\left[\ddot{h} + 2\zeta\omega_h\dot{h} + \omega_h^2 h\right] = \tfrac{1}{2}\rho U^2(2B) \times\left[K^2 H_4^* \frac{h}{B} + KH_1^*\frac{\dot{h}}{U} + KH_2^*\frac{B\dot{\alpha}}{U} + K^2 H_3^*\alpha\right] \tag{24}$$

$$I\left[\ddot{\alpha} + 2\zeta\omega_\alpha\dot{\alpha} + \omega_h^2\alpha\right] = \tfrac{1}{2}\rho U^2(2B^2) \times\left[K^2 A_4^* \frac{h}{B} + KA_1^*\frac{\dot{h}}{U} + KH_2^*\frac{B\dot{\alpha}}{U} + K^2 A_3^*\alpha\right] \tag{25}$$

Knowing the structural properties of a bridge deck, i.e. mass *m,* mass moment of inertia *I,* natural frequencies in vertical and torsion motion ω_h, and ω_α and the structural damping ζ the task is to determine the flutter coefficients $H^*_{1..4}$ and $A^*_{1..4}$ which are functions of the reduced wind speed *U/fB* = $2\pi/K$. Once the flutter coefficients are known, equations (24) and (25) can be solved for the wind speed *U* assuming that at flutter, the deck section will oscillate at a common frequency in the vertical and rotational degree of freedom. The procedure is detailed in [4] for the eight coefficient formulation (24), (25).

Discrete vortex computations of aerodynamic lift and moment on a section forced in vertical and rotary motion at a number of non-dimensional wind speeds allows the flutter coefficients $H^*_{1..4}$ and $A^*_{1..4}$ to be determined as transfer functions between imposed motion and resulting lift and moment. In equations (26) - (29) C_L and C_M are the lift and moment coefficients, i.e. total cross wind lift force and total twisting moment about the section elastic

centre normalized by $\frac{1}{2}\rho U^2 B$ and $\frac{1}{2}\rho U^2 B^2$ respectively. h and α are the amplitudes of the imposed vertical (h) and rotary (α) motions and φ is the phase angle between the motion and force signals.

$$i \cdot H_1^* + H_4^* = \frac{C_L(\cos\varphi - i \cdot \sin\varphi)}{2(2\pi)^2 h/B}\left(\frac{U}{fB}\right)^2 \quad (26)$$

$$i \cdot H_2^* + H_3^* = \frac{C_L(\cos\varphi - i \cdot \sin\varphi)}{2(2\pi)^2 \alpha}\left(\frac{U}{fB}\right)^2 \quad (27)$$

$$i \cdot A_1^* + A_4^* = \frac{C_M(\cos\varphi - i \cdot \sin\varphi)}{2(2\pi)^2 h/B}\left(\frac{U}{fB}\right)^2 \quad (28)$$

$$i \cdot A_2^* + A_3^* = \frac{C_M(\cos\varphi - i \cdot \sin\varphi)}{2(2\pi)^2 \alpha}\left(\frac{U}{fB}\right)^2 \quad (29)$$

5.2. Non-linear flutter analysis

The flutter assessment following the above classical procedure is by nature linear and was originally developed in the field of aeronautics where flutter coefficients could calculated for thin airfoils using potential flow theory. Bridge deck sections are bluff with massive flow separation in comparison with air foil sections. It can thus not be expected that linear theory will yield the correct flutter speed even though the flutter coefficients accounts for the effects of flow separation in some average sense. An alternative approach to the linear analysis is to include the mass and elastic properties of the bridge in the discrete vortex simulation and successively turn up the flow speed until the cross section enters into 2DOF flutter motion, similarly to what is done in wind tunnel testing. The advantage of this process is that non-linearity's in the flow are included and their effect on the elastic response captured. A drawback is that individual simulation runs at different wind speeds are lengthy and it thus becomes quite time consuming to pinpoint the flutter speed as compared to the linear approach.

6. FLUTTER ANALYSIS OF BRIDGES

Following the outline of the discrete vortex method as developed for aerodynamic response analysis of bridges, examples of flutter analyses for 2 suspension bridges and one continuous beam bridge will be presented and compared to experimental results obtained from model scale wind tunnel tests.

6.1. Storebælt suspension bridge

The Storebælt suspension bridge in Denmark, figure 1, designed by the authors company was opened to traffic early June 1998 [5]. The girder of the suspended spans, which is of interest for flutter computations, is designed as a single trapezoidal steel box, 4.4 m deep and 31.0 m wide.

Figure 1. The Storebælt suspension bridge, Denmark. Main span 1624 m.

The shape of the girder and the layout of railings is apparent from figure 2, which shows the 1:80 scale section model used for flutter tests during design of the bridge.

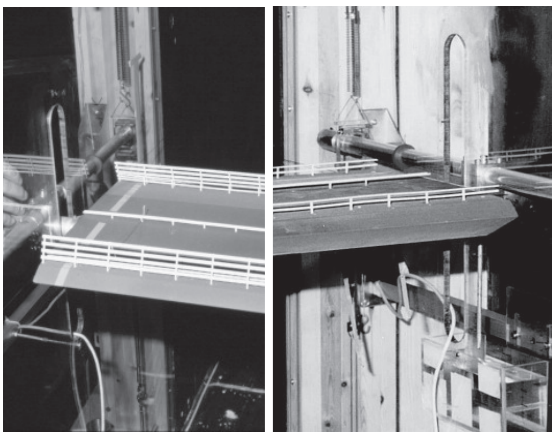

Figure 2. Section models used for flutter tests of the Storebælt Bridge. Left: With optional large wind screens, not installed. Right: As built

The structural properties of the bridge girder including the cables and flutter mode shapes identified from finite element calculations are summarized in Table 1.

Table 1. Dynamic properties of Storebælt Bridge

Vertical bending mode		Torsion mode	
			
m [kg/m]	f_h [Hz]	I [kgm]	f_α [Hz]
$22.74 \cdot 10^3$	0.10	$2.47 \cdot 10^6$	0.28

Panel models of the Storebælt bridge cross section simulating the current deck configuration is composed of 200 individual panels forming the basic trapezoidal deck shape. The optional deck configuration carrying 3.5 m high wind screens composed of longitudinal slats yielding 50% open area ratio was simulated by adding four small

rectangles with gaps in between at either side of the roadway, figure 3. Each of the rectangular cross sections of the windscreen slats are modelled by 25 individual panel elements.

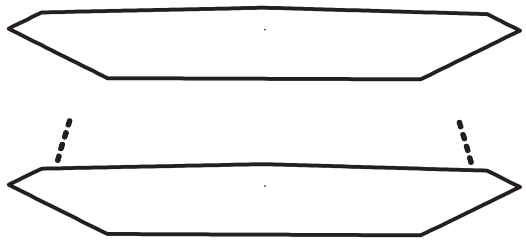

Figure 3. Panel models for flutter computations of the Storebælt bridge.

A first result compares flutter coefficients $H^*_{1..4}$ and $A^*_{1..4}$ as function of non-dimensional wind speed U/fB obtained from discrete vortex simulations to measured coefficients obtained from the section model shown in figure 2.

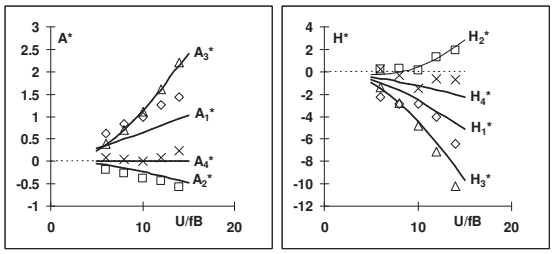

Figure 4. Flutter coefficients obtained from discrete vortex simulations (marker) and tests (line) for section A) without wind screens.

A fair comparison of simulated and measured flutter coefficients is demonstrated in figure 4, except for the H^*_4 and A^*_4 which have little influence on the resulting critical wind speed for obtained from solving equations (24), (25). The critical wind speed of the bridge is calculated as U_c = 77 m/s for the cross section without wind screens and U_c = 72 m/s for the section including wind screens which compares very favourably to U_c = 70 m/s - 75 m/s obtained directly from observing the onset of flutter for the elastically suspended section models.

The alternative approach to the linear flutter analysis based on calculated flutter coefficients, involves simulation of the flow about the elastically supported panel model at successively increasing wind speeds. In order to be representative of the prototype bridge, the panel model must be assigned identical non-dimensional rotary and translatory inertia $I/\rho B^4$, $m/\rho B^2$. The rotary and translatory spring constants k_α and k_h of the elastic supports are adjusted to reflect the non-dimensional wind speeds $U/f_\alpha B$ and $U/f_h B$ of the simulation:

$$k_\alpha = \left(2\pi \frac{f_\alpha B}{U}\right)^2 \frac{I}{\rho B^4} \quad k_h = \left(2\pi \frac{f_h B}{U}\right)^2 \frac{m}{\rho B^2} \quad (30)$$

For sake of illustration the elastically suspended simulations of the cross section with and without wind screens was run at a full scale wind speed of 80 m/s. As noted from the time series of torsion (α) and vertical (h) response displays a coupled divergent behaviour typical of 2DOF flutter.

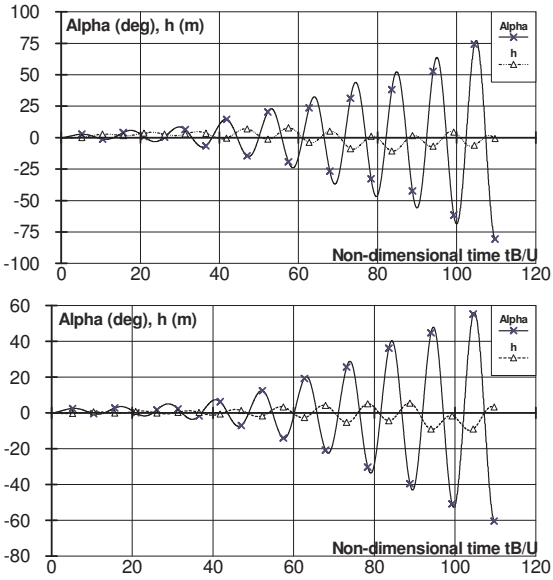

Figure 5. Simulated time histories of torsion and vertical response for the Storebælt cross section without (top) and with wind screens (bottom).

Observing the response diagram's it is of interest to note that the cross section without wind screens oscillates to higher angles of attack than the section including wind screens does. A behaviour attributed the higher aerodynamic damping caused by the presence of the wind screens.

6.2 Messina Strait suspension bridge

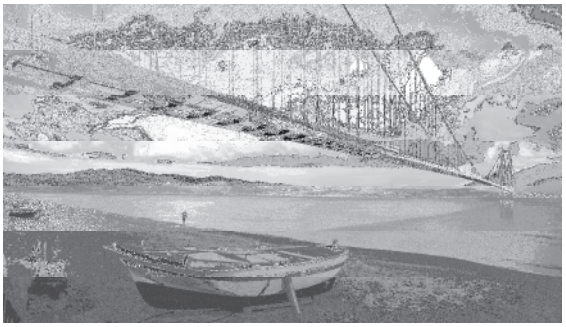

Figure 6. Artists impression of the Messina Straits Suspension bridge. Main span 3300 m.

The suspension bridge planned for crossing of the Messina Strait in Italy, figure 6 will, with a

main span of 3300 m, be the worlds longest suspension bridge when completed [6]. The authors company was involved in carrying out tender design for the successful contractor during the autumn of 2005 and Progette Definitivo design works in 2010. With the current political situation in Italy the future plans for building of the bridge are uncertain.

The railway is located on a central girder and the longitudinal girder assembly is interlocked by heavy cross beams yielding an over all width of 60 m. In addition to the split longitudinal girders, the deck is equipped with wind screens for shielding of the traffic which are fitted with longitudinal airfoils to further enhance the aerodynamic torsion damping. An impression of the complexity of the deck is obtained from the 1:80 scale section model built for tender design flutter testing, figure 7.

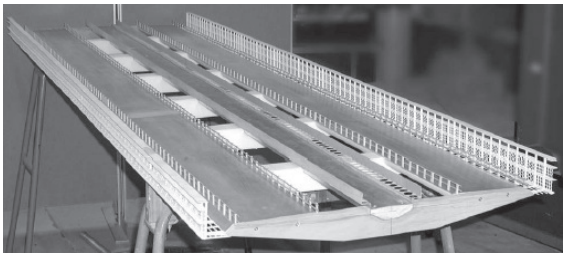

Figure 7. Wind tunnel section model of Messina Bridge deck showing the complex layout with split carriageways, wind screens and stabilizers.

The structural properties of the bridge girder including the cables and flutter mode shapes identified from finite element calculations are summarized in Table 2.

Table 2. Dynamic properties of Messina Bridge

Vertical bending mode		Torsion mode	
			
m [kg/m]	f_h [Hz]	I [kgm]	f_α [Hz]
$53.2 \cdot 10^3$	0.066	$26.5 \cdot 10^6$	0.084

The panel model of the Messina bridge cross section, figure 8, is composed of 25 individual members locked to move as an entity. Each of the individual girders are composed of 200 panels each, while the rectangles simulating the wind screens, crash barriers, the airfoils dampers and service lane grillage floors are each made up from 25 - 50 individual panels. Messina is by far the most complex bridge cross section investigated to date.

Figure 8. Panel model of Messina Tender Design cross section

The critical wind speed of the bridge deck calculated by the linear approach using the flutter coefficients $H^*_{1..4}$ and $A^*_{1..4}$ obtained from discrete vortex simulations yields a critical wind speed U_c = 83 m/s. The wind tunnel tests in comparison gave U_c = 81 m/s, indeed a close match. As a matter of interest, the authorities design requirement to the critical wind speed for onset of flutter is 75 m/s.

Similarly to the Storebælt bridge, elastically suspended simulations of the Messina cross section was run at a full scale wind speed of 85 m/s to check the linear results, figure 9. As noted from the time series of torsion (α) and vertical (h) response displays a coupled oscillatory motion. A distinct divergent behaviour as in figure 5 is not seen within the time interval simulated. However, the regular oscillatory time traces indicates that the cross section is on the verge of entering into 2DOF flutter.

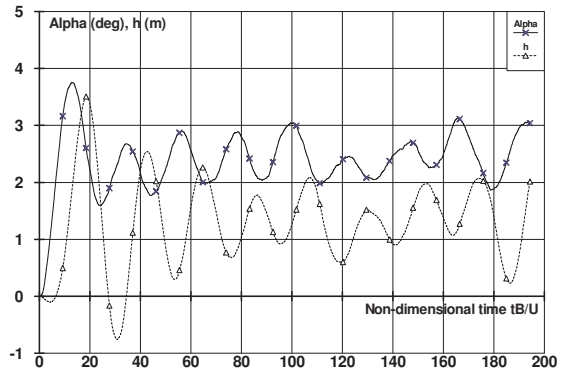

Figure 9. Simulated time histories of torsion and vertical response for the Messina cross section.

6.3 Volgograd multi span beam bridge

On 20 May 2010 the newly completed motorway bridge across the river Volga at Volgograd, Russia, figure 10, was observed to oscillate quite heavily. The authors company was invited to participate in a rush investigation into the course for the oscillations with a view to propose mitigating measures. The bridge oscillations were filmed by eye witnesses and put on YouTube. This allowed easy determination of frequency and amplitude, figure 11.

Figure 10. Volgograd bridge. A multi span continuous girder motorway bridge spanning 120 m - 150 m between piers.

Figure 11. YouTube video clip taken along the Volgograd bridge displaying vertical oscillations.

Consecutive frames from the YouTube video allowed estimation of the peak - peak amplitude as 0.8 m - 0.9 m and at a frequency of 0.43 Hz. Review of the eigenmode computations run during the design of the bridge revealed a first vertical bending frequency of 0.41 Hz at which the long centre spans were moving out of phase as shown in figure 11, i.e. a behaviour very similar to the observations. Reports of the wind conditions during the day yielded a wind direction perpendicular to the bridge line and a mean wind speed of 12 m/s. Based on the video clips vortex shedding excitation was speculated to be the cause of the oscillations which was confirmed by discrete vortex simulations.

First a simulation was run for a fixed cross section panel model yielding a strong oscillatory lift coefficient at a non-dimensional frequency fB/U = 0.23. Assuming that the vortex shedding action locks on the first vertical eigenfrequency of the bridge, yields a mean wind speed of 13 m/s in very good agreement with observations. Upon completion of the fixed simulations, the panel cross section model was loaded with the equivalent mass / unit length of the bridge m = 8.6 t/m and suspended by a vertical numerical spring which stiffness was adjusted to yield a natural frequency of 0.43 Hz of the assembly. A flow simulation running for approximately 115 periods of oscillation is shown in figure 12. Maximum amplitudes of approximately 0.45 m are noted.

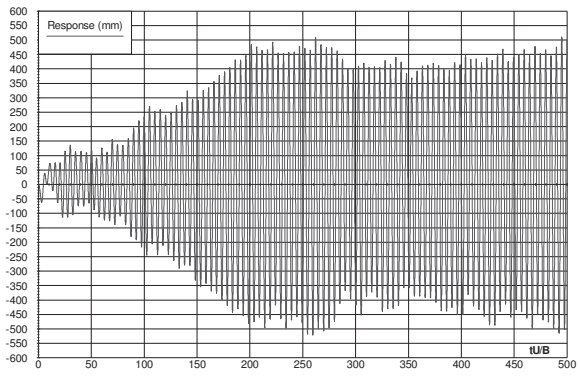

Figure 12. Discrete vortex simulation of the vertical oscillations of the Volgograd bridge.

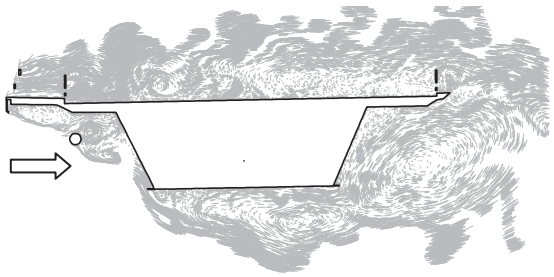

Figure 13. Large vortex structure (in grey) forming in the wake of the cross section panel model in close proximity of the girder surface.

The cause of the oscillations becomes clear when viewing a series of consecutive flow plots made as part of the simulation, figure 13. A large coherent vortex is formed in the wake of the cross section. This vortex is observed to be formed in the dead air region situated close to the inclined side panel and under the cantilevered roadway. When the vortex first forms, it spins counter-clockwise. When grown to fill the dead air region, it sheds and drifts downwind, leaving the dead air region open to be filled by a new growing vortex now spinning clock-wise. The vortex formation and shedding process is rhythmic. Large oscillatory motions of the girder results at the wind speed where the vortex formation and shedding frequency locks on to the bending frequency of the bridge girder. The same conclusion was reached by an independent investigation using grid based CFD techniques [7].

REFERENCES

[1] Lewis, R.I. 1991: *Vortex element methods for fluid dynamic analysis of engineering systems.* Cambridge University Press.

[2] Kuethe, A.M. and Chow, C., 1986: *Foundation of aerodynamics.* John Wiley and Sons.

[3] Carrier, J., Greengard, L. and Rokhlin, V. 1988: A fast adaptive algorithm for particle simulations. 669-686. *SIAM Journal of Scientific and Statistical Computation, 9*.

[4] Larsen, A. 1997: "Prediction of aeroelastic stability of suspension bridges during erection", (72) 265-274. *Journal of wind engineering and industrial aerodynamics*.

[5] Gimsing N.J. (Ed.) 1998: *East Bridge*. The Storebælt Publications, Storebæltsforbindelsen A/S, Copenhagen.

[6] Brancaleoni. F., Diana. G. et. al. 2010: *The Messina Strait Bridge*. A challenge and a dream. Stretto di Messina, CRC Press.

[7] Rutman, U.L., Meleshko, V.A. 2011: Cause of vibration of the Volgograd Bridge. *Structural Mechanics and Analysis of Structures, No. 3*. (In Russian).

Conference on Modelling Fluid Flow (CMFF'12)
The 15th International Conference on Fluid Flow Technologies
Budapest, Hungary, September 4-7, 2012

ANALYSIS OF THE LOCAL VERSUS NONLOCAL BEHAVIOUR OF THE MIXING OF HEAT IN THE CONVECTIVE ATMOSPHERIC BOUNDARY LAYER

Árpád BORDÁS[1], Tamás WEIDINGER[2]

[1] Corresponding Author. Department of Meteorology, Eötvös Loránd University. Pázmány Péter sétány 1/A, H-1117 Budapest, Hungary. E-mail: abordas@caesar.elte.hu
[2] Department of Meteorology, Eötvös Loránd University. Pázmány Péter sétány 1/A, H-1117 Budapest, Hungary. E-mail: weidi@caesar.elte.hu

ABSTRACT

Description of the atmospheric boundary layer (ABL) characteristics and modelling of turbulent mixing processes plays importnat role in atmospheric modelling. In the convective ABL buoyancy is the domminat mechanism driving the turbulence. Large range of turbulent eddyes, from small scale subgrid to large scale supergrid plums originating in the surface layer and rising up to the top of the boundary layer, are effective during convective conditions. The goal of our study is to analyse local versus nonlocal behaviour of the mixing of heat in the convective boundary layer, as well as to test the designed 1D (single-column) ABL model which simulates small and large scale heat mixing processes simultaneously. The model was tested in controlled offline numerical experiments and using field experiment databank (Wangara experiment).

Keywords: 1D model, atmospheric boundary layer, convective conditions, local and nonlocal turbulent mixing

NOMENCLATURE

F	$[Km/s]$	kinematic buoyancy flux
K	$[m^2/s]$	vertical eddy diffusivity
L	$[m]$	Monin-Obukhov length scale
M	$[1/s]$	mixing rate
R_c	[-]	ratio between local and nonlocal mixing processes
Ri_b	[-]	bulk Richardson number
T_0	$[K]$	average potential temperature in surface layer
$\underline{U}$	$[m/s]$	horizontal wind speed
a	[-]	semi empirical constant
b	[-]	semi empirical constant
g	$[m/s^2]$	acceleration due to gravity
h	$[m]$	height of the boundary layer
k	[-]	von Kármán constant
t	$[s]$	time
u_*	$[m/s]$	friction velocity
w_*	$[m/s]$	convective velocity scale
z	$[m]$	vertical coordinate
Φ	[-]	profile function
β	$[m/s^2K]$	stability parameter
γ_h	$[K/m]$	gradient adjustment term
θ	$[K]$	potential temperature

1. INTRODUCTION

Atmospheric boundary layer (ABL) is the lowest part of the atmosphere where the direct effect of the Earth's surface is noticeable. Formation of the ABL is a consequence of the interactions between the atmosphere and its underlaying surface. Atmospheric movements in the boundary layer are of great interest because of their essential impact upon nature, peple (almost all human activities take place in it) and economy. Understanding of turbulent mixing processes and description of the ABL properties are important for weather prediction, air pollution and environmental modelling.

Turbulent mixing can be generated mechanically by shears and convectively by buoyancy. Buoyantly generated boundary layers tend to be more uniformly mixed than ones driven mechanically, because anisotropy in convection favors vertical motions, while shear anisotropy favors horizontal motions. The mixed layer in the atmosphere dominated by buoyant turbulence generation is called a convective ABL.

1D (single-column) models are very useful tools in investigation of ABL characteristics. Using such models we can simulate turbulent mixing processes, illustrate basic characteristics of the layer and compare different parameterization procedures. When coupled to 3D models 1D models can

provide detailed and accurate simulations of the boundary layer structure and turbulent processes. Simulation of the convective ABL processes represents a significant source of uncertainty in modelling. Much of the difficulty stems from the large range of the turbulent scales that are effective in it. Both small scale and large scale turbulent eddies are importnat for the vertical transport in convective ABL.

Assuming that the turbulence is analogous to molecular diffusion different types of the local eddy diffusivity schemes simulate exclusively the small scale (subgrid) mixing processes. Neglecting local mixing the nonlocal mixing schemes [1, 2] describe turbulent processes as functions of large scale (suprgrid) gradients. Limitations of the both conceps are well known [3]. Combined (local and nonlocal) mixing schemes [4-6] were designed with the idea to bridge the local and nonlocal concepts simulating subgrid and supergrid mixing processes simultaneously.

The aim of our study is analyse the local to nonlocal behaviour of the turbulent mixing of heat in the convective ABL, as well as to represent and test the designed 1D boundary layer model. The model simulates mixing of heat during convective conditions as combined process. Mixing of heat during stabile conditions and mixing of momentum, independently on stability, is simulated as local process [7]. Model tests were done by controlled offline experiments and using Wangara Experiment [8] dataset.

2. THEORETICAL INTRODUCTORY

Transport of heat by large eddies plays important role in the vertical mixing of heat in convective ABL. Certain ABL models [7, 9, 10] include the nonlocal behaviour of the mixing of heat adding a gradient adjustment term (γ_h), to the eddy diffusion equation. The modified equation can be written in the following form:

$$\frac{\partial\theta}{\partial t}=\frac{\partial}{\partial z}\{w'\theta'\}=\frac{\partial}{\partial z}\left[-K_h\left(\frac{\partial\theta}{\partial z}-\gamma_h\right)\right], \qquad (1)$$

where θ is the potential temperature, $\{w'\theta'\}$ represents the kinematic heat flux and K_h denotes the vertical eddy diffusivity for heat. Following [5] the ratio between the local and nonlocal mixing processes in the convective ABL (R_c) can be defined as:

$$R_c=\frac{K_h\dfrac{\partial\theta}{\partial z}}{K_h\gamma_h}. \qquad (2)$$

The gradient adjustment term can be estimated in the form [11]:

$$\gamma_h=\frac{aw_*\{w'\theta'\}_0}{w_m^2 h}, \qquad (3)$$

where a is a semi empirical constant, w_* is the convective velocity scale, $w_m=u_*\Phi_m^{-1}$ (u_* represents the friction velocity and Φ_m denotes the profile function for momentum), as well as h is the height of the ABL. The gradient adjustment term vanishes under neutral conditions, for which $w_*=0$. Defining the convective velocity in the form [5]:

$$w_*=u_*k^{-\frac{1}{3}}\left(-\frac{h}{L}\right)^{\frac{1}{3}}, \qquad (4)$$

where k is the von Kármán constant (k = 0.4), L represents the Monin-Obukhov length scale, as well as approximating the surface heat flux as:

$$\{w'\theta'\}_0=-k\frac{u_*z_s}{\Phi_h}\frac{\partial\theta}{\partial z}, \qquad (5)$$

where $z_s=0.1h$ and Φ_h is the profile function for heat, we can estimate ratio between local and nonlocal mixing processes for heat (R_c) as:

$$R_c=\left[0.1ak^{\frac{2}{3}}\left(-\frac{h}{L}\right)^{\frac{1}{3}}\frac{\Phi_m^2}{\Phi_h}\right]^{-1}. \qquad (6)$$

The Monin-Obukhov length scale we estimate in the following form:

$$L=-\frac{u_*^3}{\beta k\{w'\theta'\}_0}, \qquad (7)$$

where β is the stability parameter ($\beta=g/T_0$, g represents the acceleration due to gravity and T_0 denotes the average potential temperature in the surface layer). Using Dyer's type profile functions for momentum and heat [12]:

$$\Phi_m=\left(1-16\frac{z}{L}\right)^{-\frac{1}{2}} \qquad (8)$$

and

$$\Phi_h=\left(1-16\frac{z}{L}\right)^{-\frac{1}{4}}, \qquad (9)$$

the ratio between local and nonlocal processes for heat in the convective ABL can be estimated as:

$$R_c = \left[0.1ak^{\frac{2}{3}} \left(-\frac{h}{L} \right)^{\frac{1}{3}} \right]^{-1} \cdot \quad (10)$$

Following [11] the value of the semi empirical constant (a) is set to 7.2. Figure 1 shows how the ratio between local and nonlocal processes (R_c) defined by Eq. (10) behaves as a function of h/L. Sensitivity analysis for Eq. (10) was done modifying the value of the semi empirical constant by ± 20%. Results of the analysis are shown in Figure 1, also.

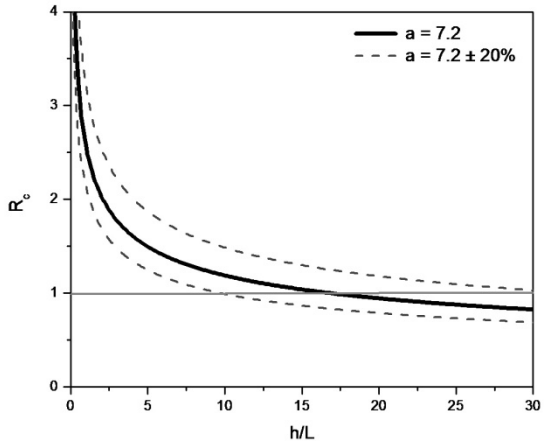

Figure 1. Ratio between local and nonlocal processes (R_c) as a function of stability

3. MODEL DESCRIPTION

Designed 1D model describes mixing of heat during convective conditions as a combined process employing mixing scheme [6]. Calculating ratio between local and nonlocal mixing of heat (R_c) for every time step the total mixing is split between subgrid and supergrid components. Mixing of heat during stable conditions and mixing of momentum, independently on conditions of stability, is simulated as local process. It still needs to be determined whether is it possible to neglect the nonlocal mixing of momentum in the convective boundary layer, while the nonlocal mixing of heat is applied. However, it is not yet clear how the inclusion of the nonlocal mixing of momentum can improve general properties of an ABL model such as growth of the boundary layer height (h) [10]. Including nonlocal mixing of momentum it is possible to correct inconsistency in description of turbulent mixing, as well as to predict more realistic wind profile in the convective ABL [13, 14]. In this study we will not analyse wind profiles.

Mixing scheme used for simulation of combined mixing processes [6] describes subgrid processes by standard eddy diffusivity scheme, and supergrid processes by Blackadar scheme [1]. The Blackadar scheme simulates effects of large scale eddies mixing material directly from the surface layer with every other model layer as it is shown in Figure 2. Combined vertical eddy diffusivity for heat (K_{ch}) and combined average mixing rate (M_c) we calculate as:

$$K_{ch} = \frac{R_c}{R_c + 1} K_h \quad (11)$$

and

$$M_c = \frac{1}{R_c + 1} M, \quad (12)$$

where M represents the standard average mixing rate.

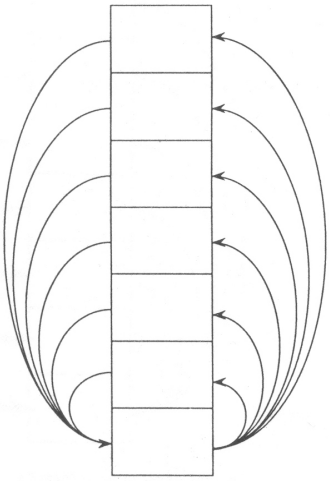

Figure 2. Schematic representation of the Blackadar scheme

Vertical eddy diffusivity for heat (K_h) and average mixing rate (M) can be defined using different parameterization methods. During model tests the vertical eddy diffusivity for heat, which depends of height, was estimated as [7]:

$$K_h(z) = k \frac{u_* z}{\Phi_h(z_s / L)} \left(1 - \frac{z}{h} \right)^2 \cdot \quad (13)$$

For unstable conditions z_s = min (z, 0.1h), for stable conditions $z_s = z$. The standard convective mixing rate was calculated as [5]:

$$M = \frac{F_1}{(h - z_1)(\theta_1 - \theta_2)}, \quad (14)$$

where F_1 represents the kinematic buoyancy flux at the top of the lowest model layer and z_1 is the height of the lowest model level. The buoyancy flux can be defined in the following form:

$$F_1 = K_{h1}\frac{\theta_1 - \theta_2}{\Delta z_1}, \qquad (15)$$

where Δz_1 represents the thickness of the lowest model layer. Combining Eqs. (14) and (15) yields convective mixing rate:

$$M = \frac{K_{h1}}{(h - z_1)\Delta z_1}. \qquad (16)$$

Height of the boundary layer (h), one of the fundamental parameters to characterize its structure, shows a strong diurnal development. The model determines it by specifying a critical value of the bulk Richardson number Ri_b defined by:

$$h = Ri_b \frac{|\underline{U}_h|^2}{\beta(\theta_h - \theta_1)}, \qquad (17)$$

where $\underline{U}_h$ is the horizontal wind speed, and θ_h is potential temperature, at $z = h$. For unstable conditions the boundary layer top predicted by Eq. (17) occurs just above the well mixed region. In this reason first the top of the convectively unstable layer z_{mix} is found as the height at which the potential temperature is equal to the near surface potential temperature θ_s calculated as [7]:

$$\theta_s = \theta_1 + b\frac{\{w'\theta'\}_0}{w_m}, \qquad (18)$$

where b is a semi empirical constant (b = 8.5 [9]). The bulk Richardson number is then defined for the entrainment layer above z_{mix} such that:

$$Ri_b = \beta(h - z_{mix})\frac{\theta_h - \theta_s}{(\underline{U}_h - \underline{U}_{mix})^2}, \qquad (19)$$

where $\underline{U}_{mix}$ is the wind speed at z_{mix}. The top of the ABL is diagnosed as the height where bulk Richardson number is equal to the critical Richardson number which value was set to 0.25.

4. MODEL TESTS

The 1D ABL model presented in the previous chapter was tested by controlled offline experiments and using Wangara Experiment [5] database. Wangara experiment was one of the first field experiments to define universal characteristics of the ABL. It was conducted in July and August 1967 near Hay (New South Wales, Australia). Pilot balloons were released hourly, radiosondes every 3 hours to provide temperature and humidity profiles.

Figure 3. shows the course of the potential temperature (θ) of the lowest model level, changing from 290 K to 300 K, during 12 h long period in controlled offline experiment. The initial vertical potential temperature profile as well as profiles obtained after 3rd and 6th hour of simulation are presented in Figure 4. Comparison of potential temperature profiles obtained by changing ratio between local and nonlocal processes (R_c), semilocal (R_c = 1) and local ($R_c \to \infty$) approach is shown in Figure 5. As it was expected profiles obtained by combined mixing concept are more realistic. Vertical model resolution in presented offline tests was 50 m.

Potential temperature profiles obtained after 6th hour of simulation by different vertical resolution (25 m, 50 m and 100 m) and the same time step are presented in Figure 6. Results show some dependence in the shape of the lowest part of the profile. Figure 7 shows the time evolution of the ABL height estimated by different vertical resolutions. There is no significant difference for different vertical model resolutions.

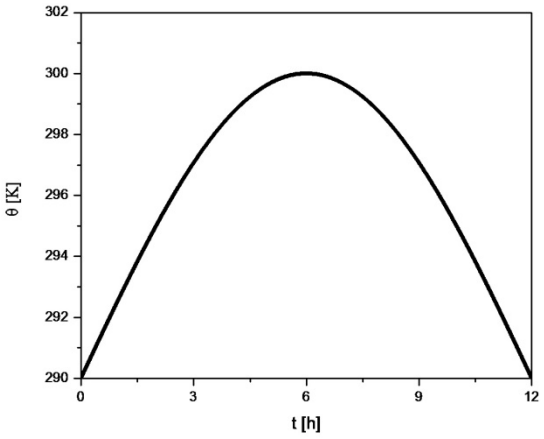

Figure 3. Course of the potential temperature (θ) of the lowest model level during controlled offline experiment

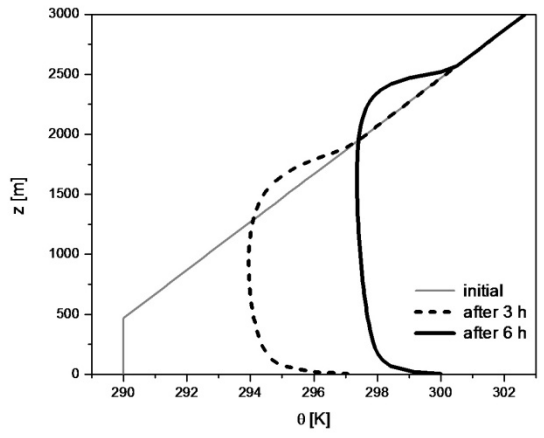

Figure 4. Potential temperature profiles obtained after 3rd and 6th hour of simulation

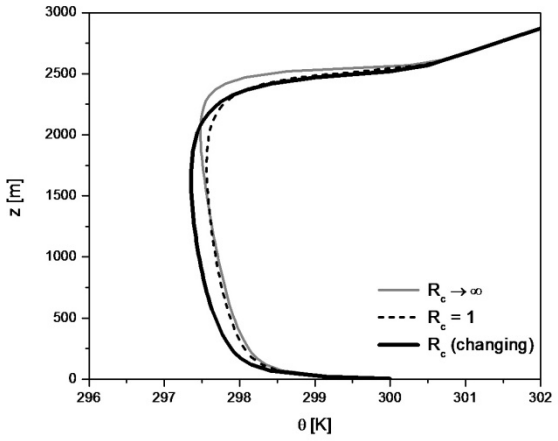

Figure 5. Comparison of potential temperature profiles obtained by different values of ratio between local and nonlocal processes (R_c) after 6th hour of simulation

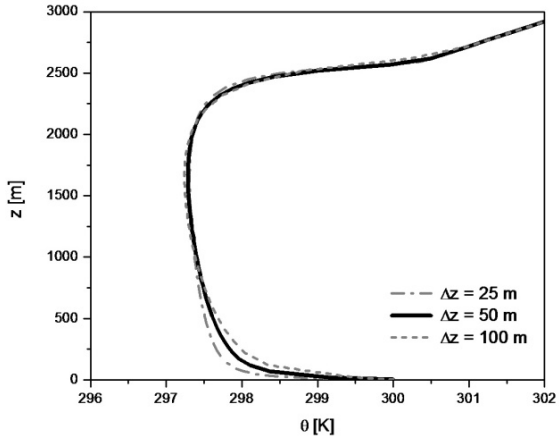

Figure 6. Comparison of potential temperature profiles obtained by different vertical resolution after 6th hour of simulation

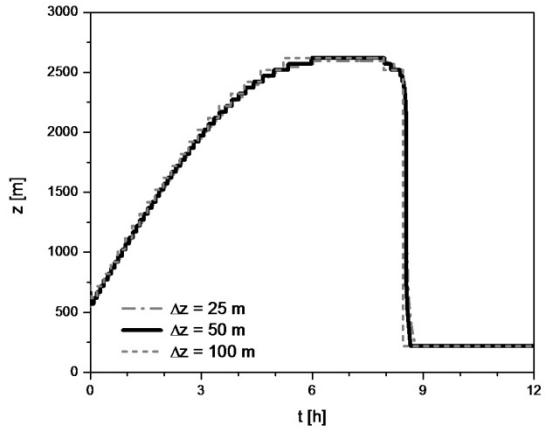

Figure 7. Variation of the ABL height estimated by different vertical resolutions

The model was tested using Wangara dataset (Day 33). Starting from measured potential temperature profile at 0900 LT (local time) model calculations were done by 50 *m* vertical resolution. Vertical resolution of the measured data is 50 *m* from the land surface to 1000 *m*, as well as 100 *m* from 1000 *m* to 2000 *m*. Potential temperature (θ) of the lowest model level was estimated by linear interpolation between measured data points as it is shown in Figure 8. Simulated and measured potential temperature profiles at 1200 LT and 1505 LT are presented in Figure 9 and Figure 10, respectively. Figure 11 compares computed and measured ABL heights. We conclude that the model calculations are in good agreement with measurements.

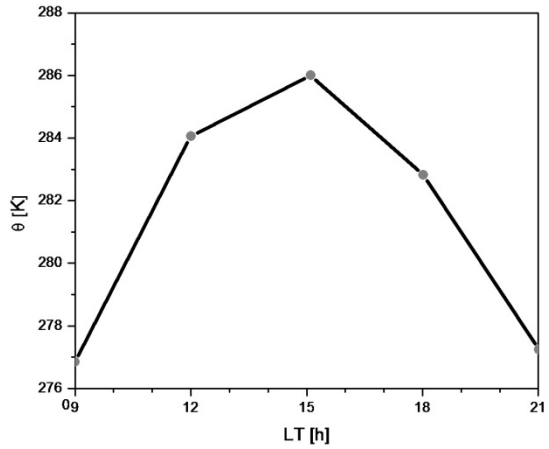

Figure 8. Variation of the potential temperature of the lowest model level from 0900 LT to 2100 LT

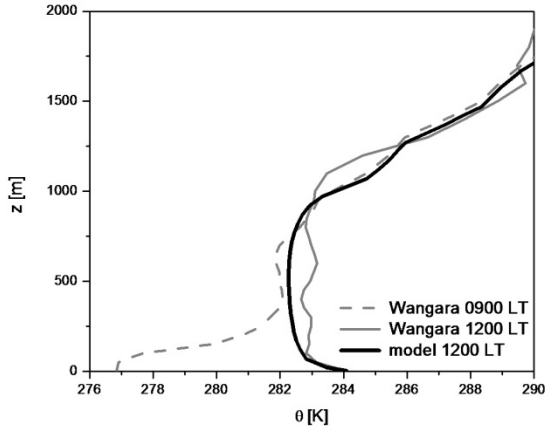

Figure 9. Calculated and measured potential temperature profiles at 1200 LT

5. SUMMARY

The ratio between local and nonlocal turbulent mixing of heat (R_c) during convective conditions was defined and the designed 1D model was presented. The model simulates mixing of heat

during convective conditions as a combined process. Calculating ratio between local and nonlocal processes in every time step the total mixing is split between subgrid and supergrid components. Mixing of heat during stable conditions and mixing of momentum, independently on conditions of stability, is described as local process. The model was tested by controlled offline experiments and using Wangara field measurement data. Model calculations are in good agreement with measurements.

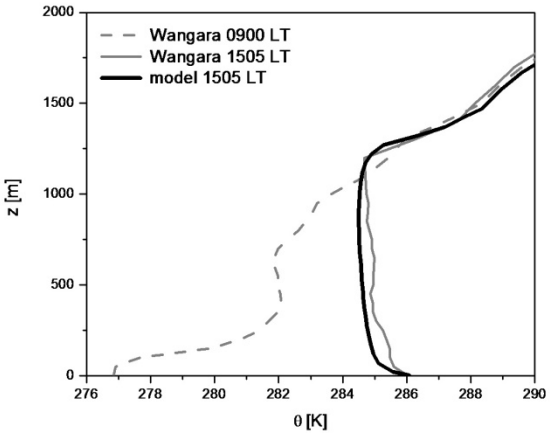

Figure 10. Calculated and measured potential temperature profiles at 1505 LT

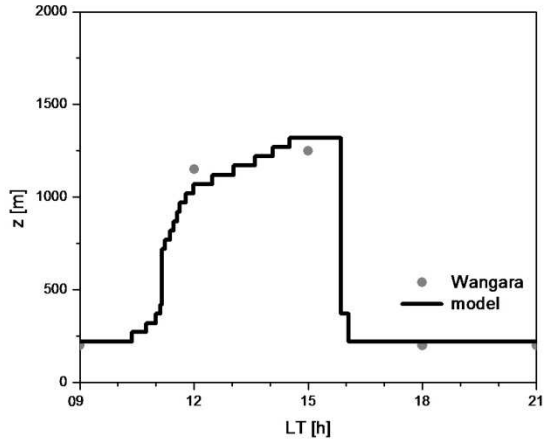

Figure 11. Variation of the ABL height from 0900 LT to 2100 LT

ACKNOWLEDGEMENTS

The authors thank the European Union and the European Social Fund for the financial support (grant agreement no. TÁMOP-4.2.1/B-09/1/KMR) during the preparation of the paper.

REFERENCES

[1] Blackadar, A. K., 1978, "Modeling Pollutant Transfer During Daytime Convection", Proc. *4th Symposion on Atmospheric Turbulence, Diffusion and Air Quality*, Reno, NV, USA, pp. 443–447.

[2] Zhang, D., and Anthes, R. A., 1982, "A High-Resolution Model of the Planetary Boundary Layer – Sensitivity Tests and Comparison with SESAME-79 Data", *J Appl Meteor*, Vol. 21, pp. 1594-1609.

[3] Stull, R. B., 1988, *An Introduction to Boundary Layer Meteorology*, Kluwer Academic Publishers

[4] Stull, R. B., 1984, "Transilient Turbulence Theory. Part I: The Concept of Eddy-Mixing Across Finite Distances", *J Atmos Sci*, Vol. 41, pp. 3351-3367.

[5] Pleim, J., 2007, "A Combined Local and Nonlocal Closure Model for the Atmospheric Boundary Layer. Part I: Model Decription and Testing", *J Appl Metorol and Climat*, Vol. 46, pp. 1383-1395.

[6] Bordás, Á., 2008, "One-column Vertical Turbulent Mixing Model for the Atmospheric Convective Layer", *Phys Scr*, Vol. T 132, 014032 (pp.5.)

[7] Troen, I. B., and Mahrt, L., 1986, "A Simple Model of the Atmospheric Boundary Layer; Sensitivity to Surface Evaporation", *Bound-Layer Meteor*, Vol. 37, pp. 129-148.

[8] Hess, G. D., Hicks, B. B., and Tamada, T., 1981, "The Impact of the Wangara Experiment", *Bound-Layer Meteor*, Vol. 20, pp. 135-174.

[9] Holtslag, A. A. M., and Boville, B. A., 1993, "Local versus Nonlocal Boundary-Layer diffusion in a Global Climate Model", *J Climate*, Vol. 6, pp. 1825-1842.

[10] Noh, Y., Cheon, W. G., Hong, S. Y., and Raasch, S., 2003, "Improvement of the K-profile Model for the Planetary Boundary Layer Based on Large Eddy Simulation Data", *Bound-Layer Meteor*, Vol. 107, pp. 401-427.

[11] Holtslag, A. A. M., De Bruin, E. I. F., and Pan, H.-L., 1990, "A High Resolution Air Mass Transformation Model for Short-Range Weather Forecasting", *Mon Wea Rev*, Vol 118, pp. 1561-1575.

[12] Dyer, A. J., 1974, "A Review of Flux-profile Relationships", *Bound-Layer Meteor*, Vol. 7, pp. 363-372.

[13] Frech, M., and Marth, L., 1995, "A Two-Scale Mixing Formulation for the Atmospheric Boundary layer", *Bound-Layer Meteor*, Vol. 73, pp. 91-104.

[14] Brown, A. R., and Grant, A. L. M., 1997, "Non-Local Mixing of Momentum in the Convective Boundary Layer a Review of Flux-profile Relationships", *Bound-Layer Meteor*, Vol. 84, pp. 1-22.

Addenda
Invited Lectures

Conference on Modelling Fluid Flow (CMFF'12)
The 15th International Conference on Fluid Flow Technologies
Budapest, Hungary, September 4-7, 2012

OPEN ROTOR AEROACOUSTIC MODELLING

Edmane Envia[1]

[1] Corresponding Author. Acoustics Branch, NASA Glenn Research Center. M.S. 54-3, 21000 Brookpark Road, Cleveland, Ohio 44135, U.S.A. Tel.: +1 216 433 8956, Fax: +1 216 433 3918, E-mail: edmane.envia-1@nasa.gov

ABSTRACT

Owing to their inherent fuel efficiency, there is renewed interest in developing open rotor propulsion systems that are both efficient and quiet. The major contributor to the overall noise of an open rotor system is the propulsor noise, which is produced as a result of the interaction of the airstream with the counter-rotating blades. As such, robust aeroacoustic prediction methods are an essential ingredient in any approach to designing low-noise open rotor systems. To that end, an effort has been underway at NASA to assess current open rotor noise prediction tools and develop new capabilities. Under this effort, high-fidelity aerodynamic simulations of a benchmark open rotor blade set were carried out and used to make noise predictions via existing NASA open rotor noise prediction codes. The results have been compared with the aerodynamic and acoustic data that were acquired for this benchmark open rotor blade set. The emphasis of this paper is on providing a summary of recent results from a NASA Glenn effort to validate an in-house open noise prediction code called LINPROP which is based on a high-blade-count asymptotic approximation to the Ffowcs-Williams Hawkings Equation. The results suggest that while predicting the absolute levels may be difficult, the noise trends are reasonably well predicted by this approach.

Keywords: asymptotics, CFD, FW-H, open rotor

NOMENCLATURE

Ai, Ai'	[-]	Airy function and its derivative
B	[-]	rotor blade count
c_0	[m/s]	ambient speed of sound
e_j	[-]	unit vector component in the radiation direction
f_j	[N/m^2]	blade force per unit area
G	[$1/m\text{-}s$]	free-space, moving-medium Green's function
g_c	[-]	convective phase factor
M_{0_R}	[-]	medium Mach number in the radiation direction
M_{tip}	[-]	rotor tip rotational Mach number
N	[rev/s]	rotational speed
n_j	[-]	surface unit normal vector
$p'(\underline{x},t)$	[Pa]	acoustic pressure
$p'(\underline{x})$	[Pa]	Fourier harmonic component of acoustic pressure
p	[Pa]	blade surface pressure
$\mathcal{Q}$	[Pa]	acoustic source amplitude
R	[m]	distance between source and observer
S	[m^2]	rotor blade surface
S_B	[m^2]	reference blade surface
T_{jk}	[N/m]	Lighthill stress tensor
t	[s]	observer time
U_{0_j}	[m/s]	medium velocity components
V	[m^3]	volume exterior to the rotor blades
v_n	[m/s]	normal component of blade surface velocity
$\underline{x}$, x_j	[m]	observer Cartesian coordinates
$\underline{y}$, y_j	[m]	source Cartesian coordinates
δ	[-]	Dirac delta function
κ	[-]	convective amplitude factor
ρ_0	[kg/m^3]	ambient air density
τ	[s]	source (i.e., retarded) time
Φ	[rad]	rotor phase function
φ, φ_s	[rad]	observer and source azimuthal angle coordinates
Ψ	[rad]	convective phase factor
Ω	[rad/s]	rotor angular speed

Subscripts

1, 2	front and aft rotor indices
j	principal coordinate directions
s	typical source point
$\mathcal{T}$	thickness noise designator
$\mathcal{L}$	loading noise designator

1. INTRODUCTION

Open rotors are inherently more fuel-efficient than fans due to their very high propulsive efficiency. With the rising fuel cost and the increasing restrictions on carbon emissions (CO_2 emissions are directly related to fuel burn) there is renewed interest in developing open rotor systems for commercial aviation applications.

The fuel burn advantage of open rotor propulsion systems was convincingly demonstrated in the past (for example, in the late 1980s and early 1990s as part of a NASA effort called the Advanced Turboprop Project [1]). A model scale open rotor developed by NASA and General Electric (GE) under that project and the subsequent engine demonstrator developed by GE, called the unducted fan (UDF), are shown in Figure 1. At that time, some of the fuel burn margin of UDF was traded off in order to meet the noise regulations of the time. Today, with the advent of high-fidelity, three-dimensional aerodynamic simulation tools it has become possible to design open rotor systems that can meet the current noise regulations (which are more stringent than the 1990s rules) without giving up any of their fuel burn advantage.

As a result, both the United States and Europe have been pursuing the development of the next generation open rotor propulsion systems. In particular, in the U.S., a joint effort between NASA and GE Aviation was initiated to investigate the aerodynamic and acoustic performance of modern blade designs. An important element of this effort has been the assessment of existing tools for predicting the aerodynamic and acoustic performance of open rotors. For that purpose a baseline, vintage 1990s, blade design called the historical blade set (also known as F31/A31) was selected for evaluating various prediction tools. F31/A31 has 12 front rotor blades and 10 aft rotor blades. Comprehensive aerodynamic, flowfield, and acoustic data sets were acquired in the NASA wind tunnels for a ~0.65*m* diameter sub-scale model of this blade set. The test campaign included both low speed testing in the NASA 9-foot x 15-foot (i.e., 2.7*m* x 4.6*m*) wind tunnel to investigate the aero/acoustic performance at operating conditions in the approach to take-off range as well as high speed testing in the NASA 8-foot x 6-foot (i.e., 2.4*m* x 1.8*m*) wind tunnel to analyse the aerodynamic performance in the speed range between climb and cruise conditions [2]. Data was acquired in an un-installed configuration, as well as at angles of attack and with a generic pylon for some conditions. In all, a sizable matrix of rotor blade setting angles, tip speed, and tunnel Mach number combinations were investigated. In this paper, the focus is on a small subset of the un-installed (zero angle of attack) configurations that were run in the low speed regime at one set of blade angles, and one tunnel Mach number. The testbed F31/A31 open rotor is shown installed in the NASA 9-foot x 15-foot wind tunnel in Figure 2.

Figure 1. Top: GE/NASA Unducted Fan (UDF) model installed in NASA wind tunnel (1985). Bottom: GE UDF engine demonstrator installed on the MD-80 testbed aircraft (1987). UDF had equal blade counts, eight each on the front and aft rotors.

Figure 2. Model scale F31/A31 historical baseline blade set shown installed in the NASA 9-foot x 15-foot wind tunnel (2010). The front rotor of F31/A31 has 12 blades and its aft rotor has 10 blades. Traversing inflow microphone system used for sideline acoustic pressure measurements is visible on the left.

2. AEROACOUSTIC MODELLING

The methodologies for predicting open rotor noise can be categorized into three main groups. The most basic approaches are empirical in nature which, as the name suggests, are based on curve fits to database(s) of measured noise as a function of the geometry and operating parameters of open rotors. Once developed these are relatively easy to use and are often employed for trend studies in the early phases of the design process. Their shortcoming, however, is that they cannot be reliably used to predict noise for configurations or operating conditions that are well outside of the envelope of the databases used for developing the models in the first place.

On the opposite end of the spectrum are the high-fidelity numerical approaches that can be used to solve for the unsteady flowfield of the open rotor and include, as part of the solution, the noise field of interest. These types of methods typically require sizable computational resources due to the huge differences in the flow scales involved. For example, whereas the background flow pressure levels may be at the ambient atmospheric level, the acoustic perturbation levels of interest are easily three to four orders of magnitude smaller. This disparity necessities highly resolved grids nearly everywhere in the domain of interest thus driving up the computer memory and computational time requirements.

It is in the middle ground between these two extremes where most of the current state of practice resides. Typically, the issue of scale disparity is circumvented by linearizing the equations of motion thus separating the nonlinear aerodynamic field from the linear acoustic field. In the linearized methods, the nonlinear aerodynamic field is specified, measured, or computed *a priori* and is introduced as source terms in the linearized equations governing the acoustics. Computational fluid dynamics (CFD) is most often used for that purpose. Once this input information is specified, the acoustic equations can be solved to estimate the acoustic field. The solution could be affected by solving the linearized equations numerically, but most often the solution is obtained using the Lighthill's acoustic analogy approach whose extension to the moving surfaces is the Ffowcs-Williams Hawkings (FW-H) equation. This equation describes the acoustic field as temporal and spatial integrals over aerodynamic source regions of interest (e.g., rotor blades and the surrounding flowfield). The approach used in this paper for predicting open rotor noise is based on an asymptotic approximation to the FW-H equation with the necessary aerodynamic input obtained via a commercial CFD code.

2.1. Acoustic Modelling

The FW-H equation, see Eq. (1a), is an exact formal solution of the general equations of motion accounting for all of the underlying physics. It expresses the sound field $p'(\underline{x},t)$ as integrals of the aerodynamic source distributions. These source distributions are traditionally called the thickness, loading, and quadrupole sources, corresponding to the three terms on the right hand side of Eq. (1a), respectively. v_n is the normal velocity of the blade, $f_j d\,S$ is the blade force, and T_{jk} (the Lighthill stress tensor) represents the fluctuating stresses in the flowfield surrounding the rotor blades. Here only the inviscid parts of f_j and T_{jk} are implied, since viscosity does not significantly contribute to the open rotor noise field. In fact, we shall neglect the contribution of the quadruple source entirely since the focus of this paper is on the low speed operating conditions for which the quadrupole source does not significantly contribute to the noise field.

$$
\begin{aligned}
p'(\underline{x},t) = &-\int_{-\infty}^{\infty}\int_{S(\tau)} \rho_0 v_n(\tau)\frac{D_0 G}{D\tau} dS(\underline{y})\,d\tau + \\
&\int_{-\infty}^{\infty}\int_{S(\tau)} f_j(\tau)\frac{\partial G}{\partial y_j} dS(\underline{y})\,d\tau + \\
&\int_{-\infty}^{\infty}\int_{V(\tau)} T_{jk}(\tau)\frac{\partial^2 G}{\partial y_j \partial y_k} d\underline{y}\,d\tau
\end{aligned}
\qquad (1a)
$$

$$
\frac{D_0}{D\tau} = \frac{\partial}{\partial \tau} + U_{0_j}\frac{\partial}{\partial y_j}
$$

In this equation, G is the free-space, moving-medium Green's function given by

$$
\begin{aligned}
&G(\tau) = \frac{1}{4\pi\kappa R}\delta\left(t-\tau-g_c R/c_0\right) \\
&g_c(\tau) = \frac{1}{\beta_0^2}\left(\kappa - M_{0_R}\right) \\
&\kappa(\tau) = \sqrt{{M_{0_R}}^2+\beta_0^2}, \quad M_{0_R}(\tau) = M_{0_j} e_j \\
&e_j(\tau) = \frac{\left(x_j - y_j\right)}{R}, \quad R(\tau) = \left|\underline{x} - \underline{y}(\tau)\right| \\
&\beta_0 = \sqrt{1-M_{0_j}^2}, \quad M_{0_j} = \frac{U_{0_j}}{c_0}
\end{aligned}
\qquad (1b)
$$

where g_c and κ are factors that embody the effects of medium convection on the propagation time $g_c R/c_0$ and spherical spreading rate $1/R$. Where

applicable, the explicit dependence of various variables on the source time τ is indicated. Assuming that the geometry of the rotor blades, their loading distributions, and the surrounding flow field are known, the integrals in Eq. (1a) can be explicitly integrated to provide an estimate of the sound field generated by the open rotor.

While in principal, Eq. (1a) can be computed explicitly by carrying out the indicated spatial and temporal integrals using appropriate quadrature schemes, e.g., see Farassat [3] and Brentner [4], most often this equation is tackled in the frequency domain and by assuming that the observer is in the farfield. This assumption results in considerable simplification of the integrands in Eq. (1a) leading to semi-analytic formulas. See, for example, the models due to Hanson [5] and Parry [6]. The strategy used in this paper for carrying out the integrals in Eq. (1a), while frequency-domain based, does not require such simplification and the resulting formulas are valid for any observer (in the nearfield or in the farfield).

Specifically, the formulas used in this paper are extensions of the single rotation ones developed in [7] to account for the counter rotation configuration. The main difference between the single and counter rotation versions is the treatment of the loading noise. Another feature of the extended theory is that, owing to the linearity of the sound field, the analysis is carried out for each rotor separately and the resulting sound fields superimposed at the end. The derivation of the working expressions will closely follow that described in Reference 7 and will use essentially the same notation. The details of the derivation are included in the Appendix A and only final formulas are given here.

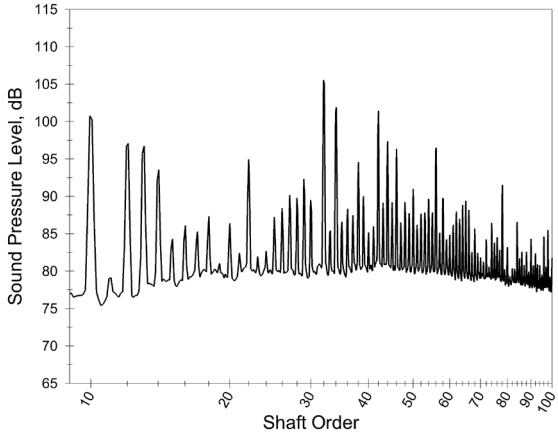

Figure 3. Sound pressure level (SPL) of the model scale F31/A31 blade set 1.524 *m* away and 90^o from the open rotor axis. The SPL is plotted versus the multiples of the open rotor shaft frequency (i.e., shaft orders). The shaft frequency is 107.3 Hz for this case.

Owing to the dominance of the open rotor spectra by tone noise (see Figure 3), in this study the modelling is focused on the tonal component of the noise spectrum. Let the blade counts and rotational speeds of the two rotors be denoted, respectively, by $B_1 \,\&\, B_2$ and $N_1 \,\&\, N_2$, where the subscript "1" refers to the front rotor. It should be noted that the open rotor blade counts or the rotational speeds of the two rotors need not (and frequently are not) equal. The tonal acoustic field of the front rotor is given by the following formula

$$4\pi p'(\underline{x},t) = \sum_{m=-\infty}^{\infty} p'_{T_m}(\underline{x}) e^{-imB_1\Omega_1 t} + \sum_{m=-\infty}^{\infty}\sum_{k=-\infty}^{\infty} p'_{L_{m,k}}(\underline{x}) e^{-i(mB_1\Omega_1 + kB_2\Omega_2)t} \tag{2a}$$

where p'_{T_m} is the thickness noise harmonic amplitude given by the expression

$$p'_{T_m}(\underline{x}) \simeq iB_1 \sum_{n=1}^{2} \int_{S_{B_1}} e^{mB_1(\mu_T - i\Psi_T)} \times \left\{ d_{0,n} \frac{Ai\left[(mB_1)^{2/3}\gamma_T^2\right]}{(mB_1)^{1/3}} + d_{1,n} \frac{Ai'\left[(mB_1)^{2/3}\gamma_T^2\right]}{(mB_1)^{2/3}} \right\} ds \tag{2b}$$

$$\Psi_T = \frac{1}{\beta_{0_1}} M_{\mathrm{tip}_1} M_{0_1} \chi_s + \varphi_s - \varphi$$

with $\Omega_1 = 2\pi N_1$ denoting the angular frequency of the front rotor and $M_{\mathrm{tip}_1} = \Omega_1 R_{\mathrm{tip}_1} / c_0$ its tip rotational Mach number. γ_T and μ_T are defined by Eq. (A.11) in the appendix. The Airy function Ai and its derivative Ai' give an accurate asymptotic approximation to the integral over τ appearing in the Eq. (1a). That integral represents the radiation efficiency of a source point over one period of its revolution about the axis of the rotor. Thus, the expression inside the curly bracket provides a closed form formula for the radiation efficiency of a given source point. Note that, Eq. (2a) indicates that thickness noise is produced at the harmonics of the front rotor blade passing frequency $B_1\Omega_1$. The larger the parameter mB_1 is, the more accurate this approximation becomes.

Similarly, the loading noise harmonic amplitude $p'_{\mathcal{L}_{m,k}}$ is given by

$$p'_{\mathcal{L}_m}(\underline{x}) \simeq iB_1 \sum_{n=1}^{2} \int_{S_{B_1}} e^{(mB_1 - kB_2)(\mu_{\mathcal{L}} - i\Psi_{\mathcal{L}})} \times \left\{ d_{0,n} \frac{Ai\left[(mB_1 - kB_2)^{2/3} \gamma_{\mathcal{L}}^2\right]}{(mB_1 - kB_2)^{1/3}} + d_{1,n} \frac{Ai'\left[(mB_1 - kB_2)^{2/3} \gamma_{\mathcal{L}}^2\right]}{(mB_1 - kB_2)^{2/3}} \right\} \quad (2c)$$

$$\Psi_{\mathcal{L}} = \frac{1}{\beta_{0_1}} \eta_{\mathrm{CRF}} M_{\mathrm{tip}_1} M_{0_1} \chi_s + \varphi_s - \varphi$$

$$\eta_{\mathrm{CRF}} = \frac{mB_1 + kB_2 \Omega_2 / \Omega_1}{mB_1 - kB_2}$$

where $\Omega_2 = 2\pi N_2$ is the angular frequency and $B_2\Omega_2$ the blade passing frequency of the aft rotor. As before, $\gamma_{\mathcal{L}}$ and $\mu_{\mathcal{L}}$ are defined by Eq. (A.11) in the appendix. Eq. (2c) shows that, in general, loading noise is produced at the frequency combinations $mB_1\Omega_1 + kB_2\Omega_2$ where *m* is called the acoustic harmonic and *k* the loading harmonic. For $k = 0$, Eq. (2c) reduces to the isolated rotor loading noise formula derived in Reference 7. Note that the loading noise harmonic amplitude is a function of the difference parameter $mB_1 - kB_2$. As will be discussed in the results section this parameter plays a crucial role in determining the magnitude of the various loading noise tones.

Nearly identical expressions for the aft rotor tone noise field can be derived but with (B_1, Ω_1) pair interchanged with (B_2, Ω_2) pair in Eqs. (2a) through (2c). Once the contributions from both rotors have been computed, the resulting sound fields can be superimposed to estimate the tonal sound field of the counter-rotating open rotor. Eqs. (2a) through (2c), and their counterpart for the aft rotor, are the working expressions used for computing the tone noise of F31/A31 blade set reported here. These expressions were incorporated into an existing NASA Glenn Research Center propeller noise code called LINPROP to predict the tone noise of open rotors. The original LINPROP code was developed in early 1990s based on the single rotation theory described in Reference 7.

2.1. Aerodynamic Calculations

The computational tool used in this paper for the aerodynamic calculations is the commercial CFD software package FINE^{TM}/Turbo developed by NUMECA International.[*] FINE^{TM}/Turbo is a turbomachinery CFD simulation software package with integrated meshing and post-simulation analysis tools. It is a structured, multi-block, unsteady Navier-Stokes solver which offers several solution algorithm choices along with several acceleration strategies. The simulations can be run in full unsteady mode though this could be quite resource intensive. To reduce the computational time requirements for the time-dependant simulations, FINE^{TM}/Turbo can also be run in the nonlinear harmonic (NLH) mode [8] which solves for a finite number of the blade passing frequency harmonic components of the time-dependent solution, but ignores all the other unsteady components. This is a targeted approach focusing on the relevant frequency content of the underlying unsteady flow. The net result is a very significant reduction in the computational time requirements. This is the approach employed in this paper for the purpose of computing the aerodynamic response. In results to be presented later in the paper, the blade loading perturbation pressures associated with the first three harmonics of the blade-passing frequency for each rotor were retained in addition to the blade mean pressure field. Only three loading harmonics were chosen to keep the computational cost reasonable while still ensuring that the relevant tones up to 50th shaft order could be modelled (see Figure 3). The implications of this choice will become clear when the acoustic predictions are discussed later in the paper.

The FINE^{TM}/Turbo computational domain used in generating the results presented here includes one passage each of the two blade rows and their associated ancillary domains like the spinner, hub, farfield, etc. (See Figure 4 below). The total mesh size is slightly over 27.1 million grid points with the farfield boundary set seven tip radii away. The computations were run in parallel mode and depending on the particular simulation, the domain was partitioned either into 39 or 42 blocks to achieve optimum computational load balance.

In total, six tip speeds were considered ranging from the approach RPM to the nominal takeoff RPM. Table 1 shows the rotor tip speeds modelled in this paper. All cases considered had equal RPMs on the front and aft rotors. The nominal blade setting angles were 40.1^{o} for the front rotor and 40.8^{o} for the aft rotor in all cases. The tunnel Mach number (i.e., open rotor "forward flight speed") was also fixed at 0.2. As was mentioned in the introduction, these cases represent a small subset of a very large matrix of configurations for which aerodynamic and acoustic data was acquired in the wind tunnel tests.

[*] Additional information regarding FINE^{TM}/Turbo software package may be found at http://www.numeca.com.

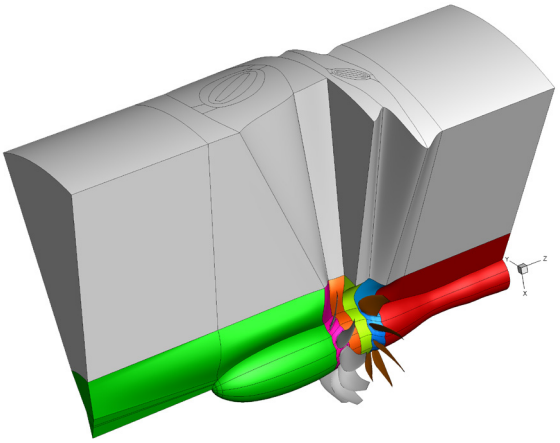

Figure 4. The computational domain and grid blocks used for nonlinear harmonic FINE™/Turbo simulations. Block regions are distinguished by different colours with the "farfield" blocks shown in gray.

Table 1. Rotor RPMs Considered in This Study

Case	Front Rotor RPM	Aft Rotor RPM
1	4620	4620
2	5268	5268
3	5551	5551
4	6068	6068
5	6303	6303
6	6436	6436

The starting point for the simulations was the highest tip speed condition, which was converged first. It took a total of 4000 iterations (3000 of them in NLH mode) to converge the solution. The maximum residual, thrust, torque, and pressure ratio had all settled after 3500 iterations, but the simulation was run another 500 iterations to ensure complete convergence. The acoustic calculations based on the 3500 and 4000 iteration solutions were nearly identical also. Once convergence had been achieved for this RPM, the next lower tip speed condition was run starting with this converged solution as the initial solution. Typically, it took 2500 iterations to achieve full convergence. The process was repeated for the next lower tip speed condition until all cases were computed. The simulations typically used between 14 and 16 cores of a 48-core compute node that is part of a NASA Glenn computer cluster each compute node of which has 128 GB of RAM.

Figures 5 and 6 show comparisons of total thrust and torque ratio predicted by FINE™/Turbo against the wind tunnel data. The agreement for thrust is quite good with an average discrepancy of 1.6%. The torque ratio comparison is only fair with an average error of roughly 9%. It should be noted that no tweaks were performed to adjust the blade angle, rotor tip speeds, or the tunnel Mach number

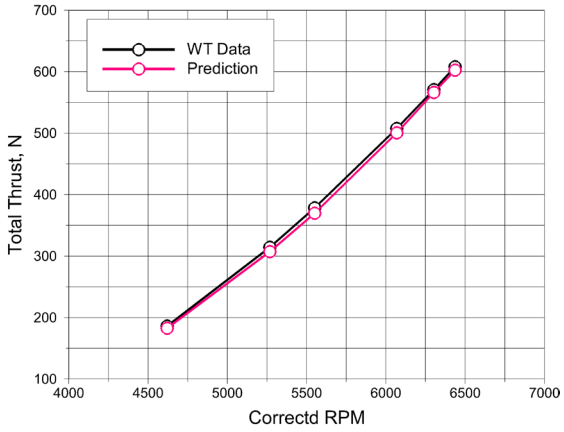

Figure 5. Measured and predicted F31/A31 rotor thrust. Combined thrust produced by both rotors is plotted.

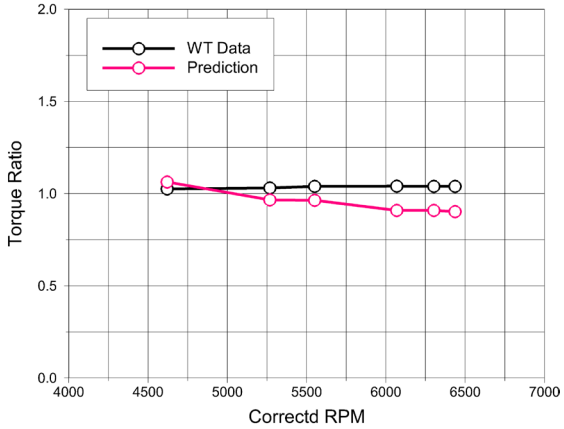

Figure 6. Measured and predicted F31/A31 rotor torque ratio.

to achieve a better match with the data. In other words, the simulations represent true "predictions".†

Figure 7 shows the contours of predicted magnitude of the mean and first blade passing frequency harmonic of the static pressure distribution on the front and aft blade rows as well as on the hub. Note the change in scale of the contour levels between the mean and perturbation contours. A close examination of the levels on the front and aft row shows that, while the mean loading levels on the front and aft rotors are comparable, there is a significant difference between the magnitudes of perturbation pressures on the two blade rows. The aft row clearly experiences much higher levels of pressure fluctuations owing to the impingement of the wakes of the front rotor, whereas the front rotor is only

† The blade shapes at the max climb condition supplied by GE were used at all speeds studied here. Thus, the small variations in the hot blade shape due to the changes in centrifugal force as a function of RPM difference from the max climb condition were ignored.

weakly affected by the potential field of the aft rotor. Another noteworthy feature is that the suction side perturbations are larger than the pressure side. The second and third harmonic pressure perturbations show similar trends to the first harmonic component, but they are smaller than the first harmonic component by roughly a factor of two and four, respectively.

By plugging the blade geometries and aerodynamic pressure distributions for each rotor into the Eqs. (2b) through (2c) the harmonic amplitudes of the thickness and loading tone noise were calculated and combined to estimate the sound field of F31/A31. The noise prediction results are discussed in the next section.

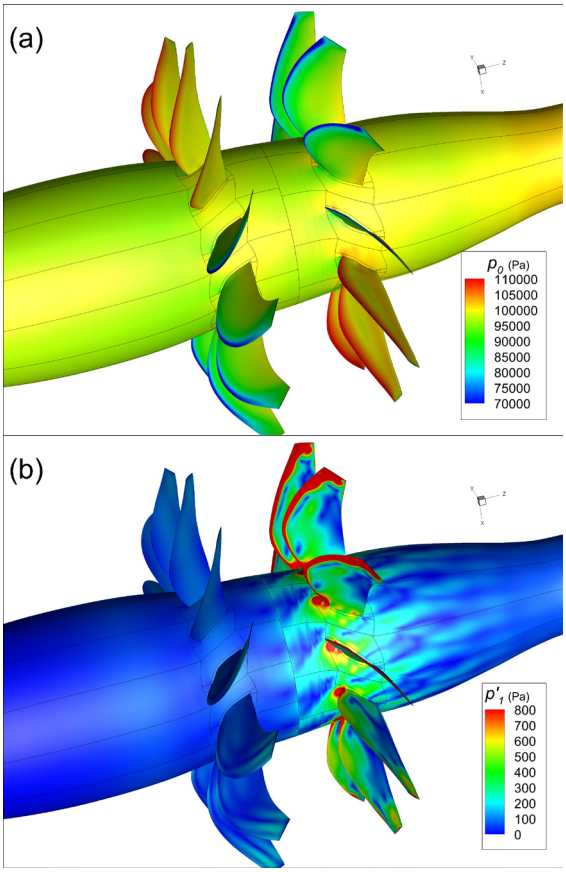

Figure 7. Contours of predicted pressure distributions on the hub and rotor blades for F31/A31. (a) shows the mean pressure level and (b) the blade passing frequency harmonic level.

3. ACOUSTIC PREDICTIONS

The modified LINPROP code was run for all of the tip speed conditions considered in this study. The calculations were performed for observer (i.e., microphone) positions that are located in a horizontal plane containing the open rotor axis and on a sideline parallel to the axis of the open rotor and 60 inches (i.e., 1.524 *m*) displaced from it. This layout duplicates exactly the test arrangement in the NASA 9-foot x 15-foot wind tunnel shown in the sketch in Figure 8.

During the test, the sideline acoustic data was acquired at 18 microphone positions ranging between 18° and 140° from the open rotor axis as shown in the figure. The data was acquired using a traversing inflow microphone (see Figure 2). Spectral data was computed from 15-second long time series acquired at 200 kHz sampling rate with a 2^{14} point FFT resulting in a frequency bin width of 12.2 Hz. Consequently, the measured tone energy is spread across multiple bins (see Figure 3). Therefore, to compare the measured levels to the predicted ones (which have an effective bin width of zero), it was necessary to sum the tone energy in the bins over which the tone is spread for the measured data.

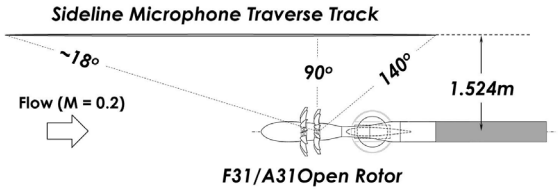

Figure 8. Sketch of the F31/A31 open rotor testbed and the sideline traversing microphone track as they were installed in the 9-foot x 15-foot wind tunnel. Acoustic data was acquired at a total of 18 microphone stops between the observer angles 18° and 140°.

As for the predictions, the loading component dominates the total level in all cases, hence only the predicted total is presented here. In any case, the experimental data cannot be parsed into constituent thickness and loading components. Also, while the data was acquired at 18 observer angles, the predictions were computed on a finer angular resolution of 51 observer angles to ensure that the nuances of the tone directivities were well captured. Lastly, given the number of the RPM and tone combinations, only highlights are presented here.

Figure 9 shows a representative comparison of the predicted tone sound pressure level (SPL) from the LINPROP code with the measured level for the highest tip speed (i.e., 6436 RPM) at the broadside microphone location (i.e., observer angle of 90°). Predictions for the tones in the range from approximately 1 kHz to 5.3 kHz are shown (shaft frequency for this tip speed is 107.3 Hz). This is because, the FINE™/Turbo simulations include the mean and only the first three blade passing frequency harmonics of the blade pressure loading for each row, which determines how many open rotor tones could be calculated based on the relationship $|mB_1\Omega_1 \pm kB_2\Omega_2|$. Therefore, the noise

predictions are restricted to the tones for which the loading harmonic k does not exceed 3.

The tones are labelled based on whether their origin is the front rotor, aft rotor, or if they are produced as a result of the interaction of the two. The frequency for each tone is given by $|mB_1\Omega_1 \pm kB_2\Omega_2|$ where $m, k = 0,1,2,3$.‡ The predicted levels include the complex conjugate contributions corresponding to the associated negative frequencies $-|mB_1\Omega_1 \pm kB_2\Omega_2|$. Before discussing the data-theory comparisons, it is important to note the following in order to better understand the comparisons.

As indicated in Figure 9, most tones can be produced by either the sum or difference frequency combinations. In fact, while there is only one sum combination for a given tone, there are infinitely many difference combinations possible. However, tones corresponding to virtually all frequency difference combinations have extremely low radiation efficiencies and do not contribute to the tone SPL in a significant way. This is most easily seen by examining the terms inside the curly bracket in Eq. (2c).

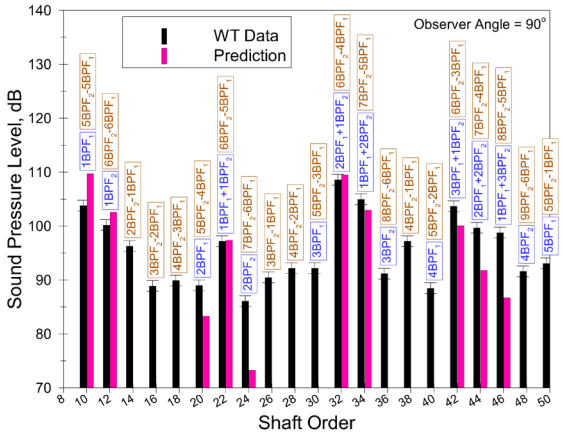

Figure 9. Comparison of measured and predicted tone SPL at the broadside microphone location (i.e., observer angle 90°) at 6436 RPM. Tones are labelled according to their origin (i.e., front rotor tones, aft rotor tones, or interaction tones). The labels are colour coded according to whether the tones are based on sum (blue) or difference (brown) combinations.

Note that since for a given frequency combination $|mB_1\Omega_1 \pm kB_2\Omega_2|$, the tone amplitude is a function of the index combination $|mB_1 \mp kB_2|$, there can be substantial difference in the radiation efficiency of the sum and difference tones. To elucidate the point, let's contrast two tones, one with the frequency $|12\Omega_1 + 10\Omega_2|$ and the other with the frequency $|12\Omega_1 - 10\Omega_2|$. The amplitudes of these two tones according to Eq. (2c) will be functions of the index combinations $|12+10|$ and $|12-10|$, respectively. Since, Ai and Ai' decay rapidly as their arguments increase, the amplitude of the sum tone will far exceed the amplitude of the difference tone. The plot in Figure 10 depicts the point graphically. The plot shows the dependence of the terms in the curly bracket in Eq. (2c) on the parameter $|mB_1 - kB_2|$ for a source on the tip of the blade. The terms are each normalized by their value for zero argument and plotted on a logarithmic scale. A number of tones for which the parameter $|mB_1 - kB_2|$ falls in the range 0 to 40 are identified on the abscissa. Tones whose frequencies are above 14 kHz are not noted since beyond that limit no discernible tones are detectable above the broadband level in the measured spectra. Note the rapid fall of the Ai and Ai' as their arguments increase. It is easy to see from this plot that sum tones have far higher radiation efficiencies than do the difference tones. In fact, there are only three difference tones in the range plotted. The radiation efficiencies of higher order difference tones are effectively negligible.

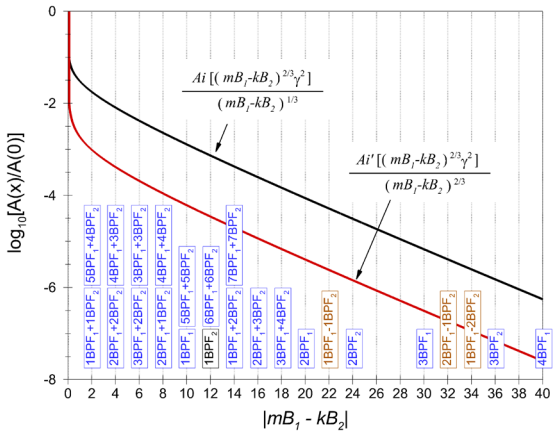

Figure 10. Radiation efficiency of sum and difference tones as a function of the index $|mB_1 - kB_2|$.

Another notable aspect of this plot is that it shows that the radiation efficiencies of several interaction (sum) tones are significantly higher than the radiation efficiencies of the individual rotor blade passing tones (i.e., BPF_1 and BPF_2). As a result, even though the magnitude of the blade loading's higher harmonics, which drive the interaction tones, are much smaller than the mean loading, which drives the blade passing tones, their comparatively much higher radiation efficiencies

‡ m=k=0 does not result in an acoustic tone.

compensate for their source amplitude deficit (recall Figure 7) thus making their levels, especially those for the low order interaction tones, on par or even higher than the blade passing frequency tone levels. Finally, it should also be noted that the higher harmonic tones of the individual rotors (i.e., nBPF$_1$ and nBPF$_2$) also have comparatively smaller radiation efficiencies and thus are expected to fall off rapidly in amplitude as seen in this plot.

Returning to Figure 9, note that the low order interaction tones 1BPF$_1$+1BPF$_2$, 2BPF$_1$+1BPF$_2$, and 1BPF$_1$+2BPF$_2$, are well predicted by the LINPROP code with discrepancies of 1 dB or less, when considering the experimental uncertainty in the measured levels which is ±1 dB. The next set of interaction tones, 3BPF$_1$+1BPF$_2$, 2BPF$_1$+2BPF$_2$, and 1BPF$_1$+3BPF$_2$, show larger discrepancies when compared with the measured levels and the discrepancy grows as the tone order (i.e., its frequency) increases. Since, as mentioned earlier, the interaction tones are driven by the harmonics of the unsteady loading on the blades, it is likely that to predict higher order tones more computational grid resolution may be needed to achieve better accuracy of the blade pressure loading harmonics.[§]

As for the individual rotor tones, the theory over-predicts the blade passing frequency tones BPF$_1$ and BPF$_2$, but under-predicts their harmonics, i.e., nBPF$_1$ and nBPF$_2$. Theses discrepancies may be explained by the following observation. The experimental data show a preponderance of tones at all shaft orders (recall Figure 3) including both odd and even order ones. Yet, the theory only predicts even order tones (whether sum or difference ones) since the blade counts are even numbers. The paradox can be explained by noting that the theory (aerodynamic or acoustic) assumes that all of the blades in each rotor disc are identical and that they all experience the same loading time history over the course of each rotor revolution, but displaced spatially and temporally from that of the reference blade. This assumption results in acoustic energy being distributed amongst a subset of shaft orders. The actual blades in a given rotor disc, however, are not exactly the same as they are hand finished (they are made of composites) and they may not experience exactly the same time history due to inherent unsteadiness of the flow. Perhaps more importantly, the setting angles for the blades in a given rotor disc vary within a small range (typically in the ±0.1^o range for F31/A31 [9]) in a random fashion around the rotor disc thus slightly modifying the loading distribution on each blade. Therefore, for the actual rotors the precise phasing assumed by the theory does not occur, a consequence of which is that the acoustic energy is distributed amongst all shaft orders rather than just those singled out by the theory. As a result, some of the energy that according to the theory would have amassed in BPF$_1$ and BPF$_2$ tones is leaked into their harmonics nBPF$_1$ and nBPF$_2$. The same mechanism could explain the measurable levels for the difference tones (e.g., 2BPF$_2$-2BPF$_1$, 3BPF$_2$-2BPF$_1$, and 4BPF$_2$-3BPF$_1$), for which the theory predicts very small radiation efficiencies and, thus, levels that would be too small to be visible in Figure 9.

Next, the variations of SPL on the sideline as a function of observer angle for the BPF$_1$, BPF$_2$, and BPF$_1$+BPF$_2$ tones are examined (See Figure 11). While it is difficult to draw general conclusions about the data-theory comparisons on the absolute level basis, the trends in data appear to be reasonably well predicted except for the far upstream and far downstream angles for the BPF$_1$ and BPF$_2$ tones. It should be noted that the predicted rapid falloff of the SPL for BPF$_1$ and BPF$_2$ away from the vicinity of the respective planes of rotation (i.e., ~90^o observer angle) is consistent with measured single rotation results. It is not clear then, why the measured blade passing tone levels for the individual rotors of F31/A31 should level off (or even increase) below about 70^o and above approximately 130^o.

The data-theory comparisons look similar for the other tip speeds, so results corresponding to those presented in Figures 9 and 11 for lower tip speeds will not be presented here. Instead, the comparisons as a function of tip speed will be shown on the basis of the overall sound pressure level (OASPL). The principal reason for choosing the OASPL metric goes back to discussion earlier regarding the acoustic energy being distributed amongst all shaft order tones rather than just those orders that the theory predicts. It could be argued that in that sense the OASPL should be a good metric to use regardless of how the acoustic energy is distributed amongst the various tones. It should also be noted that since the measured levels include both tone and broadband content, it is necessary to subtract the broadband levels from the measured data before calculating the OASPL. Lastly, based on the discussion of the results in Figure 11, the OASPL comparisons will be restricted to the observer angles in the 70^o to 130^o range.

Figure 12 shows the dependence of the OASPL on the rotor tip speed. Both measured and predicted OASPLs are shown from the highest tip speed (6436 RPM) on the top of the figure to the lowest tip speed (4620 RPM) on the bottom of the figure. Generally speaking, the data-theory agreement is reasonable at the higher tip speeds, but it deteriorates as the tip speed is reduced. The basic trend of decreasing OASPL with decreasing tip speed in the measured data is captured by the theory though not uniformly for all observer angles in that

[§] This was partially borne out by comparing the results to those from a single case that was run with a mesh resolution of 42M grid points. However, the grid packing in the vicinity of the blade may be a more important factor than grid resolution alone.

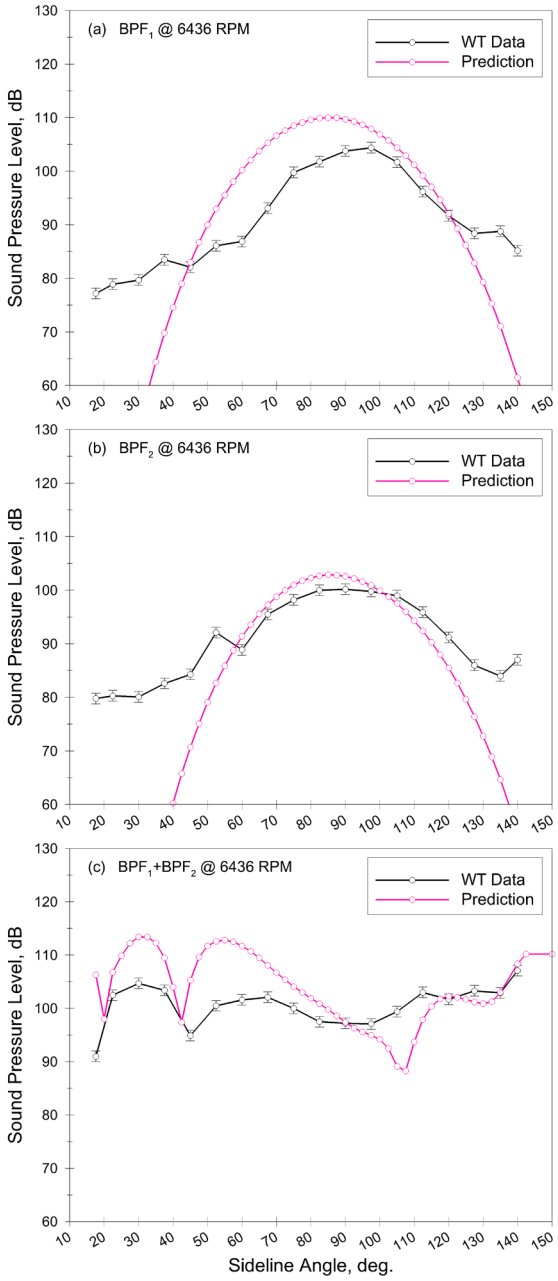

Figure 11. Sideline variations of SPL as a function of observer angle for (a) BPF_1, (b) BPF_2 and (c) BPF_1+BPF_2 tones at the 6436 RPM condition.

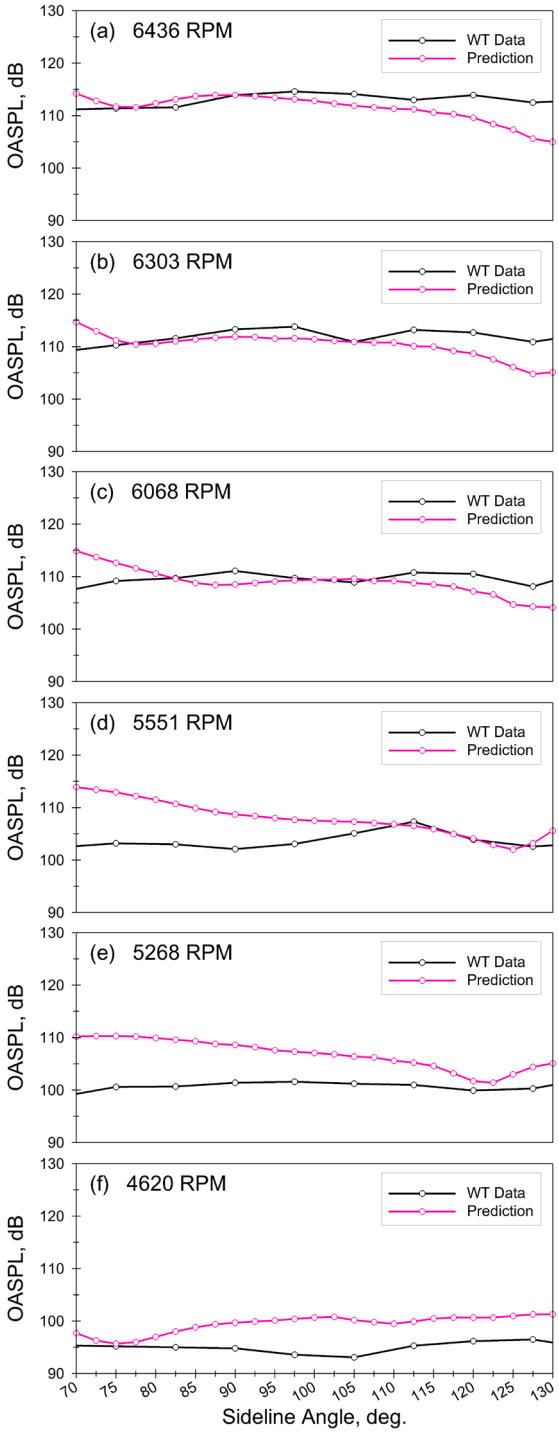

Figure 12. Sideline variations of OASPL as a function of the observer angle on the sideline. Panes (a) through (f) show the variations of OASPL with tip speed. Comparisons for observer angles in the range 70° to 130° only are shown.

the decrease in the predicted levels is slower than that in the measured data.

4. CONCLUSIONS

The results discussed in the previous section suggest that absolute level predictions on a tone-by-tone basis for open rotors (or any turbomachinery system, for that matter) may be out of reach using the existing suite of tools (i.e., CFD + acoustic analogy). This may be true even when more sophisticated numerical methods that directly compute the noise field from the field equations are brought to bear. This is a consequence of the fact that any model that assumes identical blades in each blade row, experiencing spatially- and temporally-shifted time histories, is incompatible with the real geometries, for which there always exist small manufacturing and installation variations as well as

flow non-stationarity, which could in measurable ways alter the acoustic response of the blades. Nevertheless, the basic trends seem to be reasonably well predicted using the combination of CFD and acoustic analogy (specifically, in this case, FINE^{TM}/Turbo and LINPROP). This is enough of a capability for analysis and optimization ultimately aimed at developing low-noise open rotor designs. It may also be possible to modify the existing noise models (such as that underlying the LINPROP code, for example) to accommodate small, randomized variations in the geometry and loading distributions on a blade-to-blade basis to mimic the real physics. The basic question here is whether the size of required variations to get more realistic tone spectra would turn out to be consistent with the expected variations in the actual geometries. It is the aim of a future study to investigate this approach and its consequences.

ACKNOWLEDGEMENTS

This work has been supported by the Subsonic Fixed Wing Project of the NASA Fundamental Aeronautics Program.

APPENDIX A

Taking advantage of the tonal nature of the sound field, one can write for the front rotor

$$p'(\underline{x},t)=\sum_{\ell=-\infty}^{\infty}p'_{T_\ell}(\underline{x})e^{-i\ell\Omega_1 t}+\sum_{\ell=-\infty}^{\infty}\sum_{k=-\infty}^{\infty}p'_{\mathcal{L}_{\ell,k}}(\underline{x})e^{-i\ell'\Omega_1 t} \qquad \text{(A.1a)}$$

$$\ell'=\ell+kB_2\left(1+\Omega_2/\Omega_1\right)$$

where p'_{T_ℓ} and $p'_{\mathcal{L}_{\ell,k}}$ are the thickness and loading harmonic amplitudes. Based on Eq. (1a), these are given by

$$p'_{T_\ell}(\underline{x})=\frac{\Omega_1}{2\pi}\times\int_0^{2\pi/\Omega_1}e^{i\ell\Omega_1 t}\left[\int_{-\infty}^{\infty}\int_{S_1}\rho_0\hat{v}_n\frac{D_0G}{Dt}ds\left(\hat{\underline{y}}\right)d\tau\right]dt \qquad \text{(A.1b)}$$

$$p'_{\mathcal{L}_{\ell,k}}(\underline{x})=-\frac{\Omega_1}{2\pi}\times\int_0^{2\pi/\Omega_1}e^{i\ell'\Omega_1 t}\left[\int_{-\infty}^{\infty}\int_{S_1}\hat{p}_k n_j\frac{\partial G}{\partial x_j}ds\left(\hat{\underline{y}}\right)d\tau\right]dt \qquad \text{(A.1c)}$$

Note that thickness noise involves only the rotational frequency of the front rotor since the surface (i.e., source) velocity $\hat{v}_n$ is not in any way influenced by the aft rotor. In contrast, loading noise depends not only on the front rotor rotational rate, but it is also affected by the rate at which the aft rotor blades pass by a given blade on the front rotor. In other words, the most general frequency of noise produced by the loading source depends on the combinations $\ell\Omega_1+kB_2\left(\Omega_1+\Omega_2\right)$. In the absence of the aft rotor, or when considering only the mean loading on the aft rotor, (i.e., $k=0$), the loading noise frequency reduces to the harmonics of the front rotor rotational frequency as expected.

In writing Eqs. (A.1b) and (A.1c), f_j in Eq. (1a) has been replaced with its inviscid part pn_j, and the source coordinates have been switched from the stationary frame of reference to the ones in a rotating frame fixed to the rotor, i.e., $\underline{y}\rightarrow\hat{\underline{y}}$. The integration over the time dependant rotor surface $S_1(\tau)$ has been correspondingly replaced with integration over the time-independent rotor surface S_1, which denotes the aggregate surface of all the blades in the rotor disc. The transformation is length preserving and hence its Jacobian is unity. The source amplitudes $\hat{v}_n$ and $\hat{p}_k$ are also expressed in the blade fixed coordinate system.

Finally, the derivatives of the Green's function with respect to the source coordinate in Eq. (1a) have been replaced with those with respect to the observer coordinates via

$$D_0G/D\tau=-D_0G/Dt \qquad \partial G/\partial y_i=-\partial G/\partial x_i \qquad \text{(A.2)}$$

Assuming that all the blades in the rotor disc are identical, the integration over the rotor surface S_1 can then be reduced to one over the surface of the reference blade S_{B_1}, since the contribution to the harmonic amplitude p'_{T_ℓ} from the q^{th} rotor blade is related to that from the reference (i.e., 0^{th}) blade through the spatial phase shift $e^{2\pi iq/B_1}$. Therefore, Eq. (A.1b) can be rewritten as

$$p'_{T_\ell}=\frac{\Omega_1}{2\pi}\sum_{q=0}^{B_1-1}e^{2\pi i\ell q/B_1}\times\int_0^{2\pi/\Omega_1}e^{i\ell\Omega_1 t}\left[\int_{-\infty}^{\infty}\int_{S_{B_1}}\rho_0\hat{v}_n\frac{D_0G}{Dt}ds\left(\hat{\underline{y}}\right)d\tau\right]dt \qquad \text{(A.3)}$$

The summation over the blade index q is non-zero only when ℓ is an integer multiple of the blade count B_1. When $\ell = mB_1$ (m being an arbitrary integer), the summation is equal to B_1 times the contribution from the reference blade. Thus, Eq. (A.3) reduces to

$$p'_{T_m}(\underline{x}) = \frac{B_1\Omega_1}{2\pi} \times \int_0^{2\pi/\Omega_1} e^{imB_1\Omega_1 t} \left[\int_{-\infty}^{\infty} \int_{S_{B_1}} \rho_0 \hat{v}_n \frac{D_0 G}{Dt} ds(\underline{\hat{y}}) d\tau \right] dt \quad \text{(A.4)}$$

which shows that thickness noise is produced at the harmonics of the blade passing frequency $B_1\Omega_1$.

The blade pressure loading $\hat{p}_k$ has, in general, the form

$$\hat{p}_k(\tau) = \hat{\hat{p}}_k e^{-ikB_2(\Omega_1+\Omega_2)\tau} \quad \text{(A.5)}$$

since, due to the influence of the adjacent blade row, the blade loading is always unsteady even in a rotor-fixed coordinate system.

Next, note that the loading distribution on the q^{th} blade at any time is related to the loading distribution on the reference blade via the spatial phase shift $e^{2\pi iq/B_1}$, which accounts for the location shift, and the temporal phase shift $e^{2\pi iq/B_1(\Omega_1+\Omega_2)}$, which accounts for the time lead. Therefore, Eq. (A.1c) can be rewritten as an integral over the reference blade surface as follows,

$$p'_{\mathcal{L}_{\ell,k}}(\underline{x}) = -\frac{\Omega_1}{2\pi} \sum_{q=0}^{B_1-1} e^{2\pi iq(\ell+kB_2)/B_1} \int_0^{2\pi/\Omega_1} e^{i\ell'\Omega_1 t} \times \left[\int_{-\infty}^{\infty} \int_{S_{B_1}} \hat{\hat{p}}_k e^{-ikB_2(\Omega_1+\Omega_2)\tau} n_j \frac{\partial G}{\partial x_j} ds(\underline{\hat{y}}) d\tau \right] dt \quad \text{(A.6)}$$

where, as before, the summation over the blade index q is non-zero only when $\ell + kB_2$ is an integer multiple of the blade count B_1. When $\ell + kB_2 = mB_1$, the summation is equal to B_1 times the contribution from the reference blade. Thus, Eq. (A.6) simplifies to

$$p'_{\mathcal{L}_{m,k}}(\underline{x}) = \frac{-B_1\Omega_1}{2\pi} \int_0^{2\pi/\Omega_1} e^{i(mB_1\Omega_1+kB_2\Omega_2)t} \times \left[\int_{-\infty}^{\infty} \int_{S_{B_1}} \hat{\hat{p}}_k e^{-ikB_2(\Omega_1+\Omega_2)\tau} n_j \frac{\partial G}{\partial x_j} ds(\underline{\hat{y}}) d\tau \right] dt \quad \text{(A.7)}$$

which shows that, in general, loading noise is produced at the frequency combinations $mB_1\Omega_1 + kB_2\Omega_2$.

Next, the chain rule can be used to show that

$$\frac{\partial G}{\partial x_j} = \mathcal{D}_j G$$

$$\mathcal{D}_j = -\left[\frac{1}{c_0\kappa}\left(e_j - g_c M_{0_j}\right)\frac{\partial}{\partial t} + \frac{1}{\kappa^2 R}\left(\beta_0^2 e_j + M_{0_R} M_{0_j}\right) \right] \quad \text{(A.8)}$$

which, in turn, can be used to remove the spatial derivatives in Eqs. (A.4) and (A.7). Afterwards, the integrations over t can be easily carried out since they involve Dirac delta functions. The results are

$$p'_{T_m}(\underline{x}) = \frac{B_1\Omega_1}{8\pi^2} \int_0^{2\pi/\Omega_1} \int_{S_{B_1}} \left(\sum_{n=1}^{2} \frac{\mathcal{Q}^{(n)}_{T_m}}{R^n} \right) \times e^{imB_1\Omega_1(\tau + g_c R/c_0)} ds(\underline{\hat{y}}) d\tau \quad \text{(A.9a)}$$

$$p'_{\mathcal{L}_{m,k}}(\underline{x}) = \frac{B_1\Omega_1}{8\pi^2} \int_0^{2\pi/\Omega_1} \int_{S_{B_1}} \left(\sum_{n=1}^{2} \frac{\mathcal{Q}^{(n)}_{\mathcal{L}_{m,k}}}{R^n} \right) \times e^{i(mB_1\Omega_1+kB_2\Omega_2)(\tau + g_c R/c_0)} e^{-ikB_2(\Omega_1+\Omega_2)\tau} ds(\underline{\hat{y}}) d\tau \quad \text{(A.9b)}$$

where $\mathcal{Q}^{(1)}_{T_m}$ and $\mathcal{Q}^{(2)}_{T_m}$ are the farfield and nearfield thickness source amplitudes, and $\mathcal{Q}^{(1)}_{\mathcal{L}_{m,k}}$ and $\mathcal{Q}^{(2)}_{\mathcal{L}_{m,k}}$ are the farfield and nearfield loading source amplitudes. These are given by Eq. (A.9c).

Note that, the limits of integration over τ in Eqs. (A.9a) and (A.9b) have been set to $(0, 2\pi/\Omega_1)$, since one period of the observer time maps exactly into one period of the source time. In what follows it will be assumed that the mean flow is aligned with the open rotor axis, i.e., $(M_{0_1}, 0, 0)$.

$$\mathcal{Q}_{T_m}^{(1)} = -\frac{1}{\kappa^2} imB_1\Omega_1\rho_0\hat{v}_n \times \left[1-\frac{1}{\kappa}M_{0_j}\left(e_j - g_c M_{0_j}\right)\right]$$

$$\mathcal{Q}_{T_m}^{(2)} = -\frac{1}{\kappa^3}\rho_0\hat{v}_n M_{0_j}\left(\beta_0^2 e_j + M_{0_R}M_{0_j}\right) \tag{A.9c}$$

$$\mathcal{Q}_{\mathcal{L}_{m,k}}^{(1)} = -\frac{1}{c_0\kappa^2} i\left(mB_1\Omega_1 + kB_2\Omega_2\right)\times \hat{\hat{p}}_k n_j\left(e_j - g_c M_{0_j}\right)$$

$$\mathcal{Q}_{\mathcal{L}_{m,k}}^{(2)} = \frac{1}{\kappa^3}\hat{\hat{p}}_k n_j\left(\beta_0^2 e_j + M_{0_R}M_{0_j}\right)$$

Grouping terms together and introducing a change of variable from τ to a new variable θ, both the thickness and loading terms can be cast in the form given by

$$p'\left(\underline{x}\right) = \frac{B_1}{8\pi^2}\sum_{n=1}^{2}\int_{S_{B_1}} e^{-i\lambda\Psi}\mathcal{I}_n\left(\underline{\hat{y}}\right)ds\left(\underline{\hat{y}}\right)$$

$$\mathcal{I}_n = \int_0^{2\pi}\frac{\mathcal{Q}^{(n)}(\theta)}{R^n(\theta)}e^{\lambda\Phi(\theta)}d\theta \tag{A.10a}$$

$$\theta = \Omega_1\tau + \varphi_s - \varphi$$
$$\Phi(\theta) = i\left(\theta + a_s\sqrt{1-b_s\cos\theta}\right)$$
$$b_s = \frac{2rr_s}{\chi_s^2 + r^2 + r_s^2},\quad \chi_s = \frac{1}{\beta_{0_1}}\left(x_1 - \hat{y}_1\right) \tag{A.10b}$$

where for thickness noise**

$$\lambda = mB_1$$
$$a_s = \frac{M_{\text{tip}_1}}{\beta_{0_1}}\sqrt{\chi_s^2 + r^2 + r_s^2}$$
$$\Psi = \frac{1}{\beta_{0_1}}M_{\text{tip}_1}M_{0_1}\chi_s + \varphi_s - \varphi \tag{A.10c}$$
$$M_{\text{tip}_1} = \frac{\Omega_1 R_{\text{tip}_1}}{c_0}$$

and for the loading noise

$$\lambda = mB_1 - kB_2$$
$$a_s = \frac{\eta_{\text{CRF}}M_{\text{tip}_1}}{\beta_{0_1}}\sqrt{\chi_s^2 + r^2 + r_s^2}$$
$$\Psi = \frac{\eta_{\text{CRF}}}{\beta_{0_1}}M_{\text{tip}_1}M_{0_1}\chi_s + \varphi_s - \varphi \tag{A.10d}$$
$$\eta_{\text{CRF}} = \frac{mB_1 + kB_2\Omega_2/\Omega_1}{mB_1 - kB_2}$$

Here η_{CRF} is a factor denoting the influence of the counter-rotation kinematics on the loading noise. Note that for $k=0$, i.e., when considering the influence of only the mean loading from the aft rotor on the noise of the front rotor, Eqs. (A.10c) and (A.10d) have identical forms, which is to say that the thickness and loading noise components have the same frequency content. This result is in agreement with the isolated rotor results developed in Reference 7. In general, however, loading noise for a given rotor is strongly influenced by its neighbour. It should be noted that in circumstances for which $mB_1 = kB_2$, the loading term parameters have the following simpler forms

$$\Phi(\theta) = ia_s\sqrt{1-b_s\cos\theta}$$
$$\lambda = mB_1$$
$$a_s = \frac{\eta_{\text{CRF}}M_{\text{tip}_1}}{\beta_{0_1}}\sqrt{\chi_s^2 + r^2 + r_s^2}$$
$$\Psi = \frac{\eta_{\text{CRF}}}{\beta_{0_1}}M_{\text{tip}_1}M_{0_1}\chi_s \tag{A.10e}$$
$$\eta_{\text{CRF}} = 1 + \frac{\Omega_2}{\Omega_1}$$

As shown in Reference 7, the integral $\mathcal{I}_n$ in Eq. (A.10a) can be accurately estimated using the method of steepest descent when the parameter λ is large which is the generally the case due to the large blade counts of modern open rotors. The essential steps are two fold: (1) conformably map the phase function Φ into a suitably constructed polynomial which facilitates the analysis immensely; (2) extend the domain of analysis to the complex domain through the change of variable $\nu = \theta + i\sigma$ which allows the path of integration to be deformed into appropriate steepest descent paths. In the neighbourhoods of the saddle points of these paths, the integral $\mathcal{I}_n$ can then be accurately estimated using closed form analytical expressions. The intermediate steps are described in detail in Reference 7. The final result for a generic source term is given by

** The definition of the parameter a_s as given in the Reference 7 is incorrect.

$$\mathcal{I}_n \simeq 2\pi i e^{\lambda\mu}\left\{ d_{0,n}\frac{Ai\left(\lambda^{2/3}\gamma^2\right)}{\lambda^{1/3}} + d_{1,n}\frac{Ai'\left(\lambda^{2/3}\gamma^2\right)}{\lambda^{2/3}}\right\}$$

$$d_{0,n} = \frac{\Gamma_n(\gamma)+\Gamma_n(-\gamma)}{2}$$

$$d_{1,n} = \frac{\Gamma_n(\gamma)-\Gamma_n(-\gamma)}{2\gamma} \qquad \text{(A.11)}$$

$$\mu = \frac{1}{2}\left[\Phi\left(\nu^+\right)+\Phi\left(\nu^-\right)\right]$$

$$\gamma^3 = \frac{3}{4}\left[\Phi\left(\nu^+\right)-\Phi\left(\nu^-\right)\right]$$

$$\Gamma_n(\zeta) = \frac{\mathcal{Q}^{(n)}\left[\nu(\zeta)\right]}{R^n\left[\nu(\zeta)\right]}\frac{d\nu}{d\zeta}$$

$$\frac{d\nu}{d\zeta} = \frac{\gamma^2-\zeta^2}{\Phi'\left[\nu(\zeta)\right]}$$

where $\nu^{\pm}$ denote the location of the saddle points in the complex plane and μ, γ, and Γ_n are parameters that define the conformal map. $d_{0,n}$, and $d_{1,n}$ are the source amplitudes at the saddle points. Note that the actual values of these parameters depend on whether thickness noise or loading noise is being considered.

The Airy function Ai and its derivative Ai' provide an accurate asymptotic approximation to the integral $\mathcal{I}_n$. The approximation is uniformly valid at subsonic, transonic, and supersonic tip speeds. It is also uniformly valid whether the observer is in the nearfield or farfield. The approximation is formally accurate for large values of the parameter λ, but it turns out to be surprisingly accurate even for values of λ as low as 2.

With the integral $\mathcal{I}_n$ computed, the integration over the blade surface S_{B_1} in Eq. (A.10a) can now be carried out to compute the harmonic amplitudes of the thickness and loading noise sources. For general blade shapes, this integrals is not tractable analytically, but can be easily computed using a quadrature scheme by dividing the blade surface into small elements over which the integral can be accurately estimated (see Reference 7). For the acoustic results presented in this paper, the surface grid generated as part of the FINE^{TM}/Turbo simulations was used in the surface quadrature calculations.

REFERENCES

[1] Hager, R., D., and Vrable, D., 1988, "Advanced Turboprop Project", NASA SP-495.

[2] Van Zante, D., E., Gazzaniga, J., A., Elliott, D., M., and Woodward, R., P., 2011, "An Open Rotor Test Case: F31/A31 Historical Baseline Blade Set", *20th ISABE Conference*, Gothenburg, Sweden, paper no. ISABE-2011-1310.

[3] Farassat, F., Dunn, M., H., Tinetti, A. F., and Nark, D., M., 2009, "Open Rotor Noise Prediction Methods at NASA Langley–A Technology Review," AIAA Paper 2009-3133, *15th AIAA/CEAS Aeroacoustics Conference*, Miami, Florida.

[4] Brès, G., A., Brentner, K., S., Perez, G., and Jones, H., E., 2004, "Maneuvering Rotorcraft Noise Prediction", *J. of Sound and Vibration*, Vol. 275, Issues 3-5, pp. 719-738.

[5] Hanson, D., B., 1985, "Noise of Counter-Rotation Propellers", *Journal of Aircraft*, Vol. 22, No. 7, pp. 609-617.

[6] Parry, A., B., 1988, "Theoretical Prediction of Counter-Rotating Propeller Noise", *Ph.D. Dissertation, Dept. of Applied Mathematical Studies, University of Leeds*.

[7] Envia, E., 1994, "Asymptotic Theory of Supersonic Propeller Noise", *AIAA Journal*, Vol. 32, No. 2, pp. 239-246.

[8] He, L. and Ning, W., 1998, "Efficient Approach for Analysis of Unsteady Viscous Flows in Turbomachines", *AIAA Journal*, Vol. 36, No. 11, pp. 2005-2011.

[9] Van Zante, D., E., Private communications.

Conference on Modelling Fluid Flow (CMFF'12)
The 15th International Conference on Fluid Flow Technologies
Budapest, Hungary, September 4-7, 2012

THE APPLICATION OF PIV TO INVESTIGATE TURBULENT FLOWS

Jerry WESTERWEEL[1,3], Gerrit ELSINGA[1], Ronald ADRIAN[2]

[1] Laboratory for Aero & Hydrodynamics, Delft University of Technology, Mekelweg 2, 2628 CD Delft, The Netherlands.
[2] School for Engineering of Matter, Transport and Energy, Arizona State University, Tempe AZ 85287, U.S.A.
[3] Corresponding Author. Tel.: +31 15 278 6887, E-mail: j.westerweel@tudelft.nl

ABSTRACT

Particle Image Velocimetry (PIV) is currently the only experimental technique that yields information on the instantaneous spatial structure of instationary flows, in particular turbulent flows. In the last two decades, results from PIV measurements have provided new insight in the role of coherent flow structures. Yet, the information has been restricted primarily to a planar cross section of the flow. Very recent developments in image calibration, camera technology, and computer hardware and software, made it possible to extend the measurement from the planar to the volumetric domain. By means of a tomographic reconstruction of the scattering field in the object domain it has become possible to obtain the instantaneous three-component velocity field with a data density in excess of 10^5 points in a single measurement volume. This provides access to the full deformation tensor that characterizes the flow field. This provides new capabilities to investigate turbulent flows. This will be illustrated by several recent experiments and measurements on wall-bounded and free-shear turbulent flows.

Keywords: coherent structures, PIV, turbulence, volumetric measurements

1. INTRODUCTION

In the past two decades, *particle image velocimetry*, or PIV, has become a standard tool in experimental fluid mechanics [1,2,3]. The principal characteristic of PIV that has made it so useful is its ability to measure the instantaneous velocity field simultaneously at many points, typically of the order of 10^3–10^5, with spatial resolution sufficient to permit the computation of the instantaneous fluid *vorticity* and *rate-of-strain*. To date, PIV is the only experimental method that provides such information in rapidly evolving flows. PIV measurements are most commonly snapshots of the two- or three-component velocity vector field on a planar section of the flow, but in recent years new developments have made it possible to measure the velocity over volumetric domains [4] and to measure sequences of velocity in time at rates sufficient to resolve the temporal evolution. Undoubtedly, PIV has significantly advanced experimental fluid mechanics, especially the study of flows in complex geometries and turbulent flows, providing resolution and detail that can compete with modern numerical methods, such as *direct numerical simulation*, or DNS [5].

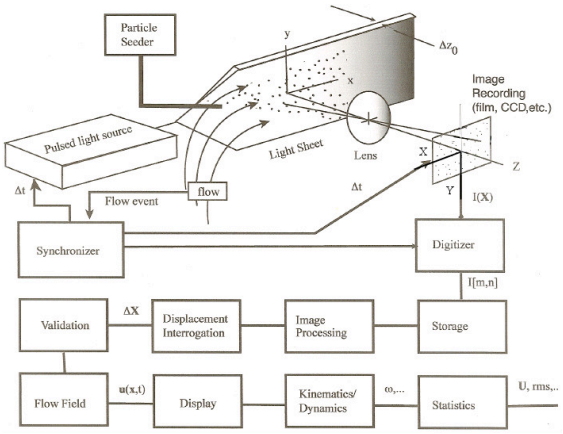

Figure 1 Components and processing steps of a planar 2-D PIV system. From: Adrian & Westerweel [6].

Among the many applications of PIV, turbulent flows are some of the most comprehensively demanding, owing to their three-dimensionality, unsteadiness and wide ranges of length and velocity scales.

One of the unique features of PIV is its ability to measure quantitatively the instantaneous spatial derivatives of the flow velocity field. Turbulence, the small scales in particular, is associated with dissipative and swirling motions and both quantities involve velocity gradients rather than the velocity itself. Therefore, there has been a long-standing

interest in fully three-dimensional velocity measurement capabilities, as this allows determining all nine components of the velocity gradient tensor.

For planar PIV (Figure 1), where two velocity components are measured in a planar cross-section of the flow, only four out of nine derivatives (and five out of nine for an incompressible fluid) can be measured, but this still enables determination of the component of the instantaneous vorticity vector that is normal to the measurement plane. With *stereoscopic* PIV [6] the views of two cameras are combined, which makes it possible to reconstruct all three velocity components in a planar cross section, while *dual-plane* PIV provides access to the full deformation tensor in a planar cross-section of the flow [7]. Volumetric approaches include *scanning planar* PIV [8,9], *holographic* PIV [10], volumetric PTV [11,12], and *tomographic* PIV [4]. The latter method is the most recent and advanced approach, and it will be discussed in detail in Section 3.

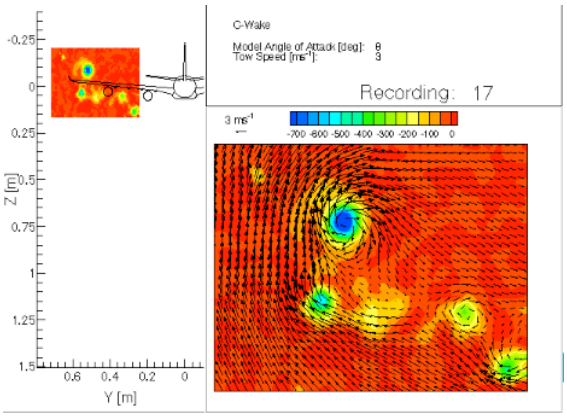

Figure 2 PIV measurement of the vortical structures in the wake of a model Airbus A340-300. From: Scarano *et al.* [13].

2. PLANAR PIV

The basic components and processing steps for a basic PIV system are shown in Figure 1; a detailed description is given by Adrian & Westerweel [6]. The ability of PIV to measure unstationary vorticity was, for example, utilized in the measurement of one of the trailing vortices of a 1:48 model of the Airbus A340-300 [13], which made it possible to determine its strength and position over an elongated domain.

Planar PIV was used to obtain quantitative information on coherent flow structures in turbulent flows; for example to demonstrate the presence of hairpin vortices in a turbulent boundary layer for Reynolds numbers (based on the momentum-loss thickness θ) between $Re_\theta = 930$ and 6845 [14]. This was well beyond values of Re_θ that were represented in contemporary DNS studies. The main advantage was that the measured spanwise vorticity permitted direct visualization of the hairpin vortices. This study demonstrated the strength of PIV for the analysis of coherent flow structures in turbulent flows.

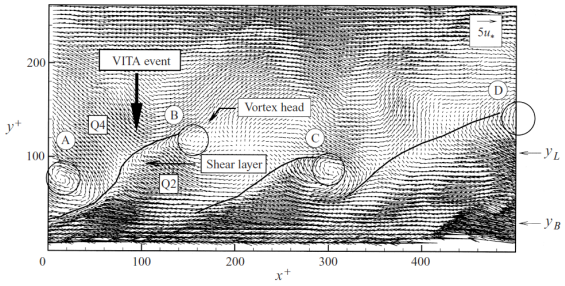

Figure 3 PIV result in the near-wall region of a turbulent boundary layer (Re_θ = 930) showing four hairpin vortex signatures. From: Adrian *et al.* [14].

Moreover, PIV enables the turbulence production terms, and other turbulence properties, to be evaluated even in highly complex flow geometries, such as in turbomachinery [15] and in stirred reactors [16].

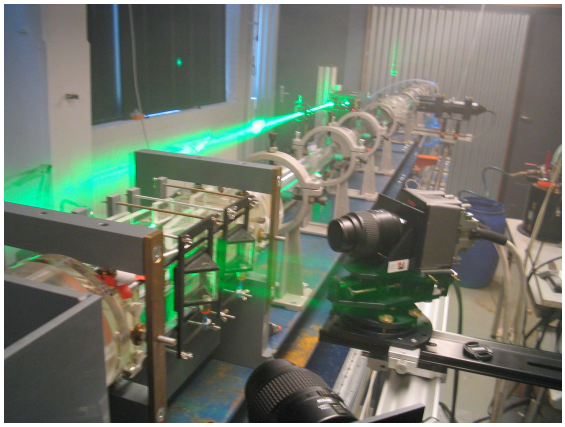

Figure 4 Stereoscopic PIV system for the measurement of pipe flow. Cameras have Scheimpflug mounts and observe the pipe flow through liquid prisms to minimize optical distortions.

Positioning the light sheet normal to the main flow direction, in combination with stereoscopic PIV using high-speed cameras, provides a means to determine the quasi-instantaneous flow structures as they are advected through the measurement plane [17]; see Figure 4. This approach revealed the first experimental observation of new solutions, in the form of *traveling waves*, for the Navier-Stokes equations in a pipe geometry [18]. These time-sequences, in combination with Taylor's *frozen field* hypothesis, can be used to reconstruct the quasi-instantaneous 3-dimensional vortical structures in the flow, such as for localized turbulence (or 'puffs') in transitional pipe flow [17,19] (as shown

in the bottom part of Figure 5) or 'vortex packets' in a turbulent boundary layer [20].

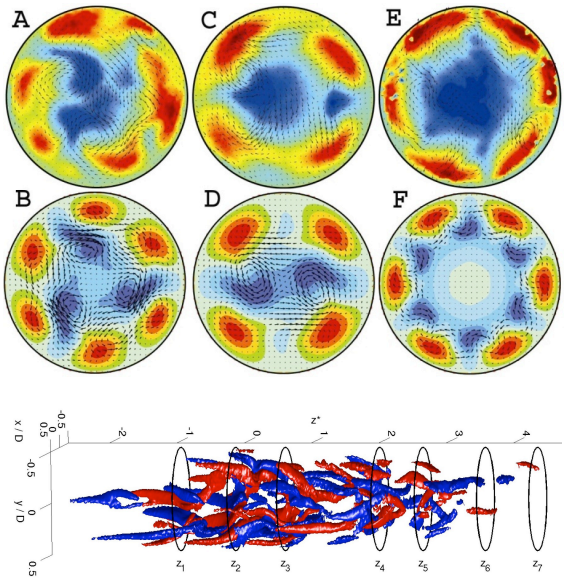

Figure 5 (top) Comparison of experimentally observed (A-C-E) instantaneous patterns of the secondary flow in transitional and turbulent pipe flow by means of stereoscopic PIV with corresponding so-called exact traveling wave solutions (B-D-F) of the Navier-Stokes equations in a pipe. The red and blue colors indicate whether the axial velocity is higher and lower, respectively, relative to the Hagen-Poiseuille velocity profile. From: Hof & van Doorne *et al.* [18]. (bottom) Visualization of the iso-contours of the stream-wise vorticity in a quasi-instantaneous reconstruction of a puff from time-resolved stereoscopic PIV data. From: van Doorne & Westerweel [17,19].

The same approach can be used to observe the flow at much higher Reynolds numbers, as shown in Figure 6. However, in these situations the reconstruction is based on flows where the mean velocity advects the flow structures through the measurement plane, which is only possible for a limited number of cases. The use of a scanning light sheet plane [6,8,9] makes it possible to record the (quasi-) instantaneous 3-D flow structure in other applications, as shown in Figure 7.

Multiple-plane PIV has made it possible to measure derivatives perpendicular to the planes. Two parallel planes generated by two separate dual-laser systems in combination with a dual stereoscopic PIV system (i.e., with four cameras in total) can be utilized in various ways [7]. Besides arrangements that reduce the measurement uncertainty due to large out-of-plane motion, one can record all three components of the velocity at the same instant in time at two nearby measurement planes. This requires the appropriate arrangement of the laser-beam polarization, polarization filters, and cameras. However, the planar measurement of all nine components of the instantaneous velocity gradient tensor becomes possible. This was utilized by Ganapathisubramani *et al.* [21] to characterize the flow structure in the log-region of a turbulent boundary layer.

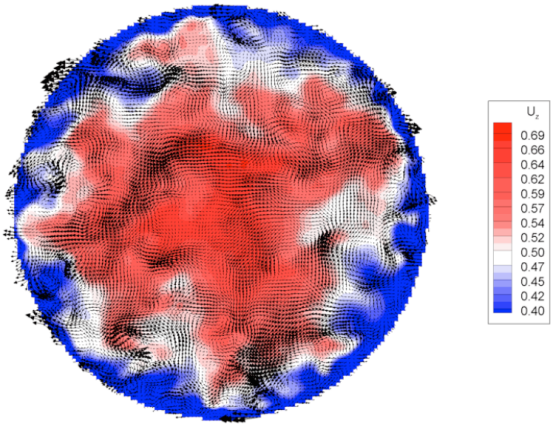

Figure 6 Typical velocity field measured by stereoscopic PIV in turbulent pipe flow at *Re* = 20,000. The measurement plane is normal to the pipe axis. The arrows indicate the in-plane components of the velocity, while whereas the color indicates the axial velocity component.

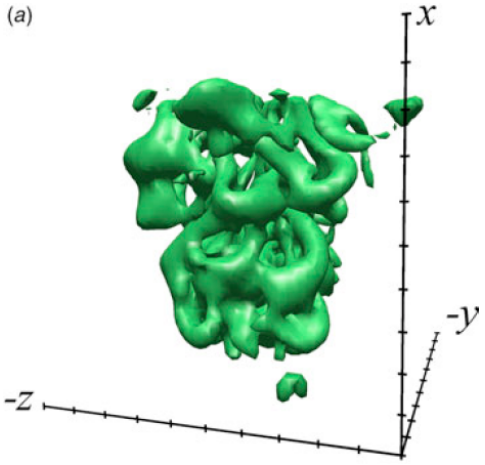

Figure 7 Surface of constant vorticity magnitude for a turbulent jet at *Re* = 1000, determined by means of scanning-plane stereoscopic PIV. From: Hori & Sakakibara [9].

Single-camera and multiple-camera PIV systems with appropriate optics and filters and advanced image processing make it possible to separate various optical data, based on (tracer/particle) size or separation of light wavelength. This can be used to investigate particle-laden turbulent flows [22-24] or mixing in a turbulent flow by means of combining *laser-induced fluorescence* (LIF) and PIV [25,26]. The latter approach was also used to investigate the

turbulence statistics relative to a strongly convoluted turbulent/non-turbulent interface [27-29]; see Figure 8.

The accuracy and spatial resolution of current 2D planar PIV data are sufficient to make estimates of acoustic sources for certain simple geometries [30], as show in Figure 9.

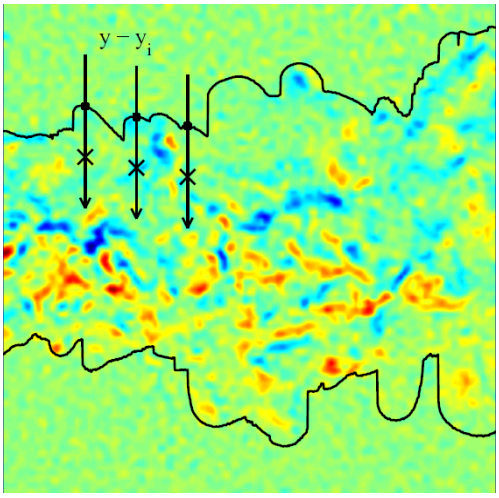

Figure 8 The fluctuating vorticity (color) of a turbulent jet at *Re* = 2000. The black curves indicate the outer envelope of the turbulent fluid that was emitted by the jet nozzle. From: Westerweel *et al.* [29].

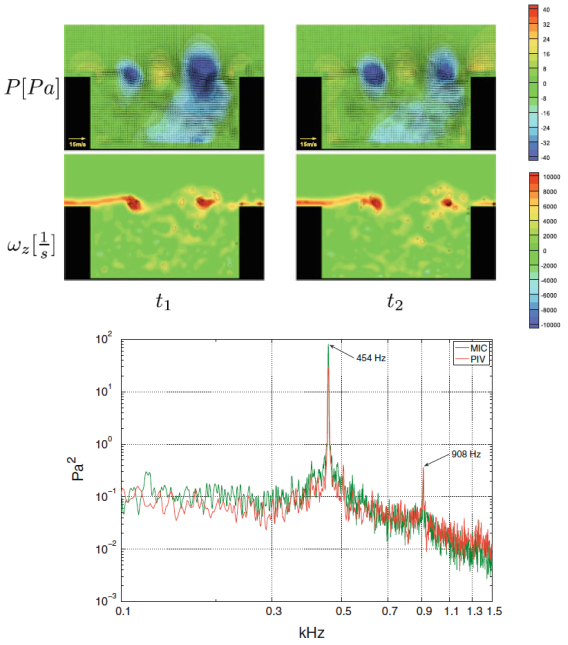

Figure 9 PIV measurement of air flow over a cavity at *Re* = 24×10^3, showing the reconstructed instantaneous pressure levels (*P*) and vorticity (ω_z) normal to the measurement plane, at to consecutive instants of time (t_1,t_2). Bottom graph shows the power spectrum of the sound pressure estimated from the PIV data compared to microphone measurements. From: Koschatzky *et al.* [30].

3. TOMOGRAPHIC PIV

Most recently tomographic PIV (Figure 10) was introduced as a promising new method for measuring the instantaneous three-dimensional velocity field [4]. In this approach the tracer particles are illuminated within a volume, and the light scattered by these particles is recorded from several viewing directions simultaneously, typically using 4-6 digital cameras. In order to keep all particles within the volume in focus, it is generally required to employ Scheimpflug adapters [3,6] and to use a small aperture, or large $f^{\#}$, for the camera lenses. From the recordings the particle distribution is reconstructed as a 3-D light intensity distribution discretized onto *voxel* elements, which are the volumetric equivalent of pixels. A tomographic algorithm solves this reconstruction problem iteratively [4].

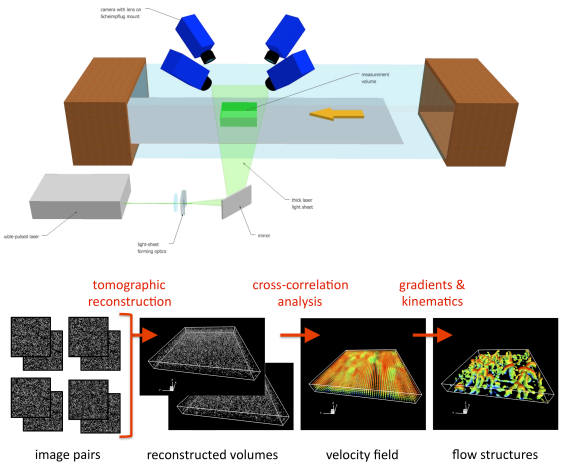

Figure 10 Working principle of tomographic-PIV. (top) Arrangement of a four-camera tomographic imaging system. (bottom) Data processing steps. From: Westerweel *et al.* [1].

While maintaining the advantages of the simple optical arrangement of 3-D PTV, the new tomographic-PIV approach proved to be more robust for two main reasons. Firstly, tomography does not rely on any particle detection, thereby relieving constraints on the particle image density and image quality that are inherent to 3-D PTV. As a result, the particle image seeding density achieved in tomographic PIV is typically increased by an order of magnitude with respect to volumetric particle tracking, which substantially improves the spatial resolution. Secondly, the cross-correlation analysis of the particle displacement typically has lower noise compared to particle tracking methods and is comparable to stereoscopic PIV and only slightly above the noise level for standard planar PIV [31].

3.1. Applications of Tomographic PIV

The variety of applications achieved to date clearly demonstrates the versatility of tomographic PIV, explaining its growing importance. The technique has been used in different flow facilities covering a velocity range from only a few mm per second in a water tank [32] all the way up to 510 m/s in a supersonic wind tunnel [33,34].

Furthermore, it is capable of measuring anywhere from millimeter-sized volumes when employing a microscope objective with four ports for imaging [35] (see Figure X), to meter-sized volumes, as demonstrated in a large-scale convection cell by Kühn *et al.* [36]. Extensions to tomographic time-resolved PIV have been achieved by employing high-speed lasers and imaging systems [37,38].

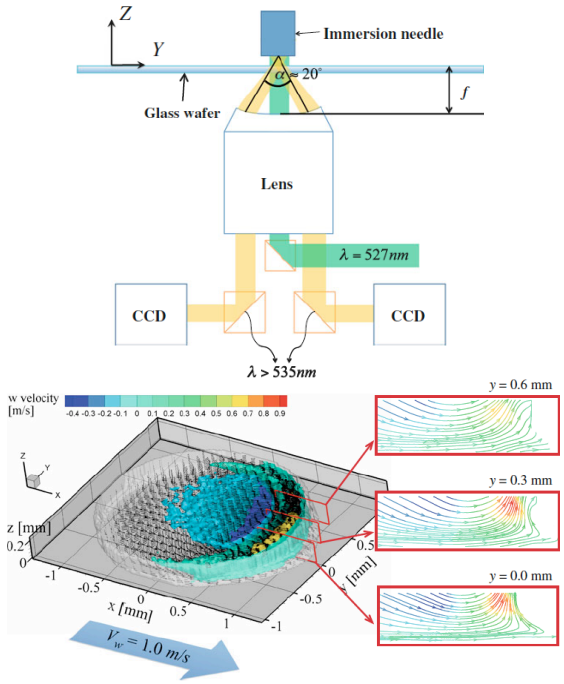

Figure 11 Optical arrangement (top) and PIV result (bottom) for the measurement of the internal 3-D flow of a liquid immersion droplet sliding over a glass wafer at 1 m/s. The measurement volume is about 2×2×0.2 mm^3. From: Kim *et al.* [35].

Many of the earlier studies focused primarily on the quantitative visualization of the coherent structures in various turbulent flows, based on data similar to those presented in Figure 12.

Studies of turbulent boundary layers revealed the spatial organization of three-dimensional vortical structures at different scales [39] or the rapid growth of an ejection event [40]. Such data has been used to validate or to improve existing structural models for the specific turbulent flow. In all these cases the three-dimensional approach avoids the ambiguities inherent in the inference of three-dimensional structures from planar data. More recently, however, tomographic PIV has been used to actually quantify the relevant flow variables related to the velocity gradients. For example, Worth & Nickels [32] determined the joint probability density function of enstrophy and dissipation in homogeneous isotropic turbulence, and Elsinga & Marusic [39] evaluated the material derivative of the invariants of the velocity gradient tensor, which define a characteristic topology time scale.

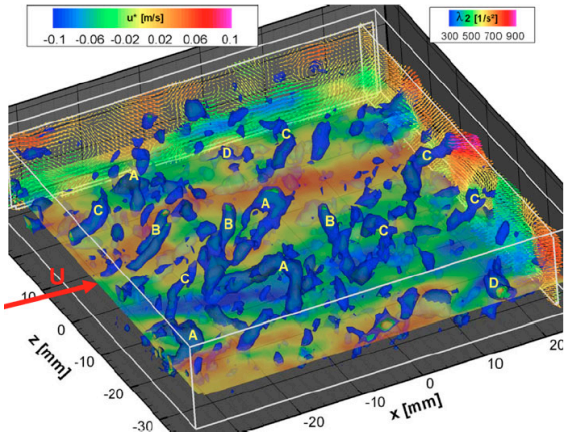

Figure 12 Instantaneous 3D velocity volume of a turbulent boundary layer at Re_θ = 2460, extracted from a time series depicting flow structures by iso-surfaces of swirling strength (blue) and selected planes depicting velocity, with the plane parallel to the surface at y^+ = 75. From: Schröder *et al.* [38].

It should be noted that sufficient spatial resolution is critical when it comes to the accuracy of the measured velocity gradients, as shown in actual measurements [41]. However, for the next generation of PIV systems it is required to achieve a fundamental breakthrough in achieving an improvement by an order or magnitude in measurement accuracy [1].

4. SUMMARY

It is anticipated that the experimental quantification of the different terms in the continuity and Navier-Stokes equations will become more common in the near future. This will likely produce valuable new insights into the interaction between the terms. In this context one can think of, for instance, the balance between turbulence production and dissipation, especially in spatially evolving flows or fully three-dimensional and turbulent flows that cannot be easily represented in a DNS. However, direct comparisons of the velocity-gradient statistics between results from numerical simulations and experiments are still of interest, even in canonical cases, and are presently sparsely available. It should be noted that sufficient

spatial resolution is critical when it comes to the accuracy of the measured velocity gradients.

ACKNOWLEDGEMENTS

RA acknowledges the support of the U.S. National Science Foundation and Los Alamos National Laboratory. JW would like to thank S. Grosse, D.J. Kuik, and E. Overmars for contributing the turbulent pipe flow data for Figure 6.

REFERENCES

1. Westerweel, J., Elsinga, G.E. and Adrian, R.J., 2013, "Particle Image Velocimetry for Complex and Turbulent Flows" *Annu. Rev. Fluid Mech.*, Vol. 45.
2. Adrian, R.J., 1991, "Particle-imaging techniques for experimental fluid mechanics" *Annu. Rev. Fluid Mech*., Vol. 23, pp. 261-304.
3. Adrian, R.J. and Westerweel, J., 2011, *Particle Image Velocimetry*. Cambridge University Press, Cambridge.
4. Elsinga, G.E., Scarano, F., Wieneke, B. and van Oudheusden, B.W., 2006, "Tomographic particle image velocimetry" *Exp. Fluids,* Vol. 41, pp. 933-947.
5. Moin, P. and Mahesh, K., 1998, "Direct numerical simulation: a tool in turbulence research" *Annu. Rev. Fluid Mech*., Vol. 30, pp. 539-578.
6. Prasad, A.K., 2000, "Stereoscopic particle image velocimetry" *Exp. Fluids*, Vol. 29, pp. 103-116.
7. Kähler, C.J., and Kompenhans, J., "Fundamentals of multiple plane stereo particle image velocimetry" *Exp. Fluids*, Vol. 29, pp. S70-S77.
8. Brücker, Ch., 1997, "3D scanning PIV applied to an air flow in a motored engine using digital high-speed video" *Meas. Sci. Technol*., Vol. 8, pp. 1480-1492.
9. Hori, T. and Sakakibara, J., 2004, "High-speed scanning stereoscopic PIV for 3D vorticity measurement in liquids" *Meas. Sci. Technol*., Vol. 15, pp. 1067-1078.
10. Katz, J. and Sheng, J., 2010, "Applications of holography in fluid mechanics and particle dynamics" *Annu. Rev. Fluid Mech*., Vol. 42, pp. 531-555.
11. Maas, H.G., Gruen, A. and Papantoniou, D., 1993, "Particle tracking velocimetry in three-dimensional flows. Part 1. Photogrammetric determination of particle coordinates" *Exp. Fluids*, Vol. 15, pp. 133-146.
12. Pereira, F., Gharib, M., Dabiri, D. and Modarress, D., 2000, "Defocusing digital particle image velocimetry: a 3-component 3-dimensional DPIV measurement technique. Application to bubbly flows." *Exp. Fluids*, Suppl., pp. S78-S84.
13. Scarano, F., van Wijk, C. and Veldhuis, L.L.M., 2002, "Traversing field of view and AR-PIV for mid-field wake vortex investigation in a towing tank" *Exp. Fluids*, Vol. 33, pp. 950-961.
14. Adrian, R.J., Meinhart, C.D. and Tomkins, C.D., 2000, "Vortex organization in the outer region of the turbulent boundary layer" *J. Fluid Mech.*, Vol. 422, pp. 1-54.
15. Soranna, F., Chow, Y.-C., Uzol, O. and Katz, J., 2010, "The effects of inlet guide vane-wake impingement on the boundary layer and the near-wake of a rotor blade" *J. Turbomach*., Vol. 132, 041016.
16. Sharp, K.V. and Adrian, R.J., 2001, "PIV study of small-scale flow structure around a Rushton turbine" *AIChE J*., Vol. 47, pp. 766-778.
17. van Doorne, C.W.H. and Westerweel, J., 2007, "Measurement of laminar, transitional and turbulent pipe flow using stereoscopic-PIV" *Exp. Fluids*, Vol. 42, pp. 259-279.
18. Hof, B., van Doorne, C.W.H., Westerweel, J., Nieuwstadt, F.T.M., Faisst, H., Eckhardt, B., Wedin, H., Kerswell, R.R. and Waleffe, F., 2004, "Experimental observation of nonlinear traveling waves in turbulent pipe flow" *Science*, Vol. 305, pp. 1594-1598.
19. van Doorne, C.W.H. and Westerweel, J., 2009, "The flow structure of a puff" *Phil. Trans. R. Soc. A*, Vol. 367, pp. 489-507.
20. Dennis, D.J.C. and Nickels, T.B., 2011, "Experimental measurement of large-scale three-dimensional structures in a turbulent boundary layer. Part 1. Vortex packets" *J. Fluid Mech.*, Vol. 673, pp. 180-217.
21. Ganapathisubramani, B., Longmire, E.K., Marusic, I. and Pothos, S., 2005, "Dual-plane PIV technique to determine the complete velocity gradient tensor in a turbulent boundary layer" *Exp. Fluids*, Vol. 39, pp. 222-231.
22. Kiger, K.T. and Pan, C., 2000, "PIV technique for the simultaneous measurement of dilute two-phase flows" *J. Fluids Eng*., Vol. 122, pp. 811-818.
23. Khalitov, D.A. and Longmire, E.K., 2002, "Simultaneous two-phase PIV by two-parameter phase discrimination" *Exp. Fluids*, Vol. 32, pp. 252-268.
24. Poelma, C., Westerweel, J. and Ooms, G., 2006, "Turbulence statistics from optical whole field measurements in particle-laden turbulence" *Exp. Fluids*, Vol. 40, pp. 347-363.
25. Webster, D.R., Roberts, P.J.W. and Ra'ad, L., 2001, "Simultaneous DPTV/PLIF measurements of a turbulent jet" *Exp. Fluids*, Vol. 30, pp. 65-72.
26. Fukushima, C., Aanen, L. and Westerweel, J., 2002, "Investigation of the mixing process in an axisymmetric turbulent jet using PIV and

LIF" in: *Laser Techniques for Fluid Mechanics* (Eds. R.J. Adrian *et al*.), Springer, pp. 339-356.
27. Westerweel, J., Fukushima, C., Pedersen, J.M. and Hunt, J.C.R., 2005, "Mechanics of the turbulent/nonturbulent interface of a jet" *Phys. Rev. Lett.*, Vol. 95, 174501.
28. Holzner, M., Liberzon, A., Guala, M., Tsinober, A. and Kinzelbach, W., 2006, "Generalized detection of a turbulent front generated by an oscillating grid" *Exp. Fluids*, Vol. 41, pp. 711-719.
29. Westerweel, J., Fukushima, C., Pedersen, J.M. and Hunt, J.C.R., 2009, "Momentum and scalar transport at the turbulent/non-turbulent interface of a jet" *J. Fluid Mech*., Vol. 631, pp. 199-230.
30. Koschatzky, V., Moore, P.D., Westerweel, J., Scarano, F. and Boersma, B.J., 2011, "High speed PIV applied to aerodynamic noise investigation" *Exp. Fluids*, Vol. 50, pp. 863-876.
31. Atkinson, C., Coudert, S., Foucaut, J.M., Stanislas, M. and Soria, J., 2011, "The accuracy of tomographic particle image velocimetry for measurements of a turbulent boundary layer" *Exp. Fluids*, Vol. 50, pp. 1031-1056.
32. Worth, N.A. and Nickels, T.B., 2011, "Time-resolved volumetric measurement of fine-scale coherent structures in turbulence" *Phys. Rev. E*, Vol. 84, 025301.
33. Humble, R.A., Elsinga, G.E., Scarano, F. and van Oudheusden, B.W., 2009, "Three-dimensional instantaneous structure of a shock wave/turbulent boundary layer interaction" *J. Fluid Mech.*, Vol. 622, pp. 33-62.
34. Elsinga, G.E., Adrian, R.J., van Oudheusden, B.W. and Scarano, F., 2010, "Three-dimensional vortex organization in a high-Reynolds-number supersonic turbulent boundary layer" *J. Fluid Mech*., Vol. 644, pp. 35-60.
35. Kim, H., Grosse, S., Elsinga, G.E. and Westerweel, J., 2011, "Full 3D-3C velocity measurement inside a liquid immersion droplet" *Exp. Fluids*, Vol. 51, pp. 395-405.
36. Kühn, M., Ehrenfried, K., Bosbach, J. and Wagner, C., 2011, "Large-scale tomographic particle image velocimetry using helium-filled soap bubbles" *Exp. Fluids*, Vol. 50, pp. 929-948.
37. Scarano, F. and Poelma, C., 2009, "Three-dimensional vorticity patterns of cylinder wakes" *Exp. Fluids*, Vol. 47, pp. 69-83.
38. Schröder, A., Geisler, R., Staack, K., Elsinga, G.E., Scarano, F., Wieneke, B., Henning, A., Poelma, C. and Westerweel, J., 2011, "Eulerian and Lagrangian views of a turbulent boundary layer flow using time-resolved tomographic PIV" *Exp. Fluids*, Vol. 50, pp. 1071-1091.
39. Elsinga, G.E. and Marusic, I., 2010, "Evolution and lifetimes of flow topology in a turbulent boundary layer" *Phys. Fluids*, Vol. 22, 015102.
40. Schröder, A., Geisler, R., Elsinga, G.E., Scarano, F. and Dierksheide, U., 2008, "Investigation of a turbulent spot and a tripped turbulent boundary layer flow using time-resolved tomographic PIV" *Exp. Fluids*, Vol. 44, pp. 305-316.
41. Tokgöz, S., Elsinga, G.E., Delfos, R. and Westerweel, J., 2012, "Spatial resolution and dissipation rate estimation in Taylor-Couette flow for tomographic PIV" *Exp. Fluids* (online).

Authors' Index